DAE-BRNS

# Indian Particle Accelerator Conference (InPAC 2019)

November 18-21, 2019

Inter-University Accelerator Centre (IUAC), New Delhi

# PROCEEDINGS

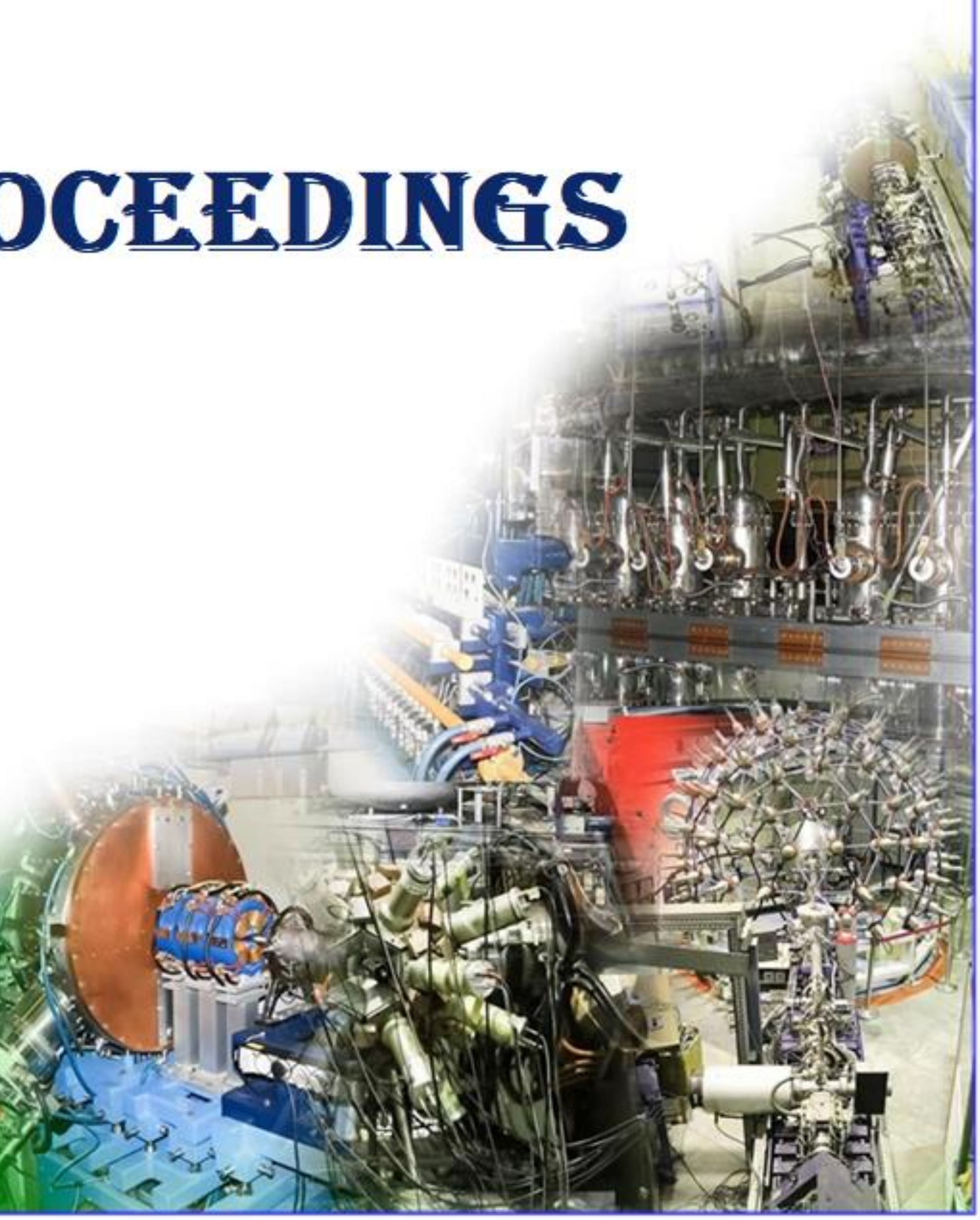

# PLENARY SESSION

# COMMISSIONING OF THE LEHIPA 3 MEV RFQ

S V L S Rao*[1], Jose V Mathew[1], S K Singh[1], M R Mishra[1], Rajesh Kumar[1], Mentes Jose[1], Hitesh Kewlani[1], Sandip Shrotriya[1], B V Rama Rao[1], Rajni Pande[1], Shweta Roy[1], Roushan Abhishek[1], Piyush Jain[1], Alok Ghosh[1], Deepak Mathad[1], Sumit Garg[1], Aman Bajaj[1], P Bhumeshwar[1], A Shiju[1], Pallavi Priyadarshini[1], Sonal Sharma[1], A Basu[1], Sherry Rosily[1], V K Kotak[1], N R Patel[1], Laxman Tayade[1], Pravin Parate[1], G N Singh[1], S K Bharade[1], C I Sujo[1], H Shukla[1], R T Keshwani[1], M M Pande[1], Paresh Motiwala[1], Alok Agashe[1], Gopal Joshi[1,2], Srinivas Krishnagopal[1,2]

[1]Bhabha Atomic Research Centre, Mumbai, India-400085

[2]Homi Bhabha National Institute, Mumbai, India-400094

*Abstract*

A 3 MeV Radio-Frequency Quadrupole (RFQ) was designed and developed for the Low Energy High Intensity Proton Accelerator (LEHIPA) at BARC. This RFQ is designed to accelerate the proton beam from 50 keV to 3 MeV in a length of 4 m with a vane voltage of 68 kV. We have accelerated 2 mA beam to 3 MeV, with a transmission of around 65 %. In this paper, we present details of the successful commissioning of the RFQ, and some results on beam measurements

## INTRODUCTION

In the first phase of the Accelerator Driven System (ADS) programme in India [1, 2], it was planned to develop the normal-conducting front-end of the ADS accelerator. This was conceptualized as the Low Energy High Intensity Proton Accelerator (LEHIPA), which is a 20 MeV, high average current proton linac, [3], comprising a 50 keV ECR ion source, a 3 MeV Radio-Frequency Quadrupole (RFQ) [4, 5] and 20 MeV Drift Tube Linac (DTL) [6]. The RFQ is a 4 m long structure and fabricated in 4 segments. These segments are coupled via coupling cell. We coupled the RF power of nearly 520 kW (Cavity power) to the RFQ using two iris couplers. Recently, we have commissioned this RFQ to its full energy of 3 MeV. The commissioning details are discussed in this paper.

## QUALITY FACTOR MEASUREMENTS

After completing the bead pull measurements, the RFQ was coupled to the klystron and then we measured the quality factor (Q) using the reflection ($S_{11}$) method, shown in Fig. 1. We calculated the loaded ($Q_L$) and unloaded ($Q_0$) quality factors [7] to be around 1,863 and 2,944, taking into consideration the series coupling losses only. The $Q_0$ measured was very low when compared to simulations, so we disassembled the RFQ and cleaned it thoroughly with citric acid and rinsed with water after which it was cleaned with acetone and alcohol. After cleaning, we reassembled and measured $Q_0$ using the transmission method ($S_{21}$) as shown in Fig. 2. During these $S_{21}$ measurements the iris wave guides were terminated with $\lambda/4$ transmission lines and we used two coupling loops whose couplings are very weak ($\beta \leq 0.05$). The $S_{21}$ signal from Fig. 2 is in the noise level; to reduce the noise we have increased the power level and also done averaging. We took the raw data of $S_{21}$ and after averaging calculated the transmission coefficient and fitted the Lorentzian function and calculated $Q_L$ to be around 4,802 [8]. The $Q_0$ is calculated to be around 5,040, by using the formula $Q_0 = Q_L(1 + \beta)$. From the simulations, for this value of $Q_0$ we calculate that an RF power of 520 kW needs to be provided to the cavity in order to establish the design vane voltage of 68 kV.

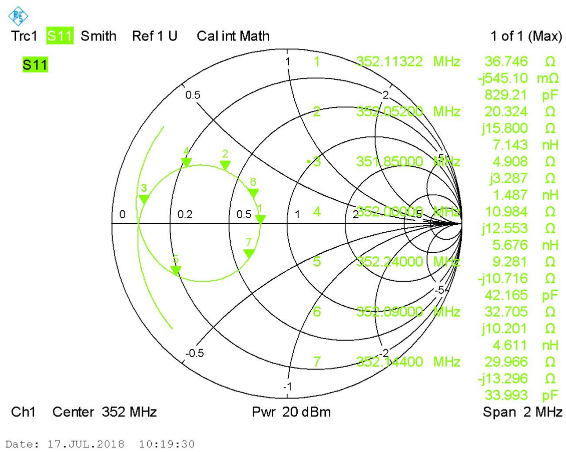


Figure 1: Smith Chart of $S_{11}$.

## KLYSTRON RF PHASE MEASUREMENTS

After completing the cold test, the RFQ was connected to the klystron and we started conditioning at very low power levels (tens of kW). We found large variations in the forward and reflected powers within the pulse as shown in Fig. 3.

The RF phase of klystron output was measured and found to be varying by around 80-100 deg within the pulse and also randomly from pulse to pulse, as shown in Fig. 4. We traced this problem to poor regulation (~ 10%) of the 2 MW CW Regulated High Voltage Supply (RHVPS), which is used as the cathode supply to the klystron.

We therefore replaced the CW RHVPS with a pulsed RHVPS (bouncer-type pulse modulator) developed by RRCAT. After installing the pulsed RHVPS, we again mea-

* svlsr@barc.gov.in

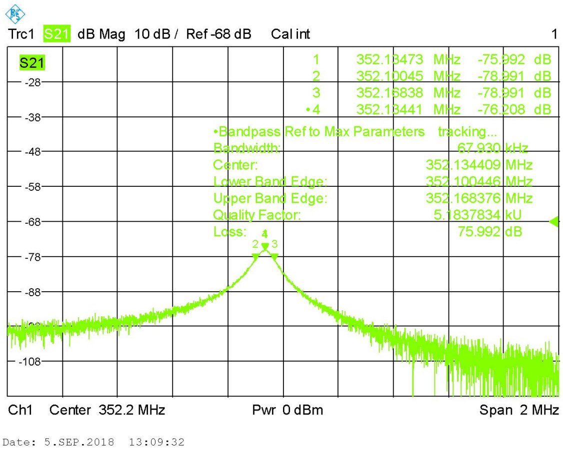


Figure 2: Transmission measurement $S_{21}$.

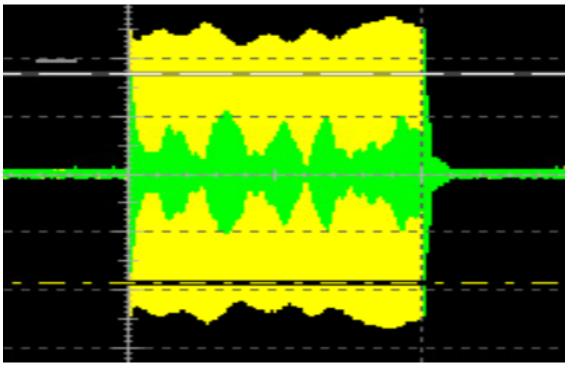

Figure 3: Forward (yellow) and reflected (green) powers with CW RHVPS.

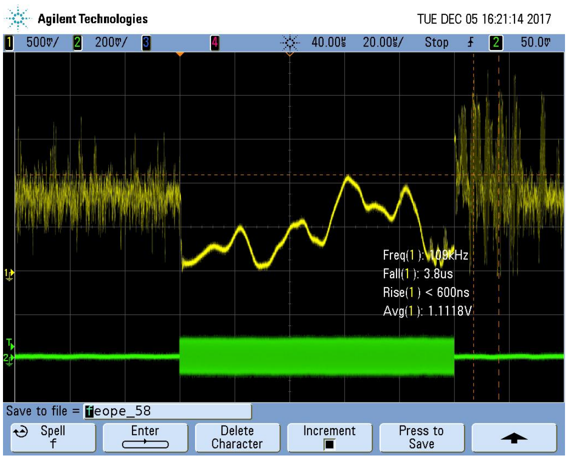


Figure 4: Klystron output phase variation.

sured the RF phase of klystron output which now varied only by 1-2 deg. The forward and reflected RF power signals of the klystron, after connecting with the pulsed RHVPS, are shown in Fig. 5. It can be seen that there is a substantial improvement in the stabilty of the RF power.

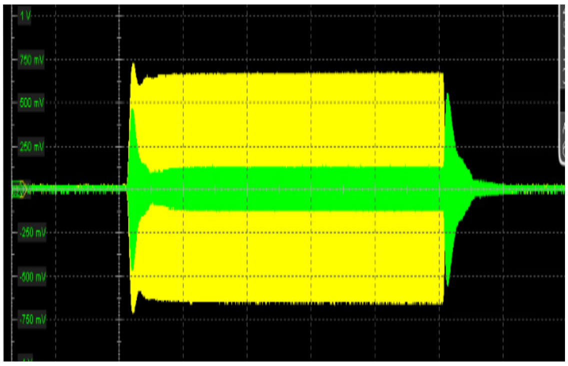

Figure 5: Forward (yellow) and reflected (green) powers with Pulsed RHVPS.

## X-RAY MEASUREMENTS

After connecting the pulsed RHVPS to the klystron, we started conditioning the RFQ. At low power levels of 50-100 kW (cavity power) we determined the vane voltage as function of the cavity power using the X-ray endpoint energy measurements, employing an Amptek CdTe X-Ray detector. We had calibrated the detector using the standard sources Am-241 and Cd, and took X-ray spectra at two power levels of 50 and 100 kW, which are shown blue and brown plots in Fig. 6. The vane voltage was calculated to be around 22.37 and 31.32 kV. Unfortunately, the detector malfunctioned after these two measurements, and so we could not get more data. However, extrapolating from the existing data, the power required for 68 kV vane voltage is $\sim$ 467 kW, which is 5.6% less compared to our predictions from the $Q_0$ measurements.

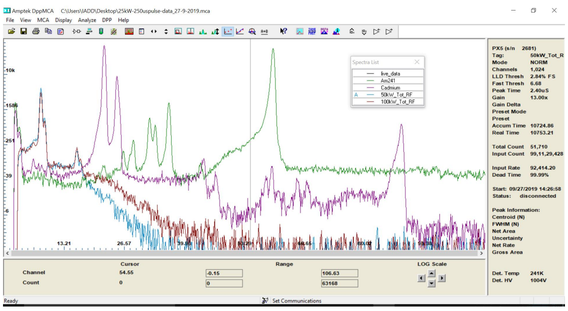

Figure 6: X-Ray spectra for two RF power levels.

## HIGH POWER CONDITIONING

The RFQ with power couplers and various diagnostic elements, is shown in Fig. 7. The pulsed RHVPS is capable of generating the DC power of 400 $\mu$s and 2 Hz rep rate. We started with a pulse width of 25 $\mu$s and 1 Hz repetition rate. Above 500 kW of the forward RF power, the klystron RF power was not stable, as shown in Fig. 8. In order to go above 500 kW, we had operated in the negative slope region of the klystron gain curve, which we call the overdrive mode. When the klystron was operated in overdrive mode, we could go up to a power level of 600 kW forward power (FP). The overall reflected power (RP) at this power level was nearly 14%.

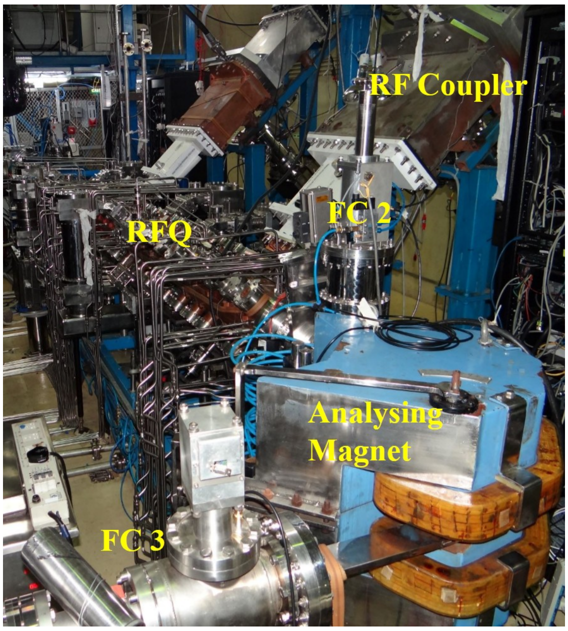


Figure 7: RFQ beam line.

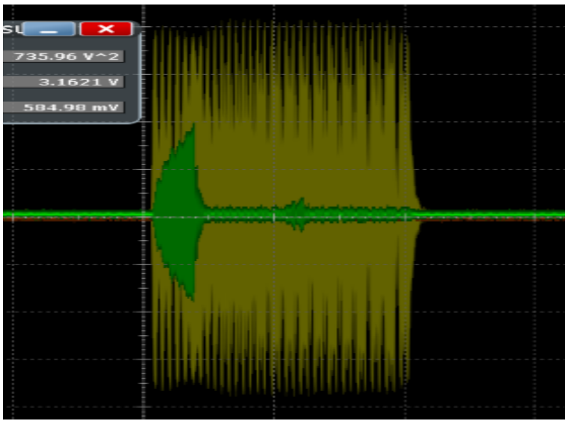


Figure 8: Klystron instability at over 500 kW.

## BEAM ACCELERATION

After establishing a stable RF power of around 520 kW in the cavity, we injected the 50 keV proton beam into the RFQ. The proton beam pulse width was 1 ms, so that in our case the RF pulse sits within the beam pulse. Before installing the RFQ in the beam line the ECR ion source was characterized fully [9]. During beam acceleration trials through the RFQ, the ion source parameters were set to the have a current of around 2 mA at the entrance of the RFQ. In order to measure the output beam energy we have installed a bending magnet (BM) at the exit of the RFQ, and to measure the transmitted and accelerated currents, we have installed two Faraday cups (FC2 & FC3) at the entrance and exit of the BM. The bending magnet was calibrated before the beam trails and the calibration curve is shown in Fig. 9.

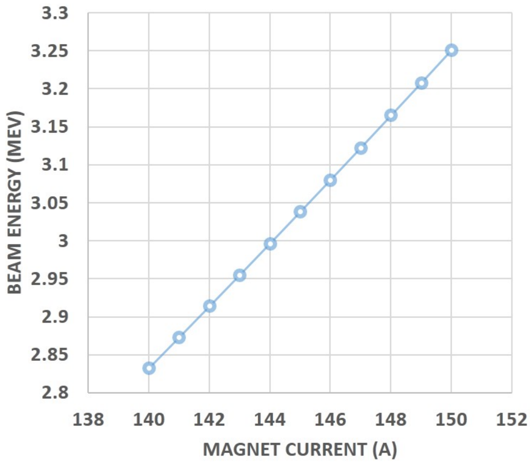


Figure 9: Bending Magnet calibration.

We set the BM current at 144 A, corresponding to 3 MeV protons, and saw a clear signal on FC3 (after the BM) as shown in Fig. 10. This shows that the energy of the beam is 3 MeV. To study the energy distribution of the accelerated beam, we varied the BM current and noted the FC3 reading at each BM setting. We repeated this for different values of the RF power in the cavity. The results are shown in Fig. 11. For a cavity power of 520 kW, we can clearly see a monoenergetic peak. The width of the peak depends on various factors such as the intrinsic energy width supported by the RFQ, the resolution of the BM, etc. As the power is reduced, i.e. the vane voltage is reduced, one gets a quasi-continuous energy distribution with very low beam current at 3 MeV, and below a cavity power of 475 kW, there is no accelerated beam at 3 MeV (though there is a continuum at lower energy). These measurements are in excellent agreement with detailed multi-particle simulations.

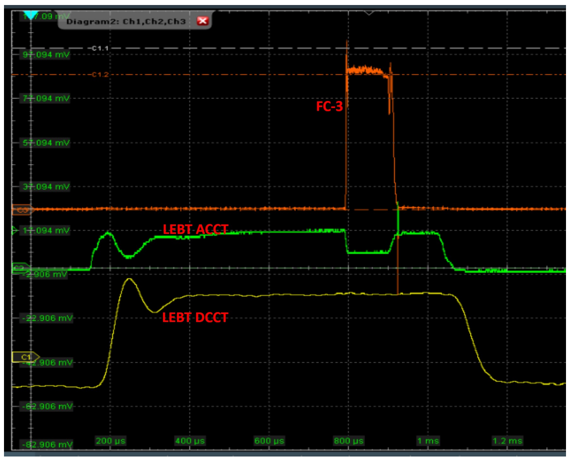


Figure 10: Accelerated beam signal on FC3.

After successful completion of first run, we reconditioned the RFQ for a longer pulse duration (ie., 100 $\mu$s and 1 Hz rep rate). During this run, after taking FC3 current signal, we removed the BM and placed the indigenously developed coax-

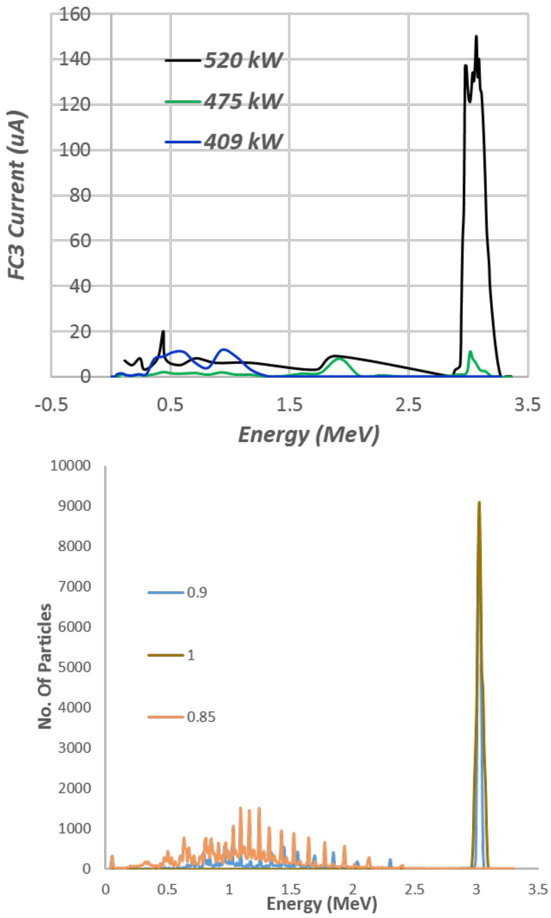

Figure 11: Beam energy spectra at different RF power levels, (a) experimental, and (b) simulation.

ial Fast Faraday Cup (FFC), to measure the bunch width [10]. The beam bunches are shown in Fig. 12. The preliminary measurements gave a bunch width ($\sigma$) of 140 ps, which is in good agreement with simulations.

After a second round of conditioning and regulatory approval, we increased the beam pulse width to 200 $\mu$s and repetition rate to 2 Hz and measured the beam energy using the Time of Flight (ToF) method. For this measurement we have used two Fast Current Transformers (FCT's). During this long pulse operation, we noticed a droop in power level nearly 20% along the pulse, which is shown in Fig. 13.

Because of this droop in the power along the pulse, the power at the end of the pulse is below the threshold required for 3 MeV acceleration, as explained above. Indeed, the FCT signals show good beam formation at the beginning of the pulse, Fig. 14, but none towards the end.

In order to reduce the droop in the power level along the pulse, we implemented the Low Level RF System (LLRF). However, in order to implement the LLRF, we had to operate the klsytron in the regular, positive slope, region, since the LLRF system was not design to handle negative slope. To our pleasant surprise, probably due to constant operation of the klystron, we found that the klystron instability that had

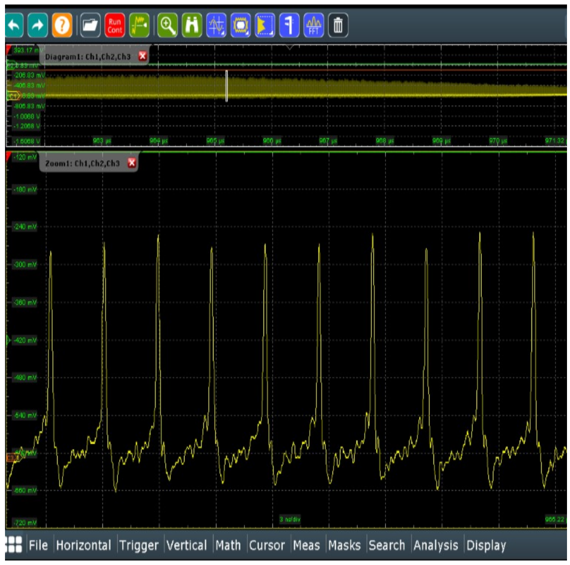

Figure 12: Time structure of accelerated 3 MeV proton bunches.

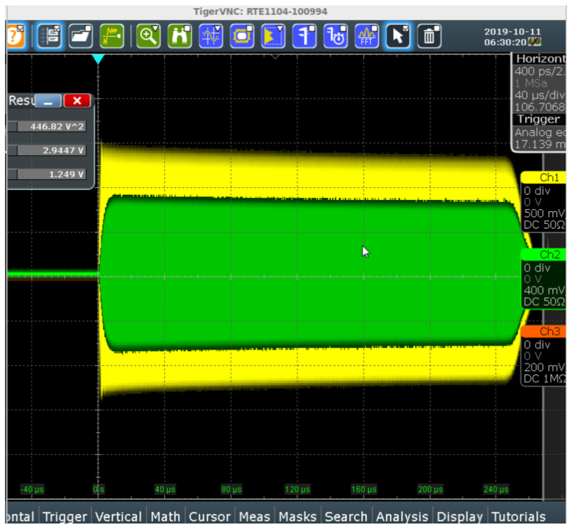

Figure 13: Klystron forward power droop along the pulse.

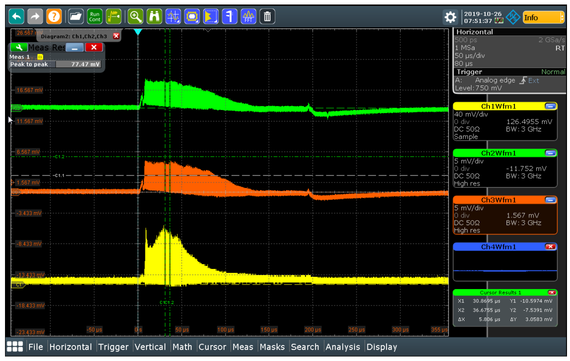

Figure 14: Beam macro-pulse signals on the two FCTs (green and orange) and the FFC (yellow), without LLRF.

earlier set in at around 500 kW, was now setting in only at around 600 kW. This is just at the threshold having 3 MeV acceleration through the RFQ. By using the LLRF system at this power level, we were able to eliminate the droop in the RF power within the pulse, and correspondingly beam signals was observed in the FCT over the entire RF pulse, as shown in Fig. 15 and Fig. 16. .

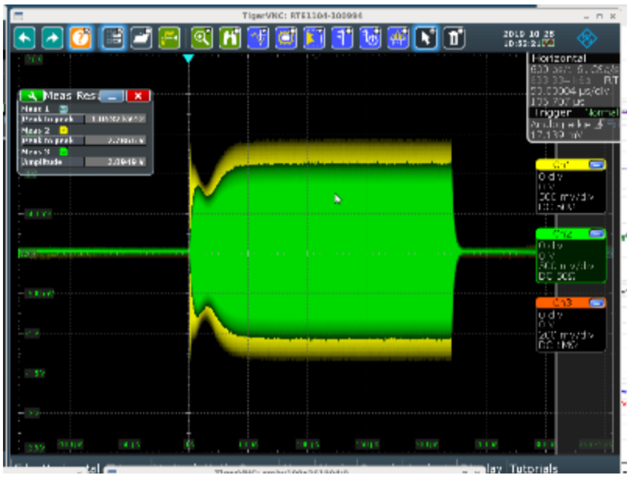

Figure 15: Klystron pulse with LLRF.

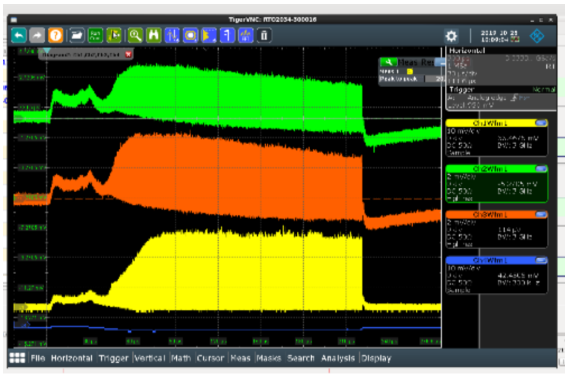

Figure 16: Beam macro-pulse signals on the two FCTs (green and orange) and the FFC (yellow), with LLRF.

.

The distance between the two FCT's was 27.8 cm. If the beam energy is 3 MeV the delay between the two FCT signal should be around 262 psec. Whereas the preliminary measurements was giving it to be nearly 350 psec as shown in Fig. 17, which corresponds to a beam energy of 2.95 MeV, assuming no errors in the distance measurement between FCTs. This is consistent with the BM value of 3 MeV, within the errors of the ToF measurement.

## SUMMARY AND CONCLUSIONS

We have accelerated beam through the RFQ to 3 MeV with an accelerated current of around 2 mA, in 200 $\mu$s pulses at 2 Hz repetition rate, corresponding to an average current of 0.8 $\mu$A. Detailed characterization of the accelerated beam

Figure 17: Time delay between two FCT's.

is in progress. We plan to increase the average current to 1 $\mu$A, and make beam available to users for experiments. We are also testing a new CW RHVPS, and once it is operational we will be able to go to much longer pulse widths.


## ACKNOWLEDGEMENTS

We would like to thank RRCAT for providing us with the pulsed RHVPS (pulse modulator). Thirteen Divisions in BARC, and over 100 personnel, have contributed to the development and operation of LEHIPA, and we thank each and every one of them for their important contributions to this important programme. A special thanks to the technicians in IADD for their extensive contributions in making LEHIPA work.


## REFERENCES


[1] Kapoor, S.S. (Ed.), Roadmap for Development of Accelerator Driven Systems, BARC Internal Report BARC/R/004 (2001).

[2] P. Singh et al., Accelerator development in India for ADS programme, Pramana-J. Physics **68**,331 (2007).

[3] T Basak et al., Physics design of LEHIPA, BARC/2004/I/007.

[4] S V L S Rao and P Singh, Design studies of a high current radio-frequency quadrupole for accelerator-driven systems programme, Pramana-J. Phys. **74**(2) 247-259 (2010).

[5] P V Bhagwat et al., Beam acceleration through proton radio frequency quadrupole accelerator in BARC,' 2016 JINST, **11**, T05001 (2016).

[6] S Roy et al., Electromagnetic and beam dynamics studies of a high current linac for LEHIPA, JINST 9 P06007.

[7] Edward L Ginzton. Microwave measurements, McGraw-Hill, 1957.

[8] Manas R Mishra et al., RF Characterization of 3 MeV LEHIPA RFQ, Presented in this Conference.

[9] Hitesh Kewlani et al., Operation and characterization of ECR ion source beam in LEHIPA, Presented in this Conference.

[10] Jose V Mathew et al., Bunch Shape measurements of 3 MeV RFQ, Presented in this Conference.

# HIGH POWER RADIO FREQUENCY (HPRF) ACTIVITIES AT BARC FOR NORMAL AND SUPERCONDUCTING RF ACCELERATORS

Manjiri Pande, Sandip Shrotriya, J. K. Mishra, Ramarao Rao, Niranjan Patel, Shiju A, Snigdha Singh, Muthu S, Shyam Sunder Jena and Gopal Joshi

Accelerator Control Division, Bhabha Atomic Research Centre, Trombay, Mumbai 400 085, India

*Abstract*

Radio frequency (RF) normal conducting (NC) or super conducting (SC) accelerator is a complex machine. For uninterrupted and reliable operation of an accelerator, all its sub systems including high power RF (HPRF) systems must perform for very long durations without trips/ faults. So HPRF needs demonstration of high technological performance with quality, safety and reliability. Challenges faced are enormous, like failures in components, devices due to arcing, thermal issues, over voltages and over currents etc. Additional problems encountered are due to ripple in DC bias, noise, grounding, radiated and conducted emissions, breakdowns, multipactoring, field emission, vacuum failures etc. At BARC, high power RF systems based on klystron and tetrode have been used to power deuterium radio frequency quadrupole (RFQ) and proton RFQ NC accelerators respectively. In order to power superconducting accelerator (e.g. single spoke resonator), LD MOSFET based high efficiency solid state RF systems have been designed and developed. All these high power RF systems have been developed by applying multidisciplinary knowledgebase in the fields of high voltage, RF, Vacuum, thermal, applied physics, innovative designs with their experimental validation, application of stringent qualification standards during their development and operation with accelerators.

This paper gives the overview of RF power systems and techniques applied, standardization and qualifications tests applied to the performance optimized RF power systems designed and developed for accelerators at BARC

## INTRODUCTION

The main purpose of the RF power source in normal conducting (NC) or superconducting LINAC is to provide the power for long term beam acceleration. So, the high power RF (HPRF) systems must be reliable, rugged, with high availability, easy maintainability and should be highly controllable. For large accelerators, the capital and operating cost of the RF system dominates the capital and running cost of the accelerator. So, HPRF systems must be compact and provide high electrical efficiency '$\eta$', which in turn reduces the economical impact. Indigenous HPRF systems for accelerators are designed and developed taking into account all these factors.

## DEVELOPMENT OF SOLID-STATE RF AMPLIFIERS FOR SUPER CONDUCTING SPOKE RESONATORS OF HIGH INTENSITY PROTON ACCELERATORS

Advancement in cryogenic technology and super conducting RF (SCRF) cavities for modern accelerators has brought down the RF power requirement by orders of magnitude compared to room temperature accelerators. Hence, the solid-state RF power amplifiers have become increasingly suitable for the super conducting accelerator applications.

On solid-state RF power devices front, the rapid advancements in high efficiency Laterally Diffused Metal Oxide Semiconductor (LDMOS) technology in VHF/UHF band have pushed the power output to higher scale. The solid-state RF power amplifiers (SSRFPA) have many advantages like simple start-up procedure, no warm-up time low voltage operation, low power circulators, graceful degradation of power etc. Due to its modular nature, it can deliver the partial output power to accelerator even though few of its power modules are down or by reconfiguring the specific number of its modules for the desired power output.

Department of Atomic Energy (DAE) laboratories are entrusted to develop two high energy proton accelerators viz., Indian Spallation Neutron Source (SNS) and Indian Accelerator Driven sub critical System (ADS). Bhabha Atomic Research Centre (BARC) is developing solid state power amplifiers at 325 MHz for these two proton accelerators as well as for its international collaborator (Fermilab) under Indian Institutes and Fermilab Collaboration (IIFC).

### *Solid-state RF amplifiers at 325 MHz*

For the superconducting accelerator program, BARC has successfully indigenously designed, developed and tested high efficiency and compact 3, 7 kW and 20 kW solid state RF systems at 325 MHz [1] as per international qualification standard. Some of their salient features are high AC to RF efficiency, high power gain, compact, low harmonics and can operate in both CW and pulse mode. These RF power amplifiers [2] will be coupled to Single Spoke Resonator1 (SSR1). Based on the technology of 7 kW, 325 MHz [3] RF amplifier developed at BARC (figure 1), the mass production of the same is being done at Electronic Corporation of India Ltd. (ECIL), Hyderabad (fig 1). The RF power waveforms obtained under CW and pulse mode of operation are shown in figure 2 and 3 respectively.

Figure 1: Solid state RF amplifier 325 MHz, 7 kW amplifier at ECIL and at BARC


Figure 2: RF power (7 kW) waveforms in CW mode

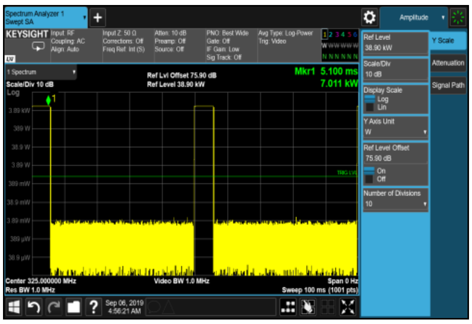


Figure 3: RF power (7 kW) waveforms in pulse mode

### *Qualifications standardization in RF Amplifiers*

Application and validation of stringent qualifications tests of individual subsystems of an RF system is an important and critical aspect of its development. It improves RF system performance for accelerator operation. The subsystems of 7 kW RF amplifier (figure 1) have been tested successfully the various qualification tests like, RE test (IEC-60068-2-3) and CE test (IEC-60068-2-4, Temperature (IEC-60068-1&2), Shock (IEC-60068-2-27), Transport Vibration (IEC-60068-2-64), Humidity test (IEC-60068-2-78). The RF sub systems undergoing qualification tests are shown in figure 4.

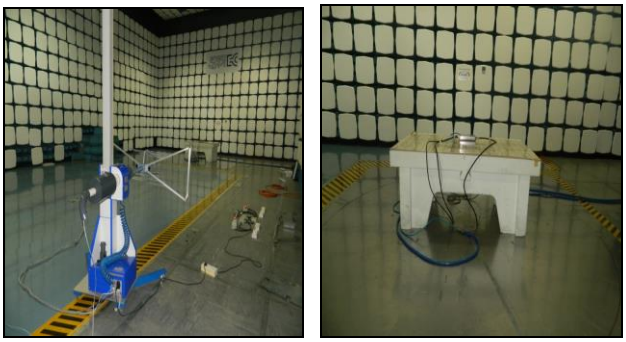

Figure 4: Qualification testing of RF modules

### *Development of 20 kW, 325 MHz solid state RF power amplifiers for proton accelerator*

RF power requirement from the RF systems increases as energy and beam current of accelerator goes up gradually. Accordingly, RF power capacity of solid state RF amplifier needs to be increased. So considering this need and as a next development stage of 7 kW RF amplifier, a prototype 20 kW RF power amplifier [4] (figure 5) at 325 MHz has been designed and developed for CW and pulse mode of operation. It uses 22 nos. of 1 kW power amplifier (PA) modules, which are combined using a (22:1) single power combiner.

Figure 5: Solid state RF amplifier 325 MHz, 20 kW

The other sub-systems like PA modules, power dividers, driver amplifier, DC P/S, water cooling systems, etc. have been designed, developed indigenously, characterised and tested before their assembly in the rack. Amplifier employs a protection system for its safe operation. It has been tested under pulse operation up to power of 20 kW (figure 6) with duty cycle up to 50 % and been tested up to 19.5 kW (figure 6) in CW operation. Some of its tested parameters are, DC to RF efficiency 61.8 % at 19.5 kW and overall gain 90.4 dB. An improved version of the same is under progress.

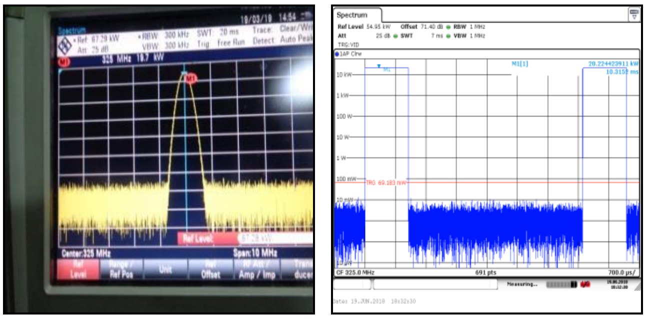

Figure 6: RF power (7 kW) waveform in CW and pulse mode

### *Solid state RF power amplifiers (150 MHz) for superconducting LINAC at TIFR*

As superconducting LINAC of TIFR, Mumbai is being upgraded, all its electronics inclusive of existing solid state RF amplifiers will be replaced with upgraded and higher power RF amplifiers. So design and development of high efficiency, compact and high gain RF amplifiers at 150 MHz with latest RF devices, technologies, high efficiency and improved reliability suitable for superconducting accelerator operation has started.

The 150 MHz, 300 Watt RF amplifiers [5] will be powering the 28 SCRF cavities of SC LINAC. In addition to power and frequency, the other targeted design specifications of this amplifier are efficiency > 65%, overall gain~ 44.8 dB, bandwidth ± 5 MHz etc. To fulfil this requirement, innovative RF design methods and heat pipe based efficient methods of cooling at this power rating have been studied and designed. This 150 MHz RF amplifier have been designed and its development is in progress.

## DEVELOPMENT OF HIGH RF AMPLIFIERS FOR NORMAL CONDUCTING HIGH INTENSITY PROTON ACCELERATORS

### *Solid-state RF power amplifier (10 KW, 352.21 MHZ) for buncher cavity of MEBT of proton accelerator of LEHIPA*

In LEHIPA, between 3 MeV RFQ and 10 MeV drift tube linac (DTL), a medium energy beam transport (MEBT) having buncher cavity is used. Buncher cavity requires RF power of around 10 kW at 352.21 MHz. So a solid-state RF power amplifier [6] has been developed, commissioned and coupled to buncher cavity via a coupler and coaxial 3-1/8” transmission line (TL) in between the buncher and amplifier. The commissioned transmission line has insertion loss of 0.36 dB, return loss at the input of RFPA (inclusive of buncher, coupler, TL) is 33 dB. After characterising the total system, the RFPA has been energised and buncher has been RF conditioned in pulse mode up to 10+ kW. The RF power waveforms of amplifier are shown below in figure 7. The 10 kW RF amplifier coupled to buncher cavity in LINAC tunnel of LEHIPA is shown in Figure 8.

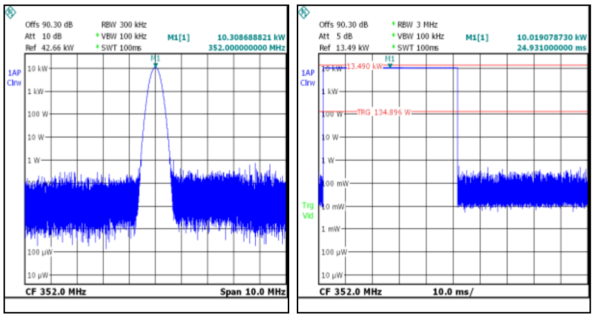

Figure 7: The 352 MHz RF power (10 kW) waveforms at 352.21 MHz of the amplifier in CW and pulse mode

Figure 8: The 352.21 MHz RF power (10 kW) coupled to buncher cavity via coaxial transmission line

### *Performance Testing, Evaluation of 1 MW, 352.21 MHz klystron RF system with pulse modulator and its power coupling for 3 MEV RFQ accelerator of LEHIPA*

Low energy high intencity proton accelerator (LEHIPA) have three accelerating cavities. One of them is 3 MeV radio frequency quadrupole accelerator (RFQ). This RFQ is designed to accelerate the H+ beam from 50 keV to 3 MeV in a length of 4 m and needs 68 kV of vane voltage

In 2016-17, a 1 MW, 352 MHz klystron was tested and commissioned in long pulse mode using Regulated High voltage Power supply (RHVPS). This klystron had coupled the RF power of around 540 kW [7], to the 1.2 MeV [8] [9] proton radio frequency quadrupole (RFQ) accelerator of the low energy high intencity proton accelerator (LEHIPA). A high amount of ripple was observed in the high voltage output of RHVPS (cathode bias supply), which severally affected the phase stability of RF power output of klystron. Hence recently, a pulse modulator with low ripple (<1 %) (Pulse modulator Specifications, 100 kV, 24Amp, Pulse width : 400 µsec, PRR: 1 Hz) was used as a cathode bias supply in place of RHVPS. The response time of pulse modulator as cathode bias supply is in the range of few tens of µsec. In order to match the response time of pulse modulator, high voltage interface system (HVIS) and anode biasing of klystron have been modified to get the desire results.

After incorporating proper modifications in HVIS and anode biasing system, the klystron system was successfully tested and commissioned with pulse modulator across RF Load. Output RF power phase stability measured has been measured below the 2° (degree). The klystron RF power was then coupled to two coupling ports of the 3 MeV RFQ accelerator via wave guide distribution line. A rigorous RF power conditioning of 3 MeV RFQ has been done before proton beam acceleration. The klystron (figure 9) has been operated for around 3 months continuously at around 600 kW during RFQ accelerator commissioning and 3 MeV proton beam has been accelerated. Test results and waveforms of RF power obtained at RFQ end of klystron system during 3 MeV proton beam acceleration are shown figure 10. Three klystron RF systems housed in Klystron gallery of LEHIPA are shown in figure 11. Waveforms recorded of proton beam measurements are shown in Figure 12.

Figure 9: Klystron RF system and its waveguide distribution for transport of RF power to RFQ

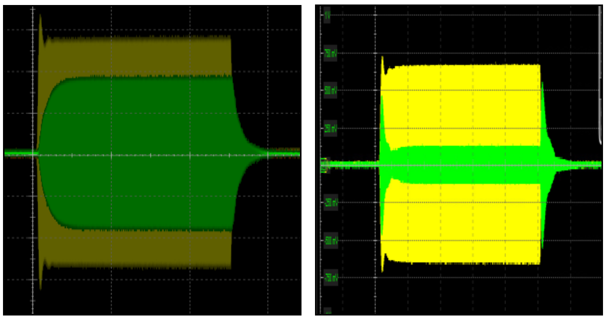

Figure 10: Forward and reflected RF power waveforms at RFQ end ((Waveform Courtesy IADD)

Figure 11: Klystron RF systems in klystron gallery

A 1 mA beam was accelerated to 3 MeV, with total RF power of around 540 kW into the RFQ, and with a transmission of around 65%.

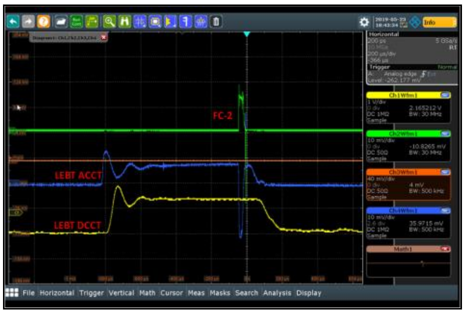


Figure 12: Beam acceleration across 3 MeV RFQ (Waveform Courtesy IADD)

## EFFICIENCY

Efficiency is a very important criterion for both NC and SC accelerators. Energy efficiency of ADS depends on efficiency of both accelerator and reactor. Efficiency is a very essential criterion and has crucial impact on economics of accelerator.

For Accelerator, wall plug efficiency ($\eta_{acc}$ , $\eta_{acc} = \eta_{dc} * \eta_{RF} * \eta_{Beam} * \eta_{other}$) is very important. $\eta_{dc}$ is AC to DC conversion efficiency, $\eta_{rf}$ is DC to RF conversion efficiency, $\eta_{beam}$ is RF to beam conversion efficiency and $\eta_{other}$ is the additional contribution of other power sources. For CW, normal conducting RF accelerators an achievable wall plug efficiency is between 10 to 20 %. For CW, superconducting RF accelerators, it is between 20 to 40%. Latest and advance RF device technology has improved the $\eta_{RF}$ close to 68 to 70%. Further increase in $\eta_{acc}$ can be achieved by improving AC to DC conversion efficiency of DC supplies, and efficiency of RF device. Use of modern pulse width modulation (PWM) based modular DC supplies over conventional supplies increases AC to DC conversion efficiency further. Overall system efficiency can be increased further by having appropriate amplifier configurations. Use of Multi beam high efficiency klystrons, high efficiency IOTs are some of the solutions for higher device efficiency.

## CHALLENGES AND REMEDIES INVOLVED IN HPRF

### *In tube based RF power systems*

Presence of high power, high voltage, high current and high temperature environment make the tube based amplifier configuration complicated. Vacuum tubes like tetrodes, klystrons are sensitive devices and require stringent protections in high RF power and across high voltage bias power supplies. Use of high frequency filters in control circuitry, use of proper isolation at high voltage / high current monitoring, requirement of high thermal management are the additional challenges faced. Because of presence of multi-electrodes, requirement of multi-bias supplies lead to bulkiness and complexity. The DC bias supply is the main energy source for the RF power device. Conventional DC bias supplies require higher size output filters for less voltage ripple and crowbar for protection of tubes against the stored energy This leads to bulkiness and unreliability under transient conditions.

The remedial measures include, use of (stored) energy less, PWM based modular DC bias supplies, which avoids stored energy and crowbar and also have high AC to DC efficiency. Use of RF devices like klystrons, IOTs, injection magnetron having high DC to RF efficiency is the latest trend. These measures have removed the drawbacks and can make the tube based RF systems effective.

### *In solid state high power amplifiers*

Challenges faced by SSRFPAs are, thermal management issues at high power, choice of amplifier architecture, unavailability of circuit models of LDMOS devices, high RF power per unit volume, reliability at around above 100 kW etc. Junction temperature of LDMOS devices is very sensitive to any variation in temperature increase. So for higher power operation regime, use of effective cooling techniques is a challenge. Lifetime of semi-conductor devices heavily depends upon their die temperature, thus making reliability of the amplifier dependent on temperature. All these factors lead to unstable and unreliable operation of SSRFA.

Use of appropriate amplifier architecture having a trade off between power, heat dissipation and phase noise of PA module is one of the remedial measure. In addition to individual PA phase adjustment, incorporation of amplitude and phase trimmers within the power combiner can be an effective solution so that effect of the amplitude/phase imbalance can to be reduced.

Of late, inductive output tubes (IOTs) seems to be best choice for HPRF systems because of their high conversion efficiencies i.e. approximately above 70% in class ‘C’ operation even at reduced drive power. Its linear phase characteristics are v good for phase control. IOTs have substantial higher gain than tetrodes (lower than a klystron). They are much smaller in size and lighter in weight compared to an equivalent klystron. But these parameters are comparable to a tetrode.

Its lifetimes are comparable to klystron and much larger than the tetrode, have substantially lower power requirements than a Klystron or tetrode. They are substantially smaller and cheaper, require less drive power than the tetrode, have much lower cooling requirements compared to Klystron and tetrode and have reduced sensitivity to variations in supply power

## INDIGENOUS DEVELOPMENT OF HPRF COMPONENTS / SUB SYSTEMS

As a part of efforts for indigenous developments of RF components of HPRF systems, various components are being designed and developed via collaborations with different institutes and private parties. Some of the components that are either developed or being developed are wideband RF driver, Graphane based RF switches & arc detector, circulator, various waveguide components, RF loads etc.

## CONCLUSION

HPRF systems are critical to any NC / SC accelerator because of their multi-displinary nature, complexity involved, their cost of development as well as operating cost, their efficiency and their impact on accelerator down time. In BARC, indigenous HPRF systems based on klystron and solid state devices have been successfully designed and developed after facing and overcoming various challenges

## ACKNOWLEDGEMENT

Authors thank Director, MRG for his constant support and encouragement**.** We also thank Head, IADD / LEHIPA – In-Charge, Technical coordinator of IIFC, for their support. Authors wish to thank Shri. Jagadish Bowlekar, Shri Hitesh Kadam of ACnD and teams of IADD and ACnD for their assistance in mechanical, assembly work, cabling and other work.

## REFERENCES

[1] Manjiri Pande et al, Invited talk, “RF power for 325 MHz superconducting cavities”, Workshop on ‘Technology development for superconducting cavities’, at RRCAT, Indore, India, July 2017

[2] Manjiri Pande et al, Invited talk, “Development of 325 MHz solid-state RF amplifiers for superconducting spoke resonators of high intensity proton accelerators” Asian Federation for Accelerator and Detectors (AFAD) 2019, at IUAC, New Delhi, India, February 2019

[3] J.K. Mishra et al, “High efficiency RF amplifier development over wide dynamic range for accelerator application”, Nuclear Inst. and Methods in Physics Research, A 868 (2017), 48–52

[4] JK Mishra, “Development and testing of prototype 20 kw, 325 MHz solid state rf power amplifier for accelerator program”, in this conference InPAC 2019, IUAC, N Delhi, India

[5] Snigdha Singh, “Design of a 300 W, 150 MHz Solid State RF Power Amplifier for SC accelerator”, in this conference InPAC 2019, IUAC, N Delhi, India

[6] BV Rama Rao, et al” Coupling and energising of 10 kW, 352 MHz solid-state rf power amplifier for buncher cavity of proton accelerator“ in this conference InPAC 2019, IUAC, N Delhi, India

[7] Sandip Shrotriya et al, “Operating experience of radio frequency power testing of klystron at 352 MHz ”, InPAC 2018,RRCAT, Indore, India

[8] Manjiri Pande et al, “Development, testing and performance of high power Radio frequency system during radio frequency Quadrupole accelerator operation of LEHIPA of ADS”, InPAC 2018,RRCAT, Indore, India

[9] P.V. Bhagwat et al., Beam acceleration through proton radio frequency quadrupole accelerator in BARC”, Journal of Instrumentation (JINST), IOP science, May 03, 2016

# NEUTRAL BEAM INJECTOR – PRESENT AND FUTURE

Mainak Bandyopadhyay* on behalf of NNBI team,
ITER – India, Institute for Plasma Research, HBNI, Bhat, Gandhinagar, 382428, Gujrat, India.

*Abstract*

Neutral beam injector (NBI) is one of the most successful auxiliary heating systems for a fusion device. In last few decades, majority of NBIs which are still operational are based on positive ion source technology with gas based neutralizer (PNBI). Their beam energies are restricted to ~ 100keV per nucleon. For larger fusion machines (like LHD, JT60U in Japan) having higher plasma density, energetic NBIs of having beam energy > 200keV per nucleon are required to have enough penetration depth in the fusion plasma to heat the core of it. Because the efficiency of neutralization of positive ions in a conventional gas based neutralizer is significantly low at energies above ~100 keV per nucleon, these NBIs are based on negative ion source technology (NNBI) and are also successfully operational for many years. Larger fusion devices such as ITER, DEMO, needed for future, beam energies of the order of ~ 500 keV per nucleon or higher are required and so NNBIs are the obvious choice for it. Some major technical issues need to be addressed to ensure long pulse commercial fusion reactor grade NNBIs. The challenges are mainly from power efficiency, negative ion yield, Caesium catalyst dynamics and neutron induced damage perspectives. Power efficiency issues are addressed at different functional component level starting from plasma production mechanism in the ion source, neutralization mechanism in the neutralizer and also in ion filtration technique in the residual ion dump (RID). To withstand harsh nuclear environment the integrity of the NNBI system needs to be assured for all operational scenarios including normal and accidental events. In this regards various aspects such as materials, component layout and their operational responses to different possible conditions including remote handling tools for maintenance are critical. The manuscript gives an overview on some of these technical aspects highlighting IPR and its national collaborator's contributions for NNBI related technology development. In addition, some fundament studies through innovative developments in the fields of efficient plasma source and Cs handling are being carried out.

## INTRODUCTION

To produce sustainable power from a magnetic confinement fusion device, the plasma therein need to be heated sufficiently. Neutral beam injector (NBI) is one of the most successful auxiliary heating system for it [1]. The fusion reactors mainly rely on the reaction between two isotopes of hydrogen: deuterium (D) and tritium (T). NBI heating is based on injecting equivalent energetic ≥ 10KeV neutral D atoms in to the fusion plasma which eventually get converted into ions in the plasma due to collisions and confined by the magnetic field and become part of the plasma. This heating scheme can be understood like, warming up the cold water by pouring in hot water. The penetration of the neutral beam depends on the effective collisional mean free-path due to the processes: (i) ionization and (ii) charge-exchange primarily. For higher beam energy, collision cross-sections are low; as a result mean free path become longer. Due to that the penetration depth of the neutral beam particle is deeper with higher beam energy. The beam intensity $I$ spatial profile inside the plasma along the beam direction can be represented as, $I = I_0\ exp(-x/\lambda)$, where $I_0$ is the beam intensity before entering into the plasma and $\lambda$ is the penetration depth. Penetration depth $\lambda$ can be estimated as [2], $\lambda=[(E_b/A_f)/(18n_e)]$ in meter. Plasma density $n_e$ is in $10^{19}\ m^{-3}$ unit, $A_f$ is the atomic mass of the neutral atom of the beam in amu, $E_b$ is the beam energy in keV unit. The above equation indicates that beam energy $E_b$ need to be optimized based on plasma density available inside the fusion device, otherwise undesirable high shine-through or edge heating is expected, if beam energy is higher or lower than the optimized value respectively. The maximum injectable beam energy $E_{max}$ need to be chosen considering the torus size of the fusion device. Smaller the machine, lower will be $E_{max}$ for the same plasma density. Smaller machines whose major radius (R) is < 5m are primarily engaged to study the fusion grade plasma dynamics and different power coupling mechanisms for plasma heating and current drive including their technological feasibility. For efficient fusion power generation large machines (R > 8 m) with higher magnetic fields are needed [3]. International Tokamak Experimental Reactor (ITER) [4], having R = 6.2m is currently under construction at Cadarache site in France under a global collaborative project, where India is a partner. However, production of electricity from fusion will be attempted in the demonstration fusion reactor (DEMO) machine. Many countries are having their own DEMO program considering success of ITER mission. Beyond DEMO, commercial fusion reactor is envisaged for commercial production of electricity. In all these future machines large amount of (tens of MW) NBI power is required to heat the fusion plasma to reach the burning stage and to sustain the extended pulse length for few 1000s or few hours or even for continuous mode operation by beam driven current drive. For long pulse operation copious amount of 14MeV neutrons will be generated from D – T reaction in the fusion plasma which may damage most of the materials around through transmutation. Therefore, to withstand harsh nuclear environment the integrity of the

* mainak@ipr.res.in

NNBI system needs to be assured for all operational scenarios including normal and accidental events. In this regards various aspects such as materials, component size, layout and their operational responses to all possible conditions including remote handling tools for maintenance are critical. Massive R&Ds on 1MV NBI for ITER are being carried out in Padova, Italy [5].

This paper discusses the future technological trend to address the challenges and related physics for a NBI system including India's contribution in this field.

## TECHNOLOGICAL CHALLENGES AND RELATED PHYSICS FOR IMPROVED EFFICIENCY

Improvement in efficiency in a NBI system lies in different areas: (A) Plasma and negative ion production, (B) Neutralization, (C) Residual ion dump (RID) filtration.

### *(A) Ion source*

The efficiency of a negative hydrogen ion source depends on the yield of negative ion production, which is linked with the plasma production and Caesium (Cs) dynamics. Filament discharge [6] and later RF discharge [7] based ion sources are used so far for NBIs. ITER sources are based on ~ 1MW, 1MHz RF negative ion source. The plasma production efficiency in RF source is significantly low ~ 10% or even less [8]. Eddy current losses in the metallic structure (Faraday shield) and electromagnetic radiation losses are the main responsible route for low RF power efficiency. Helicon plasma in RF frequency range and electron cyclotron resonance (ECR) plasma in microwave (MW) frequency range are two possible candidates which have potential to be considered as alternate technologies for future NNBI ion sources. Large size plasma sources equivalent to ITER type ion source has already been demonstrated with argon plasma using permanent magnet based multiple helicon plasma units [9] and permanent magnet based multiple ECR plasma units [10]. The efficiencies of both types are significantly more (nearly an order) than that of inductively coupled plasma (ICP) based RF ion source [11]. Permanent magnet arrangement does not need electrical and cooling water interfaces and make the ion source system simple and easy to maintain in a nuclear environment. However, such larger sources are not yet tested for negative hydrogen ion source operation with Cs vapour injection. IPR and its national collaborators are working on these technologies [10, 11, 12].

### *(B) Neutralizer*

Neutralizer is placed just after the extractor and accelerator system of the ion source. It plays a big role to determine the efficiency of a NBI system. Higher neutralization efficiency $\eta$ of extracted and accelerated ion beam is desirable for higher NBI efficiency, i.e higher injected neutral beam current per unit power used to produce it. Considering the neutralization efficiency (as shown in fig.1), it is clear that for beam energy $E_b$ >150keV, negative ion based NBIs are the only choice. There are several ways of neutralization of the ion (Hydrogen/Deuterium) beam can be carried out. For PNBI - neutralization by gas target charge-exchange collision mechanism is mainly responsible by attaching an electron to the ion species. For NNBI – there are more options to detach the loosely bound (~0.75eV) electrons from the negative ion either by collisions with the background gas molecules (Gas target neutralizer) or by plasma electrons (plasma neutralizer - $H/D^-_f + e = H/D_f^0 + 2e$) or by laser photo-detachment (Photo neutralizer - $H/D^-_f + h\nu = H/D_f^0 + 2e$). The symbols *H, D, f, e, - and 0* stands for hydrogen atom, deuterium atom, fast or energetic component, electron, negative ion and neutral component respectively. The last two neutralization processes are highly efficient.

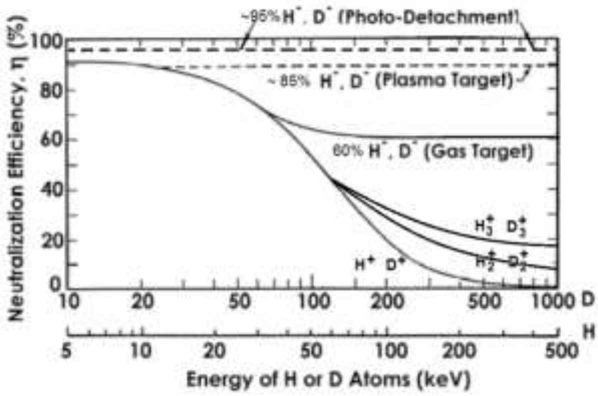


Figure 2: Neutralization efficiency η of different type of hydrogen ions having different energy considering various neutralization techniques [2].

In a gas target neutralizer, an optimum pressure profile is created and ion beam is allowed to pass through it. Fast ions are converted into fast neutral atomic beam in the transit. Those fast neutrals may again be re-converted into positive ions (known as re-ionization) if further collisions take place. The optimum target thickness for neutralization is calculated considering counter acting reactions. Some details can be found in the ref. [1].In case of high energy (>150keV) NNBI, conventional gas based neutralizer can provide maximum ~60% neutralization efficiency [2] which means ~40% of the extracted beam power is lost and dumped into the residual ion dump (RID). A gas neutralizer also demands efficient cryo-pumping to avoid stripping losses in the accelerator and re-ionization loss in the beam line and duct region.

A multi-cusped microwave ECR based plasma-neutralizer [13] can reach up to 80% neutralization. ECR plasma contains energetic electrons to perform electron detachment collisions with the accelerated negative ions and converted them into energetic neutral atoms. Gas requirement in plasma neutralize, particularly ECR based is less compared to that of gas based neutralizer and so requirement of cryo-pumps and corresponding reionization loss will be reduced significantly.

Photo neutralizer was first proposed by Fink [14]. Based on his calculation method it can be derived that ~95% neutralization is possible by pure photo-detachment considering available laser and mirror technology. The laser power "P" required can be estimated from the formula given by M. Kovari et.al. [15]. To achieve 95% neutralization efficiency in a neutralizer of width ~0.25m for 1MeV energy $D^-$ ion beam with a high power CW laser of wavelength $\lambda$ lies between 700nm to 1200nm, ~1 MW laser power is needed. Microchannel cooled high power laser diodes array bar (~150W CW per bar) of wavelength ~ 800 nm [16] is a suitable compact laser solution for photo-neutralizer purpose. Maintenance of the laser diode assembly and cavity mirror quality is a serious issue for long pulse operation, particularly in nuclear environment. SIPHORE [17] testbed in CEA, Cadarache is working on this technology.

### *(C) Residual ion dump (RID) filter*

Conventionally magnetic field ~ few 100G is used in most of the operational NBIs to filter out un-neutralized or re-ionized ions from the neutral beam by deflecting the ionic part by either 90º or 180º with respect to the original beam direction coming out from the neutralizer, utilizing Lorentz force "$q(\boldsymbol{v}\times\boldsymbol{B})$". ITER RID design (ERID) considers electric field instead of magnetic field [4] to deflect negative ions and re-ionized positive ions by < 90º angle in opposite direction and dumped on water cooled pates (see fig. 2a). The concept is compatible to ITER's four-channel beam geometry. The electric field $\boldsymbol{E}$ is created by applying negative high voltage between two consecutive plates of the ERID channel ($\boldsymbol{E}$ $\sim 10^5\ Vm^{-1}$ corresponding to 20kV applied between ERID channels for heating NB or HNB and $\boldsymbol{E}$ $\sim 5\times10^4\ Vm^{-1}$ corresponding to 8kV for that of Diagnostic NB or DNB). Due to negative HV, collision induced plasma electrons from the neutralizer are unable to travel downstream along the beam. However ERID has one major issue. Plasma formation takes place inside the ERID channels due to ionization collisions by the beam particles with background gas. The formation of plasma would screen the effective electric field and may modify ERID deflection properties. It may even destroy the ERID functionality and so possess a threat on NBI performance [18, 19]. To make $\boldsymbol{E}\sim0$ the critical plasma formation rate inside ERID channel is $\sim1.4\times10^{21}\ m^{-3}s^{-1}$ for HNB and $\sim 5\times10^{20}\ m^{-3}s^{-1}$ for DNB. Considering HNB and DNB operational scenarios, it is estimated that total rate of plasma formation is $\sim 1.2\times10^{19}\ m^{-3}s^{-1}$ & $\sim 5.4\times10^{19}\ m^{-3}s^{-1}$ respectively and within the safe limit [19]. However, gases desorption and also secondary electrons generated by the energetic ions falling on the ERID surfaces, getting accelerated in the electric field would enhance plasma formation significantly. These additional factors may lead to further reduction of ERID safety factor which will be tested in both the facilities, in Italy [5] and India.

To prevent such ERID failure one has to increase the sheath thickness significantly by reducing the electron motion towards the electrodes. In this regard a concept proposal is discussed qualitatively below. A transverse magnetic field (orthogonal to the applied electric field and the beam direction; i.e. parallel to the plane of the ERID plates) sufficient to magnetized electrons only and not the ions, will help to restrict electron motion towards ground potential plate and also restrict secondary electrons from escaping from negative potential plate. Therefore, plasma formation will be reduced and effectively sheath thickness will be more which effectively will improve ERID functionality. A schematic of magnetically enhanced ERID (MERID) concept is shown in figure 2 (b, c).

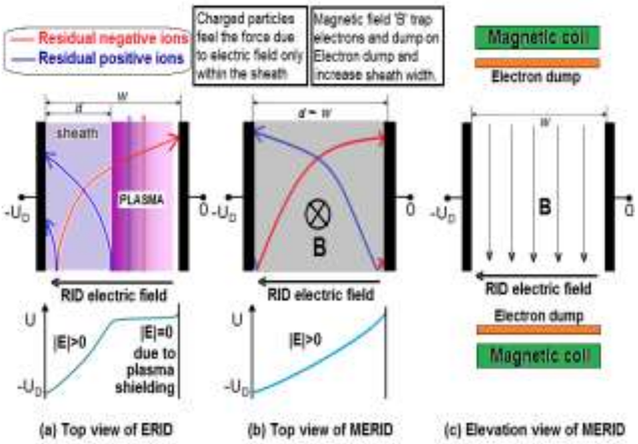


Figure 2: Schematic representation of ERID and MERID functionality and direction of electric and magnetic field.

The energy efficiency of a NBI system can be improved, if power can be extracted from the residual ion current collected by the RID by charging a capacitor bank in a resonant modular convertor. Details of such energy recovery systems suitable for PNBI beamlines can be found in the literature [20], but there is no such working system for negative ion beamline. Since photo-neutralizer neutralizes 95% negative ion beam current, energy recovery system hardly improves the efficiency and so may not be needed for future negative ion based NBIs. The new concept of MERID will be experimentally attempted in ROBIN testbed.

## CONTRIBUTIONS FROM IPR AND ITS NATIONAL COLLABORATORS

The journey started in 1995. A PNBI of ~1.7MW neutral beam power is designed and developed for steady state tokamak (SST-1) machine. Testing of individual components has been done [21,22]. All the beamline components, power supplies and control system are developed indigenously. The experience learnt in SST-1 PNBI gives confidence to accept the responsibility to deliver ITER-DNB. An Indian test facility (INTF) to test ITER-DNB with full specifications is under commissioning [23]. After joining ITER in 2005, IPR's NNBI program started with ROBIN (Rf Operated Beam source in India for Negative ion research).The roadmap of IPR's technology development under NNBI program towards ITER-DNB delivery is shown in fig.3.

Operation of ROBIN [24] test bed was started in the year 2011 and it has provided the desired experience and also helped to realize the requirements of various interfaces: like power supplies, hydraulics, diagnostics, gas feed system, Cs vapour injection system, pumping, and automated data acquisition and control (DAC) system. $H^-$ ion current densities of ~27mA.cm$^{-2}$ with an electron to ion current density ratio, $je/jH^- \sim 2$. Efforts are underway to increase the current density to the desired value of 30 mA cm$^{-2}$ with $je/jH^- \sim 0.5$ by Cs optimization, impurity control and RF matching utilizing various diagnostics (probes, optical emission spectroscopy, Doppler shift spectroscopy) [25, 26]. ROBIN has identified an interlock scheme based on electron dynamics (bias plate current) for RF generator, suitable for radiation environment (ITER type) where optical fiber based signal transmission is restricted due to material damage possibility [27]. Neutral beam from ROBIN source is envisaged incorporating a futuristic magnetically enhanced ERID (MERID).

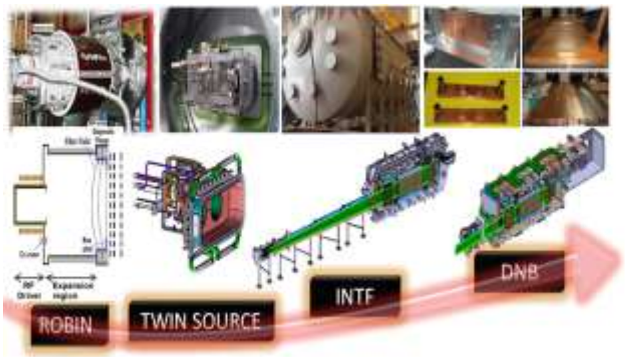


Figure 3: Roadmap of IPR's technology development under NNBI program towards ITER-DNB delivery.

In parallel to ROBIN operation, the design of TWIN source (TWo driver based Indigenously built Negative ion source) was started in 2011 onwards [28]. The aim of TWIN source is to establish inductive coupling of the RF power simultaneously to two drivers using a single RF generator, similar to ITER DNB configuration. TWIN source has two inductively coupled RF driver source. It is 1/4$^{th}$ the size of the ITER DNB source which has eight RF drivers. TWIN source design is unique from two perspectives. (a) All the embedded cooling channels in the source (even in grid, to be manufactured) are realized using vacuum brazing techniques instead of conventional copper electro-deposition [29], (b) RF driver pair can be operated both in air and under vacuum and for these two operational scenarios, the vacuum vessel is also manufactured accordingly with high voltage bushing interface for RF coupling. TWIN source manufacturing is completely indigenous and carried out by an Indian company, *M/S Hind High Vac (HHV)* in Bangalore. Till date, 50kW RF power is coupled to individual coil and 35kW in pair-configuration in air-mode without extractor and accelerator system integrated.

The aim of INTF is to characterize the ITER DNB with full specifications; i.e, ~2MW neutral beam power from 60A H- ion beam of 100keV energy with 5Hz modulation having 3s ON – 20s OFF duty cycle. The beam propagation distance is ~ 20.6 m from the extraction plane, same as that of DNB in ITER. INTF vessel of ~4.5m diameter, fabricated by *M/S Vacuum Techniques, Bangalore* is already installed [30]. The fabrication of the most challenging components – DNB ion source and its beamline components (BLC) are being carried out by internationally reputed companies following strict ITER quality protocols and corresponding fabrication statuses are 70% and 85% respectively. Auxiliary systems are either procured or under procurement. Expected starting date of ion source operation is Q2 2020, after the availability of ion source. Subsequently, installation and commissioning of BLCs will be carried out inside INTF vessel for full-fledged neutral beam operation till its delivery to ITER in 2023.

In parallel to DNB component fabrication, indigenous capabilities to manufacture these NNBI components are established in the form of prototypes. *Non-Ferrous Materials Technology Development Centre (NFTDC), Hyderabad* has develop the fusion grade coveted CuCrZr material as per ITER requirements for the BLCs and also established deep drilling for embedded straight long (>1m) cooling channels & electron beam welding (EBW) technology for dissimilar material joining [31, 32] for MW class high heat flux endured heat transfer elements (HTE). Regarding indigenous grid manufacturing, copper elctro-deposition technology to realized narrow (~ 2mm dia) wavy embedded cooling channels on large area grid structure is the stumbling process. Success in small scale prototype grid manufacturing based on Cu-electrodeposition was achieved in collaboration with Raja Ramanna Centre for Advanced Technology (RRCAT), Indore [33]; however large size electrodeposition is still a dream for in-house grid development. To overcome this hurdle, another innovate route is being carried out based on Laser Additive Manufacturing (LAM) technique in collaboration with same institute RRCAT.

Few more in-house, as well as collaborative efforts are being pursued for efficient plasma source development aiming better negative ions production. IPR has established a single module of permanent magnet based helicon plasma driver [11], a building block for a large size power efficient negative ion source. The large size ECR plasma source having multiple permanent magnet based small ECR source module [10] is being developed by Indian Institute of Technology, Delhi (IITD) in collaboration with IPR. A novel surface assisted volume negative source using Cs coated dust particles has been developed in Centre of Plasma Physics (CPP), Guwahati [12]. The concept has proved that negative ion yield can be large and equivalent to conventional cesiated ion source plasma without contaminating the hydrogen plasma with large amount of Cs. High voltage systems with proper data acquisition system for negative ion beam extraction is under commissioning in CPP laboratory.

## SUMMARY

NBI is one of the most successful auxiliary heating systems for a fusion device. Several present day technologies need significant upgradation to cope with ITER and then DEMO relevant nuclear scenarios and R&D efforts are being carried out globally including in India. IPR is engaged in NBI related R&Ds since long time. Its NNBI program got thrust after joining ITER program to deliver a 100keV DNB. IPR has developed many ITER relevant technologies in collaboration with international as well as national labs and companies. Indigenous capabilities to manufacture fusion grade NNBI components are established in the form of prototypes. Few alternate routes to develop more efficient negative ion source for futuristic NNBI are being persuaded in few national R&D institutes under collaborative umbrella.

## REFERENCES

[1] E. Speth, "Neutral beam heating of fusion plasmas",Rep. Prog. Phys. 52, 57-121, (1989).
[2] D.R.Sweetman, Nucl. Fusion, 13, 157, (1973).
[3] Fusion physics, ISBN 978-92-0-130410-0, IAEA, Vienna, (2012).
[4] ITER Design Description Document N53 DDD 29, "Neutral Beam Heating and Current Drive (NBH & CD) System" [Vienna: IAEA,2003].
[5] V. Toigo et.al., "Progress in the realization of the PRIMA neutral beam test facility",Nucl. Fusion 55, 083025, (2015).
[6] Y. Takeiri, et. al., Nuclear Fusion 46, S 199, (2006).
[7] E. Speth, et. al., "Overview of the RF source development programme at IPP Garching", Nuclear Fusion 46, S220, (2006).
[8] M. Dalla Palma et al. / Fusion Engineering and Design 84, 1460–1464, (2009).
[9] H. Torreblanca, "Multitube helicon source with permanent magnets" PhD Thesis UCLA, (2008).
[10] A. Ganguli, and R.D. Tarey, "System for Production of Large Volume High Density Plasmas for Industrial Applications Using Compact ECR Plasma Sources", Indian Patent # 992/DEL/2006.
[11] A. Pandey, et.al., "Characterization of hydrogen plasma in a permanent ring magnet based helicon plasma source for negative ion source research" Plasma Phys. Control. Fusion 61, 065003, (2019).
[12] B. Kakati, S. S. Kausik, M. Bandyopadhyay, B. K. Saikia & P. K. Kaw, "Development of a novel surface assisted volume negative hydrogen ion source", Nature Scientific Reports, volume 7, Article number: 11078 (2017).
[13] M. Hanada et.al. RSI, 75, 1813, (2004).
[14] J.H.Fink, et.al.,LLNLab report,UCRL,16844, (1975).
[15] M. Kovari and B. Crowley, Fusion Engineering and Design 85, 745–751, (2010).
[16] www.as.northropgrumman.com/ceolaser.
[17] A. Simonin, et.al., "R&D around a photoneutralizer-based NBI system (Siphore) in view of a DEMO Tokamak steady state fusion reactor",Nuclear Fusion 5, 123020, (2015).
[18] E. Surrey, Nucl. Fusion ,46 S360, (2006).
[19] L. Rossi, F. Castejon ., C. Moreno, Nucl. Fusion 49, 015002, (2009).
[20] R. McAdams et.al.,AIP Conf. Proc.1515,559, (2013).
[21] (a) S. K. Mattoo et al., "Neutral Beam Injector System for Steady State Tokamak-1," J. Korean Phys. Soc., 49, S25 (2006). (b) S. K. Sharma et.al., "Characteristics of the positive ion source at reduced gas feed', Rev. Sci. Instrum. 85, 113504, (2014). (c) Ch. Chakrapani, et.al., "Long pulse pumping behavior of a cryopump for the neutral beam injector", Jnl of Vac. Sc. & Technol. A 25, 90 (2007). (d) U. K. Baruah, et.al., "Power supply system for 1000s neutral beam injector", Proc. 17th IEEE/NPSS Symp. Fusion Engg, (1997).
[22] G. B. Patel, et.al., "Control system for 5MW neutral beam ion source for SST1" Rev. of Sci. Instrum. 77, 013501 (2006).
[23] M.J. Singh et al, "R&D status of the Indian test facility for ITER diagnostic neutral beam characterization", Nucl. Fusion, 59, 096034, (2019).
[24] M.J.Singh, et. al, "RF - Plasma Source Commissioning in Indian Negative Ion Facility", AIP Conference Proceedings 1390, 604 (2011).
[25] K. Pandya et al. "System upgradation for surface mode negative ion beam extractionexperiments in ROBIN", Fusion Engg. and Design 114, 187, (2017).
[26] M. Bandyopadhyay, et. al., "Performance evaluation of various diagnostics developed for a negative ion based neutral beam injector program in IPR", Nucl. Fusion, 59, 085001,(2019).
[27] M. Bandyopadhyay, et.al., "RF generator interlock by plasma grid bias current – An alternate to Hα interlock", AIP Conf. Proc. 1869, 030034 (2017).
[28] M. Bandyopadhyay, et. al," Two RF Driver Based Negative Ion Source Experiment", IEEE Trans. on Plasma Sc., 42, 624, (2014).
[29] R. Pandey, et.al.," Indigenous Manufacturing Realization of TWIN Source and Its Auxiliary", IEEE Trans. Plasma Science, 45, 2375, (2017).
[30] J. Joshi, et.al., "Manufacturing experience and commissioning of large size UHV class vacuum vessel for Indian test facility (INTF)", Fusion Engg. Design., 146, 1377, (2019) .
[31] C. Rotti et.al., "Establishing ITER-Grade Properties in CuCrZr: The Indian Experience",Fusion Science and Technology , Volume 65, 205, (2014).
[32] H. Patel et.al., "Manufacturing experience of beam dump for SPIDER facility", IEEE 26th Symp. on Fusion Engg. (SOFE), (2015).
[33]https://conferences.iaea.org/indico/event/151/papers/6055/files/4603-M_R_Jana-FEC2018.pdf.

# CONTRIBUTORY ORAL

# OPERATIONAL STATUS OF *K*130 VARIABLE ENERGY CYCLOTRON

P. S. Chakraborty#, A. Dey, Partha S Chakraborty, S. Ghosh, P.K. Behera, M. Dash, R. Kumar, R. Ming, R. Rasala, V.V. Rasankar, F. Tabassum, A. Das, A. Kumar, K.D. Rao, S.R. Raghuwanshi, B.N. Janavathu, D. Sinhamahapatra, A. Goswami, A. Bandyopadhyay and S. Som
Variable Energy Cyclotron Centre, Kolkata


## *Abstract*

The *K*130 cyclotron is presently equipped with two ion sources, namely electron cyclotron resonance (ECR) ion source and penning ion gauge (PIG) ion source. ECR ion source is producing high charge state heavy ions and for experiments requiring high intensity light ions, the internal PIG ion source is used while keeping the heavy ion central plug and the axial injection beam line in-place. This is an important and new development which required completely new beam tunes for light ions produced from PIG ion source. However this has significantly reduced the switch-over time between two ion sources from months to within a week. This paper describes the development of heavy ions, its internal beam profile, light and heavy ion beams energy range and beam intensities available from the cyclotron for experiments.


## INTRODUCTION

The *K*130 variable energy cyclotron is the first large circular accelerator commissioned in June, 1977. *K*130 cyclotron, also known as room temperature cyclotron, has been operating round the clock and delivering light and heavy ions for producing radio-isotopes, radiation damage studies and nuclear physics experiment etc., among the research institutes across the country. Initially cyclotron used to accelerate alpha, proton and deuteron beams. The cyclotron then started delivering high charge state heavy ions for experiments in early 2000. An indigenously developed 6.4 GHz ECR ion source was used for the production of high charge state heavy ions and later on another ECR ion source of 14.4 GHz was coupled to it. An up-gradation and modernization program of cyclotron sub-systems was under taken in the year 2007. PIG ion source was re-introduced and from then cyclotron started operating as primary source of light ions for the rare-ion beam facility apart from regular other experiments. In the year 2017, a shutdown was taken for acceleration of heavy ions again in cyclotron. In March, 2018, cyclotron has extracted heavy ions and various experiments have been performed with nitrogen, oxygen and neon beams. In March, 2019, PIG ion source was re-introduced for light ions acceleration and various experiments are presently being performed.

### *Axial injection system*

An indigenously developed 14.45 GHz ECR ion source and a new axial injection beam line has been commissioned for the production and transport of high charge state heavy ions to cyclotron. Axial injection line comprises of solenoid magnets and one 90 degree analyzing magnet that guides the beam up to inflector. The inflector is a simple mirror type inflector which bends the vertical beam to horizontal plane for further acceleration in cyclotron [1]. The inflector can also be also used as faraday cup for measuring beam current coming from ECR ion source through axial injection beam line. Three gridded single harmonic heavy ion beam buncher, developed in-house is the last element above the cyclotron yoke in the injection line.

#prodyut@vecc.gov.in

## HEAVY ION DEVELOPMENT

In March, 2017 heavy ion development program started. Oxygen beam of charge state 6 was developed in ECRIS and transported to cyclotron for further acceleration but there was no signature of beam even at the inner radius. Operational parameters like central region positions, inflector voltage, trim coils of inner radius etc. were extensively tuned in the process of beam tuning which consumes a significant time. It was observed that proton beam up to 9.0 MeV can be accelerated and extracted but more than 10 MeV proton beam, acceleration was possible up to few inches at inner radius and could not be tuned further as there was a sudden fall of the beam current. Alpha beam operation was also tried but beam could not be measured in the inner radius. From the above result, it realized that higher magnetic field may be causing some instability in beam acceleration and in case of alpha and oxygen magnetic field requirement is much higher than proton. This phenomenon could be verified if oxygen and alpha are accelerated in a magnetic field which is comparable to the magnetic field of proton. This condition requires cyclotron to be operated in higher harmonics of RF where the required magnetic field is 1/3$^{rd}$ and projectile's energy will be 1/9$^{th}$ compare to fundamental mode of operation. Third harmonic operation of oxygen 6+ beam has been performed at 5.8 and 7.0 MHz of RF, internal beam was obtained, beam current could be measured at innermost radius and then accelerated near to extraction radius. The above operation was performed for alpha which was also accelerated near to extraction radius. This indicated that beam acceleration beyond a certain magnetic field level was not possible. This could happen if the magnetic field in the central region is higher than required field, then beam will be oscillating in vertical direction with longer amplitude and may be lost in the accelerating chamber itself. Internal PIG ion source was re-introduced for tuning light ions and to have understanding about the magnitude of the magnetic field. The necessary modification in central region was carried out for PIG ion source while the central plug for heavy ion acceleration remained intact. Proton beam was extracted up to 10 MeV, alpha beam could be accelerated and measured at inner radius but there was sharp beam loss at outer radius. The above result indicated that the magnetic field at central region may not be proper and for proper field, central plug position has to be re-checked and adjusted, if required. An arrangement was made to vary the central plug position (~5mm) without disturbing the vacuum in cyclotron and axial injection beam line. Beam tuning was carried out at different positions of central plug with respect to mechanical median plane and its position was finalized with the optimum beam current. Then alpha beam was tuned using internal PIG ion source and 30 to 50 MeV alpha beam were accelerated and extracted. Later on proton beam was also tuned and extracted up to 15 MeV with about 5.0 micro-amp beam current. Having the position of central plug finalized, axial injection beam line was commissioned again and necessary modifications were also carried out in cyclotron central region for heavy ion acceleration. By the end of August, 2017 the cyclotron has developed internal beam of heavy ions. Oxygen and neon beams were developed at various energies but beam extraction could not be done and it was also realized that heavy ion extraction trial may take some more time. PIG ion source was introduced and several experiments with light ions have been performed [2].

### *Heavy ion extraction*

In March, 2018 heavy ion extraction trial started. Initially cyclotron operation started with alpha produced from ECR ion source and successfully extracted out. This operation gives some information about the positioning of the extraction electrodes and central region parameters. Beam extraction trial then started with oxygen 6+ beam and by optimizing the earlier developed operational data and adjusting the extraction electrodes position, oxygen 6+ beam of 120 MeV could be extracted out. Then neon 6+ of 150 MeV and 7+ of 203 MeV were also extracted out. The internal beam profiles of oxygen, neon beam of various energies are shown in Fig.1, Fig.2 respectively.

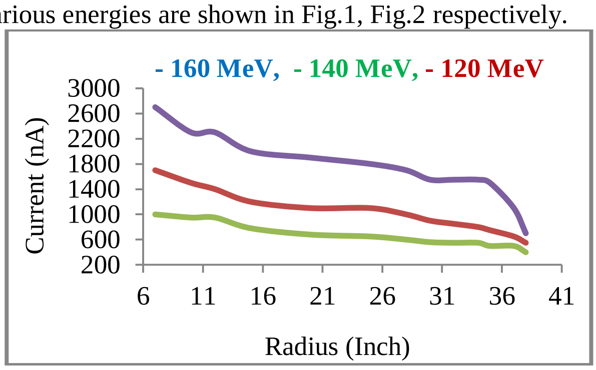


Figure 1: Internal beam profile of oxygen 6+ beam

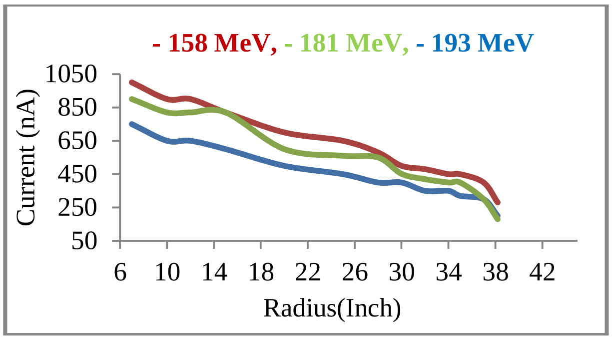


Figure 2: Internal beam profile of neon 7+ beam

## LIGHT ION DEVELOPMENT

For light ion acceleration with PIG ion source, the cyclotron central region has a geometry that consists of a Dee, Dee-insert, Dummy-Dee, Dummy-Dee-insert and PIG ion source which is located off-cantered. Here to mention that the central region geometry for heavy ion acceleration is different compare to light ion acceleration using PIG ion source. All the components of central region mentioned above for PIG ion source are there but differs in geometrical shape and PIG ion source is replaced by a mirror inflector which is located at the centre of the cyclotron. The mirror inflector bends the vertical beam by $90^0$ into the horizontal plane and directs towards dee for further acceleration. The central plug used for heavy ion acceleration is different in shape from the light ion acceleration plug. Since the axial injection line was kept in place along with heavy ion central plug, initially beam could not be obtained with the earlier light ion data. The major task was obtaining internal beam first and accelerate it further to higher radius by correcting the field of the isochronous coils called trim coils and these coils are spreading over the radius. Central region parameters like slit rotation, radial and azimuthal position of ion source has played a vital role for centering of the beam. Beam centering was checked at every higher radius during tuning. Beam centering was confirmed by shadowing technique using two current measuring probes. Internal beam was obtained after optimizing of various operational parameters which consumes a substantial amount of time. The internal beam profiles of alpha and proton beam of various energies are shown in Fig.3 and Fig.4 respectively.

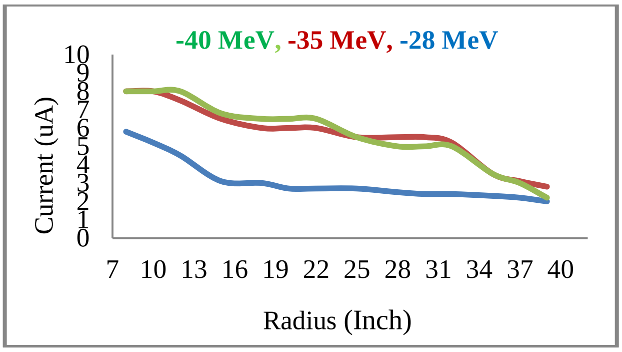


Figure 3: Internal beam profile of alpha beam

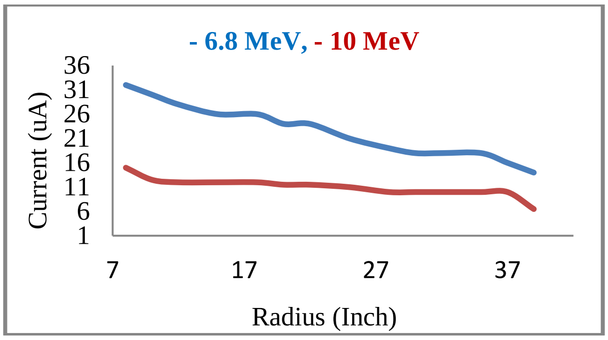


Figure 4: Internal beam profile of proton beam

### *Available Projectiles*

The cyclotron has developed heavy and light ions and the beam energy range of the above projectiles available for the experimental purpose is shown in Table 1.

Table 1: Projectiles

| Ions | Energy (MeV) | Current (nA) |
|---|---|---|
| Oxygen 6+ | 116 - 162 | 300 |
| Neon 7+ | 145 - 203 | 120 |
| Nitrogen 5+ | 101 – 142 | 400 |
| Alpha | 28 – 50 | 700 |
| Proton | 7 - 13 | 5000 |

### *Cyclotron activity and performance*

From April - October, 2018 various experiments have been conducted with heavy ions. Alpha beam was also developed in ECR ion source and delivered for INGA experiments. In January, 2019 PIG ion source was re-introduced again and high intensity proton beam was extensively used for radiation damage studies and other experiments. In middle of March, 2019 cyclotron was shut down for few planned activities and sub-systems maintenance work. In the first week of June, 2019 sub-systems made on and cyclotron operation started. Cyclotron beam made available for experiments from the second week of June, 2019 and continuing till date. During the period, April 2018 - March, 2019 the beam availability from cyclotron was 5160 hours. The performance chart of *K*130 cyclotron is shown Fig.5.

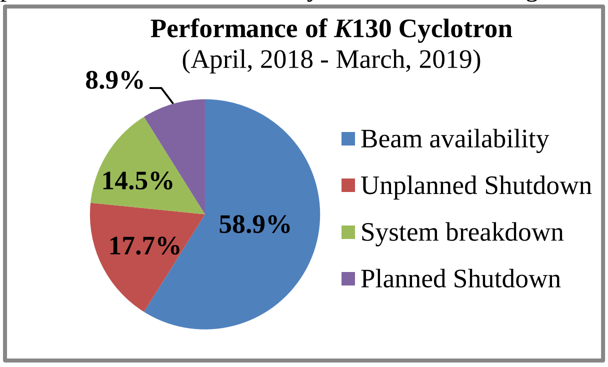


Figure 5: Performance chart

### *Cyclotron users*

During the above said period, the facility has been utilised by the experimentalists of VECC, SINP, Materials Division BARC, AchD/BARC, UGC-DAE-CSR-Kolkata, IIEST-Shibpur, Calcutta University, TIFR, University of Mumbai, Nuclear Physics Division BARC, CEBS - Mumbai etc.

## FUTURE PLAN

- Presently cyclotron central region is equipped with a mirror inflector having gridded wire mess. This inflector has certain limitations like poor beam inflection efficiency and requires high deflection voltage almost equal to ECR injection voltage. The wire mess breaks due to beam exposure and requires replacement in certain interval. It has been planned to replace the mirror inflector by spiral type inflector which has inflection efficiency more than 90%, no wire mess and voltage required for beam deflection is much less compare to mirror inflector.
- It has also been planned to accelerate ions of mass number more than twenty (20). ECR ion source has developed recently sulphur and chlorine beam of various charge states. Argon beam will also be developed and these ions will be accelerated and made available for the experiments.

## CONCLUSION

During the course of heavy ion acceleration various operational parameters have been obtained which has contributed subsequently to develop other ions of various beam energies. The reproducibility of the operational parameters like trim coils, central region parameters etc. are significant. One of the important achievements is the development of light ions using the central plug that is used for heavy ion acceleration. Operating cyclotron with two ion sources is also important in the senses that with the same plug both heavy ions and high intensity light ions can now be accelerated and the axial injection beam line need not be disturbed. Use of same central plug has reduced considerably the work complexity involved and cyclotron downtime.

## ACKNOWLEDGEMENT

Authors thankfully acknowledge the support and help provided by the team members of ECR ion source facilities section, Accelerator Technology Development (M) section, Cyclotron control section, Vacuum section, LCW section, Electrical section, Workshop, Power supply development section, Power electronics and magnet coil development section, Accelerator instrumentation section, RF section, Mechanical engineering section, Air conditioning section and Health Physics unit.

## REFERENCES

[1] P.S. Chakraborty et. al., proceedings of InPAC-2018
[2] P.S. Chakraborty et. al., proceedings of InPAC-2018

# DEVELOPMENT AND COMMISSIONING OF COMPACT DIGITAL LLRF SYSTEM FOR INDUS-2 SRS

Nitesh Tiwari*, Pritam S. Bagduwal, Dheeraj Sharma, Nitesh Mishra and Mahendra Lad
RF Systems Division, RRCAT, Indore

*Abstract*

Indus-2 is a 200 mA, 2.5 GeV Synchrotron Radiation Source. To increase the energy of electron beam and to compensate for synchrotron radiation losses, 505.8 MHz RF system is used. Indus-2 had been operating for a long period with four RF stations to suffice the requirement of beam lines at bending magnets. In last few years three insertion devices have been installed and two more are expected in future. This will increase the radiation losses and to cater this requirement two more RF stations have been installed in Indus-2. RF area of Indus-2 is very crowded due to installation of additional two Solid State Power Amplifiers. Considering the lack of space, FPGA based compact Digital LLRF system has been designed and developed in a single 32U rack that caters the requirement of station 5 and 6 simultaneously. This rack consists of two RF processing unit of 3U height. In a single PXIe chassis two FPGA card each having two high speed ADC and DACs are used for digital algorithm implementation. A common GUI has been created in LabVIEW that provides control and monitoring of important parameters for both stations and serves as local panel for Digital LLRF system. To interface with existing MCR control system a separate FPGA module is used. This Digital LLRF system has been successfully installed and commissioned in station 5 & 6 of Indus-2 RF system. With this compact Digital LLRF system Indus-2 is being regularly operated at its designed energy. In this paper work related to development, installation and commissioning of this system is described.

## INTRODUCTION

Development of Indus-2 a 2.5 GeV, 200mA Synchrotron Radiation Source (SRS) was planned in two phases. First with four RF stations for synchrotron radiation losses and in later phase it was planned to incorporate two more RF stations for insertion devices. Initially Indus-2 RF systems were based on klystron amplifiers. However due to aging and limited availability of the klystrons, they were replaced with Solid State Power Amplifiers (SSPA). SSPA requires more space compared to the klystrons and it was also not part of initial floor plan at RF area of Indus-2. Installation of two new RF stations and replacement of klystrons with more space consuming SSPA, lead to overcrowding of the RF area as shown in Figure 1. Considering this space crunching a compact Digital LLRF system for RF station #5 and #6 has been designed and developed. This LLRF system can cater the requirement of two RF stations from a single 32U rack. Layout of Indus-2 RF system is shown in Figure 2. In this paper various aspect related to design, development and installation of compact digital LLRF system in Indus-2 will be presented.

Year 2010 Year 2019

**Figure 1: Indus-2 RF Area in 2010 and in 2019**

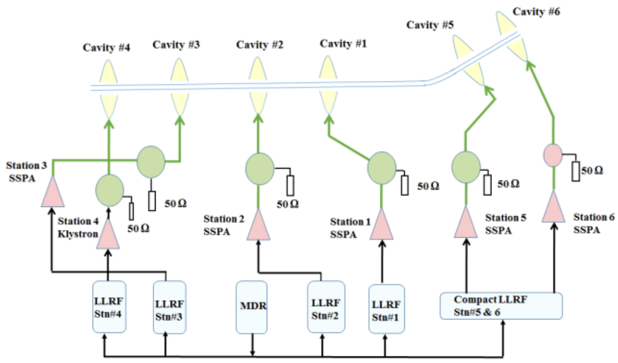


**Figure 2: Layout of Indus-2 RF Area**

## COMPACT DIGITAL LLRF SYSTEM

A compact Digital LLRF system consisting of amplitude and phase feedback control loops for both stations #5 and #6 has been designed and developed. A detailed block diagram of compact DLLRF is shown in Figure 3. LLRF system receives a common synchronized RF signal from main distribution rack, which is split in to four part two are used to drive the LLRF systems of station #5 & #6 and remaining two are diverted to the interlock units for implementation of "RF Available" interlock. Reference RF signal is processed in the RF signal processing units of respective stations before driving the high power amplifiers. Compact Digital LLRF system has a NI make PXIe chassis which houses the required digital hardware for implementation of necessary digital algorithms.

### *RF Signal Processing*

505.8 MHz, RF cavity sense signal is difficult to directly sample therefore RF signal is down converted to a suitable Intermediate Frequency (IF). RF cavity sense signal of 505.8 MHz RF is mixed with synchronized LO of 537.4 MHz to give 31.6 MHz IF signal. Synchronized clock of 25.8 MHz for I/Q sampling and LO signal of 537.4 MHz is derived from RF signal itself.

*nitesh@rrcat.gov.in

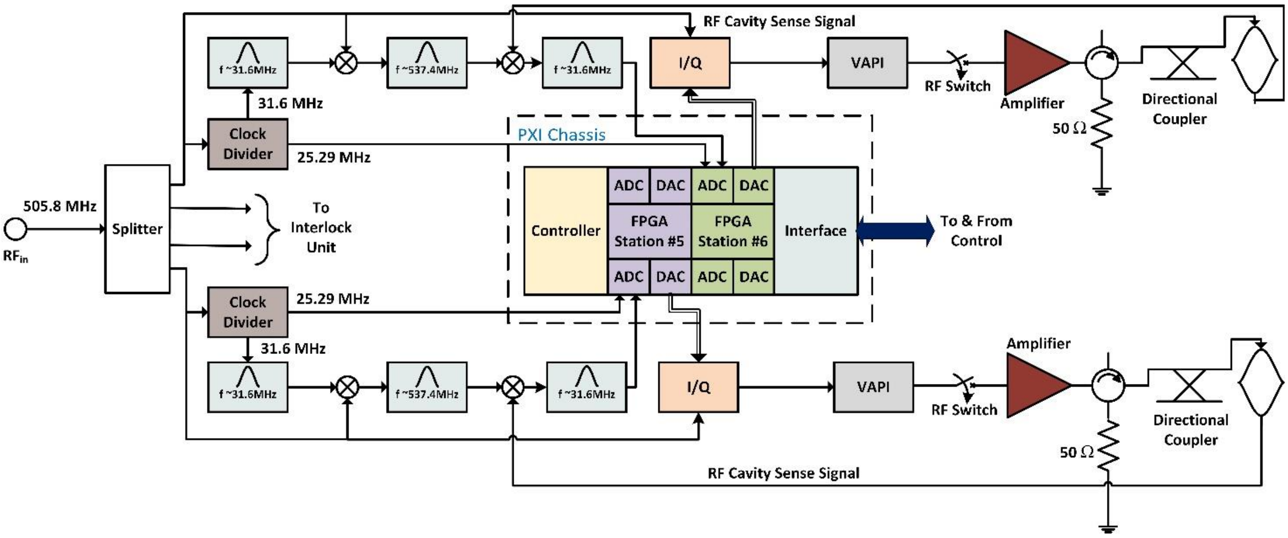


**Figure 3: Block Diagram of Compact DLLRF System**

To avoid any DC offsets, band pass filter of 31.6 MHz is used before feeding the IF signal to ADC for I/Q sampling. RF signal processing unit also consist of I/Q modulator which work as actuator to control the amplitude and phase of the main line RF signal.

**Figure 4: RF Signal Processing Unit**

Two such units shown in Figure 4, have been developed and installed in a single 32 U, 19 " rack.

## *Digital Signal Processing*

For detection of amplitude and phase from down converted RF signal and implementation of required PI controller to generate correction signals, a PXIe based digital processing system has been used. In Figure 5, shown is the photograph of digital PXIe unit installed in compact digital LLRF rack.

**Figure 5: PXIe based Digital Processing Hardware**

For compact LLRF system development, two FPGA modules with high speed ADCs (≥ 100 MSPS) and DACs (100 MSPS) are used in a single PXIe chassis. One multifunctional FPGA module having slow ADCs & DACs is used to send and receive the important signal to and from VME based control system. This single multifunction module serves for both the RF stations. Chassis is also equipped with a controller for implementation of host GUI, RF power calibrations and other operational features. A common TAB based GUI for both the stations (#5 and #6) has been developed in LabVIEW which work as local panel for the compact digital LLRF system (Figure 6).

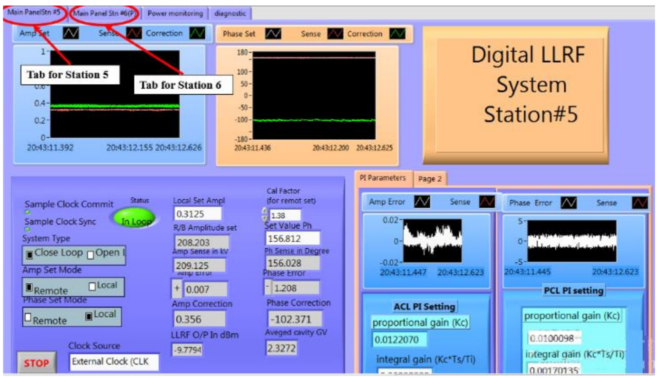


**Figure 6: Common GUI for Station #5 & #6**

## INSTALLATION AND COMISSIONING

A common RF drive signal has been used to ensure the synchronized RF signal for both the stations. A Variable Amplitude & Phase Insert (VAPI) has been used at the output of DLLRF system before driving the RF amplifier. This VAPI is used to keep the operating point of the loop same for any changes in the systems.

After the installation, RF stations are powered in open loop mode and output of LLRF is restricted to ensure the safe operation of RF amplifier and RF cavities. After that closed loop testing for amplitude and phase control is done.

PI parameters of the loops are optimized to achieve the required stability and response time. To facilitate the operation from remote control room, interfacing of digital LLRF system with VME based Main Control Room system is done

**Figure 7: Compact DLLRF Rack of Station #5 & #6**

Cavity gap voltage calibration of both the RF stations is done to ensure correct net power being fed to the RF cavities. Operating phase of both stations are optimized with respect to remaining four RF stations to accomplish the appropriate power sharing among stations. Figure 7, shows the Actual photograph of Compact Digital LLRF system.

To avoid wrong logging of phase error under RF OFF conditions modifications in digital algorithm is done, which ensure the display of phase error only after some level of gap voltage is achieved.

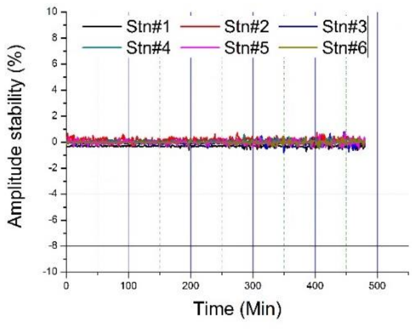


**Figure 8: Amp Stability Data of All stations**

Installation and commissioning of compact digital LLRF system for operation of station #5 and #6 has been done. With this Indus-2 has been operating at 2.5 GeV in round the clock manner. Amplitude and phase stability data of these stations along with other station are shown in Figure 8 and Figure 9.

Amplitude stability and phase stability of better than ±1% and ± 1degree respectively has been achieved in RF stations 5 and 6 which is also at par with other stations and Indus-2 requirement

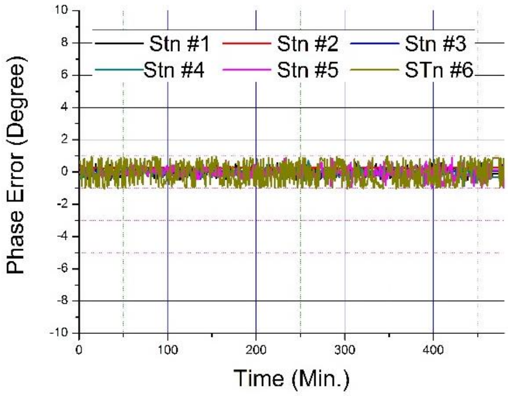


**Figure 9: Phase Stability of All RF Stations**

## CONCLUSION

A compact digital LLRF system has been successfully installed in Indus-2. This LLRF system is used for implementation of amplitude and phase feedback control loops of station 5 and station 6. PI parameters of both the stations are separately optimized for required stability and response time. Cavity gap voltage calibration and optimization of operating phase has been done for proper operation. With this compact digital LLRF system of station #5 and #6, Indus-2 is being operated regularly at designed energy of 2.5 GeV in round the clock manner.

## ACKNOWLADGMENT

Authors wish to acknowledge the efforts of Shri D. Suresh and Shri Sudarsan Kishan during installation and commissioning of compact digital LLRF system in Indus-2. Without their support it wouldn't have been possible to install the system is such a short time.

## REFERENCES

[1] Nitesh Tiwari, Pritam S. Bagduwal, M. Lad and P. R. Hannurkar, "Development of Prototype Digital LLRF system at RRCAT"InPAC-2013.

[2] Pritam S. Bagduwal, Dheeraj Sharma, Nitesh Tiwari,M. Lad and P. R. Hannurkar, " Fast Digital Feedback control system for accelerator RF system using FPGA". PCaPAC-2012

[3] Lad M., et al., "Upgradation of RF Technology in Indus-2 Synchrotron", Indian Particle Accelerator Conference InPAC 2018, RRCAT Indore, Jan., 9-12, 2018

# PHYSICS DESIGN STUDY FOR PROPOSED HIGH BRIGHTNESS SYNCHROTRON RADIATION SOURCE (HBSRS) IN INDIA

Ajay Ghodke*, Pramod Radheshyam, Ali Akbar Fakhri, Pradeep Kumar, Riyasat Husain, Abdurrahim, Saroj Kumar Jena, Pradeep Kant, Vijay Kumar Meena and D K Tyagi
Accelerator Physics Section
Raja Ramanna Centre for Advanced Technology

*Abstract*

The High Brightness Synchrotron Radiation Source (HBSRS) is a 6-GeV electron storage ring based light source which is capable of generating an ultra-low emittance electron beam is under design and extensive studies at RRCAT, Indore. Such an electron storage ring based light source is proposed to be built in India. Its ultimate goal is to provide a superior brightness of photons by reducing emittance of electrons to very small values. For reducing electron beam emittance, a multi-bend lattice scheme has been adopted. In this paper we will introduce the status of the HBSRS linear and nonlinear lattice design and other related physics studies, including storage ring design, injection system design, beam instabilities, collective effects and impact of machine errors on the beam dynamics etc. The storage ring will use a booster, as its full energy injector. In this paper we also report the status of lattice design and physics studies of the HBSRS booster, including the status of beam-injection, error studies, eddy current effects etc.

## INTRODUCTION

The High Brightness Synchrotron Radiation Source (HBSRS) is a 6-GeV, nearly one kilometer sized very low emittance storage ring based synchrotron radiation source proposed to be built in India. This source is now is under design consideration. One of the fundamental goals of these studies is to evolve a 'baseline ' lattice design for the HBSRS, and thus to study the associated accelerator physics issues and ensure the feasibility of building the HBSRS source from beam dynamics point of view and provide some major beam parameter list and tolerance budget for different hardware systems. After discussions with potential synchrotron radiation users in India, the goal emittance of the HBSRS storage ring lattice design is fixed to obtain a natural emittance less than 250 pm.rad. The basic key hardware techniques and related physics issues, a hybrid-7BA(H7BA) lattice with a emittance of ~149 pm.rad and having a large ring acceptance suitable for the conventional beam injection schemes is proposed as a baseline lattice design. Based on this lattice, we carry out associated and essential physics studies for the HBSRS, including collective beam instability effect study, error and tolerances studies, injection system design, injector design & pre-injector requirements, etc. In addition to this, we are continuously optimizing the lattice for further better performance. In this paper we report the status of the lattice design, and recent progress in accelerator physics related issues.

## LATTICE DESIGN STUIDES

An electron storage ring with beam emittance <250 pm.rad at 6 GeV with 200 mA stored beam current is desirable to achieve the required brightness of 10 [20-22] [photon/sec./mm2/mrad2/0.1%BW] in the photon energy range of few keV to 200 keV, [1]. In an electron storage ring the beam emittance is scaled as $\varepsilon_x \propto \gamma^2\theta^3$ or $\varepsilon_x \propto E^2/N_B^3$, where E is the electron beam energy, $\theta$ is the bending angle per dipole and $N_B$ is the number of bending magnets in the ring. Therefore, to achieve lower beam emittance, more number of bending magnets with smaller bending angles and independent strong field quadrupoles are required to focus the lattice optical functions at the centre of the dipole magnet. A recent trend in lattice design is based on the multi-bend achromats (nBA)[2], where n is the number of bending magnets per super-period. Recently, 7BA and H7BA are rigorously being studied for new light source projects and up-gradation of the existing facilities all over the word. A H7BA lattice has been adopted by ESRF-EBS [3] and APS-U[4], using strong transverse and longitudinal gradient incorporated in the bending magnets, which not only provides smaller electron beam emittance but also better control on the stability of nonlinear dynamics. In such low emittance storage rings, a large negative chromaticity will be generated since very strong field quadrupole magnets are being used. For chromaticity correction, strong nonlinear field sextupole magnets are included in the lattice. The sextupoles are typically placed at high dispersion locations for efficient chromaticity correction with relatively weaker nonlinear sextupole fields. Optimization of the lattice is based on several considerations namely, the betatron phase advance between a pair of sextupoles if separated by –I transform , this will help to cancel the geometric effects generated by the sextupoles[5]. Sufficient number and length of the straight sections are desirable for installation of injection, RF systems and insertion devices equipments. We consider 32 numbers of straight sections each of length ~6 m. The quadrupole magnets, grouped in eight families with various lengths and strengths, bending magnets with strong transverse gradient are used to optimize the beam emittance, dispersion function specifically at the sextupole locations, beta function at injection point or at the centre of the insertion devices etc. are to be optimized Thus, the design optimization of the HBSRS storage ring lattice is a class of multi-objective optimization problem. A multi-objective differential evolution (MODE) algorithm [6] is used to optimize the HBSRS lattice. The optical functions

*ghodke@rrcat.gov.in

of one H7BA over one super-period of length 28.5 m are shown in Fig. 1

The beam injection efficiency and adequate beam lifetime in such a low emittance storage ring are very challenging tasks. In order to ease these issues, the dynamic aperture (DA) in both the transverse planes of the ring must be as large as possible for both on and off-momentum particles. For numerical optimization of DA, five sextupole families, three in achromat and two in dispersion free sections are used.

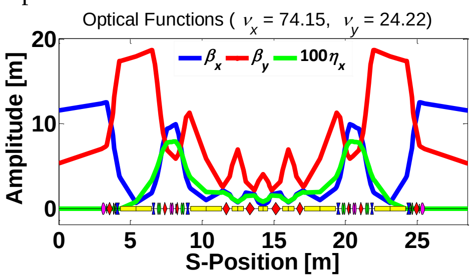


Figure 1: Lattice optical function over one super-period of H7BA lattice. yellow rectangles :bending magnet, red: focussing quadrupole, blue: defocussing quadrupoles magnets, magenta: focussing sextupole and green: defocussing sextupole magnets.

The relevant lattice parameters for the optimized HBSRS storage ring lattice are given in Table 1.

Table 1: List of parameters of the H7BA lattice at 6 GeV.

| Parameters | Values |
|---|---|
| Circumference, $C$ | 911.8 m |
| Emittance, $\varepsilon_x$ | 150 pm |
| Beam current (multi-bunch) | 200 mA |
| No./length ID sections | 32 / 6 m |
| Energy loss/turn | 2457.2 keV |
| Hor. Damp. Partition, $J_x$ | 1.703 |
| Betatron Tunes | 74.15,24.22 |
| Chromaticity:Natural | -109.6,-80.9 |
| Corrected | +4, +4 |
| Beam size at ID[$\sigma_x\sigma_y$] | 41.4, 2.8 μm |
| Beam sizeat BM[$\sigma_x\sigma_y$] | 10.9, 2.4 μm |
| Energy spread | 1.02 x $10^{-3}$ |
| Mom. compact factor | 9.6 x $10^{-5}$ |

The optimized on-momentum DA calculated based on single particle tracking for 5000 turns (twice the damping time) After systematic optimization of both linear and nonlinear dynamics, as shown in figure. 2 and 3, the 'effective' on momentum dynamic aperture (DA) and off momentum acceptance (MA) are 10 mm and 4 mm in x and y planes, and ~4% at ID locations respectively.

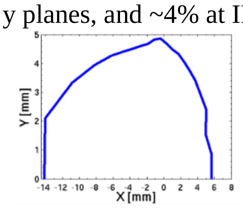


Figure 2: On momentum DA of a single particle tracked for 5000 turns at injection point.

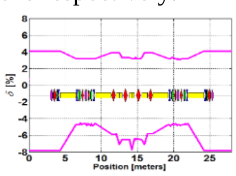


Figure 3: Transverse MA over one super-period tracked for 5000 turns at different point.

This large ring acceptance makes it feasible to use off-axis multipole injection method in the HBSRS storage ring. Further studies related to improvement in the DA with longitudinal gradient in the dipoles are in progress. These techniques will also useful in further lowering of beam emittance.

## BEAM INJECTION

The injection scheme presently under consideration is the off-axis beam injection using pulsed higher multipole kicker. We studied the dedicated scheme of pulsed sextupole magnet (PSM) kickers. In this scheme, the injected beam passes off-axis through PSM while the stored beam pass through its centre and thereby insignificantly affect the beam during frequent top-up injection. The location of PSM is very stringent and optimized using the simulation code Accelerator Toolbox (AT) [7], Kicker pulse used in the simulations is trapezoidal in shape with a total pulse width of 6μs and flat top of 2.1 μs. It requires a maximum sextupole gradient of 4300 T/m$^2$ considering length of the PSM as 0.3 m. In the preliminary studies using calculated DA without field errors, this injection scheme is found to be suitable for storage ring . An alternative to this scheme, a longitudinal on-axis injection is also being studied.

## CLOSED ORBIT DISTORTION

Due to very compact design of the storage ring, a very strong focusing quadrupoles will be used in the design of very low-emittance storage ring design, the ring performance is sensitive to various errors, such as the alignment error, magnetic field error, etc. The main contribution in Closed Orbit Distortion (COD) comes from misalignment errors of quadrupoles and dipole magnetic field errors and roll angle errors etc. In the presence of COD, acceptance for residual oscillation will reduce. Therefore, in the presence of large and finite COD, the beam injection efficiency and beam lifetime will be reduced. Simulations show of closed orbit amplification for the quadrupole misalignment is ~138 and ~142 in horizontal and vertical plane respectively. We are further studding the effect of following errors shown in table-2 on the COD in storage ring.

**Table-2: Set of errors for COD analysis**

| Errors | Δx | Δz | ΔΦ |
|---|---|---|---|
| Units | μm | μm | μrad |
| Dipole | 100 | 100 | 500 |
| Quadrupole | 50 | 50 | 200 |
| Sextupole | 50 | 50 | 500 |

## COLLECTIVE EFFECTS

### *Intra Beam Scattering (IBS)*

The impact of Intra-beam scattering (IBS) which may causes the degradation in beam quality has been studied and found to be its impact on the beam emittance is found to be negligible. The large angle coulomb scattering known as Touschek scattering which causes the electron loss. The estimated Touschek scattering related beam life time at 200 mA beam current at 6 GeV and considering 1% betatron coupling is ~50 hours with vacuum lifetime of ~22 hr @ 1.0 ntorr pressure total beam lifetime is ~15 hrs.

### *Single bunch instabilities*

Assuming longitudinal broad band impedance Z‖/n = 0.344 Ω (ESRF-EBS) [3] storage ring. Simulation using ELEGANT [8] code, shows that the strongest single bunch instabilities is found to be the transverse mode coupling instability. Its threshold bunch current of ~ 0.2 mA at zero chromaticity. The same could be increased with higher positive chromaticity and using 3$^{rd}$ harmonic RF cavity the simulation carried out using mbtrack [9] code shows that using 3$^{rd}$ harmonic cavity bunch can be lengthened from 20 psec to 200 psec thus diluting the particle density.

### *Coupled bunch instabilities*

The simulation of coupled bunch beam interaction with the higher order modes (HOMs) in the RF cavity using CLINCHOR [10] code. We use Indus-2 505 MHz RF cavity modes for these studies, Simulation shows that there is fast growth of beam instability. The growth rate of instability is ~3.5 times higher than the synchrotron radiation damping rate thus leads to beam instability which may be cured by RF cavity temperature optimization. The growth time of resistive wall instability [11] assuming typical wake field of 2.2×1015 V/C/m (APS-U) and zero chromaticity is ~4 msec. much smaller than radiation damping time of 14.8 msec. This instability can be control if the storage ring is operated at higher chromaticity of +4.

## BOOSTER SYNCHROTRON

A 6 GeV booster synchrotron having a bam emittance ~3.5 nm.rad will serve as an injector for the storage ring of HBSRS. It contains 86 unit cells of modified FODO lattice. The lattice functions of one unit cell are shown in figure 5, which contains a focusing quadrupole, a bending magnet with defocusing quadrupole component, focusing and defocusing sextupole magnets [12]. The parameters are shown in table-3.

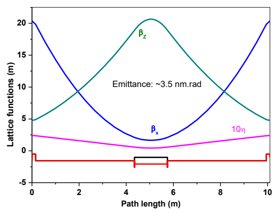


Fig. 5: Lattice functions of synchrotron for a unit cell

**Table-3: Main parameters of booster synchrotron**

| | |
|---|---|
| Circumference | 868.6 m |
| Injection energy | 200 MeV |
| Extraction energy | 6 GeV |
| Betatron tunes (x, z) | 30.27, 14.165 |
| Natural emittance | 3.5 nm.rad @ 6 GeV |
| RF Frequency | 505.667 MHz |

(x: horizontal, z: vertical)

In the booster, the effect of eddy current induced sextupole on chromaticity is studied and found that a sinusoidal ramp profile with a rep-rate of 1-2 Hz is suitable [13]. The preliminary studies of COD reveals that magnet to magnet alignment tolerances are ~40 μm [14]. At final energy, the beam will be extracted from booster with the help of fast extraction kicker for beam injection into the storage ring with specially designed beam transport line [15].

## CONCLUSIONS

The low emittance storage ring similar to ESRF-EBS type. The design of linear optics satisfies the requirements of the very low emittance, large enough DA and sufficient MA. There is a possibility of further improvement both the linear and the nonlinear beam dynamics. The design which is presented in this paper can be served as a baseline design of HBSRS project which can be used for the future optimization and relevant studies.

## REFERENCES


[1] A. D. Ghodke etal. InPAC-2018

[2] D. Einfeld, et al., J. Synch. Rad., 21(5):856–861, 2014

[3] ESRF-EBS Storage Ring Technical Design Report(September-2018).

[4] APS upgrade project preliminary design report.

[5] J. Bengtsson, The sextupole scheme for Swiss Light Source (SLS): An analytical approach, SLS note 9/97.

[6] R. Storn, K. Price, J. Global Optimization 11, 341(1997).

[7] A. Terebilo, Accelerator Toolbox for MATLAB, SLAC-PUB-8732, May 2001

[8] M. Borland, ELEGANT: APS LS-287,Sept. 2000.

[9]J. Borthwick, et. el."mbtrack: Multi-bunch tracking code". 2015.

[10] User's Guide to program CLINCHOR, L. Emery, July 2016.

[11] Pradeep Kumar, D. K. Tyagi and A.D. Ghodke, Study on Coupled bunch beam instability due to Resistive wall of vacuum chamber and its cure in HBSRS, this conference

[12] Pradeep Kant, Ali Akbar Fakhri and A D Ghodke, FODO lattice for booster of High Brilliance Synchrotron Radiation Source, this conference.

[13] Pradeep Kant, Ali Akbar Fakhri and A D Ghodke, Effect of eddy current induced sextupole during ramping in booster synchrotron of HBSRS, this conference.

[14] V. K. Meena, A.A. Fakhri and A.D. Ghodke, Closed orbit distortion and its correction at injection energy for booster synchrotron of HBSRS, this conference.

[15] Pramod R, Pradeep Kant, A.D. Ghodke, Conceptual Design of Transport Line from Booster to Storage Ring for HBSRS, this conference.

# LOW EMITTANCE OPTICS OPTIMIZATION DURING OPERATION OF INDUS-2

Ali Akbar Fakhri[1], Pradeep Kant[1], Aakash Deep[2,5], Surendra Yadav[2,5], Rahul Rana[3], KVANPS Kumar[4], Riyasat Husain[1,5], S. K. Prajapati[1] and A. D. Ghodke[1],[1]Accelerator Physics Section, [2]Beam Diagnostics Section, [3]Accelerator Control Systems Division, [4]Ultra High Vacuum Technology Section, Raja Ramanna Centre for Advanced Technology, Indore, India-452013,
[5]Homi Bhabha National Institute, Anushakti nagar, Mumbai, India–400094

*Abstract*

Indus-2 storage ring is a 2.5 GeV synchrotron radiation source, which is working as a national facility for synchrotron radiation users. In order to satisfy the requirement of users, its brightness is increased by reducing its horizontal emittance during operation from ~135 nm-rad to ~45 nm-rad at final beam energy. In this mode of operation, sensitivity towards various errors are increased, as a result vertical beam emittance is slightly reduced. Further photon beam brightness at the location of bending magnet is also not significantly increased due to higher value of vertical twiss parameters at its location. In order to overcome these limitations, a new optics is evolved and implemented at final beam energy. In this article, criteria for deciding this optics, experience during its implementation and further strategy for reducing the beam emittance are discussed.

## INTRODUCTION

Inuds-2 a 2.5 GeV synchrotron radiation source is extensively used by synchrotron radiation users belong to different institutes, universities all over the country. To satisfy requirement of certain users, photon brightness of synchrotron radiation produced by dipole magnets and insertion devices has to be increased. This brightness can be increased by reducing the beam emittance and with the help of proper choice of vertical twiss parameters (β, α governing width and divergence of the electron beam) at the location of bending magnet and insertion device.

In Indus-2, the brightness is increased by reducing its horizontal emittance to one third with the help of a switch over procedure [1] at 2.5 GeV. In this procedure, required current is accumulated at 550 MeV using the moderate optics (optics-M) having beam emittance of 135 nm-rad, after increasing the beam energy up-to final beam energy, its horizontal emittance is reduced to 45 nm-rad by changing the optics (strengths of quadrupole and sextupole magnets). In this procedure, reduction in vertical emittance is negligible due to higher value of transverse betatron coupling and spurious vertical dispersion function. These terms are slightly corrected [2] with the help of existing four skew quadrupole magnets. Further at the location of bending magnet, vertical beam size and its divergence are also not reduced due to higher value of vertical twiss parameters. The synchrotron radiation user of bending magnet are more interested to have a smaller vertical beam size and beam divergence thus, they are slightly benefited.

In order to further increase the brightness, vertical beam emittance and twiss parameters at the bending magnet location have to be reduced. For this, a new optics is evolved and implemented at 2.5 GeV with the help of the switch over procedure.

In the article criteria for deciding the new optics, which is referred as optics-B and its comparison with previously implemented low emittance optics (optics-A) is discussed The experimental results during implementation of optics -B along with measurements of beam dynamics parameters are also covered. Future plan for further reducing the transverse emittance will also be discussed.

## THEORY

The vertical beam emittance ($\varepsilon_y$) is mostly governed by horizontal beam emittance ($\varepsilon_x$), spurious vertical dispersion function and transverse betatron coupling between horizontal and vertical planes. The vertical dispersion function and transverse betatron coupling are generated by rotation of quadrupole and dipole magnets, vertical displacement of quadrupole and vertical orbit offset at sextupole locations. The coupling constant is estimated with the help of equation (1).

$$\kappa = \frac{\varepsilon_y}{\varepsilon_x} = \frac{j_x\langle H_y\rangle}{j_y\langle H_x\rangle} \quad (1)$$

Here $\langle H_z\rangle = \int \left(\gamma_z\eta_z^2 + 2\alpha_z\eta_z\eta_z^{/} + \beta_z\eta_z^{/^2}\right) ds/2\pi\rho,$ z denotes either x (horizontal plane) or y (vertical plane), s is the longitudinal distance in a bending magnet at which twiss parameters beta, alpha, dispersion and derivative of dispersion are $\beta_z, \alpha_z,\ \eta_z$ & $\eta_z^{/}$ respectively. $\rho$ is the bending radius and $j_z$ is the partition number.

The horizontal beam emittance can be reduced by reducing the $\langle H_x\rangle$ function and to do this, profile of $\beta_x$ & $\eta_x$ in the bending magnets have to be optimized. The vertical emittance can be controlled with the help of reducing following parameters such as strength of sextupole magnets, vertical orbit offset at sextupole locations, values of vertical twiss parameters at bending magnet location as well as amplification factors of vertical closed orbit distortion.

## OPTICS OPTIMIZATION

In Indus-2, beam emittance is reduced with the help of switch over procedure, in which beam is stored using the optics-M, its optical functions is plotted in Figure 1. In order to reduce the both horizontal and vertical beam emittance a suitable optics has to be evolved. At final beam energy, optical function of optics-M has to be switch over to new optics with the help of adjusting strengths of quadrupole and sextupole magnets in such a way that during this process linear and non-linear resonances should not be excited otherwise partial beam current loss may took place. For this, an objective function is optimized with the help of least square and Lagrangian multiplier method in step by step by using computer code Burhani [1] so that the trend of change of optics can be regulated.

The unit cell of Indus-2 consists one quadrupole magnet triplet (QD1-QF1-QD2) in the insertion straight section and another quadrupole magnet triplet (QF2-QD3-QF2) in the double bend achromat section. Here, QF and QD denotes horizontal focussing and defocusing quadrupole magnet respectively. The achromat section has two focusing (SF) and two defocusing (SD) sextupole magnets.

A new optical solution (optics-B) to get lower beam emittance in both horizontal and vertical plane is obtained with optimization of optics-M by varying strength of QF1, QD2 and QF2 families. The difference between previously implemented low emittance optics (optics–A) which is obtained with the help of varying the strength of (QD2 QF2, QD3) families and optics-B are discussed.

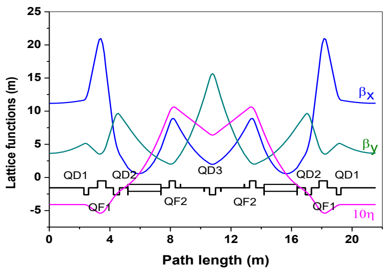


Figure 1: Lattice functions for the optics-M.

Twiss parameters for optics-A and B are shown in Figure 2 and 3 respectively and a comparison of twiss parameters between two optics are tabulated in Table-1. This table indicates that in optics-B vertical Twiss parameters at the center of bending magnet location is smaller as compared to optics-B. As a result at bending magnet location in vertical plane, electron beam size and divergence and quantum excitation due to spurious vertical dispersion function will be reduced as compared to the optics-A.

In the optics-B, in vertical plane sensitivity towards various errors will be reduced due to decrease in maximum vertical beta function and increase in vertical beta function at SD location. In Table-2, the maximum percentage change in amplification factors of closed orbit distortion, beta beat, strength variation of quadrupole and sextupole magnets from the moderate to low emittance optics are tabulated. This table indicates that in vertical plane percentage change in amplification factors of closed orbit distortion, beta beat and sextupole strengths are lower in optics- B as compared to optics-A. Thus in optics B transverse betatron coupling constant and spurious dispersion function, which are arising due to orbit offset at the sextupole location will be remain smaller as compared to optics-A.

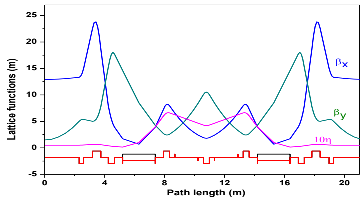


Figure 2: Lattice functions for the optics-A

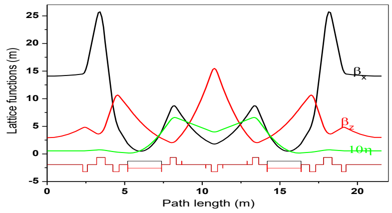


Figure 3: Lattice functions for the optics B

Table 1: Comparison between the moderate and low emittance optics

| Parameters | Optics-M | Optics-A | Optics–B |
|---|---|---|---|
| $\beta_{x,\max}, \beta_{y,\max}$ (m) | 19.8, 14.8, | 22.8, 17.6 | 25.7,15. 5 |
| $\beta_{x,ins}, \beta_{y,ins}$ (m) | 11.1, 3.6, | 13, 1.4 | 14.1, 2.9 |
| $\beta_{x,cbm}, \beta_{y,cbm}$ (m) | 0.8, 4.7 | 0.8,7.6 | 0.8,4.7 |
| $\varepsilon_x$ nm-rad@ 2.5 | 135 | 45 | 44 |

Here $\beta_{x,ins}$ and $\beta_{z,cbm}$ denotes β-function at center of insertion device and bending magnet respectively.

For the insertion devices, the spectral brightness and effect of these devices on beam dynamics are also governed by $\beta_{y,ins}$. In optics-B, $\beta_{y,ins}$ is almost two times higher as compared to optics-A. This will lead to reduction in the spectral brightness of photon beam from the center of existing three insertion devices (namely U1, U2 and U3 undulators) nearly by 20%. Effect of insertion devices on beam dynamics in optics-B will also increase in proportional to $\beta_{y,ins}$.

Table 2: Comparison between the moderate and low emittance optics

| Parameters | Optics-A | Optics-B |
|---|---|---|
| $\langle x_{CO}/\Delta x\rangle$, $\langle y_{CO}/\Delta y\rangle$ | -11%,14% | -8.5%, -15% |
| $\left\langle \frac{\Delta\beta_x/\beta_x}{\Delta k/k}\right\rangle$, $\left\langle \frac{\Delta\beta_y/\beta_y}{\Delta k/k}\right\rangle$ | 5%,43%, | 9%,-1.6% |
| $\Delta K_{QP}/K_{QP}$, $\Delta K_{SP}/K_{SP}$ | 7% , 183% | 4.5%, 64% |

## RESULTS AND DISCUSSION

Nearly >100 mA beam current was initially stored at 2.5 GeV using the optics-M. Thereafter in different machine operations, optics- A and B is executed by synchronously changing the strength of quadrupole and sextupole magnets according to look up table for optics-A and B respectively. These tables were generated and applied through the ramp software. It was observed that at higher beam current in the transition period from moderate to low emittance at few places temperature of vacuum chamber was found to be increased due to variation of the closed orbit distortion during the switch over process. In order to overcome this betatron tune and orbit correction was carried out.

The betatron tune is corrected by using tune feedback system with the help of quadrupole families of QF1, and QD2 in intermediate few steps of transition from moderate to low emittance optics. Based on this exercise, horizontal tune variation reduces to 0.004 from 0.045 and vertical tune variation reduced to 0.002 from 0.07. The look-up table was modified according to the p/s settings of tune feedback correction. The slow orbit feedback was also utilized during transition from moderate to low emittance optics as well as at low emittance optics for orbit correction and to maintain it at predefined reference orbit as per beam-lines user requirement.

In nominal optics as well as for both the low emittance optics, beta function, dispersion function in both transverse planes and horizontal beam emittance are estimated with the help of LOCO program. The betatron coupling was measured with the help of quadrupole scan method [3]. Its detail results are tabulated in Table-3

Table 3: Statistics of the optics results before correction

| Parameter | Optics-M | Optics-A | Optics-B |
|---|---|---|---|
| $\left\langle \frac{\Delta\beta_x/\beta_x}{\Delta k/k} \right\rangle$ | 5% | 7.2% | 9.6% |
| $\left\langle \frac{\Delta\beta_y/\beta_y}{\Delta k/k} \right\rangle$ | 2.4% | 4.6% | 3.6% |
| $\kappa$ | 0.2% | 0.7% | 0.4 % |
| $\langle \eta_y \rangle$ [mm] | 13 | 23 | 12 |
| $\varepsilon_x$ nm.rad | 144 | 43 | 49 |
| $\varepsilon_y$ nm.rad | 0.3 | 0.3 | 0.2 |

The result indicates in optics-A and B distortion of betatron function and transverse betatron coupling are increased as compared to the optics-M The transverse betatron coupling in optics- B is smaller (0.4%) as compared to optics-A (0.7%). In optics-B, vertical dispersion function over the ring as well at BM's location are significantly reduced as compared to optics-A. The vertical emittance is governed by the horizontal emittance, betatron coupling and spurious vertical dispersion function. In Table-3, reduction in vertical beam emittance is tabulated by taking consideration of betatron coupling, the effect of vertical spurious dispersion function is not taken into account. In case of optics-A, betatron coupling as well as rms vertical dispersion both are increased as compared to optics-M. Thus for optics-A, vertical emittance reduction will be negligible. It leads that the vertical emittance in optics-B will be reduced more than 33% as compared to the optics-A. In nut shell, these result that in optics-B vertical emittance is smaller as compared to optics-M and optics-A.

For both optics, in transverse planes distortion of beta beat and dispersion functions are corrected with the help of LOCO method, after correction desired horizontal emittance (45 nm.rad) is obtained. The photon brightness with these parameters indicate that in optics-B, photon brightness at bending magnet and insertion device locations with respect to optics-A are increased by 70% and 15% respectively.

## FUTURE STRATEGY

In both transverse plane, emittance can be further reduced by allowing finite value of horizontal dispersion function into the insertion straight section. In this case, the required strength of sextupole strengths will be drastically increased, due to higher value of chromaticity and smaller dispersion function at the location of sextupole. Thus, it is expected that betatron coupling constant and spurious vertical dispersion function will be increased. Since in optics-B, sextupole strength and amplification factor for various errors will be increased less as compared to optics-A. Thus further reduction of beam emittance can be performed with less difficulties by using optics-B as compared to optics-A. The vertical emittance can be further reduced with the help of betatron coupling and vertical spurious dispersion correction, for this location of skew quadrupoles are finalized and their development are under progress.

## CONCLUSIONS

In order to increase spectral brightness of photon beam from the center of insertion devices and bending magnet, the low emittance optics (optics-B) is evolved and implemented. With this optics, vertical emittance and vertical beta function at bending magnet location are reduced as compared to optics-A. In optics-B, photon brightness at bending magnet and insertion device locations with respect to optics-A are increased by a factor of 70% and 15 % respectively. The beam parameters are estimated with the help of quadrupole scan method and LOCO method.

## REFERENCES

[1] Ali Akbar Fakhri, Pradeep Kant, Gurnam Singh and A.D.Ghodke "Beam emittance reduction during operation of Indus-2" Review of Scientific Instruments, 86, 0333304 (2015).

[2] R. Husain and A.D.Ghodke "Betatron Coupling Measurement and Its Correction in Indus-2 Storage Ring", in this proceedings.

[3] S. Yadav et. al. "Development of Software for Automatic Measurement of Betatron Coupling in Indus-2", in this proceedings.

# BETATRON COUPLING MEASUREMENT AND ITS CORRECTION IN INDUS-2 STORAGE RING

Riyasat Husain[1,2,*] and A D Ghodke[1]

[1]Accelerator Physics Section, Raja Ramanna Centre for Advanced Technology (RRCAT) Indore

[2]Homi Bhabha National Institute, Training School Complex, Mumbai

*Abstract*

Brightness is an important parameter for any synchrotron radiation source. Correcting the emittance coupling is a one of the way to increase photon beam brightness. The main source of this effect is betatron coupling resulted from the skew quadrupolar errors. Indus-2, which is a storage ring based synchrotron radiation source, being operated regularly at RRCAT, Indore for synchrotron radiation users, Tune split and Linear Optics from Closed Orbit (LOCO) techniques are used to measure the betatron coupling. In this paper, we discuss the measurement of betatron coupling and its correction in Indus-2 storage ring using 4 number of power supplies, as the knobs, driving the skew quadrupole windings located on the SF and SD families of the sextupoles. The measured coupling coefficient of ~0.75% closely matches with the coupling coefficient obtained from the LOCO fit model. LOCO is used to find the suitable skew quadrupole power supply settings to correct the betatron coupling. The emittance coupling can be reduced to ~0.4% by this method. Based on simulation studies it is found that if more skew quadrupoles are employed, emittance coupling can be reduced to very small value.

## INTRODUCTION

Generally, the electron storage ring, which are dedicated as synchrotron radiation sources have the finite horizontal beam emittance and beam size. The radiation damping and quantum excitation at finite dispersion decide the horizontal beam emittance, which is given by [1]

$$\varepsilon_x = C_q \gamma^2 \frac{\langle \mathcal{H}_x/|\rho|^3 \rangle}{J_x \langle 1/\rho^2 \rangle}, \tag{1}$$

$$\mathcal{H}_x = \gamma_x \eta_x^2 + 2\alpha_x \eta_x \eta_x' + \beta_x {\eta_x'}^2, \tag{2}$$

where $C_q \approx 3.832 \times 10^{-13}$ $(m)$, $\gamma$ is the relativistic factor, $\hbar = h/2\pi$ is the Planck constant, $c$ is the speed of light, $m$ is the electron mass, $\rho$ is the bending radius of the dipole magnets, $\eta_x$ is the horizontal dispersion function, ($\alpha_x$, $\beta_x$, $\gamma_x$) are twiss parameters in horizontal plane and $J_x$ is the horizontal damping partition number.

The emission of synchrotron radiation also results in fininite energy spread in the beam. The energy spread of the electron beam is given by [1]

$$\sigma_\delta^2 = C_q \frac{\langle 1/|\rho|^3 \rangle}{J_E \langle 1/\rho^2 \rangle}. \tag{3}$$

Here, $J_E$ is the longitudinal damping partition number.

The dispersion function couples the phase spaces in the horizontal and longitudinal planes. The resultant horizontal beam size is the quadrature sum of beam sizes due to emittance and energy spread. For an ideal electron synchrotron the horizontal beam size is given by [1]

$$\sigma_x = \sqrt{\varepsilon_x \beta_x(s) + (\eta_x \sigma_\delta)^2}. \tag{4}$$

In vertical plane for an ideal electron storage ring, the vertical dispersion is zero, then the corresponding vertical beam emittance is zero, $\varepsilon_{y0} = 0$. However, even in the ideal synchrotron, the vertical beam size does not damp to zero. It is because the quanta of synchrotron radiation are emitted with finite vertical momenta, and the electrons must recoil. This vertical excitation of the electron beam results in the quantum limit of vertical emittance, and we write [2]

$$\varepsilon_{yq} = C_q \frac{\langle \beta_y/|\rho|^3 \rangle}{J_y \langle 1/\rho^2 \rangle}, \tag{5}$$

where $\beta_y$ is the vertical betatron function , $J_y$ is the vertical damping partition number and its value is 1 for an ideal electron synchrotron.

In an ideal synchrotron, the vertical dispersion and betatron coupling are zero; therefore vertical phase space is completely decoupled from horizontal one. The vertical beam size for an ideal machine is given by $\sigma_y = \sqrt{\varepsilon_{yq}\beta_y(s)}$. For the case of Indus-2 at nominal optics, the calculated value of quantum limit of the vertical emittance is $\varepsilon_{yq} \sim 1.4\, pm.rad$, which corresponds to the vertical beam size of 1.7 μm, which is significantly smaller than the measured value of ~52 μm. Therefore, we must consider coupling of the vertical phase space to the horizontal phase space. In a real machine, there is non-zero even though small, vertical dispersion, $\eta_y$. It gives non-zero vertical emittance $\varepsilon_{y0}$, given as [2]

$$\varepsilon_{y0} = C_q \gamma^2 \frac{\langle \mathcal{H}_y/|\rho|^3 \rangle}{J_y \langle 1/\rho^2 \rangle}, \tag{6}$$

where $\mathcal{H}_y$ is the dispersion invariance in vertical plane.

This vertical emittance together with vertical dispersion leads to the vertical beam size of [2]

$$\sigma_y = \sqrt{\varepsilon_{y0} \beta_y(s) + (\eta_y \sigma_\delta)^2}. \tag{7}$$

Recently a low emittance (45 nm.rad) optics has been implemented in Indus-2 storage ring to enhance the photon beam brightness [3]. However in order to get real advantage of the low emittance to enhance the brightness of the photon beam, vertical emittance or beam size also need to be controlled. The vertical beam size is dominated by the linear betatron coupling and by the spurious vertical dispersion (Eqn. 7). The sources of coupling are mainly the quadrupole rotation errors, vertical beam offsets in the sextupoles and the spurious vertical dispersion is generated due to rotation errors of the dipole magnets and the finite horizontal dispersion at the sextupole locations.

*riyasat@rrcat.gov.in

In Indus-2, the horizontal and vertical closed orbit distortion (COD) have been reduced to better than 300 μm, which minimises the effects of the sextupoles on the coupling. This orbit is maintained for the beamline users by applying slow orbit feedback. The measurement of the linear betatron coupling was performed in Indus-2 using minimum tune separation approach. In this method, the driving currents in the group of quadrupoles is changed and the betatron tunes are measured. The coupling factor is calculated using following formula [4]:

$$\kappa = \frac{\varepsilon_y}{\varepsilon_x} = \frac{|\Delta\upsilon_{min}/\Delta|^2}{[2+|\Delta\upsilon_{min}/\Delta|^2]}, \tag{8}$$

where $\Delta\upsilon_{min}$ is the minimum tune separation and $\Delta = \upsilon_x - \upsilon_y - p$. For Indus-2, $\upsilon_x = 9.292$; $\nu_y = 6.192$; and $p=9-6=3$.

The measurement of the tunes with variation of the current in Q2F family of quadrupoles are shown in Fig.1. Based on this measurement, the minimum tune separation at coupling resonance is $\Delta\upsilon_{min}$ ~0.015. The measured coupling (at low emittance optics) was found to be ~0.75%, which is much larger from the nominal coupling of 0.23% at operating lattice of 135 nm.rad.

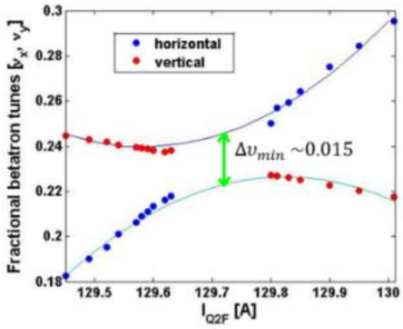


Figure 1: Measured fractional part of the betatron tunes with change of current in Q2F family of the quadrupoles.

The measured result was compared with the estimated value of the coupling using LOCO code [5]. Using LOCO code based on analysis of measured orbit response matrix (ORM), a realistic machine model was generated by fitting quadrupole strengths, rotation errors of the quadrupoles, and skew quadrupole components at the sextupole locations (as an outcome of vertical beam offsets). The estimated value of the linear betatron coupling was found to be ~0.8 %. The measured and estimated value of linear betatron coupling are close to each other.

## BETATRON COUPLING CORRECTION

### *Correction using available four skew power supplies*

Before embarking on the coupling correction, the linear lattice correction will be beneficial. This will also correct the coupling partially. Based on the LOCO analysis, the resulted deviations in the quadrupoles strengths were corrected using all 26 quadrupole power supplies to minimize the beta beat, restore horizontal dispersion and correct the spurious vertical dispersion function. Based on the analysis of the measured ORM after applying correction, there is a very small correction in the vertical dispersion, which also reduces the beam size marginally. Most dominant contribution to the vertical beam size comes from the coupling. To correct the coupling, four skew quadrupole supplies driving the skew quadrupole windings on SF and SD families of the sextupoles are fit. These fit values are applied in Indus-2 to correct the coupling, and hence the vertical beam size. As a result, coupling was reduced to ~0.4 % and vertical beam size was reduced to 40 μm from 52 μm. It was not possible to reduce the coupling further with the available limiting skew correction knobs i.e. four skew quadrupole power supplies.

### *Correction using more skew power supplies: A simulation study*

In order to achieve best control and correction of the linear betatron coupling, a simulation study was carried out by considering various combinations of the skew quadrupole knobs. Here we consider:

A. *Presently available four skew quadrupole supply driving the group of skew windings on SF and SD family of the sextupoles,*
B. *Independent power supply for each SF families of sextupoles (total 16 power supplies),*
C. *Independent power supply for each SD families of sextupoles (total 16 power supplies)*
D. *Independent power supply for each SF and SD families of sextupoles (total 32 power supplies)*

### *Simulation studies*

In simulation using multi-objective genetic algorithm (MOGA), the betatron coupling, beam size and the emittance are minimized, with available four skew quadrupole power supplies as the knobs. The total number of generation are taken to be 100 and initial population 500. The optimized results at the last generation are given in Fig. 2(a). It can be seen that the betatron coupling can be minimized up to earlier quoted value of ~0.4 % and the vertical beam size to ~ 40 μm. This is very close to the measured results for betatron coupling and vertical beam size after applying the LOCO fit results of the skew quadrupoles. It is not possible to reduce further the betatron coupling and hence the vertical beam size. In Fig. 3, the correction of the spurious vertical dispersion for all solutions at the last generation are given and it can be observed that the dispersion correction is insignificant with four skew power supplies.

In Fig. 2(b), the results using 16 independent power supplies driving skew windings at the SF family of the sextupoles are given. These 16 independent knobs compared to only four, provide a very good correction of the linear betatron coupling. In addition, the correction of spurious vertical dispersion is significant, which in addition to coupling decides the vertical beam size. It can be observed that the betatron coupling reduces to ~ 0.08 % and vertical beam size reduces to ~ 18 μm (uncorrected 52 μm). The results for 16 independent power supplies at SD family of the sextupoles are given in Fig. 2(c). This combination provides relatively better correction compared to 16 power supplies at SF families of the sextupoles. The optimized results with 32 independent power supplies driving each skew windings on SF and SD families of the sextupoles are shown in Fig. 2(d). The betatron coupling upto ~0.02 % is achievable, vertical dispersion correction (Fig. 3) is very effective which reduces the vertical beam size to ~10 μm. In Table 1, comparison of correction efficiency of different schemes for various parameters are summarized.

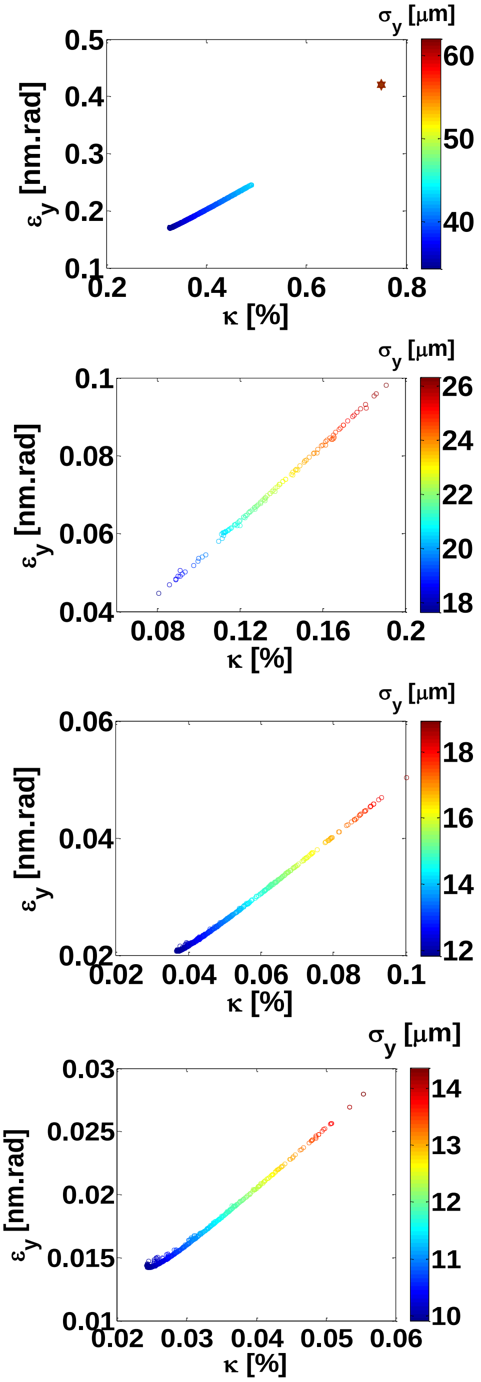


Figure 2: The optimized results for the minimization of the vertical beam emittance, betatron coupling and vertical beam size in Indus-2 from top to bottom for (i) case A, (ii) case B, (iii) case C and (iv) case D. The uncorrected value of the low emittance optics is marked by square in top two figures.

Table 1: Beatron coupling, vertical dispersion, beam emittance and beam size with different correction schemes.

| Param. | Units | Before corr. | After correction using different number of P/S case | | | |
|---|---|---|---|---|---|---|
| | | | A | B | C | D |
| $\kappa$ | % | 0.75 | 0.35 | 0.08 | 0.04 | 0.02 |
| RMS $\eta_y$ | mm | 12.3 | 12 | 8.5 | 5.5 | 5 |
| $\varepsilon_y$ | pm.rad | 396 | 170 | 45 | 20 | 14 |
| $\sigma_y$ | μm | 52 | 35 | 18 | 12 | 10 |

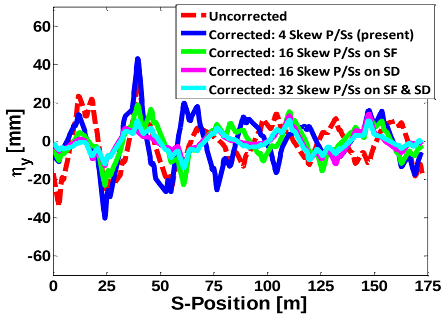


Figure 3: The spurious vertical dispersion function over the ring showing uncorrected (red line), corrected with power supply combinations: A (cyan colour), B (magenta colour), C (blue colour) and D (green colour).

## CONCLUSIONS

In Indus-2, the correction of betatron coupling κ was done with available four power supplies driving the skew windings on the SF and SD families of the sextupoles. The measured value of betatron coupling was found to be ~ 0.75% for a low emittance optics in Indus-2. However, its correction is only limited to ~0.4% with available knobs. In order to correct the betatron coupling sufficiently, a simulation study was performed including more skew power supplies. Using independent power supply for all 16 skew windings on the SD family of the sextupoles; or 32 power supplies for all skew windings on SF and SD families of sextupoles, a very good correction of κ up to < 0.05% can be achieved. Therefore, it is recommended to increase the number of power supplies from 4 to 16 or 32 driving skew windings independently on the sextupoles.

## REFERENCES


[1] S. Y. Lee, Accelerator Physics, Third Edition, World Scientific, New York, (2011).

[2] A. Wolski, Beam Dynamics in High Energy Particle Accelerators, Imperial College Press (2014).

[3] A. A. Fakhri et al., Low emittance optics optimization during operation of Indus-2, these proceedings.

[4] A. D. Ghodke et al., Rev. Scientific Instrum. 83, 103303 (2012).

[5] J. Safranek, Experimental determination of storage ring optics using orbit response measurements, Nucl. Instrum. Methods Phys. Res. A 388, 27 (1997).

[6] K. Deb, Multi-Objective Optimization using Evolutionary Algorithms, Wiley (2001).

# DESIGN STUDIES FOR A THz-FEL AT RRCAT

R.S. Saini*, Sona Chandran, Saket Kumar Gupta, Arvind Kumar, B. Biswas, Shankar Lal and K.K. Pant, RRCAT, Indore, India

### *Abstract*

A user facility is being built at RRCAT to facilitate experiments using FEL radiation in the wavelength range from 10 μm to 300 μm and beyond. The IR-FEL, which is presently in an advanced stage of commissioning, is designed to lase in the 12.5 - 50 μm wavelength range, and plans are underway on extending this wavelength range into the THz region in the near future. Two options have been studied to achieve this – augmentation of the IR-FEL for operation at THz wavelengths and building a new THz-FEL. Design studies have been performed to evaluate both these options, which are discussed in this paper. A new THz-FEL setup has been designed to include two injector systems – a conventional thermionic electron gun based injector for FEL studies and a photocathode RF gun based injector for accelerator physics experiments, both with very different electron beam properties. A common electron beam transport line has been designed for the lossless electron beam transport from both the injector systems up to the beam dump. This paper discusses the two options for the extension of the operation wavelength available at the FEL user facility to the THz region, and the physics design of the proposed new THz-FEL setup.

## INTRODUCTION

THz radiation, which lie between the Infrared and microwave regions of the electromagnetic spectrum, has emerged as a powerful tool for probing low-energy excitations at meV energy scale in condensed matter physics. Many rotational and vibrational modes exists in the THz region. In the past decade, there has been a rapid progress in THz radiation sources such as solid state oscillators, quantum cascade lasers, optically pumped solid state devices and novel free electron devices [1]. The Free Electron Laser (FEL) based THz sources, known as THz-FEL, is one of the most powerful radiation sources in this wavelength region. Tunability, high power and flexible picosecond-pulse time structure of THz radiation make the THz-FEL a very attractive THz source of coherent radiation [2].

An Infra-Red Free Electron Laser (IR-FEL) is presently in an advanced stage of commissioning at RRCAT, and a user facility is being built to use IR radiation from this FEL for research in different areas of science [3]. In the near future, it is proposed to extend the wavelength of radiation available to users to the THz region (100 – 300 μm). Two options have been studied to achieve this. Option-1 is the extension of the operating wavelength of the present IR-FEL into the THz region, with the same injector linac system, transport line, and undulator/optical cavity. Option-2 involves setting up of a new THz-FEL set up in a dedicated facility from where THz radiation will be transported to a common user facility built for the IR-FEL. This paper discusses results from design studies undertaken to evaluate both these options.

*rssaini@rrcat.gov.in

## THE IR-FEL SETUP OPERATING AT THZ WAVELENGTH

Table 1: Design parameters and results from FEL simulations (GINGER) for operation of the IR-FEL setup at 100 and 150 μm wavelength.

| Wavelength | 100 μm | 150 μm |
|---|---|---|
| RMS Normalized emittance, $\varepsilon_N$ | 30 mm mrad | 30 mm mrad |
| Beam Energy | 11 MeV | 9 MeV |
| Peak current | 30 A | 30 A |
| RMS pulse width | 1.2 mm | 1.2 mm |
| RMS energy spread | 0.5% | 0.5% |
| RMS electron beam size (mm) | $\sigma_x$ = 1.5<br>$\sigma_y$ = 0.489 | $\sigma_x$ = 1.7<br>$\sigma_y$ = 0.489 |
| Undulator period ($\lambda_u$) | 50 mm | 50 mm |
| Undulator length | 2.5 m | 2.5 m |
| RMS undulator parameter (K) | 1.0 | 1.0 |
| Undulator gap | 30.5 mm | 30.5 mm |
| Optical cavity length | 5.04 m | 5.04 m |
| Mirror radii of curvature | 2.62 m (d), 2.93 m(u) | |
| Mirror Hole diameter | 3.5 mm | 3.5 mm |
| Net round trip gain (GINGER) | 91 % | 74 % |
| Out coupled Energy | 30 μJ | 21 μJ |
| Detuning | 200 μm | 150 μm |
| Start-up time | 0.84 μs | 1.38 μs |

The IR-FEL at RRCAT is designed to operate in the 12.5 – 50 μm wavelength band with a 15-25 MeV electron beam and a 2.5 m long, pure permanent magnet undulator with 5 cm period. The IR-FEL has a 5.04 m long optical cavity in a near-concentric configuration, with a 3.5 mm diameter hole in the downstream mirror for out-coupling of FEL radiation. More details of the FEL design simulations for the IR-FEL are given in Ref. [4]. The undulator vacuum chamber has a race-track internal geometry with a vertical internal aperture of 17 mm and horizontal internal aperture of 74 mm, which have been optimized based on FEL simulations to obtain the desired gain for the electron beam and optical beam parameters available in the IR-FEL setup. Since it is now proposed to extend the operating region to THz wavelength, which is expected to result in larger loss due to diffraction, FEL simulations have been repeated considering the electron beam quality achievable in the IR-FEL setup and considering the same optical cavity and undulator vacuum chamber, but with a lower electron beam energy. From these studies, it emerges that the IR-FEL operation can be extended to a maximum of 150 μm wavelength without making any modifications in the setup. Table 1 above summarizes the typical results obtained from FEL simulations using the code GINGER [5], considering the electron beam, undulator and optical cavity parameters from the IR-FEL setup.

Since the IR-FEL injector system and its electron beam transport line have been designed for operation at 15 – 25 MeV energy, injector linac simulations and beam transport studies were repeated to ensure the achievement of the desired electron beam parameters at 11 MeV and 9 MeV for operation at 100 µm and 150 µm respectively. Table 2 summarizes the results of the IR-FEL injector simulations for operation at 10 MeV. It also summarizes the desired electron beam parameters at the undulator entry, which are achieved by tuning the beam transport line.

Table 2: Beam parameters from the IR-FEL injector linac system operating at 10 MeV, and the desired beam parameters at the undulator entry.

| Beam Parameters | Linac exit | Undulator entrance |
|---|---|---|
| Beam Energy (MeV) | 10 | 10 |
| Emittance ($\varepsilon_x, \varepsilon_y$) mm mrad | 1.38, 1.38 | 1.30, 1.30 |
| Beta function ($\beta_x, \beta_y$) m | 4.45, 4.82 | 1.76 , 0.15 |
| Alpha function ( $\alpha_x, \alpha_y$ ) | -2.20, -2.39 | 1.00, 0.00 |
| RMS Energy spread (%) | ±15 | ± 0.5 |

Considering the electron beam parameters at the linac exit as obtained from the injector linac simulations, transport line simulations have been performed considering only the electromagnets available in the present IR-FEL beam transport line with an aim to match the beam parameters at the undulator entry. This transport line has a beam slit after the first bending magnet (BM1) as shown in Fig.1, and the ratio of the contribution to the beam size at this location from the dispersion term, to that from the betatron term, has been tuned to be a maximum to select an optimum beam slit opening to pass only the beam particles with ± 0.5% RMS relative energy spread, as required for FEL operation. The lattice parameters are shown in Fig.1.

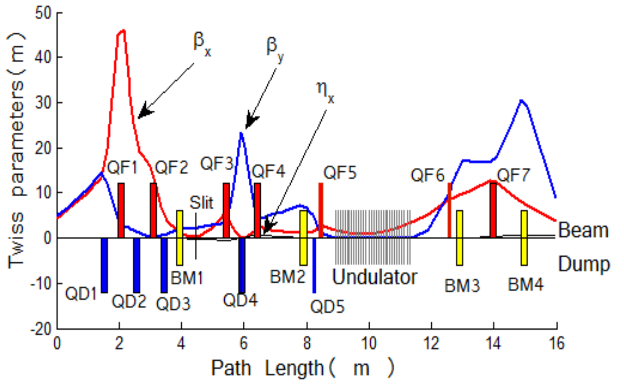


Figure 1: Lattice functions in the IR-FEL transport line

The FEL simulations, and the associated injector and beam transport studies show that the longest wavelength up to which operation of the existing IR-FEL setup can be extended without any modification is 150 µm.

## DESIGN OF A NEW THZ-FEL

Initial design studies for a new THz-FEL have been carried out in order to further extend the wavelength of light available for user experiments up to 300 µm. This THz-FEL is proposed to be built inside a dedicated radiation shielded area that is proposed to be built inside the newly constructed THz-FEL building. From a study of the available literature on existing THz-FELs, and from some initial studies on the possible configurations for a THz-FEL, a beam energy of 13.3 MeV has been considered in order to work with a higher value of the undulator parameter *K*.

FEL simulations show that diffraction effects become dominant above a wavelength of 150 µm, resulting in higher losses and poor overlap between the electron beam and the optical radiation leading to a low net gain. The option of waveguiding in the optical cavity region is presently being studied to restrict the optical radiation to a small transverse size, and two different resonator configurations are presently being studied - partially waveguided and fully waveguided. These studies include the optimization of the waveguide parameters and the undulator/optical cavity length to achieve the desired gain. It is proposed to develop the injector linac system for this FEL in-house, and the beam energy of 13.3 MeV considered in these studies is achievable employing available structures, and will facilitate operation with a high *K* parameter to generate up to 300 µm radiation.

This injector system will employ a Sub-Harmonic Pre-Buncher (SHPB), Fundamental Frequency Pre-Buncher (FFPB), Accelerating Buncher (AB) and a 12-cell Plane Wave Transformer (PWT) linac structure, all developed and qualified in-house. The source of electrons for this injector linac system will be an old pulsed thermionic electron gun that will be re-deployed for the purpose. Table 3 summarizes the results of the injector linac simulations for the THz-FEL. It also summarizes the desired electron beam parameters at the undulator entry, which are to be achieved by tuning the beam transport line to be built for this FEL.

Table 3: Expected electron beam parameters from the thermionic electron gun based injector system.

| Beam Parameters | Linac exit | Undulator entrance |
|---|---|---|
| Beam energy/peak current | 13.3MeV/ - | 13.3 MeV/ 30A |
| Emittance ($\varepsilon_x, \varepsilon_y$) mm mrad | 1.21, 1.21 | 1.20, 1.20 |
| Beta function ($\beta_x, \beta_y$) m | 0.36, 0.55 | 1.68, 0.18 |
| Alpha function ( $\alpha_x, \alpha_y$ ) | -0.11, 0.10 | 0.80, 0.00 |
| RMS Energy spread (%) | ± 13.8 | ± 0.5 |

In addition to this injector linac system for the THz-FEL, it is proposed to house another photocathode RF gun based injector linac inside the same radiation shielded area. Since the THz-FEL is also proposed to be built in an oscillator configuration, which consequently dictates a requirement of a train of micro-pulses in each macro-pulse to achieve lasing, the photocathode RF gun based injector will not be used for the THz-FEL application.

Electron beam from this injector system will be used only for beam physics experiments in the future. The design of the electron beam transport line for the new THz-FEL setup has been done considering the requirement of lossless transport and tuning of electron beams from two different injector systems from the exit of these injectors up to the beam dump. The code TRANSPORT [6] has been used for matching the beam phase space parameters from the two injectors. Beam parameters at the linac exit and at the undulator entry for the thermionic electron gun based injector system are given in table-3, while the same for the photocathode RF gun based injector system are summarized in Table 4.

Table 4: Expected electron beam parameters from the photocathode RF gun based injector system.

| Beam Parameters | Linac exit | Beam Dump |
|---|---|---|
| Beam energy/peak current | 14.34 MeV/ 100 A | 14.34 MeV/ 100 A |
| Emittance($\varepsilon_{x,}$ $\varepsilon_y$) mm mrad | 0.09, 0.09 | 0.09, 0.09 |
| Beta function ($\beta_{x,}$ $\beta_y$) m | 6.98, 6.76 | 15.03, 7. 62 |
| Alpha function ( $\alpha_{x,}$ $\alpha_y$ ) | -0.17, -0.13 | -12.52,-29.5 |
| RMS Energy spread (%) | ±0.5 | ±0.5 |

An achromatic as well as isochronous electron beam transport line has been designed to match the beam parameters from both the injector systems at the undulator entrance. A beam slit (Slit1) after the first bending magnet (BM1) in this transport line is employed as shown in Fig.2 and at this slit location, the ratio of the contribution of the dispersion term to the beam size to that of the betatron term is maximised. The beam slit opening is optimized to pass beam particles having energy spread within ± 0.5 %. Similarly another beam slit (Slit2) is also employed in this transport line after the bending magnet 3 (BM3) to carry-out the experiments for beam energy spread measurement for the electron beam from the photocathode injector system. The lattice functions for the transport line are shown in Fig.2.

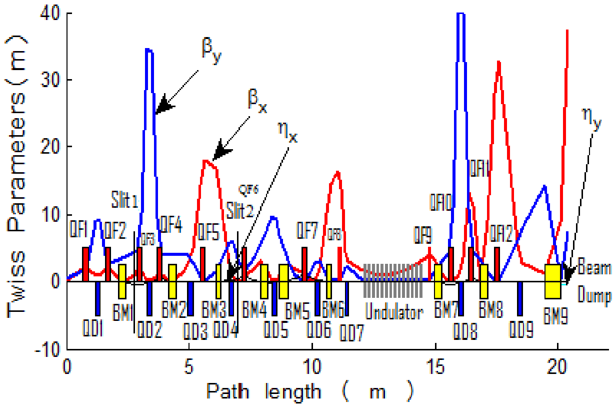


Figure 2: Lattice functions in the transport line.

A layout of the new THz–FEL set up inside its proposed radiation shielded area is shown in Fig.3, which shows the two injector systems, a common transport line from the exit of these two injectors up to the beam dump and locations of Slit1 and Slit2 in this transport line.

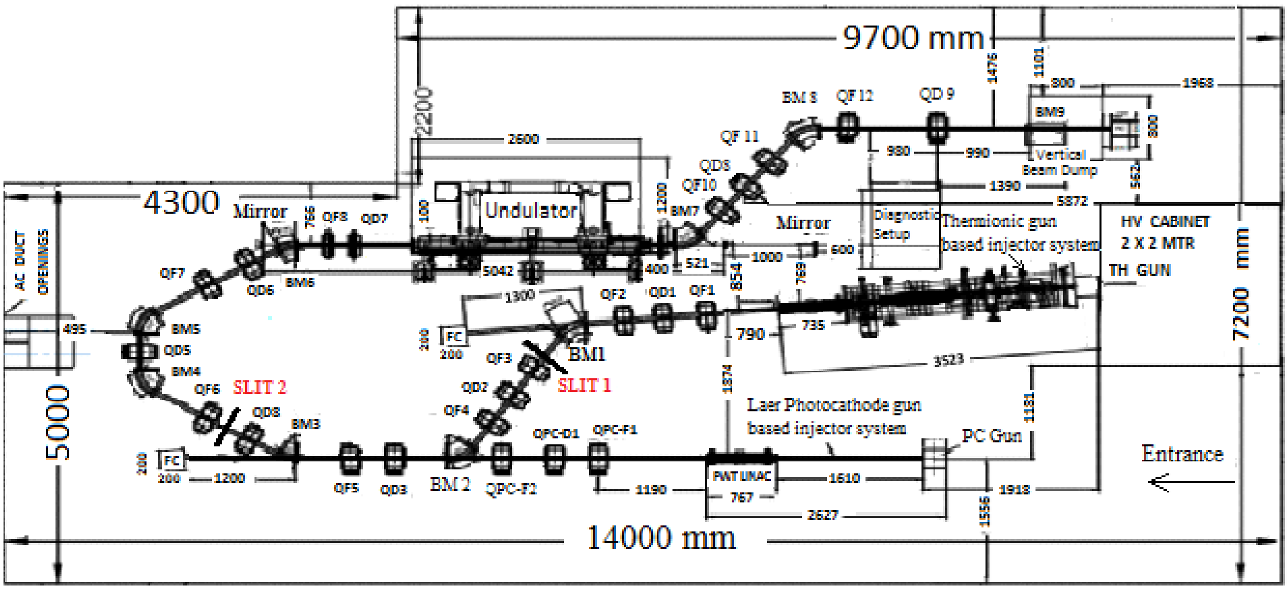


Figure 3: Layout of the new THz-FEL set up inside the shielded area.

## CONCLUSION

Two options have been studied for extension of the wavelength available at the RRCAT FEL facility from the IR into the THz region. The studies reveal that the longest wavelength at which IR-FEL operation is feasible without any changes in the existing configuration is 150 µm. Studies have also been performed on a possible configuration of a new THz-FEL setup, employing a thermionic electron gun based injector system. This setup has been designed with an additional photocathode RF gun based injector system, which will not be used for FEL experiments but which will be used for beam physics experiments. A common electron beam transport line has been designed from both the injector systems for lossless transport of the electron beam up to the beam dump, and for matching the parameters of the electron beam from the thermionic injector system to those required at the undulator entry for FEL operation.

## ACKNOWLEDGEMENT

One of the authors, S.C, gratefully acknowledges Dr. Vinit Kumar for several illuminating discussions.

## REFERENCES

[1] G.P. Gallerano et al. “Overview of Terahertz Radiation Sources” Proceedings of the 2004 FEL.

[2] Tan P, et al. “Terahertz radiation sources based on free electron and their applications” Sci. China Inf. Sci. January 2012, vol. 55 No.1.

[3] K. K. Pant, et al., Current Science, Vol. 114, No.2 (2018).

[4] V. Kumar, et al., “Design of an infra-red free-electron laser at RRCAT,” in Indian Particle Accelerator Conference (InPAC), IUAC, New Delhi, India, 2011.

[5] W Fawley, A user manual for GINGER and its 764 post-processor XPLOTGIN LBNL-49625-Rev. Ist edn 765 (Lawrence Berkeley National Laboratory, Berkeley, 766 1997).

[6] D C Carey, Third order TRANSPORT with MAD Input, TM-1546 (1988).

# PERFORMANCE STUDIES OF 1 MW CW KLYSTRON UNDER PULSED OPERATING CONDITION USING 100 KV, 20 A LONG PULSE CONVERTER MODULATOR

T. Reghu#, V. Mandloi, J.Mulchandani, P.Mohania, A.Mahawar, Hargovind Singh, Vikas Rajput and Purushottam Shrivastava

RF Systems Division, Raja Ramanna Centre for Advanced Technology, Indore, M.P., 452013, India

*Abstract*

Research and development activities of high power microwave sources for powering RF cavities of Indian Spallation Neutron Source and Accelerator Driven Subcritical Systems are underway at RRCAT. Front end accelerating structures such as Radio Frequency Quadrupoles and Drift Tube Linac demands pulsed RF power up to 1 MW. A 1 MW pulsed RF system based on TH 2089 klystron amplifier at 352.2 MHz with pulse width capability up to 1.6 ms has been developed. A compact 100 kV, 20 A converter type modulator with pulse width capability up to 1.6 ms has been used to energize the klystron. The performance of the klystron in pulsed mode operation has been studied and presented. The variation in the RF output power was measured and it is within ± 0.75 %. The phase variation of RF output power within pulse and pulse to pulse is less than ±2.5 degrees.

## INTRODUCTION

High power klystron amplifiers are widely used for powering Radio Frequency (RF) cavities of high energy particle accelerators [1]. They are available in both CW and pulsed mode operation. High voltage pulsed sources are required for powering the klystron amplifier and such sources are known as modulators. The advancement in technology of semiconductor switches with high voltage, high current, high switching frequency capabilities lead to the development of advanced solid state modulators [1]. Recently new type of modulators viz., converter and Marx type are gaining usage for long pulse (up to 5 ms pulse width) and high average power applications. Among the two, converter type modulators are more popular for driving klystrons for the development of high energy particle accelerators for spallation neutron sources. Additionally converter type modulators are compact, inherently energy limited and there is no need of any high voltage crowbar switch [2]. RRCAT, Indore, has been pursuing research and development (R&D) activities on the long pulsed klystron modulators [2-6].

Very recently,the work on the development of 100 kV, 20 A, 1.6 ms long pulse modulator for driving 1 MW klystron has been reported [5]. Such modulators are relatively new and their effects on the performance of the continuous wave (CW) klystrons are not well studied. In order to study the pulsed mode performance of a klystron driven by long pulsed modulator and to test various RF components of accelerator subsystems, an RF test stand has been developed. In this paper we will describe the details of test stand and performance characteristics of klystron amplifier in pulsed mode operation. The operational parameters of the RF test stand are given in table 1.

| | |
|---|---|
| RF output power (peak) | 1 MW |
| Pulse width (max) | 1.5 ms |
| RF frequency (nom) | 352.2 MHz |
| Droop | ±0.75 % |
| Phase stability (in pulse) | ±2.5 degrees |
| Phase stability (pulse to pulse) | ±2.5 degrees |
| Modulator output power | 2 MW |
| PRR capability | 1-30 Hz |

Table 1. Operational parameters of RF test stand

## DESCRIPTION

The simplified block diagram of pulsed RF test stand is shown in Fig.1. It consists of a 2 MW (-100 kV, 20 A) pulsed modulator, 1 MW klystron, WR 2300 waveguide transmission system, RF measurement system, solid state input amplifier and water loads to dissipate the microwave power. The modulator is based on IGBT switched DC-DC converter topology. High frequency high voltage transformers in conjunction with high frequency inverter and a series of fast recovery diodes generate the high voltage long pulses [5]. The desired output pulse width is achieved by gating the gate drive by the desired pulse width. The converter switching frequency is 20 kHz. The high voltage and high frequency transformer has been developed using Fe based nanocrystalline core material [6]. Fast recovery epitaxial diodes are used in six pulse rectifier. The 'phase shift control' in tandem with feed forward correction scheme has been employed for droop correction of the output pulse. With this technique, droop less than ± 0.75 % has been achieved. Finer details about the modulator are given in the reference [5]. The klystron amplifier, TH 2809, (Thales Electron Devices make) is a high power linear beam vacuum tube device that amplifies RF signal. It has 1.1 MW output power capability at nominal frequency of 352.21 MHz with -1 dB bandwidth of 1 MHz. The tube has five integrated cavities, two integral electromagnets for focusing the

*Work supported by RRCA T, DAE

#traghu@rrcat.gov.in

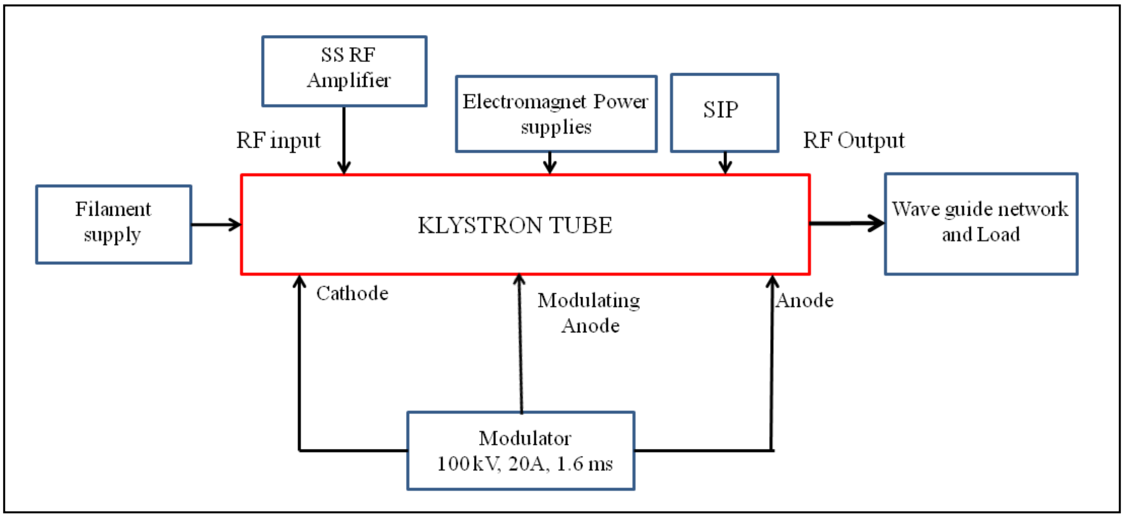


Fig.1. A simplified block diagram test set up

beam within the klystron and a modulating anode to adapt specific operating conditions. While passing through the cavities, the energy of the electron beam amplifies the input signal applied to the first cavity. The catcher cavity at the other end of the tube delivers the amplified output. The electrons are finally captured by anode.

A 200 W solid state pulsed amplifier based on LDMOS devices has been developed to energize input of the klystron. A precision signal generator has been used for driving the amplifier. The output RF power from klystron is coupled to water (LCW) load through WR2300 waveguide network. A three port circulator suitable for 352 MHz and high power operation has been used for isolation between source and load. In waveguide network, full height to half height tapered section has been used to reduce the overall size and to couple E-plane half height magic tee. 1 MW pulsed RF power is finally dumped into four numbers of 250 kW water loads. These four loads are connected at the output ports of magic tees. One more 250 kW load has been connected at the termination port of the circulator to absorb the reflected power, if any. Directional coupler has been used at the klystron output to measure both forward and reflected power. Boonton make pulsed power meter, model 4542, has been used for measurement peak power.

The cathode heater filament of klystron is powered by a 30 V, 35 A DC power supply that is 120 kV isolated as the cathode is floating at high voltage pulse. DC powering to klystron heater is preferred due to the absence of ac magnetic field generated by ac heater current near cathode area. The vacuum inside the klystron is maintained by SIP. The coils of focusing electromagnets of the klystron have been powered by 250 V, 20 A DC power supplies. The supply to modulating anode of the klystron has been derived from same cathode supply and it is kept at 71 % of the cathode voltage. The LCW flow circuit, vacuum status of klystron, cathode heater, and focussing coil power supplies are interlocked with the main modulator to avoid any failure of former systems.

## RESULTS AND DISCUSSIONS

Klystron is a nonlinear high power microwave amplifier and the output power not only depends on cathode voltage and RF input power as in conventional amplifiers, the power also depends on other parameters. The variation of output power with respect to cathode voltage has been studied and plotted in Fig.2. The output RF power has a following relation with cathode voltage,

$$P = \eta P_{\mu} \times 10^{-6} V^{\frac{5}{2}},$$

where η is the efficiency, Pμ is the microperveance and V is the cathode voltage. At higher cathode voltages the output power changes rapidly due to the power function

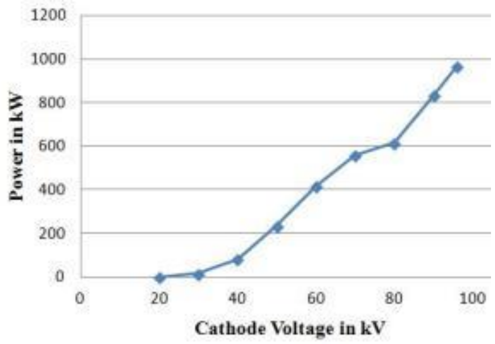


Fig. 2 RF Output power versus cathode voltage

relationship between output power and cathode voltage. Output power of 968 kW at 352.6 MHz has been extracted from the klystron. Fig. 3 and 4 shows the temporal shape of the cathode voltage, beam current and RF power at maximum cathode voltage of 96 kV. It is observed that the variation in the RF power is within ± 0.75 %. The klystron has a diode like characteristic and beam current varies as three–and-a-half power of the voltage. The relation between beam current and cathode voltage is given by

$I_b = PV^{3/2}$ , Where Ib is the beam current, P is the perveance of the klystron tube and V is the cathode voltage. Fig. 5 shows the observed relationship between beam current and cathode voltage under pulsed operating conditions.

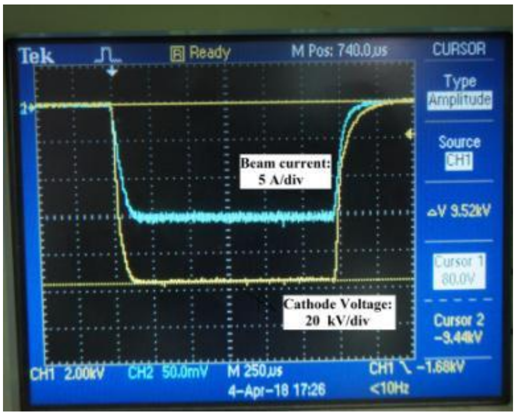


Fig. 3 Temporal profile of the RF output of klystron

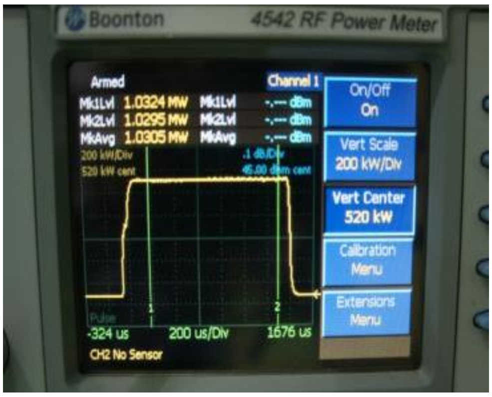


Fig. 4 Temporal profile of the RF output

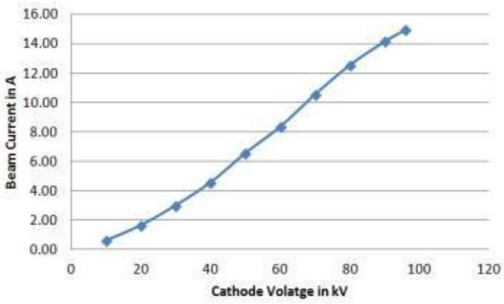


Fig. 5 Beam current versus cathode voltage

Maintaining RF phase of output pulse for a stable particle beam is important during the accelerator operation. A phase detector based on Analog Devices make AD8302 IC was used to measure the ‘in pulse’ and ‘pulse to pulse’ phase variation of the klystron output power. Unlike conventional modulators the flat top region is not ripple free due to the inherent characteristic of the converter type modulator.

The output RF phase within the pulse has been measured in a single pulse to observe the phase variation. A peak to peak variation of ±2.5 degrees was observed within the flat top portion of the pulse as shown in Fig.6. Similar result was observed even in the case phase stability of pulse to pulse.

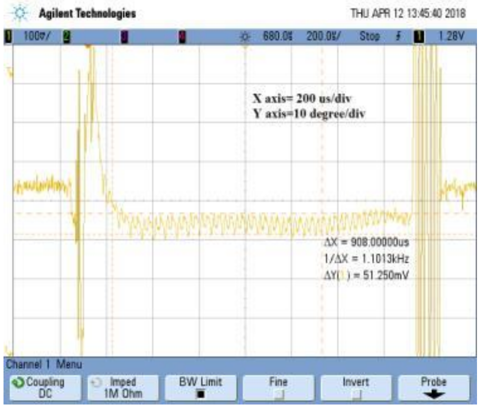


Fig. 6 RF output phase variation within the pulse

## CONCLUSION

A 1 MW pulsed RF test stand has been successfully developed and tested. Using the test stand, performance of 1 MW, CW klystron under pulsed operating condition has been studied and presented. The RF output phase variation of ±2.5 degrees within the pulse has been achieved and pulse to pulse phase stability over hundreds pulses are also in the same order. The RF test stand can also be used to test various RF components of particle accelerator.

## REFERENCES

[1] AkiraTokuchi, Fumiyoshi Kamitsukasa, Kazuya Furukawa, Keigo Kawase, Ryukou Kato , Akinori Irizawa , Masaki Fujimoto, Hiroki Osumi, Sousuke Funakoshi, Ryouta Tsutsumi, Shoji Suemine, Yoshihide Honda, Goro Isoyama, Development of a high-power solid-state switch using static induction thyristors for a klystron, Nuclear Instruments and Methods in Physics Research A, 769(2015), 72-78.

[2] T. Reghu, V. Mandloi and Purushottam Shrivastava, “Development of a 33 kV, 20 A long pulse converter modulator for high average power klystron,” Review of Scientific Instruments, 85(2014), 055102-1-055102-6.

[3] Mahesh Acharya, Purushottam Shrivastava, A 100 kV, 20 A, 1 ms long pulse solid-state Marx modulator for klystron, Nuclear Inst. and Methods in Physics Research, A, 905 (2018) 96–103.

[4] Acharya M and Shrivastava P. Design and development of a prototype 25 kV, 10 A long pulse Marx modulator for high power klystron. Review of Scientific Instruments, 87(2016), 025114-1 - 025114-6,

[5] T. Reghu , Vagesh Mandloi, and Purushottam Shrivastava, A Solid-State Converter Topology, −100 kV, 20 A, 1.6 ms, Modulator for High Average Power Klystron Amplifier, IEEE Transactions on Plasma Science, 46, NO. 10(2018), 3700-3707.

[6] T. Reghu, V. Mandloi, and Purushottam Shrivastava, Compact high voltage, high peak power, high frequency transformer for converter type modulator applications, Review of Scientific Instruments, 87(2016), 045109-1-045109-6.

# Design, development and testing of High Voltage and High frequency Transformer for high power DC Accelerator

R. Patel*, D.K. Sharma, P. C. Saroj, R.I. Bakhtsingh, R. N. Rajan, S. Dewangan, S.H. Das, N. Thakur, N.K. Lawangare

APPD, BARC, MUMBAI – 400085, INDIA

*Abstract*

This paper presents the design of 90 $kV_P$, 10 kHz, 125 kVA transformer for powering a 15-stages symmetrical Cockroft Walton Multiplier for 1MeV, 100kW DC Accelerator. A novel approach has been implemented for the simultaneous handling of higher frequency skin effect and current sharing problems; so that the high frequency 4 turns primary winding can handle 353.5 $V_{rms}$ and 339.4 $A_{rms}$ current at 10 kHz. Further concern of design is 90 $kV_P$, 10 kHz, 720 turn secondary winding with HV insulation and to achieve low reflected secondary winding capacitance referred to primary side for high step up ratio of 180. The selection of core material and suitable stacking scheme has achieved for transferring power from primary to secondary winding at high power and high frequency. A new cooling approach has been implemented for limiting the temperature rise of the transformer during continuous operation at full load. The high voltage transformer has tested up to 40 $kV_P$, 0, -40 $kV_P$ at No-Load and the complete test analysis of the developed transformer is presented in the paper including the protection from high voltage surges from the multiplier column. The specially designed and fabricated components developed for this project are primary bobbin, secondary bobbin, core support cage, silver plated primary lugs and terminals, C shape copper cooling coil and HV terminal bushings.

## INTRODUCTION

The development of 15-stages symmetrical Cockroft Walton Multiplier of 1MeV, 100 kW DC Accelerator for waste water treatment has required 90 $kV_P$, 10 kHz, 110 kW as input parameters. The 10 kHz inverter can provide 500 $V_P$ output voltage, therefore 125 kVA transformer has requirement of 180 step up ratio at 10 kHz frequency. This paper presents the cooling coil design of HV transformer of ONWF scheme as per BS EN 60076-2. This paper has divided in three sections, first section explains the principle and design of transformer, second section explains the testing procedure for estimating the designed parameters of the transformer and last section discusses the results and conclusion of design, fabrication and testing of the transformer.

## TRANSFORMER DESIGN

### *Core Selection*

Variety of cores are available in the market for transformer e.g. silicon steel, Metglas, Ferrites, etc [1]. The selection criterions of magnetic core for transformer are the lowest core loss at operating magnetic flux density and frequency and highest window length in the available cores. The highest window length is required for providing the HV insulation between windings and also gap insulation is required between HV winding and core. The silicon steel is the most preferred core in 50 Hz applications but for high frequency application silicon steel core is not suitable due to very heavy losses. The core loss and window length of AMCC 1000 are 91.83 $mW/cm^3$ at 0.2 T & 10 kHz and 40 mm respectively [2], similarly the core loss and window length of Ferrite core for power transformer U 126/91/20 are 70 $mW/cm^3$ at 0.2 T & 10 kHz and 70 mm respectively, therefore Ferrite core U126/91/20 and I126/28/20 has selected for application as per criterion and the permeability of UU 126/182/20 is 2000. The core type construction has been implemented for making the HV & HF transformer [3]. The special cage having 2 Nos. of Acrylic sheets, 2 Nos. of SS plates and 36 Nos. of SS rods has constructed for supporting two pairs of UIU 126/344/240 in core type structure and is shown in Fig. 1.

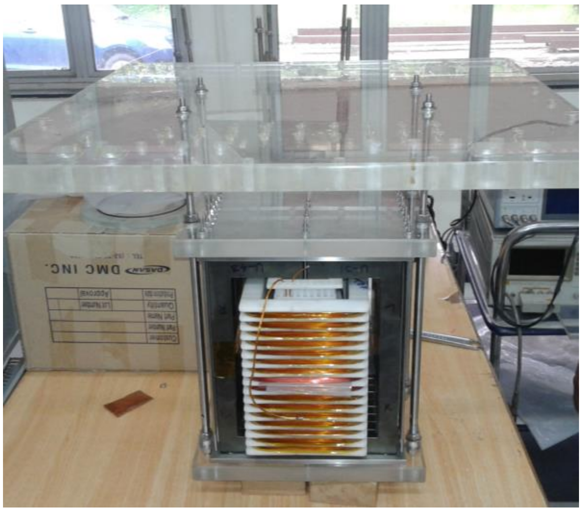

Figure 1: Winding Assembly with Core.

### *Detail Design of HV & HF Transformer*

Primary Delrin bobbin having length, width and height are 318 mm, 97 mm and 252 mm respectively. Skin depth at 10 kHz is 0.65 mm therefore 63 Nos. of Litz wire having 200 strands with 1 $mm^2$ effective cross section area has paralleled for making 4 turn primary of 712 mm MLT and 0.904 mΩ DC resistance. Secondary Delrin bobbin having length, width and height are 372 mm, 166 mm and 222 mm respectively with 16 sections has fabricated for 720 turn secondary. The SWG 17 has used

*rupeshp@barc.gov.in

in HV winding for making 5 turn in a layer and 9 layer in each section of 90 kV secondary bobbin. The MLT and DC resistance of HV winding are 983 mm and 7.1 Ω respectively. The inductance of the 4 turn primary and leakage inductance of the transformer refers to primary are 380 µH and 2.667 µH respectively and coupling factor k between primary and secondary winding with ferrite core is 0.996. The total capacitance of HV secondary winding with 16 sections and the inductance of HV winding are 13 pF and 12.3 H respectively and maximum electric field of HV winding at 45 $kV_P$ is 93.5 kV/cm [4]. The Al value of the transformer is 23.75 µH. The equivalent circuit is shown in the Fig. 2 and primary winding photo is shown in Fig. 3. The designed natural resonance frequency and the efficiency at rated kVA of the transformer are 12.6 kHz and 99.4% respectively.

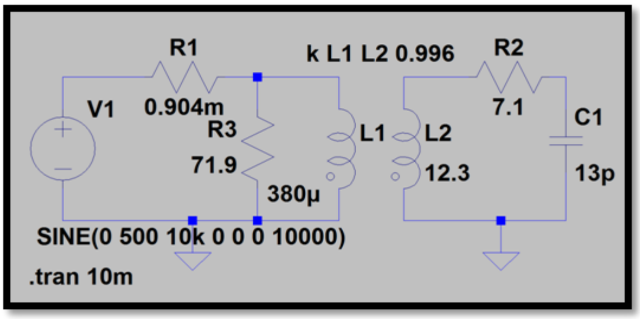


Figure 2: Equivalent circuit of Designed Transformer.

The internal dimension of MS Cubic tank is 600 mm. The maximum electric field of HV terminal at rated voltage in air is 14 kV/cm. The spark gap of 18.5 mm gap has been designed for 45 $kV_P$, 0, -45 $kV_P$ transformer from protecting the HV surges of multiplier column.

Figure 3: Primary Winding.

### *Insulation*

The HV insulation is required between primary, secondary winding and core [5]. The voltage per section of the HV winding is 6 kV and the thickness of Delrin between sections is 4 mm. The dielectric strength of Delrin is 19.7 kV/mm and the HV insulation of each section is 78.8 kV. The thickness of Delrin and HV insulation at both end of the bobbin are 5 mm and 98.5 kV respectively. Mylar having dielectric constant 3.25 at 1 kHz and dielectric strength 7.0 kV/mil has used for layer to layer to provide 625 V insulation. The voltage per turn of the HV winding is 125 V; hence no external insulation is required. The required gap for 45 kV in oil is 2.4 mm and the gap between the primary and secondary winding is 17 mm; which gives sufficient working safety factor over working voltages. There are two types of gap between HV winding and core, first gap is 15.5 mm between both end flanges of HV bobbin and core; therefore provided insulation in oil is 289.54 kV and similarly second gap is 18 mm between HV winding and core; hence the provided insulation in oil is 336.24 kV.

### *Cooling*

The estimated total losses including core and copper losses of the transformer at rated output is 760 W and the total temperature rise of the transformer including secondary and primary winding and core from ambient temperature is 32ºC. The C-shaped copper cooling coil having internal diameter 4.2 mm and length 22 m is mounted on Acrylic tank cover having dimensions 680 mm x 680 mm x 30 mm and it is designed for 1.63 lpm lcw flow at 4.82 bar pressure drop and 10 ºC temperature rises. This design presents the ONWF scheme of the transformer [6] and Fig. 4 shows the assembly details.

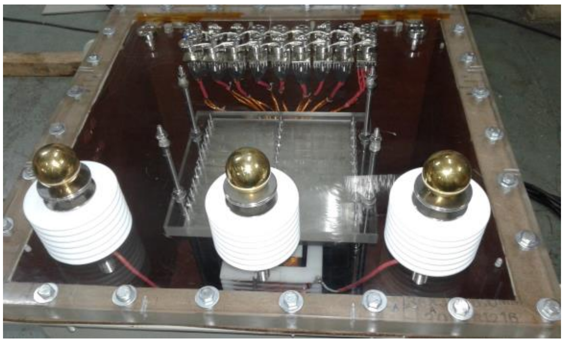

Figure 4: Assembled View of Transformer.

## TESTING AND INSTALLATION

The following measurements have been conducted for estimating the assembled HV & HF transformer in the tank with oil. The measured inductance of primary and secondary winding of the transformer after assembly in the tank at frequency 1 kHz are 413.2 µH and 12.3 H respectively and the achieved Al value is 23.8 µH. The measured leakage inductance of the transformer at primary side and coupling factor k are 2.5 µH and 0.9969 respectively. The measured resistances of winding refer to primary and refer to secondary at 10 kHz are 7.76 mΩ and 303.4 Ω respectively. The Quality factor of the secondary HV winding with measured frequency is shown in Fig. 5. The breakdown voltage of spark gap A & B of the transformer at negative polarity dc voltage are 47.2 kV and 46.4 kV respectively and hence the geometrical factor of uniformity ŋ of spark gap A & B are 0.88 and 0.87 respectively. The achieved step up ratio of the transformer at no load, 40 kV, 10 kHz is 186 and temperature rise of oil during this 1.5 hrs test run is 2.6 ºC with copper coil cooling. The step up ratio of the transformer at parallel load combination of capacitance 21 nF and wire wound resistance 348 kΩ at 12 kV, 10.8 kHz using full wave rectifier circuit is 197. The assembled 15 stage symmetrical Cockcroft – Walton HV multiplier has tested up to – 900 kV DC potential at 33.5 kV transformer voltages, 10 kHz frequency using nitrogen gas at 6 kg/cm$^2$ pressure and the step up ratio of the transformer is 204.

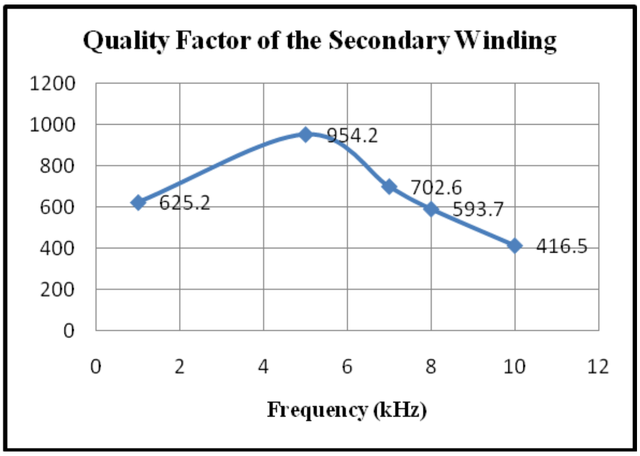


Figure 5: Quality factor of HV Winding.

## CONCLUSION

The designed and measured AL value of the transformer is 23.75 µH and 23.8 µH respectively; hence the designed air gap of 345 µm has been achieved at permeability of 2000. Similarly the designed and measured leakage inductance is 2.7 µH and 2.5 µH respectively. Therefore the measured coupling factor 0.997 of the transformer is greater than designed coupling factor 0.996. It indicates that the measured inductance of primary and secondary winding of the transformer is also greater than or equal to the designed inductance of primary and secondary winding. The output voltage of the transformer is shown in the Fig. 6. The designed step up ratio of the transformer is 180 and the measured step up ratio of the transformer at no load, load and with the HV Multiplier are 186, 197 & 204 respectively. The step up ratio is coming higher due to the stray capacitance effect like 93.2 pf capacitance between HV winding and ground at no load condition, of 150 pf capacitance at dummy load and 250 pf capacitance with the HV Multiplier. The lower and upper cut off frequency of the transformer are 20 Hz and 366 kHz respectively and the capacitance between primary and secondary winding in oil at 500 kHz is 178 pF. The performance of transformer with designed values is matching and other factors like stray capacitance effects have also been estimated for complete analysis. The heat transfer response of the transformer with copper cooling coil in the oil is also satisfactory. There is no HV discharge during the testing of the transformer.

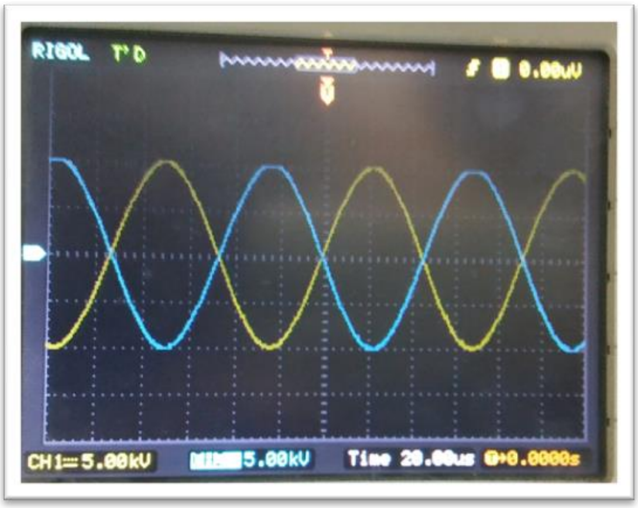


Figure 6: O/P Voltage of Transformer at No Load.

## ACKNOWLEDGEMENT

I want to give thanks to Shri R. K. Rajwat, AD BTDG & Head APPD, for their constant support and encouragement for the development of HV & HF frequency transformer.

## REFERENCES

[1] R. Patel, R. I. Bhaktsingh, D. K. Sharma, S. Dewangan, R. N. Rajan, S. Gond, N. B. Thakur, A. Waghmare, K. C. Mittal, and L. M. Gantayet, "Design Development and Analysis of High Voltage, High Frequency Tranformer for DC Accelerator Application," InPAC-2013, VECC, Kolkata, 19 – 22, November, 2013.

[2] R. Patel, D. K. Sharma, K. Dixit, K. C. Mittal, and L. M. Gantayet, "Compact Pulse Transformer for 85 kV, 3.5 µs Electron Gun Anode of Compact X – Ray Cargo Scanner" ISDEIV – 2014, Mumbai, 28 September – 3 October, 2014.

[3] McLyman, Col. Wm. Transformer and Inductor design Handbook, Marcel Dekker, New York, 1988.

[4] Snelling, E.C., Soft Ferrites, Properties and Applications, 2nd ed., Butterworths, London, 1988.

[5] Flanagan, William M. Handbook of Transformer Design And Application, Second Edition, Mc Graw Hill.

[6] Healthcote, Martin J. The J and P Transformer Book, Thirteen Edition, ELSEVIER, Newnes.

# RF ACTIVITIES AND RECENT DEVELOPMENT OF RF SYSTEMS OF VEC-RIB

H. K. Pandey, T. K. Mandi, D. P. Dutta, A. Jain, A. Bandyopadhyay and V. Naik

RIBFG, Variable Energy Cyclotron Centre, 1/AF Salt lake, Kolkata

*hkpandey@vecc.gov.in

*Abstract*

RIB facility at VECC has several heavy ion linear accelerators like RFQ, IH-LINACs and several re buncher cavity operating at 37.8 MHz and 75.6 MHz. Also, a super-conducting cryomodule housing four quarter wave resonators (QWRs) operating at 113.4 MHz is under development. The existing RF power amplifiers have been made by SAMEER Mumbai. Solid State Amplifier (SSA) modules along with proper amplitude and phase control system has been developed indigenously and tested. Along with these a superconducting electron Linac for the upcoming ANURIB facility has been developed in collaboration with TRIUMF, Canada. 1.3 GHz, 2 kW SSA and 20 kW IOT amplifier have been installed for the electron Linac. Up gradation and associated developmental work as well as the future RF activities related to the above systems will be presented in this paper.

## INTRODUCTION

An Isotope Separator On-Line type Radioactive Ion Beam (RIB) facility is presently under construction at VECC Kolkata [1-2]. Radioactive isotopes are created in a target by bombardment with energetic beams of protons or alpha-particles/ heavy-ions and subsequently ionized in an ion source. The low energy ion beams selected using an on-line isotope separator is finally accelerated to the desired energy, using Radio Frequency Quadrupole (RFQ) Linac and heavy-ion Linacs [3]. The accelerators of RIB facility are being installed for accelerating beam up to 1 MeV/u after LINAC-5. Stable beam acceleration has already been carried out up to energy of 0.4 MeV/u after LINAC-3, while RF test and characterization of Linac 4 and 5 has been completed. All the cavities have separate RF power amplifiers with a low level RF control system. To achieve efficient beam transmission and acceleration, all these RF cavities needed to be operated in phase synchronism with respect to a reference RF signal. A RF distribution system has been developed to divide the signal from the signal generator to the respective phase and level controllers of the individual transmitters [4-5]. Apart from post accelerator RIB beam line a 50 MeV, 2 mA CW superconducting electron linear accelerator (e-Linac) is also being developed at VECC for the upcoming ANURIB (Advanced National Facility of Unstable and Rare Isotope Beams) project [6]. In its first phase, a 10 MeV Injector has been developed in collaboration with TRIMUF, Canada. An e-gun with a 650 MHz RF modulated gridded cathode, floating at 100 kV has been installed and tested along with low energy beam transport (LEBT) line.

## RF SYSTEM OF RIB BEAM LINE ACCELERATORS

The RF sources for the post RIB accelerators presently consist of one 40 kW transmitter (Tx) for the RFQ, two 20 kW RF Tx for LINAC 1 and LINAC 2 and three 5 kW RF Tx operating at 37.8 MHz for RB 1(Re-Buncher), RB 2 and RB 3 and a 5 kW RF transmitter operating at 75.6 MHz for RB 4. One 20 kW 75.6 MHz amplifier is installed and tested for Linac 3, while two 20 kW 75.6 MHz Tx for Linac 4 & 5, one 10 kW and two 5 kW 75.6 MHz Tx for RB 4 and RB 5 are under development. Apart from these, four 330W 113.4MHz solid state amplifiers have been developed and tested for the upcoming superconducting QWR of post accelerator RIB beam line. A single oscillator at 37.8 MHz drives all the RF power amplifiers. This is done using power splitters which divide the RF signal to the respective power amplifiers. The schematic diagram for RF distribution is shown in figure 1. For RF cavities from LINAC-3 to QWR's, frequency multipliers are used to convert the 37.8 MHz signal to 75.6 MHz and 113.4 MHz. The forward and reflected power samples and pick-up signal from each of the RF accelerator cavities are fed to the low level RF control modules of the RF amplifiers. The amplified signals are fed to the cavities. The phase and power level for each cavity could be varied using the respective phase and level controllers of the individual transmitters. The pick-up signals from all cavities are observed with oscilloscopes during operations. The High power amplifiers for RFQ (40 kW/37.8 MHz), IH-Linac 1 & 2 (20kW/37.8MHz) and IH-Linac 3 (20kW/75.6MHz) consist of two-stage vacuum tube amplifiers. A triode tube based 1 kW amplifier is used as a driver stage and the final stage is equipped with a tetrode tube. The amplifier of RB 1 is a single stage triode tube based amplifier. All transmitters have 100 W solid state preamplifiers. The High power RF power is fed to the accelerator cavity by loop coupler through a 3-1/8" 50Ω coaxial transmission line for RFQ and IH-Linacs and 7/8" line for all buncher cavities. The driver amplifier is a class AB amplifier designed using triode 3CX5000A7 in grounded grid configuration. The design, analysis and measurement of this amplifier have been reported in. The final stage is a tetrode-tube based amplifier designed using the 4CW100000E tetrode tube. The control grid is usually negative with respect to the cathode, and screen grid is positive with respect to cathode. Because of the power handling considerations, the input matching circuit is based on lumped component, while the output is distributed matching network. A co-axial structure, one end short circuited, with centre conductor having circular cross-section and outer conductor of rectangular cross section are used as output matching tank network. The maximum output power of the tetrode amplifier is 40 kW and frequency tuning range is 32 MHz to 40 MHz. Loop couplers and frequency tuner for all accelerator cavities have been indigenously designed and built. The criticality of length of the transmission line for stable operation of amplifier connected to high Q load has been discussed and accordingly adjusted the length of feeder lines to the required value of multiple half wavelengths.

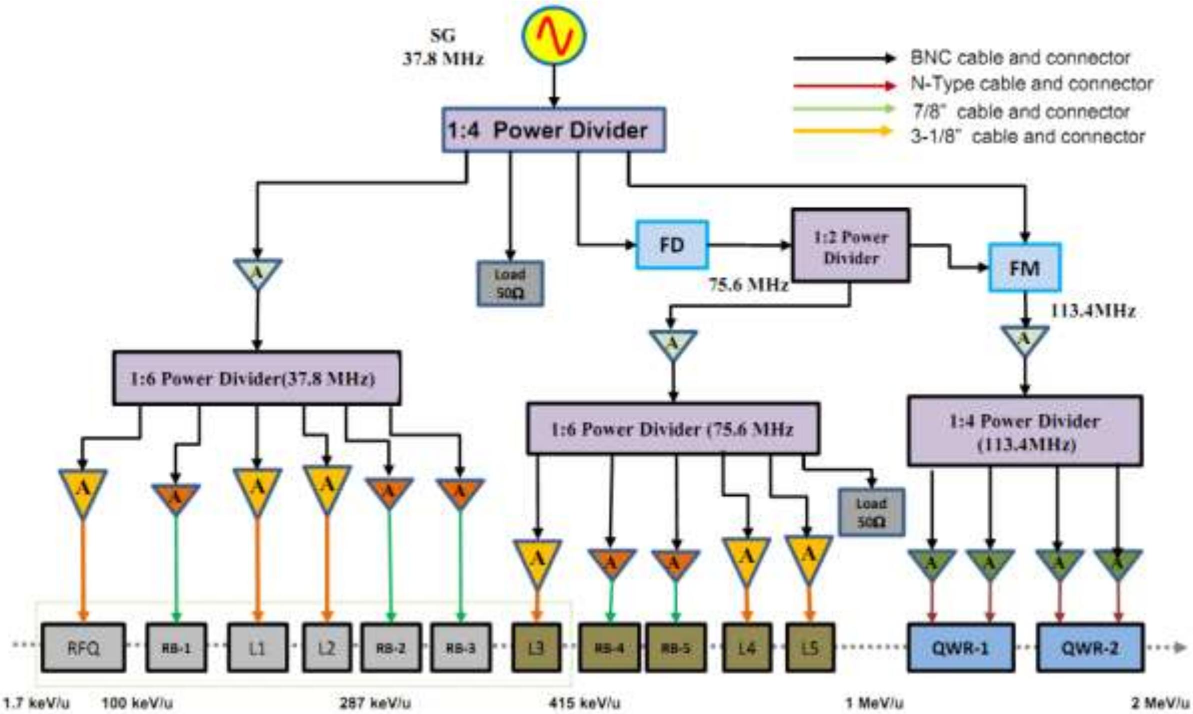


Figure 1: RF Distribution scheme for VEC-RIB accelerators

### *Low Level RF Control*

The Low Level RF (LLRF) control system regulates the amplitude and phase of the RF cavity voltage through fast electronic feedback mechanism. The frequency of the cavity is regulated by the mechanical movement of a tuner loop in appropriate direction by sensing the frequency deviation. At present the control is based on the conventional amplitude and phase loop method.

The important components in control system consists of the phase comparator (realized with double balanced mixer configured in phase comparator mode), amplitude detector (realized with Schottky diodes HP5082-2835), PI controller, voltage controlled phase shifter (realized with two 0-180˚ varactor diode based phase shifters in cascade) and voltage controlled attenuators (realized with pin diodes based π configuration circuitry). The phase detector senses the phase difference between the RF input signal and the cavity pick-up signal to produce an error signal which is fed to a PI controller to generate the control voltage. The control voltage is input to a phase shifter which brings the phase of the RF signal to the desired value. The measured phase satiability is ±0.5° and phase control range is 360°. The amplitude detector senses the level of the cavity pick-up signal and it is compared with the reference level signal to produce the error signal which is fed to a PI controller. The measured amplitude stability of the control circuit is ± 0.5% [7-8].

A mechanical tuner, which is a part of the RF cavity, is moved to tune the cavity to its resonant frequency. The detuning of the RF cavity is sensed by measuring the phase difference between the forward power sample obtained from a dual directional coupler and the pick-up signal from RF cavity. AD8302 phase detector is used to measure the phase difference. The output of the phase detector is fed to a microcontroller (ADuC841) which drives a stepper motor coupled to the tuner to achieve desired tuning.

## UPGRADATION AND REMOTE CONTROL RF SYSTEM

RF transmitter control and monitoring systems are being upgraded. The existing system is replaced by a PLC based system with provision for local as well as remote operation. The system consists of 75 digital IO and 20 analog IO. The low voltage analog signals will be processed through appropriate signal conditioning circuit to make them compatible with PLC input range.

A "Distributed Data Acquisition and Control System (DDACS)" has also been developed and installed at VECC. The remote control system is designed to control and monitor all parameters for the RIB beam line components including the RF transmitters at RIB Facility. The data acquisition and control system has a 3 layered design, namely: a) Equipment Interface Layer b) Supervisory Layer and c) Operator Interface Layer [9-10]. The Equipment Interface Layer consists of Remote Interface Modules (RIM) and Equipment Interface Modules (EIM). The RIM, realised using a 32-bit LPC 2478 ARM7TDMI, acts as the interface between the local controller of the RF Tx and the EIM. The RIM is interfaced to the EIM through RS232.

Each EIM controls a specific RIM along with a specific section of beam line support subsystems. The Supervisory layer, realised using Embedded Controllers (EC1), interfaced with EIMs through fibre optic cables, performs supervisory task of continuously sending command and acquiring data from lower level EIMs and reporting to the operator interface layer as and when requested. Operator interface layer consists of operator console formed with another embedded controller (EC2) and high performance PCs/Workstations for controlling and monitoring machine parameters.

## ELECTRON LINAC

A 50 MeV, 100 kW CW Superconducting Electron Linac (e-Linac) will be used for the production of Rare Ion Beams (RIB) for the ANURIB project at VECC. The electron Linac consists of one 10 MeV Injector stage and four subsequent 10 MeV Accelerator stages, all based on the 1.3 GHz, 2K SRF technology. The first stage of acceleration, known as the Injector Cryomodule (ICM) has been tested at TRIUMF, Canada and will be installed at VECC for further testing. Apart from the ICM, the first stage consists of a 300 kV dc thermionic electron gun (e-gun) and a 1.3 GHz buncher along with 1.3 GHz deflector cavity for beam diagnostics.

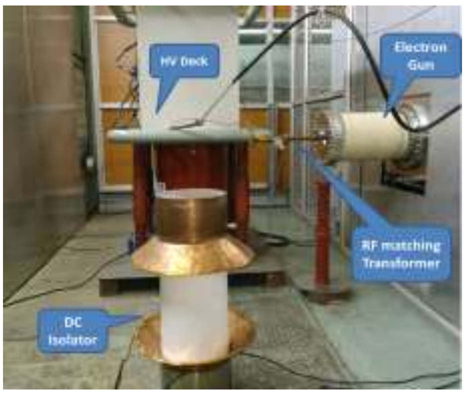


Figure 2: The electron gun set-up at VECC

The e-gun is a triode type RF modulated thermionic electron gun and has been developed at VECC. Figure 2 shows the set-up of the electron at VECC. The gun emits the beam in the form of electron bunches at a frequency of 650 MHz and conduction period of ±20 degrees. This is achieved by biasing the e-gun below cut-off and modulating the grid with 650 MHz RF voltage. The electron gun is followed by the Low Energy Beam Transport (LEBT) line. A single gap 1.3 GHz cavity acts as the electron buncher for the conditioning of the beam before insertion into the 9-cell 1.3 GHz super conducting cavity. Another 1.3 GHz RF cavity is used as a deflector for the measurement of longitudinal width of the electron beam. A RF distribution system has been devised for the ICM stage as shown in figure 3.

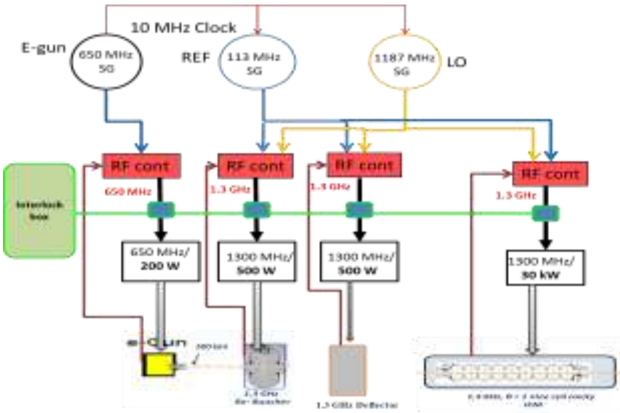


Figure 3: RF Distribution for ICM stage

## SUMMARY


The RF distribution scheme and a remote control scheme for RF transmitters have been presented. The RF systems for the VEC RIB accelerators have been developed and commissioned up to Linac 3. The low level RF control system for the RF transmitters is described in this paper. The design of the LLRF system is being improved to IQ based LLRF control. The beam test has been done for the beam of $N^{4+}$ at the IH Linac 3 exit. RF distribution scheme for the 10 MeV ICM stage has also been presented. The development of other high power RF systems of 75.6 MHz is in progress.


## REFERENCES


[1] V. Naik , et.al. RSI, 84, 033301(2013).
[2] A. Bandyopadhyay et al, Nucl. Instrum. Methods Phys. R es. A 560, 182 (2006).
[3] S. Dechoudhury, et.al. RSI, 81, 023301(2010).
[4] H. K. Pandey et al, "RF Systems of the VEC-RIB Facility", Proc. IPAC'10, Kyoto, Japan.
[5] H. K. Pandey et al., Proc. InPAC 2009, RRCAT, India, Paper ID.083.
[6] A. Chakrabarti, Nucl. Instrum. Methods Phys. Res. B 261, 1018 (2007).
[7] T K Mandi et at, InPAC 2019, Paper ID 159.
[8] D P Dutta et al, InPAC 2019, Paper ID 157.
[9] K. Dutta et al, ICAPCS'11, Grenoble, France.
[10] D-DACS Technical Manual, SAMEER, Chennai.

# DESIGN AND DEVELOPMENT OF ACCELERATING TEST TUBE FACILITY FOR DC ELECTRON BEAM ACCELERATOR

S. Dewangan*, Swati H. Das, R.I. Bakhtsingh, R.N. Rajan, S.R. Ghodke, D K Sharma, D.Jayprakash, R. Patel, S. Gond, A.G. Waghmare, S. Harer, N.B. Thakur, Mahendra Kumar, N.K. Lawangare, R. Barnwal, R. Tiwari and Dhruva Bhattacharjee

Electron Beam Centre, Accelerator and Pulse Power Division, Bhabha Atomic Research Centre, Sector-7, CBD Belapur, Navi Mumbai

*dewangan@barc.gov.in

*Abstract*

DC accelerator is suitable for high power radiation processing applications. The accelerating tube of DC electron beam accelerator are generally insulated with pressurized gas dielectrics ($SF_6$, $N_2$ or mixture of gases) from outside and inside the tube, vacuum better than $10^{-6}$ mbar is maintained. For safe and reliable operation of the high power DC accelerator, all the subsystems need to be tested at their rated parameter. For the testing of accelerating tubes, an accelerating tube test facility (ATTF) has been developed at Electron Beam Centre, Kharghar. ATTF is rated for 350kVDC, which is derived from 5 stages 50Hz CW HV multiplier. ATTF consists of Input power supply, pressure vessel, vacuum system and control system. The ATTF has been successfully tested at 350kVDC at 6kg/cm$^2$ $SF_6$ gas environment. Accelerating tubes for EBWWT (Electron Beam Waste water treatment) has been tested with ATTF. This paper describes about the salient features of the power supplies, HV conditioning and testing results of the accelerating tubes.

## INTRODUCTION

Electron Beam Waste Water Treatment (EBWWT) is under development at Electron Beam Centre Kharghar. Accelerator is rated for 1MeV and 100kW beam power. An accelerating potential of 1MV DC required for acceleration of electron-beam is developed by a 15-stages symmetrical Cockcroft Walton multiplier driven by a 45-0-45kVp, 10kHz input source and 0-500Vp, 10kHz IGBT based inverter. Electron-current is generated by a $LaB_6$ cathode based 10-15kV electron gun located on top of an accelerating column, which accelerates injected electron beam in a vacuum of $10^{-7}$ mbar.

An accelerating column has 6 numbers of accelerating tube. Each tube is made using high purity alumina rings and titanium rings diffusion bonded to hold vacuum better than $10^{-7}$mbar with a differential pressure of 7 bar. Tube has 18 dynodes with a spacing of 12.5mm. Tube is rated for 335kVdc in 6kg/cm$^2$ $SF_6$ gas environment. The working voltage on each tube at 1MVDC will be 167kVDC. It has been experienced that most of the discharges during working of the accelerator was due to discharges at the vacuum side. Each tube has to be qualified for its voltage withstand capability at vacuum side as well as pressure side. An accelerating test tube facility rated for 350kVDC, 100µA was developed to test 335kV (NEC Make) tube under 6 kg/cm$^2$ $SF_6$ gas environments outside and vacuum inside. All the tubes for EBWWT were tested at a qualified voltage in the range of 200-250kVDC.

## CONSTRUCTION OF ACCELERATING TUBE TEST FACILITY

A schematic of ATTF is shown in figure 1. It consist of (a) High Voltage Multiplier column rated for 350kV and 100µA, (b) Input Transformer rated for 25kV, 50Hz, (c) Control and measurement unit, (d) Pressure vessel, (e) Vacuum system, (f) Insulation gas 6kg/cm$^2$ $SF_6$ and (g) load-accelerating tube.

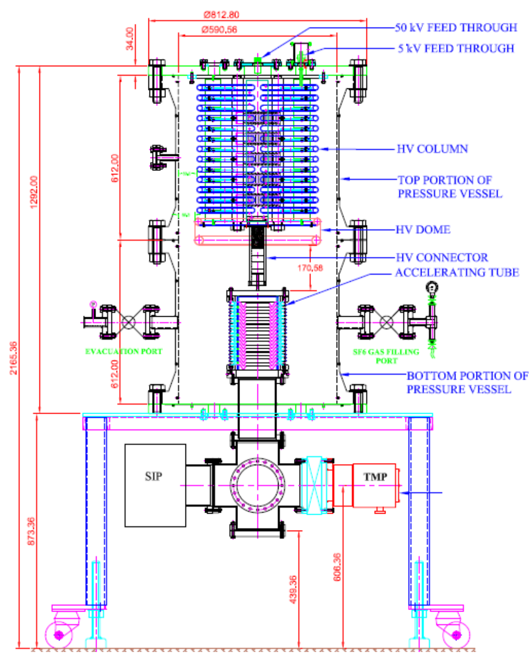


Figure 1: A schematic of ATTF

350kV DC was developed by a 5-stage conventional Cockcroft Walton multiplier at input of 25kVrms, 50Hz. Stage capacitance of 6.6nF/80kV was made using 8 numbers of 3.3nF/40kVDC ceramic capacitors. The multiplier column has 10 capacitor banks having two modules (13.2nF/40kVDC) in series. Each capacitors module is graded using 20GΩ, 60kV HV resistors. An effective grading resistance for both the HV column is 100GΩ.

The schematic diagram of the HV multiplier column is shown in figure 2.

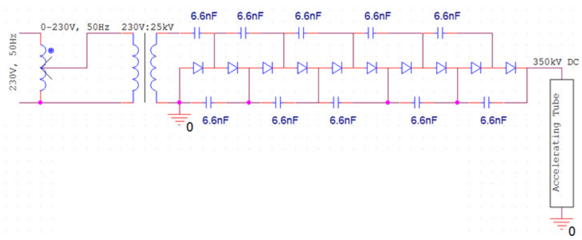


Figure 2: A schematic of HV Multiplier Column

An output voltage equation of conventional Cockcroft Walton multiplier is given by

$$Eout = 2nVi - \frac{I}{fC}\left(\frac{2}{3}n^3 + \frac{n^2}{2} - \frac{n}{6}\right) \pm \frac{I}{fC}\frac{n}{2}(n+1)$$

Where, n = number of stages, $V_{in}$ = Stage input Voltage, (peak), I= load current, C is the stage capacitance, f is the AC frequency

The multiplier rectifier stacks are rated for 148kV PIV. It is made with 16 numbers of UXFOB diodes each rated for 8kV PIV, 500mA, 50ns trr and surge current rating 20A@8.33ms. To limit the diode current during surge/arcing condition, 1kΩ HVR make bulk ceramic resistors are connected in the series of each rectifier stacks. A photograph of multiplier diodes assembled in corona cap and delrin strip is shown in figure 3.

Figure 3: Photograph of assembled rectifier stack.

A 5kΩ resistor is used in series with HV multiplier and load (tube) to limit the load current during short circuit in the load during testing. The multiplier column having a dimension of 470mm (OD), 631mm(H) is housed inside pressure vessel having a dimension of 590mm (ID) and 1224mm (H). The multiplier column has been designed for maximum electric stress of 120kV/cm at 6kg/cm$^2$ $SF_6$ gas environment. A high voltage resistive divider having division ratio of $2\times10^6$:1 was used to measure 350kVDC voltage. Output voltage is varying from 0-350kV by varying the input voltage using 0-230V, 50Hz, 120VA single phase variac. For uniform grading of the voltage across accelerating tube, high voltage resistor of 10GΩ is connected across each dynode.

## ASSEMBLY AND TESTING

The HV multiplier is assembled on the pressure vessel as shown in figure 4. Voltage divider, leakage current and grading current measurement signal were taken through HV pressure feed-through and filter board to the control and monitoring panel. Input transformer was tested at its rated voltage 230V:25kV, 50Hz. The multiplier was tested upto 176kVDC at 6kg/cm$^2$ $N_2$ gas environment and upto 360kVDC at 4.5kg/cm$^2$ $SF_6$ gas environment. Accelerating tubes are rated for $SF_6$ gas environment at 6kg/cm$^2$ pressure outside. So during testing of the tube at ATTF, $SF_6$ gas at 6kg/cm$^2$ is filled to avoid arcing outside the tube and hence ensuring the arcing at vacuum side.

Figure 4: A photograph of assembled 350kV DC Multiplier.

## ASSEMBLY OF ACCELERATING TUBE AT ATTF

The HV multiplier is assembled on the top flange of pressure vessel and accelerating tube is assembled on the bottom flanges of the pressure vessel at ATTF. The dynode spark gap spacing outside the tube was measured in the range of 1.6mm to 2.5mm. Uniform voltage distribution is ensured by 10GΩ grading resistors across each dynode. HV supply is connected to the accelerating tube using spring loaded connector having series limiting resistor to limit current during arcing inside the tube.

The pressure vessel was evacuated to 10mbar and then $SF_6$ gas is filled upto 6kg/cm$^2$ pressure. The tube was pumped down by a vacuum system (Turbo molecular pump and rotary pump) to a base pressure of $10^{-7}$ mbar.

## TESTING OF ACCELERATING TUBE AT ATTF

NEC Accelerating Tube were tested using indigenous Cockroft Walton based power supply for at least 200kV. The grading current through resistor connected across 18 dynodes is measured to observe the leakage current through the dynodes. The vacuum is maintained at $5\times10^{-6}$ level inside the tube. An experiment was carried out with one tube at a time at ATTF. The results are shown in figure 5 and Table 1.

Table 1
Testing Criteria of Accelerating Tube for 1MeV, 100kW
No load Voltage: 1200kV, No. of Tube: 6
Voltage Per tube: 200kV, Testing criteria: >220kV

| Tube No. | Initial Voltage | Final stable Voltage | Vacuum | $SF_6$ Gas Pressure |
|---|---|---|---|---|
| 1. | 318kV | 100kV | $5\times10^{-6}$ | 3.2kg/cm$^2$ |
| 2. | 235kV | 180kV | $5.2\times10^{-6}$ | 5.8kg/cm$^2$ |
| 3. | 313kV | 220kV | $3.2\times10^{-6}$ | 5.8kg/cm$^2$ |
| 4. | 295kV | 295kV | $3.8\times10^{-6}$ | 5.7kg/cm$^2$ |
| 5. | 280kV | 180kV | $4.6\times10^{-6}$ | 5.8kg/cm$^2$ |
| 6. | 257kV | 250kV | $3.5\times10^{-6}$ | 5.8kg/cm$^2$ |
| 7. | 258kV | 258kV | $7.1\times10^{-6}$ | 5.8kg/cm$^2$ |
| 8. | 260kV | 260kV | $4.7\times10^{-6}$ | 5.8kg/cm$^2$ |
| 9. | 265kV | 255kV | $5.1\times10^{-6}$ | 5.8kg/cm$^2$ |
| 10. | 250kV | 250kV | $5.7\times10^{-6}$ | 5.8kg/cm$^2$ |

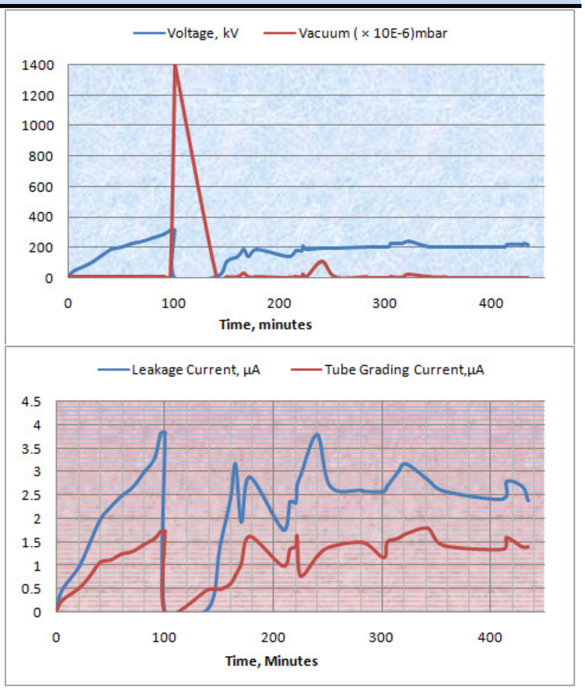


Figure: 5: Effect of HV conditioning and testing of of accelerating tube on vacuum, grading current and leakage current

It is clear from the graph and table that initial vacuum discharges at 235kV to 318kV was observed with an increase in the fluctuation in the leakage current and degradation in the vacuum. And with decrease in the applied voltage vacuum improves and leakage current decreases. After first discharges the stable voltage was found to be lower than the initial value. Sometimes arcing at higher voltage causes very low stable voltage. So for EBWWT, testing criteria more than 220kV was adopted. 10 numbers of the tubes were tested and out of which 7 tubes qualified for 1MeV, 100kW EBWWT accelerator. Figure 6 shows the assembled photograph of qualified accelerating tube at EBWWT tank.

Figure 6: Photograph of Assembled tubes at EBWWT

## CONCLUSION

The Accelerating Tube Test facility (ATTF) based on the indigenous Cockcroft Walton multiplier has been developed and successfully utilized for the testing of accelerating tube for EBWWT accelerator. 10 numbers of tubes has been tested and qualified tubes are being under assembly at EBWWT for beam trial. The setup can be modified as small accelerator for low energy radiation processing applications.

## ACKNOWLEDGEMENTS

Authors are very thankful to Shri R K Rajawat, Head APPD for constant support, guidance and encouragement in the overall DC accelerator development at Electron Beam Centre.

## REFERENCES

[1] K. Nanu, et al, “Design of 3MV/10mA DC power source for E-Beam Accelerator” Proc. Indian Particle Accelerator Conference, Centre for Advanced Technology, Indore, Feb. 3–6 (2003), p-246.

[2] T Joy, “Electrostatic Accelerator Tubes- Recent Progress and Future Directions” Proc. Nuclear Instruments and methods in physics research A287 (1990) 48-63 North-Holland.

[3] S Dewangan, et al, “Experience on High Voltage Testing and Conditioning of Accelerator tube for 3MeV DC Accelerator”, Proceedings of DAE-BRNS Indian Particle Accelerator Conference, BARC Mumbai (InPAC-2015).

# Realization of 107.5MHz, 150kW RF Power System for Re-circulating Accelerator

M K Jain#, R K Deo, M Lad, Raja Ramanna Center for Advanced Technology, Indore, India

*Abstract*

As a part of design study of the proposed high power re-circulating accelerator of output beam energy and target beam power of 7MeV and 50kW respectively; development work is underway for a RF power system with an installed RF output rating of 150kW at 107.5MHz, as required for establishing maximum RF voltage of 0.7MV between center conductor and outer conductor of shorted-ends, half wavelength coaxial accelerating cavity. Having determined various structural parameters, taking approach of microwave networks, full wave EM simulation of the RF circuit cavity structure is carried out in CST MWS and RF performance thereof in terms of input & output matching, tuning range, maximum field at various critical points etc. are verified and optimized. This paper describes the realization of RF amplifier cavity circuit structure and the EM simulation results as obtained for its satisfactory performance.

**Keywords—vacuum tubes, amplifiers**

## INTRODUCTION

In a multi-stage RF amplifier configuration, the RF power system is to be consisting of 150kW tetrode based Final power amplifier (FPA)- realized with coaxial line and parallel plate radial line based input and output cavity circuits respectively, and driven by 10kW Tetrode based driver amplifier and 1kW pre-driver amplifier based on LDMOS device. FPA of the 107.5MHz/150 kW RF power system, required for energizing shorted ends, half wavelength coaxial line accelerator-cavity of high power re-circulating accelerator, is invariably a tetrode tube based system; wherein, structure of the FPA is mounted on the coaxial accelerator-cavity so that 6-1/8"EIA coaxial output port of FPA output cavity can sit on 6-1/8"coaxial feed port of the accelerator-cavity and be matched for impedance as offered by the later. With this configuration, amplifier anode-cavity is directly coupled to the accelerator-cavity by means of a 6-1/8" coaxial through coupling line. The coupling line, in configuration, is passed through the anode-cavity near its outer cylindrical wall and is terminated to the accelerator cavity feed loop at one end for the excitation of the accelerator cavity with the RF power as coupled from the amplifier cavity; the other end is terminated with coaxial line open stub for tuning the coupling line. Therefore, the need of long high power pressurized transmission lines is avoided. This will add to compactness of the overall accelerator system for its suitability to industrial use. With this configuration, a direct ratio is established between accelerating voltage in accelerator-cavity and anode RF voltage in amplifier output cavity as excited by the tetrode. Therefore, a beam loading of the accelerator cavity can be taken care of by adjusting anode impedance loading as seen by the anode circuit; thus the RF amplifier will be operating at best efficiency. A CAD diagram of re-circulating accelerator final power amplifier (FPA) as realized is shown in figure.1

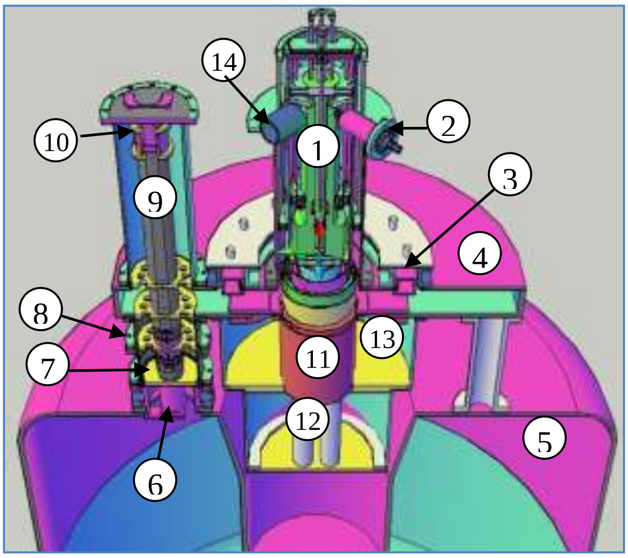


Fig.1: CAD diagram of final power amplifier (FPA) mounted on re-circulating accelerator coaxial Cavity.

[1: Input circuit Assembly of FPA; 2: Input Port of FPA; 3: output cavity tuner of FPA; 4: Output cavity of FPA; 5: Accelerator coaxial cavity; 6: accel. Cavity loop RF coupling loop; 7: Accel cavity coaxial RF window; 8: RF output port of FPA; 9: coaxial coupling line assembly; 10: variable capacitor for RF coupler tuning; 11: Tetrode tubeTH571; 12: Insulated anode water cooling channels.13: tetrode insulated support; 14: Input Air-cooling inlet].

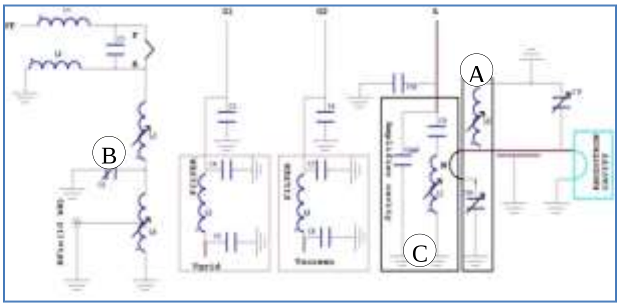


Fig 2:Equivalent circuit of FPA and through line coupler. (A: through line coupler; B: I/pt cavity; C: O/p cavity)

## DESIGN

For designing FPA, tetrode tube TH781 from Thales is considered to deliver required 150kW RF power at the central operating frequency of 107.8MHz in cathode-driven grounded–grid configuration in class AB mode, getting inherent advantage of stable operation and avoiding the critical requirement of neutralization adjustment against positive feedback between input and output circuit of the FPA. Operating parameters TH781 based FPA as designed for 150kW RF output is given in table-1. However, the tube [4] is capable of delivering more than 200kW of RF output, providing a scope of upgrading the RF power system for higher beam power operation of the accelerator.

Design parameters of the end compensated coaxial accelerator-cavity, considered for this design work, are listed in table-2. To generate 700kV of peak gap voltage between center and outer conductors of the coaxial cavity, 107kW RF power will be dissipated as copper losses inside the accelerating cavity with a maximum electric field of 2.64MV/m at mid way on the surface of center conductor of the coaxial cavity. Therefore to have a beam power of 50kW with beam energy of 7MeV, a RF power system capable of delivering 150kW at the operating frequency of 107.5MHz will be required. The circuit network of tetrode based FPA as shown in fig.2- consisting of input and output matching & tuning circuit, tube socket and bias networks, neutralization circuit, is realized in form of a integrated structure meeting the requirements of overall layout of the accelerator RF power system as shown in fig. 1.

Table 1: Operating parameters of TH781 based FPA.

| Sr. | Parameters | Sym | Value | Unit |
|---|---|---|---|---|
| 1. | Operating frequency | f | 107.5 | MHz |
| 2. | Cathode RF Drive | $V_{g1,m}$ | 400 | V |
| 3. | Anode DC Voltage | $E_p$ | 10.0 | kV |
| 4. | Anode DC current | $I_p$ | 25.5 | A |
| 5. | Output RF power | $P_o$ | 160 | kW |
| 6. | Screen grid bias | $E_{g2}$ | 1.5 | kV |
| 7. | Input RF drive | $P_n$ | 8 | kW |
| 8. | DC grid bias | $E_{g1}$ | -400 | V |
| 9. | Anode o/p impedance | $R_o$ | 200 | Ω |
| 10. | Loaded input | $R_i$ | 10 | Ω |
| 11. | Power gain | G | 13 | dB |
| 12. | Anode efficiency | η | 63 | % |

Table 2: Accelerator-Cavity Parameters as calculated.
(Material of construction: SS coated with Cu.)

| Sr. | Parameters | Sym | Value | Unit |
|---|---|---|---|---|
| 1. | Quality factor | $Q_o$ | 45600 | |
| 2. | Shunt Impedance | R | 2.275 | M Ω |
| 3. | Resonance Freq. | $f_o$ | 107.504 | MHz |
| 4. | Coaxial Cavity Dimension: | | | |
| 5.1 | ID/OD/length | | 400/1500/1473 | mm |
| 5.4 | Conical end diameter/depth | | 300/250 | mm |

## *Output Cavity Resonator*

Output circuit is realized in form of quarter-wave parallel plate radial line resonator, which, at its center, is conductively coupled to the tetrode tube between anode and screen-grid contact-ring via DC blocking capacitor formed with corona resistant FEP laminated Kepton films of type CR019 bonded with 2mil thick copper foil at both the side; and outer periphery of the parallel plate radial line is short circuited as shown in fig 1. The annular cylindrical space between anode and screen-grid inside the tube vacuum envelop, and the externally connected shorted parallel plate radial lines at normal pressure, together form the output resonator of the amplifier. The plate to screen grid ceramic insulator serves as RF window between the two regions of the output cavity circuits. Output cavity of FPA is tuned by locally changing distance between the parallel plates by mean of a small width of circular strip of desired radius; shown as item 3 in figure 1.

For designing parallel plate radial line resonator, it is seen as a formation of concentric strips of small width of ΔR of corresponding radius $R_i$. These concentric parallel strips are considered as parallel plate lines of length ΔR and width equal to its respective periphery; all connected in cascade to form parallel plate line which is short circuited at maximum-width end and loaded with screen grid- anode capacitance at the minimum- width end, forming a parallel resonance circuit. The impedance $Z_s$- offered to anode by anode-cavity equivalent of cascade connected parallel-plate-lines is determined with help of equations 1-4. This impedance is tune out by the reactance offered by anode-screen grid capacitance, $C_{pg2}$ for having resonance condition.

$$Z_{oi} = \sqrt{(\mu_o \varepsilon_o)} / (\varepsilon_o 2\pi R_i / h) \ldots\ldots\ldots (1)$$

$$m_i = \begin{bmatrix} \cos(\beta \Delta R) & jZ_{oi}\sin(\beta \Delta R) \\ j\sin(\beta \Delta R)/Z_{oi} & \cos(\beta \Delta R) \end{bmatrix} \ldots\ldots\ldots (2)$$

$$M = \prod_i m_i \ldots\ldots\ldots (3)$$

$$Z_s = M(1,2)/M(2,2) \ldots\ldots\ldots (4)$$

(h: height of the cavity; $m_i$,$Z_{oi}$: line impedance and ABCD matrix of $i_{th}$ section of parallel plate radial line)

## *Output through line Coupler*

RF output coupling from the anode output cavity is implemented using 6-1/8” rigid coaxial through line coupler, shown as item 9 in figure 1, wherein its center conductor is passed through the anode-cavity at a radial position of 361mm from the center, near cylindrical wall, considering the mechanical constraint of its mounting on accelerator cavity, with the outer conductor getting terminated on the anode-cavity flat walls outside. With one end terminated to an 6-1/8”coaxial line open stub offering a series reactance of jX, the other end of the through-line coupler serves as the anode-cavity output-port for connecting it to the accelerator-cavity feed port; The coupling impedance at the output port, determined to be 4+jX for anode loading impedance of 200 ohm, is matched to accelerator-cavity impedance at the feed port, with help of the open stub connected to coupling line and orientation of coupling loop of the accelerator-cavity. Shunted with output port, a shorted-stub is also incorporated so that output port can also be matched to

50 ohm for testing the FPA on dummy load. The equivalent circuit of the coupling line is shown in fig 2.A

### *Input- Circuit Assembly*

In configuration, input matching & tuning circuit of FPA, show in fig 2(B), forms a coaxial lines structure as shown in fig. 1 and 4a, and is designed to deliver 8kW of RF input power to cathode for generating 400V of peak RF input voltage between cathode and control grid, driving 10 ohm impedance offered by cathode as listed in table-1. The input cavity circuit is realized inform of folded $3\lambda/4$ coaxial line which is connected to control grid and cathode of the tube at one end with other end folding itself inside the central conductor to form a variable shorting stub and connected to 1-5/8" input port. Input tuning, C2 in fig.2, is carried out by means of cylindrical movable capacitor which can be varied and also positioned at required distance from the cathode ring-terminal inside the input line as required for impedance matching over a wide range. The overall structure as realized consists of DC blocking capacitor, tube base, input matching and tuning circuit as an integrated structure as shown in figure 4a.

## SIMULATION RESULTS AND CONCLUSION

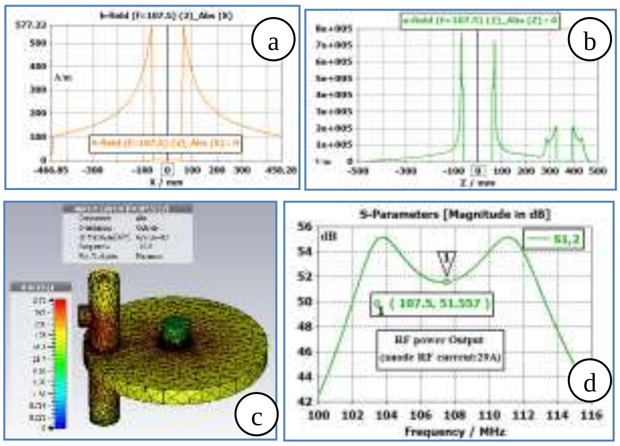


Figure 3: (a) H-field plot. (b) E Field Plot. (c) Surface current density. (d) output power V/s frequency.

Verified with the simulation results, the structure of FPA is successfully realized for 150kW of output power generated by the tetrode tube wherein the output cavity is excited by 40A of peak RF Anode current causing 8kV of peak RF voltage appearing at anode for the optimum loading of the tetrode at the operating frequency of 107.5MHz. The maximum value of the H-Field and E-filed inside the output cavity is found to be 0.8MV/m and 577A/m at the output power level of 144kW as show in figure-3d. At the sliding contacts of the tuner of output cavity, maximum surface current density is found to be less than 0.2A/mm at the maximum output power level, thus avoiding the chances of overheating of RF finger contacts- a main cause of failure at high power level. Similarly, 6-1/8" through line RF coupler used for coupling the RF power from the output cavity is found to be suitable to handle 150kW RF power for coupling to the accelerator cavity. As per the simulation results, wall losses in the amplifier output cavity, made of *Al*, is found to be less than 500W at full power level; offered $Q_o$ is 3.3k which is quite satisfactory.

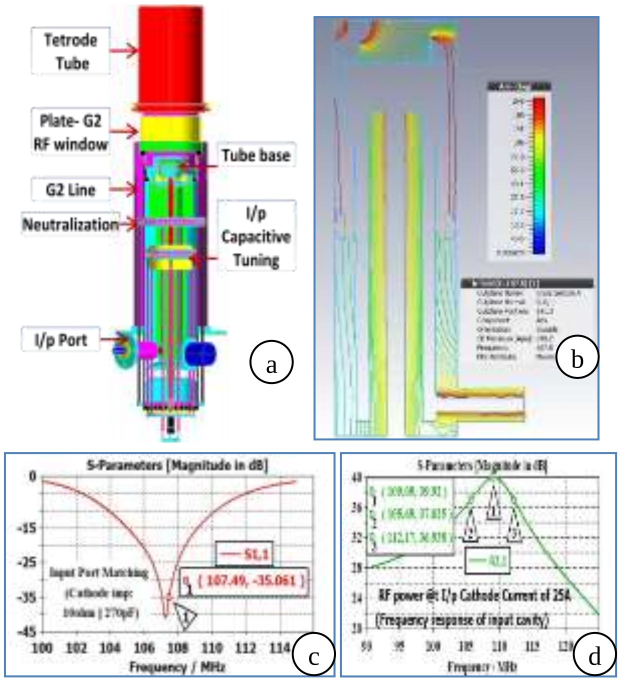


Fig. 4: (a) Input circuit assembly. (b) H-Field plot.( c) Matching at input port.(d) RF Power available to cathode.

Simulation results, shown in fig.4, confirmed satisfactory performance of I/p circuit assembly. With required RF level of 8kW at the I/p port, H-field at the sliding contacts of movable tuning capacitor and shorted stub is found to be less than 250A/m, thus the resulting surface current density is well within the RF finger stock contact rating of sliding RF contacts. 3-dB bandwidth and input matching are found to be 7MHz and 30dB respectively for a cathode input impedance range 10-25Ω. Simulation results confirmed the satisfactory performance of the RF amplifier structure realized as part of design study done for 150kW RF output at 107.5MHz.

## ACKNOWLEDGMENT

Authors would like to acknowledge the contribution of Shri Jishnu Dwivedi and Shri R S Sandha from IAD, RRCAT for their technical support and guidance in mechanical design of the structure. Authors are also thankful to Shri P Shrivastava, Director, PAG.

## REFERENCES

[1] Jain M.K., Kumar G., Deo R.K., Hannurkar P.R. Realization of 476 MHz Pulse Power cavity Amp using Planar Triode InPAC-2013 , Nov., 19-22, 2013

[2] Jain M.K., Deo R.K, Kumar G., Lad M. , "Realization of a 36-way Cavity RF Combiner at 476MHz for IR-FEL ", IEEE Applied Electromagnetics Conference AEMC 2015 , IIT Guwahati, Dec., 18-21, 201

[3] Data sheet TH781, Thales.

# HIGH STABILITY, LOW RIPPLE, PRECISION ELECTRON GUN FILAMENT HEATING DC POWER SUPPLY FLOATING AT -30 KV DC

A. Kasliwal †, V. K. Gauttam, P. Renukanath, and S. R. Tiwari
Accelerator Power Supplies Division, Raja Ramanna Centre for Advanced Technology, Indore, India.

*Abstract*

A current controlled electron gun filament heating dc power supply is required to heat the filament of an electron gun which is floated at high voltage (HV) for applications like DC accelerators, linear accelerators (LINACs), scanning electron microscope (SEM), electron beam welding etc. High stability, high energy electron beam current is required for very high resolution scanning electron microscope. This electron beam current is very sensitive towards the filament current which in turn demands a highly stable and very low ripple filament current with a setting resolution of 1 mA. A current controlled linear regulator is used in the power supply to achieve required resolution with long term stability better than ± 250 ppm of output rated current. As the supply is floating at -30 kV dc, the challenge is to control the power supply with required HV isolation of -30 kV while maintaining the desired stability and resolution. The input HV isolation is achieved by using an isolation power transformer while the HV isolation for control & read back signals is provided by optical isolators. As output current stability & resolution are greatly influenced by optically isolated analog control signal, so optical isolators with a high linearity and low temperature coefficient of gain drift are chosen.The design parameters and experimental results of the developed power supply (8V/4A) are presented in this paper.

## INTRODUCTION

The SEM is to be used for high resolution imaging of sample (specimen) surfaces being developed at BARC, Mumbai. When the specimen is irradiated with an electron beam, secondary electrons are emitted from the surface and collected by secondary electron detector. Hence, topography of the surface can be recorded by 2D scanning of electron beam over the specimen's surface. During the imaging, the electron beam current is required to be very stable. Thermionic electrons are emitted from cathode by heating of the filament and accelerated by dc electric field. The electric field is established by accelerating high voltage dc source which in turn floats the cathode & filament.  These thermo - electrons are accelerated as an electron beam. Since, the electron beam current is function of filament current, accelerating high voltage and bias voltage etc., this necessitates a high stability, high resolution filament power supply to heat the filament which is floated at high voltage. To meet the required resolution and stability with HV isolation, a hybrid power circuit topology has been chosen for low power dc application.

## POWER CIRCUIT TOPOLOGY AND HV RELATED CHALLENGES

The filament power supply (FPS) is designed and developed using hybrid power circuit topology with shielding against high electric field. It consists of a switch mode power converter as a front end pre-regulator and a current controlled series pass linear power supply as a post regulator. Basically, the pre-regulator is a switch mode isolated ac to dc power converter with fixed regulated output voltage. Since the power supply is floating at -30 kV, the major challenge is to control the power supply from ground potential while retaining the stability better than ± 250 ppm of rated output current with resolution of 1mA. Other is corona free operation with shielding against high arc current during any faulty conditions. The schematic of the power supply scheme is shown in Fig. 1.

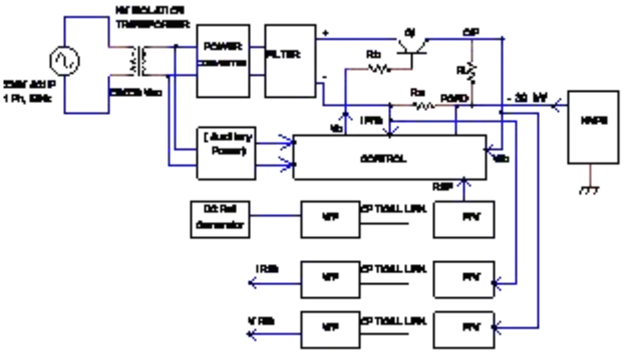


Figure 1: Schematic of power supply scheme

The rating of switch mode ac to dc converter module (power stage) is 15V/4A and is operated in voltage mode control. In second stage, a series pass linear regulator is used as a output current regulator to meet the resolution & stability requirements. The stable dc analog reference voltage is generated using LM399 IC (Max. temperature coefficient of 2 ppm/°C). This ref. voltage is converted in frequency and frequency signal is transmitted using optical link (optical fiber). At receiver end (which is floated at HV), the frequency signal is converted back to dc voltage. The received dc signal contains significant high frequency ripple which is filtered by second order active sallen-key low pass filter. Similarly, readback signals of output current & voltage are processed using optical link. Hence, HV isolation is provided for control ref & readback signals to operate the power supply from grounded system. Moreover, as the major issue in V-F / F-V conversion is nonlinearity and drift which greatly influences the accura-

† apollo@rrcat.gov.in

cy, resolution and stability of the output current. So, high linearity V-F/ F-V converter is chosen. The conversion is carried out using VFC320CP with max. linearity error of ± 20 ppm of FSR (operated in 0.01Hz to 10kHz range) & gain drift of ± 20 ppm of FSR/°C. Moreover, as the external components in V/F & F/V converter also contribute to drift with temp., so integrating capacitors with high thermal stability & custom built resistors with low temp. coeff (10ppm/°C ) are chosen. The PI controller is used in current loop for closed loop control. Since, the output current is highly sensitive towards the feedback gain, the current shunt of ± 5ppm/°C is used. The OPA27 series op-amps are used in control electronics. The design parameters of filament power supply are tabulated in Table 1.

Table 1: Design Parameters of Filament Power Supply

| S. No. | Parameter | Value |
|---|---|---|
| 1 | Output voltage | 0-8 V |
| 2 | Output current | 0 - 4 A |
| 3 | Floating voltage (max.) | - 30kV dc |
| 4 | Resolution | 1 mA |
| 5 | Type | Current Controlled |
| 6 | Stability | ± 250 ppm |
| 7 | Ac input | 230 V AC ± 10%, 50 Hz |
| 8 | Protections | O/V, O/C & Over Temp. |
| 9 | Isolation in control signals | By optically isolated V/F and F/V converters |

The HV isolation for power circuit is provided using a single phase HV isolation transformer (230/230 Vac, 100VA, 50Hz). Since filament power supply (FPS) with its power & control circuit is assembled on a PCB board which is floated up to -30 kV dc, the sharp objects in the power supply board (heat sinks, passive component's leads, soldering joints etc) leads to generation of corona discharges with hissing noise. So to curb the corona & HV discharge current, the electrostatic shielding is provided using a fabricated smooth metal box with corona ring. The filament supply is integrated with accelerating HV power supply (HVPS) in 6U height box and it is floated by HVPS. The metallic shielding of FPS greatly enhances the coupling capacitance between HV generator & FPS which give rise to significant high frequency ac component in output of HVPS and also in FPS. This capacitive coupling is eliminated by inserting a grounded metallic shield. (sandwiched in insulating epoxy sheets) between FPS & HV generator. The output connections of FPS is carried out using HV cables and a three terminal Teflon based in-house developed HV connector. The estimated max electric field at the surface of shielding box is less than 1kV/mm. All HV interconnections are made with corona free terminations.

## EXPERIMENTAL RESULTS

The power supply was initially designed, simulated and prototyped. After successful development of a table top prototype, one numbers of such power supply has been developed and tested successfully at rated power while floating at -30 kV.

Figure 2: Output current stability plot w.r.t. time.

Power supply has been tested in local mode for 5 hrs for stability test. Output current stability of less than ± 100 ppm is achieved during 5 hrs. The plot of long term stability of output current is shown in Fig. 2.

The power supply is assembled on a pcb board. The size of FPS is 150 X 200X60 mm. The developed FPS is shown in Fig. 3.

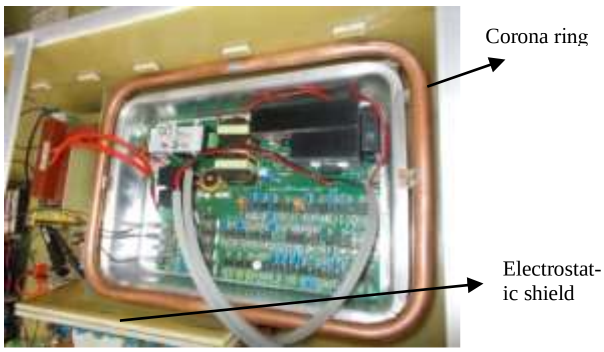


Figure 3: Developed filament power supply

The three terminal HV connector is developed using teflon as an insulating material. Corrugation is provided for required creepage path. The connector is tested up to 40 kV dc isolation with earth plate (at the centre of connector surface). The terminals are also isolated to each other up to 10 kV dc. The HV connector is shown in Fig. 4.

Figure 4: In-house developed 3 terminal teflon based HV output connector

The FPS is integrated with HVPS in a 19” rack mountable 6U height standard box. The integrated FPS with HVPS is shown in Fig. 5. The epoxy casted high voltage isolation transformer is tested up to 45 kV dc between primary & secondary. The integrated assembly is tested successfully at rated power while floating at -30kV dc.

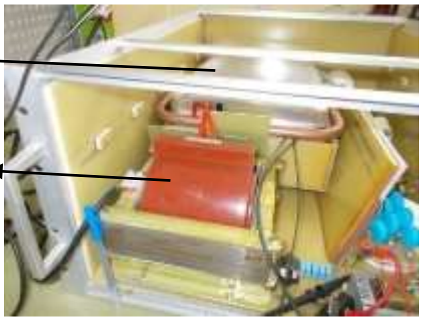


Figure 5: Integrated FPS with HVPS in a 6U box.

## CONCLUSION

The hybrid power circuit topology which include a high frequency switch mode power converter followed by a linear regulator with optically isolated reference & readback signals is well suited for high resolution, high accuracy and high stability power supply floating at high voltage for low power applications.

## ACKNOWLEDGEMENT

Authors are sincerely thankful to Mr. Amit Sahu, Mr. Deepchand, Mr. Gurupreet Singh, Mr. Nathan Singh, Mr. Milius Kujur, Mr. Chattar Singh, Mr. G. H. Ansari, Mr. M. D. Jha and Mr. Prabhu for their help in fabrication, assembly and testing of the filament heating power supply.

## REFERENCES

[1] V. K. Gauttam, Apollo Kasliwal and S. R. Tiwari, “Design and development of a high stability current controlled collimator magnet power supply with a resolution of 1mA for 10 MeV RF Linac”, Indian Particle accelerator conference (InPAC), January 9-12, 2018, RRCAT, Indore.

[2] Ajoy Sankar Banerjee, “High Precision power supply for accelerator magnets”, Proceedings of RUPAC 2012, Russia, Sept. 2012, pp. 158-160.

[3] *J. McCarthy and D. Wolff*, “Very high precision current regulated power supplies for the fermi lab antiproton source”, IEEE Transactions on Nuclear Science, vol. 32, no. 5, Oct. 1985, pp. 3778-3780.

[4] *H. Jin and S. B. Dewan*, “A combined feed forward and feedback control scheme for low ripple fast response switch mode magnet power supplies”, IEEE Transactions on Magnetics, vol. 30, no. 4, July 1994, pp. 1801-1804.

# DEVELOPMENT OF RF COMPONENTS FOR SRS INDUS-2 AND HTS

Ramesh Kumar #, Ashish K. Tiwari, Rajiv Arora, Mahendra Lad
Raja Ramanna Centre for Advanced Technology, Indore, India

*Abstract*

Six numbers of 505.8 MHz bell shaped RF cavities are installed along with RF amplifier systems in synchrotron radiation source Indus-2 at RRCAT Indore. In recent past a new indigenously developed OFE RF cavity tested up to 450kV, was commissioned in Indus-2. This cavity is working in round the clock mode with satisfactory vacuum and providing required performance during injection at 550 MeV and ramping to 2.5 GeV of the electron beam. Fabrication of spare RF cavity is also underway. A wideband (1265 MHz – 1517 MHz) stainless steel kicker RF cavity having eleven numbers of RF couplers was developed for longitudinal multi bunch feedback system (LMBFS). Eight of the coaxial couplers are shorted to ridge loaded waveguides to couple power, whereas three of them are shorted to the cavity body to damp unwanted higher order modes in the cavity. A high power Y-junction 505.8 MHz RF circulator was developed for Indus-2 using indigenous ferrites and has been in operation in one of the RF stations of Indus-2. A high power RF circulator at 650 MHz is also developed, tested and installed in the RF system of horizontal test stand (HTS). Details of the development, testing, installations, performance and important results of some of the crucial components are presented here.

## INTRODUCTION

In Indus-2 synchrotron radiation source the RF system consists of six number of RF stations connected individually to six RF cavities installed in the ring. Electron beam is injected at ~550 MeV from the existing booster synchrotron, and after accumulation the stored beam is accelerated to 2.5 GeV. RF system provides power to accelerate electron beam and to compensate for the losses due to synchrotron radiation. One of these six RF cavities is indigenously designed, developed, tested, installed and commissioned. A broadband kicker RF cavity is also developed and installed for (LMBFS) for suppressing the longitudinal multi-bunch instabilities in Indus-2 by sensing the oscillation generated from instabilities and applying suitable counteractive RF kicks through the cavity. Radio frequency components and amplifiers need protection from reflected energy at their output port. Circulators play a crucial role for these applications in RF systems where energy is isolated and directed. A three port RF circulator operating at 505.8 MHz is developed, tested and installed in one of the RF stations of Indus-2. To test and qualify high beta superconducting RF cavities at 650 MHz, horizontal test stand (HTS) facility is being established at RRCAT, Indore. To feed RF power of 40 kW at 650 MHz to SC cavity a RF amplifier is installed along with cooling water system and 6 inch high power coaxial transmission line systems developed in house. A three port RF circulator operating at 650 MHz is designed, fabricated, tested and installed at one of the RF station of HTS. Several important transmission line components for both indus-2 and HTS RF systems are developed as well.

#ramesh@rrcat.gov.in

## COMPONENTS FOR RF SYSTEM AT INDUS-2

Each RF system at Indus-2 consists of an RF amplifier either solid state or Klystron, high power circulator, RF load and transmission line system, RF power coupler, RF cavity, coolant system, low level RF system and various other control systems.

### *RF Cavity @505.8 MHz*

A bell shaped oxygen free copper RF cavity @505.8MHz was designed, developed, tested, installed and commissioned in synchrotron radiation source, Indus-2. RF cavities at 505.8 MHz earlier procured from foreign sources have been in use since 2004.

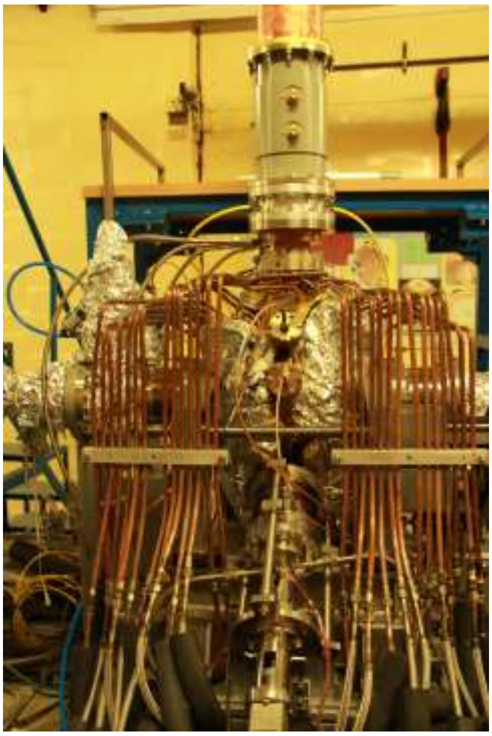

Figure 1: Installed RF cavity in Indus-2 SRS

The cavity and main power coupler parts were machined and vacuum brazed in a three stage process involving precision fixtures in each stage. RF characterization including bead pull test of the cavity were carried out before the cavity was fully integrated in a mechanical tuner along with input power coupler, several sensing couplers, higher order modes frequency shifter system, vacuum gauge and pumping system. The cavity was baked at 150ºC by recirculating hot water in situ. RF cavity was installed in the tunnel of Indus-2 and connected to a RF station through 6-1/8 inch transmission line system with installed capacity of 60kW. The cavity at fig.1 was RF conditioned and tested in CW mode up to full RF power requirements of Indus-2. After a few month of regular operation, more than 200mA at 2.5 GeV beam was achieved using contribution from this RF cavity.

### *Kicker RF Cavity*

The test RF kicker cavity to supress the longitudinal multi-bunch instabilities in Indus-2 was fabricated in stainless steel 316L with fully welded joints and ultra-high vacuum compatible coupling insertions. Alumina ceramic discs of two sizes with metallization over braze-able surfaces were used for realization of eleven number of RF couplers, all successfully brazed in hydrogen furnace and leak tested.

Figure 2: Kicker RF cavity for LMBF system

As the internal geometry of the cavity involved complicated shapes (four ridges per side), a 4 axis ball end machining followed by die sinking with electro discharge machine to remove extra material at corners, was pursued. Since the cavity is fully welded type, machining was carried out in stages to achieve good surface finish and geometrical accuracies. All the cavity parts including 11 couplers ports and 2 beam ports were TIG welded. The fully welded cavity at fig.2 was then vacuum baked at 450°C for two hours as rigorous chemical cleaning was not possible due to the multiple materials of construction and intricate inner shape of the cavity. After baking at 150°C and cool down, a vacuum level of $5x10^{-10}$ mbar in the cavity was achieved. HOMs dampening couplers were found effective in supressing the unwanted HOMs. S-parameters of the 4 set of input and output ports each were checked. In high power test the cavity could perform satisfactorily above 200 watts without heating or arcing signals. The cavity was then installed near the 6th RF cavity in LS-7 section of the indus-2 ring.

### *RF Couplers*

Couplers are crucial devices for transferring power efficiently and smoothly to an accelerating structure and also serves for sensing signals for low level RF control requirements. It essentially consist of an antenna or an inductive loop for the power coupling and a ceramic window to act as a boundary for the vacuum. A high power coupler with water cooled inductive loop and air cooled ceramic window of diameter 140 mm is developed for Indus-2 RF cavity. Several low power couplers both with antenna and loops are also developed and fitted on to the kicker RF cavity.

### *High power RF Circulator @505.8 MHz*

A high power RF circulator working at 505.8 MHz for Indus-2 RF system has been designed and developed. The circulator action is achieved by a symmetrical Y-junction strip line coupled to a magnetically biased ferrite material developed in house. Suitable transitions are used for matching the ferrite disk's lower impedance to the standard 50 Ohm impedance of the 6-1/8" EIA standard ports. The coolant tube made out of copper, bent in a complex shape was embedded in the strip line central conductor with the help of alloy and whole plate was finish machined to a high geometrical and dimensional accuracy before silver plating. Similarly the top and bottom plates of aluminium alloy supporting the ferrite discs, was provided cooling by embedding copper tube

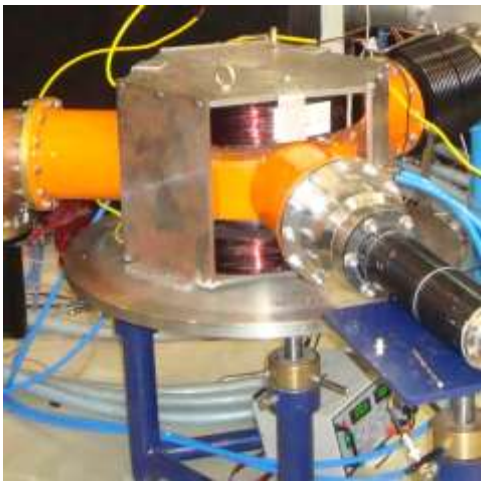

Figure 3: RF Circulator installed in Indus-2 SRS

with the help of special solder alloy in the machined channels, for getting better heat transfer. All other internal parts were silver plated and external ones were given chromate conversion coating. The mechanical assembly of circulator cavity, coaxial ports and cooling circuits were completed, followed by fixing of permanent magnet and biasing coils both sides symmetrically to the central conductor. This circulator at fig.3 is working for the last two years in RF system of Indus-2.

## COMPONENTS FOR HTS

Two 40kW solid state RF amplifiers would provide power through two power couplers to superconducting RF cavities inside HTS.

### *Transmission line system*

6-1/8 inch coaxial transmission line components are developed for erection of two sets of transmission lines from the output of the amplifiers to the cavities as shown in fig.4. Each line consists of elbows, straight sections, bellows, directional couplers, RF load coaxial to WR-1150 transition and other hardware. Similar transmission lines were also installed for two new RF cavities.

Figure 4: Transmission lines at RF cavities

### *High power RF Circulator @ 650 MHz*

A three port RF circulator operating at 650 MHz is designed and fabricated for proton accelerator applications. RF design for the matching transitions and determining cavity dimensions to house the ferrite disk was performed. These dimensions were calculated using numerical programs and closed form expressions and then finally optimized employing electromagnetic simulation software. RF parameters like VSWR/return loss, isolation and insertion loss were optimized using ANSYS HFSS and CST microwave studio. Thermal loss was calculated and cooling configuration was finalised for the central plate and ferrite. Thermal simulation in ANSYS was done to determine the optimum flow rates for central plate and ferrite cooling. After fabrication and assembly, low power measurements were found to be satisfactory. The high power test was also done where return loss of better than 22 dB and insertion loss better than 0.1 dB with isolation of 22 dB for 35 kW input power was noted with full reflection condition at output. This circulator is installed in the RF system at HTS and has been tested with RF load.

### *Coolant distribution system*

A 12 channel compact coolant distribution system is developed that controls the flow of coolant to amplifiers, circulators and RF loads with required tripping signals. Each channel is fitted with globe valve, ball valve, flow switch, temperature senor and pressure gauge for regulation. Similar systems of different size and capacity are also developed and installed at various RF stations of Indus-2.


## ACKNOWLEDEMENT

In the course of design, manufacture, chemical and vacuum processing, low and high power testing, installation and commissioning, important contributions from various groups in RRCAT, Indore is sincerely acknowledged.


## REFERENCES


[1] Ramesh Kumar, M. Prasad, A.K. Tiwari, A.K. Gupta, N. Kumar, Rajiv K. Arora, A.K. Jain, M.K. Badapanda, R.M. Pandey, V.G. Sathe, M. Lad, "High power test of indigenously developed RF cavity and RF power coupler of Indus-2", Indian Particle Accelerator Conference InPAC, TIFR, Mumbai, 21-24 December 2015.

[2] G. Mundra, S. D. Sharma, Ramesh Kumar, V. K. Bhatnagar, V. G. Sathe, R. K. Gupta, T. Veerbhadraiya, S. Sharma, K. N. Yedle, B. Sisodia, P. Ramshankar, A. K. Tiwari, M. Prasad, M.Lad, "Manufacturing of indigenous RF cavity for Indus-2", Indian Particle Accelerator Conference InPAC, TIFR, Mumbai, 21-24 December 2015.

[3] Ramesh Kumar, A.K. Tiwari, Rajiv K. Arora, M. Prasad, N. Bhardwaj, A.K. Gupta, D.K. Sharma, Akhilesh Jain, M.K. Badapanda, J.N. Rao, P. Bagduwal, Nitesh Tiwari, Ashish Bohrey, A. Karnewar, R.M. Pandey, Sanjay Gupta, R.K. Sahu, T. Puntambekar, V. Sathe, D.P. Yadav, B.K. Sindal, R. Sridhar, R.S. Sandha, Jishnu Dwivedi, Mahendra Lad, "Installation and Commissioning of Indigenously Developed RF Cavity in Indus-2", Indian Particle Accelerator Conference InPAC, RRCAT, Indore, 9-12 January 2018.

[4] Ashish Kumar Tiwari, Ramesh Kumar, Alok Gupta and Mahendra Lad, Giridhar Mundra, Sanjay Chauksey, Manjeet Ahalawat, Prashant Pareek and R S Shinde, "RF and Thermal Design, Assembly and Testing of High Power Circulator for Indus-2", Indian Particle Accelerator Conference InPAC, RRCAT, Indore, 9-12 January 2018.

# High density analog readout module on VME bus for accelerator control applications

***Abstract*—A new analog-to-digital converter, Versa Module Europa (VME) module equipped with 64 voltage monitoring channels in maximux 20V range and 12-bit resolution has been developed for accelerator control and data acquisition applications at Inter University Accelerator Centre (IUAC), New Delhi. The board design uniquely combines high density of discrete analog components with intelligent digital logic design on a 6U single width VME board. The complexity of VME slave interface for backplane bus communication along with rugged front-end (FE) analog interface controller has been implemented on a single FPGA (Field Programmable Gate Array). The board is a highest density with lowest per channel cost design on a single width 6U VME board space. The in-system programmability and reconfigurable architecture of current FPGA chips has given additional flexibility, which allows the firmware modifications through simple reprogramming. The VME slave interface, written in VHDL (Hardware Description Language), has been inducted as a core component in the firmware design, therefore eliminated the need of additional customized device for VMEbus communication. The design approach illustrates that it is inexpensive, flexible, reduce test cycle time, and gives performance comparable or superior to traditional approaches by consuming less power and board space. The analog voltage signals from the beam line devices are routed to the board with dual dynamic range of 0-10V or ±10V. The analog and memory controller design of FE analog section periodically scans all sixty-four input signals at repetition rate of 2 millisecond (ms). The electronic noise reduction in the field input signals is accomplished by adequate filtering at input stage of FE-electronics with 3dB cutoff at 39Hz. The input signal overvoltage protection is implemented by a diode clamp circuit for each channel. A four-layer PCB is designed using KiCAD software to maintain dedicated ground layer and populated with discrete surface mount devices (SMD) to accommodate high density of channels in a single width. On board DC-DC converter serves the dual purpose of high voltage requirement (5V to ±15V, 330mA) and the isolation between clean analog ground from the noise injecting digital ground. This helped in maintaining higher signal-to-noise ratio (SNR).**

***Index Terms*—analog-to-digital converter, FPGA, VME slave interface, control system**

## I. INTRODUCTION

Inter University Accelerator Centre (IUAC) [1] is a unique research facility having series of ion-beam accelerators which can deliver different ion species with energies ranging from few tens of keV (killo electron volt) to hundreds of MeV (mega electron volt) [2]. Among these facilities the major one combines 16 MV (million volt) tandem accelerator (Pelletron) with energy booster superconducting linear accelerator (SC-LINAC) [3] to deliver a powerful machine for nuclear and material science research. The research lab caters the needs of atomic and molecular physics researchers through low energy ion beam facility (LEIBF) [4]. Application based research is carried through low energy negative ion implanter (LENII) facility [5]. There is 1.7 MV horizontal tandem for accelerator mass spectroscopy (AMS) [6]. Presently all efforts has been in setting up high current injector (HCI) for SC-LINAC booster, which will considerably reduce the beam time requirement to collect useful statistics.

The diverse nature of all these aforementioned accelerators converges at the requirement of a reliable control system. A highly stable, expandable and rugged control system of an accelerator is the prime requirement for smooth functioning. Since millions of volts are involved during the machine operation, which puts stringent requirement on control system stability and reliability to avoid unwanted voltage discharges (sparks). At IUAC all these machines are equipped with indigenously developed embedded PC-based distributed control system [7]. In general, a control system mainly subdivided into two major components :

- Software component
- Hardware component

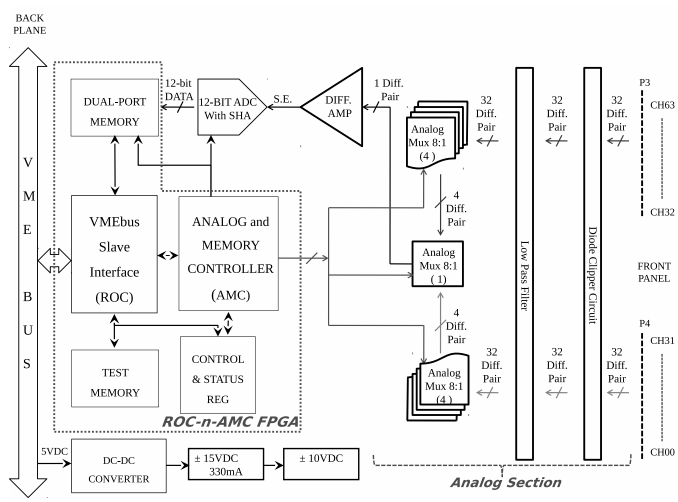


Fig. 1. Functional Block Diagram of the module

The architecture of software application program is kept similar in all of these facilities, whereas each one of them is optimized for the hardware component. The hardware configuration is decided on the basis of number of beam line devices to be monitored or controlled. With more than 1000 parameters to handle in Tandem+LINAC or HCI+LINAC combination, high density VMEbus based [8] control system is employed for this facility. The hardware component of the control system mainly integrate number of analog/digital input/output VME boards [9], [10], [11]. To cater the need of device monitoring, a high density, 64-channels, dual range, 12-bit quantization level output, analog-to-digital converter (ADC) VME board is designed. The high density of channels on a single width 6U VME board can significantly reduce the module count and hence the power consumption in round the clock operation. The higher level of stability and reliability is guaranteed by careful selection of low power consuming discrete surface mount devices (SMD). The core of the module design is implemented using reconfigurable field programmable gate array (FPGA) with maximum voltage requirement of 3.3V. The logic design on FPGA, significantly accelerate the design process of other VME bus based projects and the fuctional validation of the design is completed rapidly due to elimination of integrated circuit fabrication delays. This approach also allows adapting the functionality to account for unforeseen requirement such as additional debugging functions which can be included in the design even after completion of the circuit fabrication. With commonly available DSP (digital signal processing) blocks on modern FPGAs, a digital filter algorithms can be implemented on acquired data without additional resources on board. Due to consistently increasing fabrication capabilities of integrated circuits, the future FPGA technologies offer both higher densities and higher speeds. The overall block diagram of the module is shown in Fig. 1.

## II. ANALOG CIRCUITRY : FRONT-END DESIGN

The analog section, with 64 linear gate and stretching circuit followed by a 64:1 multiplexer are placed in the front-end (FE) of the board design. Each channel, driven from the field, is protected for over-voltage and high frequency noise using back-to-back diode circuit followed by a single pole 40 Hz noise filter. The overvoltage protected and noise free analog input is digitized by a 12-bit analog-to-digital converter, consisting of user transparent on-chip sample-and-hold (SHA), internal 10V reference, clock and output buffer stage. The fast, 12-bit ADC, with 100kSPS peak sampling allows the conversion and data storage of all the 64 channels in $\sim$ 2.0 ms ($\sim$ 33 $\mu$s per channel). The output from ADC is stored locally on dual-port memory that is implemented within FPGA. The ADC and memory control signals are generated through analog-n-memory controller (AMC) designed on FPGA device. The differential configuration gives each channel its own return path, which provides channel to channel isolation.

## III. SYSTEM DESIGN ON FPGA

### A. Read Out Controller : VME Slave interface

Instead of using application specific integrated chip (ASIC) for VMEbus communication, it is implemented on reconfigurable FPGA device along with board control logic. The advantages of this approach includes flexible functionality, lower development time and cost etc.The VMEbus slave interface on FPGA device gives freedom to change functionality at development stage according to the design requirement. VME bus interfacing is handled (for module base address decoding, successful completion of VME cycle, interrupt bus handing, bus error in case of unsucessful VME cycle etc.) by a macro residing with in the FPGA. The optimized VME core design consumes a small fraction of resources of a medium sized FPGA (e.g. XC3S400 from SPARTAN3 family). A sufficient FPGA resources remain available (after VME core macro design) for user programming to meet specific requirements. The core design of VME bus interface operates like a bridge between VMEbus and the other peripheral device controllers designed on the same FPGA device. Designing control logic on single FPGA simplifies the PCB design process to large extent. In addition using FPGA for designing the control logic reduce power consumption due to low voltage operation and interfacing (e.g., LVTTL or LVDS). All internal registers of the module can be accessed via A16/D16 or A16/D32 modes. The other modes (optional) viz. A24/D16 or A24/D32 can also be implemented in the slave design with small change in the macro (documented in the design). The core design of VME responds to VMEbus single read and single write cycles. It also responds to the block transfer BLT16 and BLT32. We have implemented the design on Xilinxs Spartan3S400 FPGA. The FPGA firmware is written as industry standard Hardware Description Language, VHDL.

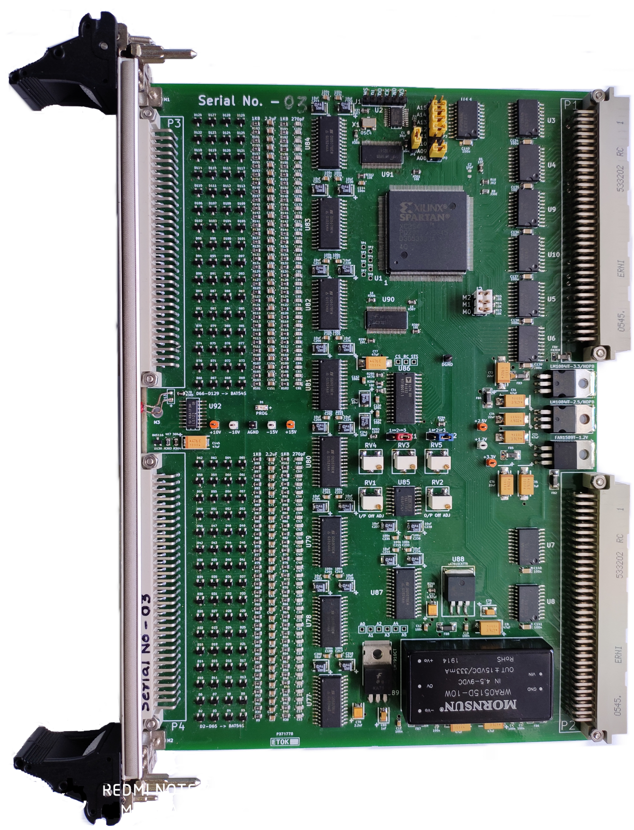


Fig. 2. (Colour online) 64-channels, analog signals readout module in VME form factor. Each channel has its own return path.

### B. Challenges faced with VMEbus interface design

As we know VMEbus interface is asynchronous, therefore any central clock does not coordinate the VME backplane signals [12]. This problem was overcome by using on board system clock and synchronized backplane signals with this system clock. VMEbus interfaces usually require delay lines to guarantee their timing parameters. These lines are not available in most FPGA chips, and so the timing parameters must be guaranteed by using external driver and receiver (buffer) chips. The buffer chips here serve two more purposes, (a) they are needed because FPGA chips lack enough drive current to drive all the VMEbus backplane signals directly and (b) they act as a level translators, since most of the VMEbus backplane signals are 5 V (TTL) compatible and FPGA signals are 3.3 V (LVTTL) compatible. The buffer chips or level translator chips are placed between the target device (FPGA) and the VMEbus connector. The synchronous RTL VMEbus interface clock is the sampling clock for the asynchronous VMEbus backplane signals and also as the system clock for the peripheral interfaces. The clock must be fast enough to sample the address and data strobes that, at their minimum low or high time, are 30 ns long. That means the minimum clock speed for the interface is 1/30 ns, or 33.333 MHz. The maximum clock speed is dependent on the data strobe skew of the backplane. The VMEbus specification limits the skew to 20 ns, which results in a maximum frequency of 1/20 ns or 50 MHz. When the VME core design is operated at the maximum speed, each read or write operation requires an average maximum of 2.5 clock cycles, or 50 ns, to complete. When the interface is connected to an equally fast MASTER controller it can operate at the maximum VMEbus data transfer rate. In our design, to keep the things simple for other peripheral interfaces, we have used 40.00 MHz crystal oscillator as the system clock.

## IV. TEST RESULTS AND DISCUSSION

The newly developed analog readout module is thoroughly tested for reliability on the test bench and sucessfully integrated with the accelerator control system. It has been installed in one of the VME servers in high current injector facility to readout beam currents, pressure values, vacuum guages etc. from beamline. It has reduced the module count to 1/4 in comparison to existing CAMAC standard, hence considerably reduced the power consumption in overall system. The power consumption is lowered further by the utilization of CMOS components in fabricating the board. Other than control system requirements, the high density VME module is useful for many applications which require a large number of differential inputs to be converted into digital form. The assembled board is shown in Fig. 2.

## V. CONCLUSION

The VMESADC64 module with 64 analog readouts and 12-bit ADC resolution has been developed successfully at IUAC. The firmware for the design is written in VHDL and ported on SPATAN3 FPGA. The module is very useful in specific to perform automation of our accelerator control and for many generic applications which require a large number of differential inputs to be converted to digital form. The features like, overvoltage protected inputs, high frequency noise filters, and jumper-selectable input signal range lend the board to fullfil majority of applications in process control, laboratory instrumentation and general data acquisition systems. The reconfigurable single FPGA carries the VME slave interface along with analog and memory controller. The high density of readout signals (64-channels) on single width VME module space is made possible with intelligent 4-layers of printed circuit board (PCB) design. Each independent channel is protected for over-voltage (+/- 12V) and high frequency noise (40 Hz single pole filter). With $\sim$ 1000 beam line parameters to monitor/control at IUAC research facility, the high density module is very helpful to lower the module count and considerably reduce the power consumption. The modularity in firmware allows the design reuse for new development prjects. The FPGA implementation allows the combination of several logic functions into one module. The higher gate-count FPGA helps in designing more complex logic applications without the need for a hardware redesign.

## VI. ACKNOWLEDGMENT

The authors (KS and Deepak Kumar Munda) acknowledge and would like to express their sincere thanks to B. P. Ajith Kumar for encouragement, Pradip Barua and Chandrapal for their help during testing of the module at high current injector, HCI, facility, and Ashok Kotahri for providing mechanical drawings in fabricating front panel of the VME module.

## REFERENCES

[1] http://www.iuac.res.in/

[2] D.Kanjilal *et al.*, "Testing and operation of the 15UD Pelletron at NSC", *Nucl. Inst. Methods in Physics A*, vol. **328**, pp. 97-100, 1993.

[3] A.Rai *et al.*, "Operational experience with IUAC Linac", *$14^{th}$ International conference on RF superconductivity-SRF2009 Proceedings*, pp. 244, 2009.

[4] Sarvesh Kumar *et al.*, "A beam optical study of new low energy ion beam facility at IUAC", *Proceedings of the DAE symposium on nuclear physics*, vol. 53, pp. 763, 2008.

[5] Devrani Devi Ksh *et al.* "Low energy Negative ion implanter facility at IUAC", *Proceedings of the seventh DAE-BRNS Indian particle accelerator conference*, vol. 47, 2015.

[6] Pankaj Kumar *et al.* "Accelerator Mass Spectrometry: an ultrasensitive dating and tracing technique", *Journal of Physics : Conference Series*, vol. 775, 2016.

[7] B. P. Ajith Kumar *et al.*, "Distributed control system for NSC tandem LINAC", *Indian Journal of Pure and Applied Physics*, vol. **39**, pp. 1-3, 2001.

[8] *VME Bus Specification VITA*, ANSI/IEEE Standard 10141987, 1987.

[9] Kundan Singh *et al.*, "VME based readout module for analog multiplexed ASICs", *International Symposium on Nuclear Physics*, vol. 55, 2009.

[10] Kundan Singh *et al.*, "High density, multi-range analog output Vera Module Europa board for control system applications", *Review of Scientific Instruments*, vol. **85**, 015105 pp. 1-6, 2014.

[11] Kundan Singh *et al.*, "64-channel optically coupled digital I/O VME board for control system applications", *DAE-BRNS National Symposium on Nuclear Instrumentation (NSNI)*, 2013.

[12] W. D. Peterson, "The VMEbus Handbook", 3rd ed: VITA, 1993.

[13] Y. N. Guo *et al.*, "A general purpose VME module", *IEEE Transactions on Nuclear Physics*, vol. **50(5)**, pp. 1752-1755, 2003.

[14] Xilinx Inc., "SPARTAN 3 FPGA Family".

# DEVELOPMENT OF DATA ACQUISITION SYSTEM FOR ECCENTRICITY MEASUREMENTSETUP OF FIVE-CELL 650MHz SCRF CAVITY

S.K.Chauhan*, S. V. Kokil, N.Nigam, B. Oraon, G.V. Kane
Raja Ramanna Centre for Advanced Technology, Indore, India

*Abstract*

RRCAT is involved in the development of multi-cell Super Conducting Radio Frequency (SCRF) cavities for high intensity proton accelerator programme. The SCRF cavities are designed to operate at a specific operating frequency with very narrow bandwidth. The cavity should be fabricated with allowable mechanical tolerances i.e. length, concentricity etc. An eccentricity measurement (EM) setup has been developed indigenously to measure the eccentricity of equatorial region of a five-cell 650 MHz SCRF cavity with respect to cavity axis. The eccentricity measurement (EM) setup consists of a set of linear potentiometer sensors, cavity rotation system and a DAQ system. A program has been developed using LabVIEW software to acquire data from potentiometers, control stepper motor to rotate five-cell cavity at different angular positions and analyze data to measure eccentricity and display it. Eccentricity of a five-cell 650MHz cavity fabricated in niobium has been measured and results were compared with co-ordinate measurement machine (CMM). The paper will discuss the details of the developed data acquisition system for eccentricity measurement setup of five-cell 650 MHz SCRF cavity at RRCAT, Indore.

## INTRODUCTION

The main function of the eccentricity measurement (EM) is to determine how close the center of each cell is to the cavity axis passing through the end flanges. In addition to this, it is also required to find how much is the centers of all cells lie w.r.t. each other. The eccentricity of the cavity cells is estimated by variation in resistance using potentiometers on eccentricity measurement setup. Sensors on EM setup touch the cavity equator region. Data is collected from START position for complete rotation in step of 5°. The voltage data from each potentiometer is used to determine the contour and centers of each cell. A program is developed in LabVIEW to acquire, analyse and display the data.

## MEASUREMENT SETUP

Major components for eccentricity measurement setup are linear potentiometers, DAQ card, cavity rotating system and LabVIEW Program (Figure. 1).

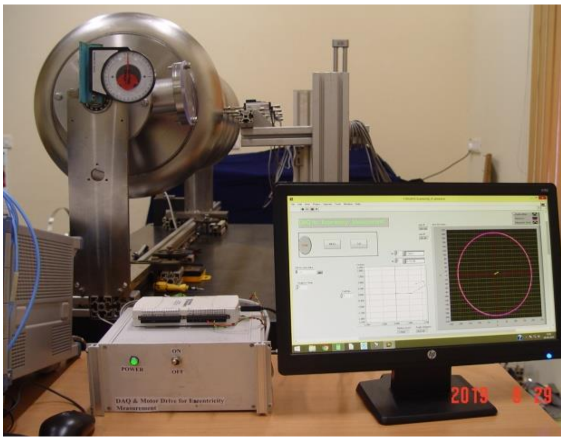

Figure 1: Eccentricity measurement setup

End flanges of cavity are assembled with flanges having self-aligning ball bearings. Flanges have accurately made holes which are used to fix with the end flanges of cavity. Positioning pins are used for aligning the centers of rotating flange and cavity flange. Special type of self-aligning ball bearings are used which help in permitting the cavity freely though it may be in deformed shape (bend, banana shape etc.). Setup has two bearing posts about which cavity rotates. One of the ends is fitted with timing belt gear drive mechanism. It helps in accurate rotation of the cavity to the desired angular position. Rotating motion is given through a geared stepper motor having a 100:1 gear ratio. A micro stepping drive is used to drive the stepper motor. The Eccentricity measurement system sensors are a single point, linear potentiometer sensors with roller. One potentiometer per cell is positioned on equatorial region using positioning setup. Potentiometer has a linear stroke of 25 mm. A pre-loading of about 3 mm is ensured while positioning them. To get good accuracy in the results, care is required to position the potentiometers passing through the horizontal plane of cavity rotating axis. An angle finder is used note down the measurement reference position.

## DATA ACQUISITION SYSTEM

An NI USB-6218, 16 Bit, 250 kS/s isolated M-Series MIO DAQ card is used to measure the potentiometers voltages and control the stepper motor.

#skc@rrcat.gov.in

The transfer function of the system is 2.5 mm/1V. To avoid common mode voltage noise differential input mode is used. A GUI is developed in LabVIEW software to control the stepper motor and acquire voltage from potentiometer at each step. This data is analysed to calculate the center of each cell and display the results. Figure 2 shows a screen shot of the GUI developed in LabVIEW software. To get good amount of data, cavity needs to be rotated for 360 degrees in steps of 5 degree each. In the measurement mode of GUI, initially, readings of potentiometers are recorded by the DAQ system as reference. Then cavity rotation start command is given by the program. At the completion of rotation step, readings of potentiometers are acquired after a delay of 1s. Delay time ensures the stable reading of the sensors. This process continues till the specified number of steps. After acquiring the full data for 360 degree along equator region, program in LabView calculate the centers of each cell and display the results.

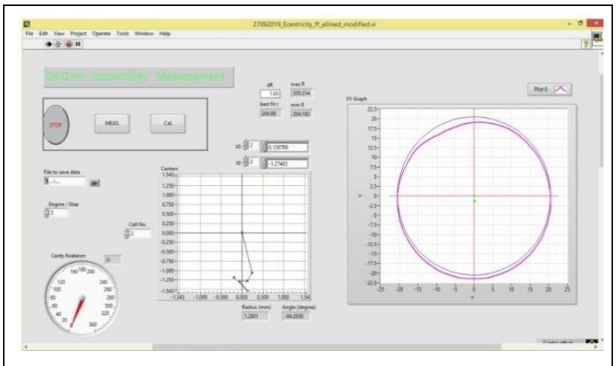

Figure 2: Screenshot of GUI of the developed software.

## CLACULATIONS

The potentiometers voltage ($V_{sensor}$) is converted into the radius r by using the following expression:

$R=r_{dummy}\pm K_{Sensor} x V_{sensor}$;
$K_{Sensor}$= 2.5 mm/V.
$x_i$ ,$y_i$ components
$x_i$ =r(cell#,i) x cos($\theta_i$) ,
$y_i$ =r(cell#,i) x sin($\theta_i$),
X= [$x_1$, $x_2$, $x_3$,…..$y_i$]
Y= [$y_1$, $y_2$, $y_3$......$y_i$]

Using "Fitting on a Sphere", these array of X and Y components are converted into the cell center.

## MEASUREMENT RESULTS

### *Dummy Cavity*

A machined dummy cavity with known eccentric disc was mounted on EM setup (Fig. 3) and measurements were carried out. In order to calibrate the system eccentricity of the dummy cavity was measured by the developed system. Eccentricity of same dummy cavity was also measured by a Coordinate Measurement Machine under same conditions. Results are found to in agreement and tabulated in Table1.

Table-1: Comparison of center of dummy cavity.

| Cell No. | Eccentricity Measurement Setup | | Coordinate Measurement Machine | |
|---|---|---|---|---|
| | X | Y | X | Y |
| Flange 1 | 0.231 | -0.201 | 0.244 | -0.263 |
| Flange 2 | 0.138 | -0.186 | 0.121 | -0.275 |
| Disc | -2.783 | -0.399 | -2.895 | -0.349 |
| Flange 3 | -0.038 | -0.163 | -0.099 | -0.299 |

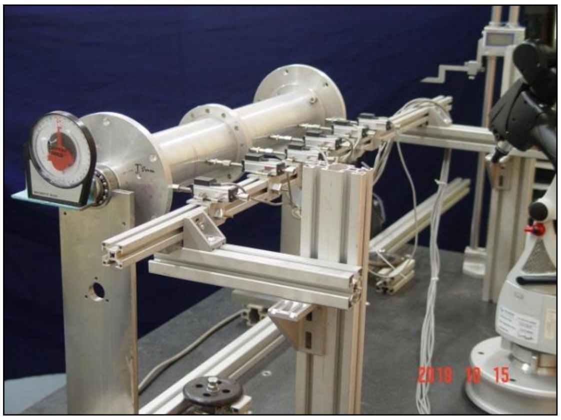

Figure 3: Eccentricity measurement of dummy cavity.

### *Five cell 650 MHz SCRF Cavity*

Eccentricity measurement of the five cell 650MHz SCRF cavity has been carried out by the EM setup and by the CMM. Eccentricity measurement of the cavity by the Coordinate Measurement Machine under same conditions is done by taking points on the equator region. However data up to 270 degrees was measured using CMM due to mechanical constraints. Table 2 shows centre coordinates of the cells measured by EM setup and Coordinate Measurement Machine.

Table-2:

| Cell No. | Eccentricity Measurement Setup | | Coordinate Measurement Machine | |
|---|---|---|---|---|
| | X | Y | X | Y |
| Cell 1 | 0.004 | -0.671 | -0.019 | -0.678 |
| Cell 2 | -0.068 | -0.790 | 0.026 | -0.856 |
| Cell 3 | -0.242 | -0.723 | -0.192 | -0.672 |
| Cell 4 | 0.006 | -0.736 | 0.048 | -0.859 |
| Cell5 | -0.315 | -0.352 | -0.242 | -0.526 |

## CONCLUSIONS

A data acquisition system for eccentricity measurement of five cell 650 MHz SCRF cavity has been developed. Measurement results of the developed eccentricity measurement setup shows close to CMM results for dummy cavity and for five-cell 650 MHz SCRF cavity.

## ACKNOWLEDGEMENT

We acknowledge Director, RRCAT and Director, PAG, Indore, for his kind support & guidance in SCRF Cavity developmental activity. We also acknowledge the support given by the colleagues of Linac Components Development Section and Superconducting Cavity Characterization and Cryogenics Section for developing the setup. We are grateful to Shri Anurag Chaturvedi who inspect the cavity by CMM and provide the measurement data.

## REFERENCES

[1] Report on Automatic Cavity Tuning Machines Project for9-cell TESLA Type Cavities

March 28, 2008 Prepared by: Ruben Carcagno, Fermilab

[2] CAVITY TUNING MACHINE CONTROL SYSTEMTECHNICAL REPORT

Contributed by:

D. Bhogadi, R. Carcagno, T. Khabiboulline, S. Kotelnikov, A. Makulski, J. Nogiec, R. Nehring, A. Quadrelli, W. Schappert

Fermilab, Batavia, IL 605

# DESIGN AND DEVELOPMENT OF LOW LEVEL RF (LLRF) CONTROL SYSTEM FOR RF TRANSMITTERS OPERATED AT 37.8 MHZ

T. K. Mandi#, H. K. Pandey, D. P. Dutta, A. K. Jain, S. Dechoudhury, A. Bandyopadhyay, V. Naik
VECC, Kolkata

*Abstract:*

A Radioactive Ion Beam (RIB) facility has been developed at VECC, Kolkata which has a beam line consisting of a series of RF linear accelerators. All the linear accelerator cavities require separate RF power amplifiers with proper amplitude, phase and resonance frequency tuning and control system. High stability of the RF amplitude and phase (~ 1.0% & ~ ± 0.5° respectively) is required in these accelerators for proper and efficient acceleration of ion beam. A Low Level RF (LLRF) is designed on amplitude and phase modulation-demodulation technique to regulate the amplitude and phase of the RF cavity voltage through a fast electronic feedback mechanism. A level and phase control circuit for four RF transmitters has been developed and tested. A GUI has been developed in NI LabView to control and monitor the amplitude and phase of the individual RF transmitters.

## INTRODUCTION

This development is related to the post-acceleration scheme of the Radioactive Ion Beam (RIB) [1-2] accelerators. The RIBs will be produced when a suitable target is bombarded with light ion beams from the cyclotron. The reaction products will be ionised and the RIB of interest will be selected using an isotope separator. The selected RIB at this stage will have energy ~1.5 keV/u. The RIB will be accelerated further using a heavy ion Radio Frequency Quadrupole (RFQ) [3] and five linear accelerators (LINACs)[4] to about 1.04 MeV/u. There will be five re-buncher cavities for longitudinal acceptance matching within this accelerator chain. All these eleven RF cavities (RFQ, five LINACs and five Re-bunchers) should be operated at the designed RF amplitude and phase for the efficient acceleration of the RIBs.

A Low Level RF (LLRF) control module has been developed and successfully tested which would ensure stability of RF power and relative phase of individual RF accelerating cavities by automatic tuning of RF input signal parameters under locked condition. In order to maintain the phase reference, the input power to all RF cavities is derived from the same signal generator. The RF distribution system distributes the signal generator output signal in 8-ways. The LLRF controller accepts the input power from the RF distribution systems. The input power is attenuated and phase shifted based on the value set by the user in the LLRF controller and fed to an RF amplifier. The output of the RF amplifier is fed to the RF cavity. The amplitude and phase of the power fed to the cavity is obtained from the RF pickup inside the cavity. This pickup signal is the feedback signal to the LLRF controller. The block diagram of the LLRF controller is shown in Figure 1.

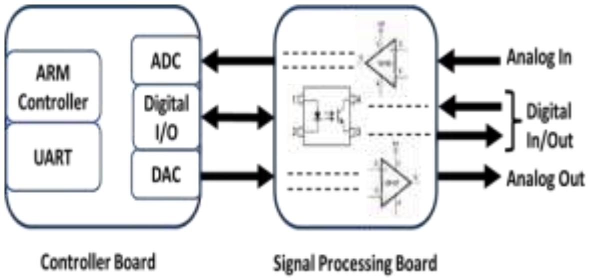


Figure 1: Schematic of LLRF control system

### *Design of LLRF control board*

At present LLRF control system is based on the conventional analog amplitude and phase modulation method, which is operates from local control panel only. The LLRF system needs to be upgraded to digital amplitude and phase modulation and demodulation based LLRF control. A schematic diagram of the digital low level control system is shown in Figure 2.

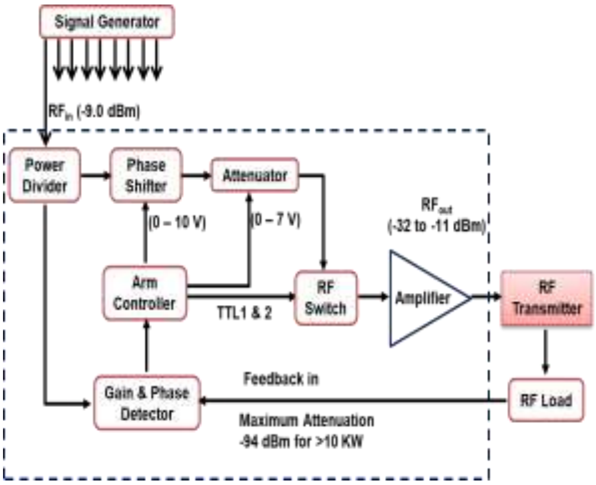


Figure 2: Schematic of LLRF control system

The frequency and voltage of the cavity may change due to cavity warming and other beam related effects. The system has been designed to compensate the input amplitude and phase with the variation of the cavity voltage and phase variations within a reasonable response time.

tkmandi@vecc.gov.in

## *Development of LLRF control board*

The control board for LLRF is designed and developed with "NXP Semiconductors" make ARM controller LPC2478 which is designed around a 32 bit ARM7TDMI-S CPU core with real time debug interfaces that includes both JTAG and embedded trace. Ten bit successive approximation type ADC with a conversion time ≤ 2.44 µs and 12-bit DAC with settling time of 8 µs have been used for the LLRF control. The controller and hardware digital I/O, which are in different voltage levels are isolated by using TLP521-6 opto-couplers. The Schematic design of control board and signal processing board is shown in Figure- 3 shows the actual picture of the fabricated boards.

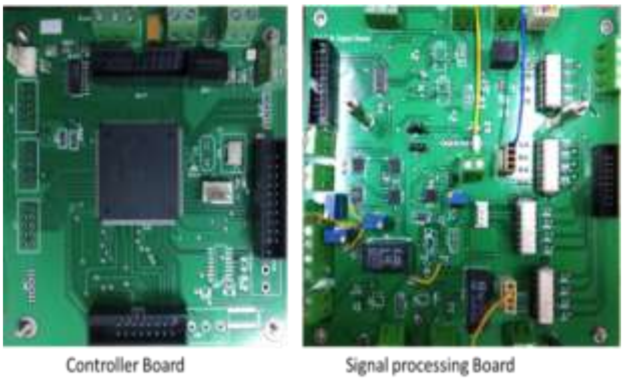


Figure 3: control board and signal processing board

The property of the voltage variable attenuator is such that when the amplitude is changed, phase also changes and likewise for voltage variable phase shifter. The aim of this control system is to control the amplitude of the RF input signal when phase is constant and vice versa. The feedback signal is processed through the controller to ensure the fine tuning of the RF parameters. The software programming for controller is written in keil-C language. The loop time of the controller is around 430 µs.

## *Development of LLRF hardware system*

The control unit with front side and rare side are shown in Figure- 4.


Figure 4: Control unit, front side and rare side.

The hardware systems developed by using voltage variable attenuator & phase shifter, RF switch, gain & phase detector module, RF amplifier etc. The RF gain detector and phase detector have been realized by using AD8302 modules. The voltage variable attenuator ZX73-2500 IC is used to control the RF output amplitude and voltage variable phase shifter JSPHS-51+ IC is used to phase shift the RF signal. RF switch RSW-2-25PA+ IC of high isolation (~50 dB) is used for fast switching. This switch is controlled by 5V TTL pulse. All the hardware has been assembled in a 19" box with all the controls at the front panel and RF input and output signal connectors at the back panel.

## *LLRF hardware Test and results*

After assembly of the hardware, the LLRF module was tested in the laboratory. During this test, external voltage variable attenuator and phase shifter were used at the output of the controller to mimic the RF load. Two phase shifter modules were used to produce a phase shift of 360˚. Amplitude was set by the voltage variable attenuator. The controller RF output power varies from – 27 dBm to -8.3 dBm at fixed RF input power of –9.0 dBm and phase variation of 0 – 360˚ as shown in Figure- 5.

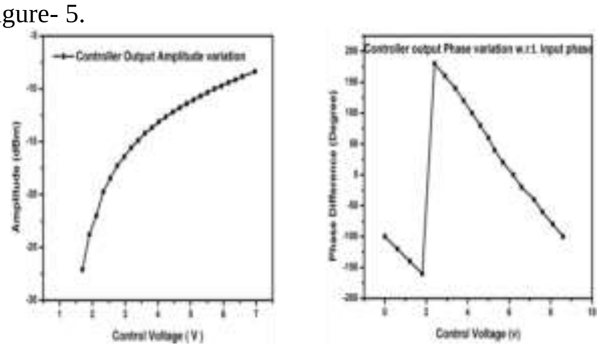

Fig-5: Amplitude and phase variation w.r.t. control voltage.

The performance of the LLRF module was also tested with a step input voltage during the laboratory test. The response of the LLRF module is shown in Figure- 6, with the level loop on condition, the output comes back fast to its original set value.

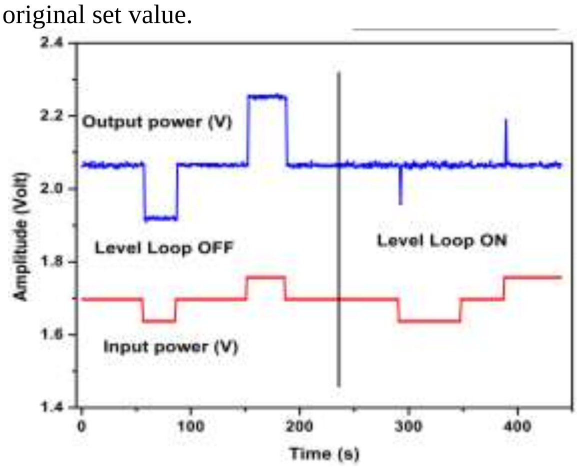


Figure-6: Performance of the LLRF module for a step inputvoltage during lab testing

### *LLRF hardware field test and results*

The LLRF module was put in to field test by connecting it to the LINAC-2 system and checked in different conditions. Performance of the LLRF controller during field testing with LINAC-2 is shown in Figure-7. Initially 2.4 KW RF power was fed to the cavity at level loop off and phase loop off (condition-1). Due to the heating of the cavity, the phase and amplitude changes with time. When both level and phase loop are off, a change of input RF phase in the controller significantly changes output amplitude (condition-2). However, when level loop is on, for a change of input phase the amplitude is constant (condition - 3).When both level and phase loops are off, a change of input level in the controller significantly changes the output phase (condition - 4). However, when the phase loop is ON (condition - 5), a change in input level does not change the output phase. When both level and phase loop ON (condition - 6) there is no change of amplitude and phase with respect to time.

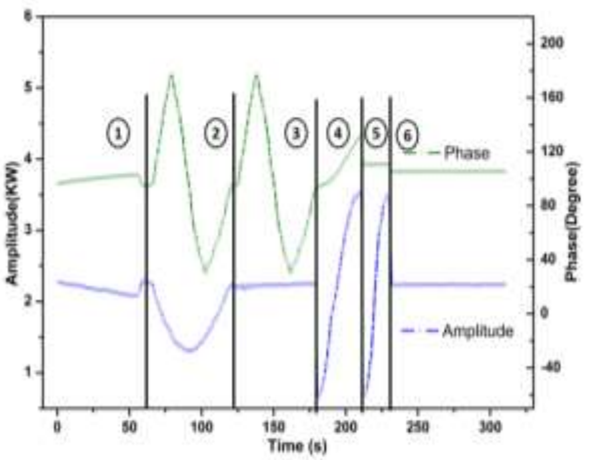


**Conditions:**

1. **Level Loop OFF, Phase Loop OFF**
2. **Level Loop OFF, Phase Loop OFF, Change Phase**
3. **Level Loop ON, Phase Loop OFF, Change Phase**
4. **Level Loop OFF, Phase Loop OFF, Change Level**
5. **Level Loop OFF, Phase Loop ON, Change Level**
6. **Level Loop ON, Phase Loop ON**

Figure 7: Field test performance of the LLRF controller

The LLRF module was further tested for different power levels. Amplitude and phase errors were introduced and the output amplitude and phase levels were monitored. Example of one such test is shown in Figure 8. The plot shows the output power level when the input power was subjected to a step voltage fluctuation of 10% while operating at 4 kW power for both loop off and loop on conditions. When the loop is on, the power comes back fast to the set value level. During long testing, the amplitude stability in this case was been found to be within ±0.5% of the set value and the phase fluctuations were within ±0.5˚ with respect to the average value.

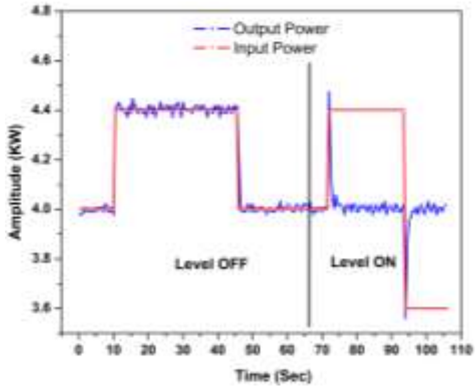


Figure 8: Response of the LLRF controller during testing with LINAC-2

### *GUI development*

The controller can be operated from local panel or remote interface through serial port. The graphical user interface (GUI) has been developed using NI LabView software shown in Figure 9. The software has provision for setting the output signal amplitude at level loop off and phase at phase loop off as well as monitors the amplitude and phase of the RF feedback signal. The GUI software has an option for store the data in text file for later analysis.

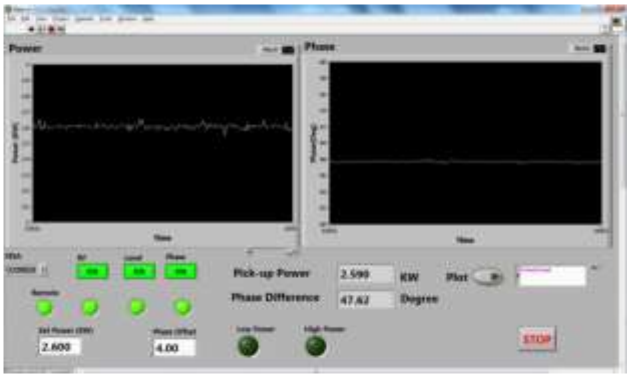


Figure 9: GUI for LLRF control and monitor

## CONCLUSION

An auto tuning method has been formulated and implemented in the controller for correction of amplitude and phase with minimum response time. The proposed tuning method is fast and does not require complex algorithm to tune. All the hardware used in the control system has been tested individually as well as testing of the integrated system along with the amplifier and cavity has been done.

## REFERENCES


[1] A. Chakrabarti, Nucl. Instr. and Meth.B 261 (2007) 1018.
[2] VaishaliNaik et al Nucl. Instr. and Meth.Phys. B (2013).
[3] S. Dechoudhury et al,Rev. Sci. Instrum. 81, 023301 (2010).
[4] A. Bandyopadhyay et al., Proc. PAC08, BC Canada.
[5] H. K. Pandey et al, Proc. IPAC’10, Kyoto, Japan.

# EPICS DAQ SYSTEM FOR BEAM POSITION MONITORING OF SPIRAL2 LINAC AT GANIL

Sandeep Bharade[#], Gurunath Randale, A.Agashe ,Paresh Motiwala, Gopal Joshi, BARC, India
Frank Pillion, Djaid Zouaoui, Dominique Touchard, GANIL, Caen, France

*Abstract*

SPIRAL2 at GANIL, France is a high intensity particle accelerator designed to produce exotic beams and driven by multi-beam superconducting LINAC. It shall accelerate lighter ions like protons, deuterons and heavy ions like nickel. A Beam Position Monitor (BPM) system is one of the most essential system for the operation of SPIRAL2, measuring various beam parameters assisting in accurate tuning of the LINAC. ACnD, BARC has designed, developed and commissioned 20 VME based BPM electronics modules with VHDL firmware and EPICS DAQ software across the LINAC of SPIRAL2. The EPICS DAQ system has been developed which adheres to SPIRAL2 command control architecture. This paper describes the detailed realization, the system performance, and the current status of EPICS DAQ system.

## GENERAL DESCRIPTION OF SPIRAL2

SPIRAL2 facility is being installed and commissioned in Caen, France. It is driven by a multi-beam superconducting LINAC designed to accelerate 5 mA deuteron beams up to 40 MeV, proton beams up to 33 MeV and 1 mA light, heavy ions (Q/A = 1/3) up to 14.5 MeV/A. In the future it shall also accelerate heavy ions Q/A = 1/6. The Linac is composed of 19 cryomodules: 12 contain one $\beta = 0.07$ cavity and 7 contain two $\beta = 0.12$ cavities. All cavities in the cryomodules operate at F = 88.0525MHz. . SPIRAL2 nominal mode of operation is planned to be C.W. mode.

## THE BPM DAQ ARCHITECTURE

### *System Layout*

The hardware architecture is based on VME form-factor with MVME5500 as controller. Each BPM sensor feeds a four input electronic module through 80m long coaxial cables [2]. The 20 BPM electronics modules are located in VME 64x crates. Each module consists of an analog board sitting on the rear side of the VME backplane and a digital board on the front side. The electronic board is able to work at 88.0525 MHz or its harmonic at 176.1050 MHz to deliver the required information.

The software architecture relies on VxWorks and EPICS. The BPM IOC, BPM Record EPICS DB, BPM record support, BPM Device Support and MVME BSP Driver correspond to the software components developed for the control and operation of the BPM system. The BPM driver interfaces the BPM hardware with the rest of the BPM IOC on Master VME CPU board. For this purpose, it uses the VME bus to exchange signals and data. The OPI is provided using CSS-BOY which access BPM custom record PV for BPM configuration and data acquisition as shown in figure 4.

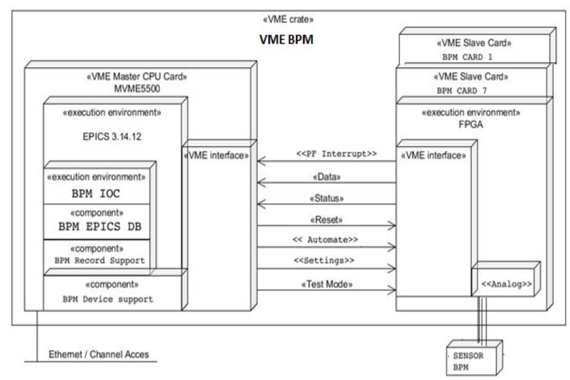


Figure 1: System Deployment View.

The EPICS system has been chosen as the basic framework for command control. The Spiral2 Control System is designed with a typical EPICS architecture, relying on OPI Clients and IOC servers communicating using Channel Access (CA) protocol. Figure 2 depicts the EPICS architecture. The highlighted parts show the custom record support, device support, interrupt service routine and database development for Bpm IOC application.

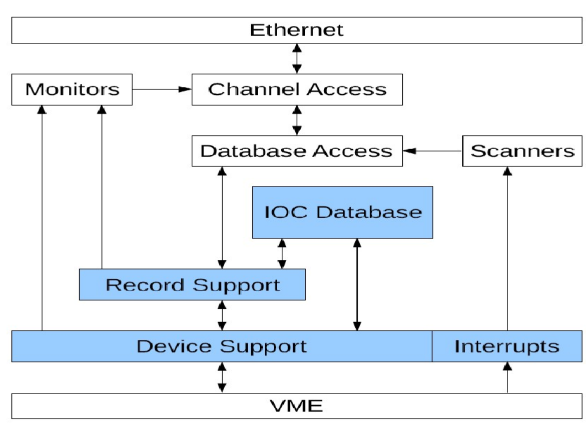


Figure 2: EPICS architecture and custom support development.

### *SPIRAL2 top Layout*

The software is being developed using SPIRAL2 topSP2 template for EPICS [1]. The following command generates SP2 template

makeBaseApp.pl -t topSP2 -i Bpm

The generated directory structure helps to adhere to standard form of application development for SPIRAL2 control system. The generated directory structure is maintained using subversion control system at GANIL server.

### *Acquisition Modes*

Data and beam parameters from each BPM system are acquired in three modes viz; Normal Interrupt, Post Mortem and Bunch shape reconstruction modes. All the modes of acquisition are supported for both pulsed and CW operating mode of the LINAC.

### *Calibration*

The BPM system is designed to meet a set of stringent specifications which is possible only if the BPM electronic cards are well calibrated before its commissioning in the accelerator system. There are a few different types of calibration procedures viz; Initialization process, Absolute K constant generation process and Cable calibration constant generation process. Initialization process is required to be carried out to generate constants for the pair of cards to equalize the differences in the four analog channels. Absolute K constant (ABS_K) is required to correctly measure absolute power of input signal in dBm. The Cable calibration constant generation process is required for compensation in cable phase due to temperature variation.

### *Gain Equalisation and Automation*

The ‘Gain Equalisation’ feature automatically equalizes vector gain of the analog channels thus guarding against drift due to temperature variations and ageing. The scheme uses an internally generated stable signal with frequency offset from that of main RF.

The system supports the feature of ‘Automation’ for automatically setting all the required settings/parameters in the system depending upon the beam intensity so that required levels of signal available at the ADC inputs results into optimum performance over the entire beam position range at a given beam intensity.

### *Normal Interrupt Acquisition Mode*

In normal interrupt modes 16 measures viz; Amplitude and phase of the four electrode signals and RF reference, corresponding vector sum, phase shift between the vector sum and the RF reference, X-Y beam positions and ellipticity are continuously acquired and stored in the internal memory of the FPGA at a rate of 10 µs. An average over N (N=2n) acquisitions as predetermined by the operator is sent to the card via EPICS. As shown in figure 3, the SF signal is timing signal which is distributed to all the SP2 equipment and indicates the presence of beam when high and absence of beam otherwise. An acquisition signal is synthesized in the FPGA which ensures start of data acquisition after delay of ΔD set by the operator via EPICS.

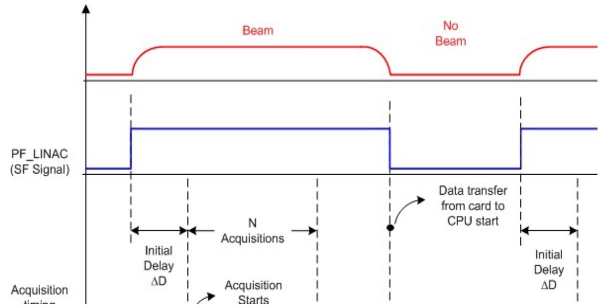


Figure 3: Normal Interrupt Acquisition Mode

The system supports multi-pulse averaging wherein it allows the operator to set the averaging value of N such that the acquisition time exceeds the pulse time and acquisition takes place in multiple pulses. The data is stored in the internal memory of the FPGA after every SF pulse and interrupt is generated to transfer the data to the VME local memory. The acquired data per pulse is further stored in circular buffer by EPICS IOC up to NO_OF_PULSES PV set by operator. The multi-pulse averaging is done in EPICS. During C.W. mode a dummy signal “SF” is distributed to fix the measurement repetition rate.

### *Post mortem Acquisition Mode*

In Post Mortem acquisition mode data corresponding to amplitude and phase of all the four channels is continuously written in external memory at 10µs rate in circular fashion. When an operating accelerator accidentally suffers from malfunction (beam breakdown for instance), a stop acquisition signal is made available to the BPM electronics by the “Machine Protection System” and the acquisition stops. An interrupt is generated by the BPM system and pre-trigger information signifying “Post mortem data” is sent to the local VME memory under DMA. Post Mortem data corresponding to 2.5s is available for analysis.

### *Bunch shape Reconstruction Mode*

A special data acquisition mode called “Bunch shape or Electrode signal Reconstruction Mode” implemented. It allows the capture of one beam bunch over 345 RF pulses (3.9µs). This special mode of operation is expected to provide information on the behaviour of the running of the LINAC.

## PERFORMANCE ANALYSIS

The shortest duration of a macro-pulse will be 100 us. The repetition rate may be as low as 1Hz and as high as 1 kHz. The intermediate configurations have to be taken in account in order to reach the C.W. operation. The step to increase or decrease either the macro pulse duration or the repetition rate will be 1us. The FPGA register size required to store the measures with a maximum averaging capability of 65536 is as shown below:

- Amplitude and Phase of the four electrodes = 8 x 33bit = 264bit

- Amplitude and Phase of the RF Reference = 2 x 33bit = 66bit
- Amplitude and Phase (w.r.t. the RF Ref) of the vector sum of the
- four electrodes = 2 x 33bit = 66bit
- Beam X&Y position = 2 x 33bit = 66bit
- The ellipticity of the beam = 1 x 33bit = 33bit
- Total = (15 measures) = 495bits

After completion of acquisition, averaged data will be written to other registers in the FPGA and will be available for transfer to VME local memory. The size of these registers required to store each set of averaged measures for each BPM system is as shown below:

- Amplitude and Phase of the four electrodes = 8 x 16bit = 128bit
- Amplitude and Phase of the RF Reference = 2 x 16bit = 32bit
- Amplitude and Phase (w.r.t. the RF Ref) of the vector sum of the
- four electrodes = 2 x 16bit = 32bit
- Beam X&Y position = 2 x 16bit = 32bit
- The ellipticity of the beam = 1 x 16bit = 16bit
- Total = 240bits (=30bytes)

Assuming a maximum of 7 BPM systems in each chassis and for a SF signal rate of 1 KHz, 210 bytes of data will be transferred to VME local memory in 1ms.

As compared to Automation scheme implemented in the EPICS code and requires number of SF pulses to automatically set the system parameters, a fast automation scheme requiring just 60µs is implemented in the FPGA firmware.

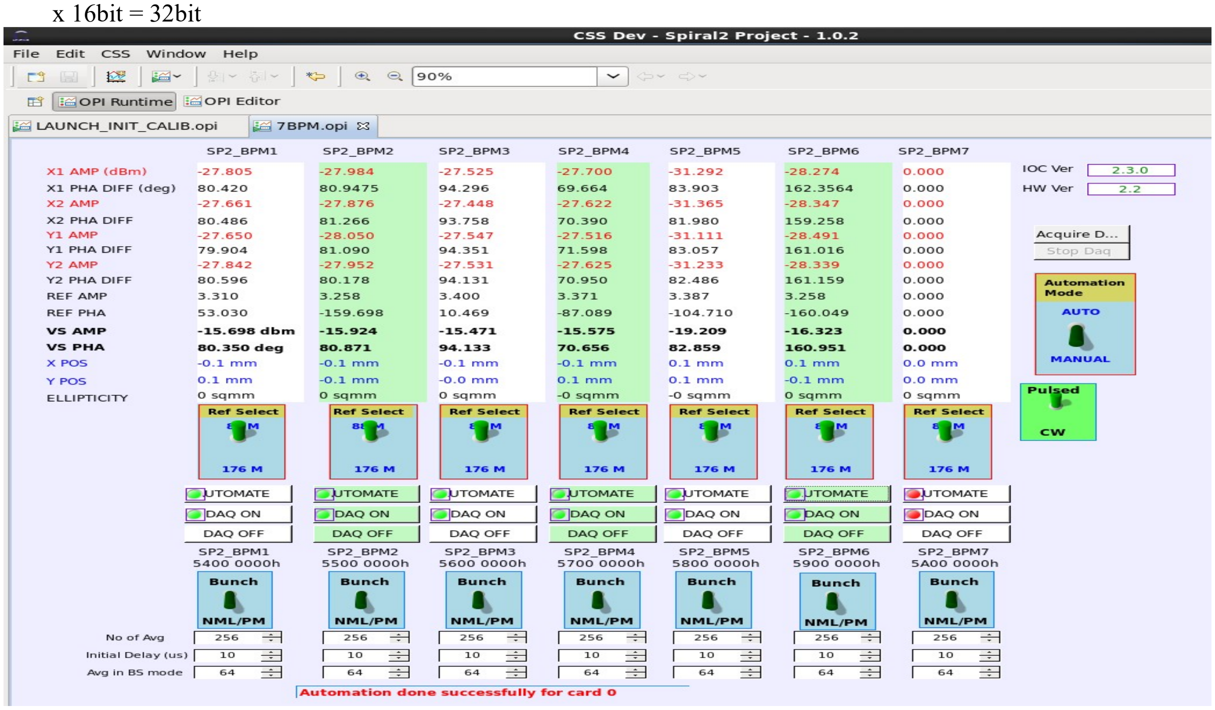


Figure 4: CSS BOY Display

## CONCLUSION

The EPICS device support, record support and bpm custom record has been implemented and one IOC can support 7 BPM system per chassis. Although the single VME board generates an interrupt, it was possible to realise each BPM as an independent system and can be operated independently.

## ACKNOWLEDGEMENT

The authors are thankful to our colleague Smt. P. Jyothi for exhaustive testing all the cards as per the Acceptance Test Procedure (ATP) before delivery to GANIL.

## REFERENCES

[1] E. Lécorché, D Touchard, et al., “JACoW, Overview Of The GANIL Control Systems For The Different Projects Around The Facility”, ICALEPCS2017, Barcelona, Spain.

[2] P. Ausset et a. “JACoW, Development of the Beam Position Monitors system for the LINAC of SPIRAL2”, WEPC15, Proceedings of IBIC2013, Oxford, UK

# FEATURES AND QUALIFICATION TESTS OF INTERLOCK PROTECTION AND MONITORING SYSTEM FOR 7KW SOLID STATE RF POWER AMPLIFIER SYSTEM

Sujo.C.I, R T Keshwani, H.Shukla, M.Afaash, S.Bharade, J K Mishra, S.Snigdha, and Gopal Joshi
BARC, Mumbai, India

G. Chamundeswari, ECIL, Hyderabad, India

*Abstract*

A 325 MHz, 7 KW solid state RF power amplifier (SSRFPA) has been developed by Accelerator Control Division (ACnD), BARC under IIFC. The RF power amplifier has been built by combining eight, 1 KW RF power modules. Protection of the RF amplifier, against any fault conditions is achieved by monitoring RF signals, analog and digital signals from each module. External signals from personal protection system, status signals from RF Protection Interlock System (RFPI) are also being monitored. If any of the parameter monitored exceeds or goes below the set limit, protective actions are taken depending on the signal. All these objectives are achieved by integrating a high speed interlock, protection and monitoring system (IPMS) with RF power amplifier. IPMS is a VME64X based system which includes seven functional modules and monitors more than eighty parameters of the RF power Amplifier. However, it needs to undergo and pass qualification tests like EMI/C, vibration, environmental, etc. as per specified standards. This paper describes the features and design principles followed in development of IPMS. Testing aspects followed by test results of some important qualification tests are also discussed in short.

## INTRODUCTION

A 325MHz, 7KW SSRFPA has been developed at ACnD, BARC combining eight RF power modules of 1KW each. Output of a driver amplifier of 50W is split into eight outputs which are the inputs to eight 1KW modules. Forward power, reflected power, drain current, drain voltage, gate voltage and temperature of each 1KW module are monitored and displayed by IPMS. 14 bit ADCs are used to digitize the signals monitored, which are placed on mezzanine cards. The monitored signals are displayed continuously on a local display and also on a remote PC. If any of these parameters (except temp.), deviates from the set value, corresponding power module is switched off. If more than one power modules deviate from set value, all the eight modules and RF input signal to the driver amplifier is made OFF. If the temperature of any module exceeds or goes below the set value, all the power supplies and RF input to the driver amplifier is switched OFF. Status of power supplies of each power module, ambient temperature, cooling water temp. and driver amplifier temp. also are monitored.

Logic interlocks have been developed with external signals from RFPI [2], safety signal etc.

## ARCHITECTURE OF IPMS

The system consists of seven 6U, VME64x based modules housed in a 19" instrumentation rack with a VME controller. Mezzanine card approach on VME carrier card has been used to design this system for modularity and easy upgradation. Two function specific mezzanine cards have been placed on each VME carrier board and the carrier board is the same for all the modules. The modules communicate to a master controller through a rear carrier board (RCB), which is called the system control module. All digital inputs are connected to system control module. RCB's have been designed to be the same in all the modules. An interface card has been designed to interface analog and digital signals from different sub systems of RF power amplifier.

Figure 1: IPMS with VME controller

SMA connectors have been used to interface RF signals to the modules and FRC connectors have been used to interface analog and digital signals to the modules.The architecture and VME carrier boards are the same as used in RFPI [2].

IPMS is installed in a 19 inch,9U, VME64x crate with advanced EMC/ESD shielding and in- built power supplies of +/-12V, 5V and 3.3V of ultra low noise. The power supplies are self protected against any failure as under/over voltage, over current, over temperature, etc. and also have passed all qualification tests.

## CONTROL SYSTEM

Analog and RF signals of IPMS are digitized and displayed continuously on the operator console at a rate of 10 Hz/100Hz through VME bus. The data transfer rate can be controlled by a timing signal connected externally to system control module.

The control system of IPMS consists of an EPICS IOC running on a Linux based MVME controller. The IPMS can be operated either in local mode or in remote mode. 7” Industrial touch panel PC has been used for local display and control of different parameters of RF power amplifier. CSS based GUI running on a PC is used for remote monitoring and control.

## QUALIFICATION TESTS OF IPMS

Careful design, layout and component selection of modules has helped IPMS to pass all the qualification tests specified. Recommended pcb layout rules have been followed in the design so that EMI/EMC tests are passed.

The VME carrier board is a fourteen layer PCB with 8 routing layers and 6 power layers having multiple power planes. All mezzanine cards and RCB are of 6 layers. The stack set up has been selected so that the signal layers are shielded. The length and bending of PCB tracks are optimised so that the track does not act as antennas. Simultaneous sampling, serial LVDS output ADCs have been selected for online data monitoring which can be configured using SPI signals. All the LVDS lines are routed as 100 ohm differential lines and all TTL lines are routed as 50 ohm lines. The differential line lengths are matched to better than 50ps delay and the terminations are placed close to FPGA. EMI gaskets have been used on the front panel groove of VME carrier board and mezzanine cards so that RF leakage is minimised. The signal ground is made common with the chassis ground so that return path is defined for Electro Static Discharges. ESD discharge strips are provided on the board at top and bottom. All the LVTTL lines have 22ohm series resistor so as to slow down the rise time.Bi-directional lines have resistors at both the ends.

Digital temperature sensors with one wire interface has been selected since these sensors are mounted close to the MOSFETs. Isolated power supplies have been used to power the temperature sensors.

The high speed digital signals, power supply and other sensitive signals are isolated by selecting suitable connectors for mezzanine cards. Samtec connectors with integral shielding has been selected for board to board interface. Samtec connectors are optimized for 100Ω differential signals. Ground pins are also located in-between two pairs of signal pins to improve the shielding effectiveness.

RF immunity testing can interfere with sensitive analog circuits, and hence a well-grounded conductive shield has been used to protect the sensitive parts. The shield that has been developed for better isolation to use with RF measurement board is shown in figure 2.

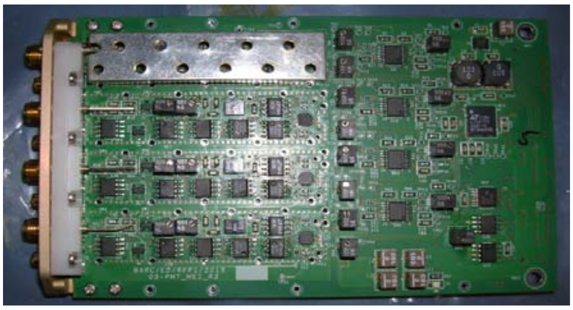

Figure 2: Shield mounted on RF measurement board.

All the analog and digital inputs from RF power amplifier and field are ground isolated using opto amplifiers /isolators.

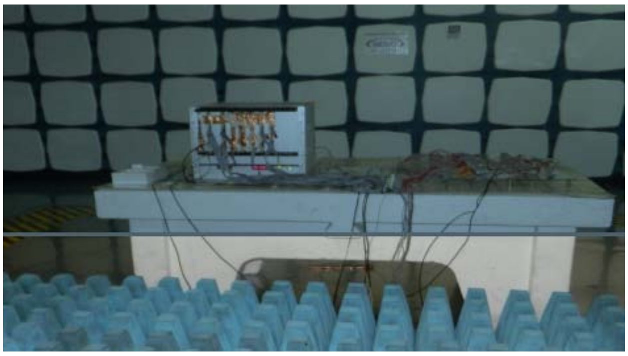

Figure 3: Test set up for IEC 61000 - 4.3

The following EMI/EMC qualification tests were conducted at ECIL.

1) Conducted/ radiated Emissions (CE & RE) test (IEC 61000-6-3 and 6-4)
2) Conducted /Radiated RF EM field immunity (CS & RS) test (IEC 61000-4-6 and 4.3)
3) Electrical fast transient/burst immunity (IEC 61000-4-4)
4) Surge immunity test as per IEC 61000-4-5
5) Voltage Dips, Short Interruptions &Voltage Variations as per IEC 61000-4-11
6) Vibration and drop tests
7) ESS tests ( thermal shock, thermal cycling, High and Low temperature tests, humidity tests)
8) Burn in tests

The system passed all the qualification tests. The VME crate was completely shielded with a perforated top cover and a back door. All the unused RF input connectors are terminated with 50 ohm and any gaps are covered with copper foils. The required inputs are connected to the system through cables running through a duct.

RE and RS tests required adequate shielding of cables and well torqued connectors. The external long cables which gives RF inputs, temperature inputs and other external inputs to the system were rerouted in order to pass these tests. CE issues are mainly because of not defining the return current paths and also due to lack of filtering at power supply. Switching power supplies may have conducted emissions issues. In IPMS it has been ensured by providing ground planes that the signal return paths are not interrupted and low impedance paths are provided for both high frequency and low frequency currents. Each VME power supply has a PI type filter with very low inductor value such that power supply drop is minimised. Combination of tantalum and multilayer ceramic capacitors with low ESR and ESL have been used so that the filter characteristics remain stable at wide frequency range. POLA power modules has been used to derive different voltages used in the modules. POLA power modules have less noise ripple and emission characteristics.

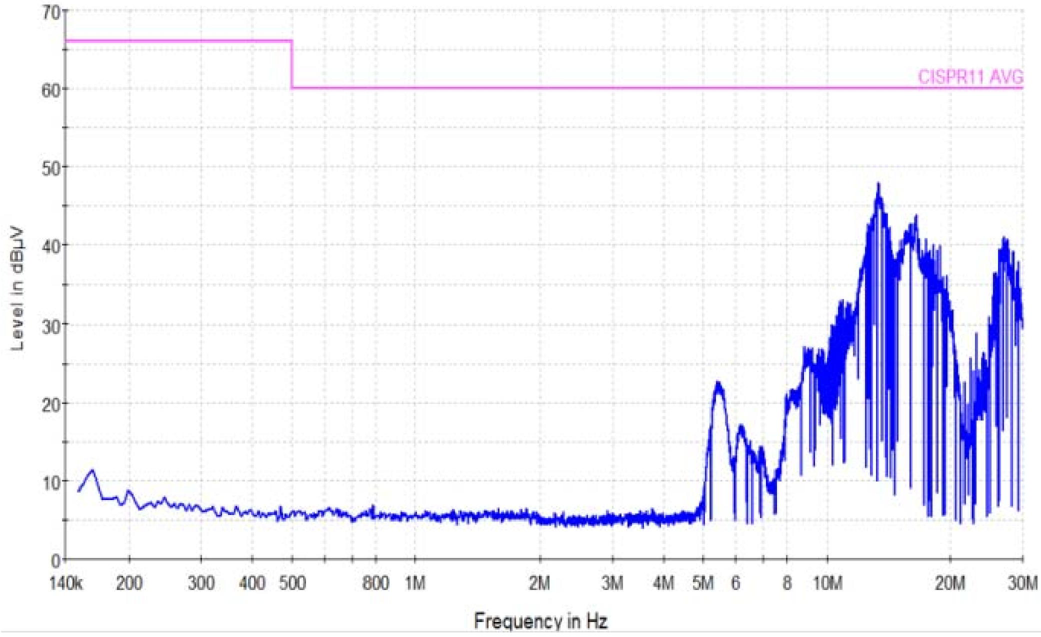


Figure 4: CE measurement 150KHz to 30MHz.

### *ESS tests*

Industrial grade components have been selected for all the modules of IPMS so that ESS tests are passed as per standards IEC 60068-2-1, IEC 60068-2-2 and IEC 60068-2-14.

### *Vibration tests*

The mezzanine card is mounted on the carrier board using M2.5 screws. One pair of screws are mounted at the rear end of the card . The card top side is fixed on to a standard PMC bezel using mounting screws (figure 2,5). The bezel is fixed to the fascia using another pair of screws. The VME modules are fixed to the crate using a pair of screws. With this arrangement vibration tests have been passed as per the standard IEC-60068-2-64. Random vibration tests were done along x,y and z directions for nearly 10 minutes.

Figure 5: Mezzannine card front panel

### *Burn in Test*

Burn in test was done at 40$^{o}$C for 48 hours and also at normal temperature integrated with RF power amplifier.

## CONCLUSION

The IPMS is qualified against all required qualification tests as per the specifications. The system is integrated with 7KW,325MHz solid state RF power amplifier and is functioning satisfactorily. The RF power amplifier will be despatched to Fermilab soon under IIFC.

## ACKNOWLEDGEMENT

We would like to thank Shri. M. M. Sutar and Smt. Charulata Shinde for their contribution in testing and realization of IPMS. We are also thankful to Shri.M. Mahesh, ECIL for his help during qualification tests.

## REFERENCES

[1] Design architecture of Interlock Protection and Monitoring System for 7KW Solid state RF power amplifier RT.Keshwani et al. Inpac 2018

[2] RF Protection Interlock System for Proton Linacs under IIFC, Sujo C.I et.al., Inpac 2018

# EPICS-based LINAC RF control system at PLF Mumbai

S. Pal[1],*, S.K. Singh[2], A. Basu[2], J.N. Karande[1], R. Palit[3], V. Nanal[3]
[1]PLF, Tata Institute of Fundamental Research, Mumbai 400005
[2]IADD, Bhabha Atomic Research Centre, Mumbai – 400085
[3]DNAP, Tata Institute of Fundamental Research, Mumbai 400005

*Abstract*
The accelerator control system of SC-LINAC booster at PLF, Mumbai has geometrically distributed architecture for RF control with modular structure. It is proposed to replace the existing control system software written as client server architecture using JAVA, with an EPICS based RF control system. A dedicated network is reserved for all the devices and computers necessary for beam operation. An Asyn EPICS driver has been developed for the existing Ethernet based crate controller. Additionally, the EPICS QT based operator interface has been developed, which is similar to previous JAVA based operator interface. The software has been tested in one local control system catering to two cryo-modules. This software has been used to control/monitor the response of various parameters. Details of this new epics-based LINAC RF control system are presented in this paper.

## INTRODUCTION

The 14 MV Pelletron accelerator was installed in December 1988 [1]. It was augmented with an indigenously developed superconducting linac booster in the year 2003 [2, 3]. The LINAC is designed for an optimum velocity $\beta_0$=0.1 at an operating frequency of 150 MHz. The superconducting linac has a modular structure with eight cryostats divided in two groups. The RF control system has been developed with Ethernet based CAMAC crate controllers (developed by ED, BARC). The DAQ related digital hardware was built around CAMAC crate controller with ISA interface controlling CAMAC Modules, e.g., DAC, ADC, DI, DO and Pulser. The control system software was written as client server architecture using JAVA as programming language, based on LINUX OS. This system is working satisfactorily for more than a decade [4,5,6].

Now we are working on the migration of the RF control system to EPICS based system [7, 8] that is a widely used and well-proven control-system framework. The substantial amount of freely available software related to the EPICS framework is also motivating this migration. A dedicated network is reserved for all the devices and computers required for beam operation. An Asyn EPICS driver has been developed for the existing Ethernet based crate controller. EPICS QT based operator interface has been developed which is similar to the previous JAVA based operator interface. The software has been tested in one local control system catering to two cryo-modules, to control and monitor the response of various parameters, namely, Loop-phase, Reference-phase, QP, Input Gain, Amplitude/Phase error, Loop on/off, Amplitude/Phase lock, and CW/Pulse mode etc.

## SYSTEM ARCHITECTURE

The LINAC control system is a distributed system. It has a multilayer architecture; there are different nodes for RF control, called Local Control Station (LCS). RF Control system has four LCSs which follow geometric distribution. Each RF LCS is connected to two cryostats. All four LCSs are connected to Master Control Station (MCS). A representative diagram is shown in Fig. 1.


Fig-1: A representative diagram of RF control system

## SOFTWARE ARCHITECTURE

Major parts of the LINAC control system are CAMAC, and Micro-controller based units consisting of electronics interface units and digital units as part of the instrument itself. The software system with CAMAC is running on QNX operating system embedded on an Intel Pentium based CPU board. Software on micro-controller based units has been developed in Assembly. An Asyn EPICS

*email: sanjoy.pal@tifr.res.in

driver has been developed for the existing Ethernet based crate controller. Each IOC writes a list of its Process Variables (PVs) and associated EPICS DB information records on this driver, which is then used by the EPICS QT based operator interface. The EPICS QT based operator interface of the LINAC RF control system is shown in Fig-2. In the new GUI, the widgets developed specifically for LINAC are using the underlying feature of the EPICS QT to communicate with the EPICS PV. The sliders are EPICS QT widgets, but they act as the sub-component of the GUI design requirement in the LINAC operator interface - which is carried out in QT. Here, the functionality of EPICS QT widget is kept intact, but additional graphics feature is included.

Fig2: EPICS QT based operator interface of the LINAC RF control system

## SUMMARY

The program to replace the existing control system software written as client server architecture using JAVA, with an EPICS based RF control system, has been initiated. An Asyn EPICS driver has been developed for the existing Ethernet based crate controller. The EPICS QT based operator interface has been developed, which is similar to previous JAVA based operator interface. The first version of the software has been tested with one local control system catering to two cryo-modules and is found to work satisfactorily over a prolonged period. The new EPICS based LINAC control system is better suited for future extensibility of the system.


## ACKNOWLEDGMENT

We thank Prof. R.G. Pillay for his guidance in the early stages work and the PLF staff for their support.


## REFERENCES


[1] K.G. Prasad Nucl. Instrum. Meth. B40/41, 916 (1989).

[2] R.G. Pillay, “Overview of the Pelletron Linac Facility”, InPAC2011 proceedings.

[3] V. Nanal et al., “Operational experience of superconducting LINAC booster at Mumbai”, HIAT09, Venice (Italy) 2009.

[4] Particle accelerator Control System, S.K. Singh et al., Proceedings of the DAE Symp. on Nucl. Phys. 55 (2010)

[5] Beam Line control System for BARC-TIFR superconducting LINAC Booster, S.K. Singh et al., InPAC2011

[6] Upgradation of Control System for Superconducting LINAC at PLF, Mumbai, S.K. Singh , InPAC2011

[7] EPICS, http://epics.web.psi.ch/software /

[8] EPICS, http://www.aps.anl.gov/epics/

# Development of Digital Feedback Control loop for 650MHz Superconducting RF cavity in Horizontal test stand

Nibandh Kumar*, Gopal Joshi, Paresh. D. Motiwala, BARC, Mumbai, India,
Brian Chase, Ed Cullerton, Phillip Varghese, FNAL, U.S.A.

*Abstract*

Under Indian Institutions and Fermilab Collaboration (IIFC) a closed loop feedback control of RF field in superconducting 650MHz, 5-cell RF cavity has been designed and developed. Digital approach is adopted for implementing the signal processing and feedback control for SC RF cavity. Use of System on Chip (SoC) based FPGA provides flexibility and configurability to the system. The complete signal chain consisting of down converter, NCO, filters, CORDIC, PI controller has been designed, modeled and simulated before implementation to achieve field stability of 0.01% in amplitude and 0.01 degrees in phase. Extensive data acquisition function for analysis and display of data is incorporated. The paper describes the design architecture and implementation of the digital signal processing in the control system.

## INTRODUCTION

A Low level RF system is responsible for maintaining a stable amplitude and phase of RF field inside an accelerating cavity which is very critical for efficient acceleration and maintaining low energy spread of beam (derived from physics experiment requirements) inside the accelerating cavity [1]. The Low level RF system is designed to maintain a field stability of 0.01% in amplitude and 0.01 degrees in phase for a 650 MHz superconducting RF cavity being brought up at RRCAT, Indore.

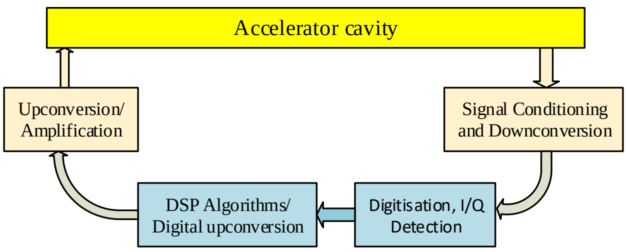


Figure 1: General description of LLRF loop

The LLRF feedback control loop is broadly described in Fig. 1. Field inside the RF cavity is picked up with an antenna probe which is translated to a lower frequency with the help of a mixer. The down-converted signal is digitized and processed inside the FPGA. The control signal is again translated to cavity resonant frequency with the help of a mixer and is fed to the cavity after appropriate amplification.

The amplitude and phase of electric field inside an accelerating cavity is kept stable with respect to a reference signal which is externally generated. The LLRF digital firmware also processes and monitors the forward signal fed to cavity and signal reflected from the cavity [2]. This monitoring is necessary to tune the coupler (responsible for coupling forward signal with cavity) and to make sure that cavity is critically coupled for the duration in which beam is present.

The LLRF system can operate in three modes

- Generator driven mode (GDR mode).
- Self-excited loop mode (SEL mode).
- Open loop mode

In GDR mode the cavity is driven with a signal with desired power and phase with respect to the reference signal. Self-excited loop mode can track the resonant frequency of the cavity within a certain bandwidth and in open loop mode, we can inject RF power corresponding to a particular power and phase into the cavity from feedforward tables.

This paper discusses the architecture of digital signal processing chain and its implementation to meet desired control and stability specifications.

## DIGITAL SIGNAL CHAIN ARCHITECTURE

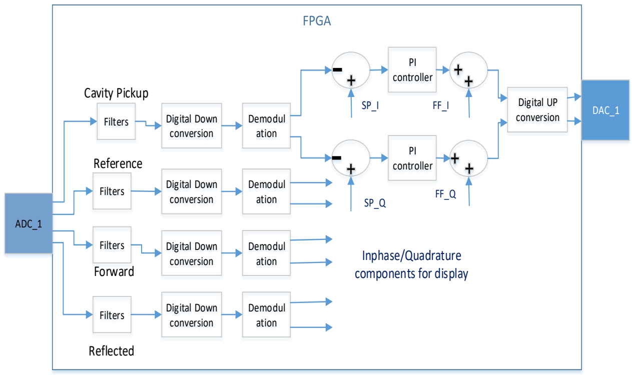


Figure 2: Digital signal chain architecture

Digital signal chain architecture is briefly described in Fig. 2. For each cavity, four signals viz; Cavity pickup, RF Reference, Forward and Reflected are processed inside the FPGA for control and monitoring purposes to obtain required functionalities from the LLRF system. All the four incoming signals to FPGA are centred at an IF of 20MHz which is digitized with a 16 bit, quad channel Analog to digital converter. Sampling frequency of the ADC is chosen to be 1320/14 MHz which is generated from a 1320 MHz mater oscillator. The incoming digitized signals are filtered inside the FPGA to remove any DC offset and provided with some processing gain by attenuating unwanted frequencies. The filtered signals are digitally down-converted to baseband using a 20 MHz digital signal synthesized from a numerically controlled oscillator which is phase locked with the RF reference signal (GDR mode).

This method of down conversion and demodulation removes the common noise introduced because of downconverter's local oscillator and ADC's sampling clock which is identical to all four input signals, within a finite bandwidth. Down conversion and demodulation scheme is shown in Fig. 3.

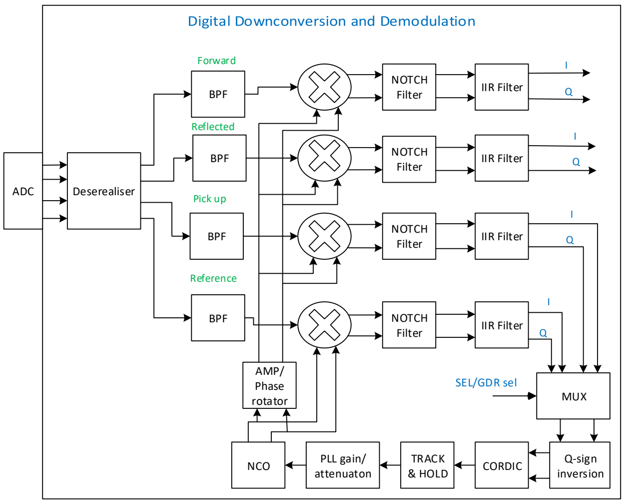


Figure 3: Digital down conversion and demodulation

Closed loop bandwidth of the LLRF loop is generally of the order of few tens of KHz. Therefore, demodulation module has been designed to cancel out common mode noise at least in the closed loop bandwidth.

## *Demodulation loop analysis*

With implemented configuration, open loop transfer function of the loop is given by:-

$$G(s) = \frac{2^{28} * f_{clk} * 6\pi * 1e5 * K}{2 * \pi * 2^{32} * s(s + 6\pi * 1e5)}$$

Here K is a programmable gain/attenuation factor present in the loop.

Total delay in the down conversion loop is around 105 clock cycles which corresponds to 1.113 µs with given sampling clock. The loop has been designed with a phase margin of 45 degrees and corresponding K value is 0.6.

Bode plot of the demodulation loop is shown in Fig. 4. The closed loop bandwidth of the loop is 78.6 KHz.

In GDR mode of operation, the demodulation loop will cancel the common mode noise in the bandwidth of 78.6 KHz which is greater than the closed loop bandwidth of the cavity and hence will help in maintaining a more stable amplitude and phase inside the cavity. The higher frequency noise which is responsible for eating up power from RF amplifier is removed by an IIR low pass filter having a 3 dB bandwidth of 300 KHz. The demodulation bandwidth of 78.6 kHz also limits the LLRF system to be able to track cavity detuning up to a range of around 80 KHz (SEL mode).

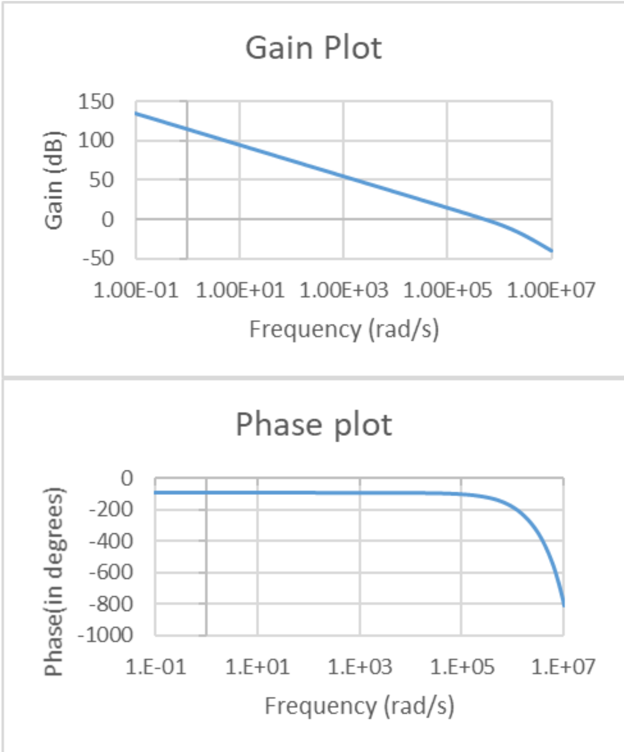


Figure 4: Bode plot of Demodulation loop.

The inphase and quadrature signal values from the demodulator are subtracted from given set point in-phase and quadrature values. The error signals are fed to the PI controller, which is digitally up converted to an intermediate frequency of 20 MHz inphase and quadrature signals. These signals are fed to a dual channel DAC which after up conversion to 650 MHz and appropriate amplification are fed to cavity.

The designed LLRF system has the provision to feed the cavity with RF power in open loop through feed forward tables. The feed forward tables can be filled with inphase and quadrature values corresponding to desired power and phase to be established in the cavity.

The PI controller's gain parameters are calculated by modelling the control loop in baseband and adjusting the gain parameters to have a phase margin of 60 degrees.

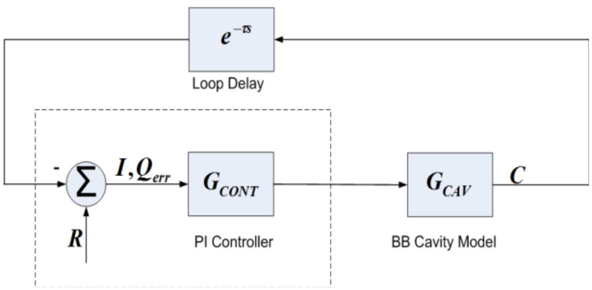


Figure 5: LLRF baseband model

The baseband model of LLRF feedback loop is shown in Fig. 5 and its open loop transfer function is given by: -

$$G(s)H(s) = \frac{K_p W_h\left(s+\frac{K_i}{K_p}\right)}{s^2+sW_h} * e^{-Ts}$$

Here, $K_p$, $K_I$ and $W_h$ (20 Hz) are proportional gain, integral gain and half bandwidth of the cavity respectively. The estimated delay in the closed loop is 3 us. Corresponding to these parameters, $K_I$ and $K_p$ values are found to be around 1.8017e7 and 1032 respectively.

An exhaustive and comprehensive data acquisition scheme has been developed for continuous acquisition of 20 waveforms at a programmable decimation rate and full sample speed acquisition of two 16 bit waveforms. Both data channels are multiplexed as of now and only one chain can remain active at a time. The data acquired from this scheme is used to confirm the Hardware and Firmware performance.

## HARDWARE IMPLEMENTATION AND TEST RESULTS

The above digital signal processing scheme is implemented on a SOC based FPGA. In absence of clock module, the required signals are generated through signal generators locked to each other through 10 MHz external reference. The analog downconverter is fed with 650 MHz pickup, reference, forward and reflected signals and a 670 MHz local oscillator locked with a 1320 MHz source which is used to generate the clock signal required by ADC for sampling. The resulting 20 MHz signals from downconverter are given to the quad channel ADC and the phase and amplitude stability of the demodulated signal is calculated with firmware operating in GDR mode with feedback loop open.

Since, noise present in demodulated signal has contribution from both amplitude dependent as well as independent sources, Hence, amplitude and phase stability is calculated with various ADC input levels. The results are tabulated in Table 1 and amplitude and phase error plot corresponding to an ADC input level of 32 % is shown in Fig. 6.

Table 1: Amplitude and phase stability

| S. No | Input level (percentage of ADC full range) | Amp error | Phase error (in degrees) |
|---|---|---|---|
| 1 | 25 % | 0.0106 % | 0.0237 |
| 2 | 32 % | 0.0094 % | 0.0233 |
| 3 | 62 % | 0.0082 % | 0.0228 |
| 4 | 78 % | 0.0077 % | 0.0230 |

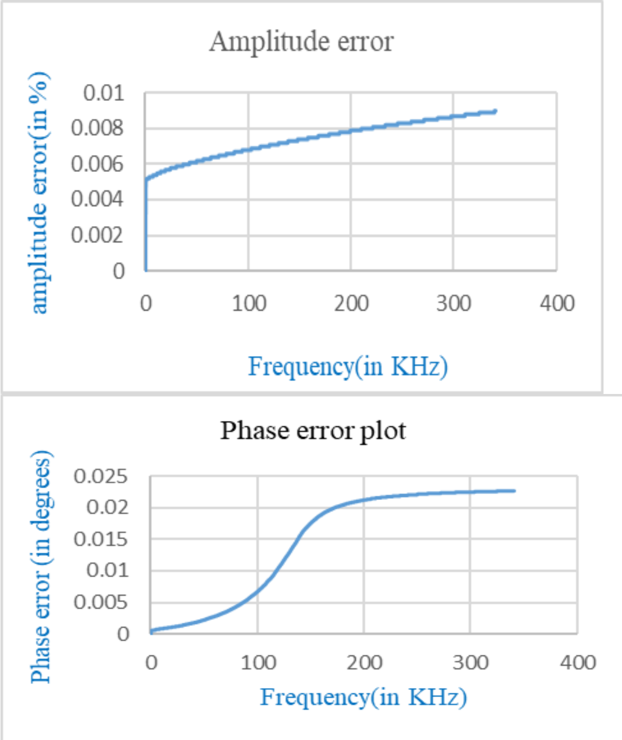


Figure 6: Integrated amplitude and phase error plot for demodulated signal

## CONCLUSIONS

The implemented signal chain meets the amplitude stability specifications for an input signal greater than 30 % of ADC full range. There seems to be some noise at very low frequency of few hertz which needs to be investigated. As is evident from phase error plot, the error up to around 80 KHz is low which is because of closed loop bandwidth of demodulation loop being around 80 KHz. The phase error increases between 80 KHz to around 300 KHz and then it flattens out. The noise outside 300 KHz bandwidth is removed by the IIR filter having a 3dB bandwidth of 300 kHz. The phase stability is a little lower, which may improve with test set up operated with clock module and further investigation of noise at very low frequency.

The data acquisition scheme can be improved to acquire both full speed and decimated signals simultaneously.

## REFERENCES


[1] Thomas Schilcher, “Vector Sum Control of Pulsed Accelerating Fields in Lorentz Force Detuned Superconducting Cavities,” Ph.D. Thesis, University of Hamburg, (1998).

[2] D.Alesini, “power coupler” LNF, INFN, Frascati, Italy.

# DIRECT OBSERVATION OF THE VISCOUS LAYER FORMATION AND BREAKDOWN DURING ELECTRO POLISHING OF NIOBIUM AND ITS CO-RELATION WITH SURFACE MORPHOLOGIES

A. Bose*[1], S.V. Kokil, S. Raghavendra
Raja Ramanna Centre for Advanced Technology, Indore, India

## Abstract

Electro-polishing (EP) of Superconducting radio frequency (SRF) cavities is an essential step that helps in removal of damaged layer, dissolution of surface contamination and provide smooth finish for the RF surface. The effectiveness of EP in achieving nano-smoothness has been linked to the formation of viscous layer whose evolution and disappearance has not been studied in detail. In fact, depending on EP parameters repeated formation and breakdown of viscous layer occurs that directly affects the surface morphology of Niobium. In this work, direct observation of such a time dependent viscous layer evolution-breakdown and its co-relation with current variation is reported. A detailed analysis of this co-relation was essential to understand the mechanisms operating during EP. The study also reports the parameters affecting the current patterns, which indirectly governs time dependent generation of viscous layer. The study finally links the viscous layer evolution pattern with surface morphologies. This study would be useful in optimization of EP parameters for SRF cavity through observation of current patterns.

## INTRODUCTION

SRF cavities are crucial for the development of high energy and high duty factor superconducting linacs [1]. The performance of these SRF cavities are measured in terms of its quality factor ($Q_o$) and accelerating gradient ($E_{acc}$ in MV/m). One of the biggest limitation towards achieving high $E_{acc}$ is the presence surface defects and roughness along with sharp grain boundary edges. In fact, presence of nano-sized defect (depth smaller than the penetration depth) has been shown to suppress the peak surface magnetic field ($B_{pk}$) [2]. In this context, electro polishing (EP) of SRF cavities becomes the most desirable surface treatment, which has evolved in to a major processing step since its inception in 1970's.

Despite its success over other polishing methods, the process exhibits lot of variability in surface topography, which may be a factor in limiting the maximum gradient. In fact, EP process itself has the potential to create defects due to a complex combination of material and electrochemical parameters [3]. The detailed understanding of these electrochemical parameters and its mechanism still alludes the SRF community. The primary reason for that is the absence of a stepwise understanding of the co-relation of the surface dynamics EP process with the current and topography evolution. Another factor affecting such analysis is the complexity of EP process, which involves many co-related parameters like voltage, current, temperature, convection, gravity, surface condition and many more. Despite such complications, the basic mechanism outlined for proper smoothening of surface has been linked to the formation of viscous layer. But, a proper co-relation between the viscous layer evolution with current variation and surface morphology is necessary which has not been studied in detail. Hence, this study was directed towards analysing the above co-relation along with its effect on surface topography.

In this work, few samples have been subjected to EP without any convection and the current pattern has been explained on the basis of online-recorded visuals of the sample surface.

## EXPERIMENTAL

### Materials

High purity Nb (RRR >490) samples (N1-N3) of sizes 10mm x 30mm x 1.8mm were cut from rolled and annealed sheet procured from M/s Ningxia, China which were used for the present study. The average grain size was ~60 µm.

### Preparation technique

The sample N1-N3 were subsequently degreased and cleaned. These samples were then mechanically polished using P400 and P600 SiC papers. These samples were again ultrasonically rinsed in Micro-90 and ultra-pure water (UPW) and subsequently buffer chemical polished (BCP) for 1min to remove surface impurities due to previous mechanical polishing, handling and other operations. It was then subjected to one EP cycle each using standard electrolyte (HF: $H_2SO_4$::1:9). This electrolyte was freshly prepared and stored ~15°C in a freezer. The sequence EP on the samples was as follows. Sample N1 was electropolished first for 80 minutes. It was followed by EP of N2 sample with the electrolyte that was already used for 80 minutes of EP on N1. In a similar manner, N3 was electropolished after N2 sample. The voltage during EP was maintained at 18V and the temperature was controlled between 18-22°C using a water-cooled chiller. In

-----------------------------------------

***aniruddha@rrcat.gov.in***

this experiment, no stirring of the electrolyte was done to avoid the effect of convection in our analysis. After electropolishing, the samples were rinsed in Micro-90 solution followed by ultrasonic rinsing in ultra-pure water (UPW) for an hour each.

The average material removed during EP for samples N1 ~0.154gms, N2 ~0.125gms and N3 ~0.166gms respectively. The distance between cathode and anode was maintained at 65 – 70 mm with the electrodes arranged in vertical orientation.

### *Procedure of analysis*

A LabVIEW program was developed for acquisition of current, voltage, and temperature during EP cycles. A simple in-situ macro videgography technique was used to support, co-relate, and conclude the complex physico-chemical processes at the metal electrolyte interface. However, such a technique has limitations to visualize samples through aged and brownish acid as well as thick viscous layers with agitated electrolytes. Despite these drawbacks, the technique was more than useful in explaining the process. The electrolyte behaviour including the viscous layer on the sample was monitored online and recorded. Finally, laser scanning confocal microscope (LSCM) was used to measure and record the surface topography and roughness of each sample before and after EP cycle.

## RESULTS AND DISCUSSIONS

The confocal images of N1, N2 and N3 surface after EP cycle is compared with pre EP surface in Fig. 1.

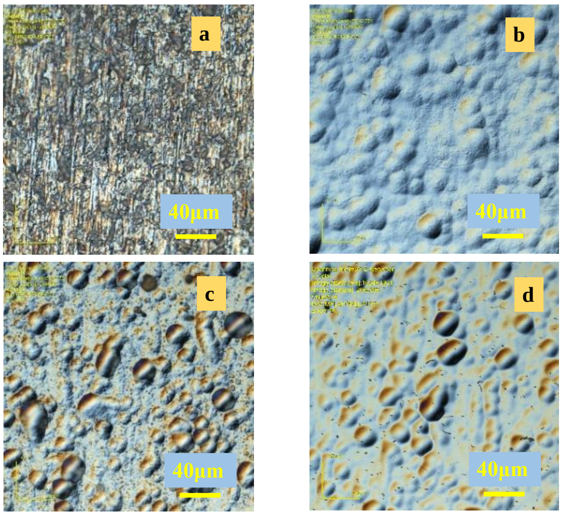


**Figure 1:** The optical images (a) before EP (P600 mechanical polish) and after 80 minutes of EP on samples (b) N1, (c) N2 and (d) N3. The same electrolyte was sequentially used starting from N1 to N3.

The change in average surface roughness (Ra) after EP on each sample along with their location is tabulated in Table 1. It is clear from Table 1, that a clear trend of roughness evolution with electrolyte aging is missing. Moreover, variation of surface roughness within the sample also exists. Hence, it can be proposed that the surface roughness evolution depends on acid aging, current pattern, as well as dynamics of the electrolyte on Nb surface.

In order to simplify this complex inter-relationship, it was necessary to understand the surface morphology by in-situ macro videography along with its co-relation to the current pattern. Such investigation revealed few interesting results, which are presented.

| Sample No. | Before EP Ra (in nm) | After EP, Ran (in nm) | | |
|---|---|---|---|---|
| | | Top | Middle | Bottom |
| N1 | 520nm | 254 | 335 | 189 |
| N2 | 510nm | 306 | 335 | 440 |
| N3 | 483 nm | 310 | 340 | 370 |

**Table 1: Comparison of Ra before and after EP on samples N1-N3**

(a) The co-relation of current pattern with the instantaneous photographs of the electrolyte dynamics on the sample surface is presented in Fig. 2. Although, the macro-video images are not extremely clear still it is clear that the layer adjacent to the Nb surface during EP changes from a bluish to light brownish colour and subsequently to an off whitish layer. The changes in colour can be related to the thickness of the reaction/ oxide layer on the Nb. Such conclusion can be made on the basis of a simple anodizing experiment which shows that the colour of the anodized Nb changes from light brown to brown to light blue to dark blue oxide with increasing thickness. Hence, from Fig. 2, it can be suggested that combination of the sulphuric acid, water content and the voltage initiate the oxide layer formation that matches well with the change in the colours observed on the Nb surface. This oxide layer subsequently reacts with HF acid, which can be co-related to the sudden current surge and the colour of the surface of Nb changing to off white. This reaction products then drips along the sample-electrolyte interface and finally mix into the electrolyte to which we would come back later.

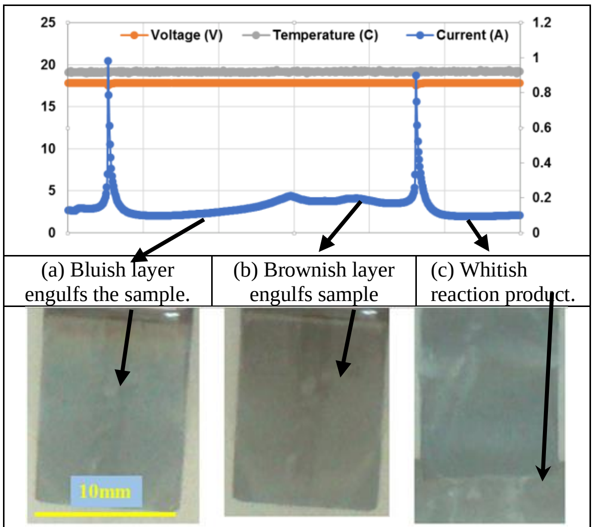


**Figure 2:** Co-relation between current pattern and surface electrolyte through in-situ images of Nb-electrolyte interface.

However, the retention of this reaction production near the sample surface was found to depend on the rate of reaction, its solubility and the viscosity at the Nb – electrolyte interface. From Fig. 3 it is clear that during EP of N1 (with fresh electrolyte), the reaction frequency is faster due to availability of F‾, leading to build up of reaction products. As the concentration of reaction product increases, it crosses the limit of its solubility in the vicinity of the viscous layer leading to its precipitation in salt form that covers the whole surface as shown in Fig. 2c. Such effect was however missing in case of N3, which clearly suggest that availability of F‾ is the critical factor. Now the efficiency of EP in surface smoothening is related to the salt layer formation and retention to induce diffusion control EP. Since, this retention effect is maximum for fresh electrolyte so the smoothening effect was better in case of N1. But, we also observed that the retention of the reaction products was non-homogeneous over the sample N1 and N2, leading to large variation in surface roughness within samples N1 and N2. However, the intra-sample variation of surface roughness in N3 was lower and requires further analysis of current pattern evolution during EP and its relation to aging.

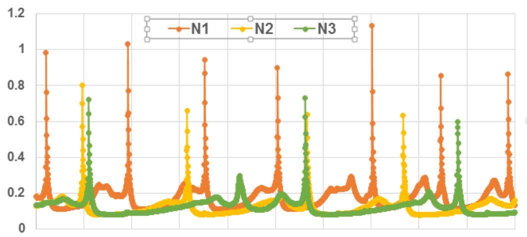


Figure 3: Current Oscillation vs time with acid aging from N1 to N3.

(b) In order to explain the above issue we plotted the snapshots of current variation profile among samples N1-N3 in Fig. 3. It is clear that the peak current values as well as the frequency of the current oscillation reduced with ageing of electrolyte (acid). Before proceeding further, it was essential to analyse the current pattern in terms of ion movement. The rise and fall of current can be co-related abrupt flow of ions into the anode followed by sudden restriction of ionic flow. In a voltage-controlled system, this implies sudden increase of resistance followed by its absence. From Fig. 3, it is clear that the maximum current approaches 0.7 – 1.2A and the minimum hovers around 0.1A. The minimum current during oscillation is similar in all cases (N1-N3) irrespective of aging of electrolyte. Such observations suggests that peak current during oscillation could be due to sudden surge of ions/ F‾. However, despite similar voltage and water content the oscillation intensity dampens with aged electrolyte. This suggests that the current peak as well as the frequency of reaction should be dominated by F‾ surge, which is known to deplete with continuous EP process. Hence, the oscillations should continue longer if HF concentration is increased from 10 % to 15% in the electrolyte. And as the acid ages, the depletion of F‾ ion from the solution should reduce the strong surge of current observed in periodic fashion as observed in Fig.2.

Hence, combining the above observations it is evident that as the electrolyte ages as in the case of EP of N3 the frequency of reaction reduces as evident from the current pattern in Fig. 3. This reduces the rate of formation of reaction product (in case of N3) which reduces the chances of it exceeding the solubility limit. It also provides time for the reaction product to slowly assimilate within the bulk electrolyte. This in turn leads to a dynamic balance between formation of reaction product, its retention on surface and its assimilation into the bulk electrolyte. Hence, the viscous layer thickness was observed to remain uniformly distributed over the sample. Such a scenario combined with current oscillation leads to more uniform EP. As a result, the intra-sample variation of surface roughness in N3 was found to be minimum.

It should be noted that such an observation is made under controlled conditions of temperature and without any electrolyte agitation. Further investigations incorporating the other features are being investigated and would a part of future work.

## CONCLUSION

The co-relation between the current pattern and the viscous layer dynamics was analysed using simple in-situ macro videgography technique. The effect of aging electrolyte on the surface topography along with current pattern and Nb-electrolyte interface dynamics was also studied. The study also highlighted the preliminary details of the mechanism involved in current oscillations. In future, the study needs to be extended to incorporate the effect of agitation of electrolyte. The baseline reason for oscillation was found to the presence of F ion when electrolyte is fresh.

## ACKNOWLEDGEMENT

We are thankful to Director RRCAT and group director for their constant support. The support from members of SCCCS with special thanks to Shri D. S. Rajpoot for his untiring help in setting up the water cooling facility for small samples highly appreciated.

## REFERENCES

[1] S. C. Joshi, S. B. Roy, P. R. Hannurkar, P. Kush, A. Puntambekar, P. Shrivastava, G. Mundra, J. Dwivedi, P. Khare and P. D. Gupta, "R&D activities on high intensity superconducting proton LINAC at RRCAT," in *Proceedings of LINAC2012*, Tel-Aviv, Israel , 2012.

[2] T. Kubo, "Field limit and nano-scale surface topography of superconducting radio-frequency cavity made of extreme type II superconductor," *Prog. Theor. Exp. Phys.*, vol. 063G01, pp. 1-12, 2015.

[3] L. D. Cooley et. al., "Impact of Forming, Welding, and Electropolishing on Pitting and the Surface Finish of SRF Cavity Niobium" IEEE Transactions on Applied Superconductivity, 21 (3), 2011.

# PHYSICS DESIGN STUDY OF MULTISPOKE RESONATORS AND THEIR COMPARISON WITH SINGLE SPOKE RESONATOR

Mukesh Kumar Pal[1#] and Rahul Gaur[1,2]
[1]Raja Ramanna Centre for Advanced Technology, Indore, India
[2]Homi Bhabha National Institute, Mumbai, India.

*Abstract*

In order to find out the most suitable choice of accelerating structure for the energy range of 40 MeV-160 MeV in the injector linac for the proposed Indian Spallation Neutron Source (ISNS), various options of spoke resonators have been explored. In this regard, the electromagnetic design of Double Spoke Resonator (DSR042) and Triple Spoke Resonator (TSR042) has been carried out at $\beta_g$=0.42 and the beam dynamics calculations have been performed using these multispoke resonators in the energy range of 40 MeV-160 MeV. Results of the design studies of these multispoke resonators and their performance comparison with the designed single spoke resonator SR042 are being presented in this paper.

## INTRODUCTION

There is a proposal to build a 1 MW proton accelerator based Indian Spallation Neutron Source (ISNS) at RRCAT [1]. It will consist of a 1 GeV $H^-$ linear accelerator (linac) and a proton accumulator ring. To accelerate the $H^-$ ions up to ~160 MeV, there are various possible options for accelerating structures to be used. Three families of Single Spoke Resonators (SSRs), i.e., SR011, SR021 and SR042 have already been designed at $\beta_g$ = 0.11, 0.21 and 0.42, for acceleration of $H^-$ ions up to 160 MeV [1]. Here, $\beta_g$ is the geometric $\beta$, which is defined as the velocity of the design particle in the unit of speed of light for which the gap-to-gap phase shift of the RF is π in the resonator. Besides this option, another option is also explored to look into the possibility of replacement of the third family of SSRs by the multi-spoke resonators. Idea of this option is generated from the thought that the multispoke resonators can provide more number of accelerating gaps in a single structure compared to SSRs. This feature could be efficiently used to reduce the linac length by replacing several SSRs by a single multispoke resonator, which can be a Double Spoke Resonator (DSR) or a Triple Spoke Resonator (TSR). However, due to more number of gaps in multispoke resonators, the velocity acceptance decreases due to narrower transit time factor profile. The European Spallation Source (ESS) project [2] has already considered the DSR scheme in the energy range of 90 MeV-216 MeV in the linac. Motivated by this, we have also explored the option of DSR and TSR to replace a group of SSRs in SR042 family for the ISNS linac.

Like SSR structure, DSR and TSR are also transverse electromagnetic (TEM) mode based accelerating structures. Unlike a single spoke conductor in an SSR, there are two spoke conductors in a DSR and three spoke conductors in a TSR, which are perpendicular to each other and transverse to the beam axis. The transverse dimension of the DSR and TSR is of the order of $\lambda/2$, where $\lambda$ is the free space wavelength of the RF. The adjacent spoke conductors in DSR and TSR are separated by $\beta_g\lambda/2$. The longitudinal length of DSR and TSR is around 1.5 times and 2 times, respectively, of the longitudinal length of SSR. Typical model of DSR and TSR are shown in Fig. 1.

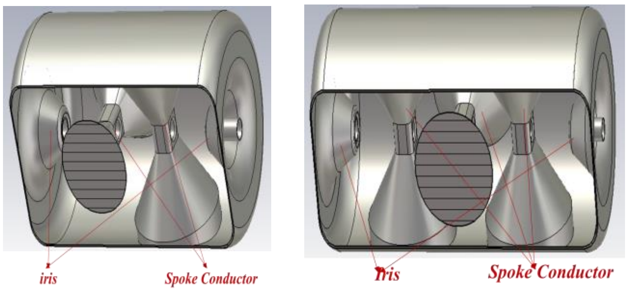


(a) (b)

Figure 1: Typical model of (a) DSR and (b) TSR.

Followed by EM design of DSR and TSR at $\beta_g$ = 0.42, i.e., DSR042 and TSR042, the beam dynamics study has been performed using their 3D field map. The performance of DSR042 and TSR042 in terms of EM field and beam dynamics has been compared with SR042, and summarized in this paper.

## EM DESIGN OF DSR042 AND TSR042

The geometrical parameters of DSR and TSR have been optimized to maximize the accelerating gradient, $E_{acc}$ of the structures. In order to maximize $E_{acc}$, the RF parameters, $E_p/E_{acc}$ and $B_p/E_{acc}$ were minimized. Here, $E_p$ and $B_p$ are the maximum electric and magnetic fields, respectively, on the inner surface of cavity. For superconducting niobium cavity at operating frequency 325 MHz, the safe limits of $B_p$ and $E_p$ have been taken to be 60 mT and 40 MV/m, respectively [3]. Besides these, other RF parameters, i.e., the shunt impedance to quality factor ratio $R/Q = V_0^2/\omega_0 U$ and the geometrical factor $G = R_sQ$, have been kept at moderate values in order to reduce the heat load of cavity. Here, $V_0$ is the accelerating voltage along the beam axis, $\omega_0$ is the angular resonant frequency, $U$ is the stored EM energy and $R_s$ is the surface resistance of superconducting structure. We would like to mention here that, for calculation of $E_{acc}$, the effective length $L_{eff}$ for DSR042 and TSR042 cavities was considered to be $1.5\times\beta_{opt}\lambda$ and $2\times\beta_{opt}\lambda$, respectively, where $\beta_{opt}$ is the optimum $\beta$ at which the transit time factor is maximum.

#mukeshp@rrcat.gov.in

The detailed geometrical optimization of DSR042 and TSR042 along with the multipacting study in the optimized geometry has been performed in the EM code CST-MWS [4]. Various geometrical parameters of a DSR are shown in Fig. 2.

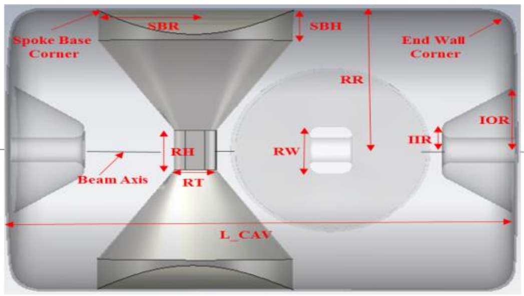


Figure 2: Geometrical parameters of a DSR.

Except *L_CAV*, all the initial geometrical parameters for DSR042 were taken to be same as mentioned in Table 1 in Ref. [5]. The beam aperture diameter for DSR042 and TSR042 has been chosen to be same as that for SR042, i.e., 50 mm. Geometrical parameters *RW* and *IIR* were optimized first by varying them simultaneously with *RW*=2×*IIR*. After getting minima of $E_p/E_{acc}$, as mentioned in Fig. 3a by black dot, we fixed *RW*, and then *IIR* was varied further to obtain the lower $E_p/E_{acc}$. After fixing the value of *IIR*, we optimized *RH* for the minimum $E_p/E_{acc}$, where the pattern of peak field ratios was found to be similar as that for *RW*. Next, we optimized *IOR* for minimum $E_p/E_{acc}$, while keeping fixed the values of *RW*, *IIR* and *RH*. Variation of peak field ratios with respect to *IOR* is shown in Fig. 3b. We restricted the upper value of *IOR* up to around half the value of ring radius *RR* such that we have sufficient space for incorporating a bending radius on the end-wall corner. Next, *SBR* was optimized for minimum $B_p/E_{acc}$ as shown in Fig. 3c. Here, we also restricted the upper value of SBR up to ~ 140 mm for the same logic as given for *IOR*. At the end, *RT* was optimized for the minimum $E_p/E_{acc}$ as shown in Fig. 3d. Note that, similar patterns of the peak field ratios with respect to various geometrical parameters were obtained for TSR042 case.

The optimized geometrical parameters and calculated RF parameters of DSR042 and TSR042 cavities are listed in Table 1 along with the parameters of SR042 for performance comparison. It can be seen that the value of maximum possible $E_{acc}$ is lower in case of multispoke resonators than SSR due to higher peak field ratios.

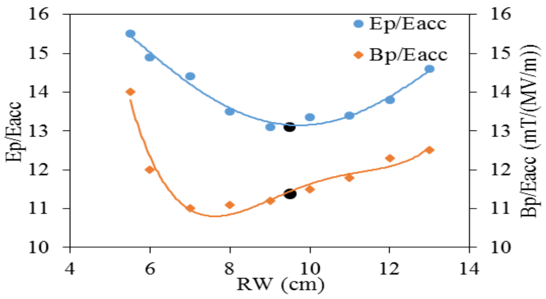


(a)

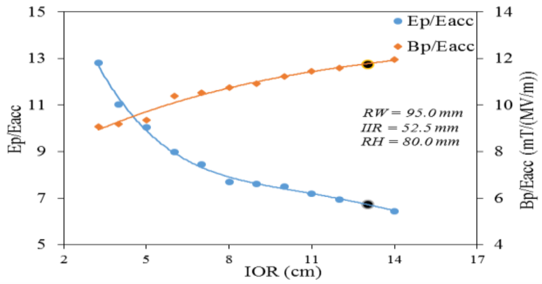


(b)

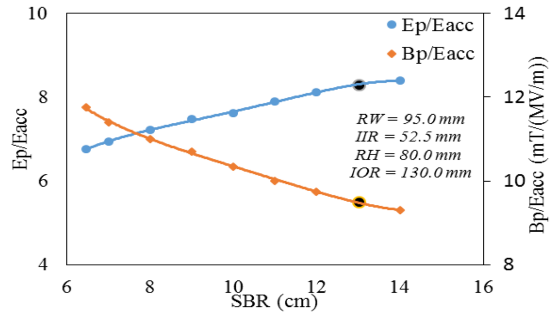


(c)

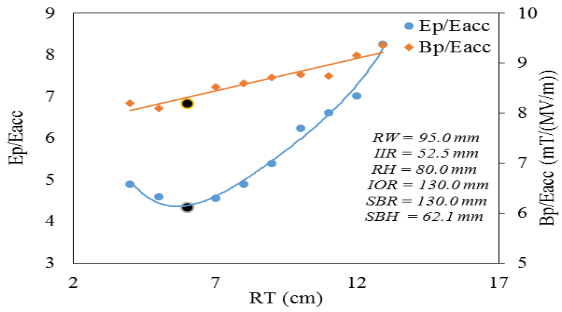


(d)

Figure 3: Variation of RF parameters $E_p/E_{acc}$ and $B_p/E_{acc}$ with (a) *RW* (b) *IOR* (c) *SBR* and (d) *RT* of DSR042.

Table 1: Optimized geometrical and RF parameters.

| **Parameters** | **DSR042** | **TSR042** | **SR042** |
|---|---|---|---|
| *RW* (mm) | 95.00 | 95.00 | 120.00 |
| *RH* (mm) | 80.00 | 80.00 | 80.00 |
| *RT* (mm) | 60.00 | 60.00 | 83.66 |
| *SBR* (mm) | 130.00 | 130.00 | 130.00 |
| *SBH* (mm) | 62.10 | 64.00 | 65.20 |
| *IIR* (mm) | 52.50 | 52.50 | 70.00 |
| *IOR* (mm) | 130.00 | 130.00 | 130.00 |
| *RR* (mm) | 283.30 | 278.10 | 271.20 |
| *L_CAV* (mm) | 719.91 | 913.74 | 520.00 |
| $E_p/E_{acc}$ | 4.4 | 4.8 | 3.5 |
| $B_p/E_{acc}$ (mT/(MV/m)) | 7.6 | 10.0 | 5.5 |
| *R/Q* (Ω) | 370 | 410 | 308 |
| *G* (Ω) | 109 | 97 | 115 |
| $E_{acc,\ max}$ (MV/m) | 8.0 | 6.0 | 10.8 |

We have also performed the multipacting calculations in the optimized multispoke resonators using the code CST-PS [4]. The end-wall corners and the spoke base corners were found to be the multipacting prone surfaces. The multipacting growth rate in both structures were found to be minimum at the end wall corner and spoke base corner radii of 10 and 0 cm, respectively. The estimated growth rate for DSR042 and TSR042 along with SR042 is shown in Fig. 4.

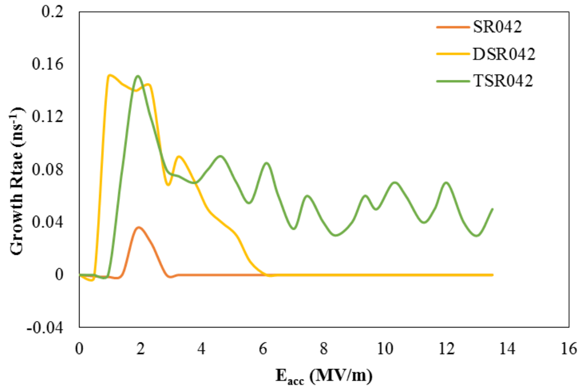


Figure 4: Multipacting growth rate in spoke resonators.

We observed that the multipacting growth rate in SR042 is significantly less compared to DSR042 and TSR042. We would also like to mention here that the quadrupole asymmetry parameter for DSR042 and TSR042 was calculated to be 0.42 and 0.45, respectively, which is of the same order of magnitude as for SR042 [6].

## BEAM DYNAMICS STUDIES FOR SR042, DSR042 AND TSR042 CAVITIES

The purpose of beam dynamics study was to select the most suitable cavity among SR042, DSR042 and TSR042 for acceleration of $H^-$ beam in the energy range 40 MeV–160 MeV on the basis of the required number of cavities, the linac length and the other beam dynamics parameters like emittance growth, halo parameter etc. The beam dynamics simulations in the energy range 3 MeV-160 MeV have been performed in the beam dynamics codes GenLinWin and TraceWin [7] using the 3D field map of the spoke resonators obtained from the code CST-MWS. For the energy range 40 MeV-160 MeV, we have considered four different lattice options- (i) four SR042 cavities per period, i.e., Drift (9.58 cm)–SR042 (50.64 cm)–Drift (9.58 cm)–SR042 (50.64 cm)–Drift (9.58 cm)–Solenoid (30 cm)–Drift (9.58 cm)–SR042 (50.64 cm)–Drift (9.58 cm)–SR042 (50.64 cm)–Drift (9.58 cm), (ii) two DSR042 cavities per period, i.e., Drift (9.58 cm)–DSR042 (68.29 cm)–Drift (9.58 cm)–Solenoid (30 cm)–Drift (9.58 cm)–DSR042 (68.29 cm)–Drift (9.58 cm), (iii) four DSR042 cavities per period, i.e., Drift (9.58 cm)–DSR042 (68.29 cm)–Drift (9.58 cm)–DSR042 (68.29 cm)–Drift (9.58 cm)–Solenoid (30 cm)–Drift (9.58 cm)–DSR042 (68.29 cm)–Drift (9.58 cm)–DSR042 (68.29 cm)–Drift (9.58 cm), and (iv) two TSR042 cavities per period, i.e., Drift (9.58 cm)–TSR042 (87.54 cm)–Drift (9.58 cm)–Solenoid (30 cm)–Drift (9.58 cm)–TSR042 (87.54 cm)–Drift (9.58 cm). Here, the length of the resonators has been taken to be $L_{eff}$ instead of *L_CAV*.

We would like to mention here that in the design of lattice for each case, a number of design criteria, as mentioned in Ref. [1], were followed, i.e., to keep the emittance growth, growth in RMS beam size and beam losses as low as possible along the linac. We would also like to mention here that the cavities of all four cases are considered to be operated at their maximum possible accelerating gradient. The Gaussian distribution with 3σ beam having $10^5$ macroparticles was assumed for the beam dynamics simulations.

The beam was found to be transmitted in the spoke resonator section without loss with less than 5% RMS emittance growth in both the planes (longitudinal as well as transverse). Also, the halo parameter was found to be less than 1 in each case. The required number of cavities and solenoids in the $\beta_g = 0.42$ section along with the linac length is summarized in Table 2 for all the four lattice options.

Table 2: Number of cavities/solenoids for $\beta_g = 0.42$ section of spoke resonators.

| Option | (i) | (ii) | (iii) | (iv) |
|---|---|---|---|---|
| **No.of Cav/Sol.** | 24/6 | 24/12 | 24/6 | 26/13 |
| **Linac length (m)** | 17.40 | 24.59 | 21.64 | 31.64 |

## CONCLUSION

It is found that as the number of accelerating gaps in spoke resonator increases, the maximum possible accelerating gradient decreases due to increasing peak field ratios. The peak field ratios for DSR in our case are found to be comparable to the DSR of ESS project [2]. This results longer linac length in case of multispoke resonators as compared to an SSR. Also, due to narrower transit time factor profile, the multispoke resonators can be used efficiently in a narrower energy range. Therefore, it is observed that the SR042 cavity is the most suitable choice among the three options for the energy range 40 MeV-160 MeV in the injector linac of ISNS due to smaller linac length, smaller number of solenoids for transverse focusing, and minimum material.

## REFERENCES


[1] Amalendu Sharma et al, RRCAT/2016-11, 2016.
[2] Ronald Garoby et al, Phys. Scr. 93 (2018) 014001, p121.
[3] M. Ball et al, “The PIP-II Conceptual Design Report”, V0.03, April 2018.
[4] CST Studio Suite 2014, www.cst.com.
[5] M.K. Pal et al, RRCAT/2015-02, 2015.
[6] M.K. Pal et al, InPAC2018, Indore, Jan 2018, ID-246.
[7] D. Uriot, “GenLinWin and TraceWin”.

# TUNING ALGORITHM FOR CURE OF MODE MIXING IN AN RFQ LINAC

Rahul Gaur# and Vinit Kumar
Homi Bhabha National Institute, Mumbai-400094, India
Raja Ramanna Centre for Advanced Technology, Indore-452013, India

*Abstract*

A four-vane type radio frequency quadrupole (RFQ) accelerator is very much sensitive to the geometrical errors, which may cause the mixing of nearby unwanted quadrupole and dipole modes to the operating quadrupole mode. This results in an undesired variation in the voltage profile of the RFQ, which may affect the beam dynamics and reduce the beam transmission. In order to tune the RFQ for the desired voltage profile, we have developed a computer program for RFQ tuning in MATLAB, using the five-conductor transmission line model of RFQ. The case study of the 3 MeV, 325 MHz RFQ for the proposed Indian Spallation Neutron Source (ISNS) project is being presented here, using CST-MWS simulations, in which the perturbation in the voltage profile due to the vane-tip modulations is corrected using the tuning algorithm. In addition to this, the tuning of the end-cells of the RFQ using a set of quadrupole rods is also being discussed in the paper.

## INTRODUCTION

Unlike other conventional accelerating structures, the Radio Frequency Quadrupole (RFQ) operates in a higher order mode, i.e., the fundamental quadrupole mode $TE_{210}$. In this case, the operating mode is surrounded by many other nearby unwanted quadrupole and dipole modes. Frequency separation between unwanted modes and the operating mode is inversely proportional to the length of the RFQ, which means that for longer structure, the unwanted modes come closer to the operating mode. It is well known that in a perfect RFQ without any fabrication and alignment error, the fundamental quadrupole mode has a flat field distribution along the RFQ length. However, in presence of any fabrication and alignment error, some component of the neighboring unwanted modes mix in the operating mode and the amount of mode mixing is inversely proportional to the frequency separation between the unwanted modes and the operating mode. The mode mixing produces an undesired variation in the voltage profile of the operating mode which may affect the beam dynamics and cause significant emittance growth and beam loss. In order to minimize the mode mixing, we have developed a computer program in MATLAB for RFQ tuning, based on the perturbative analysis of an RFQ, by considering the RFQ as a five-conductor transmission line [1, 2]. Moreover, this tuning algorithm has been extended to perform the tuning of the end-cells of an RFQ, which determines the required value of the tuning parameter of the end-cells. Here, we discuss the example of quadrupole rods, whose insertion length is considered as a tuning parameter of the end-cells.

#rahul@rrcat.gov.in

## PERTURBATIVE ANALYSIS OF RFQ

Considering the RFQ as a five-conductor transmission line, as described in Ref. [1], the normalized voltage of the operating mode of RFQ, which is perturbed due to various capacitance and inductance errors, can be written as

$$\begin{aligned}\bar{U} &= \bar{U}_{q0} + \overline{\delta U} = U_q\hat{e}_1 + U_{d1}\hat{e}_3 + U_{d2}\hat{e}_4 \\ &= (\phi_{q0} + \sum_{n=1}^{\infty} a_{qn}\phi_{qn})\hat{e}_1 + \sum_{n=0}^{\infty} a_{d1n}\phi_{dn}\hat{e}_3 + \sum_{n=0}^{\infty} a_{d2n}\phi_{dn}\hat{e}_4,\end{aligned} \tag{1}$$

where $U_{q0}$ or $\phi_{q0}$ is the normalized unperturbed voltage of the lowest quadrupole mode, and $\phi_{qn}$ and $\phi_{dn}$ are the normalized unperturbed voltages of the higher order quadrupole modes and the two polarizations of the dipole modes, respectively. Note that $\phi_{qn} = \phi_{dn} = \sqrt{1/l}$ for $n = 0$, and $\sqrt{2/l}\cos(n\pi z/l)$ for $n > 0$, where $l$ is the RFQ length. Here, $\hat{e}_1$, $\hat{e}_3$ and $\hat{e}_4$ are the unit vectors of the quadrupole, and two polarizations of the dipole components, respectively, of the modal voltage vector $\bar{U}$. The two polarizations of the dipole mode correspond to the 1-3 and 2-4 dipole modes, where the 1-3 mode couples the 1st and 3rd quadrants and the 2-4 mode couples the 2nd and 4th quadrants of the RFQ. Here, $a_{qn}$ and $a_{dn}$ are the mode mixing coefficients which denote the contribution of higher order quadrupole modes and dipole modes, respectively in the perturbed voltage of the operating mode and are given as [1]

$$\begin{aligned}a_{qn} &= -\frac{\omega_0^2}{4\left(\omega_0^2 - \omega_{qn}^2\right)}\int_0^l \phi_{q0}\phi_{qn}\left(\frac{\delta C_q}{C} + \frac{\delta L_q}{L}\right)dz, \\ a_{d1n} &= -\frac{\sqrt{2}\omega_0^2}{4(1+h)\left(\omega_0^2 - \omega_{d1n}^2\right)}\int_0^l \phi_{q0}\phi_{dn}\left(\frac{\delta C_{d1}}{C} + \frac{\delta L_{d1}}{L}\right)dz, \\ a_{d2n} &= -\frac{\sqrt{2}\omega_0^2}{4(1+h)\left(\omega_0^2 - \omega_{d2n}^2\right)}\int_0^l \phi_{q0}\phi_{dn}\left(\frac{\delta C_{d2}}{C} + \frac{\delta L_{d2}}{L}\right)dz,\end{aligned} \tag{2}$$

where the capacitance errors $\delta C_q$, $\delta C_{d1}$ and $\delta C_{d2}$ are given as $\delta C_1+\delta C_2+\delta C_3+\delta C_4$, $\delta C_1-\delta C_3$ and $\delta C_4-\delta C_2$, respectively, and similarly the inductance errors $\delta L_q$, $\delta L_{d1}$ and $\delta L_{d2}$ are given as $\delta L_1+\delta L_2+\delta L_3+\delta L_4$, $\delta L_1-\delta L_3$ and $\delta L_4-\delta L_2$, respectively; here $C_p$ and $L_p$ are capacitance per unit length and inductance integrated in length, respectively, of the $p^{th}$ quadrant with $p$ = 1, 2, 3 and 4. Here, $\omega_0$ is the angular frequency of the operating quadrupole mode, and $\omega_{qn}$ and $\omega_{dn}$ are the angular frequencies of the $n^{th}$ quadrupole and dipole modes, respectively. The parameter $h$ represents the coupling between the RFQ quadrants and is given by $(\omega_0^2/\omega_{d0}^2)$-1.

## TUNING ALGORITHM

Using perturbative analysis of an RFQ, a tuning strategy has been presented in Ref. [2]. Based on this tuning strategy, we have developed a computer program in MATLAB, which can calculate the required penetration depth of all the tuners in RFQ in order to correct the field profile error. Details of the program is described as follows.

In a real RFQ, we can measure the intervane voltage profile $V_p(z)$ of the perturbed operating mode in each quadrant $p$ of the RFQ using the bead pull method. The measured components of modal voltage vector, i.e., $V_q$, $V_{d1}$ and $V_{d2}$ can be calculated from the intervane voltage vector as $(V_1\text{-}V_2\text{+}V_3\text{-}V_4)/2$, $(V_1\text{-}V_3)/\sqrt{2}$ and $(V_2\text{-}V_4)/\sqrt{2}$, respectively [1]. These components need to be multiplied further with $\sqrt{1/l}\,/V_{q0}$ in order to obtain the normalized components of the modal voltage vector, i.e., $U_q$, $U_{d1}$ and $U_{d2}$, where $V_{q0}$ is the average value of $V_q$ over the full length of RFQ.

Knowing the modal voltage vector, the mode mixing coefficients can be calculated using Eq. (1) as follows

$$
\begin{aligned}
a_{qn} &= \int_0^l \left(U_q - U_{q0}\right)\phi_{qn}\,dz,\\
a_{d1n} &= \int_0^l U_{d1}\phi_{dn}\,dz, \qquad (3)\\
a_{d2n} &= \int_0^l U_{d2}\phi_{dn}\,dz.
\end{aligned}
$$

Considering only capacitance errors in the RFQ, the error profile can be found using mode mixing coefficients in Eq. (2) by expanding the capacitance errors, $\delta C_q$ in series of $\phi_{qn}$, and $\delta C_{d1}$ and $\delta C_{d2}$ in terms of $\phi_{dn}$, as described in Ref. [2].

In order to cancel these capacitance errors, the required inductance profile can be determined using Eq. (2). This inductance profile is achieved with the help of a set of discrete tuners distributed along the length of the RFQ in all the four quadrants. The required inductance variation $\delta L_{tp}$ of $t^{\text{th}}$ tuner in $p^{\text{th}}$ quadrant can be calculated as

$$
\frac{\delta L_{tp}}{L} = \frac{1}{l_1 + l_2}\int_{z_t - l_1}^{z_t + l_2} \frac{\delta L_p(z)}{L}\,dz, \qquad (4)
$$

where $z_t$ is the longitudinal position of the tuner. Each tuner inductance variation $\delta L_t$ is directly proportional to the variation in the corresponding tuner penetration depth $\delta h_t$. Therefore, using the relation $\delta L_t = \chi\ \delta h_t$, where $\chi$ is the tuner sensitivity parameter, the required penetration depth of each tuner can be evaluated.

## CASE STUDY OF THE RFQ FOR ISNS

In order to validate the tuning algorithm, we have performed a case study of the 325 MHz RFQ designed for the proposed Indian Spallation Neutron Source (ISNS) [3]. During EM design of the RFQ using the code CST-MWS [4], we found that the modulation on the vane-tips acts as a perturbation, which decreases the local frequency [3]. Since we have not considered any alignment or fabrication error in the model, and only a quadrant of the model is simulated with symmetry planes, the contribution of the dipole modes in the perturbed operating mode is neglected, and, hence, only the quadrupole error is considered in the perturbed operating mode. A fractional field error of ±15% was observed in the off-axis electric field at ($x$ = $y$ = 10 mm) along the RFQ length due to higher order quadrupole modes mixing even with designed modulation parameter without any error, as shown in blue color curve in Fig. 1. The fractional field error due to higher order quadrupole modes mixing is defined as $(U_q\text{-}U_{q0})/U_{q0}$. This error in the off-axis electric field causes the axial electric field to be deviated from the designed profile. In order to tune the RFQ for required field profile, there are 12 cylindrical tuners in each quadrant, which are distributed along the RFQ length [3].

We have discussed the perturbation of the operating field due to vane-tip modulation earlier in the Ref. [3], however, the tuning method presented there was based on trial and error. Here, we have used the tuning algorithm, which is described in the previous section.

For our RFQ, total capacitance per unit length is found to be 70 pF/m from the beam dynamics code PARMTEQM [5]. Therefore, using $\omega_0^2 = 1/LC$, the integrated inductance $L$ is calculated to be 3.4x10$^{-9}$ H.m. In order to evaluate the tuner sensitivity parameter $\chi$, we performed simulations in CST-MWS code, in which the inductance was calculated at various penetration depth of tuners, where all the tuners were moved simultaneously by the same amount. Inductance decreases linearly when the tuners are inserted inside the cavity, and the inductance slope or the tuner sensitivity parameter $\chi$ was calculated to be -4.57x10$^{-8}$ H.m/m.

Using the tuning algorithm, the penetration depth of all the tuners in a quadrant after two iterations was calculated to be -1.05 mm, -1.19 mm, -0.79 mm, -1.54 mm, -0.88 mm, +1.57 mm, +0.96 mm, +0.50 mm, +0.95 mm, +0.32 mm, +0.83 mm and +0.33 mm, respectively. With this setting of tuners, the off-axis fractional field error has been reduced to < ±1%, as shown by violet color curve in Fig. 1. This also resulted in the required designed axial field profile.

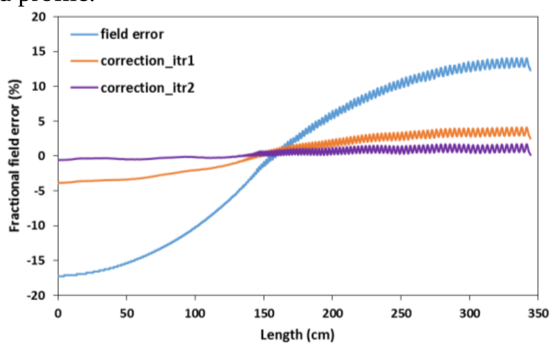


Figure 1: Fractional error of the off-axis electric field along the RFQ length.

The tuning algorithm has been validated to minimize the field perturbation due to quadrupole as well as dipole modes mixing by simulating various RFQ errors in the RFQ 3D model using CST-MWS. For example, a case study of the misalignment error of the upper vertical vane of the first section of the unmodulated ISNS RFQ was performed in order to verify if the tuning algorithm can minimize the dipole mode mixing as well. Horizontal displacement of the upper vertical vane by 200 µm resulted in the off-axis fractional field error of 8% and 11% due to mixing of the 1-3 dipole mode and 2-4 dipole mode, respectively. The fractional field error due to the mixing of 1-3 and 2-4 dipole modes is defined as $U_{d1}/U_{q0}$ and $U_{d2}/U_{q0}$, respectively. There was no field error found due to the higher order quadrupole modes. Using the tuning algorithm, the penetration depth was calculated to be -2.04 mm, +2.85 mm, +2.04 mm and -2.85 mm in the 1st, 2nd 3rd and 4th quadrants, respectively, for all the tuners. With the calculated penetration of the tuners, the off-axis fractional field error due to 1-3 and 2-4 dipole modes was reduced to 1.7% and 0.8%, respectively.

Another important case study of the vane-tip profile error in the 3D model of the modulated RFQ was performed using CST-MWS code. With a uniformly distributed random error of ±100 µm in the vane-tip profile, the off-axis fractional field error was found to be ±21%. This field error was reduced to < ±1% using the tuning algorithm, however, the longitudinal field profile was found to be distorted due to this error. Here, we have observed that, although we can obtain the desired flat profile of the off-axis electric field using the tuning algorithm, the tolerance limit on any machining and misalignment error can only be determined by statistical study based on impact of longitudinal field profile on beam dynamics.

## RFQ END-CELLS TUNING

End-cells in the RFQ are designed [3] in order to satisfy the boundary conditions of the operating $TE_{210}$ mode at the RFQ ends. Any error in the end-cell parameters may result in the mode mixing, which perturbs the field profile of the operating mode at the ends. For the tuning of end-cells, we have explored a provision of quadrupole rods, which have also been adopted earlier for IPHI RFQ [6] and Linac4 RFQ [7]. Quadrupole rods are cylindrical metallic rods attached to the end plate and inserted longitudinally to the four quadrants. These are located near the beam axis on the bisector of the quadrant. We have optimized the rod location as ($x$ = $y$ = 2 cm) in a quadrant such that these strongly affect the quadrupole mode. Diameter of the rods is chosen to be 14 mm in order to provide sufficient margin for the cooling channels. The nominal length of the rods is selected to be 30 mm in the RFQ quadrants such that the error can be corrected in both the directions of rod movement.

For tuning of the end-cells using the quadrupole rods, we have extended the tuning algorithm, described in this paper, by treating the length of quadrupole rods, instead of the penetration depth of cylindrical tuners, as tuning parameter. Here, in the end-cell region, the required capacitance profile to compensate for the error is obtained using Eq. (2). The error compensation is then achieved with the help of quadrupole rods in each quadrant.

In order to validate the tuning algorithm, we have performed a case study of the 20 cm long unmodulated model of ISNS RFQ with entrance end-cells, i.e., radial matching section. In the end-cell region, we have introduced an inductive perturbation in the form of a cylinder of diameter 50 mm inserted in the first quadrant up to 2 cm from the cavity surface. Since the perturbation was introduced in the first quadrant only, the 1-3 dipole mode was mixed in the operating mode, which resulted in the fractional field error $U_{d1}/U_{q0}$ of ~12% as shown by blue color curve in Fig. 2. Here, the field error due to the higher order quadrupole modes and 2-4 dipole modes was found to be negligible.

Since the capacitance variation $\delta C_p$ is related to the penetration depth variation $\delta h_p$ of the rod through the relation $\delta C_p = \xi\ \delta h_p$, where $\xi$ is the rod sensitivity parameter, the required penetration depth of each rod can be evaluated. Here, $\xi$ was calculated to be 37.74 pF/m/m using CST-MWS code.

Using the end-cell tuning algorithm, the penetration depth $\delta h_p$ of the quadrupole rods was calculated to be +11.62 mm, +0.36 mm, -10.86 mm and +0.39 mm in the 1st, 2nd, 3rd and 4th quadrants, respectively. With this much penetration of the quadrupole rods, the fractional field error has been reduced to ~1%, as shown by violet color curve in Fig. 2.

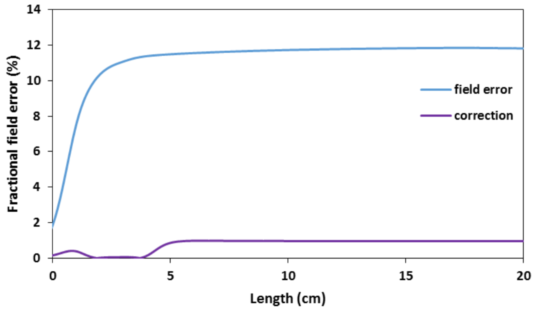


Figure 2: Fractional field error in the end-cell of the RFQ.

## REFERENCES

[1] A. Palmieri *et al.*, IPAC'10, Kyoto, Japan, May 2010, MOPEC062, p. 606.

[2] A. Palmieri *et al.*, IPAC'10, Kyoto, May 2010, MOPEC061, p. 603.

[3] Rahul Gaur and Vinit Kumar, *European Physical Journal Nuclear Sci. Technol.* 4, 9 (2018).

[4] CST Studio Suite 2014, www.cst.com.

[5] K. R. Crandall *et al.*, *RFQ Design Codes*, LA-UR-96-1836, LANL, USA, 2005.

[6] O. Delferriere *et al.*, EPAC'06, Edinburgh, Scotland, June 2006, MOPCH105, p. 285.

[7] O. Piquet *et al.*, IPAC'10, Kyoto, Japan, May 2010, MOPD027, p. 738.

[8] A. France and F. Simoens, EPAC'02, Paris, France, June 2002, p. 957.

# STUDY OF WAKE-FIELD AND LOSS FACTOR IN $\beta = 0.63$ & $\beta = 0.8$ ELLIPTICAL CAVITIES FOR HEHIPA

Alok Kumar Ghosh, Rajni Pande
Ion Accelerator Development Division, BARC, Mumbai

*Abstract*

The High Energy High Intensity Proton Accelerator (HEHIPA), a 1 GeV, 10 mA superconducting proton linac, has been designed for the Indian ADS programme. The high energy part of the linac consists of two families of 5-cell elliptical cavities with $\beta = 0.63$ and $\beta = 0.8$ to accelerate the beam from 200 MeV to 1 GeV. Calculations of wake potential and loss factors are important in designing superconducting accelerating structures. We have calculated wake potential and loss factor for a non-relativistic proton bunch passing through $\beta = 0.63$ and $\beta = 0.8$ 5-cell elliptical cavities. In the frequency domain, we have used CST eigen-mode solver to find the eigen-mode spectrum of the cavity. Using the monopole mode spectra of the cavity we have calculated the wake potential and loss factor for Gaussian bunches of different rms length. In the time domain, CST wake-field solver is used to find the wake potential for Gaussian bunchs of different rms lengths and loss factor has been calculated by integrating the wake potential over the bunch profile. Parasitic heat loss and single-bunch energy-spread due to wake fields have been estimated, from which it has been concluded that they have a negligible effect in the beam energy range of interest (200 MeV - 1 GeV).

## INTRODUCTION

A 1 GeV, 10 mA superconducting proton linac, has been designed for the Indian ADS programme. The low and medium energy section consists of an ECR ion source, a Low Energy Beam Transport line (LEBT), Radio Frequency Quadrupole (RFQ), Medium Energy Beam Transport line (MEBT) and three sets of 325 MHz single spoke resonator cavities. The high energy part includes two families of 650 MHz 5-cell elliptical cavities having geometrical $\beta$ values of 0.63 and 0.8.

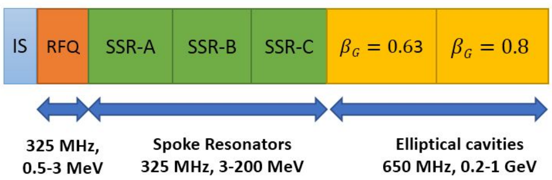


Figure 1: Schematic of the High Energy High Intensity Proton Accelerator (HEHIPA) for Indian ADS programme.

When a bunch of charged particles traverses a cavity it deposits some part of its energy as a result of its interaction with the cavity. This parasitic electromagnetic field trapped inside the cavity is known as a wake-field. The wake field generally modifies the designed field level inside the cavity and hence one must consider its effects. Wake field has both longitudinal and transverse components. In this paper we have studied the effects due to longitudinal wakefields. There are various ways through which these unwanted fields may affect the proton beam. First, the wake field produced by a particle is experienced by the trailing particles of the same bunch and they may be accelerated or decelerated relative to the source particle, leading to an energy spread in the bunch. Secondly, the EM energy lost by the bunch appears as the energy of the higher order modes, which continue oscillating inside the cavity and are dissipated producing heat on the cavity walls. The heat loss adds to cryogenic load. Here, we present the calculation of wake potential and loss factor using both methods (frequency domain and time domain), and also estimate its effect in terms of beam energy spread and parasitic heat loss.

Fine details of the wake fields are usually of lesser interest than the integrated effect of the driving bunch on a test particle travelling behind. Wake field is generally defined in terms of wake potential, which is the integrated energy change induced by a leading source particle on a unit test charge travelling on the same path at a constant distance $s$ behind, as both pass through the structure.

$$w_z(s) = -\frac{1}{q}\int_0^L dz[E_z(\vec{r}, z, t)]_{t=(s+z)/c} \tag{1}$$

Wake potential for a particle can be used as Greenâ€™s function to compute the same for a bunch of any charge distribution, as follows

$$W_z(s) = \int_{-\infty}^{s} ds'\lambda(s-s')w_z(s'), \tag{2}$$

where $\lambda(s)$ is the charge distribution of the bunch. Once the longitudinal wake potential is known, the total energy loss is calculated by integration of the wake potential over the bunch profile. Loss factor is defined as a measure of how much electromagnetic energy per unit charge a bunch leaves behind in the structure,is given by

$$k = \frac{\Delta U}{q^2} = \frac{1}{q^2}\int_{-\infty}^{\infty} ds\lambda(s)W_z(s). \tag{3}$$

## FREQUENCY DOMAIN ANALYSIS

In the frequency domain, fields trapped inside the cavity are represented as an infinite sum of fields of its eigen-modes. Since, here we are interested only in longitudinal wake fields excited by a bunch passing along the axis of the cavity, calculating the monopole modes will be enough. Modes having larger R/Q values are excited more in compared to the modes

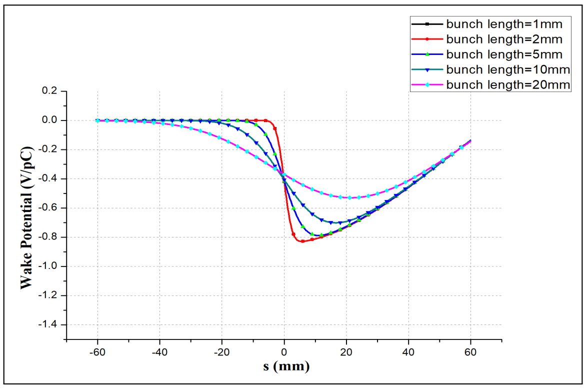


Figure 2: Wake potential induced by beam-cavity interaction in the 0.63-$\beta$ elliptical cavity for beam of different rms size.

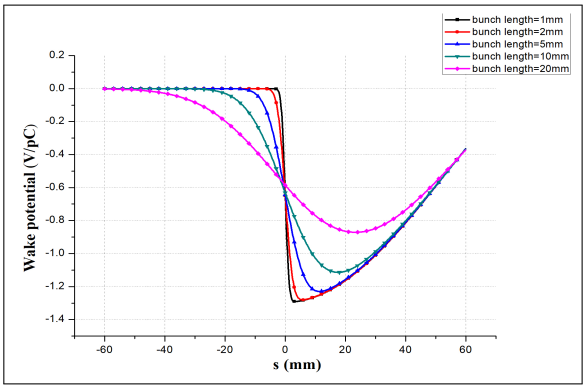


Figure 4: Wake potential induced by beam-cavity interaction in the 0.80-$\beta$ elliptical cavity for beam of different rms size.

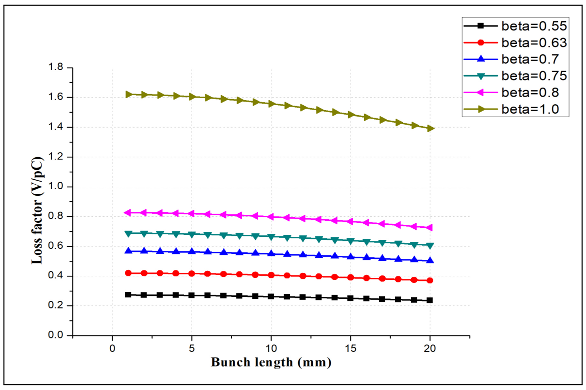


Figure 3: The total loss factor for the 0.63-$\beta$ elliptical cavity as function of bunch length calculated using frequency domain analysis.

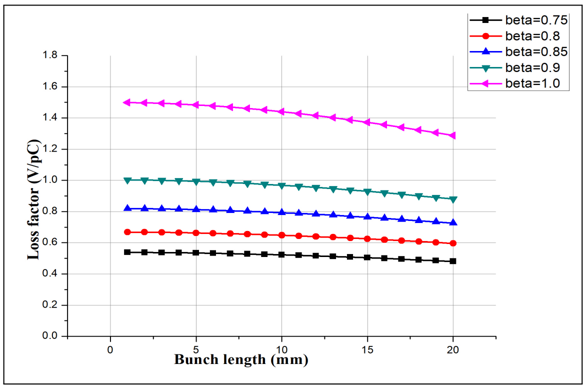


Figure 5: The total loss factor for the 0.80-$\beta$ elliptical cavity as function of bunch length calculated using frequency domain analysis.

having relatively lower R/Q value. Using the fundamental theorem of beam loading, one can show that loss factor for a particular mode excited by a point charge is given by

$$k_n = \frac{\omega_n}{4}\left(\frac{R}{Q}\right)_n \tag{4}$$

and the potential induced by a point charged particle of charge $q$ interacting with a single mode of the cavity is $V_n = -2qk_n$. So, the integrated energy variation of a unit test charge travelling at a distance $s$ behind the source will be

$$w_{zn}(s) = -2qk_n cos(\omega_n s/\beta c), \tag{5}$$

and the single-mode wake potential of a bunch having line charge density $\lambda(s)$ is given by the convolution of the point charge wake potential and the charge density function,

$$W_{zn}(s) = -2k_n \int_{-\infty}^{s} \lambda(s') cos\left(\frac{\omega_n(s-s')}{\beta c}\right) ds'. \tag{6}$$

The total wake potential is an infinite sum of individual mode wake potentials. We have calculated the wake potential taking Gaussian bunches of different rms lengths; these are plotted in Figure 2. Among the higher order modes only those having frequency below the beam pipe cut-off frequency will be trapped inside the cavity and hence contribute. The cut off frequency of our beam tube is about 2.7 GHz, below which there are 83 monopole modes. So wake potential for the first 83 monopole modes have been calculated taking a Gaussian bunch, and then summed over to get the total wake potential.

The total loss factor for a Gaussian bunch of rms length $\sigma$ can be written in the following form

$$k_{||}(\beta,\sigma) = \sum_{n=o}^{\infty} \frac{\omega_n}{4}\left(\frac{R}{Q}\right)_n e^{-\frac{1}{2}\left(\frac{\omega_n \sigma}{\beta c}\right)^2}. \tag{7}$$

The form of the equation is similar to the expression for loss factor for a particle (Eq. 4), except for an exponential factor to take into account the charge distribution of the Gaussian bunch. We have calculated the frequencies $\omega_n$ and $(R/Q)_n$ values for the first 83 monopole modes to get the loss factors for those modes and have calculated the total loss factor $k_{||}$ by summing over. The plot of integrated loss factor ($k_{||}$) as a function of rms bunch length ($\sigma$) for different beam velocities is shown in Figure 3.

With the help of the plots in Figures 2 & 4, the energy spread induced in a single bunch due to the wake field can easily

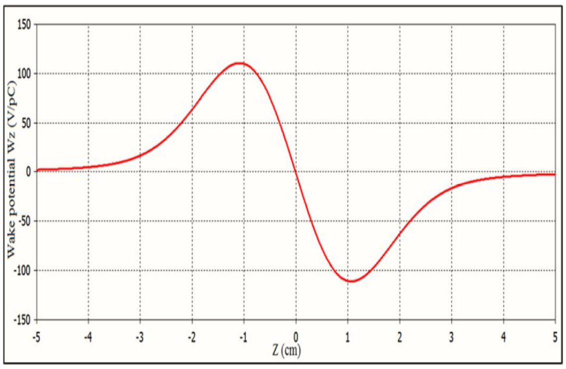


Figure 6: Result of time domain wake potential simulation using CST wakefield solver direct method in elliptical cavities.

be estimated using the following formula [1]

$$\delta\xi = -e \times q \times W_z' \times s, \tag{8}$$

where $s$ is the length of the bunch, $W_z'$ the slope of the wake potential with respect to distance $s$ and $q$ is the bunch charge. If the bunch length is 2 mm, then for a 10 mA beam current the energy spread induced in passing through 0.63-$\beta$ elliptical cavity is 10.27 eV.

We can also estimate the parasitic heat loss caused by the wake field, which is related to the loss factor ($k_{||}$) by the following formula

$$P_0 = f \times q^2 \times k_{||}, \tag{9}$$

where $f$ is the frequency or number of bunches per second, and $q$ is the bunch charge. For 0.63-$\beta$ elliptical cavities, in case of 2 mm bunch length, the average power is calculated to be 129 mW. For 0.80-$\beta$ elliptical cavity the estimated energy spread comes around 31.68 eV, and the average power dissipation is around 205 mW, as a result of passing of 2 mm Gaussian bunch with 325 MHz repetition rate.

## TIME DOMAIN ANALYSIS

We have used CST-PS wake field solver direct method in order to calculate the longitudinal wake potential for beams of velocity 0.63-$\beta$ and 0.80-$\beta$ travelling through a 5-cell elliptical cavity. In calculating the wake potential and loss factor we have followed exactly the procedure described in Ref. [2]. The functional form of the wake potential which the CST wake-field solver provides, and shown in Figure 6, contains both a static part (due to direct Coulomb forces) and a dynamic part (beam-cavity interaction). But we are interested in wake potential coming from the beam cavity interaction only. The procedure to eliminate the static part is described in Ref. [2]. One has to run two consecutive simulations with slightly different beam tube lengths. By taking the difference between the wake potentials for those two cases one can easily find the static part of the wake potential per unit length of the structure, assuming that the static part increases proportionally with the length of the beam tube.

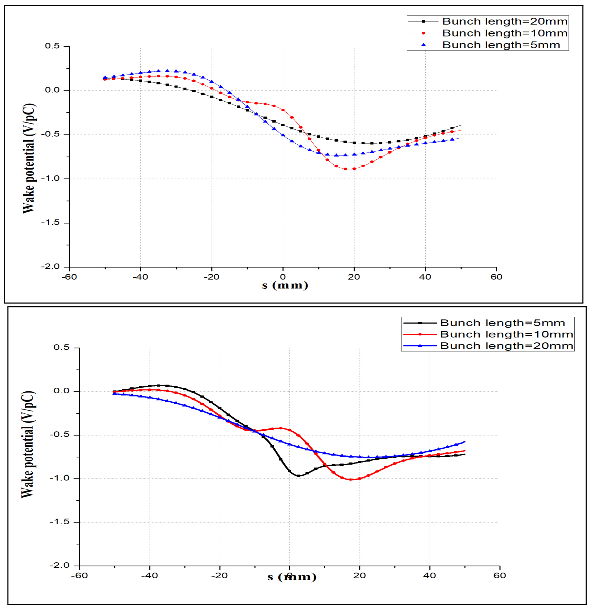


Figure 7: Wake potential (simulated in time domain) for the 0.63-$\beta$ and 0.80-$\beta$ elliptical cavities for three different bunch lengths.

By subtracting the static part of the wake potential from the total, the wake potential due to beam cavity interaction can be found out. Wake potential (simulated in time domain) for the 0.63-$\beta$ and 0.80-$\beta$ elliptical cavities for three different bunch lengths ($sigma$=5 mm, 10 mm and 20 mm) are shown in Figure 7. We have calculated the loss factor in the time domain using Eq. 3. For the 0.63-$\beta$ cavity, the loss factor for bunches of rms length 5 mm, 10 mm and 20 mm are 0.49, 0.33 and 0.33 V/pC respectively. The same for 0.80-$\beta$ cavity comes about 0.81, 0.56 and 0.53 respectively. The difference in values obtained using time domain analysis with that of the frequency domain analysis are quite small.

## CONCLUSIONS

The parasitic beam energy loss due to beam-cavity interaction in the high energy part of the HEHIPA linac has been estimated. The parasitic heat loss as a result of beam passing through both the 0.63-$\beta$ and 0.8-$\beta$ 5-cell elliptical cavities are small, and thus will not add anything to total cryolosses. In both cases, the energy spread induced in a single bunch due to wake field has also been calculated which are 10 and 31 eV respectively. The typical values of bunch energy spread in this energy range lies around hundreds of keV, with respect to which the energy spread induced as result of beam cavity interaction is negligible.

## REFERENCES


[1] Thomas P. Wangler, "RF Linear Accelerator".

[2] A. Lunin, V. Yakovlev and S. Kazakov, "CAVITY LOSS FACTORS OF NONRELATIVISTIC BEAMS FOR PROJECT X".

[3] Computer Simulation Technologies, http://www.cst.com/

# RECENT TRENDS IN HIGH POWER SOLID-STATE AMPLIFIERS FOR PARTICLE ACCELERATORS

Akhilesh Jain, D. K. Sharma, A. K. Gupta, K. Pathak, N. Kumar and Mahendra Lad

Raja Ramanna Centre for Advanced Technology, Indore, India

*Abstract*

The high-power RF amplifiers are indispensable and key technology for a broad set of commercial and strategic applications. Among these applications, the later one, meant for the high energy physics research and energy generation, embraces huge machines like particle collider, synchrotron radiation source and accelerator driven reactor. In last few years, the tremendous progress, reported for the solid-state RF amplifiers in VHF to C band, is progressively making them another promising candidate for extracting kW level of power in such applications. Along with having a clean spectrum (lowest phase noise and spurious), they offer attractive features like graceful degradation, low operating voltage, instant system start-up, modular as well scalable architecture and X-ray free operation. This article reviews the recent progress made globally and specifically, at Raja Ramanna Centre for Advanced Technology (RRCAT), in the development of high-power solid-state amplifiers. Few technology demonstrations are briefed up that have emerged from recent research and development at RRCAT.

## INTRODUCTION

For given light sources, high power RF systems decide major part of capital investment and operational cost, and directly impact overall capability and reliability. There have been regular research efforts [1] for the quest of optimum CW RF power systems for light sources. In the high average power domain, the choice is among a klystron, inductive-output tube, and solid-state RF amplifier. In last few years, the tremendous progress, reported for the solid-state RF amplifiers (SSRFA) in VHF to C band, is progressively making them another promising candidate for extracting kW level of power, with additional benefit of scalable, modular, cost effective, compact, reliable and mass-production friendly architecture.

Unlike vacuum tubes, the RF power which can be generated by a single semiconductor device is of the order of few hundreds of watts (average) and up to few kW for the pulsed operation. Hence, output power in a kW-level SSRFA is enhanced by using a combination of corporate and binary divide-and-combine architecture [2]. It incorporates multiple Power Amplifier (PA) modules, power divider and combiners. Equipped with the DC biasing, electrical hardware, cooling circuit and signal processing-control elements, it makes such architecture a standalone SSRFA. With the availability of high-power 50-65V solid-state device technology, the development of moderate power level (100W-1000W) PA module has become quite feasible for different applications.

## RECENT TRENDS AND GLOBAL SCENERIO

Recently, many institutes, including Soleil [3], PSI [4], and RRCAT [5], have harnessed the power of this cutting-edge technology by developing SSRFAs, either as a new requirement or for replacing their vacuum tube counterparts. In Soleil, four 180 kW solid-state systems are in operation at 352 MHz, with satisfactory operational availability, performance and MTBF. In PSI, a compact 500 MHz 65 kW amplifier is developed with unique optimisation algorithm at a given operating point, for system efficiency enhancement. At RRCAT, 505.8 MHz solid-state system, with total capacity of more than 250 kW, is operating in round-the-clock mode, for Indus-2 synchrotron radiation source. With these success stories, many accelerator laboratories [6] have adopted this technology. LNLS Brazil has successfully commissioned two 50 kW, 476 MHz SSRFAs in 2010. ESRF in France has already replaced some of its 1 MW Klystron with seven 150 kW, 352 MHz SSRFA. This work was executed by a French company ELTA, which had been given task of making seven 150 kW SSRFA, similar to SOLEIL design. More recently SOELIL, has built two 50 kW and 80 kW (at 500 Hz) SSRFA for ThomX at Orsay in France and for SESAME (a synchrotron light source in Jordan), respectively. Two 80 kW units are operation in SESAME since Dec 2016. Here SOLEIL tower has been replaced with cabinet type amplifier assembly, with modular power supplies, housed on the top of the cabinet. In China, an RF system using 250 kW, 166.6 MHz and 100 kW, 499.8 MHz SSRFAs are at advanced stage of development for a 6 GeV synchrotron light source. Recently, in BESSY-II, all klystrons were replaced with 500 MHz, 40 kW and 80 kW units of SSRFAs. The amplifiers are again housed in cabinets with output taken from a coaxial to waveguide type combiner. A few years ago, ESRF started R&D on cavity combiner type SSRFA, with prototype testing at 352 MHz for 85 kW power. Its design is based on amplifier modules, located around the circumference of a pill box type circular cavity. These modules are loop coupled to the cavity. Though purpose of the physical demonstration was to enhance the efficiency (56%) by eliminating RF cables, the additional problems (critical loop coupling, RF leakage, bulky single structure and poor output VSWR) jumped upon and erased this advantage. The cavity combiner based SSRFAs are under study at APS (352 MHz) and SPring-8 (509 MHz). The former is designed to combine 108 RF modules of 2 kW while the later one combines two cavity-combiner based 55 kW SSRFAs, each of which is having radial water cooled “cold plate wings” accommodating 4 RF modules of 600W. In due course of time, many designs in VHF and S band have been reported.

## SSRFA ACTIVITIES AT RRCAT

At RRCAT, three 60 kW 505.8 MHz Klystron based transmitters have been replaced in phased manner by solid state amplifiers, for Indus-2 synchrotron radiation source. Presently total installed and commissioned RF power capacity of six RF stations (five using SSRFAs and one using Klystron) in Indus-2 machine is nearly 320 kW. Other than this, 36 kW amplifiers were recently designed and commissioned at 650 MHz to power the horizontal test facility for superconducting cavities. In Indus-2 RF systems there are three 60 kW SSRFA and two 40 kW SSRFAs. 60 kW amplifier incorporates six 10 kW amplifier units (Fig. 1). Each such unit with divide-and-combine scheme, is a cluster of thirty-two RF modules (500W average), which are power combined with the help of a set of binary combiners and two 16-port radial combiners, as detailed in [5]. Its distributed control and interlock unit makes use of FPGA hardware, running LabVIEW based real-time operating system at its back-end. This 10 kW unit, along with power supplies and cooling circuit forms a basic amplifier unit which is complete in all respect from the operation point of view. The final output power of 60 kW comes from the corporate power combining scheme, combing two sets of three 10 kW units with the help of a 75 kW 2-port combiner and two 65 kW 3-port combiners (one for each set). Different high-power directional couplers were used to sample RF power at various junctions. These SSRFAs have been tested rigorously at full rated power and presently they are part of the Indus-2 machine, catering nearly three-fourth of the total power requirement for round-the-clock operation. Remaining two 40 kW amplifiers are made up of two units of 20 kW RF power. Full 20 kW power is managed in a single unit (cabinet) by using improved design of 2 kW power modules and 64 port radial combiner.

Fig. 1: 60 kW SSRFA comprising six 10 kW units

For such high power SSRFA, the analysis for studying the influence of the amplitude and phase imbalance, is mandatory. The PAs rarely have identical output (amplitude and phase) due to the tolerances of device/fabrication and variation in its impedance network. Consequently, post integration, this imbalance disturbs the even mode symmetry in power combiners.

It sets up an impedance mismatch at different interfaces. In general, the investigation of a high power SSRFA includes developing better design methodology for its building blocks and system level evaluation for the complete amplifier. PA design starts with the pertaining issues like RF transistor selection, impedance matching, load line, operating mode and device parasitic effects. The selection of the high-power RF transistor is enumerated and qualified in terms of its technical features, like the power gain, output power, linearity, efficiency, thermal management, and bandwidth. The classical scattering (S) parameters-based PA design theory is good enough and promises a best possible design for the small signal linear PA, biased for nearly full cycle conduction of drain current. For high power PA design this theory may not suffice due to several reasons [7]. Another approach for PA design is based on its operating mode and load line selection [7]. The selection of load line also depends upon the operating mode, which refers to different features which can be attributed to the PA design and characterization. Such attributes include the bias point selection (Class A, AB, B or C), selection of matching network topologies and the operating conditions of the transistor (Class E, Class S, etc.). Each set projects a specific efficiency, linearity, input drive power requirement and circuit complexity. For solid-state power modules, the traditional modes of operation [8] like Class B, Class F, inverse Class F and Class E have been very popular.

One such mode, the Class-J [9] is very popular for GaN semiconductor RF devices, offering an optimum treatment of even mode harmonics. It supports a wide band operation and simplicity in designing the output matching network. Nevertheless, this operation requires a high peak voltage at the drain terminal of the transistor. The present device technology for the UHF power MOSFETs, hardly permits this voltage to be more than twice of the rated power supply voltage. A sub-optimum solution to resolves this problem, lies in the selection of drain voltage waveform parameters' other than the optimum one. Such solutions present a feasible design space for a given device with its practicalities. Such continuous modes [10], extend the fundamental/harmonic impedance space over which power and efficiency performance of traditional modes can be maintained.

The 500 W RF PA module [11], which is a workhorse and the gain block of the 60 kW SSRFA, was designed with two similar amplifier stages, each one designed using LDMOS device BLF 573. These stages were power combined using circuit level 2-way planar Wilkinson divider and combiner. Each such stage operates in continuous Class J mode with half wave sinusoidal excitation.

A multi-way divide and combine architecture is adopted in a high power SSRFA. For N-way dividing/combining at high power, generally, a radial topology is preferred, due to their simple design and its tight control over amplitude and phase balancing among its branch ports. The radial combiners shown in Fig. 3 are 64-port structure, capable of handling 30 kW at the centre frequency of 505.8 MHz. Absence of external tuning mechanism, negligible amplitude-phase imbalance (0.2 dB and 2° respectively), and high-power combining efficiency (98.9%) makes this design repeatable, economic, and reliable. Their performance at full rated power, as measured from a batch of twenty pieces, was highly repeatable.

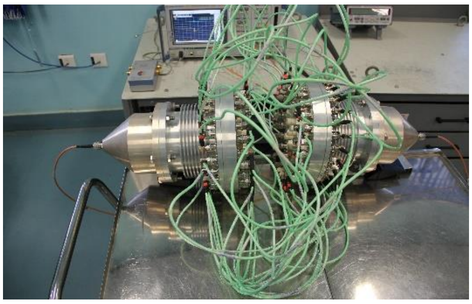

Fig. 2: Testing of 64-port radial power combiner

For high power measurement in the developed SSRFAs, different wideband (300-700 MHz) and compact directional couplers were designed to handle average powers of 1 kW, 5 kW, 20 kW and 65 kW, respectively. Their details are given in [2]. Fig. 3 shows a 60 kW coupler, developed using rectangular and non-symmetrical coaxial transmission lines.

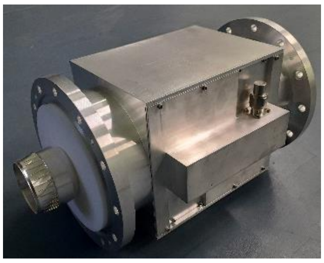

Fig. 3: 60 kW directional coupler

Other couplers at 5kW, 20 kW and 65 kW are similar in design except the coaxial media, selected to handle the rated power. They all have very low insertion loss (<0.1 dB) and directivity better than 22 dB at full rated power.

## CONCLUSION

In recent years, solid-state technology-based radio frequency and microwave amplifier, for communication as well as particle accelerators applications, have attracted a good amount of interest in the research community. Such amplifier system, operating in kW power regime, has modular and scalable architecture due to the moderate power handling capacity of active and passive RF components used therein. This review article provides a glimpse of the recent trends in the field of high-power solid-state amplifier and its constituent components viz. amplifier module, power combiner and directional coupler.

## ACKNOWLEDGEMENT

The authors are grateful for valuable guidance of Shri P. Shrivastava, Director, PAG as well as of Director RRCAT. The author acknowledges the contribution of SSRFAS and RFSD colleagues in various stages during the development of practical systems. SSRFAS team worked hard to convert the prototype version of the modules at 505.8 MHz and 650 MHz into reliable, production ready and thermally stable versions.

## REFERENCES


[1] Akhilesh Jain, "Investigations on High-Power Solid-State RF and Microwave Amplifiers for Superconducting Structures," Ph. D. Thesis, Homi Bhabha National Institute, Mumbai, 2014.

[2] Frederick H. Raab et al., "Power Amplifiers and Amplifiers for RF and Microwave," IEEE Trans. Microwave Theory Tech., vol. 50, no. 3, pp. 814-826, March 2002.

[3] P. Marchand, T. Ruan, F. Ribeiro, and R. Lopes, "Soleil RF system," Phys. Rev. special topics- Accelerators and Beams, vol. 10, no. 11, pp. 112001-112001, Nov 2007.

[4] M. Gaspar and T. Garvey, "A Compact 500 MHz 65 kW Solid-State Power Amplifier for Accelerator Applications," in IEEE Transactions on Nuclear Science, vol. 63, no. 2, pp. 699-706, April 2016.

[5] Akhilesh Jain et al., "Design and characterization of 50 kW solid-state RF amplifier," International Journal of Microwave and Wireless Technologies, vol. 4, no. 6, pp. 595-603, Dec 2012.

[6] Chaoen Wang, " Trends in RF Technology for Applications to Light Sources with Great Average Power," Proceedings of IPAC2014, Dresden, Germany, Nov 2014.

[7] Steve C. Cripps, RF Power Amplifiers for Wireless Communication, 2nd ed. Norwood MA, USA: Artech House Inc. , 2006.

[8] John B. Walker, Ed., Handbook of RF and Microwave power amplifier, 1st ed. UK: Cambridge university press, 2012.

[9] Peter Wright, Jonathan Lees, Johannes Benedikt, Paul J. Tasker, and S. C. Cripps, "A Methodology for Realizing High Efficiency Class-J in a Linear and Broadband PA," IEEE Trans. Microw. Theory Tech., vol. 57, no. 12, pp. 3196-3204, Dec 2009.

[10] Akhilesh Jain, P. R. Hannurkar, S. K. Pathak, D.K. Sharma, and A.K. Gupta, "Investigation of Class J continuous mode for high-power solid-state RF amplifier," IET Microwaves, Antennas & Propagation, vol. 7, no. 8, pp. 686 – 692, June 2013.

[11] Akhilesh Jain, A. K. Gupta, D. K. Sharma, P. R. Hannurkar, and S. K. Pathak, "Design and analysis of a high-power radial multi-way combiner," Int. J. of Microwave and Wireless Technologies, vol. 6, no. 1, pp. 83-91, Feb 2014.

# 200kV, 15mA HIGH VOLTAGE DC POWER SUPPLY CHARACTERIZATION

Amal S., Kumar Saurabh, Urmil M. Thaker, Aritra Chakroborty, Paul D Christian, Ratnesh Kumar., Mitul R Abhangi, Vala Sudhirsinh J, Praveenlal Edappala, Vismay Raulji, Rachana Rajpal, Rajesh Kumar, Ashok D. Mankani, and Ujjwal K. Baruah

*Institute for Plasma Research, Bhat, Gandhinagar -382 428*

**E-mail : amal@ipr.res.in**

***Abstract***

A compact and portable 200 kV, 15 mA High Voltage DC Power Supply has been designed and developed indigenously at IPR, Gandhinagar. High voltage part of this power supply is designed by using seven stage symmetrical Cockcroft-Walton voltage multiplier with high frequency front end converter. A 16.5 kV-0-16.5 kV, 16 kHz ferrite core transformer interfaces the voltage multiplier circuit with IGBT based half-bridge inverter having a switching frequency of 16 kHz. The high voltage power supply is tested for its functionality by connecting it to a 200 kV resistive load bank modules and the designed performance parameters are established. To study the behaviour of power supply under actual load conditions viz. an accelerator, a 200 kV hydrogen ion source has been integrated with the power supply and high voltage was applied on accelerating grid columns of ion source. This abstract describes the experimental results obtained from integration & testing of 200kV, 15mA High Voltage DC Power Supply with Ion Source and also describes the developmental aspects of the modular resistive load bank and voltage multiplier unit in detail.

## *Introduction*

The main application of the high voltage DC is to test cables having large capacitance, normally takes a very large current if it is tested with AC voltages [1]. High voltage DC also required for applications such as electron microscopes and x-ray units, electrostatic precipitators, particle accelerators in nuclear physics and so on[2] High voltages used in industry as well as research field can be divided into three classes: a) Alternating current voltages b) Direct current voltages and c) Transient voltages [1,2]. Joseph M. B. [3], has presented his paper the basic operation of voltage multiplier circuits and discussed guidelines for electronic component selection for diode and capacitor. R.Banwari, et al [4] has explained the design and developmental aspects of a -750 kV dc source for 750 keV industrial electron accelerator at CAT Indore. Juichi Tanaka, et al [6], has explained a new idea to develop 70 kV, 0.15-ampere DC power supply with a high frequency switching converter.

## *Details of Power Supply*

TABLE 1: Specification of 200kV Power Supply

| Parameters | Specification |
|---|---|
| Input voltage | 415V AC, 50Hz, 3 Phase |
| Input current | 22A per phase |
| Output voltage(kV) | 200 kV DC |
| Output current(mA) | Up to 15 |
| Nominal output power(kW) | 3 |
| Output ripple Voltage(kV) | 1.081 |
| Output ripple factor in % | 0.13 |
| Open Circuit Voltage(kV) | 220 |
| Voltage drop in multiplier(kV) | 20 |
| Inverter Frequency(kHz) | 16 |
| Multiplier Type | CW Full Wave Type |
| Polarity | Positive |
| Duty | Continuous |
| Dimensions($m^3$) | 1.3(L) x 0.5(W) x 1(H) |

## *Subsystems of Power Supply*

The design and constructional features of various subsystems of the high voltage power supply are briefly described in following subsections.

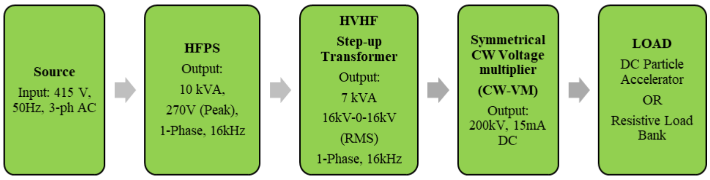


*FIG. 1. Genral Block Diagram of 200 kV, 15 mA High Voltage Power Supply*

### *Front End Converter*

The three-phase AC mains is rectified and filtered by an uncontrolled bridge rectifier and resultant DC voltage is fed to the inverter. A half bridge topology is used for the inverter with a fixed switching frequency of 16 kHz. The inverter output is controlled by changing amplitude of input AC supply using three phase variac, the position of variac is determined by reference signal. The position of variac is changed using PLC controlled VFD and inputs are fed through HMI. The output voltage of Multiplier circuit only depends on the Peak Value of the input i.e. here output voltage of the Inverter. Output Voltage of 200 kV Test Generator is measured by 300kV, 10000:1 Voltage divider.

### *High frequency Transformer*

A 7 kVA, 270 V: 16 kV-0-16 kV centre-tap transformer is an important link between the voltage multiplier circuit and the high frequency source and it plays a significant role on overall size, cost, performance and efficiency of the system. The operating frequency of the high voltage generator is chosen to be 16 kHz. The high frequency helps in reducing the size of the transformer. Ferrite cores are the ultimate choice at such frequencies having features which include high electrical resistivity, low core losses, low density suitable for light weight transformer, etc. Out of different shapes in which ferrite cores are available U core (EPCOS make U 93 core) is considered where high voltage isolation is required.

### *Voltage Multiplier Circuit*

The 7-stage multiplier circuit is realized using 3.3nF, 50 kV DC capacitors and 0.6 A, 15 kV, fast recovery diodes. A high frequency based symmetrical Cockcroft-Walton voltage multiplier circuit was chosen for generation of high voltage due to its design simplicity and economical construction. Components of the multiplier circuits along with its protective elements are distributed and arranged over Bakelite support structure. There are 7 no. of stages in voltage multiplier circuit. Spacing between the two successive stages has been maintained on the basis of high voltage consideration and practices. The electronic components of voltage multiplier circuit have been fitted on the reverse side of the top cover of the HV tank.

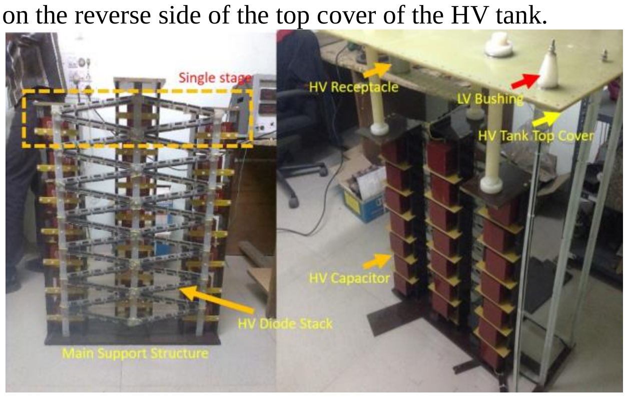


### *High Voltage Connector*

In order to connect the high voltage terminal of voltage multiplier which is inside the HV tank, to the load, flexible High Voltage x-ray cable with specially designed connector housings is utilized. The connector housing consists of R28 (225kV) Generator Receptacle fitted with Aluminium Flange and R28 (225kV) Straight Connector fitted with C2236 (250kV) High Voltage x-ray Cable.


### *High Voltage Resistive Load*

To fully test and characterize 200 kV, 15 mA DC Power Supply system an indigenously developed resistive load bank module is used. Load for 200kV rating has been built by assembling (stacking) two numbers of 100kV load bank modules in series.

### ***Expriment Setup with Ion Source***

The experimental setup mainly consist of two parts. (1) Ion source, Acceleration Column and its associated Control Systems (2) 200kV, 15mA High Voltage DC Power Supply for electrostatic acceleration column. All the components of ion source viz., Electron Cyclotron Ion Source (ECRIS) with its ion extraction system, Hydrogen gas generator, water cooling system, high voltage power supplies for Extraction of ion beam and focusing of ion beam are mounted on high voltage deck and it is kept on 200 kV floating potential. The input electric power to the entire high voltage deck assembly is provided through a DC isolation transformer (350 kV, 15 kVA). 300kV Acceleration column consists of 4 individual sections each rated for 75 kV. All the sections are connected back to back and each section have 5 electrodes. Voltage is evenly distributed using 10 nos. of 150Mohm resistors in series and demountable potential distribution rings are provided to normalise the electric field around the column. The interior of the column is maintained at negative pressure range of $10^{-6}$ torr while the exterior of column remains at atmospheric pressure. High voltage is applied for accelerating the hydrogen ion and ion acceleration depends on applied voltage. The hydrogen ion is fed from ECR ion source mounted at high voltage deck which remains at same potential as applied to the column. Beam current is measured at the end of the acceleration column using faraday cup. High voltage was applied from 0kV to 150kV in steps across the flanges, i.e, on front end of vacuum flange and other end is grounded.

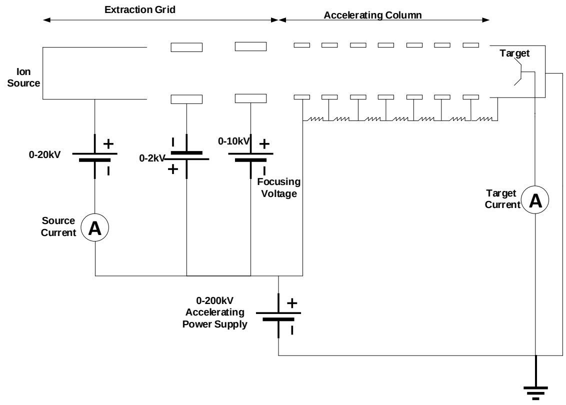


*FIG. 2. Schematic for experimental setup*

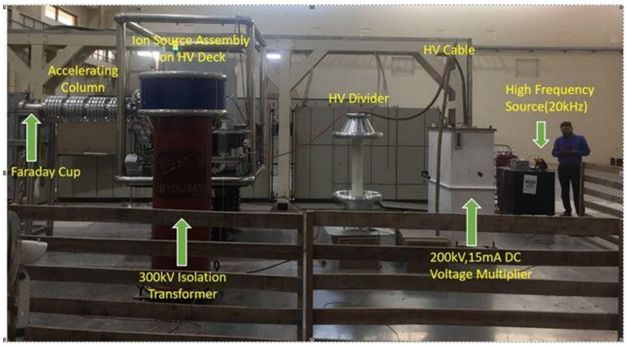


*FIG. 3. Arrangement of subsystems for experiment*

## *Expriment Results*

Initially the power supply was tested using 2 Nos. of 100kV, 10mA Load Bank Modules and results were shown in Figure 4. After that we had applied voltage across flanges of accelerating columns under no load & loaded condition. Under no load condition no ions were fed in to the column. Under loaded condition ions were fed in to the column and high voltage was applied. The load on 200kV power supply is directly depends on the ions fed to the column and the loading is adjusted using the extracting grid potential of ECR ion source. The ions fed into the column increases when the Extracting grid potential raises. The current under loaded condition was measured with faraday Cup, and the measured value is less than the actual current drawn from 200kV power supply because of the ion losses inside the column. A PLC based control system is used to control all the equipment installed on high voltage deck assembly. All the parameters like extraction voltage, focusing voltage, beam current at source and target etc. are controlled and monitored from centralized control unit. Results were shown in Figure 5.

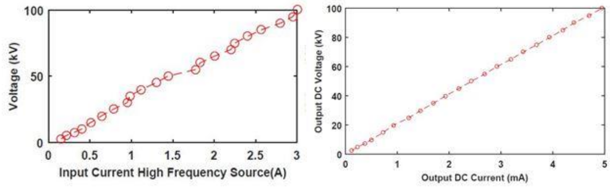


*Figure 4: Testing of 200kV DC Power Supply with 20MΩ Resistive Load Bank*

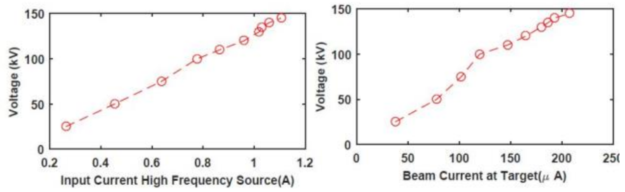


*Figure 5: Testing of 200kV Power Supply under Loaded condition with Ion Source*

## *Conclusion*

The power supply described above is an attractive scheme for generation of high voltage, high power system especially in million volts level. Various topologies / configurations to build this type of power supply were explored and studied, the Cockcroft-Walton based topology seems to be very promising owing to its simple design. In comparison with other alternative schemes, it has better performance with regards to voltage ripple and regulation.

## *Acknowledgement*

We offer sincere thanks to all colleagues of the institute for their co-operation and support in integration & testing of 200kV, 15mA High Voltage DC Power Supply with Ion Source. We would also like to thank Animesh Bhat, Transformers and High Voltage Equipments Ltd for his support during the development of power supply. Special thanks to the Director, IPR, for allowing us to develop this 200kV, 15mA power supply.

## *Reference*

[1] Kuffel, E. and M. Abdullah. (1984). High Voltage Engineering. Pergamon Press, Oxford.

[2] (Late) M.S. Naidu and V. Kamaraju, High voltage engineering, McGraw-Hill Education (India) Private Limited, 2013, pp. 152-155.

[3] Joseph, M.B. (2008) Using rectifiers in voltage multipliers circuits. Document Number: 88842 Vishay General Semiconductor.

[4] R. Banwari et al (2003). High Voltage Generator for 750 keV/ 20 kW DC Electron Accelerator.

[5] Amal S, et al (PLASMA-2014)."Design and Test Results of a 200kV, 15mA High Voltage Test Generator. Chapter 20 of Apple Academic Press, USA Pages: 321 to 338

[6] Juichi, T. and I. Yuzurihara. (1988). The high frequency drive of a new multi-stage Rectifier Circuit. Kyosan Electric Mfg. Co. Ltd., 2-29, Heian- Cho, Tsurumi-Ku, Yokohama, 230, Japan, IEEE.

# DESIGN AND DEVELOPMENT OF ICVG DISK RESONATOR BASED 650 MHz STRIP LINE FERRITE CIRCULATOR FOR PROTON LINAC

Manjeet Ahlawat†, Prashant Pareek, L. K. Aditya, Ashish Tiwari, M. Lad and R.S. Shinde, S.N. Singh

Raja Ramanna Centre for Advanced Technology, Indore, India

*Abstract*

Ferrite circulators are most widely used microwave devices to provide isolation between RF source and mismatched cavity, by circulating reflected RF power to third port terminated with matched termination. Under indigenous circulator development programme at RRCAT Indore, high power 650 MHz stip-line ferrite circulator has been designed and optimised using CST microwave studio, for RF systems of proton Linac at RRCAT. Disc resonator using Indium Calcium Vanadium Garnet (ICVG), circulator geometries, and biasing DC magnetic field have been optimised for low insertion loss and high isolation. MATLAB program is used for estimation of circulator disc-resonator radius and strip lines centre conductor geometry for 650 MHz. Thermal analysis has also been done on circulator for temperature rise at high RF power, using thermally coupled simulations. Heat resulting mainly from magnetic losses in 5 mm thick segmented ferrite resonator has been removed by implementing water cooling. Based on this design strip line ferrite circulator has been developed and tested. Excellent results with - 22 dB isolation - 30 dB reflection loss and - 0.2 dB insertion loss have been observed. Paper presents design aspects, optimisation of strip line geometry, electromagnetic and thermal simulation of ferrite circulator.

## INTRODUCTION

Ferrite circulators have been inevitable part of RF systems, used for isolation of RF source and variable or mismatched terminations. These are most widely used microwave devices which provide RF power coupling from any port to next adjacent port, and high attenuation in reverse direction. These find wide range of applications including duplexer, switch and isolator in RF systems. Operation of circulator is primarily based on tensor permeability due to ferromagnetic resonance, in magnetically biased gyromagnetic material. Disc or triangular resonators generally used in circulator, are made of gyromagnetic ferrite materials. When no dc magnetic field is applied ferrite material behaves as an isotropic medium for EM waves, but becomes anisotropic in the magnetic biased condition. In presence of dc magnetic field, spin axes of electrons of ferrite align themselves along the field. Now if RF magnetic field of propagating RF signal exists perpendicular to the spin axis, the electrons precess (wobble) about the axis of dc field. Larmor precessional frequency $\omega_L$ for the biased ferrite is given by is given by eq. 1[1].

$$\omega_L = g\frac{e}{2m_0}B = \gamma B_{dc} \tag{1}$$

$\omega_L$ = Angular precessional frequency, $B_{dc}$ = Total magnetic flux density, $ge/2m_0 = \gamma$ is gyro magnetic ratio, value of $\gamma$ for electron 27.95 GHz/T for electron.

The interaction between the spinning electrons and RF magnetic field is highest when the frequency of applied RF field is equal to Larmor precessional frequency. In this condition called ferrimagnetic resonance, maximum absorption of RF power takes place in the ferrite material. Absorbed RF energy is dissipated as heat. So this condition is avoided for non-dissipative devices like circulator.

Operation of a junction circulator is better understood by superimposition of two wave components or modes. Input RF signal can be visualized as having split in two parts (called modes) and propagate in clockwise and anti-clockwise directions. Phase difference of counter rotating modes with each other happen to be integer multiple of $2\pi$ at coupled port (for constructive interference), and odd integer multiple of $\pi/2$ at isolated port (for destructive interference) [1]. When the ferrite is not magnetized, two modes have same resonant frequency. But when a particular dc magnetic field is applied to ferrite, two (degenerate) modes resonate at different frequencies, due to different propagation speeds, causing little rotation of standing wave pattern in the ferrite resonator. Rotation of the standing wave pattern causes the maxima of electric field to be rotated towards one port, which becomes (more) coupled port, and minima closer to other port i.e. isolated port. The operating frequency of circulator is between resonant frequencies of two counter rotating modes.

## ELECTROMAGNETIC DESIGN AND MODELING

Magnetic biasing (or tuning) of the ferrite resonator is determined from the absorption plot of gyromagnetic ferrite materials as shown in figure 1. Initially material losses are observed at low values of biasing fields, which correspond to hysteresis losses. Losses are also observed in ferrimagnetic resonance region, when Larmour frequency (proportional to biasing dc field) is equal to frequency of operation. These all losses are dissipated as heat, which increase the ferrite temperature and in turn material properties.

Depending on the nature of device, RF devices are designed to work with magnetic biasing directly on, above or below resonance. Circulators are operated in either below or above resonance regions to avoid the absorption losses which may result in device insertion loss and heating.

#mahlawat@rrcat.gov.in

Circulators are designed to operate with biasing in above resonance or below resonance, primarily depending on frequency of operation.

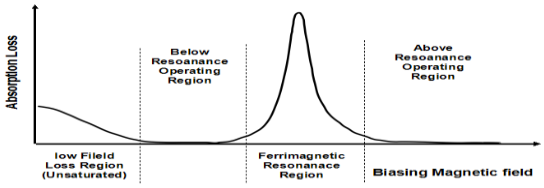


Figure 1: Magnetic biasing mode of ferrite resonator for low loss operation of circulator.

Circulators at higher GHz frequencies are designed to operate in below resonance to avoid unnecessarily high biasing fields, and are operated in below resonance at low frequencies (up to above 500 MHz) to avoid low-field losses [1].

Selection of ferrite-material for resonator is very important, which determines insertion-losses and overall performance of circulator. Low saturation magnetization is desired to reduce low-field loss region, and hence for wider below-resonance region. Ferrites with narrow resonance line width may need stringent magnetic biasing, but reduce insertion loss of the circulator, and so increase in power handling capability. This also reduces the heating of device, which may in turn change ferrite material properties. Higher spin line width gives higher RF peak power handling capability for a below resonance circulator, but not very critical for above resonance circulator (as in our case). Ferrite materials have high resistivity (~ $10^{12}$ for ICVG) reducing eddy current losses. Overall size of the junction circulator is inversely proportional to square root of its dielectric constant, which is desired to be high.

RF frequency & operating power level of the circulator are major parameters of a circulator. These parameters are crucial for a designer, to determine basic transmission geometry and type of resonator to be implemented, for successful operation.

Strip line transmission geometries are best suited due to smaller size at low frequencies (below 1GHz), while waveguide structures become unnecessarily bulky. At higher frequencies (in gigahertz range), wave-guides are preferred. Strip lines have high frequency limitations, and tend to be small & radiating. Secondly, operating power of the circulator is also important criteria for deciding basic transmission structure. Wave guides are bigger in size and have better heat dispersion as compared to isolated strip lines, so are preferred for high power (Mega Watt range), while strip line are suitable at lower power levels. At operating frequency of 650 MHz, strip line ferrite geometry is preferred, rather than bulky wave guide structure. Indium Calcium Vanadium garnet (ICVG) resonators are best suited around 500-600 MHz for low losses. Circulator is designed to operate in above resonance mode at this frequency to avoid both low field losses and also to avoid requirement of very low saturation magnetization ferrite material.

Three port circulators are most commonly used and can be cascaded together to get higher isolation & number of ports, so taken up for development.

On applying biasing magnetic field, permeability of ferrite resonator becomes tensor (Eq. 2) [3].

$$B = \begin{vmatrix} \mu & -j\kappa & 0 \\ j\kappa & \mu & 0 \\ 0 & 0 & 1 \end{vmatrix} H, \mu = 1 + \frac{\omega_0\omega_m}{\omega_0^2-\omega^2}, \kappa = \frac{\omega\omega_m}{\omega_0^2-\omega^2}, \quad (2)$$

Where μ diagonal, κ off diagonal permeability term, $\omega_m$ magnetization frequency ($\gamma 4\pi M_s$), $\omega_0$ gyromagnetic resonance frequency ($\gamma 4\pi H_{in}$), and $\omega$ operating frequency. Total internal magnetic field in the resonator, is sum of applied, anisotropic and demagnetization fields. Demagnetizing field is in reverse polarity to the applied external magnetizing force, and reduce resultant magnetic field inside the material. This is dependent on the shape of ferrite resonator used.

Circulator performance is based on total contribution of all constituent parts like resonator geometrical dimensions, and center strip line conductor width, thickness & radius, and magnetic biasing etc. The radius of the ferrite disk resonator is calculated by the visualizing the circulator as a ferrite loaded circular wave guide. Cut off frequency of dielectric loaded wave guide is calculated by standard method, solutions of which include the Bessel's function values.

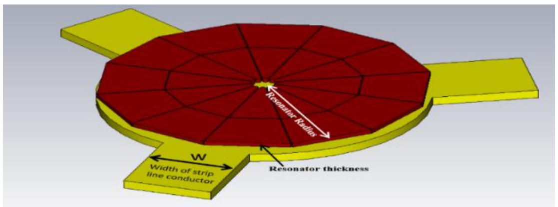


Figure 2: Ferrite disk resonator and stripline conductor dimensions indicating junction radius and strip line width.

For the dominant mode ($TE_{11}$ mode for circular waveguide), radius R (Fig. 2) of ferrite disk resonator, is given by the equation 3. [1, 2]

$$\text{Radius R} = \frac{1.84}{\omega\sqrt{\epsilon\mu_{eff}}} = \frac{1.84\,\lambda}{2\pi\sqrt{\varepsilon}}\sqrt{\frac{H_{dc}}{H_{dc}+4\pi M_s}}, \quad (3)$$

Where ferrite effective permeability= $(\mu^2 - \kappa^2)/\mu$, ε = ferrite permittivity, $M_s$ = Saturation Magnetization of ferrite material, 1.84 is first zero of derivative of Bessel's function and is product of R and wave number.

Width of the (120 degree apart) strip line conductors W as shown in Fig. 2, should be smaller than 0.75 resonator radius and 1/30$^{th}$ of wavelength [1, 2]. Strip line conductor width not to be very small, as it will lead increased losses.

Biasing magnetic field, about more than four times the resonance field, is used to bias the circulator in above resonance mode. Impedance of the strip line is matched to 50 Ω RF systems. 3D electromagnetic modeling, optimizations and thermal coupled simulation of the strip line junction circulator with sectored 166 mm diameter ferrite resonator geometry as shown in figure-3, has been carried out using CST Microwave studio. A circular central strip copper conductor is sandwiched between two partial height and segmented ferrite disk resonators, and the whole assembly is encapsulated within a metallic circular casing.

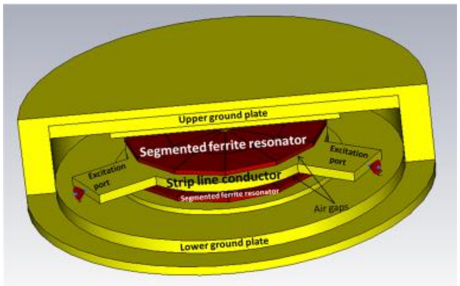


Figure 3: Designed strip-line ferrite circulator geometry using sectored 166 mm ferrite resonator modeled in CST Microwave Studio.

E-field pattern of the simulated circulator in figure-4 (left) indicates that maxima of E-field pattern is closer to the couple port, and away from the isolated port. It also shows that very low electric field pattern appears across the ferrite as compared to air gap (right).

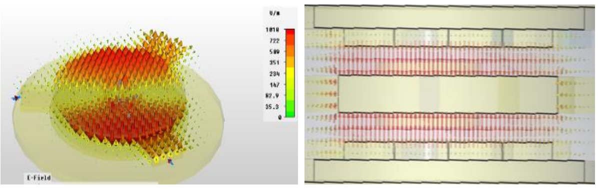

Figure 4: Top-view (left) and side-view (right) of E-field profile of the simulated circulator.

Magnetic properties of Indium Calcium Vanadium Garnet [3] such as saturation magnetization 850 gauss, and g factor 2, and dielectric constant 13 & resistivity $10^{12}$ Ω-m are used for design and modeling. Using this strip line dimensions and biasing field are optimized as shown in Table 1.

Table 1: Optimized Values of ferrite resonator and Strip Line Geometry.

| S. No. | Parameters | Values |
|---|---|---|
| 1 | Ferrite Thickness | 5 mm |
| 2 | Radius of ferrite disk | 83 mm |
| 3 | Stripline conductor width | 55 mm |
| 4 | Applied magnetic field | 1400 Oe |
| 5 | ICVG Curie temperature | 190 °C |

Thermal analysis of strip line circulator has been carried out to estimate the temperature profile and heat dispersion in circulator. Maximum observed temperature in ferrite resonator 323 K at 10 kW, which is much below than the Curie temperature of ICVG.

## MEASUREMENT RESULTS

Developed circulator has been tested at low power using Keysight Technologies E-5071 vector network analyzer, observed results are shown in figure 5. The reflection ($S_{11}$), insertion loss ($S_{21}$) and isolation ($S_{12}$) measured are ~ -22 dB, -0.2 dB, and -30 dB respectively.

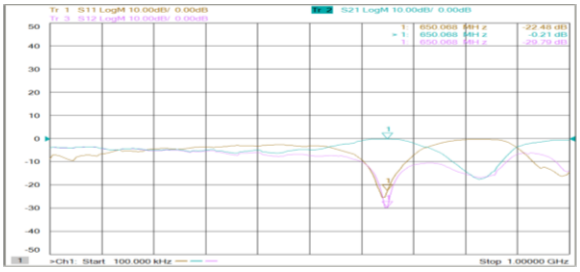

Figure 5: Measured S parameters of the circulator at low power using VNA.

As evident from this, most of the RF power input at any port is circulated to the coupled port, and very small fractions to isolated port. Also reflection from the input port is minimized to less than -20 dB.

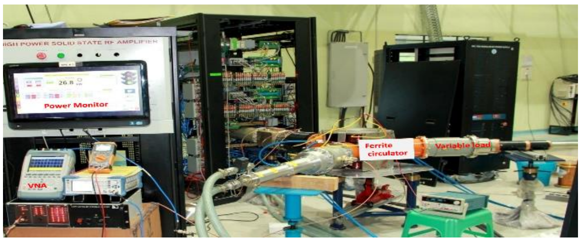


Figure 6: High power testing of the developed strip line ferrite circulator.

Port impedance matching was analyzed using smith chart, to ensure impedance matching around 650 MHz. Also high power testing of the developed circulator has been carried out as shown in figure 6, up to 36 KW satisfactorily.

## CONCLUSION

Strip line circulator with ferrite disc resonator has been designed, developed and tested. The measured reflection, insertion loss and isolation of prototype strip line ferrite circulator are ~ -25 dB, -0.2 dB, & -22 dB respectively, and around 50 MHz bandwidth. Measurement results are in close agreement with simulated data, thus realizing low loss performance, of high power circulator.

## ACKNOWLEDGMENT

Authors are indebted to Sh. A.C. Thakurta, director electron accelerator group board, RRCAT, for constant encouragement throughout the research work.

## REFERENCES

[1] Linkhart, Doughlas K., “Microwave Circulator Design”, Arctech house Inc. MA, USA 1989.
[2] Bosma, H., “On Stripline Y-circulators at UHF,” IEEE Transactions on microwave theory and techniques, January 1964, pp. 61-73.
[3] L. K. Aditya, R. Meena, M. Ahlawat, P. Pareek P. Kulshreshtha and R. S. Shinde, "Development of indium doped calcium vanadium garnets for high power CW circulators at 505.8 MHz for Indus-2" , INPAC 2018, RRCAT, Indore

# DEVELOPMENT & COMMISSIONING OF 150 KW RF AMPLIFIER FOR *K*130 RTC

Samares Kumar Manna#, Aditya Mandal, Surajit Ghosh, Sudeshna Seth, Prodyut S. Chakraborty, Saikat Paul, UmaShankar Panda, P. R. Raj,J. S. Prasad, Swarnendu Thakurtha, Umesh A Bharambe, Durjadhan Kar, Mrityunjoy Santra, Sourav Ch Pal & Dr. Sumit Som

Variable Energy Cyclotron Centre, Kolkata

## *Abstract*

The RF amplifier for K130 Room Temperature Cyclotron is to provide rf voltage across the accelerating electrodes. The rf amplifier has the frequency range of 5.5 MHz to 16.5 MHz. The power amplifier is based on Eimac 4CW 1,50,000E Tetrode Valve. The purpose of this new development is to replace BURLE 4648 based amplifier which has become obsolete. The input of the amplifier is matched using 4-Bridge-T Network mesh for wide band frequency operation. The output of the amplifier is connected to resonator tank using a kapton film based coupling capacitor. The tube used here is in grounded cathode configuration. The anode of the tube is water cooled of maximum anode dissipation 150 KW. PLC based system has been used to measure the parameters like voltage, current, RF power, water flow and air flow. PLC system ensures the turn on sequence of different power supplies for the amplifier and also provides safety interlocks. The amplifier was installed and running successfully for the operation beam tuning. This paper describes various technical aspects of the development.

## INTRODUCTION

A tetrode based 150 KW CW amplifier has been developed, tested and commissioning for K-130 RTC from frequency range of 5.5 MHz to 16.5 MHz. The amplifier will be used to accelerate different type of beam for K-130 RTC. The power amplifier is based on EIMAC 4CW150,000E tetrode. The purpose of this new development is to replace BURLE 4648 based amplifier which has become obsolete. The input of the amplifier is matched using 4-Bridge-T Network for wide band frequency operation. The output of the amplifier is connected to one end short circuited λ/4 resonator tank. The tube used here is in grounded cathode configuration. The anode of the tube is water cooled of maximum anode dissipation 150 kW. PLC based system has been used to measure the parameters and provides safety interlocks. The amplifier was installed for the operation beam tuning and running successfully.

## *Circuit configuration*

A tetrode based amplifier is chosen due to easy availability in wide range of frequency and power range. A signal generator is used to get low power signal of required frequency. The output of the signal generator is fed to a voltage regulator. Then this regulator gives signal drive to a solid state driver amplifier, which was developed in-house. The output of the driver amplifier is fed to 4 port splitter. This power is fed to the Bridge –T-Network of the input (Grid) of the tetrode tube. Anode of the tube is coupled with coupling capacitor using 3-layers (5mil each) of kapton film. Measured capacitance is 11nF, tested high voltage up to 30 kV. The amplifier is finally coupled to one end short circuited λ/4 resonator tank, which is having movable panels for operating variable frequency from 5.5 MHz to 16.5 MHz.

## *Layout of circuit*

The block diagram of the amplifier is shown in Fig 1. The circuit diagram of Eimac 4CW150,000E tetrode valve is shown in Fig.2. The characteristics curve showing different anode current by drawing load line for calculating peak anode current in Fig.3 and technical specifications like tube capacitances are given in Table 1. Electrical parameters are given in Table 2.

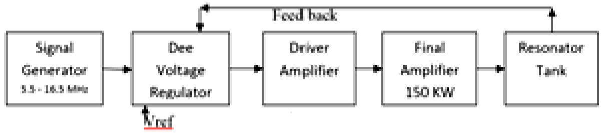


Figure 1: Block Diagram

Table 1. Tube Capacitances

| Tube inter electrode capacitance | Capacitance (pf) |
|---|---|
| $C_{in}$ | 370 |
| $C_{out}$ | 60 |
| $C_{gp}$ | 1.0 |

Table 2. Electrical Parameters

| Eletrical parameter | Volt/Current |
|---|---|
| Filament Voltage | 15V |
| Filament Current | 200A |
| Grid Voltage | -500V to - 200V |
| Plate Voltage | 18 kV |
| Plate Current | 11 A |
| Screen Voltage | 1500V |
| Screen Current | 1.5 A |

#samares@vecc.gov.in

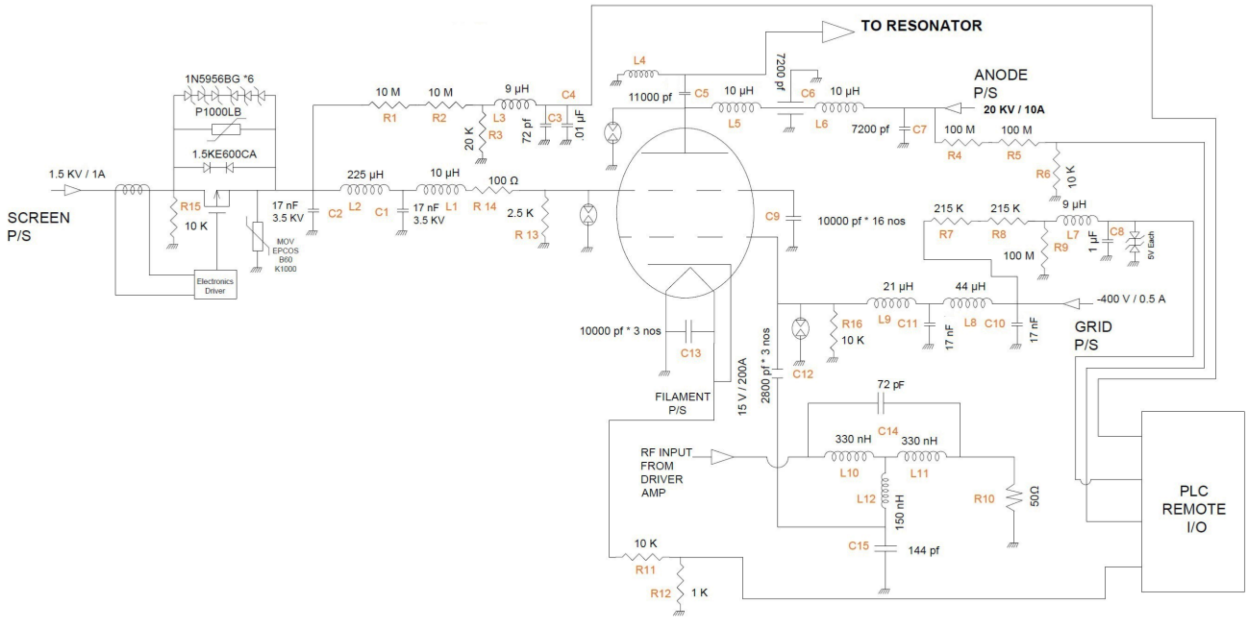


Figure 2: Circuit Diagram

*Input matching network*

A Bridge –T type network for wide frequency range of 5.5 MHz to 16.5 MHz is used. The input capacitance ($C_{in}$) as per data sheet is 370pf, in addition Miller capacitance and base & other stray capacitances. As the tube is circular in nature, to balance equal distribution of signal power four such network is used. This power is divided by 4 and given in 4 port Bridge-T networks and terminated by 50Ω water cooled load.

Different components of the amplifier are described below-

a) Anode coupling capacitor
b) RF Choke

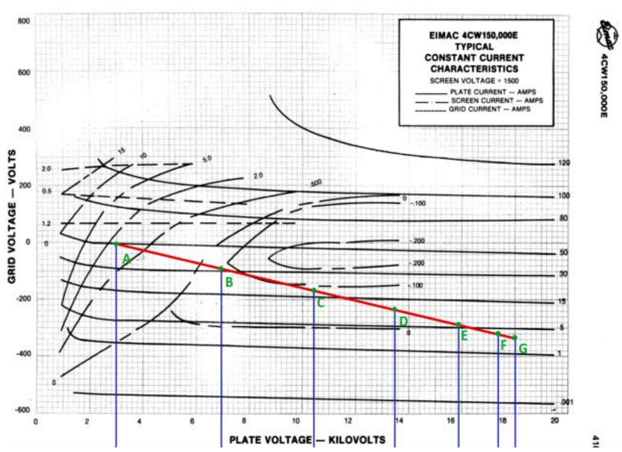


Figure 3: Load line

*Anode coupling capacitor*

A cylindrical capacitor showing in Fig.4 is designed, tested twice the operating voltage and handling high current capability at high frequency. The inner and outer conductor is separated by 3 layers of kapton film. The capacitance measured by LCR meter is 11nF and tested up to 30kV holding voltage without any spark by high voltage tester.

*RF choke*

To protect the power supply from RF interference two stages PI- type filter choke has been used having values of 10µH and 10µH with large current handling capacity. A feed through capacitor of value 3500pF is used in this PI-type filter.

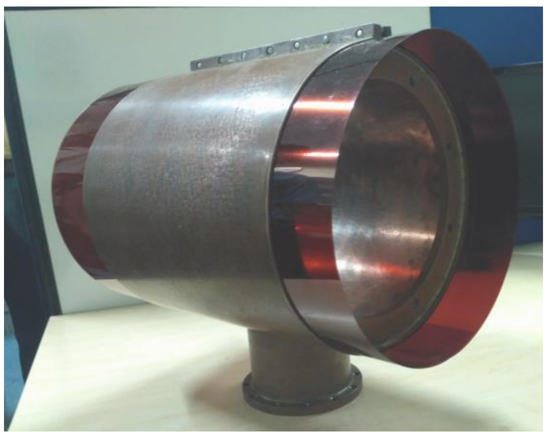

Figure 4: Anode coupling capacitor

### *PLC and amplifier protection system*

All the amplifier interlock namely under voltage, over voltage, over current, air flow, water flow, sequential operation like on/off of the amplifier tube and measurement of parameter like voltage, current, power are taken care by the PLC. Slow ramp up of filament voltage and control of other parameter of the tube and safety of the power supply is done by PLC. All interlocks are maintained failsafe and implemented in PLC.

Figure 5: Amplifier Cabinet

components like capacitors, spark gaps, RF filters is done as per schedule. The amplifier is running satisfactorily round the clock for last eighteen months since its installation.

### *RF switch*

A RF switch used in the amplifier chain to disable the RF input in case of any failure. ZFSWHA-1-20+ Mini-Circuits [3] make RF switch is used which provides more than 55 dB isolation. PLC system provides the control voltage which enables or disables the RF switch depending on tetrode amplifier status.

### *Amplifier cooling system*

Anode cooling is accomplished by circulating low conductivity water (1µsimen) using teflon tube (ID:18 mm) of proper fitting for high voltage isolation of anode terminal. The base of filament (hot terminal) also cooled by low conductivity water maintaining proper isolation. The tube and the base is fitted in a cabinet which is cooled by forced air (300 cfm). The amplifier anode dissipation 150 kW requires 110 LPM low conductivity water. Main amplifier cabinet is shown in Fig.5.

### *Anode Crowbar/ Screen Crowbar*

A fast acting crowbar system designed to operate within 3 µ sec is required to protect the RF tube in case of an overload. For this purpose a crowbar module [4] having fast switching power MOSFET with its high current driver has been designed. This deliver a high quality trigger pulse with adequate power to turn on the 5C22 Hydrogen Thyratron to trigger the series pass tube to go to the cut-off region. A simultaneous pulse is given to screen power supply using thyristors to divert the energy from the screen electrode in case of an overload in screen or anode power supply.

## CONCLUSION

During the installation and commissioning of the amplifier minor mechanical alignment was done for coupling with the resonator input port. Amplifier cooling system is made of virgin grade teflon tube. The amplifier generated required Dee voltage at different frequencies for accelerating different charged particles as required by users. Regular maintenance and cleaning of high voltage

## ACKNOWLEDGEMENT

The author(s) wish to thank all of the people who helped in development and commissioning of the amplifier. RF mechanical section fabricated the kapton based coupling capacitor as per our requirement. The authors would like to thank Power Supply Instrumentation (PSI) section and workshop for their continuous help and support.

## REFERENCES

[1] M. Kireeff Covo, et. al.,"UPG and Commissioning of the 88 inch Cyclotron Final Power Amplifier".

[2]"EIMAC 4CW150,000E" tube data sheet printed in USA by Varian EIMAC /301 Industrial Way/ San Carlos, CA 94070/ U.S.A. May 1983.

[3] https:// www.minicircuits.com/pdfs/ZFSWHA-1-0 +.pdf Datasheet ZFSWHA-1-20+ Mini-Circuits.

[4]Samit Bandyopadhyay, et.al. "Power supplies for the RF system of K-130 Cyclotron at VECC,Kolkata" Inpac 2011.

# CLOSED LOOP CONTROL OF SYMMETRICAL COCKCROFT-WALTON HIGH VOLTAGE GENERATOR


Arka Mitra, Rehim.N.Rajan

Bhabha Atomic Research Centre, Mumbai-400085, India.



*Abstract*

Symmetrical Cockcroft-Walton Multipliers are used in DC electron accelerators to generate high DC voltage. To maintain the beam energy at the specified level, its output voltage should be controlled within 2% of set value at all operating conditions. So it is of paramount importance that the output voltage of symmetrical Cockcroft-Walton multiplier is controlled in closed loop. With that objective, the dynamic characteristics of symmetrical Cockcroft-Walton voltage multiplier have been studied. A transfer function for square wave input has been obtained analytically by using discrete time model and verified by experimental setup. A controller for controlling the high voltage output of a 10 stage symmetrical Cockcroft-Walton voltage generator has been designed by dominant pole compensation method in C8051F120 micro controller environment. Experimental validation of analytically obtained closed loop response has been performed on a prototype 10 stage symmetrical Cockcroft-Walton multiplier with 20 kV, 5mA rating. The deviation of experimental result is below 10% from the analytical result for closed loop response.


## INTRODUCTION

Decades after invention of Cockcroft-Walton Multiplier, they are still widely used to generate high voltage in various applications like DC accelerator, X Rays, electron microscope etc. due to their several advantages like lower voltages stress across the diodes and the capacitors, higher voltage ratio, compactness etc [1]. Conventional voltage multipliers have relatively higher regulation and ripple which can be minimized using Symmetrical Cockcroft Walton topology [2]. To maintain the beam energy at the desired level, the voltage output of the multiplier has to be controlled in closed loop. With that viewpoint, charge transfer characteristics of symmetrical CW multiplier have been studied and a transfer function for the multiplier has been derived. That transfer function has been used for the closed loop control of the high voltage multiplier.

## DERIVATION OF TRANSFER FUNCTION

The transfer function is derived for square wave input and with certain assumptions. The load is assumed to be divided equally across each smoothening column capacitors. The capacitors are ideal and they charge and discharge instantaneously at the rising and falling edges of the input [3]. All the capacitors are of equal capacitance. The input waveform is divided into 6 segments (Fig 1) and in each time segment the voltages across the capacitors are evaluated

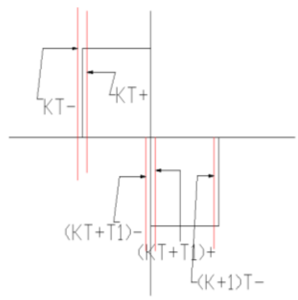


Figure 1: Input square Wave

### *Transfer function for five stages*

In Symmetrical multiplier case, each stage is affected by previous and next two stages. That's why a 5 stage multiplier is chosen as the basic block for obtaining the generalised model (Fig. 2).

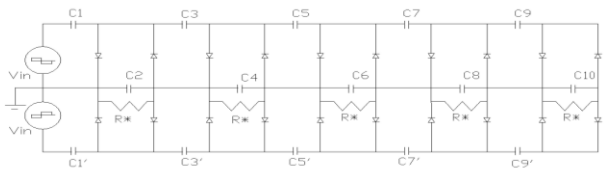


Figure 2: Five stage symmetrical Cockcroft-Walton multiplier

During positive half cycle half of the diodes will be forward biased and half of them will be reverse biased and act as open circuit (Fig. 3).

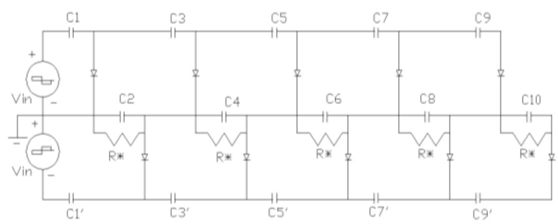


Figure 3: Multiplier during positive half cycle

In the loop containing $C_1^{'}$, $C_2$ and $C_3$, $C_1^{'}$ is charged to $-V_{in}$ in the negative half cycle. The net voltage across $C_2$ at $KT^+$ is obtained by superposing effects of input voltage $V_{in}$ and charge balance between $C_1^{'}$, $C_2$ and $C_3$ (see Eq.1).

$$V_2(kT)^+ = V_3(kT)^+ = \frac{1}{C_1^{'}+C_2+C_3}(C_3V_3(kT)^- + C_2V_2(kT)^- - C_1^{'}(2V_{in}))$$

$$= \frac{1}{3}(V_3(kT)^- + V_2(kT)^- - 2V_{in}) \tag{1}$$

For the other loops, there will be instantaneous charge balance at the rising edge. The total charge stored in the capacitors of a loop should be conserved before and after the rising edge of the input pulse. Hence the instantaneous voltages at $KT^+$ can be obtained by dividing the total stored charge in those capacitors just before the rising edge by the equivalent capacitance of the loop. Here each capacitor is having equal capacitance. So the voltage across the loop becomes average of the voltages of its capacitors just before the rising edge ($KT^-$). For example:

$$V_4(kT)^+ = V_5(kT)^+ = V_3^{'}(kT)^+ = \frac{1}{3}(V_5(kT)^- + V_4(kT)^- + V_3^{'}(kT)^-) \tag{2}$$

During the flat portion of the positive half cycle, the smoothening column capacitors will discharge through their parallel resistors and the voltages across the oscillating column capacitors will remain unaltered. The discharge time constant $K_1$ is given by $e^{-\frac{t}{CR^*}}$, where R* is total resistive load divided by number of stages.

During the negative half cycle the other set of diodes will come into conduction as shown in figure 4.

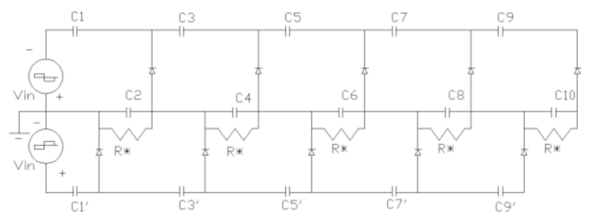


Figure 3: Multiplier during negative half cycle

The charge balance in loop containing $C_1$, $C_2$ and $C_3$' will follow the form of Eq. 1 and other loops will follow Eq. 2. During the flat portion of the negative half cycle, again the smoothening column capacitors will discharge through their parallel resistors.

The Aforementioned formulation gives following set of state equations:

$$V_2(K+1)T^- = -(\frac{2K_1}{3}+\frac{2K_1^2}{9})V_{in} + (\frac{1}{9}+\frac{K_1^2}{9})V_2(KT)^- + \frac{2K_1}{9}V_4(KT)$$

$$^- + \frac{1}{9}V_6(KT)^-$$

$$V_4(K+1)T^- = -\frac{2K_1}{9}V_{in} + \frac{2K_1}{9}V_2(KT)^- + (\frac{2}{9}+\frac{K_1^2}{9})V_4(KT)^- + \frac{2K_1}{9}V_6(KT)$$

$$+\frac{1}{9}V_8(KT)^-$$

$$V_6(K+1)T^- = \frac{K_1}{9}V_2(KT)^- + \frac{2K_1}{9}V_4(KT)^- + (\frac{2}{9}+\frac{K_1^2}{9})V_6(KT)^-$$

$$+\frac{2K_1}{9}V_8(KT)^- + \frac{1}{9}V_{10}(KT)^-$$

$$V_8(K+1)T^- = \frac{1}{9}V_4(KT)^- + \frac{2K_1}{9}V_6(KT)^- + (\frac{5}{18}+\frac{K_1^2}{9})V_8(KT)^-$$

$$+(\frac{5K_1}{18})V_{10}(KT)^-$$

$$V_{10}(K+1)T^- = \frac{1}{6}V_6(KT)^- + (\frac{5K_1}{12})V_8(KT)^- + (\frac{K_1^2}{4}+\frac{1}{6})V_{10}(KT)^- \tag{3}$$

## *Transfer function for generalised symmetrical CW multiplier:*

From Eq. 3 it can be seen that first two state equations contain input terms. The third equation shows that state voltage of 3rd stage smoothening column capacitor depends on two of its predecessor and two of its successor stages. This equation, in fact, provides the general form of a smoothening column capacitor voltage from 3rd stage to n-2nd stage where n is the total number of stages. The last two stages will have a different form of state equation because they will not have two successor stages.

Hence state equations mimicking eq. 3 can be written for n stage symmetrical CW multiplier where $V_n$ is voltage of $n^{th}$ stage smoothening column capacitor:

$$V_1(K+1)T^- = -(\frac{2K_1}{3}+\frac{2K_1^2}{9})V_{in} + (\frac{1}{9}+\frac{K_1^2}{9})V_1(KT)^- + \frac{2K_1}{9}V_2(kT)^- + \frac{1}{9}V_3(KT)^-$$

$$V_2(K+1)T^- = -\frac{2K_1}{9}V_{in} + \frac{2K_1}{9}V_1(KT)^- + (\frac{2}{9}+\frac{K_1^2}{9})V_2(KT)^- + \frac{2K_1}{9}V_3(KT)$$

$$+\frac{1}{9}V_4(KT)^-$$

For i = 3 to n-2

$$V_i(K+1)T^- = \frac{1}{9}V_{i-2}(KT)^- + \frac{2}{9}K_1V_{i-1}(KT)^- + (\frac{1}{9}K_1^2+\frac{2}{9})V_i(KT)^-$$

$$+\frac{2}{9}K_1V_{i+1}(KT)^- + \frac{1}{9}V_{i+2}(KT)^-$$

$$V_{n-1}(K+1)T^- = \frac{1}{9}V_{n-3}(KT)^- + \frac{2K_1}{9}V_{n-2}(KT)^- + (\frac{5}{18}+\frac{K_1^2}{9})V_{n-1}(KT)^-$$

$$+(\frac{5K_1}{18})V_n(KT)^-$$

$$V_n(K+1)T^- = \frac{1}{6}V_{n-2}(KT)^- + (\frac{5K_1}{12})V_{n-1}(KT)^- + (\frac{K_1^2}{4}+\frac{1}{6})V_n(KT)^- \tag{4}$$

## Experimental Validation:

The state equations given by Eq.4 are validated using a 20 kV, 5 mA rated 10 stage voltage multiplier powered by a fixed DC source via a buck chopper and a free running 10 kHz inverter. The block diagram of the voltage generator and its control loop is shown in figure 4.

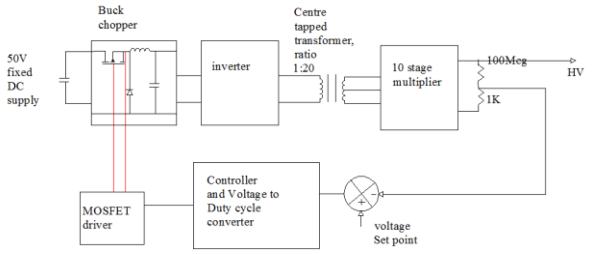


Figure 4: Block diagram of voltage control loop

The state equation of buck chopper is well documented in literature [4]. So, combining the second order chopper model and 10$^{th}$ order model for 10 stage multiplier, we obtain a 12 stage transfer function for the overall voltage generator loop.

## Controller Design:

A PI controller has been designed based on dominant pole compensation method [5]. The hardware voltage generator model has a dominant pole at 158.3 rad/s. All other poles are at least 10 times further away. So the proposed controller transfer function is: $K\frac{S+158.3}{S}$.The zero at the dominant pole location will result in pole zero cancellation. The integrator pole will contribute to a -20dB/decade slope. Hence the gcf will be controlled by the controller gain. After some iteration it is observed that at gain 0.5 we get a gain margin of 36.9 dB and a rise time of 250 ms, which is acceptable for the system.

## RESULTS AND CONCLUSION

The experimental and the analytical results for open loop step response for 15 V DC input and 70% duty cycle of the voltage generator system is shown in Figure 5.

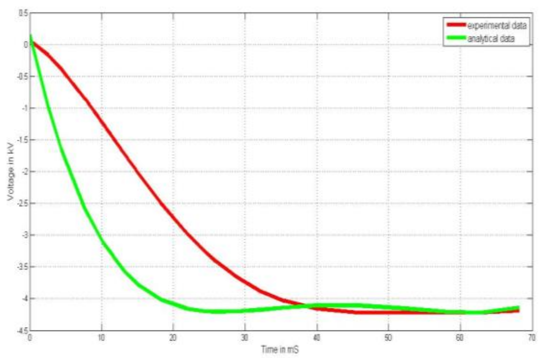


Figure 5: Comparison of open loop response at 15 V DC input and 70% duty cycle

We can see that initially the responses differ but they finally settle to same steady state value. Their rise times are also within 30 to 40 ms. The initial sluggish response for the experimental system may be due to unaccounted factors such as leakage inductance of the transformer and non square input voltage.

The closed loop response for -5.5 kV set point is shown in figure 6.

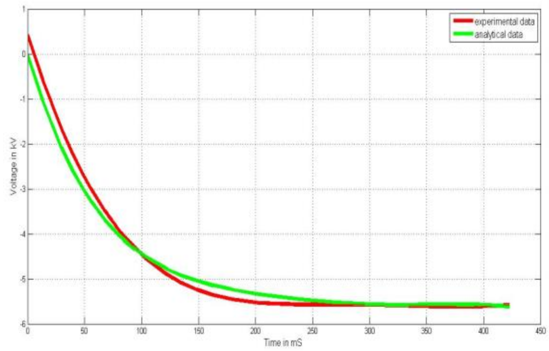


Figure 6: Comparison of closed loop response at -5.5 kV setpoint

### *Conclusion*

The transfer function of symmetrical CW voltage multiplier under square wave input has been theoretically derived. The closed loop controller for voltage control of symmetrical Cockcroft-Walton based HV DC generator system has been designed and implemented on hardware. A 20 kV, 5 mA rated 10 stage symmetrical CW multiplier has been fabricated and tested up to 15 kV HV output. The analytically obtained results have been verified by hardware testing. The closed loop controller response is found to be closely following the analytical results. This model can be used for controlling the output voltage of generalised symmetrical Cockcroft-Walton multiplier.

## REFERENCES

[1] S. Iqbal, “A hybrid symmetrical voltage multiplier”, IEEE Transactions on Power Electronics, vol. 29, no. 1, pp. 6–12, 2014.

[2] Mohsen Ruzbehani Hindawi, “A Comparative Study of Symmetrical Cockcroft-Walton Voltage Multiplier”, Journal of Electrical and Computer Engineering Volume 2017, Article ID 4805268,

[3] A. Lamantia , P.G. Maranesi , L. Radrizzani, “Small-signal model of the Cockcroft-Walton voltage multiplier”, IEEE Transactions on Power Electronics, Vol. 9, Issue 1, pp 18-25, 1994

[4] Robert W. Erickson, “Converter transfer functions”, *Fundamentals of Power Electronics*, second edition, University of Colorado, Boulder, Colorado, pp 293-300, 2004.

[5] Richard Tymerski, Loop Compensation Design Case Study: Buck DC-DC switching converter [online]. Available:https://ieeeauthorcenter.ieee.org/wp-content/uploads/IEEE-Reference-Guide.pdf

# CONTROL SYSTEM FOR FIRST TRIAL RUN OF FDG PRODUCTION AT DAE MEDICAL CYCLOTRON FACILITY KOLKATA

Umashankar Panda#1, Aditya Mandal[1], Sabyasachi Pathak[1], Suprakash Roy[1], Niraj Chaddha[1], Sudeshna Seth[1], Surajit Ghosh[1], Anirban De[1], Anindya Roy[1], Malay Kanti Dey[1], Sumit Som[1], Umesh Kumar[2], Sankha Chattopadhyay[2]

*Abstract*

DAE Medical Cyclotron Facility [1] at Kolkata was installed by Variable Energy Cyclotron Centre. There was a requirement to demonstrate the functioning of the machine for FDG production in the liquid target beam line. Complete wiring and control interface for this machine was done by our team. We developed control programs and graphical user interface indigenously without the help of the supplier. Successful trial run for demonstration of FDG production was carried out on 17th September 2018. This paper describes the control and operation approach in depth of this indigenous campaign.

## INTRODUCTION

The high-current proton cyclotron system (CYCLONE-30) is supplied by M/s Ion Beam Application, Belgium. The cyclotron has a capacity of maximum beam current of 500 μA and the beam energy within 15 to 30 MeV. There are five external beam lines – one for PET isotope production (mainly, FDG), two for SPECT isotope production and two beam lines for research and development. The commissioning of this cyclotron got delayed due to delay in building infrastructure. Due to some contractual consequences VECC had to commission this machine without involvement of the supplier.

## CONTROL REQUIREMENT

All the supplied components were assembled and installed in its desired location in November 2017- April 2018. Mechanical installations and alignments were done. Power supplies and control panel were installed. Control and power connections were done as per documentation supplied.

Process control and control interface plays an important role in the operation of such machine. Errors in the control interface can be unsafe for human and machine. There was no program supplied with the process controller and there was no control software. We had to develop it fully for remote automatic operation. We had the operation manual and the experience of VECC colleague as the source of information to build the control system. We planned the total works in phases. We build the control system for one sub-system at a time, tested and operated it before starting of another sub-system in sequence.

1 VECC / DAE Kolkata #usp@vecc.gov.in
2 BRIT / DAE Kolkata

## HARDWARES AND SOFTWARES

### *Control Hardware*

Siemens S7-400 series PLC is used in this cyclotron for control of the total cyclotron components including beam lines. There are 512 di, 288 do, 16 relay, 48 ai and 32 ao channels configured in main station. (See Fig. 1)

For control of ion source one remote I/O station is there which is at floating at -30 KV and is configured as Profibus DP slave and communicating with optical fire cable for electrical isolation. This station has 16 di, 16 do, 8 ai and 8 ao channels.

There are also 12 nos of Pfeiffer Vacuum make TPG300 vacuum gauge controllers. These controllers have Profibus DP communication and vacuum threshold relays. The relays are configured to provide vacuum level information to main PLC via the discrete inputs. PLC reads the vacuum levels through configured profibus DP communication with the TPG300 units.

### *Graphical user interface (GUI) software*

EPICS based Control System Studio [2] was selected for this machine. This is open source and quick for developing accelerator control. We used s7nodave IOC module for communicating with PLC. Control System Studio and EPICS IOC of s7nodave are time tested at several international accelerators and also at VECC cyclotrons. There are 1254 records in the EPICS IOC communicating with PLC out of which 733 are bi, 329 are bo, 149 are ai and 43 are ao records.

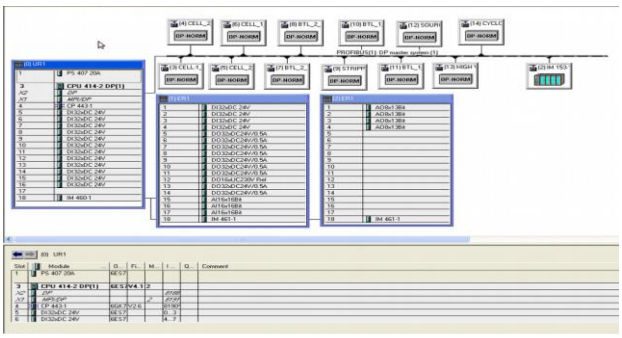

Figure 1 : screenshot of PLC hardware configuration

### *PLC Programming*

Siemens Simatic manager software [3] was used for programming. Sequential Flow Charting (SFC) language was selected for simplicity in programming and diagnostics. SFC has an advantage of quick development of process flow, easy to understand and easy for trouble shooting by team member.

All inputs and outputs were configured in PLC and GUI to display the status for run time diagnosis.

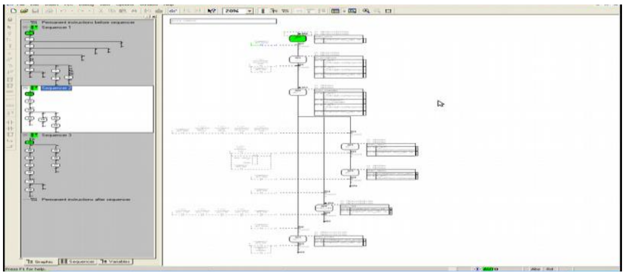

Figure 2 : SFC for main chamber vacuum

## CONTROL DESCRIPTION

### *Vacuum System*

Vacuum system control is divided into three parts. Main acceleration chamber vacuum, Ion Source vacuum and beam line vacuum. Sequential control of several valves, pumps and vacuum monitoring is done programmatically to avoid human error. Main vacuum chamber is pumped by four numbers of cyro-pumps. Injection line has a turbo-molecular pump. Ion source and beam lines are having oil diffusion pumps (ODP). These vacuum systems have four modes of operations i.e. High Vacuum, Stand-By, Off and Venting. Venting is possible when the systems are stopped. All cryo-pumps are having a regeneration facility. All these vacuum systems are backed by rotary vacuum pumps.

Interlock Fail Conditions: For all vacuum system - cooling water low flow and low fore vacuum level. In case of ODPs, high oil temperature interlocks also there.

### *Main Magnet Control*

Main magnet is having a current controlled power supply. The current can be set from 95 – 105 A via GUI. There is a fine control of +/- 1 A over and above these set point.

Interlock Fail Conditions: Cooling water low flow, Yoke not down, main magnet power supply fault, safety fail

### *Ion Source Control*

First the ion source faraday cup is put in and remote operated discharge road is disconnected from ground and flash light is put ON. There are two high voltage supply systems for ion source. One -36 KV is for ion source and another at -20 KV is for eingel lenses. These power supplies are first ramped at a ramp rate of 100 Volt per second. While stopping these system has a ramp down facility also. After these power supplies attend the set point Glasser lens power supply, Steering Magnet power supply and inflector power supply are put ON. Then the power supplies for Electron Supressor, Puller and ARC are put ON. Hydrogen gas is put ON. Then finally filament is put on with ramp rate of 0.5 A/s. Beam current is observed at Injection Faraday Cup. It should be less than 1000 micro Ampere to make the Faraday Cup out and start the particle injection.

Interlock Fail Conditions : Cooling waters low flow, Yoke not down, main magnet power supply off, beam chamber low vacuum, ion source low vacuum, vault door limit switch, ion source power cabinet door limit switch, Water temperature high, Water resistivity high, Pneumatic pressure high, power supplies fault, safety interlock fail.

Start Up Interlock : Interlock not failed, Pop Up In and Injection Faraday In.

### *RF Control*

RF system operates in an automatic sequence. If there is no interlock failure final power amplifier blower is set on. Then the filament, grid and anode started sequentially. The driver amplifier gets on after the filament of final power amplifier is on. The modulator is started when final amplifier, driver amplifier are on. The modulator is responsible for maintaining the Dee voltage and frequency at its set value.

Interlock Fail Conditions: Main magnet power supply not on, cooling waters low flow, Yoke not down, beam, chamber low vacuum, vault door limit switch, Water temperature high, Water resistivity high, Blower air flow switch, power supplies faults and safety interlock fail.

### *Stripper Control*

There are two carbon stripper foils placed inside the beam chamber by stripper control system. These are required for converting the H- beam to proton beam inside the cyclotron and deflect it to two extraction ports. There is a rotating carousal for holding 12 nos of stripper foil holders. Carousal movement is control by a d.c. motor and positioning limit switches. The stripper insertion mechanism has three types (Longitudinal, radial and azimuthal) of movements operated by d.c. motors. Limit switches and position feedbacks are used for their control. All three movements is responsible for picking of the stripper foils and then to place it inside the cyclotron high vacuum through air lock sealing and pumping assembly. There are gate valves to seal the cyclotron high vacuum from air lock assemblies when the strippers are out to the air lock position. Longitudinal movement in and out operation has slow and fast mode depending upon the limit switch positions. Radial movement is responsible for determining the extraction energy level from 15 MeV (full in) to 30 MeV (full out). Azimuthal movement moves the stripper in left or right direction. It required fine tune the placement of the beam in the extraction port. There is a stripper foil beam current monitoring system to monitor the current in the stripper foil during tuning the cyclotron beam parameters. This

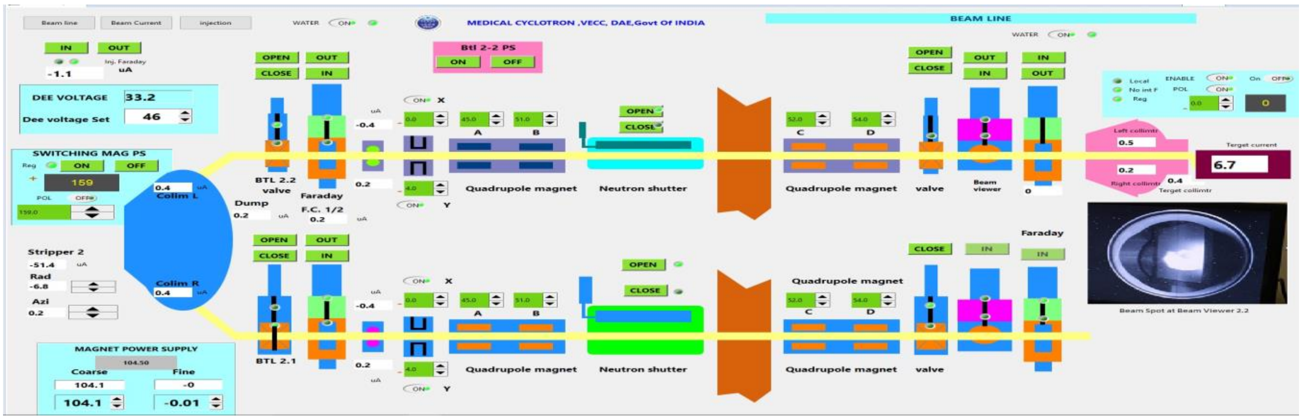


Figure 3: Screenshot of GUI showing irradiation of liquid target 2 at 6.7 micro amp

current monitoring also ensure the beam at the extraction radius and proper functioning of the stripper foil.

Interlock Fail Conditions: Cooling water low flow, air pressure low;

Insertion start up interlocks: RF Off, Magnet Off, Ion source Off;

### *Pop Up Probe Control*

This probe is inserted to beam path inside beam chamber during initial beam tuning or development to ensure proper acceleration of the beam after coming out from the inflector. The Pop Up probe is inserted to check the beam current on it. The beam current on this probe is optimised by tuning the ion source, injection magnets, focusing lens and inflectors. After tuning injection line, this probe is taken out from the beam chamber which let the beam travel to the stripper foil for extraction.

Interlock Fail conditions: Low water flow, low air pressure

### *Beam line switching magnet control*

When the H- beam is converted to proton beam using stripper it is further tuned to travel through this switching magnet. There is a beam dump at the centre of the switching magnet and in between two beam lines. There is also beam current monitoring provision at two collimators at two sides of this magnet and one at beam dump. These measurements are required to position the beam in the proper path. The magnet current of the switching magnet can be varied with a provision for polarity inversion. The value of current and polarity determines the beam transport to the desired beam line.

Interlock fail conditions: Low cooling water flow, High magnet temperature, power supply fault.

### *Beam line control*

Each beam lines have vacuum pumping stations at two ends. Two faraday cups are there, one at entry and other before the target. After first faraday cup there is a pair of drum collimators and steering magnets. Two sets of quadruple magnets are there one at the end of vault and other at start of the cave. In between vault and cave there is a neutron shutter. One beam viewer is placed before the target side faraday cup. Faraday cups and beam viewer has in and out actions with limit switch feedback. A camera is placed near the beam viewer to monitor and tune the beam to optimised shape. This image is viewed from remote monitor at control room. Beam current mentioning is also provided at drum collimators, two faraday cups and two horizontal collimators before target and final one at the target itself. Beam line magnets current are controlled as per the beam tuning need. These magnets have also a provision for polarity inversion. Neutron shutter of the beam lines opened only when it is required to pass the beam to the target caves.

Interlock fail conditions: Low cooling water flow, High magnet temperature, power supply fault, low pneumatic air pressure, low vacuum level

Start up interlock: Cyclotron high vacuum, beam line high vacuum, beam line faraday cup inserted, vacuum isolation valves opened

### *Liquid target control*

There are two liquid target lines in PET beam lines for production of F-18 irradiated liquid used for FDG production. Loading and unloading of O-18 water is done via an Ethernet controlled syringe module remotely with the help of a Siemens S7-300 PLC control system. There is a PET switching magnet to transfer the beam to the selected liquid target.

## CONCLUSION

On 17th September 2018 we had the first successful irradiation on liquid target 2 with 6.7 micro amp beam (See Fig. 3) beam for forty minutes at 18 Mev approx. F-18 produced was successfully transferred out by remote operation and with this FDG was produced at VECC.

## REFERENCES

[1] R. K. Bhandari, "Medical Cyclotron Facility at Kolkata; Cyclotrons and Their Applications 2007, Eighteenth International Conference, p.87

[2] www.epics.anl.in

[3] www.support.industry.siemens.com

# 120 MSPS VME BASED ADC CARD FOR DIGITAL BPI

R. P. Yadav, R. Rana, P. Fatnani
RRCAT, Indore, India

*Abstract*

The Beam Position Indicators (BPI) are important part of any accelerator based facility. They provide online beam position in any SRS facility. This information is used by beam physicists for studying machine dynamics. Beam position is used by active feedback control systems like Slow Orbit Feedback control systems and Fast Orbit Feedback control systems to control the beam position to the desired beam trajectory. The beam position information is contained in the button electrode signal in the form of amplitude modulated high frequency voltage signal. To digitize this processed signal in analog domain, a VME based ADC board is being developed to digitize the 505 MHz signal at 120 MSPS with 16 bit resolution. This paper presents the overall scheme and the initial characterization results obtained for this developed board.

## INTRODUCTION

The Digital BPI are used in accelerator machines around the world. The Digital BPI calculate the beam position by processing of pickup signals (4 button electrode pickup voltages) in digital domain. Efforts are put by different SRS machines towards the development of digital BPI electronics[1,2,3]. In INDUS-2, the RF frequency is at 505.8MHz and thus the pickup electrode signal also contains the beam position information in amplitude modulated form at the 505.8 MHz in about 1Mhz bandwidth. The digital BPI electronics development task needs different sub system developments like Analog Front-end (AFE) part, Digital Signal Acquisition and Conditioning (DSAC) and system bus (VME in our case) handling, signal processing in FPGA, Instrument configuration management & Control System Programming Interface (CSPI) development and High Speed Data Grouping & Sharing (HSDGS) part. Separate hardware are being developed for the AFE, DSAC and HSDGS on the VME platform. This paper discusses the DSAC design concept and some of the initial tests carried out on the first version of this board. Presently the second version of the board with modifications incorporated to address some of the issues faced in this prototype is under fabrication.

## DESIGN CONCEPT

The basic concept behind the design of the DSAC card is to build the digital processing platform on the VME bus infrastructure so that the digital signal processing requirements of DBPI can be fulfilled while keeping the flexibility of logic reconfiguration and card auxiliary resources utilization so that the same card can be used in other accelerator control system applications like LLRF signal processing and other high speed data converter applications. Spartan 6 Family based FPGA module has been chosen for providing the re-configurable logic platform to implement the filters, Digital Down Converters (DDC), Buffer Memory, IQ demodulation CORDIAC and Look Up Tables. The ADC blocks along with the VME BUS Interface Logic has been interfaced with the FPGA I/Os for seamless integration of logic fabric among the Acquisition block, processing block and data sharing block. Table 1. Lists some of the system features that are incorporated in the design.

Table 1: DSAC card features

| Sr. No. | Block Name | Feature partitioning |
|---|---|---|
| 1 | ADC Interface | 4Ch. AC-coupled, 16 bit@ 125MSPS,<br>Usable BW: 10 to 600MHz (-3db),<br>Input FS: +7dBm or +11dBm, Synchronized sampling on trigger, Trigger : External, PLL locked, on-board clock (jitter <1ps),<br>Gain error for 505.8 ± 2MHz : ≤ 0.5dB |
| 2 | Data processing Logic block | Spartan 6 LX150 family device,<br>(24 + 8) 3.3V LVCMOS I/O’s on VME P2 for interfacing to AFE and HSDGS.<br>SDRAM : DDR2 512Mbit,<br>NVRAM : 4Mbit |
| 3 | VME interface logic block | Logic fabric shared with the common pool, Upto VME 32 standard supported, DTB Slave : A32/A24/A16 / D32/D16/D8 /BLT32/BLT16, BLT : D32/D16, Interrupt : IRQ 5 vectored. |
| 4 | Timing block | PLL locking: MC / Ext. Trigger (Zero Delay Mode) / Programmable XO,<br>PLL mode : fractional + integer<br>Jitter attenuation bandwidth : 0.1 Hz to 4K Hz programmable. |

The signal processing of the DBPM is based on the under-sampling technique to sample the signal from four button electrodes with four ADCs at the rate of 119.0117MHz, which is ~69 times the storage ring revolution frequency. As a result of under-sampling, the aliased signal appears at 29.75MHz, mirrored from the 9$^{th}$ Nyquist zone. The digital signal processing is required to be implemented in FPGA to digital down convert this amplitude modulated signal from four electrodes to baseband signals using series of filters (like CIC and FIR) and decimation, TBT rate data (about ~600KHz) and lower frequency data (like 10KHz for FA and 10Hz for SA ) are needed to be calculated in steps from the four raw baseband signal channel values using the difference

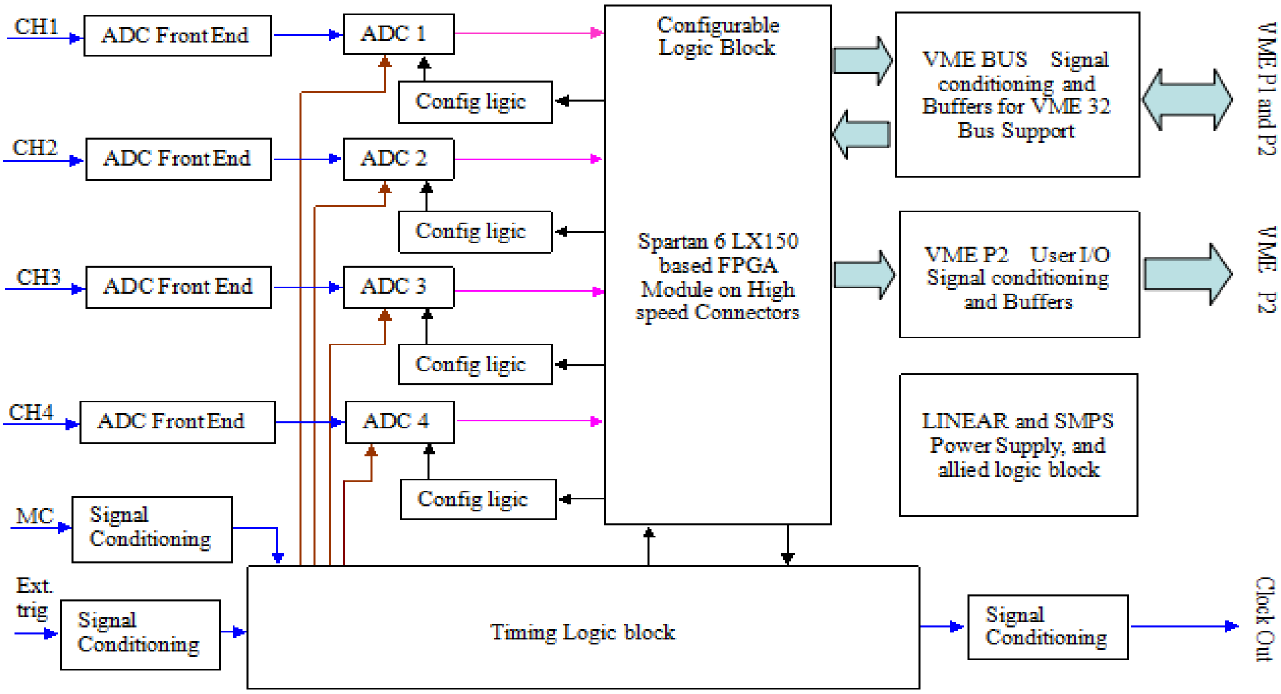


Figure 1: Block diagram of the DSAC card.

over sum (Δ/Σ) method. This multi rate data are needed to be stored in circular buffers so that it can be passed to the CPU over VME bus. The VME Bus interface is implemented in FPGA to support up to VME32 standard. The overall card design comprises of the following blocks.

- Hardware (HW)
- Software (SW)
  - Embedded Software for FPGA
  - Embedded Software for SBC

## *Hardware*

The HW is constructed to fulfill several goals :

- Ability to digitize the RF signal @505.8 MHz using the under-sampling concept for at least 4 channels.
- Use of commercial FPGA modules (so that in the initial prototypes the difficulties faced in the FPGA circuit can be avoided to speedup the process).
- 16 bit ADC should support sampling at ~120MHz for under-sampling to be achieved at ~505.8MHz. Where the sampling frequency is given by

$$f_{sample} = \frac{4}{4n+1} f_{acc}.$$

- Provision for synchronized sampling of all the four channels.
- For the case of turn-by-turn beam position measurement, The provision of ADC sampling in phase locked to bunch revolution frequency is required.
- For synchronized sampling among the distributed system of multiple BPMs the provision for sampling clock phase locking (PL) to external trigger (10MHz) is needed. Also the provision for precise generation of such trigger is required.
- Provision for Non volatile storage of ADC calibration coefficients and system configuration coefficients (like the filter coefficients, Gain and Phase compensation coefficients ) should be provided so that the card performs its functionality, if possible, independent of CPU or SBC.
- A separate data communication mechanisms are needed to be provided from FPGA fabric to AFE for seamless integration of the crossbar switching between 4 channels.
- The provision of sufficient on board RAM to support the following

Table 2 Memory partitioning

| Buffer | Capacity (K Atoms) | Capacity [MB] |
|---|---|---|
| ADC | 1024 | 8 |
| TbT | 512 | 8 |
| TbT/64 | 512 | 8 |
| LT for ADC (NV) | 65 | 0.5 |

- A separate data communication mechanism for fast data sharing from FPGA fabric to HSDGS.
- The VME interface timing should be calculated assuming that there are going to be at-least two DBPI in one VME crate.

The figure 1. Shows the block diagram of the DSAC card. The Humandata XCM-206B FPGA board with the Spartan 6 LX150 device has been selected for the board's logic block. ADC front end with double BALUN based signal coupling has been used. The capacitively coupled differential clock has been used for ADC sampling. Silicon labs Si5345A-D jitter cleaner has been used for the timing logic block along with the Silicon Labs Si570 as the programmable XO. Seeing our past experience with the commercial ICS1554 ADC PMC module the digitization section is developed based on Linear Technology's LT2209 ADC. VME bus handling logic has been implemented in FPGA of the card.

### *Software*

The embedded software for the implementation of FPGA logic is presently in the process of development. The VHDL codes are being developed for different functionality including.

- ADC triggering and data capture under different ADC operation modes,
- I2C pass-through for device configuration of PLL and XO,
- ADC data buffer interface,
- Automatic Gain Equalization,
- Automatic Phase Equalization,
- VME A32/A16, D32/D16 protocol handling,
- VME BLT32/BLT16 protocol handling,
- VME IRQ handling.
- VME Raw ADC data sharing interface.
- FPGA VME data bridge interface.

The Embedded codes has been developed on the CPU side for extending the board features to the CPU programming environment like:

- VME Driver for Raw ADC Data Access,
- VME Driver for 10KHz interrupt generation and data loop-back testing,
- VME Driver for PLL and XO configuration file downloading to device.

The other software codes are also being developed for easy characterization of the board features like.

- Automatic Function generator and Spectrum Analyzer controlling and data capturing GUI.
- PLL and XO Configuring GUI.

The overall system model for the complete system is being developed to valuate the theoretical performance of different schemes and the effect of different system parameters on the beam position resolution that can be obtained from the device.

The PCB for the first prototype board has been fabricated and populated with selective components and tests were performed in steps.

### *Initial measurements results*

Figure 2. shows the picture of the first prototype board. Figure 3. shows the amplitude response of one of the ADC channel when fed with 0dBm signal of $F_{in}$ 136MHz to 700MHz with $F_s$ of 120MHz. For the DBPI frequency band i.e. 505.8 ± 2MHz the gain flatness of less than 0.5dB has been measured. The second harmonic at 42dB down and ~72dB of noise free dynamic range was measured for the card. To improve the second harmonic

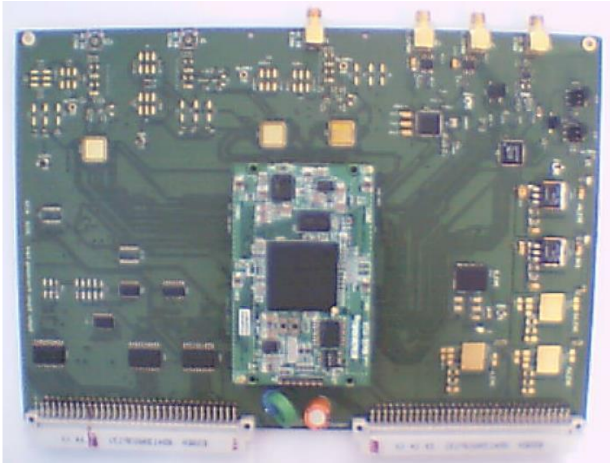

Figure 2: Prototype board with selective components mounted on it.

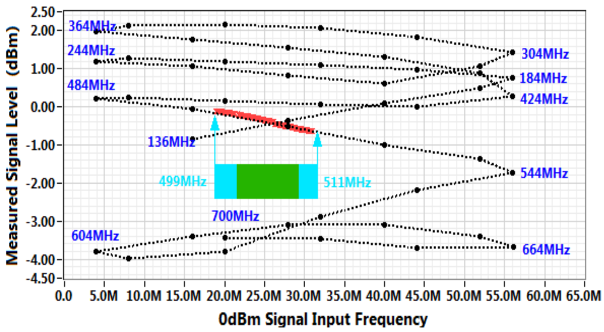


Figure 3: Amplitude response for 0dBm input signal with $F_{in}$ 136 to 700 MHz. and $F_s$ @120MHz.

response the board front end circuit layout is now revised with better track to track impedance matching, track symmetry and component re-placement. The programmable XO has now been added on board to improve the noise performance.

## CONCLUSION

The first prototype board for Digital BPI electronics has been developed. The tests were performed to characterize some of its features. The lessons learned from the first version has been incorporated in the next version of the board that is under fabrication process.

## REFERENCES

[1] Longwei Lai, et.al., "The Study and Implementation of Signal Processing Algorithm for Digital Beam Position Monitor", PAC'11, New York, 2011, p. 414-416 (2011).

[2] D. O. Tavares, et. Al.,"Development of an Open-Source Hardware Platform for SIRUS BPM and orbit Feedback", ICALEPCS2013, San Francisco, 2013, p.1036-1039(2011).

[3] G.Jug. et.al., "Development of compact electronics dedicated to beam position monitors in injectors and boosters", IBIC'13, Oxford, 2013, p. 713-715 (2013).

# DEVELOPMENT OF THERMOMETRY SYSTEM FOR QUENCH DETECTION IN 650 MHZ FIVE CELL SCRF CAVITY DURING COLD TEST

Anand Yadav*, Avinash Puntambekar, Ajay Yedle, Pralhad Kamble, Vinesh Verma
Raja Ramanna Centre for Advanced Technology (RRCAT), Indore, India
anandyadav@rrcat.gov.in

*Abstract*

Development of 650 MHz, β = 0.92 five-cell superconducting radio frequency (SCRF) cavities is ongoing at RRCAT. These multi-cell SCRF cavities are required for the proposed superconducting Proton linear accelerator at RRCAT and are also deliverable to Fermilab, USA under Indian Institutes Fermilab Collaboration (IIFC).

These SCRF cavities are tested in liquid Helium at ~ 2 Kelvin (K) in vertical test stand (VTS) facility as a part of performance evaluation test. Performance of these SCRF cavities is limited by different loss mechanisms. These loss mechanisms eventually results in power dissipation on cavity wall that causes rise of temperature at corresponding locations known as hotspots. Detection of location of these hotspots that results in quenching of SCRF cavity is important to study the cavity performance limiting mechanisms. The temperature rise at these hotspots varies from fraction of Kelvin to few tens of Kelvin. The super-fluid liquid Helium bath retracts the quench phenomenon within a time domain of few tens of milliseconds. A Silicon diode sensor based thermometry system is developed to detect location of these transient hot spots appearing on the equator region of a 650 MHz five-cell SCRF cavity. Study and analysis of the acquired data helps to sort out problem area and suggest suitable processing steps, modification and precaution in cavity fabrication and processing procedures. Initially the system was tested on 1.3 GHz single cell SCRF cavity and results were verified by microscopic examinations. Subsequently thermometry system for 650 MHz single-cell and five-cell cavity has been developed.

This paper describes the status of the development & initial test results.

## INTRODUCTION

In particle accelerators Superconducting Radio Frequency (SCRF) cavities are used to accelerate charged particles. These cavities are supposed to operate at maximum possible accelerating electric field gradients but practically gradients achieved are inferior to the theoretical limits. Performance of SCRF cavities is limited by dissipation of power by various loss mechanisms like thermal breakdown, multipacting, field emission etc. These loss mechanisms present the major problem in achieving high gradient cavities.

To understand these performance limiting mechanisms and improve the performance of cavities, cavity "Thermometry system" is a popular technique used by front end accelerator research laboratories to get quick signature of the quench location during performance evaluation test at cold. Fast readout of strategically placed thermometers in the key region of SCRF cavities (equator region) provides valuable information on SCRF cavity performance [1]. The equator region is more prone to quench as it experiences the maximum magnetic flux density along with having a welded joint in its vicinity.

The extensive study of quench mechanisms correlates the cavity performance with the issues related to its design, fabrication and processing procedure. Thermometry system identifies the location where the quench initiates and the pattern in which it propagates. These short lived thermal transients due to quench require fast temperature measurement techniques that that are not available with existing cryogenic temperature readout systems, the commercially available systems are rated for limited number of channels and low sampling rate. The reported success of this system gave the motivation to develop this system. This system is designed to locate the thermal breakdown regions quickly and precisely. Its utility of this system has been proven and is used regularly while testing SCRF cavities. Such a system is an invaluable tool for identifying and diagnosing heating issues in SCRF cavities.

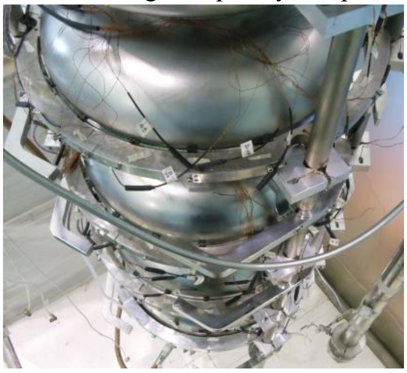

Fig.1 - 650 MHz five cell SCRF cavity equipped with thermometry bands ready for 2K test in VTS facility

## DESIGN REQUIREMENT

The RF power testing results and thermometry data reported in literature [2] reveals that temperature rise on the cavity surface varies in the range of fraction of K to few K with temperature rise in a time domain of few milliseconds. The amazingly high thermal conductivity of super fluid Helium causes thermal transients to have pulse width of the order of 100 milliseconds before the cavity regains the superconducting state. In super fluid liquid Helium hot spot temperature initially rises relatively slow up to Lambda point, after that temperature rises quickly. The cavity energises, quenches and recovers, this phenomenon repeats in a cyclic manner. As reported, defect size having radius of the order of 50μm are good enough to generate a hotspot that propagates and may result in a quench. To detect the hot spot location using thermometry system it is more relevant to acquire the relative change in temperature of various sensors rather than measurement of absolute temperature. It is essential for the application to design the FTS system to perform in two important categories: speed and sensitivity.

## SYSTEM CONFIGURATION

Based on the design requirements a fast thermometry system capable to monitor thermal disturbances in the equator region of the 650 MHz five cell cavity under test in super fluid Helium at 2K has been developed. A sixteen sensor per cell topology was envisaged with inter-sensor spacing of ~80 mm so that at-least one sensor can detect the temperature rise of propagated hot spot. Overall eighty sensors are required to scan the equator region of five-cells of multi-cell cavity. Output from each temperature sensor is sampled with a temperature resolution of 10 mK and time resolution of 125 µs (~8KS/s/ch). Higher sampling rates can be achieved after reducing the number of channels to be scanned. These sensors are connected in series configuration and excited by a stable 10µA direct current source. The measurement is taken by four wire measurement technique. The forward bias voltage of the diode sensors at 2K were transmitted to data acquisition hardware at room temperature by twisted Manganin and copper conductors through Helium leak tight vacuum compatible electrical feed-throughs. These signals are fed to data acquisition system for signal conditioning, analog to digital conversion and further processing and analysis of results.
The thermometry system comprises of following major components –

### *Thermometer assembly*

For the application Silicon diode sensors are used. These semiconductor devices in SMD package are small in size, sensitive, interchangeable, repeatable in the required temperature range and are reproducible after repeated thermal cycling. The sensing surface of the sensor is ~4.2mm$^2$ (3 x 1.4mm). The sensors were calibrated in the range 300K to 1.4K at the in-house facility available at RRCAT taking Lake-Shore make calibrated CERNOX sensor as reference. The excitation current of the temperature sensors is kept 10µA to minimize self-heating error. The forward bias voltage varies from ~0.56V at 300K to ~1.5V at 2K. The sensitivity is ~ -19mV/K to -30mV/K in the working range of 2K to 25K. These Sensors are wired in a four wire configuration after mounting it on a glass fibre epoxy fixture. This complete assembly except the sensing surface was then encapsulated in thermally conductive epoxy (Stycast-2850). This prevents direct exposure of the sensors to the super fluid Helium bath [3]. A spring loaded miniature pogo pin was attached to the thermometer assembly ensures proper thermal contact. An annular aluminium sensor support fixture for each cell supports the sixteen sensors. It ensures proper support and keeps them apart at equal spacing. These sensors are gently pressed to the cavity outer surface by radial adjustment of pogo pins of the thermometer assembly. Cryogenic thermal contact grease (Apiezon N type) is applied to the sensors sensing surface to keep them in good thermal contact with the cavity curved surface making it possible to acquire small temperature rise.

### *Signal conductors*

The output terminals of the sensors are connected to manganin conductors in a four wire measurement configuration. These conductors provides thermal resistance between the sensing element and the super fluid LHe bath at 2K, prohibiting the cool-down of the sensor element by thermal conduction. Further it was connected to a set of 20m long PTFE insulated shielded cable each having twisted pairs of copper conductor. Use of twisted conductors improves rejection to electromagnetic interference. The receiver in differential mode responds only to the voltage difference between the balanced wires. Proper grounding of shielding with these balanced lines allows low noise pick-up and crosstalk between different channels in the test facility.

### *Vacuum compatible electrical feed through box*

This Helium leak tight vacuum compatible electrical feed through box plays a vital role in transferring the electrical signals at the interface between Helium vessel of the vertical test stand (VTS) operating at ~20mbar of sub-atmospheric pressure to the instrumentation rack at atmospheric pressure. The major constraint is the number of pin outs required and limited space available between the VTS top plate and the sliding radiation shield. For this purpose a custom made feed-through box having ten numbers of 104 pin glass to metal sealed D type connectors was fabricated in-house. This feed through box was tested and qualified for Helium leak rate less than $10^{-8}$ mbar.l/Sec.

Fig.2 - Vacuum compatible electrical feed-through box

### *Data acquisition system*

The data acquisition system is intended to acquire eighty analog voltage signals in differential mode. A front end multiplexing and signal conditioning card (NI-SCXI 1102C) is used for analog signals. It has inbuilt low pass filter, cold-junction compensation sensor & programmable gain input amplifier. The sampling rate of the complete thermometry system is governed by number of channels configured by multiplexer. After configuring the data input channels these 80 analog inputs were sampled by the multiplexer in a sequential manner by the multiplexer at a sampling rate of 8kS/s/ch. This multiplexed signal is then fed to a data acquisition device having a 18 bit analog to digital converter (NI PCIe-6289). The card operates on the Peripheral component interconnect express bus of the computer. The Digitized data is buffered, organized, processed and transferred to the controller in FIFO mode. The data is fed to the controller for analysis, storage and presentation using LabVIEW software.

### *Data processing software*

The data processing, analysis and presentation is being done by using a NI- LabVIEW software based program. The software is designed to perform following major functions –

- Reproducibility check and calibration of sensors during cool down cycle of the cavity.
- Evaluation of polynomial fit equation to translate sensor voltage output to temperature scale
- Processing, analysis and presentation of data.

As a first stage the sensor calibration data is analysed and the sensor output is formulated as a function of temperature. Polynomial fit equations for each sensor are evaluated from the interpolation tables generated from the discrete data points acquired during the calibration process. These polynomial fit equations were used to translate the voltage output from sensors into the temperature.

When the desired temperature for VTS test is achieved, before exciting the RF power the response of all the sensors is recorded as a base line temperature. Temperature offset with respect to reference temperature sensor is evaluated and recorded. The acquisition of multi-channel data starts at a pre-defined data sampling rate for a running time window. Whenever any thermal disturbance is observed, a data latch option has been provided which is required to be activated to store the sensor outputs at the instance of quench. Enabling the latch switch stops further acquisition of data, stores the present data in a file with pre-defined path. The data acquired is presented on a temperature change-time plot so that thermal disturbance can be easily visualized. Finally an analysis report tracing the location of quench is generated on the basis of relative rise in temperature recorded by the sensors at different levels of RF testing.

## TEST RESULTS

A typical quench event recorded by thermometry system is presented. This was observed while testing cavity ID : RRCAT-650-B92-5001 (650 MHz $\beta$=0.92 five cell SCRF cavity). The cavity was under cold test at LHe Temperature ~ 1.94 K. During the test the thermometry system has recorded temperature rise in two adjacent sensors having identification number T02 ($\Delta$T= 0.245 K) and T01($\Delta$T= 0.16 K ) at the cell nearest to power coupler end . Both sensors indicated similar trend in temperature rise but with different magnitude. So the hot spot responsible for quench was detected nearer to T02 between the sensor location of T02 and T01.The thermal transient pulse width of ~ 250 ms & quench repetition frequency of 1.667 Hz was observed.

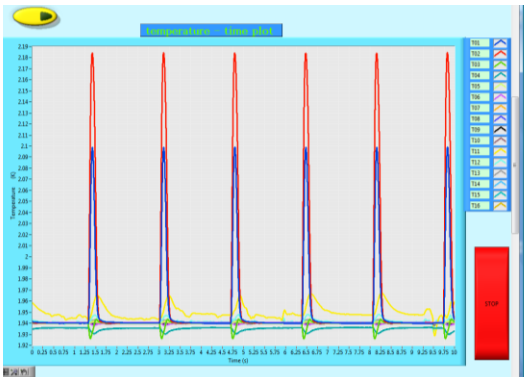

Fig.3 – Screenshot of quench detection at 1.94K

The quench instance and its repeatation rate shows concurrence with the signature of RF test signals. Later Microscopic observations also reveal a sharp step at the cavity equator weld under-bead in the region between the marked sensors.

## SUMMARY/CONCLUSION

A thermometry system for detection of hot spot locations on the equator region of 650 MHz five-cell SCRF cavity has been designed and developed. The thermometry system is operational and is used regularly while testing 650 MHz five-cell SCRF cavities. The thermometry results have shown good correlation with the RF test signals during cold test and microscopic observations performed at room temperature after cold test.


## ACKNOWLEDGMENT

We would like to express my thanks to Mr. Dmitri Sergatskov (FNAL) for his invaluable technical feedbacks, CCDD RRCAT team for sensor calibration, Mr. Viraj Bhanage and Mr. P.P. Deshpandey (LESD, RRCAT) for their technical guidance and Mr. Rajendra Adbol for his technical support required time to time in developing this system.


## REFERENCES


[1] Darryl Orris, et.al. “Fast thermometry for super-conducting RF cavity testing” Proceedings of PAC07, Albuquerque, New Mexico, USA. FERMILAB-CONF-07-245-TD

[2] S. Antipov, et.al. “Time resolved measurements of high field quench in SRF cavities” TUP112, Proceedings of SRF2013, Paris, France.

[3] “Advanced Thermometry Studies of Superconduct-ing Radio-Frequency Cavities” Jens Knobloch, Ph.D. Thesis Cornell University

# DESIGN AND DEVELOPMENT OF 1MV, 100KW SYMMETRICAL COCKCROFT WALTON GENERATOR FOR TRAMBAY DC ELECTRON ACCELERATOR FOR WASTE WATER TREATMENT APPLICATION

D.K. Sharma*, R.N. Rajan, R. Patel, S. Dewangan, A. Mitra, S. Das, S. Bairagi, A.G. Waghmare, S.A. Harer, N.B. Thakur, N.K. Lawangare, S.R. Ghodke, P.C. Saroj, V. Sharma, D. Jayaprakash, D. Bhattacharjee, S.K. Srivastava and R.I. Bakhtsingh.
Accelerator and Pulse Power Division, BARC, Mumbai.

*Abstract*

High power electron accelerators are finding numerous scientific, industrial and societal applications. Accelerator and pulse power division of BARC, Mumbai is setting up a 1MeV, 100kW DC electron beam accelerator facility for demonstration of waste water treatment at industrial scale.

High voltage generator of this accelerator is a 15stages, symmetrical Cockcroft Walton multiplier operating at 10kHz frequency, fed from a 90kV/500V, 125kVA transformer, driven by an IGBT based 500V/10kHz inverter.

The 1MV voltage multiplier is assembled in a pressure vessel and tested at 900kV output voltage in 6kg/cm2 Nitrogen gas. This paper presents salient design features, test results and further challenges ahead.

## INTRODUCTION

The 1MV, 100kW DC accelerator is based on a Symmetrical CW multiplier, fed from a Ferrite-core based 500Vp/45kVp-0-45kVp, 10kHz step-up transformer. Input power from 415V, 3-phase mains is rectified and inverted at 10kHz by an efficient IGBT based solid-state inverter. The 1MVgenerator is shown in Fig.-1.

The accelerator will be installed inside BARC premises adjacent to the upcoming Waste water treatment plant on about 12m x15m foot-print. Throughput of the accelerator facility at estimated dose of 3kGy is 2 MLD. Accelerator will be housed in concrete shielding of 1.2m thickness.

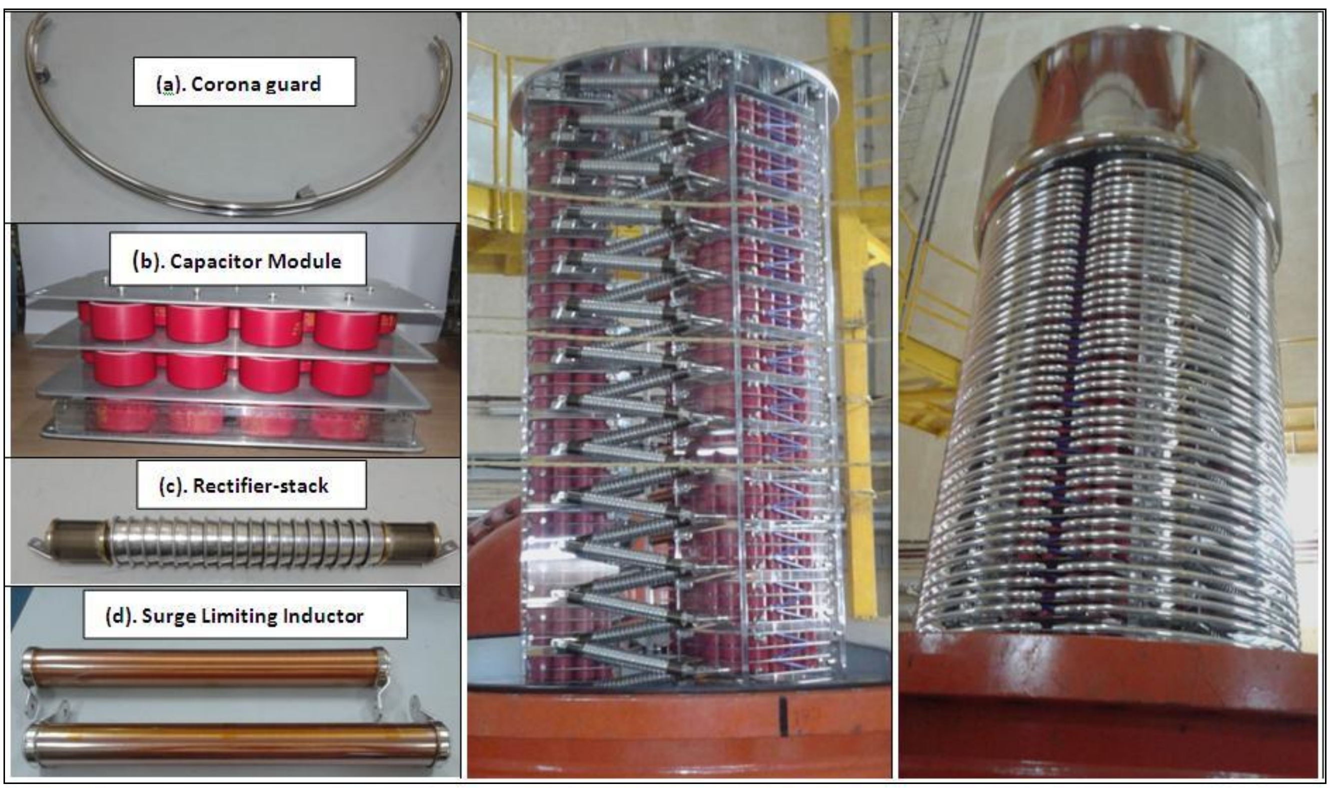


Fig.-1. (Left): Sub-systems of 1MV multiplier, (middle): Partially assembled & (right): Completely installed Multiplier.

*** dksharma@barc.gov.in.**

Water in the form of 1.5m wide, 4mm thick jet will be passed under beam exit-window for e-beam treatment. Voltage generator is housed in a pressure vessel of 1.6m ID and 3.5m internal height, filled with high purity nitrogen gas at 6kg/cm$^2$ pressure. E-beam is generated by an indirectly heated LaB6 cathode gun and accelerated through a cascade of 6nos. high-gradient accelerating tubes. Electrical schematic of voltage multiplier is shown in Fig- 2. Accelerator parameters are given in Table-1.

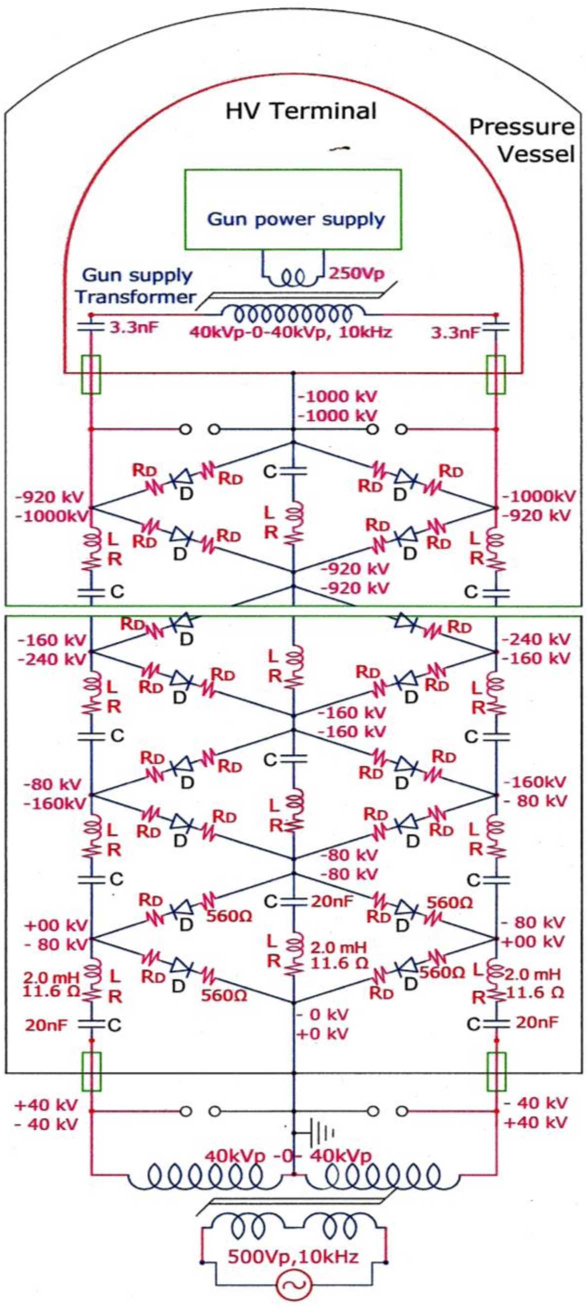


Fig. 2: Electrical schematic of 1MV multiplier.

Table 1: Design Parameters of 1MeV DC Accelerator

| Sr. No. | Description | Value |
|---|---|---|
| 1. | Beam Energy | 800 - 1000 keV |
| 2. | Beam current | 0.1 - 100mA |
| 3. | Mode of operation | Continuous (DC) |
| 4. | Width of beam scam | 1.5 m |
| 5. | Depth of penetration | 4mm (unit density) |
| 6. | Throughput | 3kGy at 2MLD |

## HIGH VOLTAGE SYSTEM

### *DCPS and Inverter*

The 3-phase, 415V, 50Hz mains input is rectified using a thyristor based converter to obtain an adjustable 500V DC output. This DC voltage is inverted at 10kHz frequency to obtain 480Vp output and supplied to HF transformer using 200 Nos. of RG-58 cables. Overall efficiency of DCPS and Inverter is about 94%.

### *High Frequency Transformer*

The 480Vp input is fed to a Ferrite-core based high frequency step-up transformer to develop 45kV$_P$ -0- 45kV$_P$ output. This transformer has 4 turns primary made of 63nos. of parallel conductors of Litz wire and a 720turns concentric secondary winding with a center-tap. Estimated 700W power-loss at rated 90kV/100kW load is removed through a water cooled copper-tube cage-type heat exchanger located inside transformer tank, immersed in the transformer oil.

## VOLTAGE MULTIPLIER

### *Support structure*

The support structure consists for 7nos. of Perspex slabs each of 226cm x28cm x24mm size, firmly secured to a 110cmx110cm square base-plate and a 110cm dia. circular top-plate. These sheets are provided with precision drilled holes for mounting the multiplier components and mirror-polished to operate at 25kV/cm of peak surface-gradient at rated 1MV output. Support- structure is designed to uplift/ shift the fully assembled multiplier, weighing nearly 1500kg for faster and easier maintenance of the accelerator.

### *Corona guards*

Specially profiled semi-circular corona-guards made of 19mm OD, 63400 aluminium-alloy tubes, to provide a 114cm OD cylindrical-shape to the multiplier. These corona guards are shaped and mirror-polished to operate at 100kV/cm peak electrical-stress in pressurized $N_2$ gas. A cross-section view of 1MV multiplier is shown in Fig. 3.

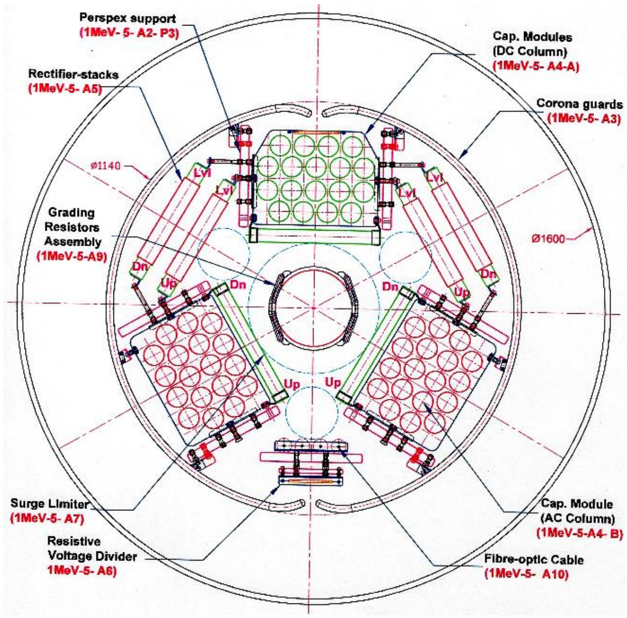


Fig. 3: Cross-sectional view of 1MV multiplier.

### *High voltage terminal*

The HV terminal is made of 3mm thick SS-304 sheet and houses electron-gun power supplies and controls for powering of electron-gun. It is designed in cylindrical-shape with 50mm edge-radii to exhibit 110kV/cm of electric stresses at the rated 1MV potential. This acts as a self discharging gap in the event of an incidental over-voltage.

### *Capacitor modules*

Multiplier consists of 45 nos. of capacitor modules each rated at 20nF/120kVDC weighing ~19kg. Each module has series-parallel assembly of 54 nos. 3.3nF/40kV ceramic capacitors located between edge-rounded, mirror-polished aluminium plates. Each capacitor has been tested for capacitance, dissipation-factor, leakage current at 40kVDC as well as controlled HV discharges.

### *Rectifier stacks*

Each rectifier-stack rated at 126kV PIV, 1A current, 200ns trr is designed to rectify 45kV stage voltage. Each stack has 34Nos. of series connected 4kV/1A diodes of closely-matched characteristics, located inside aluminium-cups for protection from stray electric-fields. These stacks are provided with 280μH, 560Ω wire-wound surge limiter on both ends for protection from fast electrical transients and sudden current in-rush.

### *Surge limiting inductors*

Each capacitor module is cascaded via a SLI of 2.0mH/ 11.6Ω, 90W rating. These inductors facilitate slow discharge of stored energy in capacitor-modules during a voltage breakdown. Each SLI is wound around a Delrin-rod using SWG-28 super-enameled copper conductor.

## INSTALLATION AND TESTING

Voltage multiplier has been installed in a pressure vessel meant for 3MeV accelerator as construction of building and fabrication of 1MV pressure vessel continued. DC power supply and Inverter have been tested at 380V, 40kW. HF transformer is tested at 42kVp-0-42kVp output. Pressure vessel is filled with high purity (IOLAR-2) nitrogen gas at 6kg/cm$^2$ pressure. Integral test with voltage multiplier has been conducted upto 900kV. Fig. 4 shows the performance parameters of 1MV generator.

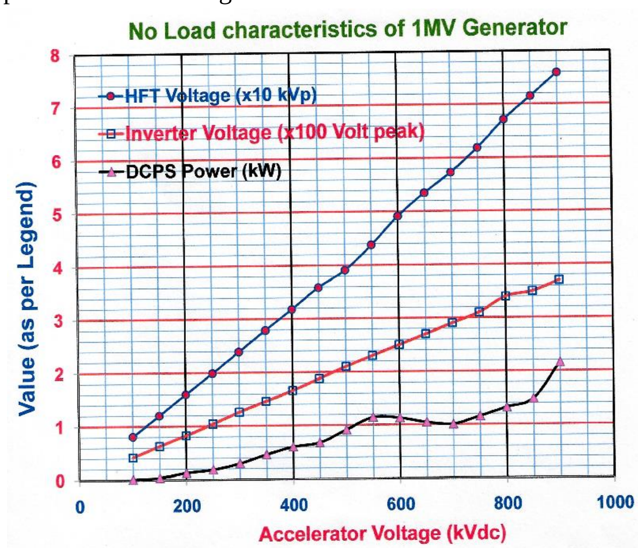


Fig. 2: Performance parameters of 1MV generator.

## CONCLUSIONS

Design and fabrication of 1MV generator for Trombay DC Electron Accelerator for waste water treatment has been completed. This generator has been integrated at transit site (EBC Kharghar) for initial testing. The voltage multiplier has been HV conditioned upto 900kV output voltage.

# STUDY OF LOW MOMENTUM COMPACTION FACTOR OPTICS AND ITS IMPLEMENTATION IN INDUS-2

Abdurrahim [a,b], AD Ghodke [a] , Arup Banerjee [a,b]
[a]Raja Ramanna Centre for Advanced Technology, Indore, India
[b]*Homi Bhabha National Institute (HBNI), Anushakti Nagar, Mumbai, India*

*Abstract*

In this paper, we present a study on low momentum compaction factor optics for Indus-2 storage ring. Indus-2 will be operated with this optics in order to obtain pico-second to sub-picosecond electron bunches. These bunches will generate the short x-ray pulses as well as coherent synchrotron radiation in THz frequency range. In this paper, the low momentum compaction factor optics, effect of power supply stability on low momentum compaction factor, simulation study for beam injection and dynamic aperture study using particle tracking will be discussed. A trial operation in Indus-2 has been performed with the low momentum compaction factor optics. The operational challenges as well as the first results obtained by applying the low-momentum compaction factor beam optics will also be discussed.

## INTRODUCTION

Operation of any synchrotron radiation storage ring with short electron pulses provides two additional tools for synchrotron radiation beamline scientists. First is the incoherent short synchrotron radiation pulses up to the X-ray regime to perform the time resolved experiments and second is the coherent synchrotron radiation in THz regime. One can achieve short electron bunches in a storage ring by various methods like femto-second laser slicing, RF deflecting cavity method and minimizing the momentum compaction factor. The method of minimizing the momentum compaction factor is the preferred one for achieving the short electron bunches as it does not require any additional hardware to be installed in the ring. Momentum compaction factor can be minimized by properly shaping the dispersion function inside the dipole magnets. The electron bunch length is related with the momentum compaction factor with the following expression [1]

$$\sigma_l = \frac{\frac{\sigma_E}{E}}{f_{rev}}\left(\frac{\alpha_c E}{2\pi h}\right)^{1/2}\frac{1}{(e^2V_{rf}^2 - U_0^2)^{1/4}} \qquad (1)$$

Where E is the beam energy, $\sigma_E$ is energy spread, $f_{rev}$ is revolution frequency, $\alpha_c$ is the momentum compaction factor, h is harmonic number, $U_0$ is radiated energy.

Momentum compaction factor is defined as the ratio of change in the path length ($\Delta L$) to the total circumference ($L$) of the storage ring due to unit change in relative momentum deviation ($\delta = \frac{\Delta P}{P}$). It is given by

$$\alpha_c = \frac{\Delta L}{L}\Big/\delta = \alpha_1 + \alpha_2\delta + \alpha_3\delta^2 + O(\delta) \qquad (2)$$

† arahim@rrcat.gov.in

Here $\alpha_1$, $\alpha_2$ and $\alpha_3$ are the first, second and third order momentum compaction factor, which are given by the following expressions [2]

$$\alpha_1 = \frac{1}{L}\oint\frac{\eta_1}{\rho}ds \qquad (3)$$

$$\alpha_2 = \frac{1}{L}\oint[\frac{{\eta_1'}^2(s)}{2} + \frac{\eta_2(s)}{\rho}]ds \qquad (4)$$

$$\alpha_3 = \frac{1}{L}\oint[\,\eta_1'(s)\eta_2'(s) - \frac{\eta_1(s){\eta_1'}^2(s)}{2\rho} + \frac{\eta_3(s)}{\rho}]ds \qquad (5)$$

Here $\eta_1$, $\eta_2$ and $\eta_3$ are the first, second and third order dispersion function, $\eta_1'$ and $\eta_2'$ are the derivative of first and second order dispersion function w.r.t path length s. $\rho$ is the radius of curvature in the bending magnet. The main contribution to the momentum compaction factor ($\alpha_c$) comes from the first order momentum compaction factor. In order to minimize $\alpha_1$, the storage ring linear optics is tuned (quadrupole strength) such that the integrated dispersion inside the bending magnets remains minimum. As $\alpha_1$ is reduced the higher-order terms contribution also needs to be minimized. The second order momentum compaction factor $\alpha_2$ is minimized using appropriately placed sextupoles in the ring. The third order momentum compaction factor $\alpha_3$ can be controlled by octupole magnets.

## LOW MOMENTUM COMPACTION FACTOR OPTICS FOR INDUS-2 OPERATION

Indus-2 is an Indian synchrotron light source, which is presently, operated at 2.5 GeV beam energy with the r.m.s. electron bunch length of 13mm. This bunch length corresponds to the momentum compaction factor of $7.2\text{x}10^{-3}$. In the storage ring, there are five families of quadrupoles, namely Q1D, Q2F, Q3D, Q4F and Q5D in a unit cell. Using the Multi Objective Genetic Algorithm [3, 4], strengths of the above five families quadrupoles are optimized to minimize the momentum compaction factor. During the optimization, constraints are imposed to ensure the good injection efficiency, adequate tune, low emittance, restricted maximum beta and low strengths of chromaticity correcting sextupoles. In present polarities of quadrupoles and sextupoles power supplies, suitable solutions are not achieved for operation as momentum compaction factor is not sufficiently small however for the changed polarities of Q4F, Q5D quadrupoles families, SF and SD sextupole families, solutions with low momentum compaction factor are found. One of the solutions, which has wide tunability of first order momentum compaction factor ($\alpha_1$) from 0.007 to a very small value of 2.71x10$^{-06}$ is chosen for implementing in Indus-2. The optical functions of this optics are shown in figure 1.

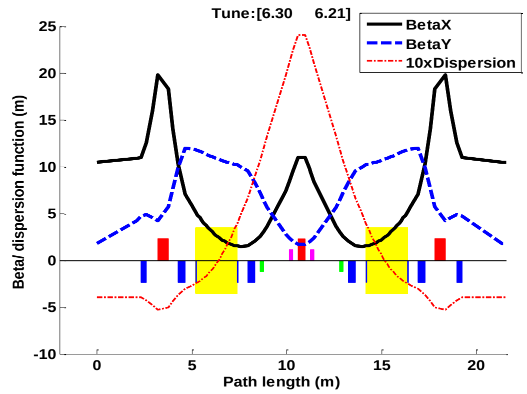


Figure 1: Optical functions of low momentum compaction optics

## *Second Order Momentum Compaction Factor*

Minimization of second order momentum compaction factor ($\alpha_2$) is important to insure the stable motion in longitudinal plane. In Indus-2 it is minimized by optimizing the strengths of chromaticity correcting sextupoles. For the low momentum compaction optics, $\alpha_2$ is reduced from -0.08 to 2x10$^{-08}$.

The important lattice parameters of low momentum compaction optics as well as present operating optics are given in table-1

Table 1: Important parameters for Indus-2 storage ring

| Parameters | Operating lattice | Low alpha lattice |
|---|---|---|
| Emittances (operating) | ~ 130 nm-rad | 381 nm-rad |
| Tune | [9.278 6.21] | [6.30 6.21] |
| Natural energy spread | 9.03x10$^{-04}$ | 9.09x10$^{-04}$ |
| Mom. comp. factor | 7x10$^{-03}$ | 2.71x10$^{-06}$ |
| Bunch length | 43ps/13mm | 2.7ps/0.8mm |
| *Betatron function[$\beta_x$, $\beta_y$] | [10.5 3.4] m | [10.5 1.79] m |
| *$\eta_x$ , $\eta'_x$ | [-0.3 m 0] | [-0.4 m 0] |

## *Dynamic Aperture*

Particle tracking is performed to study the nonlinear effects on the motion of the electron beam. Tracking is performed for 10000 turns (more than one damping time). The tracking results reveal that, there is sufficient dynamic aperture available to on and off momentum particles as shown in figure 2.

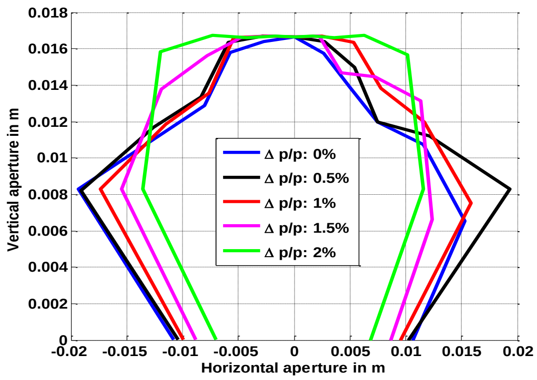


Figure 2: Dynamic aperture for low momentum compaction optics

## *Effect of Power Supply Stability on Momentum Compaction Factor*

In the low momentum compaction optics, $\alpha_1$ can be reduced to a very small value (2.71x10$^{-06}$) but during operation of Indus-2, power supply stability will put a limit on the lower value of momentum compaction factor. Effect of Indus-2 power supplies stabilities (±50 ppm) on momentum compaction factor simulated for 10000 seeds of random numbers. The simulated results reveal that lower value of momentum compaction factor for this optics will be restricted to ~ 2x10$^{-5}$(peak value). It is shown in figure 3.

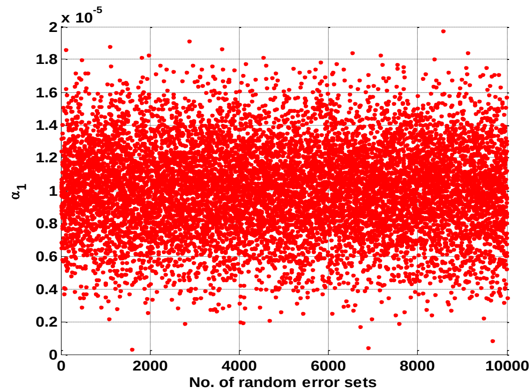


Figure 3: Effect of Indus-2 power supplies stabilities on momentum compaction factor.

## *High Momentum Compaction Factor Lattice and Injection Simulation*

Indus-2 is a booster cum storage ring, in which beam injection is carried out at ~550MeV and then beam energy ramping is performed from 550MeV to 2.5GeV. The problem of beam instability will be comparatively severe for low momentum compaction optics. Therefore, beam injection as well as beam energy ramping is preferred with high momentum compaction optics. The chosen low compaction optics has a wide tuning range of momentum compaction factor from 0.007 to extremely low value 2.71x10$^{-06}$. For injection it will be tuned to high momentum compaction factor. After reaching at final beam energy 2.5GeV, optics will be switched over to low momentum compaction optics by increasing the current of Q5D quadrupoles. To study the injection possibility in Indus-2 for high momentum compaction factor optics, tracking is carried out using the DIMAD code [5]. Four kickers, each having a half sine wave pulse of 3μs are utilized for injecting the beam. Beam is injected from 22 mm apart from the beam center axis in Indus-2. For the injection lattice, tracking results indicate about the successful injection in indus-2. The tracking results are shown in figure 4.

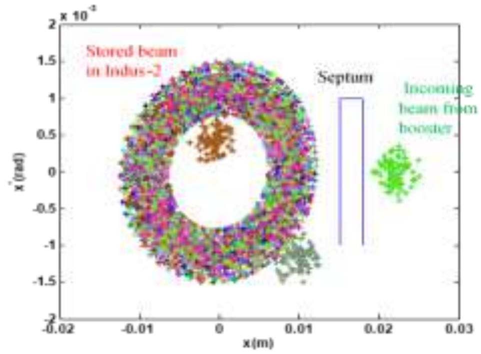


Figure 4: Injection tracking for high momentum compaction factor optics. The dots left to the septum, represent the coordinates of the injected beam in Indus-2 at septum location for 1000 turns.

## OPERATION OF INDUS-2 STORAGE RING WITH LOW MOMENTUM COMPACTION FACTOR OPTICS

Trial operation of Indus-2 is performed for implementing the low momentum compaction optics. For this, Indus-2 is tuned at injection optics of high momentum compaction factor. Injection is carried out using the four kicker magnets, installed in long straight section of the ring. For increasing the beam energy, Indus-2 magnet power supplies current were increased synchronously. Initially, there was heavy beam loss in starting of the energy ramping. After 2-3 iterations of tune corrections, beam loss was minimized. Orbit correction is also performed at injection as well as final energy. The corrected orbit at 2.5 GeV is shown in figure 5.

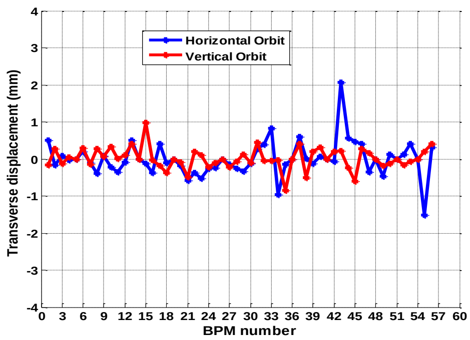


Figure 5: Corrected orbit at 2.5 GeV

### *Measurement of Synchrotron Frequency*

At 2.5 GeV beam energy, switching to low momentum compaction optics is performed by changing the strength of Q5D family quadrupoles. During switchover, betatron tunes were kept constant using the quadrupoles of Q2F and Q3D families. During switchover, synchrotron tune with Q5D quadrupoles current was measured. The momentum compaction factor derived from the synchrotron frequency is shown in figure 6. The figure depicts that measurement deviates from the model below the momentum compaction value of $2x10^{-3}$and stagnates around $3x10^{-4}$. For further reducing the momentum compaction factor, standardization of the lattice will be carried out for this optics using the Linear Optics from Closed Orbits (LOCO) algorithm. In this experiment, the momentum compaction factor is reduced by a factor of 23.

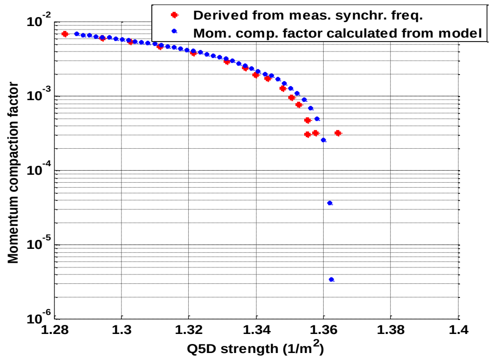


Figure 6: Momentum compaction factor (derived from synchrotron freq.) vs Q5D strength during low momentum compaction factor switch over.

## CONCLUSION

Simulation is carried out to evaluate the effect of Indus-2 power supplies stabilities on low momentum compaction optics. The simulated results reveal that due to power supply stability, lower value of momentum compaction factor will be restricted to ~ $2x10^{-5}$. Beam injection simulation indicates a successful injection in Indus-2. During trial operation of Indus-2 with the low momentum compaction optics, the momentum compaction factor is reduced by a factor of 23. For further reducing the momentum compaction factor, standardization of the lattice using the Linear Optics from Closed Orbits (LOCO) is required.

## REFERENCES


[1]. C.C. Kuo and H.J. Tsai, “Design of Low Momentum Compaction Lattices for the TPS Storage Ring”, IPAC2013

[2]. I. P. S. Martin et.al,” Experience with low-alpha lattices at the Diamond Light Source”, PRST AB 14, 040705 (2011).

[3]. L. Yang, et.al, “Application of Multiobjective Genetic Algorithm in Accelerator Physics”, ICAP09.

[4]. S. Q. Tian et.al, “A Design Approach of the Beam Optics in the Complex Storage Ring”, IPAC-10.

[5]. Roger V. Servranckx, et.al, Users Guide to the Program DIMAD.

# DESIGN OF 100 MeV PROTON ACCELERATOR FOR RADIO-ISOTOPE PRODUCTION

Shweta Roy[1], Abhishek Pathak[*], S.V.L.S. Rao[1], S. Krishnagopal[1,#]

[1]Ion Accelerator Development Division, BARC, Mumbai
[*]UM-DAE CEBS, Mumbai
[#]Homi Bhabha National Institute

Email: shwetar@barc.gov.in

*Abstract*

A 10 mA, 100 MeV proton linac is being proposed for the production of radio-isotopes for applications in nuclear medicine and research. The accelerator will comprise of a 3 MeV Radio Frequency Quadrupole linac and three sections of Superconducting Single Spoke Resonators, S11 (3-10 MeV), S21 (10-40 MeV) & S46 (40-100 MeV). The superconducting linac lattice design has been optimized and the beam dynamics studies have been performed. The design aims at minimizing the emittance and halo growth through the structure. In view of this, the phase advances have been carefully optimized in order to keep their values below 90 degrees. The phase advance per unit length is varied smoothly along the linac. Also, the resonances in the Hofmann chart have been avoided, allowing only for a few fast crossings, with no implication on emittance growth. Inter-section and inter-cryomodule matching has been done suitably to minimize emittance growth due to mismatch. The design details of the 100 MeV linac and the beam dynamics results are presented in this paper.

## INTRODUCTION

Radioactive isotopes are widely used in nuclear medicine [1] for imaging as well as therapy. Conventionally, these isotopes had been produced in reactors. However, the accelerator-produced radioisotopes yields a higher specific activity (more disintegrations per mass of desired element). Another advantage is that much smaller amount of radioactive waste is generated from charged-particle reactions. Here, we present the design of a 100 MeV, 10 mA linac for radio-isotope production.

## *Linac Layout*

The layout of the linac is shown in Fig. 1. It will consist of an Ion Source which will deliver proton beam at 50 keV. The proton beam will be matched into a 325 MHz RFQ through Low Energy Beam Transport (LEBT) line. The LEBT will consist of solenoids, and diagnostics for current, emittance and beam profile measurements. The RFQ will accelerate the proton beam up to 3 MeV. The 3 MeV beam from the RFQ will be matched into superconducting linac section, using a Medium Energy Beam Transport (MEBT) line. The MEBT will consist of quadrupole magnets and RF buncher cavities. It will also incorporate beam diagnostics. The beam from the MEBT will be further accelerated through three superconducting Single Spoke Resonator (SSR) sections, S11, S21 and S46. S11 will accelerate the 3 MeV proton beam to ~ 10 MeV. S21will further accelerate the beam to ~40 MeV and S46 up to ~100 MeV. There will be 6 cryomodules of ~7m length, one in S11 section, housing 12 cavities, 2 in S21 section housing 9 cavities each and 3 in S46 section with 6 cavities in each.

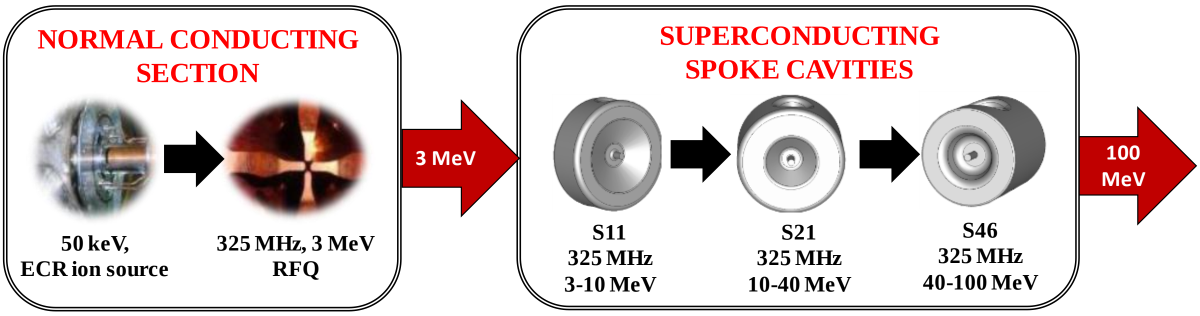


Fig.1 Layout of 100 MeV Proton Accelerator for radioisotope production.

## NORMAL CONDUCTING INJECTOR

### LEBT & RFQ

Particle-in-Cell simulations were performed with a 6 sigma Gaussian beam distribution at the input to the LEBT. The simulations were done with 5 million macroparticles. The matched beam from the LEBT was then injected into an optimised RFQ [2]. The final parameters for the designed RFQ are listed in Table-2. The beam from the RFQ was used for simulations in further linac.

Table 1. Parameters of 3 MeV RFQ

| Parameter | Value |
|---|---|
| Output Energy (MeV) | 3 |
| Frequency (MHz) | 325 |
| RF Power (kW) | 400 |
| Transmission | 99.07% |
| Output $\varepsilon_x$ ($\pi$ mm-mrad) | 0.225 |
| Output $\varepsilon_y$ ($\pi$ mm-mrad) | 0.225 |
| Output $\varepsilon_z$ ($\pi$ mm-mrad) | 0.32 |
| Vane Voltage (kV) | 80 |
| Length (m) | 4 |

### MEBT

A Medium Energy Beam Transport line is designed to be used to match the RFQ output beam into the superconducting linac section. The MEBT consists of two quadrupole doublets and three RF buncher cavities. Drift spaces have been provided for beam diagnostic and steering elements.

Table 2: MEBT Parameters

| Parameter | Value |
|---|---|
| Output $\varepsilon_x$ ($\pi$ mm-mrad) | 0.239 |
| Output $\varepsilon_y$ ($\pi$ mm-mrad) | 0.235 |
| Output $\varepsilon_z$($\pi$ mm-mrad) | 0.32 |
| Halo in x | 1.34 |
| Halo in y | 1.28 |
| Halo in z | 1.94 |

Two doublets and two RF bunchers are used to match the beam to the input of the Spoke Resonator section. The third buncher is used to minimize the emittance growth through the MEBT. The third buncher also helps in obtaining a nearly round beam at the input to the superconducting linac, where solenoidal focusing is used. The MEBT is 1.9 m long. The MEBT output parameters are listed in Table 2.

## SUPERCONDUCTING LINAC

*Design Approach*

The main criteria in designing the SC section of the linac was to minimize the emittance and halo growth while keeping the linac compact and cost-efficient. The zero current phase advances were kept below $90^0$ to avoid the envelope instability due to any mismatch in the lattice. The phase advance per metre is varied smoothly along the linac and the resonances in Hofmann chart [3] are largely avoided, allowing only for fast crossings wherever necessary.

*Linac Lattice*

The S11 & S21 linac lattice consist of a cold solenoid followed by an RF cavity, while in S46 lattice, there is a solenoid after two cavities. The lattice configuration is shown in Fig. 3. The cryomodule length is ~ 7 m in all three SSR sections. A drift of 400 mm is provided after each cryomodule due to mechanical requirements.

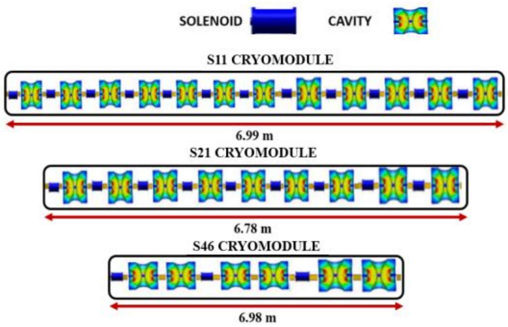


Fig. 3. Cryomodules for the three SSR sections.

*Beam Dynamics*

3D fields of the SSR cavities and solenoids were imported into the PIC code TRACEWIN [4] and the dynamics of the MEBT output beam was studied through these fields.

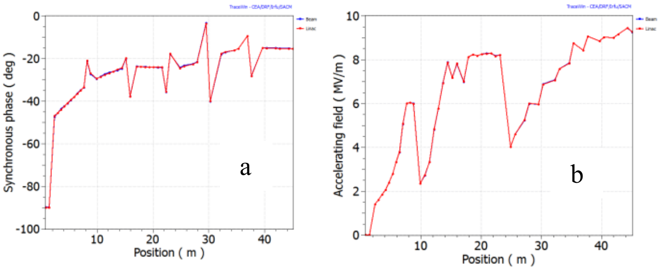


Fig. 4. (a) Synchronous Phase (b) Accelerating Field along the linac.

The synchronous phase, accelerating fields and solenoid fields were optimized to shape the longitudinal and transverse phase advances to meet the design criteria, while minimizing the number of cavities. The synchronous phase has been ramped linearly from $-47^0$ to $-30^0$, from $-30^0$ to $-20^0$ and from $-20^0$ to $-15^0$ in S11, S21, and S46 respectively, as shown in Fig.4(a). The synchronous phase was chosen such that beam bunch is well within the phase acceptance of the spoke cavities.

With the accelerating gradient shown in Fig. 4(b), and for the given energy range of 3 MeV to 10 MeV, 10 MeV to 40 MeV and 40 MeV to 100 MeV, the number of cavities required were 12, 18 and 18 respectively for S11, S21 and S46 sections respectively.

The 400 mm drift at the cryomodule break, devoid of focusing elements, has detrimental effect on the beam dynamics. Therefore, the periods preceding and following the inter-cryomodule drift were tuned in order to minimize the beam blow up. Additionally, matching was provided between different families of SSR, using the last two solenoids and cavity phase of the preceding SSR section.

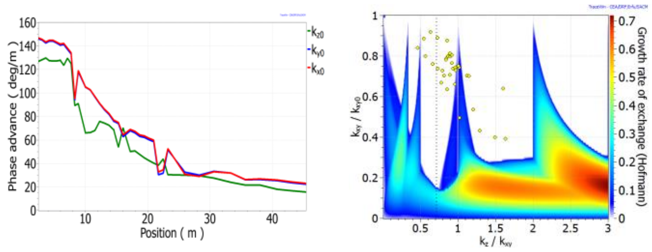


Fig. 5 (a) Phase advance per meter along the linac (b) Tune footprints in Hofmann chart.

Table 3. Parameters of Superconducting linac.

| Parameter | S11 | S21 | S46 |
|---|---|---|---|
| Energy Range (MeV) | 3-9.12 | 9.12-40.33 | 40.33-112.31 |
| Synchronous Phase | -47 to -30 | -30 to -21 | -21to-16 |
| No. of cavities | 12 | 18 | 18 |
| Cavity Length (mm) | 176 | 286 | 560 |
| $\beta_{opt}$ | 0.144 | 0.256 | 0.543 |
| Leff ($\beta_{opt}\lambda$) | 113 | 234 | 491 |
| Accelerating Gradient (MV/m) | 8 | 10 | 11 |
| Solenoid Field (T) | 3.4-4.6 | 4.6-5.1 | 5.1-5.8 |
| $\varepsilon_x$ ($\pi$ mm-mrad) | 0.245 | 0.247 | 0.248 |
| $\varepsilon_y$ ($\pi$ mm-mrad) | 0.244 | 0.258 | 0.267 |
| $\varepsilon_z$ ($\pi$ mm-mrad) | 0.320 | 0.322 | 0.335 |
| Halo in x | 1.45 | 1.57 | 1.51 |
| Halo in y | 1.40 | 1.63 | 1.58 |
| Halo in z | 1.94 | 1.89 | 1.80 |

The variation of phase advance per meter is shown in Fig. 5(a). The phase advance profile is smooth except at intersection matching. Table 3 lists the parameters of the superconducting linac. The tune footprints are shown in Fig. 5(b). It can be seen that there are fast crossings of the n=1 parametric resonances for some periods. However, this has no implication on emittance exchange between the transverse and longitudinal planes, as can be seen from Fig. 6(a). The emittance growth in the SC linac is 3.8 % in x-x', 13.6 % in y-y' and 4.6 % in z-z' planes. The beam halo growth is 12.6 % in x-x', 23.4 % in y-y' and –14 % in z-z' planes. The asymmetric emittance growth in the two transverse planes is attributed to asymmetric kicks in the two planes due to cavity fields. The halo parameter through the linac is shown in Fig. 6(b). The rms beam envelope through the linac is shown in Fig. 6(c). It can be seen that the beam size is maximum at the inter-cryomodule drifts. The aperture is everywhere 8-10 times the rms beam size.

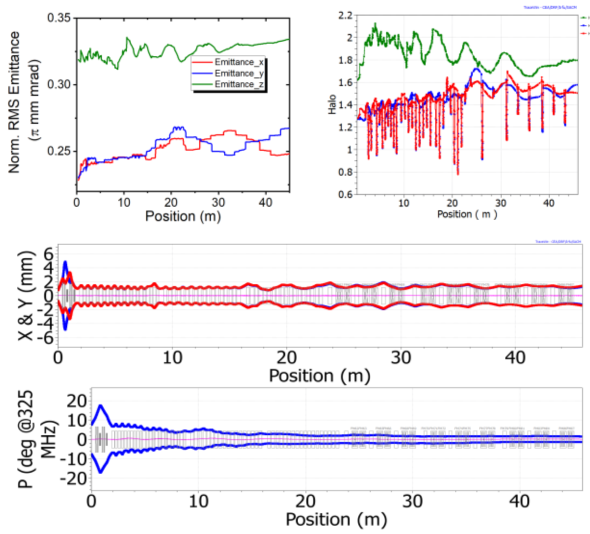


Fig. 6 (a) Emittance (b) Halo Parameter (c) Beam Envelope through the SC linac.

## CONCLUSION

A detailed beam dynamics design has been performed for a 100 MeV linac for radioisotope production. The superconducting lattice has been optimized so as to avoid parametric resonances and instabilities. An end-to-end beam dynamics simulation study has been performed for a 100 MeV linac with a six sigma Gaussian input beam distribution. The beam emittance growth through the superconducting linac is less than 15% and the beam halo growth is less than 25% in all three planes.

## REFERENCES


1. Sharma AR. Nuclear medicine in India: A historical journey. Indian J Nucl Med 2018;33:S5-10.
2. BARC, IADD, External report BARC/2016/e/016 (2016).
3. I. Hofmann, "Stability of anisotropic beams with space charge," *Physical Review E*, vol. 57, p. 4713, 1998.
4. N. P. D Uriot, "TraceWin," *CEA Saclay*, 2014.

# SAFETY REGULATION OF PARTICLE ACCELERATOR FACILITIES IN INDIA

R. K. Goyal, P. Goverdhan, Pitamber Singh*, K. Jayarajan
Bhabha Atomic Research Centre, Trombay, Mumbai 400085, India
*Ex Head, IADD, Bhabha Atomic Research Centre, Trombay, Mumbai 400085, India
(Corresponding Author: rajiv@barc.gov.in, Phone: +91-22-25590877)

## ABSTRACT

The paper describes safety regulation of particle accelerators used for industrial, research and medical purposes. Radiological and industrial safety should be considered for achieving safety of equipment as well as working personnel, the environment and the members of the public, during various stages of the project, such as siting, construction, commissioning, operation and decommissioning of accelerators. Safety of particle accelerators largely depends on type and size of the accelerator facility. Potential hazards need to be controlled by safe design and good construction, followed by safety procedures. The principal hazard associated with the operation of the accelerators is ionizing radiation (prompt radiation) produced during the operation of the accelerators. Other potential hazards include non- ionizing radiation, fire, noxious gases, and high voltage.

Safety aspects of accelerator facilities, focussing on ionizing radiation, non- ionizing radiations and industrial safety, are described in this paper. Safety principles and techniques can be applied in a graded approach, where the extent and redundancy of protective measures are commensurate with the level of hazards.

## INTRODUCTION

Accelerators are common in research, medical and industrial applications. The most widespread industrial uses of electron beam facilities are for the sterilisation of medical and pharmaceutical products, preservation of foodstuffs, polymer synthesis and modification, eradication of insect infestation and radiography. Welded joints in pipes used in critical applications can be X-rayed to ensure absence of unsafe imperfections.

Particle accelerators are the machines used to accelerate charged particles or ions to high energies. All particle accelerators have the three basic parts: a source of elementary particles or ions; a tube pumped to a partial vacuum in which the particles can travel freely; and some means of speeding up the particles. They accelerate charged particles—or ions—through an electric field in a hollow, evacuated tube. The paths of the accelerating particles may be linear, spiral, or circular. Cyclotron (spiral path) and the synchrotron (circular path) use strong magnetic fields to control the paths of particles.

Linear accelerator (linac), which is the simplest type of accelerator, was first conceived in the late 1920s. The simplest type of linear accelerator is the standing wave accelerator, in which particles travel along a cylindrical vacuum tank through a series of drift tubes, separated by gaps. As the particles cross the gaps, standing electromagnetic waves accelerate them. This type of accelerators can accelerate, particles up to 200 million electron volts (MeV). Efficiency of the linac goes down at higher energy. Physicists mainly use them as a primary accelerator that feeds into a synchrotron. In industry and medicine, they can be used as powerful X-ray machines.

Accelerator safety should be considered at the design stage itself to avoid unexpected complications, cost retrofits or impaired functionality at a later stage. Owner of accelerator facilities are primarily responsible for the safety of users, workers and environment. Therefore, they need to understand safety aspects related to their facilities and should create favourable conditions for the effective safety systems.

## REGULATORY BODIES IN INDIA

BARC Safety Council (BSC) and Atomic Energy Regulatory Board (AERB) are the bodies for radiation safety in India, which regulate the use of radiation and radioisotopes to protect the health and safety of people, worker and the environment.

**BARC Safety Council (BSC)** is the regulatory body in India responsible for Radiation Protection and Industrial Safety for the facilities under the purview of Bhabha Atomic Research Centre (BARC), which include medium and large size research reactors, reprocessing plants, research labs, irradiators, accelerators, high strength radioisotope handling facilities etc. The safety reviews of accelerator facilities under the purview of BARC are also been done by BSC.

**Atomic Energy Regulatory Board** is the regulatory body in India responsible for Radiation Protection and Nuclear Security of all facilities and activities in public domain. Its regulation for the operation of nuclear facilities covers all aspect that effects plant safety and release of radioactive material into environments. AREB guidelines for limitations of radiation exposure in the environment have been based on ALARA (as low as reasonably achievable) principle.

## ACTS AND RULES APPLICABLE FOR PARTICLE ACCELERATORS

**Legislations/Acts** There are many Legislations/Acts dealing with the safety of nuclear and radiological facilities in India, significant among them are:

**Atomic Energy Act, 1962** is to provide for the development, control and use of atomic energy for the welfare of the people of India and other peaceful purposes and for matters connected therewith. Central government has laid down the norms to prevent radioactive hazards, guarantees safety of workers, public dealing with radioactive substances and ensures safe and proper disposal of radioactive wastes under this act. A numbers of rules are promugulated from this act.

**Atomic Energy (Factories) Rules, 1996**: These rules apply to all the factories owned by the Government and engaged in carrying out the activity related to Atomic Energy.

**Atomic Energy (Radiation Protection) Rule, 2004:** It prescribes conditions to be fulfilled for giving of license, for handling radioactive material equipment etc. It prescribes the duties of Radiological Safety Officer, Employer, and Worker etc. It empowers duly authorized person to investigate, seize radioactive equipment.

**Atomic Energy (Safe Disposal of Radioactive Waste) Rules, 1987:** No person shall dispose of radioactive waste, unless he has obtained an authorization from the competent authority under these rules. It provides, “Any venture using radioactive material must appoint Radiological Safety Officer”.

**Environment Protection Act, 1986**: It provides for the protection and improvement of environment and matters connected there with. It also pitches for prevention of hazards to human beings, plants and property. The acts provide for the protection and improvement of environment and matters connected there with. Environment includes water, air and land and the interrelationship which exits among and between water, air and land, and human beings, other living creature, plants, micro organism and property.

## SAFETY ASPECTS OF ACCELERATORS

Accelerator operations present a range of potential safety and health hazards, including ionizing radiation. Ionizing Radiation can be controlled by adequate shielding, radiation detectors, warning devices, and automatic shutdown of facility. Additional potential hazards, such as non-ionizing radiation, fire, electricity (high voltage), and noxious/ toxic gas (produced from the irradiation of various materials), should be considered for safety of the workers and environment. Ventilation of accelerator facilities and air monitoring are important hazard controls to overcome accumulation of noxious gas/toxic gas. Sky-shine is a hazard with small accelerators where only shadow shields are used; or with large machines where earth cover is used.

The safety objectives of accelerators are to achieve total safety of equipment as well as working personnel, the environment and members of the public. It involves protection from both radiological and industrial hazards during the stages of siting, construction, commissioning, operation and decommissioning.

Accelerator facility shall ensure the following for safety:

a. Radiation fields and other hazardous factors in accessible areas are within the stipulated limits.

b. No one remains trapped /present in high radiation fields during operation and while the primary particle beam is switched on.

c. Protection against noxious fumes and gases that may be formed during the accelerator beam operation or in radiation processing of materials.

d. Protection from other conventional / industrial hazards, and non-ionizing radiation, which may arise from operation in various sub-systems in the facility.

e. Evolving a safety culture by means of training operators, users and other personnel working in the facility.

## IONIZING RADIATION SAFETY

Ionizing radiation is a byproduct of accelerator operations, although some accelerators, e.g. medical therapy machines, are designed to produce particular radiation fields on purpose. The yields are a function of angle of emission, primary energy and beam intensity. Even small accelerators are capable of generating radiation levels that are harmful or even lethal to humans. Two types of radiation hazard may be present in accelerators: prompt radiation and induced radiation.

**Prompt radiation** is usually generated by intentional or unintentional loss of beam in the primary beam line components, such as collimators, scrapers, stoppers, beam dumps, magnets or narrow beam line apertures. The primary beam itself may constitute prompt radiation, if not properly contained. Prompt radiation fields are present only when the accelerator is on; switching the machine off can therefore mitigate this hazard.

**Induced Radiation** is generated when primary or secondary prompt radiation interacts in the surrounding materials, especially those involving neutrons. The radiation fields generated as a result of such reactions persist even after the beam is turned off. Activation occurs mainly in beam line components exposed to large beam loss, beam dumps, collimators, injection point and narrow apertures. It can be therefore minimized by proper choices of materials used for beam line components.

### *Radiation Safety Objectives*

The objectives for enforcing radiation safety at the accelerator facility are to ensure that:

1) During normal operation, maintenance, decommissioning and emergency situations, the radiation dose to workers as well as members of the public is kept below the relevant dose limits prescribed by regulatory body.

2) All exposures are kept as low as reasonably achievable (ALARA) and in order to achieve this, the investigational limits of radiation exposure for the specified period, as directed by the regulatory bodies, are adopted.

These objectives should be met by providing the following safety features

1) Shielding;
2) Safety interlocks;
3) Access Control / Administrative control;
4) Emergency Preparedness Plan (EPP).

An authorised Radiological Safety Officer (RSO) should be available at the facility to implement the above objectives.

### *Shielding*

The shielding around particle accelerators is designed to protect personnel from intense fluxes of secondary particles (mostly neutrons) and gamma radiation. The shield is designed to attenuate high radiation intensities to permissible levels. The design of shielding is based on the estimated source term. Source term of accelerator depends on the type of particles accelerated, their energies, beam currents, target materials and the duty cycles. A realistic and justified beam loss scenario should be considered in arriving at the source term.

The shield design shall conform to the dose rate limit of 1 mSv/h in continuously occupied areas as stipulated by AERB.

Shielding of $\gamma$ and X-Rays is best accomplished using high Z materials (material with high mass numbers), usually steel or lead. Neutrons are best attenuated in materials with high hydrogen content, such as polyethylene and concrete. However, for high-energy neutrons (above 20 MeV), it is best to use a first layer of high Z material, to take advantage of inelastic process at these energies, followed by concrete or polyethylene.

### *Safety Interlocks*

Safety Interlocks are designed to protect the machine and the personnel under any abnormal/unsafe condition when the accelerator facilities are operating. Safety interlocks ensure meeting certain conditions, in a proper sequence, before the accelerator is operated. Safety interlocks of an accelerator facility should be fail-safe, redundant and testable.

Safety interlocks shall be provided for the following undesirable events which can lead to severe radiological consequences:

1) Beam Losses
2) Target Rupture
3) Vacuum Break
4) High Voltages (DC Accelerators)
5) Radiation Leak
6) Trapping of persons inside accelerator

The accelerator shall be automatically shut-down during such events.

### *Access Control System*

Access Control System consists of physical barriers with doors and access hatches that can be either locked or interlocked. A typical component of access control system is a key-bank containing many keys that allow entry to accelerator enclosure. If any key is missing from the bank, the interlock should prevent the accelerator from switching on. Access Control System also includes audio-visual warning device and warning signs. Access Control System hardware is complemented by an appropriate set of procedures specifying access protocol, enclosure, search, etc. It should be ensured that no one is trapped inside the accelerator enclosures, before the beam is switched ON. For large enclosures, search & secure buttons are used to guarantee that the search is performed in prescribed order. In addition, panic switches and ropes in accelerator enclosures enable any person accidentally trapped within to stop the beam.

### *Radiation Monitoring*

Radiation monitoring is one of the means to limit the exposure of personnel to ionizing radiation, and to verify that annual dose of the worker is within the legal limits. The radiation monitors measure the radiation dose equivalent rate at work places in supervised areas, and signal the presence of excessive radiation via local and remote alarms to alert personnel to evacuate accessible areas in case radiation levels exceed predefined radiation alarm thresholds.

Radiation monitoring in designated areas can be performed using active and passive detectors. Passive detectors such as TLD are cost effective to measure cumulative dose. They are also useful for radiation monitoring at the boundaries of the facility, to ensure that dose rates from sky-shine or direct sources do not exceed the prescribed limit. Active detectors, such as ionization chambers, proportional counters and scintillators are preferred where the information of radiation levels is needed on a continuous basis. For neutron detection, moderated detectors are used to provide coverage over a broad energy range.

Personnel monitor are mostly based on TLD detectors. All these detectors need to be carefully calibrated to specific fields encountered at the accelerator facility, because their response varies widely with the energy and type of radiation. Circumstances of personnel radiation exposures above this limit are investigated, usually as part of the institution's ALARA (Exposures As Low As Reasonably Achievable) policy.

## NON-IONIZING RADIATION SAFETY

Non-ionizing radiation may be present in many accelerator facilities. Operation of particle accelerators can generate very high electric and magnetic fields, as well as very high level of radio-frequency radiation. Klystrons and Magnetrons are the primary sources of RF in accelerator facilities. Guidelines and standards of International Commission on Non-ionizing Radiation Protection (ICNRP), and the American National Standards Institute (ANSI), should be followed to protect employees against non-ionizing radiation hazards.

Protection against Non-ionising radiation hazard can be achieved by the following means:

a. Administrative control
b. Engineering control
c. Personal protection

Emphasis should be placed on administrative and engineering control measures to minimise the need for and problem associated with personal protection.

**Administrative Control Measures** consist of the following:

i. Access Control: Access to an area should be limited to those persons directly concerned with its use.

ii. Warning Signs: Appropriate caution boards providing warning of RF and magnetic fields should be displayed at prominent places to indicate the presence of potential non-ionizing radiation hazard. Additional warning lights with hooter may be used to show that the equipment or system is energized.

iii. Distance: The user should keep far away from the non-ionizing radiation source as is practicable. The intensity of the radiation falls off as the square of the distance from the source.

iv. Limitation of exposure time: The exposure time to the radiation should be kept to the minimum, and the maximum recommended exposure limits should not be exceeded.

**Engineering Control Measures** consist of the following:

i. Sealed housings: The non-ionizing radiation should be contained within a sealed housing.

ii. Shielded Areas should be provided where the exposure process takes place external to the source housing. Persons entering the area should be adequately protected by providing a shielded area.

iii. Interlocks: Interlocks should be provided to the source housing to prevent excessive and unnecessary exposure. Interlocks are necessary where the removal of a cover from the housing could result in a high exposure. The interlocks should be fail-safe.

iv. RF Monitoring: RF leakage tests should be conducted when the system is first operated and periodically thereafter. In addition, personal protective equipment (PPE) should be used whenever required.

High magnetic fields are present at many accelerator facilities. While the health risks from magnetic fields are not well understood, health hazards do exist to persons with pacemakers or implants in metals in their body. High magnetic fields may also present safety hazards from the forces they exert on the tools made of ferromagnetic material. Perceptible or adverse effects have been produced at higher flux densities on persons with other implanted ferromagnetic medical devices (suture staples, aneurism clips, prostheses, etc.).

Disturbances caused by the high frequency signal cables and monitoring equipment (e.g. to ionization chambers, if not RF-shielded), should also be considered.

## INDUSTRIAL SAFETY

An accelerator facility, apart from being a source of nuclear radiation, will have various industrial types of activities hence calls for a program of industrial safety. The facility should have an industrial safety program in order to avoid any accident or unsafe situations. In the Department of Atomic Energy (DAE) units, AERB is responsible to over-see the adherence to the Factories Act, 1948 and the Atomic Energy (Factories) Rules, 1996. The following industrial hazard should be considered in accelerator facilities.

Details of protection from the hazards of Electrical, Fire and Toxic Gases are provided in this paper. First aid provision, along with appropriate staff trained in first aid, should be available in the facility. Periodic medical examinations should be carried out on all concerned workers to ensure that they are fit for undertaking their assigned task. Pressure vessels and vacuum systems should be periodically inspected and tested. Handling and storage of gas cylinders should be as per Gas Cylinder Rules. All hoists, lifts and lifting tackles should be subjected to periodic inspection and testing which should be certified by a competent person.

### *Electrical Safety*

Accelerators are particularly vulnerable to electrical hazards. Electrical hazards could be present in klystron, vacuum system, beam-line monitoring instrumentation and high current magnets power supplies.

High-voltage electrical systems are required to power most of the accelerator operations. High quality of earthing is a pre-requisite for protection against electric shocks. The electrical grounds as per the safety standards have to be maintained and tested periodically to ensure that the safety features are well in place. To minimise hazards due to high voltage, caution sign boards with danger signs and visual indication should be put up near such locations. Appropriate interlocked door should be available to trip high voltage during cage door opening. Specific safety requirements, such as guarding energized live parts and the use of personal protective equipment (PPE) when working on or near energized equipment, should be followed.

### *Fire Safety*

Accelerator facilities should have a comprehensive fire protection and life safety program. The facility should have the approved fire order, specifying the responsibility of the concerned officers. The facility should have suitable fire detection and alarm system (FDAS) and fire suppression systems. Fire drills and training at regular intervals, appropriate to various categories of personnel, should be carried out at regular intervals.

Emergency exit pathways should be clearly demarcated, preferably with luminescent markings, to enable the working personnel to evacuate the area in case of fire emergency, with least exposure to radiation or other hazardous situations. The emergency exit pathways should be kept free at all times.

### *Ventilation*

Industrial electron beam accelerators are commonly used for radiation processing applications of polymer materials, sterilization of health care products, colour enhancement in gemstones, etc. Irradiation of materials outside the accelerator vacuum system produces high yields of noxious gases, such as ozone and nitrogen oxides ($NO_x$). Production of ozone is related to radiation beam intensity, stopping power of the radiation beam, distance travelled in the medium, time of irradiation, and the volume of the space being considered.

Ozone is a toxic gas and exposures to excessive concentrations of ozone can cause health hazards. Necessary control measures are suggested to keep the occupational exposure of the personnel to ozone concentrations well within the Threshold Limit Values (TLV) of 0.1 ppm.

The facility should be designed for migration of the ozone. Access to the area where the concentration of ozone is likely to exceed the accepted limit should be prevented. This can be achieved by using proper ventilation system. Ventilation system in 'ON' condition should be an essential safety requirement for start-up and operation of the accelerator. The ventilation system must be kept 'ON' for a considerable duration even after shutdown of the accelerator, so as to remove ozone from the accelerator area. However, when high capacity, continuously operated ventilation system is used, the accelerator area can be accessed within a few minutes after the shutdown of the accelerator. A time delay interlock mechanism, preventing opening of personnel access doors within a preset time of termination of irradiation, must be provided to ensure depletion of ozone to an acceptable level.

## EMERGENCY RESPONSE PLANNING

The facility should be prepared and equipped to deal with any emergency situation. Emergency procedures specifying steps to alleviate the damage to personnel and property shall be available with the facility. The organisational responsibility for each action must be delineated and the required information must be displayed in the facility. The procedures should also include the name and telephone numbers of the persons to be notified for directing remedial action for example the police fire brigade, medical help, and competent authorities. In case of high radiation exposure, when specialised medical attention would be required, the competent authorities must be informed immediately. The facility management must be aware of whom to contact to secure help.

## ROLE OF REGULATION IN ACCELERATOR SAFETY

Regulator plays a significant role to provide the safe and healthy environment at accelerator facility. The prime responsibility for safety rests with the facility, but the regulator is to ensure that accelerator facilities comply with the applicable codes, standards and directives. The regulatory bodies also develop standards and provide regulatory guidance to verify, ensure and to enforce compliance with safety standards.

The regulatory authority reviews the comprehensive and systematic safety assessments, which are carried out before any consenting stage of the accelerator installation. Several documents are required at these stages to evaluate safety. Safety committees consisting of qualified experts go through these documents to evaluate safety and recommend/approve the authorisation. Certain requirements (for a particular facility) are not applicable, due to its type and nature, the same may be indicated in the application.

Depending on the size and nature of the facility, stepwise authorisations, starting from the approval of site, design and layout of the buildings, construction, commissioning, trial operation followed by regular operation are envisaged. The committee may give authorisation for trial operation at various stages of beam power.

## REGULATORY FRAME WORK FOR ACCELERATORS FACILITIES IN BARC

BARC Safety Council (BSC) is the regulatory body responsible for ensuring safety regulation in all operations involving ionizing radiation and industrial safety of all the facilities and projects under the purview of BARC. BSC is supported by an elaborate set of safety committees in different tiers. Safety regulation of particle accelerator facilities and projects in BARC is also in the scope of BSC.

BSC follows three tier review system to ensure safety of all plants and operations.BSC, along with its safety committees contributes to the safety review of accelerators. BARC has about 15 accelerator projects and facilities. BSC has constituted two safety committees exclusively for safety review of particle accelerators that is Design Safety Review Committee-Accelerator Projects (DSRC-AP) and Unit Level Safety Committee-Particle Accelerators (ULSC-PA).

DSRC-AP reviews the safety of upcoming accelerator projects. Review of the applications for siting, construction, commissioning and trial operation of accelerator projects are carried out by the DSRC. DSRCs are assisted by expert Working Groups The committee reports to BSC.

ULSC-PA is responsible for safety review of accelerators during their regular operation. The committee reports to Operating Plant Safety Review Committee (OPSRC).

Safety committees, such as DSRC-AP and ULSC-PA, constitute Regulatory Inspection Teams (RITs) for Regulatory Inspections (RI) in accelerator facilities and projects. RI helps the regulator to verify the actual condition of the facilities and the compliance of the recommendations of the safety committees. RI is also carried out before issuing regulatory consent. Facilities and projects regularly conduct fire emergency and radiation emergency exercises to verify their preparedness for emergency. BSC observer should present during the emergency exercise.

The structure of the regulatory frame work of the Particle Accelerator facilities in BARC is shown below.

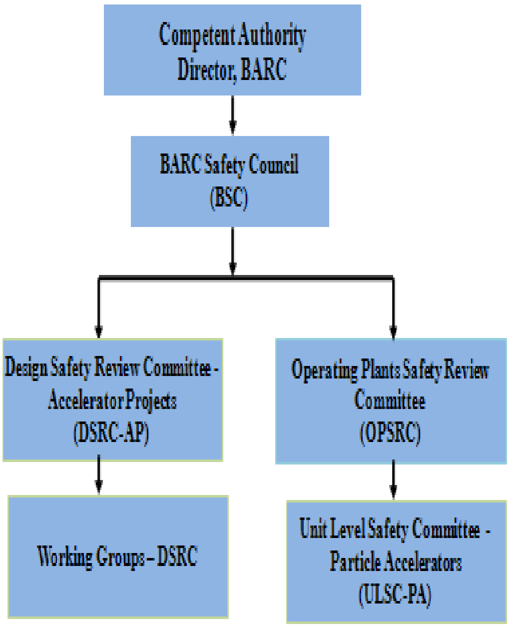


## CONCLUSION

Regulations play a pivotal role in safety of accelerators. The extent and complexity of a safety program largely depends on the type and size of an accelerator facility. Accelerators hazards can be controlled by safe design, good construction and safe operation, followed by safety procedures associated with such facilities.

Safety is of prime importance and both industrial and radiological aspects are equally important. The main difference between accelerators with reactor is the source term, vanishes when the accelerator is switches off. A safe and accident free environmental in radiological and industrial field can be achieved with the effective incorporation of safety features and proper regulation.

## REFERENCES


[1] AERB: Safety Guidelines on Accelerator (AERB/SG/IS-5).

[2] The Journey of BARC Safety Council for Strengthening Safety Culture in BARC Facilities by K. Jayarajan and V. M. Jolly; July 2017.

[3] Atomic Energy (Factories) Rules, 1996

[4] Atomic Energy (Radiation Protection) Rule, 2004.

[5] Accelerator Radiation Safety by V Vylet

[6] Radiological safety assessment of Brazilian Industrial Facilities with Electron Accelerators by M. J. M. Lourenco, A T Ramalho, F. C. A. Da Silva and J. M. O. Godoy; 2005

# STUDIES ON THE EFFECT OF RF POWER ON THE PLASMA POTENTIAL OF A 6.4 GHZ ECR ION SOURCE

M.Bhattacharjee[#], C Giri, Doddi Lavanyakumar and V.Naik

*Variable Energy Cyclotron Centre (VECC) and Homi Bhabha National Institute (HBNI),1/AF Bidhan Nagar, Kol-64*

*Abstract*

The paper describes an experimental study to determine the effect of the rf power on the plasma potential of an Electron Cyclotron Resonance Ion Source (ECRIS). A Langmuir probe has been built in-house and used to record the I-V characteristics of a 6.4 GHz ECRIS operational at the Radioactive Ion Beam (RIB) facility at VECC. This source will be used as the breeder source of a Charge Breeder Beam line presently under development at the facility. In this scheme, a $1^+$ RIB will be injected into the breeder source for the production of $n^+$ RIB. As such, an understanding of the plasma parameters of the source is vital for better capture of the incoming $1^+$ beam which would result in a good charge breeding efficiency.

## INTRODUCTION

A Charge Breeder Beam Line is under construction at the RIB facility, VECC Kolkata [1]. As described in Figure 1, it consists of a gas-jet coupled 2.45 GHz ECRIS producing $1^+$ ions that will be mass-separated and injected in a 6.4 GHz ECRIS charge breeder for producing multiply charged ions. However if the $1^+$ beam is not sufficiently decelerated, it will pass through the breeder source without getting captured.

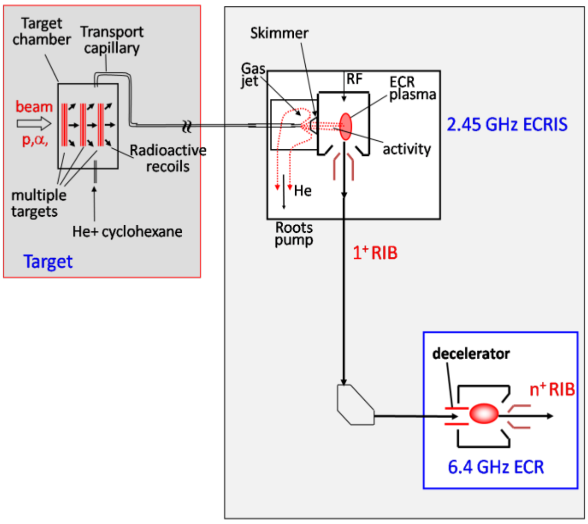


Figure 1: Scheme of the Charge Breeder Line consisting of two ion-sources in tandem. Radioactive recoils are injected via gas-jet into the first ECRIS which produces $1^+$ RIB. The $1^+$ RIB needs deceleration at the entry of the second ECRIS to a value of the order of the plasma potential of the source.

For proper capture of the $1^+$ beam by the breeder plasma, the energy of the beam has to be of the order of plasma potential so that the beam neither passes through, nor is reflected back [2].

While we design the deceleration optics to yield a final beam energy corresponding to the plasma potential of the breeder source, it is important to know how the potential changes with respect to the control parameters of the plasma. This is because; higher the plasma potential, easier it will be to transport the decelerated beam since a very low energy beam tends to blow up easily. We therefore carried out a study to determine the variation of plasma potential of the 6.4 GHz ECRIS with respect to rf power and in the process aimed to determine the maximum plasma potential.

## EXPERIMENTAL SETUP

The schematic layout of the 6.4 GHz breeder ECRIS is shown in Figure 2. Both solenoid coils and NdFeB permanent magnet have been used for magnetic confinement, microwave is injected axially. It has a maximum axial magnetic field of 1.0 and 0.7 T, at the injection and extraction side respectively, as shown in Figure 3. Radial field on the inner wall of plasma chamber is 0.7 T. The Langmuir probe is inserted axially into the plasma zone of the source. The source was evacuated to a pressure of 2 x $10^{-7}$ mbar prior to the experiment through two Turbo molecular pumps, one

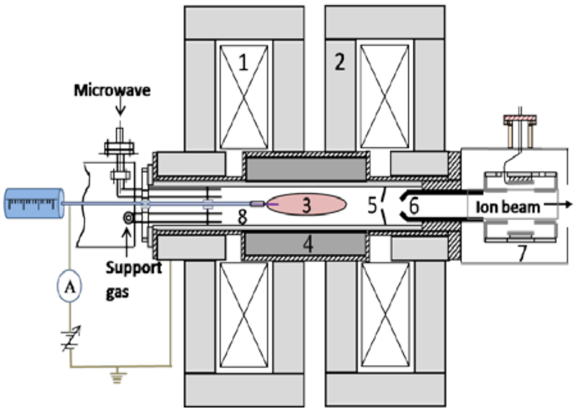


Figure 2: Schematic of the 6.4 GHz ECRIS. 1- Solenoid coils, 2- Yoke, 3- ECR plasma, 4- NdFeB hexapole magnet, 5- Plasma electrode, 6- Puller electrode, 7- Einzel lens, 8- Langmuir probe.

[#] bmahuwa@vecc.gov.in

each at the injection and the extraction end. Gas was introduced into the source in a controlled manner using a fine needle valve. The study was carried out with two different gases, namely Nitrogen and Argon. A one mm diameter Tantalum wire was used as the probe, $Al_2O_3$ was used as the ceramic coating. We used DC power supplies (Spellman EH03R33L) that could span the voltage range -100 V to +100 V. I-V characteristics as a function of rf power were recorded for different working pressures for each of the gas. The rf power was varied in the range of 0 to 500 W.

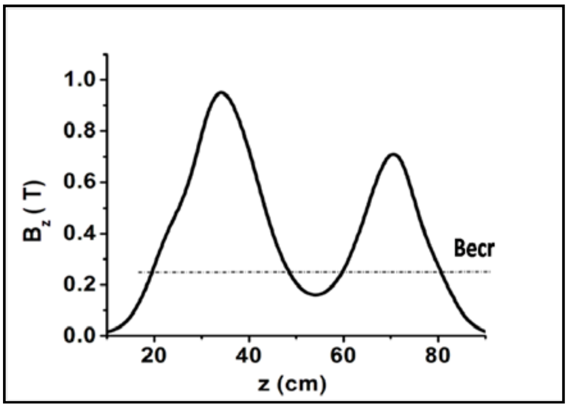


Figure 3: Axial magnetic field along the length of the ECR plasma chamber.

## DATA ANALYSIS AND RESULTS

Figure 4 shows typical Langmuir I-V curves obtained with the above experimental set-up. Since this is a magnetized plasma, collection of electrons by the probe is affected because of the gyration of the electrons along the magnetic field lines resulting in a suppression of the electron saturation current ($I_{es}$). We have therefore calculated the ion density ($n_i$ ) from the ion saturation current and assumed electron density $n_e = n_i$ applying quasi-neutrality. The plasma potential ($V_p$) is taken as the inflection point of the curve i.e the voltage where $\frac{d^2I}{dV^2} = 0$.

The electron current ( $I_e$) in the retarding region of the I-V curve is given by

$$I_e = I_{es} \exp[e(V - V_p)/KT_e]$$

where $T_e$ is the electron temperature and $K$ is Boltzmann constant. $T_e$ can be calculated from the slope of the straight line obtained by plotting natural logarithm of $I_e$ against V in the region below the plasma potential.

In ECR plasma, electrons are heated resonantly and $T_e \gg T_i$ , $T_i$ is the ion temperature. The ion saturation current in such cases is determined by the Bohm ion current [3].

$$I_{is} = I_{Bohm} = 0.6\, en_i \sqrt{\frac{KT_e}{m_i}}\, A_p$$

$A_p$ is the probe area and $m_i$ is the ion mass. From $T_e$ and $A_p$ , $n_i$ can be calculated.

The electron energy distribution function (EEDF) can be calculated from the expression :

$$f(E) = \left[\frac{(8m_e V)^{1/2}}{A_p e^{3/2} n_e}\right] \frac{d^2I}{dV^2}$$

where $f(E)$ is the function representing the EEDF, E is the electron energy and $m_e$ is the electron mass. An empirical parametrization method developed in Reference [4] was used to derive the above discussed parameters. The variation of $V_p$, $n_e$ and $T_e$ obtained thus are plotted as a function of rf power in Figure 5 and 6 for Argon and Nitrogen gas respectively.

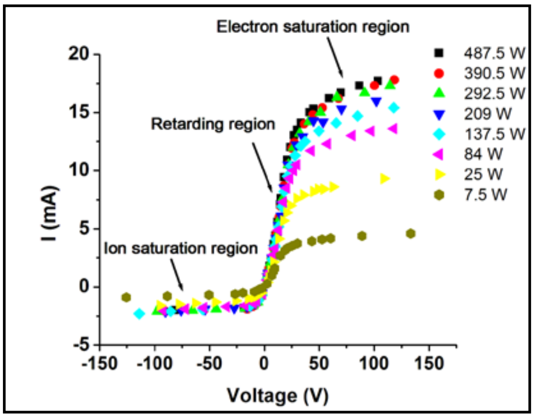


Figure 4: I-V curves for different rf powers as obtained from a nitrogen plasma in the 6.4 GHz ECRIS.

In general the plasma potential is seen to increase with rf power. The rise is rapid in the low power region and seems to slow down at higher power in most cases. The electrons in the plasma gains more energy with increasing rf power. This is expected to result in more loss of electrons from the plasma core due to large angle scattering and diffusion which in turn increases the potential of the plasma. As can be seen from the graphs, the nature of variation in the plasma potential closely follows that of the electron temperature as expected. However in most cases, there seems to be saturation effect to this rise of electron energy with power. The minimum value of the plasma potential is ~ 10 V and it reaches a peak at ~ 17-18 V in most cases. In the case of Ar gas at 9 x $10^{-7}$ mbar, a dip in both $T_e$ and $V_p$ is observed at ~ 400 V. This effect is alleviated at higher pressures and needs t to be investigated further.

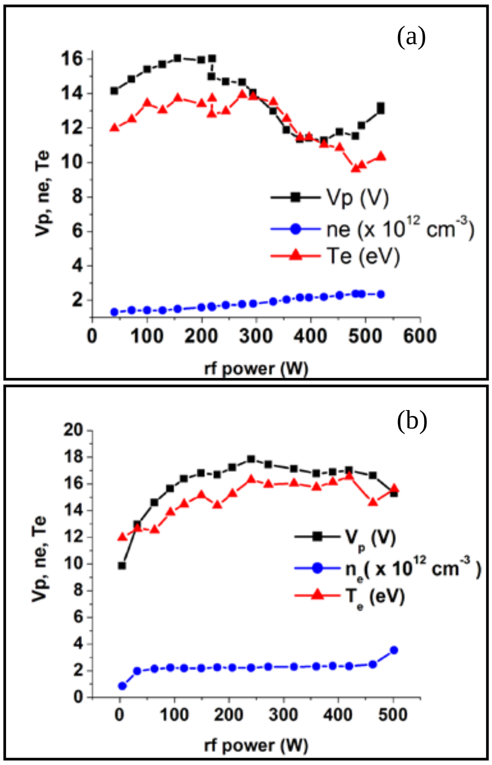


Figure 5: Variation of plasma parameters with rf power for Argon gas pressures of (a) 9 x $10^{-7}$ mbar and (b) 1.5 x $10^{-6}$ mbar.

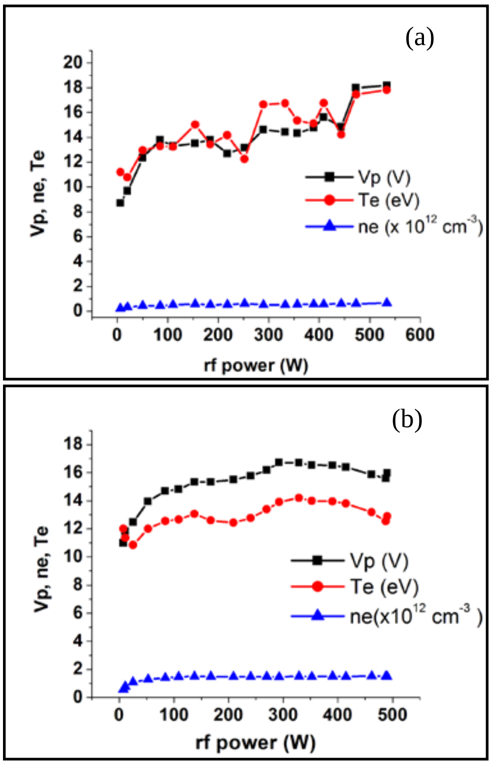


Figure 6: Variation of plasma parameters with rf power for Nitrogen gas pressures of (a) 5 x $10^{-7}$ mbar and (b) 1.25 x $10^{-6}$ mbar.

The electron density in the plasma is found to be 1-2 x $10^{12}$ $cm^{-3}$ for this range of rf power. The EEDF for one of the studies with Argon gas is plotted for a few rf powers in Figure 7. The function seems to be Maxwellian in nature with the peak shifting towards higher energy with higher power as is expected.

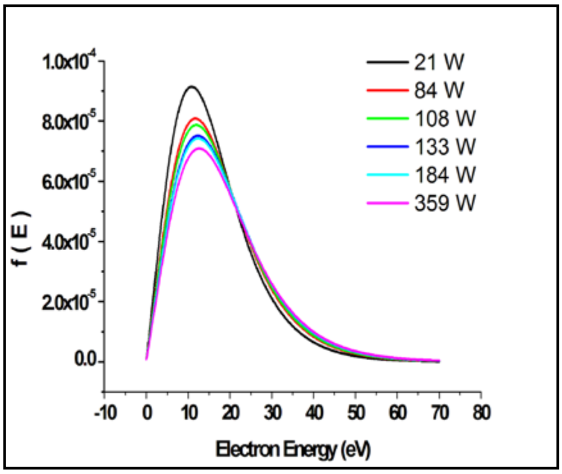


Figure 7: EEDF for different rf powers as obtained in a Argon gas plasma. Working pressure – 1.25 x $10^{-6}$ mbar.

## OUTLOOK

The variation in the plasma potential and other plasma parameters with rf power in the range of 0-500 W was studied in a 6.4 GHz ECRIS. Apart from an exception for low pressure Ar plasma, generally the potential rises and saturates at a value of 17-18 V with increasing rf power. Two gases, Nitrogen and Argon have been studied so far. The study will be taken up for a few other gases as well, to see if there is any augment in the plasma potential value. The peak value of the plasma potential hence obtained will decide the final energy of the $1^+$ beam entering the ion source and hence the design of the deceleration optics elements.

## ACKNOWLEDGEMENT

The authors would like to thank Dr. P. Roychowdhury RRF, BARC for valuable discussions on Langmuir probe measurements.

## REFERENCES

[1] M. Bhattacharjee et al,'Gas-jet coupled Charge.....' InPAC 2015, TIFR, Mumbai.
[2] T. Lamy et al, Rev. Sci. Instrum. 77, 03B101 (2006).
[3] P. Roychowdhury et al, Rev. Sci. Instrum. 84, 073303 (2013).
[4] A.A. Azooz et al, Rev. Sci. Instrum.79,103501 (2008).

# PHYSICS DESIGN STUDIES FOR ACCELERATING SECTION OF 200 MeV INJECTOR LINAC FOR HIGH BRILLIANCE SYNCHROTRON RADIATION SOURCE

Parul Arora[1, †], Nita S. Kulkarni[1] and Vinit Kumar[1, 2]
[1]Accelerator & Beam Physics Section, RRCAT, Indore
[2]Homi Bhabha National Institute, Mumbai

*Abstract*

A 3 GHz, 200 MeV linac is being considered as the injector for the proposed High Brilliance Synchrotron Radiation Source (HBSRS). In this injector linac, a 90 keV beam from electron gun will be bunched in a sub-harmonic 500 MHz pre-buncher cavity, that will be followed by a 3 GHz standing wave buncher section, which will further bunch as well as accelerate the beam upto 15 MeV. The accelerating section will be a 3 GHz, 2π/3 mode constant gradient, traveling wave linac that will accelerate the 15 MeV electron beam to 200 MeV. It will have four identical sections consisting of 114 cells each. In this paper, we present the details of electromagnetic design studies performed to optimize the geometrical and RF parameters of the constant gradient, traveling wave linac. A comparison of RF parameters estimated using simulations and analytical expressions is presented. Beam dynamics studies for accelerating section to obtain the desired parameters at the output and also to maximize the beam transmission efficiency are presented.

## INTRODUCTION

There is a proposal to build a High Brilliance Synchrotron Radiation Source, which will be a 6 GeV electron storage ring based light source with an ultra-low emittance [1]. A 3 GHz linac is being considered as the injector for the HBSRS, which will accelerate a 90 keV electron beam to 200 MeV. Fig. 1 shows the basic layout of this injector linac. The three major sections of linac will be (i) sub-haromic pre-buncher (SHPB) cavity, (ii) standing wave buncher section and (iii) constant gradient, traveling wave accelerating section.

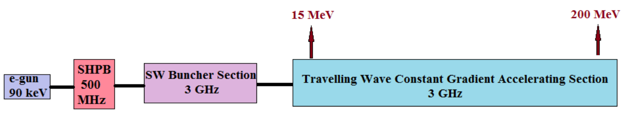


Figure 1: Schematic of injector linac for proposed HBSRS.

The beam parameters required from this injector linac are listed in Table 1. In this paper, the preliminary physics design studies are presented for the accelerating section of injector linac. It will be a 3 GHz, 2π/3 mode constant gradient (CG), traveling wave (TW) structure to accelerate the 15 MeV electron beam from buncher section to 200 MeV.

†parul@rrcat.gov.in

Table 1: Required injector linac parameters

| | |
|---|---|
| Beam energy | 200 MeV |
| Charge | 34.17 pC/bunch |
| Bunch spacing | 2 ns |
| Energy spread, rms | 0.5 % |
| Emittance, un, rms | 60 nm rad |

## ELECTROMAGNETIC DESIGN OF ACCELERATING SECTION

The accelerating section is a disk loaded, CG, TW linac. The structure parameters are listed in Table 2.

Table 2: Structure parameters for accelerating section

| | |
|---|---|
| Operating frequency | 3 GHz |
| Mode | 2π/3 |
| No of sections | 4 |
| No. of cells in each section | 114 |
| Length of each section | 3.76 m |
| Input RF power for each section | 16 MW |

The electromagnetic design studies were performed using 2D electromagnetic code SUPERFISH [2]. A cell of the disk loaded structure has five important geometrical parameters, which are cell length (*d*), aperture radius (*a*), cell radius (*b*), disk thickness (*t*) and disk edge radius (*r*). These parameters are marked on the schematic of 3-cell disk loaded structure (Fig. 2), used for SUPERFISH simulation.

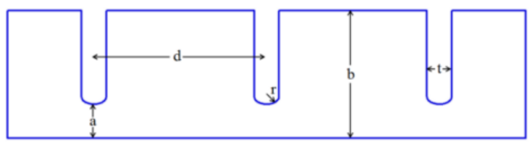


Figure 2: Schematic of 3-cell disk loaded structure.

The accelerating linac has all regular accelerating cells with $\beta_p$ = 1 ($\beta_p$ is the phase velocity in unit of speed of light). For 2π/3 mode, the cell length is calculated as 33.28 mm for 3 GHz operating frequency. The selection of disk thickness is based on the mechanical rigidity and strength of the cell. For our design, we have chosen $t$ = 5.0 mm and $r$ = 2.5 mm. Cell length, disk thickness and disk edge radius are kept same for all the cells. However, for a CG linac, aperture radius is varied over the length of the structure to obtain linearly varying group velocity, thereby achieving a constant longitudinal electric field in the absence of beam loading [3, 4]. The selection of aperture radius of cells also depends on the trade off between shunt impedance and available space for beam transmission. In our case, each accelerating section has 114 cells to achieve 200 MeV beam energy at linac output (from beam dynamics results), with the aperture radius decreasing from 13.0 mm to 10.324 mm in a manner such that the group velocity decreases linearly along the length of each accelerating section. After the estimation of aperture radius, the cell radius for all 114 cells are optimized for 3 GHz operating frequency and 2π/3 mode. In our case, the cell radius decreases from 39.839 mm to 39.134 mm. The variation in cell radius and aperture radius in each section are shown in Fig. 3 (a).

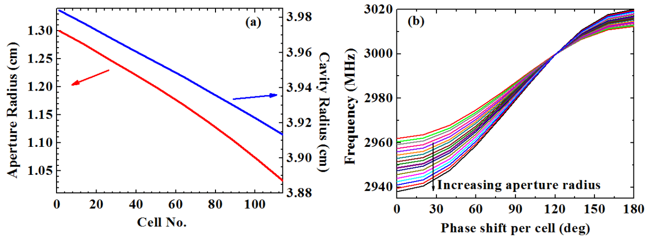


Figure 3: (a) Variation in aperture and cell radius over 114 cells in each accelerating section, (b) Dispersion curves for different cells.

### *Calculation of RF parameters*

The post-processor in SUPERFISH is used to calculate the RF parameters like quality factor ($Q$), shunt impedance ($r_{sh}$), transit time factor ($T$), attenuation constant ($\alpha$), group velocity ($v_g$) and coupling coefficient ($k$). Dispersion curves are generated for all cells (shown in Fig. 3 (b)). Table 3 lists the RF parameters for first and last cells in the accelerating linac obtained from simulations.

Table 3: Cavity RF parameters

| | First cell | Last cell |
|---|---|---|
| Frequency (GHz) | 3 | 3 |
| Quality factor | 13347 | 13286 |
| Shunt Impedance (MΩ/m) | 53.6 | 61.4 |
| Attenuation constant (Np/m) | 0.0975 | 0.218 |
| Group velocity/c | 0.0242 | 0.0109 |
| Transit time factor | 0.734 | 0.717 |
| Coupling coefficient | 0.0276 | 0.0124 |

### *Analytical calculation of RF parameters*

The RF parameters were estimated using analytical calculations as well, and compared with the simulation results. Expression for $Q$ is given by [3, 4, 5]:

$$Q=\left(\frac{\lambda}{\delta}\right)\frac{\beta_p\left[1-(t/d)\right]}{n+2.61\beta_p\left[1-(t/d)\right]}\,. \qquad (1)$$

Here, $\lambda$ is wavelength, $\delta$ is skin depth and $n$ is number of cells per wavelength for the desired mode. The value of $n$ for 2π/3 mode is 3. Expression for group velocity is:

$$\frac{v_g}{c}=\frac{2(2.405)}{3\pi J_1^2(2.405)}\left(\frac{a}{b}\right)^3\sin\theta e^{-\xi t}\,, \qquad (2)$$

where,

$$\xi=\sqrt{\left(\frac{2.405}{a}\right)^2-\left(\frac{\omega}{c}\right)^2}\,. \qquad (3)$$

Here, $\omega$ is angular frequency and $c$ is speed of light. The attenuation constant is given by:

$$\alpha=\frac{\omega}{2v_gQ}\,. \qquad (4)$$

For a traveling wave linac, the shunt impedance per unit length is:

$$r_{sh}=\left(\frac{Z_0^2}{\pi\rho_S}\right)\left(\frac{d}{b}\right)\frac{T^2}{(b+d-t)J_1^2(2.405)}J_0^2\left(2\pi\frac{a}{\beta_P\lambda}\right), \qquad (5)$$

where,

$$T=\frac{\sin\left(\frac{\theta}{2}\frac{d-t}{d}\right)}{\theta/2}\,. \qquad (6)$$

Here, $Z_0$ (=377 Ω) is vacuum impedance, and $\rho_s$ (=14.6 mΩ) is the surface resistivity . Figs. 4 (a), (b), (c) and (d) show that the simulated and analytically calculated values of quality factor, shunt impedance, attenuation constant and group velocity respectively for all the cells agree reasonably well.

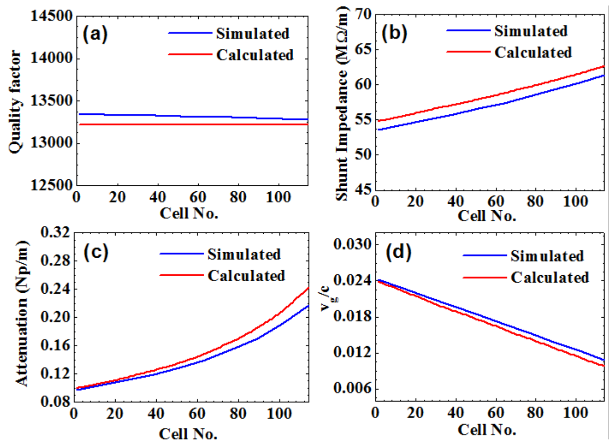


Figure 4: Variation in (a) quality factor, (b) shunt impedance, (c) attenuation, and (d) group velocity over 114 cells in each accelerating section.

## BEAM DYNAMICS STUDIES

In this section, we present the beam dynamics studies for the 3 GHz, CG, TW accelerating linac performed using code PARMELA [6]. Table 4 lists the input beam and RF parameters optimized for the required output parameters as listed in Table 1.

Table 4: Input beam and RF parameters

| | |
|---|---|
| Input RF power | 16 MW per section |
| Input beam energy | 15 MeV |
| Charge | 34.17 pC per bunch |
| Bunch spacing | 2 ns |
| Energy spread, total | ±5.0% |
| Phase spread, total | ±10° |
| Emittance, un ,rms | 0.78 μm rad |
| Twiss parameter, α | 0 |
| Beam radius, rms | 1.0 mm |

For a CG structure, aperture radius is varied over the linac length to achieve constant field gradient. However, it should be noted that, field ($E_0$) is constant in the case of no beam condition and its value is given by [3, 4]:

$$E_0^2 = \frac{r_{sh} P_0}{L}\left(1 - e^{-2\tau}\right). \qquad (7)$$

Here, $P_0$ is input RF power, $L$ is length of the structure and $\tau = \int_0^L \alpha dz$. The value of $\tau$ is 0.53 in our case.

With beam loading, the electric field along the length ($E$) is given by [3, 4]:

$$E(z) = E_0 + \frac{I_0 r_{sh}}{2} \ln\left[1 - \frac{z}{L}\left(1 - e^{-2\tau}\right)\right]. \qquad (8)$$

Here, $I_0$ is beam current. The values of electric field with beam loading effect were used in PARMELA simulations. Fig. 5 shows the TW electric field pattern along linac length generated by PARMELA at RF phase of 120°. Note that the input RF phase for each section is optimized for maximum energy gain with minimum energy spread.

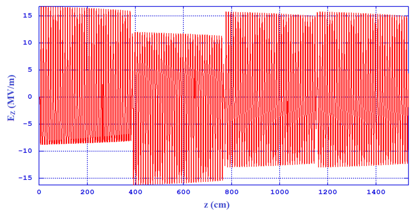


Figure 5: Field pattern as generated by PARMELA for four sections at RF phase of 120°.

Fig. 6 (a) shows magnetic field profile, used for beam focusing which is optimized for the maximum beam transmission, and also for the required beam size and emittance at linac output. Figs. 6 (b) and 7 show the growth of beam energy from 15 MeV to 200 MeV and the evolution of beam size along the linac length respectively. Note that for the beam dynamics simulations, the accelerating sections are put one after the another. However, in the real case, there will be suitable quadrupole triplets along with space for diagnostics and other devices. Fig. 8 shows beam profile, phase space plot and energy spectrum at the output of linac. Table 5 lists the output beam parameters.

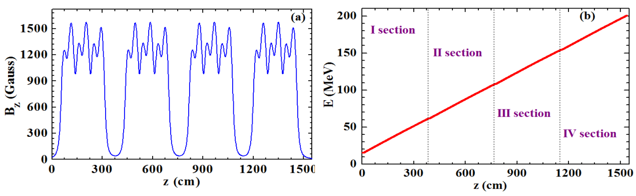


Figure 6: (a) Magnetic field profile (b) Growth of beam energy along the linac.

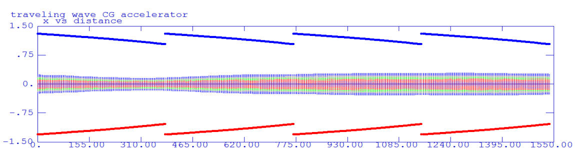


Figure 7: Evolution of beam size along the linac length.

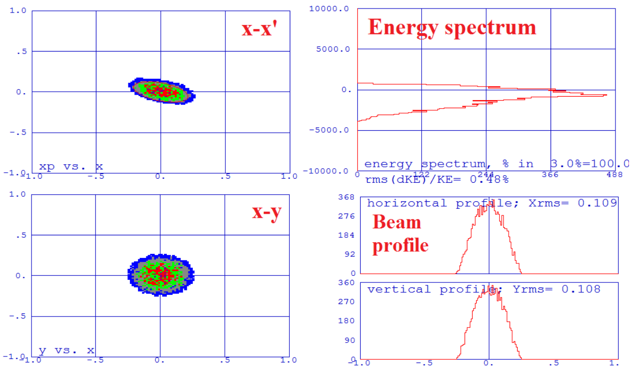


Figure 8: Phase space plot (top left), energy spectrum (top right) and beam profile (bottom) at the linac output.

Table 5: Output beam parameters

| | |
|---|---|
| Beam energy | 200 MeV |
| Charge per bunch | 34.17 pC |
| Bunch spacing | 2 ns |
| Energy spread, rms | 0.5 % |
| Energy spread (for 100% particles) | 3 % |
| Emittance, un, rms | 60 nm rad |
| Beam radius , rms | 1.1 mm |
| Beam transmission efficiency | 100 % |

## CONCLUSION

Physics design studies were performed for the 3 GHz, 2π/3 mode, CG, TW accelerating section of the injector linac considered for proposed HBSRS. It will accelerate the 15 MeV electron beam from buncher section to 200 MeV. The electromagnetic design studies were performed to optimize the geometrical and RF parameters of CG linac. The RF parameters were estimated using simulations and analytical calculations, and were found to agree well. Beam dynamics studies were performed to obtain 200 MeV beam energy with required energy spread and emittance. Complete start to end beam dynamics for injector linac will be performed and further optimization will be done based on the results. The heat load calculations will also be performed.

## REFERENCES


[1] A D Ghodke et al, “Preliminary Beam Dynamical Considerations for High Brilliance Synchrotron Radiation Source (HBSRS) ”, RRCAT Internal Report, 2017-10.

[2] J. H. Billen, and L. M. Young, “POISSION/SUPERFISH”, LA-UR-96-1834, Revised January 13, 2006.

[3] P. Lapostolle and A. Septier, “Linear Accelerators”, North Holland Publishing, Amsterdam, 1970.

[4] T. P. Wangler, “Principles of RF Linear Accelerators”, Wiley, 2008.

[5] N.S. Kulkarni et al, “Physics Design of a 10 MeV, 6 kW traveling wave electron linac for industrial applications”, Pramana, Journal of Physics, vol. 87, p. 74, 2016.

[6] Lloyd M. Young, PARMELA- LA-UR-96-1835, LANL.

# INSTALLATION, COMMISSIONING AND OPERATIONAL EXPERIENCE OF A 400KV ACCELERATOR FOR DUAL ION IRRADIATION SYSTEM

K.Suresh*#, S.Chinnathambi*, J.Navas*, C.David*, R.Govindaraj*#,M.Kamruddin*#, G.Amarendra*#, B.K.Panigrahi@#

*Materials Science Group, @Electronics and Instrumentation Group, #Homi Bhabha National Institute, Indira Gandhi Centre for Atomic Research, Kalpakkam,India.

*Abstract*

Dual beam implantations of heavy ions and helium-ions on materials emulate better the irradiation conditions of fission and fusion reactors for purposes such as material screening and evaluation of basic mechanisms or model calibration. In this regard an advanced dual beam facility which comprises of co-implantation of heavy ion beams from a 1.7 MV accelerator and helium ions from an indigenously built 400 kV accelerator has been developed. Details on beam optics design, installation, commissioning and operational experience of the 400kV accelerator and its integration with 1.7MV accelerator for dual ion beam irradiations have been presented in this paper.

## INTRODUCTION

A dual beam irradiation facility which provides co-implantation with heavy ion beams from a 1.7 MV accelerator and gaseous ions from an indigenously built 400 kV accelerator has been developed at Materials Science Group, IGCAR, Kalpakkam[1]. This dual ion irradiation facility has been set up to simulate synergistic effects of displacement damage and gaseous helium/hydrogen which is important in the context of development of radiation resistance materials for fast fission, fusion nuclear reactors and accelerator driven subcritical systems. As part of the state of art dual ion irradiation facility, an indigenous 400kV low energy accelerator with its UHV beam line with lay out as shown in Fig.1 has been established. The 400kV accelerator is an air insulated ion accelerator comprising of a 50MHz RF ion source (RFIS), pre-acceleration, acceleration stages (AT), electrostatic quadrupole triplet (QPT) lenses, double focusing 90° mass analyzing magnet (MAM), beam diagnostic devices and vacuum systems (VS). Positive ion beams of gases are extracted from the RFIS and pre-accelerated to 30keV by extraction and pre-acceleration stages mounted inside a high voltage dome (HVD). The HVD can be elevated to high voltages of 0-400kV DC. The ion beam is further accelerated to an acceleration voltage up to 400 kV DC using a 400kV DC, 3.5mA high voltage power supply (HVPS). The HVPS is an open stack, fast response, air insulated type with high stability (0.01%/hour), extremely low ripple (0.05%) and very good output regulation (<+/-0.005%). Hence, $He^{2+}$ ion beams, with a maximum energy of 860 keV can be obtained from the accelerator. The 90° bending of the ion beam and the isotope selectivity are achieved by the MAM having a mass resolution of 1 in 250, entrance and exit angle of 26.6 degrees and a bending radius of 0.4m. Post mass analysis, the ion beam is steered through a 3.7 metre long ultrahigh vacuum beam line (UHV-BL) consisting of a differential pumping section (DPS), beam optical devices (QPT, X-Y scanners, 5° neutral trap). The DPS separates the high vacuum beam line (HV-BL) operating at a vacuum level of ~ 2 x$10^{-7}$mbar and the UHV-BL operating at 4x$10^{-9}$ mbar. The samples are kept in an UHV irradiation chamber which is located at 10° UHV-BL of the 1.7 MV accelerator. The ions from the accelerator are incident on the sample at 15° to the sample normal. To implant the gaseous ions at pre-fixed depths for achieving uniform implantation, the ion beams pass through an energy degrader prior to incident on the sample. The ion fluence is controlled by measuring ion currents using Faraday cups (FC).

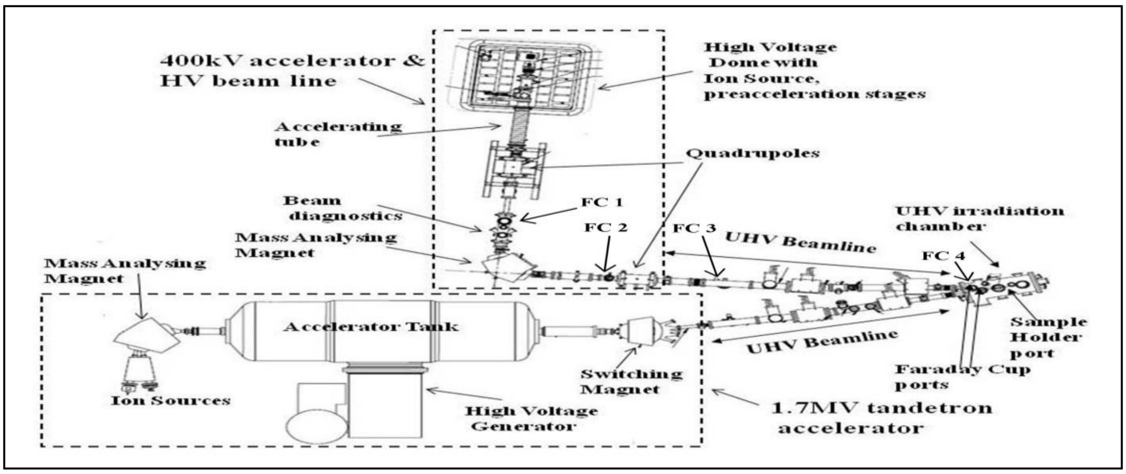


Figure 1: Dual ion irradiation layout showing details of the 400kV accelerator and its beam line

### *Beam Optics design*

First order beam optics calculations using transport matrix method was carried out to finalise the overall accelerator configuration and beam line layout[2]. An in-house developed software was used to obtain beam envelope $E(z) = \pm (\varepsilon * \beta(z))^{0.5}$ where $\varepsilon$ is beam emittance and $\boldsymbol{\beta}$ is twiss parameter in X & Y directions throughout the accelerator and the beam line. In the simulations, we used the intermediate optical components such as the RFIS, einzel lens, acceleration tube, QPTs, MAM. The settings of the einzel lens at the ion source and the setting of the QPT 1&2 were optimised to provide a 5mm beam-waist at the sample. As the passing of ion beams through the 700mm long DPS is a major factor for obtaining enhanced flux for irradiation, design of UHV-BL was done to achieve an optical transmission of 80% with a 5mm beam size at target. Typical simulation results obtained are shown in Fig. 2.

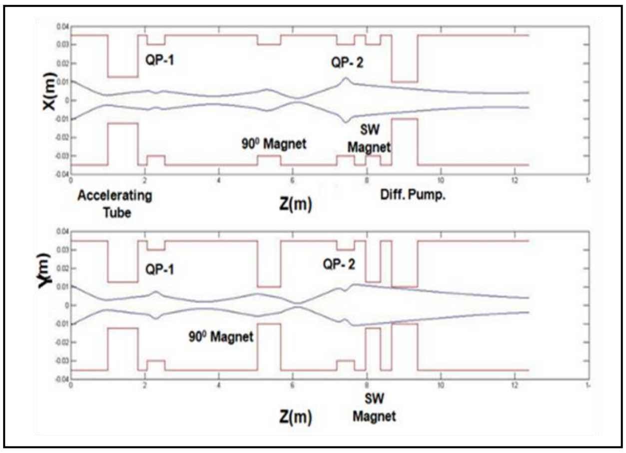


Figure 2: Results of first order beam optics calculations showing beam traces in X &Y directions. QP-1 & QP-2 - Quadrupole triplet lens 1 & 2, SW Magnet - switching magnet, Diff.Pump - differential pumping section.

### *Installation of 400kV Accelerator*

With successful beam optics design, finalisation of configuration and layout, installation of the 400kV accelerator was done in phases. In the first phase, marking and positioning of major components like HVD, HVPS and 400kV DC isolation transformer were done.Various sub-systems of accelerator like the RFIS, X-Y steerer, FC, beam profile monitor, vacuum system were assembled and aligned inside the HVD. Accurate alignment of beam line components upto the acceleration tube was done to a level of +/-1mm using the in-house developed 3 axis adjustable fixtures and an alignment telescope. Various tests were carried out to confirm the correct functionality of the beam line components, systems, etc. The functionality of gate valves, Faraday cups,vacuum pumps and gauges were checked and the accelerator was commissioned upto the pre-acceleration stage with an operating vacuum of $4.2 \times 10^{-7}$ mbar. 20 keV $H^+$, $He^+$, $Ar^+$ beams with yields upto 25uA current were obtained. The transverse emittance of the ion beam was calculated using an in-house built emittance measurement system and was found matching with the expected values. The subsequent phases of the installation included a) establishment of the HV-BL made up of the accelerating tube, $QPT_1$, gate valve, intermediate chamber, vacuum systems, 90° mass analysing magnet, Y steerer and $QPT_2$ b) installation of the UHV-BL consisting of a differential pumping section, a 5° neutral trap, an X-Y scanner, and beam diagnostic elements like BPM, RFC, various vacuum systems like turbo molecular pumps, titanium sublimation pumps, rotary pumps and ion pumps c) integration of the UHV beam line of the 400kV accelerator with irradiation end station. All the beam line components were positioned as per the beam optics calculations using aluminmiun support strctures and were coupled using standard CF150 flanges, oxygen free high conductivity (OFHC) gaskets. Necessary adpaters, bellows were used to get necessary flexibility, ease of installation, alignment and maintenance of the beam line components. The HV-BL, the UHV-BLs of 400kV, 1.7 MV accelerators and the irradiation end station was aligned to an accuracy of +/-1mm using an alignment telescope and the adjustable support structures while the beam centre of all of them were matched to 1.22m.

### *Vaccum System Design*

As the vacuum system is an important integral part of the 400kV accelerator, its design and implementation are crucial for successful production of ion beams and their transmission. During the design of vacuum system, important factors like required vacuum level, level of high voltages, ion species to accelerate, volume of the system, gas load were duly considered. The vacuum system for the beam line segment from the ion source to the differential pumping section consists of turbo molecular pumps(TMP) backed by rotary vacuum pumps to get a vaccum of the order of $2 \times 10^{-7}$ mbar. A 80 l/s TMP is used near the ion source inside the high voltage dome while three other TMPs (400-600 l/s) are used at the accelerating tube, mass analysing magnet and $QPT_2$. To maintain UHV level throughout the UHV beam line, we use two 400 l/s TMPs near the differential pumping section and X-Y scanner, air cooled titanium sublimation pumps (TSP) in combination with 400 l/s ion pumps (IP) near neutral trap and the UHV irradiation chamber.

### *Commissioning the accelerator and beam lines*

Exhaustive functionality tests were done to assess the performance of the beam line components, systems and the accelerator as a whole during commissioning of the 400kV accelerator. All the accelerator stages were vacuum leak tested and qualified with leak rates better than $1 \times 10^{-10}$ mbar-litres/sec. The standard bake out of beam line chambers was carried out at 200°C for 72 hours. With all these measures, we achieved an operating vacuum of $2 \times 10^{-7}$ mbar in the HV-BL and $4 \times 10^{-9}$ mbar in the UHV-BL. Various tests were carried out to confirm the correct functionality of the beam line components, systems, etc. The voltage holding test of the neutral trap and the X-Y scanner was done by applying upto 15kV

DC to the electrode plates and leakage currents of <0.01uA were observed over 8 hour duration. A non-linearity of <1% was observed on the high voltage riangular waves applied to the X-Y beam scanner plates, ensuring high-uniform ion implantations on the targets. Vacuum level tests were carried out with transmission of 1milliwatt ion beam. There was no change in the observed vacuum of $2.2x10^{-9}$ mbar in HV-BL and $5.1x10^{-9}$ mbar in the UHV-BL with and without beam passage. The beam profiling capability was tested by analyzing the ion beam with the beam profile monitor function in the control computer (CC).The X-Y scan area coverage test was done by scanning the beam over the four cups of the transmission Faraday cup fixed close to the sample in the irradiation station and by analyzing the on-line picture of the XYZ function in the CC.

### *Operation of the 400kV accelerator and dual ion irradiation facility*

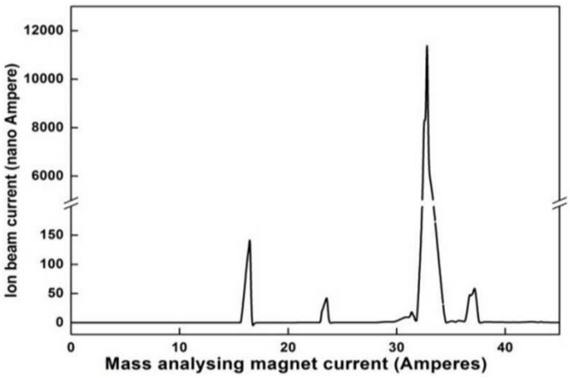


Figure 3: Mass analysis spectrum for 190 keV He+ ion beam.

After all the functionality tests, the 400kV accelerator was put into regular operation. During the warm-up test runs, many gaseous ions like $H^+$, $He^+$, $Ar^+$ were produced and accelerated to the irradiation end station. Typical yields of the ion beams obtained at the target are 6 uA of $He^+$ @ 225 keV, 70 nA of $He^{2+}$ @ 450 keV, 200 nA of $Ar^{2+}$ @ 450 keV, ~2uA of $H^+$ @ 210 keV. However the ion currents were much higher in the intermediate stages. A typical mass spectrum obtained during $He^+$ ion acceleration is shown in Fig.3. As part of calibration tests, the beam energy spread was calculated by the width of the thick target resonance yield of the $^{18}O(p,\alpha)^{15}N$ (Resonance Energy ($E_R$)=151 keV, resonance width($\Gamma_R$)=100 eV) narrow resonance reaction conducted using $Al_2O_3$ pellets enriched with 99% $^{18}O$. From this test, we obtained the values of the total broadening ($\Gamma_t$), resonance width ($\Gamma_R$) and the calculated beam broadening ($\Gamma_{beam}$) are 190 eV, 100 eV and 161 eV respectively. Thus the contributions of high voltage power supply and the inherent broadening of the RF source toward the beam dispersion at 150 keV works out to ±68 eV. Similarly we have also carried out tests to establish the accuracy of the in-house developed indirect ion fluence measurement system through implantation of 205 keV helium ions in aluminium substrates to a fluence of $2\times10^{17}$ He atoms $cm^{-2}$. The depth distribution of helium was measured using the $^4He(p,p)^4He$ proton RBS with 2.3 MeV protons. The experimental RBS spectrum is shown in Fig.4 and SIMNRA software was used to fit the experimental data with a model target scheme. The variation between the intended and the estimated fluence is found to be 5.5%. For a beam current of 1.8 µA of $He^+$ on the FC and for a dpa rate of $1\times10^{-3}$ dpa $sec^{-1}$ , the maximum He:dpa rate which can be achieved in Fe substrates using this system has been calculated to be ~50 appm $dpa^{-1}$.

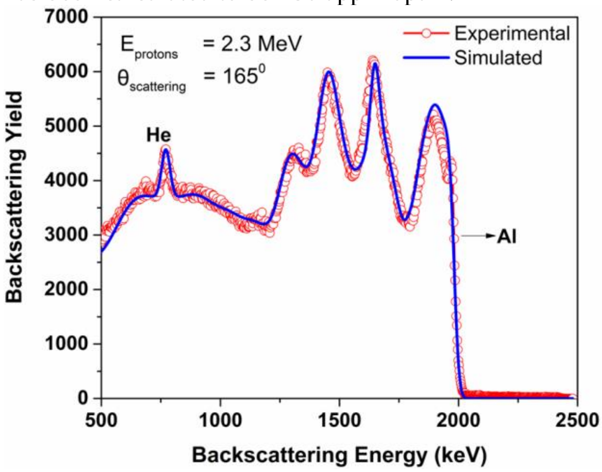


Figure 4: RBS spectrum of Al substrate irradiated with 205 keV of He ions at a fluence of $2 \times 10^{17}$atoms $cm^{-2}$

## CONCLUSIONS

A 400 kV low energy accelerator has been indigenously built and integrated with 1.7MV accelerator for the development of dual ion irradiation set up. Details on ion beam optics design, installation, commissioning and operational experience of the accelerator, its UHV beam line have been discussed. The accelerator was used to accelerate H, He, Ar ion beams in the range of and upto 450keV with yields varying from tens of nA to 12uA. Following the energy calibration of the accelerator, the accelerator was regularly operated and many dual ion irradiation experiments were carried out on reactor and other materials. Simultaneous efforts have been made to reach the full acceleration high voltage. Apart from a very few maintenance issues which were successfully resolved, the operational experience has been very satisfactory which enabled us to achieve the accelerator uptime greater than 90%.

## REFERENCES


[1] K.Suresh *et al.*, "Development of a dual ion irradiation facility for studies of radiation response in fission and fusion reactor materials", *Nucl. Instr.Meth.*,vol.447,pp. 92–99, 2019.

[2] S.K Srivastava et al., "Beam Optics Design for a dual beam irradiation setup" in Proc.Indian Particle Accelerator Conference (INPAC 2011), (2011) New Delhi, India.

# UHV PERFORMANCE EVALUATION OF INDIGENOUSLY DEVELOPED LOW CONDUCTANCE UNCOATED LONG ALUMINIUM ALLOY CHAMBER FOR UNDULATOR IN INDUS-2

S. K. Tiwari*, K. V. A. N. P. S. Kumar, B. K. Sindal, P. Bhatnagar, D. P. Yadav
Ultra High Vacuum Technology Section, RRCAT, Indore, India

*Abstract*

Spare vacuum chamber for Undulator (U1 &U2) in Indus-2 was indigenously designed and developed. Material of construction of this extruded chamber is AA6063-T6. Internal cross-section shape is race track with dimension of 81mm (width) x17 mm (height) and length of 2700 mm. Chamber is integrated with DN160 DSF (diamond shape seal flange ) at both the ends. Operating vacuum pressure ~ 1 x $10^{-9}$ mbar with stored e-beam (@2.5 GeV, 200 mA) is required to be maintained inside this chamber for longer beam life time. This conductance limited chamber will be finally coated with non-evaporable getter (NEG) coating to provide distributed UHV pumping for dynamic outgassing with stored beam condition. Before NEG coating it is imperative to assess the ultimate static vacuum performance of this chamber. With this objective, this chamber was subjected to ultimate vacuum testing in UHV lab. In order to achieve the UHV condition, chamber was baked at 170º C for 48 hours. Ultimate vacuum of ~ 4.9 x$10^{-10}$ mbar and specific out gassing rate ~ 5.1x$10^{-13}$ mbar l/s/cm$^2$ was measured after bake out.

The paper describes in brief about vacuum chamber design, UHV Qualification procedure and test results achieved. RGA spectrum of residual gas in baked and unbaked condition are also presented. This development was initiated as a step towards make in India initiative for self-reliance and import substitute for this kind of UHV chambers.

## INTRODUCTION

Indus-2 storage ring has been augmented with three undulators namely U1, U2, and U3 as part of insertion device (ID) development programme. U-1 undulator will generate synchrotron radiation having maximum flux between 6eV to 250eV for atomic, molecular and optical science (AMOS) experimental beamline. U-2 undulator will generate synchrotron radiation having maximum flux between 30eV to 600eV for angle resolved photoelectron spectroscopy (ARPES) experimental beamline. U-3 undulator will generate synchrotron radiation (SR) having maximum flux between 300 eV to 1500 eV for magnetic circular dichroism (XMCD) beamline. Vacuum chamber design of U1 & U2 undulators are identical. The minimum pole gap of these undulator is 23 mm. Spare vacuum chamber for U1 & U2 undulators was indigenously designed and developed. Like other chambers of machine required operating pressure inside these vacuum chambers is ~ 1.0 X $10^{-9}$ mbar for longer stored beam life time. This chamber will be finally coated with NEG coating ~ 1 micron thickness to provide distributed UHV pumping for dynamic outgassing with stored beam condition. Prior to NEG coating, UHV performance of the chamber was assessed on ultimate vacuum test set-up in UHV lab.

* email address sktiwari@rrcat.gov.in

## VACUUM CHAMBER DESIGN

Cross section of vacuum chamber is shown in Figure 1. Cross section dimensions are primarily driven by the minimum pole gap of undulators, beam stay clear space and minimum safe wall thickness for external atmospheric pressure loading due to evacuation. Top and bottom wall thickness of chamber is 2 mm [1]. Indigenously available Aluminium alloy 6063-T6 grade Aluminium alloy has been chosen as material of construction of this extruded vacuum chamber for its suitability for various requirements like: non-magnetic, UHV compatibility (low specific outgassing rate), extrudability, weldability, good thermal conductivity, low impedance and low residual radioactivity.

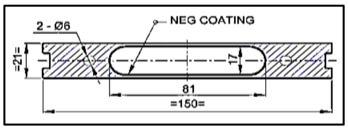


Figure. 1. Cross Section of the Undulator Chamber

The Specification of extruded undulator vacuum chamber is given in Table 1. Side holes of dia 6 mm are water cooling channels for cooling of SR heat incident on vacuum side surface from upstream dipole magnet.

**Table -1** Specification of Extruded Vacuum Chamber

| Material of Construction | AA 6063-T6 |
|---|---|
| Dimension | Race Track Internal Cross Section -81mm(W)x17mm(H) 2700mm Long (flange to flange) |
| Straightness | 0.2 mm /m |
| End Flanges | DN160 DSF |
| Molecular flow Conductance of the Chamber | 6l/s/m |

## UHV PERFORMNCE EVALUATION OF UNDULATOR CHAMBER

### *Description of Test Set-up*

AA 6063-T6 chamber was chemically cleaned as per optimised cleaning procedure prior to weld .At first, the chamber was tested alone through helium leak detector (adixen make ASM192T2D+, MDLR 1x$10^{-11}$ mbar-l/s) and was confirmed for leak-tightness in the range of ~ 5.0 x $10^{-11}$ mbar-l/s. The chamber was then assembled in test set up as shown in Figure-2a and 2b. Test set up consists of one sputter-ion pump (SIP) of pumping speed 270 l/s.One Turbo molecular pump (TMP) of capacity-250l/s (EDWARDS make) was used for roughing purpose. Two Bayard-Alpert (BA) gauges (named as BAG-1 and BAG-2; assembled at the opposite ends of Undulator chamber) and Residual Gas analyzer (Extorr make Model-XT100 (M)) were used to measure the total pressure and partial pressures of residual gases respectively. BAG-2 was located at opposite end flange of Undulator which is 3.18 m away from SIP as well as BAG-1. Data logger named as Temperature controlling & Pressure Monitoring Interface Software **(**TCPMIS**)**, an intelligent 'on /off' temperature control system, developed in UHVT Section was used to record pressure and temperature and control temperature during the entire bakeout cycle [2]. K-type thermocouple was used for measurement of temperature**.** To ensure uniform heating of Undulator chamber, Polymide insulated thin sheet flexible heaters were used. These heaters (named as heater-1,-2,-3 and -4, each having capacity 750 W) mounted on chamber are shown in Figure- 2a.Molecular flow Conductance of Undulator chamber is 6 l/s/m.

## *Outgassing Rate Evaluation*

Specific outgassing rate '$Q_s$' (mbar l/s/cm$^2$) was measured using pressure rise method and it was calculated on the basis of following formula:

$$Q_s = \frac{V}{S} \text{ x } \frac{\Delta P}{\Delta t}$$

Where V = Volume of chamber
S = Surface area of chamber
$\Delta P$ = pressure increase in time $\Delta t$

The pressure increase considered due to outgassing in the calculation is the slope of the linear fit of the respective curves plotted between pressure and elapsed time [3].

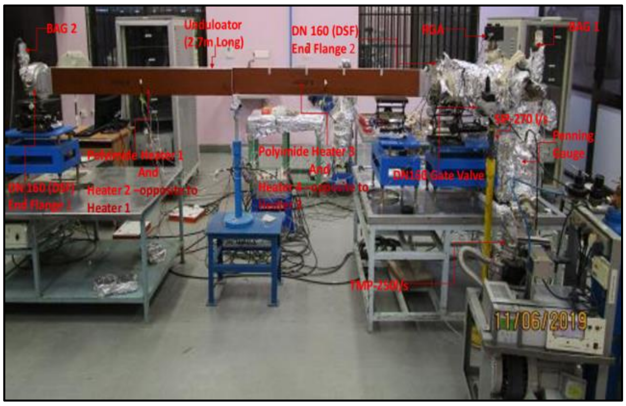


Figure- 2a: Photograph of test setup

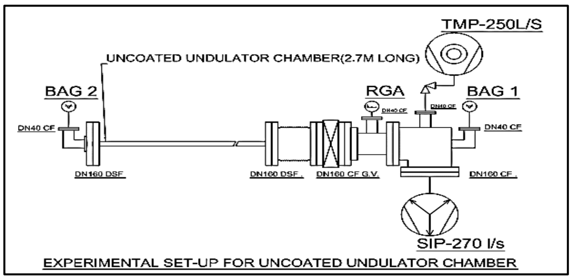


Figure -2b: Schematic of test setup

## *Procedure Adopted Before Bake-Out*

Flange-joints of assembled set up shown in Figure 2 (a) / (b) were confirmed for leak-tightness, in the range of ~8.7 x $10^{-11}$ mbar-l/s.Then test set-up was evacuated for 24 hours through TMP. Ultimate vacuum measured by BAG-1 and BAG-2 under unbaked condition followed by pumping with SIP for ~24 hrs.were 7.0 x $10^{-8}$ mbar and 3.2 X $10^{-7}$ mbar respectively. Specific outgassing rate evaluated in unbaked condition was 2.55 x $10^{-10}$ mbar.l/s/cm$^2$. Figure-3a and 3b represent the pressure trend vs elapsed time graph. Figure-4 represents screen shot of a residual gas spectrum taken at the end of experiment.

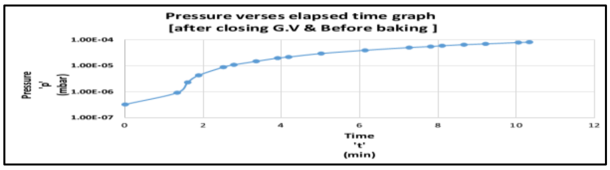


Figure-3a

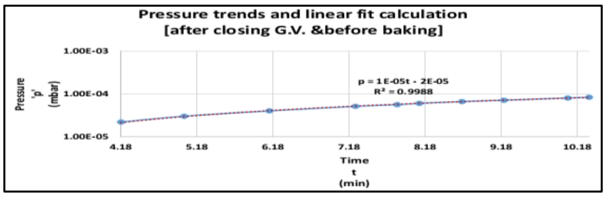


Figure-3b

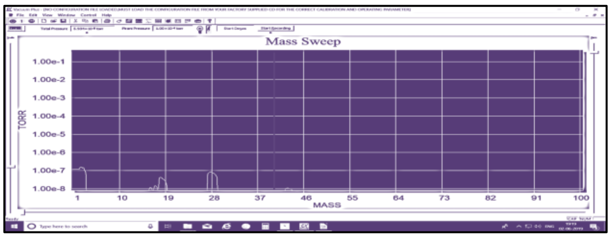


Figure-4

## *Bake-Out Procedure*

After conducting test under unbaked condition, optimized bake-out procedures, were followed. SIP and Aluminium alloy chamber as well as in-lined SS components were baked at 250°C and 170 °C respectively keeping dwell time ~ 48 hrs ( as shown in Figure 5). Rate of rise for Undulator chamber as well as in-lined SS components and SIP, were 23 °C/ hr and 32°C/hr respectively. Ultimate vacuum measured by BAG-1 and BAG-2 under baked condition followed by pumping with SIP for ~36 hrs.were 5.5 x $10^{-10}$ mbar and 4.5 X $10^{-9}$ mbar respectively.. Specific outgassing rate after 60 hrs running of SIP was ~ 5.1 x $10^{-13}$ mbar.l/s/cm$^2$. Figure-6a, and 6b represent the pressure trend vs elapsed time graph (after baking) .Figure-7 represents screen shot of a residual gas spectrum (taken after 80 hrs running of SIP).

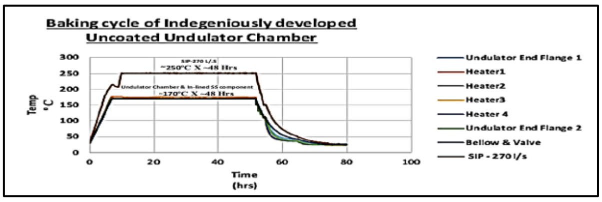


Figure-5

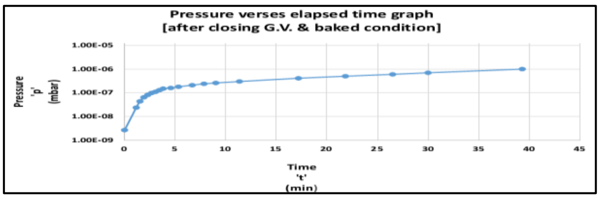


Figure-6a

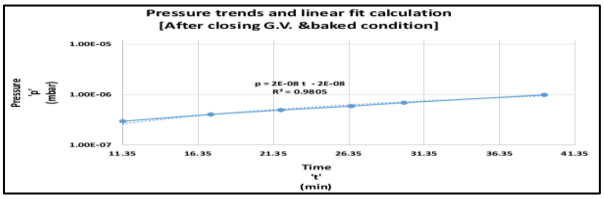


Figure-6b

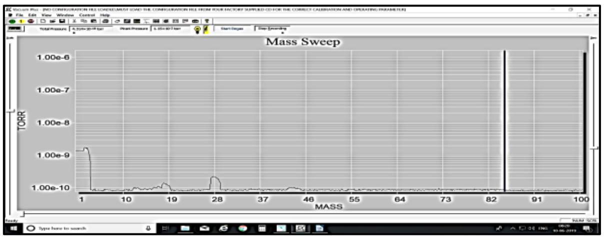


Figure-7

As BAG-1 and BAG -2 were assembled at the two extreme ends of Undulator chamber, so specific outgassing rate under steady state distributed gas load condition was also evaluated using equation $Q = C (P_1 – P_2)$ .Respective effective conductance C (Undulator as well as in-lined SS components) between the two BAGs was evaluated as1.89 l/s. Reading of $P_1$ ( BAG-1 ) and $P_2$ ( BAG-2) realised after 60 hrs running of SIP were 4.2 x $10^{-10}$ mbar and 2.7 x $10^{-9}$ mbar respectively. Vacuum exposed Surface area is 8702.64cm$^2$. Specific outgassing rate evaluated under steady state distributed load condition was 4.94 x $10^{-13}$ mbar.l/s/cm$^2$.

## COMPARISON OF SPECIFIC OUTGASSING RATE '$Q_S$' EVALUATED BY VARIOUS METHOD

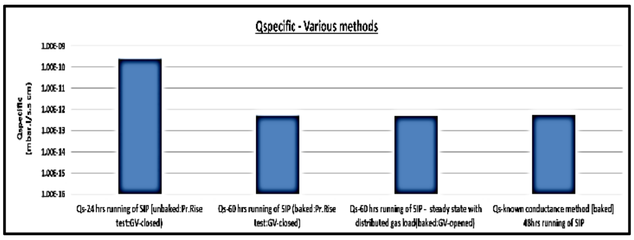


Figure-10

Bar graph shown in figure-10 represents three decade improvement i.e.~ 5.1 x$10^{-13}$ mbar.l/s/cm$^2$ in Specific outgassing rate of the spare uncoated aluminium alloy vacuum chamber for Undulator under baked condition with 60hrs running of SIP-270 l/s. Specific outgassing rate of the AA 6063-T6 Aluminium sample evaluated earlier through orifice of known conductance method (as per AVS standard) was 5.56x$10^{-13}$ mbar.l/s/cm$^2$ after pumping with SIP-270 l/s for 48 hours under baked condition [3].

## CONCLUSION

With respect to orifice of known conductance method (as per AVS standard), specific outgassing rate of the spare uncoated aluminium alloy vacuum chamber for Undulator under baked condition as well as steady state distributed gas load condition followed by 60 hrs running of SIP-270 l/s were found comparable. RGA spectra taken under baked condition shows two decade reduction in partial pressure of water vapor i.e1.4 x$10^{-10}$ torr (baked) w.r.t 3.3 x $10^{-8}$ torr (unbaked) was observed after 80 hours of SIP pumping respectively. Relatively high level of hydrogen was desorbed from the metal walls of the vacuum system. Water vapour and carbon contamination are removed to a larger extent. No peaks were observed greater than 44. In this regard Undulator chamber in terms of quantity and quality wise qualifies the UHV performance.

## ACKNOWLEDGEMENTS

Authors are extremely grateful to Shri Samiran Sarkar (Retired),Shri Tulsi Ram Meena, Shri Netram ,Shri Subda Hansdah, Shri Vishnu Pandey,Shri Navin Solanki ,Shri Hemkant Sharma,Shri M.M.Vadgama ,Shri Vijay Singh Bais,Shri K.K.Malviya ,Shri Nitin Ramdas More and Shri A.S.Yadav for their direct or indirect contributions provided during the experiments.We wish to thank Shri V.K.Bhatnagar,Head ,Fabrication facilities section and shri Dr. P. Ram Sankar,Head ,Chemical Treatment Lab for their helpful support regarding TIG welding of end flanges and chemical cleaning for the Undulator chamber respectively.

## REFERENCES

[1] D.P.Yadav et al, "Design and Finite Element Analysis of Insertion Device Vacuum Chamber for Indus-2 Storage Ring" InPAC-2015, TIFR, Mumbai, Dec., 21-24, 2015

[2] Bhange N.J., et al, "Baking system for vacuum components in INDUS-2" IVSNS-2005, IPR, Ahmedabad, 2005.

[3] Tiwari S.K.,et al, "Vacuum Performance Analysis of SR Exposed Vacuum Chamber"InPAC-2018,Jan 9-12,2018

# ANALYTICAL STUDY OF BUFFER GAS COOLING OF ION BEAMS USING VISCOUS DRAG MODEL

Paritosh Sing Babu[#], Siddhartha Dechoudhury and Vaishali Naik
VECC, 1-AF, Bidhannagar, Kolkata-700 064

*Abstract*

RFQ beam cooler is widely used for manipulating and bunching of rare ion beams. In a RFQ cooler, buffer gas medium is introduced into the segmented linear Paul trap, which will cause the ions to interact with the buffer gas through elastic scattering. The combination of electrostatic and radiofrequency fields results in a force that guides the ions towards the center of the 3D potential trap. The ion motion gets damped and finally comes into thermal equilibrium with the buffer gas in the potential minimum. We have simulated the cooling process using a macroscopic viscous drag model, where collision has been incorporated in terms of ion's mobility in the buffer gas. From the trajectory calculations the cooling times and average beam properties have been estimated. Results are presented for $^{133}Cs^+$ ions in He buffer gas.

## INTRODUCTION

Beam manipulation using RFQ cooler is a widely used technique in precision measurement of atomic nuclei such as mass spectrometry in penning trap [1], collinear laser spectroscopy [2] etc.. RFQ cooler is also employed before the high resolution separator to get better resolving power [3]. The RFQ cooler is filled with buffer gas and the electrodes are segmented and different DC voltages are applied to each segment. Inside the volume of RFQ cooler, the ions interact with the buffer gas. The ions are scattered elastically and transferred part of the energy to the buffer gas. With time, the motion of the ions is damped and finally come into thermal equilibrium with the buffer gas. The combination of DC and RF fields guides the ions towards the minimum of the potential. The beam cooling process reduces the phase space volume which helps to increase the sensitivity of the experiments mainly in the case of low intensity rare ion beams. Two collision models are generally used: one is macroscopic viscous drag model and other is microscopic Monte-Carlo method.

In this paper we have developed a viscous drag model to study the cooling of ion beams. In the viscous drag model, the collision between ion and buffer gas is included in terms of average damping force which depends on the ion's mobility in the buffer gas. Although this model can not give the detailed beam dynamics of individual ion, it can give the average behaviour of the beam such as cooling time, energy decay times, beam sizes etc. From this model one can obtain the optimal design parameters such as buffer gas pressure, frequency and amplitude of the RF voltage, electrostatic field profile etc. Results are presented for $^{133}Cs^+$ ions in He buffer gas.

[#]psb@vecc.gov.in

## METHOD

Electrodes of the RFQ cooler and buncher consists of four parallel rods of circular cross-section arranged symmetrically around the central longitudinal axis [4, 5]. The confinement of charged particles in transverse $x$ and $y$ plane is accomplished by the use of RF electric potential. The segmented rods creates a DC electric field along the axial direction and confine the particle in the $z$-direction. Before the injection into the RFQ cooler, the energy of the injected ions is slowed down from 30-60 keV to few tens of eV. The schematic view of segmented RFQ and the DC potential along the $z$-axis is shown in Fig. 1. After cooling, the ions are trapped in the axial direction near the extraction region. The end of the RFQ has fine segmentation to allow better control in the trapping region.

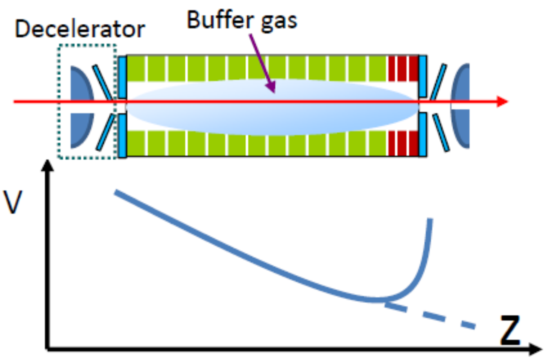


Figure 1. Schematic view of a segmented RFQ and the corresponding potentials along the $z$ axis. The solid line shows the potentials for ion trapping and the dashed line shows the extraction configuration.

The RF voltages are applied with 180 deg. phase difference to pair wise connected electrodes. The electric potential at $(x, y)$ is given by

$$\phi(x, y) = \phi_0 \frac{(x^2 - y^2)}{2 r_0^2} \tag{1}$$

where $\phi_0$ is the voltage applied between two pairs of opposite rods and $2r_0$ is the minimum separation between the opposite pair of electrodes.

If the amplitude and angular frequency of RF are $V_{rf}$ and $\omega_{rf}$ respectively then we can write,

$$\phi_0 = V_{rf} \cos(\omega_{rf}\, t + \theta) \tag{2}$$

Applying a small potential difference between adjacent rod segments will produce an accelerating field along the central axis of RFQ. Near the extraction region, different DC voltages on the rod segments can be used to generate a trapping potential. The drag and trapping potential is shown in Fig. 1. The dissipation of the ions' kinetic energy by the gas leads to their collection at the bottom of the well. In the trapping region the potential can be approximated by a parabola. Since $\nabla^2\psi = 0$, the corresponding field is given by

$$\psi(r,z) = \frac{V_{dc}}{z_0^{\ 2}}\left((z - z_m)^2 - \frac{r^2}{2}\right) \tag{3}$$

where $V_{dc}$ is the trap depth, $z_m$ is the position where potential is minimum and $z_0$ is the characteristic length and is given by the width of harmonic potential.

In a RFQ cooler, the ions interact with the buffer gas. The ions are scattered elastically and transferred part of their energy to the buffer gas. Here we have taken into account the interaction of ions with the buffer gas using viscous force. The average damping force is assumed to be proportional to ion velocity as [4]:

$$F_d = -c\,Mv \tag{4}$$

where $v$ is the velocity of ion and the proportionality coefficient $c = Q/Mk$, where $Q$ and $M$ are the charge and mass of the ion respectively and $k$ is the ion mobility. The mobility depends on the ion velocity, pressure and temperature of the buffer gas. The mobility $k$ of the ion is related to the reduced mobility $k_0$ as,

$$k_0 = k\,\frac{273.16\ \text{K}}{T}\,\frac{p}{1013\ \text{mbar}} \tag{5}$$

where $p$ and $T$ are the pressure of the buffer gas in mbar and its temperature in K respectively.

In the presence of the drag force, the equations of motion for ion in a gas filled RFQ cooler become:

$$\ddot{x} + \frac{Q}{Mk}\dot{x} + \frac{Q}{r_0^{\ 2}}V_{rf}\ \cos(\omega_{rf}\ t + \theta)\,x = 0 \tag{6a}$$

$$\ddot{y} + \frac{Q}{Mk}\dot{y} - \frac{Q}{r_0^{\ 2}}V_{rf}\ \cos(\omega_{rf}\ t + \theta)\,y = 0 \tag{6b}$$

$$\ddot{z} + \frac{Q}{Mk}\dot{z} - \frac{Q}{M}E_z(z) = 0 \tag{6c}$$

In the above equations, the damping force on the particle applies till the particle come into thermal equilibrium with the buffer gas at temperature $T$.

Using dimensionless parameters $q = 2QV_{rf}\big/(Mr_0^2\omega_{rf})$ and $\tau = \omega_{rf}t/2$, the equations of motion become:

$$\frac{d^2x}{d\tau^2} + \delta\frac{dx}{d\tau} + 2q\cos(2\tau + \theta)\,x = 0 \tag{7a}$$

$$\frac{d^2y}{d\tau^2} + \delta\frac{dy}{d\tau} - 2q\cos(2\tau + \theta)\,x = 0 \tag{7b}$$

The above set of equations are standard Mathieu equations when $\delta = 0$. Mathieu equations have both stable and unstable solutions. Ion will be confined radially when the particle is stable both in $x$ and $y$ direction. For $\delta = 0$, particle oscillation in the radial plane will be stable if $q$ is less than 0.908.

For small field gradient the average cooling time of the ion beams can be obtained from Eq. (6c) as,

$$T_{cool} = \frac{M}{Q}\int_{v_{thermal}}^{v_i} k\,dv \tag{8}$$

where $v_i$ and $v_{thermal}$ are the initial and thermal velocity of the ion respectively.

## RESULTS AND DISCUSSIONS

We present the cooling of $^{133}Cs^{+}$ ions by He buffer gas. Since RF field is used in RFQ cooler, the orientation of acceptance ellipse of the RFQ will depend on the RF phase $\theta$. Typical matched acceptance ellipse for four RF phases $\theta$ = 0, π/2, π and 3π/2 are shown in Fig. 2. Figure shows that the orientations of the matched ellipses are different for different phases and as a result the overlap area common to all the ellipses are relatively small. This overlap area also known as the RF independent phase acceptance is the effective acceptance of the RFQ (shown by shaded region in Fig. 2). We have used the RF independent phase acceptance for the buffer gas cooling of ion beams. We calculate the rms beam size and rms acceptance of the shaded region and used as input for the buffer gas cooling of ions.

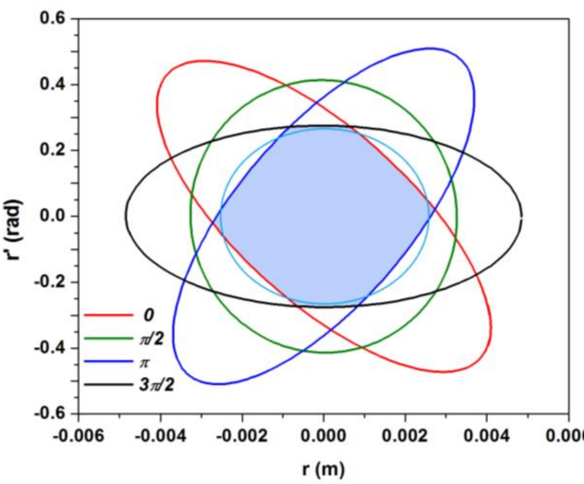


Figure 2. Sketch of acceptance ellipses at different RF phases. The shaded region shows the RF independent acceptance of the RFQ cooler. The elliptical area equivalent to RF independent acceptance is also shown (inner ellipse).

The pressure and temperature of the He buffer gas used for ion beam cooling are 300K and $p = 1.5\times10^{-2}$ mbar respectively. We consider the frequency and the peak to peak voltage of the RF are 1 MHz and 400V respectively. A DC voltage gradient of 0.1V/cm is applied along the length of the RFQ. For the present calculations, we have considered the emittance of $^{133}Cs^{+}$ ions ε = 35 π mmmrad at 60 keV, which corresponds to emittance equal to 1200 π mmmrad at 50 eV. The other parameters used in the numerical simulations are: number of ions $N$ = 7500 and time step $\Delta t$ =1ns.

The reduced mobility ($k_0$) of $^{133}Cs^{+}$ ions in He gas as a function of beam velocity is shown in Fig. 3 [6]. We can see that the mobility is constant at low velocity and it decreases sharply as the velocity of the ion increases.

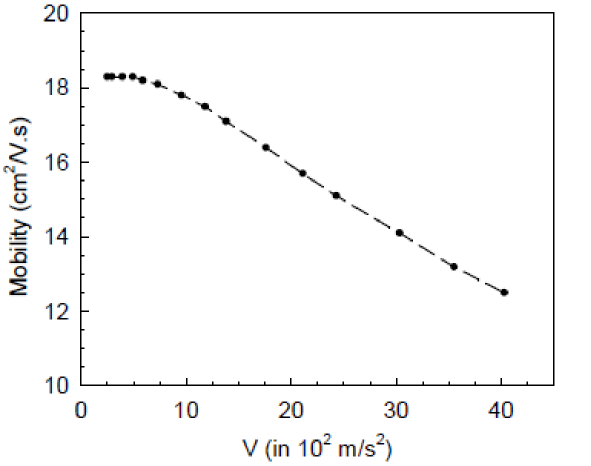


Figure 3. The mobility of $^{133}Cs^{+}$ in He buffer gas as a function of ion velocity.

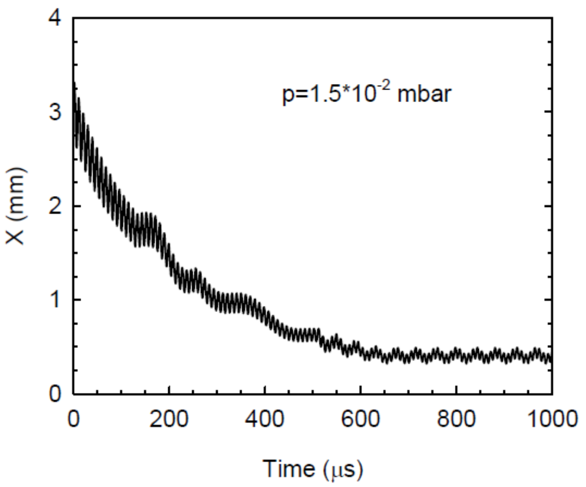


Figure 4. Damping of rms beam envelope in a RFQ cooler as obtained from viscous damping approach. The calculations have been performed for $^{133}Cs^{+}$ in He at pressure $p = 1.5\times10^{-2}$ mbar. The frequency and peak to peak voltage of the RF are 1 MHz and 400V respectively.

Figure 4 illustrates the cooling of the ions in RFQ cooler. The simulation has been performed for $^{133}Cs^{+}$ ions with Gaussian distribution in the transverse direction with initial energy 50eV. The total length of the RFQ is 90 cm and the separation between the opposite pair of electrodes is 10 mm. In Fig. 4, we have plotted the rms beam size along $x$ direction at each period of RF. We can see that the beam size is damped with time which means that the beam temperature reduces with time. After a cooling time of 550 μs, the average beam size is almost constant.

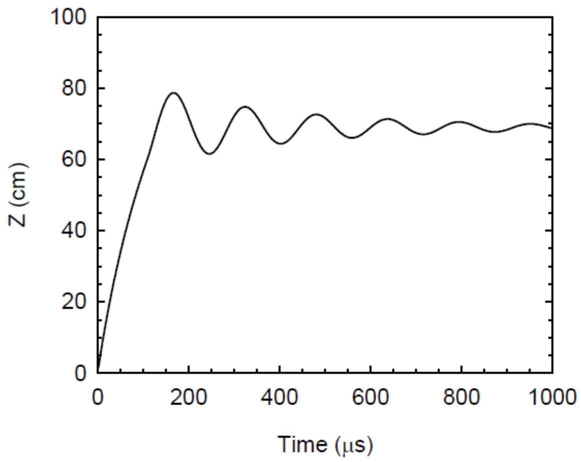


Figure 5. The axial oscillation of the centroid of the beam as a function of time.

Figure 5 illustrates the trapping of the ions in the axial direction at the potential minimum of the RFQ cooler. We have considered the DC potential well depth is 9 V. The other parameters are same as used in Fig. 4. We can see that initially the beam is guided by the DC voltage gradient and in the potential well it oscillates with respect to the potential minimum. The amplitude of the $z$ motion is damped with time and finally stopped at $z$ = 70cm.

## CONCLUSION

In this work we have studied the buffer gas cooling using macroscopic viscous drag model. In this approach, the average effect of the ion collision with the buffer gas has been approximated by a viscous force. We have presented the dynamics of $^{133}Cs^{+}$ ions in the presence of He buffer gas. Result shows that the beam is cooled and trapped in less than msec when the buffer gas pressure is in the range of ~ $10^{-2}$ mbar.

## REFERENCES


[1] V. L. Ryjkov *et al.*, Phys. Rev. Lett. 101 (2008) 012501.

[2] E. Mane *et al.*, Phys. Rev. Lett. 107 (2011) 212502.

[3] J. A. Maloney, R. Baartman, M. Marchetto, Nucl. Instrum. Methods Phys. Res., Sect. B 376 (2016) 135.

[4] F. Herfurth *et al.*, Nucl. Instrum. Methods Phys. Res., Sect. A 469 (2001) 254.

[5] T. Brunner, *et al.*, Nucl. Instrum. Methods Phys. Res., Sect. A 676 (2012) 32.

[6] M. D. Lunney, R.B. Moore, International Journal of Mass Spectrometry 190/191 (1999) 153.

# ARCHITECTURE OF LEHIPA CONTROL SYSTEM

Sudheer Kumar Singh#, Arindam Basu, Deepak Mathad, L. D. Tayade, Pravin Parate, IADD, BARC, Mumbai.
Sandeep Bharade, ACnD, BARC, Mumbai.

*Abstract*

LEHIPA (Low Energy High Intensity Proton Accelerator) is a 20 MeV, 10 mA proton accelerator, consisting of an ECR ion source, LEBT, RFQ, MEBT and DTL. The LEHIPA control system is a distributed control system. Each of these subsystems will have their own local control station which will meet their data acquisition and control requirements possibly grouped in some manner. These subsystems are to be interconnected via a Local Area Network (LAN) to the control room servers and Operator Work Stations (OWS). The Interlocks and Timing Signals are common signals, in addition to the LAN, for these subsystems. All these subsystems have to provide the required global control for LEHIPA working in a cohesive manner. For this purpose an Integrated Control System (ICS) is developed. The ICS will have to communicate with each of the Local Control Stations (LCS) and synchronize the various operations to start the accelerator, provide synchronization requirements for various subsystem during operation, tune the beam for required characteristics and shutdown the accelerator under normal and emergency condition, provide overall machine protection and interface various subsystems to the operator in a homogeneous manner for comprehensive operations, troubleshooting and maintenance in addition to archiving of data from different subsystems for future reference/provision of history.

## CONTROL SYSTEM ARCHITECTURE

Architectures help in designing, engineering, building and testing actual systems. At the same time, a better understanding of system constraints can provide input for the architecture design, and this allows future opportunities to be identified. The structure of the architecture can be made explicit through an architecture description. Extracting essential components of existing architectures such as mechanisms or the use of standards, allows the definition of a reference model. Control system architecture depicts the architecture of the plant control systems and the interface among the systems required for overall operation of process plant. The required control system is determined by the level of functionality, complexity and safety of a plant. This comprises of process control, safety instrumentation, field bus and communication protocols. The best design of the control system architecture for a plant is the one where the failure of any component/subsystem does not affect the plant safety. Control system architectures can be divided in to three categories.

#sudsing@barc.gov.in

### *Standalone System*

A standalone control system is completely self-sufficient and self-contained. Typically based on a PLC, industrial PC, hybrid PLC, or PAC (programmable automation controller), it includes I/O, a controller, an HMI, and some means of connecting its various components via a network, fieldbus, hard wiring or a bus system. Standalones are typically used to control individual unit operations. A standalone system carries out its task without direct supervision. It can be linked to other control elements in a plant if necessary, but if the communications are severed for some reason, the standalone system carries on by itself.

### *Distributed Control System (DCS)*

A DCS [1, 3] consists of multiple direct control elements, HMI workstations, SCADA systems, control processors, logic processors, I/O processors, servers, process historians, and high level software packages, all linked by networks such as fieldbus or Ethernet. A DCS is truly "distributed," with various tasks being carried out in widely dispersed devices. In general, a DCS is often used to control large processes, and it often incorporates high-level software packages, such as asset management.

### *Server-based system*

In a traditional standalone control system or a DCS, as described above, all the various control and monitoring devices, networks, HMIs and other equipment are located on the plant's premises. In a server-based system, certain non-critical parts of the control system can be located on or off the premises. While all I/O, critical controls, shutdown systems, and other real-time functions are kept in the plant, remote servers can perform all the advanced DCS-type supervisory control, SCADA, asset management, ERP, loop tuning and similar functions from afar. Such servers can be located anywhere in the world, and can be reached by secure and non-secure communication links, such as microwave, satellite, virtual private networks, the Web, dial-up modems and cell phones. Both standalones and DCSes can make use of server-based support systems.

## LEHIPA CONTROL SYSTEM ARCHITECTURE

An overall design of the LEHIPA [4] is given in figure 1. Electron Cyclotron Resonance (ECR) ion source gives DC proton beam of energy 50 keV and current of 10 mA. The low-energy beam transport (LEBT) system consists of a magnetic system comprising two solenoids that transport the beam from the ion source, and match the beam into the acceptance of the RFQ. It also has various beam diagnostic systems. For the acceleration of the proton beam at low energy, a four-vane RFQ (3 MeV, 10 mA, 352 MHz) is used. Drift-Tube Linacs (DTL) will accelerate the beam up to 20 MeV. The DTL is preceded by an medium-energy beam transport (MEBT) section. The MEBT section will consist of four magnetic quadrupoles and a rebuncher cavity that will transport the beam from the RFQ to the DTL structures that follow, and match the beam into the acceptance of the DTL. For both the RFQ and the DTL high-power CW klystrons will be used to generate the CW power of around 2 MW CW, at 352 MHz, along with high-power microwave lines to transport the RF to the accelerating structures.

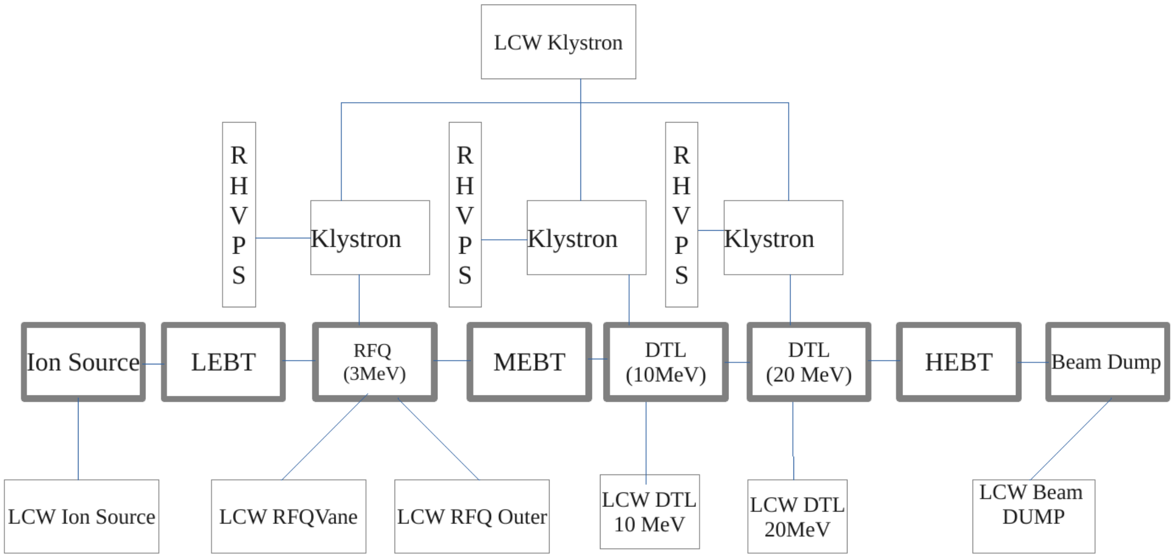


Figure 1: Schematic of LEHIPA.

The control system is mixed of standalone systems and distributed control systems. Each of these subsystems will have their own local control station which will meet their data acquisition and control requirements possibly grouped in some manner. These subsystems are interconnected via a Local Area Network (LAN) to the control room servers and Operator Work Stations (OWS). Use of High Speed redundant LAN is employed for this purpose. The Interlocks and Timing signals are common signals, in addition to the LAN, for these subsystems. All these subsystems provide the required global control for LEHIPA working in a cohesive manner. For this purpose, an Integrated Control System (ICS) is developed. The ICS communicates with each of the Local Control Stations (LCS) and synchronize the various operations to start the accelerator, provide synchronization requirements for various subsystem during operation, tune the beam for required characteristics and shutdown the accelerator under normal condition and emergency condition, provide overall machine protection and interface various subsystems to the operator in a homogeneous manner for comprehensive operations, troubleshooting and maintenance in addition to archiving of data from different subsystems for future reference/provision of history. The ICS should also provide on line help support and operator guidance. It also provides data display to wall mounted large screens. The Functional Block Diagram of LEHIPA control system architecture is explained in figure 2.

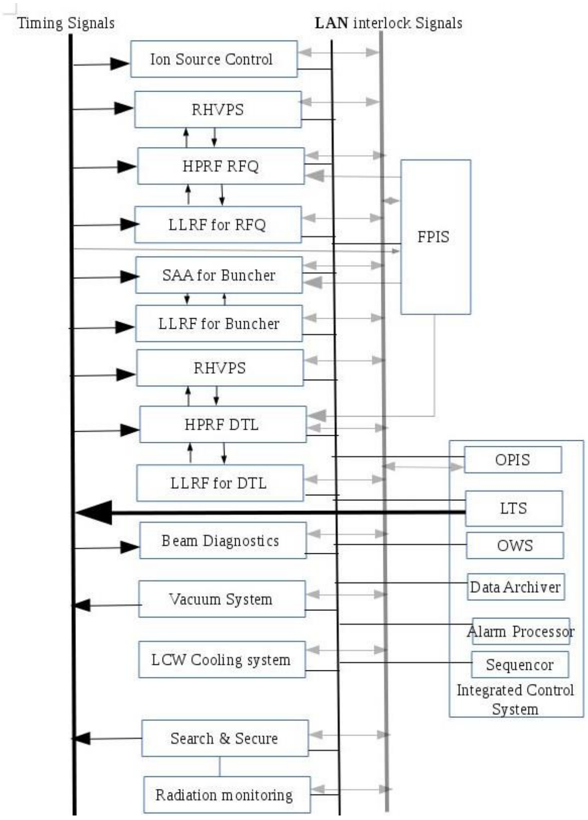


Figure 2: Functional Block Diagram of LEHIPA control system architecture.

## LEHIPA INTEGRATED CONTROL SYSTEM

Integrated control system is a functional distributed system [1,3] where all subsystems are catering to different functions of the LEHIPA. OPIS (Operational Protection and Interlock System), LTS, OWS, Data archiver, Alarm processor, Sequencer are major subsystem of ICS. ALL subsystem are communicating with each other via LAN except OPIS and LTS that provide some signals on hardwired lines to process interlocks.

Control system is implemented as a three layered architecture. Different subsystems and equipments constitute layer 1 or the Input output controller (IOC). Layer 2 is ICS Channel Access Server (CAS) which communicates with all subsystems. It supports two protocols to communicate with subsystems at layer 1 viz., MODBUS over TCP/IP and EPICS protocol. It communicates with OWS via EPICS protocol. The System Architecture of ICS CAS is given in figure 3.

LEHIPA uses different hardware systems including serial and Ethernet communication interfaces all serial interface has been connected to Ethernet LAN using serial to Ethernet converter switches. Most of the IOCS are running on LINUX based embedded PCS, cPCI systems and industrial PCS.

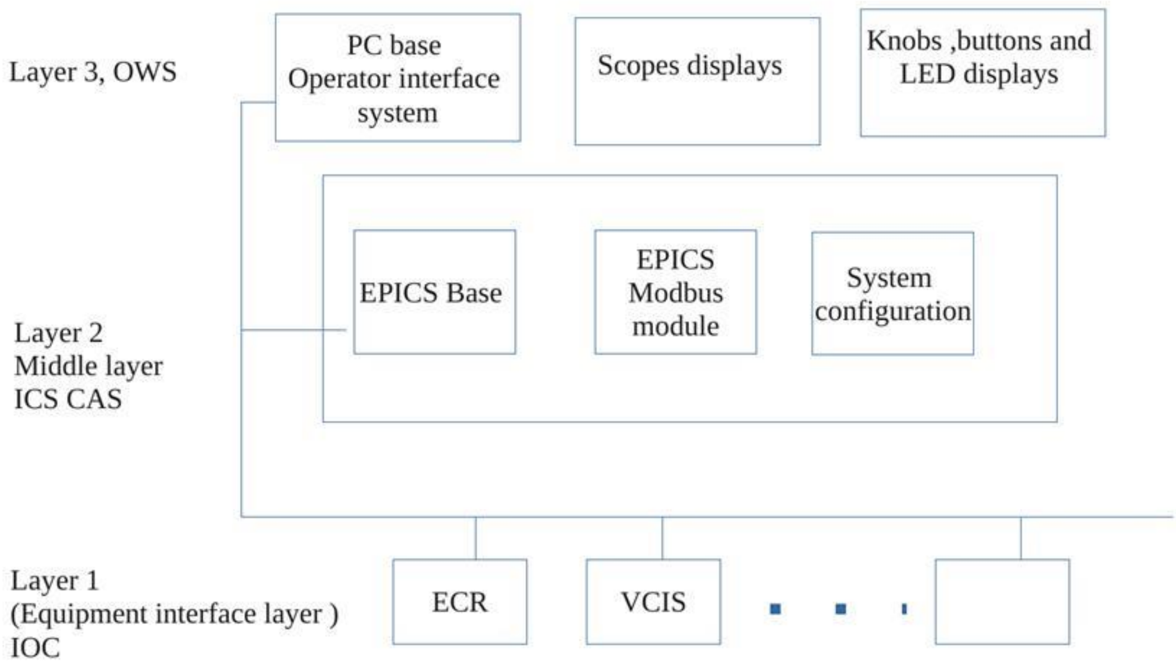


Figure 3: Architecture of Integrated Control System.

## CONCLUSION

The 3 MeV RFQ section is operational and is commissioned using the control system. The control system operated very reliably. Many suggestions have been provided by the users during operation. It will be very easy to implement these suggestions because of EPICS SCADA [2] System used in LEHIPA.

## ACKNOWLEDGMENTS

We sincerely thank Dr. S. Krishngopal, Head, IADD for his valuable suggestions and support. We are thankful to Smt. Sapna Padmakumar, Smt. Shailaja Ware and Shri. N. B. V. Subrahmanyam of FOTIA facility for their kind support during installation and commissioning of SIS system.

## REFERENCES


[1] S K Singh, “Particle Accelerator Control System”, EPAC’04, Proceedings of the DAE Symp. on Nucl. Phys. 55 (2010).

[2] Experimental Physics and Industrial Control System http://www.aps.anl.gov/epics.

[3] Control System Architecture: The Standard and Non-Standard Models, M. E. Thuot, L.R. Dalesio, Los Alamos National Laboratory, IEEE, Proc. Of the 1993 PAC, Volume 3 pp 1806-1810.

[4] P Singh et al, Accelerator Development in India for ADS Programme, PRAMANA Journal of Physics, Vol. 68, No. 2, February 2007, pp. 331-342.

# DEVELOPMENT OF REAL CODED GENETIC ALGORITHM BASED OPTIMIZATION SYSTEM FOR PERFORMANCE ENHANCEMENT OF BOOSTER SYNCHROTRON

S. Yadav[#1, 2], R. K. Agrawal[1], Y. M. Sheth[1], P. Fatnani[1], T. A. Puntambekar[1], A. C. Thakurta[1]

[1]Raja Ramanna Centre for Advanced Technology, Indore
[2]Homi Bhabha National Institute (HBNI), Training School Complex, Anushakti Nagar, Mumbai

*Abstract*

Booster Synchrotron is the injector system for Indus-1 and Indus-2 Synchrotron Radiation Sources at RRCAT, Indore, India with a Microtron as pre-injector. Microtron injects 20 MeV electron beam into the Booster Synchrotron through Transport Line-1 (TL-1). The energy of the injected beam is ramped to 450/550 MeV for beam injection into Indus-1/Indus-2, at repetition rate of 1 Hz. The accumulation rate for Indus-1 and Indus-2 depends on beam current extracted from Booster Synchrotron. Earlier, settings of more than ten parameters related to Microtron, TL-1 and Booster Synchrotron were to be optimized to maximize the accelerated beam current in Booster synchrotron. Microtron and Booster Synchrotron are pulsed systems. Even a small amount of fluctuation in any of the parameters, have its reflection on the accelerated beam current in Booster Synchrotron. Therefore, the manual optimization of parameters had always been tricky, tedious and prone to human errors. A Real Coded Genetic Algorithm (RCGA) based system is implemented to circumvent the difficulties. This has resulted in an improvement of 50-60 % in beam current of Booster Synchrotron. Using RCGA based system, an average accelerated beam current of more than 5 mA has been achieved in the Booster synchrotron. RCGA system, being auto-corrective, maintains the optimum beam current in Booster Synchrotron. It has minimized the operator's intervention for beam current optimization. The paper elaborates on details of the implementation of RCGA based system and its integration with the Indus machine control system. Results obtained of the optimization using RCGA system are also presented

## INTRODUCTION

Booster synchrotron injects the 450 and 550 Mev beam into Indus-1 and Indus-2 respectively at rate of 1 Hz [1]. The total injection time for Indus-1 and Indus-2 is related with the beam current of Booster. The beam current of Booster depends on the injected beam current from Microtron, beam parameters of injected beam and beam decay during beam energy ramping. Due to suitability of multi-objective optimization and random search technique, Genetic algorithm is used for accelerator optimizations [2-3]. For enhancement of the beam current of Booster synchrotron, Real Coded Genetic Algorithm (RCGA) based system has been developed. In this, the transmission efficiency of TL-1 is optimized by varying current in the steering coils of TL-1 [4-5]. On the optimum settings of steering coils, RCGA software maintains the cathode current for stable cathode emission. Other parameters of Microtron i.e., RF frequency, power supply current of Booster injection septum and modulator trigger delay are also scanned in the operating range and set by the software for maximized beam current in Booster .

## SYSTEM DESCRIPTION

The RCGA controller interfaces individual supervisory controllers of power supplies of TL-1 steering coils and Microtone through MATLAB server. It takes the Booster beam current, cathode emission current and FCT current as the input parameters for optimization and controls the overall system. Scheme of system is shown in figure 1.

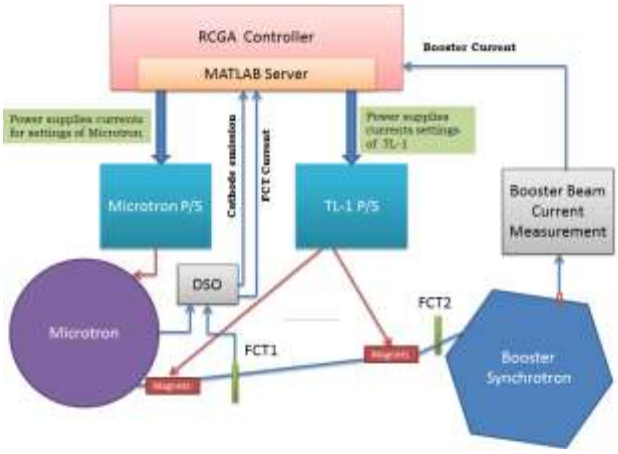


Figure 1: Scheme of RCGA based system for Booster beam current enhancement

The FCT current and Booster DCCT current are used by RCGA controller for finding the fitness of optimization system. After applying the RCGA algorithm, optimum settings of nine steering coils are applied. Throughout the optimization process, the cathode emission current of Microtron is required to be at desired level and hence sliding mode controller based online control of emission current has been implemented. For deployment of this system in Indus control room, user support system has been developed and deployed. The snapshot of the GUI is shown in figure 2.

#syadav@rrcat.gov.in

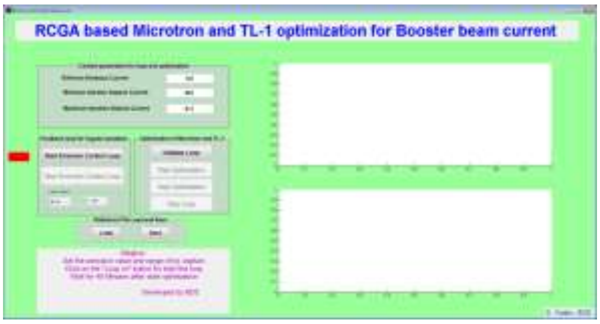


Figure 2: Snapshot of the GUI of RCGA based algorithm

The software performs the optimization as well as emission control. Optimization process starts from the routine beam operation of Microtron, TL-1 and Booster synchrotron. The steps for optimization are as follows,

- Step 1: Apply sliding mode control for keeping the stable cathode emission current of Microtron.
- Step 2: Scan and fix the P/s current of injection septum for maximum Booster current.
- Step 3: Define the boundaries of the variables based on the previous optimum values and generate the random chromosome for given population number.
- Step 4: Apply the chromosome on the machine and evaluate the fitness function as described above.
- Step 5: Use rank selection method to find the parents for next generation.
- Step 6: Apply Blend-α crossover method to create new population.
- Step 7: Apply Mutation operator on new solutions depends on probability of mutation.
- Step 8: Repeat the step 4 to step 7 for given number of iterations.
- Step 9: Adjust the boundaries of the variables according to new best optimum values of steering coils achieved during previous optimization. Repeat the step 3 to 8 for new boundaries.
- Stopping criteria: Either user stops the optimization process or beam current of Booster reaches above 9 mA.

At optimum settings, this system maintains emission current using sliding mode control (SMC). SMC is a nonlinear control method which handles the fast dynamic response of system and caters the external disturbance [6]. The setting of reference cathode emission current is available in GUI for the user. The software also identifies the optimum value of Microtron RF frequency, power supply current of Booster injection septum and the modulator trigger delay by scanning these parameters in the specified range.

## RESULT

The cost function of RCGA based optimization for online tuning of 9 Nos of TL-1 steering coil currents to achieve more than 5 mA beam current in Booster, is given as

Maximize→ $f = w1 * I_{booster} + w2 * I_{FCT1}$ or

Minimize→ Fitness value $F = 1/f$,

Where, $I_{FCT1}$ is FCT1 output current in TL-1 and $I_{booster}$ is the beam current of Booster.

The parameters for RCGA are given below,

- No. of variables = 9 (Steering coil currents)
- Population size =10
- No. of iteration = 10
- Boundary shift coefficient =0.46
- Probability of mutation =0.2;

The convergence curve and corresponding improvement in the beam current of Booster are depicted in figure 3.

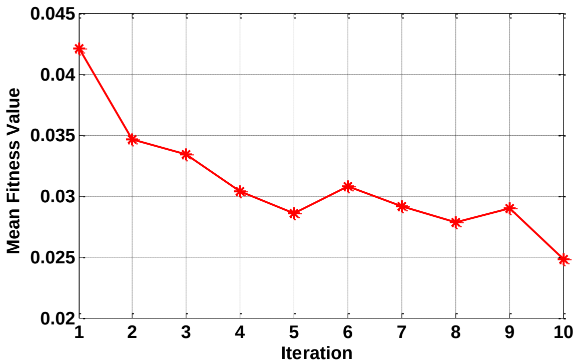


(a)

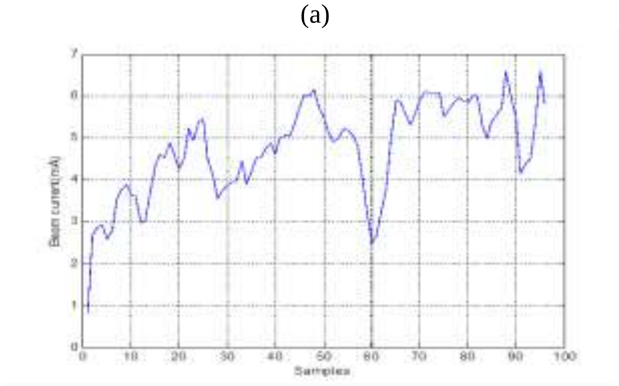


(b)

Figure 3: Typical graph for a) Convergence curve of the RCGA, b) Correspondingly improvement in Booster current

From figure 3, it is observed that convergence was achieved within 7 to 8 iterations and after this, no significant improvement was seen in beam current of Booster. During normal operation Booster beam current is ~3 to 4 mA, which by this optimization of TL-1 steering coils has enhanced to ~ 5-6 mA. This improvement helps for beam current accumulation in Indus-2. Figure 4 shows the comparative graph beam current accumulation with and without optimized TL-1 coil current settings.

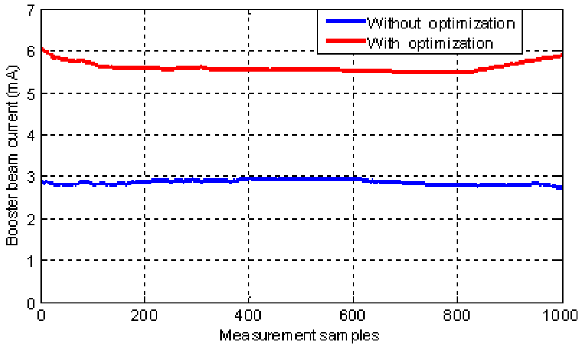


(a)

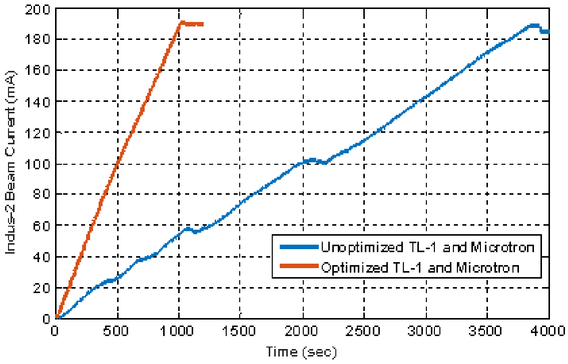


(b)

Figure 4: Typical graph for a) beam current of Booster with and without optimization for duration of ~ 3 Hrs, b) correspondingly improvement in beam accumulation of Indus-2

The improvement in the beam accumulation rate is due to enhancement beam current of Booster and slight variation in beam injection parameters of Indus-2. Figure 5 shows, effect on Booster beam current with and without RCGA controller ON.

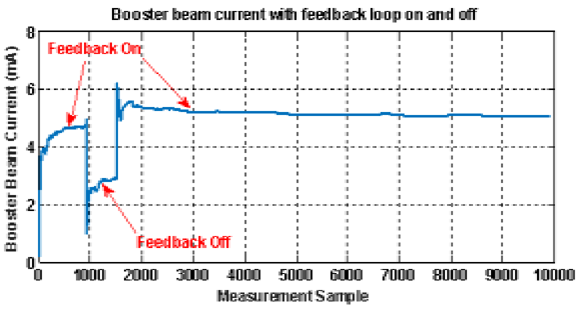


Figure 5: Typical graph for Booster beam current with and without emission loop control

Figure 5 shows an improvement of beam current by controlling the cathode emission current of Microtron.

## CONCLUSION

Real Coded Genetic Algorithm (RCGA) based system has been implemented for automatic optimization of parameters of Microtron and Transport Line-1 (TL-1) to achieve an average accelerated beam current ≥ 5 mA in the Booster synchrotron. The RCGA based system enhances the beam current in the Booster synchrotron by optimizing the parameters of the injected beam, and by improving the beam transmission efficiency of TL-1. The electron beam current from the Microtron is optimized by controlling the cathode emission, and the transmission efficiency of the TL-1 is improved by optimization of the settings of nine steering coils and simultaneously monitoring the current in TL-1. Other parameters like Microtron RF frequency, modulator trigger delay and power supply current of the Booster injection septum are also scanned and optimized by the software to maximize the beam current of Booster.

## ACKNOLEDGEMENT

The authors would like to thank the colleagues of the Beam Diagnostics Section, Accelerator Control System Division and Indus-2 operation crew members of RRCAT for their support in completion of this work.

## REFERENCES

[1] www.rrcat.gov.in/technology/accel/index.html

[2] D. Schirmer at al, Electron transport line optimization using neural networks and genetic algorithms , Proceedings of EPAC 2006, Edinburgh, Scotland.

[3] Weiwei Gao et al. , Simultaneous optimization of beam emittance and dynamic aperture for electron storage ring using genetic algorithm, Physical Review Special Topics - Accelerators and Beams 14, 094001 (2011).

[4] Mitchell, Melanie, An Introduction to Genetic Algorithms. Cambridge, MA: MIT Press. ISBN 9780585030944, (1996).

[5] N. Chakraborti, 2008. Differential Evolution: the real parameter Genetic Algorithm applied to materials and metallurgy. Kanpur Genetic Algorithms Laboratory, 2008

[6] Stephen Yurkovich and Xiaoqiu Li, Sliding-Mode Control Methodologies for Regulating Idle Speed in Internal Combustion Engines December 2005, DOI: 10.1016/B978-012170960-0/50087-6

# APPLICATIONS OF INDIGENOUSLY DEVELOPED 10 MeV RF ELECTRON LINEAR ACCELERATOR FOR DIVERSE SOCIETAL FIELDS

Nishant Chaudhary*, R. B. Chavan, M. Kumar, A. R. Tillu, D. Bhattacharjee, S. Chandan, V. Yadav, S. R. Ghodke, R. R. Tiwari, D. Jayaprakash, H. Sarukte, S. S. Gaikwad, S. H. Harer, R. K. Rajawat

Accelerator & Pulse Power Division, BARC, Mumbai

*E-mail: nishantc@barc.gov.in

*Abstract*

A 10 MeV RF electron linear accelerator (Linac) is indigenously designed and developed by APPD, BARC at Electron Beam Centre (EBC) Kharghar, Navi Mumbai, having the present capability to deliver dose rate up to 2.0 MGy/h per unit area. The radiation induced tailoring of material characteristics has been demonstrated for various research and industrial applications. The alanine-EPR as well as radio-chromic film dosimetry has been done to optimize process parameters. The irradiation of chitosan has been done on large scale to enhance the production of sugarcane through 1.3 times, by delivering 50 kGy optimized dose. The radiation hardening of solar cells was studied for ISRO with dose up to 350 kGy. The radiation damage studies of Zr-alloy have been successfully done under simulated conditions of nuclear reactor environment. The accumulated dose delivered to the samples is about 350 MGy in steps. The electrical characteristics of organic semiconductor films have been successfully modified to use these films as potential radiation dosimeter for very high radiation field. In addition the performances of these films as device, like gas sensor, have also been enhanced with delivering dose in kGy order. The reduction in reverse recovery time ($T_{rr}$) of power diode for Bharat Heavy Engineering Limited (BHEL) has been standardized and achieved 15 µs to 6 µs by imparting 4 kGy. The preservation goal for food items such as dried apricot, quince, coriander powder etc, have been achieved in dose ranging 1 kGy to 14 kGy. Multi disciplinary research experiments including nuclear data generation, activation analysis, scissioning/crosslinking of polymers, mutation of seeds, COD/BOD reduction from waste water etc., of BARC and other educational institutions have also been carried out. It satisfies the purpose to understand the electron beam (EB) induced impacts on materials and also to validate it as technical alternative of tedious conventional approaches.

*Key words:* Linac, crosslinking, chitosan, sugarcane, conducting polymer, dosimeter

## INTRODUCTION

The techniques to tailor the characteristics of materials, for societal benefits, using electron accelerators, have become very popular and economical. It has more public acceptability and outweighs over gamma irradiation or other techniques because it is simple and capable to deliver kGy dose levels in few seconds [1]. Also the system is fully controlled in nature leading to safe atmosphere. The present paper deals with the various applications including chitosan irradiation, improvements in power diode characteristics, radiation hardening studies of solar cells, food preservation and rusting studies of metal alloy, done with 10 MeV electron accelerator at EBC, BARC. We also present the performance modifications of organic thin film devices with EB.

## 10 MeV ELECTRON LINAC

A 10 MeV RF linear electron accelerator (Linac) is indigenously designed and developed by APPD, BARC at Electron Beam Centre (EBC), Kharghar, Navi Mumbai. In this Linac, oscillating electric field is established, in a series of on-axis coupled cavity, through a microwave source, klystron. The Linac is operated in pulsed mode and the beam pulses are scanned over a 1 m long titanium exit window with a scan frequency of 1 Hz. The beam pulses generated from the accelerator with a certain repetition frequency and that was set in such a way, the desired dose uniformity can be realized over the full scan length or irradiation area [2]. The output dose rate is around 1 kGy per pass in the dynamic mode keeping product speed at 1 m/min under fixed operating parameters and the dose delivery was done by setting appropriate number of passes [3]. All the irradiation experiments were carried out under normal atmospheric conditions.

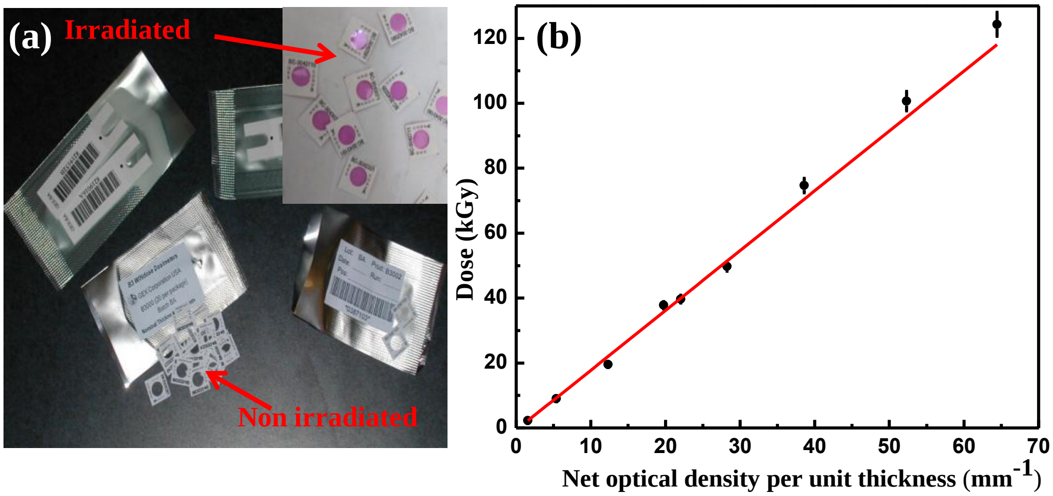


Figure 1: (a) Radio-chromic films used as routine dosimeters, (b) Routine dosimeter calibration curve generated in house with 10 MeV Linac.

## DOSIMETRY CHARACTERIZATION OF 10 MeV LINAC

Dosimetry characterization of Linac has been done by means of radio-chromic films as routine dosimeters, which is based up on radiation induced optical density change. It consists of calibration of dosimeter in house, energy verification of EB and dose profile & its correlation with beam operating parameters. The calibration of routine dosimeter has been done in house using standard alanine pellet dosimeter which is based upon electron paramagnetic resonance (EPR) technique. The calibration curve is shown in the Fig. 1.

## IRRADIATION EXPERIMENTS

### *Chitosan irradiation*

Chitosan is most promising biological macromolecules, derived from shrimp shells, having biodegradable, biocompatible, non toxic and non allergic characteristics. It is used as bio-stimulator for sugarcane to enhance production as well as to encounter the negative abiotic agents like temperature, water deficiency etc. Un-irradiated chitosan (mixed with 1% acetic acid) is in gel form and post EB treatment it becomes liquid. After multiple iterations 50 kGy has been set as optimized EB dose, to enhance the sugarcane production by around 1.3 times as compared to un-irradiated chitosan. It provides better germination, proper tillering of plant and regulate photosynthesis through minimize the transpiration from leaves & stabilizing chlorophyll levels. This experiment is going on in collaboration with Vasantdada Sugar Institute (VSI), Pune, for actual field trials.

### *Diode characteristics improvements*

The characteristics of power diode rated as 2.6 kV, 700 A, made of silicon, used as switching device in turbo generators of BHEL has been improved with 10 MeV EB treatment. The reverse recovery time (trr) has been abridged to 6 µs from 15 µs by imparting 4 kGy optimized dose. Also the leakage current and forward voltage drop are 20 mA and 2.0 V whereas those were got with gold doping as 150 mA and 2.3 V respectively. In 10 MeV facility, the exposure time required is much shorter (like 20-30 s) to complete processing of one batch having around 200 diode chips. The whole exercise is exemplary of joint partnership between industry and research institution leading to effective utilization of research expertise available within the country for manufacturing application.

### *Nodular Corrosion analysis for Zirconium alloy*

Zirconium - niobium alloy having fractional composition 0.975 Zr + 0.025 Nb is used as pressure tube in nuclear reactors which holds fuel bundles and carry the heavy water in $CO_2$ environment. The radiation induced corrosion of this metal alloy has been studied, in simulated reactor conditions, using 10 MeV Linac. The sample has been given 350 MGy accumulated dose at rate of 1.0 MGy/min with maintaining temperatures of the system as per actual reactor conditions. The corrosion has been traced after imparting dose of 150 MGy in presence of $CO_2$ and it is on rise as dose increases. The experiment is still going on and exclusive conclusion is awaited.

### *Radiation hardening studies of solar cell*

The radiation hardening studies of multi-junction solar cells (InGaP/GaAs/Ge) having 28 % initial efficiency was carried out for ISRO. In space configuration, the outer van allen belt, that is located at distance 13000 to 60000 km from the earth surface, contains very high electron (of energy ranging 0.1 -12 MeV) fluencies ~ $10^{13}$ $e^0_{-1}$ /cm$^2$. The communications satellites are located at height of 36000 km (in the same belt), called geosynchronous orbit. For a period of 15 years (normal life of satellite) it receives ~ $10^{15}$ $e^0_{-1}$ /cm$^2$. This much fluence has been delivered with Linac and the study concluded that the efficiency falls to 18 %. It is highly important to plan accordingly the solar panel matrix on a satellite.

### *Food preservation*

Electron beam irradiation of dried apricot and quince has been carried out for 4 kGy in steps of 1 kGy to enhance the self life and antioxidant characteristics. The rehydration ratio, that implies water holding capacity, decreases from 0.84 to 0.76 leading to enhance the self life. The study also suggests that sugar content increase up to 20 % along with β-carotene after receiving dose of 4 kGy [4]. Thus the EB treatment also enhances the nutritionally rich and biologically active constituent in these dry fruits.

The irradiation of coriander powder with 14 kGy optimized dose was also done. The microbial count analysis indicates that it remains nil till 1 year under normal room conditions (Fig. 2). It concludes that the storage life (in room conditions) of coriander powder enhanced up to 1 year by irradiating with 14 kGy dose. It is important because the food production cycle in India is of 1 year.

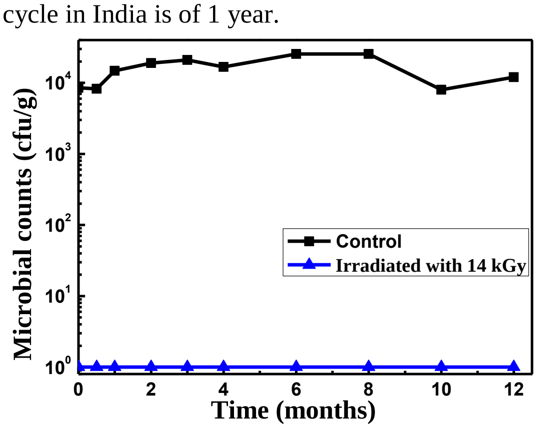


Figure 2: Microbial counts in un-irradiated and 14 kGy irradiated coriander powder in 1 year spam

### *Performance modifications of organic thin devices*

The electrical characteristics and associated performance of organic thin film based devices have been modified with 10 MeV treatments. The electrical conductance of molecular semiconductor zinc phthalocyanine (ZnPc) varied linearly with dose up to 18 kGy, facilitating it as potential radiation dosimeter [5]. Conductivity of conducting polymers nano-composites (PANI-Ag) films was enhanced by two orders after receiving dose of 30 kGy and also its sensitivity towards $H_2S$ gas sensing improved on irradiation with 100 kGy dose [6].

## CONCLUSIONS

Indigenously developed 10 MeV Linac has a broad range of utilizations and the goals have successfully been achieved for both industrial as well as basic research. The irradiation carried out on laboratory scale has potential to become applicable on actual field scale. Some of them have been applied on their actual broad scale like diode, chitosan and solar cell applications. These experiments exclusively confirmed that EB irradiation technique is a better alternative of conventional tedious approaches like chemical cross-linking, semiconductor doping, autoclave techniques etc.

## REFERENCES

[1] N. Chaudhary, A. Singh *et al.*, “Electron beam modified organic materials”, Solid State Phenomena 239 (2015) 72-97.

[2] R. H. Chilkulwar, S. D. Sharma *et al.*, “Dosimetric evaluation of an indigenously developed 10 MeV industrial electron beam irradiator” Radiat. Measur. 47 (2012) 628-633.

[3] N. Chaudhary, S. P. Koiry *et al.*, “Electron beam induced modifications in flexible biaxially oriented polyethylene terephthalate sheets: improved mechanical and electrical properties”, Mat. Chem. Phys. 189 (2017) 237-244.

[4] S. A. Rather, P. R. Hussain *et al.*, “Comparison of gamma and electron beam irradiation for using phyto-sanitary treatment and improving physico-chemical quality of dried apricot and quince”, J. Rad. Res. Appl. Sci. 12 (2019) 245-259.

[5] N. Chaudhary, A. Singh *et al.*, “Electron beam modified zinc phthalocyanine thin films for radiation dosimeter application”, Synth. Met. 231 (2017) 143-152.

[6] N. Chaudhary, A. Singh *et al.*, “Electron beam induced modifications of polyaniline silver nano-composite films: electrical conductivity and $H_2S$ gas sensing studies” Radiat. Phys. Chem. 153 (2018)131-139.

# Four Years with XCAMS at IUAC, New Delhi: Status Report

D. Khandelwal*, G R Umapathy, R. Sharma, Pankaj Kumar, S. Ojha, S. Gargari, R. Joshi, S. Chopra

Inter University Accelerator Centre (IUAC), Aruna Asaf Ali Marg, New Delhi - 110067, INDIA

* email: deekshakhandelwal44@gmail.com

## Abstract

XCAMS (The Compact $^{14}C$ Accelerator Mass Spectrometer eXtended for $^{10}Be$ and $^{26}Al$) at Inter University Accelerator Centre (IUAC), Delhi has been in regular operation since early 2015. The facility is based on NEC make 0.5MV tandem accelerator (Model 1.5SDH) having two MC-SNICS ion sources and gas detector for radioisotope detection. XCAMS facility is catering the need of researchers from the field of geology, oceanography, archaeology, atmospheric science etc. across the country and abroad. Modern standard reference samples of $^{14}C$ and standards of $^{10}Be$ and $^{26}Al$ have been measured with precision better than 0.1%, 1% and 2%, respectively. About 3000 samples of all three isotopes have been measured till now. This paper presents performance report, major maintenance related to the ion sources and accelerator. Future plans for modification and upgradation of this system will also be discussed.

## Introduction

Accelerator mass spectrometry (AMS) is an ultra-sensitive technique for counting long-lived and rare radioactive isotopes (e.g. $^{14}C$ ($T_{1/2}$= 5730 a), $^{10}Be$ ($T_{1/2}$ = 1.39 Ma), $^{26}Al$ ($T_{1/2}$ = 0.73 Ma), $^{36}Cl$ ($T_{1/2}$ = 301 ka), $^{129}I$ ($T_{1/2}$ = 15 Ma), $^{41}Ca$ ($T_{1/2}$= 103 ka) etc.). The natural abundance of these isotopes is $\sim 10^{-10}$ -$10^{-15}$ and their measurements with low energy conventional mass spectrometer poses the challenges of isobaric interferences. Accelerator based mass spectrometry technique provides high energy for removing isobaric interferences and thus helps in the high precision measurements. AMS research at IUAC started about one and half decades ago with existing 15 UD Pelletron accelerator for $^{10}Be$ and $^{26}Al$ measurements [1,2]. Later on, keeping in mind the demands of $^{14}C$ measurements in the country a dedicated 500 kV accelerator known as XCAMS was installed in 2015 [3-5].

This accelerator has been used for $^{14}C$, $^{10}Be$ and $^{26}Al$ measurements routinely. Samples of $^{14}C$ and $^{10}Be$, $^{26}Al$ are prepared in the graphitization and clean chemistry laboratory, respectively. The dating material for radiocarbon measurements mainly includes sediment, charcoal, wood, peat, shells and carbonates, bones and textile. The radiocarbon studies have helped in the paleoclimate reconstruction, establishing paleoseismic evidences and in archaeological findings etc. $^{10}Be$ and $^{26}Al$ measurements have been applied to estimate the exposure age of rocks, to determine the denudation and sedimentation rates.

## AMS system

XCAMS accelerator at IUAC is shown in figure 1. The accelerator has two MC-SNICS ion sources having 134 and 40 cathodes to produce negative ions of the cathode material. The ion source is followed by a low energy switchable electrostatic analyzer to select ions of particular E/q from any one of the ion sources. Magnetic bias sequencer (MBS) and 90° injector magnets are used to sequentially inject rare and abundant isotopes into the accelerator. An off-axis faraday cup at the entrance of the accelerator measures the low energy current of the relatively abundant isotope ($^{13}C$ in case of $^{14}C$ injection and $^{12}C$ in case of $^{13}C$ injection). Injected negative ions are accelerated towards the high energy terminal having the argon gas stripper which converts these negative ions into positive ions. Positive ions are further accelerated and charge state $1^+$ is selected using analyzer magnet. Abundant isotopes are measured in the off axis faraday cups and radioactive isotope is passed to high energy electrostatic analyzer (HE-ESA). Retractable silicon rich nitride (SRN) foil with HE-ESA and 45° magnet helps in removing of the $^{10}B$ from $^{10}Be$ in the detector. Radioactive isotope atoms are counted in a gas ionization counter having two anodes with isobutane gas medium.

## Performance of $^{14}C$ measurement

134 cathode ion source is used for routine $^{14}C$ measurements. 1 mgC is graphitized on ~5 mg iron powder using the Automated Graphitization Equipment (AGE). The graphite powder is pressed into the cathode using an automated sample press. $^{14}C$ measurements are performed at terminal potential of 460 kV and stripper pressure is kept ~27 mbar. Stripper pressure was optimized by varying it to find out optimal value of transmission (42%) and background level ($< 1 \times 10^{-15}$). In a recent study, IAEA secondary standards and Oxalic acid II (OxII) were

**Table 1:** pMC of standard samples measured using XCAMS.

| Standard Name | Expected pMC | Measured pMC |
|---|---|---|
| IAEA-C1 | 0.00 ±0.02 | 0.34±0.023 |
| IAEA-C2 | 41.14 ±0:03 | 41.476±0.194 |
| IAEA-C3 | 129.41 ±0.06 | 129.224±0.445 |
| IAEA-C4 | 0.20-0.44 | 0.337±0.0355 |
| IAEA-C5 | 23.05 ± 0.02 | 23.239 ± 0.154 |
| IAEA-C7 | 49.53 ± 0.12 | 49.361± 0.223 |
| IAEA-C8 | 15.03 ± 0.17 | 15.013 ± 0.108 |
| OxII | 134.08 | 134.17 ± 0.480 |

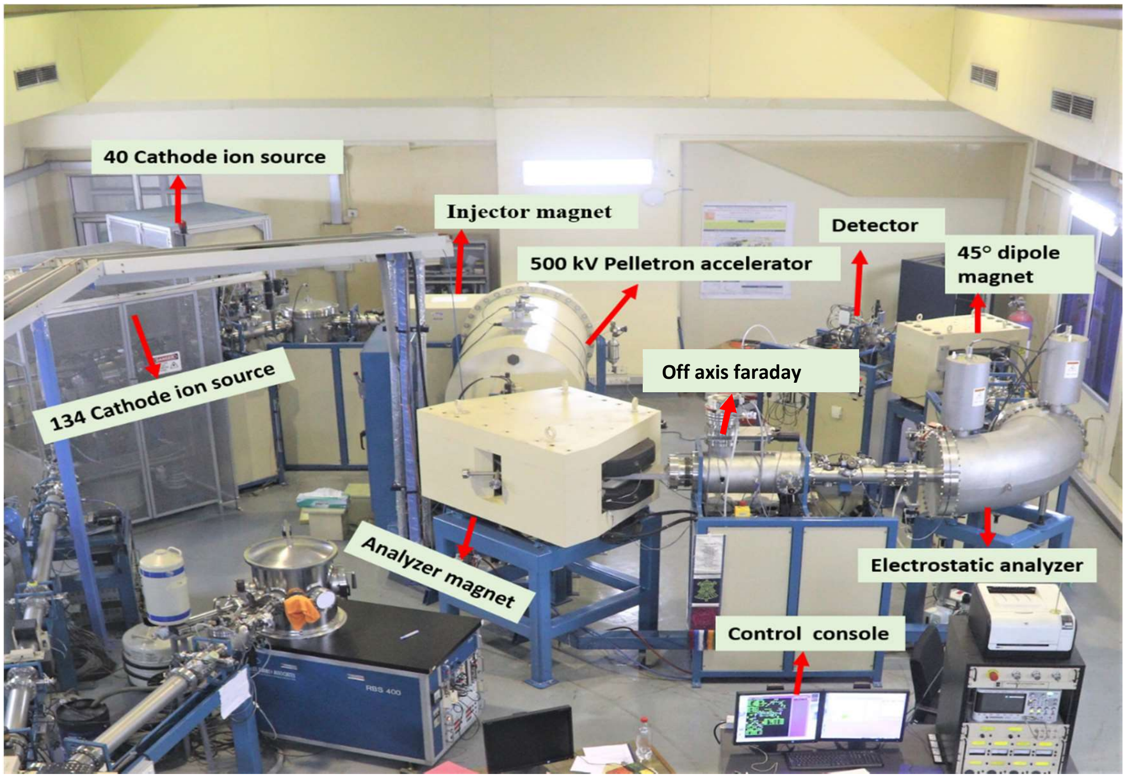


Figure 1: XCAMS system at IUAC

measured and their percent modern carbon percent modern carbon (pMC) values were compared with consensus values. Oxalic acid 1 (OxI) was used as a primary standard and Ph-blank (Phthalic anhydride, Sigma Aldrich, Purity 99%) was used as a blank. Measurements were done for about half an hour for each sample. Table 1 shows that the experimental results and their consensus values are in good agreement with each other. The same has been shown in figure 2.

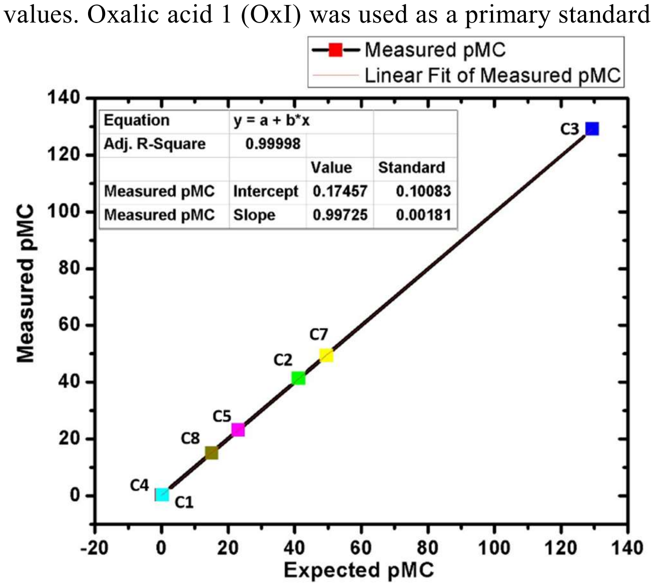


Figure 2: Graph showing expected pMC values versus measured pMC values

## Performance of $^{10}$Be and $^{26}$Al measurements

A mixture of BeO and Nb (1:3) is used as a target material for $^{10}$Be measurements. After the pre-acceleration from ion source, $^{10}Be^{16}O^-$ and $^{9}Be^{16}O^-$ are sequentially injected into the accelerator. $^{9}Be^{+1}$ current is measured in off-axis faraday cup at the entrance of the accelerator. The interfering isobar $^{10}$B is separated using a 75 nm SRN foil followed by an ESA and 45° magnet and detector. $^{10}$Be has been tried at terminal potentials of 530 kV and 550 kV and we have found that 550 kV helps in reducing $^{10}$B background. $Al_2O_3$ mixed with Nb (1:3) is used as a target material for $^{26}$Al measurement. More details regarding $^{10}$Be and $^{26}$Al measurements have been given in [4].

## Major maintenances faced in last four years

Ion sources need scheduled maintenance after several hours of operation due to deposition of cesium at its components. During the ion source maintenance, all the components are cleaned and sometimes ionizer and immersion lens need to be replaced. The varistor of the circuit providing power to rotating shaft went bad twice. Originally, circuit assembly was at an inaccessible position highlighted in figure 3, so at first instance, Pelletron tank was opened to make space available for changing the varistor. Second time, the whole assembly was shifted to an easily accessible location and

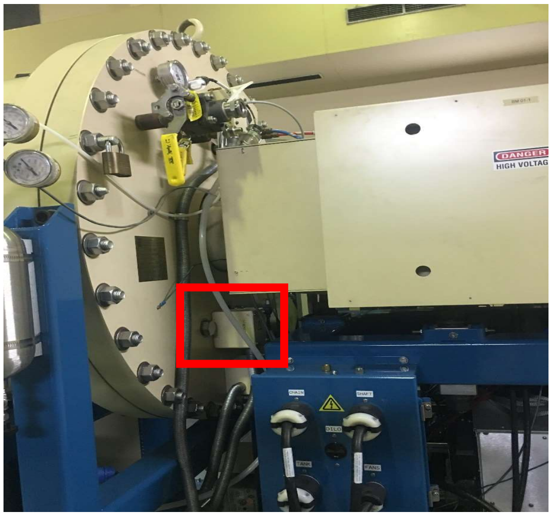

Figure 3: Location of vasistor assembly

the varistor was changed without opening the tank.

Detector outputs are processed through NIM electronics and digitized by PIXIE based data acquisition system. One of the channel (connected to anode 2) of PIXIE had gone bad and due to that 2D spectrum were not visible on the screen. We tested it using pulsar and confirmed the fault in channel 2. One spare channel (channel 3) was available at PIXIE and now anode 2 signal has been connected it.

An upward drift in 14/12 ratio was seen once during radiocarbon measurement. The problem of misalignment of cathode was found by observing the cathode under microscope as shown in figure 4. The problem was solved by the alignment of cathode wheel by adjusting the guiding rods installed at back of source 2.

**Before Alignment** **After Alignment**

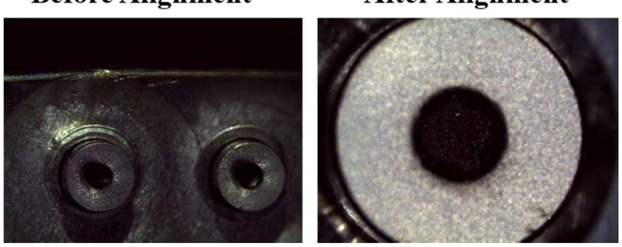

Figure 4: Cathode image observed under microscope

Failure of some other components like the failure of the turbo pump at the entrance of the accelerator, capacitor of the interface card of the control system and the stripper pressure switch interlock were also faced. These all components were replaced with the newer one.

## Future directions

One solid state surface barrier detector (SSBD) will be installed just after the ESA for radiocarbon measurements. 40 cathode ion source has provision to inject gas samples. We plan to attach gas interface for measuring small size samples.

## Conclusion

XCAMS accelerator at IUAC is in good working condition and accelerator mass spectrometry measurements of $^{14}C$, $^{10}Be$ and $^{26}Al$ are being performed satisfactorily. About 3000 samples have been analyzed since the installation of the accelerator. Major maintenances related to the system have been discussed.


## Acknowledgements

Authors are grateful to ministry of earth sciences, Govt of India for financial support (MoES/P.O.(Seismo)8(09)-Geochron/2012).


## References


[1] Pankaj Kumar *et al.* $^{10}Be$ measurements at IUAC – AMS facility, J Radioanal Nucl Chem, 290 (2011) 179-182.

[2] Pankaj Kumar *et al*. A new AMS facility at Inter University Accelerator Centre, New Delhi, Nucl. Instr. Meth. B, 361 (2015) 115 – 119.

[3] Pankaj Kumar *et al.* $^{14}C$ AMS facility at IUAC, New Delhi, InPAC – 2015.

[4] R. Sharma *et al.* AMS and upcoming geochronology facility at Inter University Accelerator Centre (IUAC), New Delhi, India Nuclear Inst, and Methods in Physics Research B (2018).

[5] R. Sharma *et al.* Operational experience with 1.5SDH Pelletron accelerator for AMS applications at IUAC, Delhi , InPAC – 2018.

# STUDY OF DIRECT TARGET APPROACH FOR THE $^{99}$MO PRODUCTION USING HIGH POWER ELECTRON ACCELERATORS

Aqsa Shaikh, Tanuja Dixit, Abhay Deshpande, R. Krishnan,

Society for Applied Microwave Electronics Engineering & Research (SAMEER)

IIT Campus, Hill Side, Powai, Mumbai -400076

*Abstract*

One of the ways to produce $^{99}$Mo is through photo neutron conversion of $^{100}$Mo into $^{99}$Mo. This can be achieved by accelerators. When an energetic electron beam hits $^{100}$Mo, bremsstrahlung photons are produced. These photons can be used to trigger the photo neutron conversion of $^{100}$Mo target to $^{99}$Mo. In this paper we have studied aforementioned method of $^{99}$Mo production by means of direct target approach. In direct target approach the production and utilization of photons take place in the same target. GEANT4 simulations are used to design and study the experiment. Molybdenum being expensive material has to be utilised very carefully. We observed that for a cylindrical $^{100}$Mo target specific activity reduces further than 1.4 radiation length. Also increasing the radius to 10mm from 4mm accounts for only 17.75% increase in activity whereas 525% increase in the overall mass. Looking at these parameters optimization of $^{99}$Mo target and activity calculation are carried out.

## INTRODUCTION

At SAMEER, development of 30MeV, 8-10 kW electron linac is underway for medical isotope production viz. $^{99}$Mo. $^{99}$Mo will be produced via photo neutron reaction using enriched $^{100}$Mo target. A study of convertor target approach in which (e, γ) reaction takes place in high Z target and (γ,n) reaction in $^{100}$Mo is reported in [1]. As per standard data reaction cross-section of (γ, n) peaks at photon energy 14-15 MeV up to 0.15 barns. 30 MeV electron linac is expected to produce enough photon flux of energies in this range, which is used for $^{99}$Mo production through $^{100}$Mo (γ, n) $^{99}$Mo reaction [1]. Enriched Molybdenum is very expensive material; a very judicial usage of the material is the key issue. As observed during simulations, direct irradiation of molybdenum target yields better results. Therefore, exhaustive simulations and comparison with standard data is carried out. Optimization of molybdenum thickness and radius for maximizing the $^{99}$Mo activity is done in this paper along with the study of activity variation with change in $^{100}$Mo enrichment level.

## EXPERIMENTAL SETUP

Beam optimization done for converter target approach is used for direct target approach as well [1]. Here 30MeV electron beam strikes directly on $^{100}$Mo target rather than on tungsten as a converter target. Molybdenum being high Z material produces bremsstrahlung photons which are used for photo-neutron conversion of $^{100}$Mo into $^{99}$Mo. Hence, in this approach electron to photon conversion and its utilization happens in the same molybdenum target.

## ACTIVITY CALCULATION

Unlike converter target approach, in direct target approach the photon flux generated is locally utilized for photo neutron conversion of $^{100}$Mo. Therefore, it is impractical to determine exact count of photons produced and their respective energies in order to calculate the activity with the help of the equation presented in [1]. As mentioned in TRIUMF, another way of activity estimation is by means of neutron flux coming out of $^{100}$Mo [2]. Neutron flux coming out of $^{100}$Mo is directly proportional to the number of photo-neutron reactions taking place inside $^{100}$Mo. This neutron flux is a result of all photo-neutron reactions like (γ, 1n) (γ, 2n) and (γ, 3n) out of which the only relevant reaction for $^{99}$Mo production is (γ, 1n) [3]. The reaction cross-sections for (γ, 1n) (γ, 2n) and (γ, 3n) reactions alongside the photon flux obtained from tungsten target is given in Figure 1.

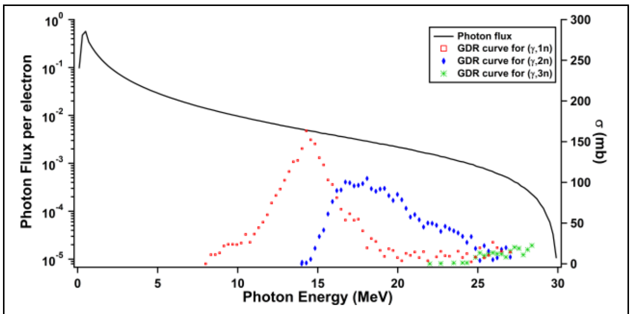


Fig. 1. The reaction cross-sections for (γ, n) (γ, 2n) and (γ, 3n) reactions on $^{100}$Mo along with the photon flux obtained from tungsten target using GEANT4 simulations.

By calculating the area under the GDR curve for three (γ, xn) reactions and photon flux curve, it is found that about 55% of the total neutron flux comes from (γ,1n) whereas the rest of the neutrons come from other (γ, xn) reaction channels. Therefore, Activity using neutron flux can be obtained as follows-

Email:skaqsa.95@gmail.com,tanuja@sameer.gov.in,abhay@sameer.gov.in,krishnan@sameer.gov.in

$$A = 0.55 N_{Mo} \qquad (1)$$

Where, $N_{Mo}$ is the neutron flux coming out of $^{100}$Mo. According to the above equation, activity calculation in direct target approach completely depends upon neutron flux obtained from GEANT4 simulations. Hence validation of neutron flux data is done by comparing values given in Barber and George [4]. For the given initial condition of 1 radiation length (r.l.) of Molybdenum target (9.594mm) hit by 34.3 MeV electron beam, neutron flux obtained from GEANT4 is $10.63\times10^{-4}$ n/e. After performing the normalization with experimental neutron flux from lead given in the table. II of [4] the neutron flux value from Molybdenum changes to $12.28\times10^{-4}$ n/e. This value can be compared with the interpolated value of $12\times10^{-4}$ n/e given in [4].

## TARGET THICKNESS OPTIMIZATION

Using GEANT4 simulation, an electron beam of 30MeV is hit on $^{100}$Mo target and neutron flux is found out. This neutron flux is used in equation (1) to estimate the photo-neutron reactions leading to the production of $^{99}$Mo. Activity calculations for different thicknesses of $^{100}$Mo target are done using equation (1) and GEANT4 simulations. The plot in figure 2 shows that for thicknesses above 1-2 radiation length of the target, there is no appreciable increase in the activity.

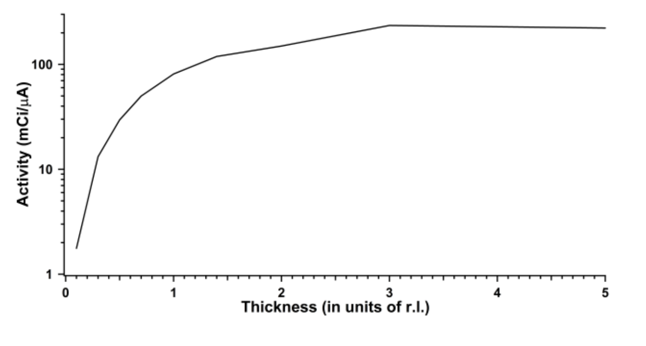


Fig. 2. Change in $^{100}$Mo activity through direct target approach with increasing thickness of $^{100}$Mo target

$^{100}$Mo is an expensive material. So, increasing its thickness beyond an appreciable length is not cost effective. It can be seen from figure 3 that increasing $^{100}$Mo thickness from 1.4r.l. to 2r.l. decreases the overall specific activity by 11.96%. Hence, 1.4 r.l. is a reasonable enough thickness for $^{99}$Mo production.

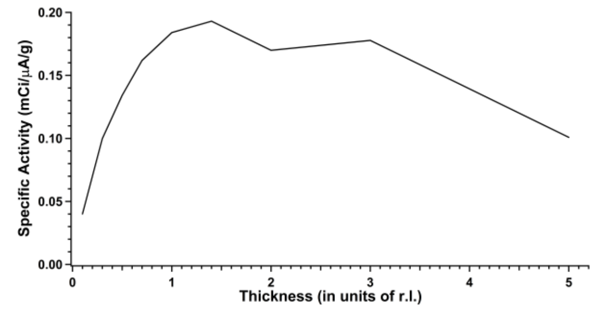


Fig. 3. Variation of specific activity of $^{99}$Mo as a function of $^{100}$Mo thickness in radiation lengths.

## RADIUS OPTIMIZATION

Angular distribution of photon flux suggests that most of the photons from 30 MeV electron beam are generated in forward direction. The radius of cylindrical $^{100}$Mo target can be reduced in order to reduce overall mass of $^{100}$Mo without drastically affecting the activity. Figure 4 compares the increase in mass of $^{100}$Mo and its activity as a function of increasing radius. It is observed that above 4mm of radius the increase in activity is only 17.75%, while mass keeps increasing as square of the radius which accounts for 525% increase in mass up to 10mm of radius. This suggests that increasing the radius of $^{100}$Mo target further than 4 mm is not cost effective for $^{99}$Mo production through direct target approach.

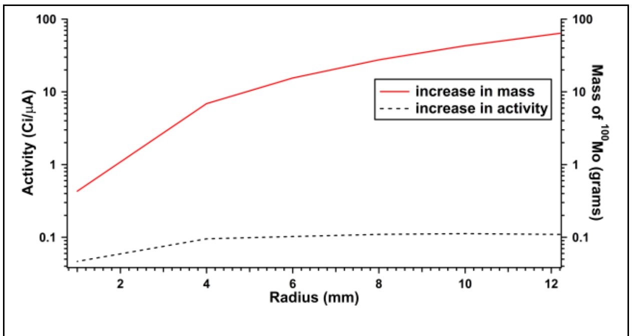


Fig. 4. Comparison of increase in mass and activity of $^{100}$Mo by varying radius of $^{100}$Mo in direct target approach.

## EFFECT OF $^{100}$MO ENRICHMENT

100% enriched $^{100}$Mo is expensive and not easily available. Therefore, it is important to find out how does various level of enrichment affect the total activity. Figure 5 shows the change in activity as $^{100}$Mo enrichment level is changed. For 90% enriched molybdenum target we have considered 10% impurity of $^{98}$Mo and likewise for other enrichment levels too. For our system the change in activity going from 90% to 100% enrichment is calculated to be 8-9%. Calculations done for our 30MeV linac system of 8-10kW the activity obtained from 90%

enrichment is 4.137 Ci/g whereas it is 4.549 Ci/g for 100% enrichment. After comparing the cost of different enriched targets the exact composition of molybdenum target for the experiment will be decided.

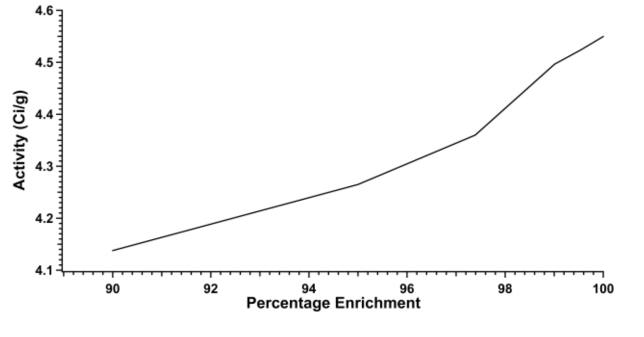


Fig. 5. Effect of enrichment level in molybdenum target on the $^{99}$Mo activity.

## RESULT

Activity calculation is done using the simulation codes GEANT4 and ROOT. For our system namely 30 MeV electron linac with average beam power of 8-10 kW, calculation for direct target geometry gives 4.549 Ci/g of activity for 100% enriched molybdenum target. This is found to be within the suggested range of specific activity by T. Ruth [5].

## DISCUSSION

Geometry of direct target approach facilitates production and complete utilization of photons in all 4 $\pi$ direction, which increases the overall activity, but cooling of molybdenum target becomes very crucial in this approach. Since, the same irradiated target is used for radio-chemistry later on therefore, design of mounting of $^{100}$Mo for irradiation is very challenging. In case of direct target approach calculations are done for $^{100}$Mo of thicknesses 1, 2, and 3 r.l. in order to compare the results with [6]. The activities for 30 MeV electron beam power obtained from equation (1) and GEANT4 simulations for the aforementioned thicknesses are 32.74 Ci/ 26.09 Ci/ 20.12Ci respectively. These values can be compared with the results presented for 50MeV electron beam in [7]. The variation in the activity values are large in most of the references either in converter target approach or direct target approach.

## ACKNOWLEDGEMENT

The author would like to thank Dr. S. V. Suryanarayan and Dr. R. Thomas of Nuclear Physics Division, BARC for their immense help. Author would also like to thank MeitY for supporting the High Energy linac activity for radio-isotope production under grant-in-aid.

## REFERENCES

[1] Aqsa Shaikh, Tanuja Dixit, Abhay Deshpande, R. Krishnan, “Study of direct target approach for the $^{99}$Mo production using high power electron accelerators”, submitted in InPAC (2019), Delhi, India.

[2] “Making Medical Isotopes,” TRIUMF, Report of the Task Force on Alternatives for Medical, Medical Isotope Production, 2008, available: https://www.triumf.ca/reportmedical-isotope-production

[3] Lee Young-Ouk , Chang Jonghwa, Kim Doohwan et al. “High Energy Nuclear Data Evaluations for Neutron-, Proton-, and Photon-induced Reaction Data at KAERI,” Journal of Nuclear Science and Technology, vol. 39, pp. 6063, 2002 available: https://doi.org/10.1080/00223131.2002.10875040

[4] W. C. Barber, W. D. George, “Neutron Yields from Targets Bombarded by Electrons,” Physical Review, vol. 116, no. 6, pp. 1551-1559, 1959, available: https://doi.org/10.1103/PhysRev.116.1551

[5] Ruth, Thomas, “The Medical Isotope Crisis: How We Got Here and Where We Are Going,” Journal of nuclear medicine technology, vol. 42, pp. 245-248, 2014, available: http://tech.snmjournals.org/content/early/2014/11/11/jnmt.1 14.144642

[6] A. Tsechanski, A.F. Bielajew, J.P. Archambault, E. Mainegra-Hing, “Electron accelerator-based production of molybdenum-99: Bremsstrahlung and photo neutron generation from molybdenum vs. tungsten,” Nuclear Instruments and Methods in Physics Research Section B: Beam Interactions with Materials and Atoms, vol. 366, pp. 124-139, 2016, available: https://doi.org/10.1016/j.nimb.2015.10.057

# FAST ELECTRON ANGULAR DISTRIBUTION FROM THIN FOIL TARGETS AT LASER INTENSITY 7 X $10^{19}$ W/CM$^2$

T. Mandal[†1,2], V. Arora[2], A. Moorti[1,2] and J. A Chakera[1,2]

[1] *HBNI, Training School Complex, Anushaktinagar, Mumbai 400 094*

[2]*Laser Plasma Division, RRCAT, Indore 452013*

***Abstract***

Intense laser produced MeV fast electrons are instrumental for the success of fast ignition concept to inertial confinement fusion along with other applications including development of high energy proton/ion beam and ultrashort duration x-rays. We have performed an angular distribution study of these fast electrons to understand their emission characteristics to be useful for various applications. The experiment was carried out on 150 TW laser facility with 25 fs, 2.2 J Ti:Sa (operated at 88 TW) laser beam focused by an off-axis parabolic mirror to an intensity ~ $7 \times 10^{19}$W/cm$^2$ on a Cu foil of thickness 7µm at an incidence angle of 40°. The electron beams were observed along laser propagation direction through the target rear surface indicating the JXB heating mechanism for fast electron acceleration. Further, highly collimated (divergence angle <10°) electron beams were also observed both along target front and rear surface direction suggesting the role of surface generated quasistatic fields in collimating and guiding the electrons along the target surface. The electron flux reduced by ~ 2.8X on reducing the laser intensity by a factor of ~2.5. Further, the electron flux reduced by a factor of ~2.4 on changing the laser polarization from p to s. The measured spectrum of electron energy extends up to ~7 MeV with a derived electron temperature of ~2.1 MeV. The fast electron emission angle changes from nearly laser propagation direction to target surface direction in the specular side with a higher beam charge on increasing the incidence angle form 40° to 70°. Further, we have observed increase in electron beam charge for s polarization compared to p. In this paper details of experimental setup and our current understanding on the results are presented.

## INTRODUCTION

Study of energetic fast electron generation in the context of ultra-high intensity laser solid interaction is a matter of prime importance due to its widespread applications ranging from ultrashort electron diffraction [1], creating warm dense matter to fast ignition approach in inertial confinement fusion [2]. Further, these electrons dictate the condition for the generation of high energy proton/ion beams [3] and ultrashort duration x-rays [4]. However, understanding the fast electron generation and acceleration mechanisms still remains one of the important and alluring subjects for researchers due to its very complex and interdisciplinary nature. Until now, a number of known generation mechanisms such as resonance absorption, vacuum heating, JXB heating [5], surface acceleration [6] has come up which are specific to various laser matter interaction conditions. However, most of the experimental observations in the literature concentrate in particular absorption mechanisms. Therefore, finding the linkage and inter-changeability between these mechanisms through variation of interaction condition is still an open issue. With the improvement of laser power to hundreds of TW to PW range, huge range of interaction conditions (in terms of laser intensity, preplamsa condition etc.) are now accessible to researchers to explore the opportunities. The experimental study reported here aims to understand the different fast electron generation/acceleration mechanisms through various laser parametric variations at laser intensity of $7 \times 10^{19}$ W/cm$^2$.

In this paper, we report experimental study of angular distribution of electrons emitted during interaction of ultrashort laser pulses with thin metal foil at the above laser intensity. A stream of energetic electrons (energy extending up to ~7 MeV with a temperature of ~2.1 MeV) was observed along laser propagation direction. The flux of these forward electrons reduced by ~ 2.8 X when the laser intensity was decreased by a factor of ~2.5. Further, highly collimated electron beams were also observed along the non-specular target surface direction both in target front and rear side. The electron emission angle changes from nearly laser propagation direction to target surface direction with a higher beam charge on increasing the incidence angle form ~40° to ~70°. The electron charge further increased when the polarization was changed from p to s which was opposite a trend for lower incidence angles.

## EXPERIMENTAL SETUP

The experiment was performed with 150TW Ti:Sapphire laser facility at RRCAT, Indore with a maximum laser energy of ~2.2J and pulse duration of 25fs (FWHM). The schematic of the experimental setup is shown in Fig 1. The laser beam was focussed using a dielectric coated off axis parabolic mirror (F/2.4) to a focal spot of 7.4µm x 5.2µm (FWHM) which contains ~24% of laser energy. The peak laser intensity was calculated to be ~7 x $10^{19}$ W/cm$^2$. The contrast of the ASE prepulse at 1ns was measured to be better than $2 \times 10^{-10}$ while for replica fs prepulse coming 11ns prior to main pulse, the contrast is measured to be $>10^{-7}$. The laser beam was focused on Cu foil targets at different incidence angle ranging from 30° - 70°.

* Work supported by the Dept. of Atomic Energy, India

† tirtham@rrcat.gov.in

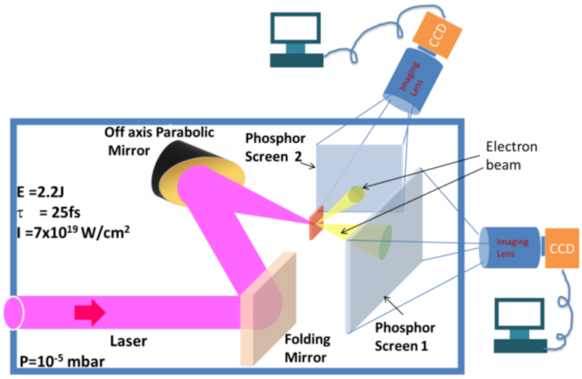


Figure 1: Schematic of the experiment setup for electron angular distribution measurement

The electron beam emanating from the target surface was detected in a single laser shot directly by $Gd_2O_2S$:Tb phosphor screens attached to CCD cameras. Two such phosphor-CCD setups were utilized to cover the nearly ~180 degrees angular range around the laser axis. One is kept in laser propagation direction and the other on side of the laser beam. The front and side setups cover an angular range of 30° to -80$^o$ and -100° to -140° w.r.t laser axis respectively. An Al filter of ~500µm thickness was kept in front of both the phosphor screens. The cut-off electron energy reaching the phosphor screen was calculated to be ~350 keV. Energy spectrum of the forward electron beam was also measured using an magnetic spectrograph. The spectrograph consists of a rectangular dipole magnet with magnetic field of ~700G and a phosphor screen as a detector.

## RESULTS

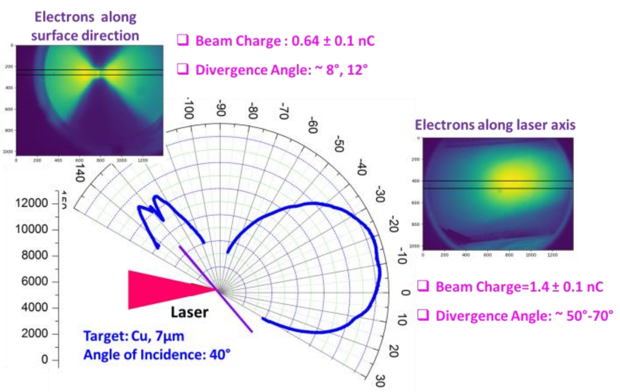


Figure 2: Polar plot of electron angular distribution with electron beam profiles as shown in insets. The flux in both direction are in arbitary unit (a.u) and are not relative to each other. The laser and the target foil is indicated by the red arrow and the purple line respectively.

Figure 2 shows the angular distribution of the emitted electrons as detected by the phosphor-CCD setups at an incidence angle of ~40°. The inset shows the actual electron beam profiles. Prominent electron beams has been observed along laser propagation direction and target surface direction. The forward electron beam is much broader with divergance angle of ~50-70° whereas the surface electron beams are much more collimated in nature with divergnce of ~8°-10°. The electron charge was calculated to be ~1.4 ± 0.1 nC and ~0.64 ± 0.1 nC for the forward beam and the surface beam respectively. Energy spectra analysis of the forward beam showed maximum energy up to ~7 MeV with a Maxwellian energy distribution having electron temperature of ~2.1 MeV.

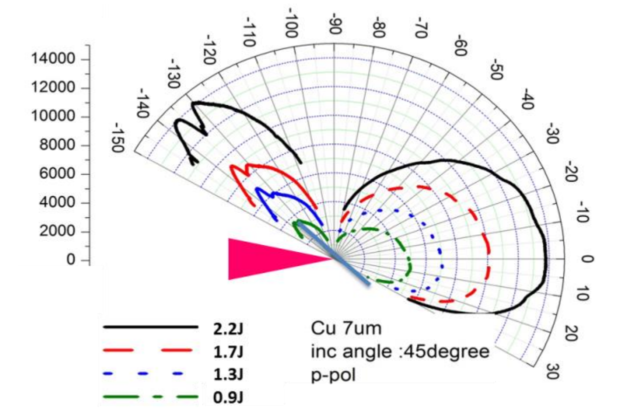


Figure 3: Polar plot of fast electron angular distribution for four different laser energy.

Figure 3 shows the polar plot of the fast electron angular distribution for four differnet laser energy from 2.2 J to 0.9 J. The corresponding change in laser intensity is from ~7x10$^{19}$ W/cm$^2$ to 2.8x10$^{19}$ W/cm$^2$. The study was done for 7µm thick Cu foil at an incidence angle of 45°. It was found that the overall electron distribution pattern remains similar throughout the laser intensity range. However, the flux of the forward and the surface electrons in incidence plane reduced ~ 2.8 X and ~4 X respectively on decreasing the laser intensity by a factor of 2.5. The result shows that the laser to fast electron conversion efficiency remains nearly same throughout the intensity varaition for the forward beam. Further, for the surface beam flux at the rear side decreased more rapidly compared to that at front side when the intensity was reduced.

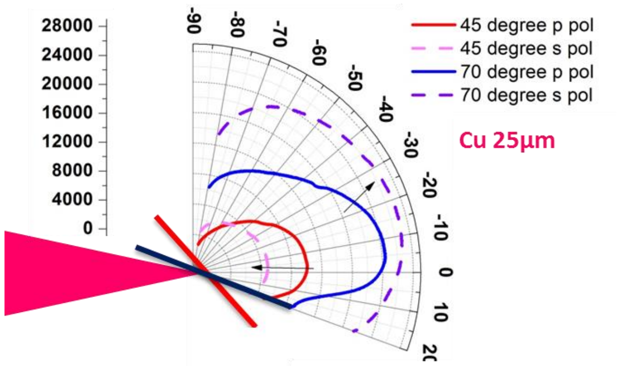


Figure 4: Polar plot of fast electron angular distribution for two different incidence angles with two different (p and s) polarization.

Figure 4 shows the polar plot of fast electron angular distribution for incidence angles of 45° and 70°. It was observed that the fast electron emission angle changes from laser propagation direction to target surface direction on increasing the incidence angle from 45° to 70°. Further, the beam flux increases with increase in incidence angle. The laser polarization was also changed from p to s for both the incidence angle by inserting a half wave plate in the laser path after compressor. Polarization dependence on electron flux showed very interesting and different trends. For example, at 45° incidence angle, the flux reduced (~ 1.6 X) whereas for 70° incidence angle, the flux increased (~ 1.1 X) on changing the polarization from p to s. It was also noted that the electron emission for s polarization for 70° was more isotropic unlike the p polarized case.

## DISCUSSION

Fast electron generation and it's angular distribution in high intensity laser foil interaction mainly depends on the laser interaction condition. At relativistic intensities (I > $10^{18}$ W/cm$^2$), the electron motions are highly directed along the laser axis and the most dominant mechanism is J X B heating where electrons are generated along laser propagation direction [5]. The observation of electron beam in the laser propagation direction for 40° incidence angle indicates that they are indeed accelerated by JxB heating mechanism. Further, the measured temperature ~2.1 MeV from the the electron spectra is close to the calculated temperature (~2.9 MeV) from ponderomotive scaling applicable for JxB heated fast electrons. This reconfirms the applicability of J X B heating mechanism in the present experimental condition.

Further, the presence of electrons along non-specular target surface direction indicates that some electrons are also guided through the push pull effect by the quasistatic electric and magnetic fields present on the surface. The quasi-static magnetic field is generated by the non-colinearity of density and temperature gradient as well as from the return current. This field tries to push the electrons in the vacuum region. On the other hand, the attractive quasi-static electric field created by the space charge on the target surface tries to pull back the electrons into the target. Under this push–pull process, some of the electrons are confined and guided along the target surface. Therefore, presence of both forwardly moving electrons as well as surface electrons in the same interaction condition indicates that multiple fast acceleration mechanisms coexists simulteneously. However, the total charge of surface electrons are much lesser than the forwardly moving electrons indicating the dominance of JXB heating over surface acceleration at 40° incidence angle.

When the incidence angle was increased to 70°, the forwardly moving electrons changes towards surface direction with higher charge. This shows the dominance of surface acceleration of electrons at higher incidence angle as more surface fileds are generated in such condition as shown by others [7].

The reduction of electron flux on changing the polarization form p to s at 45° incidence angle indicates that some polarization depenndant mechanims such as resonance absorption is responsible for generation of low energy fast electrons at lower intensity (at the rising edge of the laser pulse) which are later accelerated by the JXB heating mechanism. The increase in electron flux and near- isotropic distribution of electrons for s polarization at 70° incidence angle is a new and interesting observation which hints towards a uncommon acceleration mechnism. However, more expimentaions are required to gather more insights on this phenonmena.

In conclusion, we report the angular distribution of electrons in ultrahigh intensity laser foil interaction at intensity of ~ 7 x $10^{19}$ W/cm$^2$. MeV fast electrons were found along laser propagation direction due to JXB heating mechanism. Further, highly collimated electron beams were also observed along the non-specular target surface direction which is explained by acceleration of electrons in presence of surface fields. The near-linear reduction of electron flux with laser intensity for forward fast electrons shows that the laser to fast electron conversion efficiency is nearly same throughout the intensity range of ~7x$10^{19}$ W/cm$^2$ to 2.8x$10^{19}$ W/cm$^2$. Increase in laser incidence angle form ~45° to ~70° showed a change in electron emission angle from laser propagation direction to target surface direction. It clearly indicates a change of dominance of electron acceleration mechanisms from JXB heating to surface acceleration by the influence of quasistatic surface fields at increased incidence angle interaction.

## ACKNOWLEDGEMENTS

The authors acknowledge the laser operation support provided by Shri R.A. Khan, and Shri Ankit, and Shri D. Karmarkar for helping laser operation and providing support in setting up plasma chamber during the experiment

## REFERENCES

[1] S. Tokita, S. Inoue, S. Masuno, M. Hashida, and S. Sakabe, Appl. Phys. Lett. **95**, 111911 (2009).

[2] M. Tabak, J. Hammer, M. E. Glinsky, W. L. Kruer, S. C. Wilks, J. Woodworth, E. M. Campbell, M. D. Perry, and R. J. Mason, Phys. Plasmas 1994-Present **1**, 1626 (1994).

[3] A. Macchi, M. Borghesi, and M. Passoni, Rev. Mod. Phys. **85**, 751 (2013).

[4] T. Mandal, V. Arora, M. Tayyab, S. Bagchi, R. Rathore, B. Ramakrishna, C. Mukharjee, J. A. Chakera, P. A. Naik, and P. D. Gupta, Appl. Phys. B **119**, 281 (2015).

[5] T. Mandal, V. Arora, A. Moorti, A. Upadhyay, and J. A. Chakera, Phys. Plasmas **26**, 013103 (2019).

[6] T. Mandal, V. Arora, B. S. Rao, A. Moorti, A. Upadhyay, and J. A. Chakera, Phys. Plasmas **26**, 043105 (2019).

[7] Y. T. Li, X. H. Yuan, M. H. Xu, Z. Y. Zheng, Z. M. Sheng, M. Chen, Y. Y. Ma, W. X. Liang, Q. Z. Yu, Y. Zhang, F. Liu, Z. H. Wang, Z. Y. Wei, W. Zhao, Z. Jin, and J. Zhang, Phys. Rev. Lett. **96**, 165003 (2006).

# QUASI MONO-ENERGETIC PROTON ACCELERATION FROM THE INTERACTION OF HIGH INTENSITY SHORT PULSE LASERS WITH THIN FOIL TARGET

M. Tayyab*[1,2], S Bagchi[1], A. Moorti[1,2] and J. A Chakera[1,2]
[1] Laser Plasma Division, RRCAT, Indore 452 013
[2] Homi Bhabha National Institute, Anushakti Nagar, Mumbai 400 094

*Abstract*

High energy ion beam having some unique characteristics are generated in the interaction of high intensity laser pulse with thin foil targets. Ions are accelerated by the extremely high accelerating field (~TV/m) set up by the high energy electrons streaming at the target vacuum interface at the rear side. The acceleration process, widely referred as Target Normal Sheath Acceleration (TNSA), generally give rise to ion beam with continuous energy distribution. In this paper, we present observation of proton beam with low energy spread from thin foil target irradiated by 25 fs, 150 TW laser system. The laser pulse is focussed on an Al 0.75 µm thick target at an angle of 30° with respect to normal to a focal spot diameter 5 µm. The resultant laser intensity on the target was ~ $10^{20}$ W/cm$^2$. The ion emission was recorded along rear surface normal direction using in-house developed Thomson Parabola Ion Spectrograph (TPIS). We have observed background free quasi-monoenergetic protons of peak energy ~ 3 MeV and energy spread ~ 40% at FWHM. The laser interaction condition suggests that the collisionless shock wave generated by the intense laser pulse can be attributed for the observed plateau and peaks in proton energy spectrum.

## INTRODUCTION

Ion acceleration using high intensity ultra-short laser pulses is an interesting area of research due to its potential as a compact and cost effective ion source. The unique characteristics like ultrashort ion bunch duration (~ ps), low transverse emittance and high peak current make the laser driven ion sources even more attractive for different applications [1,2]. However, there are several challenges, viz. increasing the maximum achievable energy, reduction in energy spread and increase in laser to ion conversion efficiency; which needs to be addressed for the laser driven ion source to become a potential alternative to conventional ion accelerators.

When an intense, ultra-short laser pulse interacts with a thin foil (~µm) target, the laser pulse energy gets absorbed into the plasma through different absorption mechanism leading to generation of high energy electrons, the so called hot electrons. The hot electrons traverses through the foil material and reach at target rear side where they form a sheath field. The value of the sheath field is quite large in the range of ~$10^{12}$ V/m. The field is so strong that it ionizes and accelerates the atoms present at target rear surface. The process is widely referred to as Target Normal Sheath Acceleration (TNSA) mechanism [3]. As the accelerating sheath field is spatially and temporally non uniform, the accelerated ionic species normally exhibit broad energy distribution. Using some advanced target design, and energy selection devices, spectral narrowing of the TNSA accelerated ion beam have been demonstrated, mainly as proof of principle experiments [4,5]. In addition, few advanced acceleration mechanisms [1,2] like Radiation Pressure Acceleration (RPA) and Collisionless Shock Acceleration (CSA), are also being studied which can give rise to narrow energy spread ion beam. However, unlike TNSA, the experimental realization of these mechanisms is quite challenging. Nevertheless, there are some successful experimental demonstrations of quasi-monoenergetic ion beam using these advanced acceleration mechanisms. In this paper, we present results on quasi-monoenergetic proton bunches which were observed in our recent experiment. The experimental conditions suggest that the collisionless electrostatic shock generated during the laser foil interaction is mainly responsible for quasi-monoenergetic proton beam.

## EXPERIMENTAL SETUP

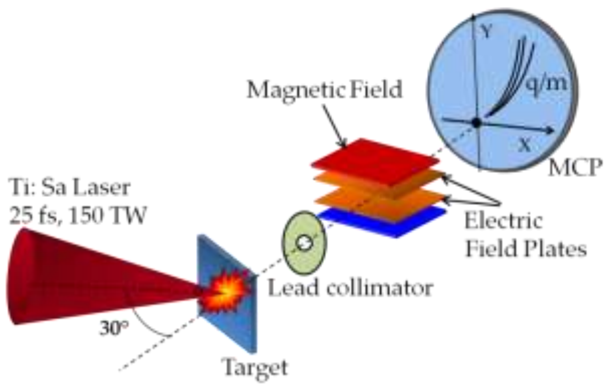


Figure 1: Schematic of the experimental setup.

The experimental scheme is shown in Fig. 1. The p-polarized, 25 fs laser pulse~~s~~ from 150 TW Ti:Sa laser system was focused using an off axis parabolic mirror on to the Al foil target of 0.75 µm thickness at 30° angle of incidence. The resulting peak intensity on to the target was ~ $10^{20}$ W/cm$^2$. During this experiment the laser pulse energy used was ~2.2 – 2.4 J i.e. ~90 - 95 TW laser power at 25 fs laser pulse duration. Ion emission was recorded along rear surface normal direction using an in-house

* tayyab@rrcat.gov.in

developed TPIS. First the ions are collimated using a lead collimator of 100 µm diameter and then deflected by parallel electric and magnetic field. A two dimensional ion sensitive detector MCP with phosphor screen is used to detect the ions. The incoming ions are dispersed into different parabolic traces as per their charge-to-mass (q/m) ratio. The deflection along a particular ion parabola gives the energy information. The light output of the phosphor is imaged by an EMCCD camera. The MCP and EMCCD combination enables the online monitoring of the accelerated ionic species on single shot basis. The captured image is then post processed using an in-house developed analysis routine to generate the ion energy spectrum.

## RESULTS AND DISCUSSIONS

A typical ion traces recorded using TPIS from 0.75 µm Al foil target is shown in Fig. 2 (a). The parabolic traces of $H^+$ (protons) and carbon ions can be clearly observed. The source of protons and carbon ions is the hydrocarbon contaminants which is normally present on the target surface at target chamber vacuum level ~ $10^{-5}$ mbar. Being lighter, protons and carbon ions are more preferentially accelerated. The proton energy spectrum is plotted in Fig. 2 (b).

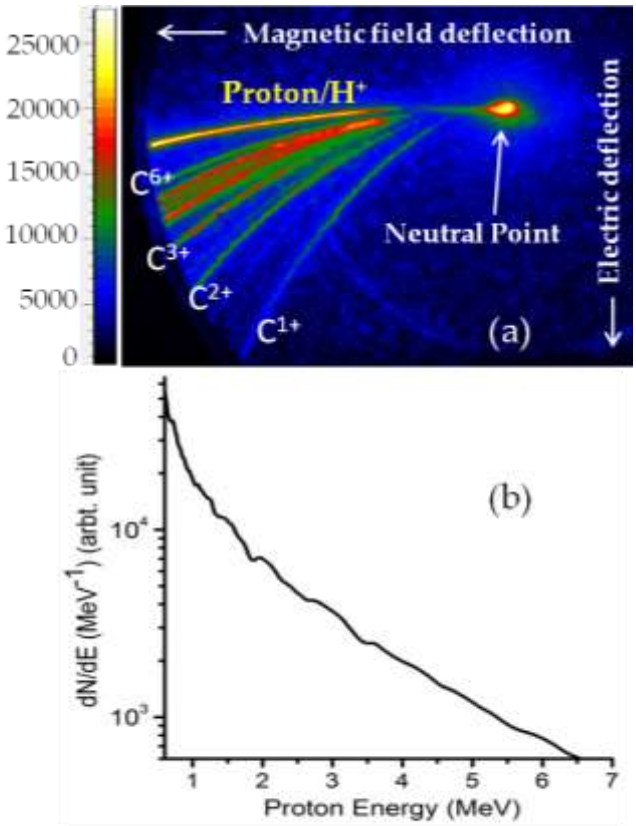


Figure 2: (a) Typical proton and carbon ion signal recorded using TPIS. The central bright spot is called "neutral point" formed due to neutral particles and photons. (b) Retrieved proton ($H^+$) energy distribution.

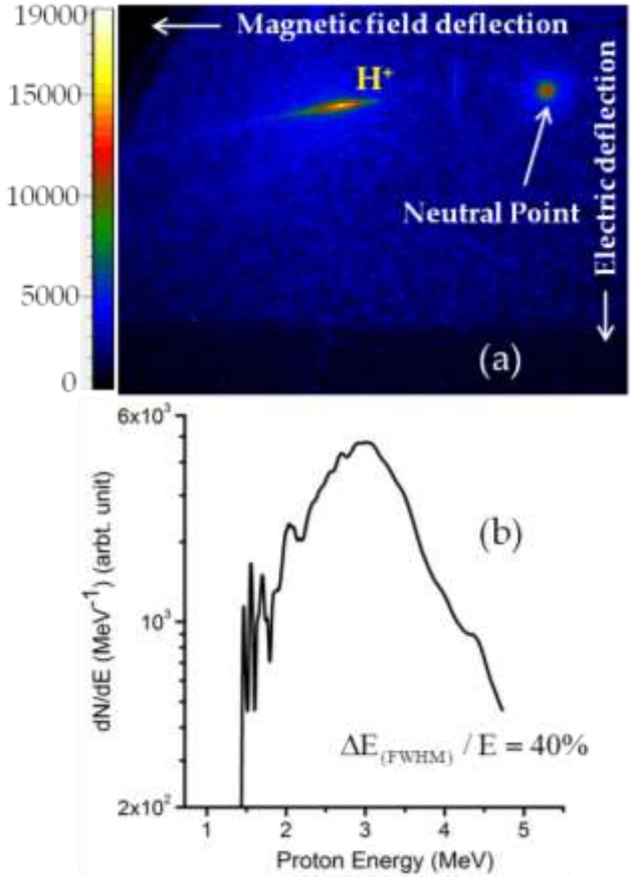


Figure 3: (a) Observation of mono-energetic H+ emission recorded in TPIS. Notably, the "neutral point" is not so bright. Under close inspection, it appears to be hollow. (b) Retrieved H+ energy distribution exhibiting a relative energy spread of ~ 40% at a mean energy around 3 MeV.

One can note that the energy spectrum is mainly continuous or have broad energy distribution with exponentially decaying profile. Along with this, during the experiment, in 35-40% of the shots we observed either plateau, a plateau with hump or clear peak in proton energy spectrum. A representative shot in which we observed background free proton bunch from 0.75 µm Al foil target is shown in Fig 3 (a). The energy spectrum is plotted in Fig. 3 (b). The energy spread (ΔE/E) is ~ 40% (FWHM) at peak energy around 3 MeV. It may be mentioned here that in our earlier experiments using 0.75 µm Al target, we did not observe similar features in proton energy spectrum, where the peak laser intensity was lower (~ $3\times10^{19}$ W/cm$^2$) as compared to present case.

The observed proton energy spectrum is unlike the TNSA accelerated proton beam which mostly exhibits broad energy distribution with exponential profile as discussed above (See Fig.2). Another acceleration mechanism which can be very effective in present experimental conditions is the Collisionless Shock Acceleration (CSA) first proposed by L. O. Silva et al. [6]. Through PIC simulation they have shown that an electrostatic shock wave can be generated in a dense plasma slab over wide range of laser and target parameters. The shock wave propagates inside the plasma slab and reflects the upstream ions with a velocity twice the shock velocity. The characteristic feature of shock acceleration is the appearance of plateau and hump in ion energy spectrum. The scheme is recently investigated by several other groups both experimentally and theoretically [7–9]. It comes out that a strong collisionless shock wave can be generated in near critical density plasma tailored in such a way so as to have exponentially decreasing density profile at target rear side. The laser pulse gets efficiently absorbed in near critical density plasma leading to strong heating of plasma volume. The heated plasma expands and due to the density discontinuity at rear side; a strong electrostatic shock is generated which can reflect the upstream ions to high velocity with nearly mono-energetic features. In such laser and target conditions the TNSA is not very effective. However, in some intermediate scenario both TNSA and CSA can be applicable and gives rise combined ion acceleration with peak and plateau superimposed on high energy side of the spectrum.

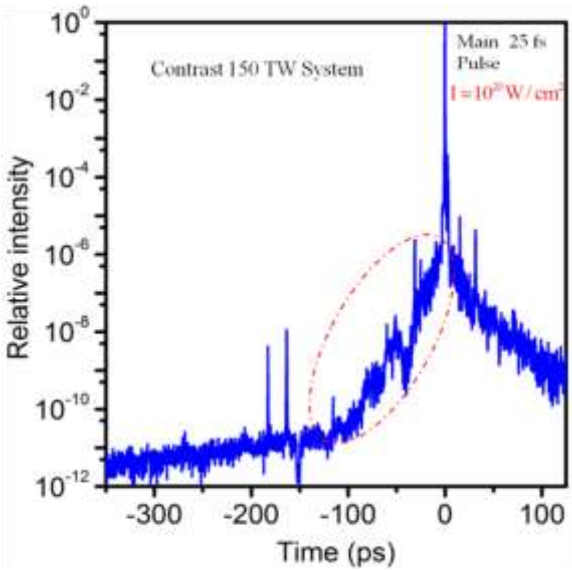


Figure 1: Laser pre-pulse contrast of 25 fs, 800 nm, 150 TW system as measured with a third order auto-correlator.

One can easily correlate the observed proton energy spectrum with the characteristic features of CSA mechanism. Now the question is what experimental parameters have led to the suitable condition for strong shock generation. A closure inspection of the laser irradiation parameters and experimental signatures strongly suggest the efficient collisionless shock generation in the present condition. Here, the peak laser intensity is quite high ~ $10^{20}$ W/cm$^2$. Even though, the laser has quite high contrast, but due to the overall increased intensity, the exponentially rising pre-pulse (Fig. 4, starting from -150 ps) is now strong enough to preheat the Al 0.75 µm thick target. The heated Al foil along with attached hydrocarbon layer expands reducing the target density. The target may eventually become a near critical density plasma. A strong evidence supporting this is the characteristic change of neutral spot image whenever peaks appears in proton energy spectrum. Reduced x-ray emission and even hallow neutral spot (compare neutral spot of Fig. 2 (a) and Fig. 3 (a)) was always observed with the appearance of quasi-monoenergetic features in proton energy spectrum. Now, when the main femtosecond laser pulse arrives, it interacts with the expanded and near critical density target plasma and thus gets efficiently absorbed. The subsequent expansion of the target leads to the generation of shock wave that reflects and accelerates the upstream protons to high velocities and with quasi-monoenergetic features.

## CONCLUSION

In conclusion, we have observed quasi-monoenergetic features (e.g. plateau, a plateau with a hump and well separated bunch) in proton energy spectra generated in intense ultra-short laser foil interaction. The laser irradiation condition suggests that the collisionless shock wave generated by the high intensity laser pulse is mainly responsible for observed plateau and peaks in proton energy spectrum.

## REFERENCES


[1] A. Macchi, M. Borghesi, and M. Passoni, Rev. Mod. Phys. 85 (2013) 751.
[2] H. Daido, M. Nishiuchi, and A. S. Pirozhkov, Rep. Prog. Phys. 75 (2012) 056401.
[3] S. C. Wilks, A. B. Langdon, T. E. Cowan, M. Roth, M. Singh, S. Hatchett, M. H. Key, D. Pennington, A. MacKinnon, and R. A. Snavely, Phys. Plasmas 8 (2001) 542.
[4] B. M. Hegelich, B. J. Albright, J. Cobble, K. Flippo, S. Letzring, M. Paffett, H. Ruhl, J. Schreiber, R. K. Schulze, and J. C. Fernández, Nature 439 (2006) 441.
[5] H. Schwoerer, S. Pfotenhauer, O. Jäckel, K.-U. Amthor, B. Liesfeld, W. Ziegler, R. Sauerbrey, K. W. D. Ledingham, and T. Esirkepov, Nature 439 (2006) 445.
[6] L. O. Silva, M. Marti, J. R. Davies, R. A. Fonseca, C. Ren, F. S. Tsung, and W. B. Mori, Phys. Rev. Lett. 92 (2004) 015002.
[7] D. Haberberger, S. Tochitsky, F. Fiuza, C. Gong, R. A. Fonseca, L. O. Silva, W. B. Mori, and C. Joshi, Nat. Phys. 8 (2012) 95.
[8] A. Pak, S. Kerr, N. Lemos, A. Link, P. Patel, F. Albert, L. Divol, B. B. Pollock, D. Haberberger, D. Froula, M. Gauthier, S. H. Glenzer, A. Longman, L. Manzoor, R. Fedosejevs, S. Tochitsky, C. Joshi, and F. Fiuza, Phys. Rev. Accel. Beams 21 (2018) 103401.
[9] F. Fiuza, A. Stockem, E. Boella, R. A. Fonseca, L. O. Silva, D. Haberberger, S. Tochitsky, W. B. Mori, and C. Joshi, Phys. Plasmas 20 (2013) 056304.

# PRELIMINARY STUDIES TOWARDS DEVELOPMENT OF AN INTEGRATED 2 K REFRIGERATION SYSTEM AT BARC*

Anindya Chakravarty [1,2,#] and D. S. Pilkhwal [1]
[1]Cryo-Technology Division, Bhabha Atomic Research Centre, Mumbai, India
[2]Homi Bhabha National Institute, Mumbai, India.

*Abstract*

Cold compressor based 2 K helium refrigerators are used for large scale superconductivity applications where superfluid helium (He II) is used as a technical coolant. A preliminary study towards development of an integrated 2 K refrigerator, using proposed up gradation of CrTD facilities at BARC, is described in the present article. The applicability of a process cycle, similar to the existing indigenously built BARC LHP50 helium liquefier, is studied and modifications are suggested to arrive at process design for a 2 K refrigerator. Finally, feasibility of developing such a system at CrTD, BARC, with the present and planned augmented infrastructure, is also briefly discussed.

## INTRODUCTION

In order to support R&D programs on superconducting accelerators and other superconducting applications, proficiency in cryogenic technology in general and helium liquefiers/refrigerators in particular, is required. With this aim of developing helium liquefier/refrigerator and associated technologies in the country, a 4.5 K helium liquefier/refrigerator (LHP50) is developed by BARC [1][2]. While operating LHP50 in the liquefier mode, liquefaction capacity in excess of 50 l/hr is achieved during recent runs. Plans are also in place to develop a new Claude cycle based 4.5 K helium refrigerator with the help of local industry. The process parameters of the new refrigerator is available in published literature [3]. In order to realize the full potential of liquid helium (LHE) as a technical coolant, refrigeration temperatures lower than that of lambda point of helium (about 2.17 K) are required (superfluid helium) [4]. Using the experience gained during development of the 4.5 K helium refrigerator at BARC, it is now decided to embark upon the development of an integrated 2 K helium refrigeration system. The work described in this article includes a preliminary study involving the process modifications required in the 4.5 K helium refrigerator/liquefier in order to achieve 2 K refrigeration. The feasibility of developing such a system at CFB, BARC is also described briefly.

## PROPOSED NEW CLAUDE CYCLE BASED 4.5 K HELIUM REFRIGERATOR

The process cycle of the proposed new 4.5 K helium refrigerator/liquefier is shown in figure 1. When compared with the already developed LHP50 [1] [2], the pre-cooling is provided by a liquid nitrogen (LN2)/ cold gaseous nitrogen (GN2) circuit instead of the high pressure (HP) turboexpander used in LHP50 [1][2]. Thus, the proposed new Claude cycle helium refrigerator is designed to operate with only two process turboexpanders as against the three used in LHP50. This is now possible to achieve because of the R&D program on centrifugal turbomachines at BARC that has enabled the development of new cryogenic turboexpanders capable of taking up high pressure ratios. The Claude cycle process consists of 8 heat exchangers in total, two of these being multi-stream (3 stream heat exchangers PFHE1 and PFHE4). The high pressure (HP) helium gas from the process compressor enters PFHE1, where it is cooled by the return low pressure (LP) helium stream as well as the GN2 stream in the LN2 pre-cooling mode. When LN2 pre-cooling is not desired, sensible heat is exchanged only between the HP and LP streams. Further, the HP stream gets cooled in the LN2 bath (in LN2 pre-cooling mode only) and subsequent array of heat exchangers from PFHE2 to PFHE7. In between, prior to PFHE3, a part of the HP stream is bifurcated and expanded through a series of two turboexpanders (TEX1 & TEX2) interspaced by PFHE4, which constitute the second of the multi-stream heat exchangers. The stream expanded through TEX meets the LP return stream at the entrance of PFHE5. BSCV4 and BSCV5 are JT valves through which the HP stream expands to LP to form helium mist. The helium mist is sent to the helium receiver vessel using a coaxial transfer line. In this receiver vessel, the mist is separated out into gas and liquid components, the liquid is collected and the gas is returned to the cold box LP interface through the transferline, thus forming the cold return stream (LP) that cools down the incoming HP stream in the heat exchangers.

## MODIFICATIONS IN THE CLAUDE CYCLE FOR 2 K REFRIGERATION

The simplest way to achieve 2 K refrigeration is to evacuate a 4.5 K liquid helium bath so that the vapour pressure is reduced to about 31 mbar. A process study for development of such a system at CrTD, using existing LHP50 as a back-up refrigerator, has also been completed [5]. The evacuation of the 2 K bath may be carried out using a series of vacuum pumps, as shown in the “bath evacuation” line in figure 2. However, the enthalpy of the cold sub-atmospheric pressure (SP) gaseous helium stream remains un-utilized in the process. For

*Work supported by Bhabha Atomic Research Centre, Mumbai, India
#anindya@barc.gov.in

refrigeration capacities lower than 100 W at 2 K, this mode of bath evacuation, due to its simplicity, is very well suited. However, as the refrigeration capacity requirement for client systems, such as that in a series of superconducting cryomodules, rises to 500 W or more, direct evacuation becomes un-economical. For such large systems, the practice is to employ a series of cold compressors backed up by a warm sub-atmospheric compressor [6][7] in the 2 K helium refrigerator process cycle.

Instead of multi-stage processes reported in literature [6][7], it is decided to develop a 2 K refrigeration process by introducing required modifications in the new Claude cycle refrigerator (4.5 K) process making use of the available compression facility at the CFB, BARC high bay area. Accordingly, few major modifications are required to be implemented as detailed below. The compression from 31 mbar (2 K bath) to the suction of the process compressor may be achieved through a set of 3 cold compressors backed up by a SP warm compressor, as shown in figure 2. From process computations, the temperature of the SP gas stream at the entry of the first cold compressor (CC1) is found to be about 3.5 K while the temperature at the exit of CC3 would be in the range 16 – 20 K. In order the utilize the enthalpy of the cold SP stream gas, an entry of the SP stream to PFHE3 would be necessitated, as the temperature at entry of PFHE4 is typically around 15 K or lower. Thus, all the heat exchangers including and upstream of PFHE3 i.e. PFHE2 and PFHE1 would have to be provided with another channel for the SP stream, when compared to the 4.5 K Claude cycle refrigerator process shown in figure 1. As shown in figure 2, the heat exchanger PFHE1 is now a 4-stream heat exchanger (1 no. each HP, GN2 return, LP return and SP return), while PFHE2 and PFHE3 are both multi-stream heat exchangers (3 streams, 1 No. each HP, LP return and SP return).

Another difference between the two processes is in the HP cold stream. While a Claude cycle liquefier/refrigerator would supply two phase helium mist to a helium receiver Dewar, the 2 K refrigerator provides a super critical cold helium (SHE) stream (3 – 5 bar, 4.5 K – 5 K) to the client 2 K cryostat, as shown in figure 2. Inside the client cryostat, after passing through a SP heat exchanger (to recover some of the cold enthalpy of SP stream before it reaches CC1), the SHE stream expands through a JT valve (BSCV12) to form helium mist (< 2 K) in the 2 K bath vessel. While the liquid component of the mist settles down, the gas is returned to the cold box SP interface through the SP heat exchanger. Inside the cold box, the same SP stream is pressurized using the set of cold compressors and the warm SP compressor, as described earlier.

From preliminary cycle analysis, it may be established that with the process compressor operating between 1.05 bara and 13 bara, for a total HP flow of 62 g/s, a refrigeration capacity of about 100 W at 2 K (~6 g/s of SP flow) is possible without considering LN2 pre-cooling. The process parameters such as state point pressures, turbine circuit flow, etc., used in the computation are same as that for the new Claude cycle refrigerator described in figure 1.

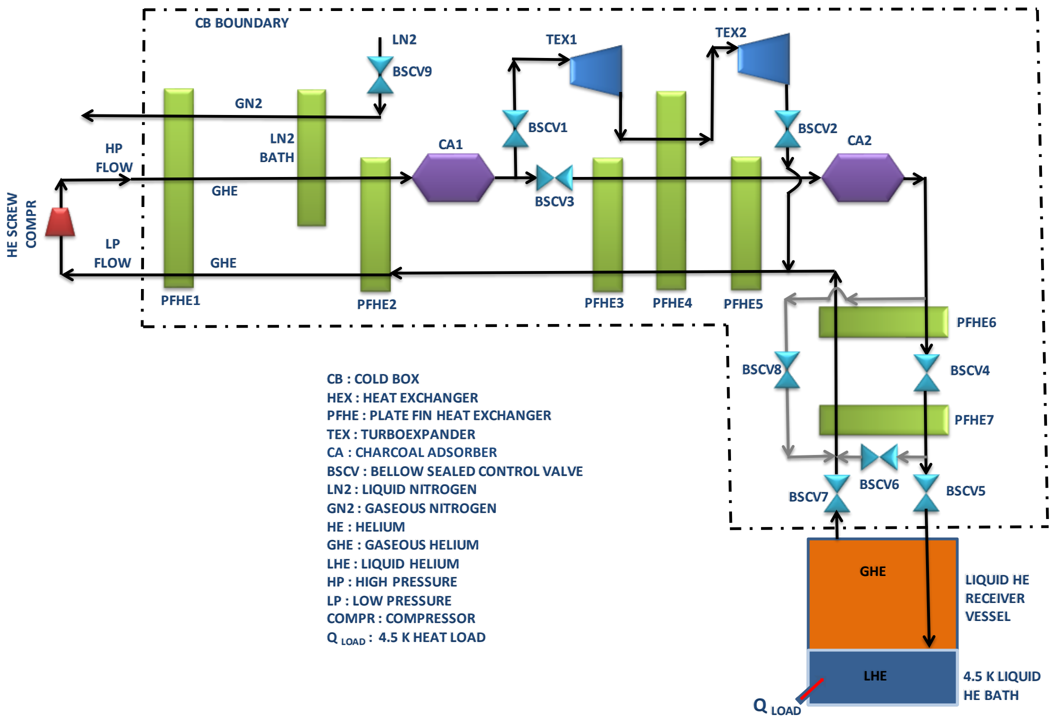


Figure 1: Process schematic of the new Claude cycle 4.5 K helium refrigerator/liquefier to be developed by BARC.

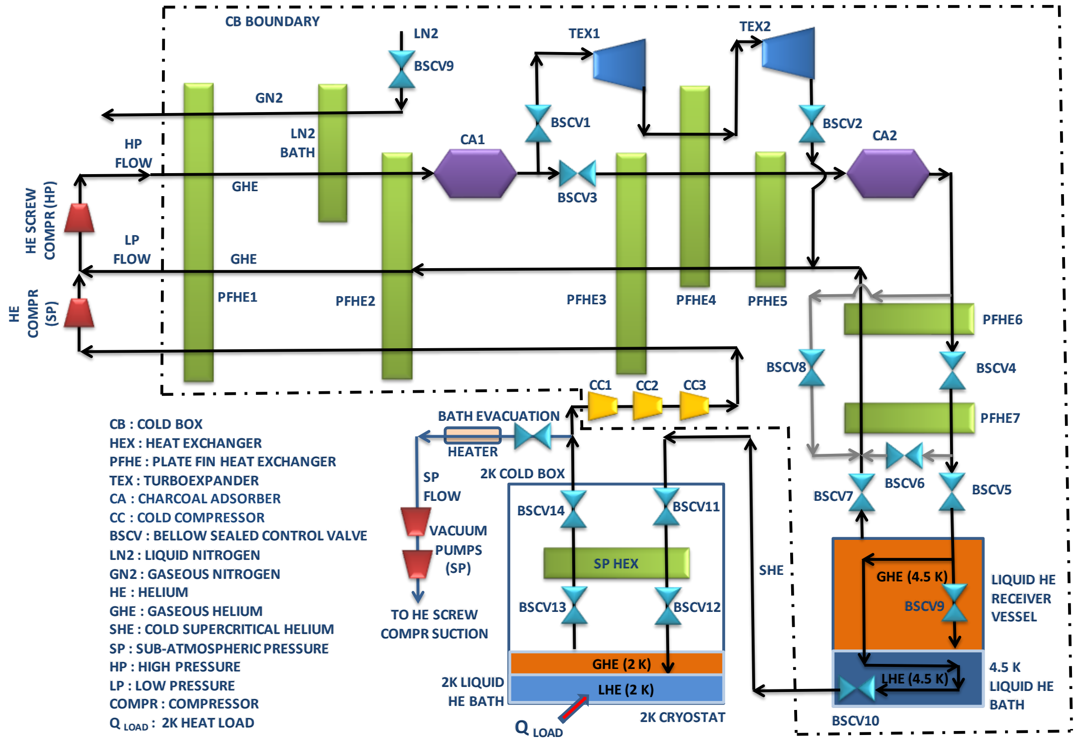


Figure 2: Proposed process modifications to the Claude cycle to achieve 2 K refrigeration at CFB, BARC.

## DISCUSSIONS

At present, the high bay area of CrTD at BARC is equipped with 3 screw compressors that may be used for helium gas. Of these, one compressor (on which the LHP50 as well as the new Claude cycle refrigerator process is based) is in service while the other two are under refurbishment. In tandem, all three would allow the process HP flow to exceed 200 g/s. Moreover, a new compressor shed, that would house a new helium compressor, is planned at the rear of CFB, BARC. Hence, soon, it is expected that the HP flow capacity would rise to about 250 g/s at CFB. With the proposed process shown in figure 2, it may be possible to raise the refrigeration capacity by 4 folds by considering 250 g/s of HP process gas flow when compared to the 62 g/s flow assumed to arrive at 100 W refrigeration capacity. Again, with LN2 pre-cooling, the refrigeration capacity may be further augmented. Increase in 2 K refrigeration capacity is accompanied by corresponding increase in SP gas flow, which would significantly bring down the design speeds of cold compressors and consequently the requirements of high speed motor drive units for the compressors, thus making the technology feasible. The turboexpander design speeds would also come down, enabling the development of more reliable rotors. Thus, on the basis of preliminary process computations, it seems that there is merit to go ahead with the development of a cold compressor based 2 K refrigeration system at CFB, CrTD, BARC.

## REFERENCES

[1] M. Goyal, A. Chakravarty, N. A. Ansari et al, “Recent improvements in the Indigenously Developed Cryogenic Systems at CrTD, BARC”, NSCS-27, IIT Bombay, Jan 2019. (under review for publication in Indian Journal of Cryogenics)
[2] N. A. Ansari, M. Goyal, A. Chakravarty et al, IOP Conf. Series: Materials Science and Engineering 171 (2017) 012007.
[3] M. Goyal, A. Chakravarty and M. D. Atrey, IOP Conf. Series: Materials Science and Engineering 171 (2017) 012091.
[4] P. Lebrun, Cryogenics 34 ICEC Supplement (1994) p. 1.
[5] A. Chakravarty, M. M. Jadhav et al, “Conceptualization and preliminary studies on the development of a 2 K refrigeration system at BARC”, NSCS-27, IIT Bombay, Jan 2019. (under review for publication in Indian Journal of Cryogenics)
[6] B. Hilbert, G. M. Gistau-Baguer and A. Caillaud, AIP Conference Proceedings 613, 225 (2002) 1472025
[7] X. L. Wang, P. Arnold et al, IOP Conf. Series: Materials Science and Engineering 101 (2015) 012012.

# DESIGN AND DEVELOPMENT OF HIGH CURRENT ELECTRON GUN FOR LINEAR ACCELERATOR

S. G. Sarkar[#], L. Mishra, D. Jayaprakash, H. K. Manjunath, J. Mondal, APPD, BARC, Trombay, Mumbai 400085, India

*Abstract*

Electron gun is an essential part of a Linear accelerator (LINAC) system. A high current electron gun has been designed, developed and tested for our electron linac system. Simulations were performed to optimize the gun geometry using 3D code CST Particle Studio. The gun has Pierce geometry with a dispenser cathode of spherical radius and a focusing electrode for focusing electron beam to a small radius. Components of the electron gun were fabricated, assembled and tested at our in-house gun test facility. The cathode was activated and tested for beam emission for two different diode configurations. For the first configuration, maximum current up to 4.3 A was extracted at 50 kV, 10 µs DC pulse voltage. The experimentally measured gun perveance was 0.39 µperv which shows very good agreement with simulated result i.e. 0.4 µperv. For another gun geometry configuration with 1.66 µperv design value, experimentally obtained perveance was 1.42 µperv which is pretty close to the design value. For this diode geometry, maximum electron beam current of 14A was obtained at 50 kV Voltage.

## INTRODUCTION

Electron Linear accelerators (Linac) have various application starting from basic science research to industrial application. APPD, BARC has taken initiative to design and develop high power pulsed electron linac for neutron production. A high power electron linac at 30 MeV is required to produce neutron source for neutron time of flight (n-TOF) application. A high current electron gun which should produce 10 A beam current at 40 KV DC pulsed voltage is required for such application.

A High current dispenser cathode based electron gun has been designed, developed and tested for this application. For simplicity, diode geometry has been considered for the gun design with focussing electrode for focussing the beam to a small beam diameter at the gun exit. For efficient electron extraction, the electron gun geometry has been optimised following beam optics simulation. Two different gun geometry having different values of gun perveance has been designed and optimized. The first gun with perveance of 0.4 µperv is designed to produce 3.2 A of beam current at 40 kV applied voltage. Another gun using the same cathode has been designed to produce gun perveance value of 1.6 µperv.

In this work we presents the design simulation results of electron gun. The paper also includes the experimental characterization results of the both the gun in detail.

## SIMULATION DESIGN OF ELECTRON GUN

Beam optics simulation of the electron gun has been carried out using "Computer Simulation technologies Particle Studio Software" (CST-PS) which analyses the charged particle dynamics in 3D electro magnetic field. The gun is designed to be operated in space charge limited mode and it has a Pierce geometry as shown in Figure 1. The cathode and focusing electrode are kept at negative potential and anode is at ground potential. The cathode used is a dispenser cathode with a spherical radius. The cathode size is selected to meet the beam current requirement.

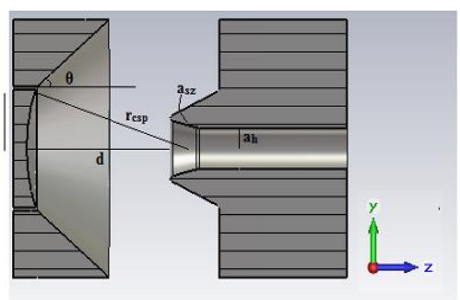


Figure 1 : Electron gun geometry

For the optimized gun design, simulation has been carried out by changing different geometry parameters such as focusing electrode angle (θ), cathode anode distance (d), anode-hole radius ($a_h$) and anode slope etc. The design goal is to achieve the optimized gun geometry to get required perveance and beam diameter at anode exit. For the high perveance gun with 1.6 µperv same anode and focusing geometry has been

*Work supported by …

[#]shreyag@barc.gov.in

used only cathode anode distance has been adjusted to arrive at the required perveance. Figure 2 represents the variation of gun perveance value with anode cathode distance.

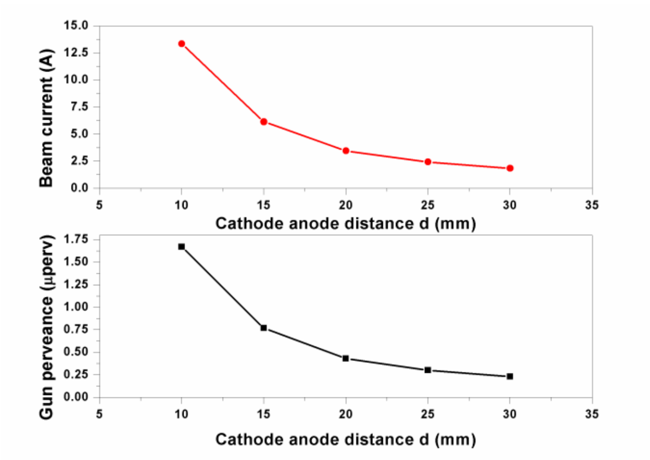


Figure 2: Simulated gun perveance and Beam current as a function of cathode anode distance

Figure 3 shows the optimized geometry of an electron gun of 0.4 µperv with trajectory as simulated by CST Particle Studio. From the figure, it is evident required focused beam of 2 mm is obtained at the anode exit. For the other gun configuration, the simulated beam diameter at anode exit is 14 mm. The simulated beam current is 12.8 A at 40 kV.

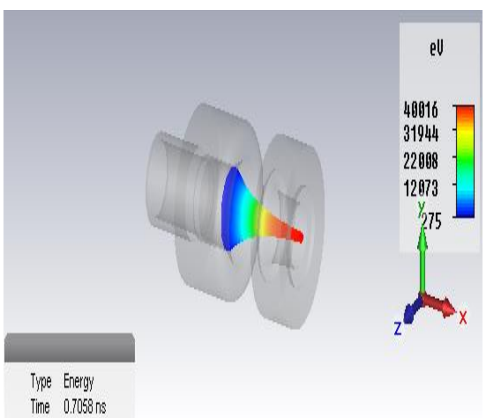


Figure 3: Simulated electron beam trajectory of the gun having 0.4 µPerv

## EXPERIMENTAL METHOD

After the optimization of geometry parameter electron gun components were fabricated, assembled and tested at our in house gun test facility specially developed for electron gun characterization. The test set up is shown in Figure 4 which consists of a vacuum chamber with pumping arrangement. The chamber provides ultimate vacuum up to $2e^{-8}$ mbar. The electron beam current was measured using Fast current transformer (FCT). The gun was operated at pulsed mode i.e. 10 µs pulse of 2 kV to 50 KV was generated using a gun modulator. Two different electron gun were constructed, assembled and tested at our gun test facility. At first, the assembled gun of 0.4 µperv was integrated with test set up and tested for beam emission after the activation of dispenser cathode. Same dispenser cathode was also used and reactivated for the second gun configuration.

Figure 4 : Electron gun test bench set up

## EXPERIMENTAL RESULTS

The beam current of the gun (I) were measured as a function of applied voltage (V) for different filament power. Figure 5 shows the trace of FCT signal of beam current (pink) and applied voltage (yellow) of the gun with 0.4 µperv. FCT has sensitivity of 1.25V/amp. The measured beam current is 3.6 A at 50 kV applied Voltage.

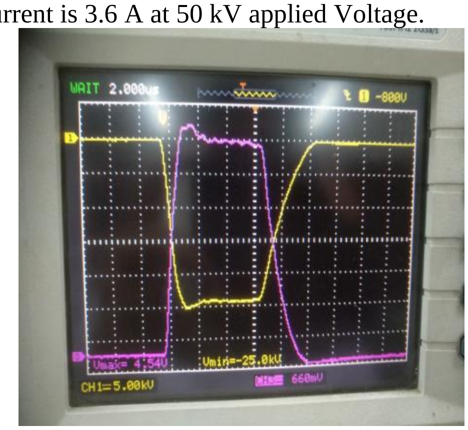

Figure 5: Beam current signal of 3.6 A from FCT at 50 kV, 10 µs pulsed Voltage .

To confirm the operation of the gun in space charge limited mode, experimentally measured beam current is plotted as a function of $V^{3/2}$ as shown in Figure 6. From the figure it is evident the gun is operated at SCL mode. The experimentally measured gun perveance as calculated from the data is 0.39 μperv. Table 1 compares the experimental and simulation result of electron gun having 0.4 μperv which are in good agreement with each other.

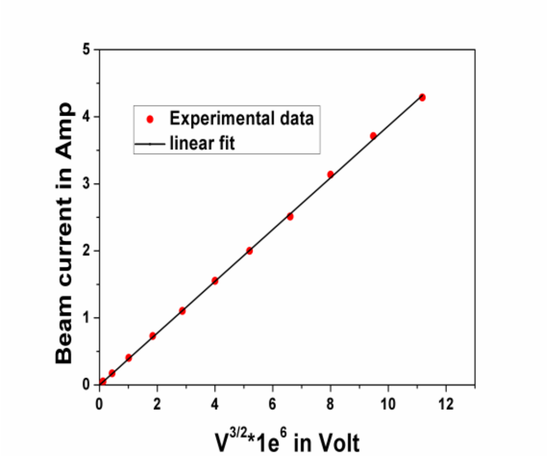


Figure 6 : Experimental and simulation data for gun of 0.4 μperv.

Table 1: Comparison of simulation and experimental results for electron gun

| Parameter | Design values | Measured Values |
|---|---|---|
| Type of Gun | Diode | Diode |
| Beam voltage | 40 kV | 40 kV |
| Beam peak current | 3.25 A | 3.14 A |
| Pulse Duration | 10 μsec | 10 μsec |
| Gun perveance | 0.41 μPerv | 0.39 μPerv |

Figure 7 represents I vs. V characteristics of the electron gun for two different configuration. The plot also compares simulation result with experimental result. From the plot it is evident that for gun having 0.4 μperv, the simulation data is in good agreement with experimental result but for the high perveance gun of 1.6 μperv, the experimental result tends to diverge from the simulation result especially at higher applied voltage. The experimentally measured gun perveance of the gun is 1.42 μperv which is 12.5 % less than the design value. Maximum current of 14 A is extracted for the gun at 50 kV DC pulsed voltage.

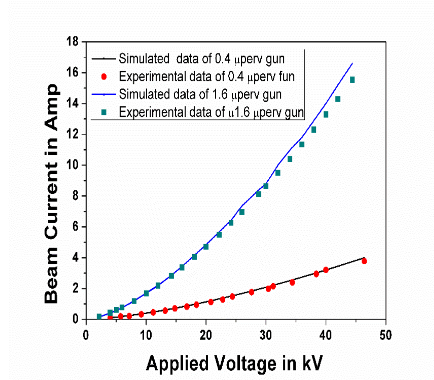


Figure 7 : I vs V characteristics of the electron gun

## CONCLUSIONS

In this paper the design optimization result of an electron gun for a proposed 30 MeV electron linac is presented. Design simulation of the gun has been done using 3D code CST Particle Studio. The gun components were fabricated and tested for two different gun configuration having different values of perveance. The experimental results for medium perveance gun of 0.4 μperv are in good agreement with the design value. The experimental results of high perveance gun of 1.6 μperv differs slightly from the design value. At 40 kV applied voltage, extracted beam current is 11.2 Amp which is 12.5 % less than the design value of 12.8 A.

## ACKNOWLEDGEMENT


The authors likes to thank, Mr. A R Tillu APPD, BTDG and his colleague Mr. H Sarukte for providing the gun modulator for electron gun characterization. Their guidance and expertise have greatly assisted our research work.


## REFERENCES


[1] C.J.Karzmark, *Medical Electron Accelerators*, Department of Radiation Oncology Stanford University School of Medicine (McGraw-Hill, New York, 1993)."

[2] J. R. M. Vaughan, "Synthesis of the Pierce Gun",IEEE T. Electron Devices 28(1), 37 (1981)

[3] B Nayak et al., "Effect of high current electron beam in a 30 MeV radio frequency linac for neutron-time-of-flight applications ", Physics of Plasmas 23 013110 (2016).

[4] CST Microwave Studio®.

# EXPERIMENTS ON A GRIDDED ION SOURCE FOR APPLICATION IN ION THRUSTERS

S. K. Sharma[#], V. Prahlad, B. Choksi, S.L. Parmar, L. N. Gupta, N. Contractor, D. Thakkar, C.B. Sumod, P. J. Patel and U.K. Baruah, Institute for Plasma Research, Gandhinagar, India
Bharat Singh Rawat, Homi Bhabha National Institute, Mumbai, India

*Abstract*

Gridded ion thrusters are used for propulsion of space vehicles in deep space explorations. In these thrusters, a beam of heavy atomic ions, e.g. $Xe^+$ is accelerated by a suitable electric field. Immediately after their extraction, the positive ions are neutralised by supplying an equal flux of free electrons. The thrust is obtained as the reaction force from the accelerated particles. A prototype ion source with magnetic bucket type plasma chamber is used for extracting and accelerating $Ar^+$ ion beam with energies of 1 – 2 keV. Argon plasma with a discharge current of 5 – 30 A is produced in the plasma chamber of the ion source. The corresponding plasma densities and electron temperature are 0.5 – $5\times10^{17}$ $m^{-3}$ and 5eV respectively. A two grid based extractor system with ~1050 apertures, each having diameter of 2 mm is utilised to extract the ion beam current upto 0.1 A. The measured divergences using a Faraday cup array are within 4 – 7 degrees. The maximum ion thrust measured by a load cell is~2.5mN.

## INTRODUCTION

The gridded ion thrusters have shown their effectiveness for the propulsion of space vehicles in deep space explorations [1 – 5]. For example NSTAR (Nasa Solar Electric Propulsion Technology Application Readiness Program) has been a very successful ion thruster used in several deep space programs [1]. NSTAR utilised 30cm ion thruster system and operated for ion beam current, 0.5 – 2.3A and ion beam energy, 1.1kV with 8200 hours of single operation [2]. In the gridded ion thrusters, beam of heavy atomic ions (e.g. $Xe^+$) is accelerated by a suitable electric field. The space charge due to ion beams is neutralised by sufficient electron flux emitted from hot filament/hollow cathodes. The main components of a gridded ion thruster are plasma chamber, extraction-acceleration system, electron emitting cathodes and neutraliser. A prototype experimental ion source, suitable for conducting experiments relevant to gridded ion thrusters, has been developed using in-house facilities at IPR (fig. 1). A magnetic bucket type plasma chamber equipped with hot filament cathode is utilised for plasma production. Two stainless steel grids is used for extraction and acceleration of $Ar^+$ ions and performing experiments relevant to ion thrusters.

[#]sksharma@ipr.res.in

## ION THRUSTER

The gridded ion thruster provides the thrust as a reaction force which is produced due to the extraction and acceleration of ions. The thrust produced due to the extraction of ion beam is defined by

$$T = \alpha F_i I_b \left( \frac{2m_i V_b}{e} \right)^{1/2} = 0.95 I_b \sqrt{V_b} \qquad (1)$$

where $I_b$ and $V_b$ are the ion beam current and acceleration voltage, $\alpha$ is the correction for the double ion content of the ion beam, $F_i$ is the correction for the beam divergence, $m_i$ is the ion mass, $e$ is the electron charge and $I_b$ is the ion beam current.

The performance of the ion thruster depends on the efficiency of plasma production and that of the ion optics i.e. extraction grids. The plasma production chamber for an ion thruster has to be optimised for higher discharge efficiency i.e. better plasma confinement. The ion source used in thrusters utilises a set of acceleration grids with an essential characteristic design to allow maximum extraction and acceleration of ions at low energies. The grids for thrusters also require features such as long term operation and lower the beam divergence. The grids needs to be designed to optimise for maximum ion transparency and enhanced life. The thermal, mechanical design and choice of suitable materials are also important so as to improve stability and prevent erosion of the grids from ion bombardment.

The screen grid is located at one end of the plasma chamber and is kept at a negative potential (-30V) with respect to plasma chamber. The ions that wander in the vicinity of the screen grid are accelerated by this potential drop, while the energetic/thermal electrons are repelled back into the plasma. A high electric field is applied between the screen grid and the acceleration grid kept at a small distance to accelerate ions to the required energies. The maximum current density that can be extracted from the ion source is space charge limited and is given by the Child-Langmuir's law as

$$J_{\max} = \frac{4\varepsilon_0}{9} \sqrt{\frac{2e}{M}} \frac{V^{3/2}}{d^2} \qquad (2)$$

where $V$ is the total voltage between the two grids and $d$ is the effective grid gap. Dependents of beam current on acceleration voltage for two sets of parameters are shown in fig 2.

Fig. 1: Prototype ion source

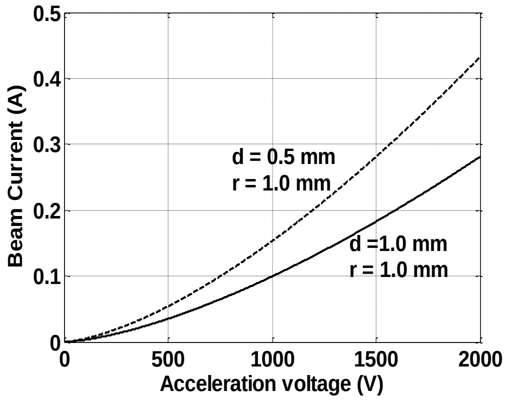


Fig. 2: Estimated beam current as a function of acceleration voltage. *d* is the gap between grids, *r* is radius of an aperture and No. of apertures are 1050.

## EXPERIMENTAL

Basic plasma production experiments have been carried out to check the performance of plasma confinement. The diameter and depth of the plasma chamber, both are 20cm. Argon plasma with a discharge current of 5 – 30A was produced using hot filament cathode. The corresponding plasma density and electron temperature were 1– $5\times10^{17}$ $m^{-3}$ and temperatures 2 – 5eV. The two grid based extractor system having ~1050 apertures distributed uniformly over both the grids is utilised to extract and accelerate ion beams at 1- 2keV energies. The gap between the two grids is 1 mm. Ion beam in the range of 20 – 100mA has been extracted from these apertures. It may be noted that the ion source developed with these parameters have applications also in other research fields such as material erosion and re-deposition.

The values of operational parameters (i.e. filament current, arc current, pressure in arc chamber and the control sequence) were optimized to achieve maximum possible beam currents without having any breakdown. Ion thrust produced by the extraction of ion beam is measured by a load cell fixed in front of the beam. Neutralisation of the ion beam has not been attempted in these experiments. The plasma formed in the downstream of the ion beam is found sufficient to compensate the space charge of the beam.

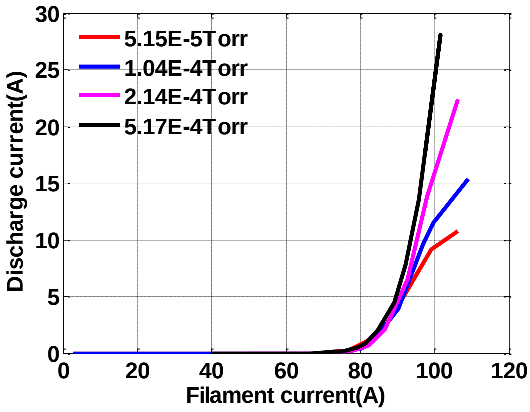


Fig. 3: Experimentally measured discharge current vs. filament current at various chamber pressures of $5\times10^{-5}$ torr, $1\times10^{-4}$ torr, $2\times10^{-4}$ torr and $5\times10^{-4}$ torr.

Figure 3 shows the variation of discharge current with filament current for various sets of pressures in the vacuum vessel (drift chamber). It is observed that there is no significant discharge current (i.e. plasma) until the total filament current reaches at ~80A. It is due to the fact that emission of primary electron starts only once the temperature of the tungsten filaments reaches beyond 2000°C. The discharge current is rapidly increased for the filament current from 80A to 105A. This behaviour can be explained by the Richardson-Dushman equation for electron emission. The maximum discharge currents for filament currents of 105A are 10A, 15, 23 and 28A for various pressures

## ION BEAM EXTRACTION

The ion beam extraction was carried out using the two grids based extraction system. The screen grid (plasma grid) and the acceleration grid are connected with the positive and negative terminals of a HV power supply. The accelerating grid is connected with the vessel via 5 kΩ resistor. The return beam current passing through the 5K resistor biases the accelerator grid at about -100 to -500 V with respect to the vacuum vessel. The negative potential is necessary to avoid the flow of back-streaming electrons and stops them entering into the plasma chamber.

The current extracted from the plasma (i.e. total current) was measured at the power supply. The beam current collected from the vacuum vessel is measured using a sensitive clamp-on-meter. The accuracy of this sensor is increased ~3mA using multiple turns in the wire. A current collector plate is also mounted at about 250mm distance from the extraction grids. The collector plate also measures the beam current incident on it. The collector current is negatively biased with respect to plasma chamber so as to reflect thermal electrons from the beam plasma. The collector current is always lesser than the beam current as only a fraction of the beam ions contributes to this current. The acceleration grid current was estimated by the difference of total current and beam current. Figure 4 shows the total extracted currents ($I_{PS}$), beam current ($I_B$), collector current ($I_C$) and acceleration grid current ($I_G$) as a function of ion acceleration voltage.

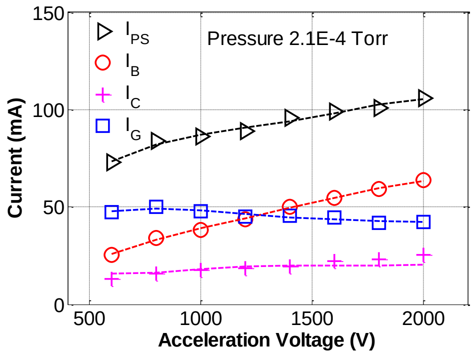


Fig. 4: Experimentally measured currents in various paths vs. ion acceleration voltage

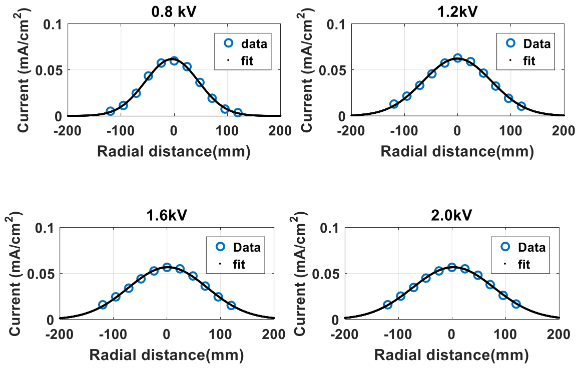


Fig. 5: Radial profiles of ion beam current density for various acceleration voltages

## DAIGNOSTICS

An array of Faraday cups (FCs) is designed and fabricated to measure radial profile of ion beam current density and angular beam divergence. The array consists of eleven FCs isolated from each other and arranged to capture radial profile of the ion beam current density. Two electrodes are fixed in front of the FCs having apertures of diameter 20 and 22 mm respectively. The first electrode is grounded. The second electrode, suppressor electrode is biased at negative potential (-30V). The purpose of the suppressor is to confine the secondary electrons within the FC. The suppressor electrode also avoids the electrons from the beam plasma into FCs. The current collected by the FCs are measured by shunt resistors connected in series. The voltages developed across the resistors are stored in a data logger. The voltage and the resistance are used to estimate the collected ion currents densities. The Faraday cup array has been installed within 200 - 800mm from the grid assembly. Typical ion beam current density profiles for various beam energies are shown in fig.5. The divergence estimated from these profiles is 4 – 6 degrees.

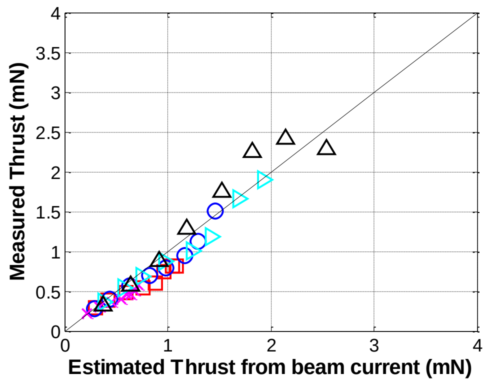


Fig. 6: Measured ion thrust vs estimated thrust

The ion thrust was measured using a rectangular aluminium plate free to move along the beam axis. The plate pushes a load cell (strain gauge) fixed with the vessel. The load cell provides the thrusts in milligram force. The thrust values were recorded for the ion beam at different beam energies. The variation of thrust is from 0.5mN to 2.5mN for beam energies 0.6 – 2.0 keV. It is observed that the thrust increases monotonically with the beam energy. The thrusts were estimated for measured beam current and beam voltage using equation 1 for Argon ions. The comparison of measured thrust with the estimated thrust is depicted in fig. 6. A good correlation between the measured and estimated thrusts is observed.

## CONCLUSION

The experimental results obtained from the developed prototype ion source suggest that this source can be used to perform thruster relevant studies. The maximum achieved ion thrust is ~2.5mN corresponding to the beam current 0.1 A at 2 keV. The source can be upgraded for the extraction of $Ar^+$ ions current exceeding 0.2A at beam energies 1 – 2keV. The extraction of $Xe^+$ is left for future work. The performance of ion source will be further improved by reducing the gap between the grids and increasing the gas flow and pumping speed.

## REFERENCES


[1] J. Brophy, Rev. Sci. Instrum. 73, 1071 (2002)
[2] J.E. Polk et al, Rev. Sci. Instrum. 83, 073306 (2012)
[3] M. Sangregorio, Chinese Journal of Aeronautics, 31(8), 1635 (2018)
[4] S. Kitamura et al, Acta Astronautica 52 (2003), 11-20
[5] G.C. Soulas, NASA report, NASA/TM-1999-209650 (1999)

# OPERATION & CHARACTERIZATION OF ECR ION SOURCE BEAM IN LEHIPA

Hitesh Kewlani[*£+], Jose Mathew[*], S.V.L.S. Rao[*], Manas Mishra[*], Deepak Mathad[*], S. H. Gharat[*], Laxman Tayade[*], S. Krishnagopal[*£]

[*]Ion Accelerator Development Division, BARC, Mumbai.
[£]Homi Bhabha National Institute, Mumbai
[+]kewlani@barc.gov.in
.

*Abstract*

Three Electrode 50 keV, 30 mA ECR Ion Source (ECRIS) was developed and commissioned for the Low Energy High Intensity Proton Accelerator (LEHIPA). Before starting 3 MeV beam acceleration trials, the pulsed ion source beam was characterized in terms of beam current, beam profile, beam position and proton fraction in the Low Energy Beam Transport (LEBT). The LEBT contains a Faraday cup, profile monitor and DCCT beam diagnostics. In the LEBT two circular apertures are used with two focusing solenoids to filter molecular ion entering to the RFQ. The ion beam profile measurement for different focusing solenoid field at two locations and the proton fraction measurement for different gas pressure, microwave power and beam pulse width were performed. Results of these experimental investigations are presented in this paper.

## OVERVIEW

At LEHIPA Three Electrode ECRIS of 50 keV, 30 mA is commissioned [1] shown in Figure 1. In LEHIPA ECR Ion source characterization and optimization has been carried out before 3 MeV beam acceleration trials [2]. The Beam characterization is done in Low energy Beam transport section. Major Focus is on beam current , beam profile measurement and proton fraction measurement. The key specifications of 3E ECRIS are mentioned in table 1.

Table 1 LEHIPA 3E ECRIS Specifications

| System | value |
|---|---|
| Energy | 50 keV |
| Current | 30 mA |
| Pulse width | 1 ms to CW |
| Proton Fraction | 80% |
| Emittance | 0.02-0.025 pi mm mrad |
| Electrode | Three ( Extractor, suppressor, Gnd) |
| Microwave | 2.45 GHz , 2kW |

## BEAM DIAGNOSTICS

The main function of LEBT (Figure 2) is to match the beam coming from ion source with Radio Frequency Quadrupole (RFQ) acceptance and diagnosis the ion beam. In LEBT the diagnostic elements are DCCT, Faraday cup, slit/wire scanner. For beam matching two solenoid magnets and two steerer magnets are used to focus and filer out unwanted higher molecular ion entering the RFQ. For proton fraction measurement 120 degree analysing magnet setup has been made which is not permanent.


Figure 1:Three electrode ECRIS at LEHIPA

## BEAM CURRENT MONITOR

After extracting the ion beam from ECRIS beam current is measure at DCCT and faraday cup before injecting to the RFQ. In table 2 beam current are listed for different microwave power at 50 keV.

Table 2 : Beam current at different point

| Microwave Power | 500 Watt | 900 Watt |
|---|---|---|
| DCCT | 6 mA | 9 mA |
| Faraday cup 1 | 2 mA | 3.5mA |
| ACCT RFQ Entry | 1.4 mA | 3 mA |

*Kewlani@barc.gov.in

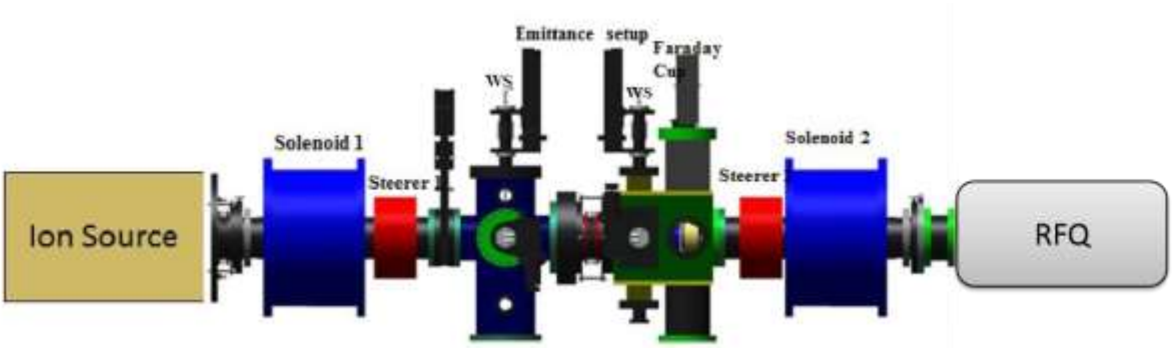


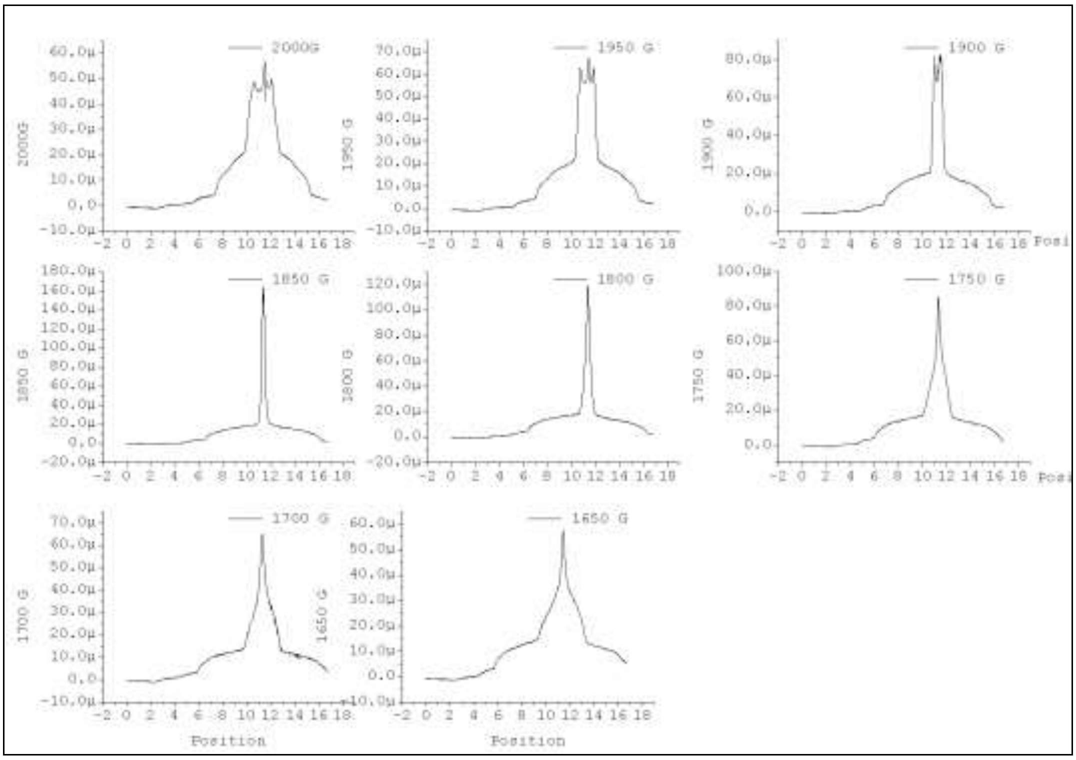


Figure 2:Low Energy Beam Transport (LEBT ) setup at LEHIPA

## BEAM PROFILE MONITOR

Beam profile measurement has been carried out using Slit scanner [Y axis] after solenoid 1 and using wire scanner [X & Y axis] after solenoid 2. Details of slit and wire scanner in mentioned Table 3.

### *Slit scanner after solenoid 1*

Beam profile experiments are carried out afeter solenoid 1 for different focusing field from 16050 Gauss to 2000 Gauss in transverse Y axis. The profile are shown in Figure 2. We got focused beam to 1850 gauss of FWHM 1.5 mm.

Table 3: Slit and wire scanner parameters

| Parameters | Value |
|---|---|
| Slit thickness | 300 micron |
| Slit width | 90 mm |
| Slit stroke | 168 mm |
| Wire thickness | 50 micron |
| Wire length | 80 mm |
| Wire scanner Stroke | 98 mm |

### *Wire scanner after solenoid 2*

Beam profile measurement (Transverse X and Y axis) are carried out by tuning the solenoid 1 to parallel the beam with field of 1250 Gauss & focusing the beam with solenoid 2 at RFQ entrance with field of 1500 Gauss. The beam profile in X and Y axis are shown in figure 3.

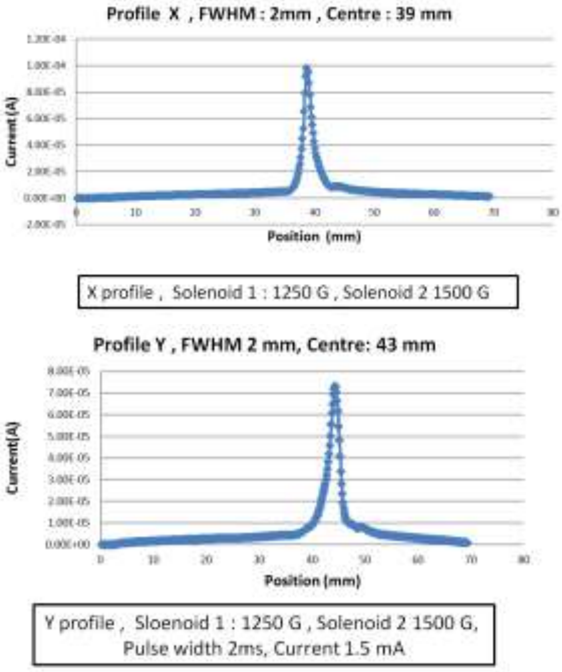


Figure 3: beam profile in Transverse X and Y axis after solenoid 2

## PROTON FRACTION MEASUREMENT

The extracted ion beam from ECR Ion source contains proton ion beam along with unwanted higher molecular ion beam ($H_2^+$ and $H_3^+$). In LEBT combination of two solenoid and two aperture, one at starting of LEBT (Dia : 42 mm) and the other at the entry of RFQ (Dia : 5 mm) are used to filter out higher molecular ion beam. By using combination of solenoid and aperture, the ion beam entering the RFQ is 99 % proton beam. In figure 4 experimental setup is shown for proton fraction measurement.

For proton Fraction measuremt first Proton ion is focused at the entry of analyzing magnet aperture and magnet scan has been taken. After that H2+ beam is focused and magnet scan has been take . Results are shown in figure 4. We have got 80 % of proton fraction at 50 keV, 6 mA.

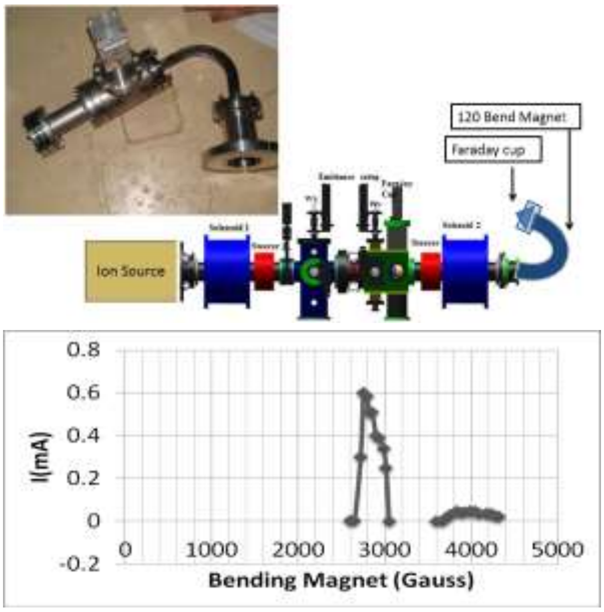


Figure 4 : Proton Fraction measurement at LEHIPA

## REFERENCES

1. P. Roychowdhury and D. P. Chakravarthy, “High intensity electron cyclotron resonance proton source for low energy high intensity proton accelerator,” Review of Scientific Instruments, vol. 80, no. 12, p. 123305, 1 12 2009.
2. P. Bhagwat, S. Krishnagopal, J. Mathew, S. Singh, P. Jain, S. Rao, M. Pande, R. Kumar, P. Roychowdhury, H. Kelwani, B. R. Rao, S. Gupta, A. Agarwal, B. Kukreti and P. Singh, “Beam acceleration through proton radio frequency quadrupole accelerator in BARC,” Journal of Instrumentation, vol. 11, no. 05, pp. T05001-T05001, 3 5 2016.
3. R. Pande, P. Singh, S. Rao, S. Roy and S. Krishnagopal, “Optimization of solenoid based low energy beam transport line for high current $H^+$ beams,” Journal of Instrumentation, vol. 10, no. 02, pp. P02001-P02001, 2015.

# DESIGN, DEVELOPMENT AND COMMISSIONING OF PERMANENT MAGNET BASED VARIABLE FIELD DIPOLE FOR BL-11, INDUS-II AT RRCAT

Elina Mishra*, Vikas Teotia, Rajesh Chimurkar and Sanjay Malhotra
*Bhabha Atomic Research Centre, Trombay, Mumbai - 400085, INDIA*
**email: elinam@barc.gov.in*

*Abstract*

High Pressure Physics and Synchrotron Radiation Division (HPPSRD), BARC is conducting study of magneto caloric effect on magneto structural materials using X-ray diffraction. BARC is having a dedicated beam line for these studies at INDUS-II at RRCAT. To understand the structural and phase transitions in such materials, measurements have to be done in the presence of variable magnetic field. Due to tight space constraints in the experimental setup, electromagnet option was ruled out. Hence, for compactness, a permanent magnet based tuneable dipole was designed, developed, qualified and installed. A variable field of 0.4 T-1 T is achieved in an air gap of 3 mm using NdFeB permanent magnets blocks. A 0.3 mm diameter capillary containing the sample to be studied is held in the centre of the air gap and is rotated at a high speed to achieve a homogeneous diffraction pattern. The pole of the magnet has been designed such that a clear angle of 33 degrees is obtained for the resultant X-rays to hit the target screen and form the diffraction patterns. Since one of the poles of the magnet and the capillary position is fixed, achieving variability in the magnetic field by varying the air gap would result in poor field uniformity at the sample. Access to the pole region was also not feasible. Shunt made of magnetic material is used to vary the reluctance of magnetic circuit to achieve variability in the field. The magnet has been designed, developed and qualified in BARC and has been commissioned in the beamline at RRCAT where initial X-ray diffraction experiments have been carried out.

Key words: Magneto caloric effect, Magneto structural material, X-ray diffraction, tunable permanent magnet dipole

## INTRODUCTION

The magnetocaloric effect (MCE) is defined as the heating or cooling (i.e., the temperature change) of a magnetic material due to the application of a magnetic field. MCE was discovered in 1881 by Warburg and explained independently by Debye and Giauque. With the construction of working refrigerators in the mid 1930's, MCE became the first method of reaching temperatures below 0.3 Kelvin.

MCE relates the magnetisation and magnetic field to entropy and temperature. The physical origin of the MCE is the coupling of the magnetic sublattice to the applied magnetic field, H which changes the magnetic contribution to the entropy of the solid. Total entropy can be defined as the sum of the entropy due to the lattice, $S_L$, the electrons, $S_E$, and the magnetic order, $S_M$[1]. At constant pressure, entropy would be a function of both temperature (T) and applied magnetic field (H) as given by the equation (1).

$$S(T,H)=S_M(T,H)+S_L(T)+S_E(T) \qquad (1)$$

The isothermal compression of a gas (apply pressure and the entropy decreases) is analogous to the isothermal magnetisation of a paramagnet or a soft ferromagnet (apply H and the magnetic entropy decreases), while the subsequent adiabatic expansion of a gas (lower pressure at constant entropy and temperature decreases) is equivalent to adiabatic demagnetisation (remove H, the total entropy remains constant and temperature decreases since the magnetic entropy increases). Fig 1 gives a schematic figure of the above phenomenon explained.

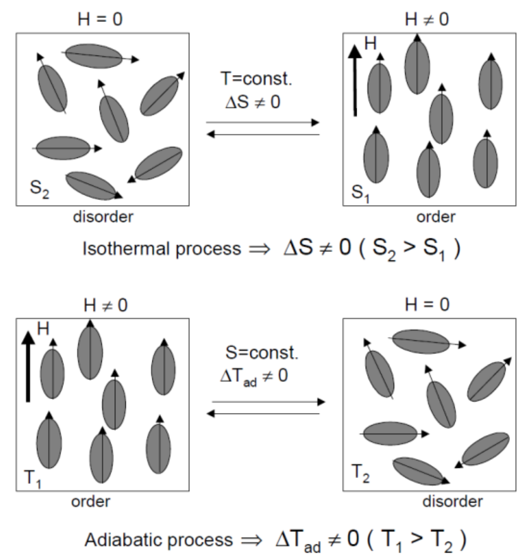


Fig 1: Model of variable field permanent magnet based dipole

The discovery and studies on MCE led to the invent of magnetic refrigerators, an alternative to the conventional gas compression technique and has several advantages. The cooling efficiency in magnetic refrigerators is very high and there are no harmful gases involved[2].

All magnetic materials intrinsically show MCE, although the intensity of the effect depends on the properties of each material. In materials undergoing first order magneto-structural transition, the structural entropy also contributes to MCE, thus giving rise to very large total entropy change. Such materials are potential candidates for MCE based refrigeration technology. In 1997, $Gd_5(Si_2Ge_2)$ was found to exhibit an exceptionally large MCE, called the giant magnetocaloric effect (GMCE). The GMCE is due to a simultaneous crystallographic and magnetic transition when the material orders magnetically that can be controlled by varying the magnetic field. Recently GMCE near room temperature was reported in $Mn_{34.5}Co_{33.1}Ge_{32.4}$ alloy, across the magneto-structural at 297 K ~1 Tesla.

To experimentally observe the magneto structural transitions in magneto caloric materials, XRD studies are done at BL-11 at RRCAT, Indore by HP&SRPD, BARC. These studies have to be done in the presence of a variable magnetic field so as to observe the magneto structural transitions.

A 1 Tesla variable field permanent magnet based dipole has been designed, developed, fabricated and installed at BL-11, INDUS-II at RRCAT, Indore by Electromagnetic Applications and Instrumentation Division, BARC. This paper discusses the electromagnetic design, analysis, measurements and results of the magnet.

## TECHNICAL SPECIFICATIONS

The beamline BL-11, INDUS-II is dedicated to material investigations under extreme conditions (high pressure/temperature). An energy dispersive beam line has been developed and commissioned at BL-11. The experimental setup consists of a synchrotron radiation beam source, a capillary tube filled with the sample under test, a variable field dipole magnet and a target screen where the X ray diffraction pattern is recorded. The sample under test is $Mn_{34.5}Co_{33.1}Ge_{32.4}$ alloy which is inserted in a 300 µm capillary tube.

Therefore, a variable field dipole magnet was required to be designed and developed for the above studies. Since there was very tight space constraint, a compact and light weight magnet system was desired. Though the most popular method of achieving variable field is an electromagnet, however the option of electromagnet was ruled out as it would make the system bulky and heavy with the copper coils and additionally need power supply. Hence, a permanent magnet based solution was considered viable.

Table 1 describes the technical specifications of the tunable dipole magnet for the diffraction experimental setup.

Table 1: Technical Specifications of tunable dipole magnet

| SN | Parameter | Value |
|---|---|---|
| 1. | Desired magnetic field in air gap | 1 Tesla |
| 2. | Range of tenability in the magnetic field | 0.35 T – 1 T |
| 3. | Capillary size | 300 µm |
| 4. | Air gap | 3 mm |
| 5. | Maximum cross section of poles (flat portion) | 10 mm x 10 mm |
| 6. | Cone angle of beam after diffraction from the sample | 33 deg in 1 direction; open in perpendicular direction |
| 7 | Beam height from the datum surface | 376 mm |

## ELECTROMAGNETIC DESIGN & ANALYSIS

To develop a variable field dipole magnet based on permanent magnets, basically two methodologies can be used. By varying the size of the air gap by moving the poles will vary the magnetic field at the centre. However, in this case, one of the poles of the magnet is fixed to the base platform. Hence moving the other pole will result in the sample not being placed at the centre of the air gap. The other option is to bypass the magnetic flux of the dipole using a shunt mechanism and varying the field at the centre[3]. This mechanism has been used in the design by implementing a soft iron shunt plate by shunting the flux.

OPERA 3D multiphysics[3]s code was used to carry out the electromagnetic design of the permanent magnet based dipole. Neodymium Iron Boron magnets were used as these rare earth permanent magnets have the highest energy density (~ 55 MGOe). Fig 2 shows the model of the dipole magnet along with the shunt iron plate.

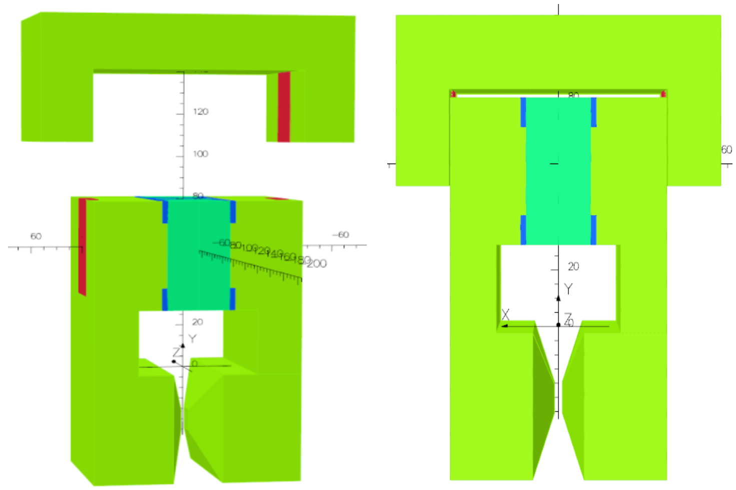

Fig 2: Model of variable field permanent magnet based dipole

The light green coloured portion is the soft iron yoke along with the poles, dark green portion is the permanent magnets and the blue portion is the aluminium bobbin. Phosphor bronze guide is provided for smooth motion of shunt. The yoke is a C shaped magnet with tapered poles to meet the field requirements. Also the pole overall dimension and tapering is also done keeping in mind the cone angle required by the diffracted beam. Six NdFeB magnets of dimensions 50 mm x 20 mm x 12 mm have been used to assemble the magnet.

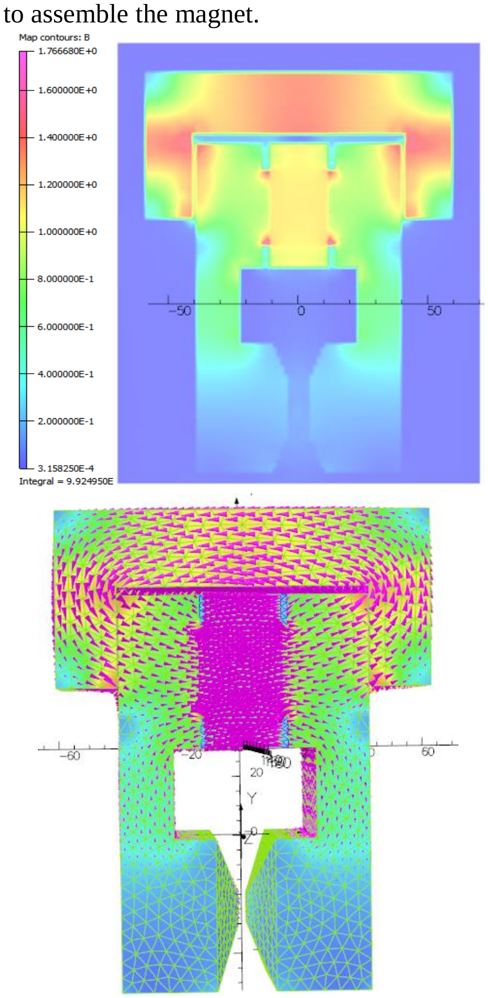

Fig 2: Contour (top) and vector plot (bottom) of magnetic field in the assembly

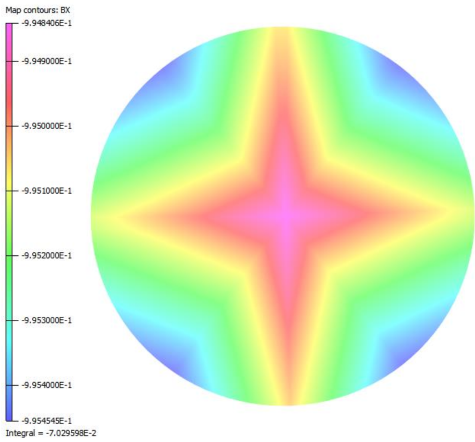


Fig 2: Contour plot of magnetic field at the air gap

A flat plate was used initially for analysis but it was observed that the tunable range is very low in such case. So legs were introduced in the plate. When the shunt plate is moved towards the magnet yoke, more and more of magnetic flux gets bypassed through the plate and thus the magnetic field at the centre decreases and vice versa. The range of magnetic field at the centre varies from 0.4 T-1 T.

Fig 2 shows the contour and vector plot of the magnet showing the magnetic field at different regions. Fig 3 shows the magnetic field distribution at the air gap when the shunt plate is at the farthest position.

## MECHANICAL DESIGN

The shunt iron plate is connected to a fixed SS top plate using a lead screw and linear bearing rod. A handle is provided at the top such that when it is rotated the shunt plate moves up and down due to the circular motion of the lead screw being converted into linear motion using guide and bearing. Phosphor Bronze railings are provided in both yoke and shunt so as to provide a guide for the motion of shunt over yoke. Entire assembly is fixed on a base platform which is placed on a XYZ stage to align the magnet to the capillary and beam. Fig 4 shows the mechanical design of the shunt plate assembly with dipole magnet.

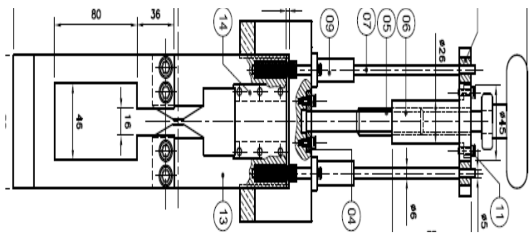

Fig 4: Mechanical design of shunt plate assembly with dipole magnet

## MEASUREMENT AND RESULTS

After the magnet was assembled, magnetic measurements were done. A miniature hall probe was placed at the air gap of the magnet and the shunt was moved to vary the field. The field varies from 0.4 T – 1 T at the air gap for the full span of shunt movement. The magnet has been installed at BL-11 of INDUS-II. XRD experiments are being carried out in Mn34.5Co33.1Ge32.4 alloy sample. At ambient conditions it exists in a mixed phase orthorhombic (Pnma) and hexagonal phase (P63/mmc). On increasing magnetic field, the percentage of hexagonal phase (paramagnetic) decreased and orthorhombic phase (ferromagnetic) increased as expected. Figures 5 show the photographs of the magnet installed in the beamline. Fig 6 shows the plot of the magnetic field at the centre vs the shunt position.

Fig 5: Photographs of dipole magnet at BL-11 at RRCAT

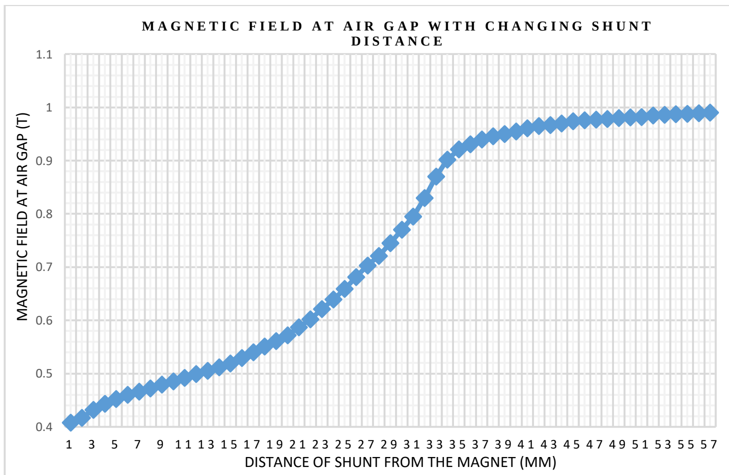


Fig 6: Plot of magnetic field with changing shunt position

## CONCLUSIONS AND FUTURE WORK

Desired range of tunability (0.4T-1T) was achieved using permanent magnets and the system was also compact & light.

## REFERENCES

[1] A M Tishin and Y I Spichkin, “The Magnetocalorific effect and its applications”, IOP publishing Ltd 2003.

[2] H. SZYMCZAK et al, “Magnetocaloric Effect. Physics and Applications”, Materials Science-Poland, Vol. 26, No. 4, 2008.

[3] David R. Barlow “Variable-Field Permanent-Magnet Dipole”, 1994 IEEE

[4] OPERA 3D reference manual

# DESIGN OF LOW-LEVEL RF SYSTEM HARDWARE BEING DEVELOPED FOR INDIAN ACCELERATOR PROGRAM AND PIP-II UNDER IIFC PROJECT

Shailesh Khole#, Gopal Joshi, ACnD/BARC
Brian Chase, Joshua Einstein-Curtis, Philip Varghese, Ed. Cullerton, Fermilab, U.S.A.

*Abstract*

The PIP-II project at Fermilab requires the Low-Level RF System (LLRF system) to regulate the phase and amplitude better than 0.01 degree and 0.01% respectively. Indian Accelerator program (ADSS and ISNS) would also have a similar performance goal for the LLRF system. This paper discusses the design choices and implementation methodology chosen for the design of digitizer system as well as the SoC based digital signal processing board.

## ARCHITECTURE OF THE LLRF SYSTEM

The overall block diagram of the RF Control and Protection System is shown below in Figure 1. The LLRF station is designed to control four cavities and has following modules a) one module of four channel Up-Converter [1], b) two modules of eight channel Down-converter [1], c) one module of four channel Resonance Controller, d) two modules of LLRF Controller. Clock Distribution unit is a separate system which provides very stable low jitter clock reference for digitization as well as down-conversion / up-conversion process.

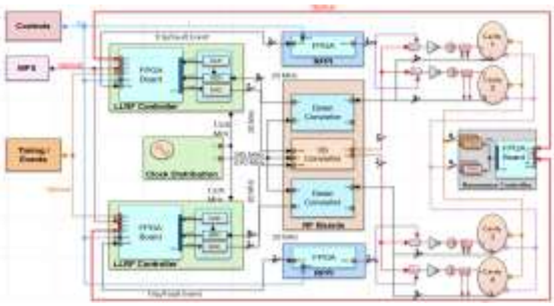

Figure 1: Block diagram representation of the RF Control and Protection System

The forward power and the reflected power at the coupler, electric field inside the cavity are monitored for all the four cavities and are down converted to a 20MHz IF signal using a suitable LO of 345MHz or 670MHz; provided by the clock distribution system. The PIP-II accelerator has 325MHz as well as 650MHz cavities in the acceleration path. A suitable phase reference line of 325MHz or 650MHz runs along the respective cavity section. The average of forward and reflected signal measured at the cavity serves as temperature compensated phase reference for RF measurement at that cavity. Two such pairs are down converted for each LLRF station.

The 20MHz IF signals are digitized by the ADC's in the LLRF controller and further base band I/Q processing is done inside the FPGA. The PI controller, Feed forward controller and other related digital signal processing is done in the FPGA before a pair of 20MHz orthogonal LLRF drive signals are generated by the DAC.

The 20MHz orthogonal IF signal is up-converted to a 325MHz / 650MHz LLRF drive signal using single side band up-conversion topology and 345MHz / 670MHz LO provided by the clock distribution module. Each of the four channels of the up-converter module drive the solid-state RF amplifier and associated RF sections up to the cavity input coupler.

The RF Protection Interlock (RFPI) system also monitors various parameters in the RF section and removes the LLRF drive to the RF amplifier on detection of a fault within 100nS.

## ARCHITECTURE OF THE SOC BASE DSP BOARD

The SoC based DSP board is designed around Cyclone-V SoC chip (5CSXFC6D6F31C6N). The SoC chip has 110k Logic elements, hundred and twelve 18-bit DSP elements, 5140Kbit of SRAM and nine 3.125Gbps transceiver channels on the FPGA side. The FPGA also has an on-board Arm Cortex-A9 dual Core Processor on the HPS side.

The block diagram of the SoC system is shown in figure 2 below. The HPS side provides 2GB of DDR3 memory running at 400MHz in 48Bit ECC mode. It also has a Gigabit Ethernet interface, USB-OTG, UART, CAN, SPI and I2C interface to link to the rest of the real world environment. SD Card, Quad-SPI Flash provide memory space which can be used either for boot mode or for storage applications. Real Time clock interface is also provided to enable time stamping of the memory data.

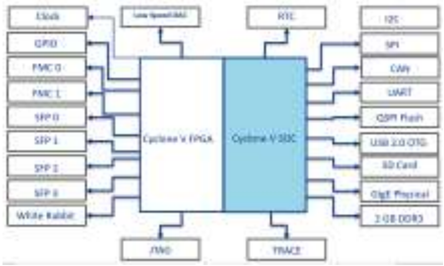


Figure 2: Block diagram representation of the of the SoC Board

The FPGA side supports the signals coming from digitizer board via the FMC connectors. Two such FMC connector supporting LP-FMC mode are provided for the same. The FPGA has nine 3.125Gbps transceivers; four of them are used for providing SFP interface. The SFP interface is the primary source for pushing raw data to the

#khole@barc.gov.in

system without involving HPS side. One of these interfaces is used for pushing data between LLRF controller and resonance controller board for implementing adaptive filter based piezo controller algorithms.

The PIP-II accelerator is to be used primarily for neutrino experiment, which will have a stringent time marking requirement for data logging. White Rabbit is the best available protocell for this purpose, a white rabbit node capable hardware has been implemented on the board.

Two channel low speed DAC is provided to output the status of various internal nodes along the signal chain implemented in the FPGA so that the signal can be viewed on the oscilloscope. JTAG and Mictor connector provide provision to debug and programme the FPGA side and HPS side on the SoC system

### *White rabbit node*

White Rabbit is an Ethernet-based network for fully deterministic data transfer and synchronization. The White Rabbit PTP core is an Ethernet MAC implementation in FPGA capable of providing precise sub-nanosecond time synchronization. The typical node functional diagram is shown below in figure 3 [2].

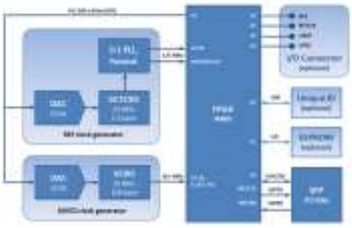

Figure 3: Block diagram representation of the of the White Rabbit node

The basic idea is to implement a Digital Dual Mixer Time Difference (DDMTD) algorithm in a NIOS core to calculate the phase difference between the SFP clock and the reference clock of 125MHz. The error signal drives the DAC and in turn the 125MHz VCTCXO to minimise the error signal. The stable clock reference for DDMTD is provided by 20MHz VCXO

The reference clock and 1pps signal are available on the board for external timing trigger. A UART interface provides access to the NIOS core for fine-tuning the loop

### *Power Supply management section*

The power supply tree is shown below in figure 4. 12V power is provided as a nominal input to the FPGA board. Two LTM4633EV, and one LTM4634EV modules provide all the necessary power for the HPS and FPGA

The low noise analog power is generated by ultra-low drop out LDO modules. The LDO modules are paced very close the actual load to minimise the noise and voltage drop due to track impedance.

The biggest power supply nuisance in a LLRF system is presence of power supply harmonics in the IF bandwidth.

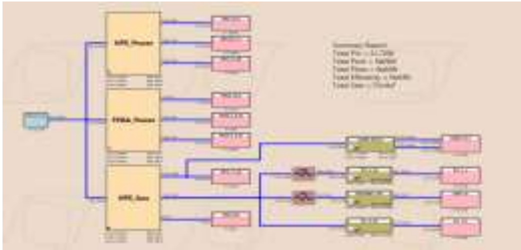

Figure 4: Power supply tree for SoC Board

LTC 6990 is a voltage-controlled oscillator which drives the clock of all LTM series power regulators. This allows the switching frequency of the LTM 4633 and LTM 4634 to be adjusted by the FPGA via a SPI interface DAC as described in figure 5 below.

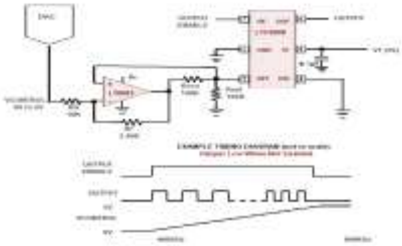

Figure 5: power supply switching frequency sweep generation

LTC 2978 based power monitoring and sequencing has been implemented to provide accurate and reliable power levels to the FPGA board.

## DIGITIZER BOARD ARCHITECTURE

The Digitizer board has eight ADC channels, four DAC channels and a clock distribution section. Two such board along with the SoC based digital signal processing board are required per station.

### *Design considerations for ADC section*

The ADC board is the heart of the entire LLRF system. The noise performance of this section decides the overall hardware performance of the system.

AD9653BCPZ-125 is chosen as the ADC for its outstanding performance around 20MHz IF range. It has an analog input bandwidth of 650MHz and has a SNR of 79.4 dBFS.at 15MHz IF and 1.3V reference. The channel to channel cross talk is -91dB.

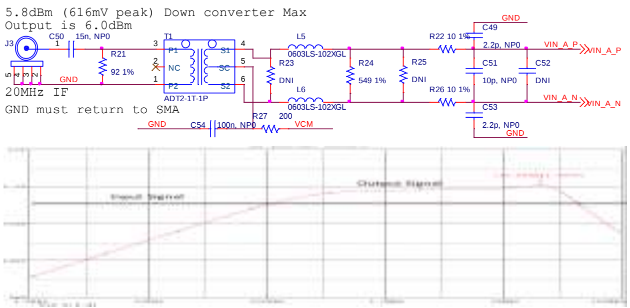


Figure 6: the input conditioning circuit and its gain-frequency response

The down-Converter provides +6dBm(616mVpeak) of signal which is boosted to 1.3V peak at ADC input by the input signal conditioning network reproduces above in figure 6. The conditioning network also, a) provides a band pass filter characteristic since the signal is having a very low bandwidth around IF and provide some resonance gain in the process (as evident in figure 6 gain plot). b). provides a smooth impedance transfer from 50Ω at input to a relative high impedance at the ADC input. The board layout is done to minimise the loop area of the signal conditioning network, channel to channel crosstalk and magnetic coupling.

The reference noise is another critical performance measure of the ADC. LTC6655-2.5 in the LS8 package is chosen for its ultra-low noise performance. The reference is scaled down to 1.3V using a resistive divider and the noise is further cut down using a op- amp based multipole low pass filter having few hertz bandwidths.

### *Design considerations for DAC section*

AD9783BCPZ, a dual channel DAC is chosen for its low noise and low intermodulation distortion (IMD) characteristics. It is capable of running up to 500MSPS and provides 80dB of SFDR for a 20MHz IF output. The DAC provides about 0.22dBm signal as against 0dBm requirement of the up converter. The board layout is done to minimise channel to channel crosstalk as well as magnetic coupling.

### *Design considerations for clock section*

The clock distribution is the most critical section in the LLRF hardware performance. LMK01801 is chosen for its multi output ultra-low additive noise performance of 50fS. It receives a 1320MHz clock from the clock distribution network and provides a 94.2457MHz clock to ADC and DAC section. The ADC DCO clock drives the LLRF FPGA allowing single cycle SERDES conversion of ADC data. A 94.2457MHz clock is also available to the FPGA. The health of the clock input is monitored using an RMS power monitor in the supervisory section.

### *Design considerations for supervisory section*

The digitizer board has a microphonic (SPU0410HR5H-1) and gyroscopic (KX023-1025) sensors for monitoring vibration induced piezoelectric signals generated on the board. The board design guideline for use of NP0 capacitors in the RF section is aimed at reducing these microphonic signal generations in the RF line.

The board also has provision for general purpose analog and digital IO line for low speed analog and digital interface to some auxiliary signals if need so arises.

## TESTING AND PERFORMANCE

The digitizer board as well as SoC based Signal Processing board has been fabricated and all subsection have been tested A picture is shown in figure 7 below. Linux 4.2 kernel has been ported on to the board. Linux kernel including the uboot and pre loader stages was built from scratch.DDR3 has been tested at full speed and full capacity. The USB, Ethernet, Quad SFP flash, I2C and SPI interface have also been tested and accessible through Linux OS.

Figure 7: Assembled LLRF Module

The digitizer board has also been tested. The SPI lines from the HPS are used for configuring the digitizer board chips. The HPS first enables the clock section, then DAC section and finally the ADC to ensure proper clocking of the system. Once the ADC clock is stable, FPGA is initialised and booted from the HPS side.

The ADC data has been de-serialised successfully and DAC has also been tested. The clock divider is working nicely. The FFT of 20MHz -7,69dBm signal is shown below in figure 8. Most of the visible peaks are sideband harmonics of 20MHz signal. The noise floor around 20MHz signal is below -120dBFS. Once thermal stabilisation and shielding is done, further improvement is expected allowing the goal of -155dBFS per Hz to be met.

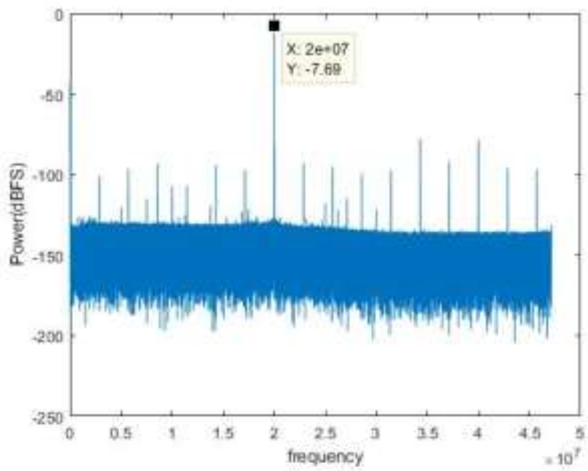


Figure 8: FFT response of 20MHz signal to ADC

The LLRF control loop is being tested and data transfer between FPGA and HPS is being optimised

## REFERENCES

[1] Design and development of 4 channel up-converter and 8 channel down converter by Mohammad Afaash, at al, published in InPAC 2018

[2] https://www.ohwr.org/project/white-rabbit/wikis/WRReferenceDesign

# DEVELOPMENT OF COMBINED FUNCTION HARMONIC SEXTUPOLE MAGNETS FOR INDUS-2

K. Sreeramulu#, S.Das, Vanshree Thakur, Ashok Kumar, Kushraj Singh, Navin Awale, Preveen Kumar, Rajesh Prasad Shah, William Amal Raj, Sudhir Kumar, Bhim Singh and Shesh Nath Singh.

Accelerator Magnet Technology Division, Raja Ramanna Centre for Advanced Technology, Indore

*Abstract*

Indus-2, a 2.5 GeV synchrotron radiation source is in round-the-clock operation mode at RRCAT. Over the years, Indus-2 has undergone several upgrades like installation of slow orbit feedback correction system, insertion devices, additional RF cavities, bunch by bunch feedback system etc. Now, it has been decided to improve the dynamic aperture of Indus-2 by suppressing the non-linearities induced from the existing chromatic sextupole magnets with the installation of a set of 32 harmonic sextupole magnets. Due to the limited space in Indus-2, it has been decided to go for compact combined function harmonic sextupole magnets having integrated additional windings to generate horizontal & vertical dipole fields for beam orbit corrections and skew quadrupole field to reduce the coupling between the two transverse planes. All the magnets have been developed with support systems and magnetically characterized & fiducialized using rotating coil method on the harmonic bench. The details of the development of these magnets with magnetic measurement results are discussed in this paper.

## INTRODUCTION

The combined function harmonic sextupole (CFHS) magnets have an aperture radius of 60 mm and overall length of 250 mm. The design of the CFHS magnet has been done using POISSON-2D and OPERA-3D codes. These magnets have the integrated field strengths of 17 T/m for the harmonic sextupole (SP) and 0.1 T for the skew quadrupole (QP) and 1.333 T-m for both the horizontal (H) & vertical (V) steering dipole (DP) fields. Prior to the series production of 32 CFHS magnets, a prototype CFHS magnet has been developed and magnetically characterized [1]. The magnetic field measurement results of the prototype magnet satisfy the specified field quality requirements. In the series magnets, about 20 % turns have been enhanced in the air cooled excitation coils for H & V - DP fields to keep margins. Figure 1 shows the cross-section of the magnet with details of various excitation coils. The magnets will be operated in slow ramping (300 mHz) mode in DC. A group of eight magnets (i.e. total 4 groups in 32 magnets) in series will be excited for the main SP component with one power supply with maximum current rating of 200A. The windings for the skew QP and H & V - DP components of each magnet will be excited separately by three bi-polar power supplies with maximum current rating of ± 15 A. The magnet assembly is made from six laminated sextant core blocks of each length 126 mm for accommodating the various field excitation coils. The details for series development of CFHS magnets are discussed below.

#sreeram@rrcat.gov.in

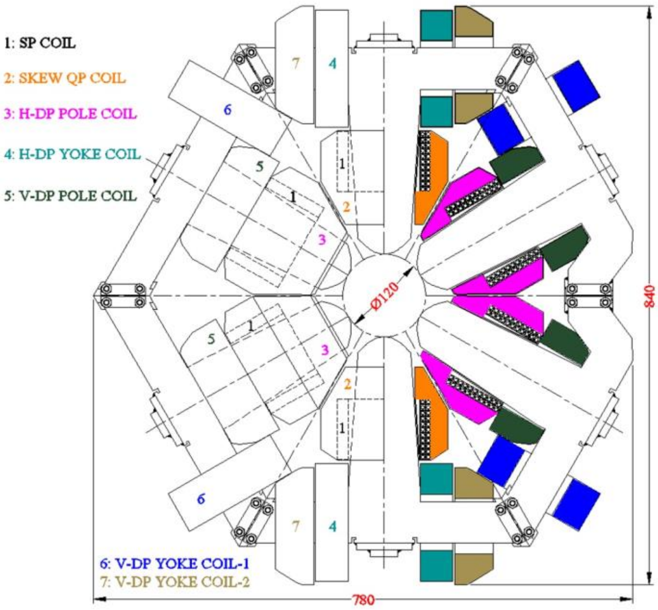


Figure 1: Details of CFHS magnet cross-section.

## MATERIALS FOR SERIES MAGNETS

The magnet cores have been made from 5.8 mm thick very low carbon steel (% C ~ 0.003 %) sheets supplied by M/s. Cockerill Sambre – ARCELOR Group, Belgium. This material has magnetic characteristics of low coercivity (< 80 A/m), high permeability at low fields ($\mu_r$ ~ 6700 at 0.9 T) and high saturation magnetic induction ($B_{sat}$ ~ 2.3 T). These sheets have a thin layer of mill scale protection – a 3 to 5μm layer of $Fe_3O_4$ oxide [2]. The main SP magnet coils have been wound from 7 mm x 7mm x ∅ 5 mm oxygen free (OF) water cooled copper conductors due to their high current density (j ~ 7 A/mm$^2$). The hollow copper conductors have been pre-insulated with 0.2 mm thick glass-fibre tape prior to the winding of SP coils. The other excitation coils (skew QP, H & V - DP field coils) are of air cooled coils (j ~ 1 A/mm$^2$) made from 3.5 mm x 3 mm enamelled copper winding strips with F-class insulation.

## SERIES PRODUCTION OF MAGNETS

### *Magnet core laminations*

About 4500 magnet core laminations have been produced by laser cutting using a 2 MW $CO_2$ laser from the local vendor. The cut laminations have extra material margins on their pole tip and mating surfaces for finish machining. Two types of laminations have been cut with suitable strip layout for minimizing the scrap from the long sheets of size 4400 x 820 mm x 5.8 mm.

### *Fabrication of sextant cores*

A rigid stacking fixture has been made to stack and compress the 5.8 mm thick laser-cut laminations to the length of 126 mm. Each laminated sextant has been fabricated by welding at few selected locations along its periphery. The machining of top and bottom faces of the fabricated sextants has been carried out to maintain the parallelism of the stack within 126 + 0.1mm. The magnet pole profile, matching/reference surfaces, V - notch for locations of guiding pins on each fabricated sextant has been machined by wire-EDM in one setting to minimize the overall geometrical inaccuracies. Few finished sextant cores have been inspected on CMM for ensuring their specified geometrical accuracies (< 0.05 mm).

### *Fabrication of magnet coils*

Each magnet assembly requires total 28 excitation coils connected in various configurations to produce the required field components. Dedicated coil winding machines have been used for fabrication of various field coils. The mechanical (geometry) and electrical inspection of each & every wound coil has been carried out as per the specifications. The electrical inspection of each coil includes the measurements of resistance (R), inductance (L) and inter-turn insulation test at a peak voltage of 500 V. All the accepted wound coils have been impregnated with epoxy resin under vacuum (< 1 mbar). The above mentioned tests have been repeated on all impregnated coils to ensure their quality. The terminals of water cooled SP coils have been brazed with nozzles for connecting with the cooling circuits and the brazed connections have been leak tested at 10 bar water pressure. Table 1 shows the details of various excitation coils in one of the CFHS magnet with values of the series magnet resistance in mΩ and inductance in mH.

Table 1: Details of excitation coils for CFHS magnets.

| **Coil type** | **Qty./ magnet** | **NI/coil in AT** | **Total R, mΩ** | **Total L, mH** |
|---|---|---|---|---|
| SP | 6 | 22 x 200 | 42.8 | 4.62 |
| Skew QP | 2 | 200 x 10 | 416 | 81.93 |
| H-DP Pole | 4 | 200 x 10 | 1430 | 337 |
| H-DP Yoke | 4 | 156 x 10 | | |
| V-DP Pole | 4 | 177 x 10 | 2090 | 412.7 |
| V-DP Yoke-1 | 4 | 208 x 10 | | |
| V-DP Yoke-2 | 4 | 143 x 10 | | |

### *Magnet assembly and inspection:*

As mentioned earlier, each magnet consists of an assembly of six laminated core sextants with associated coils. Initially, each sextant core is mounted with the associated coils and clamped in their position. Selective assembly of sextant cores has been done using special fixtures for achieving the pole aperture accuracy in each magnet within 120±0.05 mm. The sextants cores have been located with guiding pins & clamped at their ends with fasteners for each magnet assembly. The water cooled SP field coils have been hydraulically connected in series and leak tested. All the respective coils in the magnet assembly to generate the various magnetic field components are electrically connected in-series and recorded their total magnet resistance and inductance values. Finally, two fiducials along with a level plate have been mounted on the top of each magnet to represent the magnetic axis and its orientation during field measurements. The development of 32 magnets have been completed & shown in figure 2 (L).

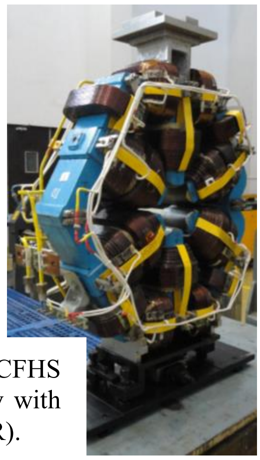

Figure 2: Completed series CFHS magnets (L) and a magnet assembly with fiducial post & positioning system (R).

### *Precision magnet positioning systems:*

Magnet positioning systems are required to hold and precisely align/position each CFHS magnet in Indus-2 ring within a tolerance of 0.1 mm in linear and 0.2 mrad in rotational axes. Compact positioning systems with the load carrying capacity of 500 kg have been developed for each magnet. Each positioning system has the translation and rotational adjustments of range ±10 mm & ± 3° respectively. The assembly of the magnet with fiducials and positioning system is shown in the figure 2(R).

## MAGNETIC MEASUREMENTS AND FIDUCIALISATION

The measurements of all 32 magnets have been carried out using rotating coil based magnetic field measurement setup developed at RRCAT [3] is shown in the figure 3. The integrated field strengths & higher order multipoles (both normal & skew) for (i) independent excitation of main SP field component and (ii) combined excitation of all the field components (SP, skew QP, H & V - DP steering fields) have been measured at various excitation levels.

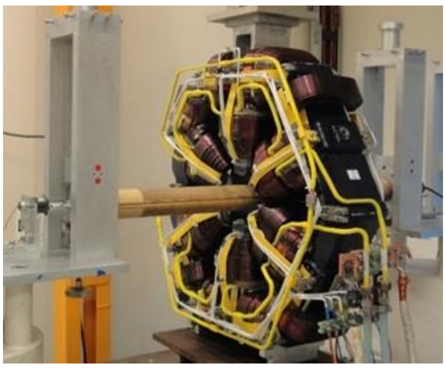

Figure 3: CFHS magnet on measurement bench.

Before taking the measurements, the magnets have been cycled from 0 to 200 A using main SP coils, while keeping the rest of coils unpowered. Initially, the magnetic axis of each magnet has been aligned w.r.t. the rotating coil axis within the precision of $\Delta_x$, $\Delta_y$ (centre deviation) < 20 µm and $\Delta_\theta$ (rotation angle deviation) of ~ 0.2 mrad at 190 A current in the SP coils. The required integrated SP field strength G′L ($d^2B_y/dx^2$.L) of 17 T/m has been achieved at ~ 160 A is shown in the figure 4. The higher order multipoles measured at 32 mm reference radius are within ± $5x10^{-4}$ of the main SP field strength and are within the acceptable limits, is shown in the figure 5.

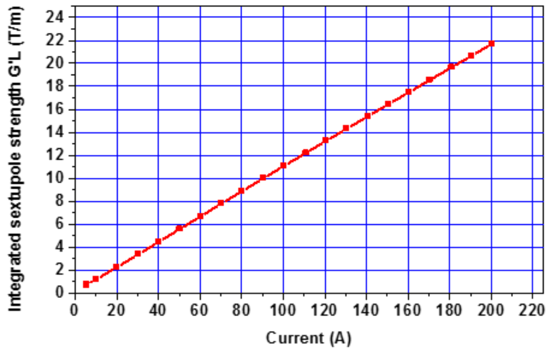


Figure 4: Variation of integrated SP strength with current.

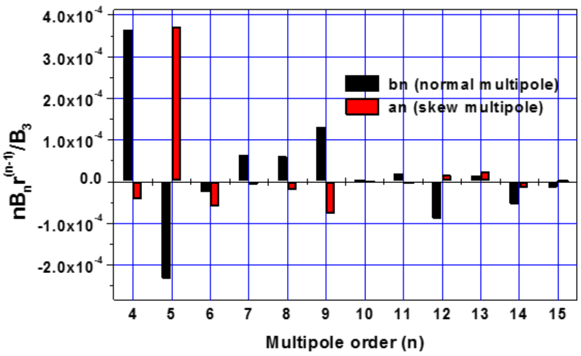


Figure 5: Integrated normal and skew multipole components at 0.032m radius normalized with SP component at 160 A.

All the 32 magnets are divided into 4 groups, each having 8 magnets. As each group of magnets will be powered by one power supply, the SP strength of all the magnets in each group should not vary beyond a specified limit.

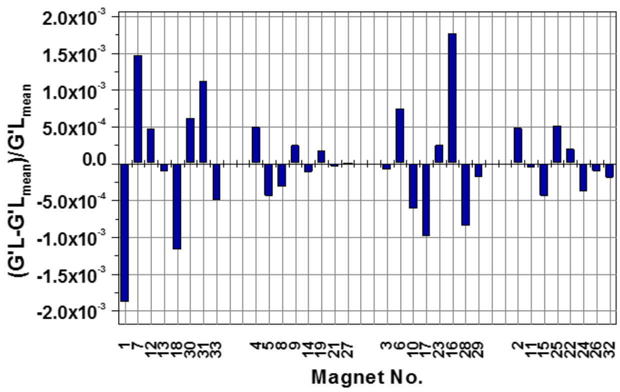


Figure 6: Deviation of the integrated SP strength from the mean integrated SP strengths within each group at 160 A.

The maximum deviation of the integrated SP strength from the mean integrated SP strength within the each group is found within ± $2x10^{-3}$ at all the excitation levels from 30 to 160 A, is shown in the figure 6. Integrated skew QP, H and V - DP steering field strengths and higher order multipoles with full combined excitation while keeping the SP current at 170A are measured, is shown in the figure 7. The measured integrated field strengths of individual field components are summarized in table 2. After the measurements, the magnetic axis has been transferred to fiducials which are mounted on the top of the each magnet.

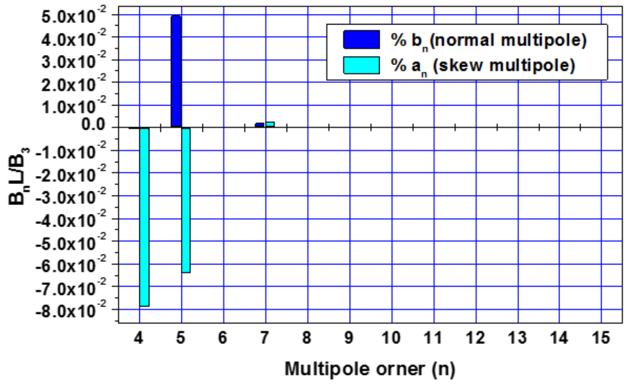


Figure 7: Integrated $b_n$ and $a_n$ multipoles at 0.032m radius for combined full excitation normalized with SP component.

Table 2: Measured field strengths (combined full excitation)

| Field component | Current (A) | Integrated strength |
|---|---|---|
| Sextupole (G'.L) | 170.5 | 17.39 T/m |
| V - DP field ( $B_y$) | 10 | 0.01453 T-m |
| H - DP field ($B_x$) | 10 | 0.01366 T-m |
| Skew QP (G.L) | 10 | 0.112 T |

## CONCLUSION

The magnetic field measurement results in each of the combined function harmonic sextupole magnets meet the required integrated field strengths and satisfy the specified field quality requirements. All the magnets have been completed and ready for installation in Indus-2 storage ring.

## ACKNOWLEDGMENTS

We acknowledge with thanks to the local venders (M/s. Artech Industries, Indore, M/s. Mistry Die-N-Tools, Indore & M/s. D&S Electric Works, Indore) for their active involvement during the successful development of these CFHS magnets.

## REFERENCES

[1] Vanshree Thakur et al, 'Harmonic Sextupole Magnets for Indus-2' Proceedings of InPac-2015 conference.

[2] F.Bertinelli et al, 'Production of low carbon magnetic steel for LHC superconducting dipole and quadrupole magnets' IEEE Transactions on Applied Superconductivity, Vol. 16, No. 2, June 2006, pg. 1777 - 81.

[3] S.Das et al, 'Development of rotating coil based magnetic measurement setup at RRCAT' InPac-2013.

# REFERENCE PHASE DISTRIBUTION SCHEME AND TEST RESULTS FOR SSR1 UNDER IIFC

Mohammad Afaash, Sujo C.I and Gopal Joshi, BARC, Mumbai, India
Edward Cullerton and Brian Chase, Fermi national Accelerator Laboratory, USA

*Abstract*

Stable acceleration through an RF accelerator demands that the phase of the RF fields remains in synchronism with the beam bunches passing through the resonators. This requires the phase of the RF field to be stabilized with respect to a common phase reference signal, which is distributed throughout the accelerator. The reference phase is distributed to the Low Level RF System through coaxial cables, which are susceptible to drifts in phase due to temperature changes and aging. The phase drifts are stabilized using phase averaging method, which requires the phase of the terminated end of the reference line remain constant. This paper describes phase reference scheme, the design of the reference phase stabilization circuit and experimental results for a reference line under different ambient temperatures, being developed under IIFC.

## INTRODUCTION

A RF reference phase signal is required by the Low-Level RF (LLRF) system, against which the phase of the electric fields inside the RF cavity is regulated. Coaxial cables are a conventional medium through which RF reference signals are distributed among the cavities in an accelerator system. A reference phase distribution system using point to point local distribution is shown in Fig.1. The reference signal is tapped using directional coupler on the RF reference line and will be routed closely with the cavity pick-up signal to the LLRF system, thereby exposing both signals to the same ambient conditions and causing identical phase drifts in both signals. However, the phase of RF signal on the reference line is susceptible to drifts due to ambient temperature variations and aging, which needs to be reduced to ensure accurate phase control of the cavity fields.

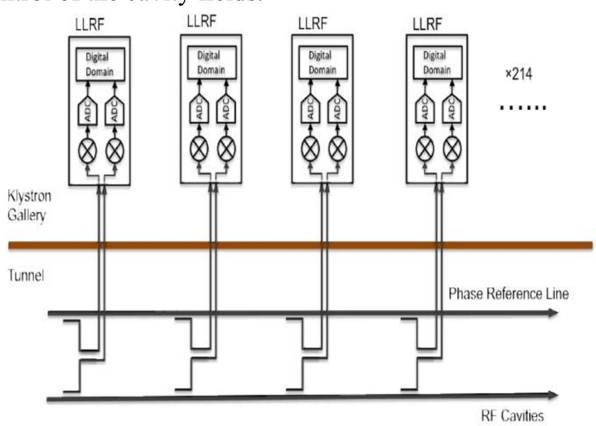


Figure 1: Distribution of RF phase reference to LLRF system

As a part of the Indian Institutions and Fermilab collaboration (IIFC), Accelerator Control Division (ACnD), BARC and FNAL are developing a reference phase distribution system using the phase averaging method.

## PHASE AVERAGING METHOD

The phase averaging method is used to stabilize the phase of the RF signal on the RF reference line. A standing wave is generated on the reference line by shorting one of its ends [1]. A phase stabilization loop is implemented at the shorted end to ensure that its phase remains constant with reference to a low phase noise Master Oscillator. Since the phase of a standing wave does not depend on its position on the reference line, the phase at any point on the reference line will remain constant, irrespective of temperature changes. The reference signal is obtained by using bi-directional couplers to obtain the forward and reflected signals and combining them to provide an RF output whose phase will be the average of phase the forward and reflected signals.

### *Phase Averaged Output*

A mathematical analysis of the RF reference line and the phase averaged output has been done, considering the effects of cable attenuation and the properties of the bi-directional coupler, which may affect faithful reproduction of the standing wave at the combiner output. A block diagram of the RF reference phase distribution system using phase averaging is shown in Fig.2. The drift in phase has been modelled as change in the electrical length of the coaxial cable, which is temperature dependent. It has been observed that the output of the combiner circuit at a point $L_1$ from the terminated end will consist of the sum of two terms as follows:

$$V_o = 2a_1 \cos\left(\frac{\phi_1-\phi_2}{2}\right) e^{j\left(\frac{\phi_1+\phi_2}{2}\right)} + (a_2 - a_1)e^{j\phi_2} \quad (1)$$

Where $\phi_1$, $\phi_2$ and $a_2$, $a_1$ are the phase and magnitude components of the forward and reflected signals input to the combiner circuit. Hence if the amplitude of the forward and reflected signals is equal, the output phase at the combiner will be the average of the forward and reflected signal phase. The parameters $\phi_1$ and $\phi_2$ contain electrical length dependent terms which are equal but both opposite in sign, hence getting cancelled out in the averaged output. The parameters $\phi_1$ and $\phi_2$ are also dependent

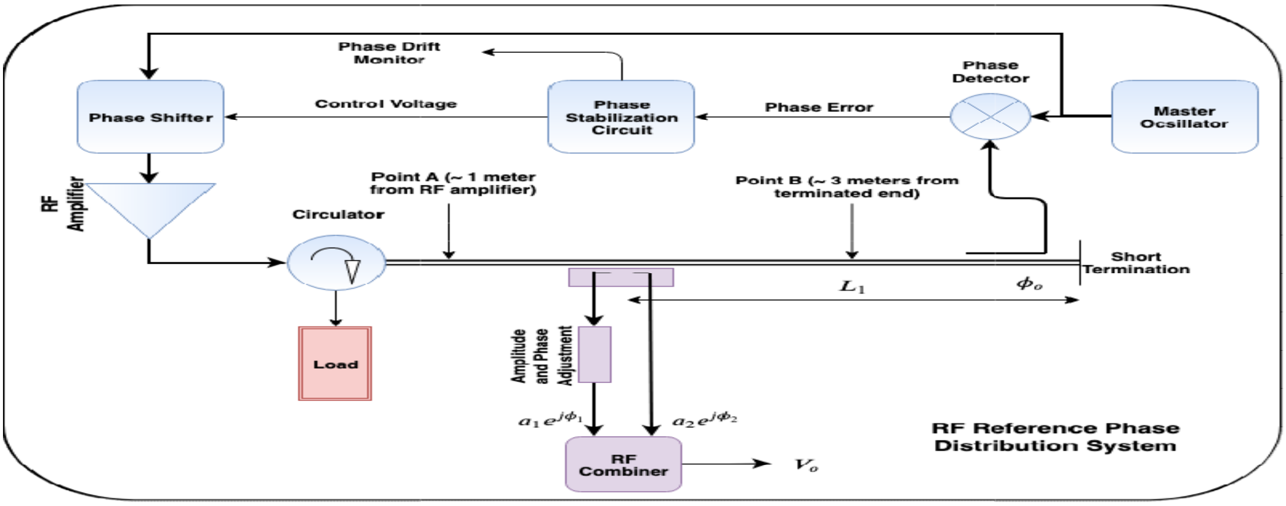


Figure 2: Block Diagram of RF Reference Phase Distribution System

the phase $ø_o$, whose drift is proportional to the length of the reference line. Hence, the phase at the terminated end needs to be stabilized using a phase stabilization loop. The phase drift contribution due to the second term of Eq.1 will depend on both the distance of the tap from the terminated end as well as phase at the terminated end. Hence the amplitude balance between the forward and reflected signal is crucial to minimizing phase drift error. The output power of the phase averaged output can be adjusted by varying the phase difference between the forward and reflected signals using an RF cable.

## DESIGN OF 325 MHZ RF REFERENCE PHASE DISTRIBUTION SYSTEM

The clock module generates the RF signals required by the LLRF system such as 325 RF reference signal, 345 MHz LO signal and 1.32 GHz clock for LLRF system clock. These signals are derived from a low phase noise oven controlled master oscillator of 162.5 MHz. The 325 MHz RF reference phase distribution system is a subsystem of the clock module which generates phase stable 325 MHz RF reference signals against which the phase of the electric fields inside the SSR1 cavity is regulated.

Phase stable 7/8” coaxial cables will be used as the reference line to minimize the phase drift on the reference line due to temperature changes. A 50 Watt amplifier provides the output power necessary to drive the RF signal along the reference line. An op-amp based phase stabilization circuit along with a drift monitor has been designed and tested. The circuit is modular in design, allowing for implementation of proportional and proportional-integral controller with control parameters which can be adjusted by changing the values of the resistor and capacitor accordingly. The master oscillator for the 325 MHz reference line is derived using a frequency multiplier which converts phase averaged reference signal from the 162.5 MHz reference line to a 325 MHz reference signal. The phase at the shorted end of the transmission line is obtained using a directional coupler. The 325 MHz master signal drives the LO of a mixer phase detector, while the feedback signal from the reference line is fed to the RF port of the mixer. The stabilization circuit produces a control output which is fed to a voltage control phase shifter, which adjusts the phase of the reference line accordingly. The drift monitor on the phase stabilization circuit configured as a non-inverting amplifier which provides the phase error voltage generated by the mixer. Low noise RF amplifiers must be used to ensure minimum added phase noise in the reference line.

### *Test Results:*

Experiments were conducted to verify the correctness of the phase averaging model and to test its effectiveness in stabilizing phase drift in a reference line. A temperature controlled enclosure consisting of a PCB heater element and air distribution fan were fabricated to produce ambient temperature variations between 35$^o$C and 45$^o$C inside the enclosure. A temperature controller with output current drive capability up-to 16A with a USB control interface has been used to regulate the current to the PCB heater element. Pt-100 RTD has been used to measure the ambient temperature inside the enclosure and is interfaced with the temperature controller. A 20 meter long RG-142 equivalent cable has been as the reference line, which was installed inside the temperature enclosure and the phase drift of the cable for a temperature between 35$^o$C and 45$^o$C was measured. The reference line was integrated with the phase stabilization loop and the phase drift between the master oscillator and the terminated end of the cable was measured using a VNA. A mixer has been used as a phase detector and care has been taken to ensure that the mixer operates in the stable phase quadrants to prevent positive feedback operation due to the 180 degree phase shift of the inverting amplifier of the controller circuit. The phase stabilization circuit was operated in proportional mode with a loop filter cut-off of 150 Hz and different proportional gain values. The drift monitor is configured as a non-inverting unity gain buffer for monitoring phase error. The plot of the phase drifts at the terminated end of the reference line is shown in Fig. 3. A phase drift of 7.6 degrees has been observed over a 10 $^{o}$C variation in temperature. The closed loop phase drifts have been measured for a proportional gain of 41.6 and 416.6 with a +23 dBm mixer, for which the phase drifts measured were 0.65 degrees and 0.05 degrees respectively. The +23 dBm mixer has been replaced with a +17 dBm mixer due to increased phase noise observed in the master oscillator signal due to additive phase noise contribution of the amplifier to drive the +23 dBm mixer. The noisy amplifier has been replaced with a low noise alternative which limits the LO drive levels achievable to +17 dBm. The closed loop phase drift using the +17 dBm mixer with a proportional gain of 416.6 has been observed to be 0.09 degrees. The marginal increase in the phase drift is attributable to the reduction in sensitivity of the mixer, thereby reducing open loop gain. The phase drift variation measured at the terminated end of the reference line is shown in Fig.3.

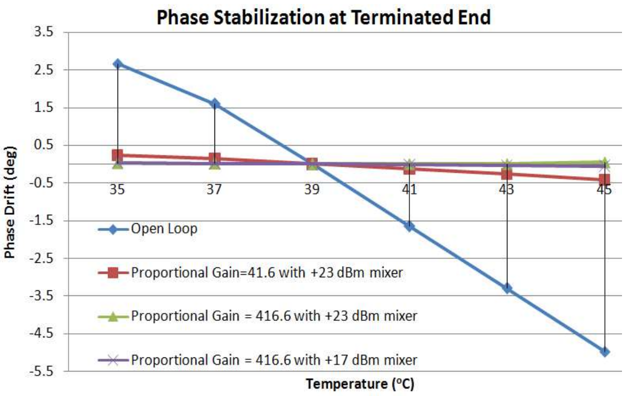


Figure 3: Phase drifts measured at terminated end of Reference Line

The drift in the phase averaged output has also been observed over the given temperature range. Careful amplitude balancing is important to obtain good phase drift suppression especially at points which are far away from the terminated end. This is due to increased contribution of the second term as a result of phase dependence on distance of the tap point from the terminated end. The phase averaged output has been measured at points close to the driving end and the terminated end of the reference line shown as points A and B in Fig.2. The phase drift near the terminated end and driving end has been measured to be 0.07 degrees and 0.4 degrees for a proportional gain of 416.6 and +17 dBm mixer phase detector. The increased phase drift at the terminated end are attributable to reflections within the reference line, which cannot be cancelled by the phase averaging scheme [2].

### *Phase Noise Measurements:*

The phase noise in the reference line will also play an important role in the regulation of electric fields by the LLRF system, as it will directly influence the jitter of the RF fields in the cavity, thereby affecting its phase accuracy. The phase noise of the 162.5 MHz OCXO has been measured as -174 dBc/Hz for a 100 kHz offset. The phase noise of the 325 MHz Master Oscillator derived from the OCXO has been measured as -161 dBc/Hz. The increased phase noise is attributable to the frequency multiplication operation as well as additive phase noise of RF amplifiers used to provide RF drive power necessary to operate the mixers. Additive phase noise measurements were done for RF amplifiers where the additive phase noise of the original amplifier and low noise amplifier were measured as -154 dBc/Hz and -164.5 dBc/Hz at 100 kHz offset respectively. The use of switching mode supplies should be avoided and cooling devices like fans must be powered using an isolated power supply to avoid switching noise and spurs in the RF output as shown in Fig.4.

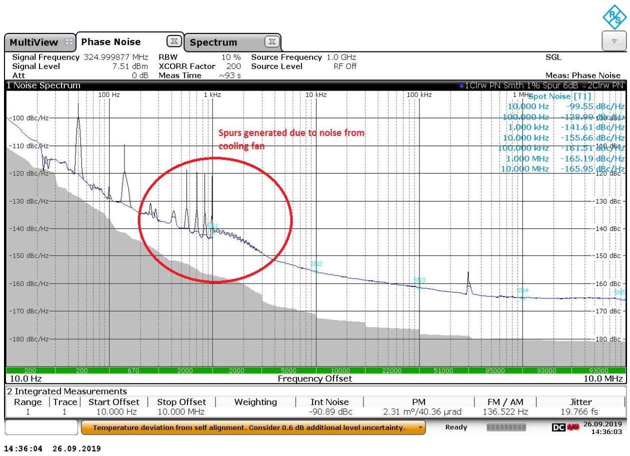


Figure 4: Phase Noise plot with spurs due to cooling fan

## CONCLUSION

The phase drift performance of the RF reference phase distribution system under varying ambient temperatures has been measured. A phase drift improvement factor of 85 has been observed for phase averaged output near the terminated end. The phase deviation due to reflections in the reference line can be reduced by ensuring use of components having good impedance match and optimization of reference line tapping point. The phase averaging circuit will require a temperature controlled enclosure to minimize uncompensated phase drift. Phase noise improvements can be achieved by restricting optimising the loop bandwidth of the phase stabilization loop.

## REFERENCES

[1] Rihua Zeng and Anders J Johansson, “Design Considerations for Phase Reference” http://docdb01.esss.lu.se/DocDB/0002/000253/001/PhaseReferenceDistribution.pdf

[2] Brian Chase and Ed Cullerton, “1.3 GHz Phase Averaging Reference Line for Fermilab’s NML” http://beamdocs.fnal.gov/AD-public/DocDB/ShowDocument?docid=3806

# POSTER PRESENTATIONS SESSION-1

# ANALYSIS OF TRAJECTORY OSCILLATION OF A CHARGED PARTICLE IN A PERIODIC FOCUSING CHANNEL BY HAMILTON-JACOBI METHOD*

B.Nayak#, BARC, Mumbai- 400094, India

*Abstract*

A systematic analysis of trajectory oscillation of a charged particle of a mismatched intense beam in a periodic focusing channel has been presented. Stability condition has been derived using Hamilton-Jacobi theory. Analytical calculation has been compared with numerical computation by taking a suitable example and results have been discussed.

## INTRODUCTION

In this paper, we have solved the KV envelope equation for a mismatched beam to find its nonlinear oscillatory behaviour in a periodic focusing channel. To make the analytical calculation simpler and self-consistent, we have taken an approximation that magnitude of magnetic field is small and so beam envelope almost remains constant ( or may be a slowly varying function of distance). Then the equation of motion for a particle in a periodic solenoidal channel can be represented by perturbed Mathieu equation . We employ Hamilton Jacobi method to find the nonlinear oscillations of the particle and found an expression for its stability which is essentially a function involving magnetic field, beam current, emitance and periodicity of magnet.

## TRAJECTORY OSCILLATION OF CHARGED PARTICLE IN PERIODIC FOCUSING CHANEEL

A strictly balanced beam is difficult to realize in practice since several conditions need to be fulfilled for this such as zero nodal component of velocity at the entrance in the uniform field region, exact value of beam radius, uniform charge density distribution. Real beams are usually unbalanced ones.The envelope equation describing beam motion in a focusing channel is

$$r'' + {k_0}^2 r - \frac{k}{r} - \frac{\varepsilon^2}{r^3} = 0 \qquad (1)$$

where $k_0 = \frac{qB}{2mc\beta\gamma}$, $B$ is the magnetic field, $\gamma$ is the relativistic factor, $\beta = \frac{v}{C}$ , $k$ is the generalized perveance, $\varepsilon$ is the emittance. Matched beam solution is $r = a$ where $a$ is matched beam radius. When the beam is not matched, the envelope radius becomes a periodically varying function of distance $z$. In the axisymmetric beam, for small amplitude oscillation $r = a + R$ where $|R| \ll a$ . Substituting it in equation (1), we get

$$(a+R)'' + {k_0}^2(a+R) - \frac{k}{a}\left(1 - \frac{R}{a}\right)\Big) - \frac{\varepsilon^2}{a^3}\left(1 - \frac{3R}{a}\right) = 0 \qquad (2)$$

As ${k_0}^2 a - \frac{k}{a} - \frac{\varepsilon^2}{a^3} = 0$ for matched beam,
The simplification of equation (2) is

$$R'' + \left({k_0}^2 + \frac{k}{a^2} + 3\frac{\varepsilon^2}{a^4}\right)R = 0$$

Total solution of the mismatched beam envelope is

$$r = a + c_1\, cos\omega_0 z + c_2\, cos\omega_0 z$$

Therefore a boundary particle periodically oscillates around the equilibrium radius $r_e = a$ with frequency $\omega_0$ when moving along z-axis.

It is possible to overcome the diverging effect of beam space charge and produce a confined beam cross-section using magnetic fields which vary periodically along the beam axis. It consists of a number of equally spaced magnetic shielded coils.

Now let us consider the oscillation of envelope of a mismatched beam in a periodic solenoid focusing channel. Cosinusoidal variation of magnetic field along the beam axis is assumed and the trajectory equation takes the form

$$R'' + \left(\left(\frac{e}{2mc\beta\gamma}\right)^2 {B_m}^2 cos^2\frac{2\pi}{L}z + \frac{k}{a^2} + 3\frac{\varepsilon^2}{a^4}\right)R = 0$$

where $B = B_m cos\frac{2\pi}{L}z$ , $L$ is period of the system and we choose $\frac{2\pi}{L}z = Z$ $e$ and $m$ are charge and mass of the particle, $k = \frac{I}{I_0}\frac{2}{\beta^3\gamma^3}$ where $I_0$ is 17 kA for electron.

Thus the particle trajectory equation becomes

$$R'' + \left(\frac{L}{2\pi}\right)^2\left(\left(\frac{e}{2mc\beta\gamma}\right)^2 {B_m}^2 + \frac{k}{a^2} + 3\frac{\varepsilon^2}{a^4}\right)R + \left(\frac{L}{2\pi}\right)^2\left(\frac{e}{2mc\beta\gamma}\right)^2 {B_m}^2(cos2Z)R = 0 \qquad (3)$$

The equation (3) resembles Mathieu Equation and can be written as $R'' + (\omega^2 + \in cos2Z)R = 0$ where $\omega^2 = \left(\frac{L}{2\pi}\right)^2\left(\left(\frac{e}{2mc\beta\gamma}\right)^2 {B_m}^2 + \frac{k}{a^2} + 3\frac{\varepsilon^2}{a^4}\right)$ =frequency of oscillation in the periodic solenoid channel and $\in = \frac{1}{2}\left(\frac{L}{2\pi}\right)^2\left(\frac{e}{2mc\beta\gamma}\right)^2 {B_m}^2$

Solution of Mathieu equation is well-known and is available in literatures. According to that, solution of this equation will have confined or growing solution depending on the value of $\omega^2$ and $\in$. These two types of solutions correspond accordingly to zones of stable and unstable focusing. Here we have tried to solve analytically this equation by Hamilton Jacobi method, a technique which is normally used to treat perturbation problems in classical dynamics. Although this analytical treatment is used by assuming smaller magnetic field but we have compared our study for higher magnetic field case also.

*Work supported by DAE, India
# nayakb@barc.gov.in

## ANALYSIS OF PARTICLE TRAJECTORY BY HAMILTON-JACOBI METHOD

Under a point transformation in trace space the simultaneous transformation of coordinates and momenta $R$ and $R'$ into canonical coordinates and momenta $Q(R,R',Z)$ and $P(R,R',Z)$ obey the Hamilton's equations of motion

$$Q_i' = \frac{\partial K}{\partial P_i} \qquad P_i' = -\frac{\partial K}{\partial Q_i} \tag{4}$$

where $K(P,Q,Z)$ is the Hamiltonian in the new coordinate system and the prime represents the derivative with respect to the Z.

We have considered $q = R$ and $p = R'$ to have consistency with the standard notations for Hamilton - Jacobi method available in literatures . Solution of the equations (4) for $p(P,Q,Z)$ and $q(P,Q,Z)$ yields the transformed Hamiltonian $K$ as a function of the old Hamiltonian $H$ as

$$K(P,Q,Z) = H(p(P,Q,Z), q(P,Q,Z), z) + \frac{\partial G}{\partial Z}$$

Let's take $H = H_0 + \breve{H}$ where $\breve{H} \ll H_0$, and $G{=}G_0(P_1, P_2 \ldots\ldots P_N, q_1, q_2 \ldots\ldots q_N, Z)$ then

$$P_i' = -\frac{\partial K}{\partial Q_i} \quad Q' = \frac{\partial K}{\partial P_i} \text{ and } K = \breve{H}$$

Let us apply Hamilton Jacobi method to solve the equation (3).

The trajectory for $\epsilon = 0$ is $q = \frac{\sqrt{2\alpha}}{\omega} cos(Z+\xi)\omega$

Hence the perturbed Hamiltonian in a periodic focusing transport channel becomes $\breve{H} = \frac{1}{2}\epsilon q^2 cos2Z$

It is found that $\alpha$ and $\xi$ are not canonical with respect to the Hamiltonian $K$, we introduce the new canonical variables $\alpha^*$ and $\xi^*$ using the generating function

$$G^* = \alpha^*[(\omega-1)Z + \omega\xi]$$

So that $\alpha = \frac{\partial G^*}{\partial \xi} = \omega\alpha^* \quad \xi^* = \frac{\partial G^*}{\partial \alpha^*} = (\omega-1)Z + \omega\xi$

Then $K = \langle\breve{H}\rangle + \frac{\partial G^*}{\partial Z} = \frac{\epsilon\alpha^*}{4\omega} cos2\xi^* + (\omega-1)\alpha^*$

Thus the motion is unstable ($\alpha^*$ is unbounded) if $\frac{\epsilon}{4\omega} > |\omega - 1|$ . On substituting our values for $\epsilon$ and $\omega$ we get the threshold magnetic field as

$$B_{mT} = \left(\frac{8mc\beta\gamma}{eL}\right)^2 \left[1 - \left(\frac{L}{2\pi}\right)^2 \left(\frac{k}{a^2} + 3\frac{\varepsilon^2}{a^4}\right)\right] \tag{5}$$

The above expression (5) tells that the threshold magnetic field highly depends upon space charge parameter , emittance of the beam , and matched beam envelope apart from magnet period (length). With increase of space charge effect (or emittance induced due to its non-linearity), value of threshold magnetic field decreases. Hence particle becomes unstable at a lesser magnetic field for a high current beam.

## COMPARISON WITH NUMERICAL RESULTS

In this section we will compare our analytical treatment with numerically evaluated results by taking a suitable example. We consider an electron beam of energy 85 kV, current 5 Amp, initial beam size ( radius) 7mm, initial divergence 10 mrad, emittance = 25 mm-mrad and period of magnet=400mm. Using these parameters, threshold magnetic field $B_{mT} \approx 50$ gauss. A program is written in C++ to solve equation (3) and we plot the variation of particle position and phase space plot with distance (upto 2m) for different magnetic fields.

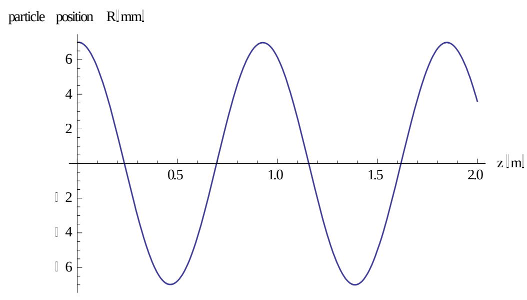


Figure 1: particle position along z-axis for B= 40 gauss

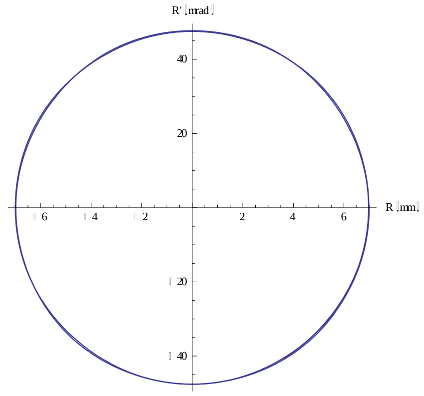


Figure 2: Phase space plot for B= 40 gauss

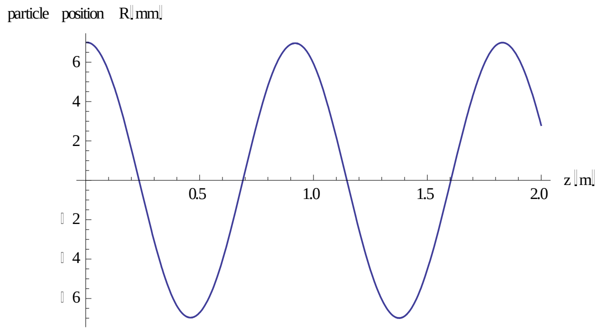


Figure 3: particle position along z-axis for B= 50 gauss

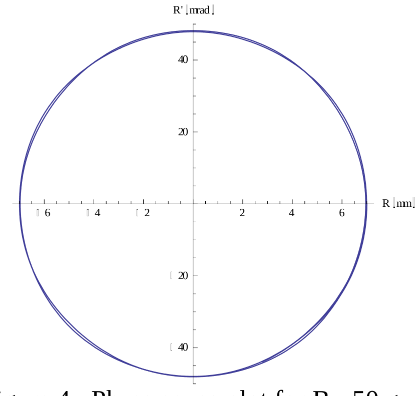


Figure 4: Phase space plot for B= 50 gauss

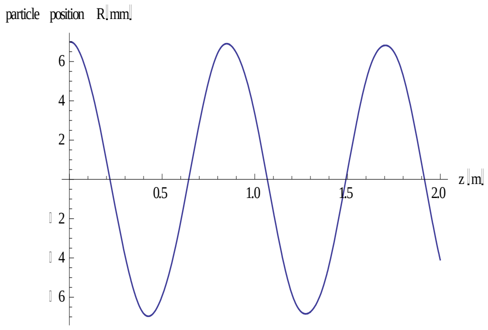


Figure 5: particle position along z-axis for B= 100 gauss

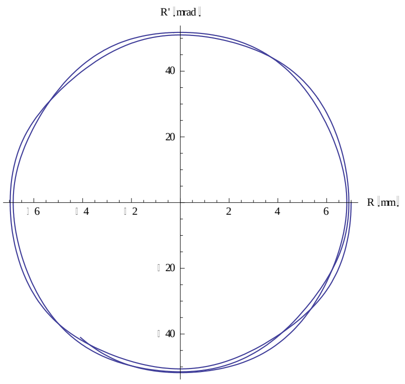


Figure 6: Phase space plot for B= 100 gauss

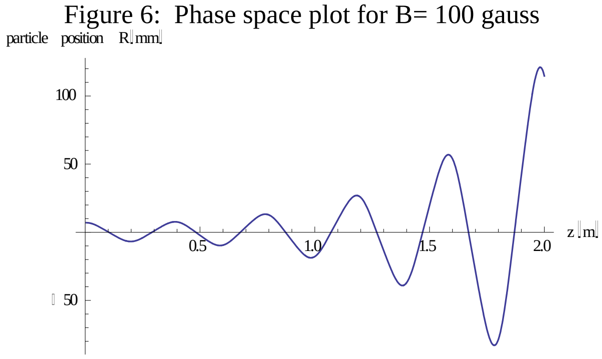


Figure 9: particle position along z-axis for B= 400 gauss

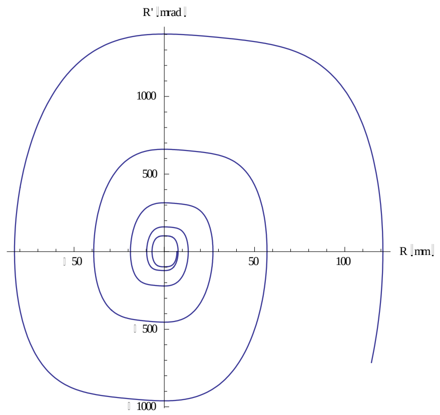


Figure 10: Phase space plot for B= 400 gauss

We observed from Figs. 1-10 that if the magnetic field is lesser than 50 gauss, beam trajectory is a stable one and phase space plot is a closed one also. But after 50 gauss, instability slowly starts e.g at 100 gauss, it can be found that there is a distortion in phase space plot . At 400 gauss, it is very clearly observed that beam trajectory goes on increasing with distance and attains a value of 150 mm at 2m distance and in phase space also ( fig. 10), beam divergence goes on increasing and becomes more than 1500 mrad . Therefore although the numerically calculated results exactly does not match to the expression (5), but it gives an idea of the value of magnetic field from which instability of the beam may develop. Now if we would like to have a stable ( bounded) motion even at 400 gauss, then magnet period can be changed to a lesser value. For example, taking $L =$ 200mm, $B_{mT} \approx 200$ gauss.

## CONCLUSION

In this paper, we have solved the oscillation of trajectory of a charged particle of a mismatched intense beam in a periodic focusing channel by Hamilton- Jacobi method. An expression is derived for the threshold value of magnetic field beyond which beam becomes unstable. This value depends upon beam current, emittance and periodicity of magnet. We have applied this theoretical study for a high current electron beam and compared it with numerically evaluated results.


## ACKNOWLEDGEMENT

I would like to express sincere gratitude to R K Rajawat , Associate Director, BTDG, BARC for the encouragement and support for this work.


## REFERENCES


[1] J. T. Mendel, C. F. Qujate, W. H. Yocom, Electron Beam Focusing with Periodic Permanent Magnet Fields, in Proceedings of the IRE, Vol.42 p.800 (1954).
[2] C. Chen and R. A Jameson, Self-consistent simulation studies of periodically focused intense charged-particle beams, Physical Review E 52, 3074 (1995).
[3] Martin Reiser, Theory and Design of Charged Particle Beams, Wiley, New York (1994).
[4] S.Y. Lee and A. Riabko, Envelope Hamiltonian of an intense charged-particle beam in periodic solenoidal fields Physical Review E 51,1609 (1995).
[5] A. H. Nayfeh, Perturbation Methods, Wiley VCH Germany (2004).
[6] R. Rand, Nonlinear Vibrations.
[7] H. Goldstein, Classical Mechanics, Addison Wesley, USA (2001).

# WAKEFIELD EFFECT OF A HIGH CURRENT BEAM IN A 25 MeV RF ELECTRON LINAC*

B.Nayak#, BARC, Mumbai- 400094, India

*Abstract*

In this paper, I have calculated the wakefields (Longitudinal & Transverse) generated due to a bunched electron beam of length 2mm and energy 4 MeV passing through a single cell of linac cavity in CST wakefield solver. Beam gains an energy of 25 MeV at the end of linac. These wakefields (including accelerating fields) are used in ELEGANT code and transverse dynamics of the beam is simulated taking into account different charges of the bunch.

## INTRODUCTION

The electric and magnetic fields carried along with the bunch induce surface charges and currents in the conducting walls of the surrounding structure and these become the sources of fields that act back on the particles in the bunch. At non relativistic velocities, the fields from the beam-induced surface charges are usually much smaller than the direct space-charge fields. Scattered electromagnetic radiation is produced when the fields moving with the relativistic particles experience geometric variations along the structure like RF cavities, vacuum bellows, and beam-diagnostic chambers. In the extreme relativistic limit, the scattered radiation cannot catch up to affect the source particles, but the radiation can and does act on trailing particles in the same or subsequent bunches. This scattered radiation is called wakefields. At lower velocities the field carried by the beam becomes more isotropic, and when the induced surface charges radiate over a length scale that is comparable to or greater than the wavelength of a particular mode, destructive interference from the different sources of the radiation reduces the energy in the corresponding wakefields . This radiated fields can be classified as short range or long range wakefields. Longitudinal wakefields may produce energy spread in the beam leading to leading to undesirable chromatic aberrations. Due to transverse wakefields, all particles (off-axis) behind the head of the bunch are deflected further away from the axis of the structure. Thus, as the bunch travels down along the pipe, the total area in transverse phase space (emittance) occupied by all the particles in the bunch will increases.

## SIMULATION RESULTS

The accelerator consists of a RF gun and one acceleratin section. After exiting from RF gun (1.6 cell, operating a 2856 MHz), beam has a rms bunch length of 2mm an energy 4 MeV. Then it passes through accelerating cavit section resonating at a frequency of 2856MHz. There are 3 accelerating cells and 34 coupling cells. Each acceleratin cell is of length 52mm.Total length of linac cavity section i 2m. Beam gains an energy of 25 MeV at the end of linac Longitudinal and transverse wake potentials of the bean passing through one single cell are simulated in CS wakefield solver and shown in Fig.1 and 2. Wakefiel pattern of the bunch is also shown in Fig.3.

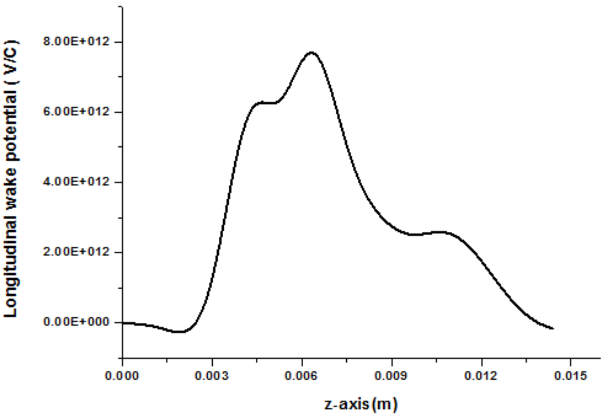


Figure 1: Longitudinal wake potential

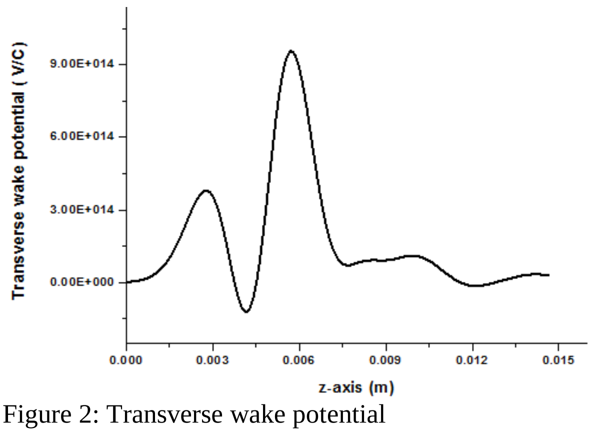


Figure 2: Transverse wake potential

*Work supported by DAE, India

# nayakb@barc.gov.in

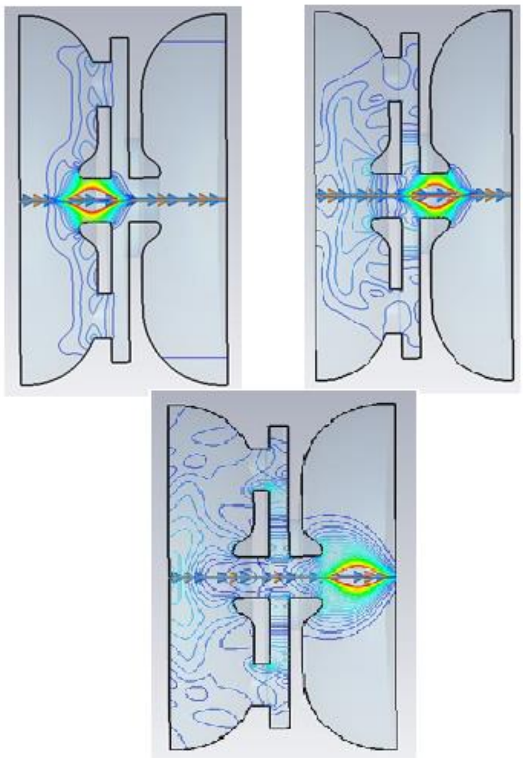

Figure 3: Wakefield pattern of the bunch as it propagate through one accelerating cell

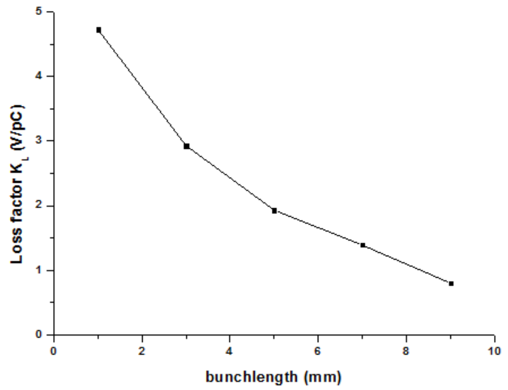


Figure 4: Loss factor

In Fig.4 and 5.,loss factor and kick factor of the beam i plot. It is observed that loss factor of the bunch decreases a bunch length increases. Also kick factor increases as bean position from centre increases. It is zero if the beam i perfectly aligned to centre (there is no translational o rotational misalignment). For 2mm shift from centre, it i 0.12 V/pC/mm.

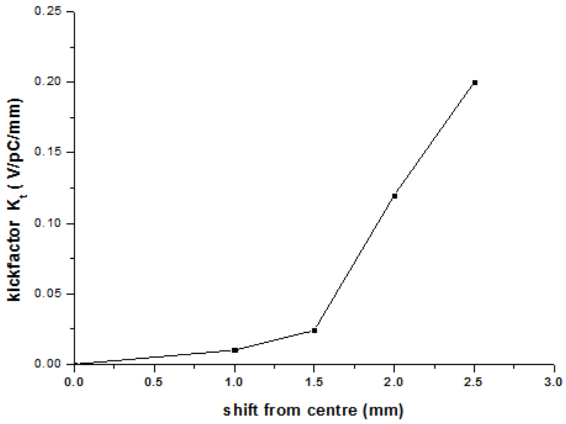


Figure 5: Kick factor

Displacement of a point on the bunch, $x(z,s)$, as a functio of z, the longitudinal position relative to the centre of th bunch ($z$ is positive toward the head of the bunch) and $s$, th distance from the beginning of the accelerator.
The transverse force at z depends on the displacement of al charges with $z^{'} > z$ and is given by
$F_x(z,s) = e^2 \int_z^{\infty} dz^{'} \rho(z^{'}) w(z^{'} - z) x(z^{'}, s^{'})$ where $\rho$ is th line density of the particles in the bunch. $e.w.x$ is th transverse field produced by a point charge displaced fron the axis by x at a distance $z^{'} - z$ behind the point charge an $s^{'} = s - z^{'} + z$ refers to the retarded time for the field.
The equation of motion for $x(z,s)$ can be written as

$$\frac{d}{ds}\left[\gamma(s)\frac{d}{ds}x(z,s)\right] + \left(\frac{2\pi}{\lambda(s)}\right)^2 \gamma(s)x(z,s) = r_0 \int_z^{\infty} dz^{'} \rho(z^{'}) w(z^{'} - z) x(z^{'}, s)$$

where $\gamma(s)$ is the energy of the beam at position s in units o $mc^2$, $m$ being the rest mass of the particle, $\lambda(s)$ is th instantaneous wavelength of betatron focusing at position and $r_0 = {e^2}/{mc^2}$ is the classical radius of the particle.

To calculate the dynamics of beam in presence o wakefields, multiparticle simulation is performed i ELEGANTcode. Longitudinal and transverse wak potentials (calculated in CST) are incorporated i ELEGANT code . To observe the effect of transverse wak field, initially beam is shifted by 2mm from centre. In Fig 6,7 & 8, transverse phase space projection of the beam i plot for 1 pC, 10 nC and 20 nC charge. For 1 pCcharge there is no further deflection of beam and with increase o charge, it increases and also emittance grows. For 20n charge, beam centre is shifted by 10mm.

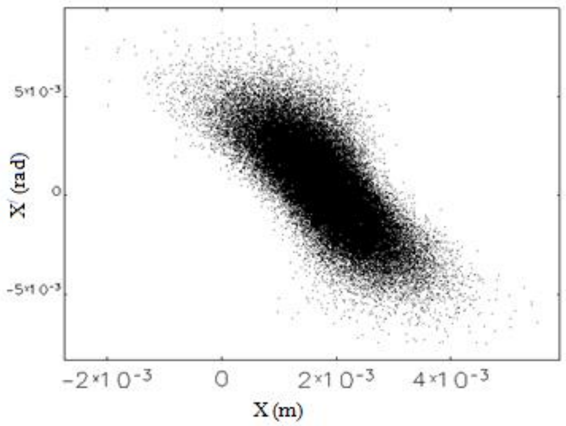


Figure 6: Phase space plot for 1pC charge

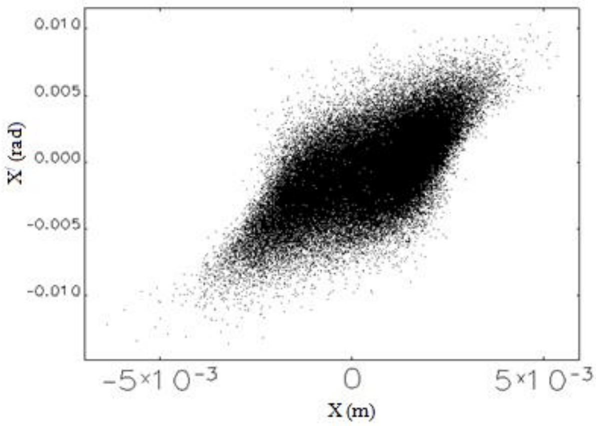


Figure 7: Phase space plot for 10nC charge

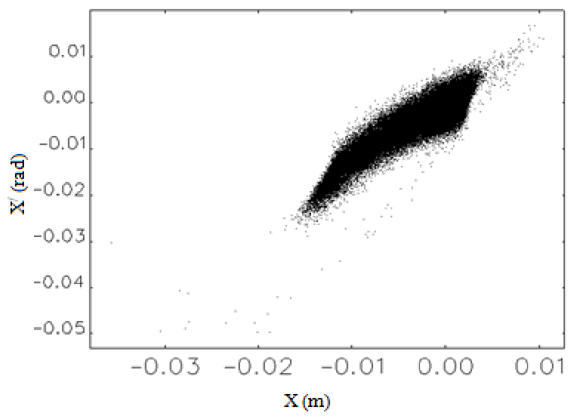


Figure 8: Phase space plot for 20nC charge

## CONCLUSION

Here wake potentials of high current bunched beam is simulated in CST wakefield Solver and using ELEGANT code, transverse beam dynamics of the beam for different charges is calculated.

## ACKNOWLEDGEMENT

I would like to express sincere gratitude to R K Rajawat , Associate Director, BTDG, BARC for the encouragement and support for this work.

## REFERENCES

[1] A.W. Chao, B. Ritcher and C. Yao, Beam Emittance Growth caused by Transverse deflecting fields in a Linear Accelerator, NIM 178 (1980).

[2] Gil A. Travis , Transverse Beam Breakup in Linear Electron Accelerators , Undergraduate thesis , January (1990).

[3] K.L.F Bane , P.B. Wilson & T. Weiland, Wakefields and Wake Field Acceleration, SLAC-3528, December (1984).

[4] , K.Y. Ng, Beam Instabilities p. 557.

[5] O. Karlberg et al., Short Range wakefields in MAX IV and FERMI Linac, Procedings of IPAC (2012).

[6] A. Novokhatski, M. Timm, T. Weiland , Single Bunch Energy Spread in the TESLA Cryomodule, TESLA 99-16, September (1999).

[7] T. Wangler , RF Linear Accelerators, Willey, New York, (1988).

[8] G.V. stupakov , Wake & Impedance, Lecture notes.

[9] M. Borland, “Elegant: A flexible SDDS-compliant code for Accelerator Simulation”, APS LS-287 (2014).

[10] CST Studio Suite www.cst.com

[11] K. Bane, “Short range wakefields in Accelerating Structures for the NLC” SLAC-PUB-9663 (2003).

[12] T. weiland and I. Zagorodnov, The short range transverse wake function for TESLA Accelerating Structure, , TESLA Report 2003-11(2003).

# DEVELOPMENT OF AN UPGRADED SYSTEM FOR THE CALIBRATION OF BEAM POSITION MONITORS OF INDUS-2

Y. Tyagi*, S. Yadav**, A. C. Holikatti, Y. Sheth and T. A. Puntambekar
Beam Diagnostics & Coolant Systems Division
**Homi Bhabha National Institute, Anushaktinagar, Mumbai - 400 094
Raja Ramanna Centre for Advanced Technology, Indore - 452 013
*Email : ytyagi@rrcat.gov.ernet.in

*Abstract*

Beam positions monitors (BPM) are non-intercepting beam diagnostic devices which are used for finding the position of beam in particle accelerators. Upgraded version of BPMs for Indus-2 synchrotron radiation source at RRCAT has been designed and developed. These beam position monitors have 4 electrodes and required to be calibrated on a test bench before installing in Indus-2 ring. The aim of calibration is to find the sensitivity and a suitable mapping function to convert induced voltage signals on electrodes into position information. The position information from these BPMs is used for correction of closed orbit distortion and maintaining electron orbit in the storage ring within few tens of microns. An upgraded calibration system has been developed indigenously with several new features. In the calibration process, the BPM is moved to different horizontal and vertical positions and induced voltage on the electrodes of BPM is recorded for respective position. The time taken to move the BPM to desired positions has been reduced to ~30 seconds compared to ~4 minutes in old system. The positional accuracy is better than 20 μm. The upgraded calibration system acquires the electrode signal data through a spectrum analyzer (Agilent E4404B) in place of RF Millivoltmeter used earlier. This modification has improved the signal to noise ratio by ~20 dB. Several new features for data analysis have been incorporated in the system software. In this paper the features of indigenously developed upgraded calibration system has been described.

## INTRODUCTION

Indus-1 and Indus-2 are two national synchrotron radiation facilities at Raja Ramanna Centre for Advanced Technology, Indore. Indus-1 and Indus-2 are regularly operated in round the clock mode since February 2010[1] [2]. Beam orbit measurement and its correction is important for getting high life time of circulating electron beam in Indus-2 storage ring. Upgraded BPMs (UPBPM) for Indus-1 and Indus-2 has been designed and fabricated for higher sensitivity and more precise beam position measurement [3][4][5]. Indigenous design and development of the upgraded version of beam position monitors and their installation in Indus-2 ring are being carried out in a phased manner. These BPMs are calibrated on a test bench in laboratory before installing in Indus-2 ring. With indigenous efforts, an upgraded calibration system has been developed to calibrate these BPMs. The aim of calibration is to validate the physics design of these BPMs and to find a suitable polynomial function to convert induced voltage signals on the electrodes of BPM into beam position information. The beam position information from BPMs is used for the correction of closed orbit distortions and maintaining the beam orbit within few tens of microns. A computer controlled fully automatic upgraded calibration system has been developed.

## CALIBRATION SYSTEM

The upgraded system consists of a 100 microns thin wire to simulate the beam path and hence electric field of beam around the cross-section of the wire. A suitable RF signal is fed to the wire. In this setup, BPM is mounted on an X-Z motion stage which is moved with the help of a stepper motor. Two stepper motors are coupled to X-Z stage to provide movement in variable step size of 50 microns to 1 mm. Two linear encoders are mounted on the X-Z stage which provides feedback of the actual movement. In earlier system [6], wire was centered manually which was time consuming and prone to errors. In new system the wire positioning is done with the help of software. The software controls the hardware which positions the wire in the geometrical centre of BPM within ~5 minutes as compared to ~50 minutes in earlier system. In the calibration process of BPM, the BPM is moved to different positions and induced voltage on the electrodes is recorded for each position. The time taken to move the BPM to desired positions was of the order of 3-4 minutes in the existing system which has been reduced to ~40 seconds with a positional accuracy of better than 20 microns. This has been achieved using a feedback loop. This upgraded calibration system acquires the electrodes signal data through a spectrum analyzer in place of RF Millivoltmeter for data acquisition. This modification has improved the signal to noise ratio by ~20 dB. The complete software has been developed in-house to control all the system devices (viz. RF signal generator, spectrum analyzer, multiplexer unit, stepper motor controller and driver unit, position feedback uniit). Mulitiple calabration data sets for same BPM can be taken by software without any user intervention for checking repeatability of calibration results.

Software modules have been developed for fitting calibration data to custom mathematical functions which are used to find position. All the calibration data is automatically saved in file for later ananlyis.

Figure 1: Photograph of upgraded calibration system for calibration of beam position monitors of Indus-2

## RESULTS

More than 35 nos. of different types of BPMs were calibrated using the developed calibation system. The measured sensitivity of these BPMs is in good agreement with design values. The system was tested for more than 72 hours continuous run and worked as per its specifications. Figure 1 and Figure 2 shows the typical horizontal and vertical response curve of upgraded beam position monitors calibrated with this system.

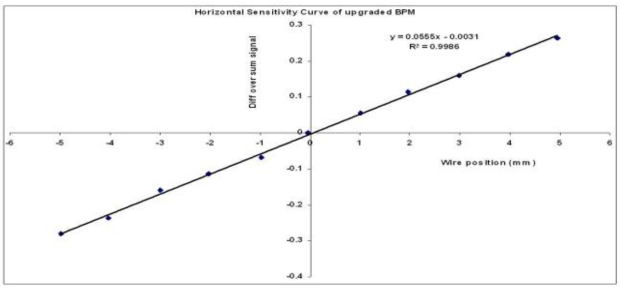


Figure 2: Horizontal response curve of upgraded BPM

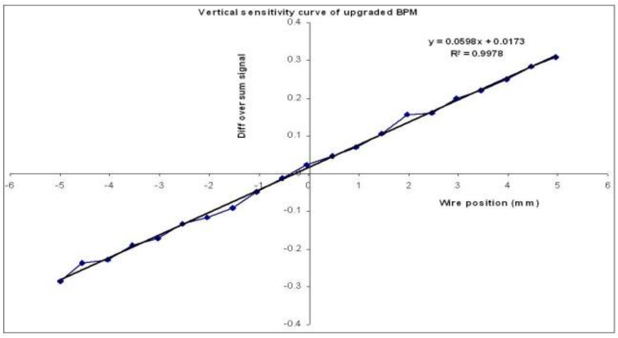


Figure 3: Vertical response curve of upgraded BPM

## CONCLUSIONS

The upgraded calibration system has significantly reduced the time required for calibration of beam position monitors from ~8 hours to ~2 hours. Signal acquisition using spectrum analyzer with modified mapping function has reduced the fitting rms error to 50 microns. More than 35 nos. of different types of BPMs has been successfully calibrated with the new system.The measured sensitivity of each BPM in both horizontal and vertical planes are in good agreement with their design values.

## ACKNOWLEDGEMENT

Authors are thankful to Shri A. K. Karnewar, Shri Lokesh Kumar Babbar, Shri Deepjwalit Vaishnav, Shri Vikram Singh Yadav, Shri Bhatu Bhika Sonawane and Shri N K Maurya for their help during the development of this system. We also thank to Shri Mukesh Kumar and Shri Akash Deep Garg for their helpful technical discussion.

## REFERENCES

[1] Singh G, Hannurkar PR, Shukla SK, Thakurta AC, Prabhu SS, Puntambekar TA, et al. Status of Indus-2 Synchrotron Radiation Source. InPAC 2011.

[2] http://www.rrcat.gov.in/newsletter/NL/nl2019/issue1/pdf/Dir.pdf

[3] L.K. babbar, Y Tyagi et.el, "Design and development of upgraded integrated type beam position indicators for dipole vacuum chambers of Indus-2 SRS", http://sircdl.cat.ernet.in:8080/dspace/handle/123456789/7697

[4] L. K. Babbar, Y Tyagi et al, "Design, development and installation of upgraded beam position indicators for Indus-2 synchrotron radiation source", http://sircdl.cat.ernet.in:8080/dspace/handle/123456789/7641

[5] L. K. Babbar, Y Tyagi et al, "Design, development and installation of ultra high vacuum compatible beam position indicators for insertion devices in Indus-2",http://sircdl.cat.ernet.in:8080/dspace/handle/123456789/7642

[6] Y.Tyagi, A.K. Karnewar et al. "Development of an Automated System for Calibration of Beam Position Monitors", National Symposium on Instrumentation (NSI-39), October 15-17, 2014, Gurukul Kangri University, Haridwar, India, Proceedings on CD.

# Theoretical and experimental studies on the resonance modes in the cavity of a 10 GHz Nanogan ECR ion source

Kedar Mal†, U.K. Rao, Y. Mathur, C. P. Safvan

Inter-University Accelerator Centre, New Delhi, India

*Abstract*

Recent experiments have demonstrated that frequency tuning is a powerful technique in ECR ion sources as it considerably influences the beam intensity and its properties. To understand the frequency tuning effect, a set of reflection coefficient measurements have been carried out at LEIBF ECR based ion source which is used for regular user experiments. The aim of this experiment was to characterize the ion source cavity in terms of possible excited resonant modes inside the evacuated cavity without the usual dc bias electrode. The reflection coefficient was measured in the frequency range 8.7-10.6 GHz in steps of 2 MHz at different tuner positions. To get the information about the resonance modes, frequency domain solver of CST Studio was used. The details of the experimental setup, measured and simulated results will be presented in this paper.

## INTRODUCTION

Electron Cyclotron Resonance Ion Sources (ECRIS) [1] are well known devices to produce high intensity beams of medium high charge states. In ECRIS, a plasma is generated and sustained through a resonant interaction between microwaves and electrons motion, and is confined by a magnetic structure called min-B structure, generated by superimposing of the fields created by axial coils with the one generated by a hexapole or octupole. The resonant interaction between microwaves and electrons motion takes place on an egg-shaped surface produced by min-B structure, called resonance surface. According to the scaling laws [1], to produce high intensity beams, higher and higher frequencies and magnetic fields are required. With the time, different techniques were discovered to boost the performances of ECRIS. The injection of two close or well separated frequencies [2,3], as well as fine tuning of a single frequency, known as frequency tuning effect [4,5]. The explanation of the frequency tuning effect is linked to the electromagnetic field distribution inside the plasma chamber which changes with frequency, as a result electron cyclotron resonance heating (ECRH) and ionization process also change [6]. Such distribution cannot be simply determined by considering the plasma chamber as a cylindrical cavity. The resonant modes in a cylindrical cavity with and without plasma have been observed and a shift of modes were seen when plasma is present [7]. Using this technique, on a 10 GHz Nanogan ECRIS [8] we studied the effect on bremsstrahlung spectra, beam intensity and shape, by sweeping the microwaves in a range of ±0.5GHz around 10GHz in steps of 10MHz. We have observed a clear dependence of beam intensity and shape from the microwave frequency feeding the plasma chamber [9]. In this experiment, we measured reflection coefficient as a function of frequency when plasma is present. The resonant modes of vacuum filled cavity without including plasma lens, rf window and waveguide assembly were calculated by eigenmode solver of CST Studio [10]. The parameter of the cavity and other assemblies were also not optimized. In this paper we present, a set of measurements of reflection coefficient with different tuner position carried out on the same 10GHz Nanogan ion source without plasma. To determine the resonant modes, frequency domain solver of CST Studio was used and simulate the cavity. A comparison between simulated and experimental results are also presented.

† email address: kedarmal@iuac.res.in

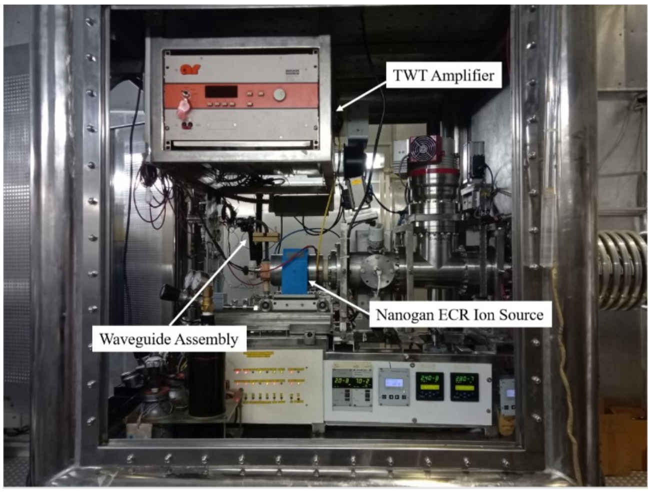


Figure 1: 10 GHz Nanogan ECR Ion Source

## EXPERIMENTAL SETUP

A 10 GHz fully permanent magnet Nanogan ECR ion source was used for the experiment as shown in figure 1. The source was bought from the Pantechnik company [8], whose typical operating frequency is 10 GHz. A detailed description of the main feature of the ion source and the facility can be found in Refs. [9], [11] and [12]. The plasma

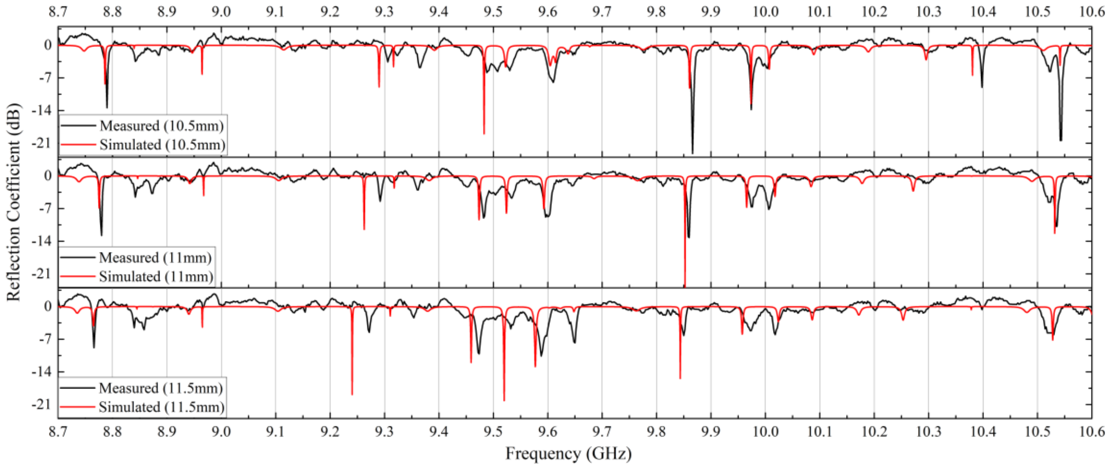


Figure 2: Reflection coefficient as a function of frequency for different tuner positions.

chamber has a cylindrical cavity of inner radius 13mm and length 140mm coupled to a RF cube and a dc bias tube positioned inside the plasma chamber. In our experiment, we have pulled out dc bias tube. The ion source was powered by a wide band (8-18 GHz) travelling wave tube (TWT) amplifier through waveguide assembly (see figure1). A Rhode and Schwarz signal generator was used to vary the frequency and in our experiment, the frequency was chosen to be varied from 8.7 to 10.65 GHz in steps of 2MHz. To measure the forward and reflected power together with frequency at each step, a C-program was written. To record stable power level, a delay of 3 second was set between each step.

## EXPERIMENTAL AND SIMULATION RESULTS

The ion source parameters were kept constant through-out the measurements and are forward power 30W at frequency 10 GHz, extraction voltage at 15kV, injection pressure 3E-7 torr and extraction pressure 2E-8 torr. With these ion source conditions the reflection coefficient data were recorded for three different positions of single stub RF tuner. The corresponding results are shown figure 2. The reflection coefficient is defined as

$$Reflection\ Coefficient = 20 * log_{10}(\frac{Reflected\ Power}{Forward\ Power}) \ldots (1)$$

where forward power is the microwave power sent to the ion source and reflected power is that reflected by ion source. We have measured both power level from TWT amplifier itself.

By analysing the reflection coefficient ($S_{11}$ parameter), it is possible to characterize the modes that exist inside the plasma chamber. In fact, the frequencies for which the minimum values of the $S_{11}$ occur represent the excited modes.

The theoretical calculation of the resonant modes and reflection coefficient of Nanogan cavity has been carried out by using frequency domain solver of CST Studio. A simulated geometry model of ion source cavity coupled to rf cube and waveguide assembly is shown in figure 3.

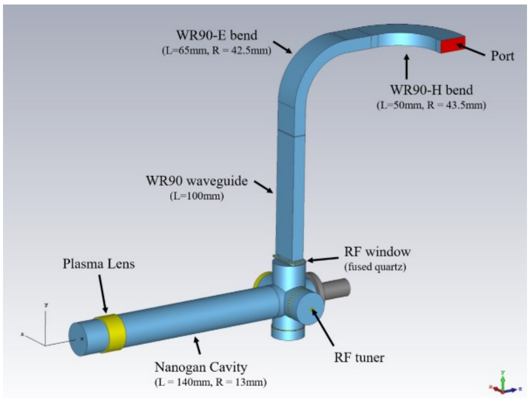


Figure 3: CST Model of the Nanogan Cavity coupled to rf cube and waveguide assembly.

To excite the geometry, a waveguide port of mode pattern TE10 was defined (see figure 3). The maximum element of the mesh size was set to 7.07mm (about $\lambda_0/4$, where $\lambda_0$ is the vacuum wavelength of frequency 10.6GHz). A detailed description about frequency domain solver is described in ref [13]. The simulation procedure started at tuner position 10.5mm, with the predefined accuracy of delta S was set to 2% to stop mesh adaption at single frequency and reduced order model accuracy was set to 1E-5 to stop broadband frequency sweep. The simulation results obtained from frequency domain solver includes $S_{11}$ parameter and resonant modes versus frequency. Furthermore, the optimization of the geometry model of Nanogan has been performed in CST studio by using Trusted Region Framework (TRF) optimizer to match the simulated results with measured one. The final goal norm in TRF optimizer was achieved 10% which shows the difference between measured and simulated data. The optimized geometry model up to WR90 H bend is shown in figure 3. The optimized $S_{11}$ parameters at different tuner positions are plotted together with measured result and shown in figure 2. The strongest resonant modes of the optimized cavity at tuner position 10.5mm, in the frequency range 8.7 to 10.6 GHz have been calculated by using eigenmode solver and defining a field monitor in frequency domain solver at positions where $S_{11}$ shows minimum value, are shown in table 1.

Table 1: Modes inside the Nanogan cavity in frequency range 8.7 to 10.6 GHz at tuner position 10.5mm.

| | Mode | Eigenmode Solver [GHz] | Frequency Domain Solver [GHz] | Measured (Reflection Coefficient) [GHz] |
|---|---|---|---|---|
| 1 | TE115 | 8.7880 | 8.7879 | 8.7900 |
| 2 | TM010 | 8.8474 | 8.8470 | 8.8420 |
| 4 | TM011 | 8.9702 | 8.9704 | 8.9680 |
| 6 | TE116 | 9.2876 | 9.2884 | 9.3060 |
| 7 | Hybrid | 9.3223 | 9.3237 | 9.3240 |
| 8 | Hybrid | 9.4809 | 9.4842 | 9.4880 |
| 9 | Hybrid | 9.5235 | 9.5214 | 9.5300 |
| 10 | Hybrid | 9.5990 | 9.6084 | 9.6100 |
| 11 | TM014 | 9.8566 | 9.8608 | 9.8660 |
| 12 | Hybrid | 9.9688 | 9.9714 | 9.9740 |
| 13 | TE117 | 10.0009 | 10.0080 | 10.0040 |
| 14 | TM015 | 10.3793 | 10.3810 | 10.3980 |
| 15 | Hybrid | 10.5372 | 10.5400 | 10.5430 |

## DISCUSSIONS AND CONCLUSIONS

A 3D simulation of the 10 GHz Nanogan cavity without plasma has been successfully performed using frequency domain solver of CST Studio. The geometry of the cavity including the rf cube, the plasma lens, the rf window and the waveguide assembly up to WR90 H bend has been taken into account. Using a TRF optimizer in frequency domain solver, we found optimum parameters for the cavity to match the simulated results with measured one by varying each parameter only by ±1% from their initial values. The optimization of parameters has been done only with tuner position 10.5mm. The results shown in table 1, confirm that the resonant modes are present in the cavity without plasma. The $S_{11}$ parameters of the optimized model at different tuner position have been compared with the measured reflection coefficient and agreement between both was about 90%. From figure 2, we can see that the peak near frequency 10.4 GHz is disappeared at tuner position 11mm and similar effect also can be seen with the corresponding $S_{11}$ parameter. Another effect of tuner can be seen in frequency range 9.95 to 10.02 GHz where both peaks starts to move far away as tuner position increased and similar effect also seen with simulated results. These results further validate the optimized model of the cavity is correct. In the future, we will study the similar results in presence of the dc bias electrode with this optimized model of ion source and also with the plasma.

## ACKNOWLEDGMENTS

The support from the colleagues of vacuum lab, workshop, beam transport lab and electronics group, are warmly acknowledged.

## REFERENCES

[1] R. Geller,"Electron cyclotron resonance ion sources and ECR plasmas", Bristol: IOP (1996).

[2] S. Biri et al., "Two-frequency heating technique at the 18 GHz electron cyclotron resonance ion source of the National Institute of Radiological Sciences", Rev. Sci. Instrum, vol. 85, p. 02B507, (2014).

[3] Z.Q. Xie et al., "Two-frequency plasma heating in a high charge state electron cyclotron resonance ion source", Rev. Sci. Instrum, vol. 66, p. 4218, (1995).

[4] S. Gammino, "3rd and 4th Generation ECRIS: Some Possible Scenarios", High Energy Physics &Nuclear Physics, S1, p. 137-141, (2007).

[5] L. Celona et al., "Observation of the frequency tuning effect in the 14 GHz CAPRICE ion source", Rev. Sci. Instrum, vol. 79 p. 023305, (2008).

[6] F. Consoli et al., "Microwave field distribution and electron cyclotron heating process", Rev. Sci. Instrum., 79, 02A308 (2008).

[7] L. Celona, et al., "On the observation of Standing Waves in Cylindrical Cavities filled by Microwave Discharge plasma", Proceedings of ECRIS08", Chicago, IL USA.

[8] P. Sortais, et al., "Latest developments on multicharged ECR ion sources at GANIL" in Proc. EPAC, 1992, p. 990.

[9] G. Rodrigues, et al., "Effect of frequency tuning on bremsstrahlung spectra, beam intensity, and shape in the 10 GHz NANOGAN electron cyclotron resonance ion source", Rev. Sci. Instrum., vol. 85, p. 02A944, 2014.

[10] CST Microwave Studio, http://www.cst.com/Content/Products/MWS/Overview.aspx.

[11] D. Kanjilal et al., "Development of a low energy ion beam facility at NSC", *Indian Journal of Pure and Applied Physics*, vol. 39, pp. 25-28, 2001.

[12] Kedar et. al, "Operation and Maintenance of ECR based Low Energy Ion Beam Facility", Proceedings of INPAC2018, RRCAT, India.

[13] Weiland, T. et al., "A practical guide to 3-D simulation", IEEE Microwave Magazine, 9(6), 62–75, (2008).

# PLASMA SURFACE PROCESSING FOR ACCELERATING STRUCTURES IN PARTICLE ACCELERATORS

P.V. Tyagi
*NPD, Bhabha Atomic Research Centre, Mumbai - 400085*

*Abstract*

Plasma surface processing for cleaning multi-cell accelerating cavities has been recently developed and proven to be successful with the improvement of the cavity accelerating gradient. The key advantage of the plasma processing is; it can be applied in-situ while accelerating cavities are installed in the accelerator tunnel. In this article, details about plasma processing and its application to multi-cell accelerating cavities as well as normal conducting LINACs will be discussed.

## INTRODUCTION

Surface contaminants present in the high gradient accelerating structures of the particle accelerators may lead to multiple issues such as field emission, degrade the vacuum level and create a discharge during their operation at high field. In this regard, inner surface of the accelerating cavities is subjected to various chemical and other post processing [1,2] to obtain a ultra-clean and smooth surface to achieve high performances and uninterrupted operations. However, sometimes performance of those accelerating cavities degrades over the time during operation.

An in-situ plasma processing had been developed for superconducting radio frequency (SRF) cavities to improve their performances at SNS, ORNL, USA [3]. The SNS high beta cavities (six cells) were suffered from field emission thus limiting their accelerating gradient. The main reason for field emission was believed to be hydrocarbon contamination present at cavity surface. Application of the plasma processing at a high beta cavity at SNS had improved its accelerating gradients. The encouraging results of the plasma processing led its deployment in the SNS cryomodules. Plasma processing involved two steps; a) plasma is ignited and tuned in the desired cell of the cavity using a base gas and 2) introducing a cleaning agent to clean the cell. The promising results of the plasma processing has also led many other labs to investigate further. Lately, plasma ignition process has also been developed for a nine cell SRF cavities for future applications [4,5] as well as applied on low beta structures [6].

In addition to application at SRF cavities, plasma processing has also been applied in the normal conducting LINACs at Daresbury laboratory, UK. These normal conducting LINACs were suffered from hydrocarbon contamination which caused a poor vacuum in the LINACs. Due to physical limitations, baking out at higher temperature than 100 $^{0}$C was not possible. Hence, the plasma processing was considered for cleaning of the LINACs. In this article, the details of the plasma processing to clean accelerating structures will be discussed.

## PLASMA PROCESSING OF MULTI-CELL SRF CAVITIES

### *Plasma ignition in a six cell SRF cavity*

For the development of in-situ plasma processing for SNS SRF cavities, it was considered to use resonant modes of the cavity and plasma in each cell of the cavity can be ignited. Neon was chosen as a base gas for plasma ignition and a small amount of oxygen was used as a cleaning agent to eradicate hydrocarbons during the cleaning of the cell. A setup for plasma processing includes two rf signal generators, a rf amplifier, gas mixer for two or more gases, vacuum system and residual gas analyser etc. Figure 1 shows the schematic of the plasma processing setup in details.

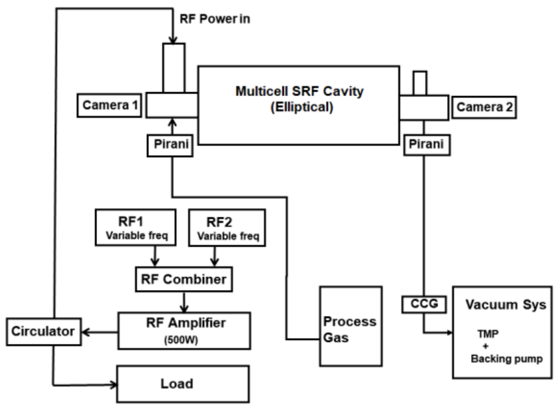


Figure 1: Schematic of plasma processing setup for multi-cell SRF cavities.

The E-field distribution in the accelerating mode (π mode) of the SRF cavity has the field level same in all cavity cells. Hence, using π mode only, it's difficult to achieve plasma ignition in each cell. That means, to achieve plasma ignition in individual cells, other modes of the cavity with the highest E-field in that cell as well their combinations along with frequency tuning to break E-field symmetry of the modes are required to be utilized.

SNS superconducting LINAC employed six cell (even no. of modes), 805 MHz medium and high beta elliptical SRF cavities. The E-field distribution of some of the modes of the cavity has found E-field symmetry in two cells. The modes with the field symmetry in two cells can be used to ignite plasma and tune in those cells after breaking the mode symmetry. This was achieved by using left and right of the resonance (off resonance) within the bandwidth of the mode. Further, another mode was combined to increase the field level in the desired cell. At last, plasma was locked in the cell using $\pi$ mode. Using this mechanism, plasma ignition in each cell was achieved successfully.

Once plasma is ignited and tuned in a cell, a cleaning agent can be introduced to clean that cell. The cleaning is live monitored through residual gas analyser (RGA) and stopped after reaching the contamination level below the background level.

### *Plasma ignition in a nine-cell SRF cavity*

After successful application of the plasma processing with performance improvement at SNS, USA, there was an interest to develop plasma processing for a nine cell SRF cavity. In contrast to SNS six cell SRF cavity i.e. even number of modes, a nine cell cavity possess nine resonant modes i.e. odd number of modes. This means that the plasma ignition mechanism for a six cell cavity cannot be applied to a nine cell cavity because the field distribution is different than six cell cavity.

The plasma ignition mechanism for a nine cell using fundamental modes of the cavity was first developed at Daresbury laboratory, UK [4]. The mechanism includes igniting plasma in first cell (coupler side) then stimulated to subsequent cells by combining a suitable mode frequency. The plasma act as a dielectric inside the cavity and perturbs the E field distribution and mode frequency. The field perturbation caused by plasma ignition was simulated using CST and a matrix plot was generated. The combining mode with corrected frequency was selected from the matrix plot having the highest E-field level in the subsequent cell. The mode is then superimposed which led plasma to stimulate to subsequent cell. This process is very straight forward to use and can be used for all types of multi-cell cavities with any number of modes (odd or even). In this process, plasma is ignited once and kept ON throughout the plasma processing of the cavity. After plasma is tuned in a cell, a cleaning agent is introduced, plasma cleaning is observed and turned off the cleaning agent after cleaning of that cell is finished, thereafter plasma is stimulated to subsequent cell and cleaning agent is introduced for cleaning of that cell. This process is repeated until all the cells have been cleaned.

At Fermilab, the plasma ignition in different cells of a nine cell cavity is achieved utilizing higher order modes (HOMs) [5]. The ignition methodology utilizes HOM coupler to ignite plasma in each cell of the cavity. The aim of utilizing HOMs of the cavity is to reduce required power for plasma ignition.

### *Improvement of surface workfunction of Nb after plasma processing*

Studies on Nb sample after plasma processing has found that Nb workfunction was increased after the plasma processing. The reported Nb workfunction is 4.3 eV whereas $Nb_2O_5$ workfunction is 5.2 eV. In most of the studies on Nb samples subjected to different surface processing including electropolishing, actual surface workfunction was measured around 4.8 eV while after plasma processing, it was increased more than 5.2 eV [7]. The SIMS (secondary ion mass spectrometry) analysis had shown that plasma is only effective to remove hydrocarbon contamination from top surface only. It was also observed that hydrocarbons from near surface region can migrate to top surface and degrade surface workfunction. It was found during the studies that multiple round of plasma processing helps to deplete hydrocarbons in near surface region thus and maintain higher workfunction for a long time. This suggested that multiple rounds of the plasma processing was required to clean cavity surface and sustain a high workfunction for a long period of time.

## PLASMA PROCESSING OF NORMAL CONDUCTING LINACS

Plasma processing has been proven to be successful for SRF cavities with their performance improvement. But, it has not been considered for normal conducting LINACs so far while high gradient normal conducting LINACs may also suffer from electron activities. One of the main reasons is that the plasma processing utilizes oxygen to eradicate hydrocarbon contaminations from cavity surface which can heavily oxidize the copper surface. Therefore, precautions are well taken to avoid plasma ignition in power coupler while applying plasma processing in SRF cavity. However, plasma cleaning is commonly used to clean copper material to be used for photocathodes development. It is observed that temperature rise during plasma processing plays a critical role in oxidation of the copper surface. Hence, to apply plasma cleaning on the copper structures, temperature rise during plasma processing should be kept low as possible to avoid unwanted copper oxidation.

Figure 2: Plasma cleaning of the normal conducting LINAC at Daresbury Laboratory. Inset shows plasma inside the LINAC.

The CLARA accelerator at Daresbury laboratory will utilized normal conducting LINACs to accelerate charged particle beam. There are total four such LINACs are planned to be commissioned. Each LINAC has 132 cells and is 4 meters long. RGA analysis of the LINACs had found hydrocarbon traces and it was not possible to achieve ultra high vacuum in the LINACs. Baking at high temperature of those LINACs was not possible because the glue used to attach cooling channels cannot sustain more than 100 $^{0}$C. Therefore, only plasma processing seemed to be a viable option to clean those LINACs. But the same plasma processing method of SRF cavities using ignition in each cell, is difficult to achieve in those LINACs. Additionally, it was difficult to monitor the plasma location with the help of cameras in such a long LINAC. Therefore, it was considered that plasma cleaning of the LINACs will be pursued but cleaning of each cell may not be necessary (see fig. 2). Plasma will target contaminated sites preferentially due to the availability of electrons more easily at contaminated sites than the cleaned sites. This will help plasma to be ignited at the contaminated cell and carry out cleaning with residual oxygen only. Once plasma is ignited in a cell, frequency tuning can be used to stimulate plasma in different cells. To avoid increase in the temperature, the forward is reduced to the lowest level keeping plasma active. This will help to avoid temperature increase thus excessive oxidation of the copper and cleaning of the LINACs can be carried out safely. Using above methodology, four LINACs were processed and no sign of hydrocarbons was found in the post processing RGA analysis. This was the first time that the plasma processing had been applied to normal conducting LINACs and was able to clean those LINACs.

## FUTURE SCOPE OF WORK

Till now, plasma processing has been applied to eradicate hydrocarbon contaminations present in multi-cell cavities, low beta cavities and normal conducting LINACs. Hydrocarbons can be present on cavity surface even after all the surface processing and assembly is carried out in high quality clean room and/or accumulated over the time during continuous operation. In both cases, plasma processing can be an important process to be used as a final surface process and/or in-situ to recover cavity performance while installed in the accelerator tunnel. Other than hydrocarbons, there can be different types of chemical contaminants present on the cavity surface for eg. sulfur is left behind after electropolishing of the cavity. In this regard, plasma processing can be a promising candidate to eradicate different types of contaminations from cavity surface. This will require development of adequate plasma chemistry for targeted type of contaminations. By changing the recipe, different types of plasma chemistry can be carried out inside a cavity thus different types of contaminants can be eradicated. Therefore, plasma processing can offer a complete solution to remove different types of contaminations present at cavity surface as a final surface treatment and/or in-situ application.

## REFERENCES


[1] P. V. Tyagi, T. Saeki, M. Sawabe, H. Hayano, S. Kato, “Influence of Electropolishing Current Densities on Sulfur Generation at Niobium Surface", Applied Surface Science, Volume 285, pages 778-782, 2013

[2] **P. V. Tyagi**, H. Hayano,, M. Sawabe, S. Kato, "Study of HPR created oxide layer at Nb surfaces" Proceedings of LINAC2012, Tel Aviv, Israel.

[3] M. Doleans, al. “In-situ plasma processing to increase the accelerating gradients of SRF cavities” Nuclear Instruments and Methods in Physics Research Section A, Volume 812, Pages 50–59, 2016.

[4] P.V. Tyagi et. al. “Plasma Ignition and Tuning in Different Cells of a 1.3 GHz Nine-cell Superconducting Radio Frequency Cavity: Proof of Principle” Nuclear Inst. and Methods in Physics Research A, Volume 893, Pages 95–98, 2018.

[5] P. Berrutti et. al. “Plasma ignition and detection for in-situ cleaning of 1.3 GHz 9-cell cavities” J. Appl. Phys.126, 023302, 2019.

[6] A.D. Wu et. al. “Vertical test results of plasma in-situ cleaning on low beta HWR cavity” Proceedings of the LINAC2018, Beijing, China.

[7] P.V. Tyagi et. al. “Improving the work function of the niobium surface of SRF cavities by plasma processing” Applied Surface Science, Volume 369, Pages 29–35, 2016.

# STUDY ON PROTON BEAM INDUCED THERMAL IMPACTS ON ROTATING SPALLATION TARGET FOR INDIAN FACILITY FOR SPALLATION RESEARCH (IFSR)

S. L. Nidhin#, N. K. Sharma[1], G. V. Kane, V. K. Senecha[1], S. C. Joshi, RRCAT, Indore, India
[1]also at, Homi Bhabha National Institute, Mumbai, India

*Abstract*

A spallation target generates neutrons upon irradiating with high energy proton beam. A Rotating Target is a novel spallation target design philosophy being considered for proposed IFSR at RRCAT. 'Semi Empirical Heat-Generation' (SEHG) algorithm, has been developed, that equips a Computational Fluid Dynamics (CFD) solver with the capability to simulate spatial energy deposition by proton beam. A thermal hydraulic analysis is carried out using the spatial energy deposition as heat load to compute the temperature rise in target material. Subsequently a thermal-structural coupled simulation is carried out to evaluate the thermal stress and deformation in the target assembly. This paper reports modifications made in the stock SEHG algorithm for time averaging of energy deposition and simulation results including energy deposition and thermal stress in rotating target assembly.

## INTRODUCTION

Spallation targets are those elements of a Spallation Neutron Source [1] that anticipates accelerated proton beam and generates neutrons. High energy proton beams, along with knocking-off neutrons deposits its kinetic energy which is anticipated as heat generation in the target materials. The target elements should have the thermal stability to withstand the high energy proton beam. Typically, static solid targets are used in low power (below 1 MW) spallation neutron source facilities. For megawatt class facilities the thermal stability of solid targets becomes vulnerable and liquid targets are preferred due to their favourable thermal hydraulics in taking away the deposited energy. Liquid targets will require a huge inventory of liquid metal (a few tens of tonnes), which is essentially radioactive. Solid targets are favourable in terms of their compact nature and radioactivity being contained in a small volume, easy to handle form. Solid targets are also famous for their high brightness behaviour which results from the compact nature of the source. Rotating Spallation targets [2] were introduced in this scenario to take advantage of both the worlds. It is essentially a solid target inheriting all its advantages and overcoming the thermal stability issue by spreading the thermal effect on a much larger volume – by rotating a solid target. Tungsten is being studied as the target material due to higher neutron yield and superior thermo-mechanical properties.

## TIME AVERAGING OF ENERGY DEPOSITION

The SEHG code [3] is modified to incorporate the dilution effect in energy deposition due to target rotation. Time averaging can be done using equation 1. $P_{avg}$ is the average power density, P is the instantaneous power density and r is the radius at which beam is interacting with target material.

$$P_{avg} = \frac{\int_{-\infty}^{\infty} P.dx}{2\pi r} \tag{1}$$

Assuming a gaussian beam,

$$P = P_0 . e^{\frac{-x^2}{2\sigma_x^2}} . e^{\frac{-y^2}{2\sigma_y^2}} \tag{2}$$

$$P_{avg} = P_0 . e^{\frac{-y^2}{2\sigma_y^2}} \left\{ \frac{1}{\sqrt{2\pi}} \frac{\sigma_x}{r} \right\} \tag{3}$$

The term inside the brackets of eqn. 3 is the time averaging factor. It can be observed that time averaging factor is inversely proportional to radius of rotation, that suggests that the dilution effect of rotation disappears as the beam penetrates deep into the target.

## ROTATING TARGET MODEL

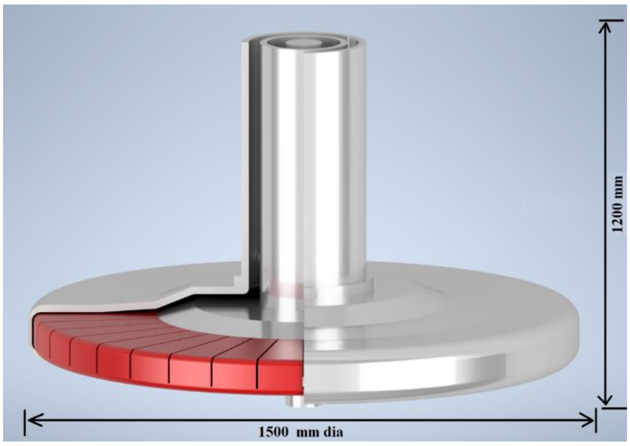


Figure 1: Rotating Target Model.

A rotating target of 1.5m diameter was modelled as shown in figure 1. Tungsten was used in segmented form

#nidhin@rrcat.gov.in

($10^{o}$ segments) which is named as tungsten blades, and 36 of them are required to cover the whole $360^{o}$. Other parameters regarding the rotating target model is listed in table 1.

Table 1: Parameter Table.

| Parameter | | Value |
|---|---|---|
| Target Disc Material | : | Tungsten |
| Casing Material | : | SS 304 |
| Target Disc Diameter | : | 1500 mm |
| Beam Energy | : | 1 GeV |
| Beam Current | : | 1 mA |
| Beam Power | : | 1 MW |
| Beam Cross Section | : | 15 mm (RMS) |
| Coolants Studied | : | Water |
| Study Type | : | Steady State |

## RESULTS AND DISCUSSION

A Fluid – Thermal – Structural coupled simulation is performed to assess the performance of rotating target under steady state time averaged loading. Water is chosen as coolant for initial design trials with a flow rate of 50 LPS. A 10 deg segment ($1/36^{th}$ of the target assembly) of the model is used for analysis to save computation time.

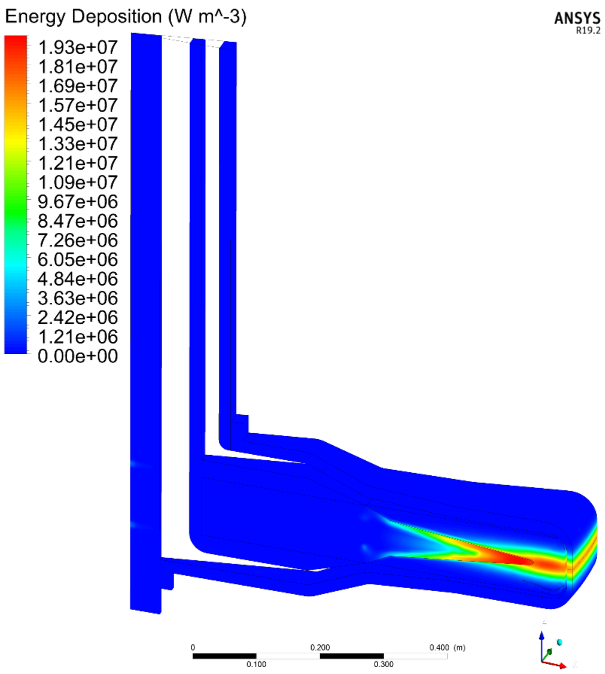


Figure 2:Energy Deposition (Heat Generation) Plot.

Figure 2 shows the time averaged energy deposition on rotating target, computed using in house developed 'Semi Empirical Heat Generation (SEHG)' algorithm. If observed carefully the radiation streaming footprints can be observed in the central shaft facing the upper and lower coolant channels. The collars of blade support shaft have a serious impact on reducing its effects to below that is acceptable. The radiation streaming footprints shows the precision of 'Semi Empirical Heat Generation (SEHG)' algorithm in simulating the beam – material interactions pertaining to target design.

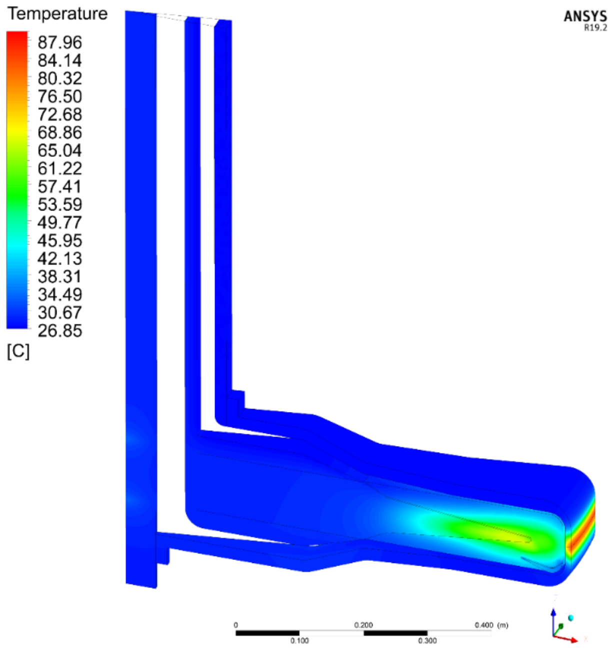


Figure 3:Temperature Rise Plot.

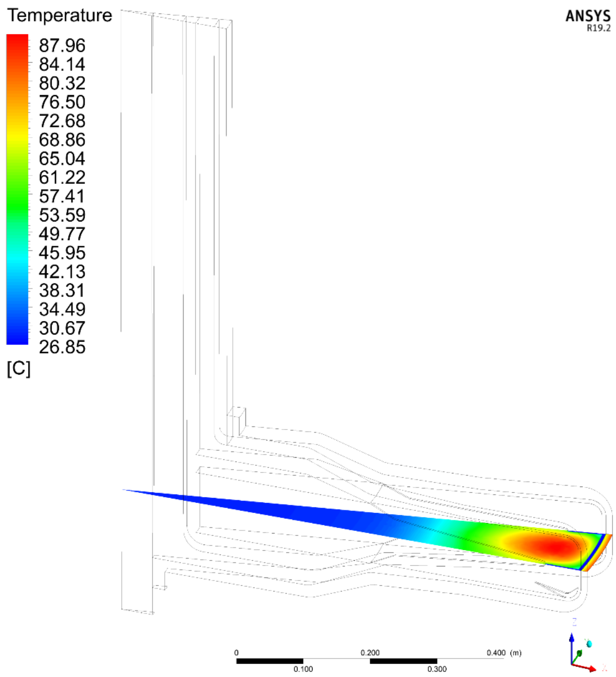


Figure 4:Temperature Plot at the plane bisecting Tungsten Blade.

Figure 3 shows the temperature plot on the target assembly. Thermal conductivity of tungsten was applied as 173 W/m.K. A peak temperature of ~ 88 °C is observed. The fluid-solid interface temperatures are within the boiling point of coolant (water). Higher temperatures were observed in the casing junction, where the beam intensity is maximum and cooling is available from only the inner surface. The temperatures are so low compared to recrystallization temperature of tungsten to cause any material impact. The temperature plot gives confidence in thermally safe operation of rotating target. Figure 4 shows the temperature contours along the central plane bisecting tungsten blade. The peak temperature (viz, 88 °C) happens to be at deep within the tungsten blade resulting in a much lower surface temperature, which reduces the fluid-solid interface temperature. The temperature contour agrees quietly with the energy deposition profile of tungsten, which suggests a peak deposition deep inside the tungsten blade than the surfaces.

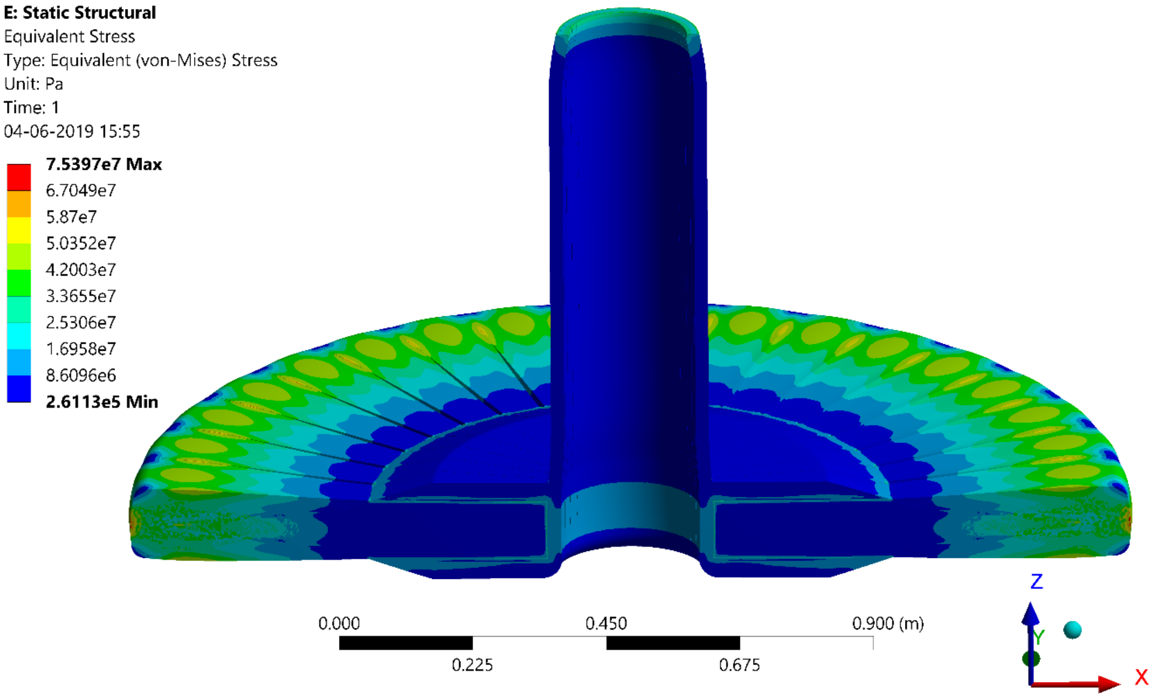


Figure 5:Equivalent Stress due to Thermal and Inertial loads.

The thermal load along with inertial load is used for structural analysis of tungsten blade and blade support shaft assembly. The young's modulus, thermal expansion coefficient and Poisson ratio of tungsten are 411 GPa, 4.5 µm/m.K and 0.28 respectively. Fig 10 shows the equivalent stress profile, the peak equivalent stress is ~76 MPa which is insignificantly small compared to the yield strength of tungsten (viz, 1600 MPa).

## CONCLUSION

The thermal impacts on a rotating target assembly is studied considering 1 GeV, 1 mA proton beam and tungsten target. Water is used as the coolant. The steady state peak temperature of 88 °C and peak equivalent stress of 76 MPa is observed. Since the temperature rise and equivalent stress are well below safety limits, the studied design configuration has achieved thermally stability.

## REFERENCES


[1] S.F. Nowicki, S.A. Wender, M. Mocko, "The Los Alamos Neutron Science Center Spallation Neutron Sources", Phys. Procedia. 90 (2017) 374–380.

[2] A. Aguilar et al. , "Design specification for the European Spallation Source neutron generating target element", Nucl. Instruments Methods Phys. Res. Sect. A 856 (2017) 99–108.

[3] S.L. Nidhin et al. , "An efficient algorithm for computation of spatial heat generation during interaction of high energy proton beam with target materials", Nucl. Instruments Methods Phys. Res. Sect. B 461 (2019) 16–24.

# ENGINEERING DESIGN ANALYSIS FOR 325 MHZ DRIFT TUBE LINAC FOR INDIAN FACILITY FOR SPALLATION RESEARCH

Pranav Paliwal, N. K. Sharma and G. V. Kane
Raja Ramanna Centre for Advanced Technology,
Indore, 452013

*Abstract*

Design and development activities are under progress for various cavities for acceleration of charged particles in Indian Facility for Spallation Research (IFSR) at RRCAT, Indore. Proton beam will be accelerated up to 1 GeV in Linac, before it is bombarded on target module for generation of neutrons. Linac consists of various cavities for acceleration of beam of charged particles. Drift Tube Linac (DTL) is a part of Linac, where beam of charged particles will be accelerated from 3 to 13 MeV at operating frequency of 325 MHz. Engineering design of DTL involves, designing stable structure and cooling path in cavity for removal of RF heat. To check the adequacy of cooing path computational fluid dynamic (CFD) studies are carried out. Thickness of DTL tank has been arrived at after iterative CFD and structural analysis.

## INTRODUCTION

Indian Facility for Spallation Research (IFSR) is an accelerator based facility which will produce neutrons upon bombardment of 1 GeV beam of protons on target material. Research and development of various components for proposed IFSR are in progress in RRCAT. Proton Linac consists of various components. It begins with ion source where $H^-$ ions are generated and transferred to radio frequency quadrupole (RFQ) through low energy beam transport (LEBT). Beam is bunched and accelerated in RFQ. After RFQ beam goes to the drift tube Linac (DTL) through medium energy beam transport (MEBT). After DTL beam goes to various superconducting (SC) cavities. From SC cavities beam goes to high energy beam transport (HEBT) to accumulator ring and finally on the spallation target for production of neutrons.

DTL [1] is a normal conducting Linac and operates at room temperature. It uses RF power source for acceleration of charged particles. Major part of RF power dissipate into walls of cavity. This heat load, leads to increase in temperature and in turn thermal stress and deformation of structures of the components. Deformation due to thermal load should be kept as minimum as possible so that it should not lead to frequency shift in DTL.

DTL consist of drift tubes and tank, which houses all the drift tubes. Tubes are suspended from top of cylinder which is maintained under vacuum. Physics design of 325 MHz, 13 MeV DTL has been carried out by Accelerator Beam Physics Section (ABPS), RRCAT [2]. Table 1 shows the design parameters for present design of DTL.

Table 1: IFSR DTL design parameters

| | |
|---|---|
| Frequency | 325 MHz |
| Particles | $H^-$ ion |
| Injection energy | 3 MeV |
| Output energy | 12.9 MeV |
| Beam current | 15 mA |
| No of drift tube | 47 |
| Total length | 4.85 m |
| Total RF power requirement | 1.337 MW |
| Duty factor | 10 % |

Based on physics design parameters, engineering design has been carried out. Cooling path has been designed for drift tubes and DTL tank and to check effectiveness of cooling path computational fluid dynamic (CFD) simulation has been carried out.

In a DTL, thermal load on structures increases along the length. Heat load on drift tubes at rear end of DTL tank is higher as compared to drift tubes which are at the beginning of DTL tank. A selective approach has been adopted for checking the effectiveness of drift tube cooling and as part of that, five drift tubes have been considered for analysis purpose. CFD simulation has been carried out for 1st, $11^{th}$, $21^{st}$, $31^{st}$ and $41^{st}$ drift tube. Objective of CFD simulation is to find fluid flow pattern (velocity and pressure) in fluid domain and temperature rise of drift tubes. This temperature distribution is input for structural analysis. Similarly, CFD simulation has been carried out for DTL tank. nd based on temperature distribution structural analysis has been carried out for estimation of stress and deformation.

## MODELLING AND SIMULATION DETAILS

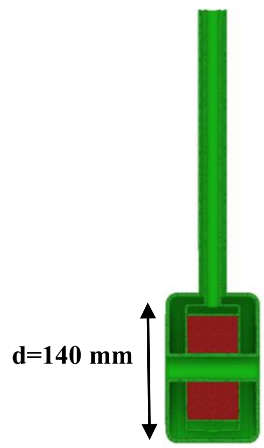


Figure 1: Cooling path for drift tube

Figures 1 and 2 show the solid model for cooling path designed for drift tube and first segment of DTL tank respectively. Various flow paths have been provided for flow of coolant in DTL tank. Circular holes throughout the length of tank, seems to be better option for heat removal as they are closer to heated surface. For better cooling of segment of tank where vacuum port is provided, serpentine flow path on outer surface of tank has been provided.

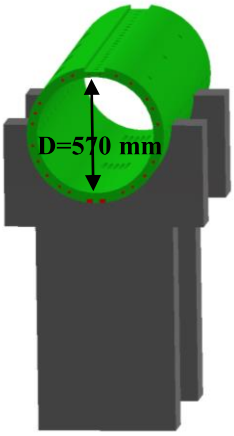


Figure 2: DTL tank model with cooling path and its support

For the purpose of CFD simulations, mesh has been prepared for drift tubes and DTL tank. To capture the near wall phenomena, very small cells near to walls has been provided. Total number of computational cells (mesh) for drift tube is ~ 1.7 lakh and for DTL tank it is ~ 4.4 lakh. Stainless steel has been considered as material for drift tube and DTL tank. Water has been considered as coolant for removal of heat from DTL. Simulations have been carried out using ANSYS. Velocity inlet boundary condition has been provided at the inlet of all cooling channels and pressure outlet boundary condition has been provided at the outlet. Heat flux is provided at the inner surface of tank. Standard k-epsilon turbulence model has been used for analysis. SIMPLE algorithm is used for pressure velocity coupling.

Structural analysis has been carried out for prediction of equivalent stress and total deformation due to various loads. For structural analysis support has been designed separately and assembly has been prepared. For DTL tank, thermal and vacuum load has been considered. For drift tubes apart from thermal and vacuum load, an internal pressure of 4 bar is also considered.

## RESULTS AND DISCUSSION

CFD simulations have been carried out for 5 different drift tubes (1st, 11$^{th}$,21$^{st}$, 31$^{st}$ and 41$^{st}$) and DTL tank. Heat load for 1$^{st}$ 21$^{st}$ and 41$^{st}$ drift tube is 0.086 kW, 0.29 kW,0.66 kW, 1.35 kW and 1.7 kW respectively at 10% duty factor. For drift tubes, inlet boundary condition is inlet velocity of 1 m/s and temperature of 300 K has been considered. This has resulted in maximum velocity of ~ 2.5 m/s for all drift tubes, which will not result in material erosion of drift tube during its operation. Figures 3 and 4 show the velocity and pressure contours, respectively for 41$^{st}$ drift tube. Velocity and pressure field distribution is similar for all drift tubes.

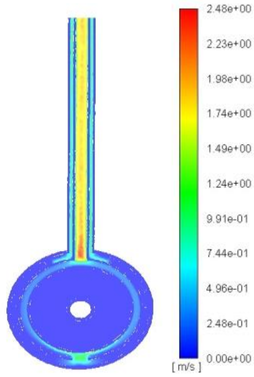


Figure 3: Velocity contour for 41st drift tube

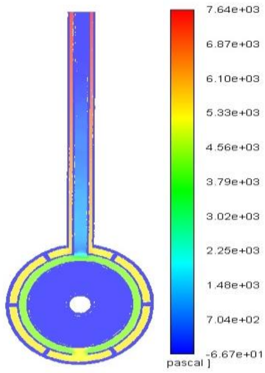


Figure 4: Pressure contour for 41st drift tube

Figure 5 shows temperature contour for 41$^{st}$ drift tube. Maximum temperature rise of 25.15 K has been observed for 41st drift tube. This is due to higher heat load for drift tubes which are at rear end of DTL.

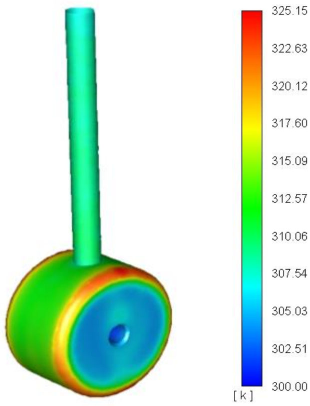


Figure 5: Temperature contours for 41$^{st}$ Drift Tube

Structural analysis has been carried out for the drift tubes. Apart from thermal load, an internal pressure of 4 bar and vacuum load also considered for analysis purpose. Figure 6 shows the stress distribution in 41$^{st}$ drift tube.

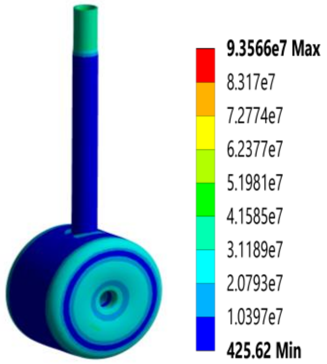


Figure 6: Stress contours for 41st Drift Tube

Stress distribution is mainly due to internal pressure in drift tube and it is similar for all the drift tubes. Value of maximum stress is ~ 95 MPa for all drift tubes. But deformation in drift tube increases with increase in temperature rise. Table 2 shows the maximum temperature on drift tube surface and deformation for various drift tube.

Table 2: Results of simulations for drift tubes

| Drift tube | Maximum Temperature, K | Maximum Deformation, mm |
|---|---|---|
| 1st DT | 301.8 | 0.036 |
| 11th DT | 305.29 | 0.038 |
| 21st DT | 311.08 | 0.05 |
| 31st DT | 324.6 | 0.065 |
| 41st DT | 325.15 | 0.074 |

Simulations have been carried out for DTL tank. Heat load for DTL tank is 49.4 kW at 10% duty factor load.

Figure 7 shows the temperature contour for DTL tank with 50 mm thickness. It can be seen that, maximum temperature occurs at inner surface of tank, near walls of vacuum port and this value is 345 K. Temperature value is high on the tank near penetrations, and all other places not much rise in temperature has been observed. This suggest coolant flow is able to remove heat and arrest the temperature rise.

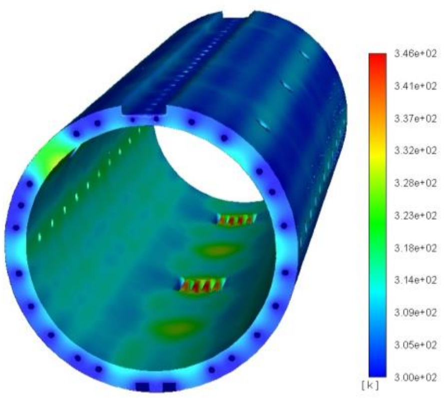


Figure 7: Temperature distribution for DTL tank

Temperature distribution on the surface of tank will exert thermal stress on tank. Apart from thermal load, vacuum load has also been considered. Figure 8 shows the stress distribution for first segment of DTL tank. Maximum value of stress is found to be 114.5 MPa. Figure 9 shows the deformation contours for first segment of DTL tank and total deformation is found to be 0.42 mm.

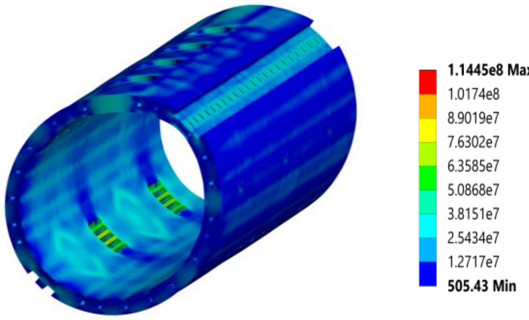


Figure 8: Stress contours for DTL tank

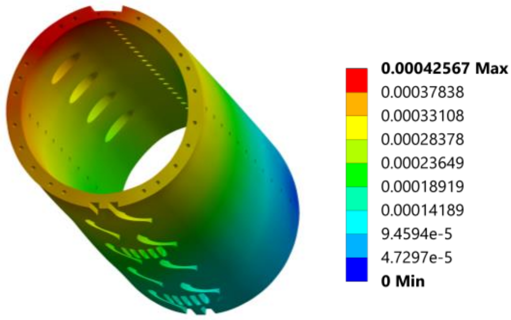


Figure 9: Deformation contours for DTL tank

## CONCLUSIONS

Cooling path for drift tubes and DTL tank has been designed and CFD simulations are carried out to estimate coolant velocity in drift tubes and temperature rise on walls of drift tube and DTL tank. This temperature distribution along with vacuum load and internal pressure is input for structural analysis. Structural analysis is carried out for the estimation of stress distribution and deformation. Maximum temperature is found to be 325 K for 41st drift. Stress distribution is similar for all the drift tubes and is mainly due to internal pressure. Maximum temperature is found to be 345 K on the inner surface of DTL tank at vacuum port. Maximum stress is found to be 114.5 MPa and total deformation is 0.42 mm. Maximum stress predicted for drift tube and tank is within acceptable limits. This study paves way for design of DTL Linac at high duty factor.

## REFERENCES

[1] Rinky Dhingra et al., “Technical Note: DTL/ABPS/2018-02: Design Data for Prototype 325 MHz Drift Tube Linac”, RRCAT, Indore India.

[2] S. C. Joshi et al., “Thermal Analysis of 350 MHz, 20 MeV CW Drift Tube LINAC Structure for Proposed 20 MeV Proton LINAC”, InPAC’ 03, Indore, February 2003, p. 99.

# MACHINING TRIALS ON VANE STRUCTURES OF RFQ OF 3 MeV, 325 MHz RFQ

T. Veerbhadraiah†, G. V. Kane, A. Chaturvedi, Sanjay Chouksey and G. Mundra, RRCAT, Indore

*Abstract*

A 325 MHz, 3.0 MeV Radio Frequency Quadrupole (RFQ) is being developed for 1 GeV proton accelerator for proposed Indian Spallation Neutron Source (ISNS) facility at Raja Ramanna Centre for Advanced Technology, Indore. RFQ is one of the important system of SNS and used for accelerating the ion beam from ion source. RFQ will be a normal conducting four vane resonating structure made of Oxygen Free Electronic (OFE) copper. One of the major challenges during development of the RFQ includes maintaining the quadrupole geometry within required tolerances during machining and assembly. Dimensions of internal features of RFQ like vane profile, width, height, flatness, straightness etc. plays an important role on field profile. In addition, surface finish on inner surface and on vanes of RFQ is more important. For this machining process plan, selection of metal cutting tools & tool materials are more important. To achieve required surface finishes on OFE copper RFQ vane surface, inner surfaces and brazing surfaces, machining parameters are optimised. In this regard few samples and a prototype RFQ segment in OFE copper were machined at machine RRCAT. Machining of actual RFQ structures structure is in progress.

The paper describes the tooling, machining process and parameters optimized and the measurement results during RFQ development.

## INTRODUCTION

RRCAT, Indore has taken up a project for development of RFQ and its sub-systems. RFQ is a four vane type RF cavity used to accelerate $H^-$ ion beam.

Process planning for machining, selection of shapes & materials of tools, optimization of cutting parameters and machining of test samples and prototype RFQ segment in copper material are explained in detail in the following sections.

## REQUIREMENTS

Total length of RFQ cavity is 3485.32 mm. Considering ease of fabrication and availability of material, RFQ is divided into 3 segments, each approximately 1.2m long. Individual segments would be coupled using metal seals and flanges. For efficient acceleration of charged particles in RFQ, critical parameters are:

- Resonating frequency of the structure
- Field profile along the length of structure
- Minimum ohmic losses on RF power transmitting surfaces
- Variation in magnitude of fields amongst the four quadrants

These parameters depends on accuracies of internal features of RFQ like:

- Vane profile accuracies
- Good surface finish on vane surfaces and inner surfaces of RFQ
- Surface finish and surface texture on brazing surfaces for good brazing joints etc.

Tolerance limits on maximum permissible errors of RFQ during the fabrication are listed in the Table 1 below:

Table 1: Permissible tolerances in RFQ structure

| | RFQ structure parameters | Tolerances |
|---|---|---|
| 1. | Longitudinal profile of the vane | ± 20 μm |
| 2. | Transverse curvature of the vane | ± 20 μm |
| 3. | Parallel and perpendicular vane tilt for a section | ± 50 μm |
| 4. | Parallel and perpendicular vane displacement | ± 50 μm |
| 5. | Surface finish on vane surfaces | ≤ 0.2 μm (Ra) |

To achieve these accuracies on assembly of RFQ after brazing, it is necessary to machine individual structure of RFQ to the following accuracies:

Table 2: Required and achievable tolerances on RFQ individual structures

| | RFQ structure parameters | Tolerances |
|---|---|---|
| 1. | Profile accuracy of the vane w.r.t. butting/brazing surfaces | ≤ 20 μm |
| 2. | Surface finish on vane surfaces | ≤ 0.2 μm (Ra) |
| 3. | Surface finish on inner surfaces of RFQ other than vane surfaces | ≤ 0.4 μm (Ra) |
| 4. | Flatness and parallelism of brazing surfaces | ≤ 20 μm |
| 5. | Scratch and burr free surfaces on brazing and inner surfaces of RFQ | |

## MACHINING OF RFQ STRUCTURES

Design of RFQ consists of two W-structures and two T-structures, brazed to form RFQ (fig.-1). To achieve stringent tolerances and high surface finish on RFQ structures, a proper machining process plan, fixtures (to hold structures at their free condition while machining, so that the tolerances of structures shall be retained after dismantling from fixture), suitable cutting tools with optimized cutting

† Email address: tvb@rrcat.gov.in

parameters and proper handling of structures to avoid scratches and dents are essential.

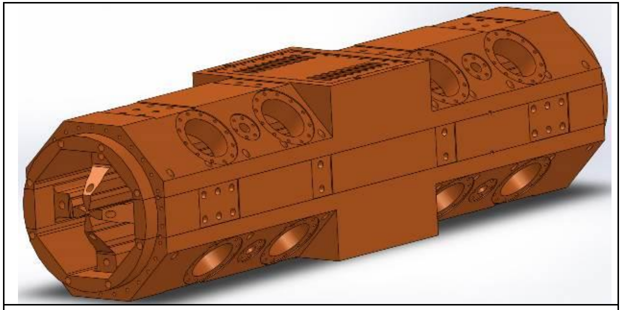

Figure-1: Solid model of RFQ

**Process planning for machining:**

1. Rough machining of RFQ structures keeping 5mm material allowance all over.
2. Stress relieving in vacuum brazing furnace so that structure dissertations are minimum at the time of brazing.
3. Semi-finish machining keeping 2mm allowance on inner, brazing and bottom surfaces of structures. Finish machining of ports on 45° surfaces and machining vacuum port slots on bottom face of W-structures.
4. Stress relieving before finish machining.
5. Finish machining of bottom surface, vacuum port on W-structures, machining of tapped holes etc.
6. Finish machining of brazing surfaces and bottom surface of T-structures.
7. Assembly of structures on machining fixtures.
8. Finish machining of brazing surfaces of W-structures.
9. Finish machining of vane, inner surfaces and ends of structures.

**Fixtures or machining of RFQ structures**:

For machining of modulated vane, inner surfaces and end profiles, fixtures are developed. They provide rigid support to structures while machining and handling (fig.2 & 3).

Figure-2: Fixture for machining of W structure on brazing surfaces, vane with undulations and inner surfaces on 5-axes CNC milling machine DMF 180

Figure-3: Fixture for machining T structure

**Brazing joints**: To establish brazing procedure suitable for RFQ structure brazing application, studies for different configurations were carried out. To validate the predicted effect, few samples were machined (Fig. 4).

Figure-4: Machined brazing samples

For the brazing filler wettability considerations, it was felt to validate the results for a small length structure. For this, four OFE copper plates measuring 250 mm long were machined. Different surface finish values viz. 0.4 µm Ra, 0.8 µm Ra etc. were maintained on the indicated surfaces. 1.1 mm wide and deep and 30 mm long grooves at specified intervals were also machined for placement of brazing filler wire. Fig. 5 shows all the parts machined for assembly brazing trial.

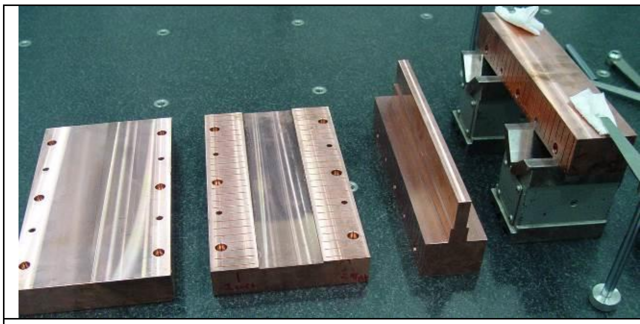

Figure-5: Components of prototype brazing structure.

**Machining of RFQ structures**

**Rough machining**: For machining of structures, side and face milling cutters with polished carbide inserts were used. Structures were machined keeping 5mm allowance on all faces and stress relieved. Subsequently structures were semi-finished keeping 2mm allowance on inner, brazing and bottom surfaces of structures. Finish machining was carried out on 45° surfaces, ports on 45° surfaces and vacuum port slots on bottom face of W-structures using different polished solid carbide cutters on Horizontal machining centre and 5-axes Vertical machining centre. Deformation due to stress relieving was observed less than 0.2 mm on the length of 1.2 m.

W-structures were machined on Vertical Machining Centre (VMC) for vacuum port slots, then on Horizontal Machining Centre (HMC) (Fig. 7) for rough and finish machining of 45° surfaces and ports on that surface, maintaining surface finish 0.4 to 0.6 µm Ra. Bottom surfaces and other features on these surfaces of the W-sections were machined on 5-axis CNC milling machine. Finish machining on bottom surface was done on free condition of the structure, maintaining the flatness 0.010 mm and surface finish was better than 0.4 µm Ra using 100 mm face milling cutter with polished Tungsten carbide inserts grade K-10 with rake angle 18°(Fig. 6)


Figure-6: Semi finished structures of RFQ


Figure-7: Machining of RFQ W- structure on Horizontal Machining Centre H 1250.

**Machining of vane with undulations**: Machining of undulations on vane of RFQ was carried out on aluminium alloy structure as shown in figure-2 and on OFE copper bars of 400 mm long as shown in figure-8, with spherical nose polished solid carbide cutter of grade K-10 of diameter 8 mm. Spherical nose cutter having shank diameter less than the tip ball diameter by 0.5 mm. Due to which shank does not come in contact with job while machining vertical surfaces. While machining, the cutter was tilted to 15° as shown in figure-2. This is essential because if the cutter is with 0° tilt angle, the tip of cutter can't machine the tip of the vane and a line gets formed. Due to tilt of the cutter, the tip of the vane was machined properly. Achieved profile tolerance of 0.012 mm and surface finish better than 0.2 µm Ra.


Figure-8: Machining of vane with undulations on OFE copper bar.

**Conclusion**: Fixtures to mount and machine RFQ structures on CNC milling machine were designed, fabricated and tested for functionality. Rough machining for first set of RFQ segment has been completed. Optimization of machining parameters was done for both rough and finish machining. Development of machining process using solid model of modulated vane has been attempted successfully. Machining trials on aluminium and OFE copper were carried out and achieved accuracies were verified on CMM machine.

**Acknowledgement:** We acknowledge whole team of Proton Linac Development Division for their encouraging support. Thanks are due to fabrication section for providing support during manufacturing. We are also thankful to maintenance group of DMTD for their support for keeping machines operational. Special thanks to Shri Hemant Jaurkar, Shri M. K. Gautam, Shri Anil Kalaskar and Shri Pawan Kumar from PMS, DMTD, RRCAT, Indore for the whole hearted support in machining of RFQ structures. Thanks are due to Shri Utpal Chatarji for supervising the machining work.

## REFERENCES

[1] G. V. Kane†, N. K. Sharma, A. Chaturvedi, B. Oraon, T. Veerbhadraiah, S. V. Kokil and S. C. Joshi, RRCAT, Indore, "Innovative Design of 3 MeV, 325 MHz RFQ structure from manufacturing consideration", InPAC 2018 held during January 9- 12, 2018 at RRCAT, Indore.

[2] S. C. Joshi, G. V. Kane, S. Raghvendra, S. Chinnathambi, B.Oraon and A. K. Jain, "Proposed Schemes For Fabrication Of 4.5 MeV, 350 MHz Prototype RFQ Structure", InPAC 2005 held during March 1- 5, 2005 at VECC, Kolkata.

[3] Anurag Chaturvedi, G V Kane, N K Sharma, B Oraon, S C Joshi, "Design for Fabrication of 325 MHz RFQ Structure", Indian Particle Accelerator Conference (InPAC-2015) held at BARC, Mumbai, from Dec 21st to Dec 24th 2015.

# COLD MODEL TESTING OF THE SCALED PROTOTYPE OF PROTON RFQ FOR ANURIB PROJECT*

C. Das #, T. Mandi, Suvadeep Roy, H.K. Pandey, S. Dechoudhury, V. Naik and A. Chakrabarti,
Variable Energy Cyclotron Centre,1/AF Bidhan Nagar, Kolkata 700 064, India
Homi Bhabha National Institute, Anushakti Nagar, Mumbai 400094, India

*Abstract*

As a front-end accelerator for proton driver of the ANURIB facility 80MHz, 800 keV, 5mA proton RFQ has been envisaged. RF structure of the extended rod type RFQ has been optimized using CST Microwave Studio. RF optimization was based on the optimization of the configuration of the stems for desired eigen-mode frequency as well as minimum assymetry of the quadrupolar field. The stem width was optimized considering the cooling channels embedded within it. For RF testing a scaled prototype of the RFQ has been fabricated in-house. Low power RF measurement of the prototype made of Aluminium has been performed.

## INTRODUCTION

An 800 keV, 5 mA proton RFQ has been proposed as the front-end accelerator of the proton driver for ANURIB project [1]. Beam dynamics as well as RF design of the RFQ resonating at frequency 80 MHz has been completed [2]. RF structure optimization was done by using CST Microwave Studio [3]. The goal of RF optimization was to get desired frequency, higher value of shunt impedance and quality factor, high dipole mode separation as well as minimum asymmetries of the quadrupolar electric field. The frequency was achieved by putting stem of optimized width and height in optimized distance apart. The maximization of Quality factor and shunt impedance and minimization of the field asymmetry has been done by playing with the stem cut angle [2]. The rod type RF structure of the proton RFQ resonating at 80 MHz is unique in its own. Hence validation of the optimization of RF parameters was necessary before going to fabricate the full scale modulated one. For this purpose, a scaled prototype of RFQ with unmodulated vanes has been fabricated in-house.

In this paper the results of CST simulation and low power RF measurements of the scaled unmodulated RFQ will be described.

## RF SIMULATION OF THE SCALED MODEL

The original RF structure of the RFQ has 18 posts to hold four modulated vanes each of length 3.41 m. For low power measurement of the RF parameters we have decided to fabricate a scaled model having 8 posts to hold four unmoduled vanes each of length 1.54 m. As the RF parameters of RFQ majorly depends on the structure of a single cell , we have kept the post configuration as well as the length of the vane over-hang on both sides same as in the original one. The structure is made of aluminium.

This structure is analysed using CST Microwave studio considering that the structure is made of Aluminium. The following figure shows that the structure has the quadrupolar electric field pattern at eigenmode frequency of 77.16 MHz. We can calculate the quadrupolar assymetry (QA) and the dipole component (DC) percentage at a particular radial position from the axis at every longitudinal position by knowing the electric fields $E_1$, $E_2$, $E_3$, $E_4$ in four quadrants [depicted in Figure 1] at equal distances from the centres. The formulae we have used for *QA* and *DC* are as follows:

$$QA = \frac{(E_1 - E_3)/2}{(E_1 + E_2 + E_3 + E_4)/4} \times 100$$

$$DC = \frac{(E_1 - E_3)/2}{E3} \times 100$$

Hence QA as well as DC will be described in ±% as per our formulation.

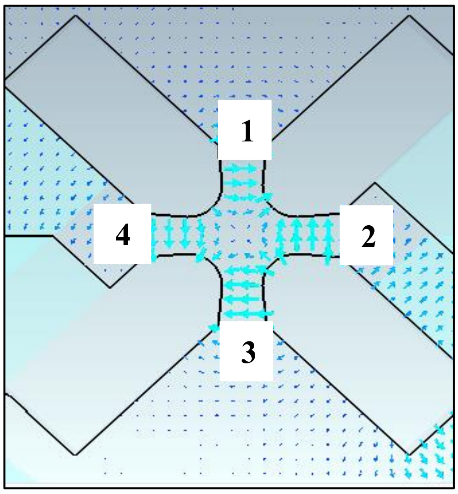


Figure 1: CST- simulated electric field pattern of the cold model

The results of the simulation is summarized in the following table 1:

*Work supported by Department of Atomic Energy, India
# chiranjib@vecc.gov.in

Table 1: CST simulated RF parameters of the Proton RFQ cold model

| Parameters | Simulated value |
|---|---|
| Eigenmode frequency (MHz) | 77.16 |
| Quality factor | 7010 |
| Shunt impedance (kΩ) | 69.3 |

## RF MEASUREMENTS

The cold-model has been fabricated in-house in VECC. RF structure parameters have been measured using vector network analyzer (VNA). The resonance frequency is measured to be 77.8186 MHz. The nearest dipole modes for the two structures are ~34.5 MHz apart. The Q-value (Unloaded) measured (-57dB) is about 3450. The measured results are summarized as well as compared with the simulated values in the following table [Table 2].

Table 2: Experimental results of lower power testing

| RF parameters | values measured/simulated |
|---|---|
| $f_0$ (Quadrupolar mode) | 77.8186/77.16 MHz |
| $f_1$ (Quadrupolar mode) | 113.8926/ 113.3583 MHz |
| $f_2$ (dipole mode) | 116.6215/ 116.0978 MHz |
| Q-value (un-loaded) | 3450/7010 |

The screenshot of the $S_{21}$ log magnitude plot on VNA featuring the quadrupolar and nearby higher order modes has been depicted in the following [Figure 3].

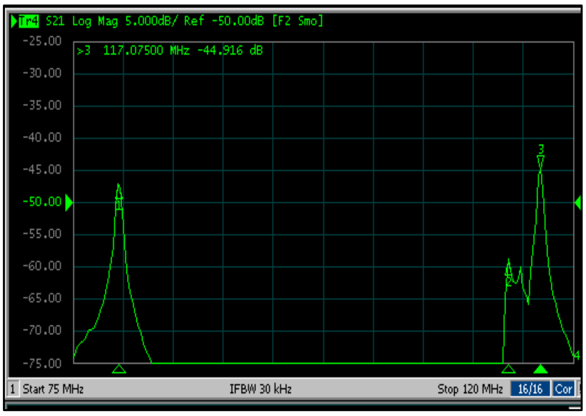


Figure 3: The measured Eigen mode frequencies

### *Bead-pull measurements set-up*

To measure the electric as well as magnetic field patterns in any cavity bead-pull measurement is performed. A small dielectric or metallic bead when placed inside a cavity the field pattern gets modified locally. This gives a change of the resonant frequency of the cavity. The change in the frequency depends on the size and properties of the bead and the intensity of the local fields. Hence the details of the field can be known by measuring the frequency shift for a known bead.

In RFQ, the horizontal component of electric field, $E_x$ is only along vertical axis (y-axis) and the vertical component of electric field, $E_y$ only along horizontal axis (x-axis). Hence using dielectric samples in form of discs/pill with circular dimension aligned along the field direction would give maximum frequency shift, as frequency shift is proportional to $r^3$, '$r$' being the radius of the pill. Moreover if the thickness of dielectric sample is kept around 1-2 mm, the positional accuracy along the axis would be in this range. To hold these pill/ disc we need a fixture that can smoothly move within the four vanes. We have used a fixture made of Teflon (dielectric constant = 2.1). A fixture [Figure 4] was made from a Teflon block by machining with a CNC machine during the fabrication of the cold model. The mobility of the fixture within the four vanes was checked thoroughly. The fixture has slots for the disc type beads, symmetrically placed in the four wings at radii 7mm, 14 mm and 20 mm. We have made a disc type dielectric bead made of $BaTiO_3$ in our Nuclear Target Laboratory. The measured dielectric constant of the bead being 12.5, we get appreciable phase shift (hence frequency shift) with the bead at r = 7 mm also.

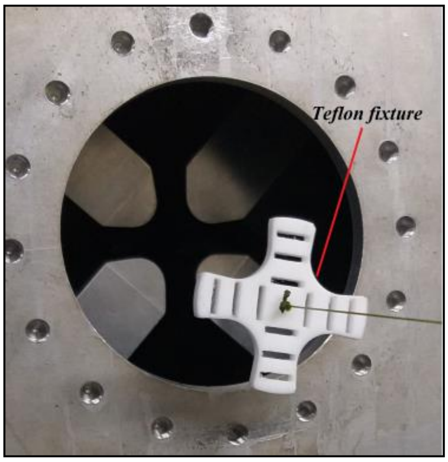


Figure 4: The Teflon fixture

The phase shift due to the Teflon fixture alone as well as the fixture with $BaTiO_3$ bead in all the slots was measured throughout the whole longitudinal length in regular interval. For each measurement average of 20 data has been taken. Thus the average phase shift ($\Delta\phi$) only due to the bead will be known. Knowing the phase shift we can get the fractional frequency shift ($\frac{\Delta f}{f_0}$) as well as the normalized electric field ($E/\sqrt{U}$).

$$\frac{\Delta f}{f_0} = \frac{\tan(\Delta\phi)}{(2Q)} \qquad \frac{E}{\sqrt{U}} = K\sqrt{\frac{\Delta f}{f_0}}$$

Where 'Q' is the unloaded Q- factor of the cavity and 'K' is a factor which depends on dimension, orientation and the dielectric constant of the bead.

The bead-pull measurement was carried out with an automated bead-pull measurement set up already developed in VEC [4]. The set-up comprising of a VNA and a stepper motor controller can be used to take phase data throughout the length of RFQ with definite length steps.

### *Bead-pull results*

The normalized electric fields in all the four quadrants have been calculated from the measured change in phase ($\Delta\phi$) at different longitudinal position. Figure 5 shows the calculated electric fields $E_1$, $E_2$, $E_3$ and $E_4$ (at positions 1, 2, 3, 4 in Figure 1) together along z for radial position r = 20 mm.

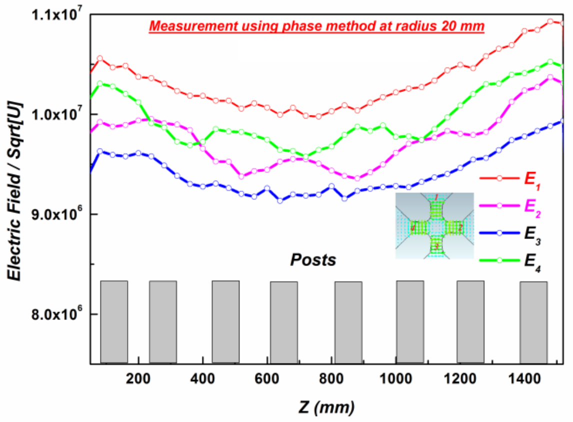


Figure 5: Normalized electric field along z in four quadrants at 20 mm radius

Quadrupolar asymmetry as well as dipole component at radial distance of 7 mm, 14 mm and 20 mm along the length of the RFQ have been calculated with the calculated $E_1$, $E_2$, $E_3$ and $E_4$.

Using the bead pull data in the transverse direction, we can calculate the R/Q value for the cavity using the following formula [5]:

$$R/Q = -\frac{2S^2}{(2\pi f)V\varepsilon\varepsilon_0}\left(\frac{\Delta f}{f}\right)$$

where '*S*' is the distance between the vane, '*V*' is the bead volume, 'ε' dielectric constant of the bead while '$\varepsilon_0$' is the free space permittivity.

The results have been summarized in the following table [Table 3]. The table shows that the experimental results are in good agreement with these of the simulation.

Table 3: Bead-pull measurement results

| RF parameters | Measured value | CST simulated value |
|---|---|---|
| QA (at 7 mm) | ±2.97% | ±2.9 |
| QA (at 14 mm) | ±3.52% | ±3.49% |
| QA (at 20 mm) | ±4.2% | ±4.1% |
| DC (at 7 mm) | ±3.15% | ±3.1% |
| DC (at14 mm) | ±3.58% | ±3.52% |
| DC (at 20 mm) | ±4.5% | ±4.2% |
| R/Q | 9.5 Ω | 9.9Ω |

## CONCLUSION

The paper describes the RF simulation results of the scaled model of the RFQ made of aluminum. The simulation results have been compared with low power RF measurement results. The $BaTiO_3$ beads used in bead-pull experiment have been made in-house. Unloaded Q value obtained in the experiment is around 50% of the simulation, whereas the measured R/Q ratio is more or less same of the simulated one. The experimental study shows that the detrimental field asymmetries at 20mm are within ±4.5%. However the proton beam will see field asymmetry within ~ ±3.5% as the beam radius within RFQ aperture is less than 7 mm.

## REFERENCES


[1] A. Chakrabarti et.al, *The ANURIB project at VECC - Plans and preparations*, **Nucl. Instrum. Meth. B 317 (2013) 253.**

[2] C. Das et.al, *Physics Design of rod type proton RFQ linac*, **2017 *JINST* 12 T 02005**

[3] CST Microwave Studio, ***CST Studio Suite*™, (2011).**

[4] T.K. Mandi et.al, *RF measurements and characterization of linac cavity using an automated bead-pull measurement system*, **Indian Particle Accelerator Conference ( InPAC 2009), RRCAT, Indore, India, Feb 10-13, 2009**

[5] H. Fujiswa, *A CW 4- rod RFQ linac*, **NIM A 345 (1995) 23**

# LOW BETA NIOBIUM QUARTER WAVE RESONATOR FOR THE SUPERCONDUCTING LINAC AT BARC-TIFR PLF, MUMBAI

N.K. Mishra[1], P.V. Tyagi[1], A.A. Shinde[2], A.D. Singh[2], S.P. Singh[2], A. Bhattacharyya[1], S. Pal[2], R. Palit[3], B. Srinivasan[1], V. Nanal[3], B.K. Nayak[1] and R.G. Pillay[4]

[1]*NPD, Bhabha Atomic Research Centre, Mumbai - 400085*

[2]*PLF, Tata Institute of Fundamental Research, Mumbai 400005*

[3]*DNAP, Tata Institute of Fundamental Research, Mumbai 400005*

[4]*Dept. of Physics, Indian Institute of Technology, Ropar, Rupanagar- 140001*

### *Abstract*

The superconducting LINAC at the Pelletron LINAC Facility, TIFR has been operational for more than a decade, delivering a variety of beams (C to Cl) for heavy ion research. The LINAC consists of seven cryo-modules, where each module is a liquid helium cryostat housing four lead coated (2 µm) copper quarter wave resonators (QWR). The QWR is designed for $\beta_{opt}$=0.10 and nominal operating frequency of 150 MHz. To widen the acceptance of the LINAC to heavier beams, it is planned to install low beta ($\beta_{opt}$=0.07) superconducting Niobium QWRs in the first module. The basic electromagnetic design of the Nb-QWR has been completed. The fabrication of a stainless steel/copper prototype has been initiated to optimize the sheet metal forming process, design the dies and fixtures and most importantly to simulate the welding geometry. The prototype will also serve as benchmark to validate the electromagnetic characteristics, such as: resonant frequency, accelerating field profile, stored energy, mechanical vibrational modes, etc. The design of the die-punch setup for the fabrication of the components of the resonator is in progress. This paper will discuss the electromagnetic design of the QWR along with details of fabrication of the prototype components.

## INTRODUCTION

A superconducting linear accelerator, indigenously developed to boost the energy of heavy ion beams delivered by the Pelletron at Pelletron LINAC Facility, TIFR. The Pelletron is a DC electrostatic machine, capable of operating both as a stand-alone accelerator and as an injector to the superconducting LINAC booster [1]. The LINAC consists of seven liquid helium cryostats, each housing four lead (Pb) coated (2 µm) copper quarter wave resonators (QWR). The base material is OFHC copper chosen for its high thermal conductivity at low temperature. Ion beams up to Ni have been accelerated by the existing LINAC. The resonators in the LINAC are designed to operate at 150 MHz with $\beta_{opt}$=0.10. Internationally, both lead and niobium have been used successfully for superconducting cavities, whereas the superconducting properties are superior for niobium as compared to lead. Some of the laboratories where bulk Nb QWRs are being used are in the LINAC at IUAC, New Delhi, ALPI at INFN, Legnaro and TRIUMF, Canada [2, 3, 4]. In order to extend the mass range it is planned to retrofit the first cryo-module with low beta ($\beta_{opt}$=0.07, 150 MHz) superconducting Niobium QWRs. This retrofitting includes fabrication of four Nb QWRs using high purity (RRR 300) Nb sheets followed by installation in the first cryo-module of the superconducting LINAC.

## DESIGN OF RESONATOR

### *RF design*

The resonating frequency is kept same as the Pb coated cavities i.e., 150 MHz with $\beta_{opt}$=0.07. The aim currently is to comprehend the engineering processes involved in the fabrication of Nb-QWR. Therefore, to ascertain the dimensions of the resonator for the design resonant frequency and $\beta_{opt}$, electromagnetic simulation was carried out using CST Microwave Studio/ COMSOL. No optimisation of parameters like $E_p/E_{acc}$, $H_p/E_{acc}$ etc. was attempted. The resonator model and E-field distribution based on these simulations is shown in Figure 1.

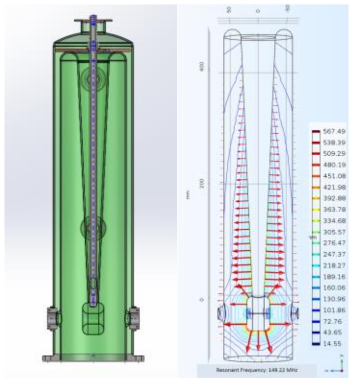

(a) (b)

Figure 1: (a) Schematic of QWR (b) Contour of electric field distribution (arrows depict the intensity of E-field (V/m) at the surface).

### *Mechanical design*

Mechanical stability is a very important requirement as the field in the cavity has to be locked to a fixed amplitude and frequency to be functionally useful. The resonator RF frequency can be modified mainly by mechanical noise in the environment like vibrations from turbo pump, and by liquid helium pressure fluctuations. In addition to the electromagnetic parameters, the design of the resonator must aim to increase the frequency of the lowest mechanical Eigen-mode as high and as far away from 50 Hz as possible, to reduce micro-phonic-induced RF frequency jitter. The design must also ensure that liquid helium-induced pressure fluctuations do not deform the resonator substantially, which may result in large changes in its resonance frequency [5]. In our case the mechanical vibrational frequency of lowest mechanical Eigen-mode is 113 Hz well above 50 Hz. Simulations show that the resonant frequency changes by 1.66 kHz/µm for changes in the diameter of central conductor and by -0.331 kHz/µm for changes in the diameter of outer conductor, other dimensions remaining constant.

## FABRICATION PROCEDURE

Superconducting niobium QWRs can be fabricated using different techniques. The most common is to take Nb sheet, apply sheet metal forming procedures in order to get the required geometry of the components and join them by electron beam welding (EBW) in vacuum. EBW facility and vacuum furnace for heat treatment of the resonators has been setup at TIFR [6]. There are several components which needs to be formed using die-punch setup whereas some components like the donut can be machined. Various components of the Nb QWR assembly are shown in Figure 2. In order to maintain the purity of Nb material, EBW is used for all welding joints. To ensure proper alignment, concentricity and to minimize the distortion, customized fixtures are required to hold the assembly during welding. The first step would be to form the Nb sheet in two halves and fabricate the inner conductor as well as outer conductor with two seam welds. Appropriate weld preparation of the components is essential to achieve the necessary tolerances.

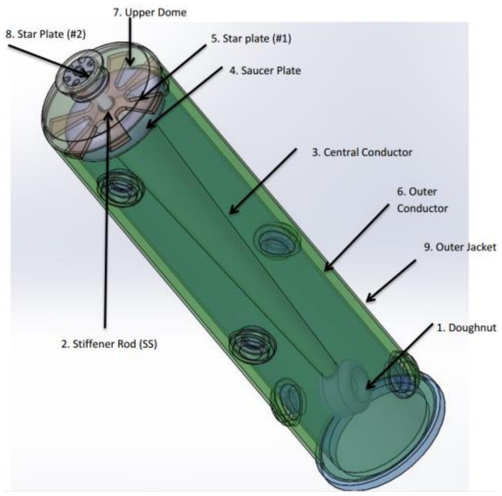


Figure 2: Schematic of QWR with different components.

### *Prototype fabrication*

Since Nb material is expensive, it was decided to make a prototype of stainless steel/Copper to study the engineering processes and determine the resonant frequency and field profile using bead test. Accordingly, a stainless steel prototype, or rather, a simple scale model has been constructed to study the various geometric profiles which will be encountered during EBW of the resonator components.

In the SS prototype the central conductor was machined starting from a rod. The ports on the outer conductor and jacket were made using tube drawing techniques, incorporating appropriate fixtures to minimize distortions. The various fabricated components of the stainless steel prototype are shown in Figure 3. Since the sheet metal properties of Cu and Nb are similar, a copper prototype of the resonator is also being planned and will be constructed in due course.

(a) (b) (c) (d)

Figure 3: (a) Donut (b) Saucer Plate (c) central and out conductor of the QWR (d) QWR assembly

## REFERENCES

[1] Pillay R G, InPAC 2015 Proceedings.
[2] S. Ghosh et al, Proc. HIAT 2012, Chicago, 185(2012)
[3] Bisoffi et al, 2007 SRF07 (Beijing, China) paper M0404
[4] Laxdal R E, Proc. EPAC 2006, Edinburgh, 1556(2006)
[5] Facco A, Particle Accelerators, 61, 265(1998)
[6] Shinde A A et al, InPAC 2018 Proceedings

# BEAM DYNAMICS IN THE INJECTOR SECTION OF A 30 MeV RF ELECTRON LINAC FOR n-TOF APPLICATION*

B.Nayak#, A.S. Dhavale, BARC, Mumbai- 400094, India

*Abstract*
Longitudinal and transverse beam dynamics studies in the injector section of 30 MeV, 10 Amp, 10 nsec RF electron linac for neutron production has been carried out in this paper. To properly consider space charge effect, multiparticle simulation is performed in PIC code ASTRA. Gun extraction voltage is considered as 85 kV and the beam is subsequently injected to prebuncher and buncher section. Solenoids are used to confine the beam to achieve maximum transmission efficiency. Also we showed that by increasing beam current in the presence of buncher of field 10 MV/m, capture efficiency decreases. Threshold beam current due to BBU has also been calculated.

## INTRODUCTION

High current accelerators are used as neutron sources to gain precise knowledge of neutron cross sections over a broad energy range, in many nuclear applications related to nuclear energy like the transmutation of nuclear waste, the thorium-based nuclear fuel cycle and accelerator driven systems (ADS). In a TOF facility, a short pulse of high-energy particles bombard on a neutron-producing target. The impinging particles can be: electrons that create neutrons via the production of bremsstrahlung and consecutive photonuclear reactions ((e,γ) (γ,n) reaction) or protons that generate neutrons via the spallation reaction[1,2]. The electron accelerator with energy higher than 10 MeV can yield neutrons by the photo-nuclear reaction. Currently many such neutron sources are operating around the world. The n-TOF-facility GELINA at Belgium has been especially designed and built for high-resolution cross section measurements. Keeping this in mind, design of a high current pulsed RF electron Linac has been undertaken by BARC, India to produce 30 MeV, 10Amp, 10nsec beam for n-ToF applications[4,5]. It will be used as a neutron generator and will produce ~ $10^{12}$-$10^{13}$ n/sec. This paper presents the detailed beam dynamics studies in the injector section of such linac (starting from entrance of prebuncher to end of buncher section) by analytical calculations as well as simulation in ASTRA code .

## INJECTION SECTION

A 85 kV Thermionic triode electron gun/ field emission gun serves as the source of electron beam. Emitted electron beam then enters to the bunching system which consists of a pre-buncher and buncher. The pre-buncher is a re-entrant type of standing wave cavity resonating at 2856 MHz with central bore radius, r=10 mm. To study beam dynamics in the buncher section, buncher cell design of 10 MeV RF Linac is used [3]. It consists of three buncher cells and one accelerating cell. The buncher consists of 'OMEGA' shaped cavities with bore radius of 5 mm and resonant frequency 2856 MHz. The schematic of the injector section is shown in Fig.1. The required parameters of the accelerator are given in Table 1.

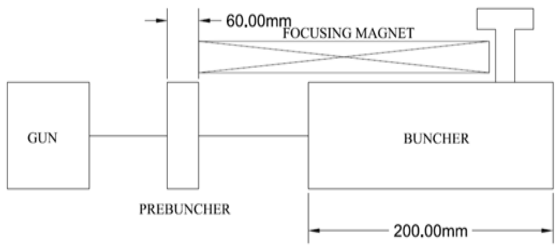


Figure 1. Schematic of injector section

Table 1: Parameters of the Accelerator

| | |
|---|---|
| Beam energy (MeV) | 30 |
| Energy spread (MeV) | ±1.5 |
| Beam current (A) | 10 |
| RF frequency (MHz) | 2856 |
| Pulse width (nsec) | 10 |
| PRF (Hz) | 300 |

## PREBUNCHER DESIGN

Pre-bunching an electron beam by a modulation cavity followed by a drift space is frequently used before synchronous bunchers for electron linacs. A very high modulation amplitude presents some difficulties and a high convergence of the prebuncher can deteriorate the characteristics of the bunch at the output of buncher. Too low modulation leads to long drift spaces and the space charge effects reduce the longitudinal bunching and increase the radius of the beam if the axial magnetic field is low.

Pre-buncher is a re-entrant cavity resonating in $TM_{010}$ mode at a frequency of 2856 MHz. Pre-buncher cavity dimensions are optimized using SUPERFISH. Figure 2 shows field distribution in a quarter of a pre-buncher cavity. Figure 3 shows the variation of axial electric field, $E_z$ in the prebuncher cavity as function of gap, g between nose cones. Gap is varied from 15 mm to 35.18 mm. The electric field magnitude increases with reduction of gap. Thus, for beam dynamics study a cavity with 15 mm gap

*Work supported by DAE, India
# nayakb@barc.gov.in

is used. To reduce the effect of beam loading, cavity will be made up of stainless steel.

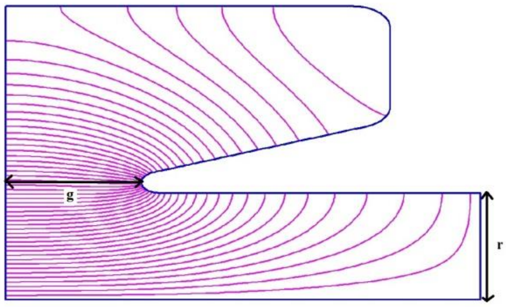


Figure 2. Field distribution in Prebuncher cavity

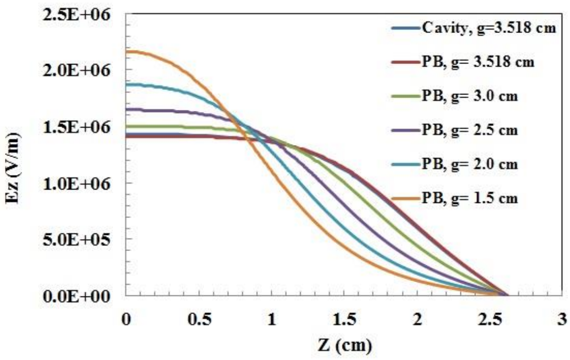


Figure 3. Variation axial electric field in buncher with g

Beam dynamics calculations are carried out in ASTRA by assuming Injection energy of electron beam to be 85 keV and beam current 15 A [6]. Electron beam bunch width is assumed to be 360 psec at the entrance of pre-buncher. Total 25000 no. of particles are taken for simulation. By varying modulation voltage in the pre-buncher cavity from 10 kV to 20 kV bunch compression at the exit of pre-buncher is studied. For 15 kV modulation voltage, bunch width reduces to 60 psec which is suitable for injection to buncher section. The compressed bunch contains 75% of the total particles. The maximum bunching distance is 110mm from centre of prebuncher. The results are shown in Fig.4.

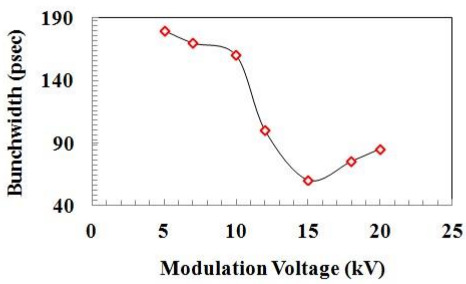


Figure 4. Variation of bunch width with modulation voltage

Longitudinal phase space plot and bunch distribution for modulation volatge of 15 kV and beam current 15 Amp is shown in Fig. 5a and 5b.

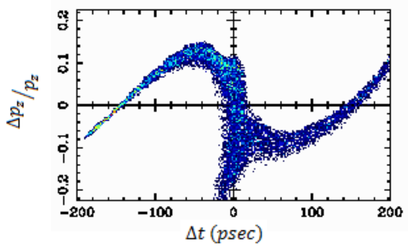


a)

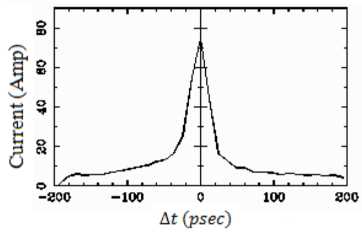


b)

Figures 5a and 5b. phase space plot and bunch distribution for 15 Amp beam current

## ANALYTICAL CALCULATION

After bunching in pre-buncher, beam enters buncher section consisting of four cells. In this section, we have calculated the effect of space charge on the capture efficiency of particles in the potential well created by the buncher. On increasing beam current, because of longitudinal space charge effect, potential well decreases[7]. The equation which governs the evolution of bunch length is

$$\varphi'' + {k_{l0}}^2\left[(1-\mu_l)(\varphi-\varphi_s) - \frac{(\varphi-\varphi_s)^2}{2\tan(-\varphi_s)}\right] = 0 \qquad (1)$$

where ${k_{l0}}^2 = \frac{2\pi q E_0 T \sin(-\varphi_s)}{mc^2\beta^3\gamma^3\lambda}$, Space Charge Factor,

$$\mu_l = \frac{3qI\lambda f}{4\pi\epsilon_0\gamma^3\beta^2 mc^3\sigma_x\sigma_y\sigma_z {k_{l0}}^2} \qquad (2)$$

where $\varphi_s$ is the synchronous phase, $\beta$ and $\gamma$ are relativistic factors, $\lambda$ is the wavelength of rf field, $I$ is the beam current, $\sigma_x, \sigma_y, \sigma_z$ are bunch size in three directions respectively. Using equation 2, $\mu_l$ is calculated for different values of beam current, I. At, zero beam current $\mu_l$ is zero. At I =15 Amp, assuming, $E_0T = 10MV/m$ ,$\varphi_s = -30^0$ ,$\beta$ and $\gamma$ correspond to 85 keV , $\lambda = 0.105m$ ${k_{l0}}^2 \approx 3000$ and beam parameters at the input of buncher $\sigma_x = \sigma_y = 2\ mm$ ,$\sigma_z = 10\ mm$ ,$f = 0.05$, $\mu_l \approx 0.22$.

Using equation (1) potential $V(\varphi)$ is calculated for different values of beam current.

$$\varphi - \varphi_s = \Delta\varphi \qquad (3)$$

$$\text{Potential, } V(\varphi) = \frac{{k_{l0}}^2}{2}(1-\mu_l)\Delta\varphi^2 - \frac{{k_{l0}}^2}{3.45}\Delta\varphi^3 \qquad (4)$$

Two cases corresponding to I=0 and I= 15 Amp are shown in figure 6a and 6b respectively.

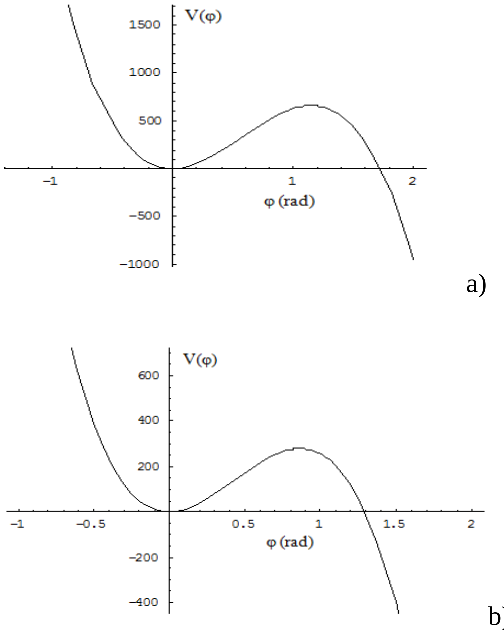


Figure 6: Potential well, a) I =0, b) I =15 Amp

Case 1: I = 0, $\mu_l = 0$
At $\varphi_s = -30^0$ and zero beam current, total width of the bucket (separatrix) is $3\varphi_s = -90^0$ .
Case 2: I =15 Amp, $\mu_l = 0.22$
Separatrix width $= -70^0$

From figure 6a and 6b it is clear that width of separatrix as well as depth of potential decreases with increase in beam current. At a beam current of 15 Amp height of potential well is reduced by a factor of two.

## SIMULATION WITH ASTRA CODE

Growth of transverse emittance and self-field effects in linac should be kept minimum to increase the transmission of the linac. The solenoid magnetic fields are adopted for the beam focusing against the space charge effect thereby preventing beam loss in rf cavity. A multiparticle simulation is performed in PIC code ASTRA incorporating space charge effect. For all the simulations presented in the following, we have used 2.5 x $10^4$ macro particles. Gaussian distribution is taken in all transverse dimensions with FWHM 5.0 mm each. A prebuncher is placed between electron gun and buncher section, a drift space of 110 mm is kept between pre-buncher and buncher. Synchronous phase of buncher is chosen as -$30^0$ to maximise the energy and minimise the energy spread. Injected beam from gun is of energy 85 keV and prebuncher gap voltage is 15 kV. From simulation, we found that beam energy at the end of buncher is 1.3 MeV with energy spread as 750 keV. Figure 7 shows the plot of Transmission efficiency, T as function of solenoid different beam currents. We observed that at a beam current of 15 Amp, T increases from 30% to 73% by increasing B from 1000 G to 2000 G, further increase in B results in reduction of T due to over focussing. Similarly, for 20 Amp beam current, T increases from 22% to 55% and then decreases.

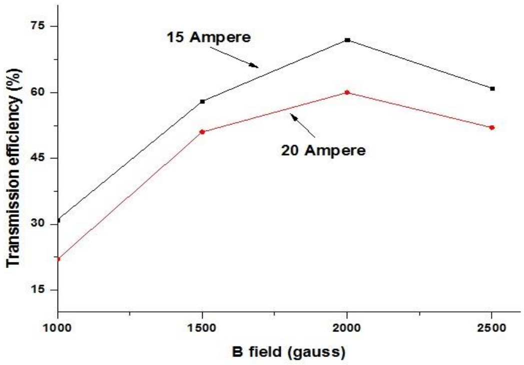


Figure 7. Variation of transmission efficiency with solenoid field, B

Threshold current for excitation of regenerative beam break up (BBU) is given by $I_{th} \approx \left(\frac{\pi}{L}\right)^2 \frac{\lambda_d \beta\gamma\left(\frac{mc^2}{q}\right)}{4Q\left(\frac{R_\perp}{Q}\right)} F_a$.

Dipole mode is excited at 4.316 GHz. At $Q = 8000\,, \frac{R_\perp}{Q} = 11.0$ $\beta\gamma = 60.0\,, F_a \approx \frac{1}{3}$ $L = 0.2m$ calculated $I_{th}$ ~ 21 Amp.

## CONCLUSION

In conclusion, for the transmission of high current, short duration pulses through the linac with optimum transmission efficiency, pre-buncher with solenoid magnetic field is required. As the beam current increases space charge effect become dominant and magnetic field is required to confine the beam. Peak current in the bunch should be less than 21 Amp so as to avoid BBU.

## ACKNOWLEDGEMENT

We would like to express sincere gratitude to R K Rajawat, Associate Director, BTDG, BARC for the encouragement and support for this work.

## REFERENCES

[1] Bensussan, J.M. Salome, GELINA. A modern accelerator for high resolution neutron time of flight experiments, Nucl.Instrum.Meth. 155 (1978) 11-23.
[2] Yunlong Chi et al., Beam dynamics studies on the 100 MeV/100 kW electron linear accelerator for NSC KIPT neutron source, in Proc. IPAC, (2011).
[3] R.C.Sethi, V.T.Nimje, A.J.Dabeer NEE A.S.Dhavale, Design of RF structures for 10 MeV, 10 kW Industrial RF Electron Linac, Internal Report, RFAS/APPD/03/2001.
[4] A.S.Dhavale et al., Beam dynamics study and design of 348° compression magnet for neutron time of flight (n-TOF) facility, JINST 9 (2014).
[5] V.T.Nimje et al., Design and development of a 30 MeV, 3 kW RF electron linac, APAC (2007) .
[6] ASTRA, A Space charge Tracking Algorithm, <http://www.desy.de/~mpyflo> .
[7] Thomas P.Wrangler, RF Linear Accelerators,2nd ed.,Wiley-VCHVerlag GmbH & Co, Weinheim, (2008).

# MODIFIED SET UP FOR HIGH PRESSURE RINSING OF NIOBIUM 650 MHz JACKETED CAVITY

S.K. Suhane, Kinsuk Das, S K Chouhan, Anurag Chaturvedi, Md. Asif Hussain, D.S. Rajput, Khileswar Prasad, Ravindra Jain, S Raghavendra, RRCAT, Indore (MP), India

*Abstract*

High Pressure Rinsing (HPR) with ultrapure water is a standard recipe for final cleaning of bare as well as jacketed (with helium vessel) niobium superconducting RF cavities. The existing HPR facility for 650 MHz 5-cell bare cavities at RRCAT has been suitably modified and augmented for rinsing of jacketed cavity which is 10% larger in diameter and 50% higher in weight. The HPR system encompasses base structure, cavity holding fixtures, linear and rotary movement mechanisms with drive and control, high pressure water pump and associated piping, class 100 clean enclosure and ultrapure water generation plant. The existing HPR base structure has been suitably strengthened to support 150 Kg load of jacketed cavity. New holding fixtures for jacketed cavity have been designed, fabricated and tested. The rotary tray mechanism has been modified to accommodate 450 mm diameter jacketed cavity. New fixtures have been designed, fabricated and assembled with a cleanroom cart of higher load capacity for loading the cavity on HPR setup. Class 100 clean enclosure has been augmented with additional FFU's for improving the cleanliness in the adjoining area. Arrangement for hand HPR of the external surface of cavity has been made. Paper describes the salient features of modified high pressure rinsing system and details of mock trial of prototype jacketed multi cell 650 MHz niobium cavity.

## INTRODUCTION

Raja Ramanna Centre for Advanced Technology (RRCAT) has taken up R&D activities related to the development of a 1GeV superconducting pulsed $H^-$ ion linac that will be required to build the Indian Spallation Neutron Source (ISNS) for research purposes in the multi-disciplinary area [1]. A 1 GeV energy proton linac would comprise of a large number of superconducting niobium cavities including spoke resonators and elliptical shaped cavities. Facilities for niobium cavity fabrication, processing and testing have been set up at RRCAT Indore. The cavity processing includes centrifugal barrel polishing, electro polishing, thermal processing, high pressure rinsing and cleanroom assembly.

After fabrication the cavity is subject to various processing steps to improve the surface quality. Any surface impurity or foreign particle on the internal surface of processed cavity may cause the emission of secondary electrons called field emission, which results into reduced accelerating gradient in the cavity. To get rid of this problem the final processing step in the cavity processing is high pressure rinsing. In HPR, The cavity internal surface is subject to impact of high velocity jets of ultrapure water in a cleanroom environment, which helps in dislodging micron size impurity from the surface and prevents further contamination of the clean surface. The 650 MHz 5-cell niobium bare cavity, after initial performance qualification in VTS cryostat is jacketed with a titanium vessel through which the liquid helium flows for cooling the cavity. Titanium jacket is welded to the cavity filled with argon gas. After welding the jacketed cavity is required to be high pressure rinsed to remove the surface contaminants from the inside surface. For rinsing of jacketed cavity of 450 mm diameter (10 % larger than bare cavity) having weight of 150 kg (30 % higher than bare cavity) the existing HPR set up designed for bare 650 MHz 5 cell cavity has been suitably modified and augmented. The modified structure can easily switch between bare as well as jacketed cavity types. The paper described details of the modifications done in the existing HPR system.

## FACILITY DESIGN DESCRIPTION

A 650 MHz 5-cell niobium cavity welded with helium jacket is shown in figure 1a.

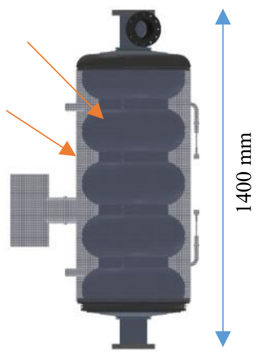


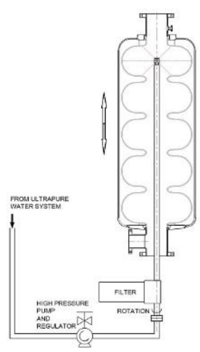

Figure 1a: Jacketed cavity
Figure 1b: Schematic of HPR

In high pressure rinsing the cavity is held in a fixture and moved vertically up and down around a coaxial rotating wand fitted with fan jet nozzles through which ultrapure water is sprayed and thus the entire internal surface of cavity is thoroughly cleaned. The process is carried out in a class 100 cleanroom [2]. Schematic diagram of HPR process is shown in figure 1b.

### *HPR Base Structure*

In order to accommodate the jacketed cavity on the base HPR structure, the existing tubular structure has been modified. Vertical frame of base structure has been stiffened with additional tubular members anchored to the wall, in order to minimize deflection of structure due to heavier cantilever load of jacketed cavity. The welded

#suhane@rrcat.gov.in

structure fabricated from square tubes of stainless steel grade 316. 3-D view of jacketed cavity mounted on the support structure is shown in figure 2.

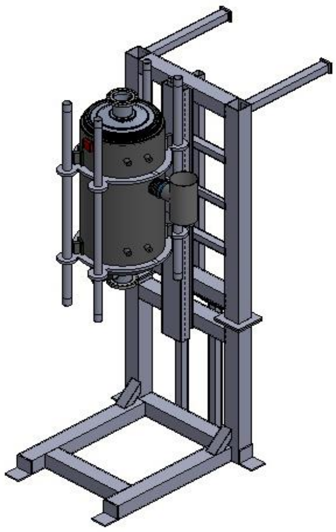

Figure 2: 3-D view of jacketed cavity on HPR structure

## *Adjustable wand arrangement*

Different cavity sizes (diameter) require different spacing between the cavity vertical frame structure and the wand. To accommodate jacketed cavity, wand with rotary tray is required to be moved away from the base structure. To facilitate this, additional brackets with tapped holes have been welded to the base structure which are used to fix the rotary tray at a larger distance. The wand has provision to be shifted closer to base structure when bare cavity is required to be rinsed. Fan jet nozzles are provided at the top of wand. Nozzles are fixed $180^0$ opposite to each other so that the forces of the water jets sprayed from the nozzles balance each other and wand will not deflect when high pressure jets are turned on.

## *Rotary Drive Mechanism*

The rotary tray with wand is moved using DC geared motor through a timing belt drive. The motor speed can be varied between 2 to 20 rpm using a speed controller. Shifting of rotary tray for accommodating larger cavity size requires the drive mechanism to be adaptive to variable distance. To facilitate this, the motor mounting arrangement has been modified. The motor is mounted on a slotted stainless steel plate in such a way that motor with timing pulley can be moved as per the distance requirement of bare or jacketed cavity.

## *Cavity Mount*

For mounting the jacketed cavity on the HPR structure, special cavity holding arrangement has been designed and fabricated. It is a four bar structure made of stainless steel pipes held together with spiders made of stainless steel grade 316. The spiders are made in two halves. The spider halves are clamped around the cavity jacket and held together using threaded fasteners. Two spiders have been used to hold the cavity in vertical orientation. In order to avoid slippage of cavity the spiders attach to the lugs welded on the jacket and hold the cavity firmly in place using special clamps made of stainless steel bolted together with the spiders. All the components have been electro polished to minimize the dust particle attraction. For attaching the clamped cavity to the structure, a frame grip assembly made of aluminium alloy 6063 has been made and fixed to the carriage plate of linear actuator.

Cavity mounting arrangement is shown in figure 3.

Figure 3: Cavity mounting fixture

## *Cavity Drive System*

To move the cavity vertically around the rotating wand, it is attached to a linear actuator through the holding fixture. For jacketed cavity a higher load capacity cleanroom compatible actuator has been procured. It is a ball screw driven actuator moved by an AC servo motor. Operation of actuator is controlled using a PLC controller. Operator can set the speed and direction of the motor. Limit switches placed along the linear rails sense the limit of travel and its direction is automatically reversed.

## *Cavity Loading Cart*

Safe handling of 150 Kg jacketed cavity within the confined space of cleanroom without hampering the required cleanliness level is a challenging activity. For loading of jacketed cavity on the rinsing set up a new cavity handling arrangement of higher load capacity has been made. The cavity assembled with the spider frame is mounted on a frame grip assembly made of aluminum alloy 6063. The cavity frame is attached to the grip assembly using high capacity toggle clamps made of stainless steel 304. The clamps enable quick assembly and dis-assembly of the cavity and thus reduces the time gap between elctropolishing and high pressure rinsing of the cavity. It is recommended that the cavity should not be allowed to dry in-between EP and HPR. The frame grip assembly is bolted to a rotating cavity mount which permits 360° rotation in steps of 45° increments. This makes the cavity handling easy while switching from horizontal to vertical position. The whole assembly is mounted on a specially procured cleanroom compatible lift cart. The new cart is of higher load capacity and longer vertical travel than the existing one. The cart made of stainless steel frame and aluminum alloy mast rolls on PU wheels. It is driven by a rechargeable battery encased in SS casing. The lift cart with the cavity fixture has been load tested for 110% of cavity weight to ensure safe handling of cavity. Loading of cavity jacket on HPR set up is shown in figure 4.

Figure 4: Loading of cavity jacket on HPR structure

## EXTERNAL HPR

A new hand operated HPR system has been added to the existing facility in the cleanroom. It is used for high pressure rinsing of external surface of cavity as well as hardware required for cleanroom preparation of jacketed cavity. The system comprises of a trigger gun, a 0.5 micron pore size sintered stainless steel filter in a SS 316 housing, fan jet nozzle made of hardened stainless steel and a PTFE lined stainless steel flexible hose. The operator can turn on and off the water stream by pressing the trigger. The filter removes any particulates generated from the trigger gun. Hand HPR arrangement is shown in figure 5a. Manual rinsing of 5-cell cavity is shown in figure 5b.


Figure 5a: Hand HPR Arrangement

Figure 5b: Manual rinsing of bare cavity

## CLEANROOM AUGMENTATION

For improving the cleanliness level around the HPR set up, the clean enclosure has been augmented with an ante-room adjoining the HPR area and final cavity assembly area. The area has been covered with anti-static PVC curtains on all four sides (to minimize particle attraction) and ceiling has been covered with fan filter units (FFU) and blank panels of polycarbonate sheet. The structural support comprises of aluminum extruded sections of various sizes. The floor has been re-coated with anti-static epoxy paint to fill fine crevices and smoothen the surface which otherwise attract dust particles. All the joints have been sealed with silicon sealant.

## WATER FILTRATION

The ultrapure water used for rinsing of cavities is finally passed through fine filters to remove particulate contamination. The UPW is passed through a polisher unit having a 0.2 micron filter and finally 0.05 micron filter. The final filter is located just after the rotary coupling of the wand. UPW for hand HPR is passed through a 0.5 micron filter located just after the trigger gun.

## HPR PROCESS FOR JACKETED CAVITY

The bare 650 MHz 5-cell niobium cavity after qualification in VTS cryostat, is opened in cleanroom for vacuum venting and backfilled with ultra-pure argon gas before titanium jacket welding in the glove box. This is necessary to prevent any possible particulate contamination of cavity during jacket welding. After welding the jacketed cavity is shifted to HPR area for high pressure rinsing with ultrapure water. The cavity is dried in cleanroom and afterwards prepared for further testing and qualification in HTS cryostat.


## CONCLUSION

Existing High pressure rinsing facility for bare multi-cell niobium cavity has been modified to accommodate 650 MHz 5-cell jacketed cavity. Necessary infrastructure has been created. Mock-trial of mounting cavity jacket on rinsing set up has been carried out. Set up can be easily switched between bare and jacketed cavity rinsing as per the requirement.

## ACKNOWLEDGEMENT

We acknowledge the useful discussions with and support received from colleagues from SCDD and DMTD, RRCAT during development of modified HPR set up.

## REFERENCES

[1]. S C Joshi, et al. "Development of Superconducting Cavities and Related Infrastructure for High Intensity Proton Linac for Spallation Neutron Source", 27th Linear Accelerator Conference, 31 August- 5 September, 2014, Geneva, Switzerland

[2] Suhane S.K. Raghavedra S., et al., "Development of high pressure rinsing set up for 650 MHz, 5-Cell superconducting RF cavity cleaning", Indian Particle Accelerator Conference (InPAC-2015), Mumbai, Dec., 21-24, 2015

# X-RAY ANALYSIS AND RF MEASUREMENTS OF LINEAR ACCELERATORS AT VECC RIB FACILITY

Pratanu Chakraborty#, Dipta Pratim Dutta, Tapan Kumar Mandi, Arihant Kumar Jain,
Dr. Hemendra Kumar Pandey, Dr. Arup Bandyopadhyay
Variable Energy Cyclotron Centre, 1/AF Bidhan Nagar, Kolkata 700064, India

*Abstract*

Development of an ISOL post-accelerator type of RIB facility is going on at VECC. A post-acceleration scheme consisting of RFQ, five IH LINACs and eight super conducting Quarter Wave Resonators (QWRs) along with other focusing and beam line elements will be used to accelerate RIBs to a final energy of 2 MeV/u out of which acceleration from 99 KeV/u to 1.043 MeV/u will be done using IH LINAC 1 to 5. The first three IH LINACs have already been commissioned and the fourth and fifth LINAC is ready for commissioning. The Inter-digital H-mode or IH LINACs are special types of resonating structures based on H-mode (TE) operation and preferred for acceleration of beams with low β and charge to mass ratio. This paper discusses the results of the X-ray analyses of these LINACs to get various important parameters like shunt impedance. Apart from this, various RF measurements have been done on these LINACs, results of which have also been reported in the paper.

## INTRODUCTION

An ISOL type Radioactive Ion Beam (RIB) Facility has been developed at VECC campus [1]. RIB accelerator facilities have opened up new frontiers of research both in the fields of basic and applied sciences. It has applications in a wide range of areas from nuclear physics to medical sciences. RIBs are basically ions of β-unstable nuclei with half-lives in the order of micro-seconds to milli-seconds. Light ion beams (p, α) produced in K130 cyclotron will be used to bombard suitable target elements to produce various species of RIBs. The produced RIBs will be ionised to higher charge states using on-line ion sources and the particular RIB of interest will be selected using an on-line isotope separator. The RIBs will be accelerated using different types of linear accelerators in stages. A 37.8 MHz heavy ion Radio Frequency Quadrupole (RFQ) will be used to accelerate RIBs to an energy of 98.8 KeV/u. Then acceleration up to an energy of 289.1 keV/u will be done using two 37.8 MHz IH LINACs. Three more IH LINACs operating at 75.6 MHz will be used after that to achieve acceleration up to 1.043 MeV/u. The final acceleration of the beam to 2 MeV/u will be achieved using eight SCQWRs to be operated at 113.6 MHz. The accelerators up to the third IH cavity have been designed for a charge to mass ratio of ≥ 1/14 and thereafter for ≥1/7. A charge stripper followed by an analysing section will be used after IH LINAC 3 for this purpose. This RIB acceleration scheme uses several quadrupole magnet doublets and triplets for transverse focusing and rebuncher cavities for longitudinal bunching. The RFQ, five IH LINACs and three intermediate buncher cavities have already been developed and delivered to the project site. Beam testing up to the end of third IH cavity have been performed. The schematic layout of the VECC RIB facility is shown in figure 1.

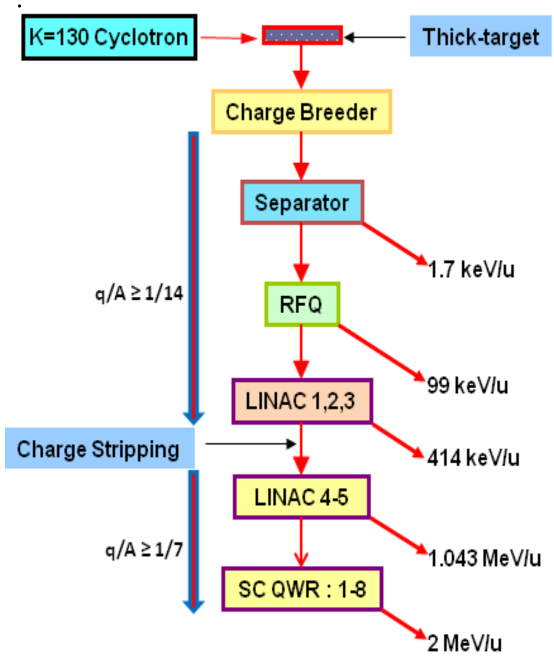


Figure 1: Schematic of RIB acceleration scheme

This report presents the X-ray analysis, high power testing and low power RF measurements for IH LINACs at VECC RIB project.

## X-RAY MEASUREMENT FOR IH LINACS

The bremsstrahlung X-ray analysis of IH Linac-1 and 2 has been done for VECC RIB project. The main aim of this analysis is to find out the peak RF voltage in a cavity for different input RF powers from the knowledge of the end-point energy of the continuous X-ray spectra. The final goal is to establish a calibrated relationship between input RF powers and peak RF voltage in a cavity and subsequently to determine the shunt impedance experimentally.

A CdTe solid state detector with 25 $mm^2$ exposure area is used for X-ray measurement. Measurements were done for different configurations of aluminium and copper slits and tantalum absorbers.

#pratanu@vecc.gov.in

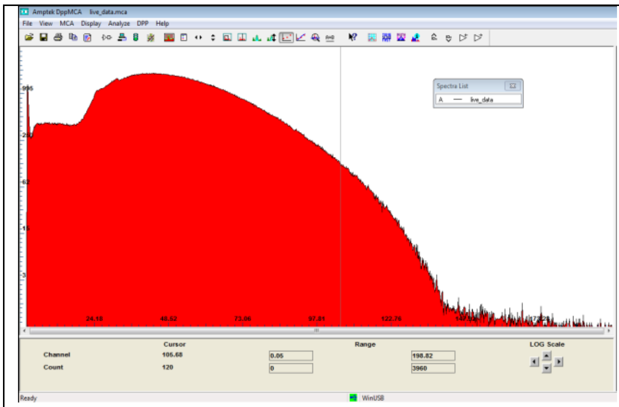

Fig.2 X-spectrum for LINAC 1 at 7 KW

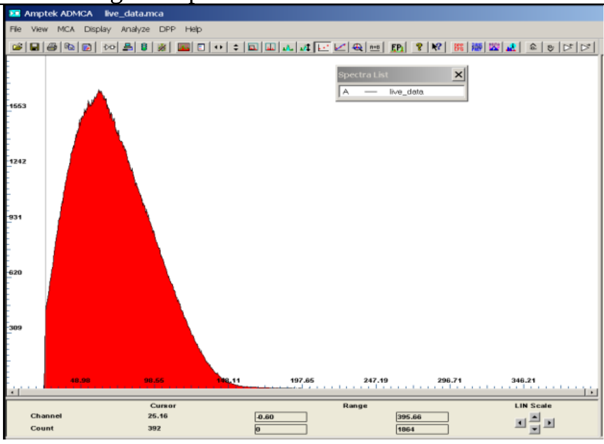

Fig.3 X-spectrum for LINAC 2 at 8 KW

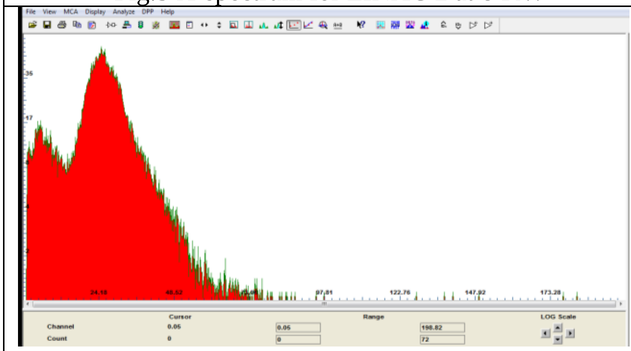

Fig.4 X-spectrum for LINAC 4 at 3 KW

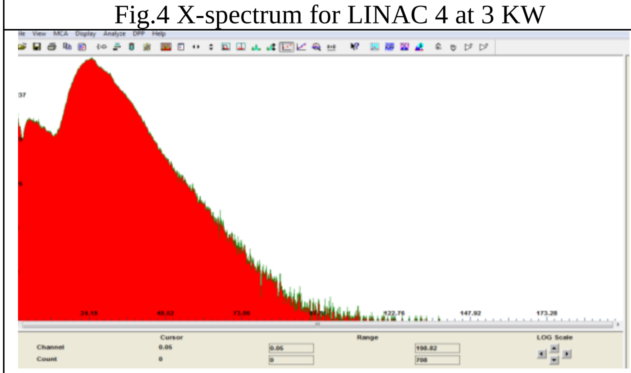

Fig.5 X-spectrum for LINAC 5 at 1.8 KW

A code has been developed for analysis of the experimentally obtained x-ray spectra using MATHCAD[R]. The main purpose of the code is to fit the experimental spectra with a theoretical one so that the endpoint energy of the fitted spectra can be considered for peak RF voltage measurement of the cavity. The theoretical fitting formulation is based on standard x-ray theory and also incorporates detector efficiency, absorber thickness and the absorption coefficient of the absorbing material [3].

This X-ray analysis code has fit the experimentally obtained X-ray results quite well and given the endpoint photon energies which can be considered for calibration and for getting shunt impedances for the cavities as given in table 1.

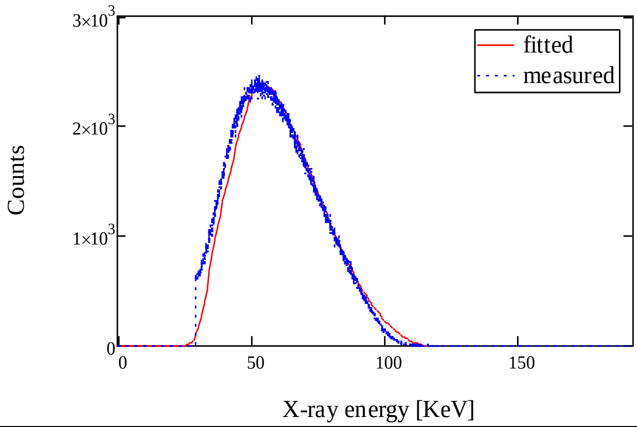


Figure 6: Fitting of X-ray spectrum

Table 1: Shunt impedances for LINACs

| IH LINAC No. | Shunt impedance in MΩ/m |
|---|---|
| Linac 1 | 236 |
| Linac 2 | 462 |
| Linac 4 | 163 |
| Linac 5 | 282 |

## LOW POWER RF MEASUREMENTS AND HIGH POWER TESTING FOR IH LINAC 4 AND 5

IH LINAC 4 and 5 are independently energised with RF power from indigenously developed amplifiers systems. The resonance frequency of both the LINACs is 75.6 MHz. The low power tests were performed for both the cavities to find out important RF parameters and to study variation of frequency with tuner. The detailed results are shown in table 2 and fig. 7 and 8.

Table 2: Low power RF measurements for LINACs

| RF parameter | Unit | LINAC 4 | LINAC 5 |
|---|---|---|---|
| Loaded Q | | 8679 | 9762 |
| Unloaded Q | | 17445 | 19719 |
| S11 | dB | -46 | -40 |
| SWR | | 1.01:1 | 1.02:1 |
| Input impedance | Ohm | 49.3 | 50.7 |

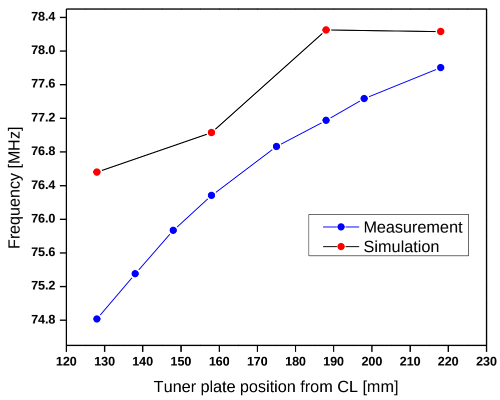


Figure 7: Frequency variation with tuner for LINAC-4

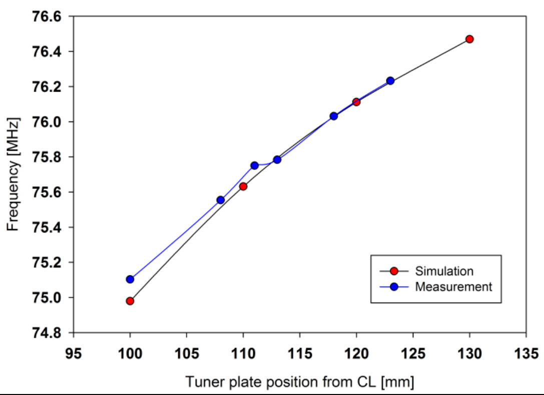


Figure 8: Frequency variation with tuner for LINAC-5

In the next step, the LINAC-4 and 5 cavities were conditioned. Initially it was done in pulsed power mode. Typically the duty cycle is increased from 5% to 30% in increment of 5% before switching over to CW mode. During this process, the cavity vacuum and the RF reflected power were carefully monitored.

During high power conditioning, Bremsstrahlung X-ray spectra were captured using CdTe detector. The aim of these measurements was to find out the maximum voltage on the drift tube from the X-ray end point energies and to find out Shunt impedance of the LINAC cavity subsequently.

## OPTIMIZATION OF TUNERS FOR LINAC 1

There was a need to tune the frequency of LINAC 1 due to the shift of fundamental frequency of operation to 37.87 MHz. Hence the tuner plates were redesigned to change the frequencies. Simulations in HFSS were done for this. A new tuner plate with diameter 100 mm has been fabricated, installed and tested for LINAC 1.

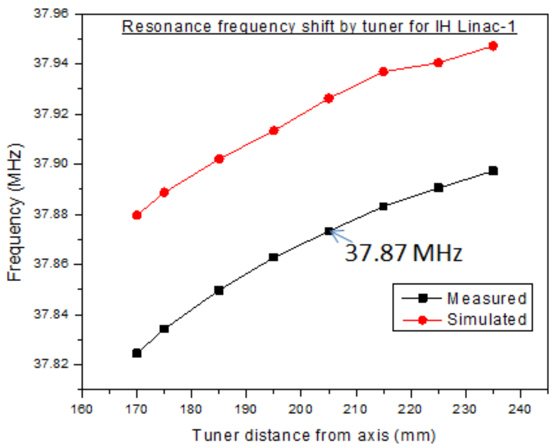


Figure 8: Frequency shift vs. tuner position for LINAC 1

## SUMMARY

This paper discusses the results of X-ray measurements and various necessary RF measurements done on IH LINACs at VECC RIB site. The measurements will help us in smooth operation of the accelerators.

## REFERENCES


[1] Alok Chakrabarti *et al*, Curr. Sci. **108**, 22 (2015)
[2] V Naik *et al, Rev. Sci. Instrum.* **84**, 03301 (2013)
[3] J P Duke *et al, XX International Linac Conference.*
[4] R. H. Pratt *et al*, Atomic data and Nuclear data tables 20, 175-209 (1977)

# PHYSICS DESIGN OF A LOW ENERGY HIGH CURRENT H- CYCLOTRON

Atanu Dutta#, U Bhunia, Malay K Dey, J Debnath, S Saha, C Nandi, A Duttagupta, A Bandopadhyay, VECC,Kolkata

*Abstract*

We have designed a fixed frequency cyclotron magnet considering the physics requirements. It is to accelerate H- ions up to 18 MeV energy with beam current ~100 micro-ampere. This type of cyclotron is particularly suitable for the production of PET radio isotopes. Extracted beam (H+) energy can be varied in the range of 15 to 18 MeV using stripping method of extraction. This method provides 100% extraction efficiency. In this paper we have presented the issues related to the designing the cyclotron magnet and the engineering issues affecting the physics design. The design was verified by tracking the charge particle from centre up to the extraction.

## INTRODUCTION

There are basically three key design features- isochronism, axial stability and radial stability. Isochronism ensures that the ion revolution period remains same for all radii. Combination of axial and radial stability ensures the containment of ions within a specified aperture. To achieve isochronism, average magnetic field is increased radially as a function of increasing energy. Most popular way of increasing average magnetic field is by increasing the pole angular width with radius or by using a combination of trim coils and pole angular width. Axial and radial stability are controlled by suitably adjusting magnetic field index and flutter. The main aim of this work is to design the cyclotron and study and settle various physics and technological issues..

In our design [Table 1] there are four magnet sectors. We have kept maximum magnetic field of 16.8 KG at the hill centre, and an average magnetic field of 10.725 KG, which correspond to a particle revolution frequency of 16.332 MHz for H-. The hill gap is 30 mm and the valley gap is 1100 mm, same as the distance between the upper and lower pole caps. A rectangular iron block is added at the centre to provide extra vertical focussing at the central region. For the injection system, one hole is provided at the center. We have provided four holes in the four valleys, two of them will be used for vacuum pumps and the rest two will be used for the RF cavities vertically. The harmonic mode *h* of operation is equal to 4. The magnet design combines the advantages of solid pole cyclotron and separated sector cyclotron. A high flutter provides strong focusing in the vertical direction. The main idea was to provide the vertical betatron tune > 0.5 at all radii. This is necessary to handle high current operation. In order to meet the isochronism, the shaping of the azimuthally averaged magnetic field was done with the help of varying the sector angular width along the radius.

## DESIGN STEPS

Detail design was done using 3D field simulation. But before that approximate pole shapes and betatronic tunes are obtained from hard edge calculations [1,2,3]. The process is outlined briefly.

For an *N* sector cyclotron with magnetic fields $B_H$ and $B_V$ in the hill and valley respectively, the angles of turning of orbits η and ξ can be given as

$$\eta = \frac{B_H B_V}{B_H - B_V}.\frac{2\pi}{N}(\frac{1}{B_V} - \frac{1}{\gamma B_0}), \xi = \frac{2\pi}{N} - \eta$$

where γ is the usual relativistic term and $B_0$ is the central magnetic field. One can easily obtain the angular widths of the hill and valley η0 and ξ0 on an equilibrium orbit for a given energy by solving

$$\cot(\frac{\eta_0}{2}) = \cot(\frac{\pi}{N}) + \frac{B_H}{B_V}(\cot(\frac{\eta}{2}) - \cot(\frac{\pi}{N}))$$

$$\xi_0 = \frac{2\pi}{N} - \eta_0$$

In order to calculate betatron tunes we need entry and exit angles to the hill (which becomes the exit and entry angles for the valley), which are given by

$$\phi_1 = \varepsilon_1 + \frac{\eta - \eta_0}{2}$$

$$\phi_2 = \varepsilon_2 - \frac{\eta - \eta_0}{2}$$

$$\tan \varepsilon_2 = \tan \varepsilon_1 + R.\frac{d\eta_0}{d\gamma}.\frac{d\gamma}{dR}$$

Here $\varepsilon_1$ is the spiral angle at the entry of the hill, which is zero in the present case. The effective spiral angle $\varepsilon_2$ at the exit of the hill includes spiral angle as well as flaring effect [2]. We have used the well-known matrix method to estimate the betatron tunes. Here hills and valleys are treated as bending magnets of lengths $\eta.\rho_H$ and $\xi.\rho_V$ having focusing strengths of $1/\rho_H$ and $1/\rho_V$, $\rho_H$ and $\rho_V$ being the radius of curvature in the hill and valley respectively. The flaring and the edge effects are introduced by using thin lens matrices at each hill-valley boundary. The radial and vertical betatron tunes $\nu_r$ and $\nu_z$ can be easily obtained from:

$$\nu_r = \frac{N}{2\pi}\cos^{-1}[\frac{1}{2}Tr(V_R.H_R)]$$

$$\nu_z = \frac{N}{2\pi}\cos^{-1}[\frac{1}{2}Tr(V_V.H_V)]$$

#atanuphy@vecc.gov.in

Table 1: Optimised parameters of the magnet

| | |
|---|---|
| Injection/ Extraction Energy | 30 KeV/15 to 22 MeV |
| No of Sectors | 4 |
| Hill gap/Valley gap | 30 mm/1100 mm |
| Hill/Valley field at extraction | 16.8 KG/1 KG |
| Extraction radius for 15/18/22 MeV | 512 /560/620 mm |
| Pole radius/RF frequency | 670 mm/65.328 MHz |
| Iron weight | 30 Ton |
| No of turns | 2x330 |
| Operating main coil current | 110 A |

Here $\mathbf{H_R}$, $\mathbf{H_V}$ and $\mathbf{V_R}$, $\mathbf{V_V}$ are the transfer matrices for horizontal and vertical motions in the hill and valley respectively. Care has been taken to keep betatron tunes $\nu_r$ and $\nu_z$ sufficiently away from the resonance.

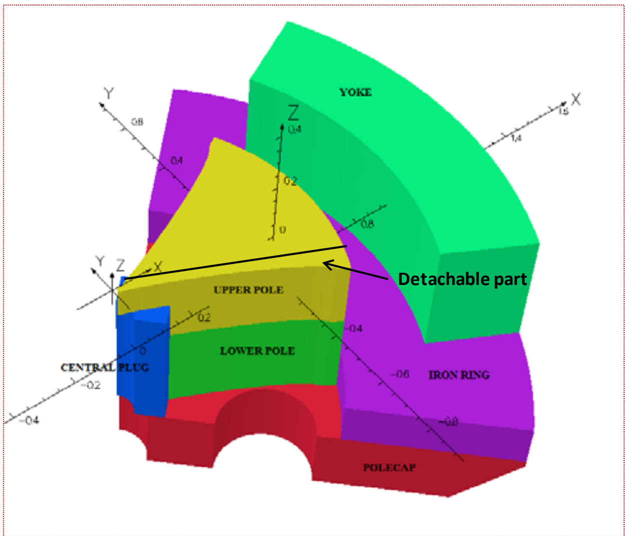


Figure 1: 3D Model (1/8th sym) of the Cyclotron Magnet.

## *Magnet Design*

A 3D software OPERA [4] was used to model the cyclotron magnet [Figure 1]. 1/8th symmetric part was simulated to make fine mesh and reduce the solution time. Following design goals were incorporated and achieved in the simulation

- To make the cyclotron compact and suitable for Hospital environment, maximum hill field ~16.8 KG at room temperature was fixed. This high field helps to keep the pole radius within 670 mm.
- To reduce the power consumption in main coil pole to pole gap was also kept small and fixed to 30 mm.
- Central plug size, positioning and pole angular widths were optimised to achieve frequency error and integrated phase error within a reasonable limit of $\pm 5.0\text{x}10^{-4}$ and $\pm 10^{\circ}$ respectively.
- A deviation of ±4 gauss of isochronous average magnetic field will cause beam loss in the extraction radius [Figure 2,3].

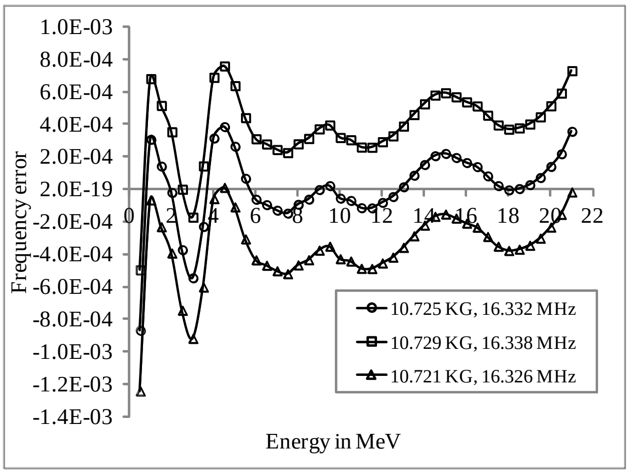


Figure 2: Frequency error at the designed field of 10.725 KG and at ± 4 gauss field deviation .

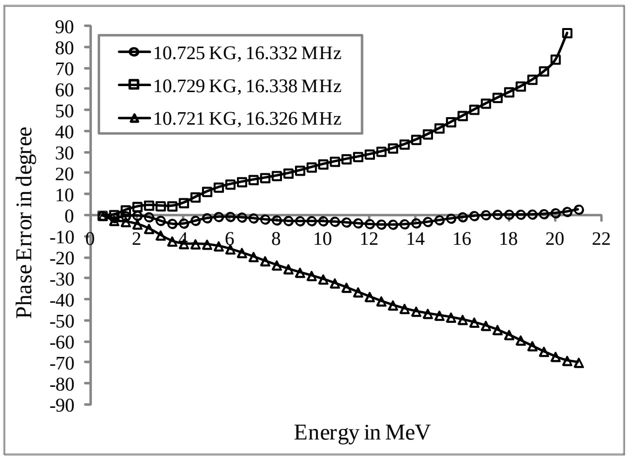


Figure 3: Integrated phase error at the designed field of 10.725 KG and at ± 4 gauss field deviation .

## *Engineering Challenges*

A detail simulation was carried out to simulate pole machining tolerance. It was found that pole edge should be machined within ± 25 micron accuracy and similar tolerance should be maintained for assembly also [Figure 4]. It was found that B-H characteristic of the iron material is playing a very crucial role in determining the shape of the pole profile. A case was studied using iron with grade AISI 1010 and AISI 1006. Pole profile was optimised with 1010. When the same profile was simulated with AISI 1006 BH it was found that integrated phase error deviates from our target value [Figure 5]. Pole profile was again optimised to get the required integrated phase error. Even for same grade of material, it was found that depending on the manufacturing process BH characteristics are different. This is will cause the final field to deviate from designed value. To handle this challenge poles were made in two parts and a separate cut section was introduced in the upper part so that if any modification is required that can be done on the detachable part and reassemble again easily.

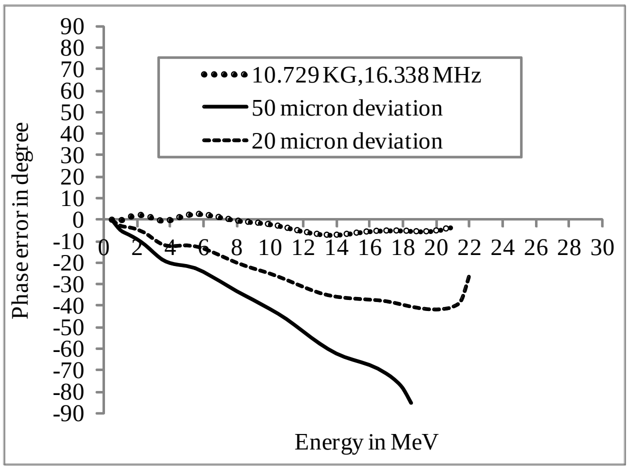


Figure 4: Integrated phase error at the designed field and for angular width deviation of 50 micron and 20 micron.

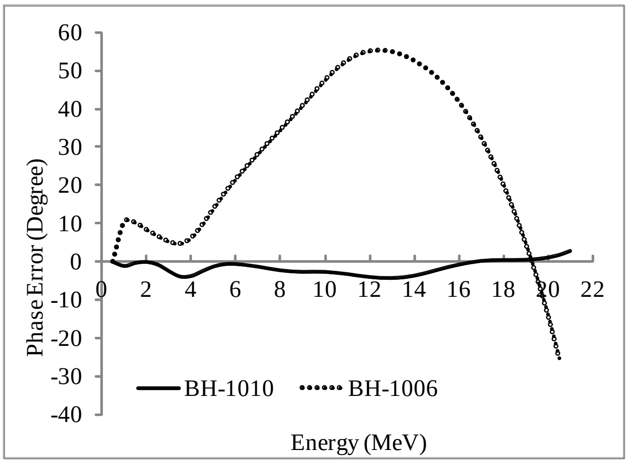


Figure 5: Integrated phase error at the designed field with BH-1010 and with BH-1006 for the same pole profile.

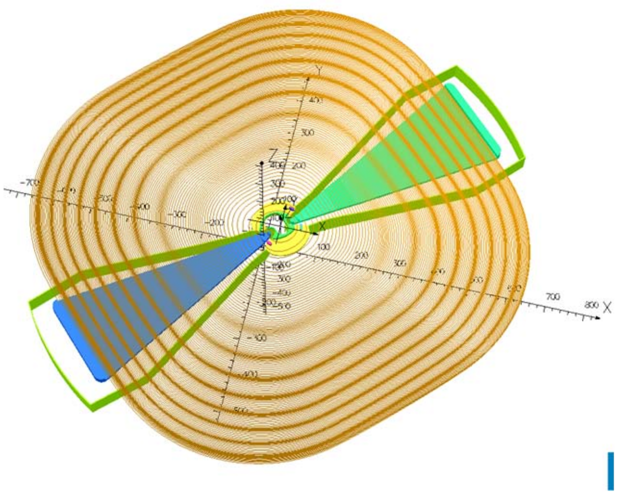

Figure 6: Particle orbits in combined electric and magnetic field with the designed field up to extraction.

*Design Verification by charged particle tracking*

To verify the design, H- ions were tracked in combined electric and magnetic field up to extraction radius using the operating conditions [Figure 6] in OPERA [4]. Accelerating components i.e, Dees and central region with beam defining posts were modelled and simulated. Positioning of the accelerating components were optimised. Beam centring was within acceptable limit. Confinement of ion beam in the vertical direction was within ±3mm which is very small compared to the available aperture [Figure 7].

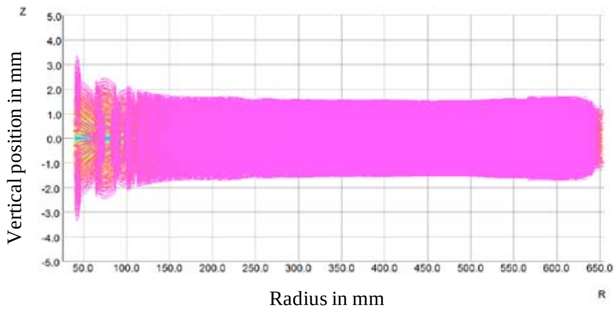


Figure 7: Radius Vs Vertical oscillation.

## CONCLUSION

Present study provides the confidence to design and manufacture a cyclotron magnet suitable for radio isotope production without any beam loss in the acceleration zone. It is also possible to estimate the sources of error arising due to material mismatch, machining and assembly limitation. Concept of detachable part in the pole is also very useful to correct the accumulated magnetic field errors arising from all the sources.


## ACKNOWLEDGEMENT

We are thankful to Draftsman Sutripta Sur and Nityanand Prasad for conceptualising the three dimensional details of the cyclotron magnet and accelerating components.


## REFERENCES


[1] J. R. Richardson, “Sector Focusing Cyclotrons”, Progress in Nuclear Techniques & Instrumentations, Vol. 1, North Holland (1965).

[2] J. J. Livingood, “Principle of Cyclic Particle Accelerators”, D. Van Nostrand Comp. (1961)

[3] A. Goswami, P. Sing Babu and V. S. Pandit, “Behaviour of space charge dominated beam in a high current compact cyclotron”’ Nuclear Instruments and Methods A 562 (2006) 34.

[4] OPERA, 3D software, COBHAM, Version 16R2

# DEVELOPMENT OF Ti Gr-2 COMPONENTS FOR HB 650 MHz SCRF CAVITY DRESSING

V. K. Srivastava*, T. Maurya, Ashish Singh, V. Vijayakumar, S. Maulali, Manish Bagre, V. K. Jain, Avinash Puntambekar

Raja Ramanna Centre for Advanced Technology, Indore, India

*Abstract*

R & D activities are going on at RRCAT for development of 650 MHz β=0.92 five-cell superconducting radio frequency (SCRF) cavities required for proposed high energy superconducting proton accelerator [1]. In addition, these cavities will be a part of deliverables from RRCAT to Fermilab under Indian Institutes Fermilab Collaboration (IIFC). Each SCRF cavity, made of high RRR niobium, is enclosed within helium vessel and welded at either ends using end cap/adaptor ring and bellows. The vessel will contain liquid helium, to cool the cavity up to 2K temperature. Precision fabrication of these Ti gr-2 components involves multiple challenges to protect base material from ambient contamination during fabrication which involves forming, welding and machining. Helium vessel and MC end cap/adaptor ring are cold formed and machined to achieve desired tolerance. Bellows are made of 0.4 mm thick sheet by hydro-forming and edge welded using micro TIG welding. All the weld joints have been qualified as per ASME section IX. To ensure sufficient toughness/ductility of welds at 2K temperature, as per AWS G2.4M, the oxidations (discoloration) of welds were minimized [2][3]. This paper discusses the design requirements, manufacturing processes involving forming, welding, machining and qualification of 650 MHz SCRF cavity dressing components.

## INTRODUCTION

Each 650 MHz β=0.92 five-cell SCRF cavity is fabricated, processed and tested at 2K in vertical test stand (VTS) for performance evaluation [1]. For dressing, a VTS qualified cavity is co-linearly aligned and inserted into helium vessel. At main coupler (MC) side, the MC end cap and at field probe (FP) side, bellows and adaptor ring serve as transition to enclose the cavity in helium vessel. The annular space between cavity and vessel contains liquid helium, to cool the cavity up to 2K temperature. The rolling pads (4 No.) lifting lugs (4 No.), tuner adaptors (2 No.), two phase port transition (1 No.) have been welded on vessel, at their respective locations, using electron beam (EB) welding. Necessary modification were made in rolling pads, lifting lugs, tuner adaptors and two phase port transition to suit the EB welding requirements. Rolling pads lifting lugs and tuner adaptors were fillet welded all around. Two phase port transition was joined using 3D full penetration welding with variable focus. Ti bellows are used to deal with axial displacement for cavity tuning and compensates the differential expansion/contraction between niobium cavity and Ti vessel due to cooling from 300K to 2K temperature and vice versa. The components are assembled over the cavity as per dressing plan using insertion fixture and tack welded.

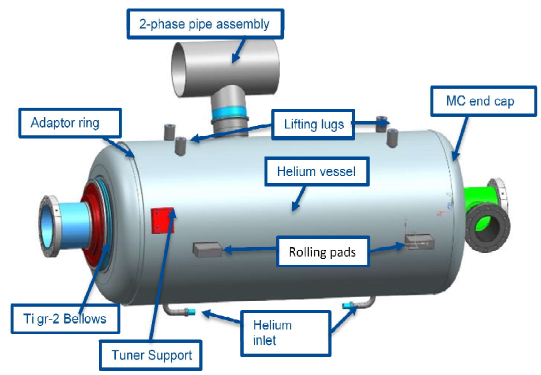


Figure-1: Ti gr-2 components in a dressed cavity

Finally, they are TIG welded in a glove box. The components for cavity dressing are –

- Helium vessel
- Bellows
- Main coupler end cap and adaptor ring

All the components are made of Ti gr-2 material conforming to ASTM B265. Ti gr-2 was opted for welding high RRR niobium (the cavity material) with it using Ti-45Nb alloy as transition and very less difference in its linear coefficient of thermal expansion w.r.t. high RRR niobium [4][5].

These components sustain together, after dressing –

- the entire load of cavity, and tuner force
- the internal pressure of confined liquid helium
- increases stiffness of cavity.

## DESIGN PARAMETERS

Design criteria of components are –

- Helium vessel design satisfies the requirements of the ASME Boiler and pressure vessel code section VIII division 2. The MAWP is 4 bar at 2K and 2 bar at ambient. The single ‘V’ groove longitudinal weld joint design satisfies the ASME section IX and AWS G 2.4M requirements.

  Inside Diameter: 440 +0.5 mm
  Outside Diameter: 450 +0.5 mm

*vks@rrcat.gov.in

Length: 942 +2 mm
Over all cylindericity: 1 mm
Leak Rate qualification : ≤ 2E-10 mbar-l/s

- Bellows are designed as membrane to qualify EJMA10 requirements [6]. The MAWP is 4 bar at 2K and 2 bar at ambient. The seam and J-scuff weld joints also satisfy AWS G 2.4M requirements.
  Inside Diameter: 234 ± 0.3mm
  Outside Diameter: 252.6 ± 1.0 mm
  Leak Rate qualification : ≤ 2E-10 mbar-l/s
  Free Length: 33.6 mm
  Axial movement: ± 2 mm
- Main coupler end cap and adaptor rings are flanged type heads, designed to satisfy the requirements of ASME BPVC section VIII division 2. The MAWP is 4 bar at 2K and 2 bar at ambient.
  MC end cap inside diameter: 336 +0.1 mm
  MC end cap outside diameter: 443.5 -0.3 mm
  Length: 56.5 mm
  Wall thickness: 8mm

  Adaptor ring inside diameter: 260 +0.5 mm
  Adaptor ring outside diameter: 443.5 -0.3 mm
  Length: 90 mm
  Wall thickness: 5mm

## FABRICATION

Prototyping and series production (for 6 sets) of Ti gr-2 components were carried out at different industries.

### *Helium vessel*

The vessel is made by progressive forming/rolling of 5mm thick Ti gr-2 sheet. Fixtures, radius templates were used for cylindricity corrections, at different stages. Single 'V' groove was machined and long seam fit up was made. Before welding WPS, WPQ and PQR were carried out. Welding coupons/specimens were made to qualify for discoloration, weld radiography, tensile test, root and face bend tests. Radiography was done using X-ray source with IQI sensitivity 2T seen. ASME section VIII division 1 mandatory appendix 4 was applied for acceptable porosity limit of radiograph. The acceptance criterion for discoloration was as per AWS G2.4M and for tensile test was conforming to ASME IX, QW-153 and table QW-422 (tensile strength ≥ 345 MPa).

Figure-2: Longitudinal welding of helium vessel

The acceptance criteria for bend test was conforming to QW-163 and for hardness test is –

Hardness of weld ≤ Hardness of Ti gr-2 plate + 30

The longitudinal seam welding was done by TIG welding process using ERTi-2 filler. Cylindricity corrections were done after root pass and final welding using fixtures and radius template. Silvery appearance (discoloration) of weld bead was maintained by trail shielding and back purging in all four weld passes. After length machining, vacuum leak rate measurement was carried out. Finally, ports for helium inlet and outlet were machined.

Figure-3: Helium vessel with rolling pads, lifting lugs, tuner adaptors and ports

### *Bellows*

Ti gr-2 bellows are fabricated by seam welding and hydro-forming of 0.4 mm thick sheet/blank. Later, machined end rings were welded at either ends. Welding was carried out by micro-TIG Welding process using ERTi-2 filler. After ends machining to remove distortion and bellows cleaning, vacuum leak rate measurement was carried out.

Figure-4: Ti gr-2 bellows and adaptor rings

### *Main coupler end cap and adaptor ring*

The MC end caps and adaptor rings are made by cold forming of 12mm and 10mm thick Ti gr-2 plates respectively. The forming was done using die and punch method at 200°C in two stages to minimize spring back thus better control of formed dimensions [7]. Later, the entire surface was machined to remove forming errors and achieve the final dimension and tolerance. The end caps and adaptor rings were machined down to 8mm and 5mm thickness respectively. To ensure the outer and inner surfaces crack free, as per ASME section V, die penetrant test was carried out.

## INSPECTION AND QUALIFICATION OF COMPONENTS

After fabrication, all the components were properly cleaned then inspected for dimensions and qualified for respective tests.

### *Helium vessel*

The entire weld length of each vessel was radio-graphed. Then the vessels were chemically cleaned. The visual examination was done followed by CMM inspection for dimension and tolerance.

Figure-5: CMM inspection of helium vessel

Later, the vessels were qualified for leak Rate: ≤ 2E-10 mbar-l/s.

Figure-6: Leak rate measurement of helium vessel

### *Bellows*

The bellows were chemically cleaned. The visual examination was done followed by inspection for dimension and tolerance.

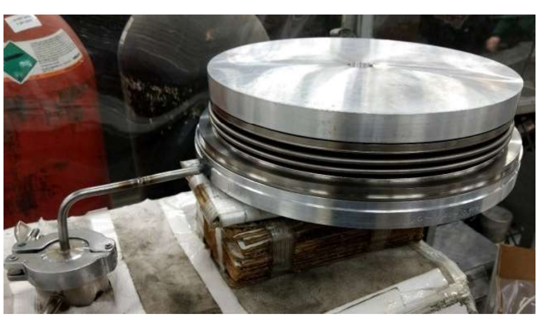

Figure-6: Leak rate measurement ofTi gr-2 bellows

Later, the bellows were qualified for pressure test at 43.5 Psig for 1 minute and for vacuum leak Rate: ≤ 2E-10 mbar-l/s.

### *Main coupler end cap and adaptor ring*

The MC end cap and adaptor rings were chemically cleaned. The visual examination was done followed by inspection for dimension and tolerance. Later, all the MC end cap and adaptor rings were qualified for die penetrant examination.

## RESULTS

The Ti gr-2 dressing components were developed and fabricated successfully for 6 cavities.The components were meeting the dimension and tolerance and other functional qualifications as specified.

## FURTHER WORKS

The experience gained in design, fabrication and qualification of components will be useful to refine the design and fabrication for improved quality and economy. Electron beam welding could be explored for fabrication of vessels and bellows. The glove box is commissioned for oxygen <10ppm and RH <15% in which final welding of dressed cavity using these components will be done.


## ACKNOWLEDGEMENTS

We acknowledge the efforts of different industries to carry out prototyping and fabrication of components. We also acknowledge the efforts of staff and support of ‘Design and Manufacturing Technology Division’ and ‘Superconducting Cavity Development Division’, in development of these components.


## REFERENCES


[1] Development of infrastructure facilities for superconducting RF cavity fabrication, processing and 2K characterization at RRCAT, S. C. Joshi et al. 2017 IOP Conference series, Material science and engineering.

[2] Ti welding technology, Tadayuki Otani, Nippon steel technical report No.95 January 2007.

[3] Welding of Ti alloys, Tim Pasang et al. ICPMMT 2017.

[4] New helium vessel and lever tuner for the 650 MHz cavities for project X, I. Gonin et al. page 841-843, Proceedings of PAC2013, Pasadena, CA USA.

[5] Technical specification for welding Ti helium vessels at Fermilab, 5500-ES-371040, 13th August 2007.

[6] Design analysis and shape optimization of metallic bellows for nuclear valve applications, A. K. Dureja et al. SMiRT 21, 6-11 November, 2011, New Delhi, India.

[7] Forming of Ti and Ti alloys, Joseph D. Beal et al. page 656-669, ASM Handbook, volume 14B.

# DEVELOPMENT OF LIGHT ION BUNCHED BEAM FACILITY FOR FOTIA DC ACCELERATOR

B M Kukreti*, Arun Agarwal.
Ion Accelerator Development Division
Bhabha Atomic Research Centre, Mumbai - 400085, India.

*Abstract*

To extend the functionality of the 6 MV Folded Ion Tandem Accelerator (FOTIA) facility at BARC, a light ion bunched beam facility is being setup. On completion, this multi-pronged bunched beam facility will meet timing related requirements of FOTIA users. Accordingly, design & development of a Low Energy Buncher (LEB) has been undertaken at 20.3125 MHz RF frequency and is based on single gap & multi harmonic principle-called multi harmonic buncher (MHB). At present, development of MHB and its low level RF system on digital platform (dLLRF) has been completed. Work related to the other subsystems, such as RF system, are under active development.

This paper will present the overall R&D status in setting up the light ion bunched beam facility

.

## INTRODUCTION

Commissioned during 2000, the 6 MV Folded Ion Tandem Accelerator (FOTIA) facility at BARC [1], has been delivering light ion DC beam to the large user base, R&D institution and universities, in the country. The facility caters to the varying R&D requirements of users such as nuclear physics, material science, life science experiments etc. In order to extend the facility functionalities for timing structures measurements of nuclear physics experiments especially (p,n), (d,n), (n,n),(n,$\gamma$) reactions, a road map [2] has been setup to establish the light ion bunched beam facility.

With the emerging application of high intensity proton Linac technology especially to the frontiers of nuclear waste incineration (long-lived minor actinides), thorium utilisation [3], production of medical isotope [4], material science etc, light ion bunched beam facility development is being undertaken to also have synergy to the offline technology development R&D for the key components of high intensity SC proton Linac namely low $\beta$ (0.10) SC resonators, using in-house resources [2]. Accordingly, development scheme of light ion bunched beam facility is to be done, in two phases with availability of sub nano second bunched beam (~ 500 ps) at 3.0 MeV proton energy, in the later phase [Fig.1.0]. This multipronged approach will also facilitate R&D in offline technology development and physics/engineering design validation to the efficient low beta SC cavity structures right after the 3.0 MeV RFQ of proposed 1.0 GeV high intensity proton Linac [3].

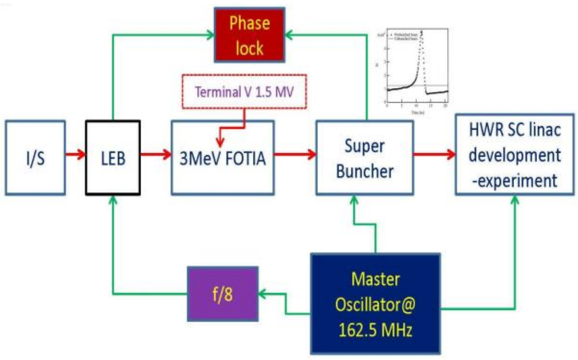


Fig.1.0: Proposed road map for setting up FOTIA light ion bunched beam facility

Accordingly, in synergy to the immediate objectives as well long term objectives of offline, high intensity proton Linac technology development, design & development of low energy buncher (LEB) also called multi harmonic buncher (MHB) is being done at 20.3125MHz. Fig.2.0 represent the schematic view studied [5] for MHB based light ion bunched beam at the terminal of FOTIA DC accelerator.

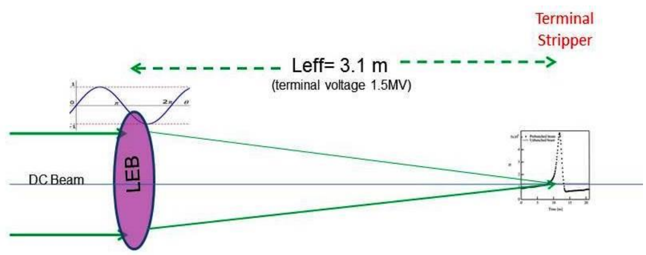


Fig.2.0: Time focus scheme on FOTIA DC accelerator

Further design study including optimal injection energy to FOTIA DC accelerator, has been presented elsewhere [2] and includes feasibility of offline technology development to the case of 40MeV SC proton Linac.

## SUB-SYSTEM DEVELOPMENT STATUS

### *Low Energy Buncher (LEB)*

After completing the physics & RF design of single gap multi harmonic buncher (MHB) , the prototype has been fabricated and presented on Fig.3.0. Technical design details of this work is presented elsewhere [6]. The characterised results to MHB prototype, for the case of three harmonic spectrum, has been done in the lab and

*kukreti@barc.gov.in

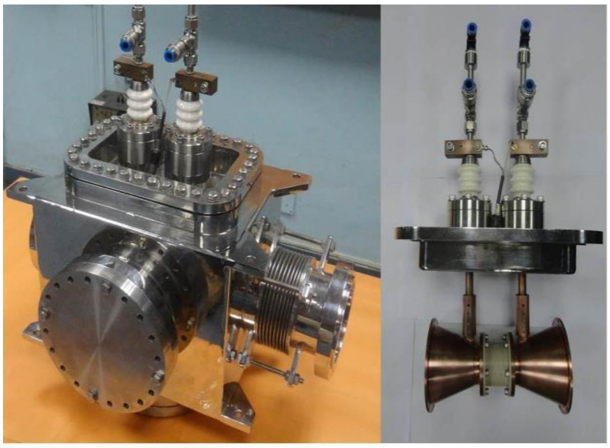

Fig.3.0: Fabricated MHB prototype


Fig.4.0: Low level characterisation of MHB prototype

presented in Fig.4.0. Results, shows for the case of first harmonics (20.3125 MHz) , the effective grid capacitance ~30pF, much on the expected line.

The required electronic support for implementing the MHB commissioning scheme to light ion bunched beam facility, is schematically presents on Fig.5.0.

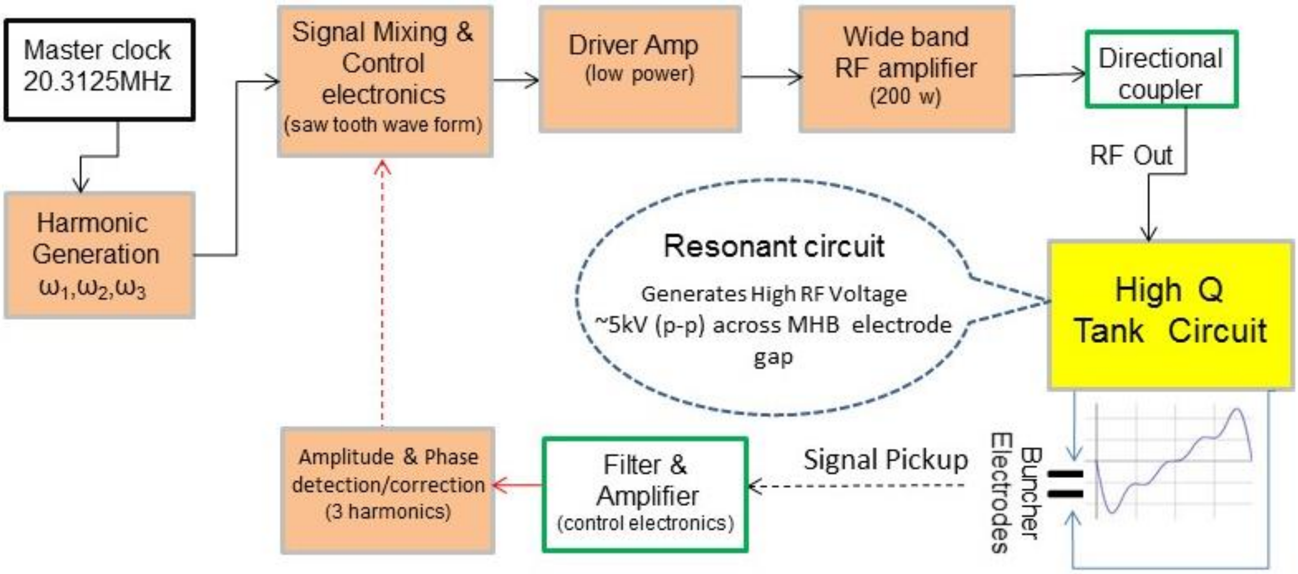


Fig.5.0: MHB electronics: Implementation strategy

## *Fast Faraday Cup (CFFC)*

To measure the fast rise time bunched beam signal, as a consequence of introduction of MHB, one requires fast faraday cup with matching bandwidth to resolve the signal. The require design of 3.0 GHz wideband, 50 ohm fast faraday cup (CFFC) in coaxial geometry, was simulated in CST. The cup design reflects the constraints of working FOTIA DC proton beam current limitation typical ~100nA. And to avoid loss of bunched beam signal, cup dia has been chosen 25mm. The resulting bandwidth is sufficient to resolve the sub nano second bunched beam. Fig.6.0 shows the fabricated fast faraday cup (air cooled) prototype, undergoing lab test. Characterised results presented on Fig.7.0, qualify the desired bandwidth (3.0 GHz) & signal transmission for the prototype. Device response to the fast timing signal has been tested using 3GHz sinusoidal signal in Fig.8.0, confirms compatibility to sub nano second bunched beam signal.

The designed CFFC prototype has been planned to undergo, bunched beam trial to that of HCI beamline at IUAC, New Delhi and LEHIPA beamline at BARC (depending upon availability of bunched beam time), so as to validate the device performance, under deployed conditions. The test performance to the larger extent, will not only give better understanding of design parameters

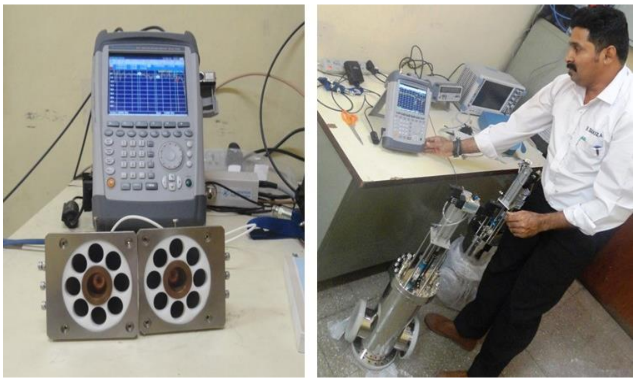

Fig.6.0: Prototype CFFC undergoing lab test

but will also help in undertaking development of high precession diagnostic components at the local industry level.

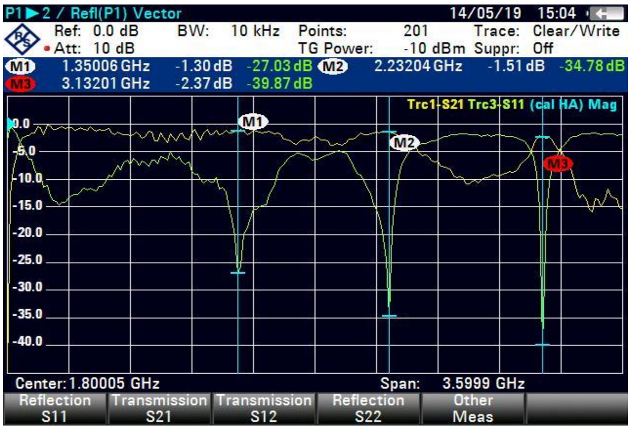


Fig.7.0: S parameters test for Fast Faraday cup

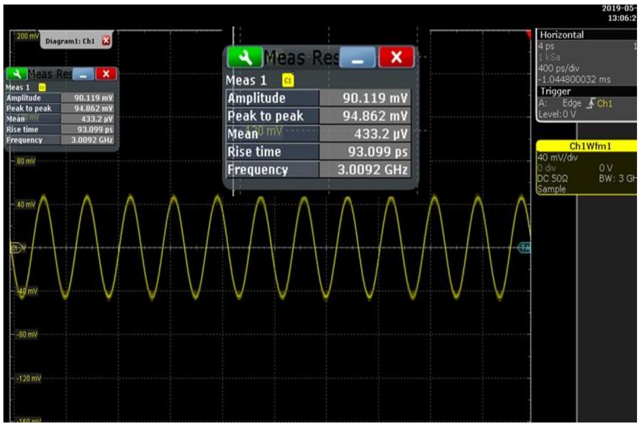


Fig.8.0: Signal rise time test on Fast Faraday cup

### *RF Tank Circuit*

RF excitation of MHB, is to be achieved with suitable design development of RF tank circuit at desired frequencies. In this regard, a 3D conceptual design, having full mechanical compatibility to MHB prototype is presented on Fig.9.0 (both top & bottom view). Recalling the characterised result of Fig.4, a preliminary study on resonant analysis for three exciting harmonics of MHB, is being initiated. In this regard, prototyping of desired high voltage RF test coil, is under active study with fabrication of prototype high voltage test coil [Fig.10].

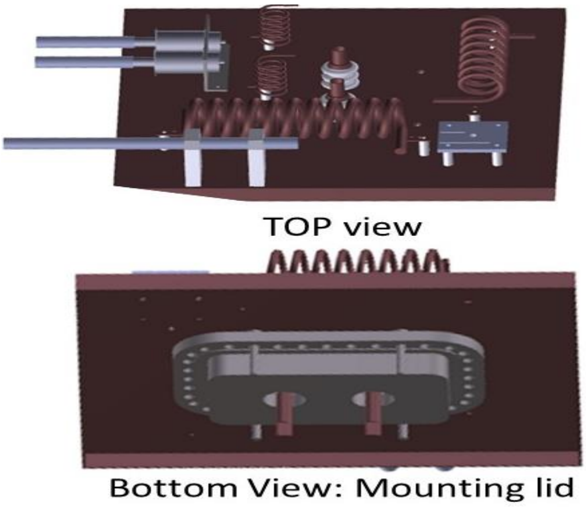


Fig.9.0: 3D Mechanical design of RF tank circuit.

Fig.10: Prototyping of high voltage RF TEST coil

### *Other subsystem*

The status of other related subsystems is as follows. Procurement of high fidelity 200 watt, 0.1-100 MHz broadband RF amplifier has been completed and tested for the rated power. Required accessories procurement namely RF power meter, directional coupler, high speed signal amplifier to CFFC, has also been completed. Design and development of low level RF controller shown in the block diagram of Fig.5.0, has also been completed on digital platform using FPGA and satisfactory tested for the required saw tooth wave form generation.

## FURTHER ACTION PLAN

To established FOTIA light ion bunched beam facility, satisfactory progress has been achieved in design, developing of most of the subsystem. To design RF tank circuit prototype, active R&D is under progress. Procurement of required critical material namely vacuum variable capacitor (01-30pF, 15kV), RF cables etc. has been readily completed. With planned test run on high voltage RF coil prototype, fabricated in the lab, will give better understanding of resonant performance for the three harmonics of RF tank circuit. Subsequently, all the subsystem will be integrated to MHB prototype for beam trial.

## ACKNOWLEDGEMENT

While working on this developmental activity, authors wish to acknowledge the valuable support received at the different stage of work from number of contributors/colleagues. We wish to thank team IUAC at New Delhi, for their valuable input/suggestion during the discussion meet especially Dr P.N Prakash, Dr A.Sarkar, Dr Sarvesh Kumar. To the working colleagues at BARC, we are thankful to Shri N K Prasad & team (EmA&ID) for extending the required workshop support. Our sincere thanks to participating task leaders of ACnD for their valuable support. At divisional level, critical suggestion by Dr Rajesh Kumar, during the lab testing of CFFC and logistic support extended by HEAD IADD, is wishfully being acknowledged.

## REFERENCES

[1] P. Singh et al. “Status report on the folded tandem ion accelerator at BARC”, Pramanna J. Phys,**59**, (2002).

[2] B.M.Kukreti et al. Proc of 7th InPAC-2018, RRCAT, Indore, India, Jan (2018)

[3] P. Singh et al. "Accelerator Development in India for ADS Programme", Pramanna J. Phys,**68**, (2007).

[4] B.M.Kukreti et al. "Medical isotope production using high intensity proton accelerator technology" ,SSNTD-20 , Mysuru, India, Oct ( 2017).

[5] Skorka SJ.,3rd Int conf IEEE-NS,US,(1981).

[6] B.M.Kukreti et al.,27th NSCS, IITB, Mumbai, India Jan (2019).

# Development and Testing of Tuner and Its Subsystems for 650 MHz Superconducting RF Cavity

K. K. Singh*, A. Yedle, A. Yadav, V. K. Jain, D.V. Ghodke and A. Puntambekar
Raja Ramanna Centre for Advanced Technology, Indore, India
*kksingh@rrcat.gov.in

*Abstract*

Tuners are essential components of dressed superconducting RF (SCRF) cavity, which are required to tune (or to detune) the cavity during accelerator operation. Tuner for SCRF cavity is very important as the cavity quality factor is very high, so cavity becomes very sensitive to small external influence (such as microphonics) or internal influence (such as Lorentz Forces on cavity walls). RRCAT is developing SCRF cavity lever tuner and its subsystems under Indian Institutions and Fermilab Collaboration (IIFC). As per IIFC design, five numbers of tuners have been fabricated with the help of Indian industry. Maintaining strict mechanical tolerance and controlling the magnetic permeability of SS316L are some of the challenges in tuner fabrication. This tuner uses stepper motor and piezo actuators for slow and fast tuning actuations. Stepper motor controller along with driver is developed to drive the motor in cryo-environment for slow tuning. Piezo controller along with driver is also developed to drive the piezo in pulse mode. A dedicated tuner test set up is also designed and fabricated for pre-qualification of tuner and its control electronics. Lever tuner is characterized for its tuning range, hysteresis and resolution at no load and full load at room temperature and cryogenic temperature up to 77K. This paper brings out design requirements of tuner and their control, fabrication of tuners, test set up and pre-qualification at room temperature and up to liquid nitrogen temperature.

## INTRODUCTION

Development of tuner for 650 MHz, $\beta = 0.92$ five-cell super- conducting radio frequency (SCRF) cavities are ongoing at RRCAT. These multi-cell SCRF cavities are required for the proposed superconducting Proton linear accelerator at RRCAT and are also deliverable to Fermilab, USA under Indian Institutes Fermilab Collaboration (IIFC) [1]. Due to narrow bandwidth of ~30 Hz of this superconducting RF cavity, it becomes very sensitive to small perturbation as cavity sensitivity is ~160 Hz/µm [2]. The perturbations may arise in the cavity due to dynamic Lorentz forces at cavity walls (due to pulse operations of the cavity) and microphonics (external vibrations). In order to compensate the detuning due to these perturbations, proper tuning mechanism is required.

There are two types of tuning operation viz. slow tuning (range of 200 kHz, resolution of 2 Hz) and fast tuning (range of 1 kHz, resolution of 0.5 Hz)[2]. Slow tuning is used for initial adjustment such as manufacturing error and cool-down conditions. Different types of slow tuner are Saclay / TTF tuner, KEK slide jack tuner, KEK coaxial ball screw tuner, DESY blade tuner and lever tuner etc. Geared stepper motor is used for slow tuning operation. Fast tuner is used to compensate dynamic Lorentz force detuning and microphonics. Piezo actuators, assembled with slow tuning mechanism, are used for fast tuning operation. Resonance control system controls the operation of slow and fast tuning mechanism and minimizes RF power loss during accelerator operation.

In order to test the tuning operation, lever tuner is assembled on a specially designed and developed tuner test stand. Tuner controller is also developed to drive the motor as well as Piezo-actuators.

## LEVER TUNER DEVELOPMENT

The 3D model of lever tuner is shown in Fig. 1. Tuner assembly is attached on helium vessel at tuner lug support. This mechanism consists of double lever arrangement, with approximately 20:1 ratio. Geared stepper motor guides the thin lever (yellow) which spins around bearing A and move bearing B in order to move thick lever (Red). Thick lever is in connection with transition ring connected to the cavity. So, stepper motor transmits force through thick liver. Two piezo actuators, assembled at the centre between transition ring and red lever, transmit force directly to the cavity [3].

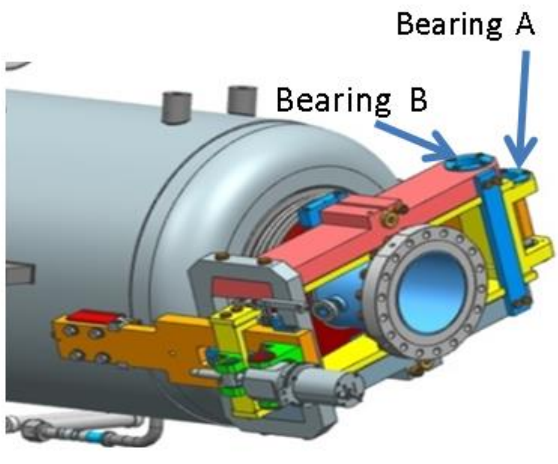


Figure 1: 3D model of lever tuner

Five numbers of lever tuners have been fabricated based on IIFC design [3]. Required mechanical tolerances are achieved in fabrication process. Machining of SS is subjected to magnetization of tuner component. It is require to maintain the magnetic hygiene ($\mu_r$) below 1.05. Higher magnetic hygiene leads to increase in surface resistances of the superconducting cavity which reduces quality factor. In the machined component magnetic hygiene below 1.05 is achieved by annealing process. After annealing, Tuner component are assembled.

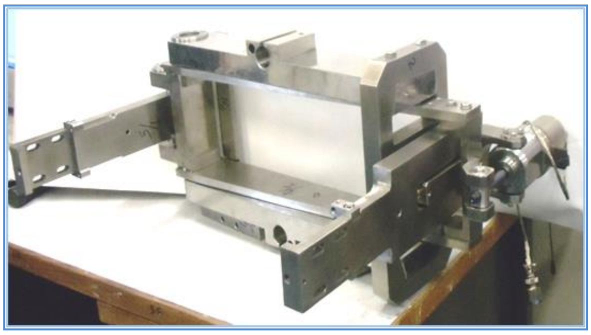

Figure 2: Lever tuner assembly

Lever tuner assembly is shown in Fig.2 In order to test tuner function and tuner stiffness, tuner is mounted on a test stand. Test stand is designed and fabricated.

## TUNER CONTROL

The tuner control system is used for driving the motor as well as piezo actuator for slow and fast tuning operation. The schematic of tuner control system is shown in Fig.3. GUI for stepper motor and piezo control is shown in Fig.4a and 4b. Stepper motor driver (35 V and 1 amp per phase), drive the motor in bipolar mode. Current controlled driver has been developed to drives the motor in cryogenic conditions as well as room temperature.

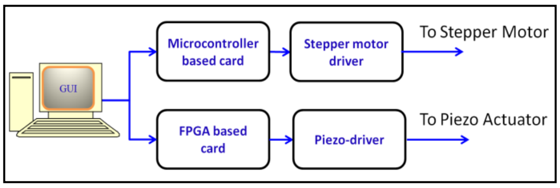


Figure 3: Tuner control system

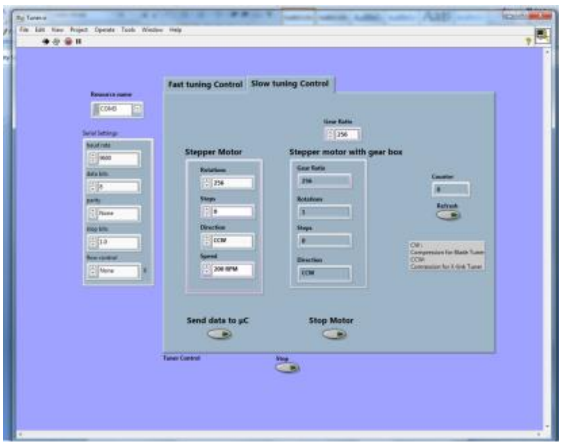


Figure 4a: GUI for stepper motor control

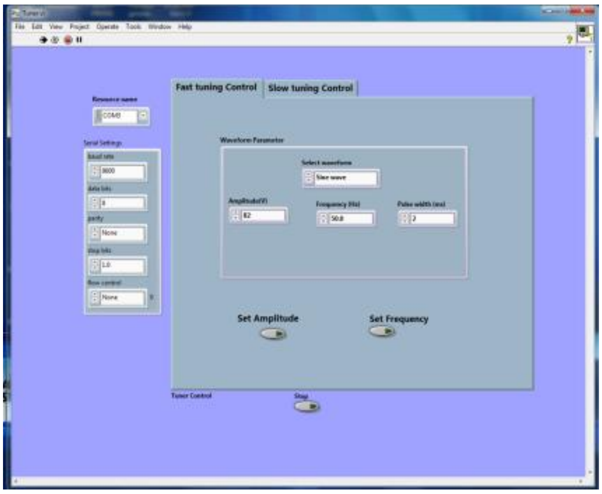


Figure 4b: GUI for Piezo control.

Half sine wave is used to drive the piezo-actuators in order to compensate Lorentz force detuning [4] in feed forward loop. In view of this, Piezo-controller using Spartan-3 based FPGA board has been developed to generate half sinusoidal waveforms (0-5V amplitude, 1-50 Hz repetition rate and 1 -10 ms pulse width). Piezo driver used to drive the piezo-actuators by amplifying the low level signal upto 100V, @2A. Developed piezo driver board is shown in Fig.5.

Figure 5: Piezo driver board

## TESTING AND RESULTS

Lever tuner assembled with test stand has been tested at room temperature for its tuning range and hysteresis initially at no load and then at full load. During testing geared stepper motor (gear ratio 1:256) is rotated by developed controller and displacement at centre location (cavity force transfer location or Piezo location) and motor location recorded with dial indicators. Thereafter experiment is repeated by rotating the motor in reverse direction. It is found that for a displacement of 1 mm at the centre, the displacement at motor location is 18.6 mm no load, which also matches with tuner design parameter.

In order to estimate the tuner stiffness, the tuner is loaded with spring load (Belleville spring stiffness 5.6kN/mm) which is more than cavity stiffness of 4.2 kN/mm. Similar tuner experiment is repeated and data of both no load and full load is plotted as shown in Fig.6. Hysteresis of 23 µm is observed at full load. Tuner stiffness of ~40 kN/mm is estimated using the experimental values. Further the estimated resolution of ~250nm/motor rotation was found.

Developed Piezo controller is also tested by driving the PI make piezo actuators with half sinusoidal waveform (of 100 V amplitude, 1 ms – 100 ms pulse width and 1 Hz - 50 Hz repetition rate) with dummy load. The generated half sinusoidal waveform of 100V amplitude, 1 ms pulse width and 50 Hz repetition rate is shown in Fig.7.

After tuner qualification at room temperature, tuning setup is tested at $LN_2$ temperature. Test setup is shown in Fig. 8, where the tuner with test stand is kept inside a $LN_2$ vessel and dial indicates ate placed above the vessel for displacement measurement. It is observe that displacement at full load at $LN_2$ temperature is same as room temperature displacement. The cryo-compatibility of tuner and its control is verified and this control system can be implemented for 2K testing as well.

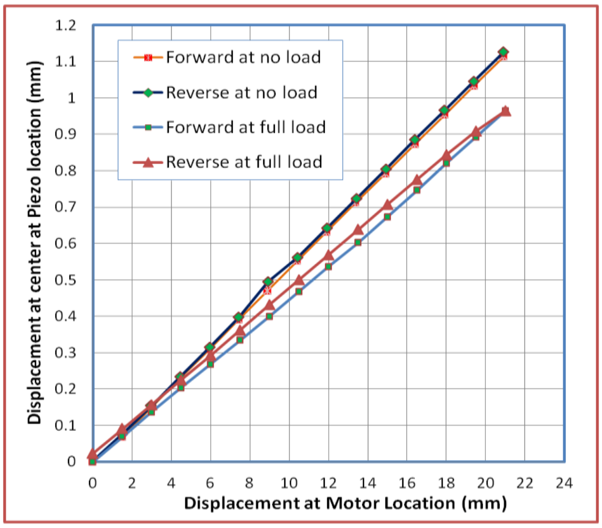


Figure 6: Displacement at centre vs. displacement at motor location at no load and at full load during 300K (room temperature) test

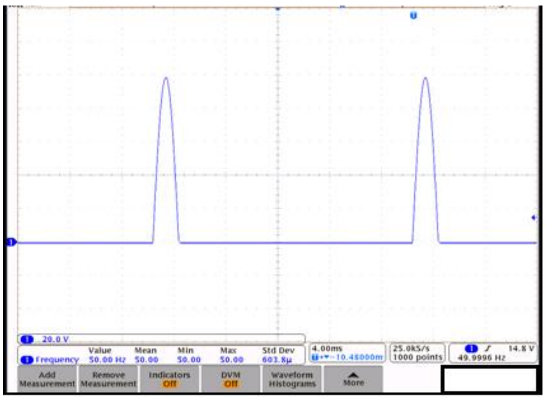

Figure 7: Half sinusoidal waveform of 100 V amplitude, 1 ms pulse width and 50 Hz repetition rate

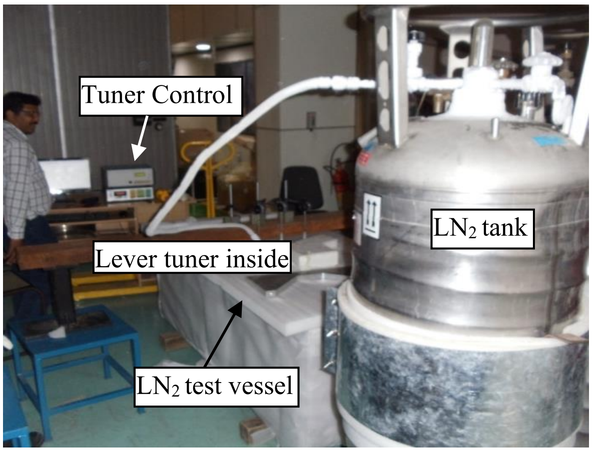


Figure 8: Tuner testing setup at $LN_2$ temperature

## SUMMARY

Lever tuner has been fabricated and tested at room temperature for its tuning range and stiffness. Open loop tuner control system has been design and developed for slow and fast tuning operation. Piezo was operated with narrow pulse width upto 1 ms @100V, 50Hz. Testing of lever tuner with dummy load is an important step in tuner qualification. After testing of tuner with dummy load, it will be mounted on 5-cell 650 MHz SCRF cavity during dressing of the cavity and further tuner qualification will be done in cryo-module.

## ACKNOWLEDGMENT


This work is carried out from the feed-back from IIFC collaborators at FNAL. The authors are grateful for the support of Mr. K. M. Khare, Mr. R. B. Adbol and Mr. K.G. Vaishnava.


## REFERENCES


[1] Amalendu Sharma, et al "Reference Physics Design for 1 GeV Injector Linac and Accumulator Ring for Indian Spallation Neutron Source", https://arxiv.org/abs/1609.04518

[2] V. K. Jain, et al., "650 MHz Elliptical Superconducting RF Cavities for PIP-II project", Proceedings of NAPAC2016, Chicago, IL, USA

[3] Pischalnikov Y., et al., "Design of 650 MHz tuner for PIP-II project" 9th International Particle Accelerator Conference, IPAC2018, Vancoer, BC, Canada

[4] Crispin Contreras., "Resonance Control for Superconducting RF Cavities" https://indico.fnal.gov/event/19221/material/slides/0.pdf

# FE analysis of SCRF cavity weld joints and its experimental verification


Syed Moulali[1]*, Vikas Jain[1], Manish Bagre[1], Vijaya Kumar[1], Ashish Singh[1], Anand Yadav[1], Avinash Puntambekar[1], Vinay Namdeo[2]

Raja Ramanna Centre for Advanced Technology, Indore, India

Samrat Ashok Technological Institute, Vidisha.



*Abstract*

Superconducting (SC) Radio frequency cavity plays a vital role in High intensity SC proton linac. At RRCAT work is ongoing to develop technology for fabrication of 650MHz five-cell SCRF cavities. These cavities are fabricated using high RRR Niobium material and joined by electron beam welding. Weld shrinkages and deformation during Electron beam (EB) welding, specially at iris and stiffing ring locations, affects the RF frequency. Proper weld parameter development and their optimization is one of the key factor in successful cavity fabrication to control and predict these deformations. Efforts have been made to simulate and analyse the weld parameters using Simufact weld software. As a case study simulation of beam tube linear butt joint of five-cell SCRF cavity has been carried out. Studied the maximum temperature of the fusion zone and cool-down time cycle (thermal cycle plot) of the weld joint estimated. The results of simulation, weld fusion zone cross section has been co-related with the micrograph of EB welded test coupon sample. This paper presents the weld parameter optimization, simulation results and their experimental verification.


## INTRODUCTION

Superconducting (SC) Radio frequency cavity is a key element of SC proton linac. At RRCAT work is ongoing to develop technology for fabrication of 650MHz five-cell SCRF cavities. These cavities are fabricated using high RRR Niobium material and joined by using in-house EBW machine. The fabrication of five-cell cavity is a challenging task on account of strict mechanical tolerances with corresponding frequency [1]. Typically a five-cell cavity consists of 38 weld joints joined in stage wise manner as shown in Fig. -1.

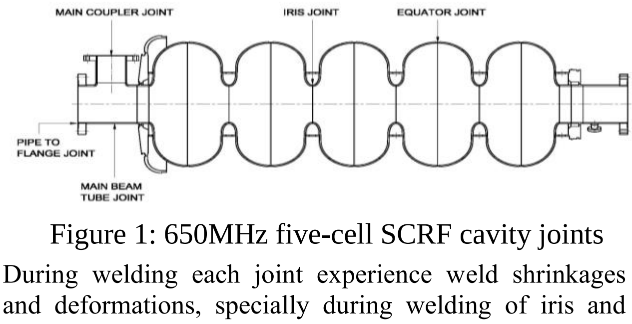


Figure 1: 650MHz five-cell SCRF cavity joints

During welding each joint experience weld shrinkages and deformations, specially during welding of iris and stiffening ring. It affect the mechanical length / geometry and hence the frequency. This result in change in cavity total length and frequency, which is governed by the RF sensitivity at equator 1MHz/mm [2]. To meet the goal of final RF tolerances and mechanical length of cavity, proper and optimised EB weld parameters are needed for obtaining desired weld bead quality, predictable and repeatable weld shrinkages. Optimisation of EB weld parameters experimentally is a time consuming process and expensive. Simulation of EB welding process enables us to estimate the fusion zones, peak temperature profiles, stress, deformations and cooling time etc. and helps in various weld parameter optimisation. However, the weld simulations are not an easy task, because it involves association of thermal, mechanical and metallurgical phenomena. It is important to get familiar with thermal process of welding for analysis of welding pool geometry, mechanics, microstructure and controlling weld quality. A FE analysis has been carried out using Simufact weld simulation software for SCRF cavity joint beam tube. A 3D model of the actual test coupon geometry of linear butt joint with fixture and applied required clamping force for simulations. To simulate the actual EB welding process, the conical volumetric Gaussian heat source model is used, effect of beam current on the weld geometry is analysed through a series of simulations for 35 mA, 48 mA and 58 mA currents and parameters are optimised for minimum power and deformation for the given weld thickness. All time peak temperatures profile are examined by simulations and experimentally verified the cross-section of fusion zone with micrograph examination.

## HEAT SOURCE FOR SIMULATIONS

Study of literature survey shows development of various heat sources such as point, line, circular, hemispherical surface, ellipsoidal, double-ellipsoid and conical heat sources and associated work carried out in welding simulations. For the high energy welding process like an electron beam welding and laser beam welding a 3D Gaussian conical heat source is used to model of power source. In this heat source, the input energy is applied in radius of effected surface (Surface heat source) and by the through depth (volumetric heat source) as shown in Fig. -2 [3]. The Simufact weld software offers comprehensive functionality for structural welding simulation. The software covers different welding processes of Arc welding, Laser, and EB welding [4]. With help of this software in the present study estimated the temperature field distribution, fusion zone, cool down analysis. In


*msyed@rrcat.gov.in

Simufact software the conical heat source is modelled as a combination of volumetric and surface heat source.

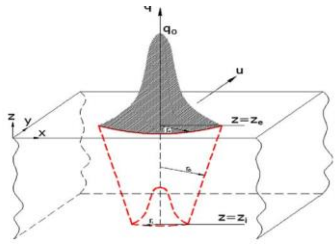

Figure 2: Typical Gaussian conical heat source

The heat source parameters mainly depend upon the upper conical radius, lower conical radius, depth and Gaussian parameter M. Which range from 0-3, where 0 represent the constant distribution and 3 the bell curve become stiffer. These values are optimised by running series of simulations and the peak temperature profiles are by varying the upper radius and lower radius as well Gaussian parameters. The optimised heat source parameters for simulations considered for seal pass and full pass the volumetric heat source parameters as shown in the Fig. 3.

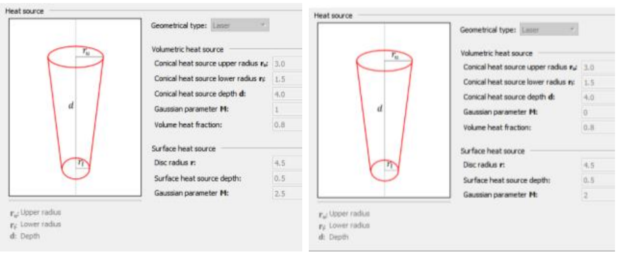

Figure 3: The heat source parameter for seal and full pass.

## SIMULATION OF LINEAR BUTT JOINT:

The 650 MHz five-cell cavity beam tube joint is a linear butt joint. The simulation of weld joint is carried out based upon the actual sample size, fixtures assembly, considering the close to actual welding. The weld simulation trail of Nb plate 200 x 50 x 4 mm two plates and the fixture material aluminium assigned for simulations as a input parameter and assembled as show in Fig. - 4.

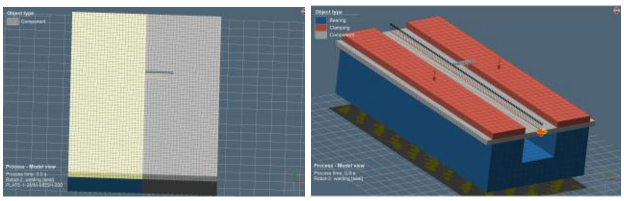

Figure 4: Nb plates and Clamping.

The mesh parameters for simulations considered element type hexahedral with no. nodes 7878 and element 5000 for plate. The reaming parts such as bearing and clamp considered element type hexahedral size 5 mm each respectively. The thermal boundary conditions applied for simulations in which convective heat transfer co-efficient: 0 W/m$^2$ K recommended for vacuum environment, contact heat transfer co-efficient: 3 W/m$^2$ K, Emissivity: 0.35 [5]. In Simufact weld software Nb material is not listed and created Nb material temperature dependent properties file for running the simulations. The material properties considered as per the Table -1 [6].

Table 1: Material properties of Niobium at 300k

| Properties | Values |
|---|---|
| Density , Conductivity | 8570 kg/m$^3$, 53.55 w/m-k |
| Specific heat capacity | 261 J/kg-k |
| Enthalpy of liquid at melting point | 285x10$^3$ J/kg |
| Melting Point | 2741 K |

The weld parameters applied for simulation to optimise weld parameter as per Table 2. Where V (Beam voltage (kV)), I (Beam current), F (weld speed), $R_{up/}$ $R_{DW}$ (Ramp up and Ramp down). The energy applied during welding is in two pass known as seal pass (S) and full pass (F). The seal pass will act as a pre heat the material. The duration between seal pass and full will be minimal.

Table 2: Input parameters used for simulations

| Trial Run | Weld Parameters | | | | | |
|---|---|---|---|---|---|---|
| | V (kV) | I (mA) | | F (mm/min) | | $R_{up}$/ $R_{Dw}$ |
| | | Seal | Full | Seal | Full | |
| 1 | 110 | 30 | 35 | 750 | 400 | 50 % of total power |
| 2 | | 30 | 48 | 750 | 400 | |
| 3 | | 30 | 58 | 750 | 400 | |

The observations of weld simulation run are given in the Table 3. Where DOP (depth of penetration), Maximum temperature ($^0$C), all time peak temperature ($^0$C). The fusion zone top bead, bottom bead and angle of fusion zone values obtained from simulations. The angle of fusion zone 90$^0$ will form a full fusion and a good under bead.

Table 3: Output parameters from simulations

| Trial Run | DOP (mm) | Max. Temp | Peak temp. | Fusion Zone | | |
|---|---|---|---|---|---|---|
| | | | | Top bead | Bott. bead | Angle (deg) |
| 1 | 2.2 | 2530.98 | 4348.29 | 1.58 | No | - |
| 2 | 3.8 | 3192.62 | 5565.05 | 4.53 | 2.67 | 76.91$^0$ |
| 3 | Full | 3706.65 | 6371.57 | 5.76 | 4.30 | 81$^0$ |

The simulation results - 3 shown full penetrations. In seal pass beam current 30 mA (I) observed the penetration up to 2 mm and in full pass beam current at 58mA obtained full depth of penetration. The cross section of fusion zone of seal and full weld pass as show in Fig. - 5.

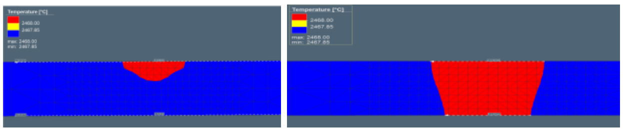

Figure 5: Seal pass and full pass fusion zones

The maximum temperature and all time peak temperatures as shown in Fig.-6.

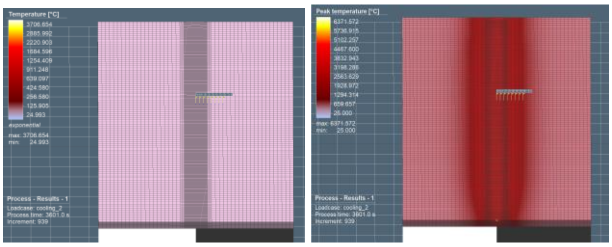

Figure 6: Maximum temperature, All peak temperature

### *Cool-down time simulations:*

After welding, it is allowed to cool-down in vacuum environment up to below 100 deg temperature. Because Niobium is a reactive material and it is highly affinity to impurities during hot condition and the contamination degrade the RRR (residual resistivity ratio) properties. In order to estimate the time required to cool to near about room temperature placed at 8 probe particles at distance of 2 mm in simulation on mid of welding zone to heat effected zone area. The graph plotted temperature Vs time as shown in Fig. -7.

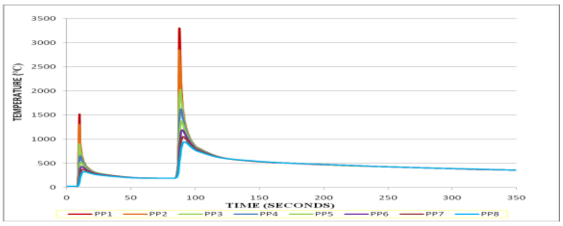


Figure 7: Cooling profile of seal and full pass after weld

It shows that a minimum time of 30 min is needed to cool the component below 100$^0$C for venting the chamber. The curve shows the exponential cooling behaviour after welding.

## EXPERIMENTAL VALIDATION:

The parameters optimised in the simulations are experimentally validated with an EB welding of plate sample as shown in Fig.-8.

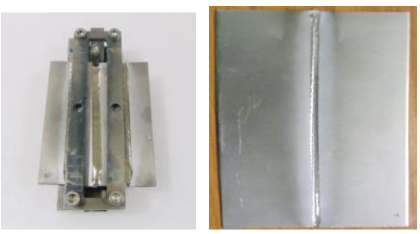

Figure 8: Nb- Test coupon fixture and sample

The test coupon weld bead microscopic examination has been carried out to compare the fusion zones of the micrograph and simulations are as shown in Fig. - 9. The fusion zones of experimental Vs simulations shows that the upper conical radius nearly 6.5 & 5.76, lower conical radius ~ 5.4, 4.3 and the depth 4 mm respectively.

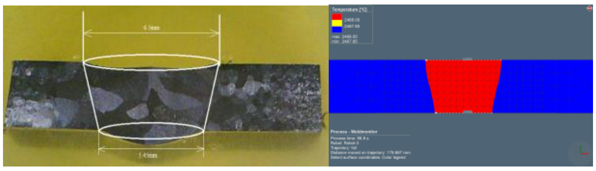

Figure 9: Fusion zones of EB weld sample and simulation fusion zone

## SUMMARY

During the EB welding of SCRF cavity each joint will be subjected to weld shrinkages and deformations. It affects the geometry and hence the changes the RF frequency. Beam tube joint has been simulated using Simufact weld software. For simulation the equivalent conical heat source is modelled for actual heat input during welding. Further, simulated the beam tube linear butt joint and optimised the weld beam current keeping other parameters constant. It is observed that the beam current (I) at 35 mA results lack of penetration. At 48 mA, got full penetration near to bottom, but found small fusion zone angle. Further, increasing the beam current to 58 mA, results in full penetration with the angle of fusion zones close to 90 deg. The fusion zones of the same weld parameters of experimental vs. simulations achieved very close. The error between the simulation and experimental ~12% observed, which shows a good agreement. Also estimated the cooling time after welding and below 100 $^0$C temperature reached in ~ 30 minutes. The benchmark of software established with experimental data. It will helpful to simulate the other joints of SCRF cavity.

## REFERENCES

[1] Avinash Puntambekar et.al "Indigenous development of First Five cell 650 MHz SCRF cavity and Series manufacturing plan" InPAC-2018 , Indore, Jan., 9-12, 2018, p. ID-34.

[2] Mohania P, Mahawar A, et.al "Room temperature RF characterization of 650 MHz Niobium cavity structures for development of Beta-0.92, 5-Cell SCRF cavity" InPAC-2018 , Indore, Jan., 9-12, 2018, p. ID-353.

[3] Bradac J. "Calibration of heat source model in numerical simulations of fusion welding" Machines, Technologies, Materials, IISN 1313-0226, Issue 11/2013.

[4] Simufact Welding "www.simufact.com/applications - modules-Simufact-welding.html#thermal.

[5] M.Letiner, G.pottlacher "Density of Liquid Niobium and tungsten and the estimation of critical point data" Metallurgical and materials transaction springe nature, volume 50A, August 2019-3653.

[6] Z.sun, R. Karppi "The application of electon beam welding for the joining of dissimilar metals: an over view" Journal of material processing technology SSDI 0924-0136(95)02150-k.

# A NEW METHODOLOGY FOR MULTIPHYSICS ANALYSIS OF 325 MHZ RFQ STRUCTURE

N. K. Sharma[#], A. Chaturvedi, C. P. Paul, G. V. Kane
Raja Ramanna Centre for Advanced Technology (RRCAT) Indore

*Abstract*

RRCAT is involved in the development of a 325 MHz, 3 MeV RFQ structure for proposed 1 GeV proton linac. During high power operation, Radio Frequency (RF) induced heating results in temperature rise, thermal deformations and frequency detuning of RFQ structure. Therefore thermal stability of RFQ is an important issue during design stage. A novel multi-physics analysis methodology using ANSYS Mechanical code has been developed and implemented for designing an efficient cooling scheme for RFQ structure. Methodology consists of a complete 3D-RF-fluid-thermal-structural-RF coupled multi-physics analysis to predict temperature rise, deformations and frequency shift for RFQ structure. During analysis, conservation of mass, momentum and energy equations are solved simultaneously for computing velocity, pressure and temperature fields. Novelty of the methodology lies in the fact that direct coupled fluid thermal analysis is integrated with RF analysis at both ends for evaluating thermal induced frequency detuning of RFQ structure. Details of analysis methodology and cooling scheme design for thermal management of pulsed RFQ structure at various duty factors (≤10%) are presented in paper.

## INTRODUCTION

RRCAT is involved in the development of a 1 GeV high intensity proton linac for proposed Indian Facility for Spallation Research (IFSR). A 325 MHz 3 MeV Radio Frequency Quadrupole (RFQ) will be used as a front end injector for proposed facility. RFQ will be a four vane resonating structure made of OFE copper. Physics design of a 325 MHz, 3 MeV, 4 Vane RFQ has been carried to accelerate $H^-$ particles from 50 keV to 3 MeV with a beam peak current of 20 mA [1].

During operation of RFQ, RF induced heating results temperature rise, thermal deformations and subsequent frequency detuning of RFQ structure. Therefore, effective cooling of RFQ is essential to maintain its thermal stability. The thermal management becomes more critical at high duty factor due to higher energy input. A new multi-physics analysis methodology for numerical simulation of RFQ structure has been developed. The methodology consists of a complete 3D-RF-fluid-thermal-structural-RF coupled analysis for predicting temperature rise, thermal deformations and frequency shift of RFQ due to RF heating. All analyses (RF, fluid, thermal, structural) and their coupling are carried out within ANSYS Mechanical software. A water cooling scheme for RFQ was designed and cavity temperature rise, deformation and frequency shift were evaluated using developed methodology. The cooling schemes were designed for 3, 5, 7 and 10 % duty factors.

## METHODOLOGY

A 3D-RF-fluid-thermal-structural-RF coupled multi-physics analysis methodology was developed for RFQ structure. The methodology consists of five steps, namely model development, RF analysis for initial geometry, fluid-thermal coupled analysis, structural analysis and final RF analysis for deformed geometry. Fig. 1 shows flow chart for analysis methodology [2].

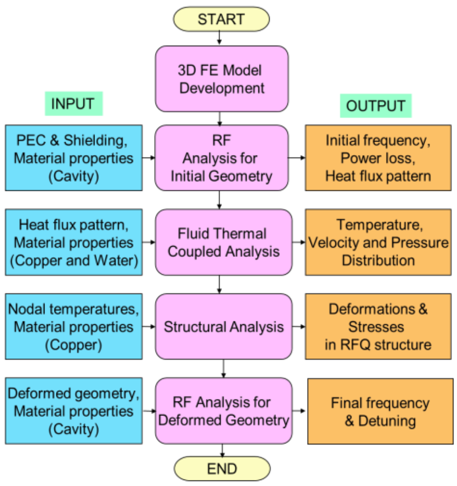


Figure 1: Flowchart for analysis methodology

## RESULTS AND DISCUSSIONS

The coupled multi-physics analysis methodology was implemented to design a cooling scheme for RFQ structure. The cooling channel locations, flow velocities and wall thickness were optimized to achieve minimum temperature rise, thermal deformations and frequency shift for RFQ structure [3]. Analyses were performed for quarter model of RFQ and results were expanded to show complete cross section of RFQ structure.

### *3-D FE Model Development*

During model development, 1.16 m long segment of RFQ was created using ANSYS Programming Development Language (APDL) script. One quarter of RFQ was modelled to reduce computational time and symmetry conditions were applied. Fig. 2 shows the model developed for coupled analysis. The RFQ model

[#]navneet@rrcat.gov.in

consists of three domains namely, vacuum, copper walls and fluid domain. RF analysis for initial and deformed cavity geometry was performed within vacuum domain. Fluid thermal coupled analysis was performed within fluid and copper walls domain and structural analysis was performed within copper wall domain. During meshing, domains which were irrelevant for a particular analysis were meshed with ANSYS Mesh 200 elements. These are dummy elements where nodes and elements exist within that domain but they do not participate in the analysis and used to perform selective analysis of required domains during coupled analysis problems.

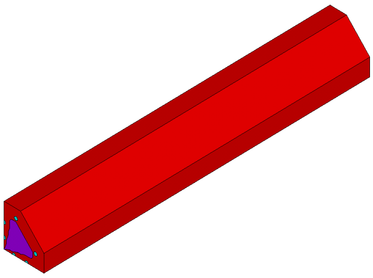

Figure 2: RFQ model for analysis

### *RF Analysis*

High frequency electromagnetic (RF) analysis of RFQ was performed for vacuum domain. During analysis, vacuum domain was meshed with HF 120 elements and copper walls and fluid domain were meshed with Mesh 200 elements. The relative permittivity and permeability for vacuum domain were defined as unity. RF analysis was performed to evaluate RFQ frequency, quality factor and electromagnetic field distribution. RFQ frequency and quality factor was found to be 325.085 MHz and 10565 respectively. Fig. 3 shows normalized electric field distribution for RFQ cavity. A macro based on APDL script was developed to evaluate surface heat fluxes and power loss for RFQ structure. Fig. 4 shows heat flux distribution for RFQ walls for 3% duty factor with 30% margin. The power loss for one quadrant of RFQ was evaluated as 902 W.

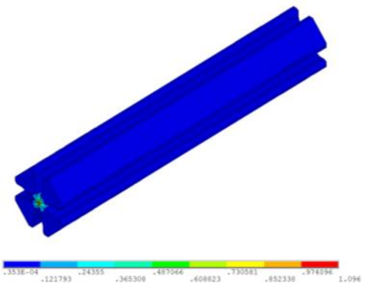

Figure 3: Electric field distribution

### *Fluid-Thermal Coupled Analysis*

Fluid-thermal coupled analysis of RFQ was performed to predict temperature rise in RFQ structure for 3% duty factor. The Mesh 200 elements within copper wall and fluid domain were converted in to Fluid 142 elements and elements within vacuum domain were switched to Mesh 200 elements. Heat fluxes evaluated from RF analysis were applied as a thermal loading for RFQ. At the inlet of each cooling channel, the flow velocity of 2.0 m/s with bulk water temperature of $25^0$ C was applied. The maximum flow velocity for cooling channels was restricted to 2 m/s to avoid material erosion. At the outlet of cooling channels, zero gauge pressure conditions were applied. No slip boundary condition was incorporated for fluid solid interfaces. After applying material properties and boundary conditions, the fluid thermal coupled analysis of RFQ was performed.

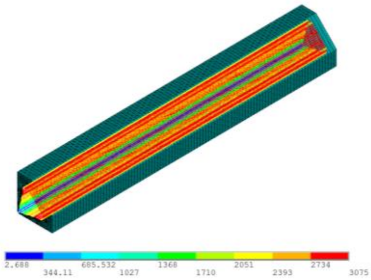

Figure 4: Heat flux distribution

The two equation k-ε model was used to compute turbulent kinetic energy, dissipation rate and effective viscosity for modelling the effect of turbulence on mean flow. During fluid thermal coupled analysis, mass, momentum and energy equations were solved simultaneously to evaluate velocity, pressure and temperature fields. Fig. 5 shows pressure distribution along the length of cooling channels. The maximum gauge pressure of 4367 Pa was evaluated at the inlet of cooling channels. The 3-D temperature profile for RFQ structure is shown in fig. 6. The maximum temperature for RFQ were evaluated as 26.24 °C. As expected, RFQ temperatures at outlet cross section are higher than inlet due to increase in cooling water temperature along the length of RFQ.

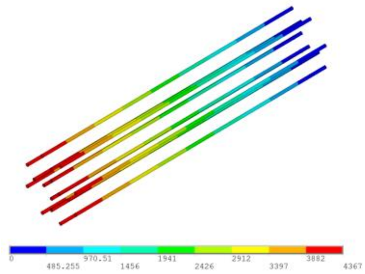

Figure 5: Pressure distribution

### *Structural Analysis*

After thermal analysis, structural analysis was carried out to evaluate thermal deformations and stresses developed in RFQ structure. During analysis, elements within copper wall domain were switched to structural elements, whereas elements within vacuum and fluid domains were switched to Mesh 200. Temperature distribution evaluated from thermal analysis was applied as input load for structural analysis. RFQ was constrained in longitudinal direction at inlet and symmetry constraints were applied for transverse and vertical directions. Structural analysis of RFQ was performed and deformation and stress distribution were evaluated. Fig. 7 shows displacement pattern for RFQ structure. Maximum deformation in RFQ structure was found to be 16 microns. The deformations developed would result in frequency shift for RFQ structure.

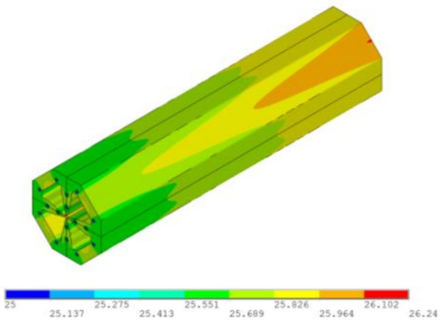

Figure 6: Temperature distribution for RFQ

### *RF Analysis for Deformed Geometry*

After structural analysis, the cavity geometry was updated to model deformed geometry. RF analysis of updated geometry was performed to evaluate new frequency of RFQ cavity. Thermal induced frequency detuning for RFQ was evaluated as a difference between new and initial frequency and found to be - 2.50 kHz. During frequency and field tuning of RFQ, the cavity will be tuned with an additional margin to compensate for predicted thermal induced frequency shift.

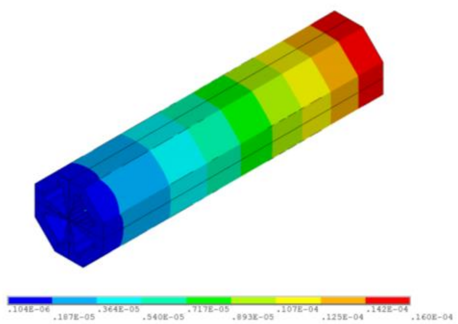

Figure 7: Deformation pattern for RFQ

### *RFQ Analysis for Various Duty Factors*

Multiphysics analysis of RFQ was performed for higher duty factor namely 5%, 7% and 10%. It was evaluated that temperature gradient, deformations and frequency shift increases at higher duty factors. Therefore thermal management would be more critical at higher duty factors. Studies were also performed to investigate the RFQ frequency sensitivity with cooling water temperatures. The cooling water will remove heat from RFQ and it will also be used for frequency control during high duty factor operation. Cooling water temperatures will be varied to restore designed frequency during RFQ operation. Table 1 summarizes the analysis results for higher duty factors.

Table 1: Results for Higher Duty Factors

| **Description** | **Duty Factor** | | | |
|---|---|---|---|---|
| | **3%** | **5%** | **7%** | **10%** |
| Power loss (W) | 902 | 1503 | 2105 | 3007 |
| Heat flux (W/m$^2$) | 3075 | 5126 | 7176 | 10252 |
| RFQ temp. ($^0$C) | 26.24 | 27.07 | 27.89 | 29.13 |
| Water temp. ($^0$C) | 25.96 | 26.61 | 27.25 | 28.22 |
| Displacement (μ) | 16.0 | 26.7 | 37.3 | 53.3 |
| Stress (MPa) | 0.55 | 0.91 | 1.28 | 1.82 |
| Detuning (kHz) | -2.50 | -4.19 | -5.87 | -8.39 |

## CONCLUSIONS

A new methodology for multi-physics analysis of RFQ structure has been developed and presented here. A script using ANSYS Programming Development Language (APDL) was developed for analysis and implemented for designing a cooling scheme for RFQ structure. A single code (ANSYS Mechanical) was used for all analyses and their couplings. It is a basic ANSYS code and various Graphical User Interface (GUI) based modules like HFSS, Workbench and Fluent with their compatible versions are not required for multi-physics analysis. The developed 3D-RF-fluid-thermal-structural-RF coupled multi-physics analysis methodology is being used for development of new high intensity RFQ accelerators for future projects. The methodology is generic in nature and can be implemented for designing various particle accelerator components (like drift tube linac, coupled cavity linac, couplers etc.) for their thermal management.

## REFERENCES


[1] R. Gaur and V. Kumar, "325MHz 3 MeV RFQ" RRCAT / ABPL / 325 MHz RFQ / 01 (internal note).

[2] N. K. Sharma, C. P. Paul, S. C. Joshi, G. V. Kane and A. Chaturvedi, "Coupled 3D Multi-physics Analysis of 325 MHz ISNS RFQ structure", Nuclear Instruments and Methods in Physics Research Section A: Accelerators, Spectrometers, Detectors and Associated Equipment, 937 (2019) 59–71.

[3] N. K. Sharma and S. C. Joshi, "Search Method Optimization Technique for Thermal Design of High Power RFQ Structure", Indian Particle Accelerator Conference-2009 (InPAC-2009), February 2009, RRCAT, Indore.

# FINITE ELEMENT ANALYSIS FOR SKIN EFFECT AND SURFACE FINISH FOR 325 MHZ RFQ STRUCTURE

N. K. Sharma#, A. Chaturvedi, C. P. Paul, G. V. Kane
Raja Ramanna Centre for Advanced Technology (RRCAT), Indore

*Abstract*

RRCAT is involved in the development of a 325 MHz RFQ for proposed 1 GeV proton linac. Due to skin effect, resistance and surface power loss in high frequency resonating structures increases with increase in operating frequency. The power loss results in temperature rise, thermal deformations and frequency detuning of RFQ structure. Electromagnetic analysis of RFQ was performed using ANSYS code to evaluate field profile and power loss in RFQ with a focus on skin depth. Skin depth for 325 MHz copper RFQ is ~ 4 microns. A mesh of 1 micron element size was created near RFQ surfaces to capture the variation of electromagnetic field and power loss within skin depth region. Simulations were performed to investigate the effect of frequency, materials and surface roughness on power loss. It was evaluated that surface finish must be one order better than skin depth to minimize power loss in RFQ structure. The analysis procedure was validated for standard pill box cavity with its analytical solutions. Analysis results provide inputs for designing cooling system for thermal management of RFQ structure. Paper presents the results of numerical simulations carried out for skin effect and surface finish for 325 MHz RFQ structure.

## INTRODUCTION

### *Radio Frequency Quadrupole*

RRCAT is involved in the development of a 325 MHz, 3.0 MeV RFQ structure for proposed 1 GeV high power Proton Linac for Indian Facility for Spallation Research (IFSR) [1]. RFQ will be a normal conducting four vane resonating structure made of OFE copper. Table 1 lists the important parameters of RFQ structure [2].

Table 1: RFQ Parameters

| S. No. | Parameter | Unit | Value |
|---|---|---|---|
| 1 | Input energy | keV | 50 |
| 2 | Output energy | MeV | 3.0 |
| 3 | Particle | - | $H^-$ |
| 4 | Peak beam current | mA | 20 |
| 5 | Duty factor | - | 1.25 % |
| 6 | Length | m | 3.48 |

### *Skin Effect*

Skin effect is the tendency of alternating current to become distributed within a conductor such that the current density is largest near the surface of the conductor and decreases exponentially in bulk material. The current flows within a small layer of conductor called Skin Depth (δ). It is a measure of the depth at which the current density falls to 1/e (e ~ 2.72) of its value near the surface.

### *Skin Effect and Surface Finish Relevance for RFQ*

The skin depth for high frequency (MHz and above) resonating structures is very small (~ microns). At these frequency, the current flows within a very small layer near the surface only. Therefore, effective cross-sectional area for current flow is reduced and effective resistance increases. This causes an increased power loss within RF structures. Also, as most of the current flows on the outer surfaces only, the length of path through which current travels will be more for rough surfaces. Therefore, the power loss would be higher for rough surfaces as compared to smooth surfaces. For RFQ and other normal conducting accelerating structures, increased power loss results higher RF power requirement, temperature rise, thermal deformations and detuning of structure from designed frequency. In present work, a finite element analysis has been performed to investigate the variation of electromagnetic field and power loss within skin depth of RFQ. Simulations were also performed to predict the effect of surface roughness, material and frequency on power loss. These studies will help in designing efficient cooling system for RFQ thermal management.

## ELECTROMAGNETIC ANALYSIS

Finite element analysis for skin effect and surface finish for a 325 MHz RFQ structure was carried out using ANSYS code [3]. The analysis aims for evaluation of electromagnetic field and power loss within skin depth region and effect of surface finish, material and frequency on RFQ power loss.

### *Analysis for Skin Effect*

Electromagnetic analysis of RFQ was carried out to study skin effect for 325 MHz RFQ structure. One eighth model of RFQ cross section with one cm length was developed and symmetry boundary conditions were used for analysis. Relative permittivity and permeability for vacuum were defined as unity. Perfect Electric Conductor (PEC) boundary conditions were applied at vacuum copper wall interfaces. After applying material properties and boundary conditions, electromagnetic analysis for cavity vacuum region was performed and electromagnetic field distribution was evaluated. Fig. 1 shows electric field distribution for RFQ cavity. It was found that electric

#navneet@rrcat.gov.in

field intensity was higher near the beam axis and decreases on moving away from beam axis. Fig. 2 shows magnetic field pattern for RFQ cavity. Magnetic field intensity is lower near beam axis and increases continuously on moving away from beam axis.

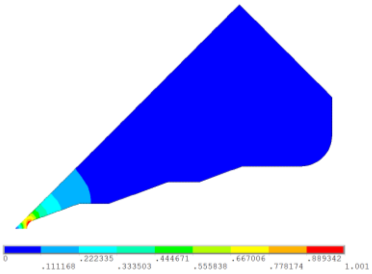

Figure 1: Electric field pattern for RFQ cavity

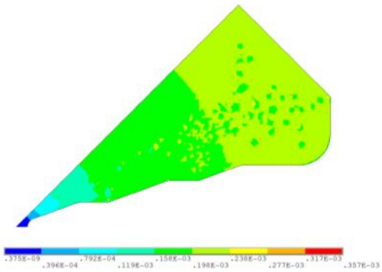

Figure 2: Magnetic field pattern for RFQ cavity

After vacuum region, electromagnetic analysis for copper wall region was performed. Magnetic field intensity evaluated from vacuum region analysis was applied as an input magnetic field for copper walls interfacing with vacuum region. A script based on ANSYS Programming Development Language (APDL) was developed to generate micron level meshing near these interfaces. The elements with one micron spacing were created to capture the variation of electromagnetic field and power loss within skin depth region.

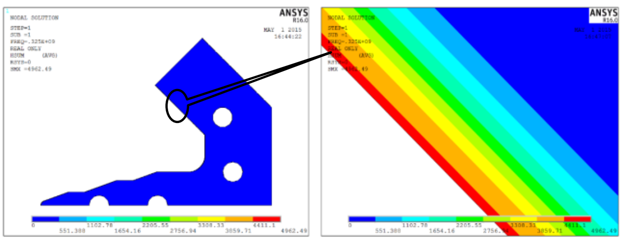


Figure 3: Magnetic field intensity for RFQ wall and its zoomed view near surface

After meshing, appropriate material properties and constraints were applied and electromagnetic analysis for RFQ was carried out. Normalized electric field, magnetic field and power loss were evaluated from analysis. Fig. 3 shows magnetic field intensity for RFQ walls and its zoomed view near vacuum-wall interface. The variation of magnetic field intensity within skin depth region is shown in fig. 4. RFQ power loss and its zoomed view near vacuum-wall interface is shown in fig. 5.

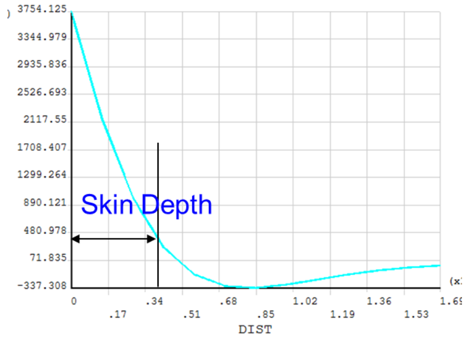


Figure 4: Magnetic field intensity profile for skin depth

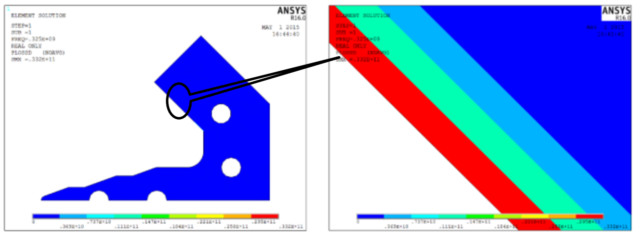


Figure 5: Power loss for RFQ wall and its zoomed view near surface

### *Effect of Surface Finish on Power Loss*

Simulations were performed to investigate the effect of surface finish on power loss for RFQ structure. One quadrant of RFQ cavity with one cm length was developed using Solid-Works code and transferred in ANSYS HFSS code for analysis. Electromagnetic simulations were carried out for smooth surfaces as well as for rough surfaces. The boundary conditions of finite electrical conductivity with layered impedance were applied for analysis. The power loss was evaluated for different surface roughness values from 0 to 4 microns. Fig. 6 shows the effect of surface finish on RFQ power loss.

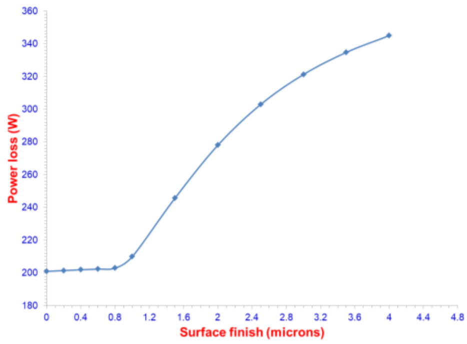


Figure 6: Effect of surface finish on power loss

It was evaluated that power loss remains nearly equal to a smooth surface for a surface roughness up to 0.8 microns. The power loss increases with further increase in surface roughness. The skin depth for OFE copper RFQ at 325 MHz is ~ 4 microns. Therefore, it can be inferred from above graph that power loss remains equal to smooth surface for a surface roughness, which is nearly one order better than skin depth of RF structure. The power loss increases ~ 70%, when surface roughness value approaches to skin depth.

### *Effect of Materials on Power Loss*

To evaluate the effect of materials on power loss, electromagnetic analyses were performed for three different materials. The materials considered for analysis were SS 304, aluminium and copper. Power loss was evaluated for one quadrant of RFQ cavity with one cm length. Table 2 shows power loss results for three materials. It was found that materials with higher electrical conductivity results lower power loss for RFQ structure. Due to highest electrical conductivity, the power loss was found lowest for copper material.

Table 2: Power loss for different materials

| S. No. | Material | Electrical Conductivity (S/m) | Power Loss (W) |
|---|---|---|---|
| 1 | SS 304 | $1.5 \times 10^6$ | 1235 |
| 2 | Aluminium | $3.6 \times 10^7$ | 249 |
| 3 | Copper | $5.8 \times 10^7$ | 201 |

### *Effect of Frequency on Power Loss*

Electromagnetic analysis of RFQ was performed to study the effect of frequency on power loss. One quadrant of RFQ with one cm length was modelled and electromagnetic field frequency was varied from 1 Hz to 10 GHz. The power losses for various frequencies were evaluated and shown in fig. 7. It was evaluated that power loss increases with increase in frequency and saturates at ~ 100 MHz frequency. This is evident because at lower frequency, current flows through the bulk of the material and hence effective resistance and power loss is less. At higher frequencies, skin depth is ~ 1-2 microns and practically all current flows from the surface only. This results an increase in power loss at higher frequencies.

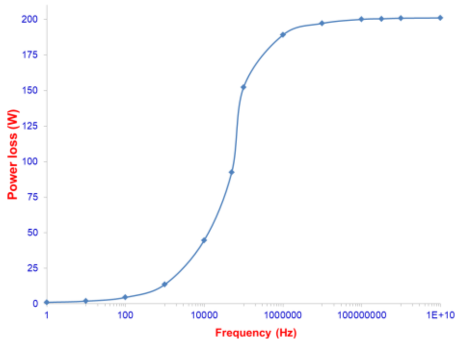


Figure 7: Effect of surface finish on power loss

## VALIDATION

Electromagnetic analysis procedure of RFQ was benchmarked with analytical solution of pill box cavity. The analytical calculations for a pillbox cavity of frequency 325 MHz were compared with finite element analysis results of a model of cavity with same dimensions. Electric and magnetic field distribution for cavity are shown in fig. 8 and fig. 9 respectively. Results of finite element analysis were compared with analytical solutions and presented in table 3.

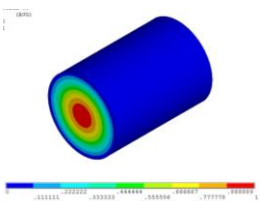

Figure 8: Electric field pattern for pill box cavity

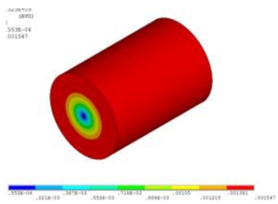

Figure 9: Magnetic field pattern for pill box cavity

Table 3: Analytical and FEA results for pill box cavity

| S. No. | Description | Analytical | FEA |
|---|---|---|---|
| 1 | Frequency (MHz) | 325.1 | 325.2 |
| 2 | Quality factor | 66147 | 65862 |
| 3 | Maximum magnetic field intensity (A/m) | 0.001544 | 0.001547 |
| 4 | Power loss (W) | $1.443 \times 10^{-8}$ | $1.448 \times 10^{-8}$ |

## CONCLUSIONS

It is well established that the skin depth is very small for high frequency resonating structures and its value is ~ 4 microns for copper at 325 MHz frequency. To the best of our knowledge, there is no work reported about the distribution of electromagnetic field and induced power loss within the skin depth domain. Also, surface finish plays a major role in power loss calculations for RF structure. An attempt has been made for predicting electromagnetic field distribution and induced power losses within skin depth of RFQ. The effects of surface finish, material and frequency on power loss were also investigated. The analysis procedure was validated for pill box cavity with its analytical solution. These studies will help in effective design of RFQ cooling system based on RF-thermal-structural coupled multi-physics analysis procedures.

## REFERENCES


[1] S.C. Joshi, S.B. Roy, P.R. Hannurkar, P. Kush, A. Puntambekar, P. Shrivastava, G. Mundra, J. Dwivedi, P. Khare, P.D. Gupta, " R&D activities on high intensity superconducting proton linac at RRCAT", LINAC 2012, Tel-Aviv, Israel.

[2] R. Gaur and V. Kumar, "325MHz 3 MeV RFQ" RRCAT / ABPL / 325 MHz RFQ / 01 (internal note).

[3] ANSYS Software online manuals.

# FREQUENCY AND FIELD FLATNESS TUNING OF FIVE CELL 650 MHZ SCRF CAVITIES

N. K. Sharma#, S. V. Kokil, G. V. Kane, N. Nigam, P. Kumar, S. K. Chauhan, B. Oraon, A. Sahu, A. Chaturvedi
Raja Ramanna Centre for Advanced Technology (RRCAT), Indore

*Abstract*

Under Indian Institution Fermilab Collaboration (IIFC), four HTS tested five-cell, β 0.92, 650 MHz Superconducting RF (SCRF) dressed cavities have to be delivered to Fermilab USA for their prototype cryomodule. For efficient beam acceleration, frequency and field flatness tuning of bare cavity is essential, primarily, at two stages, first after fabrication and second, after bulk electro-polishing. After tuning, bare cavities are processed and tested in VTS for performance characterization at 2K before dressing and testing in HTS. A semi-automatic tuning machine for five-cell, 650 MHz, SCRF cavities has been designed and developed indigenously to achieve the required resonating frequency and field flatness (> 95 %) at room temperature. Cavity tuning includes mounting cavity on tuning machine, cavity alignment w.r.t. tuning jaws, applying deformations for individual cavity cells to achieve required permanent deformation after spring back effect and intermediate bead pull measurements for electric field profile using bead pull perturbation technique. Three cavities are tuned for designed resonating frequency and field flatness > 95% using cavity tuning machine. The paper presents the tuning procedure, experience gained and challenges faced during frequency and field flatness tuning of SCRF cavities.

## INTRODUCTION

Superconducting RF cavities are designed to operate at a specific operating frequency with a very narrow bandwidth. Due to fabrication errors, the frequency and field flatness of cavity may differ from its designed values. Therefore tuning of SCRF cavity is an essential process during cavity development. A semiautomatic cavity tuning machine has been developed for frequency and field flatness tuning of five-cell 650 MHz SCRF cavities. Tuning is performed by providing plastic deformations in cavity cells near stiffener rings. A tuning algorithm was developed to evaluate the frequency corrections required for tuning of each cell. Based on tuning algorithm, the cells are either compressed or stretched by motorized tuning jaws to get required corrections. Three cavities were tuned for designed frequency and field flatness using cavity tuning machine.

## CAVITY TUNING MACHINE

A semi-automatic cavity tuning machine was developed for tuning of five-cell 650 MHz SCRF cavities. The machine is a scaled up version of earlier developed 1.3 GHz Semi-automatic tuning machine and experience gathered from previous work was utilized during this development [2]. The major subsystems of the cavity tuning machine consist of tuning jaws assembly with motor driven mechanism, base structure for mounting tuning jaws, rail guides and ball screw assembly, cavity suspension system and a bead pull measurement system. Fig. 1 shows cavity tuning machine with its major components.

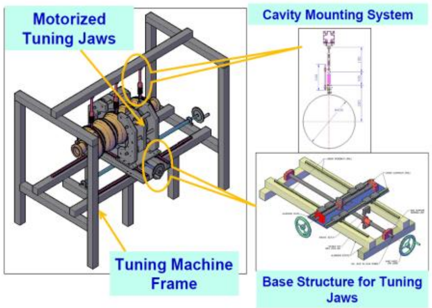


Figure 1: Cavity tuning machine with major components

## TUNING METHODOLOGY

For tuning of five-cell 650 MHz SCRF cavity, the bare cavity was mounted on tuning machine. The cavity was suspended from three locations and alignment was carried out to ensure that cavity axis coincides with axis of tuning jaws. The cavity frequency for all five modes was measured using Vector Network Analyser. Electric field profile on cavity axis was measured using bead pull perturbation technique. A stepper motor driven bead pull measurement system was used to move the bead along the cavity axis. A tuning algorithm was developed to calculate the frequency corrections required for individual cells. Based on algorithm prediction, tuning jaws were driven by stepper motor to compress / expand the cell precisely to get the required frequency corrections. The tuning jaws were moved to specific cell location using linear motion guides and ball screw mechanism. Frequency of each cell was corrected by moving the tuning jaws precisely to make permanent deformation. Frequency and field flatness were measured after each tuning step. The procedure was repeated until required frequency and field flatness was achieved.

## RESULTS AND DISCUSSIONS

Three nos. of five cell 650 MHz cavity fabricated in niobium was tuned for frequency and field flatness using

#navneet@rrcat.gov.in

indigenously developed cavity tuning machine. The tuning was performed in temperature controlled room. The temperature was maintained at $20^0$C with $\pm1^0$C variation. The first, second and third cavities were named as HB 5001, HB 5002 and HB 5003 respectively. Cavity HB 5001 and HB 5002 were tuned for a frequency of ~ 649 MHz and field flatness > 95%. Table 1 lists the frequency and field flatness tuning results for these cavities.

Table 1: Tuning of HB 5001 and HB 5002 cavities

| Cavity Name | Description | Frequency (MHz) | Field Flatness (%) |
|---|---|---|---|
| HB 5001 | Initial (as fabricated) | 649.600 | 42 |
| | After 1st tuning | 649.300 | 90 |
| | After processing | 649.105 | 78 |
| | After 2nd tuning (for VTS testing) | 649.095 | 95.9 |
| HB 5002 | Initial (as fabricated) | 649.430 | 89 |
| | After processing | 649.185 | 84.5 |
| | After tuning (for VTS testing) | 649.069 | 96.7 |

Cavity HB 5001 and HB 5002 were tuned to get required frequency and field flatness > 95%. Since cavity field flatness may degrade during further processing, dressing and performance testing, the tuning requirements were made more stringent for third cavity. A room temperature frequency of ~ 648.990 MHz with a field flatness ≥ 98% was targeted for HB 5003 cavity. Experience gathered from tuning of cavity HB 5001 and HB 5002 was utilized and HB 5003 cavity was tuned for required frequency and field flatness.

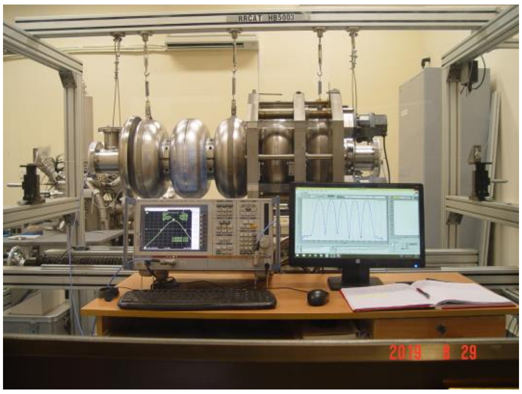

Figure 2: HB 5003 cavity mounted on tuning machine

*Tuning of HB 5003*

After fabrication, cavity HB 5003 was received for frequency and field flatness tuning. Before tuning, cavity length and cell centres were measured using coordinate measuring machine. The cavity was than mounted on cavity tuning machine and aligned with respect to centre of tuning jaws. The tuning jaws hold the cavity near stiffener rings. Clearance between tuning jaws and stiffener ring is ~ 2mm. Fig. 2 shows HB 5003 cavity mounted on tuning machine. Cavity frequency for all five modes were measured using Vector Network Analyser (VNA). Field flatness of cavity was measured using bead pull perturbation technique. The π mode frequency and field flatness for as manufactured cavity was measured as 649.988 MHz and 66% respectively. Table 2 shows cavity frequency for various modes. Fig. 3 shows frequency spectrum for all 5 modes of HB 5003 cavity. Fig. 4 shows electric field profile measurement at cavity axis for as fabricated cavity. It was measured that cavity π mode frequency is ~ 1 MHz higher than required frequency. Therefore it was decided to improve cavity field flatness by compressing cavity cells during first round of tuning. The compression process would result a decrease in cavity frequency, which is desirable.

Table 2: Cavity frequency for five modes

| S. No. | Mode | Frequency (MHz) |
|---|---|---|
| 1 | π/5 | 642.480 |
| 2 | 2π/5 | 644.389 |
| 3 | 3π/5 | 646.988 |
| 4 | 4π/5 | 649.087 |
| 5 | π | 649.988 |

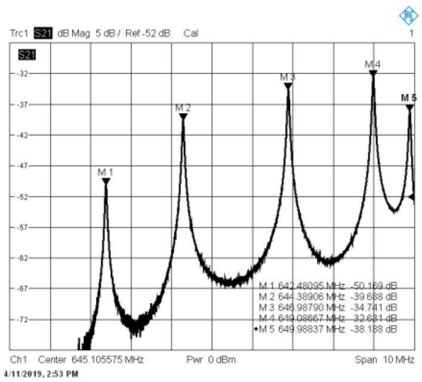


Figure 3: Frequency spectrum for HB 5003 cavity

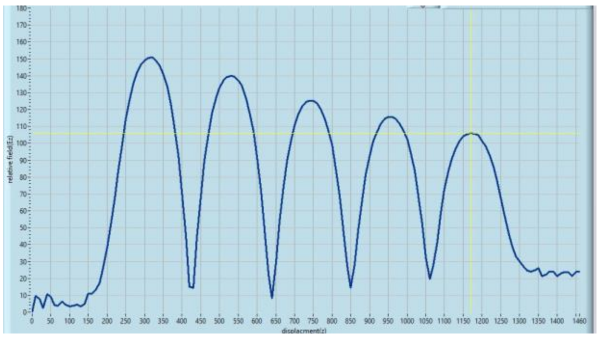

Figure 4: Electric field profile for as fabricated cavity

Based on cavity tuning algorithm, the required frequency corrections for each cell were evaluated. Table 3 shows frequency corrections required for individual cell for a target frequency of ~ 649.8 MHz during 1st round of tuning. It can be seen that cells 1, 2, 3 and 4 should be compressed to decrease their frequencies. Cell 5 requires a stretch to increase frequency ~ 1 KHz (which can be neglected). Cell 2 requires maximum compression, which will reduce cavity $\pi$ mode frequency by 62 kHz. The frequency corrections for cavity were carried out in ~ 3 to 4 rounds.

Table 3: Frequency corrections required for tuning

| Cell No. | Required frequency corrections (kHz) |
|---|---|
| 1 | -58 |
| 2 | -62 |
| 3 | -49 |
| 4 | -19 |
| 5 | 1.3 |

During first round of tuning, about 75% of required frequency corrections were applied. The cell with maximum frequency corrections was attempted first (cell 2). Other cavities were than taken one by one in series. For frequency corrections of - 62 kHz for cell 2, tuning jaws were moved on cell 2. The cell was deformed (compressed) by motorized tuners to get a frequency decrease ~ 80 kHz, held in compression state for ~ 2 minutes and released. Cavity frequency was measured after release and it was found that deformation was elastic and due to spring back effect, no change in cavity frequency was measured. The amount of compression was increased carefully in steps to get in-elastic deformation and permanent change in cavity frequency. It was observed that if deformation causes a frequency change ~ 125 kHz, than a permanent frequency change of ~ 20-30 kHz occurs. The tuning was performed for each cell to get required corrections in ~ 3 to 4 rounds. After tuning, cavity $\pi$ mode frequency was measured as 649.789 MHz and field flatness was improved to 87.6%.

After first round of tuning, cavity was taken up for processing. Bulk electro-polishing (~120 microns), annealing and high pressure rinsing processes were carried out. Processing resulted a decrease in frequency and deterioration of field flatness. The cavity frequency and field flatness were measured as 649.587 MHz @ 20 $^0$C and 88.9% respectively after processing.

After processing, cavity was again mounted on tuning machine to achieve a target frequency of 648.990 MHz ± 25 kHz with a field flatness ≥ 98%. Frequency corrections required for each cell were evaluated using tuning program. Individual cells were tuned to get required plastic deformations and frequency changes. Cavity frequency and field flatness were monitored in each stage. After getting field flatness ~ 95%, the individual cell was compressed / expanded with extra care to avoid excessive corrections for cavity frequency in either direction. The required correction as predicted by tuning algorithm were carried out in very small steps. After final tuning, cavity frequency and field flatness was measured as 648.998 MHz @ 20 $^0$C and 98.2 % respectively. Fig. 5 shows electric field profile for HB 5003 cavity after final tuning.

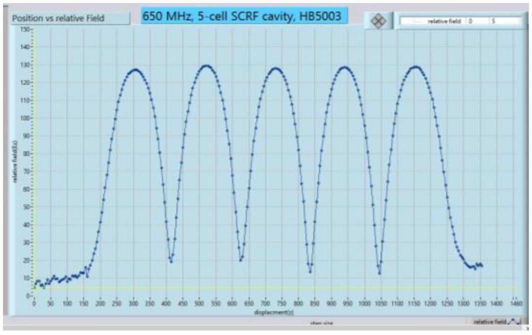


Figure 5: Electric field profile for tuned cavity

## CONCLUSIONS

Indigenous development of a semiautomatic cavity tuning machine for tuning of five cell 650 MHz SCRF cavities has been carried out. Three nos. of five cell 650 MHz niobium cavities were tuned using tuning machine. Fist two cavities were tuned for a field flatness > 95%. Using experience gathered from two cavities, third cavity was tuned for a field flatness ≥ 98%. Tuning of five cell 650 MHz SCRF cavity for designed frequency and field flatness is an essential process for cavity development. Indigenous development of cavity tuning machine, establishment of tuning procedure and tuning of five cell 650 MHz SCRF cavities are important milestones in the field of SCRF cavity technology development in India for future programs.

## REFERENCES

[1] N. K. Sharma, G. V. Kane, N. Nigam, S. V. Kokil, S. K. Chauhan, B. Oraon, P. Kumar, A. Sahu, A. Chaturvedi and S. C. Joshi “Indigenous development of a tuning machine for five cell 650 MHz SCRF cavities” Indian Particle Accelerator Conference 2018 (InPAC-2018), RRCAT, Indore.

[2] N. Nigam, S. V. Kokil, N. K. Sharma, G. V. Kane, S. K. Chauhan, S. Raghavendra, A. Sahu, O. Prakash, P. Kumar, B. Oraon, A. Chaturvedi and S. C. Joshi “Tuning of nine cell 1.3 GHz RF cavity using indigenously developed semi-automatic cavity tuning machine” Indian Particle Accelerator Conference 2015 (InPAC-2015), TIFR, Mumbai.

# BEAM INJECTION STUDIES IN A SEPARETED SECTOR CYCLOTRON FOR ANURIB PROJECT

Santanu Paul†[1,2], Animesh Goswami[1,2], Uttam Bhunia[1], Chiranjib Das[1,2], Atanu Dutta[1], Jayanta Debnath[1,2], Malay Kanti Dey[1], Arup Bandyopadhyay[1,2]
[1]VECC, 1/AF Bidhan Nagar, Kolkata 700064, India
[2]HBNI, Mumbai, India

*Abstract*

ANURIB Project at VECC, Kolkata will require a Separated Sector Cyclotron (SSC), for post acceleration of radioactive ion beams necessary for various fields of research in nuclear and material science. In this paper the basic optical layout of the injection system is discussed. The basic parameters thus determined will be used in designing the beam injection elements of the SSC.

## INTRODUCTION

ANURIB Project at VECC, Kolkata is an upcoming national facility for post acceleration of radioactive ion beams catering various fields of research in nuclear and material science [1,2]. This requires a separated sector cyclotron with K=800, which is proposed to be a four-sectored machine with low average magnetic field, where $U^{57+}$ beam with energy 7 MeV/A will be injected and accelerated up to 50 MeV/A.

The injection system for a cyclotron, is aimed to achieve centring of the beam with respect to the cyclotron centre, and matching of the beam phase space with respect to the cyclotron acceptance, to minimize beam losses during transport and acceleration [3]. It is proposed to inject the pre-accelerated beam into the median plane of the cyclotron radially, as unlike compact isochronous cyclotrons, much more space is available to place bending and focusing devices for matching and centering. Injection at much higher energy is possible in this scheme of injection.

In this paper the basic optical layout of the injection system is discussed. Initially, the magnet is modelled using ANSYS [4] and the sector shape has been optimised for achieving necessary isochronism. In the computed magnetic field, closed orbit properties at different energy steps are determined. In order to match the beam radially at the first orbit, a matching point is chosen which corresponds to one sector magnet entry. Magnetic elements are inserted with appropriate sign and strength to modify the original sector field. The central trajectory from a point outside the cyclotron to the matching point in the first orbit is done by adjusting the positions, length and field of the elements. The basic beam line parameters thus determined will be used in designing the injection elements of the SSC.

## MAGNET DESIGNING

The preliminary dimensions of the magnet and the properties of the equilibrium orbits (EO) are first obtained using hard edge approximation. The primary size of the magnet is estimated using two-dimensional POISSON code [5]. Finally three-dimensional calculation is carried out using ANSYS code to achieve isochronous magnetic field. The profile of magnet sectors is optimized based on the computed results to get the desired values of isochronous field and betatron tunes. The required isochronous field within the tolerances is obtained after several iterations by shimming the angular width of the hill as a function of radius. Figure 1 shows the one-fourth model of the magnet sectors with all four sets of coil in place. The main design parameters of the magnet are listed in Table 1.

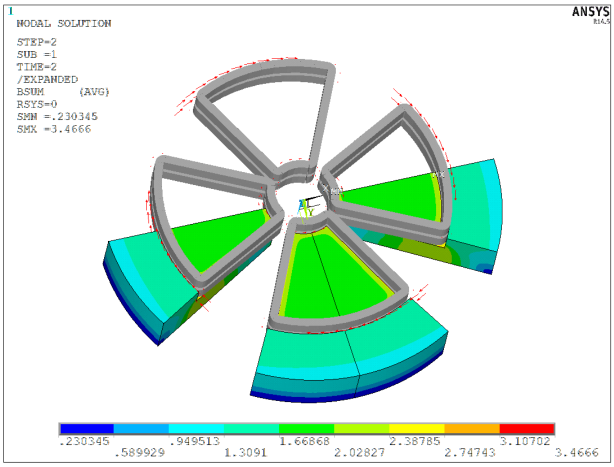


Figure 1: Model of the magnet used for field calculation.

Table 1: Optimized parameters of the magnet

| | |
|---|---|
| Injection energy | 7 MeV/A |
| Final energy | 50 MeV/A |
| Pole inner radius | 100 cm |
| Pole outer radius | 350 cm |
| Number of sectors | 4 |
| Hill gap | 80 mm |
| Sector angular width | ~ 52 deg |
| Hill field at extraction | 1.7 T |
| Valley field at extraction | 0.15 T |
| Ampere turns | 700 × (16×26) |
| Iron weight (one sector) | 288 ton |

Figure 2 shows a three dimensional contour plot of the magnetic field in the entire accelerating region of the SCC, with all the four sectors in place. The maximum hill field is kept at 1.7 T, well below the iron saturation level.

†spaul@vecc.gov.in

It is evident from Fig.2 that due to fringe effects, magnetic field extends in to the free space between the sectors.

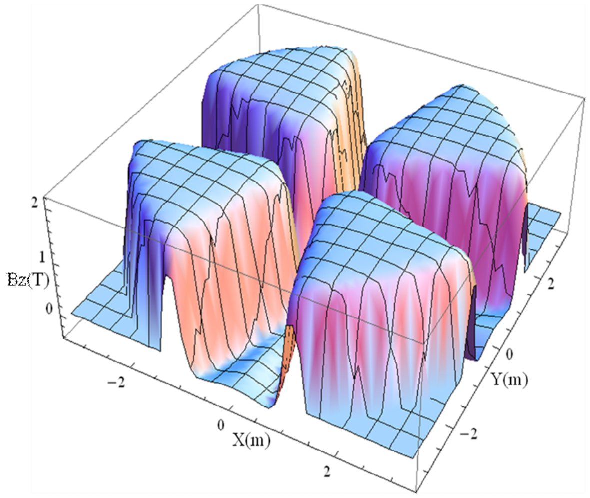


Figure 2: 3D contour plot of the magnetic field of the four sector SCC obtained from ANSYS.

## EQUILIBRIUM ORBIT

The properties of the static equilibrium orbit (EO) like the radial and axial tunes, frequency error, integrated phase shift, and average magnetic field etc. are optimized after several iterations using the equilibrium orbit program GENSPEO [6]. All the EO calculations are done at 20 energy intervals starting from 7 MeV/A. The radial variation in beam phase $\phi$ with respect to RF accelerating voltage in the acceleration zone is shown in Figure 3. The sin($\phi$) curve thus plotted is an indicator of the variation from isochronism and is sufficiently good enough for the present studies.

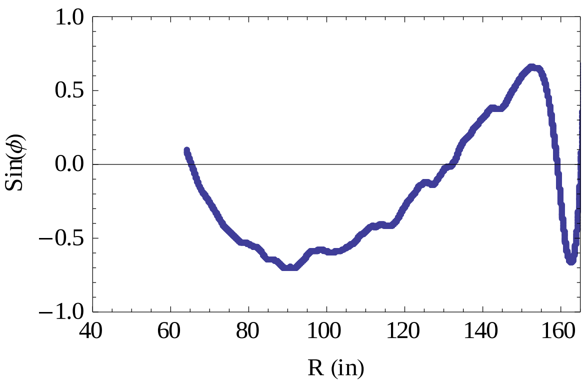


Figure 3: Beam phase varition with average radius ( in inch) during acceleration in the computed isochronous magnetic field.

The variation in radial and axial betatron tunes, $\nu_r$ and $\nu_z$ respectively, during acceleration is shown in Fig. 4. The EO in real space obtained from GENSPEO for $U^{57+}$ beam at the injection energy 7 MeV/A is depicted in Fig. 5. The isogauss contour corresponding to the magnet sectors are also shown in the plot.

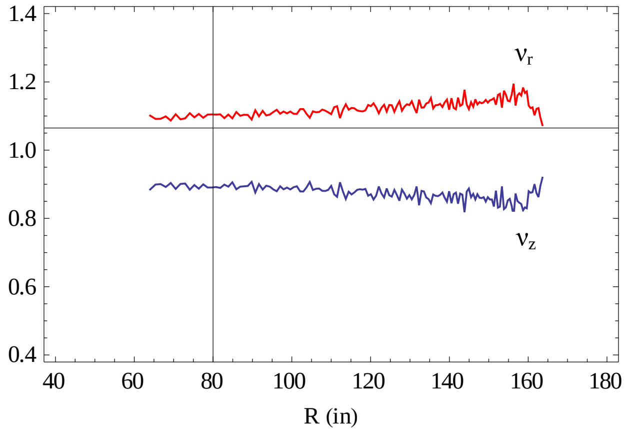


Figure 4: Betatron frequency ($\nu_r$ and $\nu_z$) variation with average radius (in inch) in computed magnetic field.

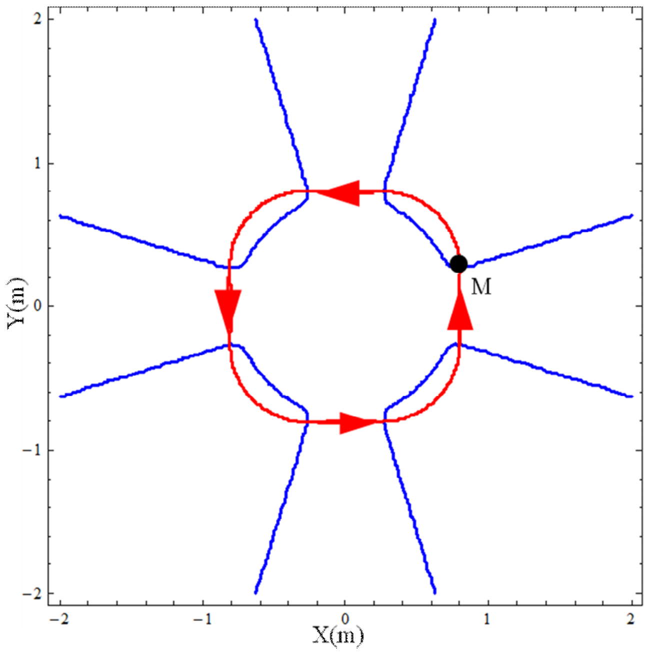


Figure 5: Projection of first EO at median plane (closed curve). Here M indicates the matching point.

## INJECTION LAYOUT

The injection system needs to transport the beam from a point outside the cyclotron ring to the first orbit suitable for acceleration. As mentioned earlier, the pre-accelerated beam enters radially along the virtually field-free central region of the SSC. A matching point has been chosen arbitrarily at one sector magnet entry to match the beam radially to the first orbit. This is shown by a point M in Fig. 5. In this section we discuss the methodology adopted to transport the central ray of the pre-accelerated beam that matches the equilibrium properties at M. A particle tracking routine has been written in MATHEMATICA [7] that integrates the equation of motion using fourth-order Runge-Kutta algorithm in the computed 3D magnetic field. A straightforward solution to the injection problem is to track backwards starting from the point M. The Cartesian coordinates and velocities along X and Y directions at M are: X0 = 1.14 m, Y0 = 0.03 m, VX0 = $3.76\times10^5$ m/s and VY0 = 3.68 $\times10^7$ m/s. In order to track the injected beam backwards, the magnetic field in the median plane is reversed. In the reversed magnetic field, particle tracking with initial coordinates (X0, Y0) and velocities (-VX0, -VY0) have been performed. Magnetic elements are inserted by superimposing their equivalent magnetic field over the original sector field. This is graphically shown in Fig. 6. The location, strength and length of the magnetostatic injection elements (B1 and B2) are adjusted so that the central trajectory from a point P outside the cyclotron matches to the point M in the first orbit. The parameters of B1 and B2 obtained are listed in Table 2. Forward tracking of the central particle starting from P, in the computed field of SSC superimposed with the contributions from B2 and B1 is shown in Fig. 7. It is easy to see from Fig. 7 that, the trajectory matches with the first EO beyond matching point M, as required for efficient injection.

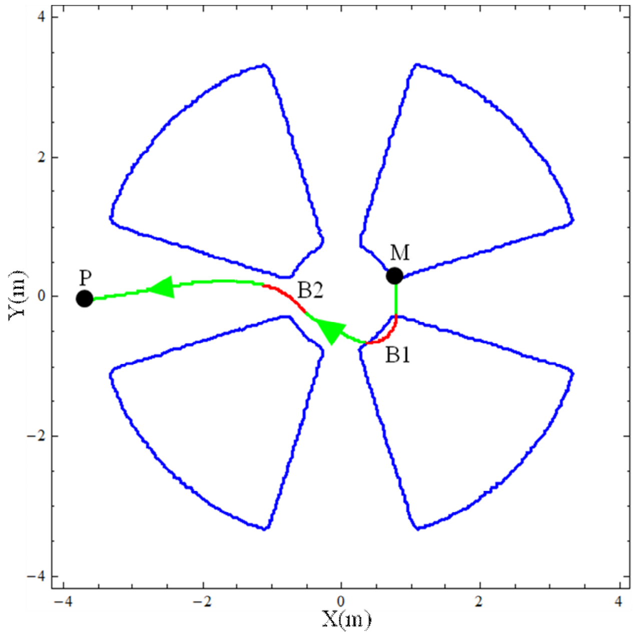


Figure 6: Backward tracking the central particle from matching point M, to a point P far away. B1 and B2 correspond to the injection elements.

Table 2: Optimized parameters of injection elements

| Element | B1 | B2 |
|---|---|---|
| Type | Magnetostatic | Magnetostatic |
| Field (T) | 0.75 | 0.8 |
| Curvature (m) | 2.12 | -1.99 |
| Effective length (m) | 1.38 | 0.57 |

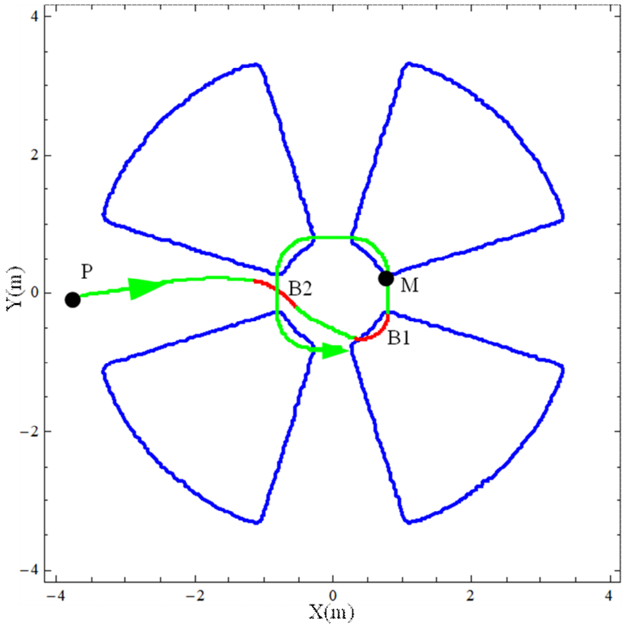


Figure 7: Forward tracking of the central particle from point P to M and matching with the first EO.

In the present study, only the central particle trajectory during injection have been determined, which specifies the basic layout of the injection system of the SCC. For more accurate analysis, it is necessary to include multi-particle dynamics and dispersion effects in the present calculations.

## REFERENCES


[1] Arup Bandyopadhyay, V. Naik, S. Dechoudhury, M. Mondal and A. Chakrabarti, PRAMANA, Journal of Physics, 85 (2015) 505.

[2] Alok Chakrabarti, Arup Bandyopadhyay, Vaishali Naik, Siddhartha Dechoudhury, Manas Mondal and P. Y. Nabhiraj, Nucl. Instrum. and Meth. B, 317 (2013) 253.

[3] A. Goswami, A. Dutta and A. Bandyopadhyay, JINST 14 (2019) P03027.

[4] Ansys Multiphysics, ANSYS v 14.0 (2012).

[5] POISSON/SUPERFISH Reference Manual, Los Alamos Accelerator Code Group MS H829.

[6] M. M. Gordon, “Computation of Closed Orbits and Basic Focusing Properties for Sector-focused cyclotrons and the Design of “Cyclops”, Particle Accelerators, 16 (1984), pp. 39-62.

[7] https://www.wolfram.com/mathematica.

# IN-HOUSE BEAM PROFILE MEASUREMENT SET-UP FOR MEASURING ELECTRON BEAM EMITTANCE USING SOLENOID SCAN TECHNIQUE

Md. Zamal Abdul Naser[1*], Siddhartha Dechoudhury[1], Sanket Haque, Shourya Mukherjee[#],
Paritosh Sing Babu[1], Arup Bandyopadhyay[1], Vaishali Naik[1],
VECC, Kolkata, [#]IIT Karagpur, [1]also at HBNI, Mumbai, India

*Abstract*

A 50 MeV, 2 mA cw superconducting electron linear accelerator (e-Linac) [1] is being developed at VECC for the upcoming ANURIB (Advanced National Facility of Unstable and Rare Isotope Beams) project. The thermionic electron gun with 650 MHz RF modulation and a gridded cathode, floating at 100 kV along with low energy beam transport (LEBT) line has been installed and tested. A YAG: Ce (Cerium activated Yttrium Aluminium Garnet) scintillation screen based beam profile measurement set-up has been developed in-house. The transverse electron beam size and centroid have been measured using developed MATLAB based software. Efforts are being carried out to measure transverse emittance using solenoid scan technique. This paper briefly reports the development of beam profile measurement set-up and preliminary results of solenoid scan for the 100 keV electron beam.

## INTRODUCTION

100 kV Electron gun along with the LEBT line [2] has been installed and tested at VECC, Kolkata as shown in Figure 1. The electron source is a DC thermionic gun, with gridded cathode. It is RF modulated [3] at 650 MHz corresponding to bunch length of 170 ps and charge 3pC/pulse at 2 mA of average electron beam current. A beam profile measurement set-up has been designed, developed and installed in the second diagnostic box which is placed at a distance of around 1.4 m after the anode entry of the electron gun. The emitted electron beam hits the scintillation screen to produce green visible light which is captured by a CCD camera via an optical flat mirror placed at $45^0$ with the beam line axis. The captured image is analyzed by in-house developed software to measure the size and centroid of the electron beam.

A ray tracing optics simulation has been carried out to optimize the configuration of the imaging optics. This configuration has been tested off line. A preliminary solenoid scan using the developed optical imaging system has also been carried out to measure the transverse beam emittance.

## BEAM PROFILE MEASUREMENT SET-UP

The beam profile measurement set-up comprises a screen holder with pneumatic actuator and an optical imaging system. The scintillation screen of diameter 50 mm and thickness 0.2 mm is mounted on a copper plate having a hole at the centre of diameter 49 mm. It is fixed by another copper plate with same configuration and both the plates are fixed by 8 nos. of screw. Copper is used to dissipate heat which is produced at the screen after hitting the electron beam. There is a provision to measure the beam current by putting a Faraday cup above the screen holder. Both the Faraday cup and the screen holder are attached with same pneumatic control. The YAG: Ce scintillation screen is oriented 45° with respect to beam axis.


Figure 1: Installed LEBT line

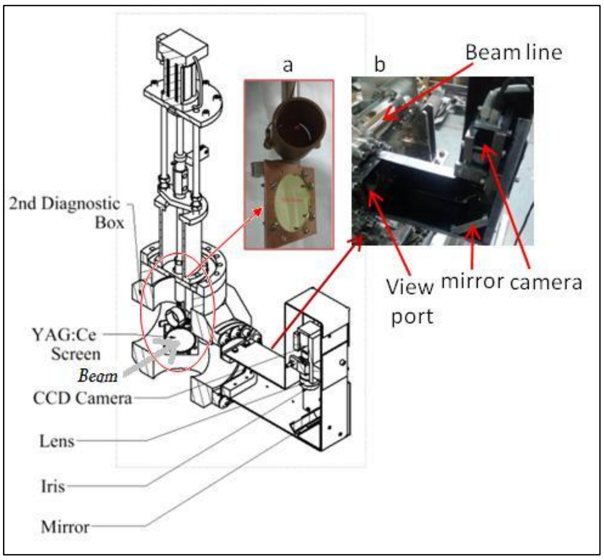


Figure 2: 2D sketch of beam profile measurement set up (inset: a) Ce: YAG scintillation screen and faraday cup b) camera box)

An optical flat mirror as shown in Figure 2 and 3 is mounted at $45^0$ to the beam line's vertical plane. The optical lens with CCD camera is placed facing downward to capture the reflected light from the mirror. The mirror, lens and CCD camera are placed inside a box as shown in Figure 2. The whole box is attached on the view port of

*zamal@vecc.gov.in

the diagnostic chamber. Inside surfaces of the box are painted black to minimize the background light into the camera. There is a provision to change the mounting angle of mirror. The camera is mounted on a separated plate which is fixed with the box by two screws. The mounting plate of camera can move up or down to adjust the field of view of camera. In this configuration the CCD camera is placed above the median plane of the beam axis to protect the sensor from the bremsstrahlung X-ray.

## OPTICAL SIMULATION

There are two main objectives of the beam imaging optics - a) to capture the full view of the scintillation screen which is of 50 mm diameter and b) to attain a maximum possible resolution with the full field of view. Since, the CCD camera is having a sensor of 12.5 mm and YAG:Ce screen has a diameter of 50 mm, the optics in between screen and CCD should have a demagnification factor of 0.25 in order to be captured full view on to the camera. A ray tracing simulation [4] has been used to determine the position of the optical elements (i.e. the positioning of the lens, mirror and CCD camera) to achieve the desired de-magnification factor. The optimized layout is shown in Figure 3 resulting in de-magnification factor of 0.24. Specifications of optical components of the imaging system are listed in Table 1.

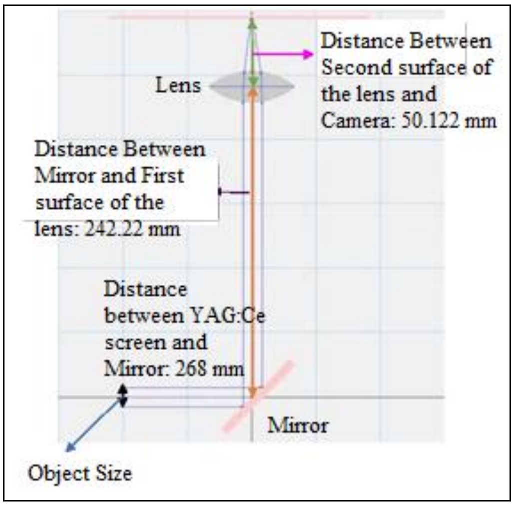


Figure 3: Layout of optical imaging system

Table 1: specifications of optical parameters

| Parameters | Specification |
|---|---|
| CCD Camera | acA780-75gm – Basler ace |
| Lens :<br>focal length<br>working distance<br>Iris<br>depth | <br>49.5±5% mm<br>Between 300 mm$^*$ to $\propto$<br>F 2.5 – F 32.0<br>25.0 mm |
| Optical flat mirror:<br>dimension<br>wavelength range | <br>75 × 75 × 12 mm<br>250 – 700 nm |

## BEAM POFILE MEASUREMENT

All the components of optical imaging system have been mounted inside the box as per the distance as shown in Figure 3. There is a provision to vary the distance between lens and the camera. A resolution target with two sets of six equispaced lines on an aluminium plate has been fabricated in-house. In one set, the lines of width 180 µm are spaced by 60 µm whereas in the other set, the lines of width 170 µm are spaced by 50 µm. The resolution target is focussed on the camera by varying the distance between lens and camera. It is seen from the Figure 4a that the lines with spacing 60 µm are well resolved with the present optical set-up. However, the required imaging resolution is 5% of the beam size. But in solenoid scan method with the resolution of 60 µm we can get very minute variation of beam sizes with solenoid current. For geometric calibration of beam image so as to transform position coordinate from pixel co-ordinates of the image, a calibration target of diameter 50 mm with holes of 80 µm spaced by 7 mm has been developed as shown in Figure 4b.

The geometric calibration has been carried out by captured images of calibration target for two positions, one perpendicular to the sight of camera and other at an angle of 45 deg have been recorded. The histogram of the image, recorded by a CCD camera, consists of intensity and pixel positions.

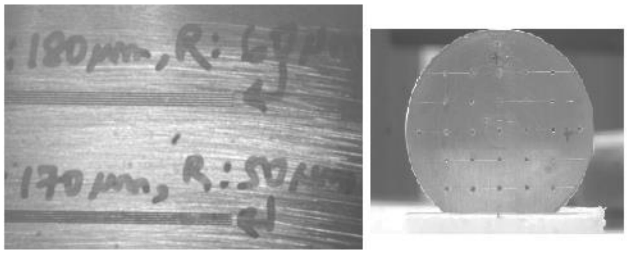

Figure 4: a) Resolved lines of resolution target, b) Calibration target

Twenty five corresponding control points from each of these two images have been selected. These set of points give the co-efficients of polynomial warping required to convert the pixel into geometric coordinates for the actual position of the screen i.e. $45^0$ to the beam axis. A software in MATLAB has been developed in-house for calibration of the beam image and finally to measure the beam size. After getting the optimized beam image, beam profile along X and Y axes has been captured. A Gaussian curve has been fitted to the image. The full width of a curve (FWHM) has been measured between those points which are at half of the maximum amplitude. The X-Y centre and FWHM of the processed image is shown in Figure 5. The beam spot shown in the figure is the processed image after subtracting the background image captured without beam.

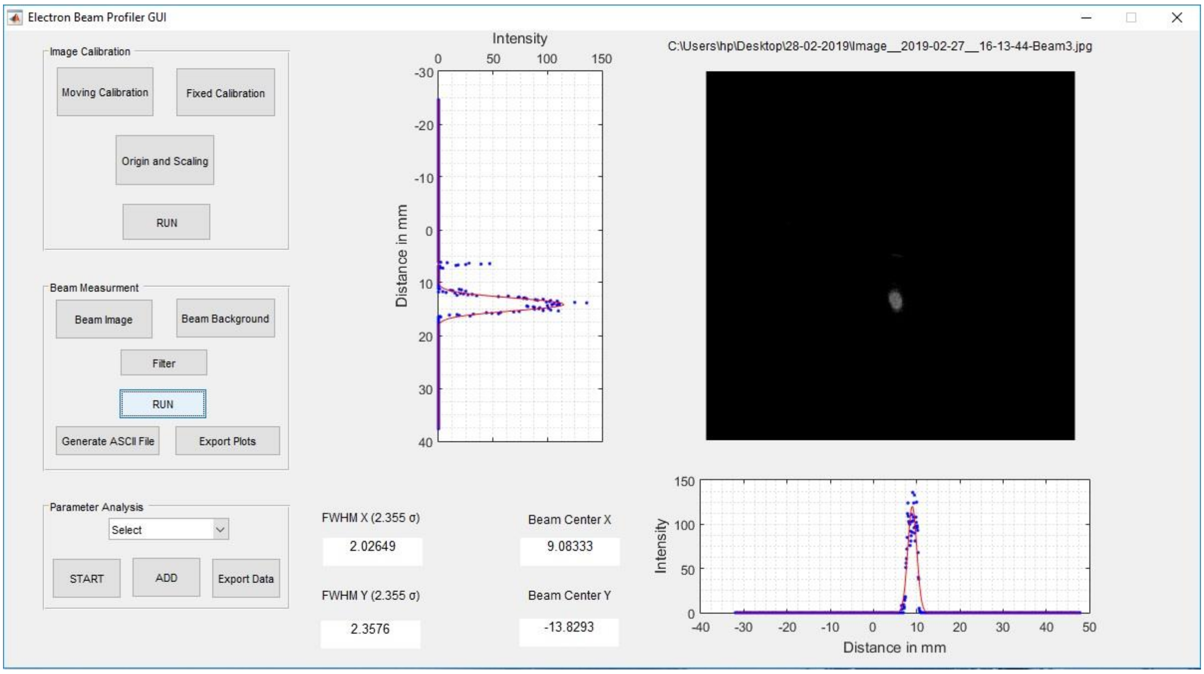


Figure 5: GUI Window of Iimage Processing Software for Electron Beam Profile Measurement (beam spot showing FWHM and beam centroid)

Electron beam current from electron gun is optimized by tuning X-Y steering magnet and solenoid magnet. Applying a grid DC bias voltage of 8 V and filament voltage of 6V, beam current of 0.5 μA is measured in the faraday cup of second diagnostic box. Preliminary solenoid scan has been carried out by noting the image size analysed from the software, by varying the field of preceding solenoid. It has been fitted with analytically calculated curve using the matrix method resulting in ellipse having emittance of 5π mm mrad as shown in Figure 6. Although a change in centroid of the beam along X and Y has been occurred (0.3 mm max.) during variation of the solenoid field of 118 G to 130 G. Further alignment of the solenoid and screen would be necessary before going for final measurement.

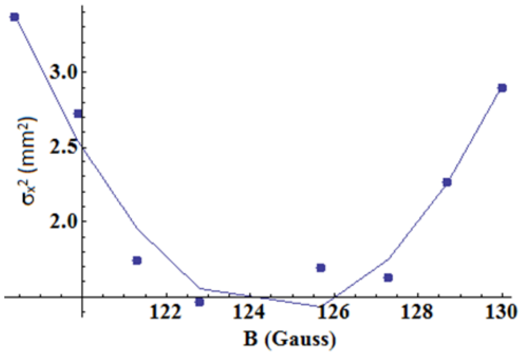


Figure 6: Variation of RMS beam size with solenoid field

# REFERENCES

[1]. V. Naik et al., " VECC/TRIUMF Injector for the ELINAC Project", Proc. LINAC (2010), 726

[2]. Md. Zamal A. Naser et al., "Characterization and testing of RF modulated 100 kV thermionic electron gun", INPAC(2015), TIFR, MUMBAI

[3]. Md. Zamal A. Naser et al., "characterization and testing of rf modulated 100 kv thermionic electron gun", INPAC(2018), RRCAT, Indore, India

[4]. https://arachnoid.com/OpticalRayTracer/

# COMPENSATION OF BEAM STEERING EFFECT IN SUPERCONDUCTING QWR


Uttam Bhunia[#], Arup Bandyopadhyay, Variable Energy Cyclotron Centre, 1/AF, BidhanNagar, Kolkata-700064

Zhongyuan Yao, R. E. Laxdal, TRIUMF Laboratory, Vancouver, Canada



*Abstract*

VECC is developing Superconducting Quarter-wave resonators (QWR) ($\beta$=0.054) operating at 113.6 MHz in collaboration with Triumf Laboratory, Canada for post acceleration of radioactive ion beams. QWRs are the preferred choice of ion acceleration because of its high accelerating electric field in the low-β region (0.001<β<0.2). Beam steering caused by the up-down asymmetry of the geometry with respect to beam axis leads to emittance growth and beam loss. There are electric and magnetic dipole field components near the beam hole, which steer the beam vertically. Electromagnetic design has been optimized in order to compensate for beam steering effect by introducing donut shaped axi-symmetric drift tube that reduces magnetic field in the gap and to reach high accelerating voltage. Further, suitable beam offset is used to introduce RF defocusing field to counteract with steering effect of transverse electric and magnetic field. This paper describes the simulation results and method proposed to minimize the beam steering effect in VECC QWR.


## INTRODUCTION

Super-Conducting (SC) Quarter Wave Resonators (QWR) of 113.6 MHz with geometry beta of 0.055 is under development for the post-acceleration of Rare Isotope Beam (RIB) at VECC, Kolkata. Each QWR module will accelerate beam up to q/A= 1/7 with accelerating gradient of 5.5 MV/m in CW mode. QWRs are asymmetric with respect to beam pipe and develop transverse electric and magnetic field along the beam axis. This unwanted field component leads to undesirable beam steering and imposes a serious problem in beam transport. The beam steering effect depends on the synchronous phase selected for beam acceleration, accelerating gradient, particle charge to mass ratio, etc. For light ions and beam with large longitudinal emittance the effect of beam steering is more serious [1]. In order to optimize the overall performance of QWR, it is essential to minimize the beam steering effect. Ostroumov [1], Facco [2], Frazer [3] already studied this problem in a generalized way and recommends different options such as introduction of donut shaped drift tube, vertical offset of beam, tilting of beam port, etc. We considered the method of vertical offset of QWR to minimize the beam steering where the RF defocusing effect counteracts the transverse electric and magnetic steering [1]. Amount of off-centering has been calculated by particle tracking through QWR and adopting an optimization approach thereof. Following the required offset of QWR, particle tracking is further carried out to qualify the result. This paper presents the details to minimize beam steering effect in 113.6 MHz VECC QWR. QWR has been modeled electro-dynamically using CST MWS [4] and 3D electric and magnetic field distribution prerequisite to study beam steering effect has been calculated.

## BEAM STEERING IN QWR

The basic geometry of QWR is as shown in figure 1. The distribution of electric field Ez, Ey and magnetic Bx on the beam axis (z-direction) through 113.6 MHz VECC QWR is simulated with CST MWS as shown in figure 2(a) and figure 2(b). Other components of electric and magnetic field has negligible effect on beam steering.

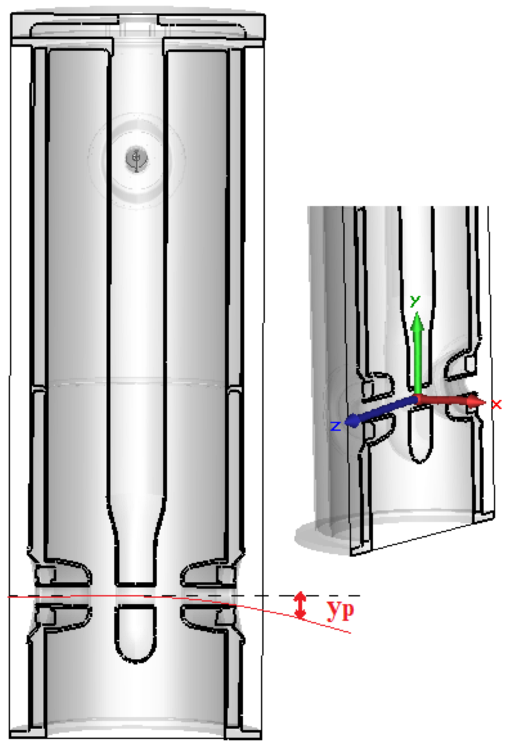


Figure 1: The geometry of the cavity and beam steering

The equation of motion to be solved in presence of electric and magnetic field may be written as

$$\frac{d\vec{p}}{dt} = \frac{q\,e}{A}\left(\vec{E} + \vec{v} \times \vec{B}\right) \quad (1)$$

where, q is the charge state of ion, A is mass number, e is elementary charge, and $\vec{v}$ is particle velocity. The beam


#ubhunia@vecc.gov.in

deflection yp can be expressed as the ratio of $p_y/p_z$, where $p_y$ is the transverse momentum kick and $p_z$ is the longitudinal momentum of beam particle. The momentum kick in vertical direction due to horizontal magnetic field Bx is given as

$$py_m = qe\beta c \int B_x(x, y, z, t)dt \qquad (2)$$

In case of transverse electric field component Ey, the momentum kick in vertical direction is

$$py_e = qe \int E_{xy}(x, y, z, t)dt \qquad (3)$$

Vertical magnetic and electric field deflection may be written as

$$y_{pm} = \frac{py_m}{pz} \;\&\; y_{pe} = \frac{py_e}{pz}$$

where, $p_z=\beta\gamma Am_0c$ is the particle longitudinal momentum.

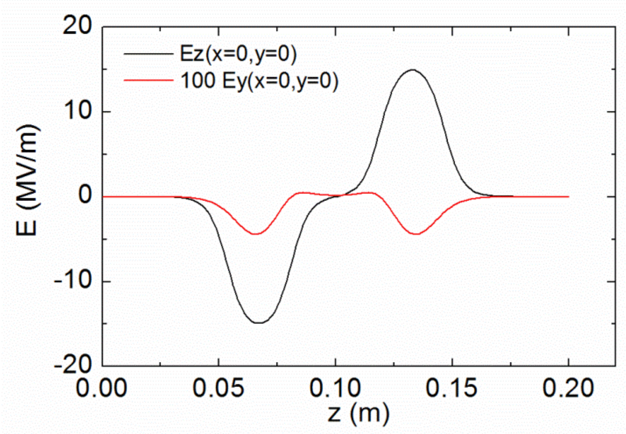


Figure 2(a): Electric field distribution along the axis of QWR

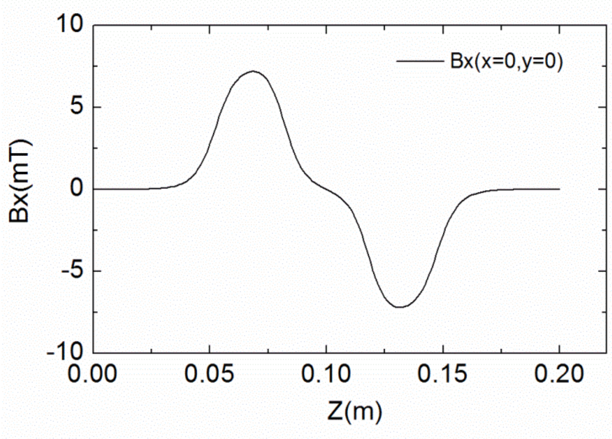


Figure 2(b): X component of magnetic field distribution along the axis of QWR

For longitudinal stability or focusing, it requires the synchronous phase to be negative.

The radial momentum impulse delivered to the particle is given by [5]

$$y_{prf} = -\frac{\pi q E_0 TL \sin\varphi_s}{mc^2\gamma^2\beta^2\lambda} r \qquad (4)$$

Because of longitudinal stability, $\varphi_s$ is negative that results vertical impulse on beam is positive. Total beam steering angle is the effect of contribution due to Bx, Ey and RF defocusing effect. General particle tracer code (GPT) [6] is used to simulate multi-particle motion in 6-dimensional phase space that take cares of all the contributions.

The 3D beam steering data for q/A=1/7, accelerated electric field Ea=5.5 MV/m, and synchronous phase of -25 degree are calculated using GPT over a range of range of particle energies ( in terms of β) and vertical offsets of QWR is as shown in figure 3. It is to be noted that all three contribution of vertical beam deflection has been taken into account in GPT simulation.

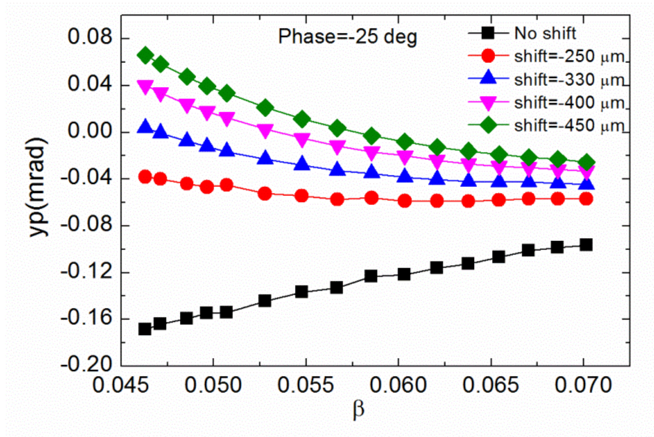


Figure 3: Beam steering over a range of particle energies for various vertical offset of QWR

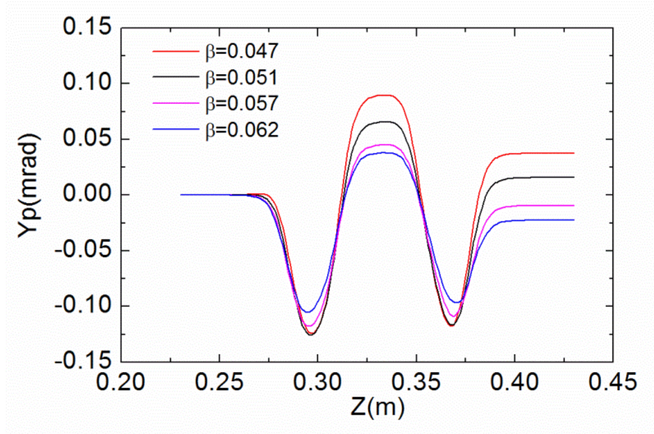


Figure 3: Steering of beam centroid along longitudinal direction

Again beam steering angle yp varies in the longitudinal direction as shown in figure 4. It is to be noted that magnitude of yp could be both positive and negative along the longitudinal direction.

## OPTIMIZATION OF BEAM STEERING EFFECT

To compensate beam steering, QWR is displaced in vertical direction with respect to accelerator axis. In order to optimize the beam steering effect over the range of particle energies of different mass to charge ratio, the objective function to be minimized may be written for chosen individually tuned synchronous phase as

Minimize

$$f(shift) = \int_{\beta_{\min}}^{\beta_{\max}} \int_{z_{\min}}^{z_{\max}} yp(shift, z, \beta)^2 \, d\beta \, dz$$

Subject to  0<=shift <=1000 µm

The upper limit of shift is chosen arbitrarily more so that magnitude of optimized shift lies within it. The limit of integration spans over the range of reduced particle velocity β (=v/c) and longitudinal distance z.

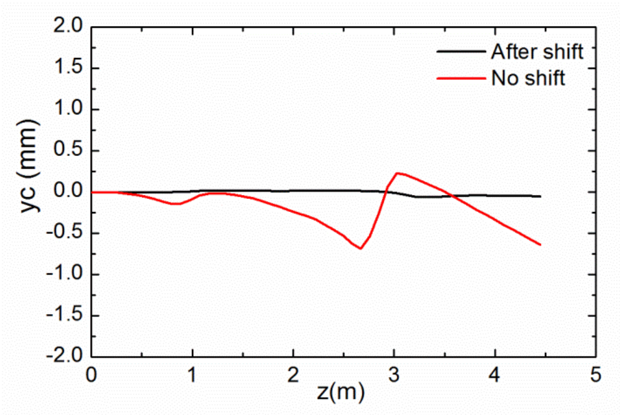


Figure 5(a): Steering of beam centroid (yc) with/ without correction for a representative ion species of q/A=1/7 at synchronous phase of -26.0 degree

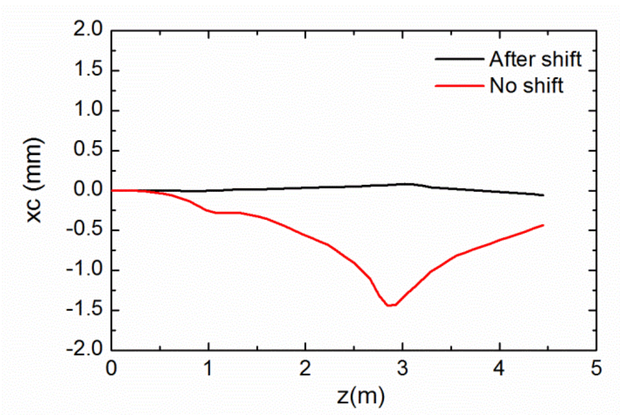


Figure 5(b): Steering of beam centroid (xc) with/ without correction for a representative ion species of q/A=1/7 at synchronous phase of -26.0 degree

For the given set of database, the optimized vertical offset is found to be 407 µm using differential evolution algorithm. With the optimized data, details multi-particle beam dynamic simulation has been carried out using General particle tracer code (GPT) to validate the result as observed in figure 5(a) and figure 5(b). Two lattices each comprises of a set of two QWRs with a focusing solenoid in between have been considered. It is to be mentoined that for a long chain of QWR, individual QWR may be given different offsets or shifts and the optimization objective function may be constructed accordingly.

## DONUT SHAPED DRIFT TUBE

The addition of donut shaped axisymmetric drift tube at the inner conductor of QWR reduces the magnetic field in the gap as cshown in figure 6. Therefore, vertical beam steering due to transverse magnetic field (Hx) reduces too.

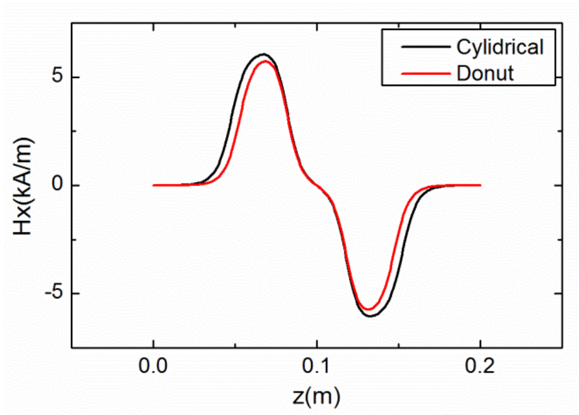


Figure 6: Horizontal magnetic field for donut (black) and cylindrical (red) central drift tube

## SUMMARY

The beam steering effect has been studied over the operating region of VECC QWR using general particle tracking code GPT. Suitable vertical offset (~400 µm) of QWR has been proposed to minimize the steering effect to around 0.02 mrad. However, it is to be mentioned that system vertical position changes during cool-down to 4.2 K by an amount of around 1.7 mm. Therefore, it is important to establish the offset value at room temperature for each QWR and solenoid so that warm position is compatible with desired cold position.

## REFERENCES


[1] P. N. Ostroumov and K.W. Shepard, Phys. Rev. ST Accel. Beams 4, 110101 (2001)

[2] A. Facco and V. Zviagintsev, Phys. Rev. ST Accel. Beams, 14, 070101 (2011)

[3] M. A Fraser, R.M.Jones and M. Pasini, Phys. Rev. ST Accel. Beams, 14, 020102 (2011)

[4] CST Microwave Studio 2014

[5] Y. S. Qin et al., "Beam Optics Verification for a QWR", 13 th Symposium on Accelerator Physics (2017), Jishou, China

# Experience on fabrication of 650 MHz five-cell SCRF cavities using Electron Beam Welding.

Manish Bagre * S. Moulali, V. Vijayakumar, Ashish Singh, , T Maurya, Umakant Srivastava, Ajay Yedle, Anand Yadav, Vinesh Verma, V K Srivastava, Sanjay Sharma, T Veerbhadraiah, G. kane,Rajeshwar Shanda, P Mohania, A. Mahawar, P Ram Sankar,A. Puntambekar

*Raja Ramanna Centre for Advanced Technology, Indore, India.*

manish@rrcat.gov.in

### *Abstract*

Development of 650 MHz (β=0.92) five-cell SCRF cavities are ongoing at RRCAT. Large number of such multi-cell cavities are required for the future high energy superconducting proton accelerators proposed at RRCAT. In addition, these cavities will be a part of deliverables from RRCAT to Fermilab under Indian Institutes Fermilab Collaboration (IIFC).Conventionally, SCRF cavities are fabricated from niobium sheet by the formation of half-cells by deep drawing, followed by machining at weld location and Electron-Beam Welding (EBW). The welding of half-cells is a elusive procedure, requiring intermediate cleaning steps and a careful choice of weld parameters to achieve full penetration of the joints. The equator welds are particularly critical. A challenge for a welded construction is the tight mechanical and RF tolerances. Using 15 KW-house EBW machine, four numbers of 650 MHz five cell SCRF cavity has been fabricated. These completed five cell SCRF cavity has been pre-qualified for dimensional measurement, vacuum leak testing and RF testing at 300K.

The paper presents the experience gained during fabrication of these cavities with revised manufacturing process sequence plan, modified weld joint design, covering weld parameters optimization, components machining & dumbbell tuning at intermediate stage of fabrication.

## INTRODUCTION

RRCAT has taken up development of prototype 650 MHz five cell (β=0.92) SCRF cavity as part of Indian Institution Fermilab Collaboration (IIFC). Large quantity of elliptical multi-cell SCRF cavities are also required in medium and high beta section for proposed Indian Spallation neutron source (ISNS) at RRCAT. Based on experience gained on Tesla Shape 1.3 GHz nine cell SCRF cavity and few single 650 MHz cell cavity, development of high beta multi-cell 650 SCRF cavities has been taken up [1].

## CAVITY MANUFACTURING PROCESS PLAN

Based on experience gained on 1.3 GHz nine cell SCRF cavity RRCAT the welding sequence plan has been made in which first dumbbell to join with dumbbell to make double dumbbell. [2] Than double dumbbell to join with double dumbbell to make Quadrupole dumbbell. Lastly the Quadrupole dumbbell assembly were joined with MC and FP end group. The first 650 cavity was made by this welding sequence plan. For SCRF cavity application, The EB welding from inside (RF-side) is recommended to ensure smooth weld bead.

Based on this observation & taking the advantage of IRIS diameter (118 mm) the process sequence plan was revised in which double dumbbell is joined first with MC and FP end groups. The final equator joint is middle of assembly with full penetration from outside (only one). Due to revised process sequence plan the risk of equator weld was reduced to 80 % & smooth under beads were obtained. The last three cavity were made by revised welding sequence plan.

***EB welding machine & RRR qualification*:** 15kW electron beam welding machine is set up in house. The weld chamber size 3800 x1500 x 1950 $mm^3$ is capable to weld from low beta to high beta energy range of proposed Linac.

High RRR (Residual Resistivity Ratio) Niobium has been preferred metal for fabrication of SCRF cavities. RRR which indicate the purity of material plays an important role for SCRF cavity performance. Heat flow at cavity inner surface depends upon thermal conductivity of cavity material which should be high enough to achieved desired performance. Thermal conductivity of niobium directly related to RRR as ($\lambda_{(4.2k)}$= 0.25 RRR).The experience shows that High RRR niobium used for fabrication of SCRF cavity is affected by vacuum level in EB welding machine.

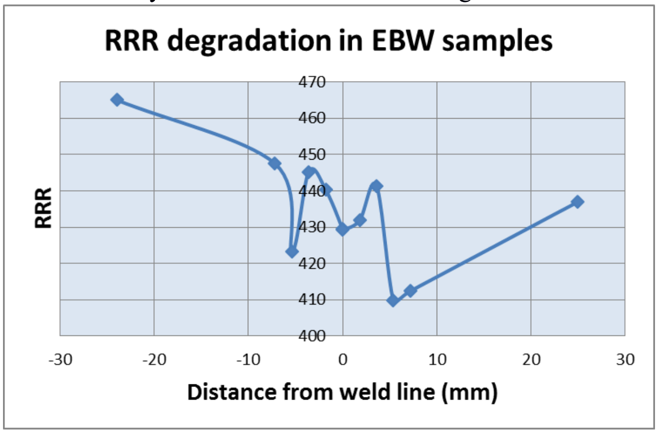


Figure 1: RRR degradation along weld seam

The welding of the all cavity joint should be carried out at pressure of < 4 x $10^{-6}$ mbar to avoid the RRR degradation. Before starting of cavity welding, RRR of Niobium welded

*manish@rrcat.gov.in

samples were determine the degradation in material due to electron beam welding and evaluation of the heat affected zone. The figure 1 shows the RRR degradation was found ~ 4.87% which is less than 10 % degradation (The pristine RRR of samples were average 451).

***Weld Parameter Development:*** Weld parameters development is vital stage for successful cavity welding. Due to high cost of niobium very restricted material is available for weld parameter optimization. A slightly defocused beam in circular pattern was used to achieve smooth inner weld bead. The weld parameter was optimized by welding on linear coupons, ring samples and dummy half cells. Numbers of test coupons were welded to develop the optimized weld parameters (beam current, accelerating voltage, welding speed and focusing current) to achieve the full penetration and desired uniform weld under-bead at the inner RF surface. The micrographs of sample weld are examined for weld penetration, weld defect like, porosity, cracks and voids etc. The figure 2 shows typical weld micrograph.

Figure 2: IRIS weld micrograph

The weld shrinkage were measured at every weld sequence which is necessary for good predication of cavity length with target frequency. It is determined on test coupons and incorporated in component machining & weldment assemblies.

## CAVITY FABRICATION

SCRF cavity Fabrication involves several steps starting from the Niobium raw material inspection, blank cutting, deep drawing forming, machining, chemical cleaning, electron beam welding and lot of intermediate QC measurement. Machining and inspection also took places at our different in-house facility. The five cell cavity is made by 8 regular cells and 2 end cells. Half-cells are made by forming a 4 mm blank in 100 tons CNC forming machine to achieve the desired elliptical geometry. Before welding Half-cells are chemically cleaned by ultrasonic cleaning and BCP process to get the cleaned surface. Half-cell machining were carried out with Indian Industry to explore for mass production.

Beam Tubes- To fabricate a tube Niobium sheets are cut to blank. After thorough visual inspection, Tubes are rolled in -house developed precision rolling machining by successive rolling method. The rolled tube was welded longitudinally with full penetration from outside only.MC end beam tube was pull-out for the power coupler by specially designed pull out fixture. In order to avoid the pull-out complexity in FP beam tube side, the weld joint design changed from 2D to 3D joint. The FP beam tube was Three – D machined for fitment of FP tube. In FP pipe 3D machined tube part was welded with full penetration from outside. The formed components are inspected thoroughly for any defect like dent, scratch and earring and waviness after that formed components are machined for final size which was further inspected geometrically and RF point of view. All flanges and transition spool are made up Niobium-Titanium and interface (end cap) from transition spool to helium vessel is made up Titanium materials.

***Electron Beam Welding of Dumbbell*:** Two half –cells are joined at the iris with an EB weld to form a dumbbell. Welding of dumbbell was performed first from outside at 80 % of depth of penetration and then 20 % from the inside for smooth under-bead. Stiffening ring are welded in between adjacent half-cell to impart rigidity against Lorentz

Figure 3: dumbbell with stiffening ring

Force Detuning and microphonic. Weld shrinkages may lead to deformation of the cell which need to be corrected by tuning & trimming at intermediate stage. [2]

***Electron Beam Welding of MC and FP End Groups:*** The end groups EB welding was taken up which consist of multiple parts with intricate shape, complex weld geometry and di-similar welding of Niobium to Niobium–Titanium (Nb-Ti) and Nb-Ti to Titanium. The dis-similar joint weld always pose challenges due to difference in melting point, thermal conductivity as well as thermal mass of the materials. The flange need to be joined by beam tube and accomplished by offsetting the beam towards niobium side. MC end group consist of the beam tube at main coupler end has a port for the RF power coupler and transition spool joined with end cap.The FC end group consist of beam pipe at tuner end and a port for RF field probe antenna. Weld shrinkages in FP & MC end group may also lead to deformation of the cell which need to be corrected by tuning & trimming.

***Equator welding*:** welds at equator is especially critical because it will exposed to high magnetic field. The required high quality of weld seam is in fact very important for SCRF performance.[3] The welding fixtures were designed to take care of every step of welding which also taking care of MC

& FP end group clocking position & stiffening ring clocking position. With revised weld sequence plan MC end group was welded with dumbbell & similarly FP end group was welded with another dumbbell. The weld parameters were listed in table: 1. Then MC end group & FP end group with dumbbell assembly was welded with another dumbbell partially from outside & inside. The last equator joint was full penetration weld from outside.

Table :1

Typical Equator weld parameter

| Welding parameter | stitch weld | Seal weld | Full weld |
|---|---|---|---|
| Beam Current (mA) | 14 | 17 | 30 |
| Voltage (kV) | 110 | 110 | 110 |
| Focusing(mA) | 960 | 960 | 1000 |
| Speed (mm/min) | 550 | 500 | 450 |
| Beam pattern | Circular | Circular | Circular |

## PRE-QUALIFICATION TESTS

The completed 650 MHz five-cell SCRF cavities were qualified for mechanical, vacuum leak check and RF measurement. [4]

Leak tightness was check with Helium mass spectrometer leak detector while blanking the all flanges except one to connect the detector. No leak was found at highest level of sensitivity of detector 9.7x10-12 mbar-ltr. /sec. The table 2 shows the filed flatness, frequency measurement at 300k, cavity length & weld shrinkage data.

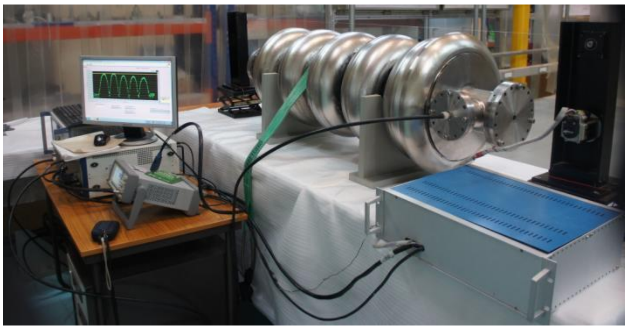

Figure 4: The frequency & field flatness measurement setup

Table :2

| Cavity ID | Length (mm) (target 1400±3mm ) | Weld Shrinkage (mm) | Frequency 300 K (MHz) (target 649.5MHz) | Field flatness as fabricated (target 95 % after tuning ) |
|---|---|---|---|---|
| 5001 | 1403.94 | 0.45 | 649.59 | 68 % |
| 5002 | 1401.33 | 0.78 | 649.405 | 87 % |
| 5003 | 1400.17 | 1.02 | 650.0 | 66 % |
| 5004 | 1401.71 | 0.73 | 649.5 | 65 % |

## SUMMARY

The electron beam welding of SCRF cavity is very vital process in fabrication. To achieve the desired field flatness, target frequency & right length the weld shrinkage & weld parameter are play very important role in fabrication of SCRF cavities. Experience shows that sometimes holes can be burned though by EBW. The burn hole repair procedure developed & demonstrated. The knowledge gained in electron beam welding of multi-cell 650 MHz SCRF cavity will be useful for series production of SCRF cavities which are deliverable under IIFC collaboration.

## ACKNOWLEDGMENT

We would like to acknowledge the corporation received from our all group members & our international Fermilab collaborator’s.

## REFERENCES

[1] M Bagre, A Puntambekar, et al, “Development of 1.3 GHz Nine-cell SCRF cavities at RRCAT”, InPAC 2015

[2] A Puntambekar, SC Joshi, “Indigenous development of first five-cell 650 MHz SCRF cavity and series manufacturing plans” in InPAC2018.

[3] M Bagre, A Puntambekar, et al Process parameters for Electron Beam Welding of various parts of a 650 MHz five cell SCRF cavities in InPAC2018.

[4] P Mohania, “Challenges of Frequency Measurement and their Control during Fabrication of 650 MHz, Five-Cell SCRF Cavities” in this conference.

# DESIGN AND MODELLING OF A SPIRAL INFLECTOR FOR K130 CYCLORON AT VECC

Animesh Goswami*, Suvadeep Roy, C. Nandi, D. Sinhamahapatra, A. Dey, P. S Chakraborty, S. Ghosh, P. K. Behera, R. Kumar, R. Ming, M. Dash, T. Fatma, K. D. Rao, A. Das, A. Kumar, S. Raghuwanshi, Prodyut Sankar Chakraborty and Arup Bandhopadhyay
VECC, 1/AF, Bidhannagar, Kolkata-700064

*Abstract*

In this paper we have discussed the design and development of a spiral inflector to be used in K130 cyclotron at VECC, Kolkata. In addition, we have presented the beam dynamics through the spiral inflector for more realistic electric field map produced by the code RELAX3D using linear transfer matrix technique.

## INTRODUCTION

The variable energy cyclotron with K=130 at Kolkata is presently accelerating different types of light heavy ion beams for doing research in different fields. A 14.4 GHz ECR ion source produces variety of ions at an extraction voltage ~ 8-10 kV. At present, the beam from the ion source is vertically injected into the central region of the cyclotron by using a gridded mirror inflector. The mirror inflector requires almost same voltage as the injection voltage for the inflection of ions. Another disadvantage is that the grid wires tend to break after being exposed to beams over a long period. The grids also cause beam degradation and transmission loss. Nowadays a spiral inflector is the most widely used inflection device because of its large acceptance, low voltage requirement and almost 100% transmission efficiency [1].

In this work we have carried out a detailed design study of a spiral inflector that can able to inflect heavy ions that are presently being accelerated using a mirror inflector. Central ion trajectory data of the spiral inflector is used to make the modelling of the spiral surfaces of electrodes facing to each other. Fabrication of the inflector has been done using computer aided machining. We have also checked the orbit centering of the injected beam using a central region code. Beam dynamics through the inflector using RELAX3D field has also been discussed.

## SPIRAL INFLECTOR DESIGN

The spiral inflector consists of a pair of biased electrodes housed in a ground shielding. Its design is mainly governed by two leading parameters, the inflector height $A$ which is same as the electrical radius of the particle in the absence of the magnetic field and the tilt parameter $k'$. The electrical radius, the magnetic radius and the parameter $K$ are given by following expressions,

$$A = \frac{2T}{qE} \quad , \quad R_m = \frac{p}{qB} \text{ and } \quad K = \frac{A}{2R_m} + k'$$

where, T is the kinetic energy, $p$ is the momentum and $q$ is the charge of the particle. $E$ and $B$ are the electric and magnetic fields respectively. The important thing to be considered while designing an inflector is to have off-centering of the beam as minimum as possible at the exit of the inflector. It must be compatible with the requirement of the central region for proper centering of the beam orbit for further acceleration.

We have designed a spiral inflector that can able to inflect $O^{5+,\,6+}$ , $Ne^{6+\,,\,7+}$ etc ions that are presently being accelerated using a mirror inflector. In this case the spiral inflector operates in scaling mode which demands that the magnetic radius $R_m$ of the ion must be constant i.e.

$$R_m\,(\mathrm{cm}) = \sqrt{20.88 A_m V_{ext}\,(\mathrm{kV}) / Q B_0^2\,(kG)} = \mathrm{const.},$$

where $V_{ext}$ is the extraction voltage, $Q$ is the charge state, $A_m$ is the mass number and $B_0$ is the central magnetic field. We have chosen the representative ion as $O^{6+}$ with $B_0 = 10.49\,\mathrm{kG}$ , $V_{ext} = 6.41\,\mathrm{kV}$ . The value of $R_m$ in this case is 1.8 cm. If we want to use the same spiral inflector for another kind of ion, $V_{ext}$ and $B_0$ for that kind of ion can be obtained by scaling according to the above equation. Large height ($A$) of the inflector is always preferable to reduce fringe field effect. However it is limited by the space available in the central region. The gap between electrodes $d_0$ is chosen ~ 5 mm to ensure the loss free bending of the beam. The aspect ratio $\xi$ , defined as the width of the electrode divided by gap between the electrodes is generally chosen 2 to avoid the effect of the fringe field. In the present design $\xi$ is taken 1.5 due to space constraints in the central region.

We have designed the spiral inflector first analytically and then numerically using computer code CASINO [2]. With the CASINO output, the INFLECTOR [3] program is executed to display the electrode shape. The electric field distribution in the inflector has been numerically calculated by the program RELAX3D [4]. These fields are then used in CASINO to calculate the ion trajectories through the inflector. In the present design, the optimized height and tilt of the inflector is $A$ = 1.6 cm and $k'$ = 0.58. The maximum required inflector voltage is ±2 kV.

Figure 1 shows geometrical positing of the spiral inflector in the central region of the K130 cyclotron. The *x-y* projection of the central ion trajectory (green line), schematic shape of the biased electrode's projection is shown in Fig. 1. It is evident from the plot that the beam can be injected and easily positioned in the central region with existing Dee and Dummy Dee inserts. The grounded

*animesh@vecc.gov.in

plates parallel to the inflector entrance and exit are placed 3 mm away from the inflector such that opening of these plates coincide with the opening of the inflector at the entrance and exit. Figure 2 shows the central ray though the inflector and in the central region, location of the Dee insert and Dummy Dee insert in the *x-y* plane and few turns of the accelerated orbits of $O^{6+}$ ions from 38.45 keV to 3 MeV. It is easy to see from Fig. 2 that the beam is well centered with the input condition provided by the spiral inflector at the matching point.

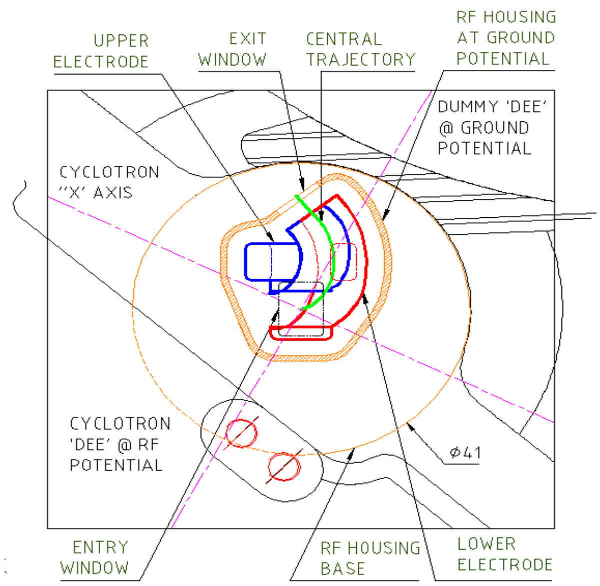


Figure 1: Spiral inflector position at central region of K130 cyclotron.

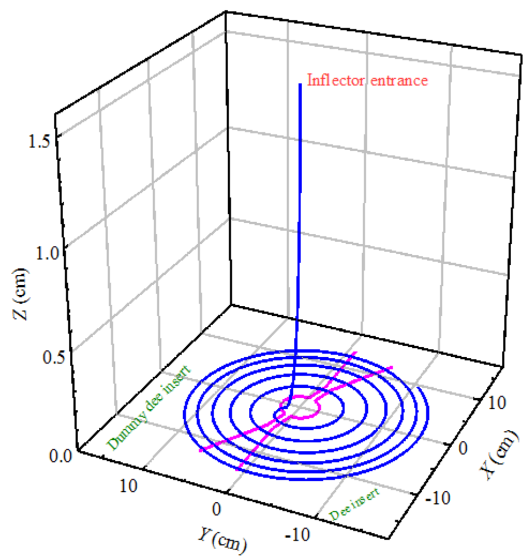


Figure 2: Central ray in spiral inflector and central region. Positions of the electrodes are also shown.

## DEVELOPMENT OF INFLECTOR

As mentioned earlier, the spiral inflector system has to be compatible with the space and operational constraints of existing central regions of the K130 cyclotron. The mounting interface of the entire subsystem was required to be identical with the internal-ion source shaft and should be quickly demountable.

### *Design of electrodes and RF cover*

The coordinates of the central trajectory is plotted in 3D and the tilt angle and gap between electrodes are evaluated at few cardinal points on the central trajectory. Spacing between these points is taken as 1mm. An UCS is fitted at this point with its Z axis aligned with the small line segment of central trajectory. Line of intersection between X-Y plane of UCS and global X-Y plane is created. The UCS now rotated to align its X axes with the line of intersection. The electric field direction vector is represented by the Y axis of the UCS at these cardinal points. Two parallel line segments, representing the electrode surface section, are drawn perpendicular to Y axis and separated by a gap between the electrodes at this location. The length of the line segments was taken as 1.5 times of the gap. The endpoints of these lines are joined with a 3D polyline. A pair of spiral helical surfaces are created using loft between line segments and 3D polylines. The edges of these surfaces are projected on the median plane or its parallel planes to form a wireframe network. Two bounded volumes for two electrodes are created by combining the spiral helical surface and surfaces created from the wireframe network.

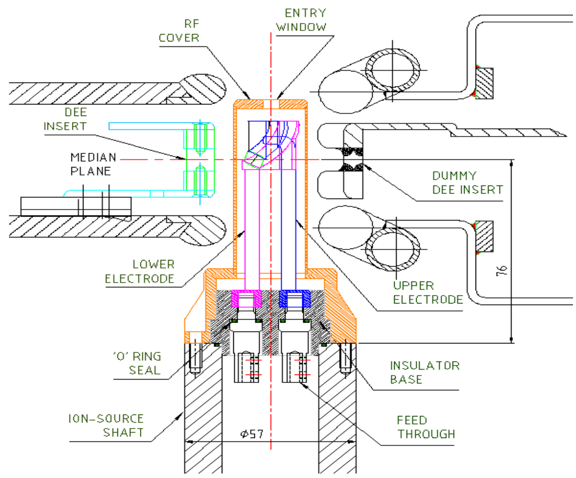


Figure 3: Sectional view of inflector within central region.

The top of the existing inflector shaft is 76 mm apart from the medial plane. The electrodes are connected to ± 5kV DC potential through a feed through mounted within an insulator base at the bottom the electrodes, shown in Fig. 3. The insulator base also houses the broader D shaped bottom end of the electrodes geometry to make the electrode assembly more stable. D shaped bottom end spiral-helical top of the electrodes are connected though a slender stem of 5 mm × 3 mm section and 50 mm length. The stem shape is optimized to maximize the rigidity within the allowable space and reliable against unforeseen shocks or mishandling. Electrode top and stem are enveloped within a hollow RF housing of 0.8 mm wall thickness (Fig. 1). The contoured profile of the housing was designed considering a gap of 2.2 mm or more from the inflector electrodes and 5 mm gap from the Dee insert. The top of the RF housing is covered with similar contoured flange having 7.6 mm × 5.4 mm entry port at center. A 6 mm × 5 mm exit port tilted at $30^{O}$ angle is machined through the side wall of the housing just in front of the electrodes exit. The bottom of the RF cover is a thick flange which covers and holds the insulator base on the vacuum seals at the top of ion source shaft.

### *Fabrication and testing*

The electrodes with integrated stem and base are machined from Aluminium-6061 rods using a CNC Mill-turn machine. Fabrication of the integrated stem electrodes is the most challenging part for the entire development due to lack of rigidity of the slender stem. In order to prevent the distortion under cutting force, an oversized cylindrical rod is used as stock material and a dummy stem is added in the model at symmetrically opposite position of the original stem.


Figure 4: Spiral inflector assembly developed at VECC

The dummy stem is useful to minimize the distortion to a great extent and removed at the final stage of machining. The complicated 3d contoured spiral helical surface of the electrodes is machined with ball end milling cutter using a rotary drive as the $4^{th}$ axis to impart The surface roughness of the functional surfaces of the electrodes is measured between 0.35μm to 0.6μm. The insulator base is made of macor and RF housing is made of ETP copper. RF housing is fabricated in three parts which are brazed together using a fixture. The spiral inflector assembly, shown in Fig. 4 is tested for vacuum leak test and high voltage. Global vacuum leak rate is found below $1\text{x}10^{-9}$mbar-l/sec and electrodes withstood upto ± 8.5kV potential difference without any breakdown when tested within a vacuum of $1.6\text{x}10^{-6}$ mbar.

## BEAM DYNAMICS IN INFLECTOR

Linear transfer matrix technique is used to study the beam dynamics through the spiral inflector. To obtain the inflector transfer matrix **M**, the five linearly independent paraxial rays are tracked through the spiral inflector using CASINO code. The beam sizes in the *u* (vertical) and *h* (horizontal) plane at a point *s* can be obtained by using sigma matrix method. To estimate the beam sizes in the spiral inflector, the paraxial ion trajectories of 100 representative particles belonging to the boundary of the input emittances of 80 mmmrad with $U(0) = H(0) = 2$ mm, $P_u(0) = P_h(0) = 0$ mrad in each plane were run through the inflector. The resulting paraxial ion trajectories in *u* and *h* planes within the inflector electrode are shown by solid lines in Fig. 5 for RELAX3D field. The dashed lines indicate the electrode apertures. Here we have used $s_{in}$ = 0 cm and $s_{out}$ = 4.4 cm so that electrode entry is at s = 1.4 cm and exit is at s = 3.9 cm. It is cear from Fig. 5 that beam has a divergent characteristic in the *u* plane and converging behaviour in the *h* plane. As the available electrode aperture in the *u* plane is less than that in the *h* plane, we expect more beam loss in the *u* plane due to restricted aperture. A careful optimization of the injected beam at the input of spiral inflector is thus necessary to keep beam sizes remain within a reasonable limit in both the transverse planes.

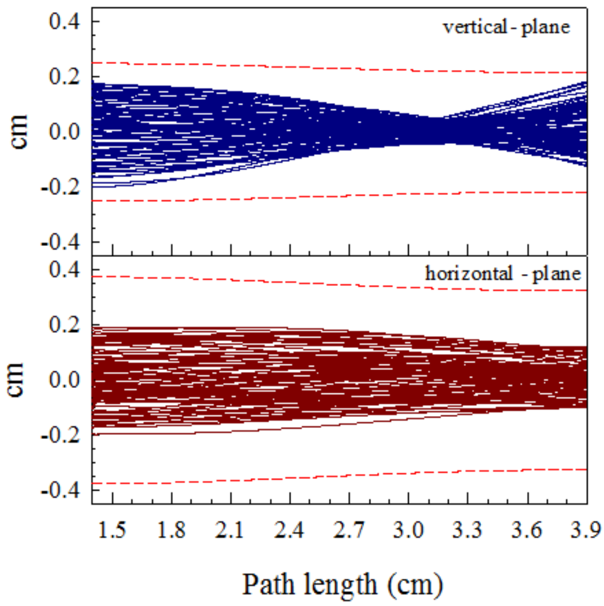


Figure 5: Paraxial ion trajectories through the spiral inflector in both planes for RELAX3D electric field.

## REFERENCES

[1] A Goswami et al., Nucl. Instrum. Meth. A **693**, 276 (2012).

[2] F B Milton and J B Pearson, CASINO User's Guide and Reference Manual, TRI-DN-89-19, (Vancouver, 1989).

[3] L M Milinkovic, RELAX3D Spiral Inflectors, TR30-DN-89-21, (Vancouver, 1989).

[4] C J Kost and F W Jones, RELAX3D User's Guide and Reference Manual, TRI-CD-88-01, (Vancouver, 1988).

# BEAM OPTICS DESIGN OF A HIGH RESOLUTION SEPARATOR FOR ANURIB PROJECT

Animesh Goswami*, Santanu Paul, Ankur Agrawal, Md. Zamal Naser, Atanu Dutta, Uttam Bhunia and Arup Bandhopadhyay
VECC, 1/AF, Bidhannagar, Kolkata-700064

*Abstract*

This paper describes the beam optics design of a High Resolution Separator to be used for selecting the desired radioactive beam in the ANURIB project at VECC. The proposed design consists of two 90-degree magnetic dipoles, two electrostatic quadrupoles and a multipole arranged in a symmetric configuration to minimize aberrations. A detailed description of the design and results of extensive simulations are presented. Higher order corrections are also discussed.

## INTRODUCTION

VECC is planning to develop a radioactive ion beam facility ANURIB [1, 2] at the upcoming new campus at New Town in Kolkata. In general, the production techniques in this facility may produce multiple radioactive species composed of slightly different masses. In order to separate the undesired radioactive species that contaminates the downstream beam lines a mass selection technique is therefore necessary.

In this paper the optical layout of a High Resolution Separator (HRS) with mass resolving power of 20000 has been presented. Initial beam optics has been designed using the code TRANSOPTR [3] and the final design of the separator has been done with the code COSY-Infinity [4] up to fifth order. An electrostatic multipole located in the center of the HRS allows for fine-tuning the second order correction. Higher order aberrations are corrected by introducing an octupole, decapole and duodecapole component in the multipole. Simulation results of $U^{238}$ beam with energy 60 keV is presented.

## HRS OPTICS

The High Resolution Separator (HRS) system requires an entrance and exit slits and two 90 degree dipole magnets for mass separation. The basic first order optical design has been obtained from simulations using code TRANSOPTR. The bending radius of the dipole magnets is chosen 1.25 meters to obtain large mass dispersion and spacing between the dipoles is kept 1.5 meters to accommodate the whole system within the space available for the HRS. For the given dipole radius and spacing, shaping of the entrance and exit faces of the magnetic dipoles is needed to get vertical focusing cause by the magnetic dipole fringe fields. Two electrostatic quadrupoles (EQ) are used to obtain beam focusing. The positions and pole-tip voltages of the electrostatic quadrupoles system were used to fit the linear optics of the HRS. To correct non-linear effects (aberration) in the beam and improve transmission and resolution an electrostatic multipole corrector is also implemented. Lineal resolution of the HRS system is given by,

$$R = \left| \frac{(x|\delta)}{2(x|x)D_e} \right| \tag{1}$$

where (x|x) and (x|δ) are the horizontal magnification and dispersion terms, respectively, from the first order transfer matrix. Here $D_e$ represents the half-width of the beam at the HRS entrance slit. The first order beam optics is finalized by optimizing point to point and parallel to parallel focusing from the entrance to exit slits. The parameters for the HRS system are listed in Table 1.

Table1: Parameters for High Resolution Separator (HRS)

| **Parameter** | **Value** |
|---|---|
| Drift from source slit to EQ | 13 cm |
| Drift from EQ to Dipole | 64 cm |
| EQ length | 12 cm |
| Dipole edge angle | 25.70 deg. |
| Dipole vertical full gap | 7 cm |

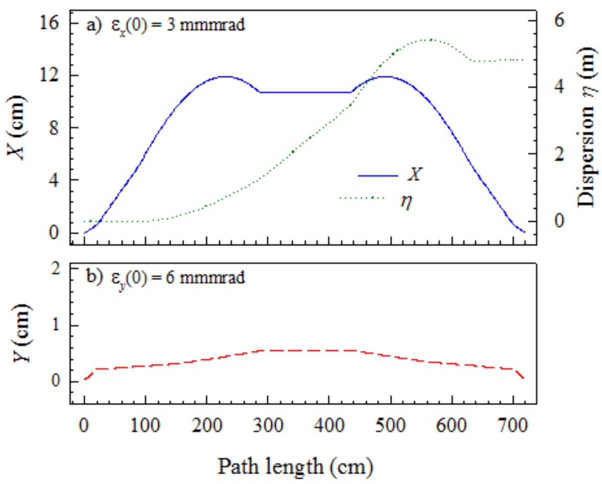


Figure 1: Plot shows (a) horizontal beam size $X$ and dispersion $\eta$; (b) vertical beam size $Y$ along the length of the HRS from slit to slit.

Simulation results of first order beam optics calculation for a beam with mass $A$ = 238, beam energy of 60 keV is shown in Figure 1. The input horizontal and vertical

*animesh@vecc.gov.in

emittances are 3 mmmrad and 6 mmmrad respectively. We see from Fig. 1(a) that the maximum extent of the beam size $X$ (blue, solid line) along horizontal direction is at the middle of the dipole magnet and is given by 12 cm for present input beam condition. It is also evident from the plot that the dispersion $\eta = (x|\delta)$ at the exit slit is 4.8 m. Using Eq. (1) the calculated value of the lineal resolution is 22,500 for source slit of full size 0.2 mm. The maximum envelope size $Y$ along vertical direction (red, dashed line), shown in Fig. 1(b), is 8 mm which is well below the pole gap.

## HIGHER ORDER CORRECTION

The resolution of the HRS system is limited by the nonlinear effects (aberrations) caused naturally by the geometry of the magnets as well as the fall-off fringe field from both the magnetic and electrostatic elements. Then the actual resolution can then be expressed by

$$R_{actual} = \frac{|(x|\delta)|}{\Delta x_{actual}} \qquad (2)$$

Here $\Delta x_{actual}$ is the final beam width that depends on the initial parameters of the beam as

$$\Delta x_{actual} = (2|(x|x)D_e| + |(x|x^2)D_e^2| + |(x|xa)D_e A_e| + \cdots) \qquad (3)$$

where $(x|x^2)$ and $(x|xa)$ are 2nd order coefficients of the transfer map of HRS and $D_e$ and $A_e$ represent the half width and the initial divergence of the beam at the entrance (source) slit.

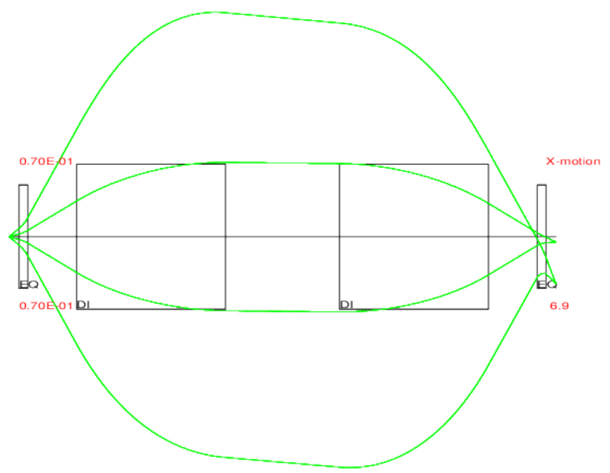


Figure 2: COSY Simulation of horizontal beam motion for the pure separator portion of the HRS.

COSY infinity code is used to determine the coefficients of the transfer map of HRS. By using the basic uncorrected HRS model in COSY, the largest nonlinear effects were identified. Figure 2 shows the effect of second order aberration on the beam at the HRS system. It is easy to notice from the plot that the rays are deviated from the optical axis at the exit slit due to aberration.

Transfer map of the HRS system obtained from COSY code are used to calculate the phase space at the slit location. The horizontal phase space ($x$, $p_x$) at the source and image slit location are shown in Figure 3. The input beam is chosen upright with size 0.1 mm and emittance 3 mmmrad. We see that at the image slit the phase space is distorted due to non liner effect and only few particles are within the ± 0.1mm aperture. Higher order corrections are therefore necessary to increase the beam transmission.

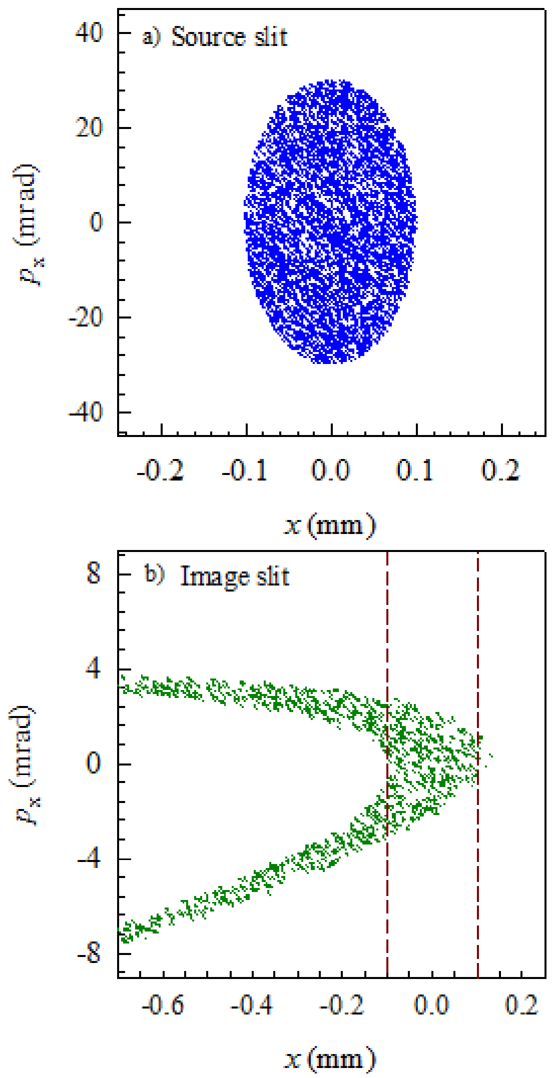


Figure 3: Horizontal phase space ($x$, $p_x$) plot at (a) source slit and (b) image slit location.

Higher order corrections of the beam optics are done by minimizing the coefficients of the transfer map given in Eq. (3). The second order aberrations effecting horizontal beam width in HRS beam line are initially corrected by introducing curvature of 0.636/meters to the dipole entrance and exit faces. Residual 2nd order aberrations that could not be minimized via this curvature are corrected by introduction of a sextupole field with the multipole corrector with a pole tip voltage of about 0.0988 kV based on a 15 cm aperture. The multipole corrector placed at the centre of the HRS system with length 30 cm. The multipole corrector is also used to correct the largest 3rd order aberration to final horizontal position via introduction of octupole fields. Additional corrections of the largest 4th and 5th order aberrations could be accomplished by introducing decapole and duodecapole fields in the corrector. Voltages required to obtain these corrections are listed in Table 2.

Table 2: Pole-tip voltages of multipole component

| Multipole (MP) component | Voltage (kV) |
|---|---|
| Sextupole | 0.0988 |
| Octupole | 0.0103 |
| Decapole | 0.0083 |
| Dodecapole | -0.00068 |

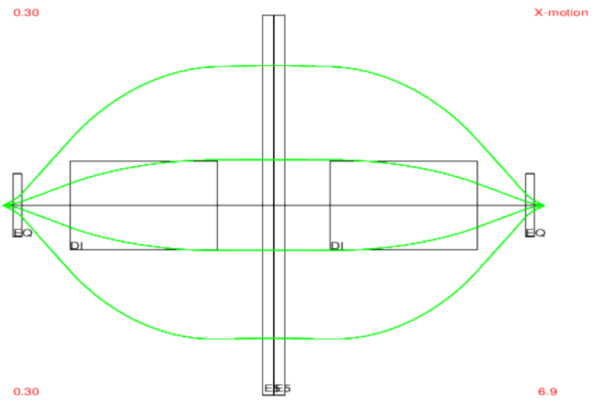


Figure 4: COSY simulation of horizontal beam motion for HRS with corrections up to 5th order.

Figure 4 shows the ray tracing through the HRS system obtained by COSY code with higher order corrections. It is evident from the plot that the rays are now close to the optical axis at the exit slit. The horizontal phase space ($x$, $p_x$) for 2000 particles at the image slit location is shown in Figure 5. The effects of these corrections can also been seen from plotting the results for a particle distribution. We see that at the image slit the phase space is not distorted and particles are well within the ± 0.1 mm aperture.

Figure 6 shows the results for distributions of 2000 particles with horizontal emittances of 3 mmmrad (using a uniform distribution for position and angle) for the target mass and +/- Δmass/mass of 1/20000. These results are based on the transfer maps generated from the simulations at 5th order in COSY. It is easy to notice from Fig. 6 that three masses are well separated at the slit location of the HRS system.

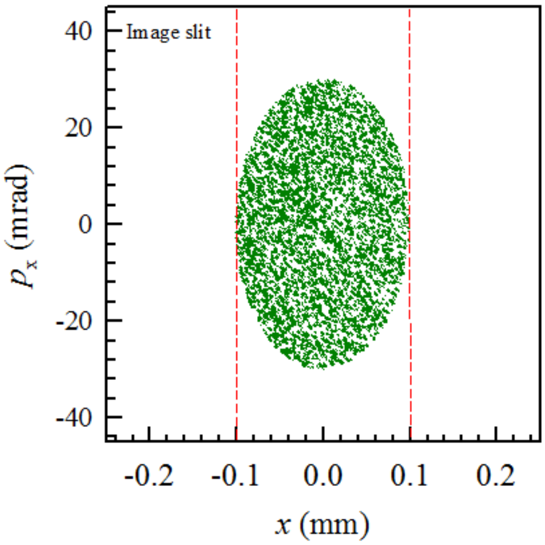


Figure 5: Horizontal phase space ($x$, $p_x$) plot at image slit location with corrections up to 5th order.

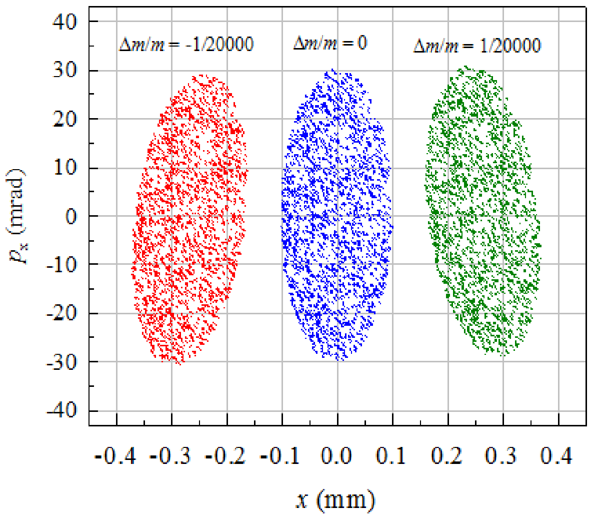


Figure 6: Final phase space for two masses differing by 1/20000 with respect to target mass at exit slit for pure HRS separator with a horizontal emittance of 3 mmmrad.

## REFERENCES

[1] Arup bandyopadhyay, V. Naik, S. Dechoudhury, M. Mondal and A. Chakrabarti, PRAMANA, Journal of Physics, 85 (2015) 505.

[2] Alok Chakrabarti, Arup Bandyopadhyay, Vaishali Naik, Siddhartha Dechoudhury, Manas Mondal and P. Y. Nabhiraj, Nucl. Instrum. and Meth. B, 317 (2013) 253.

[3] M S de Jong and E A Heighway , IEEE Trans. on Nucl. Sci. NS-30, 2666 (1983).

[4] K. Makino and M. Berz, "COSY Infinity Version 9," Nucl. Instrum. and Meth. A 558 (2005) 346.

# STUDY OF LONGITUDINAL BEAM PROFILE USING MULTI-HARMONIC BUNCHER FOR HIGH CURRENT INJECTOR AT IUAC

A. Sarkar*, Sarvesh Kumar, P.S. Lakshmy, Y. Mathur, S.K. Suman, V.V.V. Satyanarayana, S.Venkataramanan, G.O. Rodrigues

Inter University Accelerator Centre, Aruna Asaf Ali Marg, New Delhi- 110067, India
*email: abhi031264@gmail.com

*Abstract*

The multi-harmonic buncher (MHB) is operational for last two years and is able to provide beam bunches of the order of few ns for different ion beams produced by the ECR source in the HCI beamline. It is operated with the fundamental frequency of 12.125 MHz and its two harmonics at 24.25 MHz and 36.375 MHz which results in having an approximated saw-tooth waveform across an RF gap 3mm between two molybdenum grids. The dc ion beam of energy 8 kev/u from the ECR source is injected into MHB which gets bunched at a distance of 3m at the entrance of a radio frequency quadrupole (RFQ). A co-axial 50 ohm fast Faraday cup (FFC) is used to measure the bunch width as well as the beam current. Since the RFQ was operated at a lower power level (less than 20KW) than its designed value, $O^{6+}$ and $N^{5+}$ with A/q less than 6 were bunched and accelerated through the RFQ. The MHB saw-tooth was steady during all tuning operations as observed by the pick-up signal (differentiated saw-tooth). The beams were bunched with few watts of RF power employed to high Q tank circuits connected to the bunching grids. The measurements of longitudinal bunch profiles of ion beams and operational experience of MHB are explained in this paper. These measurements are crucial for the successful commissioning of the RFQ and DTL cavities for acceleration of beam through HCI.

## INTRODUCTION

The theory of beam bunching by a saw-tooth voltage across a single gap is well established over four decades [1]. This saw-tooth is approximated by a sinewave of 12.125 MHz and its two harmonics (24.25 MHz and 36.375MHz). This approximated saw-tooth is applied across a pair of Molybdenum grids placed in the beam line. The grid assembly along with all accessories are housed inside a vacuum chamber [2]. The capacitive pick-up signal from the grids is used for monitoring and tuning the MHB. The saw-tooth is generated, controlled and maintained by a specially wired electronic controller [3] and amplified by a broad band 100 watt amplifier. The amplified composite RF signal containing 12.125MHz and its harmonics from the controller is applied to the grids through high Q tank circuits. The tank circuits for operating the buncher were tuned for 12.125 MHz and its harmonics with less than 2% reflected power using vector network analyser.

The MHB is placed in the LEBT section of the HCI just after the ECR source and the A/q selector bending magnet. The criterion for the transverse beam waist formation on the buncher grids was confirmed by the beam optics calculations prior to the installation.

A commercial fast faraday cup fitted with a 50 dB gain MITEQ pre-amplifier is used to measure the FWHM of the beam bunches. A strip-line fast faraday cup developed in-house placed after the RFQ and energy analysing bending magnet was also tested. . The location of MHB and FFC in the LEBT section of HCI is shown in Fig-1.

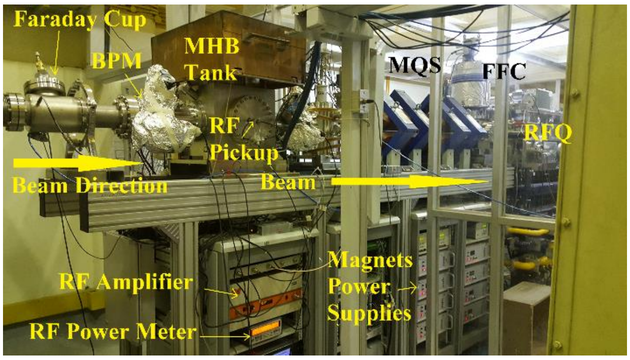


Figure1: Location of MHB and FFC in HCI beamline

## CRITERIA FOR BEAM BUNCHING OPERATION AND MEASUREMENTS

Since the ultimate goal of the HCI is to inject beam into the existing superconducting Linac operating at 97 MHz, the fundamental frequency of MHB was chosen at a sub-harmonic ie.12.125 MHz. Moreover the pre-bunching of beam using MHB was required before injection of beam into the 48.5 MHz RFQ as the RFQ was designed for a shorter length without bunching section. The criteria for optimum bunching and measurement are as follows:

1. The ion beam should have a sharp waist in transverse dimension at the RF gap formed by the grids of the buncher.

2. The electric field must be uniform across the pair of grids forming the RF gap.

3. The energy spread of the beam from the ECR source must be minimum for proper bunching.

4. The bunching grids, tank circuit coils, and RF amplifier should be water cooled for continuous operation to avoid any temperature related drifts.

5. The saw-tooth voltage responsible for bunching must be stable in terms of amplitude and phase. This is ensured by monitoring the pick-up signal triggered by the master clock.

6. The beam hall environment should be noise free in order to measure the beam bunches on CRO using the amplified signal from the fast faraday cup.

## PROBLEMS ENCOUNTERED

The problems that were encountered during the operation of MHB and measurement of beam bunches are as follows:

1. The FFC signal for measuring bunch width was very sensitive to any noise and RF pick-up. The background signal were minimized by averaging over 50 – 100 samples for stable measurements.

2. The pre-amplifier coupled to the FFC is also very sensitive and prone to damage for any RF pick-ups. It was thus turned off whenever RFQ was on. The measurement of beam bunches were made only when RFQ was off.

3. For cooling of the grids and tank circuit coils, the flow and temperature of the de-ionised water cooling system had to be maintained accurately for smooth operation.

4. All the bunched width measurements were done on a 500 MHz oscilloscope. Measurements of FFC timing signals on 4 - 6 GHz oscilloscope would yield much better results.

## LONGITUDINAL BEAM PROFILE MEASUREMENTS

Several beam tests were conducted using the MHB. It was observed that optimum bunching required proper beam tuning. Whenever beam was tuned arbitrarily, bunched width increased. When systemically beam was tuned according to the beam optics calculations with symmetric beam profiles before and after MHB ensuring a beam waist at the bunching grids, it was observed that changes made in transverse optics did not have any effect on the longitudinal beam profile. $N^{5+}$, $O^{6+}$ and $Ne^{8+}$ beams were bunched using the MHB. The FWHM of the optimized beam bunches varied from 2ns to 4ns as observed by the FFC timing signal directly on the 500 MHz oscilloscope. FFC signals observed on 4 - 6 GHz oscilloscope shall give a better timing resolution. The different bunched beam spectra along with the differentiated saw-tooth pick-up signals are shown in figures 2, 3 and 4.

Figure2: Bunched spectrum of $N^{5+}$

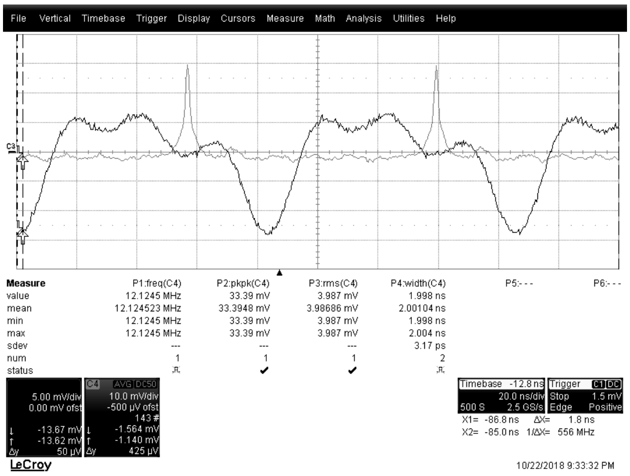

Figure3: Bunched Spectrum of $O^{6+}$

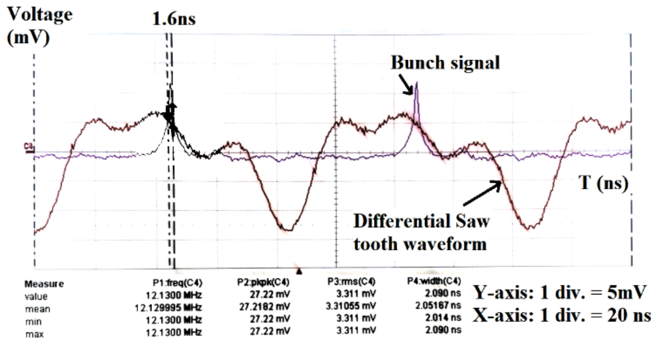


Figure 4: Bunched Spectrum of $Ne^{8+}$

We also tested an in-house developed strip-line FFC by placing it after the RFQ and energy analysing magnet and was able to detect beam bunches as shown in figure5.

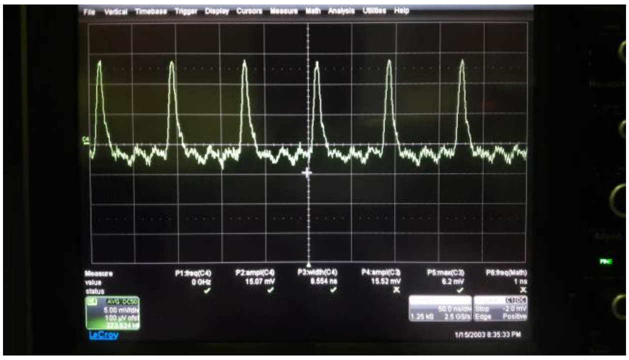


Figure5: $N^{5+}$ bunches as seen by Stripline FFC after RFQ and bending magnet

## CONCLUSION

The results shown are of the few initial tests. The optimisation of the beam parameters and the other beam optics elements in the beam line to get the best performance of the buncher are in progress. With proper beam tuning before and after the buncher and observing the FFC timing signal on a 6 GHz oscilloscope better FWHM can be achieved in future.

## ACKNOWLEDGEMENTS

The authors would like to acknowledge the help received from Rajesh Kumar, P.Barua, A. Kothari, R.Ahuja, and A.J.Malyadri during the different phases of the project. The encouragement and help received from Dr. Ajith Kumar B.P, Dr. C.P. Safvan, R. Mehta.and Prof A. C. Pandey is also acknowledged.

## REFERENCES

[1] F.J. Lynch et al., “Beam Buncher for Heavy Ions”, Nuclear Instruments and Methods, 159 (1979) 245 – 263

[2] A.Sarkar et al, “Development and testing of a multi-harmonic buncher for high current injector at IUAC, Proc. of Inpac 2015

[3] Rajesh Kumar et al, “Development of low level RF based controller for single-gap multi-harmonic buncher”, Proc. of Inpac 2015

# DESIGN AND DEVELOPMENT OF HEAT EXCHANGER FOR 1MV DC ELECTRON BEAM ACCELERATOR FOR WASTE WATER TREATMENT

R. Barnwal[#], S. R. Ghodke, M. Kumar, S. Nayak, D. Jayaprakash, R. L. Mishra, Accelerator and Pulse Power Division, BARC, Trombay, Mumbai, 400085, INDIA

*Abstract*

1MeV DC electron beam accelerator is planned in BARC for waste water treatment by reducing COD and BOD to a desired level. The accelerator is housed inside pressure vessel and it is currently under development. Heat exchanger is one of the essential parts of accelerator to remove the heat generated in nitrogen gas at 6bar pressure inside vessel. This paper discussed about selection of heat exchanger, detailed design, CFD analysis, fabrication and testing method involved. The fin tube heat exchanger is selected for cooling nitrogen gas because of large heat transfer area associated with fins. Coolant side chilled process water is selected. The heat transfer design is done after formulating the fin tube configurations. This design has been validated by CFD modelling of heat exchanger. Fabrication and quality control is done to make system as per specifications compliance. Fan is also fabricated with design to work under 6bar pressure in nitrogen. The preliminary testing of heat exchanger assembly is done in open atmosphere to measure fan capacity, motor current, and water flow rate and verifies heat transfer design.

## *Introduction*

In electron beam treatment of waste water, chemical transformation of pollutants occurs by ionizing radiation. These transformations can result in complete decomposition of substance at sufficient absorbed doses.

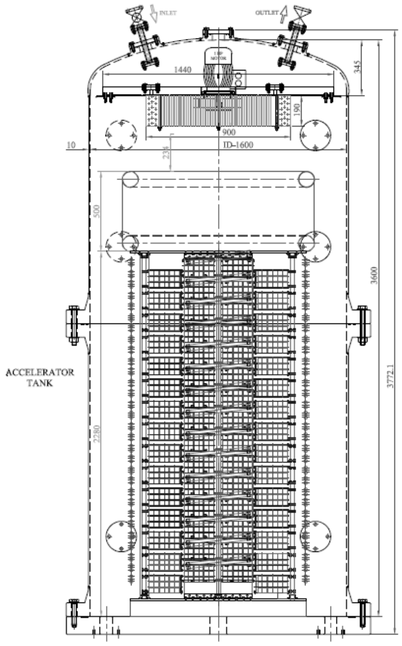


Figure 1: Schematic of DC electron beam accelerator

[#]rbarnwal@barc.gov.in

BARC is planned to setup a 1MeV DC electron beam accelerator based demonstration plant for waste water treatment. Fig. 1. shown is the schematic of DC accelerator inside pressure vessel. There is continuous heat generation from HV column, Electron gun and other electronic components in nitrogen gas at 6bar pressure inside vessel. Total heat load estimated to be about 5kW. Heat exchanger, fan and motor assembly is placed at the top of assembly inside vessel as shown in schematic.

## *Selection of heat exchanger and design details*

Compact heat exchangers are typically used when a large heat transfer surface area per unit volume is desired and at least one of the fluids is gas. Many different tubular and plate configurations have been considered, where differences are due primarily to fin design and arrangement. Heat transfer and flow characteristics have been determined for specific configurations. The high density fins increases the heat transfer area associated with gas flow from heat exchanger. Centrifugal fan is mounted at centre takes gas from the centre opening and discharge radially outward over the fin tubes. In the cold side cooled water is flowing through the heat exchanger tubes.

| | |
|---|---|
| Size of HX assembly | 900X900mm |
| Depth | 190mm |
| Tube configuration | 6X3 staggered tubes pitch 25mm |
| Tubes details | Φ12mm, 20SWG, SS304L |
| Fin detail | Al fins size 75X190mm and spacing 2mm |
| Fan Flow rate | 200cfm |
| Cooled water input | 60 lpm at 24$^0$C |

## *Thermal design and CFD model*

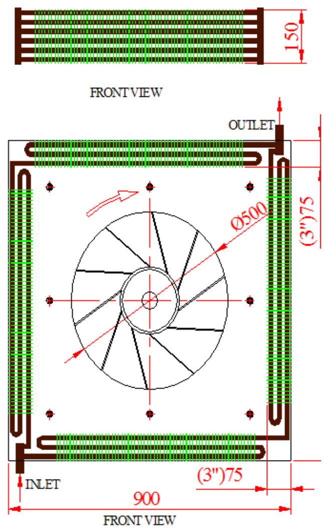


Figure 2: Heat exchanger tubes configuration.

Cold water side heat transfer coefficients have been calculated by following Nusselt number correlation for pipe flow given in reference [5]:

$$Nu_D = 0.023\,(Re_D)^{\frac{4}{5}}(Pr)^{0.4} \tag{1}$$

In gas side heat transfer coefficients has been determined by Nusselt number and Colburn j-factor correlation for N≥ 2 plain fin tube heat exchanger given in reference [1] as

$$Nu = j.Re_{D_C}.Pr^{\frac{1}{3}} \tag{2}$$

$$j = 0.086 Re_{D_c}^{P3} N^{P4} \left(\frac{F_p}{D_c}\right)^{P5} \left(\frac{F_p}{D_h}\right)^{P6} \left(\frac{F_p}{X_T}\right)^{-0.93} \tag{3}$$

From this calculation the overall heat transfer coefficient is evaluated. Effectiveness NTU (ε) method is used for calculating the heat transfer capacity of this type of heat exchanger as given in reference [3]

$$\varepsilon = \frac{1}{C^*}\left[1 - e^{-3KC^*}\left(1 + C^*K^2(3-K) + \frac{3(C^*)^2K^4}{2}\right)\right] \tag{4}$$

Pressure drop have been determined using following correlation of friction factor as given in reference [1] for plain fin tube heat exchanger

$$f = 0.0267 Re_{D_c}^{F1}\left(\frac{X_T}{X_L}\right)^{F2}\left(\frac{F_p}{D_c}\right)^{F3} \tag{5}$$

$$\Delta P = \frac{G_c^2}{2\rho_i}\left[(1+\sigma^2)\left(\frac{\rho_i}{\rho_o} - 1\right) + \frac{fA_o}{A_c}\frac{\rho_i}{\rho_m}\right] \tag{3}$$

This design of plain fin tube heat exchanger has been validated through CFD model in ANSYS Fluent. Only a sector of fin tube geometry is model because of symmetry nature of flow. Symmetry conditions are also considered on the mid planes between two fins. Boundary layer mesh is incorporated around the tube wall.

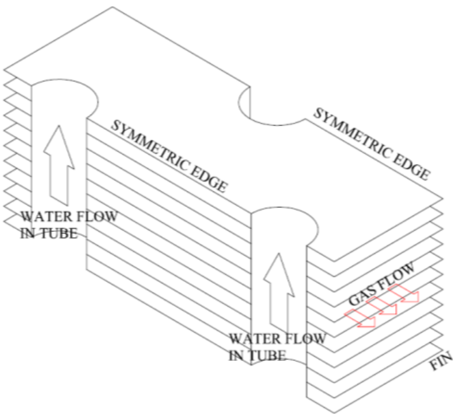


Figure 3: CFD heat exchanger gas flow model description.

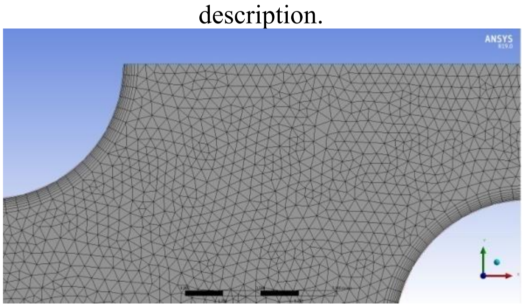


Figure 4: Boundary layer mesh around tube face.

Nitrogen gas property at 6bar pressure is used in the model. At the upstream boundary (inlet), uniform flow with constant velocity and constant temperature are taken based on design flow rate from fan and gas temperature. At the downstream end of the computational domain (outlet), stream wise gradient (Neumann boundary conditions) for all the variables are set to zero. No-slip boundary condition is used at the fins and the tube surfaces. Among various turbulent models available, k-ω model is used which showed the best convergence of model and closed matching with the numerical calculations. In the cold side tube walls are imposed with heat transfer coefficients at the water inlet temperature based on numerical calculation obtained in equation (1). The model is solved for continuity, momentum, and energy equations in ANSYS Fluent CFD solver.

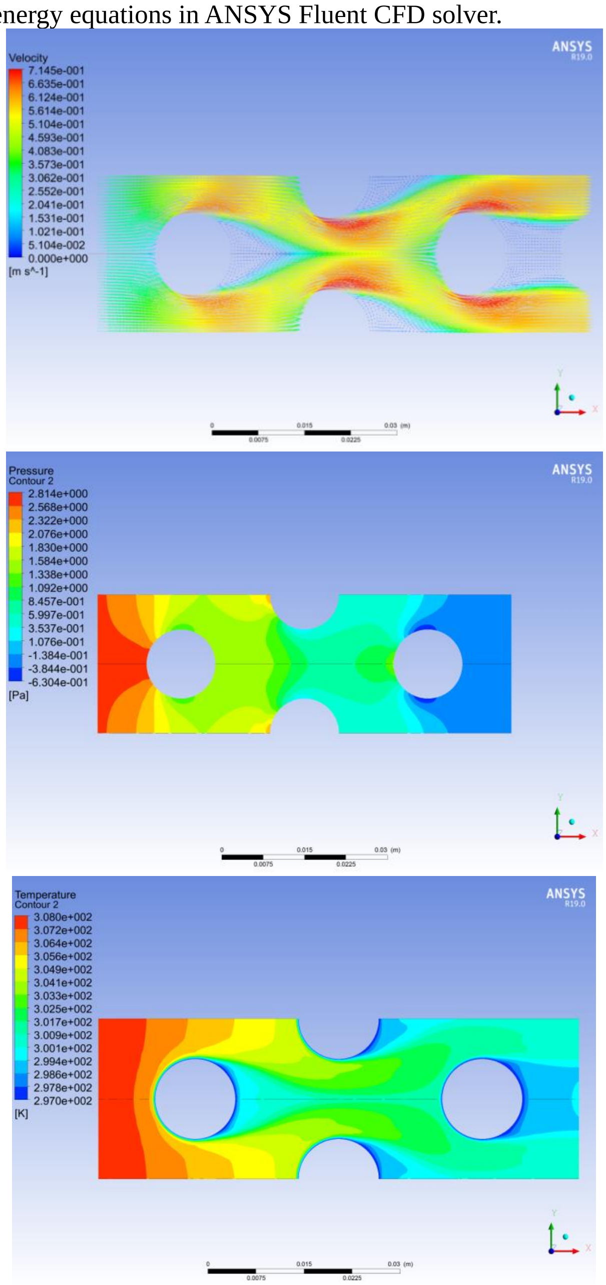


Figure 4: Velocity, pressure and temperature distribution in heat exchanger

### *Fabrication, quality control and preliminary testing*

The heat exchanger was locally developed. Materials of the tubes are SS304L and all tube joints are made by TIG welding with suitable electrode and fillers. All welding connections are checked by dye penetration tested for detecting the welding defects. Final integrity of heat exchanger tube assembly is tested by pneumatic test at 10bar pressure. The helium leak test by mass spectrometer leak detection in sniffer mode ensures a leak rate of 7.2 x$10^{-6}$ mbar l/s. After fabrication of heat exchanger it is assembled with fan and motor. The trial run test of fan is conducted and checked the fan, motor performance.

Figure 5: Heat exchanger, fan and motor assembly.

Figure 6: Fan air flow velocity measurement

### *Results and discussion*

Table 1: Results summary

| | **From correlation** | **CFD model** |
|---|---|---|
| Capacity(Q) | 4.84 kW | 4.95 kW |
| Temperature drop gas side | 7.63K | 7.81K |
| Pressure drop across heat exchanger | 2.785 Pascal | 2.814 Pascal |

Plain fin tube heat exchanger capacity calculation by effectiveness NTU method and correlation provided for Colburn j-factor and Nusselt number found to be in line with the CFD model. Pressure drop and friction factor correlation across heat exchanger is also validated with CFD model and results show a good proximity. Fan capacity is also measured and derated to half of its motor RPM using variable frequency drive to get the desired design flow. Adequacy of motor power at desired flow in nitrogen at 6bar pressure is also verified.


### *Acknowledgements*

The authors are thankful to Sri R. K. Rajawat, AD, BTDG for encouragements and supports. The authors also thank the entire DC accelerator team for their motivation and helps during this work.


## REFERENCES


[1] Chi-Chuan Wang, Kuan-Yu Chi, Chun-Jung Chang, Heat transfer and friction characteristics of plain fin-and-tube heat exchangers, part II: Correlation, International Journal of Heat and Mass Transfer 43 (2000) 2693-2700.

[2] Chi-Chuan Wang, Kuan-Yu Chi, Heat transfer and friction characteristics of plain fin-and-tube heat exchangers, part I: new experimental data, International Journal of Heat and Mass Transfer 43 (2000) 2681-2691

[3] Thomas PERROTIN, Denis CLODIC, “Fin efficiency calculation in enhanced fin-and-tube heat exchangers in dry conditions”, International Congress of Refrigeration 2003, Washington, D.C.

[4] Arafat Ahmed Bhuiyan, A K M Sadrul Islam, “CFD analysis of different Fin-and-Tube Heat Exchangers” Department of Mechanical and Chemical Engineering, Islamic University of Technology (IUT), Board Bazar, Gazipur-1704, Bangladesh. Proceedings of the 13th Annual Paper Meet 25 September 2010, Dhaka

[5] Incropera and Dewitt, “Fundamentals of Heat and Mass transfer”

[6] Frank P. Bleier, “Fan handbook”

[7] ANSYS Fluent Tutorial Guide, ANSYS, Inc.

# CHALLENGES OF FREQUENCY MEASUREMENT AND THEIR CONTROL DURING FABRICATION OF 650 MHz, FIVE-CELL SCRF CAVITIES

Praveen Mohania*, Ashish Mahawar, Adarsh Pratap Singh, Rajkumar Namdeo, Vikas Rajput, Syed Moulali, Avinash Puntambekar, Anand Yadav, Tilak Maurya, Manish Bagre, V.K. Srivastava, Vijayakumar V., Ashish Singh and Purushottam Shrivastava, RRCAT, Indore

*Abstract*

Development of 650 MHz, Beta-0.92, five-cell, niobium super conducting RF (SCRF) cavities is ongoing at RRCAT and fabrication of four such cavities have been completed. These cavities will be part of deliverables from RRCAT to Fermilab, USA under Indian Institutes Fermilab Collaboration (IIFC). Similar 650 MHz SCRF cavities are also planned to be used in future high energy SC proton accelerators proposed at RRCAT. A major challenge in cavity fabrication is to keep the cavity frequency, final length and field flatness within strict tolerance. A multi-cell cavity is fabricated by electron beam welding of several half-cells, dumb-bells and end groups in multiple steps. Each of this affects the geometry and hence frequency. In order to ensure that the final welded cavity resonates at the correct frequency for the given length and has good field flatness; measurement and stage wise corrections of resonant frequency is conducted at various development stages (half-cell, dumbbell, end-cell). This paper describes the challenges and shares the experience gained and mechanism developed for identification and correction of frequency errors to meet the desired parameters.

## FABRICATION OF MULTICELL CAVITIES

The cavity fabrication starts with formation of half-cells followed by their precise machining. These half cells are either welded together to form a dumb-bell structure or welded with beam pipes, coupler and pick up ports to form the end groups. Four dumb-bells and two end groups are then joined together to form a 5-cell cavity. During cavity fabrication RF measurements for each half-cells dumb-bells and end-cells are carried out to ensure that the final five-cell SCRF cavity resonates at frequency conforming to its length. The analysis of the RF measurements helps us to identify the amount of trim and tune to take appropriate corrective action. Dumb-bell measurements are especially challenging as not only the π-mode resonant frequency of the structure, but also frequency of the individual cells also has to be identified. A novel approach has been developed at RRCAT which has been successfully used to correctly identify the asymmetry between cells.

Dumbbells are fabricated by first welding two half-cells at syed after which a stiffing ring is welded on outer walls. Fig. 1 shows a 650 MHz, Beta-0.92, dumbbell structure with stiffing ring welded.

Fig.1. A pair of two 650 MHz dumb-bells with stiffing ring welded at the iris side of half cells.

The stiffing ring welding is usually the main deformation agent, and causes both asymmetry between resonant frequency of individual half cells of dumbell and also shifts the pi-mode resonant frequency of the dumbbell. The below table illustrates the effect of the stiffing ring welding on the pi-mode resonance frequency of dumb-bells.

Table A: Effect of stiffing ring welding on length and π-mode resonance frequency of the four dumbbells used in fabrication of second 650 MHz five cell cavity **HB650-RRCAT-5002.**

| Dumb-bell ID | Length and π-mode frequency before stiffing ring welding | | Length and π-mode frequency after stiffing ring welding | |
|---|---|---|---|---|
| | Length (mm) | Frequency (MHz) | Length (mm) | Frequency (MHz) |
| N19-N11 | 217.47 | 646.1596 | 213.88 | 644.6795 |
| N9-N10 | 217.58 | 646.7754 | 214.03 | 645.269 |
| N20-N12 | 217.8 | 646.6396 | 214.21 | 645.2772 |
| N17-N1 | 217.59 | 646.3172 | 214.25 | 644.7803 |

## IDENTIFICATION OF ASYMMETRY AND ITS CORRECTION

A novel method has been developed at RRCAT in which an half cell of the dumbell is shorted using an antenna close to the half cell length. The frequency so measured is now only due to the dimensions of the other half cell and thus by alternate using of antenna on both

*praveenmohania@rrcat.gov.in

sides of the dumbell, the assymetry between the half cells precisely can be estimated. The uniqueness of this method is that unlike perturbation method commonly used to identify the assymetry between cells the method can be used with less precise test setup. The following figure show the experimental setup used for quantization of asymetery between half cells. In the experimental setup the dumb-bell cavity is sandwitch between two conducting plates to form an RF enclosure and then an antenna long enough to effectively short top half cell is used to measure S11 on a VNA.

Fig.6 The setup used for RF characterization of dumb bell. The RF laminate attached to granite slab using tapes.

The cavity characterization setup shown above uses an RF laminate for providing RF contact to the bottom plates as the RF laminates have very high dimensional accuracies these provides a good RF contact. The same VNA and RF laminates based setup are used to measure half-cells and end-cells. To ensure proper RF contact weights are also placed. The asymmetry so measured is then rectifed by either pressing or stretching an half cell. A dedicated setup for which has been developed by SCDD, RRCAT and the details of which are also presented in the conference.[5]

After the asymmetry correction the sequencing of the dumbbells and end-cells is done in a manner so as to have minimum deviation from the design value of resonant freuqency for each complete cell of the five cell cavity. The approach used here is to join the half cells with positive residual error with half cell with negative residual error as far as possible.

## RESULTS AND EXPIERENCE GAINED

The measurement and correction setup as described above has been developed in house at RRCAT and has been successfully utilized during fabrication of first four 5-cell cavities developed at RRCAT. The method has been gradually evolved and has helped in producing reproductible performance in the formed cavity. The pi-mode resonance frequencies of the first four as formed (without tuning) cavities at RRCAT are given below in Table B. which shows the repeatibility in the process. The frequency requirement for five cell cavities is 649.2 MHz ± 0.5 MHz. The high frequency obtained in cavity 5003* was identified to be due to an offset error in measurement resonant frequency which was later taken care of.

Table B: Pi-mode resonant frequency obtained for first four 5-cell cavities.

| Cavity No. | Pi-mode frequency | As fabricated length (in mm) | As fabricated field flatness |
|---|---|---|---|
| 5001 | 649.59 MHz | 1401.33 | 68% |
| 5002 | 649.41 MHz | 1401.33 | 85% |
| 5003 | 650.00 MHz* | 1399.04 | 86% |
| 5004 | 649.50 MHz | To be measured | 78% |

## ACKNOWLEGEMENTS

The authors acknowledge the efforts of Shri P. K. Bajpai, Shri Akhilesh Rajak and Shri Jitendra Parate of RFSD, and Shri V. K. Verma, SCDD RRCAT during measurement and preparation of test setup. The authors would also like to thank Shri S.C. Joshi former director RRCAT, for his constant support in the SCRF cavity development program.

## REFERENCES

[1] S. C. Joshi, S. Raghvendra, S. Suhane, M. Kumar, P. Mohania, A. Chauhan, P. Fatnani, P.Shrivastava, P. K. Kush and P. D. Gupta, Proceedings of LINAC 2014, Geneva, Switzerland

[2] P. Shrivastava, P. Mohania, K.A.P. Singh," Performance of the RF system for qualification of 650 MHz/1300 MHz SCRF cavities in VTS at RRCAT", InPAC2015, TIFR, Mumbai, Dec, 21-24, 2015.

[3] Mahawar A., Mohania P., Singh K.A.P., Namdeo R.K., "Design and development of S-Band, 2 kW pulsed solid state amplifier for energizing pre-buncher cavity of IRFEL injector" Proc. of InPAC-2018, RRCAT, Indore, Jan 9-12,2018,p.1040

[4] P. Mohania, A. Mahawar, Kunver A. P. Singh, R.Bhati, Purushottam Shrivastava, “Development of Solid State Amplifier Based High Power RF System for Testing SCRF Cavities in RRCAT VTS”, HPRFM-2013, IPR, Ahmedabad, 4-6 September 2013.

[5] Manish Bagre et al., “Experience on fabrication of 650 MHz (β=0.92) five-cell SCRF cavities using Electron Beam Welding”, this conference

# A FARADAY CUP ARRAY FOR THE MEASUREMENT OF ION CURRENT DENSITY PROFILES FOR GRIDDED ION THRUSTER

Bharat Singh Rawat#, Homi Bhabha National Institute, Mumbai, India
S. K. Sharma, V. Prahalad, B. Choksi, S.L. Parmar, U.K. Baruah, Institute for Plasma Research, Gandhinagar, India

*Abstract*

Gridded ion source based thrusters have applications in deep space missions. In these thrusters, a beam of heavy ions (e.g. $Xe^+$) is accelerated to desired energies (e.g.1keV) by a suitable electric field applied between the extraction grids. A prototype ion source for conducting relevant experiments for obtaining an in-depth understanding of characteristics of gridded ion thrusters has been developed at IPR. This ion source has been operated for extracting an argon ion beam of 0.1A at energies of 1-2keV. The angular divergence of the ion beam should be kept low so as to generate maximum thrust and avoid erosion of grids. A Faraday Cup array has been developed to obtain the ion current density ($Ar^+$, $Xe^+$) profile and estimate the divergence for ion beams of 1-2keV, 0-20mA/cm$^2$ and beam diameter of 110 cm. The design aspects and characterization of the Faraday Cup array are discussed. The effects of source's plasma parameters acceleration voltage and background pressure on the ion density profiles are investigated.

## GRIDDED ION THRUSTER

The gridded ion thrusters have shown their effectiveness for the propulsion of space vehicles in deep space explorations [1]. In the gridded ion thrusters, beam of heavy atomic ions (e.g. $Xe^+$) is accelerated by a suitable electric field. The ion beams is neutralised by sufficient flux of primary electron emitted from hot filament/hollow cathodes kept near the downstream of beam. A prototype experimental ion source relevant for research related to gridded ion thrusters has been developed at IPR. The ion source consists of a magnetic bucket type plasma chamber, hot filaments and two stainless steel grids required for extraction of argon ions. The maximum current density that can be extracted from a particular configuration is space charge limited and is given by the Child-Langmuir's law as

$$J_{\max} = \frac{4\varepsilon_0}{9}\sqrt{\frac{2e}{M}}\frac{V^{3/2}}{d^2} \qquad (1)$$

where $V_T$ is the total voltage across the sheath between the two grids, $d$ is the effective grid gap. Figure 1 shows the schematic of experimental set for measuring ion beam profiles.

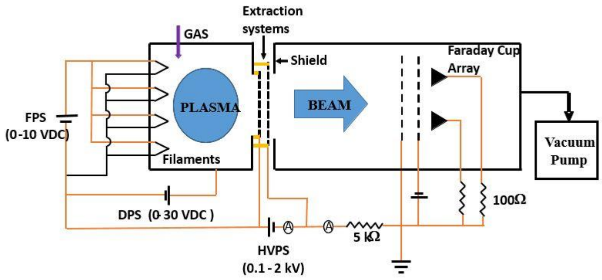


Figure 1: Experimental set up for gridded Ion source

## FARADAY CUP ARRAY

A Faraday Cup (FC) array has been designed and developed to measure ion beam densities and beam profile of the ion source/thrusters. The beam profile is utilised to estimate beam divergence. The beam divergence as a function of source parameters has also been studied.

The extracted ion beam causes the ionisation of back ground gas. The plasma produced in the beam line is called neutraliser plasma. The electrons produced due to the ionisation of background gas can be attracted towards the Faraday cup. The beam current, measured by metallic collectors of the Faraday cup array will comprise of current due to ion as well electrons. The error in the measurement of the ion current caused by the electrons can be significant due the high mobility (low mass) of the electrons. The primary electron current to the Faraday cup will cause a reduction in the measurement of ion current as compared to the actual current. To suppress these electrons, a negatively biased electrode/grid is placed before the Faraday cups. The negatively biased electrode is called the suppressor electrode. Another electrode is placed before the suppressor electrode, called ground electrode. The potential between ground electrode and suppressor electrode reflects the incoming thermal electrons. The ground electrode is used to stop the flow of plasma towards the Faraday cups. There could be another error possible due to the emission of secondary electrons. Schematic representation of biasing the suppressor and ground electrodes of faraday cup are shown in Fig. 2. The charge collected by the FC collector is measured by shunt resistors (100 ohm each) connected in series with all the Faraday cups to measure the current/current density of the ion beam. The voltages across the shunt resistors are recorded by a data logger.

bharat.rawat@ipr.res.in

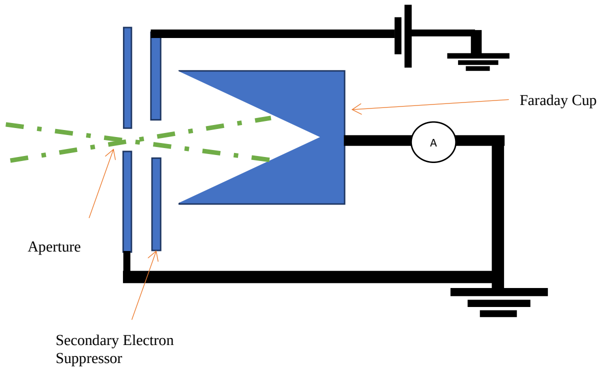


Figure 2: Schematic of a Faraday Cup

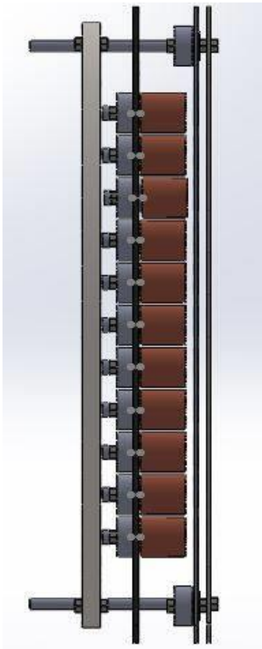

Figure 3: Faraday cup array

The Faraday cups are fabricated with copper and the conical shape is given to each cup to enhance the trapping of the secondary electrons produced inside the Faraday cups. The aperture of suppressor electrode is 21 mm in diameter whereas that of the FC is 22mm. The size of the aperture of the ground electrode is kept 20 mm. Eleven cups fabricated in-house are mounted on a stainless steel frame with the help of ceramic isolators. The two electrodes (suppressor and ground), made up of stainless steels, are attached with main frame. The 3D CAD drawing of faraday cup array is shown in fig. 3.

Figure 4 shows the particle trajectories in the FC simulated using SIMION code [4]. The $Ar^+$ ions of 1keV are represented by brown colour. The plasma electrons are shown by blue and the secondary electrons are shown by green colour. It can be observed that the suppressor electrode (at -30V) repels back the plasma electrons and also suppresses the secondary electrons emitted from the inner surface of FC. Based on this simulation the FC was designed and fabricated.

The effect of the suppressor grid has also been studied by varying its potential from -30V to 0 V. It has been observed that the measured current reduces by increasing the negative potential of the suppressor grid. This can be explained by the suppression of secondary electrons produced due the impingement of energetic ions on the copper surface of the Faraday cup. The role of the primary electrons is not understood in these experiments and requires more dedicated experiments.

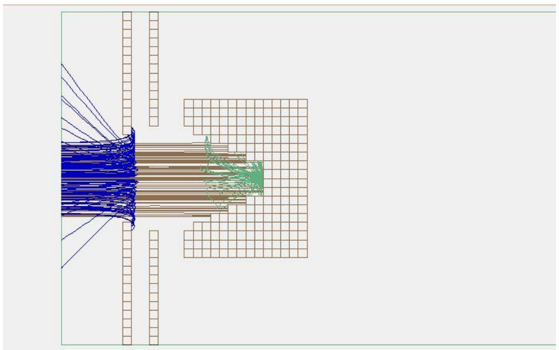

Figure: 4 Simulation of Faraday cup using SIMION. Suppressor is at -30V.

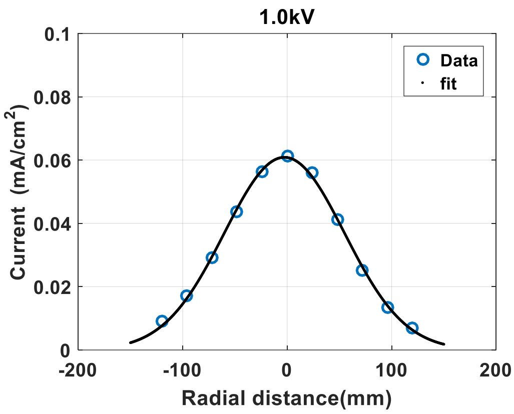


Figure: 5 Beam profile for 1kV acceleration voltage

## BEAM PROFILE MEASUREMENT

The Faraday cup array is fixed in the drift chamber in front of the extraction system. The array is mounted in such a way that it measures the radial profile of the ion beam. The current intercepted by each FC is recorded during the whole pulse lengths each about 15s.The current density is obtained by dividing the measured current by the exposed areas of the Faraday cups. The current density at an arbitrary point of time is plotted in Fig. 5. The Gaussian fitting is also plotted in the same figure. Angular beam divergences are estimated from the Gaussian profiles obtained from the fitting as shown in figure 5. The beam divergences are estimated by taking 1/e width of the Gaussian fitting profiles. The ion beam density is measured by the FC array at ~600mm distance from the extraction grids. The beam divergence estimated in this way is called 1/e fold divergence [3]. The 1/e fold divergence is defined as the angle

$$\alpha = \tan^{-1}\left(\frac{D-d}{z}\right) \qquad (2)$$

where $\alpha$ is the beam divergence in radians, $D$ is the inferred beam diameter in mm from the Faraday Cup, $d$ is the beam diameter in mm at the grid exit and $z$ is the distance in mm at which the beam profile is measured. The experimental beam divergences as a function of acceleration voltage are plotted in figure 6.

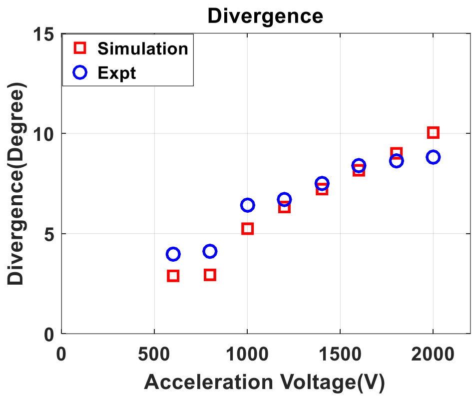


Figure 6: Experimentally measured and the simulated beam divergence as a function of acceleration voltage

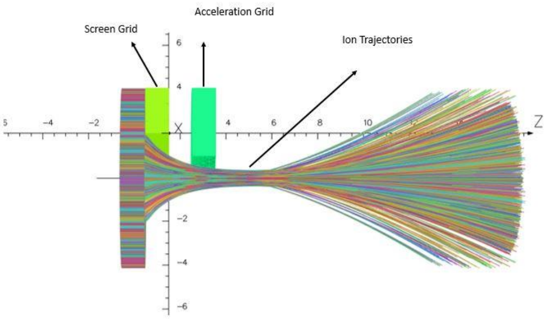


Figure 7: Simulated Ion trajectories in OPERA

The beam divergence are also confirmed by simulating ion trajectories (as shown in fig. 7) using Opera 3D-SCALA code [2]. The code is used to estimate the divergence for a single beam let for argon ion beam. The 2-grid optics/extraction system is simulated for the experimentally measured current densities corresponding to acceleration voltages varying from 0.6 – 2 keV. These results are compared with the experimentally measured beam divergence from with the Faraday Cup array as shown in figure 6. The behaviour of divergence on accelerating voltage is similar in experiment and simulation.

In OPERA-3D SCALA code, plasma free surface type emitter (type-103) was selected for simulation. In the model current density, relative meniscus voltage and the ion temperature are specified as per the experimental values. A self-consistent space charge limited current flow forms beyond the meniscus and the program adjusts the meniscus position until the plasmas specified density is equal to the self-consistent space charge limited current density. The meniscus voltage was set to -2.16V with a current density equal to the experimentally measured density (0.5 - 1.5mA/cm$^2$).

It has been observed that the total current estimated from the current density measured from Faraday cup array is about 30% higher as compared to the directly measured current. The reduction in the total current is possibly due to underestimating the exposed area of the Faraday cups. The low energy ions produced in the beam plasma can fall from the sides. It suggested the requirement of the modification in the Faraday cup design. The design of the new Faraday cup array is under process.

## CONCLUSION

A Faraday Cup array has been developed to estimate beam divergence of the Ar$^+$ ion beam produced by the prototype ion source. The eleven channel Faraday cup was utilised to measure current densities along radial direction of the ion beam. The beam divergences were estimated using the Gaussian fit of the experimental data. The beam divergence varied from 4 - 10 degrees for accelerating voltage 0.6 – 2.0 keV. The experimentally estimated beam divergences were compared with beam divergence estimated from the simulation of ion trajectories using OPERA-3D SCALA code. A good comparison of the values and behaviour with source parameters e.g. accelerating voltages is observed.

## REFERENCES


[1] Fundamentals of Electric Propulsion: Ion and Hall Thrusters by Dan M Goebel,Ira Katz

[2] OPERA-3D, Cobham plc, Brook Road, Wimborne, Dorset,BH212BJ,UK,[Online].Available:http://operafea.com/

[2] H.K.Chiu, R.M.Hong, J.T.Scotville 36th Symposium on Fusion Engineering (2009) Calculated Beam profiles for the DIII-D off axis and long pulse neutral beam upgrade

[4] D. Manura, D. Dahl. SIMION (R) 8.0 User Manual (Scientific Instrument Services, Inc. Ringoes, NJ 08551, <http://simion.com/>, January 2008).

# BEAM DYNAMICS STUDY OF 30 MEV MEDICAL CYCLOTRON KOLKATA

J. Debnath*[1], M.K. Dey, U. Bhunia, S. Paul[1], A. Dutta and Arup Bondopadhay[1]
VECC, 1/AF, Bidhan Nagar, Kolkata -700064, India
[1]also at HBNI, Mumbai,India

*Abstract*

The high current medical cyclotron, IBA CYCLONE-30 has been commissioned at Chakgaria Campus, VECC Kolkata [1]. It can produce proton beam up to 500 μA with a maximum energy of 30 MeV. There are five external beam lines, one for PET isotope production (mainly, FDG), two for SPECT isotope production (Ga-67 and Tl-201 etc) and two beam lines for research and development. It is important to understand the beam behaviour in details in order to operate it efficiently. It is a four sector machine with deep valley configuration operating nearly at 65.5 MHz. The paper describes the detailed beam dynamical behaviour using measured magnetic field data along with simulated magnetic field data. The equilibrium orbit properties, the betatron tunes, effect of 1st harmonic field, acceptable range of frequency detuning, phase history etc have been studied.

## INTRODUCTION

The Cyclone-30 accelerator is a fixed field, fixed frequency cyclotron that accelerators negative ions ($H^-$) up to 30MeV. The energy of the extracted beam can vary between 15 to 30MeV by positioning of a stripper foil at the radius corresponding to the required energy.

Figure 1: Medical Cyclotron Cyclone-30

Cyclone-30 has features of compact cyclotron as well as Separated Sector Cyclotron. It has small hill gap and large valley gap, giving strong vertical focusing required for large beam intensity. There are two 30° "Dees" operating on 4th harmonic mode at radio frequency ~ 65.5 MHz. Uniform magnetic field at the center allows a low axial injection energy.

The basic parameters of the cyclotron are given in table-1.

| Table-1 | Parameters |
|---|---|
| No. of Sectors | 4 |
| No. of Dees | 2 |
| Sector angle varying | 55-60 degrees |
| Hill gap | 30 mm |
| Valley Gap | 1200 |
| Pole Radius | 810 mm |
| Iron weight | 45 Tons |
| Hill field | 17 kG |
| Valley field | 1.2 kG |
| Betatron frequencies<br>(2 MeV & 30 MeV) | H: 1.04 – 1.06<br>V: 0.50 – 0.65 |

## SIMULATION

The closed orbit properties have been studied with GENSPEO Code [2] using the mapped magnetic field. Also the magnetic field has been simulated using TOSCA Code.

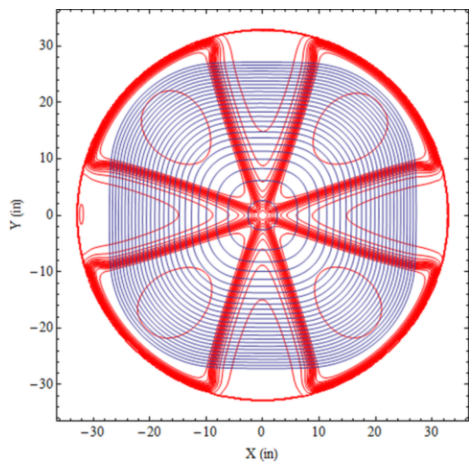


Figure 2: Iso-Gauss Contours and closed orbits

The isogauss contours and the closed orbits at different energy steps are shown in Fig 2. This is a 4-sector

---

*jdebnath@vecc.gov.in

machine. The average magnetic field and the main $4^{th}$ harmonic field are shown in Fig 3. It also shows the small amount of imperfection field present in the machine.

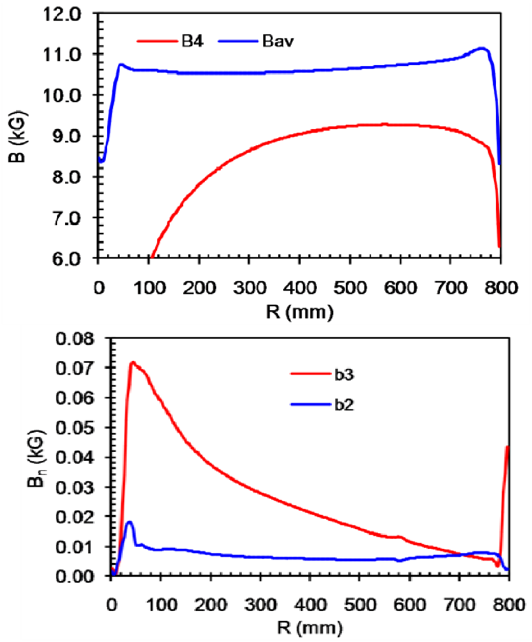


Figure 3: (a) The average magnetic and the $4^{th}$ harmonic field profiles (b) b2 and b3 are $2^{nd}$ and $3^{rd}$ harmonic imperfection fields present.

The calculated frequency error which is shown in Fig 4 is within 0.05% as a result the phase curve is very flat within ±5°. The betatron frequencies are shown in Fig 5. The tune diagram shows that the operating zone (18 to 30 MeV) is away from resonances. The axial focusing frequency (~0.6) is large enough to handle space charge effect due to large beam current.

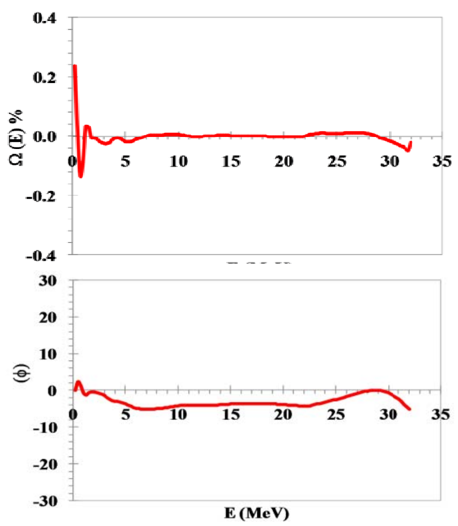


Figure 4: The frequency error and the phase curve profiles.

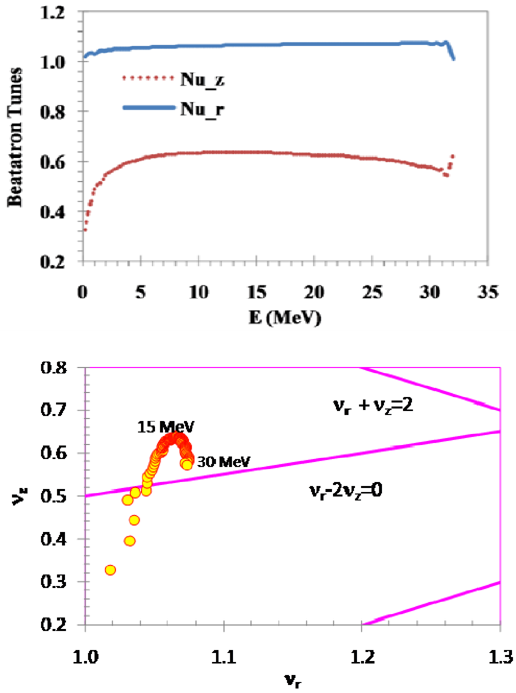


Figure 5: Radial and vertical oscillation frequencies and the tune diagram.

The Smith-Garren method [3] measures the dependency of the beam bunch canter phase on the orbit radius by detuning the amplitude of the main magnetic field or the RF frequency until both the phase shift at the location of the radial probe reaches ±90° and the probe current decreases by 50%.

Smith-Garren procedure has been simulated by detuning the radio frequency. It shows that if the Radio frequency is detuned by only ±35 kHz, 50% beam will be lost due to phase loss as shown in Fig 6.

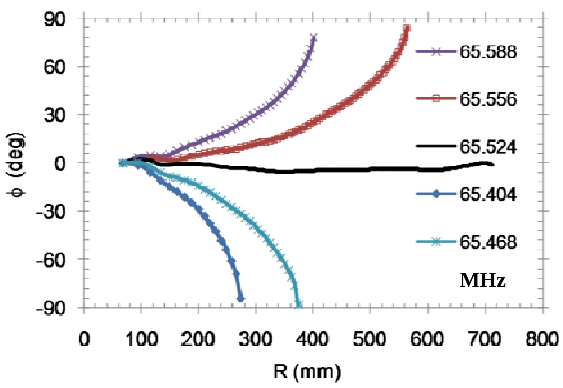


Figure 6: Smith-Garren Method for Cyclone-30

The accelerated orbit properties have been studied integrating the equation of motion in the mapped magnetic field. Fig 7 shows the turn separation profile. At energy more than 15 MeV the turn separation is of the order of 2 mm only. Therefore, multiple turns will fall on the stripper-foil at a given radius. The extraction is done by putting stripper-foil at different radius depending on the required energy of the beam. The radius vs. energy plot has been shown in Fig 7 also. After stripping the $H^-$ beam becomes proton beam and comes out from the cyclotron. Since the extraction is done by stripping and the beam is away from any harmful resonances so it has been found that the small imperfection field (b2 and b3) does not affect the extraction process.

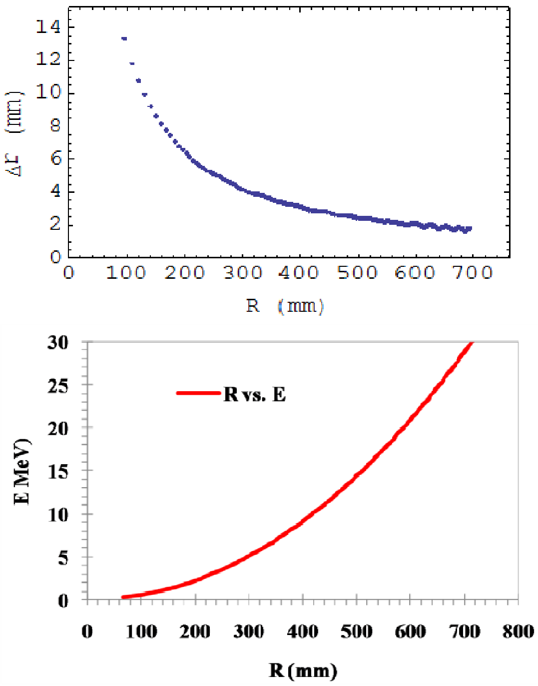


Figure 7: (a) Radius vs. Turn separation plot, (b) Radius vs. Energy plot.

The excursion of the beam centre for the reference particle has been found to be within 0.5 mm as shown bellow.

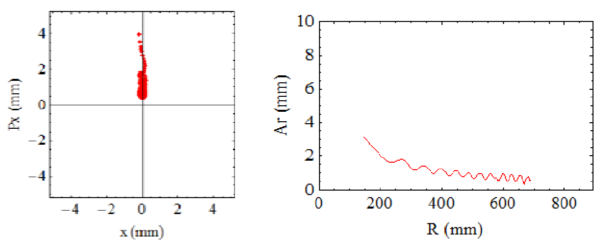


Figure 8. (a) Excursion of the beam centre (b) Coherent oscillation amplitude.

The Accelerated orbits for the reference particle have been plotted in Fig 9.

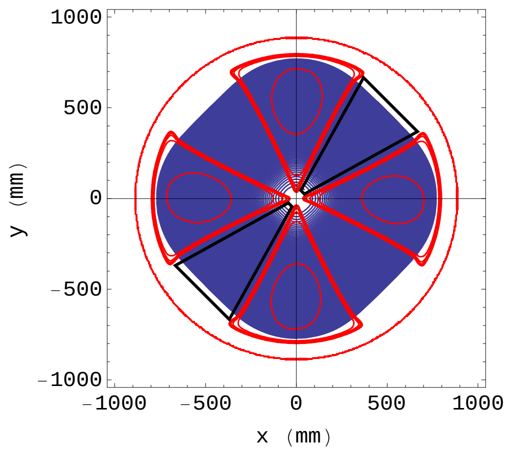


Figure 9: Accelerated orbits for the centred particle.

## CONCLUSIONS

Closed orbit properties have been simulated and ion trajectories are also studied. It is found that the machine is very stable for high current operation (up to few hundred micro Amp). Only during the initial tuning time the RF and the magnetic field should be tuned carefully since there may be phase loss due to slight radio frequency mismatch.

VECC commissioned the cyclotron with 50 micro Amp current (with 18 to 30 MeV energy) in PET and SPECT Beam lines.

## REFERENCES


[1] R.K. Bhandari et al, “Medical Cyclotron Facility At Kolkata” Cyclotrons and Their Applications 2007, 18th International Conference.

[2] M. M. Gordon, “Canonical treatment of accelerated orbits in sector-focused cyclotrons”, Particle Accelerators, 14 (1983) 119

[3] A.A. Garren, L. Smith, "Diagnosis and Correction of Beam Behavior in an Isochronous Cyclotron", CYC63

# ANALYSIS OF UNCERTAINTY IN MEASUREMENT OF QUALITY FACTOR AND ACCELERATING FIELD GRADIENT OF 650 MHz, 5-CELL SUPERCONDUCTING RF CAVITYIN RRCAT VERTICAL TEST STAND

*KunverAdarsh P. Singh*, Praveen Mohania,Vikas Rajput, Ashish Mahawar, DeodattaBaxy and Purushottam Shrivastava*

*Radio FrequencySystem Division, Raja Ramanna Centre for Advanced Technology, Indore - 452013, INDIA*

***Abstract***

To test and qualify the bare SCRF cavity, a specialized test set up known as the Vertical Test Stand (VTS) is developed at RRCAT whichmaintains the required operating conditions (cryogenic temperature, radiation shield, etc.) and is equipped with RF measurement system.[1] The VTS qualification procedure consists of determination of variation of intrinsic quality factor ($Q_0$) of the cavity with respect to increase in accelerating electric field ($E_{acc}$) inside it. A multi-cell or single cell SCRF cavity equipped with two couplers (input power coupler and pick up coupler) is first cooled to 2K after which the accelerating field inside it is gradually increased and the values of $Q_0$ and $E_{acc}$are recorded. The accuracy of these values depends upon power measurement errors and reflection from cavity, which is dependent on coupling of input power coupler. The paper here presents the analysis of uncertainty in RRCAT VTS RF qualification of SCRF cavities.

## UNCERTAINTYANALYSISTHEORY

### *Uncertainty*

The uncertainty of the result of a measurement reflects the lack of exact knowledge of the value of the measurand. The result of a measurement after correction for recognized systematic effects is stillonly an *estimate* of the value of the measurand because of the uncertainty arising from random effects andfrom imperfect correction of the result for systematic effects.[2]

### *Combined standard uncertainty*

The appropriate expression for the combined standard uncertainty in a measured quantityY i.e.$u(y)$ associated with the result of uncorrelated measurements [2] is given by

$$u(y) = \sqrt{\sum_{i=1}^{N} \left(\frac{\partial f}{\partial x_i}\right)^2 u^2(x_i)} \qquad (1)$$

*y is the estimate of Y and* $x_i$ *is the estimate of* $X_i$

Where

$$Y = f(X_1, X_2, \dots\dots.. X_N)$$

$u(x_i)$ is uncertainty associated with measurement of $X_i$

* adarshsingh@rrcat.gov.in

## UNCERTAINTY IN VTS TESTRESULTS

In qualification of SCRF cavity at VTS, measurement of $Q_0$and its variation with $E_{acc}$ is recorded. $E_{acc}$ and $Q_o$ are calculated using equations given below:

$$P_{loss} = P_i - P_r - P_t \qquad (2)$$

$$Q_o = \frac{Q_2}{P_{loss}} P_t \qquad (3)$$

$$\mathrm{E_{acc}} = \mathrm{kappa}\sqrt{\mathrm{Q_2 P_t}} \qquad (4)$$

Where $Q_2$ = Probe coupler's quality factor

kappa = cavity constant

$P_t$ = Transmitted power of cavity

$P_{loss}$ = Power loss inside cavity

$P_i$ = Incident power

$P_r$ = Reflected power

From above equations it is obvious that $E_{acc}$ and $Q_o$are calculated using power measurements, so accuracy of resultsdepends on power meter's uncertainty and uncertainty in determination of $P_{loss}$and$Q_2$. $Q_2$ is measured by decay measurement and its uncertainty depends upon both accuracy of decay time measurement and measurement of power loss and transmitted power. Measurement of $Q_2$ is done only once at low Eacc where the quality factor of cavity remains constant throughout the decay period. Thus, uncertainty in $Q_2$ is constant throughout test and it depends upon uncertainty in $P_{loss}$and decay time measurement at the start of test.

Uncertainty in power measurements is dependent upon power meter used and for our case it comes to be 4%. Power measurement accuracy also depends upon the accuracy of cable calibration, since for calibration of incident, reflected and transmitted cables power meters are used thrice for each cable. Then using equation (1) uncertainty in cable calibration for incident, reflected and transmittedpower can be calculated, which comes to 7%.

Uncertainty in $E_{acc}$ can be calculated using equation (1) and (4) as

$$\frac{\Delta \mathrm{E_{acc}}}{\mathrm{E_{acc}}} = \frac{1}{2}\sqrt{\left(\frac{\Delta \mathrm{Q_2}}{\mathrm{Q_2}}\right)^2 + \left(\frac{\Delta \mathrm{P_t}}{\mathrm{P_t}}\right)^2} \qquad (5)$$

Uncertainty in $E_{acc}$ is depends on probe coupler's quality factor($Q_2$) measurement and transmitted power measurement uncertainties. Since both these uncertainties are fixed therefore uncertainty in $E_{acc}$ is always fixed. Following plot shows the typical plot of $E_{acc}$ with uncertainty.

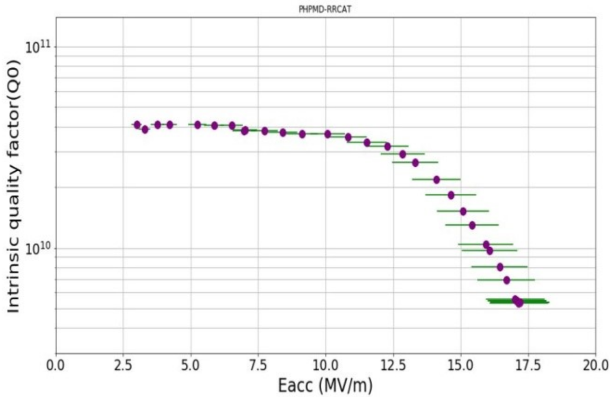


Figure 1: Uncertainty in $E_{acc}$ measurement of first 5 -cell, 0.92 Beta, 650 MHz SCRF cavity tested at RRCAT VTS. The uncertainty in measurement is 8%.

Uncertainty in $Q_o$ can be calculated using equation (1) and 3 as

$$\frac{\Delta Q_o}{Q_o} = \sqrt{\left(\frac{\Delta Q_2}{Q_2}\right)^2 + \left(\frac{\Delta P_t}{P_t}\right)^2 + \left(\frac{\Delta P_{loss}}{P_{loss}}\right)^2} \qquad (6)$$

Uncertainty in $Q_o$ is depends on uncertainties of probe coupler's quality factor ($Q_2$), transmitted power and power loss inside cavity. Uncertainties in $Q_2$ and $P_t$ are fixed but uncertainty in $P_{loss}$ varies with respect to change in coupling of input power coupler. Since the $Q_o$ varies during tests due to increase in $E_{acc}$, the coupling factor for input power coupler and hence reflected power from cavity varies during test. A typical graph between error in $Q_o$ and coupling factor is given below.

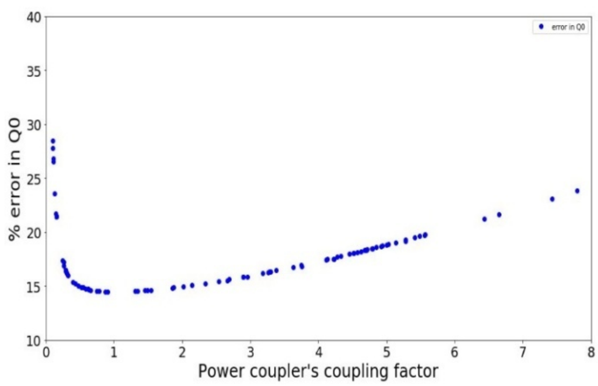


Figure 2: Uncertainty in $Q_o$ measurement with respect to coupling factor of second 5-cell 650 MHz SCRF cavity

In the Fig. 2 we can see that uncertainty is minimumwhen the cavity is critically coupled.

Now during tests, the input coupler is typically over coupled initially, and with increase in $E_{acc}$ the $Q_o$ decreases resulting in input coupler being first critically coupled and then under coupled. The uncertainty in $Q_o$ is thus higher at low gradients then it reduces and in case drop in $Q_o$ values increase once more. For optimum accuracy it is desired to have input coupler critically coupled to cavity, however as cavity quality factor is not constant a trade-off has to be made, if coupler is critically coupled to cavity at high $E_{acc}$ peak power requirement would be minimum, while accuracy of $E_{acc}$ will suffer as $Q_2$ is measured at low gradients.

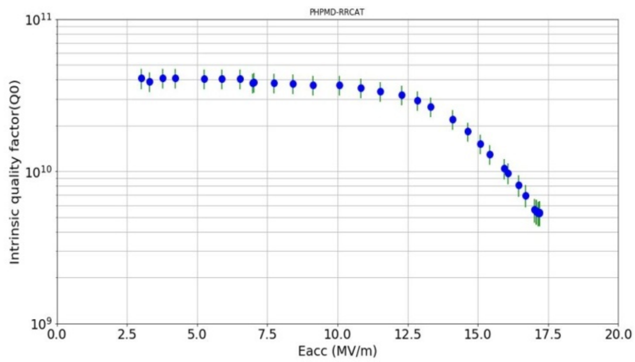


Figure 3: Uncertainty in $Q_o$ measurement of first 5-cell 650 MHz SCRF cavity. At low $E_{acc}$ uncertainty was 15% and at higher $E_{acc}$ it was around 19%. Lowest uncertainty was measured 14% (critically coupled condition)

## ACKNOWLEDGMENT


The authors are thankful to Shri P.K. Bajpai and Shri Rajkumar Namdeo of MICTL, RFSD for their technical support during cavity tests whose data was used for analysis. We are also thankful to Shri S. Raghvendra and all other members of VTS team for their support and encouragement during cavity tests. Special thanks are due to S.C. Joshi Ex-Director, RRCAT for constant inspiration and encouragement for this work.


## CONCLUSION

Uncertainty analysis of VTS test results for many cavities has been performed using method as described above. This uncertainty analysis gives qualification points for accelerating field gradient and quality factor of SCRF cavities. The analysis has been done assuming uncorrelated measurements and has been helpful in optimizing the input coupler parameters for trade-off between RF processing and result accuracies.

## REFERENCES


[1] S. C. Joshi, S. Raghvendra, S. Suhane, M. Kumar, P. Mohania, A. Chauhan, P. Fatnani,P.Shrivastava, P. K. Kush and P. D. Gupta, Proceedings of LINAC 2014, Geneva, Switzerland.

[2] GUM 1995 with minor corrections, Evaluation of measurementdata — Guide to the expressionof uncertainty in measurement, JCGM 100:2008.

[3] P. Mohania, A. Mahawar, Kunver A. P. Singh, R.Bhati, Purushottam Shrivastava, "Development of Solid State Amplifier Based High Power RF System for Testing SCRF Cavities in RRCAT VTS", HPRFM-2013, IPR, Ahmedabad, 4-6 September 2013.

[4] Ashish Mahawar, Praveen Mohania, Purushottam Shrivastava, Anand Yadav and AvinashPuntambekar, "Room temperature RF Characterization of Nb make super conducting radio frequency cavities at RRCAT", InPAC-

2018, RRCAT,Indore, Jan 9-12, 2018.

[5] Purushottam Shrivastava, Praveen Mohania, AdarshPratap Singh, AshishMahawar, Vikas Rajput,DeodattaBaxyand Raj Kumar Namdeo, “Performance of the Radio frequency system for qualification of 650 MHz/1.3 GHz superconducting RF cavities in Vertical Test Stand at RRCAT”,InPAC2015, TIFR, Mumbai, Dec 21-24, 2015.

[6] Hasan Padamsee, RF Superconductivity: Science, Technology, and Applications, Wiley-VCH VerlagWeinheim, 2009, ISBN 978-3-527-40572-5.

[7] P.Mohania, V.Rajput, D.Baxy, A.Mahawar, P.Shrivastava Indian Particle Accelerator Conference, 2011 (InPAC2011), IUAC, New Delhi, Feb., 15-18, 2011.

[8] T.J. Powers, Proceedings of the 12th International Workshop on RF superconductivity, Ithaca NY, July 2005.

# DESIGN AND ELECTROMAGNETIC SIMULATION OF THIRD HARMONIC RF CAVITY FOR INDUS-2

M. Prasad#, Pritam S. Bagduwal, Nitesh Tiwari and Mahendra Lad
Raja Ramanna Centre for Advanced Technology, Indore-452013, INDIA

*Abstract*

In Indus-2 storage ring, increasing the Touschek-dominated beam lifetime can be further enhanced by addition of RF system at third-harmonic (1.517 GHz). With the new system it will be possible to control the bunch length and charge density profile independently of the RF bucket height, improving the Touch-dominated beam lifetime. The main design requirements is to obtain a relatively low R/Q factor with quality factor Q as high as possible. A spherical shape of the cavity central body has been chosen as an optimum compromise between a high Q resonator and a low R/Q factor. Third harmonic cavity at resonant frequency of 1517.5 MHz has been designed and optimized with nose cone geometry for higher shunt impedance. Six openings are provided on the cavity: two beam ports in the end caps and four ports in the spherical body section (a tuner port, pick-up port, coupling port and a spare port which may be used for a fixed tuner).

The design and electromagnetic simulation of RF cavity has been carried out with the help of SUPERFISH and 3D-CST Studio Suite codes. Resonant frequency, quality factor and shunt impedance have been calculated for fundamental mode as well as for higher order modes up-to beam pipe cut-off frequency. Simulated values of quality factor and shunt impedance at resonant frequency (1517.5 MHz) are 23000 and 1.88 MΩ respectively. Simulation for tuner diameter, tuning stroke and tuning range is also carried out. This paper describes the design and electromagnetic simulations results of the third harmonic RF cavity.

## INTRODUCTION

Indus-2 is a 2.5 GeV third generation synchrotron radiation source operating regularly around stored beam current of 200mA. Minimum gap voltage requirement in indus-2 with over voltage factor of 2.5 is 1500kV. To fulfil this requirement storage ring is commissioned with six RF cavities with operating frequency ($f_{RF}$) of 505.8 MHz.

One of the basic requirement of synchrotron light sources is to have large beam lifetime. Large-angle intra-beam (Touschek) scattering dominate the beam life time in machine like Indus-2. To improve beam life time and maintain a high quality of electron beam in Indus-2 storage ring, a third harmonic RF cavity is required.

Harmonic cavity controls the bunch length, either lengthening or shortening by adjusting the phase of harmonic cavity gap voltage. This cavity also provides Landu damping for suppressing the longitudinal coupled bunch instability, thereby reduction in energy spread of the bunch. In Indus-2, RF gap voltage of harmonic cavity will be used to cancel the longitudinal focusing, which lengthens the bunch size and reduces the charge density. Due to bunch lengthening energy spread is reduced, which results in the longer beam life time.

The RF cavity can either be operated in active or passive mode. Active harmonic RF cavity requires dedicated RF power source at harmonic frequency to control the bunch length. However simpler passive harmonic RF cavity does not require any external power source, it is powered by the beam current itself.

## HARMONIC CAVITY

Voltage seen by electron beam in RF cavity is given by

$$V(z) = V_{rf}[\sin\left(\frac{\omega_{rf}}{c}z + \Phi_s\right) + k\sin\left(n(\frac{\omega_{rf}}{c}z + \Phi_h)\right) \quad (1)$$

Where z represents the position of the synchronous particle in the longitudinal direction. $V_{rf}$ is RF voltage at fundamental RF frequency (505.8 MHz), n represents harmonic number and $k$ is the ratio of fundamental RF voltage to harmonic RF voltage. Value of $k$ is given as follows

$$k = \sqrt{(\frac{1}{n^2} - \frac{(U_0/V_{rf})^2}{n^2-1})} \quad (2)$$

$$\sin(n\Phi_h) = -\frac{(U_0/V_{rf})^2}{n^2-1} \quad (3)$$

Where, $U_0$ is energy radiated per turn. $\Phi_h$ is the phase of harmonic voltage. The synchronous phase, $\Phi_s$ , is given by

$$\sin(\Phi_s) = \frac{n^2}{(n^2-1)}\frac{U_0}{V_{rf}} \quad (4)$$

The bunch distributions can be changed by adjusting the value of k and $\sin(n\Phi_h)$ [1], [2]. Phase of the harmonic voltage signal is tuned in such a way that slopes of the main and harmonic voltages will be added instead of cancelling, this would result in the bunch shortening. For life time improvement operation in same phase shall be avoided.

The choice of harmonic number is mainly governed by space availability in Indus-2 storage ring, which has the RF system of 505.8 MHz[3]. The size of Harmonic RF cavity should be as small as possible however very small size is impractical as the size of cavity may become comparable to the size of beam pipe. Hence RF cavity of fourth and above harmonic is impractical to use in Indus-2. Use of second harmonic cavity leads to longer flat region for beam, this will result in more bunch lengthening. As the size of the harmonic RF cavity is half of the fundamental frequency of Indus-2 RF cavity, required voltage will also be half of the fundamental voltage ($V_{rf}$) which is comparatively large. Total voltage requirement for third harmonic is even less and size is smaller too, so for these reasons, the third harmonic at 1.517 GHz is most suitable frequency to develop harmonic RF cavity for Indus-2. The required RF

# mprasad@rrcat.gov.in

parameters of third harmonic cavity are given in Table-1. Number of cavities will be decided by the available space in the storage ring. However, four RF cavities is preferred for the ease of design and operation point of view.

Table -1: Third harmonic cavity system parameters

| | | |
|---|---|---|
| Frequency ($f_h$) | 1517.5 | MHz |
| Total Voltage($V_h$) | 480 | kV |
| Shunt Impedance ($R_{sh}$)* | 1.8 | MΩ |
| Quality factor ($Q_0$) | 22000 | |
| R/Q | 80 | Ω |
| Number of cavities | 3/4 | |
| Power loss/Cavity | 7.0/4.0 | kW |

*$R_{sh}=V^2/2P$

## DESIGN OF RF CAVITY

For the design of RF cavity, spherical central body has been chosen as an optimum compromise to achieve high shunt impedance with relatively low R/Q. Third harmonic cavity at resonant frequency of 1517.5 MHz has been designed and optimized with nose cone geometry for higher shunt impedance [4]. Several geometries with different diameters and curvatures on the end plates were studied. The spherical shape is simple to fabricate and compact in size for the RF cavity of given frequency. Cross-sectional view of quarter part of optimized RF cavity and its dimensional details are shown in Fig.1. This cavity is designed with two tuning plungers for tuning the fundamental mode as well as Higher Order Modes (HOMs)

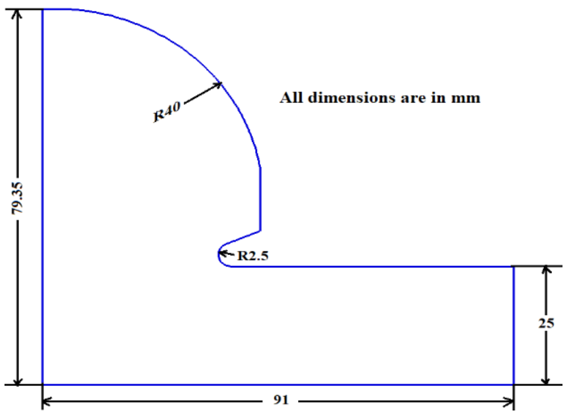


**Figure 1: Cross-sectional view of quarter part of RF Cavity**

of RF cavity. First plunger can be used for online tuning with a suitable mechanism for fundamental mode. It will compensate the beam loading and thermal effects of the cavity fields during operation in the storage ring. Second tuner can be used as a fixed tuner for coarse tuning. In RF cavity, input coupler port is located on the top of the cavity equatorial region whereas two tuning ports of same diameter are located 120° ccw and cw from input coupler port. Sensing port of smaller diameter is located opposite to input coupler port. Model of third harmonic cavity with port details is shown in Fig. 2.

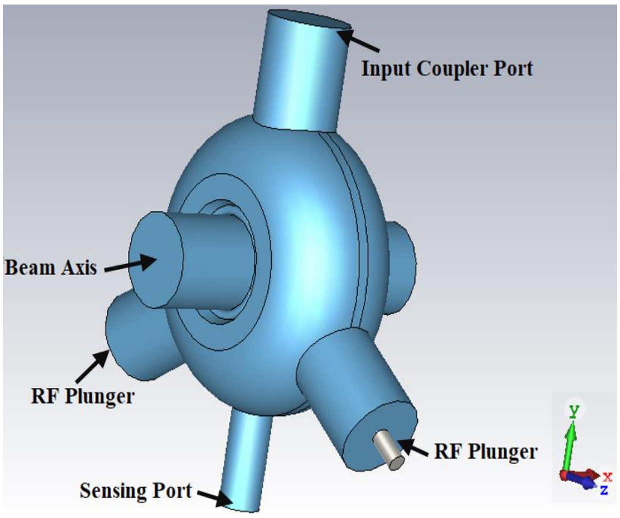


**Figure 2: Model of third harmonic RF cavity**

## ELECTROMAGNETIC SIMULATION OF THIRD HARMONIC RF CAVITY

### *RF Cavity Simulation*

Initial simulation for the design of third harmonic RF cavity has been carried out with 2D SUPERFISH code. For harmonic cavity fundamental mode resonant frequency (1517.5 MHz), quality factor, shunt impedance and transit time factor have been computed. Simulations have been carried out for accelerating voltage of 120 kV and 160 kV. Considering the reduction in fundamental frequency due to opening of ports, harmonic cavity is initially designed at slightly higher resonance frequency. For 3D simulation, aim is to design the RF cavity at resonance of 1517.5 MHz with all ports. Simulation of RF cavity parameters with inclusion of ports and plungers in RF cavity have been carried out. Power loss and power loss density have also been calculated at gap voltages of 120 kV and 160 kV. Fig. 3 shows the simulated electric field in the harmonic RF cavity for fundamental mode of 1517.5 MHz. Design parameters of third harmonic RF cavity are given in Table-2.

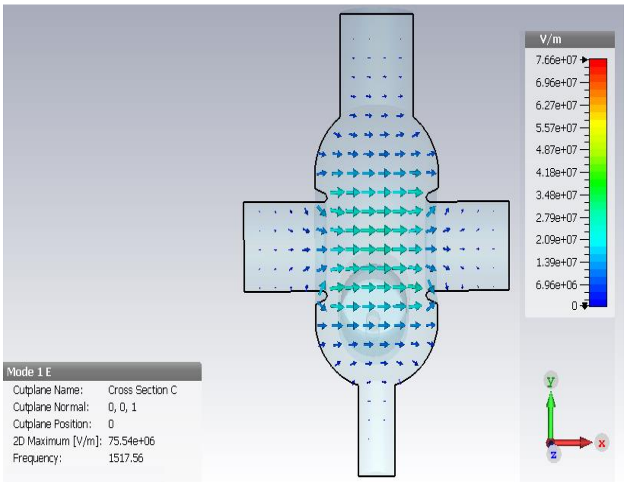


**Figure 3: Electric field plot for fundamental mode.**

Table -2: Design parameters of third harmonic RF cavity

| | | |
|---|---|---|
| Frequency ($f_h$) | 1517.56 | MHz |
| Shunt impedance ($R_{sh}$) | 1.88 | MΩ |
| Quality factor ($Q_0$) | 23000 | |
| R/Q | 83.7 | Ω |
| Tuning range/plunger | ±3.64 | MHz |
| Gap voltage (kV) | 120 | 160 |
| Power loss (kW) | 3.8 | 6.8 |
| Power density (W/cm$^2$) | 7.1 | 12.6 |

## *Tuner Optimization*

Tuners locations on the circumference of the cavity are preferred for ease of operation and for higher tuning range. Two tuners are located 120° opposite to each other. The diameter and stroke of tuners are taken Φ47 mm and 20 mm respectively. Tuners locations, size, stroke were simulated using CST MW Studio. The tuning range of 7.28 MHz has been computed for plunger movement from –5mm to +20mm with plunger position on the cavity surface is taken as 0 mm. Variation of resonant frequency vs tuning plunger movements for one tuner is shown in Fig. 4.

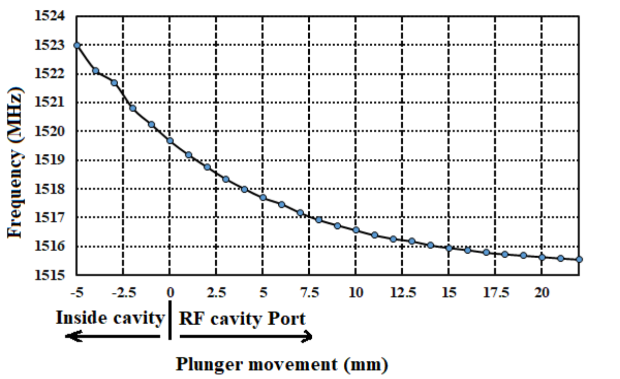


**Figure 4: Variation of resonant frequency vs tuning plunger movements.**

## *Higher Order Modes*

Multiple iterations are carried out using simulation codes to collect information about frequency, quality factor, shunt impedance and R/Q for higher order longitudinal modes and dipole modes of third harmonic RF cavity up to beam pipe cut-off frequency [5]. The dipole modes may get splitted in horizontal mode (H) and vertical mode (V) due to asymmetry in the RF cavity. Electric field plot of first dipole mode is shown in Fig.5. The calculated frequencies, unloaded quality factor ($Q_0$), shunt impedances ($R_{sh}$) and (R/Q) of longitudinal modes ($TM_{0nl}$) as well as dipole modes ($TM_{1nl}$) are listed in Table-3 and Table-4.

Table-3: Parameters of longitudinal higher modes

| Frequency (MHz) | $Q_0$ | $R_{sh}$ (MΩ) | R/Q (Ω) |
|---|---|---|---|
| 2603.174 | 21200 | 0.521 | 24.559 |
| 3270.299 | 22600 | 0.004 | 0.175 |
| 4214.050 | 34700 | 0.160 | 4.623 |
| 4372.073 | 18700 | 0.034 | 1.823 |

Table-4: Parameters of dipole higher modes

| Frequency (MHz) | $Q_0$ | $R_{sh}$ (MΩ/m) | R/Q (Ω/m) |
|---|---|---|---|
| 2207.808(H) | 21400 | 1.131 | 52.837 |
| 2213.174(V) | 19950 | 1.068 | 53.514 |
| 2348.426(V) | 22670 | 21.666 | 955.73 |
| 2363.419(H) | 21740 | 19.914 | 916.00 |
| 3133.597(H) | 18100 | 21.013 | 1138.28 |
| 3136.874(V) | 18460 | 21.319 | 1154.89 |
| 3553.615(V) | 18420 | 0.868 | 47.118 |
| 3569.518(H) | 19090 | 1.348 | 70.637 |
| 3573.993(H) | 29300 | 0.439 | 14.981 |
| 3654.172(V) | 37300 | 0.709 | 19.015 |
| 3699.351(V) | 24300 | 0.258 | 10.616 |
| 3814.222(H) | 28400 | 0.185 | 6.512 |
| 4098.954(V) | 23100 | 0.151 | 6.551 |
| 4135.555(H) | 24300 | 0.186 | 7.673 |

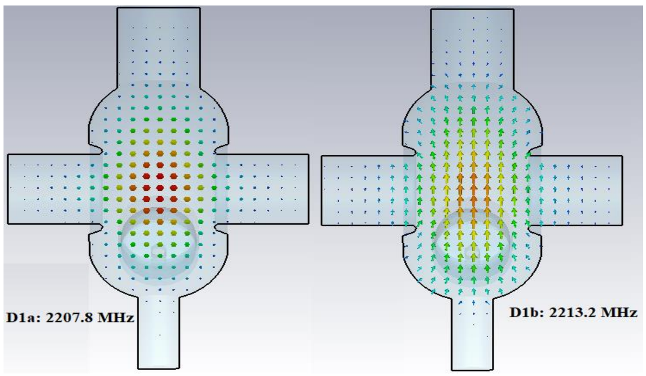


**Figure 5: Electric field plots of first dipole mode (split)**

## CONCLUSION

The third harmonic RF cavity for Indus-2 storage ring has been designed. This RF cavity is optimized for maximum shunt impedance (1.88MΩ) and quality factor (23,000). Power loss calculations have been done at different gap voltages. Simulated tuning range for each plunger is ±3.64 MHz. Frequency, $R_{sh}$, $Q_0$ and R/Q of HOMs have been computed for longitudinal and dipole modes up to beam pipe cut-off frequency.

## REFERENCES


[1] J. M. Byrd, et al., "Design of a higher harmonic RF system for the Advanced Light Source",Nucl. Inst. Meth. A (439) 1(1999) pp. 15-25.

[2] M. Georgsson, et al., "Landau cavities at MAX II", Nucl. Instr. and Meth. A 416 (1998) 465.

[3] Lad M., et al., "Upgradation of RF Technology in Indus-2 Synchrotron", Indian Particle Accelerator Conference InPAC 2018, RRCAT Indore, Jan., 9-12, 2018

[4] M. Prasad, et al., "Design, Electromagnetic Simulation and RF Characterization of Broadband Kicker RF cavity for longitudinal multi bunch feedback system for Indus-2", InPAC-2018, RRCAT, Indore, Jan., 9-12, 2018.

[5] M. Prasad, et al., "Design and Electromagnetic Simulation of HOM Damped RF Cavity for Low Emittance Storage ring", InPAC-2018, RRCAT, Indore, Jan., 9-12, 2018.

# STABILITY TESTS OF THE PHASE LOCKING ELECTRONICS FOR THE PULSED BEAMS FROM PELLETRON ACCELERATOR AT IUAC

A. Sarkar*, V.V.V. Satyanarayana, Sarvesh Kumar, A. Sharma, A. Pandey, B.K. Sahu, R. Joshi

Inter University Accelerator Centre, Aruna Asaf Ali Marg, New Delhi- 110067, India
*email: abhi031264@gmail.com

*Abstract*

The pulsed beams from the Pelletron accelerator at IUAC, produced by a multi-harmonic buncher and a chopper at the low energy section of the accelerator, are phase locked with the buncher in a very special RF modulation technique. This phase locking takes care of the fluctuations in the beam phase due to all the fluctuations in the different parameters of the accelerator and maintains the centroid as well as FWHM of the beam bunches throughout the user experiment. This system is operational for almost two decades and is successful in delivering phase stable pulsed beams during pulsed beam runs including all Linac runs for a wide variety of users. Presently due to some unknown reason there was some instability in the phase lock and the beam was going out of lock frequently making it difficult for conducting user experiment. In order to find the root cause of this problem it was decided to do a thorough test of the electronics by proper simulation technique. The electronics was tested by simulating the beam signal and was found to be quite steady. The details of the test procedure and results are discussed in this paper.

## INTRODUCTION

The beam pulsing system of the Pelletron accelerator at IUAC consists of a multi-harmonic buncher (MHB), [1] a low energy chopper (LEC) and a travelling wave deflector deflector (TWD). These are all located in the pre-acceleration region of the Pelletron accelerator. The beam pulsing system also includes a spiral loaded phase detector located at the post acceleration region of the Pelletron for detection of phase from the bunched beams. This is used for the phase locking of the buncher using RF modulation technique. The positions of the different sub-systems of the beam pulsing system are shown in figure-1.

The Multi-harmonic buncher operating at 12.125MHz bunches the dc beam into sharp bunches of 1 – 2 ns FWHM using an approximated saw-tooth voltage applied across a single gap. The dark current between the bunches are removed by the help of the low energy chopper. The low energy chopper works at 4.04 MHz and chops the dc beam through a slit producing chopped pulses of 40 to 50 ns. The chopper phase is synchronized with the buncher phase using a varialble delay adjustment. With proper phase adjustments the chopped pulses of 40 – 50 ns are bunched tightly into 1-2 ns bunches leaving no dark current between the bunches at a repetition rate of 4.04 MHz. The TWD is used occasionally for reducing the repetition rate further as per the requirement of the user experiment. The spiral loaded phase detector cavity resonates at 48.5 MHz whenever a bunched beam passes through it and produces signals giving information about the bunched beam phase. This signal is utilised by a special RF modulation technique to generate the phase error signal used for the correction of the buncher phase. The frequencies of all the sub-systems of the beam pulsing system are all sub-harmonics of the Superconducting Linac frequency ie. 97 MHz. The relative phases of the chopper, buncher and phase detector is shown in figure-2. An electrostatic potential (ESP) is super imposed on the chopper RF to define the chopper window with a repetition rate of 4.04 MHz.

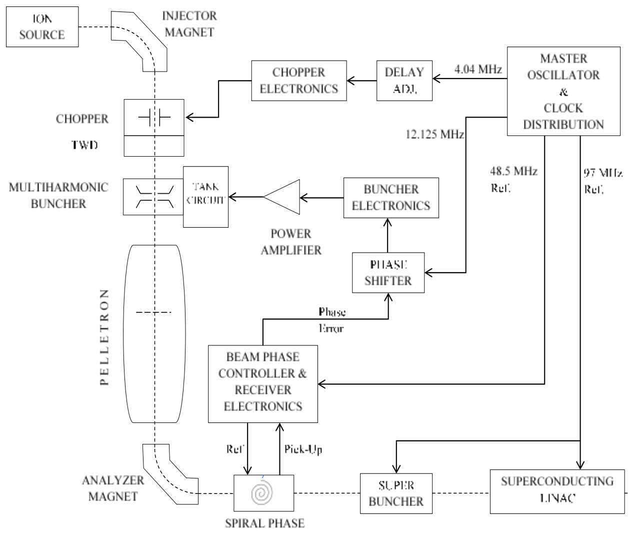


Figure 1: Block Diagram of Beam Pulsing System

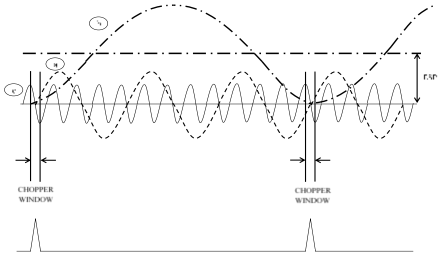


Figure 2: Relative Phases of Buncher (a), Chopper (b), and Phase Detector (c).

## RF MODULATION TECHNIQUE

The 48.5 MHz resonant cavity can be used as a phase detector when excited by a bunched beam and a reference signal which is phase modulated 180° (± 90°) at an audio rate.[2] The resulting signal in the resonator can be represented as the vector sum of the two driving signal as shown in figure 3.

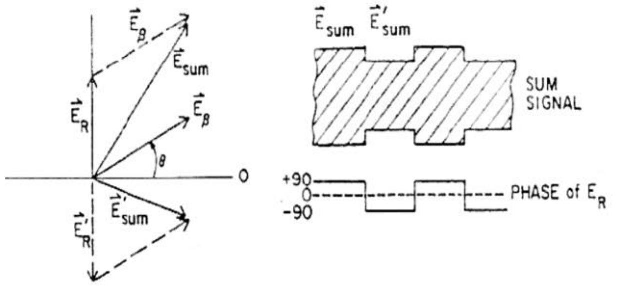


Figure 3: Vector diagram showing the amplitude modulation resulting from the addition of a beam signal ($E_B$) and a reference signal ($E_R$ , $E_R'$ ) which is phase modulated ± 90°; and schematic RF envelope related to the phase modulation timing of the reference signal.

The resulting signal is given by:

$$E_{SUM} = (E_B^2 + E_R^2 \pm 2E_B E_R sin\theta)^{1/2} \qquad (1)$$

This implies an amplitude modulation on the sum signal which will be at a minimum when the beam signal is 90° out of phase with the reference and maximum when the two are in phase. Synchronously detecting the sum signal generates a dc voltage proportional to the phase error between the two signals. The control system nulls this error signal, forcing the phase of the beam-induced signal to be orthogonal to the detector reference.

Further examination of the above equation reveals that for a fixed reference signal amplitude, the maximum amplitude modulation of the sum signal when the beam and reference signals are in phase is proportional to the beam signal amplitude. The amplitude of the signal induced by the beam is proportional to the average electrical current in the beam for a fixed bunch waveform. Measuring the peak envelope level under these conditions will indicate the average beam current. Figure 4 illustrates such a condition and shows the modulation envelope of the sum signal.

The 48.5 MHz reference signal is phase modulated at 500 Hz and 1 kHz rates at mutually orthogonal directions and fed to the phase detector. The pick-up signal from the phase detector which is the sum of the beam induced signal and the reference signal is an amplitude modulated signal containing modulation envelopes giving information about beam phase and beam current. The 500 Hz modulation which contains the phase information is synchronously detected and used for generating the phase error signal. The 1 kHz modulation component, which contains the beam current information, is detected by a peak detector and compared with the reference to generate a beam on/off signal.

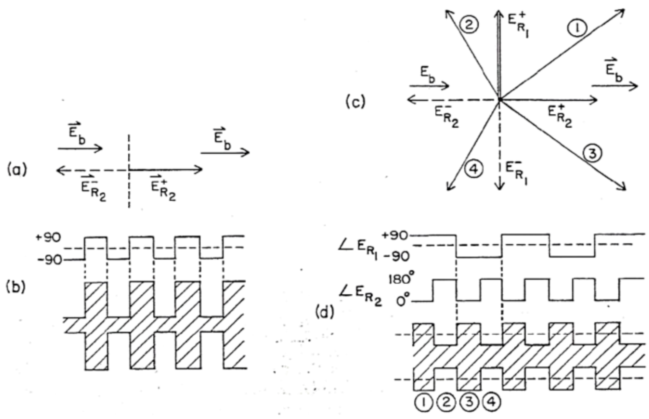


Figure 4: (a) Vector addition of a phase-modulated reference and in-phase beam signal. (b) rf envelope produced, related to modulation timing. (c) Vector addition of two phase- modulated references and beam signal. (d) rf envelope related to reference timing.

The circuit based on the technique described above was implemented into the beam pulsing system. A block diagram of the controller is shown in figure 5.

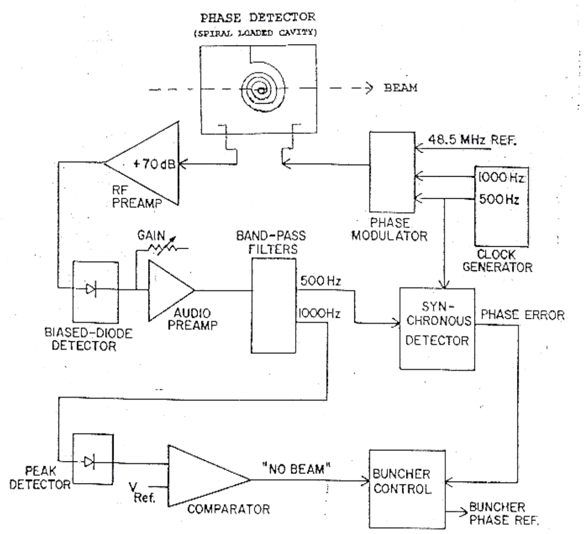


Figure 5: Block diagram of beam phase and amplitude control systems.

## TESTING OF PHASE LOCKING ELECTRONICS BY BEAM SIMULATION

The stability of the electronics for the phase locking was tested off-beam by a beam simulation technique. The block diagram for the simulation is shown in figure 6. The whole circuitry for input RF phase modulation, synchronous detection of the amplitude modulated pick-up signal, generation of phase error signal and a beam-on signal is done by two specially wired NIM modules viz. Beam Phase Controller and Beam Phase Receiver.

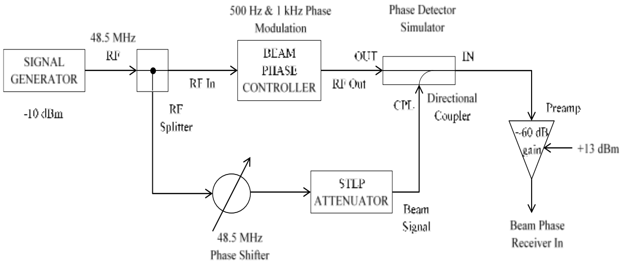


Figure 6: Block diagram of the beam simulation test.

The simulation test was done taking a 48.5 MHz signal from the Signal generator and splitted into two parts. One part was taken as reference rf and phase modulated at an audio rate. The other part was used as the beam signal passing through a variable attenuator and phase shifter to control the baem amplitude and phase respectively. The two signals were then summed in a directional coupler in the way shown in fig.6. The directional coupler was used in this configuration as the phase detector simulator. The output signal which showed the amplitude modulation was fed to the beam receiver for synchronous detection of the modulation envelope and thereby generation of the phase error signal. The phase error signal was monitored for several hours in a data logger and was found to be stable. The amplitude modulated output as seen on the CRO is shown in figure 7. Two spare modules developed earlier were also tested in the Laboratory by the same beam simulation method.

The data logger output is shown in figure 8.

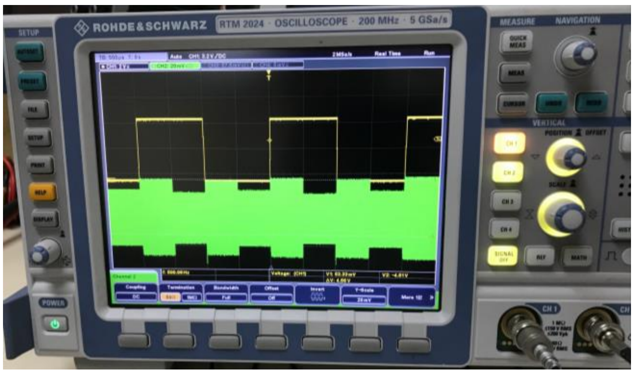


Figure 7: Amplitude modulated output as seen on the CRO.

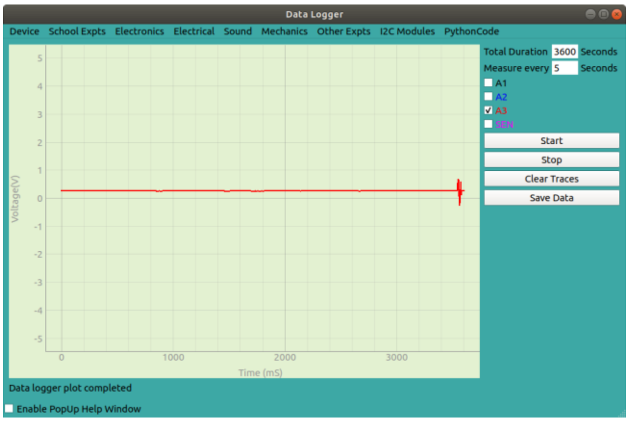


Figure 8: Data logger output showing steady phase error signal.

## CONCLUSION

There are several factors for the instability of beam phase and beam going out of phase lock. By doing this off-beam test it was concluded that the electronics for the phase lock was stable and worked well according to its design parameters.

## ACKNOWLEDGEMENTS

The authors would like to acknowledge the help received from the Pelletron group members for their co-operation. The encouragement received from Prof. A. C. Pandey is highly acknowledged.

## REFERENCES

[1] A. Sarkar et al, “Single –gap multi-harmonic buncher for NSC pelletron”, Indian Journal of Pure & Applied Physics, 39 (2001) 15 – 19

[2] M. Waterson and B.E. Clifft, “Improved rf modulation technique for bunched beam detection”, Rev. Sci. Instrum. 57 (5), May 1986, 792

# Analysis of Beam Measurement and Magnetic Median Plane Data in the Central Region of Superconducting Cyclotron (SCC)

Jedidiah Pradhan[†], Malay Kanti Dey, Anjan DuttaGupta and Arup Bandyopadhyay

Variable Energy Cyclotron Centre
1/AF, Bidhan Nagar, Kolkata-700 064
[†]jpradhan@vecc.gov.in

*Abstract*

The magnetic median plane in the cyclotron often does not coincide with the geometrical mid-plane of magnetic system. This produces radial field in the mid-plane causing vertical shift of beam and eventually leads to beam loss generally in the central region of cyclotron. This radial field is difficult to measure in presence of large vertical component however it is estimated indirectly from the position of median plane obtained from circular search coils under different conditions. These median plane positions are compared to match with the possible positional error (asymmetry) of each magnetised iron pieces in the central region. The corresponding radial field distribution is calculated by assuming uniform magnetisation of shifted iron pieces. This field is used for trajectory calculations and compared with the behaviour of beam current in the central region of superconducting cyclotron. This paper presents the methodology used for obtaining radial field and comparison of particle trajectories with the observed beam characteristics.

## INTRODUCTION

The superconducting cyclotron (SCC) at Kolkata is three sectors, three dees machine with bending limit of K=500. In many of our beam measurement in the central region of the cyclotron, beam does not move in the plane of symmetry of the cyclotron magnet. This shows the shift of magnetic median plane with respect to the mid-plane of the magnetic system whcih causes additional beam loss in vertical direction owing to small axial focussing of the beam in the centre of cyclotron. The vertical shift of the beam is driven primarily by the radial field $B_{rav}$ , but it is difficult to measure. The challenge of measurement of radial component of magnetic field is to cancel the crosstalk from the large vertical field component. However it is estimated indirectly from the position of median plane obtained from circular search coils under different situations [1]. The central region of cyclotron has several magnetic components like circular plug, circular trim coil, hill plugs (small and large) which may creates radial field, if not placed properly. The possible vertical positional error ( asymmetry) of each components is estimated from the integrated median plane positions obtained from circular search coils. The radial field is calculated from these asymmetries considering uniform magnetisation of iron for each components. This field is used for trajectory calculations and compared with the behaviour of beam current in the central region of superconducting cyclotron. This paper describes the methodology used for obtaining radial field and comparison of particle trajectories with the observed beam characteristics.

## MATERIALS AND METHODS

### *Median plane measurement set-up:*

Here the system consisting of two annular search coils (inner and outer) in a G10 base plate, fixed with inflector shaft and pneumatic drive system [2]. The signal is generated during the vertical movement of the coil. The vertical position of the coils is accurately measured with respect to mechanical median plane using fiducial points on the coil surface.

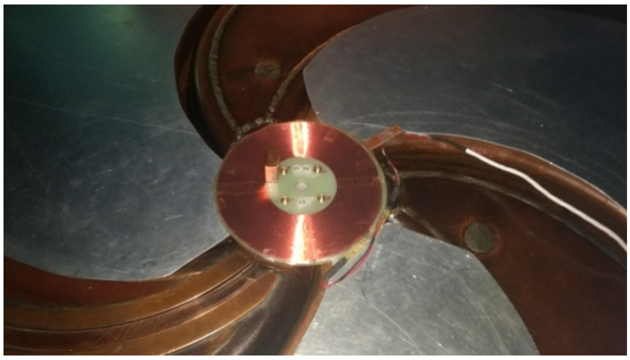

Figure 1. Search coil mounted in the central region of SCC

The pneumatic system has a stepper motor based drive for vertical positioning of search coil and an off-the-shelf digital integrator (DI). A PC based user interface is developed for search coil positioning, scanning of the central region magnetic field and acquiring data from DI. The system is validated in a 3-D magnetic field mapping test bed using standard magnet and eventually applied to measure the magnetic median plane in the central region of SCC.

### *Radial field estimation:*

The symmetry of the magnetic system is determined from the radial components of the magnetic field in the geometrical mid-plane of magnetic system. In this case the magnetic median plane is not physically the geometrical mid-plane of the system. An analytic expression [3] of the median plane position can be derived by imposing median plane condition $B_r = 0$ in the expression of total radial field for each component under given vertical offsets. However central region

[†]jpradhan@vecc.gov.in

consists of circular plug (*cplug*), hill extension (*hill ext.*) and circular trim coil (*tcoil*) and has the following expressions for median plane relative to geometrical mid-plane.

$$Z_{eff.} = Z_{cplug} + Z_{hill\ ext.} + Z_{tcoil} + Z_{others}$$

$$Z_{cplug} = \delta_{cplug} \frac{\frac{\partial B_{cplug}}{\partial r}}{\left(\frac{\partial B_{Total}}{\partial r} + \frac{\partial B_{tcoil}}{\partial r}\right)}$$

$$Z_{hill\ ext.} = \delta_{hill\ ext.} \frac{\frac{\partial B_{hill\ ext.}}{\partial r}}{\left(\frac{\partial B_{Total}}{\partial r} + \frac{\partial B_{tcoil}}{\partial r}\right)}$$

$$Z_{tcoil} = \delta_{tcoil} \frac{\frac{\partial B_{tcoil}}{\partial r}}{\left(\frac{\partial B_{Total}}{\partial r} + \frac{\partial B_{tcoil}}{\partial r}\right)} - \frac{h}{2} \frac{\Delta I/4\, I_{lower}}{1 + \Delta I/4\, I_{lower}} \frac{\frac{\partial B_{tcoil}}{\partial r}}{\left(\frac{\partial B_{Total}}{\partial r} + \frac{\partial B_{tcoil}}{\partial r}\right)}$$

$$Z_{others} = \delta \frac{\frac{\partial B_{others}}{\partial r}}{\left(\frac{\partial B_{Total}}{\partial r} + \frac{\partial B_{tcoil}}{\partial r}\right)}$$

$$\Delta I = I_{upper} - I_{lower} = I(U) - I(L)$$

where

$Z$ – Median plane with respect to mechanical centre line
$\delta$ - Asymmetries of each component
$h$ - Vertical distance between upper and lower coils
*others*- Other components

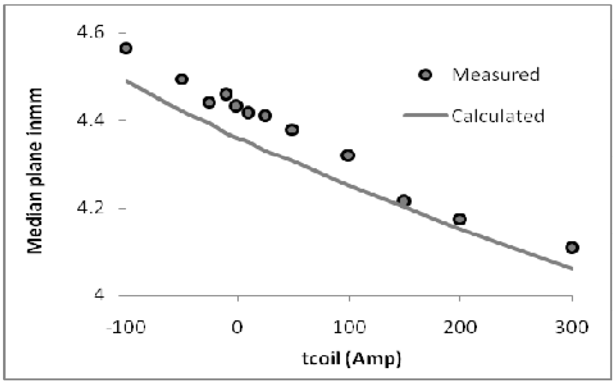


Figure 2. Median plane under different symmetric excitations of circular trim coil

The median planes are measured under different currents of circular trim coil in both symmetric and asymmetric excitations as shown in figure 2 and figure3 respectively. The circular trim coil has two coils as upper and lower coil and is excited independently. The integrated median plane as seen by each search coil is calculated using the above relationship and minimised its deviation from measured data. The field is obtained for each components assuming uniform magnetisation of iron.

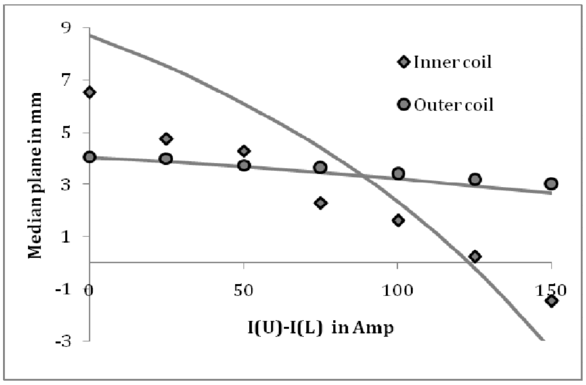


Figure 3 Median plane under different asymmetric excitations of circular trim coil

The integrated median plane position for calculated shifts $\delta$ of each component are also shown alongside in figure 2 and figure 3. The inner search coil (radius ~45mm) could not locate the median plane in symmetric excitation of trim coil due to measurement limitations. The radial field in the mechanical mid-plane is calculated from these asymmetries $\delta$ and is shown in figure 4 for three different excitations of trim coil. It is clear that the asymmetry in upper and lower part of trim coil produces different radial field under different excitations (figure 4).

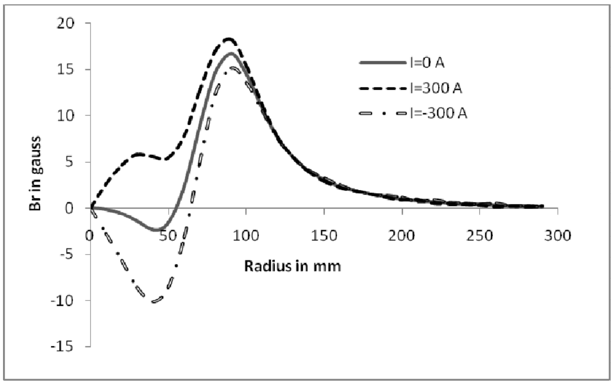


Figure 4 Radial field distributions in the mechanical median plane under three different excitations of trim coil

*Beam measurement and particle tracking:*

In the central region of the cyclotron, with no azimuthally varying field, vertical force is generated in the charge particle by the radial magnetic field and beam follows the position of the median plane. Different beam measurements allow understanding the impact of median plane shift and radial field. Our measurement of median plane shows the position of magnetic median plane is about 5 mm above the mechanical symmetry plane. This supports the observation from the reading of three finger probe where beam oscillates between top and middle fingers but zero current in bottom finger in the central region of SCC.

Charge particle tracking is carried out for $N^{2+}$ beam under h=2 operation in presence of radial field for different initial conditions. The tracking is carried out upto about 180mm, as all the beam current is measured from R > 150 mm. It is assumed 6 mm aperture in inflector hole and vertical divergence of ±50 mrad (maximum). The average vertical gap in the central region is about 26 mm beyond which beam hits the liner. The peak oscillation amplitude corresponds to maximum deviation from median plane. The median plane is varied by asymmetric excitations $\Delta I = I(U) - I(L)$ of upper and lower circular trim coil at the centre. A qualitative comparison is made with experimental beam current data in central region to understand the overall beam behaviour under varying median planes. It is reasonable to assume the reduction of beam current is solely due to vertical loss in the central region.

The maximum vertical oscillation amplitude for (z, $P_z$) = (± 3mm, ± 50 mrad) is simulated under different asymmetry of trim coil current and correlation is made with experimental beam current under similar situations. The beam current is maximum for ΔI ~200A and decreases on both sides (figure 6). It is observed that at ΔI~200A the oscillation amplitude is minimum which results reduction of vertical beam loss. In case of ideal symmetric condition the beam current should decrease on both sides of ΔI=0, similar to the oscillation amplitude.

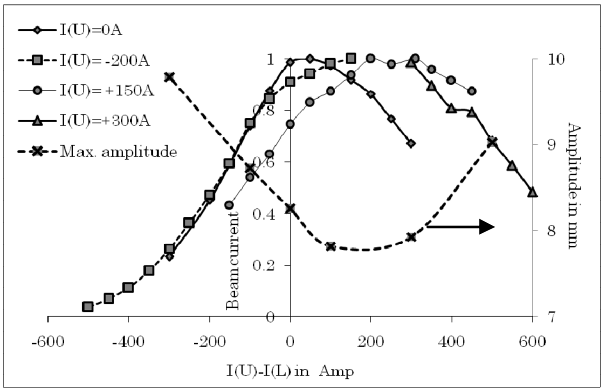


.

Figure 6 Beam current profile and vertical oscillation amplitude under different asymmetry of trim coil current

During beam measurement it is observed the improvement of beam current by lowering inflector height, however we do not have the quantitative measurement data. Particle tracking with the radial field obtained from median plane measurement indeed shows the improvement of vertical oscillation by lowering the inflector height.

The change of vertical oscillation under two different dee-voltages is simulated and shown in figure 8. It shows that higher dee voltage produce more vertical focussing. However, maximum and minimum dee voltage is limited by the presence of different posts in the central region. Specifically for $N^{2+}$ beam under h=2 operation this window is about 28 kV to 32 kV, and beam current decreases on both sides of this window (of voltage) as shown in figure 9.

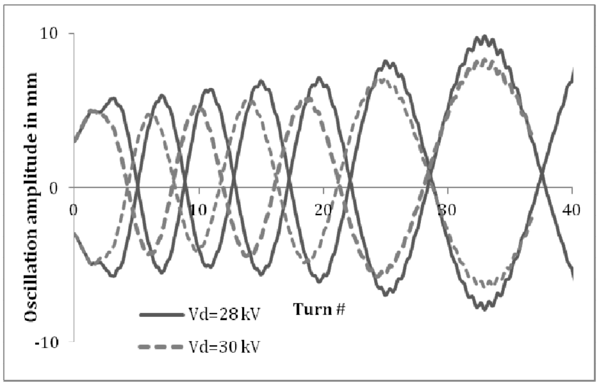


Figure 8 Increase of vertical focussing with dee voltage in the central region.

Beam current variation ( at R~160mm) with respect to dee voltage(power) under symmetrical and asymmetrical current settings of circular trim coil is experimentally measured. The optimum dee voltage corresponds to maximum beam current shows minimum voltage at ΔI ~ 200 A. This assymetric excitation of circular trim coil corresponds to minimum radial field in the central region. However with higher voltage ( outside window) beam current decrease, inspite of reduction of oscillation amplitude due to the presence of posts.

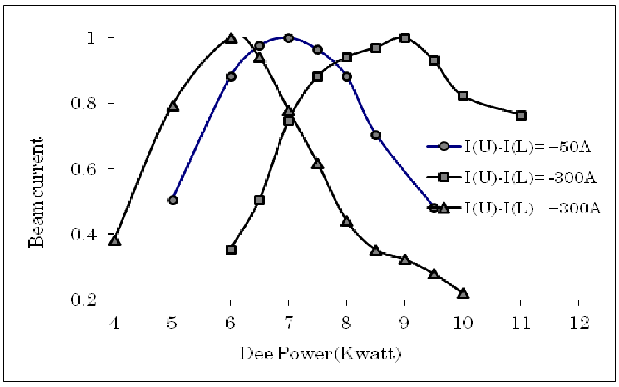


Figure 9 Beam current with respect to dee voltage under three different asymmetric excitations of trim coil

**References:**

1. G. Karamysheva et al., Proc. Cyclotron 2010, Lanzhou, China p. 206-208
2. J Pradhan et al., INPAC-2018, Indore, India
3. J J.I.M. Botman and H.L.Hagedorn, IEEE Trans. On Nucl. Science, Vol. NS-28, No.3, p. 2128-2130

# STOPPING EFFICIENCY OF AN ECR PLASMA FOR AXIALLY INJECTED IONS

Paritosh Sing Babu[#] and Vaishali Naik
VECC, 1-AF, Bidhannagar, Kolkata-700 064

*Abstract*

Isotope separator on line facilities requires charge breeders for efficient acceleration of rare isotope beams and to match the limit in mass to charge ratio of the post accelerator. Electron cyclotron resonance ion source (ECRIS) based charge breeder is widely used to produce rare isotope beams with a high charge state. In ECR, the low energy $1^+$ ions lose their initial energy and diffuse in velocity space by Coulomb collision with ECR plasma ions. In this paper we have used Monte-Carlo based simulation technique to include the Coulomb collision between ions and ECR generated plasmas. We have studied the stopping of $Ar^{1+}$ ions in Oxygen plasma for different parameters. Result shows that the capture and thermalisation of the ion beam is affected by the kinetic energy and emittance of the beam.

## INTRODUCTION

Isotope separator on line (ISOL) facilities requires charge breeders for efficient acceleration of rare isotope beams. For this electron cyclotron resonance ion source (ECRIS) is widely used for the charge breeding of stable and rare ion beams [1]. In ECRIS charge breeder system, the low charge state ions are injected and trapped in to the plasma region and their charge state is increased by electron impact ionization. The advantage of ECR based charge breeder is that it can be readily operated either in continuous or pulsed mode.

In ECRIS, the low energy $1^+$ ions lose their energy by Coulomb collision with ECR plasma charged particles and diffuse in velocity space. The collision between the injected ions and plasma is significant if the velocity of beam ions is approximately equals to the thermal velocity of the plasma ions. In the ECR, the temperature of electron is high in the range of keV and temperature of plasma ions is ~eV. So, the effect of electrons in the stopping process of ion beams is negligible in comparison to plasma ions. The injected ions will be captured if the energy of the incoming $1^+$ beam is ~ eV. The stopping of injected ions in the plasma is very crucial for the efficient charge state breeding by the electrons. The time for the slowing down is ~ several tens of micro-second and the time required for charge breeding from $1^+$ to $n^+$ is order of milliseconds.

We have estimated the stopping efficiency of the ECR plasma for externally injected 1+ ions in the presence of Coulomb collision with the ECR generated plasma charged particles using Monte-Carlo collision. Simulation results are presented for $Ar^{1+}$ ions in oxygen plasma for various parameters.

[#] psb@vecc.gov.in

## METHOD

In an ECR based charged breeder system, $1^+$ ion beam with kinetic energy $E = eV_b$ enters the plasma of the charge breeder. This ECR ion-source floats at a potential $V_s$ that is lower than the 1+ ion-source's potential $V_b$. We have assumed that the test ion collides with plasma whose velocity distribution is Maxwellian. We consider the energy loss of the externally injected ions with the plasma charge particles due to the Coulomb-interaction and do not consider ionization, excitation and charge exchange process. We also consider that the intensity of the injected beam is very small.

In the plasma the beam ions undergo multiple long range Coulomb collision with plasma ions and electrons. As a result beam ions slow down and diffuse in velocity space. The momentum loss of a test ion (labelled by $\alpha$) moving with velocity $\mathbf{v}_\alpha$ through background particles in the plasma (labelled by $\beta$) with Maxwell velocity distribution is given by [2-4]

$$\frac{d\mathbf{v}_\alpha}{dt} = -\nu_s^{\alpha/\beta}\mathbf{v}_\alpha \tag{1}$$

where $\nu_s^{\alpha\backslash\beta}$ is the slowing down collision frequency. The expression for $\nu_s^{\alpha\backslash\beta}$ is,

$$\nu_s^{\alpha\backslash\beta} = \left(1 + \frac{m_\alpha}{m_\beta}\right)\psi\left(x^{\alpha/\beta}\right)\nu_0^{\alpha/\beta} \tag{2}$$

where $m_\alpha$ and $m_\beta$ are the mass of beam ion and charge particle of the plasma respectively. The term $\nu_0^{\alpha\backslash\beta} = n_\beta z_\alpha^2 z_\beta^2 \ln\Lambda_{\alpha\beta} \big/ (4\pi\varepsilon_0^2 m_\alpha^2 \mathrm{v}_\alpha^3)$, where $n_\beta$ is the density of species $\beta$, $\ln\Lambda_{\alpha\beta}$ is the Coulomb logarithm, $z_\alpha$ and $z_\beta$ are the charges of species $\alpha$ and $\beta$ respectively and $\psi(x) = 2\pi^{-1/2}\int_0^x t^{1/2}e^{-t}dt$.

The rate of diffusion in the transverse direction of the test ion is given by,

$$\frac{d}{dt}\left(\mathbf{v}_\alpha - \bar{\mathbf{v}}_\alpha\right)_\perp^2 = \nu_\perp^{\alpha/\beta}\mathrm{v}_\alpha^2 \tag{3}$$

where, $\nu_\perp^{\alpha/\beta} = 2\left(\psi + \psi' - \psi/(2x)\right)\nu_0^{\alpha/\beta}$ is the collision frequency and $\bar{\mathbf{v}}_\alpha$ is the average velocity.

Here we have used above equations in Monte Carlo method to include the effect of Coulomb collision. At each step, collision involves first choosing a new direction for the velocity randomly using the Monte Carlo scattering operator and then choosing a new magnitude for the velocity using the energy scattering operator.

The new velocity after the scattering is related to old velocity as [2]

$$\mathbf{v}_{new} = \left(1 - \frac{v_\perp \Delta t}{2}\right)\mathbf{v}_{old} + \sqrt{\frac{v_\perp \Delta t}{2}\left(1 - \frac{v_\perp \Delta t}{4}\right)}\left(\pm\hat{\varphi} \pm \hat{\theta}\right)v_{old} \qquad (4)$$

here, $v_{old} = |\mathbf{v}_{old}|$ and $\hat{\varphi}$ and $\hat{\theta} = \hat{\varphi} \times \hat{v}$ are unit vectors normal to velocity spherical coordinate system.

The new magnitude of the velocity can be obtained from the energy scattering operator and is given by [2],

$$v_{new}^2 = \left(1 - \frac{2v_s^\alpha \Delta t}{1 + \frac{m_\beta}{m_\alpha}}\right)v_{old}^2 + \frac{4v_0^\alpha \Delta t}{\sqrt{\pi}}v_{th}^2 e^{-x} \pm 2\sqrt{\frac{v_{th}^2 v_{old}^2 v_s^\alpha \Delta t}{1 + \frac{m_\alpha}{m_\beta}}} \qquad (5)$$

## RESULTS AND DISCUSSIONS

We present the result $Ar^{1+}$ ions in Oxygen plasma. We have chosen the magnetic field configuration of 14.5 GHz ECR based charged breeder [5]. The magnetic field of the charge breeder consists of longitudinal solenoid field and a transverse hexapole field. The superposition of the two fields forms the B-minimum geometry, where the magnetic field increases in any direction from the centre to the wall. The magnetic field distribution due to solenoid along the longitudinal direction is shown in Fig. 1. The maximum solenoid field at the injection and extraction locations are 1.177 T and 0.793 T respectively. The minimum field at the centre of plasma chamber and resonant field are 0.352 T and 0.518 T respectively. The other parameters are: beam emittance $\varepsilon$ =30 $\pi$ mm mrad at 60 keV, length of ECR chamber = 30 cm, electron density $n_e = 6\times10^{17}$ per m$^3$, average charge state of Oxygen plasma = 3.5, plasma ion temperature $T_i = 1\text{eV}$.

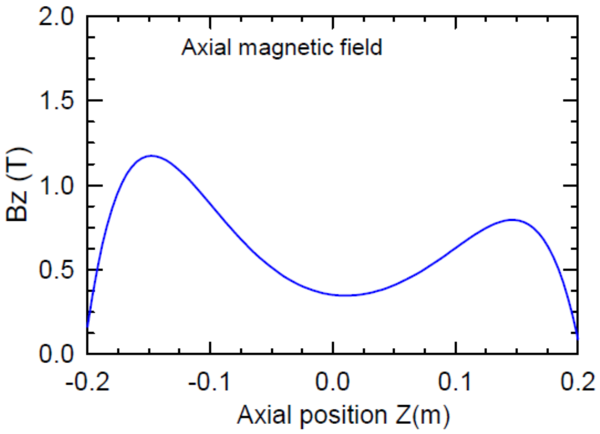


Figure 1. Variation of the longitudinal solenoid magnetic field along the axial direction.

We have performed the simulation of slowing down of $Ar^{1+}$ at different values of initial injection energy. We have found out that energy below 20 eV the ions captures into the plasma. The evolution of the average location of the beam distribution for $E$ = 5eV and 11.5 eV is shown in Fig. 2. The beam stopped at different longitudinal location in the plasma depending on the energy of the ion. We can see that the centroid of beam distribution stops at the centre of the plasma when the energy $E$ ~ 11.5 eV.

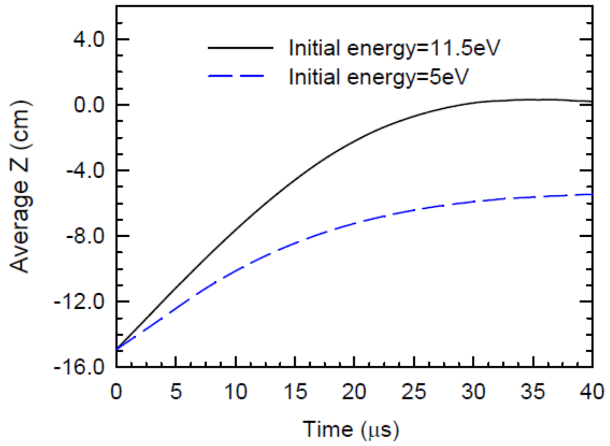


Figure 2. Temporal variation of the particles average position in the longitudinal direction. The simulation results are displayed for a time interval of 40 μs.

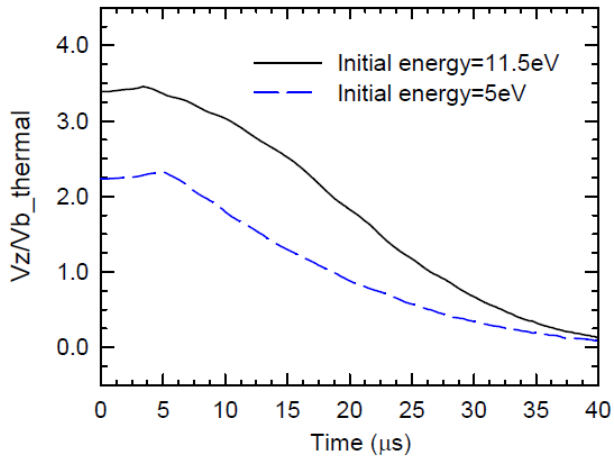


Figure 3. Time history of the average velocity of the ensemble of ion beams. The velocity is normalised to the thermal speed of the ion at energy 1 eV. The average velocity is computed over an ensemble of 7500 ions.

Figure 3 shows the evolution of the average axial velocity of the ion beam. The simulation has been performed for ions at two different energy 5 eV and 11.5 eV. It can be seen from the figure that the directional velocity in the longitudinal direction is constant before entering the plasma region and then the average axial velocity of the beam decreases due to collision with the plasma ions. The rate of decrease of velocity is small when the energy of the ion beam is very large or very small in comparison to the thermal velocity of the plasma ions. At the starting position we have considered the average velocity components of the ensemble of ions in the $x$ and $y$ direction is zero and it remains almost zero during the collision with the plasma. Simulation shows that the ions almost stop after a time of 32 μs and 38 μs for E= 5eV and 11.5 eV respectively.

The distributions of ions in the real space and phase space in transverse and longitudinal planes at time $\tau = 40\,\mu\text{s}$ is shown in Fig. 4. We have performed the simulations with 7500 particles for initial Gaussian distribution in the transverse direction of the beams. We have considered equal energy spread in both transverse directions. The emittance of the ions is $\varepsilon = 30\,\pi$ mm mrad in both the transverse planes. The injection energy and longitudinal energy spread of the beam is 11.5 eV and 0.02 eV respectively. The initial transverse energy spread is greater than and longitudinal energy spread is less than thermal energy spread of the ions at 1 eV. The real space plot in ($x$, $y$) space in Fig. 4(b) is triangular in shape due to the hexapole magnetic field in the radial direction.

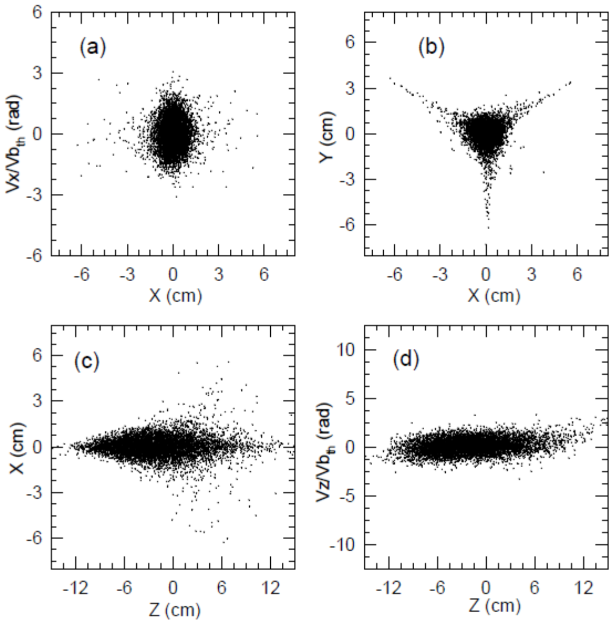


Figure 4. The real and phase space distributions of the ions at time $40\,\mu\text{s}$ with initial Gaussian distribution in transverse phase space. Plots (a) and (d) shows the phase space distributions of the ions in transverse and longitudinal phase space respectively. Plots (b) and (c) show the real space distributions. Calculated distributions of the ions after a time interval of $40\,\mu\text{s}$ .

Figure 5 shows the temporal evolutions of the velocity of test ions as it undergoes random Coulomb collisions with background plasma ions. It is evident from the figure that as time progresses, the velocity of ions in velocity space are randomly scattered. The average velocity of the ensemble of the ions with different beam energy will come to rest but all the particles will not be stopped to zero velocity and it leads to diffusion in velocity space.

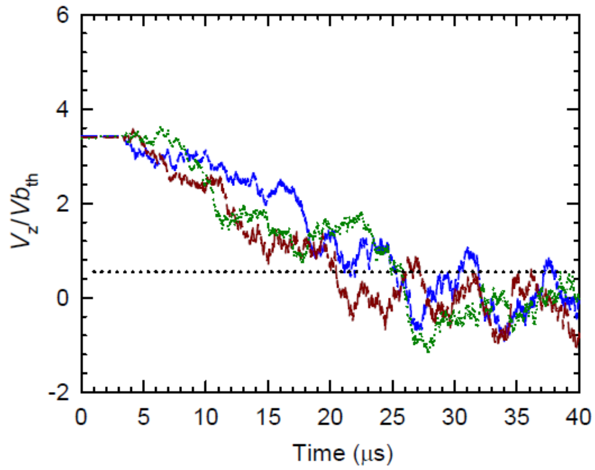


Figure 5. Temporal evolution of three test ions as it undergoes random Coulomb collisions with background plasma ions.

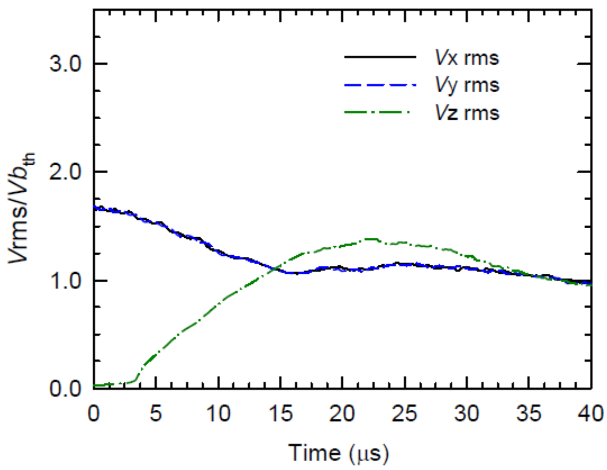


Figure 6. Evolution of the rms velocity of the ensemble of $Ar^{1+}$ ions in three directions. The velocity is normalised with respect to the velocity of the ions at energy 1 eV (energy of the ions in the plasma).

Figure 6 shows the time history of the rms velocity in the radial and $z$- direction. The $z$-component of rms velocity is maximum at 22 μs and saturates after 36 μs. After saturation the temperature in all three directions are same and equal to the temperature of plasma ions.

## REFERENCES


[1] P. Delahaye, O. Kester, C. Barton, T. Lamy, M. Marie-Jeanne, and F. Wenander, Eur. Phys. J. A 46 (2010) 421.

[2] Paritosh Sing Babu and Vaishali Naik, Phys. Plasmas 26 (2019) 033101.

[3] J. D. Huba, NRL Plasma formulary, NRL/PU/6790-16-614 (2016).

[4] A. H. Boozer, Phys Plasmas 9 (2002) 4389.

[5] A. Galatà, D. Mascali, L. Neri, G. Torrisi, and L. Celona, Rev. Sci. Instrum. 87 (2016) 02B507.

# 3D PARTICLE-IN –CELL SIMULATION OF ELECTRON AND ION DYNAMICS IN 3 MEV ROD PINCH DIODE *

Rakhee Menon, Romesh Chandra, Amitava Roy, Sonali Parashar, Archana Sharma
APPD, BARC, Trombay, Mumbai 400085, India
*Homi Bhabha National Institute, Mumbai 400094, India

*Abstract*

Pulse Power Systems generating 2-3 MeV electron beams utilizes Rod Pinch (RP) diodes as the suitable candidates for Flash X-ray generation. The RP diode has a cylindrical geometry with 1-3 mm diameter high Z anode rod extending through a cathode aperture with a suitable radial Anode Cathode Gap. The electrons generated from the cathode by explosive field emission are space charge limited (SCL) at low voltages, progress to a weak pinch as the current increases and finally to parapotential flow due to self magnetic insulation and forms a strong pinch at the anode tip. The ion space charge formed at the anode surface plays a crucial role in the formation of the pinch. This PIC simulation study is to optimise the RP source geometry varying the parameters like anode rod diameter and length, cathode emission length and diameter for 2-3 MeV, peak electron energies. For a beam energy of 3 MeV, only weak pinch is observed when there is no presence of ions due to anode plasma. With ions present, a strong pinch is observed even at energy levels of 2 MeV and 30 kA beam currents. This paper presents the electron and ion dynamics in the anode cathode gap that leads to weak to strong pinch at the anode tip. A small spot size is necessary to obtain a good resolution radiographic source.

## INTRODUCTION

Flash X-rays (FXR) for dynamic radiography [1] are generated using intense relativistic electron beams (IREB) of few tens of nanosecond duration (FWHM) and few hundreds of keV peak energy. Electron beams are extracted from the cold cathode plasma generated on the cathode surface by the process of explosive electron emission. Qualities of the IREBs generated are key to efficient FXR generation. Hard X-rays of few tens of nanosecond duration are generated by impinging intense electron beams on a high Z via Bremsstrahlung conversion. APPD, BARC has developed several FXR systems with maximum electron beam energies ranging from 300 keV to 1 MeV [2, 3]. Recently APPD has taken up development of FXR source upto 3 MeV electron energy. The figure of merit of such a source is proportional to (dose @ 1 m)/(source size)$^2$. A source with the highest possible dose in the smallest spot size is desirable for high spatial resolution. The Rod-Pinch (RP) diode consists of an annular cathode and a small-diameter anode rod that extends through the hole in the cathode. The emission is initially space charge limited and as current approaches the critical current, beam pinches due to self magnetic insulation and current enters magnetically limited (ML) regime. The pinching of the electron beam is aided by the ion current generated due to anode plasma formation at the anode. The modelling of Flash X-ray device using Particle-In-Cell and Monte Carlo simulation techniques in tandem has already been carried out for the Cable fed compact FXR system upto 500 keV electron beam energy [4]. In this paper, beam dynamics of positive polarity RP diodes operating in 2-3 MV diode voltage is evaluated by 3D PIC simulation. By varying the Anode Cathode gap (A-K gap), anode rod length, cathode emission length and ion current at anode, weak to strong pinch at the anode has been studied.

## POSITIVE POLARITY RP DIODE

The high voltage positive pulse is applied to the anode rod and the cathode is grounded. The schematic of the RP diode used in the simulation is as illustrated in Fig. 1. Three metal discs of 1 mm thickness which are at 4 mm distance from each forms the cathode and the Anode rod is of 3 mm diameter with a taper point of 2 mm.

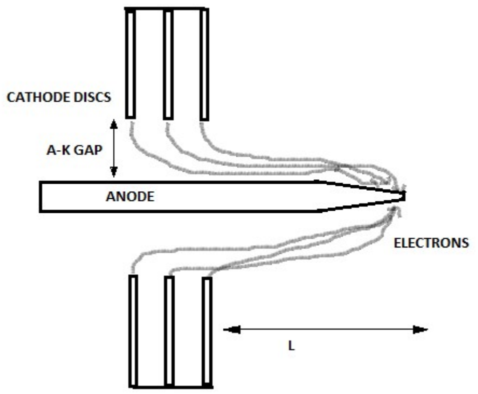


Figure 1: Schematic of the diode. The lines labelled ‘electrons’ are suggestive of ML electron flow. ‘L’ is the extension of the anode rod from the cathode disc.

The critical current, $I_{crit}$ above which beam pinching starts is given by [1]

$$I_{crit}(kA) = \frac{8.5\alpha(\gamma^2 - 1)^{1/2}}{\ln(r_c / r_a)} \qquad (1)$$

Where, $\gamma$ is the electron relativistic factor and $r_a$ and $r_c$ are the cathode and anode radii respectively. ‘$\alpha$’ is an empirical scaling factor for the critical current. Models describing the evolution of the rod-pinch-diode impedance from space-charge-limited (SCL) flow at low voltage, through weakly pinched flow; to magnetically limited (ML) flow have been reported [5].

mm and 19.5 mm radial A-K gaps. Table. 1 depicts the different diode parameters and pinch formation results.

Table 1: Electron beam diode parameters as obtained using PIC simulations.

| Voltage V (MV) | Diode Cuurent I (kA) | A-K Gap (mm) | Anode Extension L (mm) | Ion Current $I_a$ (kA) | Remark |
|---|---|---|---|---|---|
| 1.5 | 28.5 | 19.5 | 19 | 10 | Strong pinch |
| 2.5 | 50 | 19.5 | 19 | 10 | Strong pinch |
| 3.0 | 60 | 19.5 | 19 | 10 | Strong pinch |
| 1.8 | 34.5 | 19.5 | 19 | 4 | Weak pinch |
| 3.3 | 52 | 19.5 | 19 | 4 | pinch |
| 2.4 | 34 | 19.5 | 19 | 2 | Weak pinch |
| 3.0 | 42 | 19.5 | 19 | 2 | No pinch |
| 3.0 | 42 | 19.5 | 15 | 2 | Weak pinch |
| 3.0 | 34 | 19.5 | 19 | 0 | No pinch |
| 1.2 | 31 | 13.5 | 19 | 10 | pinch |
| 1.9 | 37 | 13.5 | 19 | 10 | pinch |
| 2.4 | 46 | 13.5 | 19 | 10 | Strong pinch |
| 2.8 | 52 | 13.5 | 19 | 4 | pinch |

## RESULTS & DISCUSSION

The beam dynamics of the RP diode has been carried out using (i) three-dimensional (3D) Particle-In-Cell (PIC) simulation [3].

In IREB diodes, electrons hitting the anode cause anode plasma formation and the ions from this plasma moves towards the cathode. The ion emission from the anode has been modelled by proton emission from the anode surface by DC emission with a rise time of 1 ns. Electron beam energies from 1.5 – 3 MeV have been analysed for 13.5 mm and 19.5 mm radial A-K gaps.

Even for lower voltages of around 1.2 MV, if the ion current is 10 kA at the anode surface, a strong pinch can be formed. Whereas, even at 3.0 MV, with no ions and a lower ion current of 2 kA, no pinching of the beam is observed. Weak pinching is observed for 4 kA ion current at 1.8 MV. So for the electron pinching to happen, an anode plasma formation at the early phase is essential. If we increase the cathode emission length using multidiscs, anode plasma formation can be initiated in the early part of the pulse which will make the current ML and aids beam pinching thus providing a smaller, intense FXR source.

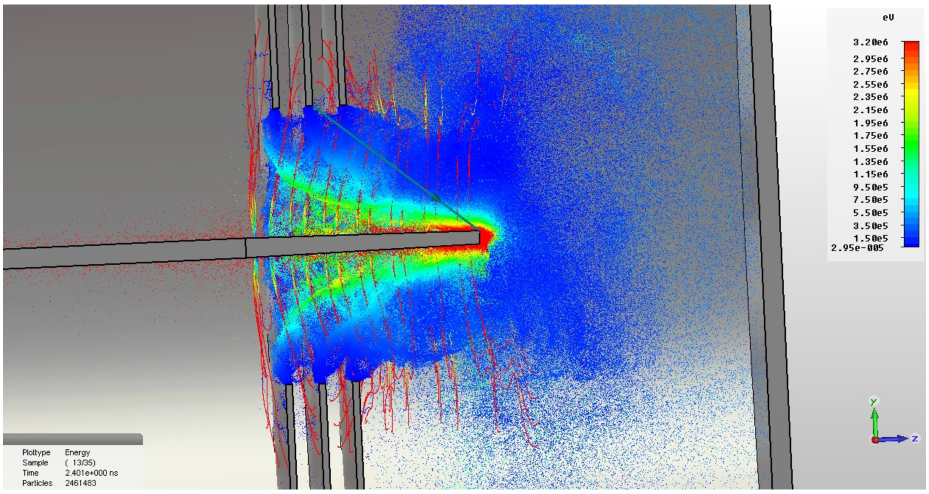


Figure 2: Snapshot of electron beam dynamics for 3 MV diode voltage with 10 kA ion current. The line colors in the picture represent energy of the particles.

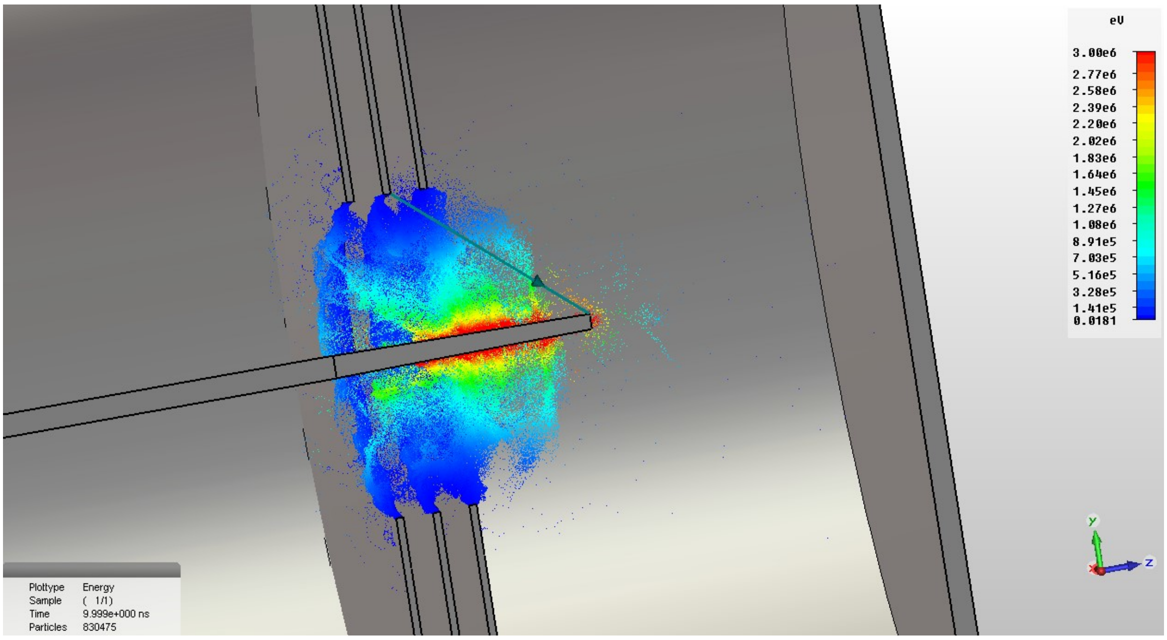


Figure 3: Snapshot of electron beam dynamics for 3 MV diode voltage with no ion current.The line colors in the picture represent energy of the particles.

## CONCLUSIONS

APPD, BARC has taken up design and development of a 3 MeV FXR source for dynamic radiography. For efficient dynamic radiography using the FXR source the X-Ray pulse width (FWHM) should be around 20-25 ns. In such cases the early ion current or the anode plasma formation is very critical during the rise time of the accelerating pulse. A PIC simulation study has been carried out for the 3 MeV FXR diode with the emphasis on the influence of the ion current from the anode plasma for a strong electron beam pinch formation. It was observed that the electron beam pinch formation is strongly dependent on the extent of the ion current irrespective of the diode voltage and current. Therefore, to produce a smaller spot size and intense FXR source it is required to increase the cathode emission length using multidiscs, thereby enhancing the anode plasma formation at the early stage of the diode voltage pulse.

## ACKNOWLEDGEMENS

Authors are thankful to R. K. Rajawat, Head APPD and AD BTDG, BARC for his constant encouragement and support. Authors are also thankful to Dr. Debabrata Biswas and Dr. Raghwendra Kumar, AM&TPS, BARC for their valuable suggestions during the simulation process.

## REFERENCES

[1] J. Maenchen, G. Cooperstein *et al.*, “Advances in Pulse Power Driven Radiography Systems”, Proceedings of the IEEE, VOL. 92, NO. 7, JULY 2004.

[2] Rakhee Menon , Amitava Roy *et al.*, "Generation and Dose Distribution Measurement of Flash X-ray in KALI-5000 System", Review of Scientific Instruments 79, 103301, (2008).

[3] Rakhee K Menon, Sabyasachi mitra *et al.*, "Development of Cable Fed Flash X-ray (FXR) System", Review of Scientific Instruments 88, 083307 (2017).

[4] R. Kumar, G. Singh, *et al.*, "Modeling of Flash X-ray device using Particle-In-Cell and Monte Carlo simulation techniques in tandem", BARC/MP&RThS/05/2016, (2016).

[5] G. Cooperstein, J. R. Boller, *et al.*, “Theoretical modelling and experimental characterization of a Rod-Pinch diode” Physics of Plasmas, vol.8, No.10, 4618 (2001).

# OPTIMIZATION OF PROCESS PARAMETERS FOR UNIFORM NEG FILM DEPOSITION IN LONG LOW CONDUCTANCE VACUUM CHAMBER

Tripti Bansod, Vijay Singh Bais, B K Sindal, S. Raj Mohan[1], Prateek Bhatnagar, Nilesh Bhange, D P Yadav

***UHVTS, [1]LMPD, RRCAT*, Indore, *India***

*email: tripti@rrcat.gov.in

## Abstract

The 2.5 GeV, Indus-2 synchrotron radiation source consists of three undulator devices, having racetrack profile long vacuum chambers of aluminium alloy material. Typical length of undulator chambers is ~ 2 to 3 m. Internal cross section dimension of the chamber is 81mm (width) X17mm (height) and provides very low molecular flow gas conductance. Operating vacuum pressure ~ 1 x $10^{-9}$ mbar with stored e-beam (@2.5 GeV, 200 mA) is required inside this chamber for longer beam life time. This conductance limited chamber requires uniform non-evaporable getter (NEG) coating of Ti-Zr-V thin film of ~ 1 µm thickness on vacuum exposed surface throughout the length to provide distributed UHV pumping for achieving the ultra-high vacuum (UHV) condition for long beam life time. To develop the NEG coated spare undulator chambers, a large NEG coating system, based on DC magnetron sputtering technique was developed in house in UHV lab. Prior to coating of actual spare chamber, process parameters were optimized for the uniform thickness of NEG coating inside the long conductance limited chamber by experimental coating trials. The coating thickness uniformity in whole chamber length achieved was within ± 30%.

This paper describes coating system description, design of cathode arrangement, operational experience for achieving stable discharge in ~ 3m long chamber with solenoid positioning and measured data of film thickness along the length of vacuum chambers.

## INTRODUCTION

The Indus-2 synchrotron light source is a booster cum electron storage ring with beam energy of 2.5 GeV. Its circumference is 172.4m. The vacuum system is made of aluminium alloy chambers with pumping by means of Sputter Ion Pump (SIP) and Titanium Sublimation Pump (TSP). A unit cell layout of Indus-2 machine consists of two dipole chambers, long and short straight sections along with pumping arrangement can be found in reference [1].

To produce the high brilliance radiation, three low gap NEG coated vacuum chambers with race-track profile of 17mm x 81mm were installed inside the minimum gap undulator magnets at the three long straight sections to provide distributed pumping [2]. These limited conductance vacuum chambers are pumped using NEG deposited film. NEG film behaves like getter pumps which are able to chemisorb the active gases on their activated surfaces. The titanium (Ti), zirconium (Zr) and vanadium (V) are the most commonly used getter elements in the accelerators. Ti-Zr-V coating does not require an additional space to install, having very low desorption yield by both thermal and photon induced. It can be activated during the normal bake out process, as the film have low activation temperature [3]. The indigenously developed DC magnetron sputter coating system was tested for stable discharge in long low conductance vacuum chambers before coating. The coating parameters optimized for deposition of approximate 1 µm thickness with uniformity of ±30% in long vacuum chambers by overlapping of solenoid positioning. The deposited film thickness were measured by mechanical stylus profilometer and elemental composition of the film was analysed by the EDXS. Repeatability of film thickness uniformity was also demonstrated for the same set of process parameters.

## DESCRIPTION OF NEG COATING SYSTEM

The large NEG coating system based on DC magnetron sputtering technique is shown in Fig. 1. It can be used to coat long vacuum chambers up to 3.5m.

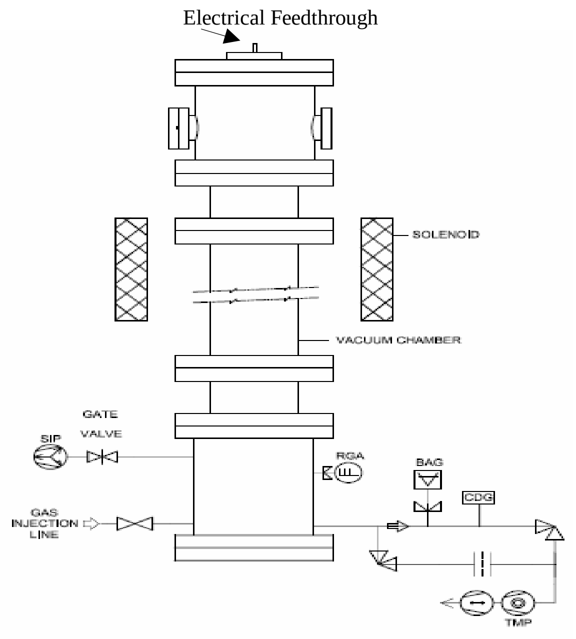


Figure 1: Schematic diagram of the setup used for coating of long vacuum chambers.

The vacuum chambers to be coated is mounted in vertical orientation. Solenoid of 1m length, with magnetic field uniformity of ±2% from the centre point to the ± 0.4m along the length, used to get the discharge at low sputtering gas pressure. Solenoid can be moved up and down along the length of vacuum chamber. Vacuum components are installed at the manifold chamber as per testing requirements, like ultimate vacuum and thin film deposition. One BA Gauge (BAG) and capacitance manometer gauge (CDG) are installed at manifold chamber to measure the pressure in $10^{-10}$ mbar range while ultimate vacuum testing and for sputtering gas pressure measurement respectively. System pumping is provided using Turbo molecular pump (TMP) backed by the dry roughing pump, connected to the manifold chamber through right angle valve. This pumping arrangement is used for evacuation, during baking of system and coating. One sputter ion pump is also installed along with the gate valve at manifold chamber to check the ultimate vacuum of the system along with the chamber to be coated before, after baking and after NEG deposition. Residual gas analyser (RGA) is installed to analyse the residual gas composition [4].

## SAMPLE MOUNTING AND TARGET ASSEMBLY

In order to optimize the various coating parameters for ensuring the uniformity of film thickness over the length of chamber, a sample holding arrangement was designed to deposit the film on the test coupons in 17mm x81mm profile of ~ 2.3m length. To put coupons along the length in small cross section, cage assembly was fabricated and test coupons were mounted inside it as shown in Fig. 2. For thickness measurement, substrate material selected for test coupons is glass. Aluminium sample was also mounted for evaluation of thin film chemical composition. The magnetic field is generated by a coaxial solenoid coil, which can generate magnetic field up to 550 Gauss.

Target was made of 1mm diameter wires of getter elements Ti, Zr & V. These three wires were inter-twisted after mechanical and ultrasonic cleaning. Two targets were suspended from the top flange through a vacuum electrical feedthrough. Targets parallel to each other were kept straight by hanging two solid cylindrical copper block at the bottom of each target using ceramic insulators.

Figure 2: Samples holding cage

## MAGNETRON SPUTTERING PROCESS

The vertical coating system have the provision to coat approximate 3.5m long vacuum chamber of different geometry. In low gap chamber to get the deposition, magnetic field was applied in the axial direction [4]. All the process controls, required for deposition were kept at the bottom end of the system. During the coating process gas flow was kept dynamic. The flow of sputtering gas was adjusted and controlled through the variable leak valve. System was operated at different pressure for different setting of magnetic coil current to maintain the same discharge voltage and current. At a low pressure to get the discharge at constant discharge voltage and discharge current, magnetic field has to be increased. To confirm the pressure at the two extreme ends of the low conductance long vacuum chamber, pressure were monitored using capacitance manometer gauges mounted at the top and bottom end of the chamber to be coated. From 1 mbar to $3x10^{-3}$ mbar pressure range, both the CDG pressure readings were plotted, shown in Fig. 3. Pressure from 1mbar to $8x10^{-3}$ mbar range at two extremes end of the low gap chamber remain same.

Before start of deposition process, the NEG coating system was evacuated using TMP and $9x10^{-9}$ mbar ultimate vacuum was achieved in unbaked condition. Gas line was baked and buffer chamber was filled with argon gas at 800mbar. Before coating test coupons were glow discharge cleaned at 300V discharge voltage and $1x10^{-2}$ mbar argon gas pressure. For deposition, sputtering gas filled in the coating setup, target was kept at negative potential, vacuum chamber and samples were kept at ground potential.

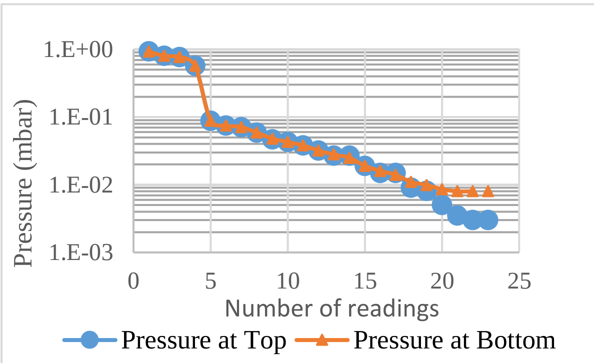


Figure 3: Sputtering gas pressure at two extreme end of 3m long, low gap chamber.

## DEPOSITION AND FILM THICKNESS CHARACTERIZATION

To optimise the process parameters for uniform thickness coating, four coating trials were conducted on DC magnetron sputtering coating setup. In first two coating trials, 1m long vacuum chamber assembled with samples mounted at slotted vacuum chamber of 17mmx 81mm profile. At $1x10^{-2}$ mbar argon pressure, -600V discharge voltage, 200 Gauss magnetic field, discharge was sustained with 100mA discharge current. The deposited film thickness with the magnetic field uniformity is shown in Fig. 4. In the uniform magnetic field the film thickness of 0.55µm to 0.537µm was deposited. But at the 50mm away from the physical end of the magnetic coil only 0.045µm thickness was deposited of Ti-Zr-V. In second coating trial, to check the repeatability of the thickness and coating parameters, system was run at same set of coating parameter and found the thickness of 0.45µm at centre of solenoid.

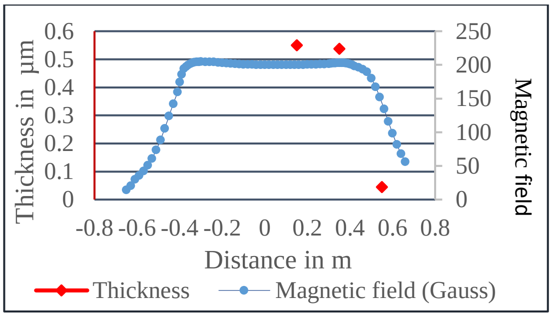


Figure 4: Deposited thin film thickness with magnetic field strength along the length of vacuum chamber

The third coating trial was also performed using argon gas to check the thickness uniformity with the overlapping of solenoid positioning, coating was done on test coupons mounted in 1m length with two extension chambers. NEG film thickness achieved was 1.32 µm to 0.82 µm in 1m length, which is ± 30% uniformity range. In fourth NEG coating trial, to check the uniformity of film thickness in 3m length, 3.5m long targets were prepared and test coupons arranged in sample holding cage. Final sputtering gas is being used for deposition purpose is Kr, as there is less efficiency to be trapped by the growing film than Ar [5]. Coating was performed in three steps by maintaining the uniform magnetic field of 250G around the chamber to be coated. In fourth NEG coating trial, the achieved film thickness along the length of chamber is shown in Fig. 5 and process parameters, film surface analysis details are given in Table-1.

Table 1: Deposition process parameters and NEG film characterization

| Sputtering Gas | Kr |
|---|---|
| Discharge Voltage | -600 V |
| Discharge current | 150mA |
| Kr Gas pressure | 8 x $10^{-3}$ mbar |
| Film thickness | 1 µm± 30% |
| Elemental composition (at%) | Ti- 32.9%, Zr-19.7%, V-47.4% |

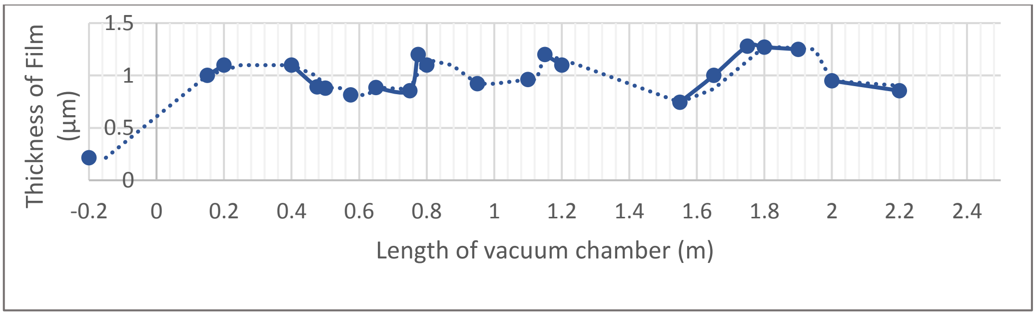


Figure 5: Thickness uniformity along the length of long vacuum chamber

## CONCLUSION

Ti-Zr-V film in low conductance long vacuum chamber were successfully deposited in vertical DC magnetron sputtering system. The film thickness uniformity along the length depends on the magnetic field uniformity. At the edges thickness is drastically reduced, however solenoid overlapping length was optimized to get the thickness in required range. Repeatability of the coating process and thickness uniformity were ensured by successive coating trials. Film thickness within ± 30% uniformity for the long undulator profile vacuum chamber was achieved.

## ACKNOWLEDGMENT

Authors express sincere thanks to colleagues of UHVTS who were involved directly or indirectly in this development work. Contributions of Shri Vinod Vishkarma for preparing the drawing, Shri Vishnu Pandey and Navin Solanki for electrical/electronic support, T. R. Meena and Shri Subda Hansdah for mechanical supports are duly acknowledged. Smt. Rashmi Singh from LFMD, RRCAT is also acknowledge for her support extended for compositional studies.

## REFERENCES

[1] Tripti Bansod, Proceeding of InPAC 2013 , VECC, Kolkata, Nov., 19 - 22, 2013.

[2] C. Benvenuti, R. Calder, O. Grobner, Vacuum 37 (1987) 699.

[3] C. Benvenuti, J. Vac. Sci. Tech. A 19 (6) Nov/Dec 2001.

[4] P. Coasta Pinto, Presented at 2nd TS Workshop, France, May 24-May 26, 2005

[5] S. Amorosi, M. Anderle, C.Benvenuti, S Calatroni, at.al, vacuum 60 (2001) 89.

# STUDY OF CARBON NANOTUBE BASED FIELD EMISSION CATHODE FOR ELECTRON BEAM GENERATION IN LINEAR ACCELERATOR

S. G. Sarkar[#]*, L. Mishra, D. Jayaprakash, H. K. Manjunath, J. Mondal, APPD, BARC, Trombay, Mumbai 400085, India
R Kar, L&PTD, BARC, Trombay, Mumbai 400085, India
[*]Homi Bhabha National Institute, Mumbai 400094, India

*Abstract*

The field emission based electron beam source has garnered a lot of attention since the advent of nanotechnology. The nanostructure due to their intrinsic geometry are very good candidate of field electron emission source. Nanostructures like carbon nanotubes (CNT) when used as a field emitting cathode source can have the advantage of having lower turn-on voltage and high emission current density compared to traditional microstructure field emitter. In this paper we present the experimental results of electron emission from CNT directly grown on inconel substrate. A new experimental set up for field emission study has been designed, fabricated and assembled. Different CNT samples with different growth condition and nanostructures have been studied for field emission and their performance has been compared as a field emitter.

## INTRODUCTION

After the advent of nanotechnology field emission cathodes based systems have garnered new found interest. Such field emission system have various applications such as field emission display, microwave amplifier, X-ray source, particle accelerator sources etc. The advantage of using field emission based system is that it can be made compact and it is theoretically possible to extract high current from such systems.

Nanostructures like nanotubes, nanocones, nanowires etc. can be used to design field emission based electron source owing to their inherent geometrical features. Nano structures like carbon nanotube (CNT) are high aspect ratio emitters which enables enhancement of field at their tip which in turn make field emission possible at lower applied voltage. CNT based cathodes can be used to construct a room-temperature electron gun for linear accelerator systems. The field emission current extracted from a CNT sample depends on CNT geometry and it differs from sample to sample. It is difficult to theoretically predict current density obtained from a sample which is a complex function of sample size, CNT size and geometry and CNT density etc. In order to design an electron gun of required current rating, it is important to estimate its emission current density in advance. Emission current density from a particular sample can be experimentally measured in order to check their suitability for particular application.

In APPD, BARC initiative has been taken to construct a field emission based electron gun for our linear accelerator system. As a first step, suitable samples of CNT should be developed and their field emission characteristics should be experimentally measured. In this paper we present experimental results of field emission test performed on different CNT cathode samples. The study has been conducted to select the best material for electron beam generation which will be able to meet the design criterion.

## EXPERIMNETAL METHODS

### *Carbon nanotube synthesis*

Carbon nanotubes (CNT) are robust field emitters which can be grown on suitable substrate by different means. For this application, Multi-walled CNTs (MWCNT) were directly grown on Inconel (600) substrate. Metallic substrate is ideal for CNT growth since they offer low turn-on field, high emission current and good stability of emission. For growth of the sample, Plasma enhanced chemical vapour deposition (PECVD) technique has been used. The samples were grown in an in house developed MPECVD set up where microwave assisted plasma was generated in a mixture of $C_2H_2$ and $H_2$ gases. Inconel substrate were oxidised and pre-treated in MPCEVD chamber before CNT deposition. Different samples were deposited under different growth condition. Samples were grown under various substrate temperature and time of deposition has also varied. For two samples microwave reflector also has been used. Different growth conditions ensure different CNT geometry and CNT density. Figure 1 shows a CNT sample directly deposited on an Inconel substrate with substrate temperature of $900^0$ C and with deposition time of 1 hour. The Inconel substrate is a circular disc of 0.5" diameter and 1mm thickness.

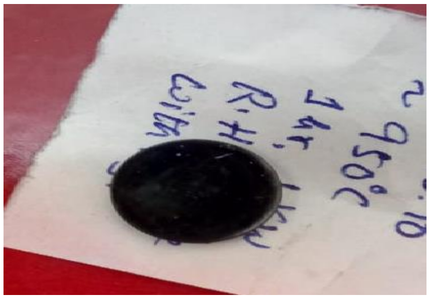

Figure 1 : CNT sample deposited on inconel

### *Field emission experimental setup*

The field emission characteristics of different samples were measured using an in house developed field emission measurement set up. The set up consists of a vacuum chamber with TMP and SIP pump. The cathode substrate holder is made of SS 304 and is isolated from the chamber (as shown in Figure 2). The sample is fixed to the cathode sample with conducting graphite paste. Cathode is floated at a negative potential. DC voltage up to 10 kV can be applied to cathode. The set-up also has a provision of applying pulsed voltage from DC to 200 ns pulsed voltage. The anode is a flat circular plate which is isolated from the chamber body. The anode is movable and can be adjusted to change the cathode distance for variation of field. The minimum gap of 50 micron and maximum gap up to 60 mm can be provided between cathode and anode. Current is measured using an electrometer. The measurements were done at a base pressure of $4e^{-8}$mbar. Field emission current is measured with nanoampere accuracy.

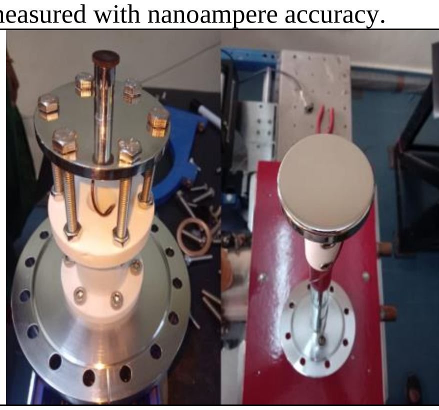

Figure 2 : Cathode and anode assembly

## RESULT AND DISCUSSIONS

### *Characterization of CNT*

After deposition of CNT on Inconel substrate the CNT sample were characterised by Scanning electron microscopy (SEM) and raman spectroscopy. SEM images of one of the sample is shown in Figure 3. From the image it is evident that bundles of CNTs are present in the sample. The CNt samples are randomly oriented. The average nanotubes has diameter of 20-40 nm. Presence of nanotubes with diameter of 100 nm were also seen.

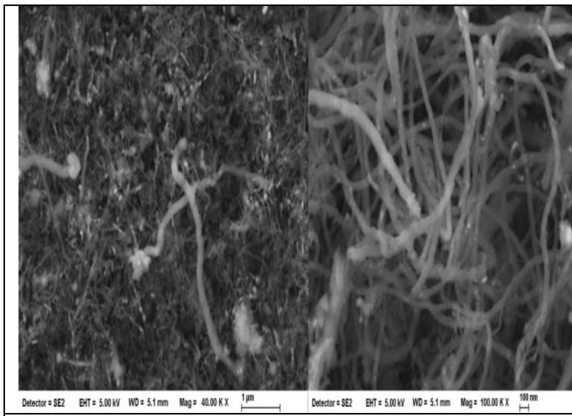

Figure 3 : SEM image of sample with different magnification

### *Field emission measurement of samples*

Field emission current density extracted from a sample is governed by Fowler–Nordheim equation. According to FN theory, the emission current density (J) from a protrusion is expressed as a function of the applied microscopic field at the tip and the work function (φ) of the emitter

$$J = aE^2 \exp(-b/E)$$

Where $a=1.42e^{-6}\exp(10.4/\varphi^{1/2})/\varphi$ and $b=-6.56e^9\varphi^{3/2}$ . Work function value is taken as 4.7 eV. The microscopic field E is related to the macroscopic applied field $E_a$ by a dimensionless factor called field enhancement factor (β) as $E= \beta E_a$ . The value of β depends on emitter geometry and it can be experimentally determined from the slope of the FN plot.

Three different samples were tested for their field emission property Field emission current of these samples were measured at different applied voltage. First sample of CNT was grown when substrate was pre-treated at $950^0$C temperature. The first sample had the least CNT density. The FE characteristics of these samples are shown in Figure 4 which confirms with Fowler Nordheim theory. The field level at which 10 µA current is extracted is defined as the turn on field.

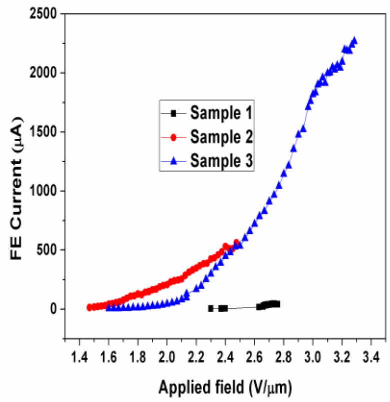


Figure 4 : FE characteristics of CNT samples

Table1: Comparison of FE characteristics of different samples

| Parameters | Turn on field in V/µm | Maximum FE current in µA | Applied field at Maximum current |
|---|---|---|---|
| Sample 1 | 2.55 | 45 | 2.75 |
| Sample 2 | 1.42 | 561 | 2.475 |
| Sample 3 | 1.76 | 2265 | 2.28 |

Table 1 shows a comparison of FE characteristics of different CNT samples. From figure 4 it is evident that sample 1 is not a good choice for cathode. During measurement the sample 1 was destroyed due to successive arcing. Sample 2 shows the least turn on field but only 560 A current was drawn from the sample. Among all the samples, Sample 3 exhibits best FE characteristics with maximum current up to 2.26 mA extracted from the sample.

Field emission measurement were repeated several time for each sample. Figure 5 shows the FE characteristics of sample 2 in successive run. CNTs of sample 2 were grown with a substrate pre-treatment at $1050^0$ C temperature. Figure 5 represents the I vs. $E_a$ characteristics of the sample. The 1 st run shows lower onset voltage at 1.07 V/µm. In successive runs the sample shows stable slightly higher applied voltage but stable FE characteristics. It is evident from Figure 5 that for run 2, 3 and 4, emission current graphs are coinciding with each other.

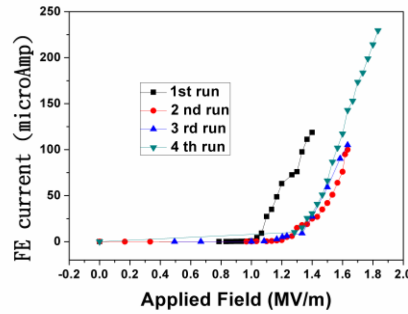


Figure 5 : FE characteristics of CNT sample 2

## CONCLUSIONS

In this paper we have presented the result of field emission characteristics study conducted on suitable cathode material. This study will help developing a practical field emission gun by using improved CNT-cathode. Randomly oriented multi-walled carbon-nanotubes grown on oxidized inconel substrate which show good field emission property. Field emission current up to 2.26 mA is obtained at 2.28 KV DC voltages from the best CNT sample. The emission currents for the samples remain fairly constant during the experiment.

## REFERENCES


[1] H. Talapatra S, Kar S, Pal SK, Vajtai R, Ci L, Victor P, et al, "Direct growth of aligned carbon nanotubes on bulk metals", Nat Nanotechnol 2006;1:112–6.

[2] Y. Hozumi et al., "Devepoment of electron gun of carbon nanotube cathode", Proc. of the PAC05,Knoxville,Tennessee, May 2005, pp. 1392-139

# DESIGN OF STRIPLINES FOR TUNE MEASUREMENT IN INDUS-1

Mukesh Kumar [#1], A.K. Karnewar[1], S. Yadav[1,2], Y. Sheth[1] and T. A. Puntambekar[1]
[1]Beam Diagnostics & Coolant Systems Division Raja Ramanna Centre for Advanced Technology, Indore
[2]Homi Bhabha National Institute, BARC Training School Hostel Building, Anushakti Nagar, Mumbai
#mukeshk@rrcat.gov.in

***Abstract***

Striplines are widely used for the controlled excitation and measurement of the transverse coherent oscillations of the charged particle beam in an accelerator for betatron tune measurement. Two striplines i.e. kicker and pickup are designed for the development of betatron tune measurement system for Indus-1. In the design, the geometries of the pickup and kicker striplines are optimized to achieve 50 Ω characteristic impedance. Important characteristic parameters like transverse shunt impedance of the kicker stripline and transfer impedance & position sensitivity of the pickup stripline are also obtained through electromagnetic simulations using CST Studio Suite. The paper presents conceptual design and simulation results of both the striplines designed for the betatron tune measurement for Indus-1 ring.

## INTRODUCTION

Indus-1 [1] is a 450 MeV Synchrotron Radiation Source (SRS). Resonance of transverse oscillations can result into partial or complete loss of the beam. Therefore, online betatron tune measurement is very important in cyclic accelerators like Indus-1. Two striplines [2] are required for online non destructive tune measurement system in Indus-1. The betatron oscillations will be independently excited in horizontal and vertical planes using one stripline. The other stripline will detect and measure the frequency these oscillations in both the planes. The rf frequency of Indus-1 is 31.6 MHz. The tune measurement system will operate at 126.4 MHz i.e. 4th harmonic.

Two striplines namely pickup stripline and kicker stripline have been designed for Indus-1 tune measurement system. The geometries of the striplines are optimized to get 50 Ω characteristic impedance for minimum reflections between striplines and external electronics (power amplifier and BPM electronics). Simulations of pickup and kicker striplines are carried out using CST PARTICLE STUDIO [3] to obtain transfer impedance, position sensitivity and transverse shunt impedance which serve as figure of merit of these devices. Conceptual design and simulation analysis of pickup and kicker striplines are presented in following sections.

## PICKUP STRIPLINE

For independent horizontal and vertical tune measurement, the pickup stripline consists of four electrodes. The electrodes are placed at $45^0$ angle with respect to horizontal and vertical axes as shown in Fig. 1. The azimuthal width of each electrode is $60^0$. Optimum length of electrode for maximum pickup signal is $L = \frac{c}{4f}$ that is ~593.35 mm for $f$=126.4 MHz. Due to limitation of space, the actual length of electrode is taken to be 180 mm which gives ~46% of the maximum signal. Pickup signal of stripline whose upstream port is matched with its characteristics impedance does not depend on the load at downstream end [2]. Therefore, to simplify the mechanical design, the downstream ends of the electrodes are shorted with vacuum chamber. The other advantage of this configuration is that it eliminates the requirement of impedance matching at the downstream end. Electrodes orientation of pickup stripline is shown in Fig. 1 and the physical dimensions of various parts are given in table 1.

Table 1: Physical Dimensions of Various Parts of Pickup and Kicker Striplines

| Sr. No. | Parameter | Pickup Stripline | Kicker Stripline |
|---|---|---|---|
| 1 | Azimuthal width of electrode (ϕ) | $60^0$ | $60^0$ |
| 2 | Radius of electrode ($R_s$) | 30 mm | 30 mm |
| 3 | Length of electrode (L) | 180 mm | 180 mm |
| 4 | Thickness of electrode (ts) | 2 mm | 2 mm |
| 5 | Radius of outer enclosure ($R_0$) | 38.5 mm | 56 mm |
| 6 | Azimuthal gap between electrode and grounded electrode(φ) | --- | $7.5^0$ |

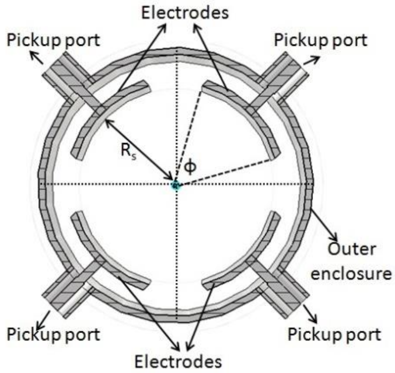

Figure 1: Cross section of pickup stripline showing electrodes orientation.

### *Characteristic impedance*

Characteristic impedance of a pickup electrode is a function of physical dimensions of the electrode and the outer enclosure. Microwave Studio (MWS) of CST STUDIO SUITE is used to optimize separation between outer enclosure and pickup electrode to get ~50 Ω characteristic for each electrode in pickup mode (even mode). Simulation of port impedance in CST MWS gives line impedance which is equal to the characteristic impedance for matched stripline. Therefore, to obtain characteristic impedance, the other end of the stripline has been matched using waveguide port. The line impedance which is also the characteristic impedance of full stripline containing all (four) electrodes is shown in Fig. 2. Characteristic impedance of single electrode is equal to the characteristic impedance of full stripline multiplied by the number electrodes. Simulation shows that the characteristic impedance of full stripline is ~12.52 Ω. Thus, the characteristic impedance of single electrode is ~50.1 Ω.

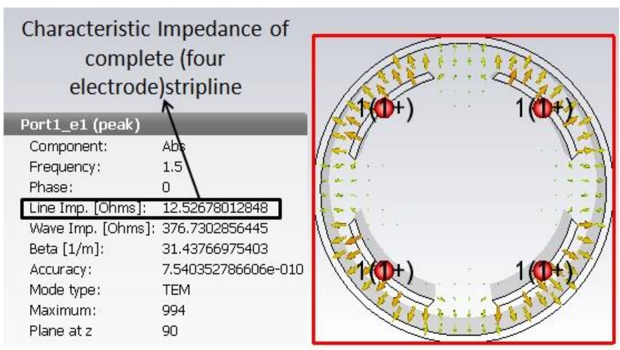

Figure 2: Line impedance of full stripline containing four electrodes. Characteristic impedance of single electrode is ~50.1 Ω (see text for detail).

### *Transfer impedance and position sensitivity*

The effectiveness of pickup stripline for detection of transverse oscillations is proportional to the product of transfer impedance and position sensitivity. These parameters (transfer impedance and position sensitivity) are obtained using wakefield solver of CST PARTICLE STUDIO (CST PS). Variation of transfer impedance with frequency is shown in Fig. 3. The transfer impedance ($Z_T$) of pickup stripline at 126.4 MHz is 4.9 Ω. Position sensitivity of pickup stripline (defined through equation (1) ) is 0.047 mm$^{-1}$.

$$S_x = \frac{1}{\Delta x}\frac{(V_A+V_B)-(V_C+V_D)}{(V_A+V_B+V_C+V_D)} \text{.................(1)}$$

Here $\Delta x$ is beam shift along x-axis and $V_A$, $V_B$, $V_C$, $V_D$ are pickup signals as shown in Fig. 4.

Due to $90^0$ rotation symmetry about stripline axis, the position sensitivity of pickup stripline is same in both transverse planes. For $Z_T$=4.9 Ω and $S_x$=0.047 mm$^{-1}$, the difference signal (($V_A$+$V_B$)-($V_C$+$V_D$)) at pickup electrodes is ~ -65 dBm for 100 mA average beam current and 1 μm beam offset.

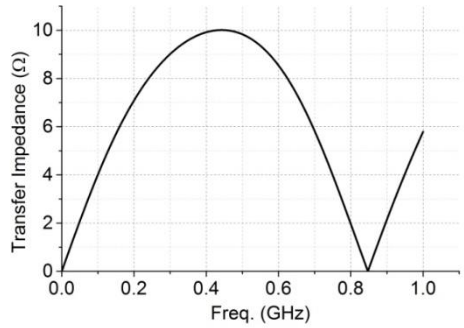

Figure 3: Transfer impedance of pickup stripline.

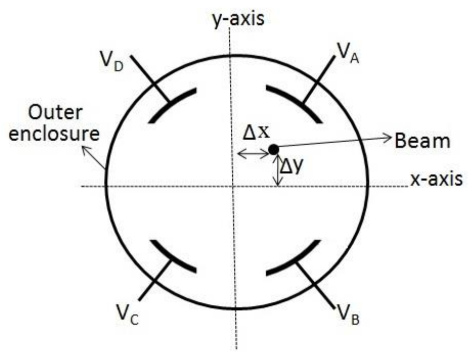

Figure 4: Nomenclature of pickup signal used for defining position sensitivity (see text).

## KICKER STRIPLINE

Similar to pickup stripline, the kicker stripline also consists of four electrodes for independent measurement of horizontal and vertical tunes. Each electrode has $60^0$ azimuthal width and placed at $45^0$ angle with respect to horizontal and vertical axes. The ground conductor (outer enclosure) is extended between two consecutive electrodes to reduce inter electrode coupling and get similar characteristic impedance in kicker (odd) and pickup (even) modes. Cross section of kicker stripline is shown in Fig. 5 and various dimensions are given in table 1.

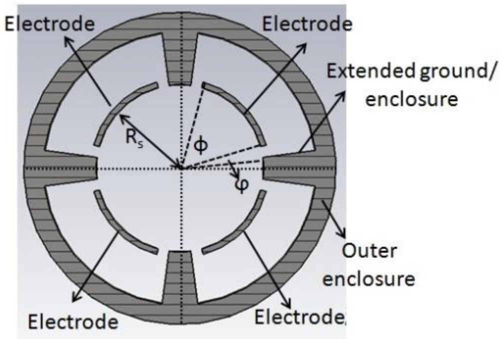

Figure 5: Cross section of kicker stripline showing electrodes orientation.

### *Characteristic impedance*

Kicker stripline can be excited in different modes. For vertical tune measurement, the electrodes above the horizontal plane are excited with $180^0$ phase difference with respect to electrodes below the horizontal plane (Fig. 6a). This mode of excitation is called vertical kicker mode. Similarly, for horizontal tune measurement the electrodes on right hand side of vertical plane are excited with phase difference of $180^0$ with respect to electrodes on left hand side of vertical plane (Fig. 6b). This mode of excitation is called horizontal kicker mode. Due to $90^0$ rotation symmetry about stripline axis, the characteristic impedance of kicker stripline is same in both modes.

Transverse geometry and dimensions of kicker stripline is optimized using CST MWS to get ~50 Ω characteristic impedance in kicker mode. The characteristic impedance obtained through simulation is ~49.9 Ω in vertical/horizontal kicker mode and 55.4 Ω in pickup mode (all electrodes at same potential).

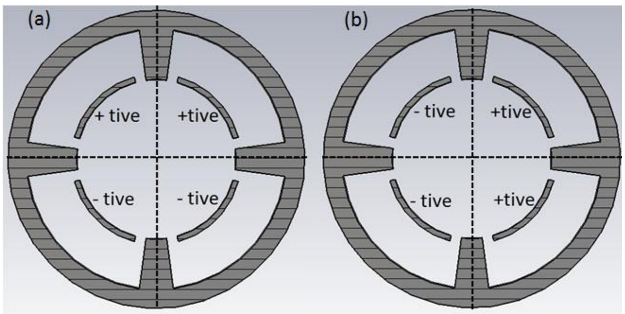

Figure 6: Vertical and horizontal modes of excitation of kicker stripline; (a) vertical mode (b) horizontal mode.

### *Transverse shunt impedance*

Efficiency of the kicker stripline is governed by its shunt impedance. The relation between transverse kick ($\theta_{kick}$), power ($P$) fed into the kicker and shunt impedance ($R_{sh}$) of a kicker is given by [4]

$$\theta_{kick} = \frac{e}{E}\sqrt{2PR_{sh}} \text{ .................(2)}$$

Here $e$ and $E$ are charge and energy of particle passing through the kicker.

Analytical expression of transverse shunt impedance at frequency 'ω' is given by [5]

$$R_{sh} = 2Z_0 \left(\frac{g_\perp c}{\omega R_s}\right)^2 sin^2\left(\frac{\omega L}{c}\right) \text{ ............(3)}$$

Here $L$ is electrode length, $c$ is velocity of light, $Z_0$ is characteristic impedance of single electrode, $R_s$ is radius of electrode and $g_\perp$ is geometry factor given by

$$g_\perp = \frac{8}{\varphi\pi} sin\left(\frac{\varphi}{2}\right) sin\left(\frac{\varphi+\phi}{2}\right) \text{ ..........(4)}$$

Transverse shunt impedance of kicker stripline is also obtained through simulation using CST PARTICLE STUDIO. Fig. 7 shows variation of shunt impedance with frequency obtained through simulations and equation (3). At 126.4 MHz, the transverse shunt impedance is ~1665 Ω.

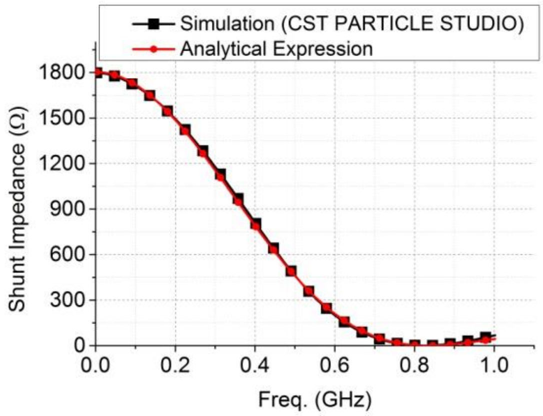

Figure 7: Shunt impedance of kicker stripline.

## SUMMARY

Design of kicker and pickup striplines for non destructive tune measurement for Indus-1 is presented. Transverse geometries of the striplines are optimized to get 50 Ω characteristic impedance for impedance matching between striplines and external electronics. Important parameters like transfer impedance, position sensitivity and shunt impedance are also obtained through simulations using CST MWS and CST PS. Simulation results are in very good agreement with those obtained from analytical expression.

## REFERENCES

[1]http://www.rrcat.gov.in/technology/accel/isrf_index.html#
[2] R.E. Shafer, Beam position monitoring, AIP Conference Proc. 212, pp. 26 (1990).
[3] CST STUDIO SUITE website: http://www.cst.com
[4] U. Iriso, T.F. Gunzel and F. Perez, Design of the stripline and kicker for ALBA, Proceeding of DIPAC09, Basel, Switzerland, pp. 86-88.
[5] D. Olsson, Design of stripline kicker for tune measurement in MAX IV 3 GeV ring, PIERS proceedings, Stockholm, Sweden, August 2013, pp. 1095-1099.

# PHYSICS DESIGN OF BEAM COLLIMATORS FOR TRANSPORT OF 1 GEV H- BEAM

Chirag Bhai Patidar# and Amalendu Sharma, ABPS, RRCAT, Indore, India

*Abstract*

The proposed configuration of Indian Spallation Neutron Source at RRCAT consists of a 1 GeV superconducting H- linac, followed by a proton accumulator ring, along with the required beam transport lines. High energy beam transport (HEBT) line transports the beam from the linac, and matches it to the accumulator ring. One of the main functions of HEBT line is to remove the halo particles coming from the linac, to minimise the uncontrolled beam loss. For betatron halo removal, betatron collimation system is located in the Linac to Achromat Matching Section (LAMS) of HEBT. It consists of two sets of horizontal scrapers (carbon foils), two sets of vertical scrapers (carbon foils) and two secondary absorbers, each absorber for both the transvers planes. Momentum collimation system consists of one set of horizontal scraper (foil) and one secondary absorber in ACHROMAT section of HEBT, to remove the longitudinal halo. Locations of scrapers and secondary absorbers are optimised to enhance the resolution of collimation system, in order to minimise the emittance of escaping halo particles from the collimators and, to achieve higher collimation efficiency, i.e. greater than 95%. In this paper, we present the physics design of betatron and momentum collimators in HEBT.

## INTRODUCTION

Optics design of HEBT line and its schematic is described in Reference [1]. HEBT consists of three sections namely Linac to Achromat Matching Section (LAMS), ACHROMAT section and Achromat to Ring Matching Section (ARMS). A major requirement for all parts of the 1 GeV proton/H- accelerators is that the uncontrolled beam loss should be < 1 W/m, to allow hands on maintenance of the accelerator. To achieve such a low beam loss, the beam halo coming from the linac is required to be removed in the HEBT, using collimators.

Betatron collimators, as well as momentum collimators are used in the HEBT line, which are located in the LAMS and ACHROMAT sections, respectively. The schematic arrangement of betatron collimators in LAMS is shown in Fig. 1. It consist of four sets of carbon foils of ~5 μm thickness, and two 1.2 m long halo absorbers of iron, each absorber for both the transverse planes.

Momentum collimators consist of one set of momentum scraper (foil) and a secondary absorber. The schematic arrangement of momentum collimators in ACHROMAT section is shown in Fig. 2.

First, Details of the betatron collimation scheme is presented and then the momentum collimation scheme is described.

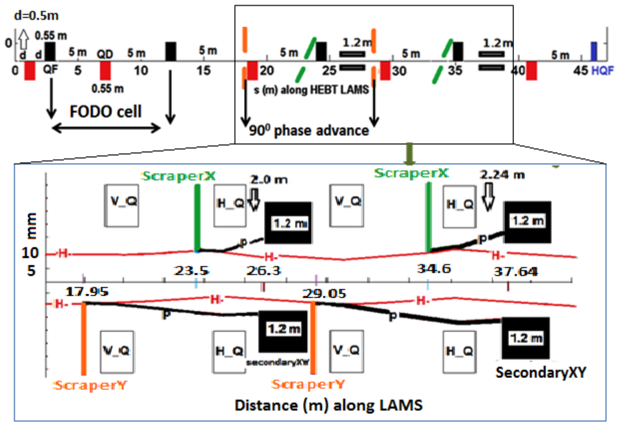


Figure 1: Schematic arrangement of betatron collimators in LAMS of HEBT. Red trajectory is for H- ion, which hits the foil and gets stripped. Thick black trajectory is for the converted proton, which goes to the absorber. V_Q and H_Q are vertical focusing and horizontal focusing quadrupoles, respectively.

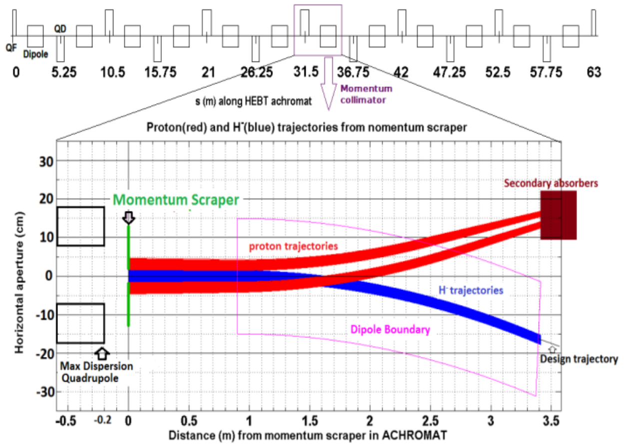


Figure 2: Schematic arrangement of momentum collimators in ACHROMAT section of HEBT.

## BETATRON COLLIMATION SCHEME

For understanding the collimation scheme, consider two horizontal foils (primary collimators), both having same normalized aperture $\pm X_{foil}$, and located at a distance of π/2 phase advance from each other. Here, $X_{foil} = x_{foil}/\sqrt{\beta}$, and $\pm x_{foil}$ and $\beta$ are the foil aperture and beta function respectively, at the foil location, which may be different for the two foils. We have chosen $x_{foil}$ as four times the rms beam size at the foil location, to ensure that only halo particles hit the foil.

#chirag@rrcat.gov.in

The H- particles, which hit the first foil, are beyond the vertical straight lines at a horizontal distance of normalized foil aperture $\pm X_{foil}$ in the normalized phase plane (Fig. 3a). Downstream to this foil location, all the particles will rotate in the normalized phase plane, and will be confined within the horizontal lines at a vertical distance of $\pm X_{foil}$, after a phase advance of $\pi/2$ (Fig. 3b) [2]. At this location, again, H- particles lying beyond the vertical straight lines, at a horizontal distance of $\pm X_{foil}$ will be scrapped by the second foil. Thus the H- particles lying inside the region made by black and red lines will pass through the foils, without getting scrapped, and the remaining particles will get scrapped. For the most general case, if the two foils are kept at a phase advance of $\theta$, this system will scrap all the halo particles having emittance beyond $\epsilon_{x,un,max} = 32\epsilon_{x,un,rms}\left(\frac{1+|\cos\theta|}{\sin^2\theta}\right)$. The value of $\theta$ is chosen as $\pi/2$ in order to minimize $\epsilon_{x,un,max}$. The two-foil system thus scraps all the halo particles having emittance beyond $32\epsilon_{rms}$, i.e., 5.66 mm-mrad, as shown in Fig. 3 for one transverse plane. The H- particles scrapped by these foils get converted into protons. Due to downstream quadrupoles (at a distance of 25 cm after each foil) in LAMS, protons and H- beam separate well due to their opposite charges, i.e. halo is separated from the beam, and can be collected at the suitably located secondary absorbers. Separation of halo protons from the normal H- beam makes it easy to remove them at the absorber, due to the large impact parameter (distance between the impact position of proton and the inner edge of absorber).

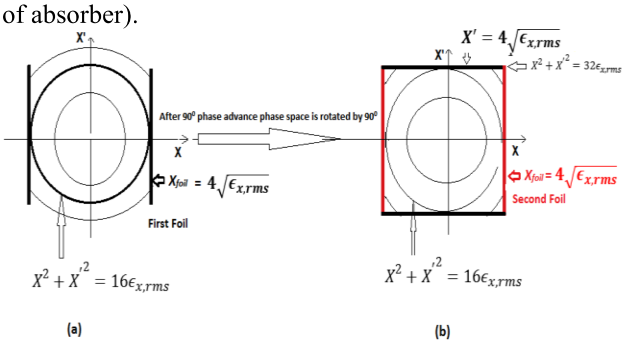


Figure 3: Normalized phase space at (a) the first foil location, and at (b) the second 2nd foil location.

It is preferable to put the foils at the location of higher beta function for the given transverse plane, to enhance the cleaning resolution [3]. Hence, the foils have been placed near quadrupoles, where beta function is high for the respective transverse plane. Locations of secondary absorbers were decided based on the ray trajectories of protons from each foil. As the secondary absorber is combined function for both horizontal and vertical plane, we looked for the location where ray tracing from foils provide maximum aperture (also maximum separation of protons and H- beam) for absorber in both the transverse planes. Fig. 4 shows the ray trajectories of protons from foils and optimised location of secondary absorbers in LAMS. The aperture of secondary absorber is kept at least $\pm 8\sigma$ throughout the entire length of 1.2 m.

Next, we discuss the calculation of collimation efficiency. Collimation efficiency is defined as the ratio of number of particles that are collected at the secondary absorber, divided by the number of particle that intercepted this absorber [3]. To calculate the collimation efficiency, 500,000 H- particles were generated at HEBT input which have Gaussian distribution with rms properties of the linac output beam, given in Table 1. Thereafter these H- particles were tracked upto 2nd secondary absorber using PARMELA [4] code. Absorption of the particles, which collided on each secondary absorber, is obtained using ORBIT code [5].

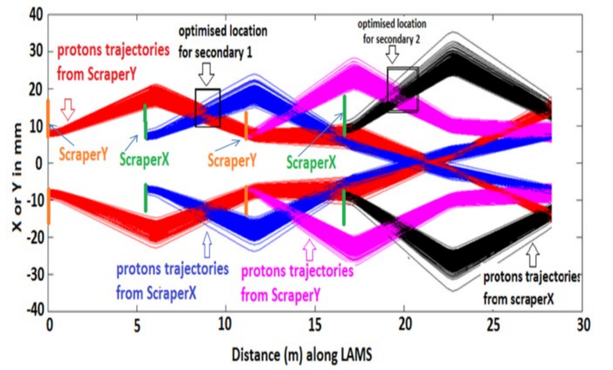


Figure 4: Ray tracing of protons from foils and optimised location of secondary absorbers.

Table 1: Beam Twiss Parameters at HEBT input

| | |
|---|---|
| $\alpha_{x/y}$ | -0.188/-1.25 |
| $\beta_{x/y}$ (m/rad) | 26.56/40.22 |
| $\varepsilon_{x/y,\ un,\ rms}$ (mm-mrad) | 0.177/0.178 |
| $\alpha_z$ | -0.17 |
| $\beta_z$ (deg/MeV) | 1.276 |
| $\varepsilon_{z,rms}$ deg-MeV | 0.1258 |
| $\delta_{rms/100\%}$ | 0.023%/0.1% |

In order to consider the effect of each foil, tracking of particles from HEBT input to 2nd secondary absorber was done in steps, updating the effect of a foil set, in a step. At each foil set, it is assumed that all the H- particles, which hit the foil, convert in protons, and then the multi coulomb scattering of these protons in the foil is computed by a self-written program, based on the foil scattering routine of ORBIT code.

Protons and H- particles at the beginning edge of each secondary absorber is shown in Fig. 5. This figure shows the separation of the H- particles and proton halos at the beginning edge of 1st and 2nd secondary absorbers. Due to the separation in H- particles and halo protons, only halo protons are lost at the secondary absorber and higher collimation efficiency is obtained.

As can be seen in Figure 5, very few protons hit the secondary absorbers, resulting into poor statistics for the calculation of collimation efficiency. In order to increase the number of proton hits at secondary absorbers, we displaced the H- beam centroid at HEBT input, either in horizontal direction by 5 mm or in vertical direction by -8 mm. For each centroid displacement, few thousand halo protons hit the secondary absorbers and then get absorbed. The obtained collimation efficiency for all above cases is more than 99.75%.

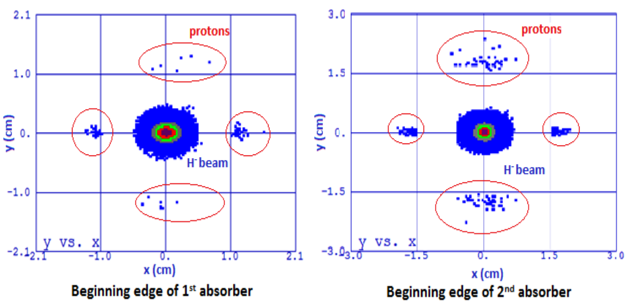


Figure 5: Separation of H⁻ beam and halo particles (converted to protons) at beginning edge of secondary absorbers of betatron collimators.

## MOMENTUM COLLIMATION SCHEME

In this scheme, we have a momentum halo scraper (foil) located at suitable location. The scraper strips off momentum halo H⁻ particles into protons. After stripping, the protons are bent in the opposite direction relative to H⁻ beam by the nearby downstream main dipole, and are collected at the secondary absorber (dump) outside the main line as shown in Fig. 2. The entire vacuum chamber for the dipole magnet is designed to pass the H⁻ beam particles and proton halo particles. Collimation efficiency is nearly 100%, as the absorber is located outside the main line. Here, we have assumed that all the H⁻ particles, which intercept the scraper, get converted to protons.

Let us assume that a foil having horizontal aperture of $\pm x_{\mathrm{foil}}$ is kept at a location having the normalized dispersion $D_x/\sqrt{\beta_x}$. The particles that *pass through* the scrapper foil, will have normalized momentum deviation (i.e., momentum deviation divided by momentum) between $\pm\delta_2$, where $\delta_2$ is given by

$$\sqrt{\beta_x \varepsilon_x} - D_x \delta_2 = x_{foil}.$$

However, due to the finite beam size, not all the particles having normalized momentum deviation between $\pm\delta_2$ will necessarily pass through the foil. Only the particles having normalized momentum deviation between $\pm\delta_1$ are guaranteed to pass through, where $\delta_1$ is given by

$$D_x \delta_1 + \sqrt{\beta_x \varepsilon_x} = x_{foil}.$$

Particles in between these two momentum deviations might get scraped, or pass through, depending on the betatron phase and emittance of the particle. This window of momentum deviation, for which there is an uncertainty in getting scrapped or passing through, is given by

$$\delta_2 - \delta_1 = \delta_{window} = \frac{2\sqrt{\beta_x \varepsilon_x}}{D_x}$$

The $\delta_{window}$ depends on the inverse of normalized dispersion, and is independent of foil aperature. Higher normalized dispersion makes this window of momentum deviation small, and is thus ideal location for placing the momentum scraper. Therefore, we have placed momentum scraper in ACHROMAT section where normalized dispersion $(\frac{D_x}{\sqrt{\beta_x}})$ is sufficiently high, at 20 cm downstream to maximum dispersion quadrupole.

At the location of momentum scraper, $D_x$ = 6.48 m, $\beta_x = 16.19\, m$ and maximum emittance of particle coming from betatron collimator is $\varepsilon_{x,max} = 5.66\, \pi\, mm - mrad$. Thus the window of momentum deviation $\delta_{window}$ is 0.3%. If we set the aperture of our momentum scraper ±16.05 mm, then $\delta_1$ = 0.1% and $\delta_2$ = 0.4%. The reason to set this value of foil aperture is that the full momentum spread of the beam coming from the linac is 0.1% and the desirable momentum spread in accumulator ring during injection is less than 0.5%.

A program was written to calculate trajectories of protons and H⁻ beam starting from foil. The trajectories information is required for deciding the dipole vacuum chamber dimensions to contain both proton and H⁻ beam. Fig. 2 shows the trajectories of protons (red) and H⁻ beam (blue) starting from momentum scraper for emittance and momentum deviation upto 5.66 mm-mrad and ± 0.6%, respectively.

## CONCLUSION

We have designed betatron and momentum collimation system for HEBT. The location of secondary absorbers and foils were optimised for efficient halo removal. The maximum emittance of halo escaping from betatron collimation system is 5.66 mm-mrad. The collimation efficiency of the betatron collimation is nearly 99.8% for $4\sigma$ and $8\sigma$ apertures of foils and secondary collimators, respectively.

The maximum momentum of halo escaping from momentum collimation system is 0.4% which meets the requirement of accumulator ring during injection. The normal momentum spread of the beam coming from the linac is not affected by the momentum collimator.

## ACKNOWLEDGEMENT

We thank Vinit Kumar for very useful discussions.

## REFERENCES

[1] Chirag Bhai Patidar and Amalendu Sharma, "Beam optics design studies of the ISNS high energy beam transport line", InPAC 2018, RRCAT, Indore.

[2] N. Catalan-Lasheras and D. Raparia, "The collimation system of the High Energy Beam Transfer (HEBT) Line", BNL/NSNS Technical Note 097, July 27, 2001.

[3] Sarah M. Cousineau, "Understanding space charge and controlling beam loss in high intensity synchrotrons", Ph.D. thesis, Indiana University, February, 2003.

[4] Lloyd M. Young, "computer code PARMELA, Los Alamos National Laboratory Report No. LA-UR-96-1835, 1996.

[5] J. D. Galambos, J.A. Holmes and D. K., "ORBIT User Manual", SNS/ORNL/AP TECHNICAL NOTE Number 011, July 16, 1999.

# CHARACTERIZATION OF THE 90 keV ELECTRON BEAM AND LOW ENERGY BEAM TRANSPORT IN THE UPGRADED IR-FEL INJECTOR

Sona Chandran†, Arvind Kumar, B. Biswas, R. S. Saini, Pravin Nerpagar and K. K. Pant

RRCAT, Indore, M.P., India

### *Abstract*

The injector linac system of the infra-red free electron laser (IR-FEL) at the Raja Ramanna Centre for Advanced Technology (RRCAT) has recently been upgraded with a new thermionic electron gun, low energy beam transport line and RF accelerating structures. Initial electron beam trials have been conducted for a detailed characterization of the 90 keV electron beam from the gun, which is space charge dominated, and for qualification of the low energy beam transport line. This paper discusses the techniques employed for the measurement of the different parameters of the non-relativistic electron beam from the gun, and presents results from the initial beam trails for the measurement of these parameters, and for transport of the 90 keV electron beam from the electron gun to the entry of the main linac. The measured results agree well with those predicted from design simulations.

## UPGRADED IR-FEL INJECTOR

An Infra-Red Free Electron Laser (IR-FEL) is presently in an advanced stage of commissioning at the Raja Ramanna Centre for Advanced Technology, Indore, and the first lasing in this system has been achieved with an indigenous injector system [1]. This injector system comprised a 90 keV thermionic electron gun, a 476 MHz sub-harmonic prebuncher (SHPB), and two cascaded Plane Wave Transformer (PWT) linac structures capable of accelerating the beam up to 20 MeV [2]. Three solenoid magnets and two combined function steering magnets were used in the low energy beam transport from the 90 keV electron gun to the PWT linac structure. The maximum peak current obtained from this injector system, after selection of the electrons with an rms energy spread ~ 0.75% using an energy selecting slit, was ~ 26 A. The maximum pulse repetition rate (PRR) and macro-pulse widths that could be obtained using this injector system restricted the Continuous Wave (CW) average electron beam power to be < 0.7 W.

IR-FEL design simulations dictate a requirement of > 30 A peak current with a relative energy spread < 0.5%, which could not be achieved with this injector system even after further optimization of the injector system parameters. Improvements were required on both the fronts: the peak current (> 30 A) and the relative energy spread (< 0.5%). Table 1 summarizes the design requirements of electron beam parameters of the IR-FEL [3]. Consequently, the IR-FEL injector linac system was recently upgraded with additional pre-buncher and buncher structures, and with the two cascaded PWT Linac structures replaced with a single 3 m long travelling wave linac structure. The expected improvements in electron beam parameters from the upgraded injector linac system are summarized in ref. [4-5] and in Table 2 below. Further, by operating the injector system with a larger macro-pulse width and a higher pulse repetition rate, it is expected to deliver a CW average electron beam power ≥ 7 W, to ultimately deliver higher CW average FEL output power.

Table 1: IR-FEL design parameters

| Parameter | Value | Unit |
|---|---|---|
| Energy, E | 15-25 | MeV |
| Emittance, $\varepsilon_n$, rms | 30 | mm-mrad |
| Charge, q | 0.3-0.5 | nC |
| Pulse width (FWHM)) | 10 | ps |
| ΔE/E | <0.5 | % |

Table 2: Electron beam parameters of the indigenous versus upgraded IR-FEL injector system

| Parameter | Indigenous injector system (Measured) | Upgraded injector system (Design) |
|---|---|---|
| Energy, E (MeV) | 18.3 | 15-25 |
| RMS normalised emittance, $\varepsilon_n$ (mm-mrad) | 40-50 | 20 |
| Charge, q (nC) | 0.26 | ≥ 0.5 |
| Pulse width (FWHM) (ps) | 10 | 10 |
| ΔE/E (%) | 0.75 | <0.5 |

Design details for the upgraded injector linac system are given in ref. [6]. It starts with a thermionic electron gun capable of delivering a 90 keV beam with up to 1.5 nC charge in 1 ns (full width at half maximum, FWHM) pulses. The gun is followed by 476 MHz and 2856 MHz prebuncher structure, which bunches the 1 ns beam to ~30 ps before it is injected into the accelerating

†sona@rrcat.gov.in

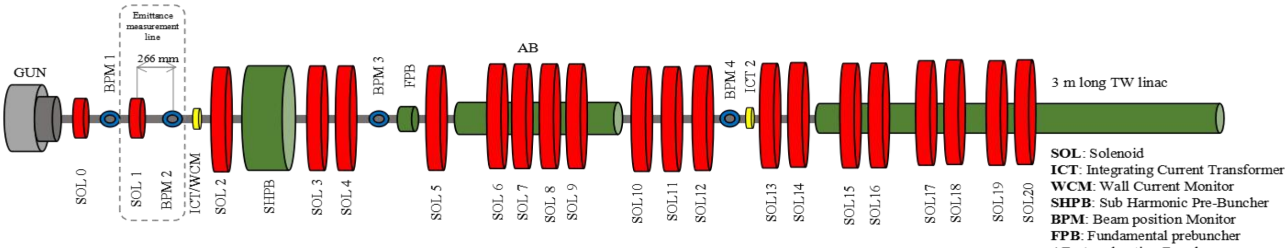


Figure 1: Schematic of the upgraded IR-FEL injector linac system

buncher (AB) for further bunching to ~10 ps and pre-acceleration to 3 MeV. The 3 m long travelling wave linac subsequently increases the energy of the bunches to 15-25 MeV. Since the upgraded injector linac system is proposed to be operated with a higher charge-per-pulse, a new LEBT has been designed and developed for the lossless transport of the non-relativistic (90 keV) electron bunches from the exit of the electron gun up to the first few cells of the main linac. Nineteen pancake solenoid magnets and seven combined function steering magnets are used in this LEBT, which extends up to the first few cells of the travelling wave linac. Figure 1 shows a schematic of the upgraded injector linac system and fig. 2 shows a picture of the upgraded system that is presently being commissioned.

Figure 2: Upgraded IR-FEL injector installed inside the tunnel

## CHARACTERIZATION OF THE LOW ENERGY, SPACE CHARGE DOMINATED ELECTRON BEAM

Lasing in an FEL critically depends up on the quality of the electron beam propagating through its undulator. Hence, it is essential to qualify the electron beam at different locations of the setup, particularly in the injector linac system and after the selection of charge with the desired relative energy spread. This section discusses the different electron beam diagnostics employed in the LEBT for the measurement of the transverse beam size, micro-pulse width, macro-pulse width, charge per micro pulse, and transverse beam emittance. The position of the beam diagnostic elements in the upgraded IR-FEL injector linac system is shown in the schematic layout in Fig. 1.

### *Beam size measurement*

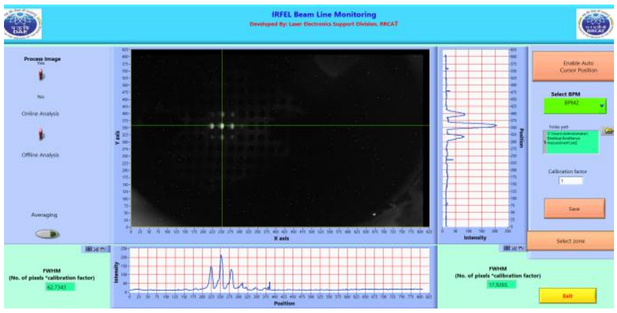


Figure 3: Beam spot at BPM 2 and the Gaussian fit on both horizontal and vertical planes

The LEBT employs three Beam Profile Monitors (BPM) to view the transverse profile of the electron beam at different locations. Another BPM is located just before the main linac. Image acquisition and analysis systems coupled to these BPMs help in the measurement of the transverse beam size at these locations. Each BPM consists of a Chromax screen mounted at an angle of 45 degrees on a linear motion feed-through. The feed-through itself is mounted orthogonal to the electron beam axis, and it facilitates movement of the screen in and out of the electron beam path. A camera, mounted in the diametrically opposite direction, is employed to view the chromax screen with the beam profile. The linear motion feed-through is operated remotely from the control room, and the fluorescence emitted by the screen when an electron bunch is incident upon it is imaged by the camera and viewed in the control room. Since the upgraded injector system operates with high charge per bunch, it causes a saturation of the Chromax screen as well as of the Charge Coupled Device (CCD) camera. While appropriate Neutral Density (ND) filters are employed between the fluorescent screen and the camera to avoid CCD saturation, the saturation of the screen itself is controlled by mounting a 0.3 mm thick screen of Stainless Steel (SS) AISI 304 grade on top of the Chromax screen. This SS screen has a network of 1.5 mm diameter holes that are spaced at a distance of 2.5 mm. Electrons in each bunch that pass through the holes to hit the Chromax screen produce fluorescence, while those hitting the SS screen are conducted to the electrical ground, thereby reducing the amount of fluorescence produced and consequently preventing the saturation of the screen. A Labview based image acquisition and analysis program developed by the LCID, RRCAT is employed for the online viewing of the beam spot, and for the online/offline analysis of the transverse beam size. More details are provided in Ref. [7]. For pixel calibration, total numbers of pixels between the two adjacent peaks are counted along horizontal as well as vertical directions. The known separation between mesh holes is divided by the pixel numbers to obtain the calibration factor. One pixel in horizontal and vertical plane are 94 and 63.5 microns respectively. Figure 3 shows a typical beam spot at BPM 2, and the Gaussian fit generated by the image acquisition software in both the planes to calculate the 'Full Width at Half Maximum' beam size. Using this setup, the electron beam size has been measured at two different locations along the LEBT, and the measured rms beam size at BPM 1 and BPM 2 are 2.34 mm and 1.25 mm respectively for the experimental set of parameters of the LEBT.

*Emittance measurement*

Measurement of the electron beam emittance has been done using a 'solenoid scan' method by employing BPM2 for measurement of the transverse beam size while scanning the magnetic field of SOL1 in the LEBT. The technique involves the comparison of the measured variation of the envelope for different solenoid settings with the theoretical variation of the beam envelope for the same solenoid settings, but considering different initial emittances for the electron beam. The actual emittance is considered as the value where best agreement is observed between the measured and theoretical plots. The rms envelope equation [9] is numerically integrated by employing the Newton Cotes rule with 4$^{th}$ order to determine the beam size and divergence at the BPM 2 location. This method duly considers the contribution of the space charge term, which is expected to be significant for the operation parameters of our electron gun.

Emittance has also been determined using the matrix method [10], which is a linear method and does not take space charge forces into consideration. Results obtained from both the methods have been compared with values predicted by the electron gun design simulations by the supplier, and with measurements performed by the supplier at the time of development of the electron gun. For 1.5 nC per bunch, the rms normalised emittance from the matrix method was 10 mm-mrad, while the envelop equation approach gives a measured value of 15-20 mm-mrad. It matches well with the design emittance of ~ 10 mm-mrad, and the value of 15-20 mm mrad measured by the electron gun supplier during factory acceptance tests. The emittance of the electron gun can be measured any time in the future using these electron beam diagnostic elements installed in the LEBT.

*Charge, micro-pulse and macro-pulse width measurement*

Figure 4: (a) Single micro-pulse and (b) 1 μs long macropulse from the gun.

The micro-pulse width from the electron gun can be varied from ~ 0.7 ns to a maximum of 1 ns (FWHM) by varying the corresponding settings on the grid pulser. Similarly, the macro-pulse width from the electron gun can be varied from a few 10s of ns to > 10 μs. Two Integrating Current Transformers (ICT), (Bergoz,ICT-122-015-5.0), installed over ceramic breaks in the vacuum beam pipe of the LEBT, are employed to measure the charge per micro-pulse, spacing between micro-pulses (repetition rate) as well as the macro-pulse width of the electron beam at two different locations along the LEBT. Figure 4a shows a single micro-pulse with the charge in the micro-pulse derived from the area under the curve and fig. 4b shows a typical electron beam macro-pulse, with micro-pulses within each macro-pulse, measured using the ICT. The charge per micro-pulse has been further confirmed using a Beam Charge Monitor [Bergoz, BCM-RFC] and very good agreement is observed between the results from BCM measurement and direct measurement from the ICT by determining the area under the curve corresponding to each micro-pulse. The time constant (~ 5 ns) of the ICT is sufficient to measure the micro-pulse spacing (~ 33.613 ns at a micro-pulse repetition rate of 27.75 MHz), and the macro-pulse width. However, it cannot be employed to measure the micro-pulse width of the electron bunches.

A Wall Current Monitor (WCM) has been developed by the BD&CSD, RRCAT for the measurement of the micro-pulse width, and it has also been installed over a ceramic break in the LEBT.

Initial experiments have been performed for qualification of the device for different micro-pulse width of bunches from the electron gun, and reasonably good agreement has been obtained between the measured micro-pulse width and the setting of micro-pulse width on the grid pulser of the gun. Figure 5 shows a typical signal from the WCM as seen on a high bandwidth oscilloscope (Make Agilent, Infiium, DSO90254A, 2.5 GHz). For a pulse width setting of 0.995 ns on the grid-pulser, the measured pulse width using the WCM is ~ 0.890 ns.

Figure 5: WCM signal for a pulse width setting of 995 ps

### *Characterization of the LEBT*

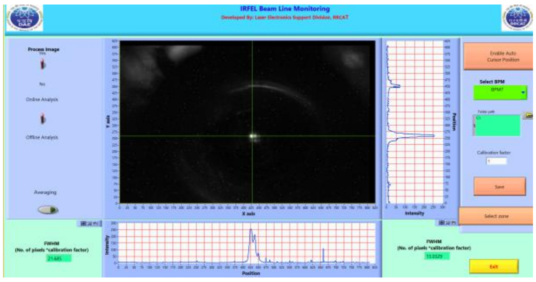

Figure 6: Beam spot at BPM 3 at the entrance of the FPB

The LEBT of the upgraded IR-FEL injector linac system has been successfully commissioned to transport the 90 keV electron beam with 1.5 nC charge per micro-pulse from the exit of the gun up to the entry of the main linac with <15% loss, which is in very good agreement with the predictions from beam dynamics simulations of the LEBT. The LEBT has sections where the physical apertures are very small (~ 11 mm inside diameter) and the magnetic field settings along the LEBT have been designed to deliver the desired small transverse electron beam size at these locations. Figure 6 shows a typical electron beam profile at the BPM3, which is just before the fundamental frequency pre-buncher with a 11 mm inside beam port at its entry. The measured rms beam size at BPM3 is 0.84 mm, which is in good agreement with design value of beam size at BPM 3. The LEBT has three BPMs and two ICTs for electron beam diagnostics, which have been successfully commissioned and employed to characterize the electron beam during transport from the electron gun to the entry to the main linac.

## CONCLUSION

The 90 keV electron beam from the gridded pulsed thermionic electron gun for the upgraded IR-FEL injector has been transported from the electron gun up to the entry of the main linac using the new LEBT that has been built and commissioned for the purpose. The space charge dominated, non-relativistic electron beam has been characterized using the electron beam diagnostic elements provided in the LEBT, and the measured beam parameters have been found to be in good agreement with predictions from design simulations.


## ACKNOWLEDGEMENT

The upgrade work was done under a collaborative effort of different divisions of RRCAT in areas of vacuum, magnets, power supply, alignment, workshops, RF power and controls. The WCM used to measure the pulse width was built by the BD&CSD, RRCAT. The technical assistance provided by Mr. Ravi Kumar Pandit, Mr. Rajkumar B. Bhowate and Mr. Sarbeswar Sardar is gratefully acknowledged.


## REFERENCES


[1] K. K. Pant, et al., Current Science 114, 2 (2018).

[2] Arvind Kumar, In Proceedings of InPAC, RRCAT, Indore, (2009).

[3] Vinit Kumar, B. Biswas, U. Kale, A. Kumar, Shankar Lal and K. K. Pant, In Proceedings of InPAC, IUAC, New Delhi,(2011).

[4] Sona Chandran, et al., "Commissioning and validation of the injector and electron beam transport systems for the IR-FEL at RRCAT", Pramana – J. Phys., 2019.

[5] Sona Chandran et al., In Proceedings of InPAC, RRCAT, Indore, (2018).

[6] Arvind Kumar et al., In Proceedings of InPAC, RRCAT, Indore, (2018).

[7] Priyadarshini Priya et al., In these proceedings.

[8] S. Barabin et al., 26th Russian Particle Accelerator Conference, RUPAC2018.

[9] Martin Reiser, "Theory and design of charged particle beams", Wiley, (2008).

[10] T. Melkumyan, "Transverse Beam Emittance Measurement Via Solenoid Scan Technique", Candle.

# SIMULATION STUDY AND MEASUREMENT OF LONGITUDINAL COUPLED BUNCH INSTABILITIES AND ITS CURE USING LONGITUDINAL BUNCH BY BUNCH FEEDBACK SYSTEM IN INDUS-2

Pradeep Kumar*, A.D. Ghodke, S. Yadav, Rajiv Arora, Akash Deep, M. Lad and T.A. Puntambekar
Raja Ramanna Centre for Advanced Technology, Indore
*e.mail :pksharma@rrcat.gov.in

*Abstract*

The bunched electron beam circulating in synchrotron light source storage ring generally induce wake fields when they pass through Radio Frequency cavity due to the interactions between circulating electrons with the Higher Order Modes of RF cavities. At higher accumulated beam current, the induced wake fields generated by leading bunch will decelerate the trailing bunches, causing them to have different synchrotron oscillation phases, if these oscillations grow then it leads to longitudinal coupled bunch beam instability. In this paper we report the beam dynamics simulations carried out for the study of the evolution of longitudinal phase space, energy and phase oscillations in presence of longitudinal coupled bunch instability in Indus-2 storage ring with 200 mA accumulated beam current at beam injection energy 550 MeV. For the control of longitudinal instability, bunch by bunch feedback system which damp the excited phase or energy oscillations of coupled bunch mode has been installed in one of the long straight sections in Indus-2. The simulation studies carried out for the control of longitudinal beam instability using feedback system are presented. The longitudinal coupled bunch instability in Indus-2 was measured by measuring the variation of the arrival time of synchrotron radiation using streak camera installed in visible diagnostic beamline. The measured results in Indus-2 without and with longitudinal feedback system are also presented in the paper.

## INTRODUCTION

The electron beam circulating in synchrotron light source storage ring will induce wake fields when it pass through the Radio Frequency (RF) cavities due to the interactions between circulating electrons with the Higher Order Modes (HOMs) of the RF cavities. Filling time of RF cavity $\tau_f = 2Q_l/\omega_{rf}$ (where $Q_l$ is the loaded quality factor of RF cavity and $\omega_{rf}$ is the angular frequency of RF cavity mode) is long for RF cavities of high quality factor. The wake fields due to the leading bunches decay exponentially according to the cavity filling time. The electro-magnetic fields remain in RF cavities when the trailing bunches arrive in the cavities. Due to these wake fields the trailing bunches decelerate and have different beam energies from the nominal values. These wake fields increases as the beam current increases, the energy deviation of trailing bunches will be gradually increased as the accumulated beam current is increased and it may lead to longitudinal coupled bunch beam instabilities. In all synchrotron radiation facilities, there is a requirement from synchrotron radiation users to provide high intensity stable photon beam but there is limitation to store higher beam current due to the longitudinal and transverse coupled bunch instabilities. To control the beam quality and storage of higher beam current in storage ring, active feedback systems in transverse and longitudinal plane [1] are applied. In this paper we present simulation studies and measured results carried out without and with longitudinal feedback system in Indus-2.

## Simulation of longitudinal coupled bunch instability [2-3]

With consideration of the wake field effect, the equation of motion for a macro-particle is

$$\frac{d^2\tau_n(t)}{dt^2} + 2\left(\frac{1}{\tau_d} - \frac{1}{\tau_g}\right)\frac{d\tau_n(t)}{dt} + \omega_s^2\,\tau_n(t) = 0 \qquad (1)$$

where $\tau_d$ the synchrotron damping time in longitudinal plane, $\tau_g$ is the growth time due to the wake field and $\omega_s$ is synchrotron oscillation frequency. The motion of the macro-particle is not stable if $\tau_g < \tau_d$. In the longitudinal phase space, the electron motion at different revolutions can be represented by equations as

$$\tau_{n+1} = \tau_n - \alpha\, T_{rev}\, \varepsilon_n \qquad (2)$$

$$\varepsilon_{n+1} = \varepsilon_n\left(1 - \frac{2T_{rev}}{\tau_d}\right) - \frac{2\pi \nu_s^2}{h\alpha} Sin\left(\omega_{rf}\, \tau_{n+1}\right) \qquad (3)$$

where $n$ :number of revolutions, $T_{rev}$ :revolution time, $\nu_s$: synchrotron tune, $E_s$ :synchronous energy, $\alpha$ : momentum compaction factor and $\omega_{rf}$ :RF frequency.

A simulation study on the deviation in beam arrival time and energy in presence of longitudinal coupled bunch beam instabilities at 200mA beam current at beam injection energy 550MeV in Indus-2 has been carried out using above equations. For the simulation, the growth rate of one longitudinal coupled bunch mode due to RF HOM is 1ms which is less than the natural damping time

~212ms. The tracking of particle up to 5000 revolutions in presence of instabilities was carried out considering initial condition of time and energy deviation $\Delta t = 0.001ns\ and\ \Delta E = 0.0$ of macro-particle with respect to the synchronous particle. The evolution of longitudinal phase space, time deviation and energy deviation with number of revolutions are shown in Figure 1(a-c) respectively which clearly indicate the instable beam without any corrective action.

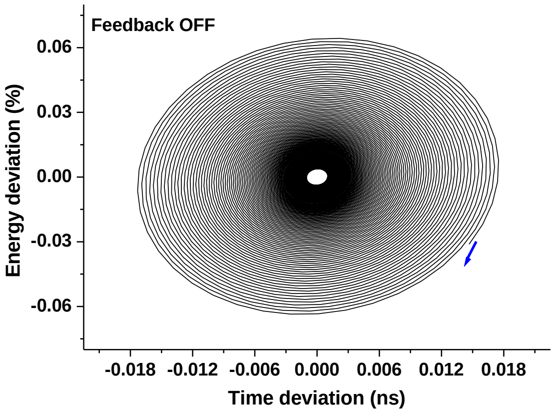


Fig. 1(a): Evolution of longitudinal phase space

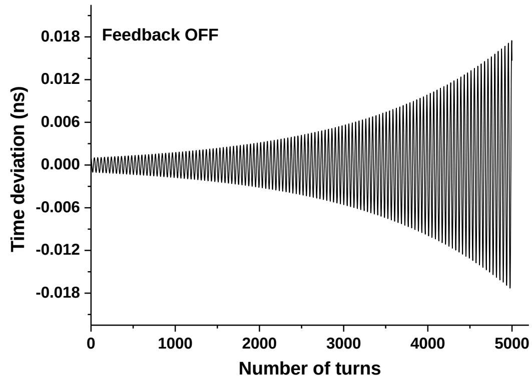


Fig. 1(b): Growth in time deviation with revolutions

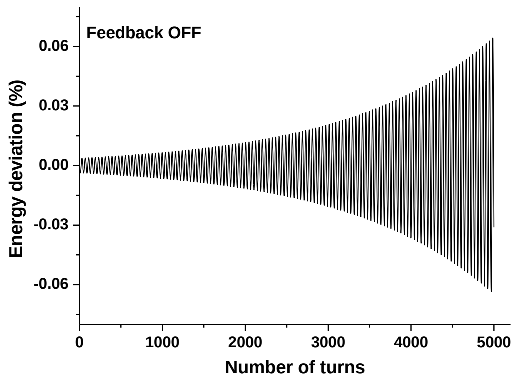


Fig. 1(c): Growth in energy deviation with revolutions

## Simulation study with longitudinal feedback system [2-3]

To arrest the growing oscillations in time and energy, a longitudinal feedback which damp the oscillations to be applied. Introducing damping effect of the longitudinal feedback in the equation of synchrotron motion as

$$\ddot{\tau}_n(t) + 2\left(\frac{1}{\tau_d} - \frac{1}{\tau_g} + \frac{1}{\tau_{lfb}}\right)\dot{\tau}_n(t) + \omega_s^2\,\tau_n(t) = 0 \qquad (4)$$

$\tau_{lfb}$ is the damping time of longitudinal feedback system.

Considering feedback damping time 0.1ms, particle tracking with feedback system was carried out. The effect of feedback system on longitudinal phase space, time deviation and energy deviation are shown in Figure 2(a-c) respectively which clearly indicates the damping of synchrotron oscillations with the application of longitudinal feedback system.

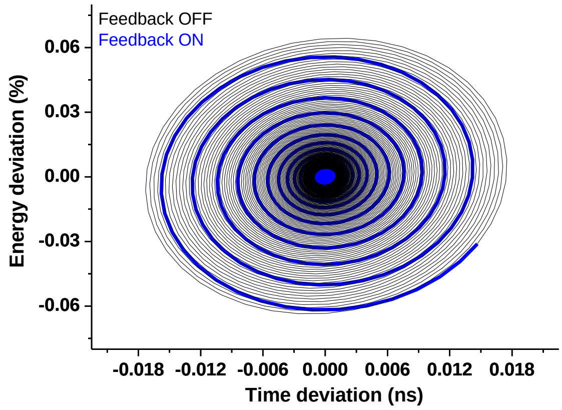


Fig. 2(a): Phase space without and with feedback

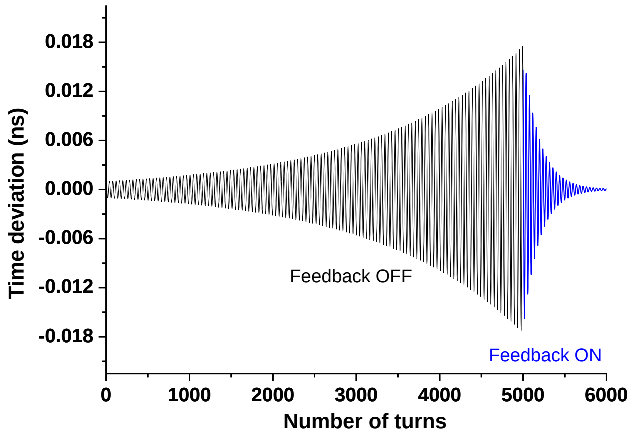


Fig. 2(b): Oscillations without and with feedback

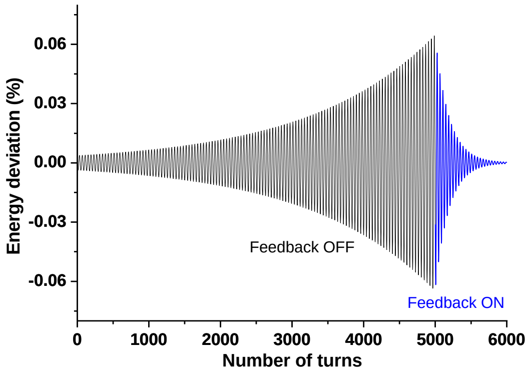


Fig. 2(c): Oscillations without and with feedback

## Measurement of Instabilities without and with longitudinal feedback system

After the installation of longitudinal multi-bunch feedback (LMBF) system in Indus-2 as shown in Figure.3, preliminary experiments with beam were conducted for the observation of excited longitudinal coupled bunch mode and its control by applying energy kick via longitudinal kicker cavity installed in one of the long straight section in Indus-2 ring.

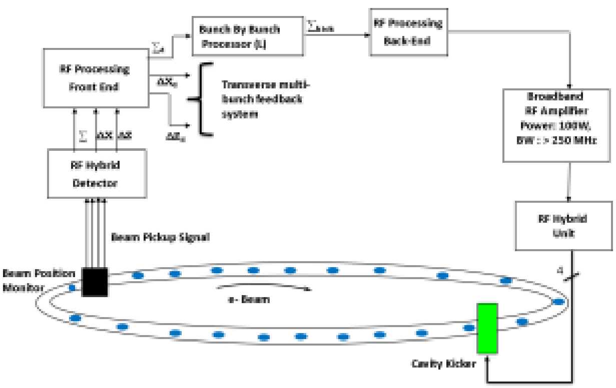


Fig.3: Longitudinal multi-bunch feedback in Indus-2

The longitudinal coupled bunch instability was measured by using spectrum analyser to observe excited coupled bunch mode and simultaneously by measuring the variation in the arrival time [4] of photon beam using streak camera installed in visible diagnostic beamline BL-23. In presence of longitudinal coupled bunch instability, the excited coupled bunch mode number 65 as observed from spectrum analyser is shown in Figure 4(a). In the present condition, longitudinal kick using LMBF system was applied and measurement was taken. The measurement of coupled bunch mode with LMBF system ON is shown in Fig. 4(b). It clearly indicate the control of longitudinal coupled bunch mode number 65 by the application of longitudinal multi-bunch feedback system.

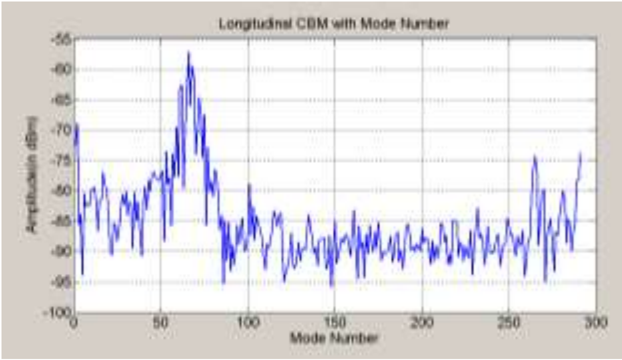


Figure. 4(a): Longitudinal excited mode without feedback

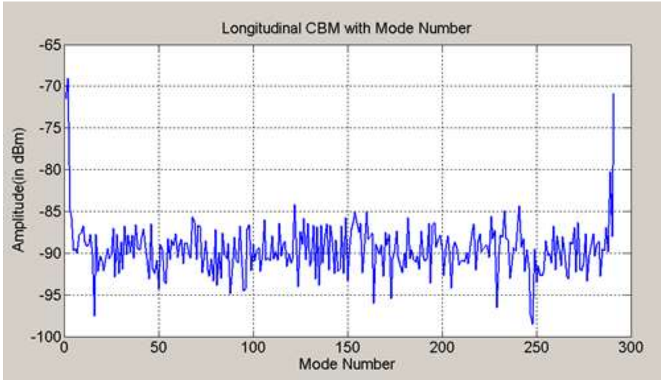


Figure. 4(b): Longitudinal mode with feedback

## CONCLUSION

A simulation study on the longitudinal coupled bunch instability and its cure using longitudinal feedback system in Indus-2 was carried out. Preliminary beam experiments were also carried out successfully to see the effect of feedback system on the control of longitudinal beam instabilities in Indus-2 ring. The feedback system is very useful for the storage of higher beam current and also for the improvement in photon beam quality for synchrotron radiation users.


## ACKNOWLEDGEMENTS

Authors are thankful to Sh. Nitesh Tiwari, Sh. M. Prasad, and Sh. H. Vaishnav from RFSD, Sh. A.C. Hollikatti, Sh. Avnish Ojha, Sh. Rahul Jain from BD&CSD and all shift crew members for fruitful discussion and support during the experiments conducted without and with longitudinal feedback system.


## REFERENCES


[1] S.Khan, T. Knuth, Longitudinal and Transverse feedback systems for BESSY-II

[2] Wenzhong Wu, Ph.D. Thesis on Feedback Systems for control of coupled bunch instabilities in the Duke Storage ring.

[3] M. Lonza, Multi-bunch feedback systems.

[4] S.Khan, Collective phenomena in Synchrotron Radiation Source, Springer-Verlag 2006.

# COUPLED BUNCH BEAM INSTABILITY DUE TO RESISTIVE WALL OF VACUUM CHAMBER AND ITS CURE IN HIGH BRILLIANCE SYNCHROTRON RADIATION SOURCE

Pradeep Kumar*, D.K. Tyagi, A.D. Ghodke
Raja Ramanna Centre for Advanced Technology, Indore
*e.mail :pksharma@rrcat.gov.in

*Abstract*
To design an ultra-low emittance electron storage ring for High Brilliance Synchrotron Radiation Source (HBSRS), there is a need of high strengths of quadrupole and sextupole magnets. To attain these strengths of magnets, small bore radii of the quadrupole and sextupole magnets are essentially desired, thus the vacuum chamber of HBSRS has a small aperture. For enhancement of photon beam brightness, in-vacuum undulators magnet of vertical gap ~5 mm will be required. Due to narrow vertical gap and finite electrical conductivity of chamber, the impedance due to resistive wall of the vacuum chamber become very significant, due to which beam motion become unstable. In this paper we report the longitudinal loss factor and bunch centroid motion in transverse plane in presence of long range resistive wall wake field generated due to small vertical gap ~5 mm of undulators magnet using tentative lattice parameters of HBSRS with 200 mA beam current at beam energy 6 GeV. The transverse resistive wall instability can be controlled by increase in chromaticity. How effectively the chromaticity is controlling the transverse resistive wall beam instability is also presented in the paper.

## INTRODUCTION

The beam instability due to resistive wall of vacuum chamber is mainly the transverse coupled bunch instability arising due to long range resistive wall wake fields. The long range transverse resistive wall wake field is zero when t ≤ 0, otherwise scales as $1/\sqrt{t}$ , with the prefactor determined by summing up the contributions from various chambers around the ring. The long range resistive wall dipolar wake field along vertical plane is given as [1]

$$W_D(t) = \sum_m \frac{g_m \beta_{y,m}}{\pi b_m^3} \sqrt{\frac{Z_0 \rho_m}{\pi}} \frac{c L_m}{\sqrt{ct}} \quad (1)$$

where $\beta_{y,m}, b_m, \rho_m, L_m$ are average beta function, vertical aperture, resistivity and length of vacuum chamber $m$, $g_m$ is the geometrical factor which is unity for round chambers and $\pi^2/12$ for elliptical insertion device chamber. The wake field along horizontal plane is given by similar expression with a change $\beta_{y,m}$ to $\beta_{x,m}$ and the factor $g_m$ is unity for round chambers and $\pi^2/24$ for elliptical chambers. The longitudinal wake field is given as

$$W_z(t) = \sum_m \frac{1}{4\pi b_m} \sqrt{\frac{Z_0 \rho_m}{\pi c}} \frac{L_m}{t^{3/2}} \quad (2)$$

## Estimations of Transverse and Longitudinal Wake functions in HBSRS [2-4]

The transverse and longitudinal wake functions were estimated considering the lattice functions of candidate lattice of circumference of ~912 m which consists of 32 periodic unit cell. A unit cell consists of 7 bending achromat (7BA) [5] of length ~28.5 m is shown in Fig.1.

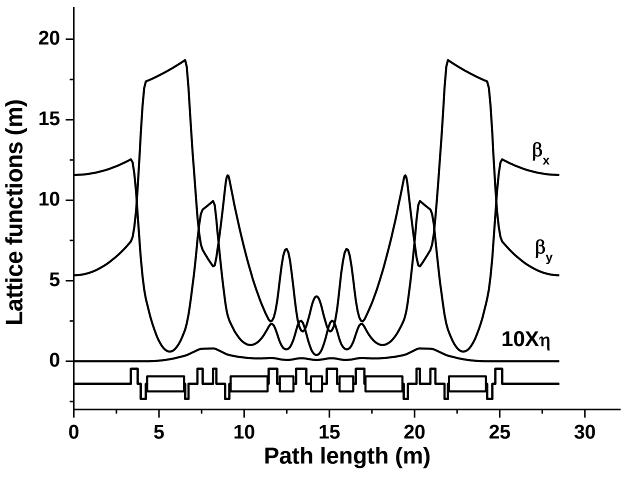


Fig.1. One unit cell of HBSRS lattice

Using the above analytical formulations, wake functions along horizontal, vertical and longitudinal plane was estimated by considering vacuum chamber material and dimensions as taken for Advanced Photon Source-upgrade storage ring. Out of 912m circumference ~16% length is taken for flat chamber for installation of in-vacuum undulators of pipe radius 2.5mm of aluminium alloy of resistivity $3.16\times10^{-8}$ Ω.m., ~14% of length is taken for round chamber of copper of pipe radius 11mm of resistivity $1.7\times10^{-8}$ Ω.m. and the rest ~70% of length is considered of round chamber of radius 11mm of aluminium alloy. The long range resistive wall wake functions along the horizontal, vertical and longitudinal planes are shown in Fig. 2(a-c) respectively. Due to narrow gap, the long range resistive wall wake functions is strong along vertical plane as shown in Fig. 2(b).

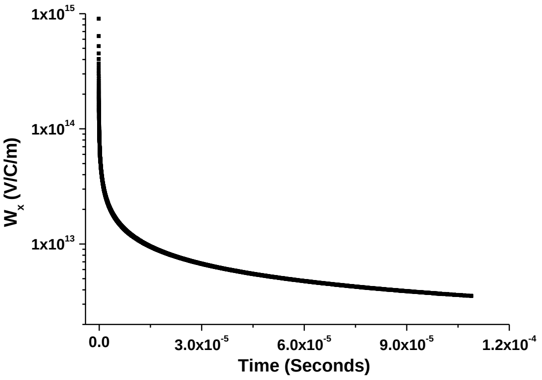


Fig. 2(a). Wake function along horizontal plane

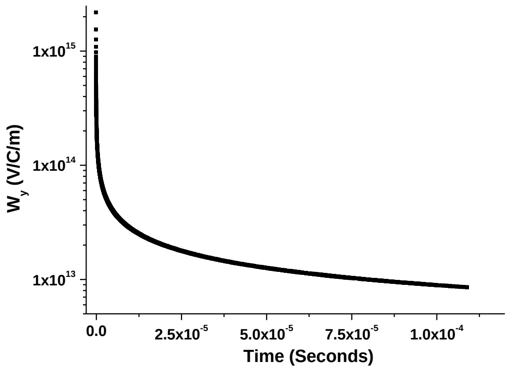


Fig. 2(b). Wake function along vertical plane

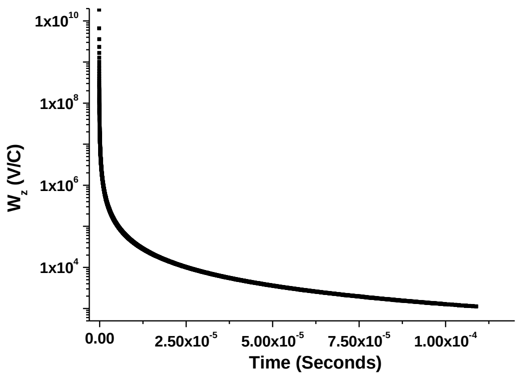


Fig. 2(c). Wake function along longitudinal plane

## Simulation study of beam motion in presence of long range wake function

Considering RF frequency 505.025MHz, harmonic number 1536, the multi particle tracking [6] was carried out assuming 10,000 electrons in one bunch and 1000 RF buckets are filled uniformly with 10,000 electrons in each RF buckets so the motion of a total of $1\times10^7$ electrons were tracked up to 5000 turns which is nearly equal to one damping time in vertical plane. For tracking the multi-particle, ELEGANT [7] code was used. The phase space in vertical plane of 10,000 electrons in one RF bucket and repeated in 1000 RF buckets used for tracking is shown in Fig. 3.

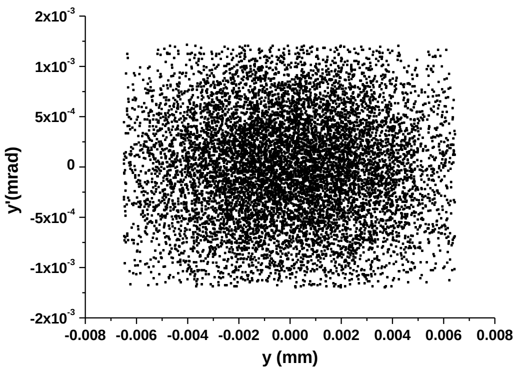


Fig.3. Phase space in vertical plane

The tracking was carried out assuming the rotation of beam about longitudinal axis is 0.2mrad, applied kick of 50μrad in both horizontal and vertical planes and $\Delta p/p$ is 0.001 at first reference bunch. The effect of long range wake functions on the motion of beam centroid of first reference bunch in six dimensional phase space was studied with zero chromaticity of machine in both transverse planes. The beam centroid motion in vertical plane with zero chromaticity is shown in Fig. 4(a). It shows that the beam is unstable if operated at zero chromaticity because the growth time of coupled bunch mode oscillation is less than the damping time. By increasing the strengths of chromaticity correcting sextupole, the chromaticity was increased to +1 in both planes and the particle tracking was carried out. The beam centroid motion with chromaticity +1, +2 in both planes are shown in Fig. 4(b-c) respectively. The tracking results show that the beam is unstable and if the machine is operated +2 chromaticity.

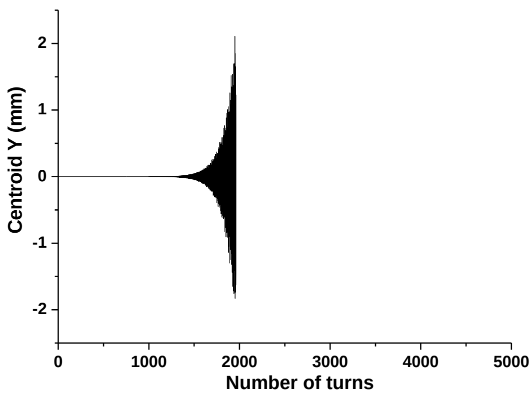


Fig. 4(a). Beam centroid motion with zero chromaticity

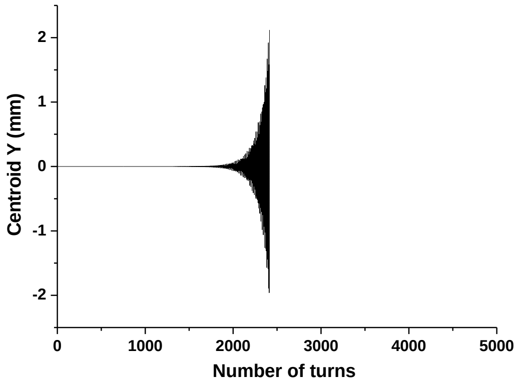


Fig. 4(b). Beam centroid motion with +1 chromaticity

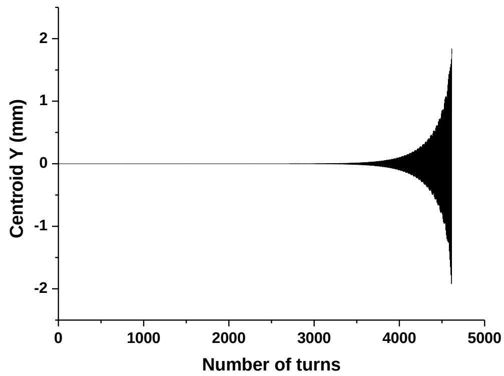


Fig. 4(c). Beam centroid motion with +2 chromaticity

With chromaticity +3, the growth time of coupled bunch mode oscillation is greater than the damping time so beam is stable.

## Heating due to longitudinal resistive wall wake function [2]

Due to longitudinal resistive wall, heating of chamber takes place for which we need cooling arrangement. The heating power $P_{rw}$ is given as: $P_{rw} = \frac{k_l I_t^2}{f_{bunch}}$ ; $k_l$ , $I_t$ , $f_{bunch}$ are longitudinal loss factor, total beam current and bunch frequency respectively. Longitudinal loss factor $k_l$ is

$$k_l = \frac{Z_0}{8\pi^2 b c}\Gamma(3/4)\left(\frac{2}{\sigma_c \mu_0}\right)^{1/2} \sigma_t^{-3/2}, \quad \Gamma(3/4)=1.2254$$

where $c, b, \sigma_c, \mu_0, Z_0, \sigma_t$ are light velocity, half vertical gap, electrical conductivity, permeability of pipe, characteristic impedance of vacuum and bunch length respectively.

Heating power per unit length for one In-vacuum undulator of aluminium alloy with a minimum gap $2b = 5mm$, total current 200mA and RF frequency ~505.025MHz is given by $P_{Rw}/L$ ~$10.5\ Watt/meter$.

## CONCLUSION

The simulation study of bunch centroid motion were carried out in presence of long range resistive wall wake functions considering same vacuum chamber materials and dimensions as used in Advanced Photon Source upgrade machine and using the lattice parameters of HBSRS candidate lattice. The results indicate that the growth time of coupled bunch mode oscillation is less than radiation damping time if machine is operated at ≤ +2 chromaticity in both planes. The instability can be controlled either by increasing the chromaticity or by the application of transverse bunch-by-bunch feedback system. If we increase the chromaticity there is reduction in dynamic acceptance for stable motion of beam so an active device i.e. transverse bunch-by-bunch feedback will be used for the control of beam instability.

## ACKNOWLEDGEMENTS

Authors would like to thank, Dr. M. Borland and Dr. Ryan Lindberg from Advanced Photon Source, USA for fruitful discussion and guidance for using PELEGANT code for study on resistive wall instability in ultra-low emittance storage ring. We also acknowledge Mrs Alpana Rajan, Sh. P.K. Thander, Sh. G. Saxena, Sh. D.K. Verma, Sh. Rajesh Verma, Sh. D.K. Kushwaha and Sh. Pankaj from Computer Division for their help, support and cooperation to install and run the ELEGANT and PELEGANT code on Amogh and Kshitij scientific server.

## REFERENCES

[1] A.W. Chao, M. Tigner, Handbook of Accelerator Physics and Engineering, world scientific publishing Co. Pte. Ltd

[2] N. Nakamura, Resistive wall impedance effects for the new KEK Light Source, IOP Conf. Series: Journal of Physics: Cof. Series 874 (2017) 012069.

[3] Yoshihiro Shobuda, Yongo Ho Chin, Resistive wall impedances of a thin non evaporable getter coating on a conductive chamber, Proj. Theor. Exp. Phys. 2017, 123401.

[4] Su-Youn Lee, Ji-Gwang Hwang and Eun San Kim, Effect of the resistive wall impedance in the PLS-II storage ring, Journal of the Korean Physical Society, vol. 56, No.6, June 2010 pp 1957-59.

[5] A.D. Ghodke etal., Physics design study for proposed high brightness synchrotron radiation source (HBSRS) in India, in proceedings of InPAC19.

[6] M.Borland, T.Bernc, L.Emery, R. Lindberg, Simultaneous Simulation of Multi-particle and Multi-bunch collective effects for the APS Ultra-Low Emittance Upgrade, in proceedings of ICAP2015.

[7] M. Borland, Elegant: A flexible SDDS-compliant code for accelerator simulation, Advanced Photon Source LS-287, 2000.

# CONCEPTUAL DESIGN OF TRANSPORT LINE FROM BOOSTER TO STORAGE RING FOR HBSRS

Pramod R*, Pradeep Kant, A.D. Ghodke
Accelerator Physics Section
Raja Ramanna Centre for Advanced Technology, Indore - 452 -013 (M P), India

*Abstract*

The High Brilliance Synchrotron Radiation Source (HBSRS), a kilometre scale storage ring based light source with the energy of 6 GeV is proposed to be built in India. The storage ring is being design to deliver ultra-low equilibrium horizontal beam emittance (~150 pm rad). A 200 MeV electron linear accelerator (Linac) will be used as a pre-injector to the full energy 6.0 GeV booster which will be used as an injector to the 6.0 GeV storage ring in top-up mode. The results of the preliminary studies on lattice design of 34 m long beam transport line connecting booster extraction point to storage ring injection point are presented. Based on the linear optics design using simulation beam optics code TRANSPORT, effects of misalignments of magnets, and systematic and statistical errors of magnetic fields, as well as the effects of the initial beam positions on the central trajectory and on the transverse beam emittance dilution studies carried out are also presented.

## INTRODUCTION

Presently, proposal to design a 6.0 GeV electron storage ring as a high brightness synchrotron radiation source (HBSRS) is under consideration at RRCAT with low emittance (~150 pm rad). It will provide photon beam brilliance up to the order of $10^{20}$ to $10^{22}$ in the photon range of 1keV to 200 keV with matchless stability [1]. A 200 MeV electron linear accelerator (Linac) will be used as a pre-injector to the 6.0 GeV booster synchrotron. This 6.0 GeV booster synchrotron will be used as a full energy injector to the 6.0 GeV storage ring. This paper describes the preliminary design of conventional beam transport line from booster synchrotron to the storage ring.

The proposed beam transfer line (henceforth the line will be named as BTR -booster to ring transfer line) transports electron beam from 6.0 GeV booster synchrotron to 6.0 GeV storage ring. In the proposed layout, the booster ring is inside the storage ring and has a clear radial distance of 7.0 m relative to the storage ring [2]. The BTR transfer line from booster extraction point to the injection point of the storage ring has length ≈ 34 m with effective bending angle of $16.5^0$.

Schematic diagram of the layout of various magnetic elements of BTR transfer line are shown in Figure 1. It includes one $6^0$ extraction magnet, three bending magnets (BM1, BM2 and BM3), thick septum, thin septum and 12 quadrupoles (6 focussing and 6 defocussing). It is proposed to put five beam profile monitors(BPM) and few button position monitors in the line for the beam position measurement. The screen monitor, which is a destructive monitor is mainly used in commissioning trials. Two screen monitors are to be put between extraction septum and BM1 to see the extracted beam from the booster and to measure the profile and position of beam.

For the same reason three BPMs are to be put between BM2 and injection septum to adjust the beam injection condition. The location of the diagnostic and the correction elements are yet to be finalised.

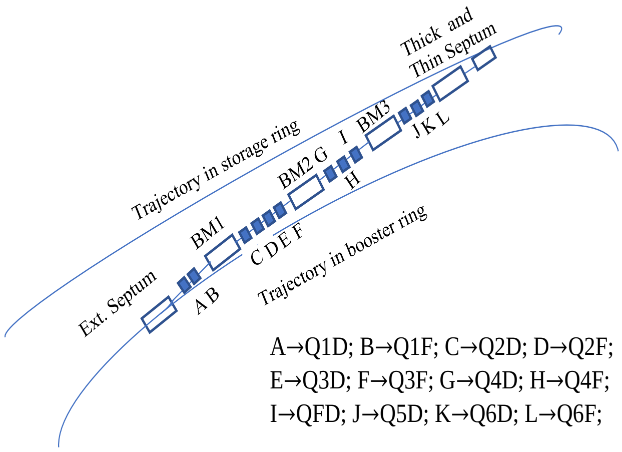


**Figure 1: Layout of BTR transfer line**

It is proposed to installed a beam dump after bending magnet BM1[3,4]. The extracted beam from booster will go straight to the beam dump by turning off the power to the magnet. The beam properties of the extracted beam can be studied without interacting with the main storage ring.

## DESIGN PHILOSOPHY

BTR transfer line has been designed in such a way that minimum loss of particles take place during the transport process. It is achieved by focussing the beam using the proper combination of quadrupole lenses. The optics of BTR transport line has been carefully managed show that the β functions of the whole line are below 100 m in both transverse planes.

In order to improve the efficiency of injection into the storage ring, phase space parameters of the beam are matched at the point of injection by using suitable arrangements and strengths of quadrupoles. In addition, it is also used to regulate the dispersion function and its derivative at the injection point to meet the requirements of the injection process.

*pramod@rrcat.gov.in

Dispersion function $\eta$ and its derivative $\eta'$ are made equal to zero at the injection, as this reduces the septum aperture requirements and more number of turns can be injected in the same aperture. To take into account the dispersion introduced by the injection septum, a bending magnet BM3 of the same polarity as the septum magnet is introduced. By changing the strengths of a quadrupoles Q4D-Q6F, $\eta$ and $\eta'$ are made equal to zero

## PROCEDURE FOR DESIGNING

After extracting the beam from the booster, beam is having finite dispersion function ($\eta$) and its derivative $\eta'$, for ease of calculation and also to keep the beam size small these are made equal to zero using quadrupoles. First quadrupole doublet Q1F and Q1D and bending magnet BM1 after the extraction septum of the booster is optimized to make the horizontal dispersion and its derivative zero, so that their contribution in the rest of the line remain zero [5].

The injection process requires that dispersion function and its derivative should be zero at the point of injection. The last section of the BTR line has six quadrupoles, one $5^0$ bending magnets and thick and thin septum magnets. As (n) and (n') will be generated due to septa, a bending magnet is introduced in the last section of line to take care of it. The quadrupoles match the beta, alpha in both the planes and makes the dispersion function and its derivative zero as required at the injection point of the storage ring. To achieve this, strength of quadrupole triplets QD-QF-QD and QF-QD-QF placed on either side of the bending magnet have been optimized.

An unmatched FODO lattice is inserted between bending magnets BM1 and BM2 to take care of mismatch between proposed length and actual length after the assembly of components of both the rings. The beta functions in both the plane at the entrance of bending magnet BM2 is same as that at the exit of bending magnet BM1.

## RESULTS

The beam parameters at the entrance of the BTR transfer line and required parameters at the injection point just after the thin septum are listed in Table 1.

**Table 1: Beam parameters at extraction and injection point in BTR**

| *Beam parameters* | *Extraction Location* | *Injection location* |
|---|---|---|
| beta function $\beta_x$ (m) | 1.8910 | 11.4805 |
| beta function $\beta_y$ (m) | 20.28240 | 4.19370 |
| alpha function $\alpha_x$ | -0.6845 | 0.0008 |
| alpha function $\alpha_y$ | 2.5994 | -0.0047 |
| Dispersion function $\eta$ (m) | 0.41 | 0.0 |
| Derivative of $\eta$ | 0.034 | 0.0 |

x, y: transverse planes (horizontal & vertical respectively)

The computer code TRANSPORT [6,7] is used for designing various magnetic element of the BTR transfer line.

The maximum $\beta_x$=64 mm, just after Q1F corresponds to the beam size ($6\sigma_x$) ~3.2 mm for give emittance $\varepsilon_x$ of 2 nm rad and energy spread of 0.126 %

$$\sigma_x = \sqrt{\beta_x \varepsilon_x + (n_x \frac{\Delta P}{P})^2}$$

Similarly, the maximum $\beta_y$=64 mm, just after Q4D corresponds to beam size ($6\sigma_x$) ~2.15 mm for give emittance $\varepsilon_y$ of 2 nm rad.

$$\sigma_y = \sqrt{\beta_y \varepsilon_y}$$

The dispersion function is below 0.45 m throughout the BTR transfer line. Adequate space has been left for installation of various diagnostic elements and steering magnets in the line.

Table 2(a), 2(b), 2(c) and 2(d) show the simulated parameters of the BTR transfer line.

**Table 2(a): Parameters of the BTR transfer line**

| | |
|---|---|
| Operational energy | 5.0 GeV |
| Total length including septum | 34.2 m |
| Number of bending magnets (excluding septa) | 03 |
| Number of quadrupoles | 12 |
| Maximum quadrupole gradient | 24.4 T/m |

**Table 2(b) Parameters of Bending magnets**

| Parameters | BM1 | BM2 | BM3 |
|---|---|---|---|
| Magnetic length | 2.5 m | 2.0 m | 2.0 m |
| Deflection | $6^0$ | $5^0$ | $5^0$ |
| Magnetic Field | 8.4 kG | 8.7 kG | 8.7 kG |

**Table 2(c) Parameters of Septa magnets**

| Parameters | Extraction Septum | Thick Septum | Thin Septum |
|---|---|---|---|
| Magnetic length | 2.5 m | 2.5 m | 1.5 m |
| Deflection | $6^0$ | $5^0$ | $1.5^0$ |
| Magnetic Field | 8.4 kG | 7 kG | 3.5 kG |

**Table 2(d) Parameters of Quadrupoles**

| Quadrupoles | Effective Length (m) | Quadrupole strength ($m^{-2}$) |
|---|---|---|
| Q1D | 0.5 | -0.77 |
| Q1F | 0.5 | 1.0 |
| Q2D | 0.5 | -0.70 |
| Q2F | 0.5 | 0.67 |
| Q3D | 0.5 | -0.67 |
| Q3F | 0.5 | 0.78 |
| Q4D | 0.5 | -0.81 |
| Q4F | 0.5 | 1.11 |
| Q5D | 0.5 | -0.23 |
| Q5F | 0.5 | 0.87 |
| Q6D | 0.5 | -1.22 |
| Q6F | 0.5 | 1.0 |

The matched lattice parameters are shown in Figure 2.0. The corresponding beam sizes (6 σ) in both the planes are plotted in Figure 3.0.

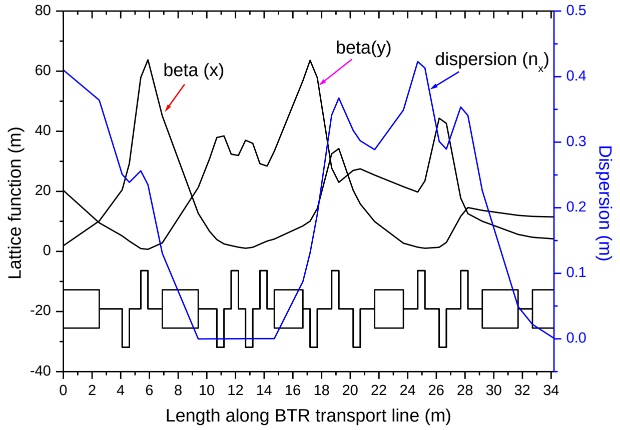


**Figure 2: Lattice parameters in the transport line**

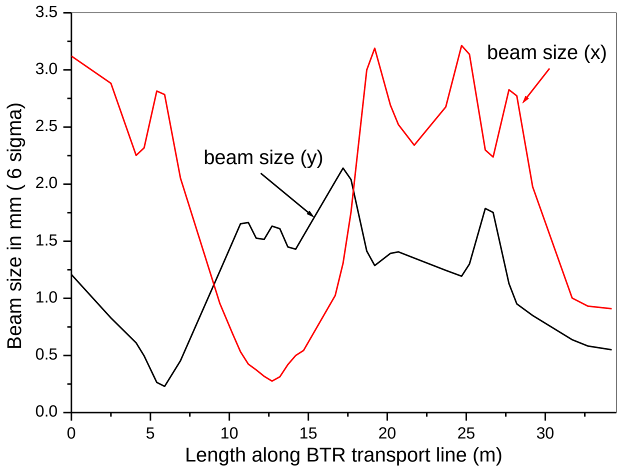


**Figure 3: Beam size along the BTR Transfer line**

## EFFECT OF ERROR ON BEAM

Magnetic field errors are unavoidable in the design and the fabrication of the magnets but they should be minimum as possible as. Similarly, the perfect alignment of the magnets is not possible, it can be done under certain limits only. Also, the beam from the pre-injector booster may have different initial position and angle as compared to the required values. All these aspects are important to study as they contribute in the centroid shit of the electron beam and due to this the beam may not reach at right position at injection point. Therefore, the tolerances are added in the estimation of the aperture of the vacuum pipe. Fine studies of all these aspects is under progress. Physical aperture of the vacuum pipe is evaluated as:

$$A=\text{Aperture}=2\ (3\sigma+\Delta)\ ,$$

where Δ is the centroid shift due to all errors.

For centroid shift upto ~ 8 mm, the physical aperture is ~24 mm. Thus an aperture of ID 24 mm has been proposed for the entire BTR line except at the bending magnets. Preliminary study of effect of displacement error and rotational error in bending magnet and quadrupole misalignment errors in horizontal and vertical is carried out. Maximum 2.5 mm centroid shift is noticed for 0.1 mm displacement error and 0.2 mrad rotational error.

## CONCLUSION

The conceptual design of BTR transfer line from 6 GeV booster to 6.0 GeV storage ring is presented. Effect of different types of errors like magnet alignment errors, beam energy jitter and magnetic field errors on the beam is yet to be evaluated. An unmatched FODO lattice between bending magnets BM2 and BM3is likely to replace by matched FODO lattice at later stage.

.

## ACKNOWLEDGEMENTS

We would like to thank Sh RS Saini for helpful discussion during the design studies of the BTR transport line.

## REFERENCES

[1] A D Ghodke et al; Preliminary Beam Dynamical Considerations for High Brilliance Synchrotron Radiation Source (HBSRS), RRCAT/2017-10

[2]. Pradeep Kant, Ali Akbar Fakhri, A.D. Ghodke; FODO Lattice for Booster of High Brilliance Synchrotron Radiation Source, INPAC 2019, Delhi

[3] NSLS-II Conceptual Design report; Chapter 5: Injection system

[4] Sirius, Design Report 02/2013, January 25, 2013

[5] Deepa Angal, Gurnam Singh; Design of Beam transfer line -3, RRCAT Internal report, CAT/99-11

[6] D,C Carey, Third order TRANSPORT with MAD input, TM-1546, (1988), Fermi Laboratory

[7] P.J Bryant Beam transfer lines CERN 94-01, Vol.1, 219-235 (1994)

# SIMULATION OF 100 keV/500 mA ELECTRON GUN USING CST PARTICLE STUDIO FOR 10 MeV LINAC

Pramod R*, A.D. Ghodke
Accelerator Physics Section
Raja Ramanna Centre for Advanced Technology, Indore - 452 -013 (M P), India

*Abstract*

At present, 50 keV electron beam from the electron gun is used as an injector to the 10 MeV linac for the Agricultural Radiation Processing facility (ARPF). This low energy electron beam from gun is severely affected by the presence of stray magnetic field of the vacuum gauges near to gun assembly, thereby reducing the efficiency of the injector system. For improving the performance of injector system, preliminary physics design of 100 keV pierce gun capable of delivering 500 mA beam current is carried out using 2-D code EGUN. Effect of geometrical tolerance and misalignment of components of gun on the beam parameters are carried out by evolving 3D model of the configuration in CST Particle studio. Parametric analysis is performed to understand the effects of variation of gun parameters such as anode-cathode gap, cathode radius, focusing angle, accelerating voltage and bias voltage on beam parameters like current, perveance, beam waist radius and its position. The paper describes the simulated results for the gun configuration using CST Particle studio as well as its comparison with EGUN code.

## INTRODUCTION

Presently, 50 keV electron beam from the electron gun is injected into 10 MeV linac. The corresponding beta ($\beta = \frac{v}{c}$ =0.41) of the electron at this energy is less than beta of the first cell ($\beta$=0.56) of the buncher cavity of the 10 MeV linac, thereby reducing the efficiency of the injector system. In addition, this low energy electron beam is severely affected by the presence of stray magnetic field of the vacuum gauges near to gun assembly. An analytical result of deflection angle and transverse shift for 50 keV and 100 keV electron beam is presented in Table 1 for a given value of uniform magnetic field and magnetic length.

**Table 1: Effect of Stray magnetic field**

| Magnetic field=5 gauss, Magnetic length=50 mm | | |
|---|---|---|
| Energy (keV) | Deflection angle (mrad) | Transverse shift (mm) |
| 50 | 33 | 0.83 |
| 100 | 23 | 0.56 |

Thus 50 keV beam introduces 33 mrad transverse kick at the injected position of the buncher cavity which is quite large. The effect can be minimized by using 100keV electron beam at the buncher cavity. Hence, it is proposed to increase the electron beam energy from the gun to 100 keV ($\beta$=0.55).

*pramod@rrcat.gov.in

## CHOICE OF GEOMETRY

To fulfil the above requirement an optimization study of modified PIERCE geometry of the gun has been undertaken. The goal was to obtain slightly convergent beam with long focal length and small focal spot which can be easily transported with the aid of a system of magnetic lenses

In pierce configuration [1], the focusing electrode is placed at an angle of $67.5^0$ from the beam edge and electron beam pursue rectilinear trajectories in the vicinity of cathode surface. The hole in the anode disturbs the electric field distribution so that the equipotential lines are not parallel to the surface of the anode but are bend up into anode aperture (behaving as diverging lens). The effect of diverging lens has been minimized using simulation.

As the starting geometry of the gun, we have taken PIERCE configuration with modified focusing electrode in order to compensate the effect of anode aperture and to have the possibility of changing the position and dimension of the focal spot.

## SIMULATION

One of the most frequent used numerical programs of this type for the calculation of electron gun is that of Hermannnsfeldt SLAC Electron Trajectory Program [2]. This program is specifically written to compute trajectories of charged particles in electrostatic and magnetostatic systems including the effect of space charge and self-magnetic fields. It is a 2D software and suitable for axis symmetric problems. Generally basic design is done using this code. Effect of geometrical tolerance and misalignment of component on the beam parameter is done by evolving 3D model of the configuration in particle studio of CST.

## STARTING CONDITIONS

The geometrical space of the gun is divided into three regions:

a. The region of the rectilinear flow, in which the Langmuir relations for space charge limited flow are used
b. A thin electric aperture lens in the vicinity of the anode
c. The emergent beam outside the gun

A schematic layout of geometry used for proposed gun is shown in the Figure 1. It has cylindrical symmetry. Beam parameters at the output of gun depends on eleven geometrical parameters ($r_k$, $d_{kw1}$, $r_1$, $w_2$, $\Theta$, $r_w$, $d_{kw2}$, $d_{ka}$ $a_1$,

$a_2$, and $a_h$) and two electrical parameters (anode and bias potential).

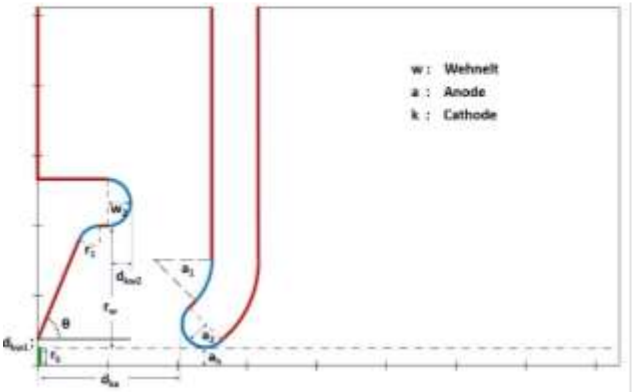


**Figure 1: Schematic layout of geometry**

Geometrical dimensions have been simulated using EGUN code to get the desired beam parameters at the given location and are listed in the Table 2.

**Table 2: Proposed specification of electron gun**

| Parameters | | Values |
|---|---|---|
| Type | | Thermionic, modified Pierce |
| Energy | | 100 keV |
| Current | | 500 mA |
| Pulse width | | 10 μs |
| Pulse repetition rate | | 300 Hz |
| Bias voltage (Negative w.r.t cathode) | | 1200 V |
| Cathode radius | Emitting surface | 4 mm |
| | Metal shield | 4 mm |
| Wehnelt | $d_{kw1}$ | 1 mm |
| | $r_1$ | 2 mm |
| | $w_2$ | 4 mm |
| | $\Theta$ | $67.5^0$ |
| | $r_w$ | 15.2 mm |
| | $d_{kw2}$ | 11 mm |
| Anode | $d_{ka}$ | 16 mm |
| | $a_1$ | 1 mm |
| | $a_2$ | 1 mm |
| | $a_h$ | 3 mm |
| Beam parameters | Beam waist position | 100 mm |
| | Beam waist radius | 0.8 mm |
| | Emittance | 6 π mm mrad |
| Maximum electric stress | | 5 kV/mm |

## CST PARTICLE STUDIO

CST Particle Studio is a specialist tool developed by Computer Simulation Technology [3] for fast and accurate analysis of charged particle dynamics in 3D electromagnetic fields. Particle Studio utilizes three different solvers called- Particle Tracking, Particle-in-Cell (PIC) and Wakefield Particle solver to focus on different kinds of charged particle problems.

Particle tracking solver [4] can simulate particle dynamics in static electromagnetic fields using Lorentz force equations. Emission under space charge limit can also be enacted using gun iterations. This solver is suitable for tracking electron trajectories in electron guns. The tracking solver uses gun iterations to simulate space charge limited emission. Thus, it does not just track the particles once through the computational domain, rather, it iteratively repeats an electrostatic computation and then tracks the particles until the desired accuracy of the space charge deviation between two successive iterations is reached.

## MODELLED GUN

The gun based on the geometrical parameters listed in Table 2 is modelled using CST particle studio and simulated results are compared with EGUN code. The figure 2(a), 2(b) and 2(c) show the modelled gun, equipotential lines and corresponding trajectory respectively. The simulated beam parameters are compared in Table 3.0.

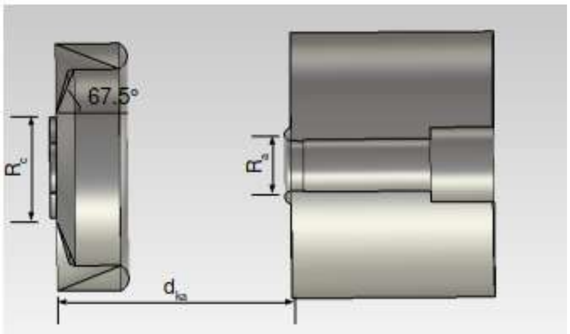


Figure 2(a): Modelled gun

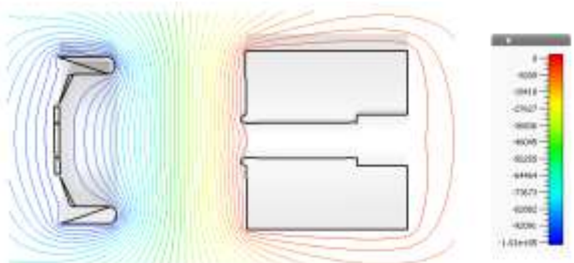

Figure 2(b) Equipotential lines

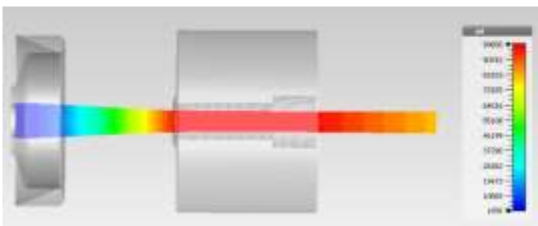

Figure 2(c): beam trajectory from modelled gun

**Table 3: Comparison of simulated beam parameters**

| Parameters | CST Particle studio | EGUN code |
|---|---|---|
| Beam waist radius | 1.1 mm | 0.8 mm |
| beam waist from cathode | 88 mm | 100 mm |
| Emittance | 15 $\pi$ mm mrad | 6$\pi$ mm mrad |
| Maximum Electric stress | 4.8 kV/mm | 5kV/mm |

## PARAMETRIC ANALYSIS

Parametric analysis of gun was performed using CST PS to understand the effects of variation of gun parameters such as anode-cathode gap, cathode radius, focusing angle, accelerating voltage and bias voltage on beam parameters like current, perveance, beam waist radius and its position [5]. Effect of change in anode-cathode gap on gun parameters is shown in Figure 3.

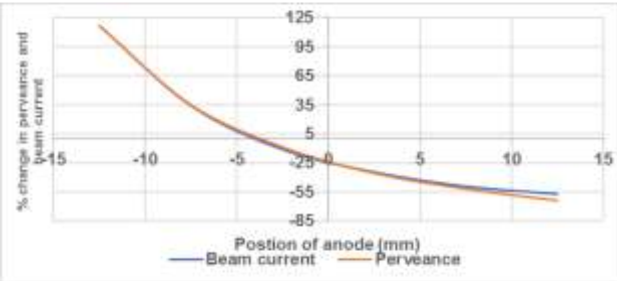


Figure 3: Dependence of gun parameters on change in position of anode

It is observed that as anode-cathode gap increases, beam waist radius becomes narrower and its position moves further and further away from the cathode. This can be attributed to the fact that current decreases as we increase the gap, due to lack of focusing.

## GEOMETRICAL TOLERANCE AND MISALIGNMENT

The knowledge of parametric analysis of gun parameters on beam current, perveance, beam waist radius and its position is used to study the effect of geometrical tolerance and misalignment of gun components. The performance of gun is severely affected, if more than 1 % of the beam current falls on anode. Excessive heating of anode may lead to unstable emission, sometimes leads to fall of beam current with time. The tolerance is fixed by varying geometrical parameters till

a. its start heating the anode or
b. beam current changes by 1 % or
c. waist radius increases by 10 % or
d. beam waist location changes by 20 mm or maximum operating electric stress becomes more than 5.5 kV/mm

When any of the above conditions are reached, the simulated geometrical dimension is considered as upper/lower limit for that gun components.

## CONCLUSION

The optimized parameters of 100 kV/500 mA gun with tolerance is summarized in Table 4. Beam parameters of electron gun obtained from simulation study will be used to design/study other beam optical elements for further transport of electron beam to the buncher cavity.

**Table 4: Optimized parameters of gun components with tolerance**

| **Parameters** | **Values** |
|---|---|
| Cathode voltage | 100 kV±1.1 kV |
| Bias voltage | 1200 V± 6 V |
| Cathode tilt | ±10 mrad |
| Wehnelt spacing, $d_{kw1}$ | 1 mm± 0.1 mm |
| Curvature radius, $r_1$ | 2 mm± 0.250 mm |
| Curvature radius, $w_2$ | 4 mm± 0.500 mm |
| Angle with respect to cathode, $\Theta$ | $67.5^0$±10 mrad |
| Radial distance from axis, $r_w$ | 15.2 mm± 0.150 mm |
| Axial distance of tip, $d_{kw2}$ | 11 mm± 0.10 mm |
| Axial distance from cathode, $d_{ka}$ | 16 mm± 0.20 mm |
| Curvature radius, $a_1$ | 1 mm± 0.10 mm |
| Curvature radius, $a_2$ | 1 mm± 0.10 mm |
| Hole radius, $a_h$ | 3 mm± 0.15 mm |
| Anode tilt | ±7 mrad |

## ACKNOWLEDGEMENTS

We acknowledge Mr. Shivam Joshi, YSRP student, SVNIIT, Surat for participating in simulation using CST particle studio.

## REFERENCES

[1] Septier Albert, focusing of high intensity beams, Focusing of Charged Particles, Chapter 3, Vol. 2.
[2] W.B. Herrmannsfeldt, SLAC 331, UC-28, 1988.
[3] Holger Spachmann, Ulrich Becker, CST GmbH Germany, Electron gun simulation with CST PARTICLE STUDIO, Nuclear Instruments and Methods in Physics Research A 558 (2006) 50–53.
[4] Space charge emission model. help tool, CST Particle Studio.
[5] Shivam Joshi, tracking of low energy electron beam in an electron gun using CST particle Studio, Internal report, YSRP-2019.

# ION-BEAM INTERACTION IN ELECTRON STORAGE RING OF HBSRS

Saroj Kumar Jena[1, 3], A. A. Fakhri[1], A. D. Ghodke[1], V. K. Senecha[2, 3]
[1]Accelerator Physics Section, Raja Ramanna Centre for Advanced Technology, Indore, India
[2]Proton Linac Development Division, Raja Ramanna Centre for Advanced Technology, Indore, India
[3]Homi Bhabha National Institute, Training School Complex, Anushaktinagar, Mumbai, India

## Abstract

The electron beam ionizes residual gases present in the vacuum chamber of an accelerator and create positively charged ions. For the ultralow emittance storage ring, the ion effect is considered as one of the very important phenomenon affecting the performance of electron beam. The ion-beam interaction in a storage ring can be categorized in two groups such as conventional ion trapping (CIT) and fast beam ion instability (FBII). The CIT lead to betatron tune shift and hinders high beam current accumulation due to partial beam loss, whereas the FBII degrades the beam quality. The CIT and FBII have been studied for a proposed 6 GeV electron storage ring of HBSRS with beam emittance of ~150 pm rad. The electron storage ring of HBSRS will be operated in different operating modes such as 1) high brightness mode in which maximum number of bunches will be filled, 2) timing mode wherein only few bunches will be filled with higher current are largely separated in the ring. and 3) round beam mode where vertical to horizontal emittance ratio is made very close to unity for achieving longer beam lifetime. In this paper, the trapping condition of various ion species and FBII growth rate are estimated for the different modes of operation. Effective mitigation techniques for these issues using partial bunch filling pattern with suitable bunch gaps are presented.

## INTRODUCTION

HBSRS is a proposed light source facility in India for which lattice design and other related studies are being carried out extensively [1]. The baseline lattice of storage ring of HBSRS is a 7 bend achromat and it is design to deliver 200 mA beam current at beam energy of 6 GeV. Relevant design parameters at the time of this study are listed in Table 1.

Table 1: Basic parameters of storage ring of HBSRS

| Parameter | Value |
|---|---|
| Energy | 6 GeV |
| Circumference | 911.8 m |
| Beam current | 200 mA |
| Emittance | 150 pm rad |
| Betatron tune (x, y) | 74.15, 24.22 |
| Energy spread | 1 x $10^{-3}$ |
| RF Frequency | 505. 025 MHz |
| Harmonic number | 1536 |
| Damping time (x,y) | 8.7, 14.8 ms |
| Beam size at ID center (x, y) | 41.4 µm, 2.8 µm ( 1% coupling) |

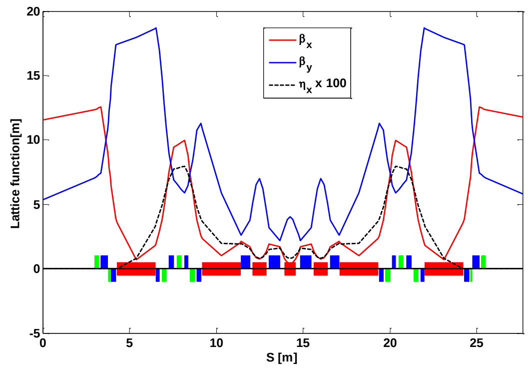


Figure 1: The lattice function and lattice structure of unit cell of HBSRS storage ring. Solid rectangle box are dipole (Red), quadrupole (blue) and sextupole (green).

Fig. 1 shows the lattice functions and lattice structure for one unit cell of the storage ring. Three bunch filling modes of operation are considered in HBSRS, mode A: high brightness mode which stores 200 mA beam current in 1000 bunches, mode B: timing mode or high resolution mode which stores 90 mA beam current in 16 bunches with a large bunch to bunch separation of 192 ns and mode C: round beam mode. In this paper, we present CIT and FBII in the storage ring of HBSRS for different filling modes of operation and their mitigation strategy. Since the beam emittance is substantially smaller than the 3rd generation light sources, problem of CIT becomes less as the strong focusing force of electron bunch over-focuses the ions in the long bunch gap. Nevertheless, FBII becomes more serious due to high bunch intensity and long bunch train.

## ION TRAPPING

In an electron storage ring, the beam produces ions via ionization of residual gas molecules. Under certain condition, they becomes trapped in the electron beam potential and this phenomenon is recognized as ion trapping. The ion trapping mainly depends on electron beam size and composition of residual gases in a storage ring. These trapped ions induces betatron tune shift in electron beam and in vertical plane it is more because of smaller beam size. The tune shift is given as

$$\Delta\nu_y = \frac{\beta_y \, r_e \, N \, \eta}{4\pi\gamma\sigma_y(\sigma_x + \sigma_y)} \qquad \text{....(1)}$$

where $\beta_y$ is the average vertical beta function of the lattice, $r_e$ is classical electron radius, N is the total number of electrons in the ring, $\gamma$ is a relativistic factor for the beam, $\sigma_{x,y}$ represents rms horizontal and vertical electron beam sizes and $\eta$ is the neutralization factor defined by the ratio of number of electrons to number of ions generated. The tune shift becomes unacceptably large ($\Delta\nu_y \sim 430\ \eta$) for HBSRS due to its smaller beam sizes. To limit this tune shift to a tolerable value, we need to control the ion density.

Based on the linear approximation of Gaussian beam field, the trapping condition of ions define a critical mass number $A_c$ for symmetric bunch filling pattern [2]. Ions with molecular mass greater than $A_c$ will be trapped in the potential well of the electron beam and the $A_c$ in horizontal ($A_{cx}$) and vertical ($A_{cy}$) plane is given by

$$A_{c\,x,y}(s) = \frac{r_p\ N_e\ L_{sep}}{2\ \sigma_{x,y}(s)\big(\sigma_x(s) + \sigma_y(s)\big)} \qquad \dots(2)$$

where $N_e$ is the number of electrons per bunch, $L_{sep}$ is bunch to bunch separation, and $r_p$ is classical proton radius. The critical mass number is decided by the vertical beam parameters as the beam size is much smaller compared to horizontal plane. Also, the critical mass along the circumference of ring varies due to strong focusing lattice and thus a given ion may be trapped in some parts of the ring, but not in others. $A_{c\,y}$ is evaluated for one unit cell of HBSRS lattice and is shown in Fig. 2 for mode A, in three different bunch filling patterns, with bunch to bunch separation of 2 ns (1536 bunches), 4 ns (768 bunches) and 6 ns (512 bunches). The figure also shows the mass number of ions of probable residual gas molecules present in a storage ring vacuum chamber at 1 nTorr pressure such as $H_2$, CO and $CO_2$. It shows that when all the bunches are filled, $CO^+$ and $CO_2{}^+$ ions are remain trapped in the beam potential, though the $H_2{}^+$ ion escaped because of lighter mass. However, as the separation between bunch increases, critical mass value goes beyond the mass of heavier gas species everywhere in the ring except few locations and hence in these modes of operation ion trapping problem can be inhibited. The ion trapping problem for mode A, can also be curbed by continuously filling 1000 bunches with 2 ns bunch to bunch separation and leaving 536 bunch gaps (equivalent to 1/3$^{rd}$ bunch gap of total bunches). In the gaps, the ions are over focused and ultimately lost to the vacuum chamber wall [2]. For this type of partial fill pattern, the critical mass cannot be estimated, but the stability analysis of ions confirms that there will be no ion trapping. The critical mass is much higher in mode B and thus no trapping is expected.

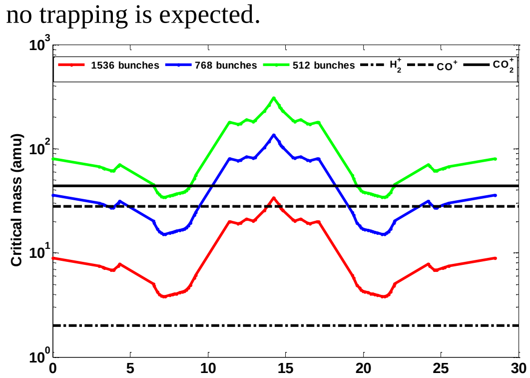


Figure-2: Critical mass in vertical plane for one unit cell of HBSRS in high brightness mode with different bunch to bunch separation.

In ultra-low emittance storage ring, the beam lifetime of stored electron beam sometimes become extremely short and in that case, round beam mode operation satisfy the operational requirements. To achieve a round beam, coupling coefficient ($\kappa = {}^{\varepsilon_y}/_{\varepsilon_x}$) is made close to unity by introducing strong skew quadrupoles in the lattice or operating the machine at difference resonance (equal fractional tune in both horizontal and vertical plane) [3]. For $\kappa = 1.0$, and 512 bunches each separated with 6 ns, the critical mass of HBSRS lattice is estimated for both horizontal and vertical plane and shown in Fig. 3. The result indicates that, in round beam mode, ion trapping occurs in the multiple sections. This phenomena can be curbed with multi train bunch filling pattern.

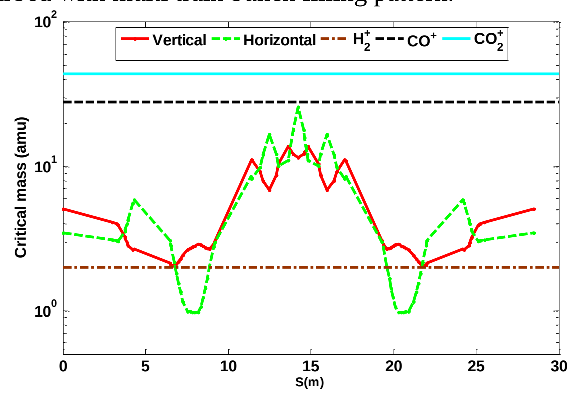


Figure-3: critical mass in both horizontal and vertical plane for round beam mode

## FAST BEAM ION INSTABILITY

With low emittance and high intensity beam, even if the ions ultimately disappear in the bunch gap, they cause single pass instability known as fast beam ion instability (FBII). Each bunch produces ions and the ion density keep on growing almost linearly over the bunch train and becomes maximum at the tail of the bunch train. This instability can hinder high beam current accumulation and may lead to beam emittance growth. The growth time of this instability is estimated by analytical formula [4] and in the vertical plane, it is given by

$$\tau_c = \frac{\gamma \sigma_y^{\frac{3}{2}} (\sigma_x + \sigma_y)^{\frac{3}{2}} A^{\frac{1}{2}}}{\sigma_{ion} d_i\ \beta_y N_e^{\frac{3}{2}} n^2 r_e r_p^{\frac{1}{2}} L_{sep}^{\frac{1}{2}} c} \qquad \dots(2)$$

where $\tau_c$ is the characteristic growth time of the FBII, A is atomic mass of the ion, n is the number of electron bunches in a bunch train, $\sigma_{ion}$ is the ionization cross section of the gas species, and $d_i$ is density of ions. This estimation is based on two following assumption, 1) the force between electron and ions increases linearly with the displacement and 2) ion oscillation frequency is constant throughout the ring. However, in a strong focusing ring, the beam size variation introduces a large spread in ion frequency and causes decoherence in ion motion. This occurrence results in Landau damping and helps in further reducing the FBII growth rate. After inclusion of the spread in ion oscillation frequency [5], the FBII growth time $\tau_{inst}$ is given by

$$\tau_{inst} = \frac{\tau_c}{c}\sqrt{2\pi}\, 4L_{sep} n\, a_{bt}\, f_i \qquad \text{....(3)}$$

$$f_i = \frac{c}{2\pi}\left(\frac{4N_e r_p}{3L_{sep}\sigma_y(\sigma_x+\sigma_y)A}\right)^{1/2} \qquad \text{....(4)}$$

where $2a_{bt}$ is the peak to peak ion frequency variation and $f_i$ is the ion frequency. For a weak focusing lattice, the parameter $a_{bt}$ has small value, whereas for the strong focusing multi-bend achromat lattice, this takes a larger value. The FBII characteristic growth time of HBSRS for the partial fill pattern is estimated using eqn. 2 as ~ 12 ns for an average vacuum pressure of 1 nTorr and beam current of 200 mA. However considering the spread in ion frequency for $CO^+$ in HBSRS as shown in Fig. 4, FBII growth time is estimated using eqn. 3 as ~0.75 ms. This shows that, even with a large ion frequency spread, the instability growth time is much less than the synchrotron radiation damping time in vertical plane.

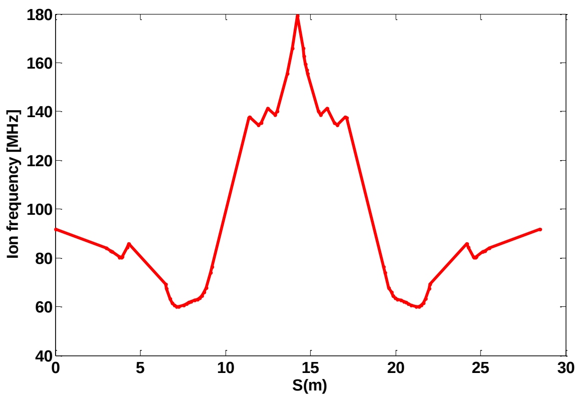


Figure-4: The spread in $CO^+$ ion frequency in HBSRS

The effect of FBII can be alleviated by reducing the density of ions in a bunch train, as its growth rate is proportional to the ion density. The line density of ions, ($\lambda_i$) increases linearly along the bunch train and becomes maximum at the tail of the bunch train which is given by the formula below and after that it decays exponentially in the bunch gap [7].

$$\lambda_i = \frac{\sigma_i N_e P\, n}{kT} \qquad \text{....(5)}$$

Where P is the vacuum pressure of gas molecules, $k$ is the Boltzmann constant and $T$ is the absolute temperature of the gas. By redistributing the bunch fill pattern into several short bunch trains with a fixed gap between them, the ion density can be reduced. Fig. 5 shows the ion density comparison for three bunch filling patterns such as single bunch train, 8 mini bunch trains and 16 mini bunch trains and each pattern consists of 1000 filled bunches. It confirms that with the introduction of bunch gaps between bunch trains, ion density reduces significantly. With the 16 mini bunch trains, FBII growth time can be increased to 12 ms (close to radiation damping time in vertical plane). Thus in combination with many short bunch trains and fast bunch by bunch feedback system, the FBII can be potentially suppressed. However, further studies of FBII using numerical methods will be carried out to get more realistic results.

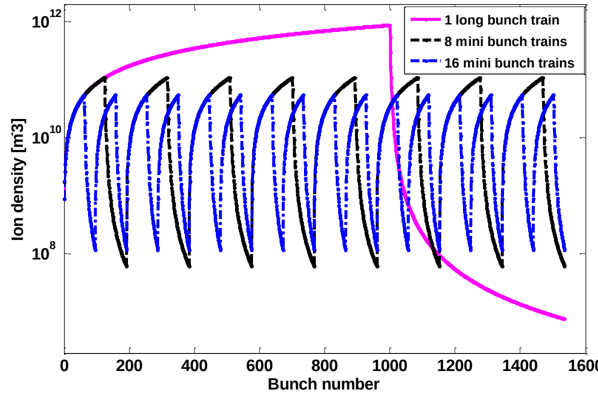


Figure-5: Ion density in different partial bunch filling patterns

## CONCLUSION

The ion trapping was studied for different bunch filling pattern using linear approximation of the beam field. The result shows that ion trapping will not be a problem for high brightness and high resolution mode of operation, though it has consequences in round beam mode, which needs to be addressed further. The FBII growth rate for HBSRS was estimated using analytical formulations. It is envisaged from the theoretical estimations that, the FBII will be a major concern in HBSRS due to its ultra-low beam emittance and very high beam intensity. Further this instability is studied using multi train bunch filling pattern as a major contributor towards ion density reduction and it shows that the growth time can be increased beyond the radiation damping time to control the instability. Also a fast bunch by bunch feedback may be used to damp the FBII.

## REFERENCES


[1] Ajay Ghodke et al., Physics design study for proposed high brightness synchrotron radiation source (HBSRS) in India, in this proceeding.

[2] C. J. Bocchetta et al., The trapping and clearing of ions in ELETTRA, Nucl. Inst. Meth. in Physics Research A, 278, 807-817 (1989)

[3] A. Xiao, et al., Experience with round beam operation at the advanced photon source, in the proceedings of IPAC, USA, 2015

[4] T.O Raubenheimer et al., Fast beam-ion instability, Linear theory and simulations, Phy.Rev.E 52 (5), 1995

[5] N. Wang, et al., Analytical estimation of the beam ion instability in HEPS, in Proceedings of IPAC2018, Canada

[6] L. Wang, et al. Ion effects in the Electron Damping Ring of the International Linear Collider, SLAC-PUB-11932, 2006

[7] Guoxing Xia and Eckhard Elsen, Update on ion studies, in proceedings of international linear collider workshop, Germany, 2007

# LINEAR LATTICE DESIGN STUDIES OF THE HIGH BRIGHTNESS SYNCHROTRON RADIATION SOURCE (HBSRS)

Riyasat Husain[1,2,*] and A D Ghodke[1]

[1]Accelerator Physics Section, Raja Ramanna Centre for Advanced Technology (RRCAT), Indore

[2]Homi Bhabha National Institute, Training School Complex, Mumbai

## Abstract

In this paper, we present a linear lattice design study based on hybrid seven-bend achromat (H7BA) configuration, for HBSRS, to achieve photon beam brightness of $10^{20\text{-}22}$ [photon/sec./mm$^2$/mrad$^2$/0.1%BW] in the photon energy range from few keV up to 200 keV. The compact storage ring with beam emittance 150 pm.rad at 6 GeV electron beam energy with stored beam current 200 mA is desirable. Based on the normal conducting technology with reasonable quadrupole gradient up to 70 T/m the optimization of various linear lattice parameters are performed to reduce the electron beam dimensions at the source points, satisfying conventional off-axis beam injection and achieving beam accumulation. Using multi-objective optimization algorithms a storage ring of circumference ~ 900 m providing 32 straight sections of 6 m length each, to install injection system, RF system and insertion devices is designed. Various design parameters for the optimized lattice are discussed.

## INTRODUCTION

To achieve the required brightness of $10^{20\text{-}22}$ [photon/sec./mm$^2$/mrad$^2$/0.1%BW] in the photon energy range of few keV to 200 keV, a storage ring with beam emittance < 250 pm.rad at 6 GeV with 200 mA stored beam current is desirable [1]. The beam emittance in the electron storage rings is given by [2]

$$\varepsilon_x = C_q\gamma^2 \frac{\langle \mathcal{H}_x/|\rho|^3\rangle}{J_x\langle 1/\rho^2\rangle}, \quad (1)$$

$$\mathcal{H}_x = \gamma_x\eta_x^2 + 2\alpha_x\eta_x\eta_x' + \beta_x\eta_x'^2, \quad (2)$$

$$C_q = \frac{55}{32\sqrt{3}}\frac{\hbar}{mc} \approx 3.832 \times 10^{-13}\ (\mathrm{m}). \quad (3)$$

where $(\beta_x, \alpha_x, \gamma_x)$ are the twiss parameters; $(\eta_x, \eta_x')$ are the dispersion and its derivative with respect to s; $J_x$ is the horizontal damping partition coefficient, $\rho$ is the radius of curvature of the dipole magnet, $\gamma$, $m$ are the relativistic energy factor and rest mass of an electron, $\hbar$ is the Plank constant, $c$ is the speed of light in vacuum.

To achieve low emittance, more dipole of smaller bending angles (or larger radius of curvature) with quadrupole gradient and independent strong field quadrupoles are needed to focussed the lattice functions in the centre of the dipole magnet. To achieve such a low emittance, the multi-bend achromats (nBA) [2], are being used, where n is the number of dipole magnets per superperiod. The quadruple bend achromat (QBA), 5BA, 7BA and hybrid combination of BAs are extensively being studied for new light source design and up-gradation of the existing facilities. MAXIV [3] is the first commissioned machine utilizing 7BA lattice and achieved the beam emittance ~300 pm.rad at 3 GeV. A hybrid 7BA (H7BA) lattice using strong transverse gradient and longitudinal gradient in the dipole magnets provides the more compact ring size, reduced emittance and above all better nonlinear dynamics performance. The ESRF-EBS [4] and APS-U [5] are the upgrades of the machines, which utilize the H7BA lattice.

As discussed above, for achieve ultra-low emittance, very strong field quadrupole magnets are generally employed which result into a large negative chromaticity. For its correction, strong field sextupole magnets are inserted in the lattice, where higher dispersion and proper phase advance between a pair of sextupole are required. First condition is necessary in view of chromaticity correction with less number of sextupoles with reduced strengths. The phase advance between a pair of sextupoles must be an odd integer multipole of $\pi$ to cancel the geometric aberrations they introduce [6]. Figure 1 shows the comparison of distribution of the dispersion function over one superperiod of regular 7BA and H7BA lattice with beam emittance ~150 pm.rad at 6 GeV. It can be observed that the amplitude of the dispersion function at sextupole location in H7BA lattice is ~ 2.5 times of 7BA lattice. The value of dispersion in the dipole magnet is almost similar in both cases, which ultimately gives the lower beam emittance. It can be noticed that the length of a super period is much smaller compared to 7BA lattice. Therefore, H7BA lattice is the choice for HBSRS storage ring in view of achieving low emittance, efficient chromaticity correction, better nonlinear dynamics and compact ring size. However, in H7BA, much strong field quadrupoles and dipoles with strong quadrupole gradient are used.

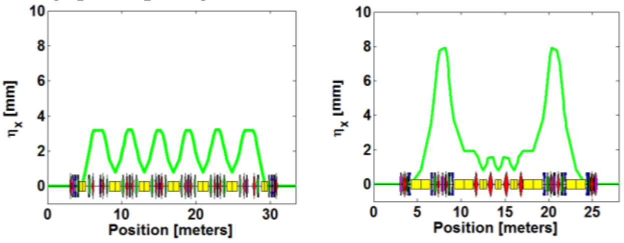


Figure 1: Distribution of dispersion function in the regular 7BA (left) and H7BA (right) lattice. The two peaks in H7BA lattice called dispersion bumps.

## LINEAR LATTICE OPTIMZATION

Number and length of the magnet free straight sections are important part of the low emittance storage ring to install injection system, RF system and insertion devices

*riyasat@rrcat.gov.in

(IDs). We consider 32 straight sections of 6 m length each. To minimize the synchrotron radiation loss to operate the RF system requiring less RF power, the dipole magnetic field in the range 0.2-0.75T are considered. In addition, a clear space of >65 mm between the magnets are provided to install the beam position monitors. Total 16 quadrupoles grouped in 8 families, 7 dipoles (four without and 3 with transverse quadrupole gradient) are used to achieve the desired beam emittance together with optimized values of beta function at injection or at the centre of IDs, dispersion function at sextupole locations etc. Therefore, lattice design of HBSRS storage ring is a class of multi-objective optimization problem. We perform the lattice optimization using multi-objective differential evolution (MODE) [7] algorithm. In optimization, 10 variables: 8-strengths of the quadrupole magnets and 2-quadrupole gradient in middle dipoles are varied in the following practically achievable limits:

- *Quadrupole gradient < 80T/m*
- *Quadrupole gradient in the dipoles < 45 T/m)*

Three optimizing objectives are used to illustrate the overall performance of a lattice: one is the beam emittance, second is the dispersion at sextupole location (required for effective chromaticity correction), and third is the absolute value of dispersion at ID centres (for effective beam size control). During optimization, following constraints and limitations are considered to achieve feasible solutions:

- *Fractional part of betatron tunes < 0.5 (avoid lower order resonances)*
- *Maximum beta function:* $(\beta_x,\ \beta_y) < 20$ *m (control natural chromaticity)*
- *Beta function at injection:* $\beta_x > 10$ *m (satisfy off axis injection)*
- *Phase advances between the sextupole pair:* $\mu_x = (2n+1)\pi$ *in the horizontal and* $\mu_y = n\pi$ *in vertical plane, where n is an integer.*

For MODE algorithm, 100 generations with 2000 population randomly generated with the quadrupole gradient and gradient in the dipole magnets upto maximum values are considered. The Accelerator Toolbox (AT) [8] is used for calculating all lattice parameters. The result of optimization at last generation are shown in Fig. 2 (top). It can be observed that the beam emittance upto 135 pm.rad could be achievable if we allow the dispersion function value of ~5 mm at ID centre with dispersion value of ~70 mm at sextupole location. This solution is disregarded in view of the following reasons: in presence of IDs, emittance may blow up, and need more strength of the sextupole to correct the chromaticity. However, in achromatic mode, the beam emittance upto 145-150 pm.rad can be achieved, with reasonably large dispersion value ~ 80 mm at sextuple location. Fig. 2 (bottom) shows the deviations in the betatron phase advances between the sextupole pairs from required conditions. Most of the solutions satisfy the required condition of phase advanced at the sextupole locations, they are only deviated by ~ 7 degree in horizontal and ~ 10 degree in vertical plane. A magnetic lattice with beam emittance ~150 pm.rad has been chosen as a baseline lattice for HBSRS storage ring.

The distribution of lattice function over 28.5 m long superperiod of the chosen H7BA lattice are shown in Fig. 3. The designed betatron tune point is shown in Fig. 4. The relevant lattice parameters for the optimized HBSRS storage ring lattice are given in Table 1. The important parameters are the circumference of the ring ~ 912 m, small SR loss per turn 2457.2 MeV. For this lattice, further studies are also being performed to qualify it for its operational feasibility.

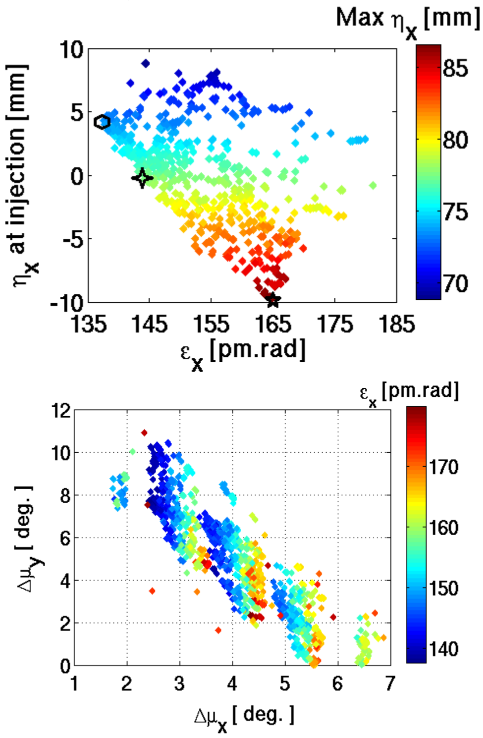


Figure 2: The optimized results at last generation of MODE algorithm showing (top) beam emittance and dispersion at injection with maximum dispersion at sextupole location, and (bottom) difference in the phase advances in respective horizontal and vertical planes at sextupole locations, colour with the beam emittance.

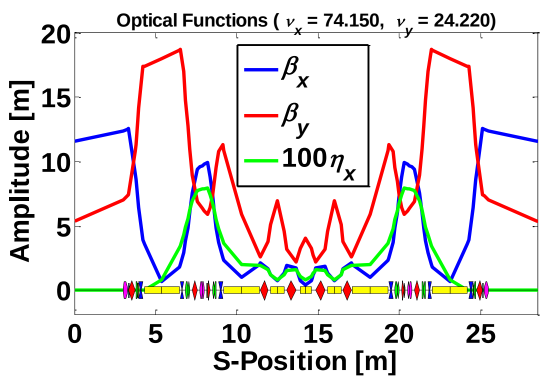


Figure 3: Lattice function over one superperiod of H7BA lattice. The rectangles show yellow-dipole magnet, red-focussing quadrupole, blue-defocussing quadrupoles magnets, magenta-focussing sextupole and green-defocussing sextupole magnets.

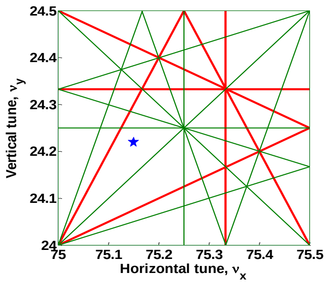


Figure 4: Tune diagram showing the designed betatron tune (blue star). Red and green lines show the 3[rd] order and 4[th] order resonance lines.

Table 1: Important parameters of HBSRS lattice at 6 GeV.

| Parameters | Units | Values |
|---|---|---|
| Circumference, C | m | 911.8 |
| Emittance, $\varepsilon_x$ | pm.rad | 150 |
| No./length ID sections | / m | 32 / 6 |
| Energy loss/turn | keV | 2457.2 |
| Hor. Damp. Partition, $J_x$ | | 1.703 |
| Betatron Tunes:[$\nu_x$, $\nu_y$] | | 74.15, 24.22 |
| Chromaticity: Natural [$\xi_x$,$\xi_y$] | | -109.6 , -80.9 |
| : Corrected | | +4 , +4 |
| Damping times: :[$\tau_x$, $\tau_y$, $\tau_\varepsilon$] | ms | 8.72, 14.85, 11.45 |
| Beta functions at ID: [$\beta_x$, $\beta_y$] | m | 11.6 , 5.4 |
| Dispersion at ID :$\eta_x$ | m | 0.0 |
| Beam size at ID: [$\sigma_x$ $\sigma_y$] | μm | 41.4, 2.8 |
| Beam size at BM:[$\sigma_x$ $\sigma_y$] | μm | 10.9, 2.4 |
| Energy spread | | $1.02\times10^{-3}$ |
| Mom. compact factor | | $9.6\times10^{-5}$ |

## PRELIMINARY NONLINEAR LATTICE OPTIMZATION STUDIES

The beam injection and beam lifetime in such a low emittance storage ring are few of the many challenging tasks. In order to ease these issues, the dynamic aperture (DA) of the ring should be as large as possible for both on and off-momentum particles. For numerical optimization of DA, MODE algorithm is used as a tool to improve the nonlinear dynamics of the lattice. We started with minimizing the resonance driving terms (RDT), amplitude dependent tunes shift (ADTS) [6], and momentum dependent tune shift by optimizing the sextupole strengths using OPA code [9]. Five sextupole families, three in achromat and two in dispersion free sections are used. Based on this optimization, a set of sextupole strengths are taken as the starting point to generate the initial population for MODE algorithm in MATLAB. Iteratively, the RDTs, ADTSs and DAs were optimised. At the last generation, one of the optimized results for ADTS and momentum dependent tune shifts are shown in Fig. 5. The on- and off-momentum DA with relative momentum errors: -2% and +2% based on single particle tracking for 5000 turns (nearly two times of the damping time) are shown in Fig. 6. The DA boundary are -10 to 6 mm in horizontal and ~4 mm in vertical plane. This may be sufficient for off-axis beam injection.

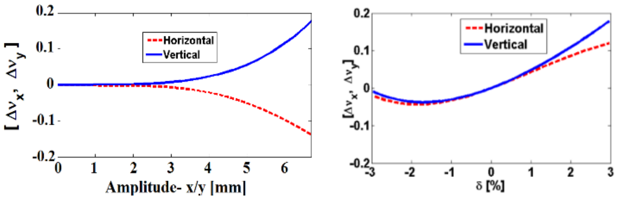


Figure 5: Amplitude and momentum dependent tune shift.

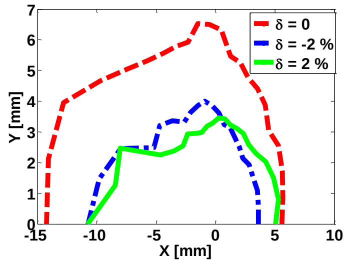


Figure 6: The DA of a single particle tracked for 5000 turns with momentum errors: 0%, -2%, +2% at injection point.

## CONCLUSIONS

The MODE algorithm was used to design a magnetic lattice for HBSRS storage ring of size 911.8 m providing 32 straight sections of 6 m length each, and with beam emittance of 150 pm.rad at 6 GeV. The storage ring utilize the strong field quadrupole magnets with gradient upto 70 T/m and generate large negative chromaticity. The strong field sextupoles at high dispersion location were used for chromaticity correction. With sextupoles, dynamics of the lattice become nonlinear and reduces the dynamic aperture. To combat the effect of nonlinearity, the optimization of linear lattice was performed to generate dispersive bumps at two extreme ends of a superperiod, where sextupoles were placed with significantly reduced strengths. The optimized dynamic aperture of the designed storage ring for HBSRS lattice appeared to be sufficient for conventional off axis beam injection and the momentum aperture is adequate to provide sufficient beam lifetime. Further studies to improve the nonlinear dynamics including octupole magnets and in presence of practical alignment and magnetic field-errors are being carried out.

## REFERENCES


[1] A. D. Ghodke etal. these proceedings.
[2] D. Einfeld, et al., J. Synch. Rad., 21(5):856–861, 2014.
[3] MAX-IV Conceptual Design Report.
[4] ESRF upgrade programme phase -II, technical design study report.
[5] Advanced Photon Source upgrade project preliminary design report.
[6] J. Bengtsson, The sextupole scheme for Swiss Light Source (SLS): An analytical approach, SLS note 9/97.
[7] R. Storn, K. Price, J. Global Optimization 11, 341 (1997).
[8] A. Terebilo, Accelerator modelling with MATLAB accelerator toolbox, PAC (2001).
[9] A. Streun, OPA Code, ver. 3.39, PSI (2012).

# CLOSED ORBIT DISTORTION AND ITS CORRECTION AT INJECTION ENERGY FOR BOOSTER SYNCHROTRON OF HBSRS

V. K. Meena†, A.A. Fakhri and A.D. Ghodke
Accelerator Physics Section
Raja Ramanna Centre for Advanced Technology, Indore-452013

*Abstract*

A booster synchrotron with a beam emittance of ~4 nm-rad at 6 GeV will serve as a full energy injector for proposed High Brightness Synchrotron Radiation Source (HBSRS). In the booster at injection energy, higher horizontal and vertical acceptance is required to accommodate higher beam emittance 60 nm-rad from 200 MeV linac. These acceptances will be reduced in the presence of Closed Orbit Distortion (COD) which is generated due to misalignment errors of quadrupoles and magnetic field errors and roll angle errors of dipoles. The COD reduces the efficiency of beam injection. Thus, the magnetic elements must be placed in the booster with great attention. The COD can be corrected using the orbit correction scheme consists of 172 Beam Position Indicators (BPIs) and 172 Combined function Horizontal and Vertical corrector magnets (CHVs). To calculate corrector kicks and estimate residual orbit displacements, we have simulated static orbit distortions due to random alignment and excitation errors for all magnets in the booster lattice. The errors have Gaussian distribution with a cut-off at three standard deviations i.e. 3σ. In this paper, a simulation study is presented to realize the effects of these errors on COD. Based on this study alignment tolerance of quadrupole and dipole magnets is estimated. A preliminary study of the orbit correction scheme is also presented.

## INTRODUCTION

Studies have been undertaken for the proposed HBSRS at RRCAT [1]. It consists of a 200 MeV linac, a full energy booster with 1-2 Hz rep-rate, 6 GeV storage ring and transport lines. In the booster a modified FODO lattice is chosen [2]. It has a focusing quadrupole magnet and a dipole magnet with embedded defocusing quadrupole components in a unit cell. This lattice with 86 unit cells is capable to provide a beam emittance of ~4 nm.rad at 6 GeV to satisfy the requirement of transparent top-up injection into the storage ring. Beam injection into the booster will be carried out using an on-axis horizontal beam injection scheme by using an injection septum and an injection kicker magnet.

For the efficient beam injection, one has to consider the practical beam dynamics aspect such as uncorrected COD as well as a residual betatron oscillations in the transverse planes. For both horizontal and vertical planes, residual betatron oscillations at the locations of dipole and quadrupole magnets for ±4σ of the injected beam are found to be ±11 mm and ±12 mm. These computations are carried out in the presence of chromaticity correcting sextupole magnets. The COD is anticipated as magnet-to-magnet dipole field errors due to the imperfections in fabrication and misalignment errors, which are governed by the installation accuracy of the magnetic element. In the presence of the COD, the residual betatron oscillations will be further increased. As a result, available room for the injected beam oscillation will be reduced. In this case, beam accumulation may be difficult or injection efficiency will be reduced due to partial beam loss. Therefore, it is necessary to estimate the alignment tolerances of magnetic elements. The estimation of COD before and after correction will play a key role for estimating the good field region of the different magnetic elements. The optical functions of the booster lattice for two unit cells are shown in Fig. 1.

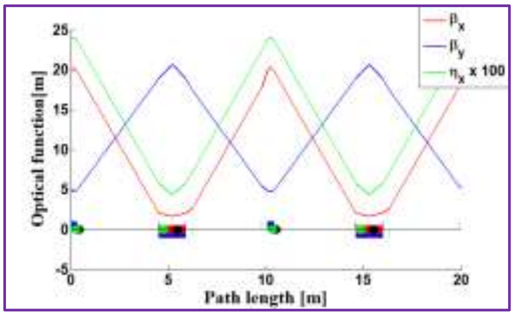


Figure 1: Optical function of two super-period of FODO lattice. The solid rectangular boxes represent bending magnet (red), quadrupole magnets (blue) and sextupole magnets (green) and position of the BPIs (black sphere) and CHVs (green sphere) also indicated.

In this paper, alignment tolerances for different magnetic elements are evolved. The orbit correction scheme is also developed by distributing BPIs and corrector magnets over the circumference. The COD before and after correction are also estimated for deciding the good field region at different magnetic elements.

## CLOSED ORBIT DISTORTION

Any unwanted dipolar kick generates distortion in ideal orbit. The effect on the orbit due to smaller error is defined as COD w.r.t. ideal orbit, it is given by

$$z_{co}(s_j) = \frac{\sqrt{\beta_{zmax}(s_j)}}{2 sin\pi\nu_z} \sum_{i=1}^{N} \theta_i \sqrt{\beta_{zi}(s_i)}\, cos(\pi\nu_z - |\psi_z(s_j) - \psi_{zi}(s_i)|) \quad (1)$$

Where $z(s) = x \; or \; y$ represents horizontal and vertical plane, $\nu_z$ is the betatron tune of the ring, and $(\beta_i, \psi_i)$ and $(\beta_j, \psi_j)$ are the beta function and the phase function for the $\theta_i$ dipolar kick and $j^{th}$ BPI respectively, and $z_{co}(s_j)$ is the orbit distortion at the $j^{th}$ BPI due to $\theta_i$ kick of the $i^{th}$ element in horizontal and vertical plane respectively. The origin of $\theta_i$ is given by

$$\theta_i = \left(\frac{\Delta B}{B}\right)_i \theta_B \;\; for \; the \; dipole \; field \; error \quad (2a)$$

$$\theta_i = (\Delta\phi)_i \theta_B \;\; for \; the \; dipole \; rotation \; error \quad (2b)$$

† vkmeena@rrcat.gov.in

$\theta_i = (kl)_i \Delta z_i$ *for quadrupole misalignment* (2c)

Where $\left(\frac{\Delta B}{B}\right)_i$, $\Delta\phi_i$ *and* $\theta_B$ are the magnetic field error, rotation error and bending angle of $i^{th}$ dipole magnet and $k_i, l_i$ *and* $\Delta z_i$ are the strength, length and misalignment of the $i^{th}$ quadrupole magnet.

Thus, COD is the overall effect of all the dipolar field errors, rotation errors and quadrupolar misalignment errors. Hence rms orbit at any point in the lattice can be obtained by the following equations

$$x_{rms}(s) = \frac{\sqrt{\beta_{xmax}(s)}}{2\sqrt{2}sin\pi\nu_x}\left\{(\Delta x)^2 \sum_i (kl)_i^2 \beta_{xi} + \left(\frac{\Delta Bl}{Bl}\right)^2 \sum_i \theta_B^2 \beta_{xi}\right\}^{\frac{1}{2}} \quad (3)$$

$$y_{rms}(s) = \frac{\sqrt{\beta_{ymax}(s)}}{2\sqrt{2}sin\pi\nu_y}\left\{(\Delta y)^2 \sum_i (kl)_i^2 \beta_{yi} + (\Delta\phi)^2 \sum_i \theta_B^2 \beta_{yi}\right\}^{\frac{1}{2}} \quad (4)$$

## Closed Orbit Amplification Factor

The effects of these errors on COD are estimated by CO Amplification Factors (AFs). Therefore, it is necessary to quantify the tolerances of magnetic field errors. It is a parameter to measure the sensitivity of these errors. The AF is a ratio of rms COD to rms error. The AFs for positioning error of quadrupoles, dipole field errors and dipole rotation errors are estimated with help of Eq. (5), (6) and (7) respectively.

$$A_z = \frac{\Delta z_{rms}^{CO}}{\Delta z_{rms}} = \frac{\sqrt{\beta_z}}{2\sqrt{2}Sin(\pi Q_z)}\{\sum_i (kl)_i^2 \beta_{iz}\}^{1/2} \quad (5)$$

$$A_x = \frac{\Delta x_{rms}^{CO}}{\left(\frac{\Delta B}{B}\right)} = \frac{\sqrt{\beta_x(s)}}{2\sqrt{2}sin\pi\nu_x}\{\sum_i \theta_B^2 \beta_{xi}\}^{1/2} \quad (6)$$

$$A_y = \frac{\Delta y_{rms}^{CO}}{(\Delta\phi)} = \frac{\sqrt{\beta_y(s)}}{2\sqrt{2}sin\pi\nu_y}\{\sum_i \theta_B^2 \beta_{yi}\}^{1/2} \quad (7)$$

## Closed Orbit Correction

The measurement of the COD will be carried out by the BPIs (which provides horizontal and vertical orbit position) and the correction will be carried out by the corrector magnets (CHVs). The corrector-to-BPI orbit response matrix (ORM) is a vital piece of information for both closed orbit correction and linear optics analysis. The basic format of the response matrix equation is

$$z = R\theta \quad (8)$$

Where column vector z contains the orbit shift produced by incremental change θ in the corrector magnets. The element of the response matrix, between BPIs and correctors, are given by

$$R_{ij} = \frac{\sqrt{\beta(s_i)\beta(s_j)}}{2sin\pi\nu}cos\left(\pi\nu - \left|\psi(s_j) - \psi(s_i)\right|\right) \quad (9)$$

The strength of the corrector magnets is computed by solving the linear equation as following

$$\theta = -R^{-1}z \quad (10)$$

Where $R^{-1}$ is the inverse response matrix.

*Distribution of BPIs and Correctors*

2 BPIs and 2 CHVs are assumed for orbit measurement and correction per super-period. BPIs are judiciously placed at high beta function locations in the lattice. To find out the best orbit correction, the corrector magnets are placed as near as possible to the generating source of orbit deviation. Thus the COD can be corrected using the orbit correction scheme consists of 172 BPIs and 172 CHVs. The tentative arrangements of the BPIs and CHVs in two super-period are shown in Fig.1.

# RESULTS AND DISCUSSION

## Amplification factors

The AFs are estimated using analytical formulae, given by Eqs. (3) & (4) for dipole and quadrupole families. The AFs for dipole and quadrupole families are shown in Fig.2. These factors are not stringent.


Figure 2: Closed orbit amplification factors

## Alignment tolerances

The simulation of maximum allowable quadrupole misalignments was performed iteratively with increasing misalignment amplitude randomly truncated at 3σ (99.73% confidence lie within this mean) for 1000 machines. This simulation is carried out with corrected chromaticity [+2, +2] in both transverse planes. In any of the cases, if COD becomes unstable, that is the limit on the misalignment. This exercise is repeated independently in horizontal and vertical planes, and the misalignment tolerances are estimated ~[100mm, 60mm] for dipole magnet and ~[65mm, 90mm] for focusing quadrupole magnet. Similarly this exercise is also carried out for maximum allowable dipolar kick in horizontal and vertical planes. The maximum magnetic field error ~$6*10^{-4}$ T and axial rotation error ~0.15 mrad are estimated. In practical case, the quadrupoles are misaligned in both planes simultaneously and combined misalignment in the horizontal and the vertical planes are limited to ~48 µm. In this case, feed down effects, which is generated due to the orbit offset at strong sextupole magnet, are shown in table-1. These results indicates that variation in betatron tune $\Delta\nu$, chromaticity $\Delta\xi$ and beta beat $\Delta\beta/\beta$ are significant. Beta beat goes up-to ~50% and ~90% in horizontal and vertical plane respectively. This is a major cause for stringent alignment tolerances. With these errors, sufficient dynamic aperture may not be available at injection energy. In order to overcome this effect, chromaticity correcting sextupole strengths have to be reduced.

For example, if natural chromaticities in both planes are corrected up-to -16 in that case feed down effects are summarized in table 2. This indicates that feed down effects are reduced as compared to the previous case thus sufficient dynamic aperture may be available for beam injection. In the above case, alignment tolerance for all magnets is also estimated, which is found to be ±100 µm. For this tolerance, the max uncorrected COD in both planes goes up-to ~13 mm.

† vkmeena@rrcat.gov.in

*COD correction*

For simulation of COD, the uncorrected COD is generated by applying the misalignment errors ~48 μm truncated at 3σ in focusing quadrupole and defocusing quadrupole magnets (embedded in dipole) for 1000 random machines. In this case natural chromaticities in both transverse planes are corrected up-to +2. The max orbit before and after correction is given in table 1. The results indicate that in horizontal and vertical plane, max orbit after correction is ~1 mm and ~1.5 mm respectively. The feed down effects after correction are also remain at higher value as shown in Table 2. Thus this scheme has to be further studied for correction.

**Table 1: Max uncorrected and corrected orbit**

| COD | Uncorrected | | Corrected | |
|---|---|---|---|---|
| @ [+2 +2] | $x_{max}$ | $y_{max}$ | $x_{max}$ | $y_{max}$ |
| Centre of BM | ~1.5 | ~5.7 | ~0.3 | ~1.5 |
| Start of BM | ~1.6 | ~5.5 | ~0.4 | ~1.5 |
| Centre of QF | ~5.1 | ~2.9 | ~0.9 | ~0.7 |
| Over the ring | ~5.1 | ~5.7 | ~0.9 | ~1.5 |

**Table 2: Feed down effect of closed orbit**

| COD | Uncorrected | | Corrected | |
|---|---|---|---|---|
| | x | y | x | z |
| **Betatron tune $\Delta\nu$** | -0.055 | -0.057 | -0.002 | -0.006 |
| | 0.051 | 0.052 | 0.028 | 0.041 |
| **Chromaticity $\Delta\xi$** | -3.66 | -1.22 | -0.08 | -0.04 |
| | 1.49 | 5.18 | 0.02 | 0.03 |
| **Beta beat $(\Delta\beta/\beta)_{max}$** | 49.4 | 92.5 | 16.3 | 25.0 |

In the previous case, it may be difficult to inject the beam thus for the misalignment tolerances of ~48 μm, natural chromaticity in both planes are corrected up-to -16, for 1000 random machines. For this maximum COD, and feed down effects before and after correction are tabulated in table 3.

**Table 3: Fed down effects**

| COD | Uncorrected | | Corrected | |
|---|---|---|---|---|
| | x | y | x | z |
| **Betatron tune $\Delta\nu$** | -0.0163 | -0.0029 | -0.0007 | -0.0011 |
| | 0.0041 | 0.0046 | 0.0040 | 0.0042 |
| **Chromaticity $\Delta\xi$** | -2.1252 | -0.2074 | -0.0199 | -0.0073 |
| | 0.7253 | 0.3835 | 0.0021 | 0.0011 |
| **Beta beat $(\Delta\beta/\beta)_{max}$** | 20.0% | 18.3% | 4.4% | 2.3 |

*Good field region*

The required good field region for the alignment tolerances of ~48 μm are estimated with the help of following equation

$$A_z = 4\sigma_z + a_z + \Delta z_{corrected}$$

Where as $\sigma_z$ beam size, $a_z$ residual oscillation and $\Delta z_{corrected}$ corrected COD.

*Focusing quadrupole magnet*

$A_x$ = 12.2+3+ 0.9~**16 mm,** $A_y$ = 5.3 + 1 + 0.7 = 7 **mm**

*Dipole magnet*

$A_x$ = 3.4 + 3 + 0.4 = **7 mm,** $A_y$ = 11.2+1+2 **~16 mm**

For the alignment tolerances of ~100 μm, the max uncorrected COD goes up-to ~[12 mm, 13mm]. If vacuum chamber is kept similar to good field region, then for the alignment tolerances of ~100 μm beam circulation even for single turn may be difficult. Therefore it is necessary to enhance vacuum aperture requirement or to keep stringent requirement on alignment tolerance, such that sufficient space for residual oscillation can be provided at the time of beam injection.

*Corrector strengths*

In order to estimate required strength of horizontal and vertical corrector magnets, COD are generated and corrected for alignment error of ±100 μm. The maximum required strength of corrector magnets are ~120 μrad and ~200 μrad for orbit correction in both horizontal and vertical planes. After COD correction, max residual COD is not reaching less than 0.5 mm. For its further reduction, this correction scheme has to be further explored. The strength of the corrector magnets for 1000 machines is shown in the left side of Fig. 3. The closed orbit before and after correction for one iteration over the ring is shown on the right side of Fig. 3.

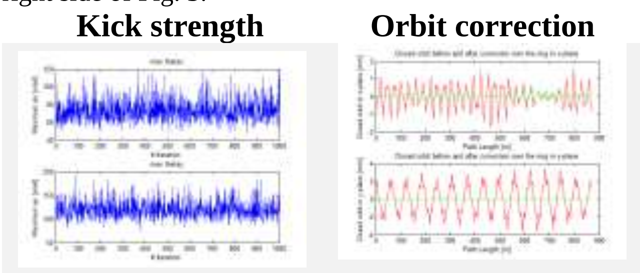


Figure 3: Required kick strength and orbit correction

## CONCLUSION

For 6 GeV, ~4 nm-rad booster synchrotron optics, alignment tolerances of all quadrupole magnets should be kept less than ~48 μm. These stringent tolerances are arising due to feed down effects, which are generated due to orbit offset in the sextupole magnet. For alignment tolerance of ~48 μm, beam accumulation may not be feasible due to feed down effects. In order to overcome this, strength of chromaticity correcting sextupole magnets have to be significantly reduced. Afterwards with orbit correction, these feed down effects can be reduced nearly one third. The required good field region for quadrupole and sextupole magnets are also estimated with the help of max corrected COD at their respective locations.

## REFERENCES


[1] A D Ghodke et al, Physics design for proposed high brightness synchrotron radiation sources (HBSRS) in India, InPAC (2019)

[2] Pradeep Kant et al, Effects of eddy current induced sextupole during ramping in booster synchrotron of HBSRS, InPAC (2019)



† vkmeena@rrcat.gov.in

# DESIGN OF HALF WAVELENGTH COAXIAL RESONANT CAVITY FOR ELECTRON ACCELERATION.

Deepak Kumar Mishra*, Subhajit Dutta, Jishnu Dwivedi
Industrial Accelerators Division, RRCAT, Indore, India

*Abstract*

RRCAT has developed and installed 10 MeV, 5KW Linac at ARPF for bulk radiation processing. This is the first step on the roadmap for reaching on industrially viable level of electron beam power for bulk processing. The next step on this roadmap include increasing the beam power to 30-50 KW level. This work is towards making preparations in that direction. Accelerator schemes making use of a large single cavity for repeated acceleration can work in cw mode and are capable of providing very high beam power with well defined energy and narrow energy spread. Such accelerator can be developed using a co-axial cavity. In this paper we will be presenting electrodynamic design of $\lambda/2$ coaxial resonant cavity.

## INTRODUCTION

The use of ionizing radiation is now a well known process in the industrial environment . Electron accelerators are widely used in a lot of industrial applications such as cross linking of polymers, processing of thermoshrinkable products, medical disposals sterilization, food preservation, etc.. When very large volumes of material require radiation treatment, demand is created for an economical, reliable and powerful radiation source . The irradiation of thick pieces of material requires a high-energy beam. J. Pottier [1] invented the recirculating electron acceleration using the single coaxial cavity, in which the electron beam passes several times along the different diameters in the median plane. After each pass the beam is made to re-enter in accelerating cavity using bending magnet. The electric field is radial and magnetic field is azimuthal having zero value in the median plane of the cavity. Ion Beam Applications(IBA)in Belgium have built several industrials models of coaxial cavity including TT100, TT200, TT300 and TT1000 providing beam power ranging from 35kW to 700kW at 10MeV beam energy. Since our aim was to go for beam power of about 50 kW. We have chosen the frequency as 107 MHz similar to TT200 for our design.

## SYNCHRONOUS CONDITION

Except the first pass, the electrons move close to the velocity of light in every other pass. Figure1 shows typical path of the electron traveling from centre of the cavity back to centre. If R is the distance between the center of cavity and entrance or exit side of bending magnet and D is the length of path taken by the electrons out side the cavity, then synchronous condition requires

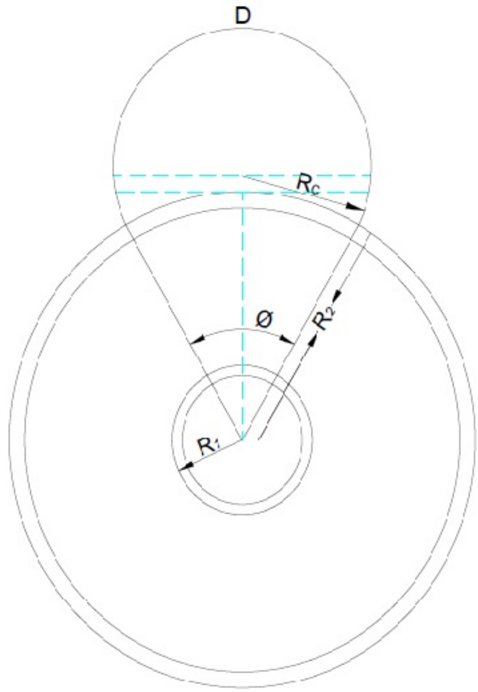


Figure 1: Cross sectional view of the coaxial cavity.

$$2R_2 + D = \lambda \tag{1}$$

If n is the number of passes, that electron beam will under go, then the angle $\phi$, as shown in figure 4 is given by,

$$\phi = \frac{\pi}{n} \tag{2}$$

If $R_c$ is the radius of the bending magnet, which has been shown as path 2 in figure 4, then the relation between $R_c$ and $R$ are given as under : –

$$R_c = R_2.tan(\frac{\phi}{2}) \tag{3}$$

The length D of path taken by the electrons out side the cavity is accordingly related as per following relation,

$$D = R_c \frac{N+1}{N} \pi \tag{4}$$

From equation (1), (2) and (3), the relation between R and $\lambda$ is derived and is given as,

$$R_2 = \frac{\lambda}{\left[2 + \frac{N+1}{N}\pi.tan(\frac{\phi}{2})\right]} \tag{5}$$

* deepak@rrcat.gov.in

From equation (5) it can be seen that $R_c$ defines $R_2$. For a particular value of $\lambda$ the value of $R_c$ and $R_2$ are related as shown in table1 below.

Table 1: Relation of $R_c$ and $R_2$ with $\lambda$

| Number of Passes N | $R_2$ | $R_c$ |
|---|---|---|
| 6 | $\lambda/2.98$ | $8.99 \times 10^{-2}\lambda$ |
| 7 | $\lambda/2.82$ | $8.1 \times 10^{-2}\lambda$ |
| 8 | $\lambda/2.70$ | $7.37 \times 10^{-2}\lambda$ |
| 9 | $\lambda/2.62$ | $6.73 \times 10^{-2}\lambda$ |
| 10 | $\lambda/2.55$ | $6.21 \times 10^{-2}\lambda$ |

For frequency f= 107 MHz, we get the value of $R_c$ and $R_2$ tabulated in table 2,

Table 2: Values of $R_c$ and $R_2$ for f=107 MHz

| Number of Passes N | $R_2$ | $R_c$ |
|---|---|---|
| 6 | 94.0 cm | 25.2 cm |
| 7 | 99.4 cm | 22.7 cm |
| 8 | 103.7 cm | 20.6 cm |
| 9 | 107.2 cm | 18.9 cm |
| 10 | 110.1 cm | 17.4 cm |

From table2 it is clear that for N=10 pases, the maximum value of $R_2$ is 110.1 cm. The actual value of inner radius of outer conductor will be less than 110.1 cm to give margin for outer conductor thickness and for placing dipole magnet.

### *Transit time factor*

The expression for transit time factor for relativistic electron is given as,

$$TTF = \frac{S_i(\theta_2) - S_i(\theta_1)}{ln(R_2/R_1)} \quad (6)$$

Where $Si(\theta)$ is the Sink function, $\theta_2 = 2\pi \cdot \frac{R_2}{\lambda}$ and $\theta_1 = 2\pi \cdot \frac{R_1}{\lambda}$.

## SHUNT IMPEDANCE

The shunt impedance is give in ref[3] as,

$$Z_s = \frac{8\pi}{\rho_s} ln^2 \frac{R_2}{R_1} \left( \frac{\lambda}{8} \left( \frac{1}{R_1} + \frac{1}{R_2} \right) + ln \frac{R_2}{R_1} \right)^{-1} \quad (7)$$

Where $\rho_s$ is the areal skin effect resistivity. For copper, $\rho_s = 2.51 \times 10^{-7} f^{1/2}$. During the transit in the gap E does not remain constant. So the useful parameter is effective shunt impedance $Z_s \cdot TTF^2$. Figure3 shows the plot of effective shunt impedance Vs. inner conductor radius for different values of outer conductor radius. From the plot it can be clearly seen that the effective shunt impedance is maximum for R1= 0.2 m to 0.25 m. From plot figure2 it can also be seen that for R1 from 0.2 m to 0.25 m there is hardly any change in transit time factor for outer conductor radius between R2=0.9m to 1.1m. So R1 can be chosen equal to 0.21 m and R2 be chosen equal to 0.96 m as reported in ref[2].

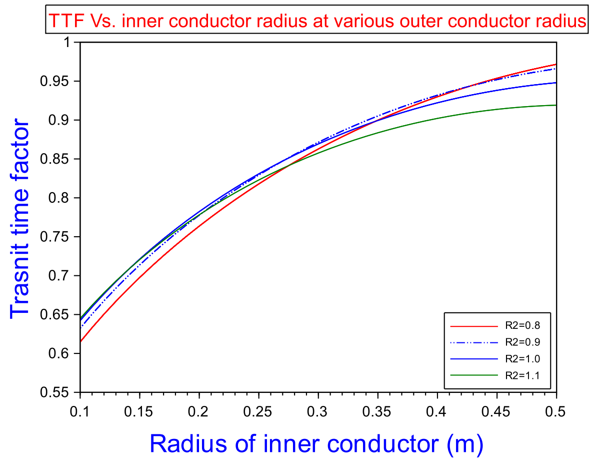


Figure 2: Plot of Transit time factor Vs. Inner conductor radius at different outer conductor radius.

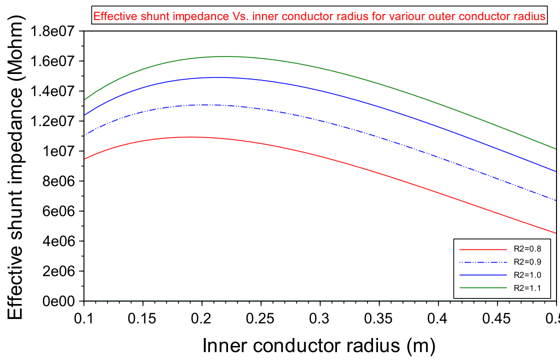


Figure 3: Plot of effective shunt impedance Vs. Inner conductor radius at different outer conductor radius.

## SHUNT IMPEDANCE IMPROVEMENT

The results plotted in figures 2 and 3 are for a cavity, in which it is assumed that both inner and outer conductor are having same dimensions form top end to bottom end. In practice the inner conductor dimensions are modified to reduce the power loss, which ultimately results in improvement of shunt impedance.

From the table shown in figure4 it can be seen that the minimum power loss is for Z=50 cm and theta = 40 degrees. The value of Q for these variables is 54552.

## CONCLUSION

The geometrical parameters of coaxial cavity have been optimized for frequency of 107 MHz. The optimized parameters of the cavity are, the outer radius of inner conductor is

**Theta (degrees)** **Quality factor.**

| Z(cm) | 5 | 10 | 15 | 20 | 25 | 30 | 35 | 40 | 45 | 50 | 55 |
|---|---|---|---|---|---|---|---|---|---|---|---|
| 25 | 49933 | 51960 | 53511 | 54525 | 54881 | 54356 | 52435 | 47040 | | | |
| 30 | 49735 | 51675 | 53257 | 54439 | 55147 | 55206 | 54281 | 51362 | | | |
| 35 | 49500 | 51293 | 52829 | 54086 | 55015 | 55512 | 55389 | 54106 | | | |
| 40 | 49232 | 50826 | 52243 | 53476 | 54494 | 55254 | 55646 | 55462 | | | |
| 45 | 48937 | 50293 | 51524 | 52640 | 53632 | 54472 | 55127 | 55503 | | | |
| 50 | 48623 | 49704 | 50707 | 51633 | 52490 | 53271 | 53970 | 54552 | 54951 | 55013 | |
| 55 | 48302 | 49092 | 49830 | 50533 | 51193 | 51825 | 52407 | 52947 | 53438 | 53838 | 54092 |

**Theta (degrees)** **Power loss (KW)**

| Z(cm) | 5 | 10 | 15 | 20 | 25 | 30 | 35 | 40 | 45 | 50 | 55 |
|---|---|---|---|---|---|---|---|---|---|---|---|
| 25 | 24.83 | 24.54 | 24.64 | 25.18 | 25.84 | 26.29 | 28.20 | 39.02 | | | |
| 30 | 24.74 | 24.21 | 24.11 | 24.27 | 24.8 | 25.89 | 27.85 | 31.74 | | | |
| 35 | 24.72 | 24.14 | 23.8 | 23.68 | 23.82 | 24.31 | 25.29 | 27.25 | | | |
| 40 | 24.75 | 24.14 | 23.69 | 23.41 | 23.28 | 23.37 | 23.74 | 24.54 | | | |
| 45 | 24.83 | 24.25 | 23.78 | 23.41 | 23.14 | 23.0 | 23.0 | 23.21 | | | |
| 50 | 24.95 | 24.45 | 24.01 | 23.64 | 23.33 | 23.08 | 22.91 | 22.82 | 22.88 | 23.20 | |
| 55 | 25.10 | 24.71 | 24.36 | 24.04 | 23.76 | 23.50 | 23.8 | 23.1 | 22.9 | 22.9 | 22.95 |

Figure 4: Tabulation of quality factor and structure power loss as a function of Angle theta at various values of Z

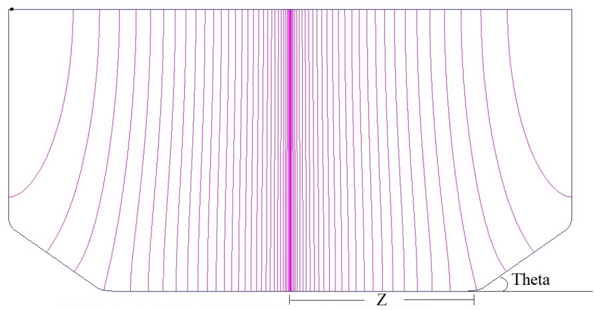


Figure 5: Geometry of coaxial cavity showing the parameter Z and Theta

21 cm, the inner radius of outer conductor is 96 cm. the value of Z and theta for lowest structure power loss and optimized Quality factor are 40 degrees and 54552 respectively.

## REFERENCES


[1] Deepak Kumar Mishra et al, Preliminary study of halfwave-length coaxial resonant Cavity operating in fundamental mode for electron Acceleration, . InPac2018.

[2] Iraj Jabbari et al.,Design study of double-layer beam trajectory accelerator based on the Rhodotron structure Nuclear Instruments and Methods in Physics Research A828(2016) 72–80.

[3] J. Pottier. “A new ty-pe of RF electron accelerator: the Rhodotron”. Nucl. Instr. Meth. Phys. Res.. Vol B40/41. pp 943-945, 1989

[4] Y. Jongen et al., The Rhodotron, a new 10 MeV, 100 kW, CW metric wave electron accelerator, Nucl. Instrum. Meth. B 79 (1993) 865.

# SIMULATION AND EXPERIMENTAL VALIDATION OF VARIOUS MEANS OF IMPROVING THE OUTPUT BEAM CURRENT OF INDUS MICROTRON

Deepak Kumar Mishra*, K.V.S. Rama Rao, Subhajit Dutta, Jishnu Dwivedi
Industrial Accelerators Division, RRCAT, Indore, India

*Abstract*

A 20 MeV Microtron is used as electron injector for the booster of the synchrotron radiation facility, Indus-I and Indus-II. The microtron operates near 2856 MHz with type 2 cavity having coupling coefficient of the order of 2.62 which resonates in TM010 mode. A cylindrical pin made of lanthanum hexa Boride ($LaB_6$) is used as electron emitter in this accelerator. The extracted beam current from microtron is about 22±2 mA. A simulation study was undertaken to understand the causes of current loss and to device various means by which the extracted beam current could be increased. With this study various means for current loss were identified and the beam current was increased to 30 mA. This paper describes the various options of increasing microtron beam current.

## INTRODUCTION

Indus-1 and Indus-2 are two synchrotron radiation facilities having electron beam energies of 450 MeV and 2.5 GeV respectively. A 20 MeV classical microtron is used as a common beam injector for these facilities. Electrons are generated and accelerated up to 20 MeV in the microtron and it is used as a pre-injector to the booster synchrotron. In the booster synchrotron, energy of the electron beam is increased from 20MeV to 450 MeV for the purpose of injection into Indus-1 storage ring and to 550 MeV for injection into Indus-2 ring.

About 22±2 mA electron beam is extracted from the $22^{nd}$ orbit at energy of 20 MeV. The beam experiments has demonstrated that there is a loss of about 50% of current from $21^{st}$ orbit to $22^{nd}$ orbit. The electron beam current injected by the electron gun is about 500 mA out of which only 24mA of current could be extracted from $22^{nd}$ orbit. A study was undertaken to understand the causes of current loss and some practical means to minimize the current loss.

## DIPOLE MAGNETIC FIELD SIMULATION

Simulations were done for the magnetic field using CST particle studio. Figure1 shows the simulated magnetic field of microtron dipole. Figure2 shows the magnetic field plot across center of dipole shown along the line CD in fig1 The field plotted in Figure 3 are magnetic field across AB indicated in figure1. Magnified magnetic field between -365 mm to 365 mm are plotted in figure4. From magnified field figure4, a field variation of about 7.5 Gauss was observed from central of dipole to the ± 360 mm.

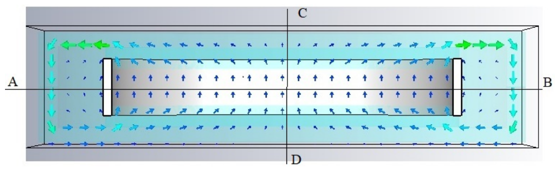


Figure 1: Magnetic field of microtron

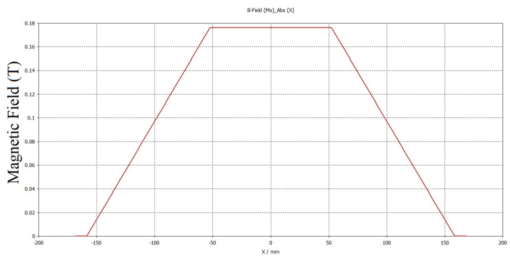


Figure 2: Magnetic field across CD

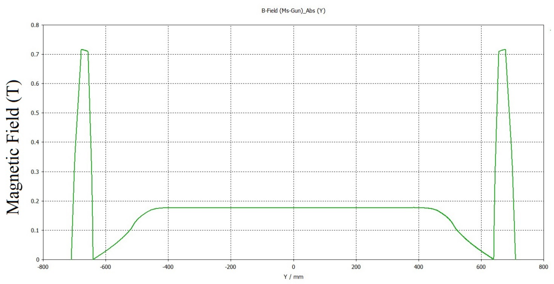


Figure 3: Magnetic field along AB

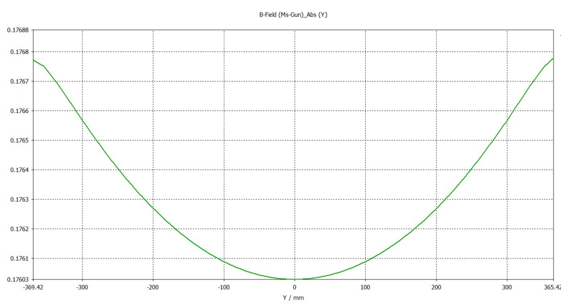

Figure 4: Magnefied plot of field between ± 360 mm

* deepak@rrcat.gov.in

## RF CAVITY SIMULATION

The Rf cavity was also simulated. Figure5 shows the details of simulated RF cavity.

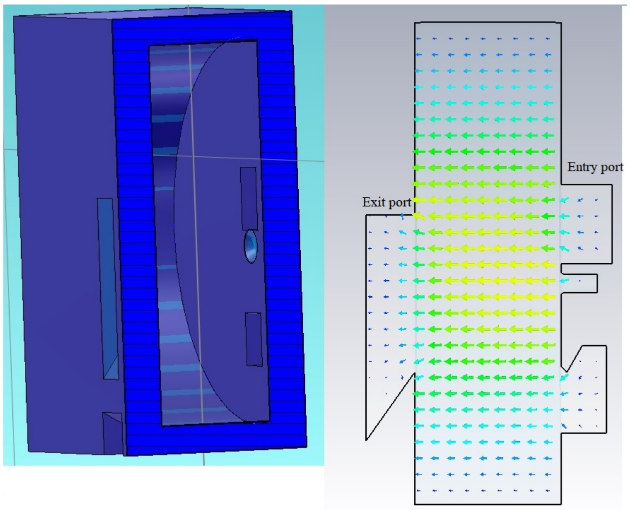


Figure 5: Simulated model of RF cavity showing different apertures including the cathode hole.

In microtron cavity the electron beam emitted from cathode comes out of cavity after performing half turns from an aperture of width 6mm, then enters in the cavity from the entry aperture of width 7mm which after getting accelerated comes out from an aperture of width 8 mm.

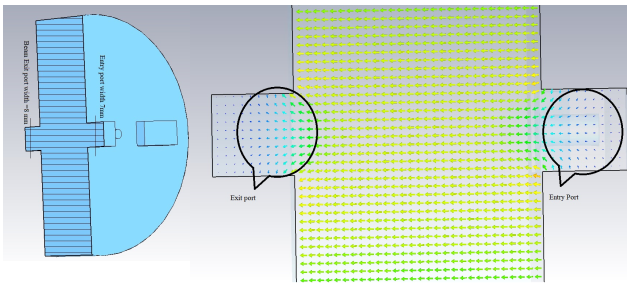


Figure 6: Electric field in RF cavity

### *Phase stability condition*

The phase stability requires that the tail of the bunch be accelerated more than the head of the bunch. This condition imply that the beam experiences a net de-focusing force after passing through cavity. As a result when beam comes out of the exit aperture, the size of beam is more than the aperture width. After reaching the entry aperture of the cavity, the part of beam is scrapped off. Figure7 below shows the electric fields of exit and entry apertures.

## PIC SIMULATION

The magnetic field and RF fields simulated above were imported in particle in Cell module of CST and the the complete acceleration was simulated. The figure8 shows the simulation result.

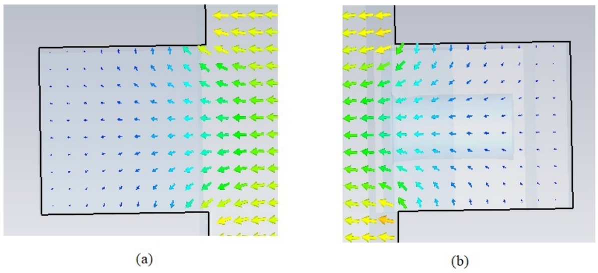


Figure 7: Radial electric fields (a) exit port (b) Entry port

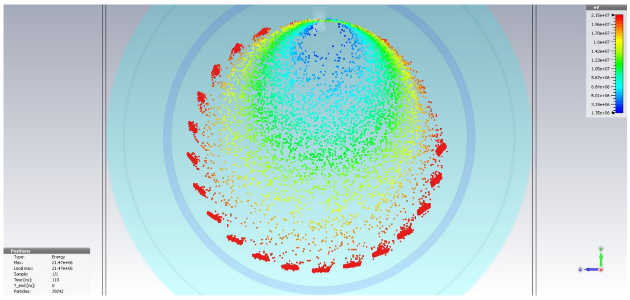

Figure 8: PIC simulated particle bunches

Initially the simulation was done for the entry width of 7mm and exit width of 8mm. The number of particles remaining after a simulation time of 110 ns were about 2000 out of 2 lakh particles. There is no scope for the focusing in the microtron so the only possible way to incerase the beam current is to avoid the beam loss at entry aperture. The major beam loss comes from the RF defocussing force, which could be reduced by increasing the exit aperture of the cavity. Several iterations of simulation were carried out by increasing the cavity exit aperture. Figure8 shows the simulation for aperture width of 13 mm. the number of particles remaining after 110ns were approximately 40,000, for the same number of initial particles as in earlier case.

## EFFECTS OF EXTRACTION AND CORRECTION RODS

The beam experiments has demonstrated that there is a loss of about 50% of current from $21^{st}$ orbit to $22^{nd}$ orbit.The presence of extraction rods, made up of low carbon steel in the extraction mechanism is expected to induce non uniform field in its vicinity. To understand the effects of extraction and correction rods, another simulation was done including extraction and correction rods. The figure9 shows the modeling with correction rods.

The simulations showed that the magnetic field in the vicinity of extraction and correction rods reduces. Figure10 shows the ideal path of electrons in $18^{th}$ to $21^{st}$ st orbit. Figure11 plots the magnetic field along ideal trajectories. In the plot the fields starts from point O shown in figure10 and moves anti clockwise reaching again to starting point O.

From Figure11 it is observed that there is a dip of about 60 Gauss in $21^{st}$ orbit as well as there are reduction in magnetic field in earlier orbits. It was suspected that the reduction in

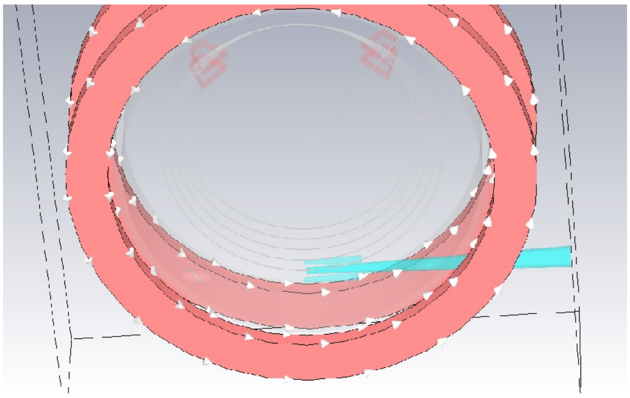

Figure 9: Model with extraction and correction rods

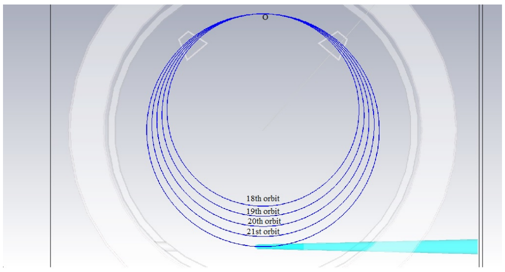


Figure 10: Path of ideal trajectories from 18th to 21st

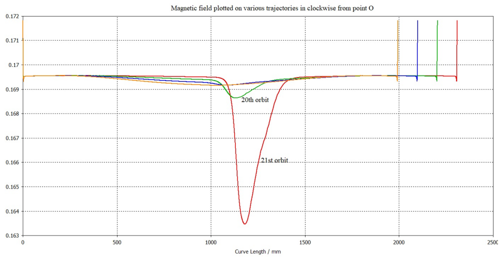


Figure 11: Magnetic field of ideal trajectories for 18th to 21st orbit

observed current loss of about 50 % in $22^{nd}$nd orbit was due to reduction in magnetic field caused by the presence of extraction and correction rods. It was thought that this reduction of mangetic field could be compensated by locally enhancing the field by installing correction coils. three correction coils were installed. One such correction coil installed in right part of the Microtron to compensate the $21^{st}$ orbit as marked with a circle in fig13. An increase of beam current from from 24 mA to 30 mA was observed at a coil current of 3A. With this correction coil an increase in current by 25% was observed.

figure12 shows the picture of the coil that was installed in microtron and figre13 shows the picture of installed correction coil in microtron.

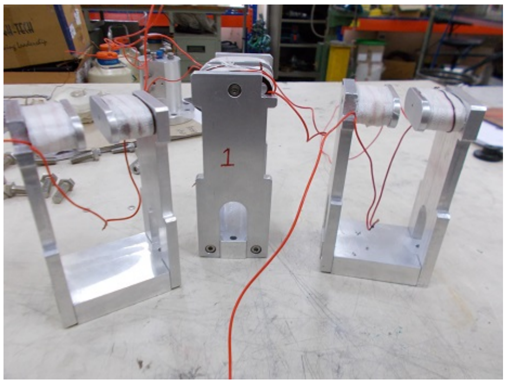

Figure 12: Picture of correction coil

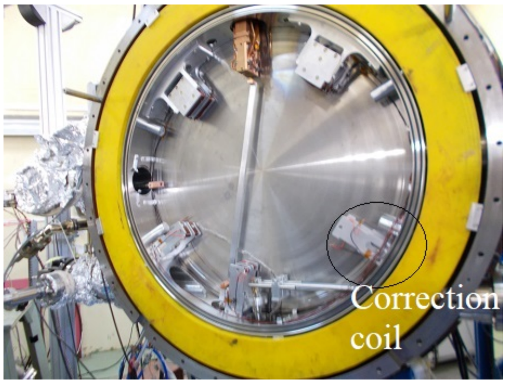


Figure 13: Picture of cil installed in microtron

## CONCLUSION

The simulations relating to reduction in magnetic filed and subsequent correction with correction coils resulted in an increase in microtron beam current by 25%. encouraged with above result, improved correction coils are being planned to install. The option of increasing the width of exit aperture for avoiding the major current loss is being explored.


## ACKNOWLEDGMENT

We wish to thank Shri A.C. Holikatti, Shri Rahul Jain and other colleagues of beam Beam Diagnostics Section who took the beam measurements.


## REFERENCES


[1] The Microtron Development and applications, Yuri M. Tsipenyuk Taylor & francis publications 2002.

[2] *Structural analysis ofthe magnetic poles ofthe 20 MeV Injector Microtron.*, Aaqib Gulzar Khan1, Shubhajit Dutta IOSR-JMCE, Volume 8, Issue 6 (Sep. -Oct.2013), PP 30-33 NJ, USA, Oct. 2014, pp. 34–52.

# FREQUENCY TUNERS FOR THE DRIFT TUBE LINAC (DTL) AT IUAC

***T.Varughese*, V.V.V.Satyanarayana and Dr. B.P Ajith Kumar***
***Inter University Accelerator Centre (IUAC), Aruna Asaf Ali marg,***
***New Delhi-110067, India***
**Corresponding author : thomas@iuac.res.in*

ABSTRACT

The upcoming Drift Tube Linac(DTL) at IUAC is planned to accelerate ion beams from 180keV to 1.8MeV in the High Current Injector (HCI) project. The DTL at IUAC have six room temperature Inter-digital H type multi gap resonator cavities. The cylindrical cavities made from mild steel is copper plated both outside and inside. The natural frequency of each resonator tank is designed at 97 MHz. There is a dynamic change in the natural frequency of tank because of change in size due to RF heating. Therefore we are using frequency tuners for stabilising the frequency of DTL tanks at 97 MHz. The design,testing and installation of these tuners in the resonator tanks will be discussed in this paper.

MECHANICAL DESIGN.

*Fixed Tuner Design*

For stabilizing the natural frequency we are using a fixed tuner and a slow tuner(Fig.1) in each tank . DTL tuners in IUAC are 300mm long and 100mm semi cylindrical copper plates of 2mm thickness. The position of the fixed tuner is decided by placing tuner plate in the tank at different positions and measuring the frequency at these positions. The position is then fixed with a few KHz up from the required 97 MHz of the tank. During operation this extra frequency is corrected to 97MHz using the slow tuner.

Fixed tuner has a central copper alloy rod which holds the tuner plate.There is a water cooling arrangement for this rod. The copper rod is cooled by chilled water at 20°C.

Each tank has slightly different natural frequencies after fabrication. So length of each tuner rod was cut after taking actual RF measurements.

*Figure 1: Slow tuner . Figure 2: Fix tuner*

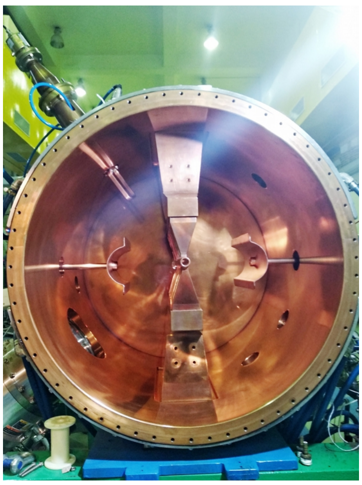

*Figure 3: DTL Tank with both tuners in position.*

*Slow Tuner Design*

Slow Tuner needs fine mechanical movements, vacuum tightness during movement, vibration free movement of Tuner plate and good RF contact with moving rod. Slow Tuner also has a copper rod and tuner plate attached to it. This copper rod is brazed to a flange which slides on linear bearings on two support rods outside vacuum. This gives vibration free smooth movement for the plate. Highly flexible Edge welded Bellows are used for vacuum sealing of copper rod. The possible travel of the tuner is 100mm.

Copper beryllium RF fingerstock is soft soldered to the mounting copper flange central hole which is grounded to the tank body. This fingerstock always makes sure the positive contact of moving copper rod and ground copper flange. Cooling of the copper rod is done by chilled water at 20°C. Non captive linear stepper motor give direct linear motion to the copper rod. The stepper motor is controlled using Rf pick-up loop. All tuner assemblies are tested for good vacuum leak rate of low $10^{-10}$ Torr.l/S before mounting on resonator tanks.

Slow tuner changes its position dynamically to adjust the natural frequency. As the plates moves in, the frequency of the tank decreases because of the increase in capacitance between Drift tubes and plate. Similarly when the plates moves out from the centre of the tank, capacitance reduces and there is an increase in frequency.We have also noticed that after certain distance, out from the centre,there is no further change in frequency.

*RF tests*

All slow tuners have a linear movement of 100mm. Fig.4 shows Frequency Vs reflected power plot on Tank No.6. Fig.5 shows Tuner position Vs frequency shift on Tank-6.

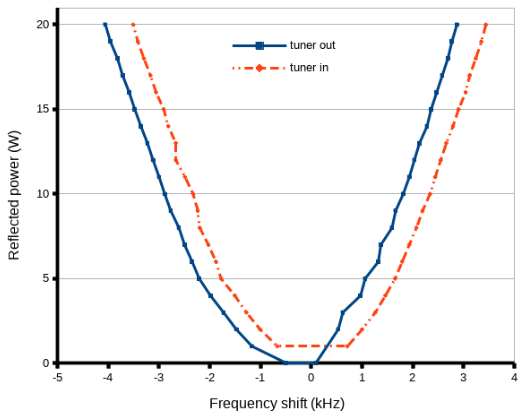


Figure 4 : Frequency Vs reflected power in Tank-6

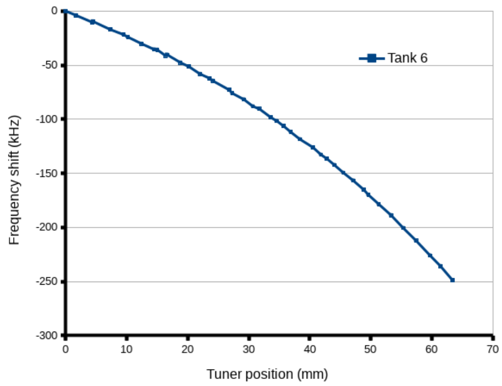


Figure 5 : Slow Tuner position Vs Frequency shift in Tank-6

## CONCLUSION

We have successfully fabricated and assembled slow tuners and fix tuners for all six DTL resonators in IUAC. We have also completed offline test with low power and found satisfactory stabilisation of tank frequency. Further studies will be done when the tanks are operated with designed RF power.

## REFERENCES


[1]. *Electromagnetic design of DTL cavity for LEHIPA .*
Shweta Roy, Rajni Pande, S.V.L.S. Rao and P. Singh Nuclear Physics Division

[2].*Tank1 of the ISAC-DTL LINAC*
Pierre Bricault, Roger Poirier, Thomas Ries, Roland Roper and Guy Stanford. TRIUMF, 4004 Wesbrook Mall, Vancouver, BC, Canada,

*Proceedings of the 1999 Particle Accelerator Conference, New York, 1999.*

# STATUS OF 18 GHz HTS ECR ION SOURCE AND LEBT OF THE HIGH CURRENT INJECTOR PROGRAMME AT IUAC

P.S.Lakshmy*, Y.Mathur, Kedar Mal, U.K.Rao, Sarvesh Kumar, A.Sarkar, and G.Rodrigues

Inter University Accelerator Centre, Aruna Asaf Ali Marg, New Delhi-110067

*Abstract*

The 18 GHz High Temperature Superconducting (HTS) ECR ion source [1] and Low Energy Beam Transport (LEBT) system of the High Current Injector programme has been continuosly undergoing tests for further acceleration of various ion beams through the RFQ and DTL accelerators. Various beams like He, N, O, Ne, Kr, Ar etc. have been extracted from the ion source and further bunched using the downstream 12.125 MHz multi-harmonic buncher. The performance of the ion source and the LEBT system will be presented and new beam developments will be discussed in detail.

## INTRODUCTION

The High Current Injector (HCI) which is being developed at the Inter University Accelerator centre will serve as an alternate facility for the existing superconducting linac and is capable of injecting high currents of ion beams of all species into the super conducting linac. The HCI consists of a High Temperature Superconducting Electron Cyclotron Resonance (HTS ECR) ion source [2], Multi Harmonic Buncher (MHB) [3], Radio Frequency Quadrupole (RFQ) accelerator, Spiral Buncher (SB), Drift Tube Linac (DTL) having six cavities, medium energy beam transport system, high energy beam transport system and beam diagnostic systems. The HTS ECR ion source, MHB, RFQ and DTL#1 have been commissioned in Beam Hall-3 and many beam acceleration tests have been carried out. The HTS ECR ion source is placed on a 200kV high voltage platform in order to match the input designed beam energy of 8keV/u at the entrance of RFQ. AS per the design, RFQ can accept beams having A/q<=6. The ECR beam gets bunched by the MHB after acceleration through HV platform before injecting into the RFQ. The bunch width is measured using a fast Faraday cup situated close to the RFQ entrance. The accelerated beam from the RFQ is again getting bunched by the spiral buncher before injecting into the DTL cavities.

## PERFORMANCE OF THE HTS ECR ION SOURCE

Figure 1. View of 18 GHz HTS ECR ion source and sub systems on the 200kV voltage platform

Figure1. shows a view of the HTS ECR ion source, associated sub systems, 30 kV extraction system, $90^0$ analyser magnet and other beam optical elements on the high voltage platform along with a 75 kV accelerating column. The Klystron amplifier operating at 18GHz, which is used to couple power to the ion source is under replacement process due to ageing related issues. Various charge states of He, N, O, Ne, Kr and Ar upto A/q<=6 have been extracted from the ion source. Source was in continuos operation for various beam acceleration tests of HCI.

### *Modifications done to the source*

During ion source testing after commissioning on the HV platform in Beam Hall-3, huge beam loss was observed due to the longer distance between ion source and the analyzer magnet. So the source was shifted towards the magnet by removing the Faraday cup and BPM and thereby reduced the distance between source and the analyser magnet by 838mm. The existing water cooled extraction system was replaced with an air cooled extraction system. The 30kV platform (small platform) for the operation of the bias power supply was re-

*plankudy@gmail.com

positioned on a rail close to the ion source and the small platform was also refurbished.

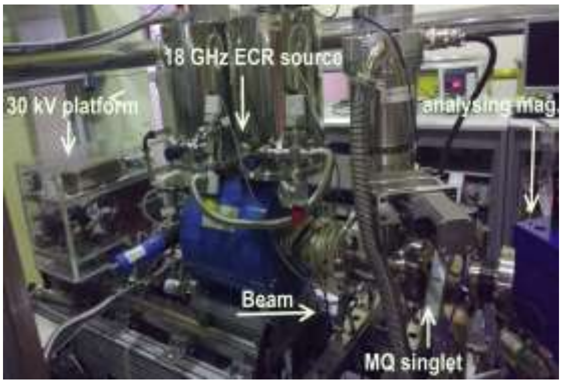


Figure 2. View of the source coupled to the analyser magnet after modifications

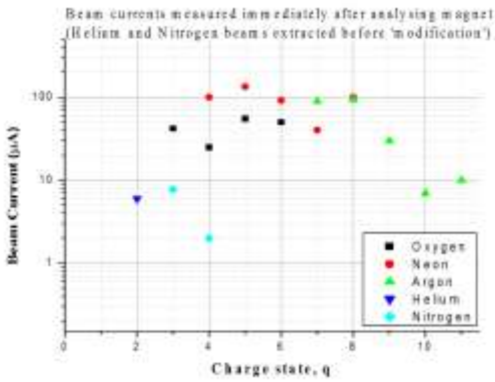


Figure 3. Beam intensities before and after modification

Figure 2.shows a view of the source after the modification carried out and Figure 3.shows a comparison of the beam intensities for various beams extracted before and after the modification. As the plot shows, beam currents have been improved by a factor of 10. A typical charge state distribution (CSD) for Ne and Kr plasma are shown in Figure 4.

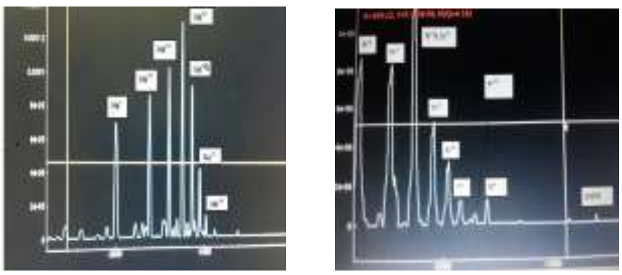

Figure 4. Charge state distributions of Ne (left) and Kr (right) plasma

The CSD spectra were recorded by scanning the analyser magnet and measuring the beam current after the analyser magnet by optimizing all the ion source parameters as shown in Table 1.

Table 1. Optimized ion source parameters for $Ne^{8+}$ beam

| | |
|---|---|
| Extraction voltage | 16.3kV |
| Bias Voltage | -160V |
| RF power | 380W |
| HTS coil 1 current | 137A |
| HTS coil 2 current | 67A |
| Injection Pressure | 1.83x $10^{-6}$ mbar |
| Extraction pressure | 5.49x $10^{-8}$ mbar |
| Analyser magnetic field | 1113 G |

### *Ion source operation with TWT amplifier*

HTS ECR ion source was in regular operation using a 17.9GHz two cavity based Klystron amplifier for HCI beam tests. Ion source has been operated with a Travelling Wave Tube (TWT) RF amplifier as well in order to study the performance of the source. It is a wide band width amplifier which can operate in the frequency range between 7.5GHz to 18GHz. Source was operated at 18GHz and various charge states of Ar beams were extracted. An enhanced X-ray emission was also observed during the source operation with the TWT amplifier.

### *Activities carried out for metal beam development*

In the HTS ECR ion source, metal beams can be produced mainly by two methods - using a micro oven and a sputtering gun. In micro oven method, the material placed inside a ceramic crucible is heated up by a coil and the metal vapours are produced and this method is used for metals with low melting point whereas the atoms of the required metals are getting sputtered out in the case of using a sputtering gun. The micro oven and the sputtering gun are biased at negative potential with 2kV isolation from the source potential. The power supply and the fiber optic communication systems have been installed on the 30kV platform and it is ready to be tested.

## LOW ENERGY BEAM TRANSPORT (LEBT) SYSTEM

LEBT mainly consists of a multi harmonic buncher, fast Faraday cup, focussing and diagnostic elements. The analysed beam is focussed at the entrance of the buncher by using electrostatic quadrupoles and accelerating column. The Multi Harmonic Buncher is a single gap grid structure operates at a fundamental frequency of 12.125 MHz. A saw tooth voltage is generated by the superposition of the fundamental and its harmonics at 24.25 MHz, 36.375 MHz and 48.5 MHz. In the present tests, the fundamental and the first two harmonics at 24.25MHz and 36.375MHz have been used. The bunch width has been measured at a distance of 3 meters downstream from the buncher, where the fast Faraday cup is placed as shown in Figure 5. MHB has been tested with N, O and Ne beams. A collimator of 3mm was also used at the entrance of the buncher for reducing the RF defocussing for beams entering off-axis. The best bunch width achieved was 1.8ns for $O^{6+}$ beam.

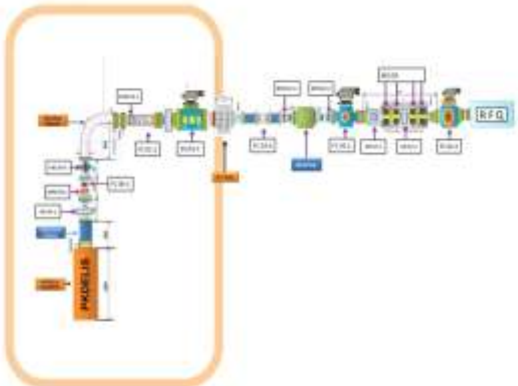


Figure 5. A schematic view of the HTS ECRIS and LEBT

The stability of the bunches was also studied. The buncher voltage and the phases of the fundamental and the harmonics were optimized to adjust the bunch position so as to have maximum transmission through RFQ. Figure 6. shows the fast Faraday cup signal having a bunch width of 1.8ns for $O^{6+}$.

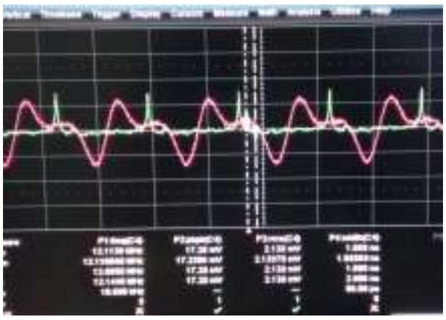

Figure 6. Preamplifier signal from the fast Faraday cup

## BEAM ACCELERATION TESTS

Different beams like $N^{5+}$, $O^{6+}$, $Ne^{8+}$ etc. have been extracted from the source and accelerated to 8kev/u through the HV platform before injecting the beam into RFQ and DTL#1. Tests have been carried out with DC as well as pulsed beam for measuring the energy gain from RFQ and DTL accelerators and also for optimizing the beam transmission through them. The beam tuning process through LEBT has been streamlined through various beam tests in such a way that the beam waist is formed at the centre of the multi harmonic buncher after the analyser magnet. The beam profiles for $O^{6+}$ and $Ne^{8+}$ after the analyser magnet are shown in Figure 7.

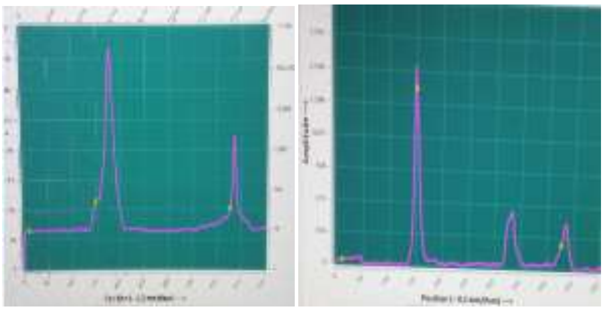

Figure 7. Beam profiles after the analyser magnet for $O^{6+}$ beam (left) and for $Ne^{8+}$ beam (right)

## SUMMARY

The HTS ECR ion source of HCI was in continuous operation for beam acceleration tests through RFQ and DTL#1. Various gaseous beams of A/q upto 6 have been extracted from the source successfully. The required bunch width also has been achieved at the entrance of RFQ by optimizing the buncher parameters and also by streamlining the beam tuning process through LEBT. Power supply installation activities on the small platform have been completed for metal beam development from the HTS ECR ion source.

## ACKNOWLEDGEMENT

The authors would like to acknowledge the members of vacuum lab and BTS lab, Mr.A.J Malayadri and Mr. S.venkataramanan for their timely support and co-operation. Valuable suggestions received from Mr. Rajeev Mehta, Dr.C.P Safvan and Dr.B.P.Ajit Kumar are highly acknowledged.

## REFERENCES

[1] G.Rodrigues, Y.Mathur, U.K.Rao, P.S.Lakshmy, A.Mandal, A.Roy and D.Kanjilal, IOP Conf. Series: Materials Science and Engineering 171 (2017) 012069.
[2] D.Kanjilal, G.Rodrigues, P.Kumar, A.Mandal, A.Roy, C.Bieth, S.Kantas, P.Sortais, Rev.Sci.Instrum.**77** (2006) 03A317.
[3] Single-gap multi-harmonic buncher for NSC pelletron. The eighth international conference on heavy-ion ccelerator technology; AIP Conf. Proc. 1999 Volume 473, pp.272.

# FODO LATTICE FOR BOOSTER OF HIGH BRILLIANCE SYNCHROTRON RADIATION SOURCE

Pradeep Kant*, Ali Akbar Fakhri & A D Ghodke
Accelerator Physics Section
Raja Ramanna Centre for Advanced Technology, Indore - 452 -013 (M P), India

*Abstract*

A 6 GeV booster, which will serve as a full energy injector for storage ring of proposed High Brilliance Synchrotron Radiation Source (HBSRS) is under design. In booster, an electron beam of higher emittance at 200 MeV will be injected from a linac and its energy will be increased up-to 6 GeV by synchronously increasing magnetic fields of all magnetic elements. At final energy, its emittance is kept small so that extracted beam from it can be injected into ring without losses. This is required from radiation safety point of view and protection of magnetic field of low gap undulators as its field may be damaged due to radiation. Its circumference is kept lower than that of the storage ring, so that it can be accommodate inside the storage ring tunnel. In this paper, the criteria for optimization of the low emittance lattice for booster are discussed. Based on these studies, a candidate lattice for booster is evolved which is capable to provide beam emittance of ~3.5 nm-rad at its final beam energy of 6 GeV.

## INTRODUCTION

It is proposed to design a High Brilliance Synchrotron radiation Source at RRCAT with an ultra-low emittance Storage Ring having an electron energy of 6 GeV and emittance of ~150 pm.rad to get a brilliance of $10^{20}$ to $10^{22}$ in the photon range of 1 to 200 keV [1]. A full energy booster along with a 200 MeV linac as a pre-injector will be used as an injector to the storage ring.

In the low emittance storage rings, which have lower dynamic aperture the conventional injection scheme is not feasible. This demands with pulse sextupole or nonlinear magnet injection scheme for which a low emittance of injected beam is required. The lower emittance will also be helpful to reduce the damage of magnetic field of low gap undulators due to radiation. In booster, electron beam will be injected from 200 MeV linac and this energy will be ramped up to 6 GeV. At injection energy, magnetic field should not be much lower, otherwise the effect of remnant magnetic field including earth's magnetic field, stability of magnetic field and driving power supplies may become prominent. Also, it is required to have an optimum synchrotron radiation (SR) loss at 6 GeV to reduce the RF power requirement for its compensation. Therefore values of magnetic fields are crucial at injection and final energies. Moreover, installing the booster on the inner wall of the storage ring tunnel will reduce the cost of building and shielding with simpler transport line design, hence, the circumference of booster and storage ring should be comparable. As beam emittance varies with the cubic power of the bending angle, a booster with large number of bending magnets (small bending angle) will help to achieve lower beam emittance as well as to lower SR loss (inverse proportionality on bending radius) resulting lower RF power requirement. The number of bending magnets along with length of unit cell will also be restricted to have a circumference comparable to the circumference of booster. These aspects have been considered carefully to choose a suitable lattice.

In this article, criteria to design for booster lattice will be discussed. A modified FODO cell has been chosen for the lattice of booster consisting of a combined function bending magnet with defocusing quadrupole component and a focusing quadrupole. Criteria for optimization of the lattice to achieve a low emittance are presented and a candidate lattice the booster has also been suggested.

## CRITERIA FOR LATTICE DESIGN

Many kinds of lattices are used in storage rings, including Double Bend Achromat (DBA), Triple Bend Achromat (TBA) and Multi-Bend Achromat (MBA) for reducing the beam emittance as well as to provide sufficiently long drift spaces for insertion devices (IDs).

The minimum emittance which can be obtained by a lattice is given by [3]

$$\varepsilon_{min} = C_q \gamma^2 \frac{I_5}{J_x I_2} \qquad C_q = 3.832\text{x}10^{-13} \quad (1)$$

Where $C_q$, $J_x$, $I_2$ and $I_5$ are Compton wavelength of the electron and horizontal damping partition number, 2nd and 5th synchrotron radiation integrals. Considering $J_x$=1 (bending magnet without gradient), and using quadrupole as thin lenses $\varepsilon_{min}$ can be approximated as [2]

$$\varepsilon_{min} = FC_q\gamma^2\theta^3, \text{ with } \theta=2\pi/N \qquad (2)$$

Where F is a factor depends on the type of the lattice. From eq. (2), it can be seen that minimum beam emittance can be reduced with the help of smaller bending angle. In this case, number of bending magnets will be increased as a result cost of the ring will be incraesed. The number of bending magnets (N) is fixed at 86 to achieve lower emittance as well as to have circumeferece of booster such that it can be installed on inner wall of the storage ring tunnel. With this, a sufficient space between bending magnet and quadrupoles is available for the installtion of diagnostic devices, vacuum pumps, corrector magnets etc. With these number of bending magnets, a comparison of minmum beam emittances ( $\varepsilon_{min}$) for different lattices can be seen in table 1. In MBA, emittance is calculated by taking 85 bending magnets to make it 5BA.

**Table 1: Minimum emittance for various lattices**

| Lattice type | F | $\varepsilon_{min}$(nm.rad) |
|---|---|---|
| 137° FODO | 1.2 | 24.7 |
| DBA | 1/4√15 | 1.33 |
| MBA, M=5 | 1/12√15 (M+1)/(M-1) | 0.69 |
| TME | 1/12√15 | 0.44 |

In MBA lattices, a severe problem of dynamic aperture is experienced because of tight focusing used to achieve low emittance; therefore these lattices are not suitable for booster where a relatively large dynamic aperture is required at injection due to large emittance of injected beam from the pre-injector linac. Moreover, in booster, the beam is injected at lower energy and ramped to the energy required for injection in to the storage ring. This necessitates a relaxed sensitivity of the lattice towards linear and nonlinear imperfections in whole ramping range. Therefore different types of lattices like FODO or modified FODO (use of gradient in bending magnets) lattices are used in booster as used in SLS, SIRIUS, Candle, TPS, HEPS etc, where comparatively higher emittance can be kept as well as straight sections can be kept smaller due to absence of IDs. Earlier, 15BA lattice with combined function dipole was chosen for HEPS booster which was changed to FODO lattice due to problem of single bunch instability [3]. As can be seen from eq. 1, the minimum achievable beam emittance of ~25 nm.rad can further be reduced by introducing the gradient in bending magnets (modified FODO) as adopted in SIRIUS[4]. The unit cell of lattice contains a focusing quadrupole and a rectangular bending magnet with defocusing quadrupole component to set linear optics (tune). For the chromatcity correction, focusing and defocsuing sextupoles will be used in ecah unit cell. The main difference with the conventional design of booster is absence of non-dsipersive sections for injection, extraction and RF systems. The concept provides a highly symmetric lattice having low emittance with reduce magnets [4]. The length of the unit cell is considered such that the circumference of booster is ~868.6 m with 86 unit cells, slightly less than that of the ring (~911.8) to utilize same tunnel for booster and storage ring having an approximate separation of 7 m, which is not only suitable for movement of equipment and personals but required for a beam transport line from booster to the storage ring.

## OPTIMIZATION OF UNIT CELL

The modified FODO unit cell is studied for different lengths of drift (between quadrupole and bending magnet) and bending magnet, keeping the cell length constant. In these studies, a global scan of defocusing strength (0-0.75 $m^{-2}$ in steps of 0.001) in bending magnet and focusing quadrupole strengths (0 - 2 $m^{-2}$ in steps of 0.01) was carried out find out the range of stable solutions with a beam emittance <5 nm.rad. In order to control over sensitivites towards linear and nonlinear imperfections as well as on required aperture for beam injection, the limit on maximum beta function is kept ≤30 m. Though the defocusing quadrupole component will be fixed in the fabrication of bending magnet but the purpose of the scaning was to vary partition function Jx, tune and beta functions through this variation and find out a good solution from the scan. Number of solutions and minimum achievable beam emittance for different bending magnet length are shown in figure 1.

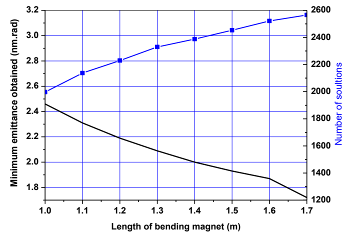


Figure 1: Minimum achievable beam emittance with bending magnet length along with number of solutions

### *Bending magnet length*

Though the achievable emittance decreaes and nomber of solutions increases with increasing length of the bending magnet but this is also important to chose a proper length of the bending magnet o have a suitable magnetic field B and lower SR loss ΔE, given by

$$B\ (T)=3.33564E\ (GeV)/\rho\ (m),$$

$$\Delta E\ (keV)=88.5E^4\ (GeV)/\rho\ (m),\ \rho\ (m)=l\ (m)/\theta\ (rad)$$

Here, l, θ and ρ define length, angle and radius of bending magnet. Since 86 bending magnets are used, only length of the bending magnet is a variable to decide the proper magnetic field and SR loss. At injection energy, in order to avoid the effect of remnant magnetic fields, which include the earth's magnetic field as well as magnetic field in surroundings, the field should not be very low. With the estimations, it is found that a length of 1.4 m is suitable on which the magnetic field at injection energy is ~350 G whereas it is ~1 T at 6 GeV. Both of these values are easily achievable and suitable for smooth control of magnetic field from injection to final energy.

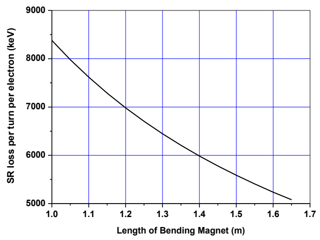


Figure 2: SR loss with bending magnet length

As can be seen from figure 2, the SR loss decreases with the bending magnet length. Therefore, looking at the reasonable value of SR loss at 6 GeV, magnetic fields at injection and final energies and reasonable number of solutions, it can be seen that a length of 1.4 m for bending magnet is suitable for the unit cell. on which a minimum emittance of ~2 nm.rad is achievable, which is ~5 times of minimum in TME.

### *Tune point and candidate lattice*

The range of emittance for combinations of strengths of focusing quadrupole and defocusing quadrupole in bending magnet is shown in figure 3 which indicates that higher strengths are required to get lower emittance, consequently higher tune values and natural chromatcities, as it is obvious from figure 4 & 5 respectively.

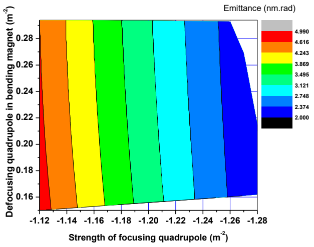


Figure 3: Range of emittance for combination of quadrupole strengths

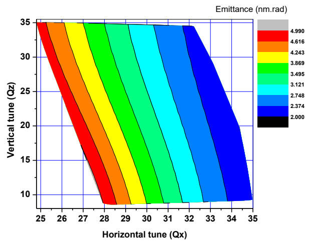


Figure 4: Range of emittance with tune points

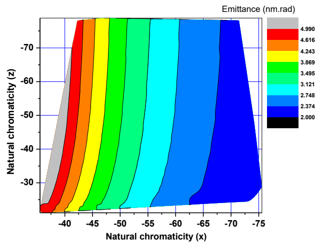


Figure 5: Range of emittance with chromaticity

Results reveal that a beam emittance of ~3.5-4 nm.rad may be obtained between the horizontal tunes of 30-31 with moderate chromaticity below -50 in both the planes to avoid higher sextupole strengths, which will affect nonlinear beam dynamics.

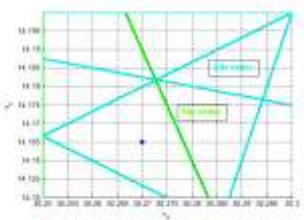

Figure 6: Tune diagram of booster up to 5$^{th}$ order resonances

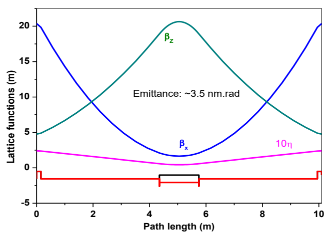


Figure 7: Lattice functions of booster for a unit cell

The tune point (30.27, 14.165) has been considered to avoid the resonances, at least up to 3$^{rd}$ order as shown tune diagram plotted in figure 6 for single periodicity. The lattice functions of unit cell and main parameters booster are shown in figure 7 and table 2 respectively.

**Table 2: Main Parameters of booster**

| | |
|---|---|
| Circumference | 868.6 m |
| Energy | 0.2-6 GeV |
| Betatron tunes ($\nu_x$, $\nu_z$) | 30.27,14.165 |
| Natural chromaticity ($\xi_x$, $\xi_z$) | -46.159 -23.051 |
| Natural emittance ($\varepsilon_x$) | 3.5 nm.rad @ 6 GeV |
| Natural energy spread | 0.128 % @ 6 GeV |
| Energy loss/turn | ~6 MeV/turn |

x, z: transverse planes (horizontal & vertical)

### *Additional defocusing quadrupole*

Though a low emittance with less number of magnets can be achieved with modified FODO but the flexibility of the lattice reduces. Hence an additional defocusing quadrupole will be used in alternate cells for flexibility.

### *Dynamic aperture*

As shown in figure-8, an initial study of the dynamic aperture is carried out for the bare lattice considering the tracking up to 5000 turns with chromaticity correction to (2,2) in both the transverse planes. A minimum aperture limitation with circular chamber of ±16 mm in in bending magnets is used in the studies, evolved from initial injection studies.

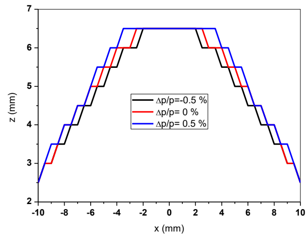


Figure 8: Dynamic aperture of booster lattice

Futher, these studies will be carried out including the multipoles and alignment errors.

## SUMMARY

A modified FODO unit cell has been evolved for the lattice of the booster to be used as an injector of HBSRS. In this the bending magnet length is optimized to have achievable magnetic field at injection and final energy along with a lower SR loss at 6 GeV. The lattice with 86 unit cell is capable to provide an emittance of 2 nm.rad but natural chromaticity increases to high values. This demands a high sextupole strength which may affect beam dynamics severely. Hence, an emittance of 3.5 nm.rad is chosen at moderate value of natural chromaticity to avoide the higher sextupole strengths.

## REFERENCES

[1]. A. D. Ghodke et al., Physics Design Studies for Proposed High Brightness Synchrotron Radiation Source (HBSRS) in India, Same proceedings

[2]. Andy Wolski, Low Emittance Machines, Advanced Accelerator Physics Course, Trondheim, Norway, August 2013

[3]. Y.M. Peng†, Status of HEPS Booster lattice design and physics studies, IPAC2018

[4]. Sirius, Design Report 02/2013, January 25, 2013

# EFFECT OF EDDY CURRENT INDUCED SEXTUPOLE DURING RAMPING IN BOOSTER SYNCHROTRON OF HBSRS

Pradeep Kant*, Ali Akbar Fakhri & A D Ghodke
Accelerator Physics Section
Raja Ramanna Centre for Advanced Technology, Indore - 452 -013 (M P), India

*Abstract*

A 6 GeV booster will be used as a full energy injector to proposed electron storage ring of High Brilliance Synchrotron Radiation Source (HBSRS). In the booster, an electron beam will be injected at 200 MeV from linac & its energy will be increased up-to 6 GeV by synchronously increasing magnetic fields of all magnetic elements. Ramping of beam energy in booster induces eddy current in the metallic dipole vacuum chambers. The generation of the eddy current is directly proportional to the ramp repetition rate, which produces an extra sextupole field in the nominal dipole fields. This leads to changes in the chromaticity. In this paper, the results of the studies of the strength of induced sextupole component for different ramp repetition rates, its effect on the beam dynamics and strategy for its correction is discussed.

## INTRODUCTION

A full energy injector with a beam energy of 6 GeV is under design for the storage ring of proposed HBSRS at Raja Ramanna Centre for Advance Technology (RRCAT). A lattice with 86 modified FODO unit cells is under consideration for this which is capable to provide a lower beam emittance of ~3.5 nm.rad at 6 GeV. In the booster, electron beam from a 200 MeV linac will be injected and then the energy will be increasd to 6 GeV by increasing the magnetic fields of magnets synchronously. In this process, due to rate of change of magnetic field, the eddy current will be generated in the metallic dipole (bending magnet) chamber, which will generate a magnetic field, opposing the change in the magnetic field that created it, as stated by Lenz's law. Therefore, it will disturb the main magnetic field of the magnets as well as will produce higher order multipoles in the magnets. The main magnetic field of bending magnets, quadrupoles and sextupoles can be corrected by keeping a provison for addional magnetic field in these magnet for its compensation. For the compensation of defocusing gradient in quadrupole, additional defocusing quadrupoles will be used.

In this paper, the effect of eddy current in the vacuum chamber of bending magnet is addressed. The eddy current in bending magnet will give rive to higher order multpoles in which the main component will the sextupoles compoenent, which will lead to change in chromatcity and hence distortion in nonlinear beam dynamics due to the tune shift of OFF energy particles. This necessiates a careful study of its effect on the beam dynamics. The estimation of eddy current induced sextupole strength for trapezoidal and sinusoidal ramping profile, the effect of vacuum chamber shape (circular or elliptical) on eddy current induced sextupole strength, its effect on chromatcity and correction is discussed in the paper. The studies are carried out by considering a smooth chamber without bellow.

## LATTICE OF THE BOOSTER

The unit cell of the lattice have a focusing quadrupole and a rectangular bending magnet with defocusing quadrupole compomnent to set linear optics. For the correction of the chromaticity, focusing and defocusing sextupoles will be used in each unit cell. The design is different than the conventional dersign which have dispersion free zone for injection, extraction & RF systems. This provides a highly symmetric lattice having low emittance with reduce magnets [1]. The lattice functions of a unit cell are shown in figure 1.

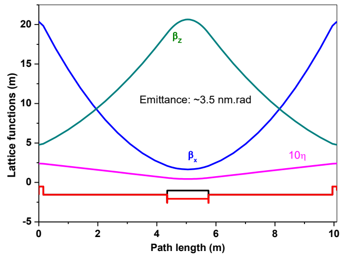


Figure 1: Lattice functions of booster for a unit cell

Though a low emittance with less number of magnets can be achieved with this, but the flexibility of the lattices reduces with this due to the use of combined function magnets. Therefore an additional defocusing quadrupole will be used in alternate cells for flexibility in setting linear optics.

## EFFECT OF EDDY CURRENT

The time varying magnetic field produces eddy currents in vacuum chamber which opposes the change of the magnetic field it self as per Lenz's law. The eddy current in bending magnet vacuum chamber disturbs the uniform field pattern of the bending magnet generating higher order multipoles, in which the sextupole is component will be dominating component. The induced sextupole component will disturb the corrected chromaticity, which at present is considered to be corrected to (2, 2) in horizontal and vertical plane. Therefore it is necessary to estimate the change in the chromaticity during ramping due to the eddy current induced sextupole component.

In order to have minimum induced sextupole component, eddy current should be minimized. The eddy current is depends on the magnetic field, rate of change of magnetic field (rep-rate) and conductivity of the vacuum chamber material and its shape. Since the magnetic field is decided by the magnetic lattice and booster will be operated at a rep-rate of 1-2 Hz, only the choice of vacuum chamber material

*pradeep@rrcat.gov.in

and shape remain as variable to minimze the eddy current. The sextupole component induced in bending magnets is given by [2, 7].

$$m = \frac{1}{2B\rho}\frac{\partial^2 B}{\partial x^2} = \frac{\mu_0 \sigma \delta}{h}\frac{dB/dt}{B\rho} F\left(\frac{b}{a}\right)$$
$$F\left(\frac{b}{a}\right) = \int_0^{\pi/2} \sin\varphi \sqrt{\cos^2\varphi + \left(\frac{b}{a}\right)^2 \sin^2\varphi}\ d\varphi \quad (1)$$

With $\mu_0$=4x10$^{-7}$, permeability of vacuum, $\sigma$= conductivity of vacuum chamber material, a= half-width, h=b is half-height & $\delta$=thickness of vacuum chamber, $\rho$=the bending magnet bending radius.

Here also, it can be seen that the induced sextupole component depends on the conductivity of vacuum chamber material, rep-rate (dB/dt) and F(b/a). This necesiates a proper choice of all these parameteres. The properties vacuum chambers in boosters of some recent synchrotron radiation sources is given in table 1 [3-8].

**Table 1: Vacuum chambers in booster synchrotron**

| Facility | Material | Thickness | h/w |
|---|---|---|---|
| HEPS | SS, Elliptical | - | 0.83 |
| ILSF | -, Circular | 1 mm | 1 |
| TPS | SS, Elliptical | 0.7 mm | 0.57 |
| SIRIUS | SS, Circular | 1 mm | 1 |

It can be seen that material of vacuum chambers has been chosen as SS (Stainless Steel) with elliptical or circular shape. The conductivity of aluminium is ~37.7x10$^6$ $\Omega^{-1}$m$^{-1,}$ as compared to the conductivity of SS ~1.35x10$^6$ $\Omega^{-1}$m$^{-1}$, conductivity, which will induce ~28 times more sextupole component as compared to SS for same magnetic field of bending magnet, rep-rate and vacuum chamber dimensions, therefore it is better to use SS for vacuum chamber of booster. It can also be seen from eq. 1, the shape of vacuum chamber - F(b/a) also maters. The aperture in the bending magnet is considered to be circular with 16 mm radius which is estimated on the basis of prelifminary studies of injection tracckings up to 1000 turns and closed orbit distortion. The thickness is considered to be 1 mm, as can be seen from Table 1 for ILSF and SIRIUS.

### *Ramp profiles for energy ramping*

For the studies, trapezoidal and sinusoidal ramping profiles are considered. The sinusoidal ramping is defined by

$$E(t)=Ef/2\ (a- b.\cos(wt)) \qquad (2)$$

Where, E(t) defines the energy at time(t), Ef is final beam energy, a=1.0333 and b=0.967 and w=2$\pi$f with f is the rep-rate. The parameters of ramping profiles along with rate of change of magnetic field are given in table 2 and the profiles for 2 Hz are shown in figure 2 for comparison.

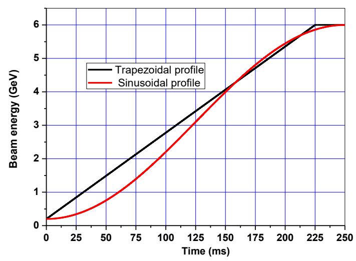


Figure 2: Trapezoidal and sinusoidal ramping profiles for the rep-rate of 2 Hz

In case of trapezoidal ramping profile, the rate of change of the magnetic field is constant from injection to final energies whereas in case of sinusoidal profile, it is lower in the regions of injection and final energies. It can also be seen that in sinusoidal profile, the rate of change of magnetic field is much lower.

**Table 2: Parameters of ramping profiles**

| | Trapezoidal Ramping | | | Sinusoidal Ramping | |
|---|---|---|---|---|---|
| Rep Rate (Hz) | Rise time (ms) | Base/Top time (ms) | dB/dt (Gauss/ms) | Rise time (ms) | dB/dt (Gauss/ms) at 1 ms after injection/ before extraction |
| 1 | 475 | 25 | 21.3 | 500 | 0.199 |
| 2 | 225 | 25 | 44.9 | 250 | 0.797 |

### *Effect of ramp profiles*

As expected, it can be seen from table 3 that the induced sextupole component (calculated from eq. 1) is higher in case of trapezoidal ramping profile and increasing much more with the rep-rate as compared to sinusoidal ramping profile. Moreover, in case of trapezoidal ramping, the induced sextupole component is maximum at injection energy (0.2 GeV).

**Table 3: Maximum induced integrated sextupole component and chromaticity during ramping**

| | Trapezoidal ramping | | Sinusoidal ramping ramping | |
|---|---|---|---|---|
| Rep rate (Hz) | Maximum integrated sextupole (m$^{-2}$) | Energy (GeV) | Maximum integrated sextupole (m$^{-2}$) | Energy (GeV) |
| 1 | 0.477 | 0.2 | 0.130 | 0.3862 |
| 2 | 1.007 | 0.2 | 0.260 | 0.3866 |

This indicates that the maximum change in the chromaticity will be at injection energy. With the rep-rate of 2 Hz, in case of trapezoidal ramping profile, the chromaticity change to (2.85, -5.61) in horizontal and vertical planes respectively which occurs at injection energy whereas in case of sinusoidal ramping profile, this change to (2.437, -1.933) in horizontal and vertical planes respectively, which occurs at ~0.386 GeV. Since the energy spread from linac is ±0.5 %, this will lead to the higher tune shift in trapezozidal ramping as compared to the sinusoidal ramping as evident from table 4. The tune shift in case of sinusoidal ramping is also calculated with the energy spread of injected beam only.

**Table 4: Tune shifts without and with eddy current**

| **Profile** | **Δp/p** | **Trapezoidal Tune shift x $10^{-4}$** | | **Sinusoidal Tune shift x $10^{-4}$** | |
|---|---|---|---|---|---|
| **Case** | **(%)** | **x** | **z** | **x** | **z** |
| Without | -0.5 | -3.0 | -5.6 | -3.0 | -5.6 |
| eddy current | 0.5 | 3.8 | 7.9 | 3.8 | 7.9 |
| With Eddy | -0.5 | -5.8 | 48 | -3.7 | 8.2 |
| current | 0.5 | 6.6 | -46 | 4.5 | -6.1 |
| With eddy | -0.5 | -2.9 | -5.9 | -2.9 | -5.9 |
| current after | 0.5 | 3.7 | 8.2 | 3.7 | 8.2 |
| correction | | | | | |

Also, at final energy, if rate of change of magnetic field is higher, as can be seen in case of trapezoidal profile, this will lead to higher sextupole component and may cause instability in the beam. Therefore it is better to use sinusoidal ramping profile for ramping.

### *Effect of shape of vacuum chamber*

Figure 3 shows, integrated sextupole component in bending magnet during ramping for circular (16 mm radius as considered from aperture requirements) as well elliptical chamber (half width of 32 mm and half height of 16 mm) for sinusoidal profile with rep-rate of 2 Hz. Though it is proposed to use circular chamber as per aperture requirement but sextupole component during ramping is higher for circular chamber as compared to elliptical chamber, which is evident from figure 3.

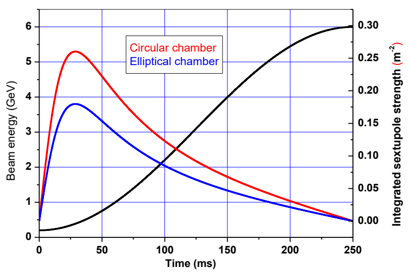


Figure 3: Eddy current induced sextupole during ramping for circular (red) and elliptical chambers (blue)

From the results, a reduction of ~30 % in the induced sextupole can be seen for the case of elliptical shape. This indicate that an elliptical shape may be better in case of trapezoidal profile.

### *Correction of chromaticity*

For circular chamber, the effect of induced sextupole component on the chromaticity in sinusoidal ramping with rep-rate of 2 Hz is calculated from computer program ESRO and shown in figure 4.

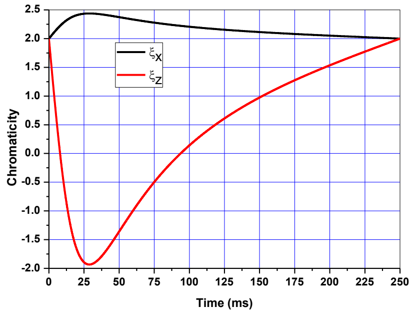


Figure 4: Effect of eddy current induced sextupole during ramping, corrected chromaticity of (2, 2) in horizontal and vertical planes disturbs

As shown in table 4, results indicate a higher increase in the vertical tune shift with the sextupole component induced by eddy current as compared to the case without eddy current. Therefore, it is needed to correct it. For this, additional strengths of ~0.002 and ~0.239 m$^{-2}$ will be required in focusing and defocusing sextupoles which can be adjusted from the sextupoles used in lattice. After correction it reaches near to the previous value but the dynamic aperture studies will have to be carried out to understand the further effect.

## CONCLUSIONS

The sextupole component induced in bending magnet due to eddy current in vacuum chamber and its effect for trapezoidal and sinusoidal ramping is studied. Results reveal a higher disturbance in the chromaticity and corresponding tune shifts in trapezoidal as compared to sinusoidal profile. Therefore, it is better to use a sinusoidal profile for ramping. The disturbance in the chromaticity can be corrected by the sextupoles used for the chromaticity correction. With elliptical shape, the sextupole component can further be reduced by ~30 %.

## REFERENCES


[1] Pradeep Kant*, Ali Akbar Fakhri & A D Ghodke, FODO lattice for booster of High Brilliance Synchrotron Radiation Source, Same Proceedings

[2] Yuemei Peng et. al, The progress of HEPS booster design, IPAC-2017

[3] H. Ghasem, E. Ahmadi, Conceptual design and expected performance of Iranian light source facility injectors, NIM A A795(2015) 228–238

[4] H. C. Chao, J. W. Tsai et al., Conceptual design of booster synchrotron for TPS, EPAC-2008.

[5] Chia-Mu Cheng, Gao-Yu Hsiung et al., Vacuum system for TPS booster, IPAC-2014.

[6] F. H. Sá#, L. Liu et al., A new booster for the SIRIUS project, IPAC-2014

[7] LACHAIZE Antoine, Estimate of eddy current effects in the vacuum chamber of the BETA-BEAM RCS, EURISOL DS/TASK 12/TN-06-08

[8] Sirius, Design Report 02/2013, January 25, 2013

# SPACE-CHARGE AND CAVITY INDUCED BEAM INSTABILITIES IN SINGLE SPOKE RESONATORS


Abhishek Pathak[2] and Srinivas Krishnagopal[1,3]
[1]Bhabha Atomic Research Centre, Mumbai.
[2]Centre for Excellence in Basic Sciences, Mumbai
[3]Homi Bhabha National Institute, Mumbai
abhishek.pathak@cbs.ac.in



*Abstract*

Most of the modern high-intensity linear accelerators employ multiple families (with the different geometric beta) of single spoke resonators at a lower velocity range. Given that the spoke cavities are pretty efficient at the lower beta range, the asymmetry introduced by the spoke lead to an unacceptable asymmetric emittance and halo growth in the presence of non-linear space-charge fields. We perform a well-organized study to determine the contribution from the non-linear space-charge field in the beam and the spoke cavities to the beam instabilities and resonances in the presence of statistical cavity and beam errors. Three-dimensional envelope equations are used to determine the stability condition of the envelope. A self-developed, fully three-dimensional particle-in-cell code PARTRACK was used to model the effect of the non-linear space-charge forces in the linac.


## INTRODUCTION

Most of the modern hadron accelerators that are intended towards high-intensity applications use Single Spoke Resonators (SSRs) for low to medium $\beta$ range. Even at these moderate velocities, particle loss because of emittance growth and halo development is of grave concern as it can significantly alter the beam flux and causes radio-activation of the system. The evolution of high-intensity beams through these linacs is an inter-play of the cavity field, non-linear space-charge field and unavoidable beam, magnet, and cavity mismatches in the linac. This article considers each of these effects and discusses the extent of beam deterioration each of them can cause in different scenarios. Here we use a self-developed code PARTRACK to perform multiparticle simulations and analyze the space-charge dominated instabilities in the presence of the three-dimensional cavity field map. The envelope instabilities, on the other hand, were investigated using the envelope equations in all three planes. To understand the role played by the space-charge and cavity field better, we have chosen the SSR-C section of the MEHIPA linac, where a high intensity (10 mA) beam is periodically confined in the radial direction against defocusing space-charge and thermal forces with the help of superconducting solenoids. The lattice under consideration is shown in Fig.1. The larger cavity size will provide enough interaction time between the beam and the SSR RF field so that the effects are clearly demonstrated.

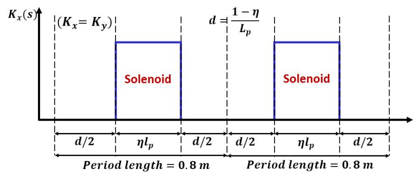


Figure 1: A lattice period for the superconducting section of MEHIPA under consideration.

## CAVITY INDUCED EMITTANCE OSCILLATION

Most of the modern high-intensity hadron linacs use single spoke cavities in the medium beta range because of its remarkable efficiency and RF performance at medium energies. As these structures are not symmetric because of the presence of the spoke, the particles in the beam suffer asymmetric transverse momentum kicks that vary for different bunch slices. Here we report a systematic study performed to investigate the contribution of the SSR RF field and particle distribution towards emittance growth in the linac.
Particle-in-cell routine of the code PARTRACK was used with the imported cavity fields to investigate the effects of the beam-field interaction using an optimized synchronous phase and accelerating field. The simulations are performed for all three SSR sections of the MEHIPA linac, but this article focuses on the dynamics of the SSR-C section. Because of the largest cavity size and maximum interaction time, the effects are dominant in this part o the linac.
A matched beam from the SSR-B section was used to perform the beam dynamics simulation, and the evolution of the transverse and longitudinal beam emittance along the linac is shown in Fig.2.
Fig. 2 clearly demonstrates the transverse emittance oscillation in x and y-direction with a maximum difference of $0.03\pi mm - mrad$ (11%). The obtained results two significant characteristics of the beam dynamics in spoke cavities: (a) oscillation of the transverse emittance along the linac and (b) introduction of beam asymmetry in x and y emittance within a solenoid channel. To better understand the role of the SSR field and beam distribution independently, we performed studies with varying degrees of initial beam asymmetry, beam distribution, and with a different RF field strength of the spoke cavity. Fig. 3(a) shows the variation beam asymmetry at the exit of the linac in terms of transverse emittance as a function of the difference in the input

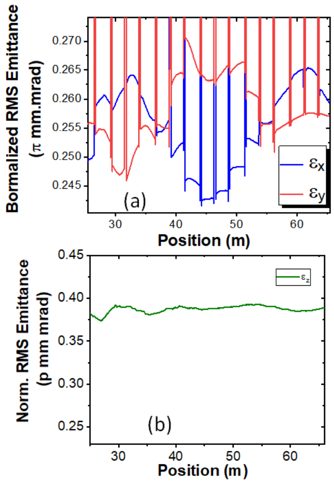


Figure 2: Evolution of the transverse emittance along the SSR-C section of MEHIPA, and (b) Evolution of the longitudinal emittance along the SSR-C section of MEHIPA.

x and y emittance. The behaviour of the average emittance oscillation amplitude with the strength of the RF field is shown in Fig. 3(b). It can be seen that with the increase in

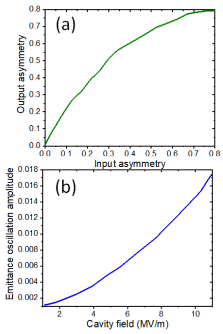


Figure 3: (a) variation beam asymmetry at the exit of the linac in terms of transverse emittance as a function of the difference in the input x and y emittance, and (b) variation of the average emittance oscillation amplitude with the strength of the RF field.

the initial emittance asymmetry in x and y-direction, the difference in the oscillation amplitude increase. The oscillation amplitude, on the other hand, is governed by the strength of the RF field in the cavity. Forces calculated over the particle at a fixed radius and varying angles using the Lorentz force equation and a Fourier series expansion suggests that the momentum imparted by the cavity field has a quadrupolar asymmetry as shown in Fig. 4. In the presence of solenoid, the phase-space rotates, leading to an oscillation in the beam divergence, beam size, and, therefore, the beam emittance. In the presence of initial asymmetry and an asymmetric SSR field, the initial difference is amplified, leading to a larger difference in the x and y emittance along the linac. With an increase in beam non-linearity, the asymmetric kick pushes the particles in the non-linear region, leading to a

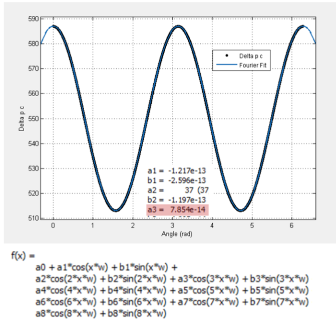


Figure 4: Quadrupolar asymmetry and Fourier series fir of the momentum kick..

higher transverse emittance of the Gaussian beam followed by parabolic, and is least for the uniform distribution. As we do not have much control over the cavity field strength because of the required output beam energy, a careful transverse beam shaping becomes an essential condition to avoid emittance oscillation in the linac.

Apart from the instabilities caused by the spoke field and the beam distribution, another factor that is of concern is the space-charge driven beam bunch instability. In the presence of an initial beam mismatch, the amplitude of the perturbed envelope grows and causes emittance and halo growth in the structure leading to a loss in beam transmission. The details of the bunch instability performed for the SSR-C section of MEHIPA is discussed in the next section.

## SPACE-CHARGE DRIVEN BEAM INSTABILITY

The space-charge driven beam instability[1] poses great threat to the high-intensity hadron accelerators by causing beam size blow-up and therefore particle loss. The problem has been studied theoretically and experimently since 1980s. However, most of the studies consider a two-dimenssional model with uniform particle distribution. Here we present a three-dimenssional macro-particle simulation studies using 3D envelope model and a Gaussian beam distribution. We also compare the instability stopband from the envelope model with the emittance growth from the self-consistent Particle-in-Cell (PIC) simulations.

The three-dimenssional envelope ina periodic lattice without acceleration is given by,

$$X'' + k_X^2 + (s)X - I_X(X,Y,Z)X - \frac{\epsilon^2}{X^3} = 0 \qquad (1)$$

$$Y'' + k_Y^2 + (s)Y - I_Y(X,Y,Z)Y - \frac{\epsilon^2}{Y^3} = 0 \qquad (2)$$

$$Z'' + k_Z^2 + (s)Z - I_Z(X,Y,Z)Z - \frac{\epsilon^2}{Z^3\gamma^4} = 0 \qquad (3)$$

With,

$$I_i(X,Y,Z) = C\int_0^\infty \frac{dt}{(\epsilon_i^2 + t)\sqrt{(X^2+t)(Y*2+t)(Z^2\gamma^2+t)}} \qquad (4)$$

$$\begin{bmatrix} X \\ X' \\ Y \\ Y' \\ Z \\ Z' \end{bmatrix} = \begin{bmatrix} 0 & 1 & 0 & 0 & 0 & 0 \\ -a_1(s) & 0 & -a_{12}(s) & 0 & -\gamma^2 a_{13}(s) & 0 \\ 0 & 0 & 0 & 1 & 0 & 0 \\ -a_{12}(s) & 0 & -a_2(s) & 0 & \gamma^2 a_{23}(s) & 0 \\ 0 & 0 & 0 & 0 & 0 & 1 \\ -a_{13}(s) & 0 & -a_{23}(s) & 0 & -a_3(s) & 0 \end{bmatrix} \times \begin{bmatrix} x \\ x' \\ y \\ y' \\ z \\ z' \end{bmatrix} \tag{5}$$

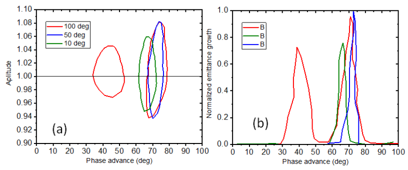


Figure 5: (a) The 3D envelope mode growth rate amplitudes as a function of depressed transverse phase advance with 100 degree, 50 degrees and 10 degrees zero current longitudinal phase advances, and (b) Normalized 6D emittance growth rate obtained using the multiparticle simulations.

where

$$a_1(s) = k_x^2 + \frac{3\epsilon_x^2}{X_0^4} - I_X(X,Y,Z) + .X_0^2 F_{XX} \tag{6}$$

$$a_2(s) = k_y^2 + \frac{3\epsilon_y^2}{Y_0^4} - I_Y(X,Y,Z) + .Y_0^2 F_{YY} \tag{7}$$

$$a_3(s) = k_z^2 + \frac{3\epsilon_Z^2}{\gamma^2 Z_0^4} - I_Z(X,Y,Z) + .Z_0^2 F_{ZZ} \tag{8}$$

$$a_1 2(s) = X_0 Y_0 F_{XY} \tag{9}$$

$$a_1 3(s) = X_0 Z_0 F_{XZ} \tag{10}$$

$$a_2 3(s) = Y_0 Z_0 F_{YZ} \tag{11}$$

The system of equations (5) are solved numerically for different degree of mismatches and with varying structure phase advance from $50^0$ to $130^0$ to obtain the region of stable operation from the point of view of emittance blowup, beam halo growth and particle loss.
If Z(s) denotes the 6 x 6 solution matrix of (5) with Z(O) = E (E = unit matrix), we may write Floquet's theorem as

$$Z(s + nS) = z(s).ZS^n \tag{12}$$

Where, Z(S) is the transfer matrix for one lattice period. if Y(s) is a solution matrix of (6), every solution z(s) of (6) can be expressed as linear combination of the column vectors of matrix Y(s). The solution of (5) can only be stable if its eigen values for the transfer matrix Z(S) remains finite for large n. Here Z(S) is a real, symplectic matrix, so the eigenvalues occur both as reciprocal and as complex-conjugate pairs. Therefore the system can only remain stable if all eigenvalues lie on the unit circle in the complex plane.
Fig. 5(a) shows the 3D envelope mode growth rate amplitudes as a function of transverse depressed phase advance for 100, 60, and 10 degree longitudinal phase advances. Fig. 5 suggests that for the zero current longitudinal phase advance below 90 degrees, the width of the instability stopband is lager for higher zero current longitudinal phase advance. For the scenario where phase advance crosses 100 degrees, the instability structure becomes more complicated with the introduction of a stopband around 40 degrees. The emittance growth obtained for the phase advances shown in Fig. 5(a) using a PIC simulation is shown in Fig. 5(b) .

## CONCLUSION

The effect of the spoke cavity field asymmetry and initial beam mismatch on the beam quality was analyzed in terms of the transverse momentum kick and mismatch growth rate with the help of a self-written code PARTRACK and 3D envelope equations. The analysis shows an introduction of transverse beam asymmetry and emittance oscillation because of the quadrupolar kicks in the spoke cavity and differences in input beam emittance. The 3D mismatch analysis shows a smooth linac operation beyond $80^0$ of phase advance and also an introduction of a stopband at a near $50^o$ higher value of longitudinal phase advance leading to an occurrence of emittance growth at higher beam current.

## REFERENCES


2. Struckmeier, J., & Reiser, M. (1983). Theoretical studies of envelope oscillations and instabilities of mismatched intense charged particle beams in periodic focusing channels. Part. Accel., 14(GSI-PRE-83-11), 227-260.

# EFFECT OF TRANSVERSE SPACE-CHARGE FIELDS ON LONGITUDINAL BUNCH SHAPING IN RADIO FREQUENCY QUADRUPOLE

Abhishek Pathak*, Centre for Excellence in Basic Sciences, Mumbai
Srinivas Krishnagopal[1], Bhabha Atomic Research Centre, Mumbai
[1]Homi Bhabha National Institute, Mumbai
Abhishek.pathak@cbs.ac.in

.

*Abstract*

Radio Frequency Quadrupoles (RFQ) are a unique kind of accelerator with their capability of bunching, focusing, and accelerating the beam at the same time. At higher intensities, the interaction of the non-linear space-charge field with the saddle potential of the RFQ has a significant effect on the bunch profile leading to the development of multiple filaments in phase-space. A detailed study was performed to investigate the impact of varying transverse particle density distribution on the longitudinal bunch profile. The results are analyzed in terms of longitudinal emittance and distortion in the longitudinal phase-space distribution. Our study also shows that the RFQ bunching process is one of such scenarios where the non-linear Columb fields are favorable over linear space-charge forces.

## INTRODUCTION

The Medium Energy High-Intensity Proton Accelerator (MEHIPA) is designed at BARC, India, as a second stage of the Indian ADS program, employs a 325 MHz RFQ as the first accelerating structure because of its unique property of bunching, focusing, and acceleration simultaneously. The MEHIPA RFQ is 4m long structure, designed for a beam current of 10 mA and accelerates a proton beam from 50 keV to 3 MeV with a constant vane voltage of 80 kV.

Most of the RFQ design consider a fixed beam current (10 mA in our case) and a 4D water-bag transverse input particle density distribution to design different section like the shaper, gentle buncher, rms, and accelerator. The beam is subjected to a sinusoidal longitudinal field that produces energy spread in the beam. The induced energy spread causes filamentation in the longitudinal phase-space leading to a bunched beam after several phase oscillations.

In practice, the matched beam from LEBT may not be a uniform distribution. Also, the preliminary tests on these accelerators are performed with a lower beam current than the designed value. A small current is chosen to ensure a successful operation and stability of the system and avoid the damage caused by the high-power beam hitting the accelerator surface at the same time.

Here we report a detailed study demonstrating the effect of nonlinear transverse particle distribution and beam current on the longitudinal bunch characteristics. We perform multi-particle simulations using DC beam with Gaussian, parabolic, conical, and uniform particle density distribution with varying beam current at the input of the RFQ to investigate the effect on the longitudinal beam dynamics. The rms beam parameters at the RFQ input also ensures maximum beam transmission with the designed beam current of 10 mA and for water-bag particle distribution.

## BEAM BUNCHING WITH DIFFERENT SPACE-CHARGE NON-LINEARITY

Bunch parameters plays a significant role in determining the beam quality, beam transmission, and accelerator efficiency of an accelerating structure. In high-intensity hadron accelerators where the beam lies in the space-charge dominated regime, an understanding of the effects resulting because of the interaction of the space-charge field with the RFQ field is indispensable. Because of the nonlinearities involved in the dynamics, a self-consistent Particle-in-Cell code Toutatis and TraceWin was used to simulate the behavior of the beam bunch within RFQ.

Fig.1 shows the longitudinal phase-space for Gaussian, parabolic, conical, uniform, and KV transverse particle distribution at the exit of RFQ for an input beam current of 1 mA, 5 mA, and 10 mA. The phase-space distribution suggests that as we decrease the beam current, the particles participating in the longitudinal filamentation do not redistribute, even after several phase oscillations. The filaments exist till the end of the RFQ, leading to a higher longitudinal emittance and beam halo. From Fig. 1 we can see that for a given beam current of 1 mA, as we decrease the degree of space-charge nonlinearity from KV to Gaussian, the localization of the particles to filaments increases. But for a given distribution say KV, as we increase the beam current from 1 mA to 10 mA, the particles start filling up the phase-space, and the filaments start to disappear. The presence of these longitudinal filaments are observed to be maximum for the KV distribution and decreases as we increase the space-charge nonlinearity to uniform, conical, parabolic, and is least for the Gaussian distribution.

With the distortion introduced because of the linear space-

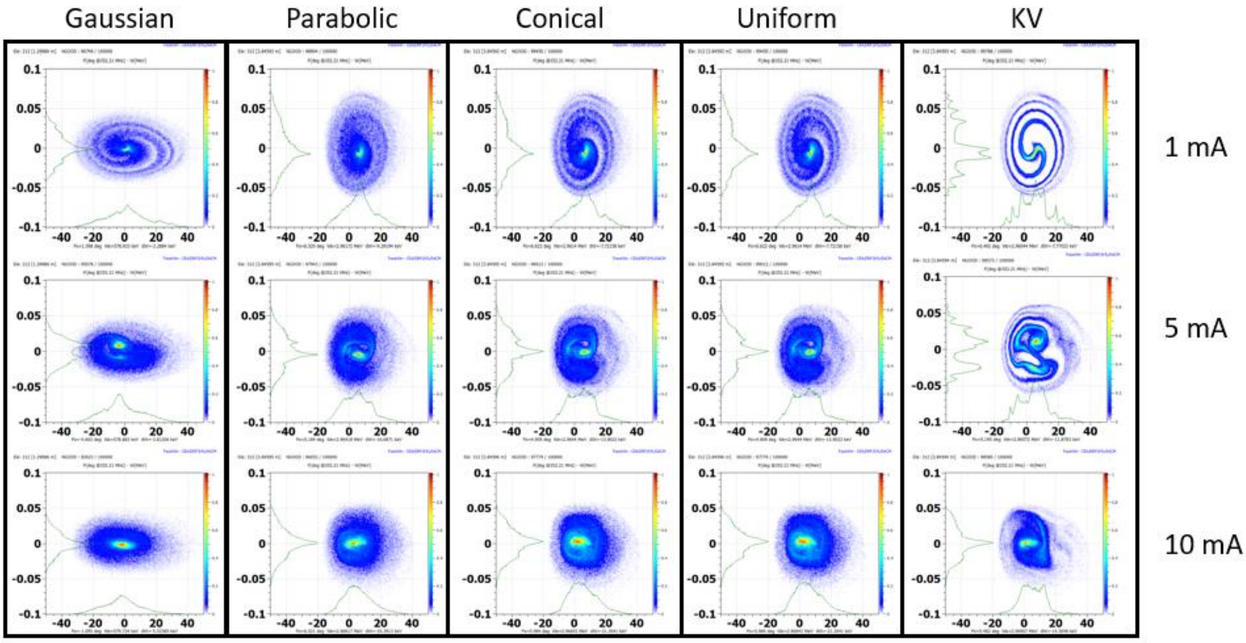


Figure-1: Longitudinal phase-space distribution at the exit of RFQ for Gaussian, parabolic, conical, uniform, and KV distribution with an input beam current of 1 mA, 5 mA, and 10 mA.

charge forces at lower beam currents than the designed value, the second and fourth moment of the beam also increase, leading to a higher beam emittance and halo. As shown in Fig. 2.

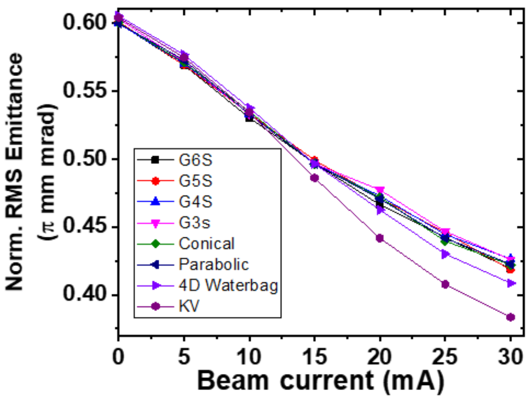


Figure-2: Variation in the longitudinal RMS normalized emittance at the RFQ exit for Gaussian(3,4,5,6 sigma), Parabolic, conical, uniform, and KV input distribution as a function of input beam current.

At lower beam current and with a lesser degree of space-charge nonlinearity, a large fraction of particles in the longitudinal phase-space is localized in filaments causing a large emittance. As shown in Fig. 1, with the increase in the beam current, the Coulombic repulsion between the particles increases, leading to a spread in the particle distribution and reduction in the second moment and, therefore, the emittance, as shown in Fig. 2. For a given beam current with the change in the input distribution from KV to Gaussian, the space-charge nonlinearity increases, causing the particles to spread out of the phase-space filaments and reduction in the longitudinal emittance. As we increase the beam current from 0 mA to 30 mA the longitudinal emittance decreases from 0.6 mm-mrad to 0.43 mm-mrad for a Gaussian distribution, 0.426 for the parabolic distribution, 0.425 for the conical distribution, 0.42 for the unfirm and the maximum reduction in the longitudinal emittance was observed for the KV distribution to a value of 0.35 mm-rad. The trend in the emittance change can be verified with the phase -space distribution shown in Fig.1. As with the increase in the beam current, the maximum changes in the particle distribution was observed for the KV distribution, the change in the emittance was also maximum for the same.

Our study suggests that change in the space-charge non-linearity not only affect the particle distribution, it also changes the phase oscillation amplitude for a given beam current. The variation in the rms phase oscillation amplitude for Gaussian, conical, parabolic, uniform, and KV distribution for the beam current of 10 mA and 1 mA is shown in Fig.3. For the designed beam current of 10

abhishek.pathak@cbs.ac.in

mA, the phase oscillation amplitude is effectively constant (1.1 mm) throughout the RFQ for all chosen input distribution, but as we decrease the beam current to 1 mA because of the occurrence of filaments till the end of the RFQ, the rms amplitude of oscillation also increases. As shown in Fig. 1, Fig.3(b) also demonstrates the maximum oscillation amplitude for the KV input distribution followed by uniform, conical, parabolic, and is least for the Gaussian distribution.

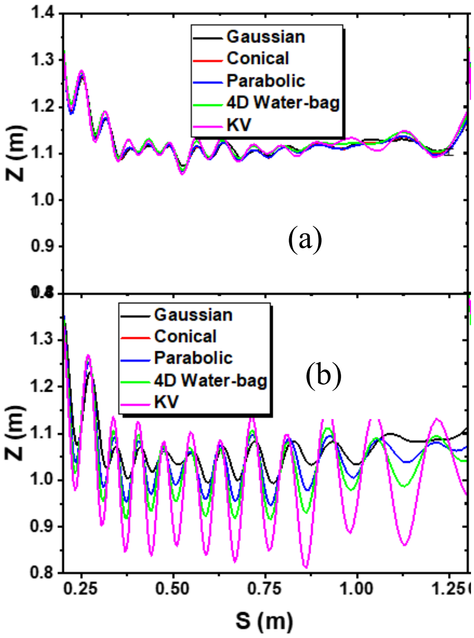


Figure-3: Variation in the longitudinal oscillation amplitude along the RFQ for Gaussian, Parabolic, conical, uniform, and KV input distribution with an input beam current of (a) 10 mA, and (b) 1 mA.

So far, all our studies use a self-consistent approach to simulate the beam dynamics during the bunching process because of the nonlinearities in the system. Another way to understand the process is by using the longitudinal component of the electric field obtained by the two-term potential[1] that is given as,

$$E_z = \frac{AV_0 k}{2} I_0(kr)\sin(kz) \tag{1}$$

Where $I_0(kr)$ is the modified Bessel function, $V_0$ is the vane voltage, k the wave vector and A is given by,

$$A = \frac{m^2 - 1}{m^2 I_0(ka) + I_0(kma)} \tag{2}$$

Where m is the modulation, and a is the minimum vane separation. We calculated the longitudinal field seen by the particles as a function of radial distance from the beam axis and the radial particle distribution, as shown in Fig. 4 to analyze the reasons behind a large number of particles in the filaments for the linear space-charge fields.

Fig.4 suggests that as the nonlinearity in the transverse distribution decreases, there is more number of particles that see an off-axis bunching field leading to a higher number of particles in the filament region of the bunch. For a Gaussian distribution where the number of particles is mostly confined near the axis, the particle density far from the bunch center is low. As the beam makes the transition from emittance dominated to space-charge dominated regime, the particles within the filaments experience a repulsive force leading to the collapse of those filaments in the later part of the RFQ.

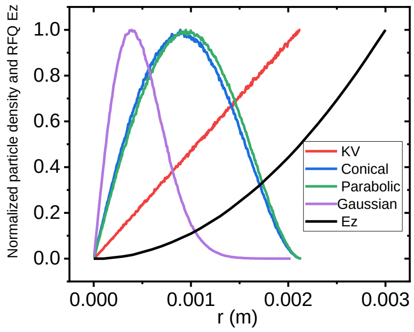


Figure-4: Radial particle distribution for Gaussian, Parabolic, conical, and KV input distribution and the longitudinal RF field seen by the particles during the bunching process.

Apart from multi-particle simulations, another way to verify these effect is by taking an energy spectrum after the RFQ. A spectrum taken at a lower beam current than the designed value will carry a signature of these filaments in the form of multiple peaks apart from the primary energy peak, as shown in the 2D profile shown in Fig.1 for different cases.

## CONCLUSION

Our study over the dependence of bunch profile on space-charge nonlinearity and beam current in an RFQ suggest that for a given RFQ with a designed beam current, the input beam current, as well as the initial beam distribution, plays a significant role in determining the longitudinal bunch profile. For an input beam with lesser nonlinearity in particle distribution, the number of particles seeing the longitudinal field away from the axis is higher, and therefore the number of particles contributing to the filamentation also increases. The filaments are found to be denser at lower beam current and start to collapse with an increase in the beam current. In addition to a higher beam emittance, a higher filament density also leads to a high-amplitude phase oscillation that may cause the particles to move out of the separatrix and loss in the beam transmission.

Analysis using the two-term RFQ potential and its overlap with the particle density distribution suggests that to obtain a bunch with a small phase oscillation, low emittance, and small halo parameters, the transverse particle density distribution should be localized as close to the beam axis as possible.

## REFERENCES

1. Wangler, T. P. (2008). *RF Linear accelerators*. John Wiley & Sons.

# EFFICIENT PHASE FOCUSING AND BEAM ACCELERATION USING OPTIMAL PHASE IN SSR-C SECTION OF MEHIPA LINAC

Abhishek Pathak[2] and Srinivas Krishnagopal[1,3]
[1]Bhabha Atomic Research Centre, Mumbai.
[2]Centre for Excellence in Basic Sciences, Mumbai
[3]Homi Bhabha National Institute, Mumbai
abhishek.pathak@cbs.ac.in

*Abstract*

For accelerating cavities like spoke resonators, the phase focusing and acceleration efficiency is an essential concern because of their broad beta acceptance range and fixed gap size. For such accelerating structures, the definition of the synchronous phase does not hold and can lead to defocusing and deceleration of the beam at lower velocities. This paper discusses the idea of using a concept of cavity dependent optimal phase that ensures an efficient acceleration and longitudinal focusing throughout the linac. We consider the analytic definition as well as optimization of the proposed optimal phase for the SSR-C section of the MEHIPA linac designed at BARC. The beam dynamics results using the definition of synchronous phase and optimal phase are compared, and the advantage of using the definition of optimal phase is demonstrated.

## INTRODUCTION

Superconducting cavities form a major part of modern high-intensity hadron accelerators in the medium and high energy range. These cavities are well optimized in terms of peak surface electric and magnetic field, R/Q, higher-order mode effect, and multipacting for an efficient RF performance. Similarly, for efficient focusing (transverse and longitudinal) and acceleration, parameters like transverse and longitudinal phase advances need optimization to achieve maximum beam energy with acceptable beam quality with a smaller number of accelerating cavities. Apart from the phase advances another parameter that governs the beam acceleration and phase focusing is the synchronous phase[1] of the beam, that is defined as,

$$\phi_s = tan^{-1}\left[\frac{\int_{S_0}^{S_0+L} E_z(s)sin(\phi(s))ds}{\int_{S_0}^{S_0+L} E_z(s)cos(\phi(s))ds}\right] \tag{1}$$

This definition is used for all accelerating structures like Radio Frequency Quadrupole (RFQ), Drift Tube Linac (DTL), etc. and works pretty well for such structures where each accelerating gap length is modified with change in the particle velocity. As far as superconducting cavities like spoke resonators and elliptical cavities are concerned, a single family of these cavities with a fixed gap length is used for a wide energy range. For such SC cavities with large $\beta$ acceptance, Eq. 1 does not provide an optimal synchronous phase for efficient acceleration.

Here we consider the SSR-C section of the MEHIPA linac designed at BARC, to investigate the effect of using the conventional definition of the synchronous phase. The SSR-C cavity accelerates the beam from 40 to 200 MeV with a designed $\beta_g$ of 0.46. The cavity geometry and transit time factor for the SSR-C cavity are shown in Fig. 1.

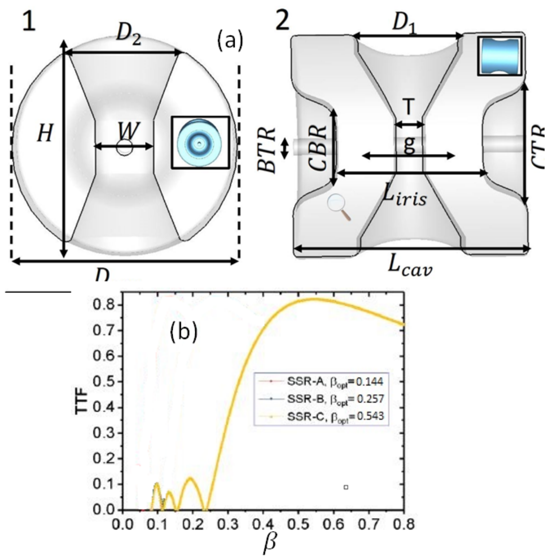


Figure 1: (a) SSR-C geometry used for the MEHIPA, and (b) the transit time factor as a function particle velocity of the optimized SSR-C cavity.

As shown in Fig. 1, for the entire energy range of 40 MeV to 200 MeV ($0.26 \leq \beta\lambda \leq 0.52$) the gap length of the spoke cavity remains the same and is 0.38 m. Fig. 1(b) suggests that for the entire $\beta$ range, the transit time factor is above 0.8, and therefore, an efficient acceleration is possible with an appropriate choice of input phase.

We performed single-particle dynamics simulations using the axial SSR-C field, with an appropriate scaling factor, to analyze the energy gain experienced by the particle for different input phases. For the SSR-C geometry, the input phase at the centre of the first gap is given by,

$$\phi_s = \phi_{0n} + \frac{2\pi \times 0.28}{0.923 \times \beta} \tag{2}$$

and the phase at the center of the second gap is calculated with a separation of 0.21 m (gap centre to gap centre). Figure 2 shows the phase seen by the synchronous particle at the center of the two accelerating gaps as a function of phase at the cavity input. From Fig. 2 it is clear that it is not possible to maintain both acceleration and bunching in both the gaps and, therefore, a compromise needs to be made between the two. Our studies to analyze the effect of the input phase

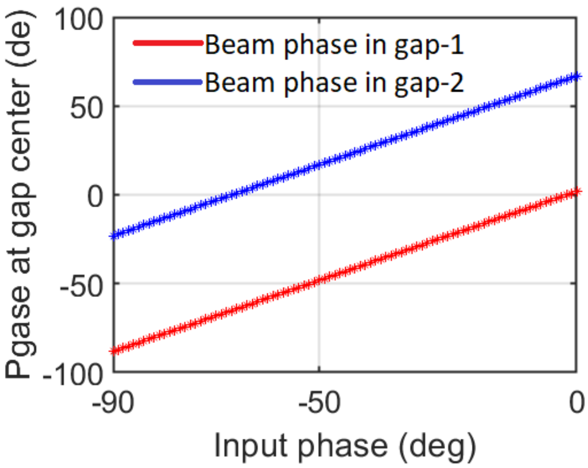


Figure 2: Beam phase at the centre of the two accelerating gaps of the SSR-C cavity, as a function of input phase.

on the energy gain and the phase oscillation suggest that, at initial velocities ($\beta = 0.25$ to $\beta = 0.45$) there are two and a half phase oscillations ($\Delta\phi = 5.1\pi$) within the SSR-C cavity. As the beam energy increases, the phase variation decreases and reduces to two full-wave oscillations ($\Delta\phi = 4\pi$) for $0.45 \leq \beta < 0.6$. Figure 3 shows the variation of the beam phase ($sin(\phi)$) along the SSR-C cavity for a constant longitudinal field and as a function of the input phase, for different particle velocities. In addition to the phase change, the spatial dependence of the longitudinal electric field was used to calculate the effective longitudinal field experienced by the beam. Figure 3 also shows the variation in the $E_z(z)$ the beam experiences as it moves along the SSR-C cavity with different velocities, as a function of the initial phase. The velocity dependence of the effective $E_z(z)$ seen by the particles for different initial phases suggests that at lower velocities, the beam is bound to see both accelerating and decelerating fields and, therefore, careful optimization of the phase is a necessity for efficient acceleration. As the velocity of the particle increases ($\beta = 0.35$ to $\beta = 0.55$), the deceleration seen by the beam can be eliminated with an injection phase between $-20^o$ and $-150^o$. The increase in the input phase leads to higher beam energy, but besides acceleration, another factor that is of concern is the bunch focusing. To obtain an optimal input phase considering phase focusing and acceleration simultaneously, we performed multiparticle simulations using the code PARTRACK.

Figure 4 shows the variation in the output energy and bunch size as a function of the input phase for the first SSR-C cavity ($\beta = 0.25$). It can be seen that with increase in input phase the energy gain in a given cavity increase but at the same time ($\phi = -80^0$) the bunch length starts to increase and

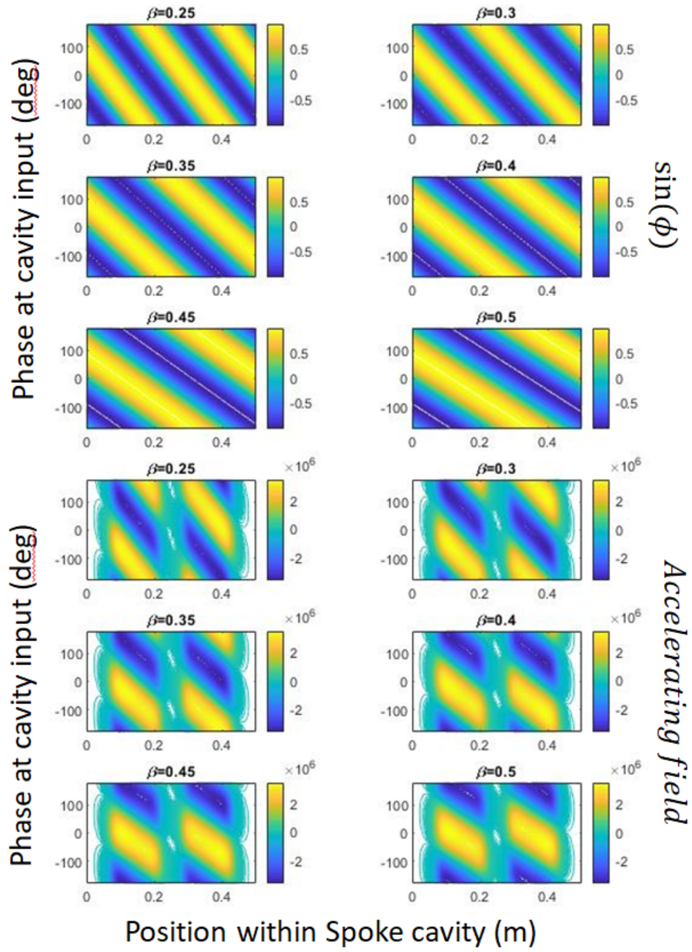


Figure 3: The phase oscillation within an SSR-C cavity as a function of input phase, for different $\beta$ values, and the effective longitudinal electric field experienced by the synchronous particle as a function of input phase, for different $\beta$ values.

therefore for the first cavity of SSR-C we settle with an input phase of $-80^o$. Identical steps were followed to optimize the input phase for all other cavities of SSR-C in the linac, and the optimized phase is shown in Fig. 4(b).

With this optimization of the input phase for each cavity, one needs only 31 SSR-C cavities for beam acceleration from 40 to 200 MeV.

## COMPARISON WITH CONVENTIONAL APPROACH

To obtain a quantitative comparison, we perform simulations considering the conventional approach where a single value of the synchronous phase is defined for a given cavity. For most high-intensity SC linacs, the synchronous phase is ramped linearly and later kept constant to keep the accelerating field designed limit. Figure 5(a) shows the variation in the synchronous phase chosen for the SC linac and the respective input phase with an assumption that the syn-

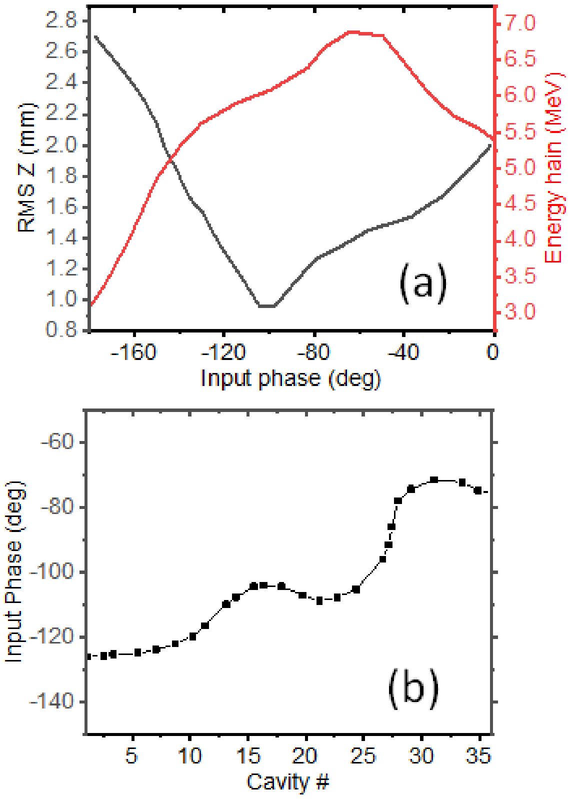


Figure 4: (a) Variation in beam energy and bunch rms size as a function of input phase for the SSR-C cavity at $\beta = 0.25$, and (b) Optimized input phase for each of the SSR-C cavities, at $\beta = 0.25$.

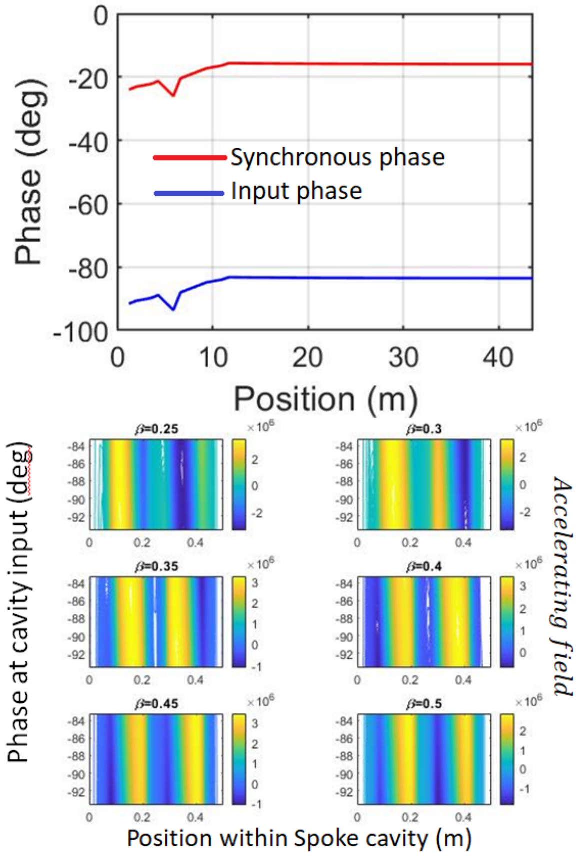


Figure 5: (a) Synchronous phase and respective input phase is chosen from conventional design, and (b) effective longitudinal electric field experienced by the synchronous particle as a function of input phase for different $\beta$ values.

chronous phase is defined at the center of the spoke cavity. Figure 5(b) shows the longitudinal field seen by the bunch as a function of the input phase (Fig.5(a)) and also as a function of distance traveled within every SSR-C cavity. The figure shows that with the conventional approach, where the usual definition of synchronous phase is adopted, the respective input phase leads to a decelerating phase for all $\beta$ values and therefore requires a larger number of the cavity of a given output beam energy. However, from Fig. 2 it is clear that an optimal choice of input phase can reduce the decelerating phase for the beam as the beam gets accelerated and even at lower $\beta$, the acceleration, as well as bunching, can be maximized by choosing the input phase between $-120^o$ and $-130^o$.

Our calculations show that the number of cavities required to accelerate the beam from 40 to 200 MeV using the input phase shown in Fig. 5 is found to be 38, which is 7 cavities more than what we require while using the optimized phase advance values.

## CONCLUSION

The synchronous phase is a well-defined parameter and is used to obtain a synchronous acceleration and phase bunching in accelerators with changing $\beta\lambda$ and, therefore, the gap length. For superconducting structures like spoke resonators that are known for their wide velocity acceptance range, the gap length remains constant for a given geometric $\beta$, and the use of synchronous phase becomes tricky. Here we have analyzed the acceleration and beam bunching efficiency in terms of output energy and final bunch rms size with changing input phase (not synchronous phase) using the field map of the SSR-C cavity used in MEHIPA.

Our study shows that with increase in the particle velocity, the decelerating field seen by the beam decreases for an input phase between $-20^0$ and $-150^o$, and, therefore, the number of accelerating cavities can be minimized by opting for an optimal input phase. As far as the bunch focusing is a concern, there exists an optimal input phase for the bunch length is minimum; therefore, the choice of input phase required a compromise between the bunch size and beam energy. Finally, we compare the results using the linearly ramped synchronous phase taken in other projects with our choice of optimal input phase. The comparison shows that for a given SSR-C cavity field and energy range (40-200 MeV), the number of cavities required is 38 with the conventional approach, but only 31 with our optimized input phase.

## REFERENCES

1. Wangler, T. P. (2008). RF Linear accelerators. John Wiley & Sons.

# STUDY OF TRANSIENT BEHAVIOUR AND ACTIVE COMPENSATION OF RF AND MAGNET FAILURE FOR MEHIPA LINAC

Abhishek Pathak*,[1] & Srinivas Krishnagopal [2,3]
[1] Centre for Excellence in Basic Sciences, Mumbai 400 098
[2], Bhabha Atomic Research Centre, Mumbai 400 085
[3]Homi Bhabha National Institute, Mumbai 400 094

*Abstract*

An application like an Accelerator-Driven Sub-critical system (ADS) demands high-energy, high-intensity hadron accelerators with exceptional reliability to avoid thermal stress on the sub-critical system under consideration. To better understand multiple factors that can cause the beam trips, an RF transient analysis was performed for the 200 MeV Medium Energy High Intensity Proton Accelerator (MEHIPA) designed at BARC. The code TraceWin and analytic modeling of the beam and RF cavity using the LCR circuit model were used to simulate potential faults that could occur in the linac components. Beam dynamics simulations were performed to quantify the effects of the failures in terms of the beam emittance and beam halo parameter, and applicable techniques are proposed to ensure smooth operation of the linac.

## INTRODUCTION

A 200 MeV, 10 mA Medium Energy High Intensity Proton Accelerator (MEHIPA)[1], has been designed at Bhabha Atomic Research Centre, Mumbai, as the second stage of the Indian ADS program [1]. Such accelerators are expected to deliver long terms operation with a small number of beam interruptions per year. The frequent occurrence of such interruptions can lead to thermal stresses and fatigue on the reactor structures, the target, or the fuel elements, leading to significant damage to the fuel claddings. Here we present a detailed transient study for the superconducting section of the MEHIPA using the LCR modeling and multi-particle simulations code TraceWin[2]. The study was performed to investigate the time interval within which dynamic compensation is essential to avoid beam quality deterioration and particle loss in the accelerator.

Our beam dynamics simulations on the reference accelerators show complete particle loss due to non-relativistic velocities, even with the failure of a single rf cavity. This loss can be avoided by retuning the fields and phases of other cavities, close to the cavity that failed, to compensate for the failed cavity. The dynamic compensation to achieve the required beam quality at the end of the linac can be implemented using a general compensation or local compensation. The general compensation algorithms require stopping the beam and retuning (RF field and RF phase) of all downstream cavities leading to a small rf margin per cavity. As long as the number of compensations is small, the general compensation technique is efficient, but with an increase in the number of faulty cavities, the compensation error increase because of the involvement of a large number of elements.

Here we have adopted the local compensation technique for MEHIPA because this method involves only neighbouring cavities and reduces the retuning error: moreover, this method does not require stopping the beam. We have used four cavities for compensation: two upstream and two downstream of the cavity that failed. As these transient effects occur within 100s of $\mu s$, the dynamic compensation should very fast and requires a predefined database containing the effect of every cavity field and phase on the final beam quality. Fig. 1 shows the normalized characterization curve for the SSR-C cavities for the final transverse and longitudinal emittances. In this paper we consider the failure of the last cavity in the SSR-B section of the linac and therefore need the characterstic curve for the SSR-C cavity only. However, in case of failure of cavities from other section, respective characterization will be required. The data presented in Fig. 1 enable us to estimate the emittance change at the output of the linac with the change in the field of a given cavity.

Once we have the database, the modelling of the beam in the presence of rf is performed using the Resister-Inductor-Capacitor (LCR) analogy where the system can be described as,

$$\frac{dV_c}{dt} = \frac{\omega(R/Q)(2I_G(t) + I_B(t)}{4} - \frac{\omega(1 - i\tan(\phi(t))V_C(t)}{2Q_L} \quad (1)$$

Where $V_c$ represents the accelerating voltage seen by the particle at the operating frequency f, $\omega = 2\pi f$, $I_B$ represents the low frequency component of the beam current (twice the average beam current), $I_G$ represents the low frequency component of the current generated by the rf generator ($= 2\sqrt{Incidentpower/(R \times incidentQ/Q)}$ ). Because of the narrow bandwidth of these cavities the fluctuations in the cavity cannot be neglected and therefore are accounted in the detuning angle, $\tan(\phi(t)) = 2\times Q_{loaded}(\frac{f_{cav}(t)-f(t)}{f(t)})$. The frequency fluctuation because of the Lorentz force, microphonics and cold tuning was calculated using the following first order model,

* abhishek.pathak@cbs.ac.in

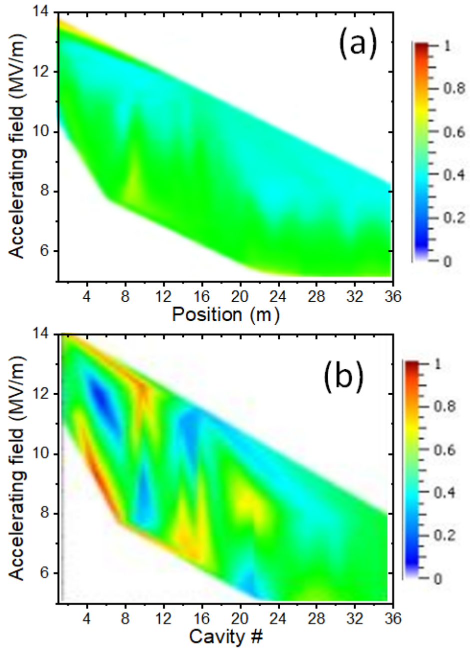


Figure 1: (a) Variation in the transverse normalized RMS emittance as a function of cavity number with varying accelerating fields, and (b) variation in longitudinal normalized rms emittance as a function of cavity number with varying accelerating fields.

$$f_{CAV}(t) = f + \Delta f_{Lorentzforce} + \Delta f_{tuningsystem} + \Delta f_{microphonics} \quad (2)$$

The solution obtained from the coupled equation (1) and (2) gives the evolution of the transient effects in the cavity in terms of the accelerating fields.

## LINAC WITH AND WITHOUT DYNAMIC COMPENSATION

The SC section of MEHIPA comprises 66 spoke cavities with 12 cavities in the SSR-A section, 18 cavities in the SSR-B section and 36 cavities in the SSR-C section of the linac. Here we chose the last cavity from the SSR-B section to perform the transient analysis. Our simulations assumed a smooth linac behaviour at t=0, followed by failure of the 30th cavity in the linac. This analysis provides an idea of the time scale we need to consider to retune the linac back to its designed beam parameters.

Fig. 2 shows the transient behaviour of the accelerating field, synchronous phase, and output energy within the failed cavity after t=0. It can be seen from Fig. 2(a) that after about 700$\mu s$, the accelerating field in the cavity goes to zero â€” also, the synchronous phase (Fig.2(b)) of the beam shifts significantly within the first 500$\mu s$ leading to a decelerating field in later cavities. As the synchronous phase changes, the beam goes out of the rf bucket, and the effects are reflected in the beam energy, as shown in Fig.

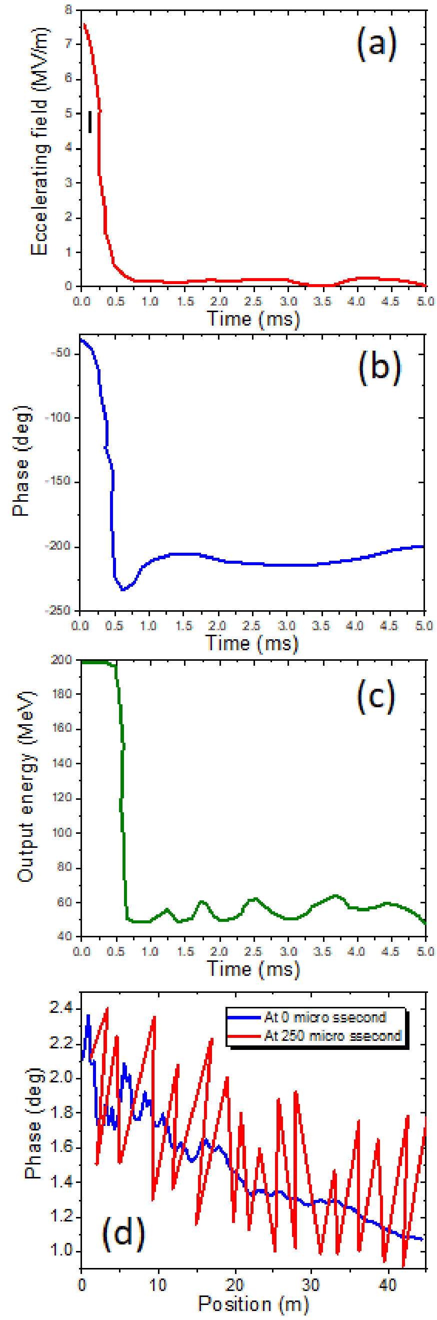


Figure 2: Transient analysis results: (a) Accelerating field within the failed cavity, (b) Synchronous phase within the failed cavity, (c) Linac output energy, and (d) variation in the beam phase width along the linac.

2(c). The energy of the beam suffers a drop of 77% from 200 MeV to 46 MeV at the end of the linac. Our study also shows that with the failure of even a single cavity, the beam phase width becomes unstable and performs large amplitude oscillations about the stable phase width, as shown in Fig. 2(d). Such large-amplitude oscillation leads to bunch instability and may cause a complete beam loss in the linac.

To investigate the dependence of the beam quality and transmission on the space-charge non-linearity, we performed multi-particle simulations with Gaussian, parabolic, and uniform particle distributions in the presence of a cavity failure. Fig. 3 shows the emittance and beam transmission, obtained for different beam distributions, along the linac after the failed cavity (cavity # 30). Fig. 3 suggests that

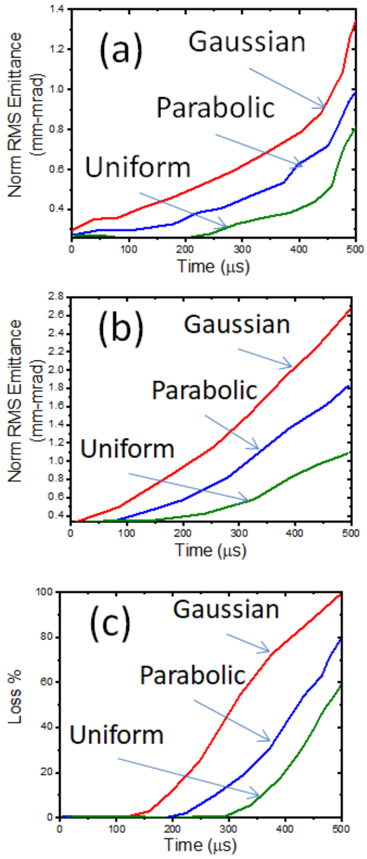


Figure 3: (a) Transient behaviour of the transverse norm. rms emittance, (b) Transient behaviour of the longitudinal norm. rms emittance, (c) Transient behaviour of beam loss for the SC section of the MEHIPA linac after the failure of the 30th spoke cavity.

the beam deterioration increases with an increase in the space-charge non-linearity. The transverse emittance blows up from 0.26 mm-mrad to 1.3 mm-mrad for the Gaussian, 1.0 for parabolic, and 0.8 for the uniform distribution. The longitudinal emittance shows similar behaviour with the space-charge non-linearity, blowing up from 0.33 mm-mrad to 2.8 mm-mrad, 1.8 mm-mrad, and 1 mm-mrad for the Gaussian, parabolic and uniform distributions respectively. As Fig. 3 shows, this emittance blow-up is observed within the first 0.5 ms of the cavity failure. With an increase in the transverse beam emittance, the particles are prone to hit the wall of the cavity, and as the longitudinal emittance increases, the particles go out of the phase-space bucket. In both cases, the beam transmission decreases, as shown in Fig. 3(c). For the Gaussian beam, we observe a complete beam loss within 0.5 ms of the cavity failure followed by parabolic and uniform distribution with a particle loss of 80% and 60%, respectively.

Our analysis shows that if we want to regain the beam quality, the compensatory measures need to be taken within 200 $\mu s$ of the cavity failure. It should be noted that this analysis has been done for the failure of only one of the SSR cavities (the last SSR-B); the transient behaviour may differ slightly for the failure of other cavities.

## FAILURE COMPENSATION

Here we adopt a local compensation algorithm to compensate for beam quality, energy, and beam transmission. For the failure of the 30th cavity in the linac, the 28th, 29th, 31st and 32nd cavities were tuned iteratively using the scan data shown in Fig. 1 to compensate for the failed cavity. The accelerating fields were increased by 10%, 5%, 18%, and 15%, and the synchronous phases were modified by +5%, -12%, -16% and +18%, for the 28, 29, 31, and 32 cavities respectively, to obtain the final beam energy of 200 MeV and 100% transmission. The transverse and longitudinal emittances were also restored to 0.26 mm-mrad, 0.27 mm-mrad, and 0.33 mm-mrad that is as same as for a linac without the cavity failure.

## CONCLUSION

The transient evolution of the beam and cavity parameters was analyzed for the SC section of the MEHIPA linac using the LCR circuit modelling and multi-particle simulations to determine the reaction time for appropriate retuning of the cavity and avoid beam loss. Our analysis shows that the detection time for such failure has to be of the order of 100s of $\mu s$, and the dynamics compensation is essential within 250 $\mu s$. In the absence of any compensation, the beam suffers complete particle loss for the Gaussian distribution followed by parabolic and uniform distributions with a loss of 80% and 60%.

Here we have adopted a local compensation algorithm that uses cavities neighbouring the failed cavity and adjusts their field and phase to regain the desired beam quality at the linac output. By choosing the 28th, 29th, 31st and 32nd cavities for the failure of the 30th cavity and increasing their field by 10%, 5%, 18%, and 15%, respectively and phase by +5%, -12%, -16% and +18%, the designed behaviour of the linac was restored.

## REFERENCES

1. IADD, BARC, External report, BARC/2016/e/916, (2016).

2. Biarrotte, J. L., & Uriot, D., Dynamic compensation of an rf cavity failure in a superconducting linac, Physical Review Special Topics-Accelerators and Beams, 11(7), 072803 (2008).

# STUDY ON UTILIZATION OF PHASE CHANGE MATERIAL NODULES FOR IMPROVING THE PERFORMANCE OF PRECISION COOLING SYSTEMS

Ram Mohan Pandey#, Manitosh Kumar Singh, Rakesh Kumar, G.R. Deshmukh, Raviparkash Shah, Bindeshwari Prasad, Yogesh Kumar

Coolant Systems & Process Control Section, BDCSD
Raja Rammana Centre for Advanced Technology, Indore, India.

*Abstract*

Indus Accelerator machine equipment are being cooled by circulating low conductivity water through their cooling circuits. If the secondary cooling water temperature increases from its operable range, performance of machine gets affected badly. This paper reports the result of an experimental study on utilization of Phase Change Material (PCM) nodules for enhancement of secondary cooling loop thermal capacity and its availability during working. A low temperature cooling media tank filled with Phase Change Material (PCM) nodules has been utilized and presented in this paper. The PCM is paraffin wax liquid filled in nodules which gets solidified at around 7-8 $^0$C temperature and absorbs around 260 kJ/kg latent heat energy during solidification. Cooling with water is only sensible heat transfer whereas cooling water with PCM nodules also involves latent heat transfer. A test set-up has been developed with refrigerating cooling capacity of 10 kW. During this study, inline cylindrical column filled with spherical nodules of PCM is used and system was tested with objective to optimize the performance of PCM nodules thermal energy system. With this set-up and improved PID tuning, water supply temperature stability of ± 0.05 $^0$C is achieved at set supply temperature alongwith 8 kW inline heater considering as system load. In this study the effect of thermal performance of the PCM nodules has been investigated. Time required for attaining the steady state condition during charging and discharging of nodules has been established. In case of tripping of operating chiller unit, using only water as a cooling media leads to continuous increase in secondary water temperature and maintaining process precision cooling temperature stability becomes difficult. When PCM nodules are used along with water, cooling media temperature remains stable for prolonged period. We conclude that using PCM nodules along with water in accelerator cooling system leads to higher thermal capacity with improved temperature stability.

## OBJECTIVE AND SCOPE OF WORK

Low conductivity water (LCW) is used as coolant for conditioning of various components of the Indus-2 accelerator. The coolant temperature and flow control system has been designed to cater the cooling demand. When accelerator beam energy is constant, the precision cooling system runs smoothly. However, when beam energy is ramped up from injection energy of 550 MeV to 2.5 GeV in nearly 12-15 mins, the cooling requirement surges due to increased heat load in a short span of time. Accordingly the cooling system responds to keep the supply temperature within the specified limit. It is well understood that a cooling system of high thermal capacity is desired to handle such thermal transient. Moreover in case of failure in running chiller unit, the standby unit starts but cooling effect delays due to time required by the compressor to load. Present study is intended to quantify and optimize the use of PCM nodules for capacity enhancement, better handling of thermal transients and to maintain the precision cooling for longer duration of time. Further the system with PCM nodules ensures availability of precision cooling till the standby compressor comes online and starts cooling. With the developed test setup supply temperature stability of ±0.05 $^0$C has been achieved.

## MATHEDOLOGY

### *Heat Transfer in PCM Nodule*

The heat transfer during change of phase of any substance is latent in nature. The PCM nodules fluid gets liquefied by absorbing the heat from process fluid (discharging) and liberate heat by dissipating the heat to refrigerated cold water (charging).[1]

### *Instrumentation and test setup*

An experimental testing system is established in thermal laboratory of CS&PCS at RRCAT. Fig. 1 shows the experimental test setup. The test setup consists of 20 kW cooling capacity refrigerating system and pumping system along with heating vessel and data acquisition system. Experimental test setup scheme layout is shown in Fig. 2. Precision cooling loop is equipped with a plate type heat exchanger and a three way PID controlled valve to maintain desired temperature in process water tank. The controlled heating system continuously refines and maintains the supply temperature at set value. With Reference to Fig. 2, The refrigerated chiller unit

# rmpandey@rrcat.gov.in

maintains the chilled water temperature between 6 to 7 $^0$C. The chilled water is circulated through primary heat exchanger and PCM nodule tank by operating chiller pump. However nodule freezing starts at around ~ 8 $^0$C and completes at ~7 $^0$C. Chilled water maintains secondary water temperature at 20 $^0$C with the help of PID controlled three way valve installed in primary loop. Water in the secondary loop is circulated through secondary heat exchanger by means of secondary pump.


Figure 1: Experimental test setup in thermal lab

During experiment the process water supply temperature at inlet to cavity tank is maintained at 40 ±0.05 $^0$C by heater bank in process loop and PID controlled three way valve in secondary loop. Process water flows through cavity tank where heat addition takes place by using heating element installed in the cavity tank. The water from the cavity tank outlet is circulated again through the secondary heat exchanger.

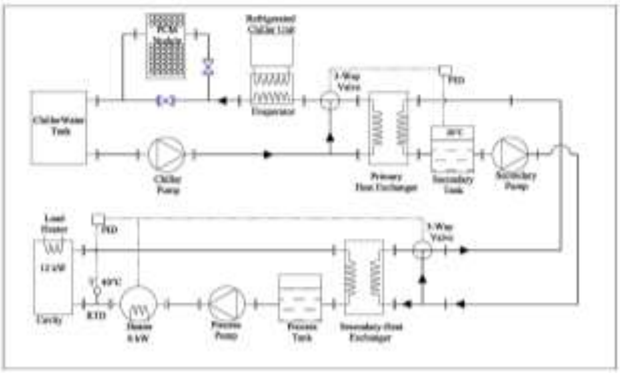

Figure 2: Experimental test set-up scheme layout drawing.

## RESULTS AND DISCUSSION

### *Cooling Backup With Nodules at Constant Heat Load*

The first test was carried out with system running in steady state condition with a constant cavity heat load and the nodules fully charged i.e. solid. The water chiller was stopped and the time was measured upto which the chilled water loop is able to maintain the secondary water temperature at 20 $^0$C. Fig. 3(a) and 3(b) depict the system response when the system was running at steady state condition with cavity heat load of (a)12 kW and (b)10 kW respectively. It was observed that after stopping the water chiller the primary loop water temperature remained low for another 1 hour for case-a and 1 hr 10 mins for case-b and then started rising. The secondary water temperature remained at 20 $^0$C for nearly 3 hrs for case-a and 3 hrs 15 mins for case-b. This is the time span when the secondary cooling was maintained by primary loop PID controller by utilizing the thermal capacity of nodule tank. The chilled water temperature remained close to 7 $^0$C for nearly 1 hour (Case-a)/ 1 hr 10 mins (Case-b) due to latent heat absorption by PCM nodules. Initially combined heat absorption capacity of nodule tank was high hence the the chilled water temperature remained low for nearly 1 hour/ 1 hr 10 mins. Afterwards the nodule tank capacity started exhausting quickly and hence the temperature started raising.

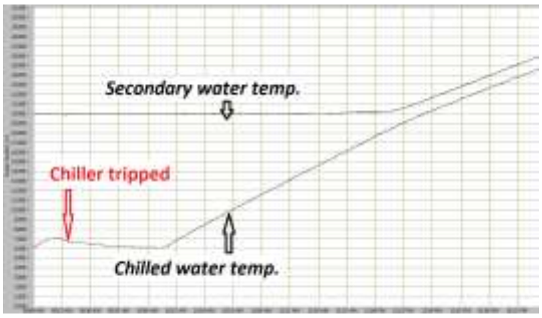


(a) Cavity heat load of 12 kW.

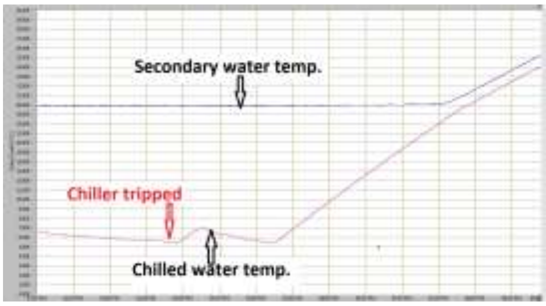


(b) Cavity heat load of 10 kW.

Figure 3: System response with nodules tank online.

### *Cooling Backup Without Nodules at constant Heat Load*

In the second test the system was operated in steady state condition at constant heat load of 10 kW in cavity and nodule tank was isolated from chilled water loop. Fig. 3 depicts the system response when the water chiller was stopped. It was observed that the primary loop water temperature started rising almost immediately. Whereas the secondary water temperature remained at 20 $^0$C for another 30 mins. Chiller water temperature started rising immediately after stopping of water chiller unit which is due to the fact that the nodule tank was isolated and hence the system heat capacity was only due to the water inventory in the chilled water loop which was significantly low.

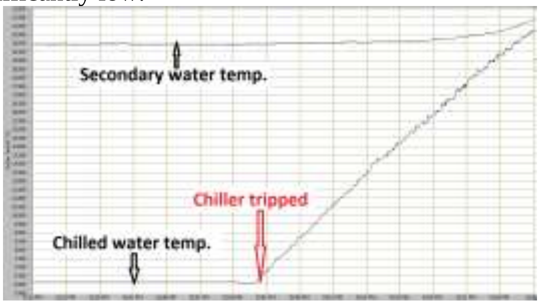


Figure 4: System response without nodules at cavity heat load of 10 kW.

### *System Response With Heat Load Ramp up*

In accelerator energy ramping the beam energy increases within short duration of time which causes transient heat dumping in the cavity. In the third test similar condition was created and the system response was observed when nodule tank was online.

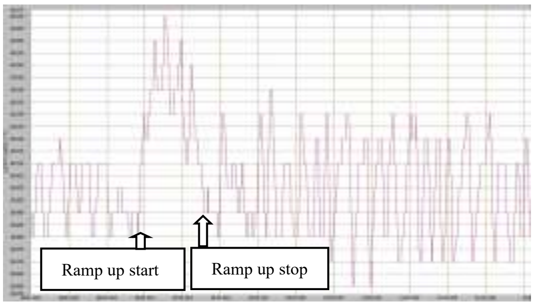


(a) Nodule tank online

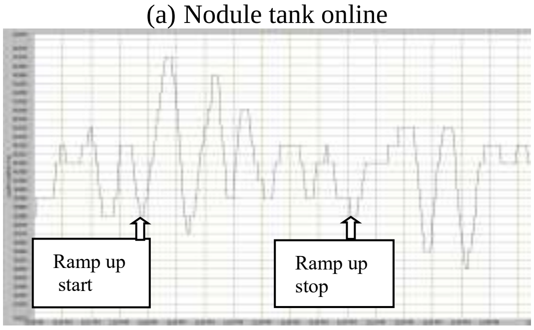


(b) Nodule tank offline.

Figure 5: System response in 2 kW ramping up

The system was operated at a constant heat load of 2 kW in the cavity and when steady state condition was reached, 2 kW heat ramp up was introduced in time span of 15 mins. Fig. 5 (a) and (b) depict the cavity supply water temperature behaviour with time during ramping. The total time of transient is nearly 20 mins and 23 mins respectively for case-a and case-b, out of which the system temperature transient was peaking up beyond precision cooling limits (40+0.06 $^{0}$C) and coming down within the limit (40 ± 0.05 $^{0}$C) for nearly 8 mins and 9 mins for case-a and case-b respectively. In 20 mins (Case-a) and 23 mins (Case-b), which includes 15 mins of ramping, the system has attained the steady state condition again and the process temperature was maintained within 40±0.05 $^{0}$C. The system response during transients due to heat load ramp up has been studied with nodule tank online and nodule tank offline. By observations it is evident that the transient dies out in shorter span of time if nodule tank is online this is due to availability of higher thermal capacity when nodule tank is online.

## CONCLUSION

In the present study it was observed that introduction of higher thermal capacity in form of PCM nodules is capable of providing sufficient time margin to start cooling with redundant chiller unit in case of tripping of running chiller unit and ensuring uninterrupted precision cooling for the cavity load during this transition. This arrangement is capable of handling the thermal transients during heat energy ramp up in a better way. After tripping of the chiller unit fall in temperature of chilled water suggests thermal capacity utilization of nodules more then required to maintain the chilled water temperature to assist cooling in secondary circuit. There is a scope of improvement in design of nodule tank for optimum utilization of PCM nodules. This observation also suggests that with a better water flow distribution in nodule tank the back up time, by using the PCM nodules can be further enhanced. Heat load ramp up capacity is limited to 2 kW for the present test setup and it does not show appreciable improvement in system response during heat load ramp up. However set up with higher heat load ramp up capacity will produce appreciable improvement in transient response of the system. Excellent precision cooling was achieved by utilizing PID controlled three way valves and the process temperature was maintained at 40±0.05 $^{0}$C.

## REFERENCES

[1] C. Uma Maheswari, R. Meenakshi Reddy, 2013. Thermal Analysis of Thermal Energy Storage System with Phase Change Material. International Journal of Engineering Research and Applications (IJERA) Vol. 3, Issue 4, 617-622.

[2] Kenenth IP, C MCIBSE, C Eng Jonathan, GATES, Andrew MILLER, MCIBSE C, 2005. Enhanced Thermal Storage Capacity of Water Storage Cylinders With Phase Change Materials. World Sustainable Building Conference, Tokyo, 27-29 September.

[3] R.M.Pandey, B.Prasad, G.R. Deshmukh, Ram Bahadur, Sanjay Gupta, 2013. Development and Operation of 65kW capacity precision cooling system for the Indus-2 RF cavities. Indian Particle Accelerator Conference (InPAC-2013)

# MACHINING CHALLENGES FOR THE DEVELOPMENT OF 650 MHz MULTI CELL SCRF CAVITIES

Sanjay Sharma[1#], Rajesh Prasad[1], Utpal Chaaterjee[1], T. Veerbhadraiah[1], Tilak Murya[2], Vijayakumar V[2], Syed Moulali[2], Manish Bagre[2], VK Srivastava[2], Sanjay Chouksey[1], G. Mundra[1]

1. Design & Manufacturing Technology Division; 2. Superconducting Cavities Development Division

**Raja Ramanna Centre for Advanced Technology, Indore – 452 013 INDIA**

#email: sanjays@rrcat.gov.in

*Abstract*

RRCAT has taken up a project on development of SCRF cavities for proton accelerator for proposed Indian Spallation Neutron Source (INSN) facility[1]. Operational performance of SCRF cavity demands special care during manufacturing and processing. Machining of SCRF cavities structure requires precision machining of various components made out of Niobium and Niobium-Titanium alloy. As the components required high geometrical and dimensional tolerances, proper planning are required at each and every stages of machining. Significant expertise has been developed in house, gaining experience from single cell to multi cell SCRF cavity machining. Various machining fixtures and required tooling have been developed for machining of SCRF cavities. Cutting parameters were optimised to achieve best results. To avoid surface contamination, special care has been taken during handling of the components during and after machining. Special coolant has been chosen for machining of the Niobium components.

The paper discusses the development of tooling and fixturing, optimization of machining parameters, machining process, precautions observed during handling of the components and the coolant used during machining of the multi cell SCRF cavities development.

## INTRODUCTION

Five cell 650 MHz SCRF cavity consists of Niobium half cells, end flanges, beam pipes with dumbbell sub-assemblies. Total number of components for single five cell 650 MHz SCRF cavity assembly consists of thirty four numbers of machined parts. Solid model of the assembly is shown (Fig. 1). These cavities are machined from high purity fine grain rolled Niobium (High RRR-300) and Nb-Ti alloy material [4].
These half cells are formed using blanks cut from niobium sheets of 4mm thickness. During initial trials these sheets were cut by EDM wire cut process. Later water jet machining was found more suitable due to no heat input during cutting process and faster cutting speed. Each assembly consists of four dumbbell sub-assemblies and two end half cells. Each dumbbell sub-assembly is formed by joining of two half cells at iris diameter. These half-cells are formed by deep drawing niobium sheets using special die-n-punch (forming tools) on a dedicated 120 Ton Hydraulic press at RRCAT.

## FORMING TOOLING AND FIXTURES

Forming toolings are machined from high strength aluminium alloy(7075-T6) material.

Fig. 2: Forming tooling (Male-punch) after machining

CNC Vertical Turning lathe (VTL) was used to generate the required profile on die and punch (Male and Female). The machined male punch is shown in figure-2 and female die in figure-3.

Fig. 3: Forming tooling (Female-die) after machining

## MACHINING OF HALF CELLS

Machining half cells was a challenge. High RRR niobium material is very soft and behaves like soft copper. Niobium while machining is difficult to machine. Chips during machining has tendency to seize to tool and gives the problem of built up edge(BUE). Nb being pyrophoric material, special care is required during machining [5]. The problem in machining of 650MHz half cell is multifold as compared to 1.3 GHz half cell as the flexibility increases in cubic order. Since direct holding of these half cells on lathe machine with conventional holding technique/device is not possible special holding fixtures were designed and developed and machining parameters were established to overcome machining problems. An important consideration of the fixture design is that should machine the entire job in single setting so that parallarilty of both the faces of machined job should be achieved better than desired tolerance of 30-40 microns. Also material selected for fixture is aluminium alloy material owing to the advantage of light weight and contamination issue with Niobium material. Since the profile accuracy of formed half cell is achieved within 0.2 mm, fixture was designed considering this fact and job /half-cell is clamped at a point where distortion is minimum during machining (Fig.4). After initial prototyping, a process plan was prepared which involved multi-stage machining operation of the cavity components to achieve the required parameters. This required coordination with the material joining ,RF measurement and tuning group at various stage of development.

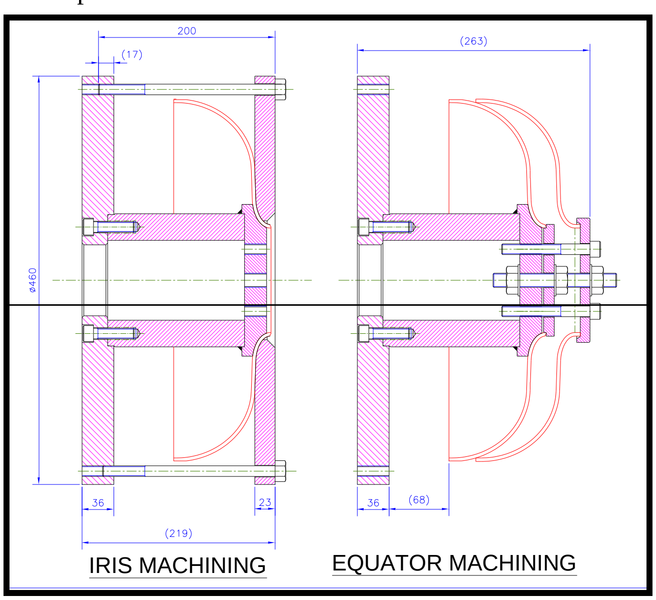


Fig.: 4 Half cell machining fixture

After machining of individual half cells (10 no’s required for one cavity).A set of half cells are joined together by 15 kW Electron Beam Welding and are welded at iris diameter to form subassemblies then are further machined with the help of another machining fixture developed for dumbbell subassembly(Fig. 5). Weld edge preparation is important to achieve correct and uniform thickness at iris and equator because it is having a direct impact on weld parameter. Dumb-bell fabrication involves challenges of controlling the mechanical dimensions with control of its frequency. Welding of stiffening result distortion of cell shape which need to be corrected by tuning and trimming.

Fig. 5 Dumbbell sub assembly during machining

### Cutting tools

As per the available literature, cutting tool materials which can be used for machining Niobium are HSS and Tungsten Carbide. Niobium machining requires skill and experience. Cutting tool angles and cutting parameters has to be adjusted to avoid heating of component which will result decrease in tool life. Trials were conducted and it was observed that formed tools of HSS gets wear and require frequent regrinding and resetting which also results poor dimensional accuracies. To solve this problem we have used WC (Tungsten carbide) uncoated polished high rake angle index able inserts with 0.2 & 0.4 nose radius with theoretical Cutting Speed of 60-90 m/min in standard tool adapters and also we have modified standard tool holder for reverse machining which is required while machining of inner diameter on equator side(Fig. 6). The optimum machining parameters are also can be found by Response Surface Methodology (RSM) in dry machining condition[3]. The main machining parameters are speed, feed and depth of cut under dry machining condition

Since the cavity is made from RRR grade high purity Niobium and any micron size defect/contamination result in SCRF cavity performance. Any foreign material contamination from tool or rough handling may result in cavity failure which can be found only during VTS testing at 2°K. Suitable hand gloves are used while handling Nb material so as to avoid any fingerprint marks on the component. These fingerprint marks cannot be easily removed even after chemical cleaning. Machines are kept in isolated clean room away from other machines. To avoid contamination machines are thoroughly cleaned before machining operations. A new set of cutting tools/inserts is used for machining of Niobium components and are preserved safely and are not allowed to be used for other material.

**Coolant/cutting oil:**

Conventional cutting oil/coolant is not used during machining. Silicon type of oils and coolant containing sulphur are prohibited, as it is very difficult to eliminate. To avoid contamination from coolant we have used high evaporative Alcohol/ Propanol coolant using mist spray which has given noticeable good results. With this particle contamination issue is also solved.

Fig-6: Tool used for reverse machining

## CONCLUSION:

The machining process of 650MHz five-cell cavity has been established and machining of half cells and dumbbells for five-cell cavity has been successfully completed. Flatness on iris surface, equator surface, parallelism of equator surface w.r.t. iris surface and surface finish has been achieved and accuracies were verified on CMM machine. After final fabrication, total length achieved was better than the required tolerance for the total length of 1400mm of five-cell cavity structure. Machining trials was done in order to optimize the machine and tool parameters by various iterations and prototype development.

## ACKNOWLEDGEMENT

We acknowledge whole team of Proton Linac Development Division for their constant encouraging support. Authors thankfully acknowledge Shri Avinash Puntambekar, Head, Superconducting Cavities Development Division for their contribution in manufacturing of 650 MHz SCRF cavity. Thanks are due to fabrication section for providing support during manufacturing. We are also thankful to maintenance group of DMTD for their support for keeping machines operational. Special thanks to Shri Suman Raj, Shri A.K. Dubey, Shri Sivadas M.V., Shri Vijay Shankar Soni, Shri Omprakash Nagar, Shri Sanjeev Sinha, Shri Prahllad Kumawat, Shri Pradeep Kumar Upadhyay, Shri Udai Narayan Sharma, Shri Kesu Marskole, Shri Kishore Patil, Shri Salaskar Vinayak Venkatray, Shri Chandra Shekhar, Shri Reetesh Kumar Jain, Shri Kalaskar Anil Subhash, Shri Lalu Prasad Munda from PMS, DMTD, RRCAT, Indore for the whole hearted support in machining of SCRF cavity components.

## REFERENCES

[1] S C Joshi et al"Development of Infrastructure Facilities for Superconducting RF Cavity Fabrication, Processing and 2 K Characterization at RRCAT". IOP Conf. Ser.: Mater. Sci. Eng. 171 012114S 2017

[2] W. Bauer Kernforschungszentrum "Fabrication of Niobium Cavities" Karlsruhe, Institut fur Kernphysik P.B. 3640, 7500 Karlsruhe, Federal Republic of German.

[3] K. Someswara Rao, C.S.P.Rao, P.S.C. Bose "Optimization of Machining Parameters for cutting temperature on turning of Niobium alloy C-103by using RSM" Department of Mechanical Engineering, NIT Warangal, Telangana, India.

[4] "Effect of different cutting techniques on the surface morphology and composition of niobium" Charlie A. Cooper, Andy Wu, Pierre Bauer, and Claire. IEEE transactions on Applied superconductivity, vol. 19, no. 3, June 2009

[5] Physical properties of Niobium and specifications for fabrication of superconducting cavities C.Z. Antoine, M. Foley, N. Dhanaraj Last Revised: August 25, 2006

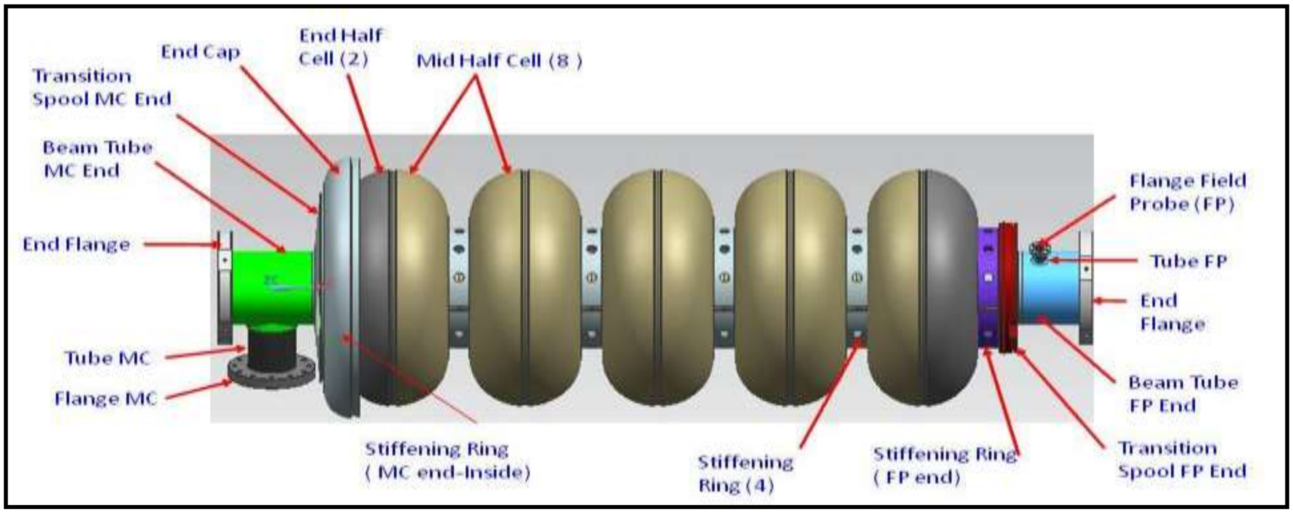


Figure 1: Solid model of 650 MHz 5-cell SCRF cavity

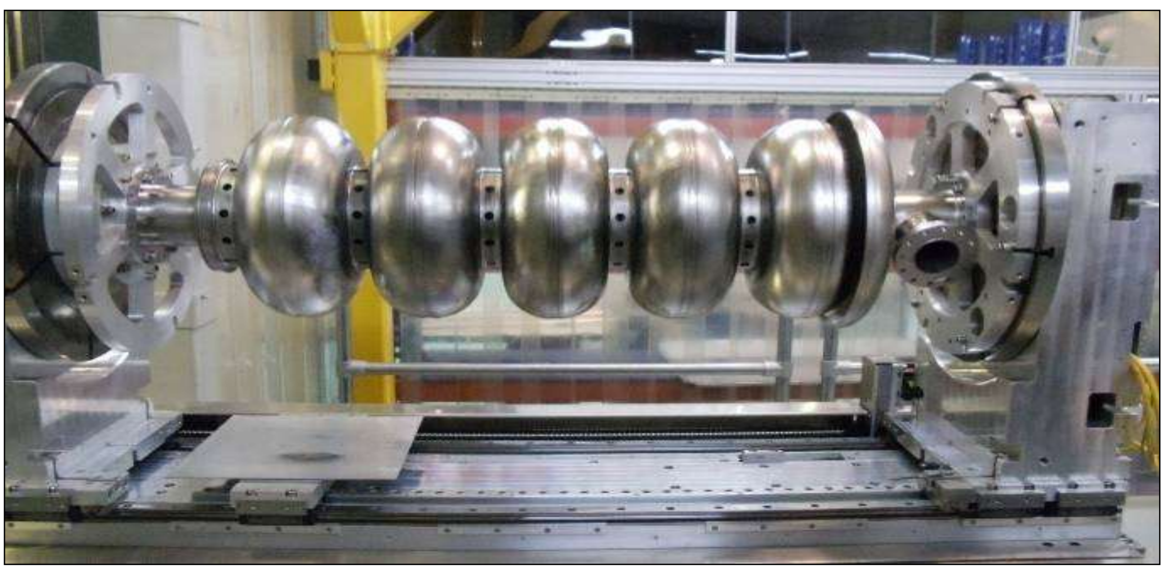

Figure 7: Actual photograph of final assembled structure

# OPERATION OF AN RF CAVITY IN THE PRESENCE OF A STATIC MAGNETIC FIELD: RF CONDITIONING AND MULTIPACTING ISSUES

Shankar Lal*,Arvind Kumar, Ravi Kumar Pandit, Pravin Nerpagar, R.S. Saini, Sona Chandran, B. Biswas, and K.K. Pant, RRCAT, Indore, India

*Abstract*

The injector linac system of the Infra-Red Free Electron Laser (IR-FEL) at the Raja Ramanna Centre for Advanced Technology (RRCAT) employs a sub-harmonic pre-buncher cavity (SHPB), which has earlier been qualified for operation at rated power levels during first lasing experiments with the IR-FEL setup. As a part of the recent injector system upgrade, a new low energy beam transport line has been installed and all the RF cavities in the injector system are now surrounded by multiple solenoids for better electron beam transmission. During commissioning experiments of the upgraded injector system, it is observed that the SHPB shows signs of breakdown at very low RF power levels and repetition rates making it difficult to operate at rated parameters, while its operation is restored to the earlier status on switching off the solenoids. This paper presents experimental observation of the effects of solenoid magnetic fields on RF conditioning of the SHPB cavity and plausible explanations.

## INTRODUCTION

An Infra-Red Free Electron Laser (IR-FEL) operating in a wavelength range of 12.5-50μm is being developed at the Raja Ramanna Centre for Advanced Technology (RRCAT) [1]. The injector system of this IR-FEL comprises a 90 keV thermionic electron gun followed by a 476 MHz sub-harmonic pre-buncher (SHPB) and multiple S-band accelerating structures [1]. The IR radiation is generated in the setup by passing the electron bunches of ~10 ps with mean energy of 15-25 MeV through an undulator placed inside an optical cavity.

The electron gun generates electron bunches of 1ns with a peak current of 1 A. These bunches are further bunched to ~50 ps by a 476 MHz SHPB before injecting into the S-band structures to further bunch and accelerate the electron bunches to desired energy. Initial commissioning and qualification of the IR-FEL has been done with accelerating structures developed in-house [1]. Considering the development of a FEL based user facility in the future, its injector system has recently been upgraded with a new electron gun and S-band structures viz. a standing wave (SW) single cell S-band buncher, a 14-cell traveling wave (TW) accelerating buncher (AB) and a 3m long TW linac [2]. To improve the beam transmission through the injector system, multiple solenoids are used in the low energy section of the beam transport line (LEBT). A schematic diagram of the upgraded injector system is shown in Fig.1, while the on-axis magnetic field profile is shown in Fig.2. Before installing in the upgraded injector system, all the accelerating structures were high power conditioned offline.

When the SHPB is energized in the upgraded injector configuration with the design magnetic field profile of the LEBT, a vacuum degradation to $10^{-7}$ mbar, from an initial base vacuum of $10^{-9}$ mbar, is observed at much lower RF power and repetition rate as compared to its operation during offline testing without a magnetic field. The accelerating voltage also drooped to a much lower value as compared to the design value for the input power. This observed degradation of vacuum and droop in the accelerating voltage prevents operation of the SHPB at desired accelerating voltage. The study of possible causes of vacuum deterioration and droop in the accelerating voltage in the SHPB are investigated and presented in the following sections.

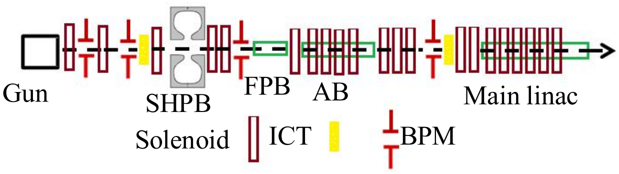


Figure 1: The layout of upgraded injector system of the IR-FEL at RRCAT.

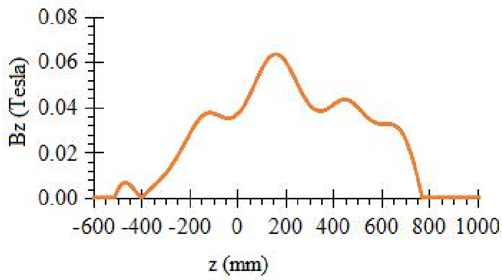


Figure 2: On-axis field profile due to the first six solenoids in the upgraded IR-FEL injector. Here zero position is referred to as the center of the SHPB.

## DESCRIPTION OF THE 476 MHZ SUB-HARMONIC PRE-BUNCHER

The SHPB is a nose cone type single-cell cavity made of Stainless Steel (SS). It has four port openings: one for RF power coupling, one for the pickup signal and two ports for frequency tuners [3]. The tuners are made of aluminum and inserted into the cavity to achieve a resonance frequency of 476 MHz. A cut view of the SHPB is shown in Fig. 3. RF power of ~ 1 kW is fed into the SHPB to establish the desired gap voltage (accelerating voltage) of ~30 kV [3]. In order to have the amplitude and phase stability required to achieve the desired beam quality, the RF pulse is ~ 50µs long (macro pulse width) and the beam pulse (macro pulse of 10 µs) is injected in to the later portion of the RF pulse with better stability [1,4]. During qualification of the IR-FEL with the in-house developed injector system, the SHPB was conditioned for RF power of ~ 10 kW with 50 µs pulse width repeating at 50 Hz. In order to measure the input and reflected RF power, a dual direction coupler (DDC) is connected at the input port, while a signal corresponding to the accelerating voltage set up in the cavity is measured using a pickup loop.

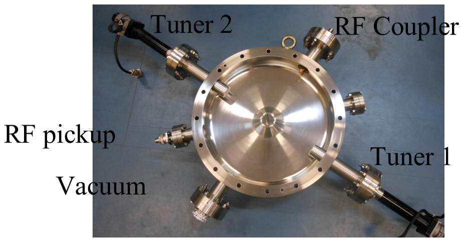


Figure 2: A cut view of the 476 MHz SHPB.

## HIGH POWER CONDITIONING OF THE SHPB: EXPERIMENTAL OBSERVATIONS

As discussed in the previous section, the SHPB was conditioned up to an accelerating voltage of ~30 kV before the solenoids were tuned on. The base vacuum in the SHPB was ~$10^{-9}$ mbar. For better control over the gap voltage (accelerating voltage) in the SHPB, a Lab-view based Graphical User Interface (GUI) is designed where the input RF power is calibrated in terms of the desired gap voltage, and the actual pickup signal, measured at a pre-defined cursor location on the RF pulse, is displayed as readout. The desired gap voltage is referred to as 'Vset', while the pickup readout is referred to as 'Vc' in the following text. During high power conditioning, the vacuum and the Vc are monitored. The cavity pickup signal is also simultaneously measured on an oscilloscope to see the macropulse shape. When the solenoids are off, the cavity pickup signal is observed for full RF pulse width of 50µs. A typical pickup signal is shown in Fig.4.

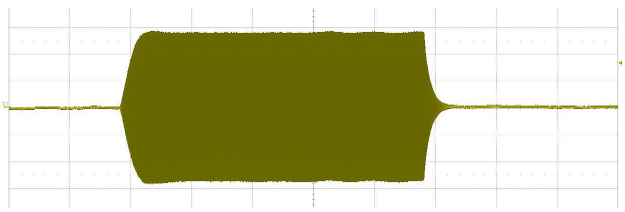

Figure 4: Cavity pickup signal (typical) measured during high power RF conditioning of the SHPB when the solenoids are off.

When the solenoids are turned on, vacuum in the SHPB suddenly degraded to $10^{-7}$ mbar. The cavity pickup signal also droops to a very low value after an initial rise time as shown in Fig.5. When the solenoids were turned off again, the vacuum improved back to $10^{-9}$ mbar and the cavity pickup signal is also restored to the full amplitude and RF pulse width.

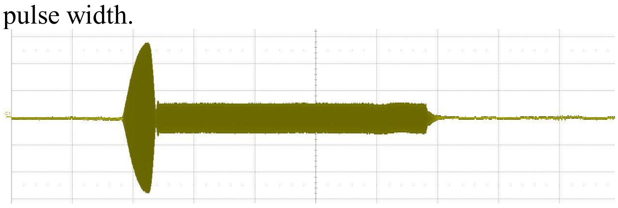

Figure 5: Cavity pickup signal (typical) measured during high power RF conditioning of the SHPB when solenoids are on.

## EXPLANATION OF THE EXPERIMENTAL OBSERVATIONS

To understand the experimental behavior of the SHPB in the presence of a magnetic field, a literature survey was carried out to study similar observations. In Ref. 5, it is reported that in the presence of an emittance compensation solenoid magnetic field of 400 G, significant vacuum activity is observed in a 113 MHz superconducting photocathode RF gun. In simulations, it has been found that the gun shows higher multipacting (MP) at a much lower voltage in the presence of the solenoid magnetic field [5]. Since the strength of the solenoid magnetic field at the location of the SHPB in our case is also of similar order (~ 400 G, see Fig.2), the possible cause of vacuum degradation could be MP. To check this, a MP study of the SHPB has been carried out with and without the solenoid magnetic field.

### *Multipacting study of the SHPB*

Multipacting simulations of the SHPB have been carried out using the Particle-In-Cell (PIC) solver of CST Particle Studio® (CSTPS) [6]. The strength of MP is determined by fitting the number of particles (electrons) with time as

$$N(t) = N(t_0)e^{\alpha(t-t_0)}, \qquad (1)$$

where N ($t_0$) is the number of particles at a time '$t_0$'when growth/decay of number of particles starts, while $\alpha$ is the growth rate expressed as $ns^{-1}$. A positive (negative) value of $\alpha$ indicates the presence (absence) of MP [7].

The MP study of the SHPB without magnetic field predicts a mild exponential growth of secondary electrons for an accelerating voltages > 25 kV as shown in Fig.7. With the solenoid magnetic field, the MP simulations predict an exponential growth of electrons from 5 kV till 30 kV as shown in Fig.7. It is clear from these simulations that MP occurs in the SHPB at a much lower voltage in the presence of the solenoid magnetic field. The MP simulation results qualitatively explain the experimental observation of vacuum degradation in the SHPB when solenoids are on, which is on account of the solenoid magnetic field provoking the MP.

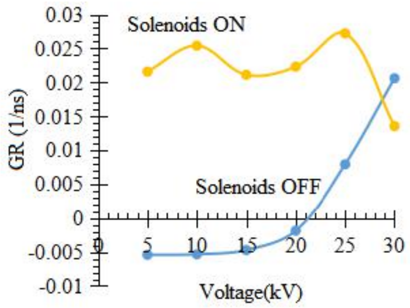


Figure 7: Secondary electron exponential growth rate vs. cavity voltage with solenoids OFF and ON.

### *Explanation for reduction in accelerating voltage in the presence of magnetic field*

The observed reduction in accelerating voltage could be explained qualitative as follows. Reference [5, 8] discuss that the reduction in cavity voltage could be due to energy taken by the multipacting electrons, which can be expressed mathematically as

$$W = W_g - W_{mp} \rightarrow W_g - \overline{w}_{mp} N_e, \qquad (2)$$

where W is the total energy stored in the cavity, $W_g$ is the energy stored in the cavity without multipacting, $W_{mp}$ is the total energy consumed by multipacting electrons and $\overline{w}_{mp}$ is the average energy of MP electrons and $N_e$ is the total number of electrons.

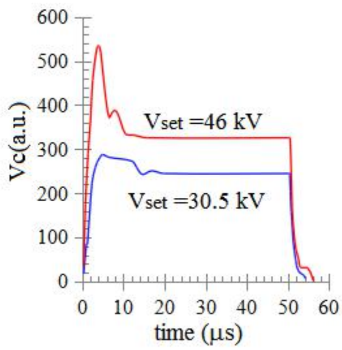


Figure 8: Cavity pickup signal for solenoid current of 50 A for set voltage of 30.5 and 46 kV.

As discussed in Ref. [9], space charge effects limit the growth of MP electrons to a steady state value after a few RF periods. Similarly, for a fixed input RF power, the energy stored in a RF cavity also attains a steady sate value after few fill times (or few RF cycles). Considering both the above facts, it is expected from Eqn (2) that the effective energy stored in a RF cavity in a case where MP takes place will also attain a steady sate value, which is lower than that in the absence of MP. This steady state value of the effective energy stored in the cavity can be increased by increasing the input RF power, which means that the cavity voltage can be set again to the desired value, but with a higher input RF power. This has been observed experimentally in the SHPB during high power conditioning in the presence of the solenoid magnetic field, as discussed in the previous section. The pickup signal (proportional to effective accelerating voltage in the SHPB) for a solenoid current of 50 A for two different input powers is shown in Fig.8, which clearly shows that it is possible to increase the equilibrium cavity voltage in the presence of MP by increasing the input RF power to the cavity.

## CONCLUSIONS

High power RF conditioning of a 476 MHz pre-buncher cavity has been carried out in the presence of a solenoid magnetic field, which increases the multipacting in the SHPB at a much lower voltage. Further investigation of the MP to determine possible methods for its mitigation are currently underway.

## ACKNOWLEDGEMENT


We are thankful to Mr. Deepak Wagmare and Dinesh Vaskel for their help in experimental studies. Authors would also like to thank Mr. R.Bhowate and Sarbeswar Sardar of FUS for their help assistance during installation and commissioning experiments. The thank is also due to teams of RFSD, APSD, AMTD and LCID for help in operation of different sub-systems.


## REFERENCES


[1] Sona Chandran et.al, “Commissioning and validation of the injector and electron beam transport systems for the IR-FEL at RRCAT”, accepted for publication in Pramana Journal of Physics.

[2] A.Kumar et. al, “Upgarde of the injector system of the IR-FEL at RRCAT”, InPAC 2018, RRCAT, India.

[3] Sanjay Chouksey et. al, “Design and fabrication of a 476 MHz sub-harmonic prebuncher cavity”, InPAC 11, IUAC, New Delhi, 2011

[4] K.K.Pant et. al, “First lasing in an infrared free electron laser at RRCAT, Indore”, Current Science, Vol. 114, No.2, 367-373, (25 January 2018).

[5] I. Petrushina et. al, “Mitigation of multipacting in 113 MHz superconducting rf photoinjector”, PRAB 21, 082001 (2018).

[6] http://www.cst.com.

[7] S. Lal et. al, “RF Design Studies of a 1.3 GHz Normal Conducting CW Buncher for European X-FEL”, in Proc. 10th Int. Particle Accelerator Conf. (IPAC'19), Melbourne, Australia, May 2019, pp. 3109-3111.

[8] R. A. Kishek, Y. Y. Lau, and D. Chernina, “Steady state multipactor and dependence on material properties”, Phy. Plasma 4(3) 1997.

[9] R. Kishek and Y.Y. Lau, “Interaction of Multipactor Discharge and rf Circuit”, Phys. Rev. Lett. 75, 1218, 1995.

# 3D VACUUM SIMULATION OF MULTI-PORT CHAMBER FOR RF BASED ION SOURCE FOR EFFICIENT EXTRACTION OF $H^-$ ION BEAM

Manish Pathak[1, *], D. V. Ghodke[1], V. K. Senecha[1,2], B Oraon[1], S.K. Sonawane[1]

[1] Ion Source & Diagnostic Section, Proton Linac Development Division, Raja Ramanna Centre for Advanced Technology, Indore 452013

[2]Homi Bhabha National Institute, Mumbai, India

*Abstract*

A Multi-cusp confined external RF antenna based $H^-$ ion source is most promising for producing low emittance $H^-$ ion beam current and desirable for high intensity proton accelerator for Spallation research application. In view of this, we have designed and developed a Multi-Port (8-ports) high conducting vacuum chamber for $H^-$ RF ion source. This vacuum chamber consists of two sections namely plasma chamber and multi-port extraction chamber. The plasma chamber is connected to the extraction chamber through an orifice of ~8 mm and desirable gas pressure in both the chambers is obtained using differential vacuum pumping systems. Since the suitable plasma density in the plasma chamber and high vacuum in the extraction chamber are crucial parameter for the efficient extraction of $H^-$ ion beam. Therefore, complete vacuum analysis over both the chambers become important task for ion source. In this paper, we present 3D modelling and vacuum simulation of plasma & multi-port extraction chamber for differential pumping. The results obtained from simulation are discussed to optimize the differential gas pressure for Efficient extraction of $H^-$ ion beam.

## INTRODUCTION

A RF based $H^-$ ion source as pre- injector to the proton Linac have been developed at proton Linac development division, RRCAT, Indore for Indian Facility for Spallation Research (IFSR) [1]. For efficient extraction of $H^-$ ion beam, there was need to develop a multiport high conducting vacuum chamber. This multiport chamber consists of 8-Ports, in which four ports is used to create vacuum in extraction as well as plasma chamber of ion source. the vacuum is created by high speed Turbo Molecular Pump (TMP). Remaining four ports are used for diagnostic purpose & four axis (X-Y-Z and angle) alignment of extracted beam current. This multiport chamber also has provision for 50 kV DC insulator for mounting main plasma generator. It can accommodate Eigen lenses, electrostatic LEBT and electrostatic chopper (Fig. 1)**.**

Since the gas pressure in different chamber of ion source are crucial for the operation of $H^-$ ion source, therefore 3D modelling & vacuum simulation of plasma & multi-port extraction chamber becomes necessary to obtain desirable pressure in both the chambers**.** we have used molecular flow module of FEM based COMSOL multiphysics simulation software to simulate pressure distribution in multiport chamber [2]. The software module provides capabilities for the accurate modelling of low pressure, low velocity gas flows in compact and complex geometries.

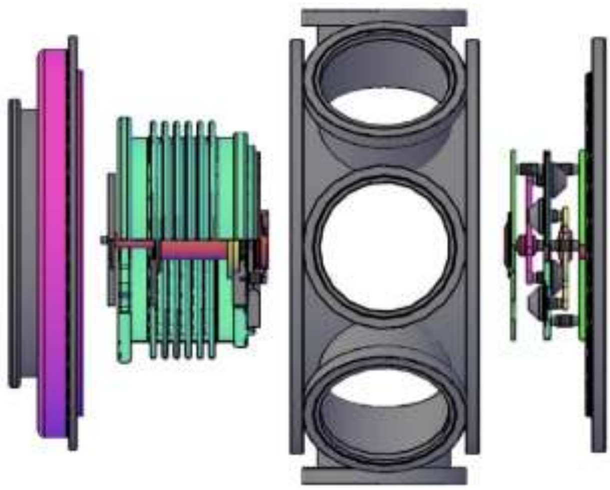

Figure 1: 3D Side of HV Insulator, Multiport Vacuum chamber and Electrode mounting back plate.

### *Modeling and simulation of multi-port chamber*

A 3D CAD model of multi-port chamber with plasma igniter was built in COMSOL geometry window using incorporated module (Fig.2). Built model has a plasma igniter of length 70 mm and 15.5 mm dia. Igniter has opening of 5 mm aperture in plasma chamber of length 103 mm. and dia. 48mm, which provides sufficient background of preliminary electrons for hydrogen gas discharge in plasma chamber. Plasma chamber is connected to the multiport extraction chamber by an office of 8 mm, where extraction electrode system is placed and beam diagnosis is done by detector. Extraction chamber is an 8-ports chamber, in which four ports have DN 200 flange & another four ports of DN 160. Four high speed Terbo molecular pumps (TMP) are coupled to the extraction

* mkpathak@rrcat.gov.in

chambers through DN 200 ports for pumping the purged $H_2$ gas. The above model is simulated in 3D COMSOL multiphysics to optimize desirable vacuum level in different chambers with gas purging.

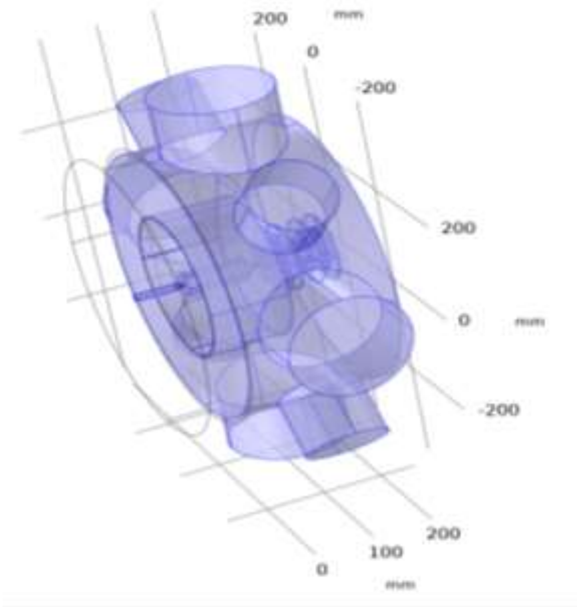

Figure 2: 3D CAD of 8 port RF chamber (Igniter + Plasma+ Extraction chamber).

The modeled geometry is simulated for different pump combination and purging rate to get optimize pressure value in plasma and multiport extraction chamber. Hydrogen Gas in ion source is purged through an igniter by 3 mm orifice. Flow of $H_2$ gas in chamber was varied from 10 SCCM to 30 SCCM (Standard Cubic Centimeters per Minute). And TMP pumping speed in simulation is varied according to available pumps in market. Simulation was started by considering small equilibrium pressure of the order of $10^{-10}$ mbar. The number density, molecular flux and gas pressure over the designed model has been computed or approximated by solving the following analytical expression of mass flow rate.

$$\dot{M} = \beta A \Delta p \tag{1}$$

Where, $A$ is mass conductance and $\Delta p$ is the pressure difference on flow port and the chamber, so that

$$\dot{M} = \beta(q_{a\infty}^2 - q_{b\infty}^2) \tag{2}$$

Here,

$$\beta = \frac{D^3}{3\pi\mu c^2}$$

$\mu$ is the gas viscosity, $D$ is the dia. of flow cylinder and $c$ is molecular mean thermal speed. The flow of the gas is assumed isothermal.

## RESULTS AND DISSCUSSIONS

### *Simulation results*

Simulated results give surface distribution of $H_2$ molecular flux, number density and pressure along the ion source different chamber. Fig. 3 shows the surface distribution of molecular flux at the ion source chamber wall. Magnitude of molecular flux has the variation of 2 order between plasma & extraction chamber. $H_2$ molecule flux of the order of $10^{22}(1/m^2 \times s)$ & $10^{20}(1/m^2 \times s)$ was found at wall of plasma and extraction chamber respectively.

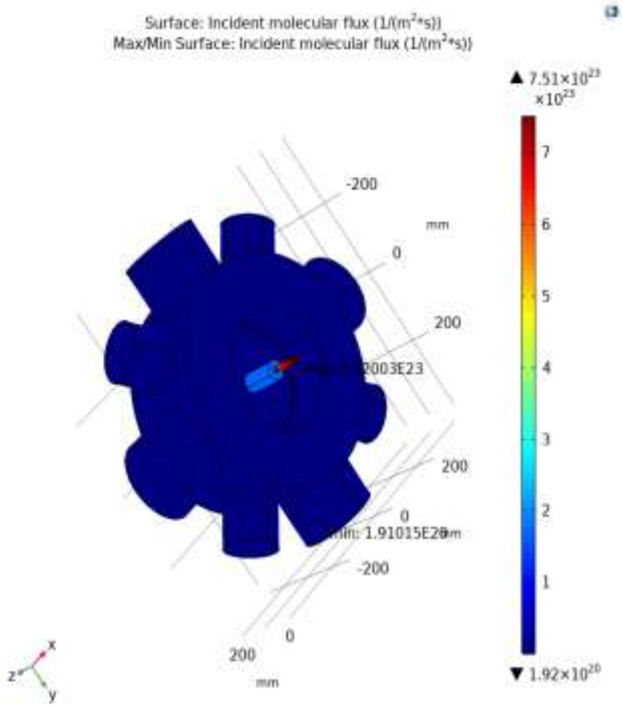


Figure 3: Surface distribution of molecular flux of $H_2$ gas in ion source different chambers at 25 SCCM gas flow rate by four TMP of total capacity 4400 L/s.

Pressure along the ion source extraction axis reduces due to effect of differential pumping. Which is shown in Fig.4. It helps to generate uniform dense plasma in plasma chamber and sustain high voltage for ion beam extraction by extraction electrodes. Number Density of $H_2$ molecule also varies in same manner as pressure along the ion source chamber, which is shown in Fig. 5. During this simulation leak, desorption and gas out gassing is not considered because quantitative load value of this gas flow in system is very less in comparison to hydrogen gas load in the chamber.

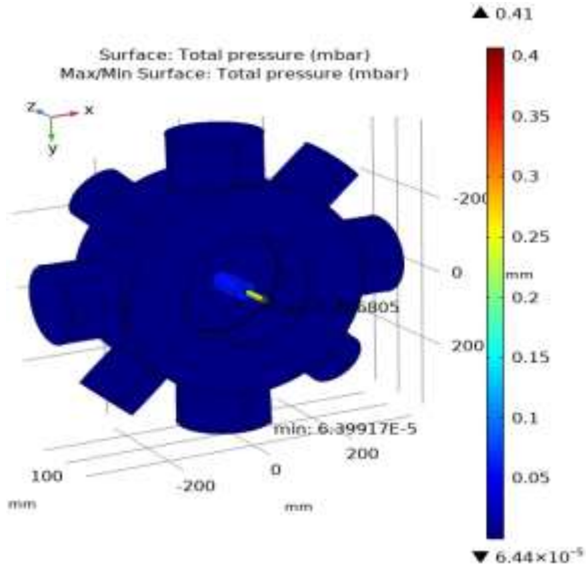


Figure 4: Surface distribution of $H_2$ gas pressure in ion source different chambers at 25 SCCM gas flow rate by four TMP of total capacity 4400 L/s.

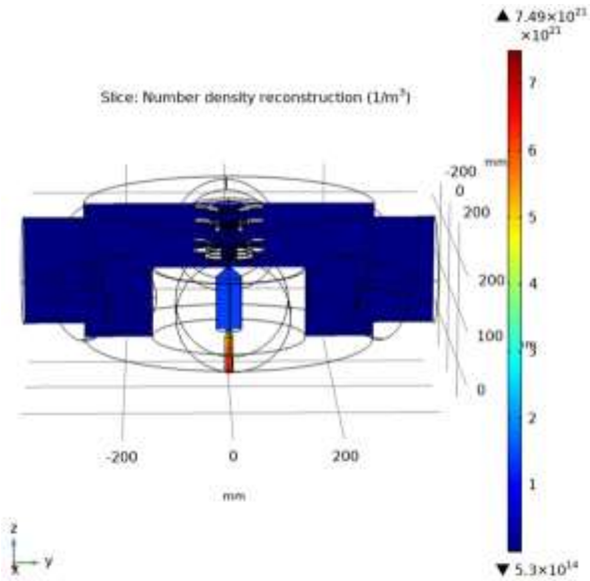


Figure 5: Surface distribution of number density of $H_2$ gas in ion source different chambers at 25 SCCM gas flow rate by four TMP of total capacity 4400 L/s.

By varying Flow of $H_2$ gas in chamber from 10 SCCM to 30 SCCM. It is found that difference of $10^{-2}$ mbar pressure between plasma and extraction chamber remain maintain against flow rate, which confirms about the proper design of ion source chamber geometry. Simulation was also performed to view the effect of no. & pump speed of TMP pumps for desired vacuum generation in multiport chamber. It was found that, there is not much change in pressure of plasma region with addition of another TMPs. But extraction pressure varies significantly. that will be more important to withstand high voltage accelerating potential. It is due to low conductance path between plasma and extraction chambers.

On the basis of these simulation results a high conducting multi-port vacuum chamber for RF based $H^-$ ion source is designed & developed, which is shown in Fig. 6.

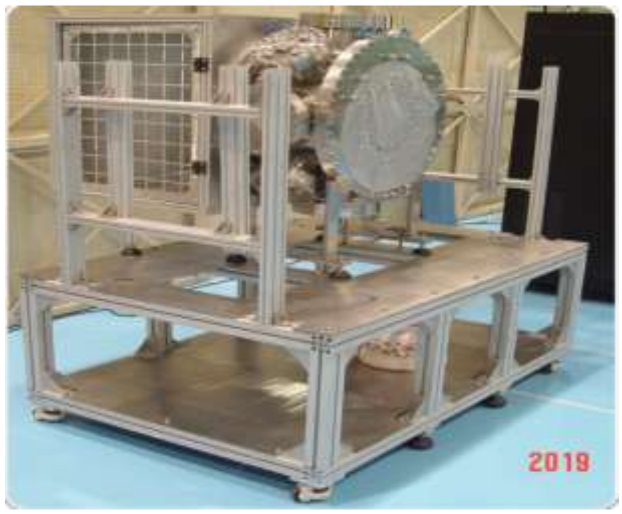


Figure 6: Fabricated Multiport (8-port) Vacuum Chamber for RF based $H^-$ Ion Source.

## CONCLUSION

The 3D modelling & differential vacuum simulation of multi-port chamber for RF based ion source for efficient extraction of $H^-$ ion beam has been successfully carried out in COMSOL multiphysics software. The simulation results are shown for $H_2$ gas pressure, number density and molecular flux on chamber wall. Comparison of pressure in different chamber with varying gas flow rate and varying pumping speed has been investigated by simulation. Number density and pressure distribution in source is governed by differential pumping phenomena between plasma & multi-port extraction chamber. Two order difference of pressure was recorded between these two chambers. Pressure of $5.6\times10^{-2}$ and $6.39 \times 10^{-5}$ mbar is obtained in plasma and multi-port extraction chamber respectively with four TMP's of 1100 L/s at 25 SCCM $H_2$ gas flow rate. Which are suitable for $H^-$ ion yield in plasma chamber and efficient extraction of $H^-$ ion beam from RF ion source.

## REFERENCES

[1] Manish Pathak, V. K. Senecha, Rajnish Kumar, D. V. Ghodke, NIM A 838, 96-102.
[2]] http://www.comsol.co.in.

# SIMULATION OF BREMSSTRAHLUNG PHOTONS AND PHOTO-NEUTRONS EMISSION FROM TUNGSTEN TARGET WITH 30 MeV ELECTRON BEAM

Rajeev Ranjan Prasad, Anupam Chakraborty, D Sunil Kumar and A John Arul
Reactor Shielding and Data Division, Indira Ghandhi Centre for Atomic Research Kalpakkam.

*Abstract*

This study reports efficiency of bremsstrahlung photons and photo-neutrons production from bombardment of 30 MeV electron beam on the thick tungsten target. Monte Carlo simulations have been carried out for electron, bremsstrahlung photons and photo-neutrons transport in thick tungsten target using the 3D particle transport code FLUKA. Along with the production efficiency of the bremsstrahlung photons and photo-neutrons the angular dependence of the bremsstrahlung photons also has been studied.

## INTRODUCTION

Now a day's electron linear accelerators (LINAC) are widely used as source of neutrons for various experimental activity in reactor physics and associated areas. The precise estimation of the strength and energy spectra of the radiation coming out from the beam target is essential not only for accuracy in performing reactor physics experiments but also for the design of the biological shield for the beam target hall. This calculation has done for generating bremsstrahlung photons and photo-neutrons from tungsten beam target with 30 MeV, 7 kW electron beam. Since the photo-neutron produced by high energy electron LINAC can be used as a selective source for application in medical physics such as boron neutron capture therapy(BNCT) for treatment of cancer cells [1]. The neutron beam from the electron LINAC can be suitably pulsed to nano-sec cycle which can be used for cross section measurement under time of flight experiment [2]. Thus Prototype Development of Electron Accelerator up to 30 MeV, with beam power of 7 kW can be used for various purposes such as fast reactor gamma streaming shielding benchmarks, neutron time of flight for cross-section measurement for nuclear materials, Medical Radioisotopes Production, Neutron Generators, and Production of Neutron rich Radioactive Nuclei. One of its applications is to generate activated sodium gamma source for validation of the shielding for fast breeder reactor (FBR). For this purpose the target is surrounded by graphite as neutron moderator followed by the sodium cell. The photo-neutrons will be used for activation of natural sodium to produce activated sodium (Na24) gamma which will be used as a source for validation of the shield models for streaming of gammas.

## PHOTO-NEUTRON PRODUCTION MECHANISM

Bombardment of high-energy electrons on a tungsten target, produces continuous spectrum of bremsstrahlung photons. These bremsstrahlung photons subsequently interact with the nucleus of the target material, resulting in the emission of the nucleons. This interaction is known as a photonuclear interaction. As the nucleons are bounded with the nucleus by binding energy 5 to15 MeV, the photon should have energy above a threshold to participate in the photonuclear reaction. Photonuclear interaction is mainly the result of three specific processes: giant dipole resonance (GDR), quasi-deuteron (QD) production and intra-nuclear cascade. From threshold to 35 MeV of energy, neutron production results mainly due to GDR. The physical mechanism can be described as one in which the electric field of the energetic photon transfer its energy to the tungsten nucleus by inducing an oscillation (known as giant resonance oscillation) which leads to relative displacement of tightly bound neutrons and protons inside the nucleus. Absorption of the incident photons excites the nucleus to a higher discrete energy state, and the extra energy is emitted in the form of neutrons. The excited nucleus comes to the ground state by emission of neutron ($\gamma$, $n$). Some contribution from double neutron emission ($\gamma$, $2n$) is also possible for higher photon energies as shown by Kumar *et al* [3]. Because of the presence of the large Coulomb barrier, proton emission is strongly suppressed for heavy nuclei like tungsten. The cross-section for this process has a maximum at photon energy between 13-18 MeV for tungsten nuclei.

## CALCULATIONS

The Modeling of the electron beam target has been done in the Monte Carlo 3D particle transport code FLUKA [4]. The electron beam of energy 30 MeV and power 7 kW were modeled in the vacuum tube of radius 1.2 cm. A cylindrical tungsten block of radius 3.6 cm and height 5.5 cm were taken as electron beam target.

The electron beam target is modeled along with the graphite moderator followed by sodium cell for production of the activation sources. In the FLUKA analysis the whole geometry is divided into 3 regions. Region-1 is target, region-2 is graphite moderator and region-3 is sodium pool. The 2D plot for the geometry of the tungsten target with graphite moderator and sodium pool is shown in Fig. 2. The production of the bremsstrahlung photons and photo-neutrons has been calculated as shown in Fig.  and 3 respectively.  The angular distribution of the bremsstrahlung photons is highly anisotropic (forward biased) shown as 2D contour plot in the Fig.4. The angular dependence of the bremsstrahlung photons is varies with energy of the photons which is shown in Fig. 5.

### RESULTS AND CONCLUSION

The primary purpose of our calculations was to estimate the efficiency of bremsstrahlung photons and photo-neutrons emission from the thick tungsten target using 30 MeV, 7 kW electron beam. The yield of the bremsstrahlung photons and photo-neutrons from the thick tungsten target with 30 MeV electrons are $5.38\text{x}10^{-1}$ photons/sec/primary electron and $2.40\times10^{-2}$ photo-neutrons/sec/primary electron respectively. The strength of the bremsstrahlung photons from the target to surrounding region is $7.81\text{X}10^{14}$ $\gamma$/s and the strength of the photo-neutron from the electron beam target to the surrounding region is $3.27\text{X}10^{13}$ n/s. The energy distribution of the bremsstrahlung photons form 1 keV to 30 MeV is given in the Fig. 3 and the energy distribution of the photo-neutron from$1\text{X}10^{-5}$ eV to 20 MeV is given in the Fig. 4. Since the emission of the bremsstrahlung photons is highly anisotropic hence angular dependence of the bremsstrahlung photons emission from the tungsten target has been calculated and shown in the Fig. 5. It shows that forward peaking of the photons is more for higher energy photons whereas lower energy photons are almost isotropic.

It is concluded that the calculation of the efficiency of photo-neutron production from the electron beam target is useful for the estimation of activation of the natural sodium for getting activated sodium gamma source. The information of the angular dependence of the bremsstrahlung photons as well as the energy spectrum of bremsstrahlung photons and photo-neutrons help in the design of the bulk shield for these radiations effectively.

## REFERENCES

**[1]** F. Rahmani and M Shahriari, " Hybrid Photoneutron Source Optimization for Electron accelerator based BNCT", Nuclear instruments and Methods in Physics Research A 618 (2010) 48-53.

**[2]** G. N. Kim, et al.," Pohang Neutron Facility Based on 100 MeV Electron LINAC", Proceedings of the second Asian PArticle Accelerator Conference, Beijing, 2001.

[**3**] V Kumar, H Kumawat, Uttam Goyal, A Polanski and P Sergey, Does the electron beam has prospects in ADSS, DAE-BRNS, Symp on Nuclear Physics held on December,26-30(2002).

**[4]** Alfredo Ferrari, Paola R. Sala, Alberto Fasso, Johannes Ranft, "Fluka: a multi-particle amulti-particle transport code", CERN-2005-010 INFN/TC05/11SLAC-R-77312, October 2005.

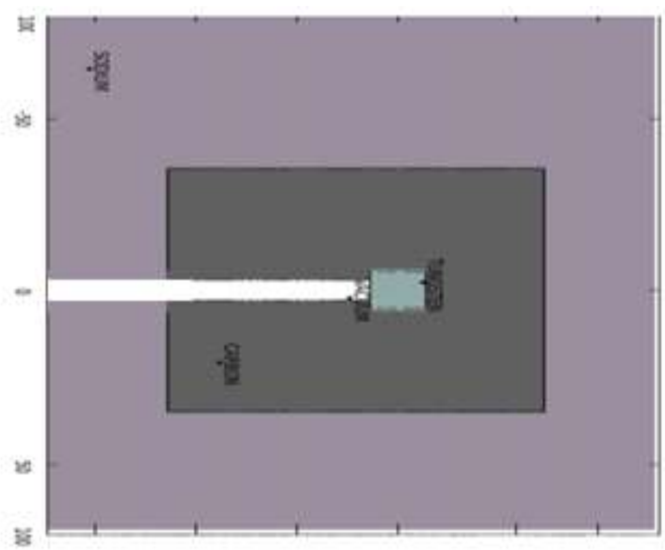

*Fig.1 Schematic of the modeling of beam target in RZ plane*

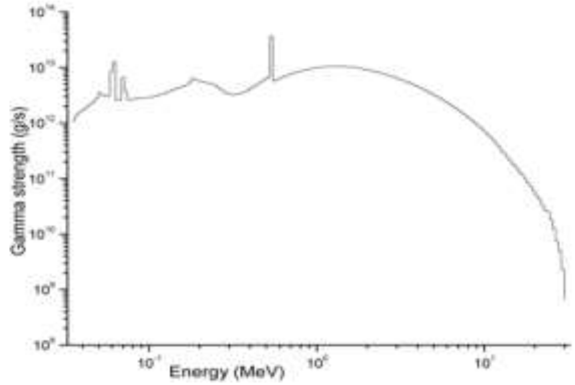


*Fig.2 Spectrum of bremsstrahlung photons at beam target*

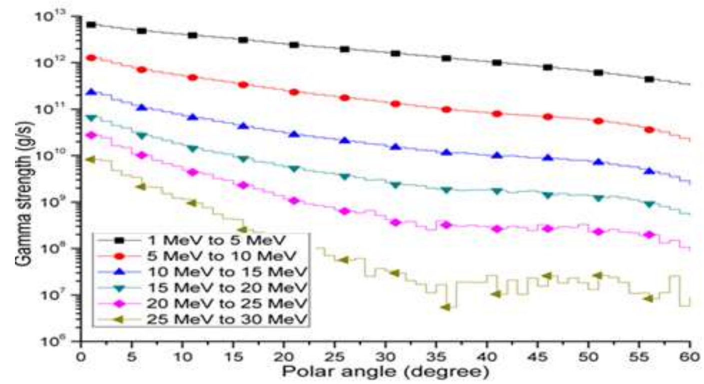


*Fig. 5 Angular dependence of bremsstrahlung photons at Beam target*

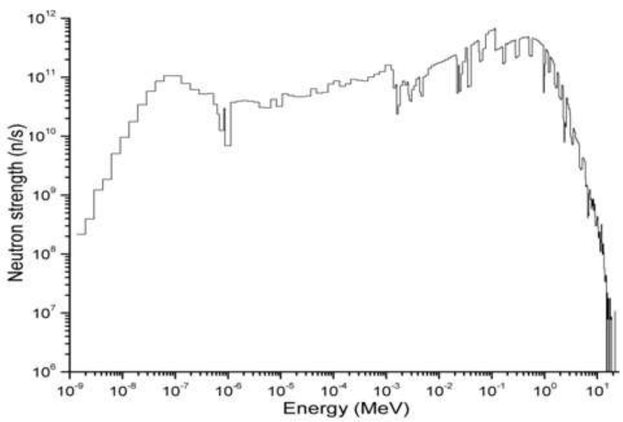


*Fig.3 Spectrum of photo-neutrons at beam target*

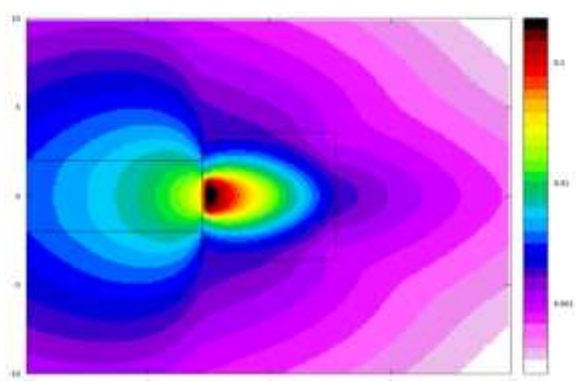

*Fig.4 2D R-Z Contour plot of bremsstrahlung photons*

# DESIGN SIMULATION OF ELECTROSTATIC BEAM DEFLECTOR CUM CHOPPER FOR H⁻ ION SOURCE

Rajnish kumar[1,2,*], D.V. Ghodke[1], Manish Pathak[1], and V.K.Senecha[2]
[1]PLDD, Raja Ramanna Centre for Advanced Technology, Indore - 452 013, India
[2]Homi Bhabha National Institute, Anushakti Nagar, Mumbai- 400 094, India

*Abstract*

A pulsed $H^-$ ion source has been developed at the Proton Linac Development Division, RRCAT. This will serve as an injector to the high current proton Linac facility for Spallation research applications. Pulse width and pulse repetition rate of this ion source can be varied from 0.5 ms to 2 ms and from 2 Hz to 50 Hz, respectively. To shape the beam in time scale so as to have a constant beam current over the pulse length. It is generally required to cut the leading and trailing edges of the ion beam pulse. Also, whenever the beam is not required for the acceleration purpose, then it should be dumped at the end of ion source before further acceleration. These requirements, can be fulfilled using an electrostatic beam deflector cum chopper with beam dumping provision. This paper reports the design simulation results of beam deflector cum chopper with beam dumping provision for the $H^-$ ion source, using OPERA-3D Multiphysics software. This software solves for the extracted ion beam trajectory under the influence of applied electric voltages and magnetic field including the beam space charge effect. In this simulation beam current density, ion temperature, electric voltages, and magnetic field due to permanent magnets used in the extraction geometry have been taken as main input parameters. Simulation results give the ion beam trajectories, total current along with the distribution of ion beam intensity in the cross-section at various location along beam axis. It also gives the electric and magnetic field distribution throughout the extraction geometry.

## INTRODUCTION

The $H^-$ ion beam pulse extracted form a pulsed cold cathode arc discharge filament based [1] and RF based $H^-$ ion source [2] usually looks like the pulse as shown in the Figure 1. The peak current does not remain constant over the beam pulse length. Initially beam takes approximately 100 µs to achieve its maximum value and at the end it again takes approximately 80 -100 µs to come to zero level. So, in order to get constant $H^-$ ion beam current over the beam pulse, leading and trailing edges of the beam pulse should be chopped. For this purpose, a design simulation study of an electrostatic beam deflector cum chopper geometry based on the beam trajectory simulations at different biasing voltage conditions at chopper electrodes has been carried out, using OPERA-3D Multiphysics simulation software [3]. The final design of the electrostatic beam chopping system has been achieved through the optimization of beam trajectories simulation in two steps. In the first step electrode geometries has been optimized for the beam trajectories simulations without applying the chopper electric field in transverse direction to the $H^-$ ion beam axis. In the 2nd step the biasing voltages required to the different sectors of chopper electrode has been optimized, so as to terminate the $H^-$ ion beam on the last ground electrode.

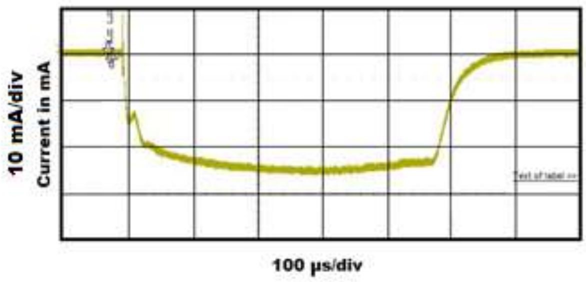


Figure 1: Typical shape of H- ion beam pulse.

## RESULTS AND DISSCUSSIONS

Implementing the chopper mechanism is that, whenever beam current is in the transition phase, the beam is deflected and dumped on the last ground electrode by applying the transverse electric field on extracted $H^-$ ion beam. This has been implemented by applying a potential difference between the upper and lower halves of the chopper electrode as shown in the Figure 2.

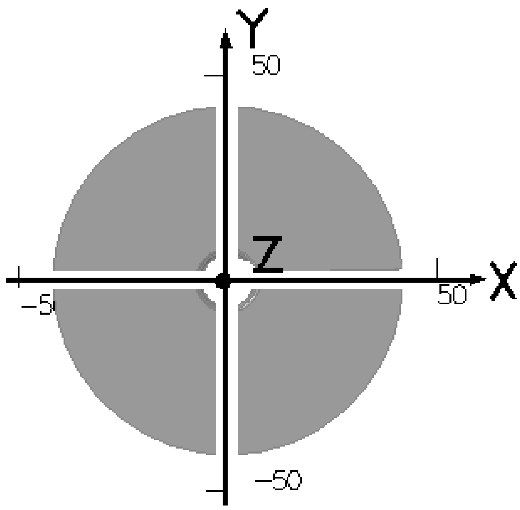


Figure 2: front view of chopper electrode.

* rajnishk@rrcat.gov.in

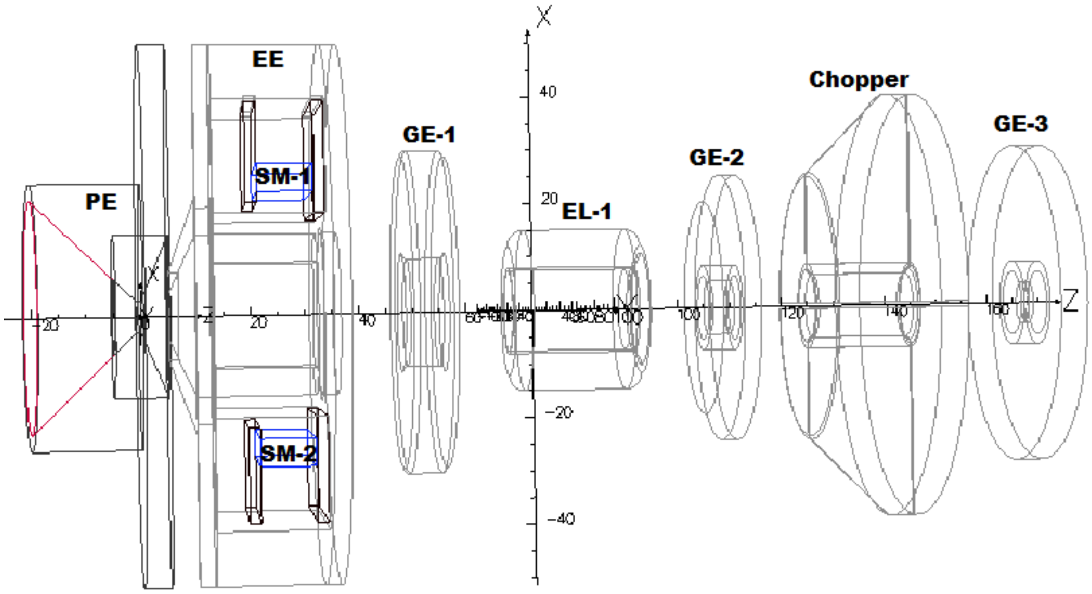


Figure 3: 3D- Model of the chopper along with extraction and beam transport systems (all dimensions in mm).

Figure 3 shows the 3D-simulation model of the chopper along with the three-electrode extraction system and electrostatic beam focusing lenses. First electrode is plasma electrode (PE) which is connected to plasma chamber and is biased at a potential of -50kV, second one is extraction electrode (EE) which is biased at 10 kV with respect to plasma electrode using a positive power supply and third one is the ground electrode (GE-1), fourth electrode is the Einzel Lens biased at -40 kV, fifth one is the ground electrode (GE-2), sixth one is the deflector cum chopper electrode divided into four equal sectors for different combination of biasing arrangements, seventh one is the ground electrode (GE-3).

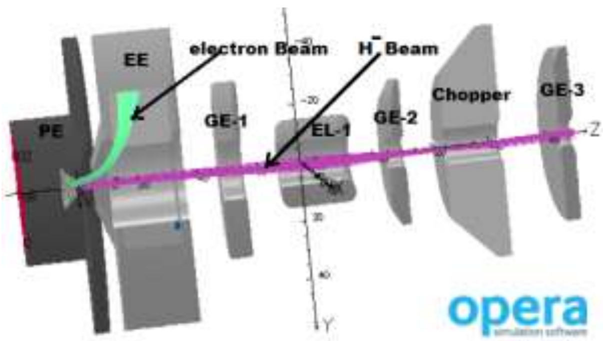


Figure 4: Electron (Green) and $H^-$ beam(pink) trajectory simulation without applying the chopper voltage

Figure 4 shows the optimized $H^-$ ion and co-extracted electron beam trajectories simulation from this geometry (here differential biasing voltage is not applied between upper and lower sectors of the chopper electrode). In this simulation PE is at -50kV, EE is at -40 kV, EL-1 at -40kV, chopper at -40 kV and ground electrodes GE-1, GE-2, GE-3 are at ground potential. The H- ion extraction must include a steering magnet for dumping of co-extracted electrons. Figure 5 shows the optimized dipole magnetic field created by these steering magnets. The 2nd reverse dipole field immediately correct a minor deflection in the $H^-$ ion beam.

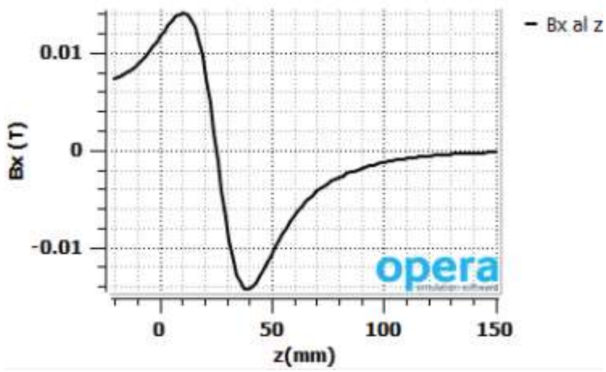


Figure 5: Variation of electron steering magnetic field along z-axis.

In order to optimize the ion extraction and transport system optics initially, a 3D-design simulation studies of this geometry have been performed and then further optimization of chopper voltage has been performed. The function of $H^-$ ion beam chopping has been achieved by applying a differential voltage pulse between upper and lower sectors of the chopper electrode as shown in Figure 6. Chopping Field will be in OFF-condition only during the constant current phase of the $H^-$ ion beam current, otherwise it will be in ON-condition including leading and trailing edges of the $H^-$

ion beam pulse. Applied voltage difference between the upper and lower sectors of the chopper electrode has been optimized by beam trajectory simulations.

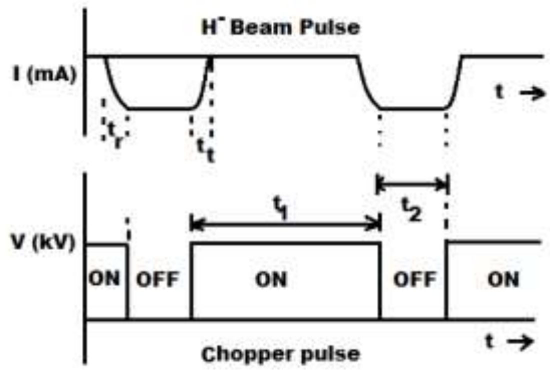


Figure 6: Typical beam chopping voltage pulse structure with respect to the H⁻ ion beam pulse.

The biasing voltage difference between upper half and the lower half of chopper electrode for achieving the transverse electric field for H⁻ ion beam chopping has been varied from 2 kV to 4 kV and 5 kV. The result of beam trajectories simulations for these cases are shown in the Fig. 7, Fig. 8 and Fig. 9, respectively. Looking at the H⁻ ion beam trajectories it is clear that 5 kV is sufficient enough to dump the H⁻ ion beam on the last ground electrode (GE-3).

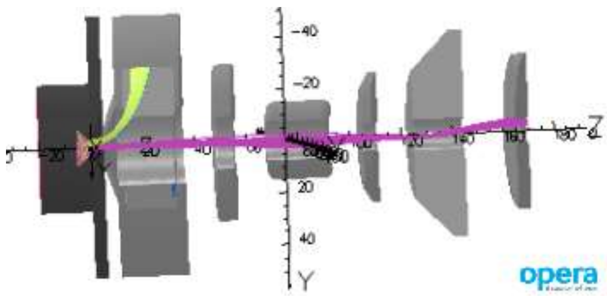


Figure 7: Electron (Green) and H⁻ beam(pink) trajectory simulation with 2 kV chopper voltage.

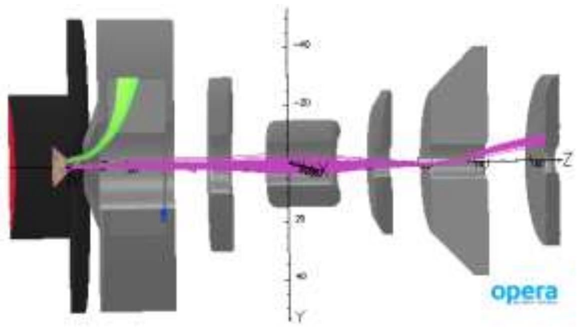


Figure 8: Electron (Green) and H⁻ beam(pink) trajectory simulation with 4 kV chopper voltage.

In all these simulations other parameters like, dimensions of various electrodes, gap between electrodes and the steering magnetic field are kept constant except the biasing between the upper and lower sectors of the chopper electrode.

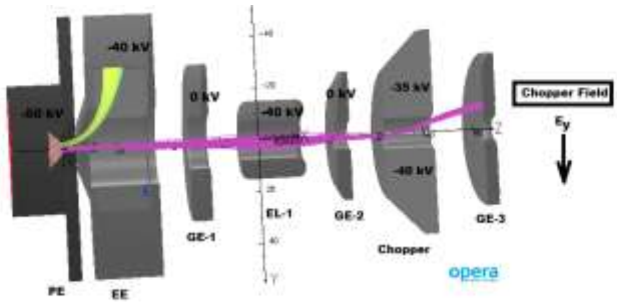


Figure 9: Electron (Green) and H⁻ beam(pink) trajectory simulation with 5 kV chopping voltage.

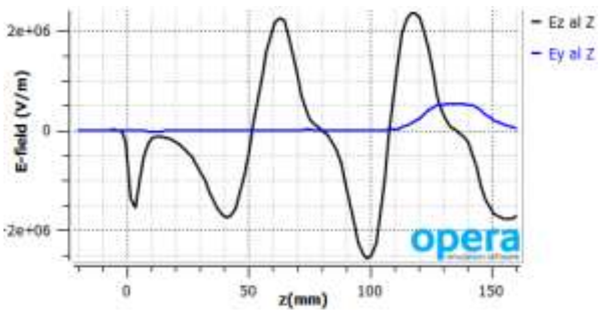


Figure 10: Variation of acceleration field ($E_z$) and transverse Chopper field ($E_y$) along Z -axis for 5 kV case.

## CONCLUSIONS

A seven-electrode beam extraction cum transport system having beam deflector cum chopper electrode has been successfully simulated and an optimum voltage required to apply between the two sectors of chopper electrode has been found through beam trajectories simulations. This is a very compact system with multiple function (extraction, transport, and chopping) in one. This geometry consists of PE, EE, GE-1, Einzel Lens (EL-1), GE-2, Chopper Electrode and GE-3. This geometry will be fabricated and tested on the exciting H⁻ ion source facilities [1,2], at RRCAT, Indore.

## REFERENCES

[1] Rajnish Kumar, D. V. Ghodke, and V. K. Senecha, Rev. Sci. Instrum. 88, 083302 (2017)

[2] D.V Ghodke et. al. “Development of a prototype external RF antenna-based H- Ion Source for Proton Linac”, InPAC-2018, RRCAT, Indore.

[3] https://operafea.com

# TESTING OF PROTOTYPE FIBER OSCILLATOR AND PREAMPLIFER FOR GENERATION OF ELECTRON BEAM IN DELHI LIGHT SOURCE

B.Karmakar, S.Ghosh, A.Sharma and B.K.Sahu, Inter University Accelerator Centre (IUAC), New Delhi, India
A. Aryshev and J.Urakawa , High Energy Accelerator Research Organization, KEK, Tsukuba, Japan
M.Washio,Waseda University,Tokyo,Japan

*Abstract*

In Delhi Light Source (DLS), the THz radiation will be generated by injecting micro-bunched electron beams into a compact undulator. The pre-bunched electron beam will be produced by the laser micro-pulses striking the photocathode. Before making the actual laser system, one prototype Yb-doped fiber based oscillator and pre amplifier have been designed and tested to validate the design of the final fiber laser system. This paper reports the design and testing of the mentioned fiber oscillator. The system has been developed at KEK and tested at IUAC. An output power of ~50mW with RMS stability of 0.6% has been demonstrated by testing the 130 MHz oscillator. Group velocity Dispersion (GVD) of the fiber has been compensated with a grating pair inside cavity to have 1028nm-1032nm BW to produce ~1.5 ps mode-locked laser pulse.

## INTRODUCTION

The concept of DLS stems from the fact that the coherent THz emission from the pre-bunched electron beams [1] can be achieved immediately from the injection point of the compact undulator magnet. This electron beam will be produced by striking laser pulses onto Cu or semiconductor photocathode. Laser pulse width will determine the width of the produced electron bunch. Therefore high power femtosecond laser pulse is required to produce proper electron beam from the photocathode. The laser oscillator should also be synchronized with the RF frequency of the electron gun.

Solid state bulk lasers are being widely used till now to generate femtosecond high power laser pulses. But these systems, notably Ti:Sa laser systems, are still complicated, sophisticated and relatively expensive. As a competitor, the Fiber laser systems have some inherent advantages e.g. rare earth doped fibers have high saturation energies. In addition, diode laser pumping via fiber make it more reliable, efficient and free from misalignment [2]. It is immune to the thermal stability problem, easy to maintain and is not expensive. Because of its superior practical features fiber laser systems are robust, futuristic, easy to maintain in long term, less expensive and can be operated at higher rep rate (MHz) easily. Therefore for multi microbunch pulse structure and later for CW operation for electron gun, this system is gaining the popularity. However it is challenging to get performance comparable to the bulk solid state laser in terms of pulse energy and duration. Therefore before making the actual laser system, it was decided that one prototype Yb-doped fiber based oscillator and pre amplifier will be made and tested to check their output performance. The main oscillator will be an Yb doped fiber to produce 1030 nm as fundamental wavelength. The repetition rate will be 130 MHz which is integer division of the main master clock (1300 MHz) to make it synchronized with the frequency of the electron gun (2860 MHz)

## OSCILLATOR AND PREAMPLIFIER DESIGN

The Oscillator is designed with a single mode LIEKKI$^{TM}$ Yb1200-4/125 Yb-doped fiber (Yb fiber 1) from nLIGHT. The schematic is shown in Figure 1 and the actual set up is shown in Figure 2.

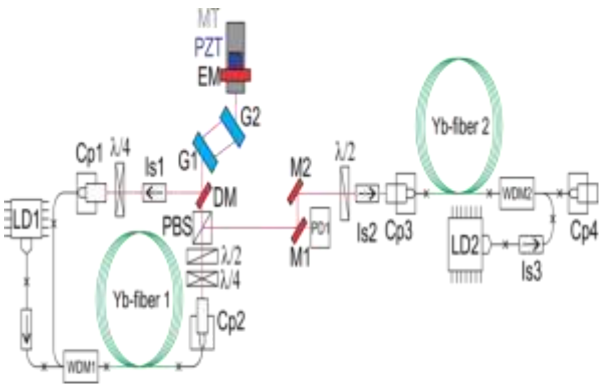


Figure 1: Oscillator+preamplifer schematic

The Yb-doped fiber (effective mode field diameter 4.4 ± 0.8μm) is pumped with a fiber coupled laser diode (LD1) delivering 450mW at 980 mm. The pump light is coupled to the oscillator cavity by a wavelength division multiplexer (WDM1). The polarization state of the mode-locked pulses is adjusted by two quarter waveplates and one half waveplate. By generating passive mode locking using nonlinear polarization evolution (NPE) inside the fiber oscillator cavity [3], sub picosecond laser pulse can be generated successfully. An isolator (Is1) is placed inside the cavity to stop the back reflection and to propagate the optical pulse in one direction. The oscillator consists of 33cm free standing path and 117 cm total in fiber path. The length was adjusted to have the oscillator repetition frequency 130 MHz.

The oscillator output is taken out by a polarized beam splitter and further amplified by another similar type Yb-doped fiber (Yb fiber 2). Yb-fiber2 is also pumped with 450 mW laser diode (LD2) delivering 980 mm as pump light. To couple the pump light WDM2 is used. We could generate up to 300mW power after pre amplifier.

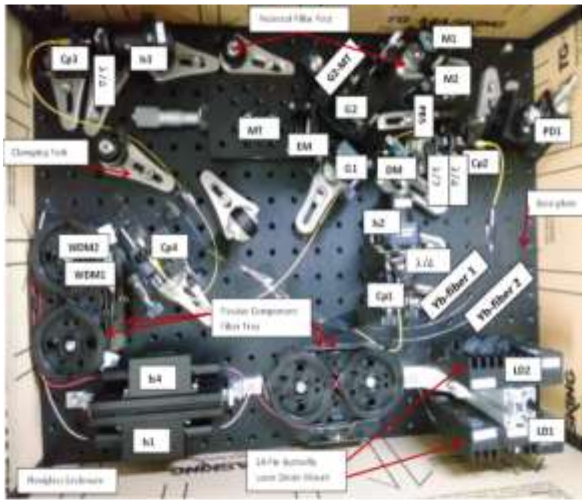

Figure 2: Actual set up on optical table

## DISPERSION COMPENSATION

It is well-known that the dispersion inside the fiber results in pulse broadening. To reduce pulse width, this dispersion should be compensated [4]. The fiber laser generated positively chirped pulse, which was compensated with a 600-groove/mm grating pair (G1, G2) in the cavity. A grating pair provides negative group delay dispersion (GDD) [5], which compensates the positive GDD of fiber in the cavity. GDD from the grating pair can be calculated by following equation:

$$\emptyset_2 = \frac{\lambda^3 Z}{\pi c^2 d^2}[1-(\frac{\lambda}{d}-\sin\theta)^2]^{-3/2}$$

Where
λ - wavelength
θ - blaze angle
d - $10^{-3}$/N , where N – number of Grooves per mm
Z- Grating-Grating separation
c - speed of light

GDD of the fiber: 0.023 $ps^2$/m
For this oscillator fiber length is 1.17m.
Therefore accumulated GDD is ~0.0269 $ps^2$

To compensate this GDD by grating with N=600, θ=17.2 deg, λ=1030nm
The separation should be Z=16.5 mm.

Therefore grating separation is adjusted to compensate the dispersion.

## TESTING AND RESULT

The oscillator and preamplifier assembly had been shifted to IUAC and had been tested successfully at IUAC. The main characteristic of the oscillator was its RMS stability and minimization of CW spectral components. The oscillator shows ~ 48mW of power at 650 mA pump current (Figure 3) with 0.68% long term RMS stability (Figure 4).

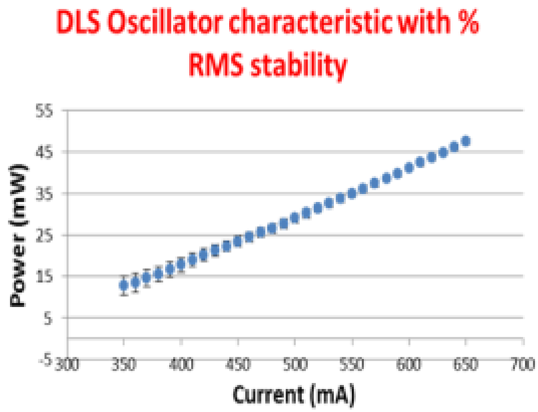


Figure 3: Oscillator output variation with pump current

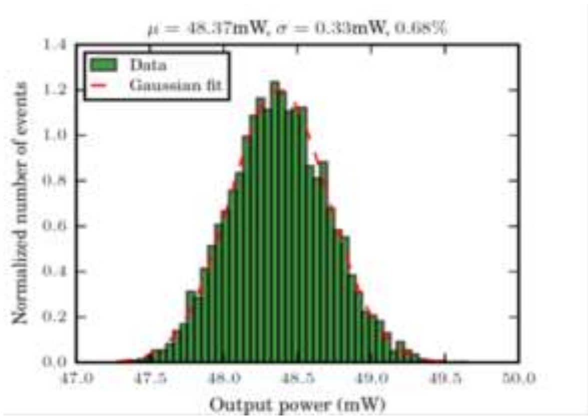


Figure 4: Oscillator RMS stability Gaussian fit

The oscillator repetition frequency is 130MHz and it is to be synchronized with the main master clock. The mirror position was adjusted to make the repetition frequency 130 MHz. The Photodiode signal (Figure 5) shows the stable mode-locking features and spectrum analyser output shows (Figure 6) 130 MHz rep rate signal.

Max RF bandwidth (99% power) was measured as 90 kHz. The central frequency stability (Figure 7) and RF BW seemed to be suitable for locking and synchronization with electron gun cavity.

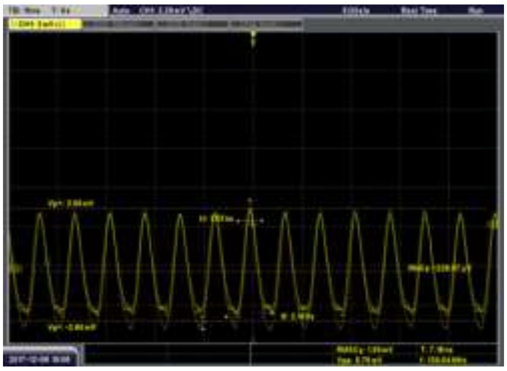

Figure 5: Mode-locked signal of the oscillator

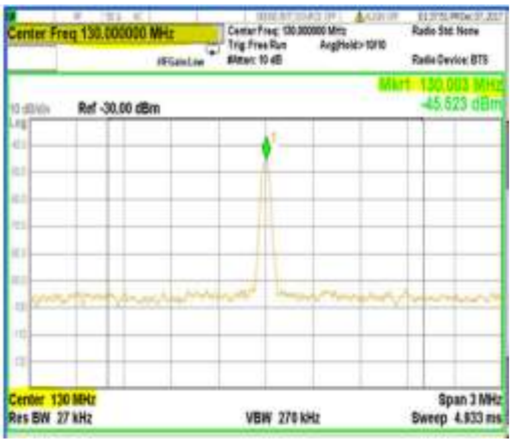


Figure 6: 130 MHz repetition frequency

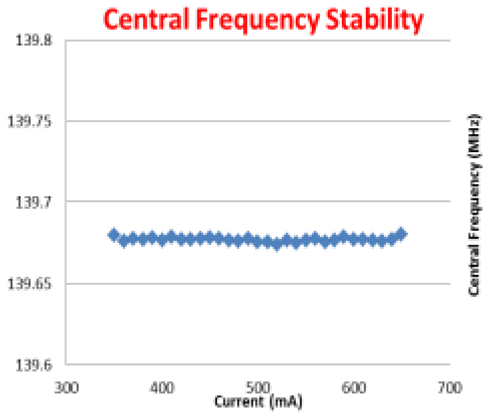


Figure 7: Repitition frequency stability

Optical Bandwidth (BW) is one of the main characteristic to produce fs pulse width. We measured optical BW (Figure 8) as 2.81 nm with full width half maxima (FWHM). With the present BW, the optical pulse width measured ~1.5 ps directly by autrocorrelator without using any external compressor. The Time Bandwidth product can tell us the transform limited pulsewidth possible with the current oscillator once we use external compressor. By assuming gaussian pulse width, Time-bandwidth product is ~0.44. Frquency BW was measured as 794 GHz which ensured the probability to get the transform limited pulse width possible ~ 554 fs.

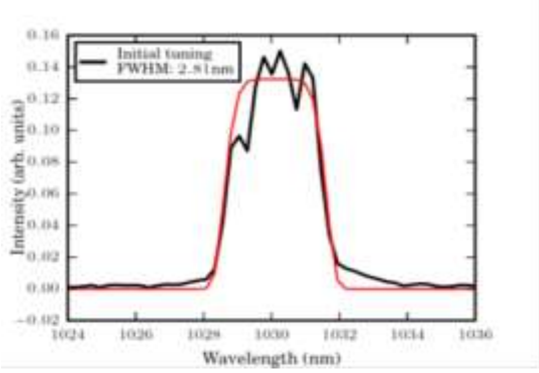


Figure 8: Optical Bandwidth

## CONCLUSION

In conclusion, we had successfully developed and tested an Yb-doped mode-locked fiber oscillator which is capable of producing fs optical pulse after compression at centre wavelength of 1030 nm and repetition frequency 130 MHz with 0.6% RMS stability. This oscillator can be synchronized with the main RF master clock of DLS to drive the electron gun. The prototype oscillator design is implemented while developing the main laser system for DLS. The optical BW can be increased more by placing a band-pass filter inside the oscillator cavity and with more efficient global tuning of the system. This will help us to generate ~200 fs pulse width from the fiber laser after compression.

## ACKNOWLEDGEMENT

The author wants to acknowledge the continuous support from the members of DLS group of IUAC, former and present Director of IUAC Dr. D.Kanjilal and Prof. A.C.Pandey respectively.

## REFERENCES

[1] S. Ghosh et al. Nuclear Instruments and Methods in Physics Research B 402 (2017) 358–363

[2] Fatih Omer Ilday, Phd dissertation “Theory and practice of high energy femtosecond fiber lasers” page 3, Cornell University,2004

[3] K. Kieu and F. W. Wise, “All-fiber normal-dispersion femtosecond laser”, 21 July 2008 / Vol. 16, No. 15 / OPTICS EXPRESS 11453

[4]H.Lim, F. O. Ilday, and F. W. Wise, “Generation of 2-nJ pulses from a femtosecond ytterbium fiber laser,”Opt. Lett. 28, 660-662 (2003).

[5] Xiangyu Zhou et. al, May 2008 / Vol. 16, No. 10 / OPTICS EXPRESS 70

# BEAM DYNAMICS STUDIES IN PRESENCE OF SUPERCONDUCTING WAVELENGTH SHIFTER FOR INDUS-2

Abdurrahim [a,b], AA Fakhri [a] , AD Ghodke [a] , Arup Banerjee [a,b]
[a]Raja Ramanna Centre for Advanced Technology, Indore, India
[b]*Homi Bhabha National Institute (HBNI), Anushakti Nagar, Mumbai, India*

*Abstract*

Indus-2 is a 2.5GeV electron storage ring, which emits the synchrotron radiation with the critical photon energy of 6 keV. The critical photon energy of the emitted radiation can be further increased with the help of inserting a high field superconducting wavelength shifter in the storage ring. For this, design and development of a 5Tesla hybrid superconducting wavelength shifter has been started at RRCAT, Indore. It will increase the critical photon energy by a factor of three. This device consists of three isolated poles, a superconducting main pole and two normal conducting side poles. Its magnetic field configuration and higher beam displacement at main pole will affect the linear and non-linear beam dynamics. Simulation has been carried out to study these effects on various beam parameters like betatron function, betatron tune, beam emittance, energy spread, bunch length and dynamic aperture. To minimize the linear effects of this device, a compensation scheme is evolved and its effect on dynamic aperture has been studied. These results will be presented in this paper.

## INTRODUCTION

Indus-2 is a dedicated synchrotron light source with nominal electron beam energy of 2.5 GeV. The lattice of Indus-2 storage ring is based on Double Bend Achromat (DBA) configuration, in which the synchrotron radiation is generated from the bending magnets with the critical photon energy of 6 keV. To perform the experiments with higher energy photons, a 5Tesla Superconducting Wavelength Shifter (SWLS) will be installed in one of the long straight section of the ring. Its design and development has been started at RRCAT, Indore. The brilliance curve of 5T SWLS along with other Indus-2 insertion devices are shown in figure 1.

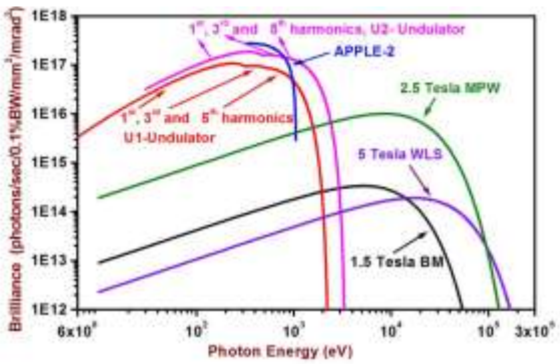


Figure 1: Brilliance curve of 5T SWLS along with other Indus-2 insertion devices

† arahim@rrcat.gov.in

The SWLS is a hybrid superconducting wavelength shifter [1], in which the main pole is superconducting where as two side poles are normal conducting. The main pole will radiate with the increased critical photon energy by a factor of three as compared to photons coming from the bending magnets of the ring. Due to its magnetic field distribution as shown in the figure 2, the beam orbit displacement at the main pole is higher. It is shown in figure 3.

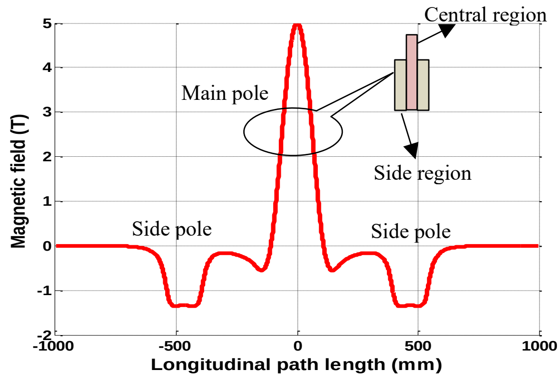


Figure 2: SWLS magnetic field distribution as a function of longitudinal coordinate. Main pole is divided in three regions (central and side regions), each modelled by a sector dipole.

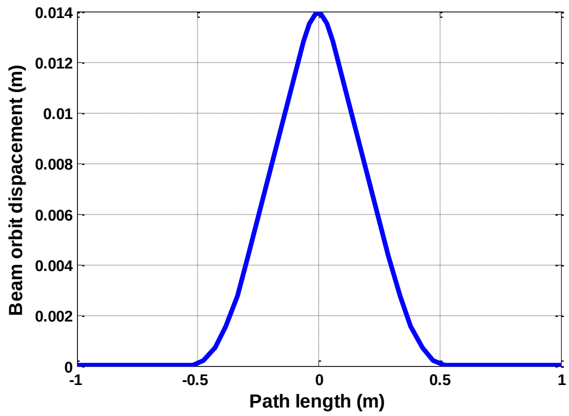


Figure 3: Beam orbit displacement due to 5T SWLS

Its magnetic field configuration and higher beam orbit displacement at main pole will affect the linear and non-linear beam dynamics. For taking in to account the focusing properties of the SWLS due to presence of the nonlinear magnetic field and big beam orbit offset as well as angle in SWLS , the wiggler model [2] of DELSY storage ring is adopted for modelling the Indus-2 SWLS..

## MODELLING OF SWLS

In the case of hybrid superconducting wavelength shifter, careful modelling of main pole is very important as it has strong magnetic field and higher orbit displacement at its location. Main pole of the SWLS is modelled by a set of three sector dipoles, satisfying the following conditions [2]. (i). Conservation of the pole bending angle, (ii). Conservation of the integral horizontal focussing, (iii). Correct representation of the wiggler radiation properties i.e. precise modelling of synchrotron integrals (mainly fourth synchrotron integral). Above criteria can be fulfilled if the lengths and bending radii of the three sector dipoles meets the following conditions

$$\alpha_w = \frac{L_1}{\rho_1} + 2\frac{L_2}{\rho_2} \tag{1}$$

$$I_{xw} = \frac{L_1}{{\rho_1}^2} - k_{z1}L_1 + 2\frac{L_2}{{\rho_2}^2} - 2k_{z2}L_2 \tag{2}$$

$$I_{zw} = k_{z1}L_1 + 2k_{z2}L_2 \tag{3}$$

Here

$$I_{zw} = -\frac{1}{B\rho}\int_{-\frac{L}{2}}^{+\frac{L}{2}} \frac{dB}{ds} x' ds \tag{4}$$

Where $L_1$ and $\rho_1$ correspond to the length and bending radius of central region of the main pole however $L_2$ and $\rho_2$ correspond to the length and bending radius of each side region of the main pole. $I_{xw}$ and $I_{zw}$ are the integrated focussing in horizontal and vertical plane respectively. $I_{zw}$ is the edge focussing, which depends on longitudinal derivative of the dipole field as well as angle of the beam trajectory (eqn. (4)). The central region of the pole is assumed to focus the beam only in horizontal plane (due to $1/{\rho_2}^2$) hence $k_{z1}L_1 = 0$. The vertical edge focussing is assigned to the two dipoles corresponding to the side region of the main pole. $\alpha_w$ and $I_{zw}$ are calculated from the field distribution of SWLS modelled in RADIA code [3]. The integrated sextupole field component of the SWLS is evaluated from the SWLS field distribution. The orbit displacement at the sextupole component will also generate the quadrupole component. The sextupole and quadrupole components are applied at the entry and exit of the main pole. Each side pole of the SWLS is modelled with rectangular magnet as the orbit displacement at the side pole locations are small and thus the sextupole components experienced by the beam will be negligibly small.

Above equations are solved by fixing $L_1$=0.0530 m and $\rho_1 = \rho_w$ =1.6667m (bending radius for 5T magnet at 2.5GeV). Based on above considerations a model for 5 Tesla superconducting wavelength shifter is developed and the relevant parameters are given in the table (1).

Table 1: Model of 5T SWLS

| Parameter | Value |
|---|---|
| $\int_{-L/2}^{+L/2} B.ds$ for main pole | 0.6209 T.m |
| $\int_{-L/2}^{+L/2} \frac{dB}{ds} x' ds$ for main pole | 0.298 T-rad |
| $\alpha_w$ | 0.0745 rad |
| Length and bending radius of central region of main pole | [0.0530 1.6667] m |
| Length and bending radius of side region of main pole | [0.0547 2.560]m |
| $k_{z1}L_1$ | 0 $m^{-1}$ |
| 2* $k_{z2}L_2$ | 0.0305 $m^{-1}$ |
| Length and bending radius of side pole | [0.2317 6.23] m |
| Sextupole component | -577.9 G/cm |
| Quadrupole comp. (due to orbit displacement) | -691.2 G |

## EFFECT ON BEAM PARAMATERS

Using the above parameters of the SWLS model in MATLAB based Accelerator Tool (AT) box, simulation is carried out to study its effect on Indus-2 beam parameters.

### *Effect on Betatron Tune and Amplitude Function*

In presence of superconducting wavelength shifter, the betatron tune shift in horizontal and vertical plane are -0.0069 and 0.0150 respectively. The maximum beta-beat is 4.5% and 10% in horizontal and vertical plane respectively. Beta-beat throughout the Indus-2 circumference is shown in figure (4). For beta-beat and tune correction, alpha matching and global tune correction technique is used. There are five families of quadrupoles used in a unit cell of Indus-2. Three quadrupoles families Q1D, Q2F and Q3D are placed in long straight section, whereas two quadrupoles families Q4F and Q5D are placed in short straight section. The two quadrupoles of Q1D family and the two quadrupoles of Q2F family, adjacent to the SWLS are used for alpha matching however the remaining Q2F family quadrupoles in the rest of the long straight sections and the Q3D family quadrupoles of all the straight sections are used for the tune compensation. In this compensation scheme, major variation in strength is shared by the local quadrupoles of Q1D and Q2F families (given in table (2)) however change in other quadrupoles strengths are very small.

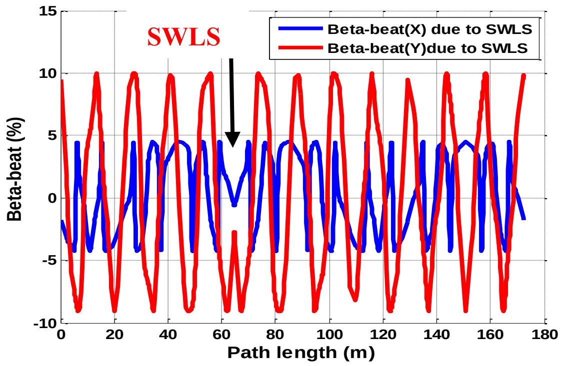


Figure 4: Beta-beat in presence of SWLS

The corrected beta-beat in both the planes are shown in figure 5.

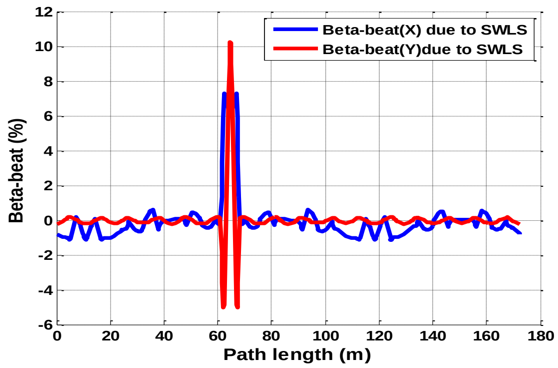


Figure 5: Beta-beat corrected using the alpha matching and global tune correction technique

Table 2: Quadrupole strength for beta beat correction

| Quadrupole (two quadrupoles adjacent to SWLS) | Quadrupole strength variation (%) |
|---|---|
| Q1D | -13.01% |
| Q2F | 3.22% |

### *Effect on Beam Emittance, Energy Spread, Momentum Compaction Factor and Bunch Length*

For the present operating optics, in presence of superconducting wavelength shifter, the emittance is reduced by 1.5%, however the energy spread is increased by 2.5%. The change in momentum compaction factor is negligibly small but due to increase in energy spread bunch length is increased by ~ 3%. In near future, Indus-2 will be operated with the low emittance (22nmrad) optics to enhance the brilliance and with low momentum compaction factor optics ($\alpha \sim 10^{-6}$) to generate the short electron bunches [4], thus the effects of superconducting wavelength shifter are studied for these optics also. Variation of important parameters for different lattices are presented in the table 3.

Table 3: Effects of SWLS on different Indus-2 optics

| Parameter | Present operating optics | Low emittance optics (22nmrad) | Low alpha optics |
|---|---|---|---|
| [$\Delta\nu_x$ $\Delta\nu_y$] | [-7 15] x$10^{-3}$ | [-11 12] x$10^{-3}$ | [-7 8] x$10^{-3}$ |
| Beta-beat (%) | [4.5 10] | [7.4 8.1] | [4.6 5.1] |
| Emittance (Δ in %) | -1.5 | 8.99 | -2.43 |
| Energy spread (Δ in %) | 2.53 | 2.82 | 2.46 |
| Momentum compaction factor (Δ in %) | ~0 | 0.09 | 82.6 |
| Bunch length (Δ in %) | 2.99 | 3.34 | 39.56 |

### *Effect on Dynamic Aperture*

Particle tracking is performed for one lakh turns to study the nonlinear effects of SWLS on dynamic aperture (at injection location). In present operating optics, the effect of beta-beat and sextupole component due to superconducting wavelength shifter is negligibly small on the dynamic aperture for on momentum particles (ΔP/P: 0%). For off momentum particles of ΔP/P 1% dynamic aperture reduces by 5.7% (12.3mm to 11.6mm) in horizontal plane. For the low emittance optics slight reduction in dynamic aperture was observed for on momentum particles as shown in figure 6. Maximum reduction in dynamic aperture is for the off-momentum particles of ΔP/P= 1%. Vertical dynamic aperture is reducing from ~ 6.4mm to ~ 5mm (~ 30 % reduction). After beta-beat and tune compensation, the dynamic aperture improves for on and off momentum particles in both the optics. In above study, the lattice multipole errors and real value of closed orbit distortion are not considered.

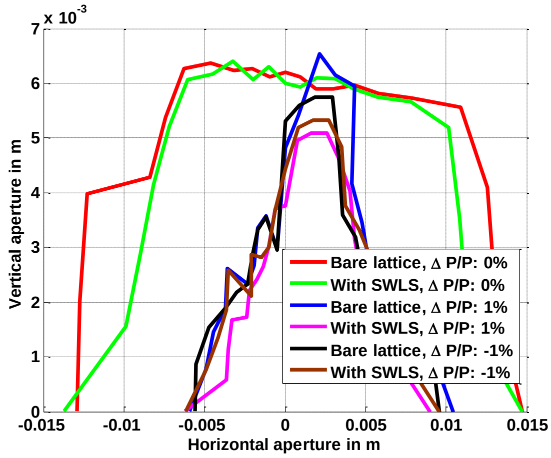


Figure 6: Dynamic aperture (low amittance optics)

## CONCLUSION

A model of Indus-2 superconducting wavelength shifter is developed. Using this model, effects on various beam parameters for different Indus-2 optics are studied. On momentum particle dynamic aperture is slightly affected in presence of SWLS for the operating as well as low emittance optics. There is maximum reduction in dynamic aperture for the off momentum particles of ΔP/P= 1% in low emittance optics. After beta-beat and tune compensation, the dynamic aperture is almost restored in every case.

## REFERENCES


[1]. Shigeru Koda et.al, "Effects of a hybrid superconducting three-pole wiggler on the stored beam at the-SAGA-LS storage ring", NIM A 682 (2012) 1–7.

[2]. P. Beloshitsky et.al, "Effect of the Superconducting Wiggler on the Delsy Beam Dynamics", NIM A 524 (2004) 13–26.

[3]. Private communication with S. Das.

[4]. Abdurrahim, AD Ghodke, Arup Banerjee, Study of Low Momentum Compaction Factor Optics and its Implementation in Indus-2, these proceedings.

# GENERATION AND CHARACTERISATION OF AN UNDER-EXPANDED SUPERSONIC GAS JET FOR BEAM-PROFILE MONITOR

Sherry Rosily, S. Krishnagopal, Homi Bhabha National Institute and Ion Accelerator Development Division, BARC

*Abstract*

Common transverse beam profile measurement techniques such as scintillators and wire scanners would be damaged by the power from beams of high intensity accelerators. Among advanced techniques currently being explored worldwide, the supersonic gas jet based method has many advantages for the linear proton accelerators. In the present work, the generation and characterisation of an under-expanded supersonic gas jet was explored in detail to study the properties of a gas jet that can be shaped into a gas sheet for 2-D transverse beam profile measurements. This paper briefly describes the experiments and simulations carried out for this purpose. Simulation of under-expanded gas jet generation using orifice nozzle in medium vacuum has been carried out using OpenFOAM tools. Flow past the skimmers in the higher vacuum region has been simulated using MolFlow+. A setup was developed for experiments on generation of the gas jet and its characterisation using impact probe. The Mach disk, a characteristic shock structure of this flow, was observed in the profiles obtained experimentally as well as through simulations.

## GAS SHEET BEAM PROFILE MONITORS

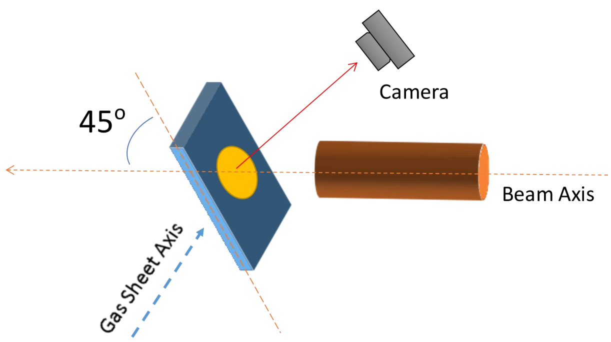


Figure 1 Scheme of a Supersonic Gas Sheet Beam Profile Monitor based on BIF

Beam profile measurements are required for controlling the beam spatial distribution and emittance measurements. Some of the common techniques developed for beam profile monitoring include Scintillating detectors and Wire scanning. However in high intensity beams these type of systems are damaged by the beam. A Gas Sheet type Beam Profile Monitor is being explored for the high intensity proton accelerators being developed by Ion Accelerator Development Division, BARC [1].

## GAS SHEET GENERATION

Gas sheets for this application can be developed using special properties of under-expanded supersonic gas jets. A focussing skimmer needs to be placed in its Zone of silence[2] to prevent the dissipation of the supersonic flow. The generation and characterisation of under-expanded gas jets was studied in detail both experimentally and through simulations for the design of a gas sheet based beam profile monitor.

## EXPERIMENTAL SETUP

The experimental setup consists of a gas source, a settling chamber and a vacuum chamber mounted with axially movable nozzle and a pitot probe mounted with radial movement with respect to the nozzle. The nozzles are holes of various dimensions ranging from 50 - 800 microns made in discs with 6 mm diameter. The vacuum chamber also has optical windows for flow visualisation setups.

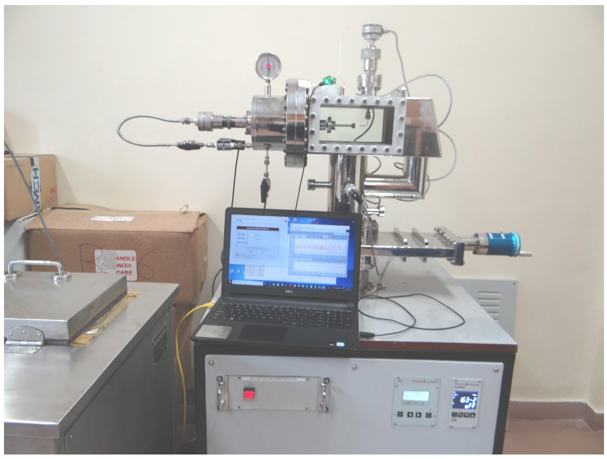

Figure 2 Setup for experiments with gas jets

The axial measurement of the dynamic pressure was measured and is plotted as a ratio with respect to settling chamber pressure in Fig. 3. The location of Mach Disk as per [2] in the experiment condition was expected to be at 11.6D where D is the diameter of the nozzle. The location of Mach Disk in the experimentally obtained plot is nearly at 13D. The location of Mach Disk indicates the successful generation of an under-expanded gas jet. The usefulness of the pitot probe measurements in the setup for obtaining the supersonic flow profile in vacuum has also been validated in the experiment.

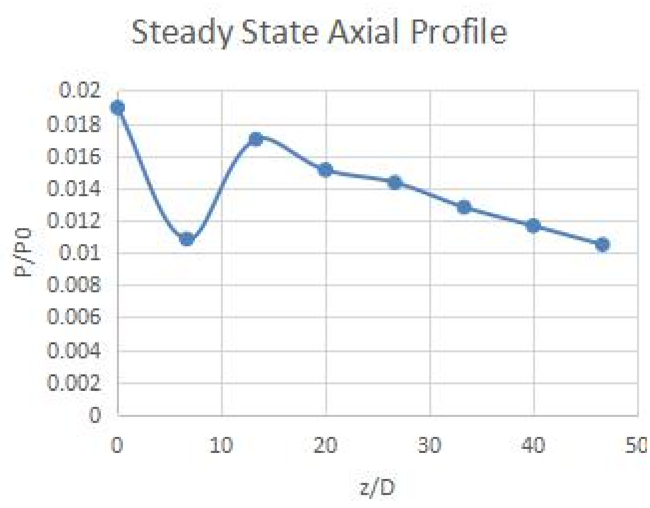


Figure 3 Dynamic Pressure to Settling Chamber Pressure ratio versus distance from nozzle to nozzle diameter ratio as recorded by the impact probe sensor in steady state

To reduce the vacuum deterioration the gas sheet would have to be operated in pulsed mode. Some technique to obtain the flow profile of the pulsed gas sheet is required.

Experiments to study the time variations of chamber pressure as well as Pitot pressure under pulsed flow has also been carried out. Fig 4. shows measurements obtained by a single pulse of 100ms duration and nine 100ms second pulses at 1Hz repetition rate. Many more experiments at different pulse rates and positions were obtained and the results are being analysed to model the gas jet flow and the dynamic response of the pitot probe to the flow. Additionally a Schlieren imaging setup is also being explored to investigate the behaviour of the pitot probe in pulsed flow and to obtain a model to make it useful for measurement of the pulsed gas jet.

## SIMULATIONS

The flow up to the skimmer is not highly rarefied flow and hence were simulated using rhoCentralFoam which is a CFD solver within the OpenFoam framework benchmarked for such supersonic flows and shock conditions[3]. Beyond the skimmer Monte Carlo based tools such as the dsmcFoam+ [4], a third party solver compatible with OpenFOAMv17, and MolFlow+ [5], were used for simulation of the gas sheet generation. The OpenFoam framework, dsmcFoam+ third party DSMC solver and ParaView result visualiser codes were installed in the Megh cloud computing facility at BARC for these simulations.

Fig. 5 shows the result of an axi-symmetric simulation of the formation of a supersonic under-expanded gas jet. The axial dynamic pressure is plotted in Fig. 6. The Mach disk location obtained in this plot is at about 7D whereas as per [2] it is 6.7D for the pressure ratio considered.

Molfow+ was used to simulate the flow past the skimmer as well as the pressure at the end of a probe in pulsed flow conditions. Molflow+ does not model interaction between gas particles and hence is fast but suitable only for very highly rarefied region.

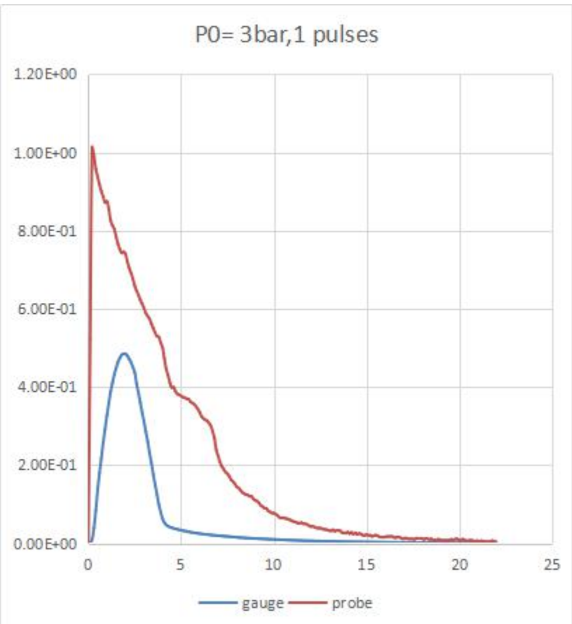


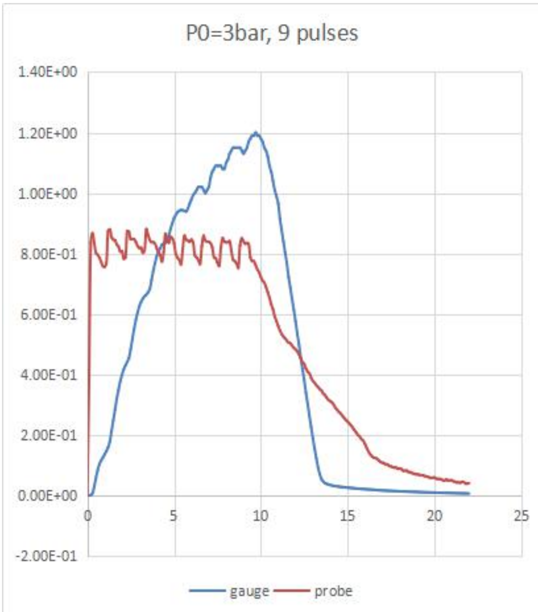


Figure 4 Plot of measured Pitot pressure (Red) and Chamber pressure (Blue) vs time for Single 100 ms pulse (Left) and Nine 100 ms pulses at 1 Hz repetition rate (Right). Units: x axis is time in seconds, y axis is mbar for gauge and x100 mbar for pitot probe

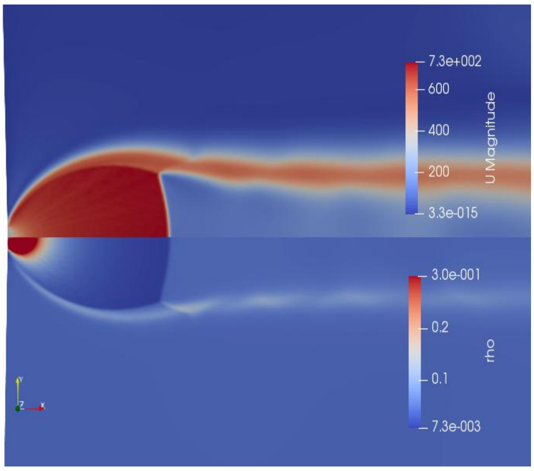


Figure 5 Screen-shot of flow profile obtained using OpenFOAM Rho Central Foam solver at 100 microseconds: Velocity profile in m/s (Upper) Density profile in kg/m3 (Lower)

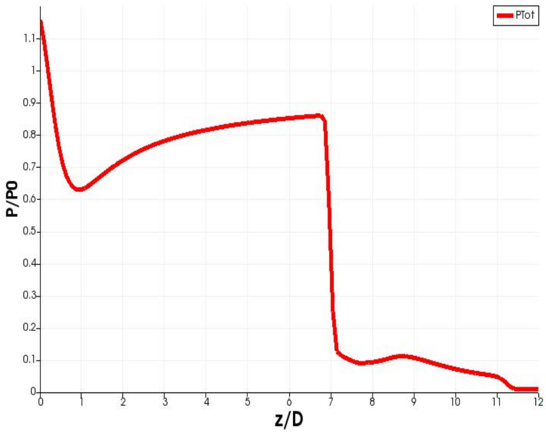


Figure 6 Computed value of Pitot pressure (dynamic pressure) to settling chamber pressure ratio vs Distance to nozzle diameter ratio from the OpenFoam simulation

DSMC tools does model this also and hence could be useful for simulating larger regions of the flow at the cost of speed and resources required.

## CONCLUSION

For development of Gas Sheet Beam Profile Monitor experiments were carried out to gain understanding about the flow of gases injected into vacuum, the properties of supersonic flow and shock structures, as well as to explore methods of characterising such flows. Familiarity was obtained in setting up and usage of CFD and Monte Carlo based software tools that help in computation and simulation of these flows. With the help of the experience gained, work has been initiated towards the design and development of a Gas Sheet based beam profile monitor for high intensity proton linear accelerators. Other challenging aspects such as flow visualisation, controllability specifications, image acquisition and background noises are also being studied.

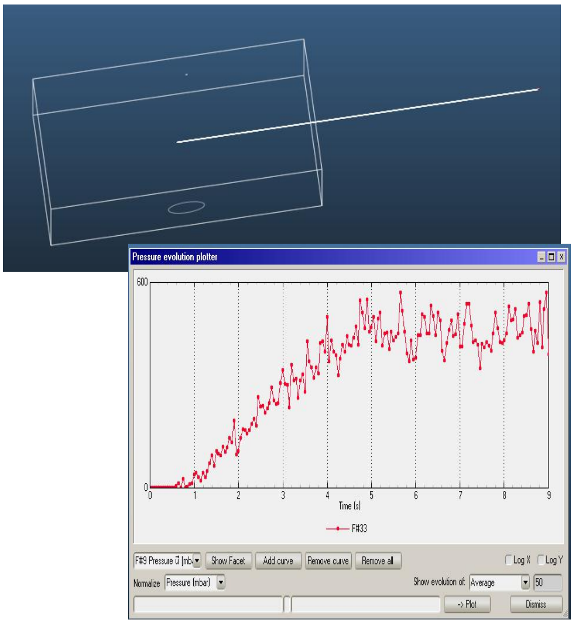


Figure 7 Simulation setup and results of Molflow+ simulation of pitot probe measurement of pulsed flow

## REFERENCES

[1] Sherry Rosily et al, "Supersonic gas jet generation and analysis for beam profile measurement application", InPAC p. 568-569 (2018)

[2] Ashkenas and Ferman, "Structure and Utilisation of supersonic free jets in low density wind tunnels", NASA-CR-60423, (1965)

[3] Luis F. Gutiérrez Marcantoni, José P. Tamagno and Sergio A. Elaskara,"High Speed Flow Simulation Using OpenFOAM", Mecánica Computacional Vol XXXI No.16, p. 2939-2959 (2012)

[4] C. White et al,"dsmcFoam+: An OpenFOAM based direct simulation Monte Carlo solver", Computer Physics Communications, Volume 224, 2018, Pages 22-43,

[5] R. Kersevan and J.-L. Pons, "Introduction to MOLFLOW+:New graphical processing unit-based Monte Carlo code for simulating molecular flows and for calculating angular coefficients in the compute unified device architecture environment", J. Vac. Sci. Technol. A Vacuum, Surfaces, Film, vol. 27, No. 4, 2009, pp. 1017–10

# SUPERCONDUCTING POST ACCELERATOR FOR LEHIPA

Pallavi Priyadarshini[1], A. Pathak[2], Rajni Pande[1], S. Roy[1] and Srinivas Krishnagopal[1,3]
[1]Ion Accelerator Development Division, BARC
[2] UM-DAE CEBS, Mumbai
[3]HomiBhabha National Institute, Mumbai

*Abstract*

In the 1 GeV linac designed for ADS, it is now proposed to use superconducting single spoke resonators (SSR) right after the 3 MeV RFQ. In order to have hands-on experience of superconducting cavity operation, the 3 MeV beam from RFQ at LEHIPA can serve as a good injector option for testing the superconducting spoke resonators. We present here the design of an SSR based 352 MHz superconducting linac after the LEHIPA RFQ to accelerate the beam to 20 MeV. The beam will be accelerated using two families of SSRs; SSR-A ($\beta_g$=0.11) and SSR-B ($\beta_g$=0.21) at 352 MHz. In this paper we discuss the physics design of the SSR-A and SSR-B cavities and the beam dynamics optimisation of the SC linac. We show that it is possible to design such a SC psot0accelerator to accelerate beam from the LEHIPA RFQ to 20 MeV, within the constraints imposed by the existing facility.

## INTRODUCTION

The Low Energy High Intensity Proton Accelerator (LEHIPA) is a normal-conducting, high intensity proton accelerator with an RF frequency of 352 MHz, presently under commissioning at BARC. As part of the DAE ADS roadmap, we have also designed a 200 MeV Medium Energy High Intensity Proton Accelerator (MEHIPA)[1], that will be superconducting and will have an RF frequency of 325 MHz (the frequency choice being driven by international collaborations). For medium beta and for lower frequency usage, Single Spoke Resonator (SSR) cavities are increasingly being used worldwide. To have hands-on experience with superconducting (SC) cavity operation with beam, it is proposed that if spoke resonators are developed at 352 MHz, then they can be tested at LEHIPA. We propose two families of SSRs: SSR-A ($\beta_g$ = 0.11) and SSR-B ($\beta_g$ = 0.21), that can be inserted after the LEHIPA RFQ, replacing the DTL tanks. The existing LEHIPA linac and LEHIPA with SC cryomodules are shown inFigure 1.

The 3 MeV beam from the existing 352 MHz RFQ can be injected into the SC linac with the help of a modified Medium Energy Beam Transport (MEBT) channel. The SC linac consists of two separate cryomodule sections, separated by a drift space of 30 cm, one with SSR-A cavities and SC solenoids and the other with SSR-B cavities and SC solenoids. This paper presents the detailed beam dynamics of the MEBT followed by SC linac using the output beam from the existing LEHIPA RFQ. The linac has been generated using GenLinWin [2] and all beam dynamics studies have been performed using the multiparticle code TraceWin [3]. GenLinWin generates the lattice for a given particle type, frequency, initial and final energy, component dimensions and cavity field map. In order to have more realistic beam dynamics of the Linac, three dimensional (3D) electromagnetic field maps of the optimized cavity and the solenoids have been used.

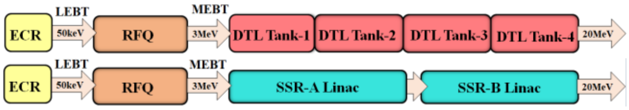


Figure 1. LEHIPA layout (top), and LEHIPA with SSR linac layout (bottom).

## MEBT DESIGN

When a proton beam is transported from the RFQ to the SSR-A linac for further acceleration, RF defocusing, space charge forces and beam mismatch can lead to beam loss due to large emittance growth and halo formation along the linac. To minimize both of these deleterious effects, it is important to match into the phase space at the entrance of the SC section.

Two quadrupole triplets have been used for transverse focusing and two double gap buncher cavities have been used for longitudinal focusing in the modified MEBT, as shown in Figure 2. In the SC linac, solenoids are used in the cryomodule for axisymmetric focusing; therefore, we have used quadrupole triplets in MEBT to ensure that the injected beam remains axisymmetric. The two-gap buncher cavity has been used to keep the voltage of the buncher cavity achievable without any electrical breakdown. Drift spaces in the MEBT are provided to accommodate beam diagnostics for measuring the characteristics of the beam coming from the RFQ.

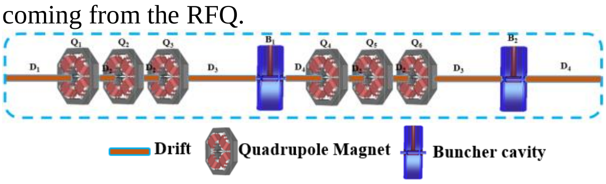


Figure 2.MEBT layout.

In any periodic structure, matched beam size plays an important role. In the ideal case, if the beam is matched at the entrance of the accelerating structure then this will remain matched throughout the periodic structure with constant beam size over each period of the structure. With this in mind, for design and optimization of the MEBT, we find the input matched ellipse at the entrance to the SSR-A cryomodule. The RFQ output ellipse is further matched to this ellipse by tuning the quadrupole gradient and the buncher cavity gap voltage of the MEBT. Optimised MEBT parameters for minimum emittance growth, halo formations and minimum beam size are presented in Table 1.

Table 1: MEBT parameters.

| Parameters | Value |
|---|---|
| Total MEBT length (m) | 1.565 |
| Quad 1 & 3 gradient (T/m) | 38.9 |
| Quad 2 gradient (T/m) | -33.9 |
| Quad 4 & 6 gradient (T/m) | 23.3 |
| Quad 5 gradient (T/m) | -23.7 |
| Buncher 1 $E_0$TL (kV) | 56.2 |
| Buncher 2 $E_0$TL (kV) | 50.7 |

## SUPERCONDUCTING SECTION

### *SSR cavity*

The two families of single spoke resonators, SSR-A and SSR-B, have been designed to accelerate the beam from 3 MeV to 10 MeV and from 10 MeV to 50 MeV respectively (though the latter will be used for acceleration only up to 20 MeV). The detailed design of the cavities is explained in Ref.[4]. Functional requirements for the cavity restrict peak surface electric field to below 40 MV/m in order to avoid field emission and the peak surface magnetic field to below 70 mT to avoid quenching of the cavity. The resonant frequency of the superconducting cavity is kept same as that of the LEHIPA i.e. 352 MHz. The fields obtained for the designed and optimized SSR-A and SSR-B cavities are listed in Table 2.

Table 2. Fields for the optimised SSR cavities.

| RF Parameters | SSR-A | SSR-B |
|---|---|---|
| $B_{peak}/E_{acc}$(mT/(MV/m)) | 7.18 | 6.59 |
| $E_{peak}/E_{acc}$ | 4.54 | 3.92 |
| $E_{acc}$ (MV/m) | 8 | 10 |
| Optimal beta ($\beta_{opt}$) | 0.142 | 0.26 |

### *Linac Structure Design*

In addition to the beam quality, the main design criterion of the SC linac with SSRs is to minimize the linac length and to reduce the number of cavities used, in order to reduce the overall linac cost. The number of cavities required for acceleration of the beam is minimised to get a range of optimal beta($\beta_{opt}$)[4, p. 12]. $\beta_{opt}$ refers to the velocity of the particle for which the Transit Time Factor (TTF) is maximum. The range of $\beta_{opt}$for SSR-A is 0.12-0.155 and for SSR-B it is 0.249-0.296. Both families of SSR are designed for $\beta_{opt}$ which fall in this range. The fields of the optimised cavities have been used in GenLinWin for linac generation and further optimisation. In both cryomodules, a SC solenoid has been used after each accelerating cavity to focus the beam in the transverse direction. Superconducting solenoids are preferred over quadrupoles because they lead to relatively shorter period length and hence, shorter cryomodules. The SSR-A cryostat, which is 6.2 m long, consists of 11 cavities and 11 superconducting solenoids, and the SSR-B cryostat, which is 4.75 m long, consists of 7 cavities and 7 solenoids (Figure 3).

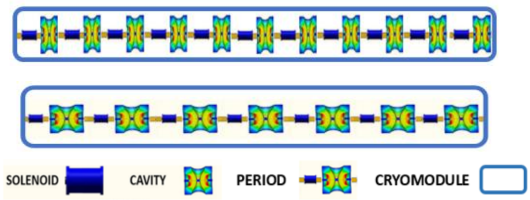


Figure 3. SSR-A (top) and SSR-B (bottom) cryomodules.

### *Beam Dynamics Studies for SC linac*

From the beam dynamics point of view, the main design criterion of the SC linac with SSRs was to minimize the emittance growth and the halo parameter when beam passes through it. This is done to avoid the possibility of beam loss induced radio activation and quenching of the cavities. To ensure minimum emittance growth and minimum halo formation, the non-equipartitioned design approach has been adopted where optimization of the phase advances is done using the fields of the cavities and solenoids. By changing the focusing field of the transverse focusing elements, the transverse phase advances have been tuned, whereas, the longitudinal phase advance is tuned using the synchronous phase and the accelerating gradient of the SC cavities [5, p. 186]. The accelerating gradient of the cavity is varied, maintaining the functional requirements of the peak surface fields, such that the structure phase advance per period is always below 90°. The synchronous phase is changed such that the beam bunch always lies inside the RF bucket [5, pp. 175-187] and the number of cavities remains minimum.

The last two cavities and two solenoids of the SSR-A section are used to match the outgoing beam to the input matched beam of SSR-B section.

## BEAM DYNAMICS SIMULATIONS

For beam dynamics studies, a fully 3D particle-in-cell code, TraceWin, has been used. All the simulations presented here start at the exit of RFQ. The beam at the exit of RFQ corresponds to 10 mA, 50 keV, and is simulated with 1 million macro particles having 3-sigma distribution [6, p. 323]at the input of the LEBT. Due to beam loss in the RFQ, the current at the entrance of the SSR-A cryomodule is 9.79 mA.

In the SC linac, the synchronous phase is ramped from -47° to -30° in SSR-A and from -30° to -21° in SSR-B, as shown in Figure 4(a). The synchronous phases of the last two SSR-A cavities are tuned to match the outgoing beam to the input of the SSR-B cavities. The phase advances per period for both transverse and longitudinal oscillations are kept below 90° as shown in Figure 4(b). In order to avoid the n = 1 resonance in the Hoffmann chart [7], phase advances in both SSR sections are varied such that the full current transverse and longitudinal phase advances do not cross each other. It can be seen in Figure 4(c) that there is a fast crossing in the Hoffman chart; this is because of matching between the two SSR sections.

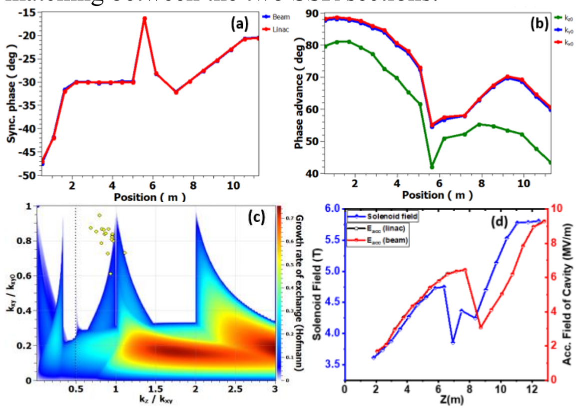

Figure 4.(a) Synchronous phase, (b) Zero current phase advances, (c) tune footprints in Hoffmann chart, and (d) Solenoid field and cavity accelerating field, along the linac.

To achieve these phase advances, solenoid gradient and cavity accelerating fields are changed as shown in Figure 4(d). As shown in Figure 5(a), the growth in emittance at the SC linac exit is 7.4%, 4.3% and 4.7% in $x-x'$, $y-y'$ and $z-z'$ plane respectively, as compared to the values at the entrance of the SC linac. The maximum halo parameter is within 1.3 for the whole linac length, as shown in Figure 5(b).

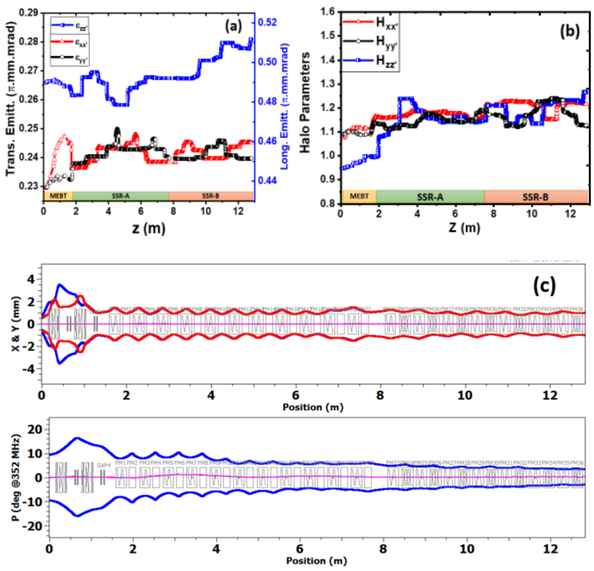

Figure 5 (a) Emittances, (b) Halo parameter, and (c) RMS envelope of the beam along the linac.

With nominal emittance and halo growth, the maximum RMS beam size for SC linac is found to be 2.12 mm at the end of the SSR-A section. Maximum RMS beam size in the MEBT is 3.86 mm. The RMS envelope for SC linac along with MEBT is shown in Figure 5(c). Final beam parameters are listed in Table 3.

Table 3. Beam parameters at the entrance to the SC linac and the exits of the SSR cryomodules.

| Beam Parameters | SC linac entrance | SSR-A exit | SSR-B exit |
|---|---|---|---|
| Beam Energy | 3 MeV | 9.92 MeV | 20.7 MeV |
| Beam Current | 9.79 mA | 9.79 mA | 9.79 mA |
| Transmission | -- | 100% | 100% |
| $\epsilon_{xx'}$ (π mm-mrad) | 0.228 | 0.242 | 0.245 |
| $\epsilon_{yy'}$ (π mm-mrad) | 0.229 | 0.244 | 0.239 |
| $\epsilon_{zz'}$ (π mm-mrad) | 0.488 | 0.497 | 0.511 |
| Halo ($H_{xx'}$) | 1.076 | 1.176 | 1.216 |
| Halo ($H_{yy'}$) | 1.091 | 1.238 | 1.128 |
| Halo ($H_{zz'}$) | 0.948 | 1.202 | 1.266 |

## CONCLUSION

Beam dynamics studies have been performed to explore the possibility of testing replacing the DTLs in LEHIPA with a superconducting post-accelerator that has two families of SSRs. This requires the LEHIPA MEBT to be modified. With the new MEBT and optimized SSR-A & SSR-B cavities, emittance growth can be kept well within 10% and halo growth can be limited to values close to one. In addition, there is no beam loss along the linac. Total length of the SSR linac is 11.2 m, which is less than that of the DTL tanks (12 m) in LEHIPA. Therefore, it will be possible to accommodate the SC post-accelerator in LEHIPA without any problem.

## REFERENCES


1. BARC External Report (BARC/2016/E/016), Mumbai, India, 2016.
2. http://irfu.cea.fr/en/Phocea/Page/index.php?id=782.
3. N. P. D Uriot, "TraceWin," CEA Saclay, 2014.
4. P. Priyadarshini, "Physics design and optimisation of SSR cavities for LEHIPA. LEHIPA/RR/2019-1," IADD, Mumbai, 2019.
5. T. P. Wangler, RF Linear accelerators, John Wiley & Sons, 2008.
6. M. Reiser, Theory and design of charged particle beams, John Wiley & Sons, 2008.
7. I. Hofmann, Phys. Rev. E, **57**, 4713(1998).

# PROGRESS ON HB650 SUPERCONDUCTING CAVITY DRESSING AND ITS INFRASTRUCTURE

Vikas Jain[1*], M. Bagre[1], S. Moulali[1], V. Vijayakumar[1], V. K. Srivastava[1], T. Maurya[1], A. Yedle[1], A. Singh[1], K. K. Singh[1], A. Puntambekar[1], S. Chandrasekharan[2], C. Grimm[2],
[1]Raja Ramanna Centre for Advanced Technology, Indore, India
[2]Fermi National Accelerator Laboratory, Batavia, IL, USA
*vikas@rrcat.gov.in

*Abstract*

Under IIFC collaboration, RRCAT is developing dressed 650 MHz 5-cell cavity. Dressing of bare superconducting RF (SCRF) cavities comprises of integrating it with encloser vessel, bellows and end caps, all made of Titanium Gr-2. Bare SCRF cavity is dressed after its performance qualification in VTS (Vertical Test Stand) and these performance parameters are sensitive and need a tight surveillance during further dressing and processing to prevent their degradation. Two types of features such as functional parameters (cavity performance) and safety parameters are important, which requires attention during dressing of SCRF cavity. A qualified SCRF cavity needs protection from any further degradation for its frequency, field flatness, voltage gradient and quality factor. Due care needs to be taken for protection of inner RF surface, support structure etc. during cavity jacketing. Important infrastructure for cavity dressing include glove box welding facility, insertion fixture unit etc. A dedicated large volume (6m$^3$) welding glove box has been designed and developed using Indian industry facilities. The environment controlled glove box welding facility has been installed and commissioned. Insertion fixture (mini bertha) has been designed, fabricated and tested with mock-assembly. RRCAT has developed TIG welding procedure for titanium welding as per code requirement. The paper presents the cavity dressing sequence with proper tooling and tests to accomplish rated performance. The paper also presents the infrastructure facilities setup at RRCAT for SCRF cavity dressing.

## INTRODUCTION

Superconducting cavity development program is aimed to develop RRCAT's strength for its superconducting LINACs for future ISNS [1]. RRCAT is collaborating with Fermilab for their PIP-II program under IIFC (Indian Institution Fermilab Collaboration). High beta (HB) cavity ($\beta$=0.92) of frequency 650 MHz has been progressed under IIFC collaboration since its conceptual design stage [2]. These HB650 cavities will increase the energy of proton from 500 MeV to 800 MeV in superconducting LINAC for PIP-II project of FNAL. Presently, 4 nos. of bare cavities have been fabricated and are under various stages of processing and VTS (Vertical Test Stand) testing at 2K. Subsequent to VTS testing, the bare cavity will be dressed.

## DRESSED HB650 CAVITY

The dressed HB650 cavity as shown in Fig. 1 consists of 4 sub-assemblies i.e. bare cavity, helium vessel, adopter ring and bellow. HB650 cavity is 1.4 m in length and 0.45 m diameter. This dressed cavity is made of high pure Nb of RRR >300, NbTi alloy and Ti grade-2 materials. HB 650 MHz dressed cavity has a total of 63 joints at various locations in bare cavity (38 nos.), helium vessel (19 nos.), bellow (2 nos.) and final assembly joints (4 nos.). All joints of bare cavity are done using electron beam welding (EBW), however helium vessel joints are completed using both EB and TIG welding. The final assembly or dressing joints uses different weld configurations using TIG welding designated as J1, J2, J3 and J4 (Fig. 2).

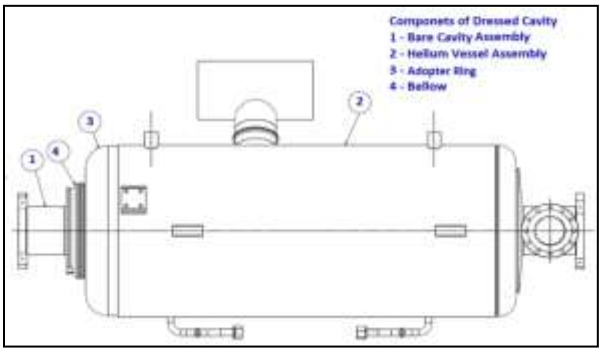


Figure 1:Dressed HB650 Cavity with various components

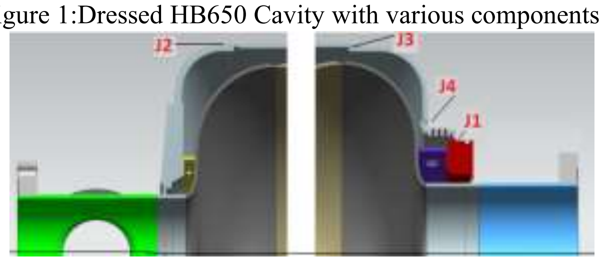


Figure 2: Cross-section of HB650 cavity showing joints at main coupler end (left) and at field probe end (right)

## CHALLENGES IN CAVITY DRESSING

Dressing of the cavity is an important stage of cavity fabrication. Protection of two types of features, viz. functional parameters (cavity performance) and safety parameters, are essential during dressing of SCRF cavity. The main challenge in dressing comes due to RF sensitivity, vacuum sensitivity and use of materials like Nb, NbTi alloy and Ti. A VTS qualified SCRF cavity needs protection from any further degradation for its frequency, field flatness, voltage gradient and quality factor. Following are main challenges of cavity dressing:-

**1. Protection of Functional Parameters**

The cavity RF sensitivity of HB650 is 160 Hz/µm and field flatness need to be maintained more than 95%, which means cavity deflection/ deformation of the order of few 100s of microns can make RF frequency out in few 10s of kHz range and field flatness degradation to less than 95%. These RF parameters pose major challenge for dressing of cavity joints J1, J2, J3 and J4 (Fig. 2) mainly due to heating of cavity cells during welding. Heating of the cavity beyond a certain limit results in plastic deformation. Due care also needs to be taken for protection of inner RF surface as it can degrade its voltage gradient and quality factor.

**2. Cavity alignment during dressing**

Alignment of cavity mechanical axis and electromagnetic axis is an important aspect of cavity dressing and a tight tolerance of ~200 microns is assigned for HB650 cavity. This requires less than 50 microns tolerance on machining of dressed cavity components.

**3. Keeping cavity protected all time**

All vacuum boundary weld joint needs to qualify for a leak rate <$1x10^{-10}$ mbar-lt/sec at room temperature and at cryogenic temperature for a dressed cavity. The dressed cavity is also tested for pressurization of upto 2 bar at room temperature as per code requirement [2, 3]. Hence the cavity need protection during vacuum tests and pressure testing using a safety bracket. Due care also required during transportation of the cavity.

Therefore any lapse/ ignorance in safety procedure during and after dressing may raze the cavity.

**4. Other issues during dressing**

Apart from the above complications, other issues are also important and needs to be taken care during cavity dressing such as weld shrinkage, weld defects (i.e. lack of penetration, porosity in weld, foreign particle inclusion, concave weld etc.), leak detection and its repair, glove box $O_2$ impurity issues, cavity handling etc.

## INFRA-STRUCTURE FOR DRESSING

Cavity dressing requires special infrastructure as described below: -

**1. Glove box or ECGB** – The environment-controlled welding inside a glove box is required to avoid oxidation in the joints of dressed cavity for welding Ti. This system is called ECGB (Environment Controlled Glove Box). Fig. 3 shows ECGB of size ~ 6m$^3$ for accommodating dressed cavity assembly for welding. It has 12 ports for gloves for welding from various locations of dressed cavity, 2 big ports for feed-through of welding cables, 2 small ports for motor and light connections, 2 ports for RF measurement feed-through for measuring cavity frequency during welding, 6 viewing windows and 2 ports for miscellaneous works. This system can be operated in manual, semi-automatic and automatic mode which can be controlled by a panel as shown Fig. 3. This displays $O_2$ and moisture level in % RH. This panel is also equipped for controlling the glove box pressure, regeneration system of the gas, rotation of cavity etc. ECGB is opened horizontally for accommodating the cavity assembly through rail system. This is also utilized for helium vessel sub-assembly joints.

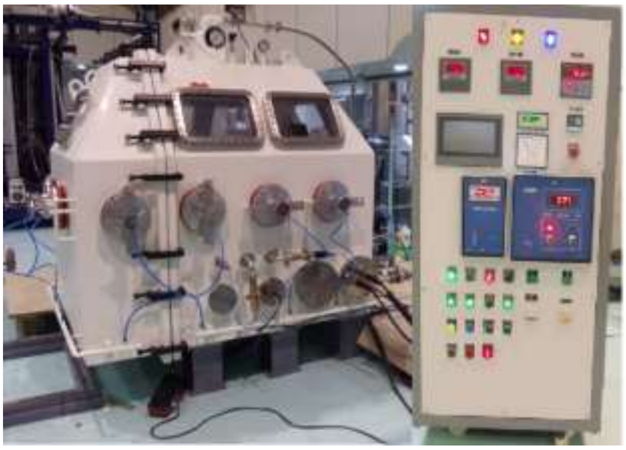

Figure 3: Environment-Controlled Glove Box for dressing of the cavity and its control panel.

**2. Insertion Fixture** – Insertion fixture also known as medium bertha, facilities in precise alignment and shimming (filling of shims between joints for concentric positioning before tacking) of bare cavity, adopter ring, bellow and helium vessel at various stages of dressing. Here the cavity is fixed on one end of ~3m long cantilever and helium vessel is rolled over the cavity as illustrated in Fig. 4.

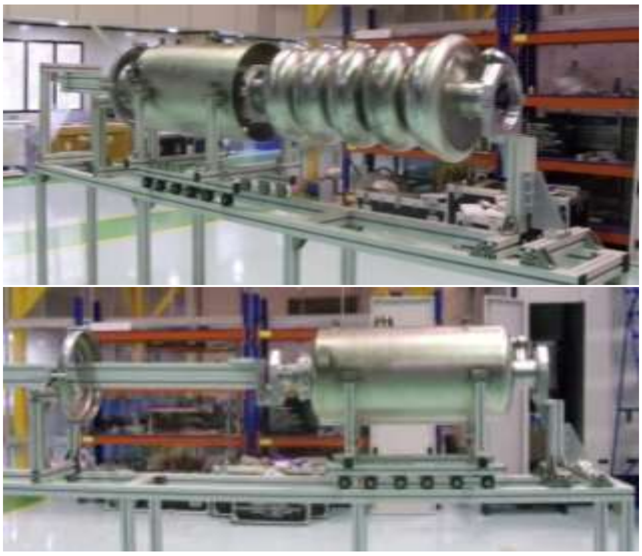

Figure 4: Insertion fixture or medium bertha

**3. Rotating cage** – This rotating cage as shown in Fig. 5 is utilized for helium vessel and dressed cavity assembly for rotation inside globe box.

Figure 5: Rotating cage showing helium vessel assembly

**4. RF frequency warning system** – This system is required during welding for protection against plastic deformation due to heating of the dressed assembly. For HB650, 100 kHz change in frequency is kept as limit for activating the alarm for warning to stop the welding.

Other infra-structures such as TIG welding machine, four bar frame structure, cavity protection brackets etc. are also needed during cavity dressing.

## PROGRESS ON CAVITY DRESSING

Components for dressed HB650 cavity are bare cavity, bellow, adopter ring and helium vessel as shown in Fig. 6. Bare cavity was fabricated using electron beam welding; all 38 different types of joints were made using RRCAT's EBW facility. Four numbers of bare cavities are fabricated and these are under different stages in processing and testing, the details of fabrication process are discussed in [4]. Bellows and end caps were fabricated in the industry and their dimensional inspection, leak testing etc. were prepared at RRCAT. Helium vessel sub-assembly components were made in various stages in industry as well as in RRCAT.

The infrastructure for dressing cavities as discussed in earlier section has been made operational. The glove box has been commissioned and achieved $O_2$ level <10 PPM and moisture level <2% RH. Preparation for joining the dressed cavity is planned in three stages; first preparation of linear weld samples and their qualification as per ASME code, second actual circular samples preparation having similar joints (J1 to J4) and mock welding inside ECGB and finally assembly of all cavity components in insertion fixture for tack welding which will be followed by full welding inside ECGB. Step 1 and 2 were completed and weld joints are qualified. The full scale circular joint trails have been completed in recently commissioned ECGB as shown in Fig. 7. The final welding of dressed cavity assembly will be taken up on VTS passed bare cavity. After dressing, the dressed cavity with safety brackets will be first vacuum leak tested for each of the joints (J1 to J4) and then it will be pressure tested at 2 bar for finalizing the dressed cavity steps.

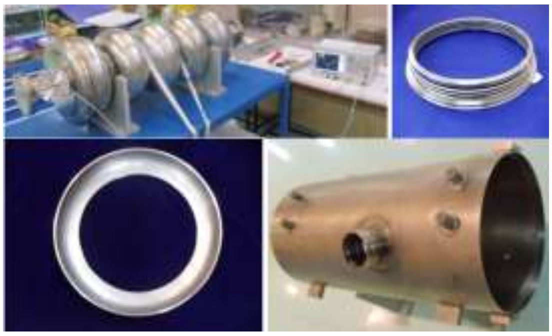

Figure 6: Bare cavity, bellow, adopter ring & helium vessel

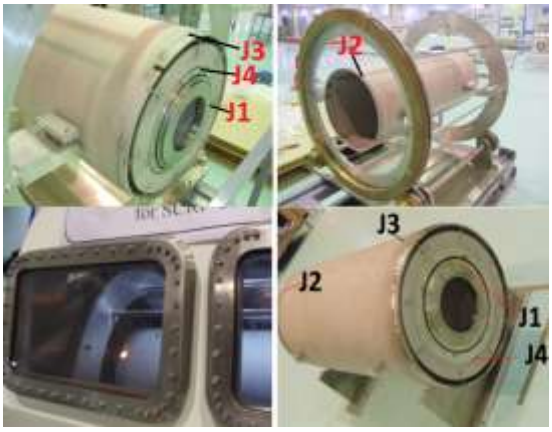


Figure 7: Preparation of mock dressing joints (J1 to J4) using dummy cylinder for welding in ECGB

## SUMMARY

Cavity dressing is an important step in dressed cavity fabrication. Infrastructure for dressing like ECGB, insertion fixture, RF frequency warning system etc. has been developed. The dressed cavity components for HB650 cavity have been fabricated. The welding trails of various joints were completed as per ASME requirement. Mock trials on Ti cylinder for various assembly joints have been completed and actual cavity dressing will be taken up next.

## ACKNOWLEDGMENT

The authors are thankful for the support given by Mr. R. Adbol, Mr. V. Verma, Mr. U. Shrivastava and Mr. K. Vaishnav.

## REFERENCES

[1] A Puntambekar, et. al.," Indigenous development of first five-cell 650 MHz SCRF cavity and series manufacturing plans", InPAC-2018, RRCAT, Indore, India

[2] V. K. Jain, et al., "650 MHz Elliptical Superconducting RF Cavities for PIP-II project", Proceedings of NAPAC2016, Chicago, IL, USA.

[3] C. Grimm, et. al. "1.3 GHz RF Nb Cavity to Ti Helium Vessel TIG Welding Process", Proceedings of SRF2009, Berlin, Germany.

[4] M. Bagre, et. al, "Experience on fabrication of 650 MHz five-cell SCRF cavities using Electron Beam Welding" in this conference.

# BEAD PULL AND RF POWER TESTING OF DRIFT TUBE LINAC (DTL) CAVITY #2 AT IUAC

V.V.V.Satyanarayana*, S.K.Kedia, Thomas Varughese and Ajith Kmar B.P.
Inter-University Accelerator Centre, New Delhi

*Abstract*

The upcoming High Current Injector (HCI) facility at Inter-University Accelerator Centre (IUAC) employs a room temperature Drift Tube Linac (DTL) to accelerate ions from 180 keV/u to 1.8 MeV/u at the output of Radio Frequency Quadrupole (RFQ), followed by a Spiral buncher. DTL consists of six room temperature Inter-digital H-type (IH) type multi-gap resonator cavities. The first cavity was installed in the beamline and successfully accelerated dc beam during recent test runs. Fabrication and assembling of DTL cavities 2 to 6 have been completed and are ready for testing. DTL #2 cavity consists of both bunching and accelerator sections in one cavity. In this cavity, there is 13 number of cells having an axial length of 69.3 cm. It is designed to operate at maximum RF power of 11 kW at 97 MHz. In the process of determining the various parameters of the cavity, bead-pull testing has been conducted to measure the electric field profile distribution inside the cavity to confirm the mechanical alignment of the inner cells is within the accuracy of 50 microns. Soon after the bead-pull test is completed vacuum system and associated interlocks have been established. After the cavity pressure measure was 6.8 x 10-8 millibar, low power testing of DTL #2 using an air-cooled RF amplifier has been initiated and it was powered up to 130 W. Later, the cavity is powered up to 6.5 kW after installing high power RF coupler and the cooling-water system is established. This paper describes the details of Bead-Pull, low power and high-power RF testing of DTL #2 cavity along with the observations and results achieved.

## INTRODUCTION

Bead pull measurement uses a non-conducting wire (like a fishing line) to pull a bead (made of dielectric/ metallic or ferromagnetic material) through a RF cavity to measure the electromagnetic field distribution on resonance inside. In the development of resonator cavities, it is required to investigate the field profile by conducting bead pull test. The field can be sampled by introducing a perturbing object and measuring the change in resonant frequency. The object must be so small that the field do not vary significantly over its largest linear dimension, and this called a perturbation method. The HCI drift tube linac (DTL) consists of six IH resonator cavities operating in cw mode at 97 MHz DTL cavity#1 is an accelerating cavity and second, third and fourth cavities includes both bunching and acceleration sections in built-in each cavity. Fifth and sixth cavities contains accelerating structures only. Bead pull test has been conducted on the cavity#2 at IUAC after completion of mechanical assembly of inside components, vacuum leak checking and Quality factor. This test has been given the data of RF field profile distribution inside the cavity as well as the idea of the mechanical alignment of drift tubes in the beam axis. Stepper motor, its controller and associated bead moving mechanism have been indigenously developed at IUAC, and the same setup has been used in the past during testing of cavity#1 parameters.

**Figure 1: DTL #2 Cavity during Mechanical assembly**

## BEAD PULL TEST SETUP

A self-excited loop (SEL) has been established to resonate the cavity. A Teflon bead is moved along the beam axis with the help of a stepper motor and supported assembly mounted on the cavity.

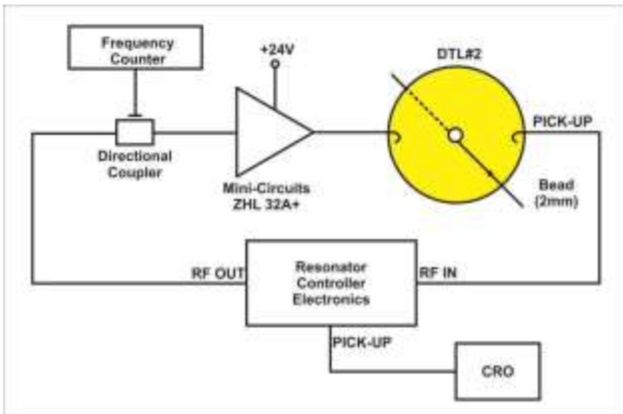


**Figure 2: Block diagram of Bead Pull Test setup**

Each time the bead is moved, frequency was measured and plotted with respect to its position along the beam axis. Figure 2 shows the block diagram of the setup used for bead pull testing. Mini Circuits model ZHL 32A+ low power RF amplifier with a gain of 25 dB and 29 dBm power output has been used to power the cavity. Self-Excited Loop (SEL) is established with the help of the cavity pickup signal and resonator controller electronics, RF amplifier and the cavity. Resonator control electronics adjusts the phase of the loop to a multiple of $360^0$ so that oscillations will takes place at the resonant frequency of the cavity. An oscilloscope is used to observe the oscillations and a HP Model 53131A Frequency counter is used to measure the frequency. A stepper motor with torque of 3 kg-cm, 0.67A at 12V has been mounted along with bead moving mechanism on one of the end plates of the cavity. A Sapphire bead of 2mm diameter is fixed on a 0.5mm thick plastic wire and this wire has been passed through a pully attached to the stepper motor and the other side of the wire is attached with a weight for stiffness of the wire. A python program will communicate with both stepper motor controller and frequency counter, each time stepper motor moved, frequency counter output will be read by this program before move the motor further. Provision of moving stepper motor in both forward and revers directions is provided in the python code. One step of the stepper motor moves the bead by a 0.6mm and almost 1150 steps are taken to complete one full move of the bead from one end of the cavity to the other end. Figure-3 shows the test setup for bead pull testing.

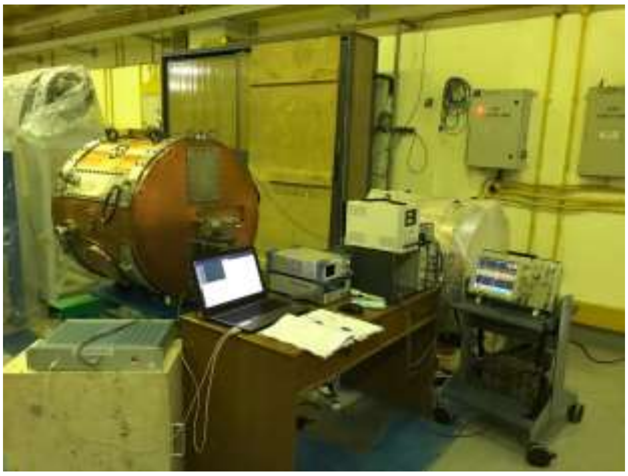

**Figure 3: Bead Pull Test Setup**

## BEAD PULL TEST RESULTS

Field profile distribution inside the cavity in forward direction of beam axis has been shown in figure 4. X-axis represents the position of the bead in number of steps of the stepper motor and Y-axis represents the frequency of the cavity in MHz.

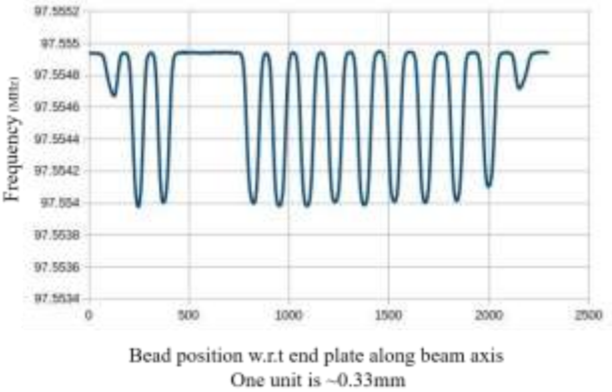


**Figure 4: Field Profile of the Cavity in beam axis**

Very small temperature raise of the cavity has been noticed and it was reflected as small frequency drift and is shown in figure 5. It was due the reason that the stepper motor's temperature was raising slightly by the time of reaching the bead from one side of the cavity to the other side, because it takes almost 20 minutes to reach the other end. Since the motor is directly mounted on one end plate of the cavity, this motor temperature is transferred to the cavity. At the same time, we have not established the cooling-water system while conducting this test. So, to minimize the temperature effect, we took the readings in the early mornings when the air conditioning system of the beam hall is more effective.

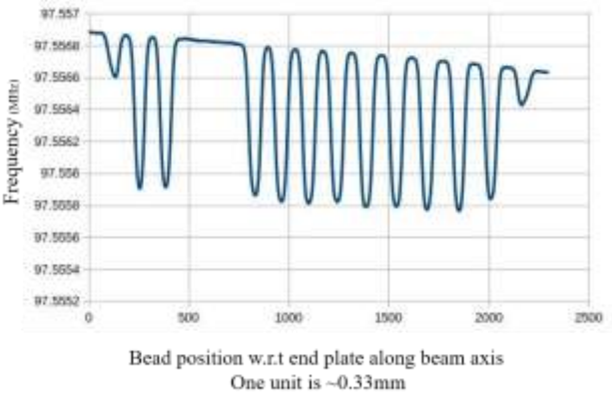


**Figure 5: Field Profile showing Frequency drift due to temperature raise of the cavity**

## RF POWER TESTING

Bead pull test results of this cavity have been confirmed the mechanical assembly of the inner accelerating components aligned with in 100 microns accuracy. RF powering has been planned after vacuum interlock and associated components have been installed. Cavity pressure was maintained better than $1.5 \times 10^{-7}$mbar. Before powering the cavity, cavity parameters have been measured and compared with the theoretical values.

Table 1: DTL#2 Measured Network Parameters

| Parameter | Measured Value |
|---|---|
| Bandwidth | 7.285 kHz |
| Frequency $f_o$ | 97.554 MHz |
| Quality Factor | 13.23856 KU |
| Loss | 52.076 dB |

Initially, the cavity was powered by using an air-cooled wide band RF amplifier (10kHz-100MHz) of Amplifier Research model 150A100B. Powering went up to ~130W with almost negligible reflected power. Cavity pressure was maintained better than $1.5 \times 10^{-7}$ mbar during this test.

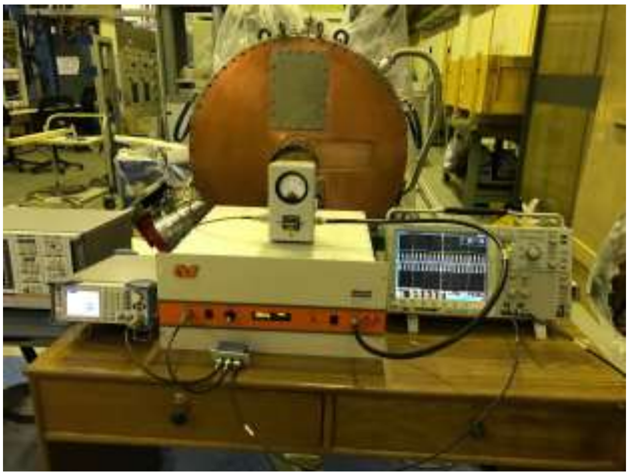

**Figure 6: Low Power Testing of DTL#2**

After low power testing is completed, power coupler and cooling-water systems were installed and once again the cavity parameters were measured before powering the cavity.

Table 2: DTL#2 Measured Network Parameters after installing RF coupler

| Parameter | Measured Value |
|---|---|
| Bandwidth | 15.975 kHz |
| Frequency $f_o$ | 97.589 MHz |
| Quality Factor | 6.10889 KU |
| Loss | 28.639 dB |

High power RF testing of the amplifier is initiated in a Self-Excited Loop (SEL) with the help of QEI, USA make 28 kW solid-state amplifier and Resonator Controller electronics and it was powered up to 6.5kW @97 MHz. During high power testing of the cavity, many times due reflected power, amplifier was tripped and finally the cavity was pulsed conditioned up to 10 kW before reaching 6.5kW CW power testing. We could not go beyond this power level due to non-availability of slow tuner and temperature monitoring were not available during this testing.

**Figure 7: High Power Testing of DTL#2**

## CONCLUSION

Bead pull test to determine the field profile distribution inside the DTL resonator cavity#2 has been completed. This test confirms the mechanical alignment of various internal components of the cavity are within the acceptable range. Field profile distribution confirms that DTL#2 cavity consists of both bunching and accelerating sections in a single cavity, theoretically. Bead pull test results of this cavity are allowed us to proceed for RF low power testing after establishing the vacuum system and associated interlock system. After RF low power testing, new RF coupler has been installed and cavity high power conditioning has been planned.

## REFERENCES


[1] RF Measurements Summary of ISAC DTL Tanks and DTL Bunchers by A.K.Mitra, TRIUMF, Vancouver, Canada at Proceedings of the 2001 Particle Accelerator Conference, Chicago.

[2] Bead-Pulling Measurement (Multi-cell Cavity Field Flatness) by Sung-Woo Lee from Oak Ridge National Laboratory.

[3] Bead-pulling Measurement Principle and Technique Used for the SRF Cavities at Jlab by Haipeng Wang.

[4] http:// www.iuac.res.in/accel/hci/dtl/index.html the (Details of DTL Proto type bead pull test).



**satya.iuac@gmail.com, vvvsatya@iuac.res.in**

# Mechanical Design of 650 MHz, beta=0.61, 5-cell, dressed SRF cavity as per functional requirement specification under IIFC collaboration

**Sundeep Ghosh[1a], Sudeshna Seth[2a], Pranab Bhattacharyya[3a], Sumit Som[4a] and Anjan Duttagupta[5a]**
*a-Variable Energy Cyclotron Centre, Department of Atomic Energy.*
*E-mail:sundeep@vecc.gov.in*

*Abstract*

VECC in presently involved in the design and development of 650 MHz low beta (β=0.61) 5-cell elliptical shape SRF cavity in collaboration with FERMILAB and other international institutes. This low beta cavity is a stepping stone for the high current, high energy proton linear accelerators required for development of ADSS and Spallation Neutron Source by DAE and for the PIP-II Project of FERMILAB. RF design of bare cavity has been completed following the technical specifications and criteria for operational parameter (LFD, dF/dP, etc) mentioned in FRS. Mechanical design of dressed cavity has been carried out in VECC taking the RF design. With an optimized stiffener ring position of 90 mm and tuner stiffness of 40 kN/mm, several finite element structural simulations of the cavity have been performed to check the safety of the cavity under normal operating and accidental loading conditions as per ASME BPV Section VIII Division 2 “Design by Analysis” guidelines.

## INTRODUCTION

DAE units are now actively involved in research and development activities on SRF cavities and associated technologies for high current, high energy proton linear accelerators, which is essential for development of ADSS and Spallation Neutron Source by DAE and for the FERMILAB PIP-II Project. Under Indian institutions-Fermilab collaboration (IIFC), VECC, Kolkata, is also involved in the design and development [1] of 650 MHz, β=0.61, 5-cell elliptical shape Superconducting RF linac cavity as per the Functional Requirement Specification (FRS) [2] consisting of specified values of EM parameters and operational parameters. An iterative process in EM design supported by teams from VECC/DAE, Fermilab and other international collaborators of Fermilab for PIP-II project, finally leads to a 5-cell elliptical shape Superconducting RF linac cavity consisting of three types of half-cells (mid-cell, end-cell and a connecting half-cell between mid and end half-cell) which satisfies different EM parameters in FRS and significantly suppresses trapped higher order modes. Using the optimized bare cavity geometry, dressed cavity model has been developed for mechanical design of dressed 650MHz cavity geometry to satisfy different operational criteria mentioned in FRS. Dressed 650MHz cavity consists of optimized bare cavity geometry with stiffener ring, helium vessel, bellows and tuner. An axisymmetric model of the dressed cavity is shown in the Figure 1. This paper describes the mechanical design of 650MHz low beta dressed cavity.

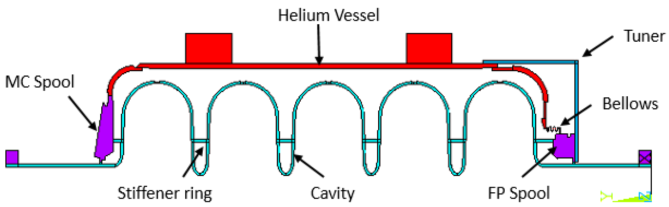


Figure 1: Several components of dressed cavity

## DESIGN METHODOLOGY

Dressed cavity model is optimized by varying cavity wall thickness, radius of stiffener rings and tuner stiffness, in order to satisfy the various operational parameters like Lorentz Force Detuning (LFD), helium pressure sensitivity (dF/dP), cavity stiffness and tuning sensitivity. This involves preparation of parametric model of the dressed cavity followed sequential EM and structural simulations to find out changes in resonant frequency modes of the cavity as it is deformed by various loads [3]. These loads correspond to Lorentz pressure, helium pressure and displacement at ends for determining LFD, dF/dP and tuning sensitivity respectively.

Variation of LFD and dF/dP with radius of stiffener rings and tuner stiffness are shown in the Figures 2-5 for simulation model of 4.2 mm cavity wall thickness. LFD, dF/dP, cavity stiffness and tuning sensitivity are found to be -2.2 Hz/ Hz/(MV/m)$^2$, 4.4 Hz/mbar, 3.1 kN/mm and 254.4 kHz/mm respectively, for wall thickness of 4.2 mm, stiffener ring radius of 100 mm and tuner stiffness of 40 kN/mm. Barring LFD all other operational parameters satisfy functional requirement specification. As VECC is going to fabricate the cavity with 4 mm of niobium sheet, structural simulations have been carried out with 3.75 mm wall thickness assuming 250 µm material removal during processing.

Final stiffener ring radius is chosen as 90 mm and the tuner stiffness is taken as 40 kN/mm. Corresponding LFD and dF/dP values for this configuration are evaluated as <2.1 Hz/(MV/m)$^2$ and <19.3 Hz/mbar respectively for cavity wall thickness of 3.75 mm. Decrease in cavity wall thickness from 4.2 mm to 3.75 mm and stiffener ring radius from 100 mm to 90 mm, will reduce cavity stiffness and increase tuning sensitivity. These two parameters at 90 mm radius thus satisfy the FRS criteria with more buffer than with 100 mm as FRS specifies cavity stiffness should be < 5 kN/mm and tuning sensitivity > 180 kN/mm.

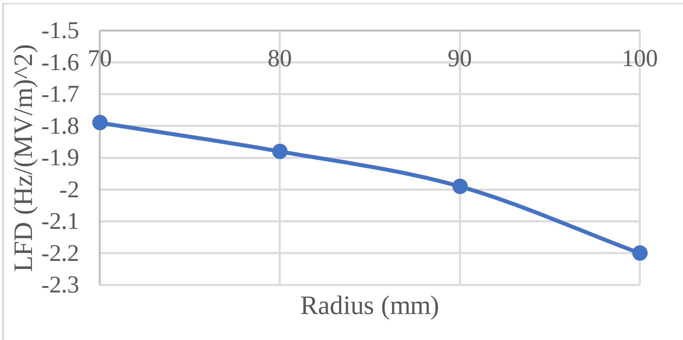


Figure 2: Variation of LFD with stiffener ring radius at fixed tuner stiffness of 40 kN/mm

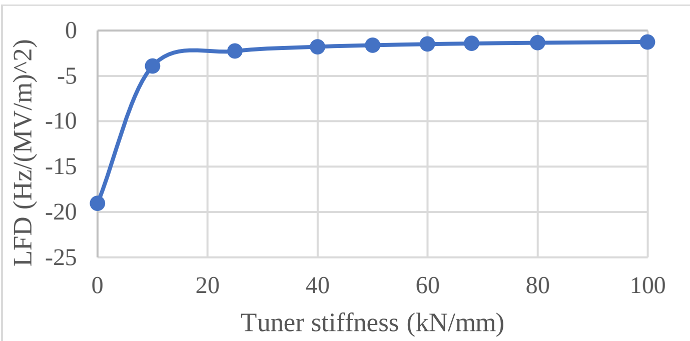


Figure 3: Variation of LFD with tuner stiffness at fixed stiffener ring radius of 70 mm

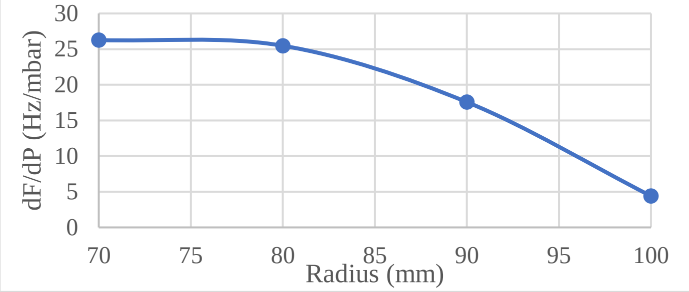


Figure 4: Variation of dF/dP with stiffener ring radius at fixed tuner stiffness of 40 kN/mm

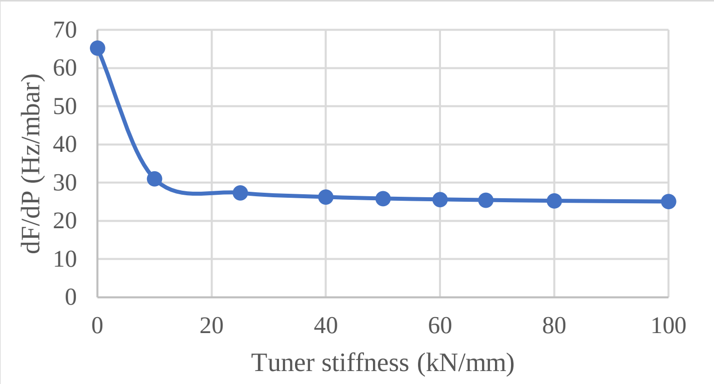


Figure 5: Variation of dF/dP with tuner stiffness at fixed stiffener ring radius of 70 mm

Magnitude of Lorentz Pressure is much higher at the iris than at the equator of the cavity [3]. As the stiffener ring is moved away from the iris the deformation near the iris also increases resulting in more frequency shift and higher LFD (Figure-2). Deformation near equator is anyhow very less compared to that that of iris. Hence, shifting the stiffener ring towards the equator (away from iris) shows no improvement on LFD. As the tuner stiffness is increased the overall system stiffness also gets increased. This causes overall lower deformation in the cavity under Lorentz Pressure and thereby reduces LFD (Figure-3). However, our study shows that making the tuner stiffness higher than 40 kN/mm gives no added advantage on LFD.

Helium pressure, unlike Lorentz Pressure, is uniform over both iris and equator of the cavity. Hence higher is the stiffener ring radius, higher is the stiffness of the cavity causing overall lower deformation and lower frequency shift. So, helium pressure sensitivity reduces with higher stiffener ring radius (Figure 4). As far as the tuner stiffness is concerned, it again has good effect (similar to LFD) on reducing dF/dP until it reaches 40 kN/mm when dF/dP remains fairly constant (Figure 5). It justifies the choice of tuner stiffness to be 40 kN/mm.

## STRUCTURAL INTEGRITY ASSESSMENT

Several safety analyses of the dressed cavity have been carried out using finite element code ANSYS [4] under various operational and accidental loading conditions of the cavity. 3D CAD model is shown in the Figure 6 along with applied boundary conditions. A simplified model of the tuner is used having hypothetical material property so that it provides an equivalent tuner stiffness of 40 kN/mm at the field probe end transition spool. Higher order 20-noded brick element is taken as the mesh element. The assembly is meshed using sweep method to obtain hexahedral dominant meshing. Mesh convergence study is performed to optimize the mesh density and to capture more accurate stress distribution across the cavity wall thickness. Chosen mesh pattern of the half-symmetry model consists of 935290 and 4418001 numbers of elements and nodes respectively. Details of all the safety analyses being performed and their results are discussed here.

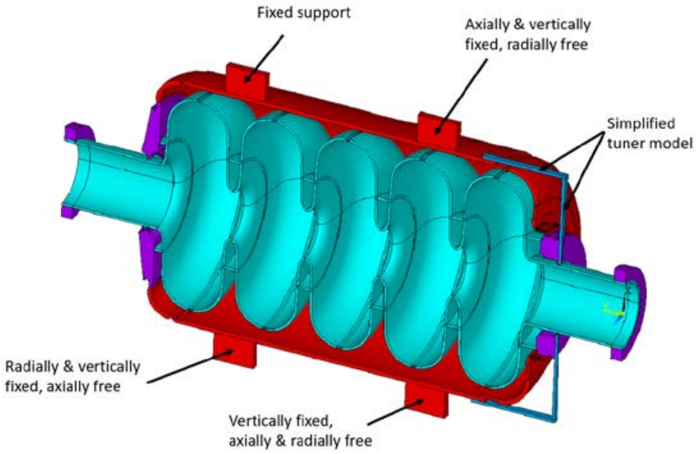


Figure 6: Solid model of dressed cavity with boundary conditions

### *Elastic Stress Analysis*

The loads on the dressed cavity consists of its self-weight, pressure exerted by helium on the external surface of cavity and inner surface of helium vessel, hydrostatic pressure head of liquid helium, thermal contraction from room temperature to 2K, compression by tuner and atmospheric air pressure. Several load cases have been envisaged taking combination of these loads, like warm pressurization, cool down, cold operation, loss of insulation vacuum, etc. It is found that the most critical condition or load case is during purging of helium gas at room temperature. Helium pressure on the dressed cavity can reach up to 2 bar during pressurization. The reason this load case is critical is because the material strength is minimum at room temperature. Steady state structural analysis of the cavity is carried out taking elastic material properties under each load case. The support lugs of the helium vessel are specified with the boundary conditions as shown in the Figure 6.

Several stress classifications lines (SCL) have been taken across the weld joint regions as shown in Figure 7. Total stress at those locations are linearly categorized into membrane and bending stresses. These linearized stresses are then compared with the allowable limits as specified in ASME BPV Code Section VIII Division 2 Subsection 5.2 depending on their potential to cause failure, as given below.

$$P_m \leq S$$
$$P_l \leq 1.5\ S$$
$$P_m + P_b \leq 1.5\ S$$
$$P_m + P_b + Q \leq 3.0\ S$$

where,

$P_m$: Primary Membrane Stress
$P_l$: Primary Local Membrane Stress
$P_b$: Primary Bending Stress
Q: Secondary Stress
S: Allowable Stress for material.

Equivalent stress distribution in the cavity vessel the most critical load case is shown in Figure 8. Excluding sharp corners and regions of singularities the maximum equivalent stress in the Nb cavity is found to be ~ 24 MPa which is less than the Yield Strength of Nb at room temperature (38 MPa). It can be seen from the figure that maximum stress in the cavity is generated around the weld joints between the stiffener rings and the half cells. Linearized stress pattern across such a location (SCL-K in Figure 7) is plotted in Figure 9. Since SCL-K is a region of gross structural discontinuity, the membrane stress at this location is compared with the local membrane stress limit (1.5S) as per ASME, whereas the membrane plus bending stress is compared with the secondary stress limit (3S).

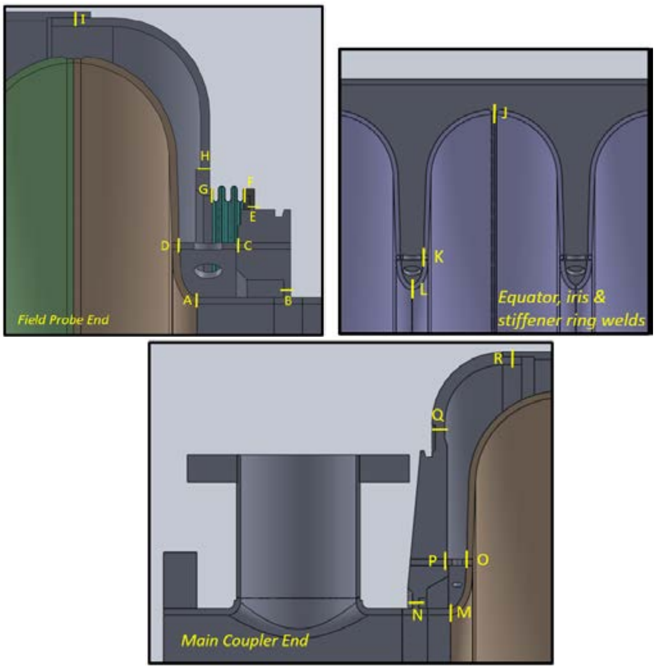


Figure 7: Location of SCLs

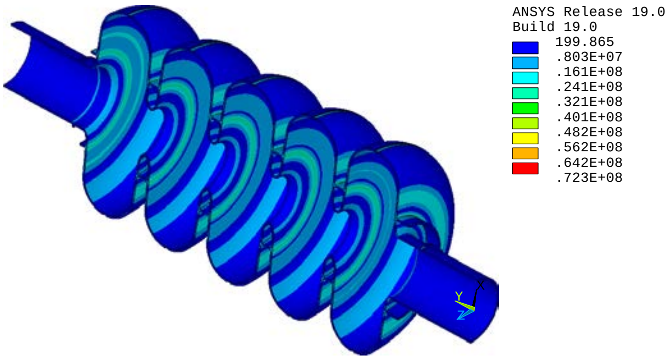


Figure 8: Von-Mises stress distribution in cavity during warm pressurization

Stress results at SCL-K under the warm pressurization condition are as follows:

$$P_l = 12.61 \leq 1.5S \text{ (22.5 MPa)}$$

$$P_m + P_b \text{ (equivalent to Q)} = 24.27 \leq 3S \text{ (45 MPa)}$$

It may be noted that the allowable strength (S) of the welded joint in the above comparison relation is obtained by multiplying the unwelded strength of Nb at room temperature (which is conservatively taken as 25 MPa) with a weld joint efficiency with 60%. Stress results for other load cases at 2K are also found to be well within the allowable limits. These load cases also have an added advantage of higher material strength than at room temperature.

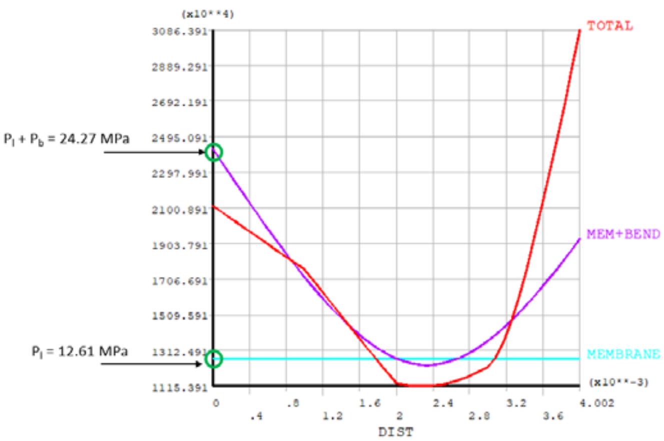


Figure 9: Linearized stress plot at SCL-K during warm pressurization (units in Pa)

## *Limit Load Analysis*

A safety check has been carried out to find out the plastic collapse pressure of the cavity under the most critical load case which is warm pressurization at 300 K. This is done by performing a limit load analysis in which the material property of Nb is assumed elastic and perfectly plastic with no strain-hardening after yielding (zero tangent modulus). Pressure inside the helium chamber is gradually increased over the analysis load steps as shown in the Figure 10. Boundary conditions are left similar to the elastic analysis.

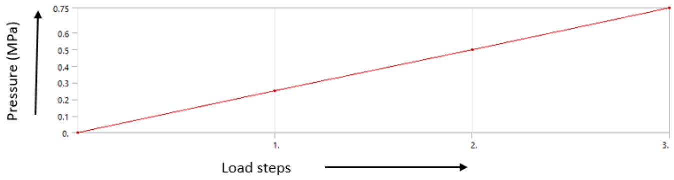


Figure 10: Variation of pressure load (MPa) with time for Limit Load Analysis

It is found that the simulation failed to converge once the pressure on the cavity exceeded 0.5 MPa. Taking a Factor of Safety of 1.5 the MAWP comes as 0.33 MPa. The unaveraged stress distribution in the cavity for last converged pressure is shown in Figure 11. The figure clearly depicts that full section yielding has occurred near the junction of stiffener rings with the half-cells. Upon further increase of pressure, the cavity lost its load carrying capacity and the solution did not converge. Considering another 20% deduction in MAWP for additional buffer, the final MAWP of the cavity is found to be 0.266 MPa which is still 30% higher than the applicable MAWP (0.205 MPa) at room temperature. This simulation study thus ensures the safety of the cavity under warm pressurization.

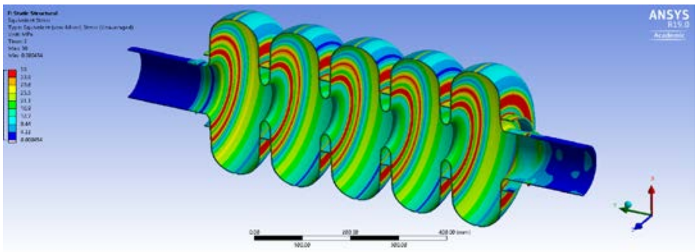


Figure 11: Von-Mises stress distribution in cavity at last converged solution

## *Buckling Analysis*

ASME Section VIII Division 2 Subsection 5.4 provides guidelines for protection against collapse from buckling. A linear elastic buckling analysis of niobium cavity is performed by applying external pressure on the cavity surface. Only the bare cavity assembly has been used and fixed boundary conditions are applied at the end flanges. Buckling calculations for helium vessel and bellows are carried out separately using design by rules based on Section VIII Division 1, so buckling analysis is not performed for these components. The lowest predicted buckled shape of cavity is shown in Figure 12. The critical pressure is found to be 12.3 MPa. Applying a design factor of 16, the critical buckling pressure comes out to be 0.77 MPa, which is 3 times higher than the MAWP of 0.205 MPa at room temperature.

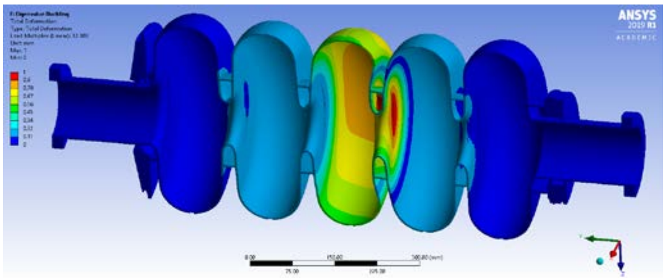


Figure. 12: First buckling mode shape at 12.3 MPa

### *Protection Against Local Failure*

The dressed cavity is checked for protection against local failure. As per ASME Section VIII Division 2 Subsection 5.3 guidelines, protection against local failure is ensured if the following condition is satisfied:

$$\sigma 1 + \sigma 2 + \sigma 3 \leq 4S$$

where, σ1, σ2 and σ3 are the principal stresses at any point in the assembly and S is the allowable stress for material at operating temperature. The simulation results of the static structural analysis under several load cases discussed earlier have been processed to obtain the sum of the three principal stresses. The results are found to be within allowable limits.

### *Fatigue Assessment*

In order to carry out the fatigue assessment of the dressed cavity the guidelines mentioned in ASME Sec VIII Div. 2 Part 5 have been followed. The load history of the cavity is determined at first which consists of pressurization, cool down and tuning cycles. The estimated numbers for cycle are as follows.

(a) Pressurization (NΔP) = 200
(b) Cool Down (NΔT) = 100
(c) Tuning (NΔTuner) = 200

Niobium cavity being an integral construction having no attachment or nozzles, the applicable criteria for fatigue assessment as per Code is as follows.

$$N\Delta FP + N\Delta PO + N\Delta TE + N\Delta T\alpha \leq 1000$$

Sum of all cycles for the dressed cavity is 500, which is less than 1000. Fatigue criteria is thus satisfied for the dressed cavity assembly and no other detailed fatigue assessment is necessary.

### *Modal Analysis*

Modal analysis of dressed cavity assembly is carried out to evaluate mechanical frequencies and mode shapes. The finite element model and boundary conditions similar to the static structural analysis is used here. Material properties corresponding to 293 K are applied. Some of the mode shapes with frequencies less 100 Hz are shown in the Figure 13.

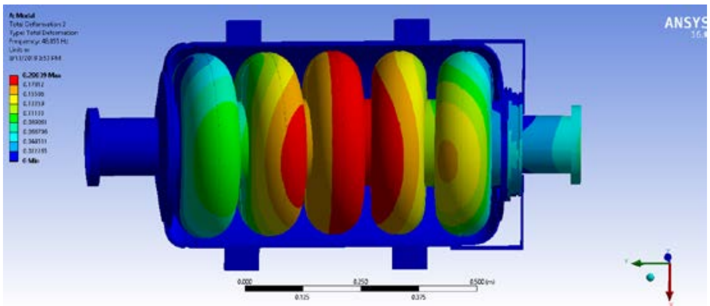


(a)

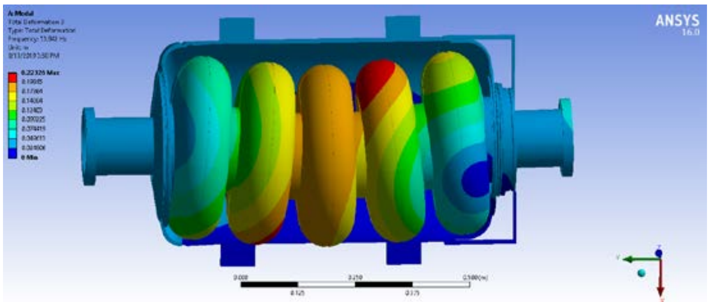


(b)

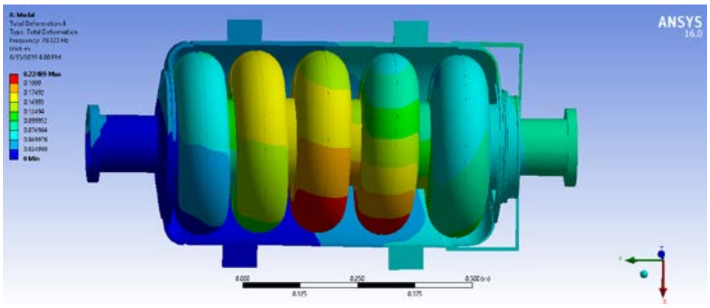


(c)

Figure 13: Mode shapes and frequencies; (a) first transverse mode at 49 Hz, (b) second transverse mode at 54 Hz, (c) first longitudinal mode at 78 Hz

## CONCLUSION

The present design consists of single stiffener ring at the same radius for all half cells. This design satisfies all operational parameters as per FRS except the LFD criteria which it exceeds by some margin. Initially, it is found out that with double stiffener rings at mid-cell, it is possible to bring down LFD within the specified limit [5]. However, the double stiffener ring cavity will be very difficult to manufacture within the desired accuracy level as demanded by SRF technology. Hence it was proposed to continue with a single stiffer ring. If the cavity is operated only in CW mode instead of Pulse mode, then the LFD criteria can be relaxed in FRS, in which case, this LFD value gets satisfied. As far as the structural integrity of the dressed cavity is concerned, the present design with single stiffener ring is found to be structurally safe under all possible operational and accidental loading conditions. The dressed cavity is also safe from plastic collapse, buckling, fatigue and local failure.

## REFERENCES

[1] S. Seth, et Al., "Test Result Of 650 MHz, Beta=0.61, Single Cell Niobium Cavity", SRF2017, LANZHOU, CHINA

[2] Functional Requirement Specification 650 MHz, Beta =.61 Dressed Cavity, TeamCenter documentED0001834,https://sangam.barc.gov.in/

[3] S. Ghosh, et. Al.," Sensitivity Study of 650MHz Five Cell SRF Cavity Under Lorentz Force", InPAC2015

[4] ANSYS, Inc. http://www.ansys.com

[5] S. Seth, et Al., " Design of 650 MHz, beta=0.61, 5-cell,dressed SRF cavity as per functional requirement specification under IIFC collaboration", InPAC2018

# RF SET POINT STUDY FOR LEHIPA DTL USING THE PHASE SCAN METHOD

Aman Bajaj*, SVLS Rao and Shweta Roy
[1]Bhabha Atomic Research Centre, 400085, Mumbai, India

*Abstract*

The Drift Tube Linac (DTL) of the Low Energy High Intensity Proton Accelerator (LEHIPA) is used to accelerate proton beam from 3 MeV to 20 MeV. The phase scan method is a common technique used to determine the RF set point i.e. the RF amplitude and phase; it also determines the input energy of beam to the DTL. We have generated the phase scan curves for Tank 1 of LEHIPA, using the PARMILA code, by varying the tank RF phase and observing the output beam phase for different values of tank RF amplitude and input energy offset to the beam. Comparing the measured phase dependence with the generated data using chi square minimization, we can tune the RF amplitude and phase. In this paper we present results for Tank 1 of LEHIPA DTL by using the simulated test experimental data generated by PARMILA, to tune the DTL tank during commissioning to within the required accuracy of 1 degree in phase and 1% in amplitude.

## INTRODUCTION

The Low Energy High Intensity Proton Accelerator (LEHIPA) being built at BARC comprises a 50 keV ECR ion source, a 3 MeV Radio Frequency Quadrupole (RFQ) and a 20 MeV DTL operating at frequency of 352 MHz [1]. The LEHIPA DTL is a 12-metre long structure, divided into four, three metre long segments. The first DTL tank (DTL Tank 1) which accelerates the beam from 3.031 MeV to 6.9174 MeV is considered for simulations in this paper.

The phase scan signature curve for a DTL tank is a curve which represents the phase of a Radio Frequency (RF) signal induced by the beam in a Beam Position Monitor (BPM) at the tank exit as a function of the phase of electromagnetic fields within the DTL tank [2]. The phase scan method is used to determine the tuning parameters such as tank electric field and tank RF phase. It also determines the input energy of the beam to the DTL tank. The determination of the RF set point, i.e. tank electric field amplitude and phase of each DTL tank, is one of the important steps during the commissioning of the DTL tank. The RF set point is determined by comparing the measured experimental data of beam phase as a function of tank RF phase with the theoretical curves generated from simulations [3].

In this paper we present results of simulations done on the LEHIPA DTL Tank 1 to develop a procedure to determine the RF set point by using the PARMILA [4] code. Simulated experiments are done using the PARMILA code to generate experimental data; these are compared with the theoretical curves to validate the procedure for RF set point determination for the LEHIPA DTL.

* amanbajaj@barc.gov.in

## SIMULATION METHOD

Simulation experiments are done on LEHIPA DTL Tank 1 which accelerates the beam from 3.031 MeV to 6.9174 MeV to obtain the experimental results of beam phase as a function of RF tank phase using PARMILA. In the PARMILA simulations we have varied the RF amplitude from 0.90 to 1.10 in steps of 0.01, where 0.90 means 90% of the design tank amplitude. The input energy deviation of beam to the tank is varied from -100 keV to +50 keV in steps of 10 keV. Now the tank RF phase is varied from $-20^o$ to $+20^o$ in steps of $2^o$ and beam phase is determined for each value of tank amplitude and input energy deviation. Phase scan curves are obtained by polynomial fitting of 10th order in beam phase as a function of tank RF phase for different values of tank amplitude and input energy deviation.

$$\phi_{Beam} = a_n(\phi_{RF}^n)$$

where n = 0 to 10.

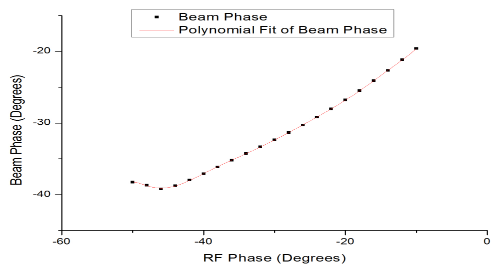


Figure 1: Beam phase at tank exit as a function of tank RF phase for amplitude 1.0 and input energy deviation 0 keV.

In our simulations we have taken five different cases where we have given some random change in design tank amplitude and deviation in the energy of incoming beam. For each case we have simulated the beam phase at the tank exit for different values of tank RF phase. Now the simulation data for all the five cases is compared with the fitted beam phase curves to determine RF set point.

## RESULTS OF PHASE SCAN METHOD

Simulation results are obtained of the beam phase at the tank exit for different RF phase shift with respect to the synchronous phase. Figure 2 shows the beam phase curves

for tank amplitudes of 0.94, 0.98, 1.00, 1.02 and 1.06 and fixed input energy deviation of -20 keV.
Figure 3 shows the beam phase curves at tank amplitudes of 0.94, 0.98, 1.00, 1.02 and 1.06 and without any deviation in the design input energy. There isn't much difference in the beam phase curves for the two cases.

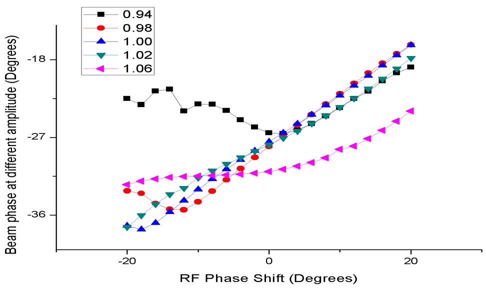


Figure 2: Beam phase at tank exit as a function of tank RF phase shift for different tank amplitudes and fixed input energy deviation of -20 keV.

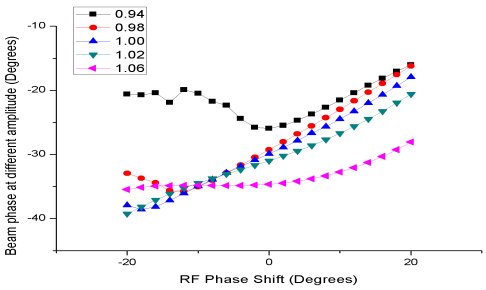


Figure 3: Beam phase at tank exit as a function of tank RF phase shift for different tank amplitudes and 0 keV input energy deviation.

Similarly Figure 4 and Figure 5 show the beam phase curves for different input energy deviation of -40 keV, -20 keV, 0 keV, +20 keV and +40 keV and at tank amplitude of 0.98 and 1.02 respectively. As shown in the figures the difference between beam phase curves increases as the amplitude increases.

In order to determine the RF set point by comparing the simulation data generated with the simulated beam phase curves, we have calculated the $\chi^2$ value with all the simulated beam phase curves of fixed amplitude and input energy deviation. Now the minimum of the $\chi^2$ corresponds to the desired tank amplitude and input energy deviation of the beam.

$$\chi^2 = \sum_{i=1}^{N} (BeamPhaseExp - BeamPhaseSim)^2 \qquad (1)$$

In order to verify the procedure for RF set point determination five examples are studied with some random shift in the

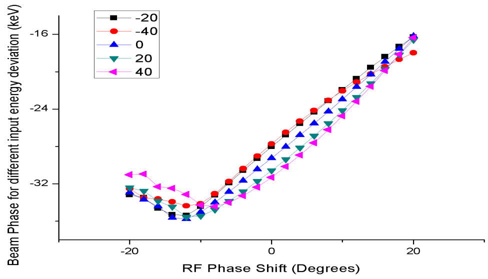


Figure 4: Beam phase at tank exit as a function of tank RF phase shift for different input energy deviation and 0.98 tank amplitude.

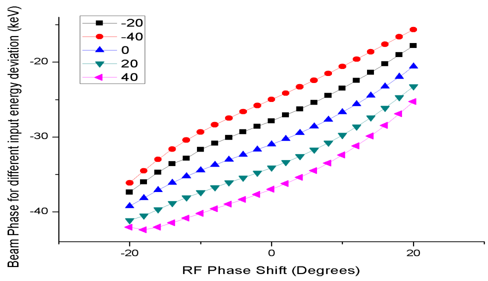


Figure 5: Beam phase at tank exit as a function of tank RF phase shift for different input energy deviation and 1.02 tank amplitude.

design amplitude and input energy. Results for five different examples are shown in Table 1 and Table 2. The determined RF set point values are close to the set values in all the cases.

Table 1: Set value and determined value of tank amplitude for different test examples.

| S.no. | Experiment Set Value | Determined Value |
|---|---|---|
| Case One | 0.973 | 0.97 |
| Case Two | 1.042 | 1.04 |
| Case Three | 0.937 | 0.94 |
| Case Four | 1.02 | 1.02 |
| Case Five | 0.984 | 0.98 |

Table 2: Set value and determined value of input energy deviation of beam for different test examples.

| S.no. | Experiment Set Value | Determined Value |
|---|---|---|
| Case One | - 26 keV | - 20 keV |
| Case Two | - 42 keV | - 40 keV |
| Case Three | + 36 keV | + 40 keV |
| Case Four | - 73 keV | - 70 keV |
| Case Five | - 12 keV | - 10 keV |

Figure 6 shows the variation of the $\chi^2$ with the tank amplitude at fixed value of the determined input energy deviation of beam for Case One; the minimum of the $\chi^2$ is the desired tank amplitude. Similarly Figure 7 shows the variation of the $\chi^2$ with the input energy deviation at fixed value of the determined tank amplitude.

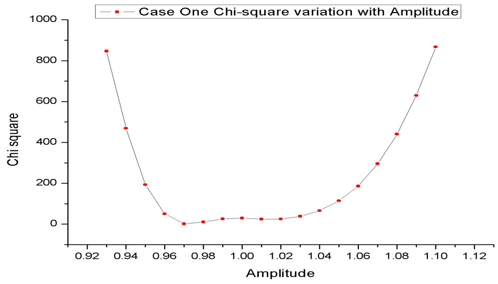


Figure 6: Chi-square variation with tank RF amplitude for case one example.

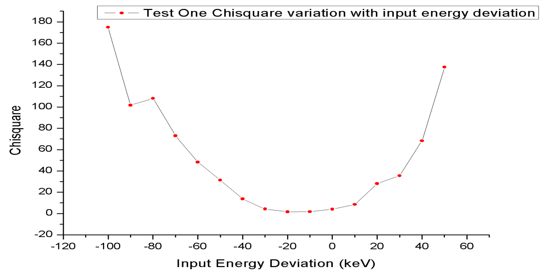


Figure 7: Chi-square variation with input energy deviation for case one example.

Once the RF set point is determined, the RF synchronous phase of the tank need to be determined. As the tank amplitude and input energy of the beam are now different from the design values, the synchronous phase need to be shifted from its design value such that the output energy of the beam from the tank is the same as the desired output energy of the tank. The RF phase is determined by using linear interpolation of the output beam energy with the tank RF phase. The RF phase at which the beam energy is same as the design output energy is the required RF phase shift in the design synchronous phase. Figure 8 shows the variation of beam energy with the shift in RF phase, from the linear interpolation the required shift in synchronous RF phase is $-4.62^o$ for Case Three in which the calculated tank amplitude is 0.94 and deviation in input energy is +40 keV. After determining the RF set point i.e. tank amplitude,

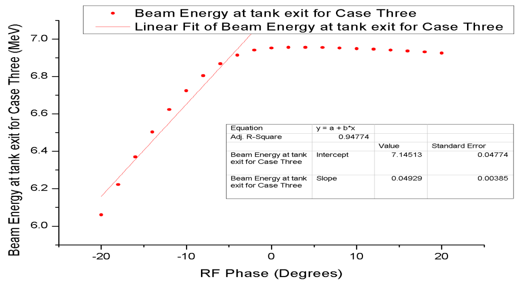


Figure 8: Output beam energy variation with the RF phase shift for tank amplitude 0.94 and input energy deviation of +40 keV.

input energy and the required RF phase shift, the tuning of LEHIPA DTL Tank 1 is complete. The determined value of amplitude is within the required accuracy of 1% and the input energy of beam is within the accuracy of 10 keV. Using the similar procedure we can tune the next DTL tank.

## CONCLUSION

We have studied the phase scan method to determine the RF set point for the LEHIPA DTL. The determination of RF set point is one of the important steps during the commissioning of the DTL tank. The procedure for tuning of DTL tank is explained and simulation results done on DTL Tank 1 of LEHIPA are shown for five different cases of the simulation experiment done using PARMILA. The determined value of amplitude is within the required accuracy of 1%, and the input energy determined is within the accuracy of 10 keV.

## ACKNOWLEDGMENTS


We would like to thank Dr. Jose V. Mathew for his guidance and support.


## REFERENCES


[1] Rao, S. V. L. S., and P. Singh. "High power accelerator development program at BARC." *Proceedings of the DAE-BRNS Indian particle accelerator conference. 2011.*

[2] Owens, T. L., et al. "Phase scan signature matching for linac tuning." *Proceedings of International Conference on Particle Accelerators.* IEEE, 1993.

[3] Jang, Ji-Ho, et al. "RF Set-up Scheme for PEFP DTL." *the proceedings of IPAC* 3835.2012 (2012): 2013.

[4] H. Takeda, "PARMILA", *LANL Report* LA-UR-98-4478 (2005).

# SIMULATION OF REBUNCHER RESONATORS AS ACCELERATING CAVITIES USING OPTIMUM PHASE FOCUSSING TECHNIQUE.

J Karmakar*, A Pandey, A Rai, A Sharma, B Karmakar, B K Sahu, D S Mathuria, G K Chaudhari, P Patra, R N Dutt, S Ghosh.

Inter-University Accelerator Centre (IUAC), Aruna Asaf Ali Marg, New Delhi- 110067, India

*joyamu13@gmail.com

*Abstract*

The Superconducting LINAC at IUAC consists of a Superbuncher (SB) to time focus the beam from 1-2 ns to 100-200 ps at the first accelerating module, followed by two more accelerating modules and finally the Rebuncher (RB) cryostat which time focus the beam at the target location. With the implementation of intelligently selecting the accelerating phases of the resonators on either positive or negative slope of the RF, acceptable time focus has been achieved at the experimental area without the use of RB resonators. With the above scheme the RB is not required for time focussing, and therefore can be used as accelerating resonators to boost the energy further. Present simulation study showed that RB resonators can be used as accelerating cavities, along with achieving acceptable time and energy focus. However, to make it happen in an optimum way the orientation of the longitudinal phase space before the RB plays an important role. The paper describes a detailed study of using the RB resonators as accelerating resonators.

## INTRODUCTION

The LINAC at IUAC consists of five cryostats viz. Superbuncher(SB) with one quarter wave resonator (QWR), three accelerating modules each with 8 QWRs and the last cryostat is the Rebuncher(RB) with two QWRs (figure 1) [1][2]. While the SB and the RB are operated at $0^o$ phase for longitudinal focussing of the beam at the first LINAC accelerating module and the experimental area respectively, the 24 accelerating QWRs are conventionally operated at $70^o$ (or $80^o$) accelerating phase which is also called Conventional Phase focussing (CPF). With the implementation of Optimum Phase Focussing (OPF) technique where some of the accelerating QWRs are operated at $110^o$ (negative RF slope) instead of $70^o$ (positive RF slope) [3][4][5], the energy and time spread at the experimental area can be minimized within acceptable limits without the use of RB. A higher beam transmission is also achieved with OPF compared to CPF. The OPF phase combination is obtained from running a FORTRAN code that does $2^n$ phase combinations of $70^o$ and $110^o$, where n is the number of accelerating QWRs. With the application of OPF scheme in the last LINAC operation, the use of RB could be avoided for longitudinal focussing along with increased beam transmission [6].

Utilizing the RB cavities as accelerating QWRs during OPF implementation to LINAC can be an optimum option for further energy gain. The feasibility for the same has been explored by simulations, which reveals that the RB can be used in accelerating mode and achieve acceptable energy and time spread, provided the longitudinal phase space at the RB has a suitable orientation.

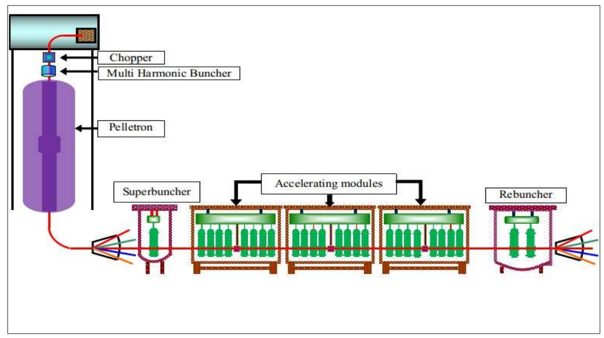


Figure1: Pelletron LINAC system at IUAC.

## DEPENDANCIES FOR TIME AND ENERGY FOCUS FROM RB

Longitudinal focussing and defocussing in general can be explained by the orientations of phase-space (figure 2) before a cavity (assuming the cavity phase is on the positive slope i.e. the field is rising with time). For phase space (PS) orientations in II[nd] quadrant as the blue one in figure 2, the higher energy particles arrive before and the lower energy particles arrive later at the QWR and is thus suitable for time focussing. Where as, for the orientations in I[st] quadrant as the orange one, the arrival of the higher and lower energy particles is reversed and will result in time defocussing.

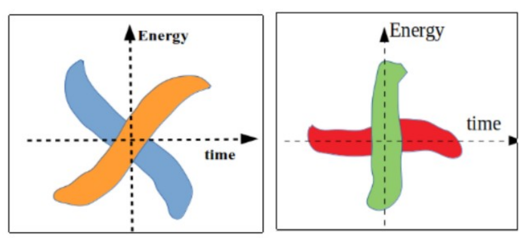


Figure 2: Different phase space orientations at a QWR.

Now assuming the PS orientation at RB is suitable for time focus (as the blue one), a reduction in energy spread can also be achieved at the experimental station (~10m from RB). This reduction in energy spread depends on the Δt and the $\Delta E_{old}$ at RB, and the resonator field. An equation stating the above can be derived for RB and is given below.

$$\Delta E=\left|\Delta E_{old}+q.E.d.TTF.\left[\sin\left(\varphi_o-\frac{\Delta t}{2}\right)-\sin\left(\varphi_o+\frac{\Delta t}{2}\right)\right]\right| \quad -(1)$$

Where, $\varphi_o$ is the synchronous phase of cavity,
$\Delta t$ is the time spread at the QWR entrance
$\Delta E_{old}$ is the energy spread at the QWR entrance
$q, E, d, TTF$ are respectively charge, QWR field, QWR effective length and the Transit time factor.

The ΔE from RB will increase or decrease depending upon the sign and magnitude of second term wrt first term in equation (1).

Now, assuming $\Delta E_{old}$ greater than magnitude of second term then,
$\Delta E < \Delta E_{old}$ if $[\mathrm{Sin}(\varphi_o - \Delta t/2) - \mathrm{Sin}(\varphi_o + \Delta t/2)] < 0$
i.e. if $-\pi/2 < \varphi_o < \pi/2$ (bunching slope)

It should be noted that for the above to be realized the Δt should not be large enough such that a later portion of the bunch see the debunching slope (i.e. beyond 90º), else the reduction in ΔE will be inefficient. For example at the synchronous phase of 70º the time spread of beam bunch should be within ~ ±0.5ns about synchronous phase, else a part of the bunch will fall on the debunching slope.

Now, if $\Delta E_{old}$ is very small (less than half magnitude of second term) then,
$\Delta E > \Delta E_{old}$ even if $[\mathrm{Sin}(\varphi_o - \Delta t/2) - \mathrm{Sin}(\varphi_o + \Delta t/2)] < 0$.

For a vertical PS orientation as in green the particles with different energies arrive at ~ same time and thus will see ~same field, and therefore $\Delta E \geq \Delta E_{old}$. The Δt for such case will also increase. Finally, for the horizontal orientation in red, the particles arrive with ~ same energy at different times, thus will see different cavity fields resulting $\Delta E > \Delta E_{old}$. The Δt for such case will decrease (assuming the QWR phase is on the positive slope).

## SIMULATION STUDIES

To explore the possibility of using RB as accelerating QWRs, the following OPF cases has been studied.

Case1: OPF of 26 QWRs (24 of LINAC & 2 of RB) optimized for minimum Δt at experimental area (NAND – National Array for Neutron Detectors).

Case2: OPF of LINAC QWRs optimized for minimum Δt at RB + RB as accelerating QWRs optimized for minimum Δt at NAND.

Case3: OPF of LINAC QWRs optimized for minimum Δt at NAND + RB as accelerating QWRs optimized for minimum Δt at NAND.

The simulations are done using the FORTRAN code that is used to find OPF combinations during LINAC operation. The parameters of the OPF cases are then used for validating the FORTRAN results using the General Particle Tracer (GPT) [7] code. To speed up FORTRAN OPF simulations, particles only on the periphery of the longitudinal phase space are considered, which is valid as the acceleration process through LINAC can be considered adiabatic, and hence Liouville's theorem will hold throughout [8].

For the simulations a pelletron beam of 122MeV $^{28}Si^{11+}$ with full ΔE ~ 30keV and full Δt ~ 1.6 ns has been used. A field of 3MV/m is used for all the accelerating QWRs. The accelerating phase pair of 70º /110º is used for OPF calculations. For comparing the final ΔE & Δt of the three cases at the experimental area (which is ~ 35m from SB), the simulation of LINAC in OPF mode with RB put off has been done for reference and the variation of ΔE & Δt is shown in figure 3.

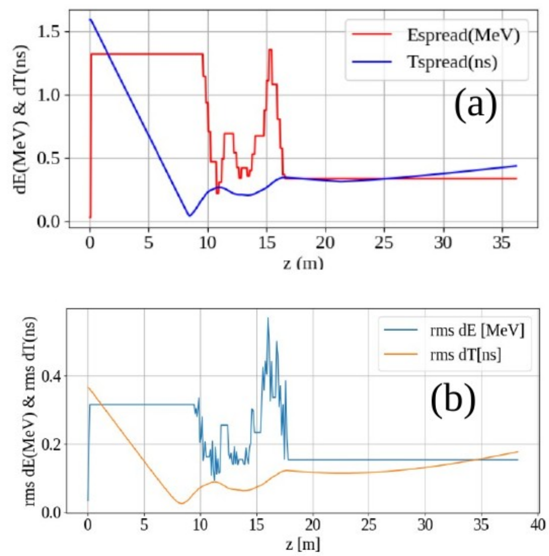


Figure 3: Variation of ΔE & Δt for OPF of LINAC QWRs with RB put off (reference case). (a) Results (base to base spreads) obtained from FORTRAN code. (b) Results (rms values) obtained from GPT. (base to base spread ~ 4 * rms value)

Table 1: Comparison of ΔE & Δt (at expt. Area) for the three OPF cases.

| | OPF with RB as accel. QWR | | | | | | OPF w/o RB | |
|---|---|---|---|---|---|---|---|---|
| | Case 1 | | Case 2 | | Case 3 | | Ref. case | |
| | Fortran | GPT | Fortran | GPT | Fortran | GPT | Fortran | GPT |
| ΔE (MeV) | 0.25 | 0.4 | 0.65 | 1.2 | 0.6 | 1.2 | 0.4 | 0.6 |
| Δt (ns) | 0.4 | 0.48 | 0.35 | 0.4 | 0.2 | 0.4 | 0.45 | 0.6 |
| $E_{total}$ (MeV) | 231 | 231 | 231 | 231 | 231 | 231 | 223 | 223 |

The results obtained from both FORTRAN code and GPT for the three cases is shown respectively in the three columns of figure 4 and also in Table 1. The ΔE from GPT is higher than what is obtained from FORTRAN code. This is expected as GPT is a particle tracking code and considers a finite beam transverse size and transverse momentum spread. The off-axis beam particles see a different electric

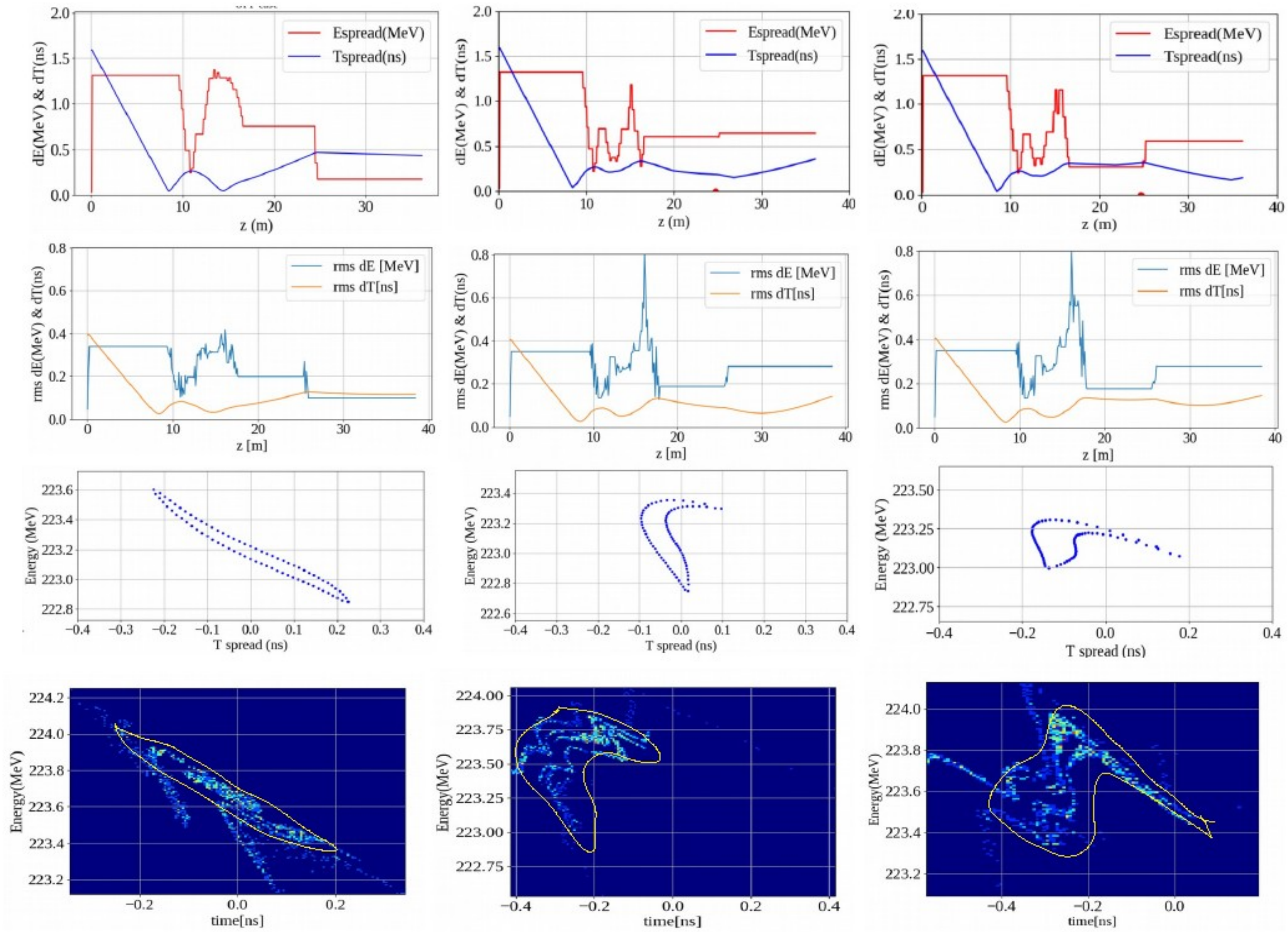


Case 1 Case2 Case 3

Figure 4: Simulation results of the three cases in three columns respectively. The first and second row are variation in ΔE & Δt through distance obtained from FORTRAN code and GPT respectively. The third and fourth rows shows the longitudinal phase space before RB obtained from FORTRAN and GPT respectively.

field than the on -axis particles and results in an additional energy spread. The FORTRAN code does not have any transverse consideration and all the particles see identical accelerating fields.

## DISCUSSION OF RESULTS

The simulations with RB as accelerating QWRs shows that apart from an increased energy gain, an acceptable Δt better than the reference case (OPF with RB put off) is achievable for all three cases as is evident from table 1. For the sake of comparison Case 3 gives the minimum Δt, where as Case 1 gives minimum ΔE. As a smaller ΔE gives a better beam transmission, Case 1 may be treated as the optimum way to accelerate the beam using 26 QWRs of LINAC and RB. This is the case where the phase space orientation (figure 4, 1$^{st}$ column, 3$^{rd}$ and 4$^{th}$ row) is similar to the blue orientation of Figure 2, and thus achieves simultaneous energy and time focus. It should be noted that the optimum choice out of the three cases is beam dependent and needs to be simulated for different beam species. The simulation results from both FORTRAN code and GPT are in reasonably good agreement, and the final verification can be done with actual beam during the upcoming LINAC operation.

## REFERENCES

[1] D. Kanjilal et al, Nucl. Instr. And Meth. A328 (1993), 97-100

[2] S.Ghosh et al, Physical Review Special Topic – Accelerator and Beams, 12, 040101

[3] V. Nanal et al, Proceedings of HIAT09, TH-07, p. 174(2009).

[4] S. Ghosh et al, proceedings of HIAT12, p. 185 (2012)

[5] J. Karmakar et al, proceedings of InPAC18, ID 206 .

[6] S.Ghosh et al, proceedings of InPAC18, ID 260.

[7] General Particle Tracer, http://www.pulsar.nl/gpt

[8] Thomas P. Wrangler, 'RF Linear Accelerators'

# PROGRESS OF THE UNDULATOR FOR DELHI LIGHT SOURCE (DLS) THZ RADIATION FACILITY

S. Tripathi*#, S. Ghosh, J. Karmakar, M. Aggarwal and A.C. Pandey
Inter-University Accelerator Centre (IUAC), New Delhi, India.
# Diamond Light Source Ltd, Diamond House, Didcot,Oxfordshire, UK.
A. Schoeps, P. Neumann, P. Vagin, M. Tischer
Deutsches Elektronen-Synchrotron (DESY), Hamburg, Germany.
E. Rial and J. Bahrdt
Helmholtz-Zentrum Berlin, BESSY II, Albert-Einstein-Straße 15, 12489 Berlin,Germany.

*Abstract*

A compact Free Electron Laser facility to produce coherent THz radiation is in the stage of commissioning at Inter-University Accelerator Centre (IUAC), New Delhi. A low emittance electron beam with 4-8 MeV range will be injected in to the undulator to produce THz radiation in the frequency range of ~ 0.18 to 3 THz. The undulator was designed by using 3D RADIA computer code.

An offer was received from Helmholtz-Zentrum Berlin (HZB), also known as BESSY, to use one of their spare undulator to produce THz radiation in the Delhi Light Source (DLS) project of IUAC. The parameters of HZB's magnet was very similar to the undulator what was designed for DLS. The recent magnetic measurements of HZB's undulator have been analyzed and has been found out satisfactory. In this paper, a brief description of the design calculation of the DLS's undulator along with the details of the magnetic field measurement of HZB's undulator will be reported.

## INTRODUCTION

The compact light source project at IUAC, known as DLS, is in the commissioning stage. In the facility, a normal conducting (NC) photocathode electron gun will be used to generate the pre-bunched electron beam which will be injected in to a compact undulator magnet to produce THz radiation [1,2]. The layout of the facility is reported in this conference [3]. Permanent magnet technology, both pure permanent magnet and hybrid design, is most common for undulator of several cm period length, while electromagnetic devices are usually built for longer period length. For a planar type undulator, the magnetic field is in the form of $B_0\, Sin(2\pi y/\lambda_u)$, where $\lambda_u$ is period length and $B_o$ the peak field amplitude of the undulator. This radiation has high intensity and the radiation concentrates into a narrow band spectrum at the fundamental wavelength of

$$\lambda = \frac{\lambda_u}{2\gamma^2}\left(1 + \frac{K^2}{2} + \gamma^2\theta^2\right) \qquad (1)$$

where $\lambda_u$ is period length of undulator, γ is Lorentz factor, and θ is observation angle. The undulator parameter $K$, representing the undulator strength, can be written as $K = 0.934 \times B_0\,(T) \times \lambda_u(cm)$ ; where $B_0$ is magnetic field at the undulator mid-plane.

Within a limited range of $g/\lambda_U$, the magnetic peak field $B$, as a function of gap $g$ and period length $\lambda_u$ can be approximated by

$$B = a\, exp\left(b\,\frac{g}{\lambda_u} + c\left(\frac{g}{\lambda_u}\right)^2\right) \qquad (2)$$

Where both $B$ and $a$ are expressed in the unit of Tesla and $b$ and $c$ are dimensionless coefficients.

## UNDULATOR DESIGN FOR DLS

The undulator for the Delhi Light Source (U50-DLS) has been designed using the code RADIA [4] with 30 periods (50 mm period length) and with the working gap varying between 16 to 45 mm corresponding to the peak magnetic field of 0.6 to 0.1 T respectively.

The undulator has magnet block of 80 mm wide, 55 mm high and 19 mm thick with 5 mm × 5 mm square cuts at the corners for clamping the block with the holders. The Vanadium Permendur poles used in this design has got a dimension of 60 mm (W), 45 mm (H) and 6 mm (T). The end sections are designed and optimised with the configuration of in terms of end pole strength [5]. The end section consists of two magnet blocks and two end poles separated by air spaces. The inner 2nd last end magnet block has the same shape as the full-size blocks, but the thickness is reduced to 75% of the thickness of the full-size blocks while the last end magnet has 25% of thickness as compared to regular magnet block. There is air space between the 2nd last magnet block & the 2nd last end pole as well as between last magnet & last pole. The shape of both end poles is identical to full size poles. The transverse field roll-off depends strongly on the transverse width of the undulator. A flat transverse roll-off reduces the higher order integrated multipoles over the good field region and reduces the effect of dynamic field integrals. In this design the width of the magnet and pole has been selected to assure a good-field region of ±10 mm about the central axis of the undulator as recommended by the beam optics calculation. The percentage of the roll-off with respect to the on-axis field at transverse positions of ±5 mm, ±10 mm, and ±20 mm is 0.05, 0.25, 2.92 and 0.30, 1.39, 8.74 percent at closed (20 mm) and open (45 mm) gap, respectively. More details of the design of the Undulator can be found in the proceedings of InPAC2018 [5].

* Email : stri_29sep@yahoo.co.in

`

## PROCUREMENT OF THE UNDULATOR

Once the design of the undulator was frozen, communication with the well reputed undulator company had been started to procure the undulator. During this time, an offer was received from our collaborator of DESY, related to the availability of a spare Undulator from HZB, Germany. It was found out that this spare undulator has got similar parameters to the designed one performed for DLS. The magnetic field measurement was recently done on the spare undulator and it was found to be in same old condition. The designed parameters of the designed undulator for DLS along with the spare undulator of HZB are shown in table-2.

Table–2. The parameters of designed & spare undulator

| **Technology** | **Designed Undulator for DLS: Hybrid , anti-symmetric** | **Available Undulator from HZB: PPM, Symmetric** |
|---|---|---|
| Magnet | Permanent NdFeB magnet ($B_r$ =1.21T) | Permanent NdFeB magnet ($B_r$ =1.21T) |
| Pole | Vanadium permendur | Not Applicable |
| Magnetic gap | 20 - 45 (mm) | 16-45 (mm) |
| Period length | 50 mm | 48 |
| No of Periods | 28 (Full) | 32 (Full) |
| Magnetic field | 0.62 - 0.11 (T) | 0.6 - 0.09 (T) |
| Undulator parameter (K) | 2.89 - 0.51 | 2.79 - 0.41 |
| Beam line height | 1.1 m | 0.5 m |
| Device length | ~1.5 m | ~ 1.7 m |

The HZB's undulator offered to IUAC has a period length of 48 mm, was built in symmetric configuration. The undulator magnet blocks are 70 mm wide, 22 mm high and 12 mm thick with 5 mm cuts at the corners with 45º angle for clamping the block with the holders. The end sections were designed and optimized with the configuration of 1/2 terms of end magnet. But by using this end configuration trajectory will get some offset from axis and for which we need some corrector coils. To make the undulator suitable for the use in DLS; with the help of RADIA [4], the end structure was modified and 1/4 magnet was added to cancel the end termination to make no offset for the trajectory. A full five period miniature model undulator of HZB with and without end-structure modification along with the magnetic fields, first integral and second integral are shown in figure 1.

The picture of the spare undulator of HZB is shown in figure 2 where the movement of the jaws of the undulator are shown in the vertical direction however, in actual operation, the jaws will move in the horizontal direction. The magnetic measurements were performed at HZB to validate the performance of the undulator. The peak magnetic field at the minimum operational gap of 16 mm was measured as 0.61 T, the plot of the vertical and horizontal magnetic fields for different gaps are shown in figure 3. The plot of the first integral to estimate the angle of deflection at the exit of the undulator and the second integral to measure the deviation of electron beam from its axis at the exit of the undulator both are shown in figure 4. After subtracting the linear background, the trajectory of the electrons at 8 MeV is plotted in figure 5. The phase error [6] of the undulator is shown in figure 6.

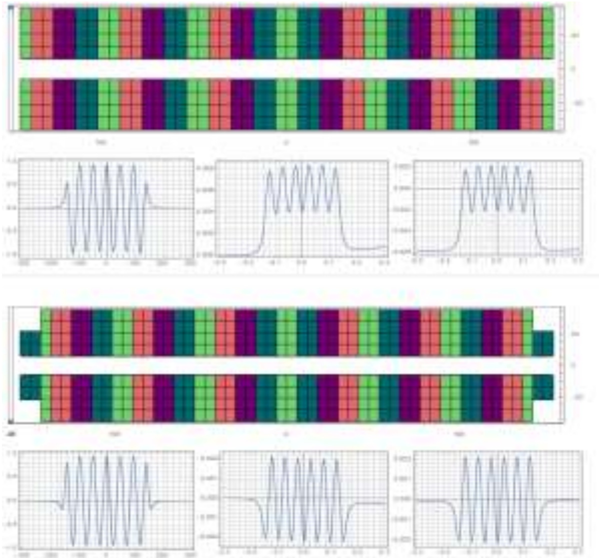

Figure 1. Top and bottom pair of figures represents the original and modified magnet end configuration along with the magnetic fields, first and second integral of the spare undulator of HZR

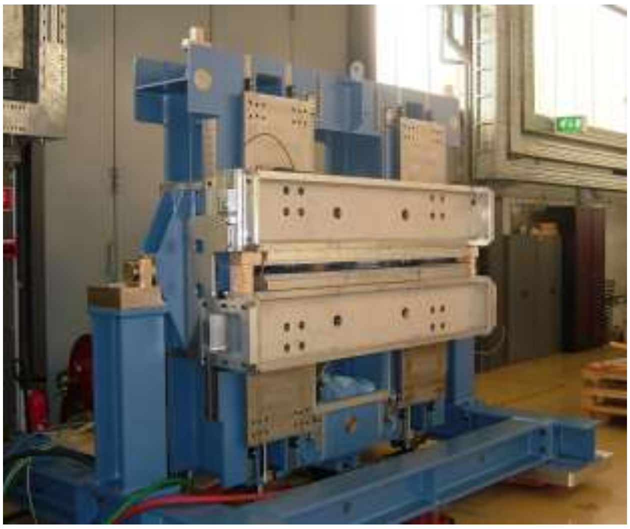

Figure 2: U48 undulator of HZB (Upward direction)

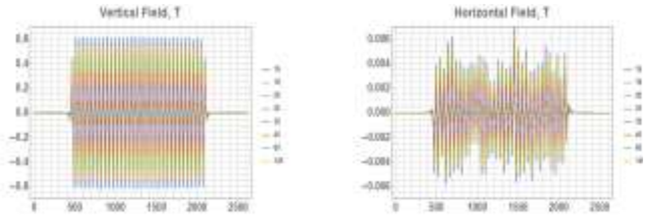


Figure 3: Magnetic field measurement (y-axis) with longitudinal distance z (x-axis) at different gaps. Here the vertical direction is the direction of moving jaws, while the horizontal direction is perpendicular to the jaw movement and the beam propagation.

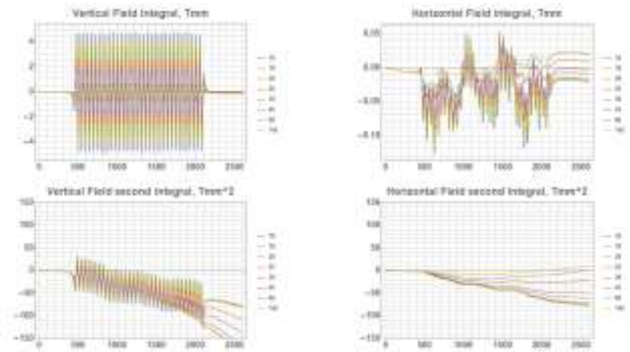

Figure 4: First and Second field integral for U48 undulator at different gaps.

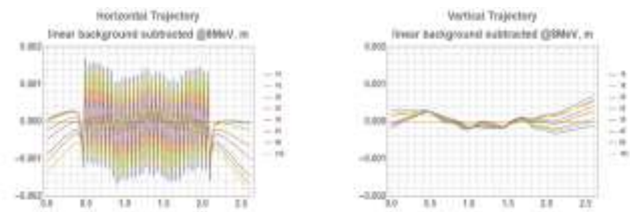


Figure 5: Trajectory plotted for U48 undulator for different gaps at 8MeV.

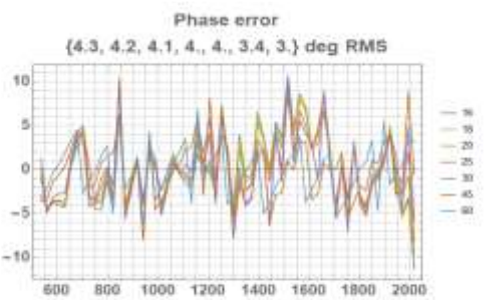


Figure 6: Phase error for U48 undulator at different gaps.

The undulator will be shifted from HZB to DESY for performing a few refurbishment jobs e.g. (i) a couple of linear encoders will be installed for accurate setting of the gaps of the undulator (ii) set of corrector coils will be installed to be able to correct the electron beam axis (iii) to perform a detail measurement of the magnetic field of the undulator and to fine tune it, if necessary and (iv) to install a new beam pipe along the axis of the undulator. All jobs are expected to be performed by the end of 2019 and at the beginning of 2020, the undulator should be shipped to IUAC.

## CONCLUSION

To produce the THz radiation from the compact FEL facility of IUAC, an undulator had been designed in the past. An undulator lying as spare at HZB, Germany has been found to be very close with the design parameters of the undulator of DLS project. The undulator has been offered by HZB to IUAC to install and to use it to produce THz radiation. The undulator needs minor refurbishment which will be done at DESY by the end of 2019. Then it will be shipped and will be installed in the beam line of DLS by the beginning of 2020.

## ACKNOWLEDGEMENT

Help received during the magnetic measurement from the staff of DESY and HZB, Germany other than the authors are highly appreciated and acknowledged.

## REFERENCES

[1] S. Ghosh *et al*., Nuclear Instruments and Methods in Physics Research – B 402, (2017), page 358-363
[2] S. Ghosh *et al*., *Proc. of this conference InPAC 2019.*
[3] P. Patra *et al*., *Proc. of this conference InPAC 2019.*
[4] RADIA, Online. Available: http://www.esrf.eu/Accelerators/groups/Insertion Devices/Software/Radia.
[5] S. Tripathi *et al., Proc. of InPAC 2018*.
[6] Richard P. Walker; PRST - Accelerators and Beams 16, 010704 (2013).

# OPTIMIZATION OF HIGHER HARMONIC RF CAVITY PARAMETERS FOR ENHANCHING THE TOUSCHEK BEAM LIFETIME IN THE STORAGE RING OF HBSRS

Deepak Kumar Tyagi†, Pradeep Kumar, A. D. Ghodke, RRCAT, Indore, India

*Abstract*

The objective of lattice design of electron storage ring for High Brightness Synchrotron Radiation Source (HBSRS) is to keep very small transverse dimensions of the circulating electron bunches for producing extremely high bright synchrotron light. The large angle intra-beam coulomb scattering due to very small transverse beam size causes short Touschek beam lifetime which is a great concern in HBSRS. In order to increase the Touschek beam lifetime a bunch lengthening RF cavity, operating at higher multiple of main RF frequency which is also known as higher harmonic cavity (HHC), is necessarily required along with the main RF cavity in HBSRS. In this paper, we report the analytical estimations of higher harmonic cavity parameters those are required for bunch lengthening in HBSRS. We also report the simulation to study the effect of passive third harmonic RF cavity on the bunch length and beam energy spread using tentative lattice parameters of HBSRS. The results show that rms bunch length will enlarge up to six times whereas energy spread remains unchanged for the optimum condition of flat potential due to harmonic RF cavity in HBSRS.

## INTRODUCTION

In order to explore the possibility for developing a high brightness synchrotron radiation source (HBSRS) in India, design study is under consideration and a preliminary candidate lattice has been evolved [1]. Alike its contemporary low emittance storage rings under design or commissioning phase such as ESRF-EBS, APS, MAX-IV etc. [2, 5-6], the beam lifetime in HBSRS is affected due to large angle intra beam (Touschek) scattering. In Touschek scattering when two electrons with in a bunch perform betatron oscillations, the transverse momenta of one electron transfer to the longitudinal one of the other. If the new longitudinal momenta of the second electron is larger than the momentum acceptance of the storage ring, it is lost. This effect becomes more intensive in an electron storage ring such as HBSRS where the charge density per bunch is very high due to small transverse beam dimensions and high beam current.

In order to improve the Touschek beam lifetime there are two options: either increase the momentum acceptance or dilute the bunch charge density. The first option is not practically possible as the momentum acceptance is limited by the storage ring lattice and also require high power source. The second option that is dilution of bunch charge density cannot be opted for transverse plane as it will degrade the photon beam brightness. Thus only longitudinal plane remains available for the bunch charge density manipulation. In the longitudinal plane however bunch charge density can be decreased by coherently exciting the synchrotron oscillations but this method is unfavourable as it increases the average energy spread of the beam which is not desirable for its effect on undulator harmonics. Another method of lowering the bunch charge density is to elongate the bunch by using a higher harmonic cavity, basic theory of which is described in [3]. The voltage of the harmonic cavity is added to the voltage of the main RF cavity in such a way that a bunch sees the net voltage with the reduced slope, which helps in the bunch lengthening. The maximum bunch lengthening is obtained at an optimum condition when the slope of the total voltage is completely zero. Harmonic cavity is operated at a frequency which is an integer multiple of the main RF frequency and do not take part in the acceleration of the beam. The voltage in the harmonic cavity is generated either by the beam itself (Passive mode) or a separate RF generator is used (Active mode). Both types of harmonic cavity have been used in other synchrotron radiation facilities [4-6] despite the fact that the optimum bunch lengthening can be achieved at a particular stored current in passive mode.

Apart from the bunch lengthening, a harmonic cavity also serve a purpose of curing the coupled bunch beam instabilities in a storage ring as it increases the synchrotron frequency spread which helps in Landau Damping. Long bunches also help in increasing the single bunch threshold current and keeping the heat load due to induced electromagnetic field in vacuum chamber elements within the tolerance limits. On the other hand harmonic cavity can be used for bunch shortening which has its important application for conducting the time resolved experiments by synchrotron radiation users.

In the present article, we have analysed the effect of $3^{rd}$ harmonic cavity (passive mode) on the bunch length in the storage ring of HBSRS. Tracking simulation has been performed using the computer code MBTRACK [7]. The effect of the bunch lengthening on the Touschek beam lifetime is also calculated.

†dktyagi@rrcat.gov.in

## BEAM DYNAMICS IN PRESENCE OF HIGHER HARMONIC CAVITY

Suppose a storage ring which consists of both the main RF cavity and a higher harmonic cavity. The complete RF voltage experienced by the bunch in presence of the harmonic cavity is given by

$$V_T = V_o[Sin(\varphi + \varphi_s) + kSin(n\varphi + n\varphi_h)] - U_o \qquad (1)$$

Where $V_0$: RF voltage in main cavity, $k$: Ratio of voltages in the higher harmonic cavity to the main RF cavity i.e. $V_h/V_0$, $\varphi_s$: Synchronous RF phase, $V_h$ and $\varphi_h$ is the RF voltage and phase in harmonic cavity, $\varphi = \omega_{RF}t$ and $U_o$ is the energy loss/turn. For lengthening a bunch, it is required to reduce the slope of the accelerating voltage near the synchronous phase. This can be achieved by proper adjustment of the phase of harmonic cavity voltage in such a way that it cancel out the slope of main RF cavity voltage. The optimum conditions that yields longest bunch are described by Hofmann [3] and can be obtained under the condition that first and second derivative of total voltage is zero i.e. $V_T' = 0$ *and* $V_T'' = 0$. From these conditions we obtain-

$$k = \sqrt{\frac{1}{n^2} - \frac{\left(\frac{U_0}{V_0}\right)^2}{n^2 - 1}} \qquad (2a)$$

$$Sin\varphi_s = \frac{n^2}{(n^2 - 1)}\frac{U_0}{V_0} \qquad (2b)$$

$$\tan(n\varphi_h) = \frac{\frac{nU_0}{V_0}}{\sqrt{(n^2 - 1)^2 - \left(\frac{n^2 U_0}{V_0}\right)^2}} \qquad (2c)$$

Considering the third harmonic cavity (n=3) and taking the parameters of HBSRS as given in table 1, the above values comes to be $k = 0.290$, $n\varphi_h = 13.06^0, \varphi_s = 145^0$.

Table 1: HBSRS storage ring (main parameters)

| Parameter | Unit | Value |
|---|---|---|
| Beam Current ($I_0$) | mA | 200 |
| Beam energy ($E_0$) | GeV | 6.0 |
| Circumference ($C$) | m | 1068.94 |
| Beam Emittance ($\varepsilon_x$) | pm.rad | ~150 |
| RF Voltage ($V_0$) | MV | 5.0 |
| RF Frequency ($f_{RF}$) | MHz | 100.124 |
| Harmonic Number ($h$) | - | 357 |
| Bunch Length ($\sigma_{\tau,0}$) | ps | 25 |
| Energy Spread ($\sigma_{\delta,0}$) | - | 9.6 x $10^{-4}$ |
| RF acceptance | % | 12 |
| Energy Loss/turn ($U_0$) | MeV | 2.548 |

### *Harmonic cavity operation in passive mode*

If we assume uniform bunch filling in the storage ring, the voltage induced by beam in the harmonic cavity is [8]-

$$V_h(\varphi) = -2I_0 F R_{sh} Cos\psi_h Cos(n\varphi - \psi_h) \qquad (3)$$

Where, $I_0$: being the stored current, $R_{sh}$: Cavity shunt impedance, $F$: Bunch form factor and $\psi_h$: Harmonic cavity tuning angle.

$R_{sh} = {V^2}/{2P}$ With V being the developed voltage and P is the beam power loss.

$\psi_h = arctan\left[2Q\frac{\Delta f}{f_r}\right]$, $\Delta f = nf_{rf} - f_r$ = Cavity detuning, where Q: Quality factor and $f_r$: Harmonic cavity resonance frequency. The relation between cavity detuning angle and phase in harmonic cavity is $\psi_h = \frac{\pi}{2} + n\varphi_h$ . In table 2 the basic parameters of harmonic cavity in HBSRS are depicted.

Table 2: Basic parameters of 3rd harmonic cavity for HBSRS

| Parameter | Value |
|---|---|
| Voltage (MV) | 1.45 |
| Quality factor | 21600 |
| Shunt impedance (MΩ) | 16.7 |
| Detuning frequency (kHz) | -29.97 |

## TRACKING SIMULATIONS

The multi particle tracking code 'mbtrack' was used for tracking. Ten thousand particles/bunch were Gaussian distributed in six dimensional phase space and tracked for 15000 turns which is more than four damping times in the storage ring of HBSRS. To study the effect of harmonic cavity on bunch length only longitudinal plane was chosen for tracking. The starting bunch length of 25ps elongates up to more than 150ps after few thousand turns. The parameters of 3HC matched with the theoretical values. In figure 1, the voltage seen by the bunch and its shape at the equilibrium with the sum of main RF and HC voltage are shown at calculated values of quality factor, shunt impedance and cavity detuning. The bunch adopts the quadratic shape for electron distribution.

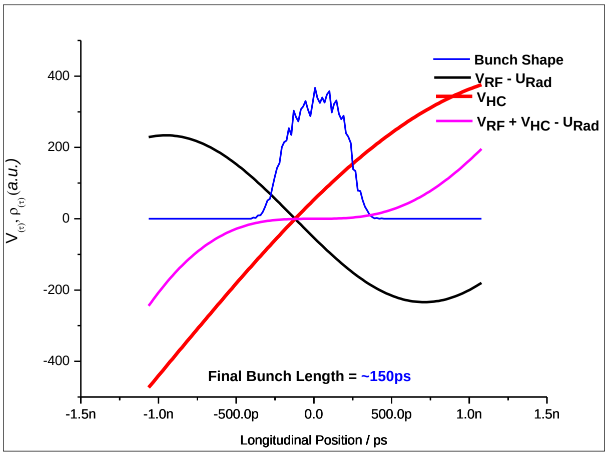


Figure-1: Bunch length under the influence of 3rd harmonic cavity

The beam filling process in presence of harmonic cavity was simulated as follows. We start with low beam current and increase it by 10mA in every 15000 turns. The increasing beam induced voltage in harmonic cavity increases bunch length from 25ps to 150ps at nominal beam current of 200mA. The effect on the bunch length over current due to the increasing harmonic cavity potential is shown in figure 2.

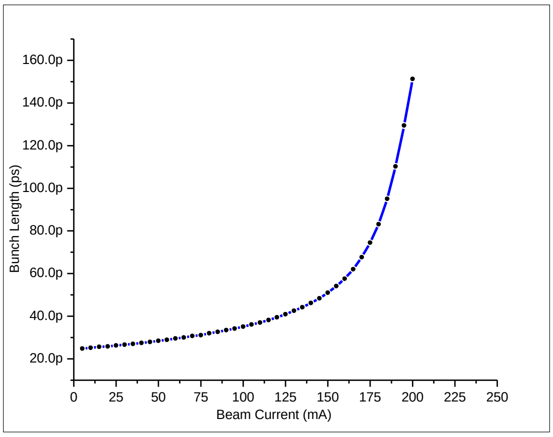


Figure-2: Effect of beam current ramp on bunch length in HBSRS

Bunch lengthening may be a consequences of increasing energy spread also. In figure 3 the energy spread over the corresponding current is shown which remains almost constant around the nominal value of 9.60 x $10^{-4}$.

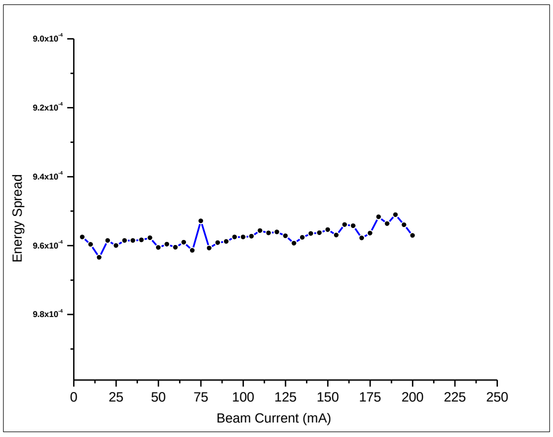


Figure-3: Energy spread under the influence of harmonic cavity in HBSRS

## BEAM LIFE TIME

The improvement in the Touschek beam lifetime is calculated from the ratio of the beam lifetimes with and without harmonic cavity voltage. The relative improvement in the Touschek beam life is defined as follows [9]-

$$\frac{\tau_{HC}}{\tau_0} = \frac{\epsilon_{HC}^2}{\epsilon_0^2} \frac{\int \rho_0^2 d\varphi}{\int \rho_{HC}^2 d\varphi} \tag{4}$$

Where, $\tau_{HC}$ and $\tau_0$ are Touschek beam lifetime with and w/o harmonic cavity respectively, ε: RF acceptance. Due the lengthening effect by third harmonic cavity in the storage ring of HBSRS the Touschek beam lifetime improves by a factor of 5.8 which is as per the expectations because the Touschek beam lifetime is directly proportional to the bunch volume i.e. $\tau \propto \sigma_x \sigma_y \sigma_z$. The transverse dimensions i.e. $\sigma_x$ and $\sigma_y$ are unaltered hence the Touschek beam lifetime is governed only by the longitudinal dimensions i.e. bunch length.

## CONCLUSIONS

The effect of third harmonic cavity to control the bunch length in the storage ring of HBSRS has been investigated and the basic parameters were obtained. Here we have analysed the effect of 3rd harmonic cavity in HBSRS taking 100MHz frequency of the main RF system and the studies are under progress with 500MHz RF system. The flat potential condition is achieved at a detuning of around 30 kHz which is almost 10% of the revolution frequency. The Touschek beam lifetime improved by a factor of ~6 due to 3rd harmonic cavity. Bunch length is calculated only due to harmonic cavity and the broadening due to wake impedance is not included.

## REFERENCES

[1] A. D. Ghodke et al., "Physics design Studies for Proposed High Brightness Synchrotron Radiation Source (HBSRS) in India", in this proceeding.

[2] N. Carmignani et al, "Harmonic RF System for the ESRF-EBS", in *Proc. IPAC'17,* Copenhagen, Denmark, paper THPAB003, pp. 3684-3687

[3] A. Hofmann, S. Myers, "Beam dynamics in double RF system", CERN, Technical Report No. CERN-ISR-TH-RF/80-26, 1980.

[4] H. Ghasem, "Bunch Lengthening in Taiwan Photon Source Using Harmonic cavity", in *Proc. PAC'09*, Vancouver, BC, Canada, paper WE5RFP005, pp. 2270-2272.

[5] M. Borland et al, "Tracking Studies of a Higher Harmonic Bunch Lengthening Cavity for the APS Upgrade", *Proc. IPAC'15*, Richmond, VA, USA, paper MOPMA007, pp. 543-545.

[6] G. Skripka et al "Commissioning of the Harmonic Cavities in the MAX IV 3 GeV Ring", *Proc. IPAC'16*, Busan, Korea, paper WEPOW035, pp. 2911-2913.

[7] J. Borthwick et al "mbtrack: Multi-Bunch Tracking Code", Sep 28, 2015.

[8] P. F. Tavaras et al, Skripka et al "Equilibrium Bunch Density Distribution with Passive Harmonic Cavities in a Storage Ring", *Phys. Rev. ST - Accelerators and Beams 17, 064401 (2014).*

[9] J. M. Byrd et al, "Lifetime increase using passive harmonic cavities in synchrotron light sources", *Phys. Rev. ST-Accelerators and Beams 4, 030701 (2001).*

# SPARK CURRENT SENSOR COIL FOR SAFE SHUTDOWN MECHANISM FOR 1MeV, 100kW ACCELERATOR

Swati H Das*, S. Dewangan, R.N. Rajan, A.G. Waghmare, N.B. Thakur and R.I. Bakhtsingh
Accelerator and Pulse Power Division, BARC, Mumbai.
* *shdas@barc.gov.in*

*Abstract*

1MeV, 100kW Electron Beam Accelerator for Waste Water Treatment is under development at Electron Beam Centre, Kharghar. High Voltage conditioning of the multiplier is under progress. The high voltage conditioning of an accelerator is accompanied by frequent discharges at different high stress locations. These high voltage discharges cause transient high voltages to appear at the input of the power supply. In case of high voltage discharges, the accelerator should get switched off to avoid over stressing of different components. These discharges are captured using spark gap and spark current is sensed through low inductance toroidal winding, Rogowski Coil. Spark current and transient voltage estimations during discharge at HV terminal have been done. The Rogowski Coil is designed and developed for 1 MeV, 100kW to detect discharge currents and trigger safe shutdown of the accelerator. The coil has been characterised in laboratory and then through in-situ testing. This paper describes about the analysis and design of the coil to its implementation in shutdown of an accelerator.

## INTRODUCTION

The high voltage generator of the 1MeV EB Accelerator employs series capacitive coupling of voltages through Symmetrical Cockcroft Walton multiplier (SCWM). The generator consist of (a) 10kHz inverter which produces voltage source with controllable duty cycle to control the current and voltage level, (b) a HV transformer and (c) voltage multiplier. An IGBT based resonant inverter sourced by 3ϕ thyristor based converter converts 415V, 50Hz 3ϕ AC voltage to 0-500V, 10kHz AC. The 10kHz voltage is stepped up by an oil insulated RF transformer to 45kV-0-45kV. The 15 stage multiplier enclosed in 6kg/cm$^2$ $N_2$ environment, sourced by the transformer multiplies the voltage in cascaded manner to 1MV. The HV terminal is provided with electric field modulated smoothened dome. The multiplier has three columns, one smoothing and two oscillating columns. An accelerator requires high voltage conditioning to achieve design voltage and thus most stable insulating strength. In high voltage conditioning, voltage is increased in steps and is associated with micro and HV discharges. Microdischarges are helpful in going to higher voltages and often not harmful for the system but HV discharges due to operating high fields results in over stressing of multiplier components. The HV discharge at dome causes maximum overvoltage and is detected using spark gap and rogoswski coil. The overvoltage at the input of the multiplier is detected and accelerator is tripped.

## ARC CHANNEL DETECTION

The major design criteria for rogowski coil is the expected current at input of the multiplier on event of HV discharge. The HV terminal, dome is a cylindrical structure surrounded by co-axial tank as ground, it forms capacitance with pressurized nitrogen gas as dielectric. The capacitance is given by,

$$C = \frac{2\pi\varepsilon_o l}{\ln\left(\frac{b}{a}\right)} \qquad (1)$$

where $l$ is the distance between HV terminal and ground in meters (arc channel length), a, b being terminal and tank diameter in meters respectively. The capacitance is calculated to be around 120pF. The arc channel length is around 200mm which is large enough to have streamer discharge. At the event of an arc, capacitance is paralleled by channel impedance consisting of series combination of spark resistance and inductance (see Fig. 1)

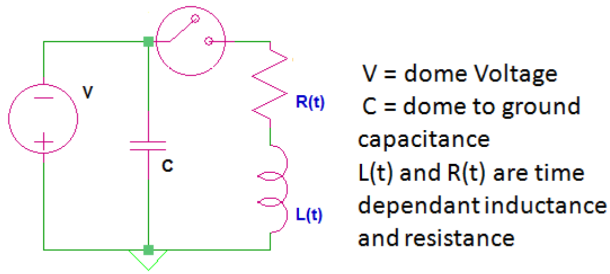


Figure 1: Schematic of an arc

The Spark channel resistance is given by

$$R = \frac{kl}{Q} \qquad (2)$$

where k is the toepler constant, $\ell$ = spark length between HV terminal and ground, in cm and Q = charge transferred through spark channel, A.sec. Toepler's constant is experimentally calculated to be $1.5\times10^{-4}$Vs/cm for 5 bar $N_2$ gas for small gap and the k value reduces for larger gaps[1]. At discharge, spark resistance changes from very high MΩ range to very low ohm range in few nanoseconds. After this time, the channel impedance is mainly determined by inductance

The Spark Channel Inductance in µH is given by[2]

$$L = 0.002l\left[\ln\frac{2l}{\rho} - \frac{3}{4}\right] \qquad (3)$$

Where ρ is the spark channel diameter in cm. For 1MeV system, $\ell$ = 20cm, dome to ground capacitance =120pF. A experimentally derived relation for ratio of ρ/ ℓ versus pressure is given by,

$$\frac{\rho}{l} = [(4.29/P) + 3.275] \times 10^{-4} \qquad (4)$$

where P is pressure in atm. At 6 atm, ρ/ ℓ is calculated to be $3.99 \times 10^{-4}$. Using this value in equation 4, spark inductance is calculated to be 310nH. The channel impedance and surge frequency can be calculated using L and C values.

The value of impedance is 55.7ohm, which gives surge current of 18kA at 1MV terminal voltage. The surge frequency of the equivalent tank circuit during arc is 26MHz.

### *Experimental and simulation results*

- The simulation results for over voltage at the input of multiplier in case HV discharge at 1MV charged dome was 240kV. The surge frequency and current are 3.4MHz and 600A respectively. This frequency is due to the tank formed by the 10µH inductor used at the input of multiplier and 200pF capacitance formed with respect to ground.
- HV discharge experiments with system at 280kV terminal voltage provided insight for expected over voltage at the input of multiplier. The surge voltage captured was 38kV with damping frequency of 3.6MHz. The value can be extrapolated for 1000kV of terminal voltage to be 135kV (see Fig. 2)

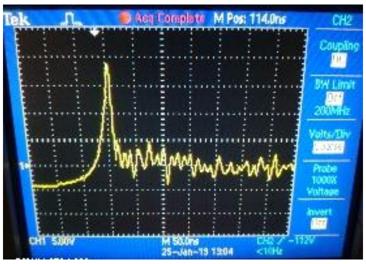


Figure 2. : Surge Voltage at multiplier input

- Protection of the transformer and inverter at the input of the multiplier from the surge voltage and surge current that may enter and harm the electronics in the inverter was necessary. The spark gap was placed at the input of multiplier with respect to ground to fire as voltage rise above set spark voltage. The firing of spark gap will allow the surge current to flow through ground. The spark response time is dependent on the rate of rise of the surge voltage. By the time spark gap fires, the voltage at transformer secondary may increase to 100kV, to prevent damaging of transformer, inductor is added in line. The inductor delays the signal to ensure avoiding of overstressing of transformer secondary till the sparking happens. The objective is to shut down the accelerator whenever there is arc in the system, to cater to this, the spark gap's current which fires in the event of system arc is picked by rogowski coil to initiate shutdown action.

## ROGOWSKI COIL DESIGN AND VALIDATION

The surge current at dome estimated in case of HV terminal discharge is 18kA, simulation result for same is 11kA. Simulation results showed current at transformer secondary to be 600A. The design of coil for capturing surge current through spark gap is done considering this current to be in kA range. The coil should have very low inductance so as to have low coil sensitivity considering high primary current. Rogowski coil is closed non-ferromagnetic toroidal one-layer homogenous winding (see Fig. 3)

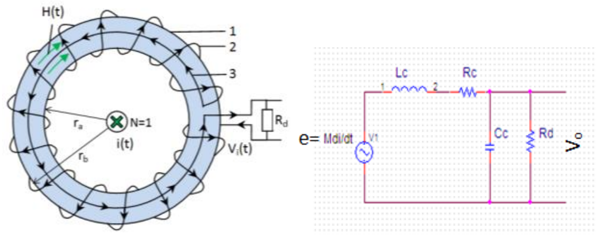


Figure 3: Schematic drawing of Rogowski coil, 1- air core former, 2- Secondary Turns, 3- compensating wire, $r_a$ and $r_b$ =inner and outer radius of former, Equivalent Circuit of coil, where $L_c$, $C_c$ and $R_c$ are coil parameters

The compensating return turn is provided to compensated the coil against any stray axial magnetic fields. In simplified form the coil can be represented by the equivalent circuit shown in Figure 3, where

$$R_c = \rho \frac{l_w}{\pi r_w} \qquad (5)$$

$$L_c = \frac{\mu_o}{2\pi} N^2 d_c \log\left(\frac{r_b}{r_a}\right) \qquad (6)$$

$$C_c = \frac{4\pi^2 \varepsilon_o (r_b - r_a)}{\log\left(\frac{r_b + r_a}{r_b - r_a}\right)} \qquad (7)$$

$l_w$ is length of coil wire, $r_w$ is wire radius, $d_c$ is core cross-section diameter. Mathematically, the circuit can be expressed though following equations,

$$i = \oint \vec{H} . \vec{dl} \qquad (8)$$

$$e = -M \frac{di}{dt} \qquad (9)$$

*i* (A) is the current enclosed, H is the magnetic field strength (A/m) , dl (m) is the infinitesimal element of path length. e is induced voltage due to current to *i*, M=$\mu_0$ An is mutual inductance of the coil, A is the turn area and n is the number of turns per unit length.
From equivalent circuit in Figure 3,

$$V_o(t) = \frac{R_d}{L_c R_d C_c s^2 + (L_c + R_c R_d C_c)s + R_c + R_d} e \qquad (10)$$

$$V_i(t) = ke \qquad (11)$$

where k is coil sensitivity (V/A)
The targeted coil sensitivity for our case considering kA range surge current was 0.01V/A. for achieving the same, designed values for coil parameters are given in Figure 4.

Figure 4: Coil placed in delrin former to isolate from aluminium shield (left) and shielded Rogowski coil (right) (Coil parameters : $r_a$ =19mm, $r_b$ =21mm, wire diameter = 1mm, core crossection = 2mm, $R_d$ =10Ω , N =26)

The coil has to work in the environment of surge prone system and stray fields, therefore 3mm shielding is provided for isolating the results from being affected by stray magnetic fields. The passive RC integration technique is used to integrate the output voltage across the termination resistor. The coil was tested without the integrator circuit using function generator which gave k value in the range of 0.1 to 0.2V/A in MHz frequency whereas calculated sensitivity was 0.6V/A for aforesaid coil parameters.

### *Surge Detection Setup testing*

The complete setup comprising of spark gap of diameter 25mm, charging capacitor and rogowski coil along with integrator circuit was tested in laboratory, results shown in Figure 4.

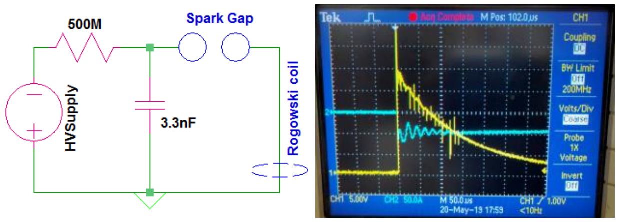


Figure 5: The circuit (left) of test setup and (right) results for arcing voltage of 23.5kV, gives output V = 24V, surge current=70A and k = 0.34 for $R_d$ of 10Ω

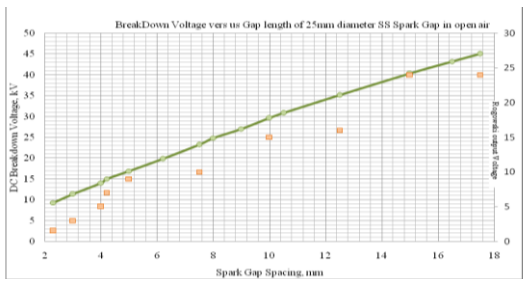


Figure 6: Breakdown Voltage Vs spark gap spacing

Experiments were done with different $R_d$ values to get k a factor lower. The spark gap (Fig. 5) spacing was varied to cause arc at different voltages and breakdown voltages are plotted for increasing 25mm spark gap spacing in Figure 6. The integrated rogowski output increases with increasing arcing voltage (see Fig. 6)

### *Installation of setup in the accelerator*

The spark gaps along with rogowski coil was installed in the accelerator tank (see Fig. 7) and experiments were conducted. The signal from the rogowski coil was given as input signal to fast trip circuit (see Fig. 7) which compares the input and generates a optical signal to trip the input HV power supply of the accelerator for safe shutdown. The dome discharge was allowed at 250kV-350kV in accelerator to capture rogowski signal and verify tripping of high voltage supply. The pulse in Fig. 7 is 800mV signal output of rogowski coil at HV terminal arc voltage of 331kV.

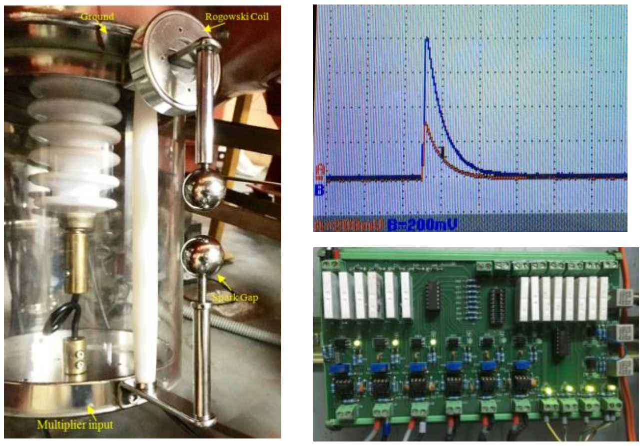


Figure 7 : The spark gap and rogowski coil assembly in the system over multiplier input feedthrough case (left), the trip signal captured at the input of fast trip circuit (right)

## CONCLUSION

This technique of surge detection through spark gap and picking the signal using rogowski coil is throughly tested at different discharge voltages. The accelerator system has been conditioned upto 900kV with number of discharge events in the process and every time it has been detected by rogowski coil and system has been shutdown safely.

## ACKNOWLEDGEMENT

Authors would like show gratitude to Shri R.K. Rajawat, Head, APPD for his constant encouragement to start the work, persevere and complete it.

## REFERENCE

[1] Santanu Singha and M. Joy Thomas, "Toepler's spark Law in a GIS with compressed $SF_6$-$N_2$ Mixture", IEEE Trans. on Dielectrics and electrical Insulation, Vol. 10, no. 3 pp. 498-505, 2003

[2] P.H. Ron, "High Voltage Sparkgaps and Switching", Proceedings of the Workshop Course on Technology of Electrical Insulation and Pulse Power Techniques, BARC, Bombay, March 1-5, 1982, p.204

# INSTALLATION OF HYDROSTATIC LEVELLING SYSTEM IN INDUS-2 AND ITS PRELIMINARY RESULTS

Vikas, Pankaj Kumar Sharma, Dinesh Barapatre, R.K. Sahu

Indus Operation Division, Raja Ramanna Centre for Advanced Technology, Indore, 452013, India

*Abstract*

Indus-2 is a 2.5 GeV synchrotron light source at RRCAT having circumference 172.47 m in which its position-sensitive magnets like quadrupoles are installed on girders. Stability of these magnets is the key requirement for stable beam of charged particles and synchrotron light emitted from them. The demand of floor and girder stability is still more crucial in future generation particle accelerators where undulator based beamlines are the dominant source of synchrotron light. Hydrostatic Levelling System (HLS) is used to online monitor the elevation differences between two points by measuring the capacitance between two surfaces. Three undulator based beamlines are coming up in near future in Indus-2. In first phase, 08 HLS sensors were mounted on quadrupole magnets of short-section girders in Indus-2 to monitor their elevation changes under different operating conditions, ground vibrations and temperature changes. To test the HLS system, a lab setup was also established in a stable underground tunnel. Stability of magnets on girders during different conditions of machine operation are reported in this paper.

## INTRODUCTION AND WORKING PRINCIPLE

A Hydrostatic levelling system is a high accuracy relative elevation monitoring system which can measure elevation difference between two points several meters apart. These types of systems are widely used in large machines like particle accelerators, survey of historic buildings structure, nuclear power stations located in seismically active areas etc. As floor/girder stability requirement in future generation particle accelerators is very stringent, similar systems have been installed in various particle accelerator facilities all around the world [1]. HLS comprises mainly two elements; capacitive sensor and a machined vessel filled with fluid. A schematic diagram of full filled HLS system with two sensors is shown in figure 1. Initially, the fluid was at rest. Due to some external disturbances, the level of fluid in both the vessels will be changed after performing damped oscillations which results in change in capacitance between sensor plate and free liquid surface [2]. Capacitance between two plates can be written as:

$$C = \frac{\varepsilon_o A}{d} \tag{1}$$

Where $C$ is capacitance between the sensor surface and free liquid surface, $\varepsilon_o$ is permittivity of air, $A$ is area of sensor plate and $d$ is the gap between two surfaces. The sensor measures the capacitance by which gap between two surfaces is determined.

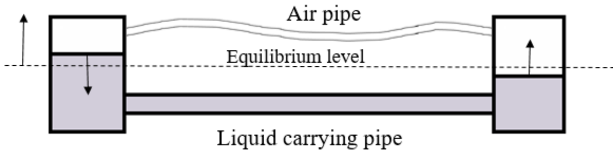


Figure 1: Schematic diagram depicting working of HLS

## LAB SETUP FOR TESTING OF HLS

A total 13 HLS sensors were bought having claimed accuracy of ± 1.1 µm with resolution of ± 0.2 µm within the measurement range of ± 1.25 mm [3]. A lab set up (05 sensors) as shown in figure 2 was established in stable underground tunnel which is a parallelopipe of 300 mm thick concrete wall. Deflection due to human movement near to sensor locations was also monitored. Movement up to ±5 µm was shown by each sensor during human movement near to it which shows the sensitivity of the system.

Figure 2: Lab set-up of HLS system

## DESCRIPTION OF INSTALLATION OF HLS SENSORS IN INDUS-2

There are 08 long and 08 short sections in Indus-2. Single girder is used in Short-section (SS) as compared to multiple girders in long section, hence, in the first phase, 08 HLS sensors (04 pairs) were installed in four diametrically opposite short-sections (one pair in each SS) of Indus-2. Figure 3 & 4 depicts the installation layout of each pair of sensor and installed sensors at site respectively. Pair 1, 2, 3 and 4 consists of HLS sensors 1-2 (mounted in SS-7), 3-4 (mounted in SS-1), 5-6 (mounted in SS-3) & 7-8 (mounted in SS-5) respectively. Mounting brackets for sensors and tubes were designed and fabricated. HLS sensors were mounted on these brackets within ±0.3 mm using optical level and tilt of these sensors was also corrected. Each pair of sensors were connected by two pipes, one is to carry the fluid and another is air pipe to equalize the pressure in each pair of sensors. All sensors with calibration & their electronics were received and the data acquired from each sensor is recorded and analysed. Due to some disturbances, relative change in elevation of any sensor is detected within sensors' capacitive measurement system.

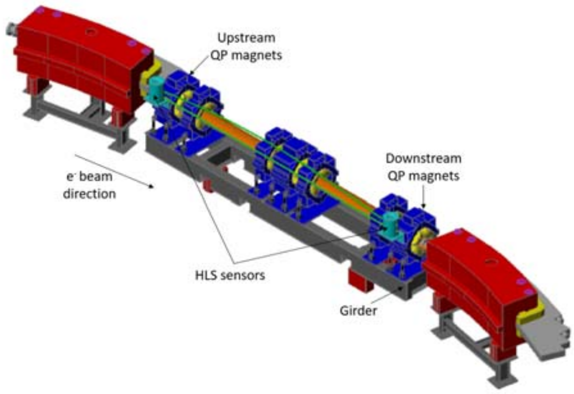


Figure 3: Layout of HLS sensors installed in short section

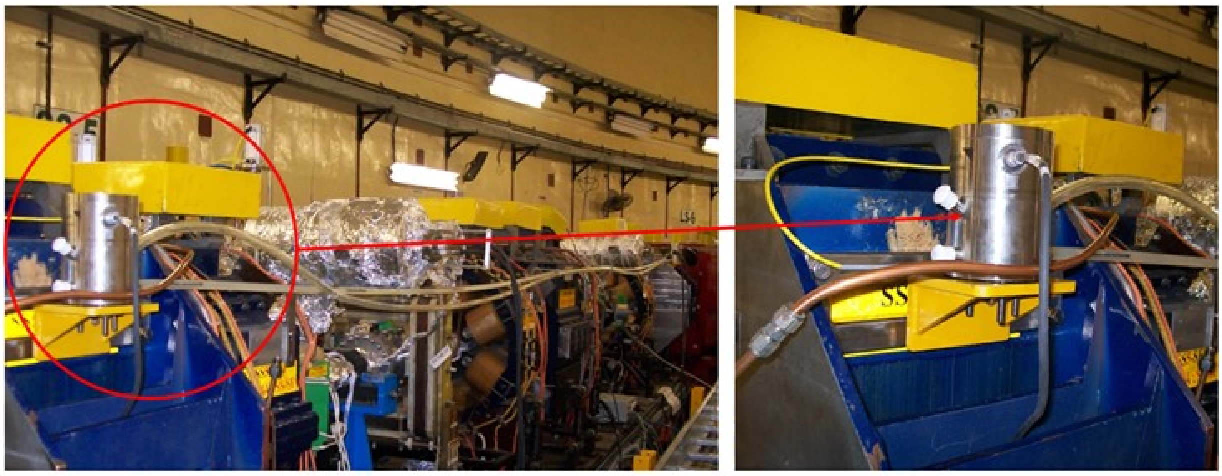

Figure 4: HLS sensors installed on Quadrupoles of short section girder.

## INITIAL RESULTS FROM HLS SYSTEM

The stability of magnets mounted on girders under various operating conditions like cycling and ramping of beam was evaluated using data collected from all the 08 sensors over five days. Relative change in elevation of sensors during cycling of current in dipole magnet's coils is given in Table 1. Data shown by either sensor of the pair was in good agreement with the other sensor of the same pair. It was analysed from the data received from each sensor that when current changes in the coils of dipole magnets under operating conditions like cycling and ramping, sensors mounted on quadrupole magnets of short-section SS1, SS5 and SS7 showed vertical movement upto ±15 µm whereas sensors installed on magnets of SS3 showed negligible deviation in height.

On the basis of our past experience and the support scheme of the short-section girder, it is considered that the upstream quadrupole magnet mounted on girder is more prone to tilt (vertical relative movement in either side). Furthermore, the vacuum chamber of upstream dipole magnet passes through the pole gap of quadrupole magnet (refer figure 3). During operation of machine under different conditions like cycling, ramping, sudden loss of power and tripping of power supply, current changes in the coils of dipole magnets and the vacuum chamber of dipole magnet experiences sudden shock due to eddy current effect. Cycling and ramping are two routine operating conditions and their effects are analysed in this paper. Upstream quadrupole magnet in each section may get disturbed due to the effect of sudden shock if there is any contact between magnet and vacuum chamber. Hence, in view of these facts, it may be possible that there is physical contact between magnet and vacuum chamber in SS1, SS5 & SS7. On the other hand, clearance may exist between magnet and vacuum chamber in SS3 even after small movement. These minute measurements/observations prompt us for physical verification at site in coming shut-down.

Table 1: Deflection data shown by each sensor during cycling

| Sr. No. | Difference in levels of each sensor (µm) |
|---|---|
| 1. | HLS-1= -10, HLS-2= 10, HLS-3= -12, HLS-4= 15, HLS-5 ~0, HLS-6~0, HLS-7 = 15, HLS-8= -12 |
| 2. | HLS-1= -6, HLS-2= 6, HLS-3= -12, HLS-4= 12, HLS-5 ~0, HLS-6~0, HLS-7 = 10, HLS-8= -10 |
| 3. | HLS-1= -10, HLS-2= 7, HLS-3= -15, HLS-4= 15, HLS-5 ~0, HLS-6~0, HLS-7 = 10, HLS-8= -12 |
| 4. | HLS-1= -10, HLS-2= 10, HLS-3= -10, HLS-4= 10, HLS-5 ~0, HLS-6~0, HLS-7 = 10, HLS-8= -10 |
| 5. | HLS-1= -10, HLS-2= 10, HLS-3= -12, HLS-4= 15, HLS-5 ~0, HLS-6~0, HLS-7 = 10, HLS-8= -10 |

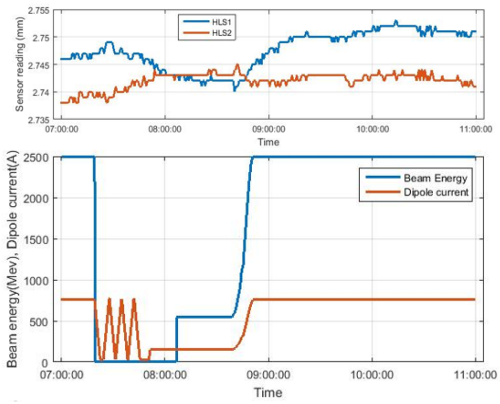


Figure 5: Deflection shown by HLS sensors 1 &2 during cycling and ramping

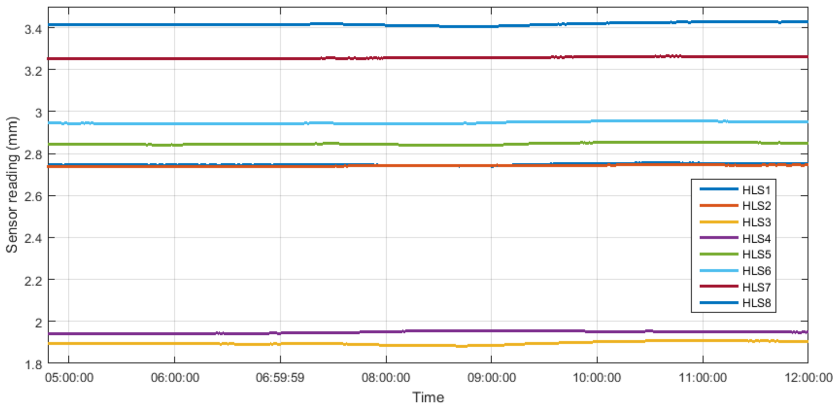


Figure 6: Level data acquired from each sensor

## CONCLUSIONS AND FUTURE WORK

Experience with a very sensitive system like, HLS in real site conditions and the care needed to respect such sensitivity finally to get reliable observations for meaningful inference from them is objective of this paper. As mentioned above, 08 HLS sensors were installed in Indus-2. The sensors installed in short-sections SS1, SS5 and SS7 showed deviation upto ±15 µm in vertical direction while sensors installed in SS3 showed negligible change in reading under operating conditions- cycling and ramping. The vacuum chamber of upstream dipole magnet experiences sudden shock due to the effect of eddy current generated due to change in current of dipole magnet coil. Transfer of shock occurs from the vacuum chamber of dipole magnet to upstream quadrupole magnet if there is any physical contact between them. In the coming long shutdown, the physical contact issue will be verified in each short section. During physical verification, if the contact between vacuum chamber and the upstream quadrupole magnet is found in SS1, SS5 & SS7 and on the other hand, clearance is found in SS3 then it can be concluded that during cycling and ramping upstream quadrupole magnet in SS1, SS5 and SS7 gets disturbed by ± 15 µm in vertical direction which needs to be dealt with.

More data will be analysed in coming year and meaningful inference will be deduced. On the basis of deduced inferences, we would decide between two options i.e. either more sensors will be installed on the magnets or the sensors will be installed on the floor of Indus-2 for fine observations. The comparison of future data & results with the present data will help us in analysing the effect of ground vibrations on floor stability as well as improve our understanding for future generation particle accelerators where required alignment tolerance is ~ 50 µm [4].

## REFERENCES

[1] James Kay, Keith A. Baker and W.J. Hoffman, “Results after one year from a Hydrostatic Levelling System installed at Diamond Light Source”, AIP Conference Proceedings 1234, (2010) 535.

[2] C. Zhang, K. Fukami and S. Matsui, “Primary hydrokinetics study and experiment on the Hydrostatic Levelling System”, IWAA’02, Japan, Nov. 2002, p. 297-307 (2002).

[3] “Validation process and calculations for HLS system”, Document sent by M/s Fogale nanotech, France (2018).

[4] Rudolf Dimper et al. “ESRF upgrade programme phase-2 (2015-2022): Technical design study”, The Orange Book.

# BEAM DYNAMICS STUDIES FOR FAULT TOLERANCE ANALYSIS OF HEHIPA

Rajni Pande, S. Krishnagopal, Ion Accelerator Development Division, BARC
rajnip@barc.gov.in

*Abstract*

A 1 GeV, 10 mA High Energy High Intensity Proton Accelerator (HEHIPA) for Accelerator Driven System (ADS) application is being designed at BARC. It consists of three families of superconducting Single Spoke Resonators (SSRs): SSR-A, SSR-B and SSR-C; and two families of 5 cell elliptical cavities. An important requirement from an accelerator for ADS is high reliability and availability. For this, suitable design philosophies like a fault tolerant design have to be adopted. In this paper, we have studied the fault tolerance of the HEHIPA superconducting linac through beam dynamics calculations. The effect of failure of each cavity and magnet on various beam parameters at the end of the linac is systematically done and its compensation using local adjustment of the fields in the adjacent elements has been studied. It is seen that failure of a cavity in the lower energy section of the superconducting linac leads to large increase in emittance. It is found that there is no loss in transmission due to the failure of any cavity in the linac beyond SSR-A. In the HEHIPA linac, focusing is done using superconducting solenoids in between the SSR cavities and warm quadrupole doublets between the elliptical cavities. Studies show that the failure of a solenoid in SSR- A, B or C leads to total loss of beam at that location in the linac while the failure of any single quadrupole in the linac leads to some beam loss and emittance increase in the linac. From simulations, it is found that the beam parameters can be brought back close to their nominal values by adjusting the fields in the adjacent elements by using local compensation technique. The results of these studies are presented in this paper.

## INTRODUCTION

The general procedure followed when a component fails in an accelerator is to shut down the beam and repair the component. However, for an application like ADS if the beam is off for more than a few seconds, it will lead to the shutdown of the reactor core. Thus the accelerators for ADS applications should have the ability to recover the beam in less than a few seconds and operate the accelerator safely. For this, fault tolerance design strategy is adopted, wherein in order to get the nominal beam parameters (transmission and energy) at the end of the linac in case of a component (cavity or magnet) failure, the accelerating gradient and phases of the cavities around the faulty cavity or the magnetic field of the magnets around the faulty magnet are adjusted [1,2].

## REFERENCE ACCELERATOR

The 1 GeV HEHIPA linac will consist of a 50 keV, 10 mA ion source, a Low Energy Beam Transport (LEBT) channel, a 3 MeV, 325 MHz Radio Frequency Quadrupole (RFQ), a Medium Energy Beam Transport (MEBT) system, three stages of 325 MHz superconducting Single Spoke Resonators (SSR-A, SSR-B and SSR-C) to accelerate the proton beam from 3 to 200 MeV and finally two stages of 5 cell elliptical cavities (Ell0.6 and Ell0.8) to accelerate the beam from 200 MeV to 1 GeV. The layout of the linac is shown in Fig. 1. The medium energy part of the linac consists of three families of 325 MHz single spoke resonators (SSR) sections: SSR-A, SSR-B and SSR-C corresponding to a $\beta_G$ of 0.11, 0.21 and 0.46 respectively. The focusing is provided by SC solenoids to minimize the period length. In SSR-A and SSR-B, a SC solenoid was used to focus the beam after every cavity while in SSR-C, there was one SC solenoid after every two cavities for focusing the beam. The high energy part of the linac consists of two sections, based on two families of elliptical cavities ($\beta_G$ = 0.6 and 0.8) operating at 650 MHz. Here, the transverse focusing is achieved by using room temperature electromagnetic quadrupole doublets in between the cryomodules containing the superconducting elliptical cavities. The focusing doublets are placed after every 3 cavities in the first section having 8 cryostats and after every 4 cavities in the second section having 13 cryostats. The main parameters of the superconducting linac are listed in Table 1.

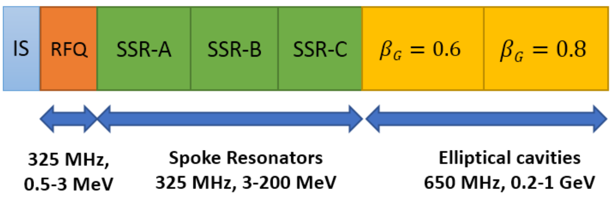


Fig.1. Layout of the 1 GeV linac for Indian ADS.

Table 1. Parameters of the 1 GeV Superconducting Linac for Indian ADS

| Section | Energy (MeV) | No. of cavities | Length (m) | Focusing |
|---|---|---|---|---|
| **SSR-A** | 3.05-10.85 | 14 | 8.42 | SC Solenoids |
| **SSR-B** | 10.85-49.69 | 20 | 18.91 | |
| **SSR-C** | 49.69-198.32 | 32 | 37.26 | |
| **Ell 0.6** | 198.32-397.43 | 24 | 47.2 | Warm Quad doublets |
| **Ell 0.8** | 397.43-1049.65 | 52 | 111.67 | |

## FAULT TOLERANCE ANALYSIS

First, the failure analysis of the superconducting linac for ADS is done. For this, systematic simulations were done and the effect of failure of each cavity and magnet on the beam parameters (beam emittance, beam energy and transmission) at the end of the linac is studied.

### Cavity Failure

Beam dynamics simulations are first done to see the effect of failure of each superconducting cavity in the linac on the beam dynamics. The percentage change in the final emittance at the end of the linac due to failure of each cavity, one at a time in the different sections of the linac are shown in Figs. 2 (a) & (b). It can be seen that failure of a cavity in the SSR A section leads to large increase in emittance. In SSR-B, the failure of a cavity in the low energy region leads to a larger increase in emittance as compared to failure in the higher energy region. In both SSR-A and SSR-B, the increase in longitudinal emittance is more severe as compared to the transverse emittance. In SSR-C, the change in emittance due to the failure of a cavity is less than 12%. In elliptical cavities, it is seen that the increase in emittance due to failure of a cavity is less than 5 % in the transverse direction and 15 % in the longitudinal direction. Beam loss due to the failure of a cavity is seen only due to cavity failure in SSR-A. The final energy in the linac also changes due to the failure of a cavity. The failure of a cavity in the high energy region leads to higher change in the value of the final energy at the end of the linac.

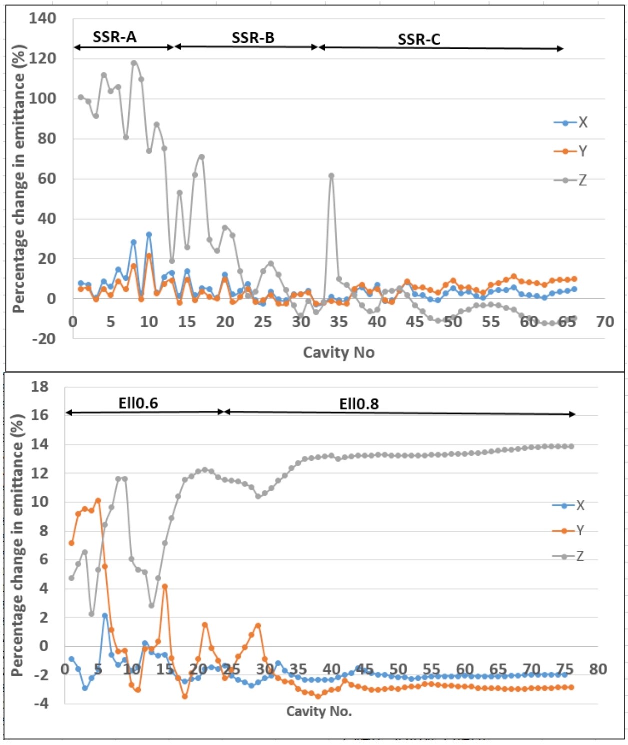


Fig. 2. Percentage change in the beam emittance at the end of the linac due to failure of a cavity in (a). SSR-A, B & C (b) Ell0.6 & Ell0.8 cavities.

In order to get the nominal beam parameters (transmission and energy) at the end of the linac in case of a cavity failure, the strategy adopted is to adjust the accelerating gradient and phases of the cavities around the faulty cavity. In the following section, some case studies have been done, where the beam parameters are brought back close to their nominal values by adjusting the accelerating gradient and phase in the adjacent cavities.

**Case study 1:** Suppose the 6$^{th}$ cavity of SSR-B fails. We see that there is no beam loss. The transverse emittances increase by 3.5 % and 4.22 % in x and y respectively while the z emittance increases by 62.22 %. By adjusting the accelerating fields in 4$^{th}$, 5$^{th}$ and 7$^{th}$ cavities, it is possible to reduce the increase in z emittance to 9.28 % with a marginal increase in the transverse emittance as shown in Table 2 and Fig. 3.

Table. 2. Beam Parameters at the end of the linac due to failure of 6$^{th}$ cavity in SSR-B and after compensating with adjacent cavities.

| | **Reference Linac** | **Failure of 6$^{th}$ cavity in SSR-B** | **After compensation using 4$^{th}$, 5$^{th}$ and 7$^{th}$ cavity of SSR-B** |
|---|---|---|---|
| **$\varepsilon_x$ (mm mrad)** | 0.2462 | 0.2548 | 0.2647 |
| **$\varepsilon_y$ (mm mrad)** | 0.2394 | 0.2495 | 0.2550 |
| **$\varepsilon_z$ (mm mrad)** | 0.319 | 0.5175 | 0.3486 |
| **Trans. (%)** | 100 | 100 | 100 |
| **Final Energy (MeV)** | 1049.55 | 1049.2 | 1049.3 |

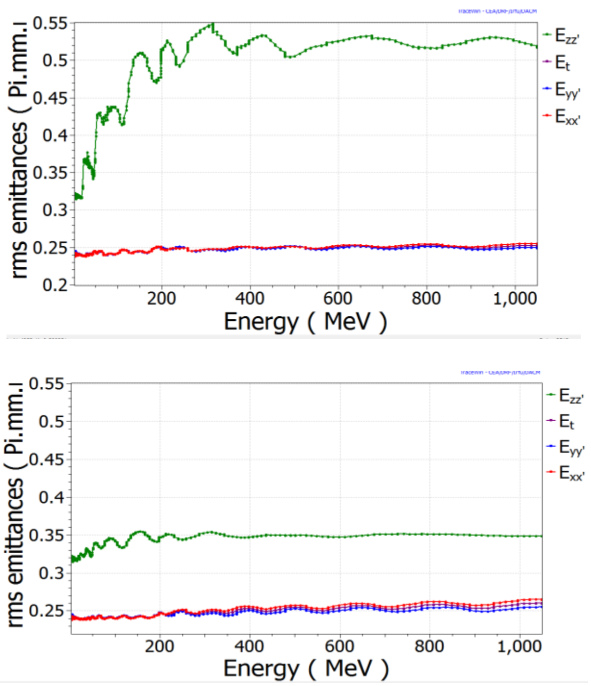


Fig. 3. Evolution of Beam emittance along the linac (a) After the failure of 6$^{th}$ cavity in SSR-B (b) After compensating the failure of 6$^{th}$ cavity in SSR-B with the adjacent cavities.

**Case study 2:** Suppose the 6th cavity of SSR-C fails. We see that there is no beam loss. The transverse emittances increase by 4.6 % and 4.01 % in x and y respectively while the z emittance increases by 10.1%. By adjusting the accelerating fields and synchronous phase in 5th and 7th cavities, it is possible to reduce the increase in z emittance to 1.38 % with a marginal increase in the transverse emittance as shown in Table 3 and Fig. 4.

Table. 3. Beam Parameters at the end of the linac due to failure of 6th cavity in SSR-C and after compensating with adjacent cavities.

| | **Reference Linac** | **Failure of 6th cavity in SSR-C** | **After compensation using 5th and 7th cavity of SSR-C** |
|---|---|---|---|
| **$\varepsilon_x$ (mm mrad)** | 0.2462 | 0.2575 | 0.2509 |
| **$\varepsilon_y$ (mm mrad)** | 0.2394 | 0.2490 | 0.2458 |
| **$\varepsilon_z$ (mm mrad)** | 0.3196 | 0.3519 | 0.3240 |
| **Trans. (%)** | 100 | 100 | 100 |
| **Final Energy (MeV)** | 1049.55 | 1048.2 | 1048.8 |

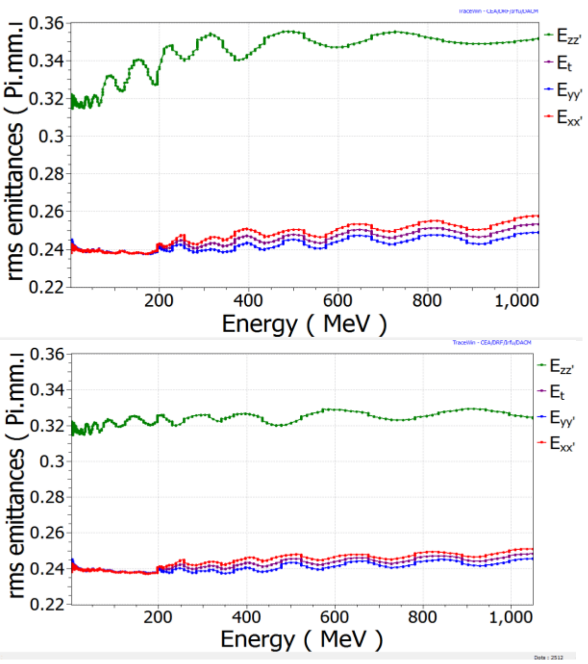


Fig. 4. Evolution of Beam emittance along the linac (a) After the failure of 6th cavity in SSR-C (b) After compensating the failure of 6th cavity in SSR-C with the adjacent cavities.

It was also seen that, for failure of any cavity in SSR-A, it is very difficult to correct with adjusting the field in the adjacent cavities. Hence, in the lower energy range, it is better to explore the possibility of a hot spare. In case of failure of any elliptical cavity in the in the high energy region, there is not much increase in final emittance and no beam loss. Minor corrections can be easily done by adjusting the adjacent cavities.

**Magnet Failure**

Focusing is done using superconducting solenoids in between the SSR cavities and warm quadrupole doublets between the elliptical cavities. Studies show that the failure of a solenoid in SSR- A, B or C leads to total loss of beam at that location in the linac. In the elliptical cavity section, if a single quadrupole from the quadrupole doublet fails, it leads to some beam loss and emittance increase in the linac. However, it is found that if a quadrupole fails, then switching off the other quadrupole of the doublet prevents loss of beam in the linac and the emittance increase is also less. This can be seen in Fig. 5.

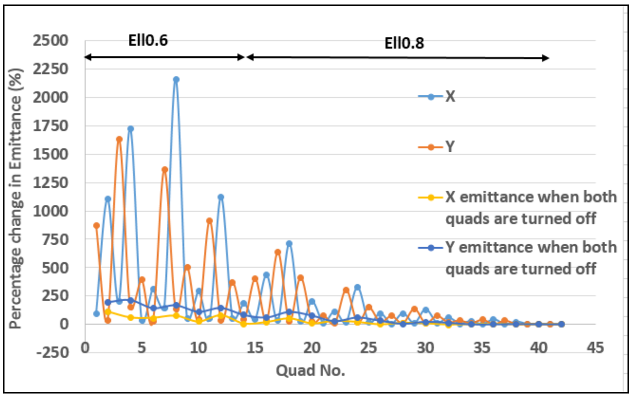


Fig. 5. Percentage change in the beam emittance at the end of the linac due to failure of a quadrupole in Ell0.6 & Ell0.8 sections & when both quadrupoles of the doublet are turned off.

## CONCLUSION

For failure of any cavity in SSR-A, it is very difficult to correct with adjusting the field in the adjacent cavities. In the lower energy range, it is better to explore the possibility of a hot spare. In case of failure of any cavity in rest of the linac, it can be corrected by varying the accelerating fields and phases of the adjacent cavities. It is found that if a quadrupole fails, then switching off the other quadrupole of the doublet prevents loss of beam in the linac and the emittance increase is also less.

## REFERENCES

[1] J-L. Biarrotte, M. Novati, P. Pierini, H. Safa, D. Uriot, Beam Dynamics Studies for the Fault Tolerance Assessment for the PDS-XADS Linac Design, EPAC 2004, Lucerne, Switzerland

[2] Biao Sun, Jingyu Tang, Fang Yan, Zhihui Li, Cai Meng, Shilun Pei, Local compensation–rematch for major element failures in superconducting linacs with very high reliability and low beam loss, Nuclear Instruments and Methods in Physics Research A 785 (2015) 77–86

# LFD AND HELIUM PRESSURE SENSITIVITY ANALYSIS FOR SSR2 CAVITY

P. Bhumeshwar[1], Piyush Jain[1,2], Srinivas Krishnagopal[1,3]
[1]Ion Accelerator Development Division, BARC
[2]Fermi National Accelerator Laboratory, Batavia, USA
[3]Homi Bhabha National Institute, Mumbai

*Abstract*

The SSR2 cavity is a $\beta_{opt} = 0.475$ superconducting spoke resonator (SSR) cavity being developed for the Indian Institutions and Fermilab Collaboration (IIFC). The basic mechanical model of the SSR2 v2.6 cavity was obtained from Fermilab [1]. It was modified slighly at BARC to optimize the cavity wall geometry to reduce multipacting. This modified model, SSR v3.0, has been used to study the Lorentz forces and the liquid helium pressure sensitivity for this cavity. The electromagnetic fields inside the cavity generate a force, called the Lorentz force, on the walls of the cavity and deform the cavity. Also, due to the liquid helium pressure fluctuations in the helium line, the cavity deforms. The cavity resonant frequency changes when the shape changes and therefore Lorentz Force Detuning (LFD) and the helium pressure sensitivity (df/dp) both need to be minimised to reduce the cavity deformation. Contributions to LFD and df/dp from different regions of the cavity to the frequency change have been studied. Different techniques such as introducing a stiffening disc on the spoke, localised increase in thickness of the helium jacket, introducing the circumferential stiffeners etc. are studied which reduce the LFD coefficient. The dependency of the pressure sensitivity on the bellow disc radius has been studied and an optimum value of df/dp is achieved. A final LFD value of −4.83 Hz/(MV/m)$^2$ and df/dp value of 1.92 Hz/mbar were achieved, which meet the Technical Requirement Specifications.

## INTRODUCTION

The resonant frequency of superconducting single spoke resonator (SSR) cavities depends on the cavity electric and magnetic field volume and the frequency of the deformed cavity changes according to Slater's rule [2],

$$\frac{\Delta f}{f} = \frac{\int_{\Delta V} (\mu_0 \vec{H}^2 - \epsilon_0 \vec{E}^2)\, dv}{\int_{V} (\mu_0 \vec{H}^2 + \epsilon_0 \vec{E}^2)\, dv} \tag{1}$$

where $\vec{H}$ and $\vec{E}$ represent the unperturbed magnetic and electric fields inside the cavity respectively. V represents the complete volume of the cavity and $\Delta V$ represents change in volume due to the deformation.

The change in frequency due to the deformations is calculated using Slater's rule above. A decrease in the electric field volume of the cavity and an increase in the magnetic field volume of the cavity, due to the deformations, reduce the frequency and vice versa. These cavity deformations need to be reduced as the bandwidth of the superconducting cavities is very low and the frequency drift needs to be within the bandwidth of the cavity.

## CAVITY DETUNING SOURCES

The Lorentz forces, generated due to the electromagnetic fields present inside the cavity when rf power is fed to it, impart radiation pressure ($P_r$) on the walls of the cavity,

$$P_r = \frac{1}{4}(\mu_0 \vec{H}^2 - \epsilon_0 \vec{E}^2).$$

This radiation pressure, or the Lorentz pressure, deforms the cavity and changes the cavity resonant frequency. This is known as Lorentz force detuning (LFD). The change in frequency is directly proportional to the square of the accelerating electric field ($E_{acc}^2$),

$$\Delta f = k E_{acc}^2,$$

where $k$ is the LFD coefficient in Hz/(MV/m)$^2$.

Liquid helium is used for cooling the cavity to attain the superconducting state. Due to the pressure variations in the helium line, the cavity gets deformed. This change in frequency is expressed in terms of helium pressure sensitivity (df/dp) and its units are Hz/mbar.

In this paper, the contributions of different regions of the SSR2 cavity to the Lorentz force detuning are studied. Various techniques used for reducing the frequency drifting, using stiffeners, are presented.

## SIMULATION PROCEDURE

A multiphysics analysis is required to analyse the cavity for different detuning sources. The procedure followed for performing the analysis [3] is summarized here:

- Use the Eigen-mode solver in multiphysics software to find the cavity resonant frequency.
- By applying proper boundary load conditions, calculate the displacement profile of the deformed cavity using the structural mechanics solver. For LFD, the boundary load will be radiation pressure (Fig. 1) and for the helium pressure sensitivity, it will be 1 bar pressure on the cavity outer surface and the helium jacket inner surface (Fig. 2).
- Find the resonant frequency of the deformed cavity using the Eigen-mode solver.

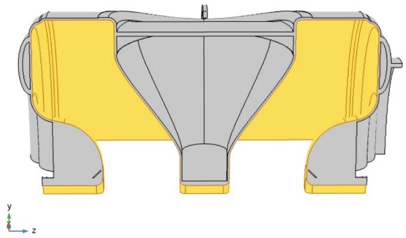

Figure 1: Boundary load for LFD.

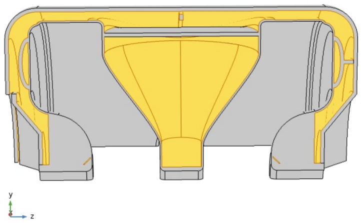

Figure 2: Boundary load for helium pressure sensitivity.

The material used for the cavity is Niobium with Young's Modulus of 105 GPa and Poisson's ratio of 0.38. For the cavity jacket, the material is Stainless Steel with Young's Modulus of 195 GPa and Poisson's ratio of 0.3.

## ANALYSIS OF CAVITY FOR LFD

The SSR2 jacketed cavity is simulated for Lorentz force detuning studies using the COMSOL Multiphysics software and the displacement profile of the cavity is shown in the Fig. 3. Three regions on the cavity are identified whose contribution to the LFD is very high: (1) end walls, (2) spoke, and (3) cylindrical surface.

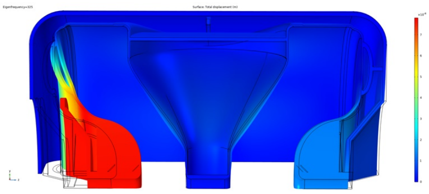

Figure 3: Displacements in the SSR2 jacketed cavity due to Lorentz forces (normalised to 1 J of stored energy).

The end walls contribute more to the LFD than other regions of the cavity. The LFD at the non-tuner end of the cavity can be improved by increasing the stiffness at that side. Having higher jacket thickness or shape optimisation can also be done to reduce the contribution. LFD at the tuner end can be totally controlled by tuner stiffness. Higher tuner stiffness can reduce the LFD contribution. LFD contribution from the spoke can be reduced by placing a disc on the spoke outer walls to reduce its deformation. Niobium thickness can be increased to reduce the contribution to LFD from the cylindrical surface.

## ANALYSIS OF CAVITY FOR HELIUM PRESSURE SENSITIVITY

For a constant liquid helium pressure, the force on the jacket disc is proportional to the area of the jacket disc (Fig. 4). The greater the area, the greater is the force acting on

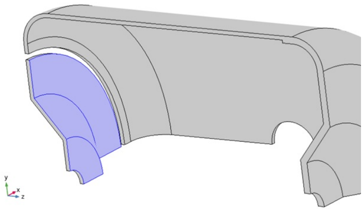

Figure 4: Jacket disc or bellow disc of the jacket (shown in colour).

the disc and thus the greater the deformation of the tuner side end wall. The helium pressure sensitivity of the cavity is optimised by varying the radius of the disc.

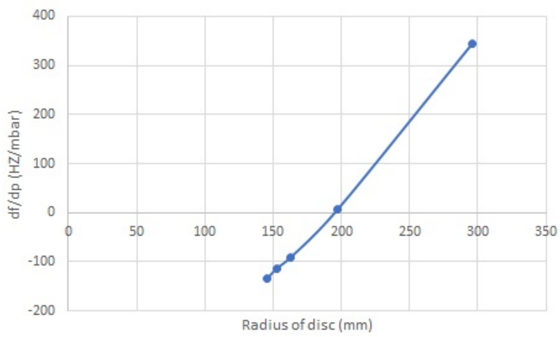


Figure 5: Variation of df/dp with bellow disc radius.

It can be seen from the Fig. 5 that the helium pressure sensitivity varies almost linearly with the disc radius. Therfore df/dp can always be controlled by varying this parameter.

## OPTIMISATION OF LFD AND HELIUM PRESSURE SENSITIVITY

Cavity thickness of 3 mm and a tuner stiffness of 40 kN/mm were chosen for the cavity model. Various techniques were implemented on the cavity model to reduce the LFD; these are discussed below.

### *Localised increase in jacket thickness at non-bellow side*

To account for the huge displacements on the end walls, the thickness of the jacket on the non-bellow side (Fig. 6) was varied, and the corresponding variation in the LFD coefficient is shown in Fig. 7. An optimal value of 12 mm for the localised thickness was chosen considering the cost and fabrication/welding problems.

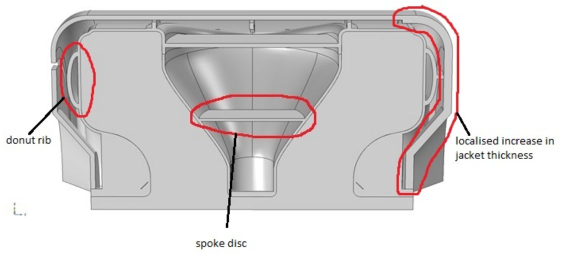


Figure 6: Three main changes made to control the LFD: localised increase in jacket thickness, spoke disc and the donut rib.

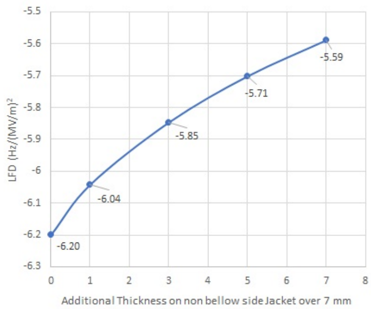


Figure 7: Variation of the LFD coefficient with localised increase in jacket thickness.

### *Insertion of spoke disc and thickening of the spoke wall*

Figure 6 shows the position of the disk inserted on the spoke external surface. The insertion of this spoke disk curbs the movement of the spoke due to the Lorentz forces. Also, spoke wall thickness was increased to 4.82 mm from the cavity thickness of 4 mm showing a slight improvement in LFD.

### *Varying the position of donut rib and placing circumferential stiffeners over the cavity*

The position of the donut rib affects the LFD coefficient and hence its position was varied to minimise the detuning. The location of the donut rib is shown in Fig. 6. When the donut rib was moved down by 5 mm, the LFD coefficient decreased and after that no improvement was observed. This change was included in the final model. The other contributing region to the LFD is the circumferential region where the deformations are reduced by placing the circumferential stiffeners over the cavity as shown in the Fig. 8.

### *Results of Simulations for LFD and Helium Pressure Sensitivity*

Table 1 summaizes the final parameters of the cavity model, after incorporating all the steps discussed above. An LFD coefficient of $-4.83\,\mathrm{Hz/(MV/m)^2}$ and helium pressure sensitivity of $-1.92$ Hz/mbar are achieved for the SSR2 v3.0 cavity with these parameters.

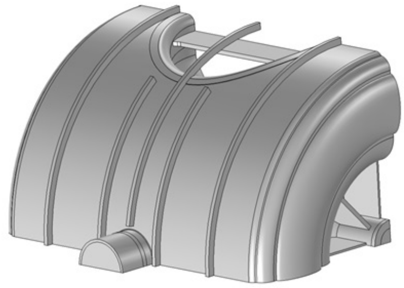

Figure 8: Circumferential stiffeners placed over the cavity.

Table 1: Details of Cavity Model

| **Parameter** | **Value** |
|---|---|
| Disc Radius | 214 mm |
| Cavity Thickness | 4 mm |
| Jacket Thickness | 7 mm |
| Tuner stiffness | 40 kN/mm |
| Jacket thickness at non-bellow side | 12 mm |
| Donut rib moved down by 5 mm | |
| Spoke disc inserted | |
| Spoke wall thickened to 4.82 mm | |

## CONCLUSION

The SSR2 v3.0 cavity has been modeled to minimise the effects of Lorentz forces and helium pressure fluctuations and their corresponding coefficients are brought down to within specifications, by employing various stiffening measures.

## ACKNOWLEDGEMENTS

We would like to thank Donato Passarelli, Leonardo Ristori and Paolo Berrutti of Fermi National Accelerator Lab, USA, for sharing their knowledge through regular discussions and meetings.

## REFERENCES

[1] Berrutti, P., Yakovlev, V. and Khabiboulline, T., 2017. Update on SSR2 Cavity EM Design for PIP-II.

[2] H. Graef, “Experience with control of frequency, amplitude and phase,” Part. Accel.,vol. 40, pp. 127–140, 1992.

[3] M. Awida, I. Gonin, D. Passarelli, A. Sukanov, T. Khabiboulline, and V. Yakovlev, “Multiphysics analysis of frequency detuning in superconducting rf cavities for proton particle accelerators,” in 2015 IEEE MTT-S International Conference on Numerical Electromagnetic and Multiphysics Modeling and Optimization (NEMO) , IEEE, 2015, pp. 1–3.

# RF CHARACTERIZATION OF THE 3 MeV LEHIPA RFQ

Manas R Mishra[1, #], Aman Bajaj[1], S. V. L. S. Rao[1], S. Krishnagopal[1,2]
[1] Bhabha Atomic Research Centre, Mumbai
[2] Homi Bhabha National Institute, Mumbai

*Abstract*

A 3 MeV proton Radio Frequency Quadrupole (RFQ) accelerator was designed and fabricated for the Low Energy High Intensity Proton Accelerator (LEHIPA) at BARC, Mumbai. The low level RF characterization of the RFQ was carried out, which mainly involves the identification of operating mode, field tuning and quality factor measurements. The fields were measured using the bead pull measurement technique and the piston tuners are used to get the required fields distribution. After several iterations, the quadrupole field levels were tuned to ± 5 % (dQ/Q0) and the dipole contributions were reduced to < 12 %. In this paper, we present detailed results of the low power measurements of the 3 MeV LEHIPA RFQ.

## INTRODUCTION

A Low Energy (20 MeV) High Intensity Proton Accelerator (LEHIPA) consisting of a 50 KeV ECR ion source, LEBT, 3 MeV RFQ, MEBT and 20 MeV DTL is being developed at BARC as a front end injector of ADS [1]. The LEHIPA RFQ is a 352 MHz, four vane type RFQ and requires 68 kV vane voltage to accelerate the proton beam from 50 KeV to 3 MeV in 4 m length. It consists of four mechanical modules, each 1 m in length and has been fabricated at Bramhos Aerospace Trivandrum Limited (BATL), Thiruvananthapuram. Dimensional error arising after fabrication process may lead to the change in the operating mode frequency and field profile as well as unloaded quality factor ($Q_0$) of the cavity. So it is necessary to carry out identification of operating mode as well as measurement of field profile and $Q_0$ value corresponding to operating mode as a measure of quality control after fabrication of RFQ cavity and minimize the measured deviation from the designed value using tuners. The next section details the measurement procedure followed for RF characterization of LEHIPA RFQ and discusses the results.

## RF MEASUREMENT AND RESULTS

As a longer RFQ is vulnerable to fabrication and alignment errors, the LEHIPA RFQ has been designed in the form of two smaller length RFQs, each comprising of two mechanical modules. Each 2 m long RFQ can be considered as an independent resonator which supports the degenerate dipole modes ($TE_{110}$, $TE_{111}$) and higher order quadrupole ($TE_{211}$) mode having frequencies close to the operating fundamental quadrupole ($TE_{210}$–like) mode. These two resonators are coupled together through a coupling cell using resonant coupling technique. This results in splitting of each mode supported by the individual resonators into two normal (structural) modes: 0 and π. The operational mode for RFQ is $TE_{210}^0$ mode which forms a transversely symmetric and longitudinally uniform field inside RFQ as required from beam dynamics design.

#manasr@barc.gov.in

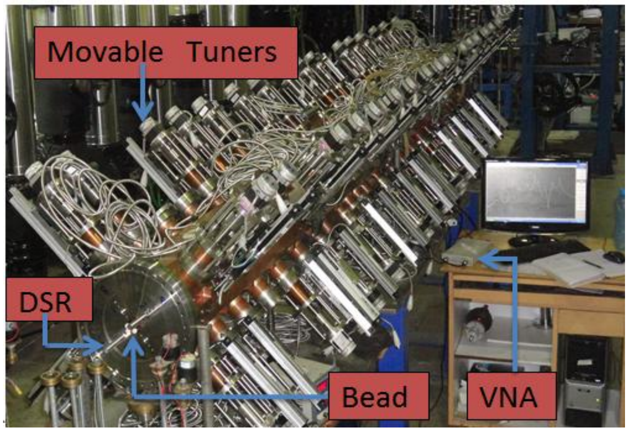


Figure 1: Bead Pull Test Bench.

The test-bench developed to perform the RF characterization of LEHIPA RFQ is shown Figure 1. It includes a vector network analyzer (VNA), the bead-pull set-up to sample the cavity field in each quadrant of the RFQ and 64 movable piston tuners for field tuning.

### *Identification of Modes*

We have used two loops to measure the cavity spectral response in transmission mode ($S_{21}$) using the VNA. The frequency spectrum for the coupled resonator under optimized tuner position is shown in Figure 2. The modes have been identified using the phase measurement technique. It involves measurement of $S_{21}$ phases in different quadrants of the RFQ relative to the feeder quadrant. The orientation of feeder and pick up loop plays an important role in this measurement technique. We have kept the orientation of both the loops in such a way that the measured $S_{21}$ phase is same in all quadrants for $TE_{210}^0$ mode. Then the other modes can be identified on the basis of the observed relative phase difference between the quadrants with respect to the feeder quadrant. The $TE_{210}^0$ mode as well as the other three nearby modes ($TE_{210}^\pi$, $TE_{211}^0$, $TE_{211}^\pi$) shown in Figure 2 have been identified using this technique. The $TE_{210}^0$ mode frequency is 352.13 MHz for the optimized tuner settings.

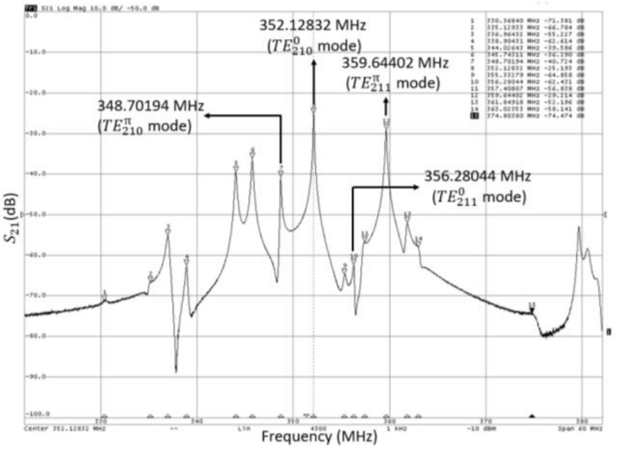


Figure 2: Frequency Spectrum of the LEHIPA RFQ for optimized tuner settings.

## *Field Tuning*

The field, in general, inside RFQ is given by $E_{real}=a_mE_m+a_{d1}E_{d1}+a_{d2}E_{d2}+a_qE_q$, where $E_m$, $E_{d1}$, $E_{d2}$, $E_q$ are the pure monopole, dipole and quadrupole fields respectively and the coefficients of each term represent their respective contributions to the actual field. These coefficients can be calculated from the cavity fields ($E_A$, $E_B$, $E_C$, $E_D$) in each quadrant using the relations $a_m=(E_A-E_B+E_C-E_D)/2$, $a_{d1}=(E_A-E_C)/\surd 2$, $a_{d2}=(E_B-E_D)/\surd 2$, $a_q=(E_A+E_B+E_C+E_D)/2$. The objective of field tuning is to minimize the dipole mode contributions in comparison to quadrupole mode contribution.

Measurement of the cavity field in each quadrant was carried out using the bead pull technique which is based on Slater Perturbation formula [2]. The cavity field in each quadrant was perturbed by moving four identical Teflon beads (6 mm dia and 4 mm length), one at a time, in all four quadrants in closed loop configuration by means of motor pulley system. The beads, supported by nylon thread (0.5 mm dia) were allowed to slide between the adjacent vanes near the vane tip where electric field is dominant. There is a change in resonant frequency as the bead enters into the cavity which can be measured in terms of $S_{21}$ phase change. The unperturbed field is proportional to the square root of change in the resonant frequency which in turn is proportional to the square root of $S_{21}$ phase change. Thus the cavity field in each quadrant can be calculated as a function of position by measuring the $S_{21}$ phase change as the bead moves inside the RFQ.

After the delivery the first two segments of RFQ by BATL, RF characterization of the first resonator was carried out using same test bench shown in Figure 1. The dipole mode ($TE_{110}$ and $TE_{111}$) frequencies were reduced much below the $TE_{210}$ mode frequency by adjusting the lengths of Dipole Stabilizer Rods (DSRs) such that the only nearby mode with frequency higher than the $TE_{210}$ mode is $TE_{211}$. The first resonator was tuned to 352.12 MHz ($TE_{210}$ mode) for the optimized field configuration. After successful high power conditioning, proton beam (50 KeV, 1 mA) from ion source was accelerated to 3 MeV using these two segments [3]. The field tuning of the second resonator was done independently in similar way. We tried to keep the tuned $TE_{210}$ mode frequency same in both resonators. The tuned $TE_{210}$ mode frequency corresponding to optimized field profile was 352.10 MHz. The advantage of this approach is that the field profile in individual tuned resonators corresponding to $TE_{210}$ mode does not change much when they are coupled together. Also the $TE_{210}{}^0$ mode frequency in coupled resonator remains almost same as the $TE_{210}$ mode frequency of the individual resonators. This makes the identification of $TE_{210}{}^0$ mode as well as the field tuning of coupled resonator involving 64 tuners less complicated.

After the two tuned resonators were coupled together, tuner lengths were adjusted iteratively to reduce the dipole contribution in comparison to quadrupole contribution. For optimized tuner settings, the field profile in all quadrants calculated from bead pull raw data is shown in Figure 3.

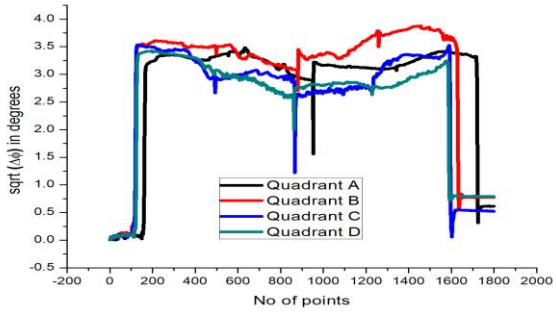


Figure3: Field profile in different quadrants of the LEHIPA RFQ.

The two points at both ends of each plot where the field changes sharply mark the beginning and end of the cavity. The point halfway the plot where the field again changes sharply marks the position of the coupling plate. We have observed a slight misalignment of vanes on either side of the coupling plate. This results in change of the transverse coordinates of the bead as it crosses the coupling plate. So there is a sharp change in field profile across the coupling plate. The same justification holds good at each mechanical joint where two segments are attached together (*i.e.* between segments 1 & 2, and between segments 3 & 4). However, there is overall reduction in field levels in lower quadrants (C and D) with respect to upper quadrants (A and B). This can be attributed to the observed sagging of the thread in lower quadrants which is around 1.5 mm in vertical direction near the midpoint of the 4 m long RFQ.

Since the start and end point of plots for all quadrants differ from each other, we took the first derivative of the raw data and found the change in the slope at the beginning and end of the RFQ and correspondingly adjusted the position in all the four quadrants. The raw data was then processed to calculate the dipole and quadrupole contribution without making any correction for bead sagging. Figure 4 shows the dipole contribution and deviation of quadrupole contribution with respect to average quadrupole contribution as functions of position. Both of them have been normalized with respect to average quadrupole contribution. From the plots, it can be concluded that, without correcting for bead sagging, the quadrupole flatness is within ± 5% and dipole contributions are within 12% for the optimum tuner settings.

We have also calculated the mode contribution using correction factor for bead sagging. The analysis assumes that the vertical displacement of the bead is maximum (1.5 mm) at the position of the coupling plate and it reduces linearly on either side with longitudinal distance, to become zero at both ends. The sensitivity of the phase variation along vertical direction was calculated to be 4.2 deg/mm. With this correction, the quadrupole flatness improves to ± 4% and dipole contributions are within 10%.

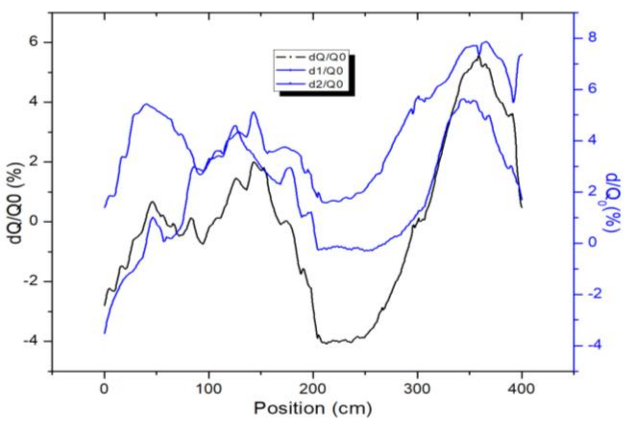


Figure 4: Field Flatness plot for the LEHIPA RFQ.

### *Quality Factor ($Q_0$) Measurement*

The loaded quality factor $Q_L$ was calculated from the $S_{21}$ plot shown in Figure 5. Since the $S_{21}$ is in the noise level (-76 dB), we have used averaging (avg factor 10) to reduce the noise floor.

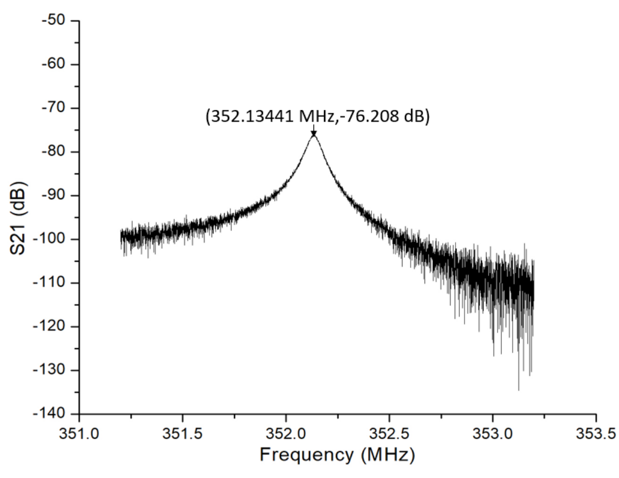


Figure 5: $S_{21}$ Plot

In order to calculate the FWHM ($\Delta f$) and resonant frequency ($f_0$) accurately, we have fitted the Lorentzian to the transmission coefficient given by $T = 10^{S_{21}(dB)/10}$. The fitted graph is shown in Figure 6. The Quality factor ($Q_L$) is calculated to be around 4,802.

The unloaded quality factor and the loaded quality factor are related by $Q_0 = Q_L\,(1+ \beta_1+ \beta_2)$, where $\beta_1$ and $\beta_2$ are the coupling coefficients of the loops. The coupling coefficient of the pick-up loop was negligibly small. The coupling coefficient of the feeder loop was found out to be 0.05 from VSWR measurement. Using all these values, the unloaded quality factor was found out to be 5,042.

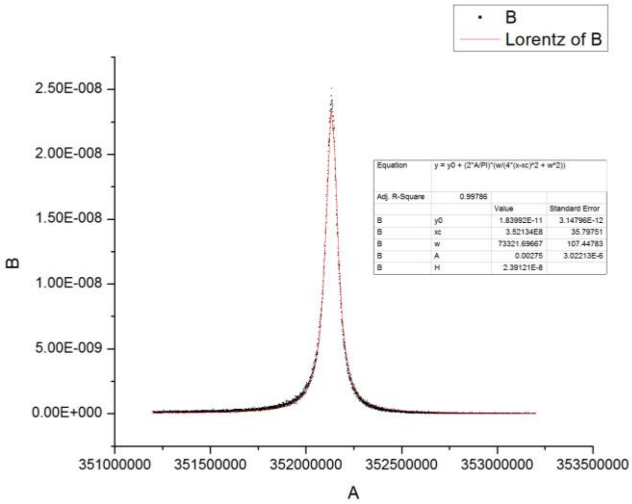


Figure 6: Lorentzian fit for the transmission parameter.

## CONCLUSION

The field tuning of LEHIPA RFQ has been successfully completed. The RFQ has been tuned to 352.12 MHz corresponding to the $TE_{210}{}^0$ mode. Field flatness ($dQ/Q_0$) of the order of ± 5 % has been achieved and dipole contributions ($d1/Q_0$, $d2/Q_0$) has been reduced to < 12%.

## REFERENCES


[1] P Singh et al., “Accelerator development in India for ADS programme”, Pramana – J. Phys.,Vol. 68, No. 2, February 2007, pp. 331-342.

[2] Slater J C., “Microwave Electronics”, D. Van Nostrand Company, New York,1950, pp. 81-82.

[3] P.V. Bhagwat et al., “Beam acceleration through proton radio frequency quadrupole accelerator in BARC”, JINST, **11**, T05001 (2016).

# DESIGN AND DEVELOPMENT OF A DUMP RESISTOR FOR A SUPERCONDUCTING ECR ION SOURCE AT VECC

Anuraag Misra# and P. Y. Nabhiraj
Variable Energy Cyclotron Centre, 1- AF, Bidhannagar, Kolkata-700 064, India

*Abstract*

Under upgradation of cyclotron systems, an 18 GHz superconducting ECR ion source (SCECRIS) is being designed and developed at VECC. Design of the magnetic system of SCECRIS had been completed and initiatives are taken for its fabrication and testing. The magnetic system consists of four axial superconducting solenoid coils and a permanent magnet based hexapole placed concentrically with the superconducting coils. The superconducting coils will store maximum upto ~50kJ of magnetic energy with an operating current of ~150A. In the event of a quench, the energy stored in the coils has to extracted and dumped quickly with a time constant of ~4s in a dump resistor of 2Ω. The dump resistor is inserted in series with the superconducting coils. As a crucial part of the quench protection system for the superconducting coils of the ECRIS a 2Ω dump resistor is designed, developed and tested. The design of the dump resistor is done to keep the voltage over the dump resistor <500 V as well as it should absorb the stored magnetic energy (~50kJ). The dump time constant is evaluated using mega current-square time integral (MIIT). For SCECRIS coil parameters an $R_{dump}$=2 Ω is calculated. The resistor is implemented using 0.8 mm thick and 530 mm long SS304 strips. They are connected in meander layout to minimize the stray inductance and increase the surface area for cooling. The thickness and spacing between the strips is optimized to keep the electromagnetic force between the strips < 50N. The assembly is tested in CW mode by dumping equivalent energy in the dump resistor. The peak temperature in the dump resistor is <50°C. The measured inductance of dump resistor is ~5μH. This paper will present the design and test results of the dump resistor for SCECRIS axial superconducting solenoid coils.

## INTRODUCTION

K-130 cyclotron is presently being modernized at Variable Energy Cyclotron Centre (VECC) to provide high charge state and high intensity heavy ion accelerated beams to the users. This demand generates a need for an ion source with a maximum operating magnetic field of up to 3 T. In order to generate the required distribution of an axial magnetic field at comparatively lower power consumption, it is optimum to use superconducting electromagnets for the Superconducting ECR Ion Source (SCECRIS) ion source [1-4]. The preliminary design of the magnetic system is done. Fig 1 shows the electrical circuit of the designed magnetic system. The electromagnets of the ion source contain four coaxial solenoids. The outer solenoids are connected to the power supply (V3) in series, while the inner solenoids have an independent power supply (V1 & V2); the current excitation in the middle solenoid is in an opposite direction to the others.

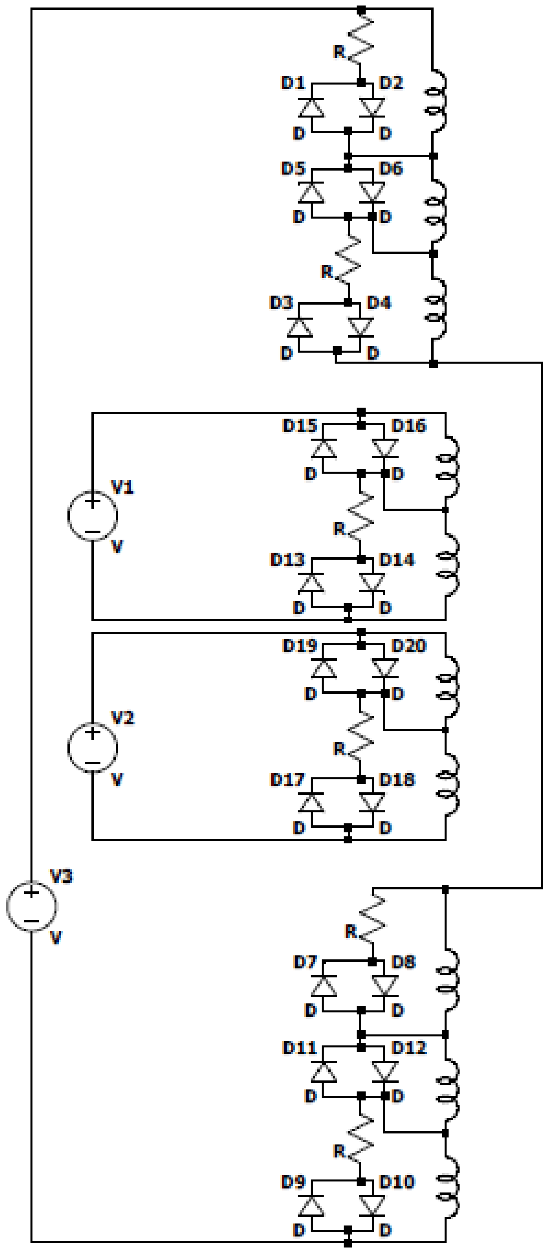


Figure 1: Electric circuit diagram of the electromagnets of SCECRIS. V1, V2, V3: power supplies, D1-D20: cold diodes, R: dump resistor.

# anuraag@vecc.gov.in

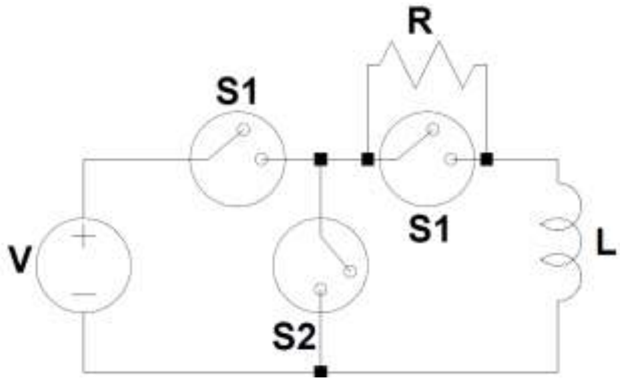


Figure 1: Schematic of quench protection system

The designed superconducting coils of the SCECRIS will store maximum magnetic energy of ~50kJ with an operating current of ~150A. In the event of a quench, the superconducting coil becomes resistive at the location of quench and the quench spreads along the coil resulting in temperature rise of the coil. During quench, energy stored in the coils has to extracted and dumped immediately in the dump resistor for the protection of superconducting coil and current leads [5-7]. A schematic for the protection system of a superconducting coil under quench is shown in figure 1. During the normal operation, circuit breaker S1 remains in closed condition and full operating current passes through it. However, under a quench circuit breaker S1 is opened and circuit breaker S2 is closed. It causes the commutation of the load current from the power supply to the external dump resistor R . The dump resistor R is generally much higher than the superconductor normal state resistance. The dump resistor R is connected across the coil and the current in the coil decays exponentially with a time constant of L/R. In this way, the magnetic energy stored in the coil is removed and gets dissipated in the external dump resistor located outside the cryostat, thereby protecting the superconducting coil from quench induced damages. This type of protection is commonly known as active quench protection. The dump resistor should be designed by taking into consideration the following key aspects. The hot spot temperature calculations of the superconducting coil must be done including the electrical and mechanical parameters of the superconducting coil composite. The maximum voltage rating of the dump resistor mainly depends on the electrical insulation of the superconducting coil. The dump resistor parameters has to be selected in such a way so that it can dissipate the total stored magnetic energy of the superconducting coil without damage. Moreover, the dump resistor should also be able to handle the heat load and electromagnetic stress produced during the process of stored energy dissipation. Based on the above mentioned design aspects and constraints, a dump resistor for superconducting coil is designed, developed and tested. In this paper, the methodology for the design of dump resistor and relevant calculations are presented. The implementation, fabrication and assembly and testing of the dump resistor is also outlined.

## DESIGN OF DUMP RESISTOR

The dump resistor is calculated using the value of maximum hot spot temperature of superconducting coil arising in the event of quench. The maximum hot spot temperature is obtained by using the adiabatic heat balance equation as given in Eq. 1

$$\int_0^t J^2(t)\,dt = \int_{T_0}^{T} \frac{C(T)}{\rho(T)}\,dT \qquad (1)$$

where, $J$(T) is the operating current density, $C$(T) and $\rho$(T) are temperature dependent heat capacity and resistivity of superconducting composite respectively. $t$ is the dump time constant, $T_0$ is the operating temperature and $T$ is the maximum hot spot temperature. The left hand side integral is a function of temperature and it is known as MIIT. The right hand side of the integral is evaluated using the specific heat of different elements used to make the NbTi superconducting coil. The data is obtained from Cryodata [8]. The resistivity of copper as a function of temperature is calculated from the relations given in [9-10]. The dump time constant $\tau_d$ is evaluated from Eq. 1 and it is calculated to be 2.5 s for SCECRIS design parameters. As the inductance of superconducting coil is 5 H, Hence the value of dump resistor is calculated to be 2Ω. SS304L is chosen for the implementation of the dump resistor due to its properties of low temperature coefficient, high density and high strength.

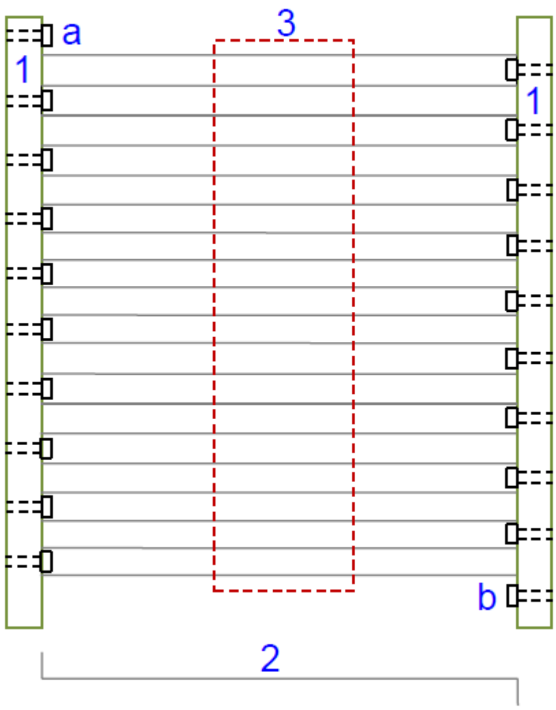


Figure 3: Top view of the assembled dump resistor. 1: G-10 clamping plate. 2: Single SS304L strip. 3: set of 20 series connected SS304L strips forming the dump resistor. a,b: dump resistor terminations.

## FABRICATION AND TESTING OF DUMP RESISTOR

Figure 3 shows the top view of the assembled dump resistor. It can be easily understood from the figure that layout of the dump resistor is done in such a way so that complete assembly of the dump resistor is compact as well as there is sufficient amount of cooling through natural convection process. The dump resistor is implemented using 0.8 mm thick and 530 mm long SS304L strips. To obtain a total resistance of 2Ω twenty number of strips are connected in series. Each single strip has a resistance of 100mΩ. A repulsive electromagnetic force is exerted between the strips during the energy dumping process. The force vector gets cancelled in the middle part of the dump resistor, however the force is maximum at the ends of the resistor. The electromagnetic force is given by Eq. 2 [11].

$$F = \frac{\mu_0 I^2}{\pi h}\left\{\arctan\left(\frac{h}{d}\right) - \frac{d}{2h}\ln\left(1+\frac{h^2}{d^2}\right)\right\} \qquad (2)$$

where, $I$ is the current, $h$ is the thickness of strip and $d$ is the distance between the two strips. The thickness and spacing between the strips are optimized to keep the electromagnetic force between the strips to be < 50 N. Figure 4 shows the photograph of the fabricated and assembled dump resistor. All the twenty strips are connected in series and mounted on a G-10 plate. At first the resistance of dump resistor is measured with a LCR meter. It is found to be 2.1 Ω , which is very close to the design value of 2Ω. Thereafter, the inductance of the dump resistor is measured for different spacing between the strips. The inductance of the dump resistor is found to be less dependent on spacing between the strips. At the design value it is measured to be only ~5μH. Finally a power supply of ~500W is connected across the dump resistor. At the maximum drawn current of 15A from the power supply the temperature rise in the dump resistor is found to be <50°C.

Figure 4: Photograph of the assembled dump resistor

## CONCLUSION

A quench protection system for a superconducting coil of SCECRIS is designed, developed and tested. The dump resistor is designed using the dump time constant calculated from adiabatic hot spot formula applied on the superconducting coil composite. A 2Ω dump resistor is implemented using SS304L material for operating at 150 A current and capable of dissipating 50 kJ of stored energy. The layout of the dump resistor is done in such a way to make it compact and ensure natural convective cooling. The measured values of temperature rise, resistance and inductance of the dump resistor are found to be in close agreement with the design objectives.

## REFERENCES


[1] S. Gammino, G. Ciavola, L. Celona, D. Hitz, A. Girard, and G. Melin," Rev. Sci. Instrum. **72**, 4090 (2001)

[2] D. Leitner, M. L. Galloway, T. J. Loew, C. M. Lyneis, I. Castro Rodriguez, and D. S. Todd, Rev. Sci. Instrum. **79**, 02C710 (2008)

[3] H. W. Zhao, L. T. Sun, J. W. Guo, W. Lu, D. Z. Xie, D. Hitz, X. Z. Zhang, and Y. Yang, Phys. Rev. Accel. Beams **20**, 094801 (2017).

[4] C. Lyneis, D. Leitner, M. Leitner, C. Taylor, and S. Abbottet, Rev. Sci. Instrum. **81**, 02A201 (2010).

[5] M. N. Wilson, *Superconducting Magnets*, Oxford Science Publications, (1983).

[6] Y Iwasa, *Case Studies in Superconducting Magnets: Design and Operational Issues*, Plenum: New York, (1994).

[7] Swati Roy *et al* 2017 *J. Phys.: Conf. Ser*. **832** 012014.

[8] "User's Guide to HEPAK Version 3.21," Cryodata Inc., P.O. Box 558, Niwot, CO80544.

[9] F. R. Fickett, "A Preliminary Investigation of the Behaviour of High Purity Copper in High Magnetic Fields," INCRA Project No. 186 (June 1972).

[10] M. S. McAshan, "MIITS Integrals for Copper and for Nb- 46.5% Ti," SSc-N-468(1998).

[11] F. C. Moon, *Magneto-Solid Mechanics*, Wiley: New York, (1984).

# DESIGN AND DEVELOPMENT OF TARGET ASSEMBLY FOR UTILIZATION OF 9 MEV RF LINAC AS PHOTO-NEUTRON SOURCE


Rishi Verma[1,5,#], Prosenjit Dhang[1], Ekansh Mishra[1], Avneesh Dubey[1], Rohit Shukla[1,5], J. Nageswara Rao[1], J. Balu Naik[1], Shobhna Mishra[1], Basanta Das[1], Manraj Meena[1], Lakshman Rongali[1], Vivek Yadav[2], Abhijit Tillu[2], Dhruv Bhattacharjee[2], Shiv Chandan[2], R. Chauvan[2], Rajneesh Tiwari[2], Mayank Shukla[3], Tushar Roy[3], M. Srihari[4], N. Hanumanthu[4], D. P. Chakravarthy[4], A. Manjula[4], G. V. Rao[4], S. R. Ghodke[2], Archana Sharma[1,2,5]

[1]Pulsed Power & Electromagnetics Division, Bhabha Atomic Research Centre, Visakhapatnam
[2]Accelerator & Pulsed Power Division, Bhabha Atomic Research Centre, Mumbai
[3]Technical Physics Division, Bhabha Atomic Research Centre, Mumbai
[4]Control & Automation Division, Electronics Corporation of India Limited, Hyderabad
[5]Homi Bhabha National Institute, Mumbai



*Abstract*

A photo-neutron target assembly has been successfully integrated in to 9 MeV RF Electron LINAC at ECIL, Hyderabad for its utilization as neutron source. The entire LINAC setup is inside radiation shielded room and it is remotely operated through a PC in control room. At full rating, the X-ray dose rate of ~22 Gy/min is produced at 1m distance from Tantalum target. The photo-neutron target assembly for neutron radiography has overall dimensions of 700mm (L) × 855mm (W) × 700mm (H) and collimation ratio (L/D) of 50. To obtain maximum thermal neutron fluence rate, two beryllium cylinders of 63mm diameter having lengths of 44mm and 84mm have been used along with 60mm HDPE moderator in between. To minimize the gamma content at image plane, collimator is placed perpendicularly in between two Beryllium targets and also the Beryllium targets are cylindrically covered with lead shielding. Collimator has 500mm length, 10mm aperture and 200mm image plane diameter. Thermal neutron flux measured at aperture and image plane were $\sim 2.7\times10^6$ and $\sim 7.4\times10^3$ neutrons/cm$^2$/second/kW e-beam, respectively. Time resolved signatures of gamma and neutron pulses (obtained using plastic and NaI scintillator detectors) confirmed that gamma emission is coincident with electron beam pulse for same duration i.e. ~5µs, whereas neutron emission is subsequently followed upon for the duration of ~35µs. For reducing gamma dose at the image plane, design and fabrication of modified ϒ-n target assembly (gamma dose <60 R/hr) has recently been completed at BARCF (Vizag) and its integration work is presently underway. This paper will cover details on design, installation and testing of our first photo-neutron target assembly along with highlights on operational intricacies of LINAC.


## INTRODUCTION

A photo-neutron target for thermal neutron radiography application using 9 MeV electron beam LINAC has recently been commissioned and tested at ECIL, Hyderabad. Neutron radiography utilizing thermal neutrons is used for imaging of light atoms (e.g. $H_2$, $D_2$, C, N etc.) in the presence of heavier ones. It's a non-destructive technique. In the utilized scheme, photo-neutron production occurs through double layer converter i.e. first layer is of thin high–Z material (e.g. W, Ta, Pb, Mo etc) and second layer is of low-Z material (e.g. Be, Be+$D_2$ etc) having low neutron separation energy [1]. The first conversion e-γ occurs when electron beam from an accelerator is incident on the high-Z target, it generates cascade shower of Bremsstrahlung X-rays [2]. In the subsequent stage, Bremsstrahlung X-rays are then directed towards the γ-n converter. Under the condition when Bremsstrahlung X-ray energy is greater than the neutron separation energy of γ-n converter target, neutrons are produced [3-5]. In the implemented scheme 'Tantalum' and 'Beryllium' have been subsequently used as first and second layer.


# rishiv@barc.gov.in


## LINAC SYSTEM HARDWARE

The pulsed coupled-cavity on-axis LINAC operates at a frequency of 2856 MHz with pulse width of ~6 µs and 200 Hz repetition rate [6]. The sub-assemblies of LINAC are horizontally aligned and the setup is shown in Fig. 1.

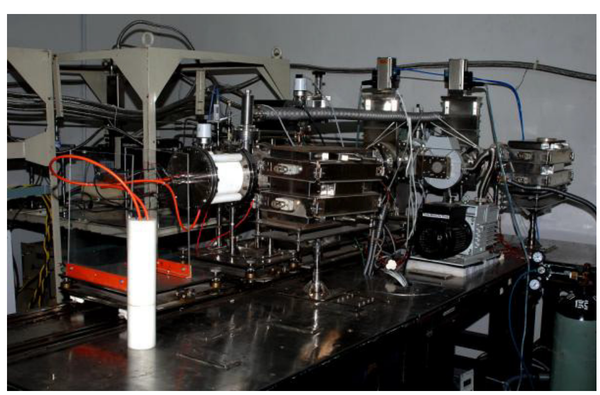

Figure 1: View of the coupled-cavity on-axis LINAC.

This LINAC has been RF-conditioned up to a peak power of 3.6 MW. A $LaB_6$-based electron gun serves as the injector of electrons into the on-axis coupled cavity LINAC, which is powered by a klystron-based RF source [6]. The electrons are accelerated to energy of 9 MeV in a length of ~1m. Fast current transformer at the end of the LINAC is used to measure the beam current. The accelerated beam of required size strikes on the water-cooled tantalum target placed at the end of the beam tube. Bremsstrahlung X-rays produced from the 'Ta' target are then allowed to fall on the 'Be' target placed inside the thermal neutron radiography setup. The main operating parameters of 9MeV LINAC are summarized in Table I.

**Table I.** Major specifications of 9MeV RF LINAC

| | | |
|---|---|---|
| Beam Energy | : | 9 ± 0.1MeV |
| Peak beam current | : | 150 mA |
| Average Beam power | : | 1.5-2 kW |
| Length of accelerator | : | ~1 meter |
| Pulse Width | : | 6μs |
| Pulse repetition rate | : | 250 Hz (maximum) |
| Injection voltage | : | 30-50 kV |
| Microwave Frequency | : | 2856 ± 2 MHz |
| Peak klystron power | : | 3.5 MW (nominal) |

Constructional schematic and photographs of the new 1.6mm thick, 50mm diameter 'Tantalum' e-ϒ target assembly has been shown in Fig. 2 and Fig. 3 respectively. For heat removal about 4.5mm wide water channel path has been provided at its backside.

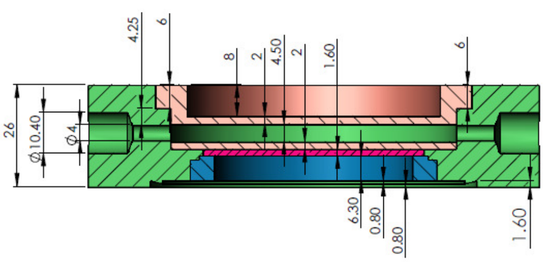


Figure 2: The water cooled e-ϒ 'Ta' target assembly.

Figure 3: The e-beam facing 'Ta' target assembly

## PHOTO-NEUTRON TARGET ASSEMBLY

The photo-neutron target is rectangular in dimensions (X × Y × Z: 700mm × 855mm × 700mm; for L/D=50). To obtain maximum thermal neutron fluence rate, two beryllium cylinders of 63mm diameter and length of 44mm and 84mm has been used along with 60mm HDPE moderator in between and a collimator (inlet aperture of 10mm and outlet aperture/image plane of 200mm) is placed after HDPE in between the two Beryllium targets in +Y direction [4]. To minimize the gamma content in image plane, thermal neutron collimator has been designed in perpendicular direction to the incident beam and also the Beryllium target is cylindrically covered with lead shielding. The detailed two-dimensional schematic of integrated target assembly is shown in Fig. 4.

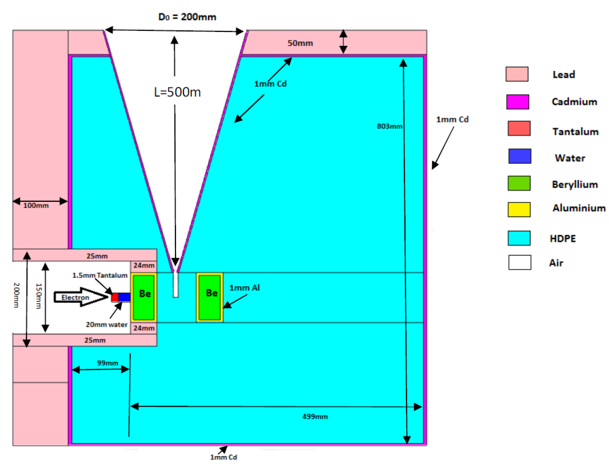


Figure 4: 2D schematic of integrated target assembly.

The dissected 3D view of the photo-neutron target assembly installation is shown in Fig. 5.

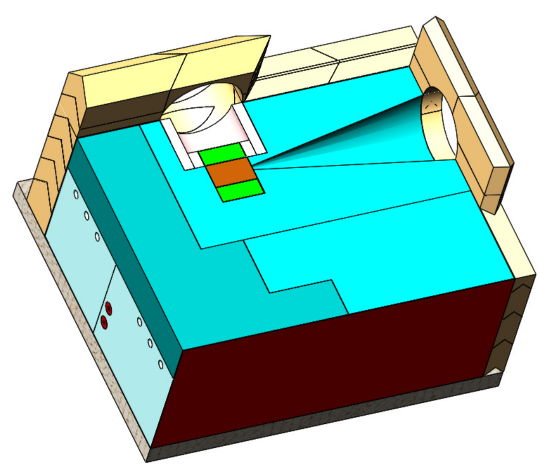

Figure 5: 3D view of photo-neutron target assembly.

The overall measure of photo-neuron target based thermal neutron radiography setup in all the three dimensions is shown in Fig. 6.

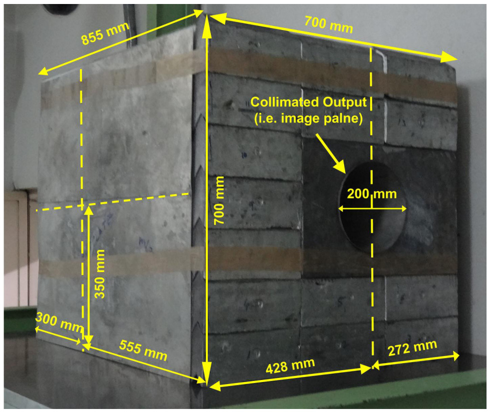


Figure 6: Measures of thermal neutron radiography setup in three dimensions.

## OPERATIONAL SAFETY INTERLOCKS

Various safety interlocks have been implemented for the safe operation of various sub-modules of LINAC. The klystron modulator has been interlocked with water flow, arc detector, klystron electromagnet current, klystron modulator door and $SF_6$ gas pressure in waveguides. In case if any of the interlock getting activated, the input trigger pulse to klystron modulator is blocked and thus no output RF power is generated. The klystron electromagnet supply is interlocked with water flow, as there is high current that can damage the electromagnet in absence of water. A relay based hardwired interlock unit has been used for implementing the above-mentioned interlocks. For the safe operation of system, the synchronized trigger generator is interlocked with vacuum and arc detector. In case of fall of vacuum pressure or arcing, the trigger going in to the system is stopped. The vacuum status of E-GUN, CAVITY and TARGET is continuously monitored and tracked during operation. In case if any of the interlock getting activated of either of the auxiliary systems, LINAC operation is self-halted.

## RESULTS AND DISCUSSION

The temporal response of measured electron beam and seeded RF power (forward and reflected) obtained on a battery powered oscilloscope is shown below in Fig. 7.

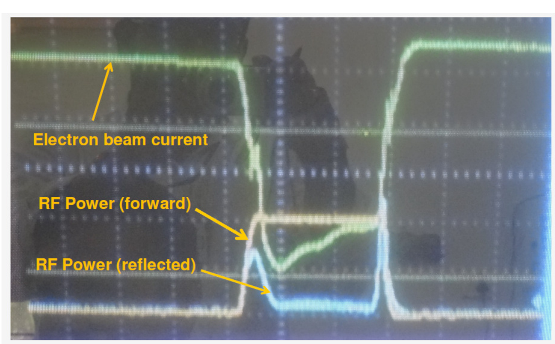


Figure 7: Temporal response of e-beam and RF power. (H Scale: 2.5μs/div, V Scale: 100mV/div)

The dose rate of x-ray produced after hitting Ta target by 9 MeV electron beam has been measured by using air ionization chamber (Model no. CC13 make IBA Dosimetry, Germany). At 250 Hz operation, the maximum x-ray dose rate of ~21 Gy/min at 1m distance from Tantalum target has been measured using air ionization chamber [7]. A biological shielding room (ordinary concrete, ρ=2.35 g/cc) had been made to shield produced X-rays. The wall thickness of shielding room is based on the regulatory dose limit of 1μSv/hr for the occupational exposure in continuously occupied areas (as per AERB Safety Directive 2/91).

Angular dose profile and energy measurement exercise was performed with the help of CaSo4:Dy TLD pellets [8]. These pellets were characterized with known dose of 1R and 100R to know the percentage standard deviation among them. Pellets having standard deviation less than 4% were chosen to maximize the measuring accuracy.

The angular dose profile (total angular span was 45° in horizontal plane with ±7.5° variation in both sides) of X-ray has been measured using CaSO4:Dy TL pellets (132mA beam current, 10Hz, beam power ~65W, exposure time 90sec). 0.05 mol% Dysprosium doped TL pellets has been used for this experiment to minimize pellet to pellet dose value variation. The measured x-ray angular dose profile is shown in Fig. 8.

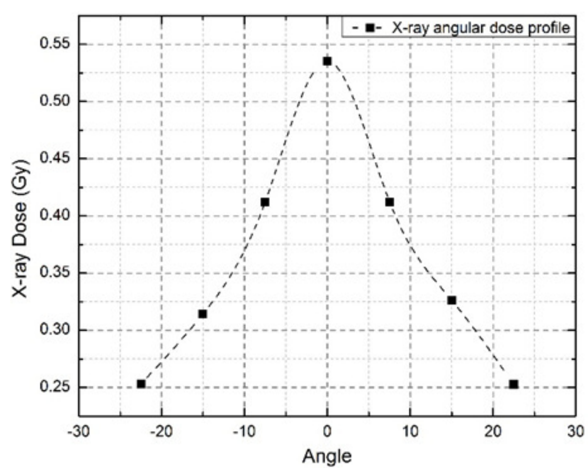


Figure 8: X-ray Angular dose distribution @1m.

To choose ideal photo-neutron target for our 9 MeV LINAC, X-ray energy spectrum has also been measured by CaSO4:Dy TL pellets. For Energy measurement copper of different thicknesses was used to know the transmitted dose by putting pellets behind them [8]. The obtained energy spectrum is shown in Fig. 9. Photon peak at ~2.15 MeV strongly suggest beryllium (photo-neutron emission threshold >1.667 MeV) as our suitable photo-neutron target.

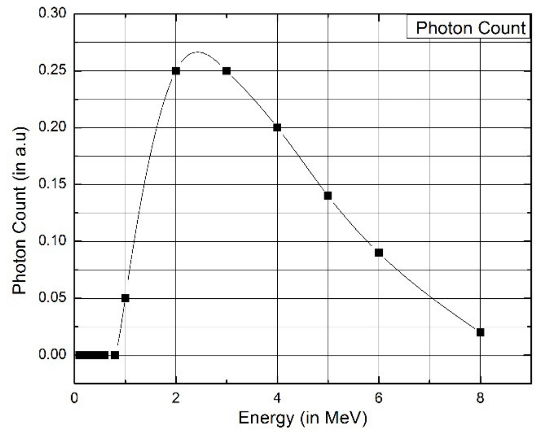


Figure 9: Measured X-ray energy spectrum.

Photo-neutrons are produced isotropically from beryllium target with the interaction of high energy Bremsstrahlung X-rays. Generated thermal neutrons come through collimator on image plane and rest are themalized by HDPE and later absorbed by cadmium sheets. Collimator length, inlet aperture diameter and diameter of the image plane were optimized by simulation in order to get the maximum thermal neutron fluence rate at the image plane and we choose L/D=50 to get better sharpness of the radiograph. The thermal neutron fluence rate calculated on the image plane is ~5.56 $\times 10^3$ n/cm$^2$/s/kW e-beam. The simulation results of neutron energy spectra on the aperture plane and image plane are shown in Fig. 10.

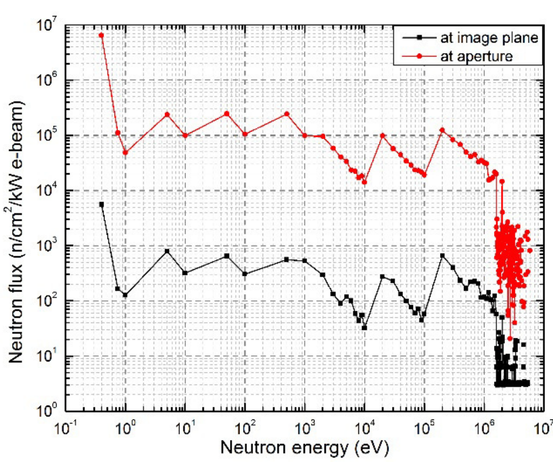


Figure 10: Neutron flux at aperture and image plane.

Thermal neutron flux at aperture (~3cm apart from the aperture) measured through Silver foil activation analysis method is ~2.2$\times 10^5$ neutrons/cm$^2$/second at 10 PRF (~2.7$\times 10^6$ neutrons/cm$^2$/second/kw e-beam). Thermal neutron flux at image plane measured through Indium foil activation analysis method is ~6.1$\times 10^3$ neutrons/cm$^2$/second at 100 Hz PRF (~7.4$\times 10^3$ neutrons/cm$^2$/second/kW e-beam). Thermal neutron beam profile at image plane was measured through Indium foil activation analysis method and the anisotropy was found to be less than 1.2 (center to peripheral).

Time resolved signatures of gamma and neutron pulses were obtained using boron loaded plastic (SPMT-1) and NaI (SPMT-2) scintillator detectors [8]. These measurements confirmed that gamma emission is coincident with electron beam pulse for same duration i.e. ~5µs, whereas neutron emission is subsequently followed upon for the duration of ~35µs.

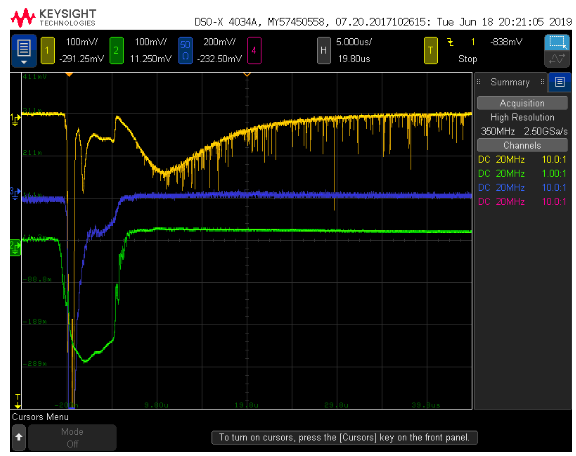


Figure 11: Time resolved measurement of x-rays and neutrons using scintillator photomultiplier detectors.

In the oscilloscope traces shown above, waveform depicted as Ch-1 is output signal of boron loaded plastic scintillator, Ch-3 is output signal of NaI scintillator detector and Ch-2 is output signal of electron beam from fast current transformer. The coincident and overlapping trace of SPMT-1 detector signal on the SPMT-2 detector signal distinct the identity of x-ray and neutrons. The negligible cross-section of NaI scintillator for neutrons is clearly evident in the corresponding trace.

## SUMMARY

A project has been taken up by Beam Technology Development Group (BTDG), BARC, to develop a 'Neutron Radiography Facility' using 9 MeV RF Electron LINAC at ECIL, Hyderabad. Recently, its operation has been restored and photo-neutron target assembly has been successfully integrated by collaborative efforts of Control & Automation Division (ECIL, Hyderabad), Pulsed Power & Electromagnetics Division (BARC, Visakhapatnam), Accelerator & Pulsed Power Division (BARC, Mumbai), and Technical Physics Division (BARC, Mumbai). The entire LINAC system is inside radiation shielded room and it is remotely operated through a PC in control room. At full rating operation, the x-ray dose rate of ~22 Gy/min is produced at 1m distance from Tantalum target. Generated thermal neutron flux from γ-n reaction with Beryllium target has been measured as ~2.7$\times 10^6$ and ~7.4$\times 10^3$

neutrons/cm$^2$/second/kW e-beam at aperture and image plane, respectively. Time resolved signatures of gamma and neutron pulses (obtained using boron loaded plastic and NaI scintillator detectors) confirmed that gamma emission is coincident with electron beam pulse for same duration i.e. ~5µs, whereas neutron emission is subsequently followed upon for the duration of ~35µs. For the purpose of avoiding gamma contribution in neutron radiograph application, procurement of a high resolution gated ICCD camera is in process.

## ACKNOWLEDGEMENT

We are very much thankful to Shri R. K. Rajawat, Associate Director, BTDG, BARC Shri Debashis. Das, Director, RRCAT & Ex-CMD, ECIL, Shri D. Venkateswarlu, Regional Director, BARCF(V) and Ms. Kavita P. Dixit, SO/H, BSCS, BARC for their guidance, support and encouragement in this project.

## REFERENCES

1. Matthew Hodges, Alexander Barizilov, Yi-Tung Chen, Daniel Lowe, *Characterization of 6 MeV accelerator driven mixed neutron/ photon source*, Physics Procedia, 90 (2017) 164-169.Lucerne, July 2004, THZCH03, p. 249 (2004); http://www.JACoW.org
2. L. Auditore, R. C. Barna, D. Loria, E. Morgana, A. Trifiro, M. Trimarchi, *Design of an e-γ converter for a 10MeV electron beam*, Particle Accelerator Conference, New York, NY, USA, 2011.
3. L. Auditore, R. C. Barna, D. De Pasquale, A. Trifiro, M. Trimarchi, *Design of a photoneutron source based on a 5 MeV electron LINAC*, Proceedings of EPAC, (2004) 2347-2349.
4. B. J. Patil, S. T, Chavan, S. N. Pethe, R. Krishan, S. D. Dhole, *Simulation of e-γ-n targets by FLUKA and measurement of neutron flux at various angles for accelerator based neutron source*, Annals of Nuclear Energy, 37 (2010) 1369-1377.
5. Tabbakh Farsid, Khalafi Hossein, *Target optimization for a 10-MeV E-beam neutron converter*, Nuclear Science and Techniques, 21 (2010) 69-71.
6. K. C. Mittal, V. Yadav, D. Bhattacharjee, *Performance of the 9 MeV RF linac for cargo scanning*, Proceedings of the DAE-BRNS Indian particle accelerator conference, 46(8), 2011.
7. Nishant Chaudhary, D. Bhattacharjee, V. Yadav, S. D. Sharma, S. Acharaya, K. P. Dixit, K. C. Mittal, *Monte Carlo simulation and measurement of X-ray dose from 9 MeV RF electron for cargo scanning*, Indian Journal of Pure & Applied physics, 50 (2012) 517-519.
8. Glenn F. Knoll, *Radiation Detection and Measurement*, Fourth Edition, 2010; Edited by John Wiley and Sons.

# A proposal for using a "plasma stripper" in the High Current Injector at IUAC, New Delhi

G. Rodrigues, Inter University Accelerator Centre, New Delhi -110067

*Abstract*

A proposal for a plasma stripper to be used as a stripping device in the High Current Injector beamline, before final acceleration through the existing Superconducting Linear Accelerator (SC-LINAC) may be a possibility to further improve the most probable charge states and beam intensities as compared to using conventional gas and/or foil strippers. From operational experience of using gas and foil strippers, it is well known that limitations arise in the lifetime of the foil especially when using heavy ions. Furthermore, the straggling effects and energy loss may deteriorate the beam quality. On the other hand, the usage of gas strippers leads to much lower available charge states as compared to using a foil stripper.

The charge state of the projectile is determined through the ionization and recombination mechanisms, which are different in a fully ionized plasma as compared to a cold gas or a partially ionized plasma. The ionization in fully ionized plasmas is mainly due to collisions with bare target ions. In cold gases and partially ionized plasma the target ions are shielded by bound target electrons, therefore the interaction is less effective. In fully ionized plasmas the recombination of the projectile is strongly reduced due to the absence of bound target electrons, which can be captured by the projectile in a cold gas or a partially ionized plasma. Due to successive ionization and the slow recombination processes, fully ionized plasma can generate highly stripped non-equilibrium charge states of heavy-ion projectiles

The advantage of using a plasma stripper is the enhanced most probable charge states when compared to foil. The beam quality emerging after passing though the plasma stripper is better controlled due to the axial magnetic field used for confining the plasma.

## INTRODUCTION

The High Current Injector (HCI) programme [1] which is currently being pursued at the Inter University Accelerator Centre, New Delhi is presently in installation and commissioning stages. In order to further achieve higher energies beyond the Coulomb barrier, a foil/gas stripper will be utilised after the exit of the DTL accelerator (1.8 MeV/u) for further acceleration through the 97 MHz SC-LINAC [2]. Although foil/gas strippers are normally used at various accelerators around the world and also in our existing 15 UD-16 MV Tandem Accelerator, the ultimate achievable charge states are still limited. If we consider other mediums like a plasma, the charge states of projectile ions are always determined by ionisation and recombination processes in the target (plasma or cold matter). The free electrons are captured by the projectile ions less probably than the bound electrons. The reason being, that in the case of a free electron capture, the excess binding energy and momentum have to be accounted for by the much lower probable processes like, radiative and dielectronic recombination or three-body recombination. The cross sections for electron capture in plasmas are smaller than those in cold matter due to fewer bound electrons in the plasma. Therefore, ions in highly ionised plasmas can attain much higher charge states than those in cold matter [3,4]. In a standard model approach, the energy loss of heavy ions in a fully ionized plasma is calculated in terms of a modified Bethe-Bloch formula given by

$$\frac{dE}{dx} = -4\pi n_e \frac{e^4 Z^2{}_{eff}}{mv^2} \ln \frac{4\pi mv^2}{h\omega_p} \qquad (1)$$

In figure 1., the stopping powers for a plasma and a cold gas are shown assuming the same effective charge in both cases [5].

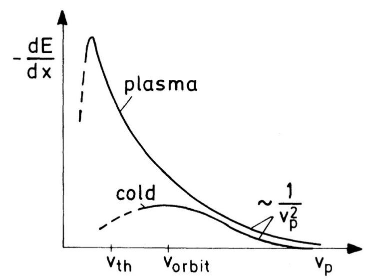


Figure 1: Stopping power as a function of projectile velocity for two cases (a) plasma and (b) cold gas [5]

## REVIEW OF EXISTING PLASMA STRIPPERS

The first experimental evidence of a stopping power enhancement in a plasma was observed for deuterons and protons [6,7]. Later, systematic energy loss measurements in a hydrogen plasma verified the difference in stopping between a highly ionized plasma and cold matter also for heavy ions. Experiments have been carried out at energies from 1-6 MeV/u for a large variety of ion species from carbon to uranium [8]. An enhancement factor of up to 3 was demonstrated.

There are various types of plasma strippers being used worldwide for achieving the most probable charge states and to further increase the beam energies. The beneficial effects of higher charge states achieved using a plasma as a stripping medium is well known.

*Plasma pinch device*

The 'plasma pinch' devices which are currently being tested by the plasma physics group from the University of Frankfurt, is basically an inductively coupled plasma where an axial magnetic field exists and there is no electrode erosion [9]. Many versions of this device have been tested, few of them like spherical theta pinch and and spherical screw pinch have been tested with beam. Figure 1. below shows the spherical theta pinch device being tested as a plasma stripper at GSI, Darmstadt. The recent experiment performed [10] during end of March 2019, shows the charge state distribution of a 3.6 MeV/u $Au^{26+}$ after passing through a hydrogen plasma in comparison to a cold gas (figure 3.). The maximum charge state with plasma is between 32+ to 34+, whereas with cold gas the main charge distribution is between 28+ to 30+.

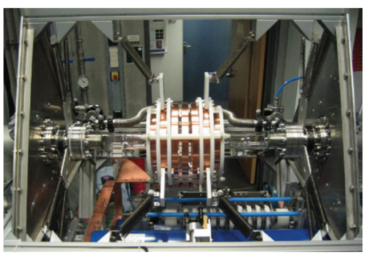

Figure 2: View of the Spherical Theta Pinch device under beam tests at GSI, Darmstadt, Germany [9]

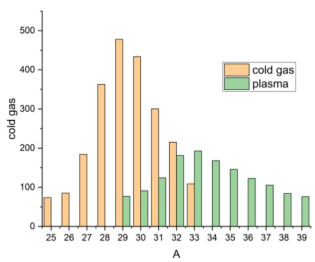


Figure 3: Charge state distribution of a 3.6 MeV/u $Au^{26+}$ beam after passing through a hydrogen plasma in comparison to a cold gas [10]

*'Laser-produced' plasma*

The feasibility of using hot plasmas as strippers for low-energy ion beams has been investigated by measuring charge state distributions of 350 keV/u ions ($^{12}C$,$^{16}O$,$^{19}F$) after their passage through a laser-produced plasma target [11]. The plasma target was produced by irradiating a small pellet of lithium hydride with a Nd-glass laser. The profiles of electron densities of the plasma target were estimated from the intensity profiles of an Ar laser refracted by the plasma. The intensities of ions with different charge states were simultaneously measured using a time-resolved magnetic spectrograph. It was found that this plasma can yield higher charge states than conventional gaseous or solid strippers.

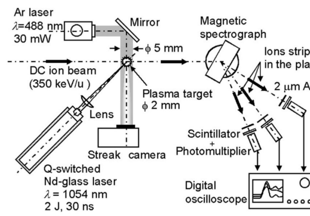


Figure 4: Experimental setup for the charge state distribution measurements and plasma target diagnostics [11].

## 'PLASMA' STRIPPER FOR HCI

The existing and planned foil/gas stripper system for the HCI will improve the charge states for further acceleration through the SC-LINAC. The charge state distributions have been calculated assuming an input beam energy of 1.8 MeV/u exiting from the last DTL cavity and passing through thin carbon foils of varying thickness positioned before the first achromatic bend. All beams extracted from the ECR ion source with A/q = 6 are assumed to have been accelerated through the RFQ and DTL accelerators. Figure 5. shows the final beam energies achieved through the SC-LINAC and their the corresponding most probable charge states. Figure 6. shows the charge state fractions after passing through a 10 $\mu g/cm^2$ carbon foil. For example, in the case of a typical beam of $^{109}Ag^{18+}$, the output beam energy emerging from a carbon foil of thickness 10 $\mu g/cm^2$ will be 1.793 MeV/u with a most probable charge state <Q> of 33.25, having a <dQ> of 1.31.

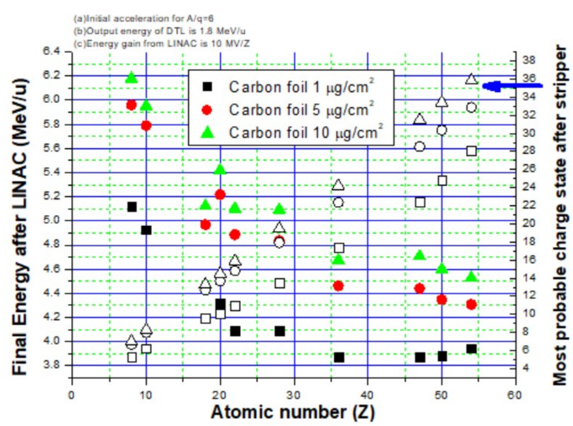


Figure 5: Final energies and most probable charge state as a function of atomic number using carbon foils of varying thickness

The final energy after acceleration through the SC-LINAC, assuming an energy gain of ~ 10 MeV per charge state is 4.87 MeV/u.

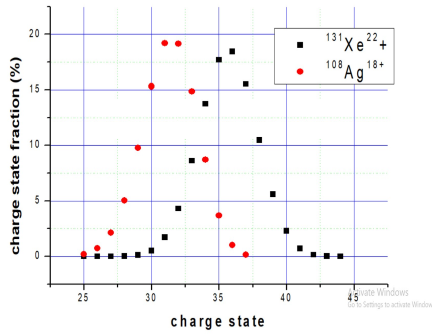


Figure 6. Charge state fractions after passing through a 10 μg/cm$^2$ carbon foil

For a plasma to be a viable stripper for slow ions, it must contain a sufficient number of fast electrons needed to attain a desired charge state during an ion dwell time. The basic idea of this scheme to inject slow, low charge state ions into an intense discharge for further stripping. However in addition to stripping, charge state reduction due primarily to charge exchange with low charge state ions and neutrals also occurs in most plasmas, a phenomenon this scheme is designed to minimize.

Considering equation (1), given above, and taking values for excitation energy for a plasma wave, $\frac{h\omega_p}{2\pi}$ = 0.083 eV at $n_e = 5x10^{18}\,cm^{-18}$ for a hydrogen plasma and comparing to the mean ionisation potential for molecular hydrogen as 19 eV, the Coulomb logarithm is larger in the case of a plasma than for cold matter and therefore leads to a higher stopping power. Therefore, the most probable charge states would be higher (as shown in figure 3.) than those calculated for carbon foils (shown in figure 5 and figure 6). A detailed modelling is being carried out for inferring the charge state distribution and thereby to know the energy losses.

The proposed plasma stripper will be re-located at the same position of the foil/gas stripper, i.e, close to the object plane of the first achromatic bend. The final goal is to compare the performance of two types of plasma strippers ; viz., induction coil type and laser-produced plasma and to see which gives the best performance in the long term scenario. One of the reasons for exploring a 'laser-produced' plasma is to rule out the effect of the magnetic field on the quality of the beam. In the first phase of installation, a 'theta-pinch' plasma will be used for initial tests and measurements to quantify the charge state distributions and whether it meets the designed goal. In the second phase, a 'laser-produced' plasma will be installed and tests will be performed.

## DISCUSSION AND CONCLUSION

The concept of using a 'plasma' stripper in the place of a conventional foil/gas stripper seems to be interesting considering the small lifetime of carbon foils and lower charge states achieved with gas strippers. The mean squared scattering angle (in units of mrad) through thin carbon foils is calculated to be, $\langle \phi^2 \rangle = 2.7 Z_i^2$ where $Z_i$ is the atomic number of the input beam of energy 1.8 MeV/u. Therefore, the option of using a laser-produced plasma or an induction coil type plasma would finally determine which system can match the goals in terms of achieving better beam quality for long duration when compared to using foil/gas strippers.

## ACKNOWLEDGEMENT

The author wishes to thank Dr.D.Kanjilal for his advice, help and constant support on developing this new technique. The author wishes to acknowledge the help received from Dr. Konstantin Cistakov from the Plasma Physics Group at the University of Frankfurt, Germany for his constant help and advice in connection with the development of the plasma stripper project, both at FAIR, GSI, Germany and for the High Current Injector development programme at IUAC, New Delhi

## REFERENCES

[1] A. Roy, Curr. Sci. 76 (1999) 149
[2] S.Ghosh et al, Phys.Rev.ST Accel.Beams,12,40101(2009)
[3] T.Peter, J. Meyer-ter-Vehn, Phys.Rev.A 43(1991)1998
[4] K.Cistakov, Univ .of Frankfurt, private communication
[5] T. Peter and J. Meyer-ter-Vehn, Phys. Rev.A 43(1991)2015.
[6] F.C.Young, D. Masher, S.J. Stephanakis, S.A. Goldstein andT.A. Mehlhom, Phys. Rev. Len. 49 (1982) 549.
[7] J.N. Olsen, T.A. Mehlhom, J. Maenchen and D.J. Johnson, J. Appl. Phys. 58 (1985) 2958
[8] K.-G. Dietrich, D.H.H. Hoffmann. E. Boggasch, J. Jacoby, H. Wahl, M. Elfers, C.R. Haas, V.P. Dubenkov and A.A. Goiubev, Phys. Rev. Lett. 69 (1992) 3623.
[9] G. Loisch, G. Xu, K. Cistakov, A. Fedjuschenko, M. Iberler, Y. Liu, T. Rienecker, A. Schönlein, F. Senzel, J. Wiechula and J. Jacoby, IEEE Transactions on Plasma Science, Bd. 42, p. 1163, 2014
[10] K.Cistakov et al., 10th International Particle Accelerator Conference, IPAC 2019, Melbourne, Australia
[11] K. Shibata, K. Tsubuku, T. Nishimoto, J. Hasegawa, M. Ogawa, Y. Oguri and A. Sakumi, Journal of Applied Physics, Vol.91,No,8,4833(2001)

# GIGABIT CAMERA INTEGRATION INTO EPICS FOR BEAM VIEWING APPLICATION AT IUAC-DLS

Ashish Sharma#, P. Patra, B. Karmakar, B.K. Sahu, IUAC, New Delhi, India.

*Abstract*

At Delhi Light Source (DLS), a CMOS gigabit ethernet based camera using GigEVision interface which supports very high throughput and a triggered acquisition process to obtain beam profile details has been selected. Its performance is compared with a USB camera at IUAC Low Energy Ion Beam Facility (LEIBF). This paper also illustrates the integration of the GigEVision camera into EPICS areaDetector environment using the aravisGigE module. EPICS base 3.15.xx which is built on OSI model has been installed and operated on Ubuntu 16.04. Operator screens for the camera have been developed using MEDM package while EPICS ADViewer plugin of ImageJ is used to display the image. More effective CaQtDM based GUI are finally deployed. A Yttrium Aluminium Garnet (YAG)-screen is placed in the beam path to obtain scintillation profile of the beam and the corresponding images taken from the cameras (USB and GigEVision interfaces) are processed through in-house developed software. Usage of this camera for observing DLS Laser spot is also explained.

## INTRODUCTION

A FEL based DLS project of IUAC is being developed to produce low emittance, narrow, bunched comb electron beam and intense THz radiation. Electron microbunches generated by striking photocathode with femtosecond laser pulse will be accelerated by a 2.6 cell normal conducting electron gun up to maximum of ~8 MeV energy. THz will be produced by injecting electron beam inside an undulator to produce THz radiation in the range of 0.18-3 THz [1].

In order to diagnose the electron beam bunch profile, and laser spot, three different beam viewers are planned. Two cameras will observe scintillation profile of electron beam on a YAG screen, and 3rd one will be employed in direct path of deflected and attenuated laser beam. This will act as a virtual cathode which will give the idea about the laser beam spot forming at the actual cathode after the electron gun [5].

This paper explains the implementation and compares the performance of Logitech C270 USB camera and FLIR's BFS-PGE-16S2C [6] GigEVision camera. Integration of camera into EPICS areaDetector [2] with control gui in CaQtDM [3], testing of setup at IUAC LEIBF is also explained. Present development is first implementation of EPICS based control system for DLS.

## USB CAMERA ACQUISITION

### *Camera Support Development*

Initial development of beam viewer started with Logitech C270 web-camera which had manual gain setting but with auto-focus and auto-trigger. Fig. 1 shows the image acquisition mechanism which is based on *linux v4l*, and *gstreamer1.0* packages. It delivered data packets from camera to local server on USB2.0 and on UDP LAN to client PC showing live image and profiles on Qt based GUI developed using python as shown in Fig. 2.

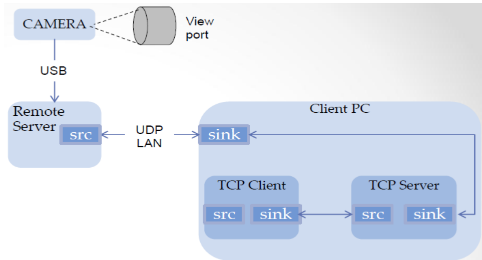


Figure 1: USB camera acquisition data flow

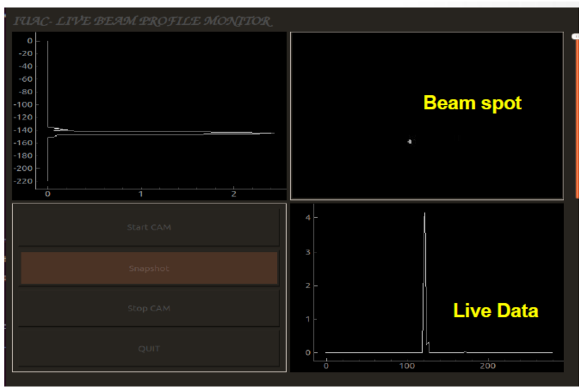


Figure 2: Control GUI for USB Camera

GUI consists of START/STOP acquisition buttons and Snapshot mode is used to display processed images with X-Y profiles. Gain and resolution settings could be changed in the back-end using *gstreamer1.0* command controls. Frame rate, exposure time, focus and trigger rate could not be changed with this camera.

## GIGEVISION CAMERA ACQUISITION

### *Camera Selection*

YAG screen size decides the Field of View (FoV) for camera, and the placement of camera on beam viewer decides Working Distance for lens selection. FoV and smallest feature size decides sensor resolution. Based on the DLS requirements, FLIR's camera [6] shown in Fig.3 with specifications listed in Table 1 was selected.

Table 1: Camera Specifications

| Property | Required Spec | BFS-PGE-16S2C with Tamron Lens (Fig. 1) |
|---|---|---|

#ashish.sharma@iuac.res.in

| | | |
|---|---|---|
| FoV | 25 mm | |
| WD | 30-60 cm | Focal Length = 50 mm |
| Sensor Resolution | 1024 × 768 (min) | 1440 × 1080 |
| Frame Rate | >30 FPS | 78 FPS |
| Exposure | Min. 10 µs | 7-30 µs |
| Shutter | Global | Global |


Figure 3: FLIR Camera and Tamron Lens

### *Camera Integration in EPICS areaDetector*

areaDetector module of EPICS [2] caters for areascan cameras from wide range of vendors like AVT, JAI, Andor, FLIR etc. having interfaces like USB3, Firewire, GigEVision. While there is a specific driver for each vendor and each type of interface, areaDetector provides flexibility to use multiple driver software in EPICS environment to connect the same camera. In order to connect to FLIR's camera using GigEVision, driver modules like ADSpinnaker, ADAravis, ADGenICam, and aravisGigE can be used in almost similar way. Present implementation is based on aravisGigE module. Firstly, *arv-tool* of aravisGigE module is used to obtain an XML file from camera upon first connection which provides a complete list of features available. This file is further used to produce a camera specific Database (.template) and control GUI .adl file understandable by MEDM. After that a new camera specific IOC was built. The *st.cmd* file was provided with maximum row (X) and column (Y) profile NDArray lengths for NDStatistics, while *aravisCameraConfig()* was called with current camera ID, and its corresponding database file was then loaded using *dbLoadRecords()*. Other databases from ADCore related to statistical analysis and common camera related plugins were also added by specifying the path to database folder using *set_requestfile_path()*. Fig. 4 shows the data flow from camera to client. NDStats and other plugins like NDProcess, NDColorConvert, NDROI etc could be enabled / disabled during runtime [4].

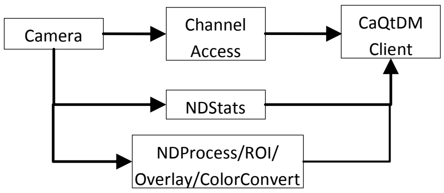


Figure 4: areaDetector data flow and plugins

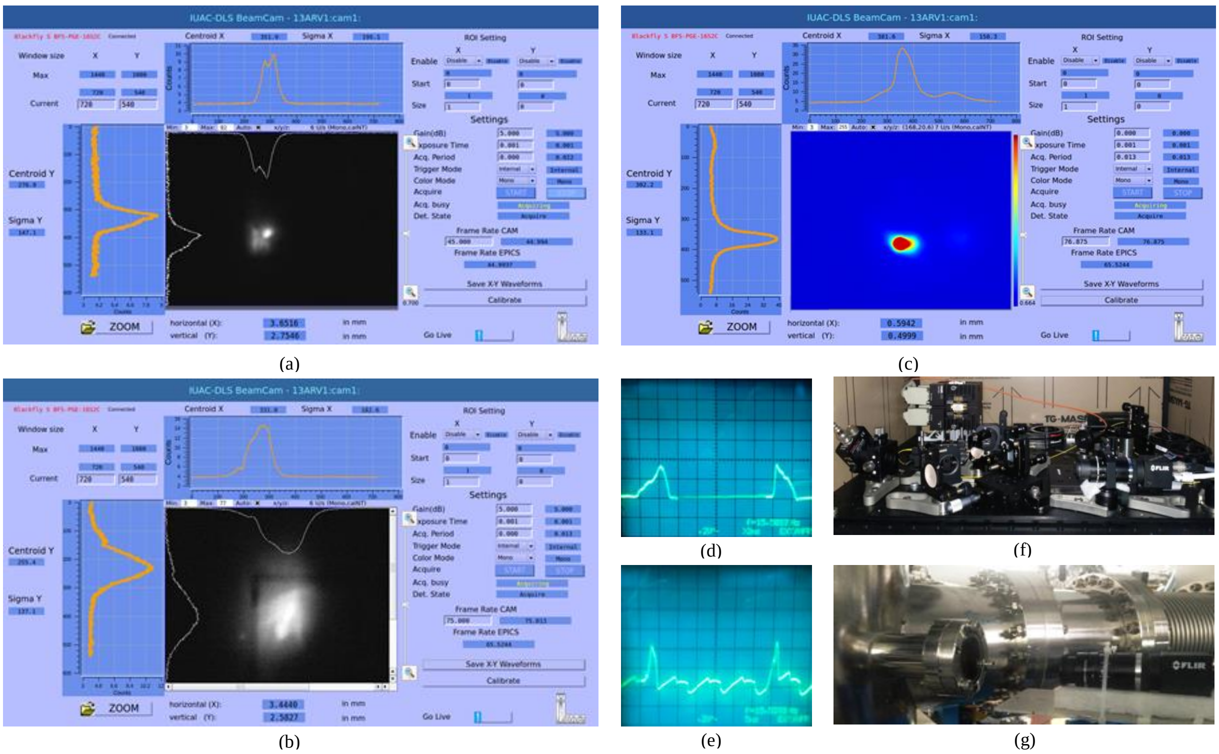


Figure 5: Beam profile of Proton H+ beam observed on (a) Camera at 70 kV, 0.4 µA, (b) Camera at 90kV, 0.4 µA, (d) BPM at 70 kV, 0.4µA, (e) BPM at 90kV, 0.4µA. IR Laser Oscillator beam spot (c) on Camera aperture as virtual cathode. Laser Oscillator setup (f) and IUAC-LEIBF beam line setup (g).

Present working setup includes 32-bit Ubuntu 16.04, with EPICS base 3.15.6, Sscan 2.10, Busy 1.6.1, Calc 3.6.1, Autosave 5.7.1, Asyn 4.36, Seq 2.2.5, and current version of Git pulled areaDetector. For GUI and image acquisition, MEDM 3.1.11 and ImageJ application is built initially and finally converted into .ui files using *adl2ui* tool and more effective and good looking CaQtDM 4.2.4 based GUI are built.

### *GUI and Image Acquisition*

The .ui file generated in above step, contains all the features available in camera which can be run by initializing the camera support in the *aravisTop.ui* file. This file can be run by *startDM* command. The main GUI for camera acquisition as shown in Fig. 5 consists of average intensity profiles in row (X) and column (Y) axes. It is also provided with information such as Centroid and Sigma of the profiles. A calibration tab is used to display the Sigma parameter in the unit of "mm". A save button is used to save the X-Y axes profile data. Camera settings like Gain adjustment, ROI setting, Image size setting, Trigger Mode, Frame Rate setting, Color mode, and Acquisition START/STOP are also provided with readbacks on the side pane. External Trigger can be provided by I/O pins of Hirose 10 connector which is used to power the camera.

EPICS caCamera widget of CaQtDM is used to display live images acquired by the camera. BPM profiles obtained by LEIBF facility Proton H+ beam run and the IR Laser oscillator profile [5] in spectrum mode are also shown. Measurement setup can be seen as well.

## RESULTS AND DISCUSSIONS

Data retrieved from both GUI can be post processed and Gauss fitted to obtain the FWHM in both profiles. Fig. 6(a) shows the profile data obtained by GigE camera with better resolution and FWHM of 3.1 and 3.8 mm respectively in X-Y axes for 70kV, 0.47μA proton beam. Fig. 6(b) shows the profile data obtained by USB camera with poor resolution and FWHM of 1.8 and 2 mm respectively in X-Y axes for 10μA proton beam. GigE camera has a better resolution with 3.75 μm pixel size as against 0.2645 mm. Good results are obtained only for high current beams with USB camera as low current scintillations could not be captured.

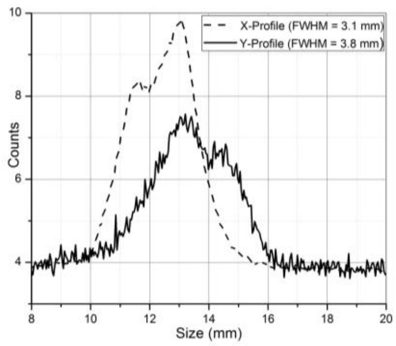


(a)

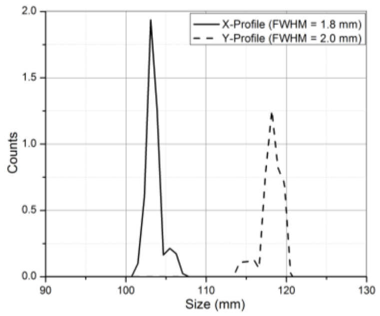


(b)

Figure 6: X-Y Profile post processed data with (a) GigEVision Camera, (b) USB camera

## CONCLUSION

Poor sensor and pixel size, very limited control on parameters, absence of trigger and low frame rate (max 30 FPS) makes USB camera unable to follow the beam variations, however, GigE camera could out-perform in all fields. Aperture control is helpful in virtual cathode application where laser beam is made to fall on camera to capture its profile. Low current profile could not be seen in USB camera. Due to larger FoV (and absence of control over it), proper shape of beam spot is not visible in USB Camera. While in case of GigE camera, FoV comparable to actual scan area is achieved with the help of external lens which is very sensitive to low current beams and will be helpful in capturing DLS electron beam spots on YAG screen even in the absence of ICT.

## ACKNOWLEDGEMENTS

Authors would like to thank Dr. Ambuj Tripathi and LEIBF group for online beam test of cameras. Dr. A. Aryshev of KEK Japan is acknowledged for helping in selection of camera. Dr. S. Ghosh is acknowledged for providing opportunity to work on the system. Prof. A. C. Pandey is also acknowledged for encouragement during this project.

## REFERENCES

[1] S.Ghosh et al., NIM-B, 402(2017)358-363.
[2] areaDetector: EPICS software for area detectors; http://cars9.uchicago.edu/software/epics/areaDetector.html.
[3] areaDetector Viewers: https://cars9.uchicago.edu/software/epics/areaDetectorViewers.html.
[4] T. Cobb, pp 794-797, Proceedings of ICALEPCS 2011, Grenoble, France.
[5] B. Karmakar et al., Proceedings of InPAC 2019.
[6] Blackfly S GigE; https://www.flir.com/products/black fly-s-gige/?model=BFS-PGE-16S2C-CS.

# PULSED ION BEAM EXTRACTION STUDY FOR DIFFERENT PULSING TOPOLOGY FOR ECRIS*

Hitesh Kewlani*+, S. H. Gharat*, Jose Mathew*, B. Dikshit#+

*Ion Accelerator Development Division, BARC, Mumbai.
#Laser & Plasma Technology Division, BARC, Mumbai
+Homi Bhabha National Institute, Mumbai

.

*Abstract*

A new 50 keV, 35 mA Electron Cyclotron Resonance Ion Source (ECRIS) is being developed for ADS application at BARC. The ECRIS is operated in both continues (CW) and pulsed mode. For initial beam acceleration trials, stable and repeatable 50 keV, 30 mA pulsed beam is required with pulse width of 1 ms at 1 Hz repetition rate. This will eventually be increased to 10 Hz, 100 Hz, and CW. The ECRIS pulsing is done in two ways. First by pulsing the ECRIS magnetron and the other by pulsing the high voltage extraction power supply. In this paper, a comparative study of both methods is presented.

## OVERVIEW

The 3E ECRIS[1] has been designed developed and commissioned for LEHIPA. The key parameters of 3e ECRIS at LEHIPA are mentioned in Table 1. At VDG, BEARC the second enhanced version of 3E ECRIS is there. At VDG 3e ECRIS research is going on for pulse and continues operation of beam extraction its effect on system beam parameters. Presently 3E ECRIS is operation is in pulsed mode for LEHIPA. The Pulse operation requirement of LEHIPA is 1ms on time with 1 Hz, 10 Hz and 100 Hz. For pulsing the ion beam there are two methods

- Pulsing the plasma with continues high voltage
- Pulsing the high voltage with continues plasma

In next sections both the methods are discussed with their experimental setup, system parameters and results

## ECR ION SOURCE

In Figure 1 3E ECRIS is shown. This is microwave based plasma generation with three electrode extraction system. Microwave generation is magnetron based at 2.45 GHz with maximum power of 2 kWatt. Microwave transmission waveguide line is WR 284. There are two coil show in figure 1 covering the plasma chamber. The function of these two coil is to generate magnetic field of 875 Gauss at the entry and exit point of plasma chamber.. this is required for ECR Plasma generation. For vacuum generation combination of dry pump and turbo pump is there erwhich gives base vacuum of 4 x $10^{-07}$ torr . For plasma generation gas is feeded into the plasma chamber through gas leak valve . The set pressure is 9 x $10^{-5}$ torr after feeding hydrogen gas to the plasma chamber. In the next section pulse beam extraction is discussed.

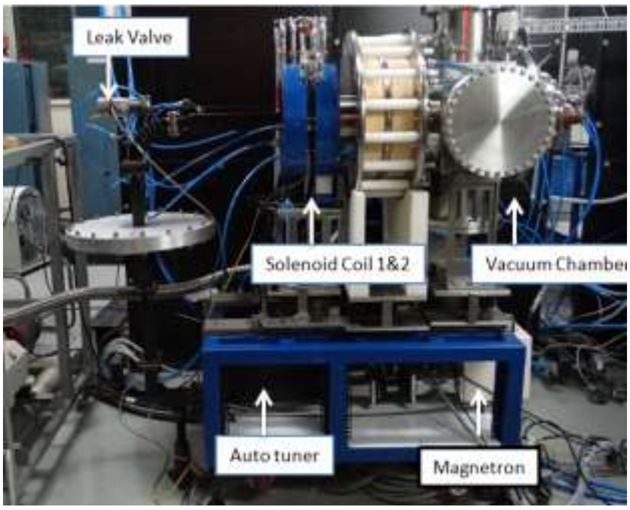


Figure 1:Three Electrode ECRIS at VDG

Table 1: 3E ECRIS Specifications

| System | value |
|---|---|
| Energy | 50 keV |
| Current | 35 mA |
| Pulse width | 1 ms to CW |
| Proton Fraction | 80% |
| Emittance | 0.02-0.025 pi mm mrad |
| Electrode | Three |
| Microwave Freq | 2.45 GHz |

## PULSING THE PLASMA

Pulse beam operation with pulsing the plasma is done by pulse operation of microwave generator. The magnetron pulse operation parameters are rise time and fall time of 50 µs, response time is 200 µs. ECRIS pulsed operation experiment conducted with pulse width from 500 µs to 2 ms ton time range with 1 Hz . Experimental layout is shown in figure 2 and results are shown in figure 3.

*Kewlani@barc.gov.in

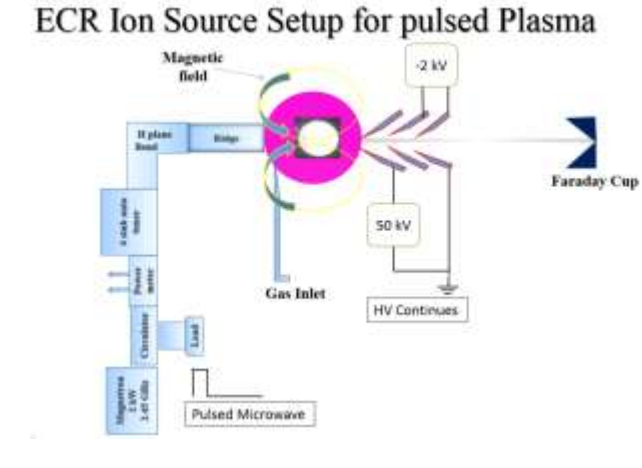


**Figure 2 : ECRIS setup for pulsed Plasma**

For pulse operation with pulsed plasma observation is

- Plasma is generated at every 1 Hz or 10 Hz
- Plasma parameters ($n_e$, $T_e$, $V_p$) are not exactly same as previous pulse
- Initial 250 µs are for plasma stabilization ( either over damped or under damped)

In figure 5(e) pulsed beam of 500 µs is shown, in which one overshoot is there at rise time after that beam current is increasing; where as in figure 5(f) 1ms beam pulse beam current is further increasing.

In figure 5(g) pulsed beam of 5ms µs is shown, in which one under damped beam current is there after that beam current achieving stable value. Where as in figure 5(h) 10 ms beam pulse beam current is further reaming at stable current level.

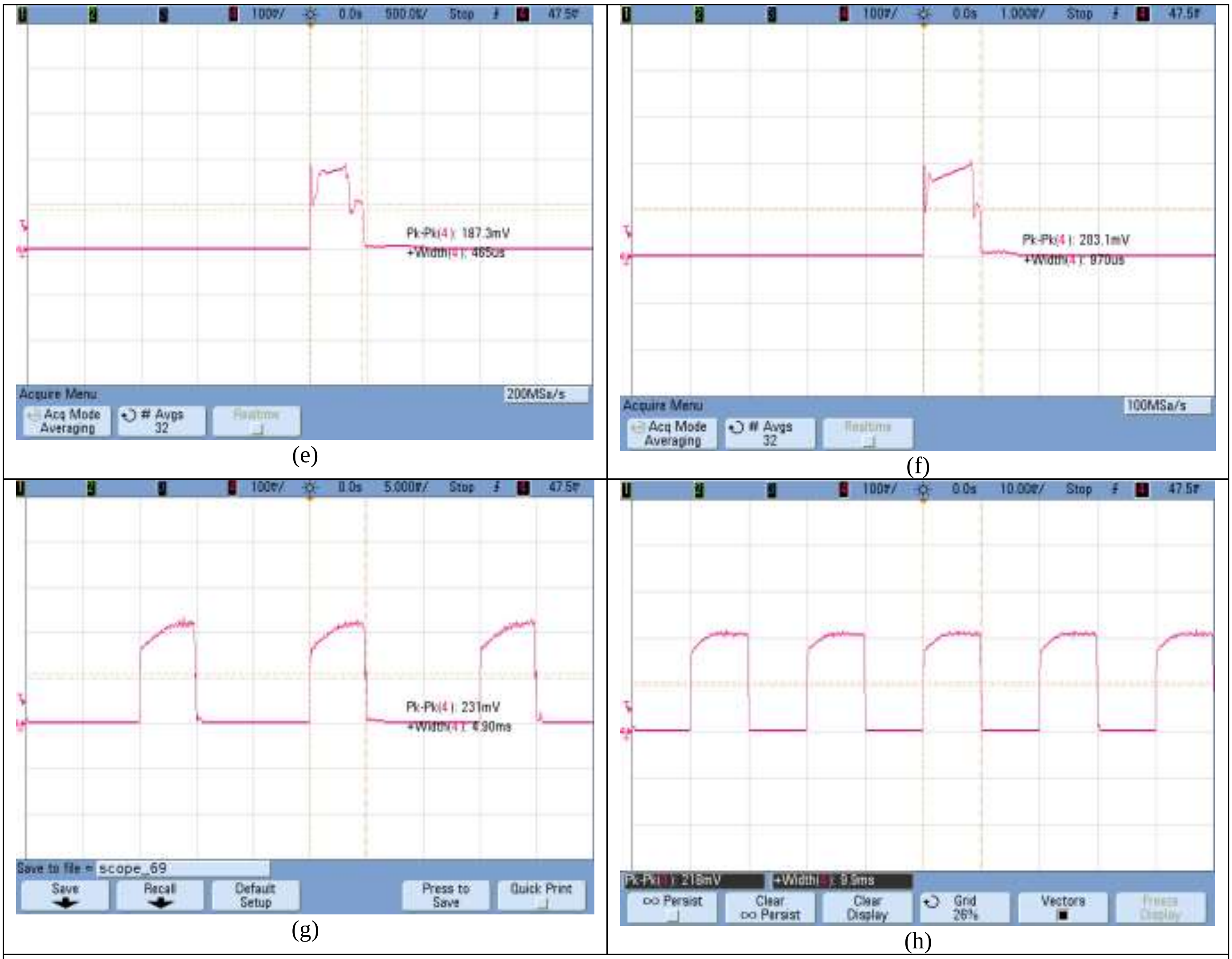


Figure 3 : ECR beam for different pulse width by pulsing the plasma

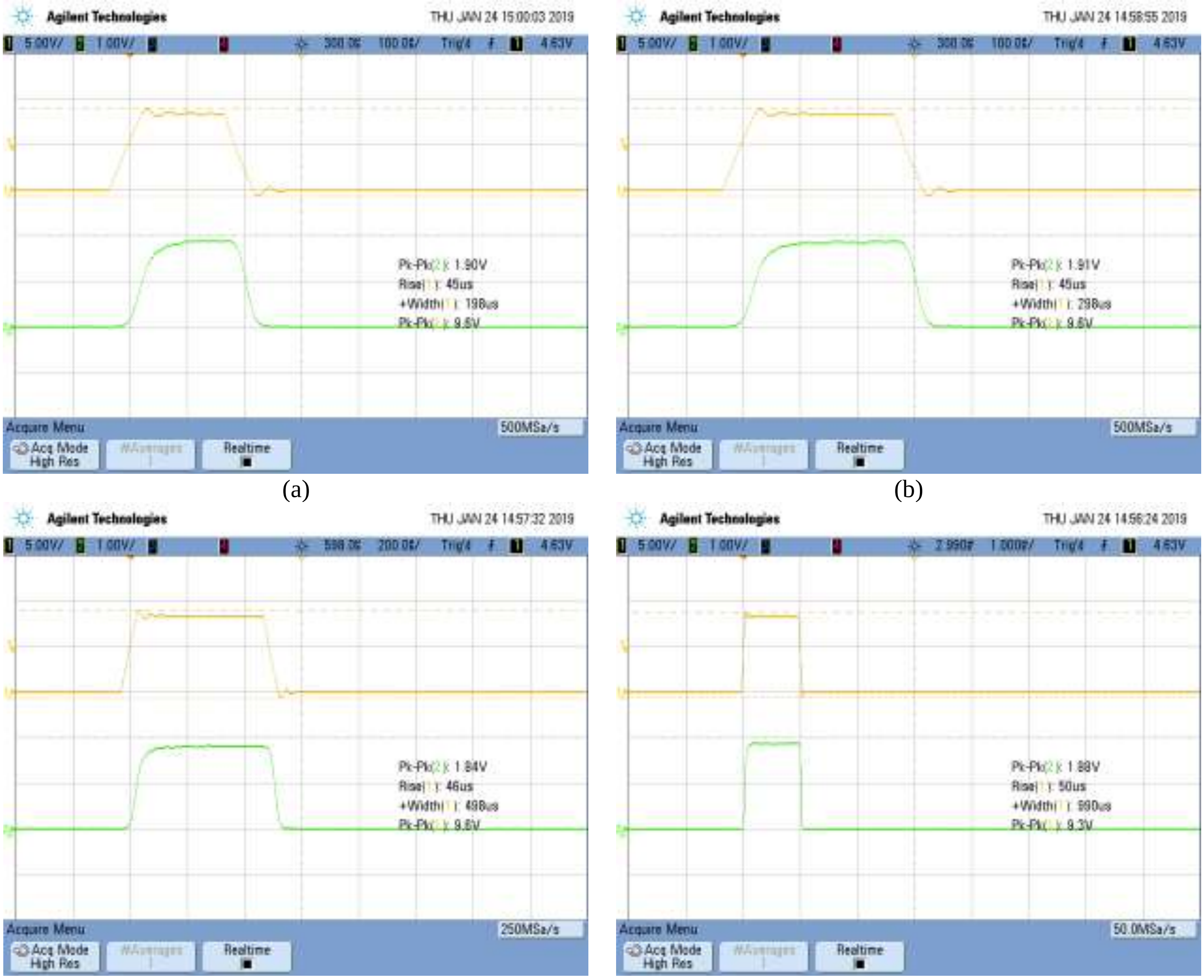

(c) (d)

Figure 5: Pulse beam extraction (a) 200 μs (b) 300 μs (c) 500 μs (d) 1ms  with CW plasma and pulsed extractor

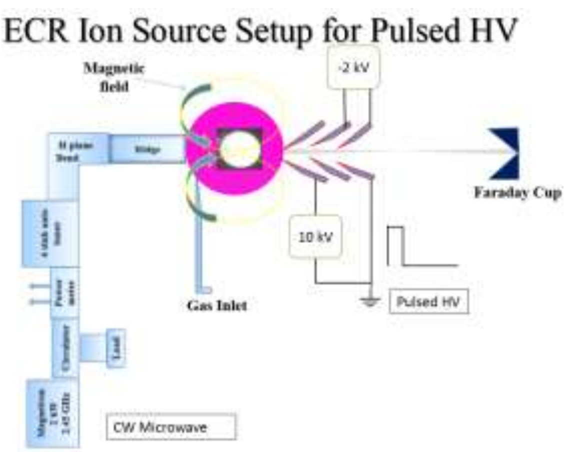


Figure 4: ECRIS set up for pulsed HV extraction

## PULSING THE EXTRACTOR HV

Pulse beam operation with pulsing the extraction high voltage with continues plasma is done by pulse operation of 10 kV High Voltage (HV) generation. The 10 kV HV generation parameters are rise time and fall time of 15 μs, slew rate of 700 V/μs. ECRIS pulsed operation experiment conducted with pulse width from 200 μs to 1 ms ton time range with 1 Hz . Experimental layout is shown in figure 4 and results are shown in figure 5.

## REFERENCES


[1] P. Roychowdhury, H Kewlani, L. Mishra, S. Gharat, R.K. Rajawat. "Emittance and proton fraction measurement in High current electron cyclotron resonance proton ion source", Nuclear Instruments and Methods in Physics Research Vol 795, Pages 45-41, 2015.

# BUNCH SHAPE MEASUREMENTS OF LEHIPA 3 MEV RFQ BEAM

Jose V Mathew*, S V L S Rao, Aman Bajaj, Deepak Mathad, Hitesh Kewlani, Sudheer K Singh, Laxman Tayade

Ion Accelerator Development Division, BARC, Mumbai 400085

*Abstract*

The LEHIPA Radio Frequency Quadrupole (RFQ) accelerates proton beam from 50 keV to 3 MeV. The time structure of the bunched beam from the 352 MHz RFQ is measured using a Fast Faraday Cup (FFC). The calibration of the FFCs are performed using Time Domain Reflectometry (TDR) technique. We are able to resolve individual beam pulses, and measure the bunch length to be around 400 ps on a 3 GHz oscilloscope. The FFC characterization and bunch shape measurement results are presented here.

## INTRODUCTION

The Low Energy High Intensity Proton Accelerator (LEHIPA) is being developed at the Bhabha Atomic Research Centre (BARC) to produce a 20 MeV, 10 mA proton beam [1]. The main components of LEHIPA are a 50 keV ECR ion source, a 3 MeV Radio Frequency Quadrupole (RFQ) and a 20 MeV Drift Tube Linac (DTL). The RF cavities operate at 352 MHz. The LEHIPA 3 MeV RFQ has been commissioned recently [2].

Different transverse beam diagnostics elements like beam profile monitors, emittance measurement systems, Faraday cups etc. have been developed for LEHIPA [3, 4]. Fast Faraday Cups (FFCs) are commonly used beam diagnostics for measuring the longitudinal beam profile [5]. The beam bunch length in LEHIPA is ~ 0.7 ns and hence the FFCs should have wide band width of a few GHz to detect the bunch signal.

Two type of FFCs are developed at BARC with a characteristic impedance of 50 Ω. One is in coaxial geometry and the other in planar (strip line) geometry. These FFCs have been tested with the LEHIPA 3 MeV beam.

† email address: josevm@barc.gov.in

In this paper the design simulations, construction, characterization and beam bunch shape measurement results using coaxial-fast Faraday cup (CFFC) are discussed.

## DESIGN AND SIMULATUONS

The coaxial FFCs are designed with a characteristic impedance, $Z_c$ of 50 Ω. The dimensions of the inner conductor, *d* and outer conductor, *D* of the FFC are calculated by, $Z_c = 1/2\pi\sqrt{\mu/\varepsilon}\ln(D/d)$ [6]. An important design parameter of FFC is the upper usable frequency (UUF) which refers to the frequency at which the first non-TEM electromagnetic wave mode comes into existent [6]. The non-TEM mode with the lowest cut off frequency, $f_c$ is $TE_{11}$ mode with $UUF = f_c = 4c/\left(d(1+D/d)2\pi\sqrt{\varepsilon_r}\right)$. For a chosen innerconductor diameter, *d* of 5.5 mm for CFFC, the UUF is 10.5 GHz. The geometry optimization simulations are performed using CST Microwave Studio (CSTMWS) [7].

Figure 1 (a) shows the CST model of the co-axial FFC. The diameter of the central conductor is tapered down to match with a standard N type connector.

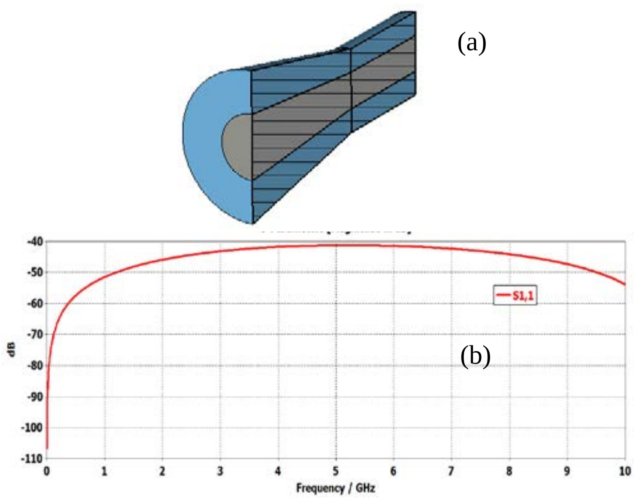


Figure 1: (a) CST simulation model of CFFC, and (b) S-parameter (S11) plot for the CFFC geometry from CSTMWS.

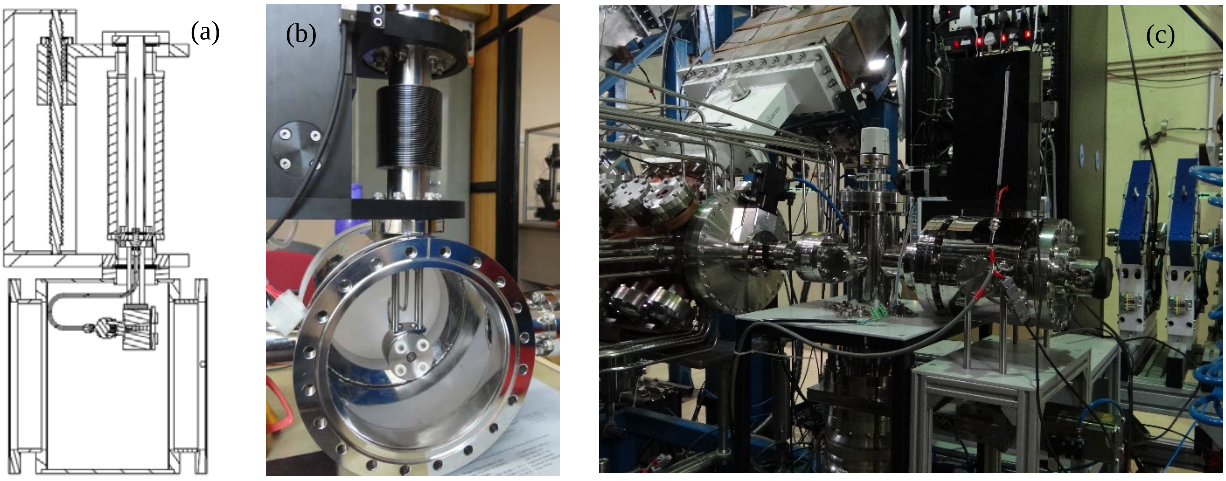


Figure 2: (a) Mechanical design of CFFC assembly, (b) picture of the CFFC assembly, and (c) CFFC assembly installed in LEHIPA beamline.

Figure 1(a) shows the CST simulation model of CFFC and Fig. 1(b) the S-parameter (S11) analysis plot of CFFC geometry from CSTMWS. The S parameter (S11) plot shows that the return loss is < -40 dB (< 0.01%) for a wide bandwidth (BW) of > 10 GHz. From the well know relation of BW with rise time, $t_r = 0.35/BW$ , the rise time of the signal is < 35 ps.

In the case of the LEHIPA RFQ, with a synchronous phase of -30$^0$, the maximum width of beam bunch or micropulse is ~ 700 ps. So, for the bunch shape measurements of the LEHIPA bunches, the designed CFFC with rise time of ~ 35 ps will suffice, provided the fabricated and design geometries are in good agreement.

## CONSTRUCTION AND CHARACTERIZATION

Figure 2(a) shows the mechanical design of the CFFC assembly. The central conductor, which acts as the beam stop, is made of copper and the outer housing is made of stainless steel. A suppressor electrode is placed in front of the central conductor for suppression of secondary electrons. Semi-rigid high bandwidth SMA cable is used to take the beam current signal from the FFC though a SMA vacuum feedthrough. The FFC is mounted on a linear movement slide for precise positioning of the FFC with reference to the beam.

The fabricated FFC assembly, shown in Fig. 2(b) has been calibrated using time domain reflectometry (TDR) technique employing a 20 GHz sampling oscilloscope (Picoscope 9341). The CFFC was tested with a step function pulse, with a rise time of ~ 40 ps and 200 mV amplitude.

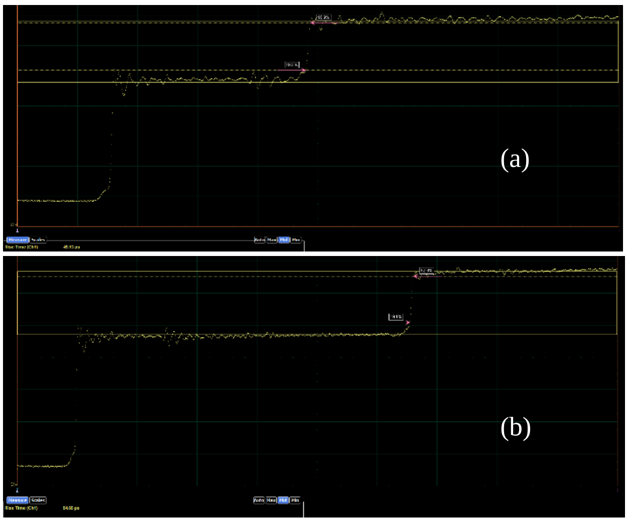


Figure 3: Time domain reflectometry (TDR) test of CFFC. a) test plot with a 50 Ω SMA cable of length 15 cm, connected to the pulse generator, b) plot with CFFC assembly connected after the 15 cm cable. The vertical scale is 29 mV/div and the horizontal scales for (a) & (b) are 635 ps/div and 1 ns/div respectively.

The time domain reflectometry (TDR) plots of CFFC in are shown in Figure 3. Figure 3(a) shows the test plot with a 15 cm SMA cable with characteristic impedance of 50 Ω connected to the pulse generator and Fig. 3(b) with the

CFFC assembly connected after the 15 cm cable. The vertical scale is 29 mV/div and the horizontal scales for are 635 ps/div and 1 ns/div respectively. A deviation from the design characteristic impedance (50 Ω) of the fabricated CFFC results in signal reflection at the interface, and by measuring the mismatch amplitude, the characteristic impedance variation can be calculated. Figure 3(b) shows no mismatch with the 50 Ω characteristic impedance cable and CFFC. The rise time of the signal from the 15 cm SMA cable (Fig. 3(a)) is 43 ps, deducting the rise time factor of the oscilloscope. With the FFC assembly attached the rise time is 52 ps. This variation is well within our acceptance limit.

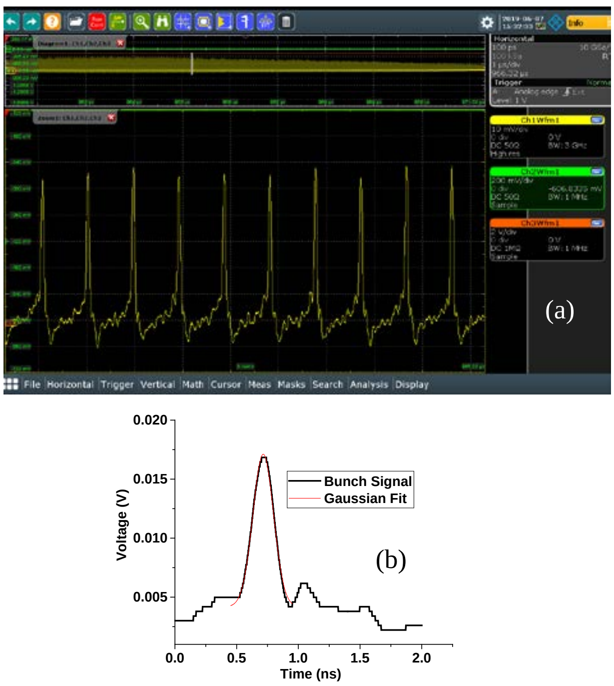


Figure 4: Beam bunch measurement using CFFC. a) individual micropulses from RFQ at time sweep of 3 ns/div. (b) Gaussian fit of an individual bunch.

## MEASUREMENT REUSLTS

The FFC assembly in the LEHIPA beam line is shown Figure 2 (c). The FFC is placed at around 250 mm from the exit flange of the RFQ.

Bunch shape measurement using the CFFC is shown in Figure 4. The bunch measurements are carried out using a 3 GHz oscilloscope. The cavity RF power was pulsed at 50 $\mu$s pulse width and 1 Hz repetition rate. As shown in Fig. 4(a), the CFFC could resolve the individual micro pulses at a time period of 2.84 ns, corresponding to the cavity RF frequency. Figure 4(b) shows the Gaussian fit of an individual micropulse or beam bunch. The beam bunch has a maximum width of 500 ps with standard deviation, $\sigma$ of around 140 ps. The measurements are repeated at different RF pulse widths and similar results have been observed.

## CONCLUSION

A compact coaxial fast Faraday cup has been designed as per the requirements of LEHIPA.The fabricated CFFC has been characterized using TDR technique and shows high bandwidth which in good agreement with the design parameters. The FFC is tested with the 3 MeV LEHIPA RFQ beam and the measurements of individual micro pulses have been carried out.

## REFERENCES


[1] P. Singh, *et al.*, *Pramana – Journal of Physics* **68**, 331 (2007).

[2] Rao, S V L S *et al.*, “Commissioning of 3 MeV RFQ”, same proceedings of InPAC-2019.

[3] Mathew, Jose V. *et al.*, “Design and development of transverse emittance measurement system for LEHIPA”. InPAC-2015, (2015).

[4] Mathew, Jose V. *et al.*, “Beam transport and characterization in the LEHIPA LEBT”. InPAC-2015, (2015).

[5] P. Strehl, “Beam Instrumentation and Diagnostics”, Springer-Verlag, Berlin 2006.

[6] D.M. Pozar, “Microwave engineering”, 2nd edition, 1998 John-Wiley & Sons.

[7] www.cst.com/

# CONCEPTUAL DESIGN FOR THz EXTRACTION, DETECTION AND TRANSPORTATION IN DELHI LIGHT SOURCE (DLS)

M. Aggarwal#, B. Karmakar, V. Joshi, A. Sharma, S. Sahu, S.K. Saini and S. Ghosh
Inter University Accelerator Centre (IUAC), Aruna Asaf Ali Marg, New Delhi, India
S.S. Prabhu, Tata Institute of Fundamental Research (TIFR), Mumbai, India

*Abstract*
Delhi Light Source is a compact pre-bunched Free Electron Laser facility being developed at Inter University Accelerator Centre (IUAC), New Delhi. In this accelerator, high quality electron beam will be produced and injected in to undulator magnet to produce radiation in the frequency range of 0.18 to 3 THz. The terahertz radiation has to be captured just at the exit of the undulator to reduce its further loss and attenuation while propagating through the vacuum chamber. At the end of the undulator, an extraction chamber equipped with a Titanium foil will be installed. The foil will reflect the THz radiation in perpendicular direction and allow the electron beam to pass through. The reflected THz radiation will be collected using a Teflon lens and then transported to the experimental stations with the help of mirrors and lenses. Along with the proposed design of THz transportation, the paper also provides a discussion on the THz detection mechanisms to be installed in the beamline.

## INTRODUCTION

The promising and emerging applications of THz radiation in medical diagnostics, non-invasive imaging, material science research, fast telecommunication and other areas have triggered the development of new sources in this part of electromagnetic spectrum. Accelerator based THz sources have been developed in different facilities of the world providing high power and continuous tunable narrowband radiation. FEL-CATS source at ENEA-Frascati, Italy [1], THz facility at University of Science & Technology, China[2], KU-FEL at Kyoto University, Japan [3] and PKU source at Peking University, China [4] are some of the compact and operational THz accelerator facilities.

A compact source of THz based on undulator is at the advanced stage of commissioning at Inter University Accelerator Centre (IUAC), New Delhi [5]. This facility, named as Delhi Light Source (DLS) utilizes a pre-bunched electron beam to generate Coherent Undulator Radiation (CUR). A laser-driven photocathode RF gun is used to emit modulated electron beam which would be accelerated to relativistic energies of 4-8 MeV. A solenoid will then focus the beam before injecting into the undulator. This electron beam would be having a multi micro-bunch structure as described in [6]. The electrons are modulated in a pre- bunched structure whose bunch length is shorter than the radiation wavelength and the longitudinal spacing between the micro- bunches is of the order of THz wavelength. Under these conditions, the radiation emitted from different micro- bunches interfere constructively and achieve super-radiant emission.

Presently, the commissioning of DLS beamline is going on and different components are at the advanced stage of procurement and installation. The paper reports the schematic design being planned for the transportation of THz from the exit of the undulator to the dedicated experimental stations. A discussion on THz detectors best suited for the facility will also be given.

## UNDULATOR RADIATION

The relativistic electron beam will be injected into the undulator magnet and produce electromagnetic radiation. The wavelength λ of n$^{th}$ harmonic of radiation is given by the famous undulator equation,

$$\lambda = \frac{\lambda_u}{2n\gamma^2}\left(1 + \frac{K^2}{2} + \theta^2\gamma^2\right)$$

where $\lambda_u$ is the undulator period, γ is the relativistic factor for electron, K= 0.0934*B[T]*$\lambda_u$ [mm] is the undulator parameter, B is the on- axis peak magnetic field of undulator and θ is the angle at which the radiation is emitted (or the observation angle) with respect to z-axis. The maximum angle at which undulator radiation is emitted can be derived from the slope of electron's trajectory inside the undulator and is given by θ~ K/γ. Angular divergence of the THz radiation has been estimated from the theoretical calculations [6] and the values are given in Table 1.

Table 1: CUR parameters and angular divergence

| **Frequency (THz)** | 0.3 | 0.6 | 1.2 | 3 |
|---|---|---|---|---|
| **Electron energy (MeV)** | 4 | 6 | 7 | 8 |
| **γ** | 8.82 | 12.74 | 14.69 | 16.85 |
| **No. of micro- bunches in 6 ps window** | 2 | 4 | 8 | 16 |
| **Average separation at undulator entrance (fs)** | 3300 | 1630 | 800 | 335 |
| **B (T)** | 0.48 | 0.48 | 0.34 | 0.12 |
| **K** | 2.15 | 2.15 | 1.52 | 0.53 |
| **θ (rad)** | 0.243 | 0.168 | 0.103 | 0.031 |

#Corresponding author:
madhuri@iuac.res.in (M. Aggarwal), bappa@iuac.res.in (B. Karmakar)

As the electron beam and radiation are confined to the dimensions of the vacuum chamber of undulator, it is important to take into account the dimensions of chamber and the angular divergence of radiation. The inner elliptical dimensions of chamber are 14 mm (horizontal) and 25 mm (vertical), where the two jaws of the undulator open and close in the horizontal direction. These dimensions are limited by the minimum undulator gap and mechanical tolerances. The length of undulator is around 1500 mm, excluding the end magnets. Since the facility is designed to be a pre-bunched FEL, so the radiation is expected to be emitted from the beginning of the undulator magnets. Thus at the calculated divergence angle (Table 1), the radiation will be striking the walls of the chamber and will get attenuated [7]. Thus it is important to collect the radiation just at the exit of undulator in order to avoid further loss and attenuation.

## EXTRACTION OF THz RADIATION AFTER THE UNDULATOR

As discussed in previous section, the THz radiation will be extracted at the exit of undulator. An extraction chamber with a Ti foil will be installed downstream the undulator to reflect the THz in orthogonal direction (Fig. 1a). The chamber is a six- port structure with two ports along the beam propagation and four ports along the perpendicular directions as shown in Fig. 1(b). A free standing 60mm x 60mm titanium foil with thickness of around 50 microns will be mounted on a holder which can be retracted with the help of a linear motion feedthrough [3]. A pumping station will be connected at the vertical port at the bottom of the chamber. Electron beam will be passing through the foil and then will be deflected by a dipole bending magnet at an angle of 60˚ and transported further to the dedicated experimental stations. The effect of foil on the divergence of electron beam is to be investigated.

The THz radiation reflected from the metal foil will pass through the DN63CF quartz window viewport separating a high vacuum of $10^{-8}$ mbar and an acrylic chamber purged with dry nitrogen. The purging with $N_2$ is important to reduce the humidity and hence absorption of THz by water molecules.

## EXPERIMENTAL DETECTION

The spatial distribution of the emitted radiation is planned to be measured using Schottky Barrier Diode (SBD) detector mounted on a linear stage (Fig. 1a). SBD detectors are very fast room temperature detectors but are expensive with a narrow detection bandwidth. For example, a typical commercially available fast SBD detector has a responsivity of 1.6 kV/W in the range of 0.26-0.4 THz with a response time of 0.1 ns [8]. To measure the spot size of emitted radiation, the parameters of the undulator source can be selected to generate the THz frequency corresponding to the detection range of SBD and the spatial distribution can be measured.

For the measurement of the THz frequency, Michelson interferometer setup will be used as shown in Fig. 2. Here

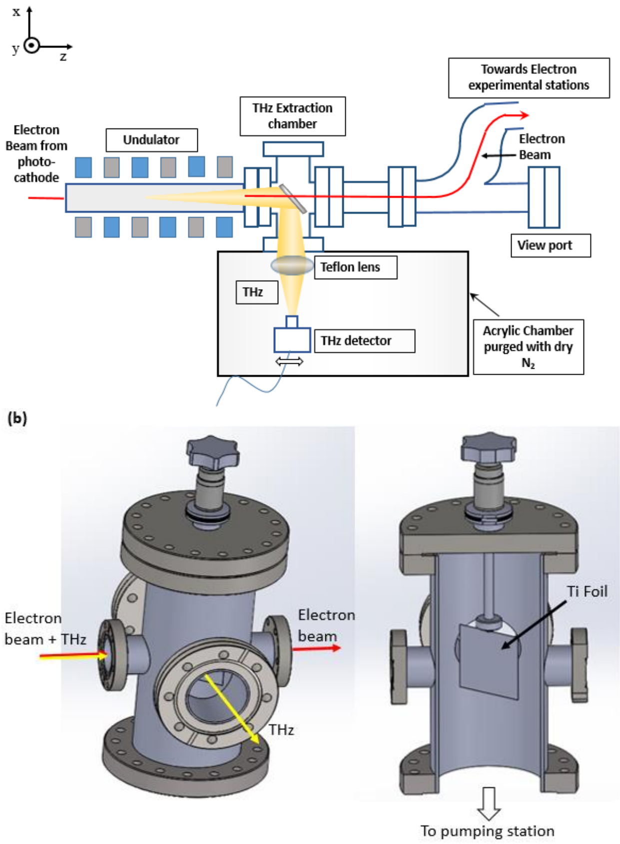


Fig 1: (a) Schematic design of the FEL beamline after the undulator (top view) and (b) Solidworks drawing of the THz extraction chamber

the detector preferred would be a broad band detector and working at room temperature. Pyroelectric detectors are a good option and they are commercially available. Typical range and responsivity of pyroelectric detector is 0.1-30 THz and 1 kV/W respectively, however, the response time is of the order of tenth of seconds [9]. For characterization of lower frequencies (0.1-1.2 THz), a set of SBD detectors can also be used as the response time is much faster [10].

An important point to mention here is that since the electron beam will be passing through the metal foil, transition radiation (TR) will also be produced along with CUR. However, TR will be emitted in two radial lobes with the intensity peaks at angle~1/γ. The difference in opening angles and the field polarization of undulator and transition radiations could be utilized to distinguish between the two. Also, the amount of TR produced can be measured experimentally when CUR is completely absent at the "fully open" condition of the undulator jaws. In this case, the detector will detect only the transition radiation.

## THz TRANSPORTATION TO EXPERIMENTAL STATIONS

There are three experimental stations being planned for the THz experiments. In order to efficiently transport the radiation to experimental stations, combination of THz mirrors and lenses are to be used. Fig. 2 shows the schematic of THz transportation line being planned. The

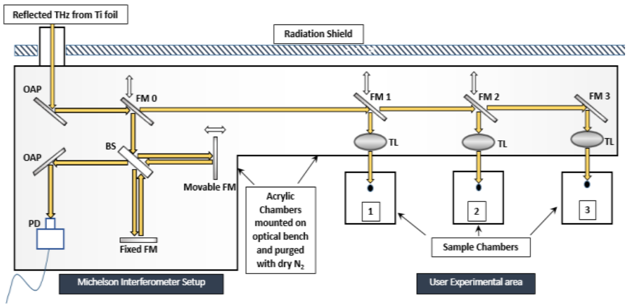


Fig. 2: Top view of schematic for the transportation line for THz. Here OAP: Off-axis parabolic mirror, FM: Flat mirror, BS: Beam Splitter, PD: Pyroelectric detector, TL: Teflon lens

radiation produced from the undulator and reflected by Ti foil is to be characterized with the help of power and frequency measurements. After the characterization, THz will be transported to the user experimental area.

The reflected THz is focused on plane mirror FM0 with the help of off-axis parabolic mirror. Mirror FM0 will be mounted on a linear stage. FM0 is to be used for the frequency measurement and to be moved from the THz path when the radiation is to be transported to experimental stations. Mirrors FM1 and FM2 will also be movable so as to select the desired experimental station. The complete path of THz will be enclosed in acrylic chambers and purged with dry nitrogen. Different type of experiments can be planned in the experimental area depending on the user requirements, such as THz pump-THz probe and circular polarization THz experiments.

## CONCLUSION

The paper provides a conceptual idea of the schematic of the THz beamline from the undulator to the experimental stations. The radiation will be extracted just at the undulator exit and detected by SBD and pyroelectric detector. A Michelson interferometer setup will measure the frequency of the radiation. Three experimental stations are planned for the terahertz experiments where the researchers can mount their samples and characterize them.

## REFERENCES


[1] Doria, A, et al., “Enhanced coherent emission of terahertz radiation by energy-phase correlation in a bunched electron beam” Phys. Rev. Lett. 2004, 93, 264801.

[2] Ruixuan Huang, et al., “Design of a Pre-Bunched THz Free Electron Laser”, Particles 2018, 1, 267–278.

[3] Sikharin Suphakul, et al., “Measurement of Coherent Undulator Radiation of Compact Terahertz Radiation Source at Kyoto University”, Int J Magnetics Electromagnetism 2017, 3:008.

[4] Xiaodong Wen, et al., “Superradiant THz undulator radiation source based on a superconducting photo-injector”, Nuclear Instruments and Methods in Physics Research A 2016, 820 , 75–79.

[5] S. Ghosh, et al., “Status of the development of Delhi Light Source (DLS) at IUAC”, Nuclear Instruments and Methods in Physics Research B 2017, 402, 358-363.

[6] V. Joshi, et al., “Theoretical and simulation study of ‘Comb’ electron beam and THz generation”, Nuclear Instruments and Methods in Physics Research A 2019, 913, 28-39.

[7] A. Sharma, et al., “Terahertz Attenuation Inside Beam Pipe of the Undulator”, Proceedings of the eighth DAE-BRNS Indian particle accelerator conference, 2018

[8] Virginia diodes www.vadiodes.com

[9] Gentec-eo www.gentec-eo.com

[10] R. A. Lewis., “A review of terahertz detectors”, J. Phys. D: Appl. Phys. 2019, 52, 433001.

# SOLID ION BEAM DEVELOPMENTS IN 14.4GHZ ECR ION SOURCE USING MIVOC METHOD

Ranjini Menon, P.Y.Nabhiraj, Mou Chatterjee, Suman Guha, Anuraag Mishra and Arup Bandyopadhyay

VECC, Kolkata

*Abstract*

Development of various ion beams of elements like Sulphur, Iron, Chlorine, Titanium etc were attempted using MIVOC (Metallic ion beam from volatile compounds) method. A separate sample injection system through the bias rod and a quartz tube is developed with in-situ heaters with multi level floating power supplies. Iron, Sulphur beams were developed from Ferrocene and Carbon di Sulfide respectively. An attempt was made to develop Ti beam from Titanium tetrachloride. A feeble intensity Ti beams and sufficiently high current Chlorine beam of both isotopes $^{35}Cl$ and $^{37}Cl$ were obtained. Preliminary trials resulted in stable high charge state ion beam of sufficient intensity enough to inject into K-130 cyclotron.

## INTRODUCTION

Figure 1: ECR Ion source that delivering heavy ion beam to room temperature cyclotron

At VECC, high charge state heavy ion beams from gaseous elements developed in 14.45 Ghz ECR ion source are routinely being injected into K-130 Cyclotron [1]. Figure 1 shows the picture of the ECR ion source assembled in the high-bay of room temperature cyclotron building. This ECR ion source is completely designed and developed in-house. Ion beam species like Nitrogen, Neon, Oxygen at energy range of ~100-200 MeV are available and are being routinely utilised by nuclear physics experimentalists. Apart from these species of ion beams, there is a requirement of ion beams of solid elements for research in the field of nuclear physics. Efforts are being made to cater this requirement and some preliminary developments are carried out using MIVOC-method (**M**etal **I**ons from **VO**latile **C**ompounds).

## MIVOC FOR PRODUCTION OF ION BEAM FROM SOLID ELEMENTS

MIVOC-method enables the production of highly charged heavy ion beams of solid elements [2]. The volatile compounds of the desired metal or solid having high vapor pressure at room temperatures is selected as sample. The sample is injected in to the plasma chamber mostly at room temperatures or slightly elevated temperatures which is broken up when enters plasma and subsequently gets ionized.

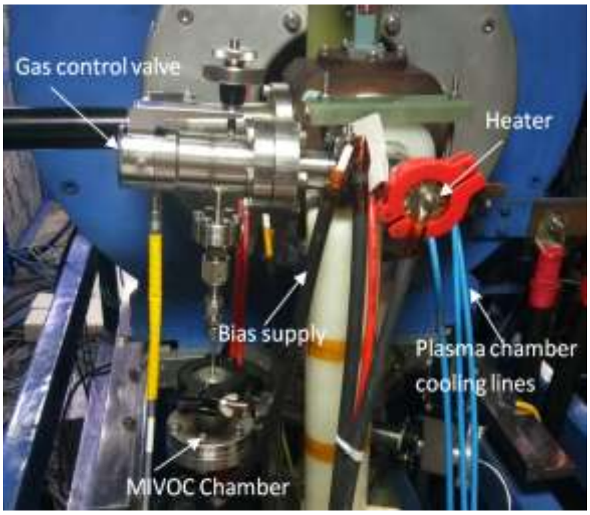


Figure 2: Experimental setup of MIVOC system

Figure 2 shows the total MIVOC setup assembled on the injection side of the ion source. Since there is a long capillary tube to feed these vapors in the plasma chamber, in order to avoid the condensation of vapour in the capillary, for some samples it is required to maintain elevated and uniform temperature throughout the length of the capillary. In order to achieve this, a separate injection system is developed with heater inserted in the quartz tube and which in turn is coaxially inserted in the bias tube which is a central conductor of microwave injection system. Also the injection system is re-designed in such a way that the flow of these vapors are directed only to the plasma chamber instead of the turbo-molecular pump on injection side to improve the efficiency of the injection. Bias and heater power supplies are galvanically isolated and floated on 10kV extraction potential.

Sulphur, Ti are developed using Carbon disulphide and Titanium tetra-chloride which are liquids.

These are filled in a chamber with quartz window. This window helps in observing the level of the liquid. Iron ion beam is produced by Ferrocene compound which is in solid form.

Two of the developed beams, Iron and Sulphur were very stable and of sufficient intensity. Figure 3 shows the typical charge state distribution of sulphur. $S^{10+}$ and $S^{11+}$ of 32 euA and 12 euA respectively were achieved. $Fe^{11+}$ $Fe^{12+}$ and $Fe^{13+}$ of 20euA, 15euA and 9euA respectively were produced. These experiments were repeated and found the results are highly repeatable and stable.

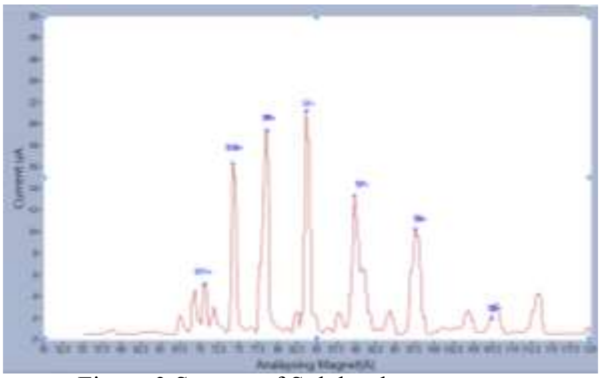

Figure 3 Spectra of Sulphur beam

Figure 4: Screenshot of control system of ion source indicating Iron beam spectrum acquision.

Figure 4 shows the typical control panel of ECR ion source where it can be seen acquiring the ion beam and charge state distribution of iron charge states.

Titanium beam was also developed. It was difficult to handle the $TiCl_4$ liquid since it forms hydrochloric acid gas as soon as it comes in contact with the moisture from the surrounding air. Very low current of of $Ti^{12+}$ and $Ti^{13+}$ were produced. More work is required to be done to produce more intense Ti beams.

Since $TiCl_4$ coumpound was used to produce Ti beam, intenses chlorine ion beams ($^{35}Cl$ and $^{37}Cl$) also could be produced.

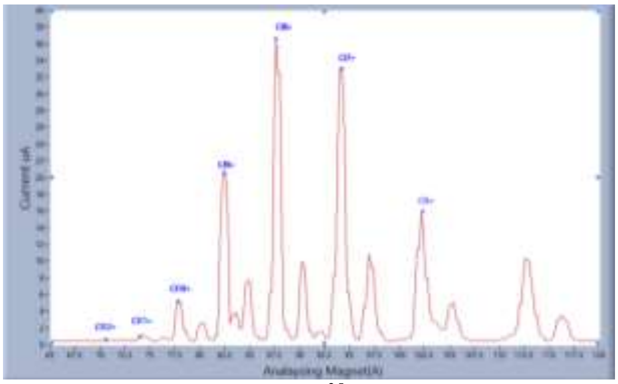

Figure 5: Typical spectra of $^{35}Cl$ ion beam

Interestingly two well separated isotopes of mass 35 and 37 of chlorine beams with sufficient intensity and stability were successfully produced. Figure 5 and 6 shows the spectra of $^{35}Cl$ and $^{37}Cl$.

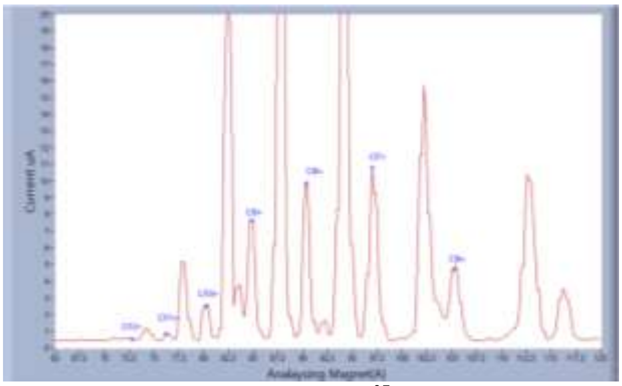

Figure 6: Typical spectra of $^{37}Cl$ ion beam

## REFERENCES

[1] P. Y. Nabhiraj, Mou Chatterjee, Ranjini Menon, Suman Guha, Anuraag Misra, et al. INPAC 2018. RRCAT, INDORE, 9-12 January, (2018) 233

[2] H Koivisto et al. Nuclear Instruments and Methods in Physics Research B 94 (1994) 291-296

# PLASMA AND IMPURITY ASSESSMENT IN ROBIN

Kaushal Pandya[1] , M.J. Singh[2] , Himanshu Tyagi[2] , Manas Bhuyan[2] , Mainak Bandyopadhyay[2,3] , Ratnakar Yadav[2] , Agrajit Gahlaut[1] , Mahesh Vupugalla[1] , Kartik Patel[1] , Hiren Mistri[1] , Bhavesh Prajapati[1] and Arun Chakraborty[1,2]

[1]Institute for Plasma Research (IPR), Bhat, Gandhinagar – 382428, India
[2]ITER-India, Institute for Plasma Research, Bhat, Gandhinagar - 382428, India
[3]Homi Bhaba National Institute (HBNI), Anushakti nagar, Mumbai 400094, India

*Abstract*

ROBIN is an inductively coupled high power (100kW) radio frequency (RF) (1MHz) operated negative hydrogen ion source facility at IPR. It is a prototype source 1/8$^{th}$ the size of ITER reference source. The ROBIN source has been operated in pure volume and surface mode (with Cesium (Cs)). Operations with Cs have helped to achieve maximum negative ion current densities 27 mA/cm$^2$ at an input RF power of 50kW and electron to ion ratio around 2. At lower current densities of 20-22 mA/cm$^2$ the electron to ion ratio improves to ~1. Operational experience on the source has shown that impurities play a significant role in stable source operation in the cesiated mode. As Cs being an electropositive alkali metal tends to form Cs compounds with impurities. This leads not only to large Cs consumption but also affects the stable operation of the source. Various diagnostics have been implemented in ROBIN to investigate the same. Three movable in house fabricated Langmuir probes are installed in the extraction region in ROBIN to monitor and characterize the plasma parameters. The probes are positioned at the top, middle and bottom in the plasma near extraction region, each separated by ~160 mm. The probes are uncompensated for RF and installed parallel to the filter field. It is also used to monitor the plasma uniformities in the source. Light collection optics for Optical Emission Spectroscopy (OES) installed in front of each moveable probe. It is used to monitor the Balmar lines of hydrogen and the O, OH, $N_2$, Cs and Cu lines to give an idea of the impurities and Cs conditioning in the source. In addition, a Residual Gas Analyser (RGA) has been connected directly to the source to assist in impurity measurements. The presentation will give an assessment of plasma parameters and impurities using implemented diagnostics.

## INTRODUCTION

The ROBIN source at IPR [1] is a RF driven single driver cesiated negative ion source test bed used to produce and characterise RF produced plasmas and $H^-$ ion beams. Studies on ROBIN are expected to provide the necessary experience and database for operating multi-driver RF based negative ion sources to be used at ITER for producing high energy multi ampere neutral beams for heating and diagnostic purposes.

Figure 1 shows the schematic of the ROBIN source at IPR. It consists of three parts i.e. driver, expansion region and extraction region. The driver is made of ceramic cylinder, inside which Faraday shield is placed to avoid the ceramic sputtering and to avoid capacitive coupling of the plasma.

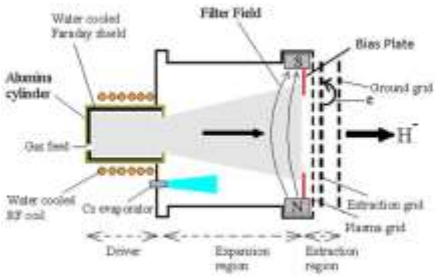


Figure 1 Schematic of the Negative Ion Source; ROBIN

Figure 2 Plasma and impurity diagnostics position in extraction region in ROBIN

The RF antenna (copper coil) is placed over the driver. A magnetic filter field of ~10mT applied between expansion and extraction region is to avoid the hot electrons (>5eV) in extraction region to avoid destruction of negative ions. The filter field flange has DN25KF ports to enable mounting of suitable diagnostics i.e. probes and OES etc. for the plasma and impurity. The extraction region consists of three multi-aperture electrostatic grids viz. the Mo plasma gird (PG), Cu extractor grid (EG) and Cu grounded grid (GG). Each grid is made in two halves. Permanent magnets are placed in EG to deflect and trap the co-extracted electrons. In the present configuration the plasma grid is lifted up to -25kV and extraction grid up to -15kV with respect to grounded grid (0kV) to extract and accelerate the $H^-$ ion beams. Only 146 apertures are opened up out of 776 in plasma grid to have similarity with identical source BATMAN [2]. The ion source remains floating when not referred to HV. In-between the ion source and the extractor accelerator system is a bias plate which is maintained at source potential. The plasma grid is biased positively with respect to source body to control the co-extracted electrons.

Plasma characterisation in the extraction region is necessary to understand and optimise the source performance with beams. Figure 2 shows the positions of the various diagnostic implemented in ROBIN to monitor and characterize the plasma in extraction region and impurity.

## LANGMUIR PROBES

The probes implemented in ROBIN are cylindrical single probes. The 0.4mm diameter and 12.5mm length probe tip is exposed to the plasma for measurements. Wilson feedthrough mechanism is used for the movement of the probes. The floating tungsten wire is biased with respect to source body. A voltage ramp (triangular wave) from +45V to -70V is applied to the probe at ramp frequency of 10 Hz. The sampling rate of the probe is 0.1 ms and data is averaged over 1ms. The probes circuit is in the closed signal conditioning rack which floats at the source potential and provides protection to the circuit against RF radiation. The middle probe has access to the beam extraction area whereas top and bottom probes are facing the bias plate.

Plasma oscillates at RF frequency and so it is difficult to estimate the plasma potential, floating potential and electron temperature using uncompensated probes. However the plasma density can be estimated through ion saturation current which is less affected in RF. The Langmuir probes measurements are reported in [3], [4], and [5]. The plasma parameters in the extraction region are correlated with the negative ion beam i.e. plasma density, asymmetry etc.

The typical Current Voltage (I-V) characteristics of the various probes are shown in Figure 3.

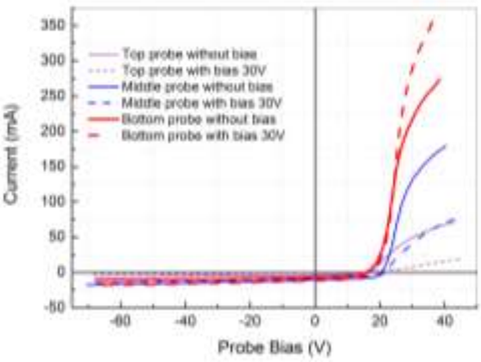


Figure 3 Typical I-V probe characteristics

Probes were moved horizontally in steps of 20 mm to achieve the plasma density profile along the horizontal direction for all 3 probe locations. Figure 4, shows the plasma densities at different locations. As seen from the figure the plasma density peaks for the middle probe and then drops off on either side of the peak value for the top and bottom probes. It is further observed that the density at the bottom probe location is a factor of ~2 as compared to the top one.

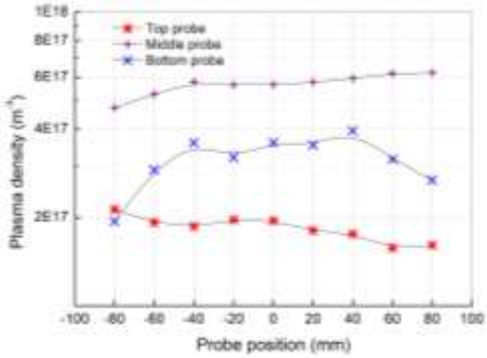


Figure 4: Plasma densities as function probe position

Bias voltage is applied during source operation to control the amount of co-extracted electrons. Studies at different bias voltages have been carried out to compare the plasma density distribution for with and without bias cases for probes at vertical centre, Figure 5.

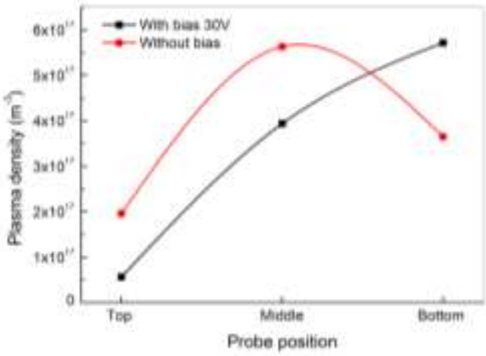


Figure 5: Plasma densities with and without bias

It is observed that the centrally peaked density distribution for the 0 V bias case changes to a gradually increasing density distribution from top to bottom for the applied bias voltage case and could be due to the E X B drift which is downward in the present experimental set up.

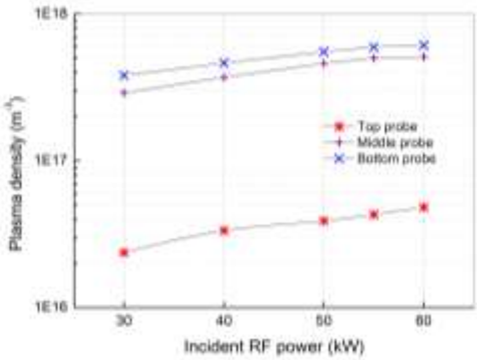


Figure 6: Plasma densities as a function of RF power

The effect of the RF power on the plasma density has also been studied at a source operational pressure of 0.6 Pa with a bias voltage of 30 V and for a power range between 30-60 kW in steps of 10 kW. Figure 6 shows the densities obtained as a function of the applied power. A factor of ~1.6 increase in the density is observed in the range of 30-50 kW. Increasing the power further resulted only in marginal increase (factor of ~1.15) in density.

## OPTICAL EMISSION SPECTROSCOPY

The optical emission spectroscopy implemented on ROBIN is a non-invasive technique to obtain line integrated measurements of the plasma density and temperature [6]. In addition it helps to provide direct online information on impurities in the source, Cs lines in surface operation mode, and Cu line which could be due to sputtering or melting due to high power loads during operation. A low resolution (1.5nm) four channels survey spectrometer, 200 to 1100 nm, is used for the same. The emitted light is collected by collimating lens (Plano convex lens of focal length 25mm and diameter 12.4mm) and focused on the fibre tip. Another end of the fibre is connected to the spectrometer. The spectrometer output is connected to a PC and monitored using software provided with spectrometer.

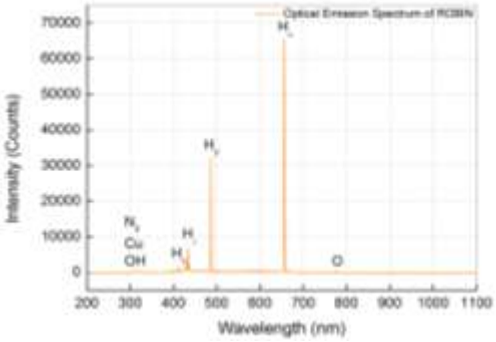


Figure 7 Typical Optical Emission Spectrum in extraction region in ROBIN

A typical OES spectrum of ROBIN is shown in figure 7. A program has been developed in LABVIEW to enable online monitoring and analysis of the emission. For each of the probe measurements reported in the paper, the corresponding emission spectra are being analysed with proper calibration factors to obtain the plasma parameters and also to enable benchmarking of the two diagnostics.

## RESIDUAL GAS ANALYSER

Monitoring of impurities is the key to successful operation of such source especially during the cesiated phase of operation which is the key to proper conditioning and obtained the desired $H^-$ densities while exercising the desired control on $j_e/j_{H^-}$ ratios. If the impurities are large, Cesium tends to form several undesirable compounds which deposit on the various components of the source and thus inhibit operation of the desired level. The ROBIN source has been recently cleaned of cesium compounds after 3 years of operation in cesiated mode. In order to monitor the impurities/ minor leaks in the source during the recommissioning phase RGA is connected to the source on the filter field flange through approximately 400mm long DN25KF vacuum bellow. It is used to monitor the water vapour and other residual gases in the source. An isolation valve is used in between to isolate the RGA from the source.

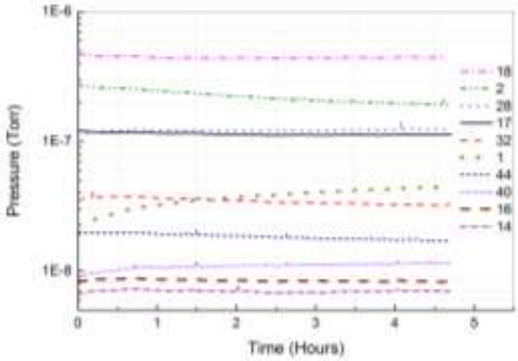


Figure 7 Measured partial pressures of various gases in ROBIN

The RGA system is lifted at source potential. However, ceramic isolator has been used in RGA line to avoid ground loops. Figure 7 shows the RGA spectrum in the source which is pumped through the grids using a 5000 l/s TMP. Water vapour and hydrogen is observed to be the major contributors to the total pressure which need to be reduced prior to Cs operation to control cesium compound formation. This shall be ensured using long hours of baking between 80-100˚C.

## SUMMARY

Various diagnostics implemented on ROBIN are discussed. Data from the three movable Langmuir probes and implemented at top, middle and bottom position in extraction region in ROBIN to monitor the plasma characteristics shows the density to be peaked when the applied bias to the bias plate is 0 V. However the trend changes with the plasma density being the maximum at the bottom and minimum at the top for an applied bias voltage of 30 V which is due to the EXB drift in the downward direction. The measurements of the optical emission spectroscopy is installed in front of each movable probe are being analysed and shall be presented elsewhere. The RGA is being effectively used to monitor the water vapour and residual gases in the source to understand the impurity level. The present conditions necessitate long hours of baking to reduce the impurity levels to make the Cs operation of the source more effective in achieving the desired results.

## REFERENCES


[1] M.J.Singh et.al., AIP Conference Proceedings 1390, 604 (2011)

[2] E. Speth et al 2006 Nucl. Fusion 46 S220

[3] Robert L. Merlino, American Journal of Physics 75, 1078 (2007)

[4] B. E. Cherrington, Plasma Chemistry and Plasma Processing, VoL 2, No. 2, 1982

[5] P. McNeely and L. Schiesko Review of Scientific Instruments 81, 02B111 (2010)

[6] U Fantz and D Wünderlich 2006 New J. Phys. 8 301

# MACHINE TOOL REQUIREMENTS FOR MAKING COMPONENTS OF PARTICLE ACCELERATOR*

Sobhan Choudhary*, Sanjay Chouksey, G. Mundra
Design and Manufacturing Technology Division
Raja Ramanna Centre for Advanced Technology (RRCAT), Indore, India
*email : sobhan@rrcat.gov.in


### *Abstract*

Particle accelerator is used for carrying out basic research in the field of medicine, diagnostics, and material science. Precision and versatile manufacturing facilities are required for manufacturing different accelerator components like microtron, vacuum chambers, microwave cavity, RF cavities, super conducting cavities and beam line components. Manufacturing of precision component (fine dimensional tolerances) with different contours and high surface finish requires precision machines. For ensuring quality of the precision components, measuring equipment's like CMM are used. General purpose lathes are used for making UHV chamber flanges, pipes, metal seals, CNC Vertical turret lathe for RF cavity and its coolant pipe grooves, Special lathe (hollow spindle lathe) used for machining SCRF cavities. Milling machines and CNC machining centers are used for machining yoke of magnet, RFQ. Horizontal boring machines used for making ports of UHV chamber. Non-conventional machines like water jet cutting machine, plasma arc cutting machine and EDM wire cut machines are mainly used for cutting materials having low machinability. Diamond tuning machines are used for machining high RF gradient linac cavities. This paper describes about the different machine tools required for manufacturing of accelerator components.


## INTRODUCTION

Accelerator components are UHV (ultra high vacuum) compatible, for good beam quality and its life. Machining of precision requires various types of machine tools like lathe, hollow spindle lathe, vertical turret lathe, Knee and column type milling machines, horizontal boring machine, jig boring machine, CNC turning center, machining center. Non-conventional machines include water jet cutting machine, plasma arc cutting machine, EDM wire cut machine.

## TURNING CENTRES

The lathe machine is primarily used to produce cylindrical surfaces and plane surfaces at a right angle to the axis of rotation. It can also produce taper surfaces & screw threads. There are two types of CNC turning centers: horizontal and vertical. Vertical turning centers are typically called a vertical turret lathe or VTL (Fig.1). CNC turning centers can have 3, 4 or 5-axes with more versatile capabilities and applications such as turning, drilling, tapping, and milling using live tools with powered rotary tool turret, sub-spindle (dual spindles), Y-axis, and multiple turrets. They are usually slant-bed type and have full machine enclosures to keep chips and coolant splashes within the machine. CNC Turning Centers with live tooling, dual spindles, Y-axis, multiple turrets meet simple to complex machining applications. Large quantity of ultra-high vacuum components like flanges (fixed, rotatable, conversion, zero length, KF), vacuum chambers, viewing windows, current feedthroughs, metallic gaskets etc. are machined on these conventional and CNC turning centres. Super conducting cavities are elliptical in shape, shall operate at 2K temperature for high accelerating gradient and quality factor are machined using CNC turning center hollow spindle CNC lathe(Fig. 2). A companion paper in these Proceedings gives details of the SCRF machining development at RRCAT.

Figure-1: Machining of Indus-2 RF cavity on CNC VTL machine

Figure 2: Hollow spindle lathe at RRCAT machining shop

## MACHINING CENTRE

Machining centers are CNC machine tools with multi-function machines equipped with automatic tool changer and are capable of carrying out milling, drilling, reaming, tapping, boring, counter boring and allied operations. Machining centers can be broadly classified into three types based on their structure i.e. horizontal, vertical, and gantry types. There are also classified based on programmable axes like three axis(Fig. 4), four axis, five axis machining Center. Pole and Yoke of various electro magnets, laminated sheets are stacked and machined on CNC machining centers as per the profile required for the various electro magnets like dipole, quadrupole, sextrapole(Fig. 3). Machining of Radio Frequency Quadrupole (RFQ) vanes modulation machining is done on precision five axis machining center using ball-end-mill cutter. A companion paper in these Proceedings gives details of the RFQ machining development at RRCAT. Double column CNC milling machines are suitable for machining 5 faces in a single setting, also for machining different angular faces, pockets, drilling and boring operations like machining of industrial LINAC components and large size UHV chambers with multi ports.

Figure 3: Pole and Yoke machined on machining centers of electro magnets

Figure 4: Vertical Machining Center (VMC)

## SINGLE POINT DIAMOND TURNING (SPDT)

The machine that does the Single Point Diamond Turning (SPDT) is an ultra precision CNC lathe with cutting tool is a diamond that has been specially prepared to cut the required surface geometry. For RF structures operating at 12 GHz and also with high RF gradient inside the cavity structure require surface better than Ra25. For RF cavity structures operating more than 100MV/m, surface finish requirement is better than 25nm. By using single point diamond turning, we can operate the structure at higher RF power without tuning. The conditioning time of the cavities is very low. With conventional machining, linac cavities are to be selected before vacuum brazing (± 10 micron). The brazed structure is to be tuned with RF measurements and mechanical deformations. The process of mechanical deformations is a rather risky operations. With accurate diamond turning, all cavities are within a tight tolerance (±2 micron) and all of the above operations can be bypassed. This leads to economical solution to accelerating structure manufacturing. Diamond turned surface also tolerate higher electric field (no discharges/arcing during operation even to high field gradients), lower RF surface loss, faster conditioning and better vacuum. For machining of Photocathode Gun and X-band accelerating and other high RF gradient structures (Fig. 5), SPDT is generally employed.

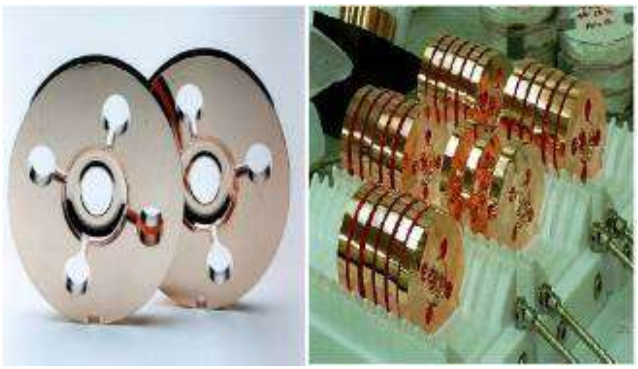

Figure 5: Machined X-band accelerating structures using SPDT

## ELECTRIC DISCHARGE MACHINING (EDM)

Electric discharge machining (EDM) is a material removal process that is especially useful for difficult-to-cut materials with complex shapes and is widely used in EDM is one of the most efficient manufacturing processes It is a non-contact thermal energy process used to machine electrically conductive components irrespective of the material's mechanical properties. In particle accelerators Pole and Yoke of various electro magnets, septum magnet are cut as per the profile requirement. Ports of multi-port chambers are also cut in the machine, as it is very fast compared to any other machining process. Large number of components for particle accelerators like Nb and NbTi rod for SCRF cavity components, reflectors for LASER light amplification, RF couplers' taper wave guides, taper waveguide cutting of RF coupler cavities,X-ray conversion targets in different sizes made out of tantalum material,HOM suppression slots in linac cavities for handling beam break-up and graphite components.

Figure 6: Kicker RF cavity using Electro Discharge Machining

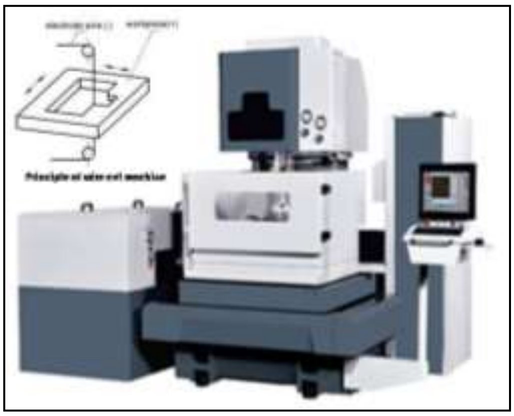

Figure 7: Submersible type Electro Discharge wire cut machine

## WATER JET CUTTING MACHINE

Water jet cutting is a non-conventional machining process in which material is removed by mechanical erosion of material. The main advantages of water jet cutting machine are very fast cutting compared to EDM wire cutting, no heat affected zone, as cold cutting and it can cut any material (metal non metal, conducting non conducting, hard and soft) . Different components that can be cut for particle accelerator punch and die blanks for 650GHz SCRF cavity, plates for electro magnet in different profile etc.(Fig. 8)

Figure 8: CNC Water jet cutting machine

## CONCLUSION

Different types of conventional and non conventional machines used for machining different types of particle accelerator components are discussed. Application of turning centres, machining centre, single point diamond turning centres and various other machine tools used for development of the precise components of particle accelerators has been discussed. In RRCAT, an in-house excellent facility has been developed for the manufacturing of particle accelerators components and sub-assemblies. We have gained experience through the development process. Various other non-conventional process like additive manufacturing process for the Ultra high vacuum vessels of complex shapes are under development.

## ACKNOWLEDGEMENT

We acknowledge whole team of Design and Manufacturing Technology Division (DMTD) for whole hearted support in machining of various accelerator components and encouraging for writing this paper. Authors thankfully acknowledge the support of various accelerators groups during manufacturing of the components.

# DESIGN AND DEVELOPMENT OF UPGRADED INTEGRATED TYPE BEAM POSITION INDICATORS FOR DIPOLE VACUUM CHAMBERS OF INDUS-2 SRS

L. K. Babbar[1*], Mukesh Kumar[1,5], Dr. B. N. Upadhyaya[2,5], V. K. Bhatnagar[3], Brahmanand Sisodia[3], Y. Tyagi[1], Rahul Jain[1], A. C. Holikatti[1], Surendra Yadav[1,5], Deepjwalit Vaishnav[1], S. Sarkar[4], S. K. Tiwari[4], D. P. Yadav[4], R. Sridhar[4] and T. A. Puntambekar[1]

[1]Beam Diagnostics Section / Beam Diagnostics & Coolant Systems Division

[2]Laser Development & Industrial Applications Division

[3]Design & Manufacturing Technology Division

[4]Ultra High Vacuum Technology Section

Raja Ramanna Centre for Advanced Technology, Indore, India

[5]Homi Bhabha National Institute, Training School Complex, Anushakti Nagar, Mumbai, India

* Email : babbar@rrcat.gov.in

*Abstract*

Four-button electrodes type beam position indicators (BPIs) are being used in Indus-2 synchrotron radiation source for the measurement of electron beam position at 56 locations, out of which 16 BPIs are integrated with 16 dipole vacuum chambers (one BPI in each chamber). Existing BPIs were installed approximately 14 years back in Indus-2 and are being used since then. In order to improve the performance of BPIs, it is planned to replace these BPIs with the upgraded version. The design and development of upgraded version of electrode assembly for integrated type BPI have been carried out for achieving higher higher transfer impedance of ~0.5 Ω at 505.812 MHz. It will enhance the electrode pickup signal strength by ~1.5 times as compared to that of the existing integrated BPI. The other improved design features are high frequency compatible 50 Ω impedance SMA feedthroughs, Nd:YAG laser welded electrode assembly, bell shaped tapered button electrode and fast decaying wake field in 50 Ω coaxial structure, which will also improve the performance of the BPI. The development of 5 BPIs has been completed which includes precision manufacturing of parts, in-house Nd:YAG laser welding of ~80 mm long SMA central conductor, TIG welding, UHV qualification and calibration by stretched wire method using X-Z stage. The flushing of button electrodes of BPI is within ±100 µm with respect to the wall of chamber. The ultimate vacuum better than 5 x 10E-10 mbar was achieved. BPI is also referred as beam position monitor (BPM), however in Indus-2, the term BPI has been used in place of BPM. The mechanical design, development, installation and initial results of upgraded integrated type BPIs have been described in this paper.

## INTRODUCTION

Today, synchrotron radiation source is an important research tool which is being used in various fields of science and technology. Indus-2 is a 2.5 GeV, 200 mA synchrotron radiation source, in operation at RRCAT, Indore, India [1]. It consists of eight super periods with a perimeter of 172.47 m. BPM is one of the important diagnostic device of a particle accelerator, however in Indus-2, we have used the term BPI to refer the BPM. There are 56 BPIs installed in a distributed manner in Indus-2 ring out of which 16 BPIs are integrated in the vicinity of dipole vacuum chambers (one BPI in each chamber). Figure 1 shows a schematic view of the locations of integrated type BPIs installed in a super period of Indus-2 (above) and dipole vacuum chamber installed in Indus-2 (below).

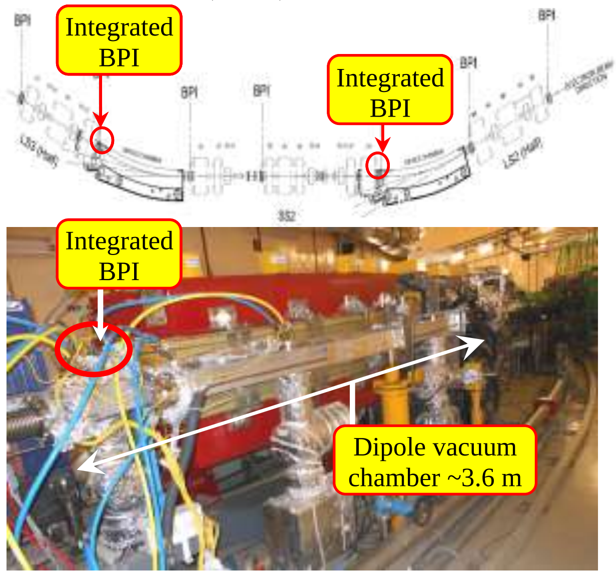


Figure 1: Schematic view of the locations of integrated type BPIs in a super period of Indus-2 (above); Dipole vacuum chamber installed in Indus-2 (below).

BPI is a non intercepting type diagnostic device, consisting of four sensor electrodes located symmetrically in beam pipe (vacuum chamber). The electron beam passing through the BPI induces voltage signals, on each of the electrodes, which are processed by a processing electronics. The beam position (charge centroid) is obtained by applying suitable algorithm on the data corresponding to four electrodes signals. These BPIs equipped with the signal processing electronics, continuously monitor the position of the beam orbit. The position data obtained is used by the control system for various activities. The schematic of electrodes configuration in BPI is shown in the Fig. 2.

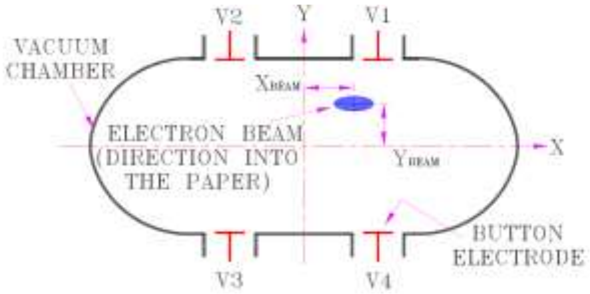


Figure 2: Schematic of electrodes configuration in BPI.

## DESIGN AND DEVELOPMENT OF UPGRADED INTEGRATED TYPE BPI

### *Conceptual Design*

The conceptual design of upgraded electrode assemblies of BPI is carried out based on its physics design and electromagnetic simulation. The quantities describing BPI's performance like transfer impedance, temporal response, frequency response, wakefield, power dissipation, linearity and coupling impedance etc have been optimized using wakefield solver of the CST Studio Suite [2]. The simulation results of upgraded electrode assembly have also been compared with that of the existing one [3]. In BPI, button electrode size is Ø 13.5 mm. The button to button distances are 33 mm and 70 mm across and along the beam path respectively. Sensitivities of BPI in the transverse x-plane and y-plane are ~0.07 per mm and ~0.05 per mm respectively. The electrode assembly of upgraded BPI has transfer impedance of ~0.5 Ω at 505.812 MHz which is ~1.5 times of the transfer impedance of the existing integrated BPI.

### *Mechanical Design*

The mechanical design of UHV compatible, non-magnetic electrode assemblies of upgraded BPI were carried out meeting the challenging requirements emerged from optimized conceptual physics design. The design of electrode assembly is carried out in such a way that bell shaped 6 mm thick SS316L button electrode, 4 mm thick insulator disc (MACOR®, dielectric constant ~6.03), ~80 mm long SS316L central conductor and 50 Ω SMA electrical feedthrough are all enclosed in a single SS316L sleeve. These four electrode assemblies of upgraded BPI will be installed in Ø28 mm ports of dipole vacuum chamber (made of AA 5083-H321), replacing the electrode assemblies of existing BPI, using de-mountable helicoflex® seal joints. Coaxial structure from button to electrical feedthrough is designed to maintain the uniform 50 Ω characteristic impedance. Improved design features of upgraded electrode assembly of BPI with respect to existing one are illustrated in Fig. 3.

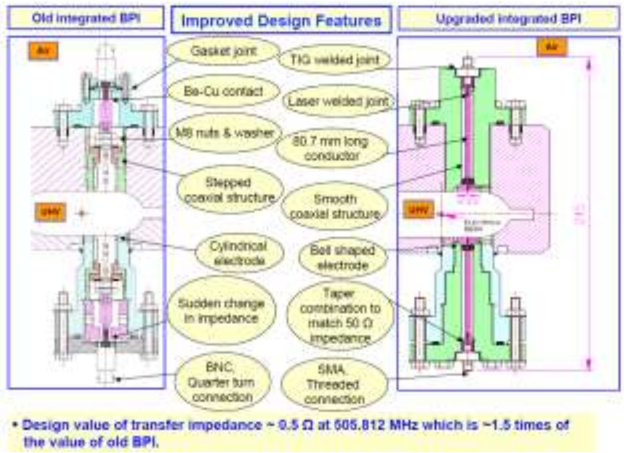


Figure 3: Improved design features of upgraded electrode assembly of BPI with respect to older one.

### *Development of Upgraded BPI*

The development of BPI involves precision machining of parts, Nd:YAG laser welding using special fixtures and TIG welding. SS316L with low relative magnetic permeability ($\mu_r \leq 1.050$ @~35 kA/m) was used for sleeves, electrodes and central conductors. Nd:YAG laser welding is used with optimized parameters as it fulfills our requirement of flexible laser beam delivery to the weld locations which were inaccessible for conventional welding methods [4]. Figure 4 shows the Nd:YAG laser welded central conductor (left); Electrode assemblies of one upgraded BPI (right).

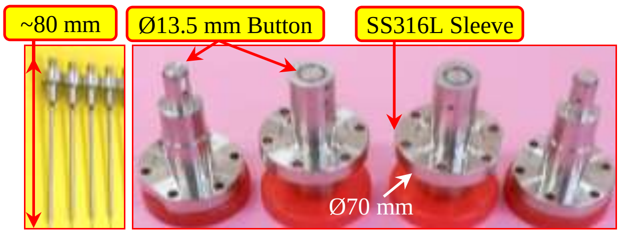


Figure 4: Nd:YAG laser welded central conductor (left); Electrode assemblies of one upgraded BPI (right).

The dedicated manifolds, made of SS316L, were designed, developed and used for the UHV qualification of the electrode assemblies of BPIs. The ultimate vacuum of ~ 2.4 x $10^{-10}$ mbar was achieved.

The design and development of dedicated calibration chamber was also carried out for the calibration of electrode assemblies. This calibration chamber, made of AA 6061-T6, has the cross section similar to the dipole chamber of Indus-2 at the location of integrated BPI. The calibration was done using coaxial stretched wire method. Position offsets and sensitivities of BPI were measured by calibration [5]. In this method, a thin wire carrying high frequency signal was stretched along the BPI axis which simulates the e-beam. Figure 5 shows the UHV testing of a batch of three BPIs using dedicated manifolds (left) and electrode assemblies of BPI during calibration (right).

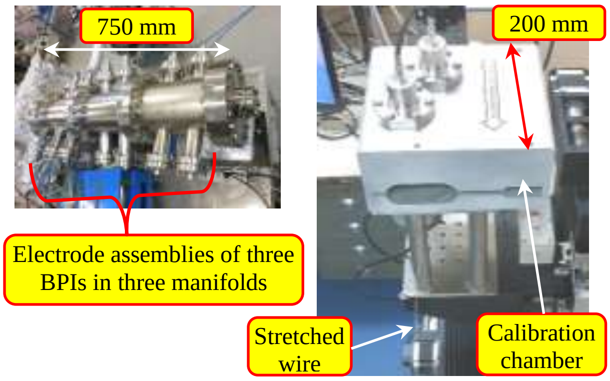


Figure 5: UHV testing of a batch of three BPIs (left); Electrode assemblies of BPI during calibration (right).

The development of first batch of five upgraded integrated type BPIs has been completed. One BPI has been installed, using de-mountable type helicoflex® seal joints, in the spare dipole vacuum chamber for the insertion device (ID) section of Indus-2 ring. Four BPIs are ready for the installation in Indus-2 ring

## RESULTS

The sensitivity of the upgraded integrated type BPIs was calculated from the slope of the curve between normalized difference signal and wire position during calibration using coaxial stretched wire method. The positional sensitivities in the transverse planes were ~0.07 per mm (x-plane) and ~0.05 per mm (y-plane). At calibration stage, a 20 dBm signal at 505.812 MHz fed to the stretched wire (terminated with 50 Ω) and electrode pickup signal strength from the upgraded integrated BPI were measured which were ~1.5 times of the signals from the existing integrated BPI. This indicates that the signal generated were close to the design value. The ultimate vacuum better than 5 x 10E-10 mbar was achieved during the UHV qualification. Residual gas analyser spectrum was also recorded and found satisfactory.

The flushing accuracy of electrodes were within ±100 µm and variation in annular gap around the signal pick-up electrodes were within ±200 µm. The value of the capacitance of the electrode assembly of upgraded integrated type BPI is ~11 pF when measured using Megger make ‘LCR131 Component Tester’ at 120 kHz.

## CONCLUSION

All the five numbers of upgraded integrated type BPIs were qualified in ultimate vacuum test. These were calibrated using stretched wire calibration setup developed indigenously. The measured sensitivity of these BPIs matches closely with the design value. The signal strength of BPI improved by ~1.5 times with respect to existing BPI, which will lead to improvement in the performance of upgraded BPI. One upgraded BPI has been installed in the spare dipole vacuum chamber of ID section of Indus-2 ring as shown in Fig. 6.

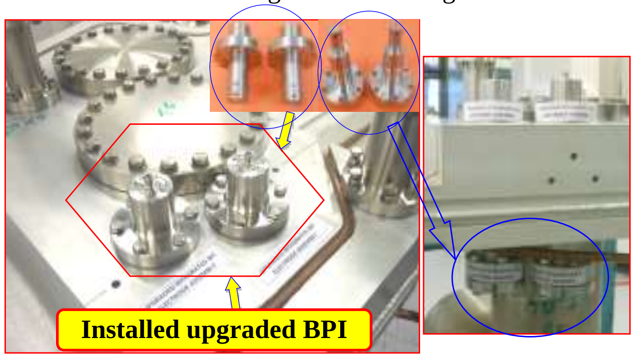


Figure 6: Upgraded integrated type BPI installed in spare dipole vacuum chamber for ID section of Indus-2 ring.

Four BPIs are ready for the installation and it is planned to install these BPIs during the major shut-down of Indus-2 ring in Dec-2019. The development of remaining upgraded integrated type BPIs is in full pace.

## ACKNOWLEDGMENT

The authors heartily wish to thank Design & Manufacturing Technology Division, Laser Development & Industrial Applications Division and Chemical Treatment Laboratory for their contribution in this work. The contributions of Shri U. P. Pandey, Shri J. C. Suthar and Shri V. K. Lal is thankfully acknowledged for UHV compatible TIG welding. The authors also thank Shri A. K. Karnewar, Shri N. K. Maurya and Shri P. K. Soni for their support for calibration and electronic testing. Contribution of the team members of Ultra High Vacuum Technology Section for the helium leak testing, ultimate vacuum testing and installation is also thankfully acknowledged.

## REFERENECES

[1] http://www.rrcat.gov.in

[2] http://www.cst.com

[3] Mukesh Kumar, “Comparative study of new and existing button electrode assemblies of integrated BPI of Indus-2”, Divisional Report, Beam Diagnostics and Coolant Systems Division, RRCAT (2017).

[4] D. K. Agrawal, L. K. Babbar, Deepjwalit Vaishnav, Rajpal Singh, B. K. Saini, Sabir Ali, Amber Choubey, R. K. Jain, Vijay Bhardwaj, S. C. Vishwakarma, Mukesh Kumar, T. A. Puntambekar, B. N. Upadhyaya and S. M. Oak, “Ultra high vacuum compatible laser welding of SMA feedthrough and button electrode with beam position indicator for accelerator applications”, DAE-BRNS 23rd National Laser Symposium (NLS-23), Dec 3-6, 2014, Tirupati.

[5] Y. Tyagi, “Calibration coefficients of prototype integrated BPI and upgraded integrated BPI of Indus-2”, Divisional Report, Beam Diagnostics and Coolant Systems Division, RRCAT (2017).

# HIGH VOLTAGE TEST RESULTS OF TRIODE TYPE ELECTRON GUN USING PLANAR CATHODE

Jyoti Mishra, Vishal Ramkar, Tanuja Dixit , Ajay Shetake, Chandrakant Nainwad, Abhisekh Waigaonkar, Akshita Tawde, Shahsikant Pokharkar, Abhay Deshpande, R. Krishnan,

Society for Applied Microwave Electronics Engineering & Research , SAMEER, IIT Campus, Powai, Mumbai - 400076

*Abstract*

A planar cathode based triode gun is assembled and tested at SAMEER for various applications. The basic design philosophy is to reuse the electron gun as many times as possible. Therefore, all the components are designed in such a way that in case of failure of any part, replacement can be done without discarding the entire assembly. In this way, many expensive and imported components can be salvaged and repairing cost can be made minimal. A planar dispenser cathode of 6 mm diameter and a Molybdenum grid of 0.1 mm thickness form the grid cathode assembly. A special jig is designed to test the beam current and beam diameter using Faraday cup assembly. Cathode temperature characteristics were studied and then Gun is tested up to 18 kV in pulsed mode and grid voltage was varied from +40 to +240 V. The measurement shows the grid control characteristics and its effect on the beam profile.

## INTRODUCTION

At SAMEER, electron linear accelerators are developed for various applications. Electron gun is the source of electrons [1]. Earlier we have used imported grid-cathode assemblies and then assembled gun at SAMEER. We faced many issues like broken filament electrodes, grid displacement, shortening of electrodes [2,3]. Therefore, efforts are made to make the assembly reusable and to make grids indigenously. A planar cathode based triode gun is assembled with a basic design philosophy to make the electron gun reusable by having replaceable parts. Hence, repairing cost comes down drastically. Efforts were made to make greater than 90 % transparent grids. Grid is made indigenously by laser cutting with very high accuracy less than 0.1 mm. Grid is mounted such that the grid-cathode distance is maintained at less than 2 mm. Gun design simulations is performed on CST software. A special jig is designed to measure the beam current and beam diameter using Faraday cup assembly with varying diameter holes in the centre. The Gun is tested up to 18 kV in pulsed mode and grid voltage is varied from +40 to +240 V. The measurement shows the grid control characteristics and its effect on the beam profile. Measurements is done using ETM (USA) make pulsed power supply. The minimum beam diameter measured is 4 mm at 15 kV at grid voltage of +240 V. Triode electron gun testing results are discussed in detail with plots of experimentally measured in the paper.

## GUN SIMULATIONS

CST Particle Studio is used to simulate the electron gun. Each part cathode, grid, focussing electrode and anode is designed and subsequently optimized in shape and size to get a nearly focussed beam at 10 mm after anode[1]. CST Particle Studio simulation of Planar Triode Gun is shown in Fig.1. Simulation gives a beam current of 79.73 mA at 15 kV and beam size of about 4 mm diameter at anode location [3].

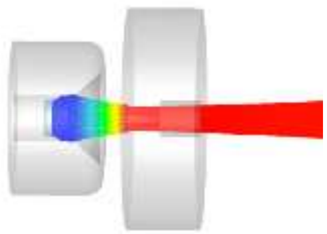

Figure 1: CST Particle Studio simulation of Planar Triode Gun

## EXPERIMENTAL SETUP

### *Assembly*

All the triode gun parts are fabricated at SAMEER except cathode. Planar cathode is tungsten matrix type of 6 mm diameter. A filament power of 10 W raises the temperature of the tungsten matrix pellet to 1100 °C. The emission current measured is 112 mA at 18 kV. Molybdenum grid is sandwiched between focusing electrode and grid support adapter. Grid is isolated from cathode and body of the electron gun. Initially distance between cathode and grid was kept 0.5 mm but some arcing was observed at high voltage operation. Therefore, cathode-grid distance was increased to almost 2 mm. Anode has an opening of 4 mm diameter to pass the electron beam. The high voltage ceramic seal can withstand voltages up to 45 kV.

All beam parameters were measured using faraday cup. Faraday cup was mounted on a linear derive so that its distance can be varied [4]. Faraday cup assembly consist

#tanuja@sameer.gov.in; jyoti160594@gmail.com

of four copper disc of thickness 1.5 mm each and having centre hole diameter of 4.5mm, 3.5mm, 2.5mm respectively and last one with no central hole. They are isolated by ceramic discs of 2 mm thickness and current is measured across the four disc using oscilloscope. Figure 2 shows the experimental setup. A sputter-ion pump of 8 lps pumping capacity is connected to the system to take care of residual outgassing during operation.

Figure 2: Experimental Setup

For cathode filament heating, DC voltage is applied across its electrodes up to 7.5 V and current of 2.2 A using ETM (USA) make power supply. It is possible to vary high voltage from 2 kV up to 20 kV continuously. Grid is pulsed maximum up to +240 V. External trigger is required to make the grid conducting. This experiment was carried out at 11 Hz pulse repetition frequency (PRF). Triggering pulse parameters used are as follows: Pulse width = 4.5 µs, Amplitude 5.0 Vp-p. To operate under good vacuum conditions, first outgassing was done at different filament voltages. Vacuum achieved is $8.5*10^{-9}$ mbar before cathode heating.

## EXPERIMENTAL RESULTS

Figure 3 shows the output pulse characteristics measured at Faraday cup and body of the jig using a current transformer (CT). The flat pulse region is about 4.5 µs. Electron beam current of 81.2 mA was obtained at 15 kV injection voltage at the faraday cup.

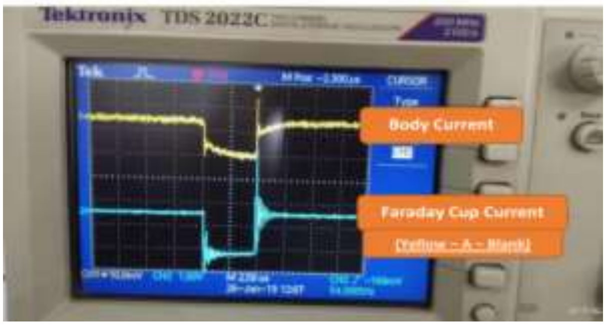


Figure 3. Body current and faraday cup current signal measured using oscilloscope

In Fig.4, Grid bias voltage is set to a fixed value of +240 V and beam current on the faraday cup is measured as a function of filament voltage. As filament voltage increases current increases but later saturates. This is due to operation in space charge dominated region.

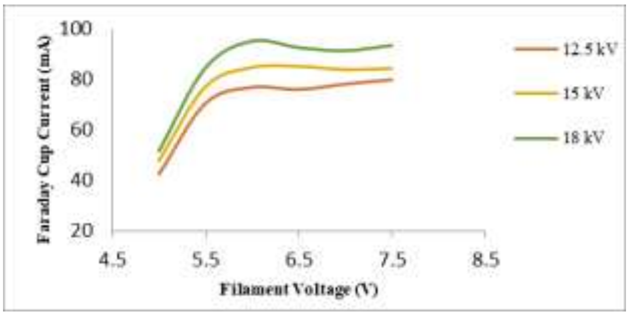


Figure. 4 Beam current variation with filament voltage at different injection voltages

We fix our operating voltage based on this plot. A value of 6.3 V is chosen as the operating filament voltage during operation of the gun.

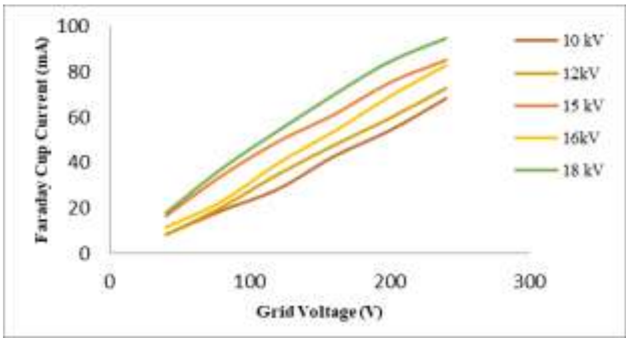


Figure 5. Faraday cup current variation as a function of grid voltage at different injection voltage

In Fig. 5, the filament voltage is fixed at 7V and variation of faraday cup current as a function of grid voltage is plotted for various injection voltage. It is observed that as grid bias voltage becomes more positive with respect to cathode, the beam current increases.

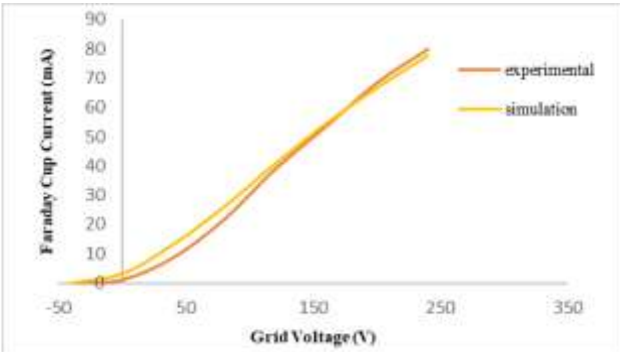


Figure 6. Measured beam current comparison with change in grid voltage using CST simulations

In Fig. 6, experimental measured faraday cup current at 15 kV with CST simulations as a function of grid voltage. In simulations, the maximum current achieved is 78 mA.

Experimentally measured beam current and simulation beam current shows 90% consistency at higher grid voltages.

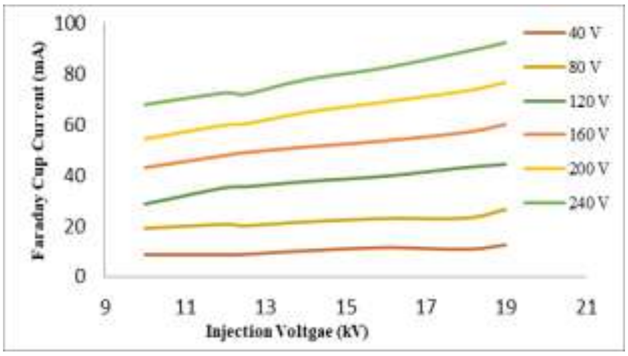


Figure 7. Beam current as a function of injection voltage at different grid voltages

Fig.7 shows the true triode characteristics, where Faraday cup current as a function of injection voltage is plotted for different grid voltages. The maximum faraday cup current measured is 92 mA.

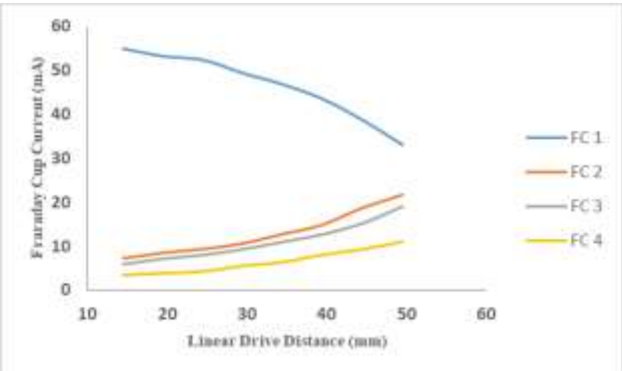


Figure 8. Faraday cup current as function of distance

Fig. 8 shows the variation in faraday cup current as a function of position of linear drive. As the distance is increased, the central collector shoes increase in current which means that the beam is focussed and aligned properly. Copper discs connected to other feedthoughs for current measurement shows less current, this indicates that the beam is not diverging.

Fig. 9 is plot of Faraday cup current as a function of $V^{3/2}$, where voltage represents injection voltgae. The slope of the graph gives perveance which is 0.02 microperve. With increase in injection voltage, the disparity between experiemental and simulation data diminutes.

## DISCUSSIONS

It is observed that the emission current measurement from the cathode is not very easy due to losses in the body. Emission current depends on cathode activation which strongly depends on vacuum condition. This gun was initially designed for 60 kV and spacings were

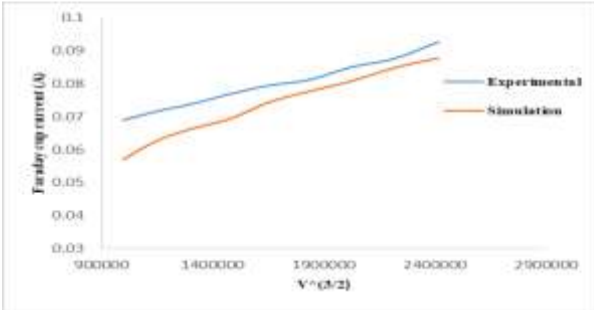


Figure 9. Faraday cup current as a function of $V^{3/2}$

adjusted accordingly. As of now we have a supply capable of delivering 20 kV, therefore the measurements are done within the supply specifications. The results are not upto the mark due to this limitation When 60 kV supply will be available then full measurements will be carried out.

## CONCLUSION

The measurements were carried out with limitations on very small beam current measurements at lower grid voltages and lower injection voltages. Cathode gets activated slowly as observed during measurements. Outgassing of gun at higher filament voltage and higher injection voltage is important to achieve good results. These results will be compared with diode configuration with the same cathode setup as a next step.

## REFERENCES


[1] Sergey Ivanovich Molokovsky, Aleksandr Danilovich Sushkov, "Intense Electron and Ion Beams", Springer-Verlag Berlin Heidelberg, (2005)

[2] Tanuja Dixit et.al., Electron gun and target design for the dual mode radiotherapy linac at SAMEER, ID 308, Proceedings of InPAC2013, VECC, Kolkata

[3] Sameer Mathe, Tanuja Dixit, et. al., “Comparative design of electron gun designs for high current linacs”, Proceedings of VEDA 2015 held at MTRDC, DRDO, Bengaluru

[4] Zhou, Zu-Sheng and He, Da-Yong and Chi, Yun-Long,"Electron gun system for NSC KIPT linac", Chinese Physics C, June 2014, p. 067006 (2014)

# DESIGN AND DEVELOPMENT OF FLANGE INTEGRATED BEAM POSITION MONITORS FOR INDUS-1 STORAGE RING AND INFRARED FREE ELECTRON LASER SET-UP

L. K. Babbar[1*], Mukesh Kumar[1,5], D. P. Yadav[2], B. N. Upadhyaya[3,5], V. K. Bhatnagar[4], Brahmanand Sisodia[4], Balkrishna Sindal[2], S. K. Tiwari[2], Y. Tyagi[1], A. C. Holikatti[1], Surendra Yadav[1,5], Ajay Kumar Soni[1], Deepjwalit Vaishnav[1], Yogendra M. Sheth[1] and T. A. Puntambekar[1]
[1]Beam Diagnostics Section / Beam Diagnostics & Coolant Systems Division
[2]Laser Development & Industrial Applications Division
[3]Design & Manufacturing Technology Division
[4]Ultra High Vacuum Technology Section
Raja Ramanna Centre for Advanced Technology, Indore, India
[5]Homi Bhabha National Institute, Training School Complex, Anushakti Nagar, Mumbai, India
* Email : babbar@rrcat.gov.in

*Abstract*

Indus-1 is a 100 mA, 450 MeV electron storage ring at Raja Ramanna Centre for Advanced Technology (RRCAT), Indore that emits synchrotron radiation covering the spectrum ranging from mid-IR to soft x-ray. It is a square ring having four straight sections (SS) with one Beam Position Monitor (BPM) installed in each. BPM is a pick up type of beam diagnostic device that has four-button electrodes. It is used for the measurement of position of electron beam passing through it. Implementation of proposed electron beam orbit correction system in Indus-1 will require eight BPMs in lieu of the four presently installed. SS of Indus-1 ring are quite occupied by the installed devices and practically there is no room available for the additional BPMs. Development of eight compact BPMs is taken up with an objective of accommodating eight BPMs in the SS. Named as "Flange Integrated BPM" (FIBPM), it has been designed in a 34 mm thick single SS316L flange having Ø152 mm outer diameter (OD). It incorporates four signal pickup button electrode assemblies, fiducial holes for alignment, tapped holes for support assembly and both sides sealing surface compatible to diamond section gasket. A prototype of the FIBPM has been fabricated, vacuum qualified and calibrated. Similarly, for another requirement, two even more compact FIBPMs have been developed in 22 mm thick SS316L flange having Ø70 mm OD with provisions for alignment and support in the flange thickness of the FIBPM. Installed in Infrared Free Electron Laser (IRFEL) Set-up at RRCAT, these 22 mm thick FIBPMs are import substitute. Mechanical design and development of FIBPMs for Indus-1 and IRFEL set-up have been described at length in this paper.

## INTRODUCTION

Indus-1 is an electron beam storage ring at RRCAT, Indore, India [1]. Perimeter of the ring is 18.96 m. It is in operation since 1999, emitting synchrotron radiation from mid-IR to soft x-ray. There are four SS in it, each having one BPM for the measurement of electron beam position. BPM is a non interceptive type diagnostic device, consists of four sensor electrodes located symmetrically. The passing beam induces voltage signals, in electrodes, which are processed by a processing electronics. The transverse beam position (charge centroid) is obtained by applying suitable algorithm on the data corresponding to four signals. The schematic of electrodes configuration in BPM is shown in the Fig. 1.

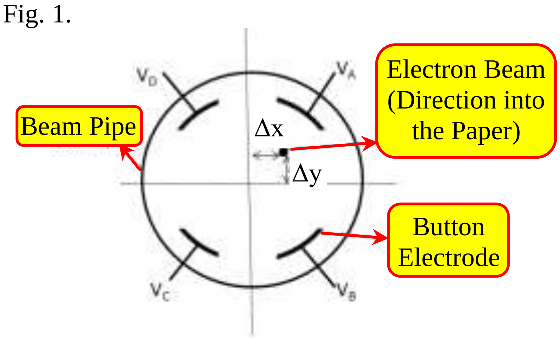


Figure 1: Schematic of electrodes configuration in BPM.

As per the present upgradation requirement regarding electron beam orbit correction in Indus-1, there is a need to use total eight BPMs (two BPMs in each SS) in lieu of ~20 years old four BPMs in use. Each SS (~3.2 m long) is too occupied to install the additional BPMs due to the already installed magnets etc. FIBPM has been designed and developed for Indus-1 in a 34 mm thick single flange Ø152 mm OD. Due to the compact design of FIBPMs, it is now feasible to accommodate eight BPMs in Indus-1.

More compact FIBPMs in 22 mm thick and Ø70 mm OD flange have also been designed, developed and installed at two places in IRFEL set-up to fulfill the requirement of a compact BPM. At RRCAT, IRFEL set-up is in advanced stages of commissioning. It is tunable in the wavelength range of 15-50 µm. It is built to serve as a 'user facility' for experiments that have initially been planned in-house in the area of Condensed Matter Physics.

## DESIGN AND DEVELOPMENT OF 34 mm THICK FIBPM FOR INDUS-1

Mechanical design of UHV compatible FIBPM has been carried out based on its physics design and electromagnetic simulation using CST Studio Suite [2], [3]. Four button electrode assemblies, 90° apart from each other, have been incorporated in 34 mm thickness of the flange which has both sides sealing faces for diamond section gasket compatible to standard UHV flanges. FIBPM has Ø20 mm SS316L bell shaped button electrode with 1 mm annular gap around it. SMA feedthrough is used to bring out connection of electrode while precisely machined Macor® disc is used as insulator in coaxial geometry of electrode assembly designed for 50 Ω impedance. The electrodes are kept flushed to Ø85 mm central bore. 34 mm thick FIBPM vacuum chamber, made of SS316L having low relative magnetic permeability ≤1.050 at ~35 kA/m magnetizing field, accommodates fiducial holes for alignment and tapped holes for its support device. Electrode assemblies are developed using in-house fiber coupled 250 W Nd:YAG laser welding with optimized parameters [4] and TIG welding. Diamond shaped seal made of Al alloy AA 6063-T5 with 60° included angle has been designed and developed by Ultra High Vacuum Technology Section, RRCAT for UHV compatible joints at both sides FIBPM. Ø152 mm OD FIBPM requires only twelve M8 bolts for its assembly in the ring. The integrity and endurance testing of the demountable joints of FIBPM using developed Al seals have also been carried out. During this, assembly was baked up to 150 °C for five repeated bake out cycles. Helium leak rate less than $6.2 \times 10^{-11}$ mbar-l/s was recorded during each cycle. During the ultimate vacuum testing of FIBPM, vacuum better than $3 \times 10^{-10}$ mbar has been achieved. Calibration of FIBPM has also been carried out using stretched wire method to find out the sensitivity. Figure 2 shows the sectional view of 34 mm thick FIBPM (left) and FIBPM developed (right).

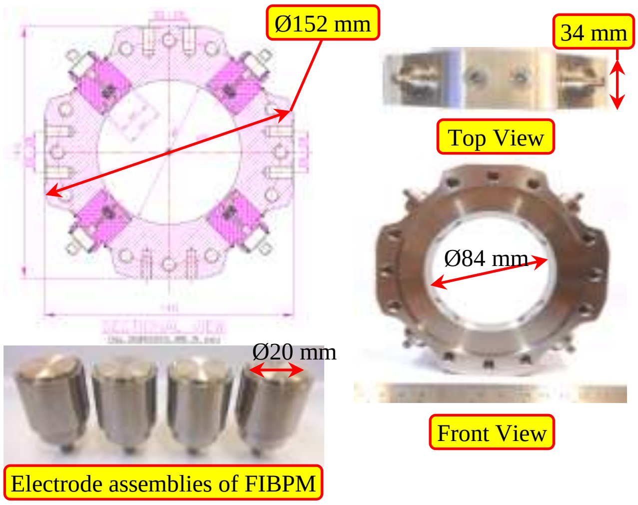


Figure 2: Sectional view of 34 mm thick FIBPM (left); FIBPM developed (right).

## DESIGN AND DEVELOPMENT OF 22 mm FIBPM FOR IRFEL SET-UP

FIBPM for IRFEL has been designed in 22 mm thick and Ø70 mm OD flange fulfilling the requirement of a compact BPM. It has both sides knife edge sealing faces similar to standard DN35CF flange for metal gasket joints. FIBPM has central bore of Ø38 mm and incorporates four numbers of Ø5.85 mm button electrodes at 30° from the vertical axis on both sides. The weld joint between the button electrode and the central conductor of SMA feedthrough is designed, considering laser welding in order to minimize the heat input thus avoiding deformation of button electrode. The provisions for alignment and support have also been made in the thickness of the FIBPM. The design of compact electrode assembly has been carried out such that it has only three components that is button electrode, SMA and sleeve. To weld the Ø1.27 mm SS304 central conductor of SMA with 1.7 mm thick SS316L button, conductor was kept protruding by ~0.2 mm above the button in order to avoid concave pit at button face. After Nd:YAG laser welding, ~0.15 mm protruded convex shaped weld bead was polished to make the button surface flat. The depth of penetration at the interface of button and conductor was measured ~0.3 mm [5]. Figure 3 shows the arrangement of button electrodes in 22 mm thick and Ø70 mm OD FIBPM (left) and machined parts along with laser welded electrode assemblies (right) .

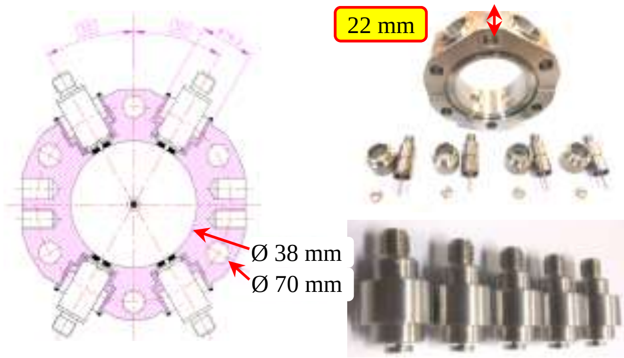


Figure 3: Arrangement of button electrodes in 22 mm thick and Ø70 mm OD FIBPM (left); Machined parts along with laser welded electrode assemblies (right).

TIG welding was used to join the electrode assembly with FIBPM flange. The ultimate vacuum of ~ $1.5 \times 10^{-10}$ mbar was achieved. Two FIBPMs have been calibrated using stretched method. Figure 4 shows the 22 mm thick and Ø70 mm OD FIBPM for IRFEL set-up.

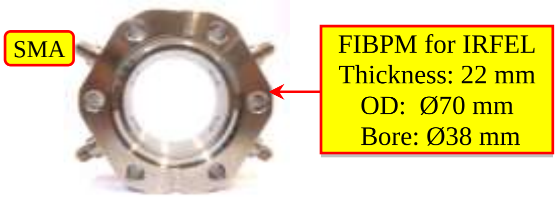


Figure 4: 22 mm thick and Ø70 mm OD FIBPM for IRFEL set-up.

## INSTALLATION of FIBPMs

The prototype of 34 mm thick and Ø152 mm OD FIBPM has been designed and developed. As per requirement, all the eight FIBPMs will be developed and installed together in Indus-1 ring for the measurement of electron beam position.

Further, two indigenously developed 22 mm thick, Ø70 mm OD FIBPMs have been installed in the pre-buncher and buncher section of IRFEL set-up. Figure 5 shows 22 mm thick and Ø70 mm OD FIBPM installed in IRFEL set-up.

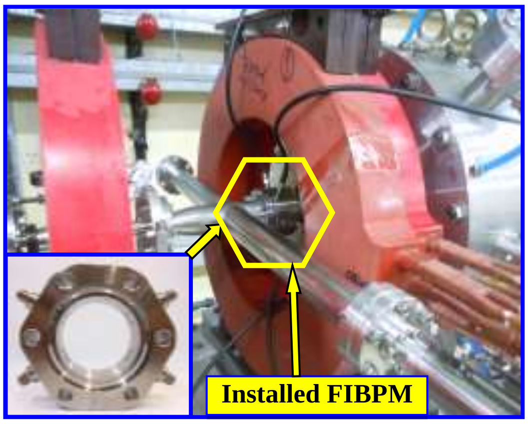


Figure 5: 22 mm thick and Ø70 mm OD FIBPM installed in IRFEL set-up.

## RESULTS

The ultimate vacuum better than 3 x $10^{-10}$ mbar was achieved during the UHV qualification of FIBPMs. The sensitivity of FIBPMs in both the transverse planes is measured using coaxial stretched wire method. The sensitivity in both the transverse planes is ~0.028 per mm (theoretical value 0.033 per mm) for 34 mm thick FIBPM. In 22 mm thick FIBPM, the measured value of sensitivities are ~0.046 per mm in horizontal plane (theoretical value 0.052 per mm) and ~0.079 per mm in vertical plane (theoretical value 0.090 per mm). In the indigenously developed 22 mm thick and Ø70 mm OD FIBPM which is an import substitute, the value of the capacitance between the button electrode and flange body is ~5 pF (nearly same in four button electrodes) when measured using Megger make 'LCR131 component tester' at 120 kHz. This value is near to the capacitance (~4 pF) of FIBPM which is being sold by foreign manufacturer in the international market. The difference in the value of capacitance might be due to the different design of coaxial structure, these FIBPMs incorporate. The flushing of the button electrodes were measured within ±50 µm with respect to the inner wall of central aperture for all the FIBPMs. The relative magnetic permeability of FIBPMs after all the machining and welding activities were found ~1.19 max, near the TIG welded joint, at the magnetizing field of ~35 kA/m when measured using the Ferromaster® magnetic permeability meter [6].

## CONCLUSION

The prototype of 34 mm thick and Ø152 mm OD FIBPM has been designed and developed for Indus-1 ring to fulfill the upgradation requirement regarding beam orbit correction. It has qualified the ultimate vacuum test. The measured sensitivity of FIBPM is near to the theoretical value. Due to the compact design of FIBPMs, the installation of eight BPMs in Indus-1 electron storage ring is possible.

22 mm thick and Ø70 mm OD two FIBPMs have also been developed indigenously and installed in IRFEL set-up at RRCAT for the measurement of electron beam position. These FIBPMs are of compact design and require only <1 inch space in assembly line for its installation. It is an import substitute, developed using in-house Nd:YAG laser welding facility. The experience gained so far will be very helpful to fulfill the new requirement of compact BPMs. Further, there is a new requirement for five more UHV compatible FIBPMs for IRFEL set-up, RRCAT in Ø114 mm OD knife edge flange.

## ACKNOWLEDGMENT


The authors heartily wish to thank Design & Manufacturing Technology Division, Laser Development & Industrial Applications Division and Chemical Treatment Laboratory for their contribution for this work. Contribution of the team members of Ultra High Vacuum Technology Section for ultimate vacuum testing and installation is also thankfully acknowledged. The authors heartily wish to thank team members of Accelerator Physics Section and Beam Diagnostics Section for their motivation to take up this activity of design & development of compact beam position monitoring devices. The technical discussion at the different stages of the development with Shri Rakesh Kaul, Dr P. Ganesh and Shri Vijay Kumar Bhardwaj is also thankfully acknowledged.


## REFERENECES


[1] http://www.rrcat.gov.in

[2] http://www.cst.com

[3] Mukesh Kumar, "Simulation results of flange integrated beam position monitor for Indus-1", Divisional Report, Beam Diagnostics and Coolant Systems Division, RRCAT, 2016.

[4] D. K. Agrawal, L. K. Babbar at el., "Ultra high vacuum compatible laser welding of SMA feedthrough and button electrode with beam position indicator for accelerator applications", DAE-BRNS 23rd National Laser Symposium (NLS-23), Dec 3-6, 2014, Tirupati.

[5] Dinesh Nagpure and P. Ganesh, "Report on weld cross-section examination", Divisional Report No. RRCAT/LMPD/MEL/13 Dec 2018, Laser Materials Processing Division, RRCAT.

[6] https://stefan-mayer.com

# ACHROMATIC BEAM OPTICS FOR THE ELECTRON BEAM TRANSFER LINE IN FEL FACILITY AT IUAC DELHI

Sarvesh Kumar*, Joydeep Karmakar, G. Rodrigues, S. Ghosh, N. Madhavan
Inter University Accelerator Center, New Delhi

*Abstract*

The Delhi Light Source (DLS), being developed at IUAC, New Delhi, will produce Tera-Hertz (THz) radiation from the wiggling motion of an electron beam passing through an undulator magnet set-up. The electron beam of energy range 4 to 8 MeV and ≈1 % energy spread needs to be deflected away from THz radiation immediately after the undulator magnet. As the electron beam will be asymmetric in the transverse plane at the exit of the undulator magnet, a momentum achromat with carefully chosen quadrupole magnets has been designed to transport the electron beam. The achromatic configuration consists of beam bending by equal and opposite angles of 60 degree using two identical dipole magnets (DM). It is of dogleg type achromatic configuration with the inclusion of minimum number of quadrupole magnets (QM). The final achromatic configuration is DM-QM-QM-QM-DM-QM-QM. At the end, two quadrupole magnets can focus the electron beam to anyone of the three successive experimental stations with the desired beam quality and ease of tunability. In this paper, the details of the electron beam achromatic optics using codes such as GICOSY and GPT will be presented.

## INTRODUCTION

The Delhi Light Source [1, 2] produces the THz radiations by wiggling motion of electron beam inside undulator. The 4-8 MeV electron beam is generated by an electron gun comprising of a photocathode, RF cavity and a solenoid. It is focused to the entrance of the undulator magnet. The horizontal undulator magnet wiggles the beam in the vertical direction and the beam comes out of the undulator is wider vertically and smaller horizontally. Now, the electron beam has to be transferred to a parallel beam line by means of an achromatic bending [3]. The dogleg achromatic bending configuration is DM1-QM1-QM2-QM3-DM2-QM4-QM5 where DM stands for dipole magnet and QM for quadrupole magnet. The electron beam can be focused to three successive experimental stations using two quadrupole magnets at the end.

There are many 90 degree achromatic bends [4] already designed at IUAC Delhi for transporting the heavy ion beams. Many labs [5, 6] have employed dogleg achromatic configurations to transport the electron beam.

* sariuac@gmail.com, sarvesh@iuac.res.in

## CRITERIA FOR BEAMLINE DESIGN

The beamline design has to satisfy few criteria so as to transport the electron beam effectively. Here are few geometrical constraints and design considerations.

1. The beamline has to follow all the geometrical constraints of the beam hall. The distance between parallel beamlines is 2 meters.
2. The beam optics should result in zero emittance growth and full transmission.
3. The energy spread is considered to be ≤ 1 % to design all the beam optical components.
4. The final beam optics solution must result into practical placements of all the beam optical components, facilitate the placement of proper beam diagnostics devices and vacuum devices etc.
5. The transfer matrix coefficient [X,D] and [A,D] for full achromatic configuration are designed to be zero at the double focusing point of the whole achromatic configuration. The dogleg configuration also requires [X,D] to be zero at the middle of the achromat.
6. The magnetic field is chosen in such a way that all the magnets can be managed by just air cooling.

## ACHROMATIC ELECTRON BEAM OPTICS

The initial beam parameters are extracted from GPT code simulations of previous section and are given in Table-1. The achromatic bending of electron beam is necessary as maximum energy spread is assumed to be around 1% in order to avoid large beam size due to dispersion of beam in bending plane.

Table 1: Initial twiss parameters at two energies, 4 MeV and 8 MeV of electron beam to design the achromatic system resulting from GPT code

| Parameters | 4 MeV | 8 MeV |
|---|---|---|
| $\alpha_x$ | -2.23 | -0.1443 |
| $\beta_x$ (mm/mrad) | 14.6 | 0.3751 |
| $\epsilon_x$ (mm-mrad) | 2.57 | 1.81 |
| $\alpha_y$ | -0.472 | -3.322 |
| $\beta_y$ (mm/mrad) | 0.105 | 7.4729 |
| $\epsilon_y$ (mm-mrad) | 2.82 | 1.661 |
| Energy Spread (%) | 1 | 1 |
| Max. beam rigidity (Tm) | 0.0134 | 0.0267 |

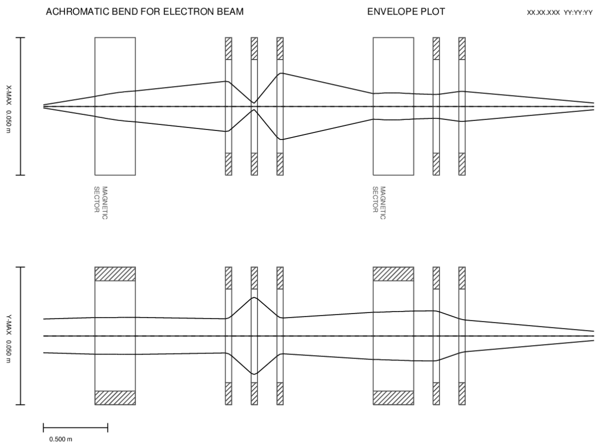


Figure 1: Beam optics of achromatic bend for 4 MeV electron beam using GICOSY code, upper plot is for horizontal plane and the bottom plot for vertical plane

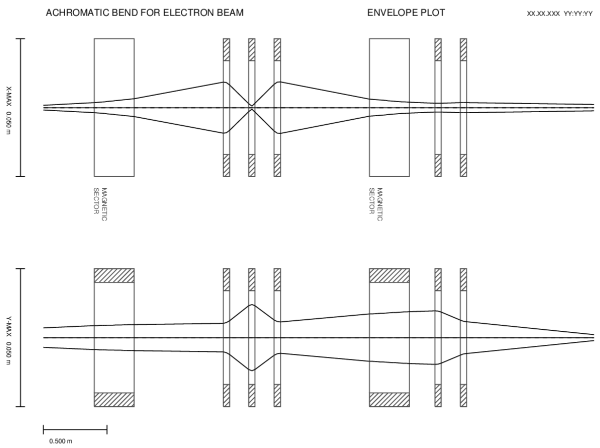


Figure 2: Beam optics of achromatic bend for 8 MeV electron beam using GICOSY code, upper plot is for horizontal plane and the bottom plot for vertical plane

Table 2: Beam optical specifications of Dipole magnets

| Parameters | Values |
|---|---|
| Bending Angle | 60 degree |
| Bending Radius | 300 mm |
| Max. magnetic Field | 1200 G |
| Magnetic Rigidity | 0.036 Tm |
| Edge Angle in non dispersive plane | 6 degree |
| Quantity | 2 |

The additional quadrupole magnets are needed to confine the beam in both transverse planes. The double focusing condition should be achieved for both transverse planes at the output. The beam optics is done using GICOSY [7] and GPT [8] codes and is shown in the Fig. 1,2,3 and 4 respectively for 4 MeV and 8 MeV electron beam. The beam

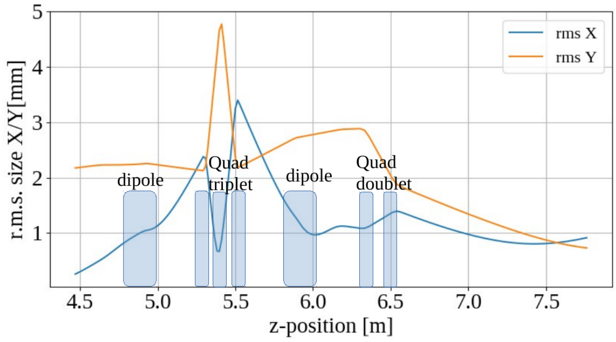


Figure 3: Beam optics of achromatic bend for 4 MeV electron beam using GPT code

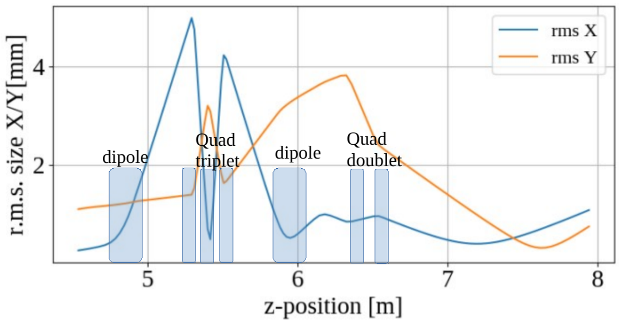


Figure 4: Beam optics of achromatic bend for 8 MeV electron beam using GPT code

Table 3: Beam tuning simulation parameters for dipole and quadrupole magnets using GICOSY code

| Parameters | 4 MeV | 8 MeV |
|---|---|---|
| DM1 (G) | -498 | -944.3 |
| QM1 (G) | -331 | -628.3 |
| QM2 (G) | 307.2 | 581.4 |
| QM3 (G) | -331 | -628.3 |
| DM2 (G) | 498 | 944.3 |
| QM4 (G) | 93.17 | 209 |
| QM5 (G) | -103.7 | -240 |

optical specifications of dipole magnet are given in Table-2. The peak magnetic fields for dipole and quadrupole magnets to handle the electron beam of energies 4 MeV and 8 MeV are given in Table-3.

## CONCLUSION

The achromatic configuration has been studied in a proper systematic way with evolution of many design options and a final design is chosen based upon various geometrical, fabrication constraints and ease of operation. The fabrication of magnets is already started at BARC Mumbai.

## ACKNOWLEDGMENT

The authors would like to acknowledge the help and support received the Director, IUAC, Delhi and all the collab-

orators from the BARC, Mumbai to fabricate the proposed magnets.

## REFERENCES


[1] S. Ghosh, V. Joshi, J. Urakawa, N. Terunuma, A. Aryshev, S. Fukuda, M. Fukuda, B. Sahu, P. Patra, S. Abhilash, J. Karmakar, B. Karmakar, D. Kabiraj, N. Kumar, A. Sharma, G. Chaudhari, A. Pandey, S. Tripathi, A. Deshpande, V. Naik, A. Roy, T. Rao, R. Bhandari, and D. Kanjilal, "Status of the development of delhi light source (dls) at iuac," *Nuclear Instruments and Methods in Physics Research Section B: Beam Interactions with Materials and Atoms*, vol. 402, pp. 358 – 363, 2017, proceedings of the 7th International Conference Channeling 2016: Charged Neutral Particles Channeling Phenomena. [Online]. Available: http://www.sciencedirect.com/science/article/pii/S0168583X17303622

[2] V. Joshi and S. Ghosh, "Multiparticle time-domain analysis of coherent undulator radiation," *Phys. Rev. Accel. Beams*, vol. 22, p. 020702, Feb 2019. [Online]. Available: https://link.aps.org/doi/10.1103/PhysRevAccelBeams.22.020702

[3] K. Steffen, "Cern accelerator school," 1985.

[4] S. Kumar and A. Mandal, "Achromatic beam transport of high current injector," *Journal of Instrumentation*, vol. 11, no. 02, pp. T02 003–T02 003, feb 2016. [Online]. Available: https://doi.org/10.1088%2F1748-0221%2F11%2F02%2Ft02003

[5] Y. Sun, "Second-order achromat design based on fodo cell," *Phys. Rev. ST Accel. Beams*, vol. 14, p. 060703, Jun 2011. [Online]. Available: https://link.aps.org/doi/10.1103/PhysRevSTAB.14.060703

[6] J. Björklund Svensson, T. K. Charles, O. Lundh, and S. Thorin, "Third-order double-achromat bunch compressors for broadband beams," *Phys. Rev. Accel. Beams*, vol. 22, p. 104401, Oct 2019. [Online]. Available: https://link.aps.org/doi/10.1103/PhysRevAccelBeams.22.104401

[7] "Gicosy code," https://web-docs.gsi.de/~weick/gicosy/.

[8] "General particle tracer software package," http://www.pulsar.nl/index.htm.

# POSTER PRESENTATIONS SESSION-2

# DESIGN OF HIGH I/O COUNT FPGA BASED MULTILAYER BOARD AND CORRELATION BETWEEN SIMULATION AND HARDWARE RESULTS OF DIGITAL DESIGN*

P. Maheshwari, P. Fatnani
RRCAT, Indore – 452013, India.

*Abstract*

Xilinx Spartan3AN 700k gates and 484 ball count **B**all **G**rid **A**rray (BGA) package **F**ield **P**rogrammable **G**ate **A**rray (FPGA) based 10 layer board is designed in-house for control applications. The board will be used for next version of **E**quipment **C**ontrol **M**odule (ECM) [1] that are presently catering to the requirements of supervisory control system for Injector Microtron. It has more functionality, features, expandability and overall better performance compared to the previous design. The digital design as per the required specifications is done in Verilog **H**ardware **D**escription **L**anguage (HDL) using Xilinx ISE 14.7. In addition to the challenges in the hardware design, challenges are also involved in the digital system design such as utilization of I/O as per their performance, resource utilization, functional validation, timing constraints and verification and many more. Before the FPGA final burn-in, it is necessary that the design is verified at various stages of the design steps to ensure validation with respect to intended functions and performance. Along with functional verification, it is important to do the timing verification to avoid serious design functional failure issues. Debugging of such failures otherwise may be quite difficult and also results in waste of time and consequently delay the projects. Highlighting the features of the board, this paper discusses the implementation of the digital design in FPGA and requirement of different types of simulations for the digital design. Discussions are also extended to how much a simulation can be correlated with the actual hardware result. The correlation is an important factor that provides a confidence level for implementation of a design in FPGA.

## INTRODUCTION

At RRCAT, Microtron is primary electron injector for Indus-1 and Indus-2 **S**ynchrotron **R**adiation **S**ources (SRS). In 2015, the supervisory and monitoring control system of Microtron was upgraded with new design from VME based centralized system to FPGA based distributed architecture and deployed in field [1]. The ECM is the main module which has the responsibility to execute various general and special functions for its sub-system. It is also responsible for taking appropriate action in case of occurrence of an event like interlock failure, supply trip, etc. All the required functions are implemented in FPGA, which is the brain of an ECM. Xilinx Spartan3, 400k gates in **P**lastic **Q**uad **F**lat **P**ackage (PQFP) – 208 pin FPGA based two layer board was designed in-house for the development of ECM. Digital design of communication controller, peripheral interface controller and various required functions have been implemented at **R**egister **T**ransfer **L**evel (RTL) through Verilog HDL. No processor system is used in the design. Since 2015, the ECMs are working satisfactorily round the clock, without any issue. But due to advancement in technology and availability of more resources in compact package like BGA, those PQFP devices may not be available in the market for very long time. Also, the **L**ook-**U**p **T**able (LUT) utilization of the device with addition of new requirements, since its deployment, had also reached to 54%. Due to its limited expandability and the need to cater to more requirements and do better performance in terms of speed, a multilayer board is being designed with Spartan3AN 700k gates FPGA. The device has 484 ball in which 372 user I/O are available which are used in the design. Except PCB fabrication, all other steps involved from schematic design, placement, layout & routing (using Altium Designer) to component mounting and board testing is done in-house. The hardware is also tested by modifying and implementing digital design in FPGA and executing all the functions in lab and field. A performance comparison is done in terms of communication speeds in both versions of boards. A comparative study between Post-route simulation of digital design and actual results from hardware is also done. This is helpful in evaluating the design performance in terms of timings and area (FPGA resources) as well as provide a measure on how much a simulation result can be helpful in predicting the actual hardware results.

## DESIGN OF HIGH I/O COUNT FPGA BASED MULTILAYER BOARD

The design of new board is based on the requirement of more programmable resources, better speed performance, system availability and better features that will be helpful in enhancing system performance and availability.

The chosen FPGA IC is Xilinx Spartan3AN series XC3S700AN-4FG484I with 484ball BGA package in which 372 balls can be configured for user I/O and rest are used for configuration pins, multiple supplies and return path. The new ECM design provides ADCs with better speed and resolution, bipolar analogue setting and read backs with isolation, increased communication speed, dual configuration mode to read status and send command and high expandability in terms of hardware and specifications are provided. A comparative study between the old board [1] and new board is shown in table 1.

*puneet@rrcat.gov.in

To design a board with high pin count devices, it is required to first estimate the number of layers needed for proper routing of all the signal nets, power and return path planes. A rough estimate for number of routing layers required for routing the signals can be calculated by equation 1 [2]:

$$\text{Layers} = \frac{\text{Signals}}{\text{Routing channels} \times \text{routes per channel}} \qquad (1)$$

Table 1: Comparison between Old and New board

| Board feature | Old | New |
|---|---|---|
| FPGA | Spartan3 – 400k gates | Spartan3AN – 700k gates |
| Package / User I/O | PQFP 208 / 141 | BGA 484 / 372 |
| No of Layers | 2 layers | 10 layers |
| External SDRAM | Not available | 256 Mb (16 x 16) |
| Isolated Analog I/O Channels | 2, Unipolar 10V | 2, Bipolar ±10V |
| ADC/DAC | 12 / 16 bits | 16 bits both |
| ADC Sampling rate / DAC Settling time | 13 SPS / 4 µs | 100 kSPS / 5 µs |
| Communication ports (isolated) | RS232/RS485 and optical | Two RS232, one RS485 & Optical |
| Standard Baud rate support | Up to 115.2 kbps on 50 m,CAT6 | Up to 921.6 kbps on 105 m,CAT6 |
| Digital I/O | 12 | 24 |
| Command and status | Potential free contacts | 10mA current drive & Potential free (both configurable) |
| RTC | Not available | With msec time |
| Expandability | 21 unused IO | More than 100 unused IO |

In our case, the ball pitch of the device is 1 mm, routes per channel are 1, number of routing channels are 84 and hence the number of signal layers required are 4.42. The number must be integer, so the required layers are 5. Separate power and return path planes for digital and analog part of the design are taken, making it total 9 layers. But due to fabrication process, the layers are always even and hence 10 layers are considered for final design. The total thickness of the PCB is 1.7 mm. Fig 1 shows layer stack-up and art work of the PCB design obtained from Altium Designer software. Plane splitting is done for various digital power supplies $V_{cc}$, $V_{ccInt}$, and $V_{ccAux}$, $V_{cco}$, $V_{ccSDRAM}$, and analog power supplies + 5 V, ±12 V, ±12 V_isolated1 and ±12 V _isolated2. All the vias used are through hole. The minimum track width and electrical clearance used for routing is 6 mil. Fig 2 shows the actual populated board in the lab and its 3D version generated from Altium Designer software.

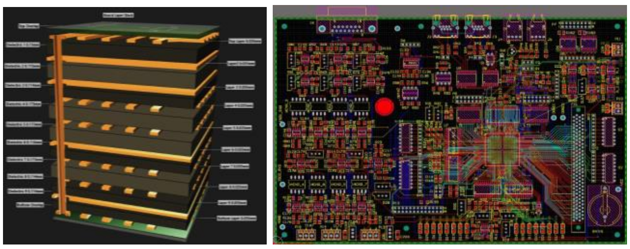

Figure 1. Layer Stack-up and PCB Design artwork

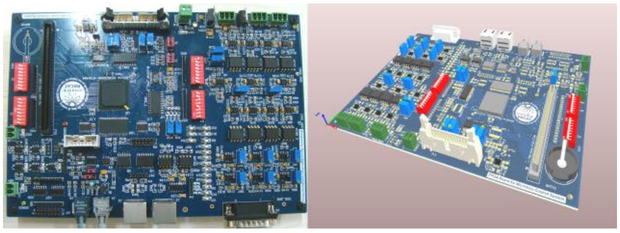

Figure 2. Actual board and 3D view from software

## DIGITAL DESIGN IMPLEMENTATION, SIMULATIONS AND ACTUAL RESULTS

The digital design used for the supervisory and monitoring control of Combined Function Magnet (CFM) power supplies is implemented in this new board with addition of some more functions. Table 2 shows the resource utilization comparison report for both the devices. It is evident from the table that the utilization of LUTs in the Spartan3AN is only 34% compared to 54%

Table 2: Device utilization summary

| Device Utilization Summary | | | | | | |
|---|---|---|---|---|---|---|
| Features | Spartan3 (XC3S400-4PQ208) | | | Spartan3AN (XC3S700AN-4FGG484) | | |
| Logic Utilization | Used | Available | Utilization | Used | Available | Utilization |
| Total Number Slice Registers | 1,945 | 7,168 | 27% | 1,827 | 11,776 | 15% |
| Number used as Flip Flops | 1,941 | | | 1,823 | | |
| Number used as Latches | 4 | | | 4 | | |
| Number of 4 input LUTs | 3,888 | 7,168 | 54% | 4,041 | 11,776 | 34% |
| Number of occupied Slices | 2,438 | 3,584 | 68% | 2,598 | 5,888 | 44% |
| Number of Slices containing only related logic | 2,438 | 2,438 | 100% | 2,598 | 2,598 | 100% |
| Number of Slices containing unrelated logic | 0 | 2,438 | 0% | 0 | 2,598 | 0% |
| Total Number of 4 input LUTs | 4,045 | 7,168 | 56% | 4,204 | 11,776 | 35% |
| Number used as logic | 3,872 | | | 4,025 | | |
| Number used as a route-thru | 157 | | | 163 | | |
| Number used for Dual Port RAMs | 16 | | | 16 | | |
| Number of bonded IOBs | 125 | 141 | 88% | 147 | 372 | 39% |
| Number of MULT18X18s | 8 | 16 | 50% | 4 | 24 | 16% |
| Number of BUFGMUXs | 4 | 8 | 50% | 1 | 8 | 12% |
| Number of DCMs | 1 | 4 | 25% | 8 | 20 | 40% |
| Average Fanout of Non-Clock Nets | 3.29 | | | 3.32 | | |

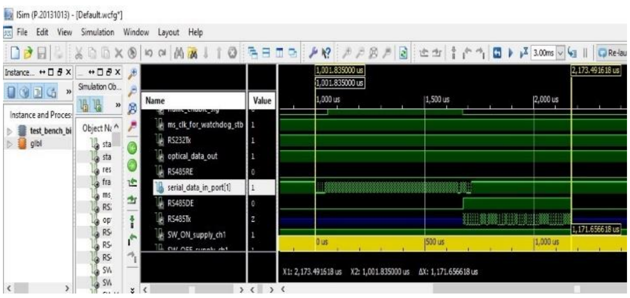

Figure 3. Timing simulation results of Post Place & Route of the design using Xilinx ISIM.

used in Spartan3. Also, bonded IOBs in Spartan3 are almost 88% used leaving limited space for hardware expansion. While new design used 39% of IOBs only. The design is synthesized and simulated using Xilinx ISE 14.7 tools. A test bench based verification approach is used and written in Verilog. Constraint vectors are provided to Unit Under Test (UUT). A communication controller is designed to communicate with SCADA running at operator console. It is a part of complete digital design, inside the FPGA. Simulation of communication controller performance is done with a test bench designed with suitable test vectors. Communication frames are sent through test bench and corresponding response frames are received by it. The data rate is 921.6 kbps and total frame length is 110 bytes. Behavioural simulation is done for functional correctness and timing results of Post Place & Route simulation of the design are shown in fig 3.

The actual hardware performance is also evaluated for the controller and instead of SCADA, a python script is designed for communication. The results are recorded on the scope, Make: Fluke, Model: 190-204/Scopemeter as shown in fig 4. Waveforms in red and blue are received and transmitted frames by controller.

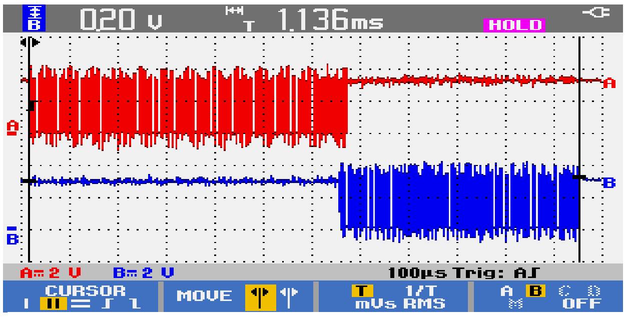


Figure 4. Actual hardware timing results for communication frame on scope.

## SIMULATION AND ACTUAL HARDWARE RESULTS

### *Post Place and Route Simulation Results:*

It is necessary to do post place and route simulation so that actual timing details can be incorporated inside simulation and more accurate timing predictions can be obtained even before implementation. The post route simulation can be useful for predicting the behaviour of actual hardware while it may still need some further analysis. In our case, we have observed timing of serial communication of 110 bytes (over RS485 interface and in RS232 protocol) in simulation which comes out to be 1.172 ms. The data rate used is 921.6 kbps.

### *Actual Hardware Results:*

The same communication frame is sent through computer via a python script at same rate. The binary waveforms are observed on the single ended pins of RS485 IC (ISO35DW, Make: TI) and the observed total time is 1.136 ms as shown in fig 4. Comparing both the timings of simulation and actual results, it is found out that both are in close relation with each other. The mismatch in total timing is in micro seconds and may be due to measurement limitations of the available scope.

## RESULTS

The new multilayer board is designed for the enhanced version of previous board to cater to more requirements, perform better and considering the device availability in market. Simulations of the digital design are done and actual hardware testing is completed in lab and field. On deployment front, an ECM with this new board is already working in field. The development with BGA package IC and multilayer PCB gives us experience of in-house design and development of complex systems.

## CONCLUSION

To design a digital system inside an FPGA, the design process includes verification and validation of the design at each step. For functional verification of the design, behavioural simulation is done. But the design's actual behaviour changes when violation of timings, usually setup and hold time, is observed after implementing the design in FPGA. One may misinterpret those issues with functional issues, if not considered during design cycle. Once there in design, the timing issues may lead to failure of the design and can be difficult to find through hardware probing. From our analysis, it is found that the timing simulations and actual results closely match with each other. Design performance and timing violations in simulation also reflect in actual design inside the device. This is an important aspect when time critical applications are designed in FPGA.

## ACKNOWLEDGEMENT

I sincerely thank Sh Yogendra Sheth, Head BDS, BDCSD and Ex-Head CIEDS, ACSD who always encouraged me to achieve the goal and helped me in solving various problems during the design and development. Sh Hemant Kumar, Sr. Technician ACSD is the team member without whom this work could not have been possible; the 10 layer PCB is designed and board population is done by him. I would also like to thank all other colleagues of ACSD who directly or indirectly helped me in the design of the new board.

## REFERENCES

[1] P. Maheshwari, Y. M. Sheth, P. Fatnani, C. P. Navathe, "FPGA based control system hardware for Microtron", InPAC 2013, Kolkata

[2] UG1099(v1), Xilinx BGA device design rules.pdf

[3] Spartan-3AN FPGA family datasheet, DS557, https://www.xilinx.com/

[4] Four and six-layer high speed PCB design for spartan3E FT256 BGA package, XAPP 489 https://www.xilinx.com/

[5] PCB stack up design considerations for Intel FPGAs, AN613, https://www.intel.com/

# STUDY OF TARGETS FOR THE $^{99}$MO PRODUCTION USING HIGH POWER ELECTRON ACCELERATORS

Aqsa Shaikh*, Tanuja Dixit, Abhay Deshpande, R. Krishnan,

Society for Applied Microwave Electronics Engineering & Research (SAMEER), IIT Campus, Powai, Mumbai 400 076

*Abstract*

In this paper, converter target method for production of $^{99}$Mo is studied. In converter target method electron beam hits a high Z target which converts electrons into bremsstrahlung photons (e,γ) and then (γ,n) reaction takes place in $^{100}$Mo target kept after the converter target. Aim of this study is to optimize experimental parameters for maximizing $^{99}$Mo activity. First parameter to optimize is electron beam energy which decides the entire design of electron linac. Study done using GEANT4 simulations shows that 25-30MeV linac is sufficient for producing $^{99}$Mo without much impurities of other isotopes. Next the design of converter target (tungsten) is optimized. It is observed that increasing the thickness of tungsten target from 0.1 to 0.8 r.l. (radiation length), flux weighted reaction cross section ($\sigma_a$) for $^{100}$Mo(γ, n)$^{99}$Mo reaction increases by 6.55% where as it starts to decrease after 0.8r.l. and for 1.5r.l. $\sigma_a$ decreases by 1.60% of the peak. In converter target method, $^{100}$Mo is kept after tungsten target. Radius and length of this cylindrical $^{100}$Mo target are optimized using GEANT4 simulation. It is found that within 1.5cm of $^{100}$Mo 50% of 30MeV photons are attenuated where as to attenuate 99% of it 9.5cm of $^{100}$Mo is required. Keeping the mass of $^{100}$Mo constant and increasing the thickness from 1.5cm to 9.5cm, increases the activity only by 20%. Detailed discussion of all these parameters along with activity calculation for our system is presented in the paper.

## INTRODUCTION

After realizing the demand of $^{99}$Mo in nuclear diagnostics, various efforts are being made worldwide to produce $^{99}$Mo using different technologies. $^{99m}$Tc is a widely used radioactive tracer isotope in Nuclear Medicine. $^{99}$Mo generators are supplied from BRIT (Board of Radiation & Isotope Technology) and also from other countries like Israel, Turkey, UK etc. The strength of the generator decides the cost, which can vary from INR 27,000 to INR 70,000. Over 70% of nuclear medical procedures include the use of $^{99m}$Tc [1]. At SAMEER, in order to produce $^{99}$Mo, a project to study accelerator based production of $^{99}$Mo using 30 MeV high beam power electron linac is undertaken [2]. A prototype of the 30 MeV electron linac is to be developed in two stages. In first stage, a 15 MeV 3-5 kW electron linac will be developed followed by an upgraded 30 MeV 10 kW beam power linac [3]. $^{99}$Mo will be produced via photo neutron reaction using enriched $^{100}$Mo target.

Cross-section of (γ, n) reaction peaks at photon energy 14-15 MeV up to 0.15 barns. 30 MeV electron linac is expected to produce enough photon flux of energies up to 30 MeV, which is used for $^{99}$Mo production through $^{100}$Mo (γ, n) $^{99}$Mo reaction.

## GEANT4 SIMULATION

GEANT4 (Geometry and Tracking) Monte-Carlo based simulation tool is used to design the target and estimate $^{99}$Mo activity. Monte Carlo simulations are estimations of quantities inferred from the chemical and physical behavior of particles sample considered representative of the whole modelled system. Validation of code is the first step before using it for producing required data. Before going ahead with the simulation, GEANT4 code validation is done using experimental results from SAMEER's medical linac. The "Siddhartha" medical electron linear accelerator, with nominal beam energy of 6 MeV was tested for dose and energy on Radiation Field Analyzer (RFA). The dose output is shown in Fig. 1. The energy was measured using J10/J20 ratio which is a standard practice in Medical Physics. Measure energy is found to be between 5.5 to 5.8 MeV. This experiment is reproduced using GEANT4 simulation. In GEANT4 simulation code, a circular electron beam of 3mm radius and 0.1mm standard deviation with Gaussian energy profile of 5.5 MeV and 0.5 MeV sigma strikes a 1.5mm thick tungsten target with 2.5mm thick copper backing. The normalized dose from the simulation output is compared with the experimental RFA data in Fig 1. It is observed that the dose pattern followed by GEANT4 output in the forward direction matches well with the experimental data.

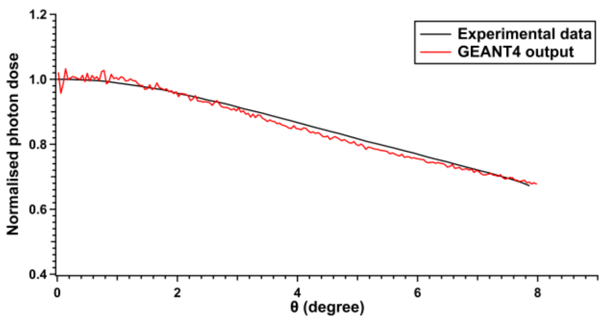


Figure 1: Comparison of experimentally obtained and GEANT4 simulation based normalized photon dose angular distribution.

*skaqsa.95@gmail.com, tanuja@sameer.gov.in

## BEAM ENERGY OPTIMIZATION

Electron beam hitting a high Z material, tungsten, produces bremsstrahlung photons. These bremsstrahlung photons are used in the production of $^{99}$Mo by means of $^{100}$Mo (γ, n) $^{99}$Mo reaction. To optimize the electron beam energy, flux weighted average reaction cross section ($\sigma_a$) is calculated [4]. In Fig. 2 normalized $\sigma_a$ is plotted against increasing electron beam energy. Maxima of the plot corresponds to 20-30 MeV electron beam and it decreases thereafter. To understand this behaviour, photon flux distribution for electron beams of energies 15 to 70 MeV hitting tungsten target is obtained using GEANT4. It is observed that, when electron beam energy is increased from 15 MeV to 70 MeV, the total photon flux and the end point energy of bremsstrahlung increases, which is expected from a typical bremsstrahlung pattern. But it is also observed that with the increase in electron beam energy there is no appreciable increase in the effective photon flux under the peak of GDR curve. Going from 30MeV to 40MeV, 50MeV, 60MeV and 70MeV increases the photon flux in the window of highest reaction cross-section for (γ,1n) by 29.47%, 48.26%, 61.29% and 71.73% whereas increase in the photon flux in the window of highest reaction cross-section for (γ,2n) reaction is 61.27%, 97.37%, 124.05% and 143.05% respectively. This shows that the increase in probability of (γ,2n) reaction almost twice as much as (γ,1n) if the electron beam energy is increased beyond 30MeV. Which is undesirable in the case of $^{99}$Mo production.

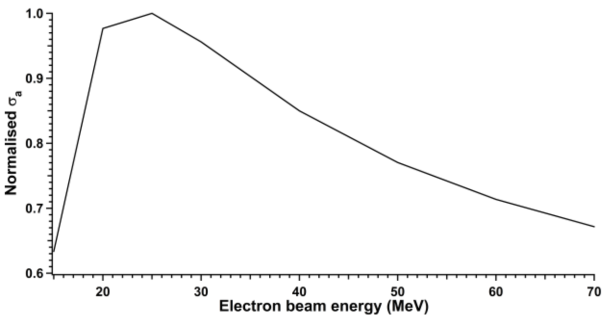


Figure 2: Normalized flux weighted average reaction cross-section ($\sigma_a$) for $^{100}$Mo (γ, n) $^{99}$Mo reaction plotted against various electron beam energies.

## METHOD OF PRODUCTION

The converter target approach to carry out $^{100}$Mo (γ, n) $^{99}$Mo reaction is studied. In this approach, a converter target is kept before $^{100}$Mo target to produce photon flux required for $^{100}$Mo (γ, n) $^{99}$Mo reaction. This converter target converts highly energetic electron beam into bremsstrahlung photons. Tungsten, being high Z material with high melting point, is suitable for electron to photon conversion.

## CONVERTER TARGET OPTIMIZATION

After beam energy optimization, geometry of converter target is optimized. The optimization is done to obtain maximum effective bremsstrahlung photons (12-17 MeV) from tungsten target. Using GEANT4, thickness of tungsten is varied from 0.1 to 5 r.l. Photon flux obtained from various tungsten thicknesses is plotted along with GDR curve in Fig. 3. As target thickness increases, photon flux also increases but soon saturates after few r.l. thickness. When thickness is increased to 1.5 r.l. the effective photon flux is found to have decreased in the region of GDR curve. This happens due to self-absorption of photon flux in tungsten. Similar to beam energy optimization, tungsten thickness optimization is done by comparing the value of $\sigma_a$ for tungsten target thickness of 0.1 r.l. to 1.5 r.l. Maximum $\sigma_a$ is obtained for 0.8 r.l. thick tungsten target. Hence, 0.8 r.l. is considered as optimized converter target thickness.

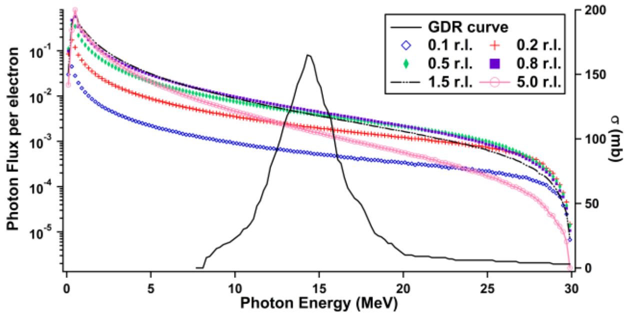


Figure 3: The GDR curve is associated with Y-axis on right hand side showing microscopic reaction cross-section (σ) in mb for $^{100}$Mo (γ, n) $^{99}$Mo reaction. Bremsstrahlung photon flux intensity per electron for various target thickness starting from 0.1 to 5.0 radiation length is plotted with GDR curve.

## ACTIVITY CALCULATION

Using photon flux data obtained from GEANT4 the following equation is used to calculate activity.

$$A = \left(1 - e^{-\lambda t}\right) V I_e \left(\frac{\omega \rho N_a}{M}\right) \int \Phi_{GEANT4}(E)\, \sigma(E)\, dE \quad (1)$$

Where, $I_e$ represents current in units of number of electrons. λ, t, V, ω, ρ, $N_a$, M, $\phi_{GEANT4}$ and σ are decay constant of $^{99}$Mo, irradiation time, volume, mass fraction, density, Avogadro's number, molar mass of $^{100}$Mo target, photons per electron hitting $^{100}$Mo and photo-neutron reaction cross-section of $^{100}$Mo respectively [5].

## MOLYBDENUM TARGET OPTIMIZATION

Photon flux coming from tungsten target hits $^{100}$Mo and triggers the photo neutron conversion reaction. These photons are of all the energies up to 30MeV. According to NIST data, to attenuate 50% of 30MeV photons about 1.5cm of molybdenum target is sufficient. Whereas to attenuate 99% of 30MeV photon 9.5cm of the same material is required [6]. Figure 4 shows the change in activity for our system as thickness of $^{100}$Mo target is increased. Keeping the mass of $^{100}$Mo constant when its length is increased by decreasing the radius, it is found that the activity increases rapidly in the beginning then slows down. By changing the length of molybdenum target from 1.5cm of length to 9.5cm only 20% of increase in activity is found. Hence, $^{100}$Mo target is optimized for 1.5cm of length.

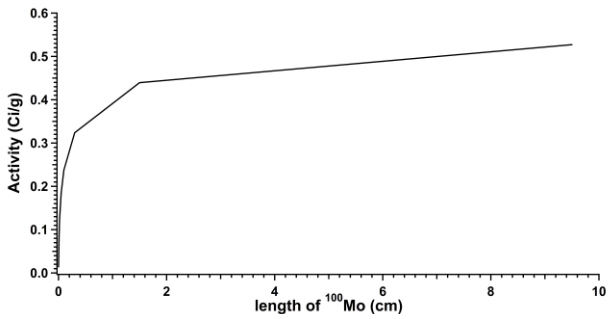


Figure 4: Increase in the $^{99}$Mo activity with increasing $^{100}$Mo target length.

Using the reaction cross-section data and GEANT4 output, in the case of optimized parameters presented in this paper, activity of 1.331 Ci/g/µA is obtained from equation (1).

## RESULT

Activity calculation is done using the simulation codes GEANT4 and ROOT. For our system namely 30 MeV electron linac with average beam power of 8-10 kW, activity estimate by converter target method is 0.439 Ci/g.

## CONCLUSION

In converter target method entire beam energy is lost due to absorption in tungsten target therefore cooling mechanism is provided only to tungsten. 30 MeV electron beam is sufficiently large to produce $^{99}$Mo through photo-neutron conversion of $^{100}$Mo with the use of 0.8 r.l. of tungsten converter target and 1.5cm of $^{100}$Mo target. There is a further need to improvise the experimental method in order to increase this activity.

## REFERENCES


[1] "Technetium-99m Radiopharmaceuticals: Status and Trends," IAEA Radioisotopes and Radiopharmaceuticals Series No. 1, STI/PUB/1405, 2010, ISBN:978-92-0-1035097, Available: https://wwwpub.iaea.org/MTCD/Publications/PDF/Pub1405_web.pdf

[2] Aqsa Shaikh, Tanuja Dixit, Abhay Deshpande, R. Krishnan, "Comparative Simulation Study of Direct and Converter Target Approach for the Production of $^{99}$Mo with 30MeV Electron Linear Accelerator," manuscript submitted in IEEE journal.

[3] A. Deshpande, T. Dixit, J. Urakawa et al, "S-band linac based X-ray source with pi/2 mode electron linac," Nuclear Instruments and Methods in Physics Research Section A: Accelerators, Spectrometers, Detectors and Associated Equipment, vol. 637, no. 1, pp. S62-S66, 2011, available: https://doi.org/10.1016/j.nima.2010.02.023

[4] Naik, H., Suryanarayana, S.V., Jagadeesan, K.C. et al. "An alternative route for the preparation of the medical isotope 99Mo from the 238U(γ, f) and 100Mo(γ, n) reactions," Journal of Radioanalytical and Nuclear Chemistry, volume 295, pages 807-816, 2012, available: https://doi.org/10.1007/s10967-012-1958-9

[5] Jang Jaewoong, Yamamoto Masashi, Uesaka Mitsuru, "Design of an X-band electron linear accelerator dedicated to decentralized 99Mo/99mTc supply: From beam energy selection to yield estimation," Physical Review Accelerators and Beams, vol. 20, no. 10, pp. 104701, 2017, available: https://link.aps.org/doi/10.1103/PhysRevAccelBeams.20.104701

[6] J.H. Hubbell and S.M. Seltzer, "X-Ray Mass Attenuation Coefficients", doi: https://dx.doi.org/10.18434/T4D01F

# BROADBAND AMPLIFIER FOR MULTI HARMONIC BUNCHER

Parmanand Singh*, Yaduvansh Mathur and S.Venkataramanan

Inter University Accelerator Centre (IUAC), New Delhi-110067

**Email:param.bitm@gmail.com*

*Abstract*

A broad band solid state RF power amplifier capable of delivering more than 100 Watts of power (CW) in frequency range of 10MHz – 50MHz (+/-1.5 dB) has been successfully developed with state of the art RF components for general purpose application. It is being used with Multi Harmonic Buncher (MHB) of High Current Injector (HCI) at IUAC. This amplifier has been developed as import substitution after repeated failure of imported power amplifiers purchased for this application. The amplifier includes various crucial protections against high VSWR, high temperature and input power drive. The requirement of broad band amplifier is essential to amplify the quasi-sawtooth input signal which is created by adding fundamental frequency and its harmonics in the frequency range of 12.125MHz to 36.375MHz. The amplifier is cascade type operating nearly in class-A mode and DMOS RF MOSFETs are used.

## INTRODUCTION

Bunched ion beams are required for Radio Frequency Quadrupole (RFQ) and others energy booster's resonating structures to enhance its energy further in HCI accelerator, which is under construction at IUAC. Bunching of ion beams is done by MHB using saw tooth voltage which gives the energy modulation required to bunch the dc beam. The frequency used in MHB is 12.125MHz (Fundamental), 24.25MHz, 36.375MHz and 48.5MHz. Commercially available air cooled broad band solid state RF amplifiers which were being used earlier to power the MHB have failed repeatedly and replacement parts are not available due to customisation. To replace these commercial amplifiers a 100W (CW) water cooled broad band solid state RF power amplifier was developed indigenously. It has been tested with the system successfully. The developed amplifier is a broadband amplifier having bandwidth in the frequency range of 10MHz – 50MHz and gain of +65dB. These amplifiers are operated nearly in class-A mode to have better harmonic suppression. We have been able to obtain best 2$^{nd}$ harmonics distortion of 14dBc down and 24% of dc to RF conversion efficiency. The amplifier gain is built across three stage cascaded pre-amplifier, driver and power amplifier sections. Its subsystems are RF switch, a compact SMPS unit, control board and a directional coupler. The CATV block QBH-2832 is used as a pre-amplifier, RF MOSFETs MRF151 and MRF151G are used as driver and power amplifier respectively. The RF MOSFETs are operated at 36V dc with gate biasing of 5V regulated by LM723, a versatile regulator chip. Amplifier control circuit is operated at +24Vdc. The power devices are mounted on copper heat spreader and in turn mounted on water cooled aluminium heat sink for high thermal stability and reliability. The power monitoring is possible with directional coupler and front panel power meter. The amplifier is housed in a 3U - 19" rack mountable standard aluminium cabinet.

## DESCRIPTION OF MODULE

The broadband solid state RF power amplifier is compact integrated assembly having three stage amplification by pre-amplifier, driver amplifier and power amplifier.

***Pre-Amplifier:*** A wideband CATV power block QBH2832 having a gain of +35dB is used to pre-drive intermediate power amplifier. It is capable to delivering ~1.5W of power in the frequency range of 0-200MHz.

***Driver Amplifier****:* Driver Amplifier stage uses single RF MOSFET MRF151with a gain of +18dB in required frequency range. The RF MOSFETs have very high gain at lower frequency, hence they tend to oscillate and get destroyed. A RC feedback network is connected between drain and gate for stable operation. This stage delivers nearly 10W drives to the final power amplifier.

***Power Amplifier****:* This final power amplifier section consists of a Gemini package RF MOSFET MRF151G, wired in push-pull configuration to achieve desired power level. The input and output impedances matching is done using a transmission line transformers made with semi-rigid coaxial cable of suitable characteristic impedance. The transformers are loaded with powdered iron core to cover the lower frequency range. Tuning capacitors at the output of the amplifiers are provided to maximize the output power. The final output power has a gain of +13dB in the mid band and delivers 100W minimum across useful bandwidth.

***RF Switch:*** The RF switch SA630D is used to break the RF path within 6uS to protect the amplifier from fault conditions like input over drive, over temperature and poor VSWR.

***Directional Coupler:*** The commercial directional coupler DCP3000FM is used at the final stage of the amplifier for measurement and monitoring of forward and reflected RF power. This directional coupler gives proportional dc voltage corresponding to both forward and reflected power level at output.

***Control Board:*** The control board has three major sections: protection, measurement/monitoring and remote read out & control. The control board process the various faults condition like over temperature, VSWR in relay sequence ladder logic. It put off the amplifier in case of any fault and the condition gets latched using the latch circuit. Over temperature protection enable at 60˚C, the input over drive actuates at +1dBm and faulty VSWR condition is set at 10% of rated output power at lower frequency. At front panel analog power meter and LEDs are provide to measure forward/reflected powers, supply voltage/current and to indicates power on/faults condition respectively. In back panel 25pin D-connector is provided for remote control and monitoring.

***DC Supply***: SMPS PBA1000F-36 is used to supply the dc power to RF amplifier and 24V SMPS RS-35-24 for control power.

***Mechanical Assembly:*** The power RF MOSFETs are mounted on surfaced finished 8.5”x2.5”x0.5” copper heat spreader and in turn mounted on 8”x6.5”x0.75” water cooled aluminum heat sink for high thermal reliability. The amplifier is assembled in a 3U height 19” rack mountable standard MS enclosures.

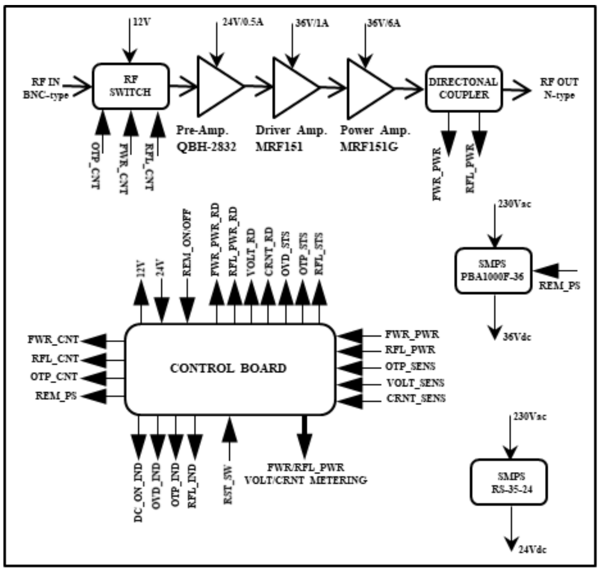


*Figure 1. Block diagram of the amplifier*

## Specifications

| | | |
|---|---|---|
| Output Power | : | 100 watts (CW) |
| Input Power | : | +3dBm max. |
| Frequency range | : | 10MHz – 50MHz (-3dB BW) peaking at 26 MHz |
| Flatness | : | ± 1.5dB |
| Gain | : | ~65 dB ( 15dB internal attn. ) |
| Phase shift | : | ±5° max. |
| Impedance | : | 50 Ω |
| VSWR | : | 1:2 |
| Harmonics | : | -37dBc ( 2$^{nd}$ ), -14dB (3$^{rd}$) at 100W |
| Efficiency | : | 18% ( AC to RF ). |
| Efficiency | : | 24 % ( DC to RF ). |
| Mode of operation | : | near Class A |
| Operating Voltage | : | +36Vdc |
| DC power | : | +36Volts/29A, +24Volts/0.5A (control card ) |
| Protections | : | Over temp. at 60°C, Over Drive +1dBm, VSWR 1:2 |
| Indications | : | DC ON, Over temp. Input over drive, VSWR. |
| RF connectors | : | BNC Male (Input), N Male (Output). |
| Cooling | : | Water cooled at least 4-6 Lpm at room temperature, Internal forced air cooling |
| Dimension | : | 19 x 5.5 x 17.5” (WxHxD) |

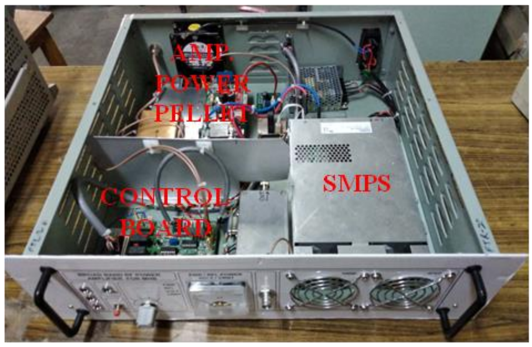


*Figure 2. Internal view of the amplifier*

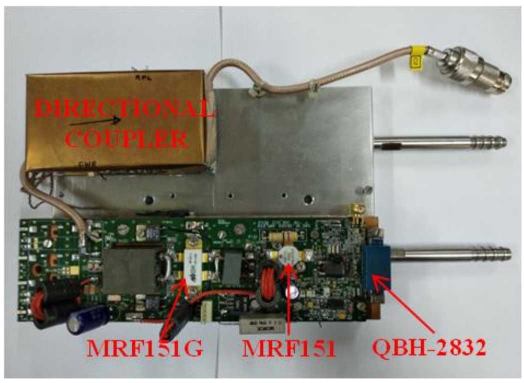


*Figure 3. Power pellet of the amplifier.*

## TEST RESULTS

After assembly of the amplifier it tested continuously with 50Ω matched load for two weeks at 100W (CW) power. The amplifier is characterized and calibrated for its different parameters. The amplifier is integrated with the MHB system of HCI at IUAC and tested.

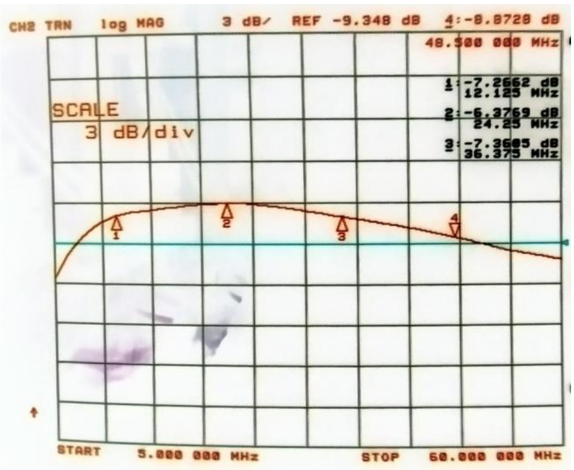


*Figure 4. Transfer characteristics of the amplifier at 100W.*

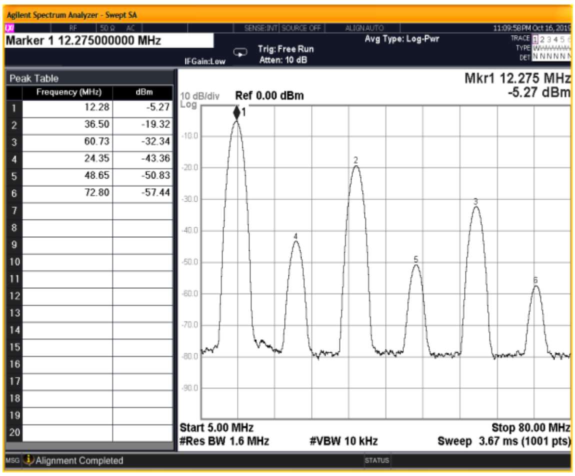


*Figure 5. Harmonics of the amplifier at 100W, at 12.125MHz.*

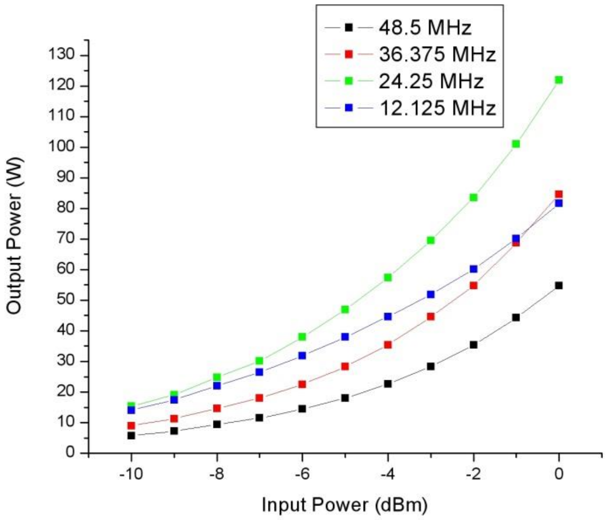


*Figure 6. Input vs output power plot*

## CONCLUSION

We have been able to successfully develop and integrate a broadband power amplifier for powering MHB of HCI.

## ACKNOWLEDGEMENT

Authors would like to thank Mr. Ajith Kumar B.P for providing the opportunity and support during the development of this module. We are also thankful to members of the workshop and utility group at IUAC for their continuous support and help.

## REFERENCES

[1] S. Ventankatramanan et al, Technical report on “400W RF Power Amplifier for Linac”. http://www.iuac.res.in/labs/erfl/vhf97Mhz400wamp.pdf

# Design Architecture of RF Interlock, Protection & Monitoring system for HTS control electronics

R T Keshwani, Sujo C I, Hitesh Shukla, Sandeep Bharade, Mayur M. Sutar, Shailesh Khole & Gopal Joshi, Accelerator Control Division (ACnD), BARC, Mumbai

*Abstract*

Horizontal Test stand (HTS) is characterization facility for superconducting cavity planned at Raja Ramanna Centre for advanced Technology (RRCAT), Indore. Besides control of field amplitude and phase, by low level RF (LLRF) control system, protection of system is an important feature needed. This is achieved by measuring parameters like RF power, optical signal due to arc, various analog and digital inputs, etc. Subsequently the RF power input to cavity being characterized is stopped in the event of parameter/s crossing the set threshold. This paper describes architecture of RF protection and interlock system tailor made for HTS protection. This system is VME64X based, modular, high density and scalable. Interfacing of this system with LLRF and other systems is discussed in short. As facility is under construction, only lab test results for some of modules are presented

## HTS

Horizontal test stand (HTS-2) is planned & being installed at RRCAT to test fully dressed SCRF cavities of 650MHz type. Superconducting (SC) RF cavities have to be qualified in test facility before installation in a cryomodule [1]. This cryostat facilitates testing of two 5-cell 650 MHz SCRF cavities, in CW or pulsed regime, for upcoming High Intensity Superconducting Proton Accelerator projects which is enabling technology for Indian Spallation Neutron Source project (ISNS).

Some important features of facility are:

1) It can house 2 SCRF cavities at a time with suitable coupler arrangement.
2) It has all required cryogenic system with associated instrumentation to test cavities at rated temperatures.
3) RF Field is to be setup and controlled in cavity to test at specified field levels using suitable power amplifier & low level RF control system.
4) While operation, facility has to be protected by provided suitable interlock systems.

In this paper, need, features and implementation RF protection & Interlock system (RFPIS) is described in short.

## RFPIS AND ITS FUNCTIONS

RFPIS is implemented with VME64x based controller in a 6U VME crate, which is compatible with 19" rack. This design is implemented using FPGA based cards [2, 3]. Mezzanine card approach on VME carrier card is used to design this system for modularity and easy upgrading. Fast and slow signals are processed using different cards/circuits to ensure safe and reliable operation. Main functions of RFPIS are as follows:

1. Acquiring, processing, logging and displaying the various measurable parameter signals .
2. Protect the cavity & RF system from faulty operating conditions
3. Handshaking of signals with external systems like LLRF, etc.
4. Facilitate communication with external systems through standard communication protocols i.e. (EPICS)
5. Stores the cavity operating parameters for diagnosis purpose.

Interlock and protection is implemented for:

1. Excessive RF power arising at any of RF measurement locations. Adjustable trip levels by end user within design set limits.
2. Excessive RF leakage from RF antenna.
3. Excessive optical signal arising from arc while cavity / coupler conditioning phase and also while normal operation. .
4. Excessive field emissions at predefined locations in RF structures.
5. Besides analog inputs like RTD (coupler temperature), IR sensor signal, etc are monitored. Digital inputs like safety permit, MPS permit, LLRF ready, SSA ready, bias supply status, are monitored.

In order to realize such as logic and fast acting protection system which monitors different types of parameters such as RF, analog, digital, contacts, etc. distributed processor/controller architecture was chosen. The modular architecture similar to that used in [3] has been adapted here and provided functional separation wherein one module monitors one or two types of parameters.

Various types of modules are:

(1) Multi-trip module.
(2) FEP-PMT module
(3) System Control cum digital input

The capacity requirement of RFPIS as needed by HTS is listed in table 1. To achieve this capacity and performance, VME64X architectures with modular distributed architecture was followed. The architecture is as seen in figure 2. Various parameters & their types monitored by RFPIS may be understood referring to figure 1.

† rtk@barc.gov.in

Table 1: Capacity of one RFPIS

| Input Parameter Type | No of signals monitored |
|---|---|
| RF signals | 08 |
| Analog Inputs | 04 |
| Digital inputs | 06 |
| PMT inputs | 04 |
| FEP inputs | 04 |
| Antenna Input | 01 |

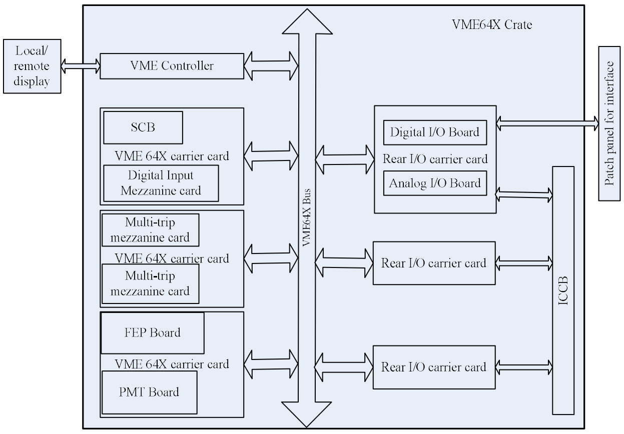


Figure 1: Architecture of RFPIS

## RFCPS FOR HTS

Protection scheme of HTS are mainly implemented in RFPIS while continuous field control scheme is implemented in LLRF. LLRF functionalities need downconverter, FPGA based PI control, upconverter and resonance control system. Suitable phase reference distribution system referred as clock module also form part of LLRF system. All these subsystems are collectively referred as RFCPS (RF control and protection system). RFCPS is housed in 38U twin rack with suitable RF and cable interconnects at top of rack. Figure 2 shows the placement of various modules in a rack. Directional coupler & splitter module is needed to monitor RF signals entering the rack and splitting them suitably to route to RFPIS and LLRFS. Purpose of LLRFS is to maintain the amplitude and phase of RF field in cavity close to set point. In case of superconducting cavity, as RF field is applied cavity deforms resulting in shift in resonance frequency. This shift is measured by resonance control system and bought close to set point using piezo tuners and stepper motor as final control element. Purpose of RFPIS is to monitor various parameters while cavity operation. In the event of parameters crossing specified limits, the RF power input to cavity is stopped by opening RF switch. This action opens input to final control element (in this solid state amplifier), thus preventing damage of RF system.

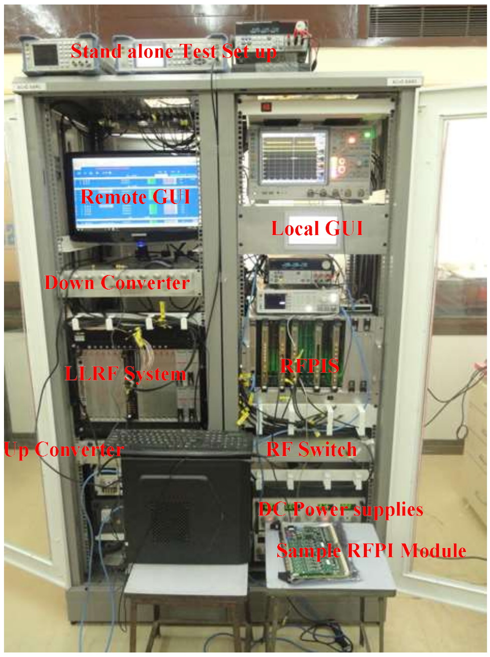


Figure 2: RFCPS rack with placed modules

## RFPIS INTERFACE

RF inputs monitored by RFPIS are forward power, reflected power and cavity pick up for a given cavity under characterization in HTS. RF power is coupled using RF coupler. The condition monitoring of coupler for its safety is carried out by measuring its temperature using RTD, arc monitoring using PMT, bias supply status signal, etc. Referring to figure 4, listed below are some features of RFPIS output signal interfaces:

1. RF INHIBIT signal is digital output (DO) from RFPIS & controls the LLRF fast switch between LLRF and SSA. It is opened in event of fault detection. This signal is generated within 1.0 microsecond after the detection of a fault condition. It is a 50 Ohm compatible TTL level.
2. SSA INHIBIT signal is DO from RFPIS & controls the internal Fast RF switch at the SSA. This inhibits the internal RF drive. This signal is generated within 1.0 microsecond after the detection of a fault.
3. SSA DC INHIBIT signal is DO from RFPIS & controls the permit to the DC supply powering the FET in case RF power is detected even when RF switch is open. It is a 50 Ohm compatible TTL level.
4. MPS signal is DO from RFPIS & controls the permit to the machine protection system that disables beam when RF is not available. This action must be carried out in less than 5 microseconds from the detection of RF fault.
5. LLRF_FAULT is DO from RFPIS & is an output TTL signal which informs the LLRF the fast switch has been opened. Subsequently LLRF can take suitable control action.

Suitable cable interconnects and cabling system is used for these different types of electrical signals. For e.g., for RF inputs a low attenuation coaxial cable (FSJ1, FSJ4, heliax brand) has been used. For analog inputs, a twisted pair cable has been planned. RFCPS has capability to interface Machine protection system (MPS) which generates trigger signal for LLRF and timing signals for RFPI.

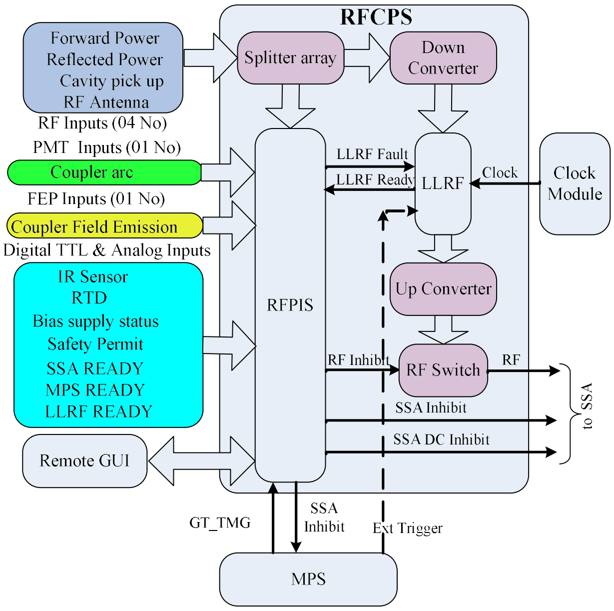


Figure 3: RFPIS interfaces

## TEST RESULTS

Lab test results are shown in figures 4 and 5. Response of RF measurement electronics to signal from RF transducer is as seen in figure 4. It is assessed from this figure that any fault detected will be processed within 500 ns by RFPIS. This guarantees the protection function as fast as 500 nsec. Response of PMT card to optical input of 1 µsec pulse signal is as shown in figure 5. It is observed that optical pulse of duration as low as 1 µsec could be detected by RFPIS.

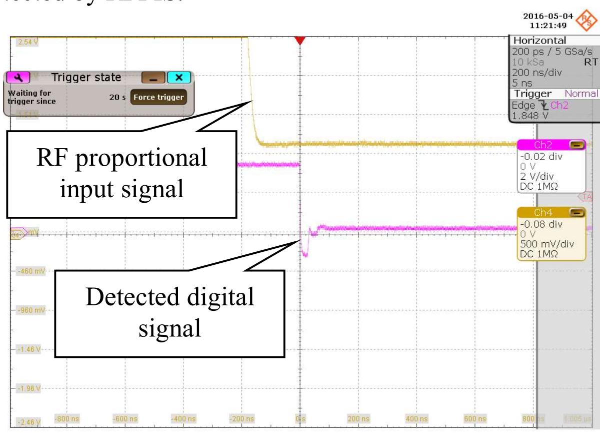


Figure 4: Response to RF input

Figure 6 shows control GUI designed for HTS RFPIS. Module-wise threshold setting, Input value display, trips, etc. are indicated. Cavity fill time is programmable from GUI to disable trips due to reflected power usually encountered while cavity filling. Status of all DI and value of AI is also displayed in GUI for monitoring by an operator. As indicated in GUI, SSA RDY, LLRF RDY, SAFETY PERMIT and MPS PERMIT must be valid DI for system to start. GUI also enables including or excluding certain parameter as contributor to overall trip logic. The PMT Power supply status is also indicated on GUI. A cable connect/disconnect indication is provided to ensure connection of each input to RFPIS.

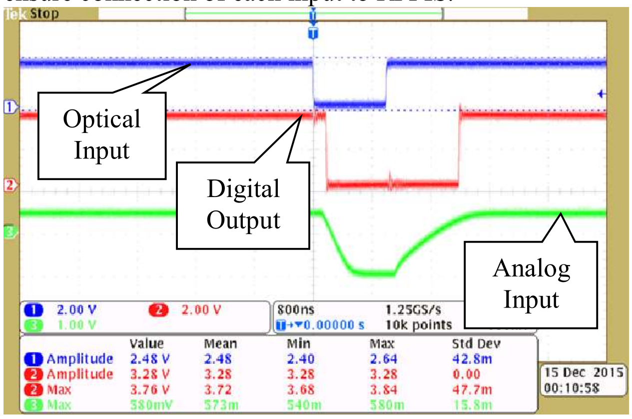


Figure 5: Response to optical input

Figure 6: Monitoring and Control GUI

## CONCLUSION

RFPIS for HTS has been tested and installed at HTS site. As understood from laboratory test results, it shall protect coupler and cavity from any abnormal situation arising while operation of cavity testing. RFPIS is suitably interfaced to other subsystems like LLRF, MPS, etc.

## REFERANCES

[1] Khare P Gilankar, et al (2016) "Design of Horizontal Test Cryostat for Testing Two 650 MHz Cavities: Cryogenic considerations", 26th International Cryogenic Engineering Conference & International Cryogenic Materials Conference, New Delhi, India.

[2] Sujo C.I. et al (2018) "RF protection interlock system for proton linacs under Indian institutions and FERMILAB collaboration" Proceedings of the eighth DAE-BRNS Indian particle accelerator conference 2018, INIS Volume: 49, INIS Issue: 14.

[3] Sujo C.I. et al (2015) "Description of RF Protection Interlock System for LEHIPA", presented at Indian Particle Accelerator Conf. (InPAC'15), December 21-24, 2015 held at TIFR, Mumbai, INIS volume 47, issue.

# ARM BASED VME CPU BOARD FOR EQUIPMENT INTERFACE LAYER OF INDUS-1 LCW PLANT CONTROL SYSTEM*

Rana R.*#, Yadav R.P.*, Fatnani P.*
RRCAT, Indore, MP-452013, India

*Abstract*

A quad core ARM based CPU is used for development of open source VME CPU board [1] that has many advantages from Motorola based 68040 CPU boards currently being used at both Equipment Interface layer and Supervisory layer of the overall three layered architecture of Indus-2 control system. The driver and application software are developed to configure the developed board for deployment in Indus-1 Low Conductivity Water (LCW) plant control system. The feasibility of this work would help facilitate higher computation powers at lower layers for local control with or without upper layer supervisory controls. This paper presents the driver and application software development details for the new VME CPU board towards Indus-1 LCW control system along with implementation strategies employed in implementation testing of the unit in the field for initial trials.

## INTRODUCTION

Indus-1 LCW control system caters for the control of cooling requirement of various Indus-1 components through control and monitoring of various signals from LCW plant. LCW components like switching of pumps and valves, monitoring and recording temperature and flow, status of pumps, valves and heat exchangers and interlock handling etc. Four types of VME based DAQ cards are used for the control and monitoring of these signals. These are, Motorola 68040 CPU card, analog input cards, opto-in cards and relay out cards. These cards are used extensively in Indus-1 and Indus-2 control systems. CPU board is responsible for control of data flow, analog input board reads analog devices and provides these values when polled by the CPU, similarly opto-in cards are used for status reading of the connected devices and relay out are used for switching ON and OFF the connected devices. These peripheral VME boards are in-house developed.

Motorola 68040 VME CPU board is in use since the beginning of the Indus-1 and Indus-2. After this long span of time the requirement to have high computational power at lower layers for implementation of intelligent control system [2] at different layers with varying control capability has arisen. This requirement along with high data rate requirement can not be fulfilled by present Motorola CPU and buying a new board would be a costlier solution as it would require the procurement of board support package (BSP) as well. Any new board purchase would also necessitate purchase of new software set as well. Also there is not full flexibility available for modification and custom development at these black box software and hardware solutions. All this leads to the motivation to develop indigenous VME CPU board that could provide high computational power along with being available with full hardware and software customization support. Open source hardware and software platforms were utilized for both hardware and software developments. The new CPU board has been developed and tested for various CPU performances [1].

This board is developed towards implementation into the existing control system and evaluate the feasibility of replacement of existing CPU board for similar functionality initially. This paper presents the details of software application development and first time implementation experience of the new CPU board into Indus-1 LCW station for acquisition of analog data only. At first only analog station is chosen to work with, in Indus-1 shutdown time, without electron beam or interlocks for hassle-free working. Work towards the implementation and trial of the new CPU board into Indus-1 LCW plant had been planned in a way that the existing hardware and software need not be modified significantly except for minor adjustments.

## HARDWARE & SOFTWARE DETAILS OF INDUS-1 LCW CONTROL SYSTEM

Two VME are used for Indus-1 LCW Control System. Station one is responsible for acquisition of analog signals and station two for control and acquisition of digital signals. These two stations house one VME CPU board each and multiple peripheral boards, ADC cards for station-1 and opto-in and relay cards for station-2. Both the stations are connected to upper layer application through a switch as shown in Fig. 1.

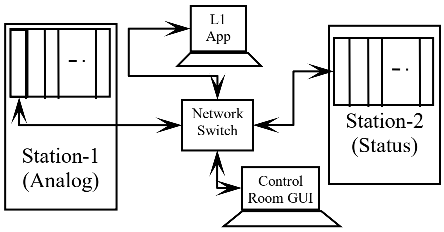


Figure 1: Hardware Layout Block Diagram of Indus-1 LCW Control System.

Seven number of 12-bit VME ADC boards are used in 32 channel single ended mode or 16 channel differential mode [3].

*Raja Ramanna Center for Advanced Technology, Indore
#rahulr@rrcat.gov.in

### *Control Software Application Details for Indus-1 LCW*

The upper layer has a LabVIEW application that sends the command string to VME stations and receives response string through TCP/IP [4]. The stations parses the command and reply accordingly by polling data through respective peripheral boards. The command format is explained in Table 1.

Table 1: L1 App and VME CPU command format

| Format | R#1 |
|---|---|
| Meaning | This command is sent by L-1 (upper layer App) to L-2 (VME CPU) STN-1 periodically for getting ADC data of all the analog devices. |
| Argument | Here 1 represents the station number. |
| Response | Two replies are sent in response:<br>"DATA" and actual 976 byte data |

There is only one C program running on the CPU which has two major functions namely, implementing socket programming and talking to Linux kernel driver for accessing VME data from ADC board [3]. It uses TCP socket to communicate with LabVIEW program running on the server PC. Logical block diagram of the software development is highlighted in Fig. 2.

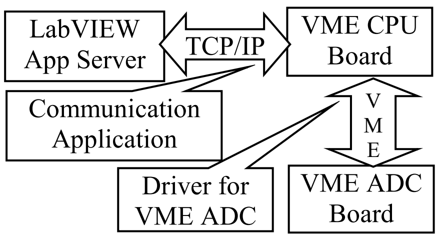


Figure 2: Logical Block Diagram of Software of Indus-1 LCW Control System.

### *Data organization for Analog Station*

To cater the requirement of all analog signals of Indus-1 LCW, 7 ADC boards are used. VME ADC Boards specifications are: 7 Nos., 32 channel, 12 bit. 12 bit data is taken in two byte (2 B) space, ignoring 4 MSBs. To accommodate the data in existing format [4] used for Motorola CPU, the data has been segregated in 4 blocks as follows:

- Block-1: For diagnostic information, like board bus-error. (7 bytes for 7 boards)
- Block-2: For first 3 ADC boards. (3×2×32 = 196 B)
- Block-3: For next 3 ADC boards. (3×2×32 = 196 B)
- Block-4: For last 1 ADC boards. (1×2×32 = 64 B)

Each block is assigned a fix size of 244 bytes, empty data padded with zero. So a total of 976 byte of data packet is formed at CPU.

### *Software Application Algorithm*

The program initiates and listens to TCP/IP socket connection on first run. After connection, it waits for the command, a read command in analog case, from the server application. On getting the command, it sends the request to VME kernel to get data from the assigned VME address. Various read and write register operations for address and data sharing are performed in communication with the kernel driver, that in turn performs various register read-write operations for communication with the VME board and get required data. It include sending request for start conversion and repeatedly reading the data locations from the ADC board. The program then packs and sends back the ADC data in desired format. It works on command basis and doesn't remain in a loop to periodically read the input cards. It is the responsibility of the upper layer application to send command on a regular basis. The polling rate employed is 1 Hz.

### *VME Driver Algorithm*

A driver in c language is developed that communicates to kernel driver of the CPU board through register read and write operations for polling VME ADC peripheral board. 16 bit of data from each ADC board's 32 channels (board is specified by 24 bit physical address assigned through on-board switches called base address and each channel is specified by the location of memory to be read after commanding start of conversion, SOC [3]) is polled in two step process. First the command of SOC is given by writing address of first channel at board's base address+2 location. Then reading the response from the base address after waiting for conversion time as per ADC board's specifications (24μs in our case).

The background communication process for VME write operation i.e. writing 32 bit of data on 32 bit address of VME board, is, calling kernel function by: writing lower 16 bit of address at certain kernel register location (0x86), writing higher 16 bit of address at kernel register location (0x87), writing lower 16 bit of data at kernel register location (0x88), writing higher 16 bit of data at kernel register location (0x89), writing 16 bit of coded data (0x800D) at kernel register location (0x8A), reading 16 bit of status data from kernel register location (0x8B) to get status of the write operation command. If it's 0x8000 then it's an error of non-receipt of DTACK signal from the VME board. 0x0000 as response means that the command was successfully executed.

The background communication process in VME read operation is, calling kernel function by: writing lower 16 bit of address at certain kernel register location (0x80), writing higher 16 bit of address at kernel register location (0x81), writing 16 bit of coded data (0x800D) at kernel register location (0x82) (it act as command) to fetch data from provided VME address, reading higher 16 bit of data from kernel register location (0x84), reading lower 16 bit of data from kernel register location (0x83), reading 16 bit of validation data from kernel register location (0x85) for checking validity of the data. If it's 0x8000 then it's an error of non-receipt of DTACK signal from VME board. 0x0000 as response means that the command was successfully executed.

*Work done towards software of the VME CPU board for Indus-1 LCW*

i. Writing C code, socket programming, for implementing Ethernet functionality. It is somewhat different from ethernet functionality for Motorola VME CPU— in the sense that the environment is Linux (Mint) instead of OS9, so the libraries and functions are different.
ii. Writing C driver code for above application for accessing VME ADC board data using two modes - as facilitated by the ADC board hardware i.e. through FIFO reading same address for all 32 channels and through reading base locations for particular channel's data after SOC command repeatedly for all channels. It involves utilizing VME driver for performing multiple read-write operations at kernel registers.
iii. Packaging the polled data and integration of the above two to send the data from VME CPU board to LabVIEW application over TCP/IP.
iv. Adjustments in the Indus-1 LCW LabVIEW code (Station-1) for accessing data from new CPU.

## INITIAL TEST TRIALS AND RESULTS

A setup was prepared in lab environment to test one ADC board (reading multiple times the same address to imitate reading multiple ADC boards with just change of addresses), opto board and relay board with new CPU board and fans installed (cooling requirement is there for the CPU board) in the VME chassis. Though the emphasis of development and testing was for ADC part of the system but, for troubleshooting, Opto and Relay boards were also used. The CPU board needs a monitor for displaying the Linux mint OS GUI and the application development is done on the CPU itself. For testing multiple configurations, ejection and re-insertion of the ADC board, it has been mounted on VME extender, outside VME chassis for ease of handling. A LabVIEW application similar to the Indus-1 LCW L1 application was build to test the data received from VME CPU. Seeing some timing issues related to TCP/IP connection and loop repetition, some timeout modifications were done at the LabVIEW applications side~~ on Indus-1 LCW Server machine in the field.~~

Application test setup was developed in lab for successfully accessing ADC board data at 1Hz rate by providing 0-10V signal voltages from DC source. The data was then transmitted to test LabVIEW application mimicking Indus-1 LCW application.

Finally the Indus-1 LCW CPU was replaced on field during shutdown period. The new setup was able to perform as the old one except that the acquired data was not correct. One ADC board was then placed on VME extension board (extender) to check for simulated signals from DC source (replicating Lab environment). That worked fine. To remove the doubt of impedance matching due to inclusion of extender, The CPU board was also checked on extender, keeping ADC boards in the chassis, but that didn't work. So it was decided to replicate the field environment in lab and analyse the system misbehavior. The system was kept in the data acquisition state with simulated signals for about half day to check the heating or any other malfunctioning. The system worked fine in this regard. The simulated data for this period is available online on SRS website.

## CONCLUSION AND FUTURE SCOPE

The necessary framework including communication and driver applications were developed and utilized to extend the quad core ARM based VME CPU board's functionality towards reading VME ADC board in lab environment as well as on field. The availability of this framework would help further development to extend the overall functionality of the new CPU board as a full fledged VME CPU board with additional opto, relay and interlock compatibility equivalent to existing CPU boards.

The future work in this direction include finding compatibility issues between new CPU board and various modes of VME ADC board, detailed characterization and timing analysis with VME ADC board, opto-in board, relay board and interlock unit. The possibility of operation enhancement by GPS time stamping of data and incorporation of intelligent control system would also be studied.


## ACKNOWLEDGEMENT

For cooperation and support towards successful completion of the activity, we thank Sh. Amit Chauhan for providing his VME CPU OS9 program details, Smt. Sampa Gangopadhyay for providing her VME ADC board's address details and Sh. Samaresh Kar for prompt assistance whenever needed.


## REFERENCES


[1] Yadav R.P. et. al., "ARM SoC based VME CPU board development using Open Source Framework for Intelligent Accelerator Control System", ICRESH-2019, IIT Madras, Jan 2019.

[2] Yadav R.P. et. al., "Intelligent Agent Based Operator Support and Beam Orbit Control Scheme for Synchrotron Radiation Sources", International Journal of Advanced Science and Technology, Vol 52, March 2013

[3] Smt. Sampa Gangopadhyaya, "VME ADC board Address Details", RRCAT Internal Document, RRCAT Indore.

[4] Sh. Amit Chauhan, "Indus-1 LCW Control System Layer-2 Scheme for Station-1 (Analog I/O)", RRCAT Internal Document, RRCAT Indore, 2010.

# DESIGN AND DEVELOPMENT OF UP-CONVERTERS AND DOWN-CONVERTERS FOR 2860MHZ RF CAVITY

G. D. Randale*, R. T. Keshwani, P. D. Motiwala and Gopal Joshi
Accelerator Control Division, BARC, Mumbai-94

*Abstract*

Eight channel Down Converters (DC) and a four channel Up Converters (UC) are designed as a part of LLRF system for control of RF field in 2860MHz RF cavity. Two types of converters have been designed and developed. These provide eight channels of isolated, linear and low noise down-conversion of 2860MHz cavity signals to either IF or baseband. The down-converted signals are further digitized and processed in SoC based FPGA module. The UC provide four isolated channels for conversion from either baseband or IF to 2860MHz RF cavity drive signals. This paper describes the design and performance analysis of the up/down converter modules developed for a 2860 MHz cavity.

## INTRODUCTION

Today, digital techniques are extensively used in the development of RF control and instrumentation for RF accelerator applications. With availability of high speed, high performance ADCs and FPGAs, implementation of digital and FPGA based designs are very attractive and have become a standard to an extent. However, the requirement of RF Analog front ends cannot be entirely ruled out, specifically for very high frequency applications. There are two approaches for converting the RF analog signals into digital form first is direct down conversion method and second is using up down converters followed by digitizers [1]. For cavity frequencies of the order of 2860MHz direct down conversion method may not be suitable because clock jitter will lead to higher phase noise. Also there is limitation that you need wideband ADC with very high sampling rates. So the second approach of Up/Down converter is attractive for such high frequency cavities. In this approach the ADC sampling frequencies can be of lower range with lower bandwidth of the converters. There are number of applications where 2860MHz cavities are used in the accelerator [2]. The DC and UC becomes integral part of such systems. In the present development baseband and IF based approaches have been implemented in hardware and performance of the modules are analysed.

## MODULE DESCRIPTION

All the modules [3] are designed to fit into 19" chassis with 3U height. The modules have all input output connections from the backside and all monitor connections are on front side.

### *8 Channel Down Converter Module*

The DC mainly consists of three major sections

- LO Input and distribution
- RF input
- Baseband I, Q output / IF output

Figure 1 shows the block diagram of the 8 channel baseband DC. The external Local Oscillator (LO) input is given at 2860MHz which is same as the RF input frequency. This LO input is distributed to all the channels through suitable splitters and amplifiers. Finally, LO input is amplified and fed to the LO port of quadrature demodulator. The RF input is passed through a low pass filter and fed to the RF port of quadrature demodulator. The baseband IQ outputs are generated by the quadrature demodulator and passed through the stages of amplification and low pass filtering. For each input and output port signal monitoring outputs are available for diagnostics. The RF input section is shielded in the aluminium shield so as to have lower crosstalk between the channels.

The IF based DC module is similar to the base-band based DC except the quadrature demodulator. In IF based approach RF mixer is used to down convert the 2860MHz RF input to IF frequency of 44.68MHz instead of baseband. The IF signal is then amplified by a fixed gain amplifier and made available as IF output after passing through the low pass filter. The LO input in the IF based DC is given as 2904.68MHz thus providing IF of 44.68MHz.

### *4 channel UP converter Module*

The baseband UC mainly consists of following major sections

- LO input and distribution
- RF Output
- Baseband I Q inputs / IF Input

Figure 2 shows the block diagram of the 4 channel baseband UC. The UC generates 2860MHz RF drive output from the baseband IQ signals and 2860MHz LO signal. The external 2860MHz LO input is distributed and given to the four channels of UC. Further the baseband IQ from the digital LLRF module (available from the DACs) are provided to the UC boards. As required by the quadrature modulator the single ended IQ signals are converted to differential signals with 800mVp-p amplitude. The baseband IQ signals are modulated by IQ modulator and the output is fed through the bandpass filter. The monitor outputs are made available for diagnostics. A high isolation non-reflective switch is

*gdr@barc.gov.in

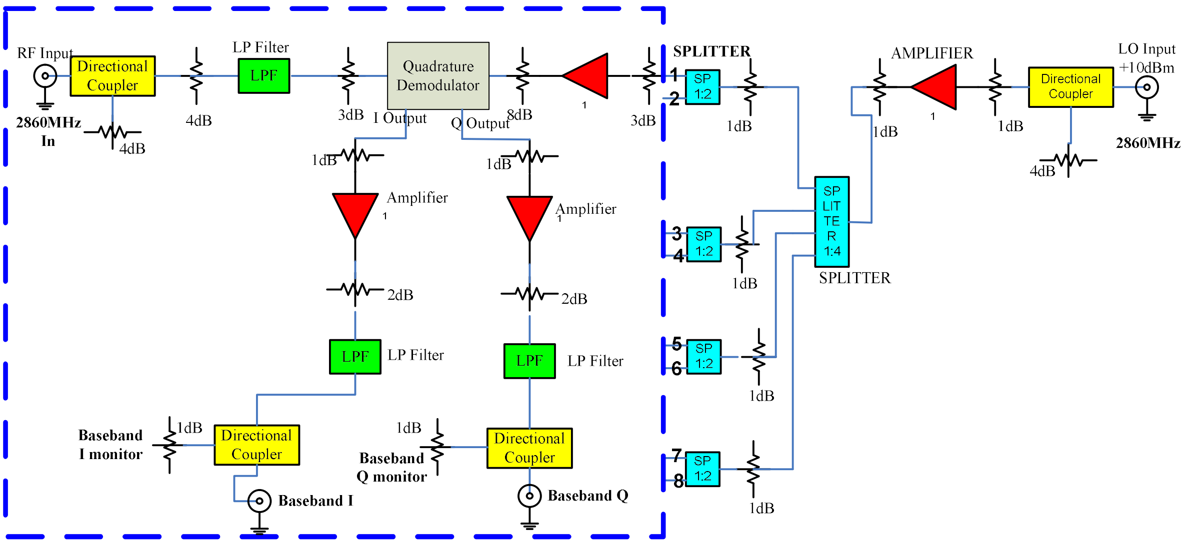


Figure 1: Block diagram of baseband downconverter module.

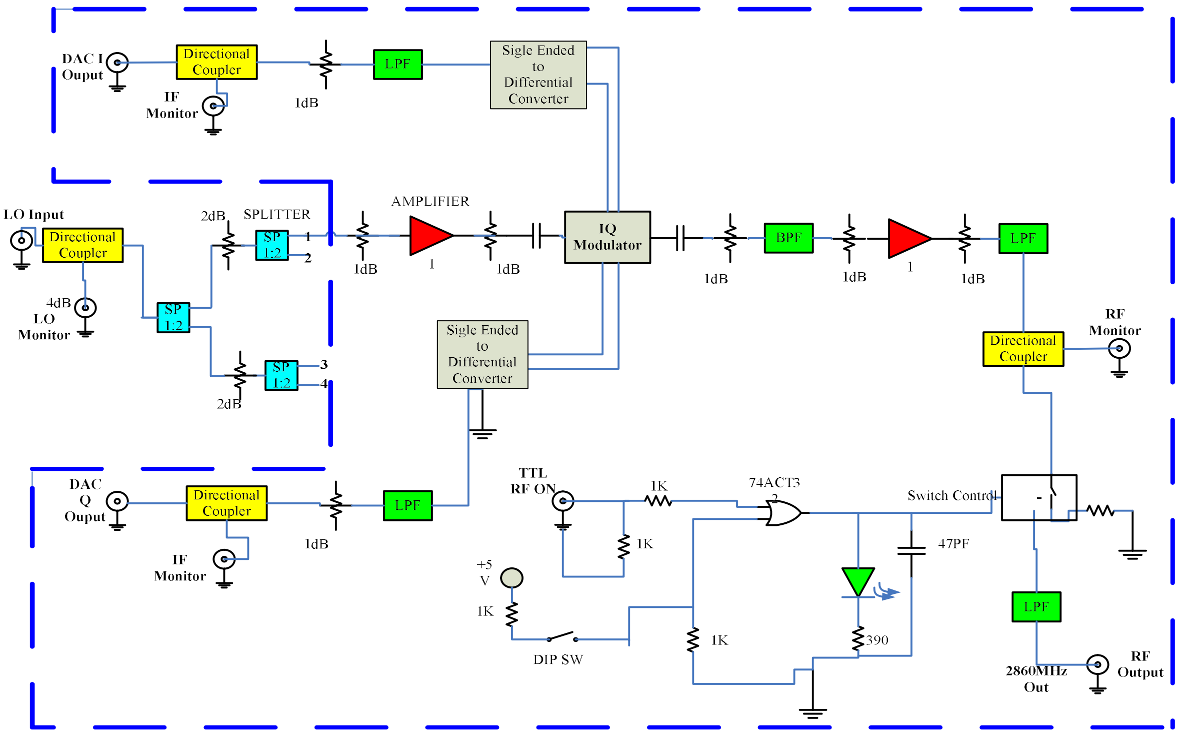


Figure 2: Block diagram of baseband Up-converter module

placed before the output port so as to cut off the RF output whenever required. The IF based UC module generates 2860MHz RF signal from the 44.68MHz IF and 2904.68MHz LO. The output from the IQ modulator is passed through the narrow bandpass filter so as to suppress the LO and the sidebands after the IQ modulator.

## PERFORMANCE ANALYSIS

Figure 3 and Figure 4 shows the photograph of the baseband 8 channel DC and 4 channel UC respectively.

### *8 Channel Down converter*

The performance of the modules is analysed for following parameters

- Channel to Channel Isolation
- Linearity of output

The channel to channel isolation for the baseband down converter is observed to be 38dB to a maximum of 93dB. In case of IF based down converter these are in the range from 41dB to 68dB. The linearity of the module is checked and it is observed that the IF based module gives better than 2% linearity upto a level of

+4dBm output. For the baseband based downconverter it gives the linear output upto a range of +4dBm.


Figure 3: Baseband Down-Converter module


Figure 4: Baseband Up-Converter module

### *4 Channel Up Converter*

The performance of the module is analysed for the following parameters

- Channel to Channel Isolation
- Linearity of RF output
- RF output spectrum
- Measurement of switch isolation

The channel to channel isolation for IF based UC is in the range from minimum 47dB to maximum 88dB with maximum RF output level of +2.5dBm. Table 1 shows measurements for the channel to channel isolation for IF based UC. For baseband UC it is in the range from minimum 53dB to maximum 66dB with maximum RF level at the output is +8dBm. It is observed that performance of the modules improves with better connections and grounding schemes. The channel to channel isolation improved significantly with the proper grounding.

Table 1: Channel to Channel isolation for IF based UC

| **O/P I/P** | **Ch1** dB | **Ch2** dB | **Ch3** dB | **Ch4** dB |
|---|---|---|---|---|
| **Ch1** | | -86.37 | -55.65 | -49.89 |
| **Ch2** | -60.77 | | -61.68 | -52.84 |
| **Ch3** | -55.79 | -58.78 | | -45.63 |
| **Ch4** | -49.07 | -55.59 | -53.38 | |

For Baseband up converter the RF output is linear within 2% for the output level of +7dBm. For IF based up converter the RF output is linear within 2% for the output level of +2dBm.

The RF output spectrum for IF based up converter contains the LO feed through which is below 50dBc and the upper sideband is below 55dBc. The RF switch isolation is measured as better than 45dB in both the baseband and IF based up converters.

The switch isolation for the IF and baseband UC are in the range of 45dB. Table 2 shows the RF output with output switch ON and in OFF condition

Table 2: RF switch isolation for baseband UC

| **RF Switch** | **Ch1 dBm** | **Ch2 dBm** | **Ch3 dBm** | **Ch4 dBm** |
|---|---|---|---|---|
| ON | 7.47 | 7.14 | 7.99 | 7.78 |
| OFF | -39.34 | -39.96 | -37.36 | -38.56 |

## CONCLUSION

The 8channel IF and Baseband based Down converter module and 4 channel IF and baseband based Up Converter were designed and their performance for the basic parameters is analysed. It was observed that the implementation meets all the design specifications. The improvement areas have been identified and to be implemented in next version of the design.

## ACKNOWLEDGEMENT

Authors wish to thank Mohammad Afaash ACnD BARC for his continuous help in testing of all the Up/Down converters. We would like to thank Smt. Charulata Shinde ACnD, BARC for her help in assembly of the modules.

## REFERENCES

[1] RF Applications in Digital Signal Processing https://cds.cern.ch/record/1100538/files/p249.pdf

[2] S. Ghosh, et al, “Status of Design and Development of Delhi Light Source at IUAC, Delhi”, MOPOW016, IPAC2016, Busan Korea.

[3] Mohammad Afaash, et al, “Design and Development of 4 channel Up-Converter and 8 channel Down-Converter”, InPAC-2018, RRCAT Indore, India

# PERFORMANCE ANALYSIS OF BPM ELECTRONICS FOR SPIRAL2, GANIL, FRANCE

G. D. Randale*, P. Jyothi, P. D. Motiwala, S. K. Bharade and Gopal Joshi
Accelerator Control Division, BARC, Mumbai-94

*Abstract*

Beam position monitor (BPM) electronics system has been designed and developed by ACnD, BARC for LINAC of SPIRAL2 which is being commissioned at GANIL. 20 such systems have been exhaustively tested at BARC as per Acceptance Test Procedure (ATP) jointly prepared by BARC and GANIL. These BPM systems have been commissioned along the LINAC. Each BPM system is coupled to a capacitive type non-intrusive sensor and measures various beam parameters such as X-Y position, amplitude-phase, ellipticity etc. at 88MHz and its harmonic at 176MHz. Various performance related parameters such as RMS noise, channel to channel cross coupling, linearity, dynamic range, calibration constants, etc. have been measured/computed to ascertain system performance. This paper describes the performance analysis of the BPM electronics modules.

## INTRODUCTION

BPM will be the only diagnostic instrument used during the operation of the LINAC thus forming a very critical diagnostic tool and is expected to provide beam position, phase and ellipticity measures at high accuracy. The BPM electronics mainly consist of a set of two VME bus based boards; digital board and analog board. The system supports all the measurements at the RF reference of 88.0525MHz and its harmonic at 176.1050MHz. The VME based hardware and EPICS based application software provides auto gain calibration to compensate for the drift due to temperature variation and aging. Full digital architecture is adopted which makes the system highly flexible and configurable. A number of data acquisition modes have been incorporated for diagnostic and performance analysis. Testing of the BPM systems was carried out at BARC as per the ATP and various parameters were measured to evaluate the performance.

## PERFORMANCE PARAMETERS

The Performance of the BPM system is analysed with the following parameters.

- System Constants
- Automation/Dynamic range
- Offset tone Dynamic range and quality
- Cross Coupling measurement
- Linearity measurement
- RMS Noise measurement
- Absolute value measurement
- Phase measurement
- Bunch shape reconstruction
- RF Input return loss measurement

### *SYSTEM CONSTANTS*

In order to get precision measurements from a BPM system it is required to generate a set of system constants specific to the BPM hardware and stored in a file which is recalled on system start-up. The set of system constants generated are:

- Initialization and calibration constants – to equalize the differences in the four analog channels.
- Absolute K constants – to measure absolute power of input signal in dBm.
- Cable calibration constants – to compensate for change in phase of the long cables due to temperature variation.
- Phase constants – to compensate for the phase difference between RF reference and input RF signals.

### *AUTOMATION /DYNAMIC RANGE*

Figure 1 shows typical measurement setup for the testing of the BPM electronics in laboratory. The measurement of dynamic range (approx. -20dBm to -65dBm) is important for the proper operation of the BPM system. The dynamic range decides the range of measurement of beam current as well as range of beam XY position measurement in the beam. The BPM electronics treats the measurement problem in two distinct parts. First part deals with the variation in beam current from few μA to 5mA. The second part deals with the large range of XY position measurement for a given beam current.

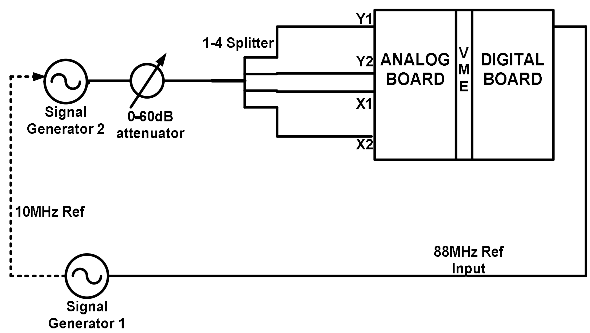


Figure 1: Setup for the Automation/Dynamic range measurement

Table 1 shows the values for the automation/dynamic range measurement for the 20 BPM modules which are commissioned at GANIL. The measurement is carried out at both 88MHz and 176MHz and at both the extremes of dynamic range. It is observed that the levels are within ±2dBm for the each range.

*gdr@barc.gov.in

Table 1: Automation/Dynamic range

| Card Set | 88MHz High (dBm) | 88MHz Low (dBm) | 176MHz High (dBm) | 176MHz Low (dBm) |
|---|---|---|---|---|
| **1** | -19.82 | -65.2 | -19.21 | -64.3 |
| **2** | -19.95 | -65.81 | -19.35 | -64.21 |
| **3** | -20.09 | -65.9 | -19.31 | -64.2 |
| **4** | -19.77 | -65.34 | -19.1 | -64.19 |
| **5** | -19.4 | -64.42 | -19.33 | -63.48 |
| **6** | -19.68 | -65.25 | -19.55 | -64.29 |
| **7** | -19.83 | -65.83 | -19.72 | -64.68 |
| **8** | -19.5 | -65.6 | -20.8 | -66.8 |
| **9** | -19.59 | -65.27 | -19.07 | -63.79 |
| **10** | -19.15 | -64.19 | -19.42 | -64.07 |
| **11** | -20.58 | -65.82 | -18.8 | -63.79 |
| **12** | -20.45 | -65.91 | -19.16 | -64.78 |
| **13** | -19.13 | -64.87 | -19.39 | -64.23 |
| **14** | -19.66 | -65.37 | -18.25 | -63.83 |
| **15** | -20.02 | -65.96 | -18.37 | -63.62 |
| **16** | -19.72 | -64.67 | -20.3 | -65.1 |
| **17** | -20.26 | -65.08 | -19.02 | -64.29 |
| **18** | -20.29 | -65.34 | -19.11 | -64.12 |
| **19** | -19.49 | -65.5 | -18.86 | -65.42 |
| **20** | -20.46 | -66.13 | -18.46 | -63.97 |

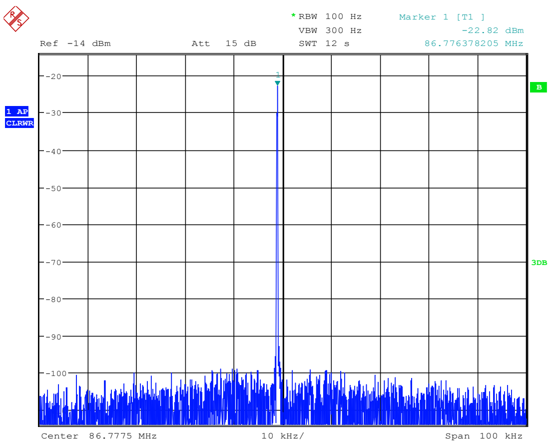


Figure 2: Offset tone spectrum

## *OFFSET TONE DYNAMIC RANGE AND QUALITY*

Offset tone at frequencies slightly away from the RF frequencies of 88MHz and 176MHz are synthesized in the digital board and their ranges are required to match the dynamic range of the system. Thus the total dynamic range of the offset tones is approximately 45dB±1dB. The quality of the offset tone greatly impacts the system performance.

Figure 2 shows the spectrum of offset tone at 86.776MHz with no spurious peaks within ±100KHz.

## *CROSS COUPLING MEASUREMENT*

Cross coupling between the RF channels impacts the XY position measurement directly. This includes coupling between the four channels and RF reference. It is observed that the channel to channel cross coupling is better than 45dB and that between RF reference and RF input channel is better than 55dB.

## *LINEARITY MEASUREMENT*

Linearity measurement is important for the proper operation of the BPM system. It determines the range of XY position measurements and corresponding RF signal variation is measured without saturation by analog frontend of the system. Figure 3 shows the graph of the measurement. It is to be noted that system behaves very linear from -80dBm to -55dBm for automation at -64dBm. Figure 4 shows the measurement done with maximum signal level. It is observed that the system is linear within 1% from -12dBm to -35dBm.

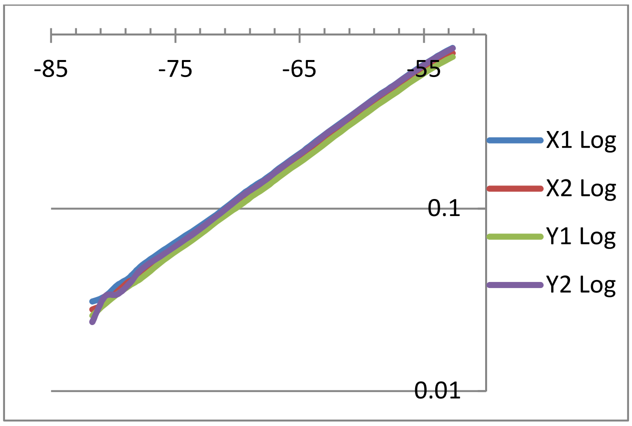


Figure 3: Linearity measurement for Maximum gain at 88MHz

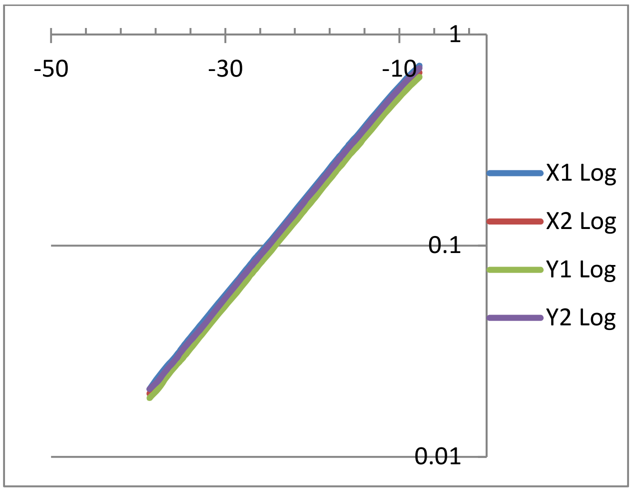


Figure 4: Linearity measurement for Minimum gain at 88MHz

## *RMS NOISE MEASUREMENT*

The RMS noise is important parameter for accurate measurement of position of the beam. The RMS noise of the measurement system plays important role when the signal levels are minimum and gain is maximum. This puts a limit on the lowest beam current for precision measurement of XY position.

Table 2 shows the RMS noise measurement for BPM modules which are supplied to GANIL. The tabulated measurements are for 88MHz. It is seen that in most of the boards phase noise is less than 0.4° with maximum gain and well below 0.05° at minimum gain. Also the amplitude noise is less than 1.5% at maximum gain and less than 0.1% at minimum gain. Similar measurements were observed at 176MHz also. The phase noise is very low when the measurement is done as the difference between the RF reference phase and the RF input phase. This cancels the common mode noise and the measurements are much better.

Table 2: RMS noise measurement

| Card Set | Amp Noise (%) | Phase Noise (Deg) | Amp Noise (%) | Phase Noise (Deg) |
|---|---|---|---|---|
| | Maximum Gain | | Minimum Gain | |
| **1** | 0.5316 | 0.3437 | 0.04234 | 0.3145 |
| **2** | 0.5095 | 1.301 | 0.04667 | 0.487 |
| **3** | 1.32 | 0.7553 | 0.04693 | 0.03636 |
| **4** | 1.491 | 0.8536 | 0.04199 | 0.02735 |
| **5** | 1.027 | 0.6148 | 0.0487 | 0.03315 |
| **6** | 1.089 | 0.6365 | 0.0556 | 0.03263 |
| **7** | 0.6552 | 0.4093 | 0.04569 | 0.03179 |
| **8** | 0.3628 | 0.2387 | 0.04517 | 0.03232 |
| **9** | 0.8509 | 0.5169 | 0.03566 | 0.03353 |
| **10** | 1.486 | 0.8767 | 0.04244 | 0.0335 |
| **11** | 0.5953 | 0.3817 | 0.03102 | 0.03187 |
| **12** | 0.552 | 1.4 | 0.04287 | 0.32 |
| **13** | 0.8178 | 0.4849 | 0.03168 | 0.03185 |
| **14** | 1.433 | 0.8211 | 0.04511 | 0.03109 |
| **15** | 0.5181 | 0.3201 | 0.04207 | 0.03171 |
| **16** | 0.6926 | 0.4387 | 0.04358 | 0.03634 |
| **17** | 0.5914 | 0.3699 | 0.05723 | 0.03215 |
| **18** | 0.895 | 0.5131 | 0.06219 | 0.03145 |
| **19** | 0.646 | 1.614 | 0.04679 | 0.3422 |
| **20** | 1.12 | 0.667 | 0.0398 | 0.0339 |

### *ABSOLUTE VALUE MEASUREMENT*

This unique measurement feature reads the power of the RF input at all the four electrodes and RF Reference. The absolute value measurements are directly linked with the beam current. It is observed that the measurement is within 0.5dB in the range from minimum (-64dBm) to maximum (-19dBm) level of automation.

### *PHASE MEASUREMENT*

The phase measurements of all the four electrodes of a BPM sensor are done with respect to the phase of the RF Reference. The measured phase is useful for determining the energy of the beam. The phase measurements are within 0.5° for all the channels.

### *BUNCH SHAPE RECONSTRUCTION*

The shape of the bunch at the electrodes of the BPM sensor is expected to be Gaussian in time domain. With limited bandwidth of the RF signal chain the system supports acquisition of data for reconstruction of the shape of the beam. A unique scheme implemented in the system that supports bunch shape acquisition on all the four electrodes in a given BPM sensor.

### *RF INPUT RETURN LOSS MEASUREMENT*

Figure 5 shows the return loss measurement at 88MHz and is observed to be 16.79dB at 88MHz. RF input return loss plays very important role in ellipticity measurement.

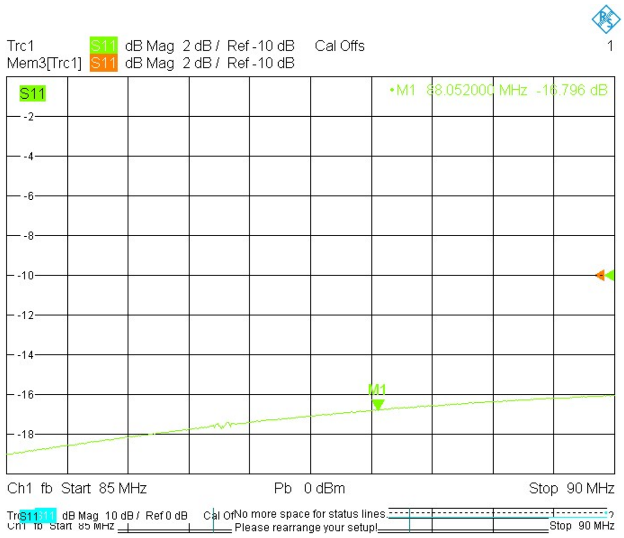


Figure 5: Return loss measurement of RF Input at 88MHz

## CONCLUSION

The 20 BPM systems supplied to GANIL gives similar performance for all the measurement parameters. Measurement resolution of 50µm is achieved over a wide dynamic range. Phase noise of the order of 0.03 deg is observed over the upper end of dynamic range. All the other parameters measured are well within the required specifications and systems are being tuned for the commissioning scheduled in 1st quarter of 2020.

## REFERENCES


[1] G. Joshi et al.,“An offset tone based gain stabilization technique for mixed-signal RF measurement systems”, Nucl. Instr. Meth., vol. A 795, 2015, pp. 399-408

[2] P. Ausset et al.,“Development of the Beam Position Monitors system for the LINAC of SPIRAL2”, WEPC15, Proceedings of IBIC2013, Oxford, UK

[3] Sandeep Bharade, et al., “EPICS DAQ system for Beam Position Monitoring of SPIRAL2 LINAC at GANIL”, InPAC 2019, IUAC New Delhi, India

# DIGITAL LLRF SYSTEM FOR MULTI HARMONIC BUNCHER

G. D. Randale*, A. A. Agashe, P. D. Motiwala and Gopal Joshi
Accelerator Control Division, BARC, Mumbai-94

*Abstract*

The paper describes the scheme developed for the closed loop control of RF field in a multi harmonic buncher (MHB). The system has three feedback control loops for three frequencies viz; 20.3125MHz and its two harmonics (f, 2f, 3f). Three digital sequences corresponding to each frequency are synthesized using lookup tables in FPGA. Three on board DACs convert these digital signals to analog, to be filtered by suitable band pass filters and combined to get single output. The output waveform is controlled by setting the amplitudes and phases of each harmonic. The resultant saw tooth waveform is provided to the buncher tank circuit after suitable amplification. The sawtooth signal will give best energy modulation required for bunching a DC beam. The received Pick up signal from the buncher is digitized and each harmonic is digitally extracted before further processing.

## INTRODUCTION

ACnD, BARC has developed a digital LLRF feedback control system for control of field in a single gap multi harmonic, low energy buncher for FOTIA, BARC. The system employs direct digitization technique for processing of the incoming pickup signal and the generation of RF drive signal for MHB.

The digital LLRF system [1] is well known to be free from limitations like DC offsets, drifts due to temperature and ageing, gain imbalance, impedance mismatch, etc. Digital system offers flexibility and powerful computational facility due to the possibility of implementing complex algorithms in FPGA. Repeatability and powerful diagnostic capabilities are additional advantages of digital and FPGA based systems.

Digital LLRF system developed for MHB employs full digital technique with direct sampling. Pickup signal from the buncher is digitized and demodulated to extract IQ components. These are then digitally processed inside FPGA and drive signal is generated with digital modulation in FPGA. Due to the implementation in digital domain cross coupling between the harmonic signals is very minimal.

## DLLRF SYSTEM DESCRIPTION

Figure 1 shows the block diagram of overall LLRF system for MHB. The heart of the system is the FPGA wherein the code for digital signal processing resides. The FPGA generates digital sequences to obtain RF signal of 20.3125MHz (f) and its two harmonics at 40.6250MHz (2f) and 60.9375MHz (3f). These three digital sequences are fed to three DACs whose outputs are suitably filtered by three independent bandpass filters to obtain three harmonically related RF signals. The filtered RF signals are combined and fed to single wideband amplifier. Since the frequencies are close, single amplifier is used. The output of the analog module is further amplified and given to the tank circuit of the MHB. The pickup signal received from the MHB is suitably attenuated or amplified and fed to the ADC in digital module. The input RF signal is digitized using on-board ADC and down converted to three quadrature signals corresponding to each frequency. The FPGA further processes the baseband IQ signals and generates three sequences corresponding to each harmonic and feeds to the DACs.

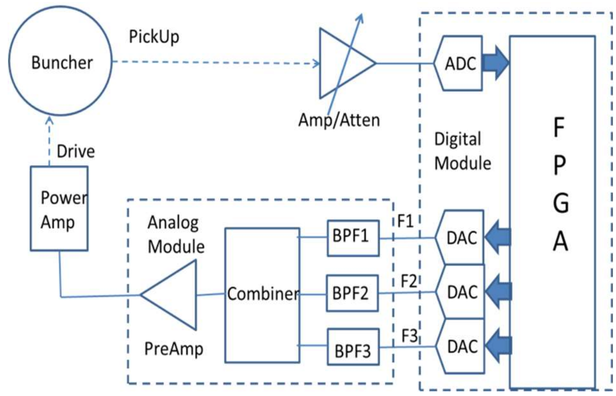


Figure 1: LLRF System for MHB

## *LLRF SYSTEM HARDWARE*

The system hardware mainly consists of a digital module and analog module. The digital module mainly consists of an FPGA and high speed ADC and DACs. The digital hardware also supports VCO based sampling clock generation logic which is required for generating suitable very low phase noise clock for the ADC.

### *FPGA & ADC/DAC Board features*

- FPGA with a capacity of 119,088 logic elements
- 32 bit 33MHZ master cPCI interface with DMA capability
- Duel VCO clock synthesizer to provide clocks to ADCs and DACs
- 14-bit 8 channel 80MSPS ADC interface
- 14-bit two channel 300MSPS DAC interface
- 10-bit three channel low speed debug DAC interface with 40MSPS update rate
- Six (1Mx16) High speed asynchronous SRAM interface
- Status indicators such as Fault, interlock, etc.

### *Analog Module features*

- Three different narrow bandpass input channels for three harmonics

*gdr@barc.gov.in

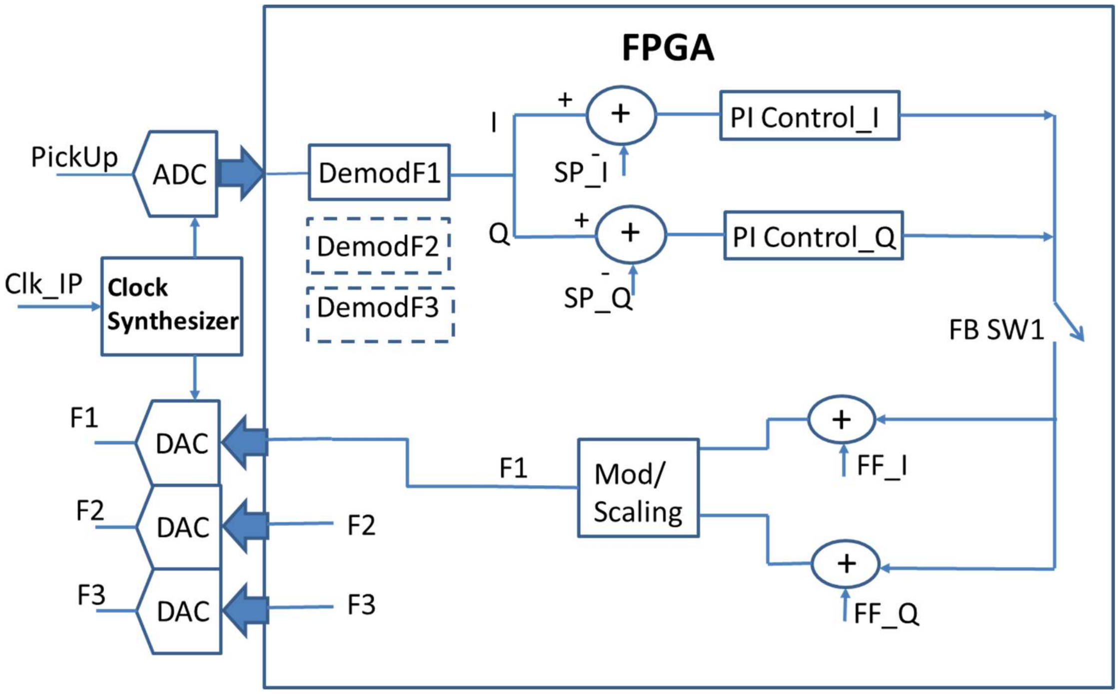


Figure 2: Block diagram of the digital implementation in FPGA for the LLRF system of MHB.

- 29dB Fixed gain single wideband pre amplifier stage
- Single regulated 24V 2A DC power supply
- Single multiharmonic amplified output signal level upto -6dBm

Figure 3: FPGA and ADC/DAC board used in the LLRF system Implementation

### *Digital Implementation details*

Figure 2 shows the block diagram of the digital implementation in FPGA. The 14bit ADC digitizes the incoming RF signal and feeds to the FPGA. Digital signal processing chain with feedback and feedforward control for the main frequency and its two harmonics is implemented in the FPGA. The first stage in the implementation is down conversion of digitized signal to baseband IQ signals by digital demodulator. There are three such demodulators corresponding to each harmonic frequency. As the digitized sequence consists of all the three harmonics the demodulation lookup table sequence is different for each demodulator. The three harmonics are demodulated with the lookup tables of 7/16 for 20.3125MHz, 7/8 for 40.625MHz and 5/16 for 60.9375MHz. The low pass filter after the demodulator is chosen such that for a given harmonic demodulator other harmonics fall at the null of the low pass filter. This way we get the demodulated IQ from each demodulator corresponding to the particular harmonic frequency. After demodulation the IQ outputs are compared with the set points. These set-points are defined based on the required output power in close loop feedback operation. There are separate set-points for both I and Q. The difference error signal between the set point and the actual IQ values is given to the PI controller. The PI controller comes in to action when the feedback switch is closed. During open loop operation the feed-forward comes into action. The feed-forward sets the suitable IQ levels for generation of the different harmonic signals. The feed-forward is then given to the digital IQ modulator which generates the appropriate harmonic signal whose amplitude is governed

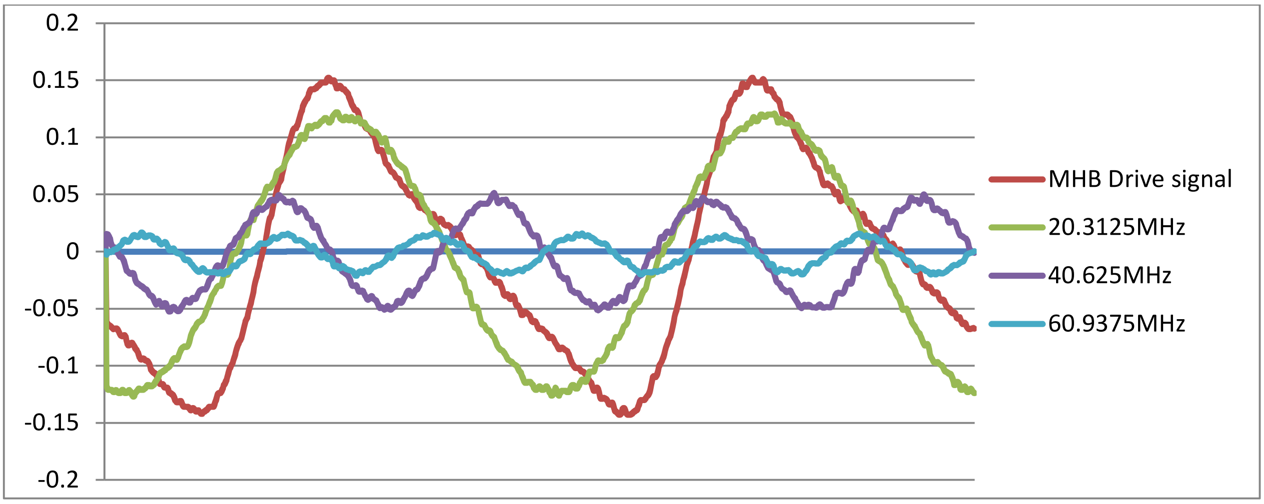


Figure 4: Sawtooth waveform and the corresponding three harmonics

by the feed-forward levels. The digital sequences used in the IQ modulation are same as those used for the IQ demodulation. When the loop is closed the correction signal from PI controller is added with feed-forward IQ levels and fed to the IQ modulator. Before IQ modulation the signals are passed through phase rotators. These phase rotators are used to match the phase between the harmonics to compensate phase change due to variation in cable lengths. In this implementation clock synthesizer plays an important role by generating low jitter sampling clocks of 46.43MHz for the ADC and DACs from the RF reference of 162.5MHz.

## IMPEMENTATION AND RESULTS

The digital module is composed of 6U CPCI based board and consists of the ADC, DACs, clock synthesizer and FPGA. Figure 3 shows the photograph of the board. The analog module is fabricated separately. The required FPGA firmware is implemented in VHDL. Graphical User Interface (GUI) based software is developed for the easy access and control of various parameters of the system.

Figure 4 shows the sawtooth waveform and the individual harmonics acquired from the system. The settings used during implementation are given in table 1. The setup is used in the open loop configuration and feed-forward levels are given through the GUI. Combination of different levels of amplitude and phase is provided and it was noted that to get the required sawtooth wave from the system, specific values of amplitude and phase need to be provided to the system. In the present system the phase of each set-point can be set within 0.2° and amplitude can be set with a resolution of 1%.

It is to be noted that the phase rotator values are subjective and depend upon the cable lengths from the digital to the analog module. This is advantage of the system that we need not to match the lengths of the cables in hardware rather we can correct the mismatch of cable lengths in the software through GUI. For performance analysis different modes of data acquisition are supported in the GUI interface. The data is acquired in the on-board SRAM memories and processed offline.

Table 1: Typical Implementation Parameters

| **Freq** | **FF amp** | **FF Phase** | **Phase Rotator** | **PowerO/P** |
|---|---|---|---|---|
| F1 | 0.18 | 0° | -11.5° | -6.5dBm |
| F2 | 0.332 | 0° | 42.5° | -15.2dBm |
| F3 | 0.074 | 0° | -62.0° | -24.35dBm |

## CONCLUSION

The digital LLRF system has been implemented successfully for the single gap multi harmonic buncher. The digital technique gives better performance with respect to amplitude and phase control of the generated harmonic signal. This leads to easier calibration of the system and better performance.

## REFERENCES

[1] Alok Agashe, P.D.Motiwala, S.K. Bharade, Shyam Mohan, Gopal Joshi, "Digital LLRF system for RFQ", InPAC-2015, Dec 21-24, BARC Mumbai.

[2] A. Sarkar, Rajesh Kumar, et al, "Development and Testing of a Multi-Harmonic Buncher for the high current injector at IUAC", InPAC-2015, Dec 21-24, BARC, Mumbai

# EPICS ARCHIVER FOR IPMS SYSTEM OF 7 KW RF POWER AMPLIFIER

Mohammad Afaash, Sandeep Bharade and Gopal Joshi, BARC, Mumbai, India

*Abstract*

ACnD, BARC has designed and developed Interlock Protection and Management System (IPMS), which protects the solid state RF amplifier from unsafe operating conditions. The IPMS consists of EPICS I/O controllers which provide measured parameter information to the control system in the form of 'Process Variables' (PV). The Archive system takes time stamped PV data samples from an EPICS IOC via Channel Access, and stores them in a relational database. Archive client programs like CSS access historic data samples in the given database and displays them in graphical form. The archive system allows optimal utilization of the database storage capacity by providing configurable sample modes and data retention lengths. This paper describes the architecture, configuration and implementation of the EPICS archiver for IPMS system of the 7kW solid state power amplifier, developed under IIFC.

## INTRODUCTION

A 325 MHz, 7 KW solid state RF power amplifier has been developed by Accelerator Control Division (ACnD), BARC under IIFC. The system has been built by combining eight 1 KW RF power amplifier modules. The amplifier parameters are monitored and protected against fault by the IPMS system. The IPMS is based on VME64X architecture and consists of a number of FPGA based modules which monitor RF, analog, digital parameters, contact inputs and outputs, and temperature signals [1]. The IPMS executes protection of the amplifier by switching off the RF input to the amplifiers or removing the DC bias of the affected RF power amplifier module. The system is controlled and monitored by means of an EPICS based SCADA running on a 7" industrial touch panel PC. The IPMS can also be controlled remotely by using a Control System Studio (CSS) based GUI application running on a remote PC. The remote PC can also be used to store historical data for fault diagnosis and reliability studies like burn-in testing. This has been done by implementing an EPICS archiver storing amplifier parameters in a relational database (RDB).

## EPICS ARCHIVER

The EPICS archiver is an archiving toolset for the Experimental Physics and Industrial Control System. It can archive any value that is available via Channel Access (CA) protocol [2]. The architecture of the EPICS archiver is shown in Fig.1. The EPICS archiver consists of the following components:

### *Sampling*

The sampling of PVs from an EPICS Input-Output Controller (IOC) is done by the ArchiveEngine which is a Channel Access client running on a computer. The ArchiveEngine supports multiple sampling options, which are configurable for the individual channels. The sampling options are:

- Monitor: Subscribes to changes and stores all the values that the IOC sends to its subscribers
- Sampled: Periodically requests a value from the CA server based on a user specified time value.
- Monitored with Threshold: Similar to monitor, but data is stored only if the changes exceed a specified threshold.

The different sampling modes allows the user to optimize usage of resources like CPU usage, disk space and network bandwidth, which is especially for channels whose data does not change significantly with time. The configuration of the ArchiveEngine is done by providing a configuration file in XML format or retrieved from the RDB. Each ArchiveEngine also contains an in-built web server to provide status information and remote control of the engine.

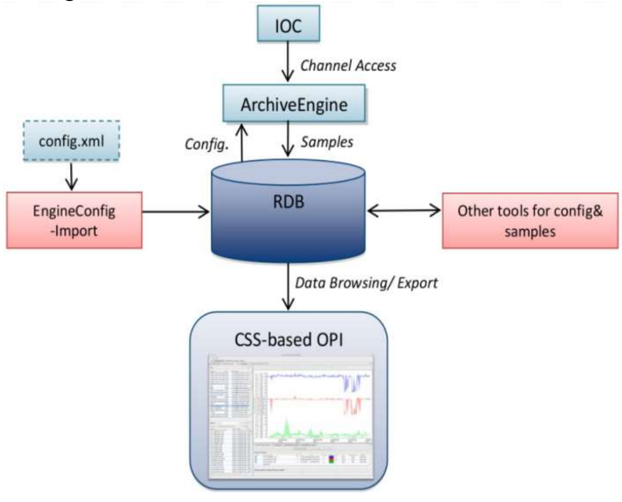


Figure 1: Architecture of EPICS Channel Archiver [3].

### *Storage*

The data sampled by the ArchiveEngine can be stored in a RDB or an XML-RPC based data server. The RDB contains table structures which stores the configuration of the ArchiveEngine such as configuration name, address of web server and list of channels to be monitored. The model of the table structure is shown in Fig.2. The database consists of three types of tables, namely Engine and Channel Configuration, Data and Alarm Settings. Configuration and sampling data of multiple archive engines can be stored within the same database. Each ArchiveEngine will contain one or more Channel Groups, each containing one or more Channels. The channel table contains the configuration of sampling mode and retention period of each channel to be archived.

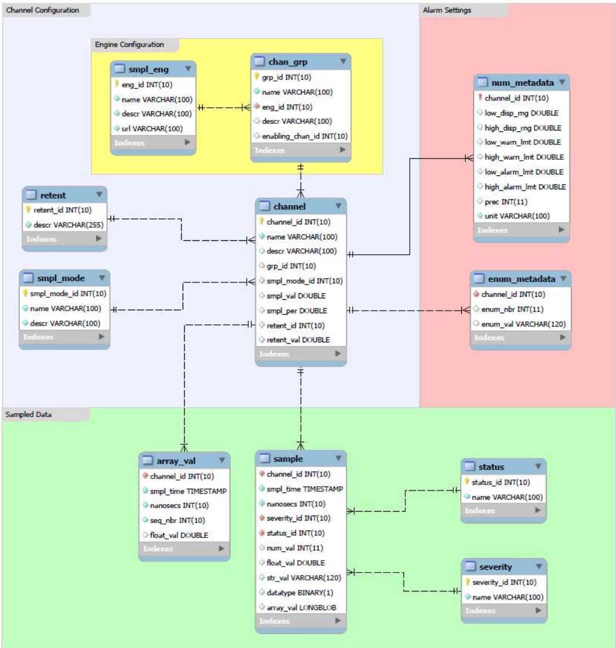


Figure 2: RDB Model for EPICS Archiver.

The sample table contains all the timestamped sampled data obtained from an IOC. The sampled data is identified and mapped to a channel by its Channel ID.

### *Retrieval*

Data stored in the database can be retrieved by RDB clients like the data browser of Code Composer Studio for the graphical representation of historical data. The data browser can also be used to convert the data retrieved from the archiver into a CSV file with timestamp.

## EPICS ARCHIVER FOR IPMS SYSTEM

EPICS archiver system has been developed and deployed for the IPMS system of 7kW amplifier which has been developed under IIFC. The block diagram of the EPICS based control system for the IPMS system is shown in Fig.3. The control system consists of an EPICS IOC running on a Linux based MVME controller. The controller also consists of a Network Time Protocol (NTP) client which ensures accurate time stamping of measured data by periodically synchronising its system time with the remote PC running a NTP server. EPICS Channel Access is used by a 7" Industrial touch panel PC for local display and control of Process Variables. CSS based GUI running on a PC is used for remote monitoring and control of process parameters. The remote PC also contains the ArchiveEngine and RDB. The archiver is configured to sample and store approximately 400 process variables. The archiver is configured to run on user-login and will run continuously until the PC is shutdown. Fig.4 shows the archived data retrieved using CSS data browser. RDB has been used instead of XML-

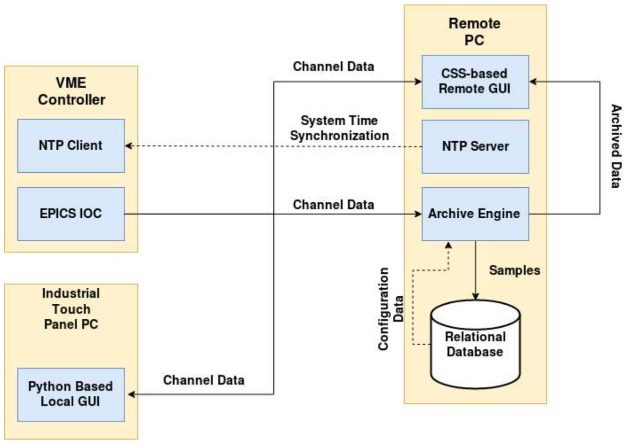


Figure 3: Block Diagram of EPICS Control System for IPMS.

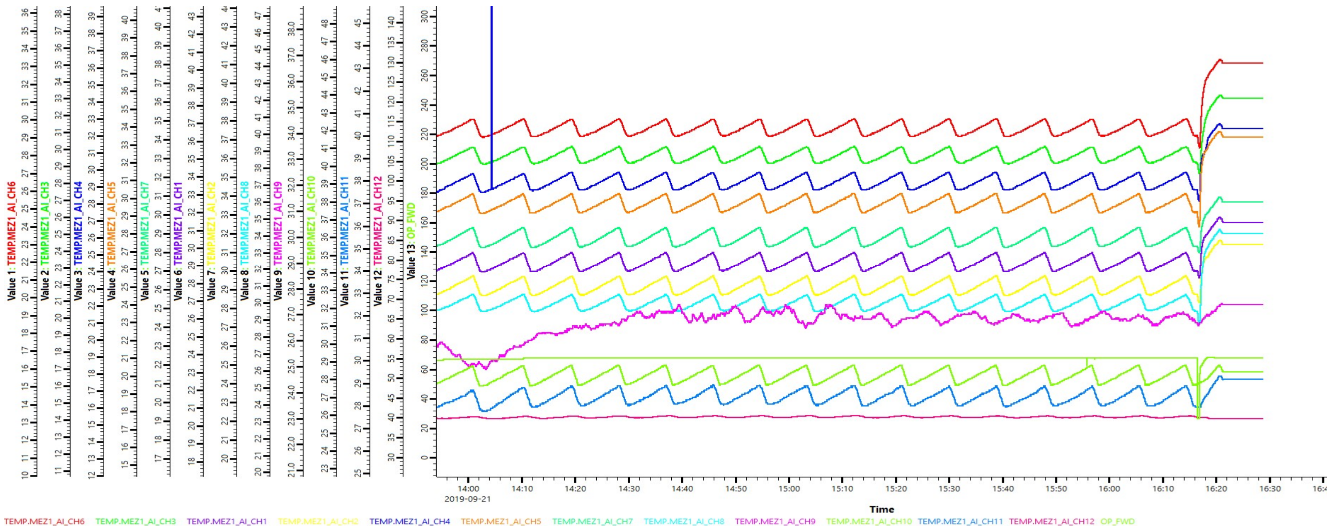


Figure 4: Graphical Representation of Archived Data using CSS Data Browser.

RPC based data server since the table structures in RDB are simple allowing custom applications can be developed by the user which query the RDB and display the retrieved data. Multiple RDB clients may exist, making the system scalar.

## CONCLUSION

EPICS Archiver system has been installed and tested at ECIL, Hyderabad, which has been used for burn-in test and reliability studies of 7 kW 325 MHz RF power amplifier. The archiver has been useful in the diagnosis and resolution of technical issues during integrated testing.

## REFERENCES


[1] R.T Keshwani et al, "Design Architecture of Interlock, Protection and Monitoring System for 7 kW Solid State RF Power Amplifier", InPAC 2018.

[2] EPICS Channel Archiver Manual, July 2016.

[3] Kay Kasemir, "Control System Studio Training-Archive System". https://portal.slac.stanford.edu/sites/conf_public/AWLC17/presentations/Kasemir_Archive_system.pdf.

# DESIGN AND DEVELOPMENT OF POWER PART OF A 300 A, 90 V SWITCH MODE POWER CONVERTER WITH INDUSTRIAL SUPPORT

Vineet Kumar Dwivedi[†1], Alok Singh[1], Mangesh Borage[1,2] and S. R. Tiwari[1]
[1]Raja Ramanna Centre for Advanced Technology, Indore 452013, India
[2]Homi Bhabha National Institute, Mumbai 400094, India

*Abstract*

A large number of power converters are required to energize electromagnets in a particle accelerator. Apart from stringent performance requirements, which are seldom satisfied by the commercial off-the-shelf power converters, various other parameters such as high reliability, easy maintainability, uniformity for standardization etc. are important that demand designer's equal attention. The Indus Accelerator Complex (IAC) at Raja Ramanna Centre for Advanced Technology (RRCAT) is arguably the largest installation of power converters for electromagnets in India. The power converters have been designed and developed in-house. While the manufacturing expertise in the industry was utilized for part-fabrication, the system integration and qualification testing was largely carried out in house. To cater to the requirement of similar systems for future accelerator projects, which are expected to be more challenging – both in terms of numbers and the aforementioned performance parameters – involvement of industry on a larger scale is necessary. Switch Mode Power Converter Section (SMPCS) of Accelerator Power Supplies Division (APSD) at RRCAT had taken initiatives towards this development of power converters of lower ratings. Moving further on this route, a power part of 300 A, 90 V switch mode power converter was recently developed and tested at Electronics Corporation of India Limited (ECIL), Hyderabad based on the design and manufacturing details provided by SMPCS, RRCAT. This paper describes the power converter, development methodology and test results.

## INTRODUCTION

A particle accelerator is a complex machine involving several inter-related multidisciplinary sub-systems such as ultra-high vacuum, magnets, radio frequency system, beam diagnostic systems, control systems, power converters for electromagnets etc. Power converters for electromagnets is an important sub-system of an accelerator. The quality and stability of magnetic field produced by an electromagnet is also governed by the current flowing through its coils. Therefore, very high stability (typically down to 0.005%) current controlled precision power converters are deployed in large numbers in an accelerator installation. Nearly 280 power converters are operational in round-the-clock mode in IAC at RRCAT. In addition, approximately 150 power converters are being developed in-house for various functionalities in IAC. The proposed accelerator projects are expected to have the power converters larger in number.

The power converters for electromagnets differ from the commercially available power converters in many ways: the output current is controlled instead of voltage; output current stability is more stringent than available with the most of the off-the-shelf solutions; power converters for electromagnets need to be operated in different modes, slow- and fast-ramping, dc, one-, two- and four-quadrant modes; operation over wide conversion range while maintaining performance parameters etc. While the industry was involved in part-fabrication of subsystems, the power converters in IAC have been largely designed and developed in-house [1], [2].

With ever increasing use of power converters in variety of other demanding applications, the expertise and maturity in manufacturing of power converters in industry is on the rise. At the same time, industry may or may not have sufficient technical expertise to design the power converter that would meet the performance specifications of a power converter for electromagnet. It is therefore prudent to explore the possibility of 'manufacturing' of the power converter as a whole, or, the 'power part' of a power converter based on the 'design' and 'manufacturing details' evolved from the design studies, simulation and in-house prototype development. Such efforts have been initiated at SMPCS, APSD of RRCAT with the successful development of 60 low-power, current-controlled, modular power converters for Infra-Red Free Electron Laser Facility (IRFEL) at RRCAT [3] and 20 similar units with enhanced features and better output current stability for beam transport line magnets of the proposed injector linac in IAC [4].

Moving further on this path with high-power rated converters, it was proposed to develop the power part of 300 A, 90 V power converter, being developed as a part of a project – technology development for low emittance storage ring – with the involvement of industry, which will be based on the design studies, simulation and manufacturing details carried out at SMPCS, APSD.

This paper reports the details of the power converter, various steps involved in the development and salient results.

## THE POWER CONVERTER

The power converter is rated to provide 300 A, 90 V maximum, while operating from 415 V, 50 Hz three-phase ac mains. It is based on switch-mode dc to dc converter topology. The scheme of the power converter is shown in Fig. 1, which shows a four-quadrant switch-mode converter, as a general case. It can be suitably configured as an

†email address: vineet@rrcat.gov.in

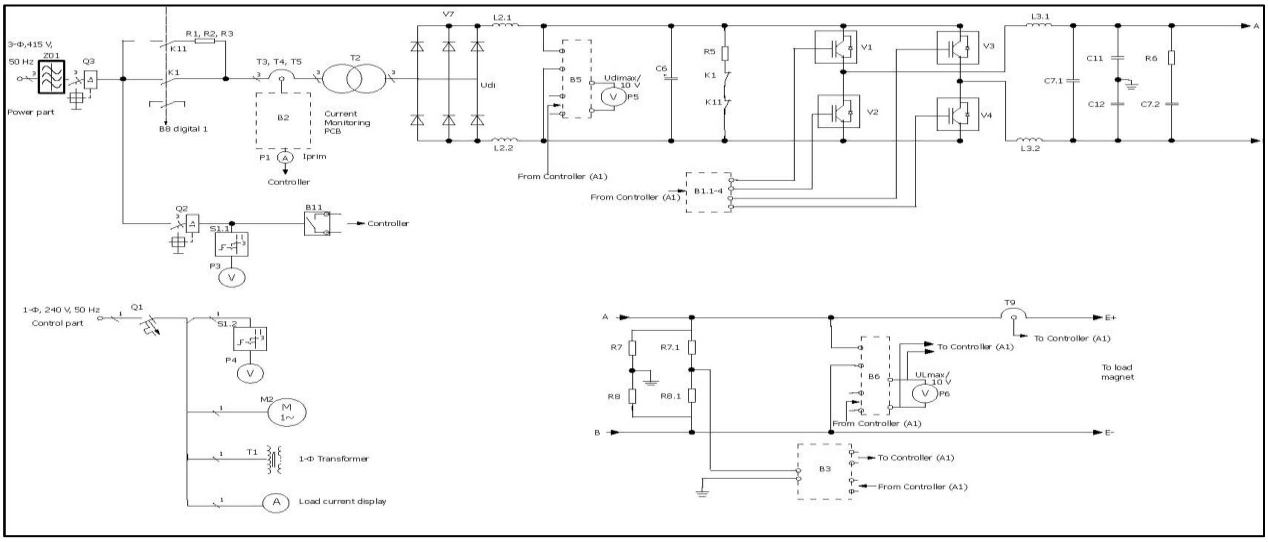


Fig.1: Schematic of the power part of power converter

one- and two-quadrant converter, depending on application requirement.

The three phase ac mains is first terminated to a three phase line filter (Z01) for reducing conducted EMI, before passing it on to miniature circuit breaker for overload protection (Q3). The main contactor (K1) and soft charging contactor (K11), together with soft charging resistors (R1, R2, R3) work in time-coordinated manner to prevent inrush current caused by the three phase transformer and dc-link filter capacitors (C6). Input line current is measured via input CTs (T3, T4, T5), which is used for metering as well as over-current protection. The ac mains is stepped down using a delta-star transformer (T2), and rectified using diode bridge rectifier (V7) and a low-pass LC filter (L2, C6), that provides unregulated intermediate dc bus. The switch- mode converter consists of a bridge circuit consisting of four IGBTs (V1-V4) followed by damped LC filter (L3, C7 and R6) to provide required regulated dc output. The converter is operated as a buck converter with 25 kHz switching frequency. The power converter is housed in a cabinet of size 0.8m x 0.8m x 2.15m.

## MANUFACTURING THE POWER PART IN INDUSTRY

### *Preparation of Detailed Documentation*

Detailed documentation is necessary to communicate the ideas and information. Detailed specifications have been prepared. Elaborative circuit diagram and wiring chart have been prepared, which was easy to understand by the manufacturer, are handed over after placement of purchase order. Placement of the component and general assembly layout of the cabinet has been made. Test procedure template to test the power converter has been prepared.

### *Defining the Scope of Work*

Defining the exact scope of work is important. The broad scope of job includes preparation of general assembly (GA) drawings, mechanical drawings, fabrication drawings, circuit diagrams, wiring details etc. for the power circuit. The procurement and fabrication of components was as per the approved bill of materials (BOM), fabrication, wiring and testing of the power circuit, transportation of the system to RRCAT, along with extensive sets of documents. Further, the manufacturer had to provide necessary support required for interfacing of a set of 'SMPCS Electronics', which is described next.

### *Integration of 'SMPCS Electronics'*

The overall electronics required for functioning/testing of the power part is supplied as free issue material (FIM) to the manufacturer for uniformity, since this set of electronics has been standardized at SMCPS are used in other existing power converters [5].

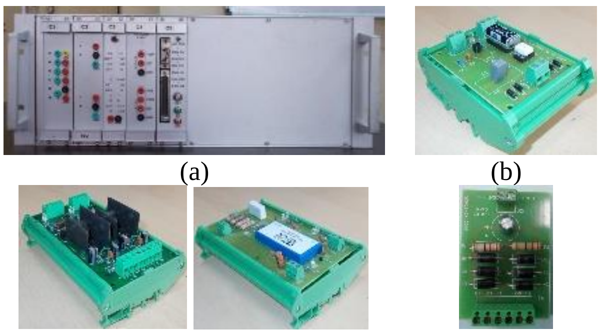

(a) (b) (c) (d) (e)

Fig. 2: (a) Control rack (b) Earth fault monitoring PCB (c) IGBT driver PCB (d) Input DC and load voltage sensing PCB (e) Input current sensing PCB

Figure 2(a) shows the photograph of control rack. The function of control rack is to provide necessary control mechanism for proper functioning of power supply. Auxiliary supply card proved power supply for various ICs, digital faults etc. DCCT supply card provides power supply to DCCT interface card. Fault card detects various faults such as over voltage, over current fault and indicates the same on the fascia. It also initiates the tripping of power supply in the event of fault. Control card provides necessary control signal for proper functioning of power supply. Local/remote card facilitates the user to operate the power supply either in local mode or in remote mode. Figure 2(b) shows the photo of earth fault monitoring PCB which is used to detect the accidental earthing of the output terminals. Figure 2(c) depicts the photo of IGBT driver PCB which is used to drive an IGBT module. Figure 2(d) shows the photo of voltage sensing PCB used to monitor intermediate DC voltage as well as the output voltage. Figure 2(e) shows the photo of input current sensing PCB which is used to sense input ac current via ACCTs.

### *Quality Assurance*

Once the necessary inputs have been given to the manufacturer from RRCAT, quality check has been assured at each and every stage. Correctness of wiring, placement of components, layouts, documentation have been checked at various stages of development. Different tests were prescribed to ensure the performance.

### *Defining Test Sequences*

Various tests have been conducted at manufacturer's premises such as functional testing, checking of the gate pulses at IGBTs, open loop test at low power to high power by monitoring the values, waveforms and temperature at various locations, close loop test at low power, tuning of control loop, close loop testing to high power on dummy inductive load to nominal current for at least 8 hours with data logging for various signals and temperatures at various locations, measurement of conducted EMI at nominal current operation on input and output terminals.

## RESULTS AND DISCUSSION

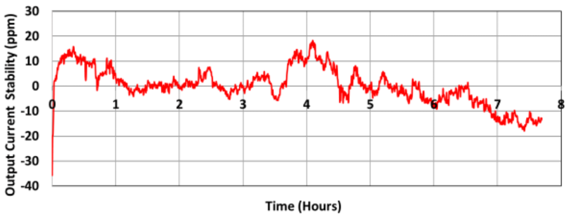


(a)

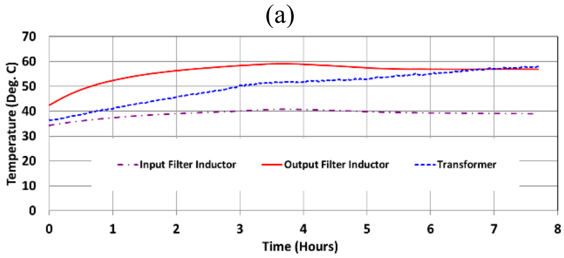


(b)

Fig. 3: (a) Output current stability of power converter measured for 8 hours, and, (b) temperature at transformer and inductors recorded during the test.

Extensive tests were performed at the manufacturer's premises. Figure 3(a) shows stability of the power converter (for 8 hours continuous operation) which is within ±30 ppm. Figure 3(b) shows the temperature at transformer and inductors, which is safe considering the Class-F insulation used in these devices. Figure 4(a) depicts photograph of power converter. EMI test result on input line side and at the output bus bar are shown in Figure 4(b) and (c), respectively, which are well below the limit lines.

(a)

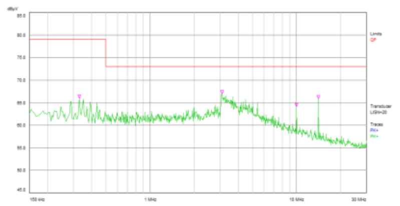

(b)

(c)

Fig.4: (a) Photograph of power converter cabinet. Conducted EMI spectrum at (b) input line, (c) output busbars.

## ACKNOWLEDGEMENT


The authors acknowledge the contribution of Shri V. W. Somkuwar and Shri M. K. Koli during the development of the power converter.


## REFERENCES


[1] Tiwari S.R., Thakurta A.C., Thipsay A.P., Pagare A., Gandhi M.L., Singh T., Singh S., Kotaiah S. Power Supplies for Indus-1Asian Particle Accelerator Conference - 1998 (APAC-98) , Tsukuba, Japan, Mar., 23-27, 1998

[2] Thipsay A.P., Kotaiah S., Thakurta A.C., Banwari R., Tiwari S.R., Singh S.N., Renukanath P. Power supply development at CAT by accelerator power supplies division
Indian Particle Accelerator Conference - 2005 (InPAC-05), VECC, Kolkata, Mar., 1-5, 2005, p. 427-430

[3] Singh A., Dwivedi V. K., Borage M. B., Tiwari S. R., Thakurta A.C., "Power supplies for IRFEL beam transport line magnets", Indian Particle Accelerator Conference (InPAC),2015, TIFR, Mumbai, Dec., 21-21, 2015.

[4] Singh A., Dwivedi V.K., Borage M. B., Tiwari S. R., "Power Converters for Transfer Line Magnets of New Injector Linac in Indus Accelerator Complex", Indian Particle Accelerator Conference-2018 (InPAC-18), RRCAT, Indore, Jan., 2018

[5] Dwivedi V.K., Singh A., Koli M.K., Borage M.B., Tiwari S.R., "Design and Development of New 20 kW Power Converters for Quadrupole Magnets in Indus-2", Indian Particle Accelerator Conference-2018 (InPAC-18), RRCAT, Indore, Jan., 2018.

DEVELOPMENT OF DIGITAL CONTROL CARD FOR HIGH STABILITY POWER CONVERTERS FOR ELECTROMAGNETS

Alok Singh†1, Mangesh Borage[1,2] and S. R. Tiwari[1]
[1]Raja Ramanna Centre for Advanced Technology, Indore 452013, India
[2]Homi Bhabha National Institute, Mumbai 400094, India

*Abstract*

A Field Programmable Gate Array (FPGA)-based prototype digital control card has been developed to achieve high output current stability within ±10 ppm in magnet power converters. It is a 4U sized card which retrofits the existing analog control card in the standardized control rack of magnet power converters being developed for / used in Indus. The digital control card mainly consists of an FPGA, Analog to Digital Converter (ADC), signal conditioning circuit, oven controller, pulse blocking circuitry, etc. This card has been programmed with high resolution feedback control scheme, evaluated and tested with a magnet power converter achieving output current stability within ±10 ppm. This paper presents the details of the digital control card, improvements made over the table-top version followed by reporting of test results.

## INTRODUCTION

Future accelerator projects in India would require magnet power converters in large numbers with stringent output current stability requirements, down to ±10 ppm. For implementation of feedback control scheme in these power converters, digital controllers are preferred over their analog counterparts as the technological advancements in digital hardware have made them more attractive due to their inherent advantages like immunity to component variations, easy implementation of sophisticated control schemes, flexibility and design standardization of digital hardware [1][2].

Towards this, activities related to the development of FPGA-based prototype digital controller for magnet power converters were taken up which led to the development of a table-top digital controller consisting of Xilinx Spartan-3AN FPGA board, EVAL-AD7634EDZ ADC evaluation board and analog signal conditioning PCB, resulting in output current stability within ±50 ppm with a prototype magnet power converter [3]. Taking this activity further towards consolidation, a 4U size prototype digital control card has been developed which retrofits the existing analog control card in the control rack module of magnet power converter. It mainly consists of an FPGA to implement Proportional-Integral (PI) based close loop control scheme along with high resolution digital pulse width modulation (DPWM), signal conditioning circuit, ADC, oven control circuit and pulse blocking circuit.

## THE DIGIAL CONTROL CARD

### *Overview*

Figure 1 shows the block diagram of current feedback loop for a magnet power converter implemented using a digital controller. For achieving high output current stability, a precision Direct-Current Current Transformer (DCCT) is used as a current sensor. The current feedback signal from DCCT is given to the digital control card which consists of analog signal conditioning circuitry which conditions the DCCT signal before feeding it to the ADC circuit. The ADC samples the signal and provides the digital feedback signal to a digital hardware for implementation of the control algorithm. This digital hardware consists of an error generation module, compensator module and high resolution DPWM module [3]. It takes digital reference and current feedback signals as inputs, processes them as per the desired control law and generates high resolution DPWM pulses to drive semiconductor switches in the magnet power converter.

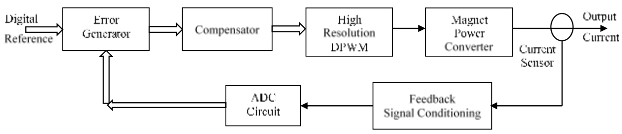


Fig. 1: Block diagram of digital controller for magnet power converter

The preferred choices for digital platform for implementation of digital controller are microcontrollers, Digital Signal Processors (DSP) and FPGAs. While microcontrollers and DSPs are software based processors, FPGAs are digital hardware based devices that contain two-dimensional array of configurable logic blocks (CLBs), programmable interconnects, input/output blocks and dedicated function blocks like DSP slice, block RAM, etc. The reprogramming capability, high throughput and reduced computation times in FPGAs due to their capability to perform high degree of parallel computations have made them popular for implementation of digital controllers for power converter applications [4].

### *Features and Composition*

The digital control card is customized on a four-layer, 4U sized PCB with thickness of 1.6 mm and copper thickness of 35 microns.

†aloksingh@rrcat.gov.in

It consists of a 32-pin euro connector for retrofitting it with the analog control card in the back-plane PCB of control rack module of magnet power converter. In addition to various circuits, the card comprises of an FPGA board which consists of a USB port, oscillators, non-volatile memory and other peripheral circuits.

The entire circuit on the PCB is divided between three categories: analog, digital and oven circuits respectively. The analog circuit includes feedback signal conditioning circuit, single ended to differential converter driver circuit and precision voltage reference circuit for ADC. The digital circuit includes FPGA board and peripherals, ADC circuit and pulse interlock circuit. The oven circuit includes oven temperature sensing and control circuit. To electrically separate analog and digital circuits, two separate ground planes are used for both. This is done to minimize the interference of high frequency digital circuit operation on the analog circuit which processes critical front-end current feedback signals. Figure 2 shows photograph of the digital control card.

## *Circuit description*

A brief description of various on-board circuits is given below:

Auxiliary power supplies generation and conditioning circuit:

The power supplies driving the three types of circuits described above are also divided into three categories, i.e., analog, digital and oven. The auxiliary power supplies required for the analog circuits are ±15 V, 5 V and 2.5 V respectively while the power supplies required for the digital circuits are 5 V and 3.3 V respectively. A separate 12 V power supply is required for the oven control circuit.

The analog supply of ±15 V is provided from the auxiliary power supplies card, through back-plane PCB, mounted in the control rack module of power converter. The incoming supply is fed to the respective analog circuits through a first-order low-pass filter. The 5 V power supply required for analog circuit like single to differential converter circuit is generated on-board from the incoming +15 V supply using regulator IC 7805. Similarly, the 2.5 V analog power supply required for ADC is generated from the 5 V power supply using regFFigulator IC ADP1706.

The digital supply of 5 V, required for the FPGA board, is also provided from the auxiliary power supplies card in control rack. It is also interfaced to the digital circuit through a first-order low-pass filter. Another digital circuit power supply of 3.3 V generates on the FPGA board and provided to the ADC circuit through interconnections on PCB. Similarly, the 12 V supply required for oven temperature sensing and control circuit is also provided from the auxiliary power supplies card.

Feedback signal conditioning circuit:

This circuit is used to condition the incoming current feedback signal by filtering, buffering, attenuation and making provisions for fine calibration of output current. A first-order RC type low-pass filter is used to filter out any unwanted high frequency pick-ups in the feedback signal coming from DCCT. The DCCT provides full scale signal of 10 V corresponding to its full scale current of 100 A but the ADC used has the maximum input range of 5 V at its two differential input pins. Therefore, the filtered feedback signal is attenuated by a factor of 2 before feeding it to the succeeding stage of single to differential converter driver circuit.

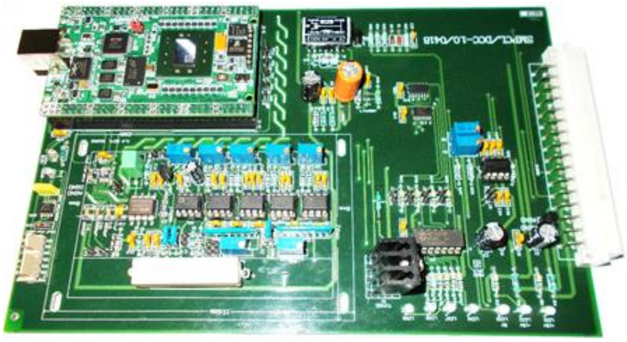

Fig. 2: Photograph of digital control card.

Single ended to differential converter driver circuit:

As the ADC accepts differential input signal therefore, the single ended feedback signal is required to be converted to differential type. This is done with the help of single ended to differential converter driver LT6350.

ADC Circuit:

A low noise, high speed, 24-bit successive approximation register (SAR) type ADC, LTC2380-24, is used in the circuit to sample the current feedback signal [5]. The maximum throughput of this ADC is 1.5 Msps. However, for digital controller implementation sampling is done at the rate of 416 ksps and only 16 MSBs of the ADC are used.

Precision voltage reference circuit:

The ADC LTC2380-24 requires an external reference to define its input voltage range. Also, the accuracy of an ADC largely depends on the accuracy of its input reference voltage. Therefore, a 5 V, low noise, precision voltage reference, VRE3050, with low temperature drift of 0.6 ppm/°C is used to provide reference voltage to the ADC.

FPGA board:

An FPGA development board, EDX-008-160T, of size 55 mm X 90 mm is used for implementation of digital controller. The board includes an FPGA, XC7K160T-1FBG484C, 50 MHz and 200 MHz oscillators, non-volatile memory, JTAG connector, status LEDs and switches respectively. It also consists of on-board regulators to generate internal voltages. A USB port is given for communication with computer and it has provision for configuration of 100 I/O (inputs/outputs). It requires a single power supply of 5 V for operation and can be easily plugged on the control card with the help of pin-headers and sockets.

Pulse interlock circuit:

The function of this circuit is to block the DPWM pulses in case of occurrence of any fault.

Oven control circuit:

The card has the provision for mounting of an oven which is used for keeping the temperature of various critical front-end electronic components constant which is essential for achieving high output current stability. The oven control circuit consists of oven temperature sensing and control circuit. The circuits housed inside the oven include feedback signal conditioning circuit, single ended to differential converter circuit, precision voltage reference circuit and ADC circuit respectively.

## IMPROVEMENTS AND RESULTS

The table-top prototype digital controller developed earlier consisted of an FPGA kit containing FPGA of Spartan-3 family, 18-bit ADC evaluation board and a general purpose PCB containing analog signal conditioning circuit as shown in Fig. 3 [3].

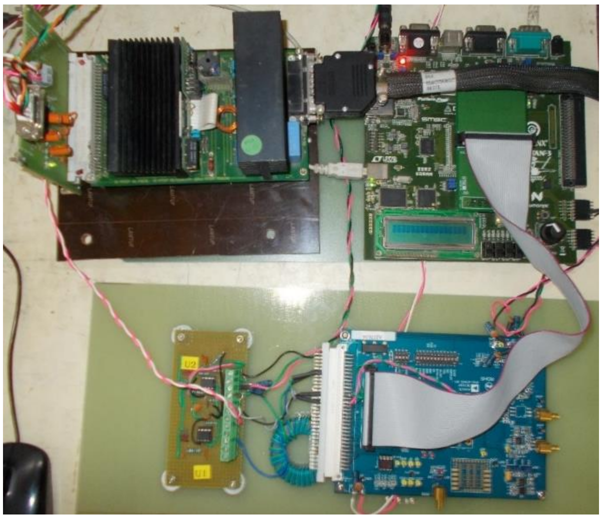

Fig. 3: Photograph of table-top digital controller [3].

The digital control card shown in Fig. 2 integrates all these circuits on a single 4U sized PCB and consists of high performance components like Kintex-7 FPGA and 24-bit ADC as mentioned earlier. In addition, the card also contains components with low temperature drifts in front-end electronics, like precision voltage reference, precision resistor arrays and precision op-amps, which are crucial to achieve high stability.

As compared to the table-top version, the digital control card has better noise immunity. Out of four PCB layers, inner two are used for analog and digital ground planes respectively which connects inside ADC. In addition, layout of the control card is judiciously planned to minimize PCB track lengths which contain high frequency digital signals. To further improve noise performance, grooves in zig-zag fashion is placed between analog and digital circuits on the card to reduce capacitive coupling.

The table-top version did not have provision for temperature controlled oven however, it is provided in the new card to improve output current stability. Further, improvements have made in the control algorithm to achieve better line regulation.

Figures 4 and 5 shows test results of digital controller with 80 A/25 V rated prototype magnet power converter with sample rate of 416 ksps, proportional ($k_p$) and integral ($k_i$) constants of 55.6 and 1068.6 respectively and 15-bit hybrid DPWM scheme. Frequency response results are shown in Fig. 4. The control loop bandwidth obtained is 1 kHz with gain and phase margins of 4.7 dB and 36.6° respectively. Figure 5 shows comparison of output current stability results for table-top version and the developed control card under similar test conditions. The stability achieved with the table-top version was ±50 ppm (blue graph) while with the new control card, stability within ±10 ppm (red graph) is achieved.

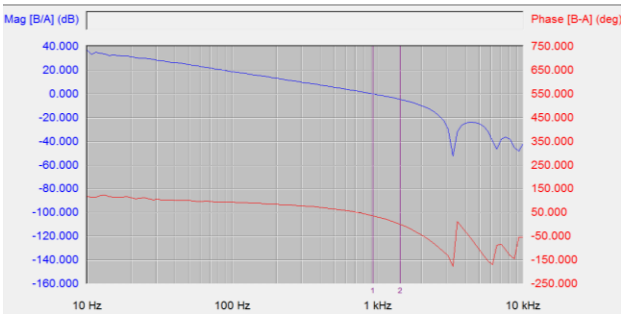


Fig. 4: Frequency response of digital controller.

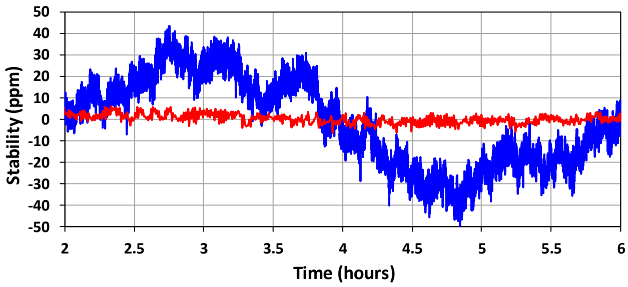


Fig. 5: Comparison of stability results of the new digital control card (red curve) with those obtained with the earlier table-top version (blue curve).

## REFERENCES


[1] K. Ogata, "Discrete-Time Control Systems", Prentice-Hall, Inc., 1987.

[2] Guang Feng, Boris Deriy, Thomas Fors and Ju Wang, "A Novel Digital Control System to Achieve High-Resolution Current Regulation for DC/DC Converters at The APS", IPAC-2010, Kyota, Japan.

[3] Alok Singh, Mangesh Borage and S.R. Tiwari, " Development of Prototype FPGA Based Digital Controller for Magnet Power Converters" Proc. Of InPAC-2018, RRCAT, Indore.

[4] Cristian A. Sepulveda, Javier A. Munoz, Jose R. Espinoza, Miguel E. Figueroa and Carlos R. Baier, "FPGA v/s DSP Performance Comparison for a VSC-Based STATCOM Control Application", IEEE Transaction on Industrial Informatics, vol. 9, no. 3, pp:1351-1360, August 2013.

[5] www.analog.com/en/products/ltc2380-24.html.

# 200 A, 85 V SWITCH MODE POWER CONVERTERS FOR MAIN SEXTUPOLE WINDING OF THE HARMONIC SEXTUPOLE MAGNETS IN INDUS-2

Alok Singh†1, Mangesh Borage[1,2], P. Renuka Nath[1] and S. R. Tiwari[1]
[1]Raja Ramanna Centre for Advanced Technology, Indore 452013, India
[2]Homi Bhabha National Institute, Mumbai 400094, India

*Abstract*

Switch-mode power converters with output ratings of 200 A /85 V and output current stability within ±500 ppm are developed to energize the main sextupole winding of the multifunction magnets, which are proposed to be installed in Indus-2 for performance improvement. These are dc, current-regulated power converters consisting of two modules of two-switch forward converters operating at 25 kHz and connected in input-parallel, output-series (IPOS) configuration. This paper describes the design principles, highlights salient features and discusses the test results of power converter.

## INTRODUCTION

It is proposed to install 32 nos. of multifunction magnets in Indus-2 for performance improvement. It is a combination of sextupole winding, vertical and horizontal steering coils, and, a skew quadrupole coil. Out of these, the main sextupole winding is required to be energized with dc current-controlled power converter. One power converter will energize main sextupole coils of 8 magnets in series. Therefore, in total 4 power converters are required to energize main sextupole coils of 32 harmonic sextupole magnets. These power converters are rated for 200 A /85 V with output current stability requirement of ±500 ppm.

## THE POWER CONVERTER

### *Topology and its Salient Features*

Figure 1 shows the block diagram of power converter which consists of front end protective components like miniature circuit breaker (MCB), contactors and inrush current limiting circuit, followed by a 3-phase diode bridge rectifier and a low pass filter. The power converter operates on 3-phase 415 V, 50 Hz ac. The dc-dc power converter consists of two modules of two-switch forward converter (TSFC) connected in input-parallel, output-series (IPOS) configuration as shown in Fig. 2. This topology has inherent load sharing capability with equal distribution of losses in two stages which helps in reduction of stresses in power devices and effective thermal management [1]. The two modules operate at switching frequency of 25 kHz in phase-staggered manner, thereby resulting in reduced ripple amplitude at the output along with frequency doubling, which helps in reduction of output filter size.

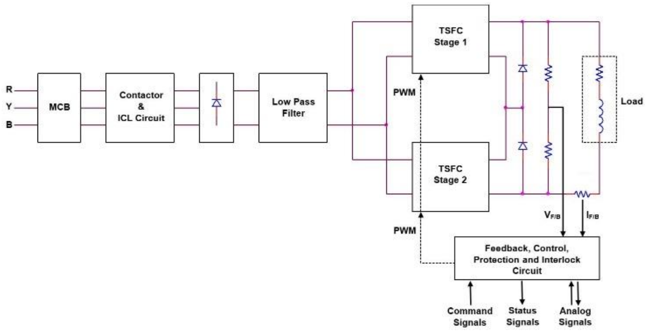


Fig. 1: Block diagram of power converter

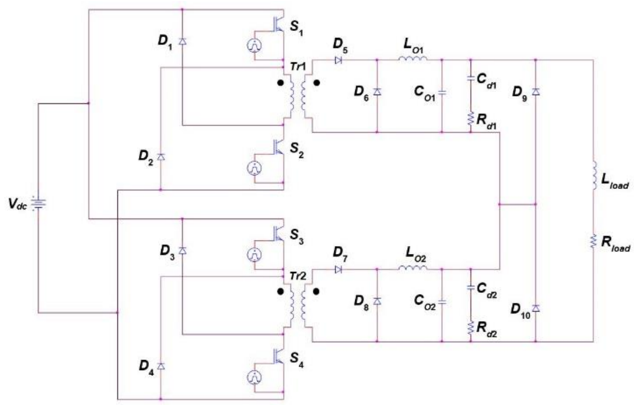


Fig. 2: IPOS configuration of two-switch forward converter modules.

The feedback controller is based on dual-loop feedback control scheme which consists of two loops: an outer current loop and an inner voltage loop. The current feedback is taken through a precision shunt made of water cooled zeranin tube, as opposed to the DCCT used in [1]. Voltage feedback is taken through a voltage divider. The feedback, control, protection and interlock circuit, shown in Fig. 1, processes various command, status and analog signal to provide interleaved gate drive pulses to the two stages of TSFC. As shown in Fig. 1, two free-wheeling diodes are connected across the output to freewheel the energy of magnet load whenever power converter turns off.

The salient features of these power converters are design modularity, smaller size, high efficiency, ease of maintenance, simple cooling arrangement, low audible noise, etc.

†aloksingh@rrcat.gov.in

*Operation*

The interleaved operation of topology shown in Fig. 2 is described with the help of 4 modes as shown in Fig. 3.

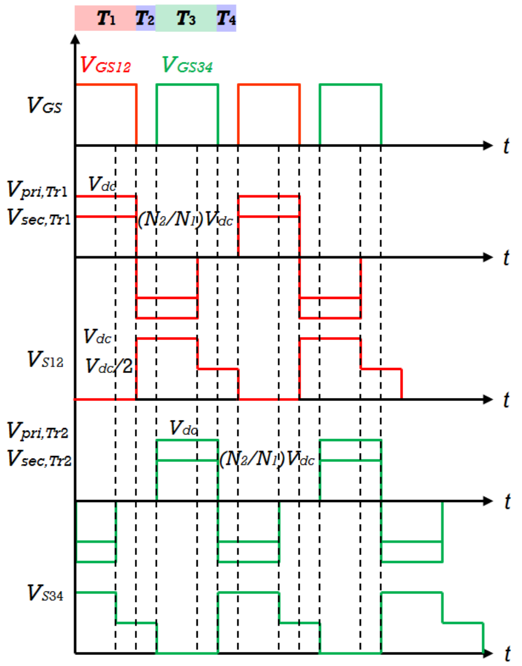


Fig. 3: Waveforms showing operation of TSFC modules in IPOS configuration.

The various abbreviations used in Fig. 3 are described below:

| | | |
|---|---|---|
| $N_1$, $N_2$ | : | Primary and secondary turns of HF transformer respectively |
| $T_1$, $T_2$, $T_3$, $T_4$ | : | Time durations of 4 modes of operation respectively |
| $V_{dc}$ | : | Input dc voltage |
| $V_{GS12}$ | : | Gate drive pulses of switches $S_1$ and $S_2$ |
| $V_{GS34}$ | : | Gate drive pulses of switches $S_3$ and $S_4$ |
| $V_{pri,Tr1}$, $V_{pri,Tr2}$ | : | Primary voltages of high frequency (HF) transformers $Tr1$ and $Tr2$ respectively |
| $V_{sec,Tr1}$, $V_{sec,Tr2}$ | : | Secondary voltages of HF transformers $Tr1$ and $Tr2$ respectively |
| $V_{S12}$ | : | Voltage across switches $S_1$ and $S_2$ |
| $V_{S34}$ | : | Voltage across switches $S_3$ and $S_4$ |

<u>Mode $T_1$</u>:

In this mode, power transfer from source to load takes place by the upper TSFC module shown in Fig. 2. Switches $S_1$ and $S_2$ are turned on simultaneously, causing energy transfer from input to output through the upper HF transformer having turns ratio of 9:2. On the secondary side, rectifier diode $D_5$ turns on causing the current to flow through the load with the help of free-wheeling diode $D_8$ in the lower TSFC module. The operation waveforms of this mode are shown in Fig. 3.

<u>Mode $T_2$</u>:

In this mode, switches $S_1$ and $S_2$ turns off while switches $S_3$ and $S_4$ remain in the off state. Diodes $D_1$ and $D_2$ turns on to reset the transformer in upper TSFC module and clamps the voltage across switches $S_1$ and $S_2$ to the dc link voltage ($V_{dc}$). At output, current through the load free-wheels through the two free-wheeling diodes $D_6$ and $D_8$ of the two modules respectively. The operation waveforms of this mode are shown in Fig. 3.

<u>Mode $T_3$</u>:

In this mode, power transfer from source to load takes place with the help of lower TSFC module while the upper module transformer is still in the reset mode. Switches $S_3$ and $S_4$ are turned on simultaneously, resulting energy transfer from input to output through the lower HF transformer having turns ration of 9:2. On the secondary side, rectifier diode $D_7$ turns on causing the current to flow through the load with the help of free-wheeling diode $D_6$ in the upper TSFC module. In the meantime, diodes $D_1$ and $D_2$ turns off when the upper module transformer is completely reset causing voltage across switches $S_1$ and $S_2$ to reduce to $V_{dc}/2$. The operation waveforms of this mode are shown in Fig. 3.

<u>Mode $T_4$</u>:

Operation in this mode is similar to the mode $T_2$. In this mode, switches $S_3$ and $S_4$ turns off while switches $S_1$ and $S_2$ remain in the off state. Diodes $D_3$ and $D_4$ turns on to reset the transformer in lower TSFC module and clamps the voltage across switches $S_3$ and $S_4$ to the dc link voltage. At output, current through the load free-wheels through the two free-wheeling diodes $D_6$ and $D_8$ of the two modules respectively. The operation waveforms of this mode are shown in Fig. 3.

## ASSEMBLY LAYOUT

The development is carried out in modular fashion by fabricating and testing three modules, namely, breaker panel module, power circuit module and control module respectively, independent of each other followed by their integrated testing, on the similar lines as described in [1]. This helps in reducing the development time as well as facilitates the maintenance.

Figure 4 shows labelled photograph of a power converter cabinet. One cabinet houses two power converters, each consisting of a separate breaker panel and power circuit modules respectively. Two, independent, control modules of both the power converters are assembled in a single, standardized 19-inch, 4U rack (Fig. 4).

The breaker panel acts as an interface between the input three phase line and the power circuit module.

The power circuit module comprises of three phase diode bridge rectifier made using three modules of SKKD100/16, input low pass filter components and the two modules of TSFC connected in IPOS configuration as shown in Fig. 1 and Fig. 2. Each TSFC module comprises of two FF150R12RT4 IGBT modules, a high frequency transformer, output high frequency inductors and capacitors, and an ultra-fast soft recovery diode module VSUD400CW60.

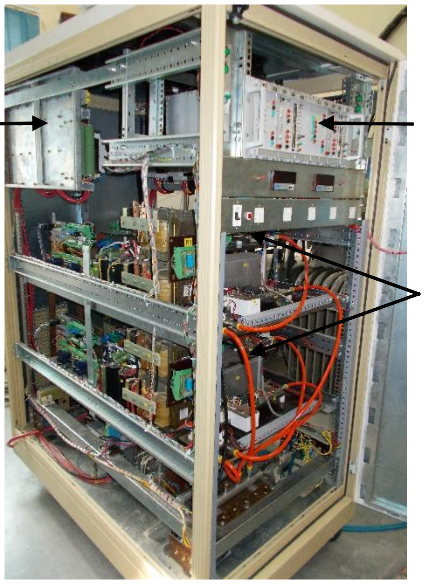


Fig. 4: Photograph of power converter cabinet.

It also consists of freewheeling diodes, SKKD162/16, connected across the output to freewheel the energy of magnet load. Various din-rail mounted PCBs like snubber card, shunt amplifier card (SAC), transformer primary current sensing cards, isolation amplifier card, IGBT driver cards, etc. are also assembled on this module. All power devices and HF transformers are mounted on water-cooled heat sinks. As mentioned earlier, a water-cooled shunt made of zeranin tube is also mounted on this module.

The control rack for each power converter performs the functions of feedback, control, protection and interlock circuit as shown in Fig. 1. It comprises of five cards namely auxiliary supply card, SAC supply card, fault-interlock card, control card and remote interface card respectively. These cards are interconnected to each other through a back-plane PCB.

## TEST RESULTS AND DISCUSSION

All modules of power converters are fabricated and tested independently using test simulators. Subsequently, these are integrated and tested as per the protocols developed for rigorous testing of power converters. Various tests include functional testing at low and high power, protections activation, remote interface tests, calibration, burn-in test, stability test, etc. Thermal imaging of critical power components is done during burn-in test to monitor their temperature and ensure that it remain within safe limits.

Figure 5 shows voltage across switches $S_2$ and $S_4$ respectively on the primary side and rectified voltage waveforms on secondary side across diodes $D_6$ and $D_8$ respectively.

Figure 6 shows that the series output configuration of two TSFC modules adds up to make the final output and their interleaved operation results in reduced ripple amplitude along with frequency doubling at the output.

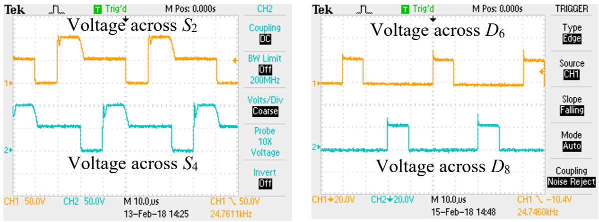


(a) (b)

Fig. 5: (a) Voltage across switches $S_2$ and $S_4$ (50 V/div), (b) Rectified voltage waveforms across diodes $D_6$ and $D_8$ (20 V/div). X-scale: 10 µs/div in (a) and (b).

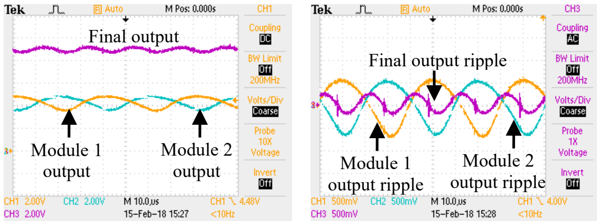


(a) (b)

Fig. 6: Output of two TSFC modules along with final output (a) Output voltages (2 V/div), (b) Ripple in output voltages (500 mV/div). X-scale: 10 µs/div in (a) and (b).

Figure 7 shows output current stability curve for more than 6 hrs of continuous operation. The output current stability is well within the required limits of ±500 ppm.

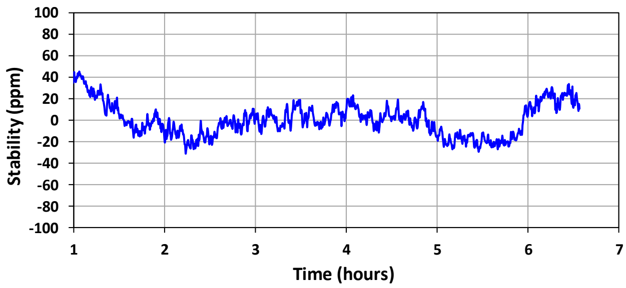


Fig. 7: Output current stability curve

So far, assembly of all modules is completed followed by their independent testing. Integrated testing of 3 power converters is completed and one of these is being used to characterize the harmonic sextupole magnets.

## ACKNOWLEDGEMENT

The authors acknowledge contributions made by Shri S. K. Prajapati, Shri Vinod Somkuwar, Shri Nathan Singh and Shri M. K. Koli in the development of power converters.

## REFERENCES

[1] Vineet Kumar Dwivedi, Alok Singh, Manohar Koli, Mangesh Borage and Sunil Tiwari, “Design and Development of New 20 kW Power Converters for Quadrupole Magnets in Indus-2”, Proc. of InPAC 2018.

# X-RAY MONITOR SYSTEM FOR SUPERCONDUCTION LINAC

*Manoj Kumar T.K[1*], J.N. Karande[1], A.N. Takke[1], S. Pal[1],
R. Palit[2] and V. Nanal[2]

[1]*PLF, Tata Institute of Fundamental Research, Mumbai 400005*

[2]*DNAP, Tata Institute of Fundamental Research, Mumbai 400005*

*Abstract*

The heavy ion superconducting linac at Pelletron Linac Facility (PLF), Mumbai employs lead plated copper cavities. These superconducting cavities emit X-rays when RF field is applied. A simple scintillator detector system, consisting of CsI crystal developed at BARC, coupled to a commercial PMT, is being setup to monitor the radiation levels around the cryostat and to enable the requisite access restriction for safety of personnel.

## INTRODUCTION

The superconducting LINAC at PLF, Mumbai has a modular structure with eight cryostats divided in two groups, with four superconducting accelerating cavities in each cryostat made up of lead plated copper [1,2]. In these superconducting cavities, Pb X-rays (~70-80 keV) are generated due to field emission, when RF field is applied. A scintillator detector system is developed to monitor the radiation levels near the cryostats and to restrict the access to the area for the safety of the personnel involved. The radiation monitor system is designed to monitor the count rate and if it exceeds the presset level, it triggers an indicator located near the hall access door.

## SYSTEM DESIGN

The radiation monitor system is designed using a scintillator detector, which produces light output directly proportional to the energy of incident radiation. A photomultiplier tube (PMT) is used to convert the light to an electrical signal. A 3mm thick 25mm diameter CsI (TI) scintillator, developed and supplied by BARC, is used to detect the incident radiation. The scintillator is optically coupled to a commercial 1" diameter PMT model R1924A [3] of M/s Hamamatsu Photonics. Instead of using dedicated bench top High Voltage power supply units, the high voltage required for the PMT operation is generated using a low cost and miniaturised high voltage module QH15-5 acquired from M/s Emco High Voltage [4]. The HV output can be varied from 0 to 1500 V, by varying the control input to the HV module. A LM-317 adjustable voltage regulator is used to vary the input voltage to the HV module. To supply the interstage voltage for each electrodes, a voltage divider network is developed in house and coupled to the PMT base. The output of the PMT is fed to a voltage amplifier designed around AD817 operational amplifier [5]. The signal is amplified to a desired level by adjusting the gain. This amplified signal is coupled to a voltage comparator circuit with adjustable threshold, which produces a TTL compatible digital signal to drive the counter circuit. Figure 1 shows the block diagram of the radiation monitor and figure 2 shows a picture of HV board (panel a) and the assembled circuit (panel b).

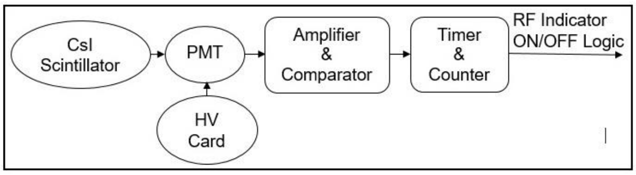


Figure 1: Block diagram

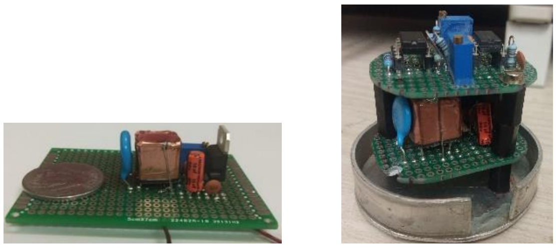

(a) (b)

Figure 2: a) HV generator circuit and b) stacked HV and amplifier card.

A simple timer and counter circuit (Fig. 3) is designed and fabricated for recording the number of counts in a specific time interval. The timer circuit consists of a 32.768 KHz crystal oscillator circuit and two 12 stage binary counters. The time interval for accumulating the counts can be set from few microseconds to several seconds. The counter logic is based on CD4040 binary counter chips. The count rate value (i.e. number of counts in a given interval) is preset at the background level and the circuit is designed to generate a logic high signal whenever count rate exceeds the preset value. At the end of each predefined time interval, the counter is reset and starts counting fresh. The overall processing time of an event is around 10µS and the unit is capable of handling around 100KHz count rate.

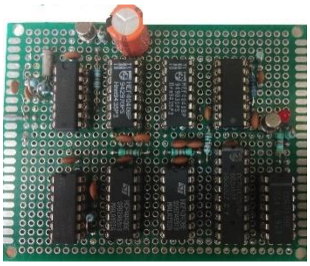

Figure 3: Timer and Counter circuit

**email- manoj@tifr.res.in*

One detector unit of the radiation monitor system has been developed using a CsI scintillator and performance has been tested with Am-241 and Ba-133 radiation sources (60 – 80 keV), in the energy range of Pb X-rays. Fig 4 shows the output from the PMT and the comparator for background (panel a), for Am-241(panel b) and for Ba-133 (panel c).

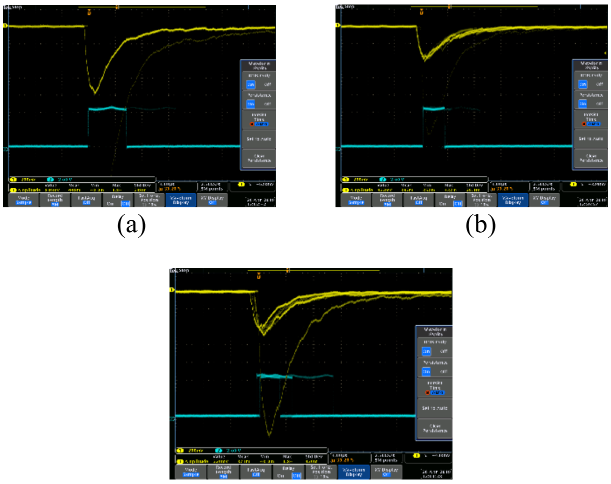

(a) (b) (c)

Fig 4: Screenshots of PMT output and the comparator output: (a) background, (b) $^{241}$Am source ( 59 keV) and (c) $^{133}$Ba source (80 keV)

It is evident that the setup works well for low energy radiation. In the accelerator hall, when RF power is turned on, the Pb X-rays will be generated and the count rate in the detector is expected to be higher that the preset background value. Thus, the logic high signal is linked to to switch on the remote RF power indicator outside the accelerator hall door.

## SUMMARY

A simple and cost effective scintillator detector system is setup to monitor the radiation levels around the cryostat. One of the CsI scintillators developed in Crystal Technology Section, BARC is coupled to the PMT and tested with few radioactive sources and the performance looked satisfactory. It is proposed to make a Complete setup of eight detectors (one for each cryostat) and logic outputs from each detector will be combined through an “OR” gate, which will be used to trigger the remote RF ON/OFF indicator outside the hall entrance door. This will be a true indicator for access restriction and will serve as an additional measure for the safety of the personnel. To display the count rate and status of the RF indicator in the control room, a standalone microcontroller read out interface will be provided in the timer and counter card.

## ACKNOWLEDGEMENT

We are grateful to Prof. R.G. Pillay for invaluable guidance in the project. We thank Dr. S. C. Gadkari, Dr T.V.C Rao and team, Crystal Technology Section, BARC for providing the CsI scintillator crystals. We would also like to thank Mr. S.P. Singh for designing an enclosure for PMT and to Mr L.V. Kamble for fabricating an aluminium box, and to the PLF staff for their support.

## REFERENCES

[1] R.G. Pillay, “Overview of the Pelletron LINAC Facility”, InPAC2011 proceedings.

[2] V. Nanal et al., “Operational experience of superconducting LINAC booster at Mumbai”, HIAT09, Venice (Italy) 2009.

[3]https://www.hamamatsu.com/resources/pdf/etd/R1924A_TPMH_1280E.pdf

[4] www.emcohighvoltage.com/datasheets/qseries.pdf

[5] https://www.analog.com/media/en/technical-documentation/data-sheets/AD817.pdf

# DEVELOPMENT OF LARGE SCALE IRRADIATION SET UP FOR INDUCED MUTATION OF GRAINS USING LARGE AREA LOW FLUX PROTONS AT BARC-TIFR PELLETRON LINAC FACILITY

J.P. NAIR#, P. SURENDRAN, HILLARY SPARROW, R.S. WORLIKAR[1] and A. K. GUPTA
*Nuclear Physics Division, BARC, Mumbai-85*
*[1] PLF, TIFR, Mumbai 400005*

## Abstract

Preliminary investigations of induced mutation studies in rice were carried out using "large area low flux Proton beam in air set up" at Pelletron Accelerator and dose required for favorable traits were identified [1] in collaboration with NABTD, BARC. Field trials require large quantities of grains to be irradiated which the present set up cannot fulfill as frequent sample changing consumes time due to beam interruption to access the beam hall. A remotely operated sample changer was developed which houses 66 samples for irradiation and is changed using a DC geared motor. The sample position is aligned with the beam port by viewing through a camera in the beam hall and monitor in the counting area. Using this technique multiple samples where irradiated to get sufficient quantity of rice for field trials in minimal time of irradiation. A remotely operated X-Y translational movement mechanism was also developed to replace the manual scanning for measurement of Proton flux for uniformity in the large area. This changing of detector position without entering the beam hall minimized the time of mapping, optimization of beam for irradiation and ease in changing of beam energy. These two developments lead to successful field trial of mutation induced rice. This paper describes the details of the set up and the results achieved.

## INTRODUCTION

Large area low flux proton beam in air set up was developed earlier to irradiate samples of large area using forward scattered proton beam taken to air through a titanium window [1]. The set up was used to irradiate grains like rice and wheat for induced mutation studies with proton flux of $10^8$/cm$^2$/sec and beam size 36mm diameter in collaboration with NABTD (Nuclear Agriculture and Bio-Technology Division), BARC. However, field trials necessitate irradiation of grains of large quantity which the existing set up is not capable of handling due to frequent changing of samples. Moreover, frequent sample changes cause beam interruptions for entering into beam hall leading to significant loss of beam time. In addition, scanning of Proton beam for flux uniformity needed changing of detector position in the beam hall resulting into further beam time loss. Thus, to overcome these problems, a new irradiation set up was developed in-house by incorporating two important features, leading to successful irradiation of large quantities of grains for mutation-induced studies, is described in detail in the following sections.

## DEVELOPMENTAL WORK

***Remotely operated X-Y movement:***

A remotely operated X and Y movement was developed to measure the uniformity of beam using a PIN diode detector. The detector encapsulated in a one mm collimator in front and graph paper behind was mounted on a X-Y movement. The detector set up was mounted on a channel rail which can be moved by a combination of a 250 mm long screw and a D.C. geared motor in vertical direction (Y direction). The above arrangement is fixed on another channel rail with a similar mechanism for movement in X direction. The position of the detector (collimator) is seen through the camera by focusing on the graph paper and the entire operation is viewed in the counting room on a TV screen (Fig:1). A controller, having features like ON/OFF, Forward/ Reverse and "DO IT" operations, was developed and operated from the counting room by observing through camera and TV interface.

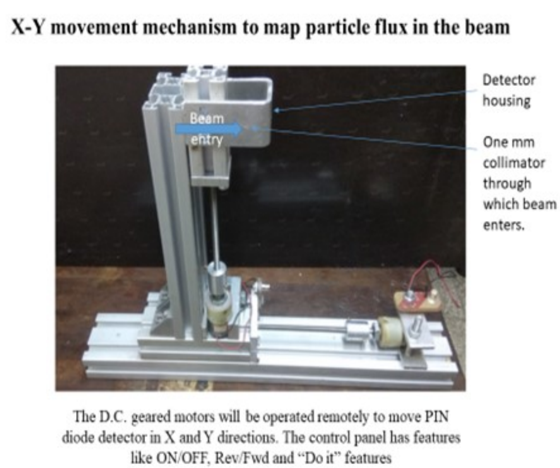


**Fig.1: Remotely operated X-Y movement**

***Aluminum wheel sample holder:***

An Aluminum wheel of 50 cms diameter, which can accommodate 66 sample holders in four concentric circles, driven by a geared D.C motor was fabricated. The four circles in the aluminum wheel accommodate 24, 20, 14 and 8 samples, respectively. After scanning the beam

# jpnair@tifr.res.in

to estimate the uniformity of the proton flux the scanning set up was replaced with aluminum wheel with samples mounted on it for irradiation (Fig:2). Each sample is aligned w.r.t the beam port by monitoring through a camera in the beam hall in conjunction with a TV in the counting area. Multiple samples of rice and wheat were irradiated to the desired dose using this set up (Fig:3).

The dose on the sample is measured by monitoring the counts on the detector mounted at 30$^o$ of the chamber. The ratio of the counts/cm$^2$/sec on detector facing the window to the counts on detector at 30$^o$ is measured before commencing of irradiation. This relative ratio is used for estimating the desired fluence on the sample from the counts registered by the detector at 30$^o$. The flux of the particles is measured by a rate meter and the fluence accumulated was estimated using a counter.

**Fig.2: Aluminium wheel mounted with samples of grains**

**Fig.3: Large scale irradiation set up on the beam line**

Recently, the newly developed system was used during the irradiation of large quantity of grains for induced-mutation studies and field trials of these grains were conducted. Besides retaining the favorable traits like early maturing and short height of rice plants herbicide resistance trait were also observed by NABTD, BARC [2,3,4].

## CONCLUSION

The newly developed "large area low flux proton set up in air", comprising user friendly features, is being utilized by NABTD, BARC, extensively. Large scale irradiation of rice and wheat were carried out, successfully. The set up is also being used for qualification of radiation hardened electronic devices for space qualification by ISRO.

The authors would like to thank Pelletron Linac Facility staff and Central Workshop, TIFR for their cooperation during these measurements.

## REFERENCES

**[1]** J. P. Nair, P. Surendran, Hillary Sparrow and A. K. Gupta, **Large area Low flux proton Irradiation set up and its applications at BARC-TIFR Pelletron Accelerator**, InPAC-2018, RRCAT, Indore.

**[2]** Chauhan Anjali, Kumar Vikash, Vishwakarma G, Iyer Preethi R, Nair J.P, Surendran P, Sparrow Hillary, Gupta A.K, Shitre A.S, Shinde A.K, Kunkerkar R.L, Sharma Deepak, Patel Ravi Raj Singh, Das B. K. **Effect of Proton beam irradiation on growth and survival parameters of Indian rice variety (Oryza Sativa L) "Indira BaraniDhan 1"** DAE-BRNS Life Science Symposium 2018.

**[3]** Chauhan A, Kumar V, Iyer PR, Vishwakarma G, Nair J. P, Surendran P, Sparrow H, Gupta A. K, Shinde A.K, Kunkerkar R.L, Sharma D, Patel R.R.S, Shitre A.S and Das B.K. **Standardisation of proton beam dose for mutagenesis of Indian rice varieties**; Abstract book of 14$^{th}$ Biennial DAE BRNS Symposium on Nuclear and Radiochemistry, Jan 15-19, 2019, BARC, Mumbai, p235.

**[4]** Anjali Chauhan, Vikash Kumar, Preethi. R. Iyer, Gautam Vishwakarma, J. P. Nair, P. Surendran, Hillary Sparrow, A. K. Gupta, A. S. Shitre, A. K. Shinde, R. L. Kunkerkar, Deepak Sharma, Ravi Raj Singh Patel and B. K. Das, **Effect of proton beam irradiation on survival and seedling growth parameters of Indian rice (Oryza sativa L.) variety 'Indira Barani Dhan 1'.** Electronic Journal of Plant Breeding, 10 (2): 490-499 (Jun 2019) ISSN 0975-928X. DOI: 10.5958/0975-928X.2019.00062.0

# SHIELDING DESIGN OF PARTICLE ACCELERATOR BASED IRRADIATION CREEP STUDY FACILITY

S.Sen, S.Balaji, S.Chinnatambi, S.K.Srivastava, B.Sundaravel, C.David, P.Gangopadhyay, R.Govindaraj, M.Kamruddin

Material Science Group, IGCAR, Kalpakkam, Tamil Nadu-603102

*Abstract*

To simulate the effect of radiation-induced creep in fast reactor materials, it is planned to use a proton beam of energy in the range 3 to 4 MeV with beam current of 30 μA in particle irradiation facility at IGCAR. The secondary neutron and gamma sources from the target material are estimated. Monte-Carlo simulations are performed using these radiation sources to compute dose rates and optimizing shields to maintain accessibility to the key areas of the facility during the experiments.

## INTRODUCTION

With fast spectrum reactors, it is possible to achieve very high levels of fuel burnup, which is important for its economical operation and burnout of long-lived transuranic radioactive wastes [1]. The main limiting factor in achieving high fuel burnup is the radiation damage to core structural and cladding materials. Fast neutrons causing atomic displacements not only degrade the material properties because of swelling and embrittlement but also lead to enhanced creep rate. The rate of plastic deformation in materials under irradiation in the fast reactor may increase many orders of magnitude above its thermal creep rate.

Particle accelerators have proved to be a feasible alternative to irradiation of materials in the fast reactor for the study of irradiation-induced creep [2]. It is easier to control the parameters governing the phenomenon in an ion beam facility than in a reactor. Energetic ion beam under well-controlled conditions is used to simulate the effect of neutron-induced irradiation creep. Furthermore, displacement rates in an ion beam facility are usually greater than ~$10^2$ times the rates achievable in a fast reactor largely improving the experimental efficiency. An important experimental constraint is the suitability of the accelerated particles in terms of its penetration distance and damage characteristics. Proton is preferred over other ions since its penetration depth is more and it's single charged state allow better beam dynamics. It is planned to use a high energy proton beam (3 to 4 MeV) to allow sufficient penetration of the beam to achieve reasonably uniform damage rates within the target.

High energy protons will be able to penetrate the Coulomb barrier of target atoms giving rise to compound nuclear emissions apart from simple Coulomb scattering. Prompt and isotropic compound nuclear emission of penetrating radiation in the form of secondary neutrons and gammas are the major radiation hazard for the occupational workers in such experimental facilities. An estimate of sources for neutrons and gammas are performed. Gamma and neutron source strengths are used in a Monte-Carlo simulation for estimation of dose rates and shield optimization. High-density concrete is used as shields because of its effectiveness to attenuate both neutrons and gammas.

The Monte-Carlo simulation method is extremely well suited with accelerator facilities because of its geometrical flexibility which allows an accurate model of the facility [3]. However, the method is computationally intensive and often requires large simulation time in order to obtain results with acceptable accuracies. The method works by simulating individual particles and records its behavior in the system in order to infer certain average characteristics of the system. The method enables a detailed simulation of the energy and angular representation of the interacting particle and thereby providing an estimate of dose rates at specified locations of interest.

## METHOD

Prompt emission of energetic neutrons and gammas from the target during irradiation is the dominant contributor to the dose rates in a short time operation of the accelerator. PACE4 uses a Monte-Carlo procedure to determine the decay sequence of an excited nucleus using the Hauser Feshbach formalism [4]. The code is used to calculate the evaporation cross-section for secondary emissions in reactions induced by protons on the D9-steel target. The sources are evaluated for incident proton beam of energy 3.4 MeV with a beam current of 30μA. The neutron and gamma sources are estimated to be 1.73 x $10^7$ n/sec and 1.41 x $10^9$ $\gamma$/sec respectively as given in Fig. 1 and 2.

The high-density concrete used for this study has significantly better performance in radiation shielding and compressive strength when compared with ordinary concrete [5]. More iron content in high-density concrete is desirable for efficient neutron attenuation in the high energy region since it is a good inelastic scatterer. In the low energy region, the elastic scattering by hydrogen in concrete is the dominant mechanism for neutron attenuation. Thermal neutron scattering by bound hydrogen in water present in concrete further enhances the effect of neutron attenuation. ENDF/B-VI.8 cross-section data at 300K is used for the simulation. Thermal scattering law data of H in $H_2O$ at 300K is used to simulate the bound atom effect. In addition, high-density concrete has moderately better gamma attenuation property compared to ordinary concrete.

In order to maintain radiation levels in the occupied areas below the acceptable level (< 1 μSv/hr) during the operation of the accelerator, a high-density concrete (3.6 gm/cc) structure is modeled around the source. Additional walls are modeled to attenuate streaming particles from the beamline opening to the control room and the workshop as given in Fig-3. The dimensions of the shields are optimized to meet the dose limits criteria outside the shields.

The present study is carried out using MCNP version 4B to simulate the transport of particles [6]. Isotropic distributed cylindrical source of neutrons and gammas is assumed with estimated source strengths as shown in the following Fig. 1 and 2. The model is simulated with several shield configurations, and an optimized shielding is arrived at satisfying the dose criterion. The standard deviation error is calculated from the simulation. The Dose Energy (DE) and Dose Functions (DF) are used to convert particle flux into the dose rate equivalent. Commonly used geometric splitting/Russian roulette technique is used here for variance reduction in dose rate estimates [3]. The sky-shine effect which results from the scattering of particles from the surrounding air is an important factor when the roof shield is not provided [7]. Streaming particles from beamline opening could result in enhanced sky-shine effect amounting to higher dose rates in regions outside of the additional shield walls, and thus reducing the effectiveness of shield thickness provided. To take care of this, walls adjacent to the workshop have been raised compared to other walls as given in Fig. 3. An array of detectors are placed in the simulation on outer regions of additional shields in order to arrive at the peak dose.

## RESULT AND DISCUSSIONS

Dimensions of high-density concrete shields are optimized for the accelerator-based irradiation creep experiment facility using MCNP simulation. A cave of wall thickness 60 cm around the source satisfied the dose criterion outside the walls. On top of the cave, the thickness of the concrete used is 10 cm mainly to reduce the sky-shine effect. Contact dose rates are estimated on the surface of the cave walls. Concrete walls are provided to restrict streaming radiation from the beamline opening from reaching the control room and the workshop as shown in Fig. 3. Doses are estimated at the height of the beamline, 140 cm from the ground level. The height of the wall adjacent to the workshop is raised up to 305 cm compared to other walls of 213 cm to reduce the sky-shine contribution in the workshop region. The peak dose in the region exterior to the additional concrete wall is away from the outer contact surface because of the sky-shine effect. The estimated dose rate peaks are at a distance of 20 cm from the outer surface of the wall towards the control room and at 75 cm from the outer surface of the cave. Peak dose rate outside the wall adjacent to the workshop is at a distance of 20 cm from the wall and at a distance of 10 cm from the front surface of the cave. The estimated dose rates for various regions are given in Table 1. The design of the shield is made in a conservative way assuming the possibility of emission from the collimator placed along the beamline. Thus, dose rates estimated in the workshop and the control room region is much lower than the required dose criterion. The region in front of the beamline entry point is not accessible up to a distance of 150 cm.

## CONCLUSIONS

Radiation sources are estimated for 3.4 MeV proton beam incident on the D9-steel target of the irradiation creep study facility. High-density concrete shields are designed to limit dose rates at contact with the outer walls of a concrete cave enclosing the source. The thickness and height of walls are optimized to limit dose rates on the outside of the walls. The optimized wall thickness of the cave is estimated to be 60 cm and roof thickness of 10 cm. An opening is provided in the front of the cave for the beamline entry. Backward streaming particles from the target through the beamline void are attenuated by concrete walls of thickness 10 cm and 25 cm provided on either side of the beamline to effectively shield the workshop and the control room.

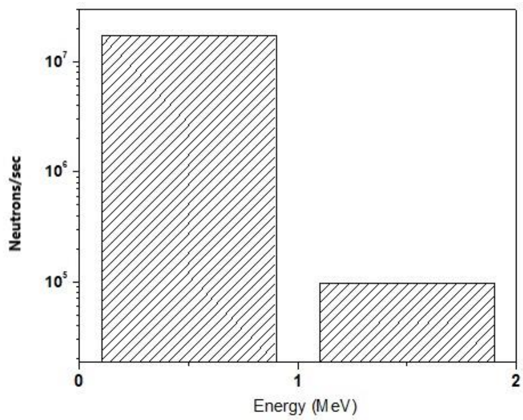


**Fig 1:** Neutron Spectrum with 3.4 MeV incident Proton on D9 target at a beam current of 30 μA

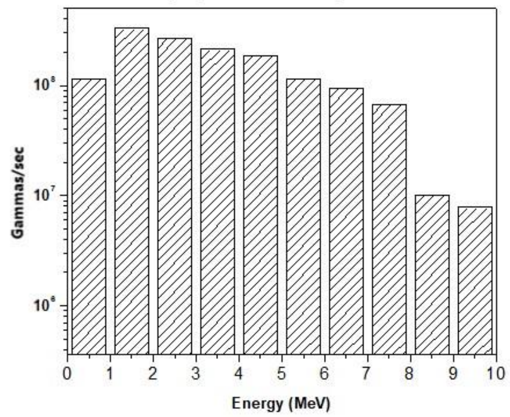


**Fig 2:** Gamma Spectrum with 3.4 MeV incident Proton on D9 target at a beam current of 30 μA

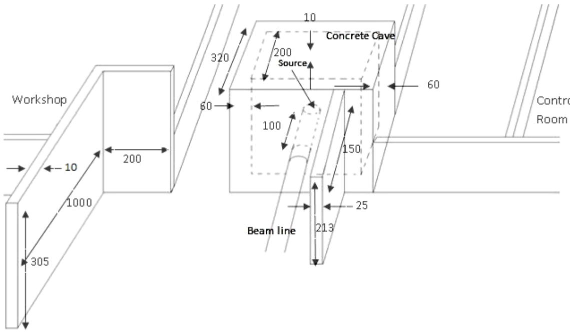


**Fig 3:** High-density Concrete Shields for Irradiation Creep Study Facility (dimensions in cm)

**Table-1.** Estimated dose rates in regions outside the shields

| **Position** | **Dose Rate (μSv/hr)** | | |
|---|---|---|---|
| | **Neutron** | **Gamma** | **Total** |
| Point of beamline entry into the cave | 119 | 195 | 314 |
| Outside the cave wall opposite to the beamline entry into the cave | 0.0044 | .651 | 0.6554 |
| The sidewall of the cave towards the control room | .0031 | .726 | 0.7291 |
| The sidewall of the cave towards the workshop | .0031 | .711 | 0.7141 |
| Peak dose rates on the outer side of the wall towards the control room | .0010 | .240 | 0.241 |
| Peak dose rates on the outer side of the wall towards the workshop | .0015 | .195 | 0.1965 |

## REFERENCES

[1] Andrew G. Osborne et.el. 'Reducing Irradiation Damage in a Long-Life Fast Reactor with Spectral Softening', Energies 2018, 11, 1507.

[2] T. C. Reiley et. al., 'The ORNL Irradiation Creep Facility', ORNL/TM-7470, September 1980.

[3] Pooneh Saidi et.al., 'Variance Reduction of Monte-carlo Simulation in Nuclear Engineering Field, Theory and Applications of Monte-Carlo Simulations', Victor (Wai Kin) Chan, IntechOpen, DOI: 10.5772/53384.

[4] O.B.Tarasov, D.Bazin NIM B 266 (2008) 4657-4664; A.Gavron, Phys.Rev. C21 (1980) 230-236.

[5] S. M. J. Mortazavi et.al., 'High-performance heavy concrete as a multi-purpose shield', Radiation Protection Dosimetry, Volume 142, Issue 2-4, December 2010, Pages 120–124

[6] J. K. Shultis and R. E. Faw, 'An MCNP primer', Dept. of Mechanical and Nuclear Engineering Kansas State University Manhattan, KS 66506, December 2011

[7] C. M. Lampley, 'The Sky-shine-II Procedure: Calculation of the effects of structure design on neutron, primary Gamma-ray and secondary Gamma-ray dose rates in the air', NUREG/CR-0781 RRA - 17901 RE, May 1979.

# SAFETY CONTROL SYSTEM FOR MEDICAL CYCLOTRON FACILITY, KOLKATA

Sabyasachi Pathak†, Suprakash Roy, Umashankar Panda, Aditya Mandal, Barun Das, Sumit Som
Variable Energy Cyclotron Centre, Kolkata, India
†spathak@vecc,gov.in

.

*Abstract*

DAE Medical cyclotron facility for production of medical isotope and research in material science is under commissioning at VECC, Chakgaria. The cyclotron facility has 5 nos. of beamlines apart from main vault where the cyclotron is installed. A dedicated beamline will be used for production of PET radioisotope, two solid target beamlines will be used for production of Ga, and Th. Another beamline is for irradiation study of different materials. This material science beamline is further splitted into one high current and one low current beamlines. Another beamline is turned vertically downward for the facility of target study with high current proton beam. Machine protection system, user safety system, radiation monitoring system of the facility has been installed to meet regulatory and safety aspect.

## INTRODUCTION

Medical cyclotron is capable of delivering beam upto 500 µA with energy upto 30 MeV [1]. Different targets have different requirements of beam current, energy and duration of irradiation e.g. PET target has a requirement of 18MeV and 35 µA beam for duration of 30 minutes to 1 hour depending on the required dose of Fluoro Deoxy Glucose (FDG).

During beam tuning and irradiation, neutrons are produced due to interaction between accelerated projectiles of different energies with beam tubes, beam stoppers, beam viewers, target materials etc. Neutrons deposit energy by collisions with protons in body tissue. Though neutrons do not take part in direct ionization but interacting with body tissue eventually causes gamma radiation. Therefore neutrons flux is very harmful to human body [2, 3]. It is only present when there is beam. Therefore concrete shielding, shield doors and safety interlocks are incorporated to avoid any exposure of personnel to neutron streaming. Also after irradiation is completed, gamma radiation prevails inside the vaults since different materials get activated during the process. It requires certain time for gamma radiation to come below safety level and necessary interlocks are provided to restrict entry to the vault and cave areas unless the gamma level is below permissible limit. Also gaseous radioactive isotopes $N^{13}$ and $O^{15}$ are produced which are to be safely handled by Air Handling Unit (AHU) that maintains negative air pressure inside the vault and the caves and use proper air filters and stack are used to emit those gas in the environment ensuring the radiation below hazardous level.

A PLC (Programmable Logic Controller) based safety control system was installed and commissioned in the Medical Cyclotron Facility. The control system and the field instruments are explained in the following section.

## AN OVERVIEW TO THE SAFETY CONTROL SYSTEM

The safety system consists of a Siemens make PLC (Safety PLC) as the main controller, GUI (Graphical User Interface) to display current status of the facility and different alarms and finally various field subsystems to collect field data and to actuate some field outputs. So, the entire control system can be classified into following categories,

1. Safety PLC
2. Neutron Shutters Interlock
3. Shield Door Interlock and Control
4. Search and Secure Protocol
5. Emergency Crash Off
6. Radiation Interlock
7. Negative Air Pressure Interlock
8. Hotcell Interlock
9. Others
10. GUI

### *1. Safety PLC*

Siemens S7 315F CPU [4] with 120 safety discrete inputs, 50 safety discrete outputs, 32 isolated discrete inputs and 16 isolated discrete outputs are configured for safety control interfacing. For safety inputs two inputs are wired separately for each signal. For example, there are two shield limit switches which get closed when the door is closed. To get the door closed signal both the limit switch should get closed within two seconds and maintain the closed state. Else the door close detection will fail. Similarly for safety outputs there is a minimum threshold current monitoring to check if the outputs are really ON. For example if “Beam ON” indication lamp is not glowing due to open circuit there will be an output failure detection in the PLC. If all the inputs and outputs are in safe state then only it will enable the main cyclotron control PLC for operating RF, Ion Source, injection faraday cup and related beam line components.

### *2. Neutron Shutters Interlock*

These are placed in every beamlines. The purpose of them is to stop neutron streaming in the unused beamlines. Therefore beam and neutrons are blocked to the cave if the respective neutron shutter is closed. Then that cave is accessible unless there is high radiation. Two redundant feedbacks are collected from each neutron shutters via limit switches to ensure the shutter is in position while entering a cave.

Figure 1: Safety PLC


Figure 2: Neutron Shutter in Beamline 2.1 (Solid Target)

## *3. Shield Door Interlock and Control*

Shield doors are concrete filled doors which allow entry to vault caves during commissioning and maintenance and otherwise block neutron and gamma during closed condition. Two redundant limit switch feedbacks are collected from each door to ensure the door is properly closed. If door is closed properly then only beam can be allowed to generate inside cave or to be travelled inside caves provided the respective rooms are secured.

Opening and closing of shield doors are done using unique keys for each room. These keys are placed in a safety key box in the control room. While any door is required to be operated, the corresponding key is to be taken out from safety key box which ensures that beam cannot travel to that room. Then this key is to be placed inside the shield door panel and can be operated.

Also opening of door is only allowed from safety PLC. It is only allowed if the gamma radiation inside vault is below permissible limit.

## *4. Search and Secure Protocol*

Before beam generation at cyclotron vault or beam transmission at any caves, corresponding rooms are to be checked thoroughly unless some person is trapped inside the rooms while beam is transmitted. Therefore, search and secure protocol is followed which involves pressing of search buttons in a sequential manner at various positions of the rooms. This ensures various areas of vault and caves to be checked thoroughly for presence of any person. Additionally, two warning lights with buzzer (inside and outside the room) glow during the search operation to warn any person inside and outside the room. There is particular timing involved with this protocol so that a person a is never allowed to start a search and secure operation and leave the room for certain time and continue which may cause unnoticed entry of some person inside the room. In such occasion search and secure operation has to be started from the beginning. The operation completes with pressing of search button within time in a proper sequence and closing of shield door. Then the shield door key has to be returned in the safety key box in control room. This will secure the room which can also be seen in the GUI.

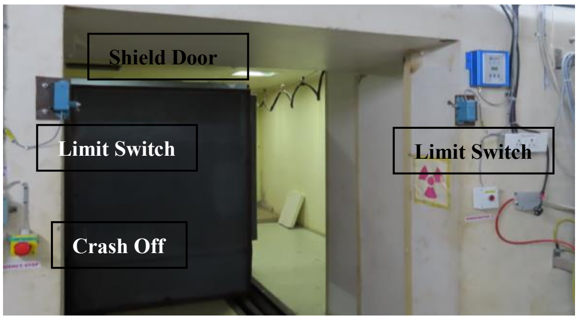


Figure 3: Shield Door of Cyclotron Vault

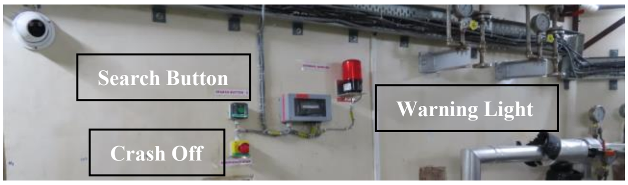


Figure 4: Search button, Crash-Off button & Internal Warning Light

## *5. Emergency Crash Off*

There are some emergency crash-off buttons placed at various locations of the facility i.e. vault, caves, control room etc. to trip the machine in emergency situations such as if any component failure noticed or some person trapped inside the vault or cave can use these to prevent the machine to be operated.

## *6. Radiation Interlock*

Two types of radiation monitors are installed for vault and each cave- a gamma monitor inside the room and a neutron monitor outside the room. Each of the monitors provides feedback for high gamma or neutron level. These are integrated with the control system. If there is high gamma inside vault or any cave then the shield door can’t be opened. If there is neutron outside the room then the machine will be tripped immediately since there should not be any neutron streaming outside the rooms during running condition.

## *7. Negative Air Pressure Interlock*

Negative air pressure is maintained inside the vault and the caves using AHU. This is done to prevent any leakage of radioactive gaseous isotopes i.e. $N^{13}$ and $O^{15}$. Negative air is sensed by BMS (Building Management System) using differential pressure sensors placed inside vault and caves and the signals are integrated with safety PLC. Beam can be generated or transmitted only if there is negative air pressure inside the concerned room.

Figure 5: Radiation Monitors & Interlocks

### *8. Hotcell Interlock*

Hotcells are lead-shielded chambers where radio-pharmaceutical processing of irradiated targets are carried out. There are two hotcells for synthesis of FDG from irradiated liquid target $H_2F^{18}$ and one reception hotcell to receive the solid target for further chemical processing. Before transfer of irradiated targets two things are ensured, the door of hotcells are closed and negative pressure is maintained inside. When both of them are okay then only the irradiated materials can be transferred. Also, during the transfer the door of the hotcell can not be opened. This is controlled by the safety control system to ensure no radiation leakage to the person working at hotcell area. Additionally, warning lights glow in the hotcell area during the transfer.

### *9. Others*

Others subsystems include the following,

- Fire interlock: Fire safety interlock is integrated with the safety PLC to trip the machine if any fire alarm is triggered.
- High Voltage & RF: High voltage supplies and RF system inside cyclotron vault is turned OFF when the shield door is opened.
- Integration with Accelerator Control System: Status of RF and Ion Source are fed from ACS. Also, these can only be turned ON if safety PLC allows ensuring the vault is secured.
- Integration with PET Control System: Irradiated liquid can only be transferred if allowed from safety PLC.

### *11. GUI*

A graphical user interface is developed and installed to display the status of the field i.e. which room is secured, shield doors are opened or closed, position of any emergency crash off button used. Also different alarms like high radiation outside room, fault in negative pressure etc. are displayed and can be acknowledged with the reset button. Some screenshots of the GUI are given below

Figure 6: GUI of Safety Control System

## FUTURE SCOPE

Further provisions are kept for future expansion. These are additional PET RnD Hotcells, which will be installed later for Research and Development Purposes. Hotcell interlock provisions are kept for two such hotcells. Also a provision gas target production is there to be accommodated in the existing safety control system.

## CONCLUSION

Therefore, the installation and commissioning of the safety system for all the beamlines and targets of Medical Cyclotron Facility is completed. During commissioning individual systems were tested and verified. Currently the safety system is running satisfactorily.

## REFERENCES


[1] R.K.Bhandari, “Medical Cyclotron Facility at Kolkata; Cyclotrons and Their Applications 2007, Eighteenth International Conference, p.87

[2] Thomas E. Johnson et al., “Health Physics and Radiological Health”, Lippincott Williams and Wilkins.

[3] Herman Cember et al., “Introduction to Health Physics: Fourth Edition”, McGraw-Hill Education.

[4] www.support.industry.siemens.com

# UPGRADATION OF TEMPERATURE MONITORING SYSTEM FOR INDUS-2 VACUUM COMPONENTS

N. J. Bhange#, Hemkant Sharma, Prateek Bhatnagar, Sujata Joshi, D. P. Yadav
Ultra High Vacuum Technology Section, RRCAT, Indore, India

*Abstract*

Indus-2, a 2.5GeV Synchrotron Radiation Source (SRS) at RRCAT, Indore consists of a large vacuum system. The vacuum envelope of Indus-2 ring is composed of sixteen dipole chambers inside of which dipole synchrotron radiation (SR) is generated. Total SR heat load of ~125 kW is generated by 2.5GeV, 200mA stored beam. Only 20% of this SR is channeled into the beam lines for use, whereas 80% of it is unused. The unused SR heat is absorbed by water cooled photon absorbers and end flanges mounted on dipole chambers. Each dipole chamber has four photon absorbers and three beam line ports. Considering this high heat load, monitoring the temperature of this vital vacuum envelope with necessary interlock is an important requirement, during machine operation. The existing temperature monitoring system is providing interlock to machine safety system, working satisfactorily for more than fourteen years. The system has not only provided safety interlock but also pointed the crucial temperature rise due to accidental beam orbit variations. It has also guided as an input for beam orbit corrections and additional cooling arrangements required for higher beam current operation. The rising temperatures generated a need to extend probing further at more locations on dipole chambers. The upgraded system of 20 units of 16 channels each supports to monitor 320 channels only taking about half the space of an existing system. The system is capable of monitoring these channels using half duplex RS485 mode of communication in modular fashion. Each module is microcontroller based 16-channel Temperature Monitoring Unit (TMU), providing alarm & trip events. The paper discusses experience of existing system, required maintenance in radiation environment as well as design & development of upgraded system.

## INTRODUCTION

At 2.5Gev, 200mA, estimated radiated power in the bending magnets is 125 kW and it has the potential to cause material damage to chamber walls. It is necessary to ensure that vacuum components temperatures are within control. This will also ascertain low out gassing rate & minimising possibility of developing a leak. TMU is 8-channel temperature monitoring unit, using K-type thermocouple for the span of 0-500ºC at the resolution of 1ºC. Temperature was monitored on the vital parts of vacuum envelope, such as dipole chambers, photon absorbers & end flanges (blocking unused beam power ports of dipole magnet) having possibility of temperature rise. Unit generates e-beam trip signal by switching off the RF cavities after temperature crosses trip set point. The trip signal activates interlock to dump the beam. These units have feature of open sensor detection & isolated RS-485 communication. These units were installed in the Indus-2 tunnel for minimising the overall cabling & susceptibility of sensor cables to noise. The units were deployed in Indus-2 on 2005 [1] & after around eight years of smooth operation total communication on RS485 bus was halted. The root cause of failure was radiation which was re-confirmed by taking measurement of radiation dose [2] at installed units. The modifications in units were done for gracefully handling communication failure. The situation was challenging considering short time for maintenance limited to only in bimonthly shut down & keeping smooth operation of interlock. To overcome this situation phase wise steps were taken, as in first phase limiting communication failure problem only to single unit, in second phase replacing the set of major components in all units with required hardware modifications & in last stage relocation of the system in Indus-2 tunnel having minimum radiation. After implementing all these modifications no communication failure has been noticed.

In consideration with requirement of additional demand of temperature monitoring at new locations especially after installation of undulators, development of prototype unit for 16-channel TMU (Shown in Figure.1) was started. The practical limitations of installed TMU were reviewed & efforts were taken for minimising its short comings in the new unit. The size was reduced almost to half of earlier unit considering limited space available for installation in Indus-2 tunnel. After testing of two prototype units forty units were fabricated & tested successfully.

## TECHNICAL DESCRIPTION

The existing system is in operation for about fourteen years 24x7 round-o-clock providing alarms & interlock to Machine Safety Interlock System (MSIS) successfully. It has activated safety interlock on more than ~30 events & alarms on several occasions after detecting temperature rise over set limits. The troubleshooting of first major


Figure 1: Front & Back Panel of TMU



#bnilesh@rrcat.gov.in,

communication failure showed that it was due to high radiation dose absorbed by a transistor (BC337) which was part of watchdog reset circuit to microcontroller. The false reset signal was enabling the half duplex RS485 driver permanently in transmit mode, resulting in total communication failure. For restricting failure to single unit in first phase the RS485 driver direction control changed to failsafe mode i.e. in case of failure RS485 driver will always be in receiving mode. In second phase the microcontroller 89C52 were replaced with 89S8253 having internal watchdog & EEPROM for remotely updating trip set point. As a first safety precaution, in software the trip set values gets updated in EEPROM only if they are within defined extreme limits i.e. 50ºC to 99ºC. As a secondary safety level, in software after power on reset the trip set points read from EEPROM cross checked to ensures they are within extreme limits otherwise default value programmed in flash memory which is 75ºC is used as trip set point. In last phase all units were located to the place having least radiation level in the tunnel.

High temperature rise was a bottleneck for operating the machine with higher beam current. At first the temperature data was studied & critical locations where temperature was increasing beyond alarm set point were noted. It was concluded that the heating of different dipole chambers at different energy level was due to change in the orbit. In first stage (Beam current ~ 90 mA) global correction for first horizontal & then vertical orbit were made & temperature data were studied. In second stage (Beam Current ~120 mA) it was observed that temperature at exit port of dipole chamber was exceeding more than 75ºC. To overcome it new water cooled copper cooling block was developed & installed on all dipole chambers. Necessary beam orbit corrections were also done to keep temperature at other locations on dipole chamber within safe limits.

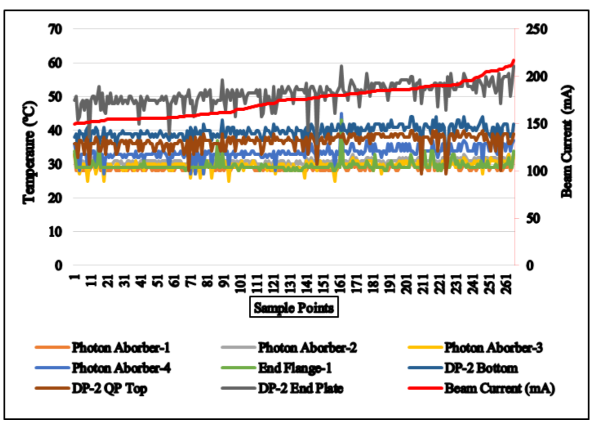


Figure 2: Sampled maximum temperature on a bending magnet chamber with beam current.

The sampled maximum temperature data (Shown in Figure 2) between the periods Jan-2018 to September-2019 along with increasing beam current from 150mA to 220mA, on a bending magnet chamber is plotted in the Figure-2. It can be seen the temperatures of all channels are within safe limits.

## DESIGN & DEVELOPMENT

Further the operation at higher beam current (~200mA) required a need to extend probing further at more locations on dipole chambers. The upgraded system of 20 units of 16 channels each supports to monitor 320 points. In new unit various provisions were added for overcoming shortcomings of existing units. For quick replacement the terminal connectors of thermocouple sensors on unit were changed to plugin type, D-connectors for RS-485 connector were replaced by RJ-45 connectors, internal address setting DIP switch has been provided on back panel. This switch also supports opting for termination resistor. Temperature measurement is done using K-type thermocouples. New units along with quick replacement feature also supports onsite firmware upgradation for reducing maintenance time as required. The other existing feature of working system are also implemented. RC filter is used for rectifying common mode & differential mode noises. The circuit is compatible for both grounded & un-grounded type of thermocouples. It also has provision for detection of open thermocouple.

ATmega328P was used as microcontroller & ADC ADS1118 was selected having a ΔΣ ADC core with adjustable gain, an internal voltage reference, a clock oscillator, and an SPI. All of these features are intended to reduce required external circuitry and improve performance. Such 8 ADC were multiplexed over SPI making design simple & compact. LM35 was preferred over inbuilt temperature sensor of ADC for CJC (Cold Junction Compensation) because it can be placed close to the thermocouple connector on front panel for minimising CJC error. The linearization of thermocouple is done with the help of lookup table. Half duplex RS485 communication is used in which all units are acting as slaves while computer in control room plays role as master. RS485 driver is optically isolated from the circuit for overcoming the ground loops & minimising the noise interference in analog measurement circuit [3]. Terminating resistors on the extreme end units are used to get rid of signal reflections.

## OPERATION AND INTERLOCK

Basic operation & interlock is similar to existing system. There is provision for two types of set points called Alarm Set Point & Trip Set Point. Both can be set point can be changed remotely. Alarm set point changed in GUI whereas trip set point is programmed in EEPROM. Since alarm has the second priority, it's raised in computer software. Trip set point is hardwired interlock (single contact). In PC software, user can identify the unit generating the alarm as this data is passed by the unit through the communication frame. In controller unit status of spare contact of trip relay is reed back & its status is sent in the frame. Considering the importance of trip relay, a maintenance frame was incorporated. After issuing this command all the trip relay will be activated & their status will be reed back. This insures normal behaviour of all trip relays from control room only. Each unit has single trip relay with failsafe logic (normally activated). The N/O (normally open) contacts of all trip relays are connected in series & single contact is given to Machine Safety Interlock System (MSIS). If any channel among 16 crosses trip set point, the trip relay is deactivated which results in opening the contacts. Necessary action will be taken through the interlock to dump the beam in the ring.

## SOFTWARE & COMMUNICATION

The microcontroller software of new units is compatible with existing & new unit (i.e.8 &16 channels). This has been kept for phase wise installation of new units in future, providing compatibility with existing GUI in control room.

Figure 3: GUI Panel for TMU

All units receives the computers query on RS485 bus & reply to it as per MODBUS protocol. Typical communication frame structure over RS485 is as given below:

| Char. No. | 1 | 2 | 3 | 4 | 5 | X | X |
|---|---|---|---|---|---|---|---|
| Character | STX | ADD | ADD | FRAME CHAR | DATA | CHK SUM | ETX |

ADD : 2 digit address,
STX/ETX: Start & End of frame,
FRAME CHAR: Frame defining charachter,
CHK SUM: Checksum

For initial testing of the operation of units in lab GUI (Shown in Figure 3) was developed in visual basic.NET. The GUI has following important features:

1. Data logging of 320 channels.
2. Selection of active units.
3. Trip signal status indication & logging.
4. Detection of open Thermocouple states.
5. TRIP test facility.
6. Trip set point programming.
7. Support for fault finding of ADC & calibration.
8. The communication on RS485, checksum verification and error reporting is done by the system. Invalid frames if received are kept in log for analysis.

Operation of units have been observed using the GUI for more than a week & found that the measurement matches with the output provided through temperature calibrator (YOKOGAWA CA-71). For the range of 0-500ºC the linearity error is none below 160ºC & within +/-1ºC between 160ºC to 500ºC.

## CONCLUSIONS

The existing system is working satisfactorily over past 14 years. Necessary steps were taken to ensure smooth operations of the system in spite of few failures due to radiation. The system has provided valuable input for achieving higher beam current operation. New units have been developed & tested successfully which will be commissioned soon in Indus-2.

## ACKNOWLEDGEMENTS

The authors are thankful to all the colleagues in UHVTS, RRCAT, especially Shri Navin Solanki for ensuring proper assembly of sensors. It will be incomplete without mentioning name of senior technician Shri Mahendra Vadgama for putting his sincere efforts in the development of prototype units, testing of new units & round-o-clock maintenance of system in Indus-2.

## REFRENCES

[1] *Distributed remote temperature monitoring system for Indus-2 vacuum chambers, Inpac-2011*
*N. J. Bhange, P. Gothwal, P. Fatnani, S. K. Shukla, RRCAT, Indore*

[2] *Dose assessment on temperature monitoring units in Indus-2 tunnel Inpac-2018*
*Gupta Dilip Kumar, Sahu T. K., Haridas, G., Bandyopadhyay T., N. J. Bhange*

[3] *National Semiconductor, Application Note 1057 by John Goldie Ten Ways to Bulletproof RS-485 Interfaces*

# IMPROVEMENTS TO VACUUM MONITORING AND LOGGING SYSTEM AT PLF MUMBAI

C. Rozario[1] *, S. Pal[1], R. Palit[2] and V. Nanal[2]

[1]*Pelletron Linac Facility, Tata Institute of Fundamental Research, Mumbai- 400005, INDIA*
[2]*Dept. of Nuclear & Atomic Physics, Tata Institute of Fundamental Research, Mumbai- 400005, INDIA*
** email: catarina@tifr.res.in*

## *Abstract*

The Superconducting Linear Accelerator, indigenously developed as a booster to the Pelletron, consists of 7 cryo-modules. The beam can be delivered to a different user stations on 7 beam lines housed in two separate experimental halls. The UHV in linac and beam lines is achieved using turbo-molecular pumps and Titanium sublimator + sputter ion pumps. A remote monitoring system for distributed vacuum measurement devices and gate-valve interlocks for vacuum safety have been installed. Since it is essential to monitor the vacuum over an extended period during accelerator operations, further improvements are carried out to the system for data logging and display. The vacuum measurement devices and custom-made gate valve monitoring devices are physically distributed and connected on the TCP/IP Ethernet bus. The monitoring and logging of the beam line vacuum parameters and the valve status has been developed using the LabVIEW.

## INTRODUCTION

The LINAC vacuum in the beam line and in the RF resonators is constantly maintained in the order of $10^{-7}$mbar. The communication to both types of monitoring devices - vacuum (Pfeiffer make wide range compact gauge sensor) and the gate valve (custom-made using PIC microcontroller) is established using serial device server that converts serial RS232 to Ethernet standards. Additional client computer allows easy local diagnostic feature.

With the use of Producer-Consumer methodology and TCP LabVIEW library for communication, we have developed an integrated GUI to process, record and display the vacuum and valve parameters. TCP VI (Virtual Instrument) ensures reliable transmission between client and server allowing multiple simultaneous connections. Time stamped data using TDMS (Technical Data Management Streaming) format allows safe access of the real time data from the same data file. We have been able to stream and store 40 channels of data numerically and graphically, with a refresh rate of 0.5Hz. The display interface is provided with a history subpanel, where the user can navigate and select the channels from the recorded files. The monitoring of current and past vacuum data has proved to be a useful tool for vacuum monitoring and troubleshooting.

## SOFTWARE IMPLEMENTATION

LabVIEW provides built-in template VIs that include the subVIs, functions, structures, and front panel objects helping to accelerate the software application.

### *Data communication using TCP VI*

TCP/IP communication provides a simple user interface that conceals the complexities of ensuring reliable network communications. The client initiates a connection to the device server using the process - opening the connection, reading/writing the information, validating for various errors in the network or device, and closing the connection. The server (device) listens for remote connections and responds appropriately. This is schematically shown in Figure 1.

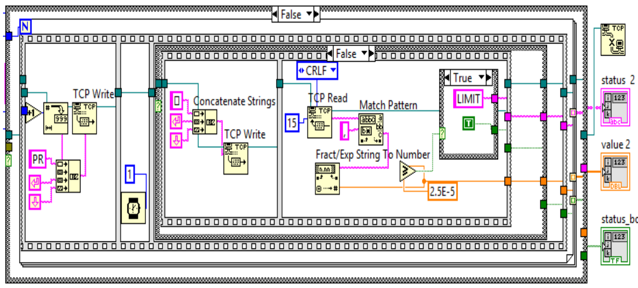


Figure 1: Block diagram of subVI for Vacuum communication

### *Producer-consumer methodology*

This methodology allows easy handling of multiple process while iterating at individual rates. The producer is the receiving module whereby the data is collected in array every one second. The Block diagram of vacuum/valve producer code screen is shown in Figure 2. The consumer is the analysis and processing module that processes, display and stores the data retrieved from the variable array.

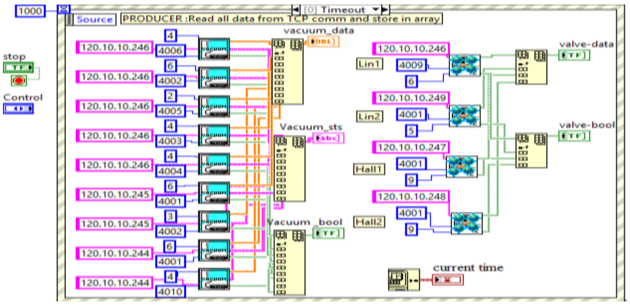

Figure.2: Block diagram vacuum/valve Producer

### *Data storage/retrieval using TDMS*

Use of TDMS allows flexible and easy data file format without designing new header structure. The TDMS allows concurrency as it has the ability to read/query and write on the same TDMS files. The TDMS file has associated time values for the acquired data channels stored in one or more explicit time channels. The TDM is also portable to other application such as Excel. The vacuum data is stored in the files every 6 seconds in a 3 layer format, interleaved and timestamped. The block diagram of TDMS write code screen is shown in Figure 3.

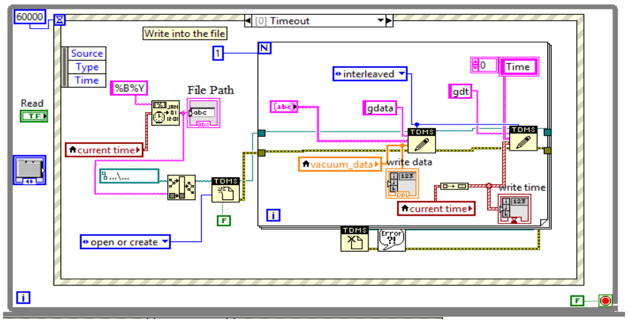

Figure 3: Block diagram of code Screen for TDMS write

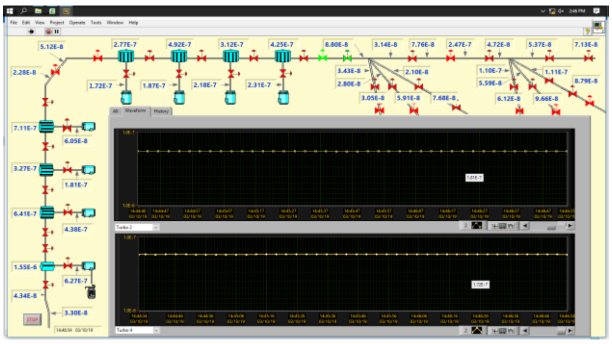
Figure 4: Front panel of Vacuum & Valve Monitoring and Logging System

User can access the channels from the history menu on prompt button and monitor any 4 channels on the graph. The front panel (Figure. 4) displays the measured vacuum and valve status on beam line diagram using color and blink (error) on the real time basis. A menu driven function- *Waveform* allows real time streaming of any two user selected vacuum data (0.5 Hz). *History* allows user to access data stored month wise in the file and plots multiple channel (#4) on XY plot (Figure. 5).

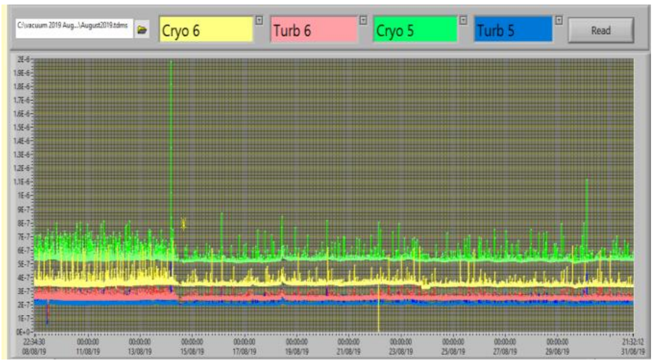

Figure 5: Multi channel XY plot from the TDMS history file

## CONCLUSION

The improvisation of the vacuum monitoring and logging system in LINAC accelerator hall and experimental halls (Hall-1 and Hall-2) has helped in troubleshooting and identifying vacuum changes in real time basis as well as long time variation provided through history files. Diagnosis of 40 vacuum parameters is now possible with an easy-to-use interface of multi-channel graph and facilitation of well-organized and documented files storage.


## ACKNOWLEDGMENT

We would like to thank Prof. R.G. Pillay, for invaluable guidance in the project. We also thank Ms. Sukanya Aldar, Ms. Mayuri Parkhe for their contribution and the PLF staff for their support.


## REFERENCES


[1] C. Rozario, *et al.* “Remote Monitoring of Vacuum and Valve Status using LabVIEW” INPAC 2015 proceedings.

[3] http://www.ni.com/product-documentation/3727/en/ the NI TDMS file format.

# ION BEAM ANALYSIS ACTIVITIES AT IUAC, DELHI

G R Umapathy#, S Ojha, S Gargari, G Raturi, Jaswant Singh, Pranav Singh ,Suraj Kumar, Mohan Nishal, N S Panwar, M P Singh, Jagdish Prasad, Rakesh Kumar , V P Patel, Mukesh Sota, K Devarani, Rajan Joshi, Sundeep Chopra, Dinakar Kanjilal

Inter-University Accelerator Center (IUAC), New Delhi, India

*Abstract*

Small and medium energy accelerators from keV to few MeV range play an important role in the field of material characterization, cultural & heritage studies, forensic analysis, biomedical elemental analysis, radio carbon dating etc. These studies are collectively known as Ion Beam Analysis (IBA). 1.7 MV Pelletron accelerator based IBA at IUAC, New Delhi is functional since 2010 and more than 15000 measurements have been performed using this accelerator. Rutherford backscattering Spectrometry (RBS), Channeling, Resonance–RBS and Elastic Recoil Detection Analysis (ERDA) measurements are performed routinely. This paper describes details of 1.7 MV based IBA facility and its applications activities in IUAC Delhi. Some of the recent experiments will also be discussed.

## INTRODUCTION

The interaction of energetic particle like $H^+$,$He^+$ or $e^-$ with material results in multiple phenomena like primary back scattering, ejection of primary knock on, and induced emissions like X rays , gamma rays and secondary emissions. These primary and secondary radiations energy analysis give specific information of the target material. The charged particle H/He when projected with few MeV to the target material few get backscatter due to close encounter with nucleus. These backscattered particles lose some of its energy on interaction and along the path of penetration. This energy information is detected using Silicon Surface Barrier Detectors (SSBD) and popularly known as Rutherford Backscattering Spectrometry. The RBS technique in ion channeling mode i. e. when projectile atoms are channeled along the direction of the plane of the crystal most of the projectile get along the crystalline plane giving track information about presence of defect/impurities in the path. The characteristic *X*-rays emitted through electron state change by projectile interaction with material with suitable *X*-ray detector called Particle Induced X-ray Emission (PIXE). In case of nuclear reaction to certain depth would emit gamma radiation which could be detected using suitable detector called as Nuclear Reaction Analysis (NRA). In case target marital having less mass then the projectile incident in grazing angle it would suffer knock on from the surface. Detecting these in forward angel referred to ERDA. All of these modes can be performed in a single scattering experimental chamber sequential or simultaneous. The RBS ,Channeling and PIXE are nondestructive where as NRA and ERDA targets would suffer partial destructive. Among IBA techniques RBS is more popular for its relevance in thin film analysis.

## INSTRUMENTATION FOR IBA

### *Ion Source and Accelerator*

Negative helium ions are generated by RF charge exchange ion source. Source primarily contains two parts. Positive ions are extracted from He plasma generated via application of RF on quartz bottle filled with helium gas. The second section of source extracted helium ions are passed through volume containing vapors of rubidium. Charge exchange occurs and negative helium ions are generated. They are extracted and focused into accelerator through injector section. The 1.7MV (NEC's model 5SDH-2) tandem accelerator with terminal voltage up to 1.7 MV is used for accelerating helium ions. At the terminal of the accelerator, a nitrogen stripper gas allows a second acceleration of the ion after converting incoming negative ion to a positive one. He ions of energy range 400 keV to 5.1 MeV are produced and delivered to experimental end station. The precise energy selection is performed by stabilized voltage at terminal and suitable magnetic field at analyzer magnet [1-3].

### *IBA Endstation*

The energetic He beam is focused on target in experimental chamber through 2 mm aperture. The target holder mounted on 4 axis motorized goniometer can hold multiple samples at a time. The goniometer can be programmed to bring the each sample in line with beam via X and Y motions and perform RBS measurement for a

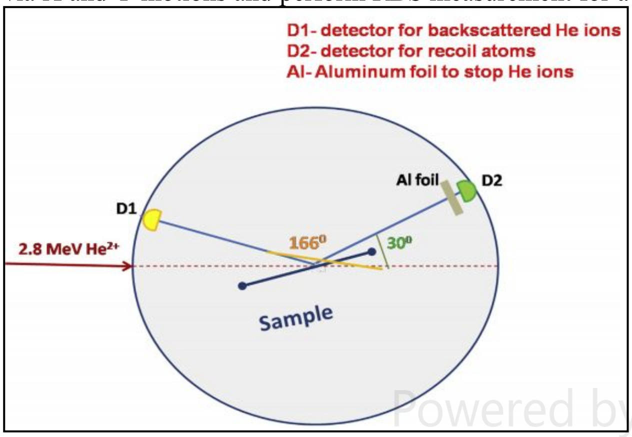


Figure 1: Schematic of the experimental setup for RBS-ERDA measurements at IUAC

#umagrphysics@gmail.com

preset charge collection. The θ and Ψ motion of goniometer is utilized to perform channeling and off axis RBS measurements. Energy of backscattered helium is measured by SSBD of 15 keV resolution mounted at $166^0$ . Facility is equipped with one movable detector ($110^0$-$30^0$) for grazing angle and ERDA measurements. The RBS and Channeling measurements are performed usually at 2 MeV and ERDA are carried at 2.8 MeV. Besides conventional measurements, resonance analysis is carried out for O, N and C at 3.037 MeV, 3.70 and 4.2 MeV's respectively for detection of lower mass elements in higher mass substrates. Simultaneous RBS-ERDA measurements are performed by placing movable detector at $30^0$ and tilting the samples to $75^0$ ($15^0$ tilt with respect to beam direction). The backscattering detector records backscattered He at $166^0$ and recoiled H spectra are measured with movable detector at $30^0$. Al or mylar stopper foil in front of movable detector stops recoiled helium and permits H to pass through it [1- 3].

## RESULTS AND DISCUSSION

### *RBS*

The energy of the backscattered projectile (He) is measured and related to the mass of the scattering nucleus and its position in the matrix. The characteristics of RBS make it particularly useful for determination of depth profile of heavier elements in light element matrices and for investigation of thin/multi-layer films. Those spectra are recorded in counts vs energy where energy, counts and FWHM of peak provide information of element, composition and thickness of layer respectively [1,4]. From Figure 2 the elements La, Sr, Co Mn and O are in the ratio $La_{1.3}Sr_{0.3}Co_1Mn_1O_6$ film thickness is 325 nm

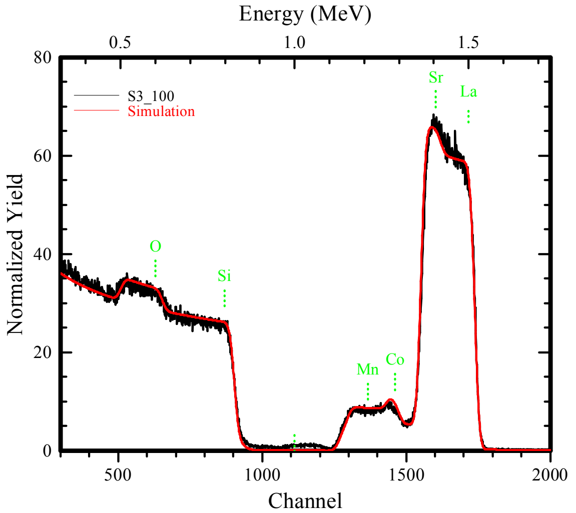


Figure 2:RBS spectra pulse laser deposited $La_{1.3}Sr_{0.3}Co_1Mn_1O_6$ thin film over Si(100) measured (black) simulation using RUMP code (red)

### *Channelling*

In channeling mode the incoming ions are confined in the periodic potential of crystalline arrangement of atomic rows. So that ions are focused only in forward direction and back-scattering yield reduced in comparison with normal recorded spectra. The back-scattered yield, depending up on channelled or dechanneled provides information about the location of impurity atoms, interstitial/substitutional positions, defect density and its depth profiles etc. RBS Channelling is most useful characterization tool in topics related to Solid phase Epitaxial Growth, Ion Beam Induced Epitaxial Crystallization, Ion Beam Mixing, diffusion profile and ion implantation in semiconductor technology [3].

### *Resonance RBS*

Enhancement of backscattering cross section can be used for detection of low mass impurities [1, 7]. Measurements at resonance energies for elements like O-3.037 MeV, N-3.70MeV, and C-4.2 MeV in heavier matrix substrates provides accurate information of their presence in minute quantities. In addition, the resonant width is only few keV, and can be used for depth profiling as a function of ion beam energy. The RBS measurement at oxygen resonance measurement at 3.045 MeV can provide information of presence of O in thin film, presence of native oxide layer on substrates and rate of oxidation of elements.

### *ERDA*

ERDA for Hydrogen detection and depth profiling can be carried out using the same setup by beam incident in gracing angle and movable detector placed at forward angle 300 with 14 µm Al Helium stopper foil in front of the detector. Figure 5 shows simultaneous RBS-ERDA set up with SSB detector placed at $160^0$ and $30^0$ . The H in any material or thin film can be probed from nm to few microns. The Figure 4 show the ERDA spectra of Hydrogen detected from GO (graphene oxide) surface on Si surface. The 30 KeV Hydrogen of dose 1E15 atom/cm2 implanted in Si(100) is used as depth calibration standard as shown in figure 4 with black line [4].

Table 1: Measurement Techniques and recent publications using IBA facility at IUAC

| Measurement | Application | Reference |
|---|---|---|
| RBS | Thin films, Nuclear targets | Lisha Raghavan et al, Thin Solid Films Vol 680, 2019, P 40-47 |
| Resonance | Near and depth probe for O*, N, and C | *Kunalsinh N. Rathod, et al, Phys. Status Solid B 2019 1900264 |
| Channelling | Single crystals, Epitaxial layer | Divya Gupta *et al* 2019 *Nanotechnol ogy* **30** 385301(2019) |
| ERDA | Thin and bulk targets | Chetana Tagyi et. al. Intern. Jou. of Hyd. Energy Vol 43, Iss 29 (2018), P-13339-47 |

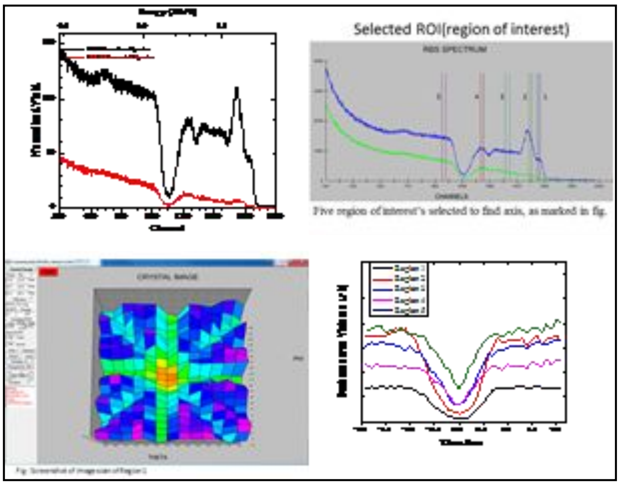


Figure 3: (a). Comparison of RBS spectra of Multi-junction solar cell random (black) and channeled (red) (b).Selection of region of interest to find axis of channeling (c).Image scan of above Epitaxial solar cell (d). Angle scan for all 5 selected region along different depth

## OPERATION SUMMARY

The stable He beam is extracted from RF source with combination of probe, extractor and bias gap lens assembly. The injector energy 24 keV remains same for all types measurements. The Terminal voltage and charge state are chosen to deliver accurate energy to end station using quadruple as focusing element and the analyzer magnet. The table 2 shows accelerator operation summery for He beam

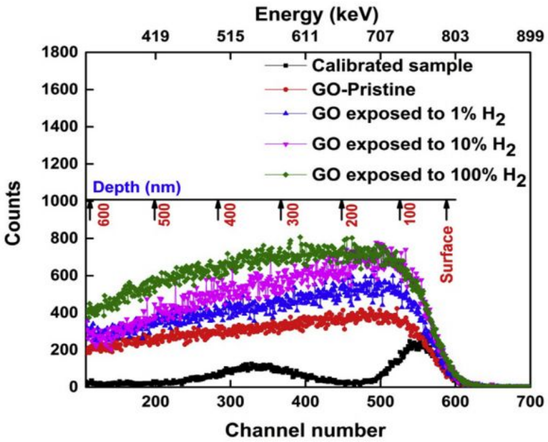


Figure 4 : ERDA plots (with energy and depth scale) showing the hydrogen content present in pristine GO, GO-1%, 10% and 100% Hydrogen gas environment. (Chetna Tagyi et al. Intern. Jou. of Hyd. Energy Vol 43, Iss 29 (2018), P-13339-47)

Table 2: The Operation details of Terminal Voltage , Charge state, Energy for different measurement technique using He beam

| **Terminal Potential (MV)** | **Charge State** | **Energy** (MEV) | **Measurement** |
|---|---|---|---|
| 0.86-0.987 | +1 | 1.8-2 | RBS and Channeling |
| 1.07-1.25 | +2 | 3.045-3.09 | O resonance RBS |
| 1.198 | +2 | 3.61 | N resonance RBS |
| 1.32 | +2 | 4.02 | C resonance RBS |
| 0.92 | +2 | 2.8 | ERDA and Channeling |

## CONCLUSION

The Pelletron accelerator based IBA facility has been developed and is being used regularly at IUAC. A large number of academic researchers from different Universities and institutes from various parts of country and abroad have been using the facility regularly. It is a compact and versatile facility which is being used for different types of measurements such as RBS, Resonance RBS, RBS-Channeling and ERDA for development of better understanding of the compositional profile and quality of the target. The facility is operational round the year and more than 15K measurements have been performed September 2019.

## REFERENCES

[1] W. K. Chu, J. W. Mayer, and M. K. Nicolet, "Back Scattering Spectrometry", Academic Press Inc, Harcourt Brace Jovanovich, 1978.

[2] Dinakar Kanjilal et. al. Testing and operation of the 15UD Pelletron at NSC, NIMA, Volume 328, Issues 1–2, 15 April 1993, Pages 97-100.

[3] L. H. Yeo, et al, Anomalous spectral-weight transfers unraveling oxygen screening and electronic correlations in the insulator-metal transition of VO2, Phy. Rev. B 91, 081112(R) (2015).

[4] R D Verda, C J Maggiore, J R Tesmer, A Misra, T Hoechbauer, M Nastasi, R W Bower, Depth profiling of hydrogen in crystalline silicon using elastic recoil detection analysis, Nucl Inst Meth in Phy Res, 183 (2001) 401-412.

[5] G R Umapathy, Sunil Ojha, Kavita Rani, Meenu Thakur, Neeraj Kumar, Ruchi Mahajan, S Chopra, D Kanjilal, Composition Profile of Thin Film Target by Rutherford Backscattering Spectrometry, DAE Symp. Nucl. Phys., (2016).

[6] G R Umapathy et al,Proceedings of the DAE Symp. on Nucl. Phys. 63 (2018)

# DESIGN AND DEVELOPMENT OF VERSATILE AND MODULAR DIGITAL CONTROL SYSTEM FOR POWER CONVERTERS OF ACCELERATOR*

H. K Khatwani[1,]*, S. N. Singh[2], M. L. Gandhi[1], R. Banwari[1] and A. C. Thakurta[3]
[1]Accelerator Power Supplies Division, RRCAT, Indore - 452013, INDIA
[2]Accelerator Magnet Technology Division, RRCAT, Indore - 452013, INDIA
[3]Electron Accelerator Group, RRCAT, Indore - 452013, INDIA
**Email: khatwani@rrcat.gov.in*

*Abstract*

A modular digital control system has been designed to standardize the control of magnet power supplies built with different topologies. The developed digital control system will be helpful to move towards a common hardware and software for control of power supplies.

This digital control system was applied to control the power circuit of a magnet field mapping power supply which uses SCR based pre-regulator and a transistorized series pass regulator. The digital control loop for load current and the collector to emitter voltage of the series pass element is implemented in FPGA XC7A35T. For current loop, the DCCT output is digitized using a 24-bit ADC and the controller output from the FPGA is sent to transistor base drive using a 16-bit DAC. The voltage between the collector and the emitter nodes of the transistor bank was sensed and digitized using an 18-bit ADC. The DSP TMS320F28379D gets the current reference data from remote through serial communication, sends it to FPGA for control loop, gets the load parameters from FPGA for protection and control the SCR firing. We achieved better than ±30 ppm of load current stability at load current of 200A after implementing this control system.

The developed digital control hardware can be used for different power converters by changing the software.

## INTRODUCTION

The Indus Accelerator complex is a national facility having two synchrotron radiation sources, Indus-1 and Indus-2. These accelerators consist of large numbers of magnets to control the electron beam in desired orbit. The power converter topologies for these magnets depend upon the required current/power specifications. Different topologies require different control schemes. For these power converters, analog control schemes have been implemented. This control configuration requires a huge amount of inventory for all the power supplies. From the functionality point of view, although these analog controlled power supplies meet the required specifications, but they have limited remote control and diagnostic capability. A control system is required which can facilitate minimum inventory, better remote control and diagnostic features. To implement this, a modular versatile digital control system has been developed which can be used in power supplies with little changes irrespective of the power converter topology. The inherent programmability of the digital control system is helpful in development of versatile power supplies control unit for all power supplies.

For digital control implementation in power converters, the Digital Signal Processors (DSPs) [1] and Field Programmable Gate Arrays (FPGA) [2] are used as the preferred options.

DSPs are software-based devices, programmed in C language. These devices have integrated modules such as ADCs, PWM, RAM and peripheral interface bus such as SPI.

FPGAs are digital hardware-based devices consisting of arrays of uncommitted digital resources such as registers, gates, memory blocks, multipliers etc. The programming of these devices is focused on configuring the logic resources and defining the interconnections between them to achieve the desired operation.

In the developed module, we have utilized the dual advantage of FPGA for parallel computing and the DSP for the complex arithmetic calculations.

## HARDWARE DESCRIPTION

The digital power supply control block diagram is shown in Fig.1. The picture of versatile digital control card is shown in Fig. 2. The DSP TMS320F28379D is used for supervisory control, interlocks and firing control of pre-regulator SCR converter. The DSP is interfaced with remote control through an Asynchronous Serial Communication Interface (ASCI) bus. The DSP gets the load current reference from remote reference and sent it to FPGA through Serial Peripheral Interface (SPI) bus. The FPGA Artix XC7A35T is used for implementing the digital control of power supply. Three different control loops have been implemented in FPGA, and these control loops can be programmed at different sampling rate. The FPGA board is interfaced to different ADCs and DACs to get the feedback signals and set the controller output using SPI bus. The sampling rate of the ADCs and update rate of DACs is decided by control loop. The current and voltage feedback signals from the power circuit are digitized using a 24-bit sigma delta ADC and 18-bit SAR type ADC. To monitor and control other parameters such as filter capacitor current and voltage across the devices, an 8-channel 18-bit ADC is used and interfaced to FPGA. There is a provision of 5 analog outputs by a 4-ch 16-bit DAC and a 20-bit DAC. The DAC outputs are used for controlling the power converter and for debugging the digital controller.

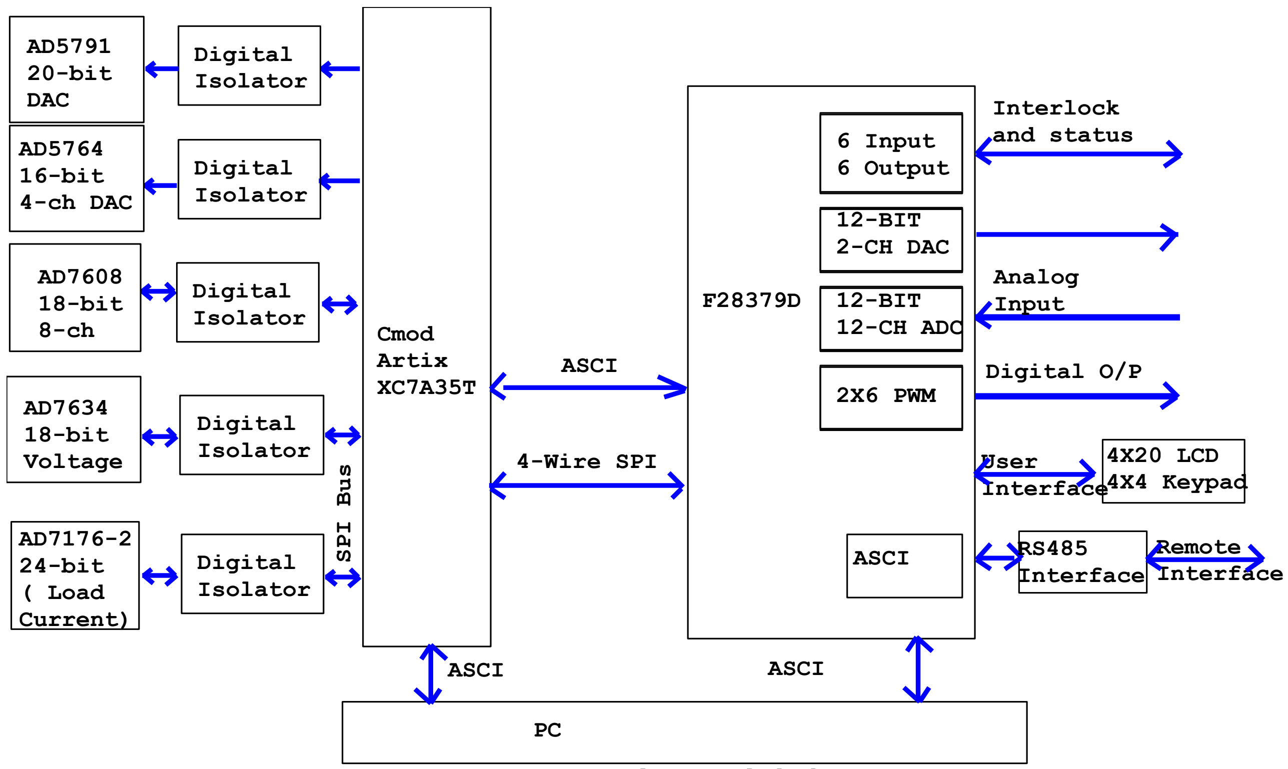

Figure 1: Power Supply Control Block Diagram

## POWER CONVERTER DESCRIPTION

The developed digital control system has been tested with a 1000A, 60V power supply. This power supply, using an anolog control system, has been used for the characterisation of dipole and other magnets for more than 20 years. In this power supply, SCR controlled pre-regulator followed by transistorised series pass circuit has been used. The existing analog control system was replaced and the new digital control system implemented. For control of load current and the voltage across series pass transistor bank (Vce) the digital PID control have been implemented in FPGA. The analog output of current loop is used to drive the transistor base and digital output of Vce control loop is sent to DSP and then DSP set the firing of SCR bridge by sensing the sync signal from mains voltage with its internal 12-bit ADC.

## DIGITAL CONTROL LOOP IMPLEMENTATION

The PID control has been implemented in the present control system. In PID control, the difference between reference and readback corresponds to the control loop error. The PID control output is the parallel sum of three paths that act, on the error, error integral and error derivative. The weight of each path is adjusted to optimise the transient response. The PID output can be represented by

$$u(t) = K_p e(t) + K_i \int_{-\infty}^{t} e(\tau)dt + K_d \frac{de(t)}{dt}$$

Conceptually the controller comprises three separate path connected in parallel. The proportion gain Kp adjust the open loop gain, the integral path accumulate the error history and derivative term used to damp the oscillation and reduce the transient.

Apart from conventional PID control algorithm some additional enhancement features incorporated in the control system such as proportional output saturation, independent reference weighing on proportional path, anti-windup integral reset and adjustable output saturation.

## CONTROLLER SELECTION

### *FPGA Board*

The Artix XC7A35T has 33,280 logic cells, 90 DSP slices and 1,800 Kb block RAM. This is sufficient to implement the required PID control loops implementation. The control algorithm has been implemented using fixed point arithmetic.

### *DSP Board*

The DSP 320F28379D has single precision floating point unit, 200 MHz internal clock speed, 24-ch 12-bit ADC, 24 PWM output. In the digital control system developed, LAUNCHXL-F28379D board [4] has been used. The control system developed has provision for 12-channel analog input and 12-channel high resolution PWM output and 12 general purpose I/O for interlocks and status signal.

### *ADC*

The 24-bit sigma delta ADC AD7176-2 has been used for sensing the load current at sampling rate of 4 ksps. An 18-bit ADC AD7634 is used for sensing the voltage with max sampling rate of 200 ksps. An 8-ch ADC AD7608 used to sense other parameters like filter capacitor current, voltage across the devices, temperature of devices etc.

### *DAC*

Two different ADCs were used to set the controlled output at different rate. One 4-channel 16-bit DAC AD5764 with settling time 10 µs and other is single channel 20-bit AD5791with settling time 1µs. The analog output is set by any of these DAC output depends upon the required controlling speed and resolution.

## IMPLEMENTATION OF CONTROL

The control algorithm has been implemented in FGPA and DSP. The DSP gets the reference from the remote and send the status of power supply to remote by asynchronous serial communication. The set reference is sent to FPGA board by SPI protocol. The FPGA check the reference whether it is within operating range and within the acceptable step change. After the validation the FPGA update the PID reference. The analog output is set by DAC and the PWM control reference is sent to DSP. Based on the set value the DSP modify the PWM output signal.

The system is versatile in the sense that the same control hardware, but with a different software, can be used to control a different power converter. A different software can be based on selection of parameters which in turn depend on nature of the power converter.

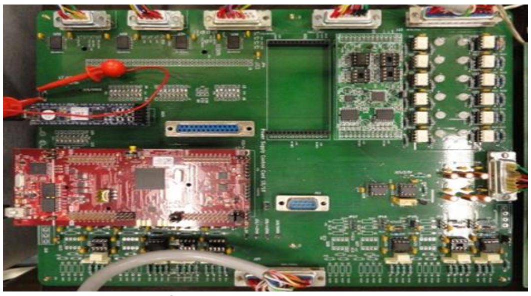

Figure 2: Pic of the Versatile Digital Control Card

## RESULTS

The developed digital control system has been tested with the field mapping power supply at 200 A with a magnet having 200 mH / 200 mΩ impedance. The observed load current was within ± 30 ppm over 8 h run of the power supply (Fig. 3).

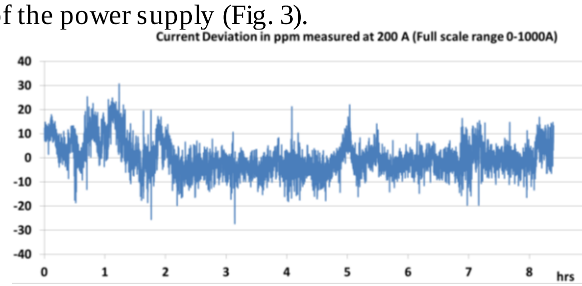


Figure 3: Measured load current data (for 8 hrs) showing stability within ±30 ppm

## ACKNOWLEDGEMENT


Authors are thankful to Vinay Kumar Maurya, Ramesh Prasad and Nathan singh for their help during system integration and testing of power supply. Authors are also thankful to other colleagues of Accelerator Power Supplies Division, RRCAT, Indore for their valuable support during the development of the versatile digital control system.


## REFERENCES


[1] Bao-Sheng Wang, et all, “THE FULLY DIGITAL CONTROLLED CORRECTOR MAGNET POWER CONVERTER”, Proceedings of IPAC’10, Kyoto, Japan p 3278.

[2] R. N. Xu, et all, “DIGITAL POWER SUPPLY CONTROLLER DEVELOPMENT BASED ON FPGA”, Proceedings of IPAC2013, Shanghai, China, p702.

[3] K. H. Park, et all, “THE MAGNET POWER SUPPLY FOR PAL-XFEL” Proceedings of IPAC2014, Dresden, Germany, P 504-507.

[4] Texas Instruments Co., www.ti.com

# Control station for remote operation of adjustable beam line slits

J. N. Karande[1*], Manoj Kumar T.K.[1], Prajakta Dhumal[1], A.N. Takke[1], S. Pal[1], R. Palit[2] and V.Nanal[2]

*[1]PLF, TIFR, Mumbai – 400005*

*[2]DNAP, TIFR, Mumbai – 400005*

* *jkarande@tifr.res.in*

*Abstract*

The heavy ion beam transport system in the PLF, Mumbai includes beam diagnostic devices and adjustable X-Y Slits (beam collimators). Presently there are two generations of Slit boxes installed in Linac accelerator and user beam lines. The first generation Slit box design is based on a DC motor while the second generation slit box design employs a stepper motor. Each slit box is a combination of four slits X+, X-, Y+ and Y-. The present slit control units have only local control and slit adjustment needs beam interruption. Hence, the slit control stations are designed for remote control and monitoring. The control hardware is developed around Silicon lab module C8051F020. The new design facilitates the slit adjustments during the beam tuning without interrupting the beam. Two control stations for DC motor type slit controllers are designed, developed and successfully installed in the Linac accelerator. One control station for the stepper motor type slits is developed and testing is in progress.

## INTRODUCTION

The superconducting LINAC at PLF, Mumbai [1] has more than 20 beam diagnostic boxes in the beam transport system. Beam diagnostic box is a combination of beam diagnostic devices, namely, BPM (Beam Profile Monitor), FC (Faraday Cup) and adjustable X-Y slits. These devices play an important role in the beam transport system. The adjustable X-Y slit set is a combination of four separate slits, X+, X-, Y+ and Y- (see Fig. 1).

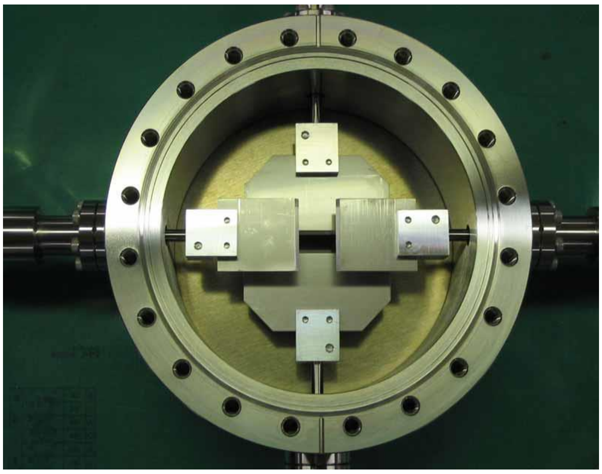

Figure 1: An inside view of the slit box

These slits provide an adjustable collimator along the beam paths and also help in defining the beam path. Each slit is connected with motor and has a displacement range of 15 mm, corresponding to -3mm to +12mm movement w.r.t. the centre of the beam line. . A variable resistor (potentiometer) is connected to the motor shaft to get an accurate position read-back, which translates to the measurement of displacement. There are two generations of slit boxes installed in the Linac and user beam lines. The first generation slit box design is based on a DC motor, while the second generation slit box design employs a stepper motor. Present controllers for these slit boxes are not suitable for the remote operation and require beam interruption for adjustments, Moreover, and the position accuracy is also limited. Therefore, a new slit controller is designed, which facilitates the slit adjustments during the beam tuning through RS232 communication. It also has improved position read back accuracy of ±1% due to four wire measurement and 12 bit ADC readout.

## HARDWARE DESCRIPTION

Electronics hardware for this control system is developed around Silicon Lab module C8051F020 [2]. This module is an enhanced version of 8051 microcontroller. It has 64 I/O pins, five timers, six external interrupts, several internal interrupts, 12 bit on-board ADCs. In addition, it has two serial ports and 64K program memory. Figure 2 gives a block diagram of the control system. In this control system, position monitoring and motor control of either DC or stepper is incorporated for 4 slits.

Silicon lab C8051F020 module is interfaced with motor driver, LCD, Keyboard, limit signals, RS232 level convertor and ADC for the Analog measurements.

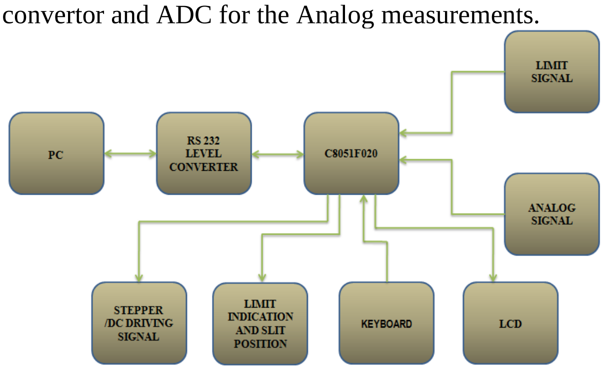


Figure 2: Block diagram of the slit control system

*email: jkarande@tifr.res.in

There are two types of drivers used in this design- a DC motor driver and a stepper motor driver. The DC motor driver circuit design is based on L293 driver IC shown in Figure 3. In a single L293D there are two H-bridge circuits inside the IC, which can rotate two dc motors independently. Two driver ICs are incorporated in the design to take care of four DC motors.


Figure 3: A picture of Slit control box (DC Motor)

In the second generation of the slit box, stepper motors are used for the movement of the slits. A stepper motor control design is based on A4988 micro stepping stepper motor driver shown in Figure 4. This driver can drive the bipolar stepper motor up to 2 A output current per coil. It has a simple step and direction control interface. This driver provides five different step-resolutions, namely, full step, half step, quarter step, eighth step (1/8) and sixteenth (1/16) step. It has inbuilt intelligent chopping control that automatically selects the correct current decay mode (fast or slow decay).

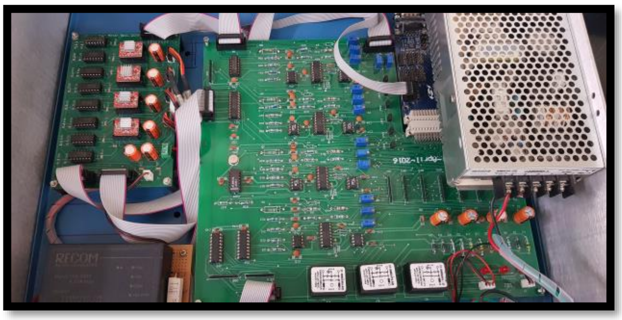

Figure 4: A picture of slit control box (Stepper Motor)

Further, over-temperature thermal shutdown, under-voltage lockout, and crossover-current protection are also available in this driver. This driver requires three digital control signals, namely, Pulse, Enable and direction. The Pulse input frequency decides the speed of the motor, while the Direction input is used for changing the direction of the motor (forward/reverse) and the Enable input is used to start/stop the motor. Three digital I/O port pins of C8051F020 are dedicated to each motor control.

The slit position monitoring is done using a 12 bit on board ADC of Silicon lab C8051F020. A Variable resistor (potentiometer) is mechanically coupled with the motor shaft for getting position read-back and Change in the resistance is directly proportional to the change in the position of the slits. Four wire measurement technique is used for position read-back, with a constant current of 1mA. The voltage across the potentiometer is measured using the 12 bit ADC and processed further to get the resistance. Before giving this signal to ADC proper signal conditioning is done to match acceptable signal level of ADC. Proper care has been taken to filter out the noise from the signal for getting position read back with accuracy better than +/- 1%. The measured resistance is then converted to fractional level and the slit position read-back is displayed as '0 to 100 %' corresponding to 0 to 15mm displacement. For the mechanical safety of the slits, limit switches are provided on slit boxes. Using these limit switches automatic motor stop logic is developed using digital gates. A 4*4 Keyboard for local control and 4*20 LCD panel for local display is also incorporated in the design. The control and monitoring from the remote PC is done via RS232 serial communication.

## SUMMARY

Slit controllers for remote operation and improved position read-back accuracy have been developed for two generations of slit boxes. The DC motor type slit controllers are successfully installed at two different location in linac beam lines and are working satisfactorily. The final testing of the stepper motor type slit controller is underway. These controllers will be installed in linac user beam lines.

## ACKNOWLEDGMENT

We are grateful to Prof. R.G. Pillay, for invaluable guidance in the project. We thank Mr. L.V. Kamble for fabrication and mechanical assembly of the slit controller units, and the PLF staff for their support.

## REFERENCES

[1] R.G. Pillay, "Overview of the Pelletron LINAC Facility", InPAC2011 proceedings.
[2] C8051F020 (www.silabs.com/documents/public/data-sheets/C8051F02x.pdf

# DEVELOPMENT OF METHODOLOGY FOR QUALIFICATION OF PERFORMANCE OF ACTIVE SHUNTS DURING THEIR MASS PRODUCTION

Aradhana Kumari*, M. L. Gandhi and A. C. Thakurta
Accelerator Power Supplies Division, RRCAT, Indore - 452013, INDIA
. * email : aradhana@rrcat.gov.in

*Abstract*

Eighty numbers of active shunts are being produced in-house at RRCAT; and they would be deployed to facilitate Beam Based Alignment in Indus-2 ring, a 2.5 GeV electron accelerator.

The active shunts would be placed across the highly interactive system which consists of a network of series connected quadrupole magnets, their driving current source and the active shunts connected in parallel to the remaining quadrupole magnets in the series connected chain of the magnets. A four quadrant converter in the output stage allows multi-quadrant operation of the shunt whereas a pulse width modulated rectifier in the preceding stage supports bidirectional utility interface enabling efficient converter operation in all quadrants. This topology generates very low line harmonics, near unity power factor operation, and facilitates regenerative utility interface along with the four quadrant operation at the output. Therefore, the performance tests related to the measurement of turn-on and turn-off transients, line harmonics, stability, power factor, converter efficiency, converter dynamics, etc. have to be executed on each active shunt to ensure closely matching behaviour amongst all the manufactured unit of the active shunts.

In this paper, the complete testing strategy, the importance of all the test parameters and method of inspection of those parameters have been explained.

## INTRODUCTION

The active shunts [1] are being produced to be placed across each Quadrupole (QP) magnets of Indus-2 storage ring for Beam Based Alignment (BBA) [2]. There are a few current sources which feed groups of series connected QP magnets. The shunt has been designed to deliver as well as sink the required current through these magnets without affecting the current in other series connected magnets.

The active shunt is a current regulated power supply rated for ±6 A, ±80 V and 500 PPM stability. In this topology, the input stage is a Pulse Width Modulated Rectifier (PWMR); followed by a Four Quadrant Converter (FQC) as the output stage. The purpose of the PWMR is to: 1) minimise the THD in line voltage and current; 2) maintain unity power factor over in the operating current region; 3) provide regenerative utility interface that allows bidirectional flow of power. The FQC allows bipolar output enabling operation in all four quadrants [1]. During BBA, magnetic field of each of the seventy-two quadrupole magnets of Indus-2 ring can be changed individually by ±3%, without affecting the field of other QP magnets. The BBA helps in reducing the **C**losed **O**rbit **D**istortion (COD) and increasing the beam lifetime. Also, the shunts can be useful in performing the **L**inear **O**ptics from **C**losed **O**rbit (LOCO) for beta beat correction and tune correction [3]

In-house development of eighty nos. of quadrupoles and their qualification is a big challenge, where it has to be ensured that all the units are assembled identically. The four stages of production involve: i) Printed board assembly; ii) Assembly and wiring; iii) Visual inspection; iv) Table top testing of essential control boards; and v) Integrated testing of the shunts. All these have to be completed within the decided timeframe under the well-planned production strategy [4]. Assessing the quality of such large numbers of units during the mass production within the strict timespan is not possible without a tactically organised approach. In order to execute this task, a stepwise procedure and a blueprint have been prepared based on certain tests, which are to be compulsorily filled during the manufacturing of the shunts. The procedure so developed is inclusive of careful blow by blow checks at each crucial stage of the shunt which includes power and control electronic circuits. In this paper methodology developed for integrated testing will be focussed.

## SEQUENCE OF TESTING PROCEDURE

The different stages in the qualification of the active shunt unit are: 1) Functional testing of PWMR and FQC blocks independently; 2) Integrated testing of PWMR and FQC as a combined unit; 3) Capturing of different waveforms, calibration test, stability data record, report generation; 4) Comparison of the test report of the unit under testing with the previous reports; 5) Taking corrective steps if the results vary beyond the expected figures arrived and recorded in previous reports.

In order to facilitate the testing of the various modules of the active shunt, a forced cooled array of power resistors with a magnetic choke has been designed. With the help of plug and socket arrangement, it becomes easy to establish the desired test circuit. It saves considerable time required for making these connections frequently during the testing. The load bank uses over temperature protection interlock. A picture depicting load and active shunt arrangement can be seen in Fig. 1.

Figure 1: Active shunt connected to load set-up

Each unit of the active shunt is qualified in a sequential manner as shown in the flowchart in Fig. 2, After completing all these stages, the supply becomes ready in all respects for commissioning at Indus Accelerator Complex (IAC).

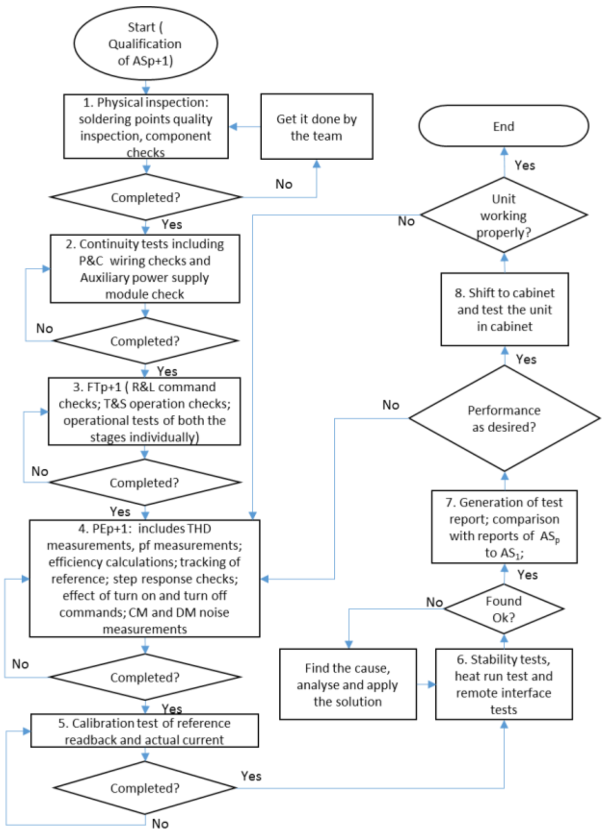


Figure 2: Flowchart for the sequence of testing and qualification of AS units; *Abbreviations: (p+1)$^{th}$ Active Shunt ~ AS$_{p+1}$; Power & Control ~ P&C; Functional Testing of (p+1)$^{th}$ unit ~ FT$_{p+1}$; Performance evaluation of (p+1)$^{th}$ unit ~ PE$_{p+1}$; Remote local board ~ R&L; Timing & sequence board ~ T&S.*

## INDEPENDENT TESTING OF PWMR

There is a specific setup for testing the PWMR stage [4]. After completing all the preliminary checks viz., gate signals, feedback ratio, polarity checks, the power analysis and harmonics analysis are carried out. The values corresponding to total harmonic distortion in line voltage and currents are recorded. In order to find out its efficiency, a standard template has been prepared.

## INDEPENDENT TESTING OF FQC

There is specific test setup for testing of FQC individually [4]. The voltage controller is the inner loop, hence it is qualified first, which includes the current and voltage ratio and polarity check with DC reference as well as the step response of voltage loop.

Thereafter, the current loop is closed and the reference and read-back are monitored at various points viz., front panel, controller card, FQC current sensing cards, etc.

## INTEGRATED TESTING

Once the PWMR and FQC stages are individually qualified, they are integrated to form a complete unit. At this point, it is essential to perform the trimming of feedforward network to minimize the turn-on transients. Through this, it is ensured that once the load switch closes and the AS unit comes in parallel to the active load of QP magnets already energised with a main power supply, minimum disturbance should be observed in the load current.

## PERFORMANCE EVALUATION TESTS

After integration of PWMR and FQC, some measurements are taken to evaluate the performance of a unit. Overall performance of the unit depends on all the tests carried out previously i.e. wiring and assembly to stepwise functional tests of individual blocks.

The major tests included in the performance evaluation of the unit have been described below:

1) Protections and interlocks, voltage polarity checks power and control wiring, remote local operations, sequence and timing check are done as shown in the flowchart in Fig. 2.

2) *PWMR testing with resistive load and DC power supplies [1]:* During the independent testing of PWMR, readings are taken for line harmonics analysis, pf measurements and power analysis, in both the rectifier and inverter mode.

3) *Testing of the complete unit with magnet load and DC power supplies [1]:* After the qualification of FQC stage independently, both PWMR and FQC are integrated. Thereafter, line harmonics measurements, pf measurements and power analysis are carried out, in both the rectifier and inverter mode.

4) *Testing of PWMR operation in the integrated unit [1]:* Here, the operation of the bridge changes from a simple rectifier to the pulse width modulated rectifier. The output voltage waveform of PWMR is captured after setting the rated current of 6 A. In this part, the voltage pattern of PWMR is analysed in co-ordination with the timing diagram [1].

5) *Voltage loop step response [1]:* In this part, the outer loop of FQC which is a current is opened and a step reference is given to the voltage loop with the help of function

generator Tektronix/AFG3102C and its response is recorded.

6) *Current reference tracking in current loop [1]:* In this test, the tracking of the load current with its reference is verified. All of these operations are time synchronized.

7) *Effect of turn on command on load current [1]:* In order to minimize the disturbance caused in load current when the load switch is closed, feed-forward trimming is carried out. The magnitude of this disturbance is captured during this test.

8) *Effect of turn off command on the load current [1]:* At the time of turn off, the load current is brought to zero at predetermined rate. The current loop remains active till the command for opening the load switch is released. This feature of AS helps in keeping the energy of the magnetic components to a minimum value so that opening of the load switch won't cause excessive stress on the circuit elements.

9) *Effect of turn off command on the PWMR output voltage [1]:* In this step, the load current of AS unit is set to the rated current value of 6 A, and the overshoot in PWMR voltage is measured. The acceptable limit is 30 %, above which overvoltage fault is received.

10) *CM and DM noise measurements [1]:* These readings are taken with the active load. Typical values have been given in the table 1.

11) *Calibration test:* A relation between the reference and the actual load current is found by taking their readings. A module is developed to measure the actual load current during this test. The same module is also used while measuring the load current stability.

12) *Stability data record:* The stability data is recorded for 12 hours with help of 6.5 DMM of Keysight/34465A.

13) *Heat run test:* The supply is kept on for 12 hours and after this tenure, the temperature at different point viz., all heat sinks, regulator ICs, driver ICs etc. are measured and recorded.

14) *Remote interface tests:* An interface board has been designed to operate the supply in remote mode. The power supply operation is verified for the remote command signals (On, Off and Reset), analog signals and the status signals. The active shunt is given an analog remote reference and its read-back is monitored with DMM.

The values corresponding to the test parameters mentioned as above are recorded in a fourteen-page test template. The data so recorded in the test report is compared with the previous results. Through this it becomes easy to ensure the quality, reliability, uniformity in all the units. Since, it is difficult to include that template in this paper, therefore the typical values of all the parameters measured has been tabulated below in table 1.

After the step of report generation, the supply is moved into the cabinet, and they are tested inside the cabinet. Thereafter the cabinet is installed and commissioned at site in IAC.

Table 1: Typical values of the test parameters for AS

<table>
<tr><th>Sr No.</th><th>Test parameters</th><th>Instruments used</th><th>Values (Typical)</th></tr>
<tr><td>1</td><td>THD in line voltage</td><td rowspan="9">DMM-4.5 digits, Agilent/ U2152B; DSO Tektronics/ TPS2024; Current amplifier Tektronics/; A DC power supply- APlab/ L12815S</td><td>≈ 4%</td></tr>
<tr><td>2</td><td>THD in line current</td><td>≈ 7%</td></tr>
<tr><td>3</td><td>Efficiency</td><td>≈ 80%</td></tr>
<tr><td>4</td><td>Rise time_ Voltage loop step response</td><td>≈ 40 µs</td></tr>
<tr><td>5</td><td>Overshoot _Voltage loop step response</td><td>≈15 %</td></tr>
<tr><td>6</td><td>Disturbance in load current during turn on</td><td>≈ 3 mA</td></tr>
<tr><td>7</td><td>Observed overshoot in voltage in PWMR during turn off</td><td>≈ 28%</td></tr>
<tr><td>8</td><td>CM noise</td><td>≈1 mA</td></tr>
<tr><td>9</td><td>DM noise</td><td>≈ 0.25 mA</td></tr>
</table>

## CONCLUSION

The methodology described in this paper has been followed for the testing of the active shunts. Due to this organised stage wise testing, fault diagnosis and rectification time has come down. A closely matching performance of all the units could be achieved. The data so recorded for each unit can be referred during commissioning as well as maintenance. So far, fifty-nine such active shunts have been made in-house, and out of these forty-six have been qualified for commissioning.


## ACKNOWLEDGEMENT

The authors acknowledge the contribution of P. Renukanath and his team in the development of the magnetic components used in the active shunts. They appreciate the roles of Deepchand and his team in the fabrication and mechanical assembly. They are also thankful to Lal Viswanath and S. C. Ghosh for their assistance during assembly and wiring of the shunts.


## REFERENCES


[1] M.L. Gandhi, Srinivas Lingam and A.C. Thakurta, "Bipolar Active Shunt with Bidirectional Utility Interface for the Quadrupole Magnet of Indus - 2," 9th In-ternational conference on Industrial and information systems (ICIIS), pp. 1-6, Dec. 2014.

[2] S.K. Jena, Riyasat Husain, M. L. Gandhi, R. K. Agrawal, S. Yadav and A. D. Ghodke "Beam Based Align-ment and its Relevance in Indus-2", AIP Review of Scientific Instruments 86, pp. 093303-1 to 093303-6, Sep. 2015

[3] Riyasat Husain and A. D. Ghodke, "Analysis and Correction of Linear Optics Errors, and operational improvements in the Indus – 2 Storage Ring", Chinese Physical Society and the Institute of High Energy Physics of the Chinese Academy of Sciences and the Institute of Modern Physics of the Chinese Academy of Sciences and IOP Publishing Ltd Chinese Physics C, Volume 41, Number 8, Apr. 2017

[4] Aradhana Kumari, M.L. Gandhi, Srinivas Lingam and A.C. Thakurta, "Development of Active Shunts for Quadrupole Magnets and their Production Status; and their Role in Indus-2", InPAC-2019

# DESIGN, INSTALLATION AND COMMISSIONING OF SMOKE EXHAUST SYSTEM FOR EXPERIMENTAL HALL AT INDUS-2 ACCELERATOR COMPLEX

Anil kumar[1,*], H. K. Khatwani[1], M. L. Gandhi[1], V. D. Sharma[1], R. Banwari[1], and A. C. Thakurta[2]
[1]Accelerator Power Supplies Division, RRCAT, Indore - 452013, INDIA
[2]Electron Accelerator Group, RRCAT, Indore - 452013, INDIA
[*] Email: anilkumar@rrcat.gov.in.

*Abstract*

Prevention of fires in any installation is an essential requirement because fires not only damage the property but also affect the health of workforces. Safe exit of occupants from the premises is the most important activity in the event of fire. The fire load of Indus-2 experimental hall, 3734 $m^2$ in size, is approximately $10^5$ MJ which can cause huge fire and smoke. The loads of Indus-2 are concentrated and so confined that it becomes necessary to install a smoke exhaust system to remove smoke and heat from the buildings in the event of a fire. A smoke exhaust system as per NFPA-92 [1] standards has been installed in the experimental hall at the Indus Accelerator Complex (IAC). This paper describes the conceptual design of the smoke exhaust system which includes selection of blowers, ducts, zonal distribution of area, air changes per hour and their control scheme. There are thirteen direct driven blowers and three belt driven blowers which cater to the requirement of six air changes per hour as per the guidelines of CFPA-E [2]. The exhaust system has been installed on the roof of IAC adjacent to windows for proper evacuation of smoke and ease of firefighting.

## INTRODUCTION

Safe escaping of occupants is the most important matter in the event of fire in the any building. Hence, how to assure the safety and reliability of escape routes is a major subject in the field of structural fire prevention research. Smoke extraction during a fire, smoke and fire gases spread through the entire building. Smoke exhaust systems are designed to remove smoke and heat from buildings in the event of a fire. These systems play a crucial role in increasing occupants' safety and allowing rescue personnel to safely enter burning buildings. In comparison to natural smoke extraction units, they work independent of external conditions and assure the full performance immediately. There was no system to exhaust smoke from Indus-2 experimental hall during large scale smoke due to fire. As per AERB recommendation a suitable smoke exhaust system has been installed in Indus-2 experimental hall.

The entire experimental hall including Radio Frequency system and Magnet Power Supplies system divided into 16 zones. Each zone contains three sectors and each sector contains seven glass windows of 800 mm x 540 mm size. Two glass windows of each sectors was used for suction. Six suction ducts of size 800 mm x 540 mm, one main duct of 400 mm diameter and one blower was used for one zone. Total 15 such type exhaust systems were installed to smoke extraction during a fire, smoke and fire gases spread through the entire experimental hall.

An exhaust system for catering these needs has been installed at IAC whose details are given in this paper.

## PURPOSE

The standard defined in NFPA-92-4.1 (2012) states the purpose as given below.

**a)** Inhibit smoke from entering stairwells, means of egress smoke refuge areas.
**b)** Maintain a tenable environment in smoke refuge areas and means of egress during the time required for evacuation**.**
**c)** Inhibit the migration of smoke from the smoke zone.
**d)** Provide conditions that enable emergency response personnel to conduct search and rescue operations, and to locate and control the fire.
**e)** Contribute to the protection of life and to the reduction of property loss.

## DESIGN OBJECTIVES

This system is designed as per design objectives defined in NFPA-92 (clause no. 4.1) as given below.
The methods for accomplishing smoke control shall include one or more of the following:

**a)** *The containment of smoke to the zone of origin by establishment and maintenance of pressure differences across smoke zone boundaries.*
From the consideration of 4.1.1, it is recommended to keep those AHUs "on" which are not affected due to smoke. This will help in maintaining the pressure difference across smoke boundaries due to intake of fresh air.

**b)** *The management of smoke within a large volume space and any un-separated spaces that communicate with the large volume space.*
As per Confederation of Fire Protection Associations in Europe (CFPA-E) guidelines if the fire compartment area is > 4800 $m^2$ and the height is 5 to 7.5 m then air change is required 6 air changes per hour.

## CALCULATION OF CAPACITY OF FAN

The Experimental hall is approximately 3734 $m^2$ with 6.95 meter height. The total volume is 26138 $m^3$ with 48 segments. The volume of smoke per segment is 545 $m^3$. Considering the height and area, since the height is 6.95 meter and the area is close to that, 6 air changes per hour have been considered. For 6 air changes per hour the volumetric flow rate per segment is 3270 $m^3$ per hour per segment. For three segments it is 9810 $m^3$ per hour. So fan selected having air flow rate of 10000 $m^3$ per hour.

## ACTIVATION OF SYSTEM

Activation of system as per purpose defined in NFPA-92 **(clause no. 4.5.2) (2012) as follows:**

***Activation of smoke control system shall be accomplished by an approved automatic means.*** So, we have kept the system on auto with actuation on auto with Fire alarm system and control of the air movements with fresh air on the opposite side of exhaust, and smoke exhaust to the atmosphere.

## POWER SUPPLY

As per CFPA-E, para 5.6, Smoke and Heat evacuation System (SHEVS) must have a source of power that is independent to the main power.

## LOCATION OF FANS AND CONTROLS

It has to be in the area which is not affected due to smoke. So, it is kept on the roof.

Other aspects are to: 1) Minimize vibrations to avoid any damage to the floor; 2) Avoid flooding of the area where fans are kept so that these remain healthy and operational; and 3) Ensure rust proof ducting and fans.

## SYSTEM DESCRIPTION

The entire exhaust system is a sturdy construction with anti-vibration pads and suitable supports to ensure freedom from vibration while running. The entire fan housing is mounted on MS channel framework and duly powder coated to prevent formation of rust. The vibration of the Smoke exhaust fans is not exceeding a peak-to-peak displacement of 100 μm. For all Fans, serrated rubber pads are provided for vibration isolation. The ducting also painted with anti- corrosion paint.

The smoke exhaust system consists of exhaust fans, control panels and ducting. The capacity of the smoke fans is selected to deliver minimum of 6 air changes. To provide effective exhaust of smoke, the existing AHUs are utilized to provide supply air opposite to the exhaust fans. On actuation of smoke detectors of a particular area, the corresponding fire dampers of the AHUs will close automatically. The outer side AHUs installed on the exhaust side wall will also trip but the inner side AHUs installed on opposite side of the exhaust shall remain in service irrespective of their present state. The mandatory condition for the operation of smoke exhaust system is that the inner AHU in operation and outer AHU in off condition. The off AHU will help to prevent spread of smoke in other areas. AHUs "on" which are not affected due to smoke will help in maintaining the pressure difference across smoke boundaries due to intake of fresh air [3].

## SCHEME FOR DISTRIBUTION OF EXHAUST FANS:

Indus-2 Experimental hall including MPS and RF area are divided into 16 zones. Each sector contains two ducts opening and connected to main duct (Sector covers a space between three columns). Three such type sectors connected to exhaust fan with control panel. Presently the electrical supply to control panel is provided from the ac mains supply of IAC. To fulfil the requirement of independent ac mains supply, a diesel generator set may be installed.

## CONTROL LOGIC

The smoke detector with cross zoning of the Experimental hall actuates the following:

- Stop the outer AHUs on the respective zone of the detector with all remaining AHUs ON.
- Switch ON all the inner AHUs on opposite side of the exhaust to supply the air at the top (if such AHUs are in "OFF" condition).
- Fire dampers on the return side of the AHUs close automatically on receiving smoke signal through Fire Alarm System.
- Put on the exhaust fan of this zone.

## FAN SECTION

The fan meets Air Movement and Control Association (AMCA) standard with following specification:

- Air flow rate : ≥ 10,000 $m^3$ per hour room temperature
- Temperature rating : 200 °C
- Suction pressure : ≥ 150 mm of water column
- Discharge pressure : Free air delivery to the exhaust with louver
- Type of fan: Centrifugal direct driven fan
- Type of blade : Backward curve
- Efficiency of fan: ≥ 75%.
- Vibration: Anti vibration pad to achieve ≤ 100 μm
- Noise : 85 dB at 3 m distance
- Rust proof fan enclosure

## MOTORS & DRIVE

Three phase 415 V / 50 Hz motors drive the fans. The selected motors have class-F insulation. It is a squirrel cage, totally enclosed motor with an integral fan, and hasIP-55 protection. As per the site requirement, both the direct driven and belt drive fans have been installed.

## DUCTING

The ducting should fit into the existing glass window frame of dimension 800 mm x 540 mm to draw suction from the experimental hall. The 400 diameter ducting of about 3.25 mm thickness is connected to the exhaust blower assembly.

## SAFETY FEATURES

Each Smoke exhaust System has safety features as described below:

- Fan and motor are mounted on a vibration pad. Base has been connected to equipment earthing provided nearby.
- All screws used for panel fixing, projecting inside the unit are covered with PVC caps to avoid human injury.
- Emergency key switch has been provided at every fan unit to cut off power while working at site.

## INSTALLATION & COMMISSIONING OF SMOKE EXHAUST SYSTEM

Fifteen smoke exhaust units (Fig. 1) have been installed on the roof of the IAC to take care of the following areas: Indus-2 experiment hall, Indus-2 RF hall & Indus-2 MPS hall in the event of fire. Three belt driven (Fig. 2) and 12 direct driven exhaust units (Fig. 3) have been installed based on availability of space on the roof. These are units integrated with existing fire detection and alarm system of Indus Complex for automatic starting of the exhaust system in event of fire as per the control logic. The exhaust system can be operated manually for regular testing of the system to check its healthiness. The system is healthy and working satisfactorily since February 2019.

Figure 1: Two zones of smoke exhaust system installed on the roof of Indus Accelerator Complex.

Figure 2: The smoke exhausts system with a belt-driven blower catering to MPS area of Indus-2 Accelerator.

Figure 3: A portion of the smoke exhausts system covering three sectors of a zone with a direct driven blower.

## ACKNOWLEDGEMENT

Authors are thankful to S. K. Sonawane, Birjesh Kumar Mishra and Vaddadi Ramesh and for their help during installation, commissioning and testing of smoke exhaust system. Authors also appreciate the support received from the colleagues of Construction and Services Division, and Accelerator Power Supplies Division of RRCAT.

## REFERENCES

[1] NFPA92 “Standard for Smoke Control Systems” 2012 Edition NFPA, 1 Battery march Park, Quincy, MA 02169-7471

[2] The Confederation of Fire Protection Associations in Europe (CFPA E) “Smoke and Heat Exhaust Ventilation Systems Planning and Design”

[3] SMOKE CONTROL, section 4/Chapter 12, SFPE Handbook of Fire Protection Engineering

# RF Cavity Heater Power controller with Safety Interlocks


Prajakta Dhumal*, J.N. Karande, C. Rozario, S. Pal
PLF, Tata Institute of Fundamental Research, Mumbai- 400005, INDIA
R. Palit and V.Nanal
DNAP, Tata Institute of Fundamental Research, Mumbai- 400005, INDIA
* prajaktat@tifr.res.in



*Abstract*

The heavy ion superconducting LINAC booster at TIFR consists of seven module cryostats, each having four superconducting RF cavities. To improve the quality factor and minimize the losses due to surface resistance of the cavity, baking at 100°C is carried out under high vacuum over a prolonged period. A dedicated heater power controller unit is developed to ensure safe baking operation with minimal human interference. The resonator heater power control unit is provided with safety interlocks to prevent exposure of lead plated superconducting cavities to bad vacuum. One unit for controlling four heaters is designed, tested and installed in the LINAC. This paper will describe the design details.


## INTRODUCTION

The superconducting LINAC booster, indigenously developed to boost the energy of the heavy ion beams from the 14 MV Pelletron accelerator at TIFR, Mumbai. The LINAC, consists of seven modular cryostats, each housing four lead plated quarter wave resonators, designed for an optimum velocity $\beta_0$=0.1 at an operating frequency of 150 MHz [1,2]. In order to achieve the maximum quality factor, and reduce losses due to surface resistance, each RF cavity need to bake at 100 °C temperature for prolonged period under ultra-high vacuum in the modular cryostat, prior to cool down. The resonators in each cryostat are fitted with special polyimide MINCO make thermos foil heaters (50Ω, 2 A) for baking and temperature measurement is done using diodes (DT400). We have developed a four channel resonator heater power control unit. Each channel is capable of heating two polyimide thermos foil heaters connected in the series combination. The heater control unit is interlocked with the vacuum controlled gate valves of each module, for vacuum isolation and safety.

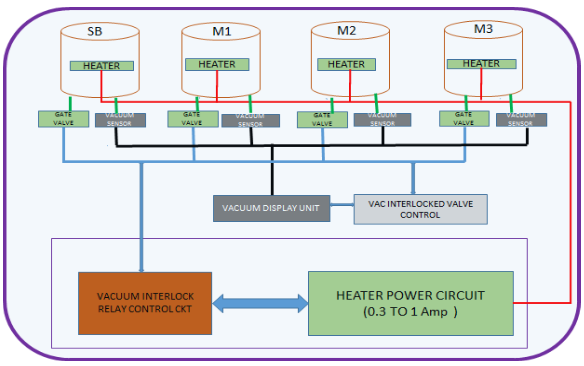


Figure 1: A Schematic layout of heater and vacuum connections

Figure 1 shows a schematic layout of the heater power control system and vacuum system with safety interlocks. Each cryostat is equipped with a turbo pump and a gate valve for isolation. Additionally, isolating valves are also provided between the modules. For measurement of vacuum, two vacuum gauges are provided on each module-one directly on the Turbo pump and other on the top of the cryostat. Appropriate interlocks are setup for different valves with the output from these vacuum gauges [3]. This safety feature is incorporated in the heater power control system design.

## HARDWARE DESIGN AND SAFETY OPERATION

Figure 2 shows a simple circuit of the heater power controller. It employs a variable alternating current source of 0.3 to 1A, which is developed using Thyristor regulators. This regulator is used to control the primary voltage of the transformer for controlling the load current. Phase angle controlled regulator is connected in the primary of the transformer circuit and secondary circuit of the transformer is connected to the load, i.e. to two thermofoil heaters connected in series. The load current of the secondary is changed by varying primary voltage using the Thyristor control. The heater current of each individual module is manually adjusted to achieve 100 °C temperature. The current accuracy is better than ± 5 % and stability is found to be better than ±2%.

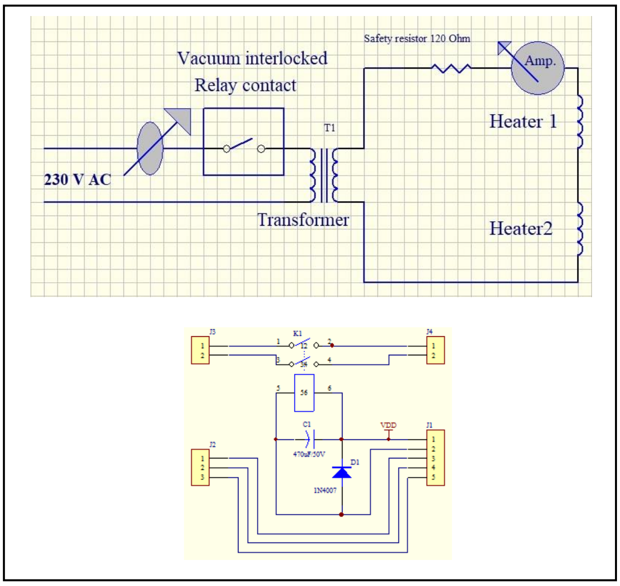


Figure **2**: Circuit of the heater controller (top panel) and vacuum interlock (bottom panel)

*email: prajaktat@tifr.res.in

Since the baking is carried out over a prolonged period, safety measures needs to any electrical and vacuum failure. The heater control unit is interlocked with the vacuum controlled gate valves of each module, for vacuum isolation and safety. A 24 V relay based control circuit is added to each channel for the control of the heater power shown in Figure 2. A micro switch connection of the gate valve is used to start or stop the heater power through the relay contact. In case of a vacuum accident during baking, the gate valve operates to isolate the module since it is interlocked with vacuum readout signals.


Figure 3: Heater Power Controller Unit – picture (top panel) and inside view (bottom panel)

Feedback from the gate-valve-closed micro-switch is connected to the safety relay to shut down the heater power. The heater power is automatically restored once the gate valve status changes to 'open' due to vacuum recovery. This helps to minimize the damage due to heating in poor vacuum. It should be mentioned that the 230V/120V transformer also helps to isolate the electrical ground. Forced air cooling is also provided for the high power transformers in this unit. One unit for controlling four heaters is designed, tested and installed in the LINAC. The second unit is under development.

## SUMMARY

A RF cavity heater power control unit is designed for the safe baking of RF superconducting cavities of LINAC at PLF, Mumbai. This unit employs the power source for heater load and safety interlocks. This unit facilitates the safe baking operation with minimal human interference. One unit for controlling four heaters is designed, tested and installed in the LINAC.

## ACKNOWLEDGMENT

We are grateful to Prof. R.G. Pillay, for invaluable guidance in the project. We thank PLF staff for their technical support.

## REFERENCES

[1] R.G. Pillay, "Overview of the Pelletron LINAC Facility", InPAC2011 proceedings.

[2] V. Nanal, "Operational experience of superconducting LINAC booster at Mumbai", HIAT09, Venice (Italy) 2009.

[3] C. Rozario. "Remote Monitoring of Vacuum and valve status using Labview", InPAC2015 proceeding

# ENHANCEMENT OF FIRE SAFETY FOR SUB-SYSTEMS OF INDUS ACCELERATOR

Anil kumar[1,*], H. K. Khatwani[1], M. L. Gandhi[1], V. D. Sharma[1], R. Banwari[1], and A. C. Thakurta[2]
[1]Accelerator Power Supplies Division, RRCAT, Indore - 452013, INDIA
[2]Electron Accelerator Group, RRCAT, Indore - 452013, INDIA
[*] Email: anilkumar@rrcat.gov.in

*Abstract*

The Indus Accelerator Complex has two synchrotron radiation sources, Indus-1 and Indus-2. These are operating in round the clock mode at 450 MeV / 125 mA and 2.5 GeV / 200 mA respectively. These accelerators contain a large numbers of components and installations with approximately $10^5$ MJ fire load in Indus-2 transformer rectifiers with area of about 280 $m^2$, $10^5$ MJ fire load in Indus-2 ring covering about 1650 $m^2$ of floor area, and $10^4$ MJ in Indus-2 MPS hall with about 950 $m^2$ of floor area.

Generation of smoke during burning of electrical cables is the major hindrance for control of the fire and the firefighting personnel which can cause severe damage to the equipment. It is essential to isolate the entire cable layouts into smaller zones so that fire is limited in a smaller area. This is done by introducing fire barrier at different intervals by sealing at all the openings with the use of adequate fire resistance materials. The fire retardant coating on electrical cables in Indus-2 Accelerator Complex reduces the propagation of fire in both horizontal and vertical directions. An intelligent modular fire detection and alarm system is installed for early detection of fire to minimize the damage of the installed property and safe evacuation from the installation.

This paper covers the details of fire barriers, fire breaks, selection of cables as passive and foam sprinkler system, fire hydrant system, smoke exhaust system and intelligent fire detection and alarm system of Indus complex as active fire protection systems.

## INTRODUCTION

The risks of fire in any building are subjected to hazards that include: direct burning due to smoking materials, arching due to defective wiring and poor periodic servicing of electrical equipment, radiation fire due to overheat of portable equipment not switched off, conduction fire due to poor house-keeping of flammable materials, and hot surface or friction due to repairing activities such as welding that may cause a fire. The fire can create serious consequences including loss of many lives, damaged properties and financial losses.

The definition of fire protection of a building refers to the ability to detect, withstand, prevent and reduce any damage caused by a sudden unexpected fire whether man made or non-man made. There are a number of ways in which Indus Accelerator Complex (IAC) can secure /safe guard from fire. The fire loads [1] of the Indus Complex are given in Table 1.

Table 1: Fire loads in IAC

| Sr. No. | The Power Supplies and the Loads | Fire load |
|---|---|---|
| 1 | RF power supply cables, cabinets motors PVC partition and plastic hoses | $10^3$ MJ |
| 2 | Rectifier transformers and capacitors banks | $10^3$ MJ |
| 3 | Dipole magnet power supply cabinet and water cooled low voltage transformer, other magnets power supply, steering coils power supply cabinets. | $10^4$ MJ |
| 4 | UHV systems (160 Sputter Ion Pumps and other pumps) and baking power supply cabinets, control system cabinets and beam lines | $10^3$ MJ |
| 5 | Dipole, quadrupole and sextupole magnets, RF cavities, insertion and control devices, vacuum pumps and heaters, septum, kicker, quadrupole, sextupole magnets steering coils and AC package unit | $10^5$ MJ |
| 6 | AHUs | $10^3$ MJ |

## FIRE PROTECTION APPROACH

### *Passive Fire Protection (PFP)*

It is an integral component of the three components of structural, fire protection and fire safety in a building [2]. PFP refers to fire resistance measures. The purpose of PFP is to maximize the time available to evacuate a property, or prevent a fire from taking hold in the first place.

### *Active Fire Protection (AFP)*

Active fire protection is a term that can be used to describe any systems or products put in place to detect or combat a fire [2]. These systems will always need some form of trigger to activate by a user. Fire can be controlled or extinguished, either manually (firefighting) or automatically.

### *The potential electrical and general ignition sources*

Electrical devices in buildings can be ignition source by way of inadequate connection, incorrect connections, spark or flame due to loss of cooling, use of under rated switchgears, power cables, oil filled transformer and capacitors banks.

### *Engineered safety futures*

- Suitable interlocks to cut off power with diverse, redundant and fail safe features and interlocks with smoke /flame/heat with suitable cross zoning.
- Making access control automatically free in case of fire, provision of emergency exhaust ventilation
- Emergency lights with exits signs for easy escape and firefighting.
- Provision of fire dampers to close on fire automatically and to trip AHUs. Suitable interlocks are provided to achieve these features

### *Informations on fire*

- Auto dial up features
- Synoptic panel, Personal Address System, Fire Alarm Control Panel
- Colour graphics, Repeater panel
- Manual call point, Telephone system, Hooters, flashers

## FIRE PROTECTION TO CABLES

Fire protection to cables is given so that spreading to other cables and also to other area is prevented. The fire protection is given by the following measures.

### *Cable laying & segregation requirement*

In order to avoid vertical or lateral spread of fire through cables, all apertures or opening, which are part of vertical or horizontal partition elements, through which cable or cable trays pass, should therefore be segregated.. This is implemented by providing fire barriers at different interval by sealing all the openings with the materials that may result in providing adequate fire resistance.

### *Fire barrier*

Fire protection is passive fire protection systems that prevent propagation of fire from one fire zone to other floor and wall penetration. The fire barriers (Fig.1) should have minimum of 3 hours fire rating, comply with NFPA 221 [2], IS-12458-1988 [3], BS-476 part 20 [4] and UL 1479 standards [5], high oxygen index greater than 60%, anti-corrosive and anti-rodent properties, gas and smoke tight, resistant to chemicals, oils and lubricants, not shrink or crack after prolonged use and should not get affected by moisture. Material after curing should be non-hygroscopic, not emit smoke under fire exposure, compatible with cable jacket material and should adhere properly to surface performs satisfactorily after remaining in contact with water and should be suitable for overhead applications.

### *Fire breaks*

Fire breaks are passive fire protection systems made of chemical coating which prevent propagation of fire in horizontal or vertical run of cables and prevent spread of fire to nearby area. This fire breaks (Fig. 1) slow down the propagation of fire for at least 30 minutes. The material selected for fire break having no deteriorating effect on current carrying capacity, water resistant, resistant to corrosive gases, acids, alkalis, hydrocarbon and chemicals, flexible and no crack on bends, mechanically strong to allow foot traffic, not emit toxic gases or flames, high oxygen index.

Figure 1: Implementation of fire barrier & fire breaks on power cables.

## FIRE ALARM SYSTEM (FAS)

The Fire detection and alarm system at IAC has been changed from 2nd generation (analogue addressable fire alarm system) to 4th generation (Intelligent 100% hot redundant fire alarm system) with latest devices. Additional areas like new users' building, beam line hutches have been included in the newly installed FAS

The system devices have been selected as per EN 54 [6], installation of devices was completed as per NFPA-72 [7] (national fire alarm code-1999), National building code: 2016 [8] and IS: 2189:2008 [9] and cables for loops laying as per NFPA 70 [10] (national electric code - 2002). This system consists three fire alarm control panels (FACP) , five synoptic panels, one repeater panel, one auto dialler, 1167 devices, 18 km fire survival loop cables, System management GUI has been installed in Indus Control room and the virtual map is installed in another room of IAC with a flasher (Fig. 2). All three FACPs, virtual map and GUI are networked (Fig.3).

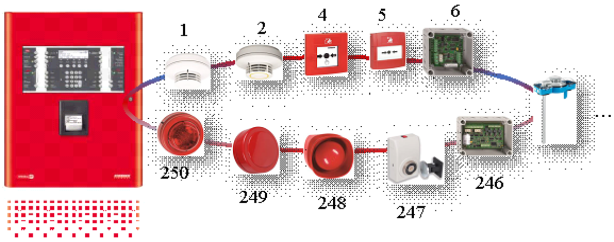


Figure 2: Fire alarm devices in loop connected with control panel

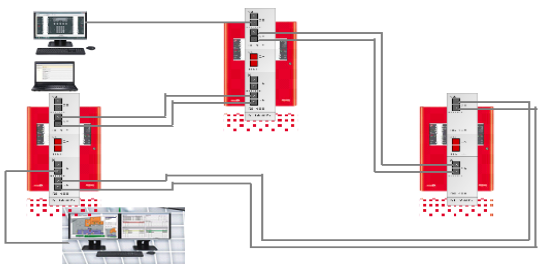

Figure 3: Communication network layout

The major features of the systems [11] are as follows:

### *Fire Alarm Control Panel (FACP) features*

- *100% Redundancy as a principle*
  All electronic elements and components are present in duplicate so that the system remains fully functional even in event of a fault occurring.

- *Hardware redundancy for a double security*
  As soon as a fault occurs in the active half of the system, the panel recognizes this immediately, and automatically switches over internally to the system which is ready for use. The fault is indicated on the operating panel, while all functions of the entire system remain completely available and unimpeded.
- *Overvoltage protection, earthing concept*
  This panel is equipped with a comprehensive, integrated overvoltage protection concept that protects all peripheral inputs as well as the mains power supply in accordance with EN50130-4 (EMC) and EN61000-6-2 (interference in industrial use).
- *Integrated short circuit isolator*
  Each detector on the loop is equipped with integrated short circuit isolator and can be fed from two sides. Thus upon short or open circuit the loop will automatically re-establish via the intact side and thus all the other detectors keep on functioning.

**FOAM SPRINKLER SYSTEM**

*Risk profile*

There is a 295 kVA transformer rectifier unit with 1290 kg of transformer and also contains additional sources of fire like crowbars and bleeders along with cooling fans and HV capacitors enclosed.. The area is closely surrounded by all sides with vital and precious installations Indus-1 & Indus-2, Indus substation and LCW plant.

*Damage Prevention measure*

Oil and fire propagation to surrounding in case of fire in one transformer has to be stopped with all measures by containing the fire and oil spill in the worst case ensuring a foam cover if oil spillage to neighboring locations still takes place. A foam (3%) mixed water spray system and the non-destructible (against fire) tubular linear heat sensing system give the signal for actuates the foam water spray system in fire event as damage prevention measure is installed. This operates after automatic cutoff of power to all the equipment on actuation of fire alarm signals as well as manual spray actuation.

Figure 4: Foam sprinklers system

This system contains one bladder tank of 2500 liter, foam spray nozzles, Deluge valve, solenoid valve for releasing foam concentrate, air expansion linear heat detection system, and control panel (Fig. 4).

**FIRE WATER HYDRANTS**

Internal Fire Water piping is already laid in Indus-2 with availability of fire water for the ring and part of the experimental hall with two fire hydrants in experimental hall & two open to sky area. Open to sky area hydrants may be used for extinguish fire in Indus-2 ring and experimental hall hydrants may be used for extinguish fire in beam line area.

Air pressure is maintained above the tank through compressor. Low pressure alarm is annunciated in control room when pressure falls lower than 4.0Kg/cm$^2$. New panel is installed near control room to indicate normal Fire water pressure.

**SMOKE EXHAUST SYSTEM**

A smoke exhaust system as per NFPA-92 [12] standards has been installed in the experimental hall at IAC so that the safety of the personnel working in this area is ensured in the event of fire and loss of the property can be minimized. The area of the hall has been divided into 16 zones covering 48 sectors. Each zone has a blower of 10000 m$^3$ per hour capacity, which receives the smoke from a duct connected to six suction openings. There are thirteen direct driven blowers and three belt driven blowers which cater to the requirement of six air changes per hour as per the guidelines of CFPA-E [13].

## ACKNOWLEDGEMENT

Authors are thankful to B K Mishra for his help during installation, commissioning and testing of Fire detection and alarm system. Authors also acknowledge the support from the colleagues of Accelerator Power Supplies Division (APSD), RRCAT.

**REFERENCES**


**[1]** V D Sharma "Conceptual design report of fire detection and protection system for Indus-2" January 17, 2003, CAT/2003-02

**[2]** NFPA 221 "Standard for Fire Walls and Fire Barrier Walls" 1997

**[3]** IS: 12458 –"Method of fire resistance test of fire stops" 1988 (Reaffirmed 2002)

**[4]** BS: 476-part20 "Method for determine nation of the fire resistance of elements of construction (general principles)"

**[5]** UL 1479 "Standard for Fire Tests of Penetration Fire stops"

**[6]** EN54 "Fire detection and fire alarm systems" 2001

**[7]** NFPA 72 "National Fire Alarm Code" 1999

**[8]** National Building Code of India 2016

**[9]** IS 2189: "Selection, installation and maintenance of automatic fire· detection and alarm system code of practice" (fourth revision)" 2008

**[10]** NFPA 70 "National Electric Code" 2002

**[11]** Modular fire safety Integral IPMX catalogue (Schrack Seconet)

**[12]** NFPA 92 "Standard for Smoke Control Systems"

**[13]** The Confederation of Fire Protection Associations in Europe (CFPA E) Smoke and Heat Exhaust Ventilation Systems Planning and Design

# DESIGN AND DEVELOPMENT OF REMOTE INTERFACE OF 10V, 300A POWER SUPPLY FOR HIGH TEMPERATURE SUPERCONDUCTOR BASED STEERING MAGNET

S. Srivastava*, A. De, Y. Kumar and S.K.Thakur
Variable Energy Cyclotron Centre, Kolkata-700064, India.

*Abstract*

A Graphical User Interface (GUI) was designed and develops for steering magnet power supplies using Labview software. Two High Temperature superconductors (HTS) based steering magnet power supply (300A/10V DC) are monitored and controlled in a single front panel with associated interlocks. The GUI communicates with the power supplies over RS232 link. The GUI has current start and stop button along with programmable ramp rate provisions. The ramp rate sets the offline quench detection circuit by adjusting the appropriate time and voltage delay. These ramp rates can be set from 1A/s to 20A/s as per the present requirement of the user. The associated interlocks such as water, door etc. are also displayed in the monitor. The refresh rate of the GUI is around 2 seconds it also a provision to record data in (Microsoft excel) file, which can be further used for the study and analysis of HTS steering magnet characteristics. The power supplies were tested upto 200A. Present paper will discuss in detail the algorithm while designing the remote interface of HTS magnet power supplies.

## INTRODUCTION

Steering magnet power supply is a essential part for providing corrective steering of beam in high energy beam line of cyclotron in both Horizontal (X) and Vertical (Y) direction. HTS based steering magnet in principle, has several advantages over low-temperature superconductor (LTS) magnet [1-2]. Figure 1 show the in house development of HTS based steering magnet system which are to be used for the external beam line facility of K500 cyclotron. With the help of cry cooler these HTS magnet is cool down around 20-30K. The X-Y HTS coils are powered by two independence high current (300A) power supplies. These power supplies have in build quench protection scheme. Only one has to set the appropriate quench voltage and time. Occurrence of quench is the severe drawback of HTS magnet. In HTS magnet coils are segmented in terms of double pancake coils and voltage taps on individual pancake coils will be monitored to detect small normal zone. The coil is protected with the usual method of resistor in parallel. Onset of quench gradually develops voltage across the power supply and the power supply is set to be tripped for voltage of more than 2 V (generally) during steady state operation. The setting of ramp rate is also very crucial in the operation of power supplies. Because high ramp rate generally make the quench very frequently due to the inductor load of HTS magnet. In the present paper the operation and monitor of two HTS steering magnet power supply GUI development will be discussed. These GUI is made in LABview based graphical programming software language [3]. The control of two X-Y magnet power supply is done by using two RS232 port using USB to RS232 expander board of Advantech make.


Figure 1: Actual view HTS based steering magnet (*a*) steering magnet dipped in liquid nitrogen chamber (*b*) Remote operating panel.

## POWER SUPPLY SPECIFICATION

High current power supply of rating 300A, ±10V is come under the system 8500 category of Danfysik make [4]. The System 8500 Precision Magnet Power Supplies are DC constant current output power supplies designed for applications requiring very high stability and low noise combined with reliability and ease of operation. This power supply is widely suited for precision spectroscopy and ion beam transport applications. The regulation is linear type with primary control SCR based pre regulator. The current stability is better than 100ppm.

*E- mail: saurabh@vecc.gov.in.

The power supply has both manual and remote operation facility. One of the main salient features is that the control and interface electronics modules are isolated from the power modules by an electrostatic and thermal shielding wall. This feature eliminates the ground loops and conducted noise between digital controls. The power supply has various interlocks such as over current protection, over temperature, water flow, external interlock protection etc. Figure 2 shows the actual photograph of X and Y steering magnet power supply.


Figure 2: Actual view of X, Y magnet power supply: (*a*) X (Horizontal steering) power supply (*b*) Y (Horizontal steering) power supply (*c*) four channel Quench setting system.

## REMOTE PROGRAMMING

The power supply can be operated in local (LOC) mode or in Remote (REM) mode. The present power supply is remotely connected with RS232 protocol. In this case the straight cable is used. i.e. Receiver pin and Transmitter pin of DB25 connector (attached with power supply) is connected to Receiver pin (pin 3) and Transmitter pin (pin 2) of the RS232 respectively. After the connection with RS232 cable one needs to set the jumper setting in main Magnet Power Supply (MPS) panel. For RS232 connection ST9 jumper should be short circuited and ST10, ST11 should be open in the power supply control panel. As the RS232 is operated in 9600baud rate switch 2 of SW1 and switch 1 of SW2 is right moved. In order to make this effective a long press of S2 button has to make. This procedure stores the current setting in the hardware. After the long press one can change switches of SW1 and SW2 to their original position. This means any changes will only be effective if long press of S2 button is made.

### *Programming*

The MPS communication protocol is built upon plain ASCII characters where each command or reply is delimited by a "Carriage Return" <CR> character. However, replies have a “Line Feed” <LF> character added before the <CR> for a friendlier display when using a terminal. The magnet power supply has Ramp profile software. The ramp profile software is an option that can be ordered with the Magnet power supply. No additional hardware is needed in order to run ramp profile software.

With the ramp profile software, it is possible to download and run a pre-defined ramp sequence that the output current must follow. The ramp sequence can be programmed in three different methods.

- a ) Arbitrary point method;
- b ) Equal timeslot method;
- c ) Auto Slew Rate Ramp Profile method.

The power supply comes with around 100 software command for remote operation. However, we have used only seven main commands for remote operation. The list of main commands that were used in the remote operation are summarizes in Table 1. In order to make the GUI easy to operate we have made our own ramp profile software, this help to used only seven main commands to operate the power supply remotely. In present ramp profile software one can made the ramp rate from 1A/s to 20A/s. User have also option to start and stop at any interval of operation from start to stop the set current. The status of power supply, which involves, over voltage, over current, door, water and external interlocks can be checked by S1 command. WA command is used to set the output current in percentage level. AD command is used to read the voltage and current output of power supply. Here X has a variable from 0 to 16. For example AD 2 is used to read output voltage and AD 8 is used to read the output current in 16 bit format.

Table 1:- Important command used in power supply

| S. No. | Command | Function |
|---|---|---|
| 1. | REM | Switch on PS in Remote |
| 2. | LOC | Switch on PS in Local |
| 3. | CMD | Read current mode of operation |
| 4. | RS | Reset interlocks |
| 5. | S1 | Read the status of interlocks |
| 6. | WA XXXXXX | Set the current in XX.XXXX% |
| 7. | AD X | Read back of V/I |

Figure 3 shows the main GUI of the remote programming of X and Y power supply. The two power supplies were communicated via RS232 protocol of COM 4 and COM5. Advantech based USB to four ports RS232 extender is used for increasing COM port. The rate of increased ramp rate can also be visualized via the graph provided in the GUI. Failure of any interlocks will blink the corresponding LED button provided at the right side of the GUI. X_Fine tuning button is provided if the user want to stop the ramping of power supply at any instance and want to fine tune with different ramp rate or with no ramp rate. The power supply is tested up to 200A.

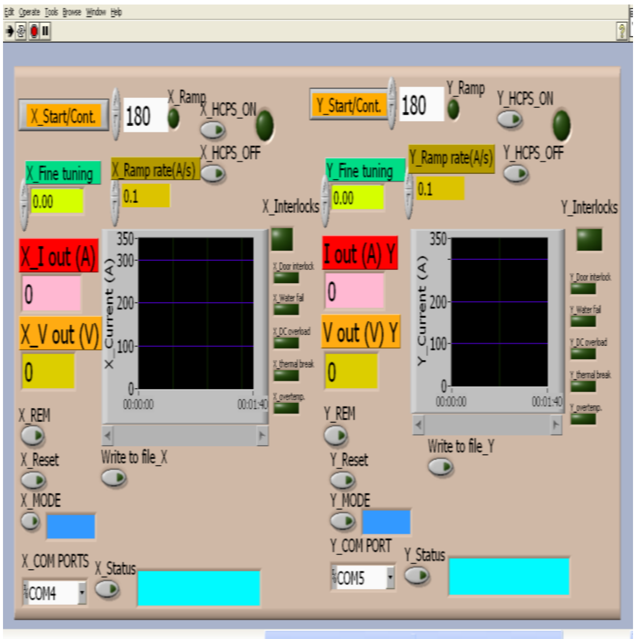


Figure 3: GUI of X, Y magnet power supplies

### *Sequence of operation*

In order to operate the power supply in safe mode one should have to follow the correct sequence of operation. First of all the main interlocks should be checked which includes door and water. The operation of remote panel should be followed as: First press *X_Reset* for resetting all interlocks, second press *X_Ramp* for putting final value of set current third set the *X_Ramp* rate. If one wants to record all the data then one has to press *Write to the file_X button*. The same procedure should be followed by Y steering magnet power supply.

## CONCLUSION

The present paper discusses the design and development of graphical user interface of two horizontal (X) and vertical (Y) HTS steering magnet power supply. The GUI is build in Labview software programming language. The in house ramp profile software is made for the control and monitoring of the power supply. With present ramp profile software one can set the ramp rate from 1A/s to 20A/s. The GUI also possesses data logging button which when long press log all the setting and current reading in Microsoft excel which can be further used for analysis purpose.

## REFERENCES


[1] Hatanaka K, Nakagawa J, Fukuda M, Yorita T, Saito T, Sakemi Y, Kawaguchi T, Noda K, "A HTS scanning magnet and AC operation", NIM-A, Vol. 616, pp 16-20. (2010).

[2] Pradhan J, Bhunia U, Roy A, Panda U S, Bhattacharyya T K, Thakur S K, Khare V, Das M, Saha S, Bhandari R K, "Basic design and test results of High Temperature Superconductor insert coil for high-field hybrid magnet", Current Science, Vol. 104, No.9 (2013).

[3] Labview programming. www.ni.com.

[4] Danfysik MPS 8500 Reference manual. https://www.danfysik.com/media/1179/user-manual-sys8500.pdf

# Simulation studies on 5kV/5A power supply using pulse step modulation technique

S. Srivastava* ,Y. Kumar and S.K.Thakur
Variable Energy Cyclotron Centre, Kolkata-700064, India.

*Abstract*

A 5kV/5A power supply is designed and simulated utilizing Pulse Step Modulation (PSM) which comprises of 10 power supply modules (SPM) based on Pulse Width Modulation (PWM). A power supply with PSM techniques is used in the accelerator technology in order to avoid crowbar, ease of maintenance etc. The PSM uses phase shifted PWM for producing final output. There are various ways to obtained phase shifted PWM like using FPGA, DSP etc. In this paper, the phase shifted switching pulses are obtained by using analog IC LTC6994 which can produce a delay of 1µs to 33.6s. The use of analog IC eases the complexity of design. Each phase shifted PWM pulse is used to turn ON and OFF the IGBT connected in each module as a Buck converter mode which is fed from a 600 VDC source. A free-wheeling diode connected at the output of the modules bypasses the current even it is in standby or non-function mode. Each SPM can produce 60V to 540V with maximum 5A depending upon duty cycle of switching pulse. Simulation is performed in MATLAB and LTspice and simulated results will be produced in the paper. Load regulation is obtained using PI controller which controls the duty cycle of phase sifted PWM pulses in all modules. The final output is the summation of voltages of modules connected in series resulting very less ripple at higher ripple frequency and thus the requirement of filter capacitor is very less. The main advantages of PSM based high voltage power supply are smaller size, very good voltage regulation, low stored energy etc.

## INTRODUCTION

PSM were first introduced by Brown Boveri [1]. The main advantage of PSM based power supply is modular design, uniform power distribution, low EMI, high bandwidth, high efficiency, very low filter capacitor at output that leads to crowbar less operation [2-5]. PSM basically consist of a series connected switching modules known as SPM. Each module has an insulated DC power supply, a semiconductor switching element IGBT/MOSFET and a free-wheeling diode. Generally in PSM phase shifted PWM pulses were used to ON/OFF the switching devices; this is generally achieved by FPGA and DSP board [6-7]. Synchronization is become tough task for obtaining phase shifted PWM signal when using more than two FPGA/DSP board. In order to overcome this problem a new approach is presented in this paper that is based on using phase shifted analog IC LTC6994-2. LTC6994-2 can produce a delay of 1 µs to 33.6*s* based on the combination of resistor network as given in datasheet [8]. Using separate phase delay circuit leads to lesser programming complexity and then the concept of whole PSM can be achieved efficiently and systematically.

## WORKING PRINCIPLE

A 5kV/5A power supply based on PSM based is aim to design and developed in VECC. According to the principle of the PSM, the control system should switch all modules on and off equally distributed, to ensure equal loading on all modules. This control method is called stage rotation [9]. This is achieved using FIFO principle. Figure 1 shows the block diagram of the working principle of 5kV/5A power supply based on PSM. The PWM pulse is produce by a commonly available SG3524 IC. This PWM pulse is phase delay by $T_d = T/N$ using LTC 6994-2 IC. $T$ is the time period of PWM and $N$ is the number of SPM module used. The feedback circuit is implemented in SG3524. The output uses very low output filter capacitor due to $N$ times switching frequency at output.

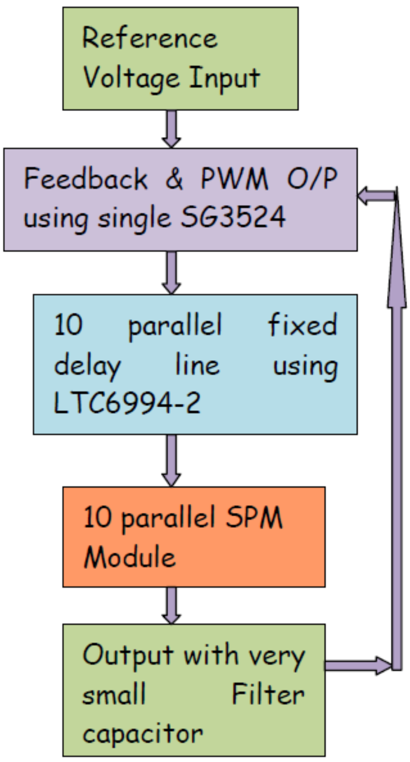


Figure 1: Block diagram of PSM based power supply.

*E- mail: saurabh@vecc.gov.in.

## *Obtaining fixed delay*

For the design of 5kV/5A 10 SPM modules were used. Each module has a rating of 600V. Total 10 module where used to produce 5kV by varying PWM. The switching frequency of SG3524 where kept at 5 kHz, this leads to the requirement of 20 µs (*T*/*N*) fixed delay in order to obtain equal loading in each SPM module. Figure 2 shows the schematics of 20 µs delay line. In LTC 6994 resistor $R_{SET}$ is used to programs an internal master oscillator frequency, setting the LTC6994's time base. The input-to-output delay is determined by this master oscillator and an internal clock divider, $N_{DIV}$, programmable to eight settings from 1 to $2^{21}$. The output follows the input after delaying the rising and/or falling transitions. The time delay is calculated by:

$$t_d = \frac{N_{DIV} \times R_{SET}}{50k\Omega}\mu s \text{ , } N_{DIV} = 1,8,64,.....,2^{21} \qquad (1)$$

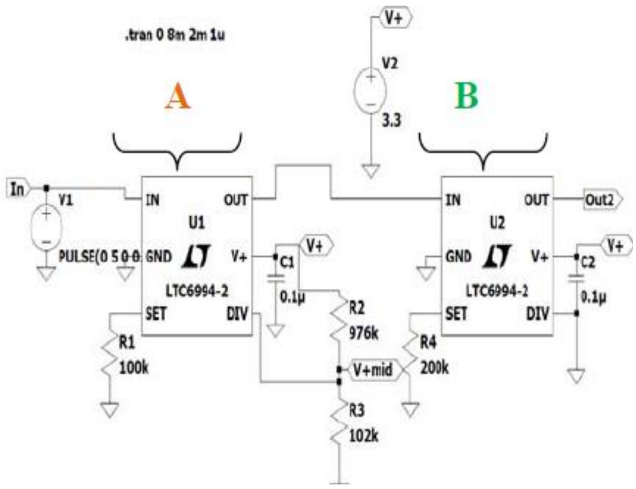


Figure 2: Schematic of delay line

The $N_{DIV}$ tells the combination of R2 and R3 that should be used in order to find the exact delay. The LTC 6994 can produce delay either from 1-8µs, or in a combination of $N_{DIV}$*(1-8µs). For example in order to produce 20 µs delay two LTC 6994-2 IC is used one (as shown in Label A in Fig 2) produce 16µs delay while the another LTC 6994-2 (Label B in Fig 2) will produce 4µs delay. Proper choice of R1 ($R_{SET}$), R2 and R3 can produce a delay of 1µs to 33.6*s*. The schematic is built in LTSpice software which is freely available. The simulation of Fig. 2 is shown in Fig. 3. In Figure 3 it can be easily seen that a fixed delay of 20µs is obtained. In order to produce this time delay one should has to assured the lower and higher value of the duty cycle. It is observed in simulation that when $T_{on}$ is less than 20µs or greater than 190µs i.e. the difference between $T_{on}$ and $T$ is within 20µs then, the delay line will not capture the rising and falling edge and fail to produce the desired delay. In the simulation output of Fig. 2 each resistance were set at maximum 10% tolerance level. So two LTC 6994-2 IC is required for producing 20µs and a total 20 LTC 6994-2 IC required in a given 5kV/5A power supply. This shifted PWM is then given to switching device (IGBT in present case) via optical fiber to turn ON/OFF the IGBT.

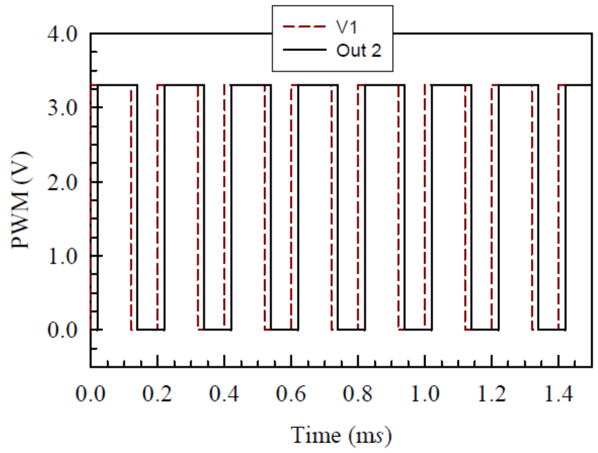


Figure 3: 20 microsecond delay circuit

## *Simulation results*

Figure 4 shows the full simulation schematics of regulated 5kV/5A PSM based power supply done in MATLAB simulink. As mention in previous subsection for obtaining fixed delay one has to limit lower and upper limit of the duty cycle of PWM. This is achieved by inserting saturation block as shown in Fig. 4. PI controller is used for regulation the load regulation response can be observed in Fig. 5. A constant 10% load is applied at 0.2*s*. From Fig. 5 one can observed that the output ripple voltage is very less i.e. 0.06% at 5kV. This load disturbance is produced with the help of circuit breaker tool in the Simulink library. In PSM based power supply the role of phase shift or delay is very crucial. It may be possible that while designing an actual circuit one get either delay greater than 20µs or less than 20µs, in that case equal loading will be hamper and one could not get the regulated output.

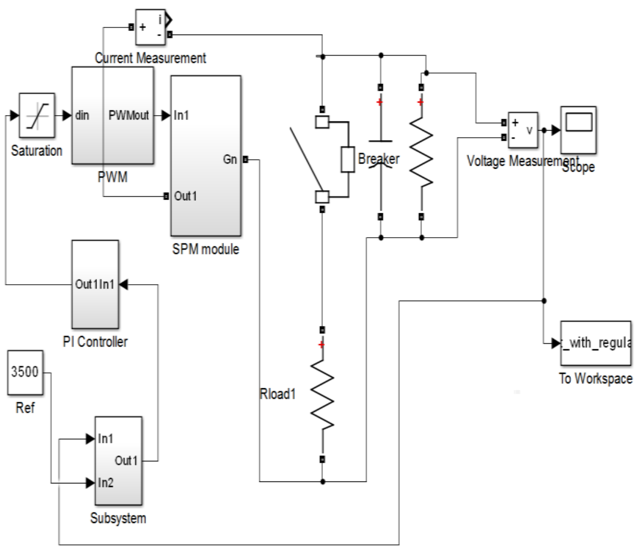


Figure 4: Simulation done in MATLAB

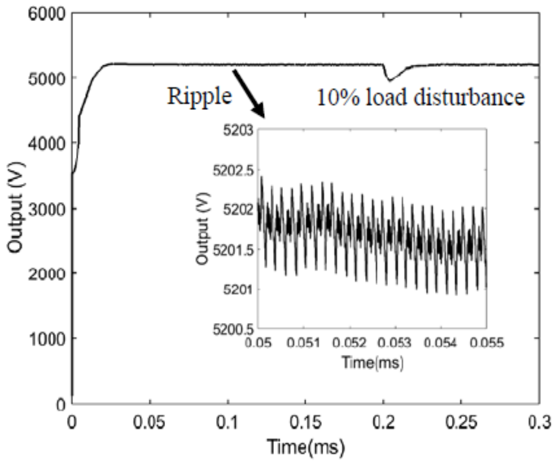


Figure 5: Simulation result

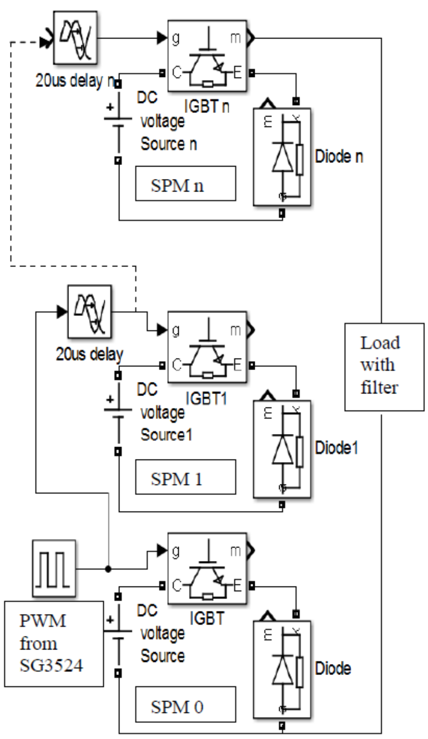


Figure 6: SPM module subsystem overview

Therefore the simulation is also performed by perturbing the delay and varying PWM frequency keeping all other things intact. In one simulation the PWM frequency is increased in a multiple of initial designed PWM frequency (5kHz). It is observed that one can increase the PWM frequency in an integer multiple up to ($N$-1)/$T$. In another simulation when the delay is increases by 4 µs the output get distorted. It is observed that when the PWM frequency is reduced to 4.5 kHz then the circuit behaves well. In another simulation the delay is decreased by 4 µs, and then this drawback can be overcome if one increased the PWM frequency to 5.5kHz. The analysis of this result is very important, as while actual designing one can play with SG3524 frequency for obtaining smooth output if there is any discrepancy occur in the design of LTC 6994-2 IC based delay circuit. Figure 6 shows the inside view of SPM module. One can easily observed that the PWM signal coming out is delayed with 20 µs and then it is given to another SPM module. So every SPM module where equally delayed with 20 µs with one another in orders to ensure equal loading.

## CONCLUSION

A 5kV/5A power supply is designed and simulated utilizing PSM technique which comprises of 10 SPM. The present scheme utilizes the analog LTC 6994-2 delay line IC for producing the fixed delay necessary to obtain phase shift. A single PWM controller IC SG3524 is used to drive PWM. The present designed is seems to be more rugged and easy to design when consider to its digital counterpart done previously.

## REFERENCES


[1] S. S W. Schminke, High-power Pulse-Step Modulator for500 kW Short-,Wave and 600 kW Medium-Wave Transmitter, Brown Boveri Rev. 73 (1985) (5) 235-240.

[2] S. M. Pan et al., "The Control System of The 100kV HVPS For NBI," 2011 IEEE/NPSS 24TH Symposium on Fusion Engineering.

[3] J. Alex and W. Schminke, "A high voltage power supply for negative ionNBI based on PSM technology," in Proc. 17th SOFE, San Diego, CA,1997, vol. 2, pp. 1063–1066.

[4] N. Tomljenovic, W. Schminke, "Solid state dc power supplies for gyrotron and NBI sources", Proc. of Symposium on Fusion Technology, 1992.

[5] Wolfgang Forster, J. Alex., "High voltage, high power, pulse-step modulators for the accurate supply of gyrotron and other heating devices" Conference Record of the Twenty-Fifth International Power Modulator Symposium, 30 June-3 July 2002, Page(s): 126 – 129.

[6] S.K.Thakur, S. K. Kumari and Y Kumar, "Design and performance analysis of a crowbar-less high voltage power supply based on PSM technique " Sådhanå (2018) 43:129.

[7] YAO Lieying et al., "A Fully Digital Controller of High- Voltage Power Supply for ECRH System on HL-2A," 2011 IEEE/NPSS 24TH Symposium on Fusion Engineering.

[8] Datasheet of LTC 6994. https://www.analog.com/media/en/technical-documentation/data-sheets/699412fb.pdf

[9] J. Alex and W. Schminke, "Fast switching, modular high-voltage DC/ACpower supplies for RF-amplifiers and other applications," in *Proc. 16th Symp. Fusion Eng.*, Champaign, IL, 1995.

# SERIES CONNECTED IGBT BASED FAST HIGH-VOLTAGE SWITCH - A PROTOTYPE

Samit Bandyopadhyay*, Ranjan Kumar
Variable Energy Cyclotron Centre, 1/AF, Bidhannagar, Kolkata, India

*Abstract*

The demand of solid-state fast operating high-voltage switches which is having a substantial advantage over crowbar is growing and also finding its application mainly in the development of dc HVPS (High Voltage Power Supply) for the high-power, high-frequency vacuum tube based RF system of any accelerator. Conventional crowbar system using fast-acting Ignitron(s) connected at the output of the HVPS is being used for the protection of the expensive electron vacuum tubes from internal arcs. Solid-state based fast high-voltage switch which disconnects the HVPS from the vacuum tubes, and will have minimum or no stress on the power components such as transformer, chock and rectifier of the power supply. This paper describes the prototype development and testing of a static and dynamic voltage balanced, fast high-voltage switch using four numbers of series-connected IGBTs.

## INTRODUCTION

With the rapid growing of the power electronics semiconductor devices in the recent years, connecting the devices in series or in parallel to withstand higher voltages and currents respectively than the individual device ratings find application in the field of modern power electronics converter designs.

Conventional electron tube (triode/tetrode) based RF amplifier systems of any accelerator are equipped with the ignitron(s) / thyratron(s) based fast acting crowbar system connected in parallel as a protective device which shorts the dc anode high-voltage power supply and diverts the energy, in case of an internal arc in tube load. High voltage solid-state based switch connected in series can also be utilized to perform as a protective device [1] in terms of fast action to disconnect the load and having no short- circuit stress on the H.V anode power supply input transformer, choke and rectifier elements. Moreover, the concept of solid-state fast-opening type (disconnect) switch using series connected MOSFETs / IGBTs provide the necessary flexibility of a modular design with no inherent limit to voltage handling.

This paper describes the in-house development of a high-voltage and power solid state disconnect switch using four numbers of IGBTs connected in series, with static and dynamic voltage balancing network. The operation of the HV switch has been reviewed with a laboratory made unregulated 4KV/10A dc power supply and the results are being reported.

*samit@vecc.gov.in

## CIRCUIT TOPOLOGY

### *Device Selection*

IGBT, IXEL 40N400 having $V_{CES}$=4KV, $I_{C110}$=40A is the best available choice for its high voltage, current and power handling capacity along with low forward voltage drop. The switch module(s) of the IGBTs fabricated in-house taking into consideration its high-voltage and power-application is shown in Figure 1.

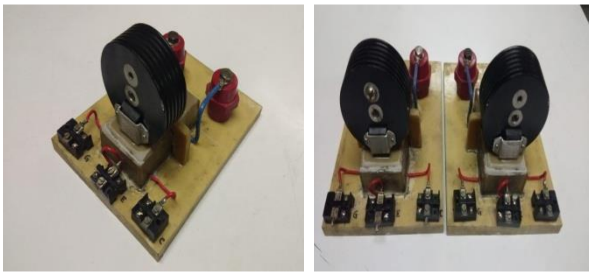

Figure 1: IGBT Module(s)

### *Series connection of IGBTs*

In order to connect number of IGBTs in series-string and to operate as a high voltage switch (connected in-series operation), it is necessary to ensure that the voltage across each IGBT is shared equally in both static (steady state) and dynamic (transient) conditions, so that no single IGBT sees the absolute maximum voltage.

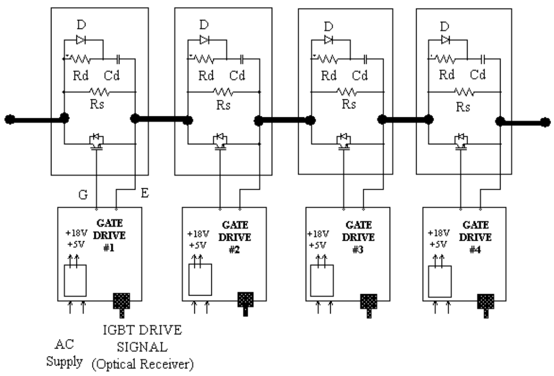


Figure 2: Series Connected IGBT switch module

Resistor-Capacitor-Diode (RCD) based voltage balancing circuit [2] is being used for the series connection of 4 nos. of IGBTs in this case. Resistor $R_s$ is being used as a static balancing component and $R_d$, $C_d$ and D (fast diode) constitute the dynamic balancing part. The diode D provides the low impedance path when $C_d$ is charged during turn-off, and $R_d$ limits the current when $C_d$ is discharged during turn-on switching.

### *Gate Drive Circuit*

Motorola MC33153 single gate driver IC that can source 1A and sink 2A has been chosen to drive each IGBT. Each IGBT driver board requires two regulated dc power supplies of +18V and +5V, for driver supply and optical fiber receiver (HFBR R-2521Z) respectively with a total maximum supply power requirement of ~2W.

### *Magnetically Isolated AC Power System*

In order to power-up, each IGBT driver module has to be insulated from the ground potential up-to the full switch voltage capability. Magnetically isolated high-voltage insulated AC power system has been developed using a 20KHz 130W class AB audio-amplifier connected to a transformer assembly having a single-turn primary winding feeding 4-nos. of ferrite toroids (CEL T-45 HP3C ) with 24 secondary turns each. Galvanic isolation is being provided and ensured by the Low-Density-High-Molecular-Weight-Polyethylene (LDHMWPE) single-turn primary, having 50kV dc continuous (20KV @ 50 Hz ac) voltage withstanding capacity.

## TEST RESULTS AND CONCLUSION

A laboratory test-bench as shown in Figure 3 integrating all the modules has been arranged for performance testing of the switch modules [3]. To achieve highly synchronized operation without any gate drive delay along with the necessary insulation, HFBR optical fibers are being used. A monoshot of variable time duration using 555 timer generates the necessary drive signal through the optical fiber transmitter (HFBR T-1524Z).

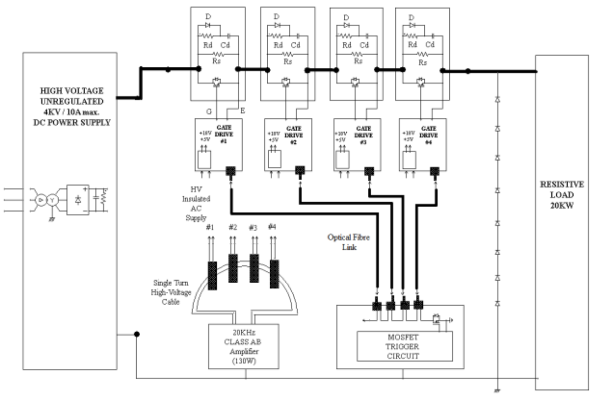


Figure 3: Laboratory Test-Bench

The test results in respect of the voltage-balancing and fast-disconnect (turn-off) operation are shown in Figure 4, Figure 5 and Figure 6. The positive test-results validate the concept of solid-state based high-voltage fast-disconnect switch and can further be explored for the up-gradation of the high-voltage bias supply of tetrode based RF system of VECC Cyclotrons.

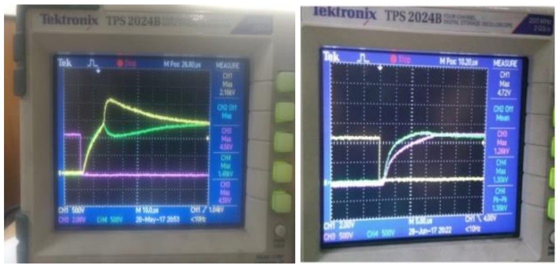


Figure 4: Voltage balancing without RCD & with RCD

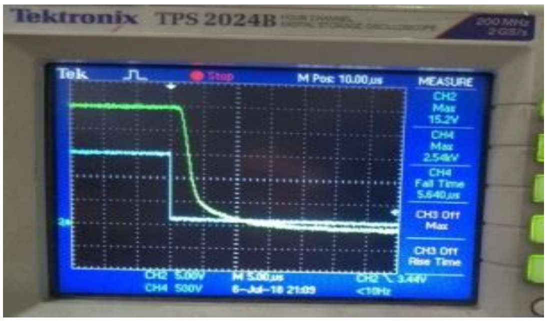


Figure 5: Output Disconnect time / Turn-off time

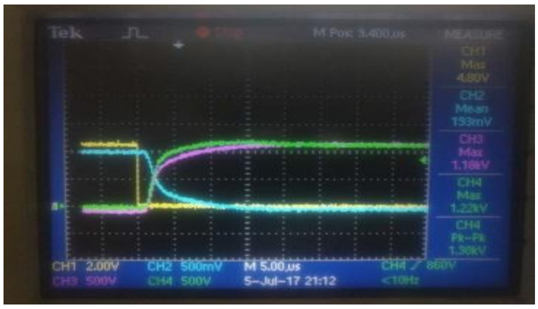

Figure 6: Yellow- Off-Signal, Blue- Output voltage, Green & Pink- Voltage across IGBTs.

## ACKNOWLEDGMENT

The authors sincerely thank all members of Power Supply Development Section, VECC and Shri Lalit Biranwar of RRCAT Indore, for fabrication and testing.

## REFERENCES

[1] Ian S. Roth et al, “A Solid-State Opening Switch for Crowbar Replacement”, Proceedings of PAC 2001, Chicago, Pages: 1459-1461.

[2] Ruchira Withanage et al, “Novel Voltage Balancing Technique for series connection of IGBTs”, Proceedings of 2007 European Conference on Power Electronics and Applications.

[3] S.Kwiatkowski et al, “Fast Disconnect Switch for ALS Storage Ring RF System High Voltage Power Supply”, Proceedings of PAC 09, Vancouver, Canada, Pages: 1745-1747.

# DEVELOPMENT OF A RESONANT HIGH-VOLTAGE DC POWER SUPPLY

Samit Bandyopadhyay*, Tapan Kumar Mandal
Variable Energy Cyclotron Centre, 1/AF, Bidhannagar, Kolkata, India

*Abstract*

High voltage dc power supplies find a wide range of applications in the field of electrostatic systems of any accelerators as well as in Laser based systems, medical diagnostic equipments and in industry for high-voltage testing of components and cables. This paper describes the in-house development of a state-of-art soft-switching based continually variable 0-20kV / 5mA max, dc-regulated power supply to operate in constant-voltage constant–current (CV/CC) mode. DC-DC converter topology based on Half-bridge resonant inverter with a resonant tank circuit followed by high-frequency step-up transformer and 4-stage Cockcroft Walton multiplier is being adopted for the development of this power supply. The converter operates at a constant frequency near resonance of the tank circuit and is controlled by PWM duty-cycle control. Functional testing of the power supply has been done and the test-results are being reported in this paper.

## INTRODUCTION

The use of a high-voltage dc power supply is commonplace in the electrostatic systems of any accelerators. Switch-mode power conversion topologies [1] operating at high frequencies along with step-up transformer and output multiplier is the basic for the development of such power supplies. One of the key components that need serious attention is the high voltage and frequency step-up transformer, which is having large secondary turns and insulation layers along with high isolation distance, leading to an increase in the leakage inductance and the winding capacitance. This inherent leakage inductance and winding capacitance results in undesired voltage and current spikes and in turn can damage the switching devices. Connection of proper snubber circuit does not improve resulting in snubber losses that in-turn reduces the efficiency and reliability of the converter system. An attractive and state-of-art solution is to integrate these transformer non-idealities into the basic converter design, using the leakage inductance and the secondary winding capacitance as the resonant tank element to ensure the soft-switching operation.

The paper describes the in-house development and the methodology adopted for the development of a high voltage dc power supply having the basic starting specifications that are as follows.

- Input Voltage: 230V ±10%
- Output Voltage: 0-20kV, DC.
- Max. Output current: 5mA max.
- Operation: CV / CC Mode.

The operation of the circuit has been tested for its performance and the results are being reported.


Figure 1: 0-20kV/5mA High-Voltage DC Power Supply.

## DESIGN AND TOPOLOGY

### *Power Converter Topology*

The schematic of the static power converter as shown in Figure 2, uses single-phase as its input due to its low output power requirement. The utility main is stepped down that is rectified and filtered to produce the unregulated dc voltage (Vd) of 240V. The unregulated dc is used to power the MOSFET based Half-Bridge inverter to convert the dc unregulated voltage to a high frequency square ac signal. The inverter output ac signal is boost-up by a high-frequency step-up transformer (1:n, n=20) followed by a 4-stage Cockroft-Walton (CW) multiplier circuit that generates the required output dc voltage.

As shown in Figure 2, the inherent high voltage transformer non-idealities act as the resonant tank element of the Inverter circuit. The resonant tank inductor Ls, is the sum of the transformer leakage inductance with the series external inductance. Similarly the parallel resonant capacitor Cp is also the sum of the parasitic capacitor of the transformer secondary reflected to the primary ($n^2$Cw, Cw is the secondary winding capacitance) with additional external capacitor and Cs forms the series resonant capacitor. Ls, Cs, Cp constitute the LCC tank element for the Half-Bridge inverter circuit [2]. Series-parallel (LCC) resonant tank topology is being adopted for the development of this power supply, which is having better characteristics in respect of its open and short-circuits load characteristics. Amongst the available dc-dc converter topologies with isolation transformer, Half-Bridge topology is selected taking in view the output power requirement which is 100W maximum in this case.

*samit@vecc.gov.in

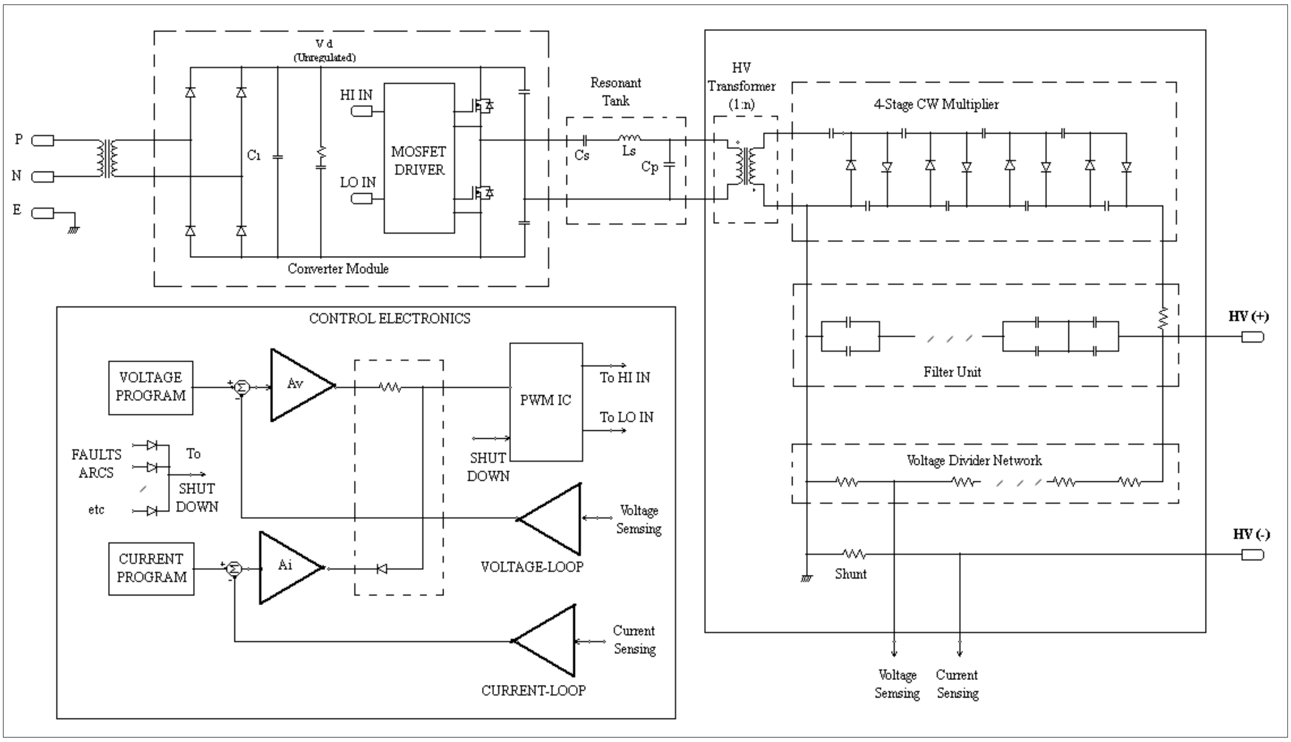


Figure 2: Schematic of 20KV/5mA Resonant High-Voltage DC Power Supply

The output 4-stage Cockroft Walton multiplier using high voltage diodes and capacitors is responsible for rectifying and filtering the transformer output to generate the dc output voltage. In addition, a low pass RC filter network has also been implemented and housed for reduction of output voltage ripple.

The dc voltage output also provides the output feedback and monitoring signal from a high voltage resistive network to divide the output voltage low enough to be processed by the power supply control circuitry for voltage regulation. A precise low value shunt-resistor is being added in the low-voltage side of the high voltage output circuit for current sensing and monitoring.

## *Control Electronics*

Control electronics consisting of regulation/control loops, monitoring and trip/shutdown circuits, needs to function together for its required operational performance. The output voltage of the power supply can be regulated by adjusting either the switching frequency (for fixed output voltage power supply) or by the amplitude of the input voltage Vd. Additional switching regulator up-line (towards mains) with fixed frequency operating inverter, will increase switching power loss and degrade its efficiency and reliability.

PWM based Duty-Cycle-Control is being adopted for the development of this required continually variable power supply operation. The operating frequency has been found by looking for the minimum peak oscillating current of the MOSFET at 240V of dc unregulated voltage (Vd) and fixed 50% duty-cycle switching, as shown in Figure 3, to get the required output voltage at full load, without closing the control loops. The switching frequency is being fixed at ~32kHz in this case.

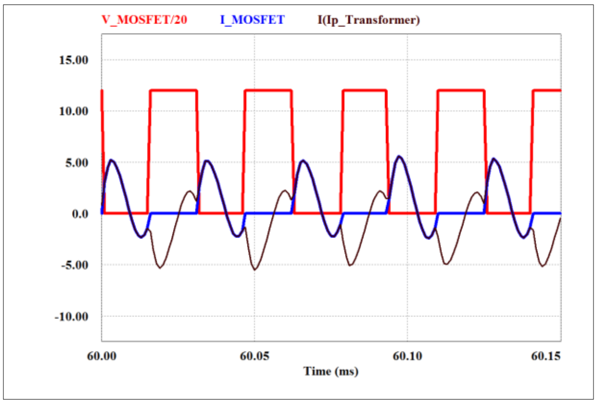


Figure 3: Resonant Switching of MOSFET and Primary-current of high-voltage transformer (Simulation Result)

The feedback signals from the output voltage and current are being compared with a reference to generate the error signal. Compensating error amplifier with high dc-gain gives the necessary control signal to SG3524 PWM regulator IC for duty cycle control. High dc- gain of the voltage control-loop ensures the overall stability of the power supply in voltage mode. As high voltage conditioning of the electrostatic system results in large current variations, the power supply is equipped with ac electronic arrangement at the output of two error amplifier chains (Av and Ai) to function as an analog exclusive-OR circuit that ensures the constant voltage/constant current (CV/CC) operation [3]. The power supply switches from voltage to current mode whenever the output current reaches the set current program value and no sooner the output current drops below the set, it recovers automatically to the default constant voltage mode of operation. Figure 4 presents the simulation result explaining the operation of the power supply in CV / CC Mode with the control loops in place.

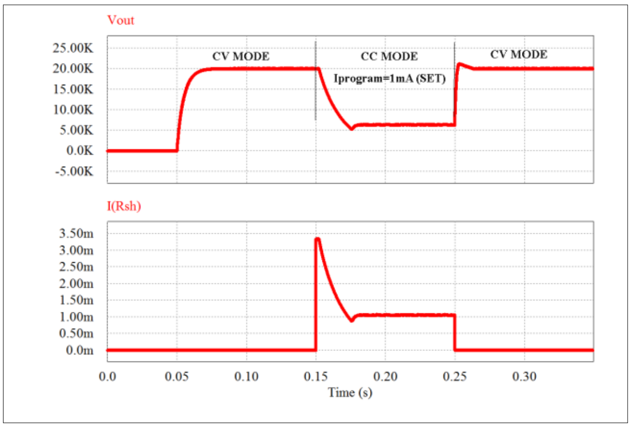


Figure 4: CV / CC Operation (Simulation Result)

The trip-circuit module protects the power supplies in the event of abnormal situations prevailing in load side, or inside the power supply unit. The shutdown pin of the SG3524 PWM regulator IC is being actuated when any one or more of these abnormal parameters are detected and the interlocks are latched on to display in the front panel.

## RESULTS AND CONCLUSION

All the modules as described, are assembled integrated and connected inside a 3U-cabinet (L=550mm, W=435mm, H=133mm), as shown in Figure 5.

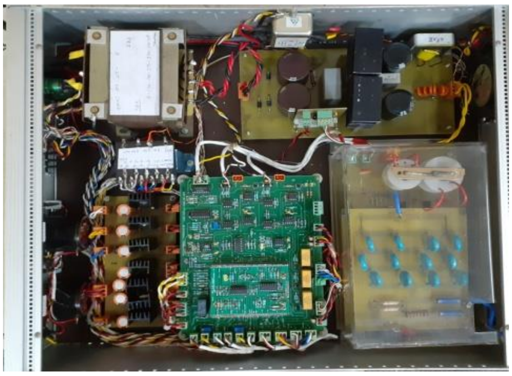

Figure 5: Power supply cabinet (Top view)

The developed 0-20kV / 5mA max., dc resonant high-power supply unit, with PWM duty-cycle control has been tested with a resistive dummy load, and the results in respect of output voltage and ripple at full load of 5mA are being shown in the Figure 6 and 7 respectively.

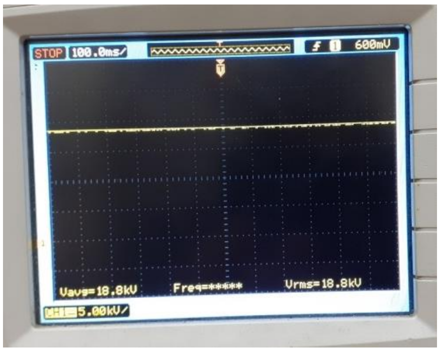

Figure 6: DC Output Voltage at Full load of 5mA

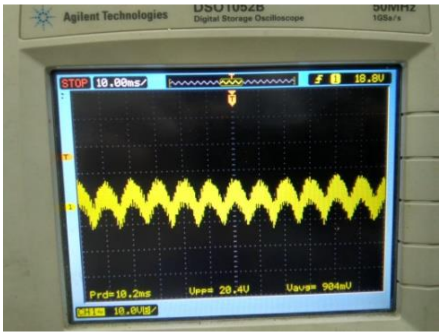


Figure 7: Output Ripple at 20kV/5mA


## ACKNOWLEDGEMENT

The authors sincerely thank all members of the Power Supply Development Section, VECC for the development fabrication and testing of this power supply.


## REFERENCES


[1] Ned Mohan, T.M Undeland, W.P.Robbins, “Power Electronic Converters – Application and Design”, 2nd Edition, John Willey and Sons. Pages: 301-319.

[2] Robert L Steigerwald, “A Comparison of Half Bridge Resonant Converter Topologies”, IEEE Transactions on Power Electronics, Vol. 3, Issue 2, April 1988, Pages: 174-182.

[3] S.Beghini et al “A compact high voltage power supply for the LNL recoil mass spectrometer”, Nuclear Instruments and Methods in Physics Research Section A: Accelerators, Spectrometers, Detectors and Associated Equipment, Volume 300, Issue 2, 15 January 1991, Pages: 328-334.

# A VERSATILE LOW ENERGY NEGATIVE ION IMPLANTER

Ksh. Devarani Devi, S. Gargari, R. Joshi, S. Ojha, M. Sota, V.Patel, GR Umapathy, J. Prasad, Rakesh Kumar, M.P.Singh, N.S. Panwar, S. Mohan, Suraj Kumar, Pranav Singh, Jaswant Singh, Gaurav Raturi, P. Barua, Ashok Kothari, Chandrapal, Rajiv Ahuja, S. Chopra

Inter University Accelerator Center, Aruna Asaf Ali Marg, New Delhi-110067, India

*Abstract*

To meet the ever increasing demand for varieties of dopant ion beams and their precision doping, a low energy ion accelerator in the energy range, 30-200KeV was developed. The facility delivers highly stable and collimated ion beam with ion currents ranging from few nA to few µA. Precision doping, control over the beam incident angle to the wafer of implantation as well as no energy contaminant, free from other impurities such as oxygen and hydrogen is possible. We present the tool overview, performance, available ion beams, new beam developments and implant results.

## INTRODUCTION

Enormous research in material synthesis, device fabrication and modifications through ion-solid interaction in nuclear energy loss regime resulted in the development of low energy ion implanter at IUAC [1, 2, 3 and 4]. For instance, the structural, electrical, optical and magnetic properties of materials are modified through ion beam irradiation in this energy range. Among various material synthesis processes, ion implantation technique is unique in its flexibility of controlling ion concentration as well as choosing the depth of dopant. These are determined by the quantity of ions collected over a time and the ion acceleration energy. The technique allows doping of any amount of dopant in any host matrices, even beyond its solid solubility limit. It gives excellent accuracy, uniformity and reproducibility. Precision doping at any ion implant angle to the wafer in a well defined space region can be achieved; careful masking can define more refined area of doping [5]. The last property can be defined at the target station while the other properties strongly depend on the ion accelerator and the ion source technology. The technique facilitates implantation with no energy contaminant and free from other impurities such as oxygen and hydrogen with the help of the analyzer magnet which selects the particular ions of interest and reject all other. We present the tool overview, performance, available ion beams, new beam developments and implant results.

## ION IMPLANTER TOOL AND ITS PERFORMANCE

IUAC developed ion implanter is of pre-acceleration type of ion accelerator. It is shown in figure 1 and figure 2. Experiments regularly conducted in the implanter facility require a broad range i.e. from low to high dose implants and energies spanning several orders of magnitudes of 30 to 200KeV. Varieties of ion species are required for various studies such as doping of P/N type ion species and others ion species for material science studies. Additionally, the facility requires a versatile target positioning capabilities to do implantation at any angle of ion beam to the wafer.


Figure 1. Ion source and acceleration column


Figure 2. Beam line and target chamber

The implanter accelerator is equipped with MC-SNICS ion source which is installed on a high voltage deck (200kV). Negative ions generated at the ion source are subsequently extracted and focused by an einzel lens in deceleration- acceleration mode. Ion source is discussed in details in the following sections. These ions are further accelerated up to 200KeV of energies by an accelerating column consisting of three accelerating tubes. The particular ion of interest are selected by using an analyzing cum switching magnet and switch over the ion beam to $90^0$ bending angle beam line. Higher mass ions with lowest energies such as 30KeV $^{197}Au$ are extremely spread out due to strong focusing by electrostatic quadrupole triplets (EQT-1). Ion beam intensity gets lost at the analyzer magnet approximately 50%. As ion beam energy increases, we observe improvement in ion beam transmission and increase in beam intensity. The energies of the higher mass ions are limited around 100keV since the analyzer magnet has a maximum rigidity, R $=mE/Z^2$ of 34 (where m- mass in a.m.u., E- energy in MeV, Z- charge state). The analyzed beam are further transported through the beam line and finally focused at the target chamber by adjusting electrostatic quadrupole triplet (EQT-2) fields and electrostatic steerers (ES-2). Ion beam diagnostics devices such as beam profile monitors and faraday cups installed at beam waist positions monitored shape of beam and measure currents.

The end station of the implanter system, the target chamber is provided with a rotator and a linear movements which allow us precision doping of any ion at any angle of wafer. An electrostatic scanner is installed in front of the target chamber to have uniform ion implantation as well as variable scan area of the samples. The optimal ion beam size obtained in the chamber is of 5mm X 5mm. The scanning method is high –speed electrostatic X-Y scanning of approximately 700 Hz (vertical) and 900 Hz (horizontal) axis. The vertical movement of target ladder is controlled by using motorized linear motion feed through while rotational one is done manually. CsI crystal doped with thallium is used to view ion beam spot.

To achieve required vacuum of the beam line, turbo molecular pumps backed by oil free scroll roughing pump are used. At proper locations of the beam line, beam line valves are positioned to isolate the accelerator system in part as and when required. The base pressure in beam line and chamber is $5 \times 10^{-8}$ torr. The entire accelerator i.e. ion source and all beam line components are controlled remotely from a centralized control console. The control system used for its operation is indigenously developed.

## A VERSATILE ION SOURCE

Ions can be produced by various methods. However, MC-SNICS (Multi Cathode Source of Negative Ion by Cesium Sputtering) which can hold 40 cathode samples at a time is the preferred choice as it delivers broad range of ion species with ion beam intensities of few nA to few μA [6,7]. It is cesium assisted sputtered based negative ion source. Negative ions are formed by capturing an electron into an electron affinity level of the atom. Therefore, an element will form negative ions provided that it has positive electron affinity and low work function. Theoretically, negative ion, $I^-$ produced from the sample surface will be given by [8]

$$I^- = I^+ A\, \eta^- \exp(-n_0 L \sigma_d)$$

$I^+$, A, $\eta^-$ are projectile ion current, sputtering yield and negative ion formation efficiency. Exp ($-n_0L\sigma d$) is a factor decreased due to electron detachment collisions. $n_0$ ,L and $\sigma_d$ are the neutral gas particle density, transport length and the electron detachment cross section for the negative ion respectively. Single electron detachment cross section, $\sigma_d$ is almost independent of negative ion energy but weakly dependent on the physical parameters of the negative ion and the target gas.

Constant current density of negative ion beams from the ion source can be controlled by cesium flow rate to the ionizer and hence Cs+ flow rate to the cathode i.e. cathode current. In general, ion source delivers approximately deliver 1 uA or more currents of ion beams for implant. Therefore, the ion source operates in high values of ion source parameters. Oven heater and line heater are on always.

All elements do not form the stable negative ions. In such cases, it is obvious to use molecular ions. However, molecular ion beams have disadvantages as they reduced final energy of the ion beam of interest. By selecting lightest possible molecule, such as hydride, reduction in energy can be minimized. Carbide, Nitride or Oxide are of interest in case hydride is not possible. The list of the typical ion beam delivered from this facility for ion implantation is given in table 1; whereas, the newly developed elemental and molecular ion beams are listed in table 2.

Table 1: Available ion species along with their ion beam intensity

| | | | | |
|---|---|---|---|---|
| $^{7}Li$<br>*100nA* | $^{11}B$<br>*400nA* | $^{12}C$<br>*1μA* | $^{16}O$<br>*1μA* | $^{27}Al$<br>*130nA* |
| $^{28}Si$<br>*1μA* | $^{31}P$<br>*1μA* | $^{32}S$<br>*200nA* | $^{48}Ti$<br>*400nA* | $^{56}Fe$<br>*150nA* |
| $^{58}Ni$<br>*1μA* | $^{59}Co$<br>*1μA* | $^{63}Cu$<br>*1μA* | $^{107}Ag$<br>*1μA* | $^{197}Au$<br>*1.1μA* |

Table 2: Newly developed ion species including the molecular beams with their beam current

| | | | | |
|---|---|---|---|---|
| $^{24}C_2$<br>*1.1μA* | $^{49}TiH$<br>*1μA* | $^{54}CrH_2$<br>*1μA* | $^{74}Ge$<br>*500nA* | $^{145}SrF_3$<br>*70nA* |
| $^{40}MgO$<br>*100nA* | | | | |

## ION IMPLANTATION EXPERIMENTS AND ITS RESULTS

In ion implantation experiment, ion fluence (or dose) determines the total doping concentration. Precisely, the implanted dose ($\Phi$ in $cm^{-2}$) is controlled by beam current (I in ampere), and implantation duration (t in second). Whereas, the incident beam direction is defined by tilt ($\theta$) and twist ($\Phi$) angle which are shown in the figure 3 below. Tilt ($\theta$) is the angle between the ion beam and the normal to the wafer surface. Meanwhile, we do not have the provision of controlling twist angle [9].

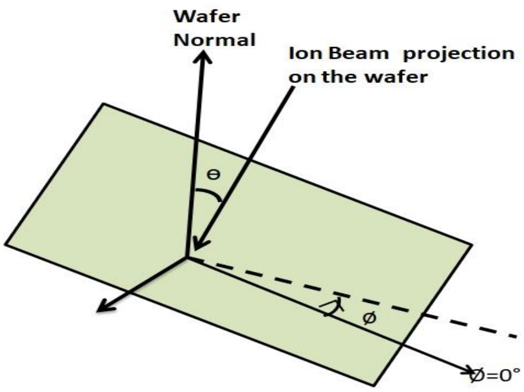


Figure 3. Tilt angle, ɵ and twist angle, ø

70keV $Au^-$ ions are implanted in quartz substrates, sizes 1cmx1cm with variable fluencies, $1x10^{16}$ions/$cm^2$ to $1x10^{17}$ions/$cm^2$ at tilt angle, ɵ=0º. The measured experimental RBS spectra for 70keV Au- ion implanted quartz substrate with different ion fluences confirm the presence of Au particles with a projected range of 35 nm inside the substrate. This is well matched with the SRIM calculated value, 34.7 nm. No other contamination other than substrate (28Si, 16O) can be seen from the RBS spectra. The good uniformity of the ion implantation on the sample surface area up to 15mm x15 mm is also achieved using an electrostatic scanner in front of the target chamber.

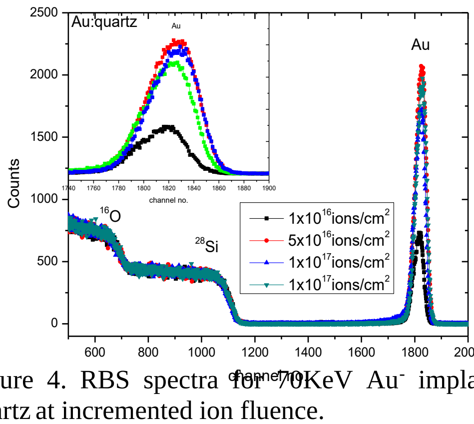


Figure 4. RBS spectra for 70KeV $Au^-$ implantation in quartz at incremented ion fluence.

## RESULT

30- 200KeV ion beams of various species having masses from 7Li to 197Au as well as molecular ion beams are developed, accelerated and transported up to the target chamber for ion implantation experiments. Doping free from impurities such as oxygen and hydrogen could be achieved. The dopant depth profiles are well matched with the calculated ones. Precision doping at any implant angle is possible.

## REFERENCES


[1] T. Trivedi et al, Physics Procedia 90 (2017) 100 – 106

[2] K. Devarani et al, InPAC-2006, DAE-BRNS Indian particle accelerator conference, 2006

[3] G. D. Alton, M.T. Johnson, Nuclear Instruments and Methods in Physics Research A328 (1993)202-206

[4] N Kumar et al, Vacuum 124, 55-59

[5] Leonard Rubin and John Poate, JUNE/JULY 2003 © American Institute of Physics, The Industrial Physicist, 12-15

[6] Ksh. Devarani Devi, InPAC-2015, DAE-BRNS Indian particle accelerator conference, 2015

[7] R. Middleton, NIM 118, p.329-336.

[8] Kshetrimayum Devarani, InPAC-2013,DAE-BRNS Indian particle accelerator conference,2013

[9] Jerald P. Dykstra et al, Nuclear Instruments and Methods in Physics Research B55 (1991) 478-481

# Digital LLRF Control System for Low Energy Buncher System At PLF, Mumbai

Shweta Prasad[1#], S. Pal[1], J.N. Karande[1], R.Palit[2], V. Nanal[2], G. Randale[3] and G. Joshi[3]
[1]PLF, Tata Institute of Fundamental Research, Mumbai 400005
[2]DNAP, Tata Institute of Fundamental Research, Mumbai 400005
[3]ACnD, Bhabha Atomic Research Centre, Mumbai 400085

*Abstract*

Development of digital LLRF system has been initiated at Pelletron Linac Facility, Mumbai, to replace the conventional analog radio frequency (RF) system for RF cavities (both normal conducting and superconducting). As a first step, the digital LLRF system is being developed on a MicroTCA.4 platform, for the LEB RF cavity operating at 18.75 MHz. This paper briefly describes the basic architecture, digital signal processing scheme, and test results of this MicroTCA.4 based system. This design will be implemented for all 3 normal conducting RF cavities of the LEB system.

## INTRODUCTION

A conventional analog radio frequency (RF) system to control amplitude and phase has been operating for RF cavities (both normal conducting and superconducting) at Pelletron Linac Facility, Mumbai [1]. In order to maintain the phase and amplitude of the electric field in the cavity, RF controller cards have been developed by AcnD, BARC for all the RF cavities which are operating at the sub-harmonics of LINAC operating frequency, f =150 MHz. The Low Energy Buncher (LEB) present at entrance of Pelletron consists of a double harmonic drift buncher operating at f/16 (9.375MHz) and f/8 (18.75MHz). And a sweeper present at the exit of the Pelletron accelerator is operating at f/32 (4.6875MHz) [2]. The present analog control system is being upgraded to digital LLRF control system as it provides many advantages over its analog counterpart, such as DC offsets, drifts, gain imbalance and impedance mismatch. In addition, the digital control system will have better diagnostics, maintenance, upgradation and stability. The design and development of DLLRF is in progress for the LEB RF cavity operating at 18.75 MHz on a MicroTCA.4 platform at PLF, TIFR, Mumbai and its details are presented in this paper.

## MICROTCA.4 BASED SYSTEM

MicroTCA is a modular and open standard for building high performance switched fabric computer systems in a small form factor. MicroTCA.4 includes a chassis with redundancy of power unit, cooling unit, MicroTCA Carrier Hub (MCH), Advanced Mezzanine Card(AMC) and Micro-Rear Transition Module (µRTM). It also has a precision clock generation and distribution system. The AMC SIS8300-L card contains 10 ADCs (16 bits, 125MHz), 2 DACs (16 bits, 250MHz) and Xilinx Virtex 6 FPGA.The µRTM SIS8900 card contains 10 analog channels,clock ports & triggering ports as shown in Fig.1.


Figure 1: Picture of SIS8300-L and SIS8900 cards of MicroTCA.4

## DIGITAL LOW LEVEL RF CONTROL SYSTEM USING MICROTCA.4

The block diagram of the digital LLRF implementation for a low energy buncher system and the digital processing are shown in Fig. 2 and Fig.3, respectively. The amplitude and phase of the pick-up signals of f=18.75MHz and 9.375MHz are matched with the amplitude and phase of the reference signals. The digital processing of signals have been carried out on Virtex-6 FPGA[3]. It mainly consists of digital I/Q demodulator, CORDIC algorithm, digital I/Q modulator and PI controller as shown in Fig.3 The I/Q demodulator, CORDIC algorithm and digital I/Q modulator have been developed and tested on MicroTCA.4.

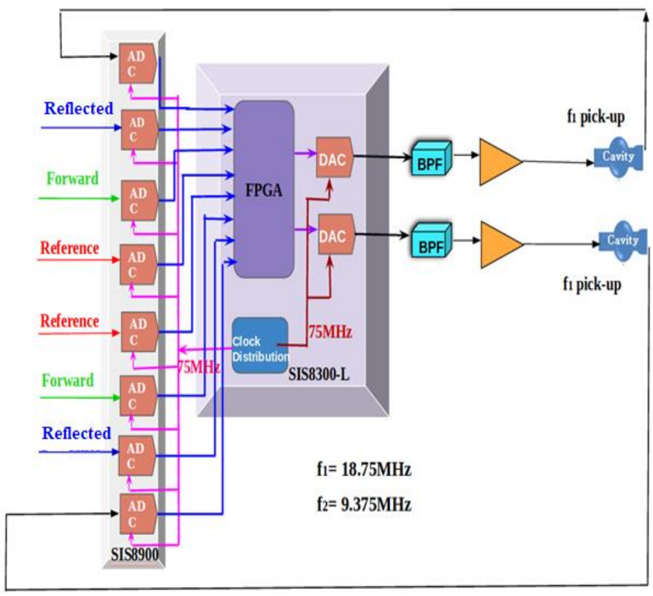


Figure 2: Block diagram of digital LLRF (DLLRF) system for LEB

#shweta.prasad@tifr.res.in

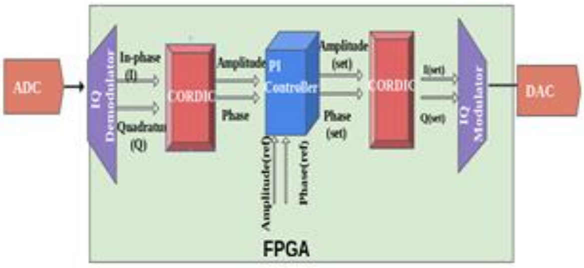

Figure 3: Digital processing flow diagram

## *Clock distribution*

The ADC clock, FPGA clock and DAC clock operate at 75MHz and are derived from 250MHz crystal oscillator by using a clock multiplier (SI5326) and a clock divider (AD9510)

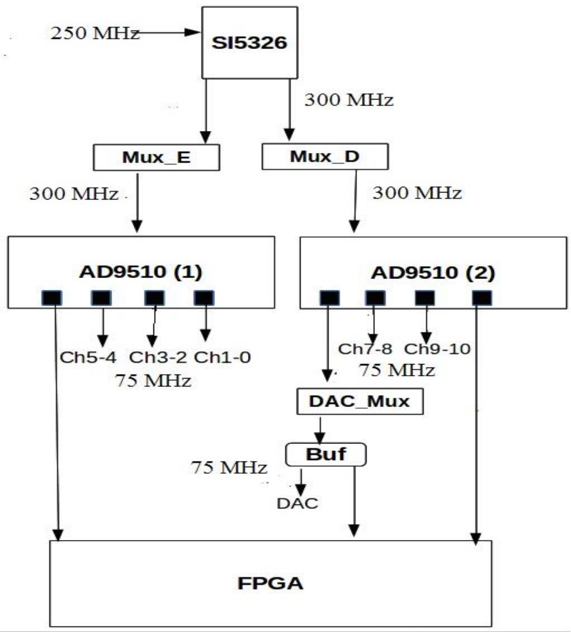

Figure 4: Clock Distribution module

## *Digital I/Q demodulator*

The polar representation of the RF signal is decomposed into its Cartesian representation, which is in-phase (I) and quadrature (Q) components by direct I/Q sampling method. The 18.75 MHz RF signal is sampled at 75 MHz by the ADCs. On the FPGA, the samples are collected and passed to CORDIC module. Fig. 5 shows the 18.75 MHz pick-up signal with its respective I and Q components.

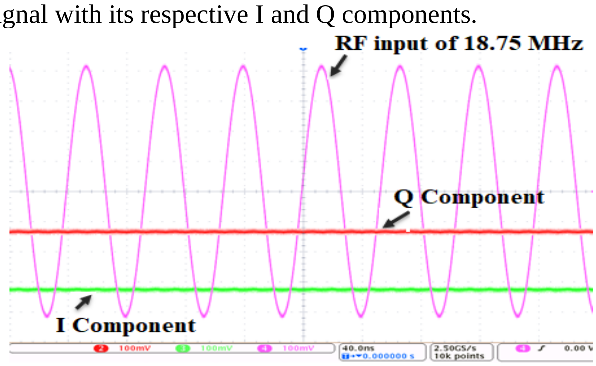

Figure 5: Digital I/Q demodulator output as seen on scope

## *Digital I/Q Modulator*

Digital I/Q Modulator is implemented by Direct Digital Synthesis (DDS).The DDS reproduces the 18.75 MHz RF signal at the output of the DAC when the clock is set to 75MHz. As is evident from the FFT, the output contains the fundamental frequency component along with its image frequencies. To extract the fundamental frequency component and to attenuate the unwanted image frequencies, an analog band pass filter of centre frequency 18.75MHz has been designed. The outputs of DAC without and with the analog filter(with insertion loss of 4.1dB) are shown in Figure 6 and Figure 7, respectively.

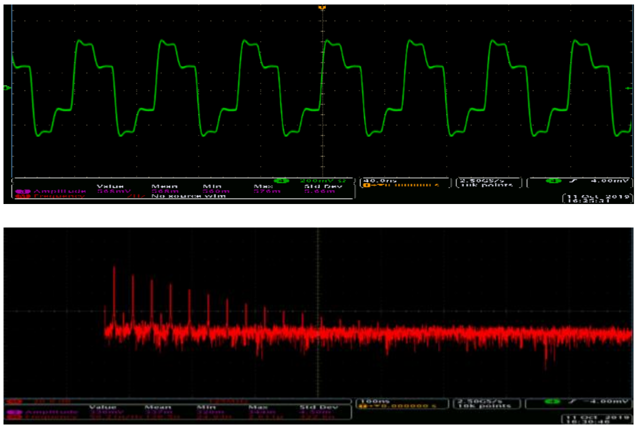
Figure 6: Digital I/Q Modulator output and its FFT.

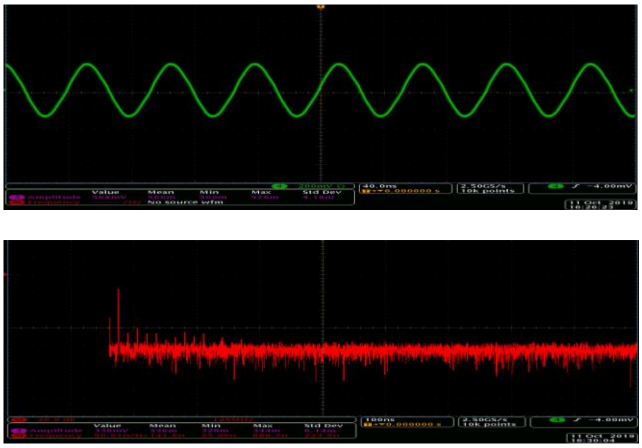
Figure 7: Digital I/Q Modulator output after filtering.

## *Magnitude and Phase calculation using CORDIC Algorithm*

The vectoring mode of CORDIC algorithm has been developed and tested for the calculation of the magnitude of 18.75 MHz RF pick-up signal and the phase difference of RF pick-up signal w.r.t the reference signal (of 18.75MHz).

In vectoring mode, the $I_0$, $Q_0$ with initial phase $\emptyset_0$ is driven to $I_n$, 0 with final phase$\emptyset_n$. At this point, the value of $I_n$ gives the magnitude (|M|) and the accumulated value of $\emptyset_n$ gives the phase( $\Theta$).

$$|M| = I_n = A_n\sqrt{(I_0^2 + Q_0^2)} \quad (1)$$

$$\Theta = \emptyset_n = \emptyset_0 + tan^{-1}(\frac{Q_0}{I_0}) \quad (2)$$

Fig. 8 shows the magnitude plot for the input pick-up signal, i.e. the plot of the magnitude measured from the RF signal generator and that calculated by the CORDIC. Similarly, Fig. 9 shows the phase plot for measured and the values calculated by CORDIC for the phase difference between the reference signal and the pick-up signal.

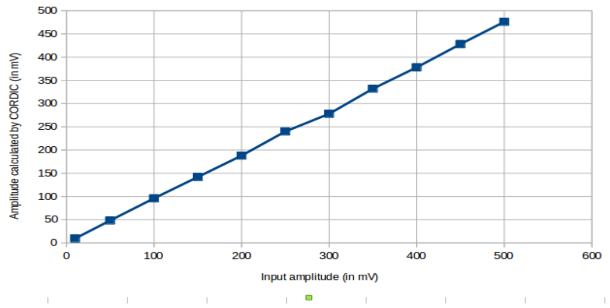


Figure 8 Magnitude Plot of input pickup signal (in mV).

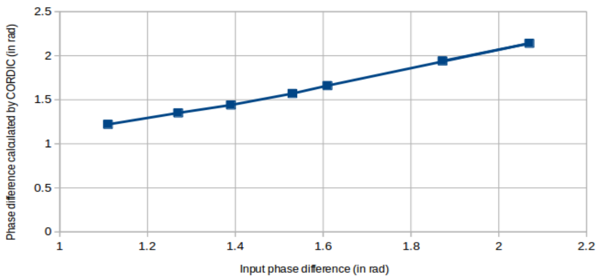


Figure 9: Phase difference plot between reference signal and pick-up signal (in radians).

### *Analog band pass filter*

An analog band pass filter of centre frequency 18.75MHz has been designed and tested. The filter parameters are given in Table-1. Fig. 10 shows the frequency response of the filter at 18.75 MHz measured with the network analyser.

Table-1: Design parameters of analog filter

| | |
|---|---|
| Centre Frequency | 18.75 MHz |
| Bandwidth | 980 kHz |
| Quality factor (Q) | 19 |

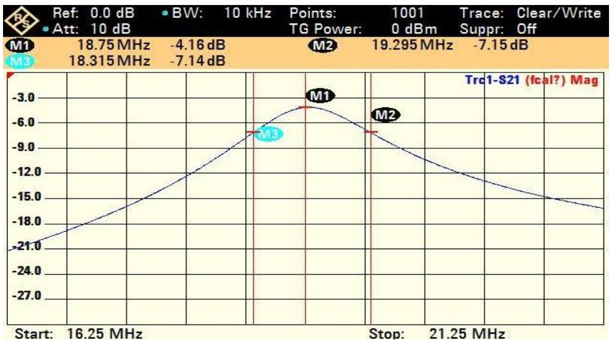


Figure 10: Measured frequency response of the filter

## TEST RESULT OF DLLRF SYSTEM

The DLLRF system test setup (block diagram as shown in the Fig. 11) consists of a dummy RF cavity, amplifier (gain= 8.9dB), a RF signal generator and a MicroTCA. The DLLRF system has been tested in open-loop mode. In the open-loop mode, the 18.75MHz input RF signal from RF signal generator is first fed to first ADC channel and the ADC output is sent to FPGA where the phase of the input RF signal is calculated. After I/Q Modulation and I/Q Demodulation the signal is passed to the DAC. The output signal of DAC after filtering and amplification is passed to the dummy cavity, which is tuned at 18.75MHz.The pickup signal from the dummy cavity is fed to second ADC channel and then to FPGA .The phase difference between input RF and pick-up is calculated.

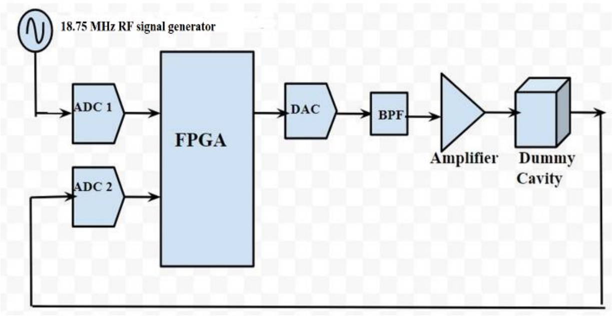


Figure 11: Block diagram of test setup in open loop mode

## CONCLUSION

The DLLRF system has been tested for 18.75MHz pickup signal. The modules of DLLRF system, namely, direct I/Q sampler, CORDIC and I/Q modulator have been implemented in the firmware of MicroTCA.4. These modules are used with the clock generation module, analog bandpass filter, amplifier and dummy RF cavity. The results of the magnitude of pick-up signal and the phase difference calculated by CORDIC are close to measured values. In open loop test, the phase difference accounting the delay between ADC and DAC has been calculated. In future,these modules will be tested in closed loop with RF control logics having PI feedback control.

## ACKNOWLEDGMENT

We would like to thank Prof. R.G. Pillay, for invaluable guidance in the project. We also thank Mr. Rajesh Sahu (NPD, BARC) and the PLF staff for their support.

## REFERENCES

[1] Gopal Joshi, C.I.Sujo, Shyam Mohan, "RF control for heavy ion linacs", InPAC2006 proceedings

[2] M.Y. Vaze *et al*. Indian Journal of Pure and Applied Phys. **35**, 193(1997)

[3] M. J. O'Farrell. Low Level Radio Frequency Control of RIA Superconducting Cavities. Master's Thesis, Michigan State University, East Lansing, Michigan, 2005

# EVALUATION TESTS OF UPGRADED HOT CATHODE IONIZATION GAUGE CONTROLLER FOR INDUS ACCELERATOR VACUUM SYSTEMS

Kumar K.V.A.N.P.S. †, Sindal B.K., Deokar D.Y., Bhange N.J., Yadav D.P.,
Ultra High Vacuum Technology Section, RRCAT, Indore, India

*Abstract*

An upgraded Hot Cathode Ionization Gauge Controller (HCIGC) has been developed and tested at Ultra High Vacuum Technology Section (UHVTS), RRCAT, Indore. HCIGCs are used for pressure measurement in the range of $10^{-3}$ to $10^{-11}$ mbar continuously using Bayard-Alpert (B-A) type HCIG heads. Pressure measurement, in Injector Microtron, Transport Lines, Indus-1 & Indus-2 Synchrotron Raditaion Sources, Beam line front end of Indus Accelerator Vacuum Systems, is performed by HCIG heads. M/s ECIL, Hyderabad make HCIG controllers have been deployed in Indus Vacuum Systems for the last 14 years for pressure measurement along with control features for protecting the vacuum systems from loss of vacuum events. Upgraded new controllers have more control features to control front end gate valve operation along with the modular approach to reduce the mean time taken to repair and increase the reliable machine availability for user community.

The upgraded controllers were calibrated on an in-house developed UHV test system and already deployed in Indus Complex. Details of UHV test system, testing procedure and results are described in this paper.

## INTRODUCTION

The Indus Accelerator Complex is equipped with ~300 metre of vacuum systems (the largest vacuum system in India)[1].The complex has six separate vacuum systems covering Injector Microtron, three transport lines, three synchrotrons. Among them Indus-1, Indus-2 are the two dedicated high energy electron synchrotron radiation sources operating at 450 MeV (beam current at 100mA) and 2.5 GeV (beam current upto 200 mA). Indus-2 is the largest vacuum facility (with the circumference of 172.46 metre) operating on 24x7 basis as a national synchrotron facility for users. UHVTS is engaged in reliable, regular operation & maintenance of Indus facility complex vacuum systems on round-the-clock 24x7 basis.

Ionization gauges are regularly used for pressure measurement in Indus complex vacuum systems. Around 85 nos., of HCIG heads are currently installed on Indus vacuum systems including beam line front ends of Indus-2. An ionization gauge comprises a sensor (gauge head), electronic circuits necessary to energize the sensor, and an in-built ion current measurement circuit in an electronic controller. In the HCIG head, electrons emitted from the cathode are accelerated by the anode potential to ionize gas molecules within the boundary of the vacuum envelope, which then produce an ion current at the collector. The value of collected ion current is related to the gas pressure, the electron emission current, and sensitivity of the gauge head

The existing version of HCIGC were designed in early 90's UHVTS, RRCAT (in association with ACD, RRCAT) first time tested the HCIGCs manufactured by M/S. ECIL, Hyderabad in the year 2001 and deployed in the year 2005 in Indus-2 complex. Presently, 74 such units are deployed in various locations of Indus Complex Vacuum System for pressure measurement and pressure interlocking and vacuum sector isolation purpose in case of any vacuum loss events due to air leaks/e-beam mis-steering.

Over the last 14 years, due to the aging of the components and requirement of additional process control features, it is felt to upgrade the controllers with (i) Modular approach to reduce the mean time taken to repair (MTTR) from few days to few hours, (ii) Must follow industrial standards of mechanical, electronics such as AVS [2] or ISO/DKD [3, 4, 5] standards, (iii) Facility to monitor emission & degas current externally for diagnostic purpose. As a result of the continuous developmental efforts by UHV Instrument lab at UHVTS [6], new upgraded HCIGs were developed with the help of Indian Industry and successfully deployed twelve new controllers in the year 2018 on Indus Complex Vacuum Systems.

### *Description of UHV Test System:*

The UHV Test system consists of DN 160 CF "I" shaped vacuum chamber with six radial DN 40 CF ports for mounting of HICG heads, UHV compatible leak valve, and all metal right angle valve for evacuation purpose. The vacuum chamber is made up of SS 304L as shown in Fig. 1(a). It is an excellent conditioned system for UHV range studies of any kind like characterisation of Mass Spectrometers, calibration of Vacuum Gauge controllers. The main UHV pumping system consists of a Sputter Ion Pump (Make: RRCAT, Pumping Speed: 270 l/s for Nitrogen), Titanium Sublimation Pump (Make: RRCAT, Pumping Speed: 500 l/s for Nitrogen) so as to reach ultimate vacuum in the range of ~$5.0\times10^{-11}$ mbar. The total volume of the experimental system was ~ 50 litres.

† kkumar@rrcat.gov.in


Figure 1(a) : UHV Test System

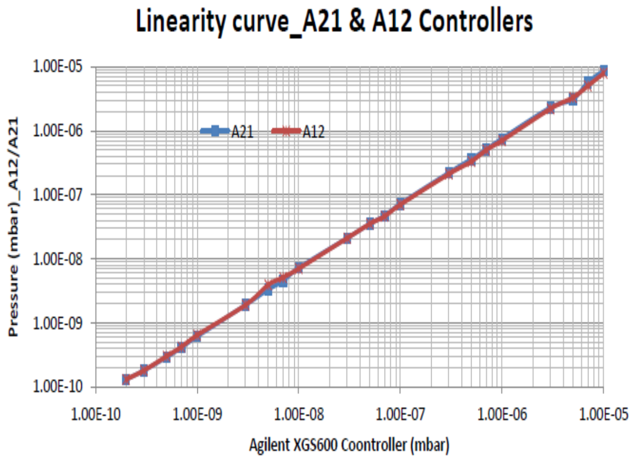


Figure 1(b): Linearity curve of A21 & A12 HCIGCs w.r.t Agilent XGS 600 Controller

Figure 1: (a) Details of UHV Test System & (b) Linearity curve of two UUTs w.r.t reference controller.

The test chamber is equipped with a HCIG (UHV24 & 24P) heads along with a factory calibrated XGS 600 controller for reference purpose. The developed controllers are connected to the other HCIG heads for testing purpose. An UHV compatible leak valve (UDV 046) was used for gas injection purpose during the calibration & linearity measurement of HICGCs. Initial evacuation is performed by a dry Turbo Molecular pumping station (Model No.: TPS Mobile) up to $1x10^{-5}$ mbar and baked the system for 24 hours at $250^{0}C$ to reach an ultimate vacuum of $\sim 5.0x10^{-11}$ mbar.

## *Calibration Procedure:*

HCIGCs were new and tested for the first time on the test setup. The tested instruments are identified as RRCAT/2017/Axx (xx refers to the serial no. of the unit). The controllers were connected to the respective HCIG heads on radial port with the reference gauge head is positioned in the between them. Prior to the calibration procedure, it is ensured that ultimate vacuum of the order of ≤ 1.0x-10 mbar maintained. The following steps were followed for calibration of each controller:

(i) Physical inspection of the HCIGC for damage of chassis, inspection of front & back panel connectors, display panel etc., Also, the connecting cables were checked for any cracks along its insulation, and labelled with the controller serial number to avoid unnecessary power trips during the testing process.

(ii) Functional checking of all the filaments, process relay LEDs, Degas function, sensitivity variation & the zero of the controller.

(iii) Switching of Filament-1 & Filament-2 and checking of the pressure measurement over each emission current range for a period of two days.

(iv) Both filaments degassing at 25 W for 15-20 minutes

(v) Checking of the Remote/Local function, Process Relay Contacts, Pressure set point using a test zig and data logging of the details by in house developed hardware & GUI program on a computer, for ensuring reliability of all control outputs.

(vi) The burn-in test is done for around seven day's period, in which linearity of pressure measurements were checked by means of gas injection into the vacuum system.

The pressure measurements by the reference unit and Unit Under Test (UUT) are logged onto the computer with a data logging rate of 1 Hz to check the stability and reliability of the UUTs.

A nearly linear relation between pressure measurements of UUTs is highly desirable. A linear response simplifies the calibration of the HCIGC and the sensitivity does not need to be determined in each decade of the whole pressure range of the gauge head. The test gas used here is "air" and injected to the vacuum system via a UHV leak valve over six decades of pressure range. The linearity was measured by means of the UUT simulating its regular operation in Indus-1 & Indus-2 systems. Each calibration at base pressure of $\sim 1x10^{-10}$ mbar and proceeded with increasing pressure to about $1x10^{-5}$ mbar typically with three calibration points per decade. Calibration data were measured for increasing and decreasing pressures in the vacuum system. In all cases, two UUTs were simultaneously tested on the system.

This procedure allowed independent verification that any anomalous behaviour observed was due to malfunction of the particular UUT. The linearity plots are given in Figure 1 (b) & Figure (2).

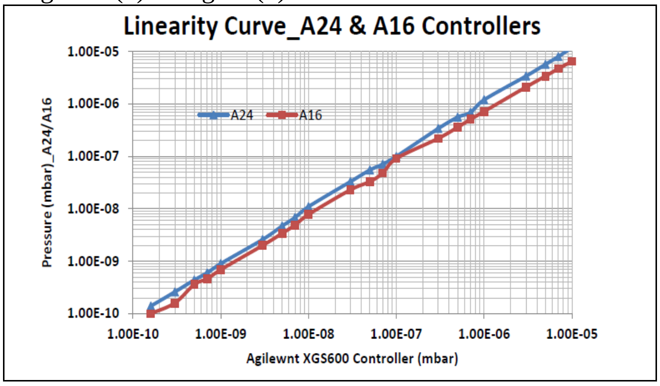


Figure 2: Linearity curve of A24 & A16 UUTs vs reference XGS 600 controller.

Figure 3: Front panel of the RRCAT/2017/A16 Controller

Figure 4: Rear panel of the RRCAT/2017/A16 controller

Figure 5: Internal view of the controller cards (modular design type)

Figures (3), (4), & (5) shows the front, rear and internal view of the upgraded HCIGC controllers.

Sensitivity of the HCIG head also measured by the Agilent XGS 600 reference controller and by the UUTs. The measured sensitivity values are in agreement with the manufacturer's data and found within 20% accuracy.

The following information was recorded both before and during calibration of the UUTs:(a) Identification of the reference gauge & UUT, including the type of HCIG head, manufacturer and the relevant parameters like emission current, sensitivity etc., (b) Date of calibration, (c) Ambient temperature, (d) Calibration gas (in our case it is atmospheric air), (e) Base pressure achieved in the system, (f) Details of gauge settings, if any required, (g) Orientation details of the HCIG head, (h) Plot of Reference gauge pressure Vs gauge under calibration (on log-log axis) under various pressure regimes, (i) Signature of the concerned agencies, (j) Recording of the type faults of the each UUT, trouble shooting of the UUT, time taken to repair each problem, frequency of occurrence of the similar type of fault etc.,

After the completion of the measurements at the final target pressure, pumping the vacuum system down to its base pressure and checked for leaks, if any cropped up during the system operation.

## CONCLUSION

The main conclusion is that the HCIGCs are very promising for reliable pressure measurement use in accelerator & laboratory UHV systems The linearity of the pressure measurement of HCIGCs found to be in agreement with the design parameters. The performance of the deployed HCIGCs are found to be very satisfactory in Indus Complex Vacuum Systems during the last 12 months. The mean time taken to repair is very less and typically two hours for trouble shooting of the controller and bringing back to its normal operation due to its modular approach.

## ACKNOWLEDGEMENT

Authors would like to thank the Director, RRCAT along Director, Proton Accelerator Group & Electron Accelerator Group for their constant encouragement in the evaluation and regular deployment of HCIGCs in the Indus Complex Vacuum Systems.

Also, we express our sincere thanks to colleagues of UHVTS for their direct/indirect support, suggestions during the development, evaluation and deployment of HCIGCs.

## REFERENCES

[1] *R.Sridhar, "Ultra High Vacuum Systems of Indus Accelerator and its Operational Experience" IVSNS-2015, TIFR, November 18-20, 2015, Mumbai.*

[2] *James A. Fedchak, Patrick J. Abbott et. A., JVST A 36, 030802 (2018); doi:10.1116/1.505060.*

[3] *ISO 27894:2009 "Vacuum Technology- Vacuum Gauges-Specifications for hot cathode ionization gauges".*

[4] *ISO 3567:2011 (E) "Vacuum Gauges-calibration by direct comparison with a reference gauge".*

[5] *Guideline DKD-R 6-2 "Part (4) – Calibration of Measuring devices for Vacuum Ionization gauges".*

[6] D. Y. Deokar, "Design, Upgradation & Development of BAG controller and its mass production", InPAC-2018, RRCAT, Indore.

# OUTPUT FILTER NETWORK AND CONTROL SYSTEM MODELING OF A CROWBARLESS HVDC BIAS POWER SUPPLY FOR RF AMPLIFIER

Manmath Kumar Badapanda#, Akhilesh Tripathi, Rinki Upadhyay, Rajeev Kumar Tyagi, Mahendra Lad and Purushottam Shrivastava
Raja Ramanna Centre for Advanced Technology, Indore, MP, India - 452013.

*Abstract*

A solid state modular -36 kV, 24 A crowbar less DC power supply with full range 24 pulsed input and low ripple output has been developed to bias vacuum tube based RF amplifiers, based on which a US patent was granted in 2018. A challenging task of development and realization of output ripple filter of this power supply was undertaken, specifically keeping its attenuation, overshoot and stringent stored energy in view. This paper presents the design, configuration, simulation and experimental results of the output filter network employed in this power supply. A combination of feed forward and feedback control system is adopted in this power supply. The attenuation provided by this output filter network at 36 kHz is 11.8 dB. The output voltage ripple of this power supply was observed to be less than 0.72 % at -36 kV, 3 A DC operating point, which is in close agreement with simulation result presented in this paper. The overshoot in the output voltage and the output voltage stability of this power supply are less than 0.15% and less than 0.5 % respectively. Suitable wire burn test has been carried out on this power supply to qualify it for biasing sensitive RF amplifiers. The output stored energy of this power supply is less than 10 Joule, thereby completely avoiding crowbar to protect RF amplifiers under their arcing condition.

## INTRODUCTION

Vacuum tube based RF amplifiers are sensitive devices which demand low output ripple and low output stored energy from their high voltage DC bias power supplies. They can handle maximum up to 20 Joules of stored energy under their arcing conditions [1], [2]. In addition to other stringent performance requirements from their bias power supplies, the over voltage handling capabilities of these devices are also quite limited, which makes their design and development, a technically challenging task. A solid state modular -36 kV, 24 A crowbar less DC power supply with 24-pulsed input system as well as low output ripple and low output stored energy is developed to bias high power RF amplifiers based on which a US patent #100, 27,122 was granted [3]. This power supply employs 72 number of 500 V, 24 A DC-DC power modules connected in series to provide -36 kV DC output. As IGBTs in inverter bridge of each DC-DC power module are operated at 18 kHz, the frequency of its rectified output is 36 kHz. A novel control strategy is implemented in this power supply for staggering of its DC-DC power modules to obtain high effective output ripple frequency i.e., 72 x 36 kHz = 2.592 MHz, thereby significantly reducing output filtering requirement. This power supply employs various sub-systems having several unique novel features but the scope of this paper includes only output filter network and control system modelling aspects of this power supply. A suitable damped passive output filter network is employed for this power supply, keeping various factors like attenuation, overshoot and stored energy in view. A combination of feed forward and feedback control system is adopted in this power supply for which suitable control system model is presented.

#mkp@rrcat.gov.in. SO-H & Head, RF Power Supplies Lab, RF Systems Division, RRCAT, Indore.

## OUTPUT FILTER NETWORK

The simulation circuit of this output filter network is shown in Fig. 1. Necessary damping elements (R1, R2) have been provided in this filter network to minimize output ripple and overshoot. Output capacitance of this filter network (C1) is intentionally kept low to reduce the stored energy in it. The resistor R2 connected in series with the output capacitor C1 further reduces the stored energy dumped into the arcing RF amplifier. Under practical conditions, the power supply output also contains an envelope of 36 kHz along with 2.592 MHz ripple component due to mismatches in power modules and mismatches in staggering instants caused by faulty power modules. To simulate this envelope, the pulsed voltage source of amplitude 750 V and frequency 36 kHz is intentionally added in series with 36 kV DC in PSpice simulation circuit.

The series equivalent parameters of damped parallel LR circuit (L1‖(L2 + R1)) of this output filter are $L_{series}$ = 5.6 mH and $R_{series}$ = 1004 Ω and its cut-off frequency is 15.03 kHz ($\omega_n$ = 94436.27 radians/sec) taking C = 20 nF. The damping ratio "ε" is given by

$$\varepsilon = \frac{R_{Total}}{2\sqrt{\frac{L_{series}}{C}}} \quad (1)$$

which comes out to be 0.97, where, $R_{total} = R_{series} + 20\ \Omega$ = 1004 Ω + 20 Ω = 1024 Ω. The transfer function of this output filter is given by

$$F(s) = \frac{\omega_n^2}{(s^2 + 2\varepsilon\omega_n s + \omega_n^2)} = \frac{8.91\times10^9}{(s^2 + 183206s + 8.91\times10^9)} \quad (2)$$

The magnitude plot and phase plot of F(s) are given in Fig. 2 and Fig. 3 respectively. The attenuation at the effective output ripple frequency of 2.592 MHz of the power supply is more than 75 dB, thereby completely eliminating this ripple component from the output and the attenuation at 36 kHz is 11.8 dB (attenuation factor of 3.89). The simulated output ripple voltage waveform of output filter network is shown in Fig. 4. The magnitude of peak to peak output ripple is 193 V at 36 kHz.

## CONTROL SYSTEM AND ITS MODELLING

A combination of feed forward and feedback control system is adopted in this power supply wherein, the feed forward control takes care of wide variations in input line voltages as well as the output set voltage requirements and an overriding feedback control is employed for the fine regulation of the output voltage. For controlling the output voltage of this power supply, the phase shift (φ) between diagonal pair IGBTs of inverter bridge employed in DC-DC power module of this power supply is varied.

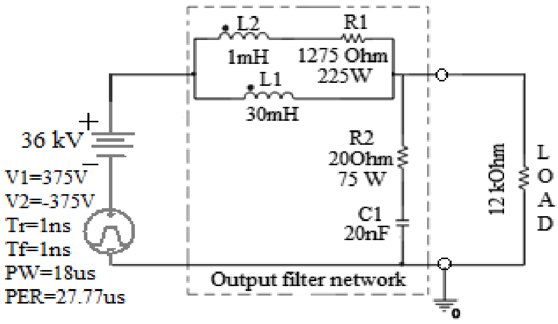


Figure 1: Simulation circuit of output filter network

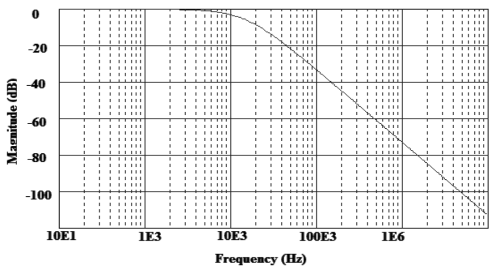


Figure 2: Magnitude plot of output filter network

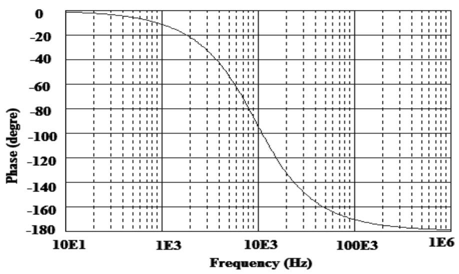


Figure 3: Phase plot of output filter network

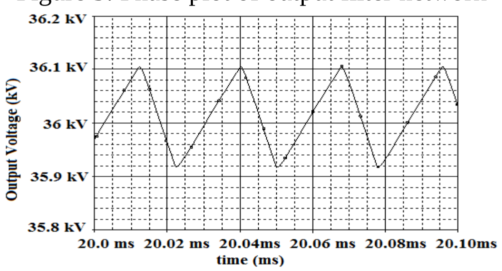


Figure 4: Simulated output voltage ripple of output filter network

With feed forward control, the phase shift is given as

$$\phi = \left(22.68V_{input} - 9334\right)A \tag{3}$$

where $V_{input}$ is the input voltage and factor "A" is the feed forward action which is given by

$$A = \left[\frac{555}{Desired\_set\_voltage}\right] \tag{4}$$

The power supply consisting of power supply plant, output filter, feed forward controller and feedback controller has been modelled as shown in Fig. 5. Here, for simplicity, the power supply plant is represented as gain K = 7200 to get 36 kV output with 5 V reference and the value of feedback factor is 1/K. Proportional integral (PI) based feedback controller is chosen for this power supply. Again, as the characteristics of a process do not change with the addition of a feed forward control hence it is omitted while doing the stability analysis of the complete power supply system for determining the parameters of feedback controller. The closed loop transfer function of the system as shown in Fig. 5 is

$$\frac{Y(s)}{X(s)} = \frac{(K_p + K_I/s) \times K \times F(s)}{1 + [K \times (1/K) \times (K_p + K_I/s) \times F(s)]} \tag{5}$$

By putting the value of F (s) from (2) in (5) and simplifying

$$\frac{Y(s)}{X(s)} = \frac{(K_p s + K_I) \times K \times \omega_n^2}{s^3 + 2\varepsilon\omega_n s^2 + \omega_n^2 s + K_p s\omega_n^2 + K_I\omega_n^2} \tag{6}$$

The closed loop characteristic equation (CE) from (6) is

$$CE: s^3 + 2\varepsilon\omega_n s^2 + \omega_n^2(1 + K_p)s + K_I\omega_n^2 = 0 \tag{7}$$

Using (ε', ω') parameterization along with a third pole at s = ω', CE may be set as

$$CE: (s^2 + 2\varepsilon'\omega's + \omega'^2)(s + \omega') = 0 \tag{8}$$

This equation (8) may be rearranged as

$$CE: s^3 + s^2(2\varepsilon'+1)\omega' + s(2\varepsilon'+1)\omega'^2 + \omega'^3 = 0 \tag{9}$$

Equating terms from (7) and (9)

$$\omega' = \frac{2\varepsilon\omega_n}{2\varepsilon'+1}, \quad K_p = \frac{\omega'^2(2\varepsilon'+1)}{\omega_n^2} - 1, \quad K_I = \frac{\omega'^3}{\omega_n^2}.$$

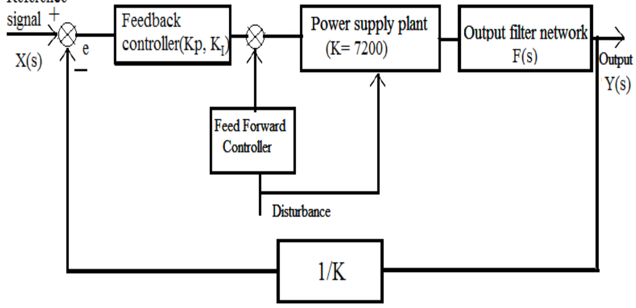


Figure 5: Power supply control system model

The power supply system with PI controller is designed for damping ratio ε' = 0.9 corresponding to the output filter damping ratio of ε = 0.97. The values of ω', $K_p$, and $K_I$ are found out as ω'= 0.693 $\omega_n$ = 65444.3 rad/sec, $K_p$ = 0.345 and $K_I$ = 0.48. The transfer function of the power supply system may be re-written as

$$\frac{Y(s)}{X(s)} = \frac{7200 \times (1+\frac{s}{91053}) \times (4282956402)}{(1+\frac{s}{65444.3})(s^2+117800s+4282956402)} \quad (10)$$

The compensated system shown by (10) has one pole at s = ω'= 65444.3 rad/sec (10.415 kHz), two conjugate poles at s = -ε'ω' ± jω'√(1-ε'²) = -58899.87 ± j28533.7 and one zero at s = $K_I/K_p$ = 82787 rad/sec (14.49 kHz). The overshoot of the system is calculated as

$$M_{overshoot} = e^{\frac{-\pi\varepsilon'}{\sqrt{(1-\varepsilon'^2}}} \quad (11)$$

which is 0.15% for ε' = 0.9. The compensated system has infinite gain margin and its phase margin is higher compared to system without PI feedback controller, thereby increasing relative stability of the power supply.

## WIRE BURN TEST

Wire burn test is conducted on -36 kV, 24 A DC bias power supply of inductive output tube (IOT) RF amplifier to ensure that stored energy in it is less than 20 Joule. An experimental set up is made employing a three terminal triggered switch in series with 33 AWG copper test wire of length 10.9 cm calibrated for 10 Joule. In this test, the arcing condition of RF amplifier is intentionally created to get an idea about the amount of fault energy dumped into the RF amplifier under arcing condition from its bias power supply and the survivability of test wire ensures that the stored energy in the bias power supply is below the energy handling capacity of RF amplifier during arcing condition. With triggering of this switch, output current protection of the power supply is activated and firing pulses to both chopper IGBT as well as inverter bridge IGBTs of all power modules are blocked causing the output voltage to collapse. The survivability of test wire ensures that the stored energy in this power supply is below 10 Joule, thereby completely avoiding crowbar.

## EXPERIMENTAL RESULTS

The peak to peak output voltage ripple of this power supply at -36 kV, 3 A operation with IOT amplifier is shown in Fig. 6. Channel 4 and channel 2 show the voltage ripple before and after output filter network. The ripple amplitude gets attenuated by a factor of 3.89 as depicted by the frequency response of output filter network. The ripple amplitude observed before output filter network is 988 V which is more than input DC voltage of single DC-DC power module due to switching noises and slight overshoots in the leading edge of each power module output, presence of ripple in input DC voltage and errors in fixing actual staggering instances of these modules. As the magnitude of ripple before

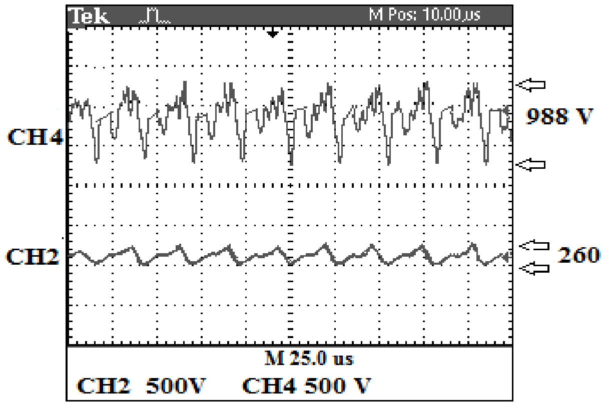


Figure 6: Output voltage ripple at -36 kV, 3 A DC

output filter network is higher, the output ripple of this power supply is also slightly higher (260 V) than the simulated value (193 V). Again, combined feed forward plus feedback control improves the performance of the system over only feed forward control or only feedback control. The stability of output voltage is found to be ≤ 3% with only feed forward control corresponding to -10% to +10% variations in input line voltage and -36 kV set output voltage, which gets further reduced to ≤ 0.5% with over-riding feedback control system.

## CONCLUSION

The output filter network employed at the output of -36 kV, 24 A DC power supply reduces the voltage ripple at 36 kHz by a factor of 3.89 and eliminates the ripple at 2.592 MHz. The output voltage ripple of this power supply at -36 kV, 3 A DC operating point is close to the simulation result presented in this paper. The observance of slightly higher ripple is due to the presence of ripple in input DC voltage of power modules, overshoot in the power module outputs and errors in fixing their actual staggering instances. The overshoot in the output voltage and the output voltage stability of this power supply are less than 0.15% and less than 0.5 % respectively. The output stored energy of this power supply is found to be below 10 Joule which qualifies it to bias sensitive RF amplifiers.

## REFERENCES


[1] M. K. Badapanda, A. Tripathi, R. Upadhyay, M. Lad and P. R. Hannurkar, “High Power RF Testing of 1 MW, 352.2 MHz Continuous Wave Klystron Amplifier,” IEEE Trans. Plasma Sci., vol. 44, no. 99, pp. 3599-3607, Oct. 2015.

[2] A. Tripathi, M. K. Badapanda, Rinki Upadhyay, Mahendra Lad, “Wire Survival Test of Crowbar Less, High Voltage DC, Klystron Bias Power Supply,” Open Science Journal of Electrical and Electronic Engineering, vol. 4, no. 1, pp. 1-9, Sep. 2017.

[3] M. K., Badapanda, “High voltage DC power supply for high power radio frequency amplifiers,” US Patent No. #100, 27,122 dated July 17, 2018.

# FPGA CONTROLLED HIGH CURRENT PULSE POWER SUPPLY FOR SOLID STATE RF AMPLIFIERS

Akhilesh Tripathi#, M. K. Badapanda, Rinki Upadhyay, Sachin Rathi and Mahendra Lad
Raja Ramanna Centre for Advanced Technology (RRCAT), Indore - 452013, India

*Abstract*

A FPGA controlled pulse power supply having forty number of output channels, each of 50 V, 80 A rating has been designed and is under development to bias pulsed solid state RF amplifiers. In this power supply, a capacitor bank is charged by a 50 V, 700 A constant current DC power supply and energy stored in this capacitor bank is discharged with the help of MOSFET switches in output channels for generating output pulses. Control and protection of this pulse power supply is implemented through Xilinx make XC6SLX9TQG144C Spartan-6 FPGA. This control-protection unit has capability to vary the pulse width and frequency of drive pulses from 100 µs to 2.5 ms and from 1 Hz to 50 Hz respectively. The load current of each output channel is sensed through a hall sensor and given to control-protection unit after suitable signal processing for blocking the gate drive signals in case of over current. Adequate steps have been taken for minimizing the overshoot in the output pulses and to keep them properly synchronised. Twenty-four number of output channels of this pulse power supply were fabricated and tested with dummy resistive load and experimental results are presented in this paper. With operation of each output channel at 80 A peak current, 2.5 ms ON time and 50 Hz operating frequency, both rise time and fall time and pulse droop of the output pulse were observed as less than 20 µs and less than 0.5% respectively.

## INTRODUCTION

Pulse solid state RF amplifier based RF systems are being developed for various particle accelerators at Raja Ramanna Centre for Advanced Technology, Indore. Each pulse solid state RF amplifier requires a 50 V pulse power supply for its biasing and draws maximum of 80 A peak current. The task of development of a 50 V, 40 x 80 A pulse power supply is taken up at RRCAT which is capable of biasing 40 number of pulsed solid state RF amplifiers simultaneously. It contains 40 number of pulse output channels where each output channel can provide 80 A peak current. Out of 40 channels, 24 pulse output channels have been developed and tested on dummy load. The pulse duration of output pulses is variable from 100 µs to 2.5 ms and frequency is variable from 1 Hz to 50 Hz. Suitable precautions are taken during fabrication of all output channels to minimize rise and fall times of output pulses and keep them synchronized. FPGA based control and protection unit is developed for the operation of this pulse power supply which is presented in this paper.

#atripathi@rrcat.gov.in. RF Power Supplies Lab, RF Systems Division, RRCAT, Indore.

## SCHEME

The pulse power supply is developed by charging a capacitor bank with the help of a constant current DC power supply and then discharging the energy stored in this capacitor bank with the help of MOSFET switches employed in pulse output channels to generate output pulses [1]. The pulse power supply has the capability to feed 40 number of pulsed solid state RF amplifiers (SSPA), each drawing 80 A peak current. The capacitance requirement at the output of DC power supply to limit the droop in output pulse is given as:

$$\mathrm{I} = C\,\frac{\Delta v}{\Delta t} \tag{1}$$

Here, $I$ is the total current drawn from the power supply during pulse ON time, $\Delta v$ is the allowed droop in output pulse and $\Delta t$ is the ON time of pulse. For pulse power supply with 40 output channels, each of 80 A peak current rating, $I$ = 40 x 80 = 3200 A, allowed droop in pulse, $\Delta v$ = 0.5% of 50 V = 0.25 V and pulse ON time $\Delta t$ = 2.5 ms, capacitance requirement is calculated as 32 F. The charge lost by this capacitor bank during ON time is calculated as $\Delta Q = I \times \Delta t$ = (40 x 80 A ) x (2.5 ms) = 8 C. The time remaining to replenish this lost charge by the DC power supply is 17.5 ms. So the current requirement from DC power supply to replenish this lost charge within 17.5 ms is, $I = (\Delta Q/\Delta t)$ = 8 C/ 17.5 ms = 457 A. Hence a 50 V, 700 A DC modular, hot swappable, regulated DC power supply having output regulation better than 0.1%, output voltage stability better than 0.1% and voltage ripple less than 0.1% is used as DC power source in this pulse power supply. For 24 output channels of 80 A peak current rating, capacitor requirement is calculated as 19.2 F. The overall scheme of pulse power supply containing 24 number of pulse output channels is shown in Fig. 1. The capacitor bank is initially charged though a slow start resistor which is bypassed after 2 minutes by means of a DC contactor of appropriate rating to facilitate slow start charging of this capacitor bank. The energy stored in this capacitor is discharged in the form of output pulses by means of MOSFET switches employed in each output channel. The schematic of 50 V, 80 A pulse output channel is given in Fig. 2. It contains an IXYS make 250 V, 170 A, n-channel MOSFET switch (IXFH170N25X3), a gate driver circuit (Power Integration make 2SC0108T2H0-17), a freewheeling ultra fast recovery diode and load. Additional 100 A DC contactors are also provided in each output channel for cutting the pulse output from SSPA load in case of

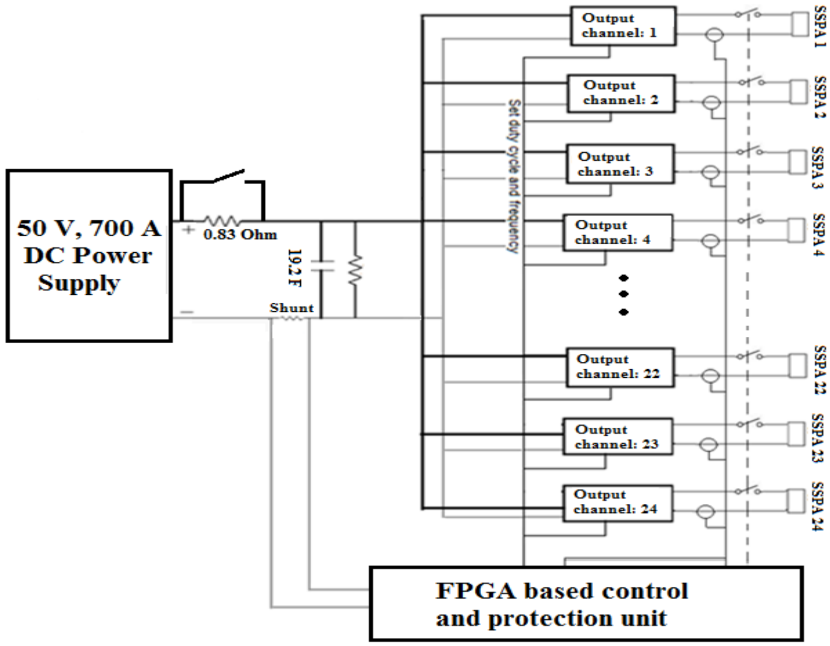

Figure 1: Schematic of 50 V, 24 x 80 A pulse power supply

failure of gate driver or MOSFET switch. During switch OFF of MOSFET switch in each output channel, the overvoltage stress appears across this switch due to $L*di/dt$, where $L$ is the inductance of physical path from capacitor $C$ to load in Fig. 2 and $di/dt$ is the slope of current flowing through the switch. The inductance $L$ is minimized by reducing the length of the physical path and employing litz wires for connecting outputs of pulse output channels to SSPA loads. The wiring lengths in the power path of all the output channels are also kept same to keep them properly synchronized.

## CONTROL AND PROTECTION SYSTEM

The control and protection of this pulse power supply is implemented through Xilinx make XC6SLX9TQG144C Spartan-6 FPGA embedded in EDGE Spartan 6 development board. The block diagram of this development board is shown in Fig. 3. The function of this FPGA is to vary the pulse width and frequency of the drive pulses of all 24 pulse channels from 100 µs to 2.5 ms and from 1 Hz to 50 Hz respectively. EDGE Spartan 6 FPGA Development board is the feature rich development board with XC6SLX9TQG144C Spartan 6 FPGA, 50 MHz clock, 8 MB SPI FLASH, 12 bit SPI ADC, 12 bit SPI DAC, USB UART bridge to communicate board with windows PC COM port interface, 20 pin expansion connector, LCD interface, 4 digit 7 segment display, 16-SPDT slide switches for digital input, 5 Push buttons for providing momentary digital inputs, 16 LEDs for displaying digital outputs, 12 bit VGA interface, a temperature sensor and a RESET switch. This board gets 5 V power from USB JATG port and contains an internal voltage regulator to provide 3.3 V supply to FPGA. FPGA can be configured either from USB JTAG using Xilinx software or by on-board SPI FLASH Memory. FPGA configured through JTAG gets erased when 5 V power supply is removed or by pressing the reset button. XC6SLX9TQG144C is a logic optimized FPGA of Xilinx Spartan 6 family with 102 IOs, 9152 logic cells and 18 Kb RAM blocks. The drive pulse generated by this FPGA for one channel is shown in Fig. 4. The over current protection of all the output channels is also implemented through this FPGA. The

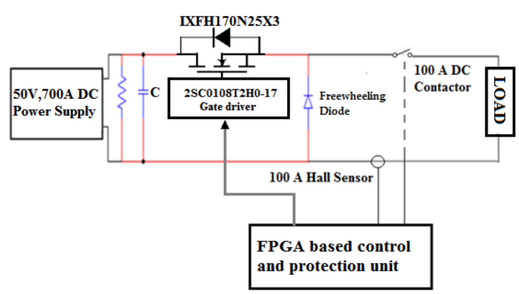

Figure 2: Schematic of 50 V, 80 A pulse output channel

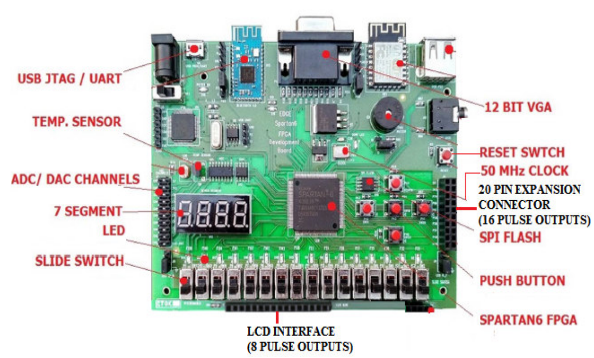

Figure 3: Block diagram of EDGE Spartan 6 FPGA board

load current of all the output channels are sensed by LEM make 200 A hall sensors (LA 150) and their corresponding voltage signals are filtered, processed and fed to FPGA through SPI ADCs. All these ADC signals are compared against a set reference and if any of these signals goes higher than the set reference, drive pulse of that particular pulse channel is blocked by FPGA. Simultaneously the DC contactor of that particular channel is also opened to make sure that SSPA load is isolated from the power supply even if the gate driver or MOSFET of that pulse channel has failed.

## EXPERIMENTAL RESULT

The developed pulse power supply is tested on dummy resistive load with all 24 pulse output channels feeding to 80 A dummy load. The ON time was kept as 2.5 ms at frequency of 50 Hz. Output pulse of one channel is shown in Fig. 5 and its rise time and fall time are shown in Fig. 6 and Fig. 7 respectively. The droop observed in the output pulse is below 0.25 V (0.5%). The rise time and fall time of the output pulse were observed as less than 20 µs. The photograph of the fabricated pulse power supply is shown in Fig. 8.

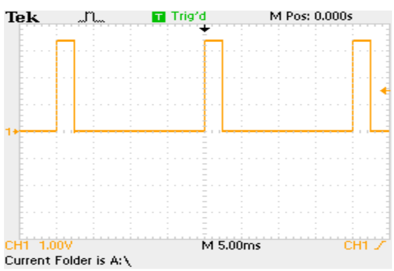


Figure 4: Pulse drive signal generated by FPGA (2.5 ms ON time and 50 Hz frequency)

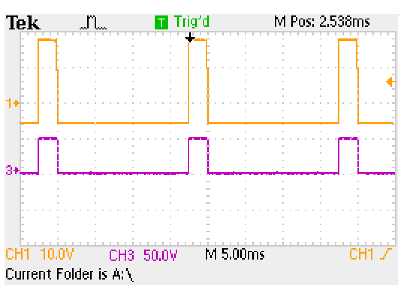


Figure 5: Gate drive signal (Channel 1) and pulse output (Channel 3). Pulse ON time: 2.5 ms; Frequency: 50Hz; Peak current: 80 A; Pulse amplitude: 50 V.

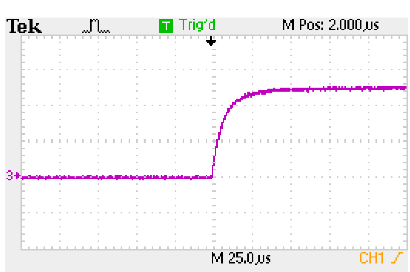


Figure 6: Rise time of the output pulse < 20 µs

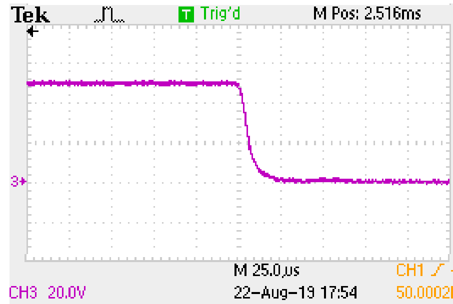


Figure 7: Fall time of the output pulse < 20 µs

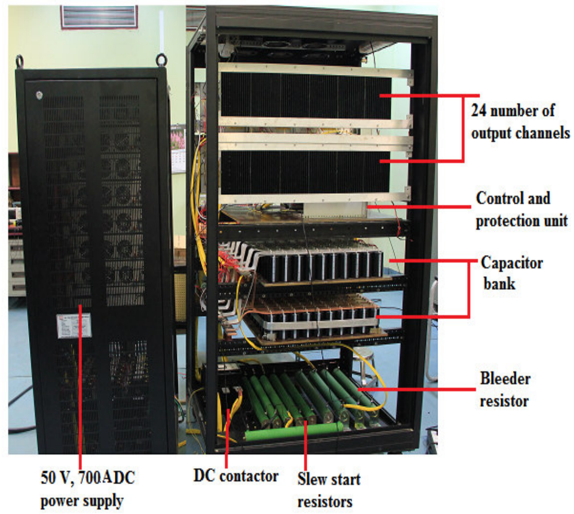


Figure 8: Photograph of 24 channel pulse power supply

## CONCLUSION

A 50 V pulse power supply with 24 pulse output channels, each of 80 A peak current rating, is designed, developed and tested on dummy resistive load. This pulse power supply can bias 24 number of pulse solid state RF amplifiers simultaneously. The control and protection of this pulse power supply is implemented through Xilinx make XC6SLX9TQG144C FPGA. Over current protection feature is employed in this pulse power supply for tripping the output channels in case of over current. The ON time can be varied from 100 µs to 2.5 ms and frequency can be varied from 1 Hz to 50 Hz. The droop in the output pulse is minimized by using sufficient capacitance at the input of pulse output channels. The wire lengths in the power paths of all the output channels are kept same to keep them properly synchronized. All the output channels of this pulse power supply were tested on 80 A dummy load with 2.5 ms ON time at 50 Hz. The rise time and fall time of the output pulses were observed as < 20 µs and droop was observed as < 0.25 V.

## REFERENCES

[1] Tripathi A., Badapanda M.K., Upadhyay R., Lad M., "Development of 50 V, 640 A pulse power supply for solid state RF amplifiers," Indian Particle Accelerator Conference, RRCAT, Indore, Jan, 2018.

# DESIGN, DEVELOPMENT AND CHARACTERIZATION OF MULTICHANNEL RF UP-DOWN CONVERTER FOR PARTICLE ACCELERATORS

Pritam S. Bagduwal*, Dheeraj Sharma, Nitesh Mishra, Nitesh Tiwari and Mahendra Lad
Radio Frequency Systems Division, RRCAT

*Abstract*

High Energy Particle accelerators use RF to accelerate the charged particles to desired energy. Amplitude and phase stability are one of the most stringent requirements for proper operation of accelerator machines. To keep the amplitude and phase of the RF field stable with-in the required limits, Low Level RF (LLRF) system having Amplitude Control Loop (ACL) and Phase Control Loops (PCL) are used. ACL and PCL can either be analog or digital. Digital LLRF system offers inherent advantages like flexibility, adaptability, repeatability and reduced long time drift errors compared to analog systems. However, it is difficult to process the high frequency RF signal directly using ADCs hence RF down converter is used. To bring back the processed signal to RF domain, RF up convertor is required. In this paper we will present the design, development and characterization of RF up down converter board. To realize multichannel RF processing, four RF Up and Down conversion channels are realized in a single board. Down conversion channel consists of active mixer that offers the advantage of low conversion loss and high LO-IF isolation. In each channel RF is mixed with appropriate LO to generate required IF signal. This IF signal contains the amplitude and phase information of RF signal. Board is also equipped with I/Q modulator based four RF up converter channels. These are used to control the amplitude and phase of RF signal through baseband I/Q signals. Using this board two channel RF processing unit has been designed, developed and tested in Lab. With slight modifications this board can be used for various digital LLRF systems in the frequency range from 150 MHz to 1000 MHz. Such multichannel high-density RF boards will be useful for future accelerators having large number of RF stations.

## INTRODUCTION

LLRF system consists of Amplitude Control Loop (ACL) and Phase Control Loop (PCL) along with other functionalities. Amplitude and phase stability of required order is key for proper operation of accelerator machines. Due to inherent advantage of digital technology, digital LLRF system are being used for implementation of ACL and PCL. Since RF signals are difficult to digitized directly with the required level of accuracy therefore it is necessary to down convert RF signal to Intermediate Frequency (IF). Down converted IF signal shall have all the amplitude and phase information of RF intact with minimum conversion loss. From the down converted IF signal amplitude and phase information is extracted and compared with set amplitude and phase values.

An appropriate controller is used to generate the base band control signal to control the amplitude and phase of

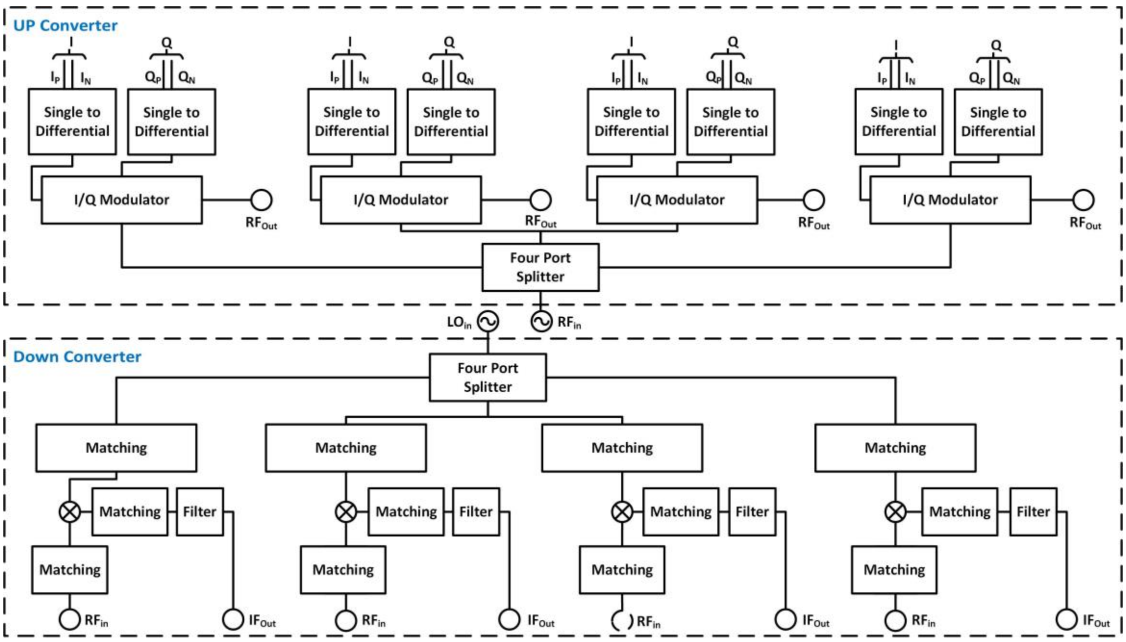


**Figure 1: Lay Out of RF Up-Down Converter Board**

*pritam@rrcat.gov.in

main line RF signal. This baseband control signal is required to be up-converted back to the RF. For this up-converter is required. Up conversion shall have required amplitude and phase control range to provide required correction for RF signal. RF board having four RF up-converter and four RF down converter channels has been designed and developed. Block diagram of board layout is shown in Figure 1. In this paper, development of board and test results will be presented.

## RF DOWN CONVERTER

Functional requirement of the down conversion is to translate the high frequency RF signal to relatively low frequency IF signal without loosing any amplitude and phase information of RF signal. Developed board has four RF down conversion channel. For down conversion mixer is used (Figure 2), where two RF signals of different frequencies ($f_1$, $f_2$) are multiplied resulting in output consisting of two side bands {($f_1$-$f_2$), ($f_1$+$f_2$)}. Both side bands contain the true amplitude and phase information of RF signal at lower or higher frequency.

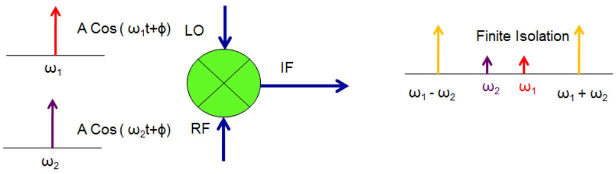


Figure 2: Mixer Functionality

Due to ease of digital processing, lower side band is used in LLRF applications. Losses occurred in the process of down conversion is called conversion loss and should be minimum. Each down conversion channel has been characterized for conversion loss (Figure 3).

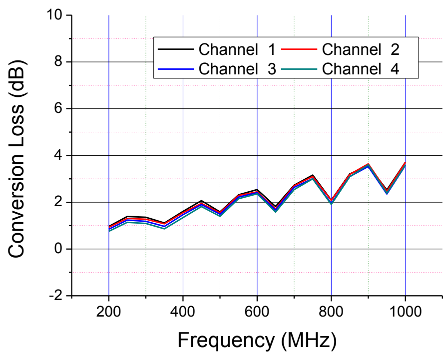


Figure 3: Conversion Loss

Linearity and monotonicity in the down conversion is desirable. For linearity measurement, amplitude and phase of RF signal is varied by known value and change in amplitude and phase of down converted IF has been observed. Results are presented in Figure 4.

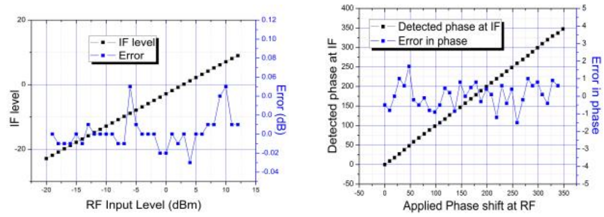


Figure 4: Amplitude and Phase Linearity in down conversion

For LLRF applications only the lower side band is required with suppression of upper side band. A bandpass filter at IF frequency is used to suppress the upper side band and other spurious components. For testing of side band rejection, RF signal of 650 MHz is mixed with LO signal of 670 MHz and spectrum of IF signal is seen on spectrum analyser (Figure 5). Upper side band or any other spurious signal are found to be around -40 dBc from lower sideband.

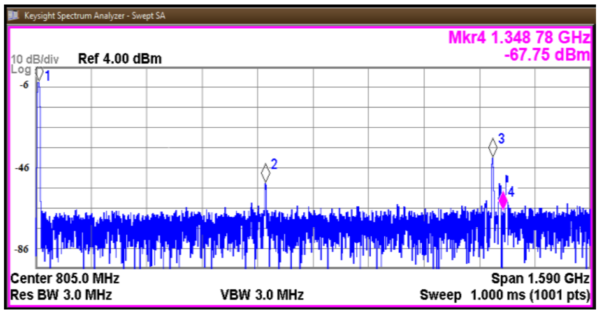


Figure 5: Spectrum of IF Signal

## RF UP CONVERTER

After processing of down conversion depending upon the discrepancy between set and sense value correction signals are generated. This correction signal is in base band. So, to convert this correction signal back to RF, I/Q modulator based up converter has been designed. I/Q modulator controls the amplitude and phase of the RF signal by changing the In-Phase and Quadrature phase components of modulator (Figure 6).

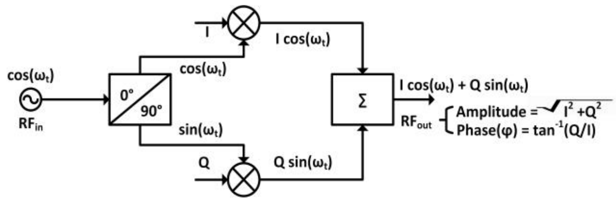


Figure 6: Functionality of I/Q Modulator

Dynamic Range over which amplitude and phase of RF signal can be controlled is measured for the frequency range of 200MHz to 1000MHz and results are shown in Figure: 7

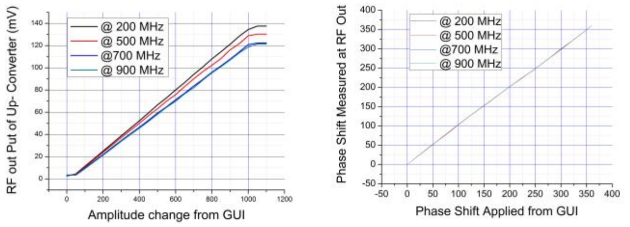


**Figure 7: Amplitude and Phase control range of I/Q Modulator**

Each channel has 360 degree of phase control and has more than 30 dB of amplitude dynamic range.

Leakage of RF input to output under zero I/Q drive condition shall be as low as possible, especially for high gain RF systems like the one used in particle accelerators. RF leakage measurement using VNA has been done (see Figure 8).

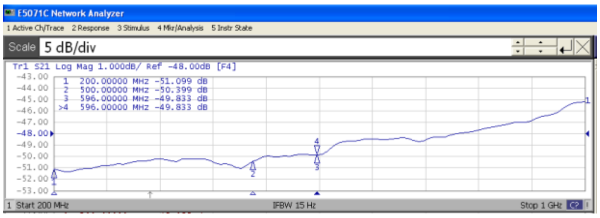


**Figure 8: RF Leakage Characterization using VNA**

Leakage under zero I/Q drive condition for all four channels better than -40 dBc in frequency range of 200 MHz to 1000 MHz.

RF output of up-converter shall only depend on the I/Q control signal and should be independent of level of RF drive in. To determfine the proper operational value of RF driving point, measurements were taken, and results are presented in Figure 9.

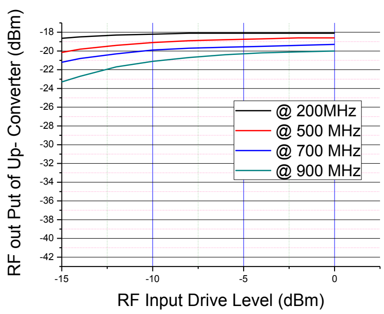


**Figure 9: Change in RF out with change in RF input drive**

At around -2 dBm of RF input level, output is independent of input drive so operation around this value is desirable.

Multichannel RF Up/Down Converter has four RF up converter channels and can operate at any frequency between 200 MHz to 1000 MHz with I/Q control bandwidth of more than 80 MHz. These ranges are enough for most of the accelerator requirements at RRCAT. Channel to channel Isolation for up converter channels are measured to be better than 90 dBc for this Board. Photograph of Multichannel RF up down converter board is shown in Figure 10.

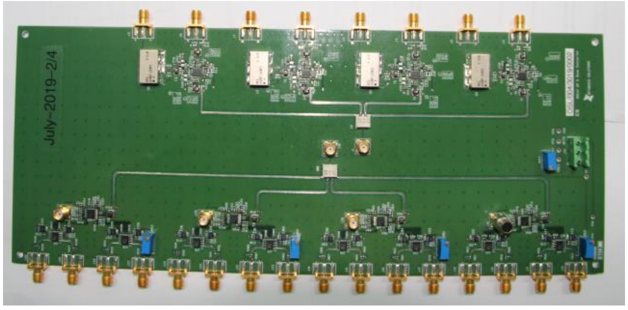


**Figure 10: Multi-Channel RF Up-Down Converter Board**

## CONCLUSION

Considering the future requirements of large numbers of LLRF systems, multichannel RF up-down converter board has been designed and developed which contains four numbers of RF up and down conversion channels on a single board. RF down conversion channel has the required linearity and monotonicity in the amplitude and phase range of 35 dB and 360 degree respectively and offers conversion loss of around 2 dB with spurious and side band down by more than 50 dB. RF board has I/Q modulator based four up converter channels. Each has amplitude and phase control range of 35 dB and 360 degree respectively over the frequency range of 200 MHz to 1000 MHz with RF leakage less than -40d Bc and control bandwidth of more than 40 MHz. With slight modifications in the matching network, RF down conversion can be used for any signal in between 200 MHz to 1000 MHz.

## ACKNOWLADGMENT

Authors are very thankful to Shri D. Suresh and Shri Sudarsan Kishan for their contribution in assembling and testing Multi Channel RF Up Down Converter board.

## REFERENCES

[1] Nitesh Tiwari, Pritam S. Bagduwal, M. Lad and P. R. Hannurkar, “Development of Prototype Digital LLRF system at RRCAT”InPAC-2013.

[2] Pritam S. Bagduwal, Dheeraj Sharma, Nitesh Tiwari,M. Lad and P. R. Hannurkar, “ Fast Digital Feedback control system for accelerator RF system using FPGA”. PCaPAC-2012

[3] Data sheet of Quadrature Modulator AD 8345 Analog devices

[4] Data sheet of Active Mixer ADL 5801, Analog devices

# INDEGENOUS DEVELOPMENT OF 20 KV, 20 A PFN CHARGING SOLID STATE SWITCH FOR LINE TYPE HIGH POWER PULSE MODULATORS

J. Mulchandani#, M.Acharya, Prem Baboo and Purushottam Shrivastava
Radio Frequency Systems Division, Raja Ramanna Center for Advanced Technology, Indore, India

*Abstract*

In line type high voltage pulse modulators, thyratron switches are used to discharge the pulse energy from pulse forming network (PFN) in to the klystron load through step up pulse transformer. The recovery time of the thyratron produces constraint on the higher pulse repetition rates for high average power applications. To resolve this problem conventionally a thyratron series switch is used to isolate the charging supply during the recovery of thyratron and to start the charging after the recovery period. An IGBT based solid state prototype switch capable of charging the PFN up to 20 kV at 20 A peak and repetition rate up to 200 Hz has been developed to replace the charging thyratron. Commercially available low voltage IGBT switches are used in series connection for this switch. The paper discusses the design, development and testing results of the developed high voltage solid state charging switch.

## INTRODUCTION

Presently a line type PFN based pulse modulator is in use for 6 MW peak power microwave system of 10 MeV electron LINAC of Agricultural Radiation Processing Facility [1,2,3]. Table 1 shows the major specifications of the microwave system and figure 1 shows the schematic of the complete microwave system. Command resonant charging scheme [4] for PFN has been used to charge it up to the voltage of 20 kV using a Thyratron switch. Second Thyratron switch is used to discharge the full energy of PFN in to the Klystron load through 1:13 step up pulse transformer. The practical problem which is seen during the vast operations of this scheme is that the charging thyratron gets misfired sometimes during the switching of discharging thyratron due to sudden spike on its respective electrodes. Though an optimized despiking network, heating of thyratron and triggering electronics is used to overcome this issue but the operating conditions of thyratron being very sensitive to the temperature and load so a minor variation in these parameters can trigger the problem. To get rid of this changing behaviour of charging thyratron, it is determined to use solid state switches in place of Thyratrons. In this direction, a prototype solid state switch has been designed and developed to replace the charging thyratron as shown in figure 1. Besides the advantage of steady switching behaviour with solid state switches, a longer life time can also be achieved.

Table 1: Major specifications of microwave system

| Parameter | Value | |
|---|---|---|
| Peak Output microwave power | 6 | MW |
| Operating microwave frequency | 2856±2.5 | MHz |
| Microwave Pulse Width | 11 | µs |
| Klystron anode voltage max. | 130 | kV |
| Klystron anode current max. | 90 | A |
| Rise time of modulator pulse | ≤ 1.5 | µs |
| Fall time of modulator pulse | ≤ 2 | µs |
| Pulse repetition rate max. | 1-300 | Hz |

## DESCRIPTION OF SWITCH AND ITS WORKING

The PFN is charged by resonant charging scheme in which it is charged to approximately twice the DC supply voltage. The charging switch is required to pass a sinusoidal current pulse of peak value 18 A for pulse duration of 1.1 ms. Before the charging pulse, the switch sees a positive voltage equal to DC supply voltage and just after the completion of charging cycle, reversal of voltage across switch appears. To handle the DC voltage up to 10 kV, a series connection of 7 numbers of 4500 V IGBT switches is used. The IGBTs are connected with fast antiparallel diode across them and the reversal of resonant current is blocked by a separate diode stack connected in series to the charging circuit as shown in figure1.

Table 2: Major specifications of developed solid state PFN charging switch

| Parameter | Value | |
|---|---|---|
| Maximum operating DC voltage | 11 | kV |
| Maximum Charging PFN voltage | 22 | kV |
| Peak charging current | 30 | A |
| Max. Charging Pulse width | 1.2 | ms |
| Turn ON delay time | 2 | µs |
| Rise time | 1.5 | µs |
| Turn OFF delay time | 5 | µs |
| Fall time | 1 | µs |
| Pulse repetition rate max. | 220 | Hz |

Table 2 shows above the major specifications of the charging switch and figure 2 shows the schematic circuit for the switch. The IGBTs with drivers and balancing network are mounted in circular fashion and cooled by forced air. Each of the IGBT is driven by a standard IGBT driver having short circuit current

#jaikishan@rrcat.gov.in

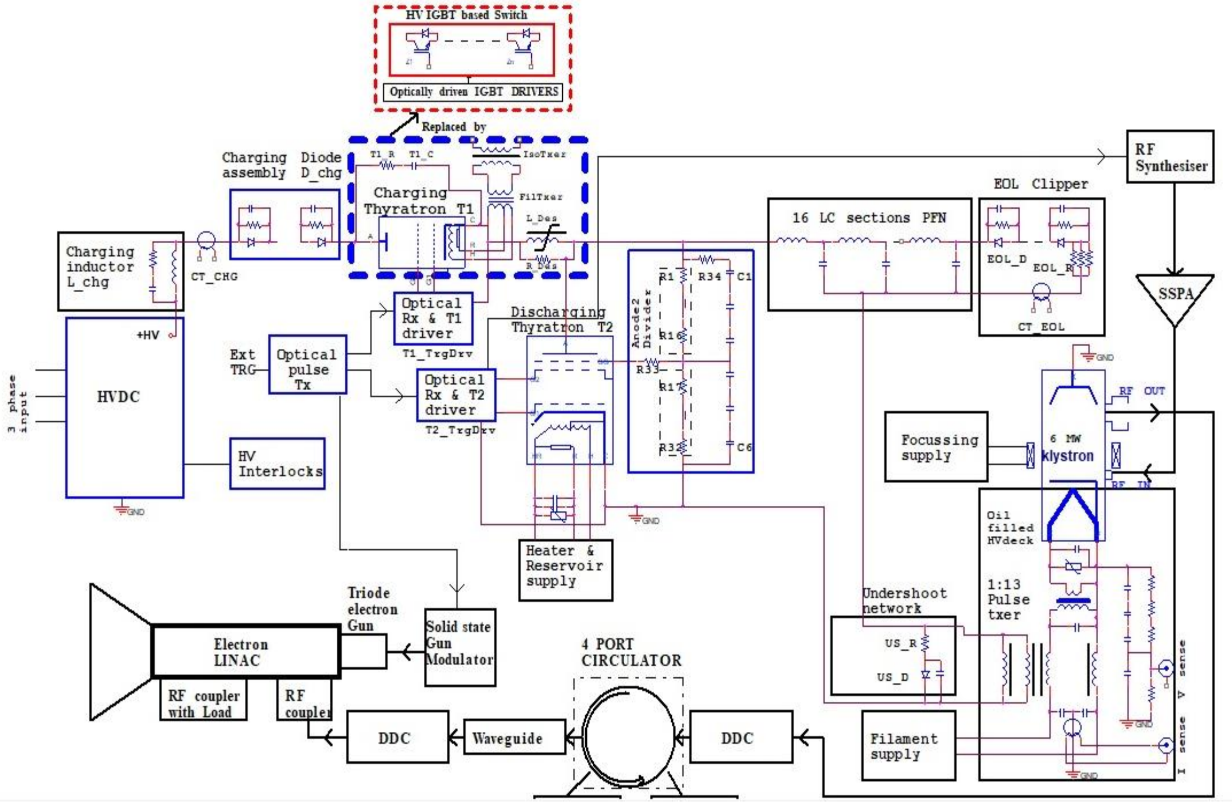


Figure 1: Complete schematic of the 6MW peak power microwave system for 10 MeV Electron Linac at RRCAT.

protection of the IGBT. In case of short circuit in the charging circuit, each driver turns OFF softly the gate supply of its IGBT for safe turn OFF of the IGBT. The power to the driver circuits is given by isolated current sources as shown in figure 2. The switching command to each driver is also optically isolated through standard optical fiber connection.

Resistors RB1 to RB7 provide static balancing voltages to the IGBTs in series. RCD networks (RC1-C1-D1 to RC7-C7-D7) provide dynamic balancing of voltage across each IGBT during turn ON and turn OFF of the IGBTs. Block varistors are also connected across each IGBT as second level of protection against any overvoltage transients across it.

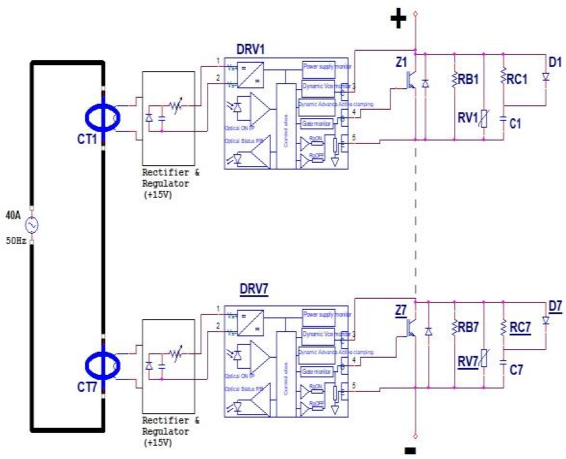


Figure 2: Schematic of 20 kV, 20 A PFN charging switch


Figure 3: **Left side :** Solid state charging switch test set up at microwave system of 10 MeV linac. **Right side:** Close view of the charging solid state switch

## TESTING OF SWITCH AND RESULTS

The gate voltage synchronisation was checked for each IGBT as shown in figure 4. The timing difference was noted to be < 100 ns. After this the switch has been tested with the microwave system of 10 MeV linac at operating conditions of 19 kV charging voltage and charging cycle repetition rate of 220 Hz. A peak current of 16 A was measured during the charging cycle. The charging inductor has been provided with block varistor network to suppress the transient voltages across it in case of sudden turn OFF of the IGBTs due to any reason in between the charging current cycle. Figure 5 shows the switch voltage and charging voltage waveforms at 220 Hz operation. The microwave output and electron beam parameters observed with this switch are found to be same as with Thyratron tube charging switch (Figure 6). The temperature distribution between the IGBTs during the above test was measured using thermal imaging camera (Figure 7). The maximum temperature of 73ºC was noted at IGBT 7 and minimum temperature of 65ºC was noted at IGBT 4. The IGBTs were interchanged but no change in temperature distribution was obtained. The reason was concluded to be the uneven distribution of air flow passing the switches.

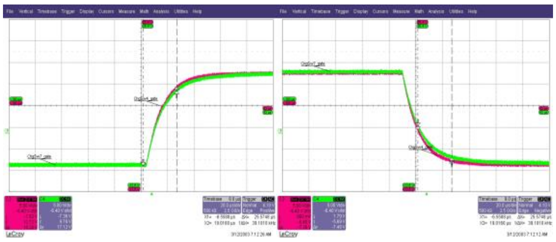

Figure 4 Synchronisation test of IGBT gate voltages : Left one showing gate voltage rise time and right one showing gate voltage fall time. **Green**: IGBT 7 gate voltage, **Red** : IGBT 4 gate voltage

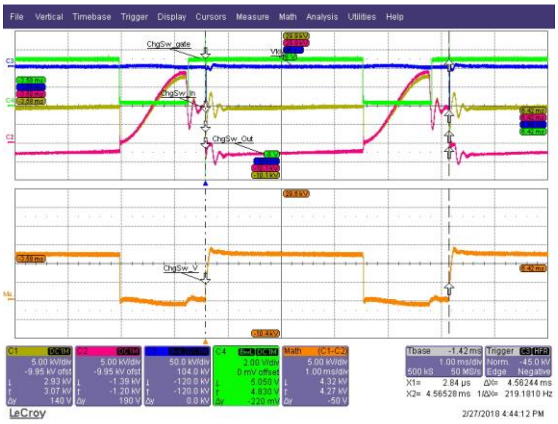


Figure 5 Charging switch waveforms at 10 kV DC operating voltage –**Green** : Switch command signal, **Orange** : Charging switch voltage, **Red** : PFN charging voltage waveform at 220 Hz PRR

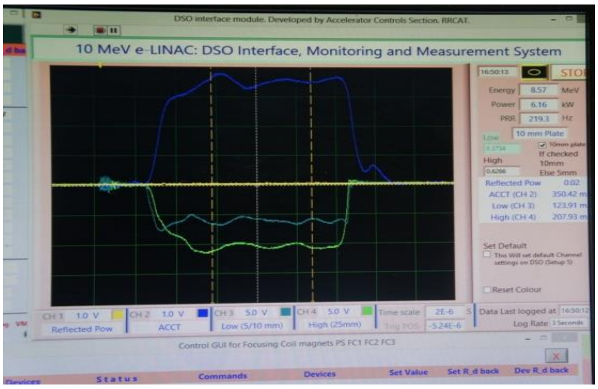


Figure 6 Snapshot of electron beam current waveforms at PC operating panel (**Blue** : ACCT @ 350 mA, **Cyan** : Low energy plate current & **Green** : High energy plate current @ beam energy of 8.5 MeV and average power of 6 kW)

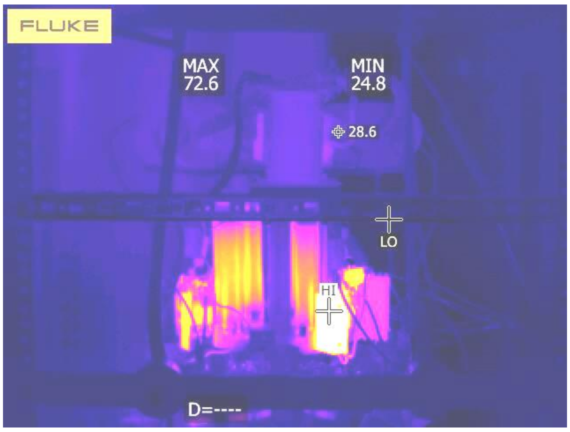


Figure 7 Thermal image of switch taken during the operation at 19 kV charging voltage at repletion rate of 220 Hz

## CONCLUSION

A prototype of 20 kV, 20 A solid state charging switch for pulse forming network of 6 MW peak microwave system has been made and tested successfully. The uneven temperature distribution of switches as seen during the tests at high PRR of 220 Hz, will be addressed in the upgraded version of the switch.

## ACKNOWLEDGEMENT


The authors acknowledge the skilful efforts from Mr. J.Y. Parate, Mr. Vinod Phadnis and Mr. Akhilesh Rajak during the assembly of the high voltage switch and its testing.


## REFERENCES


[1] Development, qualification and commissioning of high power microwave SYSTEM AND components for electron Linac program at RRCAT- Purushottam Shrivastava, J. Mulchandani, Y.D. Wanmode, M. Acharya, T. Reghu, P. Mohania, Sivananda Reddy, A. Bhisikar, Prem Baboo, H.G. Singh, INAPC-2015, Mumbai.

[2] Purushottam Shrivastava, et.al., Development of Indigenous 15MW peak 90kW average power Klystron Pulse Modulator and related technologies for 10MeV,10kW Industrial electron LINAC, Proceedings of InPAC 2005, RRCAT, Indore.

[3] Purushottam Shrivastava, et.al., Development of 6MW Peak High Average Power Pulsed S-Band Microwave Source for 10MeV, 10kW LINAC, Proceedings of InPAC 2003, CAT, Indore.

[4] K.Satoh,N.Kumazawa,O.Endoh,M.Imagawa,et.al., Development of high duty pulse power supply for S-band klystron, proceedings of JAERI-Conf 1995.

# DSP CONTROLLED PHASE STAGGERING OF DC-DC POWER MODULES FOR LOW RIPPLE OPERATION

Rinki Upadhyay#, M.K.Badapanda, Akhilesh Tripathi and Mahendra Lad
Raja Ramanna Centre for Advanced Technology, Indore-452013

*Abstract*

To validate DSP control of high voltage DC power supply with multiple modules connected in series , a scheme employing 4 number of series connected 500 V, 5 A DC-DC power modules, operating in phase shifted PWM mode, has been developed. A DSP based control-protection system developed for phase staggering of these power modules to provide low ripple output is presented in this paper. This control-protection system consists of a module controller in each power module and a central controller. Module controller provides gate drive signals to inverter bridge IGBTs in each power module and monitors the status of power module as well as communicates with central controller through RS-485. Suitable optical isolation has been provided for communication between module controller and central controller. The central controller sends phase staggering signals, shut down signals and delta correction signals to power modules during operation. In case of any abnormal condition, this control-protection system trips the entire power supply. It has capability to operate the power supply in remote mode via a PC connected through RS-232 along with fault diagnosis and data logging features. Experimental result obtained during phase staggering of power modules is also presented in this paper. This control-protection system also has capability to operate up to 64 number of power modules for the development of high voltage DC power supplies with low output ripple for RF amplifiers.

## INTRODUCTION

High power RF amplifiers demand low output ripple and low output stored energy from their high voltage DC bias power supplies. Under arcing conditions, they can handle maximum up to 20 Joules of stored energy [1], [2]. The design and development of such power supplies are complex and challenging task as reduction of output filter size and output stored energy are two contradictory requirements. Modular topology based power supplies employing a number of series connected power modules with phase staggered outputs pose a promising solution to meet both these contradictory requirements simultaneously. Various converter configuration using ZVS/ZCS arrangement are employed in such power modules to minimise the switching losses, thereby increasing the efficiency of power modules as high efficiency, high power density and high reliability are of prime importance in high power applications. This paper describes in brief the digital control-protection system developed for phase staggering 4 number of DC-DC power modules of a solid state modular 2 kV, 5 A DC power supply. This control scheme can be adopted for development of DC power supplies of higher voltage ratings for biasing high power RF amplifiers.

#rinki@rrcat.gov.in. RF Power Supplies Lab, RF Systems Division, RRCAT, Indore.

## POWER CIRCUIT

A 2 kV, 5 A DC power supply employing series connection of 4 number of 500 V, 5 A DC-DC power modules has been developed as a prototype of high voltage DC power supply for high power RF amplifier. Fig. 1 shows the power circuit of 500 V, 5 A DC-DC power module employing a single phase inverter bridge operating in phase shifted pulse width modulation mode (PSPWM) at 20 kHz switching frequency, high voltage-high frequency isolation transformer, full wave rectifier bridge, a freewheeling diode. Auxiliary LC compensation circuit has been incorporated in the power module to ensure zero voltage switching (ZVS) of IGBTs in inverter bridge to minimize their switching losses, specifically for low current application. Each power module takes 750 V DC input from a 1 kV, 12 A DC power supply and generates 500 V average DC output. The outputs of power modules are connected in series and suitably phase staggered to provide low ripple output which in turn reduces the output filter capacitor size and hence the output stored energy, one of the most critical requirement of high power RF amplifiers.

## PHASE STAGGERING OF POWER MODULES

The series connection of four power modules is shown in Fig. 2. Here each power module is represented as a DC source (V) in series with switch (S) and a freewheeling diode (D). For low ripple operation, all the power modules are operated at same duty cycle with time period T corresponding to their rectified output frequency

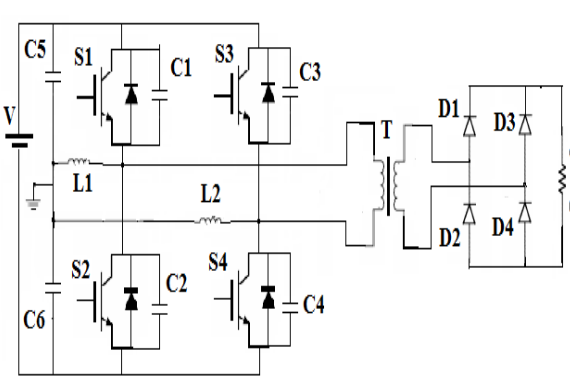


Figure 1: Power circuit of DC-DC power module

(40 kHz). Firing pulses to inverter bridge IGBTs of 1st power module are given at t = 0 and then to that of 2nd, 3rd and 4th power modules are given at delay of t = T/4, 2T/4 and 3T/4 respectively. During operation, if any power module gets faulty, load current path will be provided by its freewheeling diode. Fig. 3 shows the output voltage waveform of four power modules phase staggered at 66 % duty cycle. From this figure, it is clear that the ripple frequency of output is four times the frequency of individual power module while the magnitude of output voltage ripple is equal to the input DC voltage of individual power module. With the increase in number of power modules, the magnitude of output voltage increases but the output ripple still remains equal to input DC voltage of individual power module, thereby providing low ripple operation. The output voltage of each power module is regulated at desired level by controlling the phase shift of diagonal pair IGBTs of inverter bridge.

## CONTROL-PROTECTION SYSTEM

DSP based control-protection system has been developed for phase staggering the outputs of DC-DC power modules as shown in Fig. 4. Module controller and central controller are key parts of this control system. Provisions for data logging of events and fault history of last 32 faults have been incorporated. This system has capability to operate the power supply in remote mode via a PC connected through RS-232. In case of any abnormal conditions, the control-protection system trips the entire power supply by withdrawing the gate drive signals of IGBTs in power module and tripping the input contactor of 1 kV, 12 A DC power supply.

### *Module Controller*

The module controller consists of DSP 2023 and DSP 6011. DSP 2023 provides PWM gate drive signals, each of 20 kHz switching frequency, to inverter bridge IGBTs. It also monitors various module parameters like input DC voltage, input DC current, IGBT heat sink temperature, 15 V, 5 V DC control power supply to detect the health status of power module. Communication DSP 6011 is

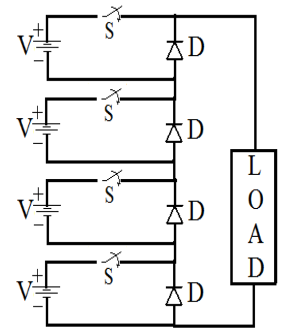


Figure 2: Equivalent circuit of four power modules in series

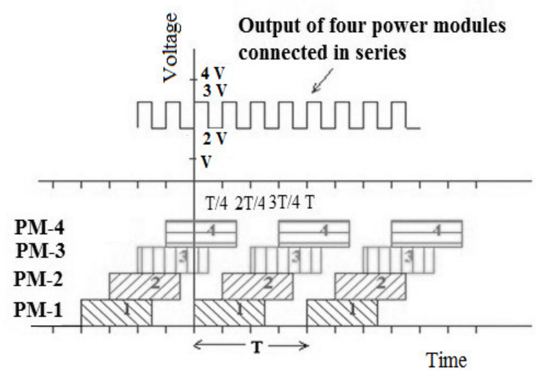


Figure 3: Output voltage waveform of four phase staggered DC-DC power module at 60 % duty cycle for low ripple operation

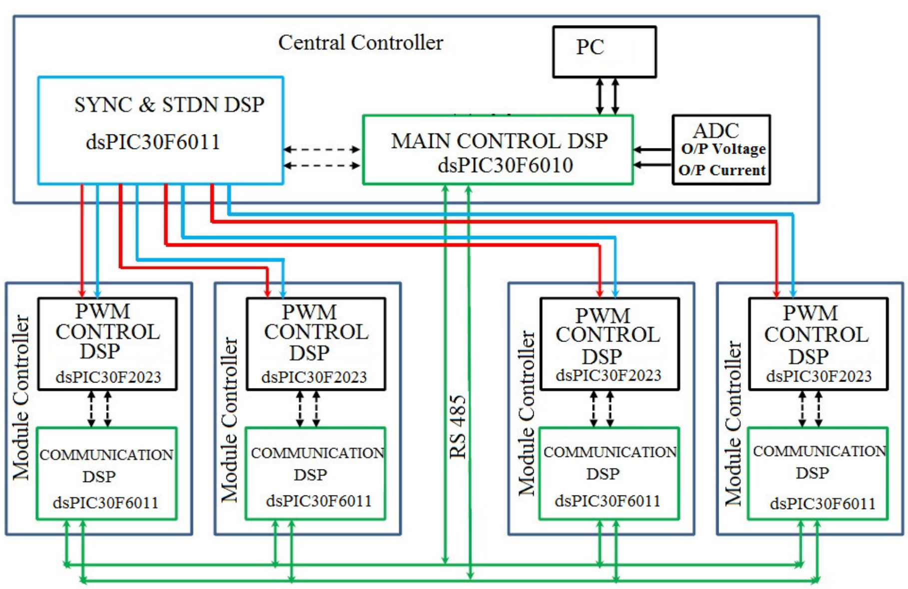


Figure 4: Control system architecture

responsible for establishing two way communications between power module and central controller through RS 485 interface. Suitable opto-coupler ICs have been employed in power module to provide optical isolation for this communication. This DSP also displays crucial parameters of power module on LCD.

### *Central Controller*

The central controller consists of DSP 6010 and DSP 6011. DSP 6011 provides phase staggering and shut down signals to the power modules. In case of failure of one power module, the phase staggering signals are auto-updated and given to remaining three power modules. With the failure of two power modules, shut down signals are given to all power modules thereby tripping the complete system. Four number of 74HC154 demultiplexer ICs, each generating 16 number of phase staggered signals have been used in the staggering circuit. Hence the control-protection system has capability to operate up to 64 number of power modules. DSP 6010 is the main control DSP of this control-protection system and is responsible for communication with both module controller as well as the user via PC. Communication with PC is established through RS-232 interface. The main control DSP also generate delta correction signal after comparing the actual output voltage with its set value and provides this signal to module controller for fine regulation of individual module output voltage.

## EXPERIMENTAL RESULTS

The developed 2 kV, 5 A DC power supply was tested on 3 A resistive load. The phase staggering signals generated by central controller are shown in Fig. 5. The output voltage of individual power module, operating at 750 V DC input and generating 500 V average DC output is a 40 kHz rectangular pulse waveform. The final output voltage waveform obtained after phase staggering of four power modules at same operating point is shown in Fig. 6. It is observed from this waveform that peak to peak output voltage ripple is approximately 750 V while the ripple frequency is found to be 160 kHz. The photograph of one unit of DC-DC power module is shown in Fig. 7.

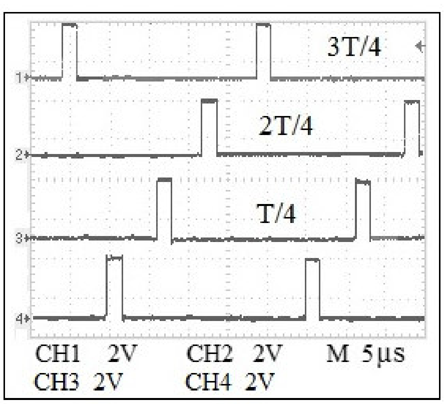


Figure 5: Phase staggering signals of power module generated by central controller

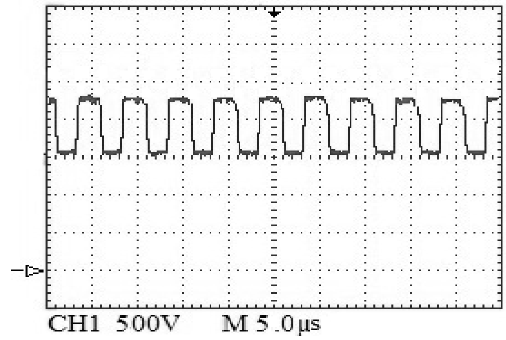


Figure 6: Output voltage obtained after phase staggering outputs of four power modules

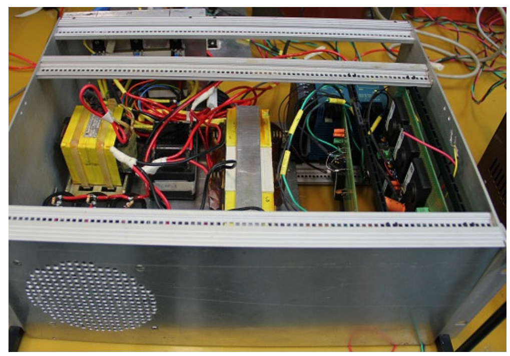

Figure 7: Photograph of DC-DC power module

## CONCLUSION

DSP based control-protection system has been developed for phase staggering the outputs of 4 number of 500 V, 5 A DC-DC power modules for low ripple operation. Module controller provides gate drive signals to inverter bridge IGBTs and monitors the heath status of power modules. Central controller provides phase staggering, shut down signals to module controller. Communication between module controller and central controller is established through RS-485 with suitable optical isolation. The performance of the control system is found to be satisfactory. The developed control-protection system has provision to stagger upto 64 number of power modules which will be helpful for the development of high voltage DC power supplies for high power RF amplifiers.

## REFERENCES

[1] M. K. Badapanda, A. Tripathi, R. Upadhyay, M. Lad and P. R. Hannurkar, "High Power RF Testing of 1 MW, 352.2 MHz Continuous Wave Klystron Amplifier," IEEE Trans. Plasma Sci., vol. 44, no. 99, pp. 3599-3607, Oct. 2015.

[2] A. Tripathi, M. K. Badapanda, Rinki Upadhyay and Mahendra Lad., "Wire Survival Test of Crowbar Less, High Voltage DC, Klystron Bias Power Supply," Open Science Journal of Electrical and Electronic Engineering, vol. 4, no. 1, pp. 1-9, Sep. 2017.

# DEVELOPMENT OF CONTROL AND MONITOR INSTRUMENTATION FOR A LOW ENERGY 400KV ACCELERATOR AND ITS UHV BEAM LINE

K.Suresh*#, J.Navas*, C.David*, B.K.Panigrahi@#

*Materials Science Group, @Electronics and Instrumentation Group, #Homi Bhabha National Institute, Indira Gandhi Centre for Atomic Research, Kalpakkam,India.

*Abstract*

A 400kV low energy accelerator has been established indigenously at Materials Science Group, Indira Gandhi Centre for atomic research, Kalpakkam as part of a state of art dual ion irradiation facility. The 400kV accelerator is an air insulated ion accelerator comprising of a 50MHz RF ion source, pre-acceleration, acceleration stages, electrostatic quadrupole lenses, double focusing mass analyzing magnet and beam diagnostic devices. This paper discusses about the in-house development of control and instrumentation for the 400kV accelerator and its UHV beam line. Starting with a simple PIC16F877A microcontroller based control system, the control instrumentation has grown into a reliable fibre optic based distributed control and monitor system using Group3 and PXI based data acquisition and field interface circuits. In Group3 system, three device interface nodes with I/O boards are interfaced to various acceleration systems. These nodes are linked to a Loop Controller at the control computer located about 25 meters away using a pair of fibre optic cables. Transacting data at 1.152 Mbaud, the system continually refreshes control outputs and scans status inputs at a typical rate of 125Hz. User-friendly control software is developed using LabVIEW.

## INTRODUCTION

A low energy 400kV accelerator has been established indigenously at Materials Science Group, Indira Gandhi Centre for atomic research, Kalpakkam as part of a state of art dual ion irradiation facility[1]. The dual beam ion irradiation facility, in which the 400kV accelerator is used for injecting Helium/Hydrogen and a 1.7MV Tandetron accelerator from M/s. High Voltage Engineering Europa, The Netherlands is used for irradiation by heavy ion beam which produces displacement damage at very high rate, is used to simulate synergistic effects of displacement damage and gaseous helium/hydrogen which is important in the context of development of radiation resistance materials for fast fission, fusion and accelerator driven subcritical systems.

### *400kV accelerator system description*

The 400kV accelerator is a low energy, air insulated ion accelerator comprising of a 50MHz RF ion source (RFIS), pre-acceleration, acceleration stages, electrostatic quadrupole lenses (QPT), a double focusing mass analyzing magnet (MAM) and beam diagnostic devices (BDD). In the 400kV accelerator, the positive ion beam (IB) produced by the RFIS is extracted and pre-accelerated to 30keV by the extraction and pre-acceleration stages. The RFIS system consists of a quartz bottle, a thermo-mechanical leak system, a 50MHz/100W RF power supply, 0-6kV DC probe supply and a 0-5A current regulated magnet power supply. A gap lens and a set of X-Y electrostatic steerers are used to focus, align and inject the IB into an accelerating tube (AT) with 16 sections. The RFIS and its systems, turbo molecular vacuum system, X-Y steerers, extraction, gap lens, beam diagnostic elements like Faraday cup and beam profile monitor are housed inside a high voltage dome (HVD). The HVD is electrically insulated from the ground using a set of ebonite insulators and two equipotential plates which also provide adequate mechanical support. A 5kVA, isolation transformer with 425kV DC isolation is used for feeding the single phase, 230V AC input power to all the systems kept at the HVD. The ion beam is further accelerated using the AT and the DC acceleration voltage (DCAV) applied between the HVD and the ground. The DCAV is provided by an air insulated 400kV DC, 3.5mA high voltage power supply with a high stability (<0.01%/hour), low ripple (0.05%) and a very good output regulation (<+/-0.005%). Hence the 400kV accelerator can provide doubly charged ions upto a maximum energy of 860 keV. The 90 degree bending MAM mass analyses the IB with a mass resolution of 1 in 250. Post mass analysis, the IB is steered through a 3.3metre long ultrahigh vacuum beam line (UHVBL) operating at a typical vacuum of $4x10^{-9}$mbar. The UHVBL consists of a differential pumping section, beam handling devices like XY scanners, steerers, neutral trap, BDD like beam profile monitor, Faraday cup and vacuum systems. Beam optics of the accelerator was optimized to achieve maximum beam transmission of about 80% through the differential pumping unit and also to obtain a focused narrow beam (< 5mm dia) on the sample mounted in an UHV irradiation chamber. Focusing of the IB is achieved using a pair of QPTs.

### *Control and monitor instrumentation development*

Electronics and instrumentation to facilitate control and monitoring the 400kV accelerator and its UHVBL have been designed and developed in-house. The control and monitor instrumentation is based on Group3 make PC based, fibre optic linked, distributed control system [2]. The control system is used to remote control the 400kV accelerator from the control room located about 25 metres away. All the parameters of the accelerator are controlled and displayed on a control computer (PC) screen. The general block diagram of the control system is illustrated in figure 1. From the control point of view, the modular control system divides the entire 400kV accelerator and its beam line into 3 major blocks a) systems at HVD dome b) systems in the high vacuum beam line (HVBL) and c) the systems in the UHVBL.

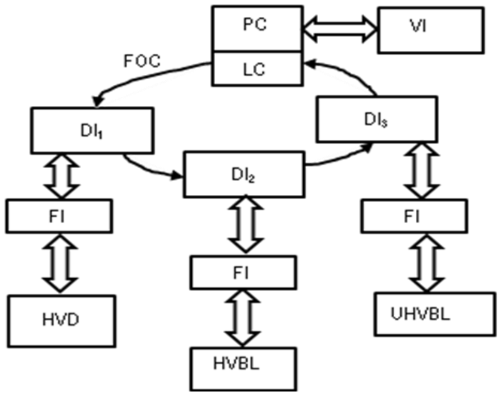


Figure 1: Block diagram of the fibre optic based distributed control and monitor system.PC-personal computer,LC-Loop Controller,VI-virtual instruments, $DI_{1,2,3}$-device interface nodes, FI-field interface circuits,HVD-high voltage dome, HVBL-high vacuum beam line, UHVBL-ultra-high vacuum beam line.

Data from the PC is sent over fibre optic cables (FOC) to three Device Interface (DI) kept at the HVD, HVBL and UHVBL. Each DI contains analog I/O, digital I/O data acquisition (DAQ) boards which are interfaced to the accelerator systems through the field interface circuits. At the PC, a PCI based central/Loop Controller (LC) with a co-processor on board handles all the communications between the PC and the DI and thus relieves the PC from handling high speed communications. The communication between the PC and the LC's co-processor is through a 2 Kbyte of dual port RAM present on the LC. To set a new control value of an accelerator subsystem output, the PC writes the necessary control data into the appropriate area of the shared dual port RAM and the co-processor on the LC formats this control data into a suitable message packet and sends it out on the FOC to the DI. The latest status data of the accelerator subsystems are obtained by the LC by continuously interrogating the DIs and updating the dual port RAM with the new status data which are subsequently read by the PC. In this manner, control and monitoring information are transmitted over the FOC at up to 1.152 Mbaud rate, continuously refreshing outputs and scanning inputs. To interface the signals from the DAQ boards in the DIs to the accelerator systems, we have developed and used a host of FIs including the signal conditioners, isolation amplifiers, and other custom circuits, etc. The main function of the signal conditioners used with each DAQ board is to shunt out any high energy transients picked up by the signal wiring to chassis ground. Further they also perform other functions like a) transient attenuation b) signal level modification c) pull-up to +5V or 24V. We have employed 4-way high performance isolation amplifiers(ISOAMP) for protecting the monitor and control signals as well as equipment from noise, transient power surges, internal ground loops, and other hazards present in the HVD. The ISOAMP does signal processing tasks like isolation, filtration, and linearization. Salient Features of the control system include: a) superior EMI/RFI noise immunity, high voltage isolation, and fast data transfer b) modular design c) small form factor d) high channel density, high resolution (16 bit for analog monitoring signals), high update rate (scan rates of up to 32,000 channels per second) e) rugged and reliable operation. General scheme of hardware used for controlling and monitoring of various accelerator parameters of the HVD,HVBL,UHVBL is illustrated in Figure 2.

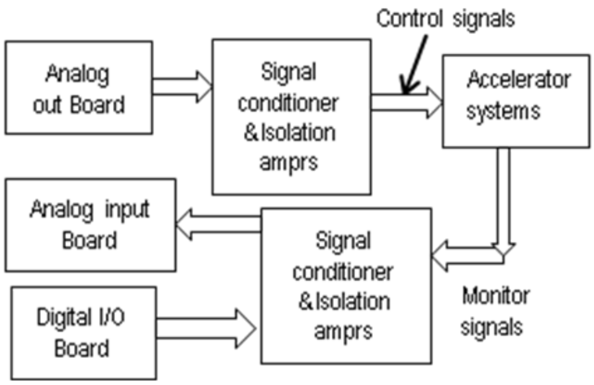


Figure 2: General scheme of hardware used for controlling and monitoring of accelerator parameters.

## *Control and Monitor system for systems at HVD*

Precision control signals in the range of 0-10V DC, required for controlling accelerator parameters of the systems kept at HVD like RFIS probe voltage, magnet current, gas feed system, extraction, X and Y steerers, and their parameters, are generated using an 8 channel high precision 14 bit analog out (AO) board kept in the $DI_1$. The AO board generates eight single ended, independent, analog control signals with a 14 bit setting resolution, 0.1% accuracy, 20mV/°C offset temperature coefficient and an update rate of 125 Hz. These control signals are buffered, filtered, and isolated by a dedicated ISOAMP before being fed to accelerator systems i.e field devices. For monitoring the RFIS and other accelerator parameters, precision 8 channel analog input (AI) boards are used. Accepting 8 differential inputs, the AI board acquires analog inputs in the range of -10V to 10V to 16 bit resolution at a rate of 125Hz per channel. Using a set of 2:1 high accuracy and precision analog multiplexers and the digital I/O lines, we have developed a scheme for monitoring 14 accelerator parameters using a single 8-channel analog input board. The RFIS and its power supplies are elevated to a potential of 30kV DC with respect to the HVD and hence the 115V AC input power is fed to the RFIS through a 3kVA, 40kVDC isolation transformer. Due to the potential difference between the HVD and the RFIS, control and monitoring of the RFIS power supplies could not be done using standard electrical wiring from the DI kept at the potential of the HVD. This problem was solved by using control and monitoring scheme shown in figure 3. In this scheme, 10mm dia x 15cm long perspex rods with a mechanical coupling assembly couple 12V DC motors at one end and control potentiometers of the RFIS power supplies at the other end with the perspex rods providing electrical isolation. Two isolated digital I/O lines with L298 based H-bridge motor controller control the speed, direction of the DC motors to increase/decrease the output of the RFIS power supplies. To monitor the outputs of the power supplies, monitoring potentiometers are coupled to the perspex rods through nylon insulated gears and the voltage outputs of the monitoring potentiometers follow the control potentiometer outputs fed to the RFIS power supplies. The monitoring signals from these potentiometers outputs are acquired by the AI board of the $DI_1$. Thus the DC motor-control potentiometer-monitoring potentiometers with the perspex mechanical coupling provide a low cost and reliable solution to the RFIS control and monitoring.

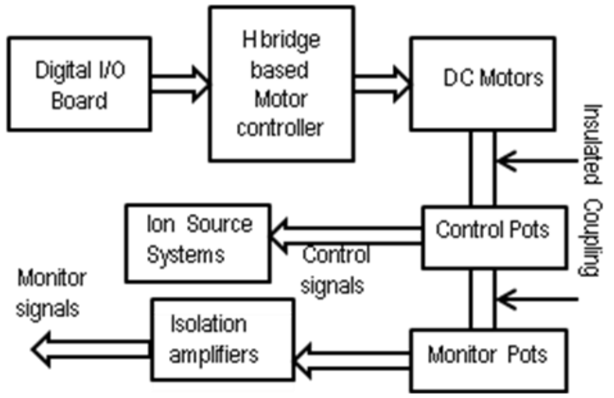


Figure 3: Hardware used for controlling and monitoring of RFIS parameters.

### *Control and Monitor systems for HVBL and UHVBL systems*

The general scheme of hardware shown in figure 2 is used for controlling and monitoring of accelerator systems in the HVBL like QPT1&2 voltages, vacuum level, Y-steerer outputs, Faraday cup position, IB current. The $DI_2$ with all AI, AO and digital I/O boards is used for this. Through an isolated RS232 bidirectional interface, the PC controls 0-120A/60V high stability current regulated power supply which energises the MAM. Similarly using the $DI_3$ with AI, AO and digital I/O boards, various parameters of UHVBL like vacuum, neutral trap voltages, X-Y scanner voltages, Faraday cup positions, IB current are controlled and monitored. A PIC16F877A based dedicated multichannel gate valve control and monitor system is used for controlling various gate valves used in HVBL and UHVBL [3]. Instrumentation for indirect fluence measurement system, high precision multichannel low current and fluence measurement system have also been developed for use with the 400kV accelerator[4][5]. Labview virtual instruments were developed for the entire control system to control and monitor the accelerator parameters[1]. Augmentation of the control system with PXI based data acquisition is under progress.

### *Testing of the control and monitor system*

All the individual blocks of the control system like DI, LC, various I/O cards, gas feed system, etc were individually tested and satisfactory performance was observed. All the channels of the AO boards were checked by generating voltages in the range of 0-10V, especially zero, full scale and a reference value at the middle of the full scale. The output resolution, precision, linearity, noise, stability, offset parameters of the control signals were found within acceptable levels. Similar tests were conducted on the AI board inputs using external simulation signals in the range of 0-10V and acceptable performance observed in terms of missing codes, differential nonlinearity, integral nonlinearity, etc. A self-check scheme of the AO-AI signal chain is used to monitor the correct functioning of the signal chains. The ISOAMPs were tested for linearity, stability, offset, isolation, etc. The individual I/O cards were integrated with DI, PC, LabVIEW virtual instruments.

## CONCLUSIONS

Using the distributed control system, the 400kV accelerator was regularly operated and 5mm dia $Ar^+$ beams of 230keV have been obtained in the initial phase up to the HVBL. Then the 400kV accelerator was integrated with the UHVBL. Various ion beams like $H^+$,$He^+$,$He^{++}$,$Ar^+$, with typical parameters of 10uA/ 450keV were obtained on target at UHV irradiation chamber. The performance of the control and monitor system has been found very satisfactory.

## REFERENCES


[1] K.Suresh *et al.*, “Development of a dual ion irradiation facility for studies of radiation response in fission and fusion reactor materials”, *Nucl. Instr.Meth.*,vol.447,pp. 92–99, 2019.

[2] Group3technology, New Zealand, https://www.group3technology.com.

[3] K.Suresh et al., “Development of a microcontroller based multi-channel gate valve and Faraday cup controller system for a 400kV low enery acclerator” in Proc.Indian Particle Accelerator Conference (INPAC 2018), (2018),Indore,India.

[4] K.Suresh et al., “Development of a simple, low cost, indirect ion beam fluence measurement system for ion implanters, accelerators”, *J.Inst.*,vol.13, P02033, 2018.

[5] K.Suresh et al., “Development of a simple, low cost, high precision multi-channel ion beam current and fluence measurement system for a low energy accelerator”, *J.Inst.*,vol.13, T05011, 2018.

# DEVELOPMENT OF FAST PULSE POWER SUPPLY FOR LOW IMPEDANCE TL MAGNET

Rajesh Barothiya#, Yashpal Singh
*Accelerator Power Supply Division*
Raja Ramanna Centre for Advanced Technology, Indore-452013, INDIA

*Abstract*

Design of fast rise pulse power sources for low impedance transmission line type magnets involves many challenges. In the present work, A 30kV / 3kA pulse power supply has been designed & developed to test a 5 Ohm transmission line type kicker magnet. This magnet is a parallel combination of five TL magnets, each have a impedance of 25 Ω. The current pulse is generated by discharging a pulse forming line into matched transmission line magnet. A high voltage thyratron CX1666 is used as a switch. A pulse current with a rise time of 45 ns and a flattop of 80 ns was obtained when exciting current was 3 kA. A rise time of ~45ns was obtained with compact cable termination & low inductance thyraron assemblies. In this paper, we discuss the specific issues related to the design of pulse forming network, compact cable termination & low inductance thyraron assembly for achieving faster rise time of the current pulse. Experimental results of the developed pulse power supply will be also presented.

## 1. INTRODUCTION

Indus1 (450 MeV) and Indus 2 (2.5 GeV) are two electron synchrotron storage rings operating at RRCAT Indore. These rings are filled with electron bunches extracted from the Booster ring (450 MeV) using lumped type kicker magnet & kicker power supply. Inductance of lumped type magnet presents a transient mismatch to the trapezoidal shape current pulse, causing poor rise time & high flat-top ripple. Low rise time with low flat-top ripple is desirable to achieve high extraction efficiency & partial loss of extracted bunches. It was planned to design and developed a transmission line type kicker magnet & pulse power supply to optimise technologically conflicting requirements and achieve the above mentioned objectives. Efforts have been put to realise fast rise and good flatness of magnetic field by (i) good matching between power supply and load (ii) reduced stray inductance (iii) reduced magnet propagation time. Design and development of a pulse power supply to energise a 5 Ω transmission line type kicker magnet has been carried out at PPSS/RRCAT, Indore. To drive a low impedance magnet was a challenge from the design point of view of the power supply.

## 2. DESIGN DETAILS

The design parameters of the power supply are listed in Table 1, whereas schematic diagram of the power supply is shown in Fig. 3. Previously a TL magnet was designed with an impedance of 25 Ω /18 Cells. This magnet was split into two halves and connected in parallel to realize an impedance of 12.5 Ω. A power supply with matched impedance was designed and TL magnet was tested with this power supply.

#barothiy@rrcat.gov.in

Table 1: Design Parameters

| Parameters | Value |
|---|---|
| Pulse Shape | Trapezoidal |
| PFN Voltage | 30 kV |
| Peak Current | 3 kA |
| PFN Impedance | 5 Ω |
| Rise Time (1 – 99%) | 45 nsec |
| Flat top Time | 80 nsec |

Figure 1: Power Supply under testing

This design of magnet was found lacking, because of unacceptable propagation delay and significant reflections in magnetic field. To overcome these limitations, it was decided to redesign TL magnet with less number of cells per magnet. A new TL magnet design comes with 25 Ω /5cells. Such five magnets are connected in parallel to realise an impedance of 5 Ω. A Pulse power supply has been developed to energize this magnet. Power supply delivers a current pulse having a rise time of 45 ns and flat top of 80 ns, when independently energizing all five modules of the magnet.

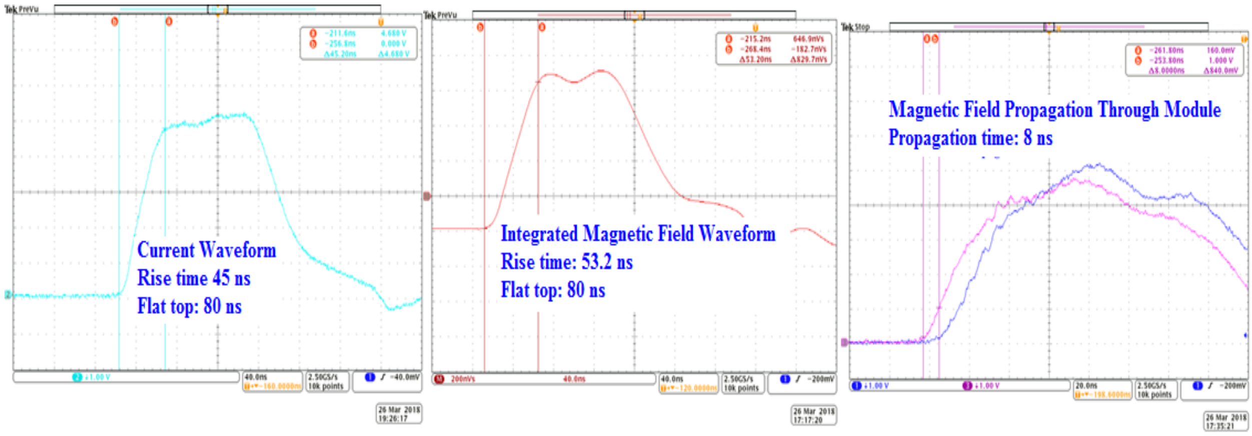


Figure 2: Current pulse & magnetic field waveforms

Design of fast rise pulse current for such a low impedance magnet involves many challenges. Decreasing the magnet impedance, increases L/2R time constant which in turn affects the rise time of current pulse. Here L is the stray inductance of the assemblies & R is the system Impedance. This requires careful design of thyratron & feed through assemblies to reduce the stray inductance, whereas strict impedance matching with the magnet is required to reduce flat top ripple due to reflections.

Figure 1 shows the photograph of power supply under testing with TL magnet. The power supply unit is composed of a command pulse charger unit, pulse forming lines (PFL), matching resistors, thyratron, and transmitting cables. A command-charging scheme is used to utilise RG217 cable for 30 kV pulse application. The charging time is set to 100 µs at the maximum charging voltage of 30 kV. If the thyratron switch fails to trigger within 110 µs of pulse charging, PFL will be discharged through bleeder network for safe operation of PFL cable.

## *2.1 Pulse Forming Line*

Trapezoidal type of current pulse can be generated by discharging a pre-charged pulse forming network in to match impedance. Generally PFL (coaxial cable) is preferred in short duration & fast rise pulses to simplify the construction of the power supply. The PFL gives fast and low ripple pulses, but low attenuation is essential.We have used ten RG217 coaxial cables connected in parallel to form an impedance of 5 Ohm. To get pulse duration of 125ns, each cable has a length of 12.5 meters. These bunches of cables are floated at 32kV during pulse generation, hence isolated cable spool was fabricated & installed to support these cables. To get the faster rise & low transient oscillation in the pulse, low inductance thyratron & cable termination assemblies were designed.

## *2.2 Thyratron Switch*

The thyratron is a key device in high voltage pulsed-power supplies. We used a thyratron model CX1666, whose maximum ratings are, the peak forward anode voltage of 35 kV and peak anode current of 10 kA. The nominal operational parameters in our application are 30 kV, 3 kA pulses at 1 Hz. To get the faster turn on time of thyratron, maximum gas pressure was optimized by increasing reservoir heater voltage up to safe specified value. This arrangement drops the hold off voltage of thyratron up to 31 kV which is acceptable in our application. The triggering scheme affects much on stability and turn-on time of the thyratron tube. Double pulsing trigger method was used to get the excellent firing characteristics of the thyraron. E2V Technologies solid-state trigger systems MA2709A is used for this application.

## *2.3 Low Inductance assemblies*

The rise time of the current is governed by the switching time of the thyratron, stray inductances and capacitances of the pulse forming line termination, matching resistors & thyratron housing. To achieve the faster rise & flat top of the current pulse a low inductance coaxial thyratron assembly was designed & fabricated. Height of the thyratron assembly was also reduced by 33% with newly designed assembly. At each stage of designing every mechanical assembly impedance was maintained within the specified limit to overcome reflections due to mismatch. Further work is going on to observe the reflections at each stage of the pulse transmission.

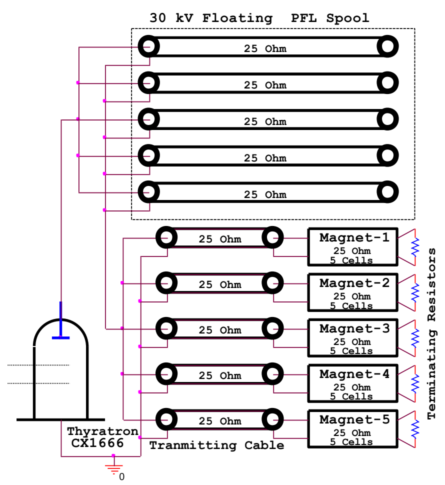


Figure 3: Schematic Diagram of the Power Supply

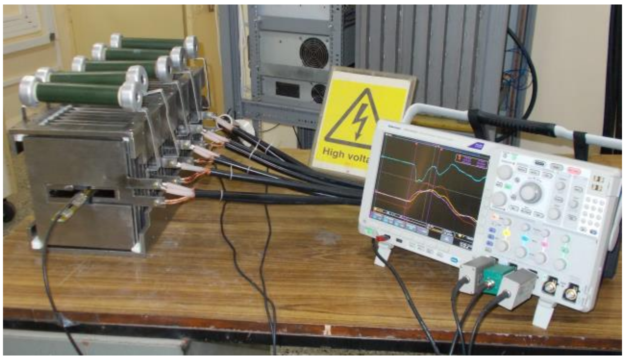

Figure 4: TL magnet testing without vacuum chamber

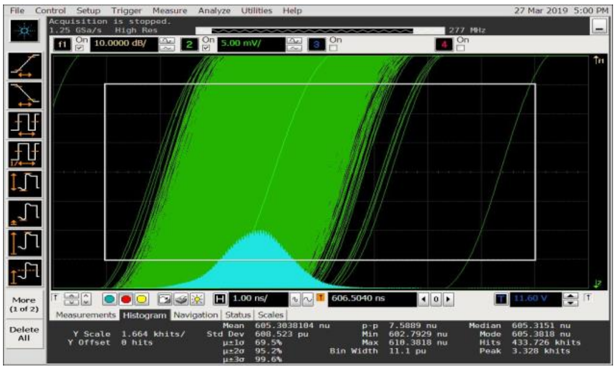

Figure 5: Jitter Measurement

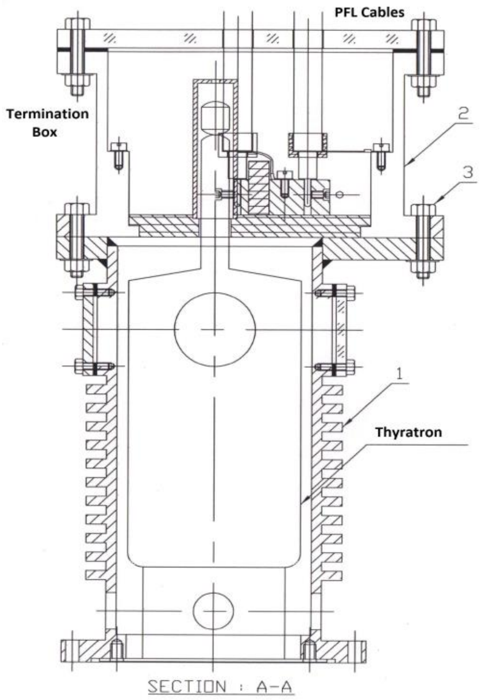


Figure 6: Thyratron & cable termination assembly

Figure 7: PFL & thyratron assembly at Initial testing

## 3. CONCLUSION

As per the designed parameters, power supply was fabricated and preliminary test have been performed on it. Test results from a lab prototype shown in figure 2, shows a close agreement with designed & simulated results. Final tuning of the current pulse will be carried out after installation of cable termination assembly & vacuum chamber of the TL Magnet

## 4. ACKNOWLEDGEMENT

Authors express their gratitude to Sh A.C.Thakurta, director, EAG for his support and encouragement. Authors would also like to express appreciation to Shri R.S. Shinde, Shri P. Pareek, Shri V. Gaud, for their fruitful technical discussion. Author would also like to thank to Shri Satyadav & Shri Yunus khan for all the precision fabrication & testing work of the power supply.

## 5. REFERENCES

[1] R.S.Shinde, etal Technical Note: “Studies of Prototype Transmission line kicker magnet”, March 2009

[2] G.N.Glasoe and J.V.Lebacqz, “Pulse Generators”, MIT Rad. Lab. Series, vol.5, McGraw-Hill, New York, 1948

[3] F.B.A. Frungel, “High Speed Pulse Technology”,(Academic, New York,1965), Vol. I-III

[4] T. Kawakubo, H. Someya, “How to decrease the rise time of a current from a thyratron housing” ,Nuclear Instruments and Methods in Physics Research A306 (1991) 426-431North-Holland

[5] G. Nissibian “ Travelling wave kicker magnets with sharp rise and less overshoot” IEEE Trans on Nuc Sci Vol NS-26 No.3 June 1979

# RADIATION DAMAGE ASSESSMENT AND PROTECTIVE MEASURES FOR TILT METERS OF UNDULATORS IN INDUS-2 RING

Dilip Kumar Gupta[1*], Haridas G[1], Gautam Sinha[2], B K Sindal[3], D.P.Yadav[3] and M S kulkarni[1]

[1]Health Physics Division, BARC, Mumbai
[2]Accelerator Magnet Technology Division, RRCAT, Indore
[3]Ultra High Vacuum Technology Section, RRCAT, Indore

*Abstract*

Three permanent magnet type undulators (U1, U2 and U3) are installed in Indus-2 storage ring to generate synchrotron radiation (SR) with enhanced brightness in comparison with bending dipole magnets. These are tuneable sources and pole gap of the undulator needs to be varied to generate SR in the desired energy ranges with enhanced intensity. These undulators are equipped with the sophisticated instruments like tilt meters and encoders to ensure the proper movement of the magnet jaws for pole gap variation. During the operation of Indus-2, electrons of 2.5 GeV and 200 mA is circulated in a 172.4 m vacuum envelope around the ring. As a result of this bremsstrahlung x-rays and synchrotron radiation are produced which form the radiation environment near the ring [1]. The sensitive equipment like tilt meters and encoders are to be protected from radiation damage if the dose received by these devices from the radiation is beyond the damage threshold. A preliminary dose assessment at locations of interest, on all the three undulators are carried out by using $CaSO_4$: Dy Thermo-luminescent (TL) dosimeters. Measurement data indicates that the accumulated dose at U1 location is higher than U2 and U3. Suitable protection scheme involving radiation shielding was evolved and deployed. Dose measurements were carried out and the results obtained before and after the implementation of radiation protection scheme is reported in the paper.

## INTRODUCTION

Indus-2 is a 2.5 GeV synchrotron radiation source at Raja Ramanna Centre for Advanced Technology, Indore. The storage ring is housed in a shielded tunnel of width 5.5 m thick and is operational up to a stored beam current of 200 mA at 2.5 GeV.

There is provision for 26 beamlines in Indus-2, out of which 16 are in operational (regular and trial). Out of 26 beamlines 5 are insertion device based beamlines. Presently three undulators named at U1, U2 and U3 are installed at three separate straight sections of the storage ring.

An undulator is an insertion device which consists of a periodic array of permanent dipole magnets. In an undulator the permanent dipole magnets are arranged in a manner such that the magnetic field direction alternates periodically along the length of the undulator. Electrons traversing through the periodic magnet structure are forced to undergo sinusoidal oscillations and thus emit radiation [3]. Photograph of an undulator is as shown in figure-1. The synchrotron radiation produced in an undulator is very intense and concentrated in narrow energy band. This radiation is guided through beamlines for experiments at the experimental station.

*dilipgupta@rrcat.gov.in

During the operation of the storage ring radiation environment within the tunnel consists of bremsstrahlung photons of the energy up to 2.5 GeV. The bremsstrahlung x-rays are generated due to interaction of the electrons with accelerator structure during beam loss and with residual gas molecules in the vacuum chamber [3].

Sensitive components like tilt meters, encoders and motors in the undulators are prone to damage if continuously exposed to ionising radiation. A detailed dose measurement at components of interest on all the three undulators were carried out by using $CaSO_4$:Dy Thermo-luminescent dosimeters(TLD). The measurement was carried out to work out the magnitude of radiation dose which causes the damage.

The paper describes the measurements, analysis and the preventive measures adopted to protect the devices.

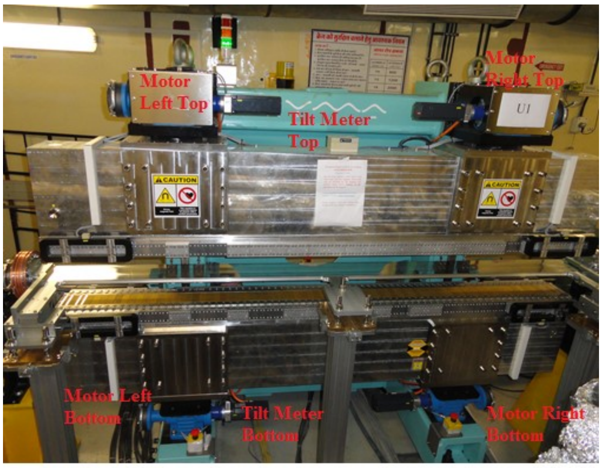


Figure 1: Photograph of undulator showing sensitive components

## MATERIAL AND METHODS

### *Calibration*

For evaluation the calibration factor, $CaSO_4$ : Dy TLDs were exposed to gamma radiation dose in the range from 4.1 mGy to 648.7 mGy from a Co-60 source. After exposure, the discs were read in a TLD reader (Intech, India). The calibration curve obtained is shown in figure 2. The calibration factor obtained is 76.96 counts/mGy, which is used for estimation of dose from exposed TL discs at I-2 tunnel .

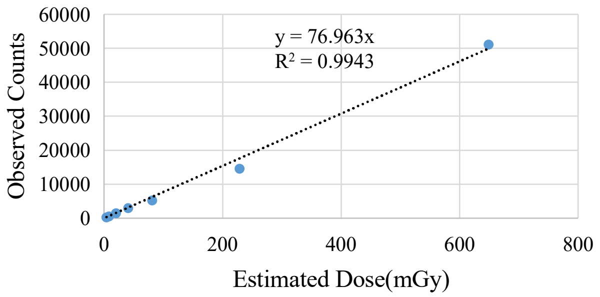


Figure 2: Calibration curve of TLD

### *Dose measurements*

In the first measurement $CaSO_4$:Dy TL discs were placed on the sensitive components in all the three undulators for the measurement of dose. Measurements were done on tilt meters and motors of U1, U2 and U3 on the top and bottom jaws. At each location two TL discs were used. The dosimeters were exposed to radiation emitted from the ring for 13 operating days. The exposed TLDs were analyzed using the TLD reader and the result are shown in Table -1.

As the tilt meter at U1 showed the maximum dose, integrated dose measurements on tilt meter and nearby areas of the undulator, U1 was carried out for a period of 16 operating days. This measurement was carried out to confirm the high dose observed during the first measurement and to find out the shield requirements to protect the tilt meter from radiation damage.

In order to see the effect of shielding on the dose at the tilt meter, a 9 mm lead shield of ~ 10 cm x 10 cm area was placed vertically in front of the tilt meter to shield radiation reaching the tilt meter. TLDs were placed symmetrically in the front and back side of the lead shield and also on the tilt meter. On the shield surface three set of TLDs were placed (at the top, middle and bottom). The TLD at the middle of the shield corresponds to the plane of the vacuum chamber between the jaws. Exposure was given for 7 operating days. The Schematic of TLDs installed at U1 is shown in figure-3 and the results of the measurement are given in Table -2 .

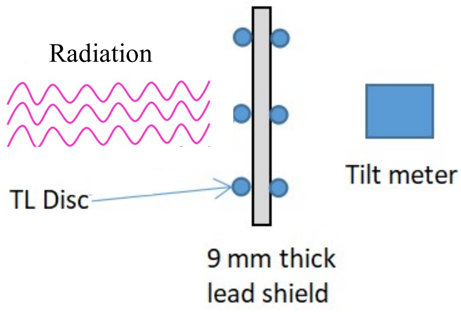


Figure 3: Schematic of TLDs installed on shield in front of tilt meter at U1

## RESULTS AND DISCUSSION

The dose recorded by the TLDs installed on undulators in ring tunnel is summarized in the Table-1 and Table-2. Table -1 gives the details of dose measurement and Table-2 presents the effect of shielding.

Table -1. Measured dose at different locations on undulators in Indus-2

| Location | Undulator | Measurement-1 | Measurement-2 |
|---|---|---|---|
| | | Total dose in 300 operating days ( Gy) | Total dose in 300 operating days ( Gy) |
| Motor Down(left side ) | U-3 | 1.15 | -- |
| Motor Down (right side) | U-3 | 1.38 | -- |
| Tilt Meter(up side) | U-3 | 1.62 | -- |
| Tilt Meter(up side) | U-1 | 1.85 | -- |
| Motor Down(left side ) | U-1 | 2.54 | -- |
| Motor Top(left side ) | U-3 | 2.77 | -- |
| Tilt Meter(up side) | U-2 | 3.23 | -- |
| Tilt Meter(down side) | U-3 | 3.46 | -- |
| Motor Down (right side) | U-1 | 3.69 | -- |
| Motor Top(left side ) | U-1 | 3.92 | -- |
| Motor Top (right side) | U-3 | 5.77 | -- |
| Tilt Meter(down side) | U-2 | 9.92 | -- |
| Tilt Meter(down side) | U-1 | 19.38 | 15.59 |

The integrated dose estimated from the first set of measurement for 300 days of operation in a year is found to be in the range 1.15 Gy to 19.38 Gy. Tilt meter placed down side on U1 and U2 is received significant high dose among the locations monitored. The data from the second set of measurement was comparable with the first set of measurement. As the radiation damage thresholds for sensitive component like transistor are reported in the range of 10 to 200 Gy [2], there are likely chances of damage to the tilt meter as it has sensitive electronic components in it.

Table-2: Measured dose at different locations around U1 after placing the shielding chamber

| Location | Dose in 7 operating days (Gy) | Dose reduction factor on account of shield |
|---|---|---|
| Pb shield_front side (top) | 799.93 | 5.12 |
| Pb shield_back side (top) | 156.30 | |
| Pb shield_front side (middle) | 103.81 | 4.34 |
| Pb shield_back side (middle) | 23.91 | |
| Pb shield_front side (bottom) | 33.65 | 5.17 |
| Pb shield_back side (bottom) | 6.51 | |
| Tilt meter_top (With out shield) | 0.45 | 3.75 |
| Tilt meter_top (With shield) | 0.12 | |

Table-2 indicates that a dose reduction of 4 to 5 is achieved with the insertion of 9 mm thick lead shield in front of the tilt meter where maximum radiation dose was measured. Based on the measurements with shield it is inferred that the dose received by the tilt meter is coming from the front direction, getting scattered and reaching the meter.

Based on these observations, a lead enclosure with 9 mm thick lead is designed, fabricated and installed on the tilt meters of all the three undulators. Figure - 4 shows the photographs of bare and shielded tilt meter.

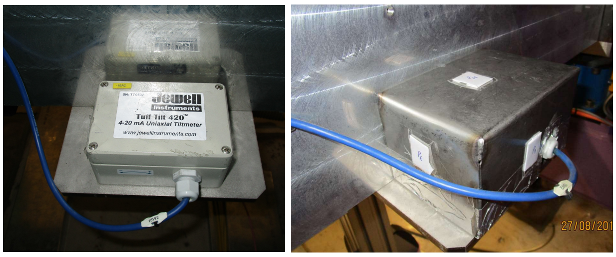

Figure 4: Photographs of bare and shielded tilt meter.

## CONCLUSION

Radiation dose on undulators installed in Indus-2 was carried out for assessment of damage due to radiation exposure. Independent measurements were carried out on sensitive components of the undulators. From the study it is concluded that

1. Bare tilt meter on U1 and U2 are receiving significant dose in comparison with U3.
2. A dose reduction of 4-5 is achieved with 9mm thick lead shield around tilt meters.
3. Shield enclosure made of 9 mm thick lead placed around the tilt meters is expected to protect them from the radiation damage.

## ACKNOWLEDGEMENT

The authors are thankful to Shri T. A. Puntambekar, Head, BDCSD, RRCAT and Shri R.K. Sahu, Head, IOD, RRCAT for the encouragement and support provided for the present work.

## REFERENCES

[1] www.rrcat.gov.in
[2] NCRP Report No.51 (1979)
[3] Herman Winick "Synchrotron Radiation Sources - A Primer"(1995)

# FPGA BASED CONTROL OF HIGH VOLTAGE POWER SUPPLY FOR GEM DETECTORS

Abhishek Singh, Sabyasachi Pathak, Dr. S.K. Thakur
Variable Energy Cyclotron Centre, Department of Atomic Energy, Kolkata, INDIA

*Abstract*

This article describes an FPGA based digital implementation of feedback control and operation of a high voltage Switch mode power supply (SMPS). A negative power supply of -5 kV, 2 mA DC voltage regulated power supply based on flyback DC-DC converter topology is designed and developed for Gas Electron Multiplier (GEM) detectors mostly used in nuclear experimentation. The SMPS control is simulated and control parameters are adjusted for desired performance using the MATLAB Simulink tool. MATLAB Simulink based Xilinx block sets are used for digital control loop and PWM logic simulation in closed loop. The feedback control system along with PWM generator is implemented on a Xilinx FPGA development board with required interfacing modules (ADCs, MOSFET driver, analog feedback isolation etc). The FPGA development board is programmed using VHDL language for digital feedback logic implementation.

## INTRODUCTION

The high voltage power supplies are used in nuclear experimentation for detection of various particles and radiations with the best possible accuracy, which requires the DC high voltage power unit to be as precise as possible. In modern nuclear experiments, the HV power supply of detectors needs to be equipped with more features than traditional power supplies, like detecting an overload fault, or a change in the detectors current and immediately trip it from the load within a few microseconds. This requires fast and reliable digital processing systems like FPGAs, DSPs etc which can handle the stringent timing requirements and accuracy of the nuclear spectroscopy systems. The modern power supplies are needed to be controlled remotely via the PC, which is another requirement of HVPS. In this project, the GEM detectors are biased by the HV power supplies, which need to be ramped up slowly upto the desired voltage level. GEM detectors are basically gaseous ionization detectors which consist of a micropattern structure of copper around the insulator [1, 2, 3].

## FLYBACK BASED HIGH VOLTAGE SWITCH MODE POWER SUPPLY

A switch mode high voltage power supply is implemented using flyback converter topology as it offers compact and isolated design for low power output. Since, the power supply output requires a high voltage with low current, the converter is operated in discontinuous current mode (DCM) i.e. magnetizing inductor current resets at the end of every switching cycle thus requiring lower value of magnetizing inductance as opposed to the continuous current mode (CCM) [4,5]. The output voltage of an ideal flyback converter operating in DCM mode is expressed as (See Eq. 1) below.

$$V_o = V_{dc} D \sqrt{\frac{RT}{2.5 L_p}} \qquad (1)$$

Where,
$V_{dc}$ = Input Voltage
D = Duty Cycle
R = Load Resistance
$L_P$= Magnetizing Inductance
T = Switching Time Period

A capacitor based voltage doubler circuit is used at the output of the converter, which in turn reduces the parasitic capacitance of secondary turns, thus reducing the spikes in the MOSFET current at the beginning of every switching cycle. The input of the converter is 50V unregulated DC which is derived from ac mains followed by the rectifier-filter chain. The switching frequency of MOSFET is 48 kHz, derived from the PWM output algorithm implemented inside the FPGA board.

The isolation of FPGA with MOSFET gate is achieved by Avago technologies based HCPL-090J IC, which provides the galvanic isolation between input and output of 2500 $V_{rms}$. It is then fed to a MOSFET gate driver.

The output voltage is regulated by varying the duty cycle of the MOSFET controlled by an FPGA based digital controller. Voltage and current feedbacks are isolated using linear optocouplers IL300 and then fed to a 2-channel ADC. The PWM output of the controller is isolated using digital isolator and then fed to a gate driver to drive the MOSFET.

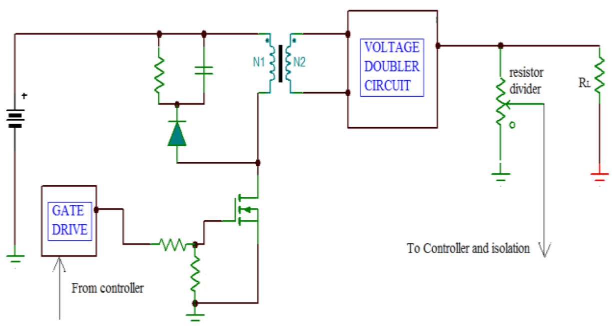


Figure 1: A -5kV, 2 mA flyback topology based HVPS

As can be seen from Fig.1, when the gate drive output is ON, the drain-source voltage is zero, and when it is in OFF condition, the drain-source voltage rises slowly to

DC input plus the output voltage divided by turns ratio preceded by a short duration transient spike of upto $2*V_{DC}$ due to the transformer primary leakage inductance.

## FPGA BASED FEEDBACK CONTROLLER SIMULATION AND IMPLEMENTATION

The control system algorithm for the voltage regulation is implemented on a reconfigurable platform which is FPGAs (Field programmable gate arrays). The FPGAs can efficiently map and implement larger digital circuits and algorithms in a concurrent manner, synchronized with the system clock.

*Simulation of the feedback control loop*

The simulation is done on a MATLAB Simulink platform using Xilinx blocksets. The PI (Proportional + Integral) controller and PWM (pulse width modulator) blocks are simulated using Xilinx blocksets, with flyback power supply unit as the plant of closed loop feedback system. Controller parameters $K_P$ and $K_I$ are chosen as integers values 5 and 2 respectively for optimum response time of 50 ms and overshoot of only 10 to 15%.

*PI controller implementation in FPGA*

The PI controller and PWM functionality is implemented on FPGA device using VHDL hardware description language. The control parameters of the PI controller can be updated online as can be seen from the RTL diagram in Fig. 2. The Good-gain method [6, 7] is adopted for tuning the PI controller using MATLAB. The digital feedback signal isolated by IL300 circuit is fed to the ADC card interfaced to FPGA, which is the "In2" input shown in Fig. 2. ADC card PMOD AD1 by Digilent Inc. is used which runs at 1 MSPS sampling rate. The set point is "In1" input which is driven by a state machine feeding the ramping data values at a rate satisfying the ramping rate set by the user.

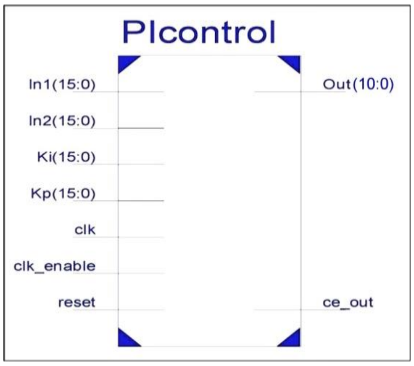


Figure 2: PI controller RTL diagram in FPGA

The PI controller output "Out" is given to the PWM module as shown in Fig. 3, which is a 11-bit data. The output of PI controller is limited internally to match the PWM input data width of 11-bits.

*PWM logic implementation in FPGA*

The PWM module is also implemented inside the FPGA, which is running at CLK_in clock synchronized with PI controller clock, while the output is synchronized by a different clock 'CLK', which is the PWM free running ramp clock chosen according to the required PWM output frequency, as can be seen from RTL diagram given in Fig. 3 below. The clock domain synchronization between the two clocks is maintained internally using a small depth FIFO block, which reads the output the data at PWM clock frequency, and accepts the input at 'CLK_in' clock domain. The PWM output of 48 kHz is derived from the FPGA system clock of 100 MHz and internal counter of 11-bits, which is same as data input width.

$$F_{pwm} = 100\ \text{MHz} / 2^{11}$$
$$= (100 \times 1000) / 2048\ \ \text{kHz}$$

which comes to approximately 48 kHz PWM output.

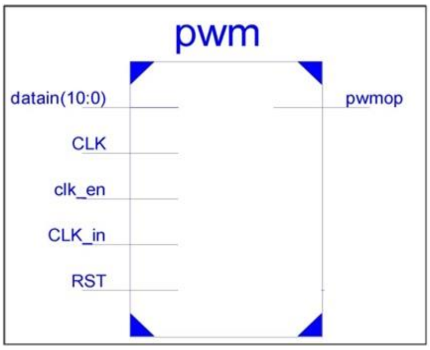


Figure 3: PWM controller RTL diagram in FPGA

*FPGA based implementation of control loop*

For our design implementation, the FPGA board chosen is Xilinx Spartan-6 based LX9 development board, with PMOD AD1 card for analog to digital conversion at a sampling rate of 1 MSPS. The analog feedback is isolated from the ADC board using Vishay semiconductor IL300 IC based opto-isolation circuit. The output from HVPS is first attenuated to a low voltage level of 5V using precise resistor dividers, followed by the isolation circuit, which is then fed to the ADC input of the FPGA board.

As shown by block diagram in Fig. 4 below, the ADC is fed with voltage feedback signal input. The digital equivalent of voltage signal is fed to the PI controller block followed by PWM block to generate the PWM signal at 48 kHz rate.

As shown in Fig. 4 below, the digital set point is given from the PC via RS-232 port, which is the digital equivalent of analog set point value. Apart from the control loop, there is a current and voltage readout logic inside the FPGA, which reads the current and voltage data, and sends it to PC via RS-232 link so as to be displayed on the GUI software.

The ramping rate and final set point also selectable from the GUI interface. The ramping rate is selectable as 20V/s, 40 V/s, 60 V/s and 80 V/s as per user requirements. Also, in the event of any failure or overcurrent situtation, the voltage is ramped down fastly at 100 V/s rate. Also GUI has a read output section for current and voltage output at the load, which updates automatically at regular interval of 500 ms to provide the online data without any user intervention.

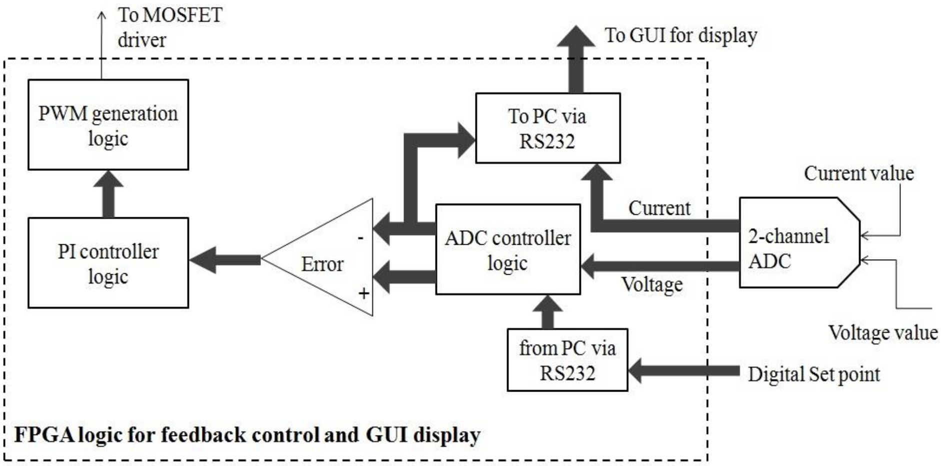


Figure 4: Block diagram of FPGA based feedback control system

Table 1: Specifications and results of implementation

| Specifications | Results |
|---|---|
| Voltage Ripple (at full load) | < 0.2 % |
| Load regulation | < 1 % |
| Line regulation | <1 % |
| Settling time (for 1 kV step input of set value) | 50 ms |

## CONCLUSION AND FUTURE WORK

As tabulated in the table 1 above, the data is gathered from the experimental results obtained from the implemented -5 kV, 2mA HVPS system developed for GEM detectors, which are acceptable to the user requirements. As is clear, that the total control system is efficiently implemented inside the FPGA board alongwith PWM generator, which is the challenging part. Maintaining the synchronization of PI control data output with the PWM clock was important for the safety requirement of GEM detectors. In the future scope, a multiple channel system of 4 such power modules are planned to be controlled using a single FPGA board.

## REFERENCES


[1] F. Sauli, "GEM: A new concept for electron amplification in gas detectors," Nuclear Instruments and methods in physics research A 386 (1997) 531-534, 6 Nov 1996, Available: https://www.lctpc.org/e8/e46/e47/

[2] Alexander Deisting, "Working principle and performance of GEM detectors" Biweekly HighRR Seminar: GEM Detectors – 12.07.2017 (A. Deisting).

[3] https://en.wikipedia.org/wiki/Gas_electron_multiplier

[4] R. W. Erickson and D. Maksimovic, "Fundamentals of Power Electronics".

[5] Ned Mohan, Tore M. Undeland, William P. Robbins, "Power electronics: Converters, Applications and Design".

[6] K. Astrom and T. hagglund, "PID Controllers: Theory, Design and Tuning".

[7] Finn Haugen, "Comparing PI tuning methods in a real benchmark temperature control system", Modeling, Identification and Control, Vol. 31, No. 3, 2010, pp. 79-91, ISSN 1890-1328.

# DESIGN AND DEVELOPMENT OF A 5 kW PULSED SOLID STATE AMPLIFIER AT 650 MHz FOR CONDITIONING AND PULSE CHARACTERIZATION OF SUPERCONDUCTING RF CAVITY AT RRCAT VTS

Ashish Mahawar*, Praveen Mohania, Raj Kumar Namdeo, Kunver Adarsh P. Singh, Deodatta Baxy and Purushottam Shrivastava

MICTL, Radio Frequency System Division, Raja Rammana Centre For Advanced Technology, Indore - 452013

*Abstract*

RRCAT has developed a vertical test stand (VTS) to test and qualify 650 MHz, multi-cell superconducting RF (SCRF) cavities[1]. At present, CW power up to a maximum of 250 W is provided via SSPA to test these cavities up to the design accelerating gradient. A 5-kW pulsed amplifier which can deliver in excess of 3 kW peak power at the cavity with up to 2 ms pulse width and 10% duty cycle has recently been developed to provide an option for fast conditioning and pulse characterization of cavities in the VTS. The amplifier has been developed using eight LDMOS transistors combined via planar combiners for final stage. The paper presents the design details and test results of the amplifier.

## INTRODUCTION

In the vertical test stand (VTS), qualification of cavities is carried out at 2 K to find the maximum accelerating gradient ($E_{acc}$) and quality factor $Q_0$. Accelerating gradient inside the cavity depends on the losses inside the RF cavity and the RF power that is provided to it. Due to cryogenic system limitations CW power is restricted up to 250 W, which is more than enough to qualify cavities. However, in some cases improvement in cavity has been observed with pulsed RF conditioning. In pulsed conditions, while the average power can remain lower to minimize losses, the peak power can still be higher. Since present amplifier can deliver only up to 250 W of peak/CW power, a new high-power pulse amplifier has been developed. The amplifier been designed to generate up to 5 kW of pulsed microwave power at 650 MHz, with up to 10% duty cycle. The amplifier is designed to be used as a gain block with gain of 15 dB and can be driven by existing amplifier in the VTS system. The amplifier is expected to help in conditioning of 650 MHz RF cavities in VTS tests and in characterization of cavities under pulsed conditions, if desired. The present paper elaborates the design and development of the said amplifier and to present the test results of the amplifier.

## AMPLIFIER CONFIGURATION

Amplifier has been developed by combining two 3 kW SSPA modules using Wilkinson combiner/divider. Each module has been developed using four 800 W LDMOS transistors, combined via Planar combiners.

Planar Wilkinson combiner/divider has been used in the design as it is simple and easier to realize on a planar circuit. It also offers very good phase and amplitude balance and isolation. Further, the 'planar' property allows these parameters to optimize more easily for a desired characteristic[4].

Fig.1 and Fig.2 show the scheme of the amplifier; one stage 1:2 Wilkinson divider is used to split input power into two parts which further divided into four parts using 1:4 divider; for each module. The power is then amplified by four individual amplifiers in each of the modules. The matching circuits of each module are fabricated using high dielectric constant (9.7) RF laminates to reduce size of the amplifiers. Since high reflections are normal in accelerator applications the output of the amplifiers is protected by using circulators at the end of each amplifier module. A 2:1 combiner then combines the power to provide 5 kW at the output. The overall gain of each amplifier module inclusive of losses due to combiners and circulators, etc. is 15 dB.

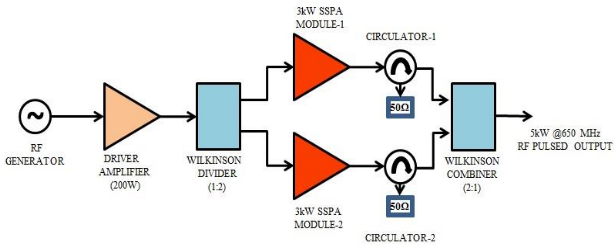


Figure 1: 5kW S-Band amplifier configuration.

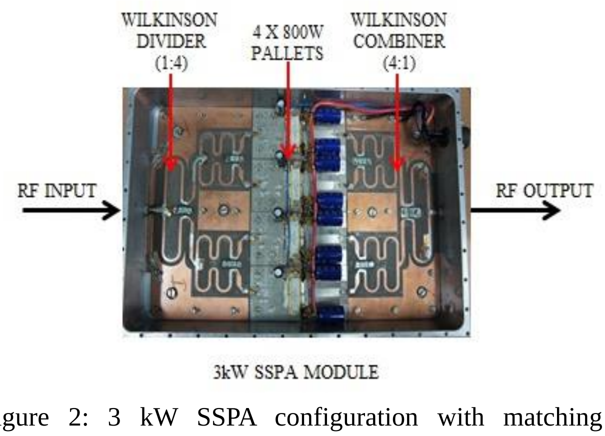


Figure 2: 3 kW SSPA configuration with matching circuits and 2-stage Wilkinson divider and combiner.

* amahawar@rrcat.gov.in

Each amplifier module can provide output power in excess of 3 kW and operates in class AB mode. As the duty cycle requirements are medium (10%), the heat generation is significant. In order to reduce heat load, devices are operated with low bias currents of ~ 80 mA, (also Drain voltage is kept at 48 V). Although this reduces linearity and gain but it increases stability of the amplifier. As the amplifier is to be operated with fixed output power, linearity is not important. A large capacitor bank of 338 mF has been used to compensate the pulse droop as the amplifier is expected to be used for long pulse widths of the order of 1 ms to10 ms.

In order to ensure better phase match between the four ports in each module, the combiner/divider has been fabricated using a substrate of dielectric constant 2.2 and thickness of 60 mils, thus allowing higher dimensional tolerance. Fig. 3 below shows the photo of the amplifier. The 1:2 divider and the combiners are mounted separately, while the 3 kW amplifiers mounted on heat sinks are placed side by side. Heat load in each module is ~ 300 W with 10% duty cycle. The amplifier being modular design allows the flexibility of using it as either a 3 kW or 5 kW amplifier. Also, in case of any future requirements, the amplifier can be upgraded to higher power with addition of more modules.

## TEST SET-UP AND RESULTS

Tests were carried out on the amplifier to determine its gain response, frequency response and pulse shape. A complete test set up consisting of signal generator, amplifier modules, Wilkinson divider and combiners, peak power analyser and programmable power supplies was prepared and the amplifier as assembled above was subjected to thorough testing.

The amplifier has been qualified for up to 50 Hz of PRR at 2 ms pulse width, although it can be operated with higher pulse width at low PRR or lower power also. It was subjected to several heat runs to evaluate its long-term stability and thermal performance. No oscillations, or pulse shape deterioration were observed. No observable rise in temperature was recorded in lab environment. Fig. 4 shows the output power pulse of the amplifier. Fig. 5 and Fig. 6 show the gain and frequency response of the amplifier, respectively.

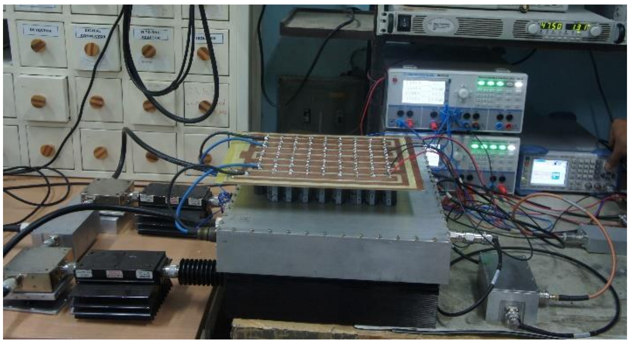

Figure 3: 5 kW amplifier assembled with combiner, divider and circulators during testing in lab.

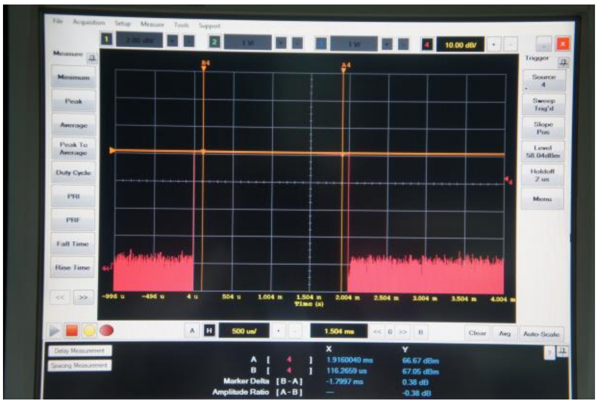

Figure 4: Output power of the amplifier with pulse width set at 2 ms. Output power is 67 dBm (5 kW), droop observed is ~ 0.38 dB.

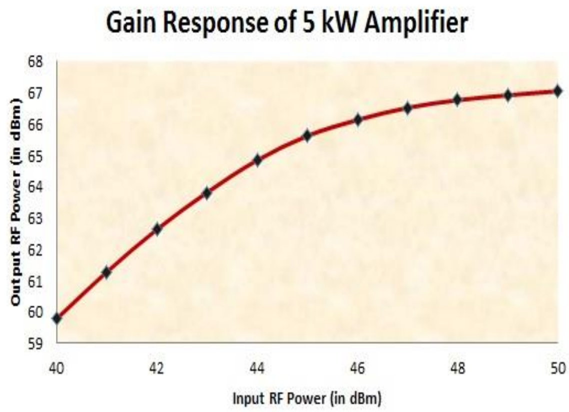


*Figure 5: Gain response of the amplifier.*

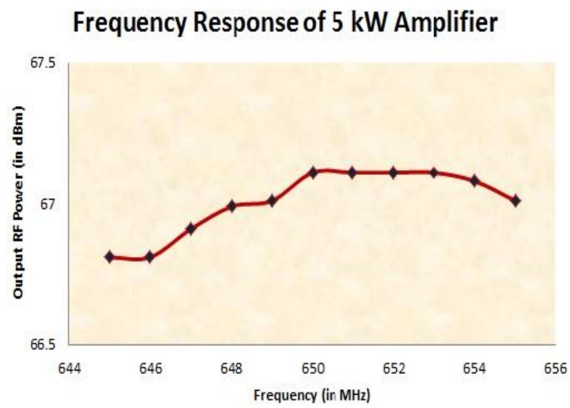


*Figure 6: Frequency response of amplifier.*

## CONCLUSION

The design and development of 5 kW SSPA has been done and it has been tested in the lab. The results are as expected. The amplifier will be incorporated in the VTS LLRF system as and when required, for cavity conditioning.

## ACKNOWLEGDEMENT

We are thankful to Shri Jitendra Parate & Shri Akhilesh Kumar Rajak for mechanical assembly work and Shri P.K. Bajpai for the assembly of the combiner/divider and amplifier modules. Their efforts were invaluable for this development work.


## REFERENCES


[1] P. Shrivastava, P. Mohania, K.A.P. Singh," Performance of the RF system for qualification of 650 MHz/1300 MHz SCRF cavities in VTS at RRCAT", InPAC2015, TIFR, Mumbai, Dec, 21-24, 2015.

[2] Mahawar A., Mohania P., Singh K.A.P., Namdeo R.K., "Design and development of S-Band, 2 kW pulsed solid state amplifier for energizing pre-buncher cavity of IRFEL injector" Proc. of InPAC-2018, RRCAT, Indore, Jan 9-12,2018,p.1040

[3] P. Mohania, A. Mahawar, Kunver A. P. Singh, R.Bhati, Purushottam Shrivastava, "Development of Solid State Amplifier Based High Power RF System for Testing SCRF Cavities in RRCAT VTS", HPRFM-2013, IPR, Ahmedabad, 4-6 September 2013.

[4] P. Mohania, A. Mahawar, P. Shrivastava, P. D. Gupta," A compact 10 kW, 476 MHz solid state radio frequency amplifier for pre-buncher cavity of free electron laser injector linear accelerator", Review of Scienctific Instruments (AIP), Vol. 84, No. 9, Sep 2013

[5] Praveen Mohania et. al, "Challenges of Frequency Measurement and their Control during Fabrication of 650 MHz, Five-Cell SCRF Cavities", this conference

[6] Manish Bagre et. al, "Experiance on fabrication of 650 MHz (β=0.92) five-cell SCRF cavities using Electron Beam Welding", this conference

[7] K.Adarsh P. Singh et. Al, "Analysis of uncertainty in measurement of quality factor and accelerating field gradient of 650 MHz, 5-cell super conducting RF cavity in RRCAT vertical test stand", this conference

# DESIGN AND DEVELOPMENT OF RF POWER DETECTION AND PROTECTION SYSTEM

Dheeraj Sharma*, Pritam S. Bagduwal, Nitesh Tiwari, Nitesh Mishra and Mahendra Lad
Radio Frequency Systems Division, RRCAT, Indore 452013, INDIA

*Abstract*

A typical RF system consists of low level RF (LLRF), high power RF amplifier, circulator, transmission line components and RF accelerating structures. Detection of any unsafe condition and protection of various RF sub-systems is essential for safe and healthy operation of such RF systems. This is one of the major and crucial functionalities of an LLRF system. A test setup is being developed in our lab to characterize the components of LLRF for superconducting cavity based RF systems. For this test setup an "RF Power Detection and Protection System" has been developed. This system consists of four RF power detection channels to monitor RF signals coming from field emission probe (FEP), RF antenna and directional coupler placed before RF cavity for forward & reflected power. This system also has four analog input channels for monitoring the signals of Photo Multiplier Tube (PMT), IR sensor and temperature sensors. Further it has sixteen digital input channels to implement interlocks for protection of super conducting RF cavity and associated sub-systems. In case of any unsafe condition it inhibits the LLRF output by operating a fast RF switch ensuring machine and personnel safety. The algorithm has been developed for both the CW and pulse mode of operation and realized on FPGA PXI card for real time monitoring, diagnostics and operation of fast RF switch in case of any fault. Design algorithm, its implementation and test results are presented in this paper.

## INTRODUCTION

With advancements in the field of Superconducting RF (SRF) cavities, they are becoming a popular choice for future particle accelerators. ISNS and IADS are two such future SRF accelerator projects being discussed in India. A typical SRF system has major components like superconducting accelerating structure, high power RF amplifier, circulator, transmission line, high power RF coupler and Low Level RF (LLRF) control system. Depending upon the requirement these SRF cavity based accelerators could either be a Continuous Wave (CW) machine like ADS or pulse machine like SNS. SRF cavities having high quality factor (Q) generally operate at high reflecting power compared to normal conducting RF cavities. Due to high RF power levels and large reflected power during operation of SRF accelerators, implementation of safety and protection features in such RF systems is very important. One of the crucial functionalities of an LLRF system is to provide a safety interlock mechanism to detect for any unsafe condition during operation and to ensure the healthy & smooth operation of the system. An "RF Power Detection and Protection System" for such functionality in LLRF, has been designed and developed in our lab. This system can continuously monitor signals (RF, Analog & Digital) coming from various sources at SRF accelerator. In the event of a fault condition it inhibits the RF signal going to the solid-state power amplifier (SSPA) by operating a fast RF switch. For real-time monitoring and hardwired operation of fast RF switch, the algorithm has been implemented on FPGA available as a PXI card. The algorithm has been designed to work for both, the CW and pulse mode of operation. With a very important advantage of easy expansion to accommodate more interlock channels (RF, Analog & Digital), the PXI platform also allows the same cards to be used along with the digital LLRF systems developed at RRCAT for its accelerator facilities like Indus-2 (CW RF) and IRFEL (Pulsed RF). A graphical interface has also been developed for configuration & diagnostics of the system to be done locally, and for data exchange with the main supervisory control system working remotely.

## SYSTEM ARCHITECTURE

Architecture of the RF Power Detection and Protection System has been illustrated in Figure 1. In a multi-slot PXI chassis, one PXI controller and one PXI FPGA card have been used. In case of any requirement to increase the number of RF, Analog or Digital channels more PXI FPGA cards can be used in the same chassis with a quick extension of the interlock algorithm. Description of various hardware units are as follows.

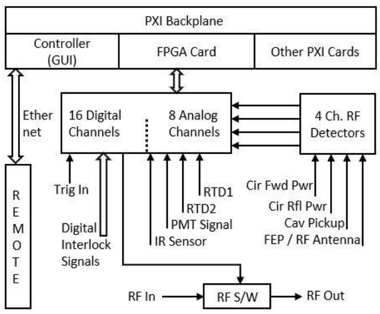


**Figure 1: Architecture of RF Power Detection and Protection System**

*dheerajsharma@rrcat.gov.in

### *RF Power Detection & Fast RF Switch Unit*

Figure 2 shows the "RF Power Detection & Fast RF Switch" unit. This unit consists of 4 logarithmic RF detectors (AD 8313) and two cascaded RF switches (ZSDR-230+). Logarithmic detectors are having large dynamic range of 70 dB and RF bandwidth (100 MHz to 2.5 GHz) allowing the system to be used for other RF frequencies also.

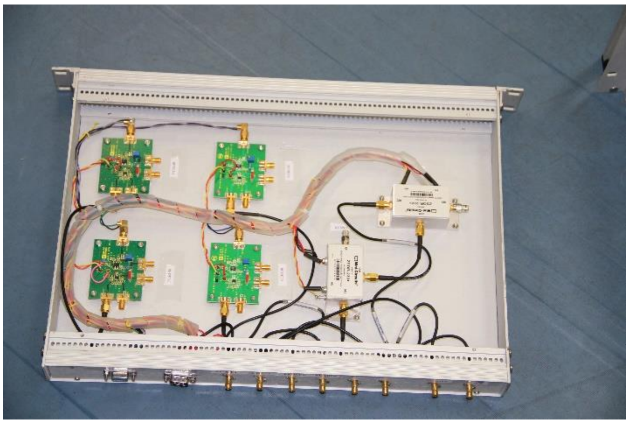

**Figure 2: Four Channel RF Detection & Fast RF S/W**

The response time of RF detectors is typically 40 ns full-scale, which makes the system fast for detecting changes in RF power levels. These RF channels can be used for detection and monitoring of the forward, reflected, transmitted, FEP or RF Antenna signals as required. For the RF output two RF switches are used in cascade to attain the RF signal isolation better than 70 dB in OFF condition.

### *Analog & Digital Channels in PXI FPGA Card*

A PXI based multifunctional & reconfigurable I/O module (NI 7841R) has been used for implementing the interlock algorithm. This module contains a user-programmable FPGA (Xilinx, Virtex-5 LX30) for fast and real-time signal processing of the interlock algorithm. The FPGA device has direct access to the analog and digital channels to ensure guaranteed and precise data capture timing. Compared to typical data acquisition hardware, in this module each analog channel has dedicated 16-bit A/D converter (ADC) for independent data acquisition up to FPGA which makes it suitable for implementing the time critical interlock systems. There are eight analog channels with sampling rate of 200 kS/s per channel in the module. Four of which are used for RF detector output signals and remaining four can be used to monitor the signals coming from Photo Multiplier Tube (PMT), IR sensor & temperature sensors at the cavity coupler and other places. There are 96 numbers of TTL compatible digital I/O channels available in the module. In the current GUI, 16 of such digital I/O channels are being used for many other interlock signals like machine access, cryomodule status, vacuum status, safety permission and signals from various sub-systems.

### *PXI Controller*

The PXI controller (NI PXIe-8135) used is an Intel Core i7, 2.3 GHz quad-core embedded controller having two 10/100/1000 BASE-TX (Gigabit) ethernet ports. The system GUI runs on this controller and can communicate with the main supervisory control system over fast ethernet link. Figure 3 shows the PXI chassis (NI PXIe-1082) with the controller and FPGA card having analog and digital inputs.


**Figure 3: PXIe Chassis with Controller & FPGA Card**

## PARALLEL EXECUTED ALGORITHM

The flow of the interlock algorithm has been shown in Figure 4. This algorithm has been implemented inside the FPGA giving advantage of parallel, fast and real-time processing capabilities for signal monitoring & control. This algorithm could be quickly extended to accommodate more analog and digital channels with the upgraded hardware module as per the requirement. All the RF, analog and digital signals are being compared parallelly with their trip limits or trip status. As soon as any faulty condition is detected it operates the fast RF switch and latches the faulty interlock signal. The algorithm has been designed to work for both the CW and trigger-based pulse mode of operation.

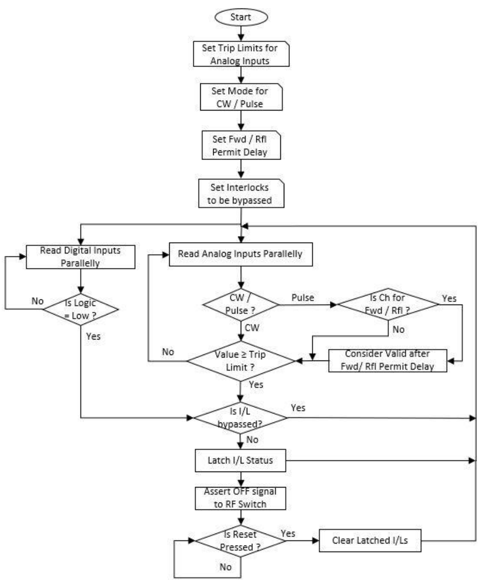


**Figure 4: Parallel Executed Algorithm in FPGA**

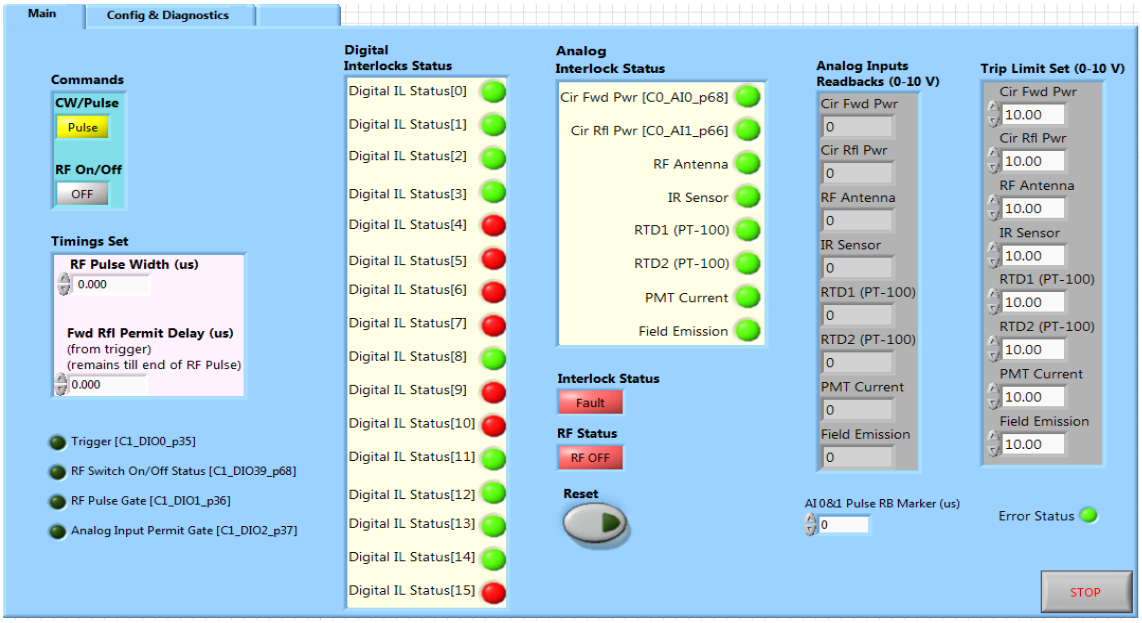


**Figure 5: Graphical User Interface (First Tab)**

## GRAPHICAL USER INTERFACE

A Graphical User Interface (GUI) has been prepared (Figure 5) to set, configure and observe various parameters of the interlock algorithm. CW mode or trigger-based pulse mode of operation can be selected. For the pulse mode of operation pulse width (in µs) can be set to generate RF pulse after the input trigger by operating the RF switch. The interlock permit window can also be adjusted for the forward and reflected power in terms of delay (in µs) from the input trigger till the end of the RF pulse. This creates a valid time duration for interlock to operate which is required to avoid undesired tripping and to ensure smooth operation in the pulse mode. For all the analog inputs the GUI shows their values and correspondingly a configuration table has been provided to set their trip limits. Provision for bypassing any interlock signal has been implemented and when done the corresponding interlock fault indicator is turned to appear as disabled. In the pulse mode of operation, a marker position (in µs) relative to input trigger can be set to show the values of analog signals at that point within the RF pulse.

## FUTURE WORKS

Work is in progress for adding extra functionality of preserving and sharing, high sampling rate data of the interlock signals around the trip condition (a short duration just before and after) for post analysis purposes.

## CONCLUSION

The RF Power Detection and Protection System has been successfully tested and is functioning at the lab as expected. After sensing any interlock signal for its fault condition, processing of algorithm and RF switch response time it takes about 4 µs to cut off the RF signal. Figure 6 shows the trip timing performance of the system where RF is cut off within 4 µs in the event of a fault occurrence.

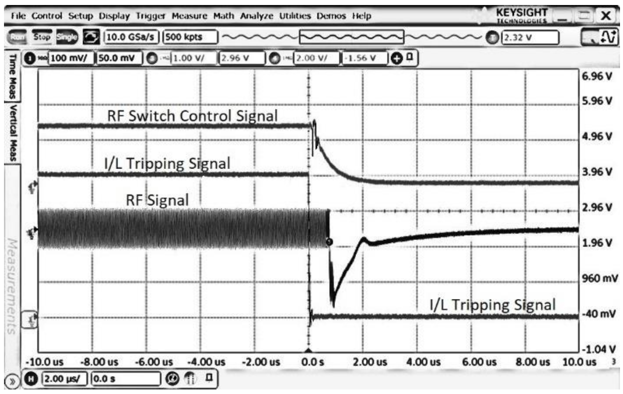


**Figure 6: Tripping OFF the RF Signal after Fault Detection**

## ACKNOWLEDGEMENTS

Authors gratefully acknowledge contributions towards development of the system from Shri D. Suresh and Shri Sudarsan Kishan of the Low Level RF Controls Lab (LLRFCL), RFSD at RRCAT.

## REFERENCES

[1] P. K. Kush *et al.*, "Design of Horizontal Test Stand (HTS-2) for SCRF Cavities at RRCAT", InPAC2011, New Delhi, Feb. 2011

[2] Sujo C. I. *et al.*, "Description of RF Protection Interlock System for LEHIPA", Inpac2015, Mumbai, Dec. 2015

[3] T. Petersen *et al.*, "Fermilab Cryomodule Test Stand Rf Interlock System", NAPAC2016, Chicago, IL U.S.A.

# RF SYSTEM FOR THE FREE ELECTRON LASER BASED DELHI LIGHT SOURCE

B. K. Sahu, S. Venkataramanan, A. Sharma, P. Singh, Y. Mathur, A. Pandey, B. Kumar, A.J. Malyadri, R. Kumar, S.K. Saini, S. Ghosh

Inter University Accelerator Centre, Arina Asaf Ali Marg, NewDelhi, India

*Abstract*

Photo cathode RF gun based compact Free Electron Laser facility named as Delhi Light Source (DLS) is under development at IUAC. The high power RF system for 2860 MHz photo cathode based electron gun consists of a 25 MW klystron operating in pulsed mode for a duration of 4 μsec (max) with repetition frequency up to 50 Hz. A solid state switch based modulator having pulse flatness suitable for beam stability requirement is used to power the klystron. The vacuum wave guide system to transport the RF Power is used to avoid any contamination of photo cathodes. The supporting fixture, cooling arrangement, electrical power connection with additional ground connection is being carried out as per operational requirements. The Low Level RF (LLRF) subsystem of the RF photo cathode is composed of cavity controller with an amplitude loop, a phase loop operating in pulsed mode along with protection for high power RF system. The present status of installation along with some initial test results is described in the paper.

## INTRODUCTION

A normal conducting photo cathode based RF gun is used to produce electron beam for the development of a compact free laser facility named as Delhi Light Source (DLS) [1]. The high power RF system required to power the electron gun consists of klystron along with suitable high power pulse modulator having a pulse flatness to match the requirement of the beam optics. The klystron supplies the required power to the electron gun. The klystron operates in the pulsed mode with maximum pulse duration of 6μs using suitable solid state modulator. Vacuum based wave guide components are used to transport RF power from Klystron to the RF Gun. Waveguide section, the supporting fixture, cooling arrangement, etc. has been optimised for trouble free reliable operation of the facility. Electrical power connection with additional ground connections has been established.

The LLRF subsystem of the electron gun complements the high power RF system using cavity controller consisting of an amplitude loop and phase loop operating in pulsed mode for entire pulse duration of the high power RF system. The choice of master clock and distribution scheme have been finalised.

## RF POWER SOURCE

The RF power source for the RF electron gun is based upon a 2860 MHz, 25 MW peak power klystron and modulator operating in pulsed mode with a duration of 4 μsec (max) . The technical specification of the RF system is listed in table-1.

**Table 1. Specification of the RF system**

| Sl. | Parameter | Value |
|---|---|---|
| 1 | Peak Output power | 25 MW |
| 2 | Average Output power | 5 KW |
| 3 | operating frequency | 2860 MHz |
| 4 | Bandwidth (-1 dB) | ± 1MHz |
| 5 | Output RF pulse duration measured at 3dB points | 0.2 μs to 4 μs |
| 6 | Pulse flatness within 4 μs | ± 0.3% |
| 7 | Maximum Operating pulse duration | 6 μs |
| 8 | Operating Pulse repetition rate | 1-50 Hz |
| 9 | Pulse to pulse stability | Within 0.01% |
| 10 | Efficiency at rated peak output power | ≥ 40% |
| 11 | Power Gain at rated peak output power | ≥ 50 dB |
| 12 | Output Wave guide | WR-284(Vacuum) |
| 13 | Output Microwave Flange | SLAC |
| 14 | Input/ Output VSWR | 1.4 :1 |

In the High Power RF systems, there are three subsystems whose details are given in the following:

1. ***Klystron:***

The klystron tube consists of an electron gun and a series of RF cavities. Typical S-band Klystron available from commercial manufacturers usually operate at a frequency of 2856 MHz [2] which was modified to 2860 MHz for the operation of DLS. In order to operate, the tube needs a source of voltage and current for heating the filament of electron gun and a DC power supply for solenoid magnets used for focusing the propagating electron beam through the tube length. The focusing electromagnet (Solenoid) has six coils which are energized by six different current from solenoid power supply. In order to produce high power output of ~25 MW, a voltage pulse in the order of tens of kilovolts (> 200 kV) and current of the order (>200 A) are needed for tube operation for which the tube cathode is connected to a step-up pulse transformer, located in the tank at the base of the assembly. The transformer coil is immersed in oil. A waveguide attached to the output cavity carries the RF power to the electron gun. A microwave ceramic window isolates the tube vacuum. The VSWR of the klystron tube is 1.4:1 to keep the klystron safe during RF conditioning.

Work supported and partly funded by DAE-BRNS

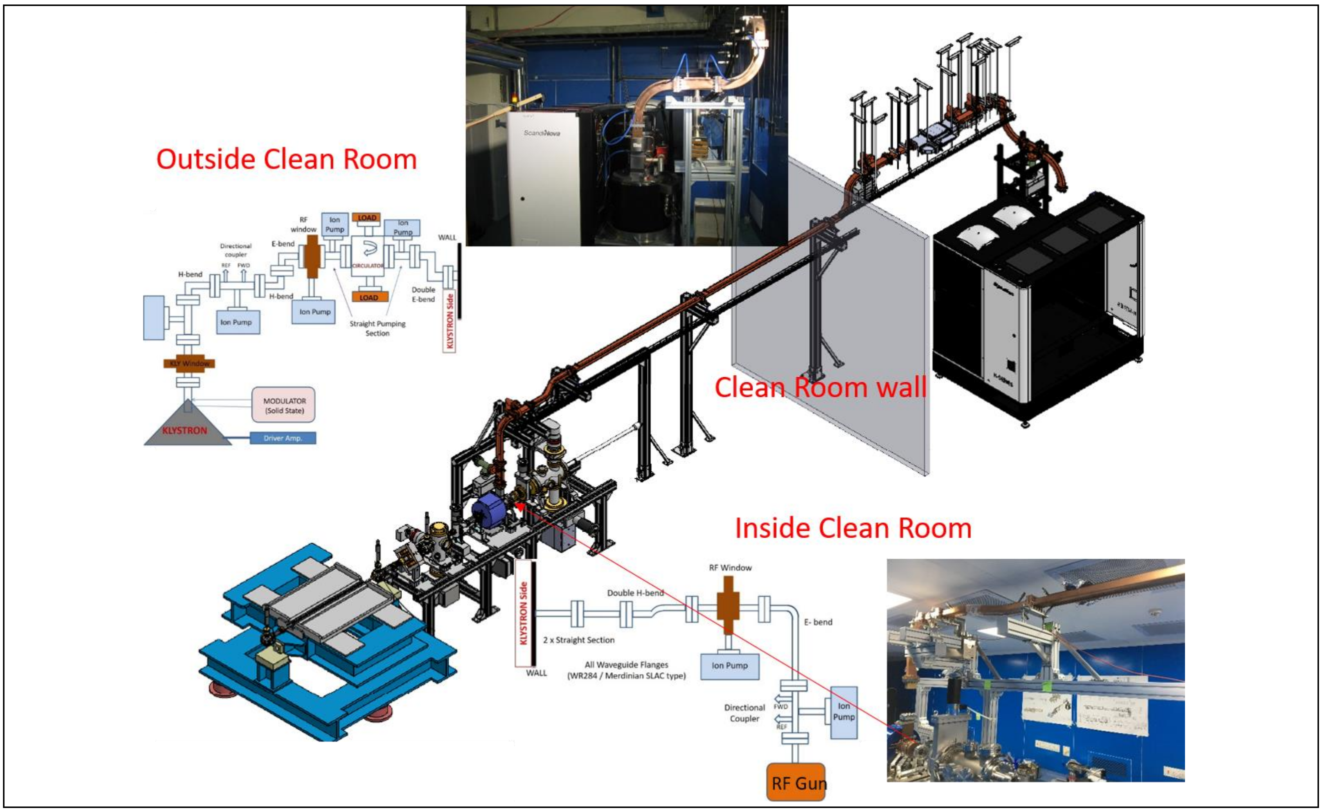


Figure 1. View of the High power RF system for DLS

***2. Modulator:***

The High Voltage (HV) pulse power source [3] consists of a HV pulse modulator, a pulse transformer and HV low inductance pulse cables connecting Isolated Gate Bipolar Transistor (IGBT) switching units and pulse transformer. It generates HV pulses of almost rectangular pulse shape required at the klystron cathode. The nominal pulse duration is 4 μs and the rise and fall times are less than 2 μs. Already during the leading edge of the high voltage pulse, when the voltage has reached 80% of the flat top level, the klystron can start to generate RF power. Although this part of the RF pulse does not meet the requirements regarding phase and amplitude stability for particle beam acceleration in the accelerator, it can be used to fill the cavities with RF. High Voltage pulse flatness is an important criteria to obtain a stable RF output to drive the RF gun. If there are a lot of ripples in the top of high voltage, that will get replicated in the RF as well. The flat top ripple is specified within ±0.3% in order to limit phase and amplitude variations of the klystron RF output during the beam acceleration. The pulse-to-pulse stability for the entire operation must keep the variation of pulses within 0.01%. Modulator control electronics is based on soft PLC system. All the important system level interlocks have been configured to stop the RF and High Voltage at different instances.

***3. Wave Guide system:***

The block Diagram of proposed RF distribution system for DLS is shown in Figure 1. The vacuum based waveguide (WR284) section is designed to have a power drop of ~ 25 W/m across the length. RF Wave guide section compromises of straight sections, E and H bends, directional couplers, RF windows and pumping sections. All the WR284 waveguide sections and special devices like RF Window, Directional Couplers etc. have Merdinian/SLAC type flange connector which is Male on one side and Female on the other side. Vacuum system with vacuum pump, power supply and controller is used to attain the necessary vacuum in the wave guide section. The most outlining parts of this waveguide system are the double E and H-bends which have been specially designed to cater the needs of height and the weight bearing capacity at the installation site. High Power Isolator consisting of circulator and load is required for the protection of klystron amplifier against the reflected power from the RF cavity [4]. The High Power Circulator which is also vacuum based and the load is rated for full power with short circuit at the output port and over the range of all possible phases of reflected power. The High Power Circulator and the load are planned to operate under all conditions of high power RF without arcing.

## TEST RESULTS

Initial integration of all the subsystems of high power RF system was carried out during Factory acceptance test (FAT) at Scandinova facility in Sweden [5]. The long straight sections could not be installed during FAT due to the space limitation. The whole RF delivery system was mounted on specially designed Aluminium channels and support structures. Each waveguide section was individually provided with efficient water cooling arrangement on either side of the body. Ion pumps were placed across the RF system at defined locations for maintaining the vacuum levels. Low power RF was fed into the RF Driver Amplifier using a RF signal generator through a triggered RF switch. The trigger for the switch was provided by same trigger generator. The output of RF switch was connected to solid state RF Driver Amplifier. The RF Driver Amplifier was used to provide necessary input to the klystron. The setup is shown in Figure 2.

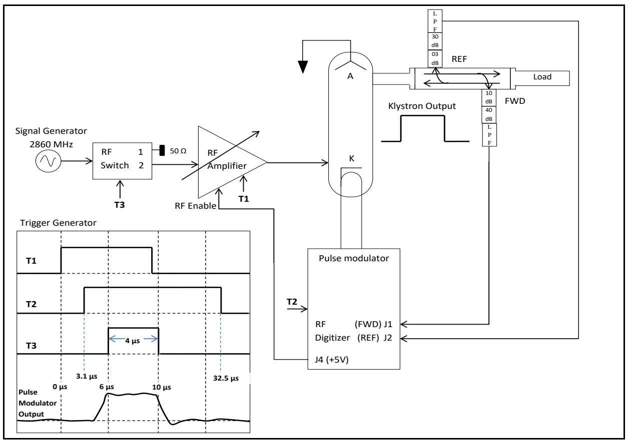


Figure 2: Set up for powering High Power RF system

The vacuum and RF conditioning of the system had been completed using the same set up. The necessary safety interlocks like reflected power, vacuum levels are done for the protection of the RF system. High Voltage pulse flatness is an important parameter to obtain a stable RF output for the RF gun. In order to achieve pulse flatness of 0.3%, tuning of pulse transformer was done using kanthal based resistive strips and copper inductance coils. Measured pulse flatness of ±0.29 % at full rated RF power is shown in Figure 3.

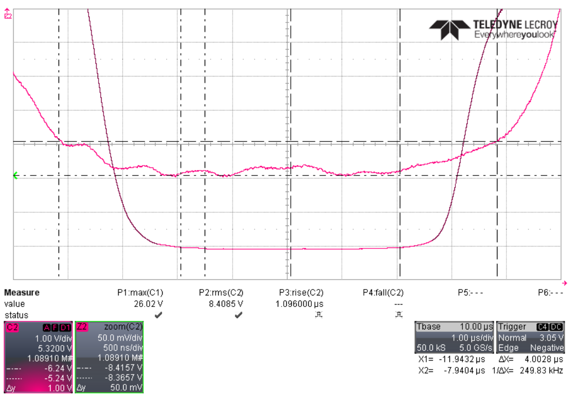


Figure 3: Measurement of Pulse flatness during testing

## LLRF SYSTEM

The requirements for low level RF (LLRF) control systems for the DLS are not only defined in terms of the stability of RF amplitude and phase but also with respect to the compatibility with high power RF system. The basic idea of any RF control system is based on feedback control in which the cavity field vector is measured and compared to the desired set-point. The resulting error vector is filtered and amplified before modulating the klystron drive and thereby, the RF power to the electron gun. However, during pulsed operation, the perturbations causes detuning and beam loading. Thus, the feedback can be supplemented by a feed-forward circuit which compensates the average repetitive error [6]. In addition, the RF gun field set-point can be implemented as a look up table to accommodate the time-varying gradient and phase during conditioning. The specification of a DSP/FPGA based LLRF system has been finalized to meet all the requirements of the DLS for the required field stability, reliability and operability. The desired amplitude and phase stability at the DLS are 0.1%, and 0.1°, respectively, which is sufficient for the stable production of electron beam and THz radiation recommended by beam optics calculation.

## PRESENT STATUS

High power RF system is being installed at IUAC with first section of wave guide consisting of H bends and the directional coupler. A good vacuum level has been achieved and the RF conditioning is started. The wave guide section from the RF Gun up to the circulator is also installed. The testing of high power RF circulator is being carried out at manufacturer site. The testing of the LLRF system will also be carried out soon. The final testing of the entire RF system with RF gun will be completed by the end of 2019.

## ACKNOWELDEMENT


The authors would like to acknowledge the help received from Prof. J. Urukawa, Prof. S. Fukuda of KEK Japan during the finalization of the technical specifications. Support and help received from Dr. G. Joshi and Dr. Manjiri Pandey, BARC, Mr. P. Srivastav, RRCAT and Dr. L.M. Joshi, CEERI, Pilani during finalization of RF system is highly acknowledged. The authors acknowledge the support and co-operation of FEL group members during installation. The encouragement and support received from Prof. A. C. Pandey is highly acknowledged.


## REFERENCES


[1] S. Ghosh et al. Nuclear Instruments and Methods in Physics Research – B 402, (2017) p. 358-363.

[2] D. Sprehn et al. Proceedings of the RF96, Kanagawa, Japan, April 8-12, 1996, P 91-99

[3] Kavita Dixit et al. Proceedings of the workshop on pulsed power modulators, 2006

[4] T. Taniuchi et. al, Proceedings of IPAC 2011 San Sebastian, Spain

[5] Technical Report IUAC/TR/AS/Ref-22/2018-19.

[6] Zhang, H et al. Proceedings of IPAC 2011, San Sebastian, Spain

# COMMISSIONING OF 1KW S-BAND MICROWAVE POWER GENERATOR AT IUAC

Yaduvansh Mathur[*, 1], U. K. Rao[1], Narender Kumar[2, 3], R.N. Dutt[1], G.O. Rodrigues[1]
[1]Inter-University Accelerator Centre, New Delhi 110067, India
[2]Department of Physics, University of Liverpool, Liverpool L697ZE, United Kingdom
[3]Cockcroft Institute, Daresbury Sci-Tech, Warrington WA2 4AD, United Kingdom

*Abstract*

A 1kW S-band, 2.45GHz Magnetron based Microwave power generator, procured from M/s Cober Muegge, Germany has been commissioned at Inter-University Accelerator Centre (IUAC) for 2.45GHz Microwave Ion source facility. It is water cooled and a continuous wave (CW) microwave power generator. It has been installed with all necessary interlocks for protection and safety of both the equipment as well as the operating personnel. This generator has replaced the 2kW microwave generator which was declared obsolete by its manufacturer. This generator is coupled to the ion source with isolator using the WR340 waveguide, DC break and many other components. The manufacturer has provided CANBUS communication to control and monitor its parameter remotely. It has no local control and power monitoring facility. Therefore, an indigenous controller was designed and interfaced with the system to control and monitors its parameters locally as well as remotely. The additional USB interface using Modbus also has been incorporated. This system has been commissioned and the facility is being used for various experiments related to materials science, atomic and plasma physics.

## INTRODUCTION

This low energy microwave ion source facility has been designed to deliver ion beams having energies in the range of a few hundreds of eV to a few tens of keV with beam currents in order of a few micro-amperes to a few hundreds of micro-amperes. In this facility, plasma is generated using the microwave heating technique. For this purpose, 1kW S-band C.W. water cooled microwave power generator has been commissioned. It is magnetron-based microwave power generator. Magnetron is crossed-field device because both magnetic and electric fields are produced in perpendicular directions so that they cross. This system was first tested on the dummy load for its rated full power for more than 24hours and then installed in the ion source facility. An indigenous controller was also developed to control and monitor parameters of microwave power generator both locally and remotely. It is interfaced to the ion source taking care of all the necessary interlocks.

*email: yaduvansh@iuac.res.in

## COMMSIONING OF MICROWAVE GENERATOR

A 1kW S-band Magnetron microwave power generator was commissioned for 2.45GHz ion source facility at IUAC [1]. It consists of magnetron head with integrated isolator and magnetron power supply. It is coupled to the ion source along with three stub tuner, directional coupler, 4 step ridge wave guide, DC break, RF window and WR340 waveguides and bends.

### *Magnetron Head*

The magnetron head is the heart of the microwave generator system. It has an integrated isolator to protect the microwave head from high reflected power due to load mismatch. It is a water-cooled structure. It requires minimum flow rate of 4l/min at 20-25degree Celsius with less than 4bar pressure. It uses a Panasonic magnetron with aluminium heat sink. It has a cavity magnetron structure.

The Cavity Magnetron has 8 cavities tightly coupled to each other. A thick cylindrical cathode is present at the centre and a cylindrical block of copper, is fixed axially, which acts as an anode. This anode block is made of a number of slots that acts as resonant cavities. The space present between the anode and cathode is called as Interaction space. The electric field is present radically while the magnetic field is present axially in the cavity magnetron. This magnetic field is produced by a permanent magnet, which is placed such that the magnetic lines are parallel to cathode and perpendicular to the electric field present between the anode and the cathode as shown in the figure1.

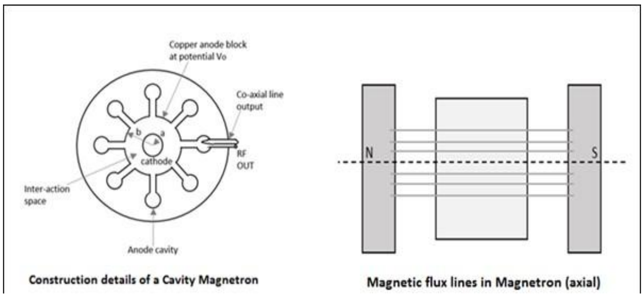


Figure1: Magnetron Magnetic Field Lines

The inside structure of the magnetron head cavity is similar to the structure [2] shown in the figure2.

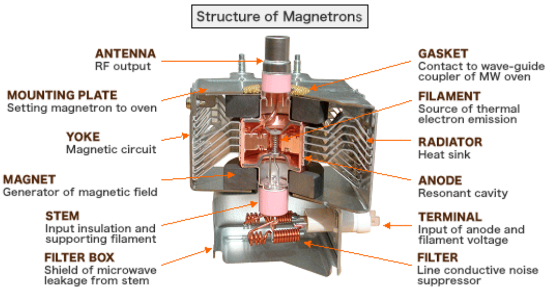

Figure2: Structure of Magnetron

### *Magnetron Power Supply*

Magnetron Power Supply of M/s Cober Muegge make model no. MX1000D-151KL has been used in this system. It is three phase 400V, 50Hz 1940VA water cooled high voltage power supply. It gives 4350V dc, 1392VA output. It also has an auxiliary output of 230VAC, 1A for filament. This power supply can be controlled and monitored remotely to vary the microwave output power.

### *Other microwave components*

This 1kW microwave generator is coupled to the ion source along with isolator 1.2kW isolator as shown in the figure3. It provides 23dB isolation to the magnetron head. It has an insertion loss of a 0.2dB. It is a water-cooled isolator.

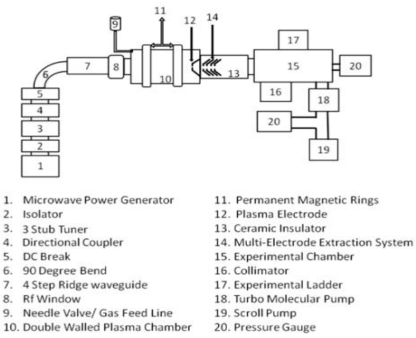

Figure3: Schematic Diagram for 2.45GHz Facility

After an isolator a three-stub tuner was installed for impedance matching of the ion source impedance with microwave power generator. The direction coupler of M/s Cober Muegge make model no. MM1010E-110AF was installed. It gives 4-20mA corresponding to 0 to 1kW microwave output power. Then we have a DC break to isolate the microwave power system from the ECR ion source potential which is at an extraction potential approx. 15kV), followed by it is a WR340 90degree E-bend. Microwave power is then coupled to the ion source using the 4-step ridge waveguide.

The simulation results as shown in the figure4 using a 4-step ridged waveguide structure show improved electric fields in the plasma chamber as compared to normal waveguide structures for coupling the RF power to the plasma chamber.

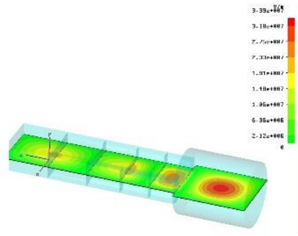

Figure4. Influence of a 4-step ridged waveguide on the electric field in the plasma chamber for $TE_{111}$ mode

### *Indigenous controller*

This 1kW microwave power generator of M/s Cober Muegge make has only the remote monitoring and control option. It does not come with any local control and local monitoring option. So, we have developed an indigenous controller which can controls and monitor this microwave power generator both locally and remotely. Figure5 shows the block diagram of the indigenously developed microwave controller. It is a 19inch 3U size unit. Using this we can monitor the absolute forward and reflected power locally on its display and can also monitor and log it remotely using the CANBUS and the MODBUS interface options. It has an USB interface option also. This controller inhibits the microwave output in the fault condition and latches it.

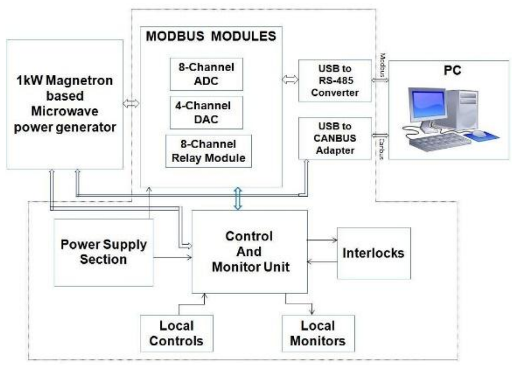

Figure5: Block Diagram of Microwave Controller

## TESTING OF MICROWAVE GENERATOR

This microwave generator was first tested for its full power with the dummy load to check its functionality. Then it was integrated with the microwave Ion source facility.

### *Testing with dummy Load*

Microwave generator was tested on the water-cooled dummy load using the CANBUS communication with GUI interface provided by the manufacturer. Figure6 shows the testing of microwave generator and the control software being used.


Figure6: Testing of Microwave Generator Using CANBUS

Microwave power generator was then tested using the indigenous microwave controller for its full rated power. All the safety interlocks were simulated during this test. Figure7 shows the test set-up block diagram. Figure 8 is the actual test set-up.

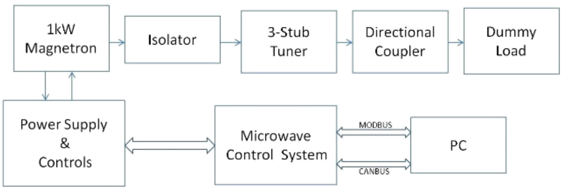


Figure7: Test Set-up


Figure8: Testing of 1kW Magnetron Microwave Generator using Microwave controller

Figure9 shows the test results. It shows the microwave generator output measured as per the control given from the indigenous microwave controller.

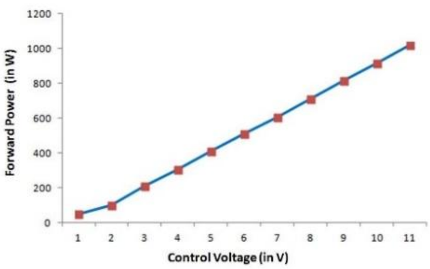


Figure9: Test Result-Forward Power Vz Controls

### *Testing with system*

This 1kW magnetron microwave power generator was then coupled with the ECR ion source system, Figure10.This system is used to generate the low energy high flux ion beams for performing various material science and plasma physics experiments.

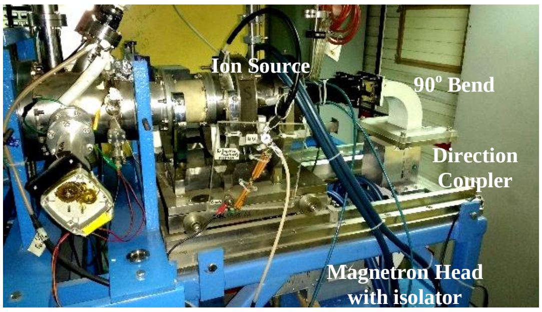


Figure10: Microwave Generator Coupled to the ion Source

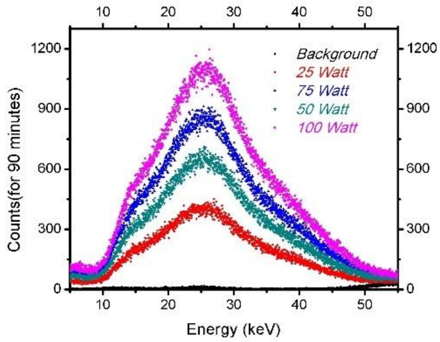


Figure11: X-ray Measurement Results [1]

Figure11 shows the x-ray measurement results obtained by generating the plasma in the 2.45GHz ion source facility using this 1kW microwave power generator.

## CONCLUSION

1kW, S-band (2.45GHz) magnetron microwave power generator has been successfully commissioned for 2.45GHz Microwave ion source facility at IUAC. It is operational and is being used to generate plasma for various plasma physics and material science studies.


## ACKNOWLEGEMENT

Authors would like to thank the mechanical workshop group and utility groups at IUAC for providing their support in accomplishing this work.


## REFERENCES


[1] Paper on “A compact 2.45 GHz microwave ion source and associated Wien filter based analyzing system for low energy ion beam facility” by Dr. Narender Kumar, G. Rodrigues, S. Kumar, Y. Mathur, U.K. Rao, R. Ahuja and D. Kanjilal, in InPAC2018.

[2] Webpage: https://steemit.com/steemstem/@proteus-h/how-the-cavity-magnetron-works-the-vacuum-tube-that-powers-microwave-oven-and-radar

# AUTOMATING RF CONDITIONING OF S- BAND LINEAR ACCELERATOR (LINAC) STRUCTURE

Gigi Joseph*, Sandesh R. Bhat#, Megha Kolhekar*, Anita Jadhav*, Mandar M. Vidwans, Sanjay N. Pethe, Sharad T. Chavan
Society of Applied Microwave Electronics Engineering & Research (SAMEER), IIT Bombay Campus, Powai, Mumbai – 400076.
*Fr. C. Rodrigues Institute of Technology, Navi Mumbai – 400703.

*Abstract*

SAMEER has been involved in the design and development of indigenous Linear Accelerators (LINAC). These structures are integrated using number of accelerating cavities, drift cavities, radio frequency(RF) feed window, target etc. During baking process where the complete tube is assembled, the oxide gas molecules trapped inside the accelerating structure get released. These oxide bubbles act as impurities that may hamper the LINAC operations at high power. This process of releasing the trapped oxide bubbles and other impurities (if any) that might be present is called RF- outgassing**.** This RF-outgassing process is carried out by applying the RF-power. The process is time-consuming and requires physical manpower to be present during the process. Hence, we propose automated monitoring of the LINAC vacuum during the outgassing process and accordingly sweep across the required RF-power as well the pulse repetition frequency (PRF). Automating this process will help to operate the system continuously without any manual intervention and simultaneously log in all the system parameters, which can also be used for debugging.

## INTRODUCTION

The linear particle accelerator is a long linear array of accelerating "cells" powered by a RF source in the megawatt power range and in the gigahertz frequency range[1]. It consists of a chain of number of resonant cavities coupled to each other. Apart from the accelerating structure, the LINAC consists of

1) Electron gun for injecting electron beam in the accelerator
2) Microwave window for feeding microwave power
3) Target for high energy X-rays emission.

A main advantage of the LINAC is its capability for producing high-energy, high-intensity charged-particle beams of high beam quality, and characteristics of the Linac include the following points.

- Strong focusing can easily be provided to confine a high-intensity beam.
- Because the beam travels in a straight line, so power loss can be minimum.
- Injection and extraction of the beam are simple.
- The LINAC can be operated at any duty factor, all the way to 100% duty or a continuous wave, which results in acceleration of beams with high average current.

### *Fabrication*

Oxygen free high conductivity copper is procured and the Linac cavities are cut using Computer Numeric Controlled (CNC) machine. Chemical cleaning is done since LINAC has to sustain ultra-high vacuum as well as hosting very high electric fields. It is followed with precise assembly, joining the parts (brazing), tuning the LINAC using the network analyser, mounting electron gun and sealing the LINAC. It is then put in a chamber where it will be pumped down to evacuate the sealed assembly to the desired vacuum level while it is kept at temperatures high enough to free up gases trapped on inner surfaces of the LINAC. This process is commonly known as Thermal outgassing or bake-out.

### *Thermal Outgassing*

The rationale behind the bake-out process is based on providing thermal energy to gas molecules adsorbed on the surface or absorbed in the inner surface of the Linac cavities to free these gases. To liberate these bonded molecules, the thermal energy provided should be higher than the binding energy for each gas. This binding energy is exponentially dependant on temperature. Thus, the more we increase the LINAC temperature, the more outgassing we achieve. Typical bake-out temperatures for copper LINACS would be in the range of 300°C to 500 °C. Typical gases that would be desorbed from the Linac's inner surfaces are $H_2$, $H_2O$, CO, $CO_2$, and $CH_4$[2]. Bake-out is a slow process that has a relatively longer cycle-time in the LINAC manufacturing flow compared to other processes. It may take 20 to 30 hours to attain vacuum levels of $10^{-8}$ to $10^{-9}$ torr.

### *High Power RF Conditioning*

Before we can begin supplying the full RF power into our LINAC we need to condition the inner surfaces of the accelerator so that it would be able to stand high fields without arcing or breaking down. Based on this consideration, the RF input power to the LINAC is increased slowly and gradually. This process is usually known as RF conditioning. Conditioning is a process of cleaning and smoothing the inner surfaces of the structure with the RF power, and driving the surface into controlled localized breakdown, and it also modifies those inner surfaces such that the Secondary Emission Yield is reduced [3].

*ggmariajoseph@gmail.com
#sandesh@sameer.gov.in

Increasing the pulse width should also be done very carefully, since the pulse width determines the amount of RF energy available to sustain an arc once it is initiated. This procedure is a slow and lengthy process. Hence, it is recommended to automate the process. In this technique, three parameters are controlled, namely:

- Average RF power
- Pulse repetition frequency (PRF)
- Modulator power

These parameters are incremented in steps until reaching the maximum power rating for the specific Linac being conditioned. This is done with the help a feedback system that continually monitors two feedback parameters: arc counts and ion pump current (indicating the vacuum level).

Uninterrupted delivery of X-ray or electron treatment requires arc-free operation of the medical accelerator. Dual Mode Multi Energy Linac being developed at SAMEER can deliver up to 18MeV of electron radiation as well as 6MV and 15MV photons. In an RF conditioning process, the pulse width, pulse repetition frequency (PRF), and peak RF power are automatically stepped up to a level higher than the maximum operational power rating [4]. This is done under the control of an optimizing technique. An algorithm is employed where the accelerator running conditions (arcing and vacuum) are being continually monitored and the above operating parameters are changed until reaching maximum programmed power. Arcing rates and vacuum levels are decisive control variables [5].

## OBJECTIVES

The objectives of the current work are:

- to automate the manual RF conditioning system
- to implement a complete control software with good operator interfaces and remote accessibility,
- to implement a data logging system to log the parameters
- to evaluate the performance of the designed RF conditioning system for the Linac tube.

## SYSTEM DESCRIPTION

### *Hardware Used*

For control and monitoring, we have developed Field-Programmable Gate Array (FPGA) based controller-Xilinx Spartan 6 LX9 as shown in figure 1. The concurrent glue logic for monitoring and controlling the field signals is implemented in VHDL. The intelligent firmware helps in fast response in case of faults and field signals crossing out of the desired limits. This controller is connected with the external world using dual channel redundant RS-485/ fibre optic channels using MODBUS protocol for communication. High speed ADC's sampling at the rate 4.5Mbps are used for the monitoring important signals, it communicates over SPI with FPGA. 16-bit DAC's are used for giving the required analog set points. In this project, MODBUS RTU (Remote Terminal Unit) mode is used as it uses binary coding and Cyclic Redundancy Check (CRC) error checking thus making it more efficient. It uses time gaps for silence in framing. The main advantage of using RTU mode is that it achieves higher throughput.

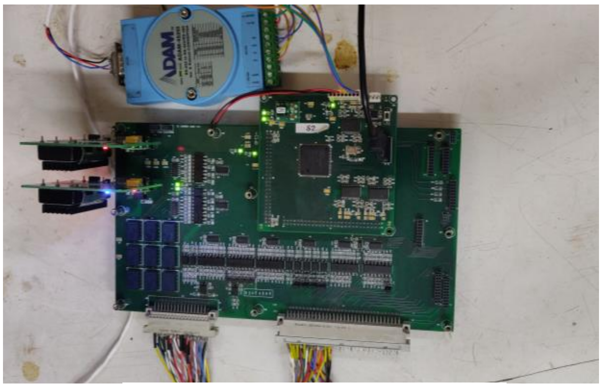

Figure 1: Xilinx Spartan 6LX9 used

### *Software used*

LabVIEW (Laboratory Virtual Instrument Engineering Workbench) is a graphical programming environment which has become prevalent throughout research labs, academia and industry. LabVIEW is designed to facilitate data collection and analysis, as well as offers numerous display options [6]. As shown in the figure 2, the developed graphical user interface has the following functions:

- Monitoring of PRF, Automatic frequency tuning voltage ($V_{tune}$), radiation dose and Linac vacuum level
- Verification of various interlocks and relays
- Setting of PRF in Hz.
- Increasing and decreasing of $V_{tune}$ voltage
- Acknowledgement of data packets with date and time is displayed.
- CRC generation and comparison is done thus validating the data packet on reception.
- Data logging in Comma-separated values (CSV) format.

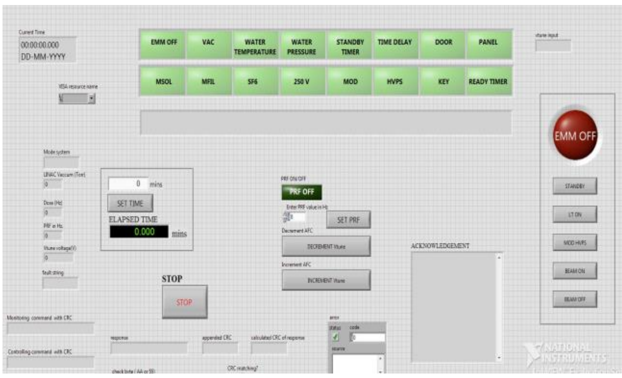

Figure 2: Front panel of the developed GUI

### *Implementation of the control design*

To control the whole RF conditioning processing efficiently it is necessary to design the control system software by focusing on the following facts –

- The algorithm of the software should be flexible for the future upgradeability.
- It should be modular, so that the debugging can be done easily with less time.
- It should have a Graphical User Interface (GUI).
- All the results and data should be archived for future analysis.

The GUI has been designed using producer consumer loop structure so as to acquire multiple sets of data to be processed in order. In the producer loop, the monitoring commands as well as controlling (user intervening) commands are framed along with appending CRC error check bits. These are then queued. In the consumer loop, these commands are extracted from the Queue and sent over the communication channel to FPGA. The response from FPGA as shown in figure 3 is read and both the received CRC and calculated CRC are matched and the response is further processed for control logic. The parameters are monitored and logged into CSV file at 100ms interval.

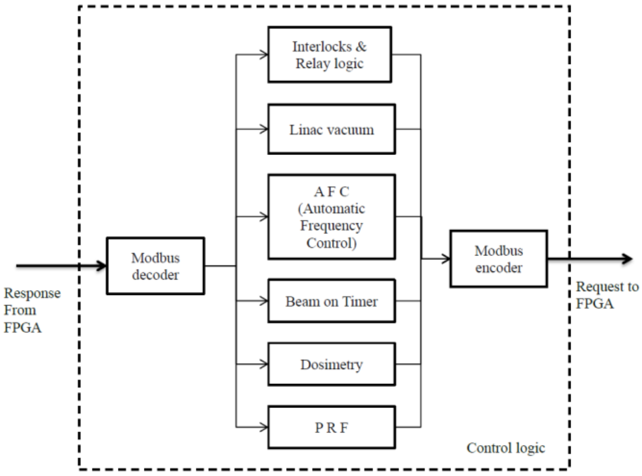


Figure 3: Functional Block diagram

Before starting the RF conditioning, all emergency interlocks must be off and the vacuum pressure should be checked to be between $10^{-6}$ to $10^{-9}$ torr. The flow and temperature of water inside the water chiller or cooling unit should also be checked. The temperature can vary between 22°C to 30°C. During the initial steps the machine will be in reset mode. After checking for water and vacuum parameters, then the machine enters the standby mode, where the command LT ON is given from the GUI and all the low power supplies are switched on and a full filament current is provided to thyratron. The lowest values of PRF and RF input power is set (10 Hz/1.8 MW).

The system warm up time of 20mins has to be elapsed before switching on the high power. The time is set for command BEAM ON or to switch on the high-power modulator. If the vacuum current is less than 5µA, then the PRF and RF power values are slowly increased step by step, until the vacuum current rises above 5µA and the system stops getting further kicks (i.e. arcing is under control).

Pressing the switch labelled ‘STOP’ in the main GUI screens finishes conditioning process and the modulator should be turned off. The data and graph for the power and vacuum should be saved for the future analysis. All the windows, programs, computers and instruments should be turned off.

## CONCLUSION

Thus, the automated RF conditioning system developed is expected to have following qualities:

- Smooth starting with gradual increase of the RF power.
- The control system will increase, decrease, hold or back off the RF power depending on the vacuum.
- RF power will be shut down during any kind of fault and the system will increase the power automatically after the fault condition is rectified.
- Auto cycling and constant power supplying should work efficiently.

## ACKNOWLEDGEMENTS

This work is supported by the Society for Applied Microwave Electronics Engineering & Research (SAMEER), Mumbai. The first author would also like to give full respect to the scientists from SAMEER for their great help in the experimental setup. The first author would like to acknowledge the assistance of her colleagues in the preparation of this paper.

## REFERENCES

[1] Hyper Physics, Retrieved September 2018,url: http://hyperphysics.phy-astr.gsu.edu/hbase/hph.html.

[2] Saamy Hanna, *RF Linear Accelerators for Medical and Industrial Applications*, Artech House; 1st edition, ISBN 13: 978-1-60807-090-9.

[3] ”*Physics And Technology Of Linear Accelerator Systems”,* Proceedings of the 2002 Joint USPAS-CAS-Japan-Russia Accelerator School, World Scientific Publishing Co. Re. Ltd. ISBN 981-238-463 -4.

[4] V.A. Dolgashev, et al., "RF Breakdown in X-Band Waveguide”., Proc. of EPAC 2002., June 2002.

[5] *Automated High-Power Conditioning Of Medical Accelerators*, Proceedings of EPAC 2004, Lucerne, Switzerland, S. M. Hanna, S. Storms, Siemens Medical Solutions USA, Inc., Oncology Care Systems Group Concord, CA 94520, USA

[6] Jovitha Jerome, *Virtual instrumentation using LABVIEW*, ISBN-978-81-203-4030-5, PHI learning Pvt. Ltd., New Delhi

# DEVELOPMENT OF HIGH PRECISION RF AMPLITUDE & PHASE MODULATION SYSTEM

Nitesh Mishra*, Pritam S. Bagduwal, Dheeraj Sharma, Nitesh Tiwari and Mahendra Lad
Raja Ramanna Centre for Advanced Technology, Indore, India

*Abstract*

RF systems are indispensable part of modern high energy particle accelerators. High stability of amplitude and phase of RF field are prerequisites in particle accelerators. Due to the stringent requirements of stability, high precision amplitude and phase measurements and their control become important. Voltage controlled RF attenuators and phase shifters introduce coupling in amplitude and phase of the RF signal which is not desirable and affects the RF system stability. In this paper development of an IQ modulator, high resolution DACs (16 bits, 100 MS/s) and VNA based high precision amplitude and phase modulation system is discussed. This system is able to modulate the amplitude well within resolution of 0.01 dB and phase well within resolution of 0.05 degree over a broad frequency range. Dynamic range for amplitude control is nearly 40 dB and phase control is 360 degree. The algorithm has been developed such that the amplitude and phase modulations are decoupled with high precision of control. The test results are presented in this paper. This precision modulation system has been used to characterize and finding out the noise sources in RF systems.

## INTRODUCTION

Primarily RF systems in particle accelerators are required for acceleration of charge particles to required energy. A typical LLRF system (shown in figure 1) consists of RF source, RF amplifier to increase the power level of RF signal, Circulator to protect the RF amplifier against any reflection, Directional coupler for power measurement and Accelerating structure like RF cavities. Charge particle interact with electric field in accelerating structures to gain the energy. Therefore stability of the RF field inside the cavity directly controls the performance of beam.

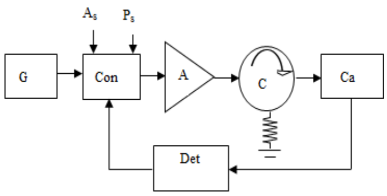


**Figure 1: Typical RF System with Feedback Loop**

Low Level RF control system is used to keep RF field stable inside the accelerating structure. A typical feedback system requires detectors for detection of amplitude and phase of RF signals, PI controller and an actuator which can control the amplitude and phase of drive RF signal. In feedback RF system, detected amplitude and phase is compared with set amplitude and phase and depending upon the error signal, a suitable control signal is generated. This signal drives the actuator to change the amplitude and phase of drive RF signal. Precision amplitude and phase control of RF signal is one of the very important aspect of any LLRF system design as it decides the precession with which the amplitude and phase of RF signal can be controlled. Conventionally Voltage Controlled Attenuators (VCA) and Voltage controlled Phase Shifters (VCPS) are used in RF systems.

In this paper, problems associated with conventional VCA and VCPS are mentioned and development of high precision RF amplitude & phase modulation system and its results are also presented.

*niteshm@rrcat.gov.in

## CONVENTIONAL VCA AND VCPS

VCA and VCPS are used conventionally for fine control of amplitude and phase of RF signal. VCA and VCPS are characterized in lab and block diagram of test set-up for VCA and VCPS characterization is shown in figure 2.

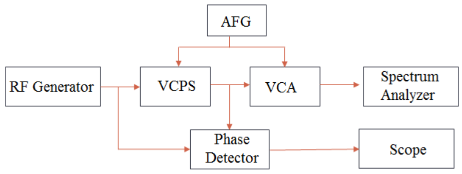


**Figure 2: Test Set-Up of Conventional VCA and VCPS**

### *Test Set-Up Results of VCA and VCPS*

Characterization of VCA and VCPS is done one by one. For the characterization of VCA, control voltage (from AFG) of VCA is varied and VCPS is held constant. While For the characterization of VCPS, control voltage of VCPS is varied and VCA is held constant. For full range of control voltage, amplitude and phase variations are observed .Results of test set-up of VCA and VCPS are shown in figure 3 & 4 respectively.

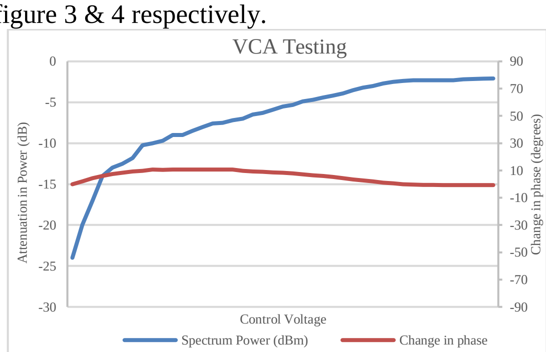


**Figure 3: VCA Characterization Plot**

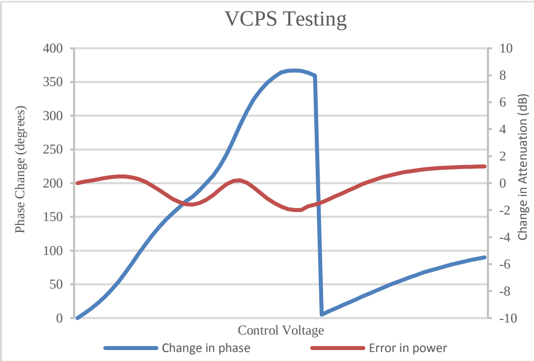


**Figure 4: VCPS Characterization Plot**

The results show, in VCA characterization, for a full range of attenuation, phase varies in between ±4° and in VCPS characterization, for a full swing of 360° phase change, attenuation varies in between ±1.5 dB. This amplitude and phase coupling could be a serious problem and it can limit performance of RF systems.

## HIGH PRECISION AMPLITUDE AND PHASE MODULATION

To avoid the above problems in conventional VCA and VCPS, a new high precision amplitude and phase system is developed. For this development, proper actuator and DAC (digital to analog converter) is to be selected. Selection of appropriate actuator is a crucial task in LLRF control. There may be numerous actuators to control amplitude and phase of RF signal, I/Q modulator is one of the most popular actuator as it can control both amplitude and phase. In I/Q modulator amplitude and phase of RF signal is controlled by changing in-phase (I) and quadrature-phase (Q) components of signal. A sinusoidal signal can be represented into their in-phase and quadrature-phase component as shown in the figure 5.

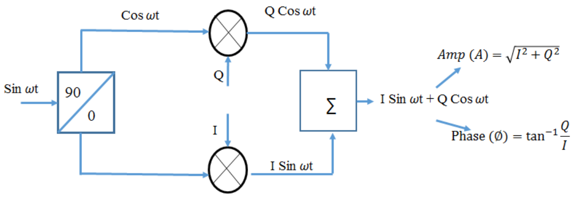


**Figure 5: In-phase and Quadrature-phase representation**

Selected I/Q modulator (AD8345) accepts the differential control inputs in the form of I ($I_p$ and $I_n$) and Q ($Q_p$ and $Q_n$) signal that modulates the amplitude and phase of incoming RF signal accordingly. Range of input differential signal lies in 0.7±0.3 V that is sufficient enough to control full 360° range of phase.

### *DAC Selection Criterion*

For a full swing of 360° phase control actuator needs 0.6 V full range *i.e.*

$$0.6\ \text{V} \sim 360°$$

For a resolution of 1° and 0.01°, minimum required voltage resolution will be:

$$\frac{600}{360} * 1000\ \mu\text{V} \sim 1°$$

$$\frac{600}{360} * \frac{1000}{100}\ \mu\text{V} \sim 0.01°$$

$$\mathbf{16\ \mu V \sim 0.01°}$$

Minimum number of bits (say n) required for 16 μV resolution for full scale range of ±1 V:

$$\frac{2\ V}{2^n} \leq\ 16\ \mu\text{V}$$

*i.e.* $$\boldsymbol{n \geq\ 16.93}$$

And 16 bits DAC will provide a resolution of

$$\frac{2\ V}{2^{16}} = 30.51\mu V$$

*i.e.* $$30.51\ \mu V \sim 0.02°$$

So, such a high resolution NI-6363 DAC (16 bits, 100 MSPS) is selected to produce fine voltage change. Flow chart of the designed algorithm is shown in figure 6.

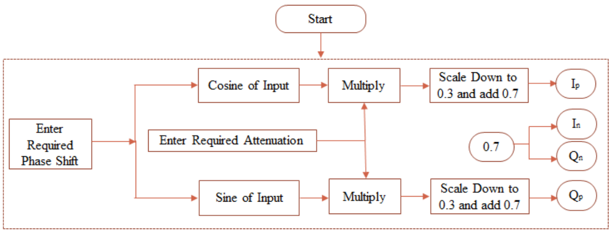


**Figure 6: Flow Chart of Designed Algorithm**

## PRECISION AMPLITUDE & PHASE MODULATION CHARACTERIZATION

For characterization of high precision amplitude and phase modulation with selected I/Q modulator and DAC, a LabVIEW based application is designed (figure 7) and a lab test set-up is developed as shown in figure 8. In test set-up, Vector Network-Analyzer (VNA) is used as both RF signal generator and RF signal detector.

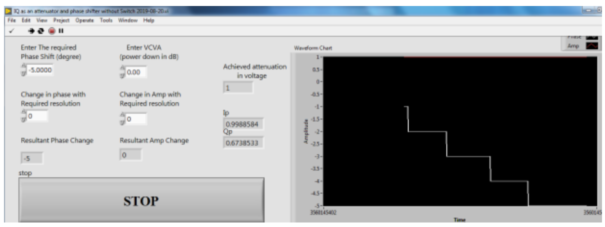


**Figure 7: Snapshot of LabVIEW Based Application**

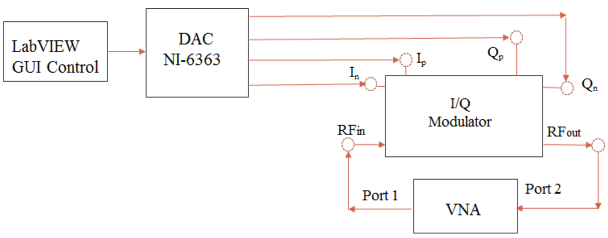


**Figure 8: Lab Test Set-Up**

*Test Set-Up Results*

Characterization results of high precision amplitude and phase modulation of RF signal at 650 MHz is presented however this system can be used for wide range of frequency band for 200 MHz to 1000 MHz. A continous data of 40 seconds to show resolution in amplitude and phase modulation is shown in the figure 9 & 10 respectively. This system is able to modulate amplitude in resolution of 0.01 dB and phase in resolution of 0.05°.

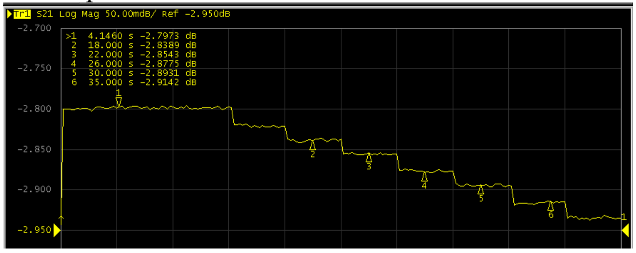


**Figure 9: Resolution in Amplitude Modulation**

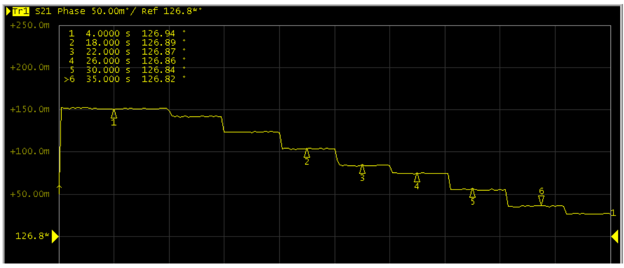


**Figure 10: Resolution in Phase Modulation**

To determine amplitude to phase coupling and full dynamic range of the system, characterization is done and a continous data of 40 seconds is shownig figure 11 &12 respectively.

Dynamic range of amplitude modulation at 650 MHz is found nearly 35 dB figure 9. In this full dynamic range of amplitude modulation, phase lies stable well with in ±0.01°.

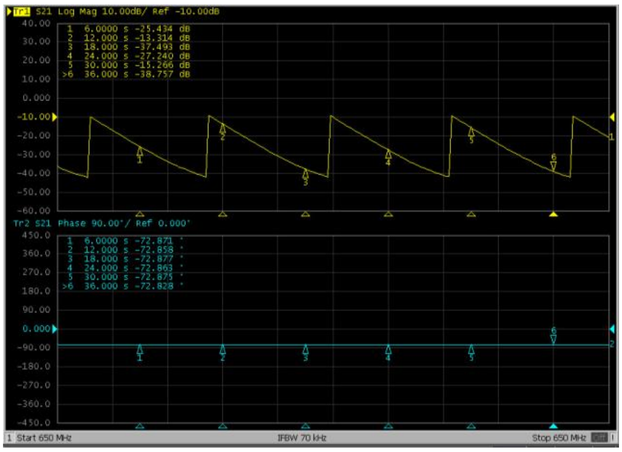


**Figure 11: Dynamic Range of Amplitude Modulation**

Dynamic range of phase modulation is achieved full 360° (figure 10) and in the full dynamic range of phase modulation, amplitude remains stable with in ±0.15 dB

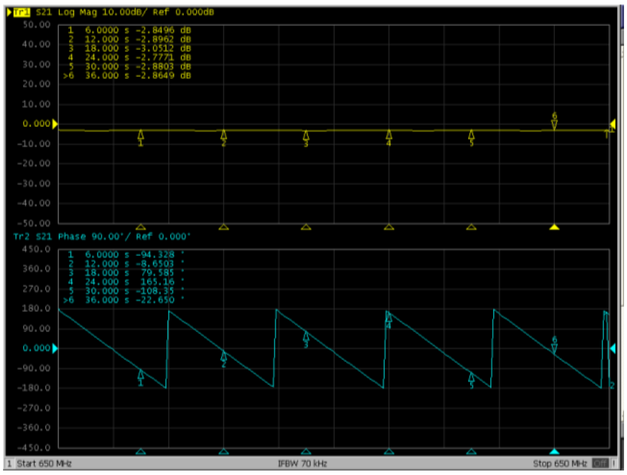


**Figure 12: Dynamic Range of Phase Modulation**

## CONCLUSION

In this paper, development of IQ modulator based high precision amplitude and phase modulation system is described. For a continuous data of 40 seconds, Test results of 0.01 dB resolution in amplitude and 0.05° resolution in phase is presented. Dynamic range of system is found nearly 35 dB in attenuation and 360° in phase. Amplitude to phase coupling is found nearly ±0.01° in amplitude modulation and ±0.15 dB in phase modulation.


## ACKNOWLEDGEMENT

The authors would like to thank our colleagues from the RF systems division at RRCAT Indore, especially Sh. Ekansh Mishra, Sh. D. Suresh and Sh. Sudarsan Kishan for their kind support.


## REFERENCES


[1] Nitesh Mishra, Pritam Singh Bagduwal, Nitesh Tiwari, Akhilesh Jain, Mahendra Lad, "Simulation, characterization and analysis of I/Q modulator for high precision LLRF systems" InPAC-2018, RRCAT Indore, M.P.

[2] Shoubhik Chakraborty, Dheeraj Sharma, Pritam Singh Bagduwal, Nitesh Tiwari, Mahendra Lad, P.R. Hannurkar, "I/Q detection scheme for indus-2 RF system" HPRFM-2013, IPR Gandhinagar

[3] Nitesh Tiwari, Pritam S. Bagduwal, M. Lad and P. R. Hannurkar, "Development of Prototype Digital LLRF system at RRCAT"InPAC-2013, VECC Kolkata.

# STUDY OF SHIELDING ADEQUACY AROUND INDUS-1 FOR ACCIDENTAL BEAM LOSS CONDITIONS IN TRANSPORT LINES

M K Nayak*[1], Ritu Rani[2], T K Sahu[1], Haridas G[1], R.K.Sahu[3], M.S.Kulkarni[1]
[1]Health Physics Division, Bhabha Atomic Research Centre, Mumbai-400085, India
[2]Atomic Energy Regulatory Board, Mumbai-400085, India
[3]Indus Operation Division, RRCAT, Indore-452013, India

*Abstract*
Indus-1 and Indus-2 are two electron synchrotron radiation sources (storage rings) for which a booster synchrotron (BS) is a common injector. Electron beam from BS is transported to the rings through transport lines, TL-2/3. Radiation field in the user hall (outside radiation shield wall) of Indus-1 storage ring during beam transport was found to be high when accidental electron beam loss occurs in the transport lines. To quantify the radiation level in the user hall and nearby control room, an experiment was performed by simulating the accidental beam loss at various transport line components at beam energy of 550 MeV. The measurement locations was judiciously selected to obtain the maximum radiation level outside the shield wall. A theoretical estimation of radiation level for the simulated beam loss conditions was also carried out at selected locations in the user hall and in control room. The experimental data is compared with the calculated one and are found to be in reasonable agreement. From the measurements, assuming an accidental beam loss for 10 min/day for 10 mA booster current, the maximum dose rate closer to the forward direction w.r.t the transport line, outside shielding works out to be 591 µSv/day. To reduce the dose rate to acceptable levels, additional shielding is suggested. The shield augmentation is found to be not required at wider emission angles w.r.t the transport line. The paper gives the details of the measurements, calculation and the conclusion drawn from the work.

## INTRODUCTION

Indus-1 and Indus-2 are two synchrotron radiation (SR) facilities at RRCAT, Indore. The facilities consists of 20 MeV Microtron, 450/550 MeV Booster synchrotron and 450 MeV Indus-1 & 2.5 GeV Indus-2 storage rings. Microtron & Booster synchrotron are connected through transport line -1 (TL-1) whereas Booster and Indus-1/Indus-2 are connected through TL-2/TL-3. Booster accelerates the electron energy from 20 MeV to 450 MeV for Indus-1 and up to 550 MeV for Indus-2. These storage rings emit synchrotron radiation which is used for various research applications. Bremsstrahlung radiation (BR), the main source of hazardous radiation, is produced due to interaction of electron beam with vacuum chamber or any other machine components during beam loss. They have broad energy spectrum up to the electron energy and angular dependent [1]. Apart from bremsstrahlung, photo-neutrons are also produced when BR photons having energy greater than the threshold for neutron production strikes the vacuum chamber. During beam injection into Indus-1 or Indus-2, two possible locations of accidental beam loss assumed are: Bending Magnet-2 (BM-2) in TL-2 and beam shutter in TL-3. The paper reports the investigation of the radiation level in the experimental hall of Indus-1 due to accidental loss of injected beam at these locations. Photon dose calculations and measurements are reported in this paper. As the cross-section of photo-neutrons production is low, typically of ~ mbarn/nucleon, they are not considered in the present study.

* nayak@rrcat.gov.in

## SOURCE TERM USED FOR CALCULATIONS

Source term is the maximum dose rate per unit electron beam power at a distance of 1 meter from a high Z thick target. It is expressed in Gy-m²/h/kW. Empirical relation for evaluation of angular bremsstrahlung source term for the calculations is given in equation (1) below.

$$\dot{D} = 2700\sqrt{E}\theta^{-1.5} \text{ (Gy /h-kW)} \quad \text{-------- (1)}$$

Where E is in MeV and θ is in degrees (> $20^0$)

The equation is valid in the electron energy ranging from 33 MeV- 5 GeV and for medium Z materials (Fe or Cu) [2].

## CALCULATIONS

### Assumptions

Seven reference points (point A to G) around Indus-1 experimental hall & control room (shown in figure 1) are selected to evaluate adequacy of radiation shielding around Indus-1 storage ring. For calculation of dose rate, accidental beam loss at beam shutter and bending magnet-2 location of transport line - 2/3 were considered. Following assumptions were used for theoretical calculation:

- Single point beam loss of extracted beam from booster.
- Two beam loss points considered are beam Shutter in TL-3 and bending magnet-2 in TL-2.
- Energy of electron beam – 550 MeV
- Booster current – 10 mA
- For photon and neutron source term calculation – Iron target is assumed for bending magnet and tungsten for Beam shutter.

### *Dose rate at reference points*

The theoretical dose rate at reference points around the shield due to accidental beam loss is given in table 1.

Table 1: Theoretical dose rates due to accidental beam loss at beam shutter & bending magnet-2

| **Reference points** | **Photon Dose rate (μSv/h)*** | |
|---|---|---|
| | **Beam shutter** | **Bending magnet-2** |
| A | 231.84 | 157.61 |
| B | 0.00 | 0.04 |
| C | 0.30 | 0.00 |
| D | 0.01 | 1.10 |
| E | 11.16 | 1.92 |
| F | 0.00 | 0.00 |
| G | 0.00 | 0.33 |

*for 10 mA booster beam current @ 550 MeV

## EXPERIMENTS

Experimental measurements were also carried out at selected reference points outside the shield. Measurements were performed using ion chamber based radiation monitors (ECIL make, model-AM4561A, 25 litre Nitrogen at 6 bars). Following were the experimental conditions:

- Accidental electron beam loss at bending magnet-2 in TL-2 at 550 MeV
- Accidental electron beam loss at beam shutter of TL-3 at 550 MeV
- Beam current of 2.5 mA (from booster synchrotron)

Seven reference points around the shield and control room are selected for the measurement. Experimentally observed dose rates are given in table 2.

Table 2: Dose rate during accidental beam loss at beam shutter & bending magnet-2 location

| **Locations** | **Photon Dose rate (μSv/h)*** | |
|---|---|---|
| | **Beam shutter** | **Bending magnet - 2** |
| Exp. Station of BL-1 (A) | 0.31 | 54.28 |
| Central hole of BL-1 | 1.73 | 842.67 |
| Exp. Station of BL-2 (B) | 0.14 | 0.79 |
| Exp. Station of BL-5 (E) | 0.31 | 0.38 |
| Indus-1 corridor | 0.02 | 0.02 |
| Control Room (F) | 0.15 | 0.17 |

*for 2.5 mA beam current from booster@ 550 MeV

Note: the alphabets A, B, E & F in parenthesis are the same reference points as in table 1.

## RESULTS AND DISCUSSIONS

The dose rate at all reference points is calculated and compared with experimental data. The present structural shielding is already considered for calculation and experimental data is recorded using area radiation monitors placed in Indus-1 experimental hall.

Table 1 shows that theoretical dose rate due to accidental beam loss at beam shutter at reference points A & E are above 10 μSv/h with the highest at location, A (231.84 μSv/h). Though the beam shutter is locally shielded it has not been considered for calculations. For the loss point at BM-2, location A (exp. area, BL-01) and E (exp. area, BL-05) shows significant dose rates, 157.61 μSv/h and 1.92 μSv/h respectively. However these dose rates are for a continuous beam loss, whereas the accidental beam loss in transport line usually occurs for a short time.

Table 2 gives the experimental data when 2.5 mA @ 550 MeV is allowed to be lost at beam shutter & bending magnet-2. The maximum dose rate observed in this case is at the central hole of BL-1, nearer to the loss points. Dose rate observed by radiation monitors were 1.73 μSv/h (beam shutter) & 842.67 μSv/h (bending magnet-2). The data indicates that among the loss points considered, loss at BM-2 showed the highest dose rate at central hole location. In this condition, exp. station of BL-01 indicated 54.4 μSv/h. Other locations showed ≤ 1 μSv/h for both the loss points.

Table 3 gives the comparison of theoretical and experimental data for the both accidental beam loss conditions at the selected reference points at 2.5 mA booster beam current.

Table 3: Comparison of theoretical and experimental dose rate (BR) for common reference beam loss points.

| **Beam loss points** | **Reference points** | **Theoretical Dose Rate (μSv/h)** | **Experimenta l Dose Rate (μSv/h)** |
|---|---|---|---|
| Beam Shutter (BS) | A | 57.96* | 0.31 |
| | B | 0.00* | 0.14 |
| | E | 2.79* | 0.31 |
| | F | 0.00* | 0.15 |
| Bending magnet-2 (BM-2) | A | 39.40 | 54.28 |
| | B | 0.01 | 0.79 |
| | E | 0.48 | 0.38 |
| | F | 0.00 | 0.17 |

*The dose rate is without considering the local shielding whereas the experimental data is with existing local shielding around the beam shutter and hence the difference.

The experimental data obtained for the case of beam loss at BM-2 is found to have good match with the theoretical data. However for the case of beam loss at beam shutter, the experimental data is not matching with the calculated value. This is due to the reason that the local shielding around the beam shutter is not considered in the calculation whereas measurement gave attenuated dose rate.

A radiation interlock provided at BL-1 and BL-05 with extraction trigger of booster which prevents such accidental beam loss in transport line. However, due to interlock failure, such loss may occur and to mitigate the consequences, additional shielding towards BL-01 & BL-02 shall be provided. Assuming such accidental loss for a duration of 10 min/day and for 10 mA booster current, the dose rate at central hole location (BL-01) works out to be 591 µSv/day (including neutron dose, less than 5%). To reduce the dose level to acceptable values (less than 80 µSv/day@10 µSv/h for shielding), 1 TVL of mild steel (10 cm) is suggested.

## CONCLUSION

Theoretical and experimental investigation of accidental beam loss at BM-2, TL-2 and beam shutter in TL-3 has been carried out. The following are concluded from the studies.

- Maximum dose rate is found during accidental beam loss at bending magnet-2 of TL-2.
- Radiation level due to beam loss at beam shutter is negligible due to local shielding around it.
- For accidental loss lasting for a duration of 10 min/day, to reduce the dose level to acceptable levels (less than 80 µSv/day), 1 TVL of mild steel (10 cm) is suggested.

## ACKNOWLEDGEMENT

The authors acknowledge the support received from Shri. A.C.Thakurta, Director, Electron Accelerator Group, RRCAT. We are also thankful to Indus shift crew members for support in experiment. We are also thankful to Shri Jamsinkumar, IOD, RRCAT for providing us drawing & useful data.

## REFERENCES

[1] Radiation protection design guidelines for 0.1-100 MeV particle accelerator facilities, NCRP No. 51.

[2] A.H. Sullivan., A Guide to radiation and radioactivity levels near high energy particle accelerators, 1992

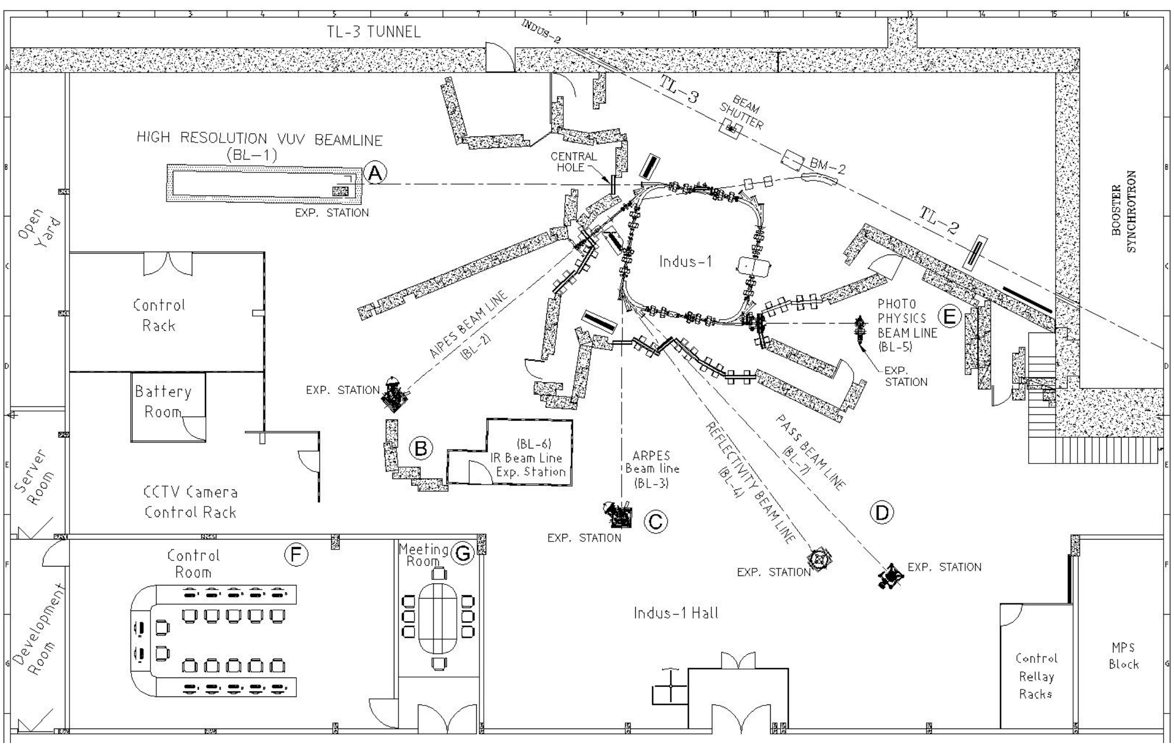


Figure 1: Layout of existing shielding with reference points (A – G) at Indus-1

# FABRICATION OF A 270° BENDING MAGNET CORE ASSEMBLY FOR ENERGY FILTERING SYSTEM OF ARPF, RRCAT

Brahmanand Sisodia[1 #], Sanjay Sharma[1], T. Veerbhadraiah[1], S.C. Vishwakarma[1], V. K. Bhatnagar[1], Sanjay Chouksey[1], G. Mundra[1], K. Sreeramulu[2], Ritesh Malik[2], S.G. Goswami[3], R. K. Soni[3], Pankaj Kumar[3], Jishnu Dwivedi[3].

1. Design & Manufacturing Technology Division; 2. Accelerator Magnet Technology Division;

3. Industrial Accelerators Division; Raja Ramanna Centre for Advanced Technology, Indore.

*Abstract*

A 270° Energy filtering system is being developed for Agricultural Radiation Processing Facility, RRCAT, Indore. This energy filtering system is necessary to limit the maximum energy of electron beam within the regulatory limits for irradiation of food and agricultural products. Total 270° bending of the electron beam will be achieved by two separate bending magnets (195° & 75°) installed on a common platform. The fabrication of magnet core assemblies for both 195° & 75° has been completed for the energy filtering system and their details of fabrication are discussed in this paper.

**Key Words** – ARPF, Travelling wave linac, Energy filtering system, Bending magnet, CNC Water jet cutting.

## INTRODUCTION

RRCAT has developed and commissioned two travelling wave Linacs of 10 MeV, 5 kW for irradiation of medical, agricultural and industrial products at Agricultural Radiation Processing Facility (ARPF), Indore. Food irradiation using ionizing radiations such as gamma rays, electrons and x-rays is a promising food processing technology that will not only reduce the large scale food spoilage, but also reduce food borne diseases by eliminating the harmful bacteria / organisms from the food & agricultural products. Electron linear accelerator as ionizing radiation source is used for food irradiation [1].

Regulatory limit is imposed on the maximum energy of electron beam for radiation processing facilities, so that, no induced radioactivity is produced in the irradiated products as well as in materials used in facility. The maximum energy of electron beam has been limited to 10 MeV in electron mode and 7.5 MeV in X – ray mode of irradiation [2]. Therefore, a 270° energy filtering system is being developed for ARPF and figure 1 shows the schematic diagram of the energy filtering system depicting the assembly details of 270° bending magnet. This dipole magnet is a doubly achromatic asymmetric type with central ($B_o$) field of 1751 Gauss & field uniformity ($\Delta B/B$) < 2 x $10^{-3}$ in the good field region of ± 30 mm on mean bending radius. This dipole magnet is of sector type with mean bending radius of 200 mm and pole gap size of 30.2 mm. The 270° bending of the electron beam will be achieved by two separate bending magnets of 195° and 75°. The details of the magnet core fabrication for both the magnets are discussed below.

## MATERIALS FOR MAGNET CORES

The low carbon steel (C ≤ 0.08 %) plates of 40 mm and 180 mm thickness have been used for fabrication of core assemblies for both the magnets. The magnet assembly parts (support structure, coil clamping elements etc.) have been made from non-magnetic materials such as austenitic grade stainless steel (AISI 316 L), aluminium.

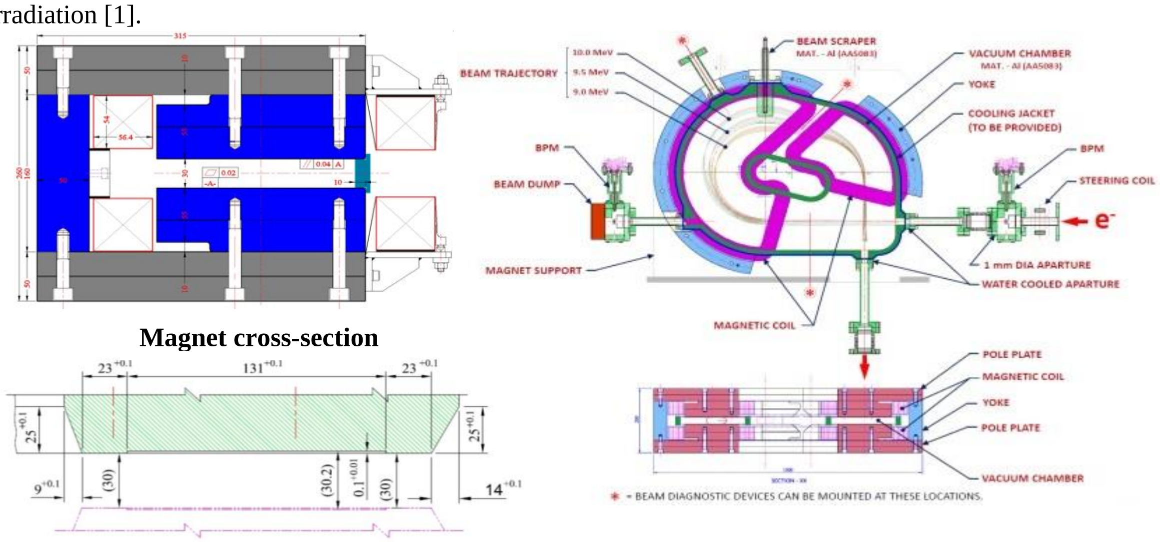


**Magnet cross-section**

**Details of pole profile**

Figure 1: Schematic diagram of energy filtering system with 270° bending magnet assembly details.

# bnsisodia @rrcat.gov.in

## MAGNET CORE FABRICATION

The yokes of both the magnets have been manufactured from 180 mm thick plate. Initially, a ring of 930 mm (OD) x 630 mm (ID) has been cut by gas cutting and machined to 830 (OD) x 730 (ID) mm x 165 mm (H) on vertical turret lathe. The specified dimensional tolerances and surface finish has been maintained on this ring. Similarly, the magnet pole assemblies have been made from four pieces of 40 mm thick plates by cutting of the rings having of 835 mm (OD) x 195 mm (ID). All the machined four pole plates have been machined and assembled together with a total height of 115 mm.

Abrasive water jet (AWJ) cutting has been adopted for cutting of the machined ring plates for making the sector assemblies of both the magnet cores. AWJ cutting is a non-conventional cutting process which utilizes high velocity slurry jet for cutting of materials. AWJ cuts produce no thermal effects on the workpiece i.e. the metallurgical structure is not altered. For this reason, this technology is often preferred to other beam technologies such as laser and plasma [3].

The profile cutting of 270° bending magnet (BM) components has been done from machined circular plates of 830(OD) x 195 mm (ID) on CNC AWJ cutting machine using MOST 2D nesting software. The CNC water jet cutting machine used for profile cutting has home position in rectangular coordinates and the MOST 2D nesting software also takes stock size in rectangular shape. To determine the home position of circular stock and desired profile cutting, a virtual stock size in rectangular shape has been assumed as shown in figure 2 and 3.

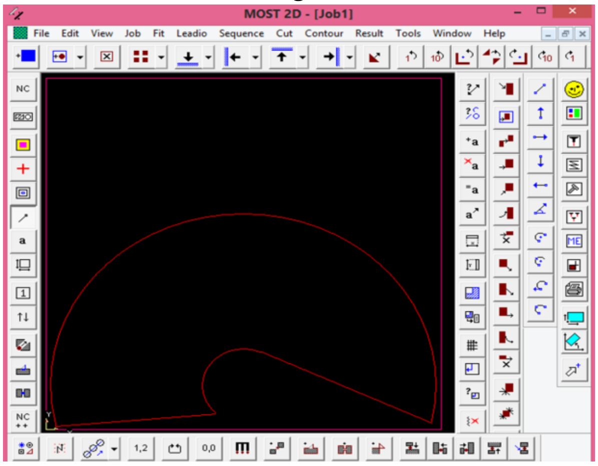


Figure 2: Nested Profile of 195 degree BM Sector.

KMT AWJ cutting calculator was used to estimate the cutting speed and water jet cutting pressure. Following cutting parameters have been used during the process:

- Water jet cutting pressure: 3500 – 4100 bar.
- Orifice diameter: Sapphire orifice of Φ 0.3 mm.
- Garnet: Almandine garnet of 80 mesh having hardness of 7 on Moh scale.
- Garnet mass flow rate: 350 – 450 g/min.
- Cutting speed: 4 - 20 mm/min.

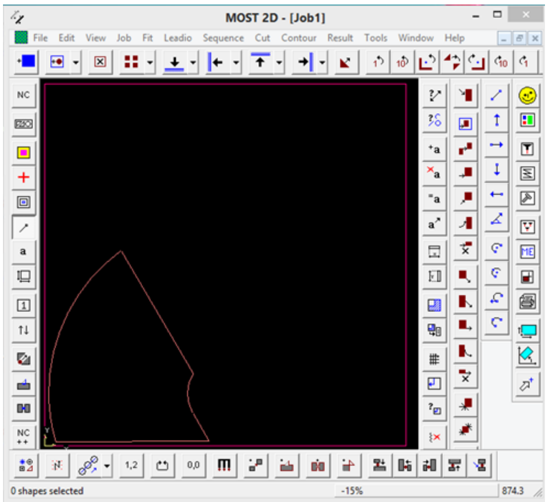


Figure 3: Nested Profile of 75 degree BM Sector.

Figure 4 shows the AWJ cutting of magnet sectors from the assembly of plates of thickness 115 mm.

Figure 4: AWJ cutting of magnet sectors.

The pole pieces and yoke pieces of 195° and 75°BMs in the thickness of 115 mm and 160 mm have been cut successfully on AWJ cutting and are shown in figure 5.

Figure 5: AWJ cut sectors of 270° bending magnet.

## MACHINING OF MAGNET CORES

To achieve the desired magnet parameters, the profile accuracies, entry & exit pole tapers have to be maintained as per the specified geometrical tolerances on the magnet cores. Also, the symmetry of top pole w.r.t. bottom pole in the core assemblies is equally important. After AWJ cutting of magnet sector shapes, doweling has been done on assembled magnet cores on 3-axis CNC milling machine to ensure their repeatability in the subsequent dis-assemblies & re-assemblies.

Then, finish machining of half assembly of the magnet cores, yokes and magnet supports have been done on 4-axes CNC Horizontal boring machine, 3-axis CNC milling machine, CNC vertical turret lathe. Coated carbide inserted face milling cutters, coated solid carbide end mill and ball mill cutters have been used for machining of sector faces, entry and exit profiles and radial taper profile on the magnet cores.

## ASSEMBLY OF MAGNET CORES

The final assembly of magnet cores of 195° and 75° has been carried out after the geometrical inspection of their half core assemblies and their corresponding magnet yokes. These assemblies have been done w.r.t previously made dowel holes on the assemblies. The overall size of the 195° BM core is 826 mm x 630 mm x 260 mm and of 75° core is 445 mm x 412 mm x 260 mm. The overall assembly inspection of both the magnet core assemblies has been carried out using CMM and found as per the specifications. Also, the pole gap inspection has been done with the standard precision bore gauges and found within ± 0.03 mm.

Finally, the magnet cores have been assembled with the respective excitation coils and shown in the figure 6.

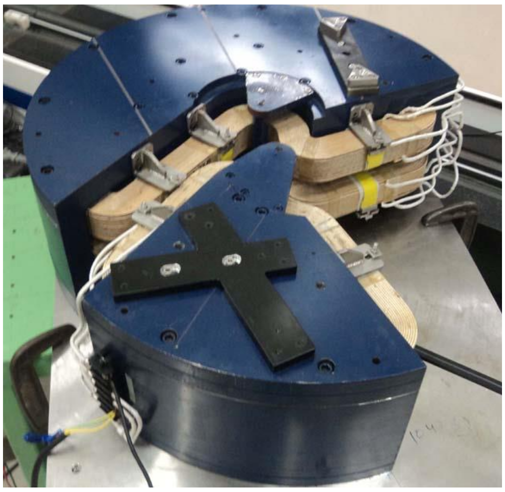

Figure 6: 270 degree bending magnet assembly.

## MAGNETIC MEASUREMENTS

The magnetic measurements have been carried out with hall probe along the electron beam trajectory. Initially, the field measurements have been done on individual dipole magnets of 195° and 75° and later on the assembled 270 degree magnet (magnet assemblies of both 195° and 75° with drift space) which is placed to form an achromatic system for further field measurements. Preliminary measurement results show the achievement of total bending angle of 270.04° on bending radius of 200 mm. The measured field uniformity ($\Delta B/B$) is within $2\times10^{-3}$ for good field region of ± 30 mm in both the bending magnets. The magnetic measurements are in progress for further investigation.

## CONCLUSION

The fabrication of both the magnet core assemblies of 195° and 75° have been completed with the specified geometrical tolerances. The initial magnetic measurement results satisfy the field quality requirements.


## ACKNOWLEDGMENTS

Authors would like to acknowledge the efforts of Shri Sunil Kumar Shukla, Shri Ashok Kumar, Shri Kushraj Singh and contributions of all other colleagues of DMTD, AMTD & IAD during manufacturing of 270 degree bending magnet. Also, they express their sincere thanks to maintenance team of DMTD for their support in successful fabrication of this magnet assembly.


## REFERENCES


[1] S. Das et al, ‘Development of magnets for beam diagnostic line of ARPF Linac, InPAC-2018, RRCAT, Indore.

[2] Pankaj Kumar et al, ‘Development of beam diagnostic line for ARPF Linac, InPAC -2018, RRCAT, Indore.

[3] Massimiliano et al, ‘Orifice coefficients evaluation for water jet applications’, 16th IMEKO TC4 Symposium, Sept. 22-24, 2008, Florence, Italy.

# MEASUREMENT AND INSTRUMENTATION SYSTEM OF DRIVER AMPLIFIER FOR 3 KW SOLID STATE AMPLIFIER

Arihant Kr Jain#, H K Pandey, Tapan Mandi, Dipta Pratim Dutta, Arup Bandyopadhyay, V Naik

VECC, 1/AF Bidhan Nagar, Kolkata-700064

*Abstract*

A 3kW/37.8 MHz solid state amplifier is under development for one of the rebuncher [1] of RIB accelerator beamline, which consists of 4 independent high power amplifier modules combined together to obtain 3 kW final power. A driver amplifier will be driving each amplifier module. This paper describes the details of driver amplifier and its instrumentation. The driver amplifier is developed using MOSFET MRF141G. The instrumentation is developed around an Arduino board. RF power detectors, current sensor and temperature sensor complete the sensing system for the amplifier. Signal conditioning circuitry has been designed to process the detectors and sensors signals to a suitable scale so as to improve measurement sensitivity. A TFT display unit displays the forward and reflected RF power, driver circuit drain current, temperature as well as VSWR. RF input has been interlocked with detectors and sensor measurement.

## INTRODUCTION

The existing amplifier to power the rebuncher is triode-based and has turned old enough to need regular maintenance and repair. Efforts are undertaken to replace it with Solid state amplifier of equivalent power output.

The driver amplifier presented in this paper will be used to drive 4 high amplifier modules combined together to obtain 3 kW final power, at 37.8 MHz. The output of driver amplifier will be split into 4 channels using a power splitter. The scheme of amplifier under development is shown in Figure 1.

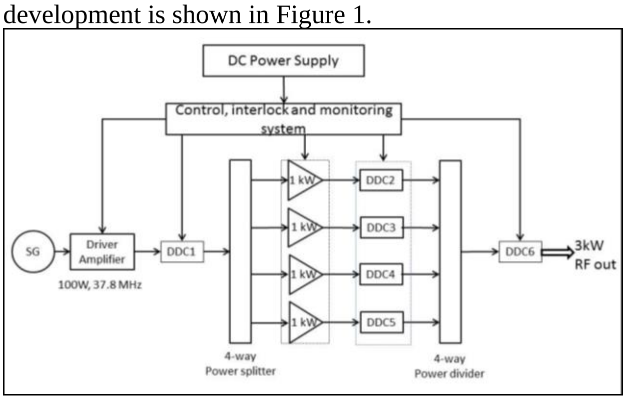


Figure 1: Scheme of 3 kW solid state amplifier

In this paper we are presenting the scheme for driver amplifier development and instrumentation system associated with it.

RF signal of 37.8 MHz frequency is fed to driver amplifier which enhances the power upto 100 watts. The output is then divided into 4 channels to input four 1kW amplifiers. Forward and reflected power at the output of driver amplifier is monitored using power detectors at directional coupler ports.

## 100W, 37.8 MHZ DRIVER AMPLIFIER FOR RIB REBUNCHER SSA

### *Scheme of Driver Amplifier*

The basic amplifier module of 100W, 37.8MHz consists of two stage amplification system. The first stage is based on RFHIC make RWP03040-10 amplifier which provides a gain of 40 dB. The second stage is based on MOSFET MRF141G which provides gain of 25dB. Important driver amplifier parameter as measured are listed in Table 1.

Table 1: Driver amplifier parameters

| | | | |
|---|---|---|---|
| Frequency, MHz | 37.8 | Gain | 65 dBm |
| Output power | 100W | Efficiency@100W | ~40% |
| Supply voltage | 28VDC | Quiescent current | 0.7A |

### *Instrumentation system and signal conditioning*

The amplifier instrumentation system (Figure 2) basically consists of a microcontroller (ATmega 2560), temperature sensor (LM35), hall-effect based current sensor (Honeywell CSLA2CD) and RF power detectors (AD8310 detector IC). ATmega 2560 is an 8-bit microcontroller with 10-bit ADC. The analog measurements are taken continuously even though display is updated at 500 ms.

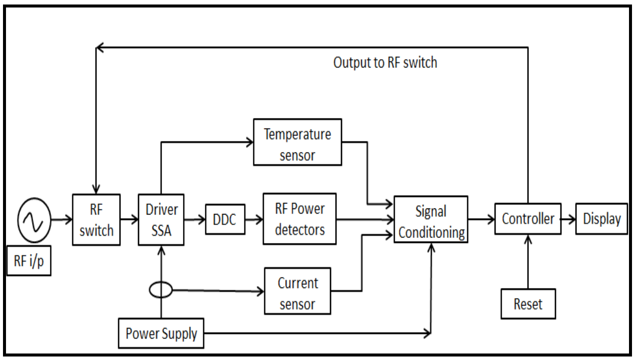


Figure 2: Amplifier instrumentation system scheme

A dual directional coupler (DDC) which is the most common device for measuring forward and reflected power is used. In DDC the power flowing in one direction of main coaxial line is coupled to the one port while the power flowing in the opposite direction is coupled to another port. Forward and reflected power coupled to DDC ports are sensed by RF power detectors. The

# ak.jain@vecc.gov.in

important parameters of DDC at 37.8 MHz are tabulated in Table 2.

Table 2: Directional coupler parameters

| DDC Parameters | Measured Value |
|---|---|
| VSWR | 1.067 |
| Insertion loss (dBm) | 0.11 |
| Forward coupling (dBm) | 49.37 |
| Reverse coupling (dBm) | 47.91 |
| Directivity (dBm) | 30.4 |

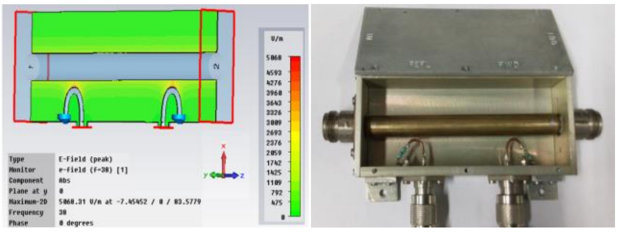

Figure 3: Dual directional coupler (simulation and developed)

The driver amplifier and its processing circuitry are placed inside a single rack. Due care has been taken to avoid electromagnetic interference with proper grounding and power supply isolation for RF and instrumentation circuit.

The detector system has been designed to measure power in the range of 10 to 100W.

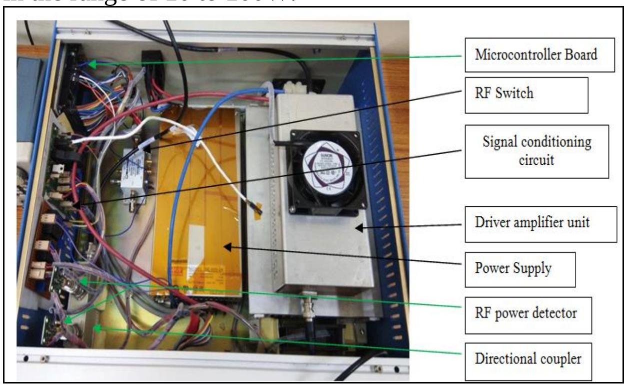


Figure 4: Photograph showing amplifier and its components

## Safety Interlocks

To protect the driver amplifier against any malfunctioning in amplifier system, provision for different safety interlocks have been implemented. Sensing and interlocking circuitry has been designed like monitoring of temperature to protect against overheating, drain current monitoring for overcurrent protection and VSWR monitoring. Safe limit of operation of these interlocks are decided on the basis of lab testing. In case of any fault, the microcontroller generates an interlock signal to open the RF switch which inhibits RF signal input to amplifier.

## Signal conditioning circuitry

The complete electronics circuitry is powered by a single 24 VDC power supply. DC to DC converters (+/- 15 VDC and 5VDC) and voltage regulators (8VDC) have been used to power the sensors and ICs. This provides the necessary isolation and well as compact form factor. Differential amplifier configuration is used for current and power measurement. This improves noise immunity and prevent sensor loading due to high input impedance of differential amplifier. Gain has been set so as to keep the amplified output within maximum input range of ADCs. Zener regulator and diode have been used to keep the input of microcontroller safe in case of op-amp output swing to maximum value. This arrangement limits the output voltage to 5.1 V and -0.7 V in case of positive and negative voltage swing respectively.

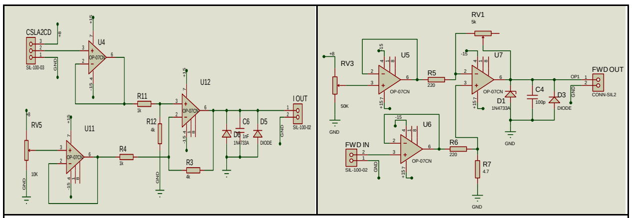

Figure 5: Signal Conditioning Circuits

## Measurement setup

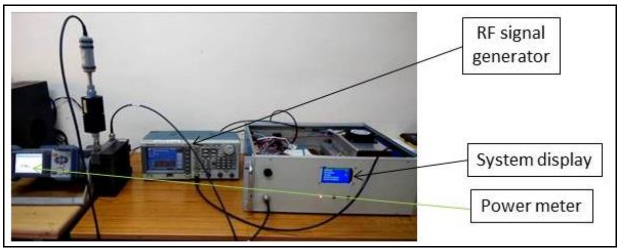


Figure 6: Power measurement calibration setup

Calibration of power measuring circuitry has been done against standard power meter (Make Rohde & Schwarz, Model NRP-Z24). The measurement setup is shown in Figure 6. The maximum deviation is within ± 1.5% over desired power range of 10 to 100W (Fig. 7).

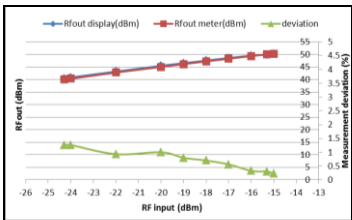


Figure 7: Measurement uncertainty plot


Figure 8: Panel display

## Amplifier characteristics

Important amplifier characteristics like power transfer characteristics, amplifier gain, harmonic and efficiency measurements have been presented till ~100W output power (Figure 8).

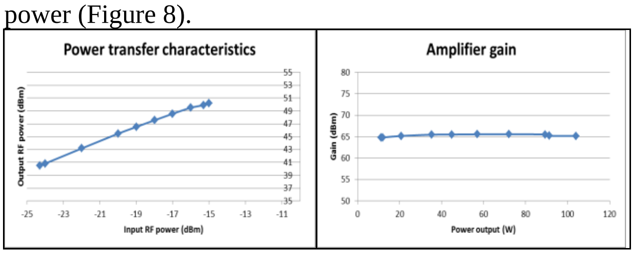

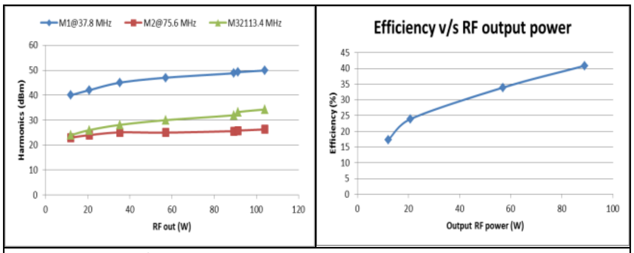


Figure 8: Amplifier characteristics

## CONCLUSION

The driver amplifier system has been tested extensively at 100W and is ready to use. It will be integrated with power splitter to drive 4 independent 1kW amplifiers. Power splitter has been developed and is under test. Work is underway to develop instrumentation and monitoring for the high power amplifier.

## REFERENCES

[1] Arup Bandyopadhyay, D. Bhowmick et al, "Rare Ion Beam Facility at Kolkata– Present State of Development", Proceedings of PAC09, Vancouver, BC, Canada, FR5REP117

[2] Sherry Rosily, Manjiri Pande and V. K. Handu, "DEVELOPMENT OF 75 MHz, 1 kW RF AMPLIFIER FOR HEAVY ION RFQ ACCELERATOR", INPAC 2011

[3] https://www.arduino.cc

[4] Hank Zumbahlen, "Basic Linear Design", Analog Devices

# AUTOMATING OF THE SHUNT IMPEDANCE MEASUREMENT SYSTEM FOR ELECTRON LINEAR ACCELERATORS

Archana Kolekar*, Sharad T. Chavan#, Sandesh R. Bhat, Mandar M. Vidwans, Ashish Harsola*, Ganesh H. Gaikwad and Sanjay N. Pethe
SAMEER, IIT Campus, Powai, Mumbai – 400 076,
*Fr. C. Rodrigues Institute of Technology, Navi Mumbai

*Abstract*

SAMEER has developed a 6 MV radiation oncology systems for the treatment of cancer patients. The radiation source is the side-coupled standing wave S-band linear electron accelerator (LINAC) is designed and developed in SAMEER. The shunt impedance of a LINAC is one of the important parameters and is measured using bead-pull method. Since, the manual measurement procedure needs a hard work and errors may occur, hence it is necessary to automate it. This paper describes the automated electro-mechanical system which has been developed for bead pull to measure the shunt impedance of LINAC, the measured and calculated results are discussed in detail.

## INTRODUCTION

The heart of LINAC is accelerating structure. The accelerating structure consists of a long series of adjacent, cylindrical evacuated microwave cavities. These cavities are characterized by intense electric fields. The energy of such fields is transferred to accelerating electron beam to produce resultant highly energetic electron beam [1,2]. The transfer of energy will obviously take place at resonant frequency of the cavities which is 3 GHz operating in $TM_{010}$ mode. So, the resultant highly energetic electron beam depends upon how intense is the electric field excited in the cavities, for a given power dissipated in the cavity is nothing but shunt impedance of the cavity. Since the output of this device (LINAC) depends upon interaction of electrons with the electric field in the cavity, measurement of shunt impedance becomes quite an important consideration [1,3].

Shunt impedance of an accelerator section is an important parameter which gives an idea about the figure of merit of the accelerating structure. For resonant type accelerating structure, it is calculated using perturbation techniques [3]. In this technique a small perturbing object is used to disturb the resonant frequency of the accelerating structure. This technique is based on Slater Perturbation Theorem.

The experimental technique for the measurement of shunt resistance $R_0$ necessitates the measurement of electric field in the cavity over the region of interest. The shunt resistance $R_0$ and $Q_0$ (Quality factor) are proportional to each other and depend upon the power dissipation in the cavity. The ratio $R_0/Q_0$ is, therefore, independent of losses and governed only by the geometrical factors. In determination of the shunt resistance $R_0$ the problem may be divided into two parts: the measurement of geometrical factor $R_0/Q_0$ and the measurement of $Q_0$. Since $Q_0$ can be measured easily, this procedure provides an indirect method of determining $R_0$.

The fact that $R_0/Q_0$ is independent of losses makes it regard to their presence. The geometrical factor $R_0/Q_0$ can be found by perturbation techniques which involve the measurement of the resonant frequency of the cavity as a function of position of certain perturbing objects. Since resonant frequency can be measured accurately, this procedure provides a simple powerful way to determine $R_0/Q_0$. In addition to the perturbation techniques, there are also several other methods to measure $R_0$, applicable to particular problems. But here only perturbation technique is used. $R_0/Q_0$ is given by [1].

$$\mathrm{R}_0/\mathrm{Q}_0 = \frac{S^2\Delta F}{K\varepsilon\Delta\tau \times 3.14 \times F_1 F_2} \tag{1}$$

Using a standard cavity with known fields e.g. a cylindrical cavity in $TM_{010}$ mode, the constant $K\varepsilon\Delta\tau$ form factor can be determined for a perturbing bead. The S is the length of the cavity and $\Delta F$ is maximum change in resonant frequency. $F_1$ and $F_2$ are maximum and minimum resonant frequencies respectively.

The final shunt impedance, R is calculated by [3].

$$\mathrm{R} = 2Z_{eff}/Linaclength \tag{2}$$

$$Z_{eff} = \left(\sqrt{R_0}T\right)^2 \tag{3}$$

Where T and $Z_{eff}$ are the transit time factor and effective shunt impedance [3] respectively.

#sharad@sameer.gov.in, *guddikolekar1995@gmail.com

In order to measure the shunt impedance of the LINAC it is necessary to move the bead (perturbing object) with an accuracy of 1 mm. It is difficult to do so manually. Hence in the present study the automated system has been designed and developed.

## DEVELOPMENT WORK AND RESULTS

The block diagram of LINAC shunt impedance measurement system is shown in Fig. 1. Typically, the system consists of Vector Network Analyzer (VNA), Microcontroller, Integrated stepper motor, computer with LabVIEW software and mechanical fixture for the bead pull and LINAC tube.

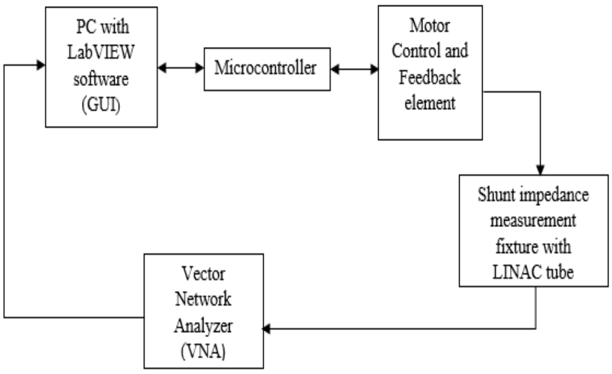


Figure 1: System Setup Block diagram.

### *Automated Setup and Measurement*

In the LINAC shunt impedance measurement setup, the bead was attached to a Kevlar thread (non-stretchable) and it was moved along the Centre of the LINAC axis with an accuracy of 1 mm. The stepper motor and alignment jig has been used for precise bead movement. The measurement set up is shown in Fig 2.

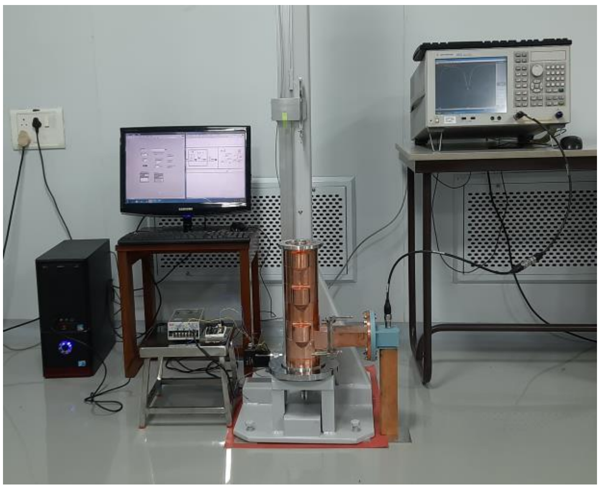

Figure 2. Shunt impedance measurement set up

Microcontroller (Arduino) is used to control the stepper motor rotation and its direction. It has been programmed through LabVIEW software to control stepper motor operation. The LINAC was connected to the vector network analyser (VNA) via coaxial to waveguide adaptor for measuring perturbed frequency. It was continuously sensing the frequency change due to the movement of bead. This perturbed frequency data acquisition from Vector Network Analyzer (VNA) has been done through LabVIEW software. This acquired data is analysed and the shunt impedance is calculated by the program which has been developed as per the flow chart shown in Fig. 3.

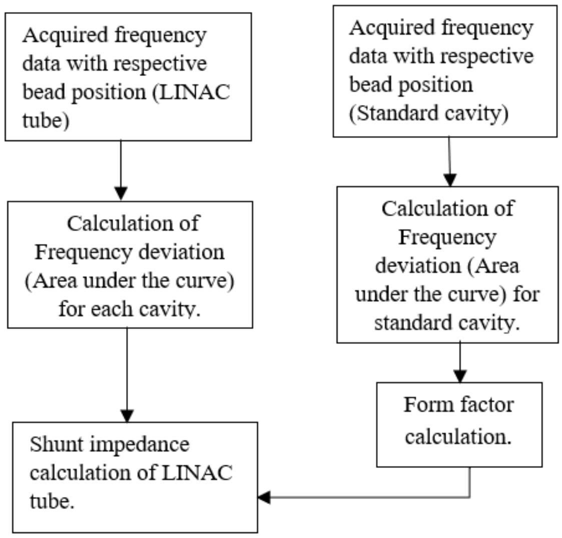


Figure 3: Calculation flow chart

The form factor is calculated using the cylindrical cavity with known value of shunt impedance which known as standard cavity. The position of the bead inside the cavity is varied in steps of 1 mm and corresponding change in resonant frequencies are recorded and acquired in computer by using LabVIEW acquisition program. The evaluated value of the form factor is as shown in Fig. 4. The calculated form factor of standard cavity is 5.324E-19.

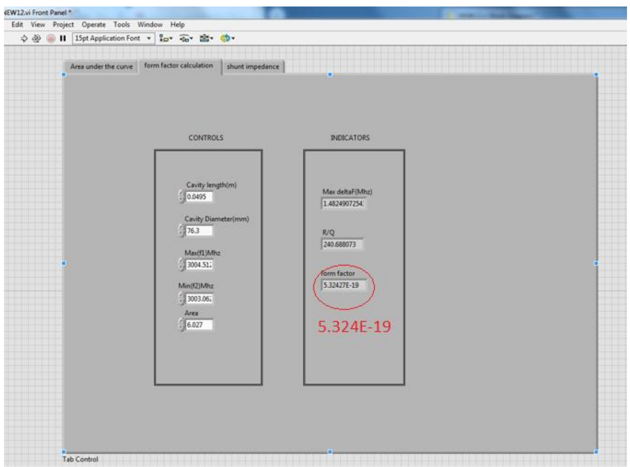


Figure 4: Evaluated form factor of standard cavity.

Calculation LabVIEW program begins with analysis of acquired data. After analysing, form factor is calculated by using Eq.1.

The standard cavity is replaced by LINAC tube whose shunt impedance is to be measured, the above procedure repeated. The graph of square root of frequency shift versus position of bead is plotted which is shown in Fig.5. The area under the curve for each cavity is calculated by LabVIEW program, which is used for the further calculations. The normalised area assuming constant field is calculated by program and it gives the frequency deviation for each cavity in LINAC tube.

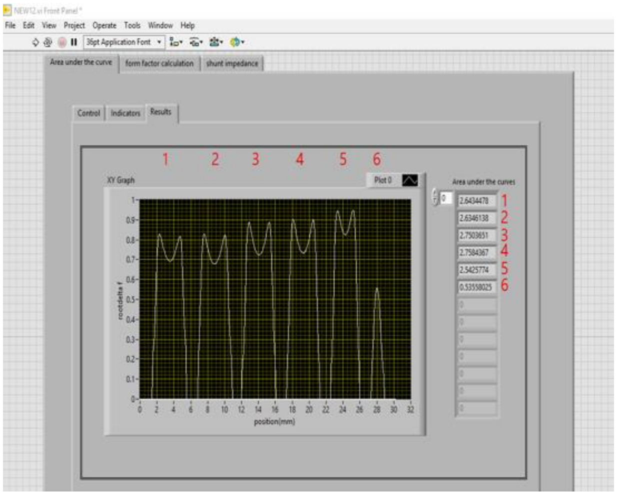


Figure 5: Measured electric field profile of the LINAC

The calculated value of LINAC shunt impedance using a metallic bead is 101.37 MΩ/m as shown in Fig. 6.

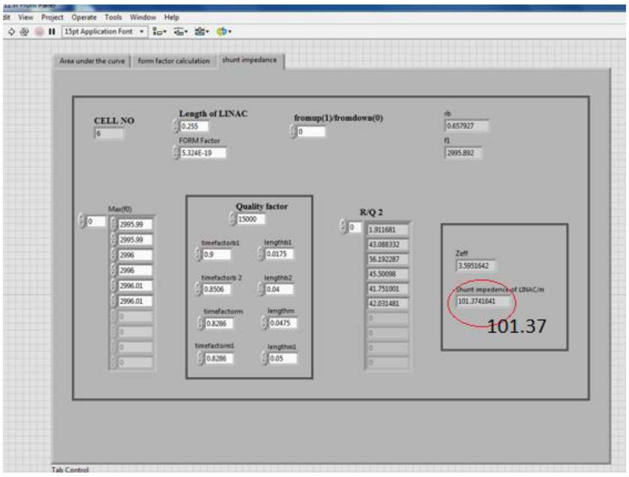


Figure 6: Measured Shunt Impedance of LINAC tube

## CONCLUSION

In conclusion, we have successfully achieved automation of shunt impedance measurement setup for LINAC tube.

## REFRENCES

**[1]** *https://www.energy.gov*. (n.d.). Retrieved April 2019, from https://www.energy.gov: https://www.energy.gov/articles/how-particle-accelerators-work.

**[2]** R. Krishnan, A.P. Deshpande, T.S. Dixit, S. Chavan, C.S. Nainwad, S.N. Pethe, T.T. Tiwari, (2017) "*'S' band linac tube development work in Sameer," in Proc.* PAC09, Vancouver, BC, Canada FR5REP083.

**[3]** T.S. Dixit, R. Krishnan, S.N. Pethe, C.S. Nainwad, A.P. Deshpande, *"Shunt impedance of a 6 MeV standing wave side coupled structure," in Proc.* PAC09, Vancouver, BC, Canada WE5PFP016.

# DEVELOPMENT OF AN AUTOMATED RF AMPLIFIER TEST BENCH

Deepak Kumar Sharma*, Akhilesh Jain and Mahendra Lad
Raja Ramanna Centre for Advanced Technology, Indore, India.

*Abstract*

An automated Radio Frequency (RF) test setup has been created for the characterization of solid state RF power amplifiers and associated RF components. The setup has been built using PC based instrument control scheme. Various instruments have been connected using applicable (RS485, USB or Ethernet) bus to a controlling computer. The acquisition and control software has been created to perform various measurement tasks rapidly, and to generate required measurement data in a report. The hardware connection provides single terminal for various operations and the software provides consistency in measurements and report generation along with help in taking care of instruments and human safety. Also, this system is aimed to provide interactive yet simple interface to the operators. This test setup was successfully used during development of different high-power solid-state RF amplifiers for IIFC, Indus-2 and IFSR RF systems.

## INTRODUCTION

The automation in the manufacturing industry is a well established technique for testing and measurement. The computerization or automation in measurements helps in testing and quality evaluation process. It reduces the test time, and improves the accuracies in the measurement, with the elimination of most of the human errors in the manual measurements. The automation in the research and development (R&D) laboratories is also important for the test quality and surety of the results. For some of the measurements under R&D activities the test or recording speed requirements are so stringent that a manual measurement can't fulfil the same. For such cases there is no substitute to automated measurements.

From the need for automation point of view, the testing and tuning of solid state RF power amplifiers [1,2] is not a different task than other R&D and manufacturing tests. It involves measurements with the help of various RF and non RF instruments including RF signal generator, RF power sensor, DC power supply, power meter, spectrum analyzer, Vector Network Analyser (VNA) etc. Each single point measurement requires taking readings from all of the above instruments and recording them for future use. As the power amplifiers are non linear, their characteristics vary with input power. Hence, measurements at a number of input power values are required, which makes it a cumbersome and time consuming task. This task is simplified with the help of automated measurement setup described in this paper.

* dksharma@rrcat.gov.in

## HARDWARE SUMMARY

Figure 1 shows a typical arrangement (in the form of a block diagram) for high power measurements, suitable for various two ports Devices Under Test (DUT). The shown RF connections are supported by the control instrumentation connections of the system controller with all the instruments. The adopters, splitters, interface convertors and control connections are not shown in the figure, to keep clarity in the diagram. Some of these detailed are listed as Table 1.

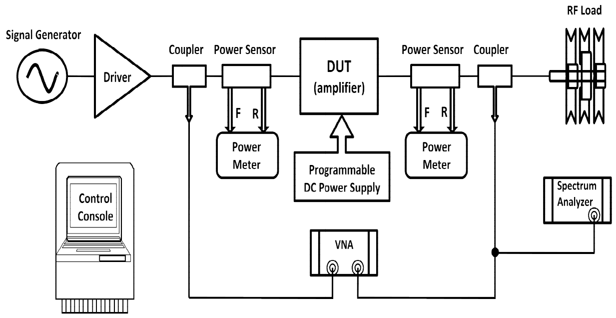


Figure 1: Block diagram of the high power RF test setup.

Due to variability of the measurement application and in order to take advantage of flexibility and economy of personal computer (PC), it has been selected as system controller. Also there is no need for real time processing or very high speed close loop algorithms; hence choice of general purpose computer is reasonable. But some of the components of the measurement system do not have an interface which is readily available in the present day's commercial computers. Hence, in order to connect them in the system, appropriate interface converters are deployed. A multi-port RS 232/ RS485 hub with USB interface, for example, is used as number of serial ports available nowadays in PCs is insufficient for the application. Selection of instruments is mostly depends on the RF performance parameters/ measurement requirements. In order to measure input and output powers of the DUT an indigenously developed 2-channel RF power sensor [3] is deployed.

Table 1: Deployed instruments and their functions

| Sr. No. | Instrument | Measurements/ Function | Remote Interface |
|---|---|---|---|
| 1. | RF Signal Generator | RF signal generation with pulse modulation | LAN |
| 2. | Driver RF Amplifier | Boost signal generator level to attain power level to drive input of DUT | Hard wired |
| 3. | RF Power Sensor | Measurement of DUT input and output powers | USB to serial |

| | | | |
|---|---|---|---|
| 4. | DC Power Supply | To DC bias the DUT (power amplifier) | LAN |
| 5. | VNA | DUT I/P to O/P amplitude ratio and propagation phase measurement | LAN |

## SOFTWARE DESIGN

### *The environment*

For this development work the software environment was selected to be National Instruments LabVIEW, running on Microsoft Windows operating system. The choice of the operating system is obvious as Windows PCs are commonly available and are easy to operate and maintain. The selection of the software development language/ environment is made based on the application to be developed and the previous experience held in such development work. LabVIEW is a well established work bench for data acquisition based application development. Based on the above criteria the software development work started with LabVIEW as a workhorse.

### *Instruments servers*

As evident from the hardware block diagram, there are variety of instruments each with varied interface requirements and response time. Hence, instrument servers have been created, one for each instrument. The instrument server is a piece of software which interacts with its associated instrument exclusively and responds to data and setting requests from its calling (main) program. Each server keeps its privet attributes corresponding to important variables of the test environment and the instrument properties or settings. In this way handling each instrument becomes easy for the next stages of the software development.

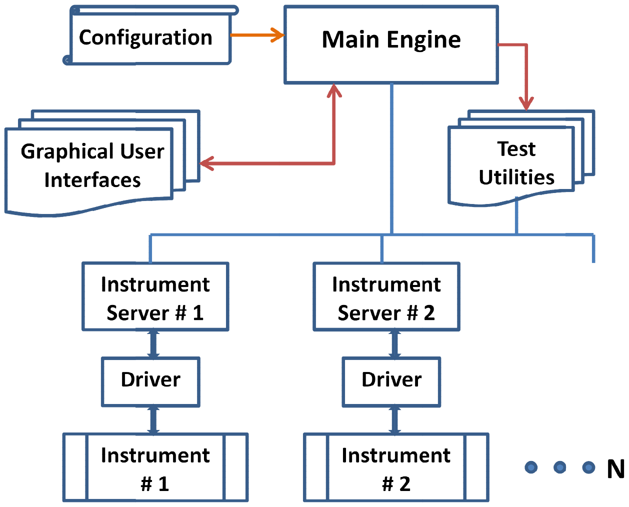


Figure 2: Architecture of the test software.

### *Software Architecture*

Figure 2 shows a block diagram representation of the overall software architecture. Instrument drivers are used to communicate with the individual instruments. On top of the drivers the instrument server resides. The main software engine is the component responsible to manage all the tasks. It communicates with instrument servers for the updated data and handles the user commands received through active (depending on the present monitor/ display resolution) operator interface. The other software components are invoked by the engine on the request of the user. The monitoring and protection functions are implemented in the main engine itself.

## FUNCTIONS AND FEATURES

As mentioned in above diagram, there are several small pieces of software (named as 'Test utilities') which work in slave mode with the main engine. They have their individual tasks and normally depend on the engine for their configuration data and access to the resources. Some of these functions are elaborated in this section, along with the important features of the system.

### *Control loops*

As depicted in figure 1, the RF generator feeds a driver amplifier output of which drives the input of the device under test (DUT). Power gain of the driver and the DUT may vary slowly with time and the operating conditions. RF power level at any point in the chain can be controlled by varying the power level of the RF generator. The level of the generator can be controlled in one of the following modes, available in the developed system:

a) **Constant generator level:** the generator level is kept constant, at a value specified by the operator, and any variation in the component gains changes the output power level (open loop).

b) **Constant DUT input:** the DUT input is constantly monitored and the RF generator level is varied to maintain the DUT input at the operator specified value.

c) **Constant DUT output:** the generator level is varied to maintain the DUT output at a value specified by the operator.

Any of the three modes can be selected by the user at run time by a click on a radio button on the user interface.

### *Power Transfer Characteristics*

Power transfer characteristics (PTC) of an amplifier, or any two terminal device under test, is a plot of variation of output power with respect to variation in the input power level. Power amplifiers are usually a non liner device and hence determination of their full range PTC curve is essential to the characterization of the amplifier. Saturated output power and 1-dB compression point are well known outputs of the analysis of the PTC curve for an amplifier. In the system described here, the PTC is measured by slowly sweeping the input power level and by recording output power (as well as other important parameters) of the amplifier. Subsequently an analysis of the recorded data is made to determine the 1-dB compression point. Finally, all the measurements with the DUT ID, test conditions and analysis results are saved in a file for the future reference.

### *Detector Characterization*

Other than characterization of amplifier modules one of the important use of the developed test bench is testing and non linear calibration of indigenously developed RF power sensors. In this application, input power to un-calibrated directional power sensor, is swept from low level to more than 500 W and sensors readings are recorded. The difference between these readings and the value of actual power is fed to the sensor's EEPROM. The EEPROM data is utilised by sensor software for point to point correction of the measured data with which the sensor is termed as calibrated. The same procedure is repeated for checking the calibration performed earlier.

### *Other Features*

Along with above functions followings are the salient features of the system:

- Through calibration for VNA
- Flexible system configuration
- Report generation
- Intelligent software
- Screen dump function
- Interactive front panel
- Save and recall configuration
- Advanced controls and indicators
- Independent front panels and block diagram etc.

## RESULTS AND CONCLUSIONS

An automated high power RF test and measurement bench is created with the help of various instruments and LabVIEW for integration and programming. Some screen shots of the user interface are shown as Figure 3 and 4.

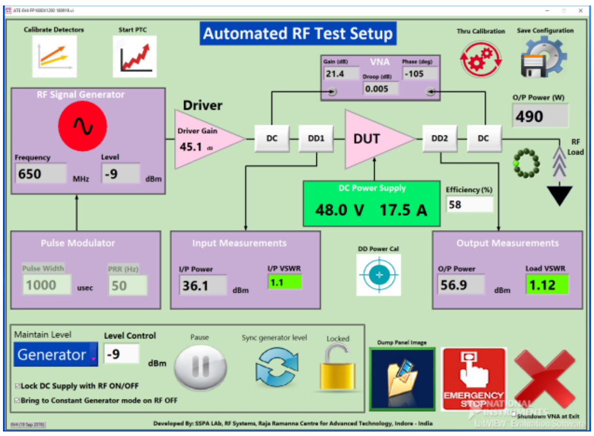


Figure 3: Screenshot of main user interface panel.

The RF test bench described in this paper has been designed and four numbers of such setups are working in our lab. So far, more than 1000 numbers of amplifiers and more than 200 numbers of power sensors have been characterised on these benches.

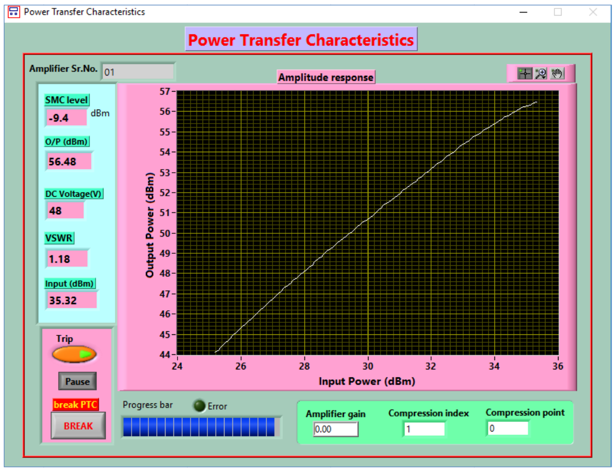


Figure 4: Screenshot of power transfer characterization.

## ACKNOLEDGEMENTS

We sincerely acknowledge the efforts of all our team members, especially Mr. Varun Bhalla and Mr. Dheeraj Verma, in the assembly and software development of the above test system. We also thank to all who have contributed to the development work by their valuable comments and suggestions.

## REFERENCES

[1] Akhilesh Jain, D. K. Sharma, A. K. Gupta, P. R. Hannurkar, S. K. Pathak, "Compact solid state radio frequency amplifiers in kW regime for particle accelerator subsystems", *Sadhna, Academy Proceedings in Engineering Sciences*, Aug. **2013**, *Vol*. 38, No. 4, p. 667-678.

[2] Akhilesh Jain, P. R. Hannurkar, S. K. Pathak, D. K. Sharma, A. K. Gupta, "Investigation of Class J continuous mode for high-power solid state RF amplifier", *IET Microwaves, Antennas & Propagation*, June **2013**, *Vol*. 7, No. 8, p. 686 – 692.

[3] Deepak Kumar Sharma, Akhilesh Jain, Kriti Pathak, Mahendra Lad, "Compact dual-channel radio frequency power sensor for solid state amplifiers", Nuclear Inst. and Methods in Physics Research, A.

# DATA LOGGING SOFTWARE MODULE FOR SOLID-STATE RF AMPLIFIER


Kriti Pathak*, Deepak kumar Sharma, Akhilesh Jain, Mahendra Lad

RRCAT, Indore



*Abstract*

This paper presents the details of design, development and deployment of a data logging software module, for high-power solid-state RF amplifier systems. At RRCAT, high-power solid-state RF amplifier systems of the power levels of hundreds of kW are developed and are in use in round the clock mode of operations in accelerators. In these RF amplifiers, embedded control system is based on real time (RT) controller running on NI Linux. Hence, this development was taken up to be able to deploy it on Windows as well as Linux based RT targets, running LabVIEW. The developed module performs logging of acquired data in binary format, data retrieval and report generation. The developed software is efficient in memory and CPU utilization. Additionally, it generates compact data log files and it is compatible for deployment on a range of targets (RT, X86 etc.). It can be adapted to different channel counts so as to maintain log efficiency for very small to fairly large channel counts. The developed software module is tested successfully with the RF system.


## INTRODUCTION

At RRCAT, synchrotron radiation facility is being run in round the clock mode for which hundreds of kW of RF power is required. Solid state RF amplifier system caters for this requirement. Since RF MOSFET is the key element in power generation which is sensitive to temperature and RF reflections, it is essential to identify and replace the device that fails to avoid its adverse effects on the system on later stage. An embedded control system takes care of proper functioning of RF system. This system is based on real time (RT) controller running NI LINUX. This huge data which is being acquired by control unit needs to be archived on a regular basis to ease analysis or system debugging offline. Although various data logging software modules are available (mostly for Windows based systems) but they cannot directly be deployed on the Linux based RT controller in use. This requirement led to the development of a general purpose data logger which can be integrated with any utility designed in LabVIEW independent of the LINUX/WINDOWS platform or RT/ general PC. The developed software module was integrated with Indus II RF amplifier system [1], Graphical User Interface (GUI) for remote operation of RF amplifier system [2] and is compatible with indigenous directional RF power sensor [3]. Desired logged data can be retrieved for a given log time and can be displayed in multiple ways to facilitate analysis.

## DATA LOG FORMAT

Data is logged in a compact binary format in different virtual channel segments. In all, there are 5 segments where each segment can store up to 250 channels data. Depending on the utility, the channel count and channel data type is different. Data logger developed for RF system, for example, logs amplifier forward and reflected powers, heat sink temperatures, system status/interlocks and power/temperature overload alarm/trips for 192 RF amplifiers. Channel segmentation for this application is mentioned in Table 1.

Table 1: Channel Data Segmentation

| **Segment No.** | **Channel Data Type** | **Channel count in use** |
|---|---|---|
| 1 | Amplifier forward powers (Analog) | 192 |
| 2 | Amplifier reflected powers (Analog) | 192 |
| 3 | Amplifier temperatures (Analog) | 48 |
| 4 | Amplifier Rack and system status signals (Digital) | 24 |
| 5 | For future use | NIL |

Data acquired is logged at the rate of 10 Hz in the form of typed defined packets. Each packet/cluster comprises two fields/elements viz. A (U8) and HL (I16) whereby value in A defines the type of data stored in HL. Table 2 shows different combinations of the two fields.

Table 2: Data Log Format

| **A (U8)** | **HL (I16)** | **Comment** |
|---|---|---|
| 0 to 249 | 0 to 32767 | A : Channel No. of a particular segment; HL : Channel data |
| 250 to 254 | 0 to 36000 | A : Segment No.; HL : No. of 100 milli seconds in a particular hour |
| 255 | 0 to 23 | A : 255; HL signifies hour of a particular day |


*kpathak@rrcat.gov.in

Segmentation allowed us to log up to 1250 channels by using just 1 byte U8 format for channel number. This considerably reduced the packet size and hence increased the storage efficiency. A separate log file is generated for each segment, each day. Files of a specific day are stored in a separate folder named by the date. This helps to directly fetch the required segment log file instead of retrieving all segments data had it been written in a single file. This approach helped decreasing CPU and memory usage and increasing efficiency.

Acquired data is first pushed in a queue and then dequeued into a data log file when queue overflows. Packets are enqueued in a definite sequence wherein hour information is stored first followed by segment no. and time information and lastly channel no. and data. While storing data in a particular segment file, the hour and seconds information is clubbed (segment no. is dropped) followed by segment's channel nos. and corresponding data.

## ALGORITHM

Developed data logger software module is not a standalone application rather it is in the form of source code which can be integrated with different utilities. Channel count and type of data (to be stored), changes depending on the utility. To accommodate for this variation, channel/segment assignment in logger module is designed to be specific to a utility but other things remain same.

Each segment is associated with its own queue and data log file. Data acquired by the data logger software module is first stored in a queue wherein each queue element is a cluster of two elements A and HL. Figure 1 explains the steps followed while storing the data in a queue in the form of a flowchart.

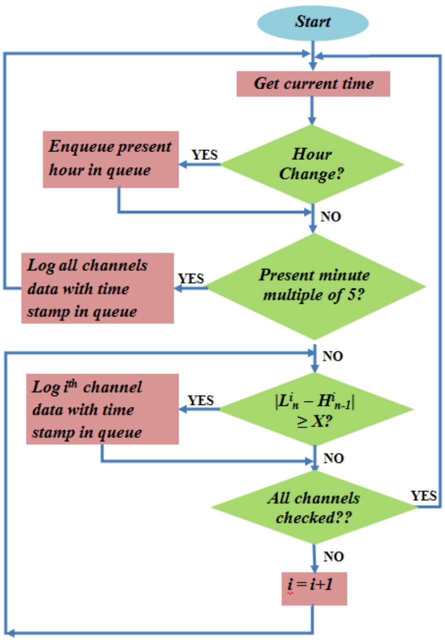


Figure 1: Flowchart depicting updation of queue.

Acquired channel data is checked at every 100 ms for a change in its present value (denoted by $L^i_n$ in Fig. 1) from the previously logged value ($H^i_{n-1}$) by an amount X. If change is more than X, channel value is stored in queue with time stamp or else value is ignored. This is done to optimize between memory and accuracy by reducing queue size and in turn data log file size; without generating significant error. Queue elements are retrieved and stored in a data log file as shown in Fig 2.

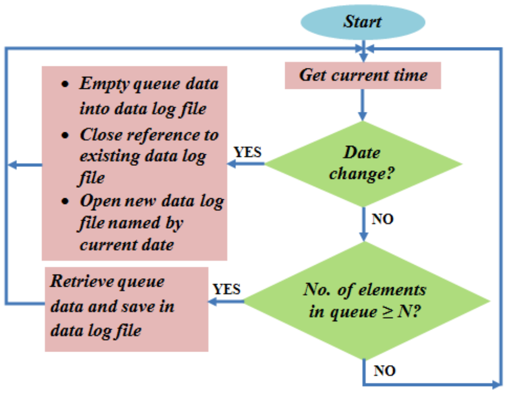


Figure 2: Data log file update.

A new data log file is generated each day for each segment. If date changes, all the data present in the queue is saved in existing log file and the file is closed. New log file is generated for the changed date. If date is not changed, data is saved in log file from queue when the no. of elements in the queue exceeds N.

## SOFTWARE DESIGN

The data logger software module is designed in LabVIEW environment. It is designed in the form of two different sub modules to ease its integration with different utilities – logger and retriever. This segregation of job also helps in debugging of designed software. Both the sub modules are again realized in the form of different functional units performing specific tasks like storing acquired data in a queue or retrieving data from a log file etc.

### *Logger Module*

Logger module performs two main functions - storing acquired data in binary format in a queue and saving the queue data in a data log file. Both tasks are performed in parallel with logging in queue given higher priority. In addition to this the module also creates new log files when date changes and closes the old ones. Figure 3 shows part of the code implemented to store data in a queue. At each hour change in the clock the code forms a packet with A=255 and HL contains hour information. This packet is enqueued. Further each channel value is checked, in sequence, for a defined change from previously logged value and if so happens it forms a packet where A contains channel no. and HL contains the channel data. All such packets are then queued up.

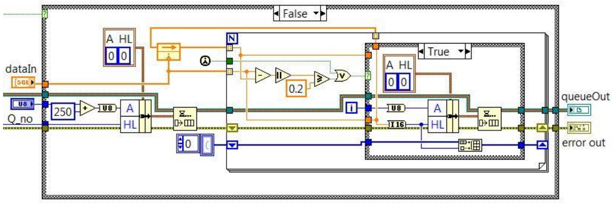


Figure 3: Code implementing queue update.

Partial code to implement retrieval of the queue data and saving into corresponding data log file is shown in Fig. 4. In this part of the code change in the date is checked. If the date doesn't change, the queue elements are retrieved and appended in the existing log file when the no. of elements in queue exceeds a definite number N. If the date changes, queue contents are appended in the existing log file irrespective of queue size. Existing log file is then closed and a new log file for the new date is generated.

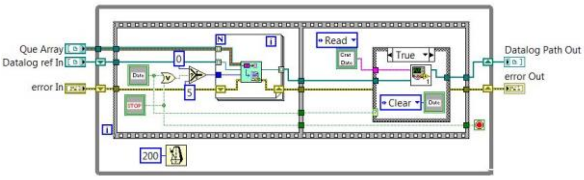


Figure 4: Code implementing log file update.

## *Retriever Module*

Retriever module implements fetching of required data from corresponding data log file. User specifies the channels to be displayed along with the time window. Data from a single day at once could be retrieved. Code shown in Fig. 5 fetches the suitable log file and filters the required channels data from that file for a given time duration. Filtered data is then displayed on the GUI with proper time stamping.

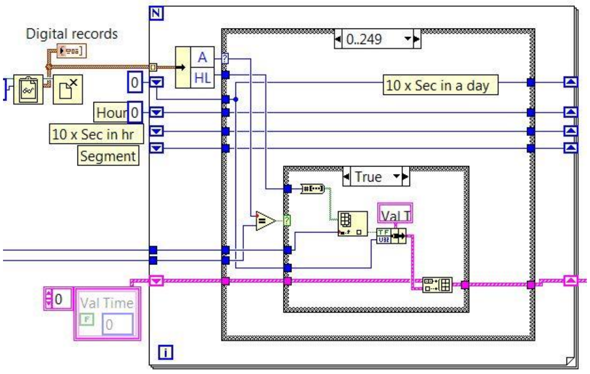


Figure 5: Code implementing data retrieval.

## RESULTS

Data logging software module developed for solid state RF amplifier system is successfully integrated with RF amplifier control system and tested for its functionality. Data is logged at a rate of 100 msec. Fig. 6 shows the front panel of the GUI designed for data retrieval. User can select the channels to be displayed with the date and time span. Data from the selected channels for a given time span is displayed in two formats – graphically and tabular. Graph can display multiple channels on y axis for the given log time plotted on x axis. In tabular format, each row corresponds to a different channel with the columns showing data of a channel at different log instants.

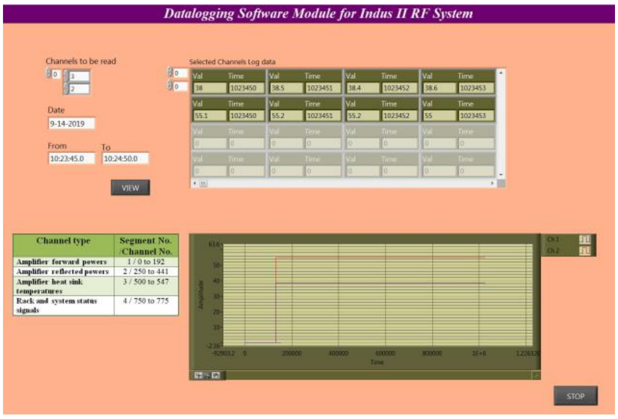


Figure 6: Front panel of the GUI for data retrieval

## ACKNOWLEDGEMENTS

Authors gratefully acknowledge the kind support and constructive feedback of Varun Bhalla in this work.

## REFERENCES

[1] Jain A., Sharma D.K., Gupta A.K., Kumar N., Pathak K. and Lad M. "Design, Development and Commissioning of High Power Solid State RF Amplifier for Indus-2 RF system", Indian Particle Accelerator Conference INPAC 2018 , RRCAT Indore, Jan., 9-12, 2018.

[2] Pathak K., Sharma D.K., Jain A., Bhalla V. and Lad M. "Design and development of a graphical user interface for remote monitoring and control of RF system", Indian Particle Accelerator Conference INPAC 2018 , RRCAT Indore, Jan., 9-12, 2018.

[3] Deepak kumar Sharma, Akhilesh Jain, Kriti Pathak and Mahendra Lad, "Compact dual-channel radio frequency power sensor for solid state amplifiers", Nuclear Instruments and Methods in Physics Research Section A: Accelerators, Spectrometers, Detectors and Associated Equipment, Volume 944, 11 November 2019, 162559. https://doi.org/10.1016/j.nima.2019.162559.

# COUPLING AND ENERGISING OF 10 KW, 352 MHZ SOLID-STATE RF POWER AMPLIFIER FOR BUNCHER CAVITY OF PROTON ACCELERATOR

B. V. Ramarao*[1], S. Muthu [1], J. K. Mishra [1], Manjiri Pande [1], Gopal Joshi [1], M. R. Mishra [2], V. M. Jose [2], S. V. L.S. Rao [2], Rajesh Kumar [2], *and* S. Krishna Gopal [2]

*1) Accelerator Control Division, and 2) Ion Accelerator Development Division*

*Bhabha Atomic Research Centre, Trombay, Mumbai 400 085*

**bvram@barc.gov.in*

*Abstract*

A 10 kW, 352 MHz solid-state RF power amplifier, which was developed has been coupled to buncher cavity of Low Energy High Intensity Proton Linear Accelerator (LEHIPA). There is a loop coupler and coaxial 3-1/8” transmission line in between the buncher and solid-state RF power amplifier. The measured transmission line has insertion loss of 0.36 dB. The return loss at the input of RFPA (inclusive of buncher, coupler, TL) is 33 dB.

## INTRODUCTION

The Low Energy High Intensity Proton Linear accelerator (LEHIPA) of BARC has basically three acceleration structures and one buncher cavity. The total rated energy is 20 MeV. There is a Radio Frequency quadrupoles (RFQ) and two stages of drift tube linacs. Recently a 3 Mev proton acceleration through RFQ is commissioned [1]. In order to have minimal losses of particles while accelerating through Drift tube Linac, in succession of RFQ, a buncher cavity is an essential component of LEHIPA. A two-gap pill box type buncher cavity has been designed. To raise the bucher gaps to the required electric field gradient the buncher needs a RF power input of 10 kW at 352 MHz. A RF solid-state power amplifier has been designed and used for this RF power requirement. Fig.1 shows the buncher system of LEHIPA. The buncher system consists of a Buncher cavity, a loop coupler, Transmission line, and a high power solid-state amplifier. The paper presents the details of the RF solid-state power amplifier and its coupling through Transmission lines etc.

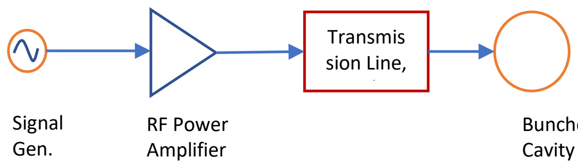


Figure 1: Buncher system.

## RF SOLID-STATE POWER AMPLIFIER

The block diagram of the solid-sate RF power amplifier is shown in Fig. 2. It consists of 16 RF power modules, two 8-way power combiners, a two-way combiner, a two-way divider, two 8-way dividers, pre-drive and drive modules, DC power supplies, sensorics, and an interlock and protection system (IPS) [2]. Total 16 modules are assembled over eight heat sinks with two modules over each heat sink. It is a two-stage combined power amplifier with a 2-way combining follows an 8-way combining. It has pre-drive and drive power amplifier stages to amplify the low-level signal from the local oscillator. The DC SMPS power supplies feed the RF modules, and these are rated at 50V, 30 A. The amplifier includes various sensor like inlet and outlet temperature sensors, flow switch, directional coupler for RF signal monitoring, voltage and current signals of RF modules etc. An interlock and protection system monitor all the sensor signals of the Solid-state RF power amplifier (SSRFPA) and protect the modules against the over voltage/current, temperature, absence of water flow etc. It provided ON/Off sequence power supplies. It protects the modules by switching off RF signal input and shut down of DC power supplies. The IPMS also display the amplifier parameters. Fig. 3 shows the assembled SSPA in a 19” 36 U rack unit. SSRFPA has been tested on a 50 Ω RF load. Fig. 4 shows the pulse test of SSRFPA at 10% duty cycle. The output is stable RF pulse with <200 W variation during the ON time. The peak power output is 10.24 kW. The pulse period is 100 ms. It has been tested with various duty factors from 0.1% to 100%. It has rise time and fall time <10 us. It has been tested in CW mode also. Fig 5 shows the CW test result with a spectrum analyser.

## TRANSMISSION LINE

The output of the solid-state RF power amplifier has been coupled to buncher through a EIA 3-1/8” transmission line. The TL consists of bends, straight sections, directional couplers etc. Fig. 6 shows the installed transmission line at LEHIPA. The measured reflection coefficient of the TL is shown in Fig. 5. The reflection coefficient is better than 13 dB. The measured insertion loss of the transmission line is 0.36 dB, which corresponds to an RF dissipation loss of 8% of the input power.

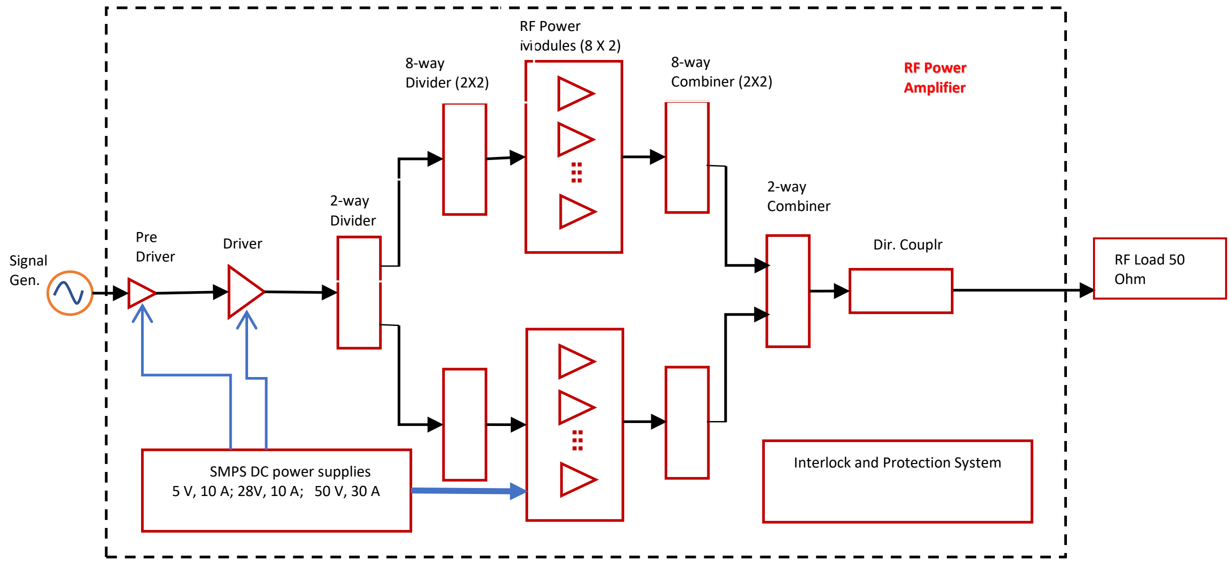


Figure 2: Block diagram of 10 kW RF

Figure 3: Installed RF SSPA at LEHIPA.

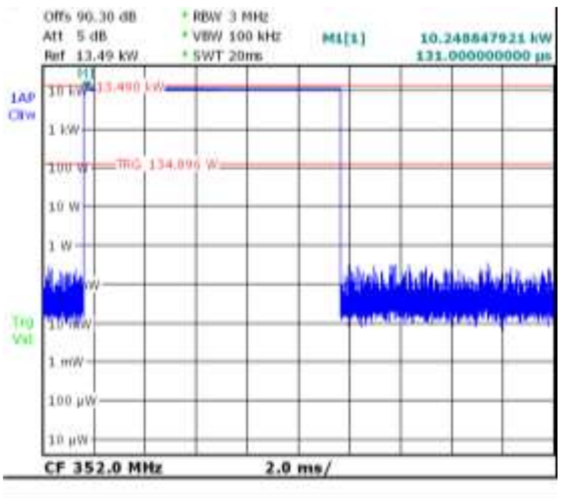


Figure 4: RF output @ 10% duty factor on 50 Ω load

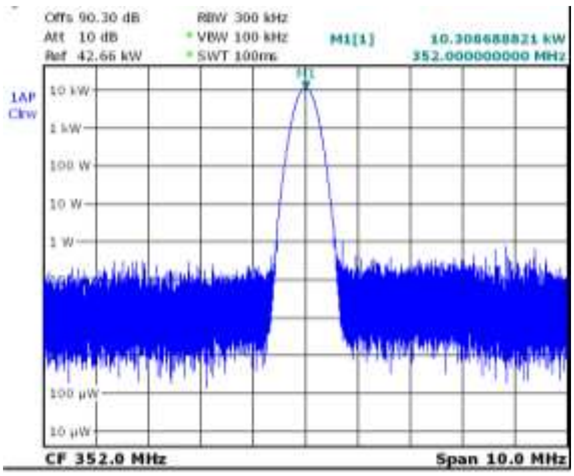


Figure 5: RF output of 10.3 kW on 50 Ω load

Figure 6: Photograph of installed RF Transmission line

After testing the RF SSPA on a 50 Ω load, it has been connected to buncher cavity. It has been coupled by using a loop coupler. The measured input reflection co-efficient $|S_{11}|$ of the coupled cavity is shown in Fig. 7. Before tuning, the input reflection coefficient is -15.31. The coupler has been retuned for minimum reflection coefficient. The minimum reflection coefficient under better tuning condition is -33.6 dB.

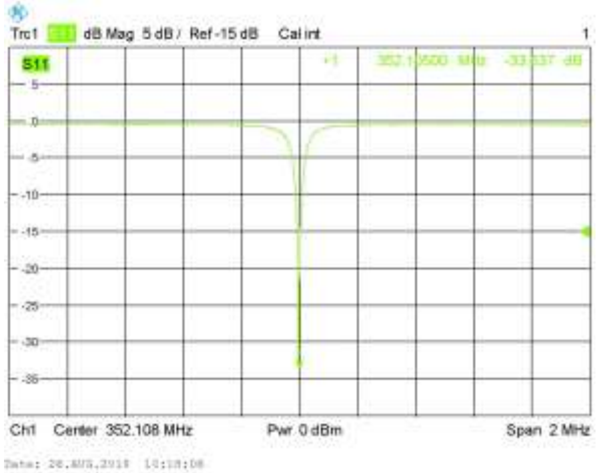


Figure 7: Measured $|S_{11}|$ after of tuning coupler

Fig. 8 shows measured input impedance of the coupled cavity. It is slightly over coupled to a 50 Ω system. The coupling coefficient of the buncher is 1.023. The loaded bandwidth of the cavity and TL system together is 52 kHz. The loaded quality factor of the coupled cavity is 6771. Intrinsic Q of the cavity is 13,542. The directional coupler is calibrated for its coupling co-efficient and directivity for measurement of incident and reflected power of the cavity.

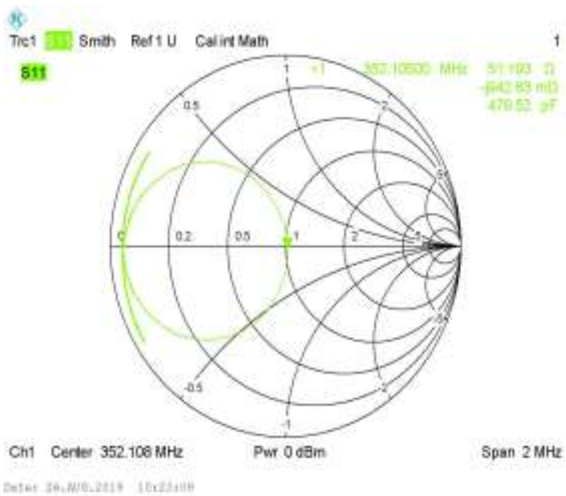


Figure 8. Measured input impedance after tuning

The directional coupler parameters in a TL are
Directivity: -27.0 dB
Coupling coefficient: 61.48 dB
Isolation: -88.54
Input Match: -13.5 (with 50 Ω termination)
Input match: -33 dB (with buncher)

## TEST RESULTS

The power amplifier has been coupled to the buncher and buncher has been conditioned in pulse operation. Initially, low pulse width and low peak input power has been applied and after observation of minimal reflection, input power has been gradually increased. The typical test waveform of the buncher RF signals are shown in Fig. 9. The pulse width has been set at 400 us and repetition frequency is 2 Hz. At 11 kW input power, the reflection is less than 20 dB. The buncher cavity is successfully conditioned and ready for beam trials. Now, the buncher cavity is installed offline to beam axis and conditioned. In due course buncher will be installed inline to beam axis and 3 MeV beam bunching trials will take place.

Figure 9: Time domain signals of forward (yellow), reflected (green), and cavity pick up (orange) signals.

## REFERENCES

[1] Manjiri Pande, Sandip Shrotriya, Niranjan Patel, Shiju A, B.V. Rama Rao, J.K. Mishra, S. Muthu, Snigdha Singh, S.S. Jena and Gopal Joshi, "Radio Frequency Power coupling to 3 MeV Radio Frequency Quadrupole Accelerator for proton beam acceleration", *in Proc of InPaC-2018*

[2] B. V. Ramarao, S. Muthu, J. K. Mishra, Snigdha Singh, S.S. Jena, Manjiri Pande and Gopal Joshi A.N. Other, "Development of 10 kW, 352 MHz Solid-state RF Power Amplifier for Buncher Cavity of Proton Accelerator", *in Proc of InPaC-2018*

# DEVELOPMENT OF SOFTWARE FOR REMOTE OPERATION OF SCANNING MAGNET POWER SUPPLY

Jatin Jotangia[†], P. Fatnani, Ashesh Gupta, Pankaj Gothwal, M. Seema, Janardhan Musuku
Raja Ramanna Center for Advanced Technology, Indore.


## *Abstract*

A 10 MeV electron linac is developed at ARPF (RRCAT) for radiation processing of agricultural and medical products. The size of electron beam at exit of accelerator window is 20 mm, which needs to be scanned inside a vacuum chamber to get wide radiation field suitable for irradiation. The electron beam, inside the vacuum chamber is scanned with time varying magnetic field which is produced with the scanning magnet power supply. A control system has been developed to feed the reference signal to the scanning magnet power supply. The scanning supply tracks the reference signal to produce the desired time varying magnetic field. The ramp current is adjustable from ±2.0A to ±10.0A with ramp-up time 50ms-1000ms and ramp down time< 5ms. During current ramping, the slope of the profile either remain constant to produce linear quick fly-back type profile or is modified to sinusoidal shape with the help of seven segmented inputs. The seven segmented feature is included to adjust the beam intensity at the extremity of scanning to achieve uniform dose distribution.

The dedicated remote control software is developed to operate the control system of scanning magnet power supply. This software gives the various facilities to user for easy operation. The main feature of this software is to set the desired reference signal remotely from any location, set reference signal can be saved for the future use and also it can be loaded from the saved file, mode selection facility, ON/OFF control for reference signal, Error logging and handling, status indications, data read-back, graphical view, data logging of each and every parameter at the repetition of 1Hz. Control scheme for generating the different types of the current profile for scanning system and detailed working of software is discussed in the present paper.


## INTRODUCTION

A radiation processing facility based on 10 MeV, electron Linear accelerator is being set up at RRCAT, Indore. The facility will be used for radiation processing of food, agricultural and medical products. The electron Linac generates pulsed electron beams with diameter typically 20 mm. The pencil electron beam is scanned inside a trapezoidal shaped vacuum chamber to obtain wide radiation field required for irradiation of the products packed in boxes. The time varying magnetic field required for scanning of beam is produced with help of the scanning magnet and associated power supply. The curt profile in the scanning magnet plays an important role in achieving uniform dose distribution inside the product under irradiation. The ramp current is adjustable from ±2.0A to ±10.0A with ramp-up time 50ms-1000ms and ramp-down time< 5ms. During current ramping, the slope of the profile either remain constant to produce linear quick fly-back type profile or is modified to sinusoidal shape with help of seven segmented inputs. The seven segmented feature is included to adjust the beam intensity at the extremity of scanning to achieve uniform dose distribution. Small ramp down time is a critical requirement to ensure that no beam pulse comes during the ramp down time.

A computer based control system has been designed developed and installed to provide suitable beam scanning during product irradiation.

## FUNCTIONAL DESCRIPTION

Remote control software establishes the serial communication with the hardware unit and at interval of every one second it will read the status, mode of operation and present value of all the parameters. If communication with the hardware unit is not established, then the error message will be displayed on the front panel of GUI software. This software also provides the auto reconnect facility if the communication is failed with hardware unit and again reconnects after some time. Software has three different window tabs to configure and to read/set the parameters. The event of recent change in parameter value performed by user will be displayed on message box along with an event time stamp.

Scan current and time is easy to change by entering the value in respective field on the GUI software.

### Functionality of software

**Mode selection:** There are 2 operation modes (single segment mode & seven segment mode) which are available for scanning magnet power supply; Software gives the option to select the appropriate mode.

**Apply settings:** To set the values of current and time for single segment & seven segment mode.

**Pulse ON** (Reference signal): To give the reference signal to scanning magnet power supply from the control room PC.

**Sequence of operation:** To give the sequence of commands for scanning power supply before actual scanning process starts.

*Sequence:*

I. Set and apply the reference signal (current and time value for respective mode of operation).
II. Give the Pulse ON command: Applied peak current and time value will be available on scanning power supply.
III. Give the Control reset command: it will bring scanning supply in ready condition.

IV. Give the Enable (Contactor ON) command:
V. Give the Load Power command:
VI. Give the Interlock Reset command:

**Save the settings of profile parameter:** To save the present current and time parameter value in the file for future use.
**Load the settings of profile parameter:** To load the current and time parameters value from the saved file.

## HARDWARE OF SCANNING MAGNET POWER SUPPLY

The Equipment Control unit consists of ramp controller card, ramp memory card, analog reference generation card and digital I/O card. User needs to provide three prime parameters that are ramp up time, retrace time and scanning magnet current set value. On reception of parameters, the processor begins the calculation and prepares digitized Look up Table (LUT) for ramp memory card and fills 8K memory locations. The ramp controller card generates timing pulses to upload the digitized ramp LUT into the DAC. The ramp start is synchronized with external trigger pulse for proper scanning of product.

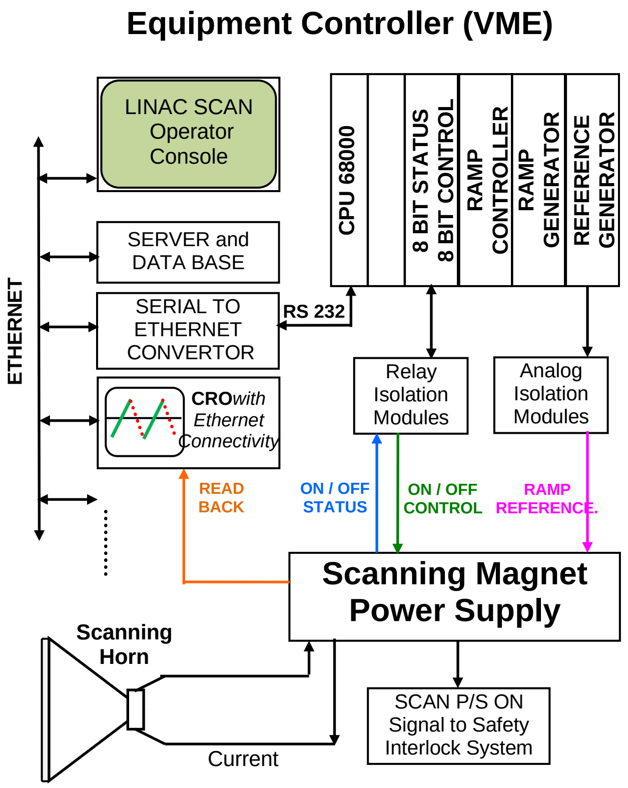


Figure 1: Hardware Architecture.

## SOFTWARE REQUIREMENTS

Scanning magnet power supply has two modes of operation one is local mode and other is remote mode of operation. Remote operation of the unit from main control room is required for ease of operation, with all events and parameters values are logged with time stamp. To keep administrative control over the change of parameter value so that only authorized operators can change the beam parameter. This software runs with the main control system to facilitate all the operation from single computer. This software also gives facility of data logging for comparison and analysis of data.

Figure 2 shows the waveform which are monitored and controlled by remote control software.

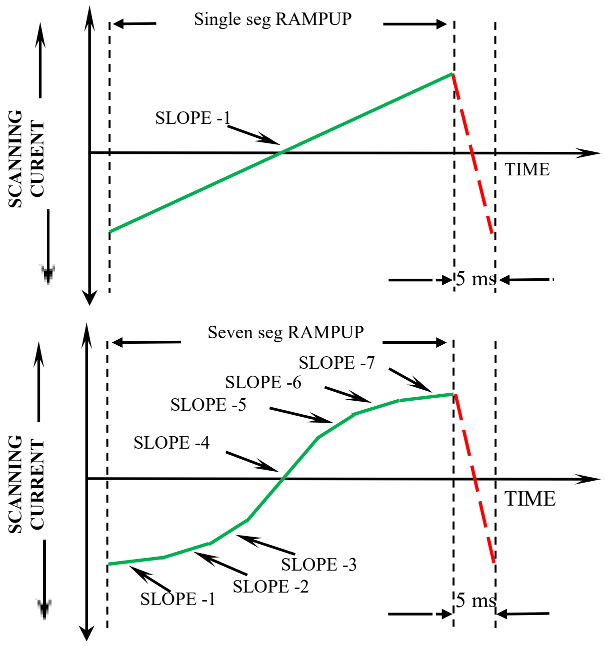


Figure 2: Scanning Waveform.

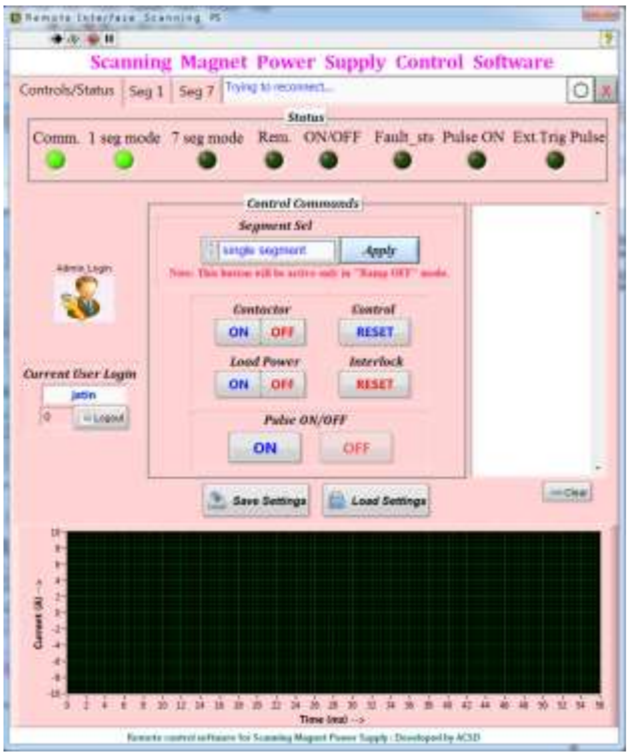


Figure 3: Front Panel GUI of Remote Control Software.

Figure 4: GUI for set parameter.

## SALIENT FEATURES OF SOFTWARE

- Graphical representation.
- Software design is modular which helps in any modifications and integration with main control system software.
- Easy to change the scanning current and time value by simple clicks.
- Mode selection for different mode of operation.
- Read-back of all parameters data.
- Error detection and recovery from the error condition.
- Data logging of all operator events and parameter statuses.

## SOFTWARE FLOWCHART

After software initialization it opens the serial communication port at baud rate of 9600kbps. Further it verifies the communication with the hardware unit, if the communication with the hardware unit is not established then the software will give appropriate error message and it will try to reconnect with scanning hardware unit. When communication port, cable and baud rate are proper then software will send the command to the hardware unit to read all the parameters, in response to the read command of software, hardware sends the string of present set of all parameters value. Once the string is received the software will extract all the parameters value and display on appropriate field of that parameter. This process will continue after programmable time interval. If during this process user wants to change the parameter from software, then change in the parameter event will generate. Software will first check the value of particular parameter, if it is within the permitted range of operation then software will send write command to hardware unit and changes are successfully applied. If the parameter value is out of range, then software will generate the error message. All the parameters are logged into database at a programmable interval, presently it is done at every one second. Figure 5 shows the flow chart of software.

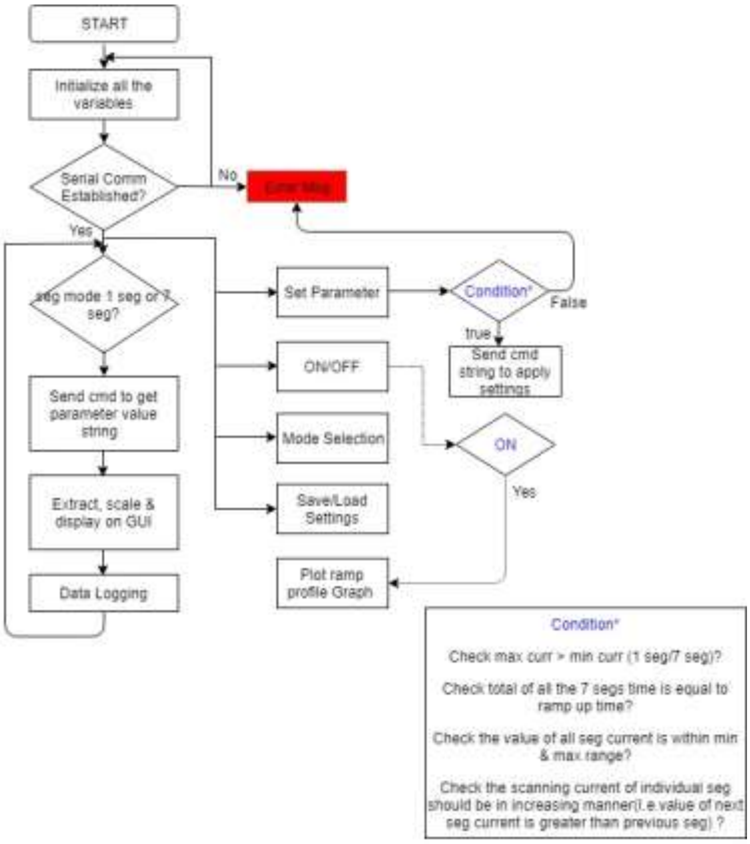

Figure 5: Flow Chart.

## CONCLUSION

The control system of scanning magnet is interfaced with actual power supply and has been tested using software and it was successfully operated in noisy environment. Software was designed and developed for remote operation. All the functionality was thoroughly tested in lab environment and all the features of hardware and software were tested. The scanning magnet hardware and software is deployed at ARPF site. The operation till now is satisfactory and reliable.

## ACKNOWLEDGMENT

The author wants to acknowledge the help of colleagues of Accelerator Controls System Division and Industrial accelerator division for understanding the functional requirements of the system. This helped me to develop the software for the system.

# FRONT-END PROTECTION SYSTEM FOR SOLID STATE RF AMPLIFIERS

Narendra Kumar Bharadwaj*, Akhilesh Jain, Mahendra Lad

Raja Ramanna Centre for Advanced Technology, Indore-452013, India.

*Abstract*

A Horizontal Test Stand (HTS) facility is set up at RRCAT for testing of dressed Super-conducting RF cavities. For operation of HTS, many sub-systems are required like RF Amplifier, LLRF, RFPI, Cryogenics, Vacuum, Radiation monitoring, Safety Interlock etc. To cater the need of RF power, a 36 kW, 650 MHz Solid State RF amplifier system has been developed in-house and installed in HTS. To ensure the safety of this amplifier against various unsafe possible conditions, Front-End Protection system has been designed, developed and deployed in the aforesaid RF amplifier system. It consists of two units, one RF processing and another electronic protection logic implementation unit. Electronic protection logic implementation unit checks different sampled (with the help of RF unit) signals for their healthy condition and allows the smooth operation of amplifier only if all these signals are found to be in desired state. Due to entirely hardware-based architecture, it ensures fast tripping of amplifier in case of any fault, with minimum propagation delay (a few micro seconds). It also monitors and displays the RF power levels at the different junctions of front-end driver amplifier. Being a front-end part of the amplifier, its reliability and fail-safe operation is important. This paper discusses about the design considerations, implementation challenges and achieved result in detail about this development work.

## INTRODUCTION

Prior to installation of a newly fabricated RF cavity, it has to be qualified for various tests. Firstly it is subjected to low RF power test at Vertical Test Stand (VTS). After successful qualification in VTS, full RF power test is performed in Horizontal Test Stand. For this HTS facility is being developed and installed at Raja Ramanna Centre for Advanced Technology (RRCAT), Indore. After commissioning, this facility will be used for the full power testing of indigenously developed fully dressed RF cavities. To generate the required RF field inside the cavity under test, an indigenously developed 36kW Solid State RF Amplifier system is deployed in the HTS. Front-End Protection System is the foremost part of the subjected solid state RF amplifier system and so it is given this name. There are basically 2 main functions of this Front-End protection system-

i) Read and display the input forward and reflected RF powers with the help of a 3 & ½ digit digital panel meter in dB scale.

ii) Safe guard the amplifier system by switching off the forward RF drive signal whenever any/some unsafe conditions in the form of interlocks viz. Forward RF Signal Overdrive, RF Inhibit or Solid State RF Amplifier not Ready arise.

The pictures of Horizontal Test Stand set up including solid state RF amplifier system are given below-

Fig1: Solid state RF amplifier system deployed in HTS

Fig 2: Cryomodule of HTS

*narendra@rrcat.gov.in

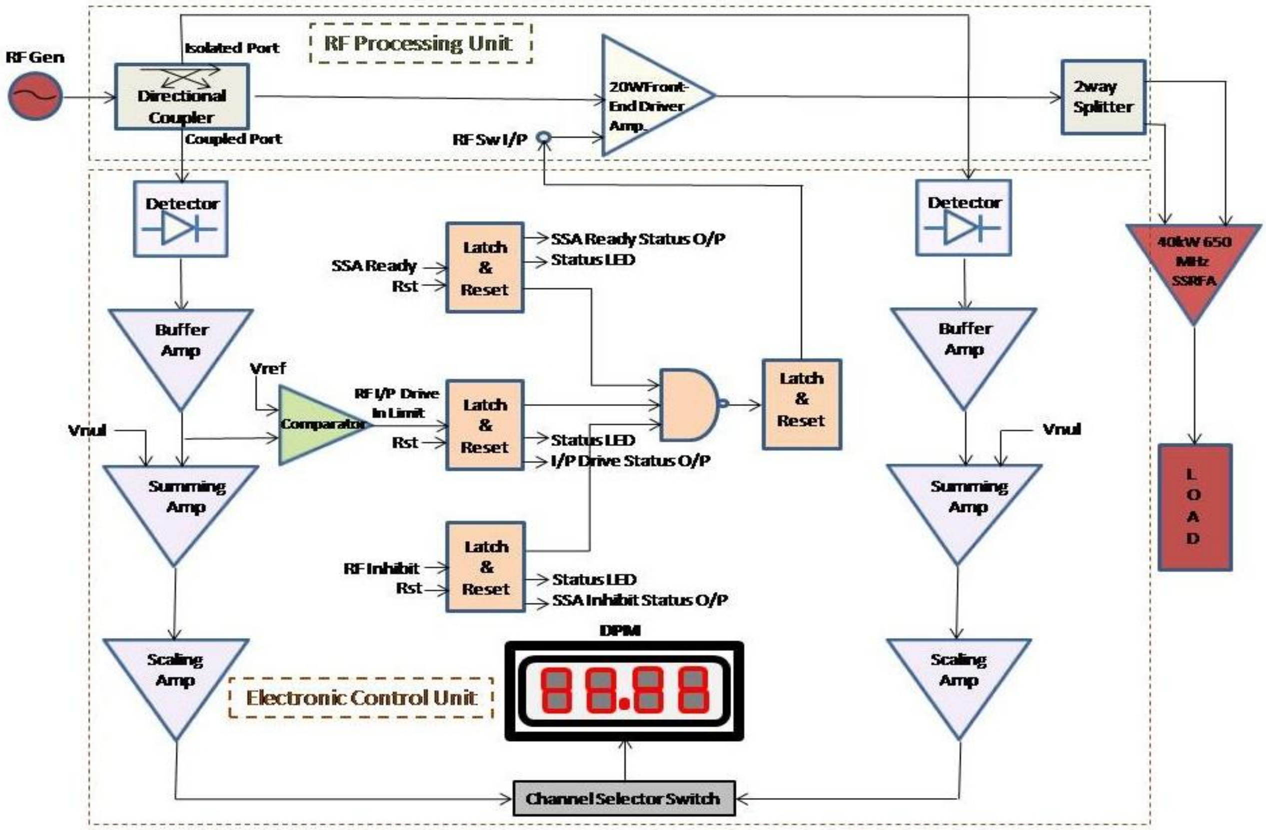


Fig3: Block Diagram of Front-End Protection System

## DESIGN AND WORKING OF FRONT-END PROTECTION SYSTEM

The design of Front-End Protection System includes RF Processing Unit and Electronic Control Unit-

### *i) RF PROCESSING UNIT:*

This unit is designed with following components-

- *Directional Coupler:* This is an indigenously designed and developed resistively coupled microstripline based directional coupler. Measured characteristic values are-

  Coupling: -22.1 dB
  Directivity: 19.2 dB
  Insertion Loss: 0.8dB
  VSWR: < 1.24 for all ports

- *20W MINICIRCUITS AMPLIFIER*
  Model ZHL- 20W-13SW+

- *2WAY INPHASE RF DIVIDER:* This is in house developed microstripline based RF power divider with following characteristics-

  Insertion Loss: 0.5 dB below 3dB
  Phase Imbalance between O/Ps: $2^0$
  VSWR: < 1.2 for all ports

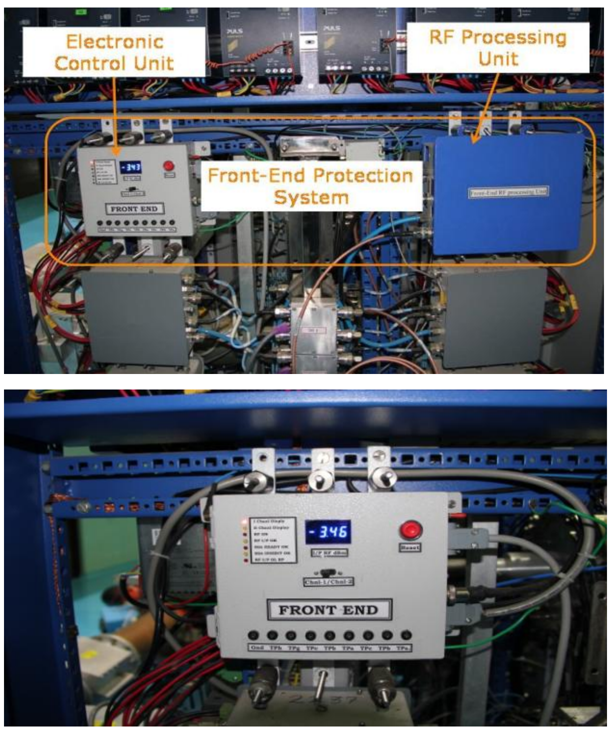


Fig 4: Front-End Protection System

### II) *ELECTRONIC CONTROL UNIT:*

This unit is meant to perform two functions basically-

i) *MEASUREMENT AND DISPLAY OF INPUT RF POWERS IN FORWARD AS WELL AS REFLECTED DIRECTIONS:*

RF signals sampled from coupled port (forward direction) and isolated port (reflected direction) of directional coupler are linearly detected (for dB scale) into DC using LT5534 and then fed to a unity gain precision summing amplifier which is calibrated to give 0.0V O/P at 0.0 dBm I/P RF with the help of negatively biased Vnul pot. Now this signal is fed to a scaling amplifier where the gain is calibrated in such a way that the O/P changes by 1V for a 1dB change in I/P. This is displayed with the help of DPM as the level of RF power. Two separate chains are used for forward and reflected RF signals. Selector switch selects the desired O/P to be displayed on DPM.

ii). *PROTECTION AGAINST UNSAFE OPERATION OF THE SOLID STATE AMPLIFIER SYSTEM:*

To safeguard the Solid State RF Amplifier System, this unit continuously monitors the various interlock signals for their state of healthiness viz. I/P RF Drive in Limit, SSA Ready and RF Inhibit OK. If any/some interlocks arise, this unit activates a RF switch which prohibits I/P RF drive to reach to the amplifier and thus protects it from damage. Corresponding interlock signal/signals are latched until these are reset manually either from local panel or remote PC. This helps in diagnosing the causes behind the faults. For the implementation of this logic, high speed CMOS ICs are used which insure the rapid and reliable interlock action. Base board and mezzanine cards topology is adopted for quick and easy maintenance of the system. A base board card and 6 numbers of mezzanine cards are used in this unit (refer fig-5). Forward/reflected RF power display DPM (in dBm), interlock status LEDs, reset micro-push-button switch, forward-RF-power / reflected-RF-Power mode selector slider switch and various important test-points are provided on the front panel itself to provide ease during operation and maintenance. ±15V power supply connector along with I/P interlock signals & O/P interlock status signals are provided on the right hand side panel which can be interfaced through two 9 pin and 15 pin D sub connector cable assemblies respectively. ±5V supplies are derived from ±15V supplies on the base board itself using voltage regulator ICs 7805 & 7905 with filters.

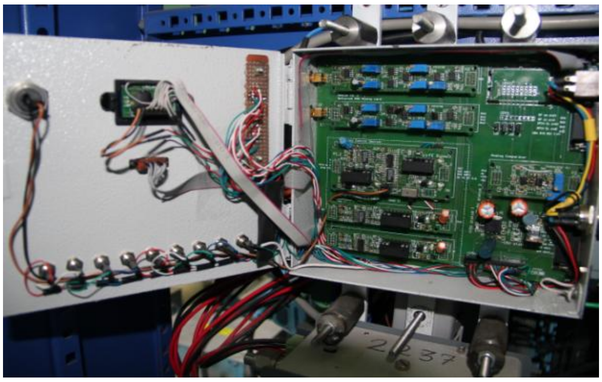

Fig 5: Base board and mezzanine cards

## RESULTS AND CONCLUSION

Front-End Protection System has been deployed in solid state RF system of HTS and is working satisfactorily. It measures & displays the I/P RF powers and trips off the RF amplifier within the measured accuracy of ±0.2 dB over the dynamic range of operation of 30dB. The measured response time from detection of an interlock signal to the action (tripping off the RF drive to solid state RF amplifier) is of the order of <15 µs for analog signal while <1 µs for TTL signal.

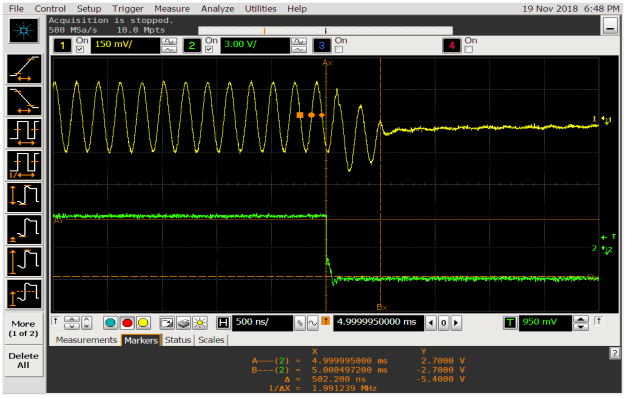


Fig 6: Screen shot of response time measured for TTL signal

## REFERENCES

[1] Narendra Bharadwaj et al., "Development & Implementation of Fast Acting 'Input RF Drive Power Overload' Interlock to Safeguard the Indus-2 Solid State RF Amplifiers", *INPAC 2018*, Indore

[2] Narendra Bharadwaj et al., "Design Modifications and Upgradations in Indus 2 RF safety interlock system for the safety of recently commissioned insertion devices U1 and U2", *INPAC 2015*, Mumbai.

[3] Akhilesh Jain et al., "High Power Solid State RF Amplifier for Indus-2 Synchrotron Radiation Source", *HPRFM 2013*, Gandhi Nagar.

[4] Akhilesh Jain et al., "Design and characterization of 50 kW solid-state RF amplifier" Int. Journal of Microwave and Wireless Technologies, vol. 4, no. 6, p. 595 603, Dec 2012.

# PERFORMANCE TESTING AND EVALUATION OF 1 MW, 352 MHZ KLYSTRON RF SYSTEM WITH PULSE MODULATOR FOR 3 MEV RFQ ACCELERATOR OF LEHIPA

Sandip Shrotriya, Niranjan Patel, Shiju A, Jagdish Bowlekar, Hitesh Kadam, Manjiri Pande and Gopal Joshi

*Accelerator Control Division, Bhabha Atomic Research Centre, Trombay, Mumbai 400 085*

*Abstract*

In 2016-17, a 1 MW, 352 MHz klystron was tested and commissioned in long pulse mode using Regulated High Voltage Power Supply (RHVPS) as cathode bias supply. This klystron had coupled the RF power of around 540 kW to the 3 MeV proton radio frequency quadrupole (RFQ) accelerator of the low energy high intensity proton accelerator (LEHIPA). A high amount of ripple was observed in the output of RHVPS, which affected the RF power stability of klystron and hence the beam acceleration of the RFQ accelerator. Then, a pulse modulator with better specifications was used as a cathode bias supply in place of RHVPS. High Voltage Interface System (HVIS) and anode biasing system had been designed for long pulse & CW mode of operation. But, the response time of pulse modulator is in the range of few tens of µsec. In order to match the response time of pulse modulator, HVIS and anode biasing of klystron have been modified to get the desire results.

This paper discusses the modifications made for converting CW or long pulse system into a fast rise and fall time pulse system and then its subsequent coupling with RF amplifier system. Test results and waveforms of klystron system during 3 MeV proton beam acceleration are discussed in this paper.

## 1. INTRODUCTION

Earlier, a 1 MW, 352MHz klystron RF system [1] was tested and commissioned in long pulse mode using Regulated High Voltage Power supply (RHVPS) as cathode bias supply. The presence of high ripple of RHVPS (~11 %) affected the phase stability and amplitude stability of RF power output of klystron which in turn affected RFQ beam acceleration.

### Initial RF phase and amplitude stability measurement

Figure 1. shows the waveform of RHVPS ripple and Figure 2. shows the phase stability of the RF Driver (100 W). Fig.3 shows effect of RHVPS ripple on phase stability waveform of RF output power from klystron.

RF Power output stability was measured using the AD 8302 phase detector circuit, which two RF inputs are required to measure the phase stability. First RF signal was sampled through a signal generator using 2-way-splitter. Other RF signal was sampled through wave guide Directional coupler at RFQ end. Both the input RF signals were compared and phase change was recorded in the DSO (fig 3).

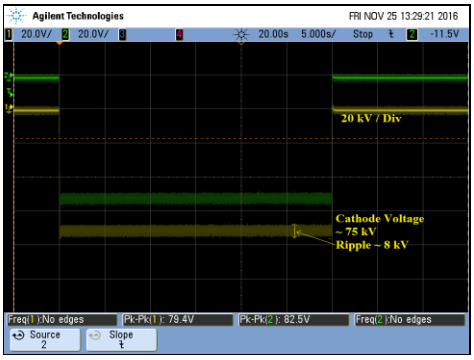


**Figure 1: RHVPS voltage ripple variation**

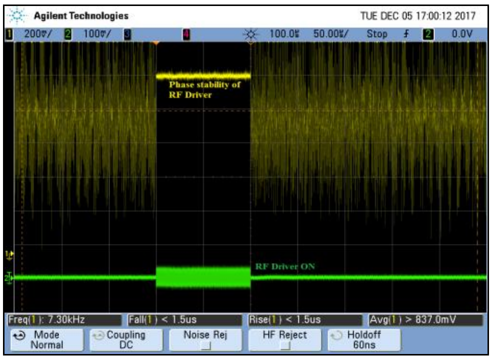


**Figure 2: Phase stability of RF output of RF Driver**

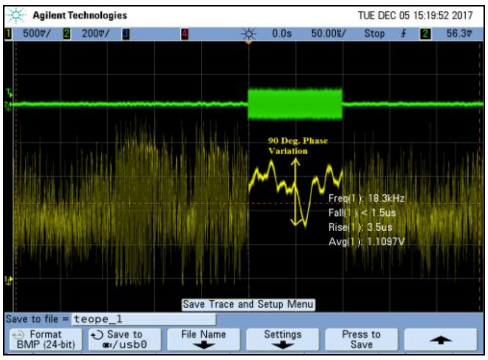


**Figure 3: Effect of RHVPS ripple on phase stability of RF output of klystron**

**System Description of Klystron**

In low energy high intensity proton accelerator (LEHIPA) set-up, klystron is located in the tunnel approximately 15 meter below the ground level and cathode bias supply is located at ground floor. RHVPS was replaced by a pulse modulator as cathode bias supply. The pulse modulator specifications are pulse width (max.): 400 µsec, pulse rise and fall time: 40 µsec, ripple: $\leq$ 1 %, PRR: 2 Hz maximum.

The distance between the cathode supply and klystron is approximately 20 meter. Cathode supply is integrated with klystron via high voltage interface system (HVIS) and HV coaxial cables. HVIS provides interface between the cathode power supply and klystron high voltage terminal. HVIS comprises of filament transformer, HV divider, dumping switch, crowbar and its protection circuitry, HV resistors, HV connectors etc.

The stray capacitances and inductances of the cathode cables and anode bias, caused substantial changes in the cathode current pulse shape.

In the previous setup, the anode bias assembly was designed for CW application and was located very near to the klystron. With this configuration, when cathode bias voltage was applied to the klystron from pulse modulator, it was observed that anode voltage settling time is higher than the cathode voltage settling time. In this condition, klystron has drawn excessive beam current (> 20 A) even at lower cathode voltage (< 60 kV). So for operation beyond this, it would have drawn more than 24 ampere and klystron would have damaged permanently. To avoid this scenario, mod anode biasing assembly was modified.

## 2. MODIFIED ANODE BIASING SET UP

The anode biasing assembly was replaced with compact, non-inductive HV resistors. These resistors were mounted and integrated inside the klystron electron gun oil tank to minimize the stray capacitance and inductance. Figure 4. shows the block diagram of the klystron system with pulse modulator and modified anode bias set up.

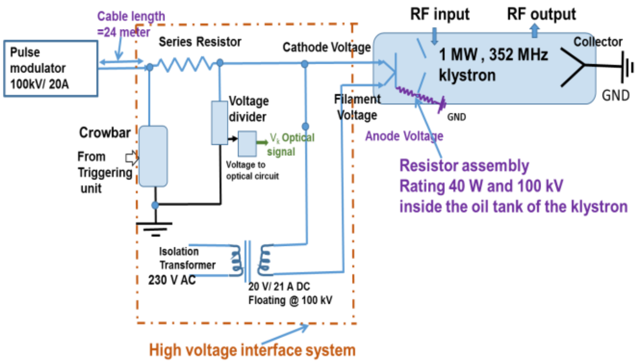


**Figure 4: Block diagram of 1 MW klystron with pulse modulator**

The HV resistors used are rated for 100 kV. The cooling for these resistors is provided by the oil inside the tank. The inside view of the klystron tank including anode basing resistors connections is given in figure 5.

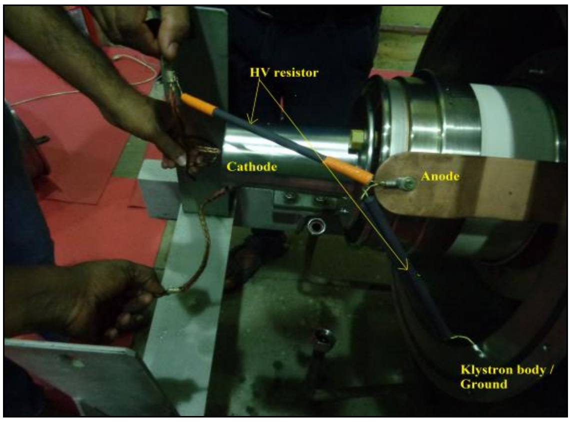


**Figure 5: Inside view of klystron tank assembly**

HV insulation test was carried out to ensure the insulation between the electrodes of klystron using 100 kV DC CW tester.

This modified anode basing set up helped to improve the anode voltage settling time. This set up will work even for low duty cycle (< 0.1 %).

## 3. TESTING OF KLYSTRON WITH PULSE MODULATOR

Control and communications signals of the pulse modulator were integrated with interlock and protection systems of the klystron. Klystron biasing was established in pulse mode. During initial testing of klystron, 16 A overshoot in the pulse waveform of cathode current was observed and is shown in figure 6.

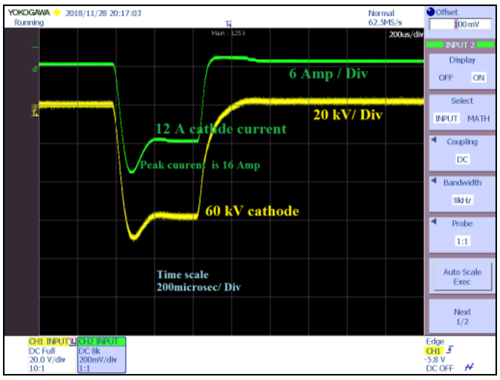


**Figure 6: Cathode Voltage & Current with overshoot**

So, HV coaxial cable lengths were optimized to reduce the stray capacitances and inductances of the cables. This has improved cathode voltage and current waveform with much less overshoot as shown in figure 7.

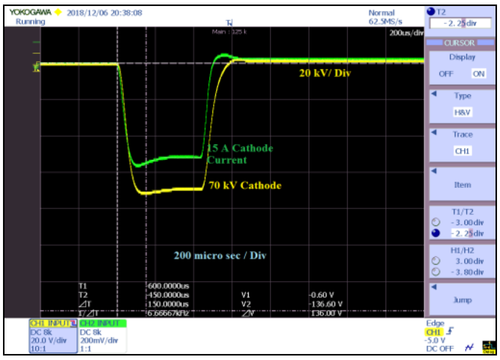


**Figure 7: Cathode Voltage & Current with reduced overshoot**

## 4. RF TESTING RESULTS

Other bias supplies of klystron were optimized and then, klystron RF system was tested using pulse modulator on matched RF load. The results obtained are shown in Table 1.

Table: 1. Klystron test results

| Sr. | Parameters | Values |
|---|---|---|
| 1 | Cathode voltage ($V_k$) | 78 kV / 17 A |
| 2 | Anode voltage | 0.66 $V_k$ |
| 3 | Filament | 17 V / 21 A |
| 4 | Electro magnet I & II | ~ 300 V / 10 A |
| 5 | DC peak power | 1.34 MW |
| 6 | RF frequency | 352 MHz |
| 7 | HV Pulse parameters | 400 µSec, PRR: 1 Hz |
| 8 | RF pulse width | 100 µSec |
| 9 | RF power | ~ 650 kW |
| 10 | Phase stability | 2 Deg. |

The improved RF power and phase stability waveforms are given in figure 8 & figure 9. The phase stability of RF output power was measured to be 2 degrees using the AD8302 phase detector.


**Figure 8: Output RF power waveform in spectrum analyzer**

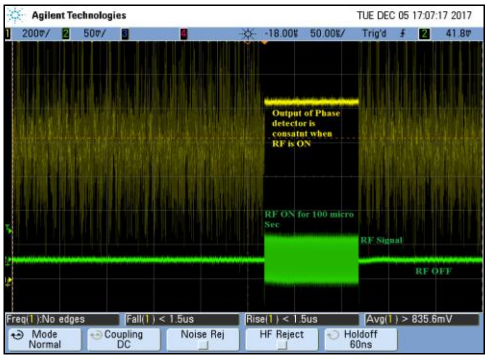


**Figure 9: Improved RF phase stability measurement**

## 5. INTEGRATION OF KLYSTRON RF SYSTEM WITH 3 MEV RFQ ACCELERATOR

The klystron RF power was coupled to two coupling ports of the 3 MeV RFQ accelerator via wave guide distribution line. A rigorous RF power conditioning RFQ was done before successfully achieving of 3 MeV proton beam acceleration.

## 6. CONCLUSION

After incorporating proper modifications in anode biasing system, the klystron system was successfully tested and commissioned with pulse modulator across RF load up to 650 kW (figure 9). Thereafter, klystron has been operated for around 3 months continuously at around 600 kW during RFQ accelerator conditioning, commissioning and then 3 MeV proton beam has been successfully accelerated.

## ACKNOWLEDGEMENT

Authors like to thank to LEHIPA team and Shri. Jaikishan, RRCAT for their assistance in assembling of HV resistors inside the electron gun, and integration of pulse modulator with klystron.

Authors wish to thank Dr. Srinivas Krishnagopal, Head, IADD and Shri Purushottam Shrivastava, Director Proton group, RRCAT for their constant encouragement support and technical expertise during the installation and testing of klystron. Authors wish to thank Dr. A. K. Mohanty, Director MRG, BARC for their constant encouragement and support.

## REFERENCES

[1] Operating experience of RF Power testing of klystron at 352 MHz Sandip Shrotriya †, Niranjan Patel, Shiju A, B.V. Rama Rao, J.K. Mishra, Shyam Sunder Jena, Manjiri Pande and Gopal Joshi Accelerator Control Division, Bhabha Atomic Research Centre, Mumbai, India, InPAC-2018.

[2] Klystron Data sheet TH 2089F

# DESIGN, INSTALLATION AND TESTING OF A DIELECTRIC WAVEGUIDE TYPE DC ISOLATOR FOR ELECTRON GUN AT VECC

D P Dutta[#], Siddhartha Dechoudhury, Md. Zamal Abdul Naser, Sanket Haque, S.K. Thakur, T. K. Mandi, H. K. Pandey, Vaishali Naik, Arup Bandyopadhyay, VECC, Kolkata 700064, INDIA

*Abstract*

A 50 MeV, 100 kW CW Superconducting Electron Linac (e-Linac) will be used for the production of Rare Ion Beams (RIB) for the ANURIB [1] project at VECC. The source of electrons for the superconducting e-Linac will be a triode type RF modulated thermionic electron gun (e-gun) housed in an $SF_6$ tank delivering 300 keV electron beam. Presently, the e-gun is operated up to a maximum anode voltage of 100 kV in air with respect to the cathode. To isolate the RF amplifier from high voltage DC and transmit the RF power at the same time, a dielectric waveguide type DC isolator has been developed. This paper describes the design, development and test results for the dielectric waveguide type DC isolator.

## INTRODUCTION

A schematic diagram of the 50 MeV, 100 kW CW Superconducting Electron Linac (e-Linac) is shown in Figure 1. The first stage of acceleration for the electron beam emitted from the e-gun is called the Injector Cryomodule (ICM) with output energy of 10 MeV [2]. The ICM is based on the 1.3 GHz, 2K SRF technology and has been developed in collaboration with TRIUMF, Canada. The ICM has been tested at TRIUMF and will be installed at VECC for further testing.

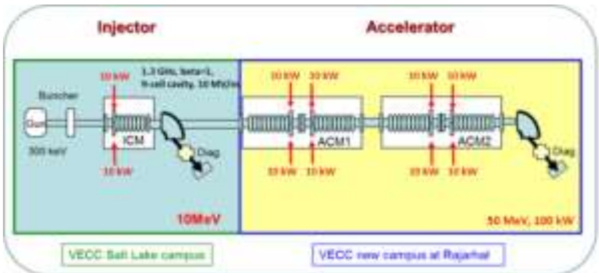


Figure 1: A schematic diagram of the 50 MeV e-Linac.

An e-gun, meant to act as the source of electron beam for the ICM, has been developed at VECC [3]. The gun emits the beam in the form of electron bunches at a frequency of 650 MHz and conduction period of ±20 degrees. This is achieved by biasing the e-gun below cut-off and modulating the grid with 650 MHz RF voltage. Although the DC power supplies for the filament and grid are floating at negative high voltage potential (-100 kV), it is advisable not to place the RF amplifier at high voltage potential [4] for protection of the device in case of a high voltage discharge. A dielectric waveguide type DC isolator has been used to isolate the RF amplifier from high voltage DC. Figure 2 shows the simulated model of the DC isolator. The DC isolator consists of two circular waveguide sections made of copper with one end of each section shorted by a copper plate. The other ends of the circular waveguide sections are joined by a dielectric rod that fits perfectly inside the circular waveguide sections. A PTFE cylinder of appropriate dimensions acts as the dielectric for the circular waveguide sections.

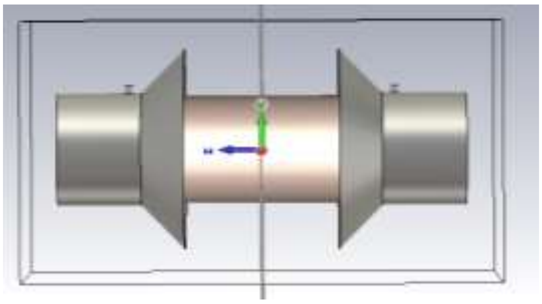

Figure 2: Simulated model of the DC isolator.

There is a discontinuity of the copper walls between the two waveguide sections, which provides the necessary DC isolation. At the area of transition from metal-dielectric to air-dielectric along the waveguide surface, conical horn type matching has been employed for efficient transmission of RF power. The DC isolator has been tested successfully for RF power transmission at an anode voltage of up to 100 kV.

## DESIGN AND SIMULATION

The design of a circular waveguide for operation at 650 MHz involves the determination of the cut-off frequency for the desired mode of RF power transmission. The ascertainment of the cut-off frequency would lead to the determination of the dimension of the waveguide. For a circular waveguide, the dominant mode with the lowest cut-off frequency is the $TE_{11}$ mode followed by the $TM_{01}$ and other higher modes. For the propagation of RF power at 650 MHz in $TE_{11}$ mode, and taking into account the fact that frequencies very close to the waveguide cut-off frequency have significant attenuation, the cut-off frequency has been assumed to be 550 MHz. The radius of the circular waveguide for the $TE_{11}$ mode for a cut-off frequency of 550 MHz may be calculated using the Eq. 1.

$$f_{c,nm} = \frac{p'_{nm}}{2\pi a\sqrt{\mu\varepsilon}} \qquad (1)$$

In Eq. 1, $f_{c,nm}$ is the cut-off frequency, $p'_{nm}$ is a root of the derivative of the Bessel function of the first kind, *n* and *m* being the number of circumferential and radial variations respectively of the transverse electric field, and *a* is the radius of the circular waveguide. Virgin PTFE with a relative dielectric constant ($\varepsilon_r$) of 2.1 has been used

[#]dpdutta@vecc.gov.in

for the fabrication of the DC isolator. The radius of the waveguide has been found to be 110 mm.

For the same radius of 110 mm of the circular waveguide, the cut-off frequency for the $TM_{01}$ mode has been found to be 719 MHz. This is well above our frequency of operation of 650 MHz. Hence, the dimension of the waveguide has been chosen such that the $TM_{01}$ mode and all higher modes become non-propagating modes and $TE_{11}$ is the only propagating mode at 650 MHz.

The wavelength of the RF wave inside the circular waveguide may be calculated using Eq. 2.

$$\lambda_g = \frac{1}{\sqrt{\mu\varepsilon}\sqrt{(f^2 - f_{c,nm}^2)}} \qquad (2)$$

In Eq. 2, $\lambda_g$ is the guide wavelength, $f$ is the frequency of operation and $f_{c,nm}$ is the cut-off frequency. For an operating frequency of 650 MHz and waveguide of radius 110 mm, the guide wavelength is found to be 600 mm.

50 Ω coaxial cables are used to feed RF power into the circular waveguide. For the excitation of RF fields inside the circular waveguide, the side launch method is used where a capacitive probe is inserted into the waveguide at a distance of $\lambda_g/4$ from the shorted end of the waveguide. Optimization of the distance of the probe from the shorted end and the depth of penetration of the probe were done using CST Microwave Studio. The optimum position of the probe has been found to be 118 mm from the shorted end with a penetration of 79 mm. In the region of transition from metal-dielectric to air-dielectric waveguide, a matching structure is required for efficient transmission of RF power. Choke-type horns were initially considered for matching purpose. However, for $\lambda_g$ of 600 mm, $\lambda_g/4$ choke transformers would become large and bulky. Simulation with conical horns, although smaller in size than $\lambda_g/4$, showed better results. Figure 3 shows the simulated 2D electric field pattern in the DC isolator with conical horn type matching.

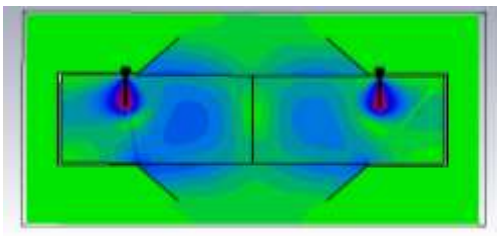

Figure 3: Simulated 2D electric field pattern in the DC isolator.

The performance of a conical horn depends on two main factors – the flare angle of the horn and the horn aperture diameter. It is known that for a fixed horn aperture, a horn flare angle of 40° – 50° gives the highest gain for the horn antenna [5]. In our case, the flare angle was fixed at 50°. It is also known that as the dimension of the horn aperture increases, a more directional beam pattern is obtained [6]. In our case, the horn aperture is 408 mm, which has been determined during simulation, with a trade-off between the size and the acceptable directivity of the horn. Optimisation of the conical horn size has been done using CST Microwave Studio.

The plots of $S_{11}$ and $S_{21}$ parameters, from simulation of the DC isolator, over a frequency range of 0.60 GHz to 0.70 GHz given in Figures 4(a) and 4(b) respectively.

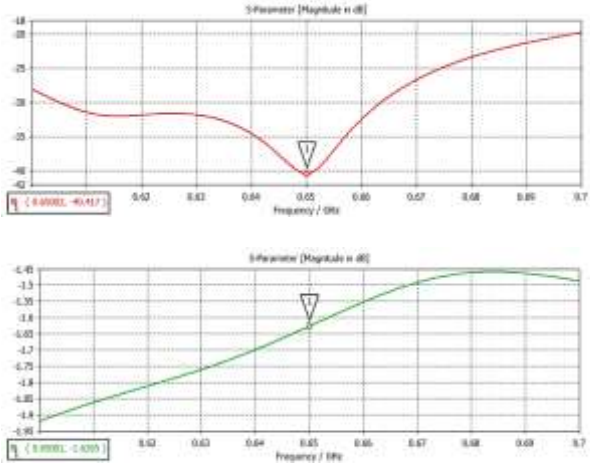

Figure 4: Simulation plot of (a) S11 parameter. (b) S21 parameter.

A polar plot of the far-field directive gain at 650 MHz for the simulated horn structure is shown in Figure 5. The polar plot shows the far-field directive gain obtained with the horn type matching, as compared to that employing an isotropic antenna in the horizontal plane. The gain increases towards the direction in which the horn is pointing and achieves a maximum value at an angle of 179°. A directive gain of 9.38 dBi is obtained in the direction of maximum radiation by using the horn type matching.

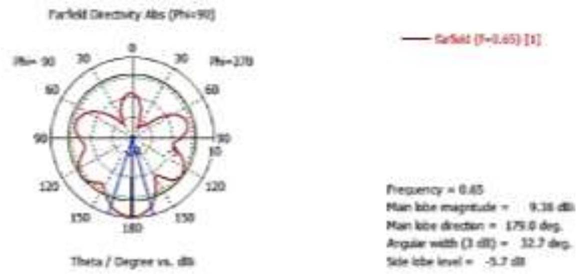

Figure 5: Polar plot of radiation pattern in the horz. plane.

## FABRICATION AND TEST RESULTS

The circular waveguide sections of the DC isolator have been fabricated using 5 mm thick copper sheets rolled to form cylindrical shape with inner diameter of 220 mm. Brazing of 5 mm thick circular copper sheets are done on one end of the circular waveguide sections to form the shorted end. The conical horn structures are made by rolling 1 mm thick copper sheets to the required dimensions so that a flare angle of 50° was maintained. All the copper surfaces were given smooth finish to reduce the surface conduction losses of RF power.

Low power RF measurements were initially done for the fabricated waveguide type DC isolator before subjecting to high voltage. The s-parameters of the DC isolator have been measured with and without the horn type matching. The simulation results and low power measurements of $S_{11}$ and $S_{21}$ are shown in Table 1.

Table 1: Simulated and measured S-parameters

| S-parameters at 0.65 GHz | Simulated value | Measured value |
|---|---|---|
| $\|S_{11}\|$ without horn | -12.0 dB | -14.5 dB |
| $\|S_{11}\|$ with horn | -40.4 dB | -17.0 dB |
| $\|S_{21}\|$ without horn | -7.49 (19 % transmission) | -7.50 dB (19 % transmission) |
| $\|S_{21}\|$ with horn | -1.63 dB (69 % transmission) | -1.71 dB (68 % transmission) |

The low power measurement of the s-parameters for the DC isolator has been done using Vector Network Analyser Agilent E5061A. The screen shots of the measurement of $S_{11}$ and $S_{21}$ are given in Figures 6(a) and 6(b) respectively.


Figure 6: Plot of measured (a) S11 parameter. (b) S21 parameter.

The DC isolator has been tested at 100 kV DC voltage and 35 W CW RF power has been applied to the waveguide type DC isolator. A better design of DC isolator is possible by using dielectric of higher relative permittivity (like Alumina, $\varepsilon_r \approx 9.6$) which will ensure better confinement of the electromagnetic wave in the air-dielectric interface. A picture of the fabricated DC isolator has been given in Figure 7.

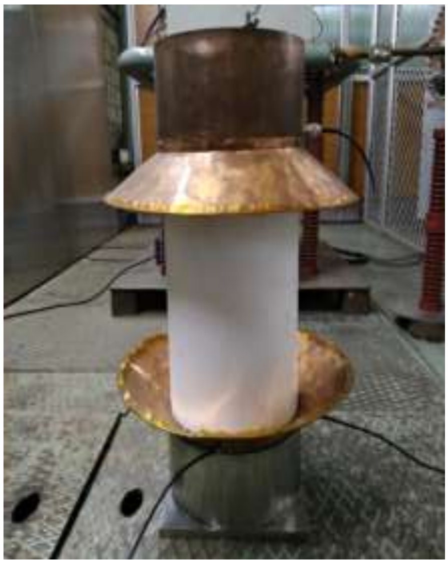

Figure 7: A picture of the fabricated DC isolator.

## CONCLUSION

A dielectric waveguide type DC isolator has been designed and developed for the purpose of isolating the RF amplifier from high voltage DC anode bias. PTFE dielectric has been used in the waveguide. Satisfactory DC isolation has been obtained along with RF transmission suitable for our requirement. Conical horn type matching has been employed to improve the transmission characteristics. The device has been tested satisfactorily. Further improvement in performance is possible by using a dielectric of higher permittivity.

## ACKNOWLDGEMENT

The author would like to sincerely thank Mr. Ken Fong, Scientist at TRIUMF, Canada for useful discussions and guidance.

## REFERENCES


[1] Alok Chakrabarti *et al.*, "The ANURIB Project at VECC - Plans and Preparations", Nuclear Instruments and Methods B 317 (2013) 253.

[2] V. Naik *et al.*, "VECC TRIUMF Injector for the E-LINAC Project", Proc. of LINAC (2010) 726.

[3] Md. Zamal Abdul Naser *et al.*, "Characterization and testing of RF modulated 100 kV thermionic electron gun", Proc. of InPAC 2018, Indore, India.

[4] K. Fong *et al.*, "Design of an RF modulated thermionic electron source at TRIUMF", Proc. of IPAC2018, Vancouver, BC, Canada, THPMK095.

[5] G. C. Southworth *et al.*, "Metal horns as directive receivers of ultra-short waves", Proc. of the IRE, Vol. 27, Issue 2, Feb 1939, p 95 – 102.

[6] A. P. King, "The radiation characteristics of conical horn antennas", Proc. of the IRE, Vol. 38, Issue 3, March 1950, p 249 – 251.

# DESIGN, INSTALLATION AND OPERATIONAL EXPERIENCE OF VACUUM SYSTEM OF 10 MeV ELECTRON LINACS

B.K. Sindal[1#], K.K. Malviya[1], K. Kumar[1], Vijay Bais[1], Smt. Sujata Joshi[1],
R.S. Sandha[2], Y. Wanmode[3] and D.P. Yadav[1],
[1]Ultra High Vacuum Technology Section
[2]Industrial Accelerators Division,
[3]RF System Division,
Raja Ramanna Centre for Advanced Technology, Indore - 452013, INDIA

*Abstract*

Raja Ramanna Centre for Advanced Technology has indigenously developed 10 MeV, 6 kW Travelling Wave (TW) electron linacs (02 nos.) for irradiation of medical, agricultural and industrial products. The required operating vacuum in linac is in the order of $10^{-6}$ mbar range and the average static vacuum in $10^{-8}$ mbar range was achieved with the help of Triode Sputter Ion Pumps (TSIP) of RRCAT make. The pressure is measured by two radiation resistant cold cathode gauges at two locations and user defined pressure safety interlock of these gauges are utilised for generating automatic trip for linacs.

The length of the entire vacuum system of linac is approximately 4.45 m and materials of construction are mainly stainless steel 304L, 316L and OFE copper. The vacuum envelop of linac mainly consists of vacuum chambers of Electron gun assembly, vacuum manifold-1, collimator assembly, accelerating linac structure with RF power input and output couplers, UHV gate valve, vacuum manifold-2, ACCT, bellow chamber, and beam scan horn subassembly.

For initial development and testing, linacs were first installed, commissioned and tested for its design parameters and trouble free prolonged operation in test vaults at RRCAT. The vacuum system was dismantled after testing and finally installed at Agriculture Radiation Processing Facility (ARPF) site near Sabji Mandi, Indore, successfully commissioned and operating at its design parameters.

This paper describes the vacuum system design and development details, installation, commissioning and operational experience of vacuum system of both the electron linacs.

Key words: Travelling wave, linacs, TSIP, and ACCT.

## INTRODUCTION

Raja Ramanna Centre for Advanced Technology has indigenously developed 10 MeV, 6 kW Travelling Wave (TW) electron linacs (02 nos.) for irradiation of medical, agricultural and industrial products.

Vacuum condition is necessary to avoid oxidation of electron gun cathode working at high operating temperature, inhibit microwave arcing and electrical breakdowns inside linac structure and minimise scattering of electron beam with residual gas molecules resulting in beam energy loss and increase in beam divergence.

#email – bksindal@rrcat.gov.in

## VACUUM SYSTEM DETAILS

The length of the entire linac vacuum system is approximately 4.45 m and materials of construction are mainly stainless steel 304L, 316L, OFE copper and alumina ceramic. The vacuum envelop of linac mainly consists of vacuum chambers of Electron gun assembly, vacuum mainifold-1, collimator assembly, accelerating linac structure with RF power input and output couplers, UHV gate valve, vacuum mainifold-2, ACCT, bellow chamber, and beam scan horn assembly. The schematic of linac vacuum system is as shown in Figure-1.

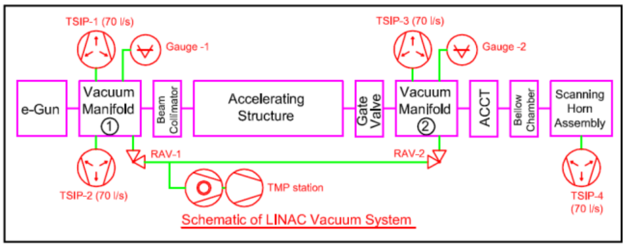


Figure 1: Schematic of linac vacuum system.

In order to minimize the vacuum gradient between different sections due to conductance limitation, distributive pumping scheme was suitably adopted. The smallest aperture of dia. 4.5 mm is available at exit port of electron gun. The electron gun section is pumped by two 70 l/s Triode Sputter Ion Pumps (TSIP) connected in vacuum manifold-1. Two TSIP were appended in electron gun for fast degassing and activation of dispenser cathode, it also provide redundancy of electron gun vacuum system with an additional pump. Figure-2 shows the internal dimensional details of beam pipe of linac Vacuum system along the beam direction.

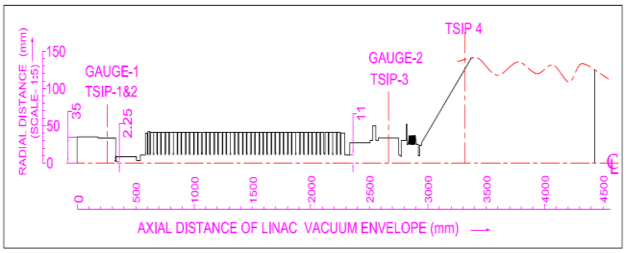


Figure 2: Internal dimension details of linac.

The vacuum system is divided into two segments using UHV gate valve, i.e. the electron gun side section with accelerating structure and scan horn side section for ease of maintenance.

One TSIP of 70 l/s is connected in vacuum manifold-2 just after the gate valve for pumping of linac structure and one TSIP of 70 l/s is provided in scanner horn assembly. TSIP and its controllers used for linacs were developed indigenously for use in accelerators at RRCAT.

Two cold cathode radiation resistant vacuum gauges are provided for pressure measurements at two locations i.e. at electron gun section (in vacuum manifold-1) and Scan horn section (in vacuum manifold-2).

User defined interlock of cold cathode gauges were utilized for safety interlock for linac. If pressure rises above $1\times10^{-6}$ mbar due to high gas load, the vacuum interlock gets activated and puts off the accelerator operation by switching off the klystron. The readouts of both the vacuum gauges were displayed and logged in control room PC.

The austenitic Stainless Steel (SS) components used were chemically cleaned, electropolished and vacuum degassed as per the UHV standards for minimise the outgassing rate to maintain the average static vacuum in the range of $10^{-8}$ mbar. Outgassing rate of copper cavities before brazing was evaluated in UHV lab using standard outgassing measurement setup as $7.02\times10^{-11}$ mbar-l/s-cm$^2$ for unbaked condition after 100 hours pumping. The outgassing rate was also evaluated after baking at 250 °C for 4 hrs as $6.43\times10^{-13}$ mbar-l/s-cm$^2$. The specific outgassing rate of SS was considered as $1\times10^{-10}$ mbar-l/s/cm$^2$ for chemically cleaned, electropolished and vacuum degassed in unbaked condition as per previously measured results.

All the demountable joints were utilised with metal gaskets, mainly OFE copper gaskets with conflate flanges, diamond shaped aluminium seals and Indium wire seal in Titanium foil window assembly to minimise the permeation gas load and avoided use of elastomer seal.

The pressure profile for unbaked condition shown in figure-3 was simulated with Ansys Software using one dimensional thermal analogy model using link elements.

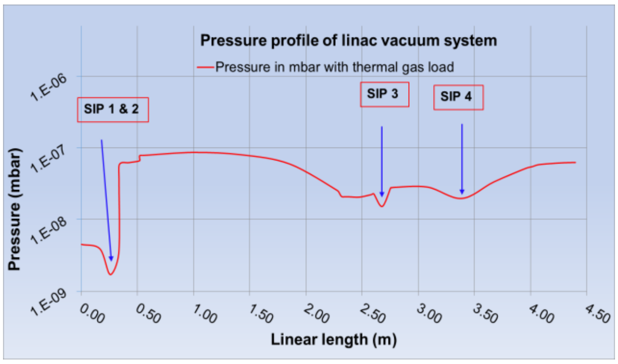


Figure 3: Simulated pressure profile.

Total volume of the system was ~70 litres, with area of vacuum exposed surfaces ~ $4\times10^4$ cm$^2$. The average specific outgassing rate was considered as $1\times10^{-10}$ mbar-l/s/cm$^2$, total effective pumping speed of TSIP's 200 l/s. Calculated average static base pressure ~ $2\times10^{-8}$ mbar considering the dominating gas load due to thermal outgassing from vacuum exposed surfaces.

## INSTALLATION & COMMISSIONING

All the components mainly linac structure, vacuum manifolds were leak tested using Helium Mass Spectrometer Leak Detector (HMSLD) for qualifying leak rate of $<5\times10^{-10}$ mbar-l/s after fabrication and cleaning. During development and testing stage the linacs were installed at RRCAT in dedicated test vaults.

The linac structure was installed on base structure using precise supports and other peripheral components like collimator assembly, RF power input and output couplers, UHV gate valve, vacuum mainifold-2, ACCT, bellow chamber, and beam scan horn assembly were assembled using appropriate metal gasket. TSIP-3, vacuum gauge-2 and all metal right angle valve were also assembled with vacuum manifold-2 and SIP-4 was assembled with beam scanning horn assembly. Complete assembly was leak tested using HMSLD.

During development process it was expected many modifications in the linac system will necessitate frequent atmospheric exposer of vacuum system which can degrade the performance of dispenser cathode of electron gun assembly. So one gate valve was also provided for isolation of electron gun vacuum system and was removed after initial testing. The electron gun assembly consists of alumina ceramic chamber, vacuum manifold-1 with two TSIP's (70 l/s), vacuum gauge, all metal right angle valve (RAV-1) and a gate valve. The electron gun assembly was always kept under vacuum for protection of cathode.

After assembly and leak detection of linac vacuum segment with scan horn assembly and other peripheral components, electron gun assembly with gate valve was connected to the linac system. A common plumbing line was assembled joining both the right angle valves (RAV-1 & 2) for connecting of TMP station. The system was again leak tested with HMSLD for newly assembled joints. Figure-4 shows the photograph of linac system in test vault at RRCAT.

Figure 4: Photograph of linac in test vault.

Initial vacuum was created with oil free Turbo Molecular Pumping (TMP) station with dry baking pump. Completely oil free TMP station is utilized to avoid any contamination in linac vacuum system. After prolonged pumping with TMP station for 10 to 12 hours attained the vacuum level in the range of $10^{-6}$ mbar, then the vacuum system shifted on SIP's after conditioning and TMP was isolated by closing the right angle valves. After 12 hours of SIP pumping, desired vacuum in the range of $10^{-7}$ mbar has been achieved. TSIP's 1 and 2 were operated with single common controller, similarly TSIP's 3 and 4 also operated with single controller for ease in operation and maintenance. The TSIP's controllers facilitate remote operation and display ON/OFF status in control room PC.

After attaining the vacuum level in the range of $10^{-7}$ mbar, conditioning of electron gun cathode was carried out under vacuum, initially the cathode gives very high gas load. The heating power was increased slowly in steps with limiting vacuum trip level of $10^{-6}$ mbar. The cathode conditioning was completed in 2 days. The cathode was also tested for evaluation of dynamic gas load at operating conditions resulting $10^{-8}$ mbar-l/s in lab after conditioning.

RF commissioning in linac structure starts with low power with 1 Hz pulse repeating rate (PRR), as unconditioned structure generates very high initial gas load, the vacuum was continuously monitored and kept below the tripping limit of $1x10^{-6}$ mbar and the RF power increased slowly upto the targeted 6 MW peak power. Repetition rate was increased in steps to reach 250 pulses per second. The RF conditioning of linac structure was completed in several days of operation.

During commissioning stage the linacs were vented to atmosphere several times to incorporate modifications. The venting was carried out with dry Nitrogen and similar evacuation procedure was adopted to obtain the desired vacuum level and linac structure conditioning every time.

In first stage linacs were operated for 1 kW beam power at 9 MeV, followed by 3 kW at 9.5 MeV in second stage, the typical vacuum readings of the system during 3 kW beam power condition with 9.5 MeV at 150 PRR was noted as $8.3x10^{-8}$ mbar in gauge-1 (e-gun side) and $2.3x10^{-7}$ mbar in gauge-2 (scan horn side). 6kW beam power was achieved with 248 PRR in final stage of commissioning with reasonable vacuum level [1].

The linacs were also tested at RRCAT for endurance and trouble free prolonged operations to meets its actual service requirements before deployment at actual site in multiple shift operation. Figure-5 shows the actual photograph of linac 1 and 2 deployed at ARPF site.

Figure 5: Photograph of linac 1 and 2 at ARPF site.

After successful installation and commissioning of both the linacs, vacuum system was dismantled, Shifted and finally installed at Agriculture Radiation Processing Facility (ARPF) site, successfully commissioned their and operating at its design parameters.

Table 1 shows the vacuum readings of Linacs 1 & 2 installed at ARPF facility.

Table 1: Vacuum readings of linacs

| Linac | e-Gun side (Gauge-1) | Scanner side (Gauge-2) |
|---|---|---|
| Linac-1 (without beam) | $4.7x10^{-9}$ mbar | $3.8x10^{-8}$ mbar |
| Linac-1 (with beam) (At 9.5 MeV, ~5 kW) | $3.8x10^{-8}$ mbar | $8.3x10^{-8}$ mbar |
| Linac-2 (without beam) | $2.1x10^{-9}$ mbar | $2.1x10^{-8}$ mbar |
| Linac-2 (with beam) (At 9.5 MeV, ~5 kW) | $1.9x10^{-8}$ mbar | $6.7x10^{-8}$ mbar |

## CONCLUSION

The vacuum system of 10 MeV, 6 kW Travelling Wave (TW) electron linacs were successfully designed, tested, installed and commissioned at RRCAT and finally deployed at ARPF site and performing satisfactorily. Both the linacs were installed and commissioned for its design parameter 10 MeV, 6 kW beam power in stages as per the test procedure at ARPF site. The simulated results of pressure profile are well within the agreement with the actual obtained vacuum level in the linacs.


## ACKNOWLEDGEMENT

Authors thankfully acknowledge the contribution of entire team of colleagues involved directly or indirectly in this linac development program. Authors Sincerely Thanks to Shri A.C. Thakurta, Director Electron Accelerator Group & Co-ordinator linac Development Program, Shri P. Shrivastav, Director Proton Accelerator Group, Shri R. Sridhar Former Head, UHVT Section, Shri Jishnu Dwivedi, Head IA Division for their constant encouragement. Supports from IA Division, RF Division DMT Division and chemical treatment facility are also acknowledged. Effort of Shri V.G. Sathe, Shri A.S. Yadav, Shri Vishnu Pandey, Shri Shambhu Ram, Shri T.R. Meena, Shri Vipin Chand Rajbar, Shri Mukesh Chand and Shri M.M. Vadgama for their respective help in completion of job is also appreciated.


## REFERENCES


[1] Development of Second 10MeV Industrial electron Linac by R.S. Sandha et.al. InPAC 2018

# INSTRUMENTATION OF HTS STEERING MAGNET FOR K500 CYCLOTRON BEAM LINE

T. Das#, T. K. Bhattacharyya, U. Bhunia, A. Roy, R. Rakshit
VECC, 1/AF, Bidhan Nagar, Kolkata-700064, India

*Abstract*

The steering magnet is required for the external beam line of K500 cyclotron to provide corrective beam steering. A conventional copper based steering magnet for high rigidity beam (maximum upto 3.3 T-m) becomes very bulky and difficult to integrate in cyclotron beam line if large steering (± 3 degree horizontal (X) and ±1.5 degree vertical (Y)) is required. Recently, commercial availability of long length (>500 m) high temperature superconductor (HTS) tape along with availability of high power cryo-cooler has opened up the opportunity to develop compact conduction-cooled HTS magnet operating at 20K or even higher. Although, many prototype magnets using HTS tape have been fabricated and evaluated, there exist only a handful of applications in the particle accelerator fields. The paper reports the instrumentation and test result of high temperature superconducting X-Y steering magnet along with details of cryostat developed in Variable Energy Cyclotron Centre (VECC), Kolkata.

## INTRODUCTION

The steering magnets are the essential part for the high energy beam line of K500 cyclotron to provide corrective steering to the beam in X-Y direction. Since the discovery of HTS material, commercialization of HTS tape for practical applications are underway. HTS is very fast becoming the ideal choice for developing magnets because of its advantages of higher operating temperature, higher specific heat leading to rare quench, etc. over low-temperature superconductors (LTS). Recently developed HTS technology along with commercially available closed cycle cryo-cooler makes the perfect duo for designing conductively cooled superconducting magnets. Although many HTS magnets are developed, application to the field of accelerator beam line is rather limited. VECC, Kolkata has initiated developing a high field HTS steering magnet of cold mass of around 300 kg and field of 6.8/3.3 kG. It is equally challenging to develop state of the art instrumentation for such magnet system. The paper describes detailed instrumentation setup, interlocks, data logging and reports the latest test results.

## SYSTEM DESCRIPTION

The magnet system consists of magnet coils and fixtures, cryostat mechanical arrangements, sensors and instrumentation, control system, interlocks, etc.

### *Coils and mechanical arrangements*

The cryostat consists of conduction-cooled BSCCO-2223 HTS coil placed inside iron yoke. Two sets of Double Pan-Cake (DPC) racetrack coils – one set for vertical field ($B_y$) and other for horizontal field ($B_x$) inside the return iron yoke are used. Coils are fabricated in-house with HTS tapes (HT-CA from M/s. Sumitomo Electric, Japan) by wet winding technique using cryogenic grade epoxy. The scheme of the conduction-cooled magnet system is as shown in Fig 1. The DPC coils are thermally connected to second stage cold head of the cryo-cooler through conductive link.

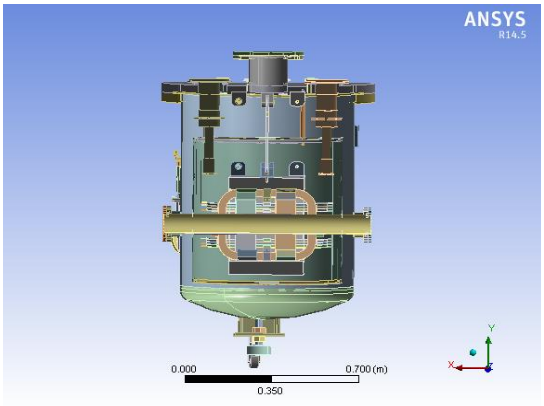


Figure 1: Mechanical arrangement of magnet cryostat

The cryostat is evacuated by turbo-molecular pump and cold mass is cooled by second stages of two Gifford McMahon cryo-coolers. The coils are suspended by glass-fibre reinforced plastic (GFRP) links to minimize heat leaks. The current lead is of a series combination of normal conductor and HTS tape based conductor (Hybrid). The entire cold mass is surrounded by intermediate thermal shield cooled by first stage of cryo-cooler. Thermal shield is wrapped by 20 layers of multilayer insulation to minimize the thermal radiation load from room temperature wall of the cryostat. Two pairs of HTS current lead with designed warm end at 60 K and cold end temperature at 20 K are used to feed the current independently to the *X* and *Y* coil. The current leads are optimized for minimum heat leak with a current of 250 A.

### *Sensor installation and Instrumentation*

The sensor installation schematic (Fig 2) shows that, mainly two types of measurements are used in the setup, e.g. temperature and voltage. For accurate and extensive measurement of the temperature during cool-down and energization of the magnet coils, temperatures at twenty two nodal points are measured. Calibrated Cernox sensors Lakeshore CX1050 are used for their extremely high sensitivity (dR/dT=30.87 Ω/K @ 20K), long range (1.4 K-400K) and minimum effect in the magnetic field.

#tanmoy@vecc.gov.in

Cernox sensors are placed on the two nodes on the *X* and *Y* magnet coils.

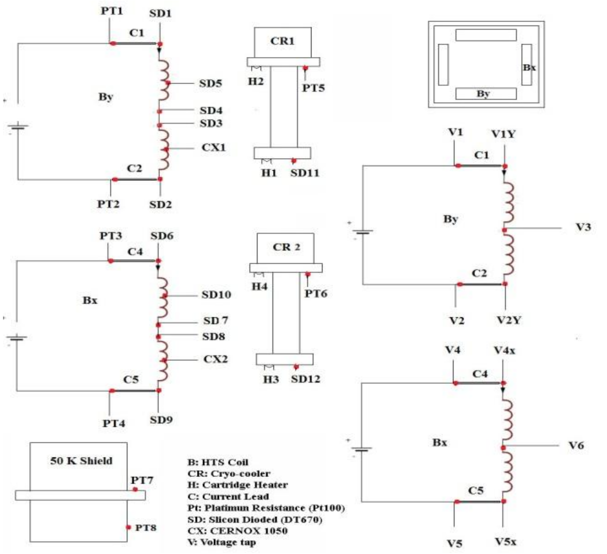


Figure 2: Schematic of sensor instrumentation

They are used in limited numbers mainly to reduce cost and to monitor coil temperature during cool-down as well as energization stage. The cooldown phase temperatures are monitored by twelve number of silicon diodes (Lakeshore DT670) placed at almost every possible nodes where the temperature may reach 20K. They are used for higher signal voltage (1.2V @ 20K) wide range of operation (1.4K -500K) and high accuracy (±0.01K).The diodes are placed at the second stages of cryo-coolers and also placed in both the coils at mirror nodes of the Cernox sensors. Two diodes are installed at both sides of each coil junction and every current lead to coil side junction. Comparatively higher temperature nodes are measured by total eight numbers of Hayashi Denko Pt100 thin film element temperature sensors with α as 0.003851 Ω/K. 50K copper radiation shield body, beam line insulation and primary stage of cryo-coolers are fitted with two such sensors. Current lead to power supply junctions are also fitted with one sensor each. All the temperature sensors are installed with cryogenic grade STYCAST 2850FT Catalyst 11LV epoxy adhesive. Power supplies are connected to *X* and *Y* coils through hybrid current leads to energize the magnet. The voltage taps interlocks are used to protect the superconducting magnet from any undesirable eventuality like quenches, etc. Three taps are taken across two coil segments connected in series for *X* and *Y*. Taps across four current leads are also taken to measure the lead voltages. Apart from temperature and voltages, vacuum is a very important parameter to be measured and maintained. Independent 'Varian' Turbo Stations are installed to maintain vacuum system ~$1\times10^{-7}$ mbar. A Lakeshore hall probe is also used to measure a fixed point magnetic field at the centre of the magnet.

## *Cabling arrangements and Noise reduction*

All the temperature sensors are connected to the Lakeshore monitor with Lakeshore make Manganin wire. It is used for its non ferromagnetic properties and lower thermal conductivity suitable for cryogenic applications. These wires are used to connect the sensor pads to terminal board fixed at 20K region of the cryostat. A Terminal board (TB) is used to reduce the conductive heat load on the system through wires and easier replacements of the sensors (Fig 3). The same wires connect TB to the vacuum insulated instrumentation feed-through pins fitted at the top flange of the cryostat. Teflon insulated wires are used to carry signals from feed-through pins to individual channel of the Lakeshore temperature monitor. The heater coils are also connected in the same way using the same wires. Voltage taps are connected to the voltage scanner using Teflon insulated copper wires via terminal block and vacuum feed-through.

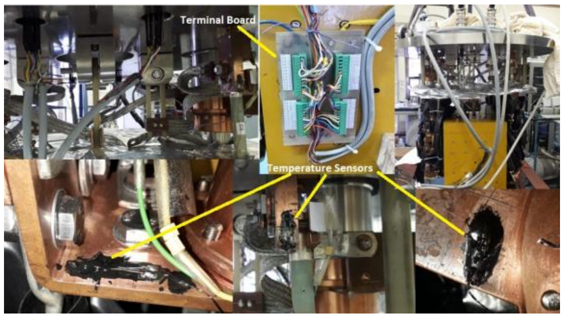


Figure 3: Sensor Installation and Cabling.

In cryogenic temperature measurement and control, there are unique challenges in addressing the many sources of potential error. Because the allowable excitation power for the sensors becomes diminishingly small as the temperatures being measured approach absolute zero. On the other hand the signal levels being measured from those sensors are extremely low. The standard methods of electrical noise reduction are followed for the set-up by adopting four wire measurements and using shielded signal cables. The cables are shielded by grounding one side of the shield with the instrumentation ground. All the instruments are also grounded from their chassis to the firm ground.

Apart from the regular precautions, recently noise-reducing circuits are incorporated by the OEM to improve cryogenic temperature controllers and their overall measurement capability. There are two major aspects of these improvements. One with adaption of specialized matched impedance input circuitry from AC resistance bridges that prevents external noise power. The other is to operate at excitation powers that are nine times lower than before, with a comparable reduction in measurement self-heating errors and an improvement in resolution, speed and overall control stability.

## *Control system and interlock*

All field sensors are connected to monitors and controllers placed on a 19 inch rack and data is fetched displayed and logged by a HMI running in a local computer in the same rack. To receive signals from temperature sensors Lakeshore model 218 monitor and Lakeshore model 332 controller are used. Temperature data is read by the HMI using RS232 communication protocol, displayed and logged.

Figure 4: Actual Setup with Instrumentation.

Advantec EKI 1524 Serial device server module is used to fetch data from multiple RS232 instruments through TCP-IP. During warm-up phase, two 25W and two 50W cartridge heaters are also controlled by the Lakeshore 332 controller. The voltage taps are connected to a Keithley switching unit 7001 multiplexer where Keithley 7064 voltage scanner cards are installed to process the voltage signal and finally the single output of the 7001 MUX is read by Keithley 2001 microvoltmeter. Voltage data is transmitted from microvoltmeter to the HMI following GPIB protocol. The HMI software is developed in-house using control studio platform and it fetches data from various instruments, displays it and log the time-stamped data in excel file. The two coils are powered by Danfysik make System 8500 power supply of 10V, 300A. The 10ppm stable power supply is custom built with current ramp, quench protection and other standard in-built interlocks. There are mainly two interlocks: one is for quench protection and the other one is for temperature interlock of the current leads. The voltage taps for the steering magnets are taken through hybrid type current leads and connected to the quench protection circuit of the power supply. The quench interlock operates at 300mV across each coil and 0.3mV across each of the current leads. For any of the mentioned condition the magnet power supply is dumped through air cooled dump resistors. If the temperature of the leads rise more than 80K the magnet power supply is dumped. This interlock is activated through the relay output of the Lakeshore temperature controller which drives the dump interlock input of the Danfysik power supply.

## TEST RESULT

The system is cooled down during Sep-Oct, 2019 and operated successfully except a few minor stoppages (Fig 5). Most of the Instrumentation part worked rather flawless. The magnetic field is measured at the centre (single point) of the magnet for the ramped up current upto 150A using Lakeshore hall probe (Fig 6).

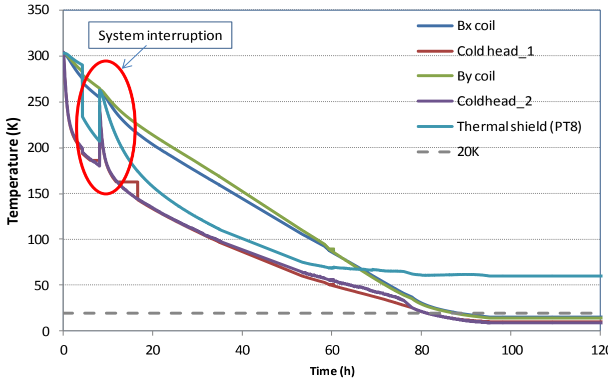


Figure 5: Cool-down curve.

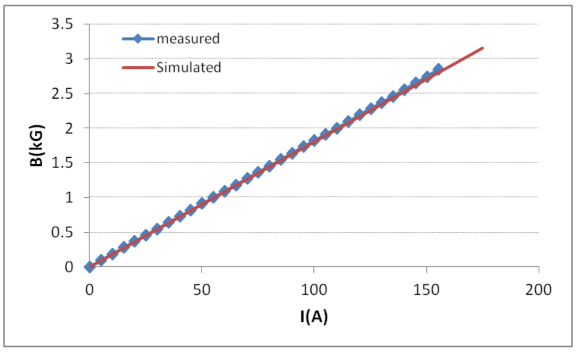


Figure 6: I vs B plot.

## CONCLUSION

The primary objective of the setup is to cool-down and test the HTS steering magnet to qualify its design aspects. From the initial data obtained from the first run the basic health of the system is found satisfactory and as per the designed specifications. The magnetic field is measured for the ramped up current upto designed value at the centre of the magnet. However the detailed magnetic field mapping is yet to be done and preparation for the activity is in progress. On successful tests, the magnet could be installed in the K500 Superconducting cyclotron beam-line. This activity has opened-up the horizon for path-breaking developments related to development of superconducting magnets for use in various field of scientific research.

## REFERENCES

[1] U Bhunia, *et.al.*, “Design of cryo-refrigerator assisted HTS steering magnet for K500 cyclotron beam line”, NSCS-25, University of Hyderabad, 8-10 Dec, 2014,

[2] V K Khare, *et.al.*, “Fabrication of racetrack-type double pancake HTS coil for K500 extraction beam line steering magnet and qualification at liquid nitrogen temperature”, NSCS-26, VECC, Kolkata, 22-24 Feb, 2017.

[3] www.Lakeshore.com

# UPGRADATION OF THE CONTROL SYSTEM OF THE 10MEV RF LINAC WITH TPLC-32 PLATFORM

R.B. Chavan*, S.T.Sonnis#, Ashutosh Mohanty#, Suraj Mukade#, Vikas Kaushik†, Umakant Yerge, Hemant.E.Sarukte, Mukesh Kumar, D.A.Roy#

Accelerator and Pulse Power Division, BARC, Mumbai, India

* rbchavan@barc.gov.in
#Reactor Control Division
†Laser and Plasma Technology Division

*Abstract*

A 10 MeV Industrial RF Electron Linac, for radiation application (Electron Beam mode or X-Ray mode) is installed at Electron Beam Centre, Kharghar, India. The accelerator is being regularly operated at 3kW average beam power for industrial and experimental irradiation applications. The control system of the same has been upgraded recently. Present control system based on RT Controller is reconfigured using an indigenously developed TPLC-32 platform. This TPLC-32 platform is qualified for Nuclear Safety Applications. There are in all 161 DI, 99 AI, 74 DO and 2 AO. Input signal are scanned at every 100msec. Data between TPLC-32 and the SCADA PC is transferred over TCP Modbus protocol. The MOVICON SCADA is used for display/monitor of the parameters. Devices of RS-232 protocol are controlled remotely through SCADA. New interface between sub systems and the TPLC-32 was developed in order to have Local / Remote operation. Pulsed Signal Measurement Circuit was modified in order to have a local display and provision of interface with TPLC-32. Datalogger tool in SCADA is used for storing the data in Database. Each table can be configured separately for logging data. Analog value signals are stored at required time interval and digital signals are stored on state change. SQL Express edition database is used for storing the data. This paper describes the salient feature of the control system with TPLC-32 Platform for 10MeV RF industrial Linac.

## BRIEF HISTORY

The former control system consists of CAMAC and a Real time controller. Replacement of the control system was planned due obsolescence of components and spares, limited signal monitoring and control capability. New Control system developed using, indigenously developed Programmable Logic Controller (TPLC- 32) will provide comprehensive signal monitoring and control with long term support.

## INTRODUCTION

A 10 MeV, 10 kW RF Electron Linac, for radiation application either in Electron Beam mode or X-Ray mode is installed and commissioned at Electron Beam Centre, Kharghar, Navi Mumbai, India. The accelerator is being regularly operated at 3kW average beam power for industrial and experimental irradiation applications[2].

An indigenously developed platform can be subjected to rigorous verification and validation procedures. Being an in-house product, long-term support for maintenance and technology up gradation is ensured[1]. The control system was developed using Indigenous Configurable Platform named (TPLC-32). It is developed as per the safety guidelines specified by AERB SG-D25 Documentation. As per the guidelines various documents like System Requirement Specifications (SyRS), System Architecture Design (SAD), Hardware Requirement (HRS), Software Requirement (SRS), Software Design (SDD), System Validation Plan and Report (SVPR) etc were prepared.

Most of the sub systems like E-Gun Filament Power Supply, Pulse measurement circuit were upgraded to interface with TPLC-32.

## SYSTEM REQUIREMENT

i) Scan Time of 100msec
ii) Fail Safe operation
iii) Easy Maintainability
iv) Ergonomics HMI
v) Database for logging the parameters/alarm/trips

## DESIGN ASPECTS

*System Architecture:*

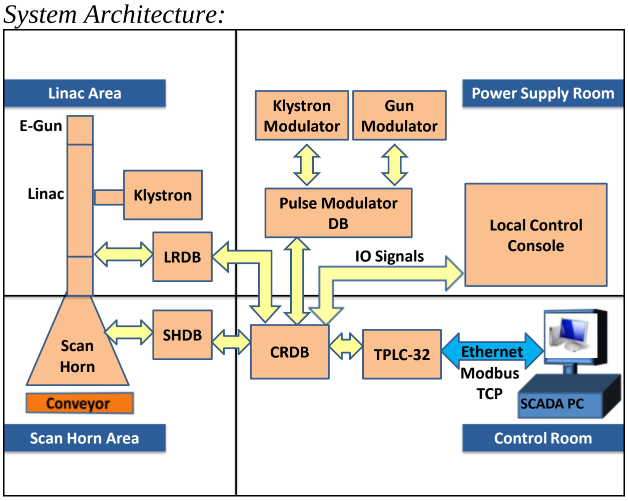


Fig 1 System Architecture

It is a centralised control system. All the signals from various location viz. Power supply room, Linac Area, Scan Horn Area are routed to control Room Distribution Box (DB). From the DB to PLC the signals are interfaced using Interface Module (IFM). Figure 1 shows the diagram of System Architecture.

*Hardware:*

The system consists of TPLC-32 platform which includes following modules. These modules are housed in two 19" Bins, one for the I/O, Control and communication modules and the other for the Analog isolation modules

| SN | Board Name | Quantity |
|---|---|---|
| 1 | CPU Board | 1 No |
| 2 | Protocol Translator Board (PTB) | 1 No |
| 3 | Analog Input Output Board (AIOB) | 4Nos |
| 4 | Digital Input Board (DIB) | 6Nos |
| 5 | Digital Output Board (DOB) | 4Nos |
| 6 | Ethernet Communication Board (ECVME) | 1 No |
| 7 | Dual Output Signal Conditioning (DOSC) Board | 16Nos |

*Local Control Console:*

Local control console was designed and developed to operate various sub systems of the Linac in local OR remote mode. Sub systems like Vacuum system, E-Gun Filament power supply etc are housed in the control console. Selector switch on the control console allows mutually exclusive local or remote operation.

*Pulse Measurement Circuit:*

Sample and Hold circuit was designed and developed[3] to measure the 5 pulsed signals (viz RF Forward Power, RF reflected power, E-Gun Voltage, Beam Current and Klystron Current of the Linac).

Sample and Hold circuit provides interface between pulse measurement circuit and TPLC-32. Pulse measurement unit consisting Sample and Hold circuit was assembled and hosed in the 19" rack mountable cabinet with local display provision as shown in Fig 2.


Fig 2 Pulse Measurement Unit

*PLC Logic development:*

The PLC logic developed was done in the software package "Application Development Environment" (ADE). ADE facilitates defining and configuring the I/O hardware boards, input / output tags, memory variables, alterable parameters, system parameters, network connections and network packets for the target TPLC-32 system. ADE Comprises of the following functions (i) System configuration (ii) FBD Editor for Logic application design in the form of Function Block diagrams (iii) Compiling the application to generate load file (iv) Downloading the load file and embedded software executables to TPLC-32 target hardware[4]. ADE also provides detailed debugging and testing of the developed application locally on EC by simulating all the field inputs and outputs. There are in all 20 FBD developed. Each sub system logic is developed in individual FBD.

*SCADA Development:*

COTS SCADA Development Package named "Movicon" was used to develop Human Machine Interface (HMI) .Fig 3 shows GUI to operate the linac from the control room.

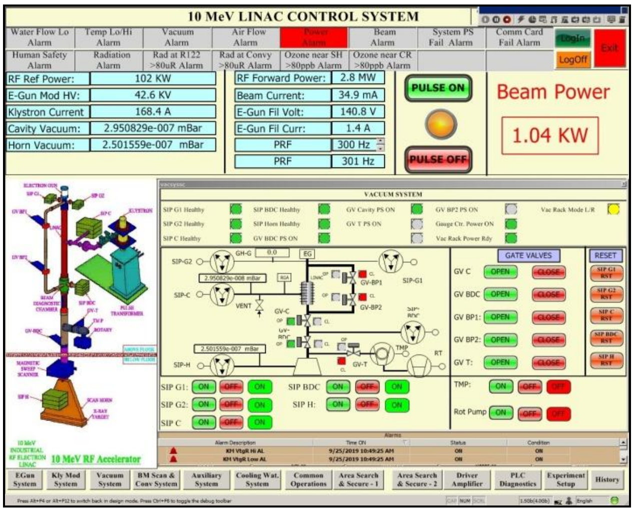


Fig 3 GUI developed in Movicon

*Database development:*

There are 8 subsystems in 10MeV RF Linac. Tables were created on basis of sub system. Entity Relationship Diagram was prepared. Individual sub system has its own DI and AI table. DI table entries are updated on-change in the state and AI tables entries are on periodically updated. Microsoft SQL Server Express Edition is used for relational database management system for storing the data. Data is stored in database with MOVICON SCADA Datalogger tool.

## TESTING AND SYSTEM INTEGARTION

Testing and integration of the control system with Linac was done in three steps

i) Offline Simulator on Engineering Console
ii) Test using I/O Simulator
iii) System Integrated Testing
iv) Commissioning

Offline Simulation mode is used to validate the PLC control logic before downloading it to actual PLC hardware. Application Development Environment (ADE) provides the feature where the inputs to the function block can be changed and outputs are checked. The testing was done as per the System Validation Plan and Report (SVPR). Offline Simulation validated correctness of the control logic.

PLC Hardware was programmed with control logic and tested using I/O simulator. I/O simulator was used to feed input (Analog and Digital) to respective boards. This test validated control logic along with PLC hardware.

Before interfacing various subsystems to the control system integrated test was carried out. In this test Voltage Input were injected at the point of interface for actual sensor before and output of the system was verified. Provision of make break of the contact was provided in place of the actual contact. With this testing field wiring was tested.

During Commissioning a sensors/contacts for each subsystem were connected and tested in incremental phased manner and complete system Validation test was performed as per SVPR.

## CONCLUSION

TPLC-32 based control system was successfully commissioned in March 2018. Since then it is working satisfactorily. Linac is being regularly operated at 3kW beam power to facilitate the user requirement.

## REFERENCES

[1] U.W.Vaidya et al , Indigenously developed Programmable Logic Controller for Safety Class IA and IB systems, SACI 2014, pp

[2] Mukesh Kumar et al, Utilization of 10MeV RF electron Linear Accelerator for research and industrial applications, Indian Journal of pure and Applied Physics Vol. 50, November 2012, pp 802-804

[3] R.B.Chavan et al, Development of control system for 10MeV Industrial RF Linac , InPAC - 2018

[4] User Manual for Trombay Programmable Logic Controller (TPLC-32) Platform, Revision 1, Pg 27

# DESIGN AND DEVELOPMENT OF DIRECT OFF LINE SMPS (20KV/15MA) USING COCKCROFT-WALTON VOLTAGE MULTIPLIER FOR RIB

Yashwant Kumar*, S. Srivastava, A. De, A. Bera, V.K. Khare, S.K. Thakur
Variable Energy Cyclotron Centre, 1/AF Bidhannagar, Kolkata, India

*Abstract*

Switch mode power supply rated 20kV/ 15mA is designed and developed indigenously for biasing the Einzel lens electrode of ECR ion source of the Rare Isotope Beams (RIB) facility at VECC. The power stage of the high voltage power supply consists of DC link converter followed by an inverter based on full wave forward topology, high frequency step up transformer and Cockcroft-Walton voltage multiplier. The power supply has feature of constant-current or constant- voltage (CC/CV) mode of operation. Output voltage/current is controlled and regulated by feedback technique. This is achieved by first sampling output voltage/current and then compared with a reference to generate an error signal. This error signal is given to a proportional and integral (PI) controller that control the duty cycle of inverter by generating appropriate pulse width modulation. Slow start, over voltage, over current and over temperature protection are some of the additional feature of the unit. The communication can be achieved either by local or by remote operation with RS232 port. Design of the power supply is simulated using PSIM and then developed in laboratory. In this paper, designed topology, function of system components, simulation and experimental result of the regulated half wave Cockcroft-Walton voltage multiplier (HWCWVM) is discussed in detail which maintained output voltage and ripple in desired limit.

## INTRODUCTION

High voltage DC power supplies are used in many applications such as particle accelerator, electrostatic systems, lasers systems, and electrostatic coating [1–4]. Cockcroft-Walton voltage multiplier (CWVM) is generally used when a DC power supply of low current and high voltage level is required. CWVM consist of several multiplying stage using capacitor and diode [3].

The main reasons to choose this topology is high voltage ratio, low voltage stress on the capacitors and diodes, small in size and high efficiency[4-5]. Furthermore, imposing equal voltage stress on every stage is the unique property of CWVM. Its construction is also simple and easy to implement [6]. Large output voltage regulation and output voltage ripple are the main drawback of the HWCWVMs [7]. These problems are overcome by designing a half wave Cockcroft-Walton voltage multipliers based on different capacitance per stage which are limited to medium voltage power supply [8]. However, in case of high voltage and high current circuit, where when output voltage goes down, the smaller capacitors (within the column) would be overstressed; therefore, capacitors of equal value should be used in a practical circuit [9].

In present days voltage multiplier are generally consists of four stages; a rectifier to produce DC link voltage, an inverter which produces high frequency AC voltage source, a high frequency step-up ferrite core transformer, and a CW voltage amplifier. In this paper a brief design of all four stages including HWCWVM are discussed, whose output voltage drop and output ripple are controlled within desired limit by controlling the duty cycle of the inverter stage switches. The power stage of this high voltage power supply [10], consists of DC link converter followed by an inverter based on full wave forward topology, and high frequency step up transformer.

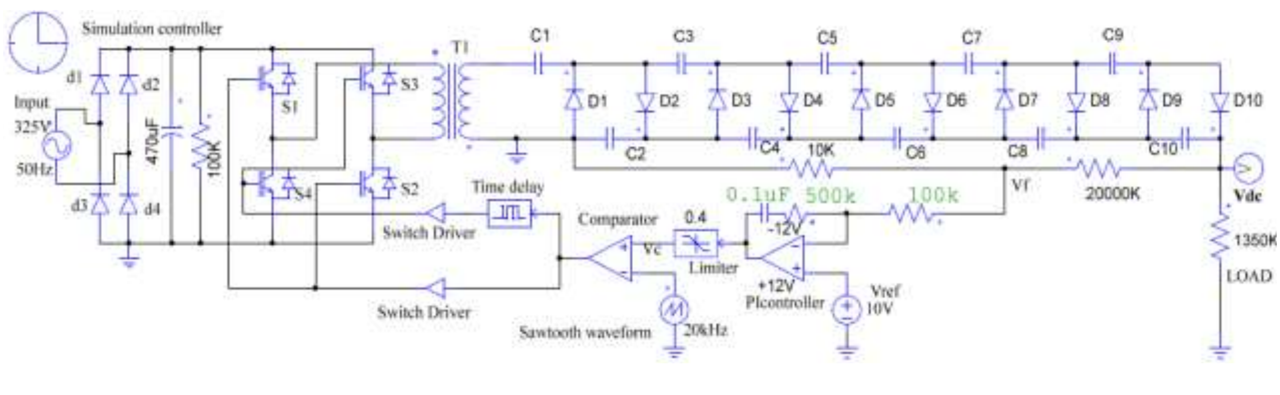


Figure1: Schematic of power supply

yashwant@vecc.gov.in

## SCHEMATIC DETAILS

The schematic diagram of the present power supply is shown in Fig. 1. In order to obtain DC link voltage, initially 230V single phase AC is first rectified with single phase full wave bridge rectifier and filtered with capacitive filter to obtain unregulated 325V DC bus. 325V DC is then switched at 20 kHz by full wave bridge inverter circuit using IGBTs ($S_1$-$S_4$) as a switch to give high frequency AC voltage. This AC voltage is fed to primary terminals of ferrite core step up transformer, which gives 2500V AC peak.

A five stage HWCWVM circuit consists of two capacitor columns, known as oscillating columns (C1,C3,C5,C7 and C9) and smoothing columns (C2,C4,C5,C6 and C10). Oscillating column capacitors are charged in first half cycle by odd numbered diodes D1-D9 and smoothing columns capacitors are charged by even numbered diodes D2-D10. At steady state and no load conditions, every capacitor in smoothing column is charged to maximum two times of output voltage (2500V) of high frequency transformer. Therefore, the maximum value of output voltage is 25kV (2 × 2500× n) at no load condition (here n=5).

Output voltage/current is controlled and regulated by feedback technique. This is achieved by first sampling output voltage/current and then compared it with a stable reference voltage to generate an error signal. This error signal is given to a proportional and integral (PI) controller to generate a control signal *Vc*. This control signal $V_c$ is compared with a 20kHz saw tooth wave form to produce a pulse width modulation (PWM). PWM pulse is used to control the duty cycle of inverter switch to follow the output voltage $V_{dc}$ with the reference voltage *Vref*. In this power supply a PWM is generated by a SG3525 Integrated Circuit.

## DESIGN OF COCK-CROFT WALTON VOLTAGE MULTIPLIER

The relations among switching frequency of the inverter i.e. frequency of transformer output $f_0$ , value of capacitor *C*, output current $I_0$, out voltage (*Vdc*) $V_0$, output voltage of the transformer $V_s$ and number of stage '*n*' are expressed by following equations [9].

The optimum number of stages expressed as:

$$n_{opt} = \sqrt{\frac{V_s fC}{I_0} \cdot \frac{4}{3} V_s} \qquad (1)$$

Maximum no load output voltage given as:

$$V_{nL} = 2 \times n \times V_s \qquad (2)$$

Drop in output voltage with load and without regulation is calculated as:

$$\Delta V_0 \cong \frac{I_0}{fC} \cdot \frac{2}{3} n^3 \qquad (3)$$

Ripple magnitude in output voltage with load and without regulation is calculated as:

$$\delta V = \frac{I_0 n(n+1)}{4 fC} \qquad (4)$$

Maximum output voltage that can be achieved with HWCWVM and the given data is calculated by equations (5).

$$(V_0)_{\max} = \sqrt{\frac{V_s fC}{I_0} . \frac{4}{3} V_s} \qquad (5)$$

Equations (3, 4) shows that, for a given value of a capacitor *C*, $V_s$ , *f* and *Io*, output voltage drop $\Delta V$ and output ripple voltage $\delta V$ depends on selected number of stages.

The capacitor used in present power supply rated as 0.02µF and 6kV. Therefore, selected value of transformer output $V_s$ is 2500V considering a safe margin of 20% (voltage stress across every capacitor). For selected switching frequency $f_0$ (20 kHz), and given output current $I_0$ (15mA), the optimum number of stages calculated from equation (1) is Eight.

Table 1: Calculation sheet for '*n*'

| S.No. | *n* | *Vnl* | $\Delta V$ | $\delta V$ |
|---|---|---|---|---|
| 1 | 4 | 20.0kV | 1600V | 187.5V |
| **2** | **5** | **25.0kV** | **3125V** | **281.25V** |
| 3 | 6 | 30.0kV | 5400V | 394.0V |
| 4 | 7 | 35.0kV | 8575V | 525.0V |
| 5 | 8 | 40.0kV | 12800V | 675.0V |

On the basis of equations (3, 4), Table 1, shows the selection of number of stage (*n*) depending on output voltage drop $\Delta V$ and output ripple voltage $\delta V$ . In present power supply selected number of stage is Five.

## SIMULATION AND EXPERIMENTAL TEST RESULT

Figure 2, shows the simulated output voltage and output ripple waveform of the power supply with respect to time. Simulated ripple waveform shows that ripple amplitude about 500V peak-peak at full load and in closed loop conditions.

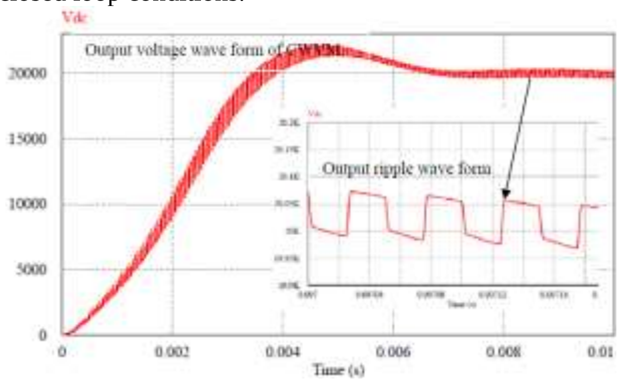


Figure 2: Simulated output voltage and ripple wave

Figure 3 shows the experimental output voltage and output ripple waveform of the power supply with respect to time. Experimental ripple waveform shows that ripple amplitude about 100V peak-peak at 50% available load load and in closed loop conditions.

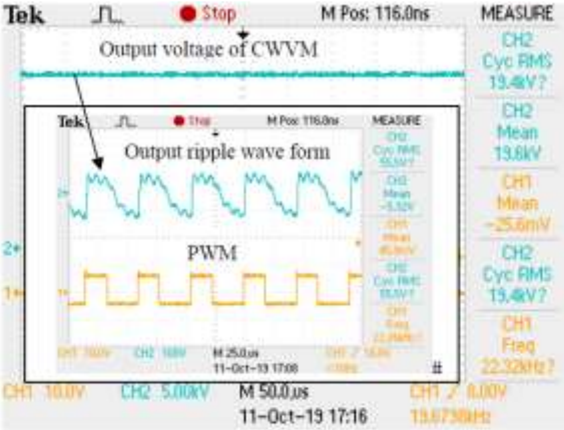


Figure 3: Experimental output voltage and ripple wave

Figure 4 shows the top view of the power supply, labeling the main part, such as power stage, high frequency transformer, HVCWVM circuit, PWM generator and auxiliary power supply.

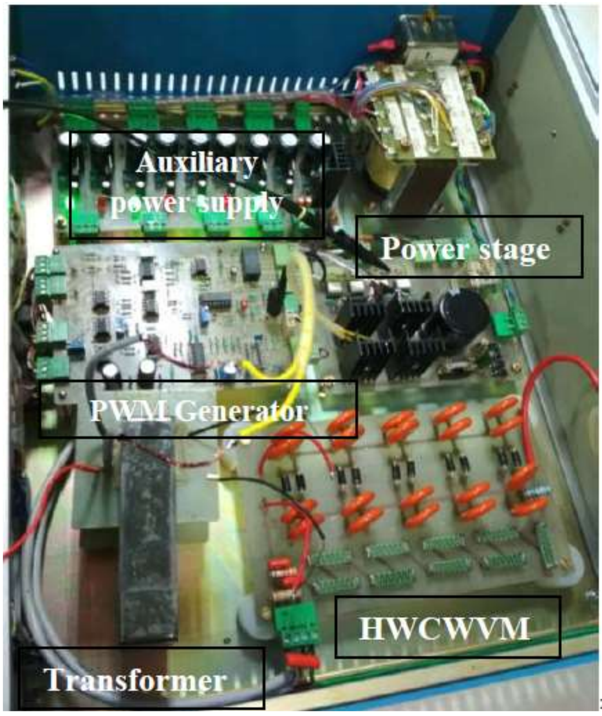


Figure 4: Photographs of the power supply (top view)

The power supply has feature of constant-current or constant- voltage (CC/CV) mode of operation. Slow start, over voltage, over current and over temperature protection are some of the additional feature of this unit. The communication can be achieved either by local or by remote operation with RS232 port.

## CONCLUSION

In this paper we have present design, simulation and development of a switch mode power supply rated 20kV/ 15mA is by using HWCWVM circuit for biasing the Einzel lens electrode of ECR ion source. The power supply has been finally tested with resistive load; various performance parameters are measured and found satisfactory. In near future this power supply will be tested with the actual load.

## ACKNOWLEDGEMENT


The authors would like to thank Mr. M. K. Gosh, Mr. A. K. Kushwaha, Mr. A. Kumar, Mr. A. Patra and Mr. V. K. Meshram technical staffs of PE & MCD Section, VECC Kolkata for their sincere supports during the development and testing of power supplies successfully.


## REFERENCES


[1] Mohsen Ruzbehani, “A comparative study of Symmetrical Cockcroft-Walton Voltage Multiplies,” Hindawi Journal of Electrical and Computer Engineering, Volume 2017, Article ID 4805268, 10 Pages.

[2] Iqbal, “A hybrid symmetrical voltage multiplier,” IEEE Transactions on Power Electronics, vol.29, no.1, pp. 6 –12, 2014.

[3] C.M. Young, M.H. Chen, S.H. Yeh, and K.H. Yuo, “A Single phase single-stage high step-Up AC-DC matrix converter based on Cockcroft-Walton voltage multiplier with PFC,” IEEE Transactions on Power Electronics, vol.27, no.12, pp. 4894–4905,2012.

[4] Z.F. He, J.L. Zhang, Y.H. Liu, Y.T. Zhang, and Y. Zhang, “Characteristics of a symmetrical Cockcroft-Walton power supplyof50Hz1.2MV/50mA,”Review of Scientific Instruments, vol.82,no.5, Article ID055116, 2011.

[5] C. M. Young, H. L. Chen, and M. H. Chen, “A Cockcroft-Walton voltage multiplier fed by a three-phase-to-single-phase matrix converter with PFC,” IEEE Transactions on Industry Applications, vol.50, no.3, pp.1994–2004, 2014.

[6] L. Muller and J.W. Kimball, “Dual-input high gain DC-DC converter based on the Cockcroft-Walton multiplier,” in Proceedings of the IEEE Energy Conversion Congress and Exposition(ECCE ’14), pp.5360–5367, IEEE, Pittsburgh, Pa, USA, September2014.

[7] H. Zhang and A. Takaoka, “Ripple due to asymmetry in symmetrical Cockcroft–Walton cascade rectifier circuit,” Review of Scientific Instruments, vol.65, no.12, pp. 3864–3865, 1994.

[8] I. C. Kobougias and E. C. Tatakis, “Optimal design of a half wave Cockcroft–Walton voltage multiplier with minimum total capacitance,” IEEE Transactions on Power Electronics, vol.25, no. 9,pp. 2460–2468,2010.

[9] C. L. Wadhwa, High Voltage Engineering, New Age International, New Delhi, India, 2007.

[10] Yashwant Kumar et al., “Design, development & testing of direct OFF line switch mode power supply for solid state amplifier”, InPAC-2018, RRCAT Indore.

# DESIGN AND DEVELOPMENT OF FPGA BASED DIGITAL TTL TRIGGER GENERATOR FOR IUAC-DLS

Ashish Sharma#, B.K. Sahu, IUAC, New Delhi, India

*Abstract*

The high power RF system of IUAC-DLS comprising of a 25 MW, S-band, 5 cell klystron, a solid state IGBT switch based pulse modulator, WR284 waveguide assembly and a 2.6 cell RF gun is currently under installation and commissioning stage. There is a requirement of multiple trigger signals for generation of synchronized high power RF pulse output from the Klystron-Modulator to accelerate the electron beam inside the RF cavity. The trigger signals are required to be in the range from 0.1 to ~35 µs width with repetition frequency in the range of 0.5 Hz till 50 Hz with a typical requirement at 6.25 Hz which is the designated repetition rate of IUAC-DLS at different delays. A system has been developed using Altera's Cyclone V Hard SoC (HPS) based FPGA which is capable of driving load in the range of 50 Ω to 1 MΩ at TTL levels. It is made with generic approach to enhance the design for including more channels in future expansions. At present, a 4-channel design has been implemented. Synchronism to reference input of Master Oscillator (MO) is also provided. Front panel controls are used to individually control each channel's pulse delay and width. Least rise time of 18 ns with a jitter of < 24 ns on falling edge and < 500 ps on rising edge is achieved. 50 ns pulse is achievable with an error of <30 ns. FPGA-HPS bridge is studied for remote control of the device.

## INTRODUCTION

High-Power RF source for IUAC-DLS consists of a Toshiba make Klystron and Scandinova make Pulse Modulator [1-2]. In order to operate the high power source in pulsed mode, 3 synchronized trigger signals for the generation of pulsed RF as shown in Fig. 1. Trigger signal T1 has to be Zero delay with ~ 9-10 µs width fed to RF Driver Amplifier, signal T2 is delayed by 3.1 µs and exits till 32.5 µs fed to the Pulse Modulator, while the signal T3 is delayed by 6 µs and exists till 10 µs owing to the 4 µs RF window as prescribed by IUAC-DLS RF requirement [1,3]. The usage and setting of signals necessitates that all the channels of Trigger Generator should be able to have a minimum resolution of 0.1 µs or better with possibility to adjust their delay and width individually.

All the Trigger signals need to be repeated at variable frequencies at various cycles of RF conditioning and operation which range from 0.5 Hz till 50 Hz with a typical requirement at 6.25 Hz which is the designated repetition rate of DLS [3]. So, the repetition rate must be at least adjustable by 0.25 Hz.

The 4-Channel TTL compatible Trigger Generator is designed and tested with high-power RF system. Design is based around Altera's Cyclone V Hard SoC (System on Chip) based FPGA (Field Programmable Gate Array) development board, which is expanded to use its SoC capabilities in the form of HPS-FPGA bridge [5] to enable remote control of the device. Following sections of the paper describes the design details and the performance results. Remote control mechanism is also briefly explained.

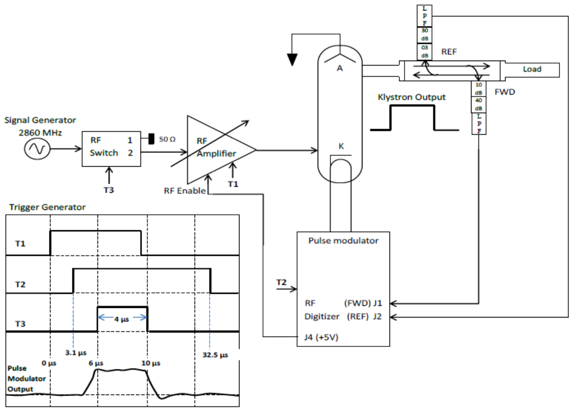


Figure 1: Layout of DLS High Power RF System

## DESIGN

### *Buffering of EXTernal Reference Signal*

An EXT reference signal from 1 MHz to 50 MHz, 3.3 $V_{pp}$ (max) is read into a General Purpose Input Output (GPIO) pin of FPGA and is used as drive input (D) to a positive-edge triggered D-flip flop implemented in VHDL inside the FPGA as shown in Fig. 2(a). A 50 MHz on board crystal oscillator serves as the clock for triggering the flip-flop. The resultant Q output of D flip-flop is further used as the main clock for whole program assembly.

### *Equal Precision Frequency Counter*

The main aim of frequency measurement in this Trigger Generator is to ensure that any frequency in the range 1-50 MHz can be used as EXT reference. It helps in derivation of minimum Time (for width and delay) and minimum Frequency resolution which are adjustable using front panel shaft encoder knobs. For a 10 MHz reference signal, a 0.1 µs time and 0.1 Hz frequency resolution is achieved.

The equal precision frequency measurement is most accurate frequency counter technique [4] wherein a gate pulse that is synchronized to the signal being measured, and is exactly an integer multiple of the measured signal period is used. Within this synchronized gate pulse, number of pulses of the system clock signal and the

#ashish.sharma@iuac.res.in

measured signal are counted simultaneously. Then the frequency of the measured signal is derived as below.

$$T = \frac{N_x}{f_x} = \frac{N_s}{f_s} \quad (1)$$

Or,
$$f_x = \frac{N_x}{N_s} f_s \quad (2)$$

Where $T$ is the synchronized gate pulse ON time, $N_x$ and $N_s$ are the number of pulses of measured signal and system clock signal respectively; that are counted simultaneously with the $T$ seconds of ON time of the synchronized gate pulse. $f_x$ and $f_s$ are the measured signal and system clock signal frequencies. In the above expressions, $T$ and $f_s$ are known beforehand, while $N_x$ and $N_s$ are computed using VHDL program as shown in Fig. 2(a). As the gate time is an integer multiple of the measured signal period, this eliminates any period error of the measured signal, as the buffered signal is fed into frequency counter module. Prior buffering of the measured signal may still cause some phase error rather than frequency error. The timing diagram of equal precision measurement is shown in Fig. 2(b).

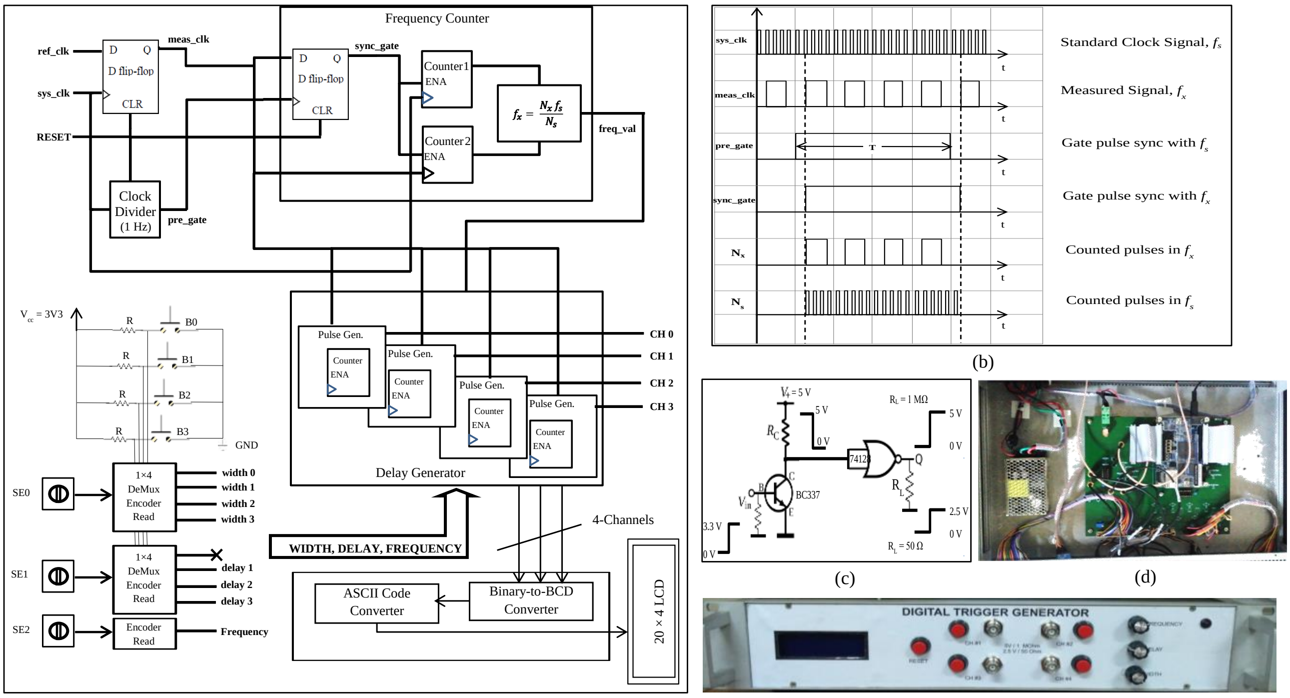


(a) (b) (c) (d) (e)

Figure 2: Complete Logic diagram of Trigger Generator (a), Equal Precision Frequency Measurement (b), 50Ω driver circuit (c), Finished PCB design (d), Front Panel of 2U×19” box with LCD, buttons, encoders and BNC Output connectors (e).

## *De-Multiplexing and Interfacing of Encoders*

In order to accept user’s input setting for pulse frequency in Hz, pulse width in μs, and pulse delay in μs, three knobs are provided on the front panel of the Trigger Generator assembly as per Fig 2(e). These knobs are used for all the channels in 1-to-4 de-multiplexed fashion. The selection of width and delay for each channel is achieved by reading the state all the 4 push buttons mounted on the front panel. Mutual exclusion is maintained among selection of any one of all the buttons at a particular instant of time. A RESET button is also provided to zero all existing settings.

The knobs are mechanical shaft encoders fed with 5V supply, which upon rotary movement of the shaft produce quadrature pulses in 2 channels which can then be easily counted inside the VHDL code. Since encoders with mechanical sensors require switch debouncing, a noise filter is used to avoid false pulsing and decoding as shown in Fig. 2(a). The pulses received from the encoder in channel A always leads channel B in case of forward movement or clockwise movement thereby counting in positive direction whereas, upon anti-clockwise movement channel B pulses lead channel A.

## *Logic implementation of Delay, Width, Period*

Each event in time domain is counted with respect to the EXT reference signal. For an EXT reference signal of typically 10 MHz, in order to produce 10 Hz repetition rate, the counter needs to count 10 MHz/ 10 Hz i.e. $10^6$ pulses. It is simply implemented by a comparator and a counter.

## *Logic implementation of Pulse Generation*

For every rising edge of the EXT Reference Signal, a tick is counted in the pulse logic implementation. A counter counts this event and checks it first with the delay value set for the particular channel from the respective knob. Once counter reaches the delay count value, the corresponding channel output is put logic ‘1’ or ‘High’ i.e. set to 3.3V. It remains as high until the counter value reaches the point of (delay + width) count from beginning. After that channel output voltage is pulled to logic '0' or 'Low'. The cycle is repeated after count corresponding to Frequency is met.

### *50Ω - 1MΩ Driving circuit*

As most of the devices offer 50 Ω termination or load which leads to increased current requirements. This current cannot be provided by the normal GPIO pins of the FPGA which are rated for around 20 mA current source. In order to facilitate driving a 50 Ω termination, an additional circuitry has been added. Here, a simple inverting amplifier circuit is built around BC337 (NPN transistor) which can offer high collector current of the order of 800 mA (DC), high bandwidth of ~ 210 MHz followed by a TTL IC 74128 (Quad 2-Input NOR 50 Ω line driver) as shown in Fig. 2 (c). Outputs are thus rated as 5V/1MΩ and 2.5V/50Ω.

### *Complete Circuit Assembly and PCB*

The design is based around Altera's Cyclone V-SoC FPGA board whose GPIO pins are read into main PCB through two 40-pin FRC cables as shown in Fig. 2(d). All the buttons, shaft encoder knobs and LCD are controlled by GPIO pins of FPGA and mounted on the front panel of a 2U×19" rack-mountable box as shown in Fig. 2(e). 3.3V EXT reference signal and the 4-channel pulse output signals are also read into and taken from GPIO pins. The 4-channel output signals drive the base of four BC337 transistors which are wired up in common emitter configuration and resulting into inverse pulse voltage output. Each of the inverse output of transistor circuit is next fed to inputs of quad 2-input NOR gate IC 74128 which acts as 50 Ω line driver.

### *Remote Control*

32-bit Lightweight HPS-FPGA bridge is used for Cyclone V HPS to communicate with FPGA via Avalon AXI bus [5]. A Qsys model of system is developed where all the delay, width and frequency parameters are modelled as PIOs/32 bit registers and memory mapped to variables in VHDL code running under FPGA fabric. A Remote ON/OFF button state is used to switch between local and remote control. All the variables are written using a C program stored in the ARM Cortex 9 HPS and used to communicate between HPS and FPGA.

## RESULTS AND DISCUSSIONS

The system has been tested with High Power RF system in the configuration shown in Fig. 1 and its performance was found to be satisfactory. All trigger requirements were 50Ω, TTL. Figures below shows the actual outputs of trigger generator captured on a 200 MHz DSO, with 10 MHz EXT reference. Outputs with 50Ω load are cleaner in comparison to 1MΩ where ringing can be seen. Rise time of 18 ns is achieved while falling edge jitter is found to be ~24 ns and rising edge jitter is ~500 ps. Sub-microsecond time adjustments are easily possible with error of around 30 ns due to fall time limitation from BC337.

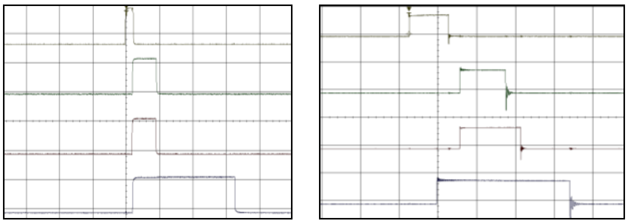

(a) (b)

Figure 3: Outputs at 50Ω load. TB = 1μs, 2V/div (a), at 1 MΩ load. TB = 2μs, 5V/div (b)

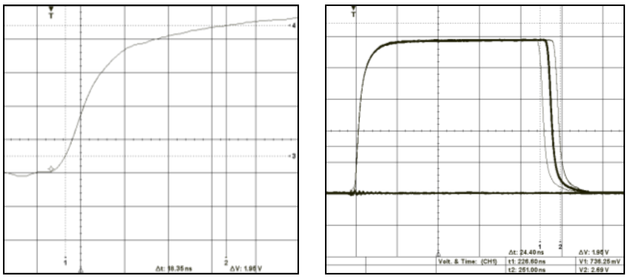

(a) (b)

Figure 2: Rise Time (a), Fall-time Jitter (b) measurements

## CONCLUSION

This Trigger Generator with achieved time related parameters like rise time, jitter etc. are found tolerable for present requirement and is tested during conditioning process of RF system. In future it is planned to be used in the operation of high power RF system of DLS with variable pulse delay, width and rep. rate. Remote control of device will be helpful during that phase.


## ACKNOWLEDGEMENTS

Authors would like to thank Dr. K. Singh for suggesting the technique for this development and Dr. S. Ghosh for providing opportunity to work on the project. Support from Prof. A.C. Pandey, Director, IUAC is also well appreciated.


## REFERENCES


[1] B.K. Sahu et al., Proceedings of InPAC 2019.

[2] A.Sharma et al., Technical Report, IUAC/TR/AS/Ref-22/2018-19.

[3] S.Ghosh et al., NIM-B, 402(2017)358-36356.

[4] Y.Y. Fang et al., SciRes, 4(2012), 696-700.

[5] Cyclone V HPS Technical Reference Manual, https://www.intel.com/content/dam/www/programmable/us/en/pdfs/literature/hb/cyclone-v/cv_54005.pdf

# APPLICATION OF EPICS CONTROL SYSTEM STUDIO IN VECC

Anindya Roy†, Shantonu Sahoo, Sarbajit Pal
Variable Energy Cyclotron Centre, Kolkata, India

*Abstract*

The PC based graphical user interface (GUI) is an essential part of the control system of complex machines like particle accelerators. A well designed multilayered user interface helps machine operators to monitor multiple machine parameters including health of the control system at various levels of interest in addition to control in a cost effective way. In VECC, *EPICS* is adopted as the control system framework for the Room Temperature Cyclotron (RTC) and Superconducting Cyclotron (SCC). The Motif Editor & Display Manager (MEDM), the GUI design tool of *EPICS* was extensively used for designing the user interface of RTC around 2008. It is based on Motif and X11and primarily designed for Linux platform. Though Windows extension of MEDM is available, but it needs a third party PC X server. Moreover MEDM is a drag & drop type development tool with limited resources. In view of the above, the *Eclipse* based latest *EPICS* GUI design tool Control System Studio (CSS) is chosen for the development of user interfaces for SCC. CSS is a rich collection of tools for designing display, diagnostics and utilities portable to Linux and Windows. Several GUIs with complex operational requirements are developed using CSS. The operational requirements, its implementation in GUI and various features of CSS are discussed in this paper.

## INTRODUCTION

There are two cyclotrons in VECC i.e. Room Temperature Cyclotron (K=130) (RTC) and Superconducting Cyclotron (K=500) (SCC). RTC is being operated round-the-clock for delivering Alpha and Proton beams at present. In SCC, beam trial is being carried out after correction of magnetic field.

The supervisory control systems of these cyclotrons are developed using *EPICS* [1], a standard open-source dual layer software tool for designing distributed control system. The Motif Editor & Display Manager (MEDM) was extensively used for developing the operator interface (OPI) of the EPICS based control system of RTC commissioned around 2008. A third party PC X server is used for running MEDM, on Windows OS based operator consoles. The inbuilt resources like GUI components, color and font options etc. are limited in MEDM. Also, there is no scripting facility in this software for implementing any operational logic, mathematical operation or file handling. Viewing these limitations and the operational requirements of SCC control system, Control System Studio (CSS) [2], java based latest *EPICS* OPI tool is selected for developing the operator interface for SCC cyclotron and in other facilities. The CSS is a feature rich tool with portability to multiple OS platforms without requiring any third party tool. The inbuilt facilities like various graphs, probe, operators' log, event based execution of Java and Python script etc. are useful designing user friendly displays, implementing complex operational logics, local file operation etc.

## CYCLOTRON CONTROL SYSTEM

The architecture of the cyclotron control system is shown in Figure 1. The device layer is composed of high current and high voltage power supplies, PLCs, beam diagnostic instruments etc. The control layer-1 consists of *EPICS* IOCs running on commercial PCs and ARM based embedded systems communicating with device layer using various types of control buses. The control layer-2 is comprised of operators' stations and control database. There is dedicated control LAN with Gigabit fiber backbone in between control layer-1 and control layer-2. The *EPICS* IOCs are running on Linux platform and operator interfaces are running on Windows platform.

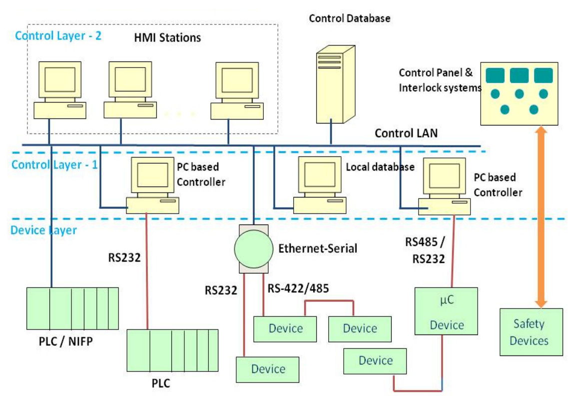


Figure 1: The architecture of cyclotron control system

### *CSS version*

The SCC control system is commissioned around 2006 and it is comprised of various in-house developed software and third party software. However the system is being upgraded with time and *EPICS* is taken up as development platform from 2008 onwards. As a result, the operators' stations are running various versions of 32bit and 64bit Windows OS. Considering the requirement of 32bit and 64bit versions of CSS, the CS-Studio 4.1.4 is chosen for implementing the SCC control interface.

### *Centralise Operator Interface Repository*

In SCC control system, a dedicated server with web interface and connected to control LAN is configured as centralise CSS GUI repository. The CSS based operator interface for various systems like Main magnet power supply, trim coil power supplies, deflector power supply ,

† r_ani@vecc.gov.in

beam line power supplies, LCW plant, Trim coil cooing system etc. are kept in centralise repository. At SCC operator console, there are six operator stations running various versions of Windows OS. In each control console, cs-studio-414 is installed and it is configured to run BOY in *No-Editing mode* with console pop-up level in *Don't Pop-up* state. The default workspace of CS-studio is configured to run the *SCC Status* page, as shown in Figure 2, while loading. The status page is designed using multiple action buttons with embedded web link for operator interface of various sub-systems kept in centralise repository. This configuration is chosen to avoid the co-existence of multiple versions of same GUI application in various operator stations.

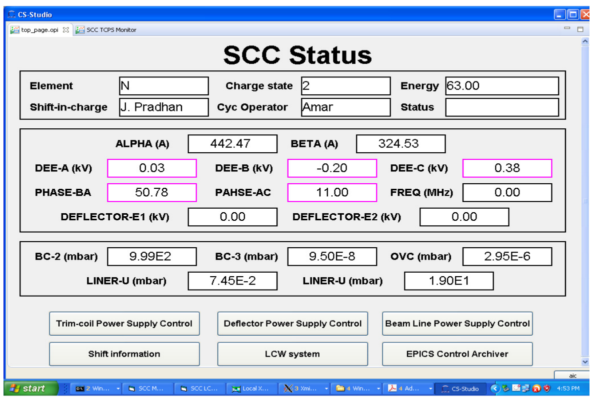

Figure 2: SCC Status page

## CSS BASED OPERATOR INTERFACE

The CSS based operator interfaces of various systems in SCC are designed in consultation with accelerator physicists through multiple iterations. The implementational complexities of individual operator interface are discussed briefly below.

### *Main Magnet Power Supply Control*

The main magnet of SCC is comprised of two superconducting coils, Alpha and Beta. These two coils are energised using two programmable DC current regulated 20V, 1000A power supplies. The control requirement includes facilities like choosing predefined

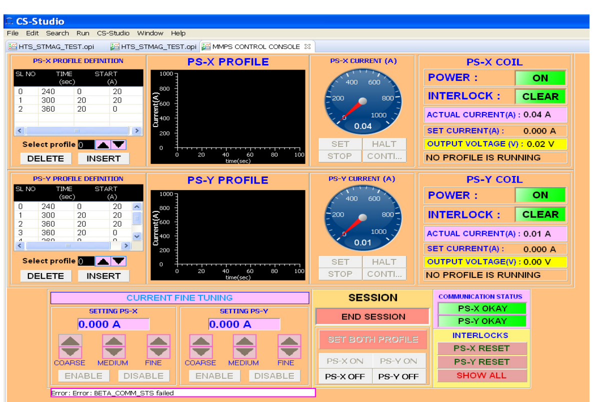
Figure 3: Main magnet control interface

ramp profile as well as editing and inserting ramp profile by the user. The ramp profiles are to be stored either in local console or centralise server. An elaborate java script with file operation and string record with special device driver are implemented for programming ramp profile, consisting of multiple string values, into the power supplies. The operator interface is shown in Figure 3. The other facilities like switching between control and monitoring mode, enabling/disabling of manual current control mode etc. are also implemented using java script.

### *Trim-coil Power Supply Control*

There are eighteen DC current regulated power supplies used to energise the trim coils of SCC. The control requirement includes facility for introducing harmonic field as per user requirement. The magnetic field and phase information for generating harmonics are stored in a file in local console. A java script involving detailed calculation of required current from field and phase value is implemented [3]. A sub-panel is also provided for changing the power supply current in harmonic mode (i.e. 1A, 1B, 1C and 13A, 13B, 13C) and display of average current as shown in Figure 4.

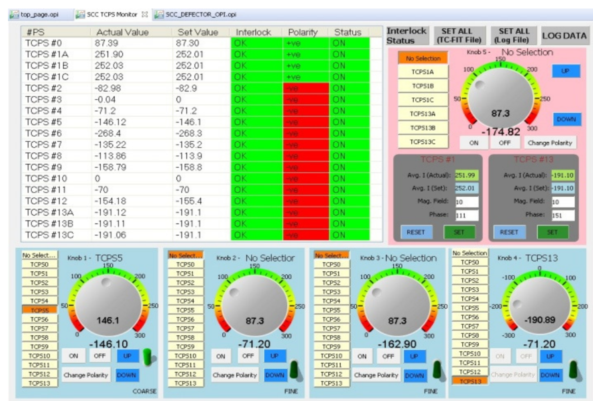
Figure 4: Trim coil control interface

### *Beam Line Power Supply Control*

The beam line of SCC is comprised of four quadrupole triplets, one steering magnet and one active magnetic channel (M9) embedded in SCC magnet. The system


Figure 5: Beam Line control interface

consisting of twelve DC current regulated power supplies are controlled and monitored over serial bus. The control requirement includes setting and monitoring of current, monitoring of interlocks and ON/OFF. The provision for fine coarse and medium level of setting is kept in the interface as shown in Figure 5.

### *Deflector Power Supply Control*

There are two high voltage deflectors, E1 and E2, in SCC for extraction of beam. These deflectors are operated using two DC voltage regulated 100 kV, 600 uA power supplies. The control requirement includes various voltage ramping options like linear ramp (RAMP), exponential ramp (AUTO), conditional ramp (CONDITIONING) as well as HALT. Though ramp options are implemented in IOC, however the power supply status, voltage current trends, ON/OFF control are implemented using various inbuilt GUI components in CSS as shown in Figure 6.

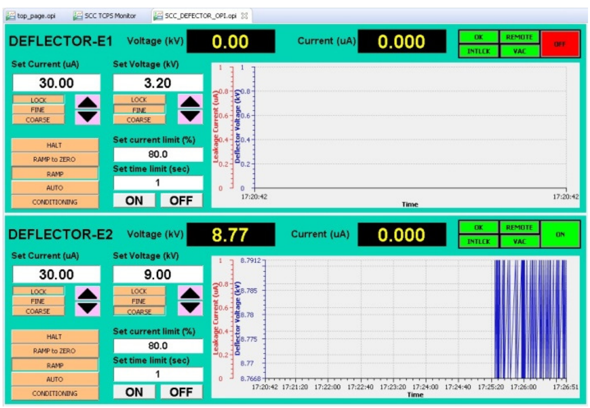


Figure 6: Deflector control interface

### *HTS Steering Magnet Test Set-up*

A High Temperature Superconductor based cryocooler assisted steering magnet is developed at VECC for the extraction beam line of K500 cyclotron [4]. The test set up of this magnet is comprised of several cryogenic temperature monitoring devices, two DC current regulated power supplies and multichannel low voltage monitoring device. The data acquisition application is developed using EPICS to introduce modular architecture for easy customization of the system. The user interface, as shown in Figure 7, is developed using CSS to implement user specific requirements like logging of time stamped data in local file, user selectable parameters for logging, scan configuration of multichannel low voltage monitoring system, configuration of temperature monitoring devices and programming of power supplies for user specified current ramp profile. These requirements are implemented through detailed java scripts associated with various widgets.

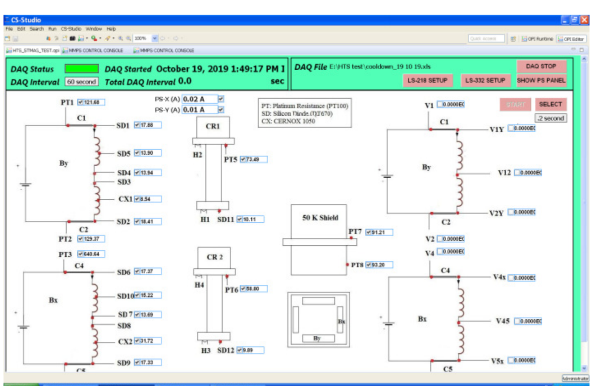

Figure 7: HTS Steering Magnet Test setup interface

## CONCLUSION

The wide collection of widgets, colors and fonts available in CSS help in designing user friendly interfaces. Application of embedded scripts associated with widgets is used extensively for implementing complex operational requirements. The embedded scripts are linked with various execution mechanisms like *Action* and *Script*. The *Action* scripts are linked to the actions like mouse click on the widget, however *Script* is linked with the change of value of associated *process variable*. The various options for opening OPI like in new window, in new tab, replace exiting are useful for controlling the number of open OPIs to ease operation. The option for opening OPI file kept in central repository through web link is utilized for version control.

## REFERENCES

[1] EPICS, http://www.aps.anl.gov/epics/
[2] Control System Studio (CSS), http://controlsystemstudio.org/
[3] S. Sahoo, et.al., "Development of EPICS based control system for Main Magnet and Trim coil power supplies", InPAC-2018.
[4] U. Bhunia, et.al., "Indigenously developed HTS steering magnet for K500 cyclotron beam line", InPAC-2019

# MODERNIZATION OF THE CONTROL SYSTEM OF 14.45 GHz ECR ION SOURCE AND INJECTION LINE ELEMENTS

Suman Kumar Guha*, Mou Chatterjee, P. Y. Nabhiraj, Arup Bandyopadhyay
Variable Energy Cyclotron Centre
1/AF Bidhannagar, Kolkata 700064, India
*suman@vecc.gov.in

*Abstract*

The 14.45 GHz ECR ion source develops multiply charged heavy ions of different species which are injected into K 500 Superconducting cyclotron for its acceleration. Several electromagnetic coils, high and low current magnet power supplies, high voltage power supply, several beam diagnostic elements along with a large numbers of vacuum pumping modules, gate valves and vacuum gauges are utilised for generation and transportation of multiply charged heavy ions. The control and data acquisition system of the 14.45 GHz ECR system was developed during the year 2002- 2003. A modernization work has been carried out during year 2018-19 for a failsafe user friendly operation. The entire control hardware is distributed into four control panels. The centralized PC based remote control system is modified for control and monitoring of each of the beam line elements, power supplies and pumping modules. Critically designed fail safe interlocks are setup according to Atomic Energy Regulatory Board (AERB) safety norms for the operation of the isolation gate valve between the cyclotron beam chamber and injection line linking with the operation of Inflector Power supply and RF screen voltage to save the system from any unanticipated failure.

The main control system is based on National Instruments' - field point modules, microcontroller based control units and a supervisory program written in NI LabView. The control unit is connected with the VECC control LAN.

**Keywords**—14.45 GHz ECR ion source, K 500 Superconducting cyclotron, Field point module, LabVIEW.

## INTRODUCTION

The K500 Superconducting Cyclotron (SCC) [1] at VECC is used for the acceleration of multiply charged heavy ions generated from 14.45 GHz ECR ion source [2]. The generation and transportation of heavy ions are being carried out utilizing several magnetic elements, beam diagnostic, power supplies and distributed vacuum pumping modules. Vacuum of the order of 1X $10^{-7}$ mbar or better is maintained throughout the injection line for better beam transportation. The centralized PC based control and operation system which was initially developed in this centre during the year 2002 -03 went through several stages of modernization during the year 2018-19 for better compatibility with the present software and hardware resources and to satisfy the design criteria of the failsafe interlock logics as per AERB norms. The upgraded system is based on distributed control panels of National Instruments field point modules, several microcontroller based control units working at field and a supervisory data acquisition – control program developed in LabVIEW. This paper describes the stages of modernization with its technical complexity.

## ECR ION SOURCE AND ITS SUB SYSTEMS

Electron Cyclotron Resonance Ion Source is a plasma device used to produce multiply charged (Z) heavy ions by allowing low charge state ions in a plasma to successive collisions (step wise ionization) with hot electrons. These electrons within plasma obtain energy from external microwave power source by Electron Cyclotron Resonance process. Plasma is confined by a B- minimum configuration inside the plasma chamber. The axial mirror field $B_z$ is produced by solenoid coils whereas the radial field $B_r$ is set by sextupole magnet. The magnetic field $B_{ECR}$ satisfies the resonance condition ie. $\omega_{ecr} = \omega_{rf.}$

The entire ECR system is comprising of the following elements: ECR Ion source, Injection line magnetic elements, Injection line beam diagnostic elements, Power supplies, Vacuum System, Microwave amplifier, LCW cooling arrangement. Figure 1 shows the schematic of the ECR Ion source along with the beam line components as presently installed for superconducting cyclotron.

## CONTROL PHILOSOPHY AND REQUIREMENT OF MODERNIZATION

The Electron Cyclotron Resonance Ion Source (ECRIS) was installed in 2008. Initially it was planned to inject the ion beam in SCC from two ECRIS to reduce the downtime while one is under maintenance. Accordingly two set of beam lines were planned to be installed hence provision was kept for more number of I/O s. Due to space constraint, a large numbers of parameters interfacing with the control channels were accommodated in a single control rack. The control hardware from M/s National Instrument which was being used till date for controlling the system parameters became obsolete hence spares and back end support became difficult to achieve. The operating system of the control console and the GUI software also became obsolete and incompatible with the existing hardware. The operation of the last gate valve (LV52) and the Faraday Cup (FC52) is highly dependent on the cyclotron safety interlocks to prevent beam injection on the cyclotron inflector when the shield door is open. The operation of the high voltage inflector power supply is also dependent on the cyclotron beam chamber vacuum and other safety interlocks.

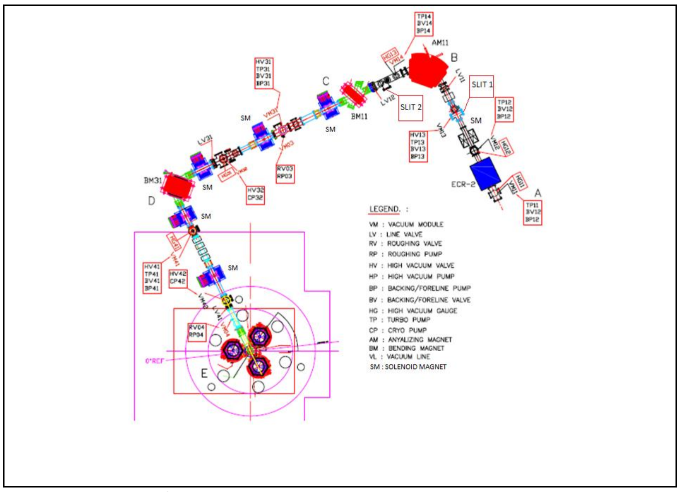

Figure 1. Layout of 14.45 GHz ECR Ion source and injection line along with beam line elements.

Hence it required an overall upgradation of the existing control system to make it suitable for use.

## HARDWARE MODIFICATION

The control hardware was upgraded from NIFP to NICFP modules [3], [4] to accommodate total 210 numbers of IOs (Digital/Analog). The complete control signals were evenly distributed among two control racks. New set of cable were laid to distribute the control cable load evenly. Figure 2 shows the complete picture of the control system before and after upgradation. For higher charge state resolution and characterization of transverse beam two jaw slit has been indigenously designed and developed in VECC. This slit is installed before the analyzing magnet as one of the beam diagnostic elements. Atmega 2560 MCU based control and monitoring system is designed and developed for the interfacing with the slit system. The system was made operational with successful beam injection in SCC.

## SOFTWARE MODIFICATION

The control console was upgraded from Windows XP to Windows 10. The proprietary GUI software (LabVIEW) version was upgraded from 7.1 to 2013. A new control tab has been added up with the present control GUI. The tab is indicating the status of the beam line vacuum components and the related interlocks. Figure 3 is showing a snap shot of this Lab VIEW front panel.

## INDUCTION OF MODIFIED INTERLOCK SYSTEM

In the earlier design, the basic interlock was designed for general interlock of ECR HV Screen, 20 kV HV extraction power supply, microwave Klystron amplifier, high current magnet power supply and vacuum system.

**Windows XP withLabview 7.1 ( Before upgradation)**

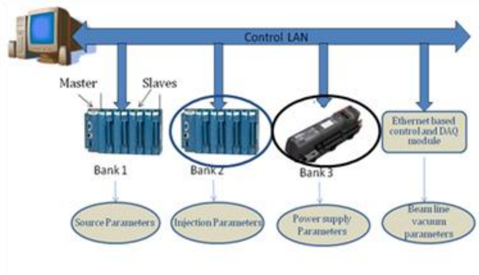


**Windows 10 withLabview 2013 ( After upgradation)**

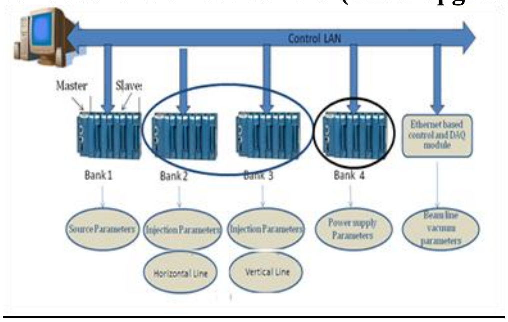


Figure 2. Hardware modification of 14.45 GHz ECR Ion source distributed control system.

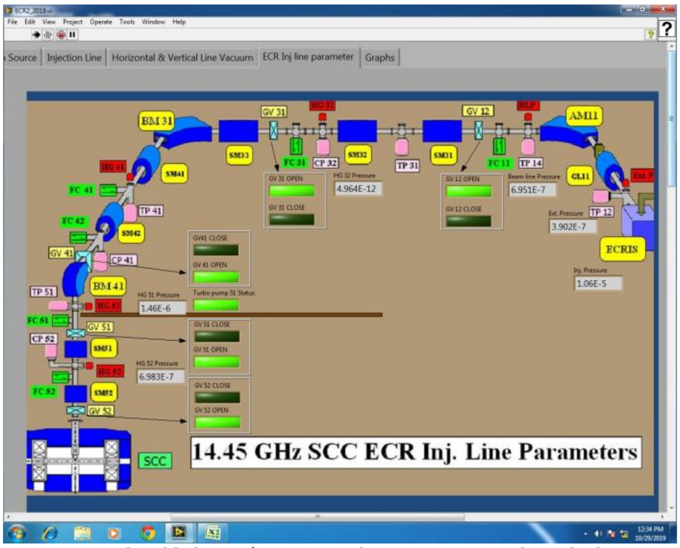


Figure 3. Newly added GUI for Injection line parameters and interlock status.

The vertical injection line vacuum system is quite different from the horizontal [5], [6] part because of frequent upper pole cap lifting and decoupling of the horizontal line from the vertical section. In this case the operation of the last gate valve in the injection line (LV52) plays a crucial role. Figure 4 may be referred for the schematic of the vertical injection line along with the beam line components. For this reason a fail-safe Interlock system was designed to maintain specific operation algorithm of the entire vertical line vacuum system and to prevent sudden inrush of air into the cyclotron beam chamber from injection side or vice versa in case of sudden leak development.

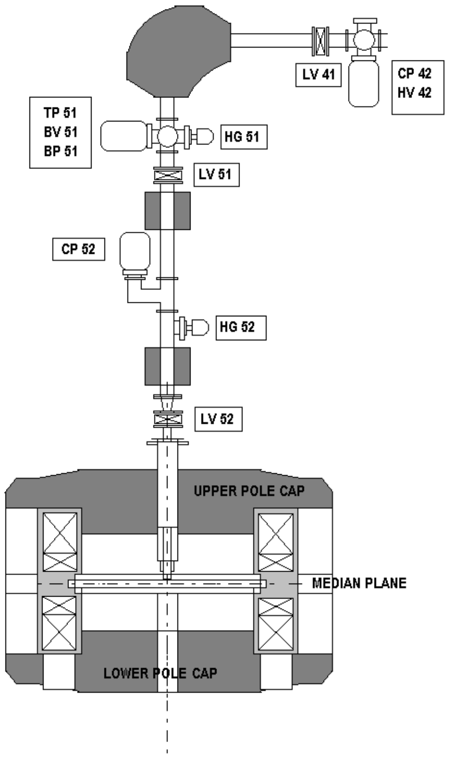


Figure 4. Schematic of vertical injection line along with SCC.

The associated interlock parameters were as follows: High vacuum gauge HG 51 and HG 52 reading, Turbo Pumping module TP 51 running status along with backing pump Rotary 51, LV51 is open/close status, Cyclotron beam chamber pressure. The previously adopted scheme for LV52 operation is shown in figure 5. In the present design the basic interlock system has been modified for the operation of Inflector power supply (20KVDC @30 mA) and LV52 considering more parameters.

*A. Inflector power supply interlock setup:*

Provisions have been kept for the associated interlocks with the operation of inflector power supply are: SCC Beam chamber pressure, Cyclotron vault & shield door status, RF screen voltage, LV52 status.

B. *LV52 operation interlock setup:*

The interlock scheme as adopted for LV52 operation considers more parameters: ECR horizontal line pressure, Cyclotron Shield door status, Cyclotron safety interlock, Status of the last Faraday Cup (FC52). The newly designed interlock scheme as adopted for LV52 operation is shown in figure 6.

## Performance Analysis and Conclusion

The 14.45 GHz ECR ion source is presently under round the clock operation generating multiply charged heavy ions. The upgraded distributed control system was tested under different conditions of operation along with the newly installed interlock schemes and was found to be working successfully. The failsafe conditions are also checked thoroughly to analyse its performance for different operational requirements. After prolonged operation if any unanticipated condition arises, necessary hard ware or software modifications will be carried out accordingly.

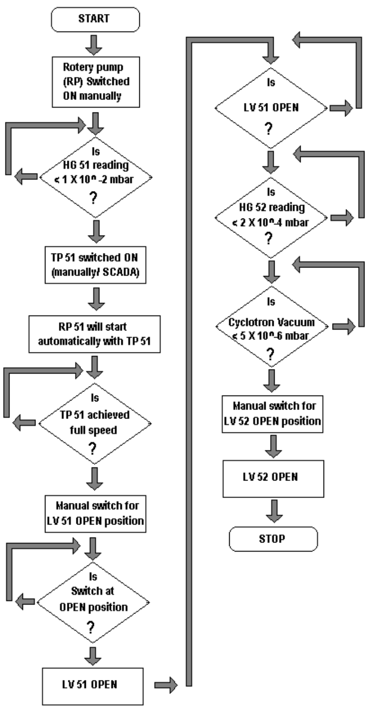


Figure 5. Previous interlock scheme as was adopted for LV52 operation.

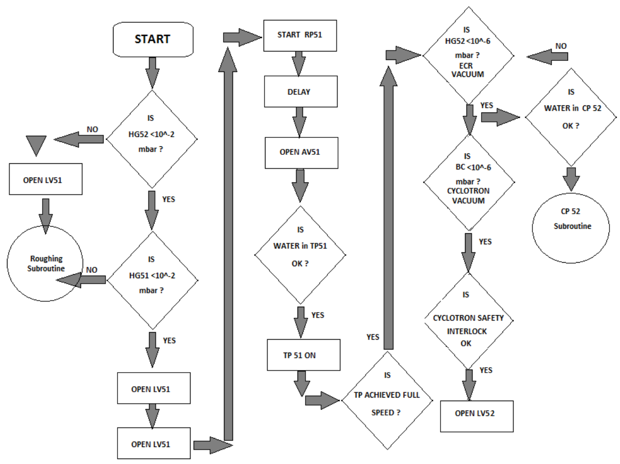


Figure 6. Modified interlock scheme of LV52.

## REFERENCES


[1] Rakesh Kumar Bhandari *, "Superconducting cyclotron project at vecc". Map India2008 -11th APAC 2007, Raja Ramanna Centre for Advanced Technology(RRCAT), Indore, India.

[2] Ian G. Brown (Ed.), "The physics and technology of ion sources". 2nd Ed. 2003 Wiley-VCH Verlag GmbH & Co.

[3] National Instruments Field point. http://sine.ni.com/nips/cds/view/p/lang/en/nid/1199

[4] Mou Chatterjee et at,"Development of an Ethernet enabled microcontroller based module for superconducting cyclotron ECR beam line control", PCAPAC 2012, VECC, Kolkata.

[5] Mou Chatterjee, Suman Guha et al. "Automation of the vacuum system of 14.4GHz ECR Ion Source and Injection line". INPAC 2013, IUAC, Delhi.

[6] Suman Guha, Mou Chatterjee et al., "Operation and interlock of vertical injection line vacuum system for superconducting cyclotron ", INPAC 2009.

# Exergy analysis for performance evaluation of a cryo-condensation based purifier integrated with helium liquefier

T. K. Maiti, A. Duttagupta, S. Pal, HBNI, VECC, Kolkata
A. Mukherjee, N. Datta, VECC, Kolkata
K.A. Jaison, V. Arolkar, K.V. Srinivasan, TIFR, Mumbai

*Abstract*

Helium purifier is an indispensible device of any helium liquefaction/refrigeration system. Helium purifiers are of two types based on their principle of operation: 1. Cryosorption, 2. Cryo-condensation. The liquefier circuit supply around 10 – 20 K coolant helium gas to cryo-condensation purifier where removal of impurity takes place by liquefaction and freezing. The product Grade 5 (99.999% helium purity) helium is then fed either to helium liquefier or stored in pressure vessel. First law of thermodynamics is widely employed for the analysis of any thermodynamic process, but this does not deal with the degradation of the quality of energy, where second law analysis or exergy study overcomes this lacuna. In this paper, an initiative has been taken to examine the exergy characteristics of an integrated liquefier-purifier device operating at Tata Institute of Fundamental Research (TIFR), Mumbai. With the help of this analysis, a process designer can identify places of thermodynamic irreversibility and find ways to make system more energy efficient.

## INTRODUCTION

With the current focus on the use of fossil fuels resulting in global warming, energy efficiency is one of the most important criteria of performance measurement of any industrial system. Cryogenic devices, being the large energy consuming systems, should be evaluated at component level to increase the efficiency of the system as a whole. The energy analysis, based on the first law of thermodynamics dealing with the conservation of energy, considers all forms of energy as equivalent. This analysis correlates the quantity between the energies, but it does not take the quality change of the energies into account during the process of energy transfer or conversion. Therefore, thermodynamic first law efficiency is inadequate for analyzing the performance of thermal systems. The exergy analysis utilizes both the first and second law of thermodynamics to correlate the quantity with the quality and effective utilization of energy by any process. Due to entropy generation characteristics below ambient temperature, exergy efficiency parameter is a good performance indicator for cryogenic processes.

Kaushik et al. [1] reviewed the energy and exergy performance analysis of different components of thermal power plant. Hafdhi et al. [2] described the exergetic analysis conducted on a power plant used in phosphoric acid factory at Tunisia. Atrey [3] conducted thermodynamic study on each component of helium liquefaction cycle and their influence on the liquefier performance. Thomas et al. [4, 5] presented the design optimization of helium liquefier applying exergy analysis method with software Aspen Hysys. Wang et al. [6] compared three configurations of helium liquefaction cycle: parallel turbines or Collins cycle, series turbines or Claude cycle, and, two parallel turbines with one expanding to intermediate pressure, using genetic algorithm.

From the literature survey, it is evident that a number of literatures are available on the exergy analysis of thermal power plant, but there is dearth of study on the exergetic analysis of cryogenic systems at liquid helium temperature. Hence, an initiative has been taken to analyse the exergy characteristics of a cryo-condensation based helium purifier presently operating at TIFR through this paper.

## CONFIGURATION AND WORKING PRINCIPLE

TIFR has an operational Linde make commercial helium liquefier L280 integrated with internal purifier. This purifier functions on the principle of condensation and freezing out of impurities by reducing the vapour pressure of impurities with decreasing temperature. Fig.1 shows the schematic diagram of helium purifier.

The purifier system comprises of Heat exchangers, Impure helium dryer, $LN_2$ separator vessel, Heater, Valves, Temperature and Pressure sensors. All of these are housed into the cold box of helium liquefier, except dryer.

The purifier achieves best performance with an impurity level of 0 - 2% nitrogen impurity by volume. The impure helium is delivered to the purifier from cylinder bank at pressure of 24 bar absolute (bar) and at ambient temperature. This impure helium passes through a dryer at node 6 and enters cold box. A high pressure cold pure helium gas stream at temperature of around 12 K is tapped from helium liquefier line and enters the purifier at node 1. This stream acts as coolant to the impure helium to be purified.

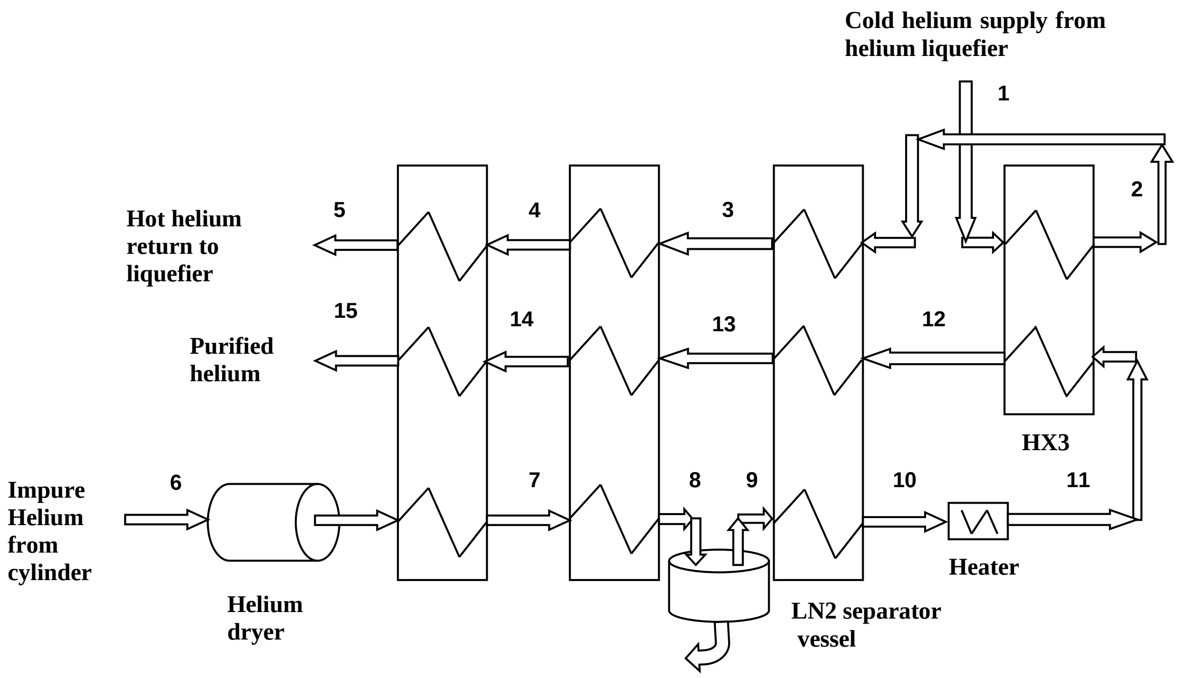


Figure 1: Schematic of cryo-condensation based helium purifier integrated with helium liquefier.

After passing through purifier, this coolant stream gets warmed up and joins low pressure (LP) line of liquefier at node 5. Impure helium passes through HX1 and then HX2B, whereafter impurities gets condensed. The condensate separates out in $LN_2$ separator vessel at node 8, which is purged out to atmosphere at certain intervals. The remaining 0.6% nitrogen at node 9 is frozen out in heat exchanger, HX2A. The now purified Grade 5 helium is warmed up in heat exchangers HX2A, HX2B and HX1 in series. The purified warm helium then joins the high pressure (HP) delivery line of screw compressor of liquefier within cold box at node 15.

During purification mode, solidified impurities continually accumulate and start blocking heat exchangers, resulting in pressure drop. On reaching the limiting value of pressure drop, purifier switches over to the regeneration mode. Regeneration of purifier is carried out by reverse flow of pure warm helium tapped from high pressure delivery line of compressor and activation of heater. The recovered gas is collected in gas bag for recycling.

## ASSUMPTIONS AND INPUT EXPERIMENTAL DATA

### *Assumptions*

1. Analysis is done at the steady state purification mode of the system.
2. Impurity of the impure helium is considered as nitrogen only. This assumption is made as nitrogen has lower boiling point than that of oxygen.
3. Heat exchangers HX2A and HX2B are combined heat exchanger where a tapping is done for removal of condensed impurity.
4. The 3-stream heat exchangers, HX1, HX2A and HX2B, are considered as 2-stream one by assuming equal temperatures for two cold flow inlets and two cold flow outlets.
5. Pressure drop of each stream at heat exchangers is 100 mbar.

The purifier under present study has limited number of sensors and transmitters to get information on the physical parameters like, pressure, temperature and mass flow rate, etc. of various nodes. The obtained experimental data and assumptions have been used as input for simulation of the purifier. The parameters of the remaining nodes have been obtained as the output. These output parameters have been used to derive the exergy characteristics for analysis.

The experimental data of the parameters of the nodes shown in Table 1 were recorded from sensors/transmitters located in helium purifier during operation.

Table 1: Temperature, Pressure and Mass flow rates of these nodes were recorded during experiment (Fig.1 is referred for location of nodes)

| | Temperature (K) | Pressure (bar) | Mass flow rate (g/s) |
|---|---|---|---|
| Node | 1, 6, 10, 14 | 1, 6,10 | 15 |

Besides above, the impurity level of pure and impure helium was obtained from measuring instruments.

Pressure and mass flow rate of impure helium considered for present study is 24 bar and 2.877 g/s respectively, with 1.50% nitrogen impurity by volume; and remaining is 98.50% helium. Temperature of nodes 1, 6, 10 and 14 has been recorded as 12 K, 300 K, 30.28 K and 80.57 K respectively; and purified helium mass flow rate at node 15 as 2.60 g/s.

## EXERGY ANALYSIS

The exergy flow for steady flow process of an open thermal system is as follows

$$\sum_{in}\dot{E}x_{flow}+\sum\dot{Q}(1-\frac{T_0}{T_j})$$

$$=\sum_{out}\dot{E}x_{flow}+\dot{W}+\dot{E}x_D \quad (1)$$

where, $\dot{E}x=\dot{m}\times ex$

Specific exergy is expressed as

$$ex=(h-h_0)-T_0(s-s_0) \quad (2)$$

And, irreversibility is expressed as

$$\dot{E}x_D=\dot{m}\times ex_D=T_0\times\Delta s_{generated} \quad (3)$$

Where $ex$ (J/g) is specific exergy or exergy transfer per unit mass, $\dot{E}x$ (W) is exergy transfer rate, $\dot{m}$ (g/s) is mass flow rate, h (J/g) is enthalpy per unit mass, s (J/g-K) is entropy. $\dot{Q}$ (W) is the rate of heat transfer across boundary at temperature $T_j$ (K). $ex_D$ is the irreversibility. $h_0$ and $s_0$ denotes the enthalpy and entropy at reference state ($T_0$, $P_0$) respectively. The ambient condition of the environment is taken as reference state, where $T_0$ = 300 K and $P_0$ = 0.10 MPa.

The purifier under present study is the combination of four heat exchangers and impurity separator, where the coolant stream and purified stream after HX3, acts as cold stream, which receives heat load from the impure hot stream and thus condensing and freezing impurities. The purifier can be considered as a combined heat exchanger where condensed / frozen impurities are removed at some stages. As the heat exchangers are employed here for refrigeration purpose, exergy transfer takes place from cold streams to hot stream. The exergy efficiency of a heat exchanger can be defined as:

$$\eta_{HX}=\frac{\dot{E}x_{C,O}-\dot{E}x_{C,I}}{\dot{E}x_{H,I}-\dot{E}x_{H,O}} \quad \text{when } T_{C,I}\geq T_{ref} \quad (4)$$

$$\eta_{HX}=\frac{\dot{E}x_{H,O}-\dot{E}x_{H,I}}{\dot{E}x_{C,I}-\dot{E}x_{C,O}} \quad \text{when } T_{C,I}\leq T_{ref} \quad (5)$$

where $\eta_{HX}$ and $\dot{E}x$ denotes exergy efficiency of heat exchanger and exergy transfer rate of a stream respectively. Subscripts H, C, I, O denote hot, cold, inlet and outlet respectively.

## RESULTS

On simulation, the temperature of node 8 has been determined as 64 K, where condensed nitrogen gets separated at separator vessel, and remaining nitrogen at node 9 is 0.62%. As temperature at node 10 is 30 K, so remaining nitrogen gets solidified and accumulated within heat exchanger HX2A, and impurity level of helium comes down to 30 ppb. Hence at this stage, quality of purified helium is Grade 5 or better.

Using the analysis methodology described above, the energy and exergy efficiency of the purifier has been determined as 5.96% and 1.39% respectively. The exergy efficiency of the heat exchangers, HX1, HX2A, HX2B and HX3 are calculated as 96.25%, 91.68%, 91.92% and 58.15% respectively.

## CONCLUSION

Above results show that exergy efficiency is quite lower than energy efficiency of the cryogenic process. So, exergy efficiency is relatively a more appropriate parameter for performance evaluation of cryogenic separation system. The purifier operating conditions, like, inlet temperture of coolant stream, impure helium temperature between HX2A and HX3, coolant stream flow, etc. may be adjusted to improve the exergy performance.

## REFERENCE


[1] Kaushik SC, Reddy VS, Tyagi SK. Energy and exergy analysis of thermal power plants: A review, Renewable and Sustainable Energy Reviews 2011; 15:1857-1872.

[2] Hafdhi F, Khir T, Yahyia AB, Brahim AB. Energetic and exergetic analysis of a steam turbine power plant in an existing phosphoric acid factory, Energy conversion and management 2015; 106:1230-1241.

[3] Atrey MD. Thermodynamic analysis of Collins helium liquefaction cycle, Cryogenics 1998; 38:1199-1206.

[4] Thomas RJ, Ghosh P, Chowdhury K. Exergy analysis of helium liquefaction systems based on modified claude cycle with two expanders, Cryogenics 2011; 51:287-294.

[5] Thomas RJ, Ghosh P, Chowdhury K. Application of exergy analysis in designing helium liquefiers, Energy 2012; 37:207-219.

[6] Wang HR, Xiong LY, Peng N, Liu LQ. The optimization on flow scheme of helium liquefier with genetic algorithm. Cryogenics 2017; 81:93-99.

# CHARACTERISTICS OF A CRYOCOOLER BASED HELIUM LIQUEFIER UNDER DIFFERENT INPUT CONDITIONS OF PRESSURE AND TEMPERATURE

Anup Choudhury, Santosh Sahu
Inter University Accelerator Centre, New Delhi, India

*Abstract*

Cryocooler based recondenser and liquefiers are being increasingly used for different applications by the Accelerator community around the world. A few of the recent developments in accelerator fields where helium condenser technology using cryocooler have been applied are (i) cooling of ECR ion source cryostat magnet in Lawrance Berkley National Laboratory (LBNL), (ii) all magnet cooling at Muon Ionisation Cooling Experiment (MICE) Brook haven national Laboratory (BNL), (iii) cooling of cyclotron gas stopper project at NSCL Michigan State university (MSU) (iv) cryostat for dark matter search at China Jinping Underground Laboratory (CJPL) China and (v) superferric superconducting magnet at RIKEN accelerator laboratory in Japan. As a general principle cryocooler based condensers find use in the places where setting up conventional cryogenics infrastructure becomes costlier during running phase and reach of normal cryogenics in the installed area is not feasible.

In the recent past a helium liquefier has been developed at Inter University Accelerator Centre using a 1.5 watt @ 4.2 K Sumitomo make cryocooler which has given a liquefaction rate of 17.5 litres per day (lpd) in the STP condition. Using integrated themosiphon technique we have been able to demonstrate a gas cooling loop from 4.2K to 300 K without any active pumping element, otherwise the gas in circulation is prone to impurity contamination. Recently we have explored the possibility of increasing production rate of this liquefier by using elevated pressure technique and by injection of lower temperature gas to the inlet of such liquefier.

This paper shall highlight the development in light of recent experiments conducted with higher pressure and lower inlet temperature of the inlet helium gas for liquefaction enhancement with the GM cryocooler liquefier.

## INTRODUCTION

Helium liquefier in conventional setup is being in use by the research community over decades for a variety of applications. With the advent of cryocooler based liquefiers, the liquefier and recondenser usage became wider due to its advantage of avoiding temperature fluctuation, vibration related problems and finite conductivity of the joining materials. By using cryocooler as a liquefier we retain the good virtues of a bath cooled system and at the same time avoid the short comings of a cryocooler system and most attractive proposition is that of its portable size.

Cryocooler based liquefier or recondenser systems used to cooldown physics experimental setups, both are normally built as an integrated setup. Cooldown of the experimental setup requires large amounts of LHe which is either supplied from the attached liquefier itself or from an external source. Using integrated cryocooler liquefier, cooldown of the bigger thermal system has been successfully attempted at MSU, where 1.2 ton cold mass cyclotron magnet was cooled down in 15 days using 3 numbers of 1.5 Watt pulse tube cryocoolers [1] using a thermosiphon type arrangement. In such a system cooldown process is much slower than the conventional external fed LHe supply model, but the main advantage of this system is zero wastage of helium gas, no helium gas handling infrastructure requirement, and contamination free process without any external pumping device.

AT IUAC we have developed a helium liquefier of 17.5 lpd capacity using a 1.5 Watt @ 4.2 K GM cryocooler with an integral thermosiphon path [2,3]. The liquefier starts producing LHe in ~2 hours time and full thermalisation takes ~4 hours time. To improve on the liquefaction rate, using the same cryocooler is always beneficial for cooling down of thermal mass connected to the system. The production rate improvement can be brought about in two ways. (i) Using elevated pressure of helium gas for producing liquid at higher temperature (<5.2K) by utilising the property of higher cooling enthalpy availability at higher temperature zones of the cryocooler and reduction of latent heat at elevated pressure. (ii) By injection of cold gas from the cooling system which shall help to reduce the thermal load on the 1$^{st}$ stage of the cryocooler and thereby improving on the production rate. Cryocooler based systems of similar nature are normally closed loop devices and when it is being cooled starting from room temperature slowly as the mass cools down the return temperature also gets colder, which can be easily fed back to the system directly near to the 1$^{st}$ stage of the cooler instead of warming up to room temperature.

A dedicated experimental setup was built to study such a cryocooler liquefier where we have studied the effect higher pressure and inlet gas temperature on the liquefaction rate.

## EXPERIMENTAL SEUP

The liquefier consists of 1.5 watt @ 4.2K cryocooler cold head whose 1$^{st}$ and 2$^{nd}$ stage was attached with highly conductive copper (OFHC) heat exchangers for transferring heat from the flowing helium gas to the cryocooler. Cold head with heat exchangers are then lowered to a thin walled liquefier body made of stainless steel and between them helium gas flows during the cooldown process. LHe is collected at the bottom of the liquefier vessel from where it is led to the thermosiphon vessel (80 cc volume) further 250 mm down and return from the vessel is fed to the inlet of the liquefier line just above the 1st stage of the cooler. The return line from the thermosiphon bottle (TSB) is a connected to the 1st stage by a flexible bellow line to take care of the thermal misalignments during connection, thermal contraction when cold and also for reducing heat load coming to thermosiphon bottle. There are two heaters in the setup (i) A 2 watt electronic heater (H1) is placed at the bottom of the TSB and the power to it is controlled by a digital precision power supply. The heater is connected in a four wire configuration to the controller for putting precision power to the heater. The activation of the heater helps to initiate the thermosiphon process where the collected LHe is converted to helium gas and returns to the top of the liquefier for restarting the journey, and thus the recycle of precious gas is done. In steady state the heater power (P) applied to this heater is a direct measure of the liquefaction rate ($L_r$) from the equation

$$L_r(lph) = \frac{P(watt)}{\rho(g/l) * L_h(J/g)}$$

where ρ is the density and $L_h$ is the latent heat of the LHe at the equilibrium pressure where the liquefaction rate is being measured.

Figure - 1, Experimental setup 3D view.

(ii) Another heater (H2) is connected to the return line above the TSB to warm up the cold helium gas up to room temperature. This heater has a maximum power of 50 Watts and with power supply voltage modulation, inlet helium gas temperature can be varied from 20K to 300K. A full view of 3D model of the setup is shown in Figure1.

Helium gas at room temperature is supplied through the top flange at the start of liquefaction process to take care of cooldown gas requirement and making adequate amount of liquid helium for experimentation. On starting cryocooler the system starts producing LHe after 2 hours but takes ~2 more hours time to fill up the dewar and to thermalise the system. When TSB is filled up with LHe (known from gas accumulation from volumetric flow meter connected to the inlet line) helium gas supply to the system is stopped and TSB bottom heater H1 is activated and powered in such a way that the system pressure stabilises initially around atmospheric pressure of 101kPa. This condition is the base working condition for liquefier where the measured liquefaction rate is 17.4 lpd .

To study variation of LHe production rate of the system at elevated pressure and with different inlet temperature, followings steps were undertaken. Initially TSB was filled up with LHe and the system pressure was stabilised by powering heater H1 in a controlled manner. The equivalent base liquefaction rate of the setup is obtained to be 17.4 lpd (525mW). At the equilibrium power the heater is put on PID control mode with the help of a controller where the input signal is that from the LHe temperature (which is integrally connected to the system pressure). The auto control is essential to take care of the local disturbances in the system which otherwise allows the system to drift apart from the intended operating condition. For higher pressure more heat is initially applied to drive away liquid to gaseous state which helps to raise the pressure of the system. At higher pressure LHe latent heat decreases, so depending on the chosen stable pressure the heater power had to be reduced for balancing the applied power commensurate to the mass flow rate.

We know that most of the sensible heat of helium gas is at higher temperature zone, so getting colder gas from the experimental chamber helps the cryocooler to spend less cold enthalpy towards cooling of incoming helium gas, thereby the cryocooler body can have lower temperature profile at the 2nd stage of the cryocooler which in turn increases the LHe production rate. In this experiment inlet gas temperature is varied by applying heater power in H2 to warm up the return cold gas from the TSB. It requires some iteration of both the heaters power adjustment before we arrive at a stabilised condition of the system. In this condition H1 power gives the flow rate and H2 power helps to vary the inlet temperature of the gas.

## RESULTS AND DISCUSSION

To get an idea of the liquefaction enhancement due to elevated working pressure in the setup a plot is drawn between the thermosiphon heater power H1 and the corresponding equilibrium pressure. Maximum pressure reached within the system with the available gas from the TSB liquid helium evaporation was 60.5 kPa(g), beyond this power the system became unstable with rapid pressure fluctuations and auto control problem. From this plot using the liquefaction formula we plotted the liquefaction rate of the system in terms of mass flow rate (g/s) and in volumetric flow rate (lpd) taking into consideration the changing density and latent heat of LHe at different pressures. This curve is shown

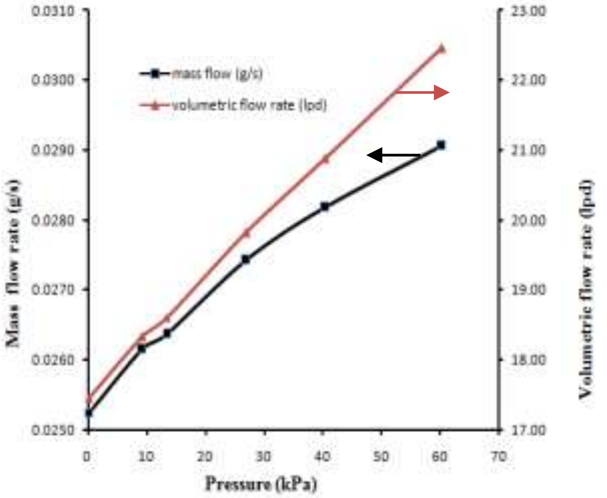


Figure -2, Production rate variation with pressure.

Figure 2. From the figure it can be observed that the volumetric flow rate increases steadily with increase in the system pressure, but mass flow tends to saturate at higher pressure. At the highest tested pressure of 60.5 kPa (g) the volumetric flow rate goes to 22.4 lpd (increases by 28.7%) compared to that at 0 kPa(g) condition (17.4 lpd). The production rate increase at elevated pressure is due to reduction of latent heat and cooling power increase at higher temperature.

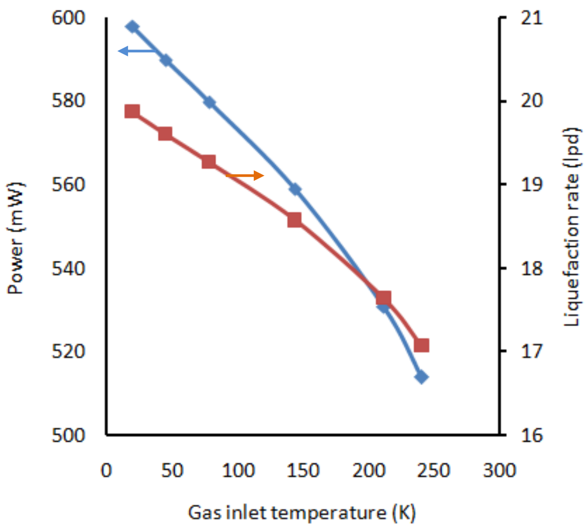


Figure -3, Production rate variation with cold inlet gas.

When cold helium gas is injected at the inlet of the liquefier near the 1st stage regenerator middle section by adjusting H2 heater the production rate increases and a plot is shown in Figure 3 between the inlet temperature and the production rate from 243K to 20K. For this case the corresponding cryocooler body temperature at 8 different positions covering the whole length of the body is plotted in Figure 4. It can be seen that in the lower half of 2nd stage regenerator both temperatures almost merge signifying very little heat transfer in that area. Overall production rate increase observed is 17.6% over the base rate with inlet temperature change from 243K to 20K at 101kPa(a) operating pressure.

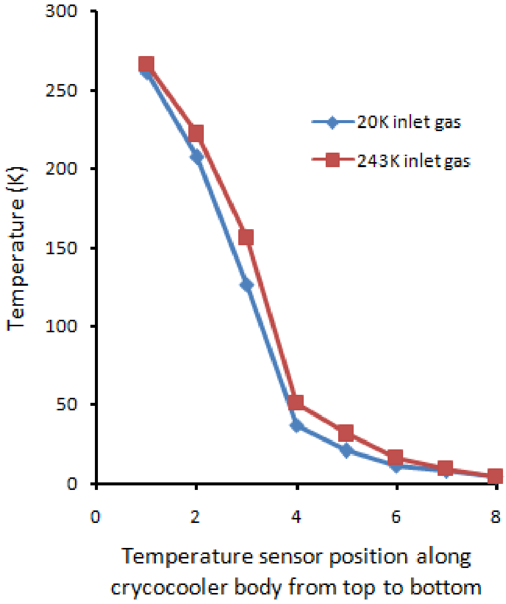


Figure -4, Cryocooler body pemperature profile

## CONCLUSION

Study setup of a portable helium liquefier using a 1.5 Watt GM cryocooler has been made has been made. The base LHe production rate at STP condition has been measured to be 17.4 lpd. Production variation study conducted under increased pressure and with colder helium gas input has shown that at 60.5 kPa(g) the production rate increase can be higher. In case of cold gas input the production rate increases by ~18% and that with higher pressure it go up by almost 30%.

The study conducted so far is not optimised and there exists scope for improvement and finding out the best solution where the system shall be able to give higher production yield with lesser stress.

## REFERENCES


[1] M A Green, et.al. "Cooing and operation of MSU cyclotron gas-stopper magnet" IEEE transactions on applied superconductivity 26(4):1-1, June 2016

[2] A Choudhury and S Sahu, Experimental helium liquefier with a gm cryocooler, Review of scientific instruments, 88, 065116(2017)

[3] Choudhury Anup, Sahu Santosh, Meena Ramcharan, "Cryocooler based helium liquefier development-A practical usage", Indian Journal of Cryogenics (2018) Volume : 43, Page 51-55

# DESIGN AND DEVELOPMENT OF HIGH VOLTAGE SWITCH USING SERIES CONNECTED BiMOSFET FOR SOLID-STATE HARD SWITCH

Mahesh Acharya#, T. Reghu and Purushottam Shrivastava
Radio Frequency System Division
Raja Ramanna Centre for Advanced Technology, Indore, MP, India

*Abstract*

In high voltage hard switch modulators, high voltage switch is an essential component. The switch can be realized using series connected low voltage solid-state switches. It is necessary to equalize the voltage across the switches during static and dynamic condition for reliable operation. A 10 kV, 8 A, 20 µs solid state series switch prototype using modified snubber scheme has been designed and developed using series connected BiMOSFET. The modified snubber scheme offers higher reliability, simplicity, fast-switching times, low loss compared to traditional voltage equalization snubber. The switch was operated and tested at 10 kV, 8 A for a pulse width of 20 µs and repetition rate of 300 Hz. Rise time of 200 ns and fall time of 2 µs have been achieved.

## INTRODUCTION

High power RF systems are the backbone of the present day high energy accelerators. Most of them requires pulse RF power to accelerate. The high voltage modulators generate the high voltage pulse for klystrons which further generates high power RF for the accelerators. Different types of techniques for generating high voltage pulses have already been reported. One of them is a hard tube modulator. In this modulator, a capacitor is charged and then discharged by a series switch for a finite duration to produce a high voltage pulse of the same duration. Conventionally vacuum tube is used as a series switch in this type of modulators. The tubes have a finite lifetime and high operating cost. Therefore, hard tube modulators are not so popular for pulse generation. After the advancement in semiconductor industries and innovation of new solid state switches like IGBT, MOSFETs and BiMOSFETs etc, it has become possible to use these switches for hard switching. These switches can be turned ON and OFF for a finite known duration. The high voltage solid state switches can replace the tube in hard switched modulator for generation of high voltage pulses. But the solid state switches are available upto a limited voltage value. Therefore, it is required to connect large number of switches in series for high voltage operation.

The series connection of high voltage switches poses a lot of challenges. One of the challenges for the series connection of high voltage switches is the voltage sharing of switches. The voltage sharing during dynamic and static condition may be unequal due to the tolerances and variation in different parameters of switches, turn ON and OFF delays. If one of the switch turns ON after some delay of turning ON of the remaining switches or the switch turns OFF before turning OFF of the remaining switches, full voltage appears across the single switch which may cause the breakdown of not only the switch, but also may fail the entire series switch configuration.

Many techniques have been reported for the voltage equalization of the series connected IGBT switches. The voltage balancing of the IGBTs can be achieved with either passive voltage equalization or active voltage equalization. The passive voltage equalization uses RCD snubber while gate side control is used in the active voltage equalization technique. The conventional RCD snubber are more reliable and simple technique for voltage equalization, but, it has higher losses and large rise and fall times. A modified snubber scheme presented here has lower losses and fast rise and fall times.

## DESCRIPTION

In a conventional RCD snubber circuit for voltage equalization, the snubber capacitor should be large enough that it can take care of switch parameters tolerance during dynamic equalization and retains the voltage across the switch within safe limits. However, the snubber capacitor is required to be small for low losses. The snubber capacitor is charged to the full voltage during turn OFF period. The capacitor energy is dissipated in the snubber resistor during turn ON period of the switch. For fast rise and fall times, the snubber capacitor should be small enough so that it would discharge completely within the pulse duration. Therefore, the conventional snubbers have large losses and large rise and fall times with the larger snubber capacitor.

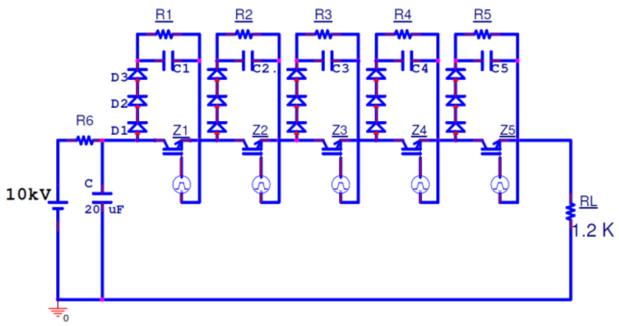


Figure 1: Schamatic of a 10 kV series switch

In the modified snubber scheme, a decoupling diode has been used to isolate the snubber capacitor from the switch during turn OFF period. In figure 1, all the snubber capacitors are charged equally due to equalizing resistors. If the switch Z2 gets delayed during turn ON and other

# email address: macharya@rrcat.gov.in

switches are already ON, then the snubber capacitor of Z2 maintains the voltage across the switch within safe limits and after that when switch Z2 turns ON, the decoupling diode isolates the snubber capacitor from the switch. The snubber capacitor discharges slowly through equalization resistor R2. Since the capacitor is not discharged through the switch, the additional stress due to discharge of snubber is avoided compared to conventional snubbers.

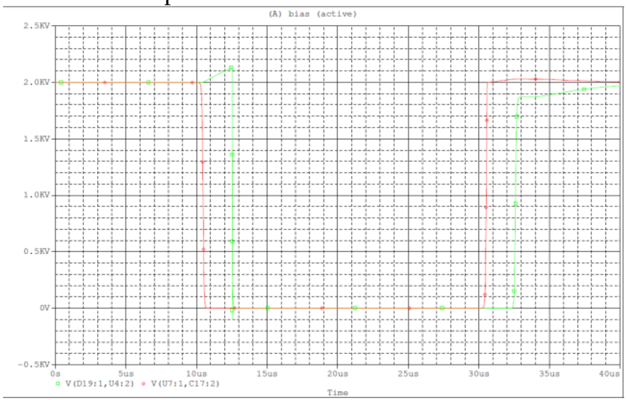


Figure 2: Simulation result of 10 kV, 8A, 20 µs series switch

A simulation was done in the PSpice for a 10 kV, 8 A, 20 µs output voltage pulse. A 10 kV series switch was used in a hard switched modulator and five switches were used for 10 kV series switch. The voltage across each switch was 2 kV in static mode. A delay of 2 µs is introduced in the gate of one switch to study the effect of snubber capacitor on the voltage across the switch. The voltage across the switch has been increased marginally to 2.03 kV. The result of the simulation is as shown in figure 2. The voltage of the capacitor increases with the $R_L C_{snubb}$ time constant. The circuit was also simulated for a missed pulse condition in which the voltage pulse of one of the switches is missed and the maximum voltage across the switch went only marginally to 2.3 kV only.

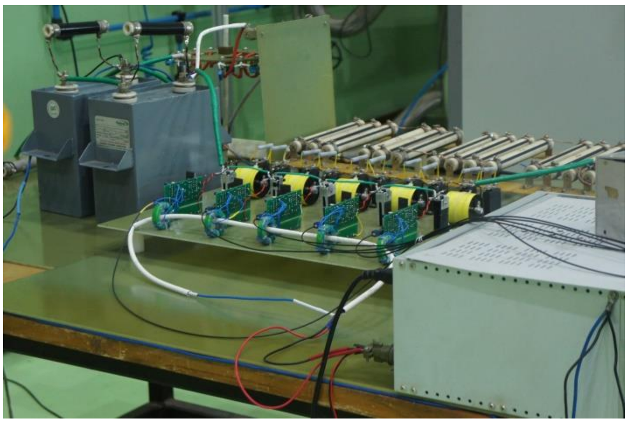

Figure 3: Test setup for testing of 10 kV, 8A, 20 µs hard switched modulator

A 10 kV series switch with driver circuit and isolation power supplies was designed, developed, and tested. The BiMOSFET has been selected for high voltage switch as it has faster turn ON and OFF times than IGBTs while lower saturation voltage than counterpart MOSFETs. The high voltage solid state switch has been realised using five BiMOSFETs. The figure 1 shows the schematic of a high voltage series switch. The high voltage switch consists of a modified snubber scheme in which three MUR 4100E decoupling diodes, a snubber capacitor and an equalizing resistor has been connected across each BiMOSFET. Driver cards for all the switches have been developed. These cards include a rectifier circuit, optical receiver and driver IC. A control circuit has been developed for controlling the switching time of the switches. All the switches should be turned ON synchronously at the same time, therefore five optical transmitters are connected in series.

A setup has been prepared for testing of high voltage series switch. A capacitor is charged by a 10 kV power supply and the same has been discharged for 20 µs pulse duration through the high voltage series switch. A 1.25 kΩ load is connected at the output. A pulse of 10 kV, 8 A , 20 µs pulse width is generated. The switch was operated at a pulse repetition rate of 300 Hz. The output voltage pulse was measured on oscilloscope using high voltage probe P6015A. Figure 4 shows the output voltage pulse waveform.

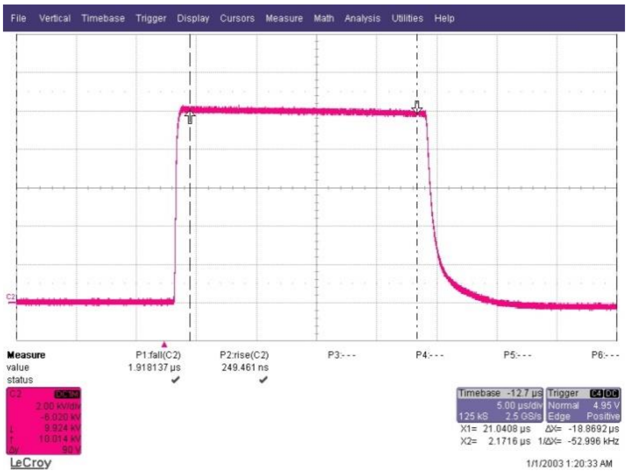


Figure 4: 10 kV, 2 A, 20 µs output pulse waveform

## CONCLUSION

A method for static and dynamic equalization of series connected IGBTs was presented. A hard switch modulator based on a 10 kV series switch was designed, developed and tested. The prototype test has shown to be good and validate the simulation and theoretical analysis. The voltage and current of the output pulse is 10 kV, 8 A. The modulator was operated with 20 µs pulse width and at a repetition rate of 300 Hz. The rise and fall times of the output voltage pulse are 200 ns and 2 µs, respectively.

## ACKNOWLEDGEMENT

The authors would like to thank Shri Debashish Das, Director of RRCAT, for his keen interest and constant support and Shri J.K. Mulchandani, for the fruitful discussions and technical support of Shri Vinod Phadnis and Harini Visvanathan.

## REFERENCES


1. Reghu T., Vagesh Mandloi, and Purushottam Shrivastava. "A Solid-State Converter Topology, -100 kV, 20 A, 1.6 ms, Modulator for High Average Power Klystron Amplifier." IEEE Transactions on Plasma Science 99 (2018): 1-8.
2. Acharya, Mahesh, and Purushottam Shrivastava. "A 100 kV, 20 A, 1 ms long pulse solid-state Marx modulator for klystron." Nuclear Instruments and Methods in Physics Research Section A: Accelerators, Spectrometers, Detectors and Associated Equipment 905 (2018): 96-103.
3. Shrivastava, Purushottam, J. Mulchandani, and V. C. Sahni. "Development of all solid state bouncer compensated long pulse modulators for LEP 1MW klystrons to be used for LINAC4 project at CERN." proc. of LINAC. Vol. 8. 2008.
4. M. Zarghani, S. Mohsenzade and S. Kaboli, "A Fast and Series-Stacked IGBT Switch with Balanced Voltage Sharing for Pulsed Power Applications," IEEE Transactions on plasma Science, vol. 44, no. 10, pp. 2013 - 2021, 2016.

# Design and development of 150 kW pulsed RF rigid coaxial line based 3-Way RF Power Combiner at 325 MHz

Alok Kumar Gupta,* Akhilesh Jain, M. Lad
SSRFAS/RFSD, RRCAT, Indore - 452013, INDIA

## ABSTRACT

150 kW pulsed RF Solid State RF Amplifier (SSPA) is under advanced development stage for energizing of Radio frequency quadruple (RFQ) for our Indian Facility for Spallation Research (IFSR) program at RRCAT. As a part of this system, rigid coaxial line based 3-port RF Power Combiner, with output power handling capacity of 150 kW pulsed RF (Pulse width: up to 5 ms and duty cycle: up to 25%), has been designed, developed and characterized. RF Power combining is a mandatory requirement of SSPAs as available output power of RF MOSFETs is quite moderate in UHF band. With the help of this 3-Way RF Power combiner, 3 nos. of 50 kW pulsed RF SSPAs at 325 MHz will be power combined to achieve 150 kW of RF output power. This 3-Way power combiner has three inputs at EIA 3 ⅛ inch rigid coaxial lines and output at EIA 6 ⅛ inch rigid coaxial line. Port to port amplitude and phase symmetry better than ± 0.1 dB and ± 1 deg. respectively, have been achieved among its three input ports successfully. This paper discusses detailed RF design aspects, cooling mechanism, low power and high power RF measurements for this 150kW pulsed RF, 3-Way RF power combiner.

## INTRODUCTION

Indian facility for Spallation Research (IFSR) will be a proton accelerator, energizing proton beam up to 1GeV.This intense beam will be bombarded on High Z target, resulting in pulsed neutron beam via Spallation. This pulsed neutron beam may be utilized for high energy particle physics experiments and will be helpful for ongoing research work of ADSS program of DAE. Radio frequency quadruple (RFQ) will energize proton beam form H- ion source up to 20 MeV. For this purpose, RF power requirement for energizing RFQ is approximately 600 kW pulsed RF with duty cycle of 25 % and pulse width up to 5 ms. It is proposed to fulfil this huge RF power requirement by four nos. of 150 kW pulsed RF SSPA based stations.

Progression of Solid State RF Amplifiers has been quite enormous at RRCAT. Advantages of SSPA technology i.e. low voltage of operation, graceful degradation and scalable architecture are optimally harnessed in design, development and deployment of 75kW CW SSPAs at Indus-2 Synchrotron Radiation Source (SRS). Installed RF power capacity of SSPAs, operating in round the clock mode, at Indus-2 has been increased up to 350 kW CW [5] [6] successfully. Recently, 75 kW CW Compact SSPA has been deployed at Indus-2 successfully with half spatial requirement as compared to previous SSPAs.

Being motivated from satisfying round the clock performance of Indus-2 SSPAs, challenge to develop SSPAs in hundreds of KW regime has been accepted for our IFSR program. Power combining is a mandatory requirement for SSPAs as output power from a basic solid state RF amplifier module is quite moderate in UHF band. Hence, large no. of these RF amplifier modules needs to power combined efficiently to achieve desired final RF output power. To achieve 150 kW of final output power, it has been decided to power combine three nos. of previously developed 50 kW- 325 MHz SSPA cabinets [2][4]. For this purpose, design of 3-Way RF power combining structure should be compact, cost effective, physically realizable and with minimal losses to maximise the efficiency of SSPA.

## DESIGN

Multiple nos. of radial, symmetrical/asymmetrical and lossless power combing structures up to 40 nos. of input ports with high power handling capacity, have been designed, developed and reported by us [1] [2] [3] [7]. An asymmetrical structure has been designed for this 3-Way power combining structure to maintain spatial layout of 150 kW SSPA compact and to have a fabrication friendly structure. This 3-Way power combiner has two symmetrical input ports at right angle of output port and third input port has been designed axially opposite to the output port, resulting in asymmetry. Coupling coefficients for these three input ports will not be identical due to this asymmetry. Hence, a suitable stub has been posted at the junction of three input ports to nullify this asymmetry. Complete three dimensional structure of this 3-port asymmetrical power combiner has been modelled and simulated in ANSYS make 3-dimensional High Frequency Structure Simulator (HFSS). It was also ensured in 3-D HFSS design that electric field at any region/discontinuity does not exceed 300V/mm in dielectric medium due to incorporation of this stub for full power of operation. Stepped impedance matching technique has been adopted to design compact impedance matching section at 6 ⅛ inch rigid coaxial line to match the impedance of junction of three inputs at 3 ⅛ inch rigid coaxial lines to system impedance. Return loss better than 30 dB was successfully achieved in simulated results. Coupling coefficient for third asymmetrical port was optimized to make all three coupling coefficients identical amplitude wise. Phase of the coupling coefficient for this asymmetrical third port was also optimized to minimize the deviation between phases of symmetrical and asymmetrical ports while maintain compactness of the structure.

## MEASURED PERFORMANCE

3-way RF Power Combiner at 325 MHz was successfully fabricated and characterized using Rhode and Schwarz's Vector network analyzer (VNA) ZNB4. Rigorous low power vector RF measurements have been performed on this 3-Way RF Power combining structure. For these measurements, output port at 6 ⅛ inch rigid coaxial line has been designated as Port No. 0 and three nos. of 3 ⅛ inch rigid coaxial line inputs were assigned as Port No. 1, 2 and 3. Spatially asymmetrical port has been designated as Port no-2. Spatially symmetrical ports have been designated as port no. 2 and 3. S-parameters measured for this 3-Way RF power combiner with VNA has been tabulated in Table-1. Return loss measurement (s00) from VNA has been displayed in Figure No. 2 in frequency span of 300 MHz. Return loss measured at 325 MHz is 21 dB and dip of s11 has been observed at 336 MHz with value of 25.9 dB. Shift of dip of s11 may be due to slight variation in value of dielectric constant (from simulated value) of commercially available Teflon. 20-dB return loss bandwidth has been measured better than 35 MHz.

Coupling coefficients between input and output ports were also measured. All three amplitudes of coupling coefficients over the frequency band of 300 MHz have been displayed in Fig. 3. Deviation between amplitudes of s20 and s30 (symmetrical ports) is measured within ± 0.015 dB at 325 MHz. Deviation of less than 0.1 dB was measured for amplitude of s10 from amplitudes of symmetrical port coupling coefficients. Symmetry among three amplitudes of coupling coefficients is quite essential for efficient power combining and has been achieved for this power combining structure. It is clear from Fig.-3, that deviation between amplitudes of symmetrical and asymmetrical ports gets wider and wider outside the 20-dB return loss bandwidth of this 3-Way power combiner. Fig.-4 depicts the insertion phase of coupling coefficients for all three input ports over the frequency band of 300 MHz. Phase of spatially asymmetrical coupling port is measured at small offset of 25˚ with respect symmetrical coupling ports. Variation of insertion phase between symmetrical ports is less than ± 0.5˚. All these low power RF measured are in excellent agreement of simulated results.

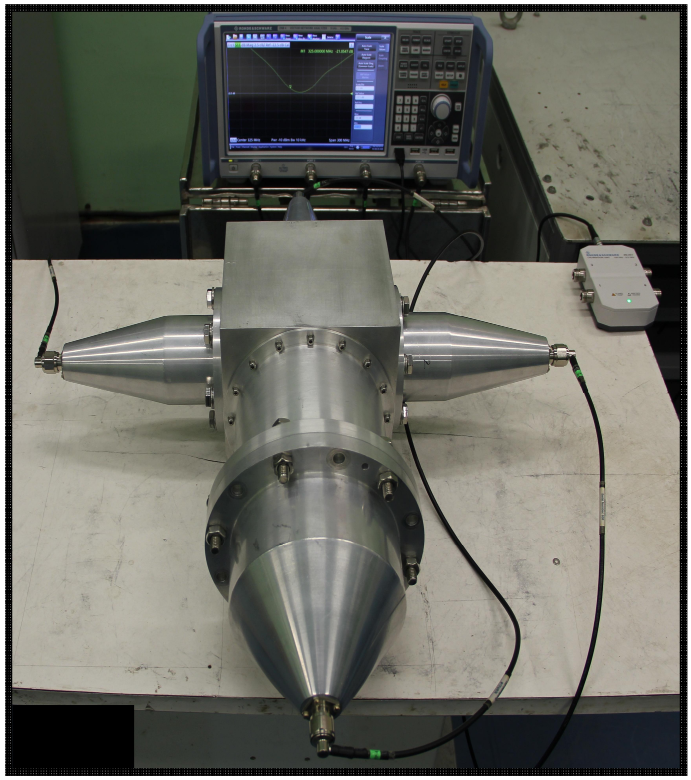

Figure 1: RF measurements of 150 kW pulsed RF 3-Way Power Combiner with R&S VNA ZNB4

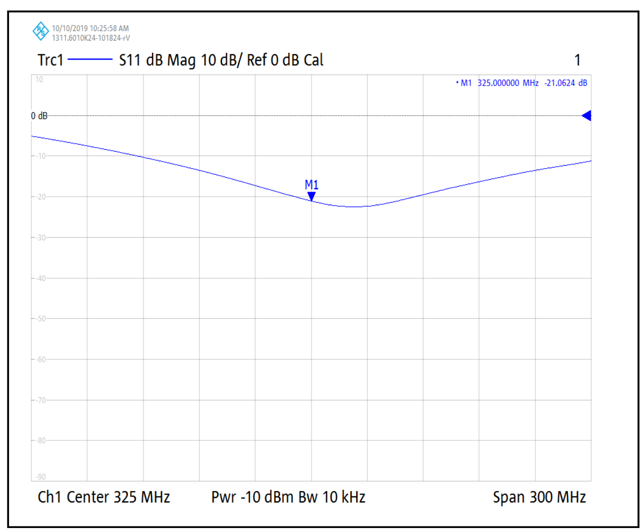


Figure 2: S11 measurement of 3-Way Power Combiner

Table 1: s-parameters of 3-Way 325 MHz RF Power Combiner

| Sr. No. | S-parameters | Magnitude (dB) | Phase (degree) |
|---|---|---|---|
| 1. | S00 | -21 | 126.2 |
| 2. | S10 | -4.78 | 55.8 |
| 3. | S20 | -4.87 | 80.0 |
| 4. | S30 | -4.89 | 79.1 |

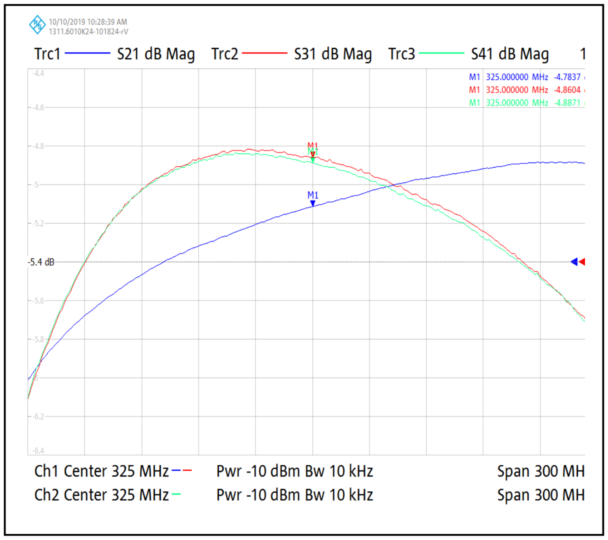


Figure 3: Amplitude coupling coefficients of 3-Way Power Combiner

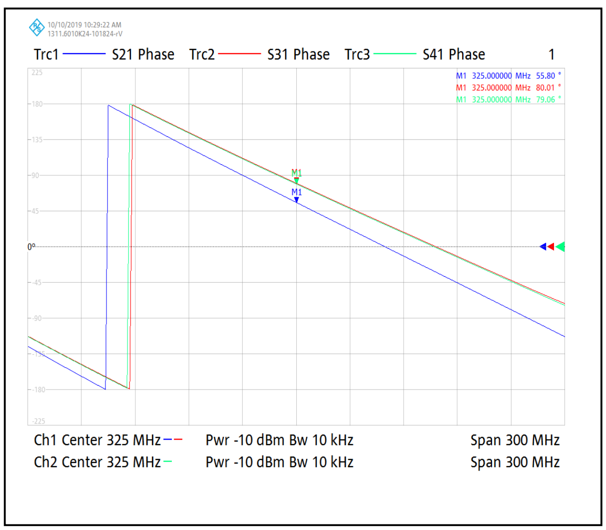


Figure 4: Phase coupling coefficients of 3-Way Power Combiner

## CONCLUSION

150 kW 3-Way asymmetrical power combiner structure at 325 MHz have been designed, realized and also characterized successfully. Power combining structure has exhibited return loss better than 21 dB corresponding to less than 1 % reflection of total fed power. Excellent amplitude symmetry among three ports has been achieved for this power combiner, required for efficient power combining. Two spatially symmetric ports have excellent phase symmetry and third port has small offset, with respect to these two symmetrical ports, which can be easily compensated with amplifier phase while power combining of SSPA racks. Insertion loss better than 0.1 dB has been observed for this power combiner, ensuring power combing efficiency to better than 97 %. Measured performance is in good agreement with theoretical and simulated results. Successful development of this compact and cost effective 3-Way power combining structure has been an important milestone achieved toward the development of 150 kW Pulsed RF Solid State RF Amplifier for energizing the Radio frequency quadruple for our Proton Accelerator program.

## ACKNOWLEDGEMENT

We are thankful to Mr. Ramesh Kumar and Mr. R. K. Arya for preparing mechanical drawings of this 3-Way RF power combiner. We are also thankful to Mr. Ravi Patel and Sameer Kumar for assembly and measurement work.

## REFERENCES

[1] Alok Kumar Gupta, Akhilesh Jain, M.Lad, Ravi Patel, and Joseph Tharayil “Design and development of 40 port coaxial line based radial RF power combiner at 325 MHz ”, in InPAC 2018.

[2] Alok Kumar Gupta, D.K. Sharma, Akhilesh Jain, and M.R. Lad “Power combining scheme for 50 kW pulsed Solid Sate RF power amplifier unit at 325 MHz”, in InPAC 2015.

[3] Akhilesh Jain, Alok Kumar Gupta, D.K. Sharma, P. R. Hannurkar, and S.K. Pathak “Design and analysis of high power radial multiway combiner ”, International journal of Microwave and Wireless technology, Vol. 06, Issue 01, Feburary 2014.

[4] Deepak Kumar Sharma, Akhilesh Jain, Alok Kumar Gupta, P. R. Hannurkar, "Development of 325 MHz 1.8 kW Pulse RF Power Amplifer" in InPAC 2013.

[5] Akhilesh Jain, P. R. Hannurkar, D. K. Sharma, A. K. Gupta, A.K. Tiwari, M.Lad, and R. Kumar, P.D. Gupta and S.K. Pathak “Design and characterization of 50 kW solid-state RF amplifier” International Journal of Microwave and Wireless Technologies, vol. 4, no. 6, p. 595 603, Dec 2012.

[6] Akhilesh Jain, P. R. Hannurkar, D. K. Sharma, A. K. Gupta, A.K. Tiwari, M.Lad, and R. Kumar, “Modular 20 kW solid state RF amplifier for Indus-2 synchrotron”, Nuclear Instruments and Methods in Physics Research A, Vol. 676, June, 2012.

[7] Alok Kumar Gupta, Deepak Kumar Sharma, Akhilesh Jain, and P. R. Hannurkar, “High Power, lossless, rigid line 2-Way RF power Combiners”, INPAC 2011.

[9] Akhilesh Jain, Deepak Kumar Sharma, Alok Kumar Gupta and P. R. Hannurkar, “Development and performance characterization of 2 kW-505.8 MHz and 4 kW-352 MHz solid state RF amplifiers”, INPAC 2011.

[10] Akhilesh Jain, Deepak Kumar Sharma, Alok Kumar Gupta and P. R. Hannurkar, “Development of solid state RF amplifiers and associated coaxial components in kW regime for particle accelerator applications”, AEMC- Dec 2009.

# GROUNDING CONSIDERATIONS FOR HIGH POWER DC ACCELERATORS

Rehim N.Rajan, Israel Bakhtsingh, Vijay Sharma, Suryaprakash Dewangan, Swati H.Das, D.K Sharma, Rupesh Patel and Archana sharma

HBNI, APPD, BARC, Mumbai-400085

*Abstract*

High power DC accelerators employ different types of high frequency power sources to excite the high voltage generator. These power sources, their loads and other auxiliary systems are spread around many rooms and floors forming a complex grounding scenario. Discharges in the high voltage generator can potentially create high frequency transients. These transients can propagate to other subsystems though the grounding system and create interference problems unless adequate measures are taken. As geometrical size of the problem is a considerable fraction of the wavelengths all grounded points can not be considered at the same potential. In this paper a brief overview of grounding system in a high power DC accelerator is described and design considerations for minimizing conducted interference through the grounding system is elaborated.

## INTRODUCTION

Industrial accelerators are widely used for applications from polymer modification to waste water treatment. They come in two different breeds namely DC accelerators and RF accelerators. DC Accelerators are preferred for lower energy regime of 300 keV to 5 MeV and RF accelerators rule the high energy category ranging from 6 to 10 MeV. DC accelerators provide continuous beam and thus the power supplies are also continuous type unlike their RF counterparts, which mostly use pulsed systems. So in a general sense, grounding requirements of RF accelerators are more stringent. However high stored energy and occasional discharges in DC accelerators make them sources of pulsed energy of very high peak amplitudes and the grounding system should ensure safety during these events. Grounding system of a 1 MeV, 100 kW symmetrical Cockroft-Walton based industrial electron accelerator at EBC kharghar is discussed here.

The power supply scheme of this accelerator involves a a symmetrical Cockroft-Walton multiplier column driven by a high frequency, high voltage supply. For this power from 3 phase mains is first processed using a Thyristor based DC power supply, which produces controlled DC link voltage of 0-480 V. This DC voltage is inverted to 10 kHz using a free running IGBT based inverter. Rectangular wave output of the inverter is smoothened by a tank circuit to produce sinusoidal voltage of 0 to 500 V peak. This voltage level is raised to 45 kV-0-45 kV using a ferrite core step up transformer. Output of the high voltage transformer is connected to the multiplier column located inside a pressure vessel with $N_2$ gas at 6 kg/cm$^2$. Electron beam produced by a floating electron gun located in the high voltage dome is accelerated through accelerating tubes located at the centre of the multiplier column. The high power electron beam up to 100 mA is taken out to atmosphere through a titanium window after scanning with an electromagnet.

## HIGH VOLTAGE DISCHARGES

The high voltage system of a DC accelerator can undergo electrical breakdown due to the high operating electric fields. The discharges are expected in the bulk gas insulation and in the accelerating tube maintained at vacuum levels better than $5\times10^{-6}$ mbar. The discharges are frequent during the initial conditioning stage and gets reduced to rare instances once the system stabilises. However discharges can be expected during occasional foil puncture, immediately after routine maintenance of the high voltage system and after long shutdown periods of the system. In all cases the system undergoes complete discharge dissipating all the stored energy in the system in protective elements, spark channel and beam ejected from the window.

Due to electrical discharges happening at the high voltage terminal, charged capacitor stack of the multiplier gets connected to ground at the HV terminal end, creating a positive going transient as shown in Figure 1.

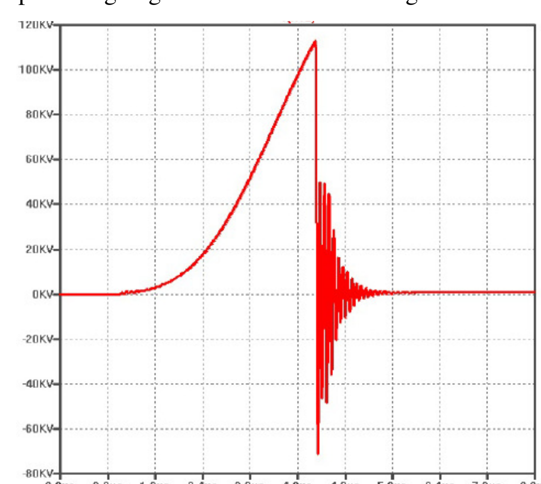


Figure 1: Transient voltage at transformer Secondary.

Since the column consists of several stages of protective impedances in series and parasitic capacitance to ground, the rising edge of this waveform is rather slow in the order of micro seconds. However if the protective elements in the multiplier is bypassed due to high over voltages across them, the rise time of the bottom most capacitor can become in the order of few tens of nanoseconds. The rising part of the waveform charges the parasitic capacitance of the high voltage transformer to much higher voltage than normal operating voltage. This phase is terminated by the action of the protective spark gaps, which clamps the transformer terminal to ground. If the spark gaps are not used, bottom end of the multiplier can raise to very high voltage resulting in insulation failure of the bottom stage insulators. The action of spark gap manifests as the fall time of the waveform shown in Figure:1, which will be in the order of few nano seconds. Following the bypass action of the spark gaps, the charged primary to secondary capacitance discharges through inductance formed by the secondary connections, spark gaps and grounding conductors. The transient voltage at the secondary terminal travels through the transformer to different parts of the system. An equivalent circuit of the transformer for common mode transient at both secondary is shown in Figure 2. The terminal to tank capacitance ($C_{tt}$), winding to core ($C_{wc}$) and connection inductances (Lc) are depicted. Direct secondary winding to primary winding capacitance is denoted by $C_w$.

## GROUNDING AND GROUND LIFTING

The accelerator and associated systems has to be adequately grounded to ensure safety to people, who are likely to operate the equipments and to provide adequate current carrying capability to conduct ground fault currents safely [1]. For this country specific standards are followed, e.g. IS-3043-1987. Here the main high voltage system is enclosed in a pressure vessel, which is grounded through the building structure itself. In addition, qualified ground referencing has to be done to ensure safety.

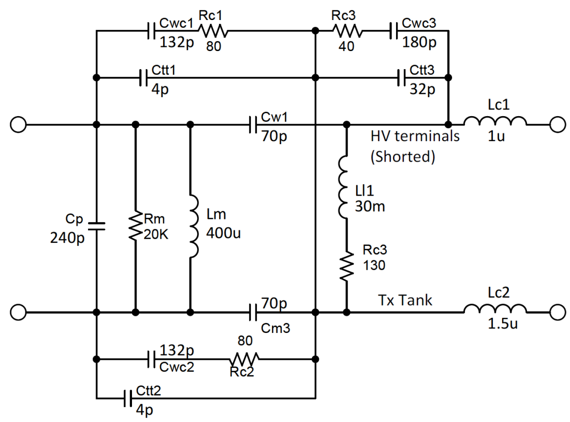


Figure 2: Common mode transformer equivalent circuit

Ground connections of the high voltage system are done using copper bus bars of 3mm X 25mm cross section. Details of this scheme are given in Figure 3. Red arrows indicate the high frequency current paths during transients. At high frequencies, the return conductors act as inductors with approximately 1.5µH/m. The location B lifts to several kilovolts by the return currents through the transformer body and centre point connections. A part of the transient current returns through the inverter producing ground lifting of point C. Secondary surge filters located in the control cabinet also will divert fault currents in the high voltage system to local ground of the control cabinet leading to

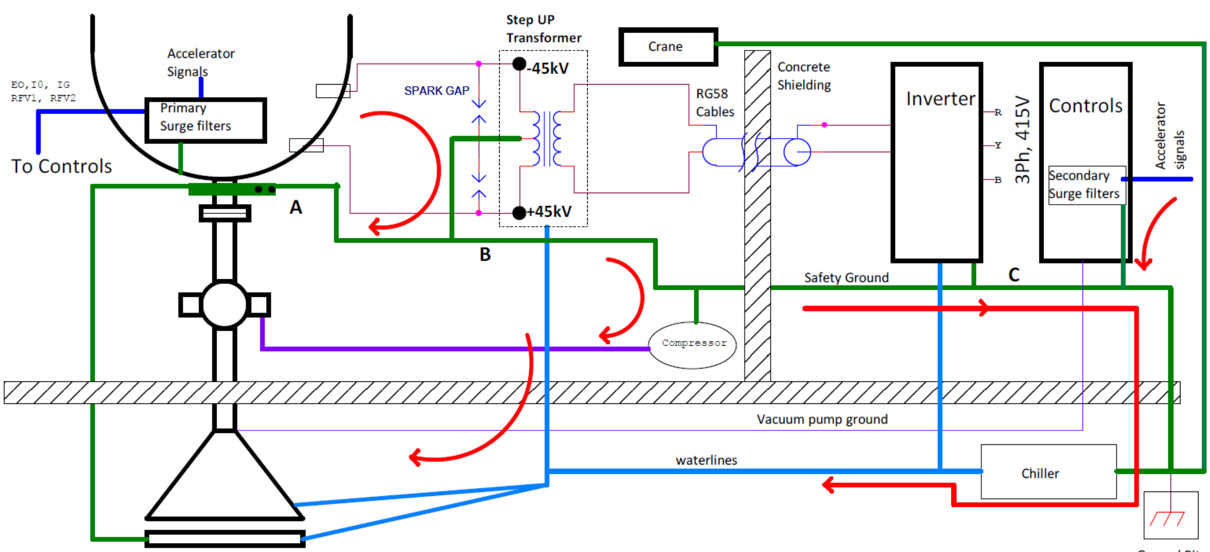


Figure 3: A grounding layout illustrating transient voltage lifting coupled through the ground conductors.

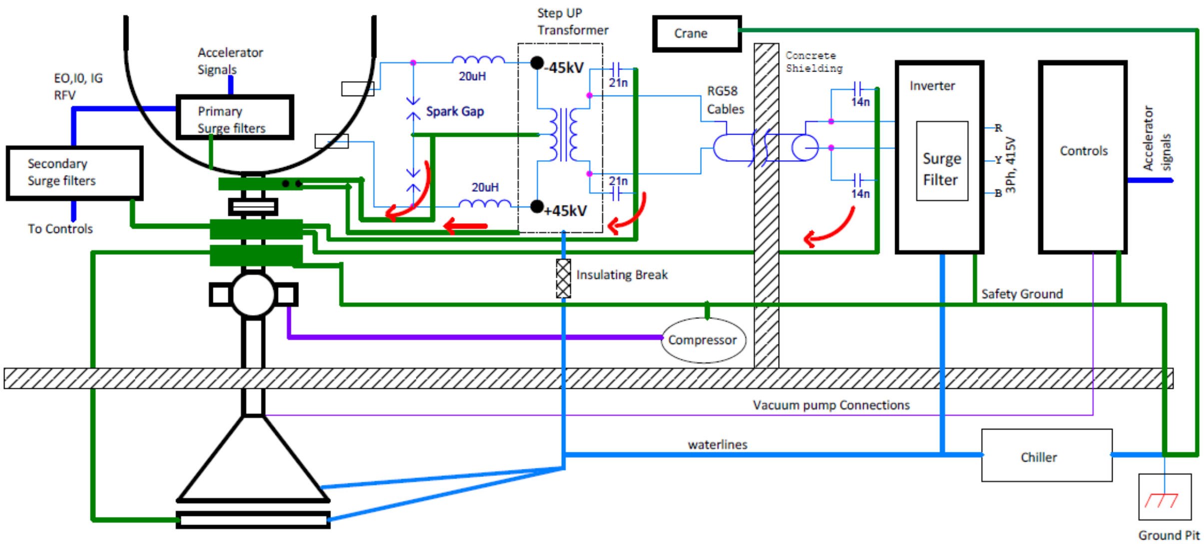


Figure 4: Modified grounding layout with dedicated conductors for high frequency return currents

local ground lifting. The transients can travel to remote locations through conductive cooling lines. During the initial trials flash over marks and damage of isolator in the inverter DC link controls was observed.

## REMEDIAL MEASURES

The cause of ground lifting is the voltage rise across return current conductors. By reducing the return line impedance and by reducing the amount of current passing through common mode impedance, the transient voltage rise can be minimised [2]. For this purpose separate return path is provided for transient currents, as shown in Figure 4. However transient current passing through inter winding capacitance still shares common impedance as shown in Figure 5. L2 shown in the equivalent circuit represents the inductance offered by ground connections between Points A and B. Inductance L1 shows the source side inductance.

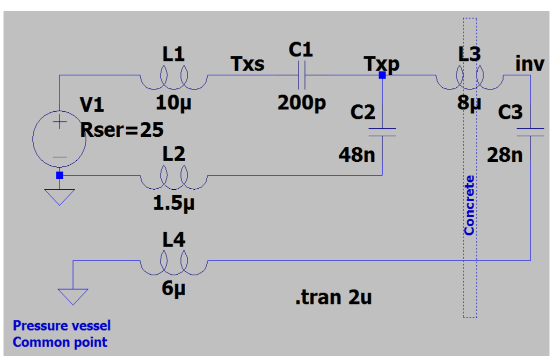


Figure 5: Equivalent circuit of ground connections

The high inter winding capacitance of the transformer makes the circuit behave as an inductive divider. By increasing value of L1 the voltage lifting at transformer primary (TXp) can be minimised. However too high inductance will practically remove smoothening effect of the transformer capacitance and will result in higher transient voltage stress at the bottom stage insulation of the multiplier. A compromise is obtained by inserting 20µH in each secondary connection to the multiplier as indicated in Figure 4. Bypass capacitors with ceramic capacitors has been incorporated at transformer primary end and inverter ends with separate return conductors. Performance of the bypass paths deteriorate due to large inductances of these long connections. High conductivity paths along the cooling lines has been broken by incorporating connections with insulating materials. With these changes, the transient voltage level at the inverter output terminals has been reduced from 10 kV level initially observed at 230 kV discharges to 1 kV at 800 kV discharges.

## CONCLUSIONS

High frequency currents should preferably return to the source through separate return conductors. By doing so potential differences due to common impedance sharing can be brought down. To bring down the transient voltage rise, suitable impedances may be inserted in the high frequency path. An electrostatic shield between primary and secondary will reduce the direct capacitance. However there are other coupling paths through the core to winding and transformer tank to terminal capacitances. Reducing the inductance of transformer tank to pressure vessel connections by multiple parallel connections or a local ground plane can greatly improve performance.

## REFERENCES


[1] Guide for Safety in AC Substation Grounding, IEEE Std 80-2000, January 2000.

[2] Fernando José González Arteche, "EMC: A mapping for the CMS experiment", Ph.D thesis, University of Oviedo, 2004.

# EPICS BASED EMBEDDED CONTROL SYSTEM ARCHITECTURE FOR ELECTRON GUN OF E-LINAC

Shantonu Sahoo, Arihant Jain, Anindya Roy

Variable Energy Cyclotron Centre, Kolkata, India

# email: ssahoo@vecc.gov.in

*Abstract*

The Electron gun system of e-LINAC consists of various components including 8 Steering Magnet Power Supply (PS), 3 Faraday Cups, 3 Vacuum Gauges, RF Generator, RF Amplifier, Filament PS, Grid PS and Cathode HV supply. For control and monitoring of these subsystems, EPICS is selected because of its distributed architecture. A modular network-based Programmable Automation Controller (PAC) with the capability of connecting I/O through backplane bus is selected as the hardware platform. The control system architecture for electron gun and details of porting EPICS in embedded PAC platform is discussed in this paper.

## INTRODUCTION

A thermionic electron gun with gridded cathode, RF modulated at 650 MHz floating at 100 keV is installed as a part of 50 MeV, 2 mA photo-fission for ANURIB facility [1]. A waveguide type DC isolator is used for feeding RF to the grid using 200 W, 650 MHz RF amplifier. Subsequent to this, a low energy beam transport (LEBT) line is installed which consists of steering magnets, solenoid magnets and Faraday Cups. Fig.1 shows a simplified block diagram of Electron gun system of e-LINAC. A computerized control system of all these components needs to be developed in order to automate the whole process.

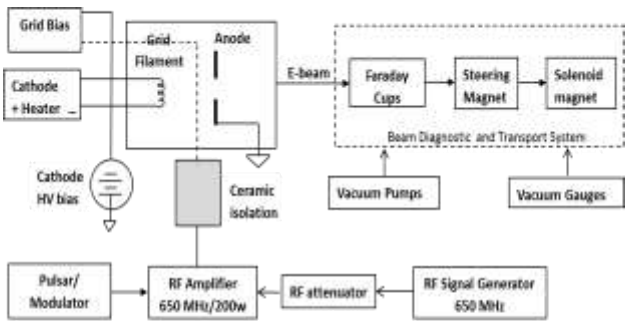


Fig. 1: Block Diagram of Electron Gun system

## I/O REQUIREMENTS

The control system for e-LINAC is distributed in nature consisting of various subsystems. The control parameters requirement is estimated and classified as Analog/Digital Inputs and Outputs. Most of the power supplies are made in-house and doesn't support any communication interface. They are controlled / monitored by analog / digital signals and readback channels. Whereas, instruments like Vacuum gauges and RF signal generator and a few power supplies have dedicated communication interface. Table 1 lists the total I/O requirements for the control system.

| S. No | Component | AI | AO | DI | DO | Protocol Interface |
|---|---|---|---|---|---|---|
| 1. | Faraday Cups (3 Nos.) | 3 | - | 6 | 6 | - |
| 2. | Steering magnet P/S (8 Nos.) | 16 | 8 | 8 | 16 | - |
| 3. | Solenoid Magnet P/S (3 Nos.) | 3 | 3 | 3 | 3 | - |
| 4. | Vacuum Gauge (03 nos.) | - | - | 3 | - | RS-232 |
| 5. | RF signal generator | - | - | - | - | LAN |
| 6. | RF amplifier | 2 | - | - | - | - |
| 7. | Filament power supply | - | - | - | - | RS-232 |
| 8. | Grid power supply | - | - | - | - | RS-232 |
| 9. | Cathode High Voltage supply | 2 | 2 | 1 | 1 | |
| | **Total** | **26** | **13** | **21** | **25** | **3 RS-232 1 LAN** |

Table 1: I/O requirements for e-LINAC Control System

## CONTROL ARCHITECTURE

Experimental Physics and Industrial Control System (EPICS) adopts a distributed control system architecture and is used worldwide in most particle accelerator labs. Due to its distributed architecture, modularity and scope for future expansibility it has been selected for development of control system for e-LINAC. Fig 2. shows the control system architecture for e-LINAC.

EPICS has a three layer architecture. In the top layer, there will be Operator Interfaces (OPI) for different subsystems like RF generator, Power Supplies, Faraday Cups etc. Middle layer is the heart of the control system i.e. an embedded system controller running EPICS Input Output Controller (IOC) on it. Bottom layer or hardware layer comprises of the analog and digital I/O modules and serial protocol converters that interfaces with the field devices.

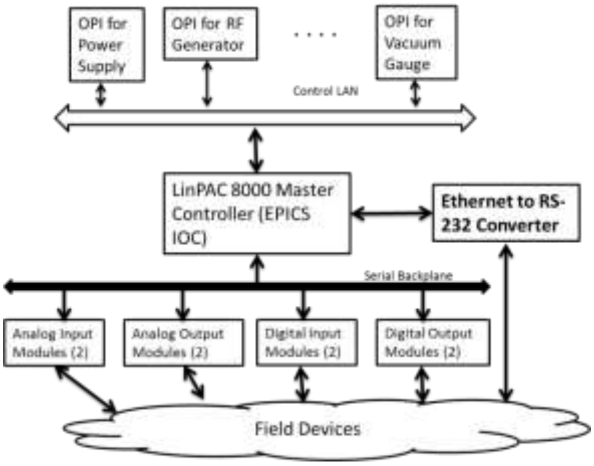


Fig. 2: Control System Architecture for e-LINAC

## HARDWARE

LinPAC-8000 Programmable Automation Controller is used as the control hardware. Fig. 3 shows the front view of the Controller being used. LinPAC-8000 has a master controller running Linux 2.6 kernel on Intel Atom CPU. Following are the list of important specifications of LinPAC-8000 controller:

- Linux kernel 2.6.33
- CPU Intel Atom Z520 CPU (1.33 GHz)
- 1 GB DDR2 RAM
- Flash 8 GB as IDE Master
- Dual Battery Backup SRAM 512 KB (for 5 years data retain)
- VGA, Ethernet and 4X USB 2.0 Ports
- I/O Expansion for 3/5/7 Slots
- Power Consumption 18 W (0.75 A @ 24 VDC)

Fig. 3: Programmable Automation Controller

LinPAC-8000 master controller is connected to other I/O modules through backplane via serial bus. Following are the list of I/O modules being installed:

1. I-8017HCW 8-channel differential Analog Input (AI) module (2 Nos.).
2. I-87024 4-channel 14-bit Analog Output (AO) module (2 Nos.)
3. I-8037W 16-channel Isolated Open Collector Digital Output (DO) Module (2 Nos.).
4. I-8050W 16-channel Universal Digital I/O (DIO) Module (3 Nos.)

Fig. 4 shows the picture of LinPAC controllers with I/O modules, Relay Units and Terminal Blocks installed on a 19" Server rack at the site.

Fig. 4: Control Server Rack installed at site

## SOFTWARE

EPICS base has been ported on LinPAC-8000. This embedded controller hosts Embedded Linux OS with GNU C library preinstalled which makes it suitable for on-board installation of EPICS base. A few library packages like libCom, readline etc needs to be built manually before EPICS installation.

After base installation, EPICS application needs to be developed. The manufacturer provides the device driver library file — libi8k.a which includes the library functions for interfacing the I/O modules connected through backplane [3]. Device support module in EPICS has been developed in C language using the libi8k.a library. The EPICS application has been successfully developed and tested on field for control and monitoring of digital and analog signals. Fig. 5 shows simplified software architecture of e-LINAC control system. Fig. 6 shows the screenshot of the EPICS application running on Embedded controller.

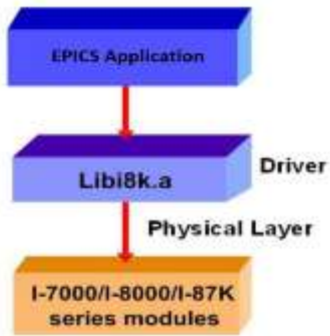


Fig.5: Software Architecture

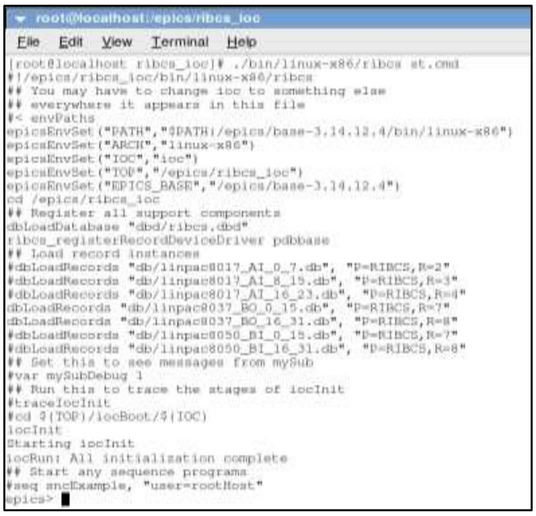


Fig. 6: Screenshot of EPICS application running on Embedded Controller

## CONCLUSION

EPICS have been selected as the control system architecture for electron gun system of e-LINAC. I/O requirement for this system has been calculated and LinPAC-8000 Programmable Automation Controller is selected as the control hardware platform. EPICS is embedded on the controller and application for controlling and monitoring of Digial and Analog I/O ports has been developed and tested successfully.

## REFERENCES


[1] Naser, Md. Zamal Abdul, et. al. "Present status of design, installation and testing of electron gun and low energy beam transport line of electron Linac at VECC." India: Bhabha Atomic Research Centre.

[2] Martin R. Kraimer, "EPICS Application Developer's Guide", EPICS Base Release 3.14.12.5.

[3] "Software Guide ICP DAS LinPAC-8X81 Series SDK", by ICP DAS Inc.

# DEVELOPMENT OF AN EPICS-BASED CONTROL AND INSTRUMENTATION SYSTEM FOR A BEAM PROFILE MONITOR FOR LEHIPA

Deepak N. Mathad*, A. Basu, Sudheer Kumar Singh, Laxman D. Tayade, IADD, BARC, Mumbai.

*Abstract*

The transverse profile of the 50 keV beam in the LEBT of LEHIPA is measured using a wire scanner. An EPICS-based control and instrumentation system has been developed for this profile monitor. The control of motion of the linear actuator for the wire scanner, beam current measurement and data acquisition system are all integrated in a single application program with a user interface. The system is synchronized with the trigger from the LEHIPA timing system. The value of instantaneous current of the beam pulse and a histogram depicting the transverse beam profile can be viewed on the user interface. This system is automated and the data captured is saved in a file at the end of the profile scan. Details of implementation of the system and sample results are discussed in this paper.

## INTRODUCTION

The Low Energy High Intensity Proton Accelerator (LEHIPA) [1] is a 20 MeV, 10 mA proton accelerator being developed at BARC. The Low Energy Beam Transport (LEBT) section is used to match the 50 keV proton beam from the ion source to the Radio Frequency Quadrupole (RFQ) using two solenoids and two sets of magnetic steerers. The LEBT also consists of beam diagnostics elements to determine the properties of the beam to optimize the operational parameters. Transverse profile being one of the important parameters of the beam is also measured in both X and Y directions in LEBT using wire scanners and slit scanners with Faraday cup mounted. A fully automated system for motion control and data acquisition based on Experimental Physics and Industrial Control System (EPICS) [2] is developed for this purpose. This presently operates in pulse mode of the beam.

## SYSTEM ARCHITECTURE

The details hardware and software architectures of the system are as follows.

### *Hardware architecture*

The hardware architecture of the system is as shown in figure 1. The current signal from the profile scanner is converted into voltage using an in-house developed multi-gain I-V converter. The gain of the I-V converter is kept fixed at a suitable value during the entire scan cycle. The voltage output is digitized by a 16-bit compact PCI (cPCI) backplane based digitizer card (cPCI-9116). It has a maximum sampling rate of 250 ks/s and the data acquisition is synchronized with the trigger from LEHIPA Timing System (LTS).

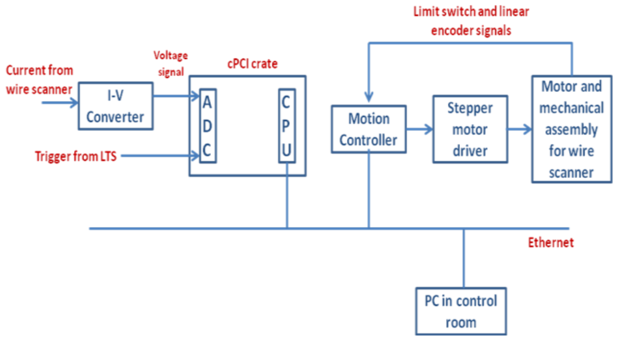


Figure 1: Hardware architecture of the system.

An Intel CPU based on cPCI with Ethernet interface is the main system controller. An Ethernet based motion controller (Galil DMC-4080) [3] is used to issue command to the stepper motor driver for moving the profile scanner in and out of the beam tube. The motion controller gets feedback from the linear encoder mounted on the mechanical assembly which determines the position of the scanner. It also has interface to the limit switches at the two extreme positions of the scanner. The system is remotely operated by a PC connected to Ethernet in the main control room.

### *Software architecture*

The software architecture of the system is as shown in figure 2.

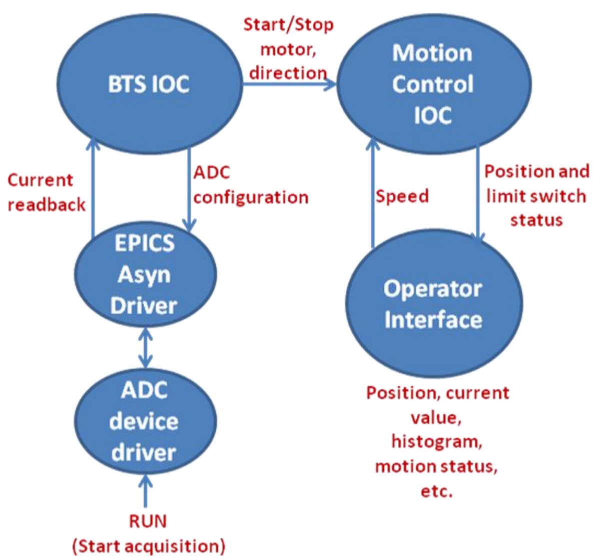


Figure 2: Software architecture of the system.

* deepaknm@barc.gov.in

Two EPICS Input / Output Controllers (IOC) are hosted on the cPCI based system controller (Linux operating system is used). The Beam Transport System (BTS) IOC controls the data acquisition through ADC and synchronizes motion of the profile scanner and data acquisition with the trigger from LTS. It also configures the ADC before data acquisition and receives back the voltage reading corresponding to the beam current. The main code for data acquisition and motion control is based on EPICS asynPortDriver class. The ADC device driver for operation in pulse mode has been developed for Linux kernel version 3.x using the available source code for kernel version 2.6. The source code for the access library is also recompiled for kernel version 3.x. The EPICS Motor Record based source code for motion control is provided by Galil. The motion control IOC hosts the process variables (PV) for control of motion of the scanner. It accepts command to Start / Stop motor and direction of movement through the PVs of BTS IOC. It takes input for speed from the operator interface. It also provides the position readback from the linear encoder and the status of the limit switches.

### *Synchronization of events with trigger*

The synchronization achieved between trigger and other events in the system is explained using a timing diagram as given in figure 3. The system gets synchronized with the trigger from LTS to the ion source when ‘Run’, a soft process variable (PV) is enabled. On the rising edge of the trigger, the beam is turned ON. Data acquisition by ADC is also started simultaneously as the same trigger pulse is input as external trigger for the data acquisition card. At this moment, the motor of the profile scanner is kept stationary as to have one-to-one correspondence of the position of the profile scanner and the value of beam current at that position. The OFF time of the beam is used for moving the sensor to the next position by turning ON the motor. It stops on the arrival of next trigger and data acquisition starts. This process will continue till the scanner reaches the limit switch. The user has to initiate the profile scan by enabling Run and issue the command to move the motor either IN to or OUT of the beam line. The rest is taken care by the system till the scan is completed. When Run is not enabled, motion control is not synchronized with the trigger pulse and it can be handled independently.

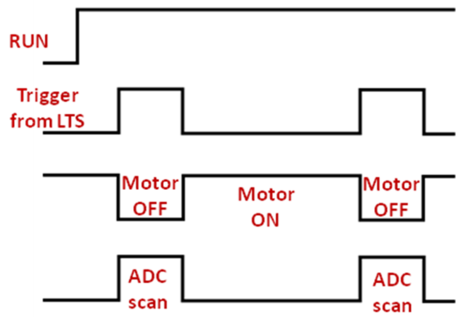


Figure 3: Timing diagram showing synchronization of different events in the beam profile monitoring system.

## GRAPHICAL USER INTERFACE

The graphical user interface (GUI) for the control of the system is developed using EPICS Qt framework. The layout of the GUI is as shown in figure 4. Push buttons for controlling the movement of the profile scanner IN / OUT of the beam tube and to stop the motion are provided. There is also a provision to set the speed of the motor. Current position of the scanner and the status of the limit switches at the two extreme positions are shown. The first plot gives the waveform of the instantaneous beam current intercepted by the profile scanner versus time in seconds. This is the output of the I-V converter (with a gain suitably set) in volts after digitization. The second plot gives the beam profile plot (beam current vs. position of the scanner). The trace is plotted online as the scan progresses. Any sample plotted on the profile plot is obtained by suitably averaging the samples of the instantaneous current. The start and stop indices of the samples to be considered for averaging are specified in the command file used to run the BTS IOC. ‘QEplotter’ widget [4] of EPICS Qt is used for plotting the instantaneous values and beam profile plot. Here, a maximum of 15 PVs can be plotted by specifying their name in the PV list.

To start a profile scan, the user has to enable Run and click on ‘Move In’ or ‘Move Out’ button. The scan will stop on its own when any of the limit switches is reached and the user will be prompted to save the data file containing scanner positions and the corresponding values of the beam current for future use. The filename will be appended with the timestamp while saving the file.

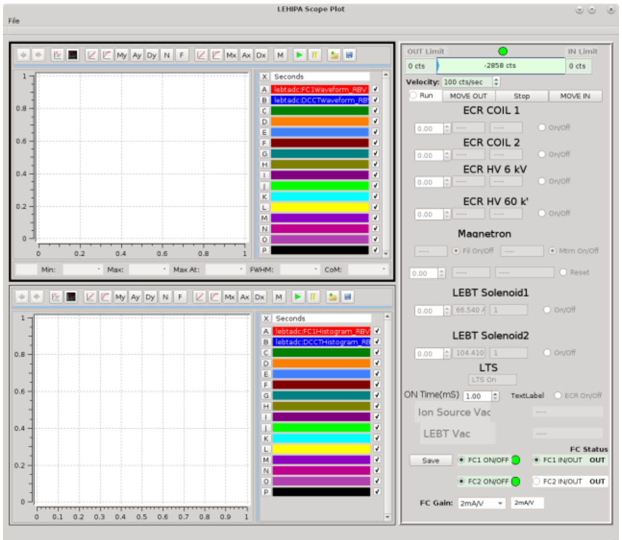


Figure 4: GUI for control of system and display of results.

Apart from display of plots and features to control motion, the control for the ion source as well as LEBT parameters is integrated in to the GUI. This all-in-one control application was useful especially during characterization of beam in LEBT. As the motion controller used here can support a maximum of 8 axes, the code and GUI can be augmented with control features for multiple axes.

## SAMPLE RESULT

This system was used during characterization of the ECR ion source beam in LEHIPA where beam profile measurements were taken for different settings of LEBT parameters for maximizing the proton fraction entering the RFQ [5]. The slit scanner with Faraday cup was used as the sensor. One of the plots obtained then is shown in figure 5. Here, the Y-axis is directly in terms of beam current in amperes. The QEPlotter widget has an alternate feature where a trace to be plotted can be a mathematical expression involving a PV present in the PV list. The PV corresponding to the output voltage of the I-V converter is multiplied by the set gain (10 µA/V, here) and the traces are plotted. The peak current is about 35 µA as seen from the profile plot.

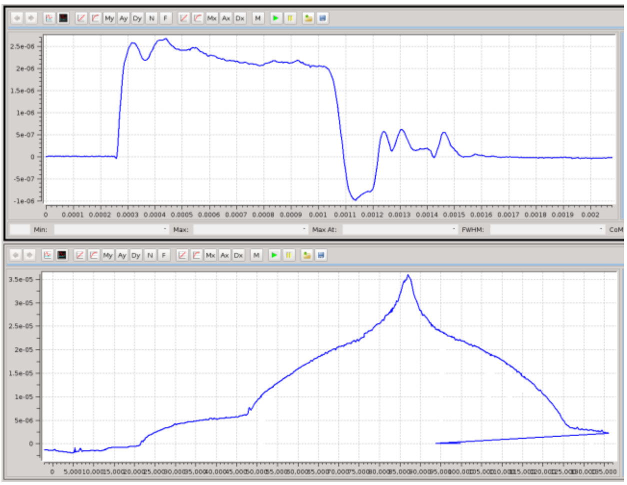

Figure 5: Plot of instantaneous value of beam current intercepted and the beam profile as displayed on GUI.

## CONCLUSION

The development of EPICS based control and instrumentation system for beam profile monitor for LEHIPA is done in this work. Code based on EPICS asynPortDriver is developed for triggered data acquisition. The motion control IOC is used to set the motion parameters. The motion of the profile scanner and data acquisition is synchronized with the trigger from LTS and controlled through BTS IOC, hence achieving one-to-one correspondence between the position of the scanner and the beam current at that position. A GUI is developed in EPICS Qt for integrated control of data acquisition, motion of scanner, ion source and LEBT parameters and display of instantaneous beam current plot and beam profile. The system developed is deployed successfully in field and was used during characterization of the ECR ion source beam in LEHIPA.


## ACKNOWLEDGEMENTS

We wish to gratefully acknowledge Dr. Jose V Mathew and Shri. Hitesh Kewlani, IADD, BARC for their inputs and feedback on the system developed. We also thank Dr. S. Krishnagopal, Head, IADD, BARC and all colleagues of IADD who supported this work.


## REFERENCES


[1] P. Singh et al, “Accelerator Development in India for ADS Programme”, PRAMANA Journal of Physics, Vol. 68, No. 2, February 2007, pp. 331-342.

[2] Experimental Physics and Industrial Control System http://www.aps.anl.gov/epics.

[3] Galil Motion Controller DMC 40x0, http://www.galilmc.com/motion-controllers/multi-axis/dmc-40x0.

[4] A. Rhyder, “QE Framework – QEGui and User Interface Design”, Australian Synchrotron.

[5] Hitesh Kewlani, “Operation & characterization of ECR ion source beam in LEHIPA”, Indian Particle Accelerator Conference, November 2019.

# SIMULATION STUDIES ON 1.5 GW X-BAND BACKWARD WAVE OSCILLATOR OPERATING IN LOW MAGNETIC FIELD REGIME

Romesh Chandra[1,2#], Rakhee Menon[1,2], Sandeep Singh[1,2], Sabyasachi Mitra[2], Senthil K[2], Ankur Patel[2], Vishnu Sharma[2], Amitava Roy[1,2], Debabrata Biswas[1,3], Archana Sharma[1,2]

[1]Homi Bhabha National Institute, Anushaktinagar, Mumbai, India-400094
[2]Accelerator & Pulse Power Division, Bhabha Atomic Research Centre, Trombay, Mumbai, India-400085
[3]Applied Mathematics and Theoretical Physics Section, Bhabha Atomic Research Centre, Mumbai, India-400085

*Abstract*

Relativistic Backward Wave Oscillators (RBWO) are the prime source of High Power Microwave generation due to its simple geometry and higher efficiency. The drawback is that it require a very high magnetic flux density >2.5 T for guiding electron beam through its slow wave structure (SWS). This magnetic field is generated either by pulsed magnetic coils or superconducting magnets. One possibility is to reduce magnetic field of operation and use permanent magnets for operation of RBWO. In this paper we are presenting a design of overmoded RBWO capable of generating 1.4 GW HPM power at 650 kV, 8.0 kA electron beam parameters. The guiding magnetic flux density is 0.74 T and output frequency is 9.45 GHz. The device efficiency is curtailed by the back streaming of the particles through the SWS as seen in 2.5 D Particle in Cell simulations.

## INTRODUCTION

High Power Microwave (HPM) find its application in electronic disruption and compatibility testing, high power RADARs, modern high gradient electron beam accelerators and plasma studies [1]. Among all the popular HPM sources Relativistic Backward Wave Oscillators (RBWO) finds an attractive place due to its simplicity of operation, higher power handling capacity, availability of devices in broader frequency range and higher efficiency [2-4].

In RBWOs, to make backward travelling microwaves radiate in the forward direction resonant reflectors (RR) are commonly used [5]. The typical efficiencies of the RR-RBWO combination range from 22-40%.

RBWO utilizes an axial magnetic field for guiding of electron beam in the direction of propagation. Beam quality and microwave conversion efficiency improves with increasing magnetic field values. But increasing magnetic field values beyond 1-1.5 T are very difficult to produce in DC mode over such a long length of RBWO. In this case 2.5 to 3.0 T pulsed magnetic coils are used. RBWO efficiency at these magnetic field values is very good. But due to pulsed nature of magnetic coil repetition rate of HPM generation gets limited. Hence there is a need to reduce the guiding magnetic field value so that either DC magnetic coil or permanent magnet could be used [6]. There is a minimum amount of magnetic field which is required for electron beam propagation through the slow wave structure (SWS) [7]. As we increase the magnetic field value above this limit RBWO efficiency increases and output power improves. Then after increasing magnetic field value further output power gets absorbed in cyclotron resonances. This happens due to overlapping of the cyclotron synchronism with the Cherenkov synchronism [8]. This region depends upon the applied magnetic field, electron beam parameters and operating mode of RBWO. This region usually ranges in between 1.0 to 1.3 T guiding magnetic field. Our aim is to operate RBWO efficiently below cyclotron resonances and above magnetic field threshold for beam propagation.

To operate RBWO efficiently in the lower magnetic field we must improve electron beam quality by reducing space charge and improve electron beam to slow wave structure coupling. For reducing the space charge in the RBWO electron beam we use a larger area beam and large diameter SWS. The problem associated with large diameter SWS is that the difference between two consecutive modes in $\omega$-$k$ space is reduced and structure becomes overmoded [9]. In an overmoded structure there is always a possibility of exciting some stray modes, which results in the poorer efficiency of the device. To avoid this we have designed a meagrely overmoded structure which is having a cross section of $1.4\lambda$ where $\lambda$ is the operating wavelength. To suppress any stray mode we have used a mode selector at the end of SWS [10]. To increase the SWS and electron beam interaction a non uniform SWS has been used with 2.4% increase in the cross section of last two cells of the SWS.

The complete designed structure is subjected to 2.5 D particle in cell simulations for 650 kV, 8.0 kA electron beam parameters. The guiding magnetic field is kept 0.74 T. The output microwave power is 1.4 GW in $TM_{01}$ mode and the output frequency is 9.45 GHz. The output microwave power diminishes for 1.1 T guiding magnetic field. The efficiency of the SWS gets limited by backstreaming of the electron beam. Further simulations are underway for the suppression of backstreaming particles.

## THEORETICAL ANALYSIS

While deciding the $B$ field magnitude required for efficient microwave generation, one has to consider minimum magnetic field requirement and microwave

#romesh@barc.gov.in

absorption in cyclotron resonances. The threshold value of the magnetic field $B$ required for electron beam propagation which is estimated to be,

$$B > (2nm/(\varepsilon_0 \gamma))^{1/2} \quad (1)$$

Here $n$ is the electron beam density, $m$ is the electron mass and $\varepsilon_0$ is the permittivity Minimum magnetic field estimated to be 0.24 T from Eq.(1). Backward microwave power gets absorbed in the cyclotron resonances if the magnetic field values are near,

$$B_{res} = \frac{2\, m\beta c}{e} \gamma \frac{\pi}{z_0} \quad (2)$$

Here $m$ is the mass of the electron, $\beta$ and $\gamma$ are the relativistic factors and $z_0$ is the pitch of SWS. From this equation magnetic flux density comes out to be 1.7 T. For the forward wave, the cyclotron resonances occur if the magnetic field values are near,

$$B_{res} = \frac{2\, m\beta c}{e} \gamma \left(\frac{\pi}{z_0} - k_f\right) \quad (3)$$

Here $k_f$ is the forward wave number of the operating mode. This value comes out to be 0.48 T for 7.5π/6 operating mode.

## DESIGN OF SWS & REFLECTOR

A seven cell nonuniform SWS is simulated for its frequency response and dispersion curve. The obtained sispersion curve and electric field profile for the desired mode of operation is plotted in Fig. 1. It may be seen in Fig 1 (c) and 1 (d) that the introduction of reflectors at the back and front end doesn't changes electric field profile much. The operating mode frequency is 9.25 GHz which in our case in unaffected by the introduction of the resonant reflector and end reflector.

The reflector is designed in the CST microwave studio using time domain analysis. The reflector is a simple waveguide structure. The reflection parmaeter $S_{11}$ and transmission parameters are shown in Fig. 2. This reflector reflects backward propagating $TM_{01}$ mode microwave into forward mode, which from the SWS end can be extracted via suitable waveguide antenna. The reflection parameters show that there is very good reflection from resonant reflector in frequency range 9.2 GHz to 9.5 GHz.

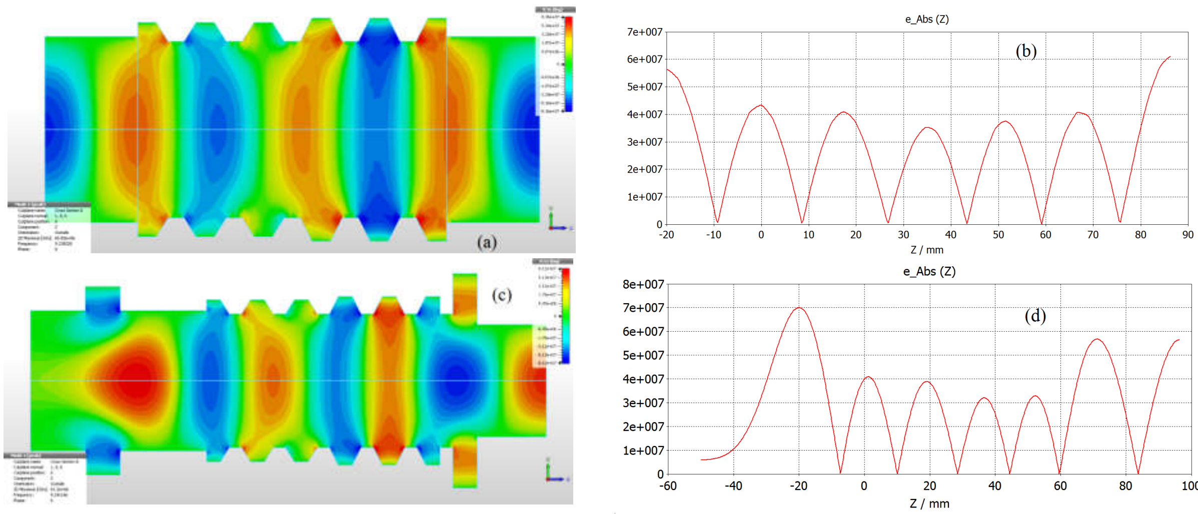


Fig. 1. (a) $E_z$ and (b) E-absolute component of the electric field in the SWS without reflector and with front and end reflector (c) and (d).

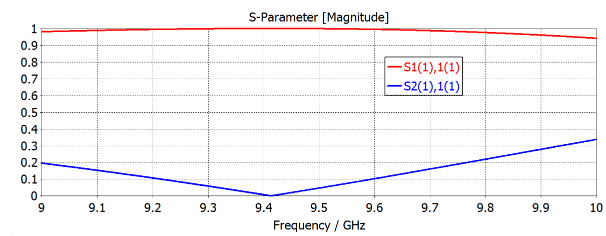


Fig. 2. *S*-parameters of the RR.

## PARTICLE IN CELL SIMULATION OF COMPLETE STRUCTURE

The complete structure is subjected to 2.5D particle in cell simulations (PIC). The operating parameters in the simulation are kept 650 kV and for 34.0 mm diameter 1.0 mm thick annular cathode, 8.0 kA electron beam current is generated. The anode cathode gap is kept to be 15.0 mm. The explosive emission electron beam generation model is used and generated beam is guided through SWS via 0.74 T guiding axial magnetic field.

The electron beam propagation in the SWS is shown in Fig. 3 for various instances. It may be seen that in low magnetic field operation whole cathode is emitting electron beams which must be avoided for better electron beam quality. We can see that once the microwave starts building up, the electron beam bunches cause defocusing of electron beam at the end of the SWS. At the end when microwave power peaks it starts grazing the SWS and finally starts hitting SWS. This beam loss curtails further microwave growth inside the cavity and microwave generation gets saturated at this point. It may be also noted from Fig. 3 that huge numbers of electrons start returning from the backend of the SWS. This results in a huge space charge build up and it disturbs the subsequent electron beam bunches. This backstreaming of electrons is due to over bunching of electron beam at the end location.

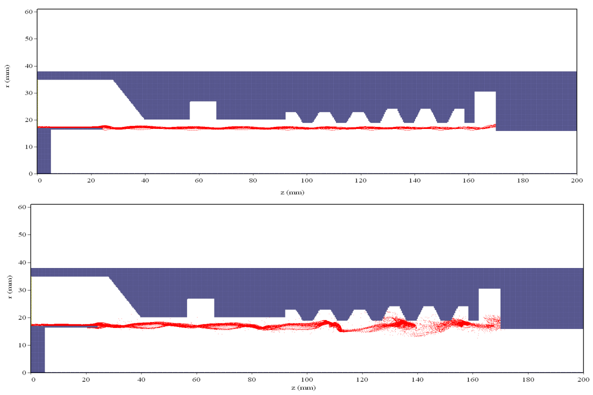

Fig. 3. Particle trajectories as obtained from PIC simulation at t=2.0 ns (top) and at t=9.0 ns (bottom).

The voltage current waveform used in the simulation is shown in Fig. 4. The maximum diode voltage is 650 kV and electron beam current is 8.0 kA. The rise time of the voltage pulse is 2.0 ns and simulation duration is set to be 20 ns.

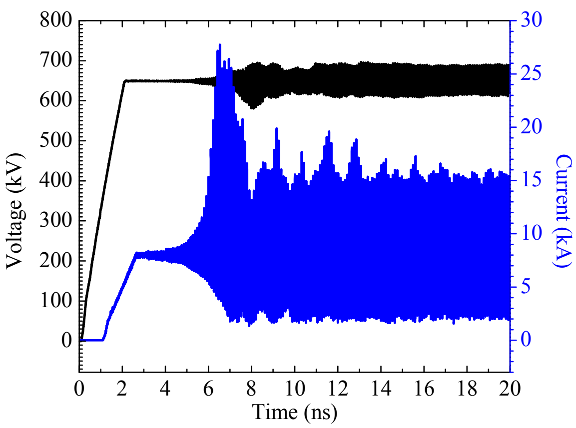


Fig.4. Voltage and current waveforms used for PIC simulation.

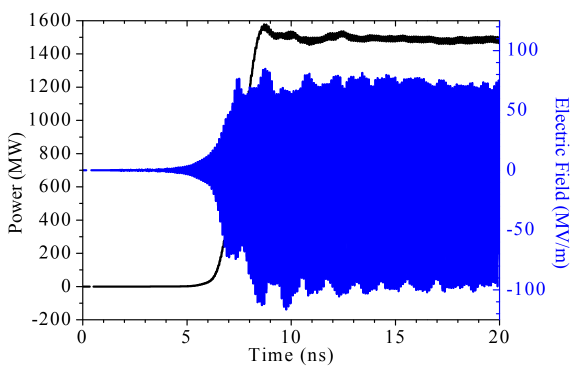


Fig.5. Time averaged microwave power (Black) and $E_z$ signal (Blue).

Obtained microwave power signal and $z$- component of the electric field at the end of structure is shown in Fig. 5. Generated microwaves get saturated at 1.4 GW microwave power level at $t$=8.5 ns. $Z$-component of the electric field has maximum magnitude of 1 MV/cm in the middle of the RBWO waveguide.

Fig.6. shows the frequency of the output microwave signal recorded outside RBWO structure. The measured frequency is 9.45 GHz in $TM_{01}$ mode. There is also a harmonic of this frequency around 19.0 GHz.

## RESULTS AND DISCUSSION

An RBWO having 9.45 GHz output frequency has been designed using time domain analysis and Particle in Cell simulations. A six cell non-uniform, overmoded SWS has been used for microwave generation. Generated microwaves travel in the backward direction where it gets reflected by a resonant reflector. The reflector was designed in such a way that its $S_{11}$ parameter is 1 near the frequency of interest. To avoid mode competition inside SWS and excitation of undesired modes, a mode selector is placed at the end of SWS such that it doesn't affect the electric field profile of the selected mode.

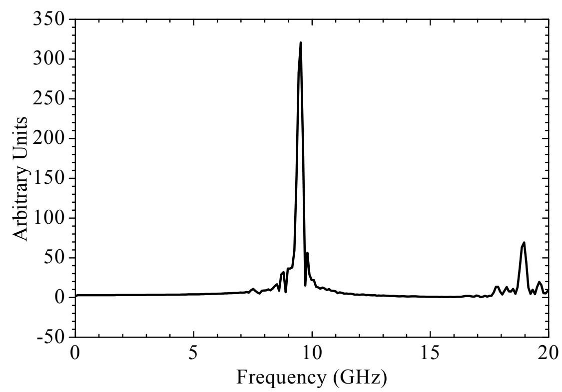


Fig.6. FFT of the output electric field signal.

The complete structure along with resonant reflector and end reflector is subjected to 2.5D PIC simulation for 650 kV, 8 kA electron beam pulse having 2.0 ns pulse rise time. The quasi-static simulations were carried out for 20 ns duration. Guiding axial magnetic flux density was kept 0.74 T for all the simulations.

The output signal frequency is 9.45 GHz as obtained from the FFT of $E_z$ component of electric field inside the output waveguide. In the PIC simulations, it was found out that output microwave power starts building up after $t$=4.5 ns and saturates to 1.5 GW at $t$=9.0 ns. The electron beam at $t$=9.0 ns gets over bunched and starts spreading and reflecting from backend of SWS. This result in the loss of electron beam from microwave cavity interaction region and limits the output microwave power. The problem of loss of electron beam from interaction region due to over bunching may be avoided by increasing the inner diameter of the SWS at the end locations, which will be attempted in future designs.

## *References*


[1]. J. Benford, J. Swegle and E. Schamiloglu, High Power Microwaves, New York, NY, *USA: Taylor & Francis*, 2006. https://doi.org/10.1201/9781420012064.

[2]. Sergei D. Korovin, Vladislav V. Rostov, Sergei D. Polevin, Igor V. Pegel, Edl Schamiloglu, Mikhail I. Fuks and Robert J. Barker, "Pulsedpower-driven high-power microwave sources", *Proc. IEEE*, vol. 92, no. 7, pp. 1082–1095, Jul. 2004. 10.1109/JPROC.2004.829020

[3]. B. V. Bunkin, A. V. Gaponov-Grekhov, A. S. Eltchaninov, F. Ya. Zagulov, S. D. Korovin, G. A. Mesyats, M. L. Osipov, E. A. Otlivantchik, M. I. Petelin, A. M. Prokhorov, V. V. Rostov, A. P. Saraev, I. P. Sisakyan, A. V. Smorgonsky and V. A. Suvorov, "Nanosecond radar system based on repetitive pulsed relativistic BWO,"in Proc. *9th Int. Conf. High-Power Particle Beams (Beams)*, pp. 195–202, May 1992. https://ieeexplore.ieee.org/document/6306489

[4]. A. Blyakhman, D. Clunie, R. Harris, G. Mesyats, M. Petelin, G Postoenko and B. Wardrop, "Nanosecond gigawatt radar: Indication of small targets moving among heavy clutters", *Proc. IEEE Radar Conf.*, pp. 61-64, Apr. 2007. 10.1109/RADAR.2007.374191

[5]. E.M. Totmeninov, I.V. Pegel and V.P. Tarakanov, " Highly efficient Xband relativistic twistron", *Laser and Particle Beams*, 34, 601–605, Dec. 2016.

[6]. I. K. Kurkan, V. V. Rostov and E. M. Tot'meninov, "A possible method of reducing the magnetic field in a relativistic backward-wave tube*", Technical Physics Letters*, vol. 24, no. 5, pp. 388–389, May 1998. https://doi.org/10.1134/1.1262101

[7]. R. B. Miller, "An Introduction to the Physics of Intense Charged Beams", Berlin, Germany: Springer-Verlag, 1982. 10.1007/978-1-4684-1128-7.

[8]. A N Vlasov, A.S. Ilyin and Y. Carmel, "Cyclotron effects in relativistic backward-wave oscillators operating at low magnetic fields", IEEE Trans. Plasma Sci., vol. 26, no. 3, pp. 605–614, Jun. 1998. 10.1109/27.700797

[9]. M.I. Petelin, "Mode Selection in High Power Microwave Sources,"IEEE Trans. Electron Dev., vol. ED-48, pp. 129-133, 2001.

[10]. Xiao, Renzhen & Li, Jiawei & Bai, Xianchen & Zhang, Xiaowei & Song, Zhimin & Teng, Yan & Hu, Yin-e & Li, Xiaoze & Sun, Jun & Chen, Changhua. (2014). An overmoded relativistic backward wave oscillator with efficient dual-mode operation. Applied Physics Letters. 104. 093505-093505. 10.1063/1.4867531.

# DESIGN OF A 300 W, 150 MHZ SOLID STATE RF POWER AMPLIFIER FOR SC ACCELERATOR

Snigdha Singh*, J.K. Mishra, Manjiri Pande, Gopal Joshi
Bhabha Atomic Research Centre, Mumbai

*snigdha@barc.gov.in*

*Abstract*

A 300 W, 150 MHz solid state RF power amplifier is being designed and developed at BARC for powering the superconducting (SC) accelerating cavities of SC linac at TIFR, Mumbai. In addition to power and frequency, the other targeted design specifications of this amplifier are efficiency >65%, overall gain~44.8 dB, bandwidth ±5 MHz etc. Based on space availability, one of the requirements for the amplifier cooling system is to avoid circulating water. To fulfil this requirement, efficient methods of cooling at this power rating have been studied. Based on this study, it has been decided to use heat pipe based cooling for this amplifier. The detailed study and design on heat pipes is in the progress. This paper discusses detailed design and simulation results of the RF power amplifier.

## INTRODUCTION

In low power (upto approximately 200 kW) segment, tube based amplifiers have been completely replaced by solid state power amplifiers. Modularity, low operating voltages which addresses the safety concerns, no radiation issues and lower size and weight are few of the advantages of solid state power amplifier. In superconducting applications, the quality factor (Q) of the cavities is quite high (~$10^{10}$ at 4 K for Niobium cavities), so RF power requirement is lowered that can be met by the solid state RF power amplifiers.

The Tata Institute of Fundamental Research (TIFR), Mumbai has an operational RF superconducting (SC) linear accelerator (LINAC) since 2002. The super conducting accelerator consists of 7 cryo modules and each cryo module has four quarter wave resonators amounting to a total of 28 accelerating (quarter wave resonators) structures in the LINAC. Each RF resonator is driven by a 150 MHz solid-state RF power amplifier. The RF superconducting accelerator is being upgraded and hence, TIFR needs upgraded Solid-state RF power amplifiers. Thus, 150 MHz high efficiency and high gain RF amplifiers are being developed at BARC for this application.

Since the RF power requirement per resonator is less (max. 300 W), a single module RF power amplifier has been designed to meet the design specifications of efficiency>65%, overall gain ~44.8 dB and bandwidth ±5 MHz.

The overall block diagram of a single module solid state RF power amplifier is shown in figure 1:

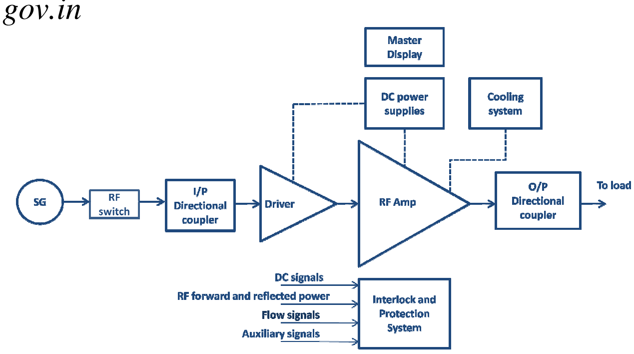


Figure 1: Block diagram of a solid state power amplifier

In this paper, RF design and thermal details of a 300 W, 150 MHz amplifier have been discussed.

## RF DESIGN

The MOSFET device for the amplifier has been selected based on the power requirement, gain, and frequency of operation among other parameters [1].

### *Amplifier gain*

For TIFR SC accelerator, the maximum available RF input to the system is 13 dBm. Considering maximum available RF input of 10 dBm (keeping a margin of 3 dBm), the gain of the subsequent stages has been calculated. Since the required output power is 54.8 dBm, it translates to a minimum gain requirement of 44.8 dB. A driver stage having maximum gain ~30 dB and power stage with gain>20 dB have been selected to meet this requirement.

After device selection, its optimum load and source terminations have been calculated and matching circuit designed accordingly. The optimum load termination required at the device output has been calculated considering the output power, drain bias supply voltage and class of operation [2].

$$Imax = \frac{3\pi * Pout(W)}{2*(Vds,DC - Vk)} \quad (1)$$

$$RLopt = \frac{3\pi*(Vds,DC - Vk)}{4*Imax} \quad (2)$$

$$\chi = \frac{Vk}{Vds,DC} \quad (3)$$

$$\eta = 0.85(1-\chi) \quad (4)$$

where, Pout is the maximum output power, $V_{ds,\ DC}$ is the drain bias voltage, $V_k$ is the knee voltage, $I_{max}$ is the maximum output current, $R_{Lopt}$ is the optimum load termination and $\eta$ is amplifier efficiency.

Using (1) and (2), the optimum load termination is calculated. The optimum matching network has been designed to offer output load impedance at the device output (drain terminal to source). The matching network has been designed using Band Pass Filter (BPF) topology with capacitors and micro strip lines. Simulation has been done using simulation tools and the output matching networks along with its results have been shown in figures 2- 4. As can be seen from figures 2 and 3, Insertion loss: 0.1 dB and Return loss: 29.7 dB respectively. The 3 dB bandwidth of the output matching circuit is 66 MHz as can be seen from figure 3.

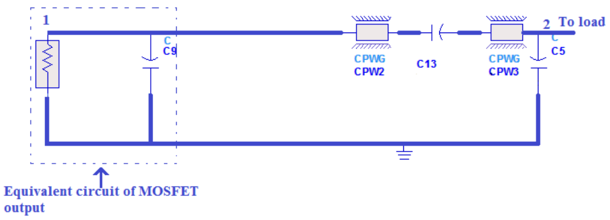


Figure 2: Output matching circuit

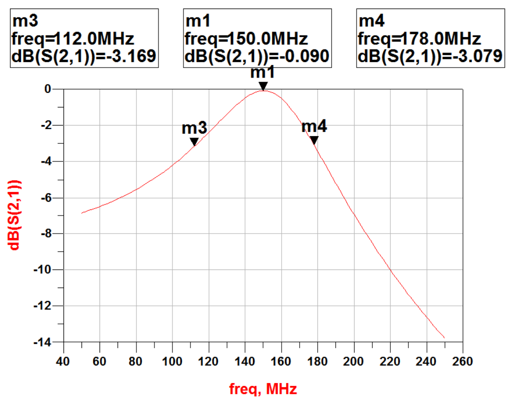


Figure 3: Insertion loss of output matching circuit

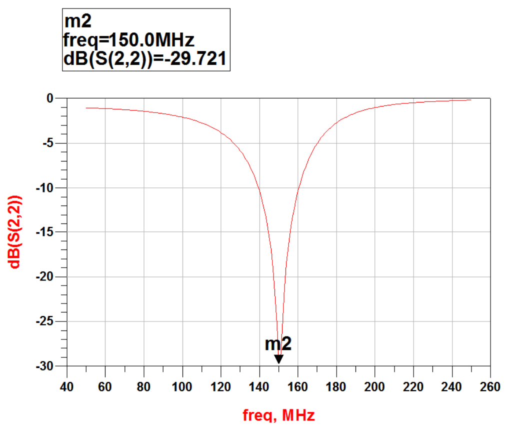


Figure 4: Return loss of output matching circuit

The input impedance to be offered at the device input (gate terminal to source) has been calculated using the values given in the datasheet after adjusting for 150 MHz operation [3]. Input matching network has also been designed using BPF topology. This has been simulated using simulation tools and the input matching networks along with its results are shown in figures 5-7. From figures 6 and 7, it can be seen that Insertion loss~ 0.4 dB and Return loss: 29.8 dB. The 3 dB bandwidth is ~16 MHz.

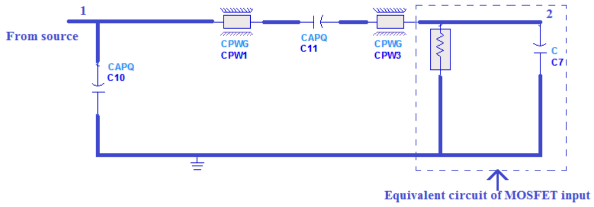


Figure 5: Input matching circuit

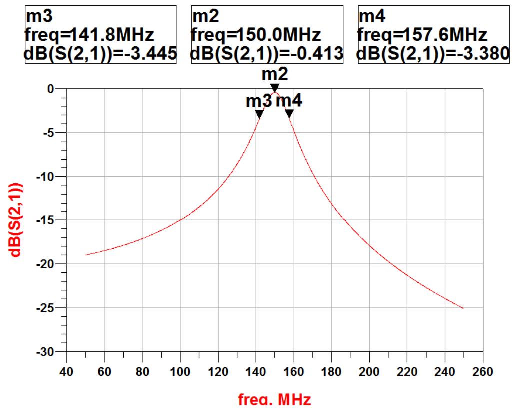


Figure 6: Insertion loss of input matching circuit

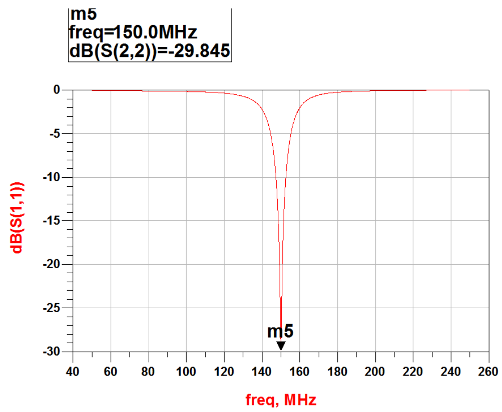


Figure 7: Return loss of input matching circuit

The values obtained i.e., Insertion loss~0.1 dB and ~0.4 dB (o/p and i/p matching network) and Return loss ~ 29.7 dB and 29.8 dB (o/p and i/p matching network) are in line with the design requirements. The PCB layout has been prepared and is being printed in a woven fiber_glass reinforced, ceramic filled, PTFE-based composite laminate.

### *Efficiency Calculation*

The efficiency of amplifier depends upon design output power, knee voltage, drain bias supply voltage and class of operation (4). Assuming class AB (close to class B) operation, the efficiency calculated is nearly 70%.

## THERMAL DESIGN

One of the requirements for the amplifier cooling system is to have a dry type cooling system. To fulfil this requirement, efficient methods of cooling at this power rating where circulating water is not used, have been studied in detail. Air cooling and heat pipe method are the two possible techniques that can be used. Based on the study, it has been decided to use cooling based on heat pipes for this amplifier. For initial functionality testing, it has been decided to use forced air cooling.

### *Option 1: Calculation for forced air cooling*

The important parameters for selecting heat sink and fans are maximum power dissipation Q (which depends on efficiency), PCB size, maximum allowable device junction temperature ($T_J$) and ambient temperature ($T_A$). The equivalent circuit for thermal resistance calculation is shown in figure 8.

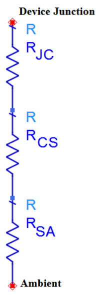


Figure 8: Equivalent circuit of thermal resistance from device junction to ambient

(Ref: www.diodes.com)

where, $R_{JC}$,$R_{CS}$ and $R_{SA}$ are thermal resistances from device junction to case, case to surface of heat sink and heat sink surface to ambient respectively.

Total thermal resistance (from junction to ambient) can then be calculated as:

$$R_{JA}= (T_J-T_A)/Q \tag{5}$$

Assuming DC to RF efficiency of 50% and the minimum ambient temperature around 40 $^OC$, the thermal resistance from junction to ambient (obtained using (5)) must be maintained below 0.37 $^OC/W$. As $R_{JC}$ is fixed for the device and can be obtained from the datasheet, (0.15 $^OC/W$ in case of selected device) the thermal resistance between device case and ambient must be lower than 0.22 $^OC/W$. Thus we selected heat sinks and fans to match this requirement.

### *Option no. 2: Heat pipes*

Heat pipes are one of the most efficient ways to move heat or thermal energy from one point to another. They use a combination of evaporation and condensation of this working fluid to transfer heat in an extremely efficient way. The heat input vaporizes the liquid working fluid inside the wick in the evaporator section. The vapour, carrying the latent heat of vaporization, flows towards the colder condenser section. In the condenser, the vapour condenses and gives up its latent heat. The condensed liquid returns to the evaporator through the wick structure by capillary action. Figure 9 depicts how this heat transfer is carried out.

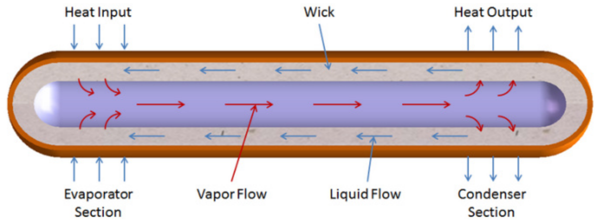


Figure 9: Heat transfer using heat pipes

(Ref: www.myheatsinks.com)

Depending on the heat to be dissipated, length of the heat pipe and the lengths of the evaporator (Le) and condenser (Lc) sections, the size and number of heat pipes required to dissipate this heat can be calculated.

The benefits of heat pipes are: High thermal conductivity, passive operation, long life with no maintenance and lower costs and therefore it has been planned to use heat pipes for thermal management.

## CONCLUSION

The RF and thermal design of Solid state power amplifier has been completed. RF simulation results are in line with the design requirements and thus PCB fabrication is under progress. As already mentioned, dry type cooling system is a prerequisite and two options for achieving the same have been explored. It is planned to conduct the bench testing using forced air cooling setup and after validation of the RF design, heat pipe based design will be incorporated.

## ACKNOWLEDGEMENT

Authors wish to thank Dr. A.K. Mohanty, Director, MRG for his continuous support and guidance.

## REFERENCES

[1] Paolo Colantonio, "High efficiency RF and microwave Solid State Power Amplifiers", Wiley Series in Microwave and Optical engineering.

[2] Jitendra Kumar Mishra, "High efficiency RF amplifier development over wide dynamic range for accelerator application", Nuclear Inst. and Methods in Physics Research, Volume 868, 1 October 2017, Pages 48-52.

[3] B.V. Ramarao, "Development of 3kW at 325 MHz solid-state RF power amplifier using four power amplifier modules" **,** Nuclear Instruments and Methods in Physics Research, Volume 735, 21 January 2014, Pages 283-290

# QUADRUPOLE MAGNET DESIGN FOR MEHIPA MEBT

Pallavi Priyadarshini, Jose V. Mathew
Ion Accelerator Development Division, BARC.

*Abstract*
A 200 MeV Medium Energy High Intensity Proton Accelerator (MEHIPA) is being designed at BARC. The MEHIPA MEBT channel consists of three buncher cavities and four quadrupoles to match the beam in the longitudinal and transverse directions respectively. The maximum magnetic field gradient required in the MEBT quadrupoles is 17 T/m for 25 mm aperture radius and effective length of 80 mm. Here, we discuss the detailed physics design and optimization studies of the electromagnetic quadrupole magnet, which will be used in the MEHIPA MEBT. Studies have been performed to optimize the quadrupole in 2D followed by a full 3D design. Harmonic analysis has been done to know multipole components of the designed quadrupole field. In addition, the effects of assembly misalignment on the multipole components have also been studied. Technique to reduce fringe field has also been proposed.

## INTRODUCTION

The Medium Energy Beam Transport (MEBT) line of MEHIPA is 2 m long, transports beam from RFQ to the superconducting SSR linac. The MEBT consists of four quadrupoles for transverse focusing and three buncher cavities for longitudinal focusing. Maximum gradient required by the MEBT quadrupole magnet is 17 T/m.

The paper starts with the design criteria, which are followed for electromagnetic quadrupole (EMQ) design. The EMQ design has been carried out in two stages: a 2D design followed by the 3D design. Understanding the mathematics of the 2D magnetic field of the quadrupole magnet is important since its 3D field, if integrated over the longitudinal coordinate, obeys the same two-dimensional differential equations. Thus, for the ease of designing the 3D magnet, detailed 2D design of pole tip, pole body, return arms and coils have been performed. The design is further optimised with pole tip shimming to improve field flatness in the aperture region. The optimized 2D design is then extended to the 3D design for effective length 8 cm. The 3D design will give a more realistic picture of an actual quadrupole magnet though the simulations are computationally expensive. Harmonic analysis has been done to know the ratio of quadrupolar to other multipolar terms. The quadrupolar fringe field is reduced by shielding the magnet with a soft iron sheet.

## FIGURES OF MERIT

Different figures of merit that describe the quality of a quadrupole magnet, which should be kept in mind while designing the magnet are as follows,

- Quadrupole gradient at an arbitrary coordinate $(x, y)$ is defined as [1]

$$g_x = \frac{\partial B_x}{\partial y} \text{ at } (x, y)$$

Due to symmetry, $g_x = g_y$. Maximum gradient G is defined as the gradient value at the Good Field Radius (GFR).

$$G = \frac{\partial B_y}{\partial x} \text{ at } (R_{GFR}, 0).$$

In 3D, the integrated quadrupole field [2]calculated at the axis $(R, 0, z)$ is given by:

$$G_{int} = \int_{-\infty}^{\infty} g dz\,.$$

- Quadrupole field uniformity is defined as

$$\delta g_x = 100 \times \frac{(g(x,0) - g(0,0))}{g(0,0)}\,,$$

Where, $g(x, y)$ is the quadrupole gradient at position $(x, y)$. The radius of the central circular region where field uniformity is within $\pm 0.5\%$ is defined as the GFR.

- The effective quadrupole magnetic length [1] is defined as:

$$L_{eff} = \frac{1}{g(0,0)} \int_{-\infty}^{\infty} g dz\,.$$

## REQUIREMENTS FOR THE DESIGN

For the MEHIPA MEBT, the design magnetic gradient is 17 T/m. The integrated gradient is 1.37 T with the effective length 8 cm and bore radius 25 mm. In addition to this, in order to keep the beam within the linear focusing region of the quadrupole magnet, good field radius of the magnet should be more than at least 50-60% of the aperture radius. For a normal quadrupole magnet it is typically required that any multipole term coefficient $(C_n)$ is suppressed relative to the quadrupolar term by a factor of at least $10^4$. Usually, the multipole terms are quoted after multiplying by a factor of $10^4$ and are said to be in "*units*".

## MAGNET DESIGN

In order to design a quadrupole, one can choose to start with the 2D or with 3D simulations. 3D simulations are computationally expensive, therefore 2D simulations are done first. To perform a first order quadrupole design and optimization, the code POISSON [3] was used that assumes that the length of the quadrupole magnet is much larger than its aperture. Symmetry condition of the quadrupole has been used; the 2D simulations have been done for one-eighth part of a quadrupole as shown in Figure 1. The optimised 2D design was further extended to 3D design with yoke length in z-direction as $l_{yoke} \approx l_{eff} - R_{ap} \approx$ 5.6 cm, where $R_{ap}$ is the aperture radius, that is 25 mm.

The 3D simulations were done for one quadrant and half the length of the quadrupole using proper boundary conditions. All 3D simulations have been performed in Magneto Static Solver of CST STUDIO SUITE [4]. The 2D and 3D models of the quadrupole magnet are shown in Figure 1.

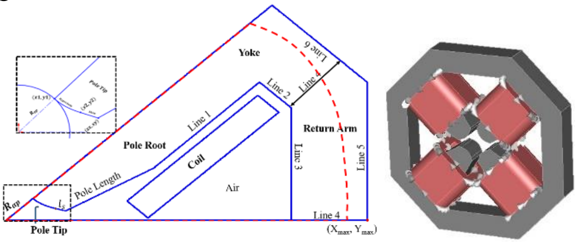


Figure 1. 2D (left) and 3D (right) quadrupole magnet designs.

## *Yoke Material*

Magnetic permeability is the ability of a material to support the formation of magnetic field within itself. Thus, the yoke material of the quadrupole is chosen to have higher magnetic permeability in order to provide less resistance path to the magnetic field due to the current carrying coil around the poles. Commonly used, Steel 1010 has been chosen for our simulations.

## *Pole Tip Design*

Ideally, the pole tips of the quadrupole magnets follow $xy = R_{ap}^2/2$ , where, $R_{ap}$ is the aperture radius of the quadrupole magnet and x, y are transverse coordinates. Pole tip of the quadrupole magnet is decided by the way we truncate the ideal hyperbolic pole tip shape. Truncation is done to prevent the pole from becoming too wide; this is necessary to leave space to accommodate the coils. As shown in Figure 1, the poles have been shimmed and optimized such that the magnetic field uniformity enhances near the centre and the hyperbolic pole tip can be terminated smoothly. Shim length $l_s$ is defined by the two points $(x_2, y_2)$ and $(s_x, s_y)$ as

$$l_s = \sqrt{(x_2 - s_x)^2 + (y_2 - s_y)^2}$$

The $l_s$ is optimised for larger extent of uniformity in the aperture region. Optimisation curve for the same is shown in Figure 2 and for the optimised pole tip the uniformity along theta θ direction is shown in Figure 2. Here, θ is the angle from x-axis. For $l_s = 7.39$ mm, it can be noticed that the uniformity is within ± 0.5% for up to a radius of 2.2 cm. This is referred to as the GFR, which is 88% of the total aperture size. In 3D design, chamfering of the pole tip can be done to improve the field quality near the aperture.

## *Pole Root and Return Arm*

Pole root and return arm have been designed such that the magnetic flux density should not be in the non-linear portion of the magnetisation curve of the yoke material (steel 1010). While designing it has been ensured that there is enough space for current carrying coils.

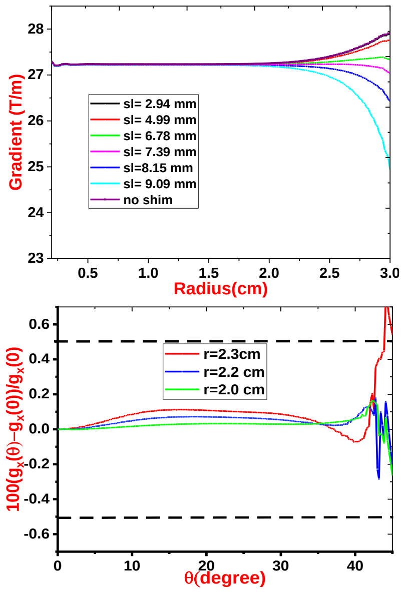


Figure 2. Plot of (a) Magnetic field gradient as a function radius (origin coinciding with the geometric origin of the quadrupole), and (b) $\boldsymbol{\delta g_x}$ variation with $\boldsymbol{\theta}$.

## *Current carrying coil*

For the ideal case of hyperbolic poles, using Ampere's law, the magneto-motive force (MMF) is given by $NI = gr^2/2\mu_0$. In reality, since the pole is not perfectly hyperbolic, for a given gradient and aperture radius, the required MMF will be higher. The value of MMF decides the wire type and number of turns for a given wire. We should choose the MMF value such that it avoids the saturation region of the gradient versus MMF curve as shown in Figure 3.

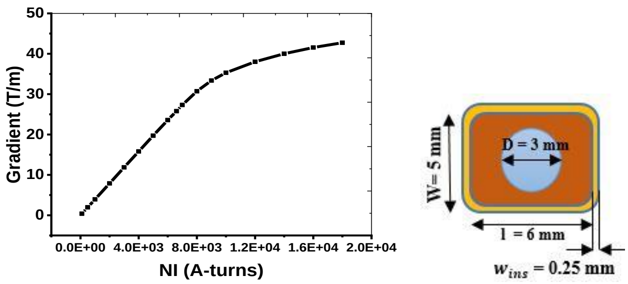


Figure 3. Gradient vs. MMF (NI) plot (left) and hollow conductor coil cross-Section (right).

For our design, we have chosen a water-cooled hollow conductor coil for the EMQ, in order to go to higher current density and thereby maintaining the compact size of the magnet. The current limit of each coil has been taken to be ~250 A based on literature survey. The hollow conductor cross section is shown in Figure 3. For simulations we have considered N= 28 turns & I = 250 A, though according to the design maximum 50 turns can be accommodated.

## *Results*

The final results of the simulations are summarized in Table 1. The quadrupole design is optimised to fulfil all the requirements posed by the beam dynamics on magnet design. The 3D absolute flux density at the edge of the magnet and in the aperture region is shown in Figure 4. The quadrupole magnet has been designed to have a gradient of 27.13 T/m. This allows for a margin in the fabrication of the magnet, so that the required gradient of 17 T/m may definitely be achieved. The harmonic analysis has been performed at a radius of 2.2 cm for the 2D design and it is found that the quadrupole term is $10^4$ times larger than the other multipoles, as listed in Table 2.

Table 1. Results for 2D and 3D magnet design.

| Parameter | For 2Ddesign | Parameter | For 3D design |
|---|---|---|---|
| NI | 7,000 A-turns | NI | 7,000 A-turns |
| G | 27.13 T/m | $G_{int}$ | 1.87 T |
| $\delta g_x$ | <$\pm$ 0.5% | $L_{eff}$ | 81 mm |
| | | $g_{max}$ | 22.63 T/m |

The MEBT channel is compactly designed and thus there is a chance of damage to the nearby beam instrumentation due to the fringe fields. Therefore, with the aim of reducing the fringe field to zero outside the magnet, soft iron shielding has been provided. Figure 5 shows a significant reduction of fringe field outside the magnet accompanied by the reduction of maximum gradient inside the magnet.

Table 2. Harmonic Coefficients.

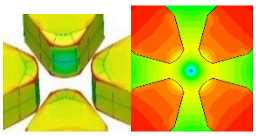

Figure 4. 3D Magnetic field.

| Harmonic Coefficients ($C_n$) | Value of $10^4 * C_n/C_2$ |
|---|---|
| $C_2$ [unit] | $10^4$ |
| $C_6$ [unit] | 0.39 |
| $C_{10}$[unit] | 3.02 X $10^{-3}$ |

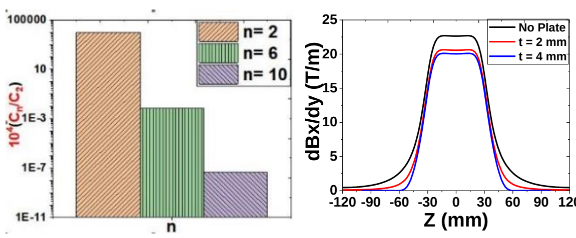


Figure 5. 3D design harmonic contents (left), and gradient along longitudinal direction for different thickness of the shielding plate (right).

## HARMONIC ANALYSIS OF ASSEMBLY MISALIGNMENT

The accelerator performance depends strongly on the quality and reproducibility of the magnets installed in the beam line lattice. There are various sources of error while fabricating and assembling the magnets. In order to study the effect of misalignment while assembling the magnet, small perturbations are introduced in the simulations and corresponding harmonic coefficients are studied.

Considering the two-piece magnet yoke design as shown in Figure 6(a), harmonic analysis due to assembly misalignment has been performed. As the yoke piece has two core halves, it provides three degrees (x, z and rotation) of freedom for the assembly errors.

On analysing the effect of displacement perturbation, it can be seen from Figure 6(b) that the dipole coefficient contribution will increase as the perturbation increases in the transverse direction (dx). Because of misalignment in the θ direction, the skew term increases, as shown in Figure 6(c). Perturbation in z does not affect the quadrupolar and dipolar contributions much, as seen in Figure 6(d), but the transverse component of the magnetic field along the z direction becomes asymmetric.

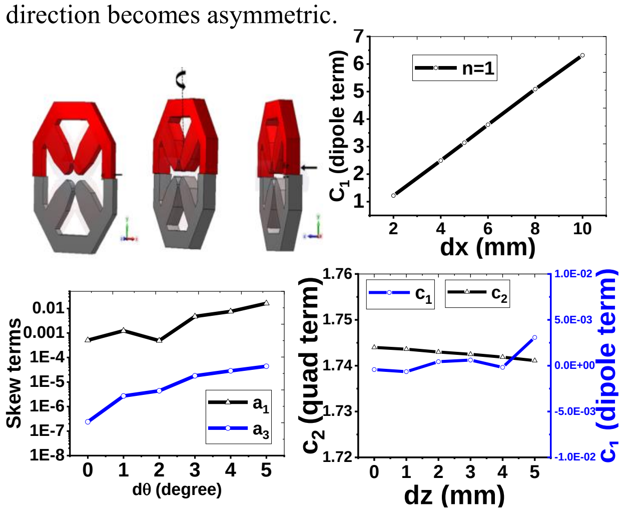


Figure 6. (a) Possible misalignments in two-piece quadrupole, (b) dipole term variation with perturbation in x, (c) skew term variation with perturbation in **θ**, and (d) quadrupole and dipole coefficient variation with misalignment in z.

## SUMMARY

The design of the quadrupole is done to satisfy the requirement posed for the transverse focusing in MEHIPA MEBT. Harmonic analysis is done to ensure the contribution of higher order field components is negligible. The introduction of shielding plate is found to reduce the fringe field significantly.

## REFERENCES


1. JT Tanabe, Iron Dominated Electromagnets.
2. D.Fernández et al., “Magnet Design & Specifications of a Quadrupole Magnet for the MEBT” ESS, 2016.
3. Krawczyk FL., et al. "The Los Alamos accelerator code group.", PAC, Vol. 4. IEEE, 1995
4. Studio, Microwave."CST-Computer Simulation Technology." Bad Nuheimer Str 19 (2008): 64289.

# DESIGN AND DEVELOPMENT OF A DIGITAL RF POWER METER

Niraj Chaddha*, Hemendra Kumar Pandey, Anindya Roy
Variable Energy Cyclotron Centre, Kolkata

*Abstract*

Digital RF Power Meter, designed and developed in VECC, is a Dual-channel RF Power measuring instrument, functioning in combination with a DDC (Dual Directional Coupler). It has two independent channels for measuring forward and reflected RF power with a dynamic range of 34dBm. Software filtered and calibrated data are available at local display as well as at serial communication line. Each channel has independent operation with different configurable coupling factor and frequency range. There are provisions of additional features through serial communication. This paper describes the design procedures during development of this instrument.

## HARDWARE

Complete hardware for this measuring instrument, starting from PCB designing to final instrument has been developed indigenously. The complete measurement system comprises of a DDC (Dual Directional Coupler) and RF power meter. DDC is mounted on the transmission line of an RF amplifier. It captures forward and reflected RF power and gives attenuated signals for the same to the measuring instrument. The attenuation or coupling factor depends on multiple parameters, though it can be fixed mechanically for a given frequency range and power.

### *Requirement*

The Power Meter was specified to measure forward and reflected RF power of a sine wave in frequency range from 30 to 120 MHz. Power measurement has been set from -14dBm to 20dBm. The coupling factor is required from 0 to 80dB. The measured power are to be displayed locally and to be communicated to a remote PC.

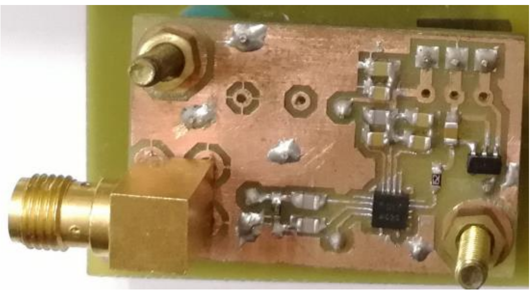

Figure 1: Sensor PCB

### *Sensor*

An RF power sensing chip is carefully selected to cater the power and frequency requirement of the instrument. A piggy back PCB module (Figure 1) has been designed to have a better shielding of this part. This sensor has a dynamic range of 47 dB to measure RF power with input frequency range from dc to 6 GHz. This sensor provides RMS voltage and envelop voltage. The rms output voltage is independent of the peak-to-average ratio of the input signal. We have used this output to calibrate the instrument in terms of input RF power.

*nchaddha@vecc.gov.in

### *Data Acquisition and Processing*

The output from sensor is buffered and filtered before it is sampled and processed by a Programmable System on Chip module (Figure 2). This module functions at a frequency of 80MHz. A high resolution built-in ADC samples the data. This data is digitally filtered again to to reduce the fluctuations. The counts acquired from ADC have logarithmic relation with input RF power (measured in dBm).

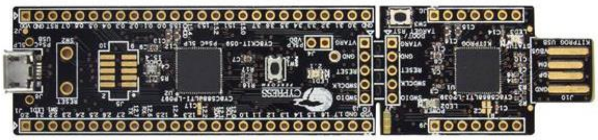

Figure 2: System-on-Chip module

Another standard RF power meter was used to find out this relation to get calibration constants. This calibration data is acquired for different frequency ranges and programmed into the chip. Power of the input channels are calculated at chip level. This module also takes care of local display, local/ manual control and remote communication.

### *Local Control*

A multipurpose knob has been provided on the panel of the instrument (Figure 3) to modify the settings manually. Coupling factors and frequency range of both the channels can be set individually through this knob. A four line LCD is also provided to display the power of two channels (Forward and reflected power) in dBm as well as in mW, W or kW.

### *Remote Processing*

As the calibration constants are available at the controller level, the power calculation is done at instrument level only. The final reading of input RF power is communicated to a PC through printable ASCII characters for display purpose. A set of communication based commands have been specified to modify the parameters like frequency range and coupling factors through serial communication.


Figure 3: RF Power Meter

## SOFTWARE

The Graphical User Interface, developed for RF power meter has two parts. The first part receives the power for both the channels from the instrument and displays it. According to value calculation, the unit of power is displayed in mW, W or kW (Figure 4).

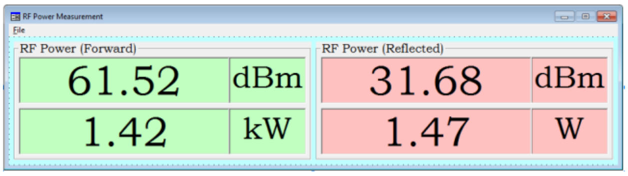


Figure 4: GUI for Power Measurement

The second part of GUI (Figure 5) is designed to modify all the configuration setting. The coupling factors and frequency ranges for both the channels can be set and monitored through a set of commands.

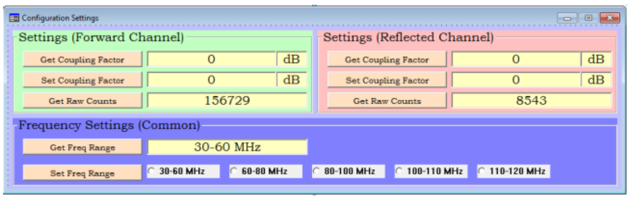


Figure 5: GUI for configuration setting

## FUTURE PLANS

The accelerator facilities in VECC Kolkata demand a very compact design of this instrument. Modification in the circuit board is required to reduce the leakage and other losses to have a durable calibration. A display-less design is also required to mount the instrument directly at the measurement point. USB or battery based powering, wireless communications are the other criteria, which will be explored on further development.

## CONCLUSION

The combination of RF power meter and Dual-directional coupler (DDC) is tested at 37.8MHz in the RF line with amplifier at the HR cave of RIB facility up to 5kW of RF power. The result is compared with another standard power meter and it is found satisfactory.

## ACKNOWLEDGEMENT

Authors would like to thank Dr. Sarbajit Pal, Dr. Arup Bandyopadhyay, Dr. Vaishali Naik and Dr. Sumit Som for their valuable guidance during development and testing of this instrument.

# DEVELOPMENT OF LOW LEVEL RF CONTROL ELECTRONICS FOR HIGH CURRENT INJECTOR RF CAVITIES AT IUAC

S.K.Suman*, Rajesh Kumar, V.V.V.Satyanarayana, C.P.Safvan, A.Sarkar and R.Mehta
Inter University Accelerator Centre, New Delhi, India
*email: sumaniuac@gmail.com

*Abstract*

The commissioning of High Current Injector (HCI) facility at IUAC is in progress. HCI consist of many phase synchronized critical RF systems such as Chopper and Deflector (CAD), Multi Harmonic Buncher (MHB) [3], one Radio Frequency Quadrupole (RFQ) [1], six numbers of Drift Tube Linac (DTL) and two numbers of Spiral Buncher (SB) cavities. To satisfy the control, safety and performance requirement of these HCI-RF devices, a Low Level Radio Frequency (LLRF) control system has been developed, which is an analog control based on GDR scheme. The performances of the developed LLRF controls have been demonstrated with RFQ at high power and these controls have also been operated with one of the DTL and SB at low power. The quantitative production with some refinements is in progress. This paper describes the design, development and test results of the LLRF controls developed at IUAC.

## INTRODUCTION

All the RF cavities of HCI have independent and identical controls except CAD and MHB. The RFQ and SB operate at 48.5 MHz and DTL at 97.0 MHz. The design of LLRF controls for both frequencies are kept same to manage the interchangeability. The LLRF controls are designed to operate under different operating modes such as conditioning, power-up sequence and normal operation. These controls are capable to detect faults within the RF system, protect equipment and personnel. Relative Phase Adjust (RPA) function is implemented to achieve the phase synchronized operation of the RF cavities as shown in figure 1.

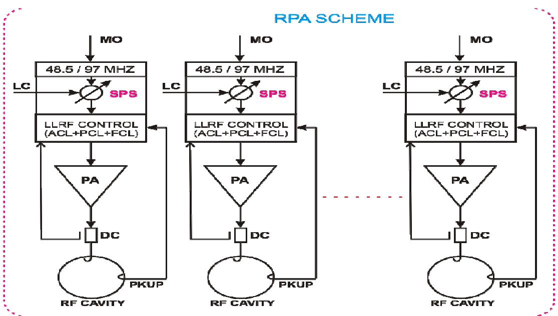


Figure 1: Phase synchronization of RF cavities

The LLRF controls for the MHB are different from the LLRF controls of RF cavities. The MHB controller is a four harmonic based 12.125 MHz saw-tooth wave generator which also maintains the phase and amplitude of the saw-tooth wave over time using feedback loops.

## LLRF CONTROLS FOR RF CAVITIES

The LLRF controls for RFQ, DTL and SB have been implemented in two distinct units, the Amplitude and Phase Control Loop (APCL) and the Frequency Control Loop (FCL) as shown in figure 2. The system built in a modular way for easy installation, maintenance and servicing. The master oscillator generation & distribution unit is common for all phase synchronized devices of HCI.

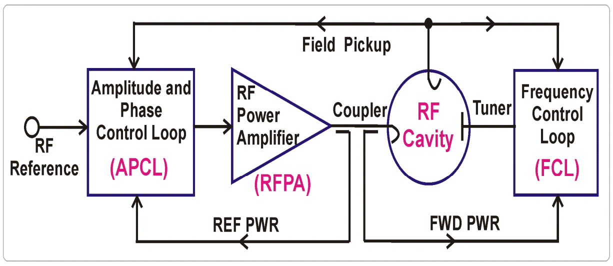


Figure 2: Outline of LLRF controls for RF cavities

### *Amplitude and Phase Control Unit*

A GDR driven amplitude and phase control loops have been integrated in a single unit as sown in figure 3. The design specifications of this controller are tabulated in table 1.

Table 1: Specifications of amplitude and phase controller

| Design Parameters | Value |
|---|---|
| RF drive control range | -20 to 0 dBm |
| Amplitude drift correction range | ± 3 dB |
| Phase drift correction range | ± 135º |
| Amplitude stability of field | < ± 0.05% |
| Phase stability of the cavity field | < ±0.05º |

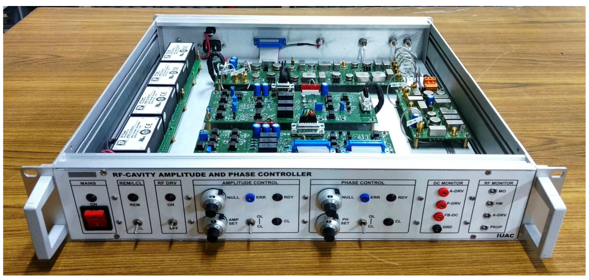


Figure 3: Amplitude and phase control unit

Amplitude and phase of the rf cavity is controlled by two Proportional Integral (PI) control loop as shown in figure 4 and it can be operated in closed loop as well as in open loop mode. In open loop mode, the amplitude control signal directly controls the rf drive of RF Power Amplifier (RFPA) without any feedback. While in closed loop operation, the rf drive is regulated as per the feedback (pickup signal) to maintain the cavity field within ±0.05% in amplitude and ±0.05º in phase. In case of perturbation in the cavity, the control automatically shifts to the open loop mode to ensure safe operation of the cavity and RF amplifier. Also the rf drive of RFPA is switched off in case of any safety interlocks appear.

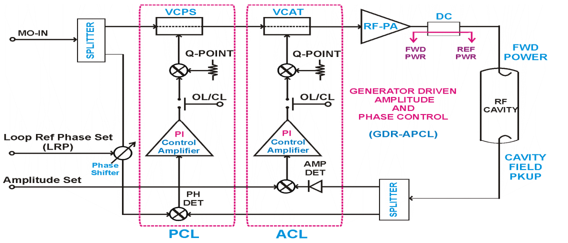


Figure 4: Block diagram of Amplitude and phase control

## *Frequency Tuner Control (FTC) Unit*

The frequency tuning loop, which has a bandwidth of a few hundred Hz, controls the cavity tuner to minimize the reflected power due to cavity warming. Rather than rely only on cooling water, a stepper motor driven mechanical tuner is used to bring the cavity back to its resonance [2]. An on/off type tuner control based on bipolar window comparator with adjustable phase hysteresis has been developed as shown in figure 5.

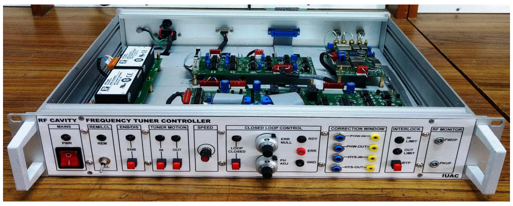

Figure 5: Frequency tuner control unit

The FTC has both open and closed loop operations. In closed loop operation, the tuner keeps the cavity tuned at its resonance frequency by comparing the phase difference of its forward and pickup power as shown in figure 6. Tuner movement reversal, tuner enable/disable and tuner extreme position limit functions are provided to make the tuner for safe operation.

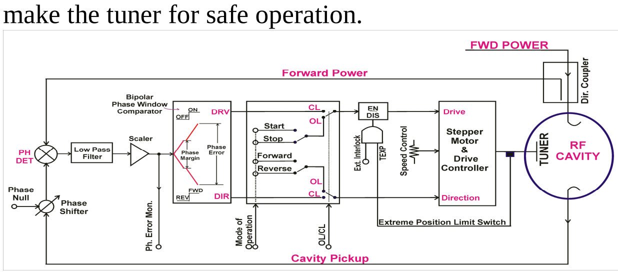


Figure 6: Block diagram of frequency control loop

## *Master Oscillator Distribution Unit*

All the phase synchronized RF systems of HCI (CAD, MHB and RF cavities) are phase locked to a reference, the Master Oscillator (MO). The MO distribution system designed in a modular and flexible way allowing for easy reconfiguration and system extension in case of need of more channels. To overcome the losses due to signal splitting and sending it over a coaxial cable, MO RF signal level is maintained at 0 dBm.


Figure 7: Master oscillator distribution unit

## LLRF FOR MULTI HARMONIC BUNCHER

The 12.125 MHz saw-tooth wave is generated by mixing the fundamental frequency 12.125 MHz with three consecutive harmonics (24.25 MHz, 36.375 MHz and 48.5 MHz) as per the equation below.

$$V(t)=Vm(\sin\omega t-0.40\sin 2\omega t+0.18\sin 3\omega t-0.06\sin 4\omega t)$$

Where ω is the angular frequency and Vm is the peak voltage of the fundamental frequency. Outline of the MHB control scheme is shown in figure 8.

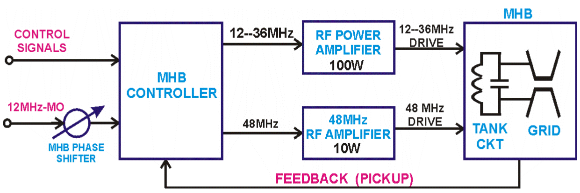


Figure 8: Outline of the MHB control scheme

The MHB controller has been designed with the specification as mentioned in table 2.

Table 2: Specification of MHB Controller

| Design Parameters | Value |
|---|---|
| RF drive control range | -16 to 0 dBm |
| Amplitude stability of tank field | < ± 0.5% |
| Phase stability of the tank field | < ±0.5º |
| Saw-tooth linearity | ~70% |

Figure 9: MHB control unit

Considering easy maintenance and servicing, the MHB electronics is divided into various modules. The block diagram shown in figure 10 depicts the modularity and inter-module signal flow of the controller.

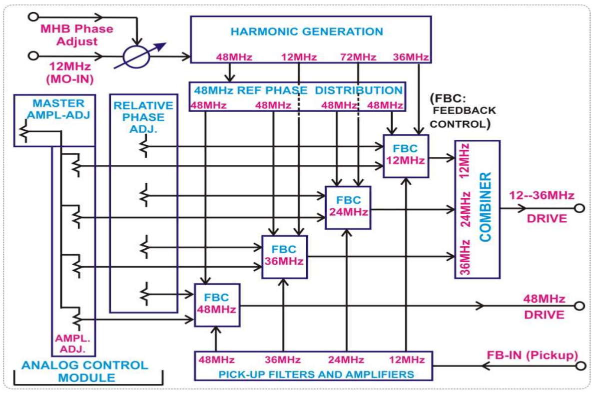


Figure 10: Block diagram of MHB controller

The output of three identical Amplitude and phase feedback control loops operating at appropriate harmonics are combined in proper phase and amplitude to get an approximated saw-tooth rf signal as shown in figure 11.

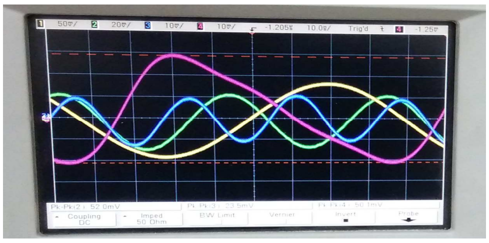

Figure 11: The generated 12.125MHz saw-tooth wave.

## TEST RESULTS

### *LLRF Test Results with RFQ*

The developed LLRF controllers are in use with RFQ since last two years. Long term rf measurement of forward power and cavity pickup of the RFQ cavity is shown figure 12.

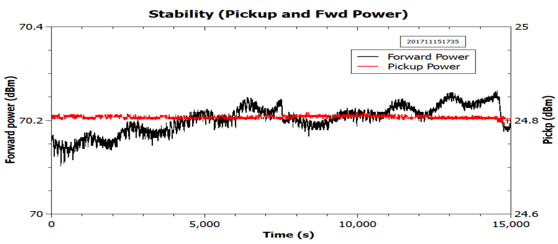


Figure 12: Forward power & pickup vs time (sec)

Amplitude and phase stability of the cavity pickup is shown in figure 13. Long term amplitude and phase error is measured less than ±0.02% & ±0.02° respectively at 25kW forward power.

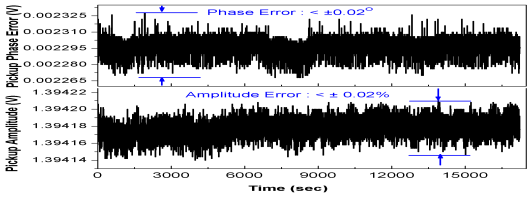


Figure 13: Amplitude & phase error vs time (sec)

Frequency locking performance of the frequency tuner controller is shown in figure 14. Tuner movement takes place at ±1° phase difference between pickup and forward power and stops at the phase difference of ±0.01°.

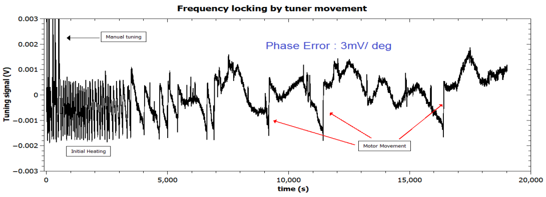


Figure 14: Frequency locking by tuner movement

### *MHB Controller Test Result*

The MHB electronics is used extensively for bunching the different beams. The saw-tooth generated at the bunching grids is stable for long term operations as seen from the pickup signal. The pick-up signal as well as the bunched spectrum for $O^{6+}$ ions is shown in figure 15.

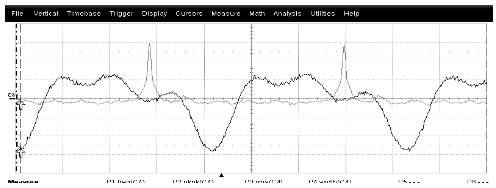

Figure 15: Ion beam bunching by MHB controller

## CONCLUSION

The LLRF system as described in this paper has been successfully developed. The MHB controller and the LLRF controls (amplitude, phase and frequency) one for each RFQ, DTL and SB have been installed in HCI. All the control units are working as per the design specifications.

## REFERENCES


[1] Sugam Kumar et al.,"Beam acceleration tests on 48.5 MHz Radio Frequency Quadrupole at IUAC", Proceedings of InPAC-2019.

[2] T. Varughese et al., " Frequency Tuners for the Drift Tube Linac at IUAC", Proceedings of InPAC-2019.

[3] A. Sarkar et al.,"Study of Longitudinal Beam Profile Using Multi-harmonic Buncher for High Current Injector at IUAC", Proceedings of InPAC-2019.

# DEVELOPMENT AND TESTING OF PROTOTYPE 20 KW, 325 MHZ SOLID STATE RF POWER AMPLIFIER FOR ACCELERATOR PROGRAM

J K Mishra*, Snigdha Singh, Shyam Sunder Jena, B V Ramarao, Manjiri Pande, Muthu S, Hitesh Kadam, Gopal Joshi BARC, Mumbai, India 400 085

*Abstract*

DAE laboratories are entrusted to develop two, high energy proton accelerators under Accelerator development roadmap. Bhabha Atomic Research Centre (BARC) is developing solid state power amplifiers at 325 MHz for these two proton accelerators as well as for its international collaborator (Fermi lab) under Indian Institution and Fermilab Collaboration (IIFC). As energy and beam current of accelerator goes up, Radio Frequency (RF) power requirement from the RF amplifier for the acceleration of charged particle also goes up. Therefore, high intensity proton accelerators require large RF power to accelerate the particle beam. A prototype 20 kW RF power amplifier at 325 MHz has been designed and developed for continuous wave (CW) and pulse mode of operation. This is being done to gain experience in high power amplifier development by combining multiple power amplifier modules. This amplifier uses 22 nos. of 1 kW power amplifier (PA) modules in a single stage power combining. All the sub-systems like PA modules, power dividers, driver amplifier, DC power supply, water cooling systems, etc. have been designed and developed indigenously. All the sub-systems have been characterised before their assembly in the rack. Amplifier has been integrated with the protection system for its safe operation. It has been tested under pulse operation up to a power of 20 kW while it has been tested up to 19.7 kW in CW operation. Through this paper, authors would like to present the test results of the amplifier.

## INTRODUCTION

BARC, Mumbai is developing solid state power amplifiers for various power levels at 325 MHz for high energy, high intensity proton accelerators (Accelerators for Indian ADS/Indian SNS and for PIP-II accelerator under international collaboration with Fermilab). As particle energy and beam current increases in an accelerator, RF power requirement for acceleration of the beam of charged particles also increases. This requires more number of amplifiers with increased power rating. This paper discusses details of the 20 kW amplifier developments and its testing in pulse and CW modes.

## DEVELOPMENT OF 20 KW, 325 MHZ AMPLIFIER

Development of 20 kW RF amplifier involves the design and development of various RF components e.g. RFPA modules, power divider and combiner, water cooling system, DC bias power supply, interlock and protection system etc. Design details of the amplifier, development and testing details of its sub-systems had been presented by Mishra et.al in [1]. A brief description of the system is presented here for the sake of continuity.

Single stage combining architecture as shown is Figure 1 is adopted for this power amplifier. It consists of 22 nos. of 1 kW PA module at 325 MHz [2] having dedicated DC bias supply, water cooling circuit for all 22 PA modules are connected in parallel, planner power divider [3] while combiner is designed in coaxial configuration [4] and Interlock and protection system (IPS) for this amplifier is presently planned with necessary protections which will be upgraded to full-fledged protection and monitoring system later. Amplifier houses directional couplers, driver, RF switch, AC power distribution system with protection against excessive load, addresses safety requirements and other electronics to complete the full system.

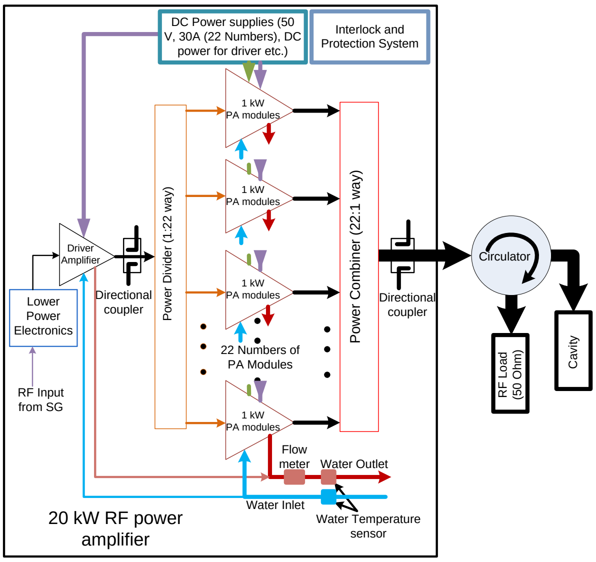


Figure: 1 Architecture of 20 kW Power amplifier [1]

## ASSEMBLY AND RACK LAYOUT

Amplifier sub-systems have been tested for their specifications [1] and assembled in a non standard rack as shown in Figure 2. Assembly of 22 nos. of 1k W PA modules are arranged on 2 sliding plate-forms. Each plate-form can house 12 nos. of PA modules 6 nos. of heat sink blocks. Each heat sink block houses 2 numbers of 1 kW PA module. Since there are only 11 heat sinks, vacant slot on one plateform is used for 220 W driver amplifier. Sliding tray design makes the assembly and maintenance process efficient. A 20 W, pre-driver amplifier and other electronics components like RF switch, low power directional couplers etc are kept just above the PA modules. AC power distribution cabinet and DC power supplies are assembled on upper part of the rack because DC power supplies are the main components releasing the heat in the air. This arrangement helps in controlling the thermal profile and heat management inside the rack. Interlock, protection system (IPS) for the amplifier is placed below the power supplies. Power combiner and dividers are placed behind the amplifier modules with suitable support arrangements.

Figure 2: Photograph of 20 kW Power Amplifier

Water cooling for all the PA modules is connected in a parallel to maintain same inlet temperature and same water flow rate as all PA modules are similar. Water cooling system uses 1" copper piping for inlet and outlet.

Figure 3 shows performance of the 1kW PA module. Amplifier gain at 1 kW output is 21.5 dB and drain efficiency up to 70% (with minimum efficiency > 65%).

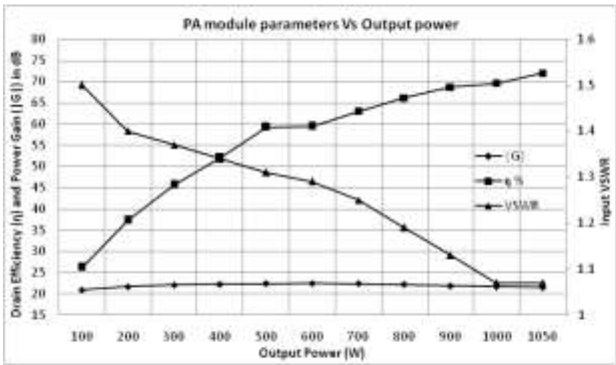


Figure 3: Measured parameters of 1 kW PA module

## INTEGRATED TESTING

Testing of the amplifier system has been planned at different levels. These are

1. Water circuit test for leak, flow rate and its instrumentation signals i.e. flow rate and water temperature.
2. AC power distribution to various sub-systems and protection functions in the systems.
3. Testing of the protection system for the amplifier.
4. In the end, testing of the amplifier for RF power.
5. Amplifier testing in pulse mode and then, testing in CW mode.

Assembled rack has been put to tests mentioned above from point 1 to 3 before starting of RF power tests. Details of RF tests are presented in this section.

### *Pulse testing*

Pulse testing of the amplifier is important to understand RF performance of the amplifier with negligible temperature effects. This study can be used to isolate thermal effects in amplifier performance. If pulse width and duty cycle are small, then this test also avoids effects of regulations in the power supplies. Amplifier has been tested in pulse mode by pulsing of the RF coming from signal generator. Pulse waveform has been shown in Figure 4. Calibration factor for the directional coupler, cable and divider has been added as offset in the R&S spectrum analyser to get amplifier power.

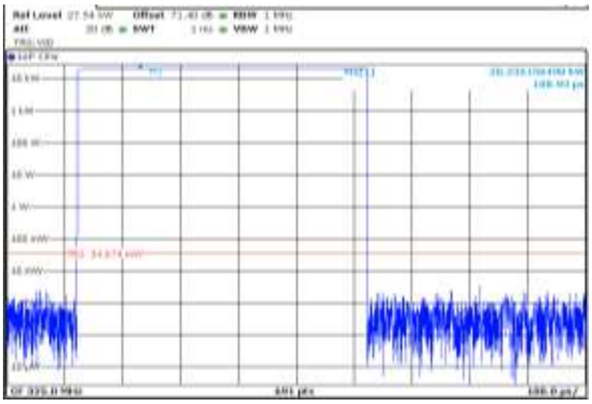

Figure 4: Pulse waveform at 20 kW

Amplifier has been tested for various duty cycles and pulse widths. Amplifier rise/fall time was measured to be less than 100 ns. Therefore any pulse width more than 500 ns ON time can easily be amplified with flat top output.

Harmonics content have also been measured in pulse mode and had been shown in Figure 5. Harmonic content is well below -49 dBc for all harmonics.

### *CW testing*

CW testing is very important to establish the amplifier's ability to work continuously under full power conditions. Some important tests are power sweep and gain compression tests, frequency sweep for amplifier BW, endurance tests, spurious and harmonics tests among others. These tests bring out

1. Thermal effects due to CW operation on amplifier gain and other parameters.
2. Effects of power supply regulation on output power and deterioration in P/S regulation due to voltage drop in cable resistance.

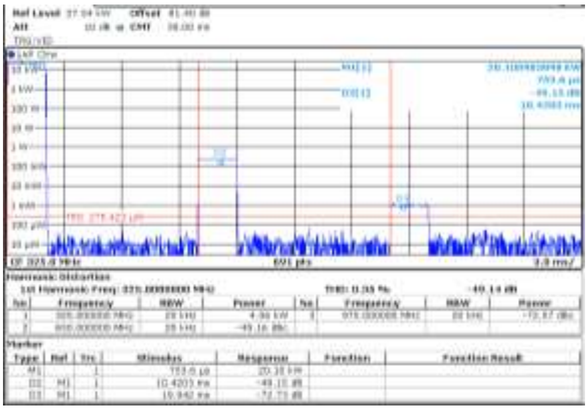

Figure 5 Harmonics measurement in pulse mode

Amplifier has been tested in CW mode up to 19.7 kW power level as shown in Figure 6. Amplifier power could not be increased further above 19.7 kW due to power supply regulation issues, reducing the amplifier saturated power level and combining losses. The bias power supply regulation is observed due to two reasons. One is power supply's own regulation and other is the voltage drop in the long DC cable from power supply to PA modules which increases with increase in RF power. This further brings down the amplifier output power and also gain compression reaches faster with power as seen in Fig. 7.

Figure 6 Spectrum of the amplifier output in CW mode

DC to RF efficiency of the amplifier has been estimated based on the combining efficiency and efficiency of the PA modules. Combining efficiency is calculated based on the magnitude and phase variation in the amplifier gain. Amplifier modules show a gain variation of +/- 0.4 dB dB and phase variation of +/- 10 degree. Using the formulae given in [5], the combining efficiency comes out to be 96.7%. DC to RF efficiency of the power stage is measured as 61.8 % at 19.5 kW. Additional power is being dissipated in the other sub-systems like driver, pre-driver and interlock circuits. This reduces the overall efficiency of the amplifier. Wall plug efficiency of the complete amplifier has been measured and found to be around 50% at 19.5 kW of output power. Power measurement accuracy is +/-5% for the measurements.

Figure 7 shows power sweep behaviour of the amplifier. Its gain increases up to 90.4 dB and then decreases due to the non-linearity in the PA modules and regulation issues in bias power supply system. Amplifier shows a gain of 89.1 dB at 18.5 kW where amplifier gain reduces by 1 dB from its maximum gain. It has been observed that the amplifier shows gain compression more than expected beyond 19 kW in CW mode due to compression in both driver and power stage.

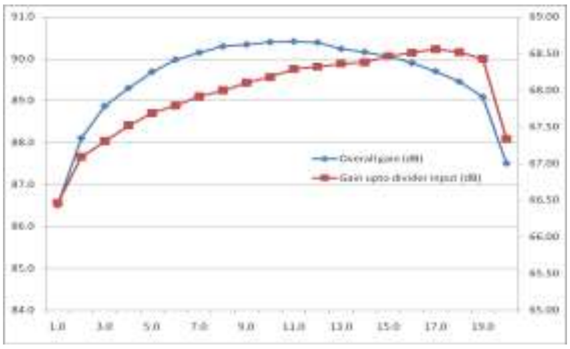

Figure 7 Power sweep measurement

## CONCLUSION

Prototype power amplifier developed for 20 kW at 325 MHz has been integrated and tested for its design parameters. In the pulse mode, amplifier works very well up to 20 kW. However, amplifier needs improvements in its CW performance beyond 19.0 kW. To achieve 20 kW output with satisfactory operation, it is planned to relook the amplifier design.

## ACKNOWLEDGEMENT

The authors would like to sincerely thank Director MRG, BARC and Head, ACnD for their encouragement and support for this development.

## REFERENCES


[1] J. K. Mishra et.al., " Design and Fabrication of 325MHz, 20 kW RF Power Amplifier for Accelerator Application," InPAC proceedings 2018.

[2] J. K. Mishra et. al., "A Compact High Efficiency 8 kW 325 MHz Power Amplifier for Accelerator Applications," Nuclear Instruments and Methods in Physics Research A, vol. A764, pp. 247-256, 2014

[3] Snigdha Singh et al., "Design and development of a 22 way splitter for 20 kW Solid State RF Power Amplifier," presented at InPAC'18, Indore, India, Jan 2018, this conference.

[4] Sonal Sharma et al.,

[5] J. K. Mishra et. al., " A novel approach for the analysis of combining efficiency for RF power amplifier," Nuclear Instruments and Methods in Physics Research A, vol. A764, pp. 247-256, 2014

# HIGH STABILITY, LOW RIPPLE, -30 KV HIGH VOLTAGE DC POWER SUPPLY FOR SCANNING ELECTRON MICROSCOPE

V. K. Gauttam†, A. Kasliwal, P. Renukanath, and S. R. Tiwari
Accelerator Power Supplies Division, Raja Ramanna Centre for Advanced Technology, Indore, India.

*Abstract*

A high stability, low ripple high voltage (HV) dc power supply is required for scanning electron microscope (SEM) being developed at BARC. For high resolution imaging, SEM demands an accelerating high voltage with ultra low ripple less than10 ppm (p-p) and short term high stability less than15 ppm. To generate this accelerating high voltage, a HV power supply is designed and developed with hybrid topology of linear and switch mode power conversion techniques. The front end is a series pass linear regulator followed by a high frequency resonant converter. The full bridge LC-LC resonant converter feeds a symmetrical 8 stage HV multiplier through a HV transformer to generate the required high voltage. The fourth order resonant converter gainfully utilizes the parasitics (eg. leakage inductance, parasitic capacitance) of the step up high frequency HV transformer as a part of resonant tank circuit. The zero voltage switching (ZVS) at turn on and lossless snubber at turn off are employed for semiconductor switches to reduce switching losses and generated EMI. The output voltage is controlled by varying the input dc of the resonant converter. The power supply is operated in closed loop with fixed frequency using voltage mode multiple control loops. The power supply uses 24V dc input to generate the high voltage of -30kV with required stability & ripple at rated output voltage and current. The design parameters, simulation and experimental results of the developed HV power supply are presented in this paper.

## INTRODUCTION

The scanning electron microscopes are used for high resolution imaging in which thermionic generated electrons from electron gun are accelerated by dc electric field to get high energy electron beam. This electron beam is scanned over specimen and emits secondary electrons. The secondary electron are detected by secondary electron detector, thus high resolution image of specimen is recorded. Since the penetration of electron beam & resolution is function of accelerating high voltage, SEM requires a high stability, ultra low ripple high voltage dc power supply to get the stable accelerating high voltage. The higher order high frequency resonant converters are very attractive for high voltage (HV) power supplies because of their features of small size, zero voltage switching (ZVS) at above resonant frequency (operating in lagging power factor mode), lower switching losses, high efficiency, low electromagnetic interference [1]. High frequency resonant converter with four resonant elements gainfully utilizes HV transformer parasitics (leakage inductance ($L_{lkg}$), winding capacitance ($C_w$)) and also absorbs the magnetizing inductance as a part of resonant network [2].

## POWER CIRCUIT TOPOLOGY

The hybrid power circuit topology is used in which a series pass linear regulator feeds the full bridge voltage source inverter (VSI). The VSI is operated at fixed duty cycle (D=0.5) with fixed frequency and it energies a center tap step-up HV high frequency transformer with sine wave output through a series resonant network. Thus series resonant network (absorbs leakage inductance) and transformer magnetizing inductance & winding capacitance forms a fourth order resonant network. The HV transformer energises an 8-stage symmetrical Cockroft Walton multiplier circuit (HV generator) to generate the high voltage. The first order low pass filter is used at the output of HV generator to reduce the high frequency ripple with in 10 ppm p-p. The block diagram of power circuit topology is shown in Fig. 1.

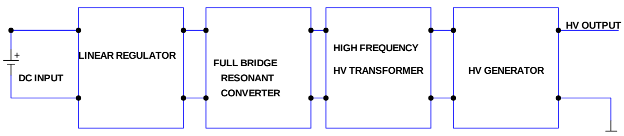


Figure 1: Block diagram of power circuit of HV power supply

The output high voltage is controlled by varying dc link input voltage of resonant converter through a linear regulator. The block diagram of closed loop control is shown in Fig. 2.

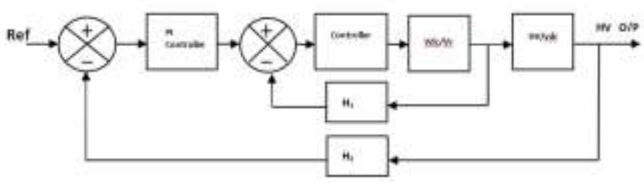


Figure 2: Block diagram of closed loop control

Since the bandwidth of outer loop is low due to slower dynamics of 8 stage HV generator, so multiple closed loop control is used with inclusion of high bandwidth linear series regulator based inner voltage loop.

† vishnuk@rrcat.gov.in

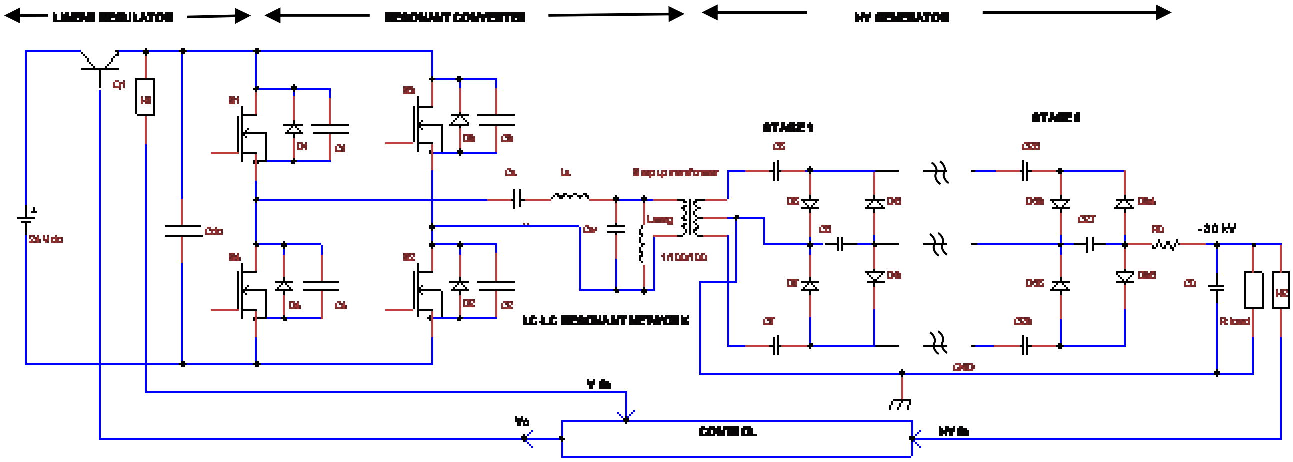

Figure 3: Circuit diagram of HV dc power supply with hybrid topology.

## ANALYSIS AND DESIGN PARAMETERS

The gain vs frequency plot of LC-LC resonant conveter is shown in Fig. 4 at different quality factor . First resonant peak ($F_{01}$) is at 33 kHz while second resonant is at 52 kHz ($F_{02}$).

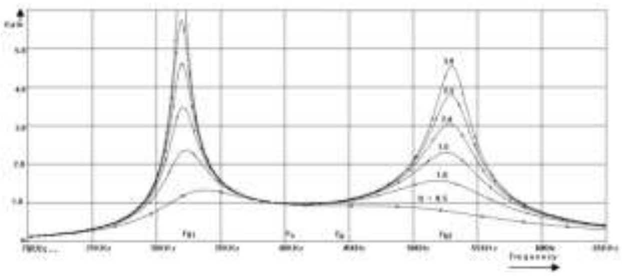

Figure 4: Plot of voltage gain vs. frequency.

The input impedance ($Z_{in}$) is plotted in Fig. 5 which shows the two soft switching regions for MOSFETs of VSI. The first soft switching region from from $F_{01}$ to $F_p$ and second is for greater than $F_{02}$. If switching frequency is $\geq F_{02,}$ then converter operates in lagging power factor and ZVS at turn on occurs. The converter is operated with fixed frequency at above $F_{02}$.

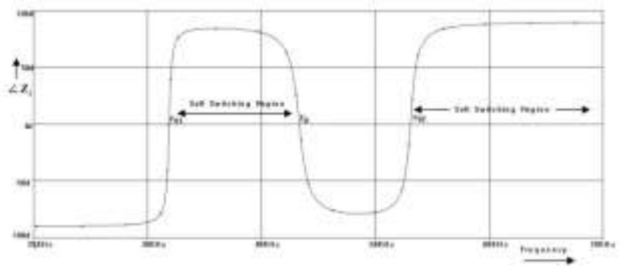

Figure 5: Phase plot of input impedance of LC-LC resonant converter.

The design parameters of high voltage dc power supply including fourth order LC-LC resonant converter are listed in Table 1.

Table 1: Design Parameters of HV Power Supply

| S. No. | Parameter | Value |
|---|---|---|
| 1 | Input Voltage | 24 V dc |
| 2 | Rated output Voltage | -30 kV |
| 3 | Output Current | 300 μA |
| 4 | Ls | 67 μH |
| 5 | Cs | 0.25 μF |
| 6 | Lp=Lm | 15 μH |
| 7 | Cp=Cw | 0.38 μF |
| 8 | $F_s$ | 40 kHz |
| 9 | $F_p$ | 44 kHz |
| 10 | $F_{01}$ | 33 kHz |
| 11 | $F_{02}$ | 52 kHz |
| 12 | Ripple(p-p) | ≤ 10 ppm |
| 13 | Stability | < 15 ppm for 10 Min |
| 14 | Protections | O/V,O/C, Arc & Over Temp. |

## EXPERIMENTAL RESULTS

The - 30kV, 300 μA high voltage dc power supply is designed, developed and tested with resistive load. The HV inter connections are carried out by HV cable and smooth metallic hemisphere are used to reduce electric field for corona free termination. A low temperature coefficient (10 ppm/c) HV divider is used for sensing of HV voltage.

The input voltage & current waveforms of HV transformer is shown in Fig. 6. The center tap step up HV transformer is fabricated on E-42/21/15 ferrite core (N87) while series resonant inductor ($L_s$) is on E -25.7/10/7 (N87).

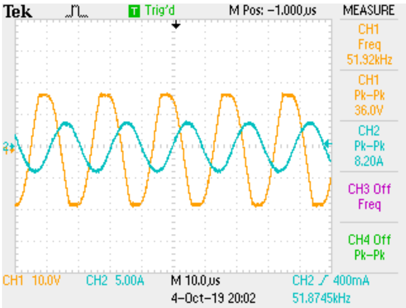


Figure 6: High voltage pulse output at -5kV of HVPPS

The HV output waveform and ripple in HV output is shown in Fig. 7. The ripple (peak-peak) less than 6 ppm is achieved at -30 kV/300 µA. The measurement of high frequency ultra low ripple in HV system is very difficult with standard HV probes due to high attenuation factor and limitation of vertical resolution of DSOs. A ripple measurement setup is designed, developed and calibrated for measurement accuracy better than 10%.

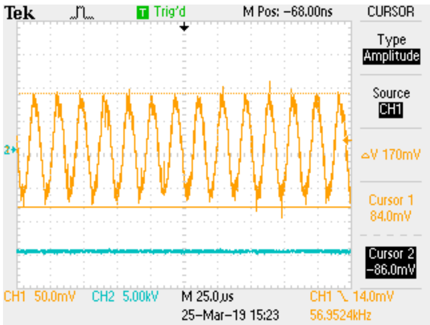


Figure 7: High voltage dc output at -30kV (ch:2, 1div – 10kV) and o/p ripple p-p < 10 ppm (ch:1,1div- 50mV)

The power supply is assembled in a standard aluminium box of size 19"(W) X 600 mm (D) X 6U(H). Top view of developed power supply is shown in Fig. 8.

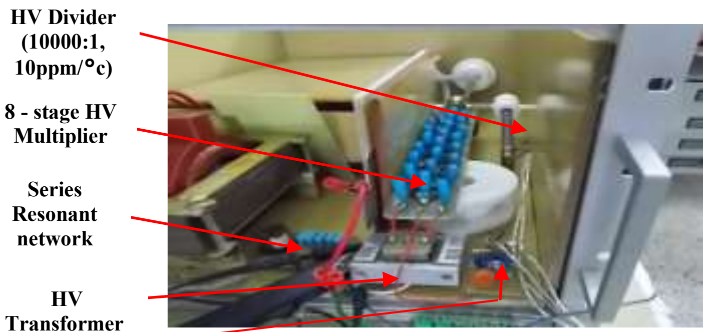


Figure 8: Developed HV power supply in a 6U height box.

The over voltage, over current, over temperature and arc protections are incorporated in the HV power supply. The stable analog reference is generated using LM 399 IC and OPA 27 series op-amps are used in control electronics. Short term stability of output high voltage is major concern in SEM applications which require a highly stable electric filed during scanning of specimen. The short term stability plot of output high voltage is shown in Fig. 9. The stability is well with in 10 ppm for 10 min operation.

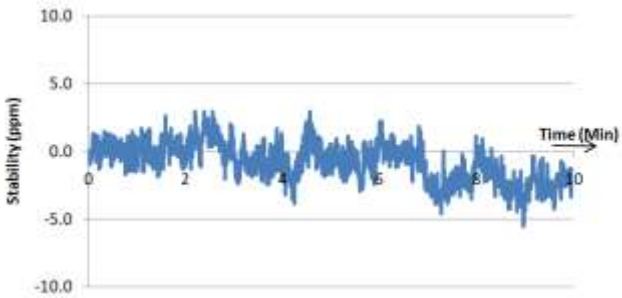


Figure 9: Short term stability at -30 kV/300 µA for 10 minute operation

## CONCLUSION

The hybrid power circuit topology which consists of a series pass linear regulator and an LC-LC resonant converter operating at fixed duty & frequency is well suited for low power HV power supplies required for SEM, mass spectrometry applications. The HV power supply is operated in closed loop using voltage mode multiple loops control. The switching frequency of resonant converter is chosen according to soft switching regions and required gain. Furthermore, the transformer parasitics and magnetizing inductance are integrated as part of resonant network in forth order LC-LC resonant topology and ZVS is achieved at turn on of MOSFET switches.

## ACKNOWLEDGEMENT

Authors are sincerely thankful to Mr. Amit Sahu, Mr. Deepchand, Mr. Gurupreet Singh, Mr. Nathan Singh, Mr. Milius Kujur, Mr. Chattar Singh, Mr. G. H. Ansari, Mr. M. D. Jha, Mr. Shriram Rout and Mr. Prabhu for their help in fabrication, assembly and testing of the high voltage dc power supply.

## REFERENCES

[1] Mangesh Borage, K. V. Nagesh, M. S. Bhatia and Sunil Tiwari, "Design of LCL – T resonant converter including the effect of transformer winding capacitance," IEEE Trans. Ind. Electron., vol. 56, no. 5, May 2009, pp. 1420–1427.

[2] V. K. Gauttam, Apollo Kasliwal and S. R. Tiwari, "Design and development of a compact -5 kV high voltage pulse power supply for IMS based detectors", Indian Particle accelerator conference (InPAC), January 9-12, 2018, RRCAT, Indore.

[3] R. P. Severns, "Topologies for three element resonant converters," IEEE Trans. Power Electron., vol. PE-7, Jan. 1992, pp. 89-97.

[4] V.K. Gauttam, A. Kasliwal, R. Banwari, T. G. Pandit and A. C. Thakurta, "A frequency controlled LCL-T resonant converter for H- ion source", Proceedings of INPAC 2013,Vecc,Kolkata.

[5] F. Hwang, Y. Shen and S. H. Jayaram "Low-ripple compact high-voltage DC power supply," IEEE Trans. on Industry Applications, vol. 42, no. 5, Sept/Oct 2006, pp. 1139–1145.

# DESIGN AND EXPERIMENTAL MEASUREMENT OF FREQUENCY RESPONSE OF HIGH BANDWIDTH VOLTAGE MODE CONTROL LOOP FOR DC – DC SWITCH MODE POWER CONVERTERS

V. K. Gauttam[1],[#] K. K. Gautam[2], A. Kasliwal[1], S. L. Sisodiya[2] and S. R. Tiwari[1]
[1]Accelerator Power Supplies Division, Raja Ramanna Centre for Advanced Technology, Indore,
[2] Shri G. S. Institute of Technology & Science, Indore, India.

*Abstract*

The current controlled dc power supplies are required to energize the collimator, steering and focusing magnets for applications in the field of particle accelerators e.g linear accelerators (LINACs) and other industrial & scientific applications. Switch mode dc- dc converters are popular because of their own advantages as low power loss, high efficiency and smaller in size & weight due to high switching frequency etc.

Usually, current controlled dc - dc converter with magnet load has multiple loop architecture which comprises of outer current loop and an inner voltage loop. But, due to large time constant of magnet load, the bandwidth of current loop is in the range of few Hz only. So it requires a high bandwidth inner voltage loop for better dynamic performance (response time) to meet the output regulation against line & load variations. The voltage mode control loop for a prototype step down buck converter is designed using type-III compensators and crossover frequency higher than output filter resonant frequency is achieved. The design parameters and simulation & experimental results of the voltage mode control loop are presented in this paper. Experimental measurement of loop gain and phase margin are also presented which are well in agreement with theoretical design and simulation results.

## INTRODUCTION

The high power, high stability current controlled focusing magnet power supplies are required to focus the electron beam of the 10MeV Linac being developed at RRCAT for agriculture radiation processing facility (ARPF), Indore. Since the magnets in the accelerators have large time constants it limits the bandwidth of current loop. So a fast correcting inner voltage loop is required to meet the dynamic & steady state specifications. However, the current loop with magnet load is effectively a first order system with dominant pole corresponding to time constant of magnet load. But inner voltage loop has second order system and requires careful design considerations to meet higher crossover frequency than output filter resonant frequency while maintaining the good phase margin ($\geq 50°$) & gain margin ($\geq 10$ db). The analysis, design and validation of a faster inner voltage loop using suitable compensators is the objective of this work.

# vishnuk@rrcat.gov.in

## VOLTAGE MODE CLOSED LOOP CONTROL

The general block diagram of a current controlled magnet power supply which consists of an outer current loop and an inner voltage loop as shown in Fig. 1

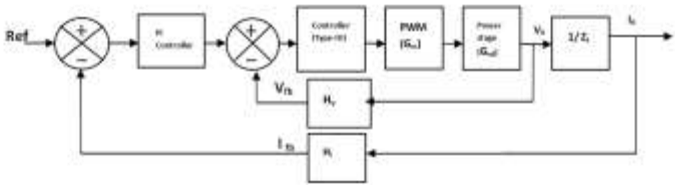


Figure 1: Block diagram of multiple control loop for a switch mode magnet power supply

The inner loop is implemented using high bandwidth voltage mode control loop for better dynamic performance of the power supply.

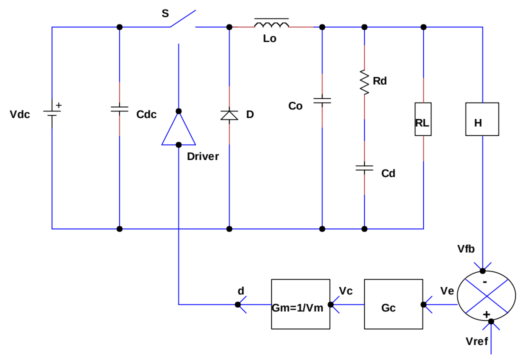


Figure 2: Power circuit of prototype dc - dc converter

The circuit diagram of prototype buck converter with its voltage mode inner control loop is shown in Fig. 2. The block diagram of inner voltage loop is explicitly shown in Fig. 3.

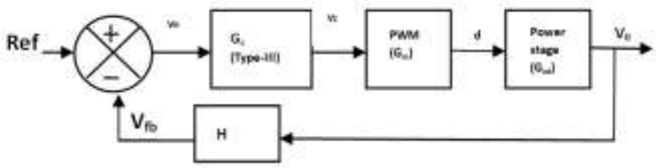


Figure 3: Block diagram of inner voltage control loop

A linear time invariant small signal model of power stage is required for analysis & design of a control loop of a switch mode power converter. The transfer function of the power stage ($G_{vd}$) and PWM block ($G_m$) is given in eq (1) & (3) respectively [1]. From Fig. 3, the transfer function of the uncompensated loop (putting $G_c$ =1) and compensated loop can be written as eq (4) & (5) respectively.

$$Duty\ to\ output\ (G_{vd}) = \frac{v_0}{d} = V_{dc}\frac{1}{1+\frac{s}{\omega_0 Q}+\frac{s^2}{\omega_0{}^2}} \quad (1)$$

$$Where,\ \omega_0 = \frac{1}{\sqrt{L_0 C_0}},\ Z_0 = \sqrt{\frac{L_0}{C_0}},\ Q = \frac{R_L}{Z_0} \quad (2)$$

$$Pulse\ width\ modulator\ (G_m) = \frac{1}{V_m} \quad (3)$$

$$Uncompensated\ loop\ (T_{uncomp}) = H G_{vd} G_m \quad (4)$$

$$Compensated\ loop\ (T_{comp}) = G_c H G_{vd} G_m \quad (5)$$

Where, $V_m$ is the peak voltage of saw-tooth carrier signal. The design parameters of voltage mode control loop for a prototype step down dc dc converters are tabulated in table 1.

Table 1: Design Specifications of Voltage Mode Control Loop for a Prototype DC-DC Converter

| S. No. | Parameter | Specification |
|---|---|---|
| 1 | Output Voltage | 20V |
| 2 | Output Current | 5 A |
| 3 | $L_o$ | 500 µH |
| 4 | $C_0$ | 10 µF |
| 5 | Resonant frequency ($f_0$ ) | 3.1 kHz |
| 6 | Loop crossover frequency ($f_c$ ) | 7 kHz |
| 7 | Phase Margin | 60° |
| 8 | Gain margin | ≥ 6 dB |
| 9 | Compensator | Type-III |

The uncompensated control loop magnitude & phase is plotted in Fig. 3 which shows the phase of -130° at $f_c$ .

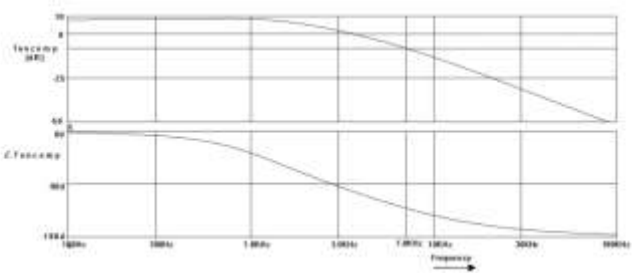

Figure 4: Magnitude and phase plot of uncompensated loop ($T_{uncomp}$)

To achieve desired control specifications, it requires a type – III compensator [2]. Since type - I compensator which has a single pole at origin while the type –II compensator has one pole & zero at finite frequency in addition to a pole at origin. Both these compensators are effectively a phase lag compensators. So, the desired phase boost of the loop can not be achieved by using either Type I or Type II. Moreover, Type- I / II are more suitable for first order systems (power stage). The loop crossover frequency is limited to power pole frequency (I[st] order plant/system) with type- I and it can be high than power pole frequency using Type-II for the required phase margin of ≥ 50°. Hence, both above compensators are suitable for outer current loop which has a lower bandwidth than inner voltage loop. The transfer function of the type -III compensator is given in eq. (6).

$$G_C = \frac{G_{C0}}{s}\frac{(1+\frac{s}{\omega_{z1}})(1+\frac{s}{\omega_{z2}})}{(1+\frac{s}{\omega_{p1}})(1+\frac{s}{\omega_{p2}})} \quad (6)$$

Where $G_{co}$ is the dc gain of compensator. The compensator has two pole & two zero at a finite frequency in addition to a pole at origin. It is effectively a phase lead compensator since it can give a max phase boost of 180°. That is why loop crossover frequency higher than power pole frequency can be achieved in a second-order systems. Usually switch mode power converters have second order output filter LC in the power stage. So loop crossover frequency ($f_c$) higher than output filter resonant frequency ($f_0$) is achieved using type-III compensator in voltage mode control loop.

It can be practically realized by two ways. One is realizing with an opamp based circuit and other is combination of a type-II and compensation in feedback sensor. The later approach is adopted for realization of type-III compensator. The one zero ($f_{z1}$), one pole ($f_{p1}$) and a pole at origin (type-II) is implemented using an op-amp while another zero ($f_{z2}$), and pole ($f_{p2}$) are realized in feedback network.

The compensator is designed in frequency domain using a K - factor method [3]. The K- factor method is a simpler frequency domain approach in which the required phase boost ($\Phi_{boost}$) at desired frequency is achieved by setting the parameter K. The parameter K and compensator pole & zero can be calculated using eq (7), (8) and (9) respectively.

$$K = tan\{45 + \frac{\Phi_{boost}}{2}\} \quad (7)$$

$$f_{z1} = \frac{f_c}{K} \quad (8)$$

$$f_{p1} = K f_c \quad (9)$$

The transfer function of controller (Gc) and feedback sensor (H) is given by eq (10) &(11) respectively.

$$G_C(s) = \frac{G_{C0}}{s}\frac{(1+\frac{s}{\omega_{z1}})}{(1+\frac{s}{\omega_{p1}})} \quad (10) \quad H(s) = H_0\frac{(1+\frac{s}{\omega_{z2}})}{(1+\frac{s}{\omega_{p2}})} \quad (11)$$

H(s) is implemented with voltage divider. The $H_0$ is the dc gain of divider. The $f_{z2}$ and $f_{p2}$ are also calculated using K-factor such that it gives max phase boost at $f_c$ and remaining boost is given by type-II stage. The design summery of voltage mode control loop with type-III compensation is tabulated in table 2.

Table 2: Design Summery of Type-III Compensation

| S. No. | Parameter | Specification |
|---|---|---|
| 1 | Loop crossover ($f_c$) | 7 kHz |
| 2 | Resonant frequency ($f_0$) | 3.1 kHz |
| 3 | Phase Margin (PM) | 60° |
| 4 | Phase of uncomp loop at fc | -130° |
| 5 | Phase lag by pole at origin | -90 ° |
| 6 | Required total phase boost | 100° |
| 7 | Phase-boost by feedback stage | 37° |
| 8 | Phase-boost by type-II stage | 63° |
| 9 | K | 4.19 |
| 10 | $f_{z1}$(kHz) | 1.67 |
| 11 | $f_{p1}$(kHz) | 29.303 |
| 12 | $G_{co}$ | 13348 |
| 13 | $f_{z2}$ (kHz) | 3.5 |
| 14 | $f_{p2}$ (kHz) | 14 |

## SIMULATION RESULTS

The designed control loop is simulated in Orcad-Pspice 16.5. The one compensator zero & pole is placed in feedback sensor. The simulated magnitude & phase plot of feedback sensor (H) is shown in Fig. 5.

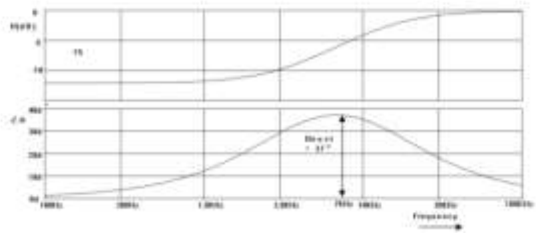

Figure 5: Simulated magnitude (in dB) & phase (in degree) plot of feedback sensor (H)

The simulated magnitude & phase plot of controller $G_c$ (s) is shown in Fig. 6. The one compensator zero & pole along a pole at origin is placed in the controller.

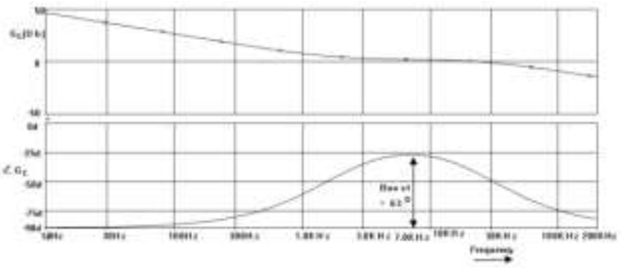

Figure 6: Simulated magnitude (in dB) & phase (in degree) plot of Controller ($G_c$)

The simulated phase plot of H shows the boost of 37° while phase plot of controller shows the boost of 63° at 7 kHz which is in good agreement of theoretical design. Hence total boost of 100° at 7 kHz is achieved. The simulated magnitude & phase plot of compensated control loop ($T_{comp}$) is shown in Fig. 7 which shows loop crossover frequency ($f_c$) of 7 kHz with phase margin (PM) of 60° & gain margin of 15 dB.

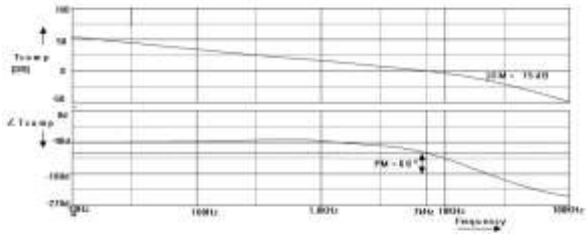

Figure 7: Simulated magnitude (in dB) & phase (in degree) plot of compensated control loop ($T_{comp}$)

## EXPERIMENTAL RESULTS

The 100W prototype buck converter is designed and developed to validate the theoretical design of type-III compensated control loop. The loop gain & phase measurement method is shown in Fig. 8[4]. The FRA injects the isolated sinusoidal voltage signal and measures the magnitude & phase of CH2/CH1 by sweeping the frequency.

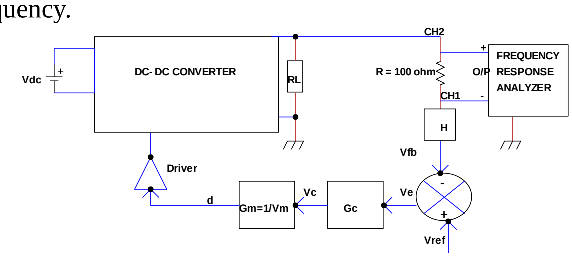


Figure 8: Diagram of loop gain & phase measurement setup

The control loop is implemented using PWM IC SG3525. The error amplifier & compensator block is implemented using its inbuilt opamp. The measured magnitude & phase of feedback sensor (H) is shown in Fig. 9.

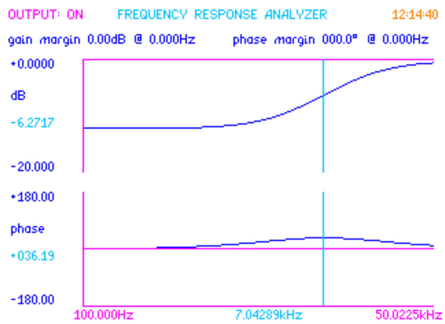


Figure 9: Experimental magnitude (in dB) & phase (in degree) plot of feedback sensor (H)

The measured magnitude & phase of controller ($G_c$) is shown in Fig. 10 which shows the phase boost of 60 ° (-30°+90°).

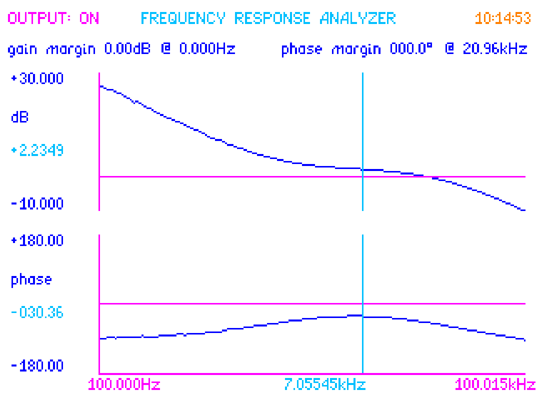


Figure 10: Experimental magnitude (in dB) & phase (in degree) plot of controller ($G_c$)

The measured magnitude & phase margin of compensated control loop ($T_{comp}$) is shown in Fig. 11 which shows the phase margin of 67.5° at loop crossover frequency (6.8 kHz) and gain margin of 15.1 dB.

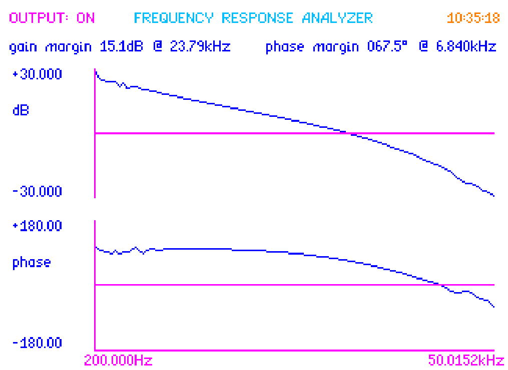


Figure 11: Experimental magnitude & phase margin plot of compensated control loop ($T_{comp}$)

The above measurements are carried out using FRA PSM 3750. The developed table top prototype dc-dc converter with type-III compensation is shown in Fig. 12.

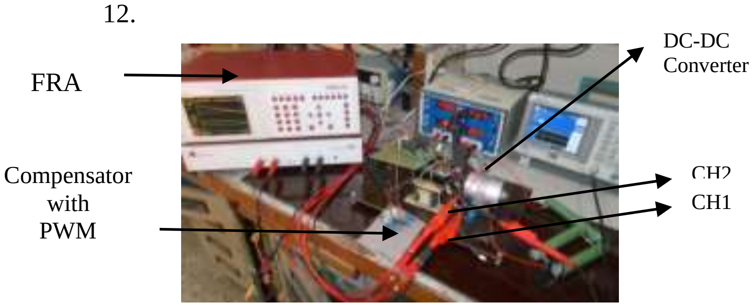


Figure 12: The developed prototype dc-dc converter with type-III compensation.

The comparison of design, simulation and measurement results of control loop is listed in Table 3.

Table 3: Comparison of Design, Simulation and Experimental Results for Control Loop

| **Parameter** | **Theoretical design** | **Simulation** | **Experimental** |
|---|---|---|---|
| Loop cross over frequency ($f_c$) | 7 kHz | 7 kHz | 6.84 kHz |
| Phase Margin | 60° | 60° | 67.5° |
| Gain Margin | 15 dB | 15 dB | 15.1 dB |
| Phase boost by $G_c$ at $f_c$ | 63° | 63° | 60° |
| Phase boost by H at $f_c$ | 37° | 37° | 36.19° |

The variation in $f_c$ and PM in theoretical & experimental results are due to practical implementation of compensator with chosen standard value nearest to design value of the components.

## CONCLUSION

The type-III compensation is suitable for high bandwidth voltage mode control loop for switch mode power converter. The bandwidth is limited to power pole frequency in type-I or II compensation with phase margin of ≥ 50 °. Hence the type-III compensation can be used for inner voltage loop in switch mode magnet power supplies for better dynamic performances. The compensation can be implemented either using an op-amp or combination of both feedback & type-II compensation. The later gives more degree of freedom for tuning of loop if required.

## ACKNOWLEDGEMENT

Authors are sincerely thankful to Mr. Amit Sahu, Mr. Gurupreet Singh, Mr. P. Renukanath, Mr. Deepchand, Mr. Nathan Singh, Mr. G. H. Ansari, Mr. Chattar Singh, Mr. M. D. Jha, and Mr. Prabhu for their help in fabrication, assembly and testing of the prototype converter with type-III compensation.

## REFERENCES

[1] Robert W. Erickson and Sragan Maksimovic, "Fundamental of power electronics", Second edition, Kluwer Academic Publishers.

[2] S W Lee, "Demystifying type II and type-III compensators using op-amp and OTA for dc- dc converters", Application Report, SLVA662, July, 2014.

[3] H. D. Venable, "The K factor a new mathematical tool for stability analysis and synthesis", Proceedings of Powercon 10, March 22-24, 1983, California.

[4] H. Choi, "Practical feedback loop design considerations for switch mode power supplies", Fairchild power seminar, 2010-11.

[5] "Testing and stabilizing feedback loops in today's power supplies", Venable instruments application note, 2017.

[6] R. B. Ridley, "Power supply design, volume 1: control", Second edition, 2012.

# COLD COMPRESSOR TECHNOLOGIES FOR 2K ACCELERATOR CRYOGENICS AT BARC

Mohananand M. Jadhav[1,2], Anindya Chakravarty[1,3] and M. D. Atrey[2]
[1]Cryo Technology Division, Bhabha Atomic Research Centre, Mumbai, India
[2] Indian Institute of Tecnology Bombay, Mumbai, India
[3]Homi Bhabha National Institute, Mumbai, India

*Abstract*

The article establishes the necessity and importance of centrifugal cold compressors (CC) for large scale sub 4.5K cryogenics. The advantages and limitations posed by the cold compressor system are brought out for a cryogenic system using typical characteristics of the cold compressors. The design of the cold compressor cartridge is studied from the point of view of heat in leak. Various modes of heat in leak are analysed and the mitigation of heat in leak through the cryogenic insulation and intercepts is deliberated upon. The resulting construction of the cold compressor system is subsequently evaluated from the point of view of rotor dynamics and stress. In addition, various sub atmospheric (Sub 4.5 K) systems and their relevance to the Indian accelerator program is described briefly in this article.

## INTRODUCTION

Modern day large accelerator projects employ superconducting magnets and cavities cooled at around 2 K. Cryogenics at 2 K, with liquid helium below lambda point (He II) as a technical coolant, has become a norm in large scale applications. The saturation temperature of helium at atmospheric pressure is around 4.2 K and hence sub atmospheric process cycles are required for catering to the needs of these 2K systems.

The simplest examples of sub atmospheric helium cryogenic cycle are the direct evacuation systems and Warm pumping systems (WPS) with sensible heat recover. The major limitation of these systems arise due to the density difference of helium between 2K and room temperature. Figure 1. Shows the volumetric capacity requirement of the WPS for the 2K refrigeration system with respect to the refrigeration wattage requirement. The commercially available WPS systems (typical capacities < 10, 000 m3/hr) can only be used for refrigeration below 100 W.

The large capacity refrigerators handle this difficulty by compressing the helium when it is dense. This is done using the cold compressors, these can either be reciprocating systems [1] or turbomachines [2]. or even Venturi injectors [3] for small capacities. The turbo compressors have advantage in cryogenic systems due to its thermally advantageous mounting, lower heat leak and compactness.

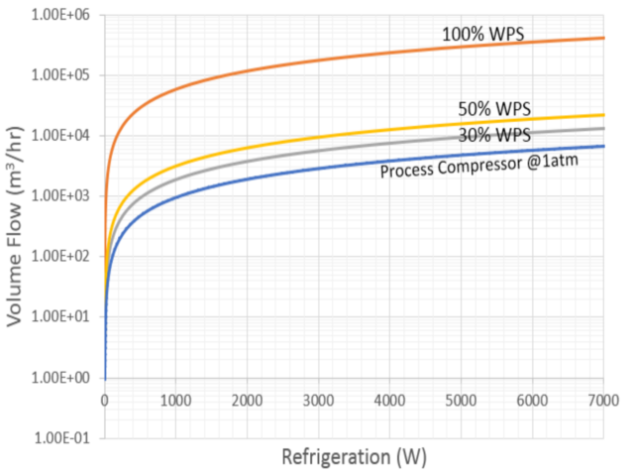


Figure 1: Volume flow requirement of Warm Pumping System for 2K refrigerator.

The turbo cold compressors typically have limited dynamic rage (cant provide same pressure ratio over range of mass flow due to instabilities) due to which hybrid cycles using both cold compressors and WPS are more suitable than the integrated Cold compressor systems. Figure 1 also shows the typical WPS capacity requirement if different percentage of compression is done through cold compressors. Since the process gas has to be further compressed after the WPS and supplied to the atmospheric refrigeration systems. It is not advantageous to reduce the WPS share of the compression below 50% percent. 50% WPS systems have also been found more economical in studies [4]. Another matter of concern for the sub atmospheric systems is the ingression of impurities. Impurity management is great concern for any cryogenic system and sub atmospheric systems requires helium guards and large purification systems. Cryocoolers are at great advantage despite of the low efficiency due to minimal cryogen handling and minimal risk of impurity ingression. Direct evacuation systems are advantages were the other 2K systems are not available. The direct evacuation system is simplest and can be ad hoc constructed from laboratory based vacuum pumping system. WPS systems with sensible recovery and gas purification system although not as simple as direct evacuation are simplest closed loop systems and can cater to continues load experiments. Table 1 summarises the typical application range of different 2K cryogenic systems discussed here.

Table 1 2K systems and application ranges

| 2K system | refr. Capacity | Limitation / Advantage | Application |
|---|---|---|---|
| **Cryocoolers** | mW | Low eff. Minimal impurity ingression | Sensor calibration, material studies, etc |
| **Direct evacuation** | <5W | Lab manageable, simplicity | Small experiments with availability. |
| **WPS with Sensible recovery** | <100 W | Large WPS, purification system | Cavity testing, equipment testing. |
| **Integrated cold compressor system.** | >200 W | Low dynamic range | single operating mode |
| **Hybrid Cold compressor Schemes** | >200 W | Large WPS, purification system | multiple operating modes |

## COLD COMPRESSOR ASSEMBLY

The cold compressor consists of a turbo-compressor impeller, a rotor bearing system, a high-speed drive and thermal isolation systems. Figure 2 Shows a proposal of centrifugal impeller based cold compressor unit. For experimental and R&D purposes the cold compressor and the diffuser assembly is required to be changed often. The proposal shown in figure 2 is based on annular diffuser cartridge configured for accessibility without cold box dismantling, suitable for the experimental and R&D requirement.

Although the cold compressor has the advantage of being compact the same results in large gradient of temperature. High speed cold compressor with small and long shaft diameters are designed to minimise thermal heat in leak. The installation cavity of the impeller and the diffuser is filled by placing convection brakes. For the 2K Cold compressor shown in figure 2, two additional thermal intercepts are used to divert the heat in leak to relatively higher temperature processes gas. For high temperature cold compressor, in later stages, only single shield can be used.

The diffuser assembly consists of combination of vane diffuser and annular diffuser. The vane diffuser is used as it gives the compact design. The annular diffuser is used for its simplicity and favourable form for the remounting application. The inlet nozzle body shown in the schematic is hollowed and filled with cryogenic insulation to reduce the thermal shorting between the inlet and exit streams of the cold compressor.

A double O-ring construction with in-between high pressure helium guard has been used at all static sealing to curtain the impurity ingression. A pressure equalisation port has been given to balance to reduce the unbalance forces on the rotor. This feature is essential for the designs where the bearing and motor assembly is kept pressurised.

The two important factors that influence the rotor dynamics of the system are the prime mover and the bearing system. BLDC motors are most suited as these are compact low weight and control friendly. However, induction motors are the cheapest option if the rotor dynamic permits. Magnetic bearings are more viable for high speed CCs as gas bearing system may lead to excessive warm gas leakage to the system.

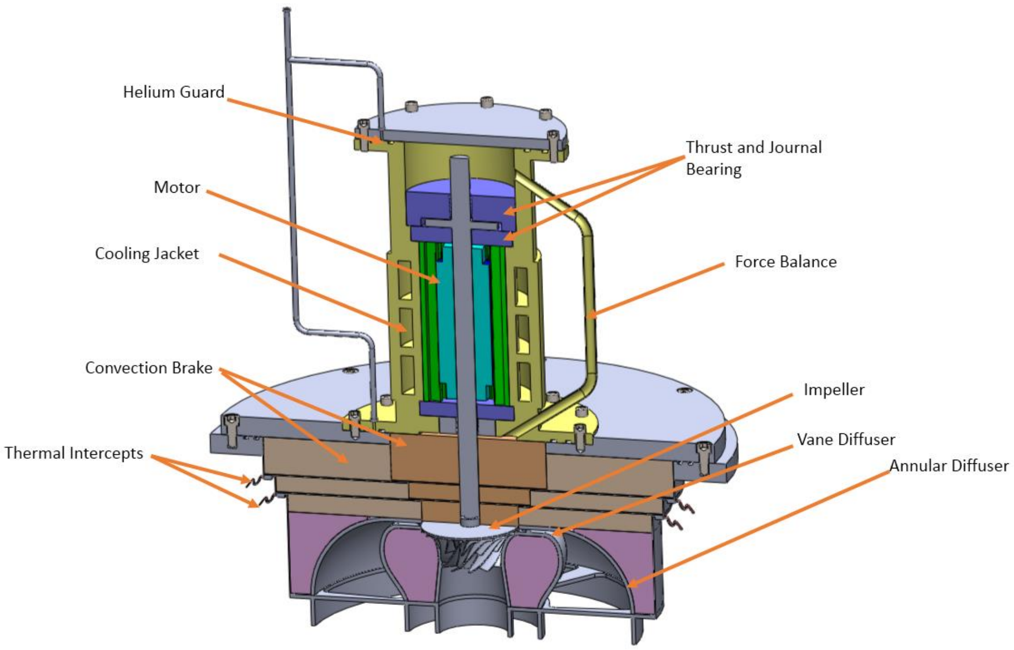


Figure 2: Schematic model of centrifugal cold compressor assembly.

## CC CHARACTERISTICS

The design of the cold compressor staging, operation and control of the system is majorly governed by the compressor 'pressure ratio - mass flow' characteristic [5]. Figure 3 shows the typical CC characteristic. The characteristic is bounded by the surge instability on low mass flow side and choked flow on the high mass flow side. The surge instability is attributed to high angle of attack at the cc inlet (fluid dynamic instability) and positive slope of the iso-speed curve (system interaction instability). For 2K cryogenic applications The system has to maintain constant pressure over the bath. Hence for the integral cold compressor cycle the mass flow variation is limited by the horizontal intersection of the constant pressure line. Whereas for the hybrid systems pressure ratio of the CC can be reduced at low mass flowrates avoiding the instability.

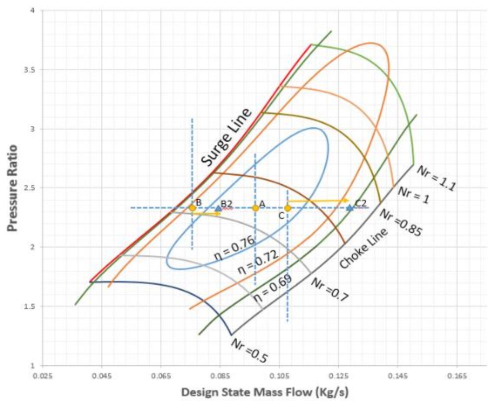


Figure 3: Characteristic of cold compressor.

For the multiple CCs connected in series the operational bounds on mass flow are further reduced. This is revealed in figure 3. For two CCs in series with characteristics as in figure 3 when the mass flow reduces from point A to point B, the first CC moves out of the high efficiency zone. This results in increased inlet temperature and the apparent mass flow of the second CC increases giving reduced pressure ratio for the given speed. This results in positive slope of the resultant characteristic curve leading to surge. On the contrary when the mass flow increases the rise in apparent mass flow cases the second CC to move towards choking. Hence the combine dynamic range of the CC train is shorter than the individual CC.

## CC DESIGN

Cold compressor is high speed turbomachinery. The design of CC is compromise between fluid dynamic requirements and manufacturing, material and rotor dynamic limitations. Figure 4 shows the effect of lean on the rotary stresses on the impeller. Optimum lean and fillet radius can reduce the rotary stresses effectively. Figure 4 also shows the splitter vane designed to accommodate more number of effective blades with confines posed by manufacturing.

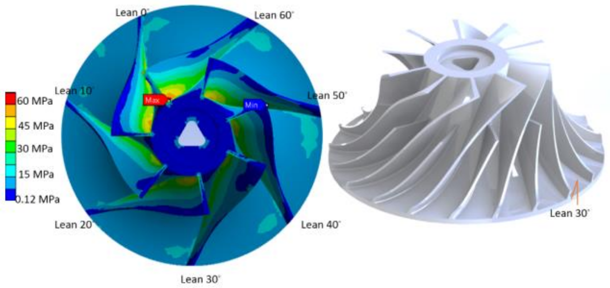


Figure 4: Rotary stress on leaned impeller

## CONCLUSIONS

Cold compressors are necessary for making large scale2K sub-atmospheric cycles compact and commercial. Different 2K systems can be selected based on application requirement and refrigeration capacity. For multiple mode large capacity application like superconducting accelerators, hybrid cold compressor systems are more suited. A cold compressor assembly with replaceable diffuser nozzle cartridge is proposed. With proper design of labyrinths and convection breaks different bearing systems and motors can be used for the cold compressor assembly. The typical pressure ratio characteristics of the centrifugal compressors governs the staging, design, operation and control of the cold compressor based systems. The overall dynamic range of the cold compressor system is further reduced by the series operation the cold compressors. With careful design good compromise between the fluid dynamic requirements and the manufacturing, material, rotor dynamics can be achieved.

## REFERENCES


[1] F. K. Miler and J. G. Brisson, "Development of a low-temperature 3He compressor for superfluid 3He-4He mixtures," *Cryogenics,* vol. 47, pp. 67-68, 2007.

[2] L. Philippe, "Cryogenic refrigeration for the LHC," MaTeFu Spring Training School, Cadarache, 2009.

[3] A. P. Shlafke, D. P. Brown and K. C. Wu, "combined cold compressor/ ejector helium refrigeration cycle," *Advances in Cryogenic Engineering,* vol. 29, pp. 487-493, 1984.

[4] C. Serge, L. Philippe and T. Laurent, "Towards Cost-to-Performance optimisation of Large Superfluid Helium Refrigeration Systems," in *International Cryogenic Engineering Confrence*, Mumbai, 2000.

[5] A. L. Klebaner, A. Martinez, W. M. Soyars and J. C. Theilacker, "Pressure field study of the Tevtron cold compressors," in *Advances in Cryogenic Engineering(CEC49)*, 2004.

# A COMPARATIVE STUDY OF TILTING PAD AND GAS FOIL DYNAMIC JOURNAL BEARINGS FOR HIGH SPEED CRYOGENIC TURBOEXPANDERS BASED ON NUMERICAL ANALYSIS

Ankit Jain[1#], Mohananand M. Jadhav[1], Anindya Chakravarty[1,2] and D.S. Pilkhwal[1]
[1]Cryo Technology Division, Bhabha Atomic Research Centre, Mumbai
[2]Homi Bhabha National Institute, Mumbai

*Abstract*

The high speed turboexpanders in medium/large scale cryogenic systems which are used for cooling superconducting RF cavities and magnets of high energy accelerators operates in the range of 3000 to 5000 Hz. Two important candidates for dynamic journal bearings in such high speed applications are tilting pad journal bearing (TPJB) and gas foil journal bearing (GFJB). The main advantage of these bearings is the lower cross-coupling forces which cause whirl instability. Another advantage is that the process fluid may be used as bearing gas to eliminate any contamination. In the present work, a steady state analysis of TPJB and GFJB is carried out and discussed with reference to a typical ultra-high speed cryogenic turboexpander for its complete range of parameters in order to achieve stable operation. Both the types of bearings are compared based on performance characteristics such as stiffness coefficients and load carrying capacity. The cross-coupled stiffness, which determines the static stability of the bearing, are compared for different bearing parameters. The dependence of stiffness coefficients on other parameters such as bearing clearance and foil stiffness is also analyzed and presented in the article.

## INTRODUCTION

An aerodynamic bearing uses relative motion between the shaft and the bearing surface for generation of forces. A plain journal bearing offers very high cross-coupled forces which give rise to instability. The two different types of aerodynamic bearings under study viz. GFJB and TPJB works by deflecting the bearing surface under pressure and reducing the cross-coupled forces.

The configuration of a bump type GFJB is shown in fig. 1. It consists of a top foil, underneath which strips of corrugated or bump foils are present. The top foil is free at its leading edge and fixed at the trailing end. When the journal rotates and top foil is subjected to pressure, the bumps act as springs which produce deflection in the top foil offering film thickness higher than that in a plain journal bearing. This construction does not allow sub-ambient pressures since the top foil will lift up to equalize the pressure on both the sides of the top foil [1]. Load carrying capacity of the bearing is generated due to the pressurized gas film between the shaft and the foil after the deflection.

#ankitj@barc.gov.in

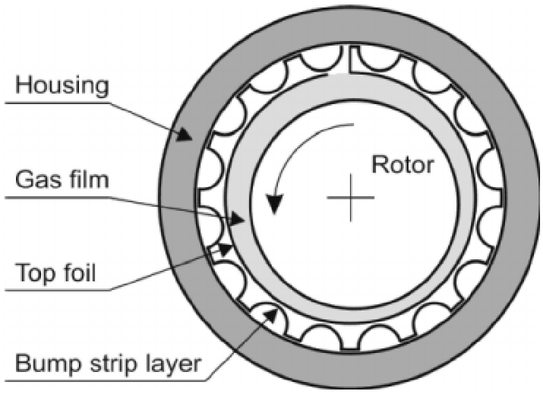


Figure 1: Gas foil journal bearing [2].

A schematic diagram of TPJB with three pads is shown in fig. 2. It can be seen as a combination of three partial plain journal bearing which are allowed to tilt around a predefined pivot to align in equilibrium position. The pad tilts to form a converging gas film between shaft and pad which generates the pressures responsible for the bearing force. The net force offered by TPJB is summation of the forces generated by all the pads.

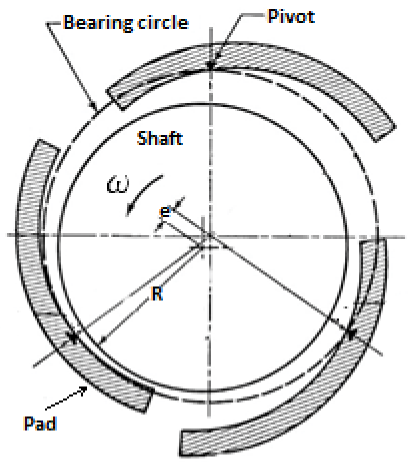


Figure 2: Tilting pad journal bearing [3].

The aim of this article is to present a comparison of GFJB and TPJB based on their performance characteristics. Variation of performance on different parameters is also studied. Nomenclature used in this article is listed in table 1.

Table 1: Nomenclature

| | | | | | |
|---|---|---|---|---|---|
| C | Radial clearance | $P$ | Dimensionless pressure | $\Lambda$ | Compressibility factor |
| E | Modulus of elasticity | $p_a$ | Ambient pressure | α | Bearing compliance |
| $e$ | Eccentricity | $R$ | Radius of shaft | $\omega$ | Speed of shaft |
| $h$ | Film thickness | $S$ | Pitch of the bumps | $\theta$ | Circumferential direction |
| $K_1$ | Structural rigidity of bumps | $t$ | Thickness of bump foil | $\nu$ | Poisson's ratio |
| $L$ | Length of the bearing | $x$ | Direction of shaft eccentricity | μ | Kinematic viscosity of gas |
| $l_0$ | Half of length of the bump | $y$ | Direction perpendicular to shaft eccentricity | $\phi_0$ | Angle of shaft eccentricity from leading edge |

## METHODOLOGY

The pressure profile on the bearing surface is computed from the film thickness profile using 1D steady state compressible Reynolds equation (see Eq. 1) [4]. The working gas is assumed to behave as an ideal gas.

$$\frac{\partial}{\partial\theta}\left(Ph^3\frac{\partial P}{\partial\theta}-\Lambda Ph\right)=0 \quad (1)$$

Where

$$\Lambda=\frac{6\mu\omega}{p_a}\left(\frac{R}{C}\right)^2$$

The variation in the film thickness in GFJB is a function of both the shaft eccentricity and the deflection of foil under pressure (see Eq. 2) [1]. The stiffness of foil is taken as uniform throughout the bearing surface.

$$h=C+e\cos(\theta-\phi_0)+K_1p_a(P-1) \quad (2)$$

Where

$$K_1=(\alpha C/p_a)$$

$$\alpha=\frac{2p_aS}{CE}\left(\frac{l_0}{t}\right)^3(1-\nu^2)$$

Whereas in TPJB, the film thickness is a function of the shaft eccentricity and the tilt of the pad (see Eq. 3) [3].

$$h=C+e\cos(\theta-\phi_0) \quad (3)$$

Where $e$ includes the eccentricity of shaft and the eccentricity generated due to tilt of the pad.

The equations are modelled using finite difference method and analysis has been carried out. The forces and stiffness components of the bearing are computed from:

$$F_x=\int_{0°}^{360°}(P-1)p_aLR\cos\theta d\theta \quad (4)$$

$$F_y=\int_{0°}^{360°}(P-1)p_aLR\sin\theta d\theta \quad (5)$$

$$K_{xx}=\frac{((F_x)_{x+\Delta x}-(F_x)_x)}{\Delta x} \quad (6)$$

$$K_{xy}=\frac{\left((F_y)_{x+\Delta x}-(F_y)_x\right)}{\Delta x} \quad (7)$$

## RESULTS AND DISCUSSIONS

The performance of bearings and its dependence on the magnitude and direction of shaft eccentricity, speed of the shaft, radial clearance and foil compliance is studied. Table 2 summarizes the basic operational and geometrical parameters used in the analysis.

Table 2: Operational and geometric parameters

| Parameter | Value | Unit |
|---|---|---|
| Radius of shaft | 10 | mm |
| Length of bearing | 20 | mm |
| Operating pressure | 1 | bar |
| Speed of shaft | 3000 | Hz |
| Kinematic viscosity of gas | 0.00002 | Pa.s |
| Foil compliance (α) | 0.276 | |
| Radial clearance | 50 | μm |
| Eccentricity | 5 | μm |
| No. of pads | 3 | |
| Angular extent of a pad | 90 | ° |
| Pivot position from leading edge of pad | 56 | ° |

Fig. 3 shows a variation of total bearing force generated for different values of angle of shaft eccentricity ($\phi_0$). The angle is taken in direction of rotation from leading edge of film for GFJB and from pivot of a pad in TPJB. A large variation is observed in case of GFJB and the bearing generates largest force when $\phi_0$ is between 180° and 270°. Also, the bearing force is almost zero when $\phi_0$ is between 0° and 90° from which it may be inferred that the shaft is unstable in this region. TPJB generates lower force as compared to the GFJB, however, the variation in force is very less. A circumferential symmetry is observed for 3 pads and the variation indicates a maximum stiffness when shaft eccentricity is towards the pivot and minimum when it is in between the pivot position of two pads.

For the rest of the analysis, shaft eccentricity is assumed to be in the opposite direction to the leading edge for GFJB and towards the pivot point of a pad for TPJB.

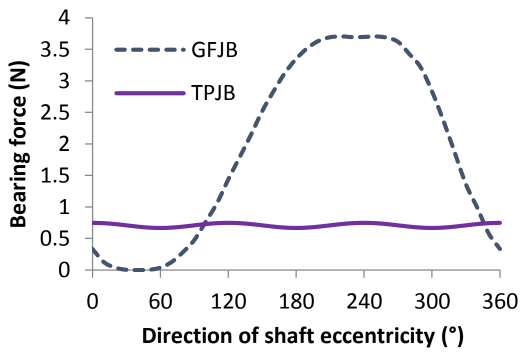


Figure 3: Variation of total force with direction of shaft eccentricity.

Fig. 4 presents the variation of $K_{xx}$ and $K_{xy}$ with speed of the shaft. For GFJB, the $K_{xx}$ values are lower than $K_{xy}$ at low speeds. But as the speed increases, $K_{xx}$ increases while

$K_{xy}$ decreases signifying a more stable bearing action at higher speeds. For TPJB, $K_{xy}$ is almost zero ensuring a stable operation at lower speeds also. The $K_{xx}$ for TPJB monotonically increases with the shaft speed.

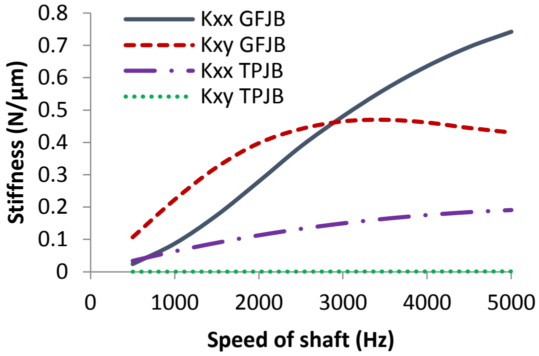


Figure 4: Variation of stiffness with speed.

Fig. 5 shows that for GFJB, $K_{xx}$ and $K_{xy}$ are of similar magnitude at low eccentricity values but at higher eccentricities, $K_{xx}$ increases while $K_{xy}$ decreases significantly, thus implying that GFJB is more stable at higher eccentricities. However, for TPJB, the $K_{xy}$ component is negligible at all eccentricity values while the $K_{xx}$ component increases monotonically with the eccentricity.

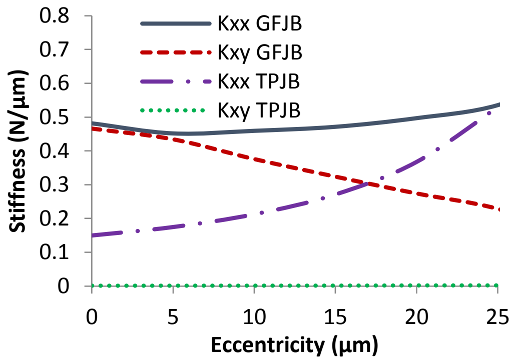


Figure 5: Variation of stiffness with eccentricity.

With decrease in clearances, $K_{xx}$ component increases for both types of bearings (fig. 6). The $K_{xy}$ component is almost negligible for TPJB while for the GFJB, it increases with clearance upto a maximum value and then decreases. The low value of $K_{xy}$ at lower clearances in GFJB is due to the effect of higher eccentricity ratio as seen in fig. 5.

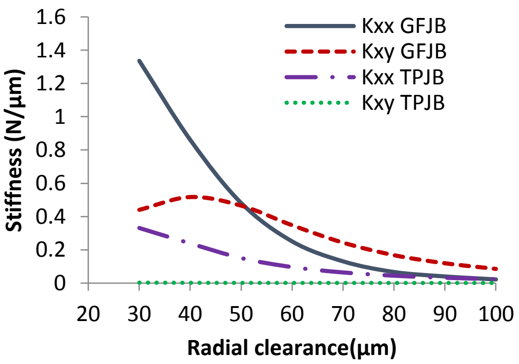


Figure 6: Variation of stiffness with radial clearance.

Fig. 7 represents a variation of $K_{xx}$ and $K_{xy}$ components, with foil compliance, for the GFJB case. Both $K_{xx}$ and $K_{xy}$ decreases monotonically. However, the ratio of direct stiffness to cross stiffness increases. Hence, a more stable bearing may be designed using more compliant foil if requirement of stiffness is compromised slightly.

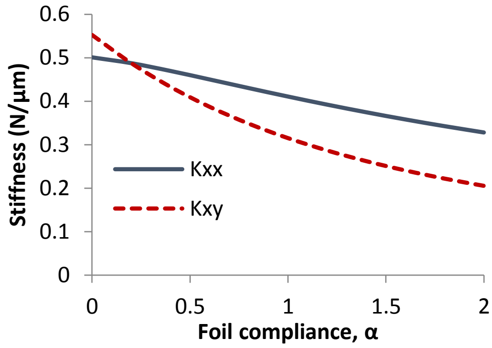


Figure 7: Stiffness of GFJB v/s foil compliance.

## CONCLUSIONS

In the analysis presented in the present article, the basic bearing characteristics of the GFJB and TPJB are studied and compared. The TPJB provides load capacity for every direction of shaft eccentricity and offers negligible cross-coupled stiffness, which is very important for stable operation. TPJB provides nearly one-third of the stiffness of GFJB under similar operating conditions. Hence, TPJB is more suitable where stiffness requirements are lower but load direction is not fixed or cyclic. In order to achieve high stiffness values in TPJB, radial clearances have to be decreased, which introduces manufacturing challenges. On the other hand, GFJB provides larger stiffness values, but due to the presence of cross-coupled stiffness and low load capacity in particular direction of shaft eccentricity, its uses are restricted to only some specific domains where a large load capacity is required in a particular direction. Cross-coupled stiffness in GFJB also decreases at very high speeds, thus making it suitable for high speed rotors. For vertical shafts or cyclic loads, different configuration of GFJB, like multiple segmented bump type or leaf type bearings can be explored.

## REFERENCES


[1] H. Heshmat, J. Walowit and O. Pinkus, “Analysis of Gas-lubricated Foil Journal Bearing,” *Journal of Lubrication Technology,* vol. 105, 1983.

[2] L. San Andrés and T. H. Kim, “Analysis of gas foil bearings integrating FE top foil models,” *Tribology International,* vol. 42, no. 1, pp. 111-120, 2009.

[3] B. Majumdar, Introduction to Tribology of Bearings, Kharagpur: Y.P. Chopra, 1986.

[4] E. J. Gunter, V. Castelli and D. D. Fuller, “Theoretical Experimental Investigation of Gas Lubricated Pivoted Pad Bearings,” *ASLE TRANSACTIONS,* 1963.

# DESIGN OF MULTIFUNCTION MULTIPOLE CORRECTOR MAGNETS

Kailash Ruwali#, Ritesh Malik, Navin Awale, Gautam Sinha and S. N. Singh

Accelerator Magnet Technology Division, Raja Ramanna Centre for Advanced Technology, Indore, India

*Abstract*

Design of multifunction Octupole and Dodecapole corrector magnets were carried out keeping in view of proposed low emittance storage ring at Raja Ramanna Centre for Advanced Technology, Indore. The results obtained using 2D and 3D calculations are presented.

## INTRODUCTION

In designing a lattice, space is always a constrain. Lattice designer needs more space to put diagnostics devices and correction magnets. Keeping this in view of proposed low emittance storage ring, design of multifunction Octupole and Dodecapole magnets are carried out.

The special feature of Octupole and Dodecapole corrector magnets are that they can generate fields in multi-function mode [1,2]. Incorporating these corrector magnets in lattice will not only save space but also allows the lattice designer to have flexibility in designing the lattice along with space for installation of beam diagnostic elements.

## MAGNET DESIGN PARAMETER

Octupole and Dodecapole magnet design were carried for a nominal gradient of 1 E+04 T/m$^3$ and 2.5 E+10 T/m$^5$ respectively. Major parameters of the magnets are given in Table 1.

## MAGNET DESIGN

Based on the magnet parameters, the cross-section of the magnet was determined by computing the field distribution with the two-dimensional magnetostatic program POISSON [3] while all 3-dimensional calculations were performed using the software OPERA-3D [4]. With the parameters mentioned in table 1, we are fabricating the magnets keeping in view of high field quality and cost effective using following procedure:

1. Readily available 40 mm thick low carbon steel plates were used as magnet core material. Using CNC wire-cut electrical discharge machine tools the steel cores will be machined with high accuracy.
2. In order to achieve the high field quality, the magnet core will be fabricated in single piece.
3. The pole profile coordinates are calculated using equations as mentioned in this paper.

### *Octupole Magnet*

The pole profile coordinates of Octupole magnet is calculated using following equation:

$$4X * Y * (X^2 - Y^2) = R^4$$

# ruwali@rrcat.gov.in

Table 1: Parameters of Octupole and Dodecapole magnet.

| **Parameter** | **Value** | |
|---|---|---|
| | **Octupole Magnet** | **Dodecapole Magnet** |
| Nominal Gradient | 1 E+04 T/m$^3$ | 2.5 E+10 T/m$^5$ |
| Aperture radius | 30 mm | 12 mm |
| Iron length | 0.103 m | 0.103 m |
| Magnetic length | 0.117 m | 0.107 m |
| Ampere-turns | 300 A | 100 A |
| No. of turns per coil | 58 (17+41) | 40 (10+10+20) |
| Current | 5 A | 2.44 A |
| Resistance per coil | 106 mΩ | 76.8 mΩ |
| Total mass | 20 Kg | 31 Kg |

Figure 1 shows the 1/16$^{th}$ view of Octupole magnet along with the co-ordinates. The Octupole magnet will have 2 coils (41 and 17 turns) per pole. The splitting of coil enables us to generate the different field modes and also to compensate the sextupole component generated during horizontal/vertical corrector mode. The modes are horizontal/vertical correctors, normal/skew quadrupoles & sextupoles and Octupole. To achieve the multi-function field, each coil will require a separate power supply.

| | X (cm) | Y (cm) |
|---|---|---|
| A | 2.771 | 1.148 |
| | 2.973 | 0.837 |
| | 3.175 | 0.661 |
| | 3.377 | 0.539 |
| | 3.579 | 0.449 |
| | 3.781 | 0.378 |
| | 3.983 | 0.322 |
| B | 4.192 | 0.275 |

| | X (cm) | Y (cm) |
|---|---|---|
| C | 11.189 | 3.173 |
| D | 12.504 | 0.0 |
| E | 16.235 | 0.0 |
| F | 13.858 | 5.740 |

| | X (cm) | Y (cm) |
|---|---|---|
| a | 5.291 | 0.132 |
| b | 6.980 | 0.831 |
| c | 6.827 | 1.201 |
| d | 5.137 | 0.501 |
| e | 10.926 | 2.466 |
| f | 10.773 | 2.835 |

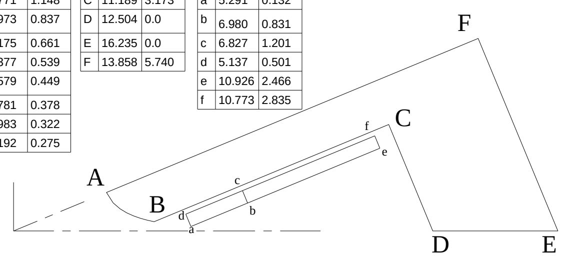


Figure 1: 1/16$^{th}$ Cross-section of Octupole magnet.

Owing to the symmetry, field calculation was carried out in 1/16 geometry. The harmonic analysis was carried out using POISSON code by interpolating 11 points over an arc of radius $r_{int}$ = 1.5 cm, with a normalization radius of 1.5 cm. The systematic harmonics are less than 1 unit.

In order to obtain the field pattern for different modes, the calculations were carried out for full 360° job. The magnetic flux lines which indicate the direction and strength of the magnetic field during the superposition of

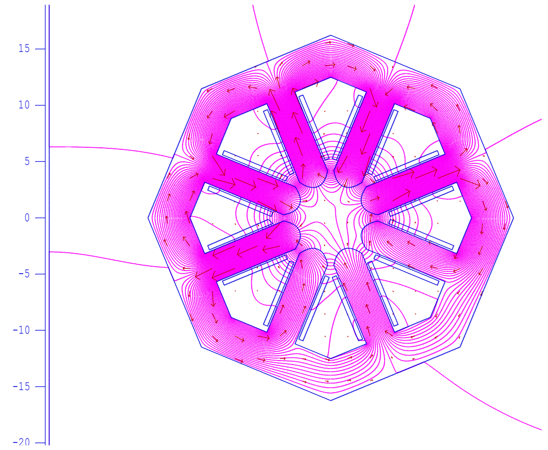

Figure 2: Superposition of four modes: Dipole corrector, quadrupole, sextupole and Octupole.

four modes: Octupole, sextupole, quadrupole and dipole corrector is shown in Fig. 2. The magnetic field values obtained using multi-function mode and single field values

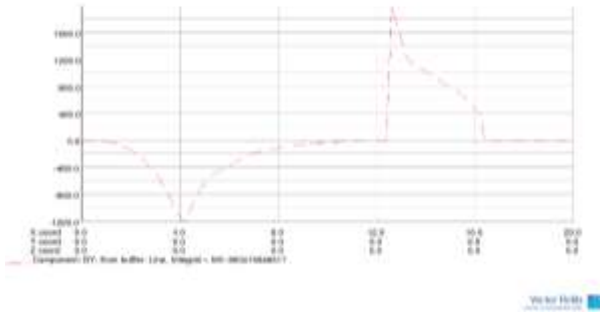

Figure 3: Magnetic field of the Octupole magnet along X-axis.

are alike.

Figure 3 shows the magnetic field distribution along X-axis (from magnet centre) for Octupole magnet. It is evident from the figure that the magnetic field component increases from the centre of the magnet according to the third power of the abscissa till 0.12 T and decreases to zero in the coil region. The magnetic field increases inside the iron yoke and becomes zero again outside the iron yoke thus indicating no leak field outside the iron yoke (iron yoke is up to 16.23 cm). Figure 4 shows the magnetic field pattern distribution along 22.5° line. Magnetic field inside core is shown in Fig. 5. Figure 6 shows magnet fabrication

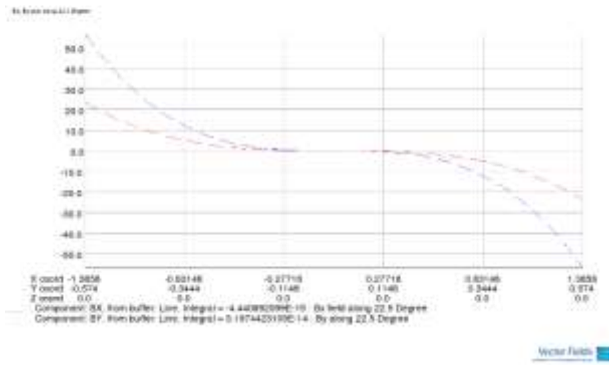

Figure 4: Magnetic field pattern in case of Octupole magnet at 22.5° line up to aperture radius.

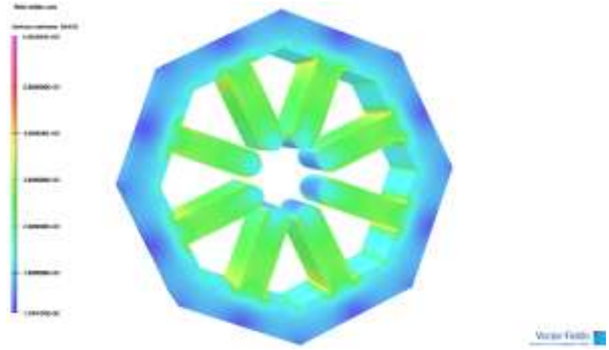

Figure 5: Magnetic field pattern inside core.

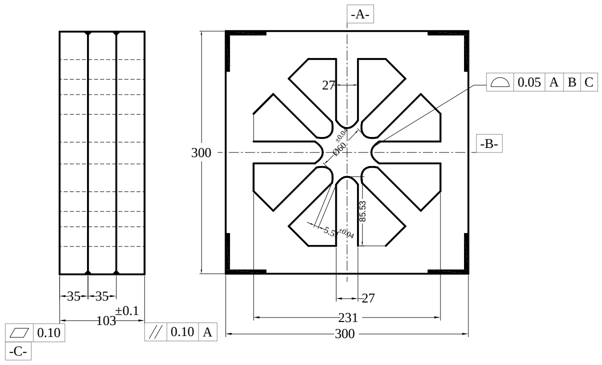


Figure 6: Magnet fabrication drawing.

drawing. The fabrication is under process. Magnetic measurement will be carried out in due course of time.

## *Dodecapole Magnet*

The pole profile coordinates of Dodecapole magnet is calculated using following equation:

$$6 * X * Y * (X^4 + Y^4) - 20 * X^3 * Y^3 = R^6$$

Figure 7 shows the 1/24$^{th}$ cross-section view of Dodecapole magnet along with the co-ordinates. The magnet has 3 coils (10, 10 and 20 turns) per pole. This splitting of coils enables us to generate different magnet modes and the superposition of these modes also. The modes are horizontal/vertical correctors, normal/skew quadrupoles and sextupoles, Octupole, Decapole and Dodecapole. To achieve the multi-function field, each coil will require a separate power supply.

| | X (cm) | Y (cm) |
|---|---|---|
| A | 1.159 | 0.31 |
| | 1.179 | 0.266 |
| | 1.189 | 0.248 |
| | 1.199 | 0.232 |
| | 1.209 | 0.219 |
| | 1.219 | 0.207 |
| | 1.229 | 0.196 |
| B | 1.239 | 0.186 |

| | X (cm) | Y (cm) |
|---|---|---|
| C | 2.746 | 0.192 |
| D | 12.455 | 2.586 |
| E | 13.148 | 0.0 |
| F | 15.529 | 0.0 |
| G | 14.488 | 3.882 |

| | X (cm) | Y (cm) |
|---|---|---|
| a | 6.393 | 0.759 |
| b | 6.51 | 0.322 |
| c | 12.432 | 0.271 |
| d | 12.87 | 0.388 |
| e | 12.343 | 2.354 |

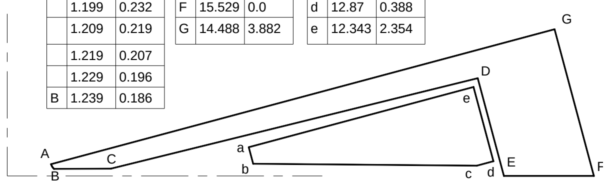


Figure 7: 1/24$^{th}$ Cross-section of Dodecapole magnet.

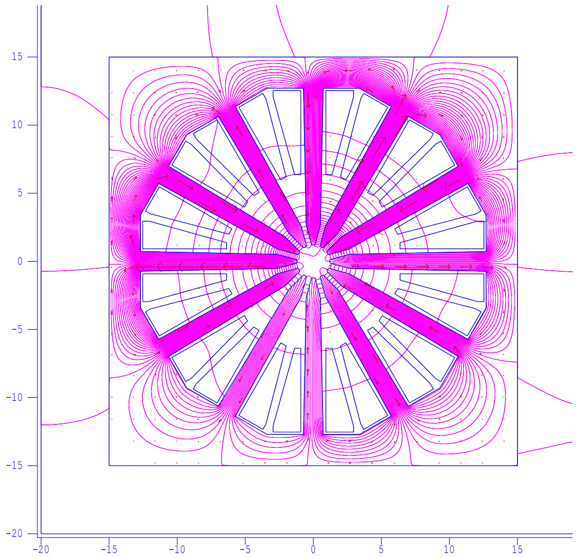

Figure 8: Superposition of six modes: dodecapole, decapole, octupole, sextupole, quadrupole and dipole corrector.

The field calculation was carried out for full geometry. The harmonic analysis was carried out using POISSON code by interpolating 360 points over an arc of radius $r_{int}$ = 0.9 cm, with a normalization radius of 0.9 cm. The harmonics are less than 6 unit. Figure 8 shows the flux line pattern during superposition of six modes. Magnetic field Bx and By along a circle of radius 0.9 cm is shown in Fig. 9.

Figure 10 shows the field pattern along X-axis (from centre). It is evident from the figure that the magnetic field component increases from the centre of the magnet according to the fifth power of the abscissa till 0.06 T and decreases to zero in the coil region. The magnetic field increases inside the iron yoke and becomes zero again outside the iron yoke thus indicating no leak field outside the iron yoke (iron yoke is up to 15.5 cm). Figure 11 shows the field inside magnet core. Figure 12 shows the fabrication drawing of the magnet. The fabrication is under process. Magnetic measurement will be carried out in due course of time.

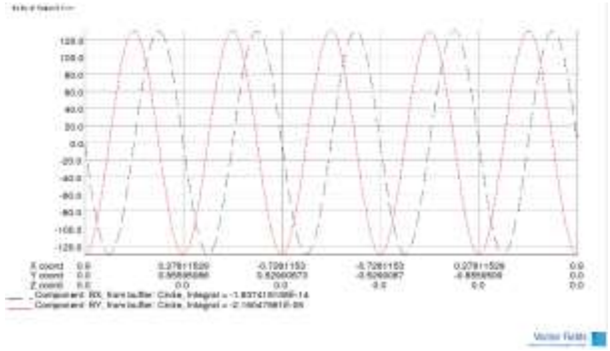

Figure 9: Bx and By field along a circle of radius 0.9 cm.

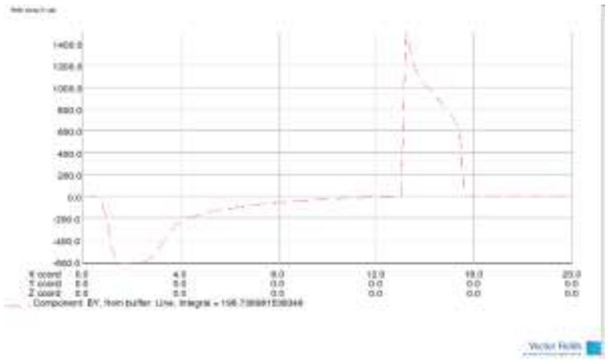

Figure 10: Magnetic field of the along X-axis.

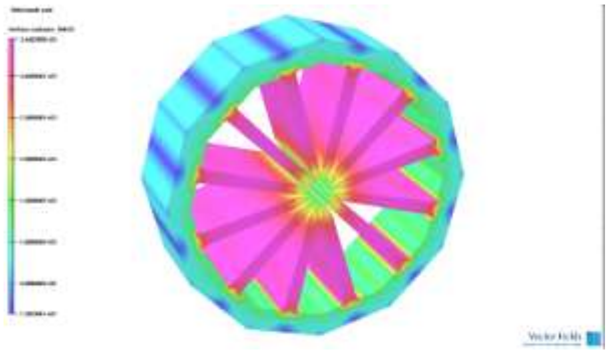

Figure 11: Magnetic field inside magnet core.

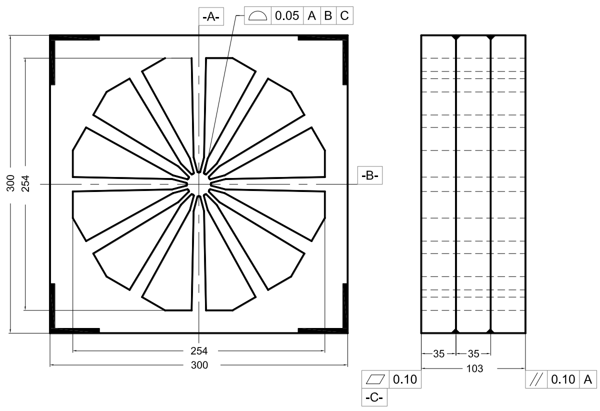


Figure 12: Magnetic fabrication drawing.

## REFERENCES

[1] L.O. Dallin and D.G. Bilbrough, "Multi-Function Corrector Magnet", IPAC 10 proceedings.

[2] Mikhail Fedurin, Paul Jines, Toby Miller, Victor P. Suller, "Multipole Design for CAMD Storage Ring", PAC 2005 proceedings.

[3] POISSON Group of Codes, Los Alamos National Laboratory, New Mexico, 86545.

[4] Vector Fields Limited, 24 Bankside Oxford, OX5 1JE. Kidlington, England.

# DEVELOPMENT OF EXTENDED POLE QUADRUPOLE MAGNET

Kailash Ruwali#, Ritesh Malik, Navin Awale, Bhim Singh, Anil Kumar Mishra, B. Srinivasan, Gautam Sinha and S. N. Singh

Accelerator Magnet Technology Division, Raja Ramanna Centre for Advanced Technology, Indore, India

*Abstract*

Development of extended pole (nose) quadrupole is carried out keeping in view of proposed low emittance storage ring at Raja Ramanna Centre for Advanced Technology, Indore. The design feature along with results obtained using magnetic measurements are presented.

## INTRODUCTION

In designing a lattice, space is always a constrain. Lattice designer needs more space to put diagnostics devices and correction magnets. Keeping this in view of proposed low emittance storage ring development of extended pole (nose) quadrupole magnet is carried out.

The special feature of extended pole or nose is the increase in the magnetic length of the magnet without increasing the physical length [1, 2]. This will save the significant space in the lattice and will allow the lattice designer to have flexibility in designing the lattice.

## MAGNET DESIGN

Main parameters of the quadrupole magnet are given in Table 1. The cross-section of the magnet was determined by computing the field distribution with the two-dimensional magneto static program POISSON [3] while all 3-dimensional calculations of the static magnetic field were performed using the software OPERA-3D [4]. The pole profile is not a true hyperbola and the poles were truncated laterally to provide space for coils. The pole tip profile is hyperbolic curve (point A-B) for obtaining good quadrupole magnet field distribution. In order to compensate for the finite pole width, tangent is provided at the end of the pole profile (point B-C). The idea of using a short flat at the end of the pole profile (point C-D) as shown in Fig. 1 is to help to improve the physical measurement of the pole spacing.

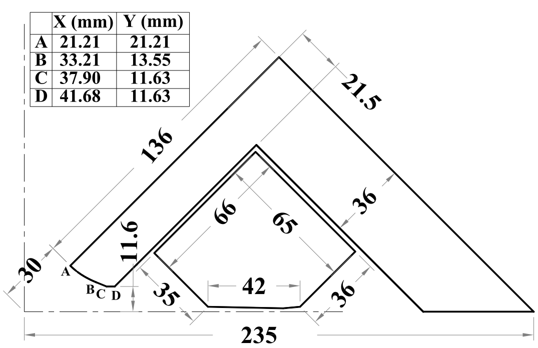


Figure 1: 1/8th Cross-section of magnet.

# ruwali@rrcat.gov.in

Owing to the symmetry, field calculation was carried out in 1/8th geometry. While designing the core cross-section, coil is kept sufficiently away from pole end so as to ease the replacement of nose pieces. The width of the nose piece is same as pole width while the height is 22 mm. The length of nose varies from 15 mm to 60 mm.

Table 1: Major parameters of the magnet

| Parameter | Value |
|---|---|
| Nominal Integrated Gradient | 2.5 T |
| Aperture radius | 30 mm |
| Iron length | 180 mm |
| Ampere-turns per pole | 5550 |
| No. of turns per coil | 370 |
| Resistance per coil | 0.6 Ω |

Figure 2 shows the magnetic field distribution along X-axis from centre. It is evident from the figure that the magnetic field component increases from the centre of the magnet linearly of the abscissa till 0.35 T and decreases to zero in the coil region. The magnetic field increases inside the iron yoke and becomes zero again outside the iron yoke thus indicating no leak field outside the iron yoke (iron yoke is up to 23.5 cm).

Figure 3 shows the nose piece with magnetic field superimposed on the iron surface. It is evident that the nose piece is not saturating. The length of nose piece is 30 mm each side. When the nose piece length is increased to 60 mm each side, saturation becomes predominant as evident from Fig. 4. For clarity, the coil is shown in one pole only in Fig. 3 and Fig. 4.

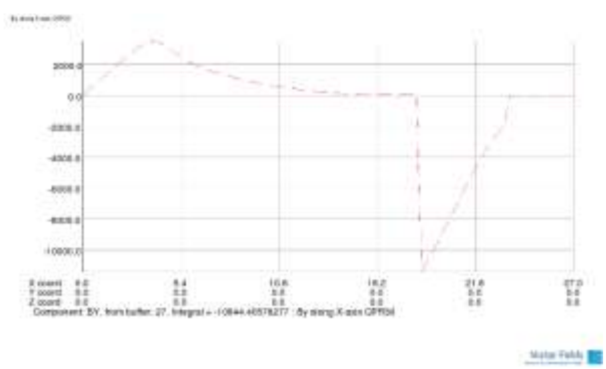

Figure 2: Magnetic field of the along X-axis.

## MAGNET DEVELOPMENT

Quadrupole magnet yoke is made from an assembly of four identical quadrants, fabricated using 40 mm thick low carbon (< 0.08 % C) steel plates. In order to achieve the required core length of 180 mm, 5 machined plates (both

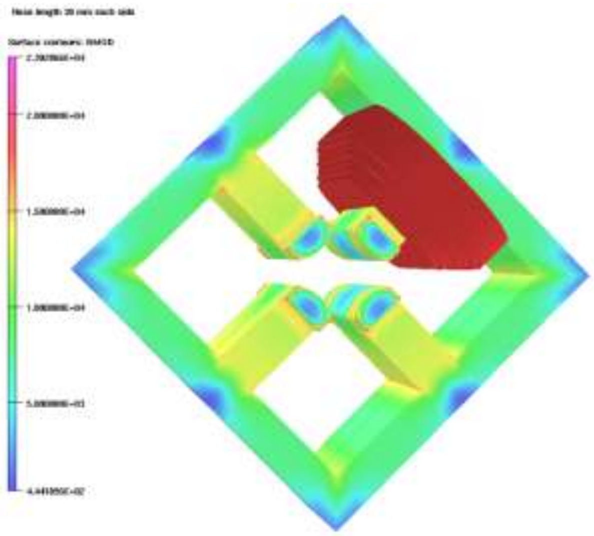

Figure 3: Magnetic model with nose not saturating.

sides) were stacked with an allowance of 2 mm at matting area and pole profile. These plates were then stacked, pressed using hydraulic press and then arc welding was carried out to get the core quadrant. A total of 4 such blocks were fabricated. The welded blocks were then machined at matting surface and pole profile using CNC milling machine. After ensuring the angular symmetry of the pole and aperture diameter to 60 ± 0.05 mm in the quadrupole magnet assembly, dowelling was done in magnet assembly for its repeatability & reproducibility for subsequent dis-assemblies/re-assemblies. Table 2 summarizes the

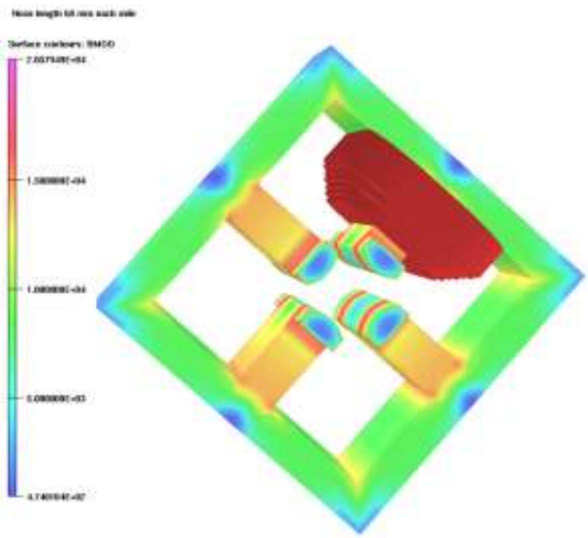

Figure 4: Magnetic model with nose saturating.

mechanical inspection report of the magnet.

The excitation coils are of air cooled type, wound from pre-insulated enameled copper strip of dimension 2 x 5 mm and varnished.

The nose pieces of length 15 mm and 30 mm were fabricated. One set of nose piece of length 15 mm were having chamfer of 5.82 x 5.82 mm. The nose pieces were upheld at pole using SS M6 bolts.

Table 2: Mechanical Inspection report

| Parameter | Value |
|---|---|
| Bore diameter | 60 ± 0.05 mm |
| Interpole distance | 23.27 ± 0.04 mm |
| Core length | 180 ± 0.03 mm |

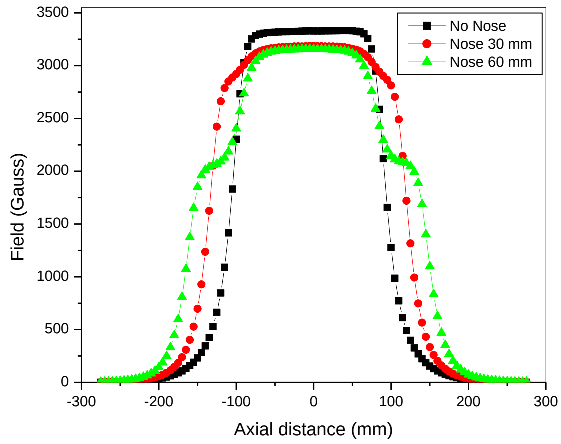


Figure 5: Measured field pattern along beam direction at a radial distance of 25 mm from the centre (x=0).

## MAGNETIC MEASUREMENT

Before carrying out the magnetic measurement (after adding/replacement of nose pieces), magnet was cycled 3 times (0 to 15 A) and measurements were carried out in forward direction of current only. In order to observe the hysteresis effect, the measurement was carried out in forward as well as in reverse direction.

The point by point magnetic field mapping was carried out with the help of a Hall probe attached to a Coordinate Measurement Machine (CMM) along the axial direction at different radial distance from magnet centre.

Figure 5 shows field pattern along axial direction at 5550 ampere turns with no nose and nose length of 30 mm and 60 mm. When the nose length is 60 mm, a prominent change in field pattern is observed where the nose piece starts which is attributed to the saturation of nose pieces as shown in Fig. 4. Only nose length of 60 mm is having a taper size of 5.82 mm x 5.82 mm.

The magnetic length, $l_{eff}$ was derived using

$$l_{eff} = \int B_y dl / B_0$$

The measured magnetic length and integrated field measured at a radial distance of 25 mm from magnet centre for different nose length measured at 5550 ampere turns are given Table 3. The increase in magnetic length and integrated field is 21% and 16% respectively when taper length is 30 mm. The decrease in gradient is 4.5% when nose length is 30 mm and becomes prominent on increasing the nose length.

The measured magnetic length is 213.1 mm with no nose and is independent of excitation level. The magnetic length decreases by 0.4%, 3.4%, 9% and 14.6% for nose length of

15 mm, 30 mm, 45 mm and 60 mm respectively with excitation from 1850 to 5550 ampere turns.

Table 3: Measured magnetic length and integrated field

| Steel length + Nose length (mm) | Magnetic length (m) | ∫Bydl (T-m) | Gradient (T/m) |
|---|---|---|---|
| 180 + 0 | 0.213 | 0.0703 | 13.35 |
| 180 + 15 | 0.239 | 0.0769 | 12.92 |
| 180 + 30 | 0.258 | 0.0820 | 12.74 |
| 180 + 45 | 0.268 | 0.0843 | 12.65 |
| 180 + 60 | 0.272 | 0.0858 | 12.63 |

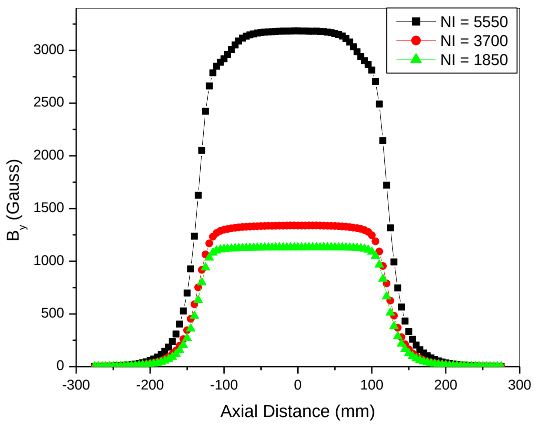


Figure 6: Axial field pattern with nose length 30 mm.

Figure 6 shows the magnetic field pattern along axial direction as a function of ampere turns for nose length of 30 mm. A gradual decrease in field along the axial direction was observed. This drop in magnetic field is dependent of excitation current as evident from Fig. 6 which ascertain saturation at nose pieces (NI=5500).

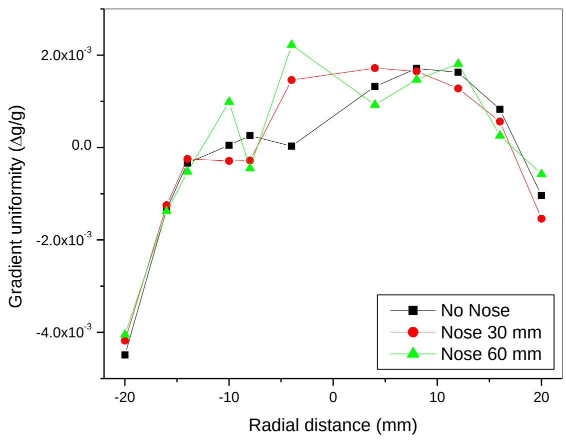


Figure 7: Gradient uniformity at magnet centre.

Figure 7 shows the measured gradient uniformity with no nose and nose length of 30 mm and 60 mm at 5550 ampere turns. The measured gradient uniformity is independent of excitation current.

The integrated gradient and higher order multipole measurements were measured using the rotating coil bench constructed by Danfysik model 690 [5]. The rotating coil of measuring radius 25.6 mm and 15 mm were used. The measuring length of the rotating coil is 550 mm. Magnetic measurements were measured up to 15A at a step of 1A. The transfer function plot is shown in Fig. 8.

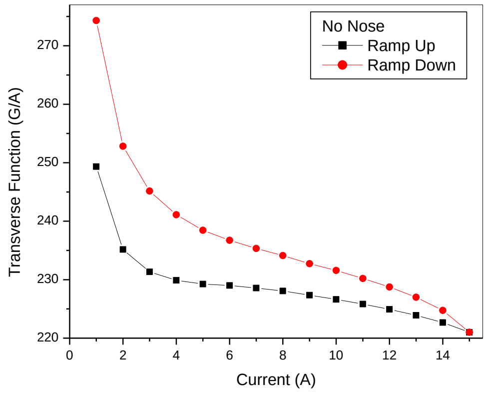


Figure 8: Transfer function plot.

Figure 9 shows the difference of integrated Dodecapole component with no nose and nose of different length. It is evident that no significant difference is observed on strength on adding nose of different length. Similar pattern was observed to other multipoles also.

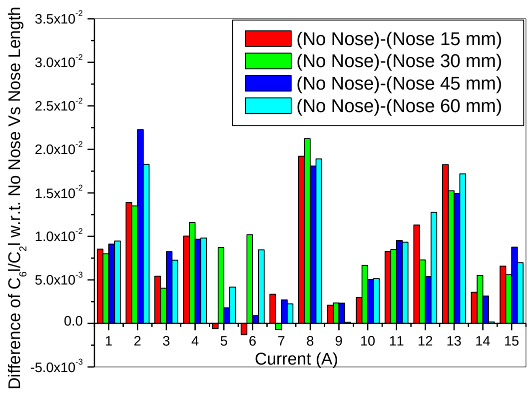


Figure 9: Dodecapole multipole dependence on nose length as a function of excitation current.

## REFERENCES


[1] R. Gupta, A. Jain, “Special magnet designs and requirements for next generation light sources”, Proc. PAC09, TU1RAI01, 614-618.

[2] Kailash Ruwali, Ritesh Malik, Gautam Sinha, “Design of Nose type magnets”, InPAC 2018 proceedings.

[3] POISSON Group of Codes, Los Alamos National Laboratory, New Mexico, 86545.

[4] Vector Fields Limited, 24 Bankside Oxford, OX5 1JE. Kidlington, England.

[5] Harmonic Bench Model 690, Danfysik, Denmark.

# DEVELOPMENT OF ASYMMETRIC SECONDARY COLLIMATOR FOR DUAL MODE RADIOTHERAPY LINAC AT SAMEER

Paresh M. Jadhav†, Sandeep S. Name, Ganesh Gaikwad, Mandar Vidwans and Sanjay Pethe
Society for Applied Microwave Electronics Engineering and Research (SAMEER),
IIT Campus, Powai Mumbai 400 076 India
†: pareshmjadhav@gmail.com

*Abstract*

SAMEER is developing a Dual Mode Dual Energy linear accelerator for radiotherapy. The system is designed to deliver photon output with energy of 6 and 15 MV. In the electron mode, the output energy will be 6, 9, 12, 15 & 18 MeV. Asymmetric secondary collimator is one of the important component of the system. It is used to shape the beam in the required rectangular size with field size ranging from 0 x 0 cm to 35 x 35 cm at iso-centre. The radiation outside of this field is absorbed by Tungsten jaws. We have successfully developed this system as per requirement. In this paper, design methodology used during development of Asymmetric secondary collimator is discussed. The complete system was assembled and tested at SAMEER, Navi Mumbai.

## INTRODUCTION

SAMEER has developed 6 MeV Linear accelerators for radiotherapy under Jai Vigyan program [1, 2]. These radiotherapy units have treated thousands of patients till date at MGIMS hospital, Wardha, Cancer Institute, Adyar, Chennai, Head & Neck Cancer Institute, Indore and Amravati Cancer Foundation, Amravati. The technology of 6 MeV radiotherapy units has been transferred to industry for production. As advancement to this technology, SAMEER has taken up a project to develop a Dual Mode Dual Energy linear accelerator for cancer therapy. The main feature of this development is to produce clinically acceptable quality electron beam and photon beam.

We developed secondary collimator for the 6 MeV electron accelerator. The asymmetric secondary collimator for 15 MeV machine is improved version of 6 MeV collimator. It has feature of dynamic wedge. Also it has upper jaw asymmetric with zero cross-over of 11 cm measured at iso-centre. All servo motors were replaced by stepper motor. It has a double feed-back system. Zero sensing precision limit switch, rotary optical encoders and linear potentiometer for absolute feed-back of jaw position are incorporated. It can give maximum 40 x 40 cm field size with clipped corner.

## CONCEPTUAL DESIGN

Fig 1 shows design methodology used during design of asymmetric secondary collimator. In this particular case of medical accelerators, the penumbra of 1 cm for a field size 10 x 10 cm at the iso-centre is permissible as per AERB Standards [3]. Hence to fulfil this requirement, the meeting faces of jaws always need to be along the radii drawn from virtual target. This condition must be satisfied for all jaw openings. To achieve this, locus of all points at various angles from virtual target keeping meeting face of the Tungsten jaws parallel to the beam was traced. Using this locus, design of guiding slots for jaws was done.

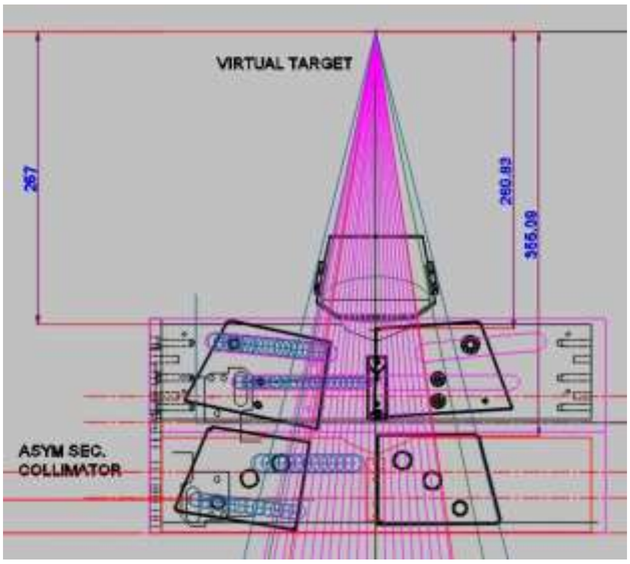


Fig 1: Design methodology of secondary collimator

This secondary collimator has four independent motors and 4 pairs of ball screws. The collinear ball screws of adjacent jaws were made in such a way that they will fit concentric to each other with concentric needle bearing. To accommodate needle bearing and to take additional load of larger zero crossing upper jaw, the diameter of ball screw ($d_m$) was increased to M20 from M16. Overall size of secondary collimator was also increased to accommodate additional feed-backs.

The general arrangement of secondary collimator is shown in the Fig. 2

It is of the dimension 630 mm x 630mm x 300mm. it has 2 pairs of independently moving Tungsten Copper jaws each having weight of 40 kg. The gross weight of total the system is about 220 kg. The entire secondary collimator can be fitted on the system with cross roller bearing in between. It can be rotated about its vertical axis as well as the horizontal axis of the gantry. All the power and signal connections were collected on D-type connector to communicate with Programmable Logic Controller.

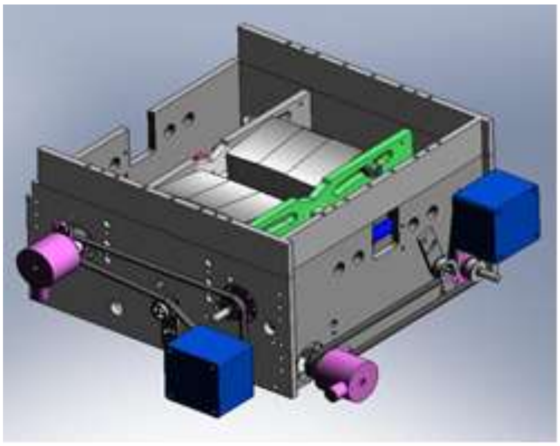

Fig 2: General arrangement of secondary collimator

For motor torque calculation, following data was considered.

Table No 1: Design Parameters

| Parameter | Value |
|---|---|
| Weight of jaw (W) | 40 kg |
| M20 ball screw diameter ($d_{m)}$ | 20 mm |
| Ball screw pitch | 5 mm |
| Actual jaw speed | 5mm / sec |
| Co-efficient of Friction between nut and screw(μ) | 0.1 |

Following formulae were used in motor torque calculation [4].

Friction angle $\Phi = \tan^{-1}(\mu)$ (1)
Helix angle $\alpha = \tan^{-1}(\text{Lead} / \pi * d_m)$ (2)
Motor speed = Jaw speed / screw pitch (3)
Motor torque($M_t$)= $W*\tan(\Phi+\alpha)*(d_m/2)$ (4)

After doing calculations, motor speed required was calculated as 60 rpm.
Motor torque required = 1.4 N-m for Factor of safety 2. Based on this calculation and keeping reserve torque on account of friction in the slots, Stepper motor of NEMA frame size of 34 having torque of 3.88 N-m was selected.
In case of secondary collimator, all the measurements are done at 1 meter distance from Virtual Target i.e. at Iso-centre but actual moving part of the collimator is at one third distance from this. Hence all the inaccuracies related to collimator are amplified to approximately 3 times. Keeping view of this, all the feedbacks used are very precise and with raesonable linearity. 24 bit multi-turn optical encoders are also used as a second feedback. For absolute zero positional feedback, special precision limit switch is incorporated. It enables collimator to auto calibrate itself every time it is turned on. For quieter operation, conventional chain driven system was replaced by timing belt driven system. In this collimator, we have used stepper motor instead of geared servo motor as in case of 6 MeV secondary collimator. The reasons being geared servo motors are noisy and produce back-lash due to gear box. Also they do not hold their position. All these disadvantages were countered by use of direct driven stepper motor with micro stepping drive. The dynamic wedge feature require programmable and precisely controlled jaw motion. Stepper motor is best suited for such application.

## METHODS

Salient features of Asymmetric Secondary collimator are as follows.

1. Max. Field size of 40x40 cm with clipped corner at Iso-centre.
2. Max. rectangular field size of 35x35 cm at Iso-centre
3. Dynamic wedge feature.
4. Zero cross-over of 11 cm for upper jaw measured at Iso-centre.
5. Use of stepper motor with micro-stepping drive.
6. Double feedback from linear potentiometer and multi-turn optical encoder.
7. Use of precision limit switch for absolute zero positional feed-back.

Actual assembly of Asymmetric Secondary collimator is shown below.

Fig 3: Actual assembly of Secondary collimator

Entire machining of components was outsourced. Assembly of asymmetric secondary collimator was done in-house. Wiring and control part was done in-house. For testing it was kept on a specially designed working table. Field optics light was projected from the top of the collimator from the calculated distance to simulate the beam. A graph paper was placed at a distance of 1 metre from Field optics to get various field sizes. The secondary collimator was run for rigorous test. After ensuring that it is running smoothly, it was calibrated for various field sizes. For it, the jaws were opened to get standard field sizes as per data from 3D model. Field sizes were measured using scale on the graph paper and the reading of both the feed-backs was recorded. We compared these actual readings with theoretical one. We repeated readings to know its repeatability. After this exercise, a look up table was generated for major readings of feedback. Intermediate readings can be calculated using interpolation. With this table, we calibrated our system and did our programming accordingly.

After this independent testing, asymmetric secondary collimator was mounted on the gantry to know its performance at various inclinations. The collimator was found working smoothly. We measured variation of readings of feedbacks due to gravity effect and applied window of tolerances for readings. After this elaborate testing asymmetric secondary collimator was integrated with our system.

## RESULTS

The readings of Linear Potentiometer for various field sizes were recorded. Similarly, readings of Rotary Encoder for various field sizes were also recorded. Encoder serves as second feed-back. The readings were plotted on Graph 1, 2, 3 and 4. In the Graph, these readings are superimposed on theoretical values to know deviation. Based on the maximum deviation, tolerance on acceptable value of feed-back was decided. It helps in health monitoring of the system. The graph shows the feed-back values are well in agreement with theoretical one.

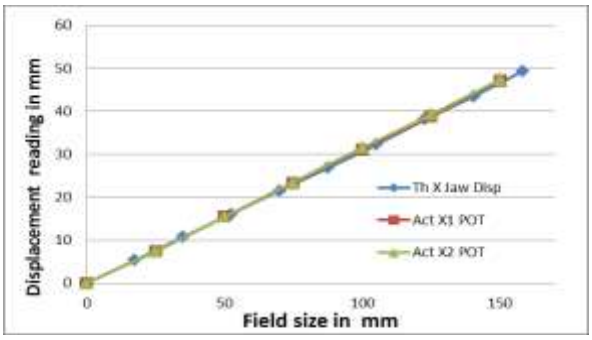


Graph 1: Upper Jaw Linear Potentimeter readings

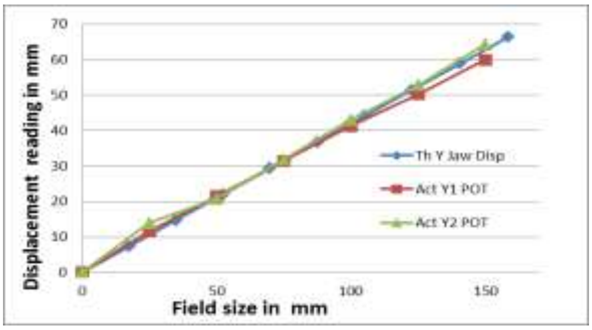


Graph 2: Lower Jaw Linear Potentimeter readings

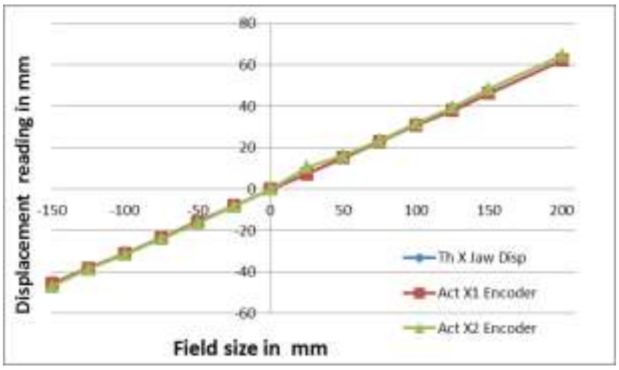


Graph 3: Upper Jaw Encoder readings

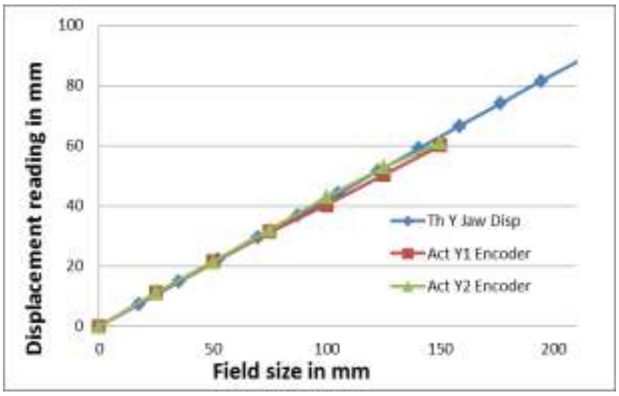


Graph 4: Lower Jaw Encoder readings

## DISCUSSION

In this way asymmetric secondary collimator for Dual Mode Radiotherapy LINAC was developed. This methodology can be used in the development of any digitally controlled system. Solidworks 3D software and Autocad were used in the design. The assembly was designed, assembled and tested at SAMEER, Navi Mumbai. We successfully calibrated and integrated it with the system.

## REFERENCES

[1] R Krishnan, A.P. Deshpande, T.S. Dixit, S. T. Chavan, C.S. Nainwad, S.N. Pethe, T.Tiwari, Proceedings Particle accelerator conference, FR5REP083 PAC’09 held at Vancouver, BC, Canada

[2] T. Dixit, R Krishnan, A.P. Deshpande, S. Chavan, C.S. Nainwad, S.N. Pethe, T.Tiwari, M.M. Vidwans, K.A. Thakur, , Proceedings of International Particle Accelerator Conference IPAC’10, Kyoto, Japan

[3] AERB Safety code No. AERB/RF-MED/SC-1 (Rev-1) March 2011

[4] V. B. Bhandari “Design of machine elements” Publication Tata McGraw Hill 2002

# LOCAL SHIELDING DESIGN FOR 30 MEV LINAC USING FLUKA

Nirupama Upadhyay*[1], Abhay Deshpande[2], K. Biju[3], Sajeev Chacko[1], Tanuja Dixit[2], R. Krishnan[2], Paresh Jadhav[2]
[1]University Department of Physics, Mumbai University,
[2]Society for Applied Microwave Electronics Engineering and Research (SAMEER), Mumbai
[3]Bhabha Atomic Research Centre, Anushaktinagar, Mumbai

*Abstract*
Technetium-99m ($^{99m}$Tc) is a widely used radioactive tracer. Traditionally, it is produced from Uranium via $^{235}$U (n, f) $^{99}$Mo reactions which depends heavily on nuclear reactors. Design studies for an alternative, cleaner approach using electron linac were initiated at SAMEER to generate $^{99}$Mo [1]. We designed a 30 MeV linac with an average current of about 350 μA at the exit of the linac. This electron beam will hit a convertor target and generate bremsstrahlung X-rays which will be bombarded on to $^{100}$Mo target to generate $^{99}$Mo. $^{99m}$Tc will be eluted from this radioactive Molybdenum.
The shielding methodology was studied to ensure safety to operator and vicinity. The existing radiation facility at SAMEER will be used with additional local shielding. We studied the (e, γ) mechanism to understand the outgoing bremsstrahlung pattern. Lead shielding is provided to ensure that the radiations are contained inside the radiation area. Lead shielding of 36 cm reduces the photon dose to permissible dose limit outside the concrete walls. Neutron flux is expected in the process and hence shielding study of neutron was also undertaken. A local shielding of HDPE and borated HDPE is proposed to help thermalize the neutrons and subsequently shield. We studied various combination and found that a combination of 39 cm of HDPE with 13 cm of 5% borated HDPE and 0.3 cm of 40% borated rubber sheet is sufficient to bring the neutron dose within the safety limits. FLUKA code was used for simulating the problem geometry and study the particle distributions at various locations with and without shield [2]. The detectors were defined using USRBIN, USRBDX and USRYIELD cards to get the particle fluence and dose values. It was found that the predictions done using FLUKA code are in agreement to the estimates obtained from analytical studies.

## INTRODUCTION

The need for particle accelerators is growing in the country mainly due to various applications in research and civilian society. In particular, the therapeutic use of electrons, protons, ions and X-rays for cancer therapy has enhanced the interest in designing and installing accelerators at various hospitals. In past decade, the number of working medical accelerators has increased substantially.
But before the treatment comes the diagnostics where radioisotopes play a crucial role. Clinical diagnosis depends heavily on imaging. Technetium-99m ($^{99m}$Tc) is a widely used radioactive tracer. Traditionally, it is produced from $^{235}$U (n, f) and $^{99}$Mo which is heavily dependent on nuclear reactors. A cleaner alternative is to explore accelerator based mechanism to generate $^{99}$Mo.
At SAMEER we are designing and developing a two stage acceleration technique to achieve a 30 MeV electron beam with an average current of about 350 μA at the exit of the linac [1]. This electron beam will hit a convertor target and generate bremsstrahlung X-rays which when bombarded on to $^{100}$Mo target will generate $^{99}$Mo and thereafter $^{99m}$Tc.
To host the accelerator, a shielded room is needed. Hence, we study the (e, γ) mechanism to find out the nature of outgoing bremsstrahlung pattern. Based on this, local lead shielding has been designed. As the energy of the electrons is large, high neutron flux will be generated. Hence, shielding study of neutron has also been done based on which, local HDPE shielding has been finalized.
The radiation field of electron accelerator includes several components such as bremsstrahlung photons, fast neutrons, positrons, etc. The production and transport of all these radiations through different targets is difficult to study, theoretically even on the basis of correct experiments. Therefore, simulations with an effective Monte Carlo code are very helpful to get information of all the particles produced in an accelerator head.

## METHOD OF CALCULATION

We have used FLUKA which is a Monte Carlo code that can simulate transport and interaction of electromagnetic and hadronic particles in any target material over a wide energy range [2]. A 30 MeV electron beam is incident on a tungsten target. The target is placed inside a local shield cube, which has a lead block surrounded by HDPE, on all sides.
We define a 0.6 cm thick cylindrical tungsten target with 0.3 cm radius. The local shielding cube consisting of lead and HDPE are defined as rectangular parallelepiped. The lead block has a thickness of 6 TVL in front direction. This lead block is surrounded by a 3 TVL regular HDPE and 1 TVL borated (5%) HDPE. In addition, a 0.3 cm thick borated (40%) rubber sheet is defined as the last layer of shielding cube. We use USRBIN, USRBDX and USRYIELD cards to define the detectors to score fluence and dose. Spatial distribution of fluence and dose was scored using USRBIN. The angular distribution of fluence was scored using USRYIELD from which we

*nirupama263@gmail.com; abhaypd@gmail.com

have calculated dose rates. The no. of primaries run are set to $10^6$.

## VALIDATION

Fig. 1 and 2 show the comparison of angular distributions of the dose rates contributed by photons emitted from tungsten and copper targets respectively. The targets were bombarded by 18 MeV, 28 MeV and 38 MeV electrons and the photon dose rates were calculated [3]. The dotted lines are from the Kosako's work whereas for similar parameters our work is represented using bold line. It can be seen that for Tungsten as well as Copper target the simulation methodology yields similar results with permissible deviation of less than 10%.

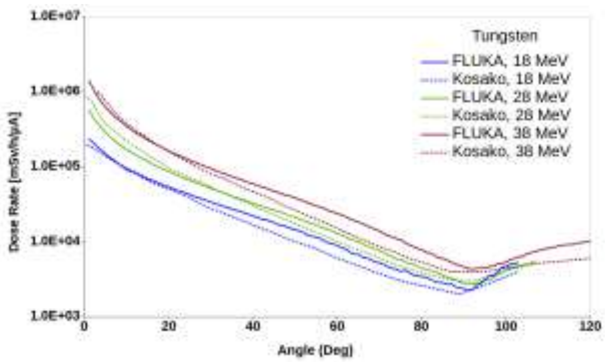


Fig. 1: Comparison of photon dose rate for Tungsten target

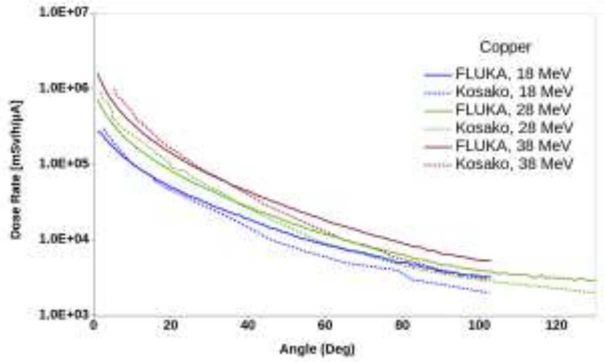


Fig. 2: Comparison of photon dose rate for Copper target

## RADIATION SHIELDING PARAMETERS

### *Source Term*

For radiation protection, conservative practice is to assume the bremsstrahlung output and neutron yields from an optimal thick target. Table 1 gives the bremsstrahlung output and photo neutron yield values from thick target [4].

### *Tenth Value Layers*

Table 2 presents the tenth value layer of bremsstrahlung and the neutron tenth value layer corresponding to fission spectra (average energy 2 MeV) in lead, HDPE and concrete [4].

Table 1: Source Term for Thick Target

| **Energy (MeV)** | **Target** | **Bremsstrahlung Output-Forward ($Gy/h/m^2/kW$)** | **Photo neutron Yield (n/s/kW)** |
|---|---|---|---|
| 30 | Tungsten | 8500 | 1.8E+12 |
| 30 | Copper | 3540 | 5.0E+11 |

Table 2: Tenth Value Layer

| **Material** | **TVLs for photons (cm)** | **TVLs for neutrons (cm)** |
|---|---|---|
| Lead | 5.3 | 88 |
| HDPE | 92 | 13 |
| Concrete | 53 | 27 |

### *Shielding*

The local shield of the target consists of 36 cm of lead in beam direction whereas 150 cm on all other sides. A 39 cm of regular HDPE with 13 cm of 5% borated HDPE surround the lead block. A sheet of 0.3 cm of 40% borated rubber layers the HDPE block and concludes the local shield. The local shielding cube is enclosed by concrete walls on all sides with a thickness of 265 cm in the forward direction.

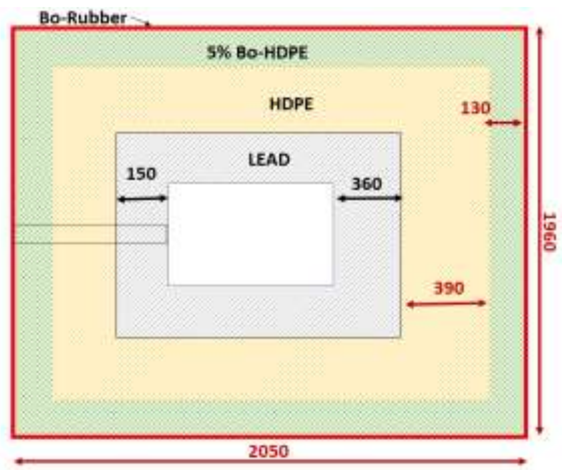


Fig. 3: Local Shielding Cube (Dimensions in mm)

## RESULTS AND DISCUSSION

Fig. 4(a) and 4(b) show the spatial distribution of photon dose outside the concrete walls for tungsten and copper targets respectively. We can see that there is negligible photon dose outside the walls in both the cases which is in agreement with the radiation safety limit of 0.1 μSv/h.

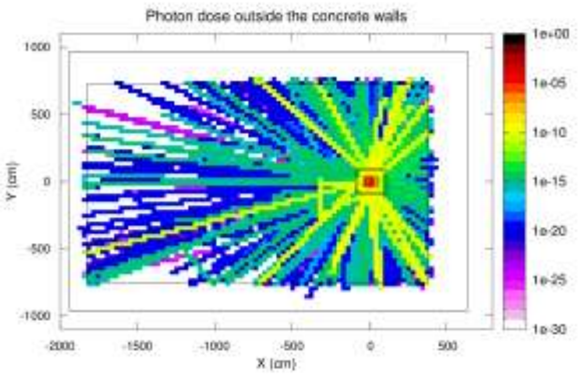


Fig. 4(a): Photon dose outside concrete walls for tungsten target

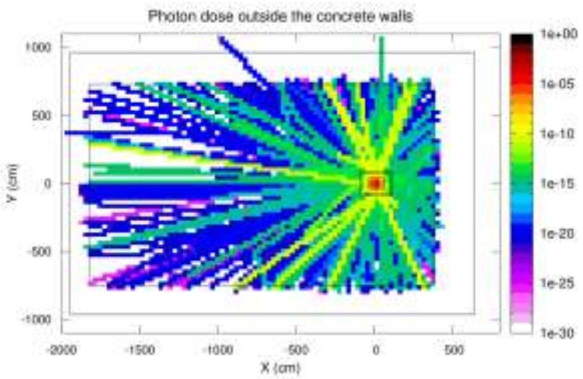


Fig. 4(b): Photon dose outside concrete walls for copper target

Fig. 5(a) and 5(b) show the spatial distribution of neutron dose inside the boron rubber sheet, which is the last layer of the local shielding cube, for the tungsten and copper targets respectively. In both the cases, there is no radiation leakage outside the concrete walls as the neutron dose is contained well within the walls.

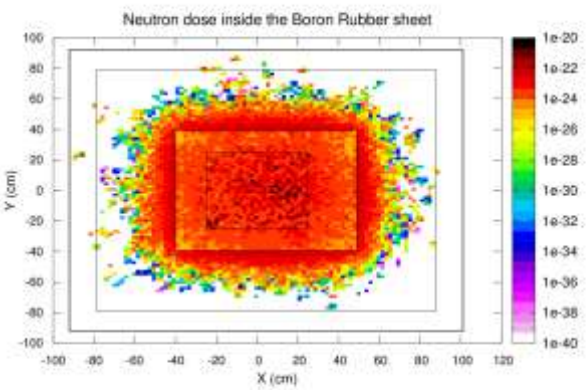


Fig. 5(a): Neutron dose inside boron rubber sheet for tungsten target

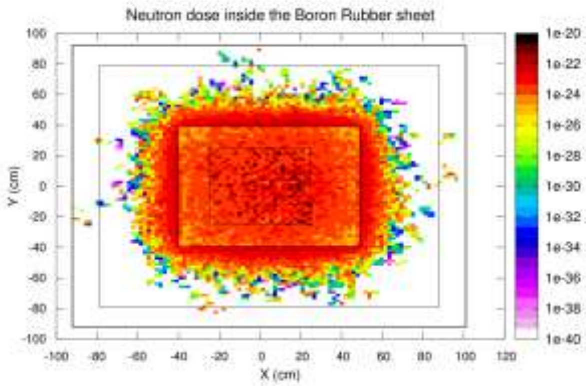


Fig. 5(b): Neutron dose inside boron rubber sheet for copper target

Based on the results, it was concluded that such a local shielding cube can be effective in reducing the leakage radiation to attain safety limits for operation.

## REFERENCES

[1] A. Deshpande, Tanuja Dixit et al, "Status of Linac based Radio Isotope Generation", Proceedings of Indian Particle Accelerator Conference InPAC 2017, Indore.

[2] A. Ferrari, P.R. Sala, A. Fasso`, and J. Ranft, "FLUKA: a multi-particle transport code" CERN-2005-10 (2005), INFN/TC_05/11, SLAC-R-773.

[3] Kazuaki Kosako, Koji Oishi, Takashi Nakamura, Masashi Takada, Kouichi Sato, Takashi Kamiyama & Yoshiaki Kiyanagi (2010) "Angular Distribution of Bremsstrahlung from Copper and Tungsten Targets Bombarded by 18, 28, and 38MeV Electrons" Journal of Nuclear Science and Technology, 47:3, 286-294.

[4] National Council on Radiation Protection and Measurements, Radiation Protection for Particle Accelerator Facilities, NCRP Report No. 144 (2003).

# Design and development of ethernet enabled high stability bipolar voltage reference for HV power supplies.

Gurupreet Singh*, Apollo Kasliwal and S. R Tiwari
Accelerator Power System Division, Raja Ramanna Center for Advanced Technology, Indore
* *gurpreet@rrcat.gov.in*

*Abstract*

This paper proposes the design and development of an ethernet enabled highly stable and high resolution analog voltage reference to be used for highly stable power supplies being developed for linear accelerators at RRCAT. It has been developed by using a SPI bus (synchronous serial communication interface) between 20 bit digital to analog converter (DAC) AD5791 of analog devices and 32 bit ARM cortex M4 microcontroller of texas instrument. The data transfer of 20 bit DAC over 16 bit SPI bus has been implemented using bifurcation techniques. The SPI is a high-speed synchronous serial input/output port that allows a serial bit stream of programmed length (2 to 16 bits) to be shifted into and out of the device at a programmed bit-transfer rate. It has been controlled by LabVIEW based user interface which communicates with microcontroller by using TCP/IP protocol through Ethernet port. Ethernet is a branching broadcast communication system for carrying digital data packets among locally distributed network devices. TCP/IP protocol is an industry–standard model and open protocol suite that can be effectively deployed in practical networking application. Main application source code and TCP/IP stack which is a vital element of the system software have been developed in C. The source code includes development of library for command sets for initialization and communication with DAC. A separate Internet protocol (IP) address was assigned to microcontroller for establishing communication link between PC and microcontroller. Hercules utility was also used for establishing and verifying the communication between microcontroller and DAC. Several methods have been followed for lossless transmission of data packet to DAC & are discussed in this paper..

## INTRODUCTION

In analog world all electronic devices must interact with real world gadgets like auto, microwave, smart TV or cell phone. To do that it must be able to map real world measurement (speed, pressure, length) to a measureable quantity in the electronic world (voltage). Of course, to measure voltage, it needs standard to measure against. That standard is voltage reference. It is a circuit element which provides a known potential as long as circuit require it. Voltage references come in many forms and offer different features, but in the end, accuracy and stability are a voltage reference's most important features, as the main purpose of the reference is to provide a known output voltage. Variation from this known value is an error. Now, high voltage power supplies used in linear and circular accelerators need to be controlled from remote location by means of various standards like RS485, RS232 and ethernet. This work involves the development of a TCP/IP (Transmission Control Protocol / Internet Protocol) based remote (Ethernet) controlled 5 ppm voltage reference to control and monitor the high voltage power supplies. As the need for faster and reliable data transfer has increased, Ethernet has provided means for handling this higher speed and high reliability with error handling capability. Ethernet's popularity has reached to the point that almost all traffic on the Internet originates and terminates with an Ethernet connection [2]. It defines data link and physical layers of the OSI (Open Systems Interconnect) reference model whereas TCP/IP defines network and transport layer of the same model. TCP/IP is a network protocol which allows one computer to talk to another computer via the internet through compiled packets of data and sending them to right location. It is designed such that each computer or device in a network has a unique IP Address and each IP address can open and communicate over up to 65535 different "ports" for sending and receiving data to or from any other network [3].

## HARDWARE DESCRIPTION

The overall system architecture which consists of three major parts is shown in figure 1 as a block diagram.

- Microcontroller based development board.
- DAC (Digital to analog converter) board.
- HV power supply

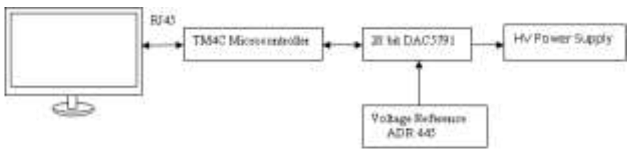


Figure 1: Block Diagram of system

### *Microcontroller based development board.*

Microcontroller has been essential part of the modern era technology which gives developer a flexibility to program the solution of a problem. In our application TM4C129nxzad microcontroller of Texas Instruments has been used which has the 10BASE-T/100BASETX ethernet controller with internal PHY, 12-bit Analog-to-Digital Converter (ADC), LCD controller, and the I2C module. It also has QSSI module which acts as a master or slave interface for synchronous serial communication with peripheral devices that have either SPI, or any other synchronous serial interfaces. The QSSI performs serial-to-parallel conversion on data received from a peripheral device. The transmit and receive paths are buffered with internal, independent FIFO memories allowing up to eight 16-bit values in Legacy mode and 8-bit values in Advanced, Bi-, and Quad-modes. The data transfer between microcontroller and 20 bit DAC has been implemented using QSSI module in advanced mode. The SPI or QSSI is a high-speed synchronous serial interface which allows transfer of serial bit stream of 2 to 16 bits to master or slave. The TM4C129nxzad microcontroller has inbuilt ethernet controller which supports 10/100 Mbps data transmission rates. The ethernet controller is made of clock control, DMA controller, MAC (Media Access Controller), TX/RX controller and PHY interface. MAC is the interface between physical layer and upper layers of OSI, This layer handles a lot of crucial tasks and as mainly responsible for error-handling, frame delimiting, identifying, transparent data transfer of LLC PDUs. In the application layer, the main challenge is dynamic IP address assignment, which is solved by lwip protocol stack. After obtaining the address, a simple TCP client-server socket application is implemented. For efficient and lossless transmission 4 byte of CRC (Cycle Redundancy Check) has been added in the end of data packet coming from upper layer. CRC is a polynomial-based block coding method for detecting errors in blocks or frames of data. A set of check digits is computed for each frame scheduled for transmission over a medium that may introduce error and is appended to its end.. The computed check digits are known as the frame check sequence (FCS). A CRC value is calculated as a remainder of the modulo-2 division of the original transmitted data with a specific 32 bits CRC generator because Ethernet uses CRC32 [1]. It is added to detect errors occurring during transmission or retrieval. If the CRC value calculated over the incoming frame matches the CRC residue then the frame is treated as error free.

Main application source code which is a vital element of the system software has been developed in C. It includes development of TCP/IP interface component using C socket library which contains function responsible for creating TCP/IP sockets for client server applications. The TCP/IP interface component binds component to its designated IP address and port number which ensures no traffic congestion. Rx and TX buffer has been used to get data and transmit data[5]. Hercules application has been used for transmitting data from desktop PC to TM4C129nxzad microcontroller and for receiving data from TM4C129nxzad microcontroller. It also has been tested with LabVIEW based user interface.

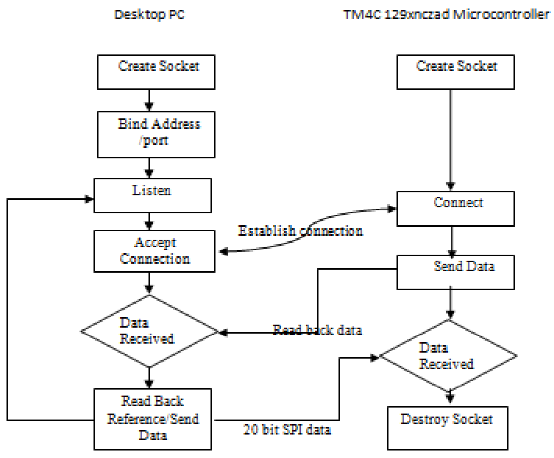


Figure 2: Flow chart of TCP/IP routine

At the microcontroller side as shown in figure 2, TCP/IP socket is created and listen the port for incoming connections. Once it connected then it starts communication with desktop PC.

### *DAC (Digital to Ana log converter) board*

The AD5791 of analog devices has been used for generating voltage reference for high voltage power supply. It is a high accuracy, fast settling, single, 20-bit, serial input and voltage output DAC device. It has very low noise of 0.6-µV peak-to-peak in the 0.1-Hz to 10-Hz frequency band and better than 0.1-ppm long-term stability over 1000 hours. It offers ±1 LSB INL and ±1 LSB DNL performance. It is designed to meet the requirements of precision control applications. Its features have been shown in Table 1.

Table 1: AD5791 Specifications

| **Property** | **Value** |
|---|---|
| Accuracy | 1ppm |
| Temperature Drift | 0.05 ppm/°C |
| Noise Spectral Density | 7.5 nV/√Hz |

It uses a versatile 3-wire serial interface that operates at clock rates up to 35 MHz and that is compatible with standard serial peripheral interface (SPI). The output range of the AD5791 is configured by two reference voltage inputs. External voltage reference to AD5791 is supplied by the ADR445 daughter card which offers ultralow noise, high accuracy, and low temperature drift performance. The voltage supplied by the voltage reference is gained up and inverted to provide the positive and negative reference voltages required by the AD5791.

Figure 3: Circuit arrangement

During initialization it goes into known output impedance state and remains in this state until a valid write to the device takes place. After initialization a 24 bits SPI data from microcontroller is transferred to the input shift register of AD5791. Data is loaded into the device MSB first as a 24-bit word under the control of a 35 MHz serial clock input. The input register consists of a R/W bit, three address bits, and twenty register bits. Each falling edge of the update clock starts the procedure of sending a new code, through the SPI interface, to the AD5791 and the rising edge updates the voltage at the AD5791 output.

## RESULT

Due to maximum 16 bits transfer limit. In our case for transferring 20 bits to DAC AD5791 bifurcation techniques has been used as shown in figure 4. It takes 3 cycles of 8 bits and transfers 24 bits meanwhile chip selects remains low for these cycles.


Figure 4: SPI data output from TM4c129xnczad

An open source application Hercules was used to establish connection with the microcontroller. After entering IP address and port number it connects with microcontroller and data transfer process initiated and is measured.

## CONCLUSION

This work describes the development of highly stable reference for precise power supplies through TCP/IP. Microcontroller communicates with the DAC board AD5791 using 24 bits SPI and generates reference for high voltage power supply. For communicating with microcontroller from desktop PC Hercules application was used and later it was verified with LabVIEW software also.

## ACKNOWLEDGEMENT

Authors are sincerely thankful to Mr. Vishnu K. Gauttam, Mr. Amit Sahu and Mr. Deepak Kumar for their help in testing voltage reference with high voltage power supplies.

## REFERENCES

[1] Charles M. Kozierok, “The TCP/IP Guide: A Comprehensive, Illustrated Internet Protocols Reference”, First edition, No Starch Press, san fransisco,2005.

[2] Jan Axelson, “Embedded ethernet and internet complete”, First edition, Lakeview Research, New york, 2003.

[3] *Dhananjay V. Gadre*, *Sarthak Gupta*, “Getting Started with Tiva ARM Cortex M4 Microcontrollers: A Lab Manual for Tiva Launch_Pad Evaluation Kit”, First edition, Springer India, 2018.

[4] Maria Rita Palattella,Nicola Accettura, Xavier Vilajosana, Thomas Watteyne, Luigi Alfredo Grieco, Gennaro Boggia, Mischa Dohler,"Standardized Protocol Stack for the Internet of (Important) Things", Communications Surveys & Tutorials, IEEE, vol. 15, pp. 1389-1406, 2013.

[5] Mr. Suyog A. Wani, Prof. R. P. Chaudhari, Ethernet Enable Digital I/O Control in Embedde d Systems", ICCEET 2012, Government College of Engineering, pp. 634-637, 2012.

# DESIGN OF COMPACT SEXTUPOLE MAGNET USING PERMANENT MAGNETS

Gautam Sinha, Ritesh Malik, Kailash Ruwali and S. N. Singh,
AMTD, Raja Ramanna Centre for Advanced Technology, Indore 452013

*Abstract*

Recently sextupole magnets of gradient 900-2200 T/mm$^2$ is proposed for the high brilliance storage ring. Keeping this in mind, sextupole magnets with gradient ranging from 1335 T/mm$^2$ to 2621 T/mm$^2$ are designed using permanent magnets (PMs). Bore radius are in the range of 25 mm to 23 mm. It is possible to calculate the magnetic field produced by PMs of finite dimension analytically. To do this equivalent charge distribution model is used and the mathematical expression of the field produced by a magnet is derived. Necessary condition to generate sextupole field using several PMs is derived. General field expression of multipole magnet is used to estimate the higher order multipoles. Effective length and other important parameters are also calculated. To verify the analytical expression simulation studies using FEM code is done.

## INTRODUCTION

Storage ring is a particle accelerator where charged particle beam revolves inside vacuum chambers guided by magnetic field. Large numbers of various magnets are used in the ring to confine the beam on the desired orbit. Sextupole magnets are used in storage ring to correct the chromaticity and to control nonlinearity in order to have large dynamic aperture. High brilliance storage ring uses sextupole magnets in the high β location for efficiently correcting the chromaticity [1]. Different families of sextupole having gradient 900-2200 T/mm$^2$ is proposed for such ring [2]. Permanent magnet (PM) based modular design of magnet is preferred for series production of such magnets.

## THEORY

In this section, field expression of cylindrical shaped PMs of finite dimension is evaluated analytically. To do this equivalent charge distribution model is used and the mathematical expression of the field produced by a magnet is derived. Magnetic field in the charge free region can be obtained by scalar potential, $\Phi_m$, formalism using the relation $\vec{B}(\vec{r}) = -\mu_0 \nabla \Phi_m(\vec{r})$. Potential can be expressed for magnetisation, $\vec{M}$ and volume v $\Phi_m(\vec{r}) = \int G(r, r') \nabla' . M(r') dv' = -\frac{1}{4\pi} \int \frac{\nabla' . M(r')}{|r - r'|} dv'$ where $r'$ the source and $r$ the observation points. Other operates are having usual meanings.

Integration is to be performed over the volume where magnetisation exists. Using divergence theorem, this can be simplified as $\Phi_m(\vec{r}) = \frac{1}{4\pi} \int_s \frac{M(r').n}{|r - r'|} ds'$ here surface, s, bounded by volume v, and $n$ is normal to surface. Here, surface charge density is related with magnetisation by $\sigma_m = M.n = M_s x. \hat{\mathrm{r}}$. Therefore, the magnetic field can be expressed as

$$\vec{\mathrm{B}}(\vec{r}) = -\frac{\mu_0}{4\pi} \int_{z_1}^{z_2} \int_0^{2\pi} \nabla \left( \frac{M_s \cos(\phi')}{|r - r'|} \right) a d\phi' dz',$$

where the magnet extends along z, from $z_1$ to $z_2$ and having radius of a. The radial component of the magnetic field $B_r$ is

$$B_r(r, \phi, z) = \frac{\mu_0 M a}{4\pi} \int_{z_1}^{z_2} \int_0^{2\pi} \cos(\phi') \left\{ r - a\cos(\phi - \phi') \right\}$$
$$\left\{ r^2 + a^2 - 2ra\cos(\phi - \phi') + (z - z')^2 \right\}^{-(3/2)} d\phi' dz'$$

3D field can be obtained by performing the numerical integration of the above equation. But in 2D, this can be solved analytically. It is preferred to study the problem in 2D and obtained necessary condition to generate sextupole field using several PMs.

If the magnet is very long along z direction as compared to its extent along x and y direction then the 2D approximation is valid. For homogeneously magnetised magnet, field at any arbitrary point $\xi_0$ produced by a magnet placed at $\xi$ can be expressed as

$$B^*(\xi_0) = \frac{\mu_0}{2\pi i} \iint \frac{j dx dy}{\xi_0 - \xi} \text{ with } \mu_0 j = \nabla \times B_r$$

$$B_r = B_{rx} + iB_{ry} \text{ and } \mu_0 j = \frac{\partial B_{ry}}{\partial x} - \frac{\partial B_{rx}}{\partial y} \text{ and } \xi = x + iy$$

$B^*(\xi_0) = \frac{1}{2\pi i} \iint \left( \frac{\partial B_{ry}}{\partial x} - \frac{\partial B_{rx}}{\partial y} \right) \frac{dx dy}{\xi_0 - \xi} = \frac{1}{2\pi i}(I_1 + I_2)$. We will use the following integration to arrive at the field expression.

$$I_1 = \left[ \int \right] \frac{B_{ry} dy}{\xi_0 - x - iy} - \int \frac{B_{ry} dx dy}{(\xi_0 - x - iy)^2}$$

After performing the integration by parts, we get $B^*(\xi_0) = \frac{1}{2\pi} \iint \frac{(B_{rx} + iB_{ry})}{(\xi_0 - x - iy)^2} dx dy = \frac{1}{2\pi} \iint \frac{B_r}{(\xi_0 - \xi)^2} dx dy$. This expression can be simplified further to

$B^*(\xi_0)=\frac{1}{2\pi}\iint\sum_{n=1}^{\infty}\frac{B_r n\xi_0^{n-1}}{\xi^{n+1}}dxdy$. If the magnetisation vector rotates by an angle $\theta$ with respect to the reference magnet, then the field generated by the modified magnet can be expressed by modifying $B_r$ by $B_r e^{i\theta}$ in the above expression.

Now, field expression will be extended for K numbers of identical magnets suitable positioned on the arc of a circle of radius $r_0$. So, the angular positions of all the magnets are $\alpha_N=(N-1)\frac{2\pi}{K}$ where $N$ varies from 1 to K .

We place the reference magnet with magnetisation vector along $x$ at $(r_0,0)$. Another identical magnet whose magnetisation makes an angle $\theta$ with $x$ placed on the circumference of the circle at $(r_o,\alpha)$.

The field produced by the magnet at $\xi_0$ can be expressed as

$B^*(\xi_0)=\frac{1}{2\pi}\iint\sum_{n=1}^{\infty}\frac{B_r e^{i\theta}n\xi_0^{n-1}}{r_0^{n+1}e^{i(n+1)\alpha}}adad\varphi$, where each magnet is having radius a. Therefore, for $K$ no. of magnets, the resultant magnetic field is

$$B^*(\xi_0)=\frac{1}{2\pi}\iint\sum_{N=1}^{K}\sum_{n=1}^{\infty}\frac{B_r e^{i\{\theta_N-(n+1)\alpha_N\}}n\xi_0^{n-1}}{r_0^{n+1}}adad\varphi=B_x-iB_y$$

Therefore, the necessary condition for generating a sextupole field using assembly of K magnets is [3]

$n=3$ and $\{\theta_N-4\alpha_N\}=3\pi/2$

To verify the theoretical prediction, simulation using FEM code is done using the above condition.

## SIMULATION RESULTS

As a proof of the theoretical model, resultant field generated by 12 identical PMs of cylindrical shape positioned on the arc of a circle is calculated using POISSON code. To generate sextupole field gradient, $\frac{\partial^2 B}{\partial r^2}$, in the range of 1335 T/m$^2$ to 3979 T/m$^2$ a modular structure is assumed. In the same mechanical structure magnets of various radius are used to generate the above field gradient. In the first example, 12 cylindrical PMs each having 5 mm radius are placed on the arc of a 25 mm radius circle. This configuration will generate 1335.2 T/m$^2$ field gradient. To understand the magnet, analysis of multipole components is important. Magnetic field of a multipole magnet can be defined as $B_y+iB_x=-\sum n(iJ_n+K_n)(x+iy)^{n-1}$ where, $J_n$ and $K_n$ are the skew and normal components for 2n pole magnets. The field on a reference radius is calculated and by doing FFT all the multipoles are evaluated. Simulation results show that all the multipoles, normalised with sextupole component, are of the order of $3\times10^{-4}$ or less. Therefore, the magnet is acceptable for accelerator application.

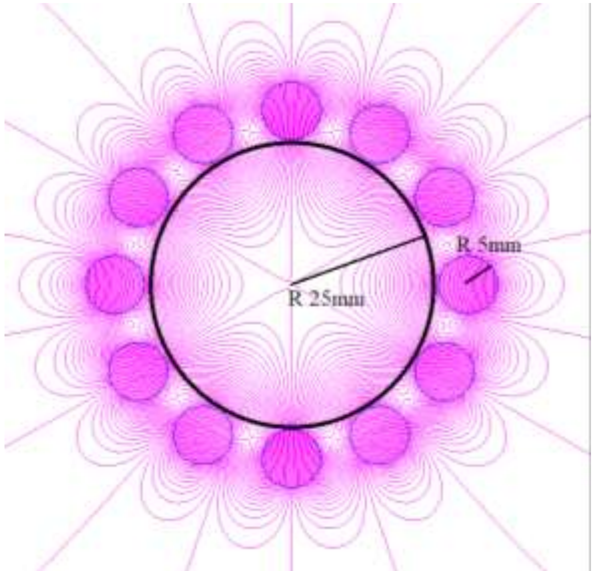


Figure1. Arrangement of 12 PMs on the circumference of a circle of radius 25 mm to generate sextupole field and field lines obtained from 2D simulation.

To generate stronger sextupole field radius of individual PMs are increase to 6 mm as shown in Fig. 2. This configuration will produce sextupole gradient, $\frac{\partial^2 B}{\partial r^2}$, of 1924.98 T/m$^2$.

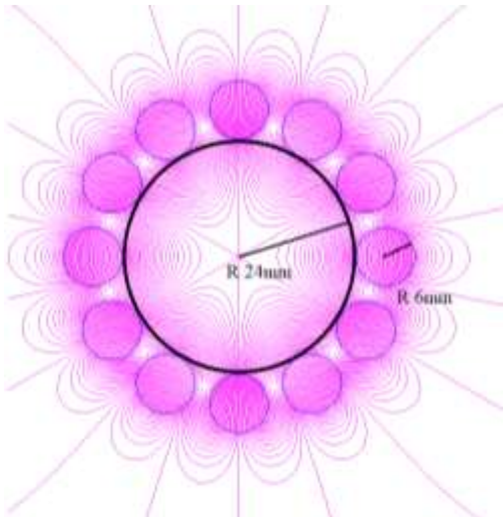


Figure 2. Arrangement of PMs with 24 mm bore radius for generating 1924.98 T/m$^2$ sextupole gradient.

In the same mechanical structure, 12 PMs each of radius 7 mm can be arranged to generate 2621.69 T/mm$^2$ sextupole gradient. Therefore, a base mechanical structure will be designed to accommodate PMs of various radius like, 5mm, 6mm and 7mm. This kind of modular design reduce time for series production of large numbers pf magnet required for storage ring. Figure 3 shows the field lines obtained using PMs each having 7 mm radius.

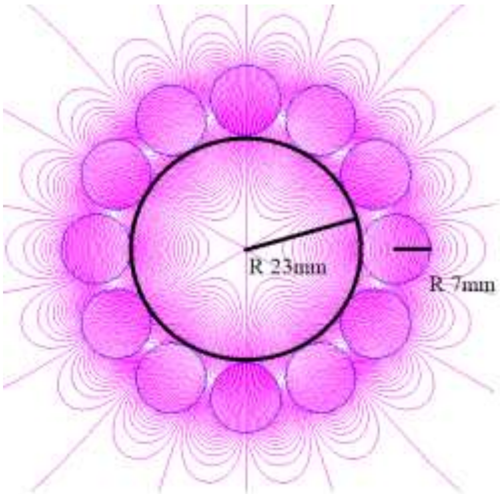


Figure 3. Arrangement of PMs each having radius of 7 mm for generating 2621.69 T/m$^2$ sextupole gradient.

There is provision to increase the gradient further in our design. In this case we have to reduce the bore radius to 19 mm and by using PMs each having 6 mm radius sextupole gradient of 3979.2 T/m$^2$ can be generated.

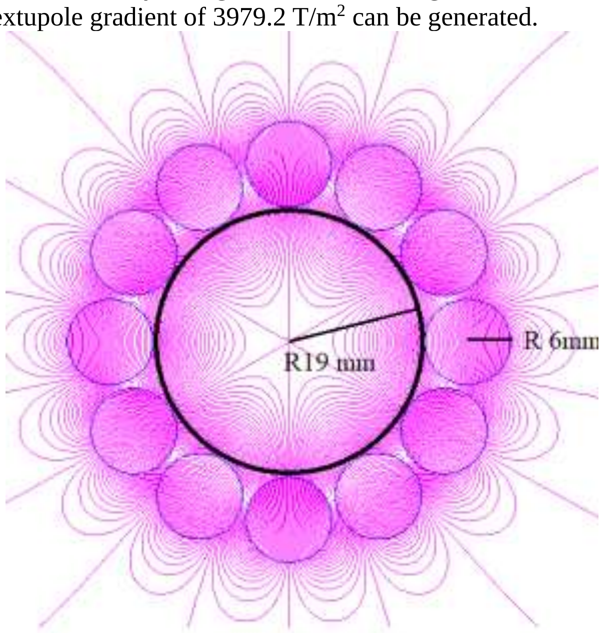


Figure 4. Generation of 3979.2 T/m$^2$ sextupole gradient for 19 mm bore radius magnet.

Similar gradient was reported for electromagnets of 19.2 mm bore radius [2]. However, PMs have its own advantages. Multipole component normalised with sextupole is plotted in Fig. 5. All the higher order components are of the order of $10^{-4}$. This is the typical requirement of accelerator magnet.

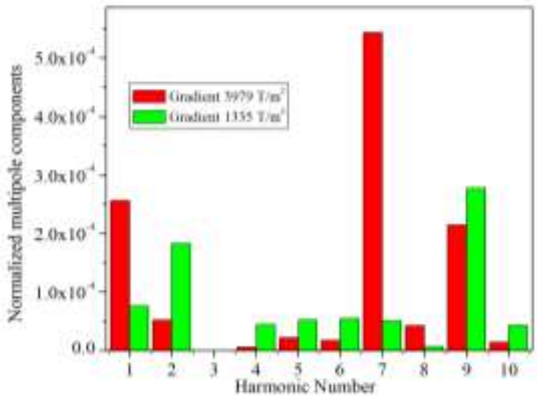


Figure 5. Normalised multipole component for different gradient of the sextupole magnet.

Table 1: Summary of the results

| Sr. No. | Bore radius | Radius of each magnet | $\frac{\partial^2 B}{\partial r^2}$ T/m$^2$ |
|---|---|---|---|
| 1 | 25 mm | 5 mm | 1335.20 |
| 2 | 24 mm | 6 mm | 1924.98 |
| 3 | 23 mm | 7 mm | 2621.69 |
| 4 | 19 mm | 6 mm | 3979.20 |

All the results are summarised in Table 1.

## REFERENCES


[1] L. Farvacque, N. Carmignani, J. Chavanne, A. Franchi, G. Le Bec, S. Liuzzo, B. Nash, T. Perron, P. Raimondi, A low-emittance lattice for the ESRF. Proceedings of IPAC2013, Shanghai, China, MOPEA008, p. 79.

[2] Philippe MARION, The ESRF upgrade phase II: the extremely brilliant source (EBS) project engineering design challenges and solutions. Presentation at NSLS II, 12 April 2016.

[3] A conceptual design of a compact high gradient quadrupole magnet of varying strength using permanent magnets, Gautam Sinha, Phys. Rev. Accel. Beams. 21, 022401 (2018).

# DESIGN OF 24 SEGMENT HEXAPOLE MAGNET FOR SUPER CONDUCTING ECR ION SOURCE AT VECC

P Y Nabhiraj, Ranjini Menon, Arup Bandyopadhyay

VECC, Kolkata

*Abstract*

An hexapole magnet with 24 segment made of NdFeB magnets is designed using a Comsol Multiphysics simulation tool for providing the radial field for Super conducting ECR ion source. Whole assembly is divided in to two layers, and in each layer high remanence and high coercivity magnets are arranged in such a way that the assembly provides highest possible magnetic field on the pole tips. This design follows non conventional angles of magnetization and positioning of magnets to achieve higher field and at the same time minimize the self demagnetization of magnets as compared to the conventional Halbach hexapole arrangement. The maximum pole tip field at the wall of plasma chamber is 1.45 T which is higher than the conventionally achievable field using the same grade of magnets. With thinner plasma chamber it is seen that Br in excess of 1.6T can be achieved.

## INTRODUCTION

Cryogen free superconducting ECR ion sources are increasingly being used for producing high charge state heavy ion beam for various applications, worldwide [1]. At VECC, an 18 GHz ECRIS is being developed for production of HCI. For HCI, it is known that better confinement of charged particle by the high magnetic field is essential. The axial field for the ECR will be provided by superconducting solenoids cooled by cryocoolers. For radial field, a hexapole assembly of NdFeB magnets will be used. The design is done in such a way that maximum field can be obtained inside the plasma chamber

## DESIGN OF HEXAPOLE MAGNET

In a typical conventional Halbach structure for ECRIS, the cylindrical Sextupole magnet is assembled from M segments permanently magnetized such that the magnetization axis of each segment advances azimuthally by an angle 8π/M with respect to a fixed coordinate system [2]. The magnetization vectors of the magnet at the poles are aligned with the radial field inside the plasma chamber. But rest of the magnet segment have an opposing field either inside or outside the chamber. Thus there is a strong demagnetization force which exists on magnets between the poles that degrades the Peak field on poles. In our design, the Halbach is modified so that none of the magnet segment faces the demagnetization force. The segments which face demagnetisation field is chosen to be made up of a material with high coercivity (High Hcj). While the pole segments can be of material with High remanence (High Br) [3].

Design of the permanent hexapole magnet with modified Halbach structure is carried out using Comsol multiphysics tool. An inner radius of 47 mm and an outer radius of 130 mm are considered as the dimension of the magnets. Since symmetry exists, $1/6^{th}$ of the assembly is considered for initial iteration which has 4 segments. Combinations of angles of first two segments are varied to find out the optimum angle for maximum field. Angles were varied from 30° to 55° for first segment and 60 to 100 degree for second segment in steps of 0.5°, i.e., ~4000 iterations were performed. Initial simulations showed that the demagnetizing force is strong near the inner side of half of the segments and it is stronger at the outer side of another set of segments. Thus design is changed so that each segment is further divided in to two pieces radially so that wherever demagnetising force is higher, magnets with high Hcj material are used, and rest of the places the high Br magnets are used. So now there are two concentric rings of 24 magnet segments each with two different materials as shown in figure 1.

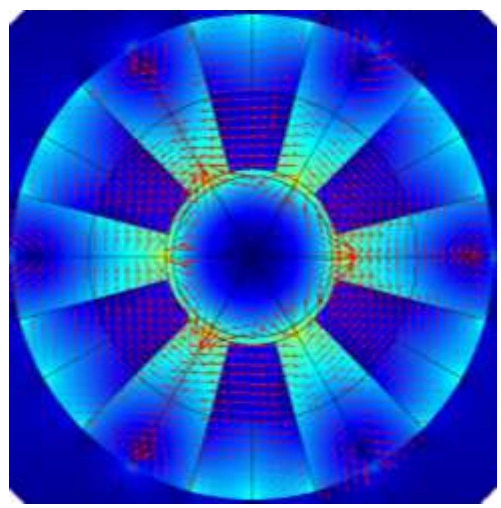

Figure 1: Radial field line distribution and the division of segments

Figure 1 shows the magnetic field lines after the complete 3D simulation of the assembly. Here the dark blue colour maps show High H field opposing the magnetisation of the permanent magnets. In this modified arrangement the demagnetising field is ~1100 kA/m as compared to 1250 kA/m in conventional one. High Br magnets considered in this simulation studies have Br > 1.4T (Hcj > 900 kA/m) and high coercive magnets have Hcj > 1900 kA/m (Br > 1.28 T), H field opposing the Magnetisation is less than Hcj of high coercive magnets and thus they are safe even at higher temperatures than $25^0$ C. Figure 2 shows the variation of maximum achievable Br at r = 43 mm, assuming a plasma chamber wall thickness of 4 mm with variations in magnetization angle of first two segments.

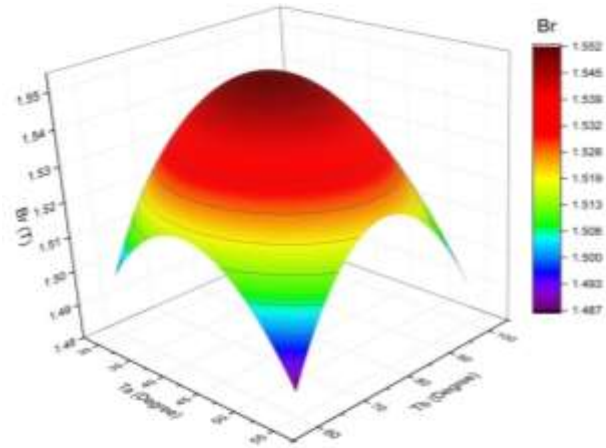

Figure 2: Dependenc of Br with the magnetization angles

## RESULTS

Magnetization angle of first segment is varied from $30^0$ to $55^0$ degree and second one from $60^0$ to $100^0$ which resulted in a variation of Br from 1.49 to 1.54 T. Figure 3 shows the comparison of Br obtained from the conventional assembly of Halbach and the current design under discussion. Max Br at r=43mm with reasonably thick plasma chamber, from conventional hexapole is 1.42 T while the other is 1.52 T. There is about 7% increase in the Br while using the same grade magnets of same volume.

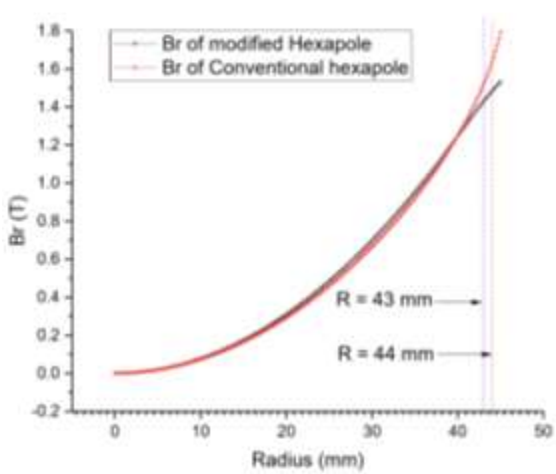


Figure 3: Variation of Br for modified Halbach and conventional Halbach

Further Besides this, the segment between the poles in conventional hexapole faces demagnetising force of slightly higher than the modified hexapole. Due to the presence of the edge of a magnet on the pole and due to $r^2$ dependence of the magnetic field from the pole, there is a significant rise in the Br near the pole of modified hexapole as shown in figure 3. Br increases by 10% and 17% at R = 44 and 45 mm respectively. In order to take advantage of this feature of modified hexapole and to attain the radial mirror ratio of more than 2, there is a plan to build a specialized thin plasma chamber. As can be inferred from the graph, the mirror ratio increases rapidly from crossover (for 18 GHz) 1.9 to 2.4 and 1.9 to 2.8 for conventional and modified hexapoles respectively. 18 GHz ECIRS experiments by Hitz et al [4] show that similar increase in radial mirror ratio improves high $Xe^{27+}$ production by > 25%.

## CONCLUSION

A magnet on pole of conventional hexapole is divided into two magnets with magnetisation direction favouring the formation of poles. The magnet between the poles also is divided into two with magnetisation direction such that there are no antiparellel demagnetising fields as seen in conventional hexapole magnet. This modification facilitates lesser demagnetisation forces on the magnets between poles which contributes to increase in the Br on the poles. The advantage of the modified hexapole is that the rate of rise of Br towards the pole is much more than that of the conventional hexapole. So by designing an innovative plasma chamber one can increase the Br significantly. It is experimentally seen that by increasing the Radial mirror ratio by 5% the high charge state production can be increased more 25%. Another important finding is that the angles of magnetisations need not be precisely controlled and thus reducing the cost of magnets significantly. Variation of magnetisation angles of $25^0$ in magnet on pole and $40^0$ on magnets between poles result in reduction of Maxim Br of < 3%. So misalignments on either direction in magnetisation does not severely impede the performance of the hexapole.

## REFERENCES

[1] Y. Higurashi et al. Rev. Sci. Instrum. 83, 02A308 (2012)
[2] A. Vassiliev et al, Rev. Sci. Instrum., Vol. 71, No. 9, (2000) 3331.
[3] P. Suominen, O. Tarvainen, and H. Koivisto, D. Hitz Rev. Sci. Instrum., Vol. 75, No. 1, (2004) 59
[4] D Hitz, A Girard and G Melin Rev. Sci. Instrum, Vol 73, No 2(2002) 509

# MEASUREMENTS AND OPTIMIZATION OF RF AND HIGHER ORDER MODE PARAMETERS OF NEW RF CAVITY IN INDUS-2

Rajiv Kumar Arora[#], Hemraj Vaishnav, Ashish Tiwari, Ramesh Kumar, Mahendra Lad
Raja Ramanna Centre for Advanced Technology, Indore-452013, India

*Abstract*

Indus-2 RF system was upgraded with installation of sixth 505.8 MHz RF cavity. The RF cavity, assembled with input power coupler, Higher Order Mode Frequency Shifter (HOMFS) and other sub-systems was installed in Indus-2 ring. Low power RF measurements of resonance frequency, quality factor, coupling coefficient, coupling of sensing couplers were performed. Coupling loop coefficient was adjusted considering with-beam operation of Indus-2 SRS at 2.5 GeV. The RF cavity was baked by circulating hot water and after cool down vacuum level of ~5x10$^{-10}$ mbar was achieved. Connection of window air and installation of transmission line from RF station to the RF cavity was done. RF conditioning of the cavity was carried out by feeding pulsed RF power initially and the cavity was finally tested in CW mode up to 35 kW power. Beam trials with sixth RF cavity in operation, along with previously installed five RF cavities were performed. RF sensing signals from cavity were observed to identify harmful Higher Order Modes (HOMs). Experiments were performed to optimize HOM parameters of the cavity. At the optimized RF and HOM settings, more than 210 mA beam was stored at injection energy and after ramping ~200 mA beam current at 2.5 GeV was obtained in Indus-2. Presently, RF cavity is working in round-the-clock mode operation in Indus-2. In this paper, details of measurements and optimization of RF and HOM parameters to obtain high beam current are presented.

## INTRODUCTION

In the synchrotron radiation source Indus-2, RF cavities are used to provide RF power to accelerate electron beam energy from ~550 MeV to 2.5 GeV and to compensate synchroton radiation losses. Considering higher RF power requirement for operation of insertion devices and to provide ease of operation, Indus-2 RF system consisting of five operational RF cavities was upgraded with installation of sixth 505.8 MHz RF cavity in April, 2018.

Table 1: Important Indus-2 and RF cavity parameters

| **Parameter** | **Value** | **Unit** |
|---|---|---|
| Operating energy | 2.5 | GeV |
| Injection energy | ~550 | MeV |
| Revolution Frequency | 1.738 | MHz |
| RF frequency | 505.8 | MHz |
| RF cavity unloaded quality factor | ~40000 | |

[#] krajiv@rrcat.gov.in

Important parameters of Indus-2 and bell-shaped imported RF cavity are listed in Table-1.

The new imported RF cavity, assembled with RF input power coupler, Higher Order Mode Frequency Shifter (HOMFS), frequency tuner system and other sub-systems was installed in the long straight section LS-7 of Indus-2 ring adjacent to already installed and operational indigenous RF cavity. The issue of higher order modes of RF cavities is very critical for operation of storage ring at high beam current. If HOMs match with beam spectra components, they generate instabilities which limit the high beam current operation. Systematic measurements of RF and HOM measurements were performed before and after the installation of RF cavity in Indus-2. Measurement data was analyzed and experiments were performed to optimize RF and HOM parameters for smooth accumulation, ramping and storage of high beam current in Indus-2. Figure 1 shows view of sixth RF cavity along with transmission line installed in Indus-2. Fifth RF cavity is also seen in the figure.


Figure 1: View of sixth RF cavity along with transmission line installed in Indus-2

## OFFLINE MEASUREMENTS AND TESTING

Offline measurements refer to without beam measurements. Before installation of the cavity, low power RF measurements of the fundamental and higher order modes were performed. Resonance frequency, quality factor, coupling of sensing couplers were measured. The resonant frequency of fundamental mode was 505.802 MHz, unloaded quality factor was ~40000. In Indus-2, the instabilities due to HOMs are avoided by shifting the HOM spectrum of RF cavities. Higher order modes can be shifted by varying precision chiller temperature or Higher Order Mode Frequency Shifter (HOMFS) position of the cavity. RF cavity has coolant channels passing over the cavity body to maintain the desired working temperature with a control of ±0.1°C and can be set in the range of 30°C to 80°C. Before installation of the cavity low power RF measurement of longitudinal and dipole HOMs of RF cavities was done. Different modes have different sensitivity as a function of temperature or HOMFS position. The data was analyzed to estimate the initial settings of temperature and HOMFS position of the cavity to avoid harmful HOMs.

The RF cavity was installed in long straight section LS-7 of Indus-2 ring. The input power coupler was adjusted for coupling loop coefficient of 3.2 considering with-beam operation of Indus-2 SRS at 2.5 GeV. Figures 2 (a) and (b) show snapshot of low power measurements.


Figure 2 (a): Snapshot of RF frequency measurement of cavity fundamental mode


Figure 2 (b): Snapshot of coupling coefficient of sixth RF cavity

Sixth RF cavity along with fifth RF cavity was evacuated and baked by circulating hot water for about 36 hours. After cool down, vacuum level of ~5x$10^{-10}$ mbar was achieved. Figure 3 shows view of sixth RF cavity during baking.

Figure 3: Sixth RF cavity along with vacuum system during baking

The cable loss at HOM frequencies from cavity pick-up probes to the RF console was measured. The coupling between input power coupler and two inductive couplers were -43 dB and -44 dB respectively. Window air cooling connection with flow switch, temperature measuring sensor, filters was made and flow was set. RF cavity was connected to the RF station outside the tunnel at other end through a fabricated 6-1/8 inch transmission line system (show in Figure 4) consisting of several line sections, elbows, flexible sections, directional couplers, RF circulator, water cooled RF load etc.

Figure 4: View of 6-1/8 inch transmission line along with components

RF conditioning was started by feeding low power in pulse mode with duty factor 0.25%. Then, pulse repetition frequency and pulse width were increased gradually to make duty factor 100% so that CW operation was reached. RF cavity was tested in CW mode up to full RF power. Adequate precautionary measures were taken throughout the cavity conditioning and measured radiation levels were with-in acceptable limits.

## ONLINE MEASUREMENTS AND OPTIMIZATION

Beam trials with sixth RF cavity in operation along with previously installed five RF cavities were performed. The precision chiller temperature and HOMFS position of new cavity were set as per theoretical estimates. Important RF parameters like cavity gap voltage, relative phases between RF cavities, vacuum level, tuning position etc. were observed and optimized. Experiments were performed to optimize RF and HOM parameters of RF cavity. RF parameters like gap voltage and phase of sixth RF cavity were fine tuned by measuring synchrotron frequency. HOM measurements with beam were done at injection energy (~550 MeV) and during ramping (up to beam energy 2.5 GeV). The signals from HOM pick-up probes of new RF cavity was observed to check harmful HOMs. The Longitudinal modes L1 (~950MHz) was observed to be harmful at high beam current. The beam instability due to L1 mode was suppressed by optimizing HOMFS position of the cavity.

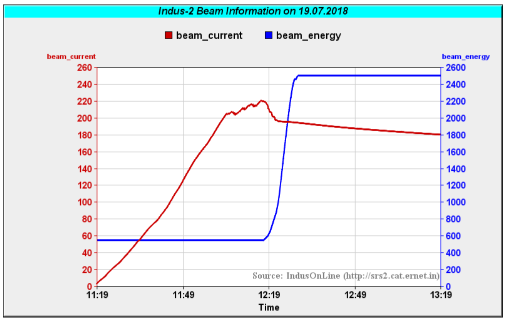


Figure 5: Indus-2 operation at high current during experiments with beam

At the optimized RF and HOM settings, 220 mA beam was stored at injection energy and after ramping ~195mA beam current at 2.5 GeV was attained in Indus-2. Figure 5 shows the snapshot of high current operation during experiments. Presently, RF cavity is working satisfactorily in round-the-clock mode operation in Indus-2. Figure 6 shows the Indus-2 operation at high current with six RF cavities.

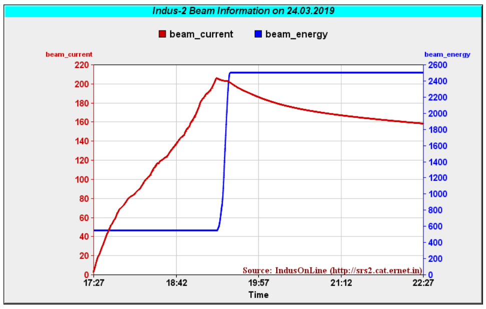


Figure 6: Indus-2 operation at 2.5 GeV with six RF cavities in operation

## CONCLUSION

RF and HOM measurements of new RF cavity were performed. The data was used to estimate initial settings of RF and HOM parameters. The parameters were further optimized during experiments with beam for injection ramping and storage of high beam current (~200mA) at 2.5 GeV. Presently, RF cavity is working at optimized settings in round-the-clock mode operation in Indus-2.

## ACKNOWLEDGEMENT

We thank RF team, high current operation team, Indus shift operation team for technical discussions and providing support during beam experiments.

## REFERENCES

[1] Rajiv K Arora, M Prasad, M Lad, P R Hannurkar, “Observations and control of beam instabilities due to Higher Order Modes in Indus-2”, InPAC-2013, Nov 19-22, 2013, VECC, Kolkata.

[2] H. S. Kang et al, “Exact determination of HOM frequency in storage ring RF cavity” NIM A 483 (2002) 629–640

[3] M. Svandrlik et al, “The cure of Multibunch Instabilities in Elettra”, PAC 95, pp. 2762-2764

[4] E. Karantzoulis et al, “Observation of Instabilities in the ELETTRA Storage Ring”, EPAC, 1994, pp.119-121.

# DESIGN OF A FOUR CHANNEL STEPPER MOTOR CONTROLLER FOR RESONANCE CONTROL OF SRF CAVITIES UNDER IIFC PROJECT

Shailesh Khole#, Gopal Joshi, ACnD/BARC
Brian Chase, Joshua Einstein-Curtis, Fermilab, U.S.A.

*Abstract*

The SRF cavities are tuned to the resonance frequency using a piezo stepper motor combination. The paper discusses design choices and implementation methodology chosen for the design of a four-channel stepper motor controller board. The controller can drive stepper motors up to 8A per phase current and can achieve 256 micro-steps within the standard 1.8 degree step size. Many other features that are available on the board are also discussed in the paper.

## TUNER ASSEMBLY

The SRF cavity have quality factor (Q) of the order of 10e8 to 10e10 resulting in a half bandwidth of the order of few Hz. Even a small imperfection during cavity fabrication would result in the resonance frequency shifting away few kHz from the desired frequency. The problem is more pronounce in multi-cell cavity owing to multiple welding and machining operations. Cavity tuning machines used during fabrication phase provide plastic deformation to the cavities so as to bring the resonance frequency within acceptable limits.

The cool-down and warm-up operation of the cavities leads to changes in mechanical dimension owing to the thermal expansion coefficients. This in turn, changes the resonance frequency of the cavities. The cavity resonance frequency also drifts slowly with time which also needs to be compensated.

A tuner assembly is usually a mechanical structure which can apply variable force to the cavity. This force causes dimensional changes within elastic limits and hence results in a reversible frequency change. The stepper motor assembly provides an electrical means to control this task. By moving the stepper motor forward and backward, the tuner assembly can compress or expand the cavity along the beam line resulting in increase or decrease of the resonance frequency.

A piezo electric module is also provided on to the tuner assembly to take care of Lorentz Force Detuning (LFD) and microphonic effects due to vibration, cavitation and fluidic motion of liquid helium around cavity. The stepper motor steps also induces jerk on every step, hence micro stepping is an essential feature of such a system.

The tuner assembly is outside the helium jacket and hence is not at liquid helium temperature. The tuner zone is a poor cooling zone and heat removal from the stepper motor as well as piezo is an issue. Care must be taken to monitor the temperature of these devices

The tuner assembly details are shown in figure 1 below and more details can be found in various presentation [1]

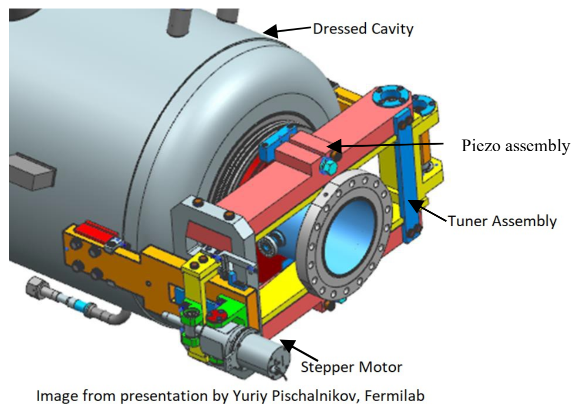


Figure 1: 3D modal of the tuner assembly

## DESIGN REQUIREMENTS FOR THE STEPPER MOTOR BOARD

The cavity stiffness is estimated to be about 45kN/mm and frequency detuning is specified as 200KHz / mm. The stepper motor is required to provide a resolution of 1 hz per step or better.

Phytron LVA 52-LCLS II-UHVC-X1 motor has been selected for PIP-II and its key specifications are listed in table 1 below.

Table 1: LVA 52-LCLS II-UHVC-X1 specs

| Description | Value |
|---|---|
| Steps per rotation | 200 |
| Gear Box Ratio | 1:50 |
| Motor stroke per revolution | 1mm |
| Tuner mechanical gain | 1:20 |

The change in mechanical dimension of the cavity for each step of the stepper motor is given by equation (1).

$$L_{step} = \frac{1}{200} * \frac{1}{50} * \frac{1}{20} = \frac{1}{200000}\text{mm} \quad (1)$$
$$= 0.005\mu M$$

The corresponding change in the resonance frequency can be given by equation (2).

#khole@barc.gov.in

$$F_{step} = 200\text{kHz /mm } {*}0.005\mu\text{M.} = 1\text{Hz per step} \quad (2)$$

## STEPPER MOTOR BOARD ARCHITECTURE

The LLRF station controls four cavities per station hence four piezo as well as stepper motor controller would be required per station. Each resonance controller chassis has four such units in addition to the LLRF FPGA board which controls the overall system.

The stepper motor controller card is 100mm by 115mm in size and has four independent stepper motor controllers as shown in figure 1 below. It also has isolated as well as not isolated digital IO lines for Limit switch sensing and for interfacing to other external signals.

The on-board ADC monitors the temperature of all the four-driver sections. The stepper motor controller provides a back-emf signal for stall detection. This back-emf signal is also monitored via the ADC. This ADC can be controlled over SPI via the CPLD.

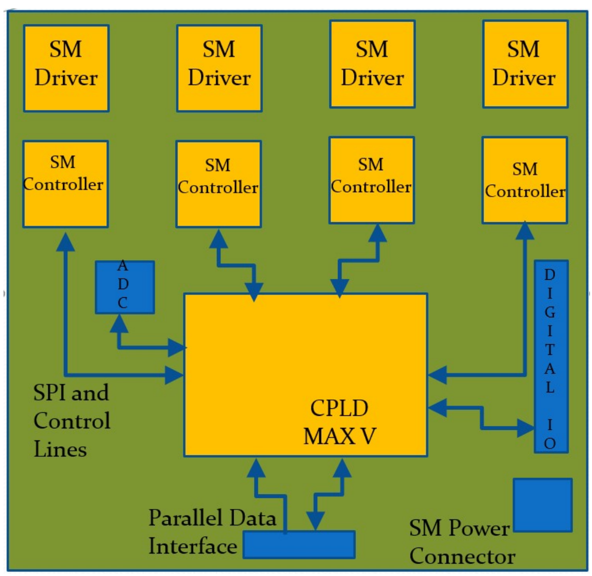


Figure 1: Block diagram representation stepper motor controller board

### *Stepper motor controller*

The stepper motor controller is designed around DRV8711 from Texas instruments. The DRV8711 requires external N-channel MOSFETs to drive a bipolar stepper motor. It can also drive two independent brushless DC motor. The chip has integrated micro-stepping indexer, which allows step modes from 1/256-step to full step.

The interface between stepper motor controller and CPLD is shown in detailed in figure 2 below. SPI serial interface is used to program the device from the CPLD. Output current (torque), step size, current decay mode, and stall detection functions can all be programed via the SPI serial interface. Internal shutdown is provided for overcurrent protection, short-circuit protection, under-voltage lockout, and over temperature conditions. Fault conditions are indicated through a common FAULTn pin. The fault source can be found by reading the dedicated fault register through SPI. Once the SPI initialisation is done the controller only requires a direction signal and a step pulse to function.

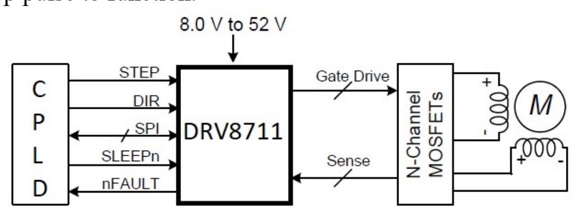


Figure 2: Interface details between stepper motor controller and CPLD

When micro-stepping, motor stall can be reported with an optional back-EMF output. The controller can operate up to 52V and hence no level shifter between controller and MOSFET driver are required.

### *Stepper motor driver*

The MOSFET bridge FDMQ86530 is N-Channel MOSFET having a voltage rating of 60 V, and a current rating of 8 A. the on state resistance is 17.5 mΩ.

The schematic of the stepper motor driver stage is shown below in figure 3. When driving a bridge section, the turn on and turn off times of the upper section are slower than the lower section. This situation is mitigated by inserting a 56Ω series resistor in the lower arm to slow it down. The current from the H-bridge is sensed and provided to the stepper motor controller for implementing stall protection and current loop implementation.

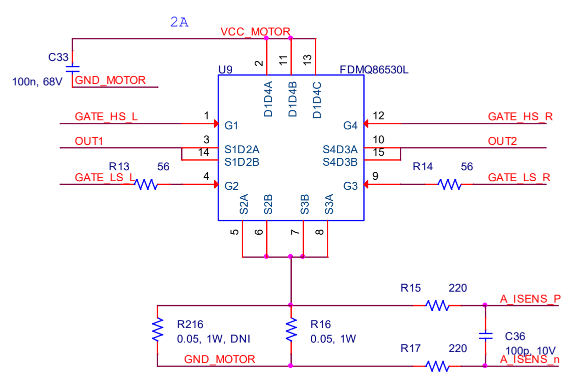


Figure 3: schematic details for stepper motor driver

The power supply decoupling capacitors are mounted very close to the chip pins for minimising the power supply impedance. All the manufacture recommendations are followed for optimal performance. The MOSFET is provided with thick and large thermal planes to dissipate heat generated due to switching action. Temperature of each MOSFET is monitored by DS60 silicon temperature monitor and is available in the CPLD after digitization.

### *CPLD*

Altera Max5 CPLD (5M2210ZF256) provides all the interface support and housekeeping operations. The CPLD initialises all the stepper motor controllers over SPI at power up as well as on any on line change command.

The CPLD also controls the ADC AD7699BCPZ through SPI interface. The ADC has eight analog input; four are used for monitoring the temperatures of motor driver and four channels monitor the back-emf voltage signal generated by the stepper motor controller.

The stepper motor mounted in the cryostat is not easily accessible and hence all kind of care has to be taken to insure smooth and reliable operation. The motor is at cryogenic temperature and hence a positional encoder type feedback is not possible. Limit switch on either extreme limit of the tuner are mounted. Eight such switches are required to be monitored. CPLD has provisions to monitor 18 such signals with galvanic isolation. CPLD also provides access to 70 I/O lines in non-isolated mode which can be used either as input or output in standard 3.3V LVTTL mode.

The frequency monitoring loop in FPGA calculates a de-tuning amount and drives the stepper motor so as to minimise the error. The micro stepping mode ensures that no jerks are transmitted to the cavity. The FPGA to CPLD interface can either be a bus type access or individual SPI mode for each stepper motor controller. When in SPI mode, the CPLD acts as a transparent buffer.

The CPLD also has a RS232 interface provided by FT232RQ; which is very useful in standalone mode. The serial interface allows the board to be linked to PC and receive commands to perform various motor control operations.

### *Power Supply*

The power supply section consists of four regulators. The CPLD needs core voltage of 1.8V, I/O voltage of 3.3V for bank connected to stepper motor controller and 2,5V for banks connected to the FPGA side. One 5V regulator is needed for ADC and temperature monitoring section. One Isolated DC/DC converter is used for powering up the isolated side of the digital isolators.

## TESTING AND PERFORMANCE

The stepper motor controller board has been fabricated and tested. All the four channels have been tested using 12V and 24V stepper motors. The initial testing was done using RS232 interface. The board has now been integrated in to the resonance controller chassis along with the FPGA board and the piezo controller board as shown in figure 4 below. Detailed testing with tuners being developed at RRCAT Indore will be done in HTS when ready.

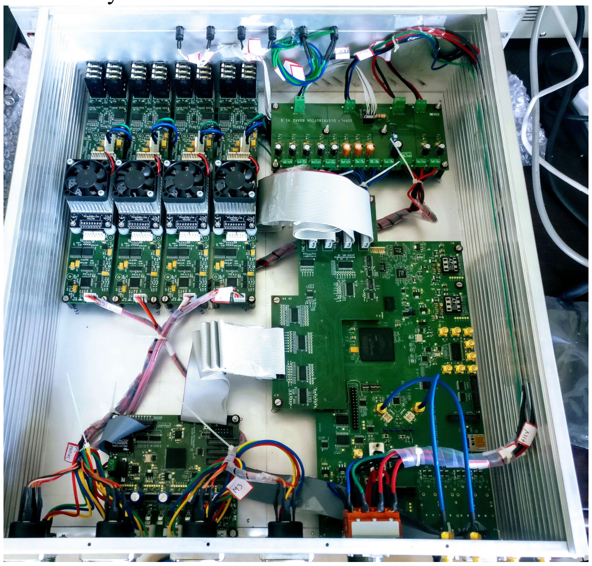

Figure 4: Assembled Resonance controller chassis

## REFERENCES


[1] https://indico.bnl.gov/event/4460/contributions /24569/attachments/20505/27483/LCLS_-PIP_tuner_talk_at_MicroWorkshop_2.pdf

# FIRMWARE ARCHITECTURE AND OPERATIONAL EXPERIENCE OF INTERLOCK PROTECTION AND MONITORING SYSTEM (IPMS) FOR 7KW, 352MHZ SOLID STATE POWER AMPLIFIER FOR FNAL.

Hitesh Shukla, Afaash Mohd., Rajesh Keshwani, Sandeep Bharade, Sujo C. I., Dr. Gopal Joshi,
ACSS, ACnD, BARC, Mumbai-94.

*Abstract*

IPMS consists of seven modules viz. one system control module, two analog modules, three mutlitrip modules and one digital output (DO) & temperature module. One IPMS system can handle upto 20 optically isolated digital inputs (DI) and outputs, 16 digital temperature sensors (DTS), 24 RF signals and 32 optically isolated analog input (AI) signals. The DI/O are configurable for contact type or TTL type. IPMS provides two DO signals SSA_READY and RF_ON_OFF. SSA_READY signal is applied to RF protection interlocks system (RFPI) informing the health of SSRFPA. RF_ON_OFF signal is applied to the switch between the RF drive and SSRFPA. In addition to the above hardwired signals, there are 12 DO, one for controlling each power supply, one for controlling the driver power supply (PS) and two for informing the machine protection system/control system regarding the SSA_READY status and RF_ON_OFF status. The detailed description of system hardware can be found in paper [1]. Development of module specific code is required due to variation in type of signals being handled.

## FIRMWARE ARCHITECTURE

State machines followed by various modules of IPMS are briefly described below:

### *System Control Module*

System control module consists of DI mezzanine card and system control (SC) mezzanine card. The SC card takes DI from DI card and inter-card communication bus (ICCB) to control the power supplies. Present operation of system evolved from SSRFPA specifications provided. I/O affecting functionality of SC board can be viewed in figure 1. DC POWER SUPPLY STATUS OK, GATE /TRIGGER, REMOTE RESETn, LOCAL RESETn, LOCAL START, REMOTE START, AUXILLIARY POWER SUPPLY STATUS, DRIVER POWER SUPPLY STATUS are DI of TTL type to DI card. SSA SAFETY PERMIT, REMOTE/ LOCALn and LOCAL RESETn are contact type signals, while rest of the signals are from different modules to SC Module. IPMS state machine generates two signals based on the different fault conditions.

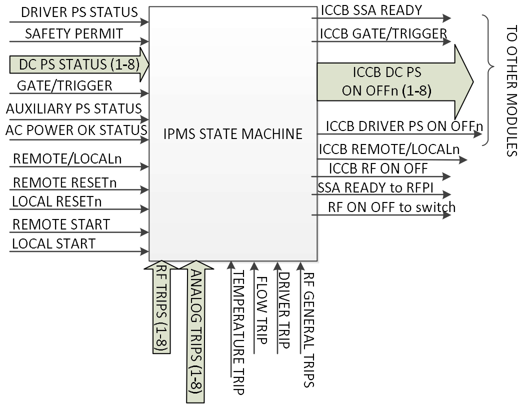


Figure 1: I/Os for system control module firmware

The state machine for IPMS is provided in figure 2. In case of fault condition, the state transits to FAULT state, while in case of a reset or falling edge of derived start signal, the state comes back to the IDLE state. Under normal condition, the state transits from IDLE to CHECK_FLOW_AND_TEMP, SWITCH_ON_PS, WAIT, ALARM_HEALTHY, CHECK_SSA_INH, WAIT_FOR_TRIPS and back to IDLE.

### *AI Module and Multi-trip Module*

Each AI module consists of two AI mezzanine card which has 8 optically isolated AI signals. Each AI signal is compared with lower limit and upper limit for over and under limit trips. The trip generation logic for AI is illustrated in figure 3. Each multi-trip module (MTM) consists of two multi-trip mezzanine board (MTB) which handles 4 RF signals. Each RF signal is compared with the upper limit value for over limit protection. The trip generation logic for MTM is illustrated in figure 4.

The limits are set by operator on the GUI which in-turn are set in corresponding registers through EPICS. The set limits are updated in DAC, every 100 µseconds through SPI protocol.

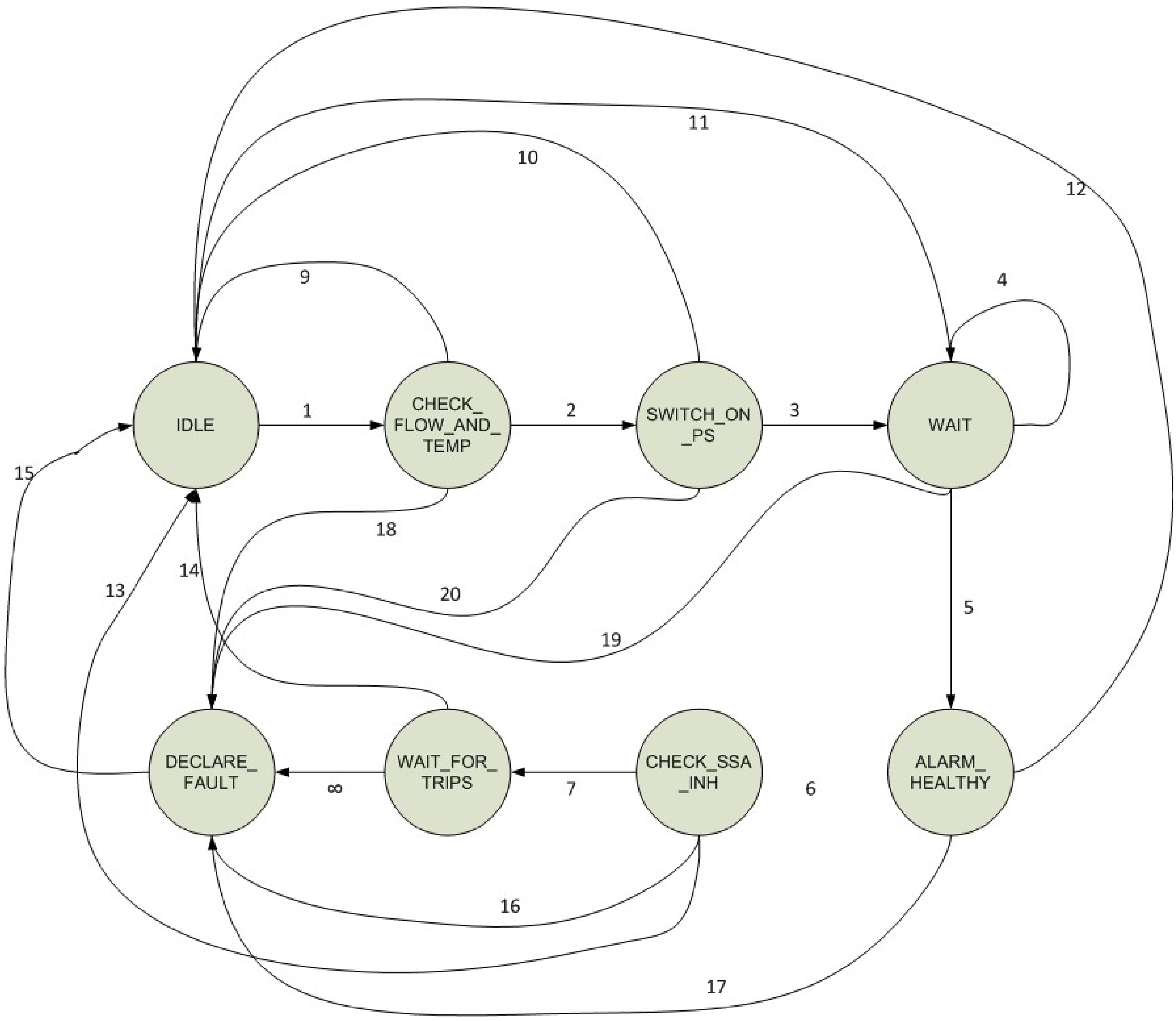


Figure 2: State machines followed by IPMS firmware

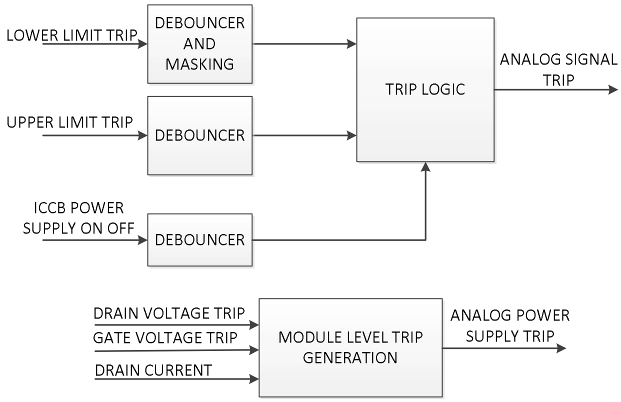


Figure 3: Trip Generation Logic for AI signals

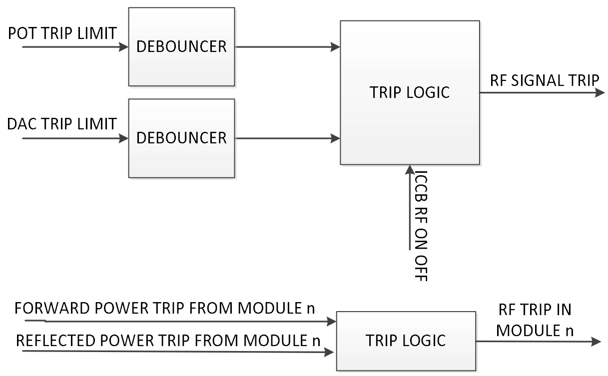


Figure 4: Trip Generation Logic for RF signals

### *Digital output and Temperature Module:*

The DO and temperature module consists of one DO mezzanine card and one DTS card. The module processes the digital control information from SC board and DTS card to control the power supplies The DTS card handles 12 DTS, each communicating the temperature value over one wire protocol from the DTS and comparing the acquired value with a digital comparator. A state machine based code has been developed for communication with one wire temperature sensor. The trip architecture is illustrated in figure 5.

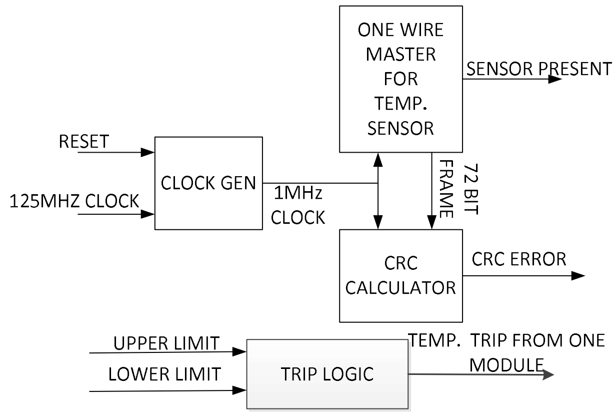


Figure 5: Trip Generation Logic for temperature signal

## *DATA ACQUISITION*:

Acquired values of AI signals and RF signals were observed to be varying by more than 10% of the full range when displayed on GUI. To reduce the displayed signal value variation, a digital filter was implemented on the sampled data coming from ADC. Variation as low as 0.1% was observed with digital filter. There are two data transfer modes for IPMS (1) online data transfer and (2) post mortem mode. In online data transfer mode, the data is acquired after digital filtering and transferred on every rising edge of the GATE/TRIGGER signal by generating an interrupt from SC board which is followed by a DMA operation by VME controller. For post mortem mode of data transfer, in case of fault, an interrupt is generated by SC board which is followed by DMA for all the modules. The pre-fault and post-fault data is each 1024 sample wide, with predefined rates as per the targeted specifications.

## OPERATIONAL EXPERIENCE

After successful working of standalone IPMS working with lab signals, it was integrated with 7KW SSRFPA. Intermittent trips at random time were observed which was not acceptable. A systematic study revealed that 100 kHz filters were not enough to filter out noise from field signals such as water flow and signals from DC power supply. Thus implementing filters in the digital domain was required. The filters were designed based on the equation 1. This solved most of the trips at SSRFPA lab at BARC.

$$0.75 * Tr \geq Tana + Tpd + Tdeb \text{ ............(1)}$$

where, *Tr* is the response time required for the signal, *Tana* is the rise time for analog signal, *Tpd* is the propagation delay from one module to the other through ICCB and *Tdeb* is the rise time of the digital filter. A stable working SSRFPA without spurious trips was thus accomplished.

A similar system was built at ECIL to be delivered to IIFC. Due to the high value of the resistors on the ICCB a coupling was observed between the GATE/TRIGGER signal and some of the trip signals that were in close proximity to GATE/TRIGGER signal on ICCB. The coupling was reduced by removing the strong pull-up of these signals in the code. This eliminated the random trip problems due to cross coupling.

It was observed that occasionally system tripped due to DTS signals. After detailed observations, it was concluded that it might be happening due to the make and break connection of one wire DTS along with the RF coupling due to high value of the pull-up resistors. As the CRC error and the absence of the temperature sensor was taken to be a trip condition in the firmware, the same started to cause the trip (shown in figure 5). As the thermal time constant of the system was of the order of more than a few seconds, it was decided to consider CRC error and connection breakage as trip condition if and only if it persisted for three seconds, while maintaining the timing for over and under temperature conditions. Firmware was updated and the same was tested with SSRFPA. Present firmware thus was arrived after several hours of testing of integrated SSRFPA.

## CONCLUSION

The firmware was tested integrating with RF power amplifier and is found to be very stable at both BARC and ECIL 7KW SSRFPA. Suitable modifications may have to be done in firmware so as to handle field signals. The RF power amplifier has been despatched to Fermilab and will be tested with RF cavity soon.

## ACKNOWLEDGEMENT

Authors would like to acknowledge, Shri M. M. Sutar of ACSS, ACnD, production team for SSRFPA and IPMS at ECIL for testing support provided at BARC and at ECIL, Hyderabad.

## REFERENCES

[1] R T Keshwani, Sujo C I, Hitesh Shukla, J K Mishra, M Afaash, M Sutar, Snigdha Singh, Gopal Joshi, "Design architecture of Interlock Protection and Monitoring System for 7KW Solid state RF power amplifier," Proceedings of Inpac 2018 in INIS Volume 49, Issue 41.

# DESIGN OF VME64X BASED DIGITAL AND ANALOG IO BOARDS

Shailesh Khole#, Gopal Joshi, ACnD/BARC

*Abstract*

A thirty-two channel each isolated digital input output board has been designed, fabricated and tested at ACnD, BARC. The board is capable of up to 10MHz I/O speed and is able to drive 2.5V LVTTL signals in 50 Ohms load as well as 5V TTL signal in high impedance load.

A sixteen channel each 16 bit analog input output board has also been designed, fabricated and tested at ACnD, BARC. The board supports 0-5V, 0-10V, ±5V, ±10V, 0-20mA, 4-20mA, ± 20mA and ± 24mA mode for input as well as output.

Both the boards can operate on internal as well as external clock, allowing clock synchronization among multiple boards. It also has internal and external trigger mechanism to allow deployment of synchronized triggered data acquisition across multiple boards.

The paper discusses the design choices and implementation methodology chosen for the design.

## NEED FOR DEVELOPMENT

All industrial and lab based process control application (including accelerators) have to monitor slow varying signals like temperature, pressure and flow, as well as to set “set-points” of various process control elements. It is also necessary to read various digital status signals and turn “on” and “off” various switchable control elements.

A lot of COTS based digital and analog cards solutions are available, even on VME platform, for use in normal process control application. Most of these COTS cards have software based trigger, which is inadequate and has large latencies. Modern Data Acquisition Systems (DAS) require a hardware based, multi-mode programmable trigger systems to meet challenging trigger requirements. Also the COTS systems, do not allow user to modify the firmware, since the schematic level information is not available. The A64-D64 data transfer modes is missing in most of the COTS systems, which can improve the overall system performance.

The Analog input and output card need to receive as well as transmit signals in voltage or current mode. Most of the COTS solution require an additional board to be designed to meet these vide variety of signal input types and ranges. Digital signals have to travel over a long distance and hence they must be capable of driving as well as receiving signals via 50Ω cables.

An VME64x compliant digital input output as well as analog input output board has been developed to address these requirements.

## DESIGN OF DIGITAL IO BOARD

The VME64x compliant digital I/O board has 32 isolated digital inputs which can drive a 5V TTL high impedance load or a 2.5V LVTTL signal in to a 50Ω load. It can also receive 2.5V LVTTL as well as 5V TTL signal with 50Ω termination. The IO connections are brought out via two pairs of mini centronic connectors. The block diagram of the 32 channel digital I/O board is shown below in figure 1.

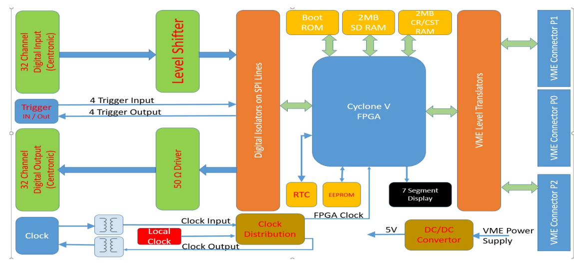


Figure 1: Block diagram of 32 channel Digital I/O Board

The board has a pair of centronic connectors on the main facia, which supports 16 digital inputs on one connector and 16 digital outputs on the second connectors. The remaining 16 inputs and 16 outputs are mounted on a dummy facia and are connected to the board via FRC cable.

### *VME64x interface*

The board supports full feature VME64x interface. It supports A16, A24, A32, A64 addressing modes. It also supports D8, D16, D24, D32, D64 data transfer modes. The board has 2Mbyte of SRAM for CR/CSR space required by advance VME data transfer modes.

SN74VMEH22501A translates 3.3V FPGA signals to VME bus compliant 3.3V signals. The chip has one 8-bit universal bus transceiver module and two 1-bit tristate capable bus transceivers. The chip is designed for 3.3V operation with 5V tolerant inputs on the VME side.

The chip has built in active bus-hold circuitry which holds unused or un driven port inputs at a valid logic state. Bus-hold circuitry is not provided on 1bit bus transceivers or on control inputs. Use of pull up or pull down resistors with the bus-hold circuitry is not recommended by the manufacturer and the same has been followed in the design.

The VME64x slave code in VHDL has been developed in-house at ACnD, BARC and the same has been used on various VME64x boards developed in the division. The same code has been ported to this board.

The data is acquired using EPICS based SCADA running on MVME5500 controller. The MVME5500 controller runs on Linux kernel 2.4.16 and supports all the required EPICS resources.

### *FPGA Interface*

The board is designed around Cyclone V FPGA in view of long term support required for these boards. The FPGA

#khole@barc.gov.in

5CEBA7F31C7N is from Cyclone V device family and has 150K logic elements and is available in 896 pin BGA package. It does not have any PCI or DDR3 hard core, thus minimising the FPGA cost. It has 156 DSP elements which can be used for implementing various types of filters for ADC /DAC data. The digital I/O board does not need this level of FPGA resources, but to retain the commonality between the boards, same FPGA has been used.

The FPGA interfaces to two memory banks of 2Mbyte static ram; one for implementing CR/CSR space and the other for storing the data generated by digital inputs and digital outputs as well as by the ADC and DAC.

The board has I2C driven EEPROM which is used for storing various parameters like board model number, board serial ID, board schematic reference number, board firmware version. The memory also stores the calibration data for each ADC and DAC channel on the Analog I/O boards.

The board also has a I2C driven real time clock (TRC) module which is used for time stamping the data received from the ADC as well as Digital Inputs. Higher precision data stamping is achieved by augmenting the RTC by local counter running in FPGA. A small 5X7 dot matrix display is available on the front panel; the status of various channels is displayed on it. The display can be programmed and updated over SPI interface by the FPGA.

### *Trigger and Clock section*

The board has four trigger inputs, which are isolated from the FPGA via ADUM160N isolator module (discussed later in detail). The trigger logic can be programmed in the FPGA as well as via GUI. The board also provides four isolated trigger outputs, which can be used for triggering additional analog as well as digital I/O boards. Trigger speeds up to 1MHz are supported when only digital I/O cards are used. When used in conjunction with analog I/O boards, the trigger rate is usually decided by the analog requirements.

The board also has provisions for external as well as internal clock reference. The external clock via SMA connector needs 0dBm to 10dBm signals. It is recommended to use at least +3dBm and above signal for reliable low jitter operation.

The external signal is isolated via a transformer and is applied to one of the input pins of 8T39S11A from IDT. The chip has been chosen for its ultra-low jitter of 35fS RMS. The second input is connected to a 125MHz xtal oscillator module. The chip is having two banks of 5 outputs each of which can be configured as LVPECL or LVDS or HCSL. Bank A outputs are used for clocking all LVDS clock inputs of the FPGA. One output from the bank B is used as a reference clock output which is brought out through transformer isolation on to an SMA connector; remaining outputs are unused. The reference clock output pin drives CDCLVC1108 which provides LVTTL compatible clock used that are used by various LVTTL clock inputs on the FPGA.

### *Digital Input*

The digital inputs from the centronic connector are terminated in a 50Ω load followed by a RC filter having a cut-off frequency of 100 kHz to eliminated glitches in the operation. This limits the speed at which digital data can be received and can easily be changed by adjusting the RC network if the need so arises.

The signal level can degrade a lot due to cable losses, hence SN74ABT241APWR is used to restore the levels to proper TTL levels. SN74ABT241APWR has a high-level input voltage $V_{IH}$ as low as 2 V on a 5V supply. Low-level input voltage $V_{IL}$ is guaranteed to be less than 0.8V, thus ensuring sufficient noise margin.

The output of SN74ABT241 drives ADUM160N which is a transformer coupled isolator. ADUM160N can operate up to 150MHz and has 6 channels per chip. The module provides 3kV RMS isolation between input and output. The propagation delay varies from 13nS to 15nS depending on the supply voltage.

Unlike other opto-coupler alternatives, dc correctness is ensured in the absence of input logic transitions. If the input side is off or in tristate mode, or the input side power supply is absent, the fail-safe output state for N0 series devices would be low.

The devices operate with the supply voltage on either side ranging from 1.7 V to 5.5 V, providing compatibility with lower voltage systems as well as enabling voltage translation functionality across the isolation barrier.

### *Digital Output*

The digital signal from the FPGA passes through an RC network, which limits the bandwidth to 100kHz. This bandwidth can be changed, if required, by changing the RC network. The I/O isolation is provided by ADUM160N, which is connected to the RC network. It also provides the required level shifting to 5V TTL level. Pull down resistors on ADUM160N ensure, that all the outputs are low when the card is powered up as well as during FPGA programming.

SN64BCT25245DW follows the isolator module and acts as a buffer. It is capable of driving 50Ω load at 2.5V LVTTL levels.

Figure 2: Fabricated Digital I/O Board

The chip is a 25Ω bi-directional octal bus transceiver designed for transmission from the A bus to the B bus or from the B bus to the A bus depending up on the logic level at the direction-control (DIR) input. The chip is capable of sinking 188-mA $I_{OL}$, which facilitates switching loads up to 25Ω. A 22Ω series resistance at the output of this chip provides a nice 50Ω source drive. The digital I/O board has been tested in lab and fabricated board picture is shown above in figure 2.

## DESIGN OF ANALOG IO BOARD

The VME64x compliant analog I/O board has 16 analog inputs. The input ranges available are 0-5V, 0-10V, ± 5V, ± 10V, 0-20mA, 4-20mA, ± 20mA, which can be individually selected for each of the input channels. The board also has 16 analog output channels; each channel can be programmed to deliver 0-5V, 0-10V, ± 5V, ± 10V, 0-20mA, 4-20mA, ± 20mA. The block diagram of the board is shown below in figure 3.

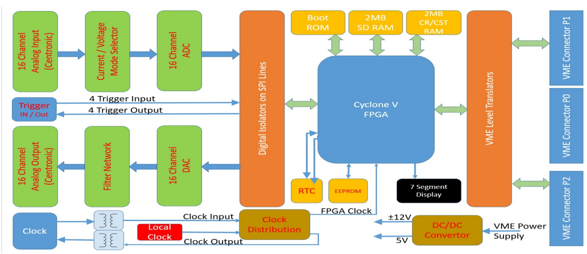

Figure 3: Block diagram of 16 channel Analog I/O Board

The design details of VME Interface, FPGA, RAM, EEPROM, RTC, Boot-rom and 7 segment display section have been discussed in detail for digital I/O board and are also applicable for the analog I/O board. The trigger and clock distribution section is also identical and has been discussed in details for the digital I/O board.

### *Analog Input*

The analog inputs from the centronic connector are terminated in 249Ω resistor which is in series with ADG1421BRMZ, an analog switch. The switch can be controlled via FPGA allowing a 4-20mA signal to be converted in to 1-5V signal, which can then be digitised by the ADC. This allows the same channel to be used for current as well as voltage inputs.

The LTC 2353-16 is a 16-bit, simultaneous sampling dual channel 550kSPS low noise SAR ADC. Both the channels of the ADC can be independently configured on a conversion-by-conversion basis to accept ±10.24V, ±5.12V, 0 - 10.24V, or 0 - 5.12V signals. This features, combined with ±1LSB INL, no missing codes at 16 bits, and 94.2dB SNR, makes the LTC2353-16 an ideal choice for our application. External voltage reference (LTC6655BHMS8-2.048) is used for driving all the ADC, thereby eliminating ratio-metric errors. Anti-aliasing filter of 275kHz at the input of ADC allows sampling speed of 550KSPS.

The output of ADC is available in SPI format with each channel providing its data on a separate MISO line but a common MOSI line. These SPI lines are interfaced to the FPGA via ADUM160N isolators to provide isolation between field signals and FPGA. The isolation is not provided at analog input stage to eliminate nonlinearity, bandwidth limitation and additive noise from the typical analog isolation modules.

The ADC data is stored in static RAM. The data can be filtered to improve the noise performance by using on board DSP elements. The span gain and offset adjustment and RTC time stamping can be applied to each data before it is stored in memory.

### *Analog Output*

The analog output stage is designed around AD5758BCPZ which provides 0 - 5V, 0 - 10V, ± 5V, ± 10V, as well as 0 - 20mA, 4 - 20mA, ± 20mA, ± 24mA ranges. The device uses an SPI interface which can operate up to 50 MHz clock. The DAC has provisions for user-programmable offset and gain compensation and it also provides advanced on-chip diagnostics, including a 12-bit ADC for housekeeping application. It has a maximum settling time of 20µS.

The AD5758 contains integrated buck dc-to-dc converter circuitry that controls the power supply to the output buffers, allowing a reduction in power consumption from standard designs when using the device in both current and voltage output modes. In current mode, the dynamic power supply management unit monitors the voltage on the DAC output and adjusts the power supply head room of the DAC accordingly

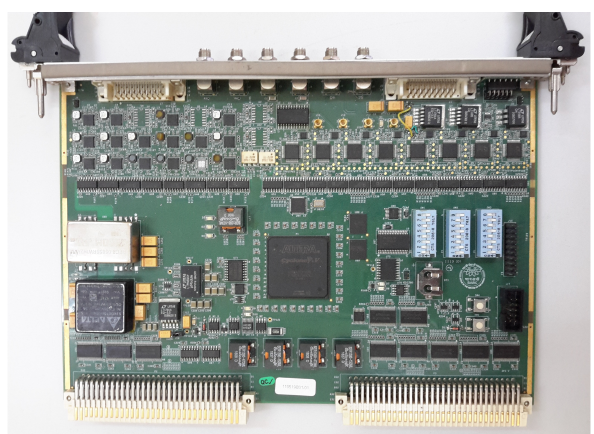
Figure 4: Fabricated Digital I/O Board

The board has been tested in lab and fabricated board picture is shown above in figure 4.

## ACKNOWLEDGEMENT

The authors would like to acknowledge Shri Sandeep Bharade, Shri Hitesh Shukla and Shri R.T. Keshwani of ACnD, BARC for their support during fabrication and testing of the boards.

# DESIGN OF DIPOLE MAGNET FOR HIGH RESOLUTION SEPARATOR

A. Agrawal*, A Dutta, A. Goswami and A. Bandyopadhyay
Variable Energy Cyclotron Centre, 1/AF Bidhan Nagar, Kolkata 700064

*Abstract*

High Resolution mass Separator (HRS) is an essential part of ANURIB project in Variable Energy cyclotron Centre, Kolkata. This facility will work as an isobaric mass separator for low energy unit positive charged radioactive ions. It consists of several electrostatic quadrupoles for focusing and matching, and two symmetrically placed dipole magnets with bending angle 90 degree as a pure separator. Requirement of high value of mass resolution of the order of 20000 puts stringent criteria for dipole magnet specification.

To achieve the required mass resolution and to accommodate maximum transverse size of beam envelope, magnet must have large pole width. To get large dispersion in the horizontal plane the bending radius of the magnet should be large. Pole face rotation and curvature at entry and exit side of the magnet is required to minimize second order aberration on the beam envelope. Our goal is then to design a dipole magnet which has minimum aberration and large dispersion to achieve the required resolution. An integral field flatness of $<10^{-5}$ is required within the good field region of the magnet. In this paper we have presented the various methods adopted while designing this dipole magnet of the HRS to fulfil the physics requirements

## INTRODUCTION

The High Resolution separator design is akin to TRIUMF's ARIEL design [1], but Dipole Magnet parameters are different here to match the beam optics requirements. The High resolution separator will be made up of 180 degree beam path, consists of matching sections with two 90 degree magnetic dipoles and a higher order harmonics corrector [2] between dipoles. Dipoles will be used as separator and its edge curvatures will decide in such a way that it corrects the second order imperfection to beam envelope [3], with facility of higher harmonics corrections in corrector. Figure 1 refers to the schematic of the beam line.

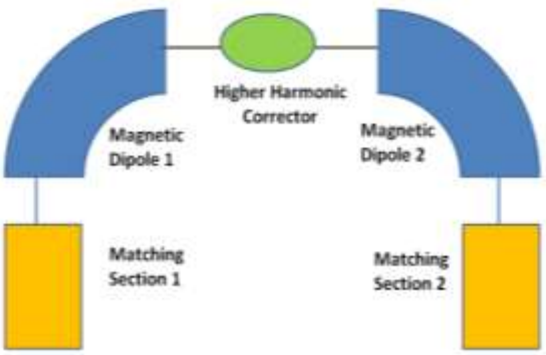


Figure 1: Schematic of High resolution separator

This combination is designed to achieve 1:20000 resolutions for a 3.125 mm-mrad (horizontal) and 6 mm-mrad (vertical) emittance. A design for the HRS dipole magnets should achieves both radial and integral field flatness goals of $<10^{-5}$.

## DESIGN CRITERIA OF DIPOLE MAGNET

The procedure of design and optimization of dipole magnet parameters to achieve field flatness of $<10^{-5}$ is motivated by the work done by Dr. Marco Marchetto in his Ph.D. thesis [4], The principle of mass separation is based on the fact that particles with different momenta have different trajectories when crossing a uniform magnetic field. If the particle is travelling in circular path in a plane with uniform magnetic field having bending radius of "ρ". The bending radius is related to the mass m of the particle according to the equation (1)

$$B\rho = \frac{mv}{q} \qquad (1)$$

The product "Bρ" is referred as the magnetic rigidity of the particle. When particles are extracted with the unit charge state at a fixed accelerating voltage V from a Ionizing source, the velocity "v" of the particles depends on the mass" m" and so we have equation (2) for bending radius

$$\rho = \frac{1}{B}\sqrt{\frac{2mV}{e}} \qquad (2)$$

This is the principle on which mass separation is based. The Dispersive property of Magnet may be used to separate beam components that differ in momenta because of difference in Mass. The accelerating voltage V applied after the Ionizing source is generally so small that non-relativistic expression may be used, assuming that input beam is of parallel in nature, as refer in figure 2, width of beam [5] at object plane is given by equation (3)

$$w_0 = D\frac{dm}{m} \qquad (3)$$

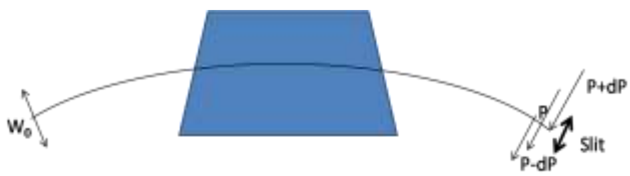


Figure 2: mass selector

Where D is called the dispersion function of the dipole magnet and m/dm is the resolving power. The dispersion function for dipole magnet is sinusoidal in nature but is directly proportional to the radius of curvature of the trajectory, in first approximation it can be written as equation (5)

$$D = \rho(1 - Cos(\theta)) \qquad (5)$$

where θ is the bending angle, Here for a 90 degree dipole the dispersion of the magnet is equal to the radius of curvature.

In order to have separation Beam maximum width $2 * x_{max}$ should be less than $w_0$. For an upright ellipse emittance "ε" of the beam can be written as "$\theta_{max}x_{max}$". using equation (4) and (5) Resolving power can be written as given in equation (6) and is inversely proportional to the emittance. Lesser the emittance better the resolving power is

$$\frac{m}{dm} \leq \frac{D\,\theta_{max}}{2\,\varepsilon} \qquad (6)$$

Magnification also played an important role as given by equation (7). So resolving power can further be improved by increase in magnification.

$$\frac{m}{dm} = \frac{P}{dP} = \left|\frac{R_{16}}{2x_{0R_{11}}}\right| = \left|\frac{R_{16}}{2x_{0M_x}}\right| \qquad (7)$$

More important, for an upright ellipse, the divergence of the beam $\theta_{max}$ is known given the emittance ε, and the maximum beam size $x_{max}$, defined by the resolution and the dispersion or can also be determined by minimum drift lenth "L" required outside the magnet in beam line, this will define the maximum divergence at the entrance of magnet. The divergence also determines good field region in pole region. The optics design is such that the minimum drift lenth "L" required outside the magnet in beam line will define the maximum divergence at the entrance of magnet as given in equation (8)

$$L\theta_{max} = L\,\frac{\varepsilon}{x_{max}} = 2\,\frac{L}{D}\frac{\varepsilon\,dm}{m} \quad (8)$$

Emittance assumed above is based on the consideration that all particles have same momenta but in actual case particles has spread in momentum, than effective emittance is higher than considered . Exact emittance can be calculated if we know spread in momentum in advance. So based on above equations $\theta_{max}$ =0.1 rad and $X_{max}$=31.25μmm choosen so emittance of 3.125 mm-mrad is taken for initial parameter calculations. Emittance larger than this still works for separator but at reduced transmission efficiency

## MAGNET DESIGN IN OPERA

Important parameters required for magnet design is obtained from the beam dynamics calculation [3] and opera design is shown in figure 3, Our design goal is to design dipole magnet as closely possible to equivalent hard edge model as shown in figure 4, as this will simplify the further studies using magnetic field. Considering the effect of fringing field, effective iron angle is taken smaller than net bending angle by a distance of pole gap at reference radius, some important design parameters are summarized in the following table.

Table 1: Parameters of the magnets

| Parameter | Value |
|---|---|
| Dipole magnet Bending angle | 90 degree |
| Bending radius | 1250 mm |
| Entrance and exit dipole hard edge angle | 25.7 degree |
| Entrance and exit dipole edge curvature radius | 1573 mm |
| Good field region width of dipole magnet | ±15 cm |
| Field Flatness required dB/B (calculated) | < $10^{-5}$ |
| Pole gap | 70 mm |
| Pole width | 1000 mm |
| Saturation level in Iron | Below 1.7T |
| Dipole Field Range ( $^{11}Li^{1+}$ to $^{238}U^{1+}$) | 0.102 to 0.480 T |

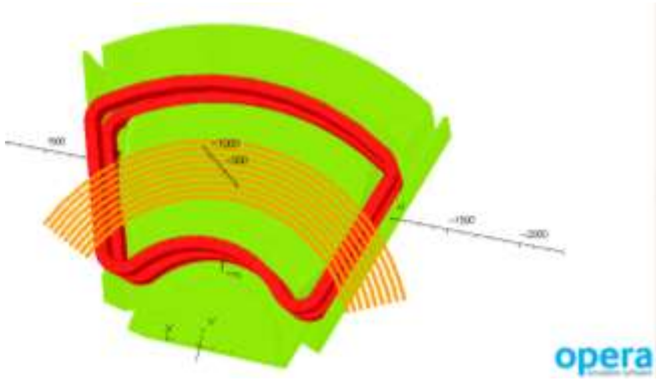


Figure 3: Dipole magnet design in opera[6]

## GOOD FIELD REGION

This $\rho\theta_{max}$ width defines the area occupied by the beam in pole region, referred in as the good field region inside the magnet.

## MINIMUM POLE WIDTH AND POLE GAP

Maximum beam envelope size in horizontal plane will define the minimum pole width, here horizontal beam size is intentially keep higher for better resolving power. And this will define the pole width. Maximum beam envelope size in vertical plane will define the minimum pole gap, also wisely chosen pole gap will be good for low current excitation and improve field quality.

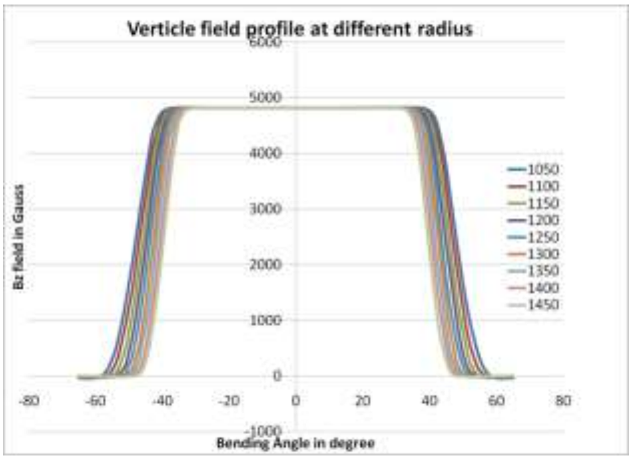


Figure 4: vertical field Bz profile at different radius

## FIELD HOMOGENEITY

The field quality requirements follow from the equation by calculating the differential in "B" and "m", is given as equation (9)

$$\frac{dB}{B} = \frac{1}{2}\frac{dm}{m} \qquad (9)$$

Field Flatness (FF) can be defined as given in equation (10), After using optimized rogowski profile at entrance and exit of pole edges, Calculated Field flatness is shown in figure 5

$$FF(r) = \frac{B_z\,(r)}{B_0} - 1 \qquad (10)$$

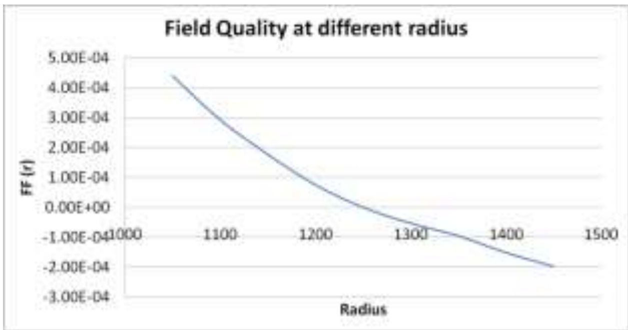


Figure 5: vertical field Bz profile at different radius

Integral ratio IRρ can be defined as given in equation (11) for a given geometric trajectory "s" as refer in figure 6

$$IR_\rho = \frac{\int_{-l}^{l} B_z(s)ds}{\int_{-l}^{l} B_0\, ds} \qquad (11)$$

The denominator of $IR_\rho$ the integral of the hard-edge case is computed only over the arc component of the geometric trajectory. while numerator is calculated at full reference trajectory. Summarized in table 2

.

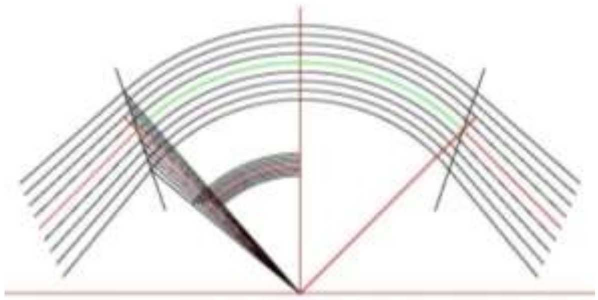

Figure 6: Reference Trajectory made up of straight and circular arc

Table 2 : Integral Ratio of reference trajectories

| Geometric trajectory P in mm | Arc length in mm | Hard edge $\int_{-l}^{l} B_0\, ds$ In T-mm | Reference trajectory $\int_{-l}^{l} B_z(s)ds$ in T-mm | Integral ratio |
|---|---|---|---|---|
| 1050 | 1846 | 889.5854 | 905.8854 | 1.018324 |
| 1100 | 1874 | 902.9963 | 919.3963 | 1.018161 |
| 1150 | 1903 | 916.7542 | 933.5542 | 1.018325 |
| 1200 | 1933 | 930.9477 | 947.7473 | 1.018046 |
| 1250 | 1963 | 945.3879 | 961.8875 | 1.017453 |
| 1300 | 1994 | 960.0830 | 976.3830 | 1.016978 |
| 1350 | 2025 | 974.9547 | 990.6546 | 1.016103 |
| 1400 | 2056 | 989.9256 | 1005.1259 | 1.015354 |
| 1450 | 2088 | 1005.083 | 1019.4838 | 1.01432 |

The paper describes the design and optimization procedure of bending magnet to achieve field quality of of $<10^{-5}$ within good field region, further improvements in integral field quality can be made using optimization of Rogowski profile around the edges of poles and minimizing the contribution of higher field harmonics.

## REFERENCES


[1] J. A. Maloney, R. Baartman, and M. Marchetto, "New design studies for TRIUMF's ARIEL High Resolution Separator", Nucl. Instr. Meth., vol. 376, pp. 135–139, 2016.

[2] Cary N. Davids *, Don Peterson "A compact high-resolution isobar separator for the CARIBU project" Nuclear Instruments and Methods in Physics Research B 266 (2008) 4449–4453

[3] A Goswami, "Beam Optics Design of a High Resolution Separator for ANURIB Project" InPAC 2019 at New Delhi

[4] "Magnetic Field Study for a New Generation High Resolution Mass Separator", Dr. Marco Marchetto. Ph.D thesis, submitted in The University Of British Columbia.

[5] P.P 26, " The optics of Dipole Magnets", John J Livingood, Academic press INC

[6] OPERA FEM Package, Version 16R1, Vector Fields, Cobham, UK

# DESIGN OF HIGH GRADIENT DIPOLE-QUADRUPOLE MAGNET

Ritesh Malik#, Kailash Ruwali, Gautam Sinha, and S. N. Singh

Accelerator Magnet Technology Division, Raja Ramanna Centre for Advanced Technology, Indore, India.

*Abstract*

This paper presents 2D and 3D design of a dipole-quadrupole magnet which is intended to be used in the high brilliance storage ring proposed to be built in RRCAT. Limited amount of quadrupole strength can be generated in dipole by tapering the poles. However, for generating strong gradient in dipole a horizontally offset quadrupole is used. In this design half of the quadrupole is used, so two of the four poles of quadrupole are optimised to make it compact and reduce the power requirement. This dipoles-quadrupole magnet is design for 0.6T peak dipole field along with 15T/m quadrupole gradient. 2D simulation is carried out using POISSON code and for 3D simulation TOSCA is used. Effect on dipole field with the change of quadrupole gradient is also studied.

## INTRODUCTION

Magnetic field is used for the bending of charge particle moving with velocity. The dipole and quadrupole magnets are used for the bending and focusing of the charge particle beam in accelerators respectively. Dipole and quadrupole magnets can be designed independently. But for the high brilliance storage ring both magnets are combined in single magnet. This combined magnet generate high gradient dipole and quadrupole field in a single magnet. These high gradient dipole quadrupole magnet are off axis quadrupole magnet. For the above purpose, off centred half quadrupole magnet are used. So, an off-centre quadrupole magnet is designed for required dipole field and field gradient. It is further optimised, for better tuning, weight reduction and power reduction.

## MAGNET SPECIFICATION

The dipole quadrupole magnet is designed for the dipole field (Bo) of 0.6T and the field gradient (G) of 15T/m. Weight of magnet should be optimise. The pole radius of magnet is 30mm. and length of magnet is 0.8m. Good field region of magnet is ±7mm for the $\Delta G/G$ less than 1e-02.

## 2-D DESIGN OF MAGNET

The magnets are design using the concept of off axis quadrupole which can generate the constant gradient of 15T/m. so, the radial distance for dipole field of 0.6T is at (0.6/15=) 0.04m from the centre of quadrupole. so, we have to design a dipole quadrupole magnet for the distance of 0.040 ± 0.007m from the centre of magnet pole.

Required NI is ~6000 Amp turns per pole to generate the gradient of 15T/m.

# goldy@rrcat.gov.in

Main coil cross section area is 75cm$^2$ (for current density 100A/cm$^2$), i.e. coil size is 7.5*10cm$^2$. And small coil size is optimised to 25 cm$^2$, i.e. 2.5*10cm$^2$. The coil size can be reduce is water cooled conductor and over size of magnet will be reduce but power losses will increases.

The pole profile of dipole quadrupole magnet is hyperbola (x*y= R$^2$/2). First, quadrupole magnet is designed in 2-D using POISSON code. After that quadrupole magnet is optimised for the offset half quadrupole magnet. Because half of the quadrupole will be used. Opposite half of dipole quadrupole magnet is designed for zero magnetic field (approximately).

First full quadrupole magnet is simulated and later on it is optimised for the off-centred half dipole quadrupole magnet. Figure 1 (a) & (b) show the quadrupole magnet cross section (in cm) and its magnetic field profile (Gauss) in horizontal plane (cm).

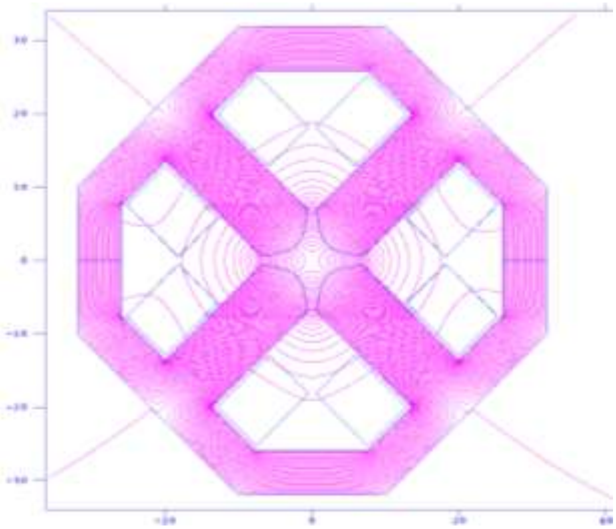

Figure 1 (a): Full quadrupole magnet cross section in cm and field contour lines, designed in POISSON.

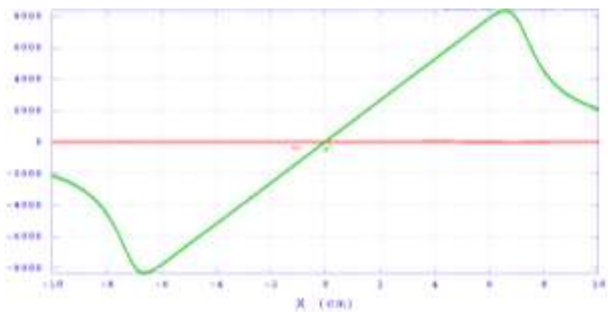

Figure 1 (b): Transverse magnetic field By (Gauss) on horizontal plan (cm).

For quadrupole magnet, beam prefer to travel thought the centre of the quadrupole where magnetic field is ideally zero, see figure 1(b). For additional dipole magnetic field, beam is travel through the horizontally offset of 4cm from the centre of quadrupole magnet at which magnetic field increase up to Bo=0.6T for field gradient of G=15T/m, see figure 2(b) & (c). To achieve this condition, offset quadrupole is used. Since half quadrupole magnet is use. So, opposite half of quadrupole magnet pole is optimised for power loss, weight, tunebility, fabrication cost, see figure 2(a). And magnetic field in this region is near to zero as desired (figure 2(c)).

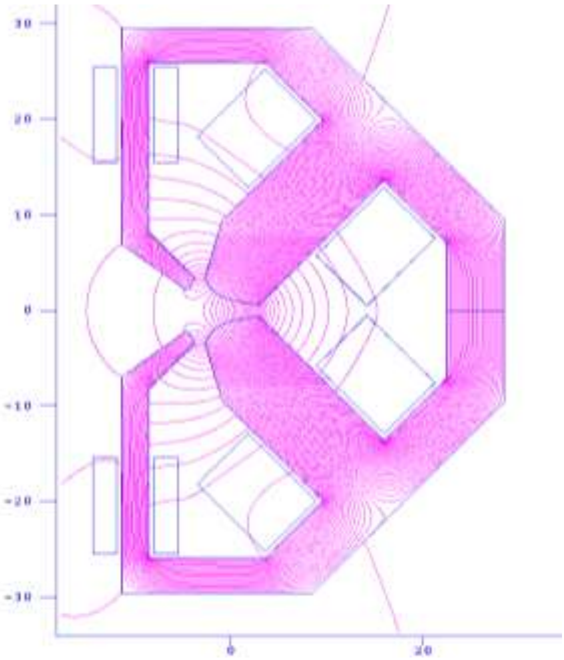


Figure 2(a). Full dipole quadrupole magnet cross section in cm for air cooled coil.

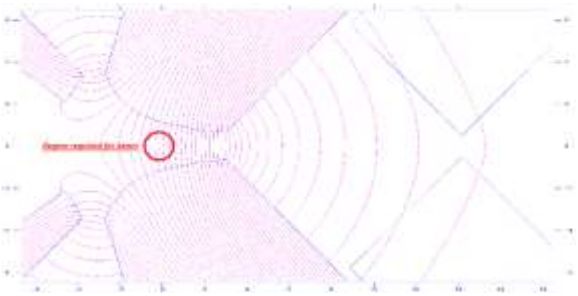

Figure 2(b). Zoom area of dipole quadrupole magnet of figure 2(a) showing the area which is used by the beam in cm.

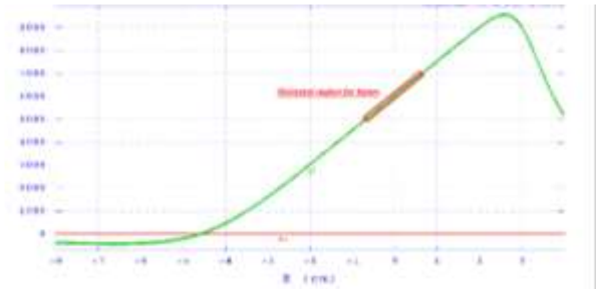

Figure 2 (c): Transverse magnetic field (By in Gauss) vs horizontal plan (x in cm) for dipole quadrupole magnet shown in offset region which is required for beam.

Dipole quadrupole magnet is successfully designed for 0.6T and gradient of 15T/m. And ΔG/G is of the order of $1x10^{-03}$ for ±0.7cm.

Length of this quadrupole is 0.8m. NI of the primary coil is 5640 Amp-turns per pole. And 1500 Amp-turns per pole for small coil used for the tuning of dipole quadrupole magnet.

For air cooled coil, if current density of $1A/mm^2$ is used then power loss is 455 watt per magnet. If coil size is reduce by increasing the current density $7A/mm^2$ (water cooled coil), power loss is increase by same factor i.e. 3.2 k watt per magnet. At the cost of power loss magnet size can be reduce i.e. Magnet weight is reduce but operational cost is increase.

The pole width of dipole quadrupole magnet is 90mm this pole is reduce to 29mm for small pole. And the width of return yoke is 60mm and reduce to 36mm for smaller pole. Magnetic field in iron core is ~1.1 T. the height of magnet is 600mm and width is 430mm for air cooled coil. The height and width of magnet is further reduce if we use water cooled coil.

3-D model is done using straight magnet using OPERA 3D MODELLER. 3D model is given in figure 3(a). Bending radius will be define later on once bending angle is specified. In 3D modelling the gradient quality ΔG/G is also less than $<1x10^{-02}$ for the region of ±10mm in respect of required ±7mm.

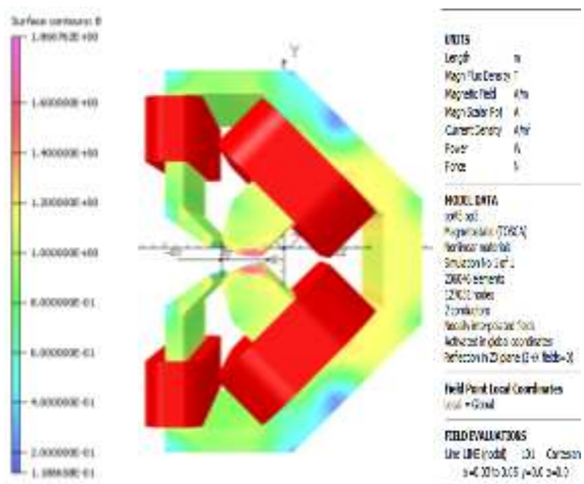

Figure 3(a). Full 3-D model (in m) of dipole quadrupole magnet with surface magnetic field contours ( in T).

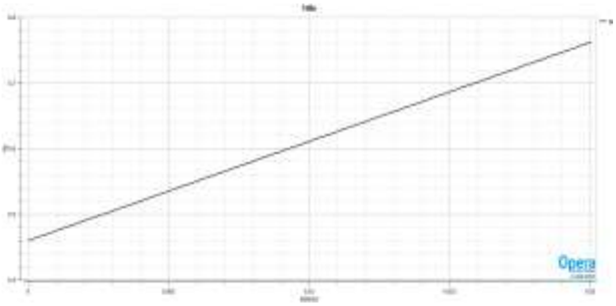

Figure 3 (b): Transverse magnetic field (T) on horizontal plan (m) for dipole quadrupole magnet at the longitudinal centre.

## CONCLUSION

Initially dipole quadrupole magnet cross section is success fully designed in 2D using POISSON code and later on 3-D modelling is done in OPERA 3D MODELLER and solved TOSCA solver. Dipole field of 0.6T and gradient of 15 T/m is obtained at offset distance of 0.04m. As well as $\Delta G/G$ is less than 1e-02 for ±7mm.

## REFERENCES

[1] POISSON Group of Codes, Los Alamos National Laboratory, New Mexico, 86545.
[2] Vector Fields Limited, 24 Bankside Oxford, OX5 1JE. Kidlington, England.

# DEVELOPMENT OF INTERNAL BEAM CURRENT MEASUREMENT ELECTRONICS SYSTEM FOR INJECTOR MICROTRON

A. C. Holikatti*, Rahul Jain, B. B. Sonawane, Y. M. Sheth and T. A. Puntambekar
Beam Diagnostics Section / Beam Diagnostics & Coolant Systems Division
Raja Ramanna Centre for Advanced Technology, Indore - 452 013
* email: anilch@rrcat.gov.in

*Abstract*

In Indus Accelerator Complex, a 20 MeV Microtron is used as an injector to Booster synchrotron of the synchrotron radiation facilities, Indus-1 and Indus-2 at RRCAT [1,2]. Internal Beam Current Measurement Electronics System (IBCMES) is developed and deployed for measurement of parameters of electron beam inside the injector Microtron. This paper describes the design and development of the IBCMES. Mechanical assembly of the Internal Beam Current Measurement system consists of two movable beam probes installed inside the Microtron for measurement of the parameters of the electron beam in last few orbits. The beam probe intercepts the electron beam of Microtron transversely and generates current signal proportional to the intercepted portion of the beam. The electronic system controls the motion of beam probes using stepper motors (SMs) and acquires beam current signal from the probes. The position of beam probes is read using linear potentiometers (LPMs) with the positional accuracy better than 100 µm. Integrator based electronics has been developed, which measures integrated current falling on the beam probe during the beam pulse with accuracy of ± 1% of the full scale value. The range of current measurement is 0.1-100 mA. The data of probe position and the beam current signal is acquired by the hardware system. This data is then collected by an application program being executed on a PC. The application program including the Graphical User Interface (GUI) has been developed in LabVIEW. The software has many features like graphical display of the acquired beam current with respect to the beam probe position, display of limit switch (LMSWs) status etc. This system is frequently used for measurement of the beam parameters during the experiments conducted for performance improvement of the injector Microtron and also after change of cathode.

## INTRODUCTION

A 20 MeV Microtron is being used as an injector for the Booster synchrotron. Microtron delivers electron beam pulsed current of 30 mA at PRR of 1 Hz. The beam of 500 nsec pulse duration is accelerated to 20 MeV and extracted through with beam extraction assembly. The extracted beam is transported through Transfer Line-1 (TL-1) and injected into the booster synchrotron. For a good injection of beam in Booster, it is important to know the beam parameters in the last few orbits of the Microtron before the beam is extracted. The internal beam parameters are measured using Internal Beam Current Measurement (IBCM) system. This is an intercepting type of beam diagnostic system. For IBCM, motion control and processing electronics system has been developed. Signals obtained from the probes of IBCM are processed by the electronics system for quantitative measurement of beam parameters such as beam current, beam size and transverse beam profile. Two numbers of IBCM systems have been installed inside the Microtron.

## IBCM SYSTEM DETAILS

Internal Beam Current Measurement (IBCM) system consists of two movable beam probes namely Probe-1 and Probe-2 mounted inside the Microtron in orthogonal directions. The probes scan the electron beam transversely. The beam probes require the motion control and current signal processing electronics for its operation. The beam probes are moved in incremental steps in the path of the beam with the help of stepper motors. The probes intercept the electron beam of Microtron transversely and generates current signal proportional to the intercepted portion of the beam. The probe position and the beam current signal are acquired by the hardware system that computes the beam profile, beam size and beam position. The scheme of Internal Beam Current Measurement system for injector Microtron is shown in Figure 1.

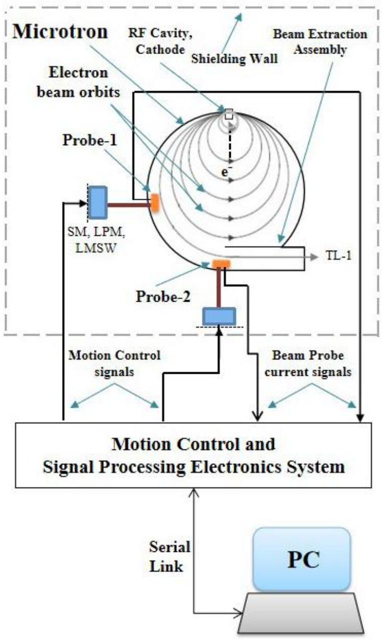


Figure 1: Scheme of IBCM system for injector Microtron.

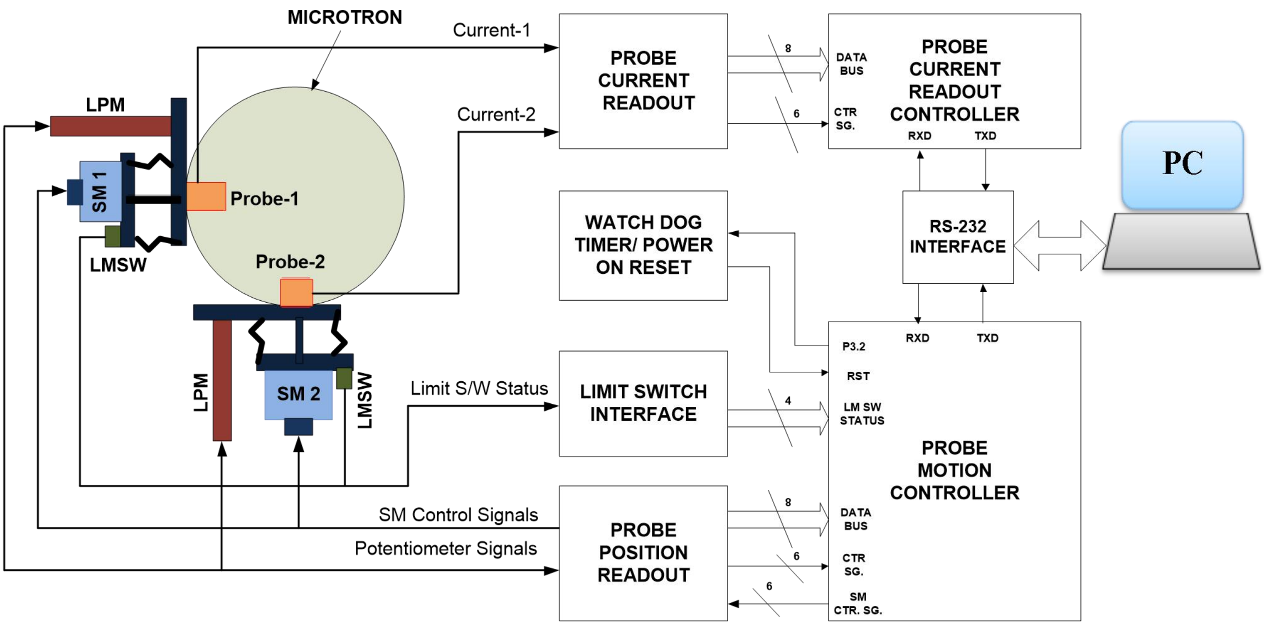


Figure 2: Block diagram of the control and processing electronics system for IBCM system.

## SYSTEM DESCRIPTION

Figure 2 shows the block diagram of the control and processing electronics system for IBCM. It is based on AT89C52 microcontroller [3]. The functions of the controller are to control the movement of the stepper motors, read the position of the beam probe from the linear potentiometer and acquires beam current signals from the probes. It also observes limit switch status to prevent the motion of probes beyond set limits which provide the safety interlocks for the system. To control the motion of probes independently, the microcontroller sends the required phase sequence to the stepper motor drivers. Speed of the stepper motos is programmable and can be varied from 3 to 80 RPM. Thus, the user can set the velocity of the probe movement. The motion controller electronics also reads and checks the status of limit switches constantly during the probe movement. The motor is stopped instantly when the beam probe reaches at its extreme positions. The action is independently taken by the dedicated limit switches. This prevents the damage to the probe mechanism.

Watchdog timer (WDT) hardware has also been configured to reset the controller in case if the system hangs or a hardware fault occurs. On the occurrence of a fault, the WDT hardware generates the reset signal to the controller which initiates corrective action i.e, parking the beam probes in a safe location, restoration of normal system operation and generation of alarm.

The linear potentiometers (Model No. PM-75-5K, make: ELAP) used for reading the position of beam probes provides linearity better than ± 0.1%. The probe position readout consists of 12-bit ADC, a voltage reference LM399 and signal conditioning circuit. The position of beam probe is read from linear potentiometer and digitized with 12-bit ADC. The digitized data is then acquired by the controller and transferred over serial link (RS-232) on request to the application running on PC. Integrator based probe current readout electronics measures integrated current falling on the beam probe during the beam pulse. The probe current readout consists of 12-bit ADC, analog switches namely HOLD and RESET and an operational amplifier [4]. The readout controller controls the timings of integrate, hold, readout and reset cycles of the integrator using RESET and HOLD switches. The beam signal integration is synchronized with the pulsed beam of Microtron. The output voltage of integrator corresponding to each beam probe is digitized by the 12-bit ADC. The readout controller acquires the digital data from ADC and sends it to the PC on RS232 serial link.

### *Software*

The data of probe position and the beam current signal is acquired by the hardware system. This data is then collected by an application program being executed on a PC. The application program, including the Graphical User Interface (GUI) has been developed in LabVIEW. The operator interface in GUI interacts with the IBCM electronics system for control of the probe motion and acquisition of integrated probe current signal data of IBCM system for injector Microtron. The software has several features like graphical display of the acquired beam current with respect to the beam probe position, probe home position setting, stepper motor rpm setting, run or stop stepper motor, reading linear potentiometer data, reading limit switch status, and communication link check etc. The GUI software also stores the acquired data with time stamp in a file in the PC. A screenshot of the

GUI of the internal beam current measurement system is shown in Figure 3.

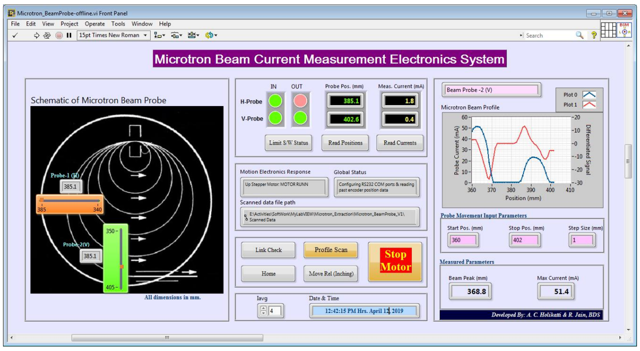


Figure 3: Screen shot of graphical user interface of internal beam current measurement system

## SYSTEM OPERATION AND TESTING

The IBCM system has been developed to remotely operate the internal beam probing system of Microtron and acquire the current, profile and position of the electron beam in the Microtron. It is operated from a PC in the control room. Figure 4 shows the photograph of installed beam probes and electronics system for Microtron.

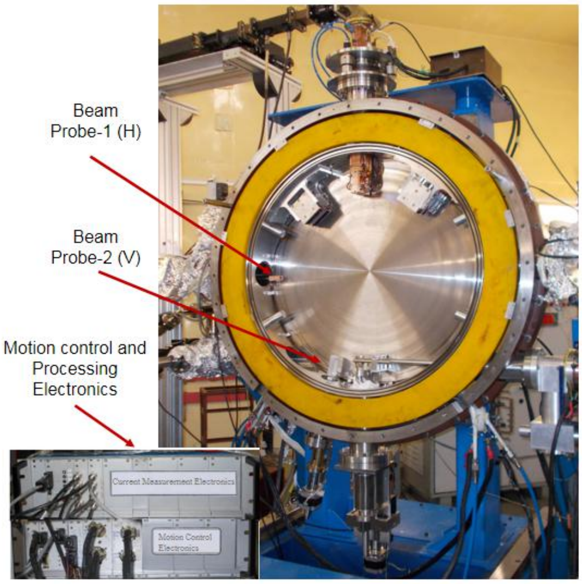


Figure 4: Photograph of installed beam probes and electronics system for Microtron.

The electronics system has been tested for the movement range of 50 mm and smooth operation under actual conditions of use. This system provides accuracy better than 100 µm in the positioning of beam probes. The movement accuracy has been verified using the dial gauge with graduation of 10 micron and linear potentiometer based position readback. The motion control interface unit is found to be working as per the requirement.

The input current measurement range of processing electronics is from 0.1-100 mA. It has been tested and calibrated in lab with a programmable current source (Model no.: 2635A, Make: Keithley) and its accuracy is better than ± 1 % of the full scale value.

## RESULT AND CONCLUSION

The beam profiles of $21^{st}$ and $22^{nd}$ (last two orbits) orbits of injector Microtron have been measured at beam current of ~ 20 mA and PRR of 1 Hz. Figure 5 shows the graph obtained by differentiating beam probe signal by using 5-point Savitzky Golay derivative algorithm, which gives the horizontal beam profile [5]. Typical FWHM values measured for the $21^{st}$ and $22^{nd}$ orbits are 4.6 mm and 4.8 mm respectively.

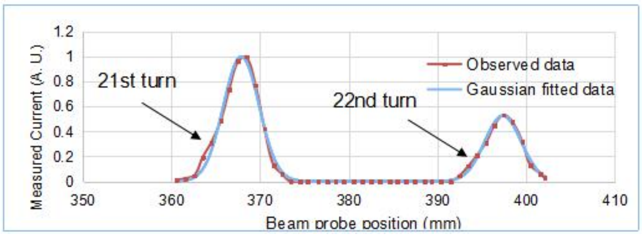


Figure 5: Typical result of beam profile of $21^{st}$ and $22^{nd}$ orbits of injector Microtron.

IBCM system is frequently used for measurement of the beam parameters during the experiments conducted for performance improvement of the injector Microtron and also after a cathode change.

## ACKNOWLEDGEMENT

The mechanical system of IBCM has been designed, developed and installed by Shri S. Dutta, Shri K.V.S.R. Rao and their team from IAD, RRCAT. The authors thankfully acknowledge their contribution and also their valuable support during testing and beam experiments. We also thank Shri Vikram S. Yadav for electronics system assembly, integration and testing.

## REFERENCES

[1] Singh G, Hannurkar PR, Shukla SK, Thakurta AC, Prabhu SS, Puntambekar TA, et al. Status of Indus-2, Synchrotron Radiation Source. InPAC 2011.

[2] Subhajit Dutta, S.G. Goswami, KVSR Rao, Pankaj Kumar, A.C. Holikatti et al. "Development and beam tests of a new 20 MeV injector microtron for Indus", Indian Particle Accelerator Conference, Dec 21-24, 2015, TIFR, Mumbai,InPAC-2015-ID-380.

[3] Atmel Corporation, "*AT89 Series Microcontroller Data Book*".

[4] Sergio Franco, "*Design with operational amplifiers and analog integrated circuits*".

[5] https://en.wikipedia.org/wiki/Savitzky-Golay_filter.

# DEVELOPMENT OF SOFTWARE FOR AUTOMATIC MEASUREMENT OF BETATRON COUPLING IN INDUS-2

S. Yadav[#1, 2], Riyasat Husain[1,2], Y. M. Sheth[1], A. D. Ghodke[1], T. A. Puntambekar[1], A. C. Thakurta[1]

[1]Raja Ramanna Centre for Advanced Technology, Indore
[2]Homi Bhabha National Institute (HBNI), Training School Complex, Anushakti Nagar, Mumbai

*Abstract*

Indus-2 is an electron synchrotron radiation source located at Raja Ramanna Centre for Advanced Technology, Indore, India. In any circular accelerator, there exist particle oscillations in transvers planes to the direction of particle motion. These are known as betatron oscillations and generally exist in transverse vertical and horizontal planes. In addition, there exists coupling between these betatron oscillations. Spurious betatron coupling which can change the vertical electron beam size is of concern in electron storage rings. Thus, for any storage ring based synchrotron light source, a precise measurement and minimization of the betatron coupling is essential for its performance improvement. Earlier, betatron coupling in Indus-2 was found out manually, which is always been an elaborate, tedious, time taking procedure and was prone to human errors. A software application is developed for automatic measurement of the betatron coupling. The application interacts with the betatron tune measurement system and MATLAB server for acquisition of the betatron tunes for various quadrupole magnet power supply settings. The application software identifies the tune values corresponding to the coupling resonance and computes the betatron coupling. A graphical user interface for operators interaction is also developed that facilitates the user to select the range of quadrupole magnet setting and display of the betatron tunes and the betatron coupling. The paper elaborates on the implementation of the algorithm for computation of betatron coupling and discusses the results obtained using this application.

## INTRODUCTION

The coupled betatron motion is an important part of any electron accelerator design. Considering linear beam dynamics, horizontal and vertical beam motion can be treated separately with perfect selection, design, and alignment of magnets. However, alignment tolerances will introduce magnetic error components, for example, rotated quadrupole components which cause a coupling of both the horizontal and vertical betatron oscillations. Betatron coupling may reduce the dynamic aperture, increase the vertical emittance in electron accelerator, and induce optics distortions, beating of the betatron motion, and shifts of the betatron tunes etc. [1-2].

The most generally used magnets that introduce coupling in beam transport systems are rotated quadrupoles and solenoid magnets. The Hill's equations in horizontal (x) and vertical (z) plane with coupling are as given as ,

$$x'' + k_x x = -k_z z + Sz' + 0.5S' z \quad (1)$$

$$z'' + k_z z = -k_x x - Sx' - 0.5S' x \quad (2)$$

Where the terms, which include S is due to solenoid field and remaining terms (including $k_x$ and $k_z$) due to quadrupole [1].

Indus-2 is an electron synchrotron radiation source located at Raja Ramanna Centre for Advanced Technology, Indore, India [3]. The skew quadruole has been installed in Indus-2 to control the betatron coupling. In this paper, we focus on automatic measurement of the betatron coupling.

## SYSTEM DESCRIPTION

A particle displaced transversely from its equilibrium orbit executes betatron oscillations about the orbit. The number of periods of oscillation in one complete turn around the machine is called betatron tune (Q). From linear difference coupling's Hamiltonian perturbation theory [1,2], let at the coupled situation betatron tune is $Q_x$ and $Q_z$ are given by

$$Q_x = Q_{x,0} - \tfrac{\Delta}{2} + \tfrac{1}{2}\sqrt{\Delta^2 + C^2} \quad (3)$$

$$Q_z = Q_{z,0} + \tfrac{\Delta}{2} - \tfrac{1}{2}\sqrt{\Delta^2 + C^2} \quad (4)$$

Where $Q_{x;0}$, $Q_{Z;0}$ are the uncoupled tunes when all coupling sources are removed. C is the coupling coefficient, which is determined by betatron tune gape between horizontal and vertical plane at coupling resonance.

Δ is the tune split of the two uncoupled tunes and given as,

$$\Delta = Q_{x,0} - Q_{z,0} - p \quad (5)$$

Where p is the integer tune split. [4].

The mode tune separation method is used in this system for betatron tune coupling measurement. The coupling ratio k can be given as [5]

$$k = \frac{C^2}{C^2 + \Delta^2} \quad (6)$$

The betatron tune measurement for different values of quadrupole magnet current is required for measurement of

[#]syadav@rrcat.gov.in

coupling. The scheme of betatron coupling measurement is shown in figure 1.

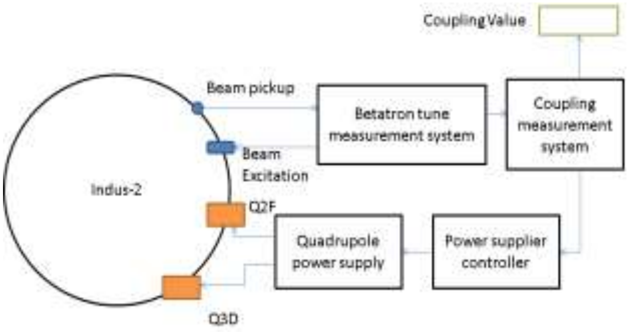


Figure 1: Scheme of betatron coupling measurement of Indus-2

The quadrupole magnet current is varied in steps to major the betatron coupling. The system performs the betatron tune measurement for each quadrupole magnet current setting. The beam excitation of betatron tune measurement is also controlled during measurement using genetic algorithm [6]. Spectrum of beam position signal in the vicinity of 505.8 MHz is analysed for finding the value of betatron tune in horizontal and vertical plane. The resolution of betatron tune measurement is 0.0005. For deployment of this system in the Indus control room, the user support system has been developed and deployed. The snapshot of the GUI is shown in figure 2.

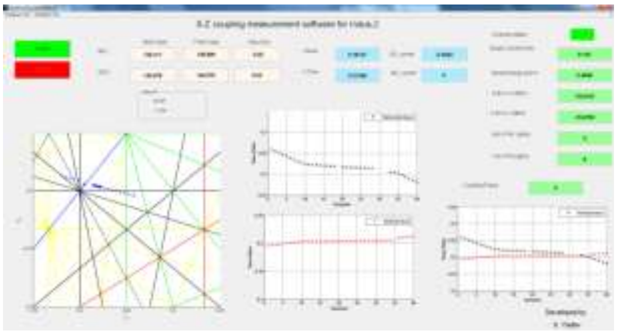

Figure 2: Snapshot of the GUI for betatron coupling measurement

The GUI has a feature to select the Q2F or Q3D family for measurement of betatron coupling. The initial step size can be decided by the user. The step by step procedure for betatron coupling measurement is shown below

- Step 1: Select focusing quadrupole (QF) or defocusing quadrupole (QD) for modifying the betatron tune towards the coupling resonance.
- Step 2: Change the Quadrupole step by step and record the betatron tune. Reduce step size near coupling resonance ($|Q_x-Q_z|< 1e-3$).
- Step 3: Analyze the betatron tune data and identify the betatron tune jump in horizontal and vertical plane.
- Step 4: Continue changing betatron tune ~~data~~ of horizontal and vertical plane even after the point as mentioned in step #3) .
- Step 5: Fit the parabola for the measured horizontal and vertical tune data and find the maxima of one plane and minima of another plane.
- Step 6: Calculate difference between minimum and maximum betatron tune at the coupling and denoted as $C= Q_{xmin}-Q_{zmax}$
- Step 7: Nominal operating tune point is $(Q_{x1}, Q_{z1})$.
- Step 8: Difference in horizontal and vertical tune point is given as
  $\Delta= Q_{x1}-Q_{z1}$
- Step 9: The betatron coupling ration k is calculated as per equation 6.

After starting the measurement process the betatron tune data with quadrupole settings are displayed on the GUI and recorded in the MS excel file.

## RESULT

In Indus-2, the experiments with the beam have been performed to measure the betatron coupling at beam energy of 2.5 GeV. The betatron tune data has been recorded for change in quadrupole. The betatron tune variation for change in quadrupole family Q2F is shown in figure 3.

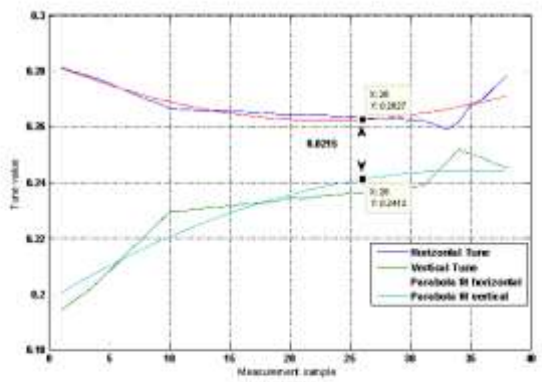

Figure 3: Typical graph of betatron tune variation with parabola fit during betatron coupling measurement

The C parameter as shown in the figure 3 is 0.0215. Total 38 betatron tune point has been measured during this experiment. The betatron coupling is ~ 0.3 % in nominal Indus-2 lattice used in routine beam operation. The measurement time with the automated setup is ~ 12 minutes, whereas it took ~1-2 hours by manual measurement. The adaptive step size of quadrupole current settings helps to achieve the resolution of 0.001 in betatron tune at coupling resonance.

The coupling has been measured at different machine conditions. The results of coupling measurement are given in table 1.

Table 1: Measurement results

| Sr. No. | Beam emittance | Coupling ratio (k) |
|---|---|---|
| 1 | $\varepsilon_x$ = 135 nm-rad | 0.2 |
| 2 | $\varepsilon_x$ = 45 nm-rad | 0.7 |
| 3 | $\varepsilon_x$ = 45 nm-rad, with modified optics | 0.4 |

The vertical beam size is a function of coupling ratio and horizontal beam emittance. Hence, the vertical beam size is lower in third beam optics.

## CONCLUSION

The coupling between the two betatron tunes has been measured with the help of the above automated coupling measurement system. The measured data are in good agreement with the beam physics design. The coupling measurement system is installed in the Indus control room for use during beam dynamics experiments.


## ACKNOLEDGEMENT

The authors would like to thank the colleagues of the Beam Diagnostics Section, Accelerator Control Systems Division and Indus-2 operation crew members of RRCAT for their support in completion of this work. The authors would also like to thank to Dr. A. A. Fakhri for applying different optics to machine during coupling measurements.


## REFERENCES


[1] H Wiedemann, Particle Accelerator Physics II Nonlinear and Higher-Order Beam Dynamics, Springer Science & Business Media, 06-Dec-2012 - Science - 472 pages

[2] G. Guignard, Betatron coupling and related impact of radiation, Phys. Rev. E 51, 6104 1995

[3] www.rrcat.gov.in/technology/accel/index.html

[4] Y. Luo et al, Measurement of global betatron coupling with skew quadrupole modulation, Physical review special topics - accelerators and beam S8, 014001 (2005)

[5] N. Kumagai et al, Estimation of betatron coupling and vertical dispersion for spring-8 storage ring, Particle Accelerator Conference, 1999. Proceedings of the 1999 Volume: 4

[6] S. Yadav, T. A. Puntambekar, P. V. Varde , Development of Adaptive Variable Boundary based Real Coded Genetic Algorithm for Online Optimization of Beam Excitation Level for Indus-2 Tune Measurement System, Journal of Instrumentation, Volume 13, July 2018

# STUDY AND ANALYSIS OF TRANSVERSE POSITION DATA OF BUNCHES IN PRESENCE OF TRANSVERSE COUPLED BUNCH MODE EXCITATION IN INDUS-2

S. Yadav[#1, 2], T. A. Puntambekar[1], P. V. Varde[2]

[1]Raja Ramanna Centre for Advanced Technology, Indore
[2]Homi Bhabha National Institute (HBNI), Training School Complex, Anushakti Nagar, Mumbai

*Abstract*

Indus-2 is an electron synchrotron radiation source located at Raja Ramanna Centre for Advanced Technology, Indore, India. In Indus-2, electron beam circulates in the form of bunches separated by ~ 2 ns. These bunches interact with each other through wake fields. This phenomenon results in the growth of instabilities of electron beam. These instabilities are known as coupled bunch instabilities (CBI). Due to the effect of transverse coupled bunch instability, every electron bunch starts oscillating with the betatron frequency in the transverse plane. The phase difference between oscillations of consecutive bunches is referred to as the mode number or coupled bunch mode (CBM). Most of the time, in the presence of transverse CBI, beam survives due to Landau damping and observation of transverse oscillation of bunches is possible. This paper describes the measurement of turn by turn beam position of bunches in Indus-2. Also presented in this paper is the analysis of position data of bunches for different levels of transverse CBMs.

## INTRODUCTION

Indus-2 is an electron synchrotron radiation source located at Raja Ramanna Centre for Advanced Technology, Indore, India [1]. The electron bunches circulating in the accelerator ring are influenced by coupled bunch instabilities and start coherent oscillations. In general, the oscillations of electron beam get dampened with natural damping processes. However, if the growth rate of the beam oscillation due to beam instabilities becomes higher than the damping rate then beam becomes unstable and every bunch starts growing oscillations with the betatron frequency in transverse plane and with synchrotron frequency in longitudinal plane. However, relative phase differences may exist between consecutive bunches, which are expressed by coupled bunch mode numbers. The phase difference $\Delta\phi$ between oscillations of consecutive bunches for $n^{th}$ coupled bunch mode is given as [2-3]

$$\Delta\phi = \frac{2\pi n}{M} \quad (1)$$

Where,
M is the harmonic number of accelerator and
n is an integer that varies from 0 to M-1.

[#]syadav@rrcat.gov.in

Different coupled bunch modes can be observed as different frequency components in the spectrum of beam pickup signal [4].

## SYSTEM DESCRIPTION

The time domain analysis of transverse positions data of bunches is performed in this paper. The phase difference between betatron oscillation of consecutive bunches has identified to estimate the dominant coupled bunch mode. The bunch to bunch separation is ~2 ns. Hence the sampling rate of ~500 MS/s and synchronization with RF signal are required for acquiring bunch by bunch position.

Measurement scheme of bunch by bunch position measurement is shown in figure 1.

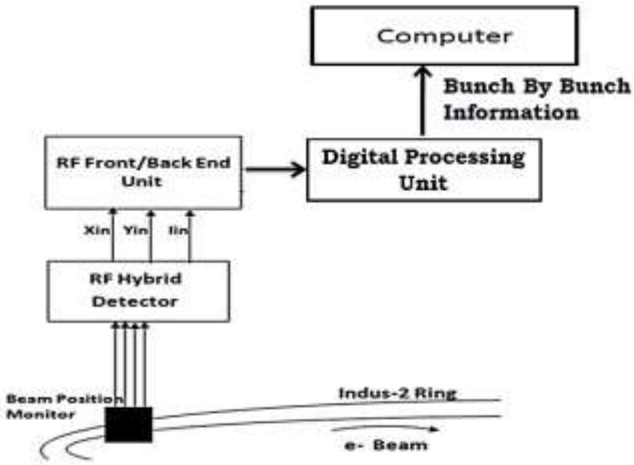


Figure 1: Schematic diagram of Bunch by bunch position data acquisition system of Indus-2

Four electrode button type beam position monitors are used for sensing the position of beam. RF Hybrid Detector is used for generating the position and intensity signal using the four electrode signals of a beam position monitor. The position signals Xin and Yin are proportional to the horizontal and vertical beam position and the signal Iin represents the intensity of the beam. RF Front/Back End Unit is used to demodulate these signals. Digital Processing Unit is used to digitize the output signals of RF Front/Back End Unit at the rate of 505.8 MS/s.

The position data are observed as constant during no beam instability. In the case of beam instability, bunch position data shows oscillation at different frequency component.

## RESULT

For the study of bunch by bunch position data, the bunch to bunch position data are acquired and recorded in ".mat" file. Total 43000 turn data of every bunch has acquired for different fill patterns. The graphs of position data for individual bunch of ~50 filled buckets for ~ 1500 turns are given in figure 2 and 3. The middle part of the graph gives the information of bunch position and rest ~241 blank buckets are shown by almost constant signal strength.

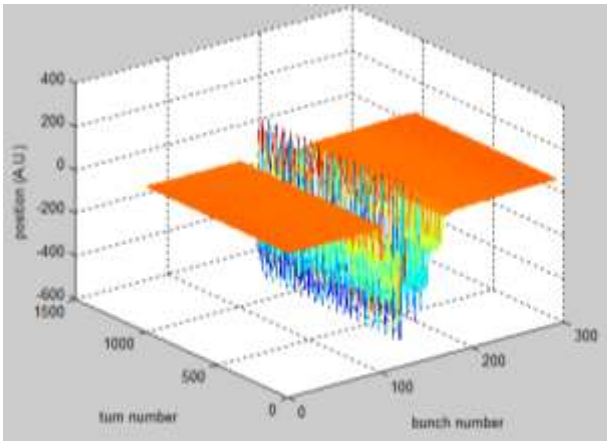


Figure 3: Typical graph of turn by turn horizontal position of 50 bunches

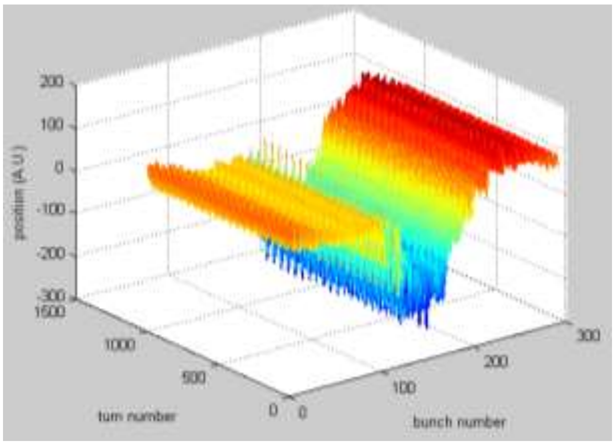


Figure 4: Typical graph of turn by turn vertical position of 50 bunches

Figure 3 and 4 shows the beam position varition turn by turn for each bunches. The value of beam position is arbitry units. The time domain oscillations of arbitarary choosen bunch no. 20 of bunch train is shown in the figure 5.

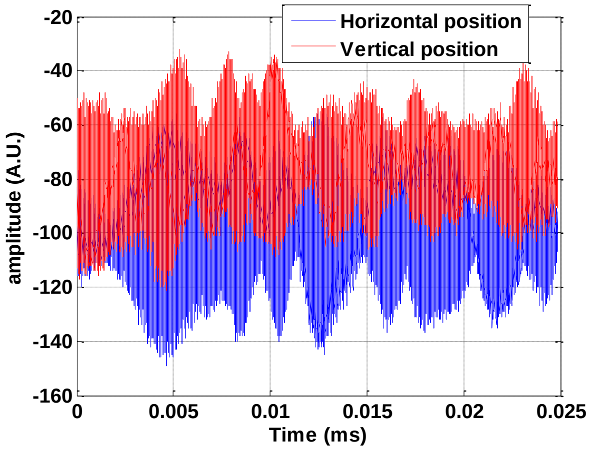


Figure 5: Typical graph of turn by turn horizontal and vertical positions of bunch no 20 of bunch train

After frequency analysis of position signal, it is found position signal contains frequencies of synchrotron sideband (~ 35 kHz), its harmonics, and horizontal and vertical betatron frequencies mainly. Hence, bandpass filter has been applied on position data to separate out the desired frequency of betatron oscillation. The filtered output is shown in figure 6.

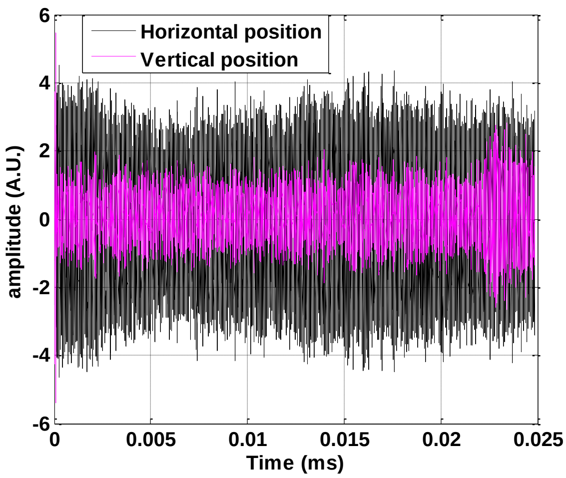


Figure 6: Typical graph of filtered turn by turn transverse positions of bunch no 20 of bunch train

From the graph it is clear that the betatron oscillation part in the beam position variation is small. Major oscillation level is due to strong synchrotron oscillation. After filtering the phase different between bunches has also been identified by Fourier analysis and given in figure 7.

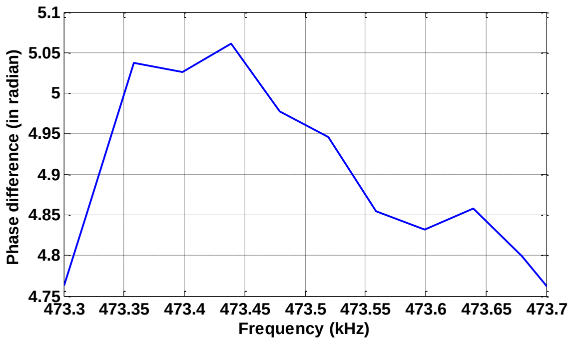


Figure 7: Typical graph of phase difference between horizontal betatron oscillations of two consecutive bunches of bunch train

The phase difference ~ 5 rad at bettron frequency of ~473 kHz has observed between consecutive bunches of bunch train. The coupled bunch mode n is calculated with equation 1 which is ~230 for this phase difference. Similarly, vertical coupled bunch mode can also identified. The observations on betatron sidebands have also taken for different bunch filling pattern. The side band levels are shown in figure 8 and figure 9.

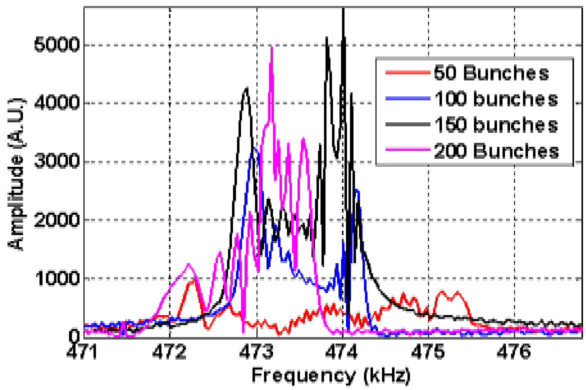


Figure 8: Horizontal betatron sideband for different bunch filling pattern.

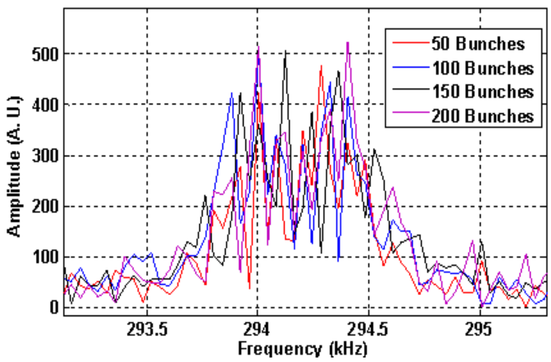


Figure 9: Vertical betatron sideband for different bunch filling pattern.

## CONCLUSION

Bunch by bunch beam position oscillations of Indus-2 have been studied in time domain to understand behaviour of bunch oscillation during different bunch filling pattern. Multiple frequencies are observed in the horizontal and vertical beam position signal of bunches. A bandpass filter has successfully applied on position signal to study betatron oscillation and relative phase difference in consecutive bunches. The impact of bunch filling pattern clearly observed on the level of horizontal betatron oscillation. Whereas, the effect of bunch filling pattern on vertical betatron oscillation level is not significant.


## ACKNOLEDGEMENT

The authors would like to thank the colleagues of the Beam Diagnostics Section for their support in completion of this work.


## REFERENCES


[1] http://www.rrcat.gov.in/technology/accel/indus2.html

[2] G A.W. Chao, “Physics of Collective Beam Instabilities in High Energy Accelerators”, New York: Wiley, 371 p, 1993

[3] Wenzhong Wu, “Feedback Systems for Control of Coupled-bunch Instabilities in the Duke Storage Ring”, Ph.D Dissertation, Department of Physics, Duke University, 2012

[4] F. J. Sacherer, “Transverse bunched beam instabilities – theory”, 9th International Conference on High Energy Accelerators, Stanford, California, USA, pages 347–351, 1974.

# WIEN FILTER VS DIPOLE MAGNET: A TECHNICAL COMPARISON STUDY FOR THE ANALYZING SYSTEM OF INDIGENOUS MICROWAVE ION SOURCE FACILITY AT IUAC DELHI

Ravi Sharma *, Hitesh Aggarwal, Jyotsna Sharma, Yaduvansh Mathur, Sarvesh Kumar
Inter University Accelerator Center, New Delhi

*Abstract*

A 2.45 GHz microwave ion source based, intense ion beam facility [1] is presently operational at IUAC, New Delhi and provides very low energy ion beams in the range 1 to 10 keV. The ECR plasma is optimized by varying the injection gas pressure, magnetic field confinement and microwave power. The extracted ion beam has to be analysed using either a dipole magnet or a Wien filter. Both options are studied in terms of ion beam optical parameters and a technical comparison is provided in the paper. The space constraints and the resolution of both devices are the main factors. The emittance of the ion source as 100 pi mm-mrad and an ion beam energy spread of 0.1 % are considered to design the beam transport system. A beam optics analysis is performed using GICOSY code to study transverse beam dynamics.

## INTRODUCTION TO INDIGENOUS FACILITY

A 2.45 GHz microwave ion source facility is available here at Inter University Accelerator Centre, New Delhi. Two NdFeB permanent magnet rings separated by a distance of 150 mm form the basic magnetic confinement structure for the microwave plasma. The axial magnetic field can be tunable by moving them with respect to each other. Each ring has six wedge shaped sectors and the pole tip has a magnetic field of $\approx$ 1T. Due to this magnetic confinement and microwave injection at 2.45 GHz using a standard WR 340 waveguide, electron cyclotron resonance heating take place to produce a plasma made up of energetic electron. The microwave cavity is fabricated using the non-magnetic stainless steel. The cooling of plasma chamber is maintained by compressed air. Different gases are injected in the plasma chamber through a capillary tube as per experiment requirement and the gaseous flow rate is controlled using the valve controller. An ion beam is generated which can be focused and bend using electromagnets or electrostatic dipoles. The paper aims to design a dipole magnet and a wien filter for the analysing system and compare them for their feasibility into real implementation in the system.

An ion beam is defined as a charged or neutral particle ensemble, each constituent particle having a larger velocity component along a fixed direction. Basically, a beam is a collection of particles in motion possessing directionality. The beam of charged particles is guided on the predefined path. For this magnetic fields are used which deflects the particles by the equilibrium of the centrifugal force and Lorentz force. Bending magnets are used for guiding a charged particle beam. There will be focusing in either transverse planes, precise nature of these focussing depending on the field configuration. There will be dispersion i.e. separation of the beam according to its momentum spread. This results in the better selection of the momentum.

* raviamity05@gmail.com, sariuac@gmail.com

## ION BEAM SPECIFICATIONS AND BASIC DESIGN CALCULATIONS

The ion beam is extracted from the microwave ion source using an Einzel lens configuration. The ion beam parameters coming out of the source are given in Table-1. These parameters will be used to design the appropriate analysing system either dipole magnet or wien filter as per the geometrical constraints and less electrical power consumption.

Table 1: Initial ion beam parameters from 2.45 GHz microwave ion source to design the analysing system

| Parameters | Values |
|---|---|
| Emittance | 100 Pi mm-mrad |
| Energy | 10 keV/q |
| Energy Spread | 0.1 % |
| Magnetic Rigidity | 0.164 Tm |
| Mass to charge ratio | 131 |

The Lorentz force on a charged particle due to electric and magnetic field is given as follows:

$$F = qE + q(vxB) \tag{1}$$

The forced due to electric field (E) and magnetic field (B) can be used to select a particular charged particles of mass (m), charge state (q) and energy (W) and is given as follows for magnetic and electric field, respectively by equation (2) and (3):

$$B.r = \sqrt{\frac{mW}{q^2}} \tag{2}$$

$$E.r = \frac{2W}{q} \tag{3}$$

Now when these two forces becomes equal, the resulting equation may be written simply as follows:

$$v = \frac{E}{B} \tag{4}$$

The equation (2), (3) and (4) form the basis to design a dipole magnet, an electrostatic dipole and a WIEN filter.

## DESIGN OF A DIPOLE MAGNET

The H shaped magnet is preferred due to symmetry of the magnet design. The maximum rigidity of magnet can be written in terms of beam parameters as follows:

$$B(T)\rho(m) = 0.1437\sqrt{\frac{M(amu)W(MeV)}{q^2}}$$

The current density in the coils is given as follows:

$$J = \frac{NI}{A}$$

Here NI are the ampere turns and A is cross-sectional area of the coil.

The resistance of the coil of total length (L) and area of cross-section (A) can be determined as follows:

$$R(ohm) = \frac{\rho_{Cu} * L}{A}$$

where

$$\rho_{Cu} = 1.72 * 10^{-8} ohm - m$$

Total power (P) required to operate the magnet is given as follows:

$$P(W) = VI = I^2 R$$

The magnetic field (B) in the pole gap (g) region of dipole magnet can be written as follows:

$$B = \frac{\mu_o NI}{g + \frac{\lambda}{\mu}}$$

Here $\mu_o$ is permeability of free space, g and $\frac{\lambda}{\mu}$ is reluctance of gap and iron, respectively. Since $\mu$ is very large, Approximately, we may write as:

$$NI = \frac{Bg}{\mu_o}$$

Based upon above design formulas, the beam optical specification of dipole magnet for air cooled configuration is given in the Table-2. If the resulting current density in the circular wire of SWG no. 12 leads to heating problems then Cu strip coils may be used for the coil windings.

Table 2: Beam optical specifications of Dipole magnets

| Parameters | Values |
|---|---|
| Bending Angle | 90 Degree |
| Bending Radius | 600 mm |
| Max. magnetic Field | 3000 G |
| Magnetic Rigidity | 0.18 Tm |
| Field Homogeneity | 0.001 |
| Number of turns per pole | 480 |
| Pole Width | 200 mm |
| Pole Height | 300 mm |
| Resistance per coil | 1.72 ohm |
| Voltage per coil | 18 V |
| Current in both coils | 10 A |
| Total Power | 180 W |
| Edge Angle in non dispersive plane | 26.5 degree |
| SWG No. of Coil wiring | 12 |

## BEAM OPTICS SIMULATIONS

The beam optics simulation are performed using code GICOSY [2] by considering the ion beam parameters given in Table-1. It is shown in Fig. 1 along with a magnetic quadrupole triplet.

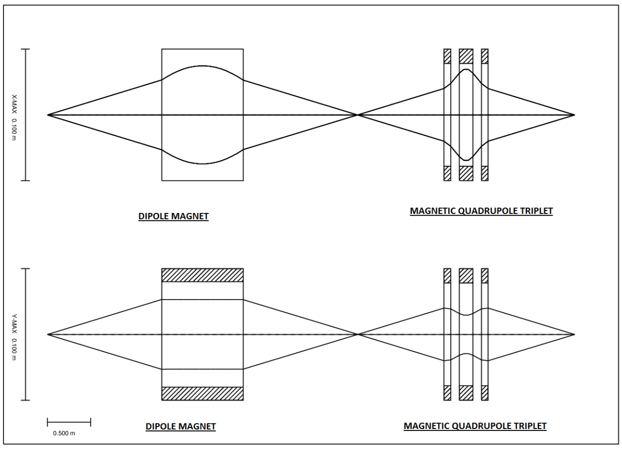


Figure 1: Beam optics using dipole magnet and a magnetic quadrupole triplet to analyse the ion beam using GICOSY code, upper plot is for horizontal plane and the bottom plot for vertical plane

## DESIGN OF A WIEN FILTER

The Wien filter is a compact design and is a combination of electric field and magnetic field to select a particular velocity of charge particle. Thus it is also known as velocity selector. The ions in the beam has same energy (10 keV/q) but due to different masses, have different velocities. Wien filter removes the undesired ion species; thus this device is called mass separator or Wien Velocity Filter(WVF). The WVF is a mass-dispersive electromagnetic optical device, with orthogonal electrostatic and magnetostatic fields both being transverse to the direction of the charged particle beam. Wien filter is used as an energy analyser as well as mass analyser. Usually Electric and Magnetic field are generated by a parallel plate capacitor and circular coils. With an appropriate choice of electric and magnetic field strength, a force set up inside the Wien Filter which in turn cancel out for the desired beam species having axial velocity v = E/B. Lorentz force for charge particle travelling with a specific velocity perpendicular to both the field vanishes. Neither mass of the particles nor the charge of the particles are important for this velocity filter. All particles of a particular velocity as given by eq. (4) will pass the Wien filter irrespective of their mass and the charge. All the neutral particles will pass the Wien filter irrespective of their velocity. In the low

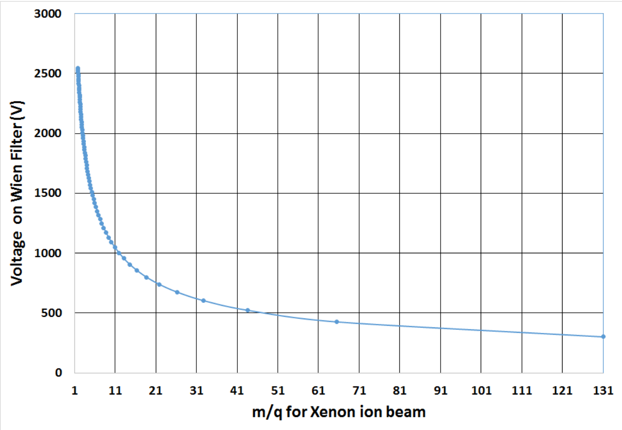


Figure 2: Wien Filter voltages versus m/q for Xenon ion beam for B=0.1 T

energy ion beam accelerator, all ions are accelerated to the same energy, therefore the Wien filters can select ions based on their masses. The Wien filter voltages [3] required for different charge states of Xenon ion beam is as shown in Fig. 2. The specifications of Wien filter is given in Table-3.

Table 3: Specifications of Wien filter

| Parameters | Values |
|---|---|
| Effective length | 70 mm |
| Max. Magnetic Field | 1000 G |
| Maximum Voltage | ± 3 kV |
| Max. beam Rigidity | 0.164 Tm |
| Max. Slit Width | ± 2 mm |
| Half Aperture | 25 mm |

## CONCLUSION

The design of both dipole magnet and the Wien filter is discussed in air cooled configuration. The dipole magnet occupies a large space whereas the Wien filter is compact in size. Since the facility is aimed to be designed as compact as possible, the Wien filter is preferred over the dipole magnet.


## ACKNOWLEDGMENT

The author acknowledge the help and support received from the IUAC office to carry out successfully the project work in the accelerator physics. The author is extremely thankful to the guidance provided by the supervisor, Dr. Sarvesh Kumar, Scientist, IUAC Delhi to carry out the project.


## REFERENCES


[1] N. Kumar, G. Rodrigues, P. S. Lakshmy, R. Baskaran, Y. Mathur, R. Ahuja, and D. Kanjilal, "Studies on the effect of the axial magnetic field on the x-ray bremsstrahlung in a 2.45 ghz permanent magnet microwave ion source," *Review of Scientific Instruments*, vol. 85, no. 2, p. 02C103, 2014. [Online]. Available: https://doi.org/10.1063/1.4852216

[2] "Gicosy code," https://web-docs.gsi.de/~weick/gicosy/.

[3] M. Schmidt, H. Peng, G. Zschornack, and S. Sykora, "A compact electron beam ion source with integrated wien filter providing mass and charge state separated beams of highly charged ions," *Review of Scientific Instruments*, vol. 80, no. 6, p. 063301, 2009. [Online]. Available: https://doi.org/10.1063/1.3125628